VOLUME I

Edited by Billy L. Edge

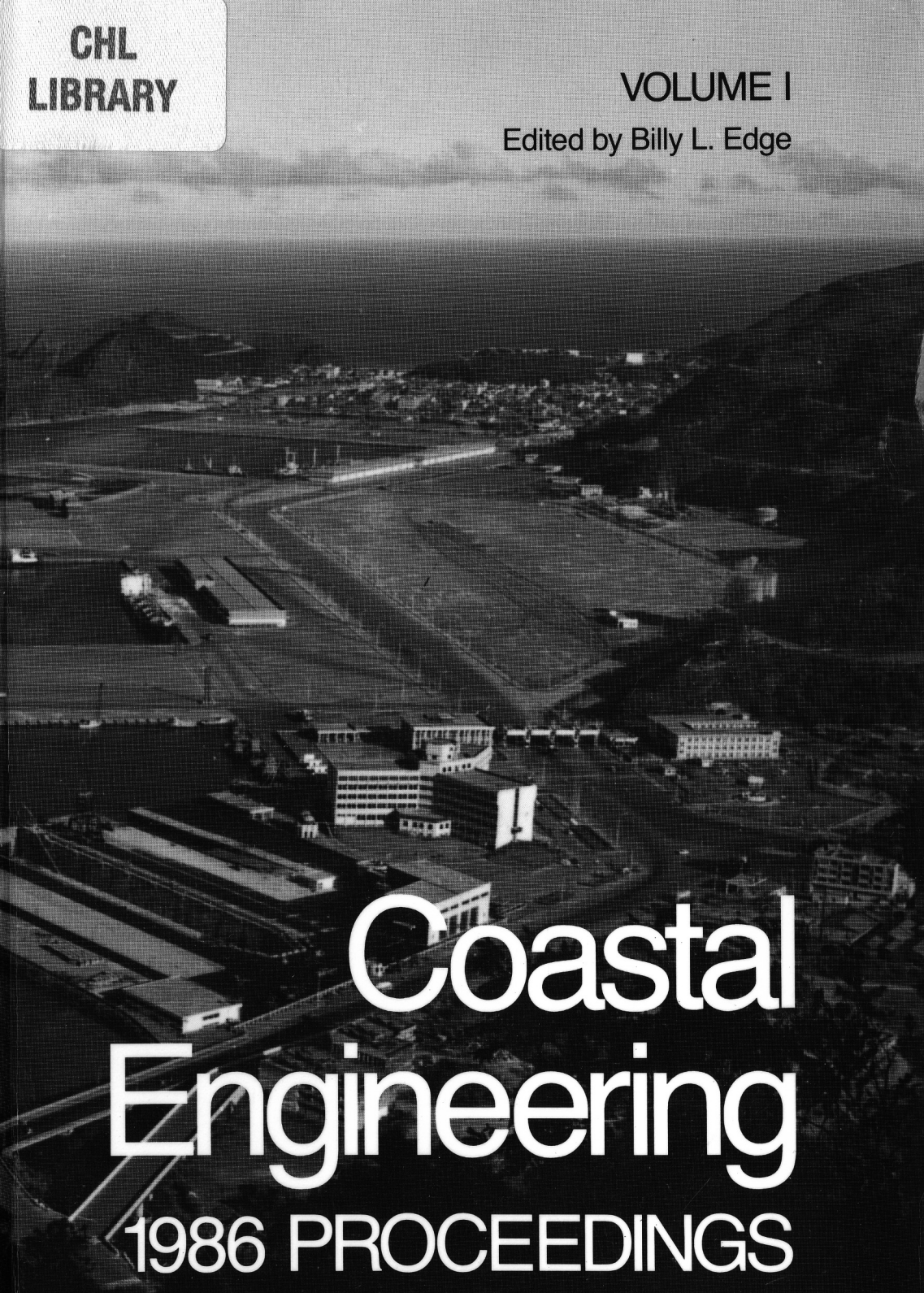

Coastal Engineering

1986 PROCEEDINGS

Twentieth Coastal Engineering Conference

Proceedings of the International Conference

VOLUME I

November 9-14, 1986
Taipei, Taiwan

Conference held under the auspices of the
Coastal Engineering Research Council
of the
American Society of Civil Engineers

Organized by the
Chinese Institute of Hydraulic Engineering

and cosponsored by the
International Association for Hydraulic Research

Edited by Billy L. Edge

Published by the
American Society of Civil Engineers
345 East 47th Street
New York, New York 10017-2398

ABSTRACT

This book contains over 200 papers presented at the 20th International Conference on Coastal Engineering. The book is divided into five parts: theoretical and observed wave characteristics; coastal processes and sediment transport; coastal structures and related problems; coastal, estuarine and environmental problems; and ship motions. Reports include the effects of wind, storms, and currents. Erosion, sedimentation and beach nourishment are covered. The papers approach these topics with theoretical studies, case reports, models, and field studies.

ISBN 0-87262-600-8
ISSN-0893-8717
Manufactured in the United States of America.

FOREWORD

Only one International Conference on Coastal Engineering has been held in the same city thus far. Moreover no country has been the venue for more than one Conference except the United States. Although repeat venues are not discouraged, the extremely time consuming activities of planning and conducting a major international conference do not encourage a second effort by the same group. Having the venue in different countries allows the participants to learn first hand about coastal problems and solutions around the world. This approach also allows those engineers and coastal scientists who could not travel to foreign countries to meet the international coastal community.

The papers in the Proceedings have been prepared by the authors who made presentations at the 20th International Conference on Coastal Engineering. The authors were asked to make their presentations and submit final papers based on review of the abstracts that were submitted well in advance of the conference. These abstracts were reviewed by a committee of four professionals including representation from the local organizing committee. These papers are eligible for discussion in the Journal of the Waterway, Port, Coastal and Ocean Division. All papers are eligible for ASCE Awards.

Venues for the 21st and 22nd conferences are Torremolinos (Malága), Spain, and Delft, The Netherlands, respectively. Countries desiring to host a future conference should contact the Secretary of the Coastal Engineering Research Council to receive information about submitting a proposal.

Billy L. Edge, Secretary
Coastal Engineering Research Council
American Society of Civil Engineers

ACKNOWLEDGEMENTS

CONFERENCE COMMITTEE

Chairman	Chi-Chang Yen
Vice-Chairmen	Pao-Chien Chi
	Chien-Hung Hu
Executive Members	Tsu-Suan Chang
	You Chen
	Za-Lee Moh
Executive Secretary	Tai-Shen Huang

ORGANIZING COMMITTEE

Chairman	Frederick L. W. Tang
Secretary	Ho-Shong Hou
Vice-Secretary	Shan-Hwei Ou

GENERAL AFFAIRS COMMITTEE

Chairman	Cheng-Chih Lin
Secretary	Hsi-Ling Yao

FINANCIAL COMMITTEE

Chairman	Ven-Young Huang
Secretary	Shih-Sheng Paul Lai

LOCAL HONORARY MEMBERS

Tsung-Wen Chen
Wen-Kuei Ku
Tai-Hai Lee
Chang-Ching Wang
Hsueh-Su Yang
Chen-Hsing Yen
Chao-Chung Yu

FOREIGN HONORARY MEMBERS

Charles L. Bretschneider
Robert G. Dean
Masashi Homma
Takeshi Ijima
Joe W. Johnson
Shiao-Kung Liu
Orville T. Magoon
Morrough P. O'Brien
Hons-W. Partenscky
D. H. Swart
Yoshito Tsuchiya
Robert L. Wiegel

COASTAL ENGINEERING RESEARCH COUNCIL AMERICAN SOCIETY OF CIVIL ENGINEERS

CONTENTS

PART I
THEORETICAL AND OBSERVED WAVE CHARACTERISTICS

PART IV
COASTAL, ESTUARINE AND ENVIRONMENTAL PROBLEMS

Twentieth Coastal Engineering Conference

Proceedings of the International Conference

VOLUME II

November 9-14, 1986
Taipei, Taiwan

Conference held under the auspices of the
Coastal Engineering Research Council
of the
American Society of Civil Engineers

Organized by the
Chinese Institute of Hydraulic Engineering

and cosponsored by the
International Association for Hydraulic Research

Edited by Billy L. Edge

Published by the
American Society of Civil Engineers
345 East 47th Street
New York, New York 10017-2398

ABSTRACT

This book contains over 200 papers presented at the 20th International Conference on Coastal Engineering. The book is divided into five parts: theoretical and observed wave characteristics; coastal processes and sediment transport; coastal structures and related problems; coastal, estuarine and environmental problems; and ship motions. Reports include the effects of wind, storms, and currents. Erosion, sedimentation and beach nourishment are covered. The papers approach these topics with theoretical studies, case reports, models, and field studies.

ISBN 0-87262-600-8
ISSN-0893-8717
Manufactured in the United States of America.

CONTENTS

PART I
THEORETICAL AND OBSERVED WAVE CHARACTERISTICS

PART IV
COASTAL, ESTUARINE AND ENVIRONMENTAL PROBLEMS

Breakwater Wave Energy Absorber, Hualien, Taiwan, ROC—R.L. Wiegel

PART I

THEORETICAL AND OBSERVED WAVE CHARACTERISTICS

Taichung Harbor—H.S. Hou

CHAPTER 1

Maximum Entropy Spectral Estimation for Wind Waves

Jorge Calderón Alvarez*
Adolfo Marón Loureiro*

Some results are presented on the application of new spectral estimation techniques using AR and ARMA models, also known as Maximum Entropy Methods, to wind wave spectral analysis. The results are compared with those obtained with conventional FFT methods. The application of some mathematical methods for model order selection is included. The relation between the optimum order and different spectral parameters is investigated.

1 INTRODUCTION

In recent years new spectral analysis methods have substituted traditional ones in many fields of science and technology. Among them, one of the most useful ones is based in the use of autorregresive models (AR), moving average models (MA) and mixed autoregressive-moving average models (ARMA). Using these models for spectral analysis is directly related with what is called Maximum Entropy Methods (MEM) for spectral estimation.

Among the possible advantages of these methods found in the literature, we can note the following ones:

1- No assumption is made about how the time series behaves outside the known interval, while FFT methods assume that the series either is zero or repeats itself indefinitely outside such interval.

2- The spectral density can be easily represented by a small number of parameters (the model coefficients).

3- Good spectral estimates can be obtained from a very short sample of the time series.

4- Real time forecasting can be easily performed.

Although wind wave spectra have been lately analysed by means of the Fast Fourier Transform (FFT), some attemps of using ARMA models have come out in publications. However, to the authors knowledge, no systematic applications for wind wave analysis have been reported.

Generally speaking, we can say that ME methods try to model a non-deterministic, discrete and stationary stochastic process $\{x(t)\}$ by an ARMA model of finite orders (m,n), whose mathematical description is as follows:

$$\sum_{k=0}^{m} b_k \, x(t-k) = \sum_{k=0}^{n} a_j \, w(t-j) \quad ; \quad t = 1, 2, 3, \ldots \qquad (1)$$

* Programa de Clima Marítimo y Banco de Datos Oceanográficos. Dirección General de Puertos y Costas. Po. Castellana, no.16, 28046-Madrid, Spain.

Where
m is the order of the autorregresive part,
n is the order of the moving average part,
a_k are the autorregresive coefficients,
b_j are the moving average coefficients and
w(t) is a zero mean white noise with variance σ^2.

The energy spectral density of the process corresponding to this model is given by the following expression:

$$S(f) = \frac{\sigma^2 \cdot A(z) \cdot A(1/z)}{B(z) \cdot B(1/z)} \quad \text{in the Nyquist range} \quad f \in [0, \frac{1}{2T}] \qquad (2)$$

where:

$$A(z) = \sum_{k=0}^{m} a_k \cdot z^k \quad , \; z = \exp(-i2\pi Tf) \; ;$$

$$B(z) = \sum_{j=0}^{n} b_j \cdot z^j \quad \text{and}$$

T is the duration of the time series.

Many different algorithms have been proposed for estimating the coefficients a_k and b_k from the data, most of them dealing with pure autorregresive models. We have selected two of the most used ones for AR models and other two for ARMA models.

First the algorithm due to Burg (1975) which tries to minimize the sample white noise variance in successive steps, beginning with an AR (1) model and increasing the order by one on each step up to a previously selected order. The method, fast and stable, is based on the powerful Levinsons' recurrence.

The second is the least square method which tries to minimize the prediction error by a least square procedure. The equations are solved by an algorithm proposed by Marple (1980). The method is easier in conception than that Burg's one but the stability of the solution is not warranted.

For ARMA models we have tried first the Box-Jenkins (1970) algorithm, but difficulties in the convergence for large series as those of wave records, make it impossible its use in a rutinary basis. Nevertheless some results are presented in this paper. At the present time we are implementing a much stable algorithm known as Yule-Walker modified method (Kay-Marple, 1982), but no results are available for this paper.

One of the main difficulties that appear when applying AR and ARMA models, is the selection of the adequate order. We have chosen for this study three criteria among those found in the literature:

a) "Final Prediction Error"(FPE): Based in the fact that for a stationary process the prediction error (σ^2) should be stationary. It gives the following performance index:

$$(FPE)_m = \frac{N + (m+1)}{N - (m+1)} \sigma_m^2 \qquad (3)$$

where: N is the total number of points in the time series and
σ_m^2 is the white noise variance for order m.

b) "Akaike's information criteria"(AIC): Assumes that data are normally distributed and tries to find the order for which the model distribution better approximates the data distribution. The following index results:

$$(AIC)_m = - N \log (\sigma_m^2) + 2m \qquad (4)$$

c) "AR Transfer function"(CAT). Tries to minimize the difference between the shape of the spectral density corresponding to an AR (m) model and the underlying AR(∞) model. The resulting index is:

$$(CAT)_m = \frac{1}{N} \sum_{j=1}^{m} \frac{N - j}{N\sigma_m^2} - \frac{N - m}{N\sigma_m^2} \qquad (5)$$

These are indexes that tend to lower values as the model fits the data better. They have performed successfully in other scientific fields. We hope that comparison of these indexes with FFT results will give a good idea about their validity.

We have not tried similar criteria for ARMA models.

2 WAVE DATA

The primary objective of the study was to evaluate the behaviour of the different algorithms when applied to real wave data in a rutinary basis. Therefore we choose a set of successive wave buoy records that were representative of the different sea states that are encountered in practice.

The total number of records is 230 and were measured by a waverider buoy moored in deep water at the Bay of Biscay (North of Spain) and covering the period of February and part of March 1984. Is in this time of the year when the worst sea states are more likely ot occur. Each record consists of 2048 sea surface elevation points with a sample rate of 2 Hz measured each three hours.

3 AR ANALYSIS OF WAVE DATA

In order to do a comparative analysis between the AR estimation algorithms and the FFT estimation,we calculated with Burg and Least squares algorithms the estimation of AR models with order varying from 1 to 40 for all the set of records.We made some tests with selected wave records trying to confirm the highest order of the AR model where the main peak of the spectrum was completely developed, finally we chose the 40.

We selected seven spectral parameters in order to characterize each spectrum:

Condition A: Direction: North West
H_s = 4.75 m
T_p = 14.5 sec.
γ = 1.4

Condition B: Direction: North
H_s = 3.50 m
T_p = 14.5 sec
γ = 1.4

The first layout has been considered only under wave condition A.

As a resume, comparisons have been made in these three cases:

Test 1: First layout and Wave Condition A
Test 2: Second layout and Wave Condition A
Test 3: Second layout and Wave Condition B

The comparison carried out with both modelling systems (physical and numerical) is based on relative significant wave height.

An example of the results of the numerical modelling and the results of the physical model can be seen simultaneously in Fig. 2

In Figures 6,7,8 comparisons of the three tests can be seen. In the horizontal axis distance in meters have been represented and in the vertical axis significant wave heights relative to the entrace are shown.

5.2.- TEST 1

The lines along which comparisons have been made can be seen in fig. 3 and the comparisons along these lines are shown in fig. 6

In all the cases the agreement is seen to be excellent.

5.3.- TEST 2

The lines along which comparisons have been made can be seen in fig. 4 and the comparisons along these lines are shown in fig. 7

In all the cases the agreement of the results of the physical and the numerical model is found to be good except for the points in which the influence of the reflection

Therefore the Maximum Entropy spectra (MES) were normalized with FFT spectra, trying to condense all the available information (40 AR models and 7 FFT estimations; raw spectrum and 3 smoothed spectra with two different windows;for each wave record).The mean and variance of normalized parameters were calculated for each possible combination. Then we could represent in graphs the spectral parameters against the order of the AR model for each FFT estimation (Figure 3).

First of all, we analysed the results obtained by both methods (Burg and Least squares),and they were very much the same,though the LS method was more unstable.Sometimes we could find records were the model did not converge and in most cases convergence is very slow compared to Burg method. Therefore the resulting conclusions for one method are valid for the other one.

The same can be said for different degrees of smoothings and smoothing windows with very similar results. Plots of normalized mean an variance can almost be superimposed.

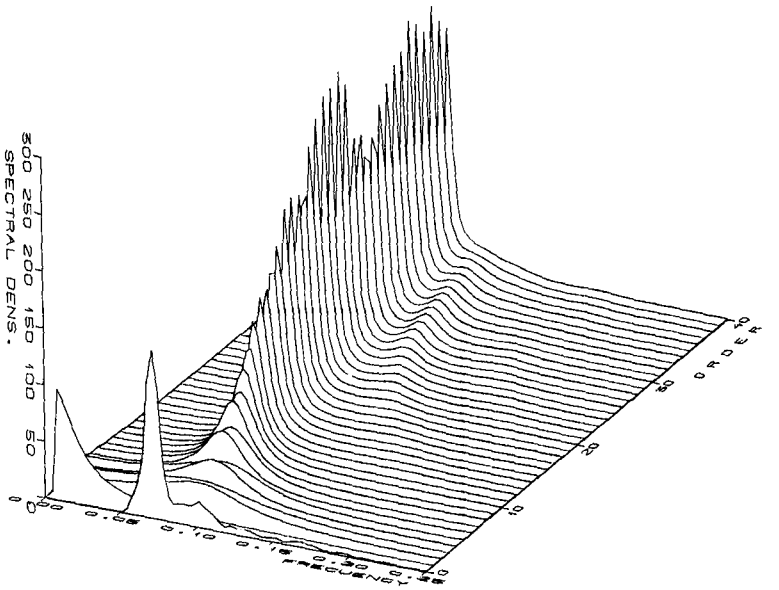

Fiture 2. Dependence of spectral shape with order of AR model. The first spectrum is the corresponding FFT spectrum.

The normalized spectral moments tend very quickly to 1,having a small variance (Figure 3),the other 3 parameters have greater variance and need higher orders to stabilize.Around 20 for Fp and more than this order for the other parameter,Qp and Smax. Obviously,the normalized Qp and

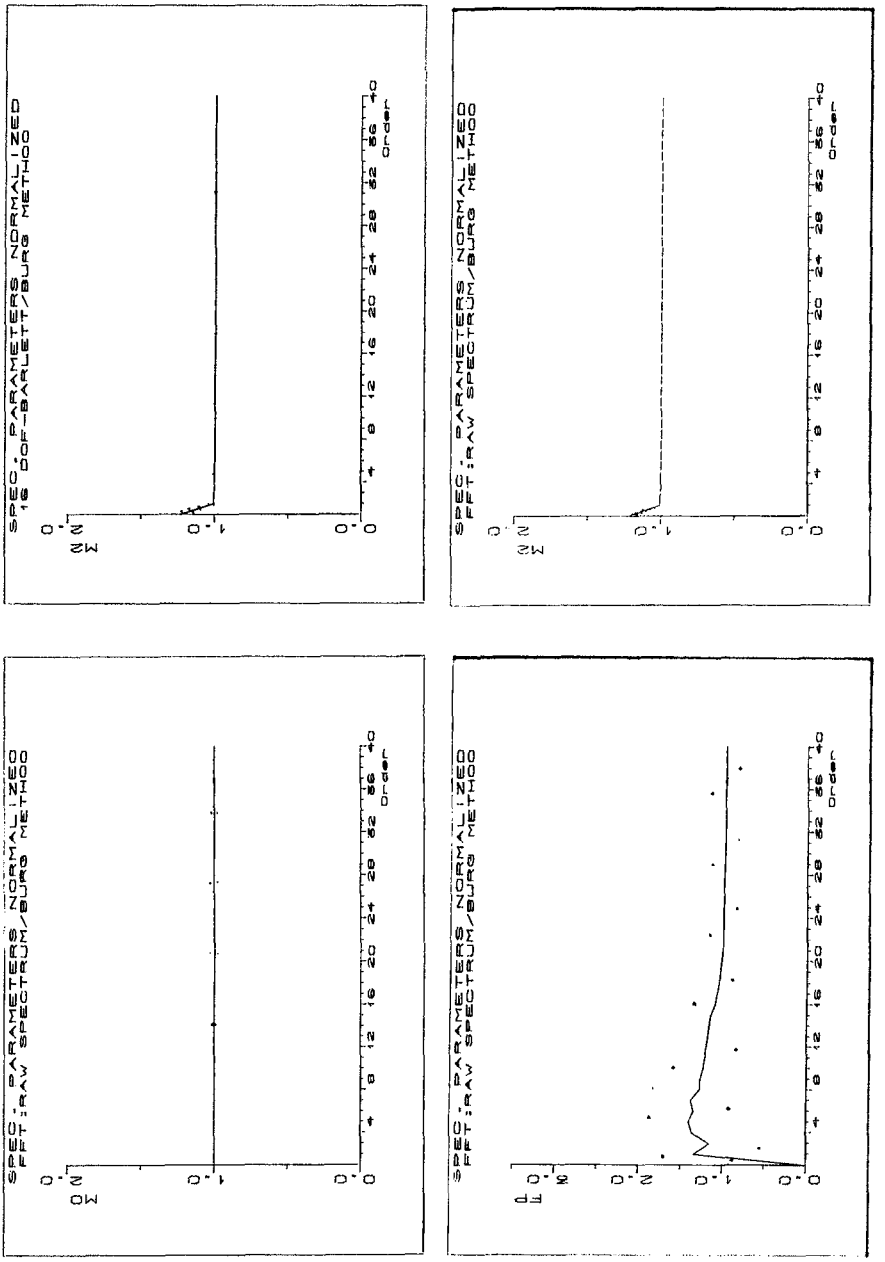

Figure 3. Examples of spectral parameters normalized.Mean (continuous - line) and standard deviation (dotted line) are represented.

Smax do not tend to 1 because their values depend largely of the degree of smoothing and the kind of used window. Though behaviour of Qp is more regular than Smax (Figure 3).

4 DETERMINATION OF THE ORDER OF AR MODELS

In order to be able to apply AR algorithms to wave data in a rutinary basis, some mathematical way of selecting the optimum order for the model should be available for its implementation in the computer. The importance of the selected order in the results is clearly illustrated in figure 2 where it can be seen how the peak frequency is converging very slowly to the true value as the order increases while it is very poorly defined for the low orders. Also some strong oscillation of the spectral value at the peak can be observed. These characteristics are common to most of the studied records.

We tried with the three criteria explained before. These criteria are based in some mathematical indexes which can be easily introduced in the programs. Theoretically, one has to evaluate such indexes for successive orders and select that order which gives the minimum value. We found actually that the indexes are monotonically decreasing when applied to waves for orders up to forty.

Therefore we choose as possible optimum order the one corresponding to the first point in the index variation curve where somo tendency to stabilization seems to happen. As a second candidate we choose the highest point were such an stabilization appears. Obviously, this method is somehow subjective and difficult to model in the computer. Actually we did the selection by hand.

Table I presents the best mean values of the normalized parameters (those nearer 1) and their corresponding standard deviations, as well as the order for which these values are obtained. The normalization is made with FFT spectra of 8 an 32 degrees of freedom. lt can be seen that different parameters need very different orders to reach an optimum.

TABLE I
RESULTS FOR BURG ALGORITHM

		M_0	M_1	M_2	M_4	F_P	S_{MAX}	Q_P
8dof	ORDER	9	33	4	5	20	40	10
	MEAN	.9999	.9998	.9978	1.0119	1.0097	1.0260	1.0442
	STD	.0025	.0164	.0064	.0195	.1600	.3180	.3120
32dof	ORDER	36	30	3	6	20	11	9
	MEAN	.9999	.9999	1.0030	.9935	.9983	1.0360	.9807
	STD	.0187	.0191	.0073	.0190	.1076	.4270	.2900

TABLE I-Results for Burg algorithm. Parameters normalized by FFT results with 8 & 32 d.o.f.(Barlett w.). Order optimun for each parameter.

In table lI the mean values of the same normalized parameters are

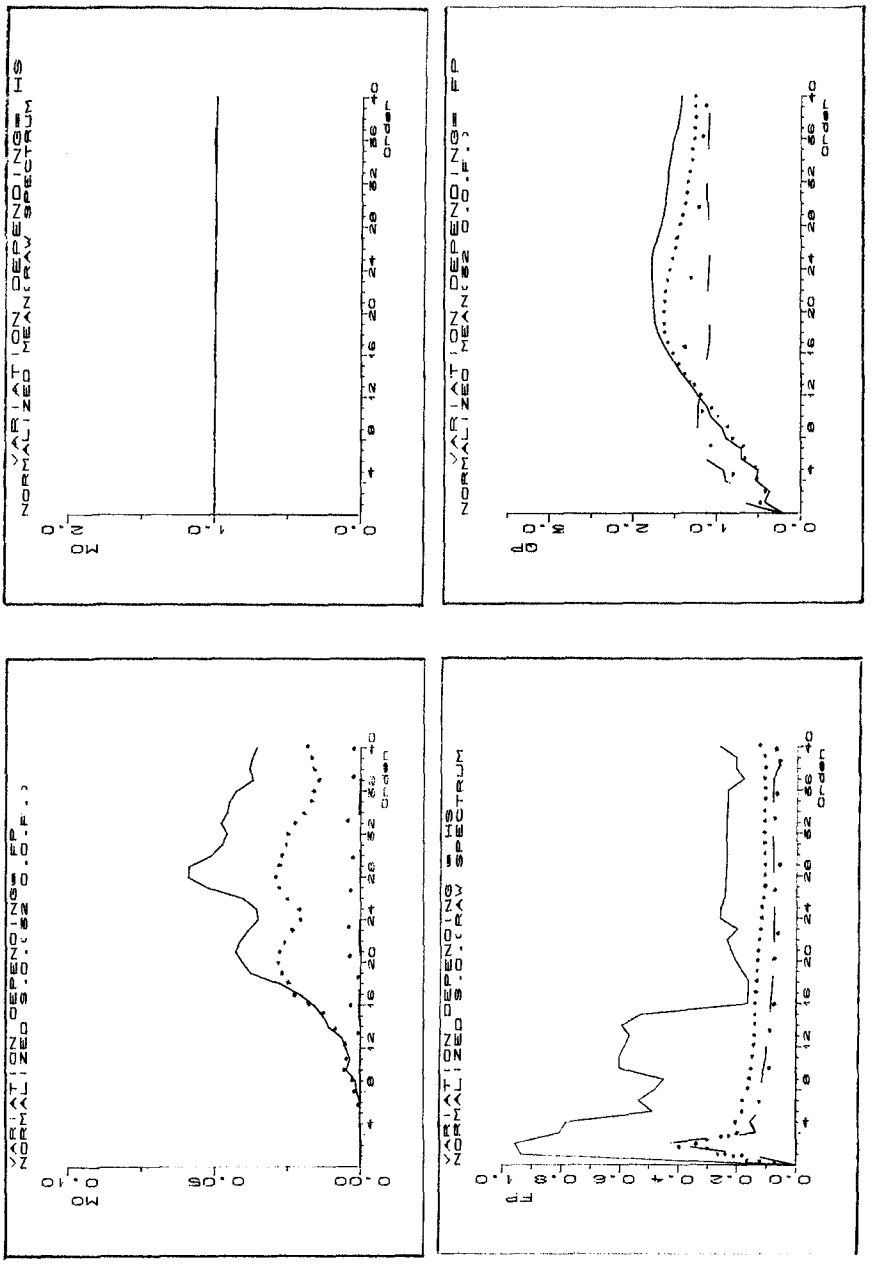

Figure 4. Variation of the order of AR model depending on different statistical parameters.

given, but in this case they correspond to the first order selected for each record by the procedure explained before when applied to the FPE criteria. Comparing both tables it can be seen that although the results obtained with the FPE orders are a little worse than the optimum ones,

TABLE II
RESULTS FOR BURG ALGORITHM
ORDER SELECTED BY FPE CRITERION

		M_0	M_1	M_2	M_4	F_P	S_{MAX}	Q_P
8dof	MEAN	.9999	.9959	.9952	.9862	1.0853	1.0177	1.3812
	STD	.0162	.0106	.0069	.0183	.2144	.4060	.3899
32dof	MEAN	.9999	.9959	.9947	.9865	1.0722	1.5653	1.4262
	STD	.0161	.0106	.0071	.0184	.1673	.5850	.4317

TABLE II-Results for Burg algorithm. Parameters normalized by FFT results with 8 & 32 dof. (Barlett w.). Order selected by FPE criterion.

the differences are not very significative except for the Qp parameter.

Of the two orders selected for each criteria we decided to deal only with the smaller one because the second one tend to be very high and no important improvement appear in the results when compared with the first one.

The three criteria gave very similar results and only a slight better performance of the FPE criteria can be mentioned.

Finally, we drew plots of the criteria selected order (mean and standard deviation) for groups of records with different values of the spectral parameters in order to see if any correlation could be found between order and spectral parameters. In general no good correlation was observed for the different parameters considered (see fig. 5 for example) and only some correlation seems to exist with the significative wave height Hs (see fig. 6). This last result is in agreement with that found by Houmb (1981) by other means.

5 VARIATION OF THE ORDER OF AR MODEL DEPENDING ON DIFFERENT STATISTICAL PARAMETERS.

We sought a possible correlation between the optimum order of the model with some spectral parameters. We first tried with significant height (Hs) and subsequently with the peak frequency (Fp).

We divided our set of data in different groups of Hs in such way that they were homogeneous, by subtracting randomly some records from those groups having more data. The five groups were divided as follows:

1.- 0. <= Hs < 1.
2.- 1. <= Hs < 2.
3.- 2. <= Hs < 3.
4.- 3. <= Hs < 4.
5.- 4. <= Hs

We repeated again the procedure described in point 3,normalizing the spectral parameters of the 40 estimated orders through Burg algorithm , via FFT estimations with 8, 16 and 32 degrees of freedom and Barlett window. In order to compare the results we represent in the same plot the curves if the mean of the five groups,and also in a separated plot the curves of the absolute value fo the standard deviation (Figure 3).

We can deduce some interesting behaviours.For the normalized spectral moments there is no distinct difference among the various groups,for both the means and the s.d., the latter ranges over a very small interval. Figure 3 shows superimposed curves corresponding to all the groups.

Concerning the Fp we found similar behaviour. The only difference found is that the first group has a turning point around the 16th. order that moves towards 1 faster than the rest of the groups,which fit into a similar shape. The s.d. for the first group is higher than for the rest of the groups but with a shape of the same sort. We cannot blame this difference to the order of the model but rather to the changing Fp, resulting from the FFT spectra for such a small Hs.

The Goda parameter behaves alike in all groups for low orders,and takes higher values for the high orders of the big groups. The s.d. is not so uniform but we did not find differences that would lead us to any conclusive result.

We tried again with the same procedure but dividing the sample in five groups according to the Fp:

1.- $0.05 \leq Fp < 0.07$
2.- $0.07 \leq Fp < 0.09$
3.- $0.09 \leq Fp < 0.11$
4.- $0.11 \leq Fp < 0.15$
5.- $0.15 \leq Fp$

We uniformized the groups not taking into account the fifth group, since it is not statistically significant for having almost no sample (Figure 4).

The means of the normalized moments do not change whichever the FFT estimation used is, but s.d. decrease in the high orders for those groups having a higher Fp. For the normalized Fp those groups with high frequencies tend towards 1 (around order 18) faster than those of low frequencies (group number 2 about order 24 and group 1 more than order 30). The behaviour of s.d. is somewhat more irregular for high orders, but we found it quite similar to that described for the normalized moments.

Finally the Qp, the normalized values of groups with higher Fp tend towards 1 faster than groups with low Fp. For the s.d.the values tend to 0. starting from a particular order but its even faster as higher the group is.

We will talk about the analysis of all these results later on when we come to the conclusions.

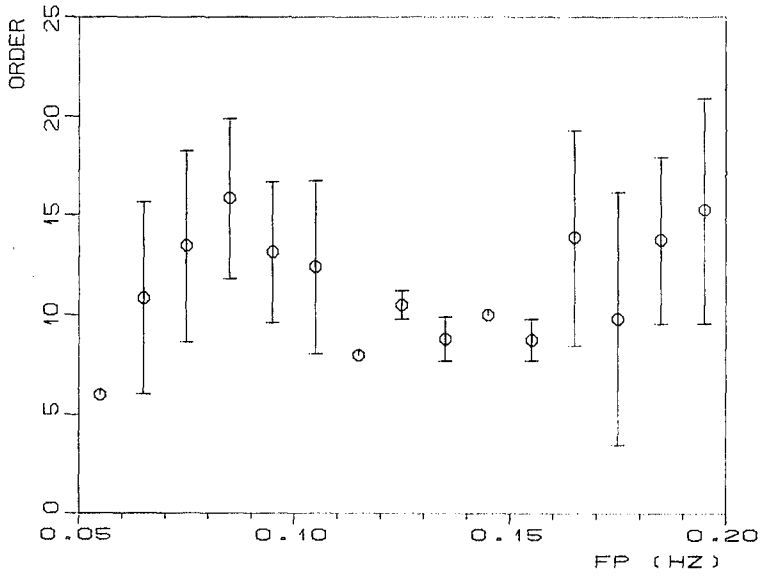

Figure 5.- Dependence of order selected by FPE criteria with peak frequency.

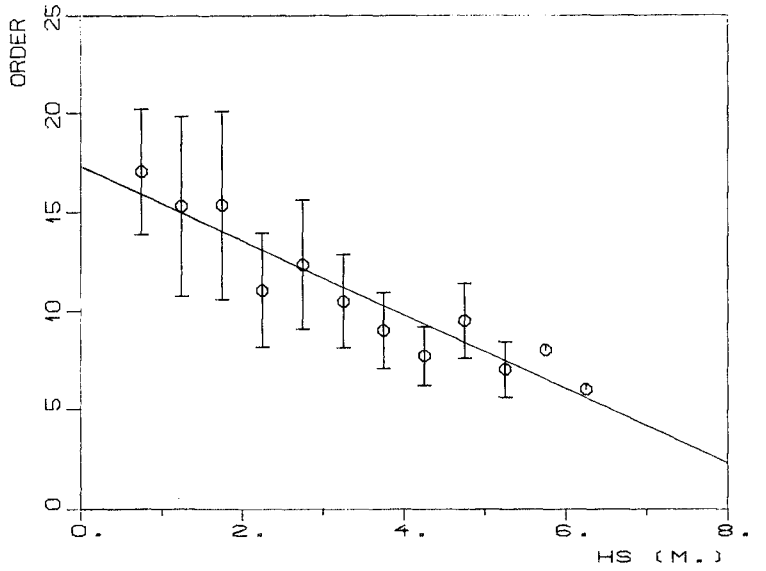

Figure 6.- Dependence of order selected by FPE criteria with significant wave height.

6 APPLICATION OF ARMA MODELS

As a first trial we selected the Box-Jenkins algorithm for ARMA model estimation, being this algorithm one of the most widely used in other fields. But we found that this algorithm performs quite poorly for the large number of data points that constitute the wave records. Computing time is prohibitive and, what is worse, the convergence to a solution is not assured giving rise to frequent running time errors.

Therefore we found it very difficult to apply this algorithm to wave data in a rutinary basis and this made it impossible to carry out a complete comparative analysis as was made for pure AR models.

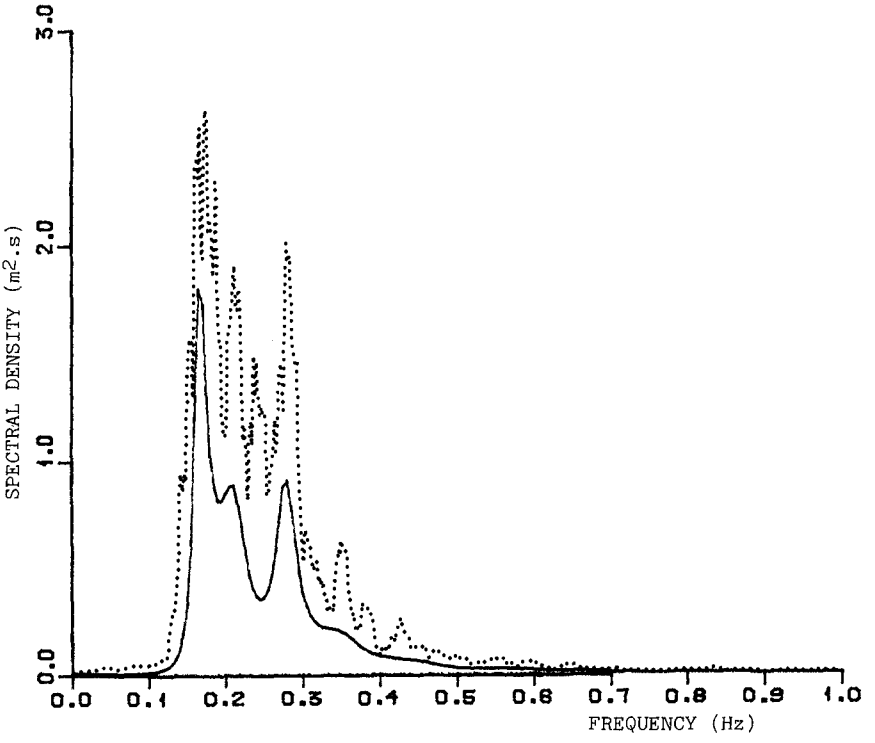

Figure 7. Example of AR spectrum obtained with an ARMA (20, 2) model (continuous line) compared with the corresponding FFT spectrum (dotted line).

We applied the algorithm to just a few cases in order to appreciate if any improvement in the spectral shape was achieved with respect to AR models. Figure 7 is one example of the results obtained using a ARMA (20,2) model to obtain the spectra of a complicated sea state. It can be seen that a very good spectrum is obtained with a very low MA order. The

same was observed for most of the particular cases studied. Specially, it is very interesting to note the way in which the sharp increase in spectral density at the low frequencies is reproduced. This differs from the pure AR models which have difficulties in modelling such part of the spectra (see fig. 1).

At present, we are implementing a new ARMA model estimation algorithm based on the Yule-Walker modified algorithm that we hope will perform much better than the Box-Jenkins one, from the computational point of view.

7 APPLICATION TO SHORT SERIES

One of the main advantages claimed for the ME methods is that they are specially well suite for application to very short time series. This fact could be very helpful in the recovery of spectral information from records where an important part of the signal is lost or distorted.

In order to study if this characteristic could be of interest in the case of wave records, we divided some of the measured records in shorter series of 128 and 256 points and compare the evolution of the estimated spectra for successive short series with that of the complete series. The same was made using FFT techniques.

We observed that AR spectra for short series had a much better resolution than the corresponding FFT spectra and from this point of view the use of AR spectra is recommended. On the other hand, it was also clear that such a small number of points was a sample too short to represent adequately the underlying sea state.

8 CONCLUSIONS

Very shortly we resume the main conclusions obtained during this study:

8.1 - Systematic application of AR models:

- The different AR algorithms used give very similar results. Burg's algorithm being faster and more stable is recommended.
- Visual comparisons between AR and FFT spectra are better made using FFT spectra smoothed to 8 d.o.f. wiht a Barlett window.
- Normalized spectral moments tend to 1 for orders over 5.
- One-peaked spectra are well represented for orders over 12, while two-peaked spectra need orders around 30. Peak frequency is well represented for orders higher than 20.

8.2 - ARMA models:

- Box-Jenkins algorithm for ARMA estimation is inadequate for waves because of long computer time and instability of the solution.
- Anyway, ARMA models seem to better represent wave spectra, mainly in the low frequency range.
- Algorithms better than Box-Jenkins' one can surely be developed.

8.3 - AR order determination:

- FPE criteria seems to behave a little better than AIC and CAT, although differences are relatively small.
- Orders selected using mathematical criteria tend to be much lower than those deduced from comparison with FFT results.
- There is some negative correlation between order selected by mathematical criteria and significative wave height. Nevertheless, the evolution of spectral parameters with order seems to indicate that the correlation should be positive.

8.4 - Relation between order and spectral parameters:

- As stated before, the dependence of model order on significative wave height is not clear. It seems that higher orders are needed to correctly represent the peak frequency for higher wave heights.
- On the other side, there seems to be a high dependence between peak frequency and model order, lower peak frequencies needing higher orders.

8.5 - Application to short series:

- Spectra for short series have higher frequency resolution than the corresponding FFT spectra.
- But, spectra obtained from short series are poor representatives of the underlying sea state.

9 ACKNOWLEDGEMENTS

Dr. Juan Jose Egozcue Rubi, professor at Barcelona University, Spain, implemented the algorithms and introduce the authors to this field. This research is part of the works carried out by the "Programa de Clima Maritimo y Banco de Datos Oceanograficos" of the Spanish Authority of Harbours and Coasts.

10 REFERENCES

BURG, J.P. (1975). Maximum entropy spectral analysis. Ph. D. Thesis, Standford U., California.

EGOZCUE RUBI, J.J (1986). Temas de procesos estocasticos y analisis espectral. Pub. of Programa de Clima Maritimo, no. 15. (Spanish).

HOUMB, O.G. and T. OVERVIK (1981). Some applications of maximum entropy spectral estimation to ocean waves and linear systems response in waves. App. Ocean Res. Vol. 3, No 4.

KAY, S.M. and S.L. MARPLE Jr. (1983). Spectrum analysis, a modern perspective. Proc. IEEE, 69, 1380-1419.

MARPLE Jr., S.L. (1980). A new autorregresive spectrum analysis algorithm. IEEE Trans. Acoust. Speech, Signal Process., ASSP -28, 441-454.

Box, G.E. and G.H. JENKINS (1970). Time series analysis: forecasting and control. Holden-Day, San Francisco.

CHAPTER 2

A re-analysis of the spectra observed in JONSWAP

J.A. Battjes , T.J. Zitman and L.H. Holthuijsen*

ABSTRACT

The frequency spectra of wind-driven waves observed during JONSWAP are re-analyzed to establish whether the Toba formulation for the high-frequency tail ($\sim f^{-4}$) fits the data better than the Phillips formulation ($\sim f^{-5}$) used originally in the JONSWAP project. The results indicate that the f^{-4}-tail provides a better fit to the observed spectra. The proportionality factor in Toba's spectrum, which is theoretically expected to be a universal constant, is found to be uncorrelated with the growth stage of the waves.

Introduction

In so-called ideal conditions of wave generation (a steady, uniform windfield at right angles to a straight upwind coastline), the spectral distribution of wave energy over the frequencies appears to have a standard shape (see e.g. Hasselmann et al., 1973). In a pioneering paper, Phillips (1958) argued that there should be a range of frequencies where the spectral density $E(\omega)$ is saturated at a level determined exclusively by the local (radian) frequency (ω) and the gravitational acceleration (g). On dimensional grounds this saturation level should obey

$$E(\omega) = \alpha\, g^2\, \omega^{-5} \qquad (1)$$

with α a universal constant. However, Hasselmann et al. (1973) showed that α varied with the growth stage, instead of being a constant, as had been inferred by Phillips.

Another approach to the formulation of the saturation range is due to Toba (1972, 1973). It is based on his so-called three seconds power law for the significant waveheight (H_s) and the significant period (T_s). Stated in spectral terms, this law implies that the integral of the spectral densities, or the variance of the surface elevation (ε), and the peak frequency (f_m) are related according to

$$\varepsilon \sim g u_* f_m^{-3} \qquad (2)$$

in which u_* is the shear velocity of the wind over the water surface.

* Dept. of Civil Engineering, Delft University of Technology, Stevinweg 1, 2628 CN DELFT, The Netherlands

On similarity grounds, Toba (1973) deduced from this that the saturation spectral density should be of the form

$$E(\omega) \cong \beta\ g\ u_* f^{-4} \qquad (3)$$

with β a universal constant.

Toba's formulation (3) and the JONSWAP-spectrum were published in the same year (1973), but the latter found initially much more recognition in the international literature than the former. This has begun to change only recently, with the presentation of further empirical evidence supporting (3) by Mitsuyasu et al. (1980), Kahma (1981), Forristall (1981), and Donelan et al. (1985), and with theoretical work of Kitaigorodskii (1983) and Phillips (1985).

In light of these developments, it was decided to re-analyse the original JONSWAP data set with the purpose of making a comparative investigation of the applicability of the formulations due to Phillips (1958) and Toba (1973). The JONSWAP data were chosen because they are supposed to represent virtually ideal generation conditions, and because the JONSWAP spectrum has widely been accepted in the oceanographic and engineering communities. Moreover, the data set is well documented.

The procedures and results of this study are only briefly described here. A full account will appear elsewhere (Battjes et al., 1986).

Data

The spectra which were analyzed in this study, obtained in the Joint North Sea Wave Project (JONSWAP, see Hasselmann et al., 1973), were kindly made available to the present authors for the purpose of a re-analysis. A total of 108 spectra from the 1969 campaign of JONSWAP was available. Nine double-peaked spectra were removed.

The spectral models

The observed spectra are studied in two frequency ranges: the high-frequency range for which the formulations due to Phillips (1958) and Toba (1973) were intended, and the full frequency range including the spectral peak. Only the results for the high-frequency range analysis are presented here.

For the high-frequency range (defined below), the following expressions are used:

$$\text{Phillips (1958)} : E(f) = \alpha\ g^2 (2\pi)^{-4} f^{-5} \qquad (4)$$

$$\text{Toba (1973)} : E(f) = \beta\ g u_* (2\pi)^{-3} f^{-4} \qquad (5)$$

Analysis procedure

Frequency range

The spectra observed in JONSWAP are given at frequencies between f_{min} = 1/128 Hz and f_{max} = 127/128 Hz, with a sample interval of 1/128 Hz. For the high-frequency range analysis, the lower and upper cut-off frequencies f_1 and f_2 were chosen as $f_1 = 1.5\ f_m$ and $f_2 = f_{max}$. For each observed spectrum, the value of the peak frequency f_m needed to determine f_1 was taken from Mueller (1976) (only for this purpose).

Parameter estimation and goodness-of-fit

The values of α and β were estimated simply as the average level of $(2\pi)^4\ g^{-2} f^5\ E(f)$ and $(2\pi)^3\ (gu_*)^{-1}\ f^4\ E(f)$ respectively, between the frequencies f_1 and f_2.

The best-fit values of α and β obtained for each observed spectrum are considered as a function of growth stage, for which the dimensionless peak frequency ν was chosen:

$$\nu = U_{10}\ f_m/g \tag{6}$$

A linear least-squares method for log scales was used to determine the coefficient r and exponent s of the assumed powerlaw relationship between α or β and ν:

$$\alpha = r\ \nu^s \tag{7}$$

and similarly for β.

To establish quantitatively which of the two models fits the JONSWAP observations best, the values of the integrated squared deviation V between observed spectral density (E') and model spectral density (E) were used:

$$V = \int_{f_1}^{f_2} [\ E'(f) - E(f)]^2\ df \tag{8}$$

However, this value is influenced by both the energy and frequency scales of the spectrum, which are irrelevant for a shape analysis. Therefore, a normalized squared deviation ($\hat{V}$) is considered:

$$\hat{V} = V\ f_m/\varepsilon_{1,2}^2 \tag{9}$$

where $\varepsilon_{1,2}$ is the total energy in the frequency range (f_1, f_2).

Results

Spectral parameters

The mean and standard deviation of the estimated values of α and β and the spectral shape parameters of the best-fit spectra are given in Table I, together with the coefficients and exponents of the power law variations with the dimensionless peak frequency (Eq. 7). A graphical impression of the variation of the scale parameters α and β with ν is given in the figs. 1 and 2.

spectral parameter		mean	standard deviation	r	s
Phillips	α	0.0204	0.0088	0.0563	1.06
Toba	β	0.129	0.0622	0.126	0.233

Table I - Mean and standard deviation of the spectral parameters α and β, and coefficients and exponents of the power law (7).

Goodness-of-fit

The joint variation of the normalized error measures $\hat{V}_P$ and $\hat{V}_T$ is given in fig. 3; the subscripts P and T refer to the Phillips and the Toba formulation, respectively. A histogram of the difference $Q = \hat{V}_P - \hat{V}_T$ is shown in fig. 4.

Discussion

Relative goodness-of-fit

It appears from an inspection of the results concerning $\hat{V}_P$ and $\hat{V}_T$ (fig. 3) and their difference $Q = \hat{V}_P - \hat{V}_T$ (fig. 4) that an f^{-4}-tail fits the observed spectra statistically significant better than an f^{-5}-tail. This is put in quantitative terms as follows. The mean and standard deviation of Q are 0.0948 and 0.0519 respectively, based on 82 observed spectra. With the Student-t test the hypothesis that the expected value of Q is larger than zero is accepted even at a confidence level as high as 99.9% (assuming the sample values of Q to be Gaussian-distributed).

The above quantitative assessment of the goodnes-of-fit of an f^{-4}- or an f^{-5}-tail cannot be compared with similar quantitative tests in the literature since such tests have not been carried out before, at least not to the knowledge of the present authors. Instead, several investigators have used a more graphic approach in which the observed spectra were multiplied with f^4 or with f^5. The functions thus obtained appeared to be more nearly a constant as a function of frequency with the f^4 multiplication than with the f^5 multiplication, e.g. Donelan et al., 1985; Forristall, 1981, Kahma, 1981; Mitsuyasu et al., 1980; Toba, 1973.

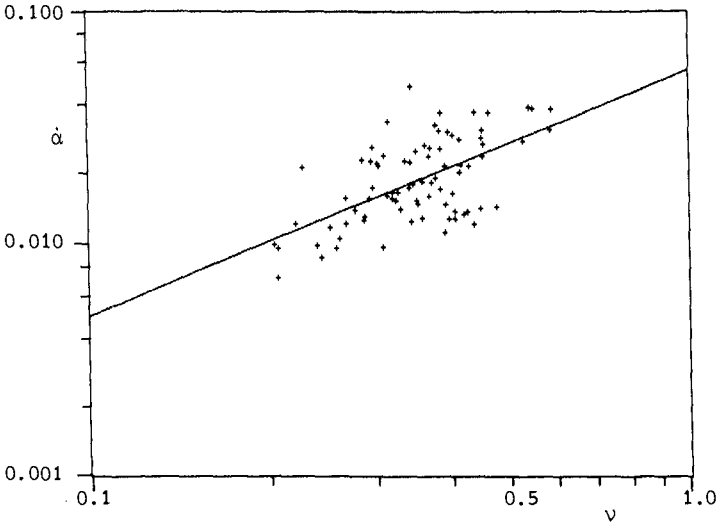

Fig. 1 - Data points: best-fit values of Phillips' α vs. dimensionless peak frequency ν. The straight line represents the best-fit power law relationship (7).

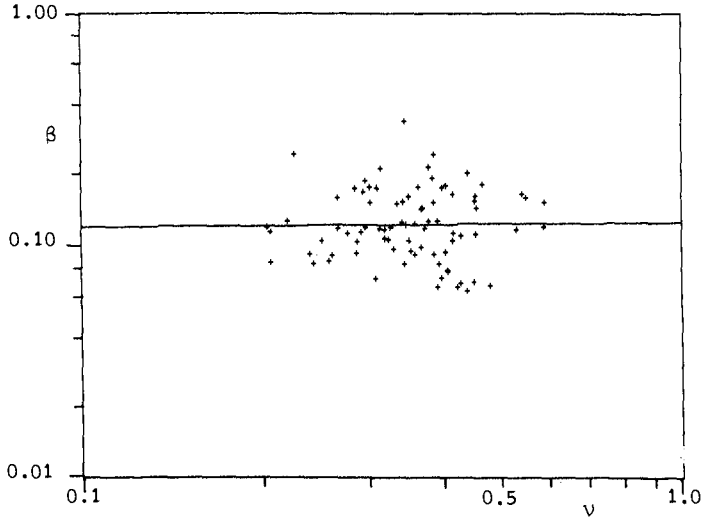

Fig. 2 - Data points: best-fit values of Toba's β vs. dimensionless peak frequency ν. The straight line represents the best-fit power law relationship (7).

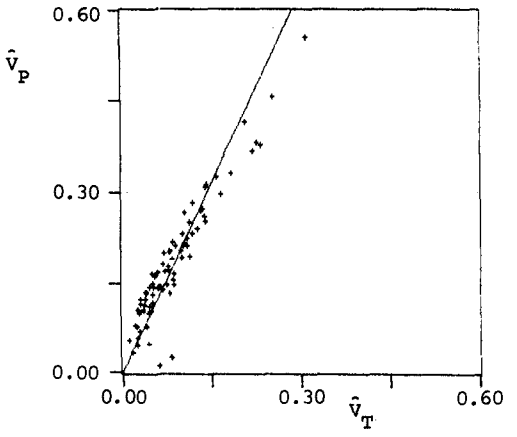

Fig. 3 - Data points: normalized error measures $\hat{V}_P$ (Phillips) and $\hat{V}_T$ (Toba) per observed spectrum. The straight line represents the best-fit proportional relationship.

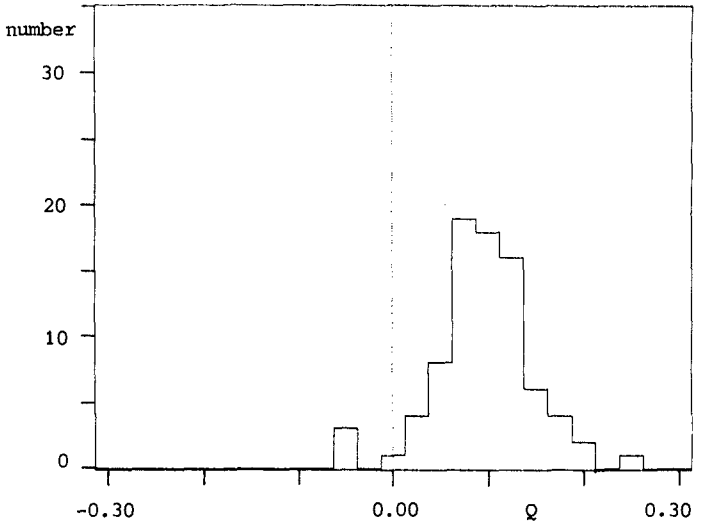

Fig. 4 - Histogram of difference in goodness-of-fit quantified with Q.

Spectral parameters

The discussion of the spectral parameters will focus on the energy scale parameter β and its possible variation with the dimensionless peak frequency ν, compared to the parameter α.

The best fit values of β have been plotted against ν in fig. 2, together with the calculated best-fitting power law relationship between the two. The data show a considerable scatter, but no trend of β with ν is visible. In fact, the hypothesis that the exponent (s) in the power-law relationship between β and ν is zero is accepted at a 99.9% confidence level, using a Student-t test (Draper and Smith, 1981). This observed lack of systematic variation of Toba's β with the growth stage parameter ν contrasts with the variation of Phillips' α (see fig. 1). It supports Toba's original model, insofar as this predicted that β should be a constant. However, in this context the unexplained relatively large scatter in the observed values is disturbing. (It is noted that the unexplained scatter did not decrease by correlating β with ν_*, the peak frequency scaled with g/u_*.)

Among the numerical results concerning Toba's β published previously, only those presented by Donelan et al. (1985) indicate a clear trend with ν. (Although Donelan et al. use a different formulation than the one used here, their results can be transformed into a relation between β and ν; the β-values so obtained have a mean value of about 0.11. Details of this transformation are given in Battjes et al., 1986.) A comparison of these results with those obtained in this paper is given in fig. 5. It is clear that the β-values found by Donelan et al. are correlated with ν, in contrast with those obtained in the present study from the JONSWAP data. The smaller scatter in Donelan et al.'s data suggests that the conditions during the observations of Donelan et al. were more homogeneous (with less unknown variability in geophysical factors) than those during JONSWAP.

The mean values of β from this study are compared in Table II with values reported in the literature. All entries in this table, except those of the present study and those referring to Donelan et al. (1985), have been obtained from Phillips (1985).

A striking outlier in Table II is the value of β from the laboratory data of Toba (1973). It is much lower than those obtained from the field data. Phillips (1985) ascribes this difference to strong wind-drift effects in the laboratory experiments. The values of β obtained from field data (except JONSWAP) vary from 0.06 to 0.11. As pointed out by Phillips (1985), there appears to be a remarkable geographically-based stratification in these results, the Pacific data being considerably lower than the non-Pacific data. The mean value of β from the present study, based on the JONSWAP observations (0.13, with a standard deviation of about 0.06) is somewhat higher than those from the other non-Pacific field data.

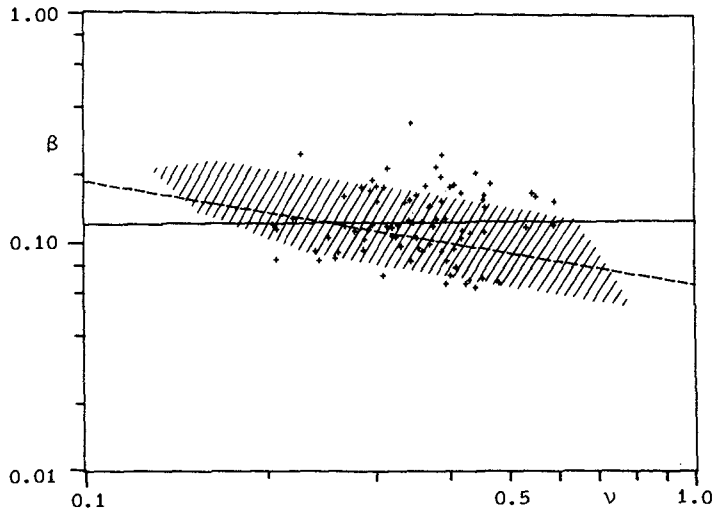

Fig. 5 - Data points and drawn line: see fig. 2. The hatched area and the dashed line represent the range of the transformed results of Donelan et al. (1985) and the corresponding best-fit power law relationship.

author	mean value of β
laboratory	
Toba (1973)	0.02
field	
Kondo et al. (1973)	0.06
Kawai et al. (1977)	0.062
Mitsuyasu et al. (1980)	0.087
Kahma (1981)	0.11
Forristall (1981)	0.11
Donelan (1985)	0.11
this study (JONSWAP)	0.13

Table II - Mean value of the energy scale parameter β from various sources.

CONCLUSIONS

A re-analysis of the original spectra measured in the JONSWAP campaign indicates that the high-frequency part of the wave spectrum can be better approximated with an f^{-4}-tail than with an f^{-5}-tail. The difference in goodness-of-fit is statistically significant at a level of confidence of 99.9%.

The estimated values of the energy scale parameter β in the Toba spectrum are found to be virtually independent of the stage of wave development represented by the dimensionless peak frequency ν. This finding is consistent with Toba's hypothesis that β should be a universal constant. However, it differs from the data of Donelan et al. (1985), whose results indicate a noticeable increase of β with a decrease in ν.

The β-values as determined from the JONSWAP data display a relatively large scatter. Their average value is slightly larger than the mean values reported in the literature.

Acknowledgements

We greatly appreciate the permission of the JONSWAP group to use their original data for a re-analysis.

REFERENCES

Battjes, J.A., T.J. Zitman and L.H. Holthuijsen, 1986, A re-analysis of the spectra observed in JONSWAP, accepted (in 1986) for publication in J. of Phys. Ocean.

Donelan, M.A., J. Hamilton and W.H. Hui, 1985, Directional spectra of wind-generated waves, Phil. Trans. R. Soc. London, A315, 509-562.

Draper, N.R., H. Smith, 1981, Applied regression analysis, sec. ed., Wiley, New York.

Forristall, G.Z., 1981, Measurements of a saturated range in ocean wave spectra, J. Geophys. Res., 86, (C9), 8075-8084.

Hasselmann, K., R.P. Barnett, E. Bouws, H. Carlsen, D.E. Cartwright, K.Enke, J.A.Ewing, H.Gienapp, D.E. Hasselmann, P. Kruseman, A. Meerburg, P. Mueller, D.J. Olbers, K. Richter, W. Sell and H. Walden, 1973, Measurements of wind-wave growth and swell decay during the Joint North Sea Wave Project (JONSWAP), Dtsch. Hydrogr. Z., A8, No. 12.

Kahma, K.K., 1981, A study of the growth of the wave spectrum with fetch, J. Ph. Oceanogr., 11, 1503-1515.

Kitaigorodskii, S.A., 1983, On the theory of the equilibrium range in the spectrum of wind-generated gravity waves, J. Ph. Oceanogr., 13, 816-827.

Mitsuyasu, H., F. Tasai, T. Suhara, S. Mizuno, M. Ohkusu, T. Honda and K. Rikiishi, 1980, Observations of the power spectrum of waves using a cloverleaf buoy, J. Ph. Oceanogr., 10, 286-296.

Mueller, P., 1976, Parameterization of one-dimensional wind wave spectra and their dependence on the state of development, Hamburger Geophysikalische Einzelschriften, 31, Hamburg University.

Phillips, O.M., 1958, The equilibrium range in the spectra of wind-generated waves, J. Fluid Mech., 4, 426-434.

Phillips, O.M., 1985, Spectral and statistical properties of the equilibrium range in wind-generated gravity waves, J. Fluid Mech., 156, 505-531.

Toba, Y., 1972, Local balance in the air-sea boundary processes I: On the growth process of wind waves, J. Oceanogr. Soc. Japan, 28, 109-121.

Toba, Y., 1973, Local balance in the air-sea boundary process III: On the spectrum of wind waves, J. Oceanogr. Soc. Japan, 29, 209-220.

CHAPTER 3

MATHEMATICAL AND PHYSICAL WAVE DISTURBANCE MODELLING COMPLIMENTARY TOOLS

by

I.Berenguer(1), P.A.Madsen(2), M.Rubjerg(3), A.Kej(4)

ABSTRACT

This paper presents comparisons between physical and numerical model reproductions on the basis of comprehensive wave disturbance studies of a major spanish port.

Mathematical modelling has reached in many cases a degree of reliability comparable to that of a physical model, but it is essential that both types of modelling systems are validated against measurements.

1.- INTRODUCTION

During the past decade, the advancement of digital computers and numerical techniques have made possible a deterministic numerical modelling of wave penetration in coastal areas and ports, i.e. a mathematical reproduction of wave time series resulting from the combined effects of refraction, diffraction and (partial) reflection of irregular waves. Such tools have now reached a degree of reliability comparable to that of a physical model. Even though further developments of the numerical tools are still needed, the coastal and port engineer is already now faced with the question whether to consider physical and numerical models as alternative or as complimentary tools.

(1) Head, Mathematical Modelling Area, Centro de Estudios de Puertos y Costas (Spain)
(2) Senior Hydraulic Engineer, Danish Hydraulic Institute (Denmark)
(3) Senior Hydraulic Engineer, Danish Hydraulic Institute (Denmark)
(4) Head, Computational Hydraulics Centre, Danish Hydraulic Institute (Denmark).

On the background of comprehensive wave disturbance studies of a major Spanish port, this paper analyses strengths and weaknesses of the two tools applied (physical and numerical model), and outline the contribution that the individual tools would make to the decision basis required by the port authority, today and in the future. The analysis contains qualitative and quantitative comparisons between physical and numerical model reproductions of the same port layout and wave conditions.

2.- PHYSICAL MODELLING

2.1.- Introduction

Complete similitude between hydraulic scale models and their prototypes is not possible unless the scale is such that the model is as large as its prototype. Some priorities must be established in order to simulate correctly the most important forces of the system considered.

In Coastal Engineering projects the forces on system elements consist of the kinetic reaction due to the inertia of an element's mass, gravity, viscous shear, surface tension, elastic compression and the pressure forces.

For overall similarity, the ratio of inertia forces, model to prototype, must equal the ratio of the vector sum of the active forces.

If gravitational forces predominate the ratio (Froude Number) model/(Froude Number) prototype, must be equal to 1, where the

$$\text{Froude Number} = \frac{V}{(gL)^{1/2}}$$

If viscous fores predominate the ratio

(Reynolds Number) model /(Reynolds Number) prototype, must be equal to 1, where the Reynolds Number = $\frac{LV}{(\mu/\rho)}$

If Surface Tension effects predominate the ratio

(Weber Number) model /(Weber Number) prototype, must be equal to 1, where the Weber Number =

If Elastic Compression forces predominate the ratio

(Mach Number) model /(Mach Number) prototype, must be equal to 1, where the March Number = $\frac{V}{(\sigma/\rho L)^{1/2}}$

2.2.- Estuary Models

There are many problem areas concerned with tidal model- ling techniques but tidal action provides the major amount of system energy, and as gravitational forces are predominant in tidal flows the Froude Number guides the modelling process.

Due to the large areas that must be simulated the use of distorted scale models is usual but the higher the degree of distortion used in the model, the greater is the roughness which is required in the model.

2.3.- Harbour Wave Action Models

Short period wind waves (T=5-20 sec) are designed in accordance with the Froude model law and are constructed geometrically similar to their prototypes.

When reproducing intermediate and long period waves (T> 20 sec) excessively large scale models are usually required because, otherwise, friction effects may be excessive and it results in excessive bottom friction losses. In such cases distorted linear scales are usually adopted. It also provides easier measurements of wave heights but wave reflection effects are increased.

Similarity of diffraction requires that the linear scales for horizontal distances on the model be equal to the wavelength scale. This ensures a correct simulation of modes of oscillation in the basins for all wave periods and, therefore, the occurrence of resonance at correct wave periods.

For long waves of small amplitude at depths smaller than 0,05 x wavelength distorted scale models reproduce wave refraction, diffraction and resonant periods accurately. For bigger depths the scale distortion has the effect of distorting the wave refraction patterns.

2.4.- Coastal erosion models.

Most of the fluid processes involved are complicated by non-linear fluid behaviour, turbulence and complex boundary conditions. In attempting to develope similitude relations, the idea of reproducing the dominant physical processes may be abandoned and attention turned to an attempt to mantain similitude of the beach profiles and longshore transport rates.

If adequate prototype data ara available and verification procedures in the model are successful we can have confidence in the results of the model although the combination of forces that occur in the prototype cannot always be reproduced exactly in the model.

3.- NUMERICAL MODELLING

3.1.- The "System 21. Mark 8"

The numerical model "System 21 Mark 8" considered here is based on the time-dependent vertically integrated Boussinesq equations of conservation of volume and momentum, assuming constant density. It is able to simulate unsteady two-dimensional flows in vertically homogeneous fluids. The Boussinesq terms account for the deviation from hydrostatic pressures distribution due to vertical accelerations and are of special interest to the short wave simulations because they make possible to consider a large range of water waves without being restricted by linear assumptions. The equations include porosity terms by means of which it is possible to consider partial reflection and wave transmission from and through piers and breakwaters. The model was described in detail by Abbott et al (1978, 1983) and the equations are included in Appendix A.

3.2.- Advantages and drawbacks of numerical modelling.

As mentioned in section 2 a general problem in physical modelling is the distorted scales. In a numerical model this problem does not exist at all and as long as you can describe the phenomena with a set of mathematical equations, prototype simulations can be made no matter how large the model area is. This is a significant advantage considering estuary models.

Often the numerical and the physical models are applied as complimentary tools. The numerical model can be used to establish the current pattern in a large area and to provide boundary conditions for a detailed physical model of a minor area of special interest.

In the numerical as well as in the physical model the accuracy of the solution will depend on the quality of the boundary data. However it is much easier to control the inflow conditions in the numerical model where the required variation of the water level or discharge simply is specified.

Another problem related to wave modelling is to control reflections in the model area. In the physical model it is very difficult to avoid reflections of long waves from the model boundaries and from the paddle generator. This is no problem in a numerical model where the wave energy can be damped out artificially along the closed boundaries or can be allowed to pass through an open boundary without any re--reflection.

Partial reflection from piers and breakwaters can also be simulated in the numerical model. You can either achieve a certain specified reflection coefficient or you can simulate the actual partial reflection from a given vertical rubble mound. Natural breakwater, however, are not always vertical and in this case experimental data is neccessary to estimate the reflection coefficients.

Finally there is the problem of data collection from the model tests. In the physical model you will have to measure for instance the velocity at certain pre-selected locations. If the scale is very distorted this cannot easily be done without affecting the flow you are actually measuring. Furthermore the data collection can only be made in a minor number of pre-selected points. In the numerical model the results will be computed in every single grid point which means that a huge number of information can be stored on a tape for later display by graphics. As an example you can determine significant wave heights in every single grid point leading to a very accurate map of isolines.

On the other hand it should of course be mentioned that the numerical model is limited by the size of the computer and wave simulations longer than 25 minutes real time are seldom made. In some situations this could be a drawback cosidering the statistics made on the results. Therefore you have to make sure that the relative significant wave heights determined do not vary with the length of the simulation.

4.- A CASE STUDY

The extension of the harbour of Bilbao has been subject to intensive studies to obtain its optimum configuration considering social, economical, and technical reasons. The port area considered for the extension covers an area of 6 by 4 km. (See fig. 1)

As part of the complete study, investigations have been carried out at the Danish Hydraulic Institute (DHI) using a mathematical modelling system (System 21 Mark 8) covering the model area with approximately 70.000 computational points.

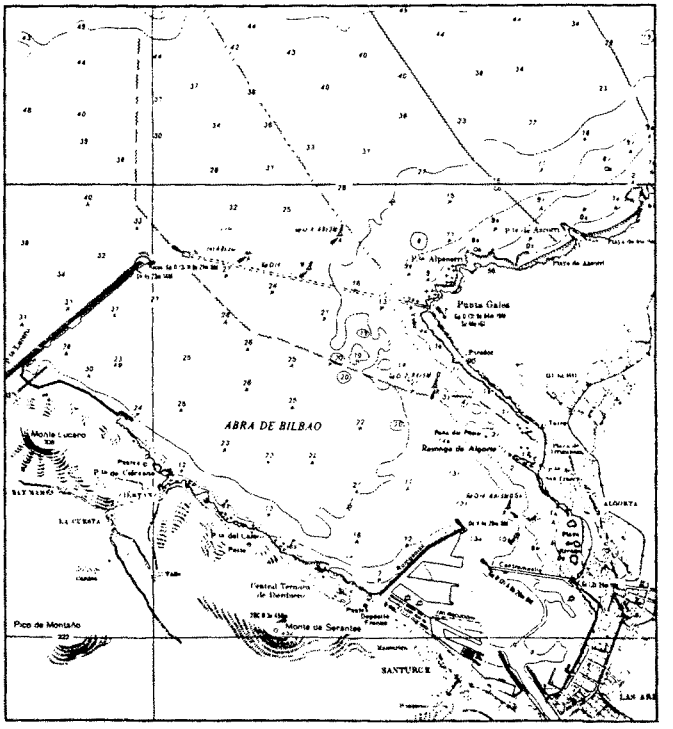

Fig. 1.- Extension Area

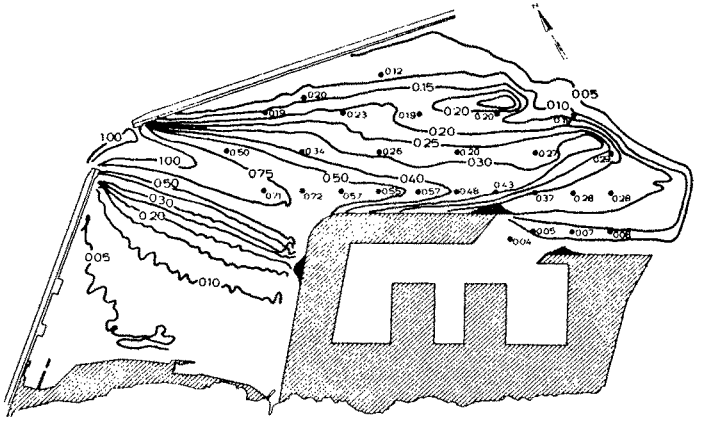

Fig. 2.- Physical and Mathematical Model Results

The grid size used for the present application was 20 m., while the time step was 1.25 seconds. This combination of grid size and time step has been considered a reasonable compromise between high accuracy of the numerical scheme for the type of waves to be simulated and realistic computer requirements.

A simulation period of 20 minutes has been chosen, allowing waves to reach the innermost parts of the harbour and to be reflected an still leave a reasonable amount of data for the following statistical analysis.

Simultaneously, studies using a physical model (scale 1:150) have been carried out at the Centro de Estudios de Puertos y Costas (CEPYC) in Madrid.

It includes the inner harbour and the area covered by the model in the laboratory is 2875 m^2.

Where partial reflection was desired a 0.33 reflection coefficient was chosen and the section obtained in some previous one-dimensional tests was constructed in the model. This section was composed of a concrete slope with stones sticked on it.

Both modelling systems (numerical and physical) have been used to reproduce time series of irregular waves synthesized on the basis of a Jonswap spectrum. A peak period of 19 seconds and a significant wave height of 4.75 m. have been considered.

5.- COMPARISON BETWEEN PHYSICAL AND NUMERICAL MODELLING

5.1.- Introduccion

Two different layouts of the harbour have been considered in this paper.

The first layout is composed of two outer breakwaters and a single operational zone close to the already existing harbour of Bilbao (Fig. 3)

The second layout is composed of the same two outer breakwaters as in the first case, but it also includes a complete development of the western side of the protected area. Additional protection is obtained through the construction of an inner breakwater with a bending of almost 90 degrees (Fig. 4 and Fig. 5)

Two different wave conditions have been considered:

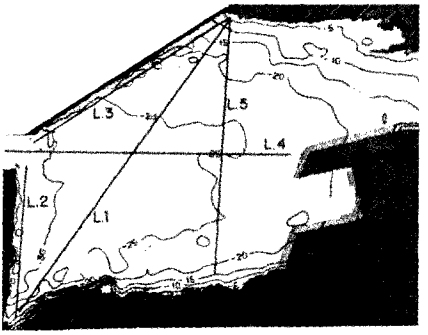

Fig. 3.- Test 1. Bathimetry and comparison lines

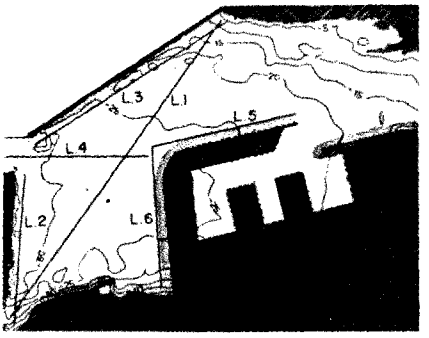

Fig. 4.- Test 2. Bathimetry and comparison lines

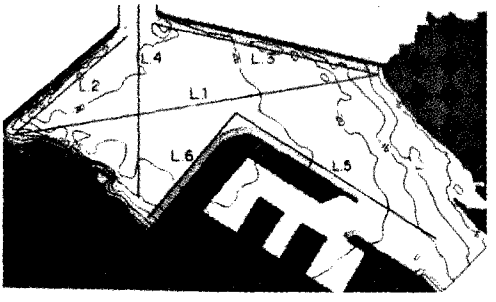

Fig. 5.- Test 3. Bathimetry and comparison lines

- Spectral Moments of order 0, 1, 2 and 4
- Peak frequency (Fp) and Spectral Density at the peak (Smax)
- Peakness Parameter (Qp) as proposed by Goda

We also had to compute the FFT spectra for comparison with the AR algorithm, the spectra computed were: the raw spectrum and smoothed spectra of 8, 16 and 32 degrees of freedom. Two spectral windows, Barlett and Rectangular, were used for each estimation.

The reason behind, this is the dependence of the chosen parameter upon the degree and shape of smoothing. Moreover, in order to get a feeling of the spectral shape, we drew graphs for a few number of wave records with one FFT estimation against the 40 AR calculated spectra, and therefore we could compare the FFT estimation with the 40 orders. Figure 2 shows an example of this kind of graph. An ordinary spectrum was selected and we ould observe some characteristics that come out in all AR estimations:

- A peak appears for high frequencies and slides towards low frequencies for higher orders of the AR model.
- A new peak is born around the 20th. order.
- We notice that we cannot increase indiscriminately the order, since for higher orders both peaks could merge.
- Difficulties in modelling the FFT results for low frequencies of the AR estimations, and reaching the Fp of the FFT for low orders of the models.

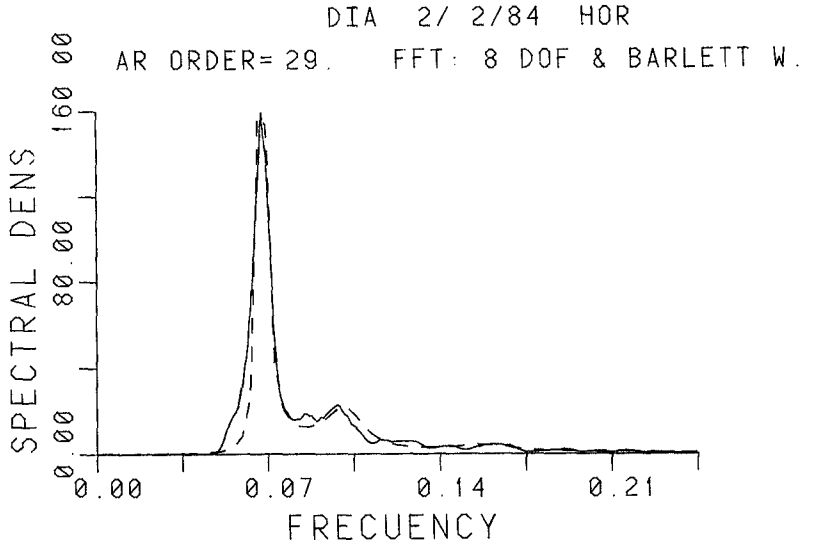

Figure 1. Comparison between FFT spectrum versus Maximum Entropy Spectrum

We could obtain in some cases fittings, as Figure 1 shows, between FFT estimation and an AR model.

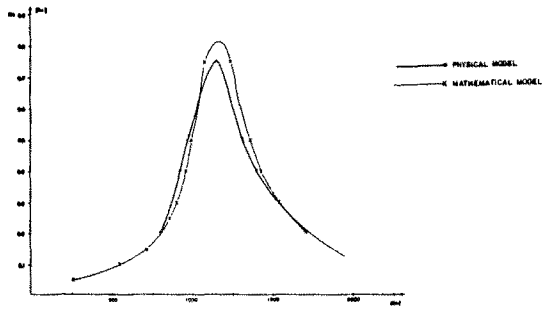

Line 1

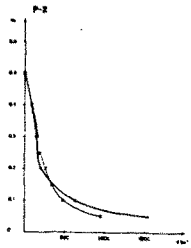

Line 2

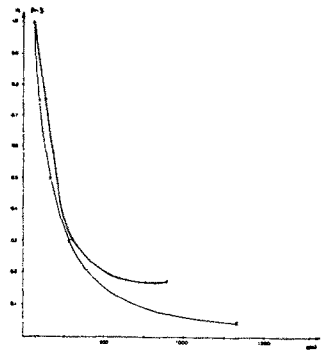

Line 3

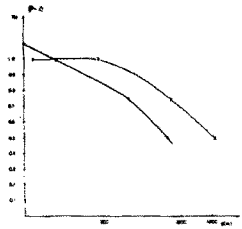

Line 4

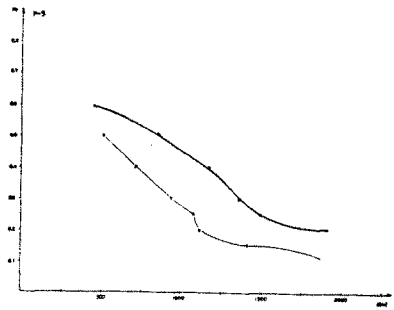

Line 5

Fig. 6.- Test 1. Comparison of results

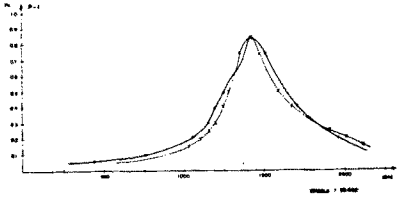

Line 1

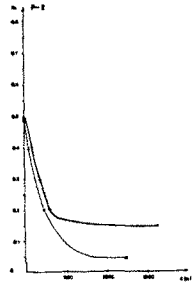

Line 2

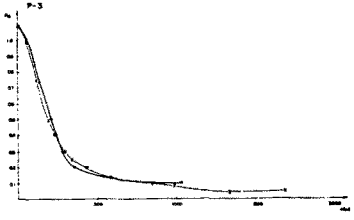

Line 3

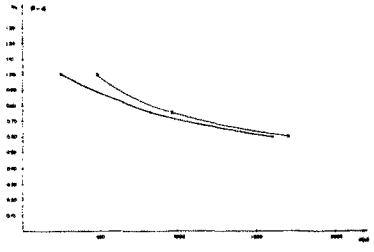

Line 4

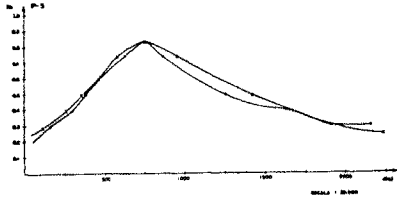

Line 5

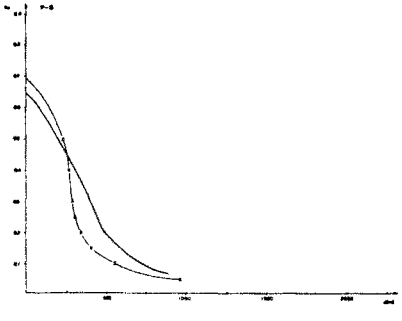

Line 6

Fig. 7.- Test 2. Comparison of results

of waves is predominant. In these cases the waves heights obtained from the physical model are higuer than those obtained in the numerical model. Hence it can be concluded that the partial reflection from the piers is different in the two systems of modelling.

5.4.- TEST 3

The lines along which comparisons have been made can be inFig. 5 and the comparisons along these lines are shown in fig. 8

As in TEST 2 discrepancies between the numerical and the physical model results appear in the points affected by the partial reflection from the bended inner breakwater in the second layout. Obviously the partial reflection coefficients achieved in the two modelling systems are different. In the physical model some preliminary one-dimensional tests have been carried out using regular waves. A table of reflection coefficients has been established as a function of depth, wave period, wave height, slope and porosity of the structure. Knowing the characteristics of the structure in the prototype some assumtions on the reflection coefficient can be made and modelled in the Laboratory.

In the numerical model the same assumptions can be applied and one can obtain the desired reflection coefficients through the specifications of the rubble mound. The equations solved by the numerical model include porosity which makes it possible to simulat the flow inside vertical porous structures. As shown by Madsen and Warren (1984), the partial reflection from vertical rubble mouds can be simulated very accurately using this method. The reflection will depend on the porosity, the diameter of stones, the width of the rubble mound, the water depth, the wave height and of the wave period. Natural breakwaters, however, are not always vertical and in this case the reflection will be different. In th numerical model, one can still obtain the reflection desired, just by changing the specifications of the vertical rubble mound, but to actually estimate the reflection for a given type of non-vertical construction, experimental data is reequiered.

On the other hand, scale effects will influence the reflections obtained in the physical model. Hence, it becomen important to validate both modelling systems directly against field measurements.

This has not been possible in the present situation and for the time being it can only be concluded that the reflections from the proposed inner breakwater in layout no. 2 are different in the physical and the numerical modelling.

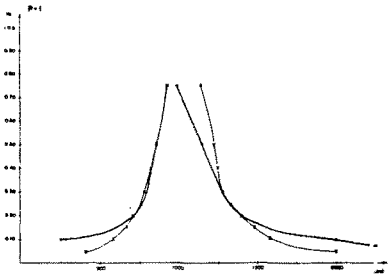

Line 1

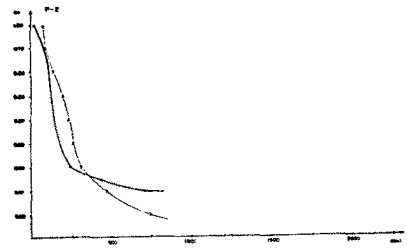

Line 2

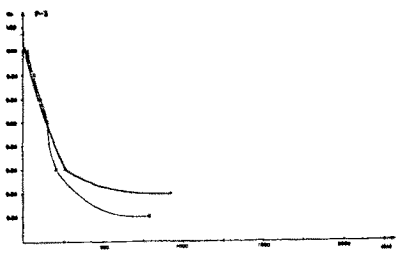

Line 3

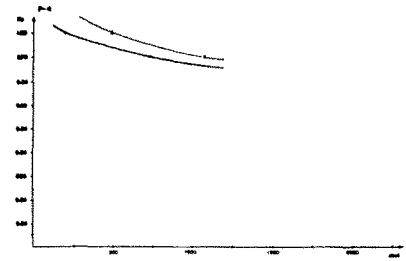

Line 4

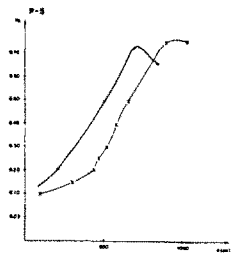

Line 5

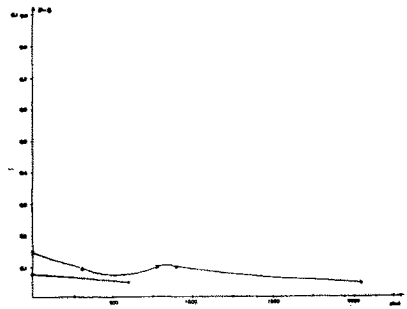

Line 6

Fig. 8.- Test 3. Comparison of results

Finally some other general tendencies can be pointed out on the basis of the three cases studied. The results obtained from the physical model are slightly higher in the more inner points at the lee of the breakwaters and slightly lower in the main direction of wave propagation than the results obtained by the numerical model. The explanation for this discrepancy can be found in the way the wave input has been specified in the two types of modelling. Firstly a one-directional input has been applied in the numerical model leading to a perfectly straight wave front at the entrance to the harbour. Secondly some variation across the entrance was observed to take place in the physical model. The reason for this variation is that part of the outer harbour bathymetry was included in the physical model. Hence along the line where the input to the numerical model was supposed to be one-directional, the wave generated in the physical model actually turned out to be directional.

Sand et al (1983) investigated the effect of directional diffraction of waves in a numerical and a physical model. Both modelling systems showed that right in the opening of the harbour the directional wave heights were smaller than the one-directional wave heights but behind the breakwaters the directional waves were clearly higher. This explains the present discrepancy between the physical and numerical model results.

6.- CONCLUSION

The transmission of waves from the sea into a harbour protected by breakwaters is a process which involves shoaling, refraction, diffraction and partial reflection processes.

This paper presents comparisons between numerical model simulations and physical model tests from a practical case study.

It is proven that engineers can confidently apply such models to the study of development projects for harbours and coastal regions. However, until now, numerical wave disturbance models have been validated primarily against results from physical models where scale effects appear. Bottom Friction, wave transmission through pervious structures, and wave reflection are phenomena that with the geometrical similarity are ill-considered in physical models and should be subject to special consideration. Hence, it is essential that both types of modelling systems (physical and numerical) are validated against field measurements.

7.- REFERENCES

1) ABBOTT, M.B., SKOVGAARD, O. and PETERSEN, H.M. (1978). On the numerical modelling of short waves in shallow water. J. Hydraul. Res. 16(3).

2) ABBOTT, M.B., McCOWAN, A. and WARREN, I.R. (1983). Extending the range of application of short-wave numerical models.

3) MADSEN, P.A. and WARREN, I.R. (1984). Performance of a numerical model. Coastal Engineering 8: 73-93

4) SAND, S.E., KIRDEGAARD, J., LERSEN, J. and RODERHUIS, G.S. (1983) Numerical and physical verification of directional diffraction of waves. Proc. Conf. on Coastal & Port Eng. in developing countries, Shri Lanka, Vol II, p. 1290-1303

8.- APPENDIX A

The equations solved by the numerical model

The numerical model is based on the time-dependent vertically integrated Boussinesq equations conserving mass and momentum. The model is described in detail by Abbott et al. (1983). The equations are given below:

Continuity

$$n\frac{\partial \zeta}{\partial t} + \frac{\partial p}{\partial x} + \frac{\partial q}{\partial y} = 0$$

x-momentum

$$n\frac{\partial p}{\partial t} + \frac{\partial}{\partial x}\left(\frac{p^2}{h}\right) + \frac{\partial}{\partial y}\left(\frac{pq}{h}\right) + n^2 gh\frac{\partial \zeta}{\partial x} + n^2 p\left(\alpha + \beta\sqrt{\frac{p^2}{h^2} + \frac{q^2}{h^2}}\right) - \frac{p^2}{nh}\frac{\partial n}{\partial x} - \frac{pq}{nh}\frac{\partial n}{\partial y} = n\frac{Hh}{3}\left(\frac{\partial^3 p}{\partial x^2 \partial t} + \frac{\partial^3 q}{\partial x \partial y \partial t}\right)$$

y-momentum

$$n\frac{\partial q}{\partial t} + \frac{\partial}{\partial y}\left(\frac{q^2}{h}\right) + \frac{\partial}{\partial x}\left(\frac{pq}{h}\right) + n^2 gh\frac{\partial \zeta}{\partial y} + n^2 q\left(\alpha + \beta\sqrt{\frac{p^2}{h^2} + \frac{q^2}{h^2}}\right) - \frac{q^2}{nh}\frac{\partial n}{\partial y} - \frac{pq}{nh}\frac{\partial n}{\partial x} = n\frac{Hh}{3}\left(\frac{\partial^3 q}{\partial y^2 \partial t} + \frac{\partial^3 p}{\partial x \partial y \partial t}\right)$$

CHAPTER 4

Statistical Modelling of Long-Term Wave Climates

Richard Burrows* and Barham A. Salih**

Abstract

The paper discusses the long-term statistical properties of ocean and coastal wave climates derived from the analysis of instrumental wave data. The aim of the work reported has been to determine the theoretical distributions, from those commonly used in analysis of wave data, which best describe the joint probability of significant wave height, Hs, and mean zero-upcrossing period, Tz. A method of modelling the wave climate in this manner has been developed utilizing parametric means of specification. The data base used in the study covers records from 18 sites around the British Isles.

Introduction

Mathematical models considered previously for this application have been examined as part of the study. Ochi (1978) proposed the use of a bi-variate (2-dimensional) Log-Normal distribution for the joint probability density function (pdf) denoted by p(Hs,Tz). This can be defined in terms of the first and second order statistical moments of the marginal pdfs of both Hs and Tz and a measure of the correlation between these wave properties. Appendix 1 presents a summary of the relevant mathematics for this and other probability distributions discussed herein.

Whilst the fit shown by Ochi for the Log-Normal distribution, applied to various data sets, was good for the bulk of the probability mass the tails, in particular that of Hs, were not well matched beyond a cumulative probability of about 0.99. It is this region which is often of interest in engineering design and a need for improved modelling of extremal (Hs,Tz) sea states has recently been identified by U.K. Department of Energy (1986).

As part of a research programme aimed at wave climate synthesis by the National Maritime Institute (NMI, but now British Maritime Technology), a development of Ochi's modelling was proposed by Fang and Hogben (1982). This involved the inclusion of a measure of the skewness in a term modifying the Log-Normal form of the marginal distribution of Hs.

The joint pdf, p(Hs,Tz), can be expressed as a product of the marginal pdf of Hs and the conditional pdf of Tz (given Hs), i.e.

*Lecturer/**Research Assistant, Department of Civil Engineering, University of Liverpool, PO Box 147, Liverpool L69 3BX, U.K.

$$p(Hs,Tz) = p(Tz/Hs).p(Hs) \quad (1)$$

Houmb and Overvik (1976) utilized the form of this equation for the description of wave climate off the coast of Norway. For both the marginal distribution of Hs and the conditional distribution of Tz, they employed a 2 parameter Weibull distribution (equivalent to the 3 parameter Weibull but with A=0, see Appendix 1). Parameters B and C in p(Tz/Hs) were then specified as functions of Hs, following regression for their sites under study.

More recently Haver (1985) has proposed a similar form of modelling to that of Houmb and Overvik but with the conditional distribution of Tp (the spectral peak period, replacing Tz) fitted to a Log-Normal distribution. The marginal distribution of Hs is described in the lower region by the Log-Normal distribution also but for the upper tail ($Hs > \alpha$, where α is a chosen threshold) a 2 parameter Weibull distribution is employed.

This latter model has not been investigated herein but the other methods described above have been applied together with several modified approaches. These include; (i) an extension of Houmb and Overvik's model by the use of the 3 parameter distribution for both marginal and conditional probability distributions, (ii) use of a mixed Weibull and Log-Normal model with p(Hs) described by the former and p(Tz/Hs) by the latter, (iii) direct specification of p(Hs,Tz) in terms of a 2-dimensional Weibull distribution. For the latter, the derivation given by Kimura (1981) for application to short-term wave climates has been utilized. Relevant equations are contained in Appendix 1.

The study has been conducted in 3 parts. Firstly, the goodness of fit of the different models to the data was investigated, the models being fitted using statistical moments of the various data samples. This provided a shortlist of preferred probability distributions. Secondly, empirical relationships between the significant wave height, Hs, and both the conditional statistics of Tz and the parameters of the different models were investigated. In this way it was hoped to improve the means of description of the Tz domain of the wave climate. By considering the degrees of exposure and wind field statistics of the different sites trends were observed and, ultimately, regression equations linking Tz statistics to the marginal statistics of Hs have been established for 2 groups of sites, loosely termed 'oceanic' and 'coastal'. The third and final part of the study has been to use the regression equations for specification of the parameters of the different models and to again assess their respective merits.

Data

The data base used in the study consisted of scatter diagrams (bi-variate histograms of the 3-hourly observation of Hs and Tz) covering periods of measurement ranging from 1 to 7 years. An example of such a diagram is given in Fig. 1. Locations of the various sites are indicated on the map in Fig. 2.

The data set is far from ideal since for few sites do recordings

exceed one or two years duration. In consequence, the effects of variability in annual wave climate will potentially cloud any 'between site' trends which may be present. Whilst these inadequacies of the data will have an unquantifiable effect on the results developed, this should not be so large as to undermine the value of the study.

FIGURE 1 BI-VARIATE HISTOGRAM, OR SCATTER DIAGRAM, OF H_s AND T_z

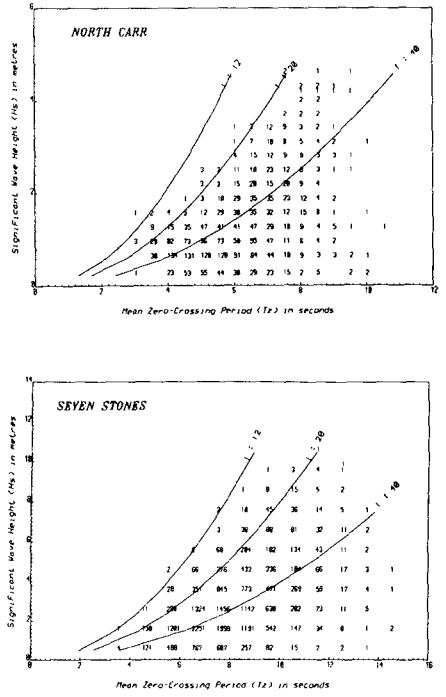

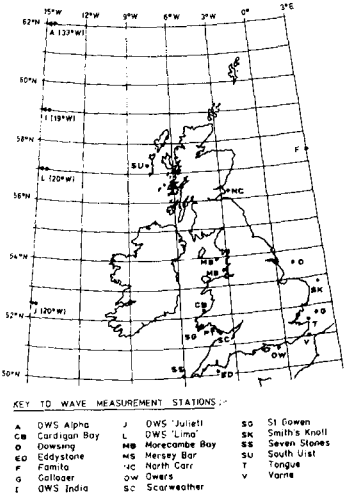

FIGURE 2 LOCATION MAP SHOWING SOURCES OF WAVE DATA

Analysis of Scatter Diagrams Forming the Data Base

The statistical properties of Hs and Tz computed from scatter diagrams for the 18 sites are listed in Table 1. These parameters (mean, standard deviation and skewness of the marginal distributions and the correlation coefficient) can be used to define each of the theoretical probability distributions referred to above (and in Appendix 1). The Weibull distribution is most conveniently expressed in terms of parameters A,B,C, each being related to the statistical moments, and these are also included in Table 1.

Marginal Distribution of Hs: The marginal histograms of Hs from the data sets have been compared against the (3 parameter) Weibull, Log-Normal and Modified Log-Normal (NMI) distributions. Fully objective 'method of moments' fitting has been used in each case. Examples, in Fig. 3, of the observed frequency histograms with theoretical distributions superimposed show each of the above to

TABLE 1 STATISTICAL PROPERTIES OF SCATTER DIAGRAMS FORMING DATA BASE

Site	Marginal Hs			Marginal Tz			ρ_{Hs-Tz}	Marginal Hs			Marginal Tz		
	$\bar{Hs}$	σ_{Hs}	λ_{Hs}	$\bar{Tz}$	σ_{Tz}	λ_{Tz}		A_w	B_w	C_w	A_w	B_w	C_w
Seven Stones	2.36	1.39	1.16	7.72	1.52	0.45	0.489	0.40	2.15	1.43	4.39	3.75	2.32
South Uist	2.44	1.33	0.96	6.33	1.42	0.20	0.706	0.37	2.31	1.60	2.53	4.27	2.90
W S Alpha	3.06	1.67	1.08	8.31	1.26	0.23	0.592	0.62	2.71	1.49	5.03	3.68	2.81
W. S. India	3.36	2.07	1.44	9.43	1.29	0.52	0.617	0.80	2.75	1.24	6.75	3.03	2.19
W. S. Juliett	3.38	2.04	1.32	9.54	1.52	0.49	0.639	0.72	2.88	1.31	6.33	3.62	2.23
Famita	2.81	1.51	1.06	7.40	1.28	0.51	0.596	0.57	2.48	1.51	4.73	3.01	2.19
Galloper LV.	1.36	0.81	1.38	4.66	0.91	0.41	0.390	0.33	1.11	1.28	2.62	2.30	2.39
Tongue LV.	0.93	0.40	0.75	4.83	0.86	0.67	-0.021	0.23	0.79	1.84	3.23	1.81	1.95
Eddystone LH.	1.17	0.81	1.59	4.83	1.12	0.74	0.646	0.23	0.99	1.16	2.84	2.24	1.84
Varne LV.	1.24	0.76	1.43	5.62	0.84	0.75	0.064	0.28	1.02	1.25	4.13	1.68	1.84
Scarweather Bk.	1.17	0.87	0.94	7.00	1.86	0.55	0.299	-.21	1.54	1.62	3.23	4.26	2.14
St. Gowan LV.	2.01	1.27	1.10	6.68	1.42	0.49	0.342	0.17	2.04	1.48	3.69	3.37	2.22
Dowsing	1.37	0.83	1.42	5.17	1.17	0.42	0.557	0.34	1.11	1.26	2.56	2.95	2.37
North Carr LV.	1.11	0.76	1.51	5.79	1.30	0.33	0.489	0.20	0.97	1.20	2.68	3.50	2.56
Smith's Knoll LV	1.09	0.67	1.31	6.40	1.04	-.15	0.523	0.21	0.96	1.32	2.40	4.39	4.36
Mersey Bar LV.	1.23	0.71	1.76	4.97	0.91	0.67	0.624	0.46	0.79	1.08	3.27	1.92	1.95
Morecambe Bay LV	1.07	0.77	1.34	3.76	1.26	0.72	0.679	-0.08	1.07	1.30	1.48	2.56	1.88
Cardigan Bay	1.01	0.69	1.19	5.89	1.47	1.25	-0.053	0.05	1.05	1.41	3.91	2.16	1.36

FIGURE 3 MARGINAL FREQUENCY HISTOGRAMS OF H_s
(note: percentage frequency $\equiv p(H_s)\Delta H_s \cdot 100$)

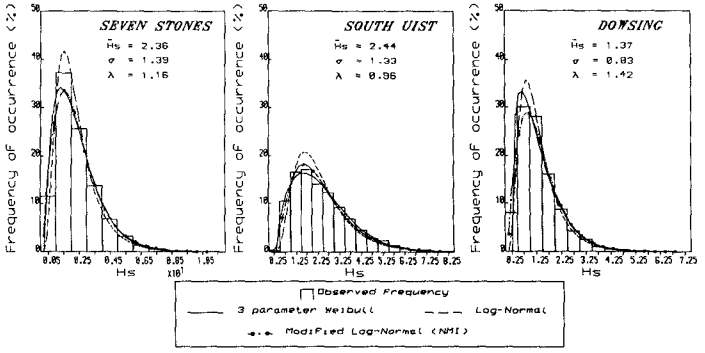

reasonably describe the main probability mass. An indication of relative performance, in terms of 'goodness-of-fit', can be obtained from an application of the χ^2 test. The χ^2 statistic is defined as:

$$\chi^2 = \sum_{i=1}^{k} \frac{(Oi-Ei)^2}{Ei} \qquad (2)$$

where Oi and Ei are the observed and expected frequencies for class (i) of (k) classes. Because, generally, the number of classes did not conform to the requirements of the standard test, for the relevant sample sizes, resulting values of χ^2 cannot be related to appropriate 'levels of significance' in the usual way. Numerical values have, therefore, been used as only qualitative indicators of

goodness-of-fit. Utilizing this approach, and making allowance for the potential departures of the Weibull fit for the lowermost classes arising from the imposition of the location parameter A, this distribution produces the best fit. Indeed, this slight limitation associated with the Weibull distribution is restricted to a region (low Hs) of little practical significance (Salih, 1986).

FIGURE 4 MARCINAL CDF's OF H_s

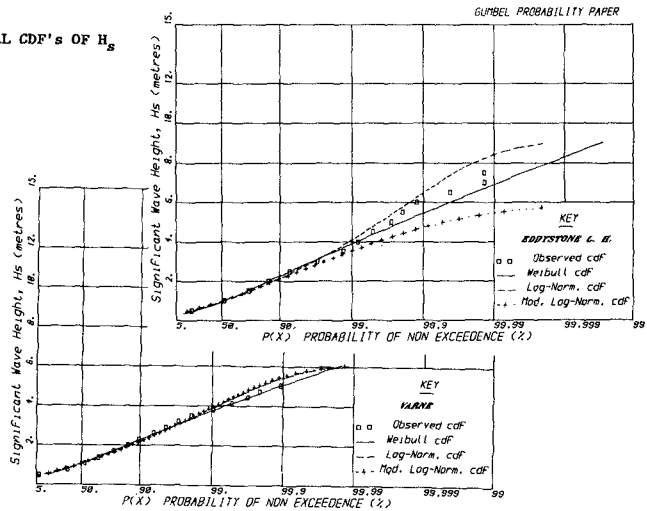

However, directing attention to the cumulative distributions of Hs the Weibull distribution is most clearly superior, as may be seen from Fig. 4. The NMI modification has not been found to improve the basic Log-Normal fit in the tails, a result which was borne out quantitatively from a Kolmogorov-Smirnov statistical test. Again, for the same reasons as those discussed above this goodness-of-fit test could not be applied rigorously. Nevertheless, the Weibull distribution performs most adequately and satisfied the test at a 5% significance level for a number of the data sets.

Marginal Distribution of Tz: The marginal distributions of Tz were treated in a similar way to that described for Hs above. In this case all three distributions showed a good fit to the data over the whole range of periods. Again, the Weibull distribution produced overall the lowest χ^2 values and generally showed the closest fit to the cdf. In view of the satisfactory behaviour of all distributions in the extreme tail the Kolmogorov-Smirnov test was not applied.

Conditional Distribution of Tz: Fig. 5 shows an example of the conditional frequency histograms of Tz for various classes of Hs forming the scatter diagrams. Both Weibull and Log-Normal distributions follow the data closely. In addition, a 2 parameter Weibull distribution and predictions from the fitted 2-dimensional Log-Normal and Weibull distributions have been considered. χ^2 estimates have been made for all conditional distributions at each site and are tabulated in (Salih, 1986). These results showed the 3 parameter Weibull and Log-Normal distributions to provide the best

fits with near equal merit. The 2 parameter Weibull distribution adopted by Houmb and Overvik is unable to locate the central probability mass in many cases and produces large χ^2 errors. Of the two 2-dimensional distributions the Weibull form was found, in this test, to consistently produce the better fit over the Log-Normal.

FIGURE 5 CONDITIONAL FREQUENCY HISTOGRAMS OF T_Z

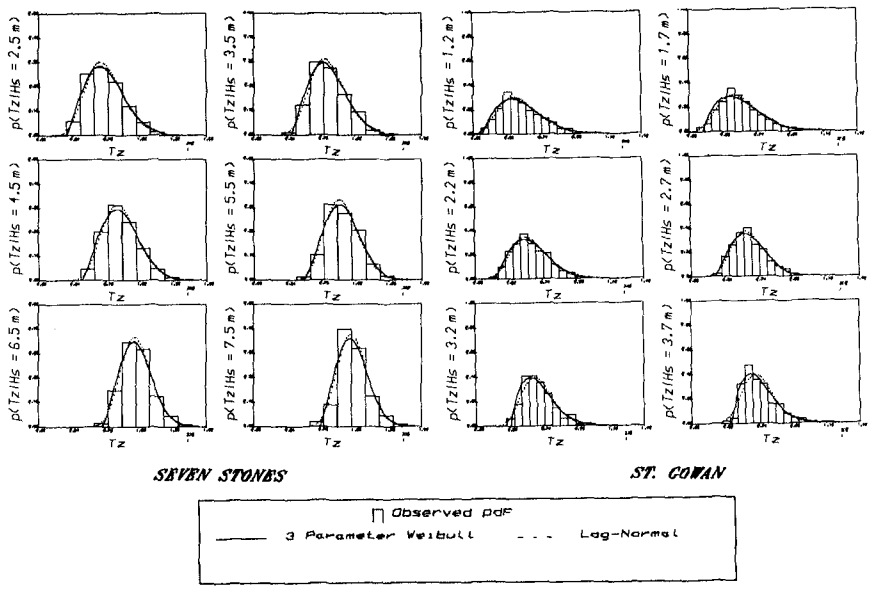

Joint Distribution of Hs and Tz: On the basis of the above findings contour maps overlaying the scatter diagrams were produced with the joint probability p(Hs,Tz) defined by:

(1) p(Hs)-Weibull, p(Tz/Hs)-Weibull; (W-W)
(2) p(Hs)-Weibull, p(Tz/Hs)-Log-Normal; (W-LN)
(3) p(Hs,Tz)-2-dimensional Log-Normal; (2DLN)
(4) p(Hs,Tz)-NMI modification to (3); (NMI)
(5) p(Hs,Tz)-2 dimensional Weibull; (2DW)

In order to establish the relative goodness-of-fits of these different approaches a 2-dimensional χ^2 computation was made. This was equivalent to the application of Eq. 2 to the conditional frequency histograms of Tz for each class of Hs in the scatter diagram with the resulting values summed to give an overall χ^2 estimate. Table 2 presents these findings which show that approach (1) above is best able to represent the characteristics of the data sets considered. Approach (2) is only marginally inferior. The Weibull distribution (5) again shows substantial improvement over the other 2-dimensional distributions.

TABLE 2
2-DIMENSIONAL χ^2 VALUES FOR COMPARISON OF SCATTER DIAGRAM OBSERVATIONS AGAINST VARIOUS THEORETICAL DISTRIBUTION FITS, USING METHOD OF MOMENTS

Site	W-W	W-LN	2DLN	NMI	2DW
Seven Stones	1243.5	643.9	2621.9	1937.6	1501.2
South Uist	17.5	36.9	97.5	98.3	101.0
W. S. Alpha	158.5	166.9	249.2	245.0	216.6
W. S. India	69.9	66.5	82.2	85.7	86.9
W. S. Juliett	30.2	29.3	88.9	131.1	42.2
Famita	313.1	281.2	714.6	690.1	517.2
Galloper LV.	155.9	170.4	696.0	528.1	240.9
Tongue LV.	51.4	139.8	266.4	402.4	196.2
Eddystone LH.	762.2	1110.6	2090.4	2105.1	1845.9
Varne LV.	71.1	71.5	146.3	135.6	180.1
Scarweather Bk.	187.7	237.4	1249.6	984.0	637.1
St. Gowan LV.	291.2	307.8	1813.2	1577.6	957.6
Dowsing	400.2	428.9	2390.6	1643.8	796.8
Smith's Knoll LV.	57.6	65.5	100.7	92.5	149.0
North Carr LV.	279.3	325.8	611.3	615.3	509.5
MERSEY BAR LV.	47.9	51.9	130.4	127.0	119.7
MORECAMBE BAY LV.	1075.7	936.1	2813.8	2747.3	1930.4
CARDIGAN BAY LV.	305.6	418.3	1065.0	997.3	877.9

Modelling the Joint Distribution of Hs and Tz

Having assessed the relative merits of the different probabilistic descriptors of p(Hs,Tz) it remains to develop means of modelling from the minimal amount of wave climate data that may be available. In this respect attention is focussed on the specification of the Tz domain, since marginal Hs statistics can be adequately established using existing methods. These include the various wave forecasting and hindcasting techniques from wind data, recently reviewed by Holtuijsen (1983) and the semi-empirical approach developed by British Maritime Technology in the U.K. and marketed as 'NMIMET' which uses both windspeed and visual waveheight archives (Andrews et. al., 1983).

A first step in this exercise is to establish empirical relationships to link the various statistical properties of Tz, in both the marginal and conditional domains, to those of Hs. From an initial investigation of this nature it was found that the data could be conveniently categorised into three groups, termed 'oceanic', 'coastal' and 'bays/estuarial' and the placements into these groups are indicated in Table 1. The statistics necessary for specification of the different probability models were then obtained for each group using 'least-squares' regression to the statistics of Hs. Due to the limited nature of the data bases, simple regression equations of the form;

$$Y = a.(\bar{Hs})^b.(\sigma_{(Hs)})^c.(\lambda_{(Hs)})^d \qquad (3)$$

were used where Y is any of the required Tz statistics and (a,b,c,d) are the regression coefficients.

In the event, due to the small size of the 'bays' group this has not been treated by regression until such time that further data sets are incorporated into the data bank. Resulting regression equations are summarised in Appendix 2 but it must be appreciated that these would

be continuously updated as new data is added. The regression equations produced mean relative errors of about 10% (3.8-17.9%) when compared with the various data sets in each group. The 'oceanic' group produced smaller errors than the 'coastal' group of sites. Dealing with each statistic in turn:-

Conditional Mean E{Tz/Hs}: Conditional mean values for each class of Hs for various sites are plotted in Fig. 6. With increasing Hs it was anticipated that the values of E{Tz/Hs} would become equivalent to the Tz values of the associated wind generated sea states, since the effects of swell would diminish. This was substantiated by the superimposition of such relationships based on the moments of Pierson-Moskowitz spectra onto the plots. In S.I. units this can be expressed as:

$$E\{Tz/Hs\} = 3.55.(Hs)^{0.5} \qquad (4)$$

Departures from this relationship for the lowest classes of Hs, therefore, give an indication of the presence of swell conditions at the different sites. A systematic variation from site to site in this respect is observed where the most exposed locations generally show the greatest departures. To model this behaviour a linear variation of E{Tz/Hs} with Hs has been assumed, defined by an intercept of the period axis κ and slope ν. Regression using the data sets for the two climate categories, as appropriate, produces the fits shown in Fig. 6. Also included here are the relationships output from the use of the relevant regression equations in the 2-dimensional models.

FIGURE 6 RELATIONSHIP BETWEEN CONDITIONAL MEAN VALUE OF T_Z, $E\{T_Z/H_S\}$, AND H_S

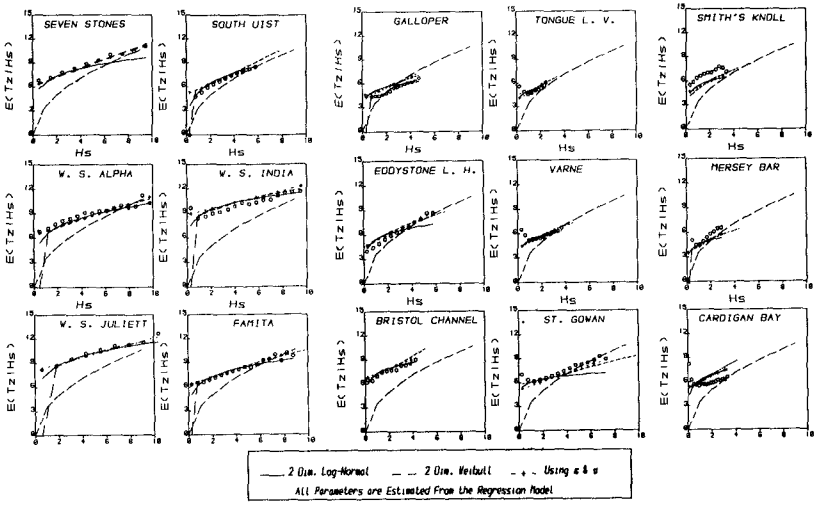

Marginal and Conditional Standard Deviations $\sigma_{(Tz)}$ and $\sigma_{(Tz/Hs)}$: Fig. 7 shows plots of the variation of $\sigma_{(Tz/Hs)}$ with Hs for sites from both groups used in the regression exercises. From the general trends

observed a quadratic variation was chosen for the 'oceanic' group and an exponential decay for the 'coastal' group. Regression equations for these are given in Appendix 2 and involve the marginal standard deviation $\sigma_{(Tz)}$ which is itself expressed in terms of a regression relationship. Resulting functions are shown on the graphs. Behaviour of the fitted 2-dimensional probability models are again included and in several instances these show serious divergence from the observed trends. This indicates the inflexibility of these theoretical functions to describe features of the scatter diagrams in close detail.

FIGURE 7 RELATIONSHIP BETWEEN CONDITIONAL STANDARD DEVIATION OF T_Z, $\sigma(T_Z/H_S)$, AND H_S

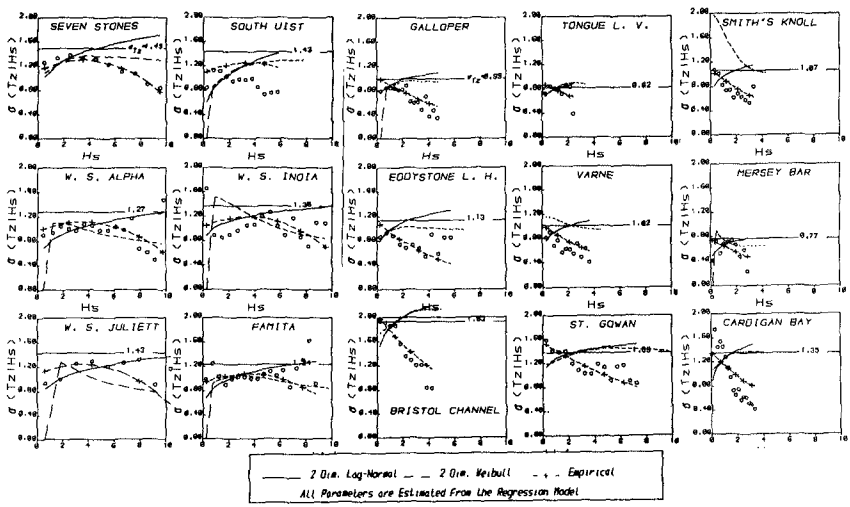

The various data sets taken individually show, in Fig. 7, significant departure from the regression functions illustrating the approximate nature of the modelling and pointing to a need for further data so that segregation into additional groupings may be made practicable.

Conditional Skewness $\lambda_{(Tz/Hs)}$ and Weibull Parameters $A_{(Tz/Hs)}$ and $A_{(Tz)}$: Definition of the 3 parameter Weibull distribution normally requires sample estimates of the first three statistical moments (see Appendix 1). However, the reliability of these estimates diminishes with the 'order' of the statistic for samples of limited size. In consequence, the computed values of skewness, λ, being a third order statistic, show much greater scatter than that shown by $E\{Tz/Hs\}$ and $\sigma_{(Tz/Hs)}$ which are determined from the first and second order moments respectively. This problem is particularly acute for the highest classes of Hs where the number of observations forming the samples are small. The scatter observed in plots of $\lambda_{(Tz/Hs)}$ against Hs (Salih, 1986) was such that no underlying trend could be detected and they are not presented here.

As an alternative approach to the full specification of the 3 parameter Weibull distribution by 'method of moments', an empirical

method was considered for definition of parameter A. Computation of remaining parameters B and C is then achieved from the first two moment estimates which are also necessary for fitting to the other probability distributions under consideration here.

Parameter $A_{(Tz/Hs)}$ represents a lower limit on the value of wave periods in the scatter diagram. If the notion of a maximum 'sea state steepness', S, is taken to be the ratio of Hs to a deep water wave length expressed in terms of this minimum wave period, it can be expressed as:

$$S = 2\pi.Hs/\{g.(A_{(Tz/Hs)})^2\} \quad (5)$$

Various steepness curves defined in this way were superimposed on the scatter diagrams, see Fig. 1, and a value of 1/12 was found to provide an upper envelope of the observations consistently for the majority of data sets. This empirical relationship has thus been incorporated into the method of modelling for the 3 parameter Weibull distribution.

A similar situation arises when employing the 2-dimensional (3 parameter) Weibull distribution since in this case an estimate of $A_{(Tz)}$, the lower limiting value of Tz from the marginal data, can render unnecessary the estimation of the sample skewnesses. In this case values of 4.0 and 3.0 have been adopted intuitively from observation of the scatter diagrams for the 'oceanic' and 'coastal' groups respectively.

Linear Correlation Coefficients $\rho_{(Hs-Tz)}$ and $\rho_{(\log(Hs)-\log(Tz))}$: These statistics are required in the specification of the 2-dimensional Weibull and Log-Normal distributions respectively. Sample estimates of the former are included in Table 1 and regression equations are given in Appendix 2.

Synthesis of Scatter Diagrams using the Regression Equations:

Test against Original Data Base: Applying the regression equations to each of the probability models provides a means of testing each approach on equal terms. The data input in these circumstances are the relevant statistics of Hs and the site exposure group, which leads to the appropriate regression equations.

Table 3 lists the 2-dimensional χ^2 values per unit observation for all sites with the exception of the 'bays' group. Overall, approach 1 (W-W) produces the minimum departures from the observed data as measured by this test whilst approach 2 (W-LN) produces the best fit in more cases. Both of these 'marginal/conditional distribution' approaches to the joint probability modelling are better than the 2-dimensional theoretical models although the Weibull form is only slightly inferior. However, although the χ^2 values do not show great disparity between any of the models, the 2-dimensional versions are significantly less able to closely represent the distributions of Tz for the higher Hs classes. This can be seen from the frequency histograms in Fig. 8 and the scatter diagrams in Fig. 9. It is immediately apparent that in the predictive mode departures from observed histograms are substantially greater than those associated

Site	W-W	W-LN	2DLN	NMI	2DW
Seven Stones	0.1278	0.1007	0.2434	0.1685	0.1185
South Uist	0.1887	0.1521	0.1836	0.1677	0.1707
W. S. Alpha	0.2286	0.2650	0.2182	0.2367	0.2165
W. S. India	0.4156	0.2564	0.1932	0.2145	0.3446
W. S. Juliett	0.0902	0.0826	0.0956	0.1228	0.0612
Famita	0.1234	0.0790	0.1289	0.1126	0.1417
Galloper LV.	0.2957	0.4904	0.7661	0.7191	0.6938
Tongue LV.	0.1657	0.1555	0.2935	0.2999	0.1817
Eddystone LN.	0.7114	0.7520	0.9474	0.9803	0.9677
Varne LV.	0.5037	0.5766	0.4047	0.4004	0.5050
Scarweather Bk.	0.2294	0.2561	0.4353	0.3550	0.2574
St. Gowan LV.	0.2109	0.2087	0.2709	0.2197	0.1486
Downing	0.1164	0.1092	0.3071	0.2877	0.1852
Smith's Knoll LV.	0.7682	0.8912	0.7454	0.7398	0.5673
North Carr LV.	0.2503	0.2816	0.2199	0.2726	0.2302
No of 'Firsts'	3	5	2	1	4
$\Sigma \chi^2$:	4.442	4.657	5.453	5.297	4.790

TABLE 3
DIMENSIONAL χ^2-VALUES, PER UNIT OBSERVATION RESULTING FROM APPLICATION OF REGRESSION MODELS TO ORIGINAL DATA BASE

TABLE 4
2-DIMENSIONAL χ^2-VALUES, PER UNIT OBSERVATION RESULTING FROM APPLICATION OF REGRESSION MODELS TO INDEPENDENT DATA

Site	W-W	W-LN	2DLN	NMI	2DW
W. S. Lima	0.1077	0.0790	0.0895	0.0808	0.1687
Owers LV.	0.4213	0.4307	0.2561	0.2523	0.2681
Cardigan Bay	0.4937	0.4842	0.5496	0.5264	0.5421

with the earlier analysis phase.

Test against Independent Data: Data sets from W.S. Lima, Owers light vessel, and Cardigan Bay (considered earlier but not used in the regression), see Fig. 2, have been compared against those synthesised by the models, Table 4 shows resulting normalised 2-dimensional χ^2 values. With such a small set of test data results cannot be conclusive but, contrary to the above findings, in these tests at least, the 2-dimensional models perform with comparable accuracy to the 'marginal/conditional' models. Further testing is clearly necessary.

FIGURE 8 CONDITIONAL FREQUENCY HISTOGRAMS OF T_z COMPARED AGAINST REGRESSION MODEL OUTPUTS

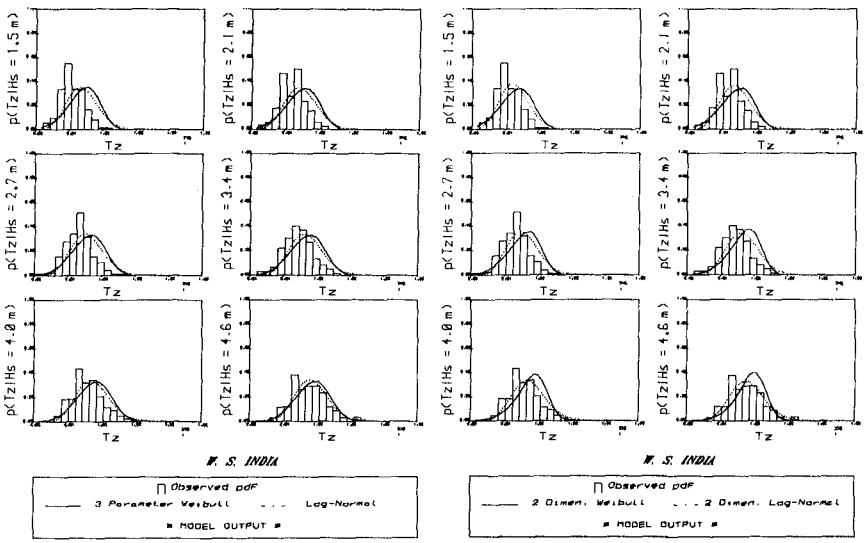

FIGURE 9 CONTOUR PLOTS FROM REGRESSION MODELS SUPERIMPOSED OVER OBSERVED SCATTER DIAGRAMS

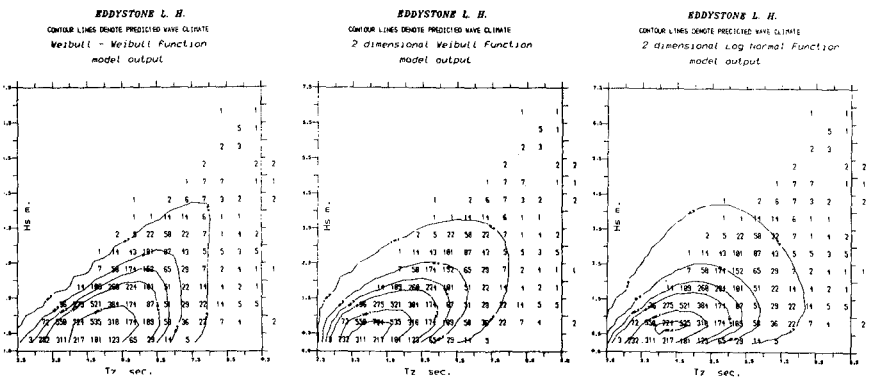

Conclusions

(1) From an analysis of scatter diagrams from 18 sites around the British Isles it has been found that the 3 parameter Weibull distribution provides a better fit than the Log-Normal distribution to the marginal properties of Hs and Tz whilst both functions describe with near equal merit the conditional behaviour of p(Tz/Hs).

(2) Regression equations linking the statistics of the various probability distributions considered to the statistical moments of Hs have been established on the basis of two categories of site exposure, loosely termed 'oceanic' and 'coastal'. Further segregation of site classification is not practicable until the data base is extended.

(3) Links between site category, exposure conditions (such as 'effective fetch' and wind field strengths) and Hs statistics are currently under investigation although preliminary findings have proved inconclusive.

(4) Synthesis of wave climates when tested against the data sets available have shown the relative accuracy of the different approaches to follow the rank order:-

1) p(Hs)-Weibull, p(Tz/Hs)-Weibull
2) p(Hs)-Weibull, p(Tz/Hs)-Log-Normal
3) p(Hs,Tz)-2-dimensional Weibull
4) p(Hs,Tz)-NMI modified 2-dimensional Log-Normal
5) p(Hs,Tz)-2-dimensional Log-Normal

(5) Limited tests of the regression based models to independent data have not clearly substantiated the above and, in consequence, further validification is necessary.

Acknowledgements

Financial support for the studies reported has been provided by the U.K. Science and Engineering Research Council through its Marine Technology Directorate Projects NW/L/1.5 and NW/L/C0A1.

References

(1) ANDREWS, K.S. et al. (1983), 'NMIMET: a global capability for wave climate synthesis'. Int. Report R149, British Maritime Technology (formerly NMI).
(2) FANG, Z.S. and HOGBEN, N. (1982), 'Analysis and prediction of long-term probability distributions of wave heights and periods'. Int. Report R146, British Maritime Technology.
(3) HAVER, S. (1985), 'Wave climate off Northern Norway', Applied Ocean Research, Vol. 7, No. 2.
(4) HOUMB, O.G. and OVERVIK, T. (1976), 'Parameterization of wave spectra'. Proc. BOSS Conf., p.144-169.
(5) KIMURA, A. (1981), 'Joint distribution of wave heights and periods of random sea waves', Coastal Engineering in Japan, Vol. 24.
(6) OCHI, M.K. (1978), 'Wave statistics for the design of ships and ocean structures'. Proc. SNAME, New York Conf.
(7) SALIH, B.A. (1986), 'Long-term probabilistic properties of wave climate'. Int. Report, Dept. Civ. Eng., University of Liverpool, Oct.
(8) U.K. DEPARTMENT OF ENERGY (1986), 'Estimating wave climate parameters for engineering applications', Offshore Technology Report OTH86-228.

Appendix 1 : Probability Distributions

The probability density function (pdf) of a random variable x is denoted by p(x) and the cumulative distribution function by P(X), where,

$$P(X) = \text{Prob}(x \leqslant X) = \int_{-\infty}^{X} p(x)\, dx \qquad (I.1)$$

The various forms of probability distribution considered herein are as follows:-

(i) Weibull Distribution

$$p(x) = \frac{(x-A)^{C-1}}{B^C} .C.\exp\left\{-\left[\frac{x-A}{B}\right]^C\right\} \qquad (I.2)$$

where A, B and C are constants, representing location, scale and shape parameters of the distribution. These parameters are related to the statistical moments of x as follows:-

$$\text{Mean}, \quad \bar{x} = E\{x\} = A + B\Gamma(1+1/C)$$
$$\text{Variance}, \quad \sigma^2_x = E\{(x-\bar{x})^2\} = B^2[\Gamma(1+2/C) - \Gamma^2(1+1/C)]$$
$$\text{Skewness}, \quad \lambda_x = \frac{[\Gamma(1+3/C) - 3\Gamma(1+2/C)\,\Gamma(1+1/C) + 2\Gamma^3(1+1/C)]}{[\Gamma(1+2/C) - \Gamma^2(1+1/C)]^{3/2}} \qquad (I.3)$$

where Γ is the Gamma function

(ii) Log-Normal Distribution

$$p(x) = \frac{1}{\sqrt{2\pi}\, xb} \cdot \exp\{-\frac{1}{2b^2}(\log(x) - a)^2\} \qquad (I.4)$$

where parameters a and b are the mean and standard deviation of log(x) and are related to the moments of x as follows:-

$$\begin{aligned} \bar{x} &= \exp\{a + b^2/2\} \\ \sigma^2_x &= \exp\{2a + b^2\}[\exp\{b^2\} - 1] \end{aligned} \qquad (I.5)$$

In the context of the paper, x can take the form of either Hs or Tz in the above equations. However, in the remaining 2-dimensional distributions it is convenient to make direct reference to the wave parameters.

(iii) 2-Dimensional Log-Normal Distribution

$$p(Hs,Tz) = \frac{1}{Hs.Tz} \cdot \frac{1}{2\pi\sqrt{1-\rho^2_{ht}}\,\sigma_h\sigma_t} \cdot \exp\{\frac{-R}{2(1-\rho^2_{ht})}\}$$

$$\text{and } R = [\frac{(h-\bar{h})^2}{\sigma_h^2} - 2\rho_{ht}\frac{(h-\bar{h})}{\sigma_h} \cdot \frac{(t-\bar{t})}{\sigma_t} + \frac{(t-\bar{t}^2)}{\sigma_t^2}] \qquad (I.6)$$

where $h = \log(Hs)$; $t = \log(Tz)$; $(\bar{h},\sigma_h)$ and $(\bar{t},\sigma_t)$ are the equivalents of (a,b) in Eq. (I.5), representing the fit parameters for the respective marginal distributions; and ρ_{ht} is the linear correlation coefficient, $\rho_{ht} = E\{(h-\bar{h}).(t-\bar{t})\}/\sigma_h\sigma_t$ (I.7)

(iv) 2-Dimensional Weibull Distribution

$$p(Hs_N,Tz_N) = \frac{m\,n}{4\beta} Hs_N^{m-1}\, Ts_N^{n-1} \exp\{-\frac{1}{2\beta}(\Phi_2 Hs_N^m + \Phi_1 Tz_N^n)\}.I_o(Hs_N^{m/2}.Tz_N^{n/2}.\gamma/\beta) \qquad (I.8)$$

where I_o is the Modified Bessel function of zero order; γ is a correlation parameter linked to the linear correlation coefficient (of the form of Eq. (I.7)) as follows:

$$\rho = \frac{\Gamma(\frac{m+1}{m})\,\Gamma(\frac{n+1}{n})\,[F(-\frac{1}{m}; -\frac{1}{n}; 1; \frac{\gamma^2}{\Phi_1\Phi_2}) - 1]}{\sqrt{[\Gamma(\frac{m+2}{m}) - \Gamma^2(\frac{m+1}{m})]\,[\Gamma(\frac{n+2}{n}) - \Gamma^2(\frac{n+1}{n})]}}\ ;\ \beta = \Phi_1\,\Phi_2 - \gamma^2 \qquad (I.9)$$

F is the Hypergeometric function; $m \equiv C_{Hs}$, $n \equiv C_{Tz}$, $\Phi_1 \equiv \frac{1}{2}(B_{Hs})^m$,

$\Phi_2 \equiv \frac{1}{2}(B_{Tz})^n$, $Hs_N \equiv (Hs - A_{Hs})$ and $Tz_N \equiv (Tz - A_{Tz})$.

Parameters A, B and C are the Weibull parameters from the marginal distributions of Hs and Tz as appropriate.

Appendix 2 : Regression Equations

In the following (O) represents the 'oceanic' group of data sites and (C) represents the 'coastal' group. Using the definition of Eq. (3), most statistics have been expressed in the form,

$$Y = a\ (H_s)^b\ (\sigma_{(Hs)})^c\ (\lambda_{(Hs)})^d$$

Y		a	b	c	d
$\bar{T}_z$	(O)	4.482	0.51	-0.11	0.70
	(C)	8.758	-0.67	0.80	-0.41
$\sigma_{(Tz)}$	(O)	11.453	-3.55	3.69	-1.40
	(C)	2.984	-1.59	1.75	-0.75
$\rho_{(Hs-Tz)}$	(O)	2.329	-2.88	4.23	-2.71
	(C)	0.348	-0.28	0.14	1.26
$\rho_{(logHs-logTz)}$	(O)	3.353	-3.73	5.48	-3.68
	(C)	0.429	-1.20	0.30	1.03
κ	(O)	2.872	0.85	-0.44	1.12
	(C)	6.510	-0.42	0.68	-0.54
ν	(O)	3.484	-2.72	2.24	-1.59
	(C)	0.326	1.05	-1.11	0.82
* μ	(C)	3.0	-1.40	1.70	-0.88
ν	(C)	-0.172	-1.10	0.305	0.531

* for 'coastal' sites: $\sigma_{(Tz/Hs)} = \mu \exp(-\nu H_s)$
  for 'oceanic' sites: $\sigma_{(Tz/Hs)} = (0.75 - 0.01 H_s + 0.07 H_s^2)\ \sigma_{(Tz)}$

CHAPTER 5

Numerical Simulation of 1964 Tsunami Across the Pacific Ocean

Michael H. Chen [1]

A two dimensional numerical longwave model using an appropriate open sea boundary condition has been developed. The use of the open-sea boundary condition makes it possible to simulate longwave propagation using a smaller region without covering the entire ocean. The numerical model is used to predict the arrival time of tsunamis resulting from the 1964 Alaskan earthquake at various stations with reasonable success.

Introduction

Tsunami is a seawave generated by a near shore shallow-water undersea ground movement. It usually causes major damage to the coastal area not only next to the epicenter of the earthquake, but also at a distance away. Due to its nature, studies of the tsunami can be classified into three categories: (1) generation, (2) propagation and dispersion across the ocean and (3) response at the coastal region. A very lengthy summary of references regarding every aspect of tsunami phenomena was presented by Wiegel (1980) in his study of tsunamis in the Philippines.

Most analytical models related to tsunamis are either limited to a one dimensional model or a two dimensional model with a constant water assumption. Mathematical models are also available for water depths which vary in some specific manner.Using an integral transform technique, Carrier (1966) developed a one dimensional analytical model to relate the wave height at the source region to a location far away. The generation of a tsunami in the region adjacent to the earthquake epicenter has been studied extensively by Hammack (1972) in his theoretic and experimental work.

Apart from the theoretic approach, many numerical models have been developed to study the longwave phenomena. Using a space-staggered implicit finite difference method, Leendertse (1967) gave a detailed discussion on the aspects of a numerical model for the longwave equation. Hwang et al. (1973) developed a numerical longwave model in spherical coordinates using methods described by Leendertse to examine the effect of the earth's curvature on the propagation of a seawave. A similiar two dimensional numerical model was also presented by Skovgaard and Jonsson (1980). In their studies, Homma's mathematical model for a longwave over a parabolic island was included.

[1]Member of Technical Staff, TRW Defense System Group, One Space Park, Redondo Beach, CA 90278

In the present study, a numerical longwave model in spherical coordinates has been developed using an alternated direction. explicit finite difference method proposed by Loomis (1973). A suitable open sea boundary condition based on the concept of matched impedance is adapted. Applying this open sea boundary condition, it is possible to investigate wave response at a particular area in the middle of Pacific Ocean without including the entire ocean.

The performance of the numerical model is verified by performing a simulation of a wave impinging upon a circular island over a constant water depth, and a real time tsunami simulation resulting from the 1964 Alaskan earthquake.

Governing Equations

With the assumption that the Coriolis force and convective terms can be neglected and the wave height, η, is small compared to the original water depth, d, the linearized longwave equations in spherical coordinates can be expressed as:

$$\frac{\partial u}{\partial t} = -\frac{g}{R}\frac{\partial \eta}{\partial \theta} \tag{1}$$

$$\frac{\partial v}{\partial t} = -\frac{g}{R sin\theta}\frac{\partial \eta}{\partial \phi} \tag{2}$$

$$\frac{\partial \eta}{\partial t} = -\frac{1}{R sin\theta}\left[\frac{\partial (du sin\theta)}{\partial \theta} + \frac{\partial (dv)}{\partial \phi}\right] \tag{3}$$

where u and v are the velocity components in the x and y direction, respectively; d and η are the original water depth and wave amplitude, respectively; θ and ϕ are the angles related to the local latitude and longitude respectively; R is the radius of the earth and t is for the time.

The above set of equations are then expressed in their finite difference forms to construct the numerical model for investigaing the longwave propagation and its response at the coastal area.

Boundary Treatment

In addition to the stability problem related to the numerical scheme, the specification of the boundary condition at the artificial boundary where the computation terminated is also very important. In his survey articles on acoustic radiation, Shaw (1970) related several physical boundary conditions to their corresponding mathematical forms. The most suitable boundary condition at the open sea is the matched impedance condition where the wave is assumed to be totally transmitted.

Applying linearized wave theory with the assumption of constant depth beyond the computational domain, the matched impedance condition becomes

$$\frac{\partial \eta}{\partial t} = -\frac{c}{R sin\theta}\left[cos\delta \frac{\partial \eta}{\partial \theta} + sin\delta \frac{\partial \eta}{\partial \phi}\right] \tag{4}$$

where c is the wave speed and δ is the angle between the wave direction and the local open boundary.

This is equivalent to the radiation condition given by Sommerfeld (1949) at the far field for the scattered wave. Equation (4) will be used at the open sea boundary where the time derivative of the wave amplitude can be related to its spatial derivative.

In addition to the open-sea condition, a treatment at the solid boundary is also required. This treatment is relatively quite simple and can be achieved by appling the null nomal derivative conditions for all flow quantities. The condition for the wave amplitude at a solid boundary is:

$$\vec{n} \cdot \left[\frac{\partial \eta}{\partial \theta}\hat{i} + \frac{\partial \eta}{\partial \phi}\hat{j}\right] = 0 \tag{5}$$

where $\hat{i}$ and $\hat{j}$ are unit vector in the θ and ϕ direction respectively and $\vec{n}$ is the local outward normal at the shoreline.With these boundary treatments, the numerical longwave model can then be formulated.

Finite Difference Scheme

The numerical model is constructed by using a space and time staggered method. The flow quantities are assigned at a location half a grid space apart. The vector quantities such as u and v are assigned at the edge of the grid element. On the other hand, the scalar quantities, d and η, are assigned in the middle of the grid element. The value at the location where a particular quantity is not computed is approximated by its average value among its four surrounding points.

Using the above arrangement for the flow quantities, the finite difference equations of the linearized longwave equations are:

$$u_{i,j}^{n+1} = u_{i,j}^{n} - \frac{g\Delta t}{R\Delta\theta}\left[\eta_{i,j}^{n+1} - \eta_{i,j-1}^{n+1}\right] \tag{6}$$

$$v_{i,j}^{n+1} = v_{i,j}^{n} - \frac{g\Delta t}{Rsin\theta_j\Delta\phi}\left[\eta_{i,j}^{n+1} - \eta_{i-1,j}^{n+1}\right] \tag{7}$$

$$\begin{aligned}\eta_{i,j}^{n+1} = \eta_{i,j}^{n} - \frac{\Delta t}{2Rsin\theta_j}\Big\{&\left[(d_{i+1,j}^{n} + d_{i,j}^{n})v_{i+1,j}^{n+1} - (d_{i,j}^{n} + d_{i-1,j}^{n})v_{i,j}^{n+1}\right]/\Delta\phi \\ &+ \left[(d_{i,j+1}^{n} + d_{i,j}^{n})u_{i,j+1}^{n+1}sin\theta_{j+1/2} - (d_{i,j}^{n} + d_{i,j-1}^{n})u_{i,j}^{n+1}sin\theta_{j-1/2}\right] \\ &/\Delta\theta\Big\}\end{aligned} \tag{8}$$

Equations (6), (7) and (8) are the basis of the current numerical model. In conjunction with the treatment of solid and open boundary, the propagation of a tsunami over an ocean can then be studied.

The actual integration in time is achieved in two stages. First, the wave amplitude, η, at $(n+1)^{th}$ step is integrated using its value at n^{th} step and the newly calculated velocities, u and v through equation (8). With this newly obtained wave amplitude, $\eta_{i,j}^{n+1}$, the velocities, $u_{i,j}^{n+1}$ and $v_{i,j}^{n+1}$, are then computed using their values at n^{th} step using equations (6) and (7), respectively. This method of integration is not exactly an explicit method but is crucial in the numerical stability. A completely explicit method is usual not stable.

Verification

It is desired to verify the performance of a numerical model by comparing the computed result with either an analytical solution or experimental data. A general solution for the wave height at the shore due to a series of monochromatic waves is given by Morse and Feshback (1953).

Such a solution for a monochromatic wave with an amplitude of one meter and a period of 4 minutes impinging upon a circular island having a radius of 18 km among a uniform depth of 4 km was presented by Vastano and Reid (1966) in their study of tsunami response at an island. A similar simulation has been performed using the present numerical model. The results of three models are shown in Figure 1.

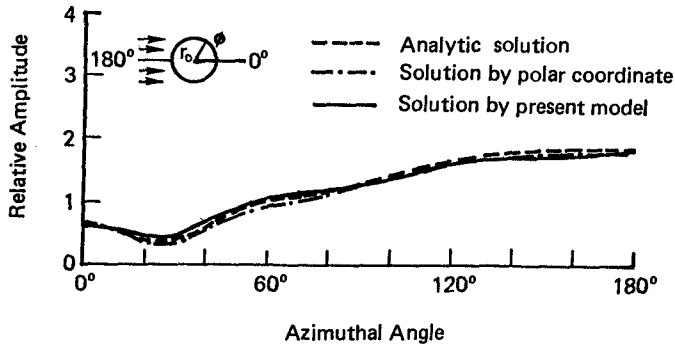

Figure 1. The comparison of maximum wave amplitude at shoreline among three models.

The predicted results by both numerical models agree quite well with the analytic solution. The use of the matched impedance condition at the open boundary transmits the progress wave outward to the open sea successfully. A similiar calculation was also presneted by Skovgaard and Jonsson (1980). In their model, the treatment on the open sea boundary is different. A known solution from the

analytical model was used at the open sea. The open-sea boundary treatment presneted in the current study is not adapted in their model.

Results and Discussions

The current numerical longwave model has been applied to simulate the destructive tsunami resulting from the 1964 Alaskan Earthquake. The original water depth is obtained from the world hydrographic chart prepared by the Scripps Institutes of Oceanography. The initial tsunamis distribution is derived from the work of Hwang and Divoky (1970) which uses the ground displacement data of the 1964 Alaskan earthquake summarized by Plafker (1969) as its data to compute the near field tsunami wave height. The computational basin is 91 $\times$ 63 (Longitude by Latitude) which covers the area from the North American continent to the Ilusian Island and from the Alaska to the equator. The grid size is 1^o by 1^o which is relatively large.

The ground displacement aftershock was illustrated by Plafker (1969). It had a broad crustal warping along a northeast - southwest trend hinge line from Prince William Sound, Alaska to Kodiak, Alaska, USA. He suggested that the axis of seabed uplift was also the axis of the source region for the generated tsunami. This axis determined the direction of the main wave. His assertion was clearly demonstrated by the numerical result. The recorded tide gage at several stations along the Pacific Ocean were presented by Spaeth and Berkman (1967). These valuable records are used to verify how well the numerical model performed.

The reported duration for the completion of ground motion was approximately 150 seconds which is very short. In other words, the initial tsunami spatial distribution could be approximated by the net undersea ground displacement, instantaneously. This assumption was adopted by Hwang and Divoky (1970) in their nearfield tsunami calculation in the earlier stage. The surface elevation at 200 seconds in their report is then converted into a 1^o by 1^o grid in spherical coordinates and is used as the initial condition in the current numerical simulation.

This initial surface height used in the current simulation is given in Table 1.

TABLE 1. THE SIMULATED INITIAL WAVE HEIGHT OF TSUNAMIS DUE TO the 1964 ALASKAN EARTHQUAKE
(unit: meter)

	152°[1]	151°	150°	149°	148°	147°	146°	145°	144°	143°	142°
59°N	⋆[2]	⋆	⋆	⋆	⋆	3.01	1.86	1.43	⋆	⋆	⋆
58°N	⋆	⋆	.402	2.45	5.86[3]	4.61	2.16	1.43	.772	.319	.038
57°N	⋆	-.49	2.68	5.19	2.55	1.09	.765	.151	.025	.001	0.00
56°N	.646	1.80	4.99	1.76	.691	.047	.003	0.00	0.00	0.00	0.00
55°N	.391	1.28	1.12	.243	.025	.000	0.00	0.00	0.00	0.00	0.00

notes:

1. It is the local longitudinal value on the western hemisphere.
2. The symbol, *, represents a zero wave height at the land.
3. The maximum initial wave height is 5.8644 meter.

The computed wave patterns show a strong seiche phenomenon in the Gulf of Alaska, resulting in very strong wave activity for as long as 10 hours after the shock. This agrees very well with the recorded result. As asserted by Plafker, the main wave propagated in a southeast direction toward the North American continent. Therefore, a portion of the wave was reflected and trapped and formed an oscillating pattern within the Gulf of Alaska. Eventually, this seiche phenomenon died out because part of wave energy was radiating outward into the open sea.

After passing through the Gulf of Alaska, the main wave continued its southeast direction and propagated toward the west coast of the North American continent. The current simulated results predict a higher maximum height at the location where there is a higher angle between the incoming wave and the shoreline which agrees with the recorded tide data. According to the tide-gage records resulting from the 1964 Alaskan earthquake, summarized by Spaeth and Berkman (1967), both Crescent City and Hilo experienced a considerably high wave activity.

The predicted wave heights are smaller than the recorded values. For comparison, the predicted and recorded tide marigrams at Crescent City, California are shown in figures (2) and (3). The predicted wave height at this location merely reaches 1 meter which is very small in comparison with the recorded value of 4 meters. This big difference is partly due to the exclusion of the contribution of the astronomical tide in the numerical simulation.

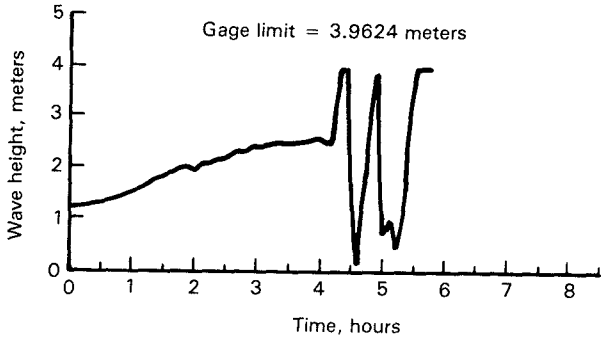

Figure 2. The tide gage record of tsunami at Crescent City, California due to the 1964 Alaskan Earthquake.

From the tide gage record, it indicates the astronomical tide is around 2.6 meters at the moment of the arrival of tsunami. If this value is used as the basis to compute the actual tsunami contribution, the estimated peak tsunami height will not exceed 2 meters. Consequently, the discrepancy between the predicted and record results is reduced considerably.

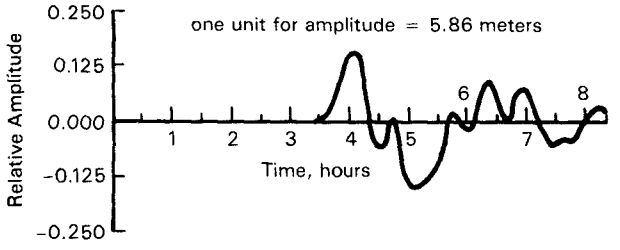

Figure 3. The simulated tsunami time history at Crescent City, California due to the 1964 Alaskan Earthquake.

From the tide marigram, the tsunami arrival time can also be calculated. The arrival time can be determined by the time either when the wave height starts to deviate from its normal state or when the first peak arrives. The former is defined as the first arrival time; the latter is defined as the first peak arrival time. Both arrival times are useful information in the tsunami warning system. The first arrival times at several stations are tabulated in Table 2.

TABLE 2. THE FIRST ARRIVAL TIME OF TSUNAMI RESULTING FROM THE 1964 ALASKAN EARTHQUAKE

Station	Long.° W	Lat.° N	Observed Hr. Min.	Predicted Hr. Min.
Yakutat, Alaska	139	59	1. 24.	0. 20.
Sikta, Alaska	135	57	1. 30.	0. 41.
Crescent City, CA	124	42	4. 03.	3. 28.
San Francisco, CA	122	38	5. 06.	4. 03.
Midway Islands	177	28	4. 51.	4. 21.
Oahu, Hawaii	160	21	5. 09.	4. 40.
Johnston Island	170	17	6. 03.	5. 33.

The difference between the recorded and computed first arrival time is approximately 30 minutes for the island stations and much higher for the stations closer

to the source region. If the arrival of the first peak is compared between the computed and the recorded results, the difference reduces to less than 15 minutes at Crescent City, California. In fact, the difference at the other stations is also reduced considerably.

In spite of a use of relatively large grid spacing, 1° by 1°; and a very rough treatment in the initial tsunami height distribution, the numerical model still predicts results comparable to the recorded data. The performance of the numerical model can be considered very good.

Conclusion and Recommandations

The major objective of the present study is to develop a suitable boundary condition for the open-sea boundary resulting from the partition of a larger area into a smaller region. With the use of this open sea treatment the large-scale propagation of a tsunami across an ocean can be investigated properly. The matched impedance condition in acoustic radiation is adapted to describe the condition at the two-dimensional open-sea boundary. This open sea boundary condition leads to a satisfactory agreement with the analytic steady-state solution for a monochromatic wave impinging upon a circular island of uniform water depth.

Using 1° by 1° spatial grid element and the bathymetry data from the world hydrographic chart, the staggered alternate-direction, explicit scheme of linearized long-wave theory is applied to simulate the 1964 tsunami. In general, the predicted first arrival time is earlier than the recorded values which is due to the difficulty in the treatment of coastal areas, especially at the source region. However, if the arrival of the maximum is used to compared the simulated and recorded data, their differences are much smaller. It indicates the use of the first arrival time as a criterion to determine the performance of the numerical model may not be appropriate. Also, we can conclude that use of a 1° by 1° grid element and linear longwave is sufficient for the prediction of tsunamis arrival time.

As pointed out by Goto and Shuto (1980), in their tsunami runup study, the predicted tsunami runup height by the nonlinear model is about 20% above that by the linear model. Based on their findings and the current result, a much finer and localized investigation should be performed using a higher order longwave equations in order to improve the predictive results at the locations such as Crescent City, California and Hilo, Hawaii where the wave amplification is important.

The conventional procedures for a small scale calculation are performed in two stages. First, a large scale calculation covering a much bigger area is performed. In this stage of calculation, all necessary flow quantities at the boundary of the smaller computational basin are stored. Second, these stored results are used as input boundary conditions in the small scale calculation. In this method, the exact effect to the computed flow quantities due to the reflection from a wall condition at the land area is not known. This uncertainity can be removed if both small and large scale calculation are performed, simultaneously.

Acknowledgments

The author wishes to thank the late G. R. Miller of the Joint Tsunami Research Effort, the University of Hawaii. This research was sponsored by a Resident Research Associateship jointly by National Research Council and National Oceanic and Atmsopheric Administration, USA.

References

1. Wiegel, R.L. (1980). Tsunamis along west coast of Luzon, Philippines. Proceedings of the 17th Coastal Engineering Conference, Sydney, Australia, The American Society of Civil Engineers, Vol. 1, pp. 652-671.

2. Carrier, G.F. (1966). Gravity waves on water of variable depth. Journal of Fluid Mechanics, Vol. 24, pp. 641-659.

3. Hammack. J.L. (1972). Tsunami generation and near field propagation. Ph.D. thesis, California Institute of Technology, Pasadena, 261 pp.

4. Leendertse, J.J. (1967). Aspects of a computational model for long-period water wave propagation. The Rand Corporation. Memorandum RM-5294-PR.

5. Hwang, L.S. et al. (1973). Rate Island tsunami model: Generation and open sea characteristics. Bull. Seismol. Soc. America, Vol. 62, pp. 1579-1596.

6. Loomis, H.G. (1973). A package program for time-stepping long waves into coastal regions with application to Haleiwa Harbor, Oahu. U.S. Department of Commerce, Technical Report NOAA-JTRE-79.

7. Skovgaard, O. and Jonsson. I.G. (1980). Transient Finite-Difference Tsunami Calculations. Proceedings of the 17th Coastal Engineering Conference, Sydney, Australia, The American Society of Civil Engineers, Vol. 1, pp. 123-137.

8. Shaw, R.P. (1970). An integral equation approach to acoustic radiation p. 143-180 in Topics in Ocean Engineering, Vol. 2, Edited by C. I. Bretschneider Houston, Gulf Publications.

9. Sommerfeld, A. (1949) Partial Differential Equations. New York, Academic Press, pp. 333-352.

10. Morse, P.M. and Feshbeck, H. (1953). Method of Theoretical Physics. New York, McGraw-Hill.

11. Vastano, A.C. and Reid, R.O. (1966). A numerical study of the tsunami response at an island. Texas A&M Univ. Technical Report No. 66-2T, 141 pp.

12. Plafker, G. (1969). Tectonics of the March 27, 1964, Alaskan Earthquake. Geological Survey Professional Paper. Vol. 543-I.

13. Spaeth, M.G. and Berkman, S.C. (1967). The tsunami of March 28, 1964, as recorded at tide stations. U.S. Department of Commerce, ESSA Technical Report CSGS33.

14. Hwang, L.S. and Divoky, D. (1970). Tsunami generation. Journal of Geophical Reviews, Vol. 75, pp. 6802-6817.

15. Goto, C. and Shuto, N. (1980). Run-up of Tsunamis by Linear and Nonlinear Theories. Proceedings of the 17th Coastal Engineering Conference, Sydney, Australia, The American Society of Civil Engineers, Vol. 1, pp. 693-707.

Notation

c = the wave speed for a longwave.
d = the original water depth.
g = the acceleration coefficient of the gravitational force.
R = the radius of the earth.
t = the time.
u = the velocity component in the θ direction.
v = the velocity component in the ϕ direction.
η = the water surface elevation.
δ = the angle between wave direction and local open boundary.
ϕ = the angle for its longitude value on earth at each location.
θ = the angle between the north pole and each location.
$\hat{i}$ = the unit vector in the θ direction.
$\hat{j}$ = the unit vector in the ϕ direction.
$\vec{n}$ = the unit outward normal vector at the shoreline.

CHAPTER 6

Tidal Computations for the Yellow Sea

Byung Ho Choi*

Abstract

A two-dimensional numerical model of the Yellow Sea has been used to compute cotidal and coamplitude charts and harmonic constants of tidal currents for the four major tidal constituents M_2, S_2, K_1, O_1 tides in the region with the mesh resolution of 1/5 degree latitude by 1/4 degree longitude finite difference grid system. An additional model incorporating dynamical grid nesting procedurc which employs a one-third grid refinement scheme was also used to reproduce the M_2 tidal regime in more detailed resolution for the part of west coast of Korea where extensive coastal development including potential tidal power and land reclamation scheme is concerned. Comparisons between observations and model result have been carried out based on coastal gauges and moored current meter data. Reasonable agreement was found between obsevations and model results, thus supporting the computed distribution of tides in the region. It was also shown that the dynamically linkaged model particularly well within 5% in amplitude and 5 degrees in phase of observed M_2 tide in the refined mesh region of the west coast of Korea.

Introduction

The tidal phenomena of the Yellow Sea are extremely complex. During the late 1920's and early 1930's extensive studies of this shelf sea area were reported and a considerable number of tidal measurements were made, from which cotidal and corange charts of diurnal and semidiurnal tides were prepared (Ogura, 1933). Russian workers (Boris, 1958; Tsiklauri et al., 1961; Stepanov et al., 1964) reported the first application of two-dimensional mathematical models on the one hand to the Yellow Sea and on the other hand, to the Gulfs of Pohai and Liautung, employing boundary value method which calls for much tidal data at external boundary points along the coast and open boundary. While the latter models were satisfactorily used to reproduce the M_2 and K_1 tides in the Gulfs of Liautung and Pohai where extensive tidal data exists, the Yellow Sea model was only used to test the sensitivity of the tides of that area to changes in the boundary tidal input data, depths along the boundaries and Coriolis parameter. Their results indicated that the computed tides in the Yellow Sea were highly sensitive to even small changes in levelling data and the depths along the boundaries.

During the past few years series of numerical tidal models (An, 1977; Choi, 1980; Shen, 1980; Xia and Wang, 1984) based on initial value method have been reported and it was demonstrated by these models that the tides

*Professor, Dept. of Civil Eng., Sung Kyun Kwan University, Suwon Campus Korea.

can be satisfactorily reproduced, thus providing general information on the tidal dynamics in this sea area. However improvement on the accuracy of the model and verification of computed tidal currents were much limited due to the lack of long-term tidal observations.

In the present paper, an initial attempt is made to provide separate tidal charts of four major M_2, S_2, K_1 and O_1 tides in the Yellow Sea from the numerical model and comparisons between model results and the observations including recently available current meter data were described. Further effort to reproduce the tides in western Yellow Sea in more detailed manner by adopting the mesh-connecting scheme for the purpose of assessing the tidal modification due to coastal development is also included.

Numerical Model

Considering the area covered by the model, the curvature of the earth and the variation with latitude of the Coriolis acceleration are taken into account by adopting spherical coordinates. The equations of motion and continuity as used in this model are (Flather, 1976):

$$\frac{1}{R\cos\phi}\left\{\frac{\partial}{\partial\chi}(Hu)+\frac{\partial}{\partial\phi}(Hv\cos\phi)\right\}+\frac{\partial\xi}{\partial t}=0, \tag{1}$$

$$\frac{\partial u}{\partial t}+\frac{u}{R\cos\phi}\frac{\partial u}{\partial\chi}+\frac{v}{R}\frac{\partial u}{\partial\phi}-\frac{uv\tan\phi}{R}-2\omega\sin\phi v+\frac{k_b u\sqrt{u^2+v^2}}{H}+\frac{g}{R\cos\phi}\frac{\partial\xi}{\partial\chi}$$

$$=0, \tag{2}$$

$$\frac{\partial v}{\partial t}+\frac{u}{R\cos\phi}\frac{\partial v}{\partial\chi}+\frac{v}{R}\frac{\partial v}{\partial\phi}+\frac{u^2\tan\phi}{R}+2\omega\sin\phi u+\frac{k_b v\sqrt{u^2+v^2}}{H}+\frac{g}{R}\frac{\partial\xi}{\partial\phi}$$

$$=0, \tag{3}$$

Eqations (1) - (3) are vertically integrated hydrodynamical equations where the notation is

t	time
χ, ϕ	east-longitude and latitude respectively
ξ	elevation of the sea surface above the undisturbed depth
h	undisturbed depth of water
$H = h + \xi$	total depth of water
R	the radius of the Earth
ω	angular speed of the Earth's rotation
g	acceleration due to gravity
k_b	coefficient of bottom friction
u', v'	components of current in the directions of χ, ϕ respectively at a depth z below the undisturbed sea level
u, v	components of depth-mean current given by $u=\frac{1}{h+\xi}\int_{-h}^{\xi}u'(z)\,dz$, $v=\frac{1}{h+\xi}\int_{-h}^{\xi}v'(z)\,dz$

These equations, formulated with a quadratic law of bottom friction, are integrated on a staggered finite difference grid using the scheme described by Roberts and Weiss (1967) which centers the advective terms in time and space. The method employed for implementing this scheme is described by Flather and Heaps (1975) and Flather (1976).

Initial and boundary condition required for the solution of equations (1) to (3) are as follows:

At $t = 0$: $u(\chi,\phi,t)$, $v(\chi,\phi,t)$ and $\xi(\chi,\phi,t)$

are specified for all positions at which the equations are to be solved. At a land boundary: the component of the flow normal to the boundary is permanently zero:

$$u\cos\theta + v\sin\theta = 0$$

where θ is the angle between the normal to the coast directed out of the sea region and χ axis. Therefore

$u = 0$ is the boundary condition at a ϕ -directed land boundary
$v = 0$ is the boundary condition at a χ -directed land boundary.

Along an open boundary, elevation is specified as a function of time and position along the boundary: $\xi(\chi,\phi,t)$ is supplied.

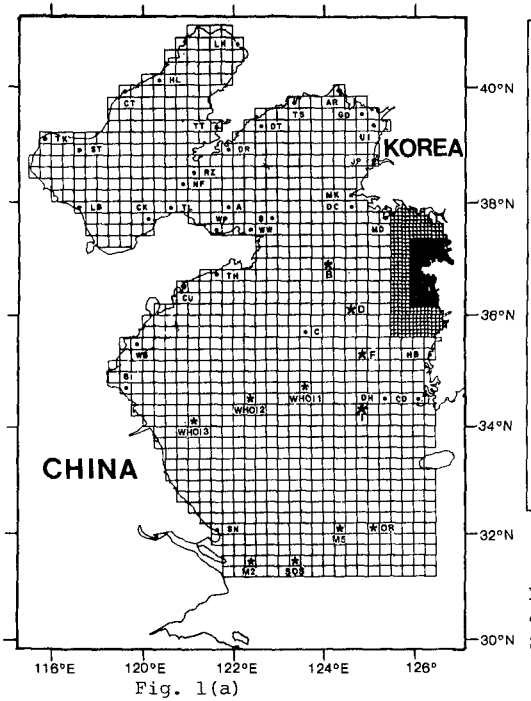

Fig. 1(a)

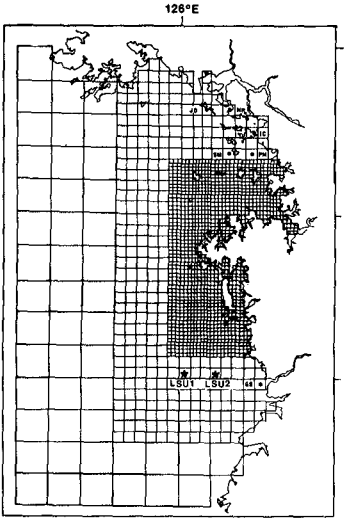

Fig. 1(b)

Fig. 1. Finite difference grid system of the Yellow Sea model.

In shallow sea areas provision is made in the numerical scheme for representing the drying of tidal flats.

The three different grid systems of the model are shown in Fig. 1. The coarse mesh has a grid resolution of 1/5 degree latitude by 1/4 degree longitude and this coarse grid has been used to compute overall tidal distribution in the Yellow Sea. This is the same grid spacing as that used in the two-dimensional shelf model of Choi (1980). The mesh size of intermediate grid system is one-third of this (1/15 degree latitude by 1/12 degree longitude) and a fine mesh system resulting from another refinement to provide a resolution of 1/45 degree latitude by 1/36 degree longitude. The dynamically linkaged model interconnecting three different grid systems has been used to compute the M_2 tidal regime of the west coast of Korea in detailed resolution.

In the model three different values of frictional parameters (0.0025 for the coarse grid and 0.0028, 0.0030 for the intermediate and fine grids) were used to give the best results for the reproduction of the tides. The open boundaries of the modcl border the line of latitude 31.2 degree North from the entrance of Changjiang River and the line of longitude 126.5 degree East. The boundary elevations were specified as a function of position and time. To satisfy explicit stability conditions, a timestep of six minutes was used for the coarse grid model and a timestep of one lunar minute was used for the dynamically linkaged model. Time and phases referred to in this study are referenced to 135 degree east longitude (time zone, -9H).

The numerical scheme employed was described prcviously (Choi, 1980) and the dynamic grid nesting procedure for joining the different grid mesh is similar to those by Owen (1979). When a computation of a variable on the one grid system in the mesh connected area requires a variable on another grid system, a linearly interpolated value is used.

Fig. 2 shows the mesh refinement grid area between two different size of meshes which are connected with an one-third refinement scheme. The finite difference scheme, which advances ξ, u, v over the entire network at time t to obtain their values at time $t + \Delta t$ is explicit and changes its scanning direction for calculation of u, v at alternate timesteps. When calculation of u, v on one grid system in the connected region requires variables ξ, u, v 's on joining grid system, a linearly interpolated values were used.

Referring to Fig. 2(a) showing mesh refinement in u-direction, u-velocities in the fine grid region are calculated as:

$$u_{i+n-1} = \frac{1}{2}\left(u_{i+n} + \frac{1}{3}(2u_{\ell} + u_{\ell m})\right) \tag{4}$$

$$u_{i-1} = \frac{1}{2}(u_{\ell} + u_{i})$$

$$u_{i+n-1} = \frac{1}{2}\left(u_{i+n} + \frac{1}{3}(2u_{\ell} + u_{\ell+m})\right)$$

The calculation of u in the coarse side of the connection requies

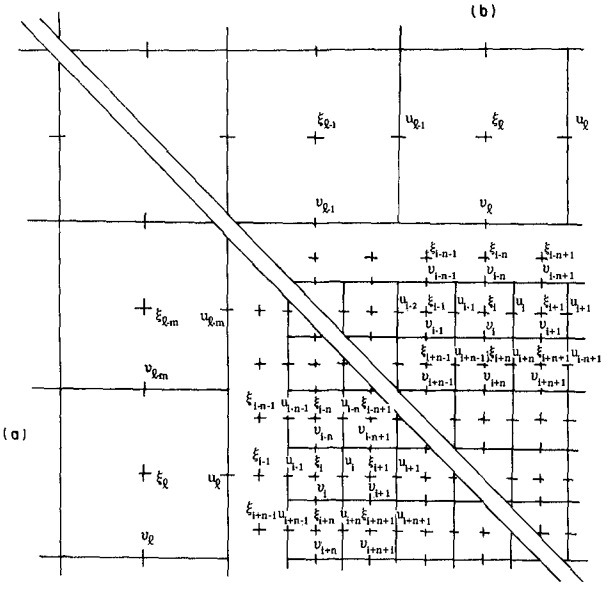

Fig. 2. Combination of two different grid system.

ξ values and v value in the fine mesh side:

$$\tilde{v} = \frac{1}{4}(v_{\ell\text{-}m} + v_{\ell} + v_{i\text{-}2n} + v_{i+n}) \tag{5}$$

$$\xi_{\ell+1} = \xi_i$$

Values of ξ along the connected regions are calculated as:

$$\xi_{i\text{-}n\text{-}1} = \frac{1}{3}\left(\frac{2}{3}\xi_{\ell} + \frac{1}{3}\xi_{\ell\text{-}m}\right) + \frac{2}{3}\xi_{i\text{-}n}$$

$$\xi_{i\text{-}1} = \frac{2}{3}\xi_i + \frac{1}{3}\xi_{\ell} \tag{6}$$

$$\xi_{i+n+1} = \frac{1}{3}\left(\frac{2}{3}\xi_{\ell} + \frac{1}{3}\xi_{\ell+m}\right) + \frac{2}{3}\xi_{i+n}$$

Referring to Fig. 2(b) showing mesh refinement in v-direction, v-velocities in fine grid region are calculated as:

$$v_{i\text{-}n\text{-}1} = \frac{1}{2}\left(v_{i\text{-}1} + \frac{1}{3}(2v_{\ell} + v_{\ell\text{-}1})\right)$$

$$v_{i\text{-}n} = \frac{1}{2}(v_{\ell} + v_i) \tag{7}$$

$$v_{i\text{-}n+1} = \frac{1}{2}\left(v_{i+1} + \frac{1}{3}(2v_{\ell} + v_{\ell+1})\right)$$

The calculation of v in the coarse side of the connection requires u values and ξ value in the fine mesh side:

$$\tilde{u} = \frac{1}{4}(u_{\ell\text{-}1} + u_{\ell} + u_{i\text{-}2} + u_{i+1}) \tag{8}$$

$$\xi_{\ell+m} = \xi_i$$

Values of ξ along the row of the connected region are calculated as:

$$\xi_{i-n-1} = \frac{1}{3}\left(\frac{2}{3}\xi_{\ell} + \frac{1}{3}\xi_{\ell-1}\right) + \frac{2}{3}\xi_{i-1} \tag{9}$$

$$\xi_{i-n} = \frac{2}{3}\xi_{i} + \frac{1}{3}\xi_{\ell}$$

$$\xi_{i-n+1} = \frac{1}{3}\left(\frac{2}{3}\xi_{\ell} + \frac{1}{3}\xi_{\ell+1}\right) + \frac{2}{3}\xi_{i+1}$$

Along the rows and columns of connected region of one grid space, nonlinear advective terms were neglected to avoid excessive interpolations.

Model Results

Tidal Elevations

The dynamically linkaged model of which the grid system is shown in Fig. 1 was run for five tidal cycles to achieve the stable tidal regime. Results of further sixth cycle was then analyzed to yield M_2 tidal harmonic constants. Subsequently the computed amplitude and phase of the M_2 elevation from the model are compared with coastal observations at various places over the Yellow Sea. The model grid points closest to these observation sites are shown in Fig. 1 as closcd circles. Table 1 shows the comparison of observed and calculated amplitude and phase of the M_2 tide for these sites. It should be borne in mind that discrepancies between values from analyses of water levels at coastal stations and values obtained by Fourier analysis of time series from the model elements occur because generally coastal stations and corresponding model points are at slightly different locations, in region where the tidal constituents change considerably over a mesh element, so that a significant error results. In addition to these limitations, the harmonic constants were derived from short period observations of water level except for a few stations. Some variability of amplitude and phase of the M_2 tide for most stations exists.

Within limitations thus imposed, however it is shown that the model generally agrees well with observation to within 10% in amplitude and 10 degrees in phase with some deterioration in Gulf of Liautung and Hangzhou Bay reaching the maximum error of 30cm. Over the coarse grid region, the results were not improved from the previous shelf model (Choi, 1980) but in intermediate and fine grid region, the area of great interest as far as potential tidal power and large land reclamation development schemes are concerned, close agreement was achieved, errors being about 5% in aplitudes and 5 degrees in phases. Fig. 3(a) shows the computed coamplitude and cophase chart of the M_2 tide from the model demonstrating good agreement with existing chart (Ogura, 1933) and previous computation from the shelf model.

The coarse grid Yellow Sea model was run for 17 days to compute S_2, K_1 and O_1 tidal distribution in addtion to previously computed M_2 tide in the Yellow Sea. For this run harmonic constants for open boundary inputs were deduced from existing tidal charts by adopting the mean values of $H_{s_2}/H_{m_2} = 0.4$, $\kappa_{S_2}-\kappa_{m_2} = 38^{\circ}$, and $H_{o_1}/H_{k_1} = 0.7$, $\kappa_{k_1}-\kappa_{o_1} = 30^{\circ}$. Harmonic analyses for each of the grid elements were performed over 15

Table 1. Comparison of observed and calculated amplitude H(m) and phase $\varkappa$ (degree referred to 135°E) for the M_2 tide.

Station	Code	Position of Station	Observed		Calculated	
			H	$\varkappa$	H	$\varkappa$
Lia Ho	LH	40°38'N 122°10'E	1.17	179	0.84	182
Hsinlutu	HL	40°08'N 120°12'E	0.13	237	0.13	190
Chinwangtao	CT	39°54'N 119°10'E	0.14	346	0.26	39
Tyoto	TT	39°54'N 121°40'E	0.65	62	0.60	49
Taku	TK	38°59'N 117°42'E	0.94	130	0.65	138
Sha-lei-tein tao	ST	38°56'N 118°31'E	0.60	96	0.38	114
Li Tsin Ho Bar	LB	37°53'N 118°40'E	0.40	208	0.30	175
Chimutao Kaochiao	CK	37°41'N 120°13'E	0.50	318	0.22	313
Ryozun	RZ	38°48'N 121°15'E	0.84	337	0.64	333
Nanfachen	NF	38°21'N 120°54'E	0.60	337	0.44	337
Tangluantsu	TL	37°59'N 120°41'E	0.56	321	0.37	328
Dairen	DR	38°56'N 121°39'E	0.99	327	0.75	317
Dai Tyozando	DT	39°16'N 122°35'E	1.32	305	1.13	297
Takushan	TS	39°46'N 123°33'E	1.93	295	1.33	287
Amnok R.	AR	40°07'N 124°24'E	0.87	1	0.89	1
Gado	GD	39°31'N 124°40'E	2.08	276	1.86	298
Unmudo	UI	39°25'N 125°07'E	2.22	337	2.00	304
Jinnampo	JP	38°38'N 125°00'E	1.56	250	1.50	246
Off Chefoo	A	37°57'N 121°55'E	0.74	332	0.53	324
Off Shantung	B	37°37'N 122°47'E	0.20	315	0.20	318
White Rock Point	WP	37°29'N 121°38'E	0.60	340	0.58	329
Weiheiwei	WW	37°30'N 122°10'E	0.59	341	0.50	344
Sangkau Bay	SB	37°03'N 122°29'E	0.70	72	0.48	74
Mongkeumpo	MK	38°11'N 124°47'E	1.12	222	0.95	217
Daechungdo	DC	37°50'N 124°43'E	0.99	178	0.89	185
Moodo	MD	37°44'N 125°33'E	1.98	158	1.75	164
Tau Tsui Head	TH	36°44'N 121°39'E	1.00	117	0.86	106
Star Reef	SR	36°23'N 120°50'E	1.20	150	0.95	143
Chintau	CU	36°05'N 120°19'E	1.25	174	0.95	148
Wang Chia Tai Bay	WB	35°32'N 119°45'E	1.20	183	1.12	183
Bamboo I.	BI	34°45'N 119°26'E	1.20	216	1.23	210
Sang Chia Chun	SN	32°01'N 121°42'E	1.10	4	0.17	21
Central Yellow Sea	C	35°39'N 123°45'E	0.83	86	0.66	83
Daeheuksando	DH	34°41'N 125°26'E	1.02	48	1.08	19
Chindo	CD	34°30'N 126°12'E	1.13	49	1.13	16
Jumundo	JD	37°39'N 126°14'E	2.70	157	2.71	169
Naeri	NR	37°38'N 126°23'E	2.80	159	2.83	169
Inchon	IC	37°29'N 126°37'E	2.92	148	3.00	168
Somoouido	SM	37°22'N 126°27'E	2.77	141	2.72	161
Palmido	PM	37°21'N 126°32'E	2.84	144	2.88	165
Gunsan	GS	36°59'N 126°43'E	2.13	109	2.15	86
Weindo	WI	36°13'N 126°02'E	1.75	103	1.78	90
Duckjuckdo	DJ	37°15'N 126°09'E	2.48	140	2.48	156
Soyado	SD	37°14'N 126°10'E	2.51	142	2.43	154
Youngheungdo	YH	37°15'N 126°30'E	2.78	141	2.79	157
Baegado	BA	37°04'N 125°57'E	2.20	132	2.30	139
Janggohang	JH	37°02'N 126°34'E	2.83	143	2.85	153
Asan	AS	36°58'N 126°47'E	3.03	144	3.09	166
Dugampo	DP	36°58'N 126°31'E	2.69	138	2.78	154
Umoodo	UM	37°02'N 126°27'E	2.62	136	2.62	151
Garolim	GR	36°57'N 126°19'E	2.40	135	2.56	144
Hagampo	HG	36°53'N 126°12'E	2.29	126	2.31	127
Chonsu Bay	CB	36°23'N 126°26'E	2.26	115	2.21	119

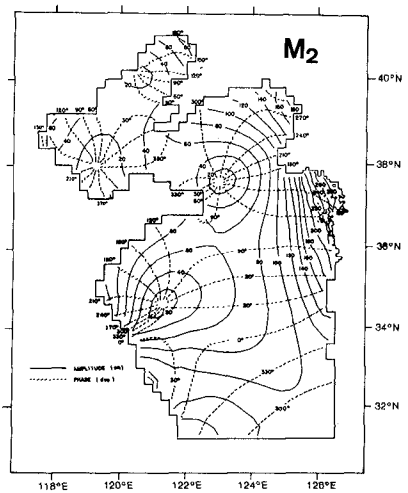

Fig. 3(a)

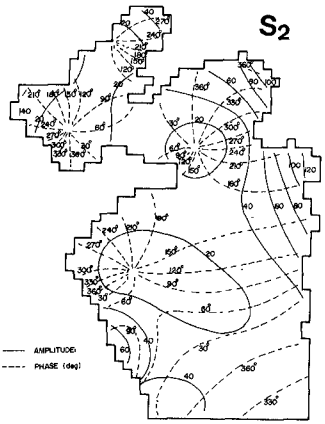

Fig. 3(b)

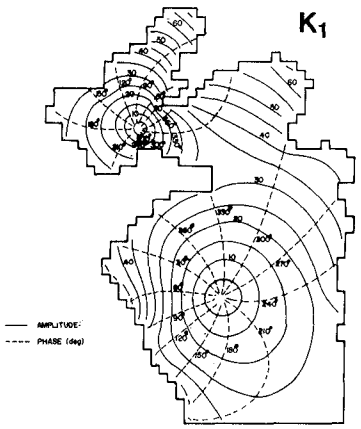

Fig. 3(c)

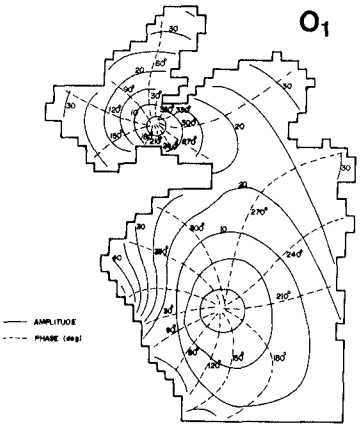

Fig. 3(d)

Fig. 3. Computed M_2, S_2, K_1 and O_1 tides from the model.

days of hourly data after discarding the first two days of data containing initial disturbances. Subsequently computed tidal charts of S_2, K_1 and O_1 tides are drawn as shown in Fig. 3(b) - 3(d). Comparison between observations and model results showed that amplitude of S_2 tide overestimated up to 30% and errors in phases of K_1 and O_1 tides were order of 10 degrees. Overall the model gave general qualitative and quantitative agreement with the existing charts and shore-based data when the crudeness of open boundary tidal data is considered.

Tidal Currents

Fig. 4 show an example of computed tidal current fields from the dynamically linkaged model at the time of lunar transit across 135°E. It can be seen from this figure that tidal currents are very strong along the coast of Taean Peninsula and to approach channel to Inchon and Asan. Sets of current vectors also undergo harmonic oscillations of tidal period, - thus the resultant velocity vectors describing the M_2 tidal ellipses are shown in Fig. 5. This chart gives an overall impression of the magnitude and direction of the M_2 tidal current distribution representing the maximum and minimum velocities as major and minor axes respectively. It is worth noting that rotating current pattern in the lower part of the Yellow Sea is in good agreement with Ogura's speculation. In near-coastal areas, elongated major axes indicates current is near-rectilinear.

In Fig. 6 the depth-mean M_2 current ellipses are plotted for the 27 stations over the Kyonggi Bay. The magnitude and time of occurrence of the maximum M_2 tidal currents, at various places are indicated in this plot. Highest currents calculated are of the order of 150 cm/sec in this area. Current observations of comparable quality do not exist over this region, but generally good agreement of the current magnitude can be expected from the fact that the model simulates the M_2 surface elevation over this region with good accuracy.

Computed depth-mean tidal currents from the extended run of coarse grid model were also harmonically analyzed to provide harmonic constants of easterly and northerly components of S_2, K_1 and O_1 tidal currents. This computed result was then compared with current observations from USA - China Marine Sedimentation Dynamics Study (shown as stations M2, M5; refer Larsen et al.,1985), LSU moored current meter data during 1982 experiment and WHOI moored current meter data during November, 1983 and USA - Korea cooperative current observations during 1986 (shown as stations B, D, F, I in Fig. 1).

Fig. 7 and Fig. 8 show comparison between observations and computed currents of M_2, K_1 tides in the form of tidal ellipses which was constructed from harmonic constants. In these figures observed ellipses are shown as solid lines and computed ellipses dotted lines. There is inherent limitation in direct comparison between observed current meter data which was measured at certain depths below sea surface and depth-averaged currents computed from the two-dimensional model, however there is general agreement between the observations and model results.

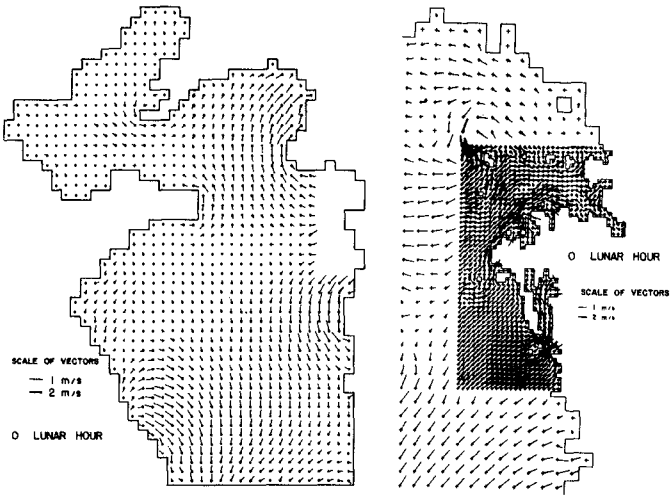

Fig. 4. Computed depth-mean M_2 tidal current from the model.

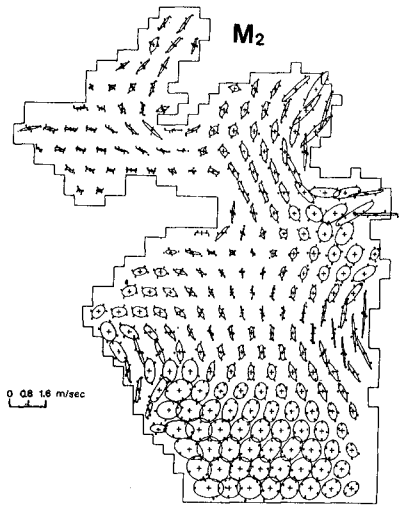

Fig. 5. Computed M_2 tidal ellipses in the Yellow Sea.

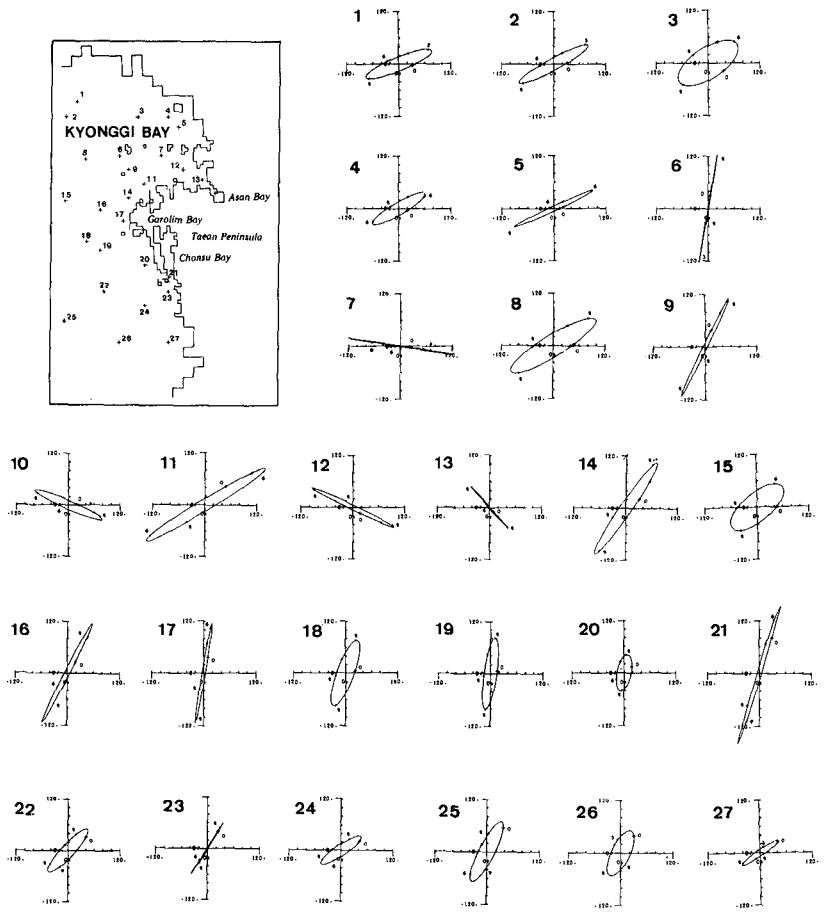

Fig. 6. Computed M_2 tidal ellipses in Kyonggi Bay.

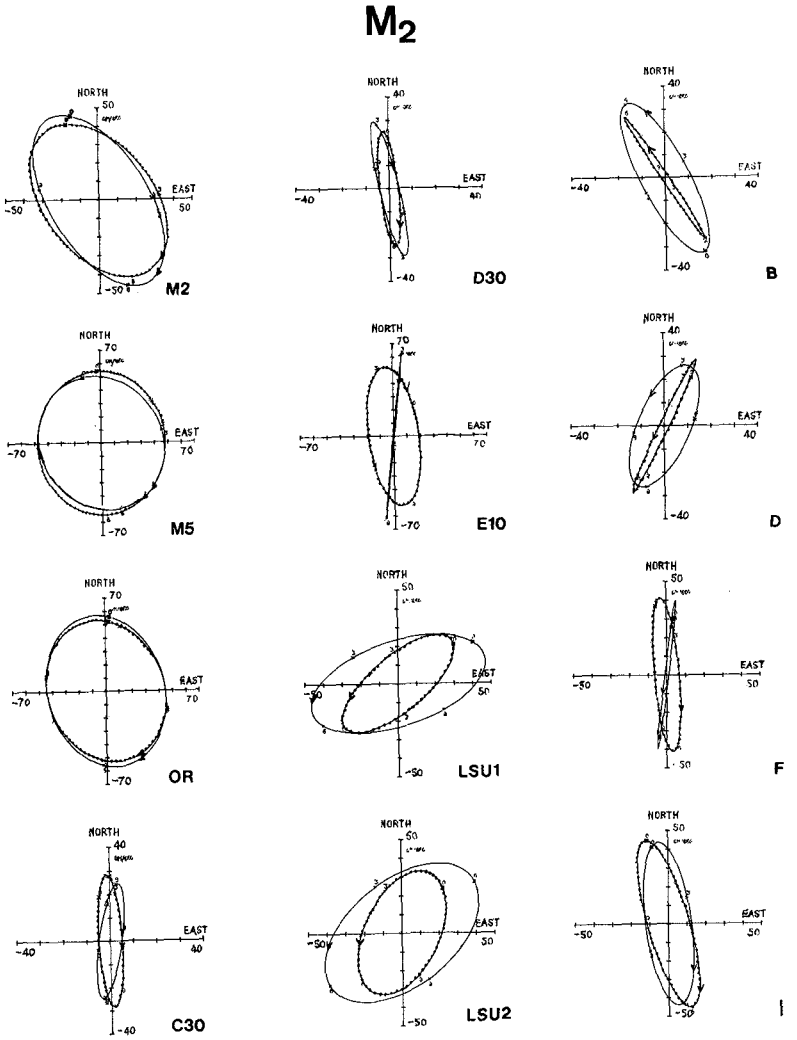

Fig. 7. Comparison of M_2 tidal ellipses between observed currents (———) and computed currents (·····). Stations WHOI 1,2,3 are shown as E,D,C.

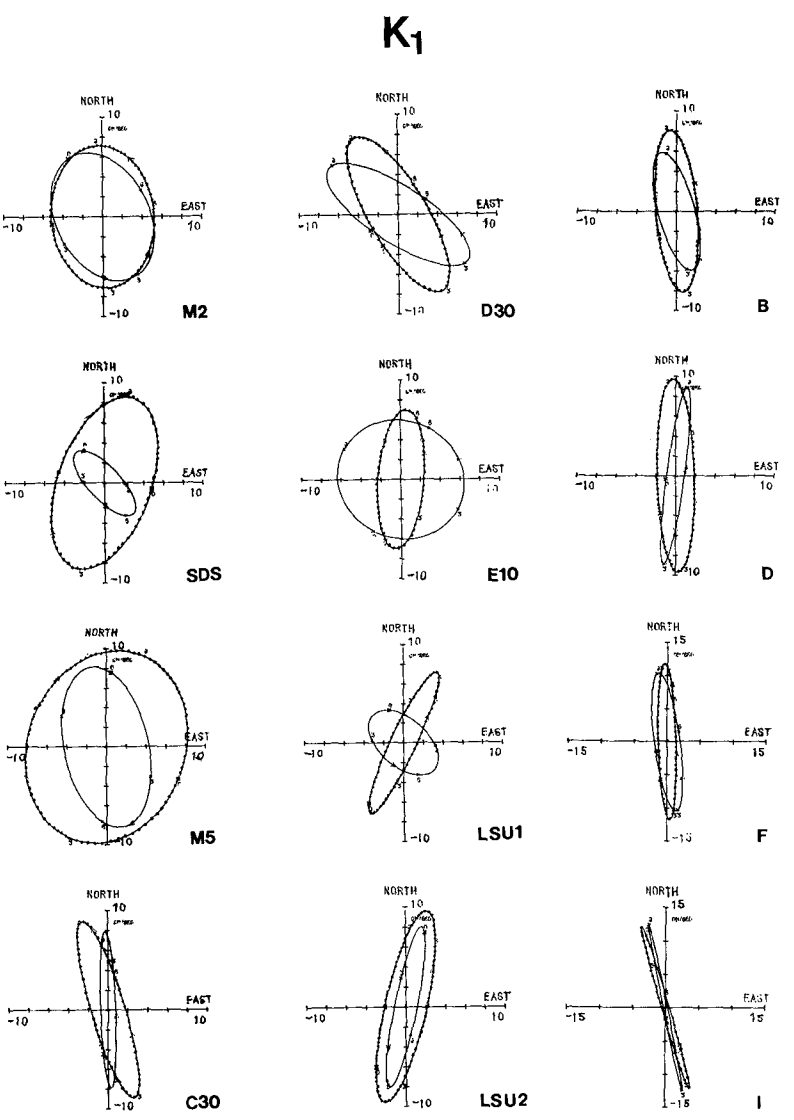

Fig. 8. Comparison of K_1 tidal ellipses between observed currents (———) and computed currents (·····). Stations WHOI 1,2,3 are shown as E,D,C.

Conclusion

Some of preliminary results from a non-linear two-dimensional model of the Yellow Sea have been presented in this paper.

The overall tidal regime of major tidal constituents in the Yellow Sea has been computed quite successfully with the coarse grid numerical model employed here. Using this coarser mesh shelf model to provide boundary data for finer mesh models in the western Yellow Sea, the near-shore variations in tides within Kyonggi Bay will be modelled in detail.

A model employing a dynamical grid nesting procedure to give fine resolution on the west coast of Korea could satisfactorily reproduced the M_2 tide in the fine mesh region in detailed manner. By this means tidal modification due to large development schemes can be evaluated.

Acknowledgements

Modelling work described here was initiated during my visit to Bidston Observatory. The author is indebted to scientists in the dynamic modelling group of Bidston Observatory. The author also wishes to thank Dr. L. H. Larsen, University of Washington, Dr. R. C. Beardsley, WHOI and Dr. J. T. Wells, South Carolina State University for making the current meter data available. Funding for this work was partially provided by Korea Science and Engineering Foundation.

References

An, H. S. (1977). A numerical experiment of the M_2 tide in the Yellow Sea. Journal of the Oceanographical Society of Japan, Vol. 33, pp. 103-110.

Boris, L. I. (1958). Calculation of the tides and tidal currents in the Yellow Sea. Trudy Leningrad Gridromet Inst.

Choi, B. H. (1980). A tidal model of the Yellow Sea and the Eastern China Sea. Korea Ocean Research and Development Institute Report 80-02.

Flather, R. A. (1976). A tidal model of the North-West European continental shelf. Memoires de la Societe Royale des Sciences de Liege, Ser. 6, Vol. 10, pp. 141-164.

Flather, R. A. and Heaps, N. S. (1975). Tidal computations for Morecambe Bay. Geophysical Journal of the Royal Astronomical Society, Vol. 42, pp. 489-517.

Larsen, L. H., Cannon, G. A. and Choi, B. H. (1985). East China Sea tide current. Continental Shelf Research, Vol. 4, Nos 1/2, pp. 77-103.

Ogura, S. (1933). The tides in the seas adjacent to Japan. Bulletin of Hydrographic Department, Imperial Japanese Navy, No. 7, pp. 1-189.

Owen, A. (1979). Tides in Bristol Channel: tidal barrage studies. Ph.D. thesis, University of Liverpool.

Roberts, K. V. and Weiss, N. O. (1967). Convective difference schemes. Math. Comput., Vol. 20, pp. 272-299.

Shen, Y. (1980). Numerical computation of tides in the East China Sea. Journal of Shandong College of Oceanology, Vol. 10, No. 3, pp. 26-35.

Stepanov, S. I. and Boris, L. I. (1964). On the effect of errors in the original data on the accuracy of the solution of boundary value problems of tidal equations. Trudy Leningrad Gridromet Inst., Rep. No, 17.

Tsiklauri, I. D. and Boris, L. I. (1961). An experiment to calculate tidal phenomena by means of "URAL-1" digital computer. Trudy Leningrad Gridromet Inst., Rep. No. 10.

Xia, Z. and Wang, Z. (1984). A numerical model of the M_2 constituent in the Huanghai Sea. Journal of Oceanography of Hunghai and Bohai Seas, Vol. 2, No. 1.

CHAPTER 7

THE INFLUENCE OF WAVES ON CURRENT PROFILES

by

Felicity C. Coffey* and Peter Nielsen**

ABSTRACT

A simple model is presented for steady current profiles in the presence of waves. The current reduction and apparent roughness increase caused by the waves are shown to depend mainly on one dimensionless parameter $\tilde{u}_*/\bar{u}_*$, i.e. the ratio between the friction velocity amplitude due to the waves and the time averaged friction velocity. The model recognises the need to apply different eddy viscosities to different flow components. Also, the thickness of the wave influenced layer near the bed is comceptually separated from the vertical scale of the wave boundary layer.

INTRODUCTION

The water motion in coastal and estuarine areas is generally a combination of wave motion and currents which can be considered steady compared to the waves. Waves and currents influence each other in mainly two ways. Firstly, variability in current strength will cause wave refraction. Secondly, vigorous wave-induced mixing close to the bed will change the current profile. In the following we shall deal only with the latter type of of interaction.

The problem was studied theoretically by Lundgren (1972), who realised that the waves change the current profile by increasing the eddy viscosity, ν_c, felt by the current in a thin layer near the bed (Figure 1), while outside this thin layer ($z > L$) the waves introduce no mixing. Hence the outer current profile is logarithmic

$$\bar{u}(z) = \frac{\bar{u}_*}{\kappa} \ln (z/z_1) \qquad \text{for } z > L \qquad (1)$$

with the only difference being that the usual zero intercept $z_o = r/30$ has been replaced by the larger z_1; r is the Nikuradse roughness of the bed and $\bar{u}_*$ is the time averaged friction velocity. Thus the wave effect on the outer current profile amounts to a constant shift:

* Coastal Studies Unit, Department of Geography, University of Sydney, Australia 2006.

** Coastal Branch, Public Works Department, N.S.W., 140 Phillip Street, Sydney 2000, Australia.

$$\Delta_{\bar{u}} = \frac{\bar{u}_*}{\kappa} \ln (z_o/z_1) \qquad \text{for } z > L \qquad (2)$$

or an apparent increase in bed roughness from $30z_o$ to $30z_1$.

A complete description of the velocity shift or z_1/z_o must contain the three basic, independent variables: $Aw/\bar{u}_*$, A/r, and φ i.e.

$$z_1/z_o = F(Aw/\bar{u}_*, A/r, \varphi) \qquad (3)$$

where A is the horizontal semi-excursion of the wave motion near the bed, ω is the angular frequency $2\pi/T$ and φ is the angle between current and wave propagation. Lundgren evaluated $\ln(z_1/z_o)$ on the basis of wave eddy viscosity measurements by Jonsson and Carlsen (1976) and assuming that the eddy viscosity felt by the current is the one caused by current alone plus the one caused by waves alone, added geometrically.

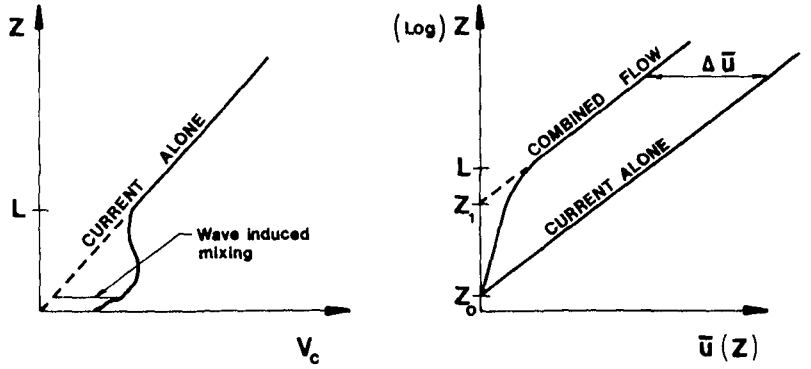

Figure 1 : Waves increase the eddy viscosity ν_c felt by the current inside a thin layer ($z \ll L$) near the bed. The resulting current profile is logarithmic for $z > L$, so the wave induced change to the outer profile amounts to a shift u or in other words, to an apparent roughness increase (from $30z_o$ to $30z_1$).

Lundgren did not consider changes in the wave boundary layer structure due to the current. Such changes were estimated later on theoretical grounds by Grant and Madsen (1979) and Christoffersen (1982). Such changes are however very minor according to empirical data and are probably without practical consequence unless the current is very strong ($\bar{u}_* \gtrsim \hat{u}_*$), see Nielsen (1985).

The models of Grant and Madsen and of Christoffersen both assume that the same eddy viscosity applies to both waves and currents, an assumption which seems altogether reasonable a priori. However, surprisingly it is not valid in general. Laboratory measurements by

van Doorn (1981) show that the eddy viscosities felt by waves and currents at the same point of the same flow can differ by as much as a factor 4, see Coffey and Nielsen (1984). The fact that different eddy viscosities must be applied to different flow components has also been observed by Bakker and van Kesteren (personal communication). In heuristic terms the phenomenon can be explained as follows : The eddy viscosity can be seen as the product of a turbulent velocity and a vertical length scale i.e.

$$\nu_T = V_\nu L_\nu \qquad (4)$$

The turbulent velocity V_ν is probably equally effective with respect to both waves and currents, but that is not the case for the vertical length scale L_ν. The length scale relevant to the current shear stress is known to grow proportionally to the distance from the bed; but the length scale relevant to the oscillatory shear stress cannot grow beyond a certain fraction of the wave boundary layer thickness or the equivalent Stokes length $\sqrt{2\nu_T/\omega}$. Hence the currents feel a larger eddy viscosity than the waves.

The implication of this is that while the eddy viscosity concept is useful as a formal parameter in simplistic flow models, the interpretation into physical terms is not as straight forward as previously imagined.

CHOSING MODEL STRUCTURE

The following section is concerned with choosing the appropriate form of the eddy viscosity felt by the current on the basis of empirical evidence. Obviously, following the remarks above, the same eddy viscosity is not expected to apply to the wave boundary layer structure.

Apart from the fairly complicated, empirical curve suggested by Lundgren (1972), two simple forms have been suggested for the eddy viscosity felt by the current inside the wave dominated layer. Christoffersen (1982) suggested a constant eddy viscosity through the bottom layer while Grant and Madsen (1979) recommended a linearly growing eddy viscosity. Both models will in general result in a discontinuity of ν_c and thus of the current gradient at the top of the wave influenced layer (z = L). See Figure 2.

For both models, it is fairly easy to obtain expressions for z_1/z_o by using the terminology of Figure 2 and the usual assumptions: $\tau/\rho = \bar{u}_*^2$ and $\bar{u}(z_o) = 0$.

For the "Christoffersen type model" (Figure 2A) we have :

$$\nu_c = \begin{cases} K\bar{u}_* z_o F & , \quad z < L \\ K\bar{u}_* z & , \quad z > L \end{cases} \qquad (5)$$

and hence :

$$\frac{d\bar{u}}{dz} = \frac{\bar{\tau}/\rho}{\nu_c} = \begin{cases} \dfrac{\bar{u}_*}{Kz_oF} , & z < L \\ \dfrac{\bar{u}_*}{Kz} , & z > L \end{cases} \qquad (6)$$

which with $\bar{u}(z_o) = 0$ gives :

$$\bar{u}(z) = \begin{cases} \dfrac{\bar{u}_*}{KF}(z/z_o - 1) , & z < L \\ \dfrac{\bar{u}_*}{K}\ln(z/z_1) , & z > L \end{cases} \qquad (7)$$

The value of z_1 is found by matching the two expressions at $z = z_oF$. We find

$$z_1/z_o = \frac{L}{z_o} e^{(1 - L/z_o)/F} \qquad (8)$$

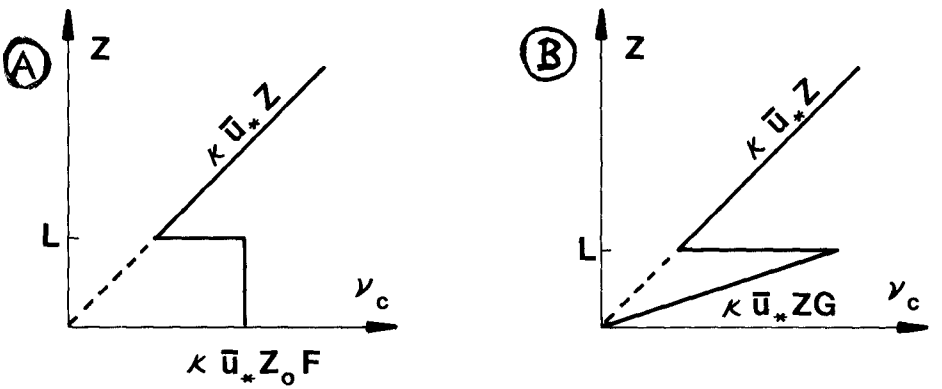

Figure 2 : Two simple previous models for ν_c in combined flows and the resulting apparent roughness change.

The analogous calculations for the model outlined in Figure 2B lead to :

$$z_1/z_o = \left(\frac{L}{z_o}\right)^{1-\frac{1}{G}} \qquad (9)$$

The two results are interestingly similar in that both expressions are assympthotically proportional to L/z_o for large values of the wave-induced eddy viscosity (large F or G). This is very interesting in view of the fact that both Christoffersen and Grant and Madsen hypothesised that L should be closely related to the wave boundary layer thickness δ. If that was true, the formulae (8) and (9) would indicate that z_1/z_o depend mainly on δ/z_o. The available laboratory data do not support this. See Figure 3.

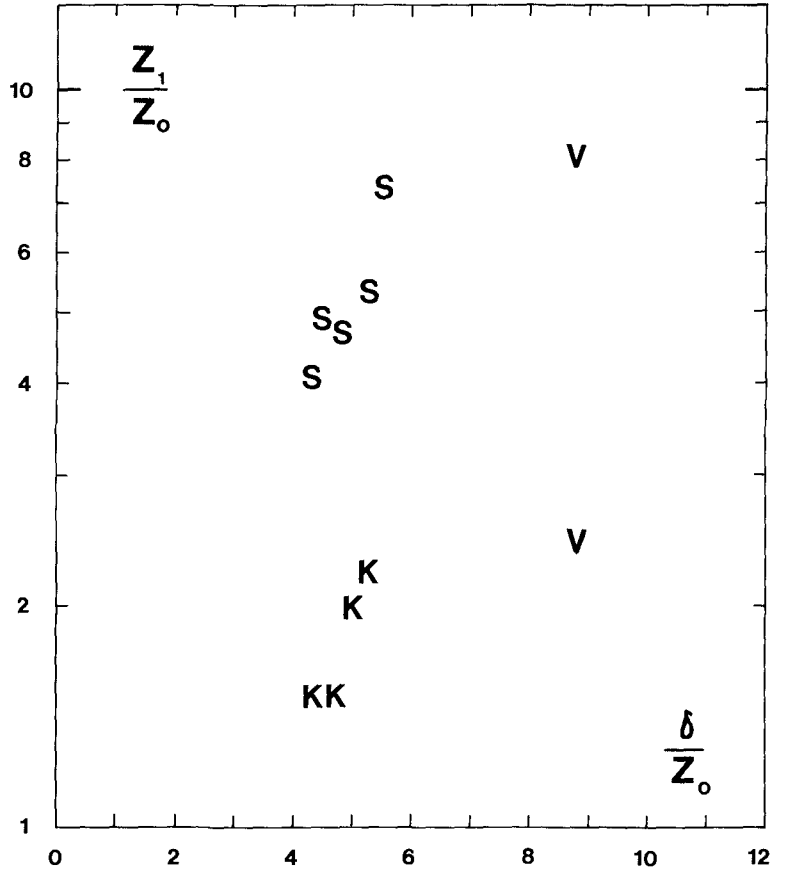

Figure 3 : Apparent roughness increase as function of dimensionless wave boundary layer thickness.

However, as Figure 4 shows, z_1/z_o depends almost exclusively on the friction velocity ratio $\tilde{u}_*/\bar{u}_*$. Such dependence will result if the thickness of the wave influenced layer has the form :

$$L = z_o F(\tilde{u}_*/\bar{u}_*) \qquad (10)$$

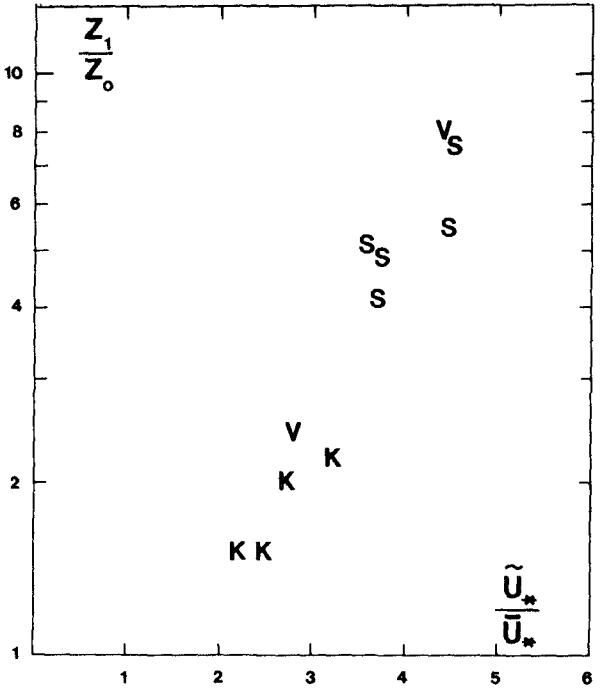

Figure 4 : Apparent roughness increase as function of the friction velocity ratio.

In the following we shall develop a simple model which is in accordance with this empirical observation and in good agreement with the available laboratory data in general. The experimental data used are summarised in Table 1.

AN EMPIRICAL MODEL

The empirical observations above support the eddy viscosity model outlined in Figure 5.

The square toe has been chosen primarily because it allows ν_c and thus the current gradient to be continuous functions of z. But also because there is some evidence (Kemp and Simons, 1982, and van Doorn, 1981, 1982) that it is somewhat more realistic than the triangular one, at least for relative roughnesses (r/A) corresponding to natural sand ripples. (See Figure 6.)

Author	Symbol	T (s)	A (m)	r (m)	$\bar{u}_*$ (m/s)	z_1 (m)
Van Doorn (1981)	V	2.0	0.085	0.021	0.016	0.0056
	V	2.0	0.085	0.021	0.026	0.0017
Kemp & Simons (1982)	K	1.0	0.011	0.025	0.018	0.0013
	K	1.0	0.015	0.025	0.019	0.0013
	K	1.0	0.018	0.025	0.020	0.0017
	K	1.0	0.021	0.025	0.019	0.0019
Kemp & Simons (1983)	S	1.0	0.011	0.025	0.011	0.0034
	S	1.0	0.013	0.025	0.012	0.0041
	S	1.0	0.016	0.025	0.013	0.0039
	S	1.0	0.021	0.025	0.013	0.0044
	S	1.0	0.024	0.025	0.014	0.0061

Table 1 : Experimental data

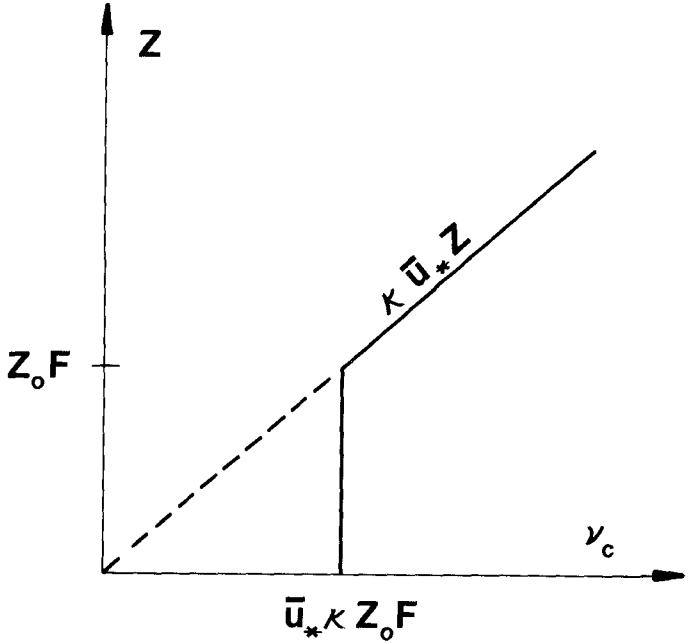

Figure 5 : Proposed distribution of the eddy viscosity felt by a steady current in the presence of waves. F is a function of the friction velocity ratio ($\tilde{u}_*/\bar{u}_*$) and possibly of the angle between current and wave propagation.

The values of ν_c observed in the horizontally homogenous layer ($z > 0.4$ centimetres) show good agreement with the form hypothesised in Figure 5.

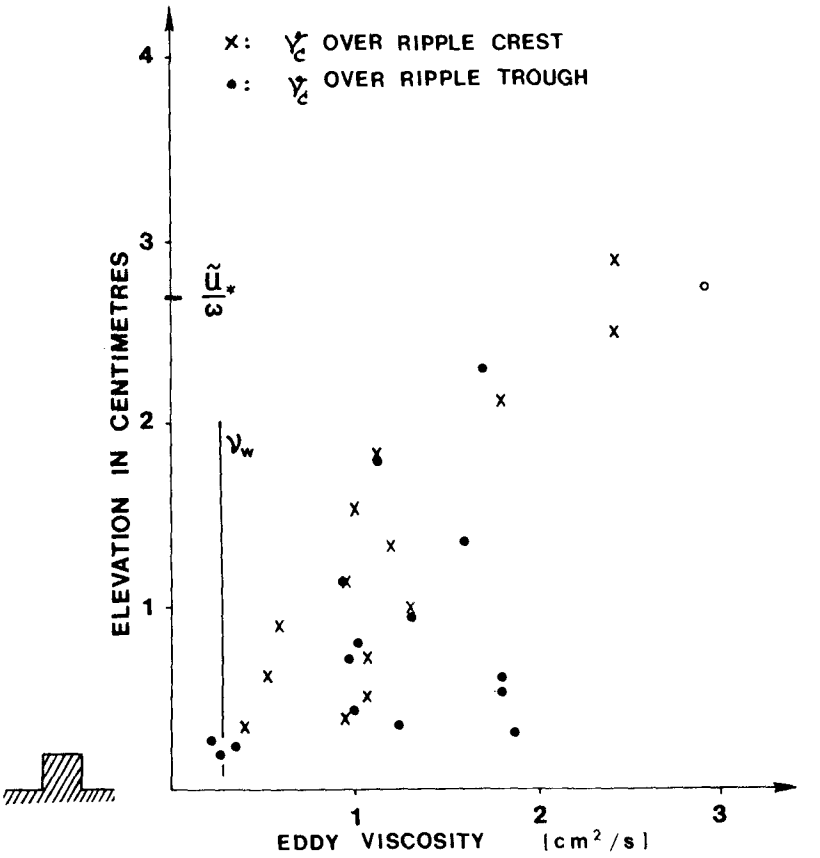

Figure 6 : Observed eddy viscosities from van Doorn (1982), Test S10. The eddy viscosity applicable to the waves (ν_w^+) is derived in accordance with Nielsen (1985) eqs 31-34.

A finite value of the eddy viscosity at the theoretical (or averaged) bed level is appropriate for rough beds. See e.g. Kajiura (1968).

With the eddy viscosity given by :

$$\nu_c^+ = \begin{cases} K\,\tilde{u}_* z_0 F & \text{for} \quad z < z_0 F \\ K\tilde{u}_* z & \text{for} \quad z > z_0 F \end{cases} \qquad (11)$$

and assuming $\overline{\tau} = \overline{u}_*^2$, we get :

$$\frac{du}{dz} = \begin{cases} \overline{u}_*/(Kz_oF) & \text{for} \quad z < z_oF \\ \overline{u}_*/(Kz) & \text{for} \quad z > z_oF \end{cases} \tag{12}$$

and with $\overline{u}(z_o) = 0$, we get :

$$\overline{u}(z) = \begin{cases} \frac{\overline{u}_*}{KF}(z/z_o - 1) & \text{for} \quad z < z_oF \\ \frac{\overline{u}_*}{K}\ln(z/z_1) & \text{for} \quad z > z_oF \end{cases} \tag{13}$$

from which z_1 can be found by matching the two expressions at $z = z_oF$. We find

$$\frac{z_1}{z_o} = F e^{\frac{1}{F}-1} \tag{14}$$

Values of the function $F = F(\tilde{u}_*/\overline{u}_*)$ which must tend towards unity for small $\tilde{u}_*/\overline{u}_*$ have been plotted in Figure 7 and for predictive purposes the curve

$$F = 1 + \frac{1}{6}(\tilde{u}_*/\overline{u}_*)^3 \tag{15}$$

has been fitted to the data.

The form of (15) is rather different from what would result from the hypotheses of Lundgren and Grant and Madsen for combined eddy viscosity, and the underlying mechanics are not understood in detail so applicability outside the experiemental range $\tilde{u}_*/\overline{u}_* < 5$ cannot be guaranteed. Also, future experimental data with different angles between current and wave propagation may call for incorporation of φ-dependence, i.e. $F = F(\tilde{u}_*/\overline{u}_*, \varphi)$.

PRACTICAL APPLICATION

In most practical cases, the problem is to estimate the current profile $\overline{u}(z)$ from knowledge of the bed roughness r and the velocities A_ω and $\overline{u}(z_r)$ at only one reference level z_r, normally one metre above the bed.

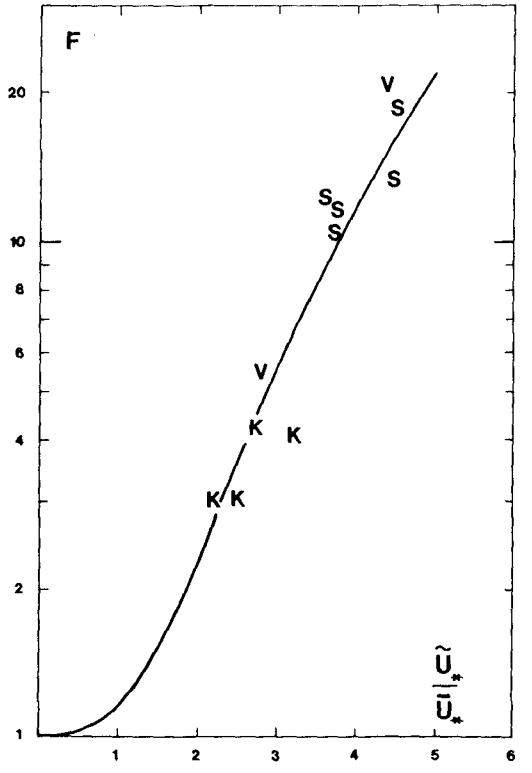

Figure 7 : Observed values of F. The curve corresponds to equation 15.

Thus $\bar{u}_*$ is unknown and must be determined iteratively from :

$$\bar{u}(z_r) = \frac{\bar{u}_*}{K} \ln \frac{z_r}{z_1} \qquad (16)$$

with the use of (14) and (15) or the direct approximation

$$z_1/z_o = 1 + 0.06\ (\tilde{u}_*/\bar{u}_*)^3 \qquad (17)$$

which leads to

$$\bar{u}(z_r) = \frac{\bar{u}_*}{K} \ln \frac{z_r}{z_o\ (1 + 0.06\ (\tilde{u}_*/\bar{u}_*)^3)} \qquad (18)$$

EXAMPLE

As an example, consider the experiment V10 from van Doorn (1981): The Nikuradse bed roughness is r = 0.021m and measurements at z_r = 0.05m give $A\omega$ = 0.257 m/s and u(0.05) = 0.090 m/s. The wave period is 2 seconds so we find A = 0.082m and hence :

$$f_w = 0.37\ (r/A)^{2/3} = 0.149 \qquad (19)$$

(Kajiura 1968) and :

$$\tilde{u}_* = \sqrt{0.5 f}\, A\omega = 0.070 \text{ m/s} \qquad (20)$$

Iterative solution of (18) then gives u_* = 0.0152 m/s, corresponding to $\tilde{u}_*/\bar{u}_*$ = 4.60 and F = 17.2. The apparent roughness increase is

$$z_1/z_o = F \exp\left(\frac{1}{F} - 1\right) = 6.7 \qquad (21)$$

and the shift of the outer velocity profile

$$\Delta\bar{u} = \frac{\bar{u}_*}{K}\ln(z_o/z_1) = -0.07 \text{ m/s} \qquad (22)$$

The velocity profile based on (13) and the above results is shown in Figure 8 together with the measured profile.

DISCUSSION

It has been shown that the apparent roughness increase (z_1/z_o) shown by the logarithmic part of current profiles in the presence of waves is mainly a function of the friction velocity ratio $\tilde{u}_*/\bar{u}_*$.

An empirical model has been established which enables estimation of the lower and the logarithmic part of a current profile from knowledge of the wave conditions, the bed roughness plus either the current friction velocity $\bar{u}_*$ or the current speed at a single evaluation $\bar{u}(z_r)$.

The central idea of the model is the same as used by Lundgren (1972), Grant and Madsen (1979) and Christoffersen (1982), namely that the waves reduce the current gradients near the bed by introducing extra mixing (eddy viscosity) below a certain level L near the bed. The effect of this, relative to a situation without waves is a constant reduction $\Delta\bar{u}$ for $z > L$ which can also be interpreted as an apparent increase of bed roughness, from $30z_o$ to $30z_1$. See Figure 1.

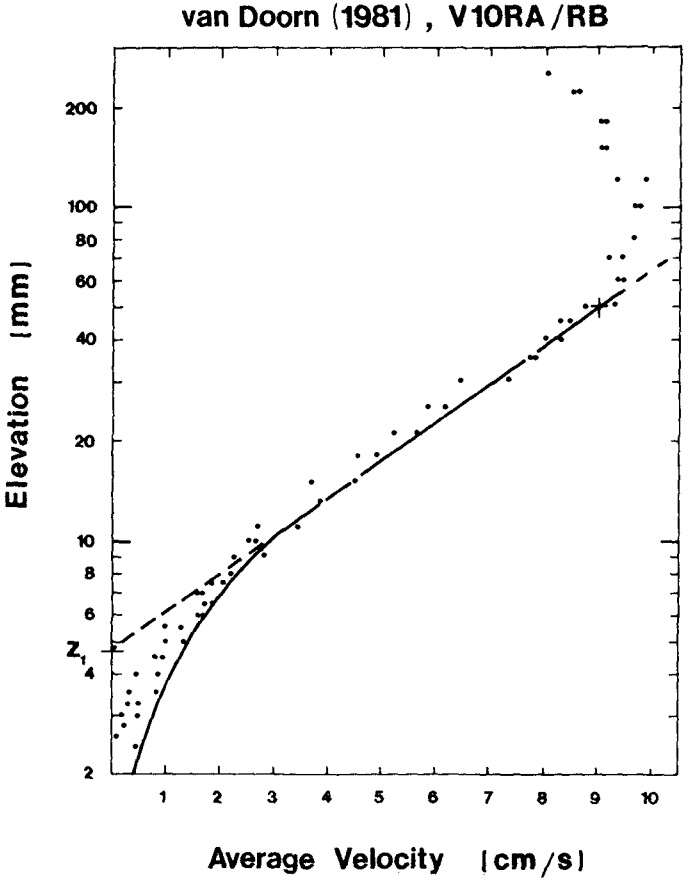

Figure 8 : Current profile predicted from the bed roughness and the velocity at a single point, $\bar{u}(0.05m) = 0.09$ m/s. Measurements by van Doorn (1981). Note that the upper part ($z > 0.07m$) of the velocity distribution is not logarithmic and therefore not covered by the model. The water depth in the experiement was 0.30 metres.

The previous idea of the bottom layer thickness L being proportional to the wave boundary layer thickness (Grant and Madsen 1979 and Christoffersen 1982) has been replaced by :

$$L = z_o \, F(\tilde{u}_*/\bar{u}_*) \qquad (23)$$

a step which is supported by the empirical data as shown in Figures 3 and 4. The conceptual separation of the wave boundary layer thickness as defined by the waves themselves and the thickness of the layer which is felt by the current to be wave influenced is essential. It is related to the fact that the vertical length scales relevant to the corresponding shear stress components are different. The length scale relevant to $\bar{u}$ is Kz, and it can grow to a considerable fraction of the flow depth. On the other hand the length scale relevant to $\tilde{u}$ is restricted to be some fraction of the wave boundary layer thickness.

Dependence of z_1/z_o on the angle between current and wave propagation has not been incorporated because experimental ver ification is not possible at the moment.

Also, the forces driving the boundary layer mass transport under progressive waves have been neglected. These are likely to dominate the profiles of weak currents (for large $\tilde{u}_*/\bar{u}_*$) but the presently available data indicate that they can be ignored for $\tilde{u}_*/\bar{u}_* \lesssim 5$.

The model is suitable for practical use within the experimental range $\tilde{u}_*/\bar{u}_* \lesssim 5$ because it is considerably simpler than previous models and in good agreement with the physical reality.

NOTATION

A	(m)	Water particle semi-excursion.
F	-	Empirical function of u_*/u_{*}, see Figure 5.
f_w	-	Wave friction factor.
L	(m)	Thickness of wave influenced layer.
r	(m)	Nikuradse roughness.
$\tilde{u}$	(m/s)	Wave induced velocity.
$\tilde{u}_*$	(m/s)	Friction velocity for waves alone.
$\bar{u}$	(m/s)	Current velocity
$\bar{u}_*$	(m/s)	Current friction velocity.
$\Delta_{\bar{u}}$	(m/s)	Wave induced current reduction.
z	(m)	Vertical co-ordinate.
z_r	(m)	Reference level.
z_o	(m)	Zero intercept height for pure current, r/30.
z_1	(m)	Zero intercept height, Figure 1.
δ	(m)	Wave boundary layer thickness.
K	-	von Karman's constant.
ν_c	(m^2/s)	Eddy viscosity felt by current
ρ	(kg/m^3)	Fluid density.
$\bar{\tau}$	(N/m^2)	Current bed shear stress.
φ	-	Angle between waves and current.
ω	(rad/s)	Wave angular velocity $2\pi/T$.

REFERENCES

Christoffersen, J.B. (1982): "Current refraction of dissipative water waves", Series Paper 30, Institute of Hydrodynamics and Hydraulic Engineering, Technical University of Denmark.

Coffey, F.C. and Nielsen, P. (1984): "Aspects of wave current boundary layer flows", Proc. 19th Int. Conf. Coastal Engineering, Houston, pp 2232-2245.

Doorn, Th. van (1981): "Experimental investigation of near bottom velocities in water waves with and without a current", Delft Hydraulics Laboratory, TOW-Report 1423.

Doorn, Th. van (1982): "Experimental onderzoek naar het snelheidsveld in de turbulente bodemgrenslaag in een oscillerende stroming in een golftunnel. Delft Hydraulics Laboratory, Report No. M1562-1a.

Grant, W.D. and Madsen, O.S. (1979): "Combined wave and current interaction with a rough bottom", Journal of Geophysical Research, Vol. 84, No. C4, pp 1797-1808.

Jonsson, I.G. and Carlsen, N.A. (1976): "Experimental and Theoretical Investigations in an oscillatory rough turbulent boundary layer", Journal of Hydraulic Research, Vol. 14, No. 1, pp 45-60.

Kajiura, K. (1968): "A model of the bottom boundary layer in water waves", Bull Earthquake Res. Inst., Univ. of Tokyo, Vol. 46, Chaper 5, pp 75-123.

Kemp, P.H. and Simons, R.R. (1982): "The interaction between waves and a turbulent current: waves propagating with the current", Journal of Fluid Mechanics, Vol. 116, pp 227-250.

Kemp, P.H. and Simons, R.R. (1983): "The interaction between waves and a turbulent current: waves propagating against the current", Journal of Fluid Mechanics, Vol. 130, pp 73-89.

Lundgren, H. (1972): "Turbulent currents in the presence of waves", Proc. 13th International Conference on Coastal Engineering, Vancouver, pp 623-634.

Nielsen, P. (1985): "On the structure of oscillatory boundary layers", Coastal Engineering, Vol. 9, No. 3, pp 261-276.

CHAPTER 8

NEAR-SURFACE ORBITAL VELOCITIES IN IRREGULAR WAVES

K.-F. Daemrich* and A. Götschenberg**

ABSTRACT

The paper deals with measurements of horizontal orbital velocities near the surface of mechanically generated waves in a wave flume.

Due to the characteristics of most velocity probes, it is difficult or impossible to measure with a fixed probe in the area above the lowest trough. As the probe is not submerged continuously, failures or uncertainties in the measurements may occur.

To overcome these limitations, a movable frame for the velocity probe was designed, which can be moved vertically up and down with the surface elevation by a disc rotor servo motor, controlled by a wave gauge. By that continuously velocities up to 3 cm below the surface could be measured.

Theoretical velocities have been calculated for comparison with different simulation methods for irregular waves, based on linear wave theory.

INTRODUCTION

Investigations and measurements of orbital velocities have been conducted for a long time. Whereas the most earlier publications were related to investigations in regular waves to check the various wave theories, the subsequent dealt with the development of simulation methods for the theoretical treatment of irregular waves. Especially the velocities in very steep and breaking waves have always been an important subject of investigations and the research on the influence of the directionality will extend, as adequate test facilities for the generation of directional waves are available now.

Due to the characteristics of most velocity probes, however, in general measurements close to the surface of the waves, especially in the wave crests, are difficult or impossible when the probe is fixed at a certain height above the lowest trough. The sensor is submerged then only a short time (especially in scaled model tests) what might create problems due to the time constants of the instrumentation or disturbing air enclosures.

* 1) Dr.-Ing., Senior Research Engineer
** 2) Dipl.-Ing., Research Engineer
both Franzius-Institut, University of Hannover, FRGermany

Earlier own measurements in irregular waves with inductive type probes had to be restricted to this area, too, and recently in a publication of SVENDSEN (1986) on surf zone turbulence it is summarized that "all investigations have concentrated on the region below trough level where measurements are available".

To overcome these limitations and to be able to perform investigations on velocities in the crest area of irregular waves, a vertical movable frame for the velocity probe was constructed. This frame can be moved up and down with the variation of the water surface by a disc rotor servo motor controlled by the output of a wave gauge. So the velocity probe is always submerged and able to measure velocities very high in the wave crest.

INSTRUMENTATION

The vertical movable frame was designed for measurements in hydraulic models with wave heights up to about 0.50 m, equivalent to the range of the often used wave gauges of the DELFT type.

It consists of a U-profiled aluminium bar sliding between guide rollers and driven via toothed rack and pinion directly connected to the servo motor (120W rated output power). A flat coil spring is used to compensate for the weight of the movable parts and the velocity probe.

Figure 1 gives a principal sketch of the set-up in the wave flume.

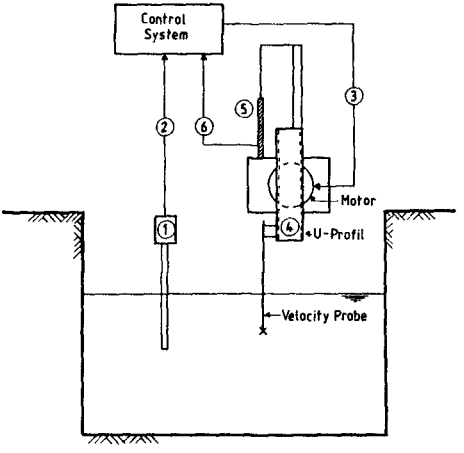

Fig. 1: Principal sketch of set-up of vertical movable frame in the wave flume

The wave gauge (1) measures the actual surface elevation of the water. Its output signal (2) provides the electronic control system which generates the set value (3) for the servo motor. The U-profiled aluminium bar (4) with the velocity probe fixed at the lower

end (and connected to the motor via toothed rack and pinion) is moved up and down by the servo motor following the set value (3). The potentiometer transducer (5) gives the actual position (6) of the U-profile (4) to the control system (actual value) and allows also to compare surface elevation and position of the probe for analysis purpose.

Figure 2 shows the device and the electronic control system, Figure 3 the set-up in the wave flume, fixed to a measuring carriage.

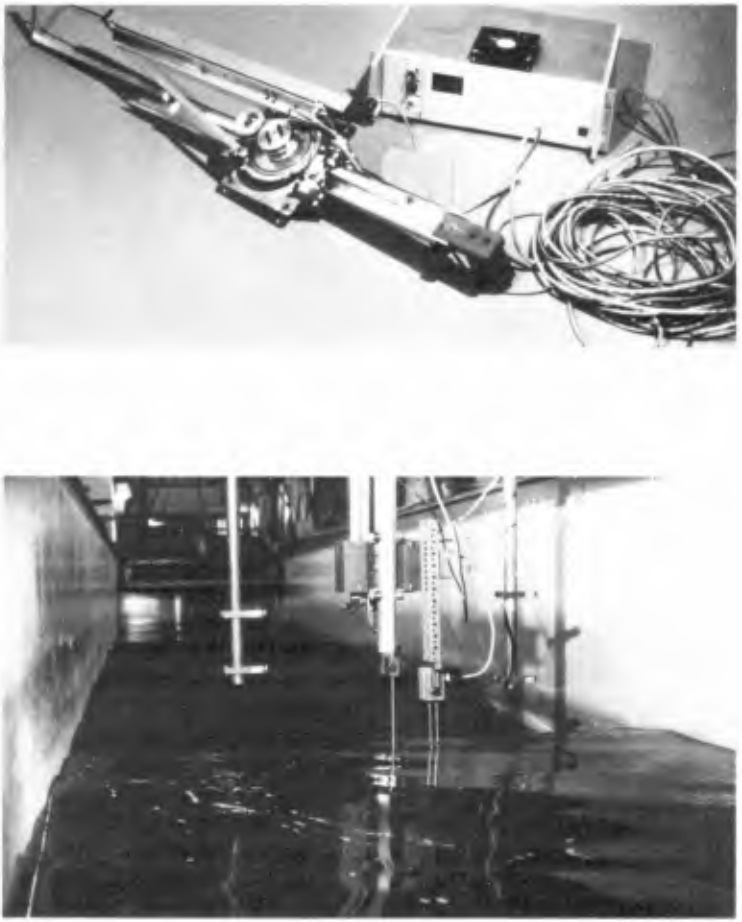

Fig. 3: Set-up of vertical movable frame in the wave flume

For a certain test, the movable frame is mechanically placed in a middle position and the velocity probe is shifted to the pretended submerged depth in still water conditions. After starting the tests the probe is then moved up and down with the surface elevation, measuring in positions approximately parallel to the surface.

Due to the characteristics of the electronic control system, the measured location is not exact constant below the wave surface. However, from the potentiometer transducer, the position of the probe can always be determined and related to the signal from the wave gauge. So the exact position as a function of time is available.

As an example, which demonstrates at the same time the limits of the system, in Figure 4 the time series of water level and probe location, and the difference between both signals, are plotted. The wave train was measured in the area of a 1:30 slope and contained steep and some breaking waves.

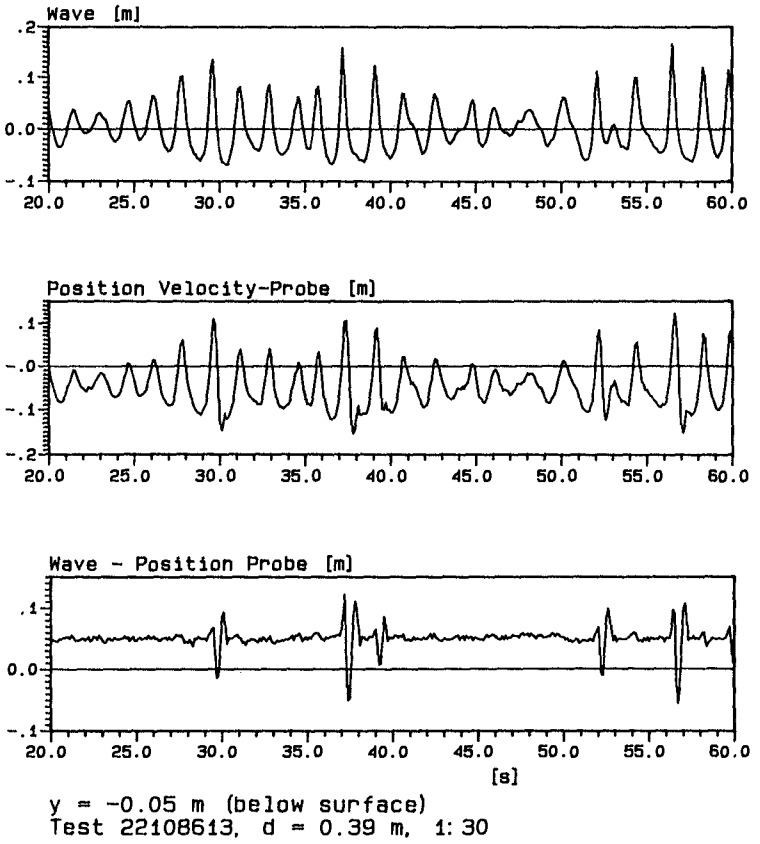

Fig. 4: Comparison of surface elevation and probe location

In the not extreme steep waves the system works with deviations of less than 1 cm. However, in the very steep waves, with the present layout of the motor and the control electronics, the system works not yet satisfying. For further measurements in steep and breaking waves, the system has to be improved by taking a stronger motor and a controller of better quality.

Finally in Figure 5 examplarily maxima (crest) and minima (trough) of the wave time-series and of the time-series of the position of the probe are compared in scatter plots.

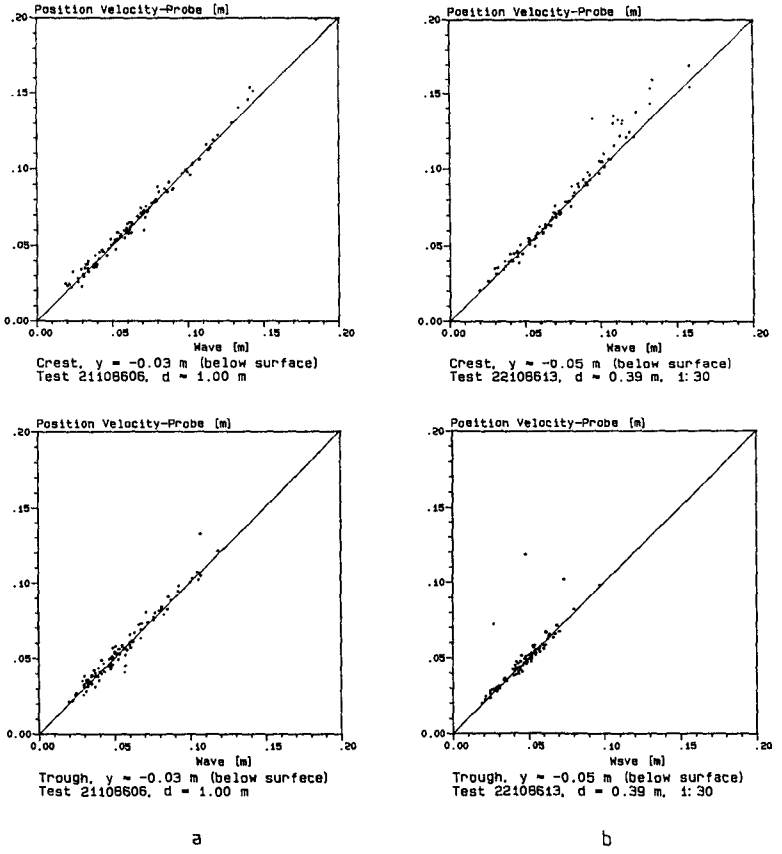

Fig. 5: Comparison of extremal values of wave surface in crest and trough and pertinent position of the probe
a) moderate wave conditions, design condition for equipment
b) very steep and breaking waves

As the motor of the system can be controlled by any external signal, the equipment can also be used for a dynamic calibration of the velocity probes. For the tests discussed in the following, a Delft Propeller Probe was used as a velocity probe. However, also a Minilab SD-12 system was available and included in the test series.

HYDRAULIC BOUNDARY CONDITIONS

The measurements discussed in the following were performed in the wave flume of the FRANZIUS-INSTITUT. The total length is about 120 m, the width 2.20 m. At the end of the flume a 1:30 slope is installed. The water depth during the tests was 1.0 m in the horizontal part.

The results presented here are from a JONSWAP spectrum with

Peak enhancement factor	$\gamma = 3.3$
Spectral peak period	$T_p = 1.8$ s
Significant wave height	$H_{m0} = 0.18$ m

The control signals for the wave machine were calculated according to the random phase spectrum method with a sequence length of 204.8 s for pusher movement of the wave paddle.

Measurements were taken in two sections:
- water depth d = 1.00 m horizontal slope (no breaking waves)
- water depth d = 0.39 m 1:30 slope (some waves breaking)

The submerged depth of the velocity probe was 3, 5, 10, and 15 cm below actual water surface with the moving frame and for comparison, 25 cm and 50 cm below mean water with a fixed height of the probe.

RESULTS OF THE TESTS

During the tests, time-series of waves, horizontal velocities, and probe locations were measured simultaneously. An HP1000/A600+ computer system was used for data acquisition and analysis.

Theoretical results, based on linear wave theory, have been calculated for comparison, with simulation methods described in detail in earlier publications (DAEMRICH, EGGERT, KOHLHASE (1980), DAEMRICH, EGGERT, CORDES (1982)).

In general for the analysis of such tests the transfer function method (or linear filtering method) would be prefered. With this method the theoretical velocity is calculated from the FOURIER coefficients of the wave train, by applying the linear transfer function and getting the time-series by an inverse FOURIER transformation.

For the measurements with the probe location varying with the surface elevation, however, this method leads to a considerable extension of the computer work, and it was decided to use for the present the complementary method, a simulation method in the time domain, which gives results of similar quality, at least in the more pronounced waves. In this method, the maxima of the orbital velocities under crest and trough of a wave were calculated from half-wave parameters. For the horizontal velocities, this half-wave

parameters are the amplitude of a wave crest or a wave trough (zero crossing wave crest height a_C and zero crossing wave trough excursion a_T) and the pertinent half-period (crest period T_C and trough period T_T). The parameter designation is according to the List of Sea State Parameters, IAHR (1986). For further explanations and definition sketches see DAEMRICH et al.(1980), (1982).

As an example, in Figure 6 measured and calculated horizontal velocity maxima for a constant submerged depth of the probe of y = 0.25 m below the mean water level are computed and plotted in scatter diagrams. It is obvious, that there is not to much difference in the tendency.

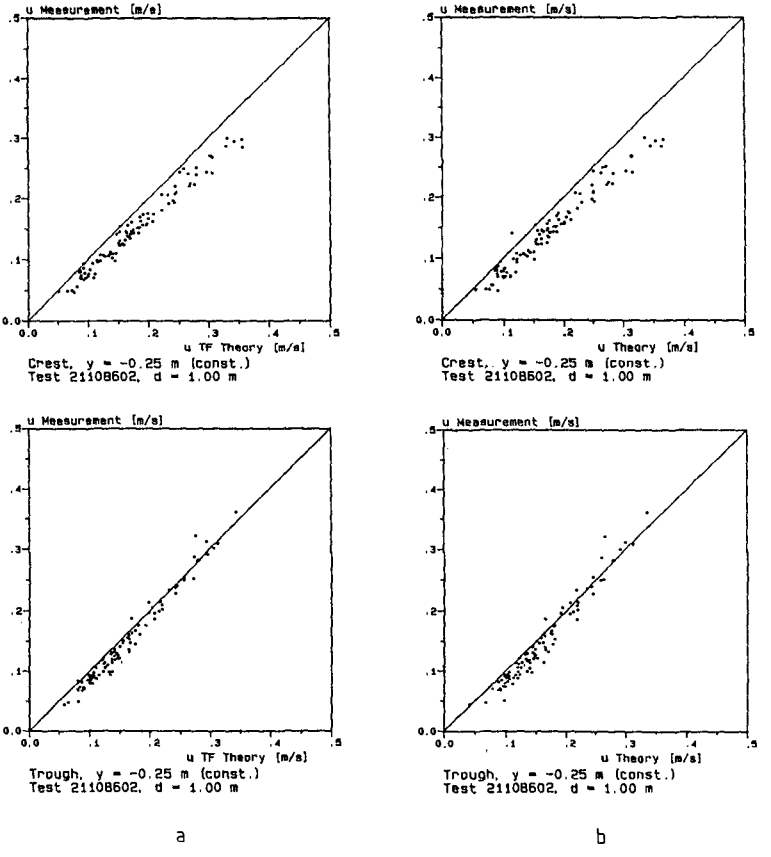

Fig. 6: Comparison of measured and calculated maxima of horizontal orbital velocities in constant submerged depth (y = 0.25 m)
a) Transfer function method b) Complementary method
upper Part: Velocities under the crests
lower Part: Velocities under the troughs

Well known and typically is the tendency of overestimating the velocities under the crests and underestimating the velocities under the troughs, which is somewhat more pronounced in the complementary method. This general deviation in the theoretical results is due to using linear wave theory without any modifications as e.g. stretching of coordinates.

In Figure 7 a part of a measured wave time-series is plotted together with theoretical velocity profiles for crests and troughs of individual waves and measured velocities 3, 5, 10, and 15 cm below the actual surface elevation. For comparison results from measurements in constant submerged depths of 25 and 50 cm below mean water level are inserted.

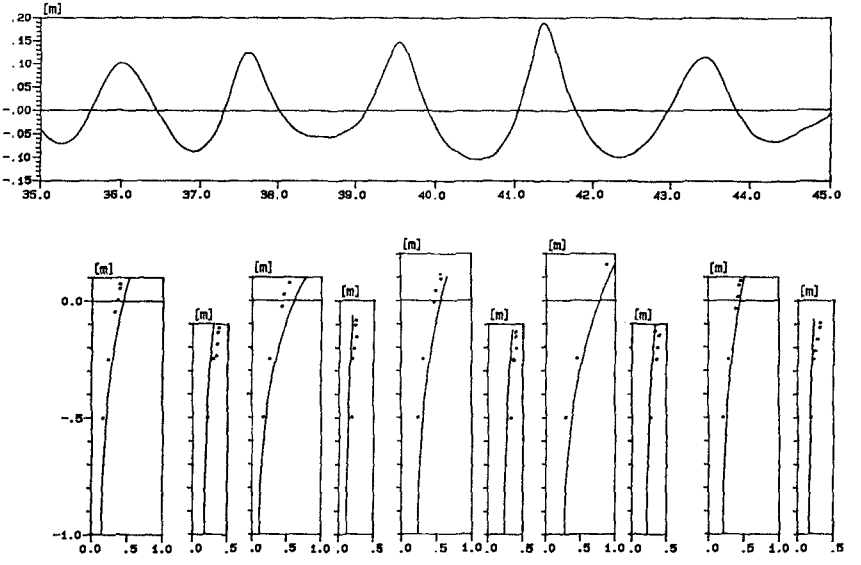

Fig. 7: Velocity profiles in crests and troughs of irregular waves (Theory: Complementary method)

The overestimation of velocities under the crests and the underestimation under the troughs are clearly visibel, however, under these wave conditions there is no change in the general trend closer to the surface.

In Figure 8 and 9 results from the complete time-series are shown as scatter plots. Compared are maxima of measured and theoretically calculated velocities in various submerged depth (upper part: wave crest data, lower part: wave trough data).

Figure 8 gives results measured in the horizontal section of the flume (water depth of 1.0 m), 10, 5, and 3 cm below the surface. The scatter of the data is not too high, also compared to earlier measurements. Overestimation and underestimation are more pronounced closer to the surface.

In Figure 9 similar results are plotted from measurements with the same wave train, but measured in 0.39 m waterdepth in the area of the 1:30 slope. Due to the steeper waves the minimum submerged depth of the velocity probe was 5 cm to avoid surfacing, the maximum submerged depth was 10 cm to avoid bottom contact. To show the trend, results from measurement in a constant submerged depth of 25 cm were added. The scatter of the data measured near the surface has increased due to some very steep or just breaking waves. The highest velocities are measured in a few just breaking waves.

MODIFICATION OF LINEAR WAVE THEORY

To consider the problem of overestimation and underestimation for design purpose the theoretical calculations were conducted exemplarily with a modification of the linear wave theory, similar to the stretching of coordinates (WHEELER (1969)).

Instead of using the actual location of the velocity probe to calculate theoretical values, e.g. 3 cm below surface elevation, we have assumed a constant location of the probe of 3 cm below mean water level for the calculation of the maxima of the near-surface orbital velocities. By this modification, the trend of over- and underestimation is clearly diminished in the complementary method and almost compensated when using the transfer function method as a simulation method.

In Figure 10 scatter diagrams are plotted exemplarily with results of those calculations.

Methods of modification of wave theories, however, have to be tested further for general application. But with the results of several contributions presented at this conference, there seems to be a good chance for simulation methods on the basis of linear wave theories.

ACKNOWLEDGEMENT

The investigation described in this paper was carried out as part of the research programme of the Sonderforschungsbereich 205 at the FRANZIUS-INSTITUT for Hydraulic Research and Coastal Engineering, University of Hannover. The authors gratefully acknowledge the Deutsche Forschungsgemeinschaft for their financial support throughout the investigations.

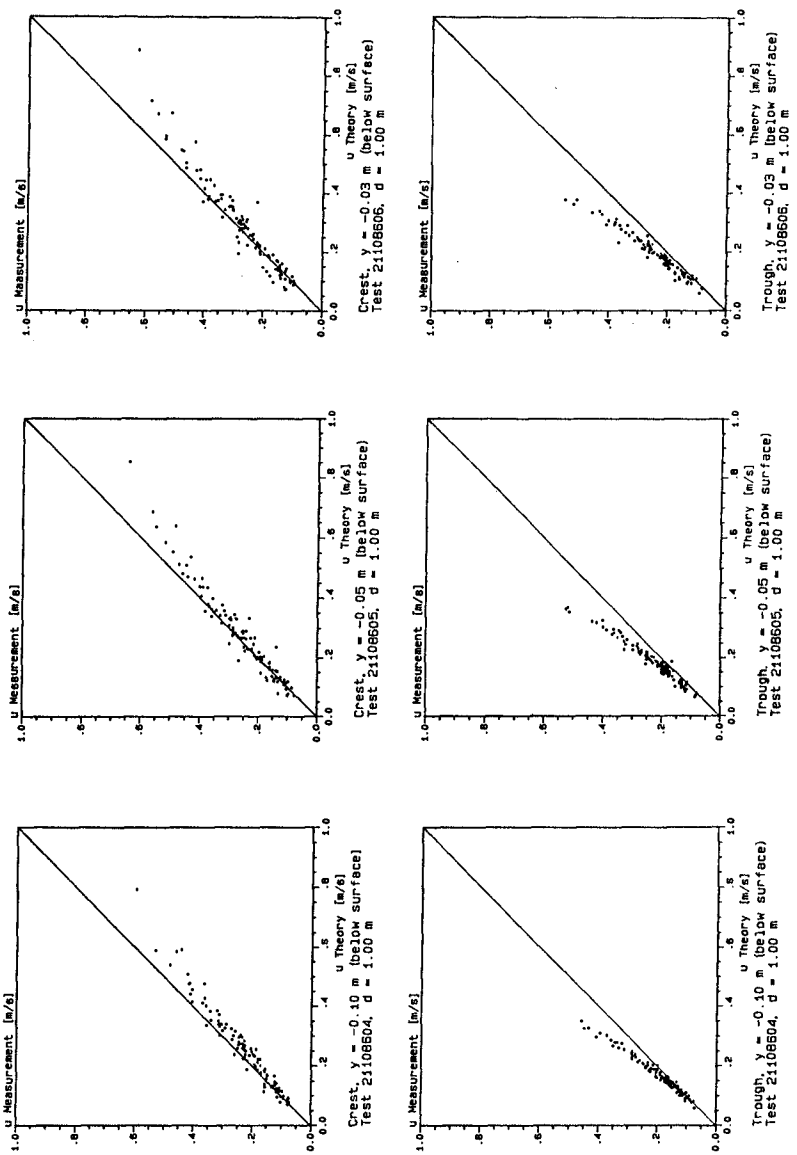

Fig. 8: Comparison of measured and calculated maxima of orbital velocities (d=1.00m)
upper part: wave crest data, lower part: wave trough data

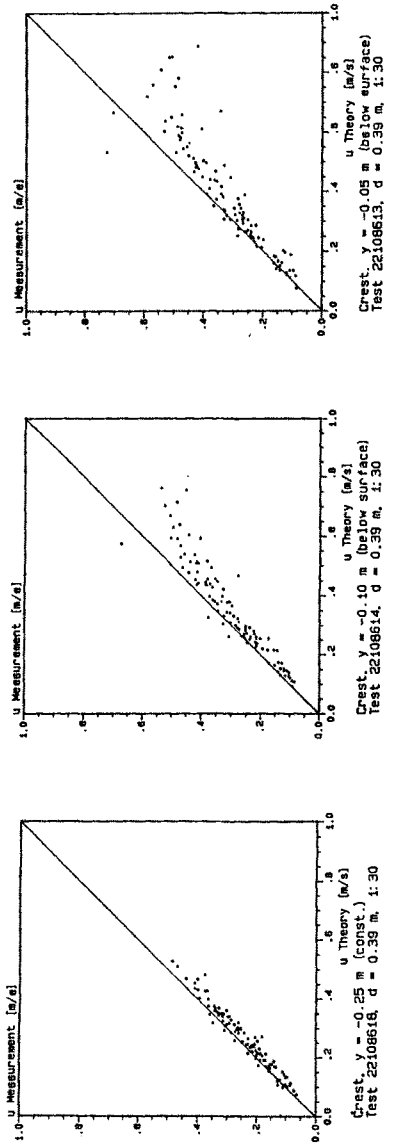

Fig. 9: Comparison of measured and calculated maxima of orbital velocities (d=0.39m)
upper part: wave crest data, lower part: wave trough data

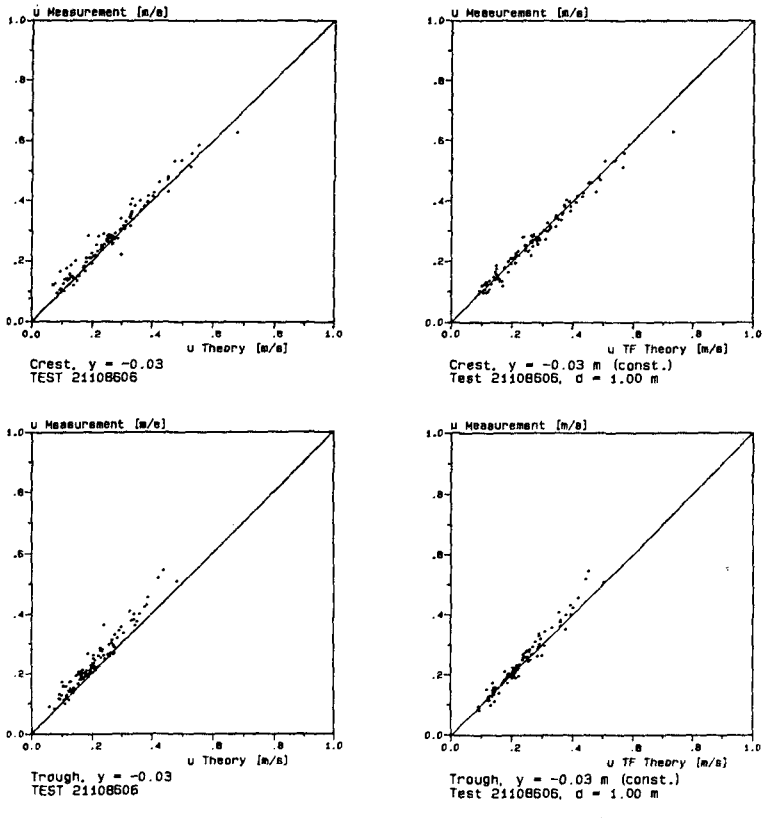

Fig. 10: Effect of modification of linear wave theory
a) Complementary method b) Transfer function method

REFERENCES

DAEMRICH,K.-F., EGGERT,W.D. and KOHLHASE, S. (1980). Investigations on Irregular Waves in Hydraulic Models. Proc. 17th Int. Conf. Coastal Engineering, Sydney, pp. 186-203

DAEMRICH,K.-F., EGGERT,W.D. and CORDES,H. (1982). Investigations on Orbital Velocities and Pressures in Irregular Waves. Proc. 18th Int. Conf. Coastal Engineering, Cape Town, pp. 297-311.

IAHR (1986). List of Sea State Parameters. Supplement to bulletin 52 (1986) PIANC. Brussels, Belgium.

SVENDSEN,I.A. (1986). Analysis of Surf Zone Turbulence. Danish Center for Appl. Math. and Mechanics, Techn. Univ. of Denmark, Report No. 330.

WHEELER,J.D. (1969). Method for Calculating Forces Produced by Irregular Waves. Preprints 1969 Offshore Technology Conference, Vol.I, Paper No. OTC 1006, pp. I-71 - I-82.

CHAPTER 9

Transformation of Random Breaking Waves on Surf Beat

by

William R. Dally[1] and Robert G. Dean[2]

ABSTRACT

Based on a previous study by the authors of regular breaking waves in the surf zone, a model for random wave transformation across the nearshore region is developed. The results of a laboratory investigation of the effect of a steady opposing current on the wave decay process are presented and a proposed governing equation verified. Surf beat effects on wave transformation are then included in the model by representing the long wave as a temporally and spatially-varying current and mean water level. The concept of an equivalent water depth, which contains the effect of the current, is introduced and then included in a stochastic form in the random wave model. Surf beat is found to noticeably increase the decay of the root mean square wave height, especially in the inner surf where the beat is strongest. Comparison of the models to two field data sets show very good agreement for Hotta and Mizuguchi (1980), but rather poor for Thornton and Guza (1983). Possible explanations for the unexpected behavior of the second data set, pertaining to filtering, are discussed. Finally, a possible explanation for the dependence of random wave decay on deepwater steepness, noted by Battjes and Stive (1985), is presented.

INTRODUCTION

The major goal of this effort is to predict the transformation of the probability density function (pdf) of wave height as random waves cross the nearshore region and surf zone. Secondary goals include investigation of the interaction of currents with the shoaling and breaking process, as well as the effects of mean wave steepness, beach slope, and surf beat on random wave transformation. Most previous invesigations, e.g. Collins (1970), Kuo and Kuo (1974), Battjes and Janssen (1978), and Thornton and Guza (1983), assume the Rayleigh pdf (or somewhat contrived modifications thereof), is valid in the surf zone. However, this assumption is not supported by laboratory and field data, with the possible exception of the measurements taken

[1]Graduate Research Assistant, Coastal and Oceanographic Engineering Department, University of Florida, Gainesville, FL 32611

[2]Graduate Research Professor, Coastal and Oceanographic Engineering Department, University of Florida, Gainesville, FL 32611 and Director, Division of Beaches and Shores, Florida Department of Natural Resources, Tallahasse, FL 32303

during the Nearshore Sediment Transport Study (NSTS) and analyzed by Thornton and Guza (1983).

The models described herein start with the Rayleigh pdf well outside the surf zone, but then numerically transform the pdf over beach profiles of arbitrary shape using the authors' regular wave model (Dally, Dean, and Dalrymple, 1984,85). A laboratory study of regular breaking waves on opposing currents is briefly reviewed and the resulting governing equation presented. Surf beat is then included in the numerical model by introducing an equivalent water depth approach. Finally, it is shown how some "observed" behavior of laboratory and field data reported in the literature might be a manifestation of 1) the analysis technique used, and/or 2) assuming a Gaussian sea in the surf zone, i.e. assuming $H_{rms} = \sqrt{8m_o}$ where H_{rms} is the root mean square wave height and m_o is the area under the energy spectrum.

RANDOM BREAKING WAVE MODEL

Formulation The basic concept of the random wave model is, starting with a known histogram of wave height at some offshore location, transform each representative wave in the histogram as if it were regular, i.e. assume there is no wave-wave interaction and let each wave shoal, reach incipient breaking, break, reform, etc. independently. Because wave period will be required to determine incipient breaking, the joint distribution of wave height and period for waves in deep water derived by Longuet-Higgins (1983) is adopted as an initial condition. This joint pdf, which yields a marginal pdf for wave height that is nearly Rayleigh in shape, is discretized into a histogram of 3600 bins, each with a representative wave height, period, and probability weight, w. Each representative "wave" is then transformed according to an improved version of the authors' numerical regular wave model.

In this new version, the approximate solution to the dispersion relation for linear waves provided by Nielsen (1984) is utilized to calculate the change in wave height due to shoaling, and the incipient breaking condition is explicitly defined as described in Moore (1982). This empirically based condition is a function of deepwater height, wave period, and local beach slope and is a hybrid of the expressions of Weggel (1972) and Komar and Gaughan (1972). The breaker decay is then calculated using the authors' previous scheme (1984,85) which was calibrated to laboratory data and is applicable on beach profiles of arbitrary shape.

On realistically-shaped bottom profiles, the question arises as to the definition of the effective beach slope, especially when bar/trough systems are present. Based on laboratory tests conducted at the University of Florida, it was observed that the bottom slope just seaward of the break point more directly affected the breaking characteristics in the trough than the local bottom configuration. Consequently, the beach slope used in determining incipient breaking is calculated by averaging the slope over the section just seaward of the point of interest, for a distance of one wave length. The negative slopes occurring on the landward side of a bar are treated as zeros in the averaging process.

Finally, at each location on the profile, the 3600 transformed waves are then ordered according to wave height from smallest to largest using a fast, "heap", sorting routine (Williams (1964)). From this ordered set of heights and associated probability weights, the behavior of any desired statistically representative wave can be calculated and monitored across the surf zone.

The information required to run the model consists of 1) root mean squared wave height and band width parameter, (ν) at the starting location, and 2) the bottom profile. If the spectrum is not available for calculating the moments required to determine the band width parameter (Longuet-Higgins, 1983) a value of ν=0.3 is used for gentle swell conditions and ν=0.6 for "confused" or storm conditions. It should be noted that the concept of addressing random wave transformation in the surf zone by monitoring a set of regular waves was also utilized by Mase and Iwagaki (1982). However, their model was limited to planar beaches, and differs significantly in the details.

Verification The random wave model was tested against the field data sets of Hotta and Mizuguchi (1980) and Thornton and Guza (1983). Hotta and Mizuguchi filmed a series of sixty wave staffs established at 2 to 3 m intervals across the surf zone. The measured bottom profile contained a large bar/trough formation, but unfortunately the cameras documenting the trough area failed during the experiment. Nevertheless, it is still an excellent data set. The bottom profile and transformation of several statistically representative waves (H_{rms}, $H_{1/3}$, $H_{1/10}$) are displayed in Figure 1. The model-predicted results generated using the values for the empirical coefficients as found in the laboratory calibration of the regular wave model (K=0.15, Γ=0.40) are also shown. The agreement is quite satisfactory, except for $H_{1/10}$ and perhaps $H_{1/3}$ in the region just seaward of the surf zone. It is believed this discrepancy is because linear theory underpredicts the rate of shoaling in shallow water, especially for waves of low deepwater steepness. Using a nonlinear theory would increase the peak value of the statistically representative wave and shift its location seaward. Even though a gap in the data in the trough region prevents verification of the wave reformation aspects of the model, the favorable comparison landward of this section lends support to the stable wave assumption of the original regular wave model (1984,85). It is noted that the random wave model predicted that the majority of the waves reformed in the trough, consistent with visual observations made during the experiment.

Figure 2 displays comparison of the transformation of the histogram of wave height as reported by Hotta and Mizuguchi (1980) with results of the model. Wave height has been nondimensionalized by the local average wave height, $\bar{H}$. Note that the Rayleigh distribution represents the actual initial histogram fairly well (station 57) but would not compare well at stations in the inner surf zone. The basic shape of the predicted pdf appears correct, especially for $(H/\bar{H}) > 1.0$. However, in the inner surf zone the model overpredicts the number of waves near $(H/\bar{H}) = 1.0$ and underpredicts for $(H/\bar{H}) < 1.0$.

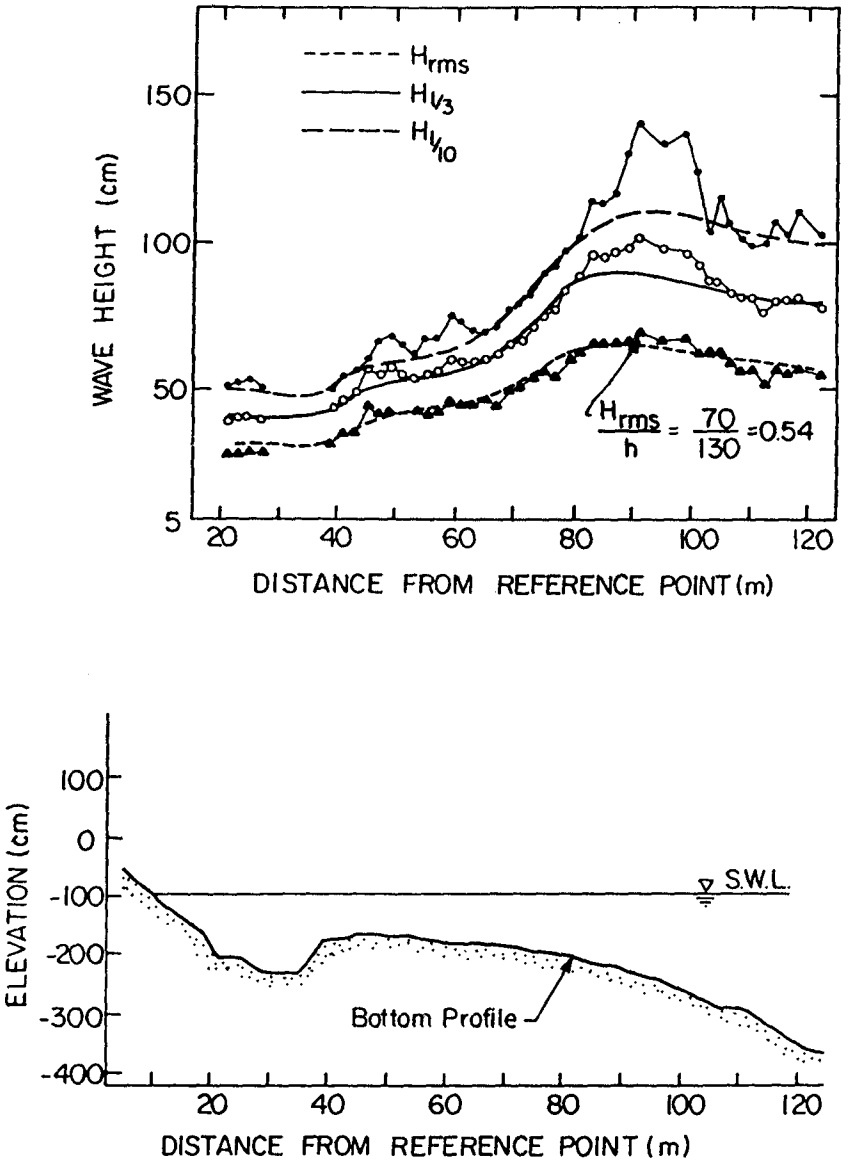

Figure 1. Comparison of transformation of statistically representative waves between model and field data of Hotta and Mizuguchi (1980).

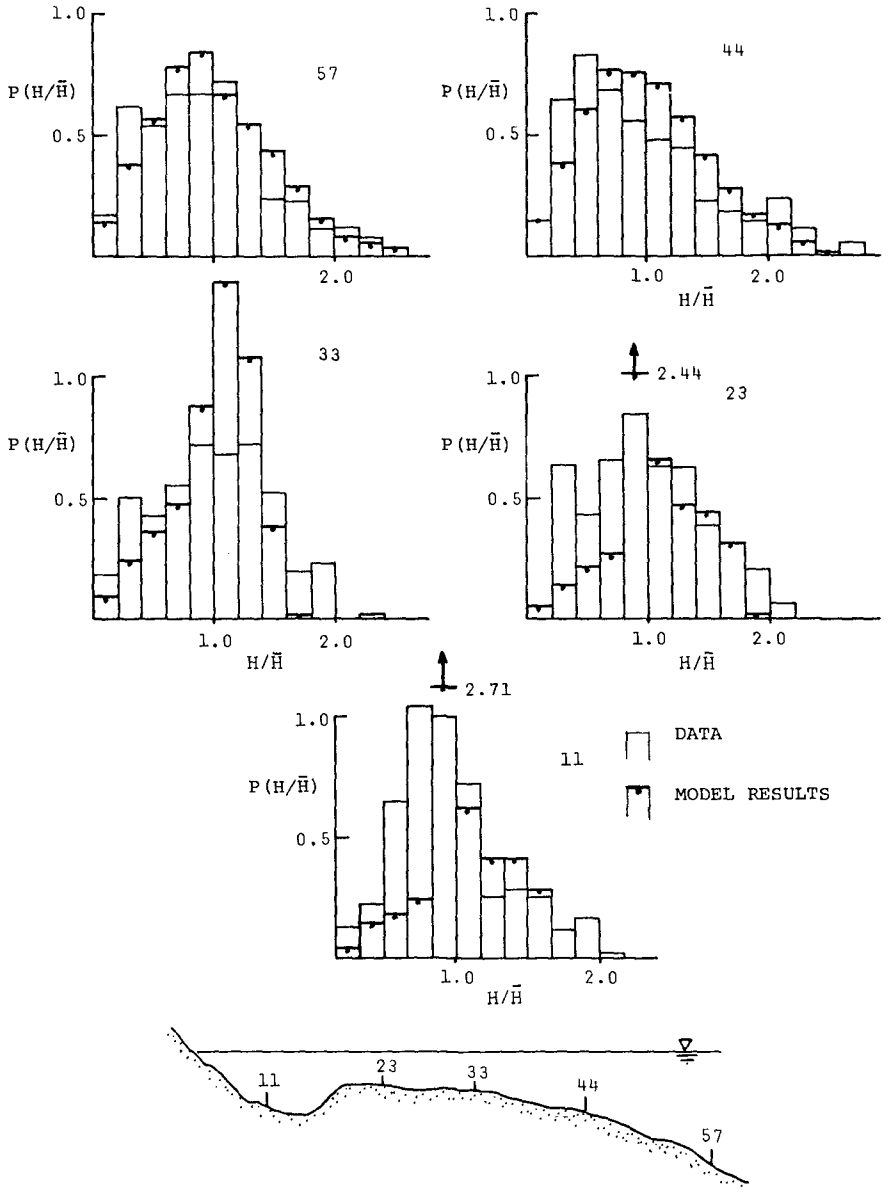

Figure 2. Comparison of transformation of histogram of wave height between model and field data of Hotta and Mizuguchi (1980).

Thornton and Guza (1983) analyzed measurements taken by resistance wire wave staffs, electromagnetic current meters, and pressure sensors during a NSTS field experiment. A typical sample of their results for the transformation of H_{rms} is presented in Figure 3 along with the local beach profile. The model comparison is also displayed, and one can see that it shows a significant discrepancy from the data. It should be pointed out that the point where H_{rms} begins to decay in the data seems to occur much farther seaward than is realistic. The mean water depth at this point was reported as 279 cm and the local ratio of H_{rms} to h was 72/279 = 0.26, which is less than half the value of the Hotta and Mizuguchi data (70/130 = 0.54). Also, it is noted that in histograms of wave height provided by Thornton and Guza, the largest wave never exceeded three times the deepwater H_{rms}, i.e. the largest wave observed anywhere during the test was approximately 168 cm in height. If this wave was just starting to break with an incipient condition H/h of say 0.78, the water depth would be about 215 cm, which is 64 cm shallower than the depth where H_{rms} began to decay.

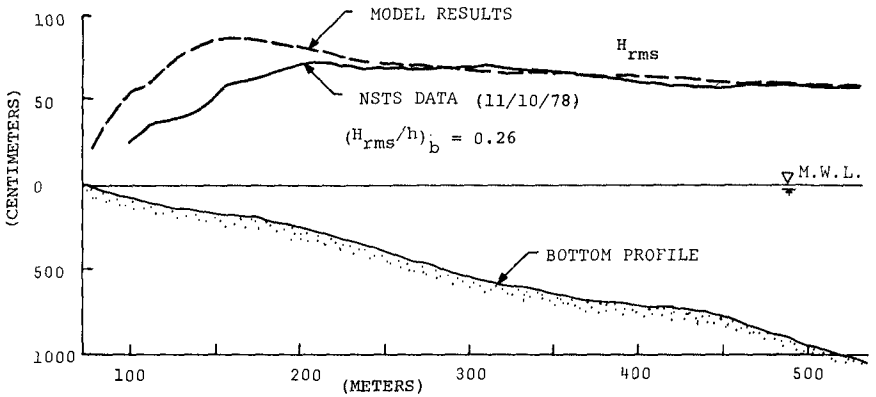

Figure 3. Comparison of transformation of H_{rms} between model and field data of Thornton and Guza (1983).

From the above observations, it is apparent that some phenomenon not included in the model and not present during Hotta and Mizuguchi's experiment was causing wave decay to occur sooner than expected. This phenomenon may be real, or an artifice of the measurement/analysis technique. A real phenomenon to which the majority of the remainder of this paper is devoted, is the interaction of wind waves with long waves such as surf beat. It is hypothesized that during the phase of the beat where the long wave water particle velocity opposes the incident waves and/or the mean water level is depressed, shoaling is accelerated and breaking initiated sooner than would otherwise occur. The opposite phase will tend to stretch the short waves and suppress breaking, but because shoaling is a conservative property while breaking is not, increased decay in average energy density (i.e. H_{rms}) should be expected. The wave conditions during the NSTS experiment

were characterized by long period, very low steepness, groupy swell, and significant long wave energy was documented, at least in the inner surf zone (Guza and Thornton, 1985). During the Hotta and Mizuguchi experiment, the waves were comparable in height to NSTS, but had a peak period less than half. They were not characterized as groupy, and only a small amount of long wave energy was documented.

Another possible source of the unexpected behavior of the NSTS data may lie in the manner the data was filtered during analysis. Although the raw data was taken at a rate of 64 Hz, it was immediately low-pass-filtered to a Nyquist frequency of 1.0 Hz, which may not be sufficient to resolve the wave height for very peaked waves, nor the front face of a broken wave. Hotta and Mizuguchi (1980) recorded on film at 5.0 Hz and did not filter before determining wave height, plus they had waves that were less peaked than NSTS and could therefore better resolve the wave height. These points are discussed further at the end of the paper.

REGULAR WAVES BREAKING ON STEADY CURRENTS

Because surf beat is an order of magnitude longer and an order of magnitude smaller than the wind waves that drive it, we assume that its effect on the short waves can be closely represented as that of a slowly oscillating current and mean water level. The effect of a slowly changing water level (depth) on shoaling and breaking is of course the essence of previous studies, but the effect of a current on a breaking wave has received relatively little attention in the literature. A governing equation for energy dissipation due to breaking on a steady collinear current and changing bottom is therefore proposed, and verified to some extent with a laboratory experiment.

Governing Equation Based on Conservation of Wave Action and linear wave theory, and the intuitive expression for the rate of energy dissipation due to breaking developed by the authors (1984,85), the following governing equation is proposed

$$\frac{\partial\left[H^2(U + Cg)/\sigma\right]}{\partial x} = \frac{-K}{h}\frac{Cg}{\sigma}\left[H^2 - \Gamma^2 h^2\right] \qquad (1)$$

where H is wave height, σ, the intrinsic wave frequency (i.e. relative to the current), U, the current magnitude, Cg, the group velocity relative to the current, h, the water depth, and x, the horizontal coordinate in the direction of wave propagation. K is a decay coefficient (0.15-0.17) and Γ is the stable wave factor (0.4-0.5). The wave number, k, is given by the dispersion relation for linear waves on currents

$$\omega = \sigma + kU = (gk \tanh kh)^{1/2} + kU \qquad (2)$$

where ω is the absolute frequency. If U is zero, these expressions reduce to the original governing equation proposed by the authors.

Verification The validity of (1) was tested by comparing numerical solutions to the results of a laboratory experiment of regular breaking waves on opposing currents. Due to space limitations the experiment will not be fully described here, but Figure 4 shows typical results of wave decay and model comparisons. The proposed governing equation appears valid, especially for mild currents. The results of this investigation are now applied to surf beat.

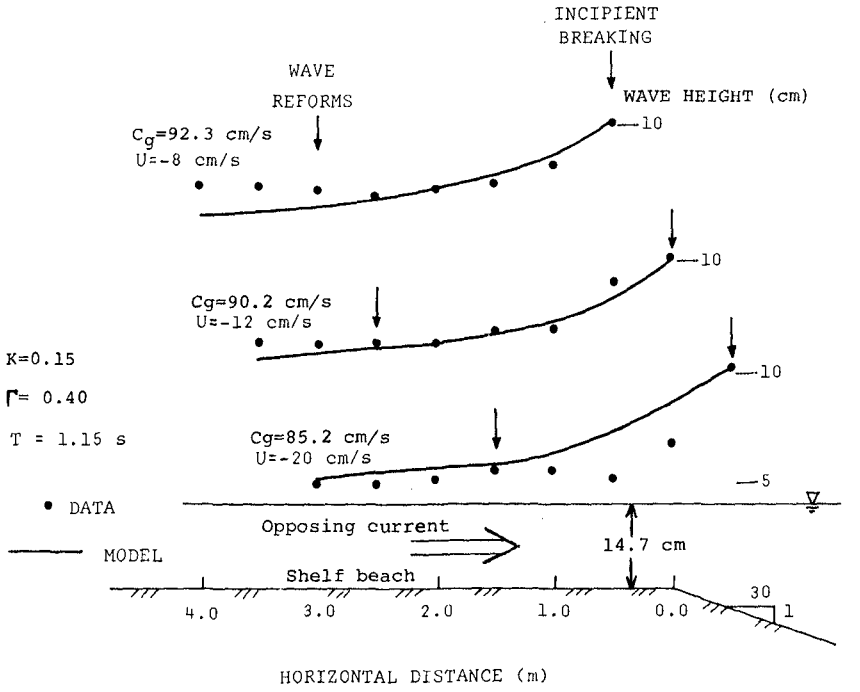

Figure 4. Sample results of wave decay on opposing currents and comparison of model (1).

RANDOM BREAKING WAVES ON SURF BEAT - THE EQUIVALENT DEPTH METHOD

The results of the laboratory investigation tend to indicate that the currents associated with surf beat are of equal or greater importance in the wave breaking process than the mean water level fluctuation. A few previous investigations have attempted to include surf beat in a random breaker model, e.g. Goda (1975) and Mase and Iwagaki (1982), but addressed only water level fluctuations.

To completely explore the problem of a short progressive breaking wave riding a partially-standing long wave, a wave tracking technique based on the method of characteristics would be required. Such a method in turn requires a time series as an initial condition, as well as complete temporal and spatial description of the surf beat.

Initial attempts found such a model numerically time-consuming, and impractical for engineering application due to the extensive input required. Therefore, a method is developed which combines the effects of the current and mean water level fluctuations, and is then included stochastically in the random breaking wave model.

Equivalent Depth The "equivalent water depth" is defined for a wave with absolute frequency ω and wave number k riding on a current as the water depth the wave would have to encounter with no current while still retaining the same wave number, i.e.

$$\omega^2 = [(gk \tanh kh)^{1/2} + kU]^2 = gk \tanh kh_e \tag{3}$$

where h_e is the equivalent water depth. A probability density function (pdf) for h_e in regards to surf beat can be developed. We first assume that the water particle velocity and mean water level associated with the standing long wave are normally distributed and uncorrelated at any location in the surf zone:

$$\text{pdf}(U,h) = \frac{1}{2\pi\sigma_u\sigma_h} \exp\left\{-\frac{1}{2}\left[\left(\frac{U}{\sigma_u}\right)^2 + \left(\frac{h-h'}{\sigma_h}\right)^2\right]\right\} \tag{4}$$

where h' is the mean mean-water level, σ_u and σ_h, are variances of the current and water level respectively.

The conditional pdf of k and h, given ω, is derived by solving the dispersion relation (2) for U and invoking a standard transformation of random variables. The joint conditional pdf of h_e and h given ω (or k_o) is then found in a similar manner by applying an approximate solution to the dispersion relation (3) given by Nielsen (1984):

$$kh_e = \sqrt{k_o h_e}\left[1 + \frac{1}{6} k_o h_e + \frac{11}{360}(k_o h_e)^2\right] \tag{5}$$

where k_o is the deepwater wave number in the absence of currents. This joint pdf is given by:

$$\text{pdf}(h_e, h/k_o) = \frac{1}{2\pi\sigma_u\sigma_h}\left|\sqrt{k_o}\left(-\frac{1}{2} h_e^{-3/2} + \frac{1}{12} k_o h_e^{-1/2} + \frac{11}{240} k_o^2 h_e^{1/2}\right)\right|$$

$$\cdot\left|(gk \tanh kh)^{1/2} - \frac{gk^2 h \operatorname{sech}^2 kh + gk \tanh kh}{2(gk \tanh kh)^{1/2}} - \sqrt{gk_o}\right| \cdot \frac{1}{k^2}$$

$$\cdot \exp\frac{-1}{2}\left[\frac{gk_o + gk \tanh kh - 2\sqrt{gk_o}(gk \tanh kh)^{1/2}}{k^2\sigma_u^2} + \left(\frac{h-h'}{\sigma_h}\right)^2\right] \tag{6}$$

where k is given by (5) as noted. A marginal pdf for h_e is then determined by integrating with respect to h over physically realistic limits (0→2h') and normalizing. In the model this is accomplished numerically using Simpson's Rule. Thus, with estimates of σ_u and σ_h, the pdf (h_e) is determined at any location across the nearshore region. An example is shown in Figure 5, where h_e has been non-dimensionalized by h'.

Stochastic Treatment of Breaking Waves on Surf Beat To include surf beat in the random breaking wave model described previously, the pdf (h_e) can be utilized to generate "equivalent profiles". In the model, the marginal probability density function of equivalent water depth at each location in the surf zone is subdivided into 10 bins of equal area, also shown in Figure 5, and the average equivalent depth of each bin is assigned to a corresponding equivalent profile. Guza and Thornton (1985) provide information from which estimates of the required variances, σ_u and σ_h, can be extracted for the NSTS experiment previously described, and several equivalent profiles are shown in dimensionless form in Figure 6.

Because of the currents, the incipient breaking condition of Moore (1982) is not applicable. A Miche-type wave steepness condition is therefore adopted to determine incipient breaking

$$\frac{H_b}{L} = 0.124 \tanh kh_e \tag{7}$$

where H_b is the wave height at incipient breaking and L the wave length. Note that when kh_e is small, (7) reduces to

$$H_b = 0.78\, h_e \tag{8}$$

In the numerical model, once incipient breaking is attained, a slightly modified form of (1) is invoked to describe wave decay

$$\frac{\partial[H^2(Cg_e/\sigma)]}{\partial x} = \frac{-K}{h'}\frac{Cg}{\sigma}\left[H^2 - \Gamma^2 h'^2\right] \tag{9}$$

where the equivalent water depth is used to calculate Cg_e on the L.H.S., and the average depth (h') used on the R.H.S. If the wave height is less than the local stable wave ($\Gamma h'$) but is greater than the incipient condition (7), the wave is simply "trimmed" to equal H_b.

Each representative wave from the original joint histogram of wave height and period is transformed across its 10 equivalent profiles and the results at each location averaged. Thus an average behavior for each wave from the original offshore histogram is calculated for given surf beat conditions.

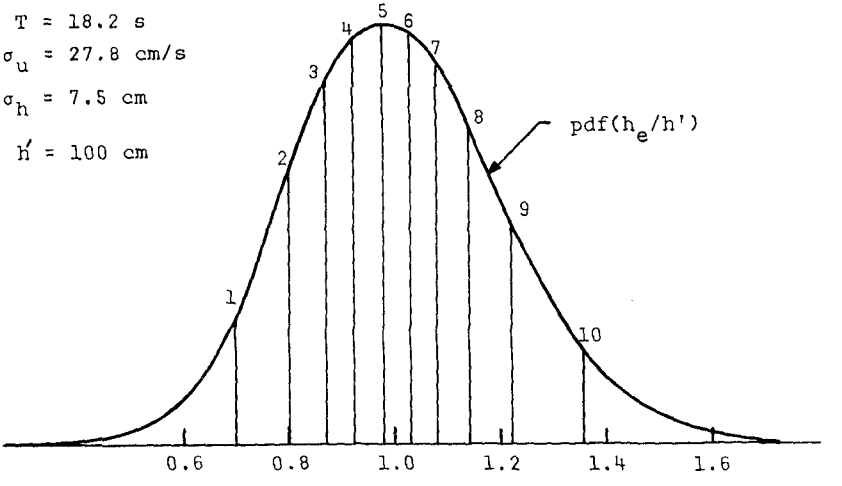

Figure 5. Example of marginal probability density function for equivalent water depth.

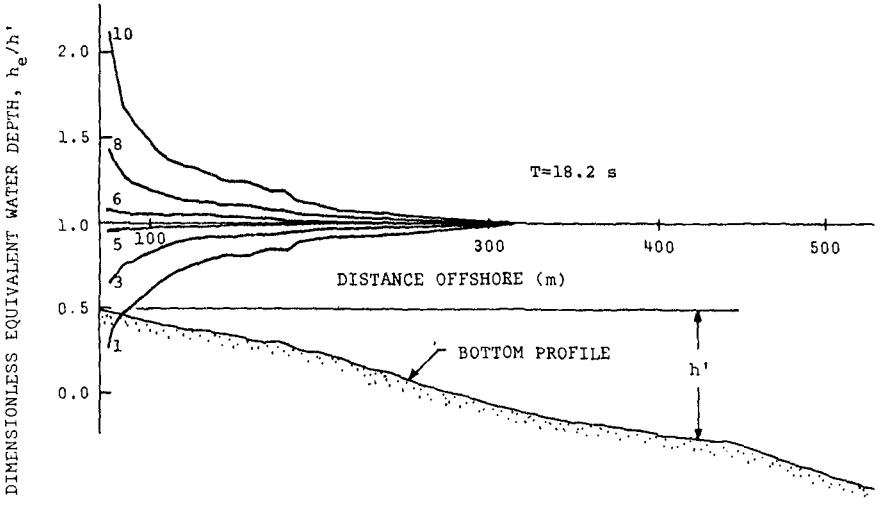

Figure 6. Example set of dimensionless "equivalent depth profiles" for NSTS data (for peak period T = 18.2 s).

Results The model including surf beat effects was run for the NSTS experiment and is compared to the data and the model results without surf beat in Figure 7. Note that surf beat did cause decay in H_{rms} to begin sooner and with greater intensity, but not to the anticipated degree. It appears that only unrealistically energetic surf beat could yield reasonable comparison of the model in its present form to this data set. Although there are some compromises encountered when adapting the decay expression (1) for regular waves on steady currents to random waves on surf beat, it is highly unlikely that they could account for the remaining discrepancy between model and data. We are now left to explore the possibility that the manner in which the data was filtered and analyzed could be responsible for the unexpected behavior.

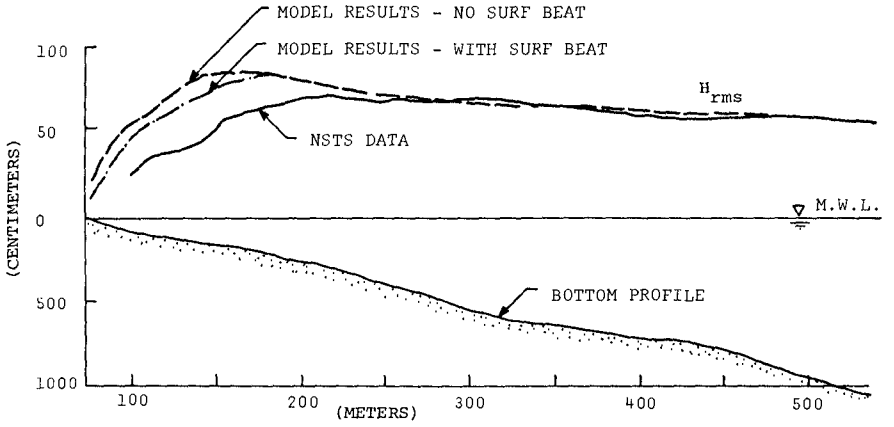

Figure 7. Comparison of H_{rms} transformation between model, with and without surf beat, to field data of Thornton and Guza (1983).

FILTERING-INDUCED "CLIPPING" OF WAVE HEIGHT

Application of the zero-up-crossing technique for analyzing wave records often involves first low-pass filtering the signal to remove higher frequency oscillations from the free surface. This high frequency "noise" increases the number of waves counted in a record by the up-crossing technique, and results in lower calculated values for statistically representative waves, such as H_{rms}. The original data for NSTS-Torrey Pines was taken at 64 Hz, block averaged which reduced the sampling rate to 8 Hz, deglitched, then low-pass-filtered "to substantially reduce energy between 0.5 and 1 Hz", and finally output to tape at 2 Hz (Gable, 1979). Thornton and Guza (1983) treated these time series further by Fourier Transforming the filtered record and zeroing the amplitude coefficients above 0.5 Hz (for gages in shallower water). The time series was then reconstructed and wave heights and periods determined using the up-crossing technique. However, if the original waves are either very peaked (as they are

when approaching the break point) or have sudden discontinuities (as is the case at the front face of a wave at incipient breaking, or the face of a bore), filtering in the above manner can significantly "clip" the wave height. As noted, wave conditions during NSTS were characterized by long-period, low deepwater steepness swell, which become very peaked in shallow water. For the peak frequency of 0.055 Hz, significant deepwater height of 79 cm, and local water depth equal 279 cm (i.e. where the data begin decay), and assuming Stream Function Theory is valid (Dean, 1974), the free surface before and after filtering above 0.5 Hz (the ninth harmonic in this instance) is shown in Figure 8. Note that the wave height was clipped by almost 25%.

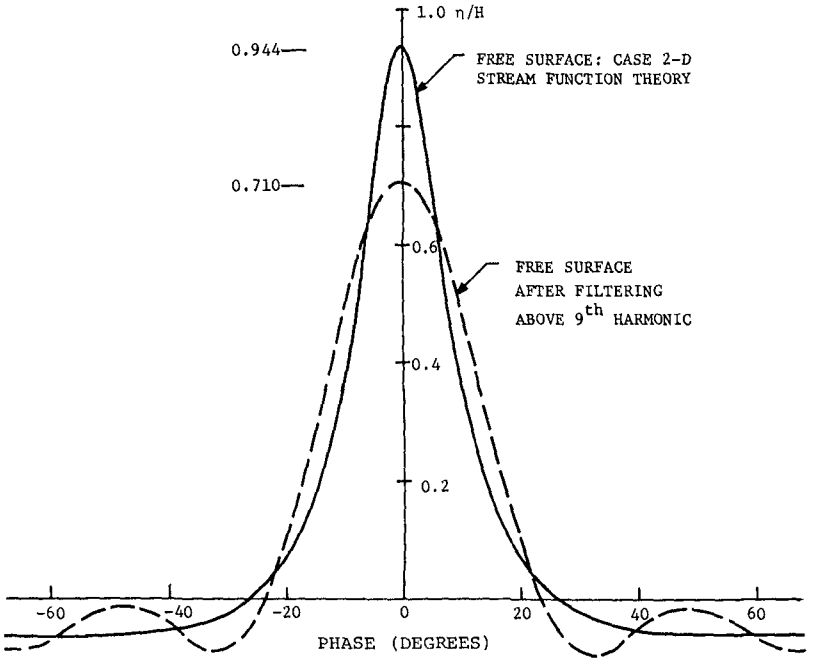

Figure 8. Wave height "clipping" due to low-pass-filtering of peaked waves. Conditions are analogous to NSTS data.

It seems the clipping artifice was induced more by the original filtering of the raw data, as one of these records from the inner surf zone was analyzed with and without the additional filtering of Thornton and Guza, and only a 6% drop in H_{rms} was found (Thornton - personal communication). This artifice is also believed by the authors to be responsible for the apparent agreement between the Rayleigh pdf and histograms of wave height in the surf zone as reported by Thornton and Guza (1983). Filtering the waves makes them appear more sinusoidal and narrow-banded, so assuming a Gaussian sea becomes, artificially, more valid. This would also appear to be why

Thornton and Guza found $H_{rms} = \sqrt{8m_o}$ to be relatively valid in the surf zone.

MEAN WAVE STEEPNESS "EFFECTS" ON RANDOM WAVE TRANSFORMATION

A few previous investigations have noted an apparent dependence of random wave decay on mean wave steepness, e.g. Battjes and Stive (1985). These models increase the decay in wave height for low deepwater steepness waves by varying empirical coefficients. The authors believe this requirement may be an artifice of assuming a Gaussian sea in the surf zone, i.e. that $H_{rms} = \sqrt{8m_o}$. A low steepness wave becomes peaked in shallow water and even though it may have the same actual height as a higher steepness wave, it contains less energy. (Steepness was found by the authors (1984,85) to have little effect on wave height decay after breaking is initiated.) Therefore, if energy is used to calculate H_{rms} rather than the actual free surface displacement between trough and crest, a lower value for wave height is produced. As a result, for the transformation of H_{rms} as defined by $\sqrt{8m_o}$, the heights of the breaking waves in the model must be artificially suppressed to obtain good fit if the measured waves were of low steepness.

CONCLUSIONS AND RECOMMENDATIONS

1) The model for random wave transformation in the nearshore region and surf zone described herein (without surf beat) appears valid in comparison to the field data of Hotta and Mizuguchi (1980), in regards to both statistically representative waves and the probability density function of wave height. However, it does not compare well to the field data of Thornton and Guza (1983). The differences are believed to be due to a "clipping" artifice induced by low-pass-filtering during the original treatment of the raw data.

2) To accurately represent surf beat in any nearshore wave model, depth and current variations should be included.

3) The stochastic model which utilizes an equivalent depth approach to represent surf beat shows that random wave transformation in the surf zone can be noticeably affected by surf beat and is characterized by an increase in breaker decay.

4) In nature, surf beat effects may be significant, but are probably limited to the inner surf zone where the surf beat is strongest.

5) In laboratory experiments, surf beat effects might be unrealistically amplified if long wave energy is trapped in the tank.

6) High frequency filtering can artificially reduce wave height, especially for waves of low deepwater steepness.

7) $H_{rms} = \sqrt{8m_o}$ is not valid in the surf zone. This is believed to be the major reason for the "observed" dependence of decay on wave steepness found in previous studies.

8) It is recommended that in data analysis, low pass filtering be used only to obtain wave periods and that the original record be used to obtain wave heights.

ACKNOWLEDGEMENT

The authors wish to express their gratitude to Dr. Edward B. Thornton, Naval Postgraduate School, for his valuable comments and assistance in the analysis of the NSTS data during this investigation.

REFERENCES

Battjes, J.A. and Stive, M.J.F., 1985, "Calibration and Verification of a Dissipation Model for Random Breaking Waves", J. Geophysical Res., Vol. 90, No. C5, 9159-9167.

Collins, J.I., 1970, "Probabilities of Breaking Wave Characteristics", Proc. 12th Conf. on Coast. Eng., ASCE, Vol. 1, 399-412.

Dally, W.R., Dean, R.G., and Dalrymple, R.A., 1984, "A Model for Breaker Decay on Beaches", Proc. 19th Conf. Coastal Engr., ASCE, Vol. 1, 82-98.

Dally, W.R., Dean, R.G., and Dalrymple, R.A., 1985, "Wave Height Variation Across Beaches of Arbitrary Profile", J. Geophys. Res., Vol. 90, No. C6, 11,917-11,927.

Dean, R.G., 1974, "Evaluation and Development of Water Wave Theories for Engineering Application", U.S. Army Coastal Engineering Research Center, Special Report No. 1.

Gable, C.G., (editor), 1979, "Report on Data from the Nearshore Sediment Transport Study Experiment at Torrey Pines Beach, California, November-December 1978", Inst. Marine Resour., No. 79-B.

Goda, Y., 1975, "Irregular Wave Deformation in the Surf Zone", Coast. Eng. in Japan, Vol. 18, 13-26.

Guza, R.T. and Thornton, E.B., 1985, "Observations of Surf Beat", J. Geophysical Res., Vol. 90, No. C2, 3161-3172.

Hotta, S. and Mizuguchi, M., 1980, "A Field Study of Waves in the Surf Zone", Coastal Engr. Japan, JSCE, Vol. 23, 79-89.

Komar, P.D. and Gaughan, M.K., "Airy Wave Theory and Breaker Height Prediction", Proc. 13th Conf. Coastal Engr., ASCE, 1972, 405-418.

Kuo, C.T. and Kuo, S.T., 1974, "Effect of Wave Breaking on Statistical Distribution of Wave Heights", Proc. Civil Eng. in the Oceans/3, American Society of Civil Engineers, Vol. 2, 1211-1231.

Longuet-Higgins, M.S., 1983, "On the Joint Distribution of Wave Periods and Amplitudes in a Random Wave Field", Proc. Roy. Soc. Lond., A389, 241-258.

Mase, H. and Iwagaki, M., 1982, "Wave Height Distributions and Wave Grouping in Surf Zone", Proc. 18th Conf. on Coast. Eng., ASCE, Vol. 1, 58-76.

Moore, B.D., 1982, "Beach Profile Evolution in Response to Changes in Water Level and Wave Height", Master's thesis, University of Delaware, Dept. of Civil Engr.

Nielsen, P., 1984, "Explicit Solutions to Practical Wave Problems", Proc. 19th Conf. Coastal Engr., ASCE, Vol. 1, 968-982.

Thornton, E.B. and Guza, R.T., July 1983, "Transformation of Wave Height Distribution", J. of Geophysical Res., Vol. 88, No. C10, 5925-5938.

Weggel, J.R., 1972, "Maximum Breaker Height", J. of Waterways, Harbors, and Coast. Eng. Div., ASCE, Vol. 98, WW4, 1972, 529-548.

Williams, J.W.J., 1964, "Heap Sort (Algorithm 232)", Communications ACM, Vol. 7, No. 6.

CHAPTER 10

A Numerical Solution to Transient Wave Induced Harbor Oscillations Using Boundary Element Technique

Vedat Demirel[1], and Shen Wang[2],

Abstract

A new numerical technique for solution to transient linear long wave induced oscillations is introduced. It is based on the boundary element method, which is well recognized by its numerical efficiency and convenience. Several harbor models are investigated. Advantages of the proposed method as compared to the existing techniques are discussed.

1. INTRODUCTION

Studies concerning harbor oscillations can be classified into two major groups, periodic wave excitations and transient wave excitations. The assumption of periodic incoming waves reduces the problem from a solution of wave equation to one of Helmholtz equation. There are a number of well-established theories available in the literature for the time harmonic case. However, only a few studies have been reported on the transient problem. The traditional approach to the transient problem is to utilize the knowledge of frequency response of the harbor and derive the solutions by means of Fourier synthesis (Carrier and Shaw, 1969). An alternative approach using finite element method (FEM) was introduced by Lepelletier (1980) to solve the problem by a time marching scheme with a time dependent ocean boundary condition.

The present study introduces a boundary element method (BEM) solution for the transient oscillations of arbitrary-shaped, constant depth harbors. Unlike Fourier synthesis approach, this method provides the required information in a natural and direct way. Moreover, this procedure requires neither internal cells nor their associated domain integrals, making the method especially attractive from the computational point of view.

2. THEORETICAL BACKGROUND

Most of the existing numerical harbor models emerge on the validity of the linear wave theory. Indeed, good agreement between the linear theory predictions and experimental results has been reported by various authors, Lee (1969) and Lepelletier (1980), for example. Hence, the problem is formulated within the framework of linear wave theory. The theory assumes irrotational flow of an inviscid, incompressible fluid, and the wave amplitude to be

[1] Graduate Assistant, University of Miami Rosenstiel School of Marine and Atmospheric Science, Division of Applied Marine Physics.
[2] Professor, University of Miami Rosenstiel School of Marine and Atmospheric Science, Division of Applied Marine Physics.

infinitesimally small. In addition, the water depth is assumed to be constant and the wave length is long enough to meet criterion for long wave approximation.

Under these conditions, the governing equation in two horizontal dimensions x and y is given by

$$\frac{\partial^2\phi}{\partial t^2} = c^2 \left(\frac{\partial^2\phi}{\partial x^2} + \frac{\partial^2\phi}{\partial y^2}\right) . \qquad (1)$$

Here ϕ is the unknown velocity potential and c is the speed of propagation. Following the long wave approximation, c is known as $c=(gd)^{1/2}$ with g and d being earth's gravitational acceleration and the water depth, respectively.

The solution of ϕ within the domain sketched in Fig-1 is sought in the present study. The configuration under consideration consists of an interior domain which will be identified as domain II and an exterior domain, domain I. Domain II is an arbitrary-shaped, constant depth harbor with vertical boundaries. It is connected to domain I with a partially or fully open entrance. Domain I represents the open ocean with semi-infinite boundaries. One part of the boundary coincides with the straight coastline extending from $-\infty$ to $+\infty$. The remaining part is a fictitious semi-circle of radius $R=\infty$, connecting both ends of the coastline.

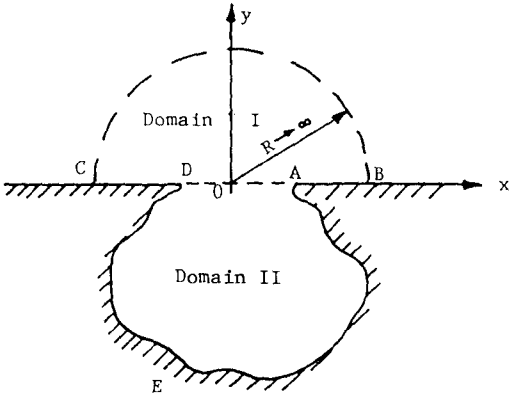

Fig-1. Geometric configuration of an arbitrary-shaped harbor.

Parallel to the time harmonic model of Lee (1969), the problem is formulated in the two regions separately. In domain I, decomposition of the velocity potential ϕ_I into components is conventional in linearized water wave problems:

$$\phi_I = \phi_i + \phi_r + \phi_s \tag{2}$$

where ϕ_i is the incident wave potential, ϕ_r is just its reflection as if the harbor did not exist, and ϕ_s is the scattered potential representing the disturbance introduced by the harbor. Since the incident wave potential is normally known, ϕ_i and ϕ_r are immediately determined. Therefore, only formulation and solution of ϕ_s will be sought in domain I.

The boundary and initial conditions are specified as:

	Domain I	Domain II	
Boundary conditions:			
	$q_s=0$ on the straight coastline	$q_{II}=0$ on DEA	(3)
	$\phi_i+\phi_r+\phi_s=\phi_{II}$	on DA	(4-a)
	$q_s=-q_{II}$	on DA	(4-b)
Initial conditions, at t=0:			
	$\phi_s = \frac{\partial \phi_s}{\partial t} = 0$	$\phi_{II} = \frac{\partial \phi_{II}}{\partial t} = 0$	(5)

Here, q is the normal derivative of ϕ, $q=\vec{n}\cdot\nabla\phi$, and $\vec{n}$ is a unit outward normal vector along the boundary.

Condition (3) assures that boundaries are impermeable by forcing the particle velocities to vanish. Conditions (4-a) and (4-b) are basically necessary to have a continuous surface elevation and fluid velocity across the boundary interface of the two domains. Notice that condition (4-b) is obtained by differentiating (4-a) with $\partial(\phi_i+\phi_r)/\partial n=0$ being understood. The negative sign in (4-b) indicates that the outward normal vectors are directed in opposite directions in I and II on DA. The last constraints are due to the hyperbolic character of the governing equation where one needs two initial conditions. They are chosen to be zero for convenience. It implies that the analysis will be started from a moment when the body of water in the harbor is at rest. However, this is not on approximation but rather a mathematical convenience; as will be seen later, a BEM formulation may include any initial state. It is worth mentioning that the radiation condition of the time harmonic problem is replaced by the causality principle to ensure the mathematical uniqueness. This constraint will be imposed in the determination of the Green's function

of the problem. For a complete derivation of the Green's function and a detailed formulation of the problem, one is referred to Demirel (1986).

3. NUMERICAL ANALYSIS

No analytical solution of the problem described in the previous section exists. On the other hand, a numerical solution is always possible by utilizing one of the solution techniques depicted in Fig. 2.

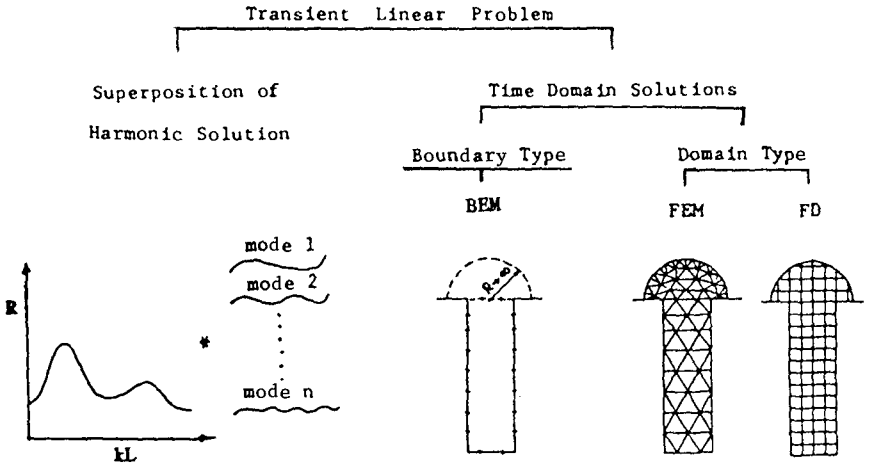

Fig-2. Classification of available solution techniques.

The first method is the traditional Fourier synthesis technique. This is a two-step procedure in which the transfer function of the harbor must be determined first. Afterwards, the transfer function and the Fourier transform of the incident wave system are convolved in the frequency domain followed by an inverse Fourier transform of the product. The second group contains time domain solution techniques. They can be sub-grouped into two categories, domain type solutions and boundary type solutions. Two major differences stand out between these categories as shown in Fig. 2. First of all, in the domain type technique, determination of the potential at any point requires the simultaneous solution of the entire domain. In contrast, in the boundary type solution technique, information of the boundary potential is sufficient to determine the interior potential at any point. Secondly, the open sea region can be extended to infinity in the boundary type method without introducing any approximation. In the domain type technique, however, the exterior domain has to be terminated at a finite distance. Because of these two reasons, BEM is used in this study. An outline of the method is summarized in the following.

The first step is to transfer the governing differential equation

to an integral form. Afterwards, the solution of this integral equation is sought. The resulting integral equation for the wave equation in two dimensions is in the following form (Mansur and Brebbia, 1982):

$$4\pi\lambda\phi(r,t) = \int_o^t \int_\Gamma \frac{\partial R}{\partial n} (\phi B + \frac{v}{c} \phi^*) \, d\Gamma \, d\tau + \int_o^t \int_\Gamma q\phi^* d\Gamma \, d\tau$$

$$+ \frac{1}{c} \int_\Omega \left(\frac{v_o}{c} \phi_o^* - \phi_o B_o + \frac{\partial \phi_o}{\partial R} \phi_o^* + \phi_o \frac{\phi_o^*}{R} \right) d\Omega \qquad (6)$$

where v denotes the time derivative of ϕ, $v = \partial\phi/\partial t$, q is the normal derivative of ϕ and R is the distance between the observation point r and the source point ξ, $R=|r-\xi|$. The parameter λ is equal to 1, 0 or 1/2 for r to be inside, outside or on a smooth part of the Γ boundary, respectively. Definition of the terms ϕ^* and B are given as,

$$\phi^* = \phi^*(r,t/\xi,\tau) = \frac{2c}{[c^2(t-\tau)^2-R^2]^{1/2}} H[c(t-\tau)-R] \qquad (7)$$

$$B = B(r,t/\xi,\tau) = \frac{2c[c(t-\tau)-R]}{[c^2(t-\tau)^2 - R^2]^{3/2}} H[c(t-\tau)-R] \qquad (8)$$

with $H[c(t-\tau)-R] = \begin{cases} 0 & c(t-\tau)<R \\ 1 & c(t-\tau)>R \end{cases}$, a unit step function .

The term ϕ^* is the Green's function for the two-dimensional wave operator, which may be considered as the effect of a source applied impulsively at $t=\tau$ located at $r=\xi$. A subscript o, as appeared in (6), indicates initial time, t = 0. Integrals over Γ are boundary integrals, while over Ω are domain integrals. All integrals are Cauchy principal-value integrals.

In order to evaluate the line integrals in (6), the boundary is discretized into a series of elements and the integrals are computed on each element piecewise. The boundary of the harbor ADE is discretized into N straight segments. In addition, the time dimension is divided into F time steps. Furthermore, functions ϕ and q in equation (6) are assumed to vary within each element and time step according to the space and time interpolation functions such that;

$$\phi(r_j,t_f) = \psi_j^T \gamma^f \phi_j^f \qquad (9)$$

$$q(r_j,t_f) = \mu_j^T \theta^f q_j^f \tag{10}$$

Here ψ_j and μ_j are space interpolation functions, γ^f and θ^f are time interpolation functions, whereas ϕ_j^f and q_j^f are column vectors containing the nodal values of ϕ and q, respectively, within the jth segment. Substituting (9) and (10) into equation (6) and applying a time stepping scheme to initiate the time integration always from the initial time yields the following set of algebraic equations:

$$\sum_{f=1}^{F} [H^{Ff}] \{\phi^f\} = \sum_{f=1}^{F} [G^{Ff}] \{q^f\} . \tag{11}$$

The elements of the matrices $[H^{Ff}]$ and $[G^{Ff}]$ are given by

$$h_{ij}^{Ff} = 4\pi\lambda\delta_{ij}\delta_{fF}\phi_i^F - \int_{\Gamma_j} \frac{\partial R_{ij}}{\partial n} \psi_j^T \int_{t_{f-1}}^{t_f} (\gamma^f B + \frac{\partial \gamma^f}{\partial \tau} \frac{\phi^*}{c}) d\tau d\Gamma$$

$$g_{ij}^{Ff} = \int_{\Gamma_j} \mu_j^T \int_{t_{f-1}}^{t_f} \theta^f \phi^* \, d\tau d\Gamma \quad . \tag{13}$$

Note that all the domain integrals in (6) are dropped out since ϕ and $\partial\phi/\partial t$ are zero in accordance with the initial conditions (5) and the time integrals are evaluated always from the initial time t=0.

Equation (11) is simultaneously applied to both domains. In each domain, the velocity potential ϕ is expressed in terms of the unknown normal derivatives of ϕ at the harbor entrance. These unknowns are determined by satisfying the matching conditions (4) on the entrance. Having obtained the derivatives of the potential along the entrance, the interior potential is calculated by letting the observation point approaching to any interior point desired.

4. NUMERICAL EXAMPLES

In the numerical computations, three model harbors were considered. A rectangular harbor and a circular harbor were taken first. Both harbors have an uniform water depth and are connected to an open-sea. The third is a model of the East and West basins of Long Beach Harbor, California. The interpolation functions ψ_j, μ_j and θ^f were taken as constant whereas γ^f was taken as linear in the computation.

The results given here were computed for two incident wave forms, an exponentially decaying cosine wave and a solitary wave:

$$\eta_i = A\, e^{-\alpha|t|} \cos(\omega_o t) \tag{14}$$

$$\eta_i = A \,\mathrm{sech}\,(mt) \tag{15}$$

where A, α, ω_o and m are the amplitude of the incident wave, a decay factor, the incident wave frequency and a dummy frequency parameter, respectively.

In the following figures, the results of the present BEM model were compared against the Fourier synthesis solutions. In each figure, the incident wave system is plotted in the upper part. The lower part is allocated for the comparison of two different approaches. The solid curve and the circles represent the results of the Fourier synthesis solution and the present theory, respectively. Coordinates of the figures were nondimensionalized by suitable parameters. For instance, values of the surface elevation were nondimensionalized by $(\eta_i)_{max}$ defined as the maximum elevation of the incident wave. Likewise, the elapsed time is nondimensionalized either by the period of the incident wave, as in the case of exponentially decaying cosine waves, or by a representative time scale for the case of a solitary wave. For a solitary wave defined by (15), the representative time scale was taken as $\bar{T}=\bar{\lambda}/(gd)^{1/2}$. Here $\bar{\lambda}$, the so-called effective wave length, is defined as twice the distance between the peak of the sech(mt) and a point at which the amplitude reduces to 0.1% of its maximum.

Case 1: A rectangular harbor

A fully open rectangular harbor with a width to length ratio b/L= 0.5 (b=2.5 feet, L=5.0 feet) and a uniform water depth d=0.5 feet was considered as the first case. The boundary of the harbor was discretized into N=32 constant elements with 6 of them placed on the entrance. The observation point was taken to be located at the back boundary of the harbor.

Fig-3 shows the time history of oscillations due to an exponentially decaying cosine wave having a frequency equal to the first natural frequency of the harbor, kL=1.1. The figure indicates that the maximum amplification for this transient wave is 3.8 and the oscillations last a little longer than 4 times the period of the incident wave system.

In the next figure, harbor response due to a solitary wave of $\bar{\lambda}/L=5.7$ was considered. As Fig-4 shows, the magnitude of the first, peak, which represents the major impact of the solitary wave, is in good agreement although there exist relatively minor discrepancies in the subsequent time steps.

Case 2: A circular harbor

The second harbor considered is a circular model previously used by Lee (1969) with a radius r=0.75 feet, a constant depth d=0.5 feet and a 60 degrees gap. For this harbor, the observation point was taken at the center of the harbor. The boundary of the harbor was discretized to N=30 straight elements with 6 of them located at the entrance.

Fig-5 shows the harbor response due to an exponentially decaying cosine wave of kr=0.5. It is seen that the peak amplitude is slightly lower but in general agrees well with the Fourier synthesis solution. Oscillations last approximately 8 cycles, reaching a maximum amplification of 2.9. The subsequent amplitudes are slightly different and decay faster in the BEM solutions.

The solitary wave induced oscillations in the circular harbor of r=0.75 were plotted in Fig-6 along with the incident wave systems. The upper part of Fig-6 represents the incident wave system with $\bar{\lambda}/2r=12.5$. The computed surface elevation at the center of the

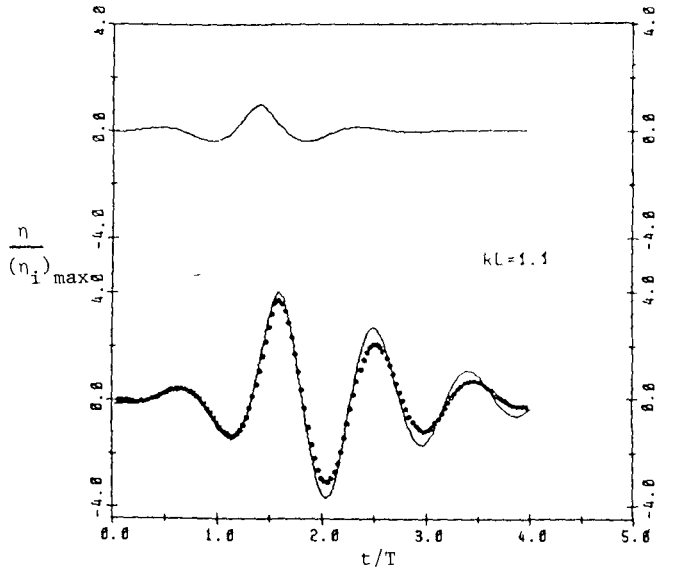

Fig-3. A comparison of time history of oscillations at the back boundary of a rectangular harbor, b/L=0.5, due to an exponentially decaying cosine wave of kL=1.1 with α=0.3.

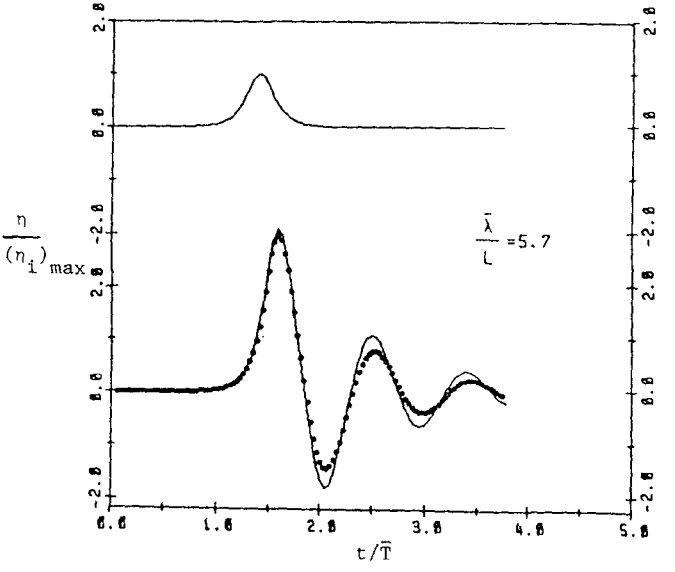

Fig-4. A comparison of time history of oscillations at the back boundary of a rectangular harbor, b/L=0.5, due to a solitary wave of $\bar{\lambda}$/L=5.7.

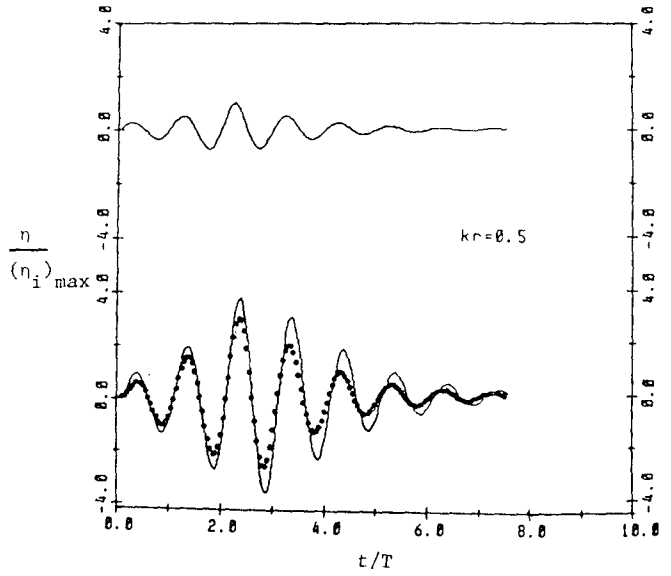

Fig-5. A comparison of time history of oscillations at the center of a circular harbor, r=0.75, due to an exponentially decaying cosine wave of kr=0.5 with a decay factor α=0.3.

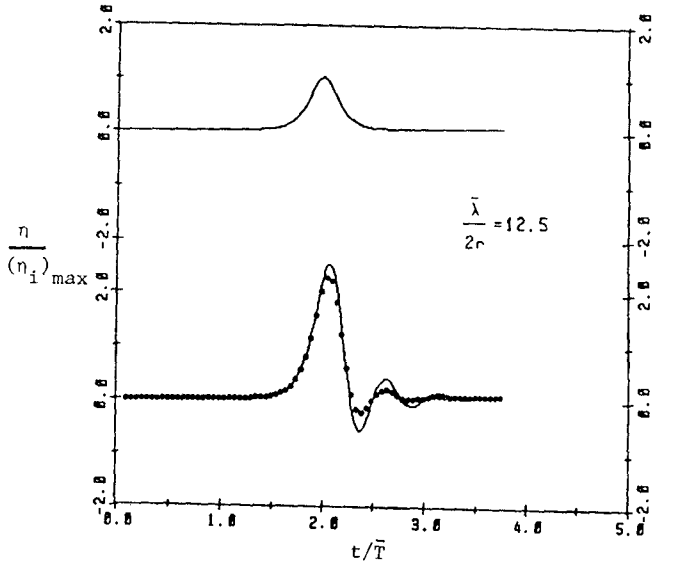

Fig-6. A comparison of time history of oscillations at the center of a circular harbor, r=0.75,due to a solitary wave of $\bar{\lambda}/2r$=12.5.

harbor is placed in the lower part of the same figure. As Fig-6 shows, the maximum amplification is 2.2 and there are few minor oscillations following this peak. This implies that the incident wave is so long that the presence of the harbor practically does not perturb the reflected wave pattern.

Case 3: Long Beach Harbor

A model of the East and West basins of Long Beach Harbor as shown in Fig-7 was considered as the last case. The same model was also used by Lee (1969). The entrance of the harbor is 0.2 feet, the water depth is d=1 feet and the characteristic length is L=1.44 feet. For this harbor, the observation point was chosen at the lower right corner of the harbor, Fig-7. The boundary of the harbor was discretized into N=75 straight elements with two elements located on the entrance.

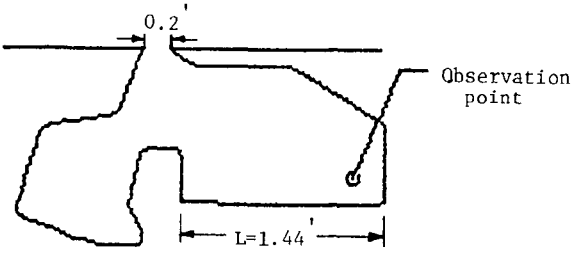

Fig-7. A model of East and West basins of Long Beach Harbor, California.

Fig-8 shows the results of a computation conducted for an exponentially decaying cosine wave input of kL=0.6. The figure indicates that the maximum amplification is 3.2 and the duration of oscillations is approximately 5 times the period of the incident wave system.

The transient response at the designated observation point of the Long Beach harbor due to a solitary wave of $\bar{\lambda}/L = 10.5$ was shown in Fig-9. It is seen that the present prediction matches well with the Fourier synthesis solution especially for the leading wave. According to the figure, the present theory estimates a maximum amplification of 2.5 and the duration of oscillations to be nearly 4 times the effective wave period $\bar{T}$.

5. CONCLUSIONS

A numerical solution to transient linear wave induced harbor oscillations using BEM is introduced. The transient linear long waves are focused in two horizontal dimensions penetrating into a constant depth, arbitrary shaped harbor. Utilizing the fundamental

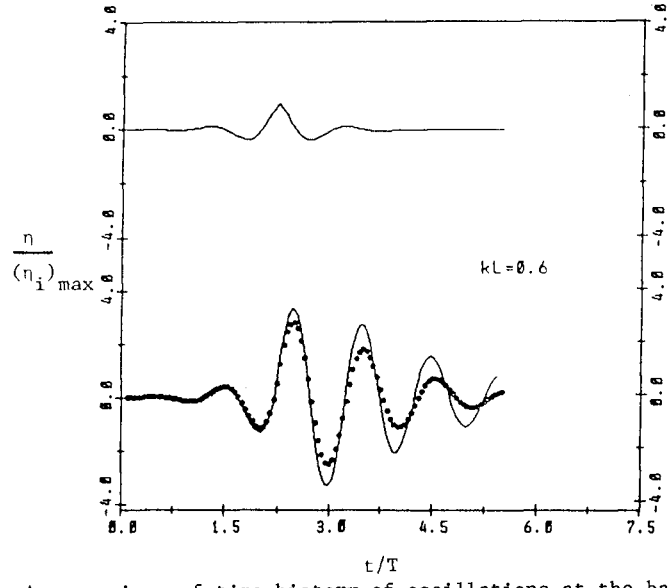

Fig-8. A comparison of time history of oscillations at the back boundary of the Long Beach Harbor model due to an exponentially decaying cosine wave of kL=0.6 with α=0.3.

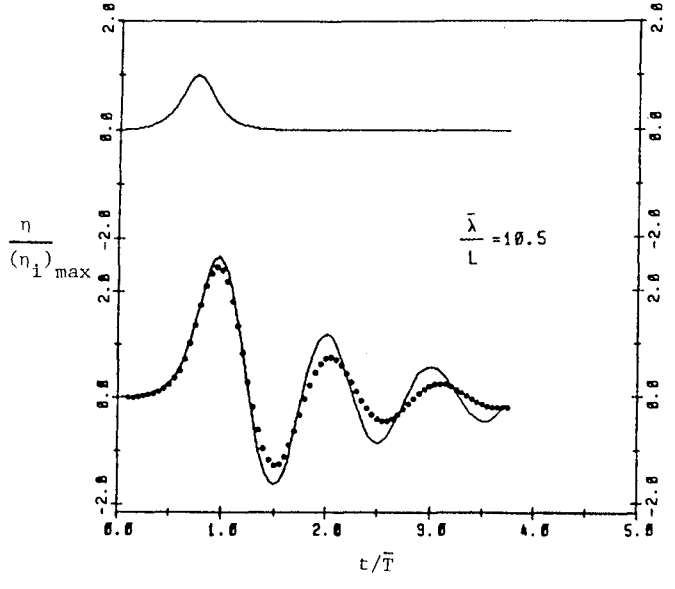

Fig-9. A comparison of time history of oscillations at the back boundary of the Long Beach Harbor model due to a solitary wave of $\bar{\lambda}$/L=10.5.

solution of Green's function for wave equation in two dimensions, only inputs of potential or surface elevation due to transient waves at the harbor entrance is required. The fluid domain is discretized into two regions but a matching technique is used at each time step to evaluate the condition at the entrance. The interior potential or elevation is obtained with only knowledge of the boundary potential.

This method has advantages over frequency domain solution in that it provides in a natural and direct way the time history of oscillations. Moreover, the computation time of the BEM solution is considerably less than that of the Fourier synthesis approach. This is because of the fact that a sufficiently large number of frequency responses are needed to carry out a proper Fourier synthesis solution.

Comparing with the theories based on the domain type techniques, the BEM approach carries forward some widely recognized priorities, such as less data preparation and reducing in the dimensionality of the problem. Also, solution in the exterior domain can be obtained easily without any approximation on the boundary conditions at the infinity. In contrast, in the FEM, a time dependent boundary condition must be specified along a large semi-circle in the open sea to avoid an artificial reflection. The accuracy of the results and the computation time are closely related to the choice of the radius of this circle.

6. ACKNOWLEDGEMENTS

The authors are indebted to Dr. John D. Wang and Dr. Chia-Chi Lu for their collaboration. Dr. Bernard Le Mehaute is also acknowledged for his valuable comments.

7. APPENDIX - REFERENCES

Carrier, C.F. and Shaw, R.P. (1969). Response of Narrow Mouthed Harbors to Tsunamis. Proc. Int. Symposium on Tsunamis, IUGG,Oct. 1969.

Demirel, V. (1986). Transient Linear Long Wave Induced Oscillations in Arbitrary-shaped Harbors: A Boundary Element Approach. M.S. Thesis, University of Miami.

Lee, J.J. (1969). Wave Induced Oscillations in Harbors of Arbitrary Shape. Report No. KH-R-20, W.M. Keck Laboratory of Hydraulics and Water Resources, Calif. Institute of Tech.

Lepelletier, T.G. (1980). Tsunamis - Harbor Oscillations Induced by Nonlinear Transient Long Waves. Report No. KH-R-41, W.M. Keck Laboratory of Hydraulics and Water Resources, Calif. Institute of Tech.

Mansur, W.J. and Brebbia, C.A.(1982). Formulation of the Boundary Element Method for Transient Problems Coverned by the Scalar Wave Equation. Applied Mathematical Modelling, Vol. 6, pp 307-311.

CHAPTER 11

EXTREME WAVE PREDICTION USING DIRECTIONAL DATA

M.C. Deo* and R. Burrows**

ABSTRACT

Potential inconsistencies in the predictions of long term wave heights can be experienced as a result of different methods of analysis possible when using directional wave data. This paper attempts to illustrate some of them. It involves analysis of two sets of directional wave data - one from a coastal location in the Irish Sea and another from an offshore location in the North Sea. An attempt is made to eliminate the discrepancies between the long term return-value wave height predictions based upon the conditional height distributions associated with different direction sectors and those derived from the omni-directional data set.

1. INTRODUCTION

The estimation of the long term wave heights is often made by fitting the wave data to a convenient probability distribution and extrapolating it upto the chosen 'return period' probabilities. A graphical technique using a probability paper is often employed.

The estimates made in this way normally do not account explicitly for the directions of the wave or those of winds generating them. It is implied by this procedure that all wave directions are equally likely to occur and that the conditions of wind speed and fetch generating the waves are directionally unbiased. If this is not the case, the method involves implicit extrapolation of sea states in direction sectors with restricted fetch beyond a physical upper limit.

Design engineers are increasingly asking for estimates of the probability of occurrence of extreme wave heights from different points of the compass. It is however observed that such estimates are not always consistent with the omni-directional estimates and it is quite

* Assistant Professor, Department of Civil Engineering, Indian Institute of Technology, Bombay-400 076, India.
** Lecturer, Department of Civil Engineering, University of Liverpool, Liverpool, L69 3BX, U.K.

possible that because of the sample size and fitting errors, the extreme wave height predictions from the worst direction may exceed the corresponding omni directional estimates.

Graham (1981) has suggested the simple factoring of the estimates from the worst direction to make them compatible with the omni-direction estimates to overcome this problem. An alternative approach is proposed here which is based on the convolution of the directional wave height distributions, that can subsequently be correlated against the omni-directional estimates to eliminate all inconsistencies.

2. DATA FOR THE STUDY

Two sets of directional wave data were available for the present studies. One set was the outcome of an earlier wave hindcasting study from seven years (1964-1970) of wind measurement at a nearshore site on the 'Mersey Bar' in the Irish Sea. The wave heights so derived have shown good correlation with observations at the site over a shorter period of one year (Burrows et al., 1985).

Figure 1 shows this site while Table 1 gives fetch length as well as corresponding estimates of significant wave height (Hs) generated from an extreme 'hurricane force' wind speed of 80 knots. It may be noted that the physical upper limit for the wave heights generated along different direction sectors varies from 4.12 to 10.06 m.

The other data set consisting of significant wave heights, average zero cross period (T_z) and wind direction, was from indtrumental recordings over the period 1975-1976 and 1980-1981 at a location in the North Sea (Figure 1). For such an open site, the fetch lengths corresponding to different directions were very large - the minimum value being 97 miles. Consequently, all of the corresponding Hs values at the 80 knots wind speed exceeded 11 m.

3. VARIABILITY IN DIRECTIONAL DISTRIBUTIONS

The data was categorized into different direction sectors and for each sector theoretical probability distributions of Gumbel, Weibull, extreme value Type III-U forms were fitted (expressions for these distributions are given in the Appendix). Estimates of the return value Hs were then abstracted.

Figure 2 shows the directional distributions of Hs values for the Irish Sea location along with selected 100-year return value probabilities. Table 1 gives the estimates of the '100 year' Hs values obtained by moments fitting to the Gumbel distribution in case of the Irish Sea data. The suitability of the Gumbel distribution fit for this

X – IRISH SEA STATION
Y – NORTH SEA STATION

FIG.1 SITES OF THE DATA COLLECTION

Table 1 Estimation of '100 Year' Hs Values

(Gumbel Distribution (All Data)

(Site : Irish Sea)

Direction sector	Fetch (Nm)	Upper limit Hs(m)	Total number of sea states	'100 Year' Hs (m)	Percentage difference w.r t omni-direction estimate
1	33.49	7.16	503	4.65	— 41.36
2	25.16	6.66	1228	4.21	— 46.91
3	11.50	4.56	797	3.03	— 61.79
4	9.31	4.27	66	1.48	— 81.34
5	9.04	4.21	870	3.31	— 58.26
6	9.01	4.12	863	3.23	— 59.27
7	8.99	4.12	2190	3.70	— 53.34
8	9.98	4.42	972	3.33	— 58.01
9	9.84	4.42	752	3.61	— 54.48
10	11.80	4.57	135	1.56	— 80.33
11	16.06	5.18	1113	4.32	— 45.52
12	25.80	6.71	1851	5.66	— 28.63
13	56.97	8.84	2958	9.86	24.34
14	68.63	10.06	1781	11.10	39.97
15	51.28	8.54	1569	6.01	— 24.34
16	56.04	8.84	1003	8.59	8.32
Omni direction			18651	7.93	0.0

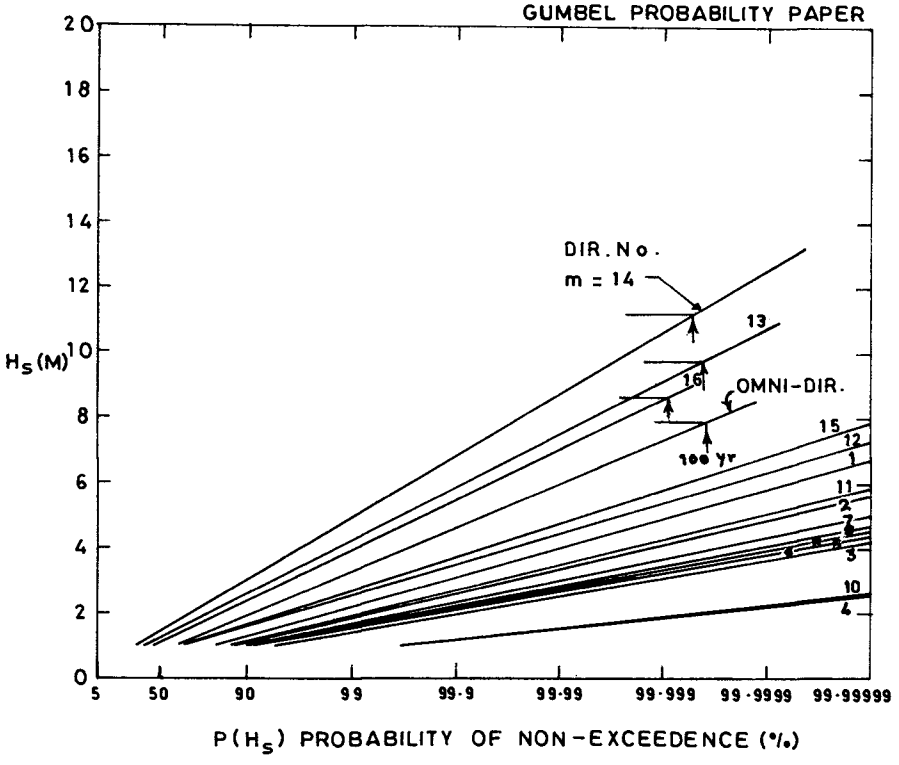

FIG. 2 DIRECTIONAL H_S DISTRIBUTIONS (Irish Sea Data)

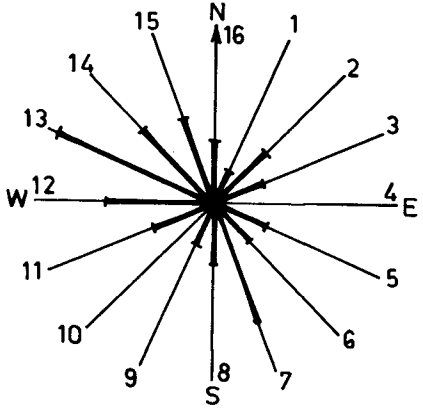

ROSE DIAGRAM INDICATING TOTAL NUMBER OF SEA STATES ALONG DIFFERENT DIRECTIONS

(SCALE – 1mm = 100 SEA STATES)

location was checked (Deo and Burrows, 1985). It is immediately seen that the total number of sea states coming from different directions is not the same and hence the assumption to that effect, made implicitly in the normal extreme wave prediction procedure is not valid.

Figure 3 shows the similar distribution fittings to the North Sea data.

Both sets of data showed that predictions of extreme wave heights from certain worst direction sectors (e g m = 13, 14, 16 in Table 1) exceed the equivalent prediction using the complete data set i.e. the normal omni-directional approach.

This outcome was found to be sensitive neither to the fitted distribution nor to the extrapolation techniques of moments or least squares. This behaviour departs from the outcome of statistical reasoning but can be explained by the different levels of uncertainty associated with the distribution fitting to data sets of different sizes.

One way to account for the above mentioned inconsistency between the directional and omni-directional estimates is to factor the former and make predictions from the worst directions compatible with the omni-directional distributions (Graham 1981) Whilst this satisfies the engineering requirements, it is not statistically correct but is nevertheless conservative. The error in this approach follows because the omni-directional predictions must exceed the worst direction values since there will generally be a finite chance of the extreme conditions (in 100 years, say) arising from other than the worst direction.

Herein, an alternative and statistically consistent technique is followed which is described in the following section.

4. CONVOLUTION OF CONDITIONAL (DIRECTIONAL) WAVE HEIGHT DISTRIBUTIONS

a) Long Term Distribution of Significant Wave Heights

The revised procedure to predict the return value estimates of Hs is as follows:

(i) Categorize the data into different direction sectors

(ii) Obtain the fitted conditional distribution of Hs for each direction

(iii) Introduce appropriate wave height ceilings to each direction sector

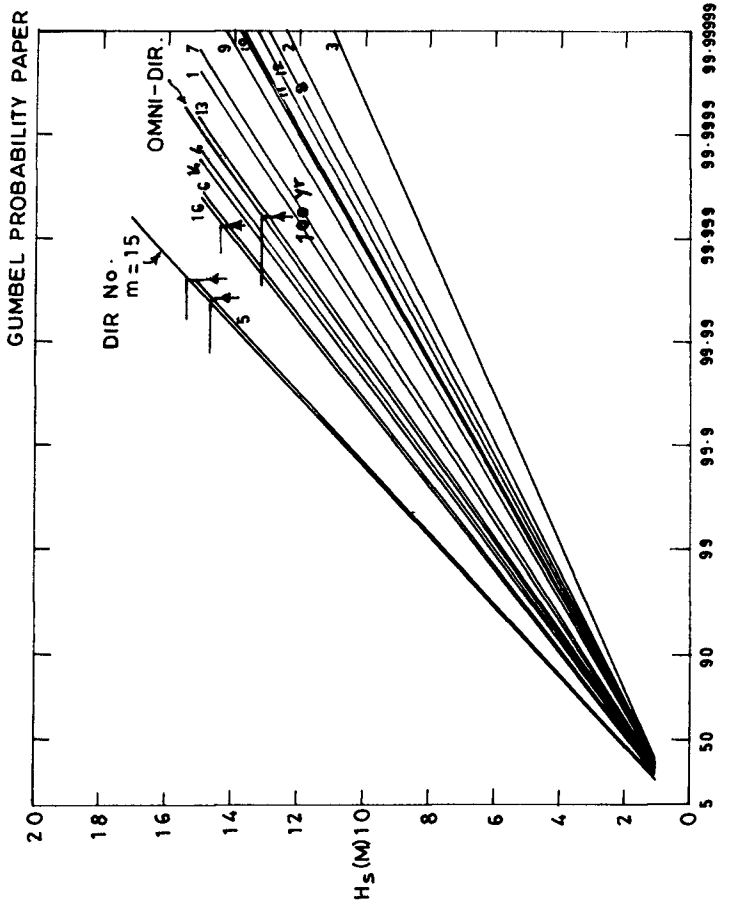

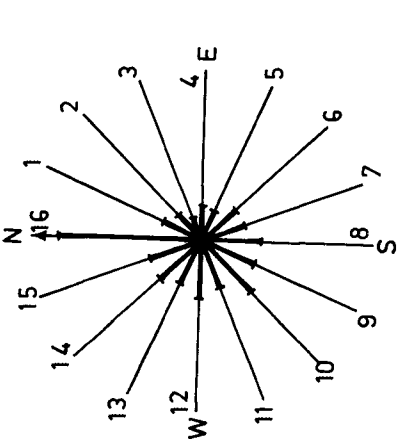

ROSE DIAGRAM INDICATING TOTAL NUMBER OF SEA STATES ALONG DIFFERENT DIRECTIONS

(SCALE–1 mm = 50 SEA STATES)

FIG.3 DIRECTIONAL H_s DISTRIBUTION (North Sea Data)

(iv) Convolute the different directional distributions and obtain an equivalent all direction distribution as follows:

$$P(Hs) = \sum_{\text{all } \theta} P(Hs/\theta)\, W(\theta) \qquad \ldots(1)$$

where

$P(Hs)$ = equivalent all direction distribution function of Hs

θ = wave direction

$P(Hs/\theta)$ = conditional distribution function of Hs for given θ

$W(\theta)$ = weighting function representing the proportion of sea states along the direction θ in the entire population.

(v) Make predictions of long term Hs values on the basis of equation (1) or if there is no directional bias in fetch or wind field, divide the all-directional Hs value obtained as the outcome of equation (1) at the appropriate return period and use this as a factor for adjustment of the directional wave height predictions. This then makes them statistically consistent with the omni-directional values which in the situation may be viewed as the most reliable estimation since it is based on fitting and extrapolation of the entire data set.

b) Long Term Distribution of Individual Wave Heights (H)

This can be made by two alternative techniques:

Method 1 : (i) Use the equivalent all direction distribution of Hs values as per equation (1) to calculate the long term distribution P(H) in the normal manner (Battjes 1970; see Appendix) or

Method 2 : (i) Use the following convolution technique to get P(H) :

$$P(H) = \sum_{\text{all } \theta} P(H/\theta)\; W'(\theta) \qquad \ldots (2)$$

where

$P(H)$ = equivalent all-direction long term distribution

$P(H/\theta)$ = conditional long term distribution of H along direction θ

$W'(\theta)$ = weighting function representing proportion of individual waves in the entire population (Deo and Burrows 1985)

(ii) Predict return individual wave heights in a similar manner to step (v) in (a) above relating to significant wave height predictions.

For each data set the equivalent all-direction distribution of Hs was obtained according to equation (1) for each year separately as well as for the total data set. These distributions were then compared with the corresponding omni-directional distributions obtained by following the normal procedure. This was repeated by varying the underlying theoretical probability distribution as well as by varying the fitting technique.

Figure 4 shows a typical outcome of this exercise and it pertains to the case of Gumbel distribution fit to the Irish Sea data using the method of moments.

It was observed that the equivalent all-direction distribution does not follow the same theoretical form as the constituent conditional distributions (Gumbel, in the present case). This result is evident also from theoretical considerations. Further the introduction of appropriate wave height ceilings along different directions, in these cases, had a negligible effect on the resulting equivalent all-direction distribution. This is probably due to the fact that this imposition did not affect any of the worst directions that dictate the extreme tail of the distribution since the most frequent wind directions fall in the sectors of longest fetch.(Refer to limiting Hs values in Table 1). In other geographical circumstances this may not be the case. In the present case the effect of applying wave height limits for each direction is certainly overshadowed by other curve fitting and extrapolation uncertainties.

It was also noted from the above mentioned comparisons that the equivalent distribution resulting from convolution technique lies on the probability paper above the one obtained on the basis of the existing (omni-direction) procedure. This indicated that it would produce conservative estimates of the design wave heights. This outcome remained unchanged in case of the North Sea data as well (Figure 5). It was also not sensitive to the choice of the theoretical distributions and the fitting techniques.

Figure 6 pertains to the equivalent all-direction distribution of individual wave heights obtained by following the methods-1 and 2 as well as by using the normal procedure. This outcome is also in line with the one discussed above in case of Hs distributions.

The values of the 100-year return period wave heights were extracted from these plots and it was found that the equivalent all-direction distribution produced conservative estimates of Hs ranging from about 5 to 20 percent for all cases involved. The corresponding overestimation of individual wave heights by the use of methods-1 and 2 was 9 to 20 percent.

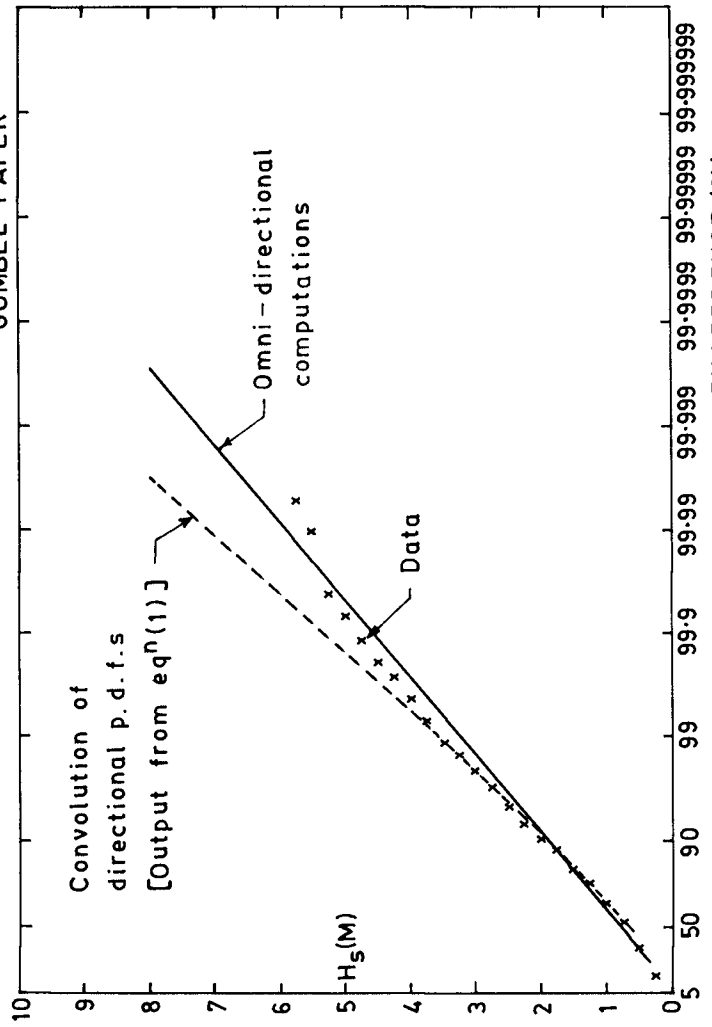

FIG. 4 COMPARISON OF H_s DISTRIBUTIONS (Irish Sea Data)

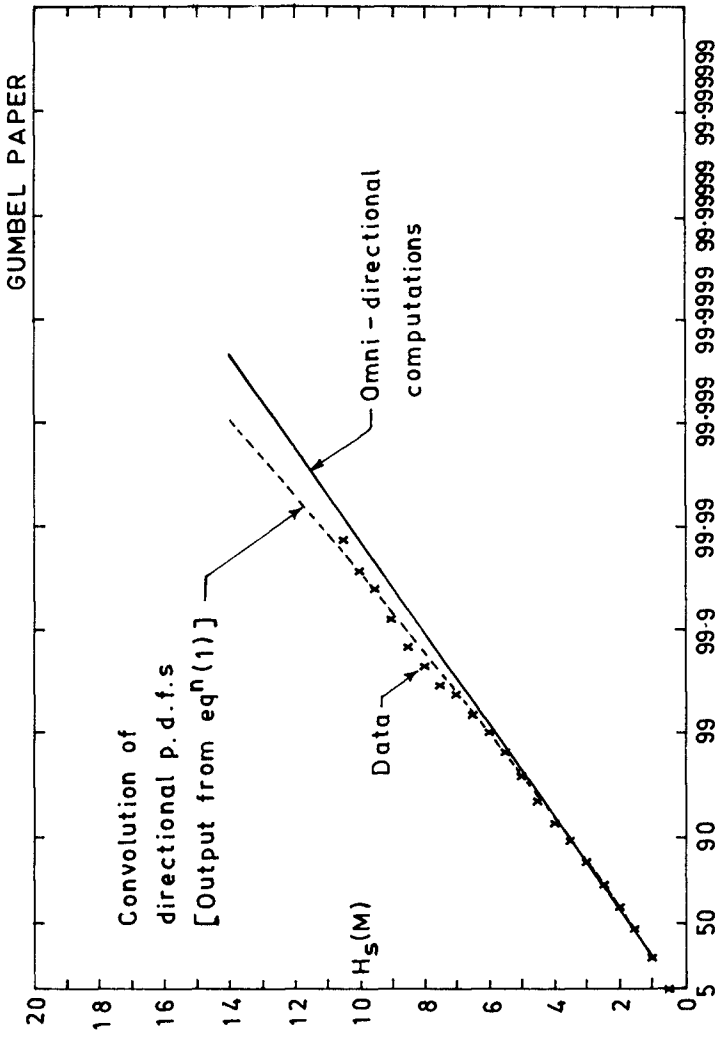

FIG. 5 COMPARISON OF H_s DISTRIBUTIONS (North Sea Data)

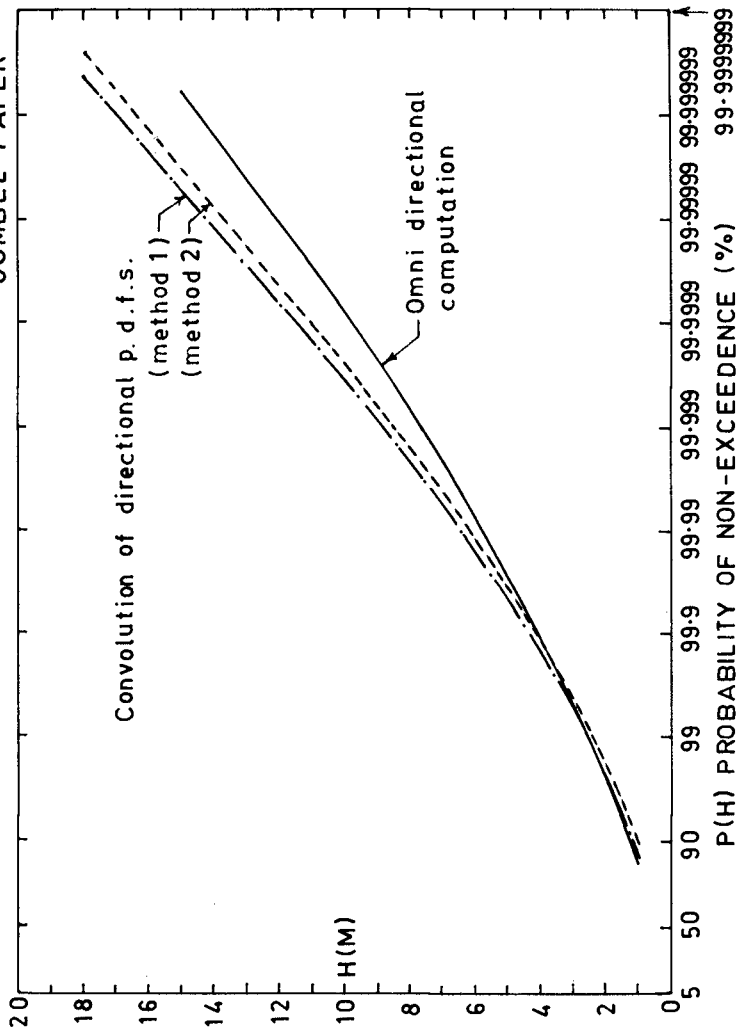

FIG. 6 COMPARISON OF 'H' DISTRIBUTIONS (Irish Sea Data)

5. CONCLUSIONS

(a) A discrepancy in the long term wave height predictions will generally arise if the directionality of the wave data is taken into account.

(b) The normal procedure to predict the long term values of the wave heights implicitly incorporates extrapolation of wave fields in certain direction sectors beyond potential physical limits. It is deficient, therefore, where severe directional bias in the fetch and wind field exists. In these circumstances, the methods presented here are more apporpriate, although they involve higher levels of uncertainties due to the smaller sample sizes considered in curve fitting and extrapolation procedures.

(c) When no such directional bias exists, the methodology enables the computation of a statistically consistent set of directional return-value wave heights which can be factored to bring them into line with the normal omni-direction calculations, having more statistical confidence due to the large sample sizes involved.

(d) Since all the procedures to predict the long term wave heights discussed here are essentially empirical in nature, their theoretical justifications are weak and hence the choice of a particular method should be left to the designer. A need for compatible sets of directional and omni-direction distributions, however, may call for the application of the methods presented herein.

ACKNOWLEDGEMENTS

The work reported herein was conducted whilst the first author was a Visiting Research Fellow at the University of Liverpool, U.K., sponsored by the TCTP scheme of the British Council. The study formed a part of the wider investigation into the probabilistic properties of wave climate supported as project (NW/L/1.5) by the UK Science and Engineering Research Council over the period 1/14-12/85.

REFERENCES

1. Battjes, J.A. (1970): 'Long Term Wave Height Distribution at Seven Stones Around the British Isles', Internal Report No. A44, National Institute of Oceanography (IOS), U.K.

2. Burrows, R. et al (1985): 'Wind/Wave Analysis and Storm Simulation Liverpool Bay', Dept of Civil Engg., University of Liverpool, U.K.

3. Deo,M.C and Burrows, R.(1985): 'Accounting for Directionality in the Prediction of Extreme Wave Heights', Report on SERC Project NW/L/1.5, Dept of Civil Engg., University of Liverpool.

4. Graham, C.G. (1981): 'Problems with the Design Statistical Approach', in Extreme Value Analysis of Directional Wind and Wave Data, Int. Conf. on Wave and Wind Directionality, Paris, Sept 1981, pp 379-401.

5. Isaacson, M. and Mackenzie, N.G. (1981): 'Long Term Distributions of Ocean Waves: A Review', Journal of WPCO, Engineering Division, ASCE, Vol. 107, No. WW2, Paper 16277, May, 1981, pp 93-109.

APPENDIX

Theoretical Probability Distributions Involved in the Analysis

1. Gumbel Distribution

(Or Extreme Value Type I Distribution)

$$P(Hs) = \exp\{-\exp[-\alpha(Hs - u)]\}$$

where $P(Hs)$ = cumulative probability distribution of Hs

α and u = constants expressible in terms of the statistical moments of the data (References 3, 5)

2. Weibull Distribution

(Or Extreme Value Type III-L Distribution)

$$P(Hs) = 1 - \exp\left[-\left(\frac{Hs - A}{B}\right)^{C}\right]$$

A, B, C = constants expressible in terms of the statistical moments of the data (References 3, 5)

3. Extreme Value Type III-u Distribution

$$P(Hs) = \exp\left[-\left(\frac{A - Hs}{B}\right)^{C}\right]$$

A, B, C = constants expressible in terms of the statistical moments of the data (References 3, 5)

4 Long Term Distribution of Individual Wave Heights, H

$$P(H) = 1 - \int_{0}^{\infty}\int_{0}^{\infty} \exp(-2H^2/Hs^2)\,\frac{\bar{Tz}^{-1}}{\bar{\bar{Tz}}^{-1}}\,P(Hs\ Tz)\,dHs\,dTz$$

where $P(H)$ = long term distribution of H

$\bar{\bar{Tz}}^{-1}$ = average number of waves per unit time in the long term

$P(Hs\ Tz)dHsdTz$ = joint probability of occurrence of Hs and Tz

CHAPTER 12

SHOALING SURFACE GRAVITY WAVES: A BISPECTRAL ANALYSIS

J.C. Doering* and A.J. Bowen*

Abstract

Nonlinearities (wave–wave interactions) play a vital role in many aspects of nearshore dynamics, such as wave shoaling and breaking, wave forces, wave–current interactions, radiation stress effects, and sediment transport. The importance of nonlinearities in the nearshore region cannot be overemphasized. At present, however, there is no wave theory that adequately accounts for these interactions, and field observations are sparse. Herein, the bispectrum is used to investigate the temporal and spatial variation of wave–wave interactions in cross-shore velocity for shoaling surface gravity waves in several nearshore environments. The implications for sediment movement of the sign of the observed wave–wave interactions for both the real part of the velocity bispectrum (which is related to the skewness of the horizontal asymmetry) and the imaginary part of the velocity bispectrum (which is related to the skewness of the temporal derivative) are discussed. A parameterization is given for the amplitude and phase evolution of the self–self sum interactions within the wind–wave peak for both planar and barred nearshore topography. The results of this paper underline the potential importance of infragravity wave energy in determining nearshore morphology.

1. Introduction

There have been a lot of papers written about the statistics and nonlinearities of sea surface elevation and slope (Srokosz & Longuet-Higgins, 1986; Longuet-Higgins, 1982, and the many references therein). Most of this literature, however, pertains only to deep water where nonlinearities are assumed to be weak in order for the problem to remain reasonably mathematically tractable. Similar theory has not been completed for shallow water as the complexities are formidable. This is particularly true near breaking where nonlinearities are generally not considered to be weak. Until the collection of data by field programs such as the Nearshore Sediment Transport Study (NSTS), and most recently the Canadian Coastal Sediment Study (C^2S^2), observations were sparse.

As waves propagate into shallow water they undergo a dramatic transformation and eventually break. Freilich and Guza (1984) have shown that a nonlinear model including triad interactions across the wind-wave frequency band can accurately predict the Fourier Coefficients (amplitude and phase) of the wave field through the shoaling region. Elgar and Guza (1985) used the bispectrum to examine the nonlinear interactions in the observed pressure field of shoaling surface gravity waves. In addition, Elgar and Guza (1986) used Freilich and Guza's nonlinear equations to model bispectral evolution through the shoaling region. The model results were qualitatively similar to the observations. The bispectral quantities examined by Elgar and Guza (1985, 1986) were plotted against depth. However, it is clear from inspection of Elgar and Guza (1985, 1986), that depth cannot provide a general parameterization of bispectral evolution. Such a parameterization would be useful, especially for modelling sediment transport since the models of Bowen (1980) and Bailard (1981) require the skewness of the velocity field as an input. Guza and Thornton (1985) computed a variety of velocity moments, including skewness, for some NSTS data, which

* Department of Oceanography, Dalhousie University, Halifax, Canada B3H 4J1

they also plotted as functions of depth. There is, however, no obvious relationship between the depth and most of the quantities they considered.

The objectives of this paper are to investigate the following aspects of the cross-shore velocity field:

i) the temporal and spatial evolution of triad interactions through the nearshore region
ii) the sedimentary implications of the observed wave–wave interactions
iii) the parametric dependence of the salient interactions

2. The Bispectrum

To investigate wave–wave interactions, the bispectrum is used. For a stationary random function of time $\zeta(t)$, the auto bispectrum is given by the Fourier Transform of the mean third-order product (Hasselmann *et al.*, 1963).

$$B(\omega_j,\ \omega_k) = \frac{1}{(2\pi)^2} \iint_{-\infty}^{+\infty} S(\tau_j,\ \tau_k) e^{-i(\omega_j \tau_j + \omega_k \tau_k)} d\tau_j d\tau_k \tag{2.1a}$$

$$S(\tau_j,\ \tau_k) = E[\zeta(t)\zeta(t+\tau_j)\zeta(t+\tau_k)] \tag{2.1b}$$

τ is a lag, ω is a radian frequency, and E denotes an expected or average operator. For digital data the (auto) bispectrum is given by Kim and Powers (1979) as

$$B(\omega_j,\ \omega_k) = A_{\omega_j} A_{\omega_k} A^*_{\omega_{j+k}} \tag{2.2}$$

where A_{ω_j} represents the complex Fourier Coefficient of radian frequency ω_j and * denotes the complex conjugate.

The bispectrum can be expressed in a normalized form known as the bicoherence (Kim and Powers, 1979).

$$b^2(\omega_j,\ \omega_k) = \frac{|B(\omega_j,\ \omega_k)|^2}{E[|A_{\omega_j} A_{\omega_k}|^2] E[|A_{\omega_{j+k}}|^2]} \tag{2.3}$$

Note that Cauchy-Schwarz's inequality ensures $b^2 \leq 1$ for (2.3); this is not true for the bicoherence expression given by Haubrich (1965). The variance of bicoherence estimates has been shown to be less than $\frac{2}{d.o.f.}$ (Kim and Powers, 1979).

The 95% level for zero bicoherence is defined by Haubrich (1965).

$$b^2 \simeq \frac{6}{d.o.f.} \tag{2.4}$$

Although the bicoherence indicates the wave–wave interactions that are significant above some chosen level, it does not provide any information regarding the relative contribution of these interactions to the nonlinearity of the record as measured by skewness. This information is, however, provided by the real part of the bispectrum. Integrating the real part of the bispectrum yields an estimate of skewness.

$$E[\zeta^3(t)] = \sum_{\omega_j} \sum_{\omega_k} \mathfrak{Re}\{B(\omega_j,\ \omega_k)\} \tag{2.5}$$

Prior to the work of Masudo and Kuo (1981) no physical interpretation had been attached to the imaginary part of the bispectrum. However, they showed that the imaginary part of the bispectrum is related to the vertical asymmetry of the waves. Moreover, Elgar

and Guza (1985) showed that the imaginary part is related to a measure of the skewness of the temporal derivative of a time series (i.e., the Hilbert transform).

$$E\left[\left(\frac{\partial \zeta}{\partial t}\right)^3\right] = \sum_{\omega_j} \sum_{\omega_k} \omega_j \omega_k \omega_{j+k} \Im m\{B(\omega_j,\ \omega_k)\} \tag{2.6}$$

Lastly, from (2.5) and (2.6) it is clear the bispectrum can be written in terms of an amplitude and phase

$$B(\omega_j,\ \omega_k) = |B(\omega_j,\ \omega_k)| e^{i\theta(\omega_j,\ \omega_k)} \tag{2.7a}$$

where

$$\theta(\omega_j,\ \omega_k) = \tan^{-1}\left\{\frac{\Im m[B(\omega_j,\ \omega_k)]}{\Re e[B(\omega_j,\ \omega_k)]}\right\} \tag{2.7b}$$

3. Data Base

The data for this investigation were collected from four nearshore environments: Pte. Sapin, New Brunswick (C^2S^2), Stanhope Lane, Prince Edward Island (C^2S^2), Queensland, Nova Scotia, and Leadbetter Beach, California (NSTS). These data provide a range of beach slopes (including a barred environment), wave periods, depths, and (significant) wave heights — see table 1 for a summary. Because of space limitations a detailed analysis of only 1 run (run 52 from Pte. Sapin) is presented. Doering and Bowen (submitted) have shown that a bispectral analysis of cross-shore velocity and pressure for the February 2, 1980 data from Leadbetter are very similar. Therefore, the reader is referred to Elgar and Guza (1985) for a detailed analysis of the Feb. 2 Leadbetter data.

The velocity data from these four environments were collected using 2-axis, 4 centimeter diameter, spherical probe, electromagnetic current meters manufactured by Marsh-McBirney Incorporated (model 512/OEM). Corrections were made for the filter characteristics of the current meter electronics where necessary.

4. Observations & Discussion

Figure 1 shows the beach profile and location of the current meters deployed at Pte. Sapin, New Brunswick during C^2S^2. The cross-shore velocity spectra for current meters C26 ($h = 3.2m$, line *a*), C23 ($h = 2.9m$, line *b*), C07 ($h = 2.0m$, line *c*) and C16 ($h = 1.7m$, line *d*) for run 52 at Pte. Sapin are given in Figure 2. Note the sharpening of the spectral peak and the relative increase in both harmonic and infragravity wave energy as the waves shoal (lines $a \rightarrow d$).

The results of a bispectral analysis of these data are plotted as 3-D plots in Figures 3-6. The following notes apply to all the 3-D plots in this paper:

1) For an auto bispectrum only $\frac{1}{8}$ of the $(\omega_j,\ \omega_k)$ frequency plane is unique (Kim and Powers, 1979). However, plotting the entire 1^{st} quadrant allows the backside of some of the peaks to be seen. For this reason, the entire 1^{st} quadrant ($\omega_j,\ \omega_k > 0$) has been plotted.
2) The origin is located at the left corner.
3) The two axes defining the frequency plane show the non-radian frequency, $f_1,\ f_2 = \frac{\omega}{2\pi}$, and both run from 0 to 0.5 Hertz.
4) There is symmetry about a 45° line ($f_1 = f_2$).

To facilitiate visualizing the bicoherence plots, only the bicoherence values above the 95% level for zero bicoherence ((2.4)) are shown. The "slab" thickness indicates the 95% value. The four panels of figure 3 show the bicoherence plots for current meters C26 (panel 1), C23 (panel 2), C07 (panel 3) and C16 (panel 4) for run 52 at Pte. Sapin. In panel 1,

TABLE 1 - DATA SUMMARY

Environment /Symbol	Beach slope	Run	Date dd/mm/yy	d.o.f.	T_p [s]	Depth(s) [m]	H_s† [m]
Pte. Sapin ▲	0.005	52	03/11/83	2048	6.6	3.2-1.7	.39
◆		62	05/11/83	1536	7.9	3.1-1.6	.69
Leadbetter ■	0.04		02/02/83	2048	15.8	5.9-1.2	.41
Queensland +	0.06	131	26/06/79	512	8.0	1.4	.16
		133	26/06/79	512	8.0	1.2	.20
		141	26/06/79	512	8.0	1.0	.20
		142	26/06/79	512	8.0	0.7	.15
		151	26/06/79	512	8.0	0.6	.13
Stanhope ●	‡	8.1	18/10/84	2560	5.7	2.5	.91
		8.2	19/10/84	1536	5.5	2.7	.67
		8.4	19/10/84	1536	5.2	2.3	.52
		9.1	19/10/84	1536	5.0	2.1	.43
		10.5	24/10/84	2560	4.9	2.2	.29
		11.6	25/10/84	2560	4.7	2.5	.32
		12.1	25/10/84	2560	6.6	1.7	.76
		12.2	26/10/84	2560	8.5	1.8	.87
		13.2	26/10/84	2048	7.5	1.8	.74
		14.3	27/10/84	1536	4.7	2.0	.31

† determined using linear theory; for the shore normal transect of sensors on Pte. Sapin and Leadbetter Beaches value given was computed using the deepest sensor.

‡ beach is concave with several shore parallel bars.

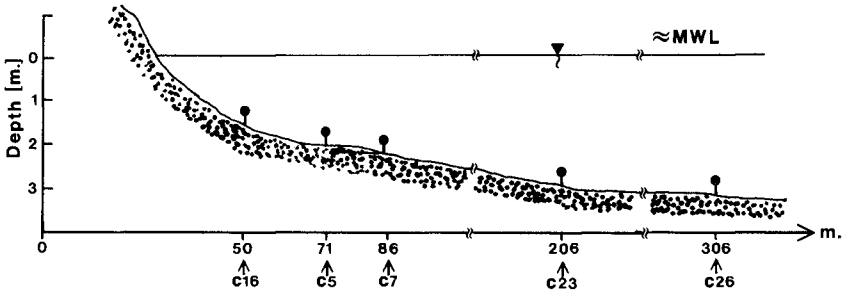

FIGURE 1. Beach profile and location of the current meters deployed at Pte. Sapin, New Brunswick.

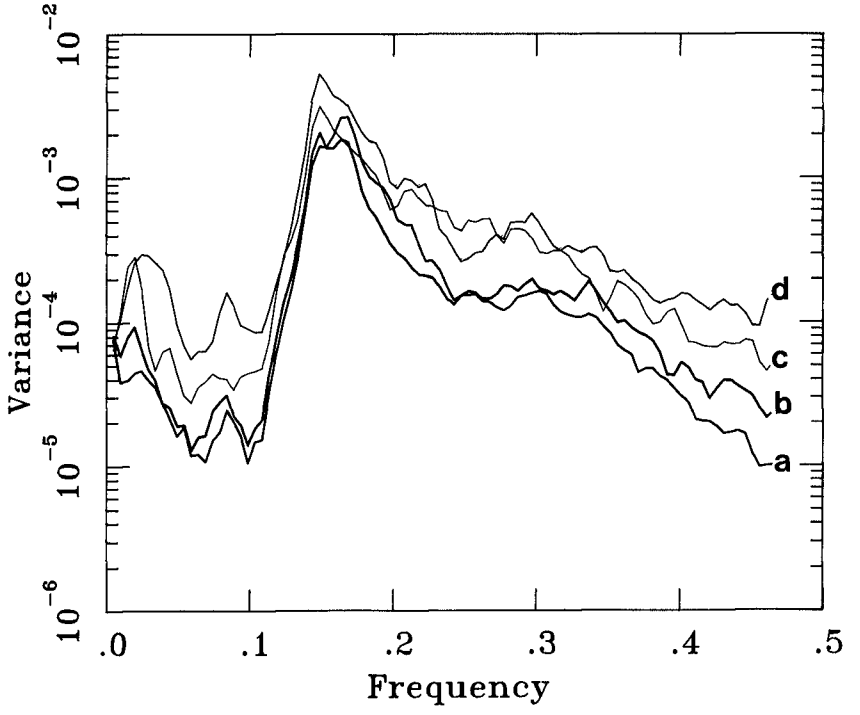

FIGURE 2. Cross-shore velocity spectra for current meters C26 (a), C23 (b), C07 (c) and C16 (d) deployed for run 52 at Pte. Sapin. *d.o.f.* = 100.

two (unique) salient peaks are noted. The peak centered at $(0.15Hz, 0.15Hz)$ indicates nonlinear phase coupling between fundamental and first harmonic frequencies of the incident waves; this interaction is hereinafter denoted (f, f). The peak at $(0.15Hz, 0.02Hz)$ indicates coupling between the fundamental and a long wave. Physically, this peak suggests that neighboring frequencies within the fundamental peak interact to form a beat or wave group, which forces a long wave, at the difference frequency; this interaction is hereinafter denoted $(f, \Delta f)$. After propagating $\sim 100m$ further shoreward, over essentially a flat bottom, panel 2 shows that very little additional coupling occurred. This is also evident from figure 2 (lines *a* and *b*). However, panel 3 indicates that additional coupling did occur after propagating $\sim 120m$ further shoreward over a gently sloping seabed. In particular, the bicoherence of the (f, f) peak increased, and broadened slightly. In addition, a new peak is present at $(f, 2f)$, indicating coupling between the fundamental and the first harmonic. The shallowest station (panel 4), which is $\sim 36m$ shoreward of C07 (panel 3), reveals several new interactions. The peaks at $(2f, 2f), (f, 3f)$ and $(3f, 3f)$ indicate sum interactions between the first harmonic and itself, the fundamental and the second harmonic, and the second harmonic with itself, respectively. Of particular interest though, are the peaks at $(2f, \Delta f)$ and $(3f, \Delta f)$. These peaks suggest that interactions within the (forced) harmonic peaks result in (harmonic) groups, which are coupled to a (forced) long wave beneath the group.

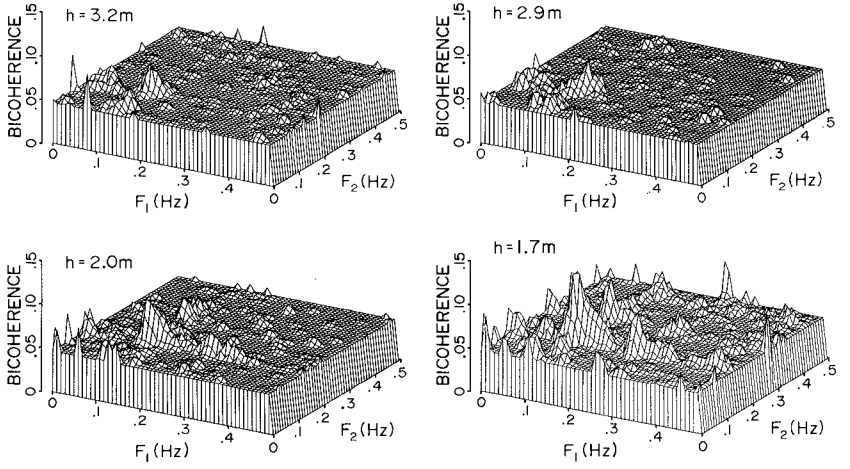

FIGURE 3. Bicoherence for current meters C26 ($h = 3.2m$), C23 ($h = 2.9m$), C07 ($h = 2.0m$) and C16 ($h = 1.7m$) for run 52 at Pte. Sapin. Only values above the 95% level for zero bicoherence (indicated by the thickness of the slab) are shown.

Figure 4 shows the real part of the bispectrum for the same four sensors as figure 3. Inspection of these four panels readily yields several points. First, the observed skewness of these cross-shore velocity time series is essentially due to the (f, f) interaction. Second, the sign of the skewness of the (f, f) interaction is opposite to that of the $(f, \Delta f)$ interaction. These observations of velocity bispectra are consistent with the pressure observations of Hasselmann *et al.* (1963) and Elgar and Guza (1985). For sediment transport this implies that the skewness of the horizontal velocity field arising from the (f, f) interaction pushes sediment in an opposite direction to the skewness arising from the $(f, \Delta f)$ interaction.

The sedimentary significance of these two interactions was noted by Wells (1967), who used Biesel's second-order solution for a discrete number of gravity wave trains to investigate the spatial variation of skewness across a beach. Wells suggested that a neutral line of zero skewness exists separating two regions, one of positive skewness in shallow water (skewed onshore), the other of negative (or seaward) skewness in deep water; he notes that, "sand in deeper water can actually be transported in a seaward direction". This mechanism was recently employed by Shi and Larsen (1983) to explain the seaward transport of fine sand and silt on the continental shelf. It is worth noting the shallow water portion of Wells' results are suspect as he extended his computations into relatively very shallow water where the underlying assumptions of the theory are no longer met.

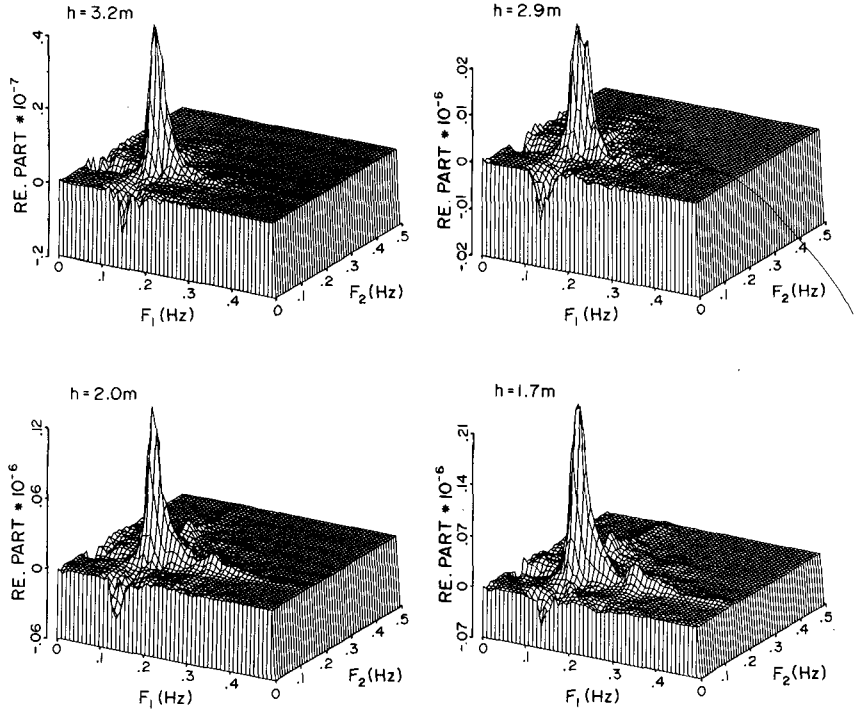

FIGURE 4. Real part of the bispectrum for current meters C26 ($h = 3.2m$), C23 ($h = 2.9m$), C07 ($h = 2.0m$) and C16 ($h = 1.7m$) for run 52 at Pte. Sapin.

Figure 5 shows the imaginary part of the bispectrum for the same four sensors as figures 3 and 4. From (2.6) it is clear that for a velocity time series, figure 5 provides information related to the wave–wave interactions that give rise to the skewness of horizontal acceleration. Note that the relative strength of the wave–wave interactions observed from these plots is biased because each imaginary estimate was not multiplied by the respective triple product of radian frequencies; as a result, the strength of the high(er) frequency interactions is deemphasized. For panel 1 the $(f,\ f)$ interaction is negative, indicating that the horizontal acceleration of this interaction is negatively skewed, therefore suggesting back-

ward tilted waves. This is, of course, not the usual direction that shoaling waves are tilted. As the waves shoaled further (panels 2 to 4) the (f, f) interaction becomes increasingly more positive (i.e., forward tilting). Although partially obscured, the $(f, \Delta f)$ interaction for panels 1 to 3 is negative, indicating that the horizontal acceleration of this interaction is skewed seaward. However, at the shallowest station, panel 4, the $(f, \Delta f)$ interaction is positively skewed. This is not the usual direction that the horizontal acceleration of this interaction is skewed, which suggests that the amplitude and phase of the Δf Fourier coefficients may include a partially reflected component.

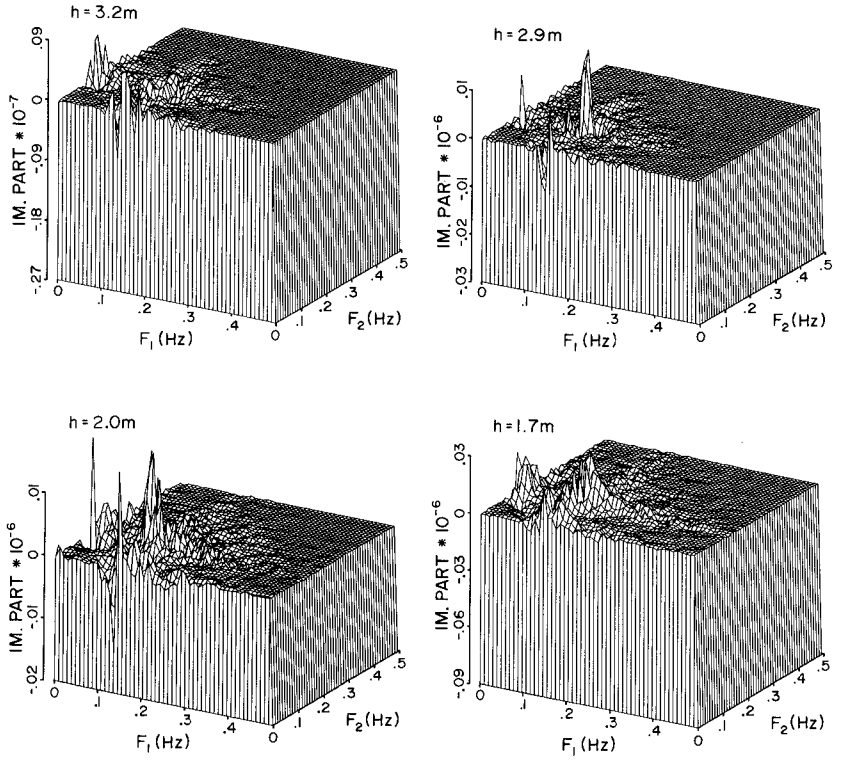

FIGURE 5. Imaginary part of the bispectrum for current meters C26 ($h = 3.2m$), C23 ($h = 2.9m$), C07 ($h = 2.0m$) and C16 ($h = 1.7m$) for run 52 at Pte. Sapin.

For progressive waves, in shallow water, it is known that sea surface elevation and the horizontal velocity in the predominant direction of propagation are strongly coherent for wind–wave frequencies (Guza and Thornton, 1980). Skewness of the horizontal acceleration resulting from vertical asymmetry of the waves, therefore, is related to the skewness of the vertical velocity. Vertical asymmetry of the waves may be an important mechanism for suspended sediment transport, since an upward skewed vertical velocity (under forward tilting waves) could balance gravitational settling, thereby maintaining suspension for advection by the mean flow (e.g., horizontal skewness).

To parameterize bispectral evolution, it is easiest to express the bispectrum as an amplitude and phase. Figure 6 shows the amplitude plots for the four previously considered sensors. Clearly, the (f, f) and $(f, \Delta f)$ interactions dominate these plots. A first-order parameterization of bispectral evolution therefore necessitates parameterizing the amplitude and phase of these interactions through the shoaling region.

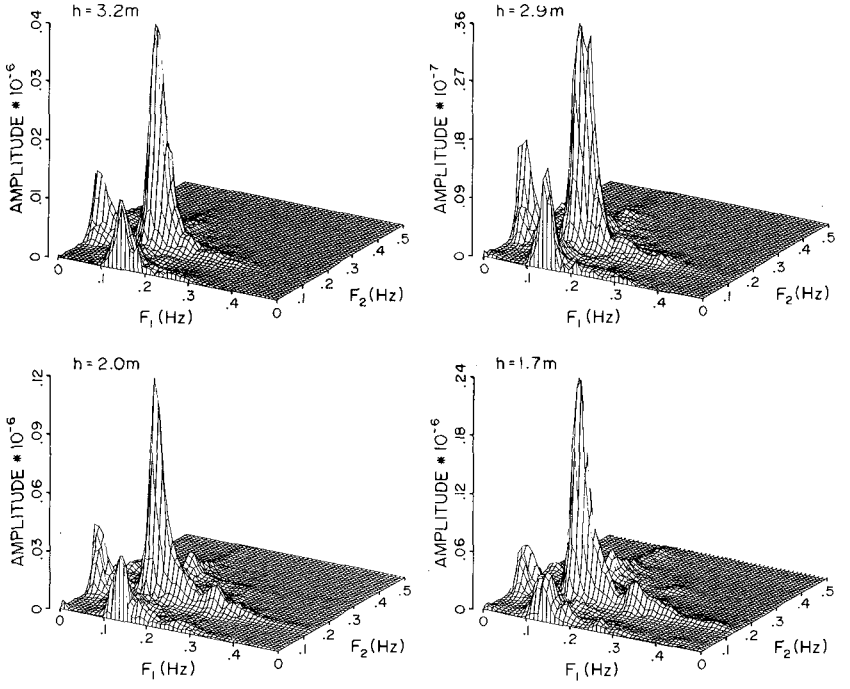

FIGURE 6. Amplitude of the bispectrum for current meters C26 ($h = 3.2m$), C23 ($h = 2.9m$), C07 ($h = 2.0m$) and C16 ($h = 1.7m$) for run 52 at Pte. Sapin.

It can be readily shown that the skewness arising from a second-order Stokes wave (a fundamental and its phase-locked, in phase harmonic) can be parameterized in terms of the Ursell number (Ursell 1953)

$$\lim_{kh \to 0} \frac{\eta^{(2)}}{\eta^{(1)}} \sim \frac{3}{4} \frac{ak}{(kh)^3} = U_r$$

In shallow water the Ursell number can be expressed as

$$U_r = \frac{3}{4} \frac{g}{8\pi^2} \frac{H_s T^2}{h^2}$$

where g is the acceleration due to gravity, H_s is the significant wave height, T is the period, and h is the local depth. Note that taking the same limit for $\frac{u^{(2)}}{u^{(1)}}$ also yields the

Ursell number. The Ursell number would seem to be a logical quantity to choose for the parameterization of the $(f,\ f)$ interaction observed in cross-shore velocity. Figure 7 shows the normalized (i.e., divided by the appropriate band integrated variance to the $\frac{3}{2}$ power) amplitude of the $(f,\ f)$ interaction for run 52, and all the other data listed in table 1, as a function of U_r. Least squares regression yields for this interaction

$$\text{Nrm. Ampl.}(f,\ f) = .48 + .31\log(U_r),\ r^2 = .92 \tag{4.1}$$

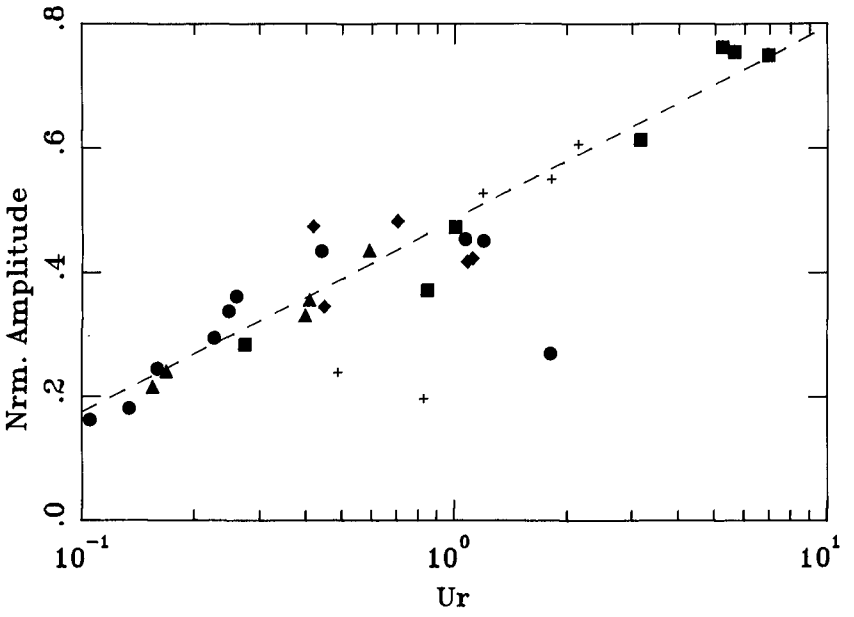

FIGURE 7. Normalized (NRM) amplitude for the self–self sum interaction of the wind-wave peak as a function of the Ursell number (U_r) for Pte. Sapin run 52 ▲, run 62 ◆, Stanhope Lane ●, Leadbetter Beach ■, and Queensland Beach +.

All of the Queensland data, which is strongly dominated by backwash, and the one Stanhope run from breaking wave conditions (circle near lower right of figure 7) were excluded from the regression. The relatively high correlation between these two quantities implies several points. First, the majority of the energy at the first harmonic is forced (ie. free energy would beat down r^2). Second, there is a relative increase in first harmonic energy as the waves shoal. Lastly, the growth of the $(f,\ f)$ interaction is dependent on depth, but apparently not on slope as U_r contains no beach slope information. Figure 7 also suggests that the relatively long period incident waves, which are commonly observed on the Pacific coast, develop much stronger nonlinearities before breaking than the shorter period waves of the Gulf of St. Lawrence or Atlantic coast.

It can be shown for a wave consisting of a fundamental and a phase-locked harmonic that the value of the $(f,\ f)$ biphase represents the phase difference, δ_1, between the fundamental and its first harmonic. Iwagaki and Sakai (1972) give a solution, correct to second-order, for the evolution of the phase shift δ_1. Their expression, which is a function of the

dimensionless quantity $\frac{\beta}{\sqrt{k_\infty h}}$, was found to be poorly correlated with the present data. However, figure 8 shows that the $(f,\ f)$ biphase was found to be well correlated with the relative depth (i.e., local estimate of kh). The two lines suggest, not surprisingly perhaps, that the evolution of the $(f,\ f)$ biphase is different for planar (dashed line) and barred (dotted line) beaches. This was not the case for the evolution of the $(f,\ f)$ normalized amplitude. Least squares regression gives,

$$\text{planar}: \quad \theta(f,\ f) = 64 + 179\log(kh),\ r^2 = .93 \tag{4.2a}$$

$$\text{barred}: \quad \theta(f,\ f) = 35 + 211\log(kh),\ r^2 = .97 \tag{4.2b}$$

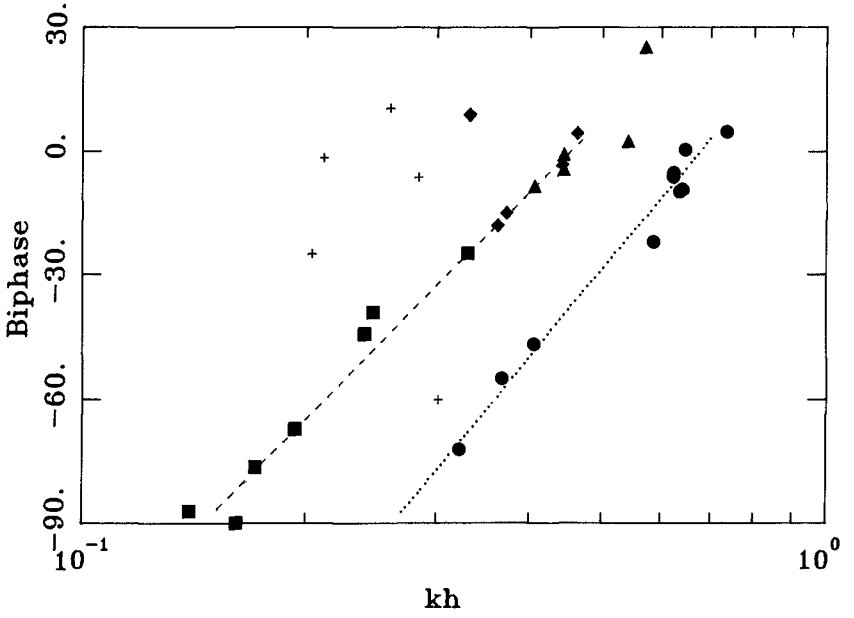

FIGURE 8. Biphase of the self–self sum interaction, $\theta(f,\ f)$, of the wind–wave peak as a function of kh for Pte. Sapin run 52 ▲, run 62 ◆, Stanhope Lane ●, Leadbetter Beach ■, and Queensland Beach +.

The Queensland data was once again excluded from the (planar environments) regression analysis. The strong backwash, noted previously, is evident in the very different biphase evolution. However, the Stanhope data point which was excluded from (4.1) has been included in (4.2*b*). This suggests (rather lightly as it is based on only one point) that $\theta(f,\ f)$ is not affected by wave breaking as strongly as as normalized amplitude was observed to be. The similar evolution of $\theta(f,\ f)$, over the steep Leadbetter Beach and gently Sloping Pte. Sapin beach suggests that $\theta(f,\ f)$ is not strongly dependent on beach slope (β). The work of Flick (1981) indicates that $-90 \leq \delta_1 \leq 0$. Therefore, equations (4.2*a*) and (4.2*b*) should be restricted to this range.

The other peak to be parameterized is the $(f,\ \Delta f)$ interaction. The observed evolution of normalized amplitude and phase suggests that the estimated Fourier Coefficients of the

low frequency (Δf) component of this interaction are complicated by reflection and possibly other sources of low frequency energy. Clearly, the estimates of amplitude and phase from a sensor beneath a partially reflected wave depends on where the sensor is located (ie. node $\rightarrow$ anti-node). Since discerning the composition of the low frequency energy in these data sets is in itself a formidable task, a parameterization of this interaction is not considered here.

5. Conclusions

Current meter data, collected from four nearshore environments, were used as an input to the (auto) bispectrum to investigate wave–wave interactions in the cross-shore velocity field of shoaling surface gravity waves. Bicoherence values indicate that as shoaling begins coupling occurs first within the wind–wave peak, i.e., (f, f) and (f, Δf) interactions. As shoaling progresses coupling occurs between the fundamental-harmonic (f, $2f$), and eventually within and between the harmonic peaks, e.g., ($2f$, $2f$), ($2f$, Δf) and ($2f$, $3f$). The real and imaginary parts of the velocity bispectrum indicate that the skewness and asymmetry, respectively, of the (f, f) interaction is usually of opposite sign to the (f, Δf) interaction.

Bispectrum amplitudes clearly show that the (f, f) interaction, and to a lesser extent the (f, Δf) interaction, are typically much stronger than the other triads. Least squares regression indicates that the normalized amplitude of the (f, f) interaction is well parameterized ($f^2 = .92$) by the Ursell number for planar and barred environments; the data provide no evidence for any strong return of energy to the fundamental frequency (as necessary, for example, for the Fermi-Pasta-Ulam instability) which might lead to wavelike horizontal variability in the (f, f) interaction, one of the suggested mechanisms for bar formation. A suitable parameterization was not obtained for the smaller amplitude (f, Δf) interaction, as the observed amplitudes and phases of this interaction were quite erratic. This suggests that the Fourier Coefficients of the Δf component are contaminated by reflection and possibly other forms of infragravity wave motion. These observations highlight the potential role that low frequency motion may play in determining seabed topography (e.g., the shore parallel bars observed at Stanhope Lane).

The biphase of the (f, f) interaction, $\theta(f, f)$, was observed to evolve differently for planar and barred environments, but for both types of beach profiles was well parameterized ($r^2 \geq .93$) as a function of kh. This implies that, like normalized amplitude, $\theta(f, f)$ does not appear to depend strongly on the beach slope. Observations indicate that the Pacific coast data (NSTS) tend to exhibit not only stronger nonlinearities prior to breaking than the east coast data (C^2S^2), but also $\theta(f, f)$ values that are much closer to $-90°$. This implies that the NSTS data develops stronger (vertical) asymmetry before breaking than the C^2S^2 data, which suggests that wave skewness/asymmetry cannot by itself be used as a breaking criteria. Since skewness/asymmetry depend on a combined functional form of kh and U_r (which is a function of kh and $\frac{a}{h}$) suggests that another or additional parameter is required to determine the inception of breaking; kh and $\frac{a}{h}$ apparently do <u>not</u> provide this information.

References

Bailard, J.A. and D.L. Inman, 1981. An energetics bedload model for a plane sloping beach: local transport. J.G.R., V. 86, 2035-2043.

Bowen, A.J., 1980. Simple models of nearshore sedimentation; beach profiles and longshore bars, <u>in</u> The Coastline of Canada, S.B. McCann, editor; Geological Survey of Canada, par 80-10, 1-11.

Doering, J.C. and A.J. Bowen (submitted to JGR). Skewness in the nearshore zone: a comparison of estimates from Marsh-McBirney current meters and "colocated" pressure sensors.

Elgar, S. and R.T. Guza, 1985. Observations of bispectra of shoaling surface gravity waves. J.F.M., V. 161, 425-448.

Elgar, S. and R.T. Guza, 1986. Nonlinear model predictions of bispectra of shoaling surface gravity waves. J.F.M., V. 167, 1-18.

Flick, R.E., R.T. Guza and D.L. Inman, 1981. Elevation and velocity measurements of laboratory shoaling waves. J.G.R., V. 86, no. 5, 4149-4160.

Freilich, M.H. and R.T. Guza, 1984. Nonlinear effects on shoaling surface gravity waves. Phil. Trans R. Soc. Lond. (A), V. 311, 1-41.

Guza, R.T. and E.B. Thornton, 1980. Local and shoaled comparisons of sea surface elevations, pressures, and velocities. J.G.R., V. 85, 1524-1530.

Guza, R.T. and E.B. Thornton, 1985. Velocity moments in the nearshore. J. Waterways, Ports, Coastal and Ocean Engr., ASCE, V. 111, no. 2, 235-259.

Hasselmann, K., W. Munk and G. MacDonald, 1963. Bispectra of ocean waves, in Time Series Analysis, edited by M. Rosenblatt, 125-139. Wiley.

Haubrich, R.A., 1965. Earth noise, 5 to 500 millicycles per second. J.G.R., V. 70, No. 6, 1415-1427.

Iwagaki, Y. and T. Sakai, 1972. Shoaling of finite amplitude long waves on a beach of constant slope. Proc. 13^{th} Int. Conf. Coastal Eng., ASCE, 347-364.

Kim, Y.C. and E.J. Powers, 1979. Digital bispectral analysis and its application to nonlinear wave interactions. IEEE transactions on plasma science, V. PS-7, no. 2, 120-131.

Longuet-Higgins, M.A., 1982. On the skewness of sea-surface slopes. J.P.O., V. 12, 1283-1291.

Masudo, A. and Y.Y. Kuo, 1981. A note on the imaginary part of bispectra. Deep sea research, V. 28A, no. 3, 213-222.

Shi, N.C. and L.H. Larsen, 1983. Reverse sediment transport induced by amplitude-modulated waves. Mar. Geol., V. 54, 181-200.

Srokosz, M.A. and M.S. Longuet-Higgins, 1986. On the skewness of sea-surface elevation. J.F.M., V. 164, 487-497.

Ursell, F., 1953. The long-wave paradox in the theory of gravity waves. Proc. Cambridge Phil. Soc., V. 49, 685-694.

Wells, D.R., 1967. Beach equilibrium and second-order theory. J.G.R., V. 72, no. 2, 497-504.

CHAPTER 13

Water-wave modulation

J.W. Dold* and D.H. Peregrine†

Abstract

Accurate numerical computations of wave trains with small modulations that grow are described. The range of wave steepness and modulation lengths that give breaking waves are determined. The number of wave crests is reduced for a time at greatest modulation but frequency downshifting is not observed. Near-breaking wave-group structure is always similar, with energy concentrated into one or two wavelengths.

1. Introduction

The ocean surface rarely, if ever, has the form of a uniform periodic travelling wave train. In part, this is due to the instabilities of such waves. The first instability to be found was the Benjamin-Feir (1967) modulational instability. Unlike other instabilities it occurs for wave trains of steepness well below the maximum steepness of steady waves at which crests approach a 120° angle, and so may be especially relevant to the evolution of ocean waves. For more recent theoretical studies of the instability itself see McLean (1982 a,b).

Experiments demonstrate that the instability leads to the formation of strongly modulated wave groups, and further evolution can lead to a recurrence of an approximately uniform wave train. One of the most striking features of experiments is that for sufficiently steep initial waves the recurrence of a uniform wave is accompanied by a decrease in frequency. (Lake et al, 1977, Melville 1982, Su et al 1982). Lake and Yuen (1978) conjecture that this frequency downshifting is related to the decrease in the dominant frequency of wind waves with fetch and duration.

Previous theoretical studies have been made with approximate equations, see Lake et al (1977), Stiassnie and Kroszynski (1982), and Lo and Mei (1985). They show strong modulation and recurrence of uniform waves, but no frequency downshifting. Since these approximations are weakly nonlinear they cannot describe the wave breaking that occurs at strongest modulation.

This work describes numerical computations of the evolution of small amplitude modulations on a uniform wave train. These computations use an efficient program solving for irrotational flow with the exact

*Research Associate and †Reader, School of Mathematics, University of Bristol, University Walk, Bristol BS8 1TW, England.

inviscid boundary conditions. The computations can continue to describe the initial overturning stage of wave breaking, and hence clearly indicate when breaking occurs.

2. Computation

The method of computation is based on a boundary-integral solution of Laplace's equation for the complex velocity $\phi_x - i\phi_y$ in two dimensions. It is based on Cauchy's integral theorem for functions of a complex variable $(x + iy)$. The method is briefly described in Dold and Peregrine (1984, 1985): a more detailed account is in preparation.

Initial conditions are chosen for the surface elevation, ζ, and velocity potential, ϕ, and were made up as follows:

(i) an initial uniform wave train on deep water; $\zeta = a \cos x$ is the relevant first approximation, but an accurate steady wave form and potential were used in units with gravity = 1, wavelength = 2π.

(ii) the computational region contained n waves, where $3 \leq n \leq 10$.

(iii) a perturbation of the form

$$\varepsilon a\left[\cos\left(\frac{n+m}{n}x - \tfrac{1}{4}\pi\right) + \cos\left(\frac{n-m}{n}x - \tfrac{1}{4}\pi\right)\right]$$

was added to ζ together with a corresponding perturbation to ϕ. This gave a modulation length of n/m waves; m was 1 or 2. The phase shift was chosen to be $\frac{1}{4}\pi$ since Stiassnie (private communication) indicated this gave the most rapid growth. The value of ε was usually 0.1 and sometimes 0.05. We did not intend to study the growth of infinitesimal perturbations.

Periodic boundary conditions were imposed on the computational region, and the effect of the above initial conditions is to give a weak periodic modulation on the wave train. The time evolution of this modulation was then followed through its initial growth until either:

(a) the computation failed because the wave crest had become too sharply curved for satisfactory resolution, which is a clear indication of the proximity of breaking. By rearrangement of computational points wave overturning could be modelled.

or (b) a near recurrence of the uniform wave state occurred. In some cases more than one recurrence was computed.

Most previous calculations with this general type of program had been for one or two periods involving no more than two waves. The present examples were for up to 10 waves followed for a hundred or more periods. Accuracy was checked in this case by running the same initial conditions with various numbers of initial points and varying the explicit tolerances for iterations and time-stepping within the computation. We aimed to find the most economical values which gave sufficient accuracy. The high-order approximations used in the method

permitted as little as 8 computational points per wave and time-steps as large as 0.1 period for the gentler waves. Figure 1 shows part of one such computation just after it has lost accuracy, together with a more accurate profile using 12 points per wavelength from the initial time.

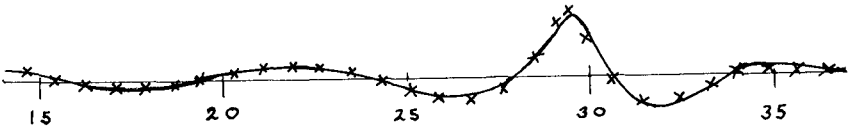

Figure 1. A partial comparison of computations of surface elevation with 8 and 12 points per wave length after 60 linear periods, i.e. $t = 120\pi$. The more accurate profile is shown with a continuous line, the computational discretization is shown for the 8 point profile. The initial steepness is 0.12, and the whole computation includes 2 modulations over 9 wavelengths. The vertical exaggeration in the figure is 5 times. The actual maximum wave slope is 23°.

3. Some examples related to wave breaking

A summary of the calculations is given in figure 2 which indicates whether or not waves grow to breaking. Some of the shorter modulations of $2\frac{1}{2}$ or 3 waves are too short to be unstable. For the instability of just two waves and its evolution see Longuet-Higgins (1978) and Longuet-Higgins and Cokelet (1978).

One important feature of all the computations is that except for a fraction of a wave period before wave breaking the linear-wave concepts of phase velocity and group velocity give a good approximation for any time interval of two or three wave periods. Hence, should anyone wish to compare any of the spatial wave profiles with wave measurements at a fixed point this is possible. The most significant point to be noted is that since for deep water waves group velocity, c_g, is half the phase velocity, c, the number of waves in a modulation on a temporal record is twice the spatial number used here; see figure 6.

Figure 3 is a representative example of cases where the small initial modulation evolved into a steep, short wave group and back to a recurrence of a near uniform wave-train. Slightly more than one modulation length of 5 waves is shown. The wave profiles are given at multiples of 10 or 20 periods since by choosing an interval of $2n$ or $4n$ periods the effects on the wave profile of both phase velocity and linear group velocity lead to a recurrence of the wave and modulation positions.

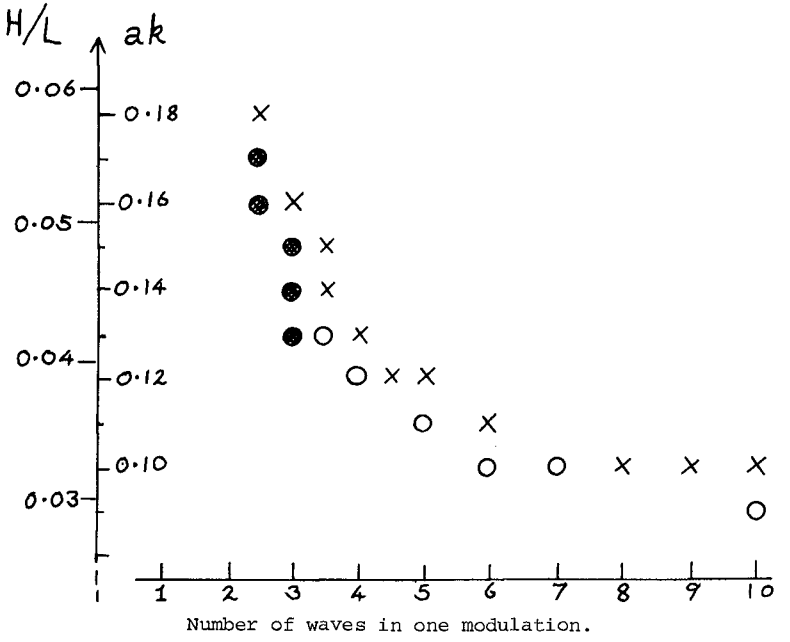

Figure 2. Summary of wave modulation computations. Crosses indicate waves grew to breaking. Open circles indicate modulation grows and uniform waves recur. Filled circles indicate no growth of modulation.

Typical features shown in figure 3 include:

(a) a short group of steep waves at maximum modulation.

(b) waves of close to zero amplitude each side of the steep waves. The modulation does have two precise zeros in the evolution.

(c) a time interval around the time of maximum modulation during which one wave crest disappears.

(d) an advance in the relative position of the peak of the modulation over that predicted by linear group velocity.

(e) a change of relative phase of waves at recurrence, but no lasting frequency downshift which requires the loss of a wave.

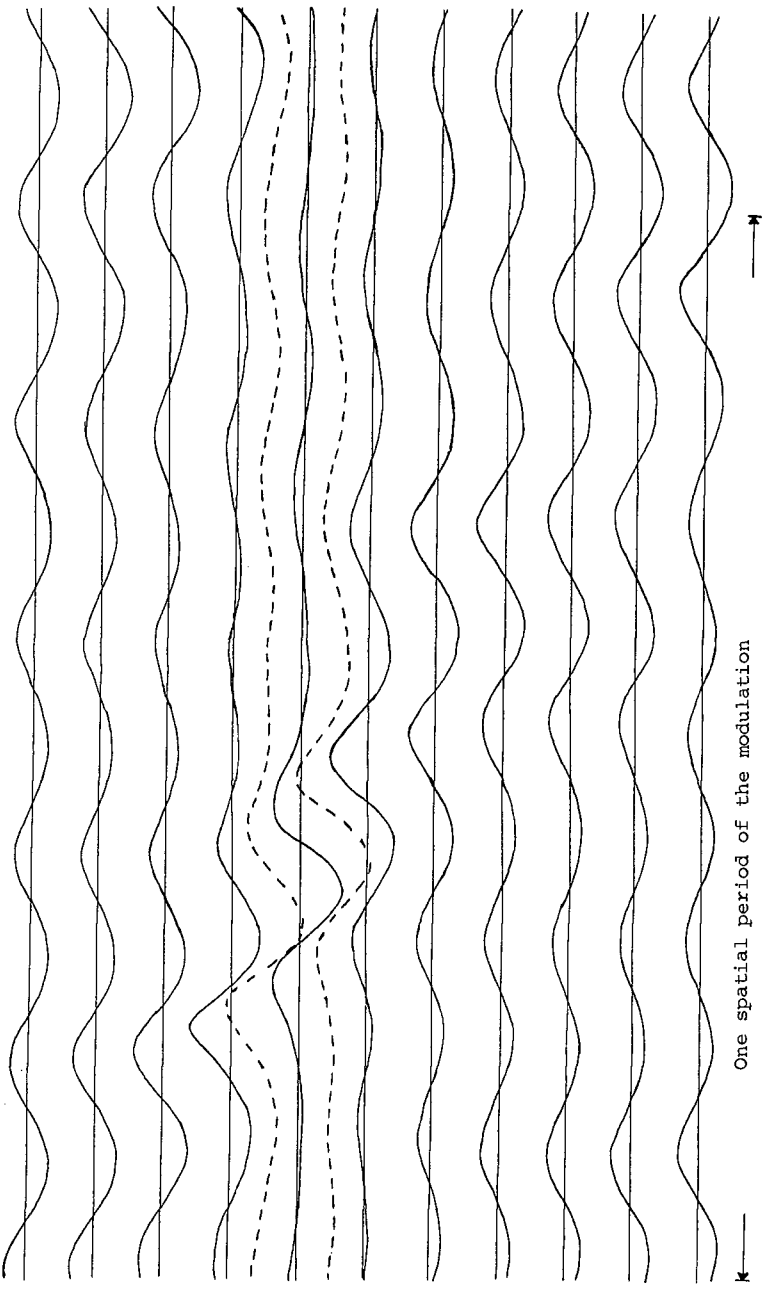

Figure 3. Evolution of the surface profile of a 5 wave modulation shown at intervals of 20 periods with supplementary profiles at 70 and 90 periods. The initial wave steepness is $ak = 0.11$, and the perturbation has $\varepsilon = 0.1$. The vertical exaggeration is 5 times.

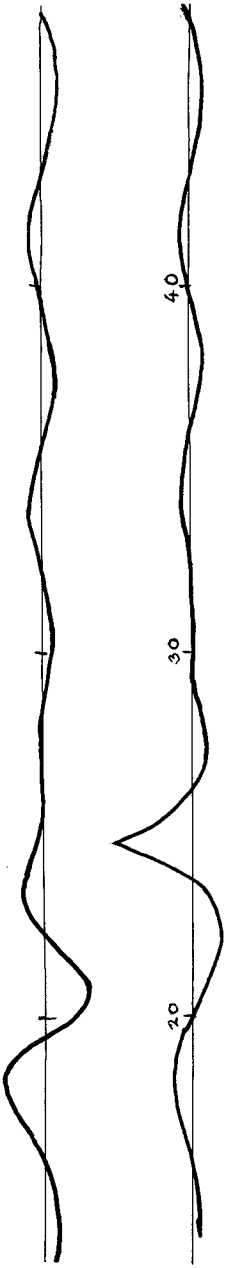

Figure 4. The surface profile of a 5 wave modulation at 60 periods and 61 periods for initial wave steepness ak = 0.12 with perturbation ε = 0.1. The vertical exaggeration is 5 times.

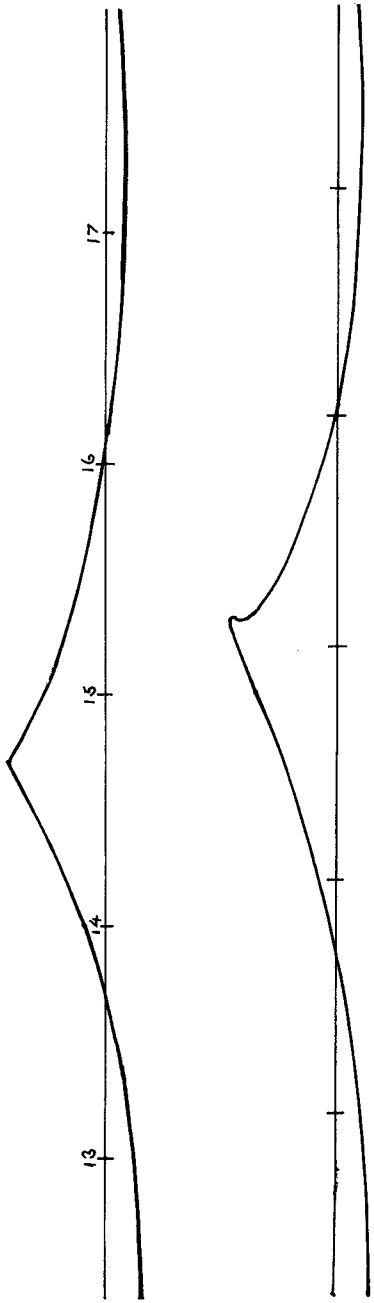

Figure 5. Computed wave profile at "breaking" for a 5 wave modulation with initial steepness ak = 0.12. (a) with initial modulation ε = 0.1 (b) with ε = 0.05. No vertical exaggeration.

Those modulations that break differ little from the first part of figure 3. This is illustrated in figure 4 which shows two profiles for the slightly greater initial wave steepness of $ak = 0.12$, compared with $ak = 0.11$ in figure 3. The first profile, at 60 periods, fits almost precisely on the supplementary profile at 70 periods in figure 3. It is significant that the ratio 70:60 is close to $(0.12)^2:(0.11)^2$ which is the relative scaling one would expect from the nonlinear Schrödinger equation. A wave trough is near the maximum point of the modulation.

The second profile in figure 4 is just one period later: the crest of a wave is now at a point close to the peak of the modulation. A very short time later the computation ceased because the wave crest was too sharp. Improved numerical resolution met the same problem. This wave crest is very close to the form of the limiting travelling wave with a corner of 120° at the crest. The maximum slopes of the waves are close to 30°. This crest is shown without vertical exaggeration in figure 5.

Also in figure 5 is a breaking wave derived from the same wave train but with the initial perturbation $\varepsilon = 0.05$ instead of $\varepsilon = 0.10$. This produced a slightly more energetic breaker at a later time.

Two isometric plots of the later stages of the computation with $\varepsilon = 0.05$ are chosen to show profiles in the time direction cutting a wave group when the peak modulation is in a trough, figure 6(a) and when it is at a crest, figure 6(b). They also show how each successive wave passes through the energy maximum.

The energy of the modulation continues to be focussed near the peak so that there is eventually one wave which either just breaks or breaks more strongly depending on the relationship between the energy focussing and wave phase. In reality each successive wave passing through such a group can break. This is reported from ocean observations by Donelan et al (1982). In a real sea the relationship between energy focussing and wave phase is likely to be even more variable, so this aspect of wave breaking has not been studied further.

The detailed shape and evolution of the short steep wave group that occurs for some periods before breaking, as illustrated in figure 6, is remarkably similar for a range of initial wave steepnesses and modulations. Profiles chosen at comparable times of wave passage through the groups can be superposed with only slight differences detectable.

4. Frequency downshifting

The problem of frequency downshifting has been examined carefully. In these calculations there is no frequency downshift at recurrence. On the other hand, at maximum modulation there is every sign of downshifting. There is normally one wave crest lost for each modulation: see figure 7 where at the end of a computation with 9 waves and two modulations only seven crests are visible. Similarly the spatial Fourier coefficients show a strong spectral shift to the lower perturbation wavenumber: figure 8 shows the time evolution of the coefficients

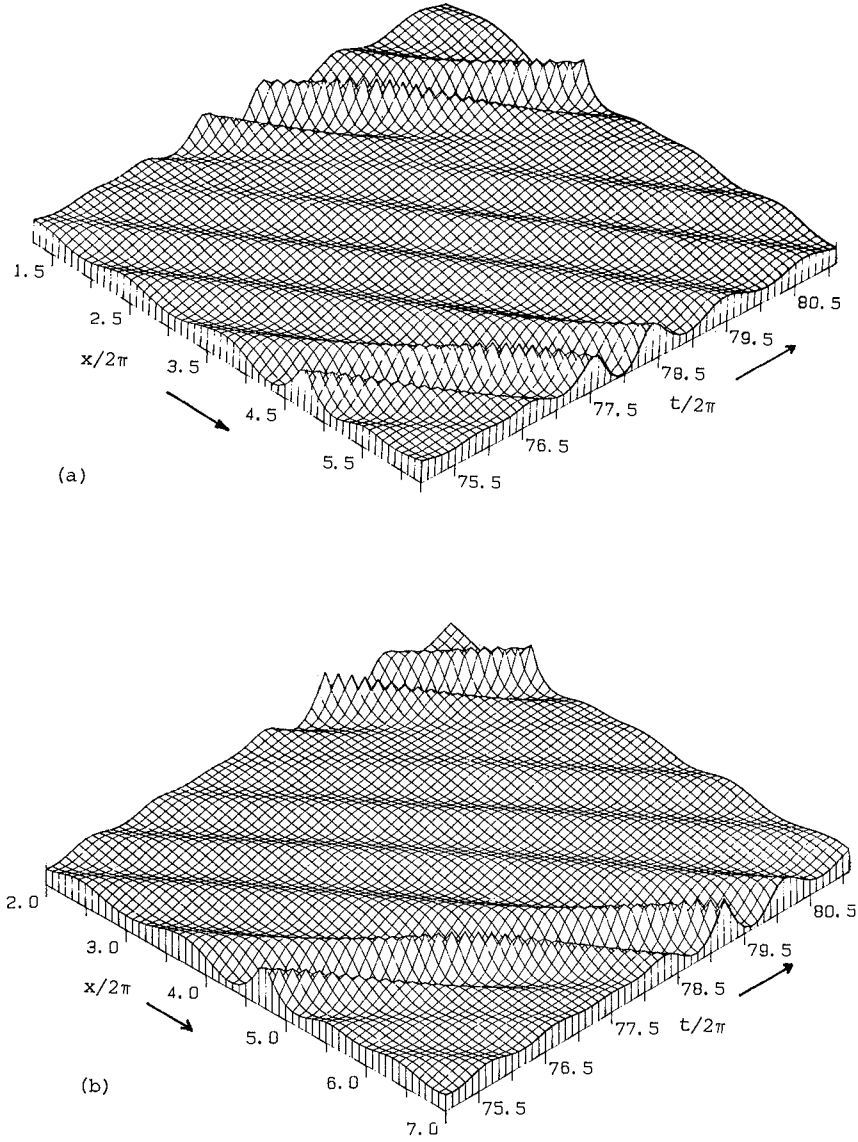

Figure 6. Isometric plots of the last 6 periods before breaking for the 5 wave modulation with initial steepness $ak = 0.12$, and initial modulation $\varepsilon = 0.05$. The "exposed" time profile has a trough at peak modulation in (a), and a crest in (b).

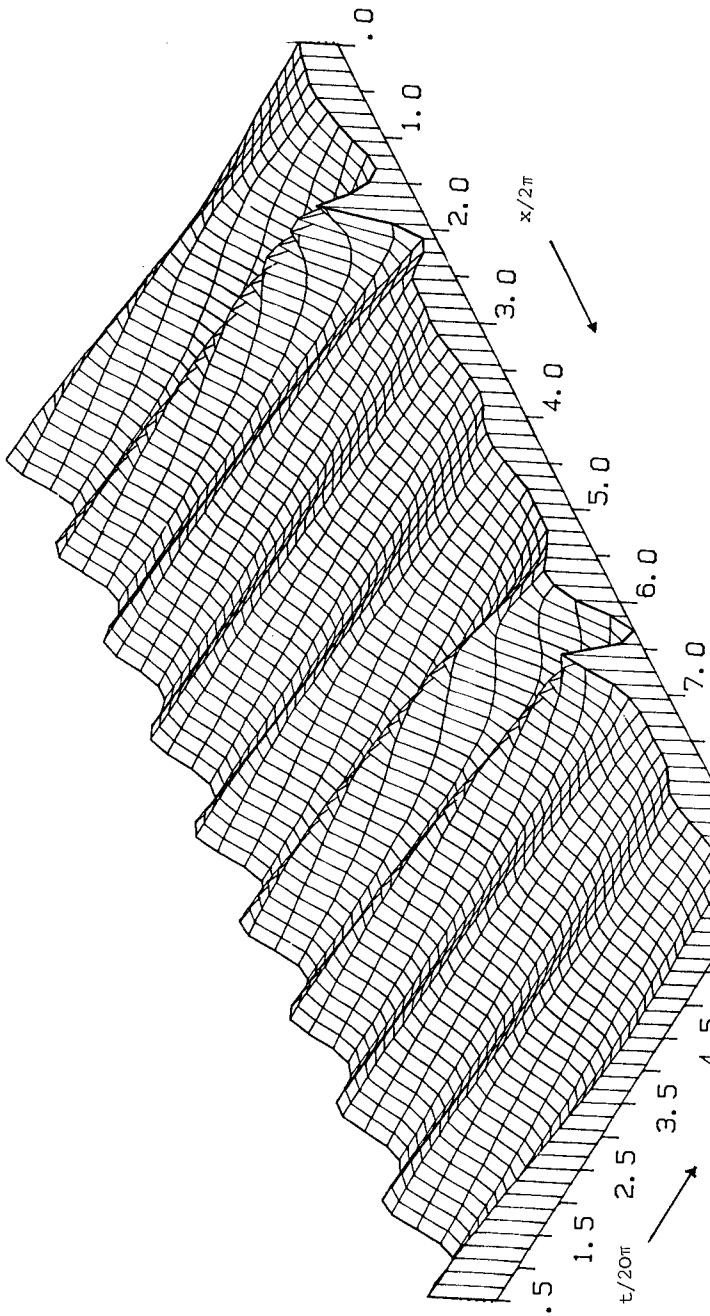

Figure 7. Plot of the time development for 64 periods of two 4½ wave modulations on an initial steepness of ak = 0.12. Phase and group velocity effects are minimised by taking data only every 2 periods. (The apparent roughness of the profiles shown is due to limitations of the plotting routine). Note the transition to 7 crests and 7 troughs.

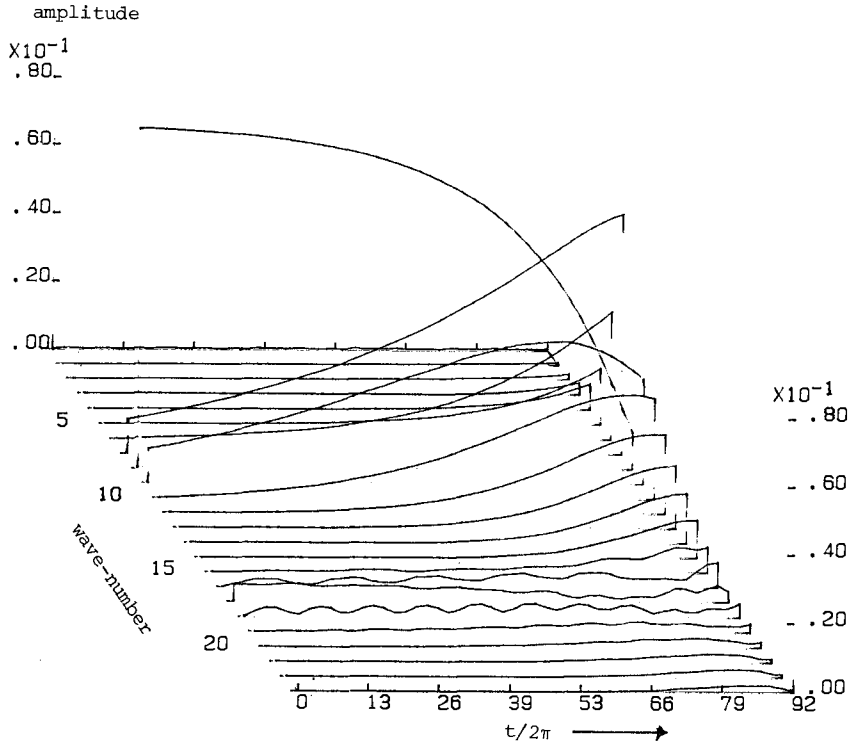

Figure 8. Time evolution of the spatial Fourier coefficients for a 9 wave modulation on waves with initial steepness 0.10. Breaking occurs at 92 periods with most energy in the "8" wave number component.

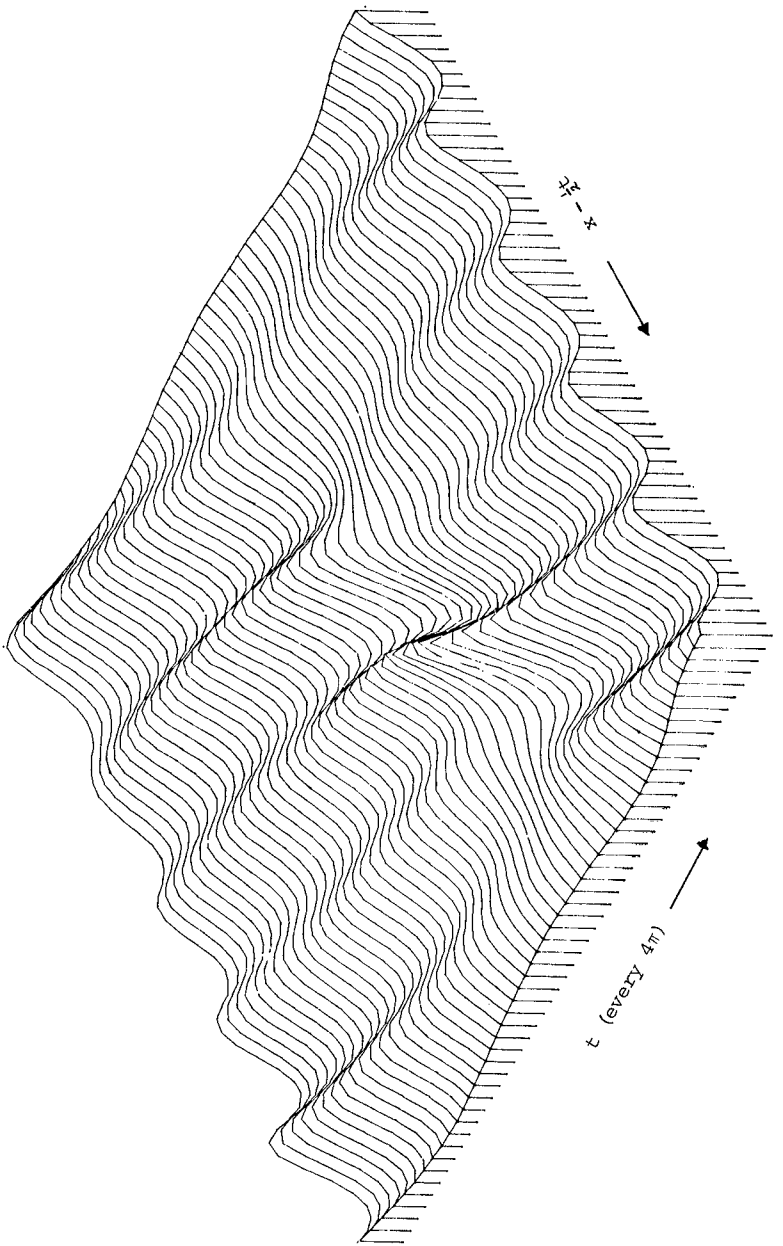

Figure 9. Evolution to recurrence, with linear phase and group velocity effects minimised, of a 5 wave modulation on wave steepness 0.11.

for a single 9-wave modulation. However, when recurrence occurs, as in figures 3 and 9 the original wavelength and period also return.

These computations support the hypothesis that breaking is essential for frequency downshift. This is consistent with experiments. However, waves actually disappear, or reappear, in the vicinity of zeros of wave amplitude. In each case of recurrence two such zeros were found at different times and one less wave can be seen during the time interval between zeros.

5. Conclusions

Computations describe many details of the evolution of weak modulations on a uniform wave train. The boundary of modulations that grow to breaking is outlined in terms of initial wave steepness and modulation length. Wave trains as gentle as $ak = 0.10$, $H/L \doteq 0.03$, can develop into breaking waves. For comparison, the energy density of a wind driven sea is equivalent to a uniform wave train, at the frequency of the spectral peak, of around $ak = 0.13$, and the limiting wave train of maximum steepness has $ak = 0.44$.

The steepest waves all occur in similar short groups a little more than one wavelength long. Such groups endure for around ten or more wave periods.

Although there are indications of frequency downshifting in the computations, the origin of the phenomenon is still obscure.

Comparisons with theory suggest:

(a) for times of a few periods linear theory gives a fair indication of wave behaviour, even for the steepest nonbreaking waves, but wave shape is nonlinear.

(b) for long time intervals, the weakly nonlinear NLS equation gives a qualitatively correct evolution, with quantitative discrepancies which are consistent with Dysthe's (1979) higher order approximation. These comparisons will be reported elsewhere.

J.W. Dold acknowledges the support of the U.K. Science and Engineering Research Council.

References

Benjamin, T.B. and Feir, J.E. 1967. The disintegration of wave trains on deep water. J.Fluid Mech. 27, 417-430.

Dold, J.W. and Peregrine, D.H. 1984. Steep unsteady waves: an efficient computational scheme. Proc. 19th Internat.Conf.Coastal Engng. A.S.C.E. Houston 1, 955-967.

Dold, J.W. and Peregrine, D.H. 1985. An efficient boundary-integral method for steep unsteady water waves. "Numerical methods for fluid dynamics II", eds: K.W. Morton and M.J. Baines, pp.671-679.

Clarendon Press, Oxford.

Donelan, M., Longuet-Higgins, M.S. and Turner, J.S. 1982. Periodicity in whitecaps. Nature 239, 449-451.

Dysthe, K.B. 1979. Note on a modification to the nonlinear Schrödinger equation for application to deep water-waves. Proc. Roy. Soc. London A 369, 105-114.

Lake, B.M., Yuen, H.C., Rungaldier, H. and Ferguson, W.E. 1977, Nonlinear deep-water waves: theory and experiment. Part 2. Evolution of a continuous wave train. J.Fluid Mech. 83, 49-74.

Lake, B.M. and Yuen, H.C. 1978. A new model for nonlinear wind waves. Part I. Physical model and experimental evidence. J.Fluid Mech. 88, 33-62.

Lo, E. and Mei, C.C. 1985. A numerical study of water-wave modulation based on a higher-order nonlinear Schrödinger equation. J.Fluid Mech. 150, 395-416.

Longuet-Higgins, M.S. 1978. The instabilities of gravity waves of finite amplitude in deep water. II Subharmonics. Proc. Roy. Soc. London A 360, 489-505.

Longuet-Higgins, M.S. & Cokelet, E.D. 1978. The deformation of steep surface waves on water. II Growth of normal mode instabilities. Proc. Roy. Soc. London A 364, 1-28.

McLean, J.W. 1982a. Instabilities of finite-amplitude water waves. J.Fluid Mech. 114, 315-330.

McLean, J.W. 1982b. Instabilities of finite-amplitude waves on water of finite depth. J.Fluid Mech. 114, 331-341.

Melville, W.K. 1982. The instability and breaking of deep-water waves. J.Fluid Mech. 115, 165-185.

Stiassnie, M. and Kroszynski, U.I. 1982. Long-time evolution of an unstable water-wave train. J.Fluid Mech. 116, 207-225.

Su, M.-Y., Bergin, M., Marler, P. and Myrick, R. 1982. Experiments on nonlinear instabilities and evolution of steep gravity-wave trains. J.Fluid Mech. 124, 45-72.

CHAPTER 14

APPLICATION OF A NESTED NUMERICAL MODEL TO IDEALISED RECTANGULAR HARBOURS

by

Roger A. Falconer[1] and Lida Mardapitta-Hadjipandeli[2]

Abstract

The paper gives details of a two-dimensional depth averaged nested numerical model and its application to a range of idealised rectangular harbours, having a constant plan cross-sectional area and varying length to breadth ratios. The main aims of the study have been to investigate the problems associated with nested numerical modelling and to apply this modelling approach to assess the influence of the shape of a harbour on its natural tidal flushing efficiency and mixing characteristics.

Introduction

In recent years there has been an increasing awareness of the tidal exchange characteristics and flushing efficiencies of ports, harbours and narrow entranced coastal basins. This incresed awareness can be attributed to a number of factors and, in particular, is partly attributable to the occurrence of poor water quality characteristics within both natural and man-made harbours and coastal basins. The main problems giving rise to poor water quality characteristics in coastal basins include such phenomena as:- low dissolved oxygen, eutrophication and low exchange rates and flushing efficiencies. The greater public concern and awareness of deteriorating water quality characteristics has partly arisen as a result of increased recreation and has led to many countries now establishing guidelines as to acceptable water quality standards within such coastal basins.

In attempting to minimise the occurrence of such phenomena as low dissolved oxygen and low tidal exchange rates, there are insufficient engineering design guidelines available to the coastal engineer faced with the task of designing a new harbour or modifying an existing coastal basin. For example, little knowledge exists in the technical literature as to:- (i) the optimum shape of harbours for maximum flushing efficiency, (ii) the ideal entrance configuration, (iii) the optimum depth for maximum flushing and minimum dredging requirements, and (iv) the effects of longshore currents on the basin's internal flow structure and exchange characteristics. Furthermore, the use of traditional physical model studies to obtain related design guidelines concerning tidal flushing and exchange characteristics for harbours is of limited

1. Lecturer in Civil Engineering, University of Birmingham, Birmingham, England.

2. Formerly Research Student, Department of Civil Engineering, University of Birmingham, England.

value, in view of the scaling problems associated with recirculating free surface flow models, i.e. Reynolds number effects. These scaling problems are particularly prevalent in harbours where the dimensions of the plan-form area, the narrow entrance width and the tidal range are such that tidal eddies occur within the basin on the flood tide.

In view of the growing concern about the water quality characteristics within narrow entranced coastal basins, such as harbours, and the problems associated with related physical model studies, there has also been an increasing use made of mathematical models for such studies e.g. Falconer (1,2). These mathematical model studies have either been undertaken for site specific studies or have been associated with related research programmes, such as:- (i) fluid mechanics and turbulence modelling, (ii) cohesive sediments and mud transport modelling, (iii) aspects of ecological, biological and chemical reaction modelling, e.g. the nitrification cycle, (iv) numerical methods, e.g. discontinuity modelling related to sewage effluent outfalls, and (v) field data acquisition and interpretation.

In earlier work reported by Falconer (1,3), a single grid-size mathematical model study was described wherein the model was specifically developed to predict the two-dimensional tide induced recirculatory velocity fields and solute transport distributions in harbours and narrow entranced coastal basins. Although reasonably encouraging agreement was obtained between the mathematical and physical model velocity and solute transport fields, at the same scale, no counter-rotating gyres - or tidal eddies - were predicted in the numerical model simulations and the dominant tidal eddy was always observed to be distinctly weaker in the numerical model predictions. The main cause of these discrepancies was attributed to the imprecise description of the velocity field at the harbour entrance and hence the main objective of this study was to develop a nested two-dimensional flow and solute transport model, with the aim of describing the velocity distribution across the harbour entrance more accurately. The model, which only required a marginal increase in the computational effort relative to the single grid-size model, was then applied to the rectangular harbours studied in an earlier research programme, by Falconer (1,3). The model was also used to investigate the effects of varying the harbour shape, entrance conditions and tidal range, with a view to establishing some fundamental engineering guidelines relating to the water quality aspects of rectangular harbours. The model included a refined turbulence model incorporating both free shear layer and bed generated turbulence, with simulations being undertaken at both prototype and physical model scales. Further physical model tests were undertaken to extend previous findings by Jiang and Falconer (4,5), and experimentally measured and numerically predicted velocity fields and exchange coefficients were compared for the physical model scale dimensions.

Governing Differential Equations

In determining the velocity and solute transport fields from the mathematical model, the depth averaged velocity components in the horizontal plane and the spatial solute distributions were obtained from the depth integrated equations of continuity, momentum - in both x and y directions in the horizontal plane - and the solute transport or

advective-diffusion equation. The full derivation of these equations is given by Falconer (6), with the equations of mass and momentum conservation being respectively given as:-

$$\frac{\partial \eta}{\partial t} + \frac{\partial UH}{\partial x} + \frac{\partial VH}{\partial y} = 0 \qquad \ldots\ (1)$$

$$\frac{\partial UH}{\partial t} + \beta\left[\frac{\partial U^2H}{\partial x} + \frac{\partial UVH}{\partial y}\right] - fVH + gH\frac{\partial \eta}{\partial x} + \frac{\tau_{bx}}{\rho} - \frac{1}{\rho}\left[\frac{\partial H\sigma_{xx}}{\partial x} + \frac{\partial H\tau_{xy}}{\partial y}\right] = 0 \qquad \ldots\ (2)$$

$$\frac{\partial VH}{\partial t} + \beta\left[\frac{\partial UVH}{\partial x} + \frac{\partial V^2H}{\partial y}\right] + fUH + gH\frac{\partial \eta}{\partial y} + \frac{\tau_{by}}{\rho} - \frac{1}{\rho}\left[\frac{H\tau_{yx}}{\partial x} + \frac{H\sigma_{yy}}{\partial y}\right] = 0 \qquad \ldots\ (3)$$

where η = water surface elevation above datum (e.g. MWL), t = time, U, V = depth mean velocity components in x,y directions, H = total depth of flow, β = momentum correction factor for non-uniform vertical velocity profile, f = Coriolis parameter, g = gravitational acceleration, τ_{bx}, τ_{by} = bed shear stress components in x,y directions, ρ = fluid density and σ_{xx}, τ_{xy}, τ_{yx}, σ_{yy} = Reynolds stress components in x,y directions.

For the bed shear stress components, the traditional quadratic friction law was used, giving (see Dronkers (7)):-

$$\tau_{bx} = \frac{\rho g U\bar{V}}{C^2} \quad \text{and} \quad \tau_{by} = \frac{\rho g V\bar{V}}{C^2} \qquad \ldots\ (4)$$

where $\bar{V}$ = depth mean fluid speed and C = Chezy roughness coefficient - evaluated in the numerical model from the Colebrook-White equation, given as:-

$$C = \frac{\sqrt{8g}}{\sqrt{f}} = -2\sqrt{8g}\,\log_{10}\left[\frac{k_s}{12R} + \frac{2.5}{Re\sqrt{f}}\right] \qquad \ldots\ (5)$$

where f = Darcy friction factor, k_s = length parameter characteristic of bed roughness, R = hydraulic radius, Re = Reynolds number = $4UR\nu^{-1}$ where ν = kinematic viscosity of fluid.

For the Reynolds stresses, the assumption was made that the direct stresses σ_{xx} and σ_{yy}, were generally small in comparison with the lateral shear stress, τ_{xy} and τ_{yx}, see Kuipers and Vreugdenhil(8) and, in the mixing zone, the lateral shear stresses were subdivided into two components. These components included turbulent shear contributions arising from free shear layer and bed generated turbulence and can be

summarised for the x-direction as follows:-

$$\tau_{xy} = \rho \left[\frac{U_1^2}{2\sqrt{2\pi R}} e^{-R/2(y^1/x^1)^2} + \frac{0.16\sqrt{g}\,\bar{V}H}{C} \frac{\partial U}{\partial y} \right] \quad \ldots\ (6)$$

where U^1 = free stream velocity, R = experimental constant and x^1, y^1 = co-ordinate axes for the mixing layer. This empirical shear stress distribution is based on the assumption of a Gaussian lateral velocity distribution in the horizontal plane and a logarithmic velocity distribution in the vertical plane. Full details of the derivation of equation (6) are given by Falconer, Wolanski and Mardapitta-Hadjipandeli (9) and Falconer and Mardapitta-Hadjipandeli (10).

The depth integrated advective-diffusion equation was attached to the hydrodynamic model, thereby enabling the transport of a conservative tracer S to be evaluated accordingly:-

$$\frac{\partial SH}{\partial t} + \left[\frac{\partial SUH}{\partial x} + \frac{\partial SVH}{\partial y} \right] = \frac{\partial}{\partial x} \left[HD_{xx} \frac{\partial s}{\partial x} + HD_{xy} \frac{\partial s}{\partial y} \right]$$

$$+ \frac{\partial}{\partial y} \left[HD_{yx} \frac{\partial s}{\partial x} + HD_{yy} \frac{\partial s}{\partial y} \right] \quad \ldots\ (7)$$

where D_{xx}, D_{xy}, D_{yx}, D_{yy} = depth mean longitudinal dispersion and turbulent diffusion tensor coefficients in x,y direction, as given by Fischer (11).

Mathematical Model Details

In numerically solving equations (1), (2), (3) and (7) an alternating direction implicit finite difference model was used, including a traditional space staggered grid scheme (see Falconer (2,3)). The difference equations were fully centred in time and space and the advective accelerations and diffusion terms were centred by a single iteration procedure (see Mardapitta-Hadjipandeli(12)). The model had no stability constraints, although it was established that the accuracy of the scheme deteriorated when the Courant number exceeded about eight, i.e. for accuracy:-

$$\Delta t \sqrt{gH}\, \Delta x^{-1} \leq 8 \quad \ldots\ (8)$$

where Δt = time step and Δx = grid spacing.

In the model, particular attention was given to the treatment of the advective accelerations, with these terms being expressed in a conservative form in both the differential and difference equations. This conservative representation of these terms allowed a more accurate simulation of the jet type flow field, associated with the flood tide flow past the narrow harbour entrance. In addition, the cross product advective accelerations were expressed in a modified form of the marker and cell technique, see Falconer et al (9), thereby allowing the momentum flux to be evaluated nearer to its position of

origin and the introduction of sufficient artificial diffusion to eliminate grid scale oscillations.

For the treatment of discontinuities, arising as the tracer contaminated fluid was advected into the region of non-contaminated fluid, sufficient artificial diffusion was introduced into the scheme to avoid the occurrence of negative concentration values. However, other than in the immediate vicinity of the discontinuity, the degree of artificial diffusion introduced into the scheme was negligible. This scheme was similar to that first outlined by Leendertse (13) and is described in more detail in Falconer (14).

Model Application

In extending work undertaken previously by Falconer et al (1)-(5), the physical and mathematical model studies were applied to idealised prototype rectangular harbours, having a flat bed, vertical sides and an asymmetric entrance. The idealised prototype harbour was assumed to have a constant plan-form area of $0.16km^2$, a mean depth of 6.0m, an entrance width of 100m, a tidal range of 5.0m and a variable length to breadth ratio - varying from 0.38 to 4.0. Each harbour shape considered was assumed to be initially contaminated uniformly within the basin by a conservative tracer of concentration 10ppm. The range of harbour shapes considered are illustrated schematically in Fig.1, which gives an illustration of the laboratory tidal tank and the harbour configuration.

For the physical model studies, the basin was modelled using a distorted Froude scale model, with horizontal and vertical length scales of 1:500 and 1:50 respectively. The resulting scaled laboratory model harbours had a plan-form area of $0.64m^2$, a mean depth of 120mm and an entrance width of 100mm. Likewise, for dynamic similarity, the corresponding velocity and time scales were 1:7.07 and 1:70.7 respectively, resulting in a model tidal period of 10.52 minutes and a range of 100mm.

In undertaking the laboratory model tests, the model harbour walls were first adjusted to give the required length to breadth ratio, for the constant plan-form area of $0.64m^2$. The overflow weir was set at the low tide level and the tidal tank was filled and the inflow rate adjusted to ensure a continuous flow over the weir for the whole model tide. After any initial circulation engendered within the basin had been dissipated, the harbour entrance was temporarily sealed and 75ml of Rhodamine B, of concentration 7.5mg/ℓ, was thoroughly mixed with the enclosed harbour fluid. The spatially averaged initial concentration was then determined from twelve evenly distributed sampling points. The temporary barrier across the harbour entrance was then removed and the tidal generator was run for three tides, after which time the generator was stopped and the temporary barrier simultaneously replaced. The spatially averaged final concentration was then determined as before and the exchange coefficient was evaluated as defined by the following equation (see Nece and Richey (15)):-

$$E = 1 - (Co/Ci)^{1/i} \quad \ldots\ (9)$$

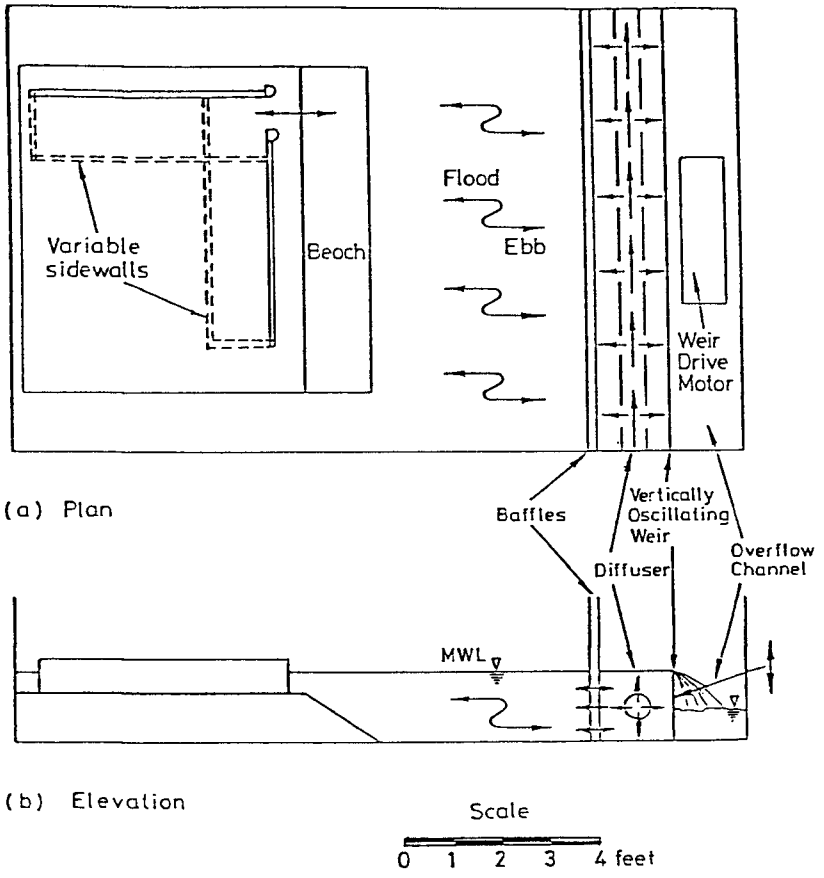

FIG.1 Details of Laboratory Tidal Tank and Harbour Configuration

where E = average per cycle exchange coefficient, Co = initial spatial average concentration, Ci = final spatial average concentration after i tidal cycles.

After the exchange coefficient had been determined, the depth mean velocity field was estimated at mean water level - for both the ebb and flood tide - using weighted drinking straws as drogues. The depth mean velocities were estimated as closely as possible at the intersecting points on a cartesian grid, which coincided with every other grid point of the mathematical model. The complete set of results for the tracer studies and velocity fields are given in Mardapitta-Hadjipandeli (12), with earlier results being given by Falconer et al (1)-(5).

For the mathematical model studies, a one-way interaction nested model was used. One-way interaction models involve the initial computation of the overall coarse-grid model which, in turn, provides the boundary conditions for the independent computation of the small-sized fine-grid model. The alternative two-way interaction models require the simultaneous computation of both grids, thus enabling the regions of different spacings to be dynamically inter-linked. The latter method therefore allows the response of the coarse-grid domain to small-scale processes occurring within the fine grid to be taken into account, giving rise to more coherent results over the computational domain. However, the dynamic coupling of the nested grid requires a more complex computational code. On the contrary, in one-way interaction models it is inherently assumed that the large scale motion of the coarse grid determines the small scale motion in the fine grid, without being affected by small scale processes occurring within the fine grid.

The overall coarse-grid domain for the rectangular harbour model studies was chosen to cover the whole plan-form area of the tidal tank and consisted of 27 x 34 grid points, of uniform grid spacing of 100mm, and with the tidal tank bathymetry being as depicted in Fig.2. At the open boundary, water elevations were presecribed according to a sine wave of the form:-

$$\eta = a \sin(\omega t + \phi) \qquad \ldots\ldots (10)$$

where a = amplitude, ω = tidal frequency and ϕ = phase angle governing the initial conditions. Since the tidal flow entered and exited the tidal tank uniformly across the oscillatory weir and in a direction normal to the open boundary, the advective accelerations were omitted along the open boundary and the tangential velocities were equated to zero. At the closed boundaries the no-slip boundary condition was implemented. A timestep of 0.84s was used in the model, giving rise to a maximum Courant number of about 9.0.

The domain of the fine grid model covered the plan-form area of the model and extended beyond the harbour entrance, as illustrated by the shaded region in Fig.2. The open boundaries of the fine-grid model were located well beyond the harbour entrance, so that small scale inaccuracies at the fine-grid open boundaries did not disturb the internal flow field predictions. The ratio of the grid scales between the coarse and fine grids in such models is arbitrary, although in practice

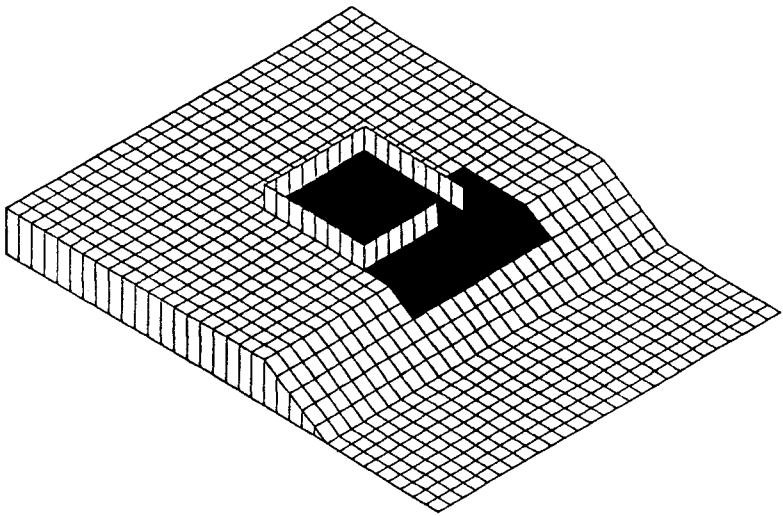

FIG.2 Isoparametric Projection of Tidal Tank Bathymetry Showing Extent of Nested Grid Domain

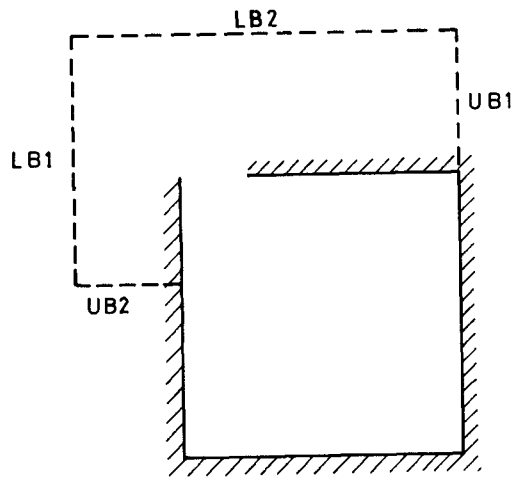

FIG.3 Schematic Illustration of Fine-Grid Open Boundaries

it has been suggested that the ratio should be kept below about 5 (see Thabet et al (16)). In this study the ratio of both the grid and time scales between the two nested grids was chosen to be 3, giving rise to a Courant number of about 9 in both grids. The decrease in the grid size and, as a consequence, in the timestep of the fine-grid model required both the time and space interpolation of the Coarse-grid model predictions in order to provide proper boundary conditions at the appropriate points along the fine-grid model boundaries. In the interpolation process, linear variations were assumed for the velocities and elevations, in both time and space.

Concerning the open boundary conditions of the fine-grid model, no guidelines were available as to the most suitable representation. Tests were therefore undertaken to determine the most appropriate combination of the open boundary conditions for this particular case study. The following combinations of open boundary conditions were tested at the four open boundaries of the fine-grid model (see Fig.3) for the square harbour configuration:-

(a) Water elevations and tangential velocity components along the lower boundaries, LB1 and LB2, and normal and tangential velocity components at the upper boundaries, UB1 and UB2.

(b) Normal and tangential velocity components at the lower boundaries, LB1 and LB2, and water elevations and tangential velocity components at the upper boundaries, UB1 and UB2.

(c) Normal and tangential velocity components at all four open boundaries.

(d) Normal and tangential velocity components along the boundaries LB1, LB2 and UB1, with water elevations being prescribed along UB2.

All four combinations gave similar velocity field predictions within the harbour, with some discrepancies occurring at the open boundaries. Combination (a) yielded the worst flow field predictions at the boundaries, where unrealistic circulation patterns were predicted along the water elevation boundaries, see Mardapitta-Hadjipandeli (12). For combination (b), grid scale oscillations were observed along the boundary UB1 and an obvious poor reproduction of the water elevation field was predicted using combination (c). The best water elevation and velocity field predictions were obtained using combination (d) and hence this inter-connecting boundary combination was used for all of the subsequent numerical model simulations.

Apart from applying the nested model to the idealised rectangular harbours at the laboratory model scale, the model was also applied to the equivalent scaled prototype harbours. The main objective of this exercise was to model directly the physical processes associated with tidal action in such harbours, thus enabling the influence of scaling in the physical model simulations to be considered. The nested model for the prototype harbours was geometrically similar to that for the physical model scale tests. The boundary conditions for the coarse and fine grid models were the same as those deployed in the physical scale model tests, with the exception of the coarse-grid model open boundary, where the

inclusion of the Coriolis term required the inclusion of a water surface slope, see Falconer et al (9). All prototype simulations were commenced from an initial state of rest, at low tide, with a timestep of 60s in the coarse-grid model and 20s in the fine-grid model - again giving rise to a Courant number of 9 in both models. As before, the computations were performed for two complete tidal cycles, with velocity, elevation and concentration fields being reproduced at every quarter of the tidal cycle.

Summary of Results

The complete set of results, for both the mathematical and physical model studies, are described in detail in Mardapitta-Hadjipandeli (12). For the nested numerical model the main finding was that the velocity field within the fine-grid model was best described by transferring only velocity information from the coarse grid model at all but one inter-connecting boundary, and by transferring water elevations at the remaining open boundary. The nested model gave better results than the non-nested model, for a similar computational effort, with the velocity fields predicted by the nested model being in much closer agreement with the physical model results. The coarse and fine grid flow structure was often significantly different between comparable simulations, with the coarse grid model incorrectly predicting a strong eddy at low tide for example. Furthermore the fine grid flow structure within the idealised harbours was not found to be strongly affected by the coarse grid flow structure, with this being best illustrated when the advective accelerations were excluded from the coarse grid model - see Mardapitta-Hadjipandeli (12).

For the laboratory scale model tests, comparisons showed a close agreement between the measured and predicted velocity and concentration distributions, as can be seen for the velocity distributions by comparing Figs. 4 and 6 respectively. An analysis of the results for the free shear and bed generated stress distributions showed that these turbulent stress components were of a similar magnitude at this scale, although from the vorticity field distributions it was confirmed that the effects of bed friction variations were not significant. Comparisons were also undertaken to establish the significance of using free slip and no slip boundary conditions at the closed boundaries, with the results confirming that the flow structure was very different for these two types of boundary condition. The no slip boundary condition gave much closer agreement with the physical model results and it was therefore concluded that this boundary condition was more appropriate in the numerical model, even though the boundary layer thickness was generally a sub-grid scale phenomenon. In terms of the flushing efficiency and exchange characteristics, the numerical and physical model results both indicated that there was a marked reduction in the exchange coefficient for aspect ratios (i.e. L/B ratios) of less than about 0.5 and greater than 2.0. The numerical model results indicated that the peak exchange coefficient occurred for an aspect ratio of unity, i.e. for a square harbour, although this was not clearly confirmed from the physical model results. Finally, for all of the comparisons undertaken at the laboratory model scale, it was evident from both types of modelling procedures that the harbour corners were always observed to be regions of poor local exchange.

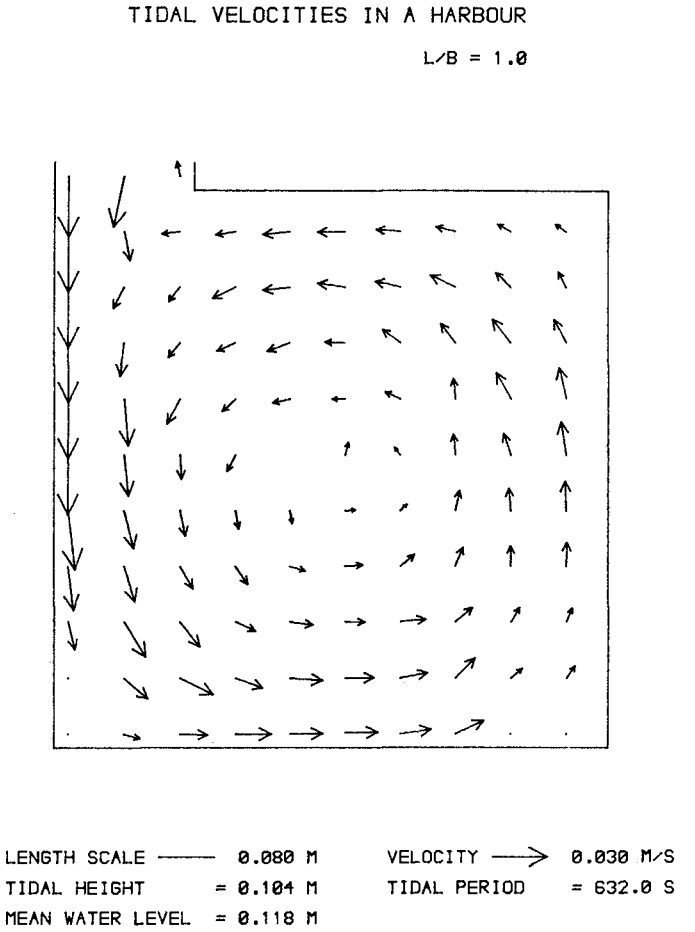

FIG.4 Experimentally Measured Velocities at Mean Water Level Flood Tide for L/B = 1.0

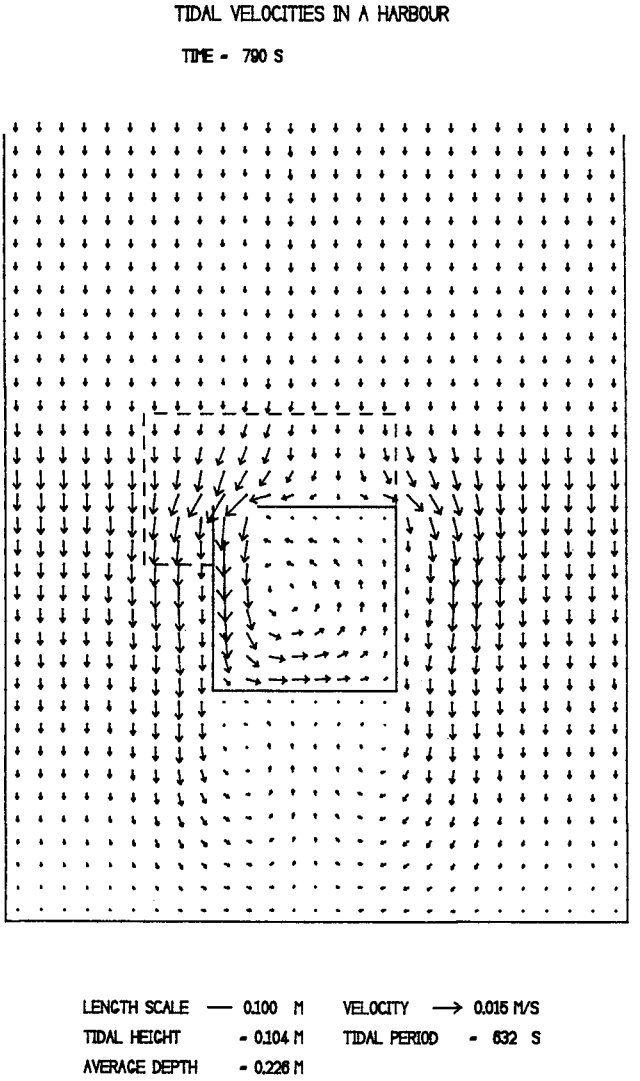

FIG.5 Predicted Coarse-Grid Velocity Field in Model at Mean Water Level Flood Tide for L/B = 1.0

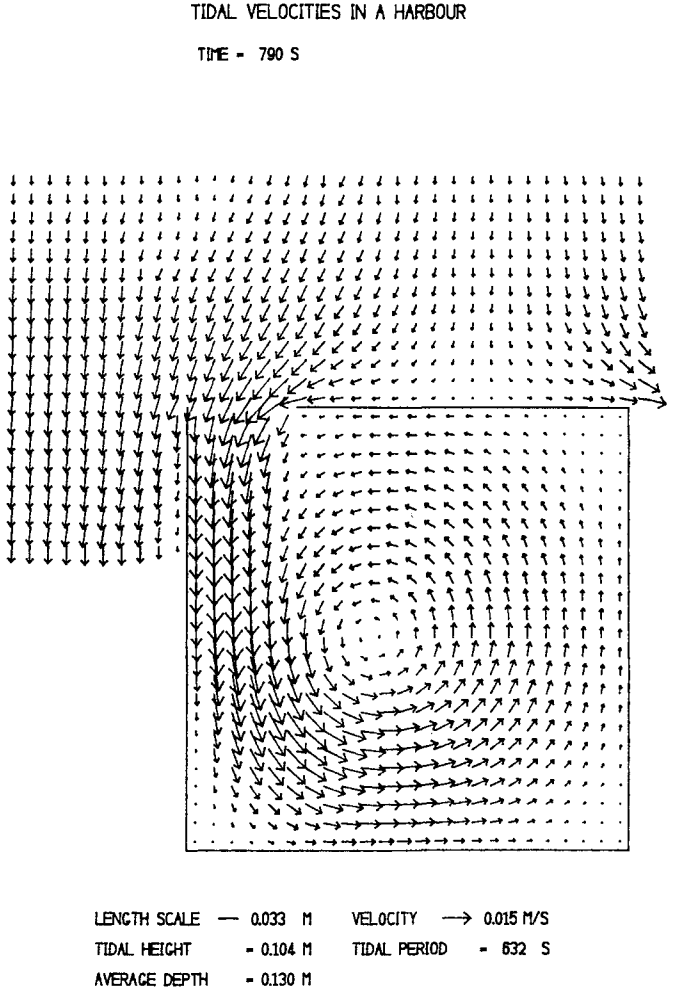

FIG.6 Predicted Fine-Grid Velocity Field in Model at Mean Water level Flood Tide for L/B = 1.0

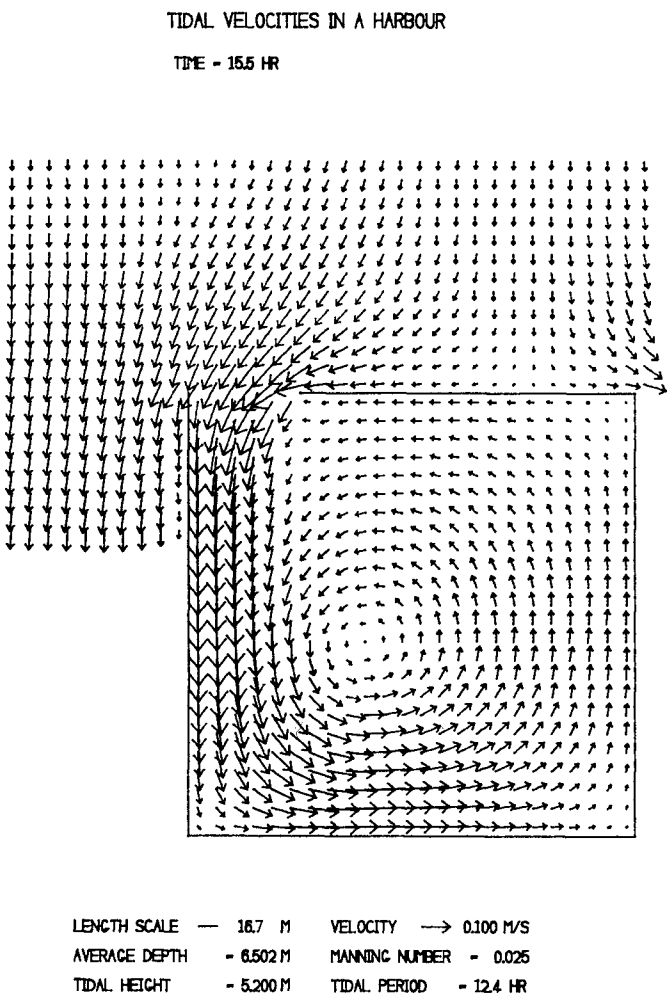

FIG.5 Predicted Fine-Grid Velocity Field in Prototype at Mean Water Level Flood Tide for B/L = 1.0

For the prototype numerical model simulations, comparisons with the laboratory model scale numerical results showed similar agreement for the coarse grid results. However, for the fine grid comparisons the velocity field patterns were often markedly different, see Mardapitta-Hadjipandeli (12). This difference between the prototype and laboratory model scale predictions was particularly pronounced during an ebb tide and was highlighted by the obvious difference in the eddy structure. Such a difference in the numerical model results for the prototype and laboratory model scale harbours has confirmed the problems associated with laboratory model studies of recirculating flows and has raised further questions as to the suitability of distorted laboratory models. As for the laboratory model scale simulations, an analysis was undertaken of the relative magnitudes of the free shear stress and bed generated stress components. The resulting comparisons showed that the free shear stress dominated over the bed generated stress in the mixing zone - unlike the laboratory model scale results - with this conclusion being confirmed by theory (12). Likewise, pronounced changes in the bed roughness coefficient were shown to have a marked effect on the vorticity structure, whereas the effects of dispersion were found to be less significant in the prototype simulations. These results also differed from the laboratory model scale predictions and confirmed the implications of a dimensional analysis study, in that vertical distortion results in an over-estimation of dispersion-diffusion processes and momentum transfer by bed generated turbulence, and an under-estimation of the effects of bed friction. Finally, the numerically predicted prototype scale exchange coefficients and flushing characteristics indicated that the optimum flushing efficiency occurred for an aspect ratio of 2.6, with a distinct reduction occurring in the exchange coefficient for a square harbour. A comparison of the corresponding standard deviation of the concentration distribution within the various shaped harbours, at both prototype and laboratory model scales, also showed that the concentrate was more uniformly mixed in the prototype harbours.

Conclusions

A nested numerical model has been developed and applied to idealised rectangular harbours to predict velocity fields, exchange coefficients and flushing efficiencies for various harbour shapes. Encouraging agreement has been obtained between the numerical model predictions and laboratory model results at the same scale, with similar prototype model simulations and comparisons highlighting the problems associated with scaling effects in distorted laboratory models. The laboratory model scale results showed that the exchange coefficient deteriorated markedly for rectangular harbours when the length to breadth ratio was less than 0.5 or greater than 2.0, whereas for the prototype model simulations the optimum exchange coefficient was obtained when the aspect ratio was about 2.6.

Acknowledgements

The mathematical and laboratory model studies reported herein were undertaken at the Department of Civil Engineering, University of Birmingham, with the study being partially funded by the Science and Engineering Research Council.

References

1. Falconer, R.A., "Numerical Modelling of Tidal Circulation in Harbours", Journal of the Waterway, Port, Coastal and Ocean Division, ASCE, Vol.106, No.WW1, February 1980, pp31-48.

2. Falconer, R.A., "A Mathematical Model Study of the Flushing Characteristics of a Shallow Tidal Bay", Proceedings of the Institution of Civil Engineers, Part 2, Vol.77, September 1984, pp.311-332.

3. Falconer, R.A., "Modelling of Planform Influence on Circulation in Harbours", Proceedings of the Seventeenth Coastal Engineering Conference, ASCE, Sydney, Australia, March 1980, pp.2726 - 2744.

4. Jiang, J.X. and Falconer, R.A., "On the Tidal Exchange Characteristics of Model Rectangular Harbours", Proceedings of the Institution of Civil Engineers, Part 2, Vol.75, September 1983, pp.475 - 489.

5. Jiang, J.X. and Falconer, R.A., "The Influence of Entrance Conditions and Longshore Currents on Tidal Flushing and Circulation in Model Rectangular Harbours", International Conference on Numerical and Hydraulic Modelling of Ports and Harbours, BHRA, Birmingham, England, Paper B4, April 1985, pp.65 - 74.

6. Falconer, R.A., "Mathematical Modelling of Jet-Forced Circulation in Reservoirs and Harbours", thesis presented to the University of London, England, in partial fulfillment of the requirements of the degree of Doctor of Philosophy, 1976, pp.237.

7. Dronkers, J.J., "Tidal Computations in Rivers and Coastal Seas", North Holland Publishing Co., Amsterdam, The Netherlands, 1964.

8. Kuipers, J. and Vreugdenhil, C.B., "Calculations of Two-Dimensional Horizontal Flow", Report No.S163, Part 1, Delft Hydraulics Laboratory, Delft, The Netherlands, 1973.

9. Falconer, R.A., Wolanski, E. and Mardapitta-Hadjipandeli, L., "Modelling Tidal Circulation in an Island's Wake", Journal of Waterway, Port, Coastal and Ocean Engineering, Vol.121, No.2, March 1986, pp.234-254.

10. Falconer, R.A. and Mardapitta-Hadjipandeli, L., "Bathymetric and Shear Stress Effects on an Island's Wake: A Computational Model Study", Coastal Engineering (in press).

11. Fisher, H.B., "On the Tensor Form of the Bulk Dispersion Coefficient in a Bounded Skewed Shear Flow", Journal of Geophysical Research, Vol.83, No.C5, May 1978, pp.2373-2375.

12. Mardapitta-Hadjipandeli, L. "Numerical Modelling of Tidal Circulation", thesis presented to the University of Birmingham, England, in partial fulfillment of the requirements for the degree of Doctor of Philosophy, 1985, pp.293.

13. Leendertse, J.J., "A Water-Quality Simulation Model for Well-Mixed Estuaries and Coastal Seas : Vol.1, Principles of Computation", The Rand Corporation, RM-6230-RC, February 1970, pp.70.

14. Falconer, R.A., "Temperature Distributions in a Tidal Flow Field", Journal of Environmental Engineering, ASCE, Vol.110 No.6, December 1984, pp.1099-1116.

15. Nece, R.E. and Richey, E.P., "Flushing Characteristics of Small Boat Marinas", Proceedings of the Thirteenth Coastal Engineering Conference, ASCE, Vancouver, 1972, pp.2499-2512.

16. Thabet, R.A.H., Verboom, G.K. and Akkerman, G.J., "Two-Dimensional Modelling of Tidal Motion for Harbour Studies", Proceedings of the International Conference on Numerical Modelling of Ports and Harbours, BHRA Birmingham, England, April 1985, pp.23-32.

CHAPTER 15

Polynomial approximation and water waves

John D. Fenton*

A different approach to the solution of water wave problems is considered. Instead of using an approximate wave theory combined with highly accurate global spatial approximation methods, as for example in many applications of linear wave theory, a method is developed which uses local polynomial approximation combined with the full nonlinear equations. The method is applied to the problem of inferring wave properties from the record of a pressure transducer, and is found to be capable of high accuracy for waves which are not too short, even for large amplitude waves. The general approach of polynomial approximation is well suited to problems of a rather more general nature, especially where the geometry is at all complicated. It may prove useful in other areas, such as the nonlinear interaction of long waves, shoaling of waves, and in three dimensional problems, such as nonlinear wave refraction and diffraction.

1. Introduction

Conventional linear wave theory, for example, uses a physical approximation which is of a low order of accuracy, neglecting terms which have a magnitude of the order of the square of the wave steepness. In most applications of this theory, however, a global spatial approximation method is used. Often the wave field is approximated by a full spectral representation (Fourier series), so that the spatial approximation is of very high accuracy, and is valid throughout the region of interest. This not only leads to an apparent large discrepancy between the accuracy by which the physical system is modelled and the numerical accuracy used in that model, but also severe limitations as to the boundary geometries which can be considered. In fact, anything other than a flat bed is usually very difficult to treat.

Long wave theory uses approximations based on the limitation that the motion have a large horizontal length scale relative to the water depth, so that the variation of velocities etc. with elevation in the fluid is relatively small. In this case there is a greater degree of harmony between the level of physical and numerical approximation. However, to higher orders of approximation, shallow water (long wave) theory quickly becomes unmanageable as the equations become complicated, and almost invariably higher derivatives occur at each level of approximation. For example, the Boussinesq equations and their relations involve third derivatives at first order, and so on. This

* Professor, Department of Civil Engineering, University of Auckland, Private Bag, Auckland, New Zealand. Work performed while a Senior Lecturer, School of Mathematics, University of New South Wales, Kensington, N.S.W., Australia 2033.

compares with the the full nonlinear equations, where there are no derivatives higher than the first in the boundary conditions. Another feature of long wave theory, as in methods which use wave steepness expansions (Stokes' methods), is that the presence of anything other than a flat bed quickly complicates the method and equations.

This paper is an initial attempt to turn in the direction of conventional numerical methods for the simulation of nonlinear waves, so that the level of physical and numerical approximation is consistent, and that as far as possible routine computational techniques can be used. In particular, local polynomial approximation methods are to be used, which are of a finite order of accuracy, but which are much simpler to use, especially in their incorporation into the full nonlinear boundary conditions. They have a further major advantage, in that they can be used to satisfy other boundary conditions locally, so that irregular boundaries can be treated, including problems of wave interactions with solid boundaries of a possibly abrupt nature, or of a gentle nature such as an irregularly varying bottom.

In this paper, it is attempted to explore where methods of local polynomial approximation might be used, by considering one problem only, that of analyzing the data obtained by a pressure transducer, and inferring other wave properties from that data, for example the surface elevation, the fluid velocity components at other points in the fluid, and possibly spectra of these and other gross quantities associated with the waves.

The information obtained by a pressure transducer is $p(t_n)$, the pressure at a finite number of instants t_n, $n = 1, 2, \ldots, N$. From these pressure readings it is simple to calculate the mean and to infer the mean depth. This can then be used as a length scale for non-dimensionalisation. Throughout the rest of this paper, all quantities are to be taken as having been non-dimensionalised with respect to the mean depth d, gravitational acceleration g, and/or fluid density ρ. (For example, pressure p is "$p/\rho gd$" in dimensional terms, horizontal velocity u is actually "$u/\sqrt{(gd)}$", and so on.) The conventional approach based on linear wave theory would be to take the signal $p(t_n)$, obtain its discrete Fourier transform P_j, for $j = 0, \pm 1, \ldots, \pm N/2$, use linear wave theory to find the corresponding harmonic components, for example U_j and V_j, of the fluid velocity, and then to obtain the actual velocities $u(x,y,t)$ and $v(x,y,t)$, in the horizontal and vertical coordinate directions x and y respectively. A limiting feature of linear theory is that all components of the waves are travelling at the speed corresponding to that phase as given by linear theory, and that there are no nonlinear interactions at all. Particularly in near-shore regions, with the observed tendency of long waves to travel as (nonlinear) waves of translation, where the individual components are bound to the main wave and travel with its speed, this is an unnecessarily limiting assumption.

This is not as critical a problem as the fundamental ill-conditioning of the problem as posed, of inferring fluid motions governed by an elliptic equation (Laplace) from boundary data specified on one level only, that of the pressure transducer. This occurs if the probe is located far below the point at which the velocities are

required or it is desired to find the surface elevations $\eta(t_n)$, from the inferred spectrum Y_j of the free surface elevation. The transfer function connecting Y_j and P_j is proportional to $\cosh k(j)/\cosh k(j)y_p$, where k is the wavenumber given by the linear dispersion relation for the jth harmonic of the signal. For higher frequency components the transfer function varies like $\exp(k(j)(y-y_p))$, and using the short wave approximation for the linear dispersion relation, this varies as $\exp(j^2\omega^2(y-y_p))$, where ω is 2π divided by the total time of the record. It is clear that the transfer function grows remarkably quickly with j, corresponding to higher frequency components. Even for smooth records with spectra P_j which decay quite quickly in j, this exponential growth of the transfer function with j completely destroys any accuracy for harmonic components shorter than the water depth. The method is really only suited to long waves in shallow water. Unfortunately it is for these conditions that linear wave theory is not particularly appropriate, as the waves are likely to be nonlinear and to be long, giving rise to the presence of higher harmonics with their attendant ability to destroy the meaningful part of the signal.

Proceeding in the other direction does not present the same set of problems, as noted above. For example, if the surface elevation is recorded, to give the Y_j, and it is desired to calculate velocities deeper in the fluid, then the transfer function works so as to dramatically reduce the U_j relative to the Y_j for higher frequency components, and the process is well-conditioned. For example, Vis (1980) and Daemrich, Eggert & Kohlhase (1980) used this approach, and found that for waves which were not high the linear theory gave good results for the fluid velocities.

Use of the spectral method outlined above does have some further practical problems. To implement the method it is usually necessary to resort to a number of techniques of data analysis, which degrade the information provided by the original signal. These techniques include trend removal, multiplying by a "window" to remove spurious components due to end discontinuities, filtering and so on.

The method used in this paper, based on local low-degree polynomial approximation does not overcome the fundamental ill-conditioning of the problem, but in water of finite depth the approach is much less susceptible to the problems described above. The application of local approximation for this problem was originated by Nielsen (1986), who used an approach based on local interpolation by trigonometric functions combined with linear theory.

2. Theory

Throughout this work it is assumed that the waves are travelling over an impermeable bed which is locally flat with coordinate origin on that bed, that all motion is two-dimensional, and that the fluid is incompressible and the fluid motion irrotational such that a complex velocity potential w exists, $w = \phi + i\,\psi$, where ϕ is velocity potential and ψ is stream function, which is an analytic function of the complex coordinate $z = x + i\,y$. The coordinate origin is taken to be on the bed, beneath the pressure probe. As the entire discussion is based on

local approximation we can introduce a local time t, which is zero at t_n, the instant at which the pressure reading is taken. The velocity components (u,v) are given by $u - i\,v = dw/dz$. The approximation is made here that the motion locally is propagating without change in the x direction with a speed c, which is as yet unknown. Hence, variation with x and t can be combined in the form x - ct. Locally, this is a reasonable assumption, as the time scale of distortion of the wave as dispersion and nonlinearity take effect is considerably larger than the local time over which the theory is required to be valid.

A principle of local polynomial approximation is adopted, such that in the vicinity of the pressure probe, throughout the depth of fluid, the complex velocity potential w(x,y,t) and the free surface η(x,t) are given by polynomials of degree M:

$$w(x,y,t) = \phi(x-ct,y) + i\,\psi(x-ct,y) = \sum_{j=0}^{M} \frac{a_j}{j+1}(z-ct)^{j+1}, \qquad (2.1)$$

where z = x + iy, and

$$\eta(x,t) = \sum_{j=0}^{M} b_j (x-ct)^j. \qquad (2.2)$$

Expansion (2.1) satisfies the governing equation for irrotational flow of an incompressible fluid (Laplace's equation) identically throughout the flow. The bottom boundary condition v(x,0,t) = 0 is satisfied if the coefficients a_j are real only, as the b_j are. It remains to satisfy the boundary conditions on the free surface, that the pressure is constant and that particles remain on the surface. Here we use the approximation again that motion is steady in a coordinate system (x-ct,y).

The steady kinematic equation that the value of ψ is constant on the surface y = η is

$$\psi(x-ct,\eta(x-ct)) = -Q, \qquad (2.3)$$

where Q is a constant. The steady Bernoulli equation is

$$R = \frac{1}{2}\left|\frac{dw}{d(z-ct)}\right|_s^2 + \eta, \qquad (2.4)$$

where R is a constant, and the subscript s denotes the surface y = η.

Also, in the frame in which motion is steady Bernoulli's equation can be written for the point $(0,y_p)$, where the pressure probe is located. The pressure around that point can be expressed as a Taylor series in x-ct:

$$p(x,y_p,t) = R - \frac{1}{2}\left|\frac{dw}{d(z-ct)}\right|_{y_p}^2 - y_p \qquad (2.5.1)$$

$$= \sum_{j=0}^{M} p_j (x-ct)^j. \qquad (2.5.2)$$

The coefficients p_j can be found from the pressure readings $p(t_n)$. Details of this will be presented further below.

Substitution of the series (2.1) and (2.2) into equations (2.3), (2.4) and (2.5) gives polynomials in x-ct. These polynomials must be valid locally for all values of x-ct, hence the coefficients of each power of x-ct must agree across the equation. This gives a system of nonlinear equations in the unknown coefficients a_0, a_1, a_2, ..., and b_0, b_1, b_2, ... The equations are in terms of the coefficients p_0, p_1, p_2, ..., which are assumed to have been calculated from the pressure readings.

It is feasible to produce the equations by hand calculation for M = 2. However for larger values of M the amount of calculation becomes prohibitive. The symbolic algebra manipulation package MACSYMA was used on the computer in the School of Mathematics at the University of New South Wales to produce solutions for M = 2 and M = 4. MACSYMA has the facility of producing executable code, and the output could be used to evaluate the full set of equations.

3. Equations

The equations can be written in the form

$$K_1 = K_2 = K_3 = K_4 = \ldots = 0, \quad D_1 = D_2 = D_3 = D_4 = \ldots = 0,$$

and

$$P_0 = P_1 = P_2 = P_3 = P_4 = \ldots = 0, \tag{3.1}$$

where the quantities K, D and P come from the kinematic equation (2.3), the dynamic equation (2.4) and the pressure equation (2.5) respectively. The subscripts 0, 1, 2 *etc.* refer to the power of x-ct of which this term is coefficient.

For a quadratic level of approximation, M = 2, the quantities are defined by:

$$K_1 = -b_0^2 b_1 a_2 + a_0 b_1 + b_0 a_1,$$

$$K_2 = -b_0^2 a_2 b_2 + a_0 b_2 - b_0 b_1^2 a_2 + b_0 a_2 + a_1 b_1,$$

$$D_1 = 2b_0^3 b_1 a_2^2 - 2a_0 b_0 b_1 a_2 + b_0^2 a_1 a_2 + b_0 a_1^2 b_1 + b_1 + a_0 a_1,$$

$$D_2 = 2b_0^3 a_2^2 b_2 - 2a_0 b_0 a_2 b_2 + b_0 a_1^2 b_2 + b_2 + 3b_0^2 b_1^2 a_2^2 + b_0^2 a_2^2 - a_0 b_1^2 a_2 + 2b_0 a_1 b_1 a_2 + a_0 a_2 + a_1^2 b_1^2/2 + a_1^2/2,$$

$$P_0 = a_2^2 y_p^4/2 - a_0 a_2 y_p^2 + a_1^2 y_p^2/2 - b_0^4 a_2^2/2 + a_0 b_0^2 a_2 - b_0^2 a_1^2/2 + p_0 - b_0 + y_p,$$

$$p_1 = a_1 a_2 y_p^2 + p_1 + a_0 a_1,$$

$$p_2 = a_2^2 y_p^2 + p_2 + a_0 a_2 + a_1^2/2. \qquad (3.2)$$

This system of equations is overdetermined, in that it contains seven nontrivial equations in the six unknowns a_0, b_0, a_1, b_1, a_2 and b_2.

For the case M = 4, where quartic variation is allowed, a system of 13 equations in 10 unknowns results. The system is similarly overdetermined. In this case, the equations are rather longer and space does not permit their inclusion here.

4. Solution of equations

The problem is, for each of the N values of the $p(t_n)$, take several adjacent values, find the local approximating polynomial by finding the p_j for $j = 0, \ldots, M$, and solve the equations to give the a_j, b_j for $j = 0, \ldots, M$. This enables a complete local solution for the velocity field to be obtained, from the a_j, and the free surface variation from the b_j.

The solution procedure is as follows.

Step 1: Initially, assume that the disturbances everywhere travel at the speed of linear long waves $c = 1$ ($c = \sqrt{g \times \text{mean depth}}$ in physical terms).

Step 2: For successive iterations until the process converges, repeat Steps 3 to 6. (In the calculations described in Section 5, 3 iterations were sufficient for four-figure accuracy).

Step 3: For each of the times t_n, n from 1 to N, perform Steps 4 and 5.

Step 4 Calculation of p_j for $j = 0, \ldots, M$: Consider equation (2.5.2) written for the point at which the pressure probe is located, $x = 0$, $y = y_p$:

$$p(0, y_p, t) = \sum_{j=0}^{M} p_j (-ct)^j. \qquad (4.1)$$

To find the coefficients in this series it would be possible to use simple finite difference methods based on the M+1 pressure readings $p(0, y_p, t_m)$ in the vicinity of t_n, for $m = -N/2, \ldots, 0, \ldots, +N/2$. (Here an ambiguous but convenient notation t_m has been used for discrete values of the local time such that $t_0 = 0$, whereas t_n will continue to be used to refer to instants at which pressure readings have been taken. This use of local time is important in the simplifications which lead to equations (4.2.1) and (4.2.2).) As it is intended that the method be used in practice, where there are likely to be irregularities in the input data, such interpolation of the pressure record is a rather dangerous procedure, as interpolating polynomials fitted to experimental points exhibit wild fluctuations. A better procedure would be to use a least-squares procedure using K points, where K is rather

greater than M+1. It can be shown (see standard numerical analysis textbooks) that the least squares procedure leads to the matrix equation

$$\begin{bmatrix} K & \Sigma t_m & \cdots \\ \Sigma t_m & \Sigma t_m^2 & \cdots \\ \cdots & \cdots & \cdots \end{bmatrix} \begin{bmatrix} p_0 \\ -p_1 c \\ \cdots \end{bmatrix} = \begin{bmatrix} \Sigma p(t_m) \\ \Sigma t_m p(t_m) \\ \cdots \end{bmatrix}.$$

In this expression all the summations are over K values of m. If approximation by a quartic is used, this matrix equation involves five equations in five unknowns, and the solution is complicated. A useful simplification can be made, however. Here and throughout the rest of this work it will be assumed that the points are obtained at equal intervals of time Δ, K is chosen to be an odd number, and points are distributed symmetrically about the point of calculation, such that m varies from $m = -(K-1)/2$ to $m = +(K-1)/2$. Then all the sums over odd powers of t_m become zero, and the system can be written as two separate systems, one of third-order and the other second-order. With a little re-arrangement they can be written:

$$\begin{bmatrix} K & \Sigma m^2 & \Sigma m^4 \\ \Sigma m^2 & \Sigma m^4 & \Sigma m^6 \\ \Sigma m^4 & \Sigma m^6 & \Sigma m^8 \end{bmatrix} \begin{bmatrix} p_0 \\ p_2 c^2 \Delta^2 \\ p_4 c^4 \Delta^4 \end{bmatrix} = \begin{bmatrix} \Sigma p(t_m) \\ \Sigma m^2 p(t_m) \\ \Sigma m^4 p(t_m) \end{bmatrix}, \tag{4.2.1}$$

and

$$\begin{bmatrix} \Sigma m^2 & \Sigma m^4 \\ \Sigma m^4 & \Sigma m^6 \end{bmatrix} \begin{bmatrix} -p_1 c\Delta \\ -p_3 c^3 \Delta^3 \end{bmatrix} = \begin{bmatrix} \Sigma m\ p(t_m) \\ \Sigma m^3 p(t_m) \end{bmatrix}. \tag{4.2.2}$$

If quadratic approximation M = 2 is used, then the last row and column of the matrices are simply deleted.

The coefficients in the square matrices are simply sums over the powers of the integers, from $m = -(K-1)/2$ to $m = +(K-1)/2$, and analytical expressions can be found for them. however the numerical values are easier to obtain by simple summation than by these complicated formulae, particularly as once the level of approximation M and the number of points K in the least squares fit are decided, the coefficients are simple integer constants for all points of all pressure records. In any case, it is easy to write down the inverses of the matrix equations presented here. That is a standard mathematical task, and will not be done here. Of course, they too are constant, once M and K are adopted.

Although the use of interpolation rather than least squares approximation is not recommended, for that case, where the number of

points is such that K = M + 1, all the matrix formulae presented above are still valid, and one is free to use either interpolation or a least-squares fit simply by choosing the value of K.

Having found the coefficients p_j, the equations can now be solved. However, the above formulae are in terms of the speed c with which the local disturbance is travelling. It is not known a priori, and has to be found iteratively, as described in Step 6.

Step 5 Solve for the a_j, b_j, $j = 0, \ldots, M$, using Method 5a or 5b below: This is the most complicated part of the solution process. To obtain the "best" solution of an overdetermined system of equations (which can never be satisfied identically because there are insufficient free variables), one procedure is to find the solution which minimises the sum of the squares of the errors. This "least-squares" procedure for the system of nonlinear equations is mentioned in Step 5b below. For the calculations described in this paper, it was found that a very simple method gave excellent results. This is described below.

5a. Direct iteration solution of the equations

In this case, sufficient of the equations were discarded, one in the case of M = 2, and three for M = 4, to give the same number of unknowns as equations, N say. Newton's method could be used for this system of nonlinear equations, and is known to converge quickly. However, it involves the calculation of a matrix, whose elements are the derivative of every equation with respect to every variable, plus the numerical solution of that matrix equation at each iteration. Fortunately, however, a much simpler method was found to work for the nonlinear system in this work, which gave results which were within 1% of those using the full overdetermined set of equations.

The solution procedure is the nonlinear equivalent of Gauss-Seidel iteration, whereby each equation is written for one unknown, whose influence dominates that equation, and the set of equations evaluated repeatedly until a solution is obtained. As the next value of each variable is calculated, its new value is subsequent equations. In the calculations it was found that the procedure worked well, both for M = 2 and M = 4.

Examining the "P" equations in (3.2) it can be seen that, for example, $P_1 = a_1 a_2 y^- + p_1 + a_0 a_1 = 0$ can be re-arranged to give the equation $a_1 = a_1 - P_1/a_0$. With initial estimates of the coefficients, the right side can be evaluated, and substituted for a_1. Other equations can be similarly rewritten. The scheme which was used in the present work was to recalculate each of the a_j from the pressure equations and each of the b_j from the dynamic equations, for j from 1 to M. In practice it was found that the order in which this was done was not important, but it is recommended that the procedure work from M to 1, so that the coefficients which are smaller in magnitude are iterated first. The P_0 equation was rewritten in terms of b_0.

If the kinematic equations are examined, it is not so obvious that any one term dominates, and it was felt that if any equations were to be deleted it should be these. The procedure adopted was, that if

locally the linear contributions were greatest, then $K_1 = 0$ should be used. At such a point, if it were a point of inflection in the pressure record, p_2 would be zero, as would all the a_2 and b_2 so that $K_2 = 0$ would be satisfied identically. Similarly near a crest or trough, the quantities with subscript 1 would be close to zero, and it would be better to use $K_2 = 0$. The criterion adopted was simply whether $|p_1|$ or $|p_2|$ was greater.

Rewriting the kinematic equations as above would give the scheme for K_1 for example, $a_0 = a_0 - K_1/b_1$. In practice, this was found to give an iteration scheme which was occasionally unstable. Luckily, a simple remedy was found to give very reliable scheme. This was to multiply the previous expression by a_0 and to take the square root to give

$$a_0 = -\sqrt{a_0(a_0 - K_1/b_1)} \text{ or } a_0 = -\sqrt{a_0(a_0 - K_2/b_2)},$$

whether $|p_1|$ or $|p_2|$ respectively was greater. The value of a_0 is negative, and of a similar magnitude to c.

To commence iteration it is desirable to have some estimate of the solution. The following were found to work well in practice:

$$b_0 = p_0 - p_2 p_0^2, \quad a_0 = -\sqrt{b_0}, \text{ and } a_j = b_j = p_j, \quad \text{for } j = 1, \ldots, M.$$

These are exact for no wave motion. In subsequent passes of the iteration terminating in Step 6, the results from the previous pass were used.

The iteration scheme can be summarised:

```
For successive iterations until solution converges
  {
  For j=M to 1 in steps of -1
     {
     a_j = a_j - p_j / a_0
     b_j = b_j - D_j
     }
  If (|p_1| > |p_2|)  a_0 = -sqrt(a_0(a_0 - K_1/b_1))
  Else a_0 = -sqrt(a_0(a_0 - K_2/b_2))
  b_0 = b_0 + P_0
  }
```

In practice it was found that convergence of this scheme was sure and rapid. Four iterations were enough to have the solution converge to four significant figures.

5b. Newtonian iteration for overdetermined systems

A more complicated but theoretically-sounder method than that described in Step 5a is to obtain that solution which minimises the errors of the complete set of equations, rather than identically satisfying some of those equations. The method is much more complicated and

takes more computational time. It was implemented by the author, but was found to give results which were little different from those obtained from the method of Step 5a. Comparisons are not presented here. It is recommended that the simpler method be used in practice.

Step 6 Recalculate the speed c: Having processed all the points n = 1, ..., N, excluding those at the beginning and end of the pressure record which cannot be treated by scheme (4.2), it is now possible to estimate the speed of propagation of the disturbances. Locally, there is no information provided by the act of measuring the pressures, and it is necessary to make rather ad hoc assumptions.

From equation (2.1), it can be easily shown that the horizontal fluid velocity in the frame of the moving disturbance, at x = 0 and t = 0 is $a_0 - a_2y^2 + a_4y^4$, hence the fluid velocity in the frame of reference of a stationary observer is

$$u(0,y,t_n) = c + a_0 - a_2y^2 + a_4y^4. \tag{4.3}$$

This provides us with a means of calculating the speed of propagation c, for if the mean current (fluid velocity) at a point of elevation y is known, denoted by $\bar{u}$, this is the mean of u over all the t_n, n = 1, ..., N. (In the absence of any knowledge of $\bar{u}$, a value of zero would be a reasonable approximation.) Substituting into equation (4.3) we have

$$c = \bar{u} - \overline{a_0} + \overline{a_2}\, y^2 - \overline{a_4}\, y^4, \tag{4.4}$$

where the $\overline{a_i}$ denotes the mean of the a_i averaged over all the n. Clearly the result shows that the value of c obtained depends upon the value of y at which the expression is evaluated. However, as the a_2 and a_4 express fluctuations of velocity about a mean, in general their means will be small and one would expect the deduced value of c to show little variation with y.

In most cases it might be rather more realistic to use the depth-integrated value of the current, denoted by $\bar{U}$. By integrating (4.3) from 0 to b_0, the surface elevation at time t_n, and taking the ensemble mean over all the n, then

$$c = \bar{U} - \overline{a_0} + \frac{\overline{a_2}}{3}\, b_0^2 - \frac{\overline{a_4}}{5}\, b_0^4 \tag{4.5}$$

With the new value of c as obtained in this step, return to Step 2, unless the process has converged. If it has converged, then

Step 7 Solution: The most useful results are the surface elevations, represented by the b_0, and the fluid velocity, given by

$$u = c + a_0 + a_1(x-ct) + a_2((x-ct)^2 - y^2) + a_3((x-ct)^3 - 3(x-ct)y^2) + a_4((x-ct)^4 - 6(x-ct)^2y^2 + y^4),$$

and

$$v = -a_1 y - 2a_2(x-ct)y - a_3(3(x-ct)^2 y - y^3) - a_4(4(x-ct)^3 y - 4(x-ct)y^3).$$

If it were desired, now a Fourier transform of the surface profile could be taken, to obtain the spectral data.

5. Results

Comparisons were made with accurate numerical solutions of steadily-progressing waves in water of constant depth. Solutions were obtained using a Fourier approximation method (Rienecker & Fenton, 1981; Fenton, 1987), giving values of pressure on the sea bed at equally-spaced intervals and the corresponding surface elevations. Using the pressure values the method of Section 4 above was applied. For both quadratic and quartic approximations 7 adjacent points were used to fit the polynomials at each point, that is, K = 7.

The family of steady waves is a two-parameter one. To obtain an idea of the accuracy of the local polynomial approximation method, a traverse through this two-dimensional space was made, considering four waves. The height/depth increased from 0.25, 0.333, 0.5, to 0.667 while the wavelength/depth simultaneously was 3, 5, 10 to 15. It would be expected that the polynomial method would work best for long waves, while for shorter waves the variation with y tends to exponential and it would not be appropriate.

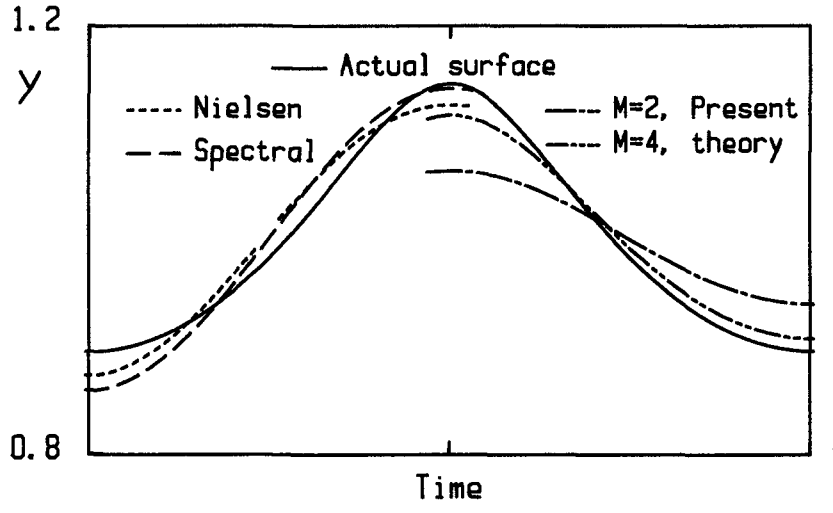

Figure 1. Actual and calculated free surface of a steady wave of height 1/4 of the depth and a length 3 times the depth.

Results are shown in Figures 1 to 4. On each figure the free surface obtained from the numerical solutions is shown as a solid line. There

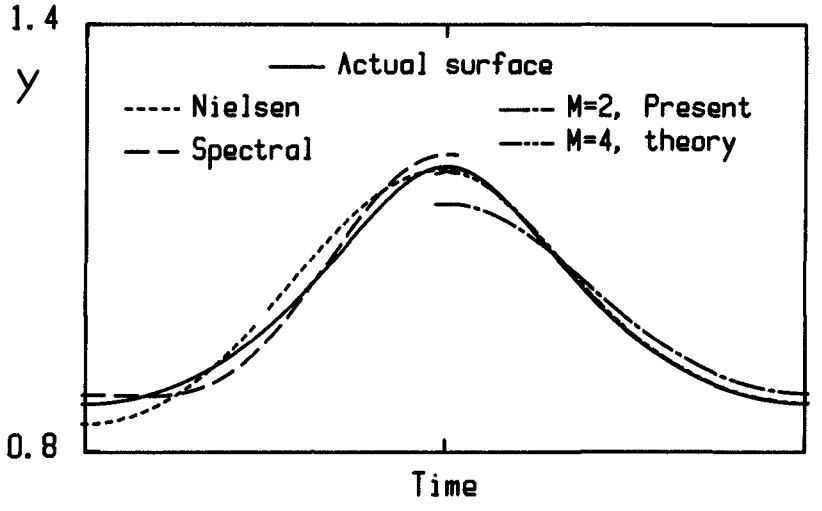

Figure 2. Actual and calculated free surface of a steady wave of height 1/3 of the depth and length 5 times the depth.

are two curves plotted on each half of the wave, plotted according to four methods of inferring the free surface from the pressure results. The actual pressure record is not shown. On the left half of the wave is shown two sets of results from linear theory. The long dashed line shows the results of applying linear wave theory using the full spectral representation. The resulting Fourier series was truncated at the last term where the successive contributions were still decreasing. After that point the results would be meaningless. The short dashed line shows results obtained from the simple empirical approximation of Nielsen (1986), able to be presented in a single formula. On the right half of the wave are shown results from the present theory, for the quadratic (M = 2) and quartic (M = 4) approximations.

It can be seen that the use of linear wave theory and a full spectral representation gives poor results for the longer and higher waves. Nielsen's local approximation method, based on fitting of a trigonometric function to part of the pressure signal is capable of good accuracy near the crest and trough of the waves. In fact, the agreement at the crests is remarkably good, considering the approximations implicit in the method. At the wave crests, the method is usually more accurate than the polynomial approximation method. Over part of the wave, however, near the inflection points, the fitting of a sinusoid breaks down, and the method gives wildly divergent results or none at all.

The results for the polynomial approximation method are shown on the right sides of the figures. For a relatively short wave (3 times the depth) the polynomial approximation is poor (Figure 1), as expected. It would be necessary to include higher order approximation

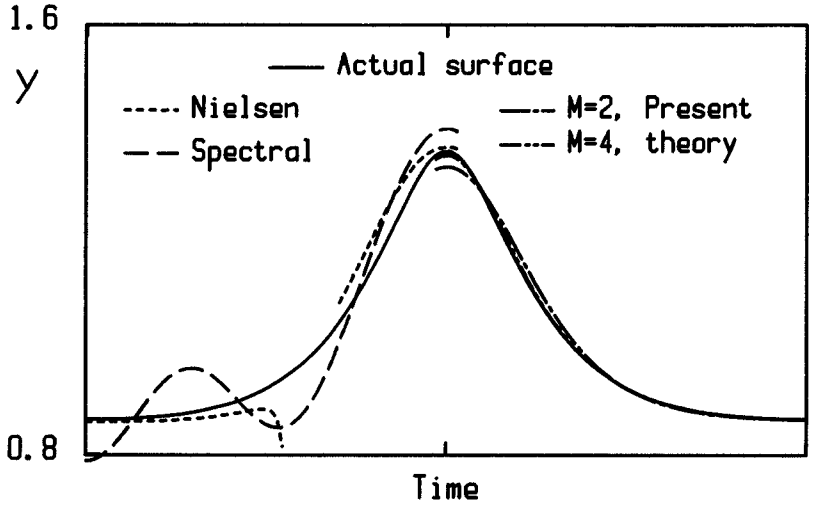

Figure 3. Actual and calculated free surface of a steady wave of height 1/2 of the depth and length 10 times the depth.

for waves this short. The situation changes quickly as longer waves are considered. For a wave which is only 5 times the water depth, Figure 2 shows that the present method is capable of high accuracy, but that it is necessary to use quartic approximation. As longer waves are considered, the quadratic approximation becomes more acceptable. Figure 3 shows a wave 10 times as long as the depth with a height of 0.5 of the depth. It is clear that the quartic approximation is excellent, usually being obscured by the surface on the plot of this scale. Finally, Figure 4 shows a very demanding case, of a wave which is 15 times the water depth in length, and a height of 2/3 of the depth. This is probably close to breaking. Except at the very crest, the M = 4 results are excellent, with the M = 2 results slightly less so. Altogether it seems that the method proposed here, with quartic approximation, is capable of high accuracy for waves up to close to the breaking point, provided that they are no shorter than about 5 times the water depth. This range of accuracy is very much greater than that of conventional wave theories and suggests that the local polynomial method, based on no approximations other than the truncation at finite degree, is capable of accurate description of steady water waves.

Peter Nielsen has kindly made available a set of his experimental results so that an indication of the robustness of the method in practice might be had. Waves were generated in a laboratory flume, and at a station two wave gauges were used to measure the free surface elevations and a pressure probe was located on the bottom. A comparison of the different methods and experimental results is given in Figure 5. The wave is high, about half the mean depth, and has the sharp crest and flat trough associated with long waves. It can be seen that Nielsen's local trigonometric approximation method works rather better

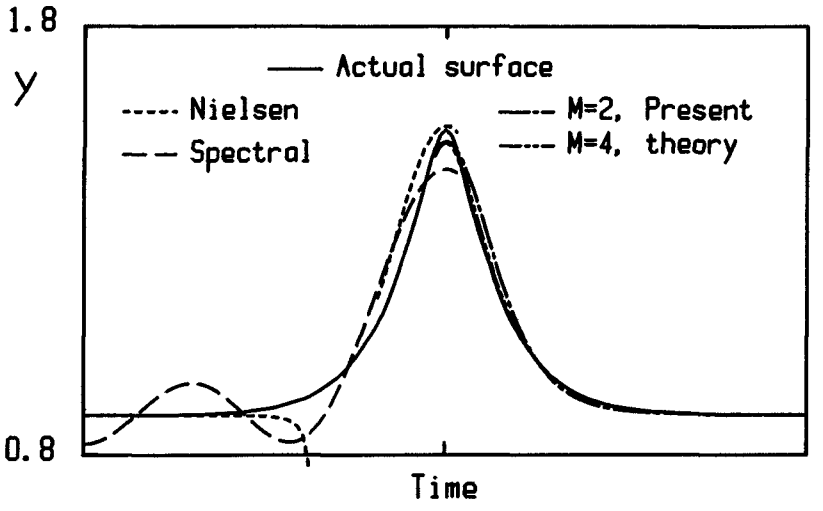

Figure 4. Actual and calculated free surface of a steady wave of height 2/3 of the depth and length 15 times the depth.

than the M = 2 approximation of the polynomial theory near the crest of the wave. However, the M = 4 level of the theory seems to be very accurate indeed. Almost everywhere the double chain-dashed line is obscured by the two lines corresponding to the wave gauge results, even at the crest. In this case, however, as the experimental results showed the expected small irregularities, it was found necessary to use the least-squares method with 13 points. For any fewer points it was found that the irregular data was such that the method of solving the equations did not converge. With 13 or more points, however, it was robust and accurate.

6. Conclusions

It has been shown that relatively low degrees of polynomial approximation can describe waves accurately in water of finite depth. This has the potential of allowing solution of wave problems by polynomial means, which allows the use of the full nonlinear boundary conditions and which may allow the incorporation of other more-general geometries.

For the problem considered here, the method has provided a technique for obtaining free surface data from pressure data, which obviates the need for Fourier transform programs and has important computational advantages over traditional methods based on Fourier analysis.

The examples presented here have not demonstrated the accuracy and robustness of the proposed method over a wide range of waves and under field conditions, however, they do suggest that the method could be used in a variety of applications.

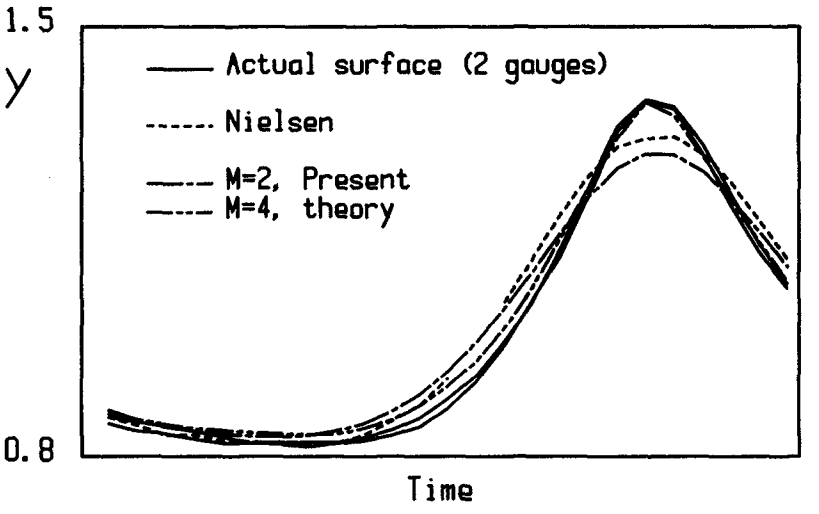

Figure 5. Experimental and computational results for laboratory wave

References

Daemrich, K.-F., Eggert, W.-D., & Kohlhase, S., 1980 Investigations on irregular waves in hydraulic models, Proc. 17th Coastal Engrng. Conf., Sydney, pp.186-203.

Fenton, J.D., 1987 The numerical solution of steady water wave problems, Computers & Geosciences 13, (to appear).

Nielsen, P., 1986 Local approximations - a new way of dealing with irregular waves, Proc. 20th Coastal Engrng. Conf., Taipei.

Rienecker, M.M. & Fenton, J.D., 1981 A Fourier approximation method for steady water waves. J.Fluid Mech. 104: 119-137.

Vis, F.C. 1980 Orbital velocities in irregular waves, Proc. 17th Coastal Engrng. Conf., Sydney, pp.173-185.

CHAPTER 16

KINEMATICS IN THE CRESTS OF STORM WAVES

George Z. Forristall*

ABSTRACT

Uncertainty about kinematics in the crests of high waves has prevented random wave simulation from being accepted as a reliable method for computing wave forces for platform design. A theoretically defensible method of calculation for wave crest kinematics has been developed recently. The method produces a potential function which fits the kinematic boundary condition specified by second order wave theory and is thus named the Kinematic Boundary Condition Fitting (KBCF) method. KBCF agreed well with measurements of mechanically generated irregular waves made by a laser Doppler current meter in a wave tank. In order to obtain further data during high, short crested storm waves, instruments for the Fulmar Wave Crest Kinematics (FULWACK) experiment were installed in the North Sea early in November 1981. During a storm later in that month, good velocity measurements at heights up to 25 feet above mean water level were obtained in over 30 waves. For comparison with this data, KBCF was extended to three dimensions. Statistics of the velocities thus simulated agreed well with statistics of the measurements. KBCF has thus been verified as a accurate method for simulating the kinematics of natural storm waves.

INTRODUCTION

Monte Carlo simulations are needed to model the dispersive and directionally spread nature of ocean waves. Forristall (1981) showed that such simulations agreed well with velocity measurements made below mean water level in storms at sea. However, heuristically motivated modifications to linear theory are necessary to produce realistic velocities above mean water level, and it is not clear which modification is best.

Forristall (1985) then developed a new method for computing the kinematics of irregular waves based on the numerical calculation of a potential function with a given kinematic free surface boundary condition (KBCF). The boundary condition was specified correct to second order using the intermediate depth interaction equations developed by Sharma and Dean (1979). Measurements made by Bosma and Vugts (1981) using a laser Doppler current meter in the Delft Hydraulics Laboratory wave tank were particularly appropriate for testing KBCF theory. Velocities were measured one standard deviation of wave height above mean water level as well as below mean water level. The waves were mechanically generated and unidirectional. The wave staff record could thus be used to specify the phases of the component wavelets, and only a two-dimensional potential function had to be calculated. The agreement found by Forristall (1985) between measured and simulated velocities was excellent. There was also good agreement between the statistics of measured and simulated velocities when only the spectral density of the waves was specified as input to the simulations.

Since KBCF is derived from the equations of wave motion using defensible assumptions, the extrapolation from laboratory scale to storm waves can be made with some confidence. Still, there is no substitute for verification with measurements made in natural short crested waves with heights comparable to those used in design. In response to this need, the Fulmar Wave Crest Kinematics (FULWACK) experiment was conducted in the central North Sea during the winter of 1981-82. Five electromagnetic current meters were mounted on taut wires stretched outboard of the north face of the Fulmar platform. Two of the meters were below mean water level and gave an estimate of the directional spectrum when used in conjunction with a wave staff. The other three meters were at nominal heights of 6, 16, and 26 feet above mean water level and gave velocity records when they were briefly immersed in the crests of high waves.

Shortly after the instruments became operational in November 1981, a pair of storms produced the most severe conditions observed during the winter. Data from these storms were digitized, and the velocity records from the second storm were used to verify KBCF wave theory. We first calculated directional wave spectra from the records. The velocity data from the wave crests were then compared with Chappelear (1961) regular wave theory and with the empirical modifications of linear theory known as stretching and extrapolation.

KBCF theory was originally developed for two-dimensional waves, and the three-dimensional problems required substantially more computational effort. The code that was developed uses the vector processing

* Shell Development Co., Box 481, Houston, TX 77001

and large storage capabilities of the Cray computer. Statistics of peak velocities simulated by the three-dimensional KBCF compare very well to the statistics of the measured velocities.

KBCF wave theory agrees with both high quality laboratory measurements and measurements made in extreme waves in a natural seaway. In the last section, we consider how the realistic simulations it produces can be used for structural design.

THE FULWACK EXPERIMENT

The Fulmar platform is located in block 31/16 in the central North Sea, within sight of the Auk platform in the same block. The platform is in 270 feet of water approximately 170 miles east of Dundee, Scotland. A Baylor wave staff and five Marsh-McBirney model 524 electromagnetic current meters were mounted just outside the north face of the platform as shown in Figure 1. The current meter support system consists of a wire rope stretched around upper and lower sheaves to form a taut wire loop. Frames for the current meters and their cables were clamped to one side of the loop and lowered to position by rotating the top sheave. The response of the taut wire system was investigated using the finite difference program described by Forristall and Hamilton (1978). Since the taut wires were clamped to the spider deck at the 20 foot level, current meters 3 and 4 were predicted to have the biggest motion: about 3 feet in a 75 foot wave. The natural periods of the taut wire sections above and below the clamps were each close to 0.5 sec.

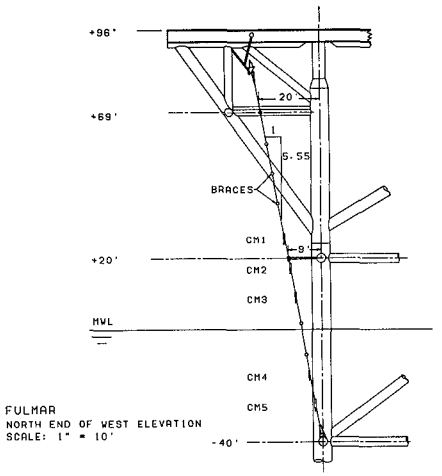

Figure 1.

The nominal locations of current meters 1–5 respectively were 26, 16, and 6 feet above mean water level, and 18 and 28 feet below it. During the data analysis, the water level on the wave staff was used to give the water level relative to the current meters. Float switches were also installed next to the top three current meters to determine the precise times of their immersions. Laboratory test showed that the response time of the switches was approximately 0.2 sec. However, the strong flow during storm waves apparently held the floats down part of the time, and the immersion times were usually determined from the wave staff signal.

The current meter axes were aligned with the platform so that a positive x-axis response indicated flow towards platform east and a positive y-axis response indicated flow toward platform north. Platform north is 18.5° counterclockwise from true north, so positive x-axis response indicated flow toward 71.5° true.

A J-Tec vortex shedding anemometer was mounted above the crown block on the drilling derrick, 345 feet above mean water level. Some possible blockage might be caused by the flare stack located to the south-southeast of the derrick. We intended to mount the anemometer so that the direction reading

would be in degrees from true north, but later comparisons between visual observation of vane position and instrument output indicated that about 15° should be subtracted from the measured directions.

The signal conditioning and recording system was manufactured by Evans-Hamilton Inc. and was housed in an instrument shelter located at the northeast corner of the cellar deck. All signals except those from the immersion switches were passed through 4 pole Butterworth filters with a cutoff frequency of 3.0 Hz. These filters replaced the output filters normally supplied with the Marsh-McBirney current meters. The Butterworth filters give a sharper cutoff as well as producing equal phase lags in the wave staff and current meter signals.

The conditioned signals were recorded on 14 channel Geotech FM analog tape recorders. Two recorders were used to give redundancy in the event of mechanical failure of one of the recorders. The recorders ran continuously at 0.03 inch/sec, and had flat frequency response to above 4 Hz. The system switched from data recording to an automatic calibration mode once each hour. During the two phases of the calibration, which lasted two minutes each, calibration signals were substituted for data and recorded through the same signal conditioning circuits. The wave staff calibration was given by two shorter bars operated by relays. The electromagnetic current meters included an internal calibration feature which fed a portion of the magnet driver excitation voltage through the channel amplifiers.

Data from two storms in November 1981 were digitized for detailed analysis. During the analog to digital conversion, the field recorded tapes were played at 3.75 inch/sec, giving a playback/field speed ratio of 125. The digitization rate was 500 Hz at playback speed, equivalent to 4 Hz at field speed. The A/D circuit had a resolution of 12 bits or one part in 4096. To avoid aliasing, the wind, wave, radar, and current meter 4 and 5 signals were filtered using 4 pole Butterworth filters with a cutoff frequency of 200 Hz at playback speed or 1.6 Hz at field speed. The immersion switch channel and current meters 1–3 were not filtered because of the intermittent nature of the signals.

The digital data were calibrated using the hourly calibration values. For each hour of field data, 6 records containing 2048 time-steps of 14 channels each were written. The effects of both the signal conditioning filters used in the field and the anti-aliasing filters were removed by multiplying the Fourier transforms of the signals by the transfer function

$$T(f) = (\tilde{f} - p_1)(\tilde{f} - \bar{p}_1)(\tilde{f} - p_2)(\tilde{f} - \bar{p}_2) \tag{1}$$

where

$$p_1 = -.3827 + .923872i,$$

$$p_2 = -.923873 + .3827i,$$

and

$$\tilde{f} = f/f_c,$$

f_c is the cutoff frequency for either of the four pole Butterworth filters, and overbars denote complex conjugation. For the filters used in the instrumentation system $f_c = 3.0$ Hz, and for the filters used during digitization $f_c = 1.6$ Hz.

Components above the cutoff frequency were removed. The current meter records were also corrected for the slight nonlinearity and non-cosine response established by tank testing of meters of this type. The calibrated current meter signal was divided by the factor r, given by

$$\begin{aligned} r &= \beta(1 - \alpha\sin 2\theta), \\ \beta &= 0.87 \quad \text{for} \quad Re < 2.51 \times 10^4 \\ &= 1.0612 - 4795/Re \quad \text{for} \quad 2.51 \times 10^4 < Re < 7.84 \times 10^4 \\ &= 1.0 \quad \text{for} \quad Re > 7.84 \times 10^4 \\ \alpha &= 0.083 - 1.5 \times 10^{-6} Re \quad \text{for} \quad Re < 5.52 \times 10^4 \\ &= 0 \quad \text{for} \quad Re > 5.52 \times 10^4. \end{aligned} \tag{2}$$

Re is the Reynolds number of the flow around the spherical sensor (4" in diameter), and θ is the direction of the flow with respect to an electrode.

THE NOVEMBER 1981 STORMS

The FULWACK system operated from November 12, 1981 to April 29, 1982, but two storms in the middle of November 1981 produced the most severe wave conditions during the experiment. The first storm developed from a low which formed east of Newfoundland and expanded as it moved to the North Sea with a minimum pressure of 972 mb. Thirty-six hours later, another low formed and followed the same track. It suddenly deepened, reaching 975 mb near the Faroe Islands (Mariner's Weather Log, 1982). The slow forward motion of the storm was partly responsible for the very high waves observed in the North Sea on November 24.

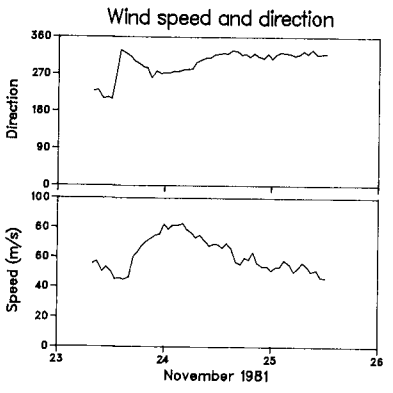

Figure 2.

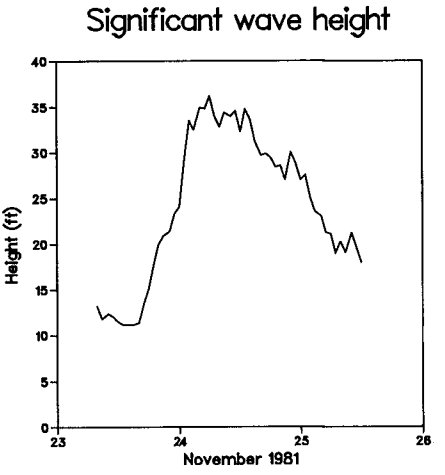

Figure 3.

Figure 2 shows the wind speed and direction measured by FULWACK during the second storm, and Figure 3 shows the significant wave height. The winds are as measured from the location at the top of the derrick. The wind speed and direction were averaged over 6 data records, giving approximately one hour averages. The wind direction has been corrected for the 15° error in instrument alignment discussed above. The wind speed reached a brief peak of 77 miles/hr on the afternoon of November 20. Then on November 24, the wind speed was near its peak of 82 miles/hr for several hours, and the direction was nearly constant.

The significant wave height in Figure 3 was calculated as four times the standard deviation of the wave signal. On November 20, the peak significant wave height was 30 feet, and on November 24 it was 36 feet. Figure 4 is a photograph taken by Mr. Mike Philpot from the Borgland Dolphin accommodations semisubmersible on November 24, illustrating the severity of the conditions. The view is toward the north face of the platform which the wave crest is approaching. The wave crest appears to be considerably higher than the spider deck located at 20 feet above mean sea level.

With two exceptions, the sensors and recording system worked very well during the storms. The y-axis of current meter 3 did not operate in either storm, and a radar wave gage installed as part of another experiment but recorded on the FULWACK system failed during the first storm.

Figure 4. A large wave on November 24

WAVE SPECTRA

We calculated directional spectra for each hour of digitized data using the methods of Forristall *et al* (1978). The information on wave direction available from a wave staff and current meter is equivalent to that from a pitch and roll buoy. It does not provide very sharp directional resolution in the sense of separating two directional peaks at one frequency. However, it can provide very good information on the mean direction of travel and amount of directional spreading for waves in each frequency band.

The co-spectra between the wave staff and current meters 4 and 5 were used to find the best estimates of the parameters in the function

$$S(f,\theta) = S(f)N(s)\cos^{2s}(\theta - \theta_o/2) \tag{3}$$

The mean direction of travel, θ_o and the spreading parameter, s, are both functions of frequency. The function $N(s)$ is included to normalize the integral of the spreading function to unity. The spectral density as a function of frequency alone, $S(f)$, was calculated directly from the wave staff data. We also calculated the rms spread, skewness, and kurtosis of the direction distribution.

With a time step of .25 sec and a record length of 2048 points, the raw spectra from a fast Fourier transform have a frequency resolution of 1/512 Hz. We took averages over 5 frequencies and ensembles of 6 spectra to give spectra with 60 degrees of freedom and a resolution of 0.01 Hz.

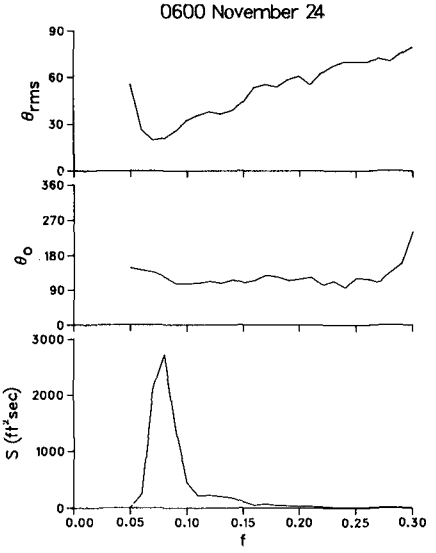

Figure 5. Directional wave spectrum at 0600

Although the energy level of the spectra varied during the storm, their directional characteristics were quite constant. Figure 5 shows the directional spectrum for 0600 on November 24, the time at which the significant wave height reached its maximum of 36.20 feet. The bottom panel of the figure shows the power spectrum, the middle panel shows the mean direction of travel, and the top panel shows the rms directional spread, all as a function of frequency. The power spectrum is unimodal with a peak at 0.08 Hz. The mean direction of travel is nearly constant with frequency, with the waves traveling toward 110° true in the mean. The rms spread is smallest at the peak of the spectrum and increases with frequency. The rms spread is related to the parameter s in equation (3) by

$$s = 2/\theta_{rms}^2 - 1 \tag{4}$$

where θ_{rms} is expressed in radians. The rms spread is a more physically appealing measure of the spreading while equation (3) is useful when a definite form of the spreading function is needed. The qualitative features of the spectrum shown in Figure 5 are typical of those computed throughout the storm.

The calculation of directional spectra from wave staff and current meter data is based on linear wave theory and gives a check on the accuracy of linear theory. The average ratios of measured to linearly predicted velocities were 0.97 for current meter 4 and 0.99 for current meter 5.

CREST VELOCITY MEASUREMENTS

The main purpose of the FULWACK experiment was to obtain velocity measurements at locations high above mean sea level where the current meters would be immersed only briefly. The behavior of the electromagnetic current meters during intermittent immersion is therefore important. Before installing the instruments on Fulmar, we conducted some immersion tests in a recirculating flume. Figure 6 shows the data recorded during one of the tests where the flow was parallel to the y-axis of the meter. Both channels of the meter had a large noise spike immediately after immersion, but then settled to the correct response after 0.6 second. The characteristics of the noise seem related to the output filter used on the current meter, which was the same in the tests and FULWACK.

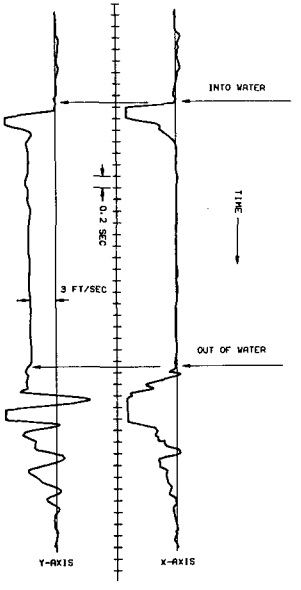

Figure 6. Current meter immersion test

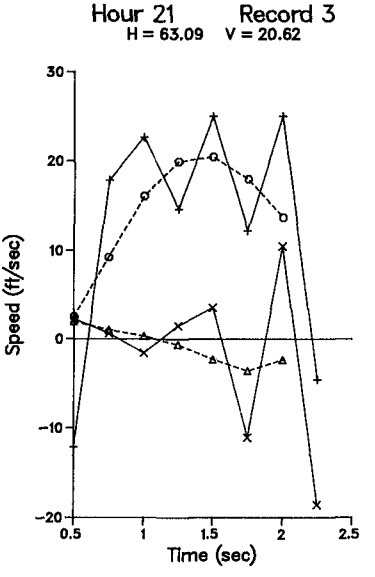

Figure 7. Kinematics of the largest wave

The flume tests indicated that reliable results could be expected only after the meter was immersed at least 0.5 sec. In order to have a few good data points for averaging or curve fitting, we selected only those waves for which a meter was immersed during at least 7 digitized samples. The meter was thus immersed longer than 1.5 sec. Applied to the top current meter, this selection scheme produced 31 waves for study from the November 24 data.

Figure 7 illustrates the quality of the actual data during the highest wave recorded. The solid line marked with + symbols is the output from the x-axis of the top current meter, and the solid line marked with × symbols is the output from the y-axis. All data points during the immersion are shown, and the origin of the time axis is arbitrary. The data has rapid oscillations and spikes with frequencies on the order of 2 Hz. This behavior was not observed in the flume tests and is not expected to be due to wave kinematics, since there is little wave energy at these frequencies. Since the natural frequency of the taut wire system is ncar 2 Hz, it is likely that the oscillations are due to relative motion between the meter and the water. Small amplitude motions can cause large relative velocities at high frequencies. The oscillations were removed by filtering.

After some experimentation with curve fitting and various smoothing schemes, we decided that the

best method for removing the noise would be a simple filter. The velocity components were filtered at $f_c = 0.5$ Hz using a filter with the amplitude response of the four pole Butterworth filter in equation (1), but with zero phase lag. The filter was applied in the frequency domain, so it was simply a real transfer function with amplitude equal to the modulus of the Butterworth transfer function. The result of the filtering is illustrated by the dashed lines in Figure 7. The filtered components seem to give a credible version of the wave velocity while eliminating the physically unrealistic oscillations.

REGULAR WAVE THEORY

The velocity components were combined vectorially and the maximum speed in the crest of each wave found for comparison with wave theories. For the wave in Figure 7, this maximum velocity was 20.62 ft/sec. The maximum speed recorded during the storm at the top meter was 21.47 ft/sec.

We first compared the measurements with the predictions of regular wave theory using the high order numerical solution of Chappelear (1961). This theory gives an excellent fit to the regular wave boundary conditions. For waves of the moderate steepness and water depth encountered by FULWACK, the solution does not differ significantly from that given by Stokes fifth order theory.

For each of the 31 waves, the period and height were computed using the zero downcrossing definition applied to the wave staff record. Figure 8 gives a comparison between the measured maximum speeds at current meter 1 and the speeds calculated by Chappelear theory. The scatter between the measured and theoretical peak speeds is considerable. The theoretical speeds are also biased about 15% to overprediction. These results are consistent with those from previous measurements made below mean water level.

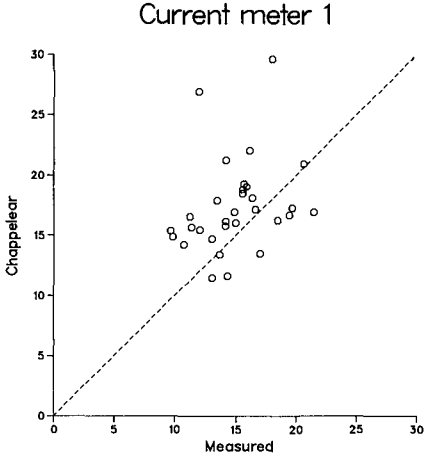

Figure 8. Peak speeds in single waves

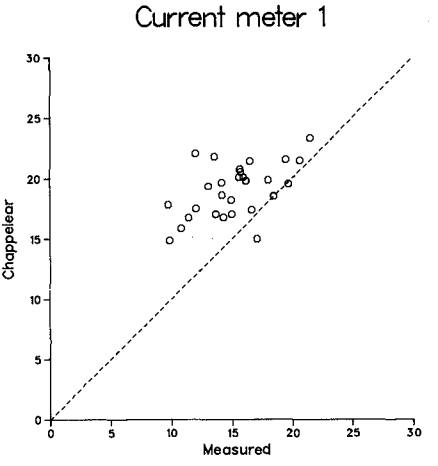

Figure 9. Peak speeds with crest defining wave

Two of the Chappelear velocities in Figure 8 are conspicuously higher than the others. These outlyers are apparently due to short zero crossing periods which do not represent the important frequencies in the wave spectrum. Daemrich and Kohlhase (1980) have suggested another way of selecting the parameters for regular waves which reduced the scatter between theory and their measurements of unidirectional irregular waves in a tank. They defined the wave by the height of the crest and the period of the crest between zero crossings. Since they used linear wave theory, the wave height and period were twice the height and period of the crest. The FULWACK waves were steep enough so that the use of nonlinear theory was advisable, so we modified Chappelear theory to converge to a specified crest height and period rather than the crest to trough height. The wave parameters were selected from the same set of 31 waves as before, and the wave by wave comparison of maximum velocities is shown in Figure 9. The scatter has indeed been reduced somewhat, mostly by the elimination of the two outlyers. The bias remains and is, in fact, larger. The improvement in the comparison is not nearly so much as reported by Daemrich and Kohlhase (1980), presumably because of the complicating effect of directional spreading in the present data.

MODIFIED LINEAR THEORIES

Forristall *et al* (1978) showed that linear simulation of the directional wave spectrum could produce velocity probability distributions which agreed well with measurements below mean water level. However, the linear superposition principle breaks down above mean water level. Empirical modifications such as stretching and extrapolation have thus been necessary to produce reasonable results. Comparisons of these methods with measurements (Forristall, 1981) have not been completely conclusive.

Wave kinematics are stretched by moving the level at which $z = 0$ in the linear wave expansion to the instantaneous free surface. In practice, a coordinate transformation is performed after the linear waves are superposed. Kinematics are extrapolated by taking the linear simulation up to mean water level and then continuing upward using the rate of increase with z calculated just at mean water level.

The simulations were made using a fast Fourier transform technique with random phases selected for each Fourier line. There were 30 directional bands at each frequency. The simulations were based on the directional spectra measured from 0200-2300 GMT. Records having the same length as the measurements were produced, and they were analyzed using the same routine. This single, literal unconditioned simulation of the storm should have the same statistical variability as the measurements. Thus, wave by wave comparisons could not be performed, and, in fact, a slightly different number of simulated waves met the immersion criteria.

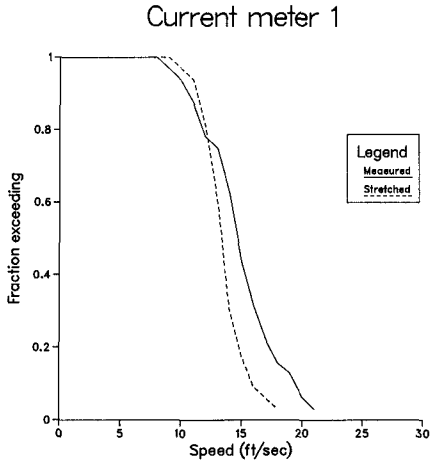

Figure 10. Distributions of measured and stretched speeds

Figure 10 shows the peak speed distribution from the stretched and simulation compared with the measurements at current meter 1. The stretched simulation agrees well with the measurements at lower velocities but is somewhat below the measurements at lower probabilities. The speeds from the extrapolated simulations (not shown) were clearly too high. These results are consistent with those found from a study of MaTS measurements in the Delft Hydraulics Laboratory. However, they disagree with the results of the measurements made at the Exxon Ocean Test Structure (OTS) as discussed by Forristall (1981).

KBCF

The Kinematic Boundary Condition Fitting (KBCF) method was developed to put the calculation of random wave kinematics on a rigorous basis. The kinematic field should be given by a potential function which satisfies Laplace's equation in the interior and the kinematic and dynamic boundary conditions on the free surface. The basic idea of KBCF is that if the shape and time derivative of the surface are known, the kinematic free surface boundary condition alone is enough to completely specify the potential as the solution to a Neumann problem. The solution can be calculated easily enough by numerical iteration. Forristall (1985) found that a specification of the surface correct to second order was sufficient to produce a solution which agreed excellently with the MaTS measurements in the Delft wave tank.

For comparison with the FULWACK measurements and for design use, it is necessary to extend KBCF to three dimensions. The second order wave interactions for infinite water depth were calculated by Longuet-Higgins (1963), and the calculations were extended to intermediate water depth by Sharma and Dean (1979). We reproduce the latter result for completeness. Let the first order water surface be given by

$$\eta = \sum_{n=1}^{N} a_n \cos(\kappa_n x - \sigma_n t + \epsilon_n) \tag{5}$$

where t is time, x is the position vector in the plane, σ_n. ϵ_n and κ_n are, respectively, the radian frequency, phase, and vector wavenumber of wavelet n, and a_n is its amplitude. The frequencies and wavenumbers are related by the linear dispersion equation

$$\sigma_n^2 = g|\kappa_n|\tanh|\kappa_n|d \tag{6}$$

where g is the acceleration of gravity and d is the water depth.

The second order correction to the wave surface given by Sharma and Dean (1979) is then

$$\eta^{(2)} = 1/4 \sum_{i=1}^{N}\sum_{j=1}^{N} a_i a_j \{K^- \cos(\psi_i - \psi_j) + K^+ \cos(\psi_i + \psi_j)\} \tag{7}$$

where

$$K^- = [D_{ij}^- - (\kappa_i \kappa_j + R_i R_j)]\sqrt{R_i R_j} + (R_i + R_j)$$

$$K^+ = [D_{ij}^+ - (\kappa_i \kappa_j - R_i R_j)]\sqrt{R_i R_j} + (R_i + R_j)$$

$$D_{ij}^- = \frac{(\sqrt{R_i} - \sqrt{R_j})\{\sqrt{R_j}(\kappa_i^2 - R_i^2) - \sqrt{R_i}(\kappa_j^2 - R_j^2)\}}{(\sqrt{R_i} - \sqrt{R_j})^2 - \kappa_{ij}^- \tanh \kappa_{ij}^- d} +$$
$$+ \frac{2(\sqrt{R_i} - \sqrt{R_j})^2(\kappa_i \kappa_j + R_i R_j)}{(\sqrt{R_i} - \sqrt{R_j})^2 - \kappa_{ij}^- \tanh \kappa_{ij}^- d}$$

$$D_{ij}^+ = \frac{2(\sqrt{R_i} + \sqrt{R_j})^2(\kappa_i \kappa_j - R_i R_j)}{(\sqrt{R_i} + \sqrt{R_j})^2 - \kappa_{ij}^+ \tanh \kappa_{ij}^+ d} +$$
$$+ \frac{(\sqrt{R_i} + \sqrt{R_j})\{\sqrt{R_i}(\kappa_j^2 - R_j^2) + \sqrt{R_j}(\kappa_i^2 - R_i^2)\}}{(\sqrt{R_i} + \sqrt{R_j})^2 - \kappa_{ij}^+ \tanh \kappa_{ij}^+ d}$$

$$\kappa_{ij}^- = |\kappa_i - \kappa_j|$$

$$\kappa_{ij}^+ = |\kappa_i + \kappa_j|$$

$$R_i = |\kappa_i|\tanh|\kappa_i d| = \sigma_i^2/g$$

$$\psi_i = \kappa_i x - \sigma_i t + \epsilon_i.$$

For infinite water depth, equation (7) reduces to equation (3.7) of Longuet-Higgins (1963) except that the latter equation is missing a factor of $1/2$. The skewness kernel is defined as $(K^- + K^+)/4$ and is a measure of the strength of the second order interaction. It is a function of the frequencies of the two interaction wavelets as well as their angular separation and the water depth. The strength of the interaction is much greater in shallow water, matching the observation that the wave profile is more skewed in shallow water. It is interesting to note that for shallow water the peak of the interaction is not for colinear wavelets, but for wavelets separated by a small angle.

The computations implied by equation (7) can be performed for a spectrum specified either in the frequency or wavenumber domain. The input spectrum is usually specified in the frequency domain, but the numerical iteration which produces the potential function is performed over a spatial grid. It is thus most convenient to transform the directional spectrum to the wavenumber domain at the start of the calculations and then transform to the spatial grid.

The input spectra from FULWACK were given for frequencies in the range $0.050 \leq f \leq 0.340$. The wavenumber grid has a resolution $\Delta\kappa = 0.002ft^{-1}$. The wavenumbers are given by $(K_x\Delta\kappa, K_y\Delta\kappa)$ where $-63 \leq (K_x, K_y) \leq 63$ so that wavenumbers up to $0.1260ft^{-1}$ can be represented. This high wavenumber cutoff corresponds closely to the high frequency cutoff in the input spectrum. Negative wavenumber components must be included since wavelets in the input spectrum can propagate in any direction.

The program begins with a linear random simulation of the type described by Forristall (1981). Linear wavelets are specified at a frequency resolution $\Delta f = 1/512$ Hz and an angular resolution $\Delta\theta = 12^o$. The amplitude of each wavelet is taken from the given directional spectrum, and the phases are taken from a uniform random distribution. The amplitude and phase are then transferred to the proper location in the wavenumber grid.

The interactions of the wavelets are then calculated according to equation (7). If the two interaction wavelets are in close to the same direction and have large wavenumbers, the interaction term at the sum of their wavenumbers will lie outside the wavenumber grid. Wavelets traveling against the main direction of propagation are expected to be small. We thus calculated the interactions only for wavenumbers $-31 \leq (K_x, K_y) \leq 31$. Even then, the calculations are formidable. There are 63 points which satisfy that inequality so approximately 16×10^6 interactions must be calculated. Because of this and the large three-dimensional grid which is used to calculate the potential function, the computations were done on a Cray computer.

The amplitudes and phases of the first and second order wavelets in wavenumber space are transformed to the spatial grid using a fast Fourier transform which was coded to take advantage of the vector processing capabilities of the Cray and is very efficient. Two transforms are taken, first by rows and then by columns. To produce better spatial resolution, we took transforms of length 256 instead of 128. The high wave number terms were set equal to zero. The spatial resolution is then

$$\Delta x = 2\pi/256\Delta\kappa = 12.27\text{ft.} \tag{8}$$

Only the 64×64 grid surrounding $(x, y) = (0, 0)$ is calculated since this gives a large enough area for the solution of the potential function.

The KBCF solution also requires specification of η_x and η_t on the grid. These quantities are easily calculated by differentiation of equations (5) and (7), and transformed in the same way as η. An initial guess for the potential function is given by the potential due to the linear waves, again computed by successive Fourier transforms in space.

A potential function which is consistent with the surface defined correct to second order can now be calculated. Define the potential ϕ such that the velocity components (u, v, w) in the (x, y, z) directions are given by

$$\begin{aligned} u &= -\phi_x \\ v &= -\phi_y \\ w &= -\phi_z \end{aligned} \tag{9}$$

The potential function satisfies Laplace's equation

$$\phi_{xx} + \phi_{yy} + \phi_{zz} = 0 \tag{10}$$

in the interior of the fluid. At the free surface η the kinematic boundary condition is

$$\eta_t + \phi_z - \phi_x\eta_x - \phi_y\eta_y = 0 \tag{11}$$

With η, η_x, η_y, and η_t specified, equations (10) and (11) define a well posed problem which can be solved numerically. However, the wave potential should also satisfy the dynamic boundary condition

$$\eta - \phi_t/g + (\phi_x^2 + \phi_y^2 + \phi_z^2)/2g = const. \tag{12}$$

on the surface. Since the surface is only correct to second order, the numerical solution will not satisfy equation (12) perfectly. KBCF theory based on the second order surface is thus an approximation to the true solution of equations (10)-(12), and its accuracy and usefulness can be verified best through comparisons with measurements.

The potential function can be found through a successive over-relaxation solution. We define a computational grid with spacing Δx in the horizontal directions and Δz in the vertical. The grid indexes are (I, J, K) in the $(x, y, -z)$ directions. Centered difference approximations to the second derivatives are then

$$\Phi_{xx} = \{\Phi(I+1, J, K) + \Phi(I-1, J, K) - 2\Phi(I, J, K)\}/\Delta x^2 \tag{13}$$

$$\Phi_{yy} = \{\Phi(I, J+1, K) + \Phi(I, J-1, K) - 2\Phi(I, J, K)\}/\Delta x^2 \tag{14}$$

$$\Phi_{zz} = \{\Phi(I, J, K-1) + \Phi(I, J, K+1) - 2\Phi(I, J, K)\}/\Delta z^2 \tag{15}$$

At each grid point, there will be a residual given by

$$r = \Phi_{xx} + \Phi_{yy} + \Phi_{zz} \tag{16}$$

At the next step, the approximate potential is replaced by

$$\Phi'(I, J, K) = \Phi(I, J, K) + \omega r/a_{kk} \tag{17}$$

where

$$a_{kk} = 2(2/\Delta x^2 + 1/\Delta z^2) \tag{18}$$

and ω is a constant chosen to speed up convergence. On our $64 \times 64 \times 64$ grid, we used $\omega = 1.87$ and found satisfactory convergence after 100 steps.

The estimates of Φ at the new step are found successively, moving through the grid in a cyclic pattern. To make use of the vector processing capabilities of the Cray, we used what is called a "black-red" ordering. The grid is divided into "black" and "red" points in a three-dimensional checkerboard pattern. The updated potential at all the "black" points is then calculated before that at any of the "red" points. Thus the updated potential is never needed, and the calculations can proceed in parallel.

The difference scheme must be modified at the boundaries. Boundary condition (11) can be rewritten as

$$\phi_n = -\eta_t(1 + \eta_x^2 + \eta_y^2)^{-1/2} \tag{19}$$

where ϕ_n is the derivative of the potential in the direction normal to the surface. To form a finite difference estimate of the normal derivative, define

$$\begin{aligned} \epsilon_x &= \eta_x \Delta z/\Delta x \\ and \quad \epsilon_y &= \eta_y \Delta z/\Delta x \end{aligned} \tag{24}$$

Then if ϵ_x and ϵ_y are both positive

$$\Phi_n = \{\Phi(I, J, K) - \Phi_c\}/\Delta z(1 + \eta_x^2 + \eta_y^2)^{1/2} \tag{21}$$

where

$$\Phi_c = (1 - \epsilon_y)\Phi_1 + \epsilon_y\Phi_2$$

$$\Phi_1 = (1-\epsilon_x)\Phi(I,J,K+1) + \epsilon_x\Phi(I+1,J,K+1)$$

and $$\Phi_2 = (1-\epsilon_x)\Phi(I,J+1,K+1) + \epsilon_x\Phi(I+1,J+1,K+1)$$

The residual at the surface node (I,J,K) is then

$$r = \eta_t + \{\Phi(I,J,K) - \Phi_e\}/\Delta z \tag{22}$$

and the new potential is

$$\Phi'(I,J,K) = \Phi(I,J,K) - \omega r \Delta z \tag{23}$$

Equation (21) must be modified in an obvious way for ϵ_x or ϵ_y negative.

The bottom boundary condition is that the normal derivative of the potential is zero. The change in the solution was insignificant when the potential at the bottom was fixed equal to the linear potential. This approximation speeded convergence somewhat, and it would be reasonable to use it at a false bottom for a KBCF solution in very deep water. The potential at the lateral boundaries of the grid was also kept constant at the linear value. Forristall (1985) showed that this condition had little effect on the solution under the wave crest in the center of the grid.

COMPARISONS WITH FULWACK MEASUREMENTS

The starting point for the KBCF calculations was the linear Monte Carlo simulation that formed the basis of the stretched and extrapolated simulations. This is the same procedure that we would be following in using KBCF for design, but it means that the simulated time series is a random realization of the process defined by the directional spectrum, and wave by wave comparisons with the data are not possible. The verification of the method is thus through a comparison of speed probability distributions.

The second order interactions tend to sharpen the crests of the waves and flatten the troughs, producing a skewed sea surface. One check of the theory can thus be made by comparing the skewness of the measured and simulated profiles, where skewness is defined as

$$\alpha_3 = m_3/m_2^{3/2} \tag{24}$$

and m_2 and m_3 are the second and third moments of the wave profile. The comparison is shown in Figure 11. Skewness is not a very stable statistic: the observed value varies significantly from one record to the next. However, there is very little bias between the measured and simulated values. The agreement is in fact somewhat better than Forristall (1985) found for the MaTS wave tank data, perhaps because the finite length of the tank affected the low frequency set down under wave groups given by the subtraction term in equation (5).

The most important result of the calculations is the comparison between the measured and KBCF simulated maximum speeds at current meters 1 and 2. Figure 12 shows the comparison for current meter 1. The simulation is an essentially unbiased predictor of the measurements: the agreement is almost perfect at the 50% level. The median value of the measured maximum speed for the sample of large waves was 14.67 ft/sec at current meter 1 and 13.80 ft/sec at current meter 2. The corresponding KBCF simulations were 15.05 ft/sec at current meter 1 and 13.24 ft/sec at current meter 2, both within 5% of the measurements. The interquartile ranges (.25% to .75% exceedance) at current meter 1 were 3.67 and 3.14 ft/sec for the measurements and 2.10 and 2.17 ft/sec for the simulations. This extra variability in the measurements might be attributed to noise which remained after the filtering process. It should be recalled that the data shown in Figure 12 came only from the 31 highest waves in 12 hours of measurement in a severe storm. All of the distribution shown in the figure thus comes from the tail of the overall speed distribution. The good match of simulated and measured peak velocity statistics constitutes a verification of KBCF theory for high, directionally spread waves.

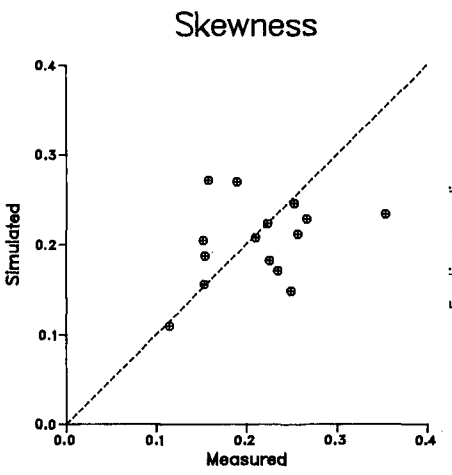

Figure 11. Wave skewness

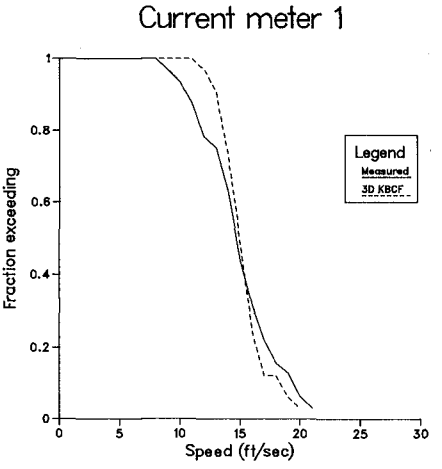

Figure 12. Distribution of measured and KBCF speeds

CONCLUSIONS

KBCF was developed as a rational approximation to the equations of motion for kinematics in the crests of irregular waves. It was compared to high quality measurements of two-dimensional waves made in a MaTS project and gave excellent results. The FULWACK experiment was designed as a full scale verification of the theory, which had to be extended to three dimensions to include the directional spreading of natural waves. Storms during November 1981 produced a good data set which included a number of waves that inundated current meters up to 26 feet above mean water level. The agreement between the velocity statistics simulated by KBCF and those measured was very good. We conclude that KBCF has been verified and is the best method of simulating the kinematic field of a complex natural seaway.

Although KBCF requires the use of a large computer, its cost is not prohibitive for simulations of individual high waves in a sea state. A number of representative waves for a design sea state could be simulated and used for static design of fixed structures. Dynamic design calculations present more of a problem, since many time steps of simulation are likely to be necessary and the cost of the simulations may become important. For these calculations and for routine design calculations on smaller computers, the best use of KBCF may be to calibrate simpler empirical models of kinematics. Rodenbusch and Forristall (1986) have developed a modification to the standard stretching algorithm which matches KBCF well in the crests of large waves.

ACKNOWLEDGEMENTS

The FULWACK project would not have been possible without the help and participation of many parts of the Shell Group. SIPM EP/23 coordinated the various activities involved. Shell Expro was extremely helpful in the design and installation of the instrument mounting system. The work of I. Middlehurst on the design and G. Grice on the installation was particularly appreciated. KSLA (Amsterdam) graciously gave us room in their instrument house, and several times loaned us spare parts from their supplies. R.C. Hamilton and T. Swarthout of Evans–Hamilton performed the instrument installation most efficiently. G. Rodenbusch and R.D. Larrabee gave helpful comments on an earlier version of this report.

REFERENCES

Bosma, J. and Vugts, J. H. (1981), Wave Kinematics and Fluid Loading in Irregular Waves, *Intern. Symposium on Hydrodynamics in Ocean Eng.*, Trondheim.

Chappelear, J. E. (1961), The Direct Numerical Calculation of Wave Properties, *J. Geophys. Res.*, **66**, 501.

Daemrich, K. F., Eggert, W. D., and Kohlhase, S. (1980), Investigations on Irregular Waves in Hydraulic Models, *Proc. 17th Coastal Eng. Conf.*, Sydney.

Forristall, G.Z. (1981), Kinematics of Directionally Spread Waves, *Proc. Directional Wave Spectra Applications*, Am. Soc. Civil Engr., Berkeley.

Forristall, G.Z. (1985), Irregular Wave Kinematics From a Kinematic Boundary Condition Fit (KBCF), *Applied Ocean Res.*, **7**, 202–212.

Forristall, G.Z. and Hamilton, R. C (1978), Current Measurements in Support of Fixed Platform Design and Construction, *Proc. of a Working Conference on Current Measurement*, Univ. Deleware, Newark.

Forristall, G. Z., Ward, E. G, Cardone, V.J., and Borgman, L.E. (1978), The Directional Spectra and Kinematics of Surface Gravity Waves in Tropical Storm Delia, *J. Phys. Oceanogr.*, **8**, 888–909.

Longuet-Higgins, M. S. (1963), The Effect of Non-Linearities on Statistical Distributions in the Theory of Sea Waves, *J. Fluid Mech.*, **17**, 459-480.

Mariners Weather Log (1982), North Atlantic Weather Log, **26**, 81.

Rodenbusch, G. and Forristall, G.Z. (1986), An Empirical Model for Random Directional Wave Kinematics Near the Free Surface, *Proc. 18th Annual Offshore Tech. Conf.*, OTC Paper 5097, Houston.

Sharma, J. N. and Dean, R. G. (1979), Development and Evaluation of a Procedure for Simulating a Random Directional Second Order Sea Surface and Associated Wave Forces, *Ocean Eng. Report 20*, Univ. Deleware, Newark.

CHAPTER 17

Mediterranean Sea Level Changes From Tidal Records

Victor Goldsmith* and Michal Gilboa*

Abstract

Of the more than 90 tide gage records in the Mediterranean, 10 representative gages were analyzed for indications of sea level rise (SLR). No definitive trend of regional sea level rise has been discerned for this area. The lack of SLR may be partially attributed to local effects on sea level such as seasonal water temperature and wind differences, and to local tectonics. The extent of these seasonal changes is in the order of tens of cms/year, and varies greatly from year to year, probably masking the trends of long-term SLR of mm/yr.

Introduction

Recent studies indicating a sea level rise on some coasts (Aubrey and Emery, 1983), together with analyses of the "greenhouse effect", have led to predictions of a future global sea level rise of 60 cm in the next 40 years (summarized in Barth and Titus, 1984). As a result, subsequent efforts have concentrated on rezoning the coasts and re-defining criteria for all coastal constructions, for the expected SLR.

In this study attention is directed at documenting and explaining seasonal sea level changes discerned in Mediterranean tide gages. These analyses are then used to help define SLR.

Tide Data

Tide records for Israel have been obtained from Israel government agencies for the following locations:

Haifa 1956-60, 1965-76
Jaffa 1955-59, 1962-73, 1975-82
Ashdod 1958-83
Eilat 1965-70, 1975-83

The first three are on the Mediterranean coast, and Eilat is on the Red Sea.

Tide records for the following locations were obtained from the Permanent Service for Mean Sea Level (PSMSL) in Liverpool, U.K.: (Fig.1):

Gibralter 1961-83
Alicante Spain (Mediterranean coast) 1960-78
Trieste Yugoslavia 1934-74
Bakar Yugoslavia 1934-74

*Israel National Oceanographic Institute, P.O. Box 8030, Haifa and Haifa University (V.G.)

Dubrovnik Yugoslavia 1956-74
Piraieus Greece 1969-82

Comparisons of concomitant tidal data at the three Israeli Mediterranean locations indicate that they have very similar tidal curves and amplitudes (30-60 cm). The similarities in these tidal curves provided a check on the efficacy of the data and on the common sea level datum (Goldsmith and Gilboa, 1985).

Seasonal Sea Level Changes

With the exception of Trieste, no clear long term sea level trends were discerned from statis tical analyses of the averages of annual sea levels. Further analyses were conducted by computing the monthly mean sea levels. From these results, strong seasonal changes of 15-20 cm were noted, with the seasonality varying around the Mediterranean. Further, the seasonality varied significantly (>5cm) from year to year.

Plots were made of the averages of all the monthly means for each of the 12 months (Fig. 2).

Temperature Effects

Along the Israeli coast there is a strong tidal seasonality with a range of 20 cm. This is approximately equal to the neap tide range, and 1/3 of the spring tide range. Highest sea levels occur at the end of summer and lowest sea levels occur at the end of winter. Heat flow data obtained over many years by the R/V Shikmona in the southeast Mediterranean continental shelf show a similar seasonality (Fig. 3). Moreover, computations of theoretical sea level changes from the measured heat flow data indicate that sea level changes based on the seasonal water temperature changes alone accounts for 2/3 of the seasonal sea level changes measured by the tide gages. This is due to changes in the water volume (i.e., cold water is denser, hence lower sea levels in winter). There appears to be a certain lag effect, with the coldest and warmest temperatures occuring at the ends of winter and summer, respectively.

A similar pattern is found in the western Mediterranean; e.g., Alicante Spain and Gibralter have a seasonality of 15 cm with highest levels in September to November, and lowest levels in February/March (Fig. 4). Here the seasonality is not so regular nor so sharp as in the eastern Mediterranean.

Wind Effects

Another factor in the seasonal sea level changes involves local wind effects, especially in on/offshore winds. In the southeast Mediterranean, very low monthly mean sea levels occur occasionally in the winter months (i.e. 20 cm below MSL). This is attributed to strong offshore easterly winds which may blow continuously for many days. In the western Mediterranean unusually high monthly mean sea levels occur in the summer months. Along the Spanish coast the

dominant winds are onshore from March to April with the highest frequency in July, and offshore from November to February, peaking in February (Sanjaume, 1984, and Figure 4). The measured monthly mean tide heights decrease from December to February at both Alicante and Gibralter, coincident with the dominance of offshore winds. Similarly, the monthy mean tide heights increase from March to October coincident with the dominance of onshore winds.

Thus the seasonal sea level changes appear to be related to a combination of sea temperature and wind effects in the Mediterranean.

Long-term Sea Level Changes From Yearly Averages

At Trieste the long-term trend is a rise in sea level, but between 1955-83 sea level was relatively stable. At Ashdod and Piraeus in the eastern Mediterranean, the annual average sea level was higher in the 1960's, and decreased by 5 cm in 1979-1980, then rose and fell again. At Gibralter and Alicante in the western Mediterranean, sea level was lower in the 1960's; it peaked higher in Gibralter in 1970-1980 and then decreased by 12 cm. (Fig. 1).

Linear regression analyses and r2 values were derived from the annual averages of the 10 tide gages. The computed trends and the r2 values are presented in the top portion of Figure 5. Only Trieste shows a clear SLR (1.3 mm/yr). Due to the many uncertainties in these tide data (including placement of the gages relative to a common datum, continuity of records, and annual variations in local climatological factors) there is some statistical uncertainty in choosing the proper limiting r2 value. Imaginary tide gage records were constructed using a random numbers table, and similar statistical computations made. In every case, r2 values were $<< 0.1$. Thus, computed sea level trends with $r2 > 0.1$ are accepted (Fig. 5). Note that at two locations, Haifa and Alicante, at opposite ends of the Mediterranean, a trend of sea level lowering is indicated.

Long-term Sea Level Changes From Monthly Averages

Because of the large seasonal range observed in the tide gage records, and the large variations from year to year in this seasonality, it appears that a better indicator of long-term changes might be discerned in the analysis of the trend for an individual month, i.e., the monthly means of all the January's for all the years of record. The results of the statistical analyses of the monthly sea level trends and concomitant r2 values are shown in the bottom half of Figure 5. Of the 120 analyses (10 gages X 12 months) only those with r2 values > 0.1 are shown.

A strong trend of rising sea level of 1-2 mm/yr is clearly shown for Trieste (especially in the summer months) and for the neighboring station of Bakar (for June and August). A weak trend of falling sea level is shown for Ashdod (August and September) and Alicante (June).

What is clar, however, is that the best results occur in the

summer months. This appears to be due to more consistant climatological factors in the summer. In the winter the Mediterranean is in the zone of westerlies with storms passing through on an average of every 7-10 days (Goldsmith and Sofer, 1983). In the summer, the subtropical low moves north and winds in the eastern Mediterranean blow every day from the northwest.

Conclusions

SLR trends in the Mediterranean are "masked" by the local processes including seasonal sea level changes from thermal expansion of the sea due to temperature changes, and from seasonal changes in the offshore/onshore winds. These seasonal changes in the sea level of 15-20 cm have large annual variations (> 5cm). Of the 10 gages analyzed only Trieste shows a definite trend of SLR amounting to 1-2 mm/yr. The location of Trieste, at the end of the Alps, suggests the importance of local tectonic effects.

To overcome the "noise" in the data resulting from seasonal effects, sea level trends of individual months, rather than annual averages, were delineated. In some cases the individual months are statistically more significant than the annual averages. The best results occur in the summer months when climatological conditions are more consistent.

The lack of consistent definitive trends in Mediterranean sea level records suggests the importance of local effects. The analyst looking for indications of SLR should be aware of local effects and take these into account before making definitive statements on SLR trends.

Acknowledgements

This research was supported by the Israel Ministry of Energy and Infrastructure and by the Israel National Oceanographic Institute. These tide data were kindly furnished by the Israel Port Authority the Israel Meteorological Service, the Israel Mapping Service, and the Permanent Service for Mean Sea Level, Liverpool U.K.

References

AUBREY, D.G., and EMERY, K.O., 1983. Eigen analysis of recent United States Sea Levels. Cont. Shelf Research Vol. 2 pp. 21-33

BARTH, M.C. and TITUS, J.G., 1984. Greenhouse effect and sea level rise: a challenge for this generation. New York, Van Nostrand Reinhold Co., 325 pp.

GOLDSMITH, V. and GILBOA, M., 1985. Development of an Israeli tidal atlas and comparison with other Mediterranean tidal data. Isr. Nat Ocean. Inst. Rep. H 8/85, Haifa, 28 pp.

HECHT, A., ROSENTRAUB, Z. and BISHOP, J., 1983. Temporal and spatial variations of heat storage in the eastern Mediterranean Sea. The Charney Workshop on Weather Modification, Ormat Turbines, Yavne Israel, and Isr. J. of Earth Sci. (in press)

SANJAUME, E., 1984. Las costas Valencianas: sedimentologia y aspectos

de morfologia litoral. Doctoral Thesis, University of Valencia, 1676 pp.

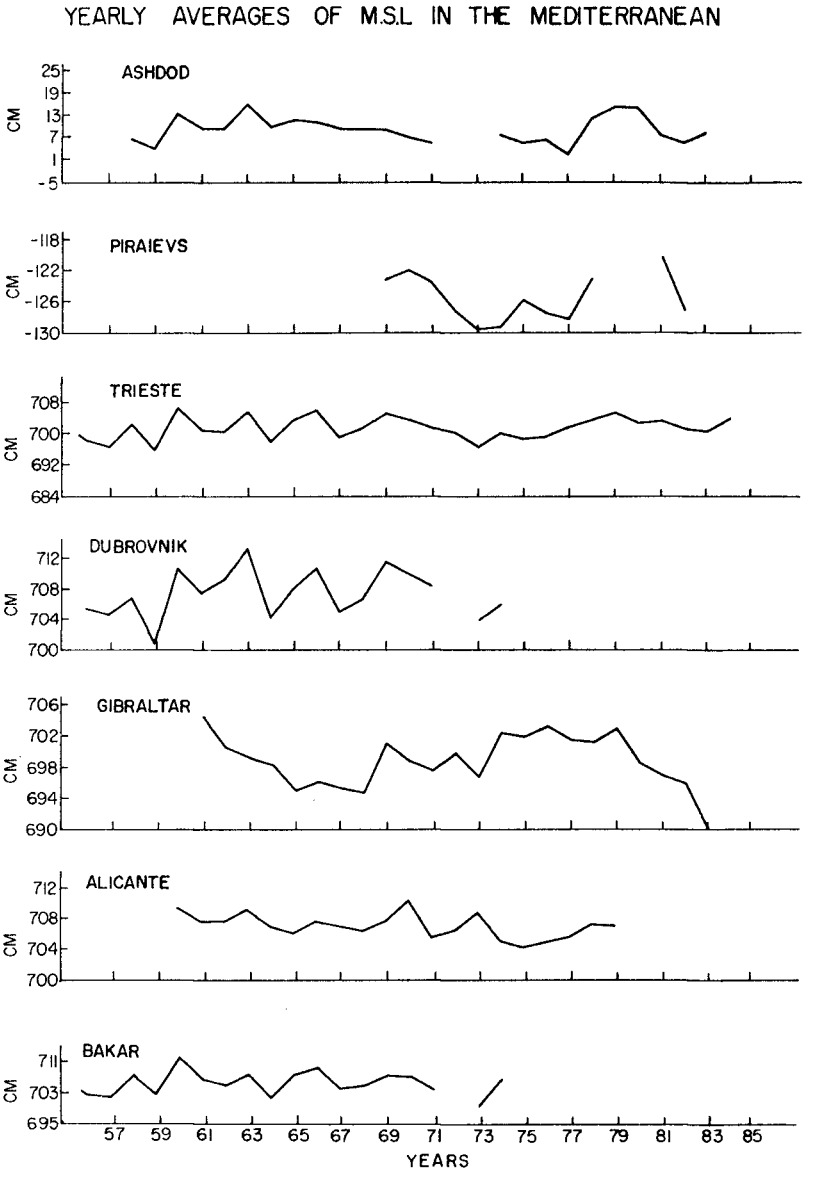

Figure 1

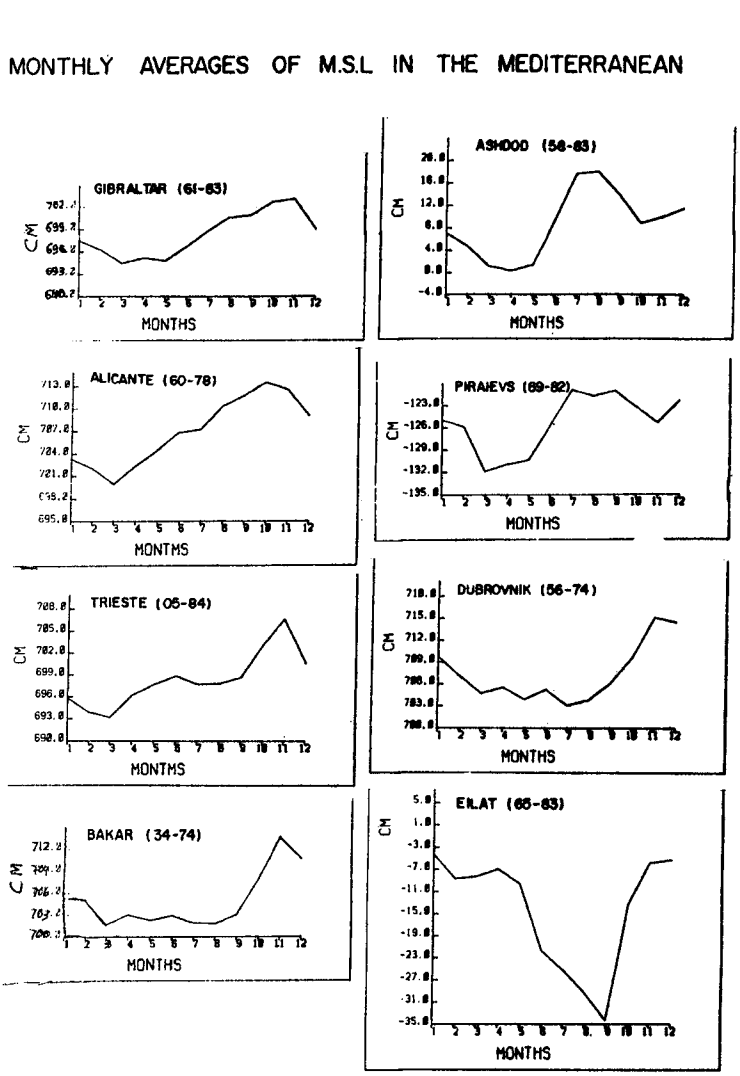
MONTHLY AVERAGES OF M.S.L IN THE MEDITERRANEAN
GIBRALTAR (61-83)
ASHDOD (56-83)
ALICANTE (60-78)
PIRAIEVS (69-82)
TRIESTE (05-84)
DUBROVNIK (56-74)
BAKAR (34-74)
EILAT (65-83)
CM
MONTHS

Figure 2

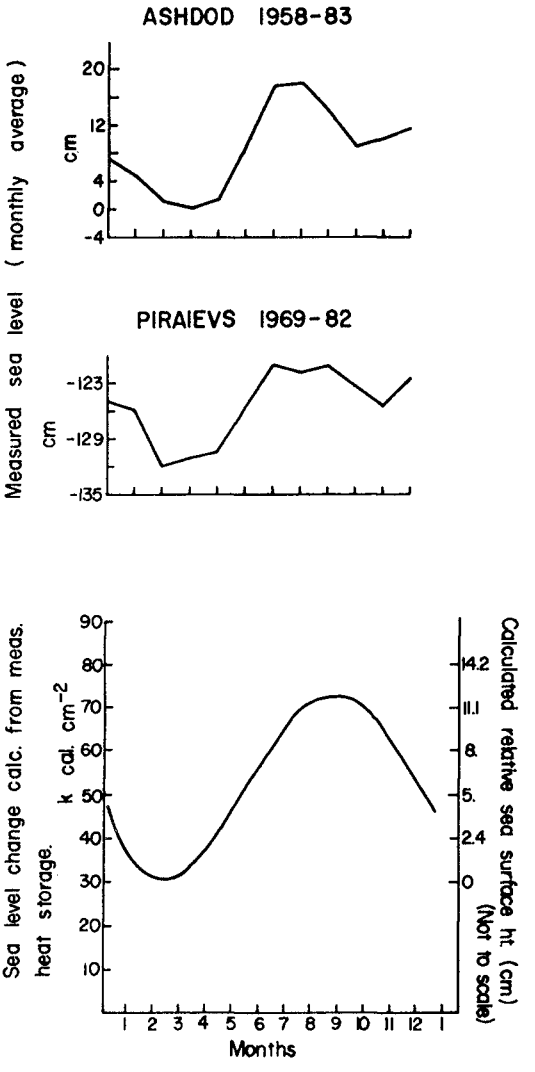
ASHDOD 1958-83
20
12
4
0
-4
cm
PIRAIEVS 1969-82
-123
-129
-135
cm
Measured sea level (monthly average)
Sea level change calc. from meas. heat storage.
k cal. cm^{-2}
90
80
70
60
50
40
30
20
10
14.2
11.1
8.
5.
2.4
0
Calculated relative sea surface ht (cm.) (Not to scale)
1 2 3 4 5 6 7 8 9 10 11 12 1
Months

Figure 3

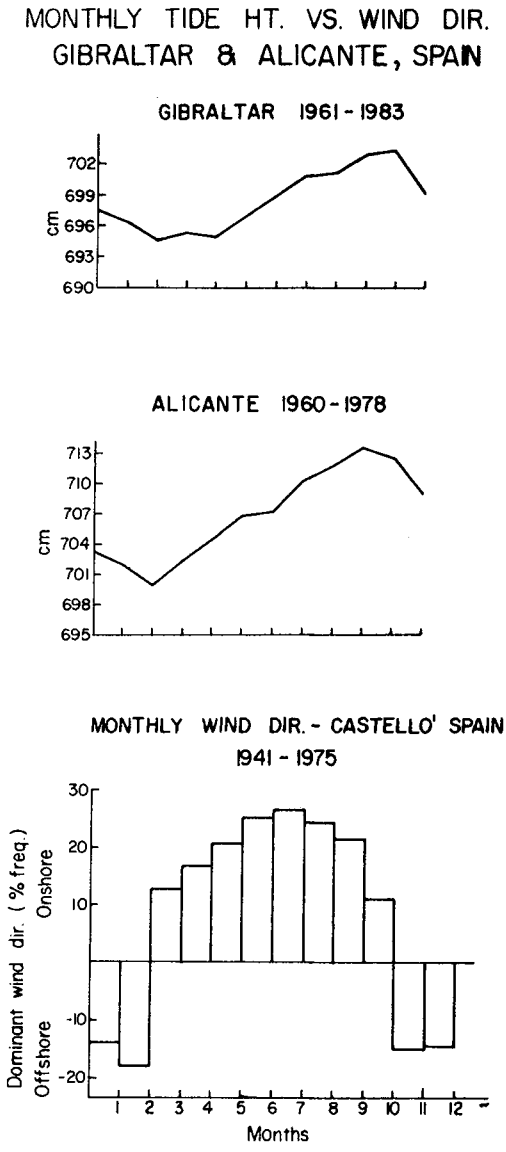
MONTHLY TIDE HT. VS. WIND DIR.
GIBRALTAR & ALICANTE, SPAIN
GIBRALTAR 1961 - 1983
cm
702
699
696
693
690
ALICANTE 1960 - 1978
cm
713
710
707
704
701
698
695
MONTHLY WIND DIR. - CASTELLO' SPAIN
1941 - 1975
Dominant wind dir. (% freq.)
Onshore
Offshore
30
20
10
-10
-20
1 2 3 4 5 6 7 8 9 10 11 12
Months

Figure 4

Tidal sea level changes in the Med. & significance yearly averages

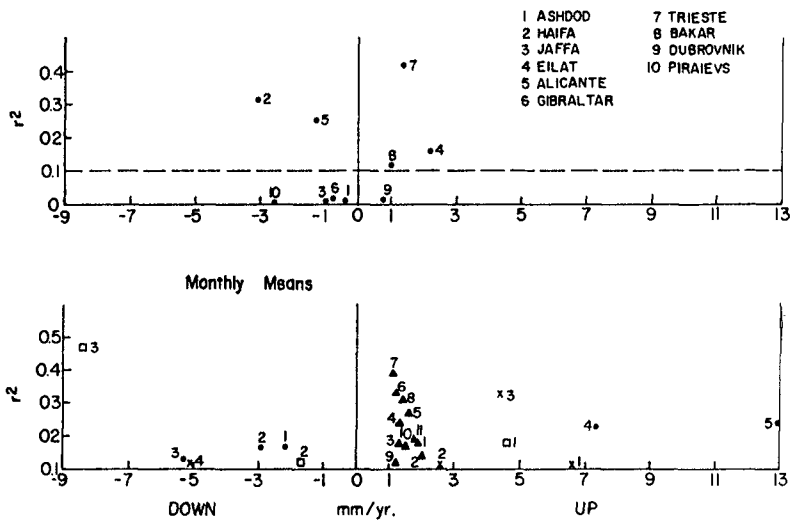

x 1. DUBRO. - FEB.
2. DUBRO. - JUNE
3. DUBRO. - SEP.
4. DUBRO. - DEC.

• 1. ASHDOD - AUG.
2. ASHDOD - SEP.
3. PIRAIEVS - FEB.
4. PIRAIEVS - OCT.
5. PIRAIEVS - DEC.

□ 1. GIBRALTAR - APR.
2. ALICA - JUNE
3. ALICA - NOV.

▲ 1. TR. - JAN.
2. TR. - FEB.
3. TR. - APR.
4. TR. - MAY
5. TR. - JUNE
6. TR. - JULY

▲ 7. TR. - AUG.
8. TR. - SEP.
9. TR. - OCT.
10. BA. - JUNE
11. BA. - AUG.

Figure 5

CHAPTER 18

EXPERIMENTAL STUDY ON THE VALIDITY RANGE OF VARIOUS WAVE THEORIES

by

Masataro Hattori*

INTRODUCTION

In the design of coastal structures and the study of nearshore dynamics, rational predictions of the wave kinematics are very important but difficult procedures. Although a large number of nonlinear wave theories have been proposed and used for computing the wave kinematics, there are no theories applicable from the deep water to very shallow water. It is, therefore, very important for coastal researchers and engineers to know which of theories describe well a wave field specified by the wave characteristics and water depth, and to select a particular wave theory for a problem of interest.

Many intensive efforts have been made to examine the validity as well as the applicability of various wave theories. However, there are still no well-accepted guidlines for the application range of the wave theories. The validity evaluation of a particular wave theory has been basically made by means of the following two versions: the analytical (mathematical) validity and the experimental (physical) validity. The analytical validity study has been conducted by various researchers (Dean, 1970; Komar, 1976; Horikawa et al., 1977; Swart, 1978) and revealed the degree of mathematical satisification to the governing equations and boundary conditions for each wave theory. The analytical validity study probably tends to show the relative applicability for various wave theories. It does not ensure that the theory describe well laboratory or field phenomena. Based on the analytical validity of various wave theories by Horikawa et al., Isobe (1985) proposed application ranges for the finite amplitude wave theories in terms of the relative water depth and relative wave height.

The experimental validity refers to how well the prediction of various wave theories agrees with actual measurements (Dean & Dalrymple, 1984). As the wave shoals, wave form becomes more asymmetrical, especially under high wave conditions of interest to design. Such nonlinearity influences greatly the wave kinematics and it makes difficult to predict readily the wave kinematics by several theories. From a practical viewpoint, it is , therefore, requested to establish the application ranges of available wave theories for shoaling waves.

In this study, laboratory data of simultaneous measurements of the

* Professor, Department of Civil Engineering, Chuo University, Kasuga 1-13-27, Bunkyo-ku, Tokyo, 112, Japan.

wave surface elevation and water particle velocities of the shoaling wave were compared with the predictions from various wave theories. On basis of degree of the overall agreement between the measured and predicted time-varying quantities, the validity range of the individual wave theory was specified.

The purposes of the present study are: (1) To propose parameters and criteria for the evaluation of wave theory validity, (2) To evaluate the validity limits for various wave theories, and (3) To determine the application ranges of available wave theories for important ranges of wave conditions of practical interest.

The wave theories included in the evaluation are listed in Table 1. The linear wave theory is the best known and widely used theory. From a practical viewpoint, the Stream Function wave theory of Dean (1965) was adopted as a representative numerical wave theory. The prediction of time-varying quantities by the ninth order irregular Stream Function wave theory, SFM9A, was performed using the measured wave profile, whereas that by the other theories was based on symmetrical profiles with the measured wave height and period.

Table 1 Wave Theories Involved in the Evaluation.

WAVE THEORY		REFERENCE
Linear wave theory	ST 1	Ippen (1966)
Fifth order Stokes	ST 5	Isobe et al. (1978) Fenton (1985)
Third order Cnoidal	CN 3	Isobe et al. (1978)
Stream Function wave theory		Dean (1965)
Fifth order of permanent waves	SFM 5B	
Ninth order of irregular waves	SFM 9A	

EXPERIMENTAL EQUIPMENT AND PROCEDURES

Experiments were performed in a glass-walled wave flume, 0.30 m wide, 0.55 m high and 20 m long. Waves were produced by a flap-type wave generator installed at one end of the flume. A sloping bottom of 1/20 was installed in the flume. Experimental conditions, given by Table 2, covered a wide range of the wave steepness. The last column of Table 2 gives the Ursell parameter, Ur_0, at the wave generator.

Simultaneous measurements of the wave surface elevation and water particle velocities were made at various locations over the slope. Range of the shallow water Ursell parameter, $Ur = gHT^2/h^2$ (H is the wave height, T is the wave period, h is the water depth, and g is the gravitational acceleration), at measuring section was from about 1 to 110. The wave surface elevation, η, was measured by resistance-type wave gages having excellent linearity and stability. The manufacture's stated frequency response of the wave gage is approximately 20 Hz, higher than the harmonic frequency range of experimental waves due to the nonlinearity. Measurements of the horizontal and vertical water particle velocities, u and w, were made using a laser doppler velocimeter of two

Table 2 Experimental Conditions.

Exp.	Run	T(s)	h_i(cm)	H_i(cm)	h_b(cm)	H_b(cm)	H_o'/L_o	Ur_o
1	1	0.80	35.0	6.5	9.0	6.0	0.068	1.14
	2	0.85	35.0	4.4	5.5	5.4	0.041	0.87
	3	1.00	35.0	3.1	5.0	4.3	0.021	0.85
	4	1.40	35.0	2.6	5.3	4.7	0.009	1.41
	5	1.20	40.0	0.9	–	–	0.005	0.30
2	1	1.00	37.5	4.7	7.0	6.1	0.032	1.19
3	1	0.80	33.0	6.5	8.5	6.8	0.068	1.22
	2	0.85	33.0	5.1	6.5	6.1	0.048	1.09
	3	1.00	33.0	3.8	5.5	5.4	0.026	1.12
	4	1.40	33.0	2.5	4.5	4.9	0.009	1.45
	5	1.20	33.0	1.1	–	–	0.005	0.47
4	1	0.80	33.0	6.5	8.5	6.9	0.068	1.22
	2	0.84	43.0	5.6	7.0	5.7	0.049	0.84
	3	0.99	43.0	4.0	5.5	5.0	0.026	0.84
	4	1.40	43.0	2.7	6.0	4.6	0.009	1.14

H_i : Wave height at the uniform water depth h_i.
H_b & h_b : Wave height and water depth at breaking point.
Ur_0 : Ursell parameter at the wave generator.

components (DISA, Model 55 X) in a vertical plane beneath the wave surface measurement. Outputs of the wave surface elevation and water particle velocities were recorded on a 7-channel analogue recorder over 70 wave periods minimally. The data were digitized by an A-D converter at a sampling frequency of 167 Hz for computer processing. After individual waves were determined from the wave gage records by means of the zero-upcrossing method, the time series data were averaged over 50 waves with respect to the phase.

DETERMINATION OF THE EVALUATION PARAMETERS

In the most previous studies (Swart, 1978), the validity of wave theory has been discussed on basis of visual comparisons between the theoretical prediction and measured values. In order to determine rationally the application range for a particular wave theory, the wave theory validity should be evaluated with appropriate criteria of non-dimensional parameters representing degree of the agreement of the theory with the measured values. We adopted the four following parameters:

(1) Ratio of the maximum values: $M_R^+ = Y_{max}/X_{max}$,

(2) Ratio of the minimum values: $M_R^- = Y_{min}/X_{min}$,

(3) Coherence between the measured and predicted time histories:

$$C_o = \sum_{i=1}^{m} X_i Y_i / \left(\sum_{i=1}^{m} X_i \sum_{i=1}^{m} Y_i \right)^{1/2}, \text{ and}$$

(4) Overall root-mean-square (rms) between the time histories:

$$E = \left[\sum_{i=1}^{m} (X_i - Y_i)^2 / \sum_{i=1}^{m} X_i^2 \right]^{1/2}.$$

X_i and Y_i, as shown in Fig. 1, are the measured and predicted values sampled at various and evenly spaced phases over one wave period of the time history. X_{max} and Y_{max}, and X_{min} and Y_{min} are the maximum and minimum values of X_i and Y_i, respectively.

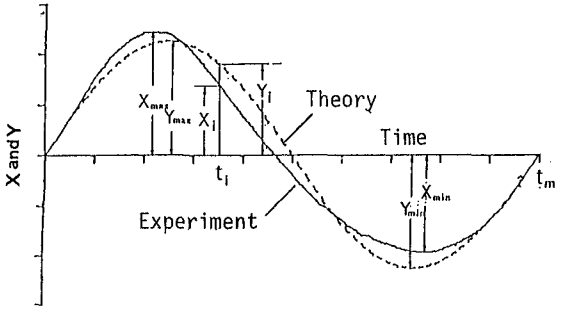

Fig. 1 Definition Sketch for Evaluation Parameters.

From a practical viewpoint, the parameter set of M_R^+ and M_R^- seems to be of a very useful in the validity evaluation. Since the coherence function C_o indicates the degree of similarity in overall profiles of time variations, the parameter set of C_o and M_R^+ is considered as a favorable measure for the validity evaluation. As the overall rms error E indicates the deviation degree of the theory from the experiment throughout the time history of one wave period, E is considered as the principal parameter for the validity evaluation.

EXPERIMENTAL ERRORS AND CRITERIA FOR THE VALIDITY EVALUATION

If experiments could be made under sufficiently well-controlled conditions, measured data are most likely contaminated with a variety kind of errors associated with the experiments. We should determine criterion for evaluation of the wave theory validity with consideration that disagreement between the theory and experiment is at least of the same order as the estimated experimental error, because the experimental validity is based on the comparison between the theory and experiment.

Prior to the determination of the evaluation criterion, it is necessary to discuss potential errors associated with experiments. The experimental errors are attributed to the following causes: experimental equipment and procedures, measuring instruments and techniques, and data processing.

Ursell parameter at the wave generator for each test run, given in the last column of Table 2, is much less than 13, and indicates that experimental waves are completely free from the secondary wave generation (Swart, 1978). Wave reflection from the sloping bottom was

one of the systematic error sources. From measurements of the wave height distribution in a part of uniform water depth, the error due to the reflection was estimated at most ± 5 % under high wave conditions.

In Fig. 2, the experimental results are shown for the variation of wave height for a series of Exps. 1 through 3. The solid line along data plots represents the theory of Shuto (1974), which is the first order Cnoidal wave theory with some second order terms retained in order to take account of the bottom slope effect. For a reference, breaking limits of Yamada and Shiotani (1968) and of Goda (1970), and the isolines of the shallow water Ursell parameter are shown. It is noticed from Fig. 2 that the experiments surprisingly agree well with the theory except for the experiments of low steepness conditions. The small deviation between the measurements and the theory is probably due to capillary effect of the water surface on thin-wire wave gages. The wave measurement error is estimated to be at most ± 2 %.

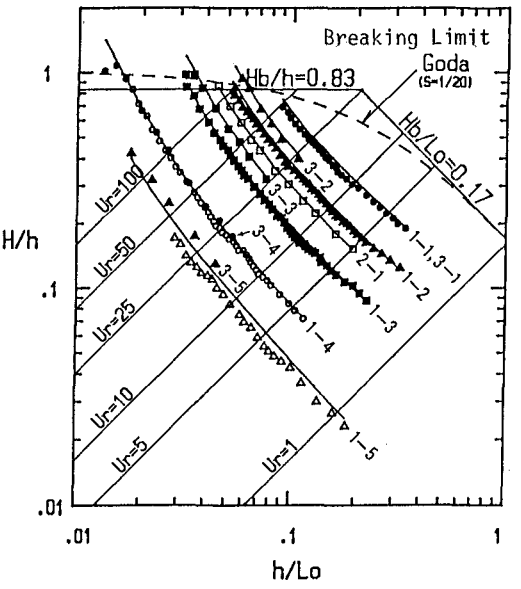

Fig. 2 Wave Height Variation.
———: Theory of Shuto (1974)

The manufacture's stated accuracy of the instruments used was much greater than that required for this class of experiments. Another potential error is due to averaging processes of the measured data, and is estimated ±0.5 % for the wave surface elevation and ± 1 % for the water particle velocity data.

Taking into consideration of the potential errors in the experiment, we determined the overall rms error of $E \leq 0.10$ as the principal criterion of the validity evaluation. Evaluation criteria of the other parameters were determined so as to be equivalent to the principal criterion and were $0.90 \leq M_R^+$ and $M_R^- \leq 1.10$ and $C_o \geq 0.995$. To substantiate the adequancy of the criteria, Fig. 3 presents an example comparison between the measured and predicted time variations of the wave surface elevation and water particle velocities. The theoretical predictions were made by using the measured wave height, wave period, and water depth. E value for the ST 5 theory is equal to the criterion of E = 0.10. Visual comparisons provide fairly well agreements between the experiment and the predictions from the ST 5 theory.

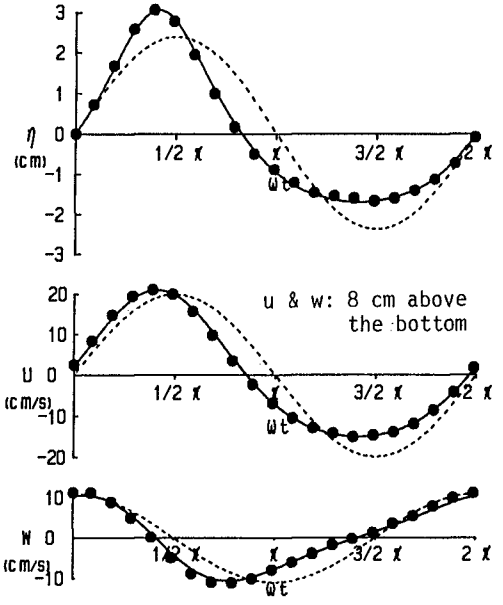

Fig. 3 Comparisons between Measured and Predicted Wave Form and Velocities for ST 1 and ST 5 Theories.
● : measured, -----: ST 1, ——— : ST 5
(Exp. 4-2: H=4.76 cm, h=12.0 cm, T=0.84 s, Ur=22.9)

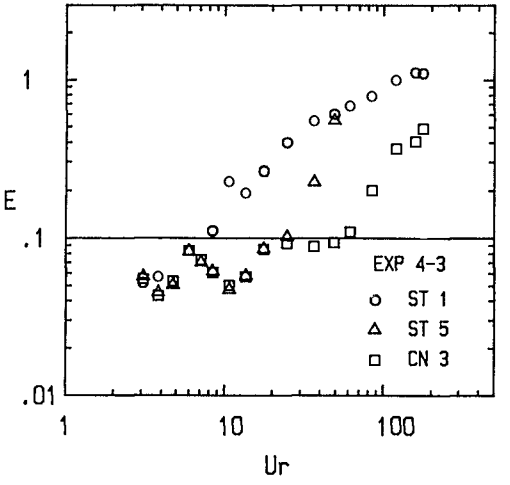

Fig. 4 Validity Limits for Wave Form of ST 1, ST 5 and CN 3 Theories in terms of E and Ur.

VALIDITY EVALUATION FOR THE WAVE SURFACE ELEVATION

Since the prediction by a wave theory is based on the measured wave height and period, the use of M_R^+ and M_R^- is not suitable for the validity evaluation of the wave surface elevation. Thus, validity examinations were performed with respect to the C_o and E parameters.

The validity limits of the ST 1, ST 5, and CN 3 theories for the wave form is shown in Fig. 4, in terms of the overall rms error E and the shallow water Ursell parameter Ur. It was found that the linear theory broke up the validity due to the wave form asymmetry about the mean water level, while the nonlinear wave theory became unable to maintain the validity due to the wave form asymmetry about the wave crest. Nonlinear effects of the shoaling wave on the wave form were discussed with the use of two types of the skewness factor for the wave form (Sekine & Hattori, 1985).

VALIDITY EVALUATION FOR THE WATER PARTICLE VELOCITIES

Since within a region of small Ursell parameter at measuring locations, the wave form is approximately symmetrical, the water particle velocities at the crest and trough phase position are predicted relatively well by either the linear or the Stokes wave theory. As the wave shoals further, the wave form becomes more asymmetrical about the crest as well as the mean water level. Due to such nonlinearity associated with the shoaling, degree of the agreement between the measurement and the prediction of the water particle velocities as well as the wave form depends on the class of wave theory applied to the computation of the wave kinematics.

Figure 5 shows an example comparison of the vertical distributions with depth for the horizontal and vertical water particle velocities under the crest and trough at a section of Ur = 22, where the wave form asymmetry becomes apparent. Under such a circumstance, the nonlinear wave theories, ST 5, CN 3 and SFM 9A, predict fairly well the measured values of the horizontal water particle velocity as seen in Fig. 5. Although the vertical water particle velocity under the crest and trough

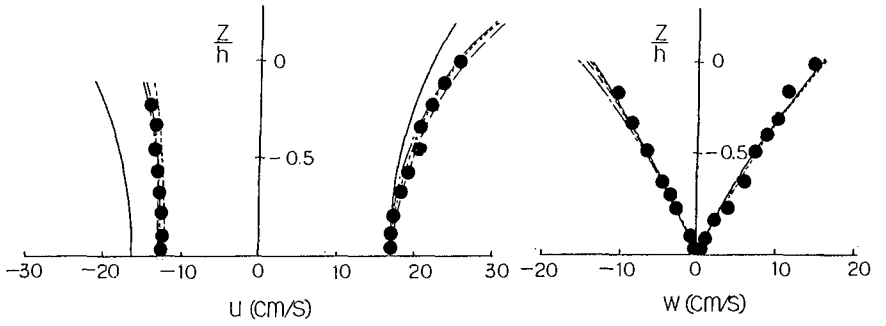

Fig. 5 Vertical Distributions of Water Particle Velocities under Crest and Trough (Exp. 2-1, Ur = 22).
———: ST 1, — — —: ST 5, — — — : CN 3, - - - - - -: SFM 9A

is represented excellently well by every wave theory as in Fig. 5, it is considered that degree of the agreement between the theory and measurements for the horizontal water particle velocity clearly depends upon the theoretical modeling for the nonlinear effect.

Based on comparisons of the vertical distributions between the measured and predicted water particle velocities, we decided to examine the wave theory validity for the water particle velocity through time history data of the horizontal water particle velocity. The validity evaluation was based on spatial distribution of the isoline of each evaluation parameter. Figure 6 is an example showing the validity limit of the ST 1 theory. The top figure is for the E value, the middle figure for the parameter set of M_R^+ and M_R^-, and the bottom figure for the parameter set of M_R^+ and C_o. The validity area is illustrated by the shaded part. The horizontal coordinate is represented by the water depth, instead of the horizontal distance from a reference point. The figure by the sloping bottom is the water depth and that in parentheses is the shallow water Ursell parameter at the measuring section. $_{max}$ and $_{min}$ are the envelop of wave height. B.P. denotes the breaking point.

As waves propagate from the intermediate to very shallow water region, the wave form is gradually translated due to nonlinear effects of the wave motion. As a consequence, the linear wave theory loses the validity for the horizontal water particle velocity as well as for the wave form. An interesting evidence is found that the validity limit for the water particle velocity broadens at the lower portions of the water column, because the bottom boundary restricts the orbital motion of water particles due to waves, especially in the vertical direction. This results degradation of the nonlinearity in the velocity time-variation. From a comparison between the top and middle figures in Fig. 6, we notice that the validity limit determined with the parameter set of M_R^+ and M_R^-, very useful in a practical use, is almost the same as that by E. In contrast, a remarkable disagreement is found between the validity limit determined by E and the parameter set of M_R^+ and C_o. Thus the parameter set of M_R^+ and C_o is not suitable for the validity evaluation. As many previous studies have pointed out, the ST 1 theory provides very good predictions of the wave kinematics even in very shallow water region, up to the breaking point.

Figures 7 and 8 show the validity limit of the nonlinear wave theories, ST 5 and CN 3. The validity limit for the ST 5 theory coincides with the nonconvergence or inapplicability of the wave theory. Although the CN 3 theory is recognized to predict reasonably well the water particle velocity in the very shallow water region, the theory becomes unable to maintain the validity due to the nonlinearity associated with the asymmetry about the maximum velocity under the crest. The CN 3 theory provides a favorable agreement with the measured wave surface elevation in the intermediate region (see Fig. 4). On the other hand, the theory tends to overpredict the horizontal water particle velocity at the crest phase position in the same region. Consequently, another validity limit appears in the intermediate water depth region, and this is expected from the assumption employed in the derivation of the Cnoidal wave theory. According to the validity evaluation for the CN 1 theory, the theory represents very poorly the

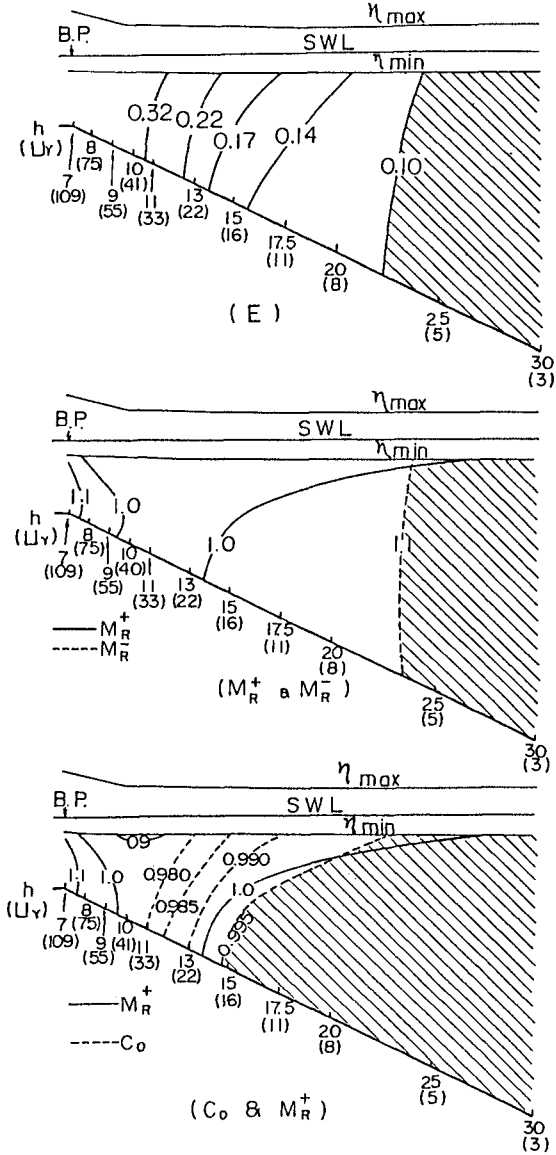

Fig. 6 Validity Limit for Horizontal Velocity of ST 1 Theory (Exp.2-1).

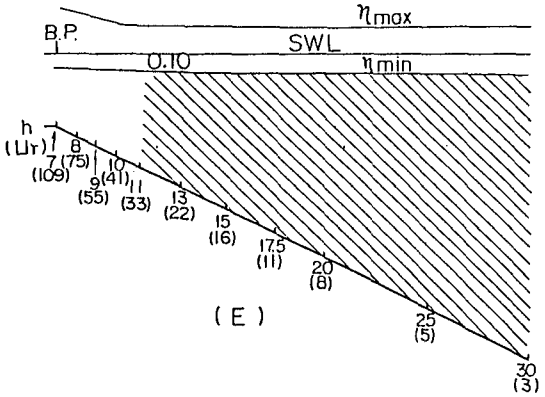

Fig. 7 Validity Limit for Horizontal Velocity of ST 5 Theory (Exp. 2-1)

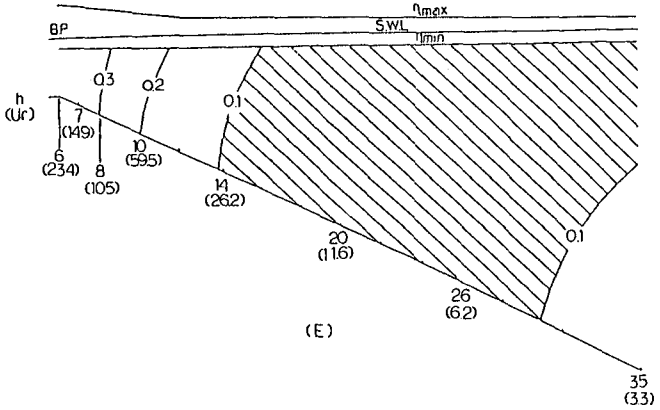

Fig. 8 Validity Limit for Horizontal Velocity of CN 3 Theory (Exp. 4-4).

measures water particle velocity. Thus the rational validity limit of the CN 1 theory could not be determine.

The irregular Stream Function wave theory, SFM 9A, provides the best agreement with the measured water particle velocity over a very wide range from the deep water to very shallow water near the breaking point. This is most probably due to the use of the measured wave surface elevation for the calculation of the SFM 9A theory.

APPLICATION RANGE FOR THE WAVE THEORIES

In the previous sections, we mainly discussed the validity limit for the wave form and the water particle velocity with the aid of the criterion of the overall rms error E = 0.10. The application range of the wave theories can be determined from intercomparisons of the validity limits for the wave form and water particle velocity, in terms of the relative water depth, h/L_0, and relative wave height, H/h, with the auxiliary parameter of the shallow water Ursell parameter, Ur. The results are presented by Figs. 9 through 11.

Application ranges of the ST 1 and ST 5 theories are presented in Fig. 9, in which the broken line is the isoline of the rms error E_T = 0.10 in the free surface boundary conditions for the wave theories, determined from the analytical validity study of Horikawa et al. (Isobe, 1986). Breaking limit by Yamada and Shotani (1968) is also shown. Circle, triangle, and square symbols denote the validity limits for the wave form and the horizontal water particle velocities near the bottom and just below the trough, respectively. According to the validity evaluation results, the validity limit for the wave form coincides with that for the water particle velocities at the upper portions of the water column. Therefore, this determines the application ranges of the ST 1 and ST 5 theories, as shown in Fig. 9.

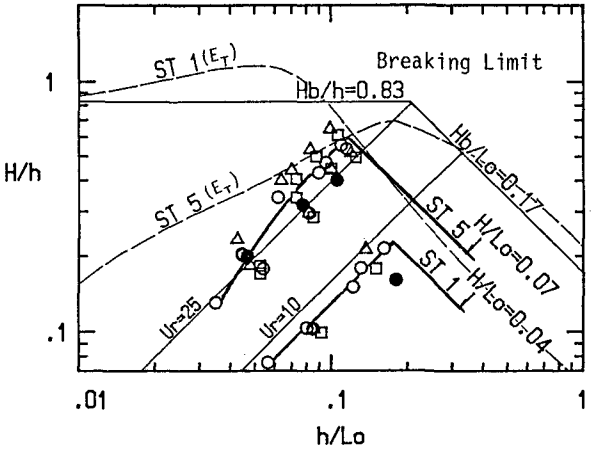

Fig. 9 Application Ranges of ST 1 and ST 5 Theories.
○ ● : the wave surface elevation, △ ▲ : near-bottom horizontal velocity, □ ■ : horizontal velocity below the trough.
—— ——: isoline of E_T = 0.10 by Isobe (1986)

A special feature found in the application range of the CN 3 theory is that the application range is confined within a region bounded by the application limits in very shallow water and in the intermediate water depth region as in Fig. 10, and provides some limitation in application of the Cnoidal wave theory. The CN 3 theory as well as the ST 5 can not represent favorably the measured values in a region of large values of

Ur, in which the asymmetry in the wave form becomes more remarkable (Iwagaki et al., 1972; Flick et al., 1981). Taking into account that there is an application limit of the CN 3 theory of Ur = 6, and that the application range of the ST 5 theory in a region of Ur > 25 is narrow, the isoline of Ur = 25 is considered as a reasonable demarcation between the applications of the ST 5 and CN 3 theories (Le Mehaute, 1976; Isobe, 1985). From Figs. 9 and 10, it is found that the application ranges determined by the experimental validity indicate a similar trend of the isoline of E_T for each wave theory, especially in the intermediate water depth.

Application range of the irregular Stream Function wave theory, SFM 9A, coincides exactly with the validity limit for the water particle velocities (Fig. 11). The SFM 5B theory, assumed the symmetrical wave form can not predict well the wave kinematics in very shallow water region because of the nonlinear effect. From a comparison between Figs. 10 and 11, we find that the application limit of the SFM5B theory is almost the same as that of the CN 3 theory in a region of large values of Ur.

To conclude the discussions in the present study, we propose a diagram representing the application ranges of the wave theories for waves propagating in the shoaling water. Figure 12 presents the application ranges in terms of h/L_0, h/H, and Ur.

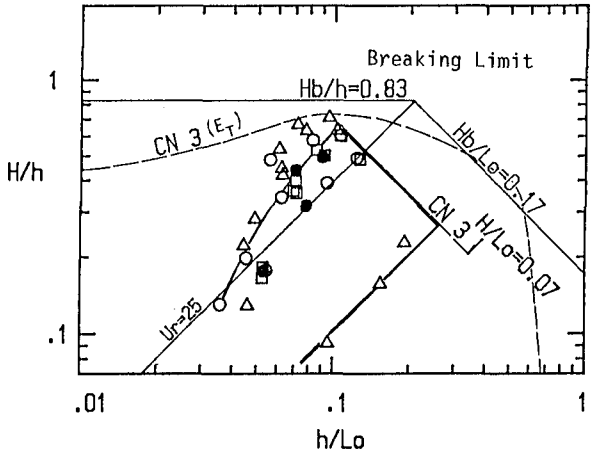

Fig. 10 Application Range of the CN 3 Theory.

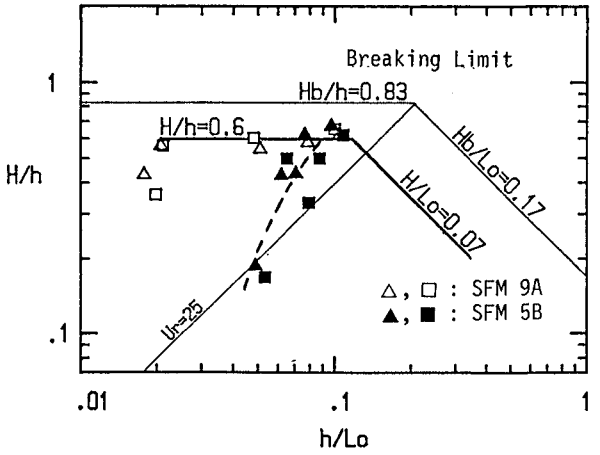

Fig. 11 Application Ranges of the SFM 9A and SFM 5B Theories.

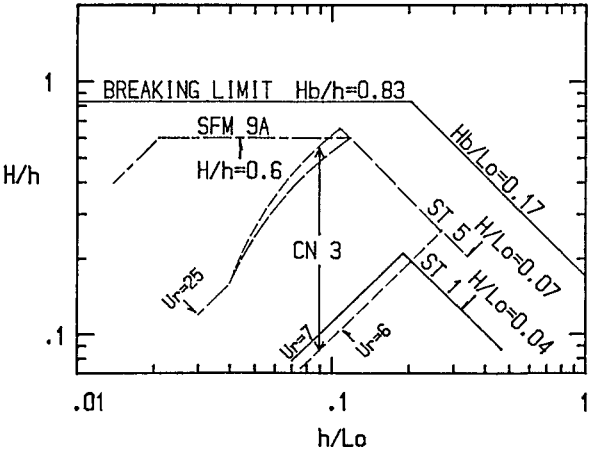

Fig. 12 Application Ranges of the Wave Theories Included in the Present Study.

CONCLUSIONS

Simultaneous measurements of the wave surface elevation and water particle velocities of shoaling waves have been performed at various locations in a wave flume with a slope of 1/20. The validity of wave theories has been evaluated by comparisons between the measured values

and predictions from the wave theories. The wave theory validity has been discussed using four parameters, representing the degree of the agreement between the measurement and theory. Based on the validity evaluation, the application ranges for the wave theories have been determined in terms of H/h, h/L_0, and Ur.

The main findings of the present study are as follows:

(1) Amongthe non-dimensional parameters for the validity evaluation, the overall rms error E plays a principal role in the determination of the validity limit of various wave theories. In addition, the parameter set of M_R^+ and R_R^- is favorable to the validity evaluation in a practical problem specified by the wave characteristics and water depth.

(2) For wave surface elevation, the validity range of analytical theory for permanent type waves is limited by the nonlinearity attributed to the wave form asymmery about the mean water level for the linear wave theory and about the crest for the nonlinear theory.

(3) The degree of agreement between the measured and predicted horizontal water particle velocity depends on the elevation above the bottom and on the value of Ursell parameter.

(4) Application ranges of the wave theories included in the evaluation are determined by the validity limits for the wave form and horizontal water particle velocity at the upper portions of water column just below the trough. Within the limit of the present study, the application ranges are determined as in Fig. 12 and Table 3.

Table 3 Application Ranges of the Wave Theories.

ST 1	$0.2 \leqq h/L_0 < 0.4$: $H/L_0 \leqq 0.04$ $0.06 < h/L_0 \leqq 0.2$: $U_r \leqq 7$
ST 5	$0.1 \leqq h/L_0 < 0.4$: $H/L_0 \leqq 0.07$ $0.06 \leqq h/L_0 \leqq 0.1$: $U_r \leqq 32$ $0.04 < h/L_0 \leqq 0.06$: $U_r \leqq 25$
CN 3	$0.12 \leqq h/L_0 < 0.4$: $H/L_0 \leqq 0.07$: $6 < U_r \leqq 25$ $0.07 \leqq h/L_0 \leqq 0.12$: $H/h \leqq 0.5$: $6 < U_r \leqq 35$ $0.04 \leqq h/L_0 \leqq 0.07$: $6 < U_r \leqq 35$ $0.02 < h/L_0 \leqq 0.04$: $6 < U_r \leqq 25$
SFM9A	$0.1 \leqq h/L_0 < 0.4$: $H/L_0 < 0.07$ $0.02 < h/L_0 \leqq 0.1$: $H/h \leqq 0.6$

ACKNOWLEDGMENTS

The author would like to express the appreciation to Dr. M. Mizuguchi, Associate Professor of Chuo University and Dr. M. Isobe, Associate Professor of Yokohama National University, for many helpful

suggestions and valuable discussions during the course of this study.

REFERENCES

Dean, R.G., 1965 : Stream function representation of nonlinear ocean waves, Jour. Geophys. Res., Vol. 70, No. 18, pp. 4561-4571.

Dean, R.G., 1970; Relative validities of water wave theories, Proc. ASCE, Jour. Waterways, Harbors, Coastal Eng. Div., WW 1, pp. 105-119.

Dean, R.G. and R.A. Dalrymple, 1984: Water Wave Mechanics for Engineers and Scientists, Prentice-Hall, New York, N.Y., 353 pp.

Fenton, J.D., 1985: A fifth-order Stokes theory for steady waves, Proc. ASCE, Jour. Waterways, Port, Coastal and Ocean Eng., No. 2, pp. 216-234.

Flick, R.E., R.T. Guza and D.L. Inman, 1981: Elevation and velocity measurements of laboratory shoaling waves, Jour. Geophys. Res., Vol.86, No. 5, 4149-4160.

Goda, Y., 1970: A synthesis of breaking indices, Trans. Japan Soc. Civil Engrs, Vol. 2, Part 2, pp. 227-230.

Komar, P.D., 1976: Beach Processes and Sedimentation, Prentice-Hall, Englewood Cliff, N.J., 429 pp.

Horikawa, K., H. Nishimura and M. Isobe, 1977: Theoretical validities of the finite amplitude wave theories, Proc. 24 th Japanese Conf. on Coastal Eng., JSCE, pp. 10-14 (in Japanese).

Ippen, A.T., 1966: Estuary and Coastline Hydrodynamics, McGraw-Hill, New York, N.Y., 744 pp.

Isobe, M., 1985: Finite amplitude wave theories and their applicable ranges, Lecture Notes of 21 st Summer Seminar on Hydraulics, Course B, JSCE, pp. 1-15 (in Japanese).

Isobe, M., 1986, Private communication.

Isobe, M., H. Nishimura and K. Horikawa, 1978: Expressions of perturbation solutions for conservative waves by using wave height, Proc. 33 rd Annual Conv. of Japan Soc. Civil Engrs., Part 2, pp. 760-761 (in Japanese).

Iwagaki, Y., T. Sakai and T. Kawashima, 1972: On the vertical distribution of water particle velocity induced by waves on beach, Coastal Eng. in Japan, JSCE, Vol. 15, pp. 35-42.

Le Mehaute, B., 1976: An Introduction to Hydrodynamics & Water Waves, Springer-Verlag, New York, 315 pp.

Sekine, Y. and M. Hattori, 1985: Experiments on validity range of various wave theories, Proc. 32nd Japanese Conf. on Coastal Eng., JSCE, pp. 11-15 (in Japanese).

Shuto, N., 1974: Nonlinear long waves in a channel of variable section, Coastal Eng. in Japan, JSCE, Vol. 17, pp. 1-12.

Swart, D.H., 1978: Vocoidal water wave theory, Vol. 2: Verification, Nat. Res. Inst. for Oceanology, Council for Scientific and Industrial Res., CSIR Res. Rept. 357, 130 pp.

Yamada, H. and T. Shiotani, 1968: On the highest water waves of permanent type, Bull. Disaster Prevention Res. Inst., Kyoto Univ., No. 18, pp. 1-22.

CHAPTER 19

DIRECTIONAL SPECTRA IN CURRENT-DEPTH REFRACTION

F. Hirosue[1] and T. Sakai[2]

ABSTRACT

According to Brink-Kjaer et al.'s discussion(1984), the expression of the wave direction change velocity is modified in our numerical model for the directional wave spectra change due to current-depth refraction (Sakai et al., 1983). The wave reflection and breaking conditions due to current are discussed from a view point of numerical analysis. Effects of the refraction term in the modified wave action equation on the directional spectra change are examined. The relative importance of current and water depth change in the directional spectra change is also examined.

INTRODUCTION

In the design of offshore structures, the wave force is the most predominant force acting on them. At present, it is usual to take into account the frequency spectra of irregular waves in the design. Recently it was pointed out that the frequency spectra were not enough for the design of some kinds of coastal structure. Usually the propagation direction of ocean waves is not uni-directional, but it spreads wide. This directional spreading influences the estimation of wave forces on structures(Battjes, 1982).

The directional spreading of ocean waves is expressed in term of the directional spectra. Several standard forms of directional spectra were already proposed for the deep-water wind waves. However the waves are transformed during propagation, and therefore the directional spectra change. Two main causes of the directional spectra change are the wave refraction due to underwater topography and that due to current. In offshore region, the latter is rather important.

A numerical model was proposed by the authors(Sakai et al., 1983) for the change of directional spectra of irregular waves due to depth-current refraction. Since then, Mathiesen(1984), Brink-Kjaer (1984), Booij et al.(1985) and Yamaguchi et al.(1985) proposed similar numerical models. All models use the following wave action conservation equation as the basic equation for the wave height change of each component composing the irregular waves.

$$\frac{\partial A}{\partial t} + \nabla \cdot \{A(U+c_{gr})\} = 0. \qquad (1)$$

---

1) Tech. Inst., Hazama-Gumi Ltd., Honmachi-Nishi, 338 Yono, Japan
2) Dept. of Civil Eng., Kyoto Univ., Sakyo-Ku, 606 Kyoto, Japan

A ($= E/\omega_r$, E is the wave energy of each component, and ω_r is the angular wave frequency relative to the current) is the wave action of each component, t is the time, $\nabla = (\partial/\partial x, \partial/\partial y)$, (x, y) is a horizontal orthogonal coordinate system, $\boldsymbol{U}$ is the vector of the horizontal current velocity, and c_{gr} is the vector of the wave group velocity relative to the current.

In the models of Mathiesen, Brink-Kjaer and Yamaguchi et al., the computation proceeds along the so-called wave ray. On the other hand, in the model of the authors, the basic equations are differentiated directly by a finite difference method. This method has a merit that values can be obtained directly on the grid points, while it is not the case in the ray method.

A steady state is assumed and therefore the local accelaration term $\partial A/\partial t$ can be eliminated in Eq.(1). Instead, a term expressing the spectral density change due to the wave direction change $\partial(A \cdot v_\theta)/\partial\theta$ is added as follows :

$$\frac{\partial}{\partial x}(A \cdot v_x) + \frac{\partial}{\partial y}(A \cdot v_y) + \frac{\partial}{\partial\theta}(A \cdot v_\theta) = 0. \tag{2}$$

This term is added to calculate the changes due to both shoaling and refraction simultaneously, which is called "refraction term" hereafter.

In Eq.(2), v_x and v_y are the x and y components of $\boldsymbol{U} + c_{gr}$ in Eq.(1) and given by

$$v_x = U + c_{gr}\cos\theta, \quad v_y = V + c_{gr}\sin\theta. \tag{3}$$

U and V are the x and y components of $\boldsymbol{U}$, and θ is the angle between the wave direction and the x axis. v_θ is a velocity of wave direction change of each component and given from the irrotational condition of wave number as follows :

$$\begin{aligned} v_\theta = {} & (\partial U/\partial x \cdot \sin\theta - \partial U/\partial y \cdot \cos\theta)\cos\theta + (\partial V/\partial x \cdot \sin\theta - \partial V/\partial y \cdot \cos\theta)\sin\theta \\ & + (\partial c_r/\partial x \cdot \sin\theta - \partial c_r/\partial y \cdot \cos\theta) \\ & + (\partial\theta/\partial x \cdot \cos\theta + \partial\theta/\partial y \cdot \sin\theta)(c_{gr} - c_r), \end{aligned} \tag{4}$$

where, c_r is the wave velocity relative to the current.

In Eq.(4), the spatial derivatives of the wave direction θ are included. The value of these derivatives is not known before the computation. In the authors' model, an approximate method was used to solve such a problem. For this problem, Brink-Kjaer et al.(1984) pointed that the differentiation resulting in Eq.(4) was not complete, and proposed Eq.(5) as a further modified form of Eq.(4).

$$\begin{aligned} v_\theta = {} & \left(\frac{\partial U}{\partial x}\sin\theta - \frac{\partial U}{\partial y}\cos\theta\right)\cos\theta + \left(\frac{\partial V}{\partial x}\sin\theta - \frac{\partial V}{\partial y}\cos\theta\right)\sin\theta \\ & + \omega_r/\sinh(2kh) \cdot \left(\frac{\partial h}{\partial x}\sin\theta - \frac{\partial h}{\partial y}\cos\theta\right), \end{aligned} \tag{5}$$

in which k is the wave number, and h is the water depth. In this equation, the spatial derivatives of wave direction do not appear, so

that the approximate method above mentioned is not necessary.

In this paper, at first, the authors' model(Sakai et. al, 1983) is introduced briefly. Subsequently, a comparison is made between the result of the numerical computation using Eq. (5) and that using Eq.(4). The wave reflection condition and breaking condition due to current are discussed from the view point of numerical model for wave directional spectra change due to depth-current refraction. These conditions are not taken account of in several models above mentioned. The relative contribution of the 1st and 2nd terms(convection terms) and the 3rd term(refraction term) in the left hand side of Eq.(2) to the wave directional spectra change is also examined. Finally, the relative effects of the current and the bottom topography on the wave directional spectra change is examined.

NUMERICAL MODEL FOR DIRECTIONAL WAVE SPECTRA CHANGE DUE TO CURRENT-DEPTH REFRACTION(SAKAI ET AL., 1983)

The basic equations for the wave refraction consist of the kinematic equations for the wave direction and the dynamical equation for the wave height. For the case of wave refraction due to current, they are the equation of condition of irrotationality of wave number and the equation of wave energy conservation in current, respectively.

In regular wave refraction, it is enough to solve these two equations separately. In irregular wave refraction, however, not only the wave height change but also the wave direction change modify the directional spectral distribution. It is , therefore, convenient to solve two equations simultaneously. The basic equation for wave height change is, as already mentioned, the equation of wave action conservation (1).

The differentiation of Eq.(2) for the numerical computation is just similar to the differentiation of Nagai, et al.(1974) for the numerical computation of directional spectra change due to underwater topography only. Fig.1 shows the grid and the definition of the quantities in the numerical computation of Eq.(2) by a finite difference method. Now it is assumed that the x-axis is normal to the shore line and all component waves propagate in the positive x direction.

The differential expression of Eq.(2) is as follows:

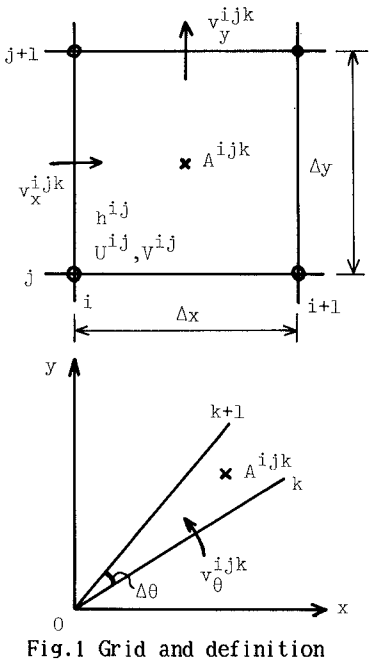

Fig.1 Grid and definition

$$a_1 A^{i\,jk} + a_2 A^{i\,j-1k} + a_3 A^{i\,j+1k} + a_4 A^{i\,jk-1} + a_5 A^{i\,jk+1}$$

$$= b A^{i-1\,jk} = B, \qquad (6)$$

in which $a_1 \sim a_5$ and b are functions of v_x, v_y and v_θ and Δx, Δy and $\Delta\theta$. The quantity $A^{i-1\,jk}$ is known because the computation proceeds in the positive x direction. If the frequency of the component waves and $i(x)$ are fixed, and $j = 1 \sim M$ and $k = 1 \sim N$, then a system of $M \cdot N$ algebraic equations is obtained. By solving this system of equations, the values of wave action A for all wave directions k and the whole range of $y(j)$ are obtained for the given wave frequency and $x(i)$. A similar computation is repeated for $i = i + 1$ until the shoreward boundary of computation is reached. These computations are repeated for each absolute frequency f of the component waves.

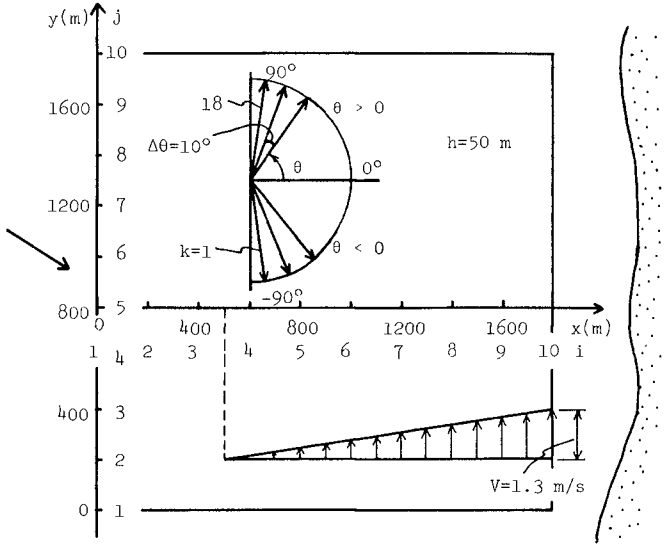

Fig.2 Computation region, water depth, current and division of wave direction

MODIFICATION OF WAVE DIRECTION CHANGE VELOCITY

A numerical computation is done under the same conditions as in the previous paper(Sakai et al., 1983), in order to compare between the computed results by using Eq.(4) with the approximate method and that by using Eq.(5). Fig.2 is the same as Fig.4 in the previous paper, and shows the computation region, the uniform water depth (h = 50m), the profile of current velocity and the division of wave direction.

As in the previous paper, the directional spectrum of Mitsuyasu et

al.(1975) is given as the deep-water directional wave spectrum on the y axis. The significant wave period is 7.0sec, the significant wave height is 3.0m and the value of the parameter S_{max} is 10. The wave frequency range from 0.09Hz to 0.71Hz, where the main part of the wave energy is contained, is divided into 19 segments, so that the logarithm of the frequency is divided with equal intervals. The other conditions are same.

Fig.3, (1) shows the distribution of directional spectral density $D(f, \theta)$ at the offshore boundary in the case of the offshore main wave direction $\theta_{po} = -60°$. In this figure, f is the absolute wave frequency. The figure (2) shows the distribution of the transformed spectral density at $x = 1{,}700$m calculated by using v_θ of Eq.(4) and the approximate method. An abnormal concentration of wave energy is found at a higher frequency region than 0.5Hz, where no energy was located in the offshore spectra(figure (1)). The figure (3) shows the distribution of the transformed spectral density at $x = 1{,}700$m calculated by using the improved wave direction change velocity as pointed by Brink-Kjaer et al.'s discussion(1984)(Eq.(5)). In this case, a slight energy concentration also can be seen in the high frequency region, but the value itself is as small as the value of the marginal part of the original energy distribution.

As seen from Eq.(4) and Eq.(5), the summation of the 3rd and 4th terms in the right hand side of Eq.(4) must be equal to the 3rd term of the right hand side of Eq.(5), which becomes zero when the water depth is constant. The summation of the 3rd and 4th terms in Eq.(4) should also become zero when the water depth is constant. In the computation of Fig.3, the water depth is constant(50m), and therefore no difference should have existed between the results in two figures (2) and (3). The difference between two figures is considered to be due to a wrong estimation of the 3rd and 4th terms in Eq.(4) by using the approximate method(Sakai et al., 1983).

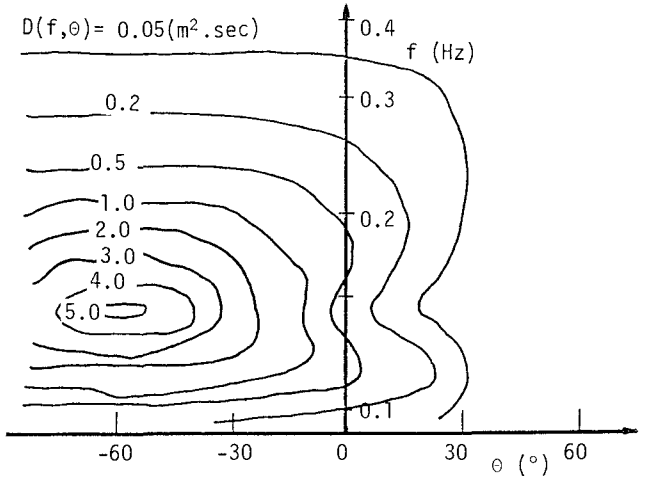

Fig.3,(1) Offshore directional wave spectrum having main wave direction of -60°

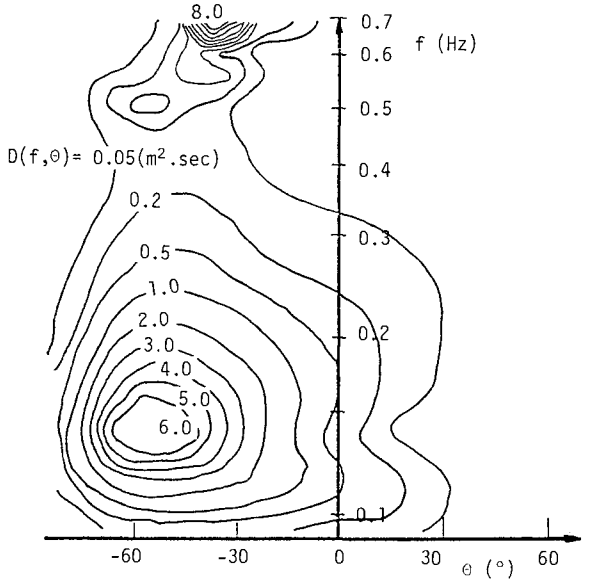

Fig.3,(2) Transformed directional wave spectrum at x = 1,700m calculated by using Eq.(4) and approximate method

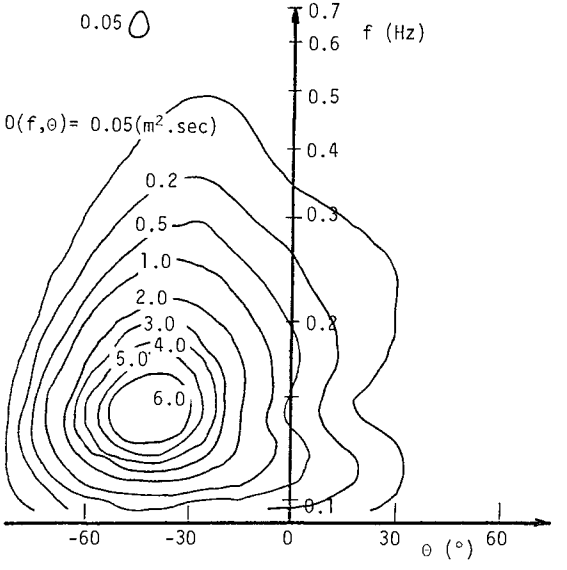

Fig.3,(3) Transformed directional wave spectrum at x = 1,700m calculated by using improved wave direction change velocity(Eq.(5))

In our previous paper, the change of the significant wave height and a representative wave direction was discussed after removing the abnormal energy concentration. Therefore, the change of these two parameters is same between in the case of using Eq.(4) with the approximate method and in the case of using Eq.(5).

REFLECTION AND BREAKING CONDITIONS

Wave reflection due to current

Longuet-Higgins et al.(1961) proposed a maximum velocity of a following current V, beyond which an obliquely incident regular deep-water waves can not penetrate the current. This limit velocity was derived from a condition that an absolute value of sine function does not exceed one in a kinematic equation governing the refraction. In this limiting condition, the wave direction becomes parallel to the current direction. Iwagaki et al.(1977) extended this treatment to a shallow water wave case, and gave the following condition.

$$\frac{V}{c_0} \leqq \frac{1 - (\sin\theta_0 \cdot \tanh\kappa h/\tanh\kappa_0 h_0)^{1/2}}{\sin\theta_0} \tag{7}$$

c is the wave velocity, and the subscript "0" indicates the quantity not in deep-water region but in no-current region. In all numerical models above mentioned, this condition is not taken into account. Tayfun et al.(1976) obtained a similar condition to Eq.(7) in his analytical treatment for the directional spectra change due to a depth and current change in one direction.

As mentioned already, our numerical model(Sakai et al., 1983) differentiates the basic equation (2) directly. The computation does not proceed along the ray of each component. So the condition (7) can not be incorporated directly into this model. In this model, the wave direction is divided as shown in Fig.2. In the computation of Fig.3, the direction of current is parallel to the y axis. This means that, if the reflection corresponds to the fact that the wave direction becomes parallel to the current direction, the wave direction of 90° corresponds to the reflection in this computation. In other words, it is expected that in this model the energy of the component parallel to the current direction at a given point becomes large.

Wave breaking due to current

There exist two kinds of idea as for the breaking of regular waves due to current in the simple theoretical treatment. One is for the case that the wave direction is parallel to the current direction. For this case, Tominaga(1967) derived a condition from a fact that a value of a quantity in a root in an equation giving the wave height change must be positive. In deep water, this condition means that an absolute value of velocity of an opposite current can not exceed the relative wave group velocity.

Another is the case that the the incident waves propagate obliquely into the current. Longuet-Higgins et al. discussed this case. Iwagaki et al. extended their result to a shallow water case. According to Iwagaki

et al., the change of wave direction θ is given by Eq.(8).

$$\frac{\sin\theta}{\sin\theta_0} = \frac{1}{(1-V/c_0 \cdot \sin\theta_0)^2} \frac{\tanh\kappa h}{\tanh\kappa_0 h_0}. \tag{8}$$

The change of wave height is given by Eq.(9).

$$\frac{H}{H_0} = \left(\frac{\sin 2\theta}{\sin 2\theta_0}\right)^{-1/2} \cdot \left(\frac{n}{n_0}\right)^{-1/2} \tag{9}$$

n is the ratio of the relative wave group velocity to the relative wave velocity. One of two cases that the wave height becomes infinite is $\theta = 0$. This case corresponds to $V = -\infty$. This means that the solution exists for any finite value of opposite current velocity. In the obliquely incident wave case, therefore, there exists no breaking condition as in the case that the wave direction is parallel to the current direction.

Tayfun et al.(1976) proposed one condition(Eq.(10)) similar to the breaking condition of regular waves propagating parallel to the current(Tominaga, 1967).

$$U \frac{k}{\kappa} > -c_{gr}. \tag{10}$$

This condition was derived from a fact that the absolute group velocity $\partial\omega/\partial\kappa$ must be positive in an equation(Eq.(11)) which gives the change of energy density of each component along the ray.

$$\Pi(\omega, \theta) = \frac{\kappa\left(\frac{\partial\omega}{\partial\kappa}\right)_0 \left(1 - \frac{U\kappa}{\omega}\right)}{\kappa_0 \left(\frac{\partial\omega}{\partial\kappa}\right)} D(\omega, \theta_0) \tag{11}$$

As seen from above discussion, it can be said that the theoretical wave breaking condition due to current is not yet clearly established. It is also questionable that the breaking condition of regular waves is applicable to each component of irregular waves. Nevertheless it is worthwhile to check the condition (10) of Tayfun et al. in the computation result shown in Fig.3, (3). It is found that component waves which do not satisfy Eq.(10) exist in the region of the slight energy concentration in Fig.3, (3).

CONTRIBUTION OF REFRACTION TERM $\partial(A \cdot v_\theta)/\partial\theta$

From the computation result obtained by using Eq.(5), the relative contribution of the convection terms and refraction term in Eq.(2) is discussed. The conditions are the same as those in Fig.3 except for the offshore main wave direction.

In this case, the water depth is constant, and the phenomena do not change in the y direction. Then Eq.(2) and Eq.(3) become as follow ($U = 0$ considered):

$$\frac{\partial}{\partial x}(A \cdot v_x) + \frac{\partial}{\partial\theta}(A \cdot v_\theta) = 0, \tag{12}$$

$$v_x = c_{gr}\cos\theta, \tag{13}$$

$$v_\theta = \partial V/\partial x \cdot \sin^2\theta. \tag{14}$$

Since c_{gr} is determined from the wave number conservation equation involving the velocity V, v_x contains the effect of the current indirectly. On the contrary, v_θ contains the effect of the current directly.

Fig.4, (1) ~ (3) compares the relative contribution of the convection term $\partial(A \cdot v_x)/\partial x$ and the refraction term $\partial(A \cdot v_\theta)/\partial\theta$ in Eq.(12) to the directional spectra change in the case of offshore main wave direction = -30°. The figure (1) shows the directional spectral density distribution at the offshore boundary. The figure (2) shows the transformed density distribution at x = 1,700m in the case that both terms are taken account of. The figure (3) shows the same density in the case that only the convection term is taken account of.

As seen from the figure (2), in the case that both terms are taken account of, the energy grows near -30° (the offshore main wave direction) where the current is opposite to the component waves. It is seen also that the energy shifts totally in the positive wave direction. On the other hand, in the case that only the convection term is taken account of(figure (3)), an abnormal energy concentration occurs in a high frequency and negative wave direction region. Except in this region, the energy distribution does not change so much from the offshore energy distribution (figure (1)).

From these results, it can be said that, at least for the case treated here, the refraction term has an important effect on the wave directional spectra change. This term explains the energy transfer between the wave components having different wave direction.

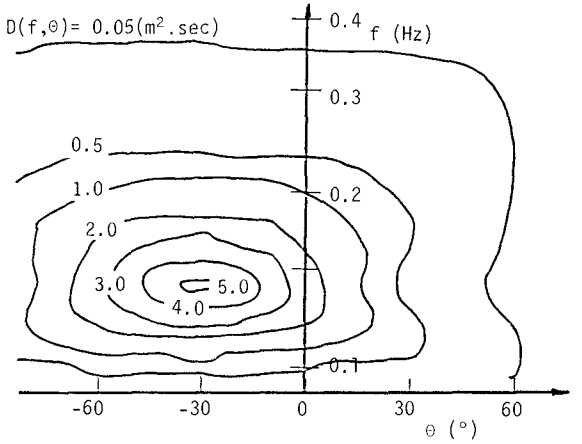

Fig.4,(1) Offshore directional wave spectrum having main wave direction of -30°

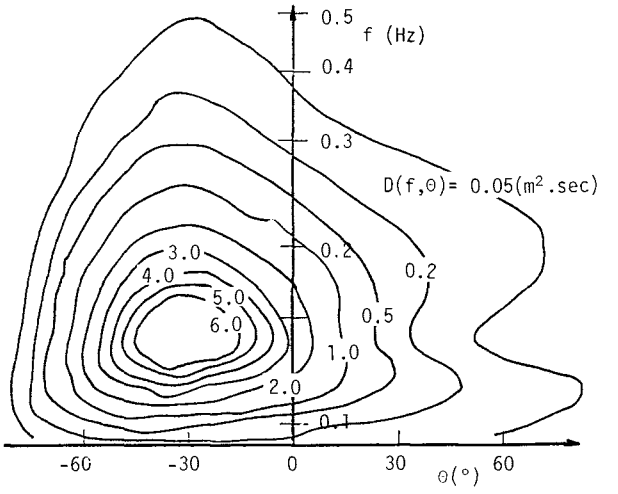

Fig.4,(2) Transformed directional wave spectrum at x = 1,700m in the case that both convection and refraction terms are taken account of

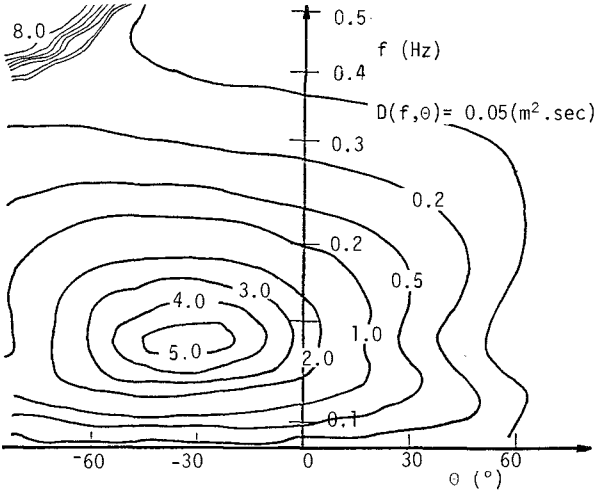

Fig.4,(3) Transformed directional wave spectrum at x = 1,700m in the case that only convection term is taken account of

COMPARISON OF EFFECTS OF CURRENT AND BOTTOM TOPOGRAPHY

Generally speaking, the lower the frequency of a component wave, the earlier the component affected by the bottom topography. It is,

therefore, expected that the effect of bottom topography is predominant for lower frequency components and the effect of current is predominant for higher frequency components. To check this, a case of plane beach of 1/40 slope is discussed in addition to the case of current in Fig.2. The water depth at the offshore boundary is 50m, and it decreases in the x direction.

Numerical computations are done for the following three cases : the current in the constant depth(50m)(Fig.2), the plane beach of 1/40 slope without current, and the same current on the beach of 1/40 slope. The offshore main wave direction is -30°. The change of directional spectra at two values of frequency is compared for these three cases.

Fig.5,(1) shows the directional spectra at a frequency f = 0.11Hz(lower than the peak frequency f_p = 1/7.0Hz = 0.14Hz) at x = 1,700m. The directional spectra in the case of current and depth change(broken line) can be explained roughly by the change in the case of depth change only(chain line). The figure (2) shows the directional spectra at a frequency f = 0.19Hz(higher than the peak frequency) at x = 1,700m. The value of the maximum energy in the case of current and depth change(broken line) can be explained by that in the case of current only(solid line), but the wave direction at which the maximum energy occurs can be explained rather by that in the case of depth change only(chain line).

Above mentioned results depends on the water depth, the beach slope, the current velocity and its profile. Still it can be said that the general trend mentioned at the first part of this section does not always hold.

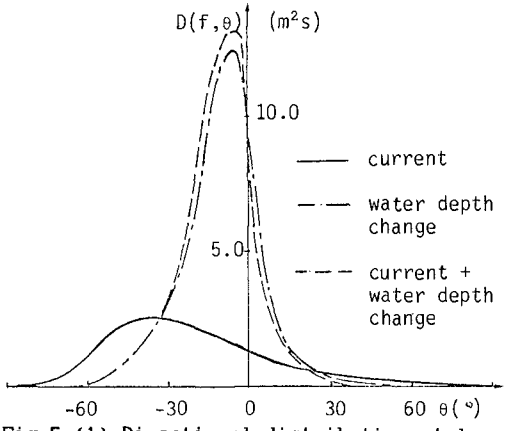

Fig.5,(1) Directional distribution at lower frequency than peak frequency(f = 0.11Hz) at x = 1,700m

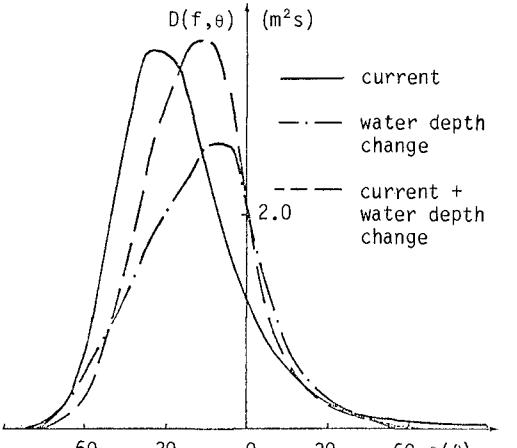

Fig.5,(2) Directional distribution at higher frequency than peak frequency(f = 0.19Hz) there

CONCLUSIONS

The expression of the wave direction change velocity, Eq.(4), in our numerical model for directional wave spectra change due to depth-current refraction(Sakai et al., 1983) was modified according to Brink-Kjaer' et al.'s discussion(1984). The improved expression, Eq.(5), shown by him was used. The wave reflection and breaking conditions due to current were discussed from a view point of numerical analysis. Effects of the refraction term $\partial(A \cdot v_\theta)/\partial\theta$ in the wave action equation, Eq.(2), and the relative importance of current and water depth change in directional spectra change were discussed by using the newly obtained numerical results.

The following conclusions are obtained:

(1) In our previous model where Eq.(4) and an approximate method were used, an abnormal concetration of wave energy occured in a high frequency region. By using Eq.(5) instead of Eq.(4) and the approximate method, this concentration disappears.

(2) The reflection condition of regular waves due to current at first given by Longuet-Higgins and Stewart(1961) can not be incorporated directly into our numerical model. It is expected that the energy density of the component parallel to the local current direction grows rapidly in our model.

(3) There are two theoretical situations for the regular wave breaking on current. One is for waves propagating parallel against the current, where a theoretical breaking condition exists. For waves propagating obliquely into the current, no theoretical limiting condition exists. For irregular waves, Tayfun et al.(1976) showed a similar condition to that for regular waves. In a region where Tayfun et al.'s condition is fulfilled on the frequency direction plane, a slight energy concentration is found in the numerical results.

(4) The refraction term $\partial(A \cdot v_\theta)/\partial\theta$ has a dominant effect on the directional spectra change compared with the convection terms $\partial(A \cdot v_x)/\partial x$ and $\partial(A \cdot v_y)/\partial y$ at least in the example treated here.

(5) Even for a frequency component having a higher frequency than the peak frequency, which is expected to be affected more by the current than by the water depth change, the change of the main wave direction is determined rather by the water depth change, at least in the example treated here.

It is believed that the numerical model proposed here for the directional spectra change of wind waves due to current-depth refraction can be used to predict more accurately the wave condition around offshore structure than the existing wave prediction models. This more accurate prediction of wave conditions will also make the wave force calculation more accurate.

ACKNOWLEDGMENT

Part of this study was supported by the Grant-in-Aid for Co-operative Research (A) '83-'84 of the Ministry of Education, Science and Culture of Japan (representative : Prof. Y. Yamada, Faculty of Engineering, Kyoto Univ.).

REFERENCES

Battjes, J. A., "Effects of Short-Crestedness on Wave Loads on Long Structures", *Applied Ocean Research*, Vol.4, No.3, 1982, pp.165-172.

Booij, N., Holthuijsen, L.H. and Herbers, T.H.C., "A Numerical Model for Wave Boundary Conditions in Port Design", *Proceedings of International Conference on Numerical and Hydraulic Modelling of Ports and Harbours*, Bermingham, U.K., BHRA, April, 1985, pp.263-268

Brink-Kjaer, O., "Depth-Current Refraction of Wave Spectra", *Proceedings of Symposium on Description and Modelling of Directional Seas*, Tech. Univ. of Denmark, paper No.C7, June, 1984.

Brink-Kjaer, O., Christoffersen, J.B. and Jonsson, I.G., " Discussion on Paper No.2 of this references", *Journal of Hydraulic Engineering*, American Society of Civil Engineering, Vol.110, No.12, Dec., 1984, pp.1871-1873.

Iwagaki, Y. et al., "Wave Refraction and Wave Height Variation due to Current", *Bulletin of Disaster Prevention Research Institute*, Kyoto University, Vol.27, June, 1977, pp.73-91.

Longuet-Higgins, M.S. and Stewart, R.W., "The Changes in Amplitude of Short Gravity Waves on Steady Non-Uniform Currents", *Journal of Fluid Mechanics*, Vol.10, 1961, pp.529-549.

Mathiesen, M., " Current-Depth Refraction of Directional Wave Spectra", *Proceedings of Symposium on Description and Modelling of Directional Seas*, Tech. Univ. of Denmark, paper No.C6, June, 1984.

Mitsuyasu, H. et al., " Observation of the Directional Spectrum of Ocean Waves Using A Cloverleaf Bouy", *Journal of Physical Oceanography*, Vol.5, No.4, 1975, pp.750-760.

Nagai, K., Horiguchi, T., and Takai, T., "Computation of Propagation of Deep-Water Waves Having Directional Spectra in Shallow Water", *Proceedings of the 21st Japanese Conference on Coastal Engineering*, Japanese Society of Civil Engineer, 1974, pp.249-253(in Japanese).

Sakai, T., Koseki, M. and Iwagaki, Y., "Irregular Wave Refraction due to Current", *Journal of Hydraulic Engineering*,, Amer. Soc. of Civil Eng., Vol.109, No.9, Sept., 1983, pp.1203-1215.

Tayfun, M.A., Dalrymple, R.A. and Yang, C.Y., "Random Wave-Current Interactions in Water of Varying Depth", *Ocean Engineering*, Vol.3, 1976, pp.403-420.

Tominaga, M., "On Current and Waves, - Waves Propagating into River Mouth and Wind Waves Generated on Current", *Coastal Disaster Res. News*, Natural Disaster Res. Group in Japan, No.6, 1967, pp.28-43(in Japanese).

Yamaguchi, M. et al., " Numerical Model for Wave Transformation due to

Current-Depth Refraction", *Proceedings of Japanese Society of Civil Engineer*, No.357/II-3, June, 1985, pp.187-196(in Japanese).

CHAPTER 20

A GRID MODEL FOR SHALLOW WATER WAVES

Leo H. Holthuijsen
and Nico Booij *)

1. INTRODUCTION

Waves in coastal regions can be affected by the bottom, by currents and by the local wind. The traditional approach in numerical modelling of these waves is to compute the wave propagation with so-called wave rays for mono-chromatic waves (one constant period and one deep water direction) and to supplement this with computations of bottom dissipation. This approach has two important disadvantages. Firstly, spectral computations, e.g. to determine a varying mean wave period or varying short-crestedness, would be rather inefficient in this approach. Secondly, interpretation of the results of the refraction computations is usually cumbersome because of crossing wave rays. The model presented here has been designed to correct these shortcomings: the computations are carried out efficiently for a large number of wave components and the effects of currents, bottom friction, local wind and wave breaking are added. This requires the exploitation of the concept of the spectral action balance equation and numerical wave propagation on a grid rather than along wave rays.

The model has been in operation for problems varying from locally generated waves over tidal flats to swell penetration into Norwegian fjords. A comparison with extensive measurements is described for young swell under high wind penetrating the Rhine estuary.

2. THE MODEL

2.1 Introduction

The representation of the wave spectrum in the model is parametric in frequency and discrete spectral in directions, that is, for each spectral direction two prognostic variables are defined: a directional energy density and a mean frequency. The model treats the

*) scientific officers, Delft University of Technology, Stevinweg 1, Delft, the Netherlands.

action balance of the waves for each spectral direction separately (the action balance is used to accommodate current effects). It is therefore a directionally decoupled parametric model.

Propagation of waves in the model is based on the linear theory for bottom and current refraction, while wave generation and dissipation is taken mostly from the literature. The balance equations for the basic wave parameters are integrated with a finite difference method on a regular grid in the study area. This approach avoids the classical problem of crossing rays and caustics frequently occurring in the more conventional wave ray technique. The computations are performed in downwave direction as in the parabolic wave propagation of Radder (1979).

2.2 Equations

Wave hindcasting models are usually based on the energy balance equation of the waves (e.g. Gelci et al., 1956; Hasselmann, 1960). However, in the presence of a mean current it is wave action that is conserved (e.g. Bretherton and Garrett, 1968). Since we wish to include in our model the influence of currents, we base our model on the action balance equation. Wave action in this balance equation is a function of time (t), space (x,y), direction (θ) and frequency (ω). Since in coastal regions a high spatial resolution is required, in view of the scale of the bottom irregularities, some parameterization of the balance equation is necessary to reduce the computer effort. In such a parameterization the directional details of the wave spectrum should be retained since the occurrence of cross-seas is an essential aspect of the wave field in coastal regions. We have therefore parameterized the action balance equation in the frequency domain only, while we retained the discrete spectral direction as independent variable. We have chosen the zero-th and first moment of the action spectrum in the frequency domain as the quantities appearing in the parameterized balance equations. The corresponding two basic wave parameters are the directional action density $A_0(\theta)$ and the mean frequency per direction $\omega_0(\theta)$:

$$A_0(\theta;x,y,t) = \int_0^\infty A(\omega,\theta;x,y,t)d\omega \tag{1}$$

$$\omega_0(\theta;x,y,t) = \frac{1}{A_0}\int_0^\infty \omega A(\omega,\theta;x,y,t)d\omega \tag{2}$$

The conservation equations for the zero-th moment $A_0(\theta)$ and for the first moment $\omega_0(\theta)A_0(\theta)$ are derived essentially by applying the definition operators (1) and (2) to the action balance equation of the waves. With some assumptions added, the results are

(Booij and Holthuijsen, 1987):

$$\frac{\partial A_0}{\partial t} + \frac{\partial}{\partial x}(c_{0x}A_0) + \frac{\partial}{\partial y}(c_{0y}A_0) + \frac{\partial}{\partial \theta}(c_{0\theta}A_0) = \frac{1}{\sigma_0} S_E - \frac{A_0}{\omega_0} S_\omega \qquad (3)$$

$$\frac{\partial}{\partial t}(\omega_0 A_0) + \frac{\partial}{\partial x}(c_{0x}\omega_0 A_0) + \frac{\partial}{\partial y}(c_{0y}\omega_0 A_0) + \frac{\partial}{\partial \theta}(c_{0\theta}\omega_0 A_0) = \frac{\omega_0}{\sigma_0} S_E \qquad (4)$$

in which c_{0x} and c_{0y} are the x- and y-components respectively of the propagation velocity c_0 at frequency ω_0 in direction θ and $c_{0\theta}$ is the rate of directional change of A_0 (i.e. refraction). $S_E(\theta)$ is the rate of change of the directional energy density $E_0(\theta)$ and $S_\omega(\theta)$ is the rate of change of the direction dependent mean wave frequency $\omega_0(\theta)$. $E_0(\theta)$ is taken to be equal to $A_0(\theta)$. $\sigma_0(\theta)$, σ_0 being the average frequency relative to the mean current. The advantage of expressing the developments of $A_0(\theta)$ and $\omega_0(\theta)A_0(\theta)$ in terms of the (direction dependent) source terms $S_E(\theta)$ and $S_\omega(\theta)$ is that these source terms can be estimated, at least to a large extent, from information in the literature.

2.3 Propagation

The conventional approach for computing refractive propagation in shallow water is to use solutions along characteristics (wave rays). However, in such an approach, which is of a Lagrangian nature, the determination of nonlinear wave generation or dissipation would require extensive numerical interactions between different wave rays. This is numerically rather inefficient since a large number of spatial interpolations between the spatially scattered wave rays would be needed. We have therefore chosen for the above Eulerian formulation of propagation i.e. refraction computations on a regular grid (e.g. Karlson, 1969; Sakai et al., 1983). All wave information required for the evaluation of nonlinear source terms is then intrinsically available at each grid point.

For coastal waters and inland waters the travel time of the waves through the area of interest is usually small compared with the time scales of wind and current (e.g. tides). The situation may then be considered as stationary so that the terms with ∂/∂ t vanish from equations (3) and (4).

In the absence of currents the second and third terms on the left-hand side of equation (3) or (4) represent propagation at the group velocity of the waves along straight lines which in varying water depths accounts for the phenomenon of "shoaling". In the presence of currents this propagation is corrected by adding the current velocity to the group velocity:

$$c_{0x} = c_0 \cos\theta + V_x \tag{5}$$

$$c_{0y} = c_0 \sin\theta + V_y \tag{6}$$

in which c_0 is the propagation speed (group velocity) at frequency ω_0 from linear wave theory relative to the mean current (V_x,V_y). The fourth term on the left-hand side of equation (3) represents the change of direction of the action transport, i.e. refraction, induced by bottom- and current variations. From linear wave theory we find the rate of directional change $c_{0\theta}$:

$$c_{0\theta} = -\frac{1}{k_0}\left(\frac{\partial\sigma}{\partial d}\right)_0 \frac{\partial d}{\partial n} - \frac{\underline{k}_0}{k_0} \cdot \frac{\partial \underline{V}}{\partial n} \tag{7}$$

in which n is the coordinate in (x,y)-space normal to the spectral wave direction θ, $\underline{V}$ is the mean current vector (V_x,V_y), $\underline{k}_0$ is the wave number vector corresponding to ω_0 with magnitude k_0 and direction θ and $(\partial\sigma/\partial d)_0$ is the depth derivative of σ for $k=k_0$.

2.4 Generation and dissipation

The generation and dissipation of the waves in the conservation equations (3) and (4) is expressed in terms of the direction dependent source terms $S_E(\theta)$ and $S_\omega(\theta)$. These source terms can be interpreted as the rates of change of $E_0(\theta)$ and $\omega_0(\theta)$ in a homogeneous situation. Each is the sum of the effects of wind wave generation, bottom dissipation, wave breaking and wave blocking on an opposing current. We therefore write the source functions $S_E(\theta)$ and $S_\omega(\theta)$ as the sum of constituent source terms.

The formulation of the source term for wave generation by wind is taken from empirical information in an idealized situation (CERC, 1973). This situation is one in which a homogeneous, stationary wind U blows over deep water perpendicularly off a long and straight coastline. Expressions are available in the literature giving the total energy and the frequency averaged over the whole spectrum as functions of fetch and wind speed. In order to obtain the source terms of wind growth as function of θ, it is assumed that in the above idealized case the energy distribution over θ is of the form $\cos^2(\theta)$, and that the averaged frequency in the idealized situation is independent of direction.

Bottom dissipation in our model is based on the conventional quadratic friction law to represent bottom shear stress. The corresponding energy dissipation for a harmonic wave

with height H and frequency ω (e.g. Putnam and Johnson, 1949) has been extended by Dingemans (1983) to random waves. The form of this expression can be seen as a measure for the orbital velocity multiplied with a measure for the bottom shear stress. The required directional version of this expression is obtained by multiplying a measure for the total orbital velocity with an expression for the shear stress based on the directional energy density and the directional mean frequency. To formulate the source term for the average frequency change due to bottom dissipation we assume a simple spectral shape and a concentration of the dissipation at the lower frequency side of this spectrum. The assumed shape of the spectrum is: zero for frequencies below the peak frequency and a ω^{-m}-tail for frequencies above the peak frequency. The result is an expression relating the source term of the bottom induced frequency change to that of the bottom induced energy change.

The source term for energy dissipation due to wave breaking caused by exceedence of steepness or exceedence of a wave height to depth ratio, is modeled after Battjes and Janssen (1978). Dissipation in this model is based on a bore model. As in the case of bottom friction, only total dissipation is obtained this way. The corresponding directional distribution of dissipation is obtained by assuming that the dissipation per direction is proportional to the energy density at that direction. The frequency change induced by breaking due to steepness is assumed to be zero. For the frequency change due to depth breaking a similar expression is used as described above for bottom friction.

In a situation with a strong opposing current some fraction of the wave energy cannot be transported upstream because the group velocity of the highest frequencies in the spectrum is less than the opposing current velocity. The lowest frequency above which this phenomenon of wave blocking occurs (the critical frequency ω_c) is the maximum frequency for which a solution exists for the wavenumber in the dispersion relationship from linear wave theory (including a mean current). In the model the "blocked" energy is dissipated with a simple relaxation model in which the total wave energy reduces eventually to the "unblocked" energy. The average frequency is similarly reduced to the average frequency of the "unblocked" energy.

3. NUMERICAL BACKGROUND

The prognostic equations for $A_0(\theta)$ and for the product $\omega_0(\theta)A_0(\theta)$, equations (3) and (4), are partial differential equations of first order with the horizontal coordinates x and y and the spectral direction θ as independent variables. Due to the nature of the equation the state in a point in (x,y,θ)-space (e.g. the value of A_0) is determined by the state upwave

from this point (upwave as defined by the propagation speeds c_{0x}, c_{0y} and the directional rate of change $c_{0\theta}$). We have therefore chosen for an upstream finite difference scheme.

The boundary conditions for these partial differential equations are in general that the incoming wave field should be given at the boundaries and that the outgoing wave field is fully absorbed by the boundaries. To fully exploit the stationarity of the wave field in our model we restrict wave directions to a constant directional sector of less than 180° (typically 120°). This seems to be acceptable for most applications of our model since waves propagate from deep water to the coast with directional changes usually less than 90° or the waves are generated by a local wind within a sector of 90° on either side of the wind direction. Since we have restricted wave directions to a sector of less than 180° and since wave information along the lateral boundaries in (x,y)-space is usually not available we assume that wave information is given only along an upwave boundary of the model in (x,y)-space (which may or may not be on land). At the other boundaries in (x,y,θ)-space we assume that no waves enter the model.

4. FIELD AND LABORATORY TESTS

Results of wave propagation in the model have been compared with observations in a large laboratory wave tank simulating swell propagation off San Ciprian (Spain), see Booij et al. (1985), and in an irregular-wave tank containing a submerged bar, see Dingemans et al. (1986). To test the model in geophysical conditions which are more realistic and complicated than in these laboratory tests, the model has been applied in an area of the Rhine estuary. This area was chosen because the model results can be compared with the results of a well documented field campaign of the Ministry of Public Works and Transport in the Netherlands (Dingemans, 1983, 1985). This campaign involved the use of 1 pitch-and-roll buoy, 1 wave gauge and 6 waverider buoys. The situation can be characterized as non-locally generated waves passing from deeper water into shallow water over a shoal with a regeneration by wind behind the shoal. Currents are practically non-existent in the chosen situation.

The bathymetry is given in fig. 1 with the location of the buoys and the wave gauge indicated. This bathymetry can be roughly characterized as a relatively shallow estuary (water depth typically 4 m – 5 m), about 10 km x 10 km in surface area. It is partly protected from the southern North Sea by a shoal of roughly 2 km x 4 km (water depth typically 1 m – 2 m) extending over half of its opening.

The computations have been carried out for a situation which occurred on October 14, 1982 at 22.00 hours (M.E.T.). The waves are locally generated in the southern North Sea with a significant wave height of about 3 m and a mean period of about 7 s at the estuary

entrance. These waves penetrate the area from north-westerly direction. They break over the shoal with a reduction in wave height to about 0.5 m over the shoal. The local wind of 16.5 m/s regenerates the waves to about 0.9 m significant wave height at the wave gauge which is located 5 km behind the shoal (see table 1).

The pitch-and-roll buoy in 16 m water depth (point 1 fig. 1) provided not only the significant wave height and the mean wave period as input at the up-wave boundary of the model (for parameter values see table 1), it also provided the mean wave direction and the directional spreading as input for that boundary. The waverider buoys and the wave gauge located at various locations in the area (points 2 to 7 in fig. 1) provided each a significant wave height and a mean wave period which can be compared with the results of the model. In fig. 2 it is shown that the pattern of the model results is consistent with the pattern of the observations (table 1; Dingemans, 1985; Dingemans, 1983), e.g. the significant wave height which at the up-wave boundary of the model (16 m water depth) is about 3.4 m, reduces gradually to about 2.5 m at 6 m depth and then very rapidly to about 0.6 m over the shoal. South of the shoal the gradual decrease in wave height continues. At the location of the wave gauge (about 5 km behind the shoal) the significant wave height is about 0.9 m. The mean wave period follows roughly the same pattern. A quantitative comparison with the observations is given in table 1.

These results are satisfactory considering that no tuning of the model is used in this complex geophysical situation. Further improvement may be expected from tuning the present model (e.g. high-frequency regeneration of waves behind a shoal should decrease the mean wave period rather than increase it as presently modelled).

Table 1
Observations and model results in the Haringvliet

location	observation		model result	
	H_s (m)	T_{mean}(s)	H_s (m)	T_{mean}(s)
1. pitch-roll buoy	3.38	7.0	3.27	7.0
2. waverider	2.90	6.3	3.19	6.8
3. waverider	2.58	6.3	2.59	6.2
4. waverider	2.68	5.9	2.54	6.1
5. waverider	0.62	2.6	0.60	4.4
6. waverider	1.05	3.7	1.14	4.5
7. waverider	1.60	5.1	1.42	4.7
8. wave gauge	0.95	2.8	0.87	3.8

5 CONCLUSIONS

The model presented here is conceptually different from the traditional approach in shallow water wave models. It is a finite difference approximation of a directionally decoupled action balance equation. Because of the finite difference approximation, classical problems of ray refraction computations are avoided and the effects of wind, currents, bottom dissipation and surf breaking are efficiently computed.

The results of the (untuned) model applied to an observed situation in the Rhine estuary showed an rms-error of about 8.3% in the significant wave height and an rms-error of about 18.7% in the mean wave period.

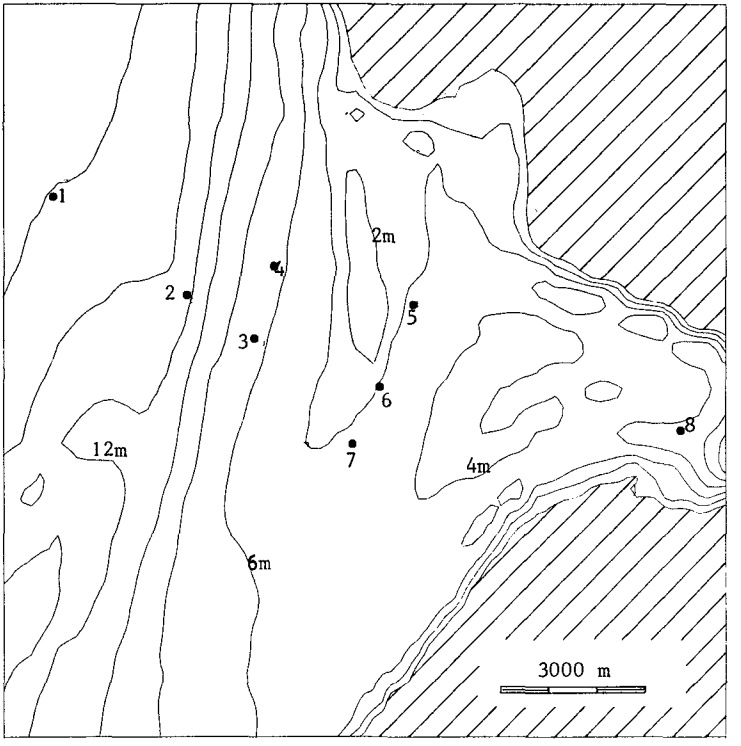

Fig. 1 Bathymetry of the Haringvliet area
in the south-west of the Netherlands.
Circles indicate locations of observation.

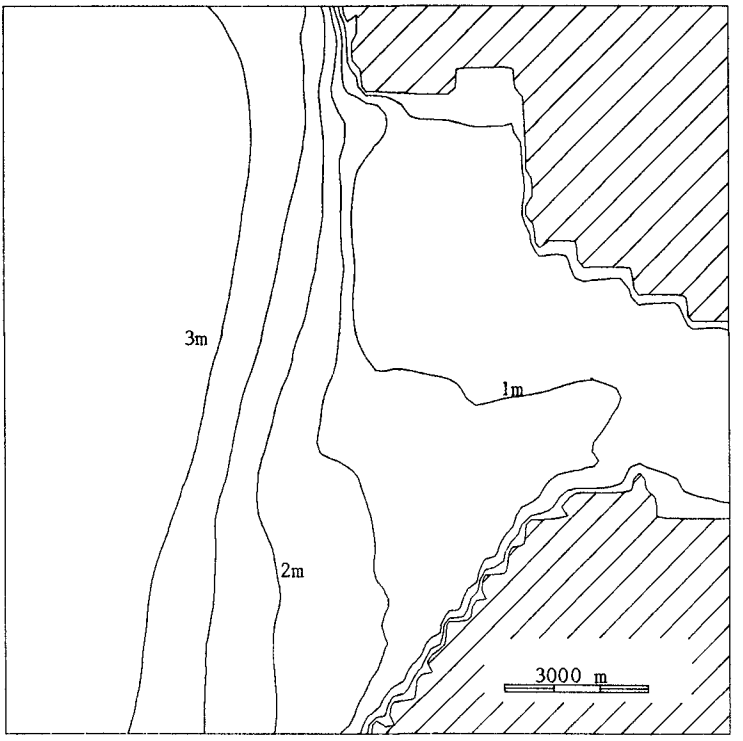

Fig. 2. Iso-lines of significant wave height.
Hatched area is land.

References

Battjes, J.A. and J.P.F.M. Janssen, 1978. Energy loss and set-up due to breaking of random waves, Proc. 16th Intl. Coastal Engineering Conference, Hamburg, ASCE, New York, pp. 569–587.

Booij, N., L.H. Holthuijsen and T.H.C. Herbers, 1985. A numerical model for wave boundary conditions in port design, International Conference on Numerical and Hydraulic Modelling of Ports and Harbours, Birmingham, 23-25 April, 1985, pp. 263–268.

Booij, N. and L.H. Holthuijsen, 1987. The directionally decoupled shallow water model HISWA, Delft University of Technology, in preparation.

Bretherton, F.P. and G.J.R. Garrett, 1968, Wavetrains in homogeneous moving media, Proc. R. Soc. London, A302, pp. 529–554.

CERC; Shore Protection Manual, 1973. U.S. Army Coastal Engineering Research Center, Corps of Engineers.

Dingemans, M.W., 1983. Verification of numerical wave equation models with field measurements, CREDIZ verification Haringvliet, Delft Hydraulics Laboratory, Rep. No. W488.

Dingemans, M.W., 1985. Surface wave propagation over an uneven bottom, Evaluation of two-dimensional horizontal wave propagation models, Delft Hydraulics Laboratory, Rep. No. W301, part 5.

Dingemans, M.W., M.J.F. Stive, J. Bosma, H.J. de Vriend and J.A. Vogel, 1986, Directional nearshore wave propagation and induced currents, Proc. 20th Intl. Coastal Engineering Conference, Taipei, ASCE, New York.

Gelci, R., H. Cazale and J. Vassal, 1956. Utilization des diagrammes de propagation à la prévision energetique de la houle, Bulletin d'information du Comité central d'oceanographie et d'études des côtes, Vol. 8, No. 4, pp. 169–197.

Hasselmann, K., 1960. Grundgleichungen der Seegangsvoraussage, Schiffstechnik, Vol. 7, No. 39, pp. 191–195.

Karlson, T., 1969. Refraction of continuous ocean wave spectra, Journal of the Waterways and Harbour Division, ASCE, Vol. 95, No. WW4, pp. 437–448.

Putnam, J.A. and J.W. Johnson, 1949. The dissipation of wave energy by bottom friction, Trans. Am. Geoph. Union, Vol. 30, No. 1, pp. 67–74.

Radder, A.C., 1979. On the parabolic equation method for water wave propagation, Journal of Fluid Mechanics, Vol. 95, pp. 159-176.

Sakai, T., M. Kosecki and Y. Iwagaki, 1983. Irregular wave refraction due to current, Journal of Hydraulic Engineering, ASCE, Vol. 109, No. 9, Paper no. 18233, pp. 1203–1215.

CHAPTER 21

ROUGH TURBULENT BOUNDARY LAYER IN SHORT-CRESTED WAVES

John R C Hsu *

Abstract

Prior to the investigation of rough turbulent boundary layer in a short-crested wave, the oscillatory laminar boundary layer at the bed is considered. Supported by numerical results of water-particle motions close to the bottom, the general patterns of kinematics in the laminar boundary layer within this wave system are reported in order to promote the understanding of the complex phenomenon. To propose a suitable method for turbulent boundary layer within such a wave system, a two-layer model using time-independent viscosity coefficient is first studied. Potential application of this model to short-crested waves is considered. From numerical results it is found that the time-invariant viscosity model is useful but can not produce velocity profile with flow reversal. It is suggested that a time-varying viscosity model may be more appropriate.

1. Introduction

Unlike progressive waves which propagate in a single direction, and standing waves that fluctuate vertically, the short-crested wave is defined as having a surface elevation which is doubly periodic in two perpendicular directions. Among many other occurrences in nature, oblique wave reflection often results in such a short-crested wave system in front of a long maritime structure. A simple reflection produces a combined progressive wave propagating along the reflecting wall (the x-direction), with a combined celerity C_s, and a standing wave component normal to it, in the y-direction (see figure 1).

Oblique approach of waves to a long rubble-mound breakwater, comprising either large precast concrete armour units or caisson superstructure, can have reflection coefficient as high as 0.8, so forming short-crested systems (Silvester 1986). The wave height of the combined wave system could be double that of the incident wave component, if a near full reflection exists. This doubled wave energy is applied to the bed, and hence can expedite the transmission of sediment along the wall. The occurrence of scour in front of seawalls is well known, and has become a common concern since it could have led to the failure of some maritime structures (Irie & Nadaoka 1984).To estimate the scour and bottom changes in front of a long breakwater, it requires the understanding of the basic mechanisms of waves and currents, particularly that within the bottom boundary layer,within which most of the sediment transport takes place (Hedegaard 1985).

The existence of a thin viscous boundary layer at the bottom in an oscillatory fluid has been extensively studied since Longuet-Higgins (1953), for both laminar and turbulent layers, particularly for two-dimensional progressive and standing waves. The term oscillatory implies that fluid velocities vary over time, so does the thickness of boundary layer. Traditionally, the description of these kinds of boundary layer in waves has been

* Department of Civil Engineering, University of Western Australia, Nedlands, Western Australia 6009, AUSTRALIA.

based upon a direct solution to momentum equations subjected to boundary conditions. This process is often laborious. Similar to the time-invariant viscosity proposed for steady turbulent flow, earlier studies of wave-induced oscillatory turbulent layer have been primarily aimed at determining the bottom shear stress and energy dissipation.

Amongst many laboratory data available for wave boundary layer, Jonsson (1963, 1966) and Jonsson & Carlsen (1976) have published experimental work which has played a significant role in the study of turbulent boundary-layer theory. Their experimental data have since been used by all workers in this area.

Kajiura (1968) developed a three-layer analytical model using the concept of time-invariant effective viscosity. This approach was followed by Noda (1971) and others to examine the turbulent boundary layer in progressive and standing waves. Employing Jonsson's (1980) new approach of velocity defect law, Brevik (1981) presented a two-layer model, which proved to be mathematically simple and yet fairly accurate compared to the three-layer model (Kajiura 1968). More recently, a time-variant effective viscosity model was suggested by Trowbridge & Madsen (1984), for fluid velocity up to second-order.

Although the turbulent boundary layer in two-dimensional waves have been studied extensively, the case for three-dimensional waves has received very little attention. For such short-crested waves, produced by full oblique reflection, the first-order Eulerian water-particle velocities and mass transport have been reported by Mei et al (1972) and Tanaka et al (1972), for a laminar boundary layer on a smooth bed. Hsu et al (1980) have derived the Eulerian water-particle velocities to second-order also for a laminar layer, and have reported experimental data available. However, the investigation of a turbulent layer has not been made previously for this wave system.

Because the wave-induced bottom layer is generally turbulent in relatively shallow water where the ocean bed is rippled and hydrodynamically rough, it is necessary to examine the rough turbulent layer in short-crested wave system, since it differs substantially from the laminar case.

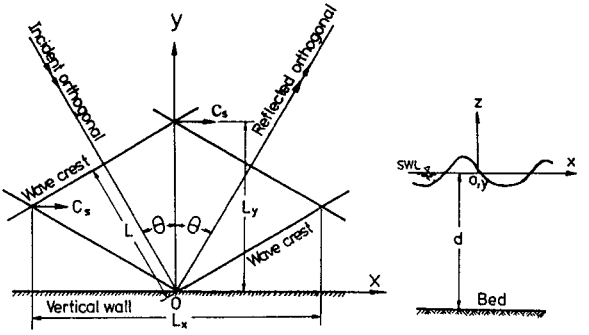

Figure 1. Definition sketch of short-crested wave system, showing co-ordinates, incident and reflected orthogonals, approaching angle θ, wavelengths L and L_x, crest length L_y, and combined wave celerity C_s.

In the present paper, Brevik's (1981) two-layer model is thoroughly studied numerically, especially the effect of varying the thickness of the lower layer (i.e. the overlapping layer of Brevik). From the results of numerical calculations, it was found that the relative velocity curves u_d/u_f and u/u_f may become discontinous upon using some improper values of the thickness of the lower layer. Minor drawback of this model is discussed. To apply the two-layer model to the short-crested waves, necessary adjustment in formulations and procedures are then proposed.

2. Laminar boundary layer at the bottom

Short-crested waves produced from 100% reflection of oblique waves can be equated to two progressive waves of the same amplitude propagating at an angle to each other. The resultant water-particle motions are very complex, varying spatially both in the vertical and horizontal directions (in the x-y plane). Water-particle motions for this simple case of two wave trains of equal height and period is shown schematically in figure 2, where it is seen that rectilinear and elliptical orbits exist along certain alignments. Along that of the combined-crest propagations (i.e. at $y/L_y = 0,1/2,1,...$) water-particle orbits are in a vertical plane. Half-way between, rectilinear horizontal oscillations occur (i.e. at $y/L_y = 1/4,3/4,...$); again half-way between (i.e. at $y/L_y = 1/8,3/8,5/8,...$), the orbits are ellipses at an angle to the vertical which depend upon their depth, being in a horizontal plane at the bed.

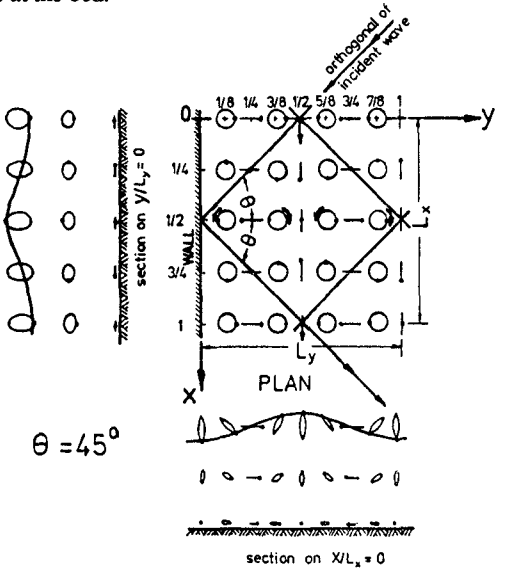

Figure 2. Patterns of water-particle motions along various y/L_y alignments in a short-crested wave system, relative to the reflecting wall.

Hsu et al (1979) have derived a third-order approximatioin of wave theory to short-crested waves by a perturbation method, for the case of full oblique reflection from a vertical wall. Irrotational motion was assumed, the fluid inviscid, incompressible and uniform depth of water. Working with non-dimensional quantities, final expressions for velocity potentials (ϕ), surface elevations (η), angular frequency (ω), and Eulerian water-particle velocities (u,v,w) in each order of approximation were derived in dimensionless form.

In studying the viscous boundary layer at the bed, Eulerian water-particle velocities at the outer edge of the bottom layer (U,V,W) are required, for both laminar and turbulent cases. These velocities are represented by the velocities on the bed from the inviscid wave theory for z = -d. The expressions of free-stream velocity (U,V,W) in the x,y and z-directions respectively are given in dimensional form as follows:

$$U = \varepsilon\phi_x \Big|_{z=-d} = \varepsilon \sqrt{(k/g)}\,(m\omega_o/\sinh kd)\cos(nky)\ \cos(mkx-\sigma t) + \varepsilon^2 \sqrt{(k/g)}\,[2m\beta_2 \cos 2(nky) + 2m\beta_3]\cos 2(mkx-\sigma t) = U_1 + U_2 + O(\varepsilon^3) \quad (1)$$

$$V = \varepsilon\phi_y \Big|_{z=-d} = -\varepsilon \sqrt{(k/g)}\,(n\omega_o/\sinh kd)\sin(nky)\ \sin(mkx-\sigma t) - \varepsilon^2 \sqrt{(k/g)}\,[2n\beta_2\ \sin 2(nky)]\ \sin 2(mkx-\sigma t) = V_1 + V_2 + O(\varepsilon^3) \quad (2)$$

$$W = \varepsilon\phi_z \Big|_{z=-d} = 0, \text{ more practically at the real bed.} \quad (3)$$

in which ε is the small perturbation parameter "ka", where "a" is the amplitude of the short-crested wave to the first-order, and "k" is the wave number $2\pi/L$, L being the wavelength of the incident or reflected wave component, σ is the angular frequency of the incident and reflected waves (i.e. $2\pi/T$, where T is the wave period in seconds), "g" is the acceleration of the gravity, "d" is the water depth in meters, "m" and "n" are the components of wave number "k" in the x and y-directions respectively as shown in figure 1, "ω_o" is the leading term of dimensionless angular frequency (i.e. $\sigma/\sqrt{(gk)}$). The full expressions to β_2 and β_3 have been presented by Hsu et al (1980). U_1 and V_1 are free-stream velocity components to the first-order, and U_2 and V_2 to the second-order.

Based upon the third-order approximation to short-crested waves, the Eulerian water-particle velocities within the laminar bottom boundary layer for a smooth and horizontal bed have been derived (Hsu et al 1980), also by a perturbation method. The procedure used was to solve the governing Navier-Stokes equations in dimensionless form subjected to various boundary conditions at the bed and at the outer edge of the boundary layer. An additional change of non-dimensional variable of kz within the bottom layer was introduced, $\zeta = (\omega_o/2)^{1/2}\,kz$. Inserting the perturbed series of fluid velocities within the boundary layer (u,v,w) and free-stream velocities (U,V,W) into the governing equations, and collecting terms of each order in ε yielded the necessary equations to each order of approximation. The solutions to Eulerian water-particle velocities to the first-order (u_1,v_1,w_1) and to the second-order (u_2,v_2,w_2) have been derived. The algebraic procedures of solving these equations were complex.

The resultant Eulerian water-particle velocities (u_1,v_1,w_1) to the first-order are given in dimensional form as

$$u_1 = \varepsilon \sqrt{(g/k)}\,(m\,\omega_o/\sinh kd)\cos(nky)\ [\cos(mkx-\sigma t) - e^{-\zeta}\cos(mkx-\sigma t+\zeta)], \quad (4)$$

$$v_1 = -\varepsilon \sqrt{(g/k)}\,(n\,\omega_o/\sinh kd)\sin(nky)\ [\sin(mkx-\sigma t) - e^{-\zeta}\sin(mkx-\sigma t+\zeta)], \quad (5)$$

$$w_1 = \varepsilon\,[(\nu\omega_o)^{1/2}\,(gk)^{1/4}/\sinh kd]\cos(nky)\ [\sqrt{2}\,\zeta\sin(mkx-\sigma t) - \sin(mkx-\sigma t+\pi/4) + e^{-\zeta}\sin(mkx-\sigma t+\zeta+\pi/4)]. \quad (6)$$

The non-dimensional variable ζ in equations (4)-(6) regulates the dimensionless distance kz within the bottom laminar layer. In dimensional form, $\zeta = z/\sqrt{(\nu T/\pi)}$, as a relative measure of vertical distance from the bed, where $\sqrt{(\nu T/\pi)} = \sqrt{(2\nu/\sigma)}$ is the usual boundary parameter. It is worth noting that the value of $\zeta = 2\pi$ corresponds to the distance at the outer edge of the laminar boundary layer, because its thickness is usually calculated by $\delta = 2\pi\sqrt{(2\nu/\sigma)} = 2(\pi\nu T)^{1/2}$.

The working procedures leading to the final expressions of the second-order Eulerian velocities (u_2,v_2,w_2) are rather lengthy and complicated. In general, they consisted of time-dependent (periodic) and time-independent (steady) terms. These were reported by Hsu et al (1980). The vertical distributions of velocity profiles vary as functions of position y/L_y (i.e. in the direction normal to the reflecting wall) and the relative time step t/T. It is useful to compare the relative magnitudes of velocity components to the first and second-order, for various y/L_y and t/T in the laminar layer within a short-crested wave. From these comparisons, it will help in obtaining an overall picture of water-particle motions within the turbulent boundary layer.

It is now desirable to show a test case of short-crested wave system produced by incident wave of period T=1 sec and 76 mm in height, with approaching angle at $\theta = 45°$ to a reflecting wall in 300 mm of water.A maximum u≈190mm/s occurs at the combined-crest alignments. Figure 3 depicts the vectorial sums of Eulerian fluid velocities (u_1,v_1,u_2,v_2),up to second-order, for specific y/L_y at various t/T. The maximum values of u and v occur at different y/L_y and t/T, for example, maximum u appears at $y/L_y = 0,1/2,1$ at t/T= 0,1/2,1; while v becomes maximum along alignments $y/L_y = 1/4$ and 3/4 at t/T=1/4 and 3/4. From figure 3, it can be observed, among various t/T, that along the alignments of combined-crest (i. e. $y/L_y = 0, 1/2,1$) water-particle motions are predominantly in the x-direction, and that along $y/L_y = 1/4$ they are mainly transverse. In the vicinity of y/L_y

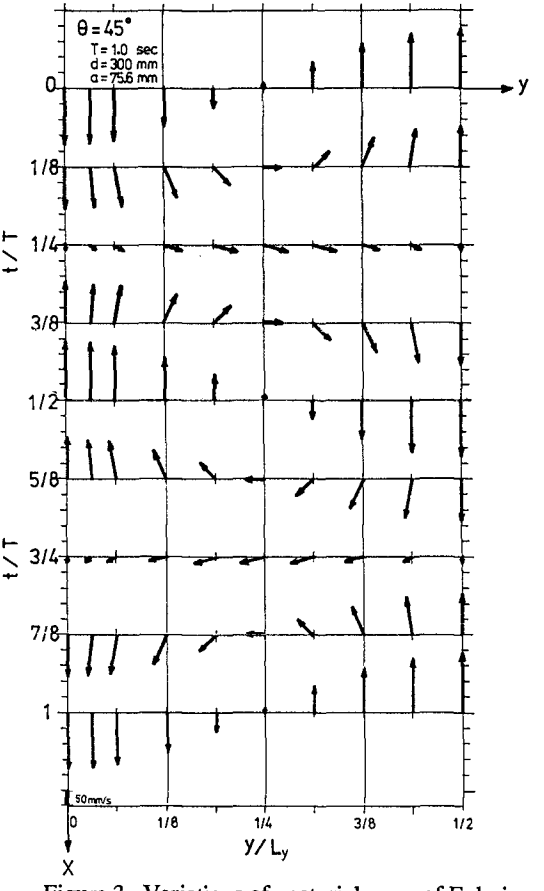

Figure 3. Variations of vectorial sums of Eulerian fluid velocities to second-order, in magnitude and direction, as functions of y/L_y and t/T, in a laminar layer.

= 1/8ths water-particle orbits rotate in ellipses. It can be observed that the orbit rotates anti-clockwise at $y/L_y = 1/8$ while it becomes clockwise at $y/L_y = 3/8$, thus reaffirming the water-particle motions sketched in figure 2.

Knowing that u and v reach their maxima at different y/L_y and t/T as noted, it is beneficial to display the vertical distribution of velocity profiles within the laminar layer as a function of time t/T for the alignments where the velocity is at its maximum as illustrated in figure 3. From figure 4, it can be seen that flow reversal exists in the lower portion of the bottom layer at certain combinations of y/L_y and t/T, even when fluid velocities to the first-order are considered. The relative ordering can be realised from the following example. The maximum ratio of u_1 and u_2 (first-order to second-order velocity) can be obtained from figures 4 and 5, where $u_1 \approx 10u_2$. Figure 5 shows the maximum magnitudes of the second-order velocities, $u_2 \approx 4v_2$, and $u_2 \approx 4w_1$, for the same wave conditions (T=1.0 sec, H=76 mm, d=300mm); in other words, $u_1 \approx 40v_2$ and $u_1 \approx 40w_1$. Further calculation shows that the maximum ratio of $w_1/w_2 \approx 10$, therefore, $u_1 \approx 400\ w_2$.

From the above example, it is clear that the vertical velocity components, w_1 and w_2, are negligibly small, particularly w_2. One may doubt the pragmatic value in which tremendous efforts have been devoted into the laborious process from which lengthy expressions are derived analytically.

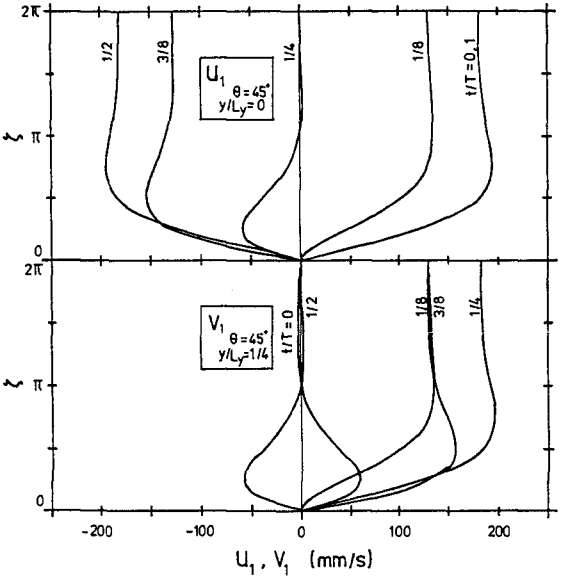

Figure 4. Profiles of Eulerian water-particle velocities u_1 and v_1, through laminar boundary layer at various time steps. waves T=1 sec, incident height H=76mm and θ=45°.

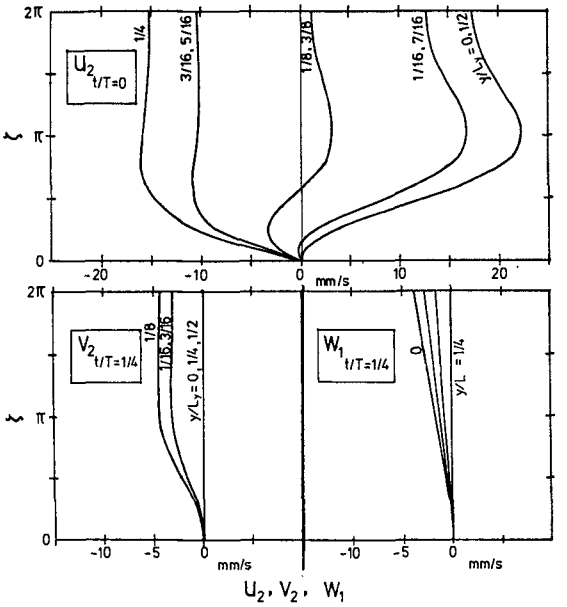

Figure 5. Profiles of Eulerian fluid velocities u_2, v_2 and w_1 through the laminar layer at various y/L_y locations and time steps t/T.

The effect of wave obliquity on the magnitude of fluid velocities is given in figure 6. From this figure, it is found that $u_1 \approx 10\,u_2$ for the case of $\theta = 60°$, and u_2 remains seemingly unchanged for all the three θ cases presented, based upon the same incident wave conditions (T=1.0 sec, H=76 mm, d=300mm) except the approaching angles. The value of u_1 decreases as θ decreases (see figure 1 for the definition of θ).

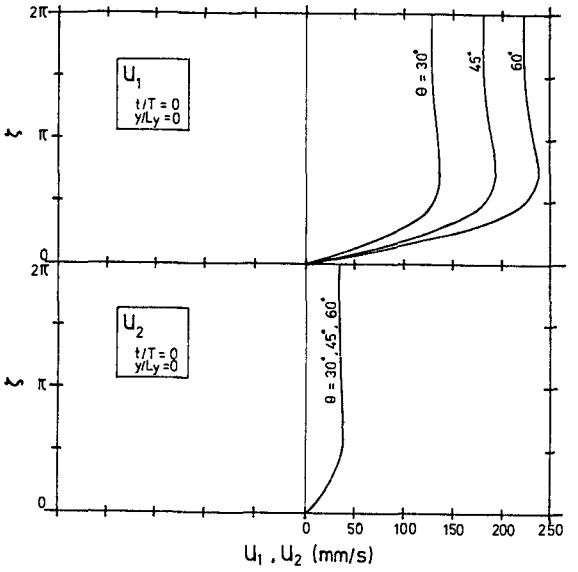

Figure 6. Profiles of the maximum fluid velocities u_1 and u_2 for the same wave conditions as in figure 4, but for various incident angles.

For the cases investigated above, the mass transport velocities (U_{M2} and V_{M2}) in dimensional value are depicted in figure 7. The forward mass transport velocity U_{M2} reaches its maximum along the combined-crest alignments, and is minimal along 1/4-ths of y/L_y, where at this latter alignment V_{M2} is zero. Therefore, all water-particles within the short-crested wave system have a net movement forward irrespective of their position along y/L_y. In the vicinity of 1/8th of y/L_y, the resultant mass-transport velocity vector is inclined towards its neighbouring alignment of combined crest.

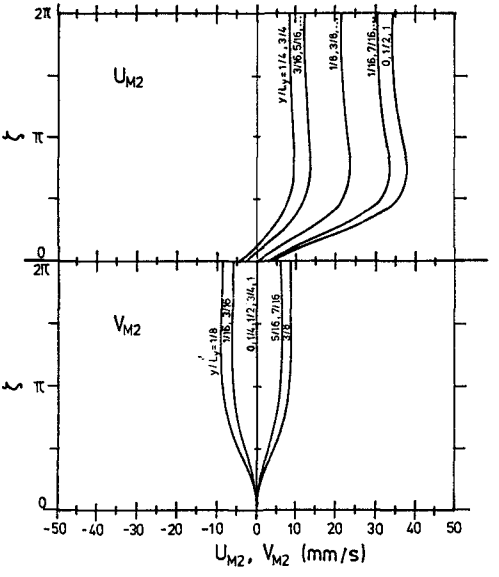

Figure 7. Dimensional mass transport velocities U_{M2} and V_{M2} through a laminar boundary layer within a short-crested wave system.

Within the laminar bottom boundary layer, the bottom shear stress τ_{bx} is defined as

$$\tau_{bx} / \rho = \nu \, (\partial u/\partial z)\big|_{z=0} \quad \text{dimensionally.} \tag{7}$$

The shear stress component in the y-direction τ_{by} can be established in a similar manner.

To the first-order approximation, substituting u_1 and v_1 into equation (7), it yields the expressions of τ_{bx} and τ_{by} as follows

$$\tau_{bx} / \rho(U_{om})^2 R_e^{-1} = \sqrt{2} \cos(\pi ky) \cos(mkx - \sigma t - \pi/4), \tag{8}$$

$$\tau_{by} / \rho(V_{om})^2 R_e^{-1} = -\sqrt{2} \sin(\pi ky) \cos(mkx - \sigma t + \pi/4), \tag{9}$$

where U_{om} and V_{om} are the maximum water-particle velocity at the bed calculated from the wave theory, R_e is the boundary Reynolds number (being $U_{om}\delta_1/\nu$), in which δ_1 is the boundary-layer parameter, $\sqrt{(2\nu/\sigma)}$. Equations (8) and (9) show a phase shift of $\pi/4$ compared to U_{om} and V_{om}. Velocity expressions up to second-order can also be used for u and v in equation (7) to derive the shear stress at the bottom.

3. Turbulent boundary layer at the bottom

Traditionally, the descriptions of an oscillatory turbulent boundary layer in waves have been based upon a direct solution to momentum equations. This process, often laborious algebraically, yields Eulerian water-particle velocities and mass transport directly (for example, Johns 1970, and many others). These approaches considered the overall bottom layer as a whole. Kajiura (1968) has given a most detailed mathematical treatment in which the whole boundary layer is subdivided into three sublayers. Each sublayer had its own characteristic mean turbulent viscosity, assumed time-invariant but as a function of vertical distance within each sublayer. Kajiura's solution agreed with experimental data available, but its mathematical expression was very complicated.

Jonnson (1980) has suggested a new approach, in which a universal law of velocities near the wall was used. After obtaining the defect velocity within the boundary layer, the fluid velocity was then calculated. This new approach was supported by velocity measurements available (Jonsson 1963, 1966; Jonsson & Carlsen 1976). Therefore, there is no need to derive the fluid velocities within a turbulent boundary layer directly from momentum equations. Brevik (1981) has applied this new approach to a two-dimensional wave case, working with dimensional quantities directly from the leading terms in the governing equation.

In this section Brevik's two-layer model is examined for the application to short-crested waves, and the differences between the laminar and turbulent cases described.

3.1 Comparison of laminar and turbulent layers

The main differences between the laminar and turbulent boundary layers are in the thickness of the boundary layer, the velocity profiles, and the mechanism of producing sediment suspension.

Jonsson (1980) suggested expressions for calculating boundary-layer thickness δ and shear friction factor f_w, for the laminar layer on a smooth wall and turbulent layer on a rough bed. He also gave ranges of Reynolds number, based on boundary-layer thickness, for these cases. A useful expression for estimating the thickness of a rough turbulent boundary layer, δ, is given by

$$(\delta/ z_o)\ \log(\delta/z_o) = 0.04\ a_{1m}/z_o\,, \qquad (10)$$

where z_o is the theoretical bed level related to bottom roughness as used by Jonsson (1980) and Brevik (1981), and a_{1m} is the maximum amplitude of the orbital motion calculated from free-stream velocity U_{1m} ($= U_{1m}/\sigma$, where σ being the angular frequency of wave, i.e. $2\pi/T$). Therefore, in a rough turbulent boundary-layer, its thickness is affected by the roughness of the bottom (from the theoretical bed level z_o) and the free-stream velocity which is governed by waves propagating above it.

In the model of time-independent viscosity coefficient, Johns (1970) reported that the overall velocity profiles within a turbulent and laminar cases are very similar, except the boundary-layer thickness of the former is about 10 times of the latter; in which for the laminar case, the boundary-layer thickness was suggested to be about $5(2\nu/\sigma)^{1/2}$. He also gave remarks on the distribution of suspended sediment within these layers. From knowledge available in boundary layer, it is therefore suggested that, for the present investigation, the thickness of a rough turbulent boundary layer at the bottom of a short-crested wave system be taken as 10 times that of the laminar case.

3.2 Two-layer model of Brevik (1981)

By employing Jonnson's approach of velocity defect law and time-invariant viscosity coefficient $\nu_t(z)$, Brevik (1981) successfully developed a two-layer model for a two-dimensional wave case. Considering only the leading terms, the governing momentum equation reduced to

$$\partial u/\partial t = \partial U/\partial t + \partial(\tau_{bx}/\rho)/\partial z, \tag{11}$$

where u(z,t) is the fluid velocity, U(t) is the free-stream velocity at the outer edge of the layer, and $\tau_{bx}(z,t)$ is the shear stress at the bed ($= \rho\nu_t \partial u/\partial z$), and the z-axis is vertically upwards from the bed. Upon assuming harmonic variations to all velocities (u, U, and defect velocity $u_d = u - U$) and bottom shear stress, in terms of $e^{i\sigma t}$, where σ is the angular frequency ($= 2\pi/T$), it yielded

$$\partial u_d/\partial t = \partial(\nu_t\, \partial u_d/\partial z)/\partial z, \tag{12}$$

or finally

$$\partial(\nu_t\, \partial u_d/\partial z)/\partial z - i\sigma u_d = 0, \tag{13}$$

where the mean turbulent viscosity $\nu_t(z)$ was assumed time independent within the boundary layer. It was also assumed that $\nu_t(z)$ is to be proportional to the distance from the theoretical bed level at $z = z_o$ within the lower layer, and became a constant in the outer layer from $z \geq \Delta$ (see figure 8, or figure 1 of Brevik 1981). The theoretical bed level at $z = z_o$ from the real bed was determined by fitting the observed velocity profile above the bed to a logarithmic distribution. Brevik (1981) proposed two different values for Δ, the first value of Δ equal to half of its boundary thickness, and the second Δ as a function of amplitude of water-particle motion close to the bed and shear friction factor f_w. It is worth noting at this stage that an improper choice of Δ will produce discontinuity to velocity profiles of u/u_f and u_d/u_f on a semi-log scale plot.

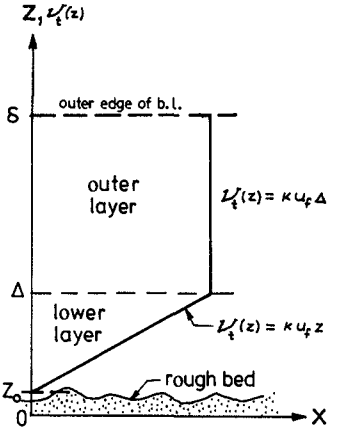

Figure 8. Assumption of the time-invariant turbulent viscosity coefficient ν_t as a function of vertical distance, in the two-layer model of Brevik (1981).

The basic equation was in dimensional form. A dimensionless variable $\xi = (4\sigma z/\kappa u_f)^{1/2}$ was then introduced into equation (13), which transformed the vertical distance z within the boundary layer, where κ is the von Karman's constant (= 0.4), and u_f is the maximum shear velocity at bed. The resultant governing equation,

$$\xi\, \partial^2 u_d/\partial \xi^2 + 2\, \partial u_d/\partial \xi - i\xi u_d = 0, \tag{14}$$

was the standard differential equation for the Kelvin functions of zero-th order, with ξ as independent variable. The solution to defect velocity u_d was related to Kelvin functions of the first and second kinds, (ber, bei, ker, kei at the specific levels of $z = z_o$ and $z = \Delta$ respectively), and generally in complex variable form. Integration constants were determined subject to boundary conditions required. After establishing the defect velocity, water-particle velocity u was found from $u(z,t) = u_d(z,t) - U(t)$, then phases calculated. The new analytical solutions to u and u_d and their phases (Brevik 1981) fit well with data of Test no.1 of Danish measurements (Jonsson 1980, Jonsson & Carlsen 1976), hence confirming the usefulness of the proposed two-layer theory. For detailed derivations and final expressions of $u_d(z,t)$ and $u(z,t)$ in each layer, see the original paper of Brevik (1981).

For calculating u_d, u and their phases numerically, it is necessary to establish a computer program which can reproduce the results of Brevik (1981). A program in PASCAL language was written with graphic ability run on a micro-computer. Expressions of Kelvin functions are obtained from Abramowitz & Stegun (1964). This program reproduced the results of u_d, u and their phases as reported by Brevik (1981) in his figures 2 to 5, using data of Test no.1 of the Danish measurements (Jonnson 1980; Jonnson & Carlsen 1976). An example of u_d/u_f and u/u_f calculated from the present program is given in figure 9 (for wave and boundary-layer conditions: T=8.39 sec, free-stream velocity U = 2110 mm/sec, max shear velocity u_f = 207 mm/sec, thickness of the turbulent layer δ = 60 mm, z_o= 0.77 mm, and $\Delta = 0.5\delta$ = 30 mm).

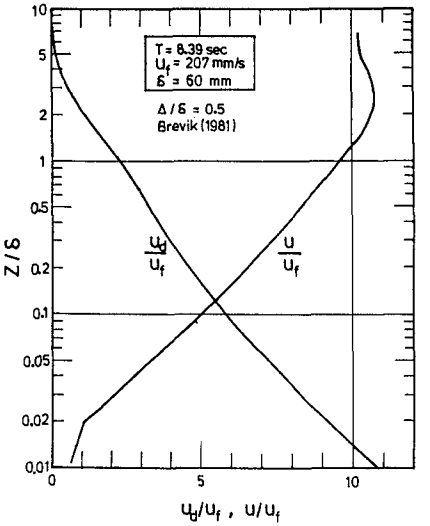

Figure 9. Profiles of relative velocities u_d/u_f and u/u_f, reproduced using data of Test no.1 of Danish measurements (Jonsson 1980, Jonsson & Carlsen 1976).

Figure 10 shows the fluid velocity u and defect velocity u_d obtained from the said conditions, previously presented in figure 9, after being converted to a normal scale plot. Because the thickness of the turbulent layer is about 10 times that of the laminar case, it can be seen that most of the changes in velocity u in the vertical direction above the bed are within the lower 25% of its overall thickness. This region is equivalent to about twice of the thickness of the laminar layer, under the same wave conditions. The remaining 75% of the thickness has rather uniform velocity profile.

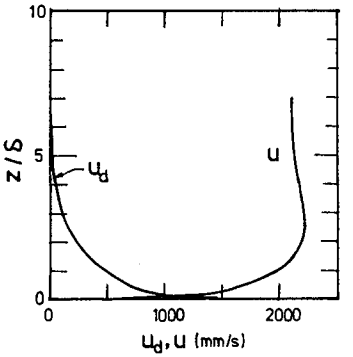

Figure 10. Converted fluid velocity u and defect velocity u_d profiles obtained from conditions specified for Test no.1 of Danish measurements (Jonsson & Carlsen 1976).

In applying Brevik's two-layer model, it is critical in able to choose a suitable thickness for the lower-layer, as can be demonstrated in figure 11. The wave and boundary-layer conditions are the same as that produced figures 9 and 10, but with variable Δ, these being Δ=1/8,1/4,1/2 and 3/4 of the turbulent boundary-layer thickness. Profound discontinuity is obvious for Δ less than half of its boundary-layer thickness. Values of Δ/δ greater than 0.5 (the case presented in figure 9) had negligible effect on the continuity just discussed, even when Δ/δ reached 0.75. The practical problem is how to select the most appropriate value of Δ/δ for each application.

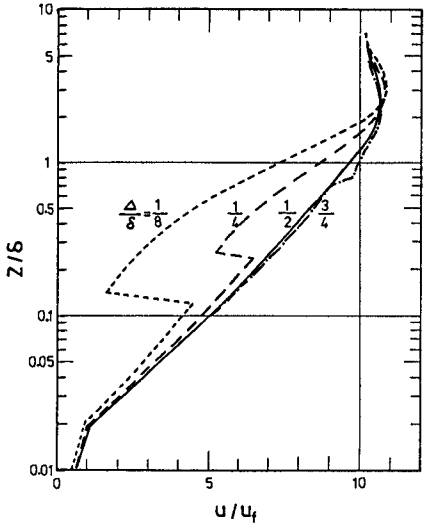

Figure 11. Discontinuity in velocity profile u/u_f on a semi-log plot, resulting from improper choices of Δ/δ, in the two-layer model (Brevik 1981).

Further study showed that the choices of the theoretical bed level z_o from bottom roughness is not critical, though affecting the boundary-layer thickness in the turbulent condition (see equation 10). Hence, this model can be applied to wave cases with reasonably rough bed. Once a proper ratio of Δ (the upper limit of the lower layer) relative to the boundary-layer thickness δ is selected, say Δ/δ = 0.5, the turning point located near the bottom of u/u_f curve in figure 9 may be shifted away from the present value of z/δ = 0.02. Given a bottom roughness 5 times the value as used by Brevik

(1981), the said turning point will be shifted to $z/\delta \approx 0.1$, modifying the slope of velocity profiles u/u_f and u_d/u_f only slightly in the region $z/\delta < 0.1$.

3.3 Application to short-crested waves

Brevik's two-layer model (1981) was derived for the case of two-dimensional progressive waves. In a three-dimensional case, the flow field is much more complex, even to the simplest case of short-crested wave system produced by full oblique reflection from a long vertical wall . Preliminary examination using only leading terms in the governing equations renders

$$\partial u/\partial t = \partial U/\partial t + \partial(\tau_{bx}/\rho)/\partial z, \tag{15}$$

$$\partial v/\partial t = \partial V/\partial t + \partial(\tau_{by}/\rho)/\partial z, \tag{16}$$

and

$$\partial u/\partial x + \partial v/\partial y + \partial w/\partial z = 0, \tag{17}$$

where (u,v,w) are the fluid velocities, (U,V) are the free-stream velocity components, τ_{bx} and τ_{by} are shear stresses at the bed in the x and y-directions respectively.

To apply the two-layer model to this short-crested wave system, dimensional expressions of free-stream velocities are required, at each order of approximation. These can be obtained from equations (1)-(3). The free-stream velocity components U and V contain trigonometric functions such as cos(mkx-σt) and sin(mkx-σt) etc. Expressing the real part of "cos(σt)" and "sin(σt)" in exponential form, such that

$$\cos(mkx-\sigma t) = \cos(mkx)\, e^{i\sigma t} - i \sin(mkx)\, e^{i\sigma t}, \tag{18}$$

and

$$\sin(mkx-\sigma t) = \sin(mkx)\, e^{i\sigma t} + i \cos(mkx)\, e^{i\sigma t}, \tag{19}$$

where $i = \sqrt{-1}$ representing the imaginary part of a complex variable. Unlike U_1 which was a constant $U_1(t)$ in a two-dimensional case, the leading term in equation (1), $U_1(x,y,t)$, is now in complex variable form. $U_1(x,y,t)$ may be split into two terms, one containing $\cos(mkx)e^{i\sigma t}$, and the other in $\sin(mkx)e^{i\sigma t}$, for example

$$\begin{aligned} U_1 &= \varepsilon \sqrt{(g/k)}\, (m\omega_o/\sinh kd) \cos(nky)\, [\cos(mkx) - i \sin(mkx)]\, e^{i\sigma t} \\ &= (\, U_{1c} + i\, U_{1s}\,)\, e^{i\sigma t}, \end{aligned} \tag{20}$$

where $U_{1c}(x,y,z)$ and $U_{1d}(x,y,z)$ relate to the time-independent velocity expressions containing "cos(mkx)" and "sin(mkx)" respectively in equation (20). Similarly, V_1 in equation (2) becomes

$$\begin{aligned} V_1 &= -\varepsilon \sqrt{(k/g)}\, (n\omega_o/\sinh kd) \sin(nky)\, [\sin(mkx) + i \cos(mkx)]\, e^{i\sigma t}, \\ &= (\, V_{1c} + i\, V_{1s}\,)\, e^{i\sigma t}. \end{aligned} \tag{21}$$

The second-order terms U_2 and V_2 in equations (1) and (2) may receive similar treatment, if higher order terms are required.

To calculate $u_{d1}(x,y,z,t)$, which is the defect velocity u_d to the first-order, at a required location (x,y,z) within the short-crested wave system, equation (15) has to be utilised twice, rendering

$$\partial(\nu_t \partial u_{d1c}/\partial z)/\partial z - i\sigma u_{d1c} = 0, \tag{22}$$

and

$$\partial(\nu_t \partial u_{d1s}/\partial z)/\partial z - i\sigma u_{d1s} = 0, \tag{23}$$

in which u_{d1c} and u_{d1s} are related to the free-stream velocity components of U_{1c} and U_{1s} in equation (20) respectively. The magnitude (or modulus) and phase of u_{d1} can be calculated for each sublayer,

$$u_{d1} = u_{d1c} + i\, u_{d1s}, \tag{24}$$

finally leading to the magnitude and phase of u_1. Adopting similar procedure, the first-order defect velocity $v_{d1}(x,y,z,t)$, in complex variable form, is given as

$$v_{d1} = v_{d1c} + i\, v_{d1s}, \tag{25}$$

and fluid velocity v_1 can be calculated after establishing v_{d1}.

Based upon the linear theory above, the flow field at a specific position within a rough bottom layer of the short-crested waves can be determined analytically and numerically. Along the combined-crests, $y/L_y = 0, 1/2, 1, \ldots$, U_{1c} and U_{1s} only are required because $V_1 = 0$; on the other hand, it needs only V_{1c} and V_{1s} along alignments $y/L_y = 1/4, 3/4, \ldots$, since $U_1 = 0$. Along other alignments, all U_{1c}, U_{1s}, V_{1c} and V_{1s} are required in calculations because U_1 and V_1 coexist.

4. Discussions

From theory and experiments available, it has been shown that the water-particle motions in the bottom layer within a short-crested wave system are quite complex, even for the simplest case produced by complete oblique reflection. The resultant wave system is most severe in its erosive capacity. To investigate the rough turbulent boundary layer at the bed, Brevik's (1981) two-layer model using time-invariant viscosity coefficient was here examined.

As revealed from the numerical calculations, Brevik's (1981) two-layer model is a valuable tool in producing a normal velocity distribution through a rough turbulent bottom layer within the short-crested wave system. But this model of assuming time-invariant viscosity coefficient $\nu_t(z)$ to each sublayer can only produce a velocity profile of u similar to that presented in figure 10. Therefore, Brevik's approach is incapable of reproducing a flow reversal in the lower portion of the boundary layer (as in figure 4).

Viewed from the time-varying velocity profiles shown in figure 4 for velocity components at the same location (x,y,z) in a short-crested wave system, a time-dependent viscosity coefficient $\nu_t(z)$ is warranted. An ideal time-dependent viscosity model will ensure the time-varying nature of the velocity profiles as demonstrated in the case of laminar layer, in both magnitude and flow reversibility. This has recently been pointed out by Trowbridge & Madsen (1984). It is suggested that a model using time-variant viscosity coefficient should be considered before a higher order theory is used for the rough boundary layer.

Although it has commonly been envisaged that a turbulent boundary layer can produce a stronger vertical velocity component, w, there is no convincing evidence, from

numerical calculation of the said model, that its magnitude is significant. It is therefore suspected other mechanisms may also be responsible for the suspension of sediments.

5. References

1. Abramowitz, M. & I.A. Stegun (1972) Handbook of Mathematical Functions, National Bureau of Standrards, Washington, D.C..
2. Brevik, I. (1981) Oscillatory rough turbulent boundary layer. J. Waterway, Port, Coastal Ocean Div., ASCE, 107 (WW3), 175-188.
3. Hedegaard, I.B. (1985) Wave generated ripples and resulting sediment transport in waves. Inst. Hydrodyn. Hydraul. Eng., Tech. Univ. of Demark, Series paper 36.
4. Hsu, J.R.C., Y. Tsuchiya, & R. Silvester (1979) Third-order approximation to short-crested waves. J. Fluid Mech., 90, 179-196.
5. Hsu, J.R.C., R. Silvester & Y. Tsuchiya (1980) Boundary-layer velocities and mass transport in short-crested waves. J. Fluid Mech., 99, 321-342.
6. Irie, I. & K. Nadaoka (1984) Laboratory reproduction of seabed scour in front of breakwaters. Proc.19th Intl. Conf. Coastal Eng., 2, 1715-1731.
7. Johns,B. (1970) On the mass transport induced by oscillatory flow in a turbulent boundary layer. J. Fluid Mech.,43, 177-185.
8. Jonsson, I.G. (1963) Measurements in the turbulent wave boundary layer. Proc. 10th Congr. IAHR, 1, 85-92.
9. Jonsson, I.G. (1966) Wave boundary layers and friction factors. Proc.10th Intl. Conf. Coastal Eng., 1, 127-148.
10. Josson, I.G. (1980) A new approach to oscillatory rough turbulent boundary layer. Ocean Eng., 7, 109-152.
11. Jonsson, I.G. & N.A.Carlsen (1976) Experimental and theoretical investigations in an oscillatory turbulent boundary layer. J. Hydraul. Res., 14, 45-60.
12. Kajiura, K. (1968) A model of the bottom boundary layer in water waves. Bull. Earthquake Res. Inst., Japan, 46, 75-123.
13. Longuet-Higgins, M.S. (1953) Mass transport in water waves. Phil. Trans. Roy. Soc. A, 245, 535-581.
14. Mei, C.C., P.L-F. Liu & T.G. Carter (1972) Mass transport in water waves. M.I.T., Ralph M. Parsons Lab., Report 146.
15. Noda, H. (1971) On the oscillatory flow in turbulent boundary layers induced by water waves. Bull. Disaster Prevention Res. Inst., Kyoto University, Japan, 20, 127-144.
16. Silvester, R. (1986) The influence of oblique reflection on breakwaters. Proc.20th Intl. Conf. Coastal Eng., ASCE, (In press).
17. Tanaka, N., I. Irie & H. Ozasa (1972) A study on the velocity distribution of mass transport caused by diagonal partial standing waves. Report, Port & Harbour Res.Inst., Japan, 11, 112-140. (In Japanese)
18. Trowbridge, J. & O.S. Madsen (1984) Turbulent wave boundary layer, 1. Model formulation and first-order solution. J. Geophys. Res., 89, 7989-7997.
19. Trowbridge, J. & O.S. Madsen (1984) Turbulent wave boundary layer, 2. Second-order theory and mass transport. J. Geophys. Res., 89, 7999-8007.

CHAPTER 22

Determination of Wind Stress (Drag) Coefficient for Coastal Waters Under Variable Meteorological and Oceanographic Conditions

S. A. Hsu*

Abstract

On the basis of a parametric model of wind stress (drag) coefficient over water surfaces and related experiments, objective procedures to obtain this coefficient under variable wind and wave conditions are outlined and recommended for oceanographic applications and air-sea interaction studies. Methods for both fully and non-fully developed sea conditions are given.

1 Introduction

Wind stress, τ, is one of the most important parameters for air-sea interaction studies see, e.g., Roll, 1965, for momentum flux; Bishop, 1984, for upwelling (current) computation . In order to obtain the magnitude of the wind stress, the drag coefficient is commonly used, i.e.,

$$\tau = \rho U_*^2 = \rho C_D U_z^2 \quad (1)$$

where ρ is the air density, U_* is the shear (or friction) velocity, and C_D is the drag coefficient, which corresponds to the wind speed, U_z, at height z above the water surface.

Variation of C_D with wind speed has been the subject of many investigations (see, e.g., a list given Blanc, 1985). An illustration is provided in Figure 1. In order to explain the increase of C_D with wind speed, Hsu (1986a) has proposed a mechanism that incorporates contributions by both wind and waves. These parameters are modeled into an aerodynamic roughness equation that has proven to be applicable in both coastal waters and open-ocean conditions.

It is the purpose of this paper to outline the procedures necessary for objective computation of the drag coefficient over coastal waters, where meteorological and oceanographic conditions are constantly changing because of variable fetch, duration, and speed of the wind, which in turn produces different characteristics of the wind waves.

2 Procedures

In order to compute C_D, the following objective procedures are recommended:

*Professor, Coastal Studies Institute, School of Geoscience, Louisiana State University, Baton Rouge, LA 70803.

(1) Obtain existing wind records, U_{Land}, from a nearby Weather Service station at a local airport in the coastal plain. Transpose U_{land} to the offshore region by an equation (shown in Fig. 2) provided by Hsu (1986b), i.e.,

$$U_{sea} = 1.62 + 1.17\ U_{land} \tag{2}$$

where the units of U_{sea} and U_{land} are in meters per second.

(2) If the anemometer at the official airport is not located at the conventional height of 10 m above the surface, correct by first using Eq. (2) and then applying the following equation:

$$\frac{U_{10}}{U_{sea}} = \left(\frac{10}{z}\right)^{0.1} \tag{3}$$

Note that if one applies Eq. (2) to the inland region the exponent should be changed. However, owing to complicated geomorphological features onshore, the value of the exponent is less certain than that of the offshore region, as shown in Eq. (2), which was verified by an experiment with tethered balloon soundings in the atmospheric boundary over the Mediterranean Sea, as shown in Figure 3 (Hsu, 1986c).

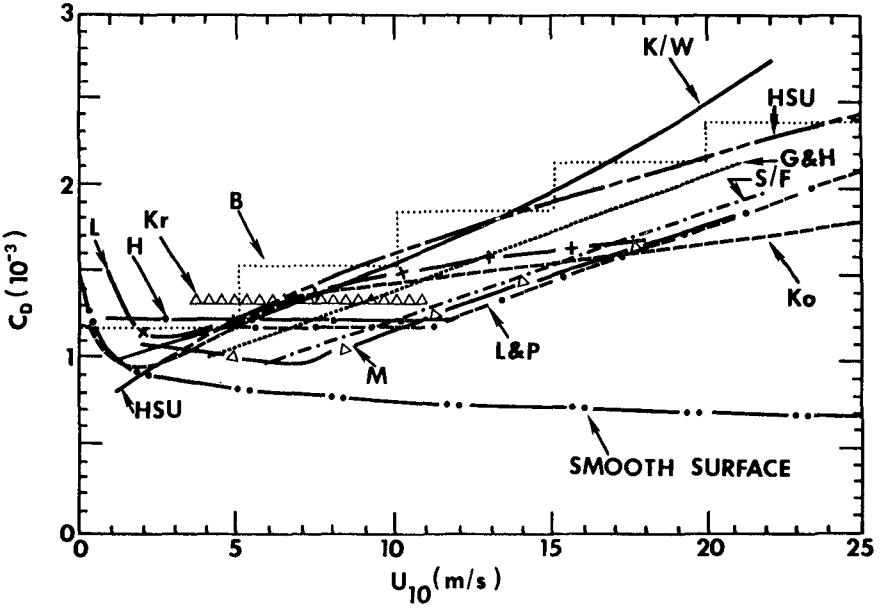

Fig. 1. Variation of the drag coefficient, C_D, with wind speed at 10 m above the sea surface from Blanc, 1985, except the curve labeled "Hsu, this study," which is based on Eq. (4) .

(3) For engineering applications, assume first that the sea is fully developed. According to Hsu (1986a, Eq. 35), we have

$$C_{10} = \left[\frac{\kappa}{14.56 - 2 \ln U_{10}}\right]^2 \tag{4}$$

where κ is the von Karman constant (= 0.4 $\pm$ 0.01; see Hogstrom, 1985).

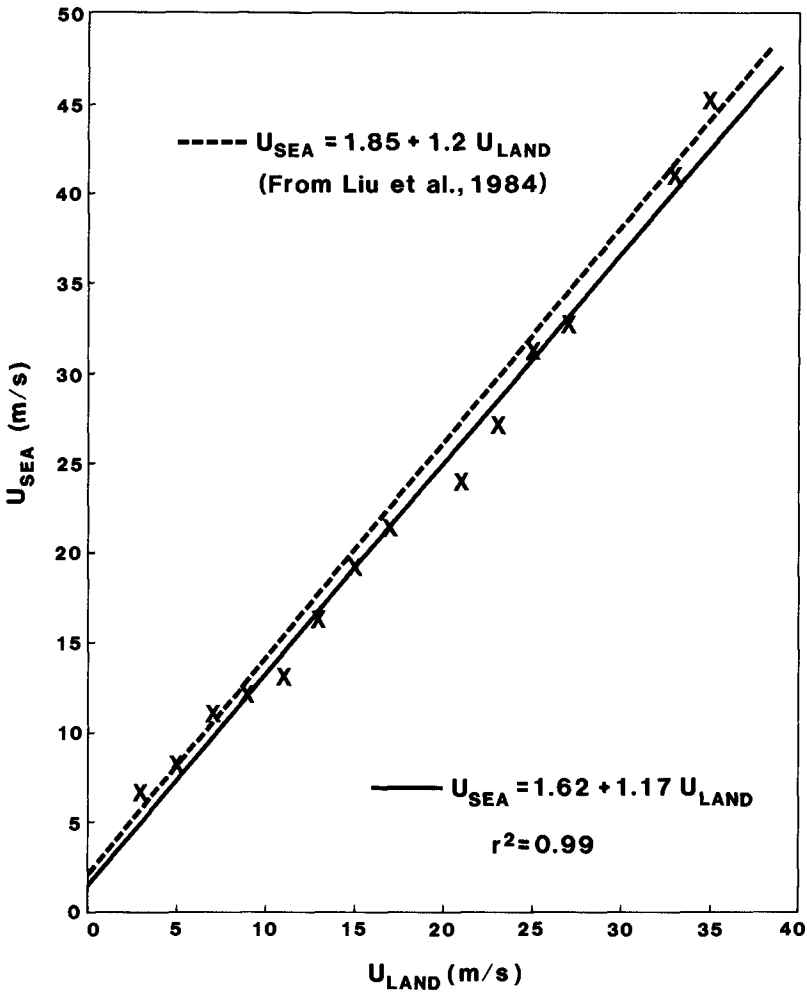

Fig. 2. Variation of U_{sea} as a function of U_{land} (from Hsu, 1986b).

This equation is shown as the curve labeled "HSU" in Figure 1, which is obtained from wind and wave parameterization and is consistent with measurements. Additional verification of Eq. (4) is given in Figure 4 as well as in Hsu (1986a).

(4) If the sea is not fully developed and detailed wind-stress estimates are needed to compute the currents, e.g., during oil spill conditions, the following procedures may be applied. From forecasted weather maps, the fetch, duration, direction, and speed of the wind near the sea surface can be obtained (see, e.g., procedures outlined in U.S. Army Corps of Engineers, 1984). On the basis of these data, wave celerity, C, and significant

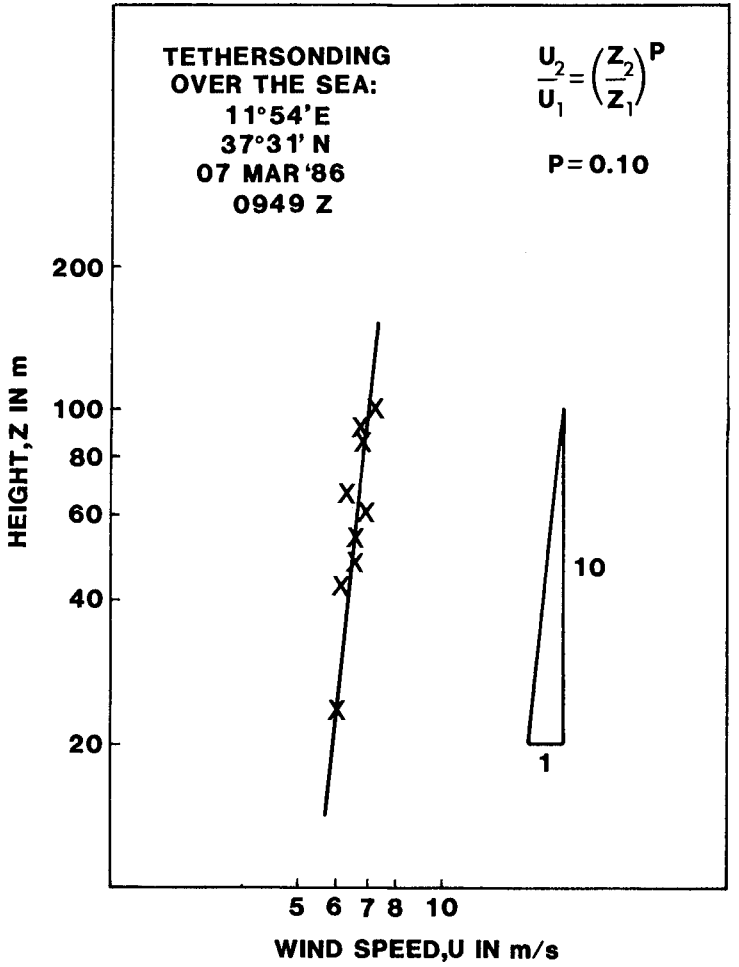

Fig. 3. A log-log plot of U versus Z over the ocean (from Hsu, 1986c).

wave height, $H_{1/3}$, can be computed. A quick way is to use the nomogram provided in U.S. Army Corps of Engineers (1984).

With wind and wave parameters, U_* can be estimated from the nomogram provided in Figure 5 (Hsu, 1976). Then, applying the following formula from Eq. (1):

$$C_D = (U_*/U_z)^2 \tag{5}$$

Note that the effect of atmospheric stability has already been incorporated in the wave characteristics (see Hsu, 1976; Janssen and Komen, 1985).

3 CONCLUSIONS

On the basis of a parametric model of wind stress (drag) coefficient and related experiments, objective procedures to obtain C_D are outlined and recommended for oceanographic applications. These procedures should be useful for coastal engineers.

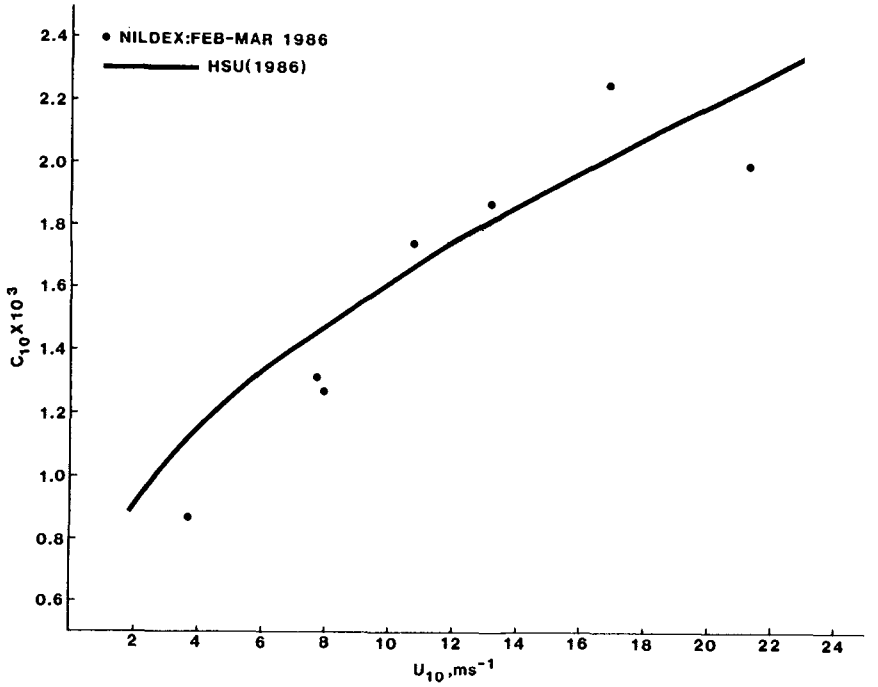

Fig. 4. Variations of C_{10} versus U_{10} as obtained from the Mediterranean Sea (see Hsu, 1986c). The solid line is based on Eq. (4).

4 ACKNOWLEDGEMENT

The 1986 Mediterranean experiment used in this study was sponsored in part by the U.S. Naval Environmental Prediction Research Facility. Additional support from the Marine Meteorology Program of the U.S. Office of Naval Research is appreciated. Travel funds to present the paper were made available by the Department of Geology and Geophysics, Louisiana State University.

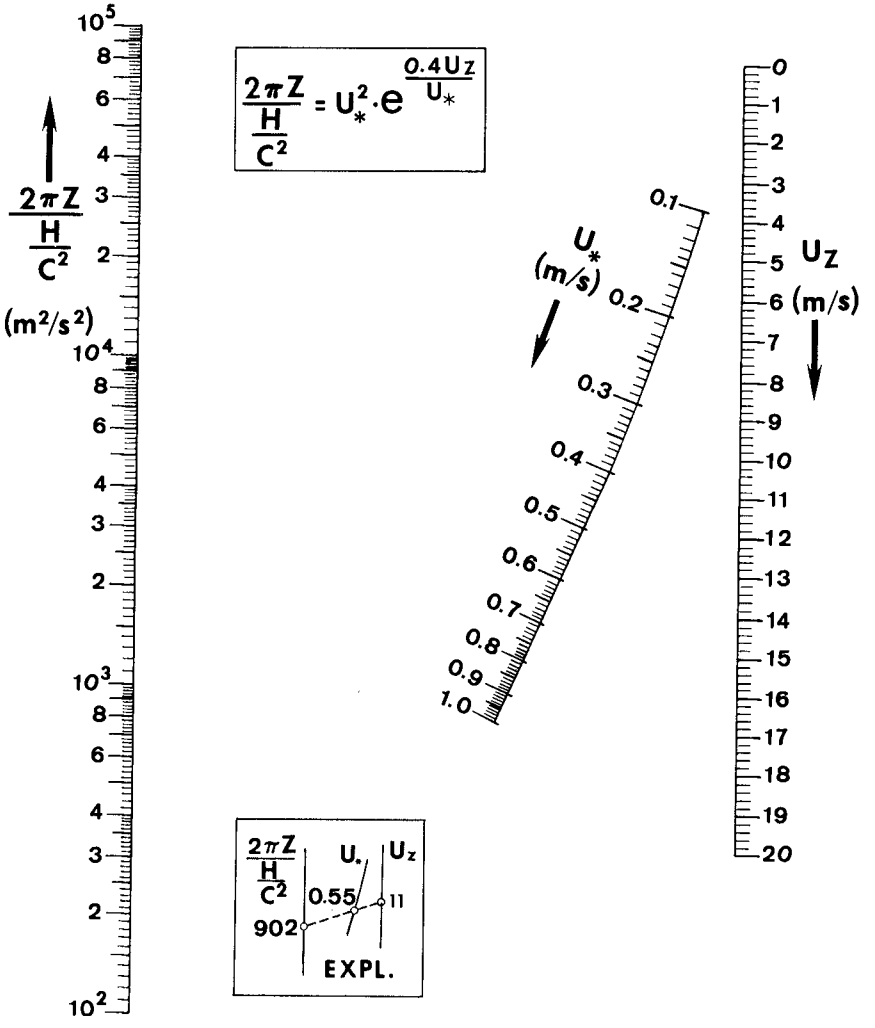

Fig. 5. A nomograph for computing U_* from wind and wave parameters for both fully and non-fully developed sea conditions. The figure gives an example of the use of commonly available wind (U_z) and wave (H and C) parameters to obtain U_* (Hsu, 1976).

5 REFERENCES

BISHOP, J.M. (1984). Applied oceanography. New York, John Wiley. 252 pp.

BLANC, T.V. (1985). Variation of bulk-derived surface flux, stability, and roughness results due to the use of different transfer coefficient scheme. Journal of physical oceanography, 15(6): 650-669.

HOGSTROM, U. (1985). Von Karman's constant in atmospheric boundary layer flow: reevaluated. Journal of atmospheric sciences, 42(3): 263-270.

HSU, S.A. (1976). Determination of the momentum flux at the air-sea interface under variable meteorological and oceanographic conditions: further application of the wind-wave interaction method. Boundary-layer meteorology, 10(2): 221-226.

Hsu, S.A. (1986a). A mechanism for the increase of wind stress (drag) coefficient with wind speed over water surfaces: a parametric model. Journal of physical oceanography, 16(1): 144-150.

HSU, S.A. (1986b). Correction of land-based wind data for offshore applications: a further evaluation. Journal of physical oceanography, 16(2): 390-394.

HSU, S.A. (1986c). Wind-wave interactions during NILDEX '86. WMCE (Western Mediterranean Circulation Experiment) Newsletter #7, Sept. 1986, pp. 22-25. Available through NORDA/NSTL, Bay St. Louis, Ms.

JANSSEN, P.A.E.M., and KOMEN, G.J. (1985). Effect of atmospheric stability on the growth of surface gravity wave. Boundary-layer meteorology, 32(1): 85-96.

ROLL, H.U. (1965). Physics of the marine atmosphere. Academic Press, New York. 426 pp.

U.S. ARMY CORPS OF ENGINEERS (1984). Shore protection manual, vol. I. Superintendent of Documents, U.S. Government Printing Office, Washington, D.C. 20402.

CHAPTER 23

Studies on the Correlation of Tidal Elevation Changes Along the Western Coastline of Taiwan

By

Dr. H.H. Hwung[1] C.L. Tsai[2] C.C. Wu[3]

Abstract

In order to understand the characteristics of tidal elevation changes along the western coastaline of Taiwan, the authors collected the tidal records at the same duration from eleven stations and made an elaborate analysis in this paper.

First step, the main tidal constituents were picked out from spectrum analysis, and the amplitudes and phase angles of these tidal constituents would be obtained by harmonic analysis. Then the variations of amplitude and phase lag of the main constituents and the variations of mean high water level and mean low water level along the coastline would be presented in the figures respectively. Finally, based on the results of harmonic analysis, the energy density of tide for every station could be calculated separately, and the location of the maximum energy density would be determined by cubic spline method.

1. Professor of Hydraulic and Ocean Engineering Department and Director of Tainan Hydraulic Laboratory, National Cheng Kung University, Tainan,Taiwan, R.O.C.
2. Assistant Researcher of Tainan Hydraulic Laboratory, National Cheng Kung University, Tainan, Taiwan, R.O.C.
3. Graduate students of Hydraulic and Oecan Engineering Graduate School , National Cheng Kung University, Tainan, Taiwan, R.O.C.

1. Introduction

Taiwan is a narrow island in the western Pacific Ocean, between the East and South-China sea. It is separated from the mainland of China by Taiwan Strait, about 130Km at the nearest part. Under this particular geographical boundary conditions, every time as the tide flooding, sea water flows into the strait from the southern and northern entrance simultaneously, and the flooding water concentrate gradually at one point of the strait until the maximum water level reaches. Then the tide ebbing, water flows back from the strait along the same route to the Pacific Ocean. Through this particular tidal movements, the amplitude of tide varies along the coastline which is only about 0.64m at the southest of Taiwan, and about 0.90m at the northest. But around Tai-Chiung coastal area which closes to the middle point of the coastline, the tidal range reaches 5.85m approximately. In order to understand the characteristics of tidal elevation changes along the western coastline of Taiwan, the authors collected the tidal records of the same duration of 11 stations from Kee-Lung, Tan-Hsui, Chu-Wei, Yung-An, Tai-Chiung, Fang-Yuan, Tai-Hsi, Wen-Kang, Chiang-Chun, Kao-Hsiung and Hsun-Kuan-Tsui shown in Fig-1.

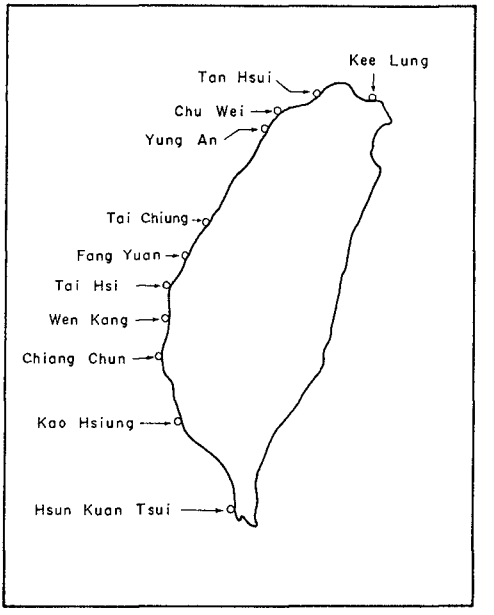

Fig-1

Based on these collected records, the main tidal constituents would be obtained from power spectrum analysis. Then the amplitudes and phase angles of these constituents were also obtained by harmonic analysis. Furthermore, the characteristics of tidal constituents along the western coastaline of Taiwan are presented in this paper.

2. Data Collection and Analysis

In order to inspect the tidal records, firstly, all the collected data for every station would be plotted as a continuous curve shown from Fig-2(a) through Fig-2(k) separately. Since the tidal records may include meteorological tide or storm surge as typhoon passing through around Taiwan island, that the abnormal tide has to be filtered from the records before all of the analysis are made.

Afterwards, the main tidal constituents can be picked out from the spectrum analysis, that 8,192 tidal records ($\Delta f=0.04394^0$/hr) were taken to do the analysis for every station. And the results were presented from Fig-3(a) through Fig-3(k) respectively.

Then based on these main tidal constituents picked out from spectrum analysis, the harmonic constants (amplitudes and phase angles) would be obtained from harmonic analysis by least square method. And after the arguement and correction coefficient of these tidal constituents were determined that the tide function could be established for every station.

3. Results and Discussions

According to the above results of spectrum analysis from Fig-2 (a) through Fig-2(k), it is well to see that the variations of water elevation along the western coast of Taiwan are dominated by semi-diurnal and diurnal tide simultaneously. And it is found that the energy of semi-diurnal tide is the highest at Tan-Hsui, Chu-Wei, Yung-An, Tai-Chiung, Fang-Yuan, Tai-Hsi, Wen-Kang and Chiang-Chun stations. But beyond the above stations, it is said, that Kee-Lung, Kao-Hsiung and Hsun-Kuang-Tsui stations are dominated both by semi-diurnal and diurnal tides.

Then, based on the spectrum analysis, we picked out twenty-five tidal constituents which the summation of energy has occupied over 90% of the tide for every station. Accordingly, the harmonic analysis by least square method was carried out for every station separately. And the results were tabulated in Table-1(a)~Table-1(k).

In general, the type of tide can be classified from the ratio ,R, between the summation amplitude of diurnal tides (K_1,O_1) and semi-diurnal tides (M_2,S_2). As $R\leq 0.25$, the tide is a semi-diurnal type, $0.25\leq R\leq 1.50$, is a mixed-type and $1.50<R$ that it is a diurnal type. Thus, from the results of harmonic analysis, the ratio,R, could be calculated for every station and listed in Table-2 respectively. And it is obviously to see that the tide between the water area of Tan-Hsui and Tai-Hsi is a semi-diurnal type, but out of this region is a mixed-type.

And the variations of amplitude and phase lag of the main constituents along the latitude of western coast from the south to the north of Taiwan island were presented in Fig-4 and Fig-5 respectively. It is obviously to see that all the amplitude of tidal constituents increas with the latitude increasing, and reach a maximum value around Tai-Chiung station, then the amplitude decreas with the latitude increasing. As for the phase lag, we can see that the tendency of variations of phase lag are the same as amplitude does along the latitude, but the larger the angular frequency of tidal constituent is, the larger the phase lag has. Likewise, the variation of the mean high water level, MHW, and mean low water level, MLW, along the latitude are shown in Fig-6.

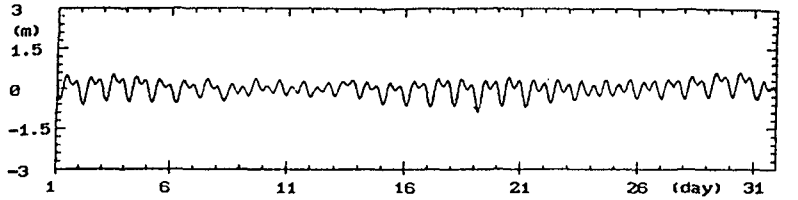

Fig-2(a) Kee-Lung JAN. 1980

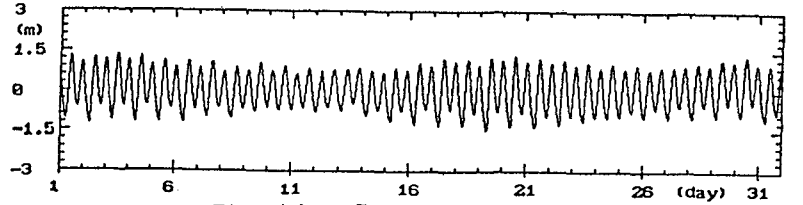

Fig-2(b) Tan-Hsui JAN. 1980

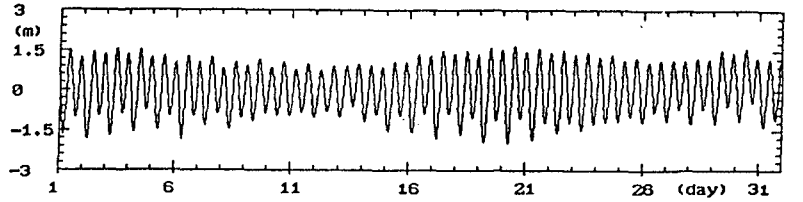

Fig-2(c) Chu-Wei JAN. 1980

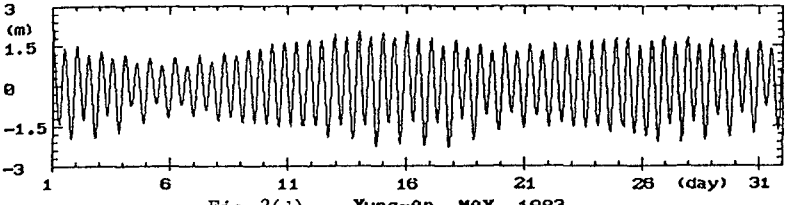

Fig-2(d) Yung-An MAY. 1983

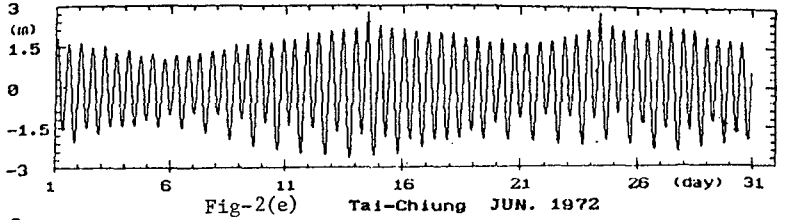

Fig-2(e) Tai-Chiung JUN. 1972

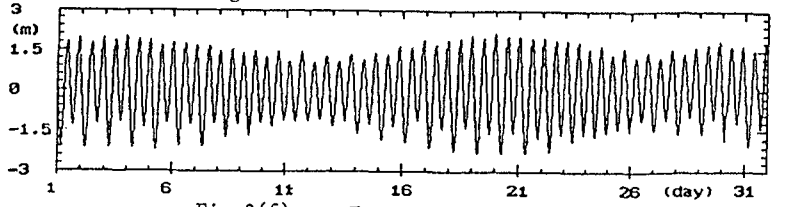

Fig-2(f) Fang-Yuan JAN. 1980

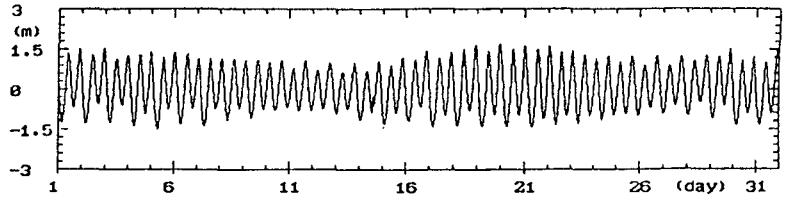

Fig-2(g) Tai-Hsi JAN. 1980

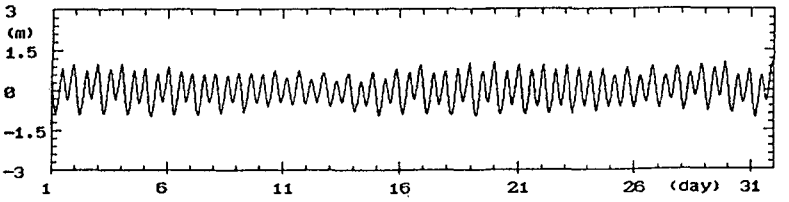

Fig-2(h) Wen-Kang JAN. 1980

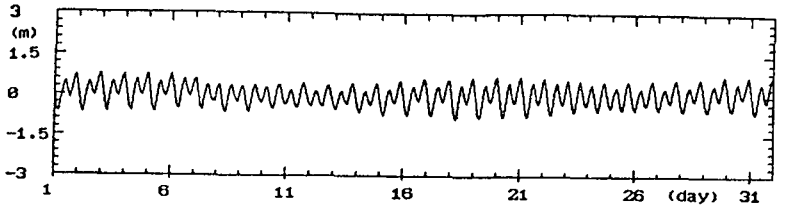

Fig-2(i) Chiang-Chun JAN. 1980

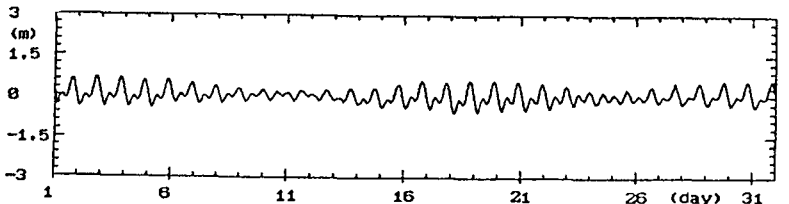

Fig-2(j) Kao-Hsiung JAN. 1980

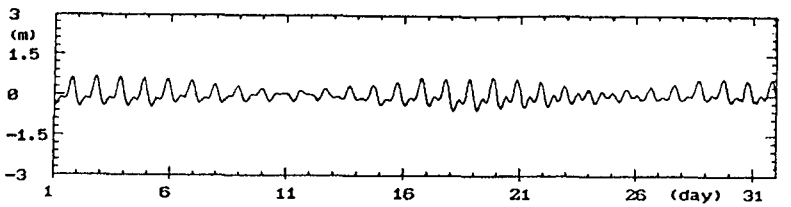

Fig-2(k) Hsun-Kuang-Tsui JAN. 1980

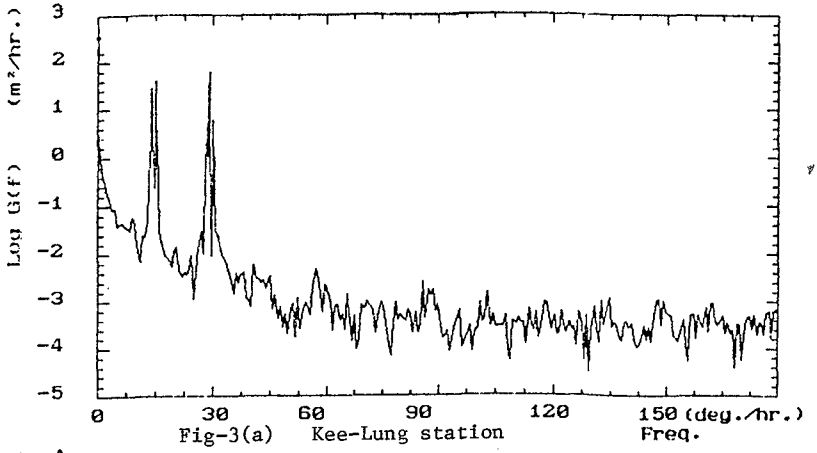

Fig-3(a) Kee-Lung station

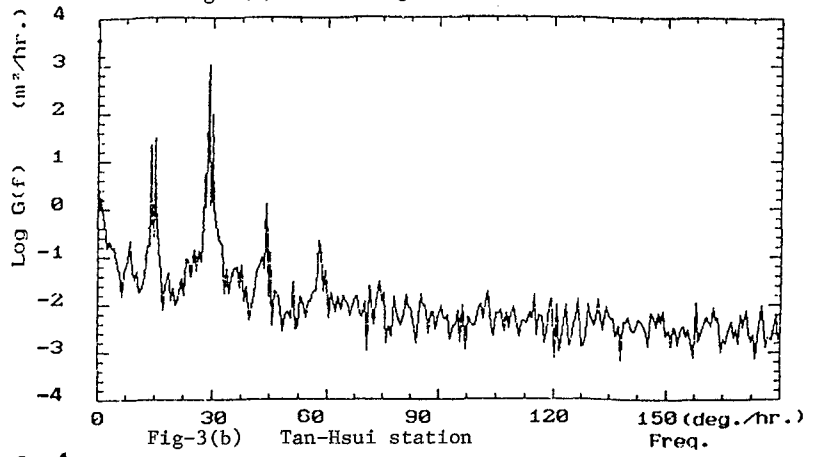

Fig-3(b) Tan-Hsui station

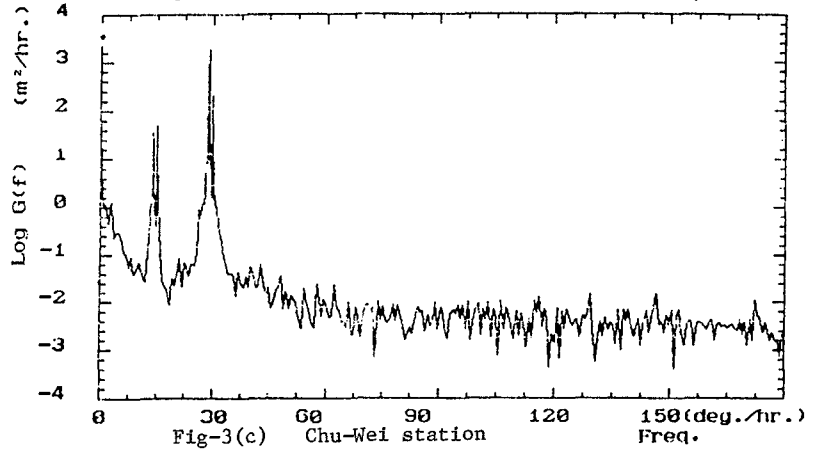

Fig-3(c) Chu-Wei station

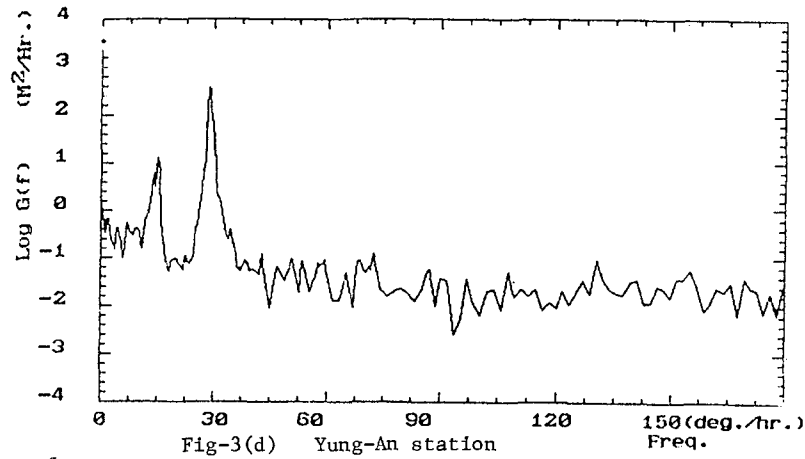

Fig-3(d) Yung-An station

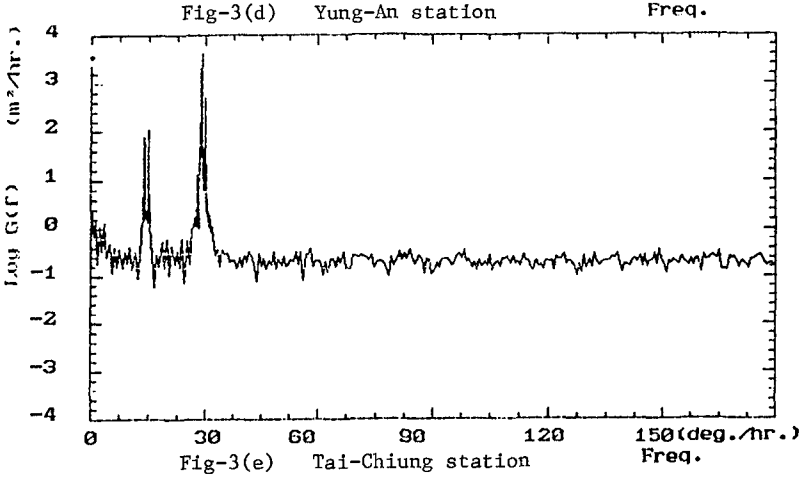

Fig-3(e) Tai-Chiung station

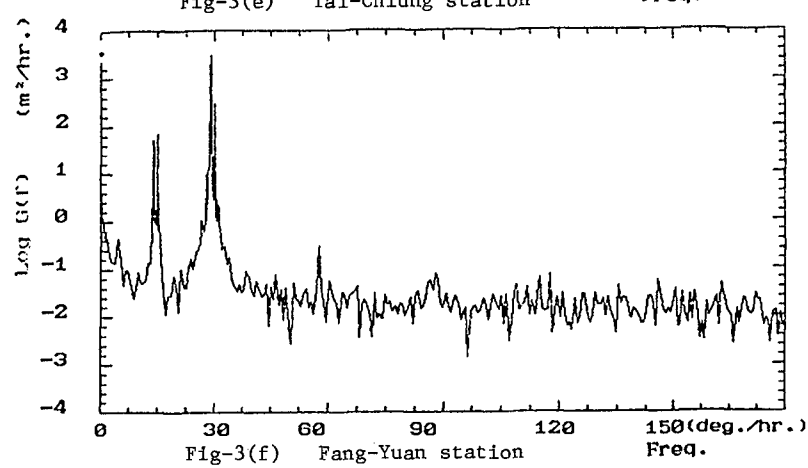

Fig-3(f) Fang-Yuan station

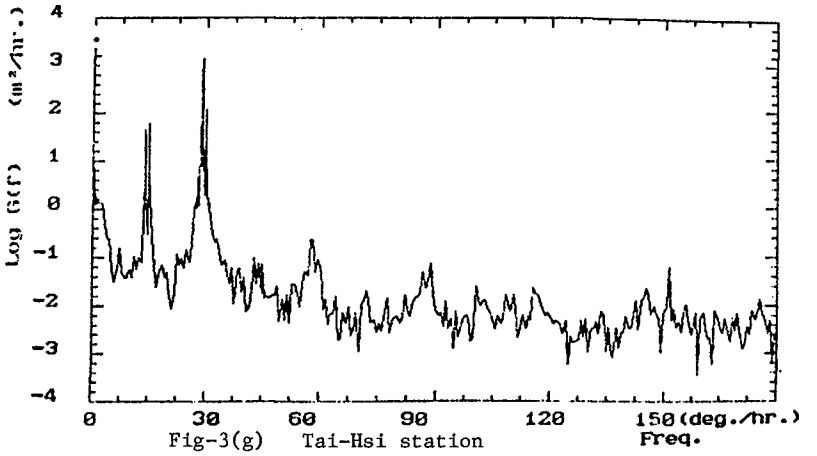

Fig-3(g) Tai-Hsi station

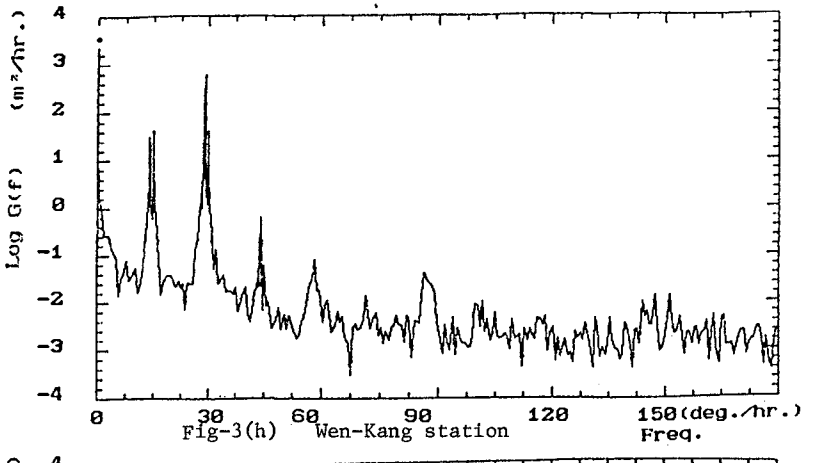

Fig-3(h) Wen-Kang station

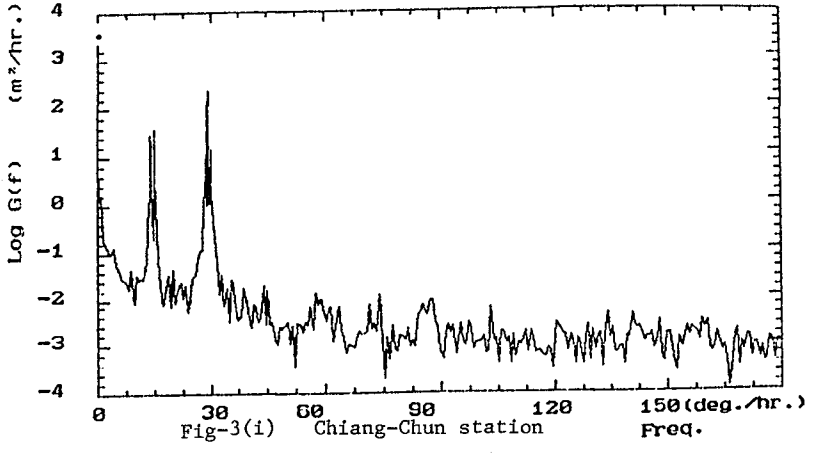

Fig-3(i) Chiang-Chun station

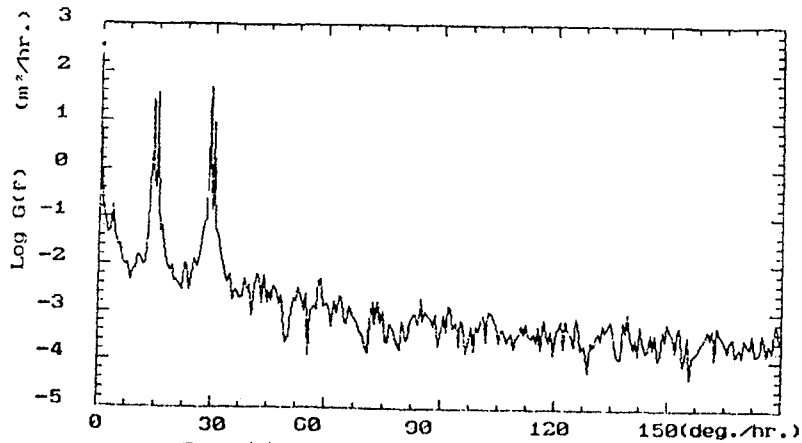

Fig-3(j) Kao-Hsiung station

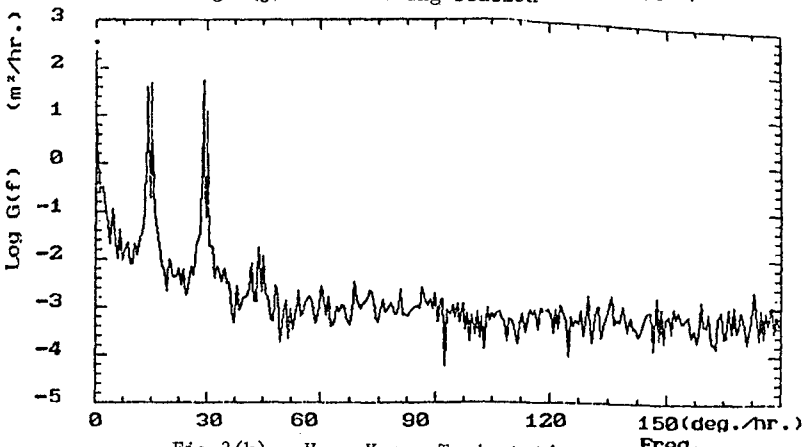

Fig-3(k) Hsun-Kuang-Tsui station

Table-1(a)

Kee-Lung			
No	Name	ampl	phase
1	M2	.2100	314.7
2	K1	.1524	220.0
3	O1	.1510	220.7
4	Sa	.1474	132.3
5	P1	.0814	229.1
6	S2	.0550	282.4
7	N2	.0520	302.0
8	Q1	.0304	223.8
9	MJU2	.0250	200.4
10	NJU2	.0147	323.5
11	Mf	.0140	33.0
12	L2	.0145	34.1
13	K2	.0140	272.1
14	M4	.0096	343.3
15	2N2	.0085	247.8
16	Mm	.0085	97.9
17	J1	.0802	232.0
18	MS4	.0077	330.0
19	Ssa	.0072	335.8
20	LUM8A2	.0070	29.1
21	Msf	.0000	294.3
22	M3	.0059	215.1
23	MNS2	.0050	179.7
24	T2	.0050	271.6
25	PSI1	.0047	101.9

Table-1(b)

Tan-Hsui			
No	Name	ampl	phase
1	M2	.8461	13.8
2	S2	.2289	29.6
3	Sa	.1715	141.1
4	N2	.1461	4.0
5	K1	.1308	257.4
6	O1	.1355	257.0
7	K2	.0670	11.0
8	P1	.0606	253.5
9	MJU2	.0562	101.4
10	M4	.0555	336.5
11	NJU2	.0400	8.0
12	L2	.0436	23.0
13	OP2	.0404	355.9
14	MS4	.0367	349.1
15	Ssa	.0352	2.0
16	MK3	.0209	249.0
17	Msf	.0204	357.5
18	Q1	.0250	254.4
19	Mf	.8238	13.4
20	Mm	.8204	48.6
21	MN4	.0202	330.0
22	MO3	.0195	240.1
23	LUM8A2	.0184	2.6
24	MNS2	.8143	180.6
25	2N2	.8125	333.8

Table-1(c)

Chu-Wei			
No	Name	ampl	phase
1	M2	1.1020	351.1
2	S2	.3172	357.0
3	N2	.2157	340.0
4	U1	.1662	245.2
5	K1	.1631	246.4
6	Sa	.1441	137.5
7	K2	.1009	1.6
8	P1	.0630	241.6
9	OP2	.0570	201.1
10	L2	.0541	355.7
11	MJU2	.0510	178.0
12	MKS2	.0430	55.3
13	NJU2	.0425	340.3
14	Ssa	.0417	51.7
15	T2	.0386	307.2
16	Q1	.0334	240.3
17	M4	.0248	209.0
18	MS4	.0222	209.0
19	A2	.0207	79.5
20	Msf	.0181	137.1
21	LUMDA2	.0136	344.0
22	MNS2	.0131	161.7
23	2SM2	.0128	240.0
24	PSI1	.0116	314.7
25	Mf	.0113	89.0

Table-1(d)

Yung-An			
No	Name	ampl	phase
1	M2	1.4170	339.4
2	S2	.4100	11.2
3	K1	.3325	230.6
4	O1	.2804	229.9
5	N2	.1071	335.6
6	M4	.0147	107.3
7	MS4	.0220	215.1

Table-1(e)

Tai-Chiung			
No	Name	ampl	phase
1	M2	1.7028	5.3
2	S2	.5100	4.7
3	N2	.3259	30.0
4	K1	.2422	232.2
5	O1	.1020	209.6
6	Sa	.1595	05.0
7	K2	.1391	290.1
8	L2	.1088	339.4
8	NJU2	.0919	330.2
10	MJU2	.0798	104.0
11	P1	.0743	289.5
12	01	.0427	334.5
13	LUMDA2	.0372	51.4
14	2N2	.0329	11.0
15	T2	.0201	10.3
16	M4	.0205	311.5
17	Ssa	.0201	255.6
18	MNS4	.0232	207.6
19	2SM2	.0229	251.5
20	MSN2	.0220	183.2
21	MN4	.0154	295.2
22	MKS2	.0151	205.0
23	MS4	.0147	207.8
24	KJ2	.0137	70.4
25	M3	.0123	113.7

Table-1(f)

Fang-Yuan			
No	Name	ampl	phase
1	M2	1.4776	352.3
2	S2	.4888	5.3
3	N2	.2575	343.9
4	O1	.1969	284.3
5	K1	.1024	270.7
8	Sa	.1537	100.4
7	K2	.0959	2.8
8	NJU2	.0870	4.7
9	MJU2	.0764	151.3
10	P1	.0729	278.4
11	L2	.0684	5.1
12	M4	.0570	270.1
13	LUMDA2	.0545	336.7
14	MKS2	.0517	100.7
15	OP2	.0427	108.4
16	Q1	.0373	265.8
17	R2	.0371	160.4
18	MS4	.0344	290.1
19	M6	.0251	264.1
20	2MS6	.0241	205.2
21	MNS2	.0231	119.8
22	MN4	.0224	272.8
23	MK3	.0204	217.8
24	2SM2	.0199	245.7
25	MSN2	.0185	188.2

Table-1(g)

Tai-Hsi			
No	Name	ampl	phase
1	M2	.8058	354.5
2	S2	.2402	11.8
3	O1	.1887	272.2
4	N2	.1827	345.1
5	K1	.1700	201.5
6	Sa	.1765	140.8
7	K2	.0894	8.7
8	P1	.0641	209.5
8	Ssa	.0519	87.4
10	NJU2	.0509	347.7
11	M4	.0406	14.4
12	LUMDA2	.0455	353.6
13	OP2	.0427	130.2
14	Q1	.0398	270.8
15	T2	.0376	311.4
18	L2	.0374	344.4
17	MS4	.0310	32.2
18	MJU2	.0291	129.7
18	MKS2	.0239	180.8
20	M6	.0225	299.1
21	MNS2	.0215	77.3
22	2MS6	.0206	321.2
23	Mf	.0206	13.5
24	MN4	.0205	357.9
25	Mm	.0204	350.8

Table-1(h)

Wen-Kang			
No	Name	ampl	phase
1	M2	.6387	352.5
2	Sa	.1043	155.3
3	O1	.1606	200.8
4	K1	.1575	287.1
5	S2	.1400	0.8
6	N2	.1299	330.4
7	Ssa	.0670	62.6
8	L2	.0521	13.9
9	P1	.0499	291.1
10	K2	.0408	10.5
11	MJU2	.0304	151.0
12	Q1	.0370	275.8
13	OP2	.0335	202.5
14	NJU2	.0291	351.7
15	MK3	.0219	226.7
18	MKS2	.0217	112.1
17	M4	.0183	349.5
18	Mm	.0174	91.5
19	M6	.0170	303.0
20	Msf	.0157	209.0
21	2MS6	.0154	331.0
22	PAI1	.0147	270.7
23	MNS2	.0146	141.6
24	2N2	.0130	296.6
25	OQ2	.0134	239.3

Table-1(i)

Chiang-Chun			
No	Name	ampl	phase
1	M2	.4241	352.6
2	O1	.1496	283.4
3	K1	.1455	298.7
4	Sa	.1458	150.8
5	S2	.0927	4.2
6	M2	.0733	344.2
7	P1	.0573	291.2
8	Q1	.0285	284.7
9	MJU2	.0269	173.2
10	MJU2	.0212	324.2
11	L2	.0176	11.3
12	K2	.0156	13.6
13	Mm	.0153	73.4
14	MKS2	.0149	157.4
15	OP2	.0147	167.7
16	MK3	.0128	227.8
17	LUMDA2	.0118	59.8
18	R2	.0117	139.7
19	MNS2	.0100	141.8
20	MS4	.0097	34.4
21	M4	.0096	.3
22	Ssa	.0093	263.6
23	J1	.0081	310.8
24	M6	.0068	332.9
25	MO3	.0079	228.8

Table-1(j)

Kao-Hsiung			
No	Name	ampl	phase
1	M2	.1826	253.6
2	O1	.1525	273.1
3	K1	.1421	284.8
4	Sa	.1208	156.1
5	S2	.0672	230.8
6	Ssa	.0588	55.7
7	P1	.0561	284.1
8	N2	.0384	258.2
9	Q1	.0328	268.3
10	K2	.0188	255.4
11	Mf	.0152	68.6
12	MJU2	.0185	214.8
13	Msf	.0088	296.5
14	2N2	.0084	269.6
15	T2	.0082	187.8
16	J1	.0073	279.7
17	OO1	.0069	75.8
18	OP2	.0066	123.8
19	NJU2	.0064	271.5
20	PSI1	.0062	75.3
21	Mm	.0061	79.3
22	SO1	.0055	188.2
23	SIGMA1	.0048	289.8
24	RHO1	.0048	273.1
25	MKS2	.0044	243.1

Table-1(k)

Hsun-Kuan-Tsui			
No	Name	ampl	phase
1	M2	.1875	235.6
2	O1	.1729	270.4
3	K1	.1629	282.8
4	Sa	.1328	158.7
5	S2	.0881	229.1
6	Ssa	.0846	69.9
7	P1	.0686	278.8
8	M2	.0355	251.8
9	Q1	.0323	277.7
10	K2	.0181	252.7
11	Mf	.0151	33.8
12	T2	.0128	253.3
13	MKS2	.0107	345.2
14	S1	.0098	59.8
15	OP2	.0095	141.8
16	PSI1	.0090	270.6
17	R2	.0088	195.3
18	Msf	.0085	301.2
19	J1	.0083	288.7
20	MJU2	.0078	244.7
21	THITA1	.0068	93.7
22	2N2	.0066	294.3
23	RHO1	.0057	263.9
24	L2	.0055	192.5
25	MP1	.0055	248.3

Table — 2

Station	R	Station	R
Kee — Lung	1.139	Tai — Hsi	0.297
Tan — Hsui	0.253	Wen — Kang	0.403
Chu — Wei	0.231	Chiang — Chun	0.571
Tai — Chiung	0.189	Kao — Hsiung	1.179
Fang — Yuan	0.206	Hsun — Kuan-Tsui	1.255

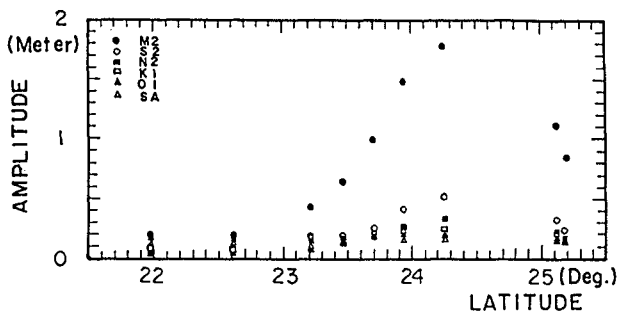

Fig-4 The relationships between the amplitude and latitude

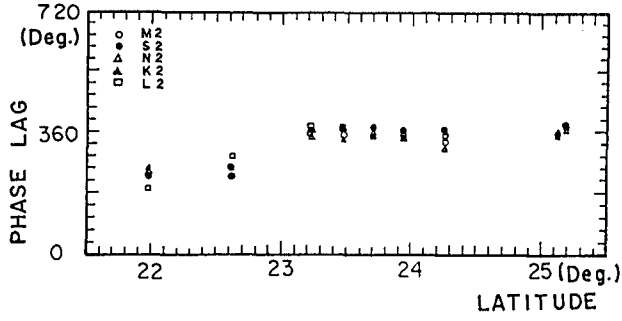

Fig-5 The relationships between phase lag of semi-diurnal and latitude

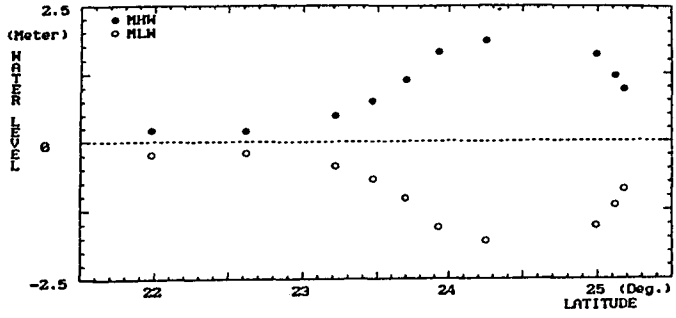

Fig-6 Variation of MHW and MLW

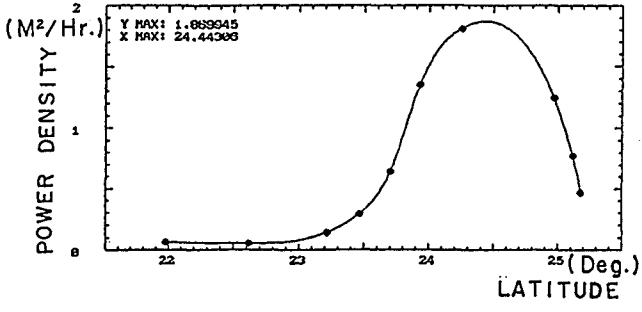

Fig-7 The distribation of energy density along the western coast of Taiwan

the location is 24° 26′, it is said that 20.9km north of Tai—Chiung station

Finally, based on the main tidal constituents obtained from harmonic analysis, the energy density of tide for every station could be calculated and the result was shown in Fig-7. Then the maximum energy density could be determined by cubic spline method, that is to say, the maximum tidal range is located 20.9Km north of Tai-Chiung station.

4. Conclusions

According to the above results, some of the remarkable conclusions would be made in this paper. They are:

(1). Along the western coast of Taiwan island, twenty-five tidal constituents picked out from the spectrum analysis are enough for engineering uses, because of the summation of energy density of these tidal constituents has occupied over 90% of the tide.

(2). The tide between Tan-Hsui and Tai-Hsi station is a semi-diurnal type which is especially dominated by M_2 constituent. However, out of this region, the tide is a mixed type which is dominated by diurnal and semi-diurnal tides simultaneously.

(3). Although the tidal records of eleven stations along the western coast of Taiwan were collected as possible as in this paper. Accordingly, the location of the maximum tidal range is determined about 20.9Km north from Tai-Chiung station. However, the more tidal stations will be provided for analysis, the more accuracy will be obtained.

5. References

1. Bendat, J.S. and Piersol, A.G. 1971, "Radom data: Analysis and Measurement Procedure." John Wiley & Sons Inc.

2. Munk W.H. Bullard E.C. 1963 "Patching the Long-wave Spectrum across the tides" J.G.R. 6812, PP. 3634-3672.

3. Zelter B.D. and Cummings R.A. 1967 "A harmanic method for prediction shallow-water tides" J. Marine Research 25.1.103-104.

4. H.H. Hwung, C.L. Tsai, 1984, "The Studies on The Tidal Frequency Analysis and Variation of Mean Sea Level", Bulletin No.69 Tainan Hydraulics Laboratory, National Cheng-Kung University.

CHAPTER 24

A PARABOLIC REFRACTION-DIFFRACTION EQUATION IN THE RAY-FRONT COORDINATE SYSTEM

Masahiko Isobe*

ABSTRACT

The parabolic equation method has been extensively used for combined refraction and diffraction problems of water waves. However, a parabolic equation is valid only when the direction of wave propagation nearly coincides with that of a coordinate; therefore, the validity ranges of the parabolic equations developed so far are restricted.

In order to achieve a wide range of validity, a parabolic equation is derived in this paper by employing a curvilinear coordinate system which has a pattern similar to that of wave rays and fronts. A computer program which is applicable to an arbitrary arrangement of coastal structures is then developed.

Results of numerical calculations are compared with available analytical solutions and laboratory data. It is proved that the present parabolic equation has a high accuracy for a wide range of incident wave direction and structure arrangement.

1. INTRODUCTION

In order to analyze the wave transformation due to combined refraction and diffraction, the mild-slope equation was derived by Berkhoff (1972). The mild-slope equation is an elliptic-type partial differential equation; hence the numerical calculation needs much computing time. Therefore, Radder (1979) and Tsay and Liu (1982) derived parabolic approximation equations which save a great amount of computing time and storage. Recently, the parabolic equation method has been modified in order to include the effects of wave nonlinearity (Kirby and Dalrymple, 1983; Liu and Tsay, 1984) and energy dissipation (Dalrymple et al., 1984; Liu and Tsay, 1985). However, the validity ranges of the parabolic equations are restricted due to the assumption that the direction of a coordinate nearly coincides with that of wave propagation.

The primary objective of this study is to derive a parabolic equation which is applicable even if the incident wave angle relative to the onshore direction and the longitudinal direction of a structure

* Associate Professor, Department of Civil Engineering, Yokohama National University, 156 Tokiwadai, Hodogaya-ku, Yokohama, 240 Japan

is large. This is done by employing a curvilinear coordinate system which has a pattern similar to that of wave rays and fronts. A computer program which can be applied to an arbitrary bottom profile and structure arrangement is developed. Results of numerical calculations are compared with available analytic solutions and laboratory data.

2. DERIVATION OF PARABOLIC EQUATION

2.1 Basic Concept

When Radder (1979) first derived a parabolic equation, Cartesian coordinates were employed. Therefore, if the incident wave angle is large, the direction of the coordinate significantly differs from that of wave propagation. In Tsay and Liu (1982), curvilinear coordinates following Snell's law were employed, which implies that the change in wave propagation direction due to refraction is taken into account. However, since the coordinates are determined independently of structures, a significant difference between the directions of the wave propagation and the coordinate occurs in the shadow region.

Waves are observed to propagate following Huygens' principle. If we define a coordinate system following this principle, the resulting coordinates must coincide with the wave ray and front pattern. We call this coordinate system a "ray-front coordinate system." Figure 1 shows an example of ray-front coordinate system. Rays 7 to 11 are incident wave rays, refracted by the change of water depth. Rays 1 to 5, and 12 and 13 are radiated from the tips of breakwaters and then refracted.

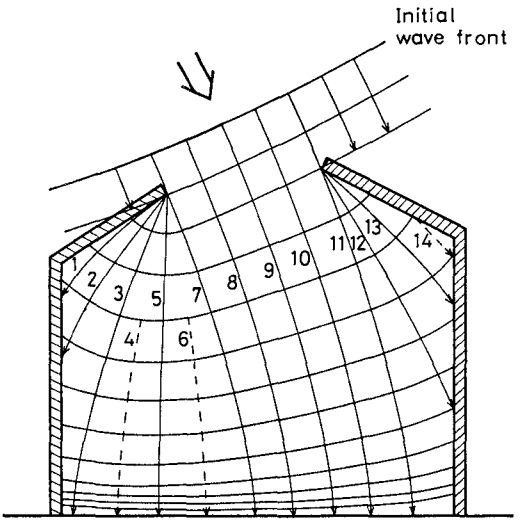

Fig. 1 Example of ray-front coordinate system.

Thus we can define a ray coordinate, and then a front coordinate from the orthogonality condition. By this definition, the direction of wave propagation almost coincides with that of the ray coordinate; therefore, the parabolic equation in this coordinate system is expected to be valid for a wide range of incident wave condition and structure arrangement.

2.2 Ray-front Coordinates

Consider curvilinear coordinates (ξ, η) as shown in Fig. 2. The directions of ξ and η respectively represent those of wave rays and fronts following Huygens' principle; thus the direction, α, of the ξ-coordinate can be determined by the following ray equation in the refraction problem:

$$\frac{1}{h_\xi}\frac{\partial \alpha}{\partial \xi} = \frac{1}{K}\frac{1}{h_\eta}\frac{\partial K}{\partial \eta} \tag{1}$$

where h_ξ and h_η are the scale factors of the curvilinear coordinates; hence $h_\xi d\xi$ and $h_\eta d\eta$ represent the lengths of short line elements. The quantity K is the wave number and usually can be calculated from the given local water depth by the dispersion relation. However, wave rays often intersects with each other for complicated bottom topographies; thus K is calculated from a slightly-modified water depth. The modified bottom topography may be taken as that with straight and parallel bottom contours, since a slight difference between the directions of the coordinate and wave propagation is allowed in the derivation of a parabolic equation. By this modification, the intersection of wave rays does not occur. The scales of axes are arbitrary; hence, we can take $h_\xi = h_\eta = 1/K$ without loss of generality, with which the values of the coordinates have the dimension of phase angle.

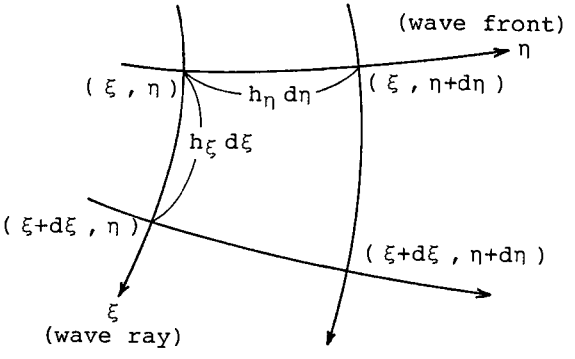

Fig. 2 Curvilinear coordinates

Once α is determined by Eq. (1), the position (x, y) along the ξ-coordinate can be calculated by

$$\frac{1}{h_\xi}\frac{d}{d\xi}(x, y)=(\cos\alpha, \sin\alpha) \tag{2}$$

If the position of a point on a front line is given, the position of the point advanced along a ray to the next shoreward front line can be determined by numerically integrating Eqs. (1) and (2) by the Runge-Kutta-Gill method. Then the η-axis can be determined as the line of ξ = const.

2.3 Parabolic Approximation

Berkhoff (1972) derived the mild-slope equation which governs the combined refraction and diffraction of periodic small-amplitude surface gravity waves over a seabed of a mild slope:

$$\nabla(G\nabla\phi)+k^2G\phi=0 \tag{3}$$

where G = cc_g (c: wave celerity, c_g: group velocity), k is the wave number calculated from the given local water depth by dispersion relation, and ∇ is the differential operator in the horizontal directions. The quantity ϕ represents the complex amplitude of the water surface fluctuation. From ϕ, the water surface fluctuation, ζ, and the velocity potential, Φ, are expressed as

$$\zeta=\phi e^{-i\omega t} \tag{4}$$

$$\Phi=\frac{g}{i\omega}\frac{\cosh k(d+z)}{\cosh kd}\phi e^{-i\omega t} \tag{5}$$

where ω is the angular frequency, g the gravitational acceleration, d the given local water depth, z the vertical coordinate measured upward from the still water level, and t the time.

Equation (3) can be reexpressed in the curvilinear coordinates (ξ, η) as

$$\frac{1}{h_\xi h_\eta}\left\{\frac{\partial}{\partial\xi}\left(G\frac{h_\eta}{h_\xi}\frac{\partial\phi}{\partial\xi}\right)+\frac{\partial}{\partial\eta}\left(G\frac{h_\xi}{h_\eta}\frac{\partial\phi}{\partial\eta}\right)\right\}+k^2G\phi=0 \tag{6}$$

which is an elliptic-type partial differential equation. In the following, we approximate the mild-slope equation (6) to a parabolic equation following Radder (1979).

Equation (6) can be rewritten as

$$\frac{1}{h_\xi}\frac{\partial}{\partial\xi}\left(\frac{1}{h_\xi}\frac{\partial\phi}{\partial\xi}\right)=-\frac{1}{Gh_\eta}\frac{1}{h_\xi}\frac{\partial(Gh_\eta)}{\partial\xi}\frac{1}{h_\xi}\frac{\partial\phi}{\partial\xi}-\left\{\frac{1}{Gh_\xi}\frac{1}{h_\eta}\frac{\partial}{\partial\eta}\left(G\frac{h_\xi}{h_\eta}\frac{\partial}{\partial\eta}\right)+k^2\right\}\phi \tag{7}$$

Here, we assume that ϕ can be splitted into two parts: the complex amplitudes ϕ^+ and ϕ^- due to incident and reflected waves, respectively, i.e.,

$$\phi=\phi^{+}+\phi^{-} \tag{8}$$

$$\phi^{\pm}\sim a^{\pm}\exp\left(\pm i\int kh_{\xi}d\xi\right) \tag{9}$$

From Eqs. (8) and (9), we have

$$\frac{1}{h_{\xi}}\frac{\partial\phi}{\partial\xi}=ik\phi^{+}-ik\phi^{-} \tag{10}$$

Then, we can eliminate ϕ^{-} from Eqs. (8) and (10):

$$\phi^{+}=\frac{1}{2}\phi+\frac{1}{2ik}\frac{1}{h_{\xi}}\frac{\partial\phi}{\partial\xi} \tag{11}$$

By taking the gradient of Eq. (11) in the direction of ξ and substituting Eq. (7), we obtain

$$\frac{1}{h_{\xi}}\frac{\partial\phi^{+}}{\partial\xi}=-\frac{1}{2ik}\left\{\frac{1}{Gh_{\xi}}\frac{1}{h_{\eta}}\frac{\partial}{\partial\eta}\left(G\frac{h_{\xi}}{h_{\eta}}\frac{\partial}{\partial\eta}\right)+k^{2}\right\}\phi$$
$$+\left\{\frac{1}{2}-\frac{1}{2ik^{2}}\frac{1}{h_{\xi}}\frac{\partial k}{\partial\xi}-\frac{1}{2ik}\frac{1}{Gh_{\eta}}\frac{1}{h_{\xi}}\frac{\partial(Gh_{\eta})}{\partial\xi}\right\}\frac{1}{h_{\xi}}\frac{\partial\phi}{\partial\xi} \tag{12}$$

On substituting Eqs. (8) and (10), we have a differential equation which contains ϕ^{+} and ϕ^{-}. Here, we further assume that $|\phi^{+}|>>|\phi^{-}|$, i.e., $\phi^{+}\fallingdotseq\phi$ and $\phi^{-}\fallingdotseq 0$. Thus we finally obtain the following parabolic equation for ϕ:

$$\frac{1}{Gh_{\xi}}\frac{1}{h_{\eta}}\frac{\partial}{\partial\eta}\left(G\frac{h_{\xi}}{h_{\eta}}\frac{\partial\phi}{\partial\eta}\right)+2ik\frac{1}{h_{\xi}}\frac{\partial\phi}{\partial\xi}+\left\{\frac{i}{Gh_{\eta}}\frac{1}{h_{\xi}}\frac{\partial}{\partial\xi}(kGh_{\eta})+2k^{2}\right\}\phi=0 \tag{13}$$

In order to make the change of ϕ slower, we transform the unknown variable from ϕ to ψ as

$$\phi=\psi\exp\left(i\int Kh_{\xi}d\xi\right) \tag{14}$$

Since K is the approximate local wave number, the exponential term in the above equation roughly represents the phase of ϕ; hence, the spatial change of ψ is expected to become slow. On substituting Eq. (14) into Eq. (13), we obtain the following parabolic equation for ψ:

$$\frac{1}{Gh_{\xi}}\frac{1}{h_{\eta}}\frac{\partial}{\partial\eta}\left(G\frac{h_{\xi}}{h_{\eta}}\frac{\partial\psi}{\partial\eta}\right)+2ik\frac{1}{h_{\xi}}\frac{\partial\psi}{\partial\xi}+\left\{\frac{i}{Gh_{\eta}}\frac{1}{h_{\xi}}\frac{\partial}{\partial\xi}(kGh_{\eta})+2k(k-K)\right\}\psi=0 \tag{15}$$

Equation (15) is parabolic; therefore, we can numerically solve it step by step from offshore to onshore if adequate boundary conditions are given. It should be noted that Eqs. (13) and (15) agree with those of Radder (1979) when they are described in Cartesian coordinates.

In deriving parabolic equations, we can adopt slightly different assumptions, obtaining different equations in high-order terms. However, the result of numerical calculation showed that the present parabolic equation has the highest accuracy among several possible equations.

2.4 Physical Interpretation of Parabolic Equation

Following Berkhoff et al. (1982), we separate the amplitude and phase of ϕ as

$$\phi = a e^{i\varepsilon} \tag{16}$$

On substituting Eq. (16) into Eq. (15), we have

$$\frac{1}{h_\xi}\frac{\partial \varepsilon}{\partial \xi} = k - K - \frac{1}{2k}\left(\frac{1}{h_\eta}\frac{\partial \varepsilon}{\partial \eta}\right)^2 + \frac{1}{2akGh_\xi}\frac{1}{h_\eta}\frac{\partial}{\partial \eta}\left(G\frac{h_\xi}{h_\eta}\frac{\partial a}{\partial \eta}\right) \tag{17}$$

$$\frac{1}{h_\xi h_\eta}\left[\frac{\partial}{\partial \xi}(a^2 k G h_\eta) + \frac{\partial}{\partial \eta}\left(a^2 \frac{1}{h_\eta}\frac{\partial \varepsilon}{\partial \eta} G h_\xi\right)\right] = 0 \tag{18}$$

from real and imaginary parts, respectively. Equation (17) can be rewritten as

$$\left(K + \frac{1}{h_\xi}\frac{\partial \varepsilon}{\partial \xi}\right)^2 + \left(\frac{1}{h_\eta}\frac{\partial \varepsilon}{\partial \eta}\right)^2 = k^2 + \left\{k - \left(K + \frac{1}{h_\xi}\frac{\partial \varepsilon}{\partial \xi}\right)\right\}^2 + \frac{1}{aGh_\xi}\frac{1}{h_\eta}\frac{\partial}{\partial \eta}\left(G\frac{h_\xi}{h_\eta}\frac{\partial a}{\partial \eta}\right) \tag{19}$$

Equation (19) corresponds to the eikonal equation in refraction problems but includes the effect of diffraction in the η-direction as seen from the last term on the right hand side.

Since $G \approx \omega c_g/k$, Eq. (18) represents the conservation of wave energy. In the first parentheses, however, the ξ-component of the wave number should appear instead of k itself. Therefore, if the direction cosine in the ξ-direction is significantly less than unity, i.e., the direction of wave propagation is significantly different from the ξ-direction, the error of the present parabolic equation will become large. Usually this does not occur, since the coordinates are determined following Huygens' principle.

2.5 Boundary Condition

The condition of complete reflection is imposed on fixed boundaries; thus the derivative of ϕ in the normal direction of the boundaries becomes zero. This can be expressed in terms of ϕ as

$$\frac{1}{h_\eta}\frac{\partial \phi}{\partial \eta} - \left(\frac{1}{h_\xi}\frac{\partial \phi}{\partial \xi} + iK\phi\right)\tan\delta = 0 \tag{20}$$

where δ denotes the direction angle of the boundary measured from the ξ-direction toward the η-direction.

The first term in the parentheses of Eq. (20) is usually small compared to the second term; therefore, it can be neglected as

$$\frac{1}{h_\eta}\frac{\partial \phi}{\partial \eta} - iK\phi\tan\delta = 0 \tag{21}$$

The accuracy of numerical caculation was higher when Eq. (21) was adopted as the boundary condition than when Eq. (20) was adopted. The reason of this result is not clear, but the error of Eqs. (18) and (21)

may cancel with each other. Hereafter, Eq. (21) will be used for boundary conditions.

For open boundaries, Eq. (21) with $\delta = 0$ was used. This means that the waves propagate in the ξ-direction just by refraction and the gradient in the η-direction is zero. If the open boundaries are located far from structures, they give no influence on the wave field around structures. However, once the disturbance from structures reaches the open boundary, the present condition induces the reflection of the disturbance.

3. PROCEDURE OF NUMERICAL CALCULATION

In order to determine the ray-front coordinates, Eqs. (1) and (2) were integrated by the Runge-Kutta-Gill method. The Crank-Nicholson scheme in which the weights for the old and new front lines are equal was applied to solve the parabolic equation (15). The weights for the two lines in the boundary condition were also taken equal.

The procedure of numerical calculation is summarized as follows:

1) Determine the position of an initial front line and the values of ϕ on the line from Snell's law.

2) Determine the position of the front line at the next step by Eqs. (1) and (2). From the tip of a structure, new wave rays are added as rays 1,2,3 and 5, or 12 and 13 in Fig. 1. If the distance between two adjacent rays exceeds a given value, new rays are also added by interpolation as rays 4,6, and 14 in Fig. 1.

3) Solve the parabolic equation (15) in order to determine the value of ϕ on the new front line.

4) Repeat 2) and 3) until the domain of calculation is covered with the ray-front coordinates.

A FORTRAN program which can be applied to an arbitrary incident wave condition, boundary condition, and bottom topography was developed.

4. RESULTS

4.1 Comparison with Analytical Solutions

In Fig. 3, circles show calculated wave height changes due to refraction. Waves are incident obliquely to a plane sloping beach with a slope of 1/10. In the figure, θ_o denotes the wave angle in deep water, d/L_o the ratio of local water depth to deep-water wavelength, and H/H_o the ratio of local wave height to deep-water wave height. In the numerical calculation shown in this figure, the grid size to wavelength ratio, Δ/L, is 1/20, which was proved to be sufficiently small by numerical experiment. Solid lines indicate wave height

changes obtained by Snell's law. The agreement is good even if the incident wave angle is large.

Next, the diffraction coefficient due to semi-infinite breakwater is examined. Figure 4 shows the diffraction coefficient along the line from A to B and from B to C. Various symbols indicate the results of the present numerical calculations with various grid sizes. The analytical solution by Penny and Price (1952) is shown by a curve. Though the small oscillation from A to B is not accurately reproduced, the agreement is good on the whole. Figure 5 compares the numerical and analytical diffraction coefficients behind a semi-infinite breakwater for various incident wave directions. The agreement is good for a wide range of incident wave direction.

Figure 6 compares the wave height distribution in front of the breakwater. Since the ray-front coordinates are defined from the direction of the incident waves, the ξ-direction can be significantly different from the propagation direction of the reflected waves. Therefore, as seen from the open triangles in Fig. 6(b), the calculated oscillation of wave height differs significantly from the analytical solution. A mirror image technique was employed to improve the accuracy of calculation in the reflective region: 1) the semi-infinite breakwater is first removed, 2) a numerical solution is obtained for a semi-infinite breakwater with θ_0=-90° (this value does not change the result significantly), and 3) the solution is folded along the given semi-infinite breakwater and superimposed. Closed symbols indicate the results; the agreement between the numerical and analytical results become much better.

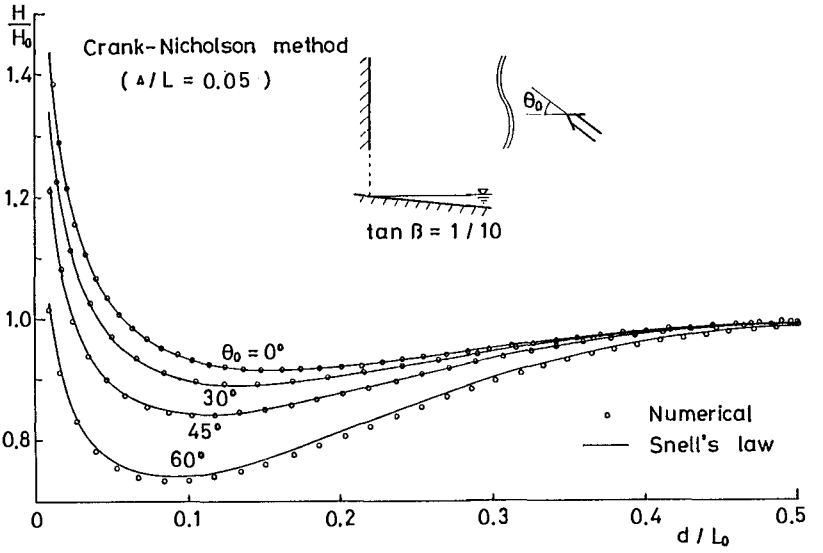

Fig. 3 Comparison of numerical and analytical wave height changes due to refraction.

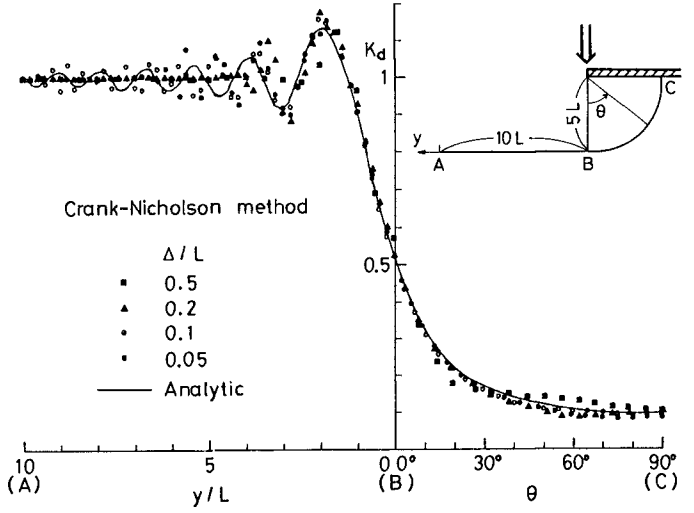

Fig. 4 Effect of grid size on the diffraction coefficient around a semi-infinite breakwater.

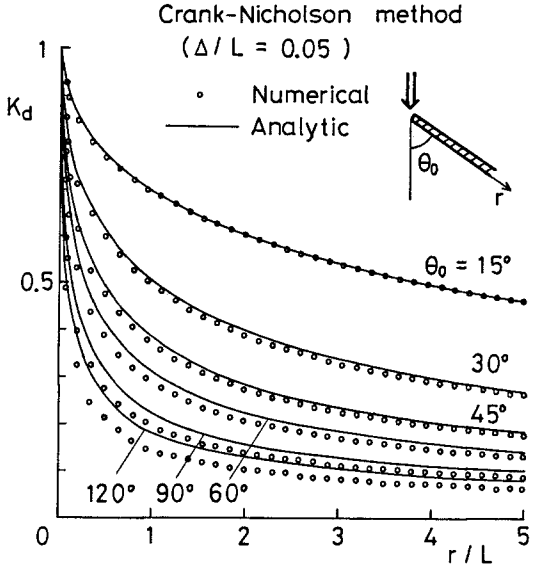

Fig. 5 Comparison of numerical and analytical diffraction coefficients just behind a semi-infinite breakwater.

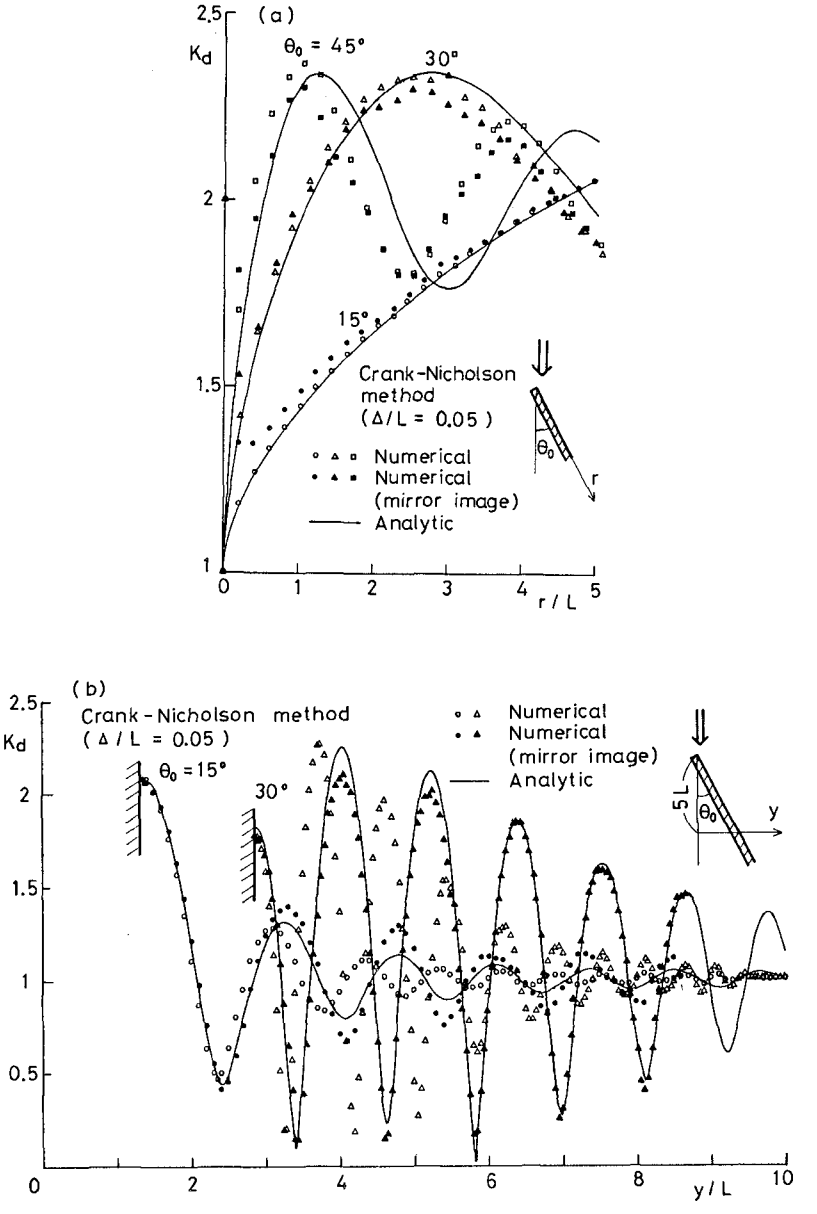

Fig. 6 Comparison of numerical and analytical wave height distributions in front of a semi-infinite breakwater.

4.2 Comparison with Experimental Data

Figure 7 shows the present experimental apparatus. A wave basin which is 9m wide and 9m long was used. As seen in the figure, a plane beach with a slope of 1/15 was attached and breakwaters were arranged on the beach. A flap-type wave maker was set obliquely to the wave basin. Capacitance wave gages were used to measure the water surface fluctuation. The incident wave height, period, and angle were 9.1cm, 0.83s, and 18°, respectively.

Figure 8 compares the calculated and measured wave height distributions from A to A' and from B to B'. The agreement is fairly good. In shallower region, time history of water surface fluctuation becomes asymmetrical due to nonlinear effect; hence comparison was not made.

5. CONCLUSION

Curvilinear coordinates which follow Huygens' principle and are named ray-front coordinates were introduced. In the coordinates, a parabolic equation for combined refraction and diffraction of water waves was derived. Numerical calculation was carried out and the results were compared with available analytical solutions and experimental data.

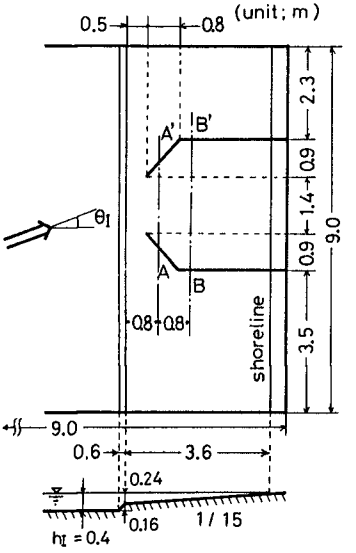

Fig. 7 Experimental apparatus.

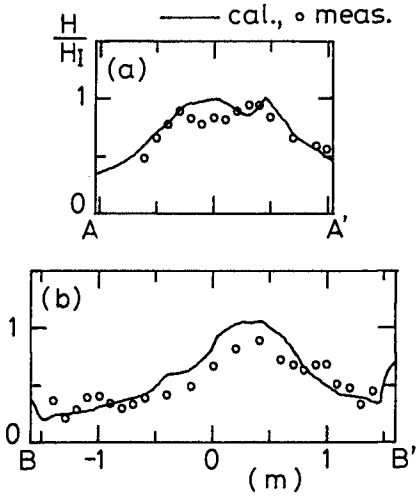

Fig.8 Comparison ofcalculated and measured wave height distributions.

The present method was proved to have a high accuracy for refraction and diffraction of linear water waves. However, in the reflective region, direct application of the parabolic equation yields a significant error because incident and reflected waves exist in the region. The accuracy of the numerical calculation was improved by employing a mirror image technique.

REFERENCES

1) Berkhoff, J. C. W. (1972): Computation of combined refraction-diffraction, Proc. 13th Coastal Eng. Conf., ASCE, pp.471-490.

2) Berkhoff, J. C. W., N. Booy and A. C. Radder (1982): Verification of numerical wave propagation models for simple harmonic linear water waves, Coastal Eng., Vol. 6, pp. 253-279.

3) Dalrymple, R. A., J. T. Kirby and P. A. Hwang (1984): Wave diffraction due to areas of energy dissipation, J. Waterway, Port, Coastal and Ocean Eng., ASCE, Vol. 110, pp. 67-79.

4) Kirby, J. T. and R. A. Dalrymple (1983): A parabolic equation for the combined refraction-diffraction of Stokes waves by mildly varying topography, J. Fluid Mech., Vol. 136, pp. 453-466.

5) Liu, P. L.-F. and T.-K. Tsay (1984): Refraction-diffraction model for weakly nonlinear water waves, J. Fluid Mech., Vol. 141, pp. 265-274.

6) Liu, P. L.-F. and T.-K. Tsay (1985): Numerical prediction of wave transformation, J. Waterway, Port, Coastal and Ocean Eng., ASCE, Vol. 111, pp. 843-855.

7) Penny, W. G. and A. T. Price (1952): The diffraction theory of sea waves and the shelter afforded by breakwaters, Phil. Trans. Roy. Soc. Lond., Ser. A, Vol. 244, pp. 236-253.

8) Radder, A. C. (1979): On the parabolic equation method for water-wave propagation, J. Fluid Mech., Vol. 72, pp. 373-384.

9) Tsay, T.-K. and P. L.-F. Liu (1982): Numerical solution of water-wave refraction and diffraction problems in the parabolic approximation, J. Geophys. Res., Vol. 87, pp. 7932-7940.

CHAPTER 25

BREAKING CRITERION ON NON-UNIFORMLY SLOPING BEACH

Takashi Izumiya* and Masahiko Isobe**

ABSTRACT

This paper deals with the breaker height on non-uniformly sloping beaches. A large number of experiments were carried out to obtain a breaking criterion on bar and step-type beaches. Based on the experimental data, a relationship among the breaker height, water depth, and wave period is investigated for various bottom configurations. As a result, the breaker height on non-uniformly sloping beaches is found to be well predicted by substituting an equivalent bottom slope in Goda's breaker index which has been obtained for uniformly sloping beaches. The equivalent bottom slope is defined as the mean slope in the distance of $5h_B$ offshoreward from a breaking point, where h_B denotes the water depth at the breaking point. The method for calculating the breaker height on natural beaches is also presented.

INTRODUCTION

The determination of the breaking point and breaker height is indispensable for planning and designing coastal structures. Theoretical investigations on the limiting wave condition of permanent waves on a horizontal bottom have been extensively done, for example, by Miche (1944), Hamada (1951), Yamada and Shiotani (1968), Schwartz (1974), and Cokelet (1977). However, there seems to be no theoretical treatment for the breaking height on sloping beaches.

Goda (1970) re-analyzed various laboratory data on the breaker height obtained by several researcheres, and proposed a breaker index. For bottom slopes less than 1/50, the index was determined to be coincident with the limiting wave condition presented by Yamada and Shiotani (1968). Since a large number of data were carefully re-analyzed, the breaker index is considered to be sufficiently reliable. However, in applying the index to the waves on non-uniformly sloping beaches such as natural beaches, it is not clear how to determine the representative value of the beach slope. This problem must be solved on the basis of empirical data because no theory adequately describes the breaking condition for such complicated bottom profiles.

---

* Research Associate, Department of Civil Engineering, Yokohama National University, 156 Tokiwadai, Hodogaya-ku, Yokohama, 240 JAPAN

** Associate Professor, Ditto

Therefore, we conducted a large number of experiments on the breaker height over non-uniformly sloping beaches. The aims of the experiments are

(1) To investigate the effect of change in bottom slope on breaker height.

(2) To propose a method to evaluate an equivalent bottom slope in order to apply Goda's breaker index to the waves breaking on non-uniformly sloping beaches.

First, the validity of Goda's breaker index is verified for uniformly sloping beaches. It is confirmed that in spite of some scatter in the data, the breaker index agrees well with experimental results. Next, from the measured values of breaker height, water depth and wave period, the apparent values of bottom slope which satisfy the equation of Goda's breaker index are evaluated. Then, the equivalent bottom slopes are approximated by a simple linear equation. The breaker height is estimated by using the equivalent bottom slope in Goda's breaker index, and compared with the experimental data.

EXPERIMENTAL SETUP AND PROCEDURE

The experiments were carried out by using a wave flume of 17m long, 0.6m wide, and 0.55m deep. Various bottom configurations were built in the wave flume by connecting steel segments, each of 1m long. The bottom profile can be changed by adjusting the lengths of columns of steel segments. For each bottom profile, regular waves with period of 0.7s to 1.6s were generated. The total number of cases amount to 670. Wave height was measured by two capacitance wave gages. The breaker point was determined as the point where the wave height was maximum.

EXPERIMENTAL RESULTS

Figure 1 compares Goda's breaker index with the experimental results for uniformly sloping beaches. In the figure, H_B denotes the breaker height, h_B the water depth at the breaking point, Lo ($=gT^2/2\pi$, g: gravitational acceleration, T: wave period) the wavelength of small amplitude waves in deep water, and S the bottom slope. The vertical axis is the breaker height to water depth ratio, H_B/h_B, and the horizontal axis is the relative water depth , h_B/Lo. The solid lines show Goda's breaker index for the bottom slopes of 1/10, 1/20, and 1/30. The open, semiclosed and closed circles denote the experimental data for the slopes of 1/10, 1/20, and 1/30, respectively. Although the experimental data for the slope of 1/10, having some scatter, show smaller values than those of Goda's breaker index, Fig. 1 shows, in general, a good agreement between the breaker index and the experimental data.

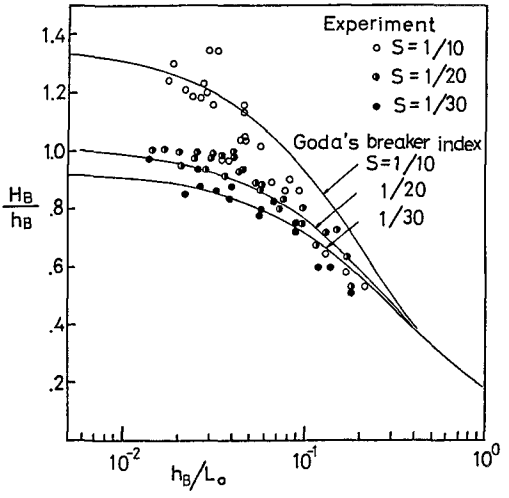

Fig. 1 Breaker index for uniformly sloping beaches.

In case of a step type beach as shown in Fig. 2, Goda's breaker index can not be applied without modification. If the incident wave height is large, the waves may break on the offshore slope S_1. As the incident wave height becomes smaller, the waves tend to break on the onshore slope S_2. In the latter case, the breaker height may be significantly influenced by the offshore slope S_1.

Figure 3 shows the relationship between the breaker height to water depth ratio and the relative water depth for bilinear bottom profiles (offshore slope S_1=1/20, onshore slope S_2=0 for Fig. 3-(a), and S_1=1/20, S_2=1/10 for Fig. 3-(b)). The curves represent Goda's breaker index for the bottom slopes, $S=S_1$ and S_2. The semiclosed circles and triangles in Fig. 3-(a) respectively denote the data for waves breaking on the slopes S_1=1/20 and S_2=0. The semiclosed squares and circles in Fig. 3-(b) respectively show the data for waves breaking on the slopes S1=1/10 and S2=1/20. In spite of some scatter in the data, most of the data lie between the two curves. This implies that the breaker height on the onshore slope is affected by the offshore slope.

In order to estimate the effect of the offshore slope on the breaker height, an equivalent bottom slope was defined and compared with the real slope. The equivalent slope, S^*, is defined as the slope which satisfies Goda's breaker index, which is approximately expressed as (Goda,1975)

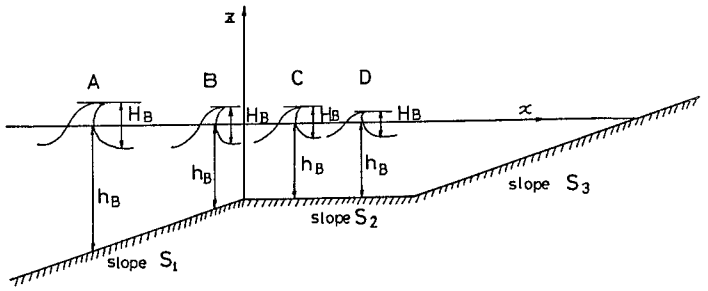

Fig. 2 Wave breaking on a step-type beach.

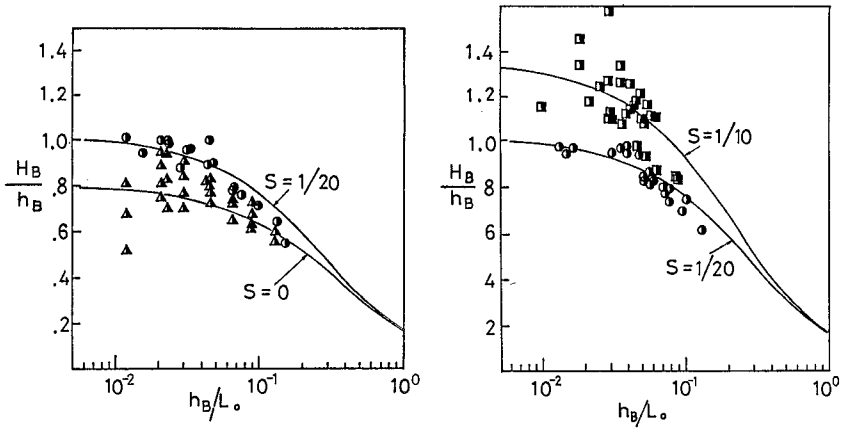

Fig. 3 Breaker index for step-type bottom profiles.

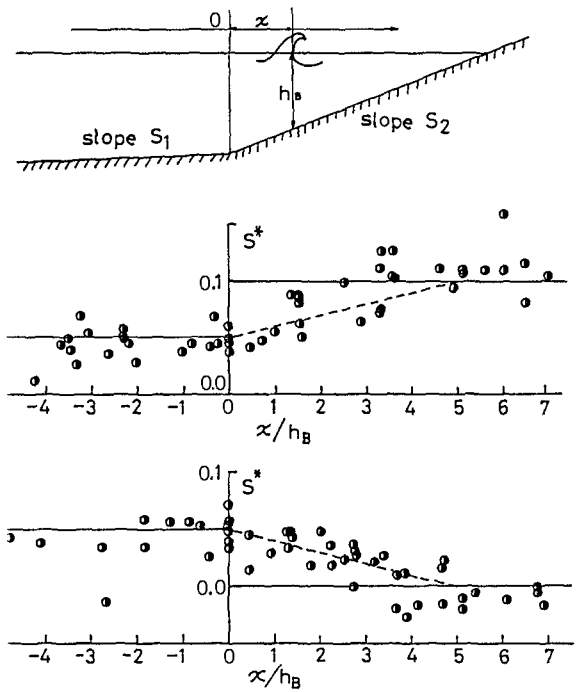

Fig. 4 On-offshore distributions of the equivalent bottom slope.

$$\frac{H_B}{h_B} = A\left\{1-\exp\left[-1.5\frac{\pi h_B}{L_o}(1+15S^{4/3})\right]\right\}\Big/\left(\frac{h_B}{L_o}\right) \qquad (1)$$

where A takes the value of 0.17 for regular waves. From Eq. (1), the equivalent bottom slope, S^*, is expressed by

$$S^* = \left\{-\frac{1}{15}\left[\frac{\ell n\left(1-\frac{1}{A}\frac{H_B}{h_B}\frac{h_B}{L_o}\right)}{1.5\pi(h_B/L_o)}+1\right]\right\}^{3/4} \qquad (2)$$

If we substitute the measured values of H_B, h_B and T into Eq. (2), we obtain a value of the equivalent bottom slope. Fig. 4 shows the on-offshore distribution of the equivalent bottom slope. The axis of the abscissa is normalized by the water depth h_B. A point x=0 is the point where the bottom slope changes. The middle figure is for the slopes of S_1=1/20 and S_2=1/10. The lower figure is for the slopes of S_1=1/20 and S_2=0. For waves breaking on the offshore slope, the values of the

equivalent bottom slope are about 0.05 as an average relation, although there is a some scatter in the data. For waves breaking on the slope S_2 , the values of S^* changes almost linearly with the increase of non-dimensional distance. It is also found that the values of S^* tend to approach the values of actual slope S_2 in the vicinity of the point $x/h_B=5$. This means that for waves breaking onshoreward of the point of $x/h_B=5$, the breaker heights are no longer affected by the offshore slope S_1. In the transition zone, the value of the equivalent bottom slope can be approximated by the linear relationship:

$$S^*=S_1+(S_2-S_1)*x/5h_B \qquad (3)$$

The equivalent bottom slope expressed by Eq. (3) is illustrated by a broken line in Fig. 5. For a bar type beach, if waves break in the trough, the breaker height must be more influenced by the water depth at the top of the bar, h_{min}, than by the breaking water depth. Therefore, h_{min} was used to define the equivalent slope:

$$S^*=\left\{-\frac{1}{15}\left[\frac{\ell n\left(1-\frac{1}{A}\frac{H_B}{h_{min}}\frac{h_{min}}{L_o}\right)}{1.5\pi(h_{min}/L_o)}+1\right]\right\}^{3/4} \qquad (4)$$

If the quantity in the curly brackets in Eq. (4) is negative, the value of S^* should take the opposite sign. It is found that Eq. (1) is nearly satisfied by substituting the equivalent bottom slope even for bar-type beaches. The equivalent bottom slope for a bar-type beach is illustrated by the broken line in Fig. 6.

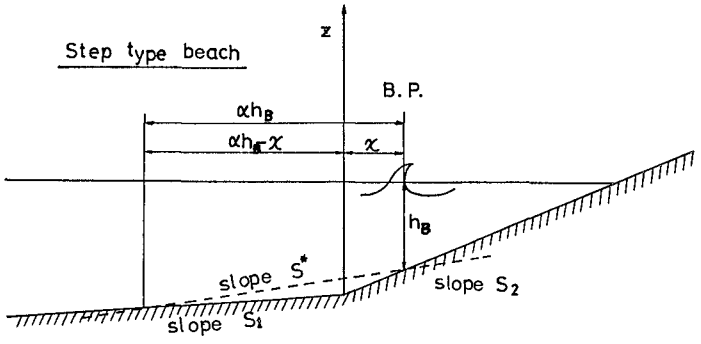

$$S^*=\frac{(\alpha h_B-x)S_1+xS_2}{\alpha h_B}=\frac{(\alpha-X)S_1+XS_2}{\alpha}$$

$$X=x/h_B \qquad \alpha=5$$

Fig. 5 Definition sketch of the equivalent bottom slope for a step-type beach.

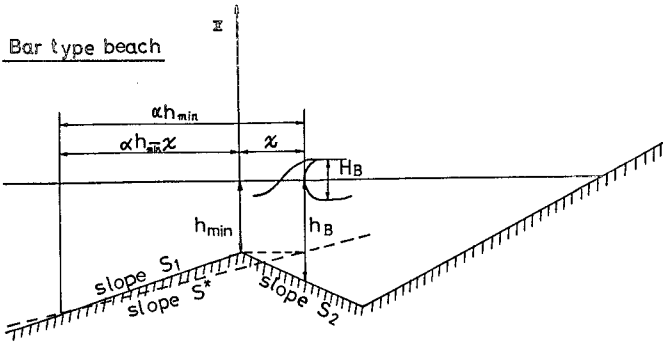

Fig. 6 Definition sketch of the equivalent bottom slope for a bar-type beach.

METHOD FOR CALCULATING BREAKER HEIGHT

On the basis of the above discussion, the method for calculating breaker height is summarized as follows:

(1) For a given site, calculate the mean slope in the range of $5h_B$ distant from that point.

(2) Calculate the breaker height, H_B, using Eq. (1) with use of the water depth, h_B, deepwater wavelength, Lo, and equivalent bottom slope S^*. For a bar-type beach, use the minimum water depth, h_{min} in stead of h_B.

Fig. 7 shows a comparison between the measured and calculated values of the breaker height for step-type beaches. The agreement between them is fairly good. For bar-type beaches, the comparison between them is shown in Fig. 8. The closed circles are for waves breaking on the offshore slope of a bar and the open circles are for waves breaking on the anti-slope of a bar. These figures show that the breaker height is well predicted by the present model.

For a natural beach, the procedure for calculating the breaker height is essentially the same as the procedure stated above. The schematic illustration is shown in Fig. 9.

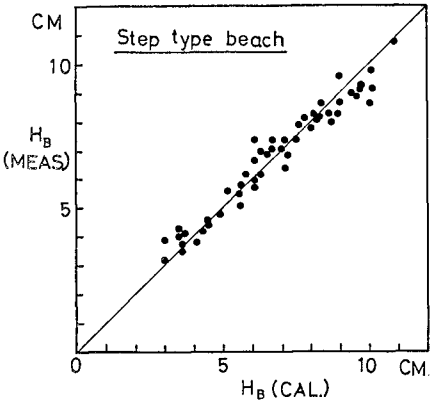

Fig. 7 Comparison between the measured and calculated values of breaker height for step-type beaches.

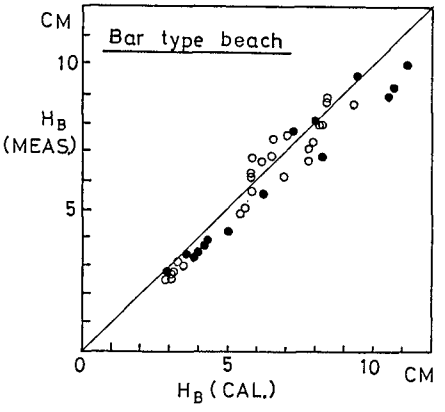

Fig. 8 Comparison between the measured and calculated values of breaker height for bar-type beaches.

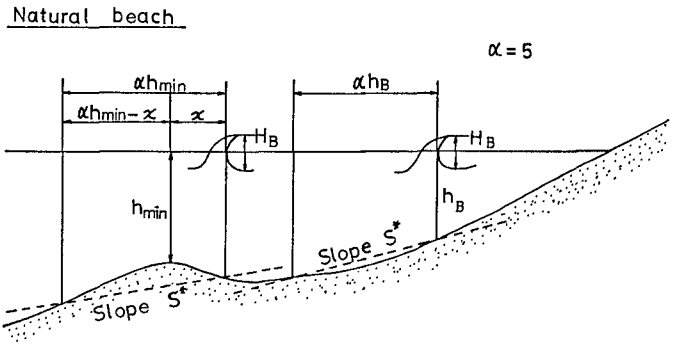

Fig. 9 Definition sketch of the equivalent bottom slope for a natural beach

CONCLUDING REMARKS

A large number of experiments were carried out in order to obtain a breaking criterion on non-uniformly sloping beaches. From the measured breaker height, water depth, and wave period, the equivalent bottom slope was evaluated by using Goda's breaker index. The spatial change of the equivalent bottom slope was examined; then it was found that the equivalent bottom slope can be determined as the mean slope in the distance of five times the water depth from a breaking point. Therefore, the breaker height on a non-uniformly sloping beach, can be predicted by substituting the equivalent bottom slope in Goda's breaker index. However, the applicability of the present model is limited because all of the data were obtained from laboratory experiments with monochromatic waves. Therefore, additional verification is necessary for irregular waves breaking on a natural beach.

ACKNOWLEDGEMENT

The authors would like to express their thanks to Mr. H. Saotome (Penta Ocean Co. Ltd.) and Mr. K. Tachibana(Pasuko Co. Ltd.) for the assistance in the laboratory experiments.

REFERENCES

(1) Cokelet, E. D. (1977) : Steep gravity waves in water of arbitrary uniform depth, Phil. Trans. Roy. Soc. Lond., Ser. A, Vol. 286, pp. 183-230.

(2) Goda, Y. (1970) : A synthesis of breaker indices, Trans. Japan Soc. Civil Engrs., Vol. 2, Part 2, pp. 227-230.

(3) Goda, Y. (1975) : Irregular wave deformation in the surf zone, Coastal Eng. in Japan, Vol. 18, pp. 13-26.

(4) Hamada, T. (1951) : Breakers and beach erosion, Rept. Trans. Tech. Res. Inst., No. 1, 165 p..

(5) Miche, R. (1944) : Mouvements ondulatoirs des mers en profondeur constante on decroissant, Annals des Points et Chausses, 114 pp. 25-78, 131-164, 270-292.

(6) Schwartz, L.W. (1974) : Computer extension and analytic continuation of Stokes' expansion for gravity waves, J. Fluid Mech. Vol. 62, pp. 553-578.

(7) Yamada, H. and T. Shiotani (1968) : On the highest water waves of permanent type, Bull. Disaster Prevention Res. Inst., Kyoto Univ., Vol. 18, Part 2, No. 135, pp. 1-22.

CHAPTER 26

Applications on Non-linear Wave Combination

J.T. Juang*

Due to the special bathymetry in Taiwan Strait, the waves off the western coast of Taiwan are considered to be composed of two-source wave system. One propagates from the central part of the Strait named main wave, and the other is generated by the local wind known as local wave which occurs along the shore. After the combination and the transformation procedure from these two-nonlinear-source wave system, the wave height distribution in Taiwan Strait should be modified. A comparison of the wave height distributions based on the present proposed method with the field data indicates that the present method yields a better result than other theorems. Furthermore, the result of application of two non-linear wave theorem to wave prediction are also presented.

Introduction

In a previous paper[11], the author proposed a theoretical expression for the wave height distribution, which was combined by using two linear source-wave system. At about the same time, Chen et.al.[1] investigated the effect of nonlinearity on the distributions of surface elevation and wave heights of random sea. In that study, it was found that the wave height distribution is effected by wave steepness and the tendencies biased toward the left and peaked toward the middle from Rayleigh distribution ($\delta_r=0$) as the value of nonlinear factor δ_r increases. Longuet-Higgins[7] also proposed a wave height distribution which was based on the joint distribution of wave periods and amplitudes in a random wave field. His wave height distribution was affected by the well-known spectral width parameter. Both of their approaches are based on single non-linear wave theorem. However, for the case where the sea wave is composed of different source-wave system, its wave height distribution should be changed. Therefore, following the same procedures as described in[11] , a two non-linear wave combination theorem was proposed.

Non-linear waves combination

According to the single non-linear wave theorem [1], the wave height distribution can be calculated by the following formula:

*Asso. Prof., Dept. of Civil Engineering, National Central University, Chung-li City, Taiwan, Rep. of China.

$$P(H)=\frac{\pi}{2}D_0^2\cdot H\cdot\left[1+\frac{D_2}{4}\cdot H^2+\left(\frac{3}{64}D_4+\frac{D_2^2}{128}\right)H^4+\frac{1}{512}D_2D_4\cdot H^6\right.$$

$$\left.+\frac{3}{32768}D_4^2\cdot H^8\right]\cdot\exp\left(-\frac{H^2}{8\overline{\zeta^2}}\right) \qquad \cdots\cdots(1)$$

In the above formula, the values of the coefficients D_i, which are functions of the root-mean-sguare of the wave steepness δ_r, are:

$$D_0=\frac{1}{\sqrt{2\pi\overline{\zeta^2}}}\left[\frac{5}{8}+\frac{1}{8}\cdot\frac{3+8(\pi\delta_r)^2\left[1-(\pi\delta_r)^2\right]^2}{\left\{1+(\pi\delta_r)^2\left[1-(\pi\delta_r)^2\right]^2\right\}^2}\right] \qquad \cdots\cdots(2)$$

$$D_1=-\frac{6\sqrt{2\pi}}{(\overline{\zeta^2})^{1/2}}\cdot\frac{\frac{3}{8}(\pi\delta_r)\left[1-(\pi\delta_r)^2\right]+\frac{1}{4}(\pi\delta_r)^3\left[1-(\pi\delta_r)^2\right]^3}{5+\frac{3+8(\pi\delta_r)^2\left[1-(\pi\delta_r)^2\right]^2}{\left\{1+(\pi\delta_r)^2\left[1-(\pi\delta_r)^2\right]^2\right\}^2}}$$

$$\cdot\frac{1}{\left\{1+(\pi\delta_r)^2\left[1-(\pi\delta_r)^2\left[1-\pi\delta_r)^2\right]^2\right\}^{3/2}} \qquad \cdots\cdots(3)$$

$$D_2=-\frac{2}{\overline{\zeta^2}}\cdot(\pi\delta_r)^2\left[1-(\pi\delta_r)^2\right]^2\left\{2-3(\pi\delta_r)^2\left[1-(\pi\delta_r)^2\right]^2\right\}$$

$$/\left[5+\frac{3+8(\pi\delta_r)^2\left[1-(\pi\delta_r)^2\right]^2}{\left\{1+(\pi\delta_r)^2\left[1-(\pi\delta_r)^2\right]^2\right\}^2}\right]\cdot\left\{1+(\pi\delta_r)^2\left[1-(\pi\delta_r)^2\right]^2\right\}^2 \cdots(4)$$

$$D_3=-\frac{D_1}{3\overline{\zeta^2}} \qquad \cdots\cdots(5)$$

$$D_4=\frac{D_2}{6\overline{\zeta^2}} \qquad \cdots\cdots(6)$$

From the above eguation, it can be found that as soon as δ_r approaches to zero, the distribution of the wave height will become Rayleigh's.

However, when the combination of two non-linear waves are considered, the above equation can be modified as

$$P(H)=u_{1,i}\cdot H\cdot\exp\left(-\frac{H^2}{u_{6,i}}\right)+u_{2,i}\cdot H^3\cdot\exp\left(-\frac{H^2}{u_{6,i}}\right)$$

$$+u_{3,i}\cdot H^5\cdot\exp\left(-\frac{H^2}{u_{6,i}}\right)+u_{4,i}\cdot H^7\cdot\exp\left(-\frac{H^2}{u_{6,i}}\right)$$

$$+u_{5,i}\cdot H^9\cdot\exp\left(-\frac{H^2}{u_{6,i}}\right) \qquad \cdots\cdots(7)$$

$$u_{1,i} = \frac{\pi}{2} D_{0,i}^2 \qquad \cdots\cdots(8)$$

$$u_{2,i} = \frac{1}{4} D_{2,i}^2 \cdot u_{1,i} \qquad \cdots\cdots(9)$$

$$u_{3,i} = \left(\frac{3}{64} D_{4,i} + \frac{D_{2,i}^2}{128}\right) \cdot u_{1,i} \qquad \cdots\cdots(10)$$

$$u_{4,i} = \frac{1}{512} D_{2,i} \cdot D_{4,i} \cdot u_{1,i} \qquad \cdots\cdots(11)$$

$$u_{5,i} = \frac{3}{32768} D_{4,i}^2 \cdot u_{1,i} \qquad \cdots\cdots(12)$$

$$u_{6,i} = 8\overline{\zeta_i^2} \qquad \cdots\cdots(13)$$

In the above formulas, $U_{1,i}, U_{2,i}, \ldots, U_{5,i}$ are the coefficients and $U_{6,i}$ are the wave energy of these two-sour-ce waves where i=1 stands for the refracted wave and i=2 represents the local wave.

Since the wave energy is proportional to the square of the wave height, we have

$$y = H^2 \quad , \quad dy = 2HdH \quad , \quad \frac{dH}{dy} = \frac{1}{2H}$$

After transformation from eq.(7), the distribution of wave energy becomes

$$P(y) = \frac{dH}{dy} P(H) = \frac{1}{2\sqrt{y}} \cdot P(H)$$

$$= \frac{u_1}{2} \exp\left(-\frac{y}{u_6}\right) + \frac{u_2}{2} y \cdot \exp\left(-\frac{y}{u_6}\right) + \frac{u_3}{2} \cdot y^2$$

$$\cdot \exp\left(-\frac{y}{u_6}\right) + \frac{u_4}{2} \cdot y^3 \cdot \exp\left(-\frac{y}{u_6}\right) + \frac{u_5}{2} \cdot y^4 \cdot \exp\left(-\frac{y}{u_6}\right) \cdots\cdots(14)$$

Under the assumption that the total energy of the combined wave is the sum of the energy of the wave associated with each source, that is,

$$z = y_1 + y_2 \qquad y_2 = z - y_1$$

the Jacobian of this transformation is

$$|J| = \begin{vmatrix} \frac{\partial y_2}{\partial z} & \frac{\partial y_2}{\partial y_1} \\ \frac{\partial y_1}{\partial z} & \frac{\partial y_1}{\partial y_1} \end{vmatrix} = \begin{vmatrix} 1 & -1 \\ 0 & 1 \end{vmatrix} = 1$$

The energy distribution for the refracted and the local wave can then be found, respectively, as

$$P(y_1) = \left[\frac{u_{1,1}}{2} + \frac{u_{2,1}}{2} y_1 + \frac{u_{3,1}}{2} \cdot y_1^2 + \frac{u_{4,1}}{2} \cdot y_1^3 + \frac{u_{5,1}}{2} \cdot y_1^4\right] \cdot \exp\left(-\frac{y_1}{u_{6,1}}\right) \cdots (15)$$

$$P(y_2) = \left[\frac{u_{1,2}}{2} + \frac{u_{2,2}}{2} \cdot y_2 + \frac{u_{3,2}}{2} \cdot y_2^2 + \frac{u_{4,2}}{2} \cdot y_2^3 + \frac{u_{5,2}}{2} \cdot y_2^4\right] \cdot \exp\left(-\frac{y_2}{u_{6,2}}\right) \cdots (16)$$

Since both distributions are mutually independent, we can obtain

$$P(z, y_1) = P(y_1, y_2) \cdot |J| = P(y_1) \cdot P(y_2) = P(y_1) \cdot P(z - y_1)$$

$$P(z) = \int_0^z P(z, y_1)\, dy_1 = \int_0^z P(y_1) \cdot P(z - y_1) \cdot dy_1 \quad \cdots (17)$$

Substituting equs.(15) and (16) into eq.(17), we have

$$P(z) = \int_0^z \left[\frac{u_{1,1}}{2} + \frac{u_{2,1}}{2} \cdot y_1 + \frac{u_{3,1}}{2} \cdot y_1^2 + \frac{u_{4,1}}{2} \cdot y_1^3 + \frac{u_{5,1}}{2} \cdot y_1^4\right]$$

$$\cdot \left[\frac{u_{1,2}}{2} + \frac{u_{2,2}}{2} \cdot y_2 + \frac{u_{3,2}}{2} \cdot y_2^2 + \frac{u_{4,2}}{2} \cdot y_2^3 + \frac{u_{5,2}}{2} \cdot y_2^4\right]$$

$$\cdot \exp\left[-\frac{y_1}{u_{6,1}} - \frac{y_2}{u_{6,2}}\right] \cdot dy_1$$

$$= \int_0^z A_1 \cdot A_2 \cdot \exp\left(-\frac{z}{u_{6,2}}\right) \cdot \exp(u \cdot y_1) \cdot dy_1 \quad \cdots (18)$$

$$A_1 = \frac{u_{1,1}}{2} + \frac{u_{2,1}}{2} \cdot y_1 + \frac{u_{3,1}}{2} \cdot y_1^2 + \frac{u_{4,1}}{2} \cdot y_1^3 + \frac{u_{5,1}}{2} \cdot y_1^4 \quad \cdots (19)$$

$$A_2 = B_1 - B_2 \cdot y_1 + B_3 \cdot y_1^2 - B_4 \cdot y_1^3 + B_5 \cdot y_1^4 \quad \cdots (20)$$

$$u = \frac{u_{6,1} - u_{6,2}}{u_{6,1} \cdot u_{6,2}} \quad \cdots (21)$$

$$B_1 = \frac{1}{2}(u_{1,2} + u_{2,2} \cdot z + u_{3,2} \cdot z^2 + u_{4,2} \cdot z^3 + u_{5,2} \cdot z^4) \quad \cdots (22)$$

$$B_2 = \frac{1}{2}\left(u_{2,2} + 2u_{3,2} \cdot z + 3u_{4,2} \cdot z^2 + 4u_{5,2} \cdot z^3 \right) \quad \cdots\cdots(22)$$

$$B_3 = \frac{1}{2}\left(u_{3,2} + 3u_{4,2} \cdot z + 6u_{5,2} \cdot z^2 \right) \quad \cdots\cdots(24)$$

$$B_4 = \frac{1}{2}\left(u_{4,2} + 4u_{5,2} \cdot z \right) \quad \cdots\cdots(25)$$

$$B_5 = \frac{1}{2} u_{5,2} \quad \cdots\cdots(26)$$

$$\begin{aligned} A_1 \cdot A_2 = & \frac{1}{2}\left[u_{1,1} + u_{2,1} \cdot y_1 + u_{3,1} \cdot y_1^2 + u_{4,1} \cdot y_1^3 + u_{5,1} \cdot y_1^4 \right] \\ & \cdot \left[B_1 - B_2 \cdot y_1 + B_3 \cdot y_1^2 - B_4 \cdot y_1^3 + B_5 \cdot y_1^4 \right] \\ = & c_1 + c_2 \cdot y_1 + c_3 \cdot y_1^2 + c_4 \cdot y_1^3 + c_5 \cdot y_1^4 + c_6 \cdot y_1^5 \\ & + c_7 \cdot y_1^6 + c_8 \cdot y_1^7 + c_9 \cdot y_1^8 \end{aligned} \quad \cdots\cdots(27)$$

$$c_1 = \frac{1}{2}\left(u_{1,1} \cdot B_1 \right)$$

$$c_2 = \frac{1}{2}\left(u_{2,1} \cdot B_1 - u_{1,1} \cdot B_2 \right)$$

$$c_3 = \frac{1}{2}\left(u_{3,1} \cdot B_1 - u_{2,1} \cdot B_2 + u_{1,1} \cdot B_3 \right)$$

$$c_4 = \frac{1}{2}\left(u_{4,1} \cdot B_1 - u_{3,1} \cdot B_2 + u_{2,1} \cdot B_3 - u_{1,1} \cdot B_4 \right)$$

$$c_5 = \frac{1}{2}\left(u_{5,1} \cdot B_1 - u_{4,1} \cdot B_2 + u_{3,1} \cdot B_3 - u_{2,1} \cdot B_4 + u_{1,1} \cdot B_5 \right)$$

$$c_6 = -\frac{1}{2}\left(u_{5,1} \cdot B_2 - u_{4,1} \cdot B_3 + u_{3,1} \cdot B_4 - u_{2,1} \cdot B_5 \right)$$

$$c_7 = \frac{1}{2}\left(u_{5,1} \cdot B_3 - u_{4,1} \cdot B_4 + u_{3,1} \cdot B_5 \right)$$

$$c_8 = -\frac{1}{2}\left(u_{5,1} \cdot B_4 - u_{4,1} \cdot B_5 \right)$$

$$c_9 = \frac{1}{2}\left(u_{5,1} \cdot B_5 \right) \quad \cdots\cdots(28)$$

Substituting eq.(27) into eq.(18), we have

$$\begin{aligned} P(z) = e^{\left(-\sqrt{u_{6,2}}\right)\cdot} \{ & c_1 \int_0^z e^{(u \cdot y_1)}\, dy_1 + c_2 \int_0^z y_1 \cdot e^{(u \cdot y_1)} \cdot dy_1 \\ & + c_3 \int_0^z y_1^2 \cdot e^{(u \cdot y_1)} \cdot dy_1 + c_4 \int_0^z y_1^3 \cdot e^{(u \cdot y_1)} \cdot dy_1 \end{aligned}$$

$$+c_5\int_0^z y_1^4\cdot e^{(u\cdot y_1)}\cdot dy_1+c_6\int_0^z y_1^5\cdot e^{(u\cdot y_1)}\cdot dy_1+c_7\int_0^z y_1^6\cdot e^{(u\cdot y_1)}\cdot dy_1$$

$$+c_8\int_0^z y_1^7\cdot e^{(u\cdot y_1)}\cdot dy_1+c_9\int_0^z y_1^8\cdot e^{(u\cdot y_1)}\cdot dy_1\} \qquad \cdots\cdots\cdots\cdots(29)$$

$$\int_0^z e^{(u\cdot y_1)}dy_1=\frac{e^{uz}}{u}-\frac{1}{u}$$

$$\int_0^z y_1\cdot e^{(u\cdot y_1)}dy_1=\frac{e^{uz}}{u^2}(uz-1)+\frac{1}{u^2}$$

$$\int_0^z y_1^2\cdot e^{(u\cdot y_1)}\cdot dy_1=\frac{e^{uz}}{u^3}(u^2z^2-2uz+2)-\frac{2}{u^3}$$

$$\int_0^z y_1^3\cdot e^{(u\cdot y_1)}\cdot dy_1=\frac{e^{uz}}{u^4}(u^3z^3-3u^2\cdot z^2+6uz-6)+\frac{6}{u^4}$$

$$\int_0^z y_1^4\cdot e^{(u\cdot y_1)}\cdot dy_1=\frac{e^{uz}}{u^5}(u^4\cdot z^4-4u^3\cdot z^3+12u^2\cdot z^2-24u\cdot z+24)-\frac{24}{u^5}$$

$$\int_0^z y_1^5\cdot e^{(u\cdot y_1)}\cdot dy_1=\frac{e^{uz}}{u^6}(u^5\cdot z^5-5u^4\cdot z^4+20u^3z^3-60u^2\cdot z^2+120uz-120)+\frac{120}{u^6}$$

$$\int_0^z y_1^6\cdot e^{(u\cdot y_1)}\cdot dy_1=\frac{e^{uz}}{u^7}(u^6\cdot z^6-6u^5\cdot z^5+30u^4\cdot z^4-120u^3\cdot z^3+360u^2\cdot z^2$$

$$-720uz+720)-\frac{720}{u^7}$$

$$\int_0^z y_1^7\cdot e^{(u\cdot y_1)}\cdot dy_1=\frac{e^{uz}}{u^8}(u^7\cdot z^7-7u^6z^6+42u^5z^5-210u^4\cdot z^4+840u^3\cdot z^3$$

$$-2520u^2\cdot z^2+5040uz-5040)+\frac{5040}{u^8}$$

$$\int_0^z y_1^8\cdot e^{(u\cdot y_1)}\cdot dy_1=\frac{e^{uz}}{u^9}(u^8\cdot z^8-8u^7\cdot z^7+56u^6\cdot z^6-336u^5\cdot z^5$$

$$+1680u^4\cdot z^4-6720u^3\cdot z^3+2016u^2\cdot z^2-40320uz+40320)$$

$$-\frac{40320}{u^9}$$

In the other hand, substituting equs.(22)to(26)into eq.(28), it becomes

$$c_1=\frac{1}{4}u_{1,1}(u_{1,2}+u_{2,2}\cdot z+u_{3,2}\cdot z^2+u_{4,2}\cdot z^3+u_{5,2}\cdot z^4)$$

$$c_2=\frac{1}{4}\{u_{2,1}(u_{1,2}+u_{2,2}\cdot z+u_{3,2}\cdot z^2+u_{4,2}\cdot z^3+u_{5,2}\cdot z_4)$$

$$-u_{1,1}(u_{2,2}+2u_{3,2}\cdot z+3u_{4,2}\cdot z^2+4u_{5,2}\cdot z^3)\}$$

$$c_3=\frac{1}{4}\{u_{3,1}(u_{1,2}+u_{2,2}\cdot z+u_{3,2}\cdot z^2+u_{4,2}\cdot z^3+u_{5,2}\cdot z^4)$$
$$-u_{2,1}(u_{2,2}+2u_{3,2}\cdot z+3u_{4,2}\cdot z^2+4u_{5,2}\cdot z^3)$$
$$+u_{1,1}(u_{3,2}+3u_{4,2}\cdot z+6u_{5,2}\cdot z^2)\}$$

$$c_4=\frac{1}{4}\{u_{4,1}(u_{1,2}+u_{2,2}\cdot z+u_{3,2}\cdot z^2+u_{4,2}\cdot z^3+u_{5,2}\cdot z^4)$$
$$-u_{3,1}(u_{2,2}+2u_{3,2}\cdot z+3u_{4,2}\cdot z^2+4u_{5,2}\cdot z^3)$$
$$+u_{2,1}\cdot(u_{3,2}+3u_{4,2}\cdot z+6u_{5,2}\cdot z^2)-u_{1,1}(u_{4,2}+4u_{5,2}\cdot z)\}$$

$$c_5=\frac{1}{4}\{u_{5,1}(u_{1,2}+u_{2,2}\cdot z+u_{3,2}\cdot z^2+u_{4,2}\cdot z^3+u_{5,2}\cdot z^4)$$
$$-u_{4,2}(u_{2,2}+2u_{3,2}\cdot z+3u_{4,2}\cdot z^2+4u_{5,2}\cdot z^3)$$
$$+u_{3,1}(u_{3,2}+3u_{4,2}\cdot z+6u_{5,2}\cdot z^2)-u_{2,1}(u_{4,2}+4u_{5,2}\cdot z)+u_{1,1}(u_{5,2})\}$$

$$c_6=-\frac{1}{4}\{u_{5,1}(u_{2,2}+2u_{3,2}\cdot z+3u_{4,2}\cdot z^2+4u_{3,2}\cdot z^3)$$
$$-u_{4,1}(u_{3,2}+3u_{4,2}\cdot z+6u_{5,2}\cdot z^2)+u_{3,1}(u_{4,2}+4u_{5,2}\cdot z)-u_{2,1}\cdot u_{5,2}\}$$

$$c_7=\frac{1}{4}\{u_{5,1}(u_{3,2}+3u_{4,2}\cdot z+6u_{5,2}\cdot z^2)-u_{4,1}(u_{4,2}+4u_{5,2}\cdot z)+u_{3,1}\cdot u_{5,2}\}$$

$$c_8=-\frac{1}{4}\{u_{5,1}(u_{4,2}+4u_{5,2}\cdot z)-u_{4,1}\cdot u_{5,2}\}$$

$$c_9=\frac{1}{4}(u_{5,1}\cdot u_{5,2}) \qquad \cdots\cdots(30)$$

Then, after certain mathematical manipulation, the energy distribution of the combined wave can be found as

$$P(z)=\frac{1}{4u}\{(E_0+E_1\cdot z+E_2\cdot z^2+E_3\cdot z^3+E_4\cdot z^4+E_5\cdot z^5+E_6\cdot z^6+E_7\cdot z^7$$
$$+E_8\cdot z^8)\cdot e^{(-z/u_{6,1})}-(E_0+F_1\cdot z+F_2\cdot z^2+F_3\cdot z^3+F_4\cdot z^4)\cdot e^{(-z/u_{6,2})}\} \quad \cdots(31)$$

$$E_0=u_{1,1}\cdot u_{1,2}-\frac{1}{u}(u_{2,1}\cdot u_{1,2}-u_{1,1}\cdot u_{2,2})$$
$$+\frac{2}{u^2}(u_{3,1}\cdot u_{1,2}-u_{2,1}\cdot u_{2,2}+u_{1,1}\cdot u_{3,2})-\frac{6}{u^3}(u_{4,1}\cdot u_{1,2}$$
$$-u_{3,1}\cdot u_{2,2}+u_{2,1}\cdot u_{3,2}-u_{1,1}\cdot u_{4,2})+\frac{24}{u^4}(u_{5,1}\cdot u_{1,2}-u_{4,1}\cdot u_{2,2}$$
$$+u_{3,1}\cdot u_{3,2}-u_{2,1}\cdot u_{4,2}+u_{1,1}\cdot u_{5,2})+\frac{120}{u^5}(u_{5,1}\cdot u_{2,2}-u_{4,1}\cdot u_{3,2}$$
$$+u_{3,1}\cdot u_{4,2}-u_{2,1}\cdot u_{5,2})+\frac{720}{u^6}(u_{5,1}\cdot u_{3,2}-u_{4,1}\cdot u_{4,2}+u_{3,1}\cdot u_{5,2})$$

$$+\frac{5040}{u^7}(u_{5,1}\cdot u_{4,2}-u_{4,1}\cdot u_{5,2})+\frac{40320}{u^8}(u_{5,1}\cdot u_{5,2}) \quad \cdots\cdots(32)$$

$$E_1 = u_{2,1}\cdot u_{1,2}+\frac{1}{u}(u_{2,1}\cdot u_{2,2}-2u_{3,1}\cdot u_{1,2})+\frac{2}{u^2}(u_{2,1}\cdot u_{3,2}$$

$$-2u_{3,1}\cdot u_{2,2}+3u_{4,1}\cdot u_{1,2})+\frac{6}{u^3}(u_{2,1}\cdot u_{4,2}-2u_{3,1}\cdot u_{3,2}$$

$$+3u_{4,1}\cdot u_{2,2}-4u_{5,1}\cdot u_{1,2})+\frac{24}{u^4}(u_{2,1}\cdot u_{5,2}-2u_{3,1}\cdot u_{4,2}+$$

$$+3u_{4,1}\cdot u_{3,2}-4u_{5,1}\cdot u_{2,2})-\frac{120}{u^5}(2u_{3,1}\cdot u_{5,2}-3u_{4,1}\cdot u_{4,2}$$

$$+4u_{5,1}\cdot u_{3,2})+\frac{720}{u^6}(3u_{4,1}\cdot u_{5,2}-4u_{5,1}\cdot u_{4,2})-\frac{20160}{u^7}u_{5,1}\cdot u_{5,1} \quad \cdots\cdots(33)$$

$$F_1 = u_{1,1}\cdot u_{2,2}-\frac{1}{u}(u_{2,1}\cdot u_{2,2}-2u_{1,1}\cdot u_{3,2})+\frac{2}{u^2}(u_{3,1}\cdot u_{2,2}-2u_{2,1}\cdot u_{3,2}$$

$$+3u_{1,1}\cdot u_{4,2})-\frac{6}{u^3}(u_{4,1}\cdot u_{2,2}-2u_{3,1}\cdot u_{3,2}+3u_{2,1}\cdot u_{4,2}+4u_{1,1}\cdot u_{5,2})$$

$$+\frac{24}{u^4}(u_{5,1}\cdot u_{2,2}-2u_{4,1}\cdot u_{3,2}+3u_{3,1}\cdot u_{4,2}-4u_{2,1}\cdot u_{5,2})$$

$$+\frac{120}{u^5}(2u_{5,1}\cdot u_{3,2}-3u_{4,1}\cdot u_{4,2}+4u_{3,1}\cdot u_{5,2})+\frac{720}{u^6}(3u_{5,1}\cdot u_{4,2}$$

$$-4u_{4,1}\cdot u_{5,2})+\frac{20160}{u^7}u_{5,1}\cdot u_{5,2} \quad \cdots\cdots(34)$$

$$E_2 = u_{3,1}\cdot u_{1,2}+\frac{1}{u}(u_{3,1}\cdot u_{2,2}-3u_{4,1}\cdot u_{1,2})+\frac{2}{u^2}(u_{3,1}\cdot u_{3,2}$$

$$-3u_{4,1}\cdot u_{2,2}+6u_{5,1}\cdot u_{1,2})+\frac{6}{u^3}(u_{3,1}\cdot u_{4,2}-3u_{4,1}\cdot u_{3,2}+$$

$$+6u_{5,1}\cdot u_{2,2})+\frac{24}{u^4}(u_{3,1}\cdot u_{5,2}-3u_{4,1}\cdot u_{4,2}+6u_{5,1}\cdot u_{3,2})$$

$$+\frac{360}{u^5}(u_{4,1}\cdot u_{5,2}+2u_{5,1}\cdot u_{4,2})-\frac{15840}{u^6}(u_{5,1}\cdot u_{5,2})$$

$$+\frac{20160}{u^7}(u_{5,1}\cdot u_{5,2}) \quad \cdots\cdots(35)$$

$$F_2 = u_{1,1}\cdot u_{3,2}-\frac{1}{u}(u_{2,1}\cdot u_{3,2}-3u_{1,1}\cdot u_{4,2})+\frac{2}{u^2}(u_{3,1}\cdot u_{3,2}-$$

$$-3u_{2,1}\cdot u_{4,2}+6u_{1,1}\cdot u_{5,2})-\frac{6}{u^3}(u_{4,1}\cdot u_{3,2}-3u_{3,1}\cdot u_{4,2}+$$

$$+6u_{2,1}\cdot u_{5,2})+\frac{24}{u^4}(u_{5,1}\cdot u_{3,2}-3u_{4,1}\cdot u_{4,2}+6u_{3,1}\cdot u_{5,2})$$

$$+\frac{360}{u^5}(u_{5,1}\cdot u_{4,2}-2u_{4,1}\cdot u_{5,2}+12u_{5,1}\cdot u_{5,2}) \quad \cdots\cdots(36)$$

$$E_3=u_{4,1}\cdot u_{1,2}+\frac{1}{u}(u_{4,1}\cdot u_{2,2}-4u_{5,1}\cdot u_{1,2})+\frac{2}{u^2}(u_{4,1}\cdot u_{3,2}$$

$$-4u_{5,1}\cdot u_{2,2})+\frac{6}{u^3}(u_{4,1}\cdot u_{4,2}-4u_{5,1}\cdot u_{3,2})+\frac{24}{u^4}(u_{4,1}\cdot u_{5,2}$$

$$-4u_{5,1}\cdot u_{4,2})+\frac{6240}{u^5}u_{5,1}\cdot u_{5,2}-\frac{6720}{u^7}u_{5,1}\cdot u_{5,2} \quad \cdots\cdots(37)$$

$$F_3=u_{1,1}\cdot u_{4,2}-\frac{1}{u}(u_{2,1}\cdot u_{4,2}-4u_{1,1}\cdot u_{5,2})+\frac{2}{u^2}(u_{3,1}\cdot u_{4,2}$$

$$-4u_{2,1}\cdot u_{5,2})-\frac{6}{u^3}(u_{4,1}\cdot u_{4,2}-4u_{3,1}\cdot u_{5,2})+\frac{24}{u^4}(u_{5,1}\cdot u_{4,2}$$

$$-4u_{4,1}\cdot u_{5,2})+\frac{480}{u^5}u_{5,1}\cdot u_{5,2} \quad \cdots\cdots(38)$$

$$E_4=u_{5,1}\cdot u_{1,2}+\frac{1}{u}(u_{5,1}\cdot u_{2,2})+\frac{2}{u^2}(u_{5,1}\cdot u_{3,2})-\frac{54}{u^3}(u_{5,1}\cdot u_{4,2})$$

$$-\frac{1656}{u^4}(u_{5,1}\cdot u_{5,2})+\frac{1680}{u^7}(u_{5,1}\cdot u_{5,2}) \quad \cdots\cdots(39)$$

$$F_4=u_{1,1}\cdot u_{5,2}-\frac{1}{u}(u_{2,1}\cdot u_{5,2})+\frac{2}{u^2}(u_{3,1}\cdot u_{5,2})-\frac{6}{u^3}(u_{4,1}\cdot u_{5,2})$$

$$+\frac{24}{u^4}(u_{5,1}\cdot u_{5,2}) \quad \cdots\cdots(40)$$

$$E_5=\frac{336}{u^3}\cdot u_{5,1}\cdot u_{5,2}-\frac{336}{u^7}u_{5,1}\cdot u_{5,2} \quad \cdots\cdots(41)$$

$$E_6=-\frac{56}{u^2}u_{5,1}\cdot u_{5,2}+\frac{56}{u^7}u_{5,1}\cdot u_{5,2} \quad \cdots\cdots(42)$$

$$E_7=\frac{8}{u}u_{5,1}\cdot u_{5,2}-\frac{8}{u^7}u_{5,1}\cdot u_{5,2} \quad \cdots\cdots(43)$$

$$E_8=-u_{5,1}\cdot u_{5,2}+\frac{1}{u^7}u_{5,1}\cdot u_{5,2} \quad \cdots\cdots(44)$$

Since $Z=H^2$ and $dZ=2HdH$, the combined wave height distribution is proposed as

$$P(H)=\frac{dz}{dH}P(z)$$

$$= \frac{H}{2u} \{ (E_0 + E_1 \cdot H^2 + E_2 \cdot H^4 + E_3 \cdot H^6 + E_4 \cdot H^8 + E_5 \cdot H^{10} + E_6 \cdot H^{12} + E_7 \cdot H^{14} + E_8 \cdot H^{16}) \cdot e^{(-H^2/u_{6,1})} - (E_0 + F_1 \cdot H^2 + F_2 \cdot H^4 + F_3 \cdot H^6 + F_4 \cdot H^8) \cdot e^{(-H^2/u_{6,2})} \} \quad \cdots\cdots (45)$$

Comparison with the measured data and the other theorems

In a study of non-linear wave height distribution, Longuet-Higgins [7] proposed a probability density function from the joint distribution of wave periods and amplitudes in a random wave field as

$$P(x) = 2x \cdot \exp(-x^2) \cdot N(\nu) \cdot F(x/\nu) \quad \cdots\cdots (46)$$

$$F(x/\nu) = \frac{1}{\sqrt{\pi}} \int_{-\infty}^{x/\nu} \exp(-\beta^2)\, d\beta \qquad (\text{error function}) \quad \cdots\cdots (47)$$

Where $x = H/H_r$, ν is a spectral width parameter; $N(\nu)$ is a normalization factor.

In a similar study, Chen et. al.[1] applied non-linear effect wave theory to obtain a dimensionless wave height distribution.

Comparison between the wave height distributions computed from the above-mentioned formulas and the field data is shown in Fig.1. It indicates that the present proposed method yields a better result.

Application

In order to apply the non-linear wave combination theorem to the prediction of wave in Taiwan Strait, the weather forecasting data, such as the weather chart, wind velocity and its direction must be available. Then, the prediction of wave can be completed using the following steps.

1. Waves from the East China Sea and Taiwan Strait are evaluated by Liang's [4] element wave prediction model.
2. The local wave height is computed by Tang's[9] shallow water wave prediction formula.
3. Since the wave steepness of two-source wave system can be calculated independently, the distribution of wave height of the combined wave using two non-linear wave combination theorem could be obtained.

The preliminary result of this prediction model is shown in Fig.2. It can be found that the results obtained by the non-linear two-source wave system are in agreement with those obtained by the two-linear source-wave system

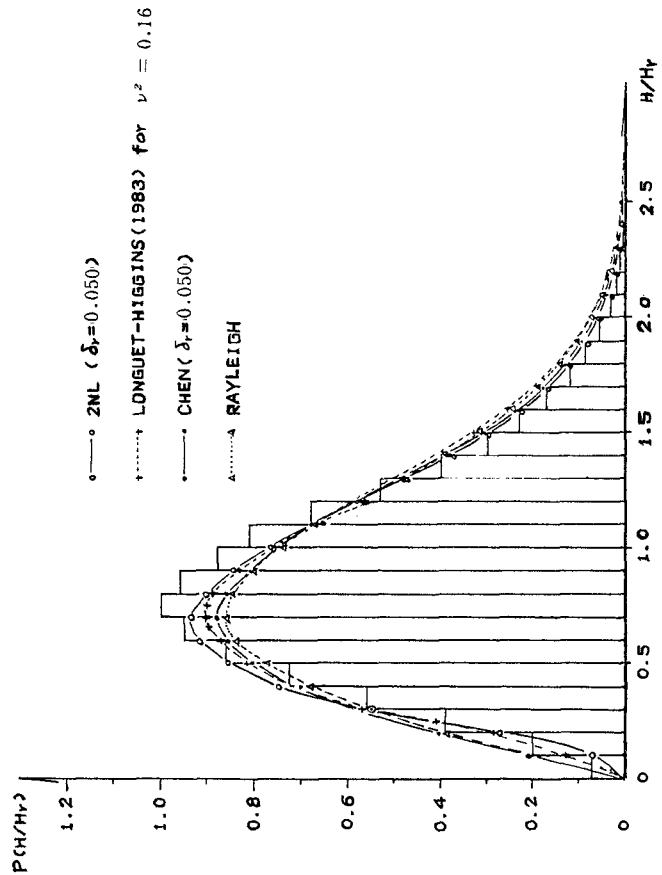

Fig.1 Comparison of the wave height distributions

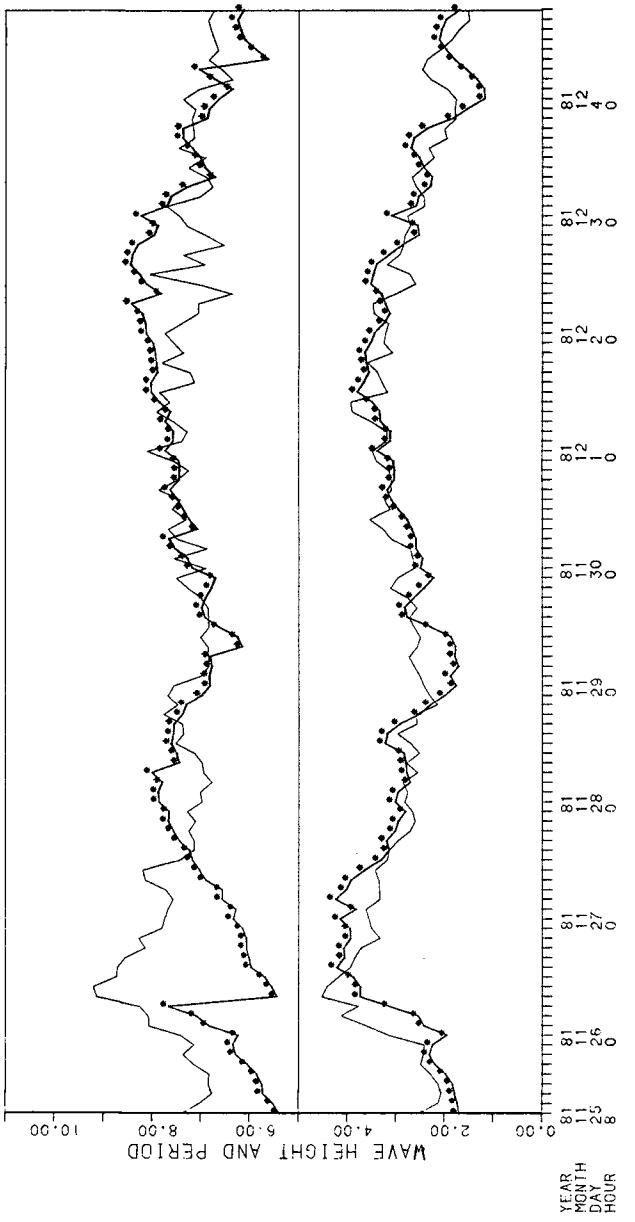

Fig.2 Results of wave prediction

including the energy loss effect. This implies that the higher-order terms in the non-linear two-source wave system are related to the energy loss.

Conclusion

In this study, the distribution of wave-height for two nonlinear source wave system is proposed, which yields the same result as those of two linear source-wave system as the wave steepness approaches zero.

From the field data, it was found that due to wave-wave interaction, some of the short-period wave will disappear which causes the mean wave height to increase and the maximum wave height to decrease. The proposed distribution can describe such a phenomenum.

Finally, it should be pointed out that although the proposed model is slightly complicated, as compared with that proposed by Chen et. al., the model is still simple to use and the computational effort does not increase significantly.

References

1. Chen,Y.Y. and F.L.W. Tang; "Non-linear Effect on The Distributions of Surface Elevation and Wave Heights of Random Sea", Proc. of 7th Conference on Coastal Engineer -ing, Taipei, R.O.C.
2. Goda, Y.;"Numerical Experiments on Wave Statistics with Spectral Simulation" ,Report of the Port and Harbour Research Institute, Vol. 9, No.3, Sep.1970.
3. Liang, N.K.,S.T. Tang and B.J.Lee; "The Wave Prediction Model of Monsoon Season for Taichung Harbour", Science Rept., NTU, 1975
4. Liang, N.K. and W.C.Lin ; "A Study on Wave Height compa -rison Between Penghu and Lukang in Taiwan Strait During Winter Monsoon Season", Science Rept., NTU, 1979
5. Longuet-Higgins, M.S. ; "On The Statistical Distribution of The Heights of Sea Waves" , J. Marine Research, 1952
6. Longuet-Higgins, M.S. ; "The Effect of Non-linearities on Statistical Distribution in The Theory of Sea Waves". J. Fluid Mechanics, 1963
7. Longuet-Higgins, M.S.; "On the Joint Distribution of Wave Periods and Amplitudes in a Random Wave Field" , Proc.R. Soc. Lond., 1983.
8. Ou, S.H., "Parametric Determination of Wave Statistics and Wave Spectrum of Gravity Waves" , Dissertation No.1, Tainan Hydraulics Laboratory, NCKU, 1977.
9. Tang, F.L.W.; "Researches on The Calculation of Waves on Long Shoaling Beaches", J. of Civil and Hydraulics Engineering, NCKU, 1970
10. Tang, F.L.W. ,S.H. Ou and J.T.Juang ; "Wave Forecasting and Wave Statistics in Taiwan Strait" , Research Thesis No.4 , Tainan Hydraulics Laboratory, NCKU, 1981
11. Tang,F.L.W. and J.T. Juang ; "Probability Density Distribution of Wave Height in Western Coast of Taiwan"

, 18th ICCE, 1982.
12. Tang, F.L.W. and J.T. Juang ; "Prediction Method for the Wave Height Distribution Off The Western Coast of Taiwan" , 19th ICCE, Houston, U.S.A., 1984.

CHAPTER 27

Measurements from a fast-moving air-cushion platform

P. Kerckaert *
A. Grobben **
P. De Candt ***

Abstract

In 1976 the Belgian Government decided to enlarge the harbour of Zeebrugge and to execute an artificial beach renourishment on the beaches at Knokke-Heist. A comprehensive survey program along the 24 km coastline was conceived using remote sensing techniques. This enabled correct momentary recordings of the beach areas, the production of differential charts and calculations of dune and beach volumes. However, the observations of the nearshore and offshore areas from ordinary survey vessels take too long so that no accurate momentary recordings of the seabottom topography can be achieved. On these grounds, in 1983, the Belgian Authorities have instructed the Eurosense Belfotop Company to develop an effective measuring method based on the use of a hovercraft.

This hovercraft platform, named "BEASAC" and designed for hydrographic surveys, is now used for monitoring the coastal morphology and the dredging activities in the access channels to the major Belgian seaports. On the basis of the "Beasac"-soundings of the nearshore area and the aerial remote sensing data of the beach, charts and differential charts of the combined beach and nearshore area are produced.

The results of this technique are very promising and will be incorporated in the further survey programs ordered by the Belgian Authorities as a substitute for the classic bathymetric vessel soundings.

* Chief Engineer - Ministry of Public Works Director of Coastal Defence Department, Ostend, Belgium
** Assistent Managing Director - Eurosense Belfotop, J. Vander Vekenstraat 158, Wemmel, Belgium
*** Director - Eurosense Belfotop, J. Vander Vekenstraat 158, Wemmel, Belgium

1. Introduction

As already reported in former conferences and technical papers, the Belgian authorities have always paid special attention to efficient shore protection of the Belgian East Coast (ref. 1,2). Picture 1 shows a Landsat-satellite picture of the Belgian Coast and the seaward side of the Westerscheldt estuary in 1984. Significant sediment movements are clearly visible around the harbour extension of the port of Zeebrugge. The Belgian East Coast is situated in the area between Blankenberge (4 km west of Zeebrugge) and the Belgian-Dutch border (10 km east of Zeebrugge).

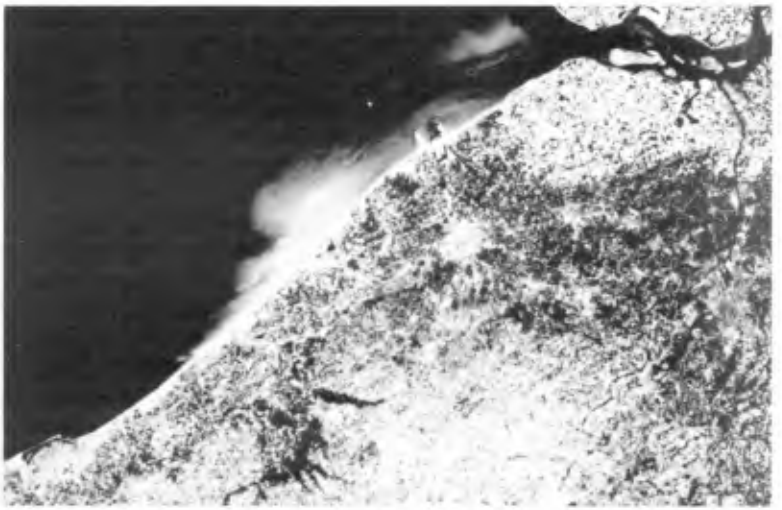

Picture 1 : satellite picture of the Belgian Coast and the Western Scheldt Estuary

The reason for the coastal protection of the Belgian East Coast is obvious : for several decades the alarming regression of the shoreline on those beaches has offered a real threat to the important tourist and residential resorts of the city of Knokke-Heist and the nature reserve "Het Zwin".

Two phenomena are the main causes for this evolution (see figure 1). First of all in front of the beaches at Knokke-Heist a gully called the "Appelzak" with a depth of about 8 m under low water level developed to within a distance of 500 m of the seawall causing important beach erosion via offshore transport. Moreover the port of Zeebrugge - built at the turn of the century - intersected the easterly flow of longshore drift so that the incoming sediment was not sufficient for natural beach replenishment.

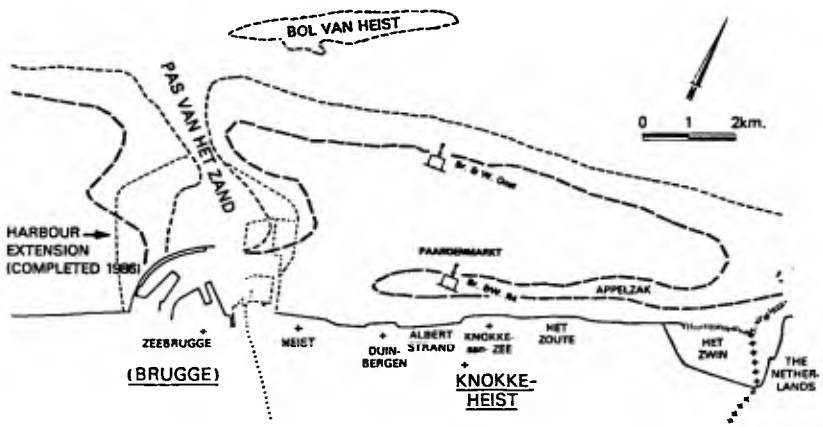

Fig. 1. : The Belgian East Coast : General Situation in 1976.

As a result, a strip of beach of only 50 to 100 m remained available in front of the seawall at low tide and the beaches disappeared nearly completely at high tide. Storms damaged the seawall on several occasions so that coastal protection works became very urgent. Picture 2 illustrates very clearly the precarious situation before 1976 when during storms, waves could overtop the existing sea-dike.

Picture 2 : During storms, waves overtop the existing sea-dike (winter 1975)

2. Coastal protection works

In 1976 the Belgian Government decided to enlarge the harbour at Zeebrugge. This included the construction of new breakwaters extending approximately 3,5 km into the sea from the existing seawall. Picture 3 gives an overall view of the harbour extension; behind them : the East Coast beaches. From the start the new expansion works of the outer Zeebrugge harbour were considered as a possible supplementary threat to the East Coast beaches. Therefore, and after a comprehensive study of the problem, it was decided to execute preventative coastal protection works on the beaches at Knokke-Heist starting at the same time with the harbour extension.

Picture 3 : The new outer harbour at Zeebrugge (1986)

In 1977 the decision was taken to execute an artificial beach renourishment of about 8,4 millions m^3 of coarse dredged sea sand. This work was completed between December 1977 and March 1979. As a result a new beach with the width of about 100 m at high tide was created. Picture 4 shows clearly the newly created beaches at Knokke-Heist. In comparison with the previous situation in 1976, the positive result is spectacular. In order to observe the evolution of the restored beaches, a comprehensive survey program along the 24 km coastline was conceived and started in june 1979. This was particularly important with regard to the influence on the beaches of the harbour extension works.

Picture 4 : Beaches at Knokke-Heist after beach renourishment

3. Coastal survey techniques

The aim of this paper is to give more details upon an important new development in the survey technique which was invented and applied to the considered coastal area. First of all it is important to know that an important contribution to the survey program was given by remote sensing techniques. This means the use of a specially conceived aeroplane, equipped with the most sophisticated cameras and multispectral scanners. These instruments are necessary in order to collect all the necessary data and to treat them by means of stereoscopic techniques. The results are then stored and ranged by specially developed computer software. The advantages of this method are obvious : speed and accuracy of measurement, the ability to provide easily assimilated results (i.e. differential charts and calculations of beach surfaces and volumes) and last but not least a correct momentary recording of a large area of observation.

In this way differential charts of the east coast beaches resulting from two aerial observations were made giving erosion and/or acretion areas.

So far, aerial remote sensing techniques in coastal engineering have been mostly limited to surface observations above the low water level especially in muddy or silty seawater areas. Sedimentological processes are however not solely restricted to the beach area itself. Important morphological phenomena occur offshore and cannot be reached by aerial remote sensing techniques. These offshore areas are even of a larger extend than the beach area and need other solutions in order to detect e.g. longshore and tidal transport.

Until now, the observation of the seabottom morphology was performed from classic bathymetric vessels. However, these vessels possess two essential disadvantages. In many cases the bathymetric soundings cannot be performed close enough to the beach so that the link with aerial remote sensing data of the beach is difficult to achieve or even impossible. Moreover, in practice, the observations from an ordinary survey vessel take too long - sometimes several months for one area - so that no accurate momentary recording of the seabottom topography can be achieved as the beginning and the end of the observations are difficult to compare.

This can result into mistakes; especially in coastal areas with rapidly changing morphological conditions. Only the use of a fast moving survey platform , capable of reaching the most shallow waters can provide an effective solution.

On these grounds, in 1983, the Belgian Authorities have instructed the Eurosense Belfotop Company to develop an effective measuring method based on the use of a hovercraft.

4. The "BEASAC"-platform

Picture 5 gives a general view of the new hydrographic measuring system, named "BEASAC".
"BEASAC" is the acronym for "Belfotop Eurosense Acoustic Sounding Air Cushion" platform.

Picture 5 : The BEASAC-platform

Although the idea to use a hovercraft for hydrographic purposes is not new, earlier attemps encountered numerous difficulties. Nevertheless the demand for hovercraft in surveying is likely to increase significantly. A first problem to be solved is the realisation of an accurate positioning system, not only with regard to the horizontal coordinates but also for the vertical location with respect to a fixed datum. Furthermore the speed of the craft leads to registration and treatment of a great amount of data, which is only feasable using special computer techniques. Finally, the craft had to be equipped as a reliable, fast and manoeuvrable high speed survey vessel.

An extended test program was set up and realised. The accuracy of the depth measurements in shallow water was checked by the terrestrial surveying of control points in the tidal zone between high and low water. The deviations between both methods were, on average, less than 10 centimers and consequently acceptable.

5. Combined charts of beach and nearshore area

On the basis of the aerial remote sensing data of beach topography and the BEASAC-platform soundings of the nearshore area a chart showing the combined beach and nearshore area was realised. Differential recordings of this total area, above and beneath the low water level line are easy to produce and give a much better insight into the morphological changes of the coastal area.

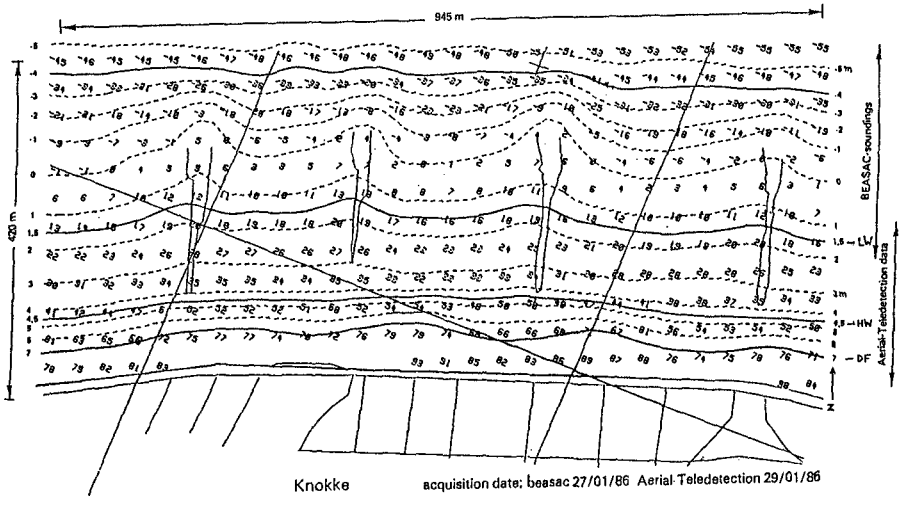

Fig. 2. : Combined chart of remote sensing and BEASAC data

Figure 2 shows the very first combined relief map realised with both aerial remote sensing techniques and Beasac soundings. The difference in data between the two methods in the overlap zone is only 10 centimeters on average.

In this way, charts of the total area east of the Zeebrugge harbour were made by a combination of remote sensing and Beasac data. While this area was normally covered by classic bathymetric vessels over a period of two to three months, it is now done by the BEASAC-platform in four to six days. Such a map can be produced on regular basis and accurate differential charts become also possible now.

After the execution of the test program, the newly developed sounding platform was accepted by the Belgian Authorities. It is now used to observe the beaches and nearshore areas of the Belgian Coast.

6. Control and monitoring surveys

The advantages of a fast moving survey platform are also obvious in other applications such as : the control and monitoring of dredging activities, and the monitoring and charting of large remote oceanographic territories. The accuracy of the measurements effected at high speeds of up to 50 km/h, in large areas such as open sea channels or sand bank configurations, was checked by classic bathymetric soundings from an hydrographic vessel. Under normal conditions the difference between both methods is less than 20 centimeters.

In this manner the Beasac platform is successfully employed for monitoring the evolution of the access channels to the major Belgian seaports, and for supervising the extensive dredging operations at these locations. The major advantages of the Beasac-system - namely the fast moving and accurate soundings - have proved to be important assets in observing and controlling sedimentological and dredging processes. More frequent charting allows evaluation of the need for, and the effectiveness of, dredging operations.

Figure 3 shows a nautical chart with absolute depth values realised with the BEASAC-platform. The represented zone is the entrance channel to the new outer harbour of Zeebrugge.

Differential depth charts of the the same area between two Beasac observation campaigns are also produced. These charts are very useful to monitor dredging operations.

The newly developed air cushion platform can indeed be considered as an important contribution towards more accurate and economical observations of morphological processes both natural and/or artificial.

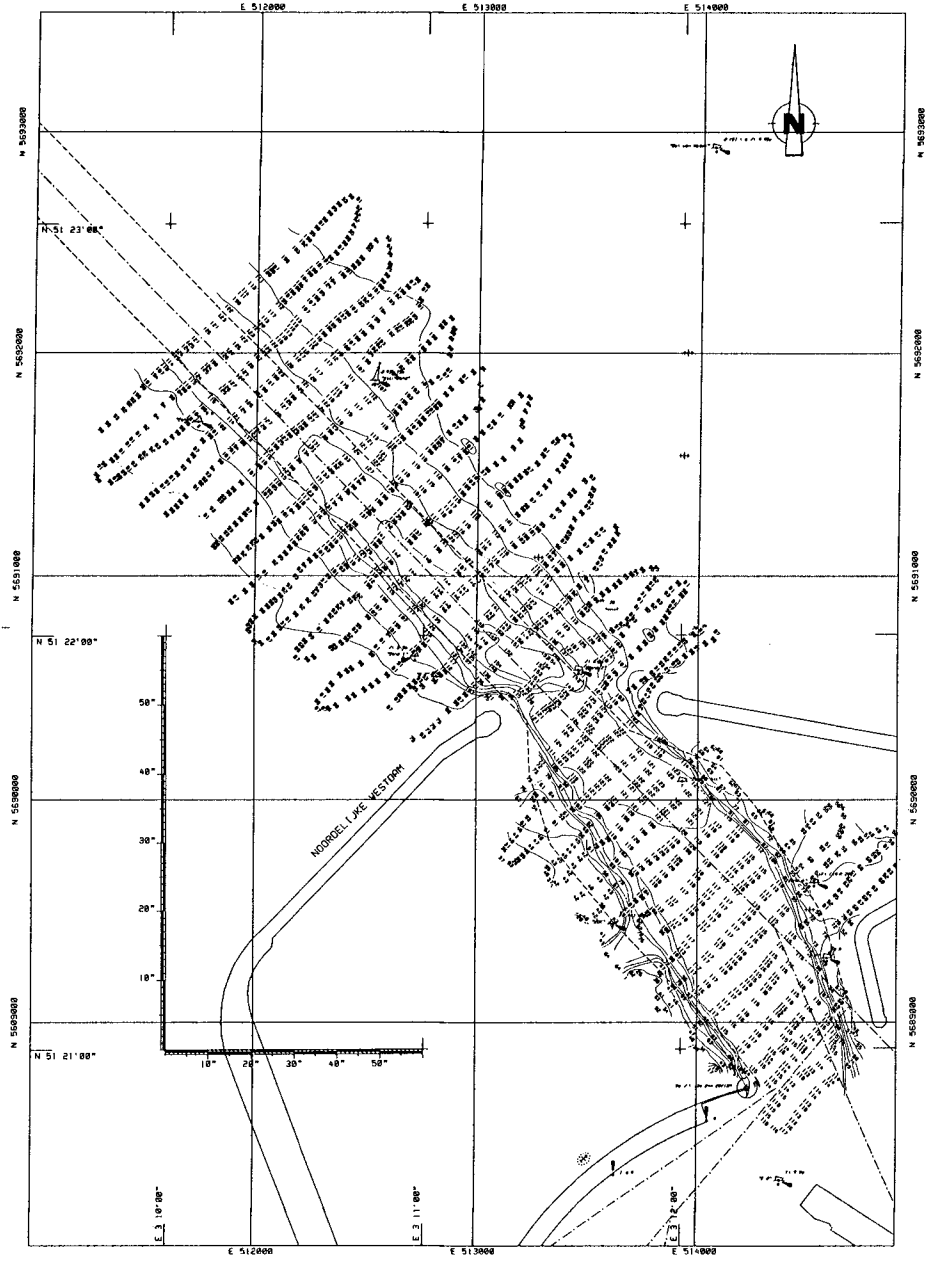

Fig. 3. : Nautical chart of the entrance channel to the port of Zeebrugge made by BEASAC

7. Survey equipment

Picture 6 shows the main cabin with the survey equipment : two Atlas Deso 20 - with 33 and 210 Khz transducers - and system control terminals are installed.

In front of the pilot, a navigation screen is mounted near the instrument panel on which the predefined tracks, the position of the hovercraft, its speed and the distance off-track are displayed.

Studies about the subject of dynamic positioning at sea resulted in the development of a very accurate and reliable positioning and navigation system, combining the use of a hyperbolic (Toran) and a circular (Trisponder) system.

Picture 6 : The main cabin with the survey equipment

On both sides of the hovercraft an acoustic transducer is installed in a stainless steel fish (see picture 7). The streamlined profile of the fish is designed for a survey speed of 27 knots, although higher speeds are possible.

The fish can be brought in or out of the water by manual or computer control. A mechanical weak link construction prevents damage to the sword or the craft in case of collision with floating objects. When approaching the shoreline the fish are retracted automatically.

Picture 7 : Stainless steel, sword and fish

In the hangar, a modern jacking system with eight jacks can lift the craft for periodic skirt inspections.

Picture 8 shows the Beasac-platform in operation near the beach. During these surveys a mobile shore beacon mounted on a jeep helps to optimise the dynamic positioning of the craft.

After each survey mission the data is transferred to the host computer system of the data center in Zeebrugge. Immediately several routine procedures are started which result in graphical and numerical reviews of the raw data. The tide-corrected data can then be plotted on a hydrographic chart.

Picture 8 : BEASAC-platform in operation near the beach

8. Conclusions

- The morphological research campaign started in 1979 on the Belgian East Coast, and, supported by aerial remote sensing techniques, it can be considered as very successful. On the basis of this campaign the decision was taken to execute a new beach renourishment of about 1 million m^3 of sand in the period March-April 1986 on locations resulting from the observations of the past survey program.

- At the same time, an important and fundamental contribution was made to more accurate observation of the nearshore and seabed area by means of a fast moving hydrographic-survey hovercraft : Beasac. The results of this new technique are very promising and will be incorporated in the further survey programs ordered by the Belgian Authorities as a substitute for the classic bathymetric vessel soundings.

Appendix - References

1. Roovers P., Kerckaert P., Burgers A., Noordam A., De Candt P. "Beach Protection as part of the Harbour Extension at Zeebrugge Belgium".
P.I.A.N.C. - 25th Congres - Section II - Volume 5 - Edinburgh 1981

2. Kerckaert P., Wens F., De Wolf P., De Candt P., De Meyer C., Grobben A.
"Beach Renourishment : A "Soft" Method for Coastal Protection"
P.I.A.N.C. - 26th Congres - Brussels 1985.

CHAPTER 28

Wind Specification for Spectral Ocean-Wave Models

M.L. Khandekar* and B.M. Eid**

Abstract

This paper investigates the utility of winds obtainable from a numerical weather prediction model for driving a spectral ocean-wave model in an operational mode. Wind inputs for two operational spectral wave models were analyzed with respect to observed winds at three locations in the Canadian east coast offshore. Also, significant wave heights obtainable from the two spectral models were evaluated against measured wave data at these locations. Based on this analysis, the importance of appropriate wind specification for operational wave analysis and forecasting is demonstrated.

Introduction

Spectral ocean-wave models based on the energy balance equation are used operationally in many areas of the world oceans at present. The spectral models are capable of providing a detailed description of the sea-state in terms of a two-dimensional (frequency-direction) wave spectrum at a given location. For real-time operations, a spectral wave model utilizes winds which are generally extracted from an operational weather prediction model.

In this study, two operational spectral wave models are chosen for which wind inputs were analyzed with respect to observed winds at three selected locations in the Canadian Atlantic ocean; also, wave products from these models were evaluated against the observed wave data at these locations. Two sets of observed wind and wave data were utilized to evaluate the model products. Based on this evaluation, the importance of appropriate wind specification for operational wave analysis and forecasting is demonstrated.

Details of Models

The two wave models used in this study are the SOWM (Spectral Ocean Wave Model) of the U.S. Navy (see Pierson, 1982) and the ODGP (Ocean Data Gathering Program) model developed by Cardone et al (1974). The SOWM is a hemispheric model which provides operational wave forecasts for the three ocean basins of the northern hemisphere; the SOWM grid is designed on a gnomonic icosahedral projection with 325 grid points in each equilateral triangle and about 1575 ocean points over the

* Research Scientist, Atmospheric Environment Service, Downsview, Ontario, Canada.
** Senior Oceanographer, MacLaren Plansearch Ltd., Halifax, Nova Scotia, Canada.

northern hemisphere. The ODGP model has a nested grid (see Figure 1) and operates over the western north Atlantic ocean with a finer grid spacing than the SOWM in deep water and half of that spacing over the continental shelf region. The ODGP model uses 24 direction bands (as against 12 used in the SOWM) while both the models use 15 frequency bands. The governing equation for both models can be expressed as

$$\frac{\partial}{\partial t} E\ (f,\ \theta,\ \bar{x},\ t) + C_g . \nabla E = (A+BE)\ (1-E/E_{PM}) \qquad (1)$$

Here E is the energy density of the wave field described as a function of frequency f, direction θ, position $\bar{x}$ and time t; C_g is the group velocity of the wave in deep water, A and B are the linear and the exponential growth terms and E_{PM} is the Pierson-Moskowitz (1964) spectrum for a fully developed sea at a given wind speed. The Pierson-Moskowitz spectrum plays an important part in modelling the transition from a growing sea to a fully developed sea. Both the models use an empirically developed dissipation term which attenuates those frequency components travelling against the winds while the nonlinear wave-wave interaction term is neglected in both the models.

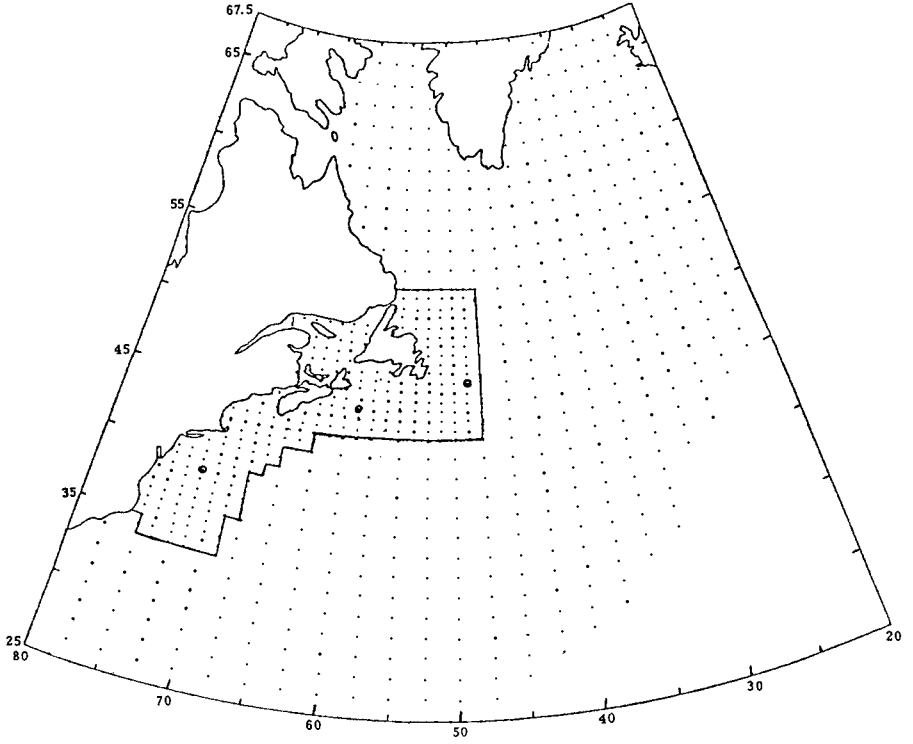

Figure 1: The operational ODGP model grid. The coarse grid has a spacing of 1.25° latitude by 2.50° longitude. The nested fine grid has half the spacing. Three circled grid points are the locations for wave model evaluation.

In SOWM, the terms A and B are modeled following the studies of Phillips (1957) and Miles (1957). The ODGP model uses an improved formulation of the term, A, following the studies of Inoye (1967) and Snyder and Cox (1966). Further, in the ODGP model, the growth algorithm was modified to allow for rapidly turning winds and the dissipation of bands travelling crosswinds was suppressed, so that at any time step no angular band is eligible for both growth and dissipation. Thus, the ODGP model has better spatial and spectral resolution and uses an improved growth algorithm than the SOWM.

Wind Input

The SOWM uses winds generated by the U.S. Navy's operational weather prediction model at Monterey, California. This operational weather prediction model is a global multi-level model which has a coupled boundary layer model where the influence of atmospheric stability is incorporated. The model generates analysis and forecast winds at 19.5m level which are then utilized to drive the SOWM; more details of the U.S. Navy's weather prediction model can be found in Mihok and Kaitala (1976).

For the ODGP model, the analysis winds are derived from the six-hourly north Atlantic surface charts prepared at the National Meteorological Centre (NMC) in Washington, D.C. (U.S.A.); these charts are reanalyzed based on latest ship weather reports and then digitized. A boundary layer model developed by Cardone (1969, 1978) is applied to generate effective neutral winds at 20m level above the ocean surface. According to Cardone (1969), a 20m-level wind speed of 24 knots under stable atmospheric conditions (air temperature warmer than water temperature) has the same effective wave generating ability as that of a 19-knot wind in neutral conditions and that of a 17-knot wind in unstable conditions (air temperature cooler than water temperature). Cardone's boundary layer model takes into account the (air-water) temperature difference at a given location and generates effective neutral winds at 20m level for driving the ODGP model. The forecast winds for the ODGP model are based on subjectively adjusted surface prognostic charts from the LFM (Limited-area Fine Mesh) model at NMC Washington; this 'man-machine mix' appears to provide an improved wind specification for the ODGP model.

Data

Two sets of wind and wave data measured at selected locations in the Canadian east coast offshore were used to evaluate the model products. The first set of data consisted of four storm events ranging from 3 to 5 days and selected from the historical weather charts dated 1 October 1983 to 31 March 1984. The movement of these storms off the Canadian coast is shown by the storm tracks in Figure 2. Each track shows the movement of the storm centre over the 2-day period which is marked on the tracks. Figure 2 also shows the three sites at which the model products were evaluated. Site 1 is near the NOAA buoy 44004 which is operated by the National Oceanic and Atmospheric Administration (NOAA), Washington. Sites 2 and 3 are near some of the oil rigs (Glooscap, Alma, Terra Nova) operated by various

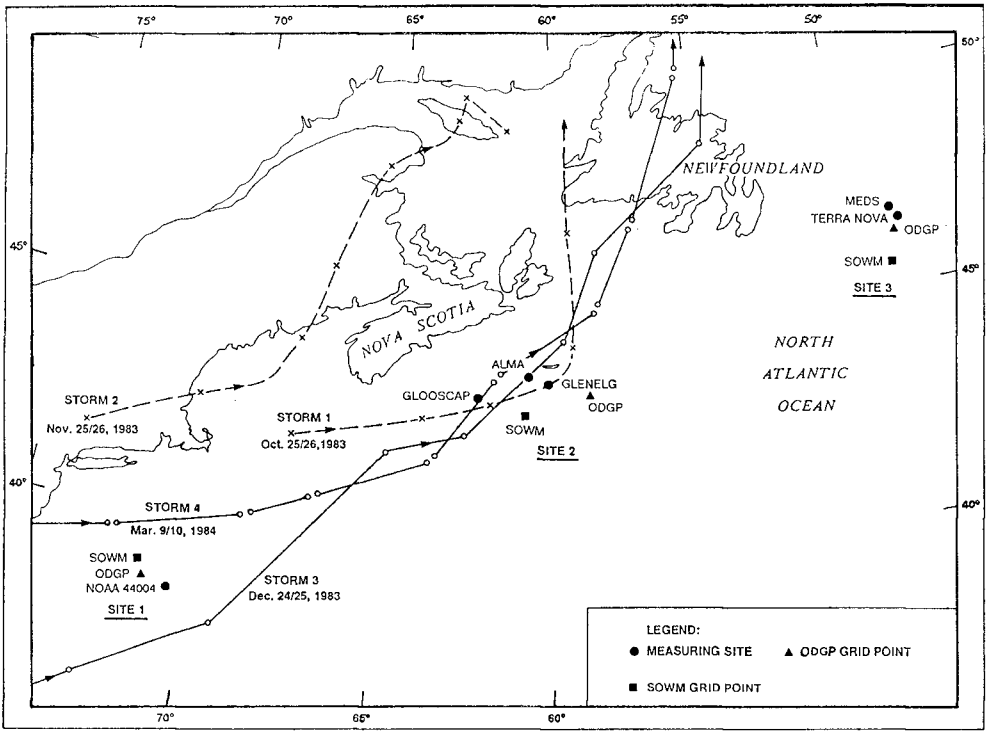

Figure 2: Locations of three sites and tracks of four storms selected for model evaluation.

oil companies. The wind and wave products generated by the two models (the SOWM and the ODGP) were evaluated for the four storm events.

The second set of data covered a two-month period from 15 January to 15 March, 1986; this was the period of a field project for the Canadian Atlantic Storms Program (CASP) during which a large amount of meteorological and oceanographic data was collected to study the evolution of winter storms that affect the Canadian Atlantic provinces. During the CASP field project, the ODGP model was run in an operational mode using two different wind inputs. One wind input was the operational wind field based on the man-machine mix as described above. The second wind input was provided by the weather prediction model of the Canadian Meteorological Centre (CMC) in Montreal. The CMC winds were extracted at the 0.998 sigma-level which corresponds to about 17m above the ocean surface in a standard atmosphere. The CMC winds were interpolated at the ODGP grid and were used without any modification, to drive the ODGP model. The CMC weather prediction model incorporates a surface turbulent flux formulation (Delage, 1985) so as to include the effect of atmospheric stability on wind variation in the vertical.

Results and Discussion

The results of the model evaluation using the first set of data are presented in Figure 3 and Table 1. Figure 3 shows a sample wind and wave plot for storm 2 covering a period November 25-30, 1983. At site 1 (in Figure 3), the maximum wind speed of 38 knots was recorded at about 18GMT, 25 November, whereas the maximum significant wave height of 9m was recorded 12 hours later at about 06GMT, 26 November. At site 2 (on the Scotian Shelf), the storm produced maximum wind and wave heights during 26 and 27 November. As the storm moved northeastward, it produced a maximum wind speed of 48 knots at site 3 (off Newfoundland) on 29 November (00GMT) and a maximum wave height of 8.5m about six hours later. An examination of the model plots shows that both the SOWM and the ODGP models produce similar wind speeds during the storm period; however, the ODGP model produces wave heights which agree more closely with observed wave heights than to SOWM wave heights. For a quantitative evaluation of the model products, a statistical analysis of the errors (model value-observed value) at all

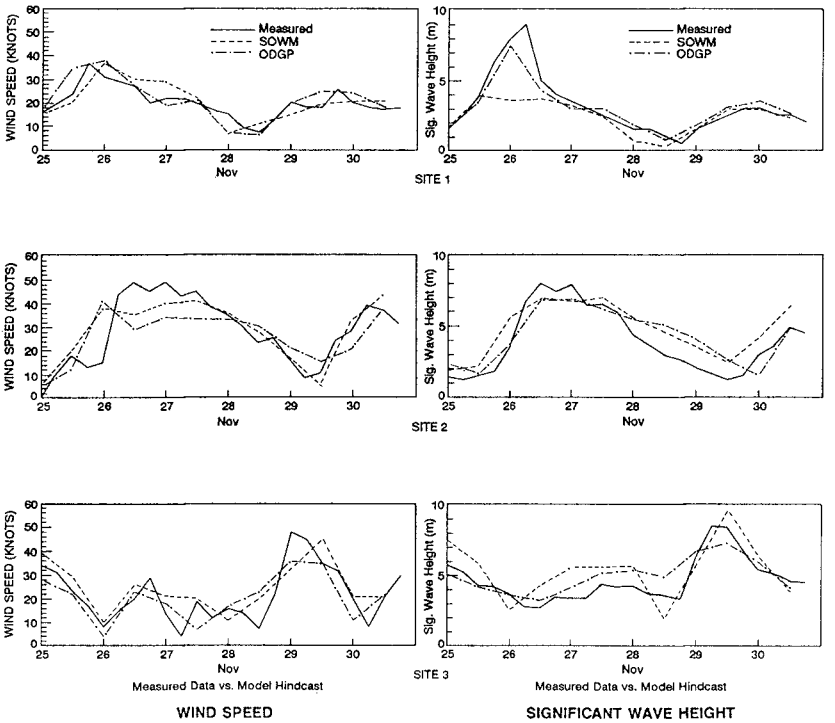

Figure 3: A sample plot showing variation of wind speed and significant wave height at three sites during the storm period November 25-30, 1983.

sites and for all 4 storm periods was made and Table 1 shows the Root Mean Square Error (RMSE) and the Mean Error (ME) together with values of the Scatter Index (SI) and the linear correlation coefficient (r) between model and observed values. The error statistics are prepared for hindcast (zero-hour forecast) products as well as for 24- and 48-hour forecast products. The results of this Table strongly suggest that the ODGP model performs better than the SOWM in a hindcast as well as in a forecast mode.

The results of the model evaluation using the CASP data set are presented in Figures 4 and 5 and in Table 2. The ODGP model was run in an operational mode during the CASP field project using the CMC winds as well as the 'man-machine mix' operational winds and the two products were designated as ODGP-CMC and ODGP-OPR respectively. In

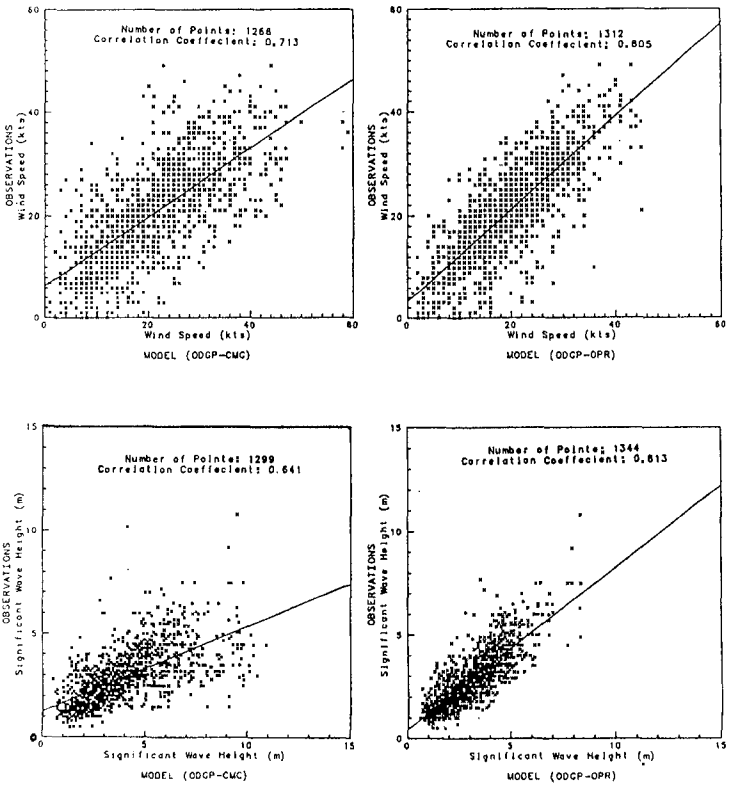

Figure 4: Scatter diagrams between observed versus model wind speed and significant wave height at all sites during the CASP field project 15 January - 15 March, 1986. The regression lines between observed and model values are also shown.

Figure 4 are shown scatter diagrams between model and observed values of wind speed and significant wave heights at analysis time (zero-hour forecasts). The data set covered the two-month period (15 January - 15 March, 1986) of the CASP field project and all three sites were included with two locations assigned to each site. The wind and wave

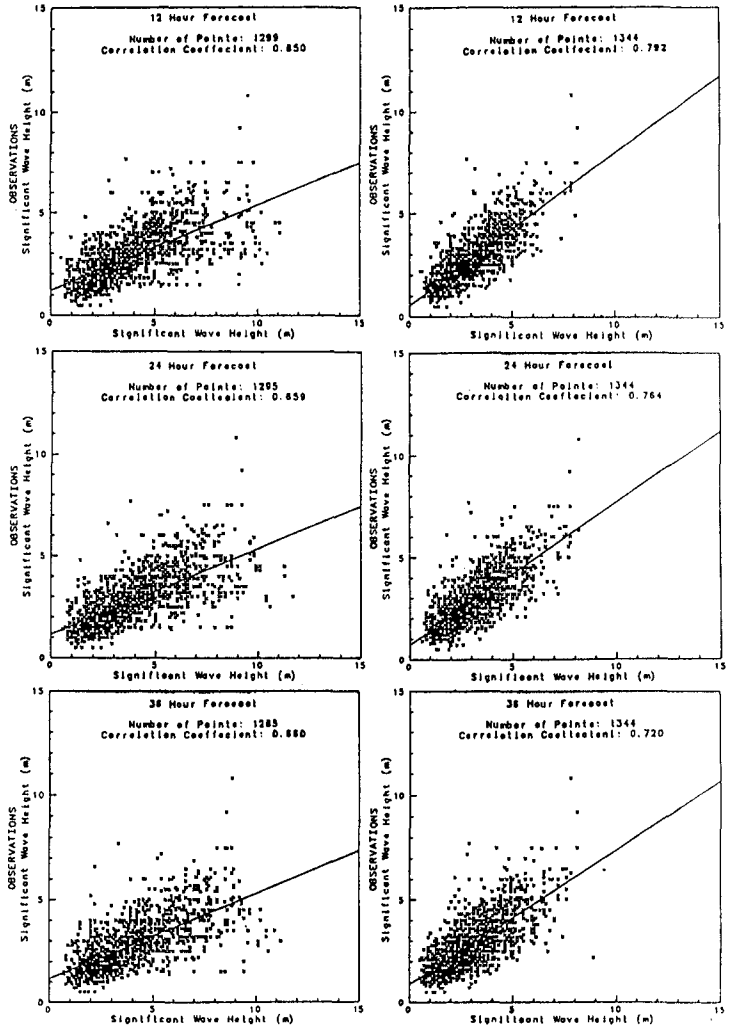

Figure 5: Scatter diagrams between observed versus model significant wave height, at 12-, 24- and 36-hour forecast times. Left: wave heights from model ODGP-CMC; Right: wave heights from model ODGP-OPR.

data were evaluated at four standard meteorological times (00, 06, 12 and 18GMT) during each day of the CASP field project; this provided a sample of 1300 or more data points (excluding missing values) for model validation. The scatter diagrams of Figure 4 suggest that at analysis time, the man-machine mix or the 'OPR' winds provide a slightly better diagnosis of winds when compared with observations at the three sites; this is also indicated by a higher value of the linear correlation coefficient between model and observed wind speeds. The scatter diagrams for significant wave height at analysis time shows that the ODCP-OPR provides significantly better values than those provided by ODGP-CMC. Figure 5 shows the scatter diagrams between model and forecast wave heights at 12-, 24- and 36-hour forecast times. In general, wave heights obtained using OPR winds provide less scatter and higher correlation coefficients with corresponding observed values than those generated using CMC winds. For a quantitative evaluation of the wind and wave products, various error statistics were calculated and these are presented in Table 2. An examination of the wind speed statistics shows that the Mean Error (ME) of the OPR winds has been significantly reduced, most certainly due to the man-machine mix procedure; this, in turn produces smaller RMSE (Root Mean Square Error) for the wind speed and consequently smaller RMSE for the wave height in analysis as well as in forecasting mode.

These error statistics, however, do not provide any information about the spatial differences in the wind fields generated by two different wind models. In order to get an appreciation of these differences, Figures 6 and 7 are presented which show a comparison of wind fields generated by the CMC and the OPR (man-machine mix) models for 16 February 1986. Both the wind fields (in Figures 6A and 6B) refer to the 00GMT analysis time while in Figure 7 are shown differences in the two wind fields obtained by subtracting the OPR wind field from the CMC wind field. The vector at each point in Figure 7 represents the difference in the wind direction while the number at the end of the vector represents the difference in wind speed. A vector parallel to the latitude lines indicates no difference in wind direction between the two wind fields. A positive number indicates that the CMC wind speed is greater than the corresponding OPR wind speed. These three Figures (namely six, seven and eight) show clearly the spatial differences in the two wind fields, particularly in the vicinity of the low pressure centre southwest of Newfoundland where the differences in wind speed and wind direction can be as large as 20 knots and 45 degrees respectively. Furthermore, it can be seen that the CMC weather prediction model in general produces surface marine winds with a definite positive bias when compared against the corresponding ODCP winds; this positive bias appears to produce larger Root Mean Square Error and Scatter Index for ODCP-CMC wave heights as shown in Table 2.

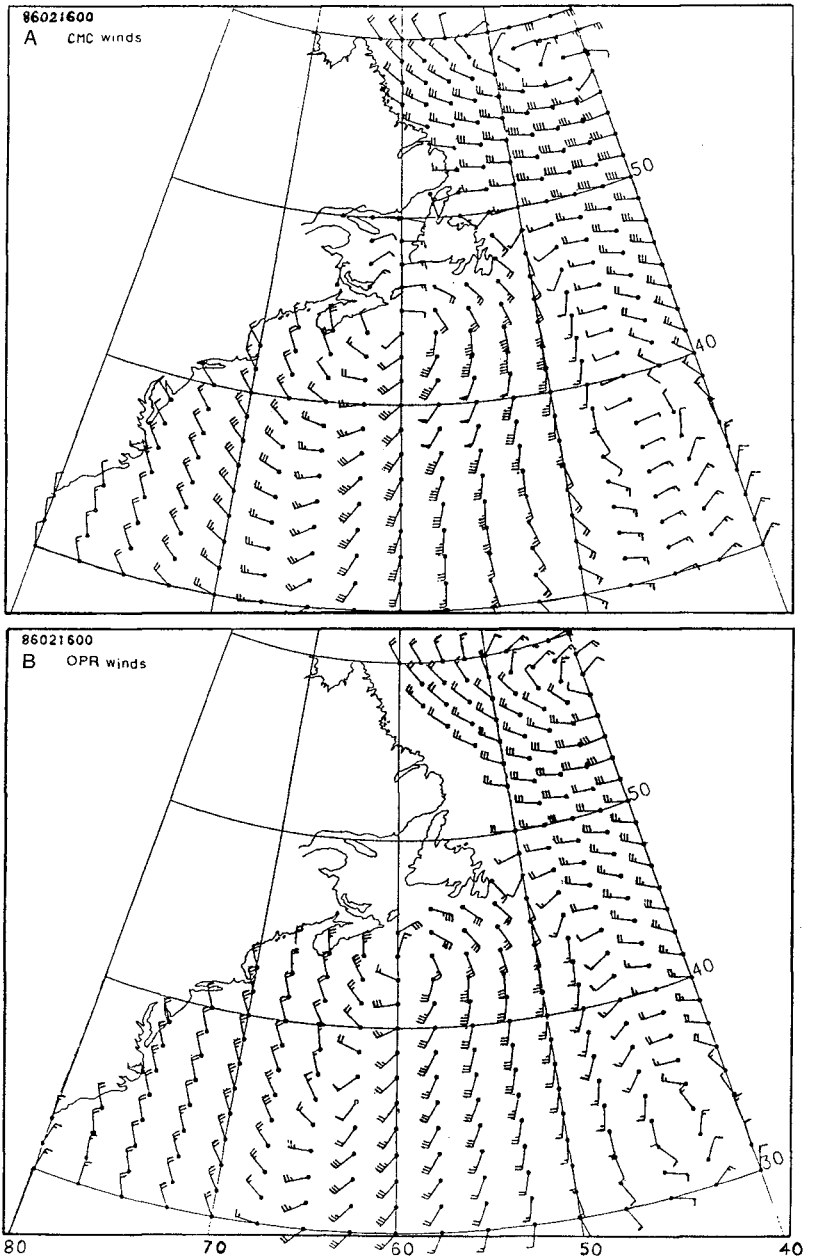

Figure 6: North Atlantic surface wind field, 16 February 1986, 00GMT. A: CMC Model; B: OPR 'Man-Machine Mix' model.

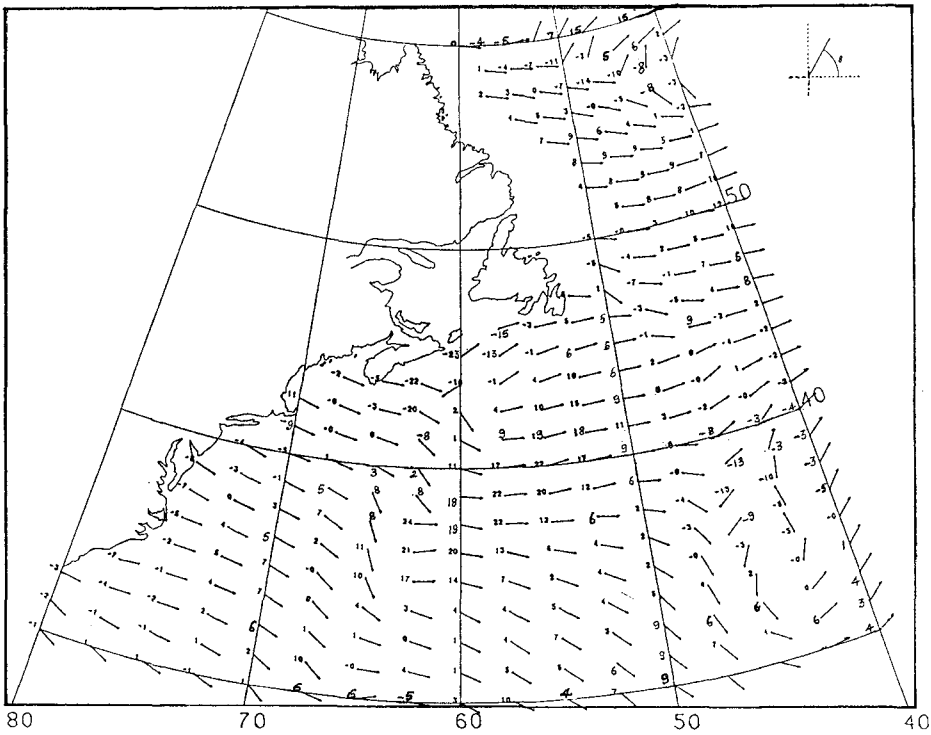

Figure 7: Scalar and vector differences between CMC and OPR wind fields. The vector represents the difference in wind direction (see inset), while the number indicates the difference in wind speed between the two wind fields.

Concluding remarks

The results presented here demonstrate the usefulness of accurate wind specification for driving an operational wave model. The man-machine mix procedure used in the operational running of the ODGP model generates winds which are superior to those produced either by the U.S. Navy's wind model or by the CMC wind model. Furthermore, the study demonstrates the need to adjust the CMC winds for application to a spectral ocean-wave model.

Acknowledgements

The evaluation of the SOWM and the ODGP was done by the MacLaren Plansearch Ltd., Halifax, on contract from the Meteorological Services Research Branch of the Atmospheric Environment Service, Downsview, Ontario. The authors are grateful to Dr. Vincent Cardone, of Ocean-weather Inc. Cos Cob, Connecticut (U.S.A.) for his valuable input in preparation of the paper. This project was supported by the Canadian Government Panel on Energy Research and Development.

TABLE 1

SUMMARY OF ERROR STATISTICS FOR SOWM AND ODGP MODELS AT ALL SITES
(Four storm cases as shown in Figure 2)

	Parameter	WIND SPEED (Knots) Forecast Time 00 hr	24	48	WAVE HEIGHT (Metres) Forecast Time 00 hr	24	48
SOWM	RMSE	11.0	13.8	14.4	1.72	2.25	2.15
	SI	53	67	68	48	63	60
	ME	4.4	5.2	4.3	0.69	0.69	0.66
	r	0.58	0.36	0.17	0.64	0.34	0.38
	n	106	103	102	133	129	127
ODGP	RMSE	10.3	11.8	12.3	1.22	1.67	1.57
	SI	50	57	59	35	47	44
	ME	2.4	5.0	4.1	0.45	0.68	0.42
	r	0.57	0.52	0.34	0.77	0.61	0.55
	n	127	127	127	158	158	158

RMSE: Root Mean Square Error

SI: Scatter Index = $\frac{\text{RMSE}}{\text{Mean Observed Value}} \times 100$

ME: Mean Error;

r: linear correlation coefficient between model and observed values

n: Number of observations

TABLE 2

ODGP-CMC vs. ODGP-OPR; SUMMARY OF ERROR STATISTICS
(CASP data, 15 January - 15 March, 1986)

	Parameter	WIND SPEED (Knots) Forecast Time 00 hr	24	48	WAVE HEIGHT (Metres) Forecast Time 00 hr	24	48
ODGP-CMC	RMSE	7.6	8.5	9.7	1.9	2.0	2.0
	SI	36	41	47	65	69	70
	ME	0.9	2.5	2.9	1.0	1.2	1.2
	r	0.71	0.67	0.56	0.64	0.66	0.64
	n	1268	1268	1228	1299	1295	1275
ODGP-OPR	RMSE	5.9	7.9	9.3	0.8	1.0	1.1
	SI	28	38	44	30	34	37
	ME	-1.3	-0.5	-1.1	0.2	0.2	0.1
	r	0.81	0.62	0.48	0.81	0.76	0.69
	n	1312	1312	1312	1344	1344	1344

References

Cardone, V.J., 1969: Specification of the wind field distribution in the marine boundary layer for wave forecasting. Report TR-69-1, Geoph. Science Laboratory, New York University, 131 pp.

Cardone V.J., C.B. Greenwood, J.A. Greenwood, W.J. Pierson, R.A. Salfi, R.A. Stacy, 1974: Development of wave hindcasting methods applicable to hurricanes. Final Report, Ocean Data Gathering Program, Analysis Phase, Submitted to Shell Development Company, U.S.A., July 1974.

Cardone, V.J., 1978: Specification and prediction of vector wind on the U.S. continental shelf for application to an oil slick trajectory forecast program. Final Report for NOAA, U.S. Dept. of Commerce, Silver Spring, Maryland, U.S.A., Nov. 1978.

Delage, Y., 1985: Surface turbulent flux formulation in stable conditions for atmospheric circulation models. Monthly Weather Review, Vol. 113, 89-98.

Inoye, T., 1967: On the growth of the spectrum of a wind-generated sea according to a modified Miles-Phillips mechanism and its application to wave forecasting. Report 67-5, Geoph. Sciences Laboratory, New York University.

Mihok, W.F. and J.E. Kaitala, 1976: U.S. Navy Fleet Numerical Weather Central operational five-level global fourth-order primitive-equation model. Monthly Weather Review, Vol 104, 1527-1550.

Miles, J.W., 1957: On the generation of surface waves by shear flows. J. Fluid Mechanics, Vol. 6, 185-204.

Phillips, O.M., 1957: On the generation of waves by turbulent wind. J. Fluid Mechanics, Vol. 4, 426-434.

Pierson, W.J., 1982: The Spectral Ocean Wave Model (SOWM), A northern hemisphere computer model for specifying and forecasting ocean wave spectra. Final report No. DTNSRDC-82/11, U.S. Naval Oceanographic Command Detachment, Asheville, North Carolina, 201 pp.

Pierson, W.J. and L. Moskowitz, 1964: A proposed spectral form for fully developed seas based on the similarity theory of S.A. Kitaigorodskii. J. Geoph. Research, Vol. 69, 5181-5191.

Snyder, R. and C.S. Cox, 1966: A field study of the wind generation of ocean waves. J. Marine Research, Vol. 14, 141-177.

CHAPTER 29

LATERAL MIXING AND WAVE DIRECTION IN THE WAVE-CURRENT INTERACTION REGION

Kyoung Ho Kim [1], Sawaragi Toru [2], Deguchi Ichiro [3]

ABSTRACT

The lateral mixing coefficient, in which the wave energy dissipation by wave breaking is taken account and the assumption of Richardson's 4/3 power law is involved, is derived for the surf zone and the diffusion of tracers injected in the wave-current interaction region is discussed experimentally to investigate the proposed lateral mixing coefficient. Furthermore measurements of velocity field on the three dimensional sloping beach of plane wave flume have been made by a bidirectional electromagnetic current meter. The results were used to investigate the characteristics of the structure of on-offshore and alongshore mean currents and the techniques for the determination of wave angle in the surf zone

1. INTRODUCTION

There are many problems which have to be solved in analyzing the nearshore currents system in the surf zone, such as the expressions for the bottom shear stress, lateral mixing, wave direction, and radiation stress and so on. Of them, especially, the lateral mixing and wave direction problems have not been clarified sufficiently.

The studies of oceanic and estuarine mixing have been performed a lot experimentally and theoretically, however, for the lateral mixing which designates the turbulent exchange of momentum few detailed studies have been made because the turbulence generated due to breaking waves is not universally defined. Wave directions have been computed on the basis of the law of conservation of waves together with the irrotationality of wave number. In laboratory, in general, by taking the angle between the shoreline and the wave crest line wave angles are determined, however, this has many problems in the surf zone because of the difficulties in the de-

1. Assistant professor, Dept. of Civil Engineering, Chungbuk National University, Cheongju, Korea
2. Professor, Dept. of Civil Engineering, Osaka University, Suita, Osaka, Japan
3. Assistant professor, Dept. of Civil Engineering, Osaka, University, Suita, Osaka, Japan

termination of the wave crest line .

In this paper, the equation for the lateral mixing coefficient in which the wave energy dissipation is taken account is proposed. Using the experimental results for longshore currents and diffusion of tracers injected in the wave-current interaction region, the validity of proposed lateral mixing coefficient is verified. The methods of the determination of wave directions are also examined by using the horizontal velocity components and the results are compared with the values obtained from other methods.

2. LATERAL MIXING

The lateral mixing term corresponding to the horizontal turbulent momentum exchange in the wave-current interaction region is an important parameter for determining the spatial distribution of longshore current with distance to the shoreline and it has been said to be dependent on the local gradient of mean currents.

In the paper, lateral mixing coefficient is derived by using the wave energy dissipation rate due to wave breaking. The dependence of the lateral mixing coefficient on the wave steepness and bottom slope are discussed. The principle assumptions are used herein as follows.

(1) Lateral mixing in the surf zone can be expressed by Richardson's 4/3 power law.
(2) The mean dissipation rate of turbulence energy is in balance to that of wave energy due to wave breaking(Battjes, 1975)
(3) The mixing scale is the same in order as mean water depth(see Iwata and Sawaragi, 1982).

From the assumption (1), lateral mixing coefficient K becomes following expression.

$$K \sim \varepsilon^{1/3}(\sqrt{\overline{Y}^2})^{4/3} \tag{1}$$

where ε is the mean rate of turbulent energy dissipation and $\sqrt{\overline{Y}^2}$ is the mixing scale. The mean dissipation rate of turbulent energy and the mixing scale are expressed from the assumptions (2)and (3)

$$\varepsilon \sim D/\rho d \tag{2}$$

$$\sqrt{\overline{Y}^2} \sim d \tag{3}$$

where D is the mean rate of wave energy dissipation, which by hypothesis equals the rate of prodection of turbulent energy. ρ is the water density and d is the mean water depth.

Sawaragi et. al.(1984) already reported that the mean dissipation rate of wave energy D can be expressed as Eq.(3) using the experimental results for the breaking waves on the sloping beach.

$$D = cF\rho^{-1/2}d^{-3/2}E^{3/2} \tag{4}$$

where c is the dimensionless constant, E is the wave energy density and F is the wave decay coefficient, which is expressed by surf similarity parameter ξ_o and the bottom slpoe S .

$$F = \begin{cases} 5.30 - 3.30\xi_o - 0.07S^{-1}, & \text{in the surf zone} \\ 0 & \text{, outside the surf zone} \end{cases} \tag{5}$$

Substituting Eqs. (2)- (4) into Eq. (1), we obtain the follwing relation

$$K = \begin{cases} AF^{1/3}\sqrt{gd}\ H, & \text{, in the surf zone} \\ 0 & \text{, outside the surf zone} \end{cases} \tag{6}$$

where A is the dimensionless constant and H is the wave height. Considering the variation of mean water level and using the coefficient γ, which is the empirical proportionality factor between the wave height and the mean water depth, Eq. (6) is transformed into Eq.(7).

$$K = \begin{cases} AF^{1/3}\gamma S^{*}x'\sqrt{gd}, & \text{in the surf zone} \\ 0 & \text{, outside the surf zone} \end{cases} \tag{7}$$

where S^* is the modified bottom slope and x' is the distance from the mean shoreline.

Perhaps the most well-known and frequently used expression for K was given by Longuet-Higgins(1970b). He suggested Eq.(8) for K by using Prandtl's mixing length theory.

$$K = N\,x\sqrt{gd} \tag{8}$$

where N is the constant which has the range of $0 < N < 0.016$. On the other hand, Battjes(1975) proposed Eq.(9) for K assuming the turbulent energy generated due to breaking waves.

$$K = (5/16\gamma^2)^{1/3}S^{4/3}M\sqrt{gd} \tag{9}$$

where M is the constant which is similar to N of Eq.(8).

Comparing Eq.(7) with Eqs.(8) and (9), we find that K in Eq.(7) comprises the wave steepness H_o/L_o, wave height-water depth ratio γ and the bottom slope S which represent

the wave characteristics. Accordingly it is thought that the constant A in Eq.(7) is more universal than the constants M and N.

To examine how K in Eq.(7) depends on wave steepness and the bottom slope, the relationship between $S*F^{1/3}$ and H_o/L_o is shown in Fig. 1. The values of $S*F^{1/3}$ are almost the function of S only and are not directly related with the wave steepnesses. Eq.(7) is similar to Eq.(9) proposed by Battjes.

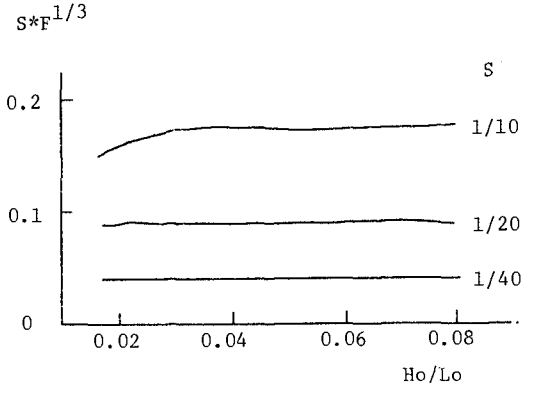

Fig. 1. Value of $S^*F^{1/3}$ versus Ho/Lo.

3. WAVE DIRECTION

Wave angle just prior to wave breaking may be the most important parameter in the surf zone for the determination of longshore currents and sediment transport. According to Longuet-Higgins(1970 a,b) good estimates of wave angle are critical for the calculation of the alongshore component of radiation stresses, particularly when the angle of incident wave is small. Sherman et. al. (1986) reported that when the wave angle is 5°, a 1° error in the angle estimate results in a 20% error in the radiation stress computation.

In the numerical calculation of nearshore current, the wave angle is computed by the law of conservation of waves together with the irrotationality of wave number. On the other hand, in the field or laboratory wave directions have been determined by using either the horizontal velocity components measured with a current meter or the angle between wave crest line and shoreline. In laboratory, in general, the latter has been used, however, this has many problems because of the difficulties in the determination of obvious

wave crest line in the surf zone. Thus the validity of the above-mentioned methods has been performed not by the comparison of the computed results with the measured results but by how the calculated currents can revive the real currents.

In the present paper, the horizontal velocity components were measured by a bidirectional electromagnetic current meter in the fixed bed of plane flume and the problems in the measurements and the calculation of wave angle are examined by comparing the results from the above-mentioned methods. The wave angle is defined by the angle relative to the shore-normal as shown in Fig. 2.

If u and v are the onshore(x) and alongshore(y) components of velocity, respectively, two methods for determining the wave angle are derived as follows.

$$\theta_p = \tan^{-1}[2\overline{(u-U_o)(v-V_o)}/\{\overline{(u-U_o)^2} - \overline{(v-V_o)^2}\}]/2 \qquad (10)$$

$$\theta_t = \tan^{-1}(v_w/u_w) \qquad (11)$$

where "$\overline{\quad}$" represents the time mean values and the subscripts o is corresponding to the time mean currents and w corresponding to the components of fluctuation.

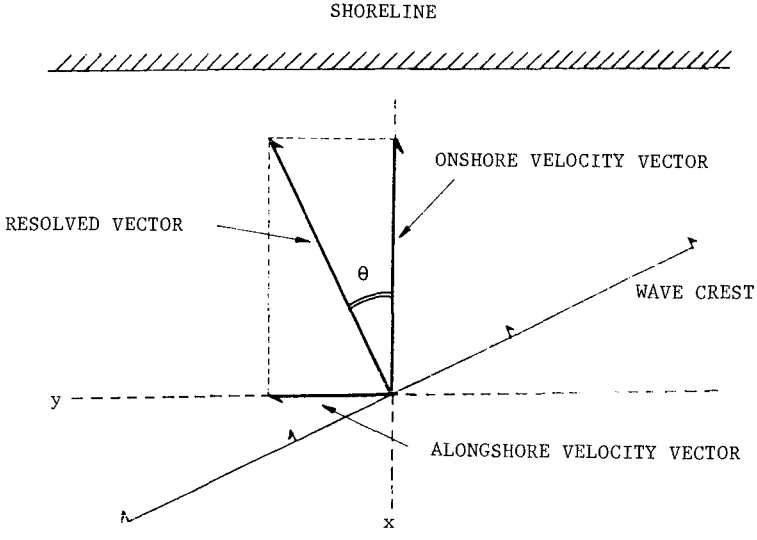

Fig. 2 Coordinate system for the wave angle.

4. EXPERIMENTS AND RESULTS

4.1 Experimental set-up and procedures

The wave facility at Osaka university was used to conduct the experiments. The plane flume is 20m long, 10m wide and 50cm deep. The waves broke on the bottom slope 1/10 (Fig. 3) and the shoreline was made in order to form the angle of 30° against the wave generating board. The wave conditons are shown in Table. 1.

Table. 1 Wave conditions

bottom slope S	wave period T(sec)	wave steepness H_o/L_o	wave height H_o(cm)	incident wave angle θ(degree)
1/10	0.91	0.052	6.70	30
	1.15	0.033	6.68	30
	1.44	0.015	6.70	30

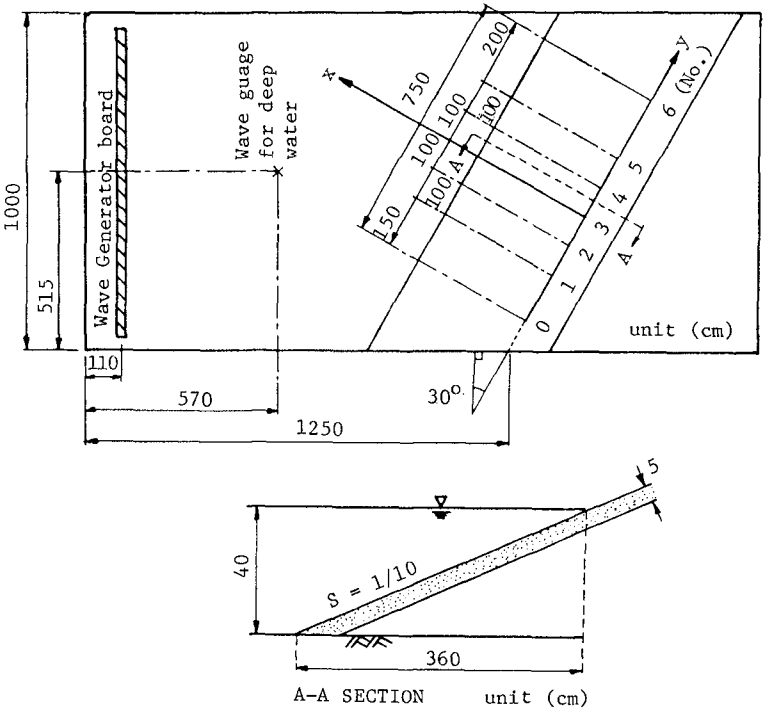

Fig. 3 Experimental set-up.

Wave profiles were measured over the surf zone at positions with an interval of 10cm or 20cm to the onshore direction(x) by means of the capacity type wave gauges. velocities were measured at 1-3 points of the vertical directions with the same measuring points of wave profiles by a bidirectional electromagnetic current meter. Simultaneously the wave crest and the diffusion of tracers injected in the flume were took photograps by a 16mm cine-camera to determine the wave direction and the coefficient of diffusion of tracer (L).

The wave profiles and the velocities were recorded as electric signals with a data recorder and they were destised at 100 hz by computer over 40 or 50 waves per each measueing point and the computer techniques were utilized to obtan the ensemble mean values. In Fig. 4-6, the example of the experimental results are shown. The upper figure shows the distributions of wave height H and the variation of mean water level $\overline{\eta}$ and the lower is the distribution of longshore current with the distance to the shoreline together with the computed values of them.

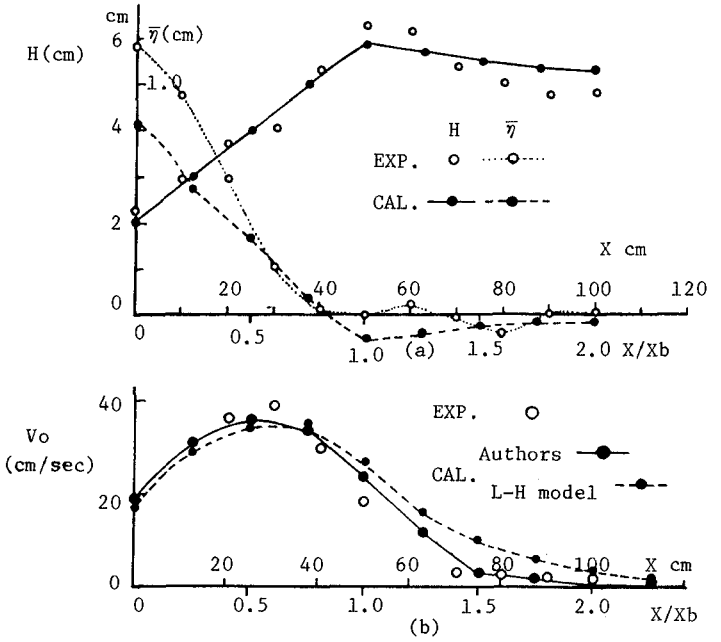

Fig. 4 Wave height, wave set-up and longshore current. (Ho/Lo = 0.015)

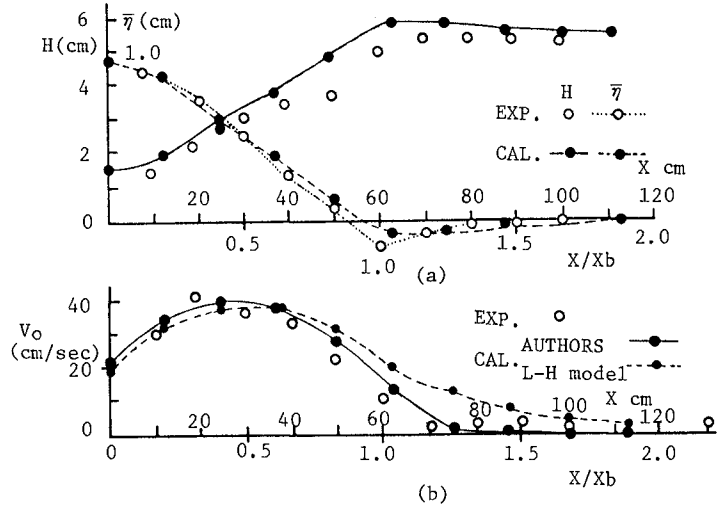

Fig. 5 wave height, wave set-up and longshore current.
(Ho/Lo = 0.033)

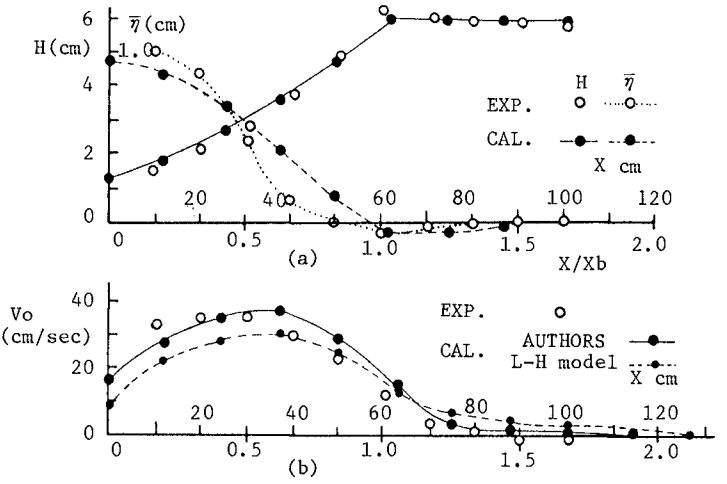

Fig. 6 Wave height, wave set-up and longshore current.
(Ho/Lo = 0.052)

4.2 Time mean on-offshore and longshore current

Fig. 7 shows the vertical distributions of time mean on- offshore(U_o) and longshore current(V_o) measured in the case in which the wave steepness H_o/L_o= 0.015. As shown in Fig. 7(a) the longshore current is almost uniform vertically at least under the wave trough. The values of longshore currents in Fig. 4-6 are the mean values of these ones.

On the other hand, the on-offshore current U_o in Fig. 7 (b) is facing the offshore directions and the magnitude of them is larger in the upper zone and smaller in the lower zone. Whether this offshore current is a kind of rip current or a compensating one for the mass transport is not clear yet. In two-dimensional sloping beach, however, Nadaoka et. al.(1982) and Svendsen(1984) already reported that steady flows compensating for the mass transport exist. The values of U_o increse as they go towards the shoreline and the maximum value of it appears within the surf zone.

Fig. 8 shows the comparisons of the offshore mean current U_o in the present experiments which is measured on the

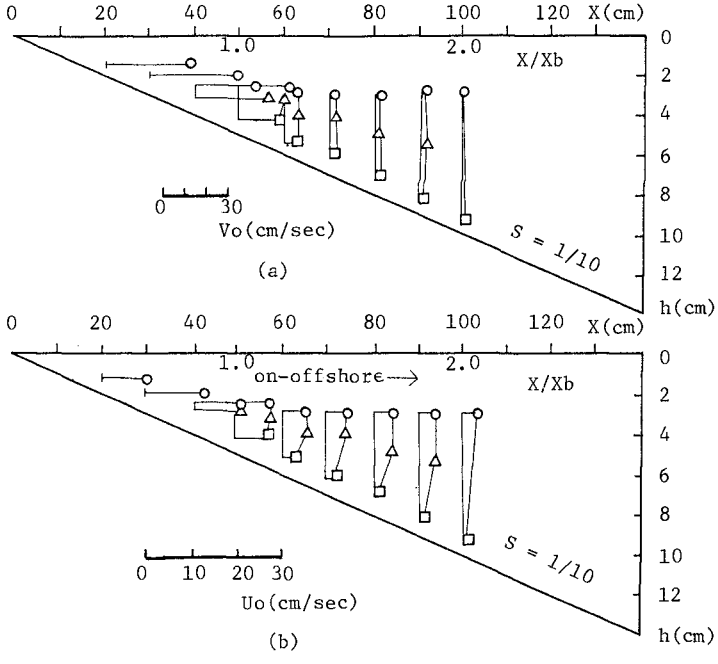

Fig. 7 Vertical distribution of on-offshore and longshore currents.

three-dimensional sloping beach with those measured on the two-dimensional sloping beach by Nadaoka et. al.(1984). The normalized values of U_o by $\sqrt{gh_b}$ (h_b is the water depth corresponding to the breaking point) are plotted with the distance to the shoreline. The results are favourably good in magnitude and direction except for the neighbourhood of the shoreline. This mean current was also measured for the cases of H_o/L_o= 0.033 and 0.052, and its maximum value is nearly $U_o/\sqrt{gh_b} \cong 0.2$ regardless of wave steepnesses. This makes us to guess that compensating flow for the mass transport exists even in the three-dimensional flow field where longshore currents occur.

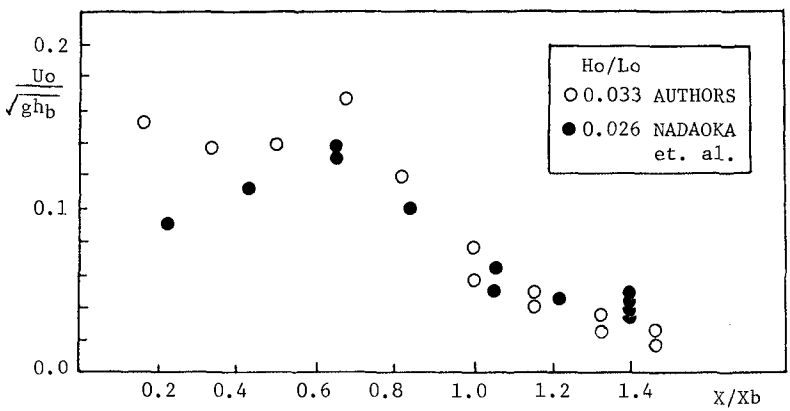

Fig. 8 Comparison of offshore current.

4.3 Diffusion coefficient

The diffusion coefficient(L) is shown in Fig. 9, which is obtained from the time variation of tracers continuously injected at positions x/x_b=1/3, 2/3, 1 and 3/2, when the longshore currents occur(x_b is the distance to the breaking point). The diffusion coefficient somewhat decreases as the wave steepnesses increase, however, the variation is small and it is in proportion to the power of 3/2 of the distance from the shoreline. it is almost zero outside the surf zone.

It was already shown that the present model for the lateral mixing in sectin 2 is in proportion to the bottom slope S, wave height-depth ratio γ, and the distance from the shoreline x. In the present experiments the value of γ, has the range of 0.8~1.2 except for the vicinity of the shoreline and the breaking point. Its local variation is larger rather than that due to wave steepnesses, that is, the diffusion coefficient may not have the obvious dependency on the wave steepness. since it is thought that the

mechanisms of the lateral mixing can be assumed to be the same, the present model for the lateral mixing, Eq.(7) is reasonable. To conform this fact, the numerical calculation for the distributions of longshore currents with the distance to the shoreline and wave deformation was performed by using the conservation equations of mass, momentum and energy together with Eq.(4) for wave energy dissipation rate and Eq.(7) for the lateral mixing coefficient.The calculated results are illustrated in Fig.4- 6 together with the experimental results. In the calculation, radiation streses, which are computed by the small amplitude wave theory for long waves , were multiplied by the reduction coefficient of 0.6-0.7 according to Stive and Wind (1984). In the figures the computed profiles of longshore currents using Eq.(8) for the lateral mixing coefficient proposed by Longuet-Higgins are also shown for comparisons. In the calculation of them the effect of wave-current interaction was considered. The computed longshore currents with Eq.(7) is in good accordance with the experimental results, particularly, outside the surf zone.

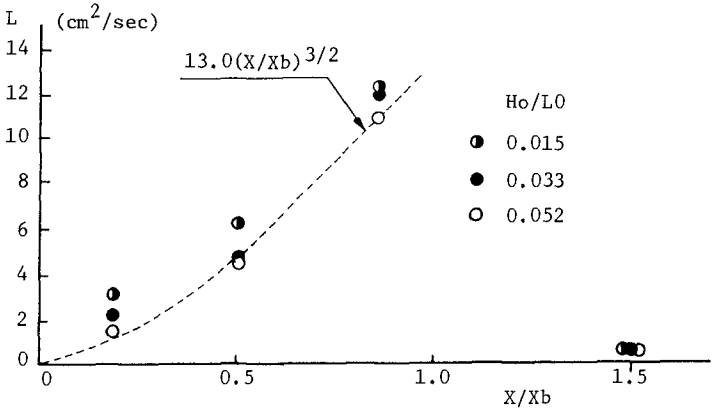

Fig. 9 Diffusion coefficient.

4.4 Wave direction

Fig. 10 shows the comparisons of wave angles obtained by using the methods mentioned in section 3. θ_m is the angle obtained by taking between the shoreline and the wave crest line taken photographsby 16mm cine-camera. θ_p is the one computed by Eq.(10). The computed values obtained by the numerical analysis are also shown for comparisons. From Fig. 10, it is found that θ_p shows a good accordance with the calculated values by the law of conservation of waves outside the surf zone. Within the surf zone the values of θ_p largely varies, however, on the average they are nearly in accordance with the calculated values considering the effect of wave-current interaction. The wave angles obtained from

the wave crest line are generally overestimated.

In Fig. 11 and 12, the phase mean velocity components of wave fluctuation u_w and v_w are vectorally plotted for the regions of $x/x_b=0.6$ in the surf zone and of $x/x_b=2.2$ outside the surf zone, respectively. In the figure(a) of each the vector(u_w, v_w) and the wave angles θ_p and θ_t are shown. Figure (b) shows the profiles of the phase mean values of the displacement of water level η_w and those of water particle velocities due to fluctuation(u_w, v_w). In the surf zone the phases of η_w, u_w and v_w do not accord well one another. Though the values of v_w were taken over thirty waves, the turbulence of it is very large. Thus the wave direction θ_t determined by the vector(u_w, v_w) greatly varies according to the phases with the range of about ±80°. On the other hand, outside the surf zone the phases of η_w, u_w and v_w show a good accordance one another, especially, the accordance of the phases between u_w and v_w is so good. Accordingly, the change of θ_t is small and it varies within the range of about ±15° . The values of θ_p is almost the same as those of θ_t in the phase in which η_w is less than zero.

From these results we see that outside the surf zone where longshore current and turbulence are not predominant, the wave direction can be determined by θ_p and θ_t, however, in the surf zone where the turbulence due to breaking and longshore current are predominant, it can not be always determined by them. The large variation of θ_p in the surf zone is thought to be caused by the turbulence of v_w and the interaction between the water particle velocities due to fluctuation and the mean currents.

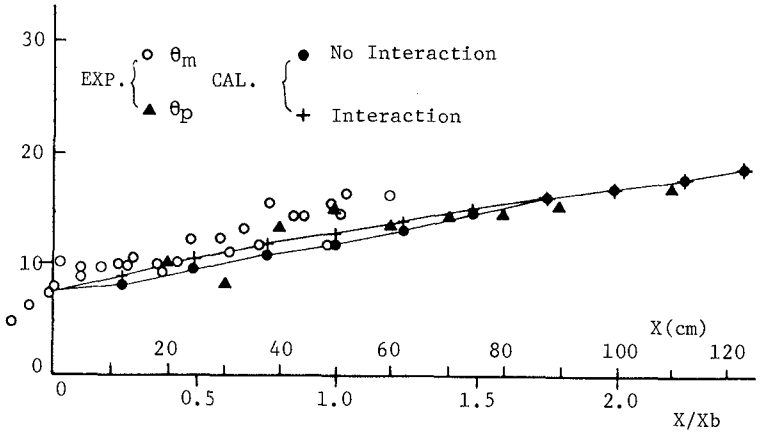

Fig. 10 Comparisons of wave angles.

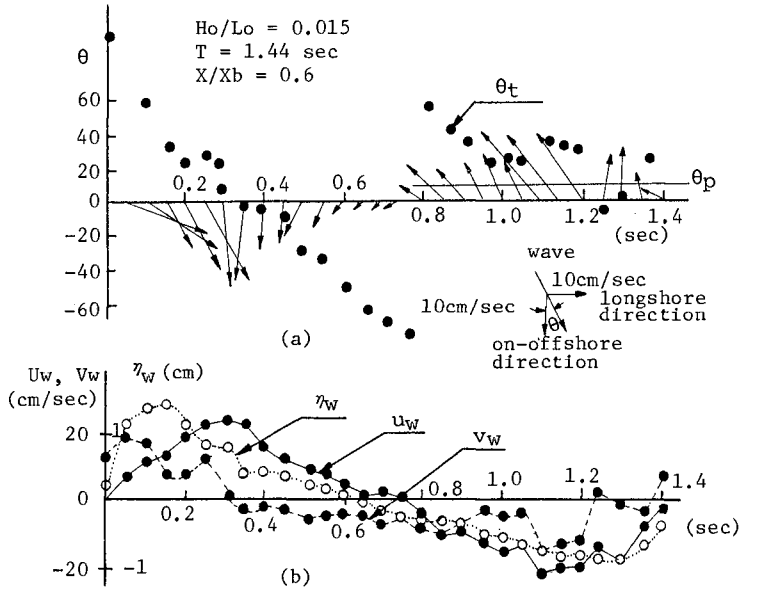

Fig. 11 Water particle velocity vector in the surf zone.

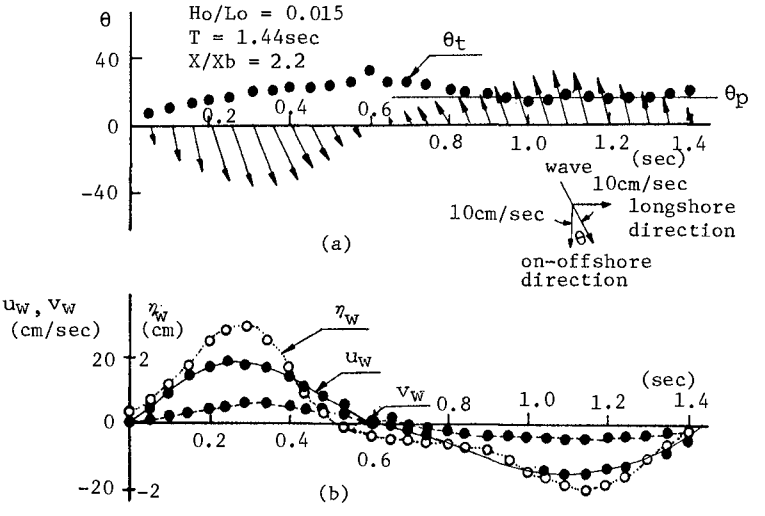

Fig. 12 Water particle velocity vector outside the surf zone.

5. DISCUSSION

In this paper, the lateral mixing coefficient, wave direction and the characteristics of on-offshore(U_O) and longshore current(V_O) are discussed. Firstly the lateral mixing coefficient is derived for the three-dimensional sloping beach where longshore current occurs. Secondly experiments are carried out to examine the wave direction, the structure of mean current in the surf zone and the diffusion of tracers injected.

The lateral mixing coefficient on the basis of wave energy dissipation is shown to be applicable for the surf zone. Wave angle θ_p caculated by the horizontal velocity compcnents and the mean currents show good estimates outside the surf zone. Within the surf zone the variation of θ_p is large, however, on the average its values are nearly in accordance with those by traditional refraction analysis of deep water waves considering the effect of wave-current interaction. Wave angles obtained by the photographic interpretation of wave crest are generally overestimated. Furthermore it is found that even on the three-dimensional sloping beach where longshore current occurs the compensating flow may exist.

6. REFERENCES

Battjes, J. A.(1975) Modeling of turbulence in the surf zone. Proc. Symp. Modeling Technique, pp. 1050-1061.

Iwata. K. and Swaragi, T.(1982) Wave deformation in the surf zone. Memoirs, Nagoya University, vol. 34, No. 2, pp.239-283.

Galvin, C. J.(1967) Longshore current velocity; A review of theory and data. Review of Geophysics, vol. 5, pp. 287-304.

Longuet-Higgins, M. S.(1970 a) Longshore currents generated by obliquely incident sea waves 1. Jour. Geophys. Res., vol. 75, No. 30, pp. 6778-6789.

Longuet-Higgins, M. S.(1970 b) Longshore currents generated by obliquely incident sea waves 2. Jour. Geophys. Res. , Vol. 75, No.30, pp. 6790-6801.

Nadaoka, K., Kondoh, T. and Tanaka, N.(1982) The structure of velocity field within the surf zone revealed by means of laser-doppler anemometry. Report, Port and Harbour Research Institute, vlo. 21, No. 2, pp. 49-106.(in japanese)

Sawaragi, T., Deguchi, I., and Kim, K. H.(1984) Energy loss and wave set-up in the surf zone. Tech. Rept., vol. 34, No. 1779, Osaka University, pp. 329-338.

Sherman, D. J. and Greenwood, B.(1986) Determination of wave angle in shallow water. Jour. Waterway, Port, Coastal and Ocean Engineering, vol. 112, No. 1, pp. 129-139.

Stive, M. J. F. and Wind, H. G.(1982) A study of radiation stress and wave set-up in the nearshore region. Coastal Engineering, vol. 6, pp. 1-25.

Svendsen, I. A.(1984) Mass flux and undertoe in a surf zone. Coastal Engineering, vol. 8, pp. 347-365.

CHAPTER 30

CIRCULATION KINEMATICS IN NONLINEAR LABORATORY WAVES

Tae-In Kim,[1] Robert T. Hudspeth,[2] and W. Sulisz[3]

ABSTRACT

A weakly nonlinear solution is presented for the two-dimensional wave kinematics forced by a generic wavemaker of variable-draft. The solution is valid for both piston and hinged wavemakers of variable-draft that may be double articulated. The second-order propagating waves generated by a planar wave board are composed of two components; viz., a Stokes second-order wave and a second-harmonic wave forced by the wavemaker which travels at a different speed. A previously neglected time-independent solution that is required to satisfy a kinematic boundary condition on the wavemaker as well as a mixed boundary condition on the free surface is included for the first time. A component of the time-independent solution is found to accurately estimate the mean return current (correct to second-order) in a closed wave flume. This mean return current is usually estimated from kinematic considerations by a conservation of mass principle

INTRODUCTION

Flick and Guza (1980) investigated the motion of a hinged wavemaker that is hinged either on or below the channel bottom using a Stokes expansion. They studied the relationship between the second-harmonic (secondary) waves forced by the wavemaker and the Stokes waves by computing the coefficients for the propagating eigenmode numerically. Their solution, like that of Daugaard (1972), neglects the interactions of the first-order evanescent eigenmodes at the free-surface boundary near the wavemaker because these evanescent eigenmodes do not contribute to the propagating waves. Furthermore, their solution as well as that of Madsen (1971) and Daugaard (1972) is not exact because they neglect the time-independent, second-order solutions which are required to satisfy exactly the boundary conditions at the wavemaker and at the free surface.

Massel (1981) attempted to extend the work of Flick and Guza (1980) by including a time-independent solution but only for the kinematic boundary condition at the wavemaker.

A closed-form solution is presented that is correct to second-order (except for the singularities at the irregular points) for the fluid motion forced by a sinusoidally moving generic wavemaker of variable draft. The generic wavemaker motion is doubly articulated and includes both piston and hinged wavemakers. The previously

[1]Asst. Prof., Dept. of Civil Engrng., Korean Military Academy, Seoul, Korea 130-09.
[2]Prof., Ocean Engrng. Program, Dept. of Civil Engrng., Oregon State University, Corvallis, Oregon 97331.
[3]Scientist, Inst. of Hydroengineering, Polish Academy of Sciences, Cystersow 11, 80-953 Gdansk, Poland.

neglected time-independent solutions required to satisfy both the nonlinear free surface and wavemaker boundary conditions are compared with the Eulerian mean horizontal momentum per unit area. The mean return current required to satisfy conservation of mass in closed wave flumes is estimated reasonably well by the time-independent, second-order solution for a broad class of planar wavemakers.

NONLINEAR WAVEMAKER THEORY

For convenience, all physical variables (denoted by superscript asterisks, *) will be made dimensionless by the following: $(x,z,h,d,b,\Delta,L) = k^*(x^*,z^*,h^*,d^*,b^*,\Delta^*,L^*)$; $(t,T) = \sqrt{g^*k^*}\,(t^*,T^*)$; $(H,\eta,S,\xi,\chi) = (H^*,\eta^*,S^*,\xi^*,\chi^*)/a^*$; $(u,w) = (u^*,w^*)/(a^*\sqrt{g^*k^*})$; $\Phi = \Phi^*/(a^*\sqrt{g^*/k^*})$; $B = B^*/(a^*g^*)$; and $p = p^*/(\rho^*a^*g^*)$ where a^* = amplitude of the first-harmonic wave component; $k^*(= 2\pi/L^*)$ = the wave number; L^* = wave length; g^* = gravitational constant; ρ^* = fluid mass density; and T^* = wave period = the period of the wavemaker oscillation.

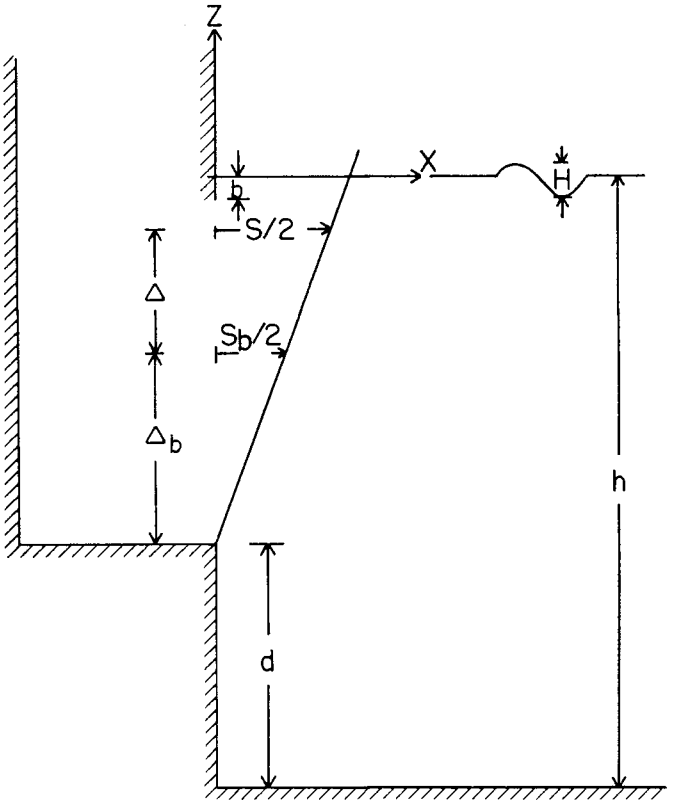

Fig. 1. Definition sketch for generic wavemaker

A generic wavemaker is shown in Fig. 1 which generates two-dimensional, irrotational motion of an inviscid, incompressible fluid in a semi-infinite channel of constant, still water depth, h. The fluid motion may be obtained from a scalar velocity potential $\Phi(x,z,t)$ by

$$[u,w] = -\vec{\nabla}\Phi \tag{1}$$

in which the two-dimensional gradient operator is $\vec{\nabla}(\cdot) = [\partial/\partial x, \partial/\partial z]$.

The velocity potential is a solution to

$$\nabla^2\Phi = 0 \qquad ; \; x > \varepsilon\chi(z,t) \; , \; -h < z < \varepsilon\eta(x,t) \tag{2a}$$

with boundary conditions (Phillips, 1977)

$$\partial\Phi/\partial z = 0 \qquad ; \; x > \varepsilon\chi(-h,t) \; , \; z = -h \tag{2b}$$

$$\frac{\partial^2\Phi}{\partial t^2} + \frac{\partial\Phi}{\partial z} - [\varepsilon\frac{\partial}{\partial t} - \frac{1}{2}\varepsilon^2\vec{\nabla}\Phi\cdot\vec{\nabla}]\left|\vec{\nabla}\Phi\right|^2 + \frac{dB}{dt} = 0; x>\varepsilon\chi(\eta,t), z=\varepsilon\eta(x,t) \tag{2c}$$

$$\partial\Phi/\partial x + \partial\chi/\partial t - \varepsilon\partial\Phi/\partial z \; \partial\chi/\partial z = 0 \quad ; \; x = \varepsilon\chi(z,t) \; ; \; -h < z < \varepsilon\eta(t) \tag{2d}$$

where $B(t)$ = the Bernoulli constant and the parameter $\varepsilon = a^*k^* << 1$. In addition, a radiation condition is required at infinity as $x \to +\infty$ in order to insure that propagating waves be only right progressing or that evanescent eigenmodes be bounded. The instantaneous wavemaker displacement from its mean position, $\chi(z,t)$, is given by

$$\chi(z,t) = \xi(z)[U(z+h-d)-U(z+b)]\sin\omega_o t = \xi(z)\Delta U \sin\omega_o t \tag{3}$$

where $U(\cdot)$ = the Heaviside step function. The amplitude of the wavemaker displacement, $\xi(z)$, for a double-articulated piston or hinged wavemaker of variable draft is given by the following equation for a straight line:

$$\xi(z) = [(S/2)/(\Delta/h)][M(1+z/h)+B'] \tag{4}$$

where $M = (1-S_b/S)$; and $B' = [\Delta/h - M(d/h+\Delta_b/h+\Delta/h)]$; in which $S/2$ = the dimensionless wavemaker stroke measured at an arbitrary elevation above the wave flume bottom at $z = -h+d+\Delta_b+\Delta$. A piston wavemaker is represented by $S_b = S$; and a wavemaker of full-depth draft is represented by $b = d = 0$ and $\Delta = h$. The dimensionless free-surface $\eta(x,t)$ and total pressure $p(x,z,t)$ are

$$\eta(x,t) = \partial\Phi/\partial t - \frac{1}{2}\varepsilon\left|\vec{\nabla}\Phi\right|^2 + B(t) \quad ; \; x > \varepsilon\chi(\eta,t) \quad , \; z = \varepsilon\eta(x,t) \tag{5}$$

$$p(x,z,t) = \partial\Phi/\partial t - \frac{1}{2}\varepsilon\left|\vec{\nabla}\Phi\right|^2 - z/\varepsilon + B(t) \; ; \; x>\varepsilon\chi(z,t) \; , \; -h<z<\varepsilon\eta(x,t) \tag{6}$$

Equations (2c & d) & (5) may be expanded in a Maclauren series by

$$\sum_{n=0}^{\infty}\frac{(\varepsilon\eta)^n}{n!}\frac{\partial^n}{\partial z^n}[\frac{\partial^2\Phi}{\partial t^2} + \frac{\partial\Phi}{\partial z} - (\varepsilon\frac{\partial}{\partial t} - \frac{1}{2}\varepsilon^2\vec{\nabla}\Phi\cdot\vec{\nabla})\left|\vec{\nabla}\Phi\right|^2 + \frac{dB}{dt}] = 0 \; ; x>0 \; , z=0 \tag{7a}$$

$$\eta - \sum_{n=0}^{\infty}\frac{(\varepsilon\eta)^n}{n!}\frac{\partial^n}{\partial z^n}[\frac{\partial\Phi}{\partial t} - \frac{1}{2}\varepsilon\left|\vec{\nabla}\Phi\right|^2 + B] = 0 \quad ; \; x > 0 \; , \; z = 0 \tag{7b}$$

$$\sum_{n=0}^{\infty} \frac{(\varepsilon\chi)^n}{n!} \frac{\partial^n}{\partial x^n} \left[\frac{\partial \Phi}{\partial x} + \frac{\partial \chi}{\partial t} - \varepsilon \frac{\partial \Phi}{\partial z} \frac{\partial \chi}{\partial z}\right] = 0 \quad ; \; x = 0 \; ; \; -h \leq z \leq 0 \tag{7c}$$

In addition, the functions Φ, η, B, p, and ω may also be expanded in the small parameter, ε, by the following:

$$\Phi(x,z,t) = \sum_{n=0}^{\infty} \varepsilon^n \, {}_{n+1}\Phi(x,z,t) \tag{8a}$$

$$\eta(x,t) = \sum_{n=0}^{\infty} \varepsilon^n \, {}_{n+1}\eta(x,t) \tag{8b}$$

$$B(t) = \sum_{n=0}^{\infty} \varepsilon^n \, {}_{n+1}B(t) \tag{8c}$$

$$p(x,z,t) = p_s(z) + \sum_{n=0}^{\infty} \varepsilon^n \, {}_{n+1}P(x,z,t) \tag{8d}$$

$$\omega t = \tau = \left(\sum_{n=0}^{\infty} \varepsilon^n \, \omega_n\right) t \tag{8e}$$

in which $p_s(z) = z/\varepsilon$ = the dimensionless hydrostatic pressure.

Substituting Eqs. (7) & (8) into Eqs. (2)-(6) and collecting terms of the same order in ε results in a set of linear boundary value problems which may be solved in successive order.

Linear Solution

The linear boundary value problem for first-order (ε^o) is

$$\nabla^2 \, {}_1\Phi = 0 \quad ; \; x \geq 0 \; , \; -h \leq z \leq 0 \tag{9a}$$

$$\partial \, {}_1\Phi/\partial z = 0 \quad ; \; x \geq 0 \; , \; z = -h \tag{9b}$$

$$\mathcal{L}\{{}_1\Phi\} + \omega_o \, \partial \, {}_1B/\partial\tau = 0 \quad ; \; x \geq 0 \; , \; z = 0 \tag{9c}$$

$$\partial \, {}_1\Phi/\partial x = -\omega_o \partial\chi/\partial\tau \quad ; \; x = 0 \; , \; -h \leq z \leq 0 \tag{9d}$$

in which the linear, free-surface operator, $\mathcal{L}\{\cdot\}$, is defined by

$$\mathcal{L}\{\cdot\} = (\omega_o^2 \, \partial^2/\partial\tau^2 + \partial/\partial z)\{\cdot\} \tag{10}$$

The solution to Eqs. (9) must also satisfy a radiation condition at infinity as $x \to +\infty$ that will admit only right progressing waves or bounded evanescent eigenmodes.

The first-order, free-surface elevation, ${}_1\eta(x,\tau)$, and the dynamic pressure ${}_1P(x,z,\tau)$ may be determined from

$${}_1\eta(x,\tau) = \omega_o \, \partial \, {}_1\Phi/\partial\tau \quad ; \; x \geq 0 \; , \; z = 0 \tag{11}$$

$${}_1P(x,z,\tau) = \omega_o \, \partial \, {}_1\Phi/\partial\tau \quad ; \; x \geq 0 \; , \; -h \leq z < 0 \tag{12}$$

A simple-harmonic solution to the linear problem requires that ${}_1B$ be identically zero in Eq. (9c). The linear solution which satisfies the radiation condition as $x \to +\infty$ is well-known and may be expressed

by the following eigenfunction expansion (Hudspeth and Chen, 1981):

$$ {}_1\Phi(x,z,\tau) = -a_1\phi_1(z)\sin(x-\tau) - \cos\tau \sum_{m=2} a_m\phi_m(z)\exp(-\alpha_m x) \qquad (13) $$

in which the orthonormal eigenfunctions, $\phi_m(z)$ in the interval of orthogonality $[-h\leq z\leq 0]$ are given by $\phi_m(z) = \cos[\alpha_m(z+h)]/n_m$; where the normalizing constants, n_m, are computed from $n_m^2 = [2\alpha_m h+\sin 2\alpha_m h]/4\alpha_m$; provided that $\omega_o^2 h+\alpha_m h \tan \alpha_m h = 0$ where $\alpha_1 = +i$.

The dimensionless coefficients, a_m, in Eq. (13) are given by

$$ a_1 = \frac{\omega_o(S/2\Delta)}{n_1} D_1(h) \; ; \; a_m = \frac{\omega_o(S/2\Delta)\, D_m(\alpha_m h)}{\alpha_m^3 n_m} \; ; \; m \geq 2 \qquad (14) $$

$$ D_1(h) = h[M(1-b/h)+B']\sinh[h(1-b/h)]-h[M(d/h)+B']\sinh[h(d/h)\cdot U(d/h)] $$

$$ - M\{\cosh[h(1-b/h)]-\cosh[h(d/h)\cdot U(d/h)]\} \qquad (15a) $$

$$ D_m(\alpha_m h) = -(\alpha_m h)[M(1-b/h)+B']\sin[(\alpha_m h)(1-b/h)] $$

$$ +(\alpha_m h)[M(d/h)+B']\sin[(\alpha_m h)(d/h)\cdot U(d/h)]-M\{\cos[(\alpha_m h)(1-b/h)] $$

$$ -\cos[(\alpha_m h)(d/h)\cdot U(d/h)]\} \; ; \quad m \geq 2 \qquad (15b) $$

where M and B' are defined by Eqs. (4) and $U(\cdot)$ = Heaviside step function which is required for negative-draft wavemakers ($d < 0$).

Second-Order Solution

The boundary value problem for second-order (ε^1) is

$$ \nabla_2^2\Phi = 0 \qquad ; \; x \geq 0 \; , \; -h \leq z \leq 0 \qquad (16a) $$

$$ \partial_2\Phi/\partial z = 0 \qquad ; \; x \geq 0 \; , \; z = -h \qquad (16b) $$

$$ \mathcal{L}\{{}_2\Phi\} + \omega_o \, \partial_2 B/\partial\tau = -2\omega_o\omega_1 \, \partial^2{}_1\Phi/\partial\tau^2 + \omega_o \frac{\partial}{\partial\tau} \left|\vec{\nabla}_1\Phi\right|^2 $$

$$ - {}_1\eta \frac{\partial}{\partial z}(\omega_o^2 \, \partial^2{}_1\Phi/\partial\tau^2 + \partial_1\Phi/\partial z) \qquad ; \; x \geq 0 \; , \; z = 0 \qquad (16c) $$

$$ \partial_2\Phi/\partial x = -\omega_1\partial\chi/\partial\tau+\partial_1\Phi/\partial z \; \partial\chi/\partial z-(\partial^2{}_1\Phi/\partial x^2)\chi \; ; \; x=0 \; , -h\leq z\leq 0 \qquad (16d) $$

The solution to Eqs. (16) must also satisfy a radiation condition at infinity as $x\to+\infty$ that will admit only right progressing waves or bounded eigenmodes. Because Eq. (16d) is an inhomogeneous Neumann condition, any constant times x may also be used for any time-independent solution.

The Bernoulli constant is ${}_2B = (a_1/2n_1)^2$ and $\partial_2 B/\partial\tau = 0$ in Eq. (16c). The first term in the right hand side of Eq. (16c) must vanish since $\partial^2{}_1\Phi/\partial\tau^2$ is a homogeneous solution of the linear operator on the left hand side of Eq. (16c) so that $\omega_1 = 0$.

It is customary in boundary value problems with inhomogeneous boundary conditions on orthogonal boundaries such as those given by Eqs. (16c & d) to linearly decompose the solution into complementary

homogeneous and inhomogeneous solutions. Accordingly, the solution to Eqs. (16) may be expressed as the linear sum of four scalar velocity potentials given by $_2\Phi = {}_2\Phi^s + {}_2\Phi^e + {}_2\Phi^f + \Psi$ in which $_2\Phi^s$ is a second-order Stokes wave potential; $_2\Phi^e$ is a near-field evanescent interaction potential; $_2\Phi^f$ is a wavemaker-forced potential; and Ψ is a time-independent potential needed to satisfy Eqs. (16c & d) exactly. This linear decomposition of $_2\Phi$ reduces Eqs. (16c & d) to

$$\begin{aligned}
&\mathcal{L}\{{}_2\Phi^s+{}_2\Phi^e+{}_2\Phi^f+\Psi\} = a_1^2 f_1(\phi_1)\sin 2(x-\tau) \\
&- a_1 \sin(x-2\tau)\sum_{m=2} a_m \exp(-\alpha_m x) f_2(\phi_1,\phi_m) \\
&+ a_1 \cos(x-2\tau)\sum_{m=2} a_m \exp(-\alpha_m x) f_3(\phi_1,\phi_m) \\
&- \sin 2\tau \sum_{m=2}\sum_{n=2} a_m a_n \exp[-(\alpha_m+\alpha_n)x] f_4(\phi_m,\phi_n) \\
&- a_1 \cos x \sum_{m=2} a_m \exp(-\alpha_m x) f_5(\phi_1,\phi_m) \quad ; \; x\geq 0 \; , \; z=0
\end{aligned} \tag{17a}$$

$$\begin{aligned}
\frac{\partial}{\partial x}\{{}_2\Phi^s+{}_2\Phi^e+{}_2\Phi^f+\Psi\} &= +\frac{a_1}{2} W_1(\phi_1,\xi,z)[1-\cos 2\tau] \\
&+ \frac{\sin 2\tau}{2}\sum_{m=2} a_m \alpha_m W_2(\phi_m,\xi,z) \quad ; \; x=0, \; -h\leq z\leq 0
\end{aligned} \tag{17b}$$

in which the nonlinear, free surface interaction terms f_1, f_2, f_3, f_4, and f_5, and the nonlinear, wavemaker interaction terms W_1 and W_2 represent nonlinear interactions involving first-order quantities that are defined in Appendix I.

The second-order Stokes wave potential, $_2\Phi^s$, must satisfy exactly Eqs. (16a & b); a radiation condition at infinity as $x \to +\infty$ requiring only right progressing waves, as well as the inhomogeneous part of the nonlinear free-surface condition in Eq. (17a) given by

$$\mathcal{L}\{{}_2\Phi^s\} - a_1^2 f_1(\phi_1)\sin 2(x-\tau) = 0 \qquad ; \; x \geq 0 \; , \; z = 0 \tag{18}$$

The well-known Stokes (1847) wave potential is simply $_2\Phi^s = -(3\omega_o/8)\operatorname{cosech}^4 h \cosh 2(z+h) \sin 2(x-\tau)$.

The near-field evanescent wave potential, $_2\Phi^e$, must satisfy Eqs. (16a & b), a radiation condition at infinity as $x \to +\infty$ requiring only bounded evanescent eigenmodes, as well as that part of the inhomogeneous free-surface boundary condition given by

$$\begin{aligned}
&\mathcal{L}\{{}_2\Phi^e\} + a_1 \sin(x-2\tau)\sum_{m=2} a_m \exp(-\alpha_m x) f_2(\phi_1,\phi_m) \\
&- a_1 \cos(x-2\tau)\sum_{m=2} a_m \exp(-\alpha_m x) f_3(\phi_1,\phi_m) \\
&+ \sin 2\tau \sum_{m=2}\sum_{n=2} a_m a_n \exp[-(\alpha_m+\alpha_n)x] f_4(\phi_m,\phi_n) = 0 \; ; \; x \geq 0 \; , \; z = 0
\end{aligned} \tag{19}$$

A solution for the near-field evanescent potential that satisfies a radiation condition as $x \to +\infty$ is assumed to be given by

$$
\begin{aligned}
{}_2\Phi^e(x,z,\tau) = a_1 \cos(x-2\tau) \sum_{m=2} a_m \exp(-\alpha_m x)[A_m \phi_1(z)\phi_m(z) + B_m \phi_1'(z)\phi_m'(z)] \\
- a_1 \sin(x-2\tau) \sum_{m=2} a_m \exp(-\alpha_m x)[A_m \phi_1'(z)\phi_m'(z) - B_m \phi_1(z)\phi_m(z)] \\
- \sin 2\tau \sum_{m=2} \sum_{n=2} a_m a_n \exp[-(\alpha_m+\alpha_n)x] C_{mn}[\phi_m(z)\phi_n(z) - \phi_m'(z)\phi_n'(z)]
\end{aligned}
\tag{20a}
$$

where

$$
\phi_1'(z) = \sinh(z+h)/n_1; \qquad \phi_m'(z) = \sin[\alpha_m(z+h)]/n_m; \qquad m \geq 2 \tag{20b}
$$

Substituting Eqs. (20) into Eq. (19) and equating coefficients of like functions gives

$$
A_m = \frac{\alpha_m^2 \omega_o^3 \{12 + 2(\alpha_m^2-1)/\omega_o^4 + \operatorname{cosec}^2\alpha_m h - \operatorname{cosech}^2 h\}}{[4\omega_o^4 + \alpha_m^2 - 1]^2 + (2\alpha_m)^2} \tag{21a}
$$

$$
B_m = \frac{\alpha_m \omega_o^3}{2} \frac{\{[4\omega_o^4 + \alpha_m^2 - 1][\operatorname{cosech}^2 h - \operatorname{cosec}^2\alpha_m h - 4] + 8(\alpha_m/\omega_o^2)^2\}}{[4\omega_o^4 + \alpha_m^2 - 1]^2 + (2\alpha_m)^2} \tag{21b}
$$

$$
C_{mn} = \alpha_m \alpha_n \omega_o^3 \frac{[1 + (\alpha_n \alpha_m/\omega_o^4) + \frac{1}{4}(\operatorname{cosec}^2\alpha_m h + \operatorname{cosec}^2\alpha_n h)]}{(2\omega_o^2)^2 + (\alpha_m - \alpha_n)^2} \tag{21c}
$$

The wavemaker-forced potential, ${}_2\Phi^f$, must satisfy Eqs. (16a & b); a homogeneous form of the linear, free-surface operator defined by Eq. (10); a radiation condition at infinity as $x \to +\infty$ requiring only right progressing waves and bounded eigenmodes; as well as that part of the inhomogeneous wavemaker boundary condition given by

$$
\begin{aligned}
\frac{\partial}{\partial x}\{{}_2\Phi^f\} + \frac{\partial}{\partial x}\{{}_2\Phi^s + {}_2\Phi^e\} + \frac{a_1}{2}\cos 2\tau \; W_1(\phi_1,\xi,z) \\
- \frac{\sin 2\tau}{2} \sum_{m=2} a_m \alpha_m W_2(\phi_m,\xi,z) = 0 \; ; \; x = 0, \; -h < z < 0
\end{aligned}
\tag{22}
$$

A solution for the wavemaker-forced potential that satisfies a radiation condition at $x \to +\infty$ is assumed to be given by

$$
\begin{aligned}
{}_2\Phi^f(x,z,\tau) = \{E_1 \cos(\beta_1 x - 2\tau) + F_1 \sin(\beta_1 x - 2\tau)\} Q_1(z) \\
- \sum_{j=2} \exp(-\beta_j x)\{E_j \sin 2\tau + F_j \cos 2\tau\} Q_j(z)
\end{aligned}
\tag{23}
$$

in which the orthonormal eigenfunctions, $Q_j(z)$, in the interval of orthogonality $[-h \leq z \leq 0]$ are $Q_j(z) = \cos\beta_j(z+h)/N_j$; where the normalizing constants are $N_j^2 = (2\beta_j h + \sin 2\beta_j h)/(4\beta_j)$; provided that $4\omega_o^2 h + \beta_j h \tan \beta_j h = 0$ and that $\beta_1 = i\beta_1$.

The coefficients E_j and F_j are

$$E_j = -\beta_j^{-1}\{\sum_{m=2} a_m[a_1(A_m+\alpha_m B_m)\langle\phi_1\phi_m,Q_j\rangle_z + \sum_{n=2} a_n(\alpha_m+\alpha_n)C_{mn}\langle\phi_m\phi_n,Q_j\rangle_z]$$

$$+ \sum_{m=2} a_m[a_1(B_m-\alpha_m A_m)\langle\phi_1'\phi_m',Q_j\rangle_z - \sum_{n=2} a_n(\alpha_m+\alpha_n)C_{mn}\langle\phi_m'\phi_n',Q_j\rangle_z]$$

$$- \sum_{m=2} \frac{a_m\alpha_m}{2}\langle W_2,Q_j\rangle_z\} \quad ; j \geq 1 \tag{24a}$$

$$F_j = \beta_j^{-1}\{\frac{3\omega_o}{4\sinh^4 h}\langle\cosh 2(z+h),Q_j\rangle_z + a_1\sum_{m=2} a_m[(A_m\alpha_m-B_m)\langle\phi_1\phi_m,Q_j\rangle_z +$$

$$+ (A_m+\alpha_m B_m)\langle\phi_1'\phi_m',Q_j\rangle_z] - \frac{a_1}{2}\langle W_1,Q_j\rangle_z\} \quad ; j \geq 1 \tag{24b}$$

where the inner product terms $\langle\cdot,\cdot\rangle_z$ in Eqs. (24) are summarized in Appendix II.

An interesting feature of the second-order problem which has not previously been given much detailed attention is the time-independent potential, $\Psi(x,z)$, which must satisfy the following:

$$\nabla^2\Psi = 0 \quad ; x \geq 0\ ,\ -h \leq z \leq 0 \tag{25a}$$

$$\mathcal{L}\{\Psi\} = \frac{\partial\Psi}{\partial z} = -a_1 \cos x \sum_{m=2} a_m\exp(-\alpha_m x)f_5(\phi_1,\phi_m) \quad ; x \geq 0\ ;\ z = 0 \tag{25b}$$

$$\frac{\partial\Psi}{\partial z} = 0 \quad ; x \geq 0\ ;\ z = -h \tag{25c}$$

$$\frac{\partial\Psi}{\partial x} = \frac{a_1}{2} W_1(\phi_1,\xi,z) \quad ; x = 0\ ;\ -h \leq z \leq 0 \tag{25d}$$

Because the time-independent solution is not a progressive wave, the radiation condition at infinity as $x \to +\infty$ is relaxed to admit bounded, time-independent velocities.

Similarly, Ψ may be decomposed into two linearly independent potentials according to $\Psi = \Psi^{fs} + \Psi^{wm}$.

The free surface potential, Ψ^{fs}, must satisfy Eqs. (25a & c); a boundedness condition as $x \to +\infty$; in addition to the inhomogeneous free surface boundary condition given by Eq. (25b). A solution which is bounded is given by

$$\Psi^{fs}(x,z) = a_1 \cos x \sum_{m=2} a_m\exp(-\alpha_m x)[b_m\phi_1(z)\phi_m(z) + c_m\phi_1'(z)\phi_m'(z)]$$

$$- a_1 \sin x \sum_{m=2} a_m\exp(-\alpha_m x)[b_m\phi_1'(z)\phi_m'(z) - c_m\phi_1(z)\phi_m(z)] \tag{26a}$$

where

$$b_m = - \frac{\omega_o^3 \alpha_m^2 \, [\mathrm{cosech}^2 h + \mathrm{cosec}^2 \alpha_m h]}{(\alpha_m^2 + 1)^2} \tag{26b}$$

$$c_m = - \frac{\omega_o^3 \alpha_m (\alpha_m^2 - 1)[\mathrm{cosech}^2 h + \mathrm{cosec}^2 \alpha_m h]}{2(\alpha_m^2 + 1)^2} \tag{26c}$$

The wavemaker potential, Ψ^{wm}, must satisfy Eqs. (25a & c); a boundedness condition on the velocity as $x \to +\infty$; in addition to a homogeneous free surface boundary condition given by

$$\mathcal{L}\{\Psi^{wm}\} = \frac{\partial \Psi^{wm}}{\partial z} = 0 \qquad ; \; x \geq 0 \; ; \; z = 0 \tag{27}$$

and an inhomogeneous wavemaker boundary condition given by

$$\frac{\partial \Psi^{wm}}{\partial x} - \frac{a_1}{2} W_1(\phi_1, \xi, z) + \frac{\partial \Psi^{fs}}{\partial x} = 0 \qquad ; \; x = 0 \; ; \; -h \leq z \leq 0 \tag{28}$$

A solution for Ψ^{wm} is given by the following eigenfunction expansion:

$$\Psi^{wm}(x,z) = \sum_{j=0} d_j \psi_j(z) [\exp(-\mu_j x) + \delta_{jo}(x-1)] \tag{29}$$

where the orthonormal eigenfunctions, $\psi_j(z)$, in the interval of orthogonality $[-h \leq z \leq 0]$ are given by

$$\psi_j(z) = \cos \mu_j (z+h) / [h/(2-\delta_{jo})]^{1/2} \qquad ; \; j \geq 0 \tag{30}$$

provided that the eigenvalues, μ_j, are given by $\mu_j = j\pi/h$.

The coefficients d_j are

$$d_j = - (\mu_j - \delta_{jo})^{-1} a_1 \{ \tfrac{1}{2} \langle W_1, \psi_j \rangle_z + \sum_{m=2} a_m [b_m (\alpha_m \langle \phi_1 \phi_m, \psi_j \rangle_z + \langle \phi_1' \phi_m' , \psi_j \rangle_z)$$

$$+ c_m \, (\alpha_m \langle \phi_1' \phi_m', \psi_j \rangle_z - \langle \phi_1 \phi_m, \psi_j \rangle_z)] \} \qquad ; \; j \geq 0 \tag{31}$$

where the inner product terms $\langle \cdot, \cdot \rangle_z$ are summarized in Appendix II.

CIRCULATION KINEMATICS

It is of interest to compare the second-order (ε), time-independent solution forced by the weakly nonlinear boundary conditions at both the free surface and the wavemaker boundaries given by Eqs. (17) with the mean horizontal momentum per unit area. The time- and depth-averaged dimensionless mean horizontal momentum per unit area is defined by (Phillips, 1977)

$$M_E = \left\langle \int_{-h}^{\eta} U_E \, dz \right\rangle_{2\pi} \tag{32}$$

where the temporal averaging operator $\langle\cdot\rangle_{2\pi} = (2\pi)^{-1}\int_0^{2\pi}(\cdot)d\tau$ and U_E is an Eulerian horizontal velocity component.

The horizontal component of the dimensionless Eulerian velocity may be determined approximately from

$$M_E = U_\Psi + U_\Phi + O(\varepsilon^2) \tag{33}$$

The dimensionless horizontal component, U_Ψ, that is forced by f_5 and W_1 in Eqs. (17) may be estimated from the time-independent velocity potential according to $U_\Psi = U_{\Psi,\infty}(d_o) + U_{\Psi,e}(a_m)$ where

$$U_{\Psi,\infty}(d_o) = -\varepsilon(2\omega_o)^{-1}\left\{\frac{n_1}{D_1(h)\phi_1'(o)}\right\}\{h[M(1-b/h)+B']\cosh b(\omega_o^2-\tanh b)$$
$$-h[M(d/h)+B']\sinh d\ \mathrm{sech}\ h$$
$$+\omega_o^6\sum_{m=2}\frac{\phi_m(o)D_m(\alpha_m h)}{n_m\alpha_m^2(\alpha_m^2+1)}[\mathrm{cosech}^2 h+\mathrm{cosech}^2\alpha_m h]\} \tag{34a}$$

$$U_{\Psi,e}(a_m) = \varepsilon\frac{\omega_o^5 n_1}{D_1(h)\phi_1'(o)}\cos x\sum_{m=2}\frac{\phi_m(o)D_m(\alpha_m h)}{n_m\alpha_m^3(\alpha_m^2+1)}\exp-\alpha_m x$$
$$[\mathrm{cosech}^2 h+\mathrm{cosech}^2\alpha_m h][\alpha_m-\tan x] \tag{34b}$$

Similarly, the dimensionless horizontal component, U_Φ, may be estimated from the first-order eigenmodes by a Maclauren series expansion about the still water level according to

$$U_\Phi = -\varepsilon\omega_o\langle(\partial_1\Phi/\partial x)(\partial_1\Phi/\partial\tau)\rangle_{2\pi} = U_{\Phi,\infty}(\omega_o)+U_{\Phi,e}(a_m)\ ;\ z=0 \tag{35a}$$

The dimensionless, far-field component, $U_{\Phi,\infty}(\omega_o)$, is given by

$$U_{\Phi,\infty}(\omega_o) = \varepsilon(2\omega_o)^{-1} \tag{35b}$$

which is the well-known Eulerian description of the dimensionless Stokes drift (Longuet-Higgins, 1953). The dimensionless evanescent component, $U_{\Phi,e}(a_m)$, is given by

$$U_{\Phi,e}(a_m) = -(\varepsilon/2)\cos x\sum_{m=2}a_m\phi_m(o)\exp-\alpha_m x\ [\alpha_m-\tan x] \tag{35c}$$

In the far-field ($x > 3h$, say), the evanescent components of the mean horizontal momentum per unit area, $U_{\Psi,e}(a_m) + U_{\Phi,e}(a_m)$, are negligible. This implies that far away from the local wavemaker effects, the mean horizontal momentum per unit area is approximately

$$M_E \sim \varepsilon(2\omega_o)^{-1}\{1-[\frac{n_1}{D_1(h)\phi_1'(o)}][h(M(1-b/h)+B')\cosh b(\omega_o^2-\tanh b)$$
$$-h(M(d/h)+B')\sinh d\ \mathrm{sech}\ h$$
$$+\omega_o^6\sum_{m=2}\frac{\phi_m(o)D_m(\alpha_m h)}{n_m\alpha_m^2(\alpha_m^2+1)}(\mathrm{cosech}^2 h+\mathrm{cosech}^2\alpha_m h)]\} \tag{36}$$

which implies that for wavemakers intersecting the free surface (i.e., b=o), the leading-order coefficient, d_o, approximately estimates the uniform return current required to insure a zero net mass flux in a closed wave flume. This may be observed by plotting the dimensionless, time-independent Eulerian velocities.

The dimensionless horizontal component of the second-order (ε), time-independent fluid motion is

$$U_\psi(x,z) = -\varepsilon \frac{\partial \psi^{wm}}{\partial x} - \varepsilon \frac{\partial \psi^{fs}}{\partial x}$$

$$= \varepsilon \sum_{j=0} d_j(\mu_j \psi_j(z) \exp -\mu_j x - \delta_{jo})$$

$$- \varepsilon \frac{\omega_o^3}{4} \frac{n_1}{D_1(h)} [1+2h \text{ cosech } 2h] \cos x \sum_{m=2} \frac{D_m(\alpha_m h)}{n_m} \frac{\exp -\alpha_m x}{\alpha_m^2(\alpha_m^2+1)}$$

$$[\text{cosech}^2 h + \text{cosec}^2 \alpha_m h][\phi_1(z)\phi_m(z)(1+\alpha_m \tan x)$$

$$+ \phi_1'(z)\phi_m'(z)(\alpha_m - \tan x)] \qquad (37a)$$

and the dimensionless vertical component is

$$V_\psi(x,z) = -\varepsilon \frac{\partial \psi^{wm}}{\partial z} - \varepsilon \frac{\partial \psi^{fs}}{\partial z}$$

$$= \varepsilon \sum_{j=1} d_j \mu_j \psi_j'(z) \exp -\mu_j x$$

$$- \varepsilon \frac{\omega_o^3}{4} \frac{n_1}{D_1(h)} [1+2h \text{ cosech } 2h] \cos x \sum_{m=2} \frac{D_m(\alpha_m h)}{n_m} \frac{\exp -\alpha_m x}{\alpha_m^2(\alpha_m^2+1)}$$

$$[\text{cosech}^2 h + \text{cosec}^2 \alpha_m h][\phi_1(z)\phi_m'(z)(1+\alpha_m \tan x)$$

$$- \phi_1'(z)\phi_m(z)(\alpha_m - \tan x)] \qquad (37b)$$

where $\psi_j'(z) = \sin \mu_j(z+h)/\sqrt{h}$.

The magnitude of the velocity $[U_\psi^2(x,z) + V_\psi^2(x,z)]^{1/2}$ is illustrated in Figs. 2 & 3 for both a piston and hinged wavemaker. Figures 2 & 3 demonstrate that the mean return current is estimated reasonably well by the leading coefficient, d_o.

ACKNOWLEDGEMENTS

Support has been provided to RTH by the Office of Naval Research under the University Research Inititative (URI) Contract No. N00014-86-K-0687; to WS (in part) by the United States-Spain Joint Committee for Scientific and Technological Cooperation under Contract No. CCA8510095; and to T-IK by the Office of Overseas Education of the Korean Army. The support of each of these agencies is gratefully

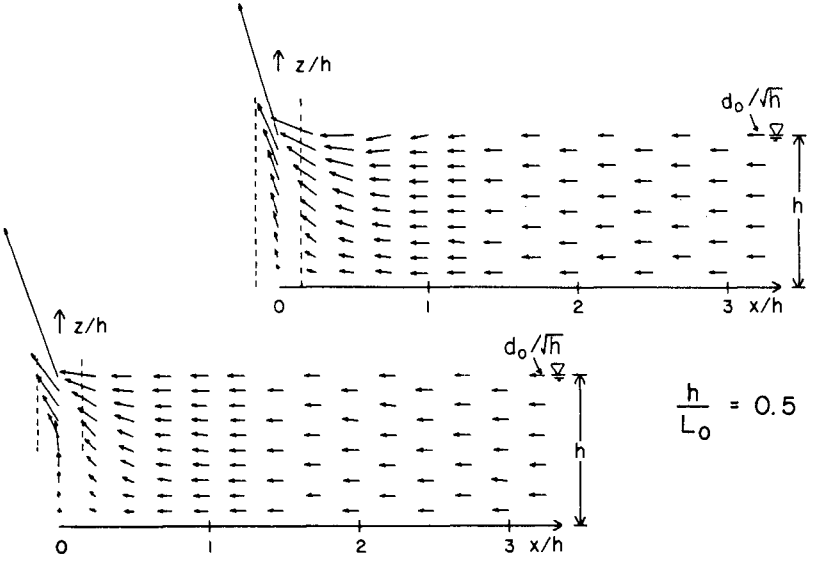

Fig. 2. Magnitude of dimensionless time-independent velocity (piston)

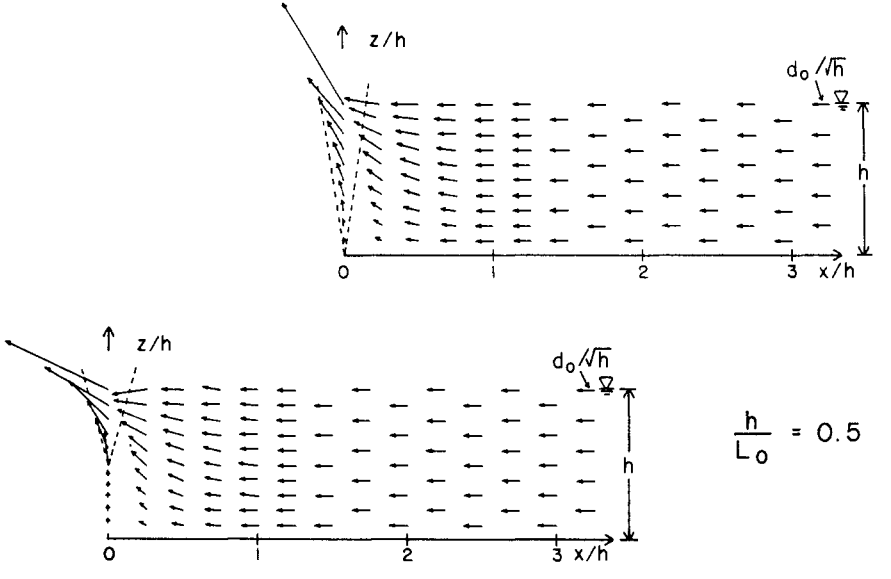

Fig. 3. Magnitude of dimensionless time-independent velocity (hinged)

appreciated. We are deeply indebted to R.B. Guenther and A.N. Williams for illuminating a number of obscure and subtle features of weakly nonlinear boundary value problems.

APPENDIX I: NONLINEAR INTERACTION COEFFICIENTS

The nonlinear, inhomogeneous free surface interaction terms in Eq. (17a) are defined from first-order quantities by the following:

$$f_1(\phi_1) = 3\omega_o n_1^{-2}/2 \tag{I.1}$$

$$f_2(\phi_1,\phi_m) = 2\alpha_m\omega_o\phi_1(0)\phi_m(0) \tag{I.2}$$

$$f_3(\phi_1,\phi_m) = \frac{\omega_o^5}{2}\,\phi_1(0)\,\phi_m(0)[\operatorname{cosech}^2 h - \operatorname{cosec}^2\alpha_m h - 4] \tag{I.3}$$

$$f_4(\phi_m,\phi_n) = \omega_o^5\,\phi_n(0)\,\phi_m(0)\,[\alpha_n\alpha_m/\omega_o^4+1+\tfrac{1}{4}\,(\operatorname{cosec}^2\alpha_m h+\operatorname{cosec}^2\alpha_n h)] \tag{I.4}$$

$$f_5(\phi_1,\phi_m) = (\omega_o^5/2)\phi_1(0)\,\phi_m(0)[\operatorname{cosech}^2 h + \operatorname{cosec}^2\alpha_m h] \tag{I.5}$$

The nonlinear, inhomogeneous wavemaker interaction terms in Eq. (17b) are defined by the following:

$$W_1(\phi_1,\xi,z) = [\phi_1'(z)\partial\xi/\partial z+\phi_1(z)\xi]\cdot[U(z+h-d)-U(z+b)] \tag{I.6}$$

$$W_2(\phi_m,\xi,z) = [\phi_m'(z)\partial\xi/\partial z+\alpha_m\phi_m(z)\xi]\cdot[U(z+h-d)-U(z+b)] \tag{I.7}$$

where $\xi(z)$ is defined in Eq. (4); ϕ_m' are defined in Eq. (20b); and

$$\partial\xi/\partial z = M(S/2\Delta) \tag{I.8}$$

APPENDIX II: INNER PRODUCTS $\langle\cdot,\cdot\rangle_z$

The inner product terms used to compute the coefficients of the second-order potential are determined from

$$\langle\cdot,\cdot\rangle_z = \int_{-h}^{o}\{\cdot,\cdot\}dz \tag{II.1}$$

These inner products are:

$$\langle\phi_m\phi_n,\Lambda_j\rangle_z = \phi_m(o)\phi_n(o)\Lambda_j(o)\left\{\frac{2(\omega_o\lambda_j)^2+\Omega_j[2\omega_o^4+\alpha_m^2+\alpha_n^2-\lambda_j^2]}{(\alpha_m^2+\alpha_n^2-\lambda_j^2)^2-(2\alpha_m\alpha_n)^2}\right\} \tag{II.2}$$

$$\langle\phi_m'\phi_n',\Lambda_j\rangle_z = \phi_m(o)\phi_n(o)\Lambda_j(o)\left|\alpha_m\right|\left|\alpha_n\right|$$

$$\left\{\frac{\omega_o^2[\alpha_m^4+\alpha_n^4-\lambda_j^2(\alpha_m^2+\alpha_n^2)+\omega_o^2\Omega_j(\alpha_m^2+\alpha_n^2-\lambda_j^2)]-2(\alpha_m\alpha_n)^2[\omega_o^2-\Omega_j]}{\alpha_m^2\alpha_n^2[(\alpha_m^2+\alpha_n^2-\lambda_j^2)^2-(2\alpha_m\alpha_n)^2]}\right\} \tag{II.3}$$

$$\langle \cosh 2(z+h), Q_j \rangle_z = \frac{4\omega_o^6 \, Q_j(0)}{(\omega_o^4 - 1)(4 + \beta_j^2)} \tag{II.4}$$

$$\langle W_1, \Lambda_j \rangle_z = \frac{S}{2\Delta} M \langle \phi_1' \Delta U, \Lambda_j \rangle_z + \langle \phi_1 \xi \Delta U, \Lambda_j \rangle_z \tag{II.5}$$

$$\langle W_2, \Lambda_j \rangle_z = \frac{S}{2\Delta} M \langle \phi_m' \Delta U, \Lambda_j \rangle_z + \alpha_m \langle \phi_m \xi \Delta U, \Lambda_j \rangle_z \tag{II.6}$$

$$\langle \phi_m' \Delta U, \Lambda_j \rangle_z = \frac{|\alpha_m|}{\alpha_m^2} [\lambda_j^2 - \alpha_m^2]^{-1} \{ \phi_m(0) \Lambda_j(0) \cos \alpha_m b \cos \lambda_j b \tag{II.7}$$

$$[(\omega_o^2 + \alpha_m \tan \alpha_m b)(\Omega_j + \lambda_j \tan \lambda_j b) + \alpha_m^2 (1 + \tan \alpha_m h \tan \alpha_m b)(1 + \tan \lambda_j h \tan \lambda_j b)]$$

$$- \phi_m [d \cdot U(d) - h] \Lambda_j (d \cdot U(d) - h) \alpha_m^2 [1 + (\lambda_j / \alpha_m) \tan(\lambda_j d \cdot U(d)) \tan(\alpha_m d \cdot U(d))] \}$$

$$\langle \phi_m \xi \Delta U, \Lambda_j \rangle_z = \frac{S}{2\Delta} M (\alpha_m^2 - \lambda_j^2)^{-2} \{ \phi_m(0) \Lambda_j(0) \cos \alpha_m b \cos \lambda_j b$$

$$\times [(\alpha_m^2 + \lambda_j^2)(1 - (\omega_o^2/\alpha_m) \tan \alpha_m b)(1 + \tan \lambda_j h \tan \lambda_j b)$$

$$+ 2(\omega_o^2 + \alpha_m \tan \alpha_m b)(\Omega_j + \lambda_j \tan \lambda_j b)] -$$

$$- \phi_m (d \cdot U(d) - h) \Lambda_j (d \cdot U(d) - h) [\alpha_m^2 + \lambda_j^2 + 2\alpha_m \lambda_j \tan(\alpha_m d \cdot U(d)) \tan(\lambda_j d \cdot U(d))] \}$$

$$+ \frac{S}{2\Delta} [M(h-b) + B'h] [\alpha_m^2 - \lambda_j^2]^{-1} \phi_m(0) \Lambda_j(0) \cos \alpha_m b \cos \lambda_j b$$

$$\times [(1 - (\omega_o^2/\alpha_m) \tan \alpha_m b)(\Omega_j + \lambda_j \tan \lambda_j b)$$

$$- (\omega_o^2 + \alpha_m \tan \alpha_m b)(1 + \tan \lambda_j h \tan \lambda_j b)]$$

$$- \frac{S}{2\Delta} [Md \cdot U(d) + B'h] [\alpha_m^2 - \lambda_j^2]^{-1} \phi_m (d \cdot U(d) - h) \Lambda_j (d \cdot U(d) - h)$$

$$\times [\alpha_m \tan(\alpha_m d \cdot U(d)) - \lambda_j (\tan \lambda_j d \cdot U(d))] \tag{II.8}$$

where

$$\Omega_j = \lambda_j \tan \lambda_j h = \begin{cases} 4\omega_o^2 & ; \text{ for } \Lambda_j(z) = Q_j(z) \text{ and } \lambda_j = \beta_j \\ 0 & ; \text{ for } \Lambda_j(z) = \psi_j(z) \text{ and } \lambda_j = \mu_j \end{cases}$$

$$\begin{Bmatrix} \alpha_1 \\ \beta_1 \end{Bmatrix} = i \begin{Bmatrix} 1 \\ \beta_1 \end{Bmatrix}$$

and ΔU is defined in Eq. (3).

APPENDIX III: REFERENCES

Daugaard. 1972. "Generation of regular waves in the laboratory." Doctoral dissertation. Institute of Hydrodynamics Engineering, Technical University of Denmark, Copenhagen, Denmark.

Flick R.E. and R.T. Guza. 1980. "Paddle generated waves in laboratory channels." J. Waterway, Port, Coastal & Ocean Div., ASCE 106(1), pp. 79-97.

Hudspeth, R.T. and M-C Chen. 1981. "Design curves for hinged wavemakers: Theory." J. Hydraulics Div., ASCE, 107(5), pp. 533-552.

Longuet-Higgins, M.S. 1953. "Mass transport in water waves." Phil. Trans. A, 245, pp. 535-81.

Madsen, O.S. 1971. "On the generation of long waves." J. Geophysical Res., 76(36), pp. 8672-8683.

Massel, S.R. 1981. "On the nonlinear theory of mechanically generated waves in laboratory channels." Mitteilungen Heft 70, 1981, Leichtweiss-Institut Fur Wasserbau der Technischen Universitat Braunschweig, West Germany.

Phillips, O.M. 1977. The dynamics of the upper ocean. 2nd edition. Cambridge University Press, Cambridge, England.

Stokes, G.G. 1847. "On the theory of oscillatory waves." Transactions of the Phil. Soc., London, 8, pp. 441-455.

CHAPTER 31

DECOMPOSITION OF NONLINEARLY REFLECTED IRREGULAR WAVES BY THE WAVE BREAKING AND DEFORMATION

by A. KIMURA*

ABSTRACT

This paper deals with a new method to decompose incident and reflected waves from the measured data of irregular standing waves. The theory by Goda et al. is extended to cope with the reflection from such a coastal structure that has a sloping surface and brings about different reflection coefficient for each incident waves. Irregular standing waves are decomposed into incident and reflected irregular waves by the short-term wave spectrum analysis method. And the reflection coefficient of the approximated zero-up-cross waves are defined as the ratio between envelopes of these irregular wave profiles. The calculated reflection coefficients can be discussed in terms of the incident zero-up-cross wave parameters such as a wave steepness, Ursell parameter, etc. An effective wave gauge system to measure irregular standing waves which have a wide band spectrum is also discussed and a method to compose the system is proposed.

1. INTRODUCTION

The theories by Kajima[1], Thornton et al.[2] and Goda et al.[3] have been commonly used to decompose incident and reflected waves from irregular standing waves formed in the vicinity of a model of off-shore structure. With these theories, irregular wave data measured at two or more different points[1] in a wave tank are firstly analyzed by the Fourier transform method and then decomposed into incident and reflected waves. The reflection coefficient is calculated for every frequency component of a spectrum. By these methods reliable reflection coefficients are calculated from an experiment of irregular waves when incident and reflected waves η_I and η_R can be written in the form

* Associate Prof. Faculty of Engg. Tottori University, Koyama Minami 4-101, Torrori, 680, Japan

$$\eta_I(t) = \sum_{n=1}^{\infty} a_{In}\cos(2\pi f_n t - \phi_{In}) \quad (1)$$

and

$$\eta_R(t) = \sum_{n=1}^{\infty} a_{Rn}\cos(2\pi f_n t - \phi_{Rn}) \quad (2)$$

in which f_n is the frequency of the n-th component. a_{In}, a_{Rn} are the amplitudes, ϕ_{In}, ϕ_{Rn} are the phases of incident and reflected waves, respectively.

In case of a breakwater made of stones or blocks, which has a sloped surface, however, the reflection characteristics of the irregular waves change almost wave by wave which are defined by the zero-up-cross method. A wave with a large steepness, for example, tends to break on a slope and loses significant part of its energy. Therefore, the resultant reflection coefficient is presumably very small for this wave. On the contrary, a wave with a small steepness is reflected with a large reflection coefficient, since it may not break on the slope. Since reflection coefficients differ wave by wave for this type of breakwater, amplitudes and phases in eq.(2) may change occasionally. There has been no established method to calculate the amplitude and phase of each wave from those reflected irregular waves. The amplitudes and phases of component waves decomposed by the ordinary Fourier transform method are, therefore, apparent ones in the analysis of reflection for this type of breakwaters. A large portion of existing offshore structures, however, somehow exhibit this type of reflection. This study aims to develop a method which facilitates the calculation of the reflection coefficient of irregular waves reflected from this type of breakwater.

2. DECOMPOSITION OF IRREGULAR STANDING WAVES INTO INCIDENT AND REFLECTED COMPONENT WAVES

For simplicity, the reflection of uni-directional irregular waves from a breakwater is treated in this study (see Fig.1). The coordinate system is shown in the same figure. Wave gauges with the interval $\Delta\ell$ are installed at a distance D from the breakwater. This breakwater is assumed to be of such a type that changes reflection characteristics according to the individual incident wave properties (e.g. steepness). Amplitudes and phases of reflected component waves in eq.(2), therefore, may be assumed constant only within a zero-up-cross interval of the wave profile. The Fourier transform method requires the constant amplitudes

and phases of component waves. However, since they are disturbed locally, data are analyzed with a data window in this study.

$$\gamma(u)=(\sqrt{2}/T')\exp[-\pi(t-u)^2/T'^2] \tag{3}$$

This window is the so called Gaussian window and has finite values only around t=u and has negligibly small values outside $t=u\pm T'/2$. Executing the convolution with wave profiles $\eta_1(t)$ and $\eta_2(t)$ measured at $x=x_1$ and $x=x_2$ in the wave tank respectively and the data window, amplitude of composed (i.e., incident and reflected) component wave is given as

$$A_{jn}(u)+iB_{jn}(u)=\frac{2}{T}\int_{-T/2}^{T/2}\eta_j(t)\gamma(u)\exp(-i2\pi f_n t)dt \tag{4}$$

in which $i=\sqrt{-1}$, $T>>T'$, $f_n=n/T$ $(n=1,2,\ldots)$ and $A_{jn}(u)$ and $B_{jn}(u)$ are

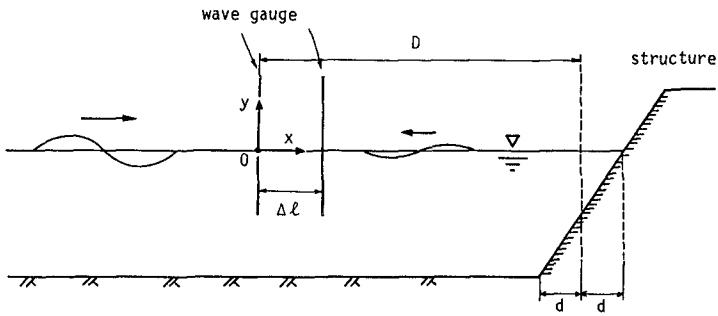

Fig.1 Illustration of wave gauges and a structure and the coordinate system.

real and imaginary parts of the n-th Fourier component of a spectrum. Subscript j indicates that those are the calculated values from the wave profiles $\eta_j(u)$ $(j=1,2)$. Substituting these components into the following equations, amplitudes and phases of incident and reflected component waves are obtained[3]:

$$a_{In}(u)=\frac{1}{2|\sin(k_n\Delta\ell)|}\{[A_{2n}(u)-A_{1n}(u)\cos(k_n\Delta\ell)-B_{1n}(u)\sin(k_n\Delta\ell)]^2$$
$$+[B_{2n}(u)+A_{1n}(u)\sin(k_n\Delta\ell)-B_{1n}(u)\cos(k_n\Delta\ell)]^2\}^{1/2}$$

$$a_{Rn}(u)=\frac{1}{2|\sin(k_n\Delta\ell)|}\{[A_{2n}(u)-A_{1n}(u)\cos(k_n\Delta\ell)+B_{1n}(u)\sin(k_n\Delta\ell)]^2$$
$$+[B_{2n}(u)-A_{1n}(u)\sin(k_n\Delta\ell)-B_{1n}(u)\cos(k_n\Delta\ell)]^2\}^{1/2}$$

$$\phi_{In}(u)= \tan^{-1}\left[\frac{-A_{2n}(u)+A_{1n}(u)\cos(k_n\Delta\ell)+B_{1n}(u)\sin(k_n\Delta\ell)}{B_{2n}(u)+A_{1n}(u)\sin(k_n\Delta\ell)-B_{1n}(u)\cos(k_n\Delta\ell)}\right] - k_n x_1$$

$$\phi_{Rn}(u)= \tan^{-1}\left[\frac{-A_{2n}(u)+A_{1n}(u)\cos(k_n\Delta\ell)-B_{1n}(u)\sin(k_n\Delta\ell)}{-B_{2n}(u)+A_{1n}(u)\sin(k_n\Delta\ell)+B_{1n}(u)\cos(k_n\Delta\ell)}\right] - k_n x_1 \qquad (6)$$

in which $a_{In}(u)$ and $a_{Rn}(u)$ are amplitudes and $\phi_{In}(u)$ and $\phi_{Rn}(u)$ are phases of incident and reflected component waves. Wave number k_n has the following relation with f_n:

$$(2\pi f_n)^2 = gk_n\tanh(k_n h) \qquad (7)$$

in which h is a water depth and g is the acceleration of gravity. Figure 2 shows an example of decomposed incident and reflected irregular wave components $a_{In}(u)$ (above) and $a_{Rn}(u)$ (below). Analyzed irregular waves are numerically simulated for the spectrum given by eq.8.

$$S(f)=2^{1/4}\exp[-\pi(f-f_p)^2\tau^2] \qquad (8)$$

In which the peak frequency f_p and the width parameter τ are 1.0Hz and 5s respectively. One hundred component waves from f=0.84Hz to 1.16Hz are composed in the simulation. The reflection coefficient of the breakwater is set to be 0.5 and no phase shift is assumed at the breakwater for all the component waves. Other parameters such as h=10cm, $\Delta\ell$ =23cm (1/4 wave length of the dominant component, f_n=1.0Hz), D=(2+0.23)m and T'=5s (eq.3) are used in the calculation. Plotted are the amplitudes of dominant frequency (f_n=1.0Hz).

Gradual changes of the incident and reflected wave amplitudes are

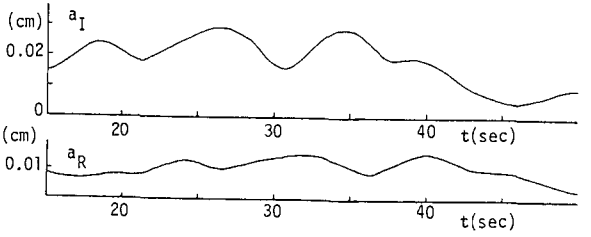

Fig.2 Gradual change in decomposed amplitudes of incident and reflected waves (f_n=1.0Hz).

observed in Fig.2. Only a time-independent single couple of incident and reflected amplitudes for individual component waves are obtained from the ordinary theories. The gradual changes in the present method are due to the leakage of a data window. The data window works not only for the emphasis of local property of data but also for the reduction of a resolution power by the Fourier transform method. If $\cos(2\pi f_0 t)$, for example, is analyzed instead of $\eta_j(t)$ in eq.(4), the calculated Fourier spectrum is not a single spike spectrum but has a spreading of spectrum values around $f=f_0$ as shown in Fig.3. This broad nature of the calculated spectrum is so called the leakage of a spectrum. The neighboring frequency components bring about this gradual change in the amplitudes (Fig.2). These changes in a_{In} and a_{Rn} are not the independent and random ones but seem to be coherent with each other since the prominent peaks in a_{In} reappear in a_{Rn} with some time interval. Although amplitude of reflected peaks reduce somehow. The averaged interval between these corresponding peaks is about 5.5s and this is the time required to go back and forth over the distance D (see Fig.1), with a group velocity of the dominant component wave (f_n=1.0Hz). The ratios between the time shifted amplitude $a_{Rn}(u-5.5)$ and the incident amplitude $a_{In}(u)$ are approximately 0.5 at any time irrespective of u. The gradual changes in the calculated wave amplitudes due to leakage, therefore, may be considered as an advantage of this method for the study of local correspondences of incident and reflected waves inspection.

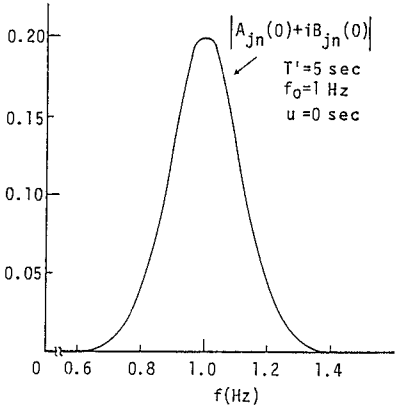

Fig.3 Leakage of a calculated spectrum.

3. THE METHOD OF EVALUATING THE LOCAL REFLECTION COEFFICIENT FROM THE ENVELOPES

Incident wave profile $\eta_I(u)$ and its envelope $E_I(u)$ are given in terms of $a_{In}(u)$ and $\phi_{In}(u)$ as

$$\eta_I(u)=\sum_{n=1}^{\infty} a_{In}(u)\cos[-2\pi f_n u+\phi_{In}(u)] \tag{9}$$

and

$$E_I(u)=[\eta_{Ic}^2(u)+\eta_{Is}^2(u)]^{1/2} \tag{10}$$

where

$$\eta_{Ic}(u)=\sum_{n=1}^{\infty} a_{In}(u)\cos[-2\pi(f_n-f_p)u+\phi_{In}(u)]$$

$$\eta_{Is}(u)=\sum_{n=1}^{\infty} a_{In}(u)\sin[-2\pi(f_n-f_p)u+\phi_{In}(u)] \tag{11}$$

Reflected wave profile $\eta_R(u)$ and its envelope E_R are also expressed in terms of $a_{Rn}(u)$ and $\phi_{Rn}(u)$ in the same way as

$$\eta_R(u)=\sum_{n=1}^{\infty} a_{Rn}(u)\cos[-2\pi f_n u+\phi_{Rn}(u)] \tag{12}$$

and

$$E_R(u)=[\eta_{Rc}^2(u)+\eta_{Rs}^2(u)]^{1/2} \tag{13}$$

where

$$\eta_{Rc}(u)=\sum_{n=1}^{\infty} a_{Rn}(u)\cos[-2\pi(f_n-f_p)u+\phi_{Rn}(u)]$$

$$\eta_{Rs}(u)=\sum_{n=1}^{\infty} a_{Rn}(u)\sin[-2\pi(f_n-f_p)u+\phi_{Rn}(u)] \tag{14}$$

Solid lines in Fig.4 show $\eta_I(u)$ (above) and $\eta_R(u)$ (below). Dotted lines are envelopes $E_I(u)$ and $E_R(u)$. Analyzed irregular waves are the same as those used in the calculation of Fig.2.

Numerically simulated incident waves and their calculated reflection waves are composed first and then decomposed into incident and reflected wave profiles again by use of equations from eqs.(4) to (6) and eqs.(9) to (14). Calculated decomposed wave profiles of incident and reflected waves show good agreements with those originally simulated ones.

Figure 5 shows the Lissajous' figure of E_I and E_R although E_R is shifted by 5.5s to adjust a time correspondence with E_I. The solid line shows the relation of $E_R=0.5E_I$. Since the reflection coefficient is set to be 0.5, this is approximately the theoretical relation in this case. Except small deviations in the small part, the agreement is found fairy good. The present method is extended to evaluate the reflection coefficient of individual waves defined by the zero-up-cross method in terms of their properties (e.g. steepness) as follows. Since E_I and E_R approximately pass the crests and troughs of waves as seen in Fig.4 and from the

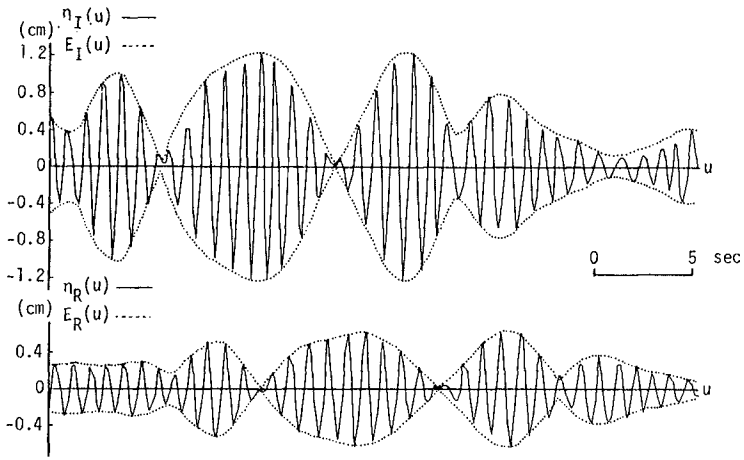

Fig.4 Decomposed wave profiles (solid lines) and their envelopes (dotted lines) for narrow-band spectrum case.

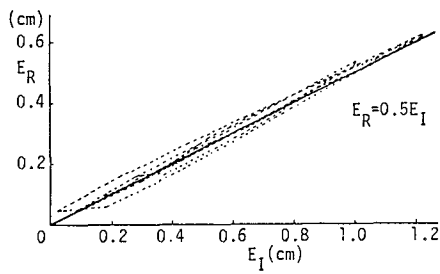

Fig.5 Lissajous' figure of E_I and E_R.

definition that an envelope is symmetrical about the u-axis, wave envelope may presumably have an instance u_i, within a zero-up-cross interval, when the twice of the envelope is equal to the zero-up-cross wave height determined in the same interval. Incident and reflected wave heights $H_I(u_i)$ and $H_R(u_i)$ are, therefore, approximated by equations

$$H_I(u_i) \simeq 2E_I(u_i), \qquad H_R(u_i) \simeq 2E_R(u_i) \tag{15}$$

The wave period of individual waves are approximated as follows. Equation 4 gives the short-term wave spectrum[4] in terms of u. The squared sum of amplitudes $| A_{jn}^2 + B_{jn}^2 |$ then changes from time to time according to the local properties of waves. The occasional zero-up-cross wave period can be approximated with $1/f_p(u_i)$ in which $f_p(u_i)$ is the peak frequency of the above squared spectrum at the instance u_i when the wave height is determined by eq.(15). The wave length is approximated by the small amplitude wave theory with this $1/f_p(u_i)$[5]. The wave steepness, for example, is determined as

$$H_I/L_I\big|_{t=u_i} \simeq 2E_I(u_i)/L_I[f_p(u_i)] \tag{16}$$

where $L_I\ [\ f_p(u_i)\ ]$ is the wave length given by

$$L_I[f_p(u_i)] = \frac{g}{2\pi f_p^2(u_i)} \tanh \frac{2\pi h}{L_I[f_p(u_i)]} \tag{17}$$

The reflection coefficient at the instance is therefore given as

$$r(u_i) = 2E_R\{u_i - 2D/C_g[f_p(u_i)]\}/2E_I(u_i) \tag{18}$$

in which $C_g\ [\ f_p(u_i)]$ is the group velocity of a frequency $f_p(u_i)$. As explained so far, the present theory uses wave envelopes instead of wave heights to calculate the reflection coefficients. Because the reflection coefficients calculated from the corresponding wave profiles may inevitably include errors to a certain degree due to a dispersive nature of irregular wave profiles. The change in the envelope, on the other hand, is rather gradual and small in comparison with the irregular wave profile itself unless the distance is large.[6] So the present method may have an advantage in the calculation of reflection coefficients. However a clear definition of the instance u_i to determine wave height and frequency (period) in eqs.(15) - (18) still has not been developed.

4. ARRANGEMENT OF WAVE GAUGES FOR THE MEASUREMENT OF IRREGULAR WAVES OF A WIDE BAND SPECTRUM

The fundamental concept of the present theory is exemplified for a irregular waves of narrow band spectrum in the former chapter. The theory is verified for irregular waves of a wide band spectrum in this chapter. In case of a wide band spectrum, there are component waves which make $\sin(k_n\Delta\ell)$ equal or nearly equal to 0 in the denominator of eqs.(5) and (6). Calculated reflection coefficients for these component waves are extremely inaccurate. The theory by Goda et al.[3] recommended an interval from $0.1\pi/k_n$ to $0.9\pi/k_n$ as an effective frequency or wave number range where reliable reflection coefficients can be calculated with eqs.(5) and (6). In this connection, a little narrower range from $0.3\pi/k_n$ to $0.7\pi/k_n$, for example, should be employed to improve the resolution. The narrower the effective frequency range becomes, however, the wider the incalculable frequency range becomes in the spectrum. To avoid this situation, the multi-wave gauge system is adopted in this study. Wave gauges are arrayed irregularly so that there is at least one suitable wave gauge pair that guarantees an effective frequency range for all the component waves in the spectrum. Intervals of wave gauges are determined as follows, if the same effective frequency range as above mentioned is adopted. The largest wave gauge interval $\Delta\ell_1$ is calculated in terms of the given low frequency bound f_d to be analyzed in the spectrum as

$$\Delta\ell_1 = \frac{0.3}{2} L(f_d) \tag{19}$$

in which $L(f_d)$ is the corresponding wave length of f_d. An upper bound of the effective frequency range f_1 for this pair of wave gauges is determined implicitly by

$$\Delta\ell_1 = \frac{0.7}{2} L(f_1) \tag{20}$$

The second largest wave gauge interval $\Delta\ell_2$ is given as

$$\Delta\ell_2 = \frac{0.3}{2} L(f_1) \tag{21}$$

since f_1 should be the lower bound of the effective frequency range for the second interval, if no overlapping of effective frequency ranges is permitted. Repeating the same procedures from eq.(19) to eq.(21) until the upper frequency bound for the i-th wave gauge interval f_i (i=1,2,...) exceeds the high frequency bound f_u to be analyzed in the

spectrum, whole intervals of the system ($\Delta\ell_i$) (i=1,2,...) can be determined. Intervals of a sample wave gauge system is listed in Table-1. Pierson-Moskowitz spectrum whose peak frequency f_p equals to 1.0Hz is used in a calculation of these intervals. High and low frequency bounds of the spectrum are set to be 0.5Hz and 3.5Hz, respectively, effective frequency interval is set to be $0.3\pi \leqq k_n < 0.7\pi$ and water depth h is set to be 10cm.

Four pairs of wave gauges are necessary to cover the entire frequency range in this case. Example arrangements of wave gauges in this case are schematically shown in Fig.6 (a), (b) and (c). The direction of incident wave is from left to right. Centers of all pairs of wave gauges coincide with each other in the system (a), one wave gauge is commonly used as a partner of the individual pairs in the system (b) and some wave gauges are commonly used twice as a partner in two wave gauge pairs in the system (c). A total number of wave gauges can be reduced in the system

Table-1 Sample of the wave gauge intervals and their effective frequency range.

f(Hz)	0.50-1.09	1.09-2.02	2.02-3.18	3.18-3.50
$\Delta\ell$(cm)	29.2	12.5	5.4	2.3

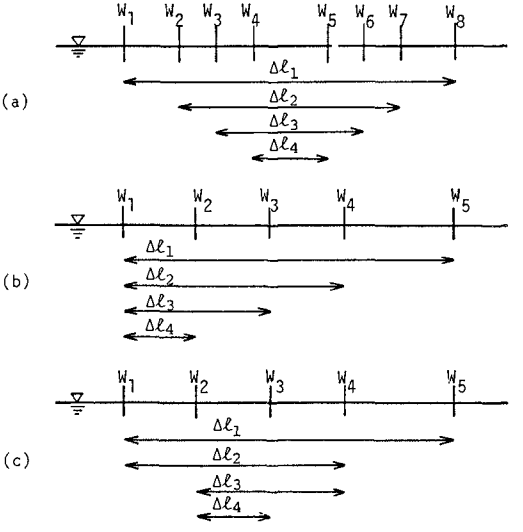

Fig.6 Samples of the wave gauge system.

(b) and (c). Judging from the numerical simulation, the resolution by the system (c) is preferable to (b). The origin of x-axis in the system (c) is preferable to set on the offshore-side a wave gauge pair which is used to analyze the dominant component. And the system is preferable to apply as close as possible to the structure.

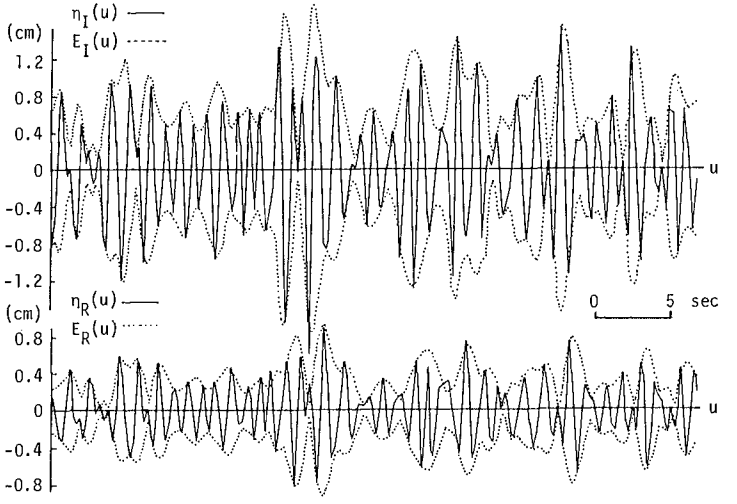

Fig.7 Decomposed wave profiles (solid lines) and their envelopes (dotted lines) for wide-band spectrum case.

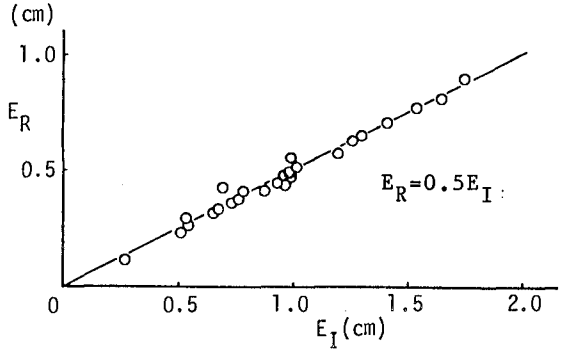

Fig.8 Relation of the values at the prominent summits in the wave envelopes for incident and reflected wave profiles.

Figure 7 shows the calculated result of incident and reflected wave profiles and their envelopes by the system (c). The distance from W-1 to the breakwater is set to be 0.3m. The reflection coefficient is set to be 0.5 and no phase is shifted for all the component waves. Notations and lines are the same as those used in Fig.4. Local disagreements between wave profiles and envelopes are a little prominent in comparison with the narrow band spectrum case. This comes from the asymmetric nature of the wave profile with the zero-level line, which irregular waves with a wide band spectrum usually have. With the ordinary method which dispenses with a data window[7], however, calculated results are almost the same as those by the present method. It can be distinguished from this figure and has been sometimes reported in the field measurements that irregular waves tend to form groups in a few waves which are enveloped by a single prominence of an envelope. Despite of the remarkable changes between incident and reflected wave profiles, the wave envelope maintains its form even after the reflection and transition. And every calculated time interval between the corresponding summits in the envelopes is almost equal to that required to go back and forth over the distance D with the group velocity of the wave around the summit. Every wave group presumably behaves as a single wave "packet[8]" in the process of reflection and transition. At the trough of an envelope, the side foot of the neighboring packets cross each other. Then the Lissajous' figure of E_R and E_I shows inevitably fluctuations around their troughs. To minimize this error, reflection coefficients are calculated only at the summit of individual prominences in E_R and E_I in

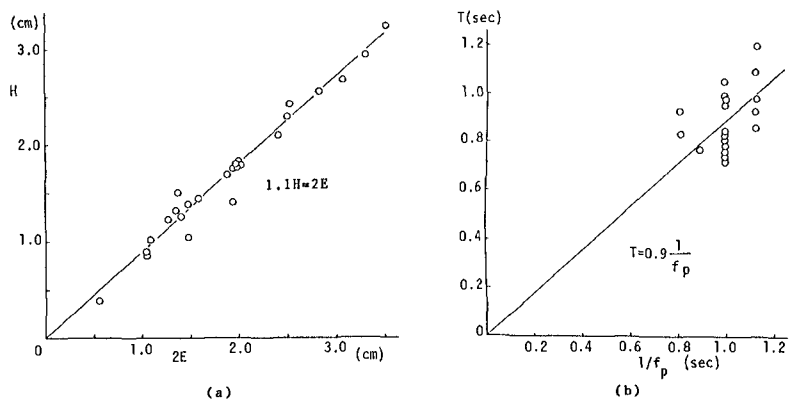

Fig.9 Comparison of (a) wave height, (b) wave period between those by the zero-up-cross method and the present definition.

this study. The relations of corresponding summits in E_I and E_R in Fig.7 are plotted in Fig.8. The solid line shows the relation of $E_R=0.5E_I$. The reliable reflection coefficient can be evaluated for those values. Wave height and period (frequency) in eqs.(15) - (17) are, then, determined at the prominent summit of the envelope. The calculated wave heights and periods, however, tend to be a little larger in this theory than those determined by the zero-up-cross method.

Figure 9 (a) shows the relation between the wave height determined by eq.(15) at the prominent summit of the envelopes and that by the zero-up-cross method just around the same instance. The solid line shows the relation $1.1H_I=2E_I$ or $1.1H_R=2E_R$. Figure (b) shows a relation of the zero-up-cross wave period to $1/f_p(u_i)$ at the prominent summit of an envelope. The solid line shows the relation of $T=0.9/f_p(u_i)$. Although the data show a little scattering, the zero-up-cross wave height and period can be approximated with the small modifications for calculated wave height and period. The calculated reflection coefficient from the present theory, therefore, can be discussed in terms of local properties of incident waves such as the steepness, Ursell number, etc. The numerically calculated constants for modifications, i.e., 1.1 and 0.9 in Fig.9 (a) and (b) respectively, are almost the same as those for wide band spectra such as Pierson-Moskowitz, Neumann and JONSWAP spectrum.

5. DISCUSSION

Since we assumed that an amplitude and a phase of a reflected wave may be constant only within a zero-up-cross interval, the width parameter of the data window in eq.(3) is desirable to be of the same order as that for a period of the dominant wave. The smaller this value becomes, however, the more uneven characteristics of the wave envelope prevail and the wider the calculated reflection coefficients fluctuate on the average. On the contrary, the larger this value becomes, the more locally the occasional nature of wave properties are averaged. Since the single wave group consists of 2-5 waves with similar properties (i.e., wave height, wave period) on the average, reflection characteristics of waves around the summit of an envelope may be assumed mutually equal. Two to five times of the dominant wave period is recommended for this value.

REFERENCES

1) Kajima, R: Estimation of an incident wave spectrum under the influence of reflection, Proc. 13th IAHR, Vol.5-1, pp.285-287, 1969.
2) Thornton, E. B. and R. J., Calhoun: Spectral resolution of breakwater reflected waves, Proc. ASCE, Vol.98, WW4, pp.443-460, 1972.
3) Goda, Y., Y. Suzuki, Y. Kishira and O. Kikuchi: Estimation of incident and reflected waves in random wave experiments, Tec. Note of P.H.R.I.M.T., No.248, 24p., 1976. (in Japanese)
4) Mark, W. D.: Spectral analysis of the convolution and filtering of non-stationary stochastic process, J. Sound Vib., Vol.11, No.1, pp.19-63, 1970.
5) Kimura, A. and Y. Iwagaki: wave length, wave velocity and shoaling characteristic of random waves, Proc. 16th ICCE, pp.320-339, 1978.
6) Kimura, A., H. Hokimoto and A. Seyama: Transition of wave groups Rept. of Faculty of Engg. Tottori Univ., Vol.14, No.1, pp.235-245, 1983. (in Japanese)
7) Rice, S. O.: Mathematical analysis of random noise, Selected papers on noise and stochastic processes, Dover, pp.133-294, 1954.
8) Kinsman, B.: Wind waves, Prentice-Hall, 1945.

CHAPTER 32

Large-angle Parabolic Equation Methods

James T. Kirby*

Large-angle parabolic equation methods for the propagation of surface water waves are discussed. The methods described here are limited to forms which are solvable by the Crank-Nicolson method, but are successful in opening the allowed range of propagation directions to ~ 50° with respect to normal incidence.

Introduction

The application of the parabolic equation method (PEM) to any relevant wave propagation problem implies that a principal propagation direction may be identified in the {x,y} plane of propagation. Then, an aperture, or window of directions with respect to the principal direction, is associated with any particular approximation, and limits the range of propagation directions which may be adequately represented by the approximation (Figure 1). The borders of a given aperture are defined only loosely and depend mainly on the amount of error the modeller is willing to allow in the wave prediction. This error may be evaluated for any given approximation by examining the approximation in terms of the related expansion of the wavenumber vector. Errors in predicted wavelengths and propagation directions may then be evaluated directly.

The purpose of this paper is to examine two methods of extending the basic parabolic equation method to include large-angle effects. The first scheme is based on the Padé approximant extension of the lowest-order scheme, following the work of Booij (1981) and Dingemans (1983). The second scheme is based on a minimax principle, and has been applied previously by Green (1984) to the problem of underwater sound propagation.

Parabolic Equations and Padé Approximants

The lowest-order parabolic equation for forward scattering of time-harmonic linear waves in the x (principal) direction in water of constant depth may be derived by substituting

$$\eta(x,y) = A(x,y)e^{i(kx-\omega t)} \tag{1}$$

into the governing Helmholtz equation to obtain

$$2ikA_x + A_{yy} = 0 + \text{higher order terms} \tag{2}$$

*Assistant Professor, Coastal and Oceanographic Engineering Department, University of Florida, Gainesville, FL 32611

where we have assumed that $|A_x| << O(k|A|)$. This approximation may be examined in light of the plane wave of permanent form

$$\eta = ae^{i(\ell x + my - \omega t)} \quad ; \quad \ell^2 + m^2 = k^2 \tag{3}$$

A(x,y) in eq. (1) is then given by

$$A(x,y) = ae^{i[(\ell-k)x + my]} \tag{4}$$

which gives

$$\frac{\ell}{k} = 1 - \frac{1}{2}\left(\frac{m}{k}\right)^2 \tag{5}$$

after substitution in eq. (2). Equation (5) in turn is the lowest order binomial expansion of

$$\frac{\ell}{k} = \left\{1 - \left(\frac{m}{k}\right)^2\right\}^{1/2} \tag{6}$$

for fixed $m/k = \sin\theta << 1$, θ being the propagation direction. The accuracy of any approximation over the range of propagation directions $0 \leq \theta \leq \theta_a$, where θ_a is the aperture width, may be evaluated by comparing predicted ℓ/k to exact $\ell/k = \cos\theta$ over the range in question. This comparison is given in Figure 2 for eq. (5). Equation (5) forms the basis of the so-called lowest-order approximation.

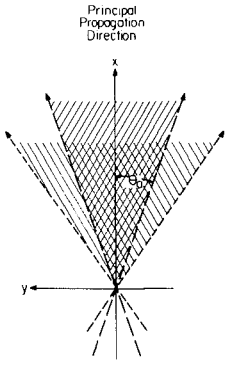

Fig. 1: Definition of aperture for parabolic approximations
//// allowed aperture: lower-order approximation
\\\\ allowed aperture: higher-order approximation (reprinted with permission of Elsevier Press)

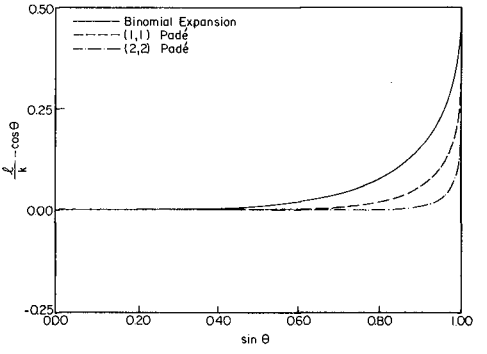

Fig. 2: Absolute errors $(\ell/k) - \cos\theta$ for several expansions of $(\ell/k) = (1 - (m/k)^2)^{1/2}$ about $(m/k) \to 0$ (reprinted with permission of Elsevier Press)

One of the simplest ways of extending the accuracy of a polynomial expansion is to construct a rational approximation consisting of the ratio of two polynomial expressions. Of the possible choices, the Padé approximant serves as the logical starting point (Baker, 1975). For eq. (6), the appropriate (1,1) Padé approximant is given by

$$\left(\frac{\ell}{k}\right) = \frac{1 - \frac{3}{4}\left(\frac{m}{k}\right)^2}{1 - \frac{1}{4}\left(\frac{m}{k}\right)^2} \tag{7}$$

The Padé approximant has the property of predicting the proper value and slope of the approximated function ℓ/k as m/k (or θ) becomes small. The approximation thus maintains the accuracy of the lowest-order approximation at small θ, and at the same time extends the accuracy of the approximation as θ increases, as shown in Figure 2. Using eq. (7) and retracing the steps of eqs. (2-5) in reverse order then gives

$$2ikA_x + A_{yy} + \frac{i}{2k} A_{xyy} = 0 \tag{8}$$

Dingemans (1983) has shown that the no-current, constant depth form of Booij's (1981) parabolic approximation is essentially equivalent to eq. (8), and proposed the Padé approximant as the relevant analysis of the splitting method employed by Booij to obtain his PEM approximation.

Padé Approximant: Computational Example

As a test of the higher-order parabolic model, we study the wave field in the vicinity of the shore-attached breakwater described in Figure 3. An extensive set of data for the wave field in the shadow zone downwave of the breakwater has been given by Hales (1980) for a number of wave periods, amplitudes, and angles of incidence. A closed form asymptotic solution in the linear, mild-slope approximation has been provided by Liu et al (1979) and has been compared to the experimental data by Liu (1982), who found qualitative agreement between the linear theory and experimental results.

The parabolic equation for the general case of uneven topography was developed according to the approximation of the previous section and is given in Kirby (1986).

For this case, we restrict our attention to the linearized theory in order to compare parabolic model results to the asympototic theory of Liu et al. The experimental results are complicated by the presence of a wave-induced current system due to the surf zone in close proximity to the measurement transects, and it is likely that neglected wave-current interaction effects have as much influence on the data as the neglected nonlinearity.

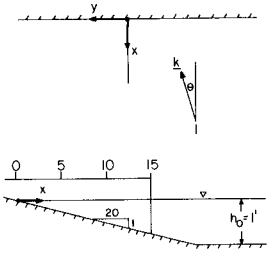

Fig. 3: Geometry of shore-attached breakwater (reprinted with permission of AGU)

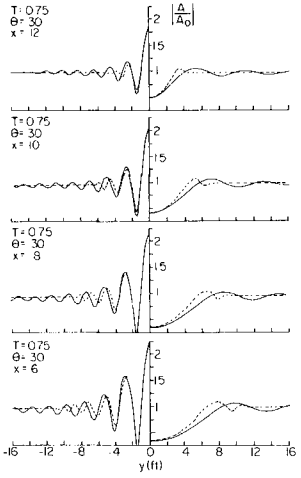

Fig. 4a: Shore-attached breakwater: comparison of lowest-order approximation and asymptotic theory of Liu et al (1979). Dashed line, lowest-order approximation; solid line, asymptotic theory; T = 0.75 s, θ = 30°. (reprinted with permission of AGU)

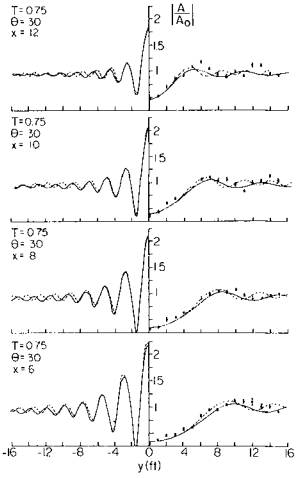

Fig. 4b: Shore-attached breakwater: comparison of higher-order approximation, asymptotic theory of Liu et al (1979), and data of Hales (1980). Dashed line, higher-order approximation; solid line, asymptotic theory, Φ experimental data; T = 0.75 s, θ = 30°. (reprinted with permission of AGU)

The geometry corresponding to the experimental arrangement consists of a plane beach with slope 1:20, extending out to a depth of 1 ft (.3048 m), beyond which the bottom is flat. The x coordinate is oriented offshore from the shoreline. The breakwater extends to x = 15 ft (4.572 m), and measured wave data in the shadow zone of the breakwater are available for the transects x = 6, 8, 10, and 12 ft (1.829, 2.438, 3.048, and 3.658 m) (Hales, 1980). Values for incident wave data are with reference to the offshore region with h = 1 ft (.3048 m).

In Figures 4a and 5a we show comparisons of the predictions of the lowest-order approximation with the asymptotic theory of Liu et al for the extremes of the test conditions T = 0.75 s, θ = 30° and T = 1.5 s, θ = 20°, respectively. In both cases it is apparent that the diffracted wave disturbance spreads laterally at a much slower rate in the lower-order approximation than in the analytic theory, which encompasses an unapproximated mild-slope equation. Both the height of the reflected wave on the upwave side of the breakwater and the wave height in the shadow zone adjacent to the downwave side of the breakwater are well predicted. However, most of the diffracted wave information is lost farther from the breakwater, well before significant amplitude modulations in the asympototic wave field die out. These results indicate that the group velocity for lateral motion of diffracted waves is too small in the lower-order approximation.

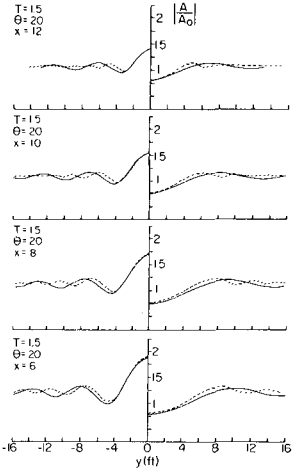

Fig. 5a: As in Figure 4a; T = 1.5 s, θ = 20°. (reprinted with permission of AGU)

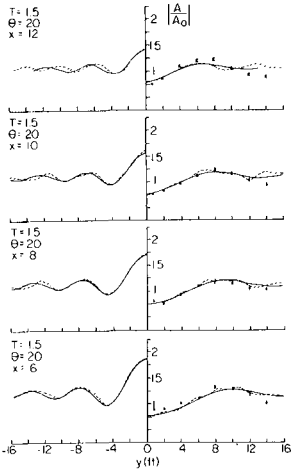

Fig. 5b: As in Figure 4b; T = 1.5 s, θ = 20°. (reprinted with permission of AGU)

For the Padé approximation, plots of results for the two test conditions are given in Figures 4b and 5b. Data in the shadow and downwave regions for these cases correspond to the lowest-amplitude runs from Hales (1980), which would be expected to correspond more

closely to the assumption of linearity. The plots indicate that the diffracted wave field is able to spread laterally in the higher-order approximation to a much greater degree than in the lower-order approximation. A comparison of the parabolic model results to the asymptotic theory indicates that the parabolic model is initially contaminated by components with large transverse wavenumber, which cause the computed amplitude modulations transverse to the breakwater to undulate more rapidly than the corresponding asymptotic results. These rapid undulations may be successfully damped using any one of several types of dissipative filters.

Minimax Approximation

Greene (1984) has suggested that improvements may be achieved while staying within the scheme of eq. (7) by relaxing the exact connection between eq. (7) and eq. (6) as $(m/k)\to 0$ in favor of adopting an approximation which minimizes the maximum error $(\ell/k - \cos\theta)$ over a prespecified aperture $0 \leq \theta \leq \theta_a$. These so-called minimax approximations may be written in the present context as

$$\left(\frac{\ell}{k}\right) = \frac{a_0 + a_1 \left(\frac{m}{k}\right)^2}{1 + b_1 \left(\frac{m}{k}\right)^2} \quad , \tag{9}$$

The coefficients of the minimax approximation are chosen so as to minimize the error

$$e = \mathrm{MAX}\left|\ell/k(\theta) - \cos\theta\right| \quad ; \quad 0 \leq \theta \leq \theta_a \quad , \quad \theta_a \text{ given} \tag{10}$$

where ℓ/k is predicted by eq. (12) and $\cos\theta = \ell/k$ is given by eq. (6). The procedure for obtaining minimax approximations is too extensive to summarize here; the reader is referred, for example, to Chapter 6 of Morris (1983). A list of values of a_0, a_1 and b_1 are given in Table 1 for aperture widths ranging from 10° to 90° in increments of 10°. The coefficient values are seen to be asymptotic to the (1,1) Padé approximant at $\theta_a \to 0$. Figure 6 gives plots of the absolute error in predicted (ℓ/k) for values of θ_a = 40°, 60° and 80°. A plot of the (1,1) Padé approximant is included for comparison. For values of $\theta_a < 60°$, the correspondence between the minimax and (1,1) Padé approximant remains close at $\theta=0$, the deviation for θ_a = 60° being $(1 - a_0) \times 100$ = 0.2%. Deviations for $\theta_a > 60°$ at $\theta\approx 0$ increase rapidly due to the difficulty in approximating eq. (7) as $m/k\to 1$. However, the advantages of the θ_a = 60° approximation over the (1,1) Padé approximant, when considered over the entire range $0 \leq m/k < 1$, are apparent. A comparison of Figures 2 and 6 indicates that the θ_a = 60° approximation attains about the same level of accuracy as $m/k\to 1$ as the (2,2) Padé approximant, with only a slight decrease in accuracy at small values of θ.

Equation (12) may be used to derive the corresponding parabolic approximation

TABLE 1. COEFFICIENTS OF THE RATIONAL APPROXIMATION DETERMINED BY VARYING APERTURE WIDTH.

Aperture	a_0	a_1	b_1
Padé	1	-.75	-.25
10°	.999999972	-.752858477	-.252874920
20°	.999998178	-.761464683	-.261734267
30°	.999978391	-.775898646	-.277321130
40°	.999871128	-.796244743	-.301017258
50°	.999465861	-.822482968	-.335107575
60°	.998213736	-.854229482	-.383283081
70°	.994733030	-.890064831	-.451640568
80°	.985273164	-.925464479	-.550974375
90°	.956311082	-.943396628	-.704401903

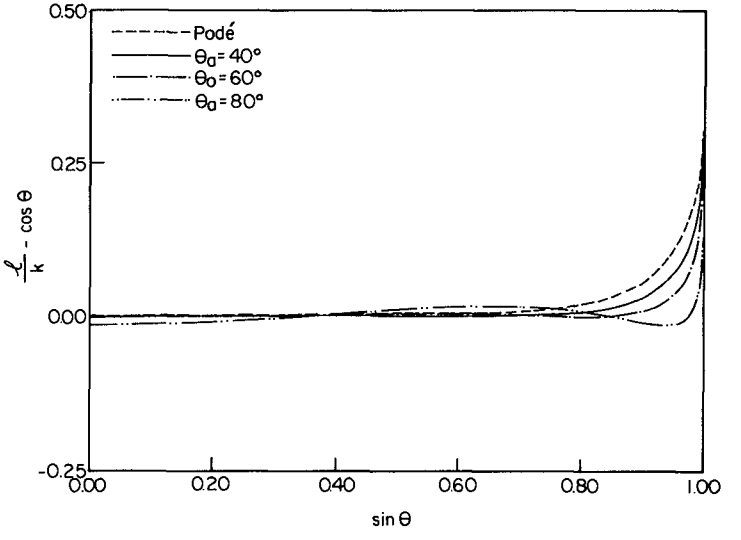

Fig. 6: Absolute errors $(\ell/k) - \cos\theta$ for various aperture widths θ_a for the minimax (1,1) rational approximation. (reprinted with permission of Elsevier Press)

$$2ikA_x + 2k^2(a_0 - 1)A + 2(b_1 - a_1)A_{yy} - \frac{2ib_1}{k} A_{xyy} = 0 \qquad (11)$$

which reduces to eq. (10) as $\theta_a \to 0$.

Tests of the Minimax Approximation at Large Angles of Incidence

The minimax approximation of the previous section has been used to develop a corresponding refraction-diffraction model including the effects of weak nonlinearity and wave current interaction: details are given in Kirby (1987). In order to test the large-angle capabilities of the model, we choose a shoal geometry given by

$$h(x,y) = \begin{cases} h_0 = 0.336 \text{ m} & ; \quad r > R \\ h_0 + 0.3 - 0.5\{1 - [(\frac{x}{5})^2 + (\frac{y}{5})^2]\}^{1/2} & ; \quad r \leq R \end{cases}$$

where R = 4 m and $r = (x^2 + y^2)^{1/2}$. The symmetry of the shoal allows the incident wave field to be rotated to any angle to the x-axis; a "correct" model will be one that causes no distortion to the resulting focusing pattern resulting from changes in θ_0, the incidence angle.

We take a rectangular grid with $\Delta x' = \Delta y' = 0.25$ m and overall dimensions $0 \leq x'y' \leq 24.75$ m. We use the incident wave period and amplitude conditions of Berkhoff et al (1982). Two incident wave directions are studied; $\theta_0 = 0°$, with the shoal centered at (x',y') = (5,10), and $\theta_0 = 45°$, with the shoal centered at (x',y') = (5,5).

For the first series of tests, we use the (1,1) Padé model to study the two incident wave angles. Figure 7 shows the wave patterns for the two incidence angles in the form of contours of surface elevation in increments of $0.5\ A_0$. The asymmetrical distortion to the focusing pattern at the 45° angle of incidence is apparent, as is a tendency for the focus to be shifted off the picture diagonal in the +x direction, or downwave in the computational sense. The distortion to the wave pattern due to the 45° angle of incidence is illustrated clearly by the superposition of wave amplitude contours in Figure 8. The superposition was obtained by rotating the wave field of Figure 7b about the center of the shoal by 36.5° in a counterclockwise sense, or 45° minus an 8.5° distortion which represents the angle between the diagonal and the line joining the shoal center to the point of maximum wave height in the focus. This 8.5° distortion accounts for the shift of the diffraction pattern in the downwave sense on the computation grid. Figure 8 shows clearly that the focus is elongated and shifted further from the shoal center than in the normal incidence case, with corresponding distortion in the diffraction fringes. Contour values in Figure 8 (and 10) are relative to incident wave amplitude.

Figure 9 shows the wave field for the 45° angle of incidence, using the $\theta_a = 70°$ minimax approximation. There is still some apparent asymmetric distortion and a shift of the focus off the diagonal in the +x direction; however, these effects are much less accentuated

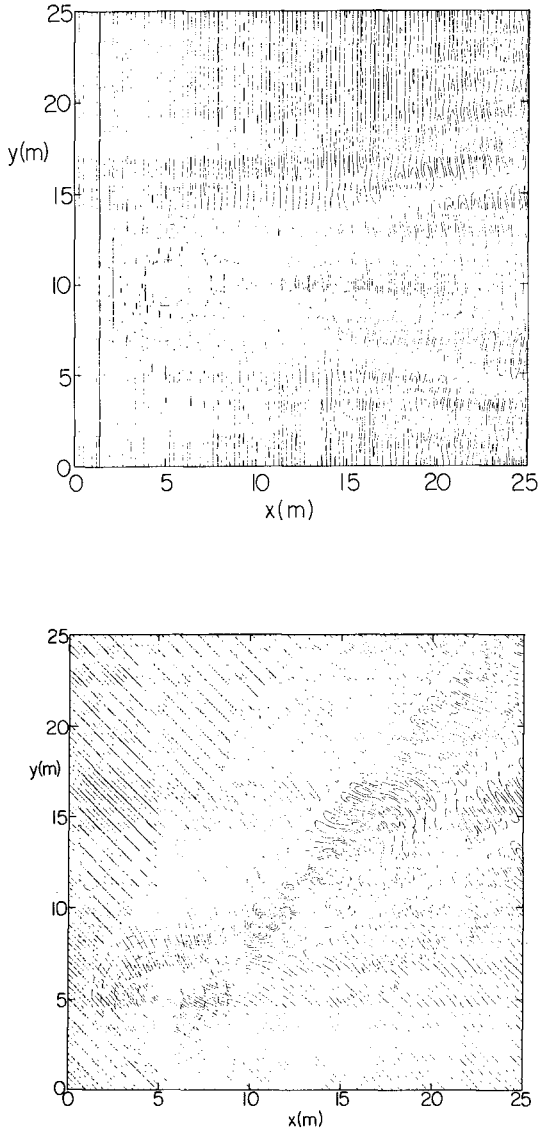

Fig. 7: Wave fields calculated using the (1,1) Padé model. Contours are in increments of 0.5 A_0 for instantaneous $\eta(x,y)$. a) $\theta_0 = 0$, normal incidence. b) $\theta_0 = 45°$. (reprinted with permission of Elsevier Press)

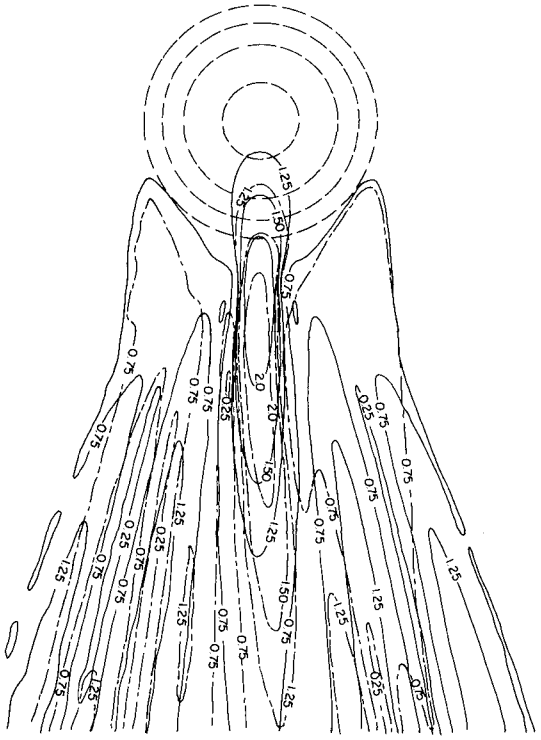

Fig. 8: Amplitude contours and topography for circular shoal. Amplitude contours $|A/A_0|$ as labelled; (1,1) Padé approximant. —— θ_0 = 0°; —•—•— θ_0 = 45°; — — depth contours. (reprinted with permission of Elsevier Press)

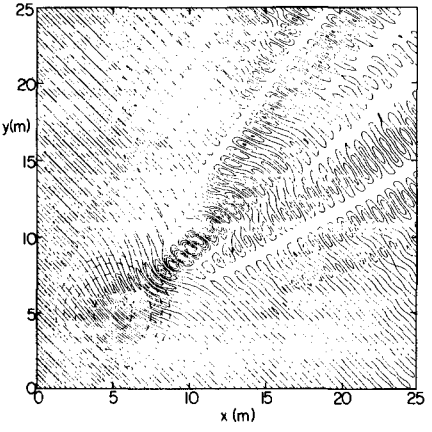

Fig. 9: Wave field calculated using θ_a = 70° model; θ_0 = 45°. Contours as in Figure 7. (reprinted with permission of Elsevier Press)

than in the Padé model. Amplitude contours for the normal and 45° incidence in the 70° approximation are superposed in Figure 10. Here the counterclockwise rotation of the 45° case is 39.75°, with a distortion of 5.25°. The two results agree reasonably well in terms of the area and extent of contours in the focus, and in the distance of the focus from the shoal center. The overall diffraction pattern is maintained reasonably well out to two maxima of the diffraction fringe away from the central focus.

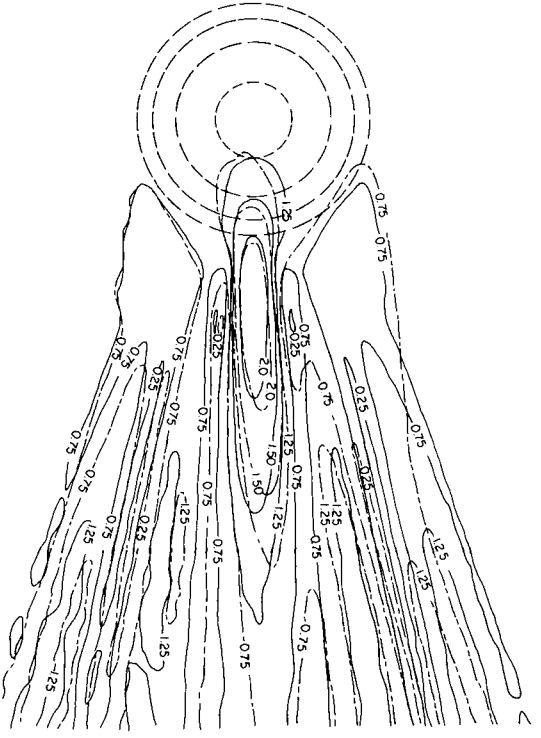

Fig. 10: Amplitude contours and topography for circular shoal, θ_a = 70° approximation. —— θ_0 = 0°; —•—•— θ_0 = 45°; --- depth contours. (reprinted with permission of Elsevier Press)

The θ_a = 70° minimax approximation clearly provides a better model for large-angle propagation than does the Padé approximant model. Further tests were conducted using the 80° approximation. This model exhibited marginally better agreement between θ_0 = 0° and 45° than did the 70° model, but caused a significant distortion to the overall extent of the focus in comparison to the Padé and 70° models.

Refraction Effects in Parabolic Approximations

For the special case of topographies varying as h(x) only, and for angles of incidence θ_0 at reference depth h_0, each of the parabolic approximations may be solved to yield an estimate of the leading-order, slowly varying wave field undergoing shoaling and refraction. Solutions for the full refraction approximation and for each of three parabolic methods follow:

Exact Refraction Solution

$$\eta = A_0\left(\frac{C_{g_0}}{C_g}\right)^{1/2}\left(\frac{\cos\theta_0}{\cos\theta}\right)^{1/2} e^{i\int k\cos\theta\, dx - my)} \tag{12}$$

Small-Angle Equation Solution

$$\eta = A_0\left(\frac{C_{g_0}}{C_g}\right)^{1/2} e^{i\int k\left(\frac{\ell}{k}\right)dx - my}\ ;\ \frac{\ell}{k} = 1 - \frac{1}{2}\left(\frac{m}{k}\right)^2 \tag{13}$$

(1,1) Padé Approximation

$$\eta = A_0\left(\frac{C_{g_0}}{C_g}\right)^{1/2}\frac{\left(1 - \frac{1}{4}\sin^2\theta_0\right)}{\left(1 - \frac{1}{4}\sin^2\theta\right)} e^{i\int k\left(\frac{\ell}{k}\right)dx - my}\ ;\ \frac{\ell}{k}\frac{1 - \frac{3}{4}\left(\frac{m}{k}\right)^2}{1 - \frac{1}{4}\left(\frac{m}{k}\right)^2} \tag{14}$$

Minimax Approximation

$$\eta = A_0\left(\frac{C_{g_0}}{C_g}\right)^{1/2}\frac{\left(1 + b_1\sin^2\theta_0\right)}{\left(1 + b_1\sin^2\theta\right)} e^{i\int k\left(\frac{\ell}{k}\right)dx - my}\ ;\ \frac{\ell}{k} = \frac{a_0 + a_1\left(\frac{m}{k}\right)^2}{1 + b_1\left(\frac{m}{k}\right)^2} \tag{15}$$

It is apparent that, with each increase in level of approximation, that the phase function of the shoaled wave becomes better approximated. Also apparent are large variations in each model's ability to reproduce the refraction coefficient $(\cos\theta_0/\cos\theta)^{1/2}$ of the "exact"solution; in particular, it is not modelled at all in the lowest-order case and is only apparent starting with the (1,1) Padé approximant method. Figure 11 gives results for computed refraction coefficients for four angles of incidence 20°, 40°, 60°, and 80° with respect to shore-normal. The minimax values are based on a chosen

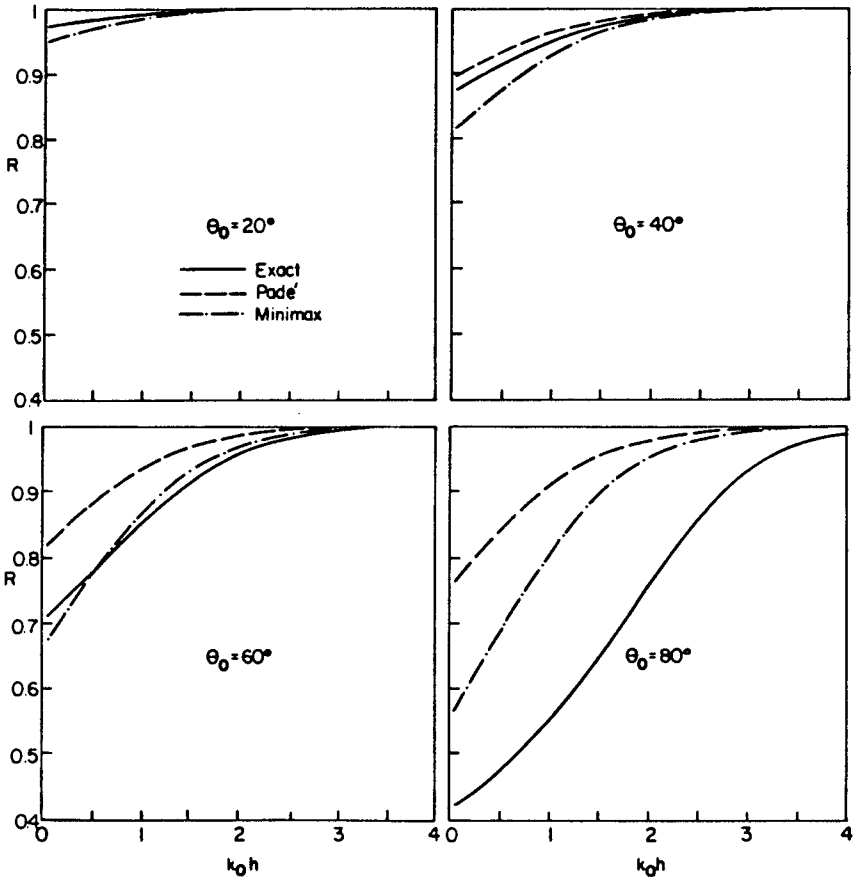

Fig. 11: Variation in refraction coefficient with deepwater angle of incidence θ_0 and water depth.

width $\theta_a = 70°$. For small angles of incidence, the (1,1) Padé approximant method exhibits favorable behavior in comparison to the minimax approximation, due to its enhanced level of accuracy as local $\theta(x) \to 0$. However, for $\theta_0 = 60°$, the minimax approximation performs quite well, while the (1,1) Padé approximant is clearly over-extended. For $\theta_0 = 80°$, the propagation angle is outside the range of both higher-order models, and each perform poorly. In each of the cases above, θ_0 is taken to be the deepwater value.

Conclusions

It has been shown that the range of wave angles which is allowable within the limitations of the parabolic approximation may be significantly increased by relaxing the local accuracy of approximations based on Padé approximants at normal wave incidence in favor of minimax approximations, which minimize the maximum error occurring over a prespecified range of wave directions. We have shown that the minimax approximations provide quantitatively accurate results for a focussing pattern developing in a wave propagating at 45° to the principal direction. This range of quantitative accuracy is seen to be well beyond the limitations of the (1,1) Padé approximant model given above. Results for wave refraction calculations suggest that it would be desirable to limit the aperture width θ_a in the minimax approximation to a value consistent with the largest expected local propagation direction, since the Padé approximant model is somewhat better at predicting the refraction coefficient at small angles of incidence.

References

Baker, G.A., 1975, Essentials of Padé Approximants, Academic Press.

Berkhoff, J.C.W., Booij, N, and Radder, A.C., 1982, "Verification of numerical wave propagation models for simple harmonic linear waves", Coastal Eng. 6, 255-279.

Booij, N., 1981, "Gravity waves on water with non-uniform depth and current", Report 81-1, Dept. of Civil Eng., Delft Univ. of Technology.

Dingemans, M.W., 1983, "Verification of numerical wave propagation models with field measurements: CREDIZ verification Haringvliet", Report W488 part 1, Delft Hydraulics Laboratory.

Greene, R.R., 1984, "The rational approximation to the acoustic wave equation with bottom interaction", J. Acoust. Soc. Am., 76, 1764-1733.

Hales, L.Z., 1980, "Erosion control of scour during construction, report 3, Experimental measurements of refraction, diffraction, and current patterns near jetties", Tech. Rep. HL-80-3, U.S. Army Eng. Waterways Exp. Stn., Vicksburg, Ms.

Kirby, J.T., 1986, "Higher-order approximations in the parabolic equation method for water waves", J. Geophys. Res., 91, 933-952.

Kirby, J.T., 1987, "Rational approximations in the parabolic equation method for water waves", Coastal Engineering, in press.

Liu, P.L.-F., 1982, "Combined refraction and diffraction: comparison between theory and experiments," J. Geophys. Res. 87, 5723-5730.

Liu, P.L.-F., Lozano, C.J., and Pantazaras, N., 1979, "An asymptotic theory of combined wave refraction and diffraction", Appl. Ocean Res., 1, 137-146,.

Morris, J.Ll., 1983, Computational Methods in Elementary Numerical Analysis, John Wiley and Sons.

CHAPTER 33

ESTIMATION OF WATER PARTICLE VELOCITIES OF SHALLOW WATER WAVES BY A MODIFIED TRANSFER FUNCTION METHOD

Hirofumi KOYAMA* and Koichiro IWATA**

ABSTRACT

This paper is intended to propose a simple, yet highly reliable approximate method which uses a modified transfer function in order to evaluate the water particle velocity of finite amplitude waves at shallow water depth in regular and irregular wave environments. Using Dean's stream function theory,the linear function is modified so as to include the nonlinear effect of finite amplitude wave. The approximate method proposed here employs the modified transfer function. Laboratory experiments have been carried out to examine the validity of the proposed method. The approximate method is shown to estimate well the experimental values, as accurately as Dean's stream function method, although its calculation procedure is much simpler than that of Dean's method.

1. INTRODUCTION

The water surface profile of shallow water waves sharpens at the crest and flattens at the trough, and generally becomes asymmetric due to shoaling on a sloping beach. The asymmetry of the water surface profile gives rise to the unsymmetrical field of the wave kinematics[1]. So far, no exact theory for asymmetrical waves has been proposed. This has prevented depicting precise characteristics of the kinematics of asymmetric regular and irregular waves. The previous investigations[2)-4)] have pointed out that the Dean's stream function method[5)] (hereafter referred to as DSFM), among several methods, predicts most accurately the water particle velocity of asymmetrical steep and near-breaking waves. However, DSFM requires a complicated iterative calculation as well as a full record of the water surface profile in order to obtain only a maximum water particle velocity. The accurate estimation of the maximum velocity is an important coastal engineering problem. Therefore, DSFM is not necessarily so useful for field engineers to estimate the kinematics of the design wave.

First of all, the difference of the water particle velocity estimated by the transfer function method using the linear wave theory (LTFM) and

---

* M. Eng., Civil Engineer, Kanazawa Office, Niigata Branch, Nippon Tetrapod, Co., Ltd., Kanazawa, Ishikawa, Japan.

** Dr. Eng., Professor, Dept. of Civil Eng., Nagoya Univ., Nagoya, Aichi, Japan.

DSFM is investigated. The linear transfer function is then modified by introducing the nonlinear effect of finite amplitude waves with the help of Dean's stream function table[6]. The modified transfer function method (MTFM) which employs the modified transfer function is proposed as a simple yet highly reliable approximate method. The calculation procedure is much simpler than that of DSFM. Lastly, laboratory experiments are carried out to examine the validity of MTFM. The experiments show that MTFM is a highly reliable approximate method to calculate the wave kinematics.

2. MODIFIED TRANSFER FUNCTION

2.1 Modified transfer function for horizontal velocity of water particle

The present authors[7] showed that a time history of the horizontal velocity u(t) is closely correlated to that of the water surface profile and that the transfer function method is an useful one to estimate the horizontal component of the water particle velocity. The transfer function $H_u(h,T,s)$ for the horizontal particle velocity is defined by

$$u(t) = H_u(h,T,s)\eta(t) . \qquad (1)$$

Equation (1) shows that the horizontal velocity is predicted from the water surface profile through a filter of the transfer function. In this paper, the water surface profile is not decomposed into Fourier component waves, whether the waves are regular or irregular; the actual water surface profile is employed as $\eta(t)$.

The transfer function $H_u(h,T,s)$ and the horizontal velocity u(t) in case of the linear wave theory are described as follows;

$$H_u(h,T,s) = \frac{2\pi}{T}\frac{\cosh ks}{\sinh kh} , \qquad (2)$$

$$u(t) = \frac{2\pi}{T}\frac{\cosh ks}{\sinh kh}\eta(t) . \qquad (3)$$

One example of comparison between the laboratory experiments and the estimation with Eq.(3) is shown in Fig.1. This figure indicates that the peak value obtained by the experiment agrees comparatively well with Eq.(3) for $\eta<0$. However, in the range of $\eta>0$, the calculated peak value is generally higher than the experimental value. This is a general tendency recognized for many data. The experimental fact implies that the nonlinear effect of finite amplitude waves which is not included in Eq.(3) should be considered in estimating the horizontal velocity, especially for the range of $\eta>0$. Then we will attempt to modify Eq.(2) so as to include the nonlinear effect.

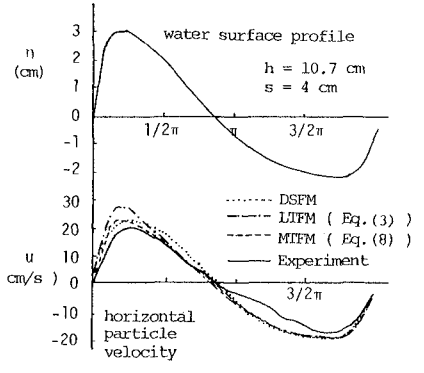

Fig.1 Comparison between measurement and calculations(Regular wave; experimental and DSFM's values are from Nadaoka et al.[4]).

We modify Eq.(2) for $\eta>0$, introducing a correction function f as expressed by

$$\left.\begin{aligned} H_u(h,T,s) &= \left(\frac{2\pi}{T}\frac{\cosh ks}{\sinh kfh}\right); \quad \eta > 0 \\ u(t) &\doteq \left(\frac{2\pi}{T}\frac{\cosh ks}{\sinh kfh}\right)\eta(t); \quad \eta > 0 \end{aligned}\right\} \text{--- (4)}$$

In Eq.(4), fh is used in place of h. The accuracy of u(t) thus evaluated for the finite amplitude waves depends largely upon how accurately f is determined.

The correction function f is formulated by using Dean's stream function table for symmetrical regular waves under various conditions. The nonlinear effect of finite amplitude waves is supposed to be predominant at the phase of wave crest. Therefore, first, the correction function f at the two locations $s=h+\eta^+$(water surface) and s=0(bottom) are determined. That is, the maximum horizontal velocities u^+ at the two locations s=0 and $s=h+\eta^+$ are first read from Dean's stream function table, where η^+ is the wave crest height. Using the second equation of Eq.(4), the values of the correction function f for various combinations of u^+ and η^+ at the locations $s=h+\eta^+$ and s=0 are calculated. The values thus calculated are given in Figs. 2 and 3 in relation to η^+/h with auxiliary parameters h/Lo and H/Lo.

According to Figs.2 and 3, the correction function f can be approximated by Eq.(5) in the range of $h/Lo \leq 0.2$.

$$\left.\begin{aligned} f &= 1+\eta^+ \quad ; \text{ for } s = 0 \\ f &= 1 \quad ; \text{ for } s = h+\eta^+ \end{aligned}\right\} \text{ for } \eta=\eta^+ . \text{ ---------- (5)}$$

Further, two assumptions are made here to formulate f for any value of s in the range of $\eta>0$;

(1) Equation (5) is extended to all positive values of η. In other words, we can substitute η (>0) for η^+.

(2) The correction function f at any depth s is expressed by a linear interporation between the values at $s=h+\eta^+$ and s = 0.

Using these assumptions, the correction function f for $\eta>0$ is formulated as

$$f = 1 + \frac{\eta^+}{h}\left(1 - \frac{s}{(h+\eta)}\right). \text{ ---------- (6)}$$

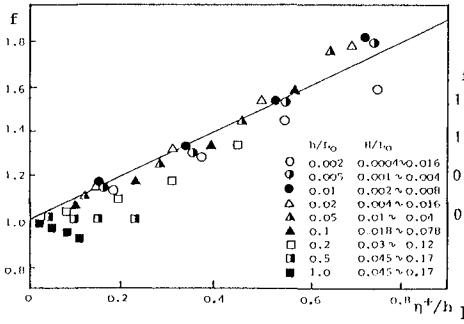

Fig.2 Value of correction function f at s = 0.

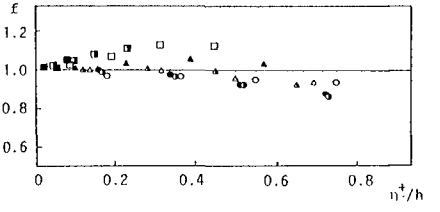

Fig.3 Value of correction function f at $s = h + \eta^+$ (symbols of calculated values are the same as those in Fig.3).

Now, let us discuss the correction function f for $\eta \leqq 0$. As already stated, Eq.(3) predicts comparatively well the experimental values for $\eta \leqq 0$. The same thing has been pointed out by Nadaoka et al. Eq.(2) is, therefore, used as the transfer function for $\eta \leqq 0$ without modification. Based on the above mentioned, the modified transfer function f proposed is given by

$$\left.\begin{aligned} H_u(h,T,s) &= \frac{2\pi}{T}\frac{\cosh ks}{\sinh(h+\eta(1-s/(h+\eta)))} ; \eta > 0 \\ &= \frac{2\pi}{T}\frac{\cosh ks}{\sinh kh} ; \eta \leqq 0 \end{aligned}\right\} \text{-------} \quad (7)$$

Using Eqs.(1) and (7), the horizontal velocity u(t) is evaluated by

$$\left.\begin{aligned} u(t) &= \frac{2\pi}{T}\frac{\cosh ks}{\sinh k(h+\eta(1-s/(h+\eta)))}\eta(t) ; \eta > 0 \\ &= \frac{2\pi}{T}\frac{\cosh ks}{\sinh kh}\eta(t) ; \eta \leqq 0 \end{aligned}\right\} \text{------} \quad (8)$$

As seen in Figs.1 and 4, the estimation with the modified transfer function method (MTFM) is in better agreement with DSFM. Then, it can be said that MTFM is much better than the linear transfer function method (LTFM).

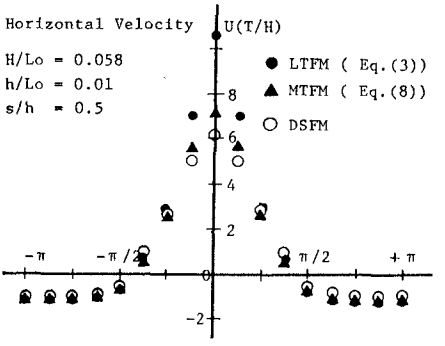

Fig.4 Comparison among DSFM, MTFM and linear transfer function method (LTFM).

2.2 Modified transfer function for vertical velocity of water particle

Judging from the conservation law of mass flux and u(t) given by Eq.(8), it can be supposed that the transfer function for w(t) should include the term $\partial\eta/\partial x$, where x is the horizontal distance. It is not desirable, however, that the transfer function involves the term of $\partial\eta/\partial x$ to avoid a complicated calculation which is not convenient to field engineers. Hence, we try to deduce a simple transfer function for w(t) as follow.

The present authors[7] have already shown that the time profile of the vertical velocity of water particle resembles that of the water surface with a certain time lag, Δt. In addition, the water surface profile can be transferred to the horizontal velocity profile of water particle by use of Eq.(8). Then, w(t) can be expressed by

$$\left.\begin{aligned} w(t) &= H_w(h,T,s)\eta(t+\Delta t) \\ &= H_{u-w}(h,T,s)u(t+\Delta t) \end{aligned}\right\} \text{----------} \quad (9)$$

where, $H_w(h,T,s)$ is a transfer function between w(t) and $\eta(t+\Delta t)$, $H_{u-w}(h,T,s)$ a transfer function between w(t) and $u(t+\Delta t)$ and Δt a time lag from a zero-upcrossing point to the next coming wave crest. The time lag Δt in Eq.(9) can be determined from a record of water surface profile.

In case of the linear wave theory, the transfer function H_{u-w} and Eq.(9) are expressed as Eq.(10) and Eq.(11), respectively.

$$H_{u-w}(h,T,s) = \tanh ks \qquad \text{---------- (11)}$$

$$w(t) = \tanh ks \times u(t + \Delta t) . \qquad \text{---------- (11)}$$

One example of comparison between the estimation with Eq.(10) and the values of DSFM is shown in Fig.5. The figure shows that the negative peak value is underestimated by Eq.(10). And, in some another cases, the positive peak value is also apart from the value of DSFM.

Therefore, we try to introduce a correction function g as expressed by

$$\left.\begin{aligned} H_u(h,T,s) &= (g \tanh ks) \\ w(t) &= (g \tanh ks) \times u(t + \Delta t) \end{aligned}\right\} . \qquad \text{---------- (12)}$$

The correction function g is formulated by Dean's stream function table, the procedure of which is the same as that of the correction function f for the horizontal velocity. Figs. 6 and 7 show the calculations of the correction functions g for positive and negative peak values in relation to the parameter of $\eta Lo/h^2$, respectively. In the figures, the correction function g calculated at s/h=0.5 is only shown. The correction functions g at other locations from the bottom up to the water surface were almost equal to that of s/h=0.5.

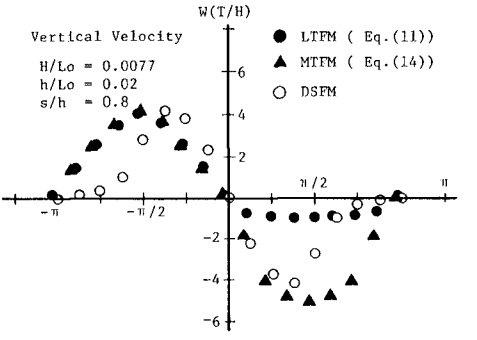

Fig.5 Comparison of vertical velocity of water particle among DSFM, LTFM and MTFM.

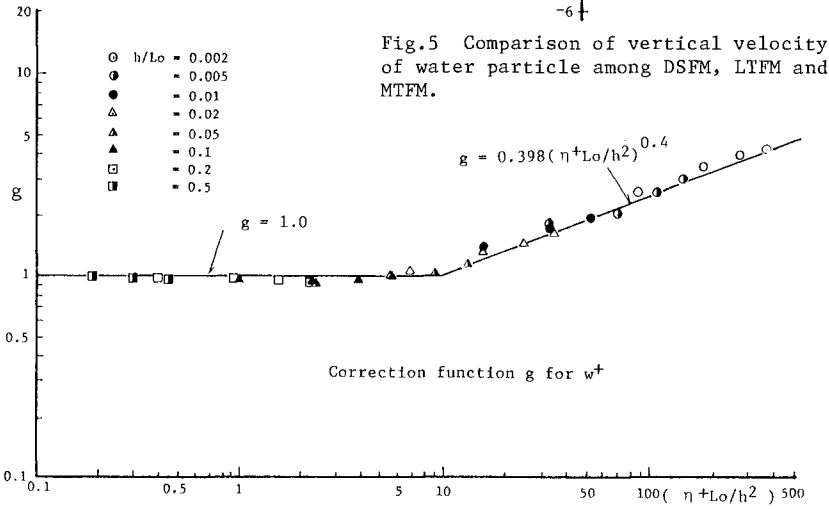

Fig. 6 Value of correction function g for w^+.

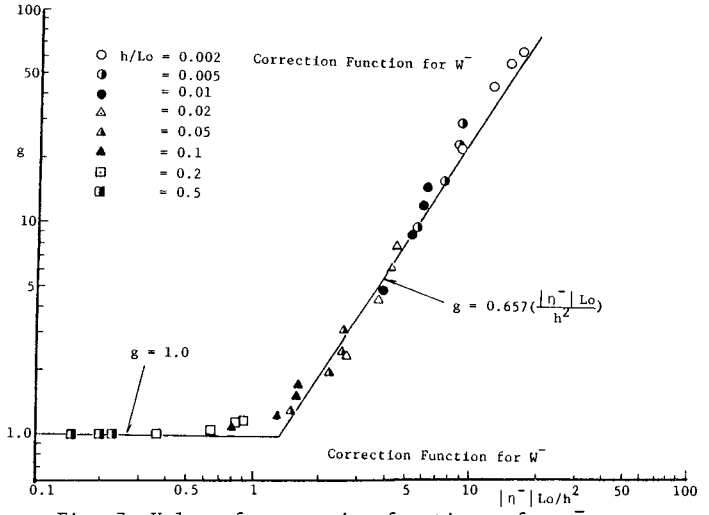

Fig. 7 Value of correction function g for w^-

According to Figs. 6 and 7, the correction function g can be approximated by

$$\left.\begin{aligned} g &= 0.398\left(\frac{\eta Lo}{h^2}\right)^{0.4} ; && \eta Lo/h^2 > 10 \\ &= 1 ; && -1.3 \leqq \eta Lo/h^2 \leqq 10 \\ &= 0.657\left(\frac{|\eta| Lo}{h^2}\right)^{1.6} ; && -1.3 > \eta Lo/h^2 \end{aligned}\right\} \quad \text{----- (13)}$$

Using this correction function, the vertical velocity of the modified transfer function method is evaluated by

$$\left.\begin{aligned} w(t) &= 0.398\left(\frac{\eta Lo}{h^2}\right)^{0.4} \times \tanh ks \times u(t+\Delta t) ; && \eta Lo/h^2 > 10 \\ &= \tanh ks \times u(t+\Delta t) ; && -1.3 \leqq \eta Lo/h^2 \leqq 10 \\ &= 0.657\left(\frac{|\eta| Lo}{h^2}\right)^{1.6} \times \tanh ks \times u(t+\Delta t) ; && \eta Lo/h^2 < -1.3 \end{aligned}\right\} \quad (14)$$

Figure 5 shows one example of comparison among DSFM, LTFM and MTFM by Eq.(14). The estimation of MTFM correspods well to that by DSFM , although there is a discrepancy between their time profiles.

Summarizing the above stated, it can be pointed out that MTFM which uses Eqs.(8) and (14) is a highly reliable approximate method to evaluate the wave kinematics.

3. LABORATORY EXPERIMENT

In the experiment, an indoor wave tank of 0.7m in width, 0.95m in depth and 25m in length at Nagoya University was used. At one end of the

wave tank, was installed a flap-type wave generator controlled by an oil-pressure servo system. At the other end of the wave tank, beach slope of 1/15 and 1/8 and a horizontal step having a slope of 1/15 at the leading edge were set, as shown in Fig.8. Experimental conditions are given in Table 1.

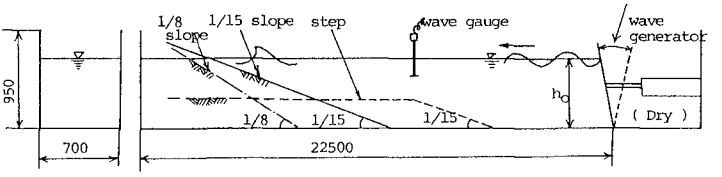

Fig.8 Schematic view of experimental set-up

Table 1 Experimental conditions

run	bottom slope i	wave period T, T1/3(s)	wave height H,H1/3(cm)	stillwater depth h(cm)	breaker depth h_b(cm)	breaker height H_b(cm)	wave
1 - 1	1/15	1.43	15.4	63	15.0	14.8	regular
1 - 2	"	1.10	10.4	"	10.9	10.9	"
1 - 3	"	0.84	11.5	"	11.3	11.3	"
2 - 1	1/8	1.10	9.7	"	10.4	10.4	"
2 - 2	"	1.00	11.8	"	11.9	11.9	"
3 - 1	step	0.89	9.0	35	10.2	10.2	"
3 - 2	"	1.06	15.4	50	16.0	16.0	"
3 - 3	"	1.00	14.1	44	14.8	14.8	"
4 - 1	1/15	1.08	11.3	63	-	-	irregular
4 - 2	"	1.32	10.3	"	-	-	"

($H_{1/3}$ anf $T_{1/3}$ are significant wave height and period, respectively)

Wave profiles were measured by capacitance-type wave gauges. The water particle velocity was measured by a cantilever type velocimeter newly devised by the present authors[8]. The water particle velocities were measured at many locations from s=0 up to nearly $s=h+\eta^+$ in the vertical direction and from h= 60cm up to h= 1cm in the horizontal direction. Time profiles of water surface and particle velocities were recorded on a magnetic tape over a period of 1 min.

4. RESULTS AND DISCUSSION

In this section, the validity of MTFM is discussed by comparing with DSFM, LTFM and the experimental values. In the calculation of DSFM, the water surface profile was divided into 20 discrete values for one wave cycle. Following Dean's method, with use of the 20 discrete values, the iterative calculation was performed 4 or 5 times until the relative error between the measured and the predicted water surface profiles becomes less than 5%.

4.1 Regular wave

(1) Time profile of water particle velocity

Figure 9 shows time profiles of the water particle velocity estimated by MTFM and DSFM, and experimental values. Figures 9(a), (b) and (c) are

the typical examples of the horizontal and vertical velocities for the waves before breaking, just at breaking point and after breaking, respectively. In case of the non-breaking wave, as in Fig.9(a), the water particle velocity predicted by MTFM is very close to that by DSFM, and both estimations are generally in good agreement with experiments. On the other hand, in case of waves just at breaking point and after breaking (see Fig.9(b) and (c)), the horizontal velocity u(t) estimated by MTFM corresponds well to that by DSFM, and the agreement of both calculations with experimantal values is very good. Concerning the vertical velocity w(t), however, a little difference between the two calculations was generally observed. In Figs.9(b) and (c), w(t) estimated by MTFM has a better agreement with experimetal values than that by DSFM.

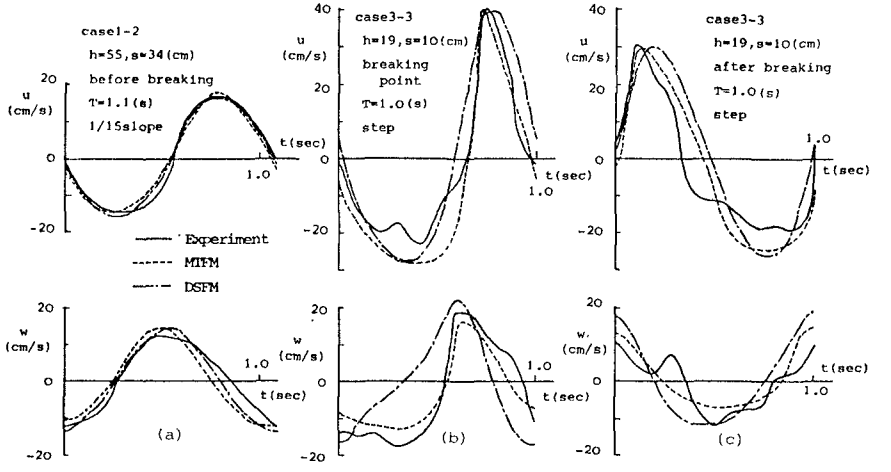

Fig.9 Comparison of time profiles of water particle velocities between calculations and experiments (for regular waves)

(2) Vertical distribution of maximum water particle velocity

Figure 10 shows some examples of the vertical distribution of the maximum horizontal and vertical velocities, where the positive and negative values of $u/\sqrt{gh}$ are, respectively, the non-dimensional onshore and offshore horizontal velocities, and the positive and negative values of $w/\sqrt{gh}$ are the non-dimensional upward and downward vertical velocities, respectively. In Fig.10, the calculated values of DSFM, MTFM and LTFM are drawn to be compared with experimental values. Using Eqs.(8) and (14), the maximum values of $u^+(s)$, $u^-(s)$, $w^+(s)$ and $w^-(s)$ by MTFM are given by

$$\left.\begin{aligned} u^+(s) &= \frac{2\pi}{T}\frac{\cosh ks}{\sinh k(h+\eta^+(1-s/(h+\eta^+)))}\eta^+ \quad (\text{for onshore velocity}) \\ u^-(s) &= \frac{2\pi}{T}\frac{\cosh ks}{\sinh kh}\eta^- \quad (\text{for offshore velocity}) \\ w^+(s) &= \frac{2\pi}{T}\frac{\sinh ks}{\sinh k(h+\eta^+(1-s/(h+\eta^+)))}\eta^+ \quad (\text{for upward velocity}) \\ w^-(s) &= \frac{2\pi}{T}\frac{\sinh ks}{\sinh kh}\eta^- \quad (\text{for downward velocity}) \end{aligned}\right\}. \tag{15}$$

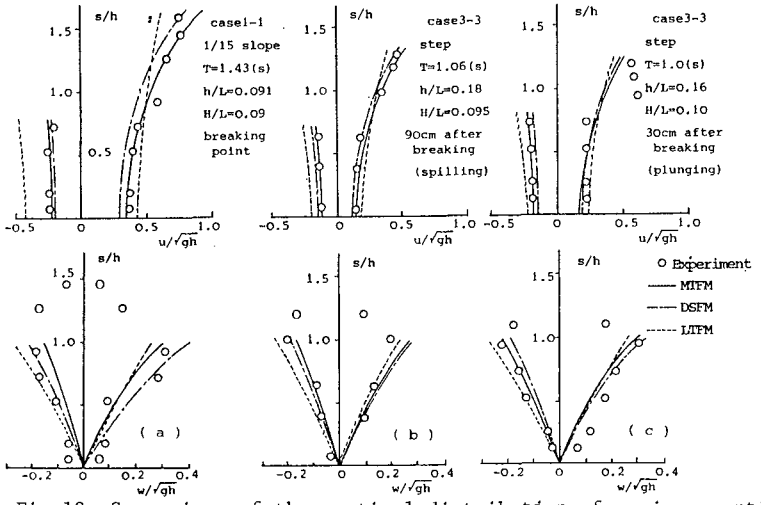

Fig.10 Comparison of the vertical distribution of maximum particle velocity between measurements and calculations (for regular waves).

In Eq.(15), η^+ and η^- are the wave crest and trough elevations, respectively, and it should be stressed that $w^+(s)$ and $w^-(s)$ are derived for $-1.3 \leqq \eta Lo/h^2 \leqq 10$.. Therefore, although they cover a wide range of wave conditions,different expressions of $w^+(s)$ and $w^-(s)$ should be used in place of Eq.(15) for the range of $\eta Lo/h^2 \geqq 10$ and $\eta Lo/h^2 \leqq -1.3$.

According to Fig.10, it can be pointed out that the vertical distributions of maximum horizontal and vertical velocities predicted by MTFM and DSFM are in good agreement with the experiments except near the free surface of the plunging breaker and the bottom. The plunging breaker has usually a bore-like character with entrainment of air bubbles. Any of the three methods does not consider the entrainment of air bubbles. This may have caused the discrepancy between the calculations and experiment for the plunging breaker. Figure 10 also shows that $w^+/\sqrt{gh}$ and $w^-/\sqrt{gh}$ near the bottom tend to be underestimated by the three methods. The reason is, as pointed out by Nadaoka et al., that the three theories assume a horizontal bottom and then they cannot exactly express the vertical component of wave motion along the bottom slope.

In Fig.10, calculated values above the stillwater level ($s/h \geqq 1$) are not indicated. The experimental values show that $w^+/\sqrt{gh}$ and $w^-/\sqrt{gh}$ decrease linearly with s/h toward the wave crest. Judging from the comparisons between the calculations and experiments including those in Fig. 10, LTFM seems to be inferior to MTFM and DSFM in predicting the maximum values, $u^+/\sqrt{gh}$, $u^-/\sqrt{gh}$, $w^+/\sqrt{gh}$, and $w^-/\sqrt{gh}$ as well as time profiles of the water particle velocity, u(t) and w(t).

4.2 Irregular wave

In evaluating the velocities of water particle u(t) and w(t), the irregular wave is not decomposed into Fourier component waves, but is treated by the wave-by-wave analysis which uses the zero-downcrossing

method. Equations (8) and (14) are applied to the individual waves in a random wave train. In calculating w(t), Δt was given by an average value of time intervals between a zero-upcrossing point and the next-coming wave crest of the wave train.

Figures 11 shows one comparison between the measurements and calculations by means of DSFM and MTFM. First, let us discuss on u(t). As seen in Fig.11, the time profiles estimated by MTFM as well as DSFM correspond well, in general, to the experimental values. However, in Fig.11, DSFM underestimates the positive peak value of u(t) for the particular waves with symbole * for which the mean water level is higher than the still-water level. On this point, MTFM can be said to be superior to DSFM. Concerning the vertical velocity w(t), both theories (DSFM and MTFM) do not predict well the experimental values. One reason of this is attributed to the method of wave definition employed, i.e. the wave-by-wave analysis like the zero-downcrossing method. The zero-downcrossing method divides the water surface profile into two parts at the zero-downcrossing point. Since the water surface profile near the stillwater level governs sensitively a peak value of w(t), the use of the zero-downcrossing method yields errors in evaluating the peak value. The same thing can be said for the zero-upcrossing method. Therefore, as pointed out by Daemrich at al.[9], the crest-to-crest method may be recommended in order to estimate the vertical velocity.

Lastly, peak values of the horizontal particle velocity u^+ at 2cm above the stillwater level are discussed. Table 2 gives peak values u^+ for successive ten waves in a random wave train, and schematic water surface profiles are shown in the second row for convenience of discussion. Comparing the calculated values with DSFM and MTFM with experimental ones, MTFM can be said to predict the experimental values much better than DSFM in general. However, it should be noted that MTFM as well as DSFM tend to underestimate u^+ of the waves which have two peaks on the water surface above the stillwater level such as No.1, No.4, No.8 and No.9.

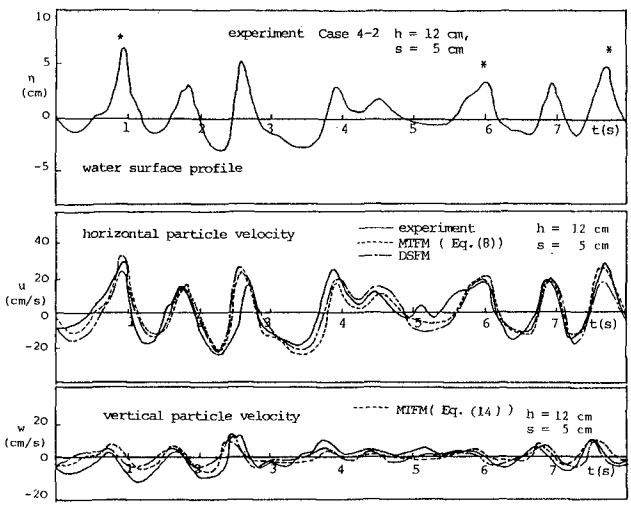

Fig.11 Time profile of water particle velocities for irregular wave (Case 4-2, h=12cm and s=5cm).

Table 2 Comparison between experimental and calculated values of horizontal particle velocity for irregular wave (Case 4-2, h = 21cm and s = 23cm).

Wave No.	1	2	3	4	5	6	7	8	9	10
water surface profile η(t) (cm)	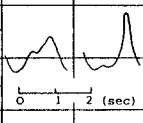									
period T (sec)	1.52	1.39	0.97	1.61	0.97	0.94	0.90	1.68	1.61	1.13
wave height H(cm)	6.4	10.7	8.8	7.5	3.5	7.6	9.2	5.5	9.1	8.7
u^+(Experiment)	40.0	56.1	50.9	46.2	26.8	48.4	46.5	44.7	46.5	43.2
u^+(DSFM)	22.7	51.7	41.3	25.0	18.7	31.0	34.5	21.9	31.0	34.4
u^+(MTFM(Eq.(8))	29.4	62.0	53.4	31.8	25.3	50.5	40.8	31.2	31.4	46.7

u^+(Experiment), u^+(DSFM) and u^+(MTFM(Eq.(8)); unit (cm/s)

Two peaks on the free surface profile will imply the existence at least two different waves. Then, it seems difficult for DSFM and MTFM proposed for a monocromatic wave to evaluate well the particle velocities for such composite waves.

As stated above, the water particle velocity estimated by MTFM is in good agreement with the experimental value of the so-called "quasi-regular waves" in a random wave train. Comparing the modified transfer function method with Dean's stream function method, it can be said that MTFM is never inferior to DSFM in evaluating accurately the water particle velocity of finite amplitude regular or irregular waves. Since the calculation procedure of MTFM is much simpler than that of DSFM, the modified transfer function method proposed in this paper is useful and highly reliable for evaluating the wave kinematics.

5. CONCLUDING REMARKS

The approximate method which uses the modified transfer function has been presented to evaluate the water particle velocity of finite amplitude waves, for engineering purposes. The approximate method (modified transfer function method) is never inferior to Dean's stream function method in evaluating the wave kinematics of asymmetrical or symmetrical finite amplitude waves in regular and irregular wave environments, although its calculation procedure is much simpler than that of Dean's stream function method. In particular, the use of the approximate method is recommended to estimate the maximum water particle velocity of finite amplitude waves in shallow water depth. However, it is found that the predominant large velocity of water particle near the free surface in the surf-zone cannot be estimated accurately by any existing method.

REFERENCES

1) Adeymo,M.D.: Velocity fields in the wave breaker zone, Proc. 12th Conf. on Coastal Eng., ASCE, pp.435-460, 1970.
2) Iwagaki,Y. and T.Sakai: Representation of water particle velocity of breaking waves on beaches by Dean's stream function method, Proc.21st Japanese Conf. on Coastal Eng.,JSCE,pp.27-32, 1974, (in Japanese).

3) Hino,M. and M.Kashiwayanagi: Application of Dean's stream function method to estimation of wave orbital velocity and wave set-down and set-up, Coastal Engineering in Japan, Vol.22, pp.11-20, 1979.
4) Nadaoka,K., Kondo,T. and N.Tanaka: Structure of velocity field within the surf zone revealed by means of Laser-Doppler anemometry, Rept. Port and Harbour Res. Inst., Ministry of Trans., Vol.21, No.2, pp.49-106, 1982.
5) Dean,R.G.: Stream function representation of nonlinear ocean waves, Jour. of Geophy. Res., Vol.70, pp.4561-4572, 1965.
6) Dean,R.G.: Evaluation and development of water wave theories for engineering application, U.S.Army Corps Eng., CERC, Spec. Rept., No.1, 1974.
7) Iwata,K., Koyama,H. and S.Futo: Experimental study on variation of wave energy after breaking, Proc.30th Japanese Conf. on Coastal Eng., pp.10-14, 1983, (in Japanese).
8) Koyama,H. and K.Iwata: Estimation of water particle velocities by a modified transfer function method, Coastal Engineering in Japan, Vol. 28, pp.1-14, 1985.
9) Daemrich,K.F., Eggert,W.D. and S.Kohlhase: Investigation on irregular waves in hydraulic models, Proc. 17th Conf. on Coastal Eng., ASCE, pp.186-203, 1980.

CHAPTER 34

Nonlinear Theory on Particle Velocity and Pressure of Random Waves

Yi-Yu Kuo* and Hwar-Ming Wang**

ABSTRACT

In this paper, to the third approximation, we used the Fourier-stieltjes integral rather than Fourier coefficient to develop a weakly nonlinear theory. From the theory, the nonlinear spectral components for water particle velocity and wave pressure can be calculated diretly from the directional spectrum of water surface displacement. Computed results based on the nonlinear theory were compared with that of experiment made by Anastasiou (1982). Furthermore, in accordance with the different characteristics of wave properties, such as wave steepness, water depth and so on, the nonlinear effects on wave kinematic and pressure properties were extensively investigated by using some standard power spectra.

1. INTRODUCTION

To the first approximation, ocean waves can be described as a superposition of statistically independent free waves which have random phases and satisfy the linear wave theory. More recently, however, it has been found by many investigators that these spectral components of ocean waves do not necessarily follow the linear wave theory, especailly in the shallow water areas. Several nonlinear random wave theories were developed by, such as Phillip (1960), Hasselmann (1962), Weber (1977) and Masuda(1979) et al. But their description were mostly confined to the spectrum of water surface displacement.

The studies on random and nonlinear characteristics with respect to the wave kinematics and pressures are seldom discussed. Hudspeth (1975) developed a simulation method to determine the uni-directional second-order sea surface characteristics; however, in his report the water particle kinematics are computed by the digital linear filter technique. Following the nonlinear wave theory developed by Longuet-Higgings (1963), Sharma (1979) proposed a second order directional wave theory by using discrete frequency component to predict the wave kinematic and dynamic property. In the present study, for similar work but to the theird order approximation, we used the Fourier-stieltjes integral rather than Fourier coefficient to develop a weakly nonlinear theory for wave kinematics and wave pressures.

2. FORMULATION

For irrotational motion of an incompressible fluid, there is a velocity potential $\Phi(x,z,t)$ governed by

$$\nabla^2\Phi(\vec{x},z,t)=0 \tag{1}$$

Here $x=(\vec{x},y)$ is the horizontal co-ordinates, z is the vertical one and t

* Professor, Department of Civil Engineering, National Chiao-Tung University, Hsinchu, Taiwan, R.O.C.

** Graduate Research Asistant, Department of Civil Engineering, National Chiao-Tung University, Hsinchu, Taiwan, R.O.C.

is the time. The solution of (1) with the condition that Φ vanishes as z=-h is given by

$$\Phi(\vec{x},z,t)=\int_K \frac{\cosh|k|(h+z)}{\cosh|k|h} e^{i\chi} dA(K) \tag{2}$$

where K denotes (ω,k). ω is angular frequency, k is wave number vector, the increment dA(K) is a random variable and $\chi=k\vec{x}-\omega t$ is the phase. The integration is over the entire ω and k space. In the same way the surface displacement η can be expressed as

$$\eta(\vec{x},t)=\int_K e^{i\chi} dB(K) \tag{3}$$

Substituting with equation (2) and (3) in the kinematic boundary condition at water surface, and using the series expasion

$$\frac{\cosh\{|k|(h+z)\}}{\cosh|k|h}=1+|k|z\tanh|k|h+\frac{1}{2}|k|^2z^2+\ldots \tag{4}$$

we can find the relationship between dA(K) and dB(K) to the third order as

$$\begin{aligned} dA(K)=&\frac{-i\omega}{|k|\tanh|k|h} dB(K) \\ &+\int_{K_1} \frac{i\omega_1\cdot k\ k_1}{|k||k_1|\tanh\{|k|h\}\tanh\{|k_1|h\}}\cdot dB(K_1)dB(K-K_1) \\ &+\int_{K_1}\int_{K_2} \frac{i\omega_1}{|k|\tanh\{|k|h\}}\{\frac{1}{2}|k_1|^2+k_1\cdot k_2 \\ &-\frac{k\cdot(k_1+k_2)k_1\cdot(k_1+k_2)}{|k||k_1+k_2|\tanh\{|k_1|h\}\tanh\{|k_1+k_2|h\}} \\ &dB(K_1)dB(K_2)dB(K-K_1-K_2) \end{aligned} \tag{5}$$

2.1 water particle velocity

The increment of water particle velocity is also defined by

$$\vec{Q}=\int_K dq e^{i\chi} \tag{6}$$

However, the particle velocity vector $\vec{Q}$ can be obtained by taking the gradient of velocity potential Φ. Therefore, from the equations (2) and (6), we have

$$dq^H(K,Z)=\frac{i|k|\cosh\{|k|(h+z)\}}{\cosh|k|h} dA(K) \tag{7}$$

where dq^H is the increment of horizontal water particle velocity. Substituting equation (5) into equation (7), we obtain

$$\begin{aligned} dq^H(K,z)=&f_1(K,z)dB(K)+\int_{K_1} f_2(K,K_1,z)dB(K_1)dB(K-K_1) \\ &+\int_{K_1}\int_{K_2} f_3(K,K_1,K_2,z)dB(K_1)dB(K_2)dB(K,K_1,K_2) \end{aligned} \tag{8}$$

where
$$f_1(K,z)=\frac{\omega k\cosh\{|k|(h+z)\}}{|k|\sinh|k|h}$$
$$f_2(K,K_1,z)=-\frac{1}{2}\left\{\frac{\omega_1 k<k,k_1>}{\tanh|k_1|h}+\frac{(\omega-\omega_1)k<k,k-k_1>}{\tanh\{|k-k_1|h\}}\right\}\frac{\cosh\{|k|(h+z)\}}{\sinh|k|h}$$
$$f_3(K,K_1,K_2,z)=\frac{\omega_1 k\cosh\{|k|(h+z)\}}{\sinh|k|h}\left\{\frac{1}{2}|k_1|^2+|k_1||k_2|<k_1,k_2>\right.$$
$$\left.-\frac{|k||k_1+k_2|<k_1,k_1+k_2><k,k_1+k_2>}{\tanh|k_1|h\,\tanh\{|k_1+k_2|h\}}\right\} \qquad (9)$$

Here $<k,k'>\equiv k.k'/|k||k'|$ denotes the cosine of the angle formed by this vectors k and k'. For further development, let the increment dB(K) is represented as the sum of primary component $dB_1(K)$, second component $dB_2(K)$ and so on. However, following a previous study (Masuda et al 1979), $dB_2(K)$ and $dB_3(K)$ can also be expressed in terms of $dB_1(K)$. Taking the mean square value of the increment dq^H and using the definition of power spectrum

$$\frac{\overline{dq^H(K)\,dq^H(K')}}{dK\,dK'}=\phi_H^q(K)\,\delta(K+K') \qquad (10)$$

we finally obtained the horizontal water particle velocity spectrum ϕ_H^q as

$$\phi_H^q(K,z)=f_1(K,z)f_1(-K,z)\phi_1(K)$$
$$+2\int_{K_1}\frac{f_1(K,z)f_1(-k,z)}{W(K)W(-K)}\{fv_2(K,K_1)\}^2\phi_1(K_1)\phi_1(K-K_1)dK_1$$
$$+4\int_{K_1}\frac{f_1(-k,z)}{W(k)}f_2(k,k_1,z)\{fv_2(k,k_1)\}\,\phi_1(k_1)\phi_1(k-k_1)dK_1$$
$$+2\int_{K_1}f_2(k,k_1,z)f_2(-k_1,-k_1,z)\phi_1(k_1)\phi_1(k-k_1)dK_1$$
$$+4\int_{K_1}\frac{f_1(-k,z)}{W(k-k_1)}f_2(k,k_1,z)\{fv_2(k-k_1,-k_1)$$
$$+fv_2(k-k_1,k)\}\phi_1(k)\phi_1(k_1)dK_1$$
$$+2\int_{K_1}f_1(-k,z)\{f_3(k,k_1,-k_1,z)+f_3(k,k_1k,z)$$
$$+f_3(k,k,k_1,z)\}\phi_1(k)\phi_1(k_1)dK_1$$
$$+2\int_{K_1}\frac{f_1(k,z)f_1(-k,z)}{W(k)}\left\{2\frac{fv_2(k,k_1)}{W(k-k_1)}+fv_3(k,k_1,-k_1)\right.$$
$$\left.+fv_3(k,k_1,k)+fv_3(k,k,k_1)\right\}\phi_1(k)\phi_1(k_1)dK_1 \qquad (11)$$

where

$$W(K)=g-\frac{\omega^2}{|k|\tanh|k|h} \tag{12}$$

$$fv_2(K,K_1)=\frac{1}{2}\{\omega^2-\omega\omega_1+\omega_1^2-\omega\omega\frac{<k,k_1>}{\tanh\{|k|h\}\tanh\{|k_1|h\}}$$
$$-\omega(\omega-\omega_1)\frac{<k,k-k_1>}{\tanh|k|h\ \tanh\{|k-k_1|h\}}$$
$$-\omega_1(\omega-\omega_1)\frac{<k_1,k-k_1>}{\tanh|k_1|h\ \tanh\{|k-k_1|h\}} \tag{13}$$

$$fv_3(K,K_1,K_2)=\frac{1}{4}\{\frac{\omega_1^2|k_1|}{\tanh|k_1|h}+\frac{\omega_2^2|k_2|}{\tanh|k_2|h}\}$$
$$+\frac{1}{2}\omega_1\omega_2\{\frac{|k_1|}{\tanh|k_1|h}+\frac{|k_2|}{\tanh|k_2|h}\}$$
$$+\frac{1}{4}\frac{\omega}{|k|\tanh|k|h}\{\omega_1|k_1|^2+\omega_2|k_2|^2\}$$
$$-\frac{1}{2}(\omega_1+\omega_2)|k_1+k_2|\{\frac{\omega_1<k_1,k_1+k_2>}{\tanh|k_1|h}+\frac{\omega_2<k_2,k_1+k_2>}{tnah|k_2|h}\}$$
$$-\frac{1}{2}\omega(\omega_1+\omega_2)\frac{|k_1||k_2|<k_1,k_2>}{|k|\quad\tanh|k|h}$$
$$+\frac{\omega}{2}|k_1+k_2|\frac{<k,k_1+k_2>}{\tanh|k_1|h\ \tanh\{|k_1+k_2|h\}}$$
$$\{\frac{\omega_1<k_1,k_1+k_2>}{\tanh|k_1|h}-\frac{\omega_2<k_2,k_1+k_2>}{\tanh|k_2|h}\}$$
$$-\frac{1}{2}\omega_1\omega_2|k|\{\frac{<k,k_1>}{\tanh|k_1|h}+\frac{<k,k_2>}{\tanh|k_2|h}\}$$
$$+\frac{1}{2}\frac{\omega_1\omega_2}{\tanh|k_1|h\ \tanh|k_2|h}\{\frac{|k-k_1|}{\tanh\{|k-k_1|h\}}<k_1,k-k_1><k_2,k-k_1>$$
$$+\frac{|k-k_2|}{\tanh\{|k+k_2|h\}}<k_1,k-k_2><k_2,k-k_2>\} \tag{14}$$

In equation (11), the first term on right is the linear component and the others are nonlinear components. $\phi_1(K)$ is the first order spectrum. Although usually difficult to obtain, the first order spectrum can often be replaced by the total power spectrum to compute the nonlinear components approximately (Masuda at al 1979). It is clear that, based on equation (11), the nonlinear spectral component of horizontal particle velocity can be calculated directly from the directional spectrum of water surface displacement.

On the other hand, from the equation (2) and (6) for vertical velocity component, we have

$$dq^V(k,z)=\frac{i|k|\sinh\{|k|(h+z)\}}{\cosh|k|h}dA(K) \tag{15}$$

where dq^V is the increment of vertical water particle velocity. Similarily, using the same procedure described above, we can obtain a formula to calculate the nonlinear spectral component of vertical water particle velocity. This formula is just as same as the equation (11) except that the functions f_1, f_2 and f_3 are completely different from equation (9). The functions for vertical velocity spectrum are shown as follows

$$f_1(K,z)=\frac{i\omega\ \sinh\{|k|(h+z)\}}{\sinh|k|h}$$

$$f_2(K,K_1,z)=-\frac{i}{2}\{\frac{\omega_1|k|<k,k_1>}{\tanh|k_1|h}$$

$$+\frac{(\omega-\omega_1)|k|<k,k-k_1>}{\tanh\{|k-k_1|h\}}\}\frac{\sinh\{|k|(h+z)\}}{\sinh|k|h}$$

$$f_3(K,K_1,K_2,z)=-i\frac{\omega\ \sinh\{|k|(h+z)\}}{\sinh|k|h}$$

$$\{\frac{1}{2}|k_1|^2+|k_1||k_2|<k_1,k_2>$$

$$-\frac{|k||k_1+k_2|<k_1,k_1+k_2><k,k_1+k_2>}{\tanh|k_1|h\ \tanh\{|k_1+k_2|h\}} \tag{16}$$

2.2 wave pressure

Neglecting the Bernoulli's constant, we have the Bernoulli's equation as

$$\frac{p}{\rho}+\frac{1}{2}(\nabla\Phi)^2+\frac{\partial\Phi}{\partial t}=0 \tag{17}$$

Here the increment of wave pressure dC(K) is defined by

$$\frac{p}{\rho}=\int_K dC(k,z)e^{i\chi} \tag{18}$$

(where p is the dynamic wave pressure, and ρ is the water density). Substituting the equation (2) into equation (17), we can obtain

$$dC(k,z)=f_1^p(k,z)dB(k)+\int_{K_1}f_2^p(k,k_1,z)dB(k)dB(k-k_1)$$

$$+\int_{K_1}\int_{K_2}f_3^p(k,k_1,k_2,z)dB(k_1)dB(k_2)dB(k-k_1-k_2) \tag{19}$$

where

$$f_1^p(K,z)=\frac{\omega^2}{|k|\sinh|k|h}\cosh\{|k|(h+z)\}$$

$$f_2^p(K,K_1,z)=-\frac{1}{2}\{\frac{\omega\omega_1<k,k_1>}{\tanh|k_1|h}+\frac{\omega(\omega-\omega_1)<k,k-k_1>}{\tanh\{|k-k_1|h}\}\frac{\cosh\{|k|(h+z)\}}{\sinh|k|h}$$

$$+\frac{1}{2}\omega_1(\omega-\omega_1)(1-\frac{<k_1,k-k_1>}{\tanh|k_1|h\ \tanh\{|k-k_1|h\}})$$

$$\frac{\sinh\{|k-k_1|(h+z)\}}{\sinh\{|k-k_1|h\}}\ \frac{\sinh\{|k_1|(h+z)\}}{\sinh|k_1|h}$$

$$f_3^p(K,K_1,K_2,z)=-\frac{\omega\omega_1\cosh\{|k|(h+z)\}}{|k|\sinh\{|k|h\}}\{\frac{1}{2}|k_1|^2+|k_1||k_2|<k_2,k_2>$$

$$-\frac{|k||k_1+k_2|<k,k_1+k_2><k_1,k_1+k_2>}{\tanh|k_1|h\ \tanh\{|k_1+k_2|h\}}-\frac{\omega_1\omega_2}{|k_2|}$$

$$(1-\frac{<k,k-k_1>}{\tanh\{|k_1|(h+z)\}\tanh\{|k-k_1|(h+z)\}})\frac{|k-k_1|k_2}{\tanh|k_2|h}$$

$$\frac{\sinh\{|k-k_1|(h+z)\}}{\sinh\{|k-k_1|h\}}\ \frac{\sinh\{|k_1|(h+z)\}}{\sinh|k_1|h} \tag{20}$$

In the same way, by using of perturbation expasion of dB(K) and the definition of power spectrum, the formula for calculating the nonlinear spectral component of wave pressure can be obtained. This formula is also as same as equation (11) except that the functions f_1, f_2 and f_3 must be replaced by functions f_1^p, f_2^p, and f_3^p (equation (20)).

3. COMPARISON WITH EXPERIMENTAL RESULTS

An experimental result concerning water particle velocities is used to verify the above nonlinear theory. The measurement was made by Anastasiou (1981) in laboratory random waves by using Laser Doppler anemometry. The random waves were simulated by using the spectral form of Pierson-Moskowitz type

$$S(\omega)=\frac{0.081}{\omega^2}\exp(\frac{-0.74\omega^4}{\omega^4}) \tag{21}$$

and generated by an irregular wave maker.

Figure 1 shows the comparison of partical velocity spectrum between the theoretically computed results and the experimental results with a water depth of 0.7m, wave steepness of 0.0478 and measurement elevation of 0.1m under water surface, where "I" denotes the measured spectrum including 95% confidence limits. From the comparison, we can find that the measured data are better consistent with the nonlinear theory than the linear theory. But in this case, the nonlinear phenomenum is not obvious because of the experimental wave conditions. In future, we will try to

make the comparison with more suitable data.

4. DISCUSSION

After normalizing the formula (11) with total energy and the peak frequency of power spectrum, we use some standard form of power spectrum in place of linear spectrum $\phi_i(k)$ in equation (11) to investigate some nonlinear characteristics of water particle velocity and wave pressure.

First, based on Pierson-Moskowitz spectrum, the influence of wave steepness on the nonlinear effect is investigated. The computational results with relative water depth (h/Lm) of 0.15, and relative measured elevation (Z/Lm) of -0.08 (measured from water surface) are shown in Figure 2. In the figures, the significant wave steepness δ is defined by significant wave height ($H_{1/3}$) and wave length (Lm), while the latter is correoponding to the peak frequency fm. The results calculated by linear theory are also shown in these figures. From the fact that the nonlinear component appear in higher and lower frequency ranges, we can learn from figure 2 that the nonlinear effect increases as the wave steepness increases.

Figure 3 shows the influence of surface displacement spectral form on the nonlinear effect for horizontal water particle velocity. Figure 3(a) and 3(b) show the results computed by using Pierson-Moskowitz spectrum and JONSWAP spectrum respectively. From the comparison between these two figures, it is found that the sharp form like JONSWAP spectrum produces clearer nonlinear effect than the milder form like Pierson-Moskowitz spectrum.

Figure 4 shows the influence of water depth on the nonlinear effect. In the figures, A_N/A_L denotes the relative magnitude of nonlinear total energy to linear total energy. The results are computed by using Pierson-Moskowitz spectrum. The breaking limit drawing with dash line in these figures is calculated from Hamada's wave breaking formula (Hamada 1951). It is shown that the horizontal velocity, vertical velocity and wave pressure all exhibite the same properties. From the figures, it is found that the nonlinear effect increases as relative water depth h/Lm decreases when the h/Lm in the range between 0.1 and 0.3. However when h/Lm is larger than 0.3, the nonlinear quantity is independent of the relative water depth. On the other hand, when relative water depth approaches 0.1, the nonlinear components approach to infinitive. In fact, in this water depth or shallower area, this formula can no longer be used because the formula is derived based on the weakly nonlinearity assumption.

Figure 5 shows the influence of measured elevation on the nonlinear effect. Z denotes the measured elevation from mean water surface. The results are computed by using Pierson-Moskowitz spectrum and with relative water depth of 0.15. For particle velocities, horizontal component and vertical component exhibite the same properties. From the figure (a), it is found that the measured elevation tends not to bear influence on the nonlinear effect. But as to the wave pressure (Figure(b)), it is found that the nonlinear effect increase as the elevation decreases.

In the above description, all simulate computational results only concern one-dimensional spectrum. In figure 6, the influence of direction-

al dispersion on the nonlinear effect is investigated with relative depth of 0.15, relative measured elevation of -0.04 and wave steepness of 0.06. The nonlinear spectral components calculated by the directional wave spectrum is compared with that of calculated by uni-directional wave spectrum. For convenience, the form of $\cos^2\theta$ was used as the wave directional distribution to calculate the nonlinear spectral components. In the computations, we found that it has to take a long computing time to integrate the directional distribution to obtain the ordinary power spectra of particle velocity or wave pressure. In Figure 6, from the comparison, it is found that the wave directional dispersion diminishes the nonlinear effect.

5. CONCLUSION

This paper is composed of two parts. First, a weakly nonlinear random wave theory in finite water depth was developed. The nonlinear spectral components for water particle velocity and wave pressure can be calculated directly from the directional spectrum of water surface displacement. The theoretical computed results were verified by experiment. Next, a simulate computation was performed. In accordance with the different characteristics of wave properties, such as wave steepness, water depth and so on, the nonlinear effects on wave kinematic and pressure properties were extensively investigated by using some standard power spectrum. From the investigation, we found some important conclusions as follows. First, the important characteristics of nonlinear effect for water particle velocity and wave pressure are similar to that for water surface displacement spectrum. Second, it takes much more computing time for directional spectrum than that for one-dimensional spectrum. Third, this theory can not be used in shallow water area when relative water depth is below 0.1.

REFERENCE

1) Masuda, A., Kuo, Y.Y. and Mitsuyasu, H. (1979). On the dispersion relation of random gravity waves. Part 1. Theoretical framework. Journal of Fluid Mechanics, 92(4): 717-730.

2) Mitsuyasu, H., Kuo Y.Y. and Masuda, A. (1979). On the dispersion relation of random gravity wave. Part 2. An experiment. Journal of Fluid Mechanics, 92(4): 731-749.

3) Hamanaka, K., et al (1980). Wave solution of irregular wave in shallow water. Proceeding 27-th Conference of coastal engineering in Japan: 16-19 (in Japanese).

4) Anastasion , K., Tiokell, R.G. and Chaplin, J.R. (1982). Measurement of particle velocities in laboratory-scale random waves. Coastal Eng., 6, 233pp.

5) Sharma, J. and Dean, R.G. (1979). Second-order directional seas and associated wave forces. OTC, Houston OTC paper 3645.

6) Hudspeth, R.T. (1975). Wave force predictions from nonlinear random sea simulation. Proc. OTC, Paper NO: OTC 2193.

7) Huang, N.E. (1971) Derivation of stokes drift for a deep water random gravity wave field. Deep-Sea Res. Vol 18: 255-259.

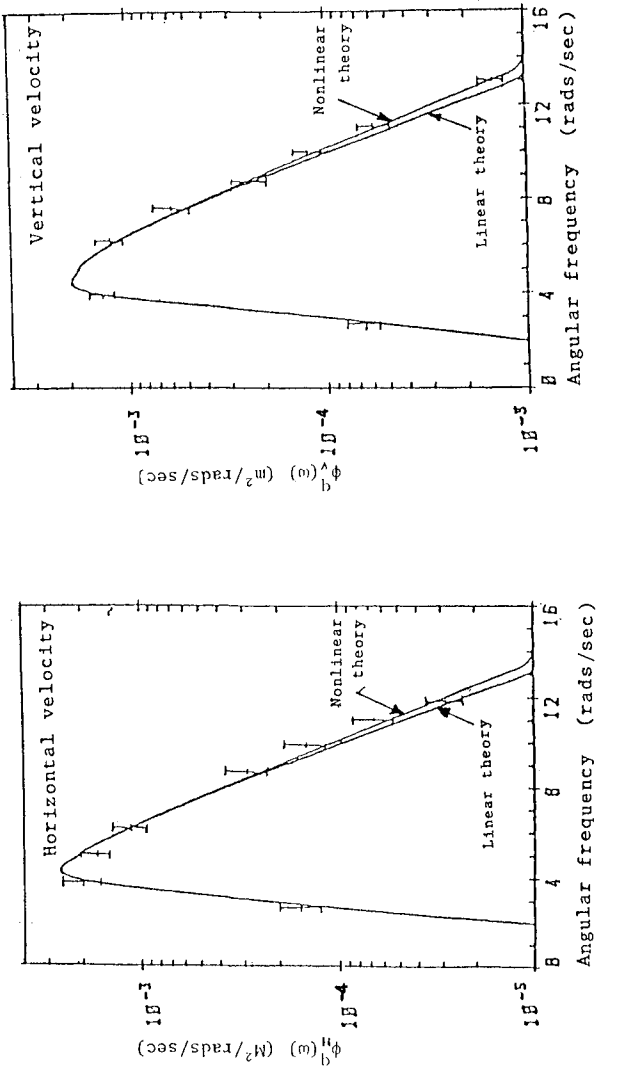

Figure 1 Comparison of the linear and nonlinear theory with the measured data

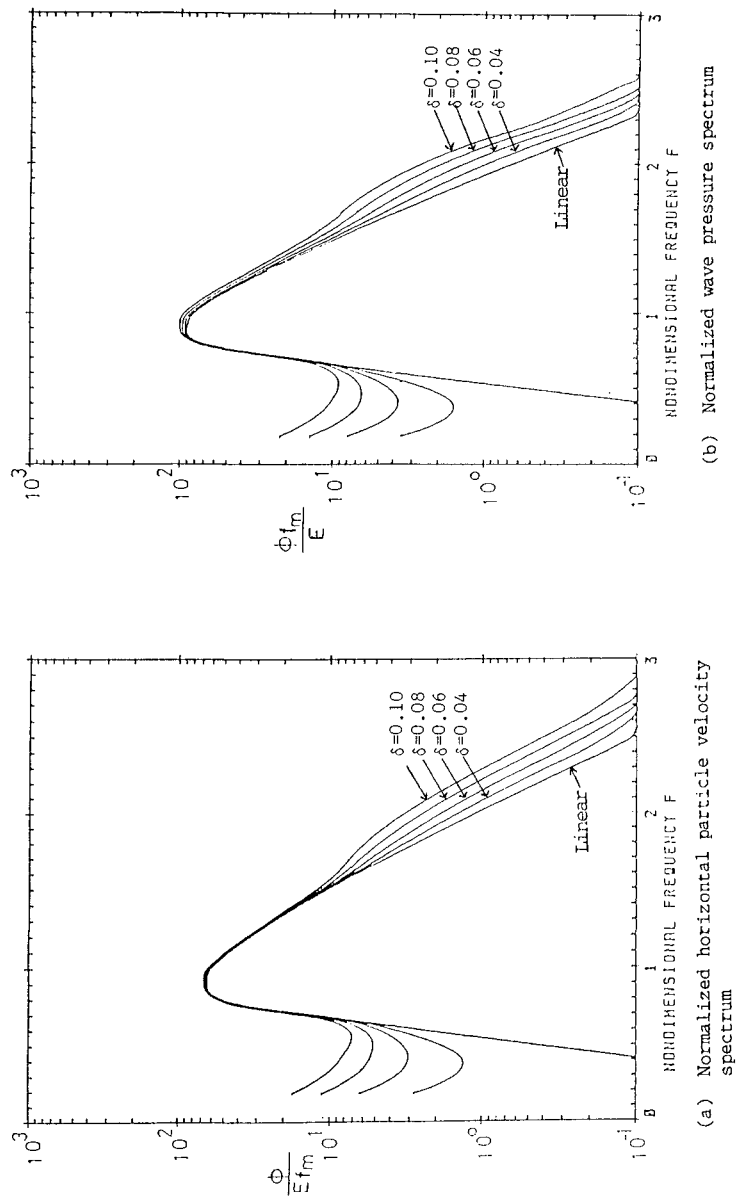

Figure 2 The influence of wave steepness on the nonlinear effect (Based on Pierson-Moskowitz spectrum)

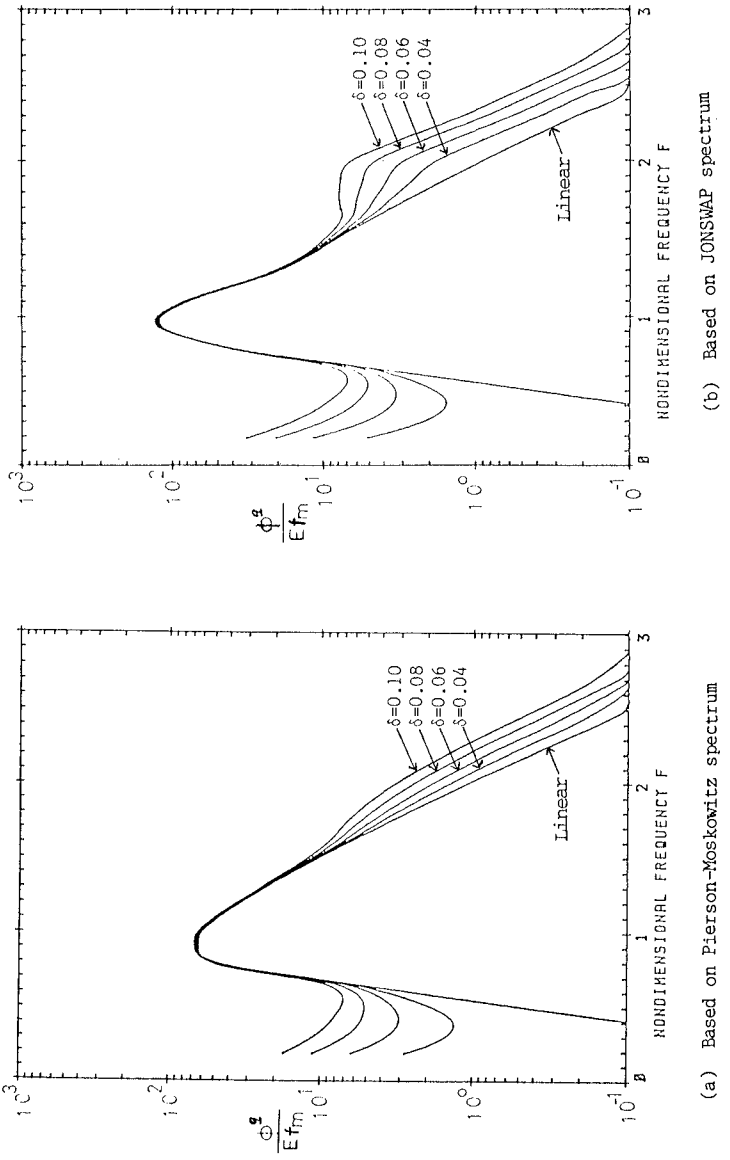

(a) Based on Pierson-Moskowitz spectrum

(b) Based on JONSWAP spectrum

Figure 3 The influence of spectral form on the nonlinear effect for horizontal water particle velocity

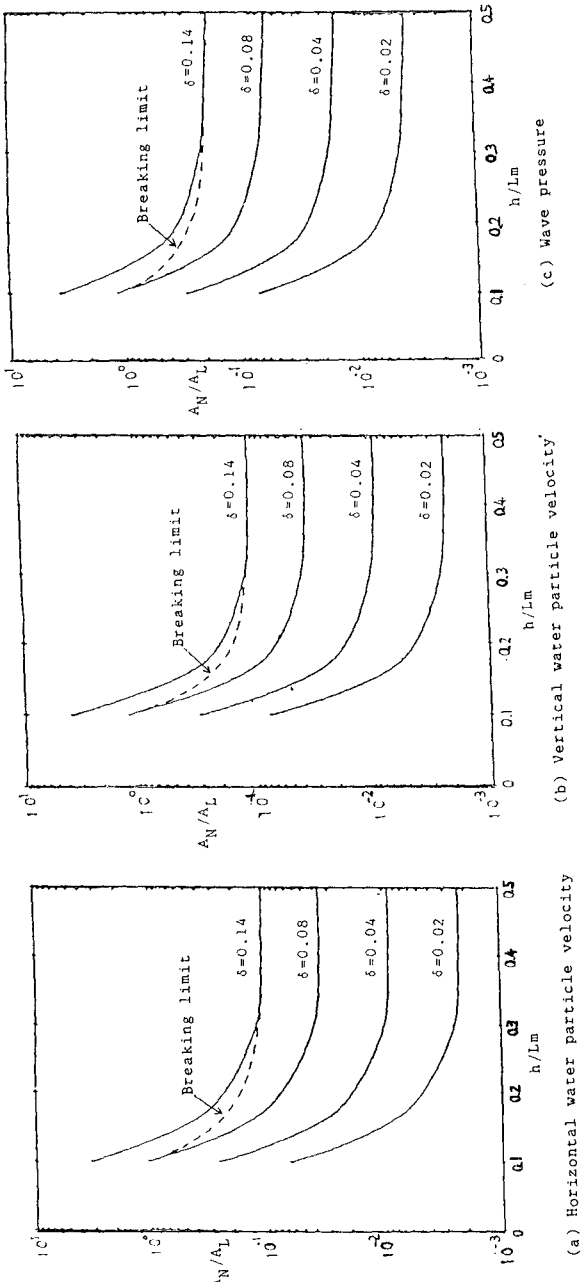

Figure 4 The nonlinear characteristics in terms of relative water depth and significant wave steepness.

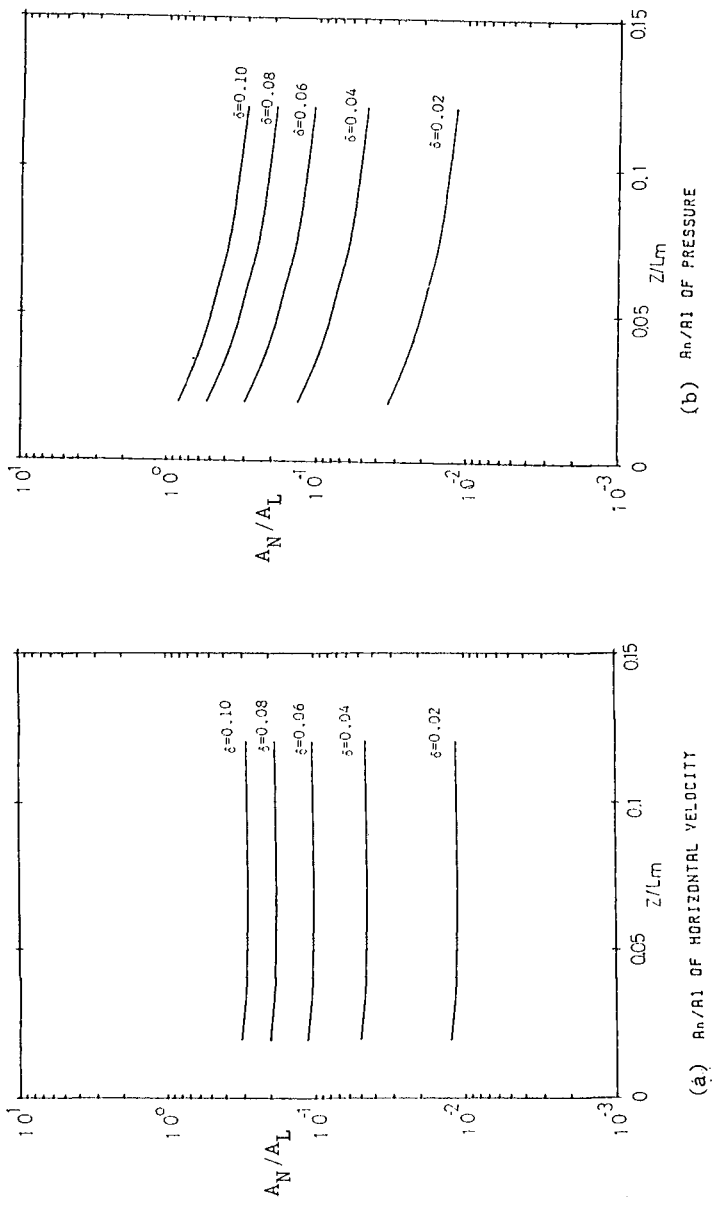

Figure 5 The influence of measured elevation on the nonlinear effect

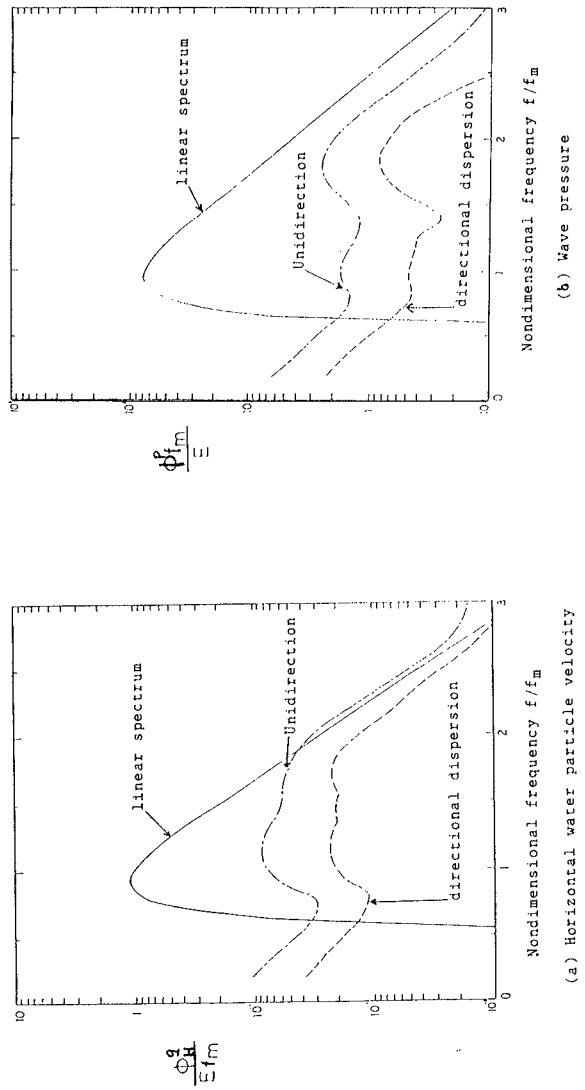

Figure 6 The influence of directional dispersion on the nonlinear effect for water particle velocity and water pressure.

CHAPTER 35

EFFECTS OF THE GULF STREAM ON NEARSHORE WAVE CLIMATE

R.J. Lai and S.L. Bales*

ABSTRACT

Large scale ocean currents, such as the Gulf Stream, Kuroshio, Peru Current, Agulhaus Current, etc., strongly modify the surrounding wave characteristics. As the Gulf Stream moves along the Continental Shelf of the southeast coast of the United States, the local ocean environment is divided into three wave climatic regimes. They are the offshore, the Gulf Stream, and the nearshore regimes. The nearshore zone is bounded by the land to the west and the Gulf Stream to the east. The distance between land and the Gulf Stream varies from 10 to 60 miles. Most of the waves in this regime are generated offshore and cross the Gulf Stream. The correlation of local wind and waves in the nearshore regime is poor except in the presence of a persistent onshore storm.

A semi-empirical approach has been developed to compute the nearshore wave climate. The hindcast/forecast directional waves from the Spectral Ocean Wave Model (SOWM) of the Navy Fleet Numerical Oceanography Center have been used as the source of the initial offshore wave conditions. After crossing the Gulf Stream, which is assumed to be a uniform current with a velocity of 2 m/s, the waves are either refracted to the nearshore regime or reflected to the offshore regime following ray theory. The onshore waves in the nearshore zone are confined to the sector from 30 to 150 degrees. The computed results are then compared with measured data with good agreement.

In summary, the Gulf Stream acts as a barrier to damp long waves and to regroup short waves. The refraction of long waves can be predicted by using ray theory. Further field experiments are needed to quantify the variation of the Gulf Stream and to investigate the interaction with approaching long waves and local wind generated short waves.

1. INTRODUCTION

The development of wave climate of a region provides the general prevailing wave conditions throughout the year. This is considered important to the design of offshore structures and for the planning of ship operations. The rapid development and large increase of population along the coastal zone makes the nearshore wave climate an urgent task for all phases of engineering works. These nearshore activities include safe ship navigation to avoid collision and

*David W. Taylor Naval Ship Research and Development Center, Bethesda, Maryland 20084-5000, U.S.A.

grounding, pollution transport, nearshore structure, beach erosion abatement, etc.

The complexity of the boundary conditions and changing dynamic parameters from the interaction of air-sea-land at the nearshore zone make the generalization of wave dynamics in coastal zones a difficult task. Furthermore, large scale ocean currents moving along major continental shelves strongly modify the approaching waves from the offshore to the nearshore. One of these regions is located at the southeast coast of the United States. The nearshore regime is bounded by the land to the west and the Gulf Stream to the east. The distance between land and the Gulf Stream varies from 10 to 60 miles (see Figure 1). The local ocean environment of this area is divided into three wave climatic regimes. They are the offshore, the Gulf Stream, and the nearshore regimes. Most of the waves in this regime are generated offshore and approach the nearshore regime by crossing the Gulf Stream. The effects of the Gulf Stream play an important role in the formation of nearshore wave climate which will be presented here.

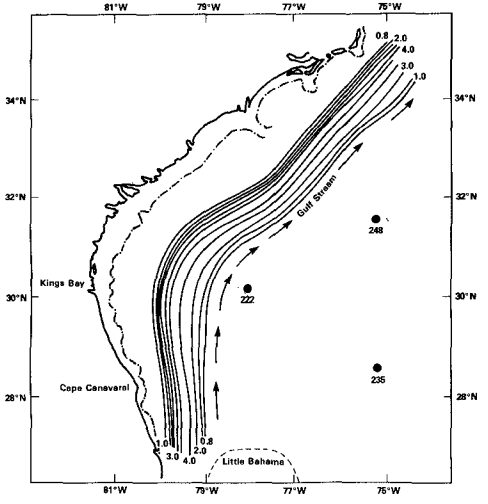

Figure 1. Map showing the Gulf Stream and SOWM grid points used at St. Marys (Kings Bay) and Cape Canaveral

2. LOCAL WAVE CHARACTERISTICS

A field measuring program has been ongoing to investigate the wave characteristics of this region since 1984. The results have been used to calibrate the Shallow Water Wave Model (Lai and Silver, 1986a) and to develop the local wave climate. The measured results of 1984 and 1985 have been published recently (Lai and Foley, 1986b). In short, submersible field stations measured directional waves four times a day at Cape Canaveral, Florida and St. Marys Inlet, Georgia. Although the data recovery rate is about 60 percent during the

measuring period, the measured data reveal many interesting local wave characteristics. These can be briefly summarized as follows:

a. Correlation of Local Wind and Wave

Strong winds imply high seas in deep water. In the nearshore zone, however, winds come from all directions and waves are limited to onshore directions; therefore, the correlation of local wind and waves becomes a difficult task. Measurements at St. Marys Inlet, Georgia provide both amplitudes and directions of wind and waves. Based on these data, wind and wave roses for the winter season of 1984 have been developed and are given in Figures 2a and 2b. Although most of the winds of the nearby shore station at the Mayport Air Station are from west, north, and northeast directions, the approaching wave directions are confined by geography to northeast, east, and southeast directions. Similar data for the summer are shown in Figures 3a and 3b for 1984. There is some correlation between the wind and wave data; however, a precise local correlation is almost impossible to establish. This has been illustrated in Figure 4 in which both daily variations of offshore and nearshore wind are compared with measured directional waves. It is clearly shown that offshore wind has better correlation with nearshore waves. This points out the fact that the wave climate in the nearshore zone is dominated by the storm and wind patterns offshore and propagates to the shore with some local wind input unless the onshore storm persists for more than 24 hours. At that time, the local wind and wave direction coincide.

b. Directional Wave Spectra

A series of measured directional wave spectra have been evaluated. The direction of long waves tends to be from the 50 to 120 degrees band while the directions of short waves are scattered. Although the same offshore storms pass through the southeast coast of Florida, the measured directional wave data at Cape Canaveral and St. Marys Inlet show different characteristics (see Figures 5 and 6). The major differences of these nearshore zones are the local topography and the heading of the Gulf Stream north (Cape Canaveral) versus northeast (St. Marys Inlet). Some of these characteristics at these two sites resulted from the effects of the Gulf Stream, which will be discussed further in the following section. While the data of Figures 5 and 6 were collected for different storms, their general characteristics are representative of each site.

3. APPROACH

The measured field data reveal the characteristics of the local waves and the poor correlation of local wind and waves. However, the data can only provide short-term wave statistics which are not enough to establish nearshore wave climatology. Therefore, hindcasting techniques have been applied here to develop the nearshore wave climate.

The U.S. Navy Fleet Numerical Oceanography Center (FNOC) has operated a Northern Hemispheric wave forecast/hindcast model, called the Spectral Ocean Wave Model (SOWM) (Lazanoff and Stevenson, 1975)

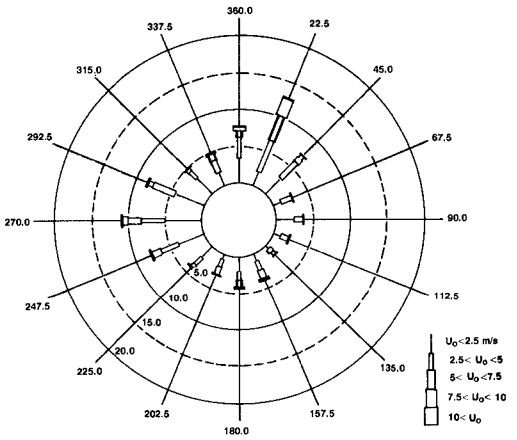

Figure 2a. Wind rose for Mayport Naval Air Base near St. Marys for winter 1984

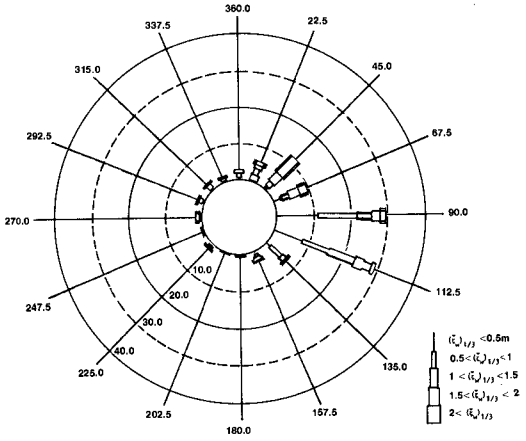

Figure 2b. Wave rose for St. Mary entrance Station 5 offshore for winter 1984

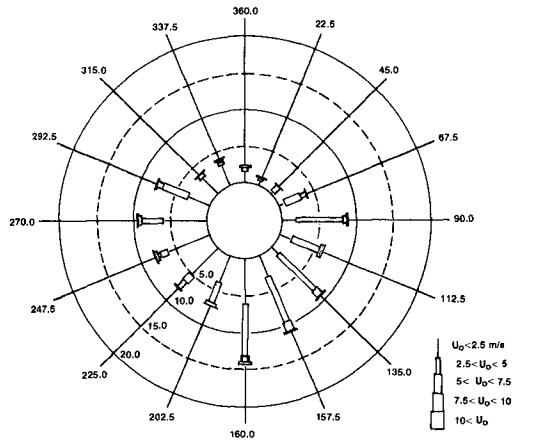

Figure 3a. Wind rose for Mayport Naval Air Base near St. Marys for summer 1984

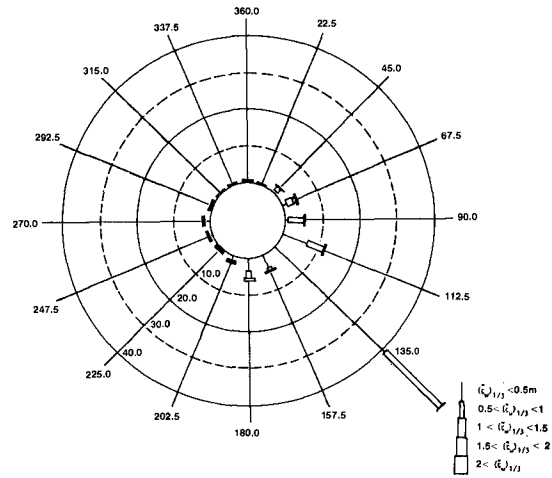

Figure 3b. Wave rose for St. Mary entrance Station 5 (offshore) for summer 1984

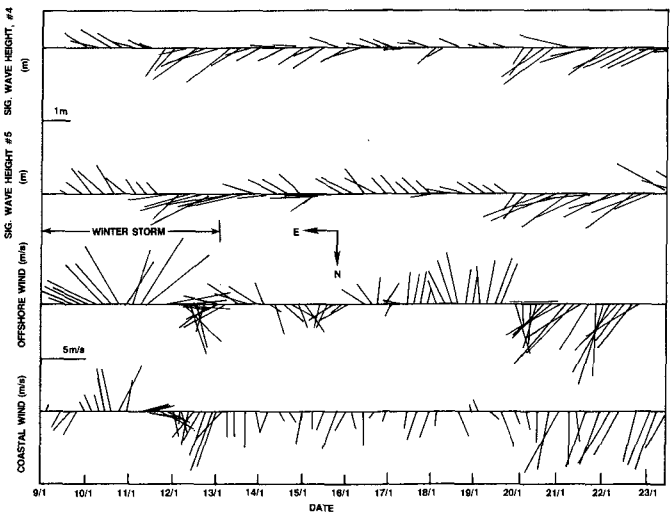

Figure 4. Measured waves at Stations 4 and 5 and winds at offshore buoy (Uo) and coastal station (Un)

from 1975 to 1985.* The deep water wave statistics derived from SOWM have been widely used at the David Taylor Naval Ship Research and Development Center (DTNSRDC), other Navy and government centers, NATO countries, and in the private sector (Bales, et al., 1982). The approach here was to transform the corresponding offshore data from the SOWM hindcast climatology to the nearshore zone to establish wave statistics over a period of 15 years.

The process of transforming waves from deep water to shallow water requires three wave parameters deirved from SOWM: significant wave height, $(\tilde{\zeta}_w)_{1/3}$; primary incident wave direction, θ_o; and incident modal wave period, T_o. Since the distance between deep and shallow water in this case is less than 120 kilometers and the uncertainty of predicting wave frequency, the shift of wave period for long waves (with $T_o \geq 6$ sec) has not been considered. Therefore, the shallow water wave periods are assumed to be the same as the hindcast ones from SOWM. The other two parameters are interrelated and are treated separately.

The correlations of significant wave height between deep (hindcast/forecast) and shallow water (measured) were developed using the given forecast wave direction and normalized by the significant wave height of the SOWM at the deep water grid points. The average of three grid points located along the central Florida east coast are used to provide the hindcast/forecast wave spectrum for both Cape Canaveral and St. Marys Inlet. These are grid points 221, 222, and

*The SOWM has now been replaced by a global model called GSOWM.

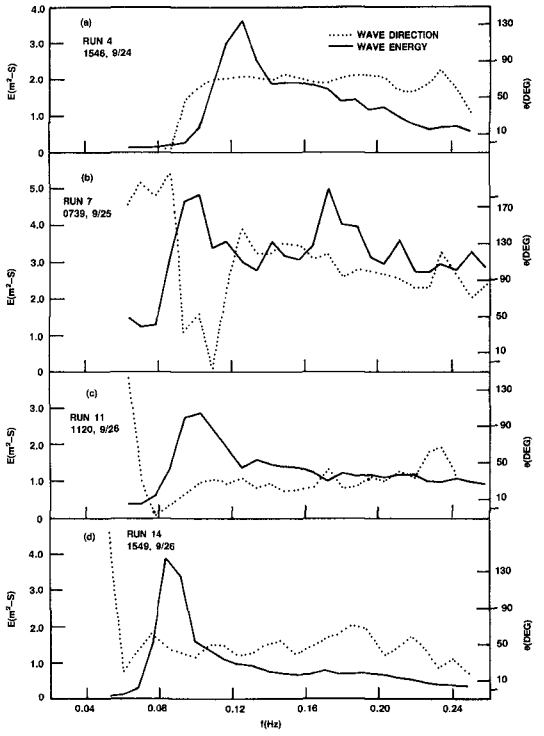

Figure 5. Measured wave spectra with mean directions at Station 2 of Cape Canaveral during the passage of the storm of 1983

235 which are located at (31.8° N, 75.1° W), (30.4° N, 77.9° W), and (28.8° N, 75.2° W), respectively, see Figure 1. The averaged spectral values of these grid points provides the overall wave forecast by the SOWM at the offshore region (Lai, et al., 1984).

The changes of approaching wave direction from deep to shallow water are complex on the Florida east coast due to the existence of the Gulf Stream, see Figure 1. Therefore, the process of transforming the forecast wave direction of SOWM into shallow water has been divided into two steps. The first step was to calculate the change in SOWM wave direction from deep water into intermediate depth by crossing the Gulf Stream. Then, by using the Shallow Water Wave Model (SWWM), the waves at the intermediate depths were transformed to the shallow water zone.

A simplified analytical solution and numerical model have been used to transform the offshore wave direction to the nearshore zone. The Gulf Stream along the Florida east coast heads northward running almost parallel to the coast line and turns to northeast direction

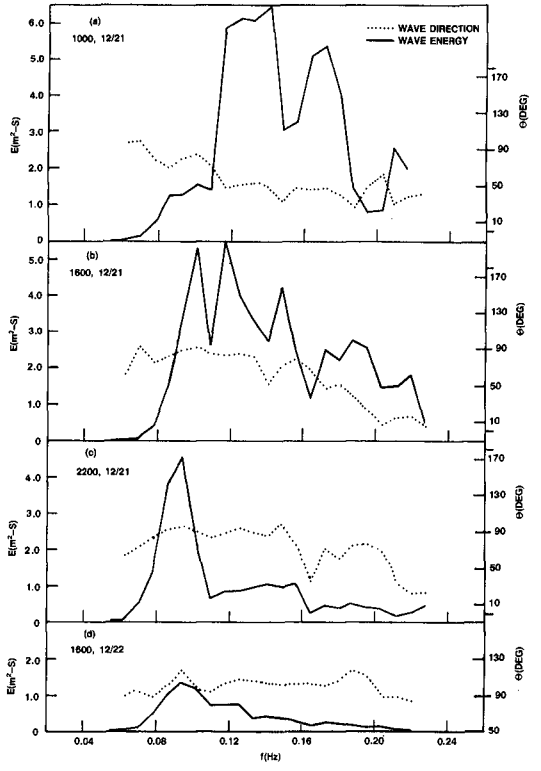

Figure 6. Measured wave spectra with mean directions at Station 5 of St. Marys during the passage of the storm of 1984

near Jacksonville, Florida. Here, it is assumed that the Gulf Stream is a uniform current, with a mean velocity of 2.0 m/s. The changes of wave direction are calculated from the following analytical solution

$$\cos\ \theta_1 = \cos\ \theta_0 / \left[1 - \frac{U_1 - U_0}{C_0} \cos\ \theta_0\right]^2 \qquad (1)$$

where θ_0 and θ_1 are the primary incident and refracted wave directions before and after crossing the Gulf Stream, respectively (Kenyon, 1971; Phillips, 1981). U_0 and U_1 are the mean currents of the deep water offshore section and the Gulf Stream, and C_0 is the original wave phase velocity. The value of U_0 was assumed to be zero in this computation.

The relationship between the parameters defined in Equation (1) are shown in Figure 7. The wave direction after refraction by the Gulf Stream is a function of the incident modal wave period, T_0, and incident direction, θ_0. The relationship between θ_0, θ_1, and T_0, with

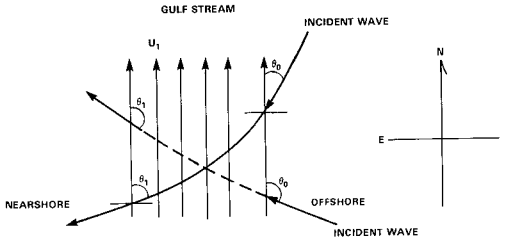

Figure 7. Change of Wave direction by the Gulf Stream where θ_0 is incident wave direction and θ_1 is predicted wave direction after crossing

assumed values of U_0 and U_1, are shown in Figures 8 and 9. In the Cape Canaveral area, as shown in Figure 8, when the waves approach from the southeast with large wave periods, the waves may reflect back to the deep water zone as shown in the upper section of the figure. This phenomenon has been discussed by Hayes (1980) and others (Chao, 1970). Furthermore, the incident waves from the north and northeast are refracted to the wave direction greater than 30 degrees. This implies that the direction of most waves (except the local wind waves in the intermediate water zone) are refracted and arrive in the nearshore zone range from the northeast, the east, and the southeast directions after crossing the Gulf Stream. In the St. Marys Inlet area, due to the change of flow direction of the Gulf Stream and the bottom bathymetry, the results are different from those of the Cape, as shown in Figure 9. Here the shoreline turns to the northeast direction near the St. Marys area, as does the Gulf Stream. The incident wave directions of the offshore zone are then confined to the 40 to 180-degree range. The changes of wave directions after crossing the Gulf Stream around St. Marys are shown in Figure 9. The offshore wave directions are limited from 40 to 160 degrees range. The nearshore wave directions range then from 70 to 165 degrees according to Equation (1).

The changes of wave directions after crossing the Gulf Stream have been computed using SWWM (Lai, et al., 1984), and will not be discussed in detail here.

4. RESULTS AND DISCUSSIONS

The wave statistics from the transformed SOWM data over a period of 15 years have been developed and published in other reports (Lai, Silver and Bales, 1984). In general, the characteristics of these wave statistics are dependent on the site chosen around the nearshore zone. Two of them are located near the field measuring sites. Thus, the measuring wave data can be used to develop short term statistics and to verify the transformation method. Two sets of short terms wave

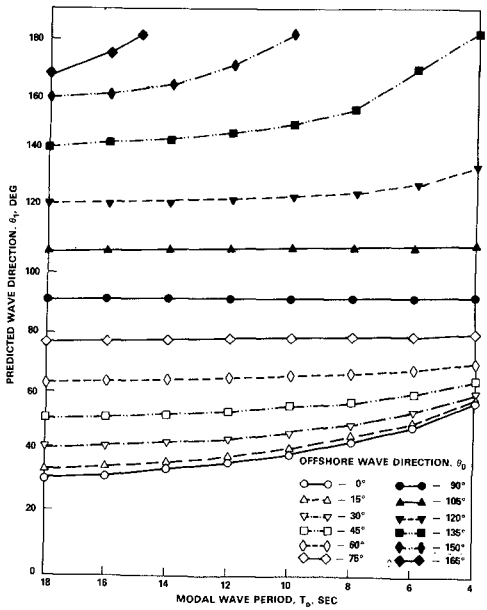

Figure 8. Predicted wave direction (θ_1) after crossing the Gulf Stream at Cape Canaveral

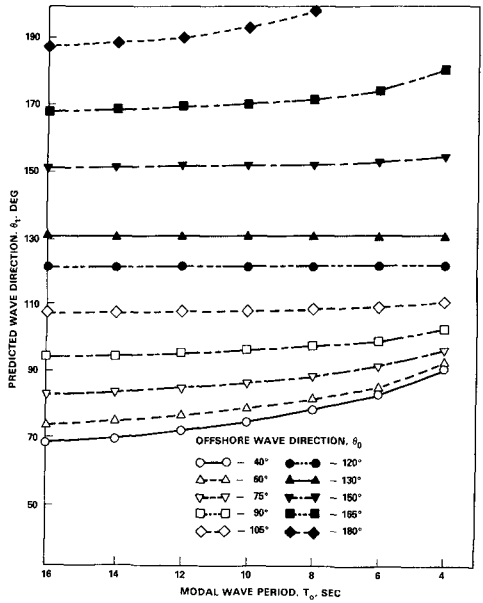

Figure 9. Predicted wave direction (θ_1) after crossing the Gulf Stream at St. Marys

statistics are presented. One is from measured field data, and the other is from the corresponding transformed SOWM data. Comparisons are made to evaluate the transformation method and to discuss the effects of the Gulf Stream on wave climate.

The wave statistics are grouped according to seasons, i.e., Winter (December to February), Spring (March to May), Summer (June to August), and Fall (September to November). Since the recovery rate of field data is around 60 percent during 1984 and 1985, it is difficult to compute wave statistics for all four seasons. The available measured and hindcast data of the rougher seasons (i.e., Winter and Fall) were chosen for comparison.

Comparison of measured and hindcast wave direction statistics are shown in Figures 10, 11, and 12. The solid lines represent the offshore hindcast data from SOWM. The dashed lines represent the nearshore transformed hindcast data, and the dotted lines represent the measured field data at the same period of time. Each figure is divided into parts (a) and (b). The data in part (b) consist of all waves. The results of part (b) show that the transformation method which takes into account the effects of the Gulf Stream and the local shoaling zone is credible. The waves from north, northeast, and east directions refract to east, normal to the shore, as predicted from the ray theory. However, the waves from south and southeast directions reflect to the offshore which is difficult to assess in the transformation process. Furthermore, when offshore waves cross the Gulf Stream, longer waves tend to follow the ray theory, and short waves are affected by the currents and local wind force. These local energy inputs interact dynamically with short waves and cause the waves to break or reorganize. This has been clearly indicated from the measured data. The analyzed results of long waves without confused sea of short waves are shown in part (a). Overall improvement for the long waves is evident especially for the waves from the north, northeast, and east directions. Here, the long waves are defined as waves with periods larger than 6.7 sec (or frequencies less than 0.15 Hz). There is only a moderate improvement on the waves from the south and southeast directions due to the complex phenomenon of wave reflection and due to less accuracy for predicting waves generated from the south near Little Bahama Basin by the SOWM (see also Figure 1).

Comparison of measured and hindcast wave period statistics is shown in Figure 13. The solid lines are from the hindcast data of SOWM and the dashed lines are from the field measured data. The wave periods from SOWM are taken from offshore region and applied to nearshore region directly. The assumption of this direct application has been discussed in a previous publication (Lai et al., 1984). The results show the direct comparison of three sets of data as referred to (a), (b), and (c) in Figure 13. The data of Figure 13(a), (b) and (c) are identical to the data of Figures 10, 11, and 12. The agreement is encouraging if one separates the long and short waves again. The overall wave period of long waves between two data sets agrees well although the distribution is not very consistent. Further research is needed to take into account the local wind force on wave evolution during the process of crossing the Gulf Stream.

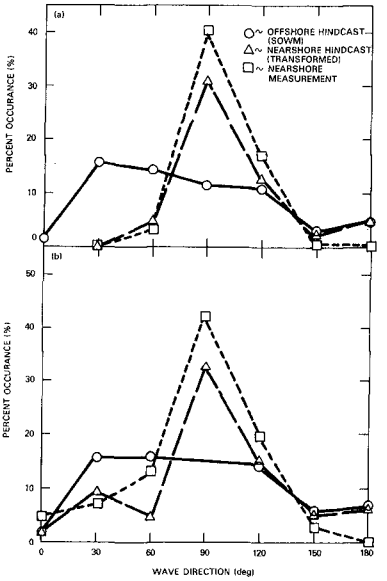

Figure 10. Comparison of measured and hindcast wave direction statistics of winter 1984 at St. Marys, where (a) for long waves, (b) all waves

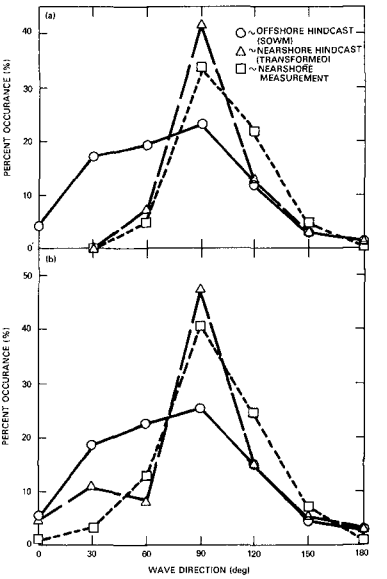

Figure 11. Comparison of measured and hindcast wave direction statistics of fall 1984 at St. Marys, where (a) long waves only, (b) all waves

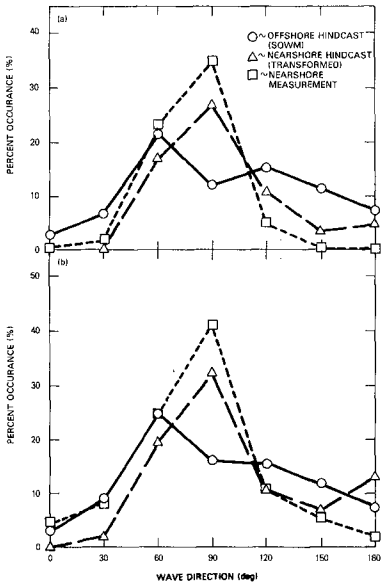

Figure 12. Comparison of measured and hindcast wave direction statistics of winter 1985 at Cape Canaveral, (a) long waves only, (b) all waves

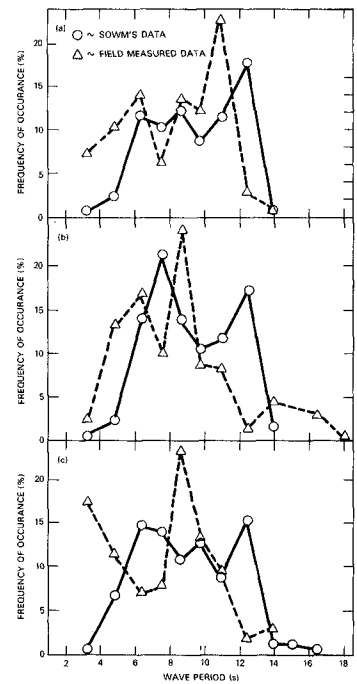

Figure 13. Comparison of measured and hindcast wave period statistics, where (a) winter of 1984 at St. Marys, (b) fall of 1984 at St. Marys, (c) winter of 1985 at Cape Canaveral

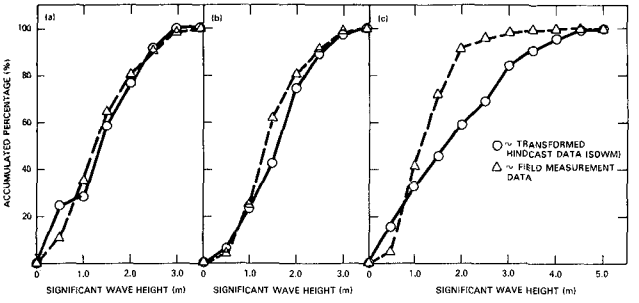

Figure 14. Comparison of measured and hindcast wave height statistics, where (a) winter of 1984 at St. Marys, (b) Fall of 1984 at St. Marys, (c) winter of 1985 at Cape Canaveral

Comparison of measured and hindcast significant wave height statistics is shown in Figure 14. The agreement between transformed hindcast data from SOWM and field measured data in the St. Marys area is very good but not so in the Cape Canaveral area. The reason for this poor agreement is not clear. However, after re-examining the data of Cape Canaveral, it was found that some stormy data during the winter of 1985 are from the south and southeast directions which may be attributed to this poor agreement. The hindcast storm data from the south and southeast directions by SOWM had been hampered by the existence of Bahama Bank to cause such discrepancy, as pointed out previously.

5. CONCLUSION

Developing nearshore wave climates require complex procedures. Shoreline structure, bottom topography, offshore wind and wave conditions and surrounding ocean current must be considered. A wave climate for the southeast coast of the United States has been developed. The offshore hindcast data from SOWM has been transformed to the nearshore zone. The transformation method takes into account the effects of the Gulf Stream and shallow water shoaling. The results have been compared with the field measured data with generally good agreement. The effect of the Gulf Stream on crossing waves should be divided into two categories, i.e., long waves and local wind waves. The refraction of long waves can be predicted by using ray theory. However, to clarify the generation and reflection of waves from the south and southwest directions further research work or field data is needed. Strong currents cause local generated wind waves (i.e., short waves) to stop, break, and reorganize. Further field experiments and research are needed in this area to predict the process of wave evolution in the ocean environment which present strong currents.

REFERENCES

1. Bales, S.L., W.E. Cummins and E.N. Comstock, 1982, "Potential Impact of Twenty Year Hindcast Wind and Wave Climatology on Ship Design," Marine Tech., Vol. 19, No. 2.

2. Chao, Y.Y., 1970, "The Theory of Wave Refraction in Shoaling Water Including the Effects of Caustics and Spherical Earth," Tech. Report 70-7, New York University.

3. Hayes, J.G., 1980, "Ocean Current Wave Interaction Study," J. of Geophys. Res., Vol. 85.

4. Kenyon, K.E., 1971, "Wave Refraction in Ocean Currents," Deep Sea Res., Vol. 18.

5. Lai, R.J., A.L. Silver and S.L. Bales, 1984, "Wave Statistics in Nearshore Zones," Proceedings Ocean Structure Dynamics Symposium '84, Corvallis, Oregon.

6. Lai, R.J. and A.L. Silver, 1986a, "Shallow Water Wave Model at Cape Canaveral, Florida and Kings Bay, Georgia," Tech. Report DTNSRDC/SPD-1190-01.

7. Lai, R.J. and E.W. Foley, 1986b, "Field Measurements of Nearshore Wave Environment at Cape Canaveral, Florida and Kings Bay, Georgia," Tech. Report DTNSRDC/SPD-1190-02.

8. Lazanoff, S.M. and N.M. Stevenson, 1975, "An Evaluation of a Hemispheric Operational Wave Spectral Model," FNWC Tech. Note 75-3.

9. Phillips, O.M., 1981, "Nonlinear Wave Dynamics," IUCEM Symposium Proceedings.

CHAPTER 36

Empirical Prediction of Wave Spectrum for Wind-Generated Gravity Waves

Jung-Tai Lin*

In the energy-containing range, an empirical frequency spectrum representing a general sea state was derived,

$$\frac{n_o^3 \phi(n)}{u_* C_o} = A_1 r \left(\frac{n}{n_o}\right)^{-r} \exp\left[-\frac{r}{r-1}\left(\frac{n}{n_o}\right)^{-r+1}\right] .$$

Experimental data were used to verify this empirical frequency spectrum. The value of A_1 was approximated to be 0.044 and the value of r is related to $n_o u_*/g$ by

$$r = 9.1 \left(\frac{n_o u_*}{g}\right)^{1/4} .$$

In the equilibrium range, the saturated frequency spectrum was approximated by

$$\frac{n_o^3 \phi(n)}{u_* C_o} = 0.08 \left(\frac{n_o u_*}{g}\right)^{-1/4} \left(\frac{n}{n_o}\right)^{-5} .$$

Experimental data were used to test whether the Phillips spectrum, $\phi(n) = \beta g^2 n^{-5}$ would serve as a better approximation of the wave spectrum than the Toba spectrum, $\phi(n) = \alpha u_* g n^{-4}$. Measurements of both the wave slope spectrum and the mean square wave slope favor the Phillips spectrum.

Introduction

Wind-Generated gravity wave has been of great interest to researchers and engineers in the field of coastal engineering because it is one of the important considerations in the engineering studies and designs for ship navigation, coastal and off-shore structures, shore protection, oil pollution control, and wave energy conversion. An accurate prediction of the wave height, wave frequency, and wave spectrum is critical to the success of these engineering studies and designs.

Based on dimensional reasoning, Phillips (20) hypothesized that in the equilibrium range, the wave frequency spectrum of wind-generated gravity waves, $\phi(n)$ is saturated and can be approximated by

*ASCE member; President, United Industries Corp., 12835 Bell-Red Rd. #120, Bellevue, WA., U.S.A. 98005

$$\phi(n) = \beta g^2 n^{-5} \quad \text{for } n_o << n << n_\gamma \tag{1}$$

where g is the gravitational acceleration, n is the angular wave frequency, n_o is the wave frequency of the dominant wave, n_γ is defined as $(4g^3/\gamma)^{\frac{1}{4}}$, γ is the surface tension per unit density and β is a non-dimensional numerical coefficient. To approximate the frequency spectrum in both the equilibrium range and the energy-containing range for fully developed wind waves in the open ocean, Pierson and Moskowitz (23) proposed the PM continuous frequency spectrum

$$\phi(n) = \beta g^2 n^{-5} \exp\left[-\frac{5}{4}\left(\frac{n}{n_o}\right)^{-4}\right] . \tag{2}$$

For a growing sea that the wind wave field has not yet reached the fully-developed stage, Hasselmann, et al, (6) proposed the JONSWAP continuous frequency spectrum

$$\phi(n) = \beta g^2 n^{-5} \exp\left[-\frac{5}{4}\left(\frac{n}{n_o}\right)^{-4}\right] \delta^\Gamma \tag{3}$$

Equation (3) was derived by multiplying the peak-enhancement function, δ^Γ, to the PM spectrum expressed in Equation (2). Here δ is the ratio of the spectral maximum to the spectral maximum derived from the PM spectrum, Γ is defined by $\Gamma = \exp\left[-(n - n_o)^2/2\sigma^2 n_o^2\right]$, and $\sigma = \sigma_a$ for $n \leq n_o$ and $\sigma = \sigma_b$ for $n \geq n_o$.

Huang, et al. (8) proposed the unified two-parameter WALLOPS frequency spectrum to approximate the frequency spectrum in the energy-containing range for a general sea state

$$\phi(n) = \frac{\beta g^2}{n^m n_o^{5-m}} \exp\left[-\frac{m}{4}\left(\frac{n_o}{n}\right)^4\right] \tag{4}$$

When the value of m is equal to 5, Equation (4) is identical to the Pierson-Moskowitz spectrum.

Based on the three-second power law (Toba, 29a) and the concept of the similarity wave spectrum, Toba (29) proposed that in the equilibrium range,

$$\phi(n) = \alpha g u_* n^{-4} \quad \text{for } n_o << n << n_\gamma \tag{5}$$

$$\phi(n_o) = \alpha_o g u_* n_o^{-4} \tag{5a}$$

where u_* is the frictional velocity of the wind, and α and α_o are non-dimensional numerical coefficients. A theoretical support for the n^{-4} equilibrium range was provided by Zakharov and Filonenko (32).

In analogy to the JONSWAP Spectrum, Donelan, et. al (4a) proposed a continuous wave spectrum which yields to the n^{-4} spectrum in the equilibrium range,

$$\phi(n) = \alpha_d g^2 n^{-4} n_o^{-1} \exp\left[- \left(\frac{n_o}{n}\right)^4 \right] \delta^r \qquad (6)$$

where α_d is a non-dimensional numerical coefficient. In a recent paper, Battjes, et. al (1a) reanalyzed the JONSWAP data and concluded that the n^{-4} spectrum may fit the data as well as or even better than the n^{-5} spectrum.

For the present study, the wave spectrum is examined by using similarity analysis. An empirical equation was provided to approximate the wave spectrum in the energy-containing range. The wave spectrum behavior in the equlibrium range was analyzed and the slope measurements were used to determine which of the n^{-5} or n^{-4} spectrum is preferrable.

Similarity Wave Spectrum

By definition, the integration of the wave frequency spectrum, $\phi(n)$, over the whole frequency range between zero and ∞ should be equal to $\overline{\eta^2}$, i.e.,

$$\int_0^\infty \phi(n)\, dn = \overline{\eta^2}. \qquad (7)$$

where $\overline{\eta^2}$ is the mean square of the vertical displacement from the mean water surface. Rewriting Equation (7) in a non-dimensional form

$$\int_0^\infty \frac{n_o \phi(n)}{\overline{\eta^2}}\, d\left(\frac{n}{n_o}\right) = 1 \qquad (8)$$

would provide an integral constraint on the function of $\phi(n)\, n_o/\overline{\eta^2}$. Mitsuyasu (14) presented similarity frequency spectra by plotting $\phi(n)\, n_o/\overline{\eta^2}$ vs. n/n_o and showed that his laboratory data had different shape of similarity spectrum from his Hakata Bay data.

Equation (7) may be rewritten in another non-dimensional form

$$\int_0^\infty \frac{\phi(n)}{\phi(n_o)}\, d\left(\frac{n}{n_o}\right) = \frac{\overline{\eta^2}}{n_o\, \phi(n_o)} \qquad (9)$$

As shown by Burling (1) and Mitsuyasu (14), the nondimensional parameter $\overline{\eta^2}/n_o\, \phi(n_o)$ can be approximated by a numerical constant, and, thus, plots of $\phi(n)/\phi(n_o)$ vs. n/n_o would present another form of similarity frequency spectrum. Donelan, et. al (1985) presented both their laboratory and field data by plotting $\phi(n)/\phi(n_o)$ vs. n/n_o, but the data cannot be collapsed into a single similarity shape.

These two forms of similarity frequency spectrum presented above have the scaling factors, including the wave characteristics, such as ϕ (n_o), n_o, and $\overline{\eta^2}$, while the wind speed, which is responsible for generating wind waves, is not explicitly included. From the point of view of predicting wave spectrum, these similarity spectrum forms may not be readily applicable. It is therefore the intention of this paper to obtain a similarity frequency spectrum that will be readily applicable in predicting wave spectrum.

In a recent paper to analyze the wind wave momentum equation

$$\rho_w g \frac{d}{dt} \left(\frac{\overline{\eta^2}}{C_o}\right) = \tau_w \tag{10}$$

Lin (11) proposed a closure approximation for the wind-wave momentum:

> The wind-wave momentum per unit area per unit weight of water, $\overline{\eta^2}/C_o$, is characterized by the wind frictional velocity u_*, and the dominant wave frequency n_o.

Here, τ_w is the effective wind wave drag and ρ_w is the density of the water. By virtue of dimensional reasoning, he derived an empirical equation

$$\frac{\overline{\eta^2}}{C_o} = A_1 \frac{u_*}{n_o^2} \tag{11}$$

where A_1 is a nondimensional coefficient, C_o is the phase speed of the dominant wave, u_* is the frictional velocity of the wind defined as $u_* = \sqrt{C_d}\ U_{10}$, C_d is the drag coefficient, U_{10} in m/sec is the wind speed at 10m above the water surface. For calculation of C_d, the empirical equations by Wu (30) were used,

$$C_d = 0.0026 \text{ for } U_{10} > 15 \text{ m/sec}$$

$$C_d = 0.0005\sqrt{U_{10}} \text{ for } 1 < U_{10} < 15 \text{ m/sec}. \tag{12}$$

Because of the importance of Equation (11) in supporting the present paper, experimental data used to verify Equation (11) are reproduced in Figure 1. These experimental data were obtained under a wide range of wind and wave conditions and in different seas around the world. The nondimensional coefficient A_1 was determined to be 0.044 for wind waves in deep waters. It is expected that the numerical value of A_1 could vary with the water depth and the current, and that it would depend on whether the wind wave field is in the growing or decaying stage. Equation (11) with $A_1 = 0.044$ may be converted to

$$\varepsilon = 1.8 \times 10^{-4} \sqrt{C_d}\ \nu^{-3} \tag{11a}$$

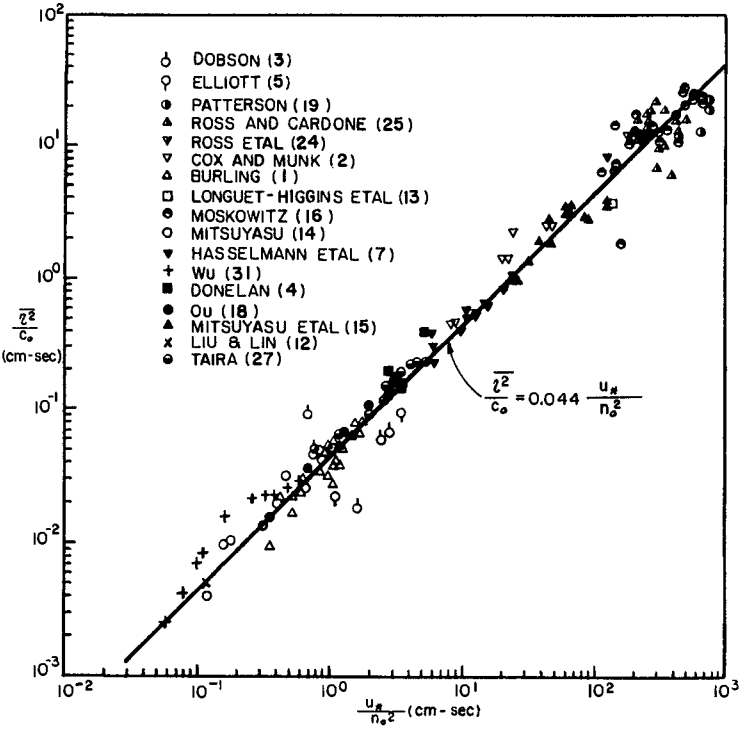

FIGURE 1 Wind - Wave Momentum Per Unit Area Per Unit Weight, $\overline{\zeta^2}/c_o$ Vs u_*/n_o^2

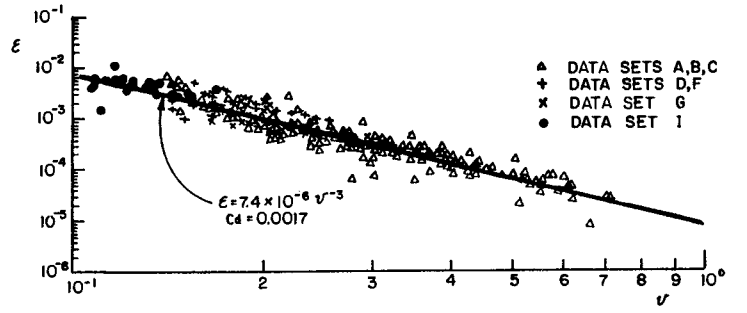

FIGURE 2 Variation of ε With ν for Wind Waves. Data Available From Hasselmann, Etal (7) and Van Müller (17)

where $\varepsilon = g^2 \overline{\eta^2}/U_{10}^4$ and $\nu = n_o U_{10}/(2\pi g)$. In Figure 2, data available from Hasselmann, et al. (7) and Von Müller (17) are replotted. A solid line representing Equation (11a) with $C_d = 0.0017$ for $U_{10} = 12$ m/sec fit the data very well.

Using Equation (11), Equation (7) is rewritten as

$$\int_0^\infty \frac{n_o^3 \phi(n)}{u_* C_o} \, d\left(\frac{n}{n_o}\right) = \frac{\overline{\eta^2}\, n_o^2}{u_* C_o} = A_1 \tag{13}$$

For wind waves in deep waters, the scaling factor of the frequency spectrum expressed in Equation (13) becomes $u_* g/n_o^4$ which is consistent with that used by Toba (29).

In Figure 3, we plot $n_o^3 \phi(n)/u_* C_o$ vs. n/n_o for wind wave data obtained in the laboratory wind-wave tanks by Mitsuyasu (14), by Toba (29), by Ou (18), and by Liu and Lin (12), and in the field by Burling (1) and Mitsuyasu (14). In Figure 4, several spectral measurements of the fully developed wind waves in open ocean conducted by Pierson (22), by Longuet-Higgins, et al. (13), by Ross and Cardone (25), and by Mitsuyasu, et al (15) are also presented in non-dimensional form as $n_o^3 \phi(n)/u_* C_o$ vs. n/n_o.

Energy-Containing Range

The energy-containing range may be defined as the frequency range in which the energy contained would represent the majority, say 95 percent, of the total wave energy. As shown in Figures 3 and 4, the slope of the rear face of the wave spectrum in the energy containing range, expressed as r in the power law: $\phi(n) \sim n^{-r}$, has a value as high as 10 for the laboratory data and it decreases as $n_o u_*/g$ decreases. To obtain the variation of the r values with $n_o u_*/g$, the experimental data plotted in Figures 3 and 4 together with additional spectral data available from Burling (1) and Mitsuyas (14) were used. The data points shown in Figure 5 may be fitted approximately by a power law,

$$r = 9.1 \left(\frac{n_o u_*}{g}\right)^{1/4} \quad \text{for } 0.017 < \frac{n_o u_*}{g} < 2.1 \tag{14}$$

The decrease of the rear face slope of the spectrum with the sea state may be attributed to the enhancement of the wave breaking process as the value of $n_o u_*/g$ decreases.

To reflect the change of the spectral shape with the sea state, an empirical wave spectrum was derived as

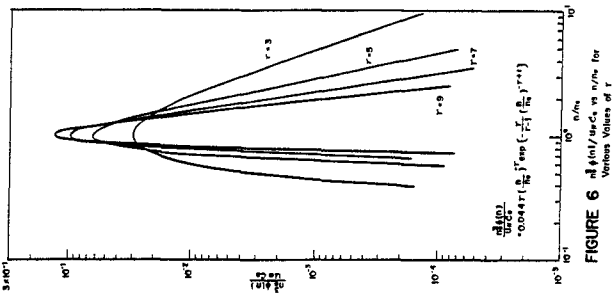

FIGURE 6 $n^3\phi(n)/u_*c_o$ vs n/n_o for Various Values of γ

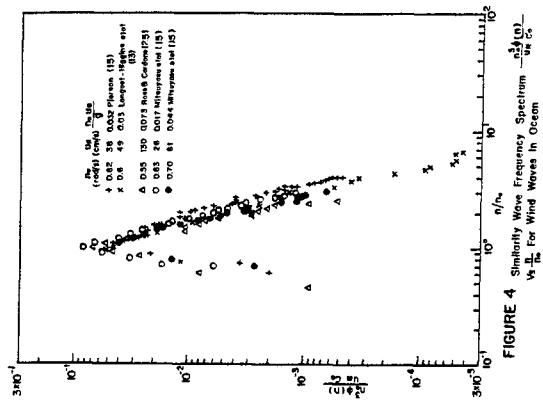

FIGURE 4 Similarity Wave Frequency Spectrum $\frac{n^3\phi(n)}{u_* c_o}$ vs $\frac{n}{n_o}$ For Wind Waves In Ocean

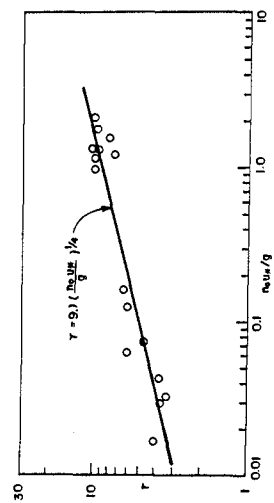

FIGURE 5 The Slope of the Rear Face of the Frequency Spectrum, γ vs $n_o u_*/g$

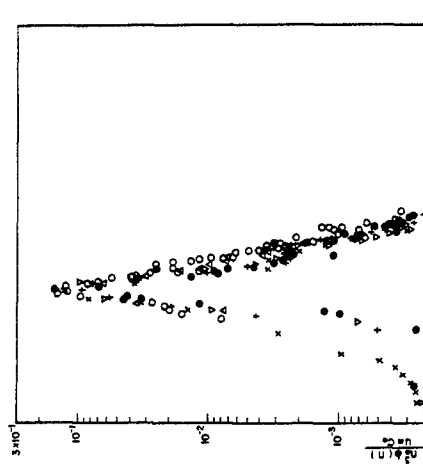

FIGURE 3 Similarity Wave Frequency Spectrum $\frac{n^3\phi(n)}{u_* c_o}$ vs $\frac{n}{n_o}$ For Fetch-Limited Wind Waves

$$\frac{n_o^3 \phi(n)}{u_* C_o} = A_1 \, r\left(\frac{n}{n_o}\right)^{-r} \exp\left[-\frac{r}{r-1}\left(\frac{n}{n_o}\right)^{-r+1}\right] \tag{15}$$

Equation (15) can readily be integrated to satisfy Equation (13), and it also satisfies the condition that the spectrum peaks at $n = n_o$. The Pierson-Moskowitz spectrum is a special case of Equation (15) when $r = 5$. Another important feature of Equation (15) is that when the value of r increases with $n_o u_*/g$ according to Equation (14), the spectral peak increases. This feature is apparently consistent with the experimental data presented in Figures 3 and 4.

To illustrate the variation of the spectral shape with r, Equation (15) is presented in Figure 6 with $A_1 = 0.044$. Also we plot $\phi(n)/\phi(n_o)$ vs n/n_o in Figure 7 as

$$\frac{\phi(n)}{\phi(n_o)} = \left(\frac{n}{n_o}\right)^{-r} \exp\left\{-\frac{r}{r-1}\left[\left(\frac{n}{n_o}\right)^{-r+1} - 1\right]\right\}. \tag{16}$$

The normalization of $\phi(n)$ with respect to $\phi(n_o)$ further accentuates the sharpening of the spectral shape when the value of r increases. In Figure 8, the analytical solutions expressed in Equation (15) for r = 10, 5 and 4 are presented for comparison with the experimental data obtained in the laboratory and in the field. The comparison is fairly well.

Equilibrium Range

In the equilibrium range, the wave frequency spectrum, according to Phillip's concept, is saturated and governed by the gravitational acceleration. By fitting the experimental data presented in Figures 3 and 4 with the n^{-5} spectrum, one may find out that the value of ß in Equation (1) is not a universal constant. On the other hand, one may also estimate the value of α as expressed in Equation (5) by fitting the experimental data with the n^{-4} spectrum. In Figure 9, the values of $ß(n_o u_*/g)^{-1}$ and α are plotted against $n_o u_*/g$. Two solid lines are drawn to approximate the experimental data as

$$ß = 0.08 \left(\frac{n_o u_*}{g}\right)^{3/4} \tag{17}$$

$$\alpha = 0.027 \left(\frac{n_o u_*}{g}\right)^{-1/3} \tag{18}$$

Since the spectral measurements of wave variances could not accurately settle the difference between n^{-4} and n^{-5} in the equilibrium range, research effort was directed to analyzing the spectral

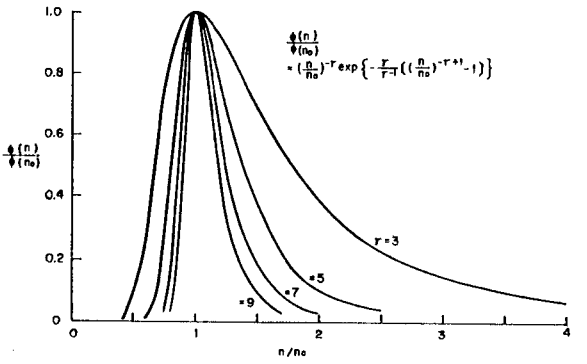

FIGURE 7 $\phi(n)/\phi(n_o)$ vs n/n_o for Various Values of r

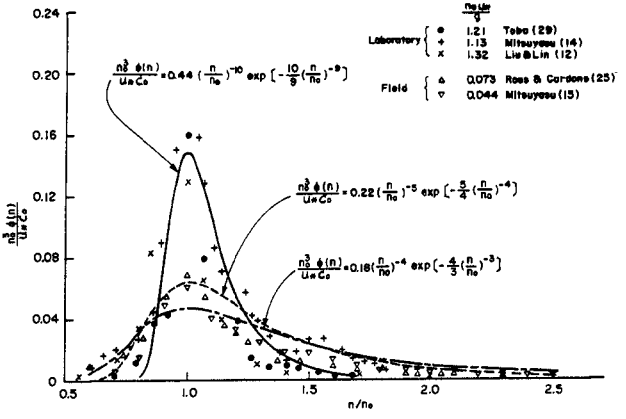

FIGURE 8 Comparsion of Analytical Solution Expressed in Equation (15) for r = 10, 5, and 4, and Experimental Data

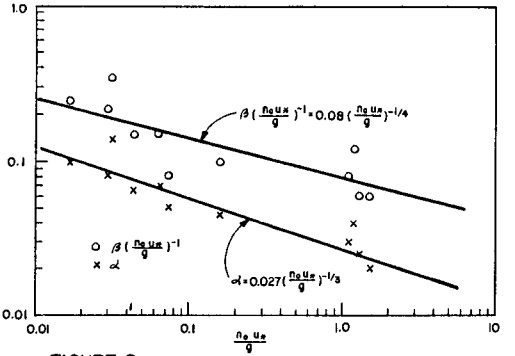

FIGURE 9 Variation of β and α With $n_o u_\pi/g$

measurements of wave slopes. Using the dispersion relation $n^2 = gk$ for gravity waves and $\phi(n)dn = \chi(k)kdk$, the wave-number spectrum $\chi(k)$ corresponding to Equations (1) and (5) are derived respectively as follows:

a) Phillips spectrum

$$\chi(k) = \frac{\beta}{2}k^{-4} \tag{19}$$

b) Toba spectrum

$$\chi(k) = \frac{\alpha}{2} u_* g^{-1/2} k^{-7/2} . \tag{20}$$

Hence, the wave slope frequency spectrum $\phi_s(n)$ in correspondence to Equations (19) and (20) are derived below:

a) Phillips spectrum

$$\phi_s(n) = \beta n^{-1} \tag{21}$$

b) Toba spectrum

$$\phi_s(n) = \alpha\frac{u_*}{g} . \tag{22}$$

Equation (22) suggests that, in the equilibrium range, the Toba spectrum would have a constant value, but this result is not supported by the limited data of wave slope spectra measured by Cox (2a) and by Long and Huang (12a).

Further testing may be made by comparing the mean square wave slope measurements and the analytical results based on Equations (19) and (20). According to Phillips (21) the mean square wave slope $\overline{s^2}$ of wind waves may be approximated by

$$\overline{s^2} = \int_{k_o}^{k_\nu} k^2 \chi(k)\, kdk \tag{23}$$

Here k_ν is the cut-off wave number, representing highest wave number of the gravity wave that could be excited by the wind. Hence, the mean square wave slope may be approximated by

$$\overline{s^2} = \frac{\beta}{2} \ln \frac{k_\nu}{k_o} \tag{24}$$

if Equations (19) and (23) are used, or by

$$\overline{s^2} = \alpha \frac{n_o u_*}{g} \left(\sqrt{\frac{k_\nu}{k_o}} - 1\right) \tag{25}$$

if Equations (20) and (23) are used.

Cox and Munk (2) conducted wave slope measurements of the sea surface covered with an artificial slick, and thus, the wave slope measurements were contributed from the gravity waves but not from the capillary waves. Since the measurements showed that wave components shorter than 30 cm were almost entirely absent (Phillips, (21)) k_ν may be approximated by $2\pi/30$ cm^{-1}. Longuet-Higgins, et al. (13) measured the wave slopes of wind waves in the open ocean. Since their measurements were filtered at 4 rad/sec, the cut-off wave number may be estimated using the dispersion relation as $k_\nu = 4^2/g$. In Figure 10, both sets of wave slope measurements are presented and compared with Equation (24) having ß approximated by Equation (17). These data are replotted in Figure 11 and compared with Equation (25) having α approximated by Equation (18). The limited wave slope measurements apparently favor Equation (24) or Phillips spectrum expressed in Equation (1) rather than Equation (25) or Toba spectrum expressed in Equation (5).

The fair agreement between the wave slope measurements and the prediction of the wave slope as expressed in Equation (24) may suggest that the remote sensing $\overline{s^2}$ could lead to estimating the wind field, u_* provided that the dominant wave frequency n_o were measured independently.

Prediction of Wave Spectrum

We have derived a general wave spectrum for the energy-containing range as expressed in Equation (15), in which the spectral density, $\phi(n)$, is scaled by $u_* C_o/n_o^3$, the wave frequency, n by n_o, and the non-dimensional coefficient r is related to $n_o u_*/g$ by Equation (14). We also determined that in the equilibrium range, the non-dimensional coefficient ß expressed in the Phillips spectrum is indeed a function of $n_o u_*/g$. Thus, the prediction of wave spectrum becomes a task of predicting $n_o u_*/g$. Because of interest in predicting $n_o u_*/g$ for fetch-limited wind waves, Lin's paper (15) is further extended for fetch-limited wind waves generated by a non-uniform wind flow.

At limited fetches, the effective wind wave drag, τ_w may be approximated by

$$\tau_w = A_2 \rho_a u_*^2 \tag{26}$$

where A_2 is a non-dimensional numerical coefficient, ρ_a is the density of the air. For a non-uniform wind flow depending on the fetch, F, or the duration, t, according to the power laws

$$u_* = u_{*o} \left(\frac{gF}{u_{*o}^2}\right)^p \tag{27}$$

$$u_* = u_{*o} \left(\frac{gt}{u_{*o}}\right)^q \tag{28}$$

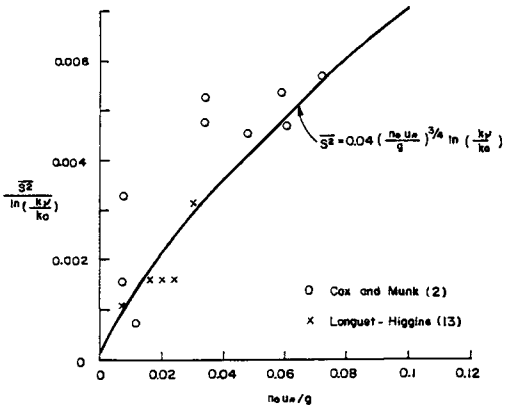

FIGURE 10 Comparsion Between the Analytical Solution Expressed in Equation (24) and Experimental Data

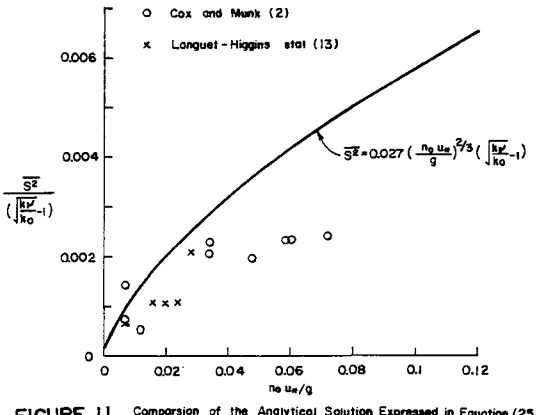

FIGURE 11 Comparsion of the Analytical Solution Expressed in Equation (25) and Experimental Data

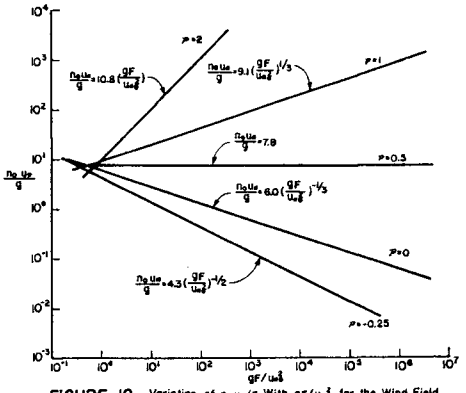

FIGURE 12 Variation of $n_0 u_0/g$ With gF/u_*^3 for the Wind Field $u_* = u_{e0}\,(gF/u_*^2)^{\frac{1}{2}}$

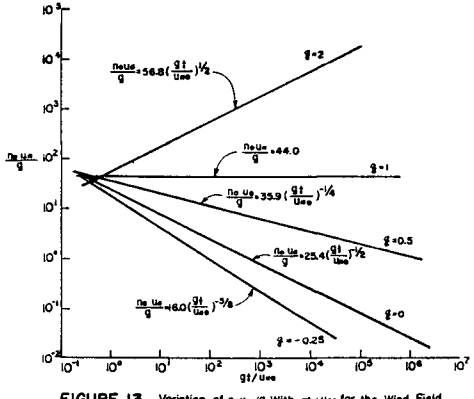

FIGURE 13 Variation of $n_0 u_0/g$ With gt/u_{e0} for the Wind Field $u_* = u_{e0}(gt/u_{e0})^{\beta}$

where u_{*o} is a reference wind speed, Equations (10) and (26) can be solved analytically and have the special solutions,

$$\frac{n_o u_*}{g} = \left[\frac{6\,\rho_a A_2}{(2+5p)\rho_w A_1}\right]^{-1/3} \left(\frac{gF}{u_{*o}^2}\right)^{-(1-2p)/3} \tag{29}$$

$$\frac{n_o u_*}{g} = \left[\frac{\rho_a A_2}{(1+2q)\rho_w A_1}\right]^{-1/2} \left(\frac{gt}{u_{*o}^2}\right)^{-(1-q)/2} \tag{30}$$

for $p > -2/5$ and $q > -1/2$. When $p \leq -2/5$ or $q \leq -1/2$, the wind wave solution is not meaningful as $n_o u_*/g$ becomes zero or imaginary. Figures 12 and 13 present $n_o u_*/g$ vs. gF/u_{*o}^2 and gt/u_{*o} respectively for a family of the parameters p and q when $A_1 = 0.044$, $A_2 = 0.057$ and $\rho_a/\rho_w = 0.0012$.

Conclusions and Recommendations

An empirical wave spectrum in the energy-containing range for a general sea state was derived as expressed in Equation (15). The Pierson and Moskowitz spectrum, as presented in Equation (2), is a special case of Equation (15). The scaling factor of the wave frequency spectrum is $u_* C_o/n_o^3$, while the scaling factor of the wave frequency n is the dominant wave frequency n_o. The non-dimensional numerical coefficient r is the only free parameter in the empirical equation and it can be estimated from the slope of the rear face of spectrum and approximated by the empirical formula expressed in Equation (14) for $n_o u_*/g$ ranging from 0.017 to 2.1.

In the equilibrium range, the saturated wave frequency spectrum is better approximated by the Phillips spectrum expressed in Equation (1) rather than the Toba spectrum expressed in Equation (5). One must point out that the wave slope data used to test the Phillips spectrum and the Toba spectrum are available from only three sources, namely Cox (2a), Cox and Munk (2), and Longuet-Higgins, et al (13). In order to establish the statistical significance of the present conclusion, additional data are required. It is recommended to perform spectral measurements of both wave variances and wave slope simultaneously at the same physical location. The wave slope can readily be measured using remote sensing technique, while the laser displacement gauge (LDG) developed by Liu and Lin (12) may be modified to measure the wave height remotely in the field.

Acknowledgement

This paper was prepared under an IR&D funding available from the Ocean Wave Energy Conservation Program of United Industries Corporation.

References

1a. Battjes, J. A., Zitman, T. J. and Holthuijsen, L. H. (1986). The JONSWAP Data Reanalyzed. The 20th Intl. Conf. Coastal Engineering, Taipei, Taiwan, R.O.C., Nov. 9-14.
1. Burling, R. W. (1959). The Spectrum of Wave at Short Fetches. Dtsch. Hydrogr. Z., 12: 45-64, and 96-117.
2. Cox, C. and Munk, W. (1954). Measurement of the Roughness of the Sea Surface from Photographs of the Sun's Glitter. J. Opt. Soc. Amer., 44 (11):838-850.
2a. Cox, C. S. (1958). Measurements of Slopes of High Frequency Wind Waves. J. Mar. Res., 16: 199-225.
3. Dobson, F. W. (1971). Measurements of Atmospheric Pressure on Wind Generated Sea Waves. J. Fluid Mech., 48:91.
4. Donelan, M.A., (1978). Whitecaps and Momentum Transfer. Turbulent Fluxes through the Sea Surface, Wave Dynamics and Prediction, Favre, A. and Hasselmann, K., eds., Plenum Press, pp. 273 - 287.
4a. Donelan, M. A., Hamilton, J. and Hui, W. H. (1985). Directional Spectra of Wind-Generated Waves. Phil. Trans. R. Soc. Lond., A315: 509-562.
5. Elliott, J.A. (1972). Microscale Pressure Fluctuation Near Waves being Generated by the Wind. J. Fluid Mech., 54:427.
6. Hasselmann, K., Barnett, T.P., et al. (1973). Measurements of Wind-wave Growth and Swell Decay During the Joint North Sea Wave Project (JONSWAP). Deut, Hydrogr.Z., Suppl. A 8, No. 12.
7. Hasselmann, K., Ross, D. B., Von Müller, P., and Sell, W. (1976). A Parametric Wave Prediction Model. J. Phys. Oceano., 6:200-228.
8. Huang, N.E., Long, S.R., Tung, C.C., Yuen, Y. and Bliven, L. F. (1981). A Unified Two-Parameter Wave Spectral Model for a General Sea State. J. Fluid Mech., 112:203-224.
9. Kitaigoroskii, S.A., Krasitskii, V.P. and Zaslavskii, M.M. (1975). On Phillips' Theory of Equilibrium Range in the Spectra of Wind-generated Gravity waves. J. Phys Oceanog., 5: 410-420.
10. Kitaigorodskii, S. A., Donelan, M.A., Lumley, J.L. and Terray, E.A. (1983). Wave-Turbulence Interactions in the Upper Ocean. Part II Statistical Characteristics of Wave and Turbulent Components of the Random Velocity Field in the Marine Surface Layer. J. Phys. Oceano, 13:1988-1999.
11a. Lin, J. T., Gad-el-Hak, M. and Lin, H. T. (1978). A Study to Conduct Experiments Concerning Turbulent Dispersion of Oil Slicks. Report No. CG-D-54-78 and AD-A058802, prepared for U.S. Dept. Transportation, U.S. Coast Guard.
11. Lin, J. T. (1985). Empirical Prediction of Wind-Generated Gravity Waves. Presented at the ASCE West Coast Regional Coastal Design Conference, Oakland, Ca., Nov. 7-8.
12. Liu, H. T. and Lin, J. T. (1982). On Spectrum of High-Frequency Wind Waves. J. Fluid Mech., 123:165 - 185.
12a. Long, S. R. and Huang, N. E. (1976). On the Variation and Growth of Wave Slope Spectra in the Capillary-Gravity Range with Increasing Wind. J. Fluid Mech., 77: 209-228.
13. Longuet-Higgins, M. S., Cartwright, D.E. and Smith, N.O. (1963). Observations of the Directional Spectrum of Sea Waves Using the Motions of a Floating Buoy. Ocean Wave Spectra, Englewood Cliffs, N.J., Prentice Hall Inc., pp. 111 - 136.

14. Mitsuyasu, H. (1968). On the Growth of the Spectrum of Wind-Generated Waves (I). Reports of Research Institute for Applied Mechanics, XVI, Vol. 55, Kyushu Univ., Japan.
15. Mitsuyasu, H., Tasai, F., Sukara, T., Mizuno, S., Ohkusu, M., Honde, T., and Rikiiski, K. (1980). Observation of the Power Spectrum of Ocean Waves Using a Clover Leaf Buoy. J. Phys. Oceanogr., 10:286-296.
16. Moskowitz, L. (1963). Estimates of the Power Spectra for Fully Developed Seas for Wind Speeds of 20 to 40 knots. Tech. Report for U.S. Navy Oceanographic Office under Contract N62306-1042.
17. Von Müller, P. (1976). Parameterization of One-Dimensional Wind waves Spectra and their Dependence on the State of Development. Max-Planck-Institute for Meteorology, University of Hamburg, West Germany.
18. Ou, S. H. (1980). The Equilibrium Range in Frequency Spectra of the Wind Generated Gravity Waves. Proc. 4th Conference on Ocean Engineering in Republic of China, Taiwan, ROC, Sept., pp. 217 - 227.
19. Patterson, M. M. (1974). Oceanographic Data from Hurricane Camille, Shell Co. Report.
20. Phillips, O.M. (1958). The Equlibrium Range in the Spectra of Wind Generated Waves. J. Fluid Mech., 4:426-434.
21. Phillips, O. M. (1966). The Dynamics of the Upper Ocean. The University Press, Cambridge, Great Britain.
22. Pierson, W. J. ed. (1962). The Directional Spectrum of a Wind-Generated Sea as Determined from Data Obtained by the Stereo Wave Observation Project. Coll. Engng, N.Y.U., Met Pap., 2, No. 6.
23. Pierson, W. J. and Maskowitz, L., (1964). A Proposed Spectral form for Fully Developed Wind Seas Based on the Similarity Theory of S. A. Kitaigorodskii. J. Geophys. Res., 69: 5181 - 6190.
24. Ross, D.B., Cardone, V.J., and Conaway, J. W. (1970). Laser and Microwave Observations of Sea-Surface Conditions for Fetch-Limited 17 to 25 m/s Winds. IEEE Trans Geosci. Electronics, GE-8, pp. 326.
25. Ross, D.B. and Cardone, V.J. (1974). Observations of Oceanic White Caps and Their Relation to Remote Measurements of Surface Wind Speed. J. Geophys. Res., 79:444-452.
26. Schule, J.J. Jr., Simpson, L.S. and DeLeonibus, P.S. (1971). A Study of Fetch-Limited Wave Spectra with an Airborne Laser. J. Geophys. Res., 76(18):4160-4171.
27. Taira, K. (1972). A Field Study of the Development of Wind Wave. J. Oceano. Soc., Japan, 28:187-202.
28. Thorton, E.B. (1977). Rederivation of the Saturation Range in the Frequency Spectrum of Wind Generated Gravity Waves. J. Phys Oceanog., 7: 137-140.
29a. Toba, Y. C. (1972). Local Balance in the Air-Sea Boundary Processes, I. On the Growth Process of Wind Waves. J. Oceano. Soc. Japan, 28: 109-121.
29. Toba, Y. (1973). Local Balance in the Air-Sea Boundary Processes, III. On the Spectrum of Wind Waves. J. Oceano. Sec. Japan, 29: 209-220.
30. Wu, J. (1969). Wind Stress and Surface Roughness at Air-Sea Interface. J. Geophys. Res., 74 :444 - 455.
31. Wu, J., (1975). Wind Induced Drift Currents. J. Fluid Mech, 68: 49-70.
32. Zakhorov, V. E. and Filonenko, N. N. (1967). Energy Spectrum for Stockastic Oscillations of the Surface of a Liquid. Soviet Phys. Dokl., 11: 881-883.

CHAPTER 37

WAVE TRANSFORMATION AND MEAN SEA LEVEL VARIATION

SHI-CHUAN LIN* JENG-SHIN HWANG*

ABSTRACT

For the practical application in coastal engineering, the universal model of water wave, momentum conservation and energy conservation equation with considering of energy loss due to bottom friction and wave breaking is adopted in this paper to evaluate the wave transformation on general slope, which including wave shoaling, breaking and attenuation after breaking as well as wave set-up and set-down during the waves advancing toward the coast.

In comparison with the results of theoretical approaches as well as experimental data accomplished by the traditional method, very good coincidence is obtained besides the mean sea level variation.

INTRODUCTION

The wave transformation and the mean sea level variation for waves propagating from deep sea toward the shore are interesting topics for coastal engineering. Conventionally, the process is divided into three parts: (1) the shoaling of the wave from deep sea till near breaking point, (2) the breaking index and (3) the wave decay and the wave set-up/set-down inside the surf zone. These problems have to be treated separately and different wave theories are to be applied in each zones because of the validity of wave theories in various water depth.

---

* Lecturer, Department of Hydraulic and Ocean Engineering, National Cheng Kung University, Tainan, Taiwan 70101, Republic of China

In the present paper, the so-called universal model of water wave derived by Chen et al. (1982) is adopted and further developed. Coupling with conservation equations of momentum and energy flux and taking bottom friction and energy dissipation due to wave breaking into consideration, the propagation characteristics of a perpendicular incident wave train on a general slope has been investigated continuously from deep sea till the shoreline. This includes the shoaling process, wave breaking, wave decay inside the surf zone and the mean sea level variation, i.e. the forementioned problems can be solved in one model.

In the model, the experimental results of the bottom friction coefficient on smooth bottom by Riedel et al. (1972) is used. The energy dissipation rate in breaking process is estimated from that in a bore of corresponding height. The limiting height of breaking from Goda (1970) is adopted for the breaker control to determine the breaking index. The results are compared with both experimental data and analytical values from other authors.

THEORETICAL ANALYSIS

1. UNIVERSAL MODEL OF WATER WAVE

For the mathematical model of water wave in uniform depth, Chen et al. (1982) proposed a new model derived from stream function, its first order exact solution in steady state are

$$\psi(x,y) = -cy + c\eta_c \frac{\sinh k(d+y)}{\sinh k(d+\eta_c)} \cos kx \qquad \cdots\cdots(1)$$

$$\eta(x) = \eta_c \frac{\sinh k(d+\eta)}{\sinh k(d+\eta_c)} \cos kx \qquad \cdots\cdots(2)$$

$$c^2 = \frac{g}{k} \tanh kd \Big/ \left[1 - k^2 \eta_c^2 \frac{\sinh^2 kd}{\sinh^2 k(d+\eta_c)} \right] \qquad \cdots\cdots(3)$$

$$H = \eta_c \left[1 + \cosh kH - \coth k(d+\eta_c) \sinh kH \right] \qquad \cdots\cdots(4)$$

where ψ is stream function, c wave celerity, $k=2\pi/L$ wave number, d water depth, η wave elevation, η_c elevation of

wave crest, H wave height.

The model is proved mathematically to be used in any case of d/L, which withdraw the restriction of application between other theories, it is to be nominated "universal model", and it is to be adopted in the paper for the wave transmission evaluation.

Dynamic properties in the wave field are definitively derived as

(1) mean kinetic energy

$$K=\frac{1}{2}\rho\overline{\int_{-d}^{\eta}\{(u+c)^2+v^2\}dy}$$

$$=\frac{1}{2}\frac{\rho c^2\eta_c^2 k}{\sinh^2 k(d+\eta_c)}\left\{\frac{\sinh 2kd}{4}+\frac{A}{B}\left\{\left(\frac{1}{B^2k^2}+\frac{1}{2}\right)\right.\right.$$

$$\left.\left.\cdot(\cosh 2kd-1)\right)\left(\frac{1}{\sqrt{1-B^2k^2}}-1\right)-\frac{1}{2}\right\}\right\} \quad \cdots\cdots(5)$$

(2) mean potential energy

$$P=\frac{1}{2}\rho g\overline{\int_{o}^{L}(\eta-\overline{\eta})^2dx}=\frac{1}{2}\rho g(\overline{\eta^2}-\overline{\eta}^2)$$

$$=\frac{1}{2}\rho g\frac{A^2}{B^2k^2}\left(\frac{B^2k^2}{(1-B^2k^2)^{3/2}}-\frac{1}{1-B^2k^2}+\frac{1}{\sqrt{1-B^2k^2}}\right) \quad \cdots\cdots(6)$$

(3) mean momentum

$$I=\rho\overline{\int_{-d}^{\eta}(u+c)dy}$$

$$=\frac{\rho cA}{Bk}\left(\frac{1}{\sqrt{1-B^2k^2}}-1\right) \quad \cdots\cdots(7)$$

(4) mean energy flux

$$F=\overline{\int_{-d}^{\eta}\left\{p+\frac{\rho}{2}\{(u+c)^2+v^2\}+\rho gy\right\}(u+c)dy}$$

$$=(3K-2P)c+\frac{1}{2}\overline{(u_b+c)^2}\{I+\rho(d+\overline{\eta})c\}+g\overline{\eta}I \quad \cdots\cdots(8)$$

(5) radiation stress

$$S_{xx} = \overline{\int_{-d}^{\eta} \{ p + \rho (u + c)^2 \} dy} - \int_{-d}^{\overline{\eta}} p_0 dy$$
$$= 4K - 3P + \rho \overline{(u_b + c)^2} (d + \overline{\eta}) \quad \cdots\cdots(9)$$

In above equations, "-" represents average over one wave length, $u_b' = u_b + c$ horizontal velocity at bottom, and

$$A = \eta_c \frac{\sinh kd}{\sinh k (d + \eta_c)} \qquad B = \eta_c \frac{\cosh kd}{\sinh k (d + \eta_c)}$$

$$\overline{(u_b + c)^2} = \frac{c^2 \eta_c^2 k^2}{2 \sinh^2 k (d + \eta_c)} \quad , \quad \overline{\eta} = \frac{A}{Bk} \left(\frac{1}{\sqrt{1 - B^2 k^2}} - 1 \right)$$

2. CONSERVATIVE EQUATIONS OF MOMENTUM AND OF ENERGY

By omitting the rate of change in time, effects of wind at surface and currents, conservative equations of momentum and of energy in two dimension show respectively

$$\frac{dS_{xx}}{dx} = -\rho g (d + \overline{\zeta}) \frac{d\overline{\zeta}}{dx} \quad \cdots\cdots(10)$$

$$\frac{dF}{dx} = \overline{P_f} + \overline{P_b} \quad \cdots\cdots(11)$$

where S_{xx} is radiation stress, $\overline{\zeta}$ set-up/down of mean water level, F energy flux, $\overline{P_f}$ energy dissipation rate due to bottom friction per unit area, $\overline{P_b}$ energy dissipation rate due to wave breaking per unit area.

3. ENERGY DISSIPATION

In non-breaking zone, the energy dissipation are dominated by bottom friction. However, mixing of air and inducing turbulence become dominant factor for energy dissipation within breaking zone of some distance. After some distance of breaking, the more shallow the depth is, the more impor-

tant is the bottom friction to energy dissipation.

P_f shows energy dissipation due to bottom friction per unit area per unit time presented by

$$P_f = \tau_{bx} \cdot u_b'$$

and $\tau_{bx}=\frac{1}{2}\rho f_w u_b' | u_b' |$ is shear stress at bottom, f_w bottom friction coefficient.

Averaging over one wave length for P_f , we get

$$\overline{P_f} = \frac{1}{L}\int_o^L \frac{1}{2}\rho f_w u_b'^2 \cdot | u_b' | dx$$

$$= \frac{2\rho f_w c^3 \eta_c^3 k^3}{3\pi \sinh^3 k(d+\eta_c)} \qquad \cdots\cdots(12)$$

For the bottom friction coefficient f_w , regression formula are worked out from the experimental data of Riedel et al. (1972) for smooth bottom. The functional form are

$$\left.\begin{aligned} f_w &= 1.993196\,(Re)^{-0.600099} && 10^2 \le Re \le 10^4 \\ \ell n\, f_w &= 74.8895 - 29.6769\,(\ell nRe) + 4.33474\,(\ell nRe)^2 \\ &\quad - 0.287814\,(\ell nRe)^3 + 0.00718364\,(\ell nRe)^4 \\ &&& 10^4 < Re \le 3.393\times 10^5 \\ \ell n\, f_w &= -3005.95 + 842.946\,(\ell nRe) - 88.6773\,(\ell nRe)^2 \\ &\quad + 4.14089\,(\ell nRe)^3 - 0.0724355\,(\ell nRe)^4 \\ &&& 3.393\times 10^5 < Re \le 3.501\times 10^6 \end{aligned}\right\} \cdots\cdots(13)$$

where R_e is Reynolds number.

For spilling breaker, its structure and energy dissipation are similar to bore, which has a strong turbulence mixed with air only near crest. Le Méhauté (1962) suggested that the energy dissipation in spilling breaker can be estimated by a bore of the same height. The average energy dissipation of breakers of unit area in unit time, $\overline{P}_b$, shows

$$\overline{P_b} = \frac{1}{4}\rho g \frac{(h_2 - h_1)^3}{h_1 h_2} Q \simeq \frac{1}{4}\rho g \frac{(\alpha H)^3}{d^2} Q \quad \cdots\cdots (14)$$

where h_1, h_2 are depths before and after the bore respectively, α breaker coefficient, Q discharge in bore per unit area.

Hwang and Divoky (1970) suggested that Q in water wave can be calculated by linear periodic bore Q=cd/L, and we can get

$$\overline{P_b} = \frac{\rho g c (\alpha H)^3}{4 L d} \quad \cdots\cdots (15)$$

NUMERICAL MODEL

In Fig.1, waves propagate from section I to section II with constant wave period T. For L=cT, we get

$$\frac{L_1}{c_1} = \frac{L_2}{c_2} \quad \cdots\cdots (16)$$

Conservative equations of momentum and of energy in finite difference form are

$$\overline{\zeta_2} = \overline{\zeta_1} - \frac{1}{\rho g (d_1 + \overline{\zeta_1})} [(S_{xx})_2 - (S_{xx})_1] \quad \cdots\cdots (17)$$

$$F_2 = F_1 - (\overline{P_f})_1 \Delta x - (\overline{P_b})_1 \Delta x \quad \cdots\cdots (18)$$

and P_b=0 for waves before breaking.

If H_1, L_1, d_1 are known in section I, we can calculate and c_1 from equation (3) and (4), and calculate F_1, $(S_{xx})_1$, $(\overline{P_f})_1$ and $(\overline{P_b})_1$ by solving equations (5)-(9), (12) and (15). Then we can get c_2, η_{c2}, L_2, H_2, $\overline{\zeta_2}$ on section II of given depth d_2 by solving equations (3), (4) and (16)-(18). Newton interaction is applied in implicit function calculation.

Critical condition for limiting waves is controlled by Goda's formula (1970), shows as follow

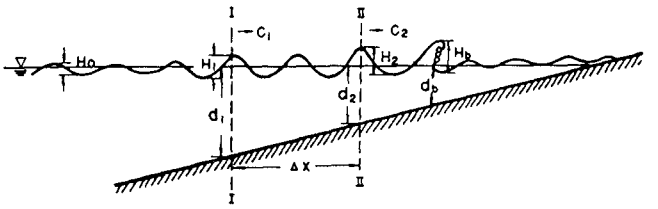
I
II
C1
C2
Ho
H1
H2
Hb
β
d1
d2
db
Δx
I
II

Fig. 1

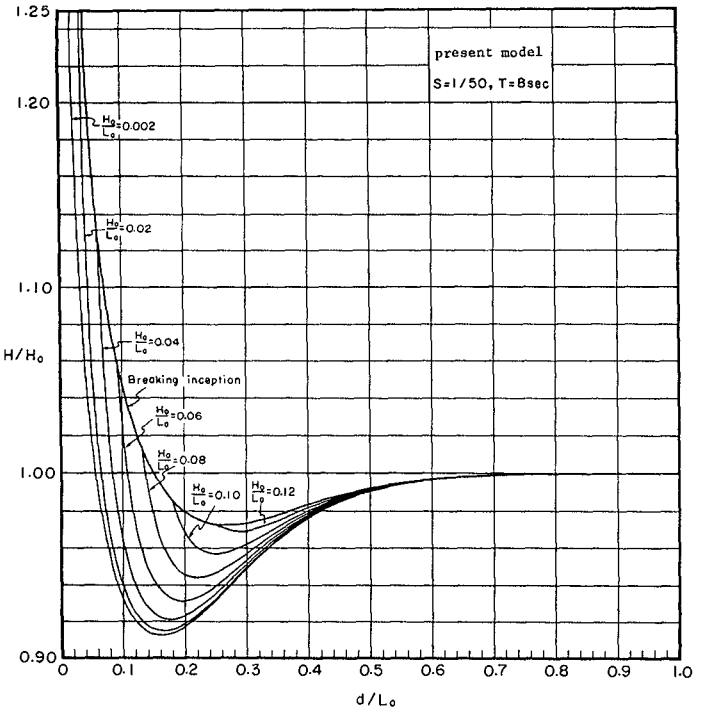
present model
S=1/50, T=8sec
Ho/Lo=0.002
Ho/Lo=0.02
Ho/Lo=0.04
Breaking inception
Ho/Lo=0.06
Ho/Lo=0.08
Ho/Lo=0.10
Ho/Lo=0.12
H/Ho
d/Lo
1.25
1.20
1.10
1.00
0.90
0
0.1
0.2
0.3
0.4
0.5
0.6
0.7
0.8
0.9
1.0

Fig. 2

$$\frac{H_b}{L_o} = 0.17 \{ 1 + \exp [-1.5 \frac{\pi (d_b + \overline{\zeta_b})}{L_o} (1 + 15 S^{\frac{4}{3}})] \} \quad \cdots\cdots (19)$$

RESULT

The present results are discussed in four parts, i.e. shoaling process, breaking index, wave decay within the surf zone and the mean sea level variation.

1. SHOALING

The change of wave height from deep sea to breaking point for five wave period T=4,6,8,10 and 12 sec. on five various bottom slope S=1/20,1/50,1/80,1/200 and 1/600 are examined by calculation. Fig.2 shows one of the shoaling diagram.

Table 1 and 2 show the shoaling coefficient $K_s=H/H_o$ between various bottom slope and between various wave period, T. K_s decreases as the bottom slope decreases. However, the differences in K_s for various bottom slope are small and it increases as the relative water depth d/L_o decreases. For given bottom slope, the differences in K_s for various wave periods are under 0.5% and can be neglected in the case of considering the effect of bottom friction.

The comparison of the present results to the experimental data from Hwung (1975) is presented in Fig. 3, it shows the present results are more close to the experimental data.

2. BREAKING INDEX

In calculating of the breaking index, H_b/H_o, d_b/H_o and H_b/L_b, the breaking criterion defined by Goda is adopted. Fig.4 - Fig.8 show the comparison of the present results to the experimental data from other authors. The tendency is well acceptable.

For a given deep water steepness H_o/L_o, the breaking index H_b/H_o and H_b/L_b decreases as the bottom slope decreases, whereas the tendency of d_b/H_o reverses. For a given bottom slope, the difference in breaking index between different

Table 2 S = 1/80, H_o/L_o = 0.04

H/Ho \ d/Lo	Period T 4.0	6.0	8.0	10.0	12.0
0.50	0.99078	0.99081	0.99081	0.99082	0.99082
0.49	0.98984	0.98986	0.98987	0.98988	0.98988
0.48	0.98880	0.98883	0.98884	0.98885	0.98885
0.47	0.98768	0.98771	0.98772	0.98773	0.98773
0.46	0.98646	0.98649	0.98651	0.98652	0.98652
0.45	0.98513	0.98517	0.98519	0.98520	0.98520
0.44	0.98370	0.98374	0.98376	0.98377	0.98378
0.43	0.98215	0.98220	0.98222	0.98223	0.98224
0.42	0.98048	0.98054	0.98056	0.98057	0.98058
0.41	0.97869	0.97875	0.97878	0.97879	0.97880
0.40	0.97677	0.97684	0.97687	0.97689	0.97690
0.39	0.97472	0.97480	0.97484	0.97485	0.97486
0.38	0.97253	0.97263	0.97267	0.97269	0.97270
0.37	0.97022	0.97033	0.97037	0.97039	0.97040
0.36	0.96778	0.96790	0.96795	0.96797	0.96798
0.35	0.96521	0.96534	0.96540	0.96542	0.96543
0.34	0.96251	0.96267	0.96273	0.96275	0.96276
0.33	0.95970	0.95988	0.95994	0.95997	0.95997
0.32	0.95679	0.95699	0.95706	0.95708	0.95709
0.31	0.95379	0.95401	0.95408	0.95411	0.95411
0.30	0.95071	0.95095	0.95104	0.95106	0.95107
0.29	0.94758	0.94785	0.94794	0.94796	0.94797
0.28	0.94442	0.94472	0.94482	0.94484	0.94484
0.27	0.94126	0.94159	0.94169	0.94171	0.94172
0.26	0.93813	0.93849	0.93860	0.93861	0.93863
0.25	0.93507	0.93547	0.93558	0.93559	0.93561
0.24	0.93213	0.93256	0.93267	0.93268	0.93271
0.23	0.92935	0.92982	0.92993	0.92994	0.92997
0.22	0.92679	0.92730	0.92740	0.92743	0.92746
0.21	0.92452	0.92508	0.92517	0.92520	0.92525
0.20	0.92261	0.92322	0.92330	0.92335	0.92340
0.19	0.92116	0.92182	0.92188	0.92195	0.92201
0.18	0.92028	0.92098	0.92104	0.92112	0.92119
0.17	0.92009	0.92082	0.92088	0.92099	0.92107
0.16	0.92074	0.92150	0.92158	0.92171	0.92181
0.15	0.92245	0.92321	0.92333	0.92349	0.92360
0.14	0.92547	0.92623	0.92640	0.92659	0.92672
0.13	0.93014	0.93089	0.93113	0.93135	0.93152
0.12	0.93696	0.93769	0.93802	0.93827	0.93848
0.11	0.94663	0.94735	0.94778	0.94809	0.94833
0.10	0.96027	0.96098	0.96154	0.96194	0.96221
0.09	0.97970	0.98050	0.98122	0.98174	0.98202
0.08	1.00836	1.00947	1.01041	1.01109	1.01138
0.07	1.05392	1.05569	1.05702	1.05788	1.05821

Table 1 T = 8sec., H_o/L_o = 0.02

H/Ho \ d/Lo	Slope 1/20	1/50	1/80	1/200	1/600
0.50	0.99061	0.99060	0.99060	0.99057	0.99049
0.49	0.98964	0.98963	0.98963	0.98960	0.98950
0.48	0.98859	0.98858	0.98857	0.98854	0.98843
0.47	0.98744	0.98743	0.98742	0.98738	0.98726
0.46	0.98619	0.98618	0.98617	0.98613	0.98599
0.45	0.98484	0.98482	0.98481	0.98476	0.98461
0.44	0.98337	0.98336	0.98334	0.98329	0.98311
0.43	0.98178	0.98177	0.98176	0.98170	0.98150
0.42	0.98008	0.98006	0.98005	0.97998	0.97975
0.41	0.97825	0.97823	0.97821	0.97813	0.97788
0.40	0.97628	0.97626	0.97624	0.97615	0.97587
0.39	0.97418	0.97416	0.97414	0.97404	0.97372
0.38	0.97195	0.97192	0.97190	0.97179	0.97144
0.37	0.96958	0.96955	0.96952	0.96940	0.96901
0.36	0.96707	0.96704	0.96701	0.96687	0.96643
0.35	0.96443	0.96440	0.96436	0.96421	0.96372
0.34	0.96167	0.96163	0.96158	0.96142	0.96087
0.33	0.95878	0.95873	0.95869	0.95851	0.95790
0.32	0.95578	0.95573	0.95568	0.95548	0.95480
0.31	0.95269	0.95263	0.95257	0.95235	0.95160
0.30	0.94951	0.94945	0.94938	0.94913	0.94830
0.29	0.94627	0.94620	0.94613	0.94585	0.94492
0.28	0.94298	0.94291	0.94283	0.94252	0.94149
0.27	0.93969	0.93960	0.93952	0.93917	0.93803
0.26	0.93641	0.93631	0.93622	0.93584	0.93457
0.25	0.93318	0.93308	0.93297	0.93255	0.93114
0.24	0.93005	0.92993	0.92981	0.92934	0.92777
0.23	0.92705	0.92692	0.92678	0.92626	0.92452
0.22	0.92423	0.92409	0.92394	0.92336	0.92142
0.21	0.92167	0.92151	0.92134	0.92069	0.91852
0.20	0.91941	0.91923	0.91905	0.91832	0.91590
0.19	0.91754	0.91733	0.91713	0.91631	0.91359
0.18	0.91614	0.91591	0.91568	0.91475	0.91170
0.17	0.91530	0.91504	0.91478	0.91374	0.91028
0.16	0.91515	0.91485	0.91455	0.91337	0.90944
0.15	0.91582	0.91548	0.91514	0.91378	0.90928
0.14	0.91748	0.91708	0.91669	0.91512	0.90992
0.13	0.92033	0.91987	0.91940	0.91755	0.91143
0.12	0.92466	0.92410	0.92354	0.92132	0.91401
0.11	0.93081	0.93013	0.92946	0.92676	0.91789
0.10	0.93929	0.93846	0.93762	0.93431	0.92343
0.09	0.95080	0.94977	0.94873	0.94461	0.93112
0.08	0.96646	0.96515	0.96384	0.95865	0.94169
0.07	0.98808	0.98639	0.98471	0.97803	0.95633
0.06	1.01904	1.01680	1.01456	1.00570	0.97709
0.05	1.06676	1.06358	1.06043	1.04796	1.00825
0.04	1.15249	1.14737	1.14230	1.12245	1.06100

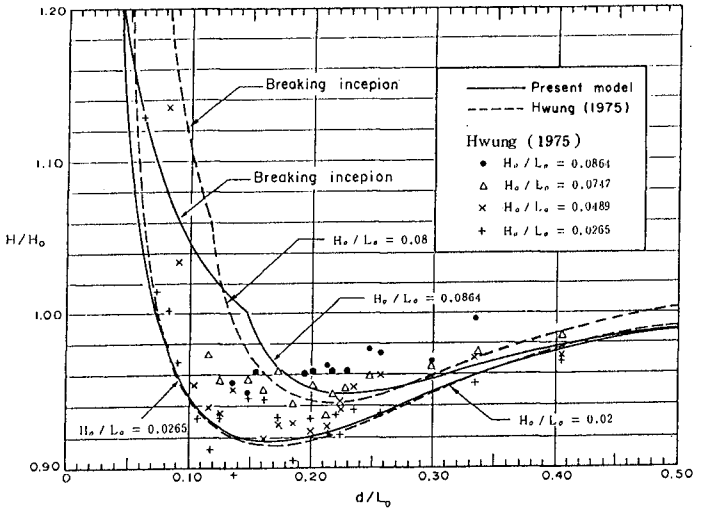
Present model
Hwung (1975)
Hwung (1975)
Breaking incepion
Breaking incepion
H/H₀
d/L₀
1.20
1.10
1.00
0.90
0
0.10
0.20
0.30
0.40
0.50

Fig. 3

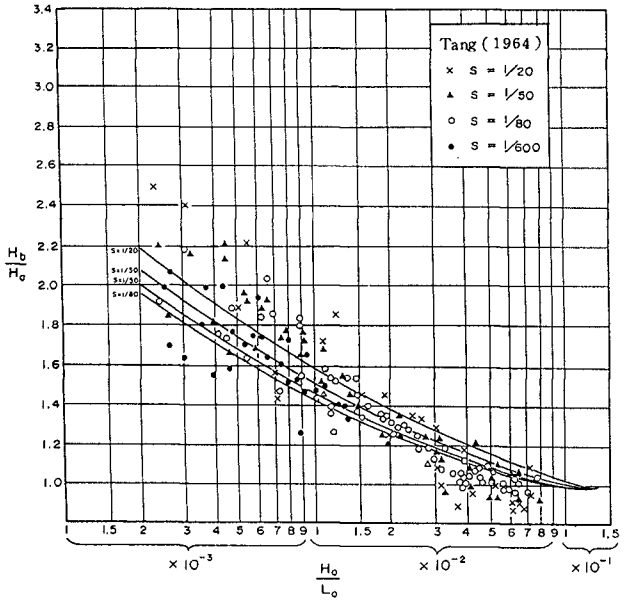
Tang (1964)
S = 1/20
S = 1/50
S = 1/80
S = 1/600
H/H₀
H₀/L₀
× 10⁻³
× 10⁻²
× 10⁻¹

Fig. 4

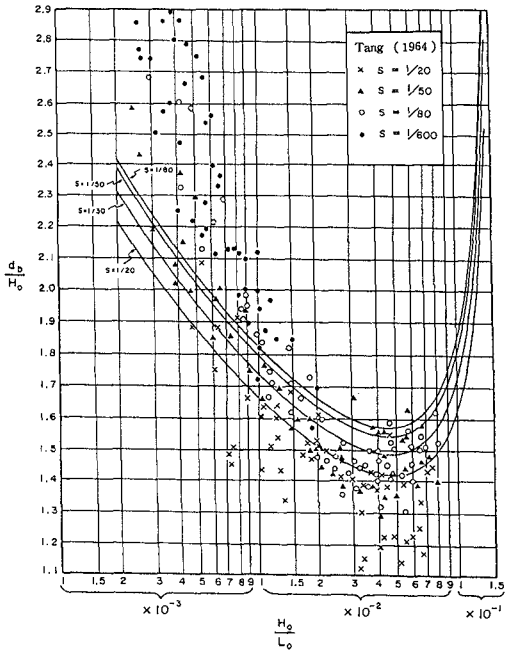
Tang (1964)
× S = 1/20
▲ S = 1/50
○ S = 1/80
● S = 1/600
S=1/80
S=1/50
S=1/30
S=1/20
$\frac{d_b}{H_o}$
× 10⁻³
× 10⁻²
× 10⁻¹
$\frac{H_o}{L_o}$

Fig. 5

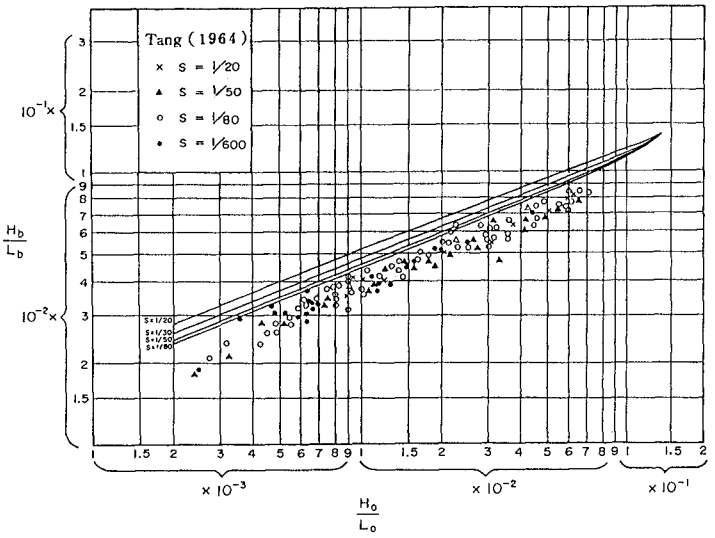
Tang (1964)
× S = 1/20
▲ S = 1/50
○ S = 1/80
● S = 1/600
10^{-1}×
10^{-2}×
$\frac{H_b}{L_b}$
S=1/20
S=1/30
S=1/50
S=1/80
× 10⁻³
× 10⁻²
× 10⁻¹
$\frac{H_o}{L_o}$

Fig. 6

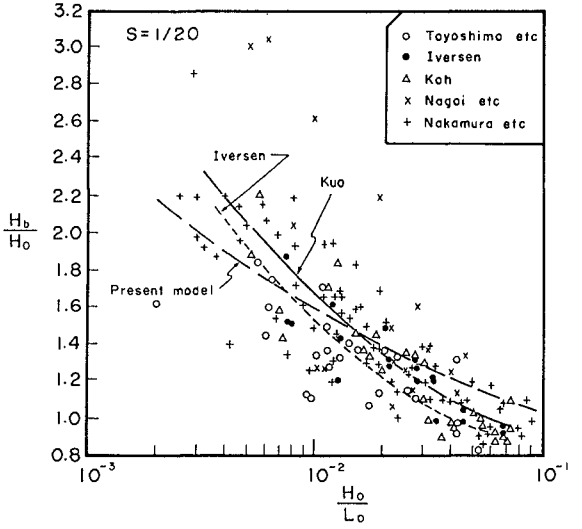
S=1/20
Toyoshimo etc
Iversen
Kah
Nagoi etc
Nakamura etc
Iversen
Kuo
Present model
Hb/Ho
Ho/Lo
3.2
3.0
2.8
2.6
2.4
2.2
2.0
1.8
1.6
1.4
1.2
1.0
0.8
10⁻³
10⁻²
10⁻¹

Fig. 7

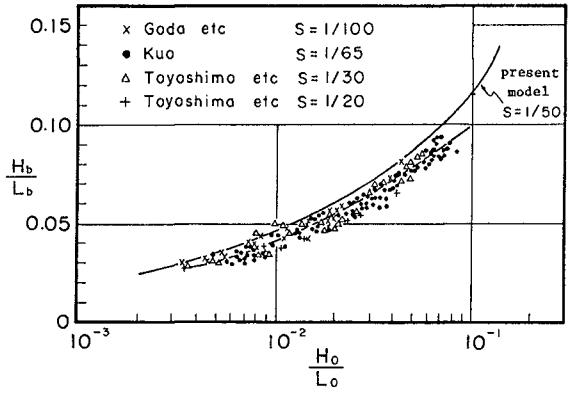
Goda etc S=1/100
Kuo S=1/65
Toyoshimo etc S=1/30
Toyoshima etc S=1/20
present model S=1/50
Hb/Lb
Ho/Lo
0.15
0.10
0.05
0
10⁻³
10⁻²
10⁻¹

Fig. 8

wave periods do not exceed 3.5%, that means the influence of wave period to breaking index is considerable small.

3. WAVE DECAY IN SURF ZONE

Fig.9 and Fig.10 show the comparison of the computational results of the relative wave height H/H_b in surf zone to the experimental data from Horikawa & Kuo (1966) and from Bowen (1968). It can be seen in the Fig.9 that there exists a residual wave height at the stillwater shoreline ($d/d_b=0$) from the computational curve. This is due to the feature of the present model, that the wave set-up can be determined simultaneously by calculating the wave height.

4. MEAN SEA LEVEL VARIATION

Fig.11 and Fig.12 show the comparison of the computational wave set-up/set-down to the experimental results from Bowen (1968) and from Sasaki & Saeki (1974). Seaward of the breaker, the experimental wave set-down can be good approached by present model, but shoreward of the breaker, there exists some difference between measured data and predicted value. However, the tendency of the predicted water level in surf zone coincides with the measured data.

CONCLUSIONS

1. The influences of bottom slope and wave period on the shoaling coefficient are small.

2. The breaking index H_b/H_o and H_b/L_b are positive related to bottom slope, but d_b/H_o is negative related. The comparison of the numerical results to the experimental data from other authors is well acceptable.

3. By proper choice of breaking coefficient α, the numerical results for wave decay in surf zone is good agreement with experimental data.

4. For the mean sea level variation, the tendency of the numerical results agrees with that from experimental data except for that near breaking point.

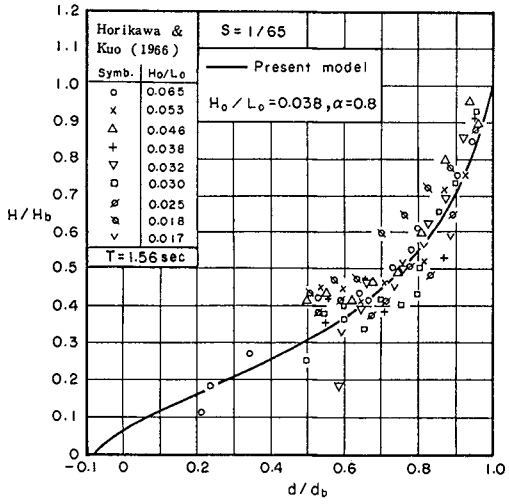
Horikawa & Kuo (1966)
S = 1/65
Present model
$H_o / L_o = 0.038, \alpha = 0.8$
Symb. | H_o/L_o
0.065
0.053
0.046
0.038
0.032
0.030
0.025
0.018
0.017
T = 1.56 sec
H/Hb
d/db

Fig. 9

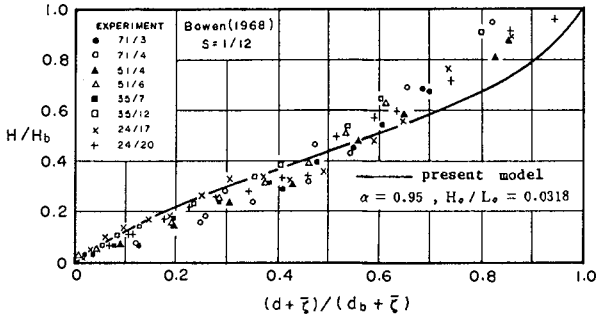
EXPERIMENT
71/3
71/4
51/4
51/6
35/7
35/12
24/17
24/20
Bowen(1968)
S = 1/12
present model
$\alpha = 0.95$, $H_o / L_o = 0.0318$
H/Hb
$(d+\bar{\zeta})/(d_b+\bar{\zeta})$

Fig. 10

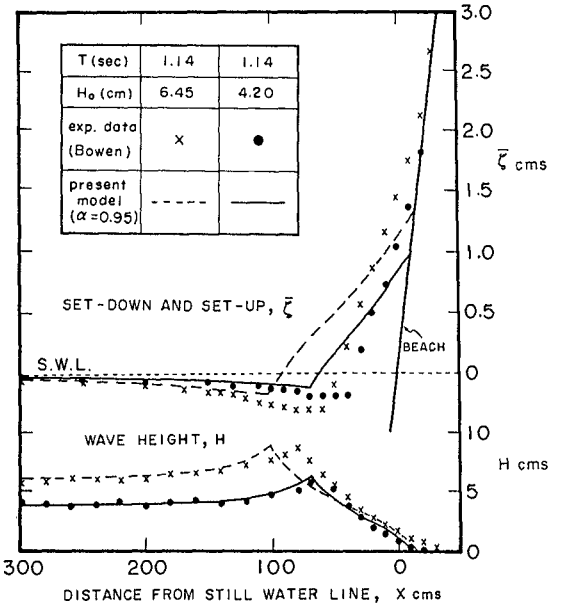
T(sec) 1.14 1.14
H_o (cm) 6.45 4.20
exp. data (Bowen) x ●
present model (α=0.95) - - - - - ——
SET-DOWN AND SET-UP, $\bar{\zeta}$
S.W.L.
WAVE HEIGHT, H
BEACH
$\bar{\zeta}$ cms
H cms
3.0
2.5
2.0
1.5
1.0
0.5
0
10
5
0
300
200
100
0
DISTANCE FROM STILL WATER LINE, X cms

Fig. 11

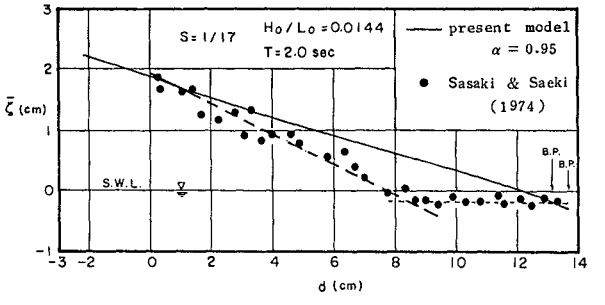
S=1/17
H_o/L_o=0.0144
T=2.0 sec
—— present model
α = 0.95
● Sasaki & Saeki (1974)
$\bar{\zeta}$ (cm)
S.W.L.
B.P.
B.P.
3
2
1
0
-1
-3 -2 0 2 4 6 8 10 12 14
d (cm)

Fig. 12

REFERENCES

1. Bowen, A.J., Inman, D.L., Simmons, V.P. (1968). Wave set-down and set-up. Journal of Geophysical Research, Vol. 73, No. 8, pp. 2569-2577.

2. Chen, Y.Y. et al. (1982). New equation of surfaoe elevation in wave motion. Proc. of 18th Conf. on Coastal Engineering, ASCE, pp. 505-522.

3. Goda, Y. (1970). A synthesis of breaker indices. Trans. Japan Soc. Civil Engineering, Vol. 2, Part 2, pp.227-230.

4. Horikawa, K. and Kuo, C.T. (1966). A study on wave transformation inside the surf zone. Proc. of 10th Conf. on Coastal Engineering, ASCE, pp.217-233.

5. Hwang, L.S., Divoky, D. (1970). Breaking wave set-up and decay on gentle slopes. Proc. of 12th Conf. on Coastal Engineering, ASCE, pp.377-389.

6. Hwung, H.H. (1975). Stokes wave in current. M.S. Thesis, Cheng-Kung University, R.O.C. 40 pp.

7. Le Méhauté, B. (1962). On non-saturated breakers and the wave run-up. Proc. of 8th Conf. on Coastal Engineering, ASCE, pp. 77-92.

8. Longuet-Higgins, M.S. (1975). Integral properties of periodic gravity waves of finite amplitude. Proceedings, Roy. Soc. Lond., A.342, pp. 157-174.

9. Riedel, H.P., Kamphuis, J.W. and Brebner, A. (1972). Measurement of bed stress under waves. Proc. of 13th Conf. on Coastal Engineering, ASCE, pp. 587-603.

10. Sasaki, M. and Saeki, H. (1974). Wave deformation in the surf zone. Proc. 21st Japanese Conf. Coastal Engineering, pp. 39-44. (in Japanese)

11. Tang, F.L.W. (1971). Planning and design of coastal engineering. Bulletin No.2, JCRR, pp. 55-64. (in Chinese)

CHAPTER 38

WAVE GROUPINESS AS A SOURCE OF NEARSHORE LONG WAVES

Jeffrey H. List

Virginia Institute of Marine Science
Gloucester Point, Virginia 23062

Abstract

Data from a low energy swell-dominated surf zone are examined for indications that observed low frequency motions are simply group-forced bounded long waves. Time series of wave amplitude are compared to filtered long wave records through cross-spectral and cross-correlation analysis. These methods are found to have limited usefulness until long waves are separated into seaward and shoreward components. Then a clear picture of a rapidly shoaling bounded long wave emerges, with a minimum of nearly one fourth of the long wave amplitude being explainable by this type of motion close to shore. Through the zone in which waves were breaking, and incident wave amplitude variability decreased by 50%, the contribution from the bounded long wave continued to increase at a rate much greater than a simple shoaling effect. Also present are clear signs that this amplified bounded long wave is reflected from a position close to the shoreline, and is thus released from wave groups as a free, offshore-progressive wave.

Introduction

Numerous recent observations have shown that waves with periods much longer than the more visually apparent wind waves often dominate the spectrum in the inner surf zone, especially during storms. However, much less clear are the origins of these infragravity motions, though a number of theories and few observations exist. Most relate in some wave to the groupiness of the incident waves. Gallagher (1971) developed a theoretical model in which edge waves could be resonantly generated by obliquely incident wave groups; Bowen and Guza (1978) substantiated this concept in a laboratory experiment. Field observations of Huntley et al. (1981) showed that low mode edge waves can dominate the low frequency motion in the longshore currents and recently Oltman-Shay and Guza (1986) have shown that in some cases as much as 50% of the shoreline runup variance is due to low mode edge waves, the size of which can be predicted from offshore measurements of the wind wave variance and wavenumber-frequency distribution.

Still, much if not most of the cross-shore current variance in the low frequency band cannot be explained in this way and appears to be either high mode edge waves or simply leaky mode standing waves. Symonds et al. (1982) provide a model by which oscillations of this

sort could be generated by long wave forcing at a time-varying breakpoint (produced by wave groupiness). However, as of yet there is no conclusive field evidence to support this model; most conspicuous is the absence of a separate standing wave zone landward of the breakpoint and a frequency dependent offshore progressive wave zone seaward of the breakpoint. Laboratory observations exist but seem conflicting. Kostense (1985) conducted a study in which changes in the wave group characteristics (wave difference frequencies, amplitude ratios, etc.) produced outgoing free waves with varying amplitudes qualitatively in accordance with the model of Symonds et al. However, in the experiment of Mansard and Barthel (1985) there seems to be a complete absence of an outgoing free wave generated at a time-varying breakpoint, although experimental conditions are largely the same except for the use of a Jonswap spectrum instead of bichromatic waves.

An alternate explanation of cross-shore surf beat motion is the direct forcing of long waves by radiation stress gradients in groupy waves. Longuet-Higgins and Stewart (1962,1964) showed that the mean water level, $\overline{\eta}$, is related to the component of radiation stress normal to wave crests, S_{xx}, by

$$\overline{\eta} = - \frac{Sxx}{\rho(gh-Cg^2)} + \text{const.} \qquad (1)$$

where h is the mean water depth, ρ is the density, and C_g is the group velocity. The negative sign indicates, for example, that a group of large waves with high S_{xx} would produce a depression of the mean (averaged over several incident wave periods) sea level. Thus the correlation between wave amplitude and long wave time series should be negative, while the corresponding cross-spectrum should show a 180^0 phase difference. Unfortunately, both the shallow water approximation of equation (1) and the spectral approach of Ottesen Hansen (1978) predict unreasonably large values of $\overline{\eta}$ in very shallow water-exactly where the size of this bounded long wave (BLW) must be known to access its contribution to surf beat motion. Nevertheless, Longuet-Higgins and Stewart found support for their theory in Tucker's (1950) observation of a time-lagged negative correlation between wave groups and long waves at an offshore station. They speculated that group bound long waves are released as free waves when incident waves break, and then are radiated offshore after reflection. A substantial shallow water BLW amplification (landward of the measurement location) could explain Tucker's observation that groups are correlated with long waves only after a time sufficient for round-trip travel to the shoreline, and not with an incoming BLW at zero lag. However, in addition to inadequate theory for the shallow water BLW size, no mechanism has been proposed by which this forced response could be released from wave groups as a free wave.

Following the work of several previous Conference authors (Huntley and Kim, 1985, Guza et al., 1985) this study examines field data in an attempt to provide some guidelines for future theoretical investigations.

Data Collection

An experiment conducted in September, 1985 at the U.S. Army Corps of Engineers Field Research Facility in Duck, North Carolina provided the data for this study. (Please see acknowledgements.) Figure 1d shows the nearshore profile and measurement locations. The morphology was fairly 2-dimensional, although some irregularities existed. All bathymetric observations were collected by the Corps using the CRAB profiling system (see Mason et al., 1985 for description). At each of the 9 measurement locations pressure and bi-axial horizontal currents were sampled synchronously for 40 minutes at 2 Hz. Pressure sensors were of the diaphragm type and flows were measured by Marsh Mcbirney electromagnetic current meters.

Waves consisted of highly grouped swell with a fairly narrow spectral peak near T=12 seconds. The angle of incidence was nearly shore-normal, although wave crests and wave groups were not very continuous alongshore.

Processing

Cross-shore currents are defined as positive onshore in order that long waves in the flows and sea-surface show the same relation with wave groups. Fourier transforms of pressure records were converted to the sea-surface by applying linear theory to each coefficient and then back-transforming to the time domain. Time series of long waves in both the sea-surface (η_L) and cross-shore currents (u_L) were found by bandpassing the data using two low-pass least squares filters (Bloomfield, 1976). An incident/long wave band cutoff was chosen at 0.06 Hz based on offshore spectra, in which it was clear that the incident band energy was confined to higher frequencies. (Changes in the η and u cross-spectrum at this frequency also substantiate this cutoff.) Additionally, energy at very low frequencies (below 0.007 Hz) was removed because certain records contained red "wall climber" type energy that was uncorrelated with other records and tended to lower the association with wave groups. Thus the low frequency time series used here contain energy from 0.007 to 0.06 Hz.

Time series of wave amplitude, A_t, were found by low-pass filtering the modulus of the high-passed, incident band sea-surface time series. In order that this series truly follow the wave amplitude, each point was then divided by $\pi/2$ to compensate for the asymmetry of a sine wave modulus. As the size of the BLW is predicted by equation (1) to be proportional to the square of the incident wave height, an additional amplitude function was calculated as the lowpass-filtered square of the incident band waves.

A groupiness factor was found from the amplitude time series as

$$GF = \frac{\sqrt{2}\sigma_{A_t}}{\bar{A}_t} \qquad (2)$$

where σA_t and A_t are the standard deviation and mean of A_t respectively. This groupiness factor has the advantage of being strictly confined between 0 (pure sine wave) and 1.0 (two beating sine waves), as opposed to factors using an amplitude function derived from the square of the incident wave (for example, see Sand, 1982).

All spectra and Cross-spectra presented here were smoothed to give 34 degrees of freedom, resulting in a 95% CI on zero coherence of approximately 0.41. Correlations between A_t and long waves were found at time lags separated by the sampling interval of 0.5 seconds to give a smooth cross-correlation function. As adjacent point in a wave time series are by no means independent, the 95% CI on zero coherence was found using a reduced number of points, N^*, given by Garret and Toulany (1981) as

$$N^{*-1} = N^{-1} + 2N^{-2} \sum_{j=1}^{N'} (N-j)\, R_{xy}(j) \qquad (3)$$

where N is the original number of points, $R_{xy}(j)$ is the lagged auto-correlation of the product of the two series to be correlated, and N' is the number of lags until R_{xy} experiences a zero-crossing. Cross-correlations presented here generally have a 95% CI on r=0 below 0.15.

Some pressure channels showed a high energy, narrow band peak in the spectra that was judged to be some sort of electronic contamination. Gaps in the results presented below represent data that was not analyzed because of this problem.

Cross-shore Statistics

Figure 1 shows the cross-shore variations in significant wave height, H_s, standard deviation of the amplitude time series, σA_t, and groupiness factor, GF. While H_s does not decrease until station 2, it is evident from σA_t and GF that initial breaking of the largest waves must begin inshore of station 6. The waves groupiness in both the current and sea-surface incident band decreases from around 0.65 offshore, a fairly high value for natural waves, to 0.45 by station 1. More importantly, the wave height variability as measured by the standard deviation in A_t, decreases by a factor of 2 across the instrument array. If the size of the bounded long wave is proportional to variations in the wave height squared, as implied by equation (1), then the BLW size might be expected to be proportional to the square of σA_t, implying a four-fold decrease from station 6 to station 1. As it turns out, this does not seem to be the case.

Cross-spectra

The cross-spectra between A_t and η_L were found as a first step in assessing the degree to which long waves in the nearshore are directly forced by wave groups. Figure 2 shows the most coherent cross-spectrum of any calculated between co-located A_t and η_L. As seen in previous

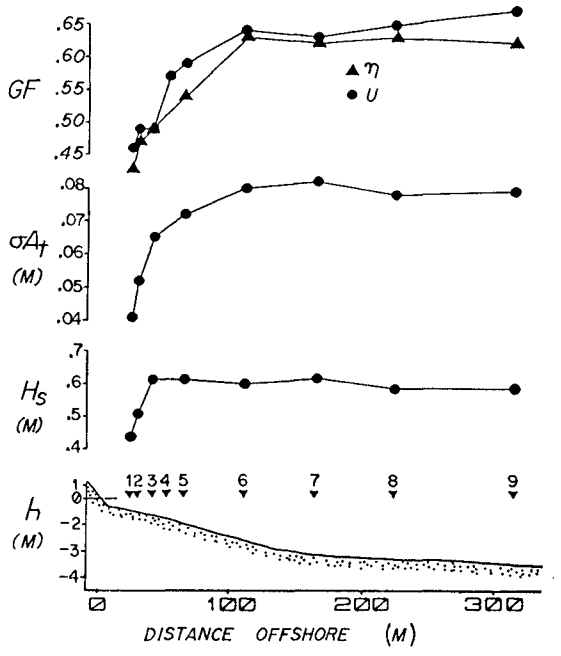

Figure 1 From top: Groupiness factor, standard deviation of amplitude time series, significant wave height (from incident band variance), nearshore profile with instrument stations.

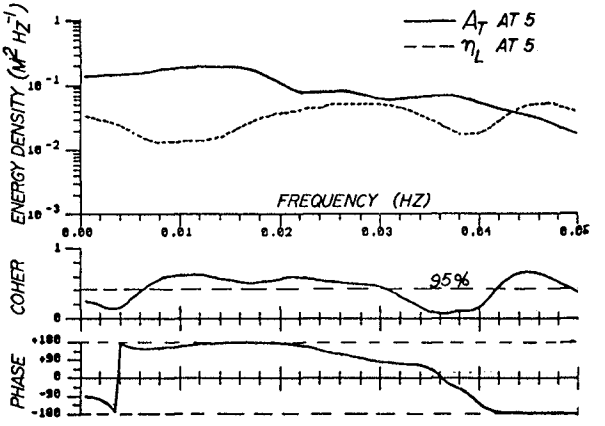

Figure 2 Cross-spectrum between amplitude time series and sea-surface long waves co-located at station 5.

studies (Huntley and Kim, 1985 and others) there is no significant frequency selection in the wave groupiness, precluding the possibility of identifying a groupiness-forced peak in the long waves. While there are some signs of the forced response (phase near 180^0 in bands of significant coherence) the relation is certainly less consistent and strong than presented by Huntley and Kim (1985). Since in addition to the incoming BLW, the nearshore long wave field may well consist of reflected long waves, waves generated at a time-varying breakpoint, and edge waves, it is not surprising Fig. 2 shows an unclear BLW signature. The Huntley and Kim measurements were taken very close to shore on a steep beach where the incoming and reflected waves would be virtually coexisting and other modes of long wave generation (other than the subharmonic) would likely be suppressed. The data presented here seems more representative of an open coast situation with waves breaking offshore and dissipating over a shallow surf zone.

Cross-correlations

In order to differentiate between group-related long wave components traveling shoreward and those either reflected or generated in the surf zone and traveling seaward, cross-correlations were calculated similar to those first presented by Tucker (1950). Figure 3a shows the cross-correlations between co-located A_t and longwaves (in both current and sea-surface) at 8 stations. The bounded long wave response is seen as a negative correlation near zero lag, which is marginally significant at station 9, strengthens to a maximum at station 3 and then decreases and disappears by station 1. That the group structure is forcing longwaves and not visa-versa is supported by a significant degree of correlation between the group structure offshore and inshore up to station 5--in other words the wave groupiness to a large extent is an original feature of the offshore waves through this zone, and is not being created by an interaction of short waves with long wave depth or current modulations. The disappearance of the zero-lag negative correlation landward of station 3 could be due to a decrease in the size of the BLW, but could also be due to this short wave/long wave effect (as has been observed by Abdelrahman and Thornton, 1985) causing a modification in the group structure and masking the ability of the cross-correlation to identify a forced response. To test this idea, the cross-correlations between the amplitude series at station 8 and long waves at 7 stations closer to shore were calculated and are shown in Figure 3b. The forced wave response, now at progressively greater time lags, appears to strengthen all the way to station 1. Solid dots in Figure 3b show the measured group travel time (from A_t cross-correlations), indicating that after waves begin breaking, the forced response tends to lag the wave groups by up to 10 seconds. The question of whether this group-correlated long wave component is still a bounded long wave or now a free wave will be addressed below.

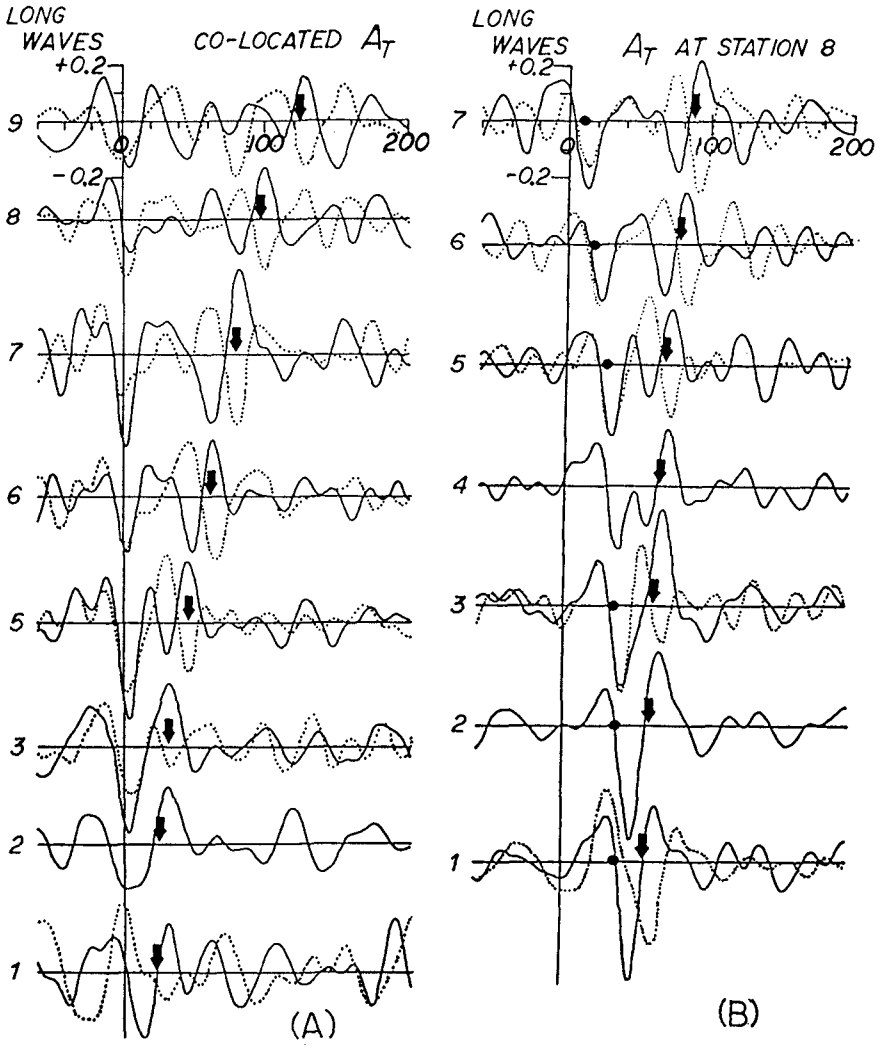

Figure 3 Cross-correlations between long wave (····· sea-surface, —— cross-shore current) and amplitude time series. Horizontal scale is the time lag in seconds, vertical scale is the correlation coefficient. Positive lags indicate a leading group structure. 95% CI on zero correlation is a maximum of 0.15. (A): cross-correlations between co-located amplitude and long waves, (B): cross-correlations between amplitude at station 8 and long waves at 7 stations closer to shore.

Another interesting feature of both Figure 3a and 3b is a series of significant peaks occurring at lags nearly matching the long wave travel time given by

$$T = \int \frac{dx}{\sqrt{gh}} \tag{4}$$

from the point of A_t measurement, to the shore, and back to the point of long wave measurement (marked by solid arrows). The signs of the η_L and u_L correlations are opposite, confirming that this signal represents outgoing wave energy. Since the correlation is negative with η_L and positive with u_L, this signal satisfies the notion that the incoming BLW is released and simply reflected as a free wave, as suggested by Longuet-Higgins and Stewart (1962,1964).

Another sometimes significant signal, appearing mostly beyond the surf zone and having the opposite sign, occurs approximately 20 seconds earlier, corresponding to a point of origin near the outer limit of the breaker zone. (A similar feature is seen in Guza et al., 1985) As it is difficult to predict exactly how a wave generated by a breakpoint forcing model might affect the cross-correlations as calculated here (see Huntley and Kim, 1984), it can only be speculated that correlations at this time lag relate to this model. In a simplistic sense, however, it would seem that since larger waves are predicted to be associated with a higher setup, long waves generated by the model of Symonds et al. (1982) should have a sign of correlation with the wave groupiness structure opposite to that of the BLW (or a recently released long wave of BLW origin). The fact that most of the significant correlations in Figure 3 fit the idea of an incident, released and reflected BLW may indicate that the breakpoint forced waves were of lesser importance during this experiment.

Since the square of the correlation coefficient gives the percent of the variability in one channel that can be predicted by another, the correlations associated with the incoming BLW in Figure 3b could ideally be used to determine the fraction of long wave height attributable to group forcing at each station, resulting in a picture of the cross-shore changes in BLW size. Unfortunately, as shown by Sallenger and Holman (1984), the infragravity variance in η or u can be dependent on the sampling location's position relative to a standing wave structure, as seems to be the case in Figure 4a. Similarly, the correlations at lags for incoming and outgoing waves may merge close to shore, distorting the values in an unpredictable manner. A method of separating the landward and seaward long wave components (Guza et al., 1985) was used to circumvent these problems.

Onshore/Offshore Long Wave Components

After Guza et al. (1985), landward and seaward progressive

long wave components in units of sea surface elevation were found as

$$\eta_L ON = \frac{\eta_L + \sqrt{h/g}\, u_L}{2}$$
$$\eta_L OFF = \frac{\eta_L - \sqrt{h/g}\, u_L}{2} \qquad (5)$$

where η_L and u_L represent each point in the η and u long wave time series and h is the average water depth. The components in units of velocity could be found similarly, but provide no additional information.

Equation (5) cannot be used with many data sets because of a number of restrictions. As noted by Guza et al., long waves must be shore normally oriented. An obliquely angled incident long wave would contaminate the offshore component and an angled outgoing long wave would contaminate the onshore component. Edge wave motions would put spurious energy into both η_L ON and η_L OFF, though probably to equal degrees. Also, long waves are assumed to follow the shallow water, linear dispersion relation, excluding bounded long waves associated with groups not in shallow water or long waves affected by steep bottom slopes.

Test showed that this data set must have largely met these conditions. For example, cross-spectra between two ON components at different stations (Figure 5a) show high coherence and the phase relations of an incoming progressive wave while cross-spectra between two OFF components (Figure 5b) show the reverse. Also, cross-correlations between separate components and A_t show a clear isolation of the incoming and outgoing long wave signals related to wave groupiness. Finally, that the ON/OFF separation has resolved problems with determining long wave heights in standing waves is evident in Figure 4b in which the H_s of ON and OFF components does not reflect the structure in the H_s of the total η_L (Figure 4a).

Cross-correlations: revisited

Correlations are now found between A_t and separate ON and OFF long wave components. The question of interest here is: how much of the long wave height at each station can be explained by a BLW type association? Thus the search is for the A_t series that can predict the most long wave variation at each station. For the onshore component stations 5,6,7,8, and 9 show the highest BLW correlations with co-located A_t; for stations 1 and 3 the highest correlations are with A_t at stations 5. For the offshore component the best correlations were always with the group structure near the maximum limit of wave breaking at station 5. Table 1 summarizes these relationships. The results differ from those presented by Guza et al. (1985) in that the maximum correlations remain negative to the most landward stations in both the ON and OFF components.

Correlations in Table 1a are squared and multiplied by the H_s of the corresponding onshore component (Figure 4b) to give estimates of

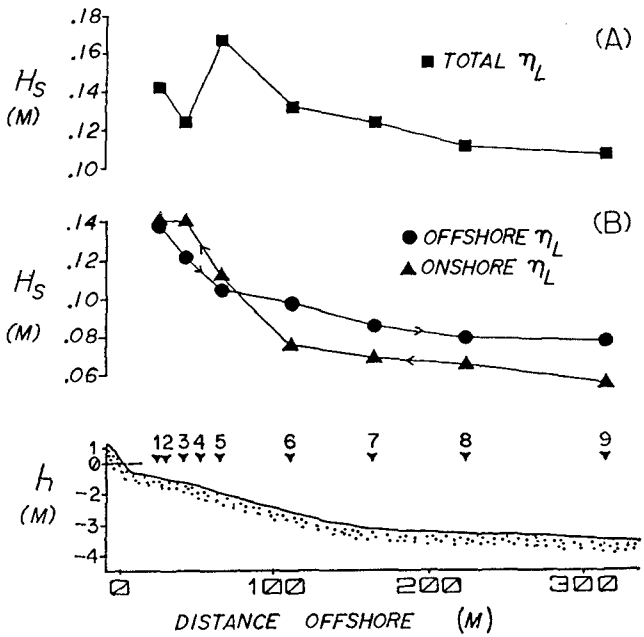

Figure 4 (A) Significant wave height from variance in sea-surface long wave band, (B) significant wave height from variance of separated onshore and offshore progressive long wave components.

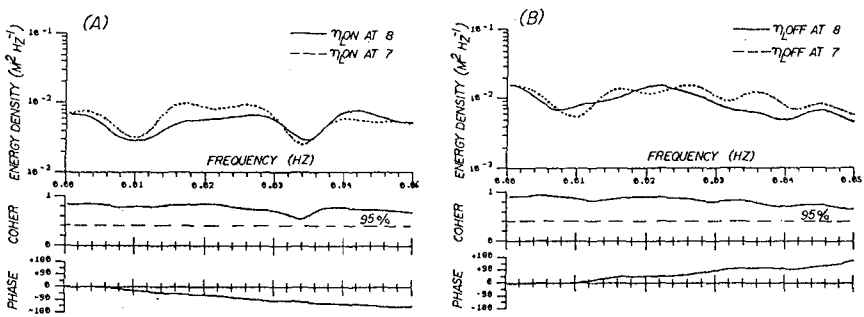

Figure 5 (A) Cross-spectrum between onshore progressive components at stations 8 and 7, (B) Cross-spectrum between offshore progressive components at stations 8 and 7.

BLW height at each station, shown in Figure 6. Values for BLW H_s found through use of the squared amplitude function are also plotted, and indicate that this method results in only a slight improvement in the analysis.

The values of BLW H_s in Figure 6 are extremely low, and probably not far from the limit of the instrument's measuring ability. However, every point is based on a correlation that is significantly different than zero at the 95% confidence level, and in most cases far better. In addition, cross-spectra calculated between the A_t and η_LON pairs in Table 1a show coherent relationships above the 95% CI. For example, Figure 7 shows that approximately 30% of the variance in η_LON at station 5 can be explained by the wave group structure. Thus it seems that the correlation values used in creating Figure 6 may underestimate the actual size of the BLW, since significant correlations seem to be predicting nearly insignificant wave heights.

Assuming that at least the relative changes in Figure 6 are real, it appears that the BLW undergoes rapid shoaling into shallow water, even through a zone in which waves are breaking. Specifically, between stations 6 and 1 the amplitude variability, σA_t, decreases by a factor of 2 (Figure 1), while at the same time the size of the estimated BLW increases four-fold. (The corresponding increase in A_t versus η_LON correlation is significant to the α=0.003 level.) Some investigators have implied that as incident waves break, the BLW also decays or is released to shoal toward shore as a free wave. However, the group-related long waves as observed here increase much more rapidly than predicted by a $(h_1/h_2)^{1/4}$ long wave shoaling, the rate being closer to $(h_1/h_2)^{5/2}$, the shallow water BLW shoaling predicted by Ottesen Hansen et al. (1981). Toward shore this group-correlated component is thus becoming a progressively larger piece of a progressively larger pie, which would not be the case for a free long wave progressing shoreward. This apparent increase in group forced long waves after incident waves have begun to break was also found by Mansard and Barthel (1985), who observed laboratory long waves increasing in size even through a constant depth zone.

The correlations with offshore components in Table 1b show that the outgoing long waves also contain a significant component related to wave groups. Close to shore these correlations are somewhat less than those for the incoming wave. This could indicate that to some degree the BLW is decreased in size before release and reflection, but could also simply be due to the greater spatial separation between the group structure and outgoing long waves. Not shown in Table 1b are positive correlations that were sometimes significant, and occurred at smaller lags than expected for a shoreline long wave reflection. While these correlations appear to be similar to those observed by Guza et al. (1985), they were never greater than the negative correlations, and were not present in the correlations with the onshore component.

A rapid shallow water increase in the forced response may explain the differences between the size of the incoming and outgoing components (Figure 4b) in the following manner. The onshore component increases rapidly past station 6 as the BLW shoals. At some point close to shore this forced wave is released and reflected as a free

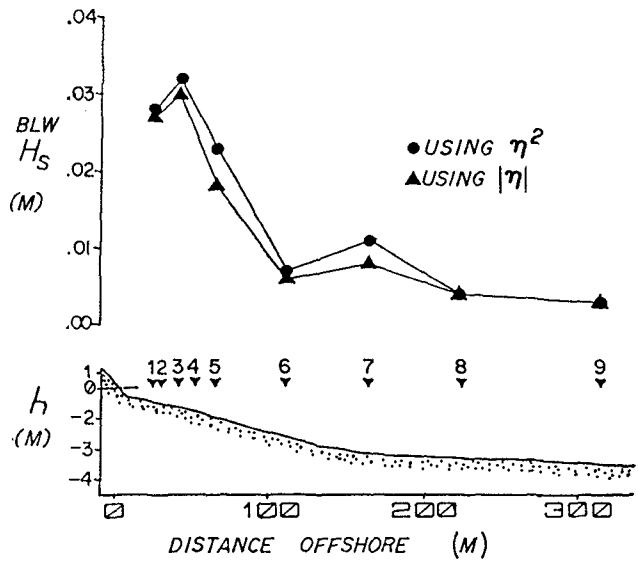

Figure 6 Significant wave height of bounded long wave inferred from correlations between amplitude time series and long waves (Table 1a). ●amplitude time series from square of incident waves, ▲ amplitude time series from modulus of incident waves.

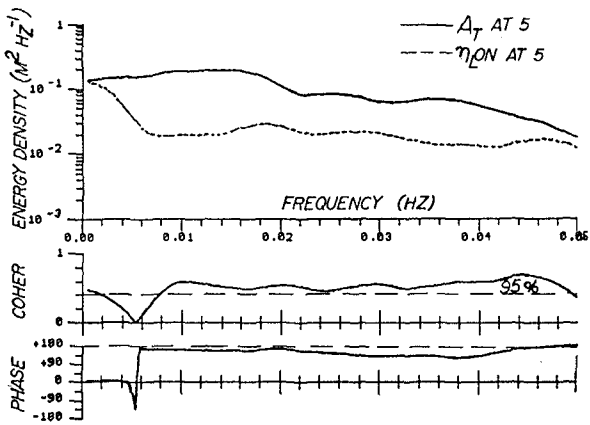

Figure 7 Cross-spectrum between amplitude time series and the onshore component of sea-surface long waves co-located at station 5. (Compare to Figure 2.)

wave which decreases in amplitude offshore at a smaller rate closer to $(h_1/h_2)^{1/4}$. Thus in deep water the offshore component is larger than the onshore component, which would explain why Tucker (1950) observed a forced response only after a large time lag. However, at the most landward stations the onshore component here is larger, implying that at least some of the incoming long wave energy decays in very shallow water with wave groups. Again the results here are different than those given by Guza et al. (1985), in which the onshore component was at all positions larger than the offshore component.

(A)

station $\eta_{L_{ON}}$	station A_t	Max r
9	9	-0.23
8	8	-0.25
7	7	-0.36
6	6	-0.29
5	5	-0.40
3	5	-0.46
1	5	-0.44

(B)

station $\eta_{L_{OFF}}$	station A_t	Max r
9	5	-0.25
8	5	-0.24
7	5	-0.31
6	5	-0.31
5	5	-0.29
3	5	-0.39
1	5	-0.37

Table 1 Maximum correlations between long wave components and amplitude time series. Integers are stations locations. Lags are at group or long wave travel time as in Fig. 3.

Discussion

Other studies of the BLW in the nearshore have exhibited a varying degree of evidence for the forced wave response. Guza et al. (1985) show that the incoming and outgoing long waves are clearly correlated to wave groups, but interestingly the negative sign of the BLW is overshadowed by positive correlations within the surf zone. Kim (1985) shows evidence of an incoming forced response, but little sign that outgoing long waves are correlated to wave groups. Huntley and Kim (1985) show nearshore long waves almost entirely forced by wave groups in a steep, reflective beach in which a separate outgoing wave cannot be distinguished. The results presented here are therefore not necessarily typical, but may represent an end member in the degree to which the BLW is clearly present in the incoming waves, and seems to be the source for at least part of the outgoing waves.

Evidence for long wave generation at a time-varying breakpoint may also exist to varying degrees throughout these studies of group-forced waves. However, it is still uncertain exactly what kind of relation these waves should show in cross-correlations or cross-spectra with wave groups. The laboratory study of Kostense (1985) showed frequency-dependent outgoing waves (never observed in the field), but this could also be an indication that the degree to which the BLW is released and reflected (instead of decayed with wave groups) is also dependent on the wave characteristics.

Certainly more theoretical work is needed to explain why the forced response seems so variable, and under what conditions the BLW becomes energetic in the nearshore, or could be released and reflected as a free wave. The observation of a BLW increase through a zone of wave breaking may find an explanation in a resonant interaction with residual wave groupiness. Long waves may be released from wave groups if the BLW satisfies the free long wave dispersion relation before incident waves break. The Model of Symonds et al. (1982) must also be

re-examined, with emphasis on possible interactions with group-bound waves, and on new methods of evaluating field data for this effect.

Conclusions

The following applies only to this study:

1. The bounded long wave, as measured by correlation coefficients with a squared wave group function, accounts for one-fourth of the incoming long wave height. This is probably a conservative estimate.

2. The bounded long wave increases in size even through a zone of wave breaking.

3. The outgoing long waves have a component correlated to wave groups with a sign and lag suggesting release and reflection of the BLW.

Acknowledgements

Many thanks to everyone at the U.S. Army Corps of Engineers Field Research Facility in Duck, North Carolina for providing an outstanding environment for field research, and for their generous data exchange policy without which this study would have been impossible. Thanks also to J. Hubertz of the U.S. Army Corps of Engineers, R.A. Holman of Oregon State University, and R.W. Sternberg of the University of Washington for allowing the use of data collected by their instruments in their field work at Duck.

References

Abdelrahman, S.M., and Thornton, E.B., 1985, Short wave modulation due to long waves in the nearshore zone, Abstracts AGU Fall Meeting, Eos Transactions, v.66, n.46, p.920.

Bloomfield, P., 1976, Fourier analysis of time series: an introduction, New York: Wiley.

Bowen, A. J., and R. T. Guza, 1978, Edge waves and surf beat, Journ. Geophys. Res., 83, 1913-1920.

Gallegher, B., 1971, Generation of surf beat by non-linear wave interactions, Journ. Fluid Mech., 49, 1-20.

Garrett, C.J.R., and Toulany, B., 1981, Variability of the flow through the Strait of Belle Isle, Journ. Mar. Res., 39, 163-189.

Guza, R. T., Thornton, E. B., and Holman, R. A., 1985, Swash on steep and shallow beaches, Proc. 19th Internat. Conf. Coastal Eng., 708-723.

Huntley, D. A., R. T. Guza, and E. B. Thornton, 1981, Field observations of surf beat. 1. Progressive edge waves, Journ. Geophys. Res., 86, 6451-6466.

Huntley, D. A., and C. S. Kim, 1984, Is surf beat forced of free?, Proc. 19th Internat. Conf. Coastal Eng., 871-885.

Kim, C.S., 1985, Field observations of wave groups and long waves on sloping beaches, Master's Thesis, Dalhousie U., Nova Scotia.

Kostense, J. K., 1985, Measurements of surf beat and set-down beneath wave groups, Proc. 19th Internat. Conf. Coastal Eng., 724-740.

Longuet-Higgins, M. S., and Stewart, R. W., 1962, Radiation stress and mass transport in gravity waves, with application to surf-beats, Journ. Fluid Mech., 13, 481-504.

Longuet-Higgins, M. S., and R. W. Stewart, 1964, Radiation stresses in water waves: a physical discussion, with applications, Deep Sea Research, 11, 529-562.

Mansard, E. P. D., and Barthel, V., 1985, Shoaling properties of bounded long waves, Proc. 19th Internat. Conf. Coastal Eng., 798-814.

Mason, C., Sallenger, A.H., Holman, R.A., and Birkmeier, W.A., 1985, Duck82--a coastal storm processes experiment, Proc. 19th Internat. Conf. Coastal Eng., 1913-1927.

Oltman-Shay, J., and Guza, R.T., 1986, Infragravity edge wave generation, Abstracts AGU Fall Meeting, Eos Transactions, v. 67, n. 44, p. 1026.

Ottesen Hansen, N. -E., 1978, Long period waves in natural wave trains, Prog. Rep. 46, Inst. Hydrodyn. and Hydraulic Engg., Tech. Univ. Denmark, 13-24.

Ottesen Hansen, N. -E., Sand, S. E., Lundgren, H., Sorensen, T., and Gravesen, H., 1981, Correct reproduction of group-induced long waves, Proc. 17th Internat. Conf. Coastal Eng., 784-800.

Sallenger, A.H., and Holman, R.A., 1985, On predicting infragravity energy in the surf zone, Proc. 19th Internat. Conf. Coastal Eng., 1940-1951.

Sand, S. E., 1982, Wave grouping described by bounded long waves, Ocean Eng., 9, 567-580.

Symonds, G., D. A. Huntley, and A. J. Bowen, 1982, Two-dimensional surf beat: long wave generation by time-varying breakpoint, Journ. Geophys. Res., 87, 492-498.

Tucker, M. J., 1950, Surf beats: sea waves of 1 to 5 minutes period, Proc. Roy. Soc. Ser. A, 202, 565-573.

CHAPTER 39

Estimating Long-Term Wave Statistics From Long-Term Wind Statistics[†]

Paul C. Liu[‡]

The Wave Climate Synthesis method, which derives long-term wave statistics from long-term wind statistics directly, is tested with four years of wind and wave measurements recorded from eight NOMAD buoys in the Great Lakes during 1981-1984. The results show that it is an excellent method for estimating long-term wave statistics and design wave height. While the method is by no means intended to replace wave hindcasting procedures, it is shown to be a useful additional tool for the coastal engineer.

Introduction

One of the first considerations when solving a coastal engineering problem is the determination of a design wave height. The usual procedure of determining a design wave height where actual wave measurements are not available consists of gathering pertinent long-term wind data, making wave hindcasts from the wind data, and subsequently performing statistical analysis on the hindcast wave data to estimate design waves. Although this conventional approach does provide useful information, it can be time consuming. In this paper we examine an alternative approach called Wave Climate Synthesis (e.g., Andrews et al., 1983) which derives long-term wave statistics directly from long-term wind statistics, bypassing wave hindcasting. This approach simplifies the process of estimating a design wave height. The validity and usefulness of this approach are demonstrated with four years of wind and wave measurements recorded from eight NOMAD buoys in the Great Lakes during 1981-1984.

Approach

The Wave Climate Synthesis method, pioneered by Hogben and collaborators (Andrews, et al., 1983, Hogben, 1987, and Hogben and Dacunha, 1985) at British Maritime Technology (formerly National Maritime Institute), is based on the concept of relating long-term marginal probabilities of significant wave height $P(H_s)$ and wind

---

[†]GLERL Contribution No. 539.

[‡]Oceanographer, NOAA/Great Lakes Environmental Research Laboratory, 2300 Washtenaw Avenue, Ann Arbor, MI 48104.

speed $P(W_r)$ by means of a parametric model of the conditional probability $P(H_s|W_r)$ as

$$P(H_s) = \Sigma P(H_s|W_r)P(W_r). \quad (1)$$

$P(H_s|W_r)$ is assumed to be represented by the Gamma distribution,

$$P(H_s|W_r) = [q^{p+1}/\Gamma(p+1)]H_s{}^p \exp(-qH_s), \quad (2)$$

where $\Gamma(.)$ is the Gamma function. The parameters p and q are given in terms of the averages and standard deviations of the wave height in each wind speed interval, H_r and v_r, respectively as

$$p = H_r{}^2/v_r{}^2 - 1, \quad (3)$$

and

$$q = H_r/v_r{}^2. \quad (4)$$

H_r and v_r, measured in m, are empirical functions of wind speed W_r, in m/s, given by

$$H_r = [(aW_r{}^n)^2 + h_2{}^2]^{1/2}, \quad (5)$$

and

$$v_r = h_2(b + cW_r + dW_r{}^2). \quad (6)$$

In the above formulations the parameters a, b, c, d, h_2, and n are all empirically obtainable from known distributions $P(W_r)$ and $P(H_s)$. From extensive oceanic studies Andrews et al. (1983), using the linear form of (6), developed recommended values of coefficients for open ocean and limited fetch conditions as listed in Table 1. One can make use of the recommended values when actual data are not available

Location	h_2	a	n	b	c
Open Ocean	2.000	0.033	1.480	0.500	0.0125
Limited Fetch	0.500	0.023	1.380	0.750	0.0188

Table 1 Recommended values of coefficients in Equations (5) and (6) according to Andrews et al. (1983)

or derive appropriate values by fitting Equations (5) and (6) to available data. In either case, once these parameters are determined

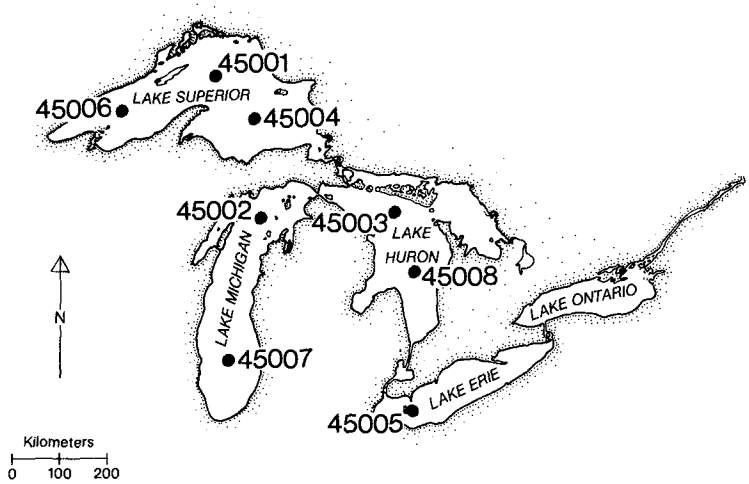

Figure 1 Location map of the eight NOMAD buoys in the Great Lakes

Gage	Lake	Lat.	Long.	Total Data in 1981-1984
45001	Superior C.	48.0 N	87.6 W	16079
45002	Michigan N.	45.3 N	86.3 W	16956
45003	Huron N.	45.3 N	82.8 W	17220
45004	Superior E.	47.2 N	86.5 W	11606
45005	Erie W.	41.7 N	82.5 W	19737
45006	Superior W.	47.3 N	90.0 W	15162
45007	Michigan S.	42.7 N	87.1 W	18448
45008	Huron S.	44.3 N	82.4 W	17286

Table 2 List of location and total data of the eight NOMAD buoys

and a long-term wind speed distribution $P(W_r)$ is given, a corresponding long-term wave height distribution $P(H_s)$ can be readily determined.

Data

To test the applicability of formulations (1) - (6) we use the long-term wind and wave data recorded from NOMAD buoys in the Great Lakes. There have been eight NOMAD buoys moored in the Great Lakes (Figure 1) since 1981 in water depths ranging from 15 m to 250 m. These buoys are boat-shaped, 6 m in length, with an electronic payload for measuring wind speed, wind direction, barometric pressure, air temperature, sea surface temperature, and surface wave spectral data. Most of the meteorological sensors are located 5 m above the water surface. Wind speed and direction, as well as air and surface water temperatures, are measured at 1-s intervals, averaged over 8.5 minutes and reported hourly. The waves are measured with an accelerometer using an on-board Wave Data Analyzer system (Steele and Johnson, 1977) that transmits acceleration spectral data via the UHF GOES satellite to a shore station. Wave frequency spectra with 48 degrees of freedom are calculated from 20 min of measurements each hour. Significant wave heights, H_s, are obtained as four times the square root of the total energy integrated over the calculated wave frequency spectrum.

The data recorded from all eight buoys during 1981 through 1984 were used in this study. The total number of data points available from each buoy ranges from 11,606 for the buoy at Lake Superior E. to 19,737 for the buoy at Lake Erie W., as shown in Table 2.

Applications

An example of applying the Wave Climate Synthesis method as formulated in Equations (1) - (6) to the Great Lakes wind and wave data is shown in Figure 2 for buoy 45004 at Lake Superior E. In Figure 2 there are four sections. The top section is the histogram for wind speed distribution, which is the required input for this method. The second section, obtained from recorded data, presents the joint distribution of wind speed and significant wave height, H_s, with the corresponding histogram for the distribution of H_s shown to the right of the joint distribution. The third section shows, in each wind speed interval, the averages and standard deviations of the wave height, defined as H_r and v_r in Equations (3) -(6), as the circles and dashed lines respectively. Equations (5) and (6) can be fitted, by the least-squares method, to yield the appropriate coefficients; and the corresponding Gamma distributions $P[H_s|H_r(W_r),v_r(W_r)]$ are also plotted. Finally, from the information derived from the above three sections, a joint distribution of wave height and wind speed and a wave height distribution, similar to the second section, can be estimated as shown in the bottom section. In general, only the histogram in the top section and a set of empirical parameters are needed to produce the estimation shown in the bottom section.

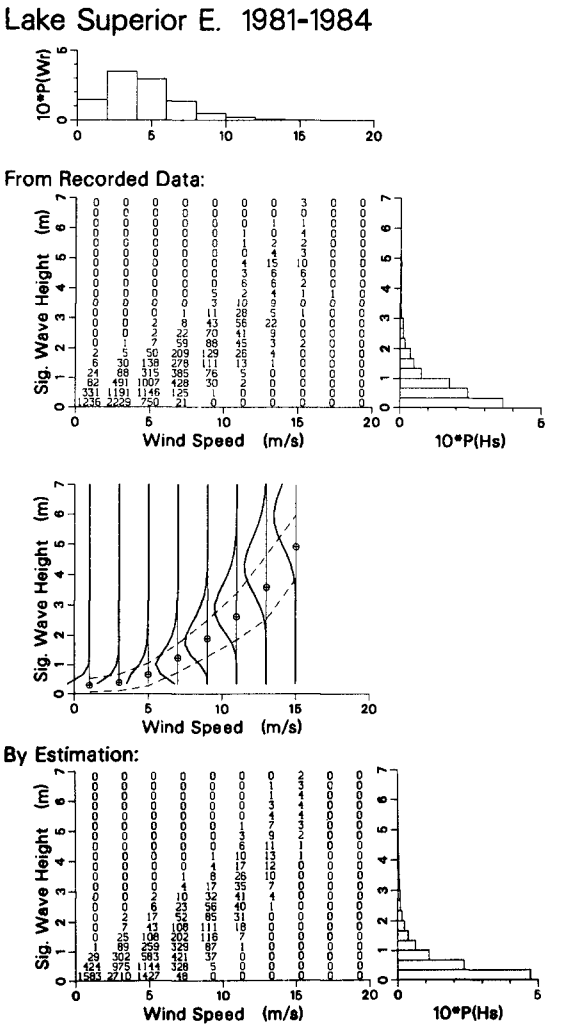

Figure 2 Long-term wind and wave histograms and joint distribution from recorded data and by estimation.

Following this approach, we derived the coefficients in Equations (5) and (6) for the eight buoy locations listed in Table 3. In the oceanic studies, h_2, in m, generally signifies the average swell activity. In the Great Lakes, however, swell is usually less significant, so in this study we simply set h_2 to the average significant wave height corresponding to the lowest wind speed interval (i.e., 0 - 2 m/s). Comparing the results given in Table 3 with the oceanic results in Table 1 indicates that for this study the values of h_2 and coefficient a are smaller while the exponent, n, is larger than those recommended by Andrews et al. (1983) for the oceanic studies. The differences are not significant since they are of the same order of magnitude as the limited fetch cases. A comparison of the fitted curves using the coefficients in Table 3 with recorded data

Gage	h_2	a	n	b	c	d
45001	0.364	0.013	2.294	0.491	0.171	-0.003
45002	0.299	0.013	2.201	0.458	0.192	-0.007
45003	0.289	0.012	2.225	0.450	0.213	-0.008
45004	0.286	0.012	2.302	0.624	0.114	0.007
45005	0.261	0.017	1.879	0.424	0.224	-0.012
45006	0.286	0.011	2.330	0.161	0.398	-0.021
45007	0.348	0.013	2.166	0.403	0.161	-0.003
45008	0.335	0.015	2.143	0.475	0.240	-0.012

Table 3 Derived coefficients for Equations (5) and (6) for all eight buoys.

for all eight buoys is shown in Figure 3. Here the model equations (5) and (6) are shown in solid lines with recorded data in dots. Although the degree of goodness of fit varies among the buoys, the model equations can be considered as providing reasonable representations for the recorded data.

Discussions

In Figure 2 the resemblance between the results from measurement and estimation, as shown in the second and bottom sections, appears to be reasonably close. A further and perhaps more effective comparison can be made by plotting the cumulative significant wave height distribution on a Weibull probability scale. This is shown in Figure 4 for all eight buoys. In this figure the recorded data are given in dots, and estimations based on coefficients in Table 3 are represented by the solid lines. The close comparison between recorded data and estimations over the higher wave heights shows that the Wave Climate Synthesis method is a viable approach for estimating long-term wave height statistics from long-term wind statistics.

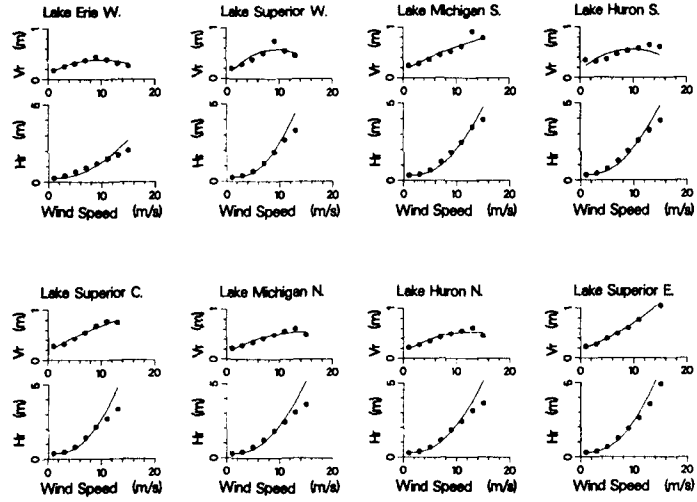

Figure 3 Fitting of Equations (5) and (6) for the eight buoys. Solid lines are estimations, with recorded data shown as dots.

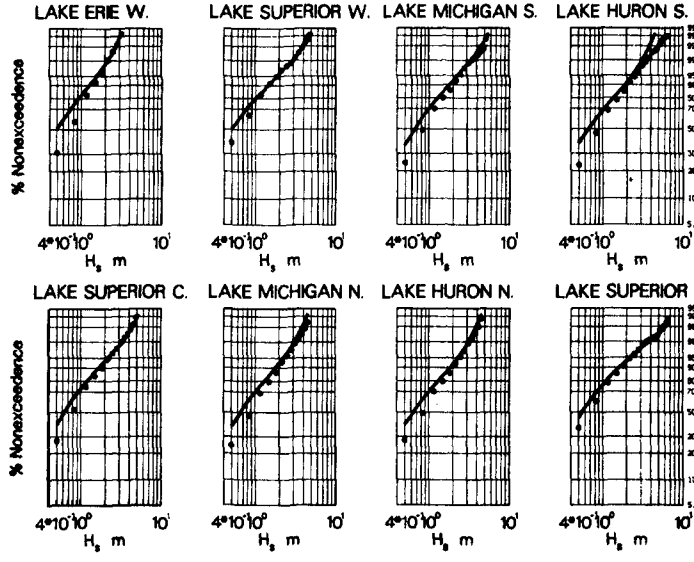

Figure 4 Cumulative distribution of significant wave heights plotted on Weibull probability paper for all eight buoys. Estimation based on Table 2 coefficients appear as solid lines, with recorded data shown as dots.

Gage	h_2	a	n	b	c
45001					0.200
45002					0.091
45003					0.091
45004	0.308	0.013	2.192	0.758	0.215
45005					0.050
45006					0.110
45007					0.099
45008					0.150

Table 4 Modified coefficients for Equations (5) and (6) for all eight buoys.

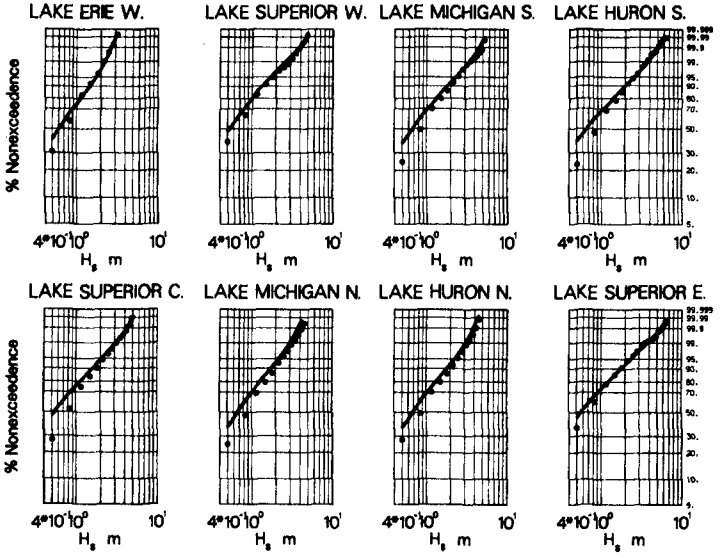

Figure 5 Cumulative distribution of significant wave heights plotted on Weibull probability paper for all eight buoys. Estimation based on Table 4 coefficients appear as solid lines, with recorded data shown as dots.

Closer examination of Figure 4 shows that sometimes the Wave Climate Synthesis method clearly overestimates the recorded data, as in the case of Lake Huron S. Sometimes, as in the cases of Lake Superior C. and Lake Superior E., the method tends to underestimate the recorded data at the high wave height end. The underestimation is especially unacceptable from a design engineer's point of view.

In an effort to rectify these unsettled cases as well as to simplify the use of different coefficients for different buoy locations, we first notice that in Table 3 the values of h_2, a and n for Equation (5) are not significantly different among the different buoys. In addition when we set d = 0 and use only the linear form of representation for the $v_r(W_r)$ function, we found that the coefficients b and c in Equation (6) vary from 0.326 to 1.138 and from 0.013 to 0.225 respectively. Assuming that the variations in b are also not significant, we then choose to use the same average values of h_2, a, n, and b for all eight buoy locations. Thus as shown in Table 4 we allow c to be the only coefficient that is different for different buoy locations. The values of c in the table are determined by trial and error.

Figure 5 presents the resulting cumulative distribution of wave height plots based on the new set of coefficients given in Table 4. This simplified version of coefficients effectively rectifies the excessive overestimation and underestimation and provides satisfactory results for practical applications. Using Table 4, for any given location in the Great Lakes where only wind statistics are available, one needs only to choose an appropriate value of the coefficient c and can then readily proceed to estimate design wave heights with justifiable accuracy.

Concluding Remarks

In this paper we examined applications of the Wave Climate Synthesis method for estimating long-term wave height statistics from given long-term wind statistics. Based on four years of data from each of eight NOMAD buoys in the Great Lakes we found that this method provides reasonably accurate and useful estimations. Many of the results presented here are preliminary in nature. The values of coefficient c in Table 4, for instance, are deduced by trial and error. More detailed analysis and data fitting as well as error analysis will be applied in subsequent studies. The model equations and coefficients will be further examined when additional longer-term data become available. While this method will not replace comprehensive wave hindcasting, it has been shown to be a useful additional tool for estimating design wave heights for coastal engineers.

References

Andrews, K.S., Dacunha, N.M. and Hogben, N., 1983: Wave Climate Synthesis. NMI Report No.R149., National Maritime Institute, Feltham, England, 143 pp.

Hogben, N., 1987: Experience from compilation of global wave statistics. Spring Meetings of the Royal Institution of Naval Architects.

Hogben, N. and Dacunha, N.M., 1985: Wave climate synthesis: Some recent advances. Proceedings, 17th Offshore Technology Conference, (OTC 4938), Vol.2, pp. 355-363.

Steele, K. and Johnson A. Jr., 1977: Data buoy wave measurements. In Ocean Wave Climate, pp.301-316. M. D. Earle and A. Malahoff Eds. Plenum Press, New York..

CHAPTER 40

EVALUATION OF A MODIFIED STRETCHED LINEAR WAVE THEORY

by

Jen-Men Lo[1] and R. G. Dean[2]

Introduction

Many experimental investigations of the drag and inertia force coefficients have relied on the determination of water particle kinematics from measured wave forms. Since the pioneering work of Airy (1845), Stokes (1847, 1880) and others, a number of wave theories have been developed for predicting water particle kinematics. Clearly, the use of a certain wave theory will lead to corresponding force coefficients. Therefore, a wave theory that provides more accurate water particle kinematics is very important.

Reid (1958) developed the simple superposition method for predicting water particle kinematics from a measured sea surface that could be either random or periodic. The method is based upon linear long-crested wave theory. Borgman (1965, 1967, 1969a, 1969b) introduced the linearized spectral density of wave force on a pile due to a random Gaussian sea. The drag force component has been approximated in the simplest form by a linear relation. This method, however, cannot calculate properties of the wave field and wave force above the mean water level.

Wheeler (1969) applied simple superposition with a stretching factor in the vertical coordinate position for hurricane-generated wave data during Wave Project II. With this method it was possible to evaluate the wave force above the mean water level.

Hudspeth, et al. (1974) compared the wave forces computed by simple superposition and irregular stream function methods. By using the simple superposition and a stretched vertical coordinate to calculate water particle kinematics, the comparison between measured and calculated forces indicates the stream function method was generally better than the linear wave theory method. The magnitudes of the difference between the theories, however, is not consistent. For maximum forces, the differences are not great. They noted that the linear

[1]Associate Research Scientist, Environmental and Earth Sciences Division, Kuwait Institute for Scientific Research, P.O. Box 24885, 13109 - Safat - Kuwait

[2]Graduate Research Professor, Coastal and Oceanographic Engineering Department, University of Florida, Gainesville, FL 32611 U.S.A. and Director, Division of Beaches and Shores, Florida Department of Natural Resources, Tallahassee, FL 32303

wave theory provides greater facility in carrying out certain mathematical operations than is possible using nonlinear wave theories.

The advantage of using the simple superposition method is that the entire measured sea surface data can be analyzed without the need to consider only one extreme wave using a nonlinear symmetric wave theory or irregular stream function theory. This paper will introduce a new mathematical stretching factor similar to the stretching factor used by Wheeler (1969). For several wave conditions, the symmetrical stream function wave theory, the stretched linear wave theory, and the new approach will be compared.

Simple Superposition

To simplify the problem, only two-dimensional wave motion will be considered. A long, irregular sequence of linear waves can be represented as an infinite sum of simple harmonic waves with closely spaced frequencies and random phase angles, i.e.,

$$\eta(x,t) = \sum_n a_n \cos (k_n x - \sigma_n t + \alpha_n) \tag{1}$$

where η is the water surface displacement; $a_n = \sqrt{2P_\eta(\sigma_n)\Delta\sigma}$; $P_\eta(\sigma_n)$ is the (one-sided) energy density spectrum of the irregular sea, varying with angular frequency σ_n; k_n is the wave number for the nth wave component ($k_n = 2\pi/L_n$); L_n is the wave length of the nth wave component; x is distance and α_n is the phase angle for the nth wave component.

When the small amplitude wave theory is used to estimate the flow regime in a wave system from the surface profile (Eq. 1), the velocity potential may be expressed by

$$\phi(x,z,t) = \sum_n \frac{a_n g}{\sigma_n} \frac{\cosh k_n(h+z)}{\cosh k_n h} \sin (k_n x - \sigma_n t + \alpha_n) \tag{2}$$

where z is referenced to the mean water surface and is positive upwards. The dispersion relationship is given by

$$\sigma_n^2 = g k_n \tanh k_n h \tag{3}$$

The horizontal water particle velocity component is given by

$$u(x,z,t) = -\frac{\partial\phi}{\partial x} = \sum_n \frac{a_n k_n g}{\sigma_n} \frac{\cosh k_n(h+z)}{\cosh k_n h} \cos(k_n x - \sigma_n t + \alpha_n) \tag{4}$$

From Eq. 4, the horizontal water particle kinematics at any given time or any given position can be found very easily. But when the position is close to the free surface, the results are not in agreement with laboratory or field data. Mathematically, Eqs. 2 and 3 are determined individually, component by component, using the small amplitude wave theory approach assuming that all wave components are independent of

each other. Fig. 1 shows a high-frequency wave component superimposed upon a low frequency wave component. Evaluating Eq. 4 at a time when both components are maximum, the vertical surface coordinate is z = $a_1 + a_2$, and it is found that the contribution of the high-frequency component to the kinematics is exaggerated by the vertical displacement due to the large low-frequency wave.

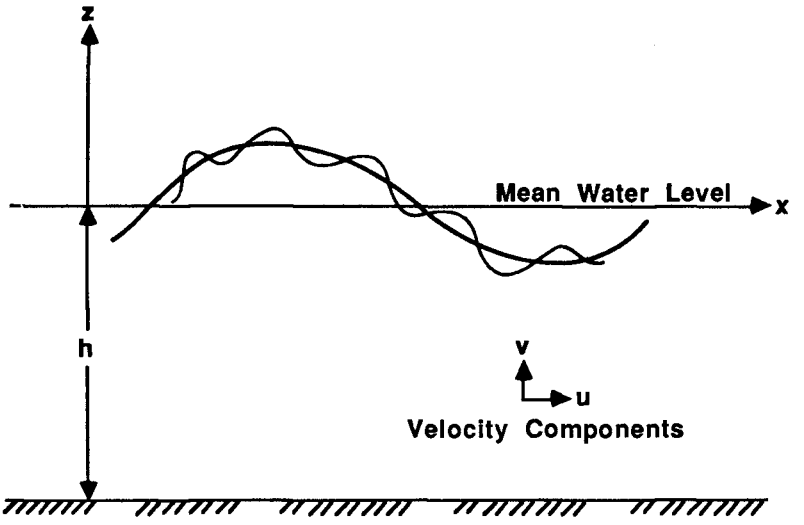

Fig. 1. Superposition of a high frequency wave on a low frequency wave.

Stretched Linear Wave Theory (SLWT)

The simple superposition technique was first developed by Reid in 1958. Wheeler applied the technique to hurricane-generated wave data in 1969. The simple superposition technique, however, predicts unreasonably large wave kinematics when it applies to locations that are above the mean water level. Therefore, Wheeler introduced an intuitive stretching factor to predict the wave kinematics by using the simple superposition method. If kinematic predictions are desired at elevation S = h + z above the bottom (where h is the mean water depth), then the stretching results in calculations being carried out at elevation S' above the bottom, where

$$S'(x,z,t) = \alpha(x,t)S \tag{5}$$

and

$$\alpha(x,t) = \frac{h}{h+\eta(x,t)} \tag{6}$$

Here $\eta(x,t)$ is the instantaneous water surface displacement measured from the mean water level. This vertical stretching is particularly significant near the free surface. It is of interest to note that the velocity potential that is stretched in this manner no longer exactly satisfies the Laplace equation.

By using the stretched linear wave theory, the kinematics (and other quantities) calculated at the actual free surface are the same as those evaluated at the mean water level in an unstretched system, thus eliminating the exaggeration of the high frequency component described previously.

Stream Function Wave Theory (SFWT)

The stream function wave theory, as described by Dean (1965), can be used to represent both theoretical symmetrical and irregular waves. In application, the theory is used to generate a symmetric wave with given parameters, such as wave height, period, and water depth. It is this symmetric form of the stream function wave theory that will be used in the comparison.

Taking a frame of reference moving with wave celerity C, the problem is reduced to a steady form. Then the kinematic free surface boundary condition becomes

$$v = \frac{\partial \Psi}{\partial x} = (u - C)\frac{\partial \eta}{\partial x} = -\frac{\partial \Psi}{\partial y}\frac{\partial \eta}{\partial x} \text{ on } z = \eta(x) \tag{7}$$

where v is the vertical velocity component and Ψ is the stream function. Eq. 7 is satisfied exactly by the equation for the stream function:

$$\Psi(x,z) = \frac{L}{T} z + \sum_{n=1}^{NN} A(n) \sinh\left[\frac{2n\pi}{L}(h+z)\right] \cos\left(\frac{2n\pi}{L} x\right) \tag{8}$$

Evaluating this expression on the free surface, i.e., setting $z = \eta$, the free surface is

$$\eta = \frac{T}{L}\Psi_n - \frac{T}{L}\sum_{n=1}^{NN} A(n) \sinh\left[\frac{2n\pi}{L}(h+\eta)\right] \cos\left(\frac{2n\pi}{L} x\right) \tag{9}$$

Since the coordinate system is moving with the wave celerity, and the pressure is zero on the free surface, the dynamic free surface boundary condition is

$$\frac{1}{2g}\left((u-C)^2 + v^2\right) + \eta = Q \text{ on } z = \eta(x) \tag{10}$$

where Q is the total head or "Bernoulli constant" on the free surface.

The numerical problem of establishing the wave theory is thus one of determining values of A(1), A(2),...., A(NN), L, Ψ_η, such that the dynamic free surface boundary condition is satisfied as closely as possible. These coefficients are determined iteratively employing a nonlinear least-squares procedure.

Modified Stretched Linear Wave Theory (MSLWT)

The SLWT was reported to be based on wave tank studies; Lo (1979) introduced a new stretching factor by using the free surface boundary conditions. Assuming that the pressure is zero on the free surface, the dynamic free surface boundary condition is

$$\frac{1}{2g}(u^2 + v^2) + z - \frac{1}{g}\frac{\partial \phi}{\partial t} = C(t) \quad , \quad z = \eta \tag{11}$$

The kinematic free surface boundary condition is

$$\frac{\partial \eta}{\partial t} + u\frac{\partial \eta}{\partial x} = v \quad , \quad z = \eta \tag{12}$$

Eqs. 11 and 12 are nonlinear partial differential equations, and the nonlinearities come from two major sources. One is the product terms in the equations, i.e., u^2, v^2 and $u\ \partial\eta/\partial x$; the other is that the equation applies to the actual free surface, $z = \eta$. The most popular technique for solving these equations is by using the Taylor series expansion to expand the value of the condition from $z = 0$ to $z = \eta$ (mean water level, a known location), then by using the perturbation procedure to solve the equations order by order. For example, the small amplitude wave theory is the solution of the first order, and the Stokes theories of various orders are extensions of the approach.

The MSLWT will be solved to the first order by using Eqs. 11 and 12 only on the free surface $z = \eta$. The solution is:

$$\eta(x,t) = a\cos(kx - \sigma t) \tag{13}$$

$$\phi_m(x,y,t) = -\frac{ag}{\sigma}\frac{\cosh k\,(h+z)}{\cosh k\,(h+\eta)}\sin(kx - \sigma t) \tag{14}$$

$$\sigma^2 = gk\tanh k(h+\eta) \tag{15}$$

Eqs. 13, 14 and 15 satisfy the boundary conditions (without the product terms in Eqs. 11 and 12) exactly. But, like the solution of the stretched linear wave theory, they no longer satisfy the Laplace equation. The effective wave number k now depends on water surface displacement. Comparing the solution for small amplitude wave theory with that for the modified stretched linear wave theory, the new stretching factor found for the modified stretched linear wave theory is given by

$$\text{Stretching Factor} = \frac{\cosh kh}{\cosh k\ (h+\eta)} \tag{16}$$

This stretching factor was established by using the boundary conditions of the wave system. For a given time, position and mean water depth, this factor will be a constant through the vertical coordinate. But under the same conditions, the stretching factor for the stretched linear wave theory (Equations 5 and 6) is a function of depth, and it has a maximum value at the free surface, a minimum value at the bottom.

To describe the statistical properties of a random water surface, it is convenient to decompose the variable of interest into Fourier components. The Fourier series representation of the water surface displacement is given by the simple superposition method as Eq. 1.

When the MSLWT is used to estimate the flow regime in a wave system from the surface profile, the velocity potential may be expressed by

$$\phi_m(x,z,t) = -\sum_n \frac{a_n g}{\sigma_n} \frac{\cosh k_n(h+z)}{\cosh k_n(h+\eta)} \sin\ (k_n x - \sigma_n t + \alpha_n) \tag{17}$$

where the dispersion relationship is given by

$$\sigma_n^2 = g\ k_n \tanh k_n(h+\eta) \tag{18}$$

and the first order horizontal and vertical water particle velocities are derived from Eqs. 17 and 18, as follows:

$$u_m(x,z,t) = \sum_n a_n\ \sigma_n \frac{\cosh k_n(h+z)}{\sinh k_n(h+\eta)} \cos(k_n x - \sigma_n t + \alpha_n) \tag{19}$$

and

$$v_m(x,z,t) = \sum_n a_n\ \sigma_n \frac{\sinh k_n(h+z)}{\sinh k_n(h+\eta)} \sin\ (k_n x - \sigma_n t + \alpha_n) \tag{20}$$

Comparison Between SLWT and MSLWT

Ohmart and Gratz (1978) presented a comparison of measured and predicted ocean wave kinematics. They found by comparing linear wave theory, Stokes Fifth Order Wave Theory and the Irregular Stream Function Wave Theory (IRSF) that IRSF yields better results. The field data were measured from the test structure (the CAGC Eugene Island 266F platform), located in the Gulf of Mexico. Mean water depth was 177 feet. A wave staff was mounted on one corner of the structure. The current meters were mounted at elevations of 5 and 20 feet below mean water level.

A 34 minute block of data was recorded each two hours or four hours depending upon the severity of the storm. The data sampling rate was at 0.5 second intervals.

Two sets of Ohmart and Gratz's data were selected for comparison with IRSF, the MSLWT, and the SLWT. Both sets were measured during storm Delia in September 1973 and in the deep water region. Figs. 2-5 present a representative comparison of the horizontal water particle velocities among the data, the IRSF theory, the MSLWT and the SLWT. The comparison shows that both the MSLWT and SLWT agree reasonably well with the data. The SLWT yields a better result (4% closer to the data) than that of the MSLWT near the crest phase angle.

Stream function wave theory (SFWT) results are known to provide a reasonably good fit with laboratory and field data. Therefore, a comparison between the SLWT, MSLWT and SFWT was also studied.

The SFWT is a nonlinear wave theory, thus the wave components given by Eq. 1 for the SLWT and MSLWT cannot be regarded as independent linear components. Rather these components are nonlinear harmonics of the fundamental. Therefore, the wave number k cannot be solved component by component using the dispersion relationship (Eq. 3) for the SLWT and Eq. 15 for the MSLWT for this condition. Only the first component can be solved for the wave number based on Eqs. 3 and 15; in general, the wave number of the nth component is nk.

Six sets of dimensionless wave conditions were selected for tabulation and evaluation from Dean's stream function tabulations (1974). Each case is characterized by values of h/L_o and H/L_o. In the present study, three values of the parameter h/L_o ranging from 0.002 to 2.0 were selected and include the relative depth range of shallow, intermediate, and deep water. The parameter H/L_o includes wave steepness ratios: 0.25 and 1.0 of the breaking wave steepness for each of the 3 h/L_o values. Fig. 6 shows the dimensionless wave conditions selected for evaluation and also indicates the referencing notation for the cases. Tables I and II present the horizontal water particle velocity comparison between the MSLWT and SFWT, and SLWT and SFWT for wave case No. 2. The wave steepness (H/L_o) for wave case 2 is 0.001564, and the relative depth (h/L_o) is 0.002 (Note: This wave is at breaking).

The percent values listed in the tables are the differences between the SFWT and the MSLWT (or the SLWT), defined as

$$\text{Percent} = \frac{\text{MSLWT (or SLWT)} - \text{SFWT}}{\text{SFWT}} \times 100 \qquad (21)$$

The main body of the table lists the dimensionless horizontal water particle velocities of the MSLWT (or SLWT). The row labelled "surface" represents the dimensionless velocities evaluated at the free surface; the percentage differences for velocities are calculated as defined above (Eq. 21). The remaining part of the table represents the dimensionless velocities and percentage differences evaluated on a grid of (Θ, S/h). The lack of entries for the higher S/h and larger Θ values (right side of page) result from the fact that the wave profile

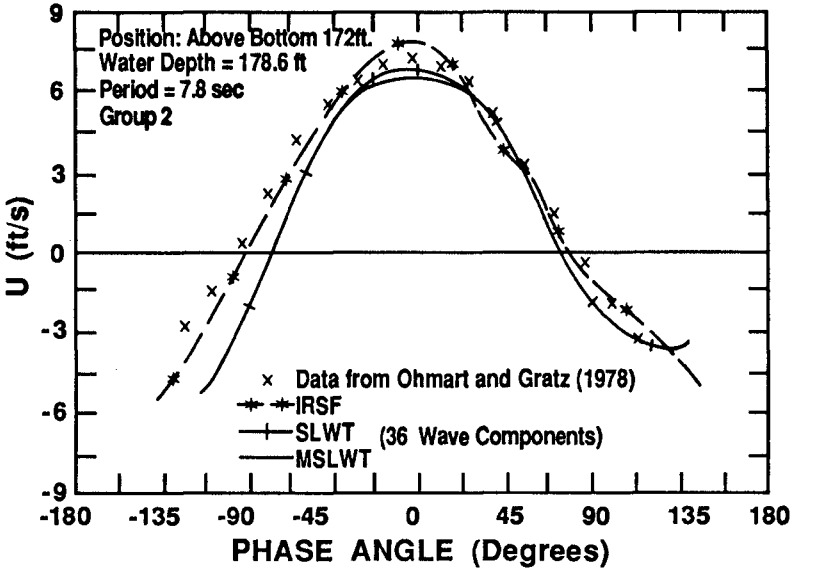

Fig. 2. Horizontal water particle velocity at a water depth of 172 feet for wave condition Group 2. Comparison of various wave theories with data by Ohmart and Gratz.

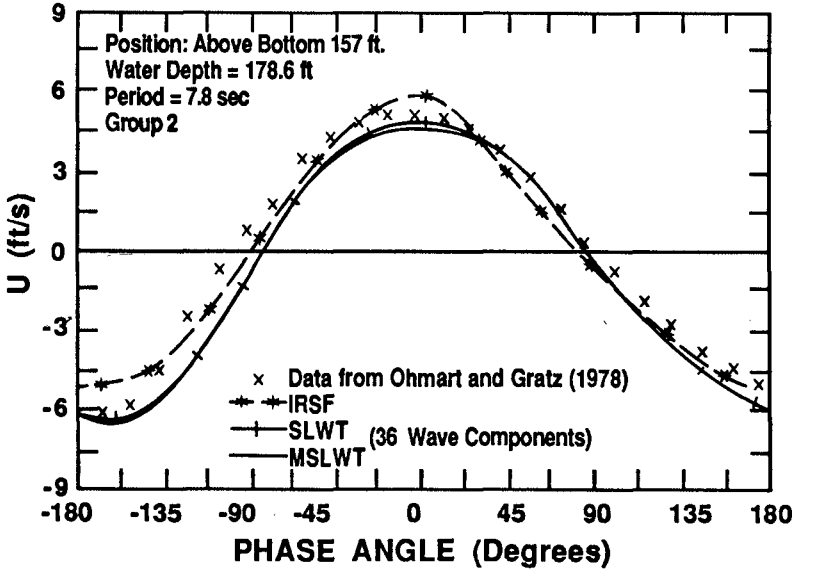

Fig. 3. Horizontal water particle velocity at a water depth of 157 feet for wave condition Group 2. Comparison of various wave theories with data by Ohmart and Gratz.

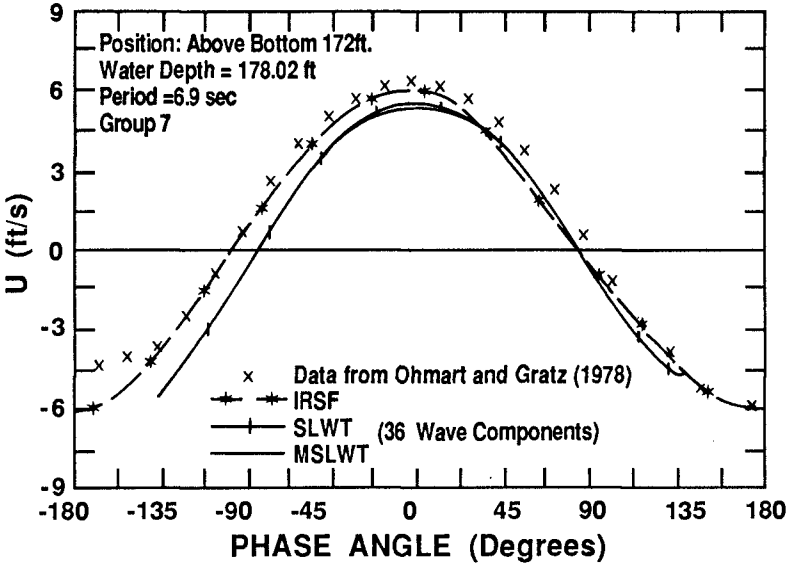

Fig. 4. Horizontal water particle velocity at a water depth of 172 feet for wave condition Group 7. Comparison of various wave theories with data by Ohmart and Gratz.

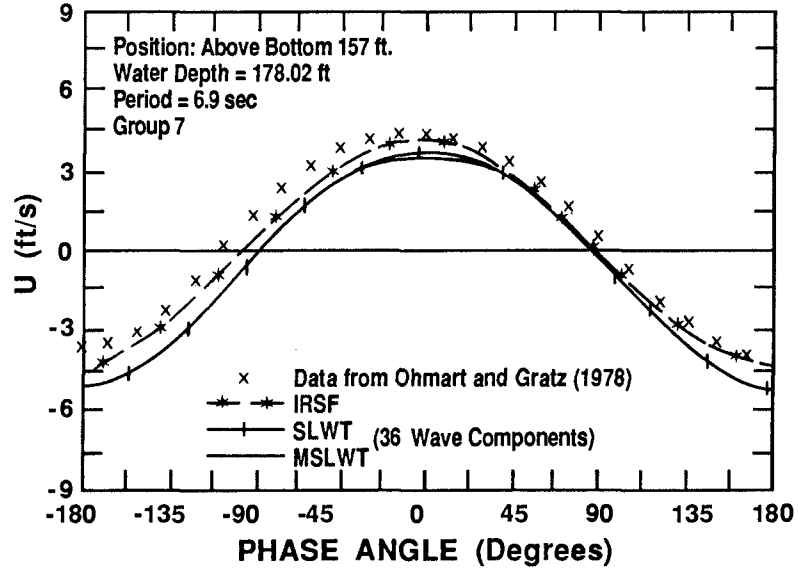

Fig. 5. Horizontal water particle velocity at a water depth of 157 feet for wave condition Group 7. Comparison of various wave theories with data by Ohmart and Gratz.

TABLE I-DIMENSIONLESS HORIZONTAL VELOCITY COMPONENT FIELD : MSLWT VS SFWT

THETA =	0.0	10.0	20.0	30.0	50.0	75.0	100.0	130.0	180.0
ETA/HEIGHT=	0.916	0.201	-.017	-.040	-.044	-.040	-.040	-.041	-.041
	-4.5%	-4.1%	18.5%	3.2%	1.2%	-0.6%	0.4%	0.3%	0.2%
SURFACE	62.477	2.874	-2.648	-2.785	-2.760	-2.237	-2.269	-2.342	-2.439
	7.8%	-76.4%	184.4%	30.4%	15.4%	10.8%	16.0%	14.5%	13.9%
S/DEPTH=1.7	61.565								
	9.5%								
S/DEPTH=1.6	56.519								
	6.6%								
S/DEPTH=1.5	52.191								
	4.3%								
S/DEPTH=1.4	48.472								
	1.8%								
S/DEPTH=1.3	45.272								
	-0.2%								
S/DEPTH=1.2	42.518								
	-1.9%								
S/DEPTH=1.1	40.149	4.212							
	-3.5%	-66.4%							
S/DEPTH=1.0	38.115	6.230							
	-4.8%	-52.1%							
S/DEPTH=0.9	36.373	7.906	-2.197	-2.660	-2.692	-2.259	-2.276	-2.340	-2.418
	-5.9%	-41.1%	205.8%	27.1%	14.1%	11.5%	15.7%	14.3%	13.6%
S/DEPTH=0.8	34.890	9.287	-1.751	-2.516	-2.611	-2.283	-2.285	-2.339	-2.394
	-6.9%	-32.5%	251.9%	23.4%	12.6%	12.2%	15.3%	14.0%	13.3%
S/DEPTH=0.7	33.638	10.417	-1.374	-2.408	-2.551	-2.301	-2.294	-2.339	-2.376
	-7.7%	-25.8%	359.3%	20.9%	11.7%	12.7%	15.0%	13.8%	13.1%
S/DEPTH=0.6	32.593	11.330	-1.055	-2.326	-2.507	-2.313	-2.301	-2.340	-2.363
	-8.4%	-20.6%	748.4%	19.1%	11.1%	13.0%	14.8%	13.7%	13.0%
S/DEPTH=0.5	31.738	12.056	-0.790	-2.263	-2.476	-2.322	-2.308	-2.340	-2.353
	-8.9%	-16.6%	******%	17.8%	10.8%	13.2%	14.7%	13.6%	12.9%
S/DEPTH=0.4	31.057	12.619	-0.575	-2.216	-2.450	-2.328	-2.313	-2.341	-2.345
	-9.4%	-13.5%	-486.1%	17.0%	10.6%	13.3%	14.6%	13.5%	12.9%
S/DEPTH=0.3	30.539	13.039	-0.409	-2.182	-2.433	-2.332	-2.317	-2.341	-2.340
	-9.7%	-11.3%	-266.3%	16.4%	10.4%	13.4%	14.5%	13.5%	12.9%
S/DEPTH=0.2	30.175	13.329	-0.290	-2.159	-2.421	-2.335	-2.320	-2.342	-2.336
	-10.0%	-9.8%	-192.0%	16.0%	10.4%	13.4%	14.4%	13.4%	12.9%
S/DEPTH=0.1	29.958	13.498	-0.219	-2.145	-2.415	-2.336	-2.321	-2.342	-2.334
	-10.1%	-9.0%	-161.3%	15.8%	10.4%	13.4%	14.4%	13.4%	12.9%
S/DEPTH=0.0	29.887	13.554	-0.195	-2.141	-2.413	-2.337	-2.322	-2.342	-2.334
	-10.2%	-8.7%	-152.6%	15.7%	10.4%	13.4%	14.4%	13.4%	12.9%

Table I. Horizontal velocity comparison between the MSLWT and SFWT for wave case No. 2.

TABLE II-DIMENSIONLESS HORIZONTAL VELOCITY COMPONENT FIELD : SLWT VS SFWT

THETA =	0.0	10.0	20.0	30.0	50.0	75.0	100.0	130.0	180.0
ETA/HEIGHT=	0.916	0.201	-.017	-.040	-.044	-.040	-.040	-.041	-.041
	-4.5%	-4.1%	18.5%	3.2%	1.2%	-0.6%	0.4%	0.3%	0.2%
SURFACE	70.899	4.015	-2.653	-2.753	-2.719	-2.199	-2.232	-2.304	-2.401
	22.4%	-67.1%	184.8%	28.9%	13.7%	8.9%	14.1%	12.7%	12.1%
S/DEPTH=1.7	70.202								
	24.9%								
S/DEPTH=1.6	66.275								
	25.0%								
S/DEPTH=1.5	62.803								
	25.2%								
S/DEPTH=1.4	59.735								
	25.4%								
S/DEPTH=1.3	57.027								
	25.7%								
S/DEPTH=1.2	54.639								
	26.0%								
S/DEPTH=1.1	52.539	5.262							
	26.3%	-58.1%							
S/DEPTH=1.0	50.700	7.159							
	26.7%	-45.0%							
S/DEPTH=0.9	49.098	8.751	-2.198	-2.626	-2.650	-2.222	-2.239	-2.303	-2.380
	27.0%	-34.8%	205.9%	25.5%	12.3%	9.7%	13.8%	12.4%	11.8%
S/DEPTH=0.8	47.712	10.077	-1.750	-2.480	-2.568	-2.247	-2.248	-2.302	-2.356
	27.4%	-26.7%	251.6%	21.7%	10.8%	10.4%	13.4%	12.1%	11.5%
S/DEPTH=0.7	46.525	11.173	-1.370	-2.371	-2.508	-2.264	-2.257	-2.301	-2.338
	27.7%	-20.4%	358.0%	19.0%	9.8%	10.9%	13.2%	12.0%	11.3%
S/DEPTH=0.6	45.522	12.068	-1.049	-2.288	-2.463	-2.276	-2.265	-2.302	-2.324
	28.0%	-15.4%	743.6%	17.2%	9.2%	11.2%	13.0%	11.8%	11.1%
S/DEPTH=0.5	44.693	12.785	-0.782	-2.226	-2.430	-2.285	-2.271	-2.303	-2.314
	28.2%	-11.5%	******%	15.9%	8.8%	11.4%	12.9%	11.7%	11.1%
S/DEPTH=0.4	44.028	13.346	-0.566	-2.179	-2.406	-2.291	-2.277	-2.303	-2.307
	28.4%	-8.6%	-479.9%	15.0%	8.6%	11.5%	12.8%	11.7%	11.1%
S/DEPTH=0.3	43.517	13.767	-0.398	-2.144	-2.389	-2.295	-2.280	-2.304	-2.301
	28.6%	-6.4%	-262.0%	14.4%	8.5%	11.6%	12.7%	11.6%	11.1%
S/DEPTH=0.2	43.157	14.058	-0.279	-2.121	-2.376	-2.298	-2.283	-2.304	-2.298
	28.8%	-4.9%	-188.4%	14.0%	8.4%	11.6%	12.6%	11.6%	11.1%
S/DEPTH=0.1	42.942	14.230	-0.207	-2.107	-2.372	-2.299	-2.285	-2.304	-2.296
	28.8%	-4.0%	-158.0%	13.7%	8.4%	11.6%	12.6%	11.6%	11.1%
S/DEPTH=0.0	42.871	14.287	-0.183	-2.103	-2.370	-2.300	-2.285	-2.305	-2.295
	28.9%	-3.7%	-149.4%	13.7%	8.4%	11.6%	12.6%	11.6%	11.1%

Table II. Horizontal velocity comparison between the SLWT and SFWT for wave case No. 2.

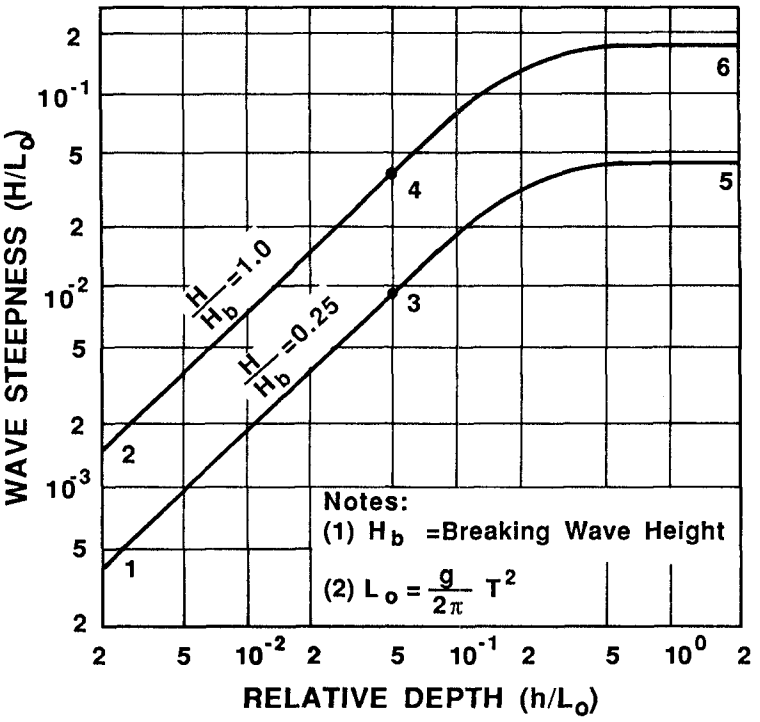

Fig. 6. Dimensionless wave characteristics selected for tabulation.

in the trough region is lower than in the crest region (left side of page). If asterisks appear, it means that the percentage differences are very large and cannot be covered by the computer output. This avoided the tabulation of very large percentages that would have been the result of division by a small number. Generally, although the asterisks indicate a large percentage error, they occur at locations where the denominator in Eq. 21 is near zero and are associated with small absolute differences. Finally, it is noted that the small percentage differences in relative water surface displacement are due to the stream function profile being used to develop a truncated Fourier series representation as an input water surface profile to both of the stretched wave theories. Figs. 7 and 8 present a comparison of the horizontal water particle kinematics between the SFWT, SLWT, and MSLWT under the crest. From this comparison, the MSLWT provides a better fit to the SFWT than for the SLWT.

Summary and Conclusions

A new stretching factor was developed based on the first order free surface boundary conditions. The simple superposition method and the modified stretched linear wave theory, provide reasonable agreement with the water particle kinematics from the Stream Function Tables. This technique is useful and convenient for the following reasons:

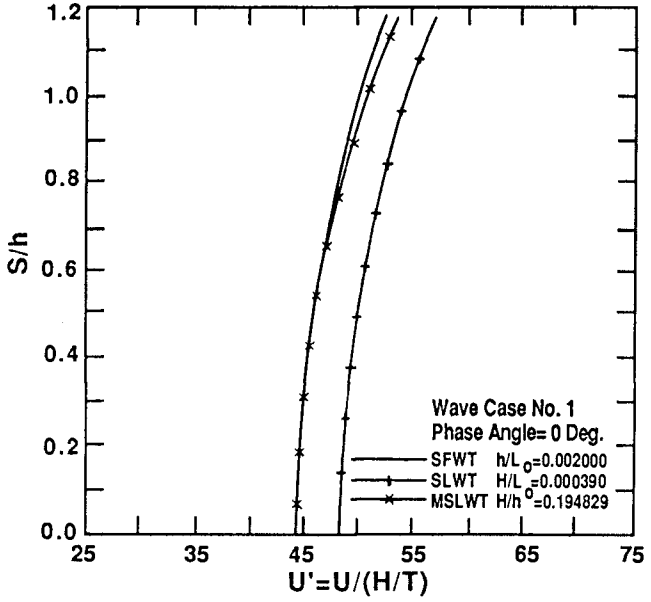

Fig. 7. Dimensionless horizontal water particle velocity distribution over depth (under the crest).

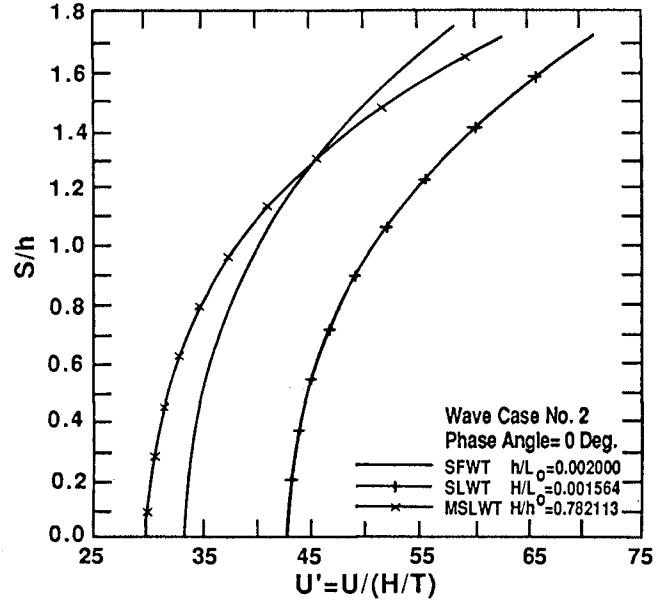

Fig. 8. Dimensionless horizontal water particle velocity distribution over depth (under the crest).

1. The simple superposition method and the MSLWT can be used to analyze any length of irregular wave records for design and dynamic studies of offshore structures. Through the superposition method, a given wave record (usually available as a function of time only) can be represented as an infinite sum of simple harmonic waves with closely spaced frequencies and appropriate phase angles.

   When the MSLWT is used to estimate the flow regime in a wave system from the surface profile, Eqs. 16, 18, 19 and 20 allow the calculation of the potential function and the kinematics.

   This method is convenient for the analysis of long and irregular wave profiles which can be characterized by power spectra and thus related to statistical wave prediction techniques that relate wave spectra to weather history for a given location.

2. Most nonlinear wave theories require a periodic wave profile, but by using the simple superposition method and the MSLWT, aperiodic wave profiles can be analyzed.

3. Based on the MSLWT, the spectral and probabilistic approaches to wave force prediction can be extended to include calculations from the sea floor to the free surface without neglecting the contribution from the mean water surface to the free surface.

4. In laboratory studies of nonlinear waves, the simple superposition method and the MSLWT will yield reasonable kinematic predictions.

5. A more extensive comparison between field data and the result of using the simple superposition method and the MSLWT is desirable and will be pursured when additional data are available. It is planned to extend the MSLWT to account for nonlinear terms included in the complete free surface boundary conditions.

References

Airy, G.B. (1845). On tides and waves. Encycl. Metropolitana, Art, p. 182.

Borgman, L.E. (1965). Wave forces on piling for narrow-band spectra. Jour. Waterways and Harbors Div., Proc. Am. Soc. Civil Eng. Vol. 91 (WW3), pp. 65-90.

Borgman, L.E. (1967). Spectral analysis of ocean wave forces on piling. Jour. Waterways and Harbors Div., Proc. Am. Soc. Civil Eng. Vol. 93 (WW3), pp. 126-156.

Borgman, L.E. (1969a). Ocean wave simulation for engineering design. Jour. Waterways and Harbors Div., Proc. Am. Soc. Civil Eng. Vol. 95 (WW4), pp. 557-583.

Borgman, L.E. (1969b). Directional spectral models for design use. Preprints 1969 Offshore Technology Conference, May 18-21, Vol. I, Paper No. 1069, pp. I-721-I-746.

Dean, R.G. (1965). Stream function representation of nonlinear ocean waves. Jour. Geophy. Res., 70(18) Sept.

Dean, R.G. (1974). Evaluation and development of water wave theories for engineering application. Vols. I and II. Special Report No. 1, U.S. Army Coastal Eng. Res. Center, Fort Belvoir, Virginia.

Hudspeth, R.T., R.A. Dalrymple, and R.G. Dean (1974). Comparison of wave forces computed by linear and stream function methods. Preprints 1974 Offshore Technology Conference, Vol. II, Paper No. 2037, pp. II-17-II-32.

Lo, J.M. (1979). Evaluation of a Modified Stretched Linear Wave Theory. Master Thesis, University of Delaware, Newark, Delaware, U.S.A.

Ohmart, R.D., and R.L. Gratz (1978). A comparison of measured and predicted ocean wave kinematics. Preprints, 1978 Offshore Technology Conference, Vol. III, Paper No. 3276, pp. III-1947-III-1957.

Reid, R.O. (1958). Correlations of water-level variations with wave forces on a vertical pile for non-periodic waves. Proceeding, Sixth International Conference on Coastal Engineering.

Stokes, G.G. (1847). On the theory of Oscillatory waves. Trans. Camb. Phil. Soc., Vol. 8.

Stokes, G.G. (1880). Supplement to a paper on the theory of Oscillatory waves. Mathematical and Physical Papers, Cambridge Univ. Press, Vol. I, pp. 314-326.

Wheeler, J.D. (1969). Method for calculating forces produced by irregular waves. Preprints 1969 Offshore Technology Conference, Vol. I, Paper No. 1007, pp. I-83-I-94.

CHAPTER 41

LIMIT WAVES ON HORIZONTAL SEA FLOOR

Chia-Chi Lu[1], John D. Wang[2], M. ASCE and Bernard Le Mehaute[3] M. ASCE

ABSTRACT

A numerical solution to periodic nonlinear irrotational surface gravity waves on a horizontal sea floor is developed using an iterative Boundary Integral Equation Method (BIEM). This solution technique is subsequently applied to determine the characteristics of limit waves for which the wave crest theoretically ceases to be rounded and become angled with an included angle of 120 degrees.

INTRODUCTION

Analytic wave theories (1,2,3) have shown that for large waves, nonlinear effects become important and wave theories that account for some of these effects give more accurate results. Most of these wave theories are based on the solutions to the irrotational monochromatic wave problem on a horizontal bottom. Application of the numerical results provided by Dean's stream function solution (4), which is of this type, is presently being recommended in the Shore Protection Manual (5) to determine forces on piles, although high order Stokes solutions have also been used. The Dean's stream function and similar solutions (4,6,7,8), are based on truncated Fourier expansions for which the accuracy of the solution decreases as the wave height approaches limit wave conditions. A limit wave has a stagnation point at the crest and, as shown by Stokes (9), the wave crest is sharp and includes an angle of 120 degrees.

A solution to limit waves based on the transformed (complex potential) plane and including terms to specifically account for the crest flow has been given by Williams (10). His solution consists of combinations of periodic motion modes and the mentioned crest terms. Since the solution is performed in the transform plane all but the dynamic surface condition are satisfied. A collocation technique satisfying the dynamic condition at discrete nodal points is used to determine the mode amplitudes. The number of modes required for accurate results and convergence depends on wave steepness and depth and was determined through empirical trial and error. Although the mode amplitudes have been calculated for a number of different wave conditions the application of the results is somewhat cumbersome and interpolation does not seem straightforward.

The numerical solution described here offers an attractive alternative method for determining limit wave parameters. The method is convergent and explicitly accounts for wave set-down.

The Boundary Integral Equation Method (BIEM), (11) solves a govern-

[1] Research Associate, Div. Applied Marine Physics, Rosenstiel School of Marine and Atmospheric Science, 4600 Rickenbacker Cswy. Miami, FL. 33149

[2,3] Professors,Div. Applied Marine Physics, Rosenstiel School of Marine and Atmospheric Science, 4600 Rickenbacker Cswy. Miami, FL. 33149

ing differential equation (e.g. Laplace equation) by evaluating the two principal dependent variables on a given physical boundary. The basic concept employed stems from the application of Green's theorem and the resulting boundary method is now firmly established as an important alternative technique to the prevailing numerical methods of analysis in continuum mechanics. The efficiency of the BIEM is attributed primarily to the fact that in non-linear problems with an unknown free surface which must be determined through interaction, it is much easier to move a few nodes on the surface for each iteration than it is to update an entire spatial grid.

In this study, a numerical solution for limit waves by means of the BIEM technique is developed. It is obtained in a coordinate system translating at wave phase speed and in which the wave motion consequently is steady. The limit waves considered here are monochromatic and periodic. They are assumed to be irrotational and symmetric around a wave crest plane. The limit wave under these conditions is taken as the wave with crest particle velocity equal to the celerity, according to Stokes criterion (9). Although Benjamin and Feir (12) have questioned the stability of a periodic solution, this study does not intend to elaborate on this aspect of the problem, but accepts it as a valuable working assumption.

THEORETICAL FORMULATIONS

Two-dimensional periodic surface gravity waves at the non-breaking limit are considered as shown in Figure 1. With horizontal coordinate x' and vertical coordinate z', the origin is on the bed and moves with the same speed as the waves so that in this moving frame all motion is steady. When the assumption of an incompressible fluid and irrotation-

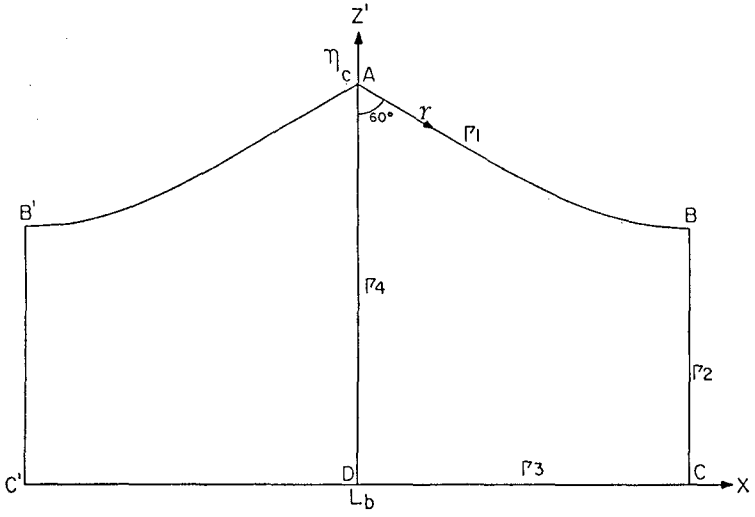

Fig. 1 Definition sketch.

al motion are incorporated, the steady-state solution is represented by a velocity potential function satisfying the Laplace equation, i.e.

$$\nabla^2\phi' = 0 \tag{1}$$

The velocity potential (ϕ') is defined in terms of velocity components u' and w' in the moving frame as

$$-\frac{\partial\phi'}{\partial x'} = u' = u - C_b \tag{2}$$

$$-\frac{\partial\phi'}{\partial z'} = w' = w \tag{3}$$

in which C_b is the speed of the limit wave and u, w are the velocity components in the corresponding fixed frame (here and in the following we use ' to designate variables measured in the translating coordinate system). The kinematic boundary condition applies to both the free surface and the bottom, i.e.

$$w' = 0 \qquad z' = 0 \tag{4}$$

$$\frac{\partial\eta}{\partial x'} = \frac{w'}{u'} \qquad z' = \eta(x') \tag{5}$$

where η is the free surface displacement.

The dynamic boundary condition on the free surface is given as

$$\eta + \frac{1}{2g}[u'^2 + w'^2] = B \qquad z' = \eta(x') \tag{6}$$

in which B is the Bernoulli constant and g is the gravitational constant.

In this study, we are specifically searching for limit wave solutions and therefore impose a further condition that the particle velocity at the crest equals the wave phase speed. This yields the well-known result that the crest has an included angle of 120 degrees and the fluid in the vicinity of the crest is characterized by a 120 degree corner flow (9), i.e.

$$\left.\frac{\partial\eta}{\partial x'}\right|_{x'=0} = -\tan^{-1}\frac{\pi}{6} \tag{7}$$

It is noted that solution of regular non-limit waves can be obtained in a very similar manner to the one described here by eliminating eq. (7) and specifying a value for B, see Lu (13).

The celerity C_b is obtained from the second definition of wave

celerity by Stokes (1), i.e.

$$C_b = -\frac{1}{d}\int_0^{\eta} u'\, dz' \ . \tag{8}$$

where d denotes the water depth.

There exists a close relationship between the celerity and the overall volume transport. If Q' is defined as the total volume rate of flow underneath the steady wave per unit width, it and the wave celerity C_b are related by

$$Q' = -d(C_b - C_s) \tag{9}$$

in which C_s is the average mass transport velocity. If pure wave motion is assumed to cause no overall volume transport of fluid (i.e., C_s=0), then $C_b = -Q'/d$.

The water depth, d*, is determined so that the crest area equals the trough area, or

$$\int_0^{L_b} \eta(x')\, dx' = d^* \tag{10}$$

in which L_b denotes the limit wave length.

Based upon the assumption of irrotationality and periodicity, the mean water level is always depressed due to existence of waves (14). The mean water level obtained by eq. (10) is lower than the undisturbed water level. The difference Δd is defined as set-down. The set-down can be determined by (see Lu (13))

$$\Delta d = \frac{1}{2g}\left[-C_b^2 + \overline{\left(\frac{\partial \phi'}{\partial x'}\right)^2 + \left(\frac{\partial \phi'}{\partial z'}\right)^2}\ \right]_{z=\eta(x')} \tag{11}$$

where overbar denotes the spatial average over a wave length along the free surface.

BOUNDARY INTEGRAL EQUATION METHOD (BIEM)

The boundary value problem defined through eq. (1) to eq. (7) can be transformed into an integral equation on the boundary only as delineated by Brebbia and Wrobel (15). Thus, the potential at a point p is given by

$$c\phi(p) = \int_\Gamma \frac{\partial \phi}{\partial n}\, \phi^* d\Gamma - \int_\Gamma \phi\, \frac{\partial \phi^*}{\partial n}\, d\Gamma \tag{12}$$

where $\partial\phi/\partial n$ and ϕ are the unknown independent variables, (normal derivative and velocity potential, respectively) and principal value of integrals is implied. The value of c is: c=1 for an internal point, c=0 for an external point, and c=0.5 for a boundary point on a smooth boundary. When the surface is not smooth at the point p, c can be

computed from eq. (12) by setting ϕ = constant over the whole domain Γ is the boundary domain, ϕ^* is the fundamental solution (Green's function) of a concentrated potential at a source point q as determined from the equation $\nabla^2\phi^* + \delta(q) = 0$ ($\delta(q)$ is the dirac delta function). For a two dimensional plane problem, the fundamental solution is $\phi = \ln(1/r)/(2\pi)$, where r is the distance from the source point to the integration point on the boundary. It is noted here that ϕ and $\partial\phi/\partial n$ are two independent variables on the boundary domain since $\partial\phi/\partial n$ cannot be determined from ϕ on the boundary only and vice versa.

For a well posed problem it is sufficient that one of the variables, ϕ or $\partial\phi/\partial n$ be prescribed along every boundary segment. In a numerical solution, the boundary is divided into a number of elements and the independent variables are described by discrete values at element nodes. Consequently a matrix form in terms of ϕ and $\partial\phi/\partial n$ can be written and solved by applying eq. (12) at each node. Once, both nodal velocity potential and normal derivative, ϕ and $(\partial\phi/\partial n)$ are known everywhere on the boundary, the velocity potential and velocity components can be calculated at any interior point as described by Ligget and Liu (16).

NUMERICAL FORMULATION AND SOLUTION

The numerical solution is obtained in the translating coordinate system in which the wave is staionary and symmetric around the wave crest plane. Thus, the model domain need only be half of the wave (i.e. ABCD) as shown in Figure 1.

In the mathematical problem the location of the surface, $\eta(x')$, is not known a priori, but must be determined as part of the solution through the use of conditions (5) and (6). In the present numerical solution an initial location of the free surface is guessed, the dynamic surface condition is imposed and an iterative technique is developed to change the position of the surface until the kinematic condition is also satisfied.

Because only wave length and wave crest elevation can be chosen independently, the problem geometry can be characterized by only a single dimensionless parameter, ξ = ratio between the limit wave crest elevation and limit wave length, making it easier to numerically cover the full range of possible conditions.

Boundary Conditions

Because the wave crest is a stagnation point, the Bernoulli constant $B = \eta_c$, where η_c is the crest elevation. The dynamic free surface condition then becomes

$$V_s = [2g(\eta_c - \eta)]^{1/2} \tag{13}$$

where V_s is the tangential velocity along the free surface. Eq. (13) can therefore be used to determine the velocity potential along a given free surface by performing a line integration along contour AB with the curvilinear coordinate γ.

$$\phi'_s(\gamma) = \int_A^{\gamma} V_s \, d\Gamma + \phi'_s\Big|_A \tag{14}$$

Taking ϕ' in the crest plane equal to 0 and noting $\gamma = \gamma(x')$

a Dirichlet condition is obtained,

$$\phi' = \phi'_S(x') \qquad \text{on } \Gamma_1 \tag{15}$$

A Neumann condition at the bottom is defined by the kinematic bottom boundary condition

$$w' = \frac{\partial \phi'}{\partial n} = 0 \qquad \text{on } \Gamma_3 \tag{16}$$

The assumption that waves are propagating without changing form implies that in the crest and trough planes vertical velocity components are zero, hence, ϕ' is constant

$$\phi' = 0 \qquad \text{on } \Gamma_4 \tag{17}$$

$$\phi' = \phi_T \qquad \text{on } \Gamma_2 \tag{18}$$

where ϕ_T obtained by eq. (14) is the velocity potential at the trough.

Initial Estimate of Surface

A cubic polynomial conforming to the known slopes at both ends (-30 degrees at the crest and 0 degrees at the trough) and passing through the crest and an arbitrarily chosen trough is used as the initial surface. Subsequently, the surface is discretized into a number of elements.

Numerical Schematization

For best possible fit a number of quadratic isoparametric elements are used along the free surface, while normal quadratic elements are used on the rest of the boundary. The nodes are located at the ends and the middle of these elements and have values of ϕ_j and $\partial\phi_j/\partial n$ associated with them, where j=1,2,3...n and n denotes the total number of nodal points.

Because the gradients are expected to be greater near the crest a variable element length is used with elements smallest at that location. Extensive testing showed that a total of 96 boundary elements provided a reasonable compromise between cost of computation and accuracy. The same grid was used for all computations regardless of the value of ξ.

Surface Iteration Technique

Based on the initial surface the BIEM can be executed. The results will in general not satisfy the kinematic boundary condition, but can be made to do so by changing the surface.

A convergent iteration technique based on "influence" solutions and a Newton-Raphson method is developed to perform the surface updating automatically. The technique first computes the change in the kinematic condition residual for unit changes in the elevation of each surface node and organizes the influence solutions in a Jacobian matrix. Based on the current residuals the Jacobian is then used in conjunction with a Newton-Raphson method to determine the optimal change to the elevation of each surface node. Because of the nonlinear nature of the problem, the Jacobian should in theory be computed every time the

surface is changed, however, we have found that in practice the Jacobian does not change much after the first few updates and need not be recomputed.

The iteration technique is continued until an error measure in the kinematic boundary condition defined as

$$\varepsilon_2(\theta) = \frac{\partial \eta}{\partial x'} - \frac{w'}{u'} \tag{19}$$

is below a threshold value. We have chosen this threshold value to be on the order of the round off errors of the method on the 36 bit UNIVAC machine employed for the computations. A flow chart of the solution method is shown in Fig. 2.

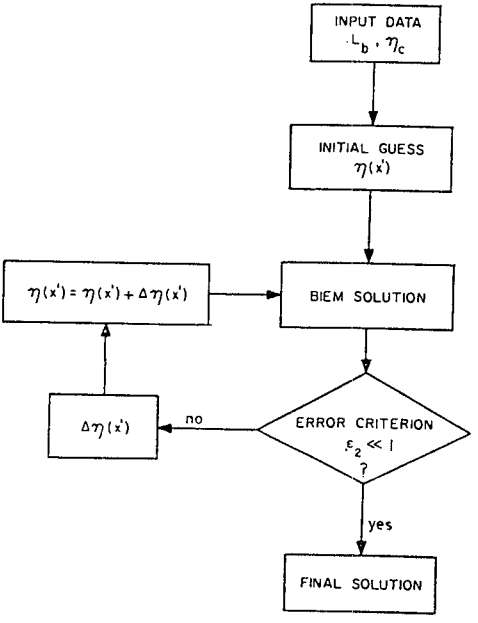

Fig. 2 Flow chart of the BIEM technique.

RESULTS

A unique limit wave is obtained with the BIEM for each discrete value of ξ. (The uniqueness is confirmed by choosing two different initial guesses of surface and obtaining an identical final solution.) However, in practical applications the crest height and wave length necessary to determine ξ are usually not known. The known or more easily obtained parameters are undisturbed water depth (d) and wave period (T). Our results can be made more amenable to practical applications by determining a relationship between ξ and the single dimensionless parameter, d/L_o, with $L_o = gT^2/2\pi$. In addition, it will be

very useful to establish relationships for L_b/L_o, H_b/L_o and η_c/L_o as functions of d/L_o to make possible direct calculation of limit wave length, wave crest elevation and wave height. Due to the assumption of limit waves unique relations can be written as

$$L_b/L_o = f_1(d/L_o) \tag{20}$$

$$\eta_c/L_o = f_2(d/L_o) \tag{21}$$

$$H_b/L_o = f_3(d/L_o) \tag{22}$$

and

$$\xi/L_o = f_4(d/L_o) \tag{23}$$

The functions f_1, f_2, f_3 and f_4 are determined numerically from our results as described in the following.

Based on the BIEM solutions and for each doublet (η_c, L_b) the limit wave height H_b can be calculated by $H_b = \eta_c - \eta_t$, where η_t is the surface elevation at the trough. Furthermore, the undisturbed water depth can be calculated from

$$d = \frac{2}{L_b}\int_0^{L_b/2} \eta(x')\,dx' + \frac{1}{2g}\left[-C_b^2 + \left(\frac{\partial\phi'}{\partial x'}\right)^2 + \left(\frac{\partial\phi'}{\partial z'}\right)^2\right] \tag{24}$$

in which the first term is the mean water level with waves and the second term is the correction for wave set-down.

Invoking the second definition of phase velocity (zero transport), the phase velocity is determined by

$$C_b = -Q'/d \tag{25}$$

in which Q' is the volume flux in the moving frame. Then, the wave period is determined by $T = L_b/C_b$. Consequently, four dimensionless doublets (L_b/L_o, d/L_o), (η_c/L_o, d/L_o), (H_b/L_o, d/L_o), and (ξ, d/L_o) are obtained for each BIEM solution. The relationship among these dimensionless parameters is plotted as shown in Figs. 3, 4, 5, and 6. Thus, for each given wave period and undisturbed water depth the input data, ξ, for the BIEM and the resulting limit wave length, wave height and crest elevation can be determined immediately.

A measure of the error committed in the kinematic boundary condition used by Dean (4) is defined by

$$E_2 = \left[\sum_{j=1}^{N} \varepsilon_2(\theta)^2\right]^{1/2} \tag{26}$$

in which N is the number of sampling points along the wave profile and $\varepsilon_2(\theta)$ is the error at each sampling point. Comparison of E_2 between the BIEM solution with 96 discretized boundary elements and those computed by Dean (4) for other existing wave theories is shown in Fig. 7.

It should be noted that the present solution satisfies the dynamic surface condition "exactly" while the other solutions have errors in

the dynamic condition. Except for very shallow water the BIEM using 96 boundary element provides results with an order of magnitude smaller error. This error could of course be made arbitrarily small by using more elements and a computer with higher precision. Direct comparison with Dean's stream function solution is not possible because it satisfies the kinematic condition exactly while containing errors in the dynamic condition, however, due to the previously mentioned convergence problems significantly better results should be expected from the BIEM solution.

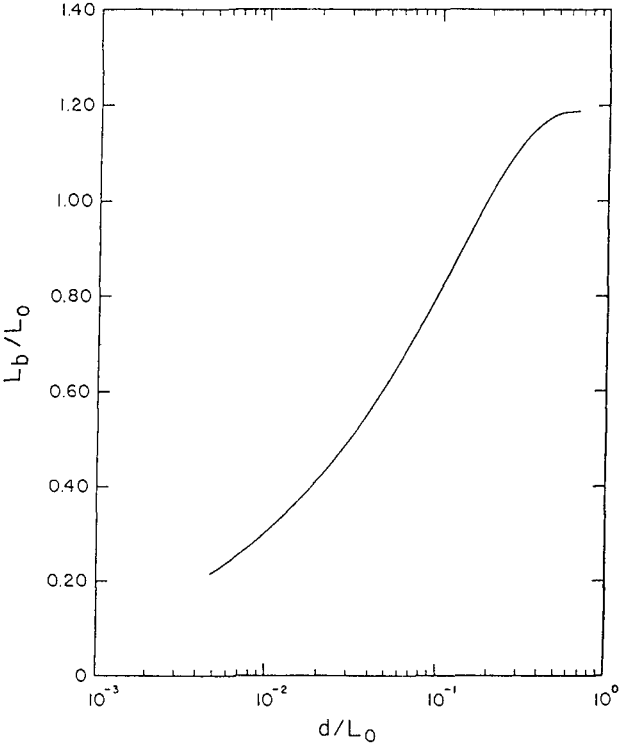

Fig. 3 L_b/L_o versus d/L_o.

The results obtained for H_b/L_o as function of d/L_o (figure 6) may be compared with the theoretical value derived by Michell (17) and Miche (18) who found $H_b/L = 0.142$ in deep water and $H_b/L = .140 \tanh (d/L)$ in intermediate depth water respectively. Due to numerical limitations that the theoretical limit of infinitely deep water cannot be calculated with BIEM approach. The deepest case calculated in this study corresponds to $d/L_o = 0.7$ and the corresponding $H_b/L_b = 0.140$. Note that these expressions use the nonlinear wave-length which is greater than L_o. An earlier study has indicated a ratio between deep water limit wave length and linear wave length of 1.2, (4), while our results yield a value of 1.186 for $d/L_o = 0.7$. As a further verification of our BIEM solutions comparison is also made with the results by

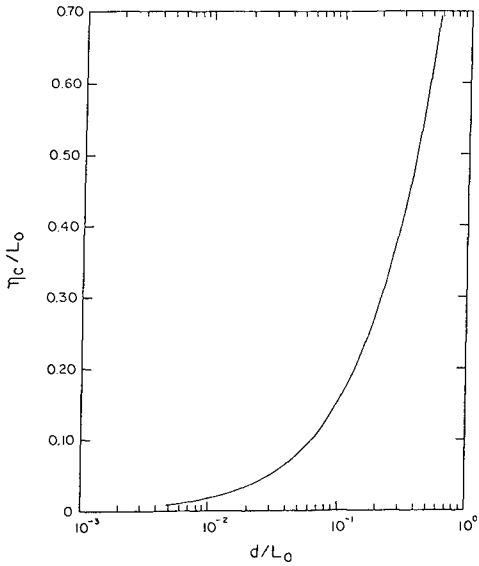

Fig. 4 η_c/L_o versus d/L_o.

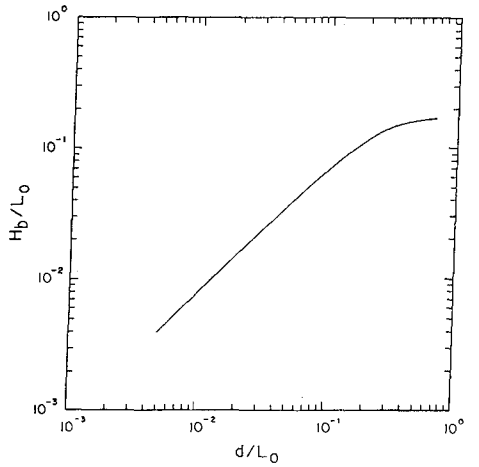

Fig. 5 H_b/L_o versus d/L_o.

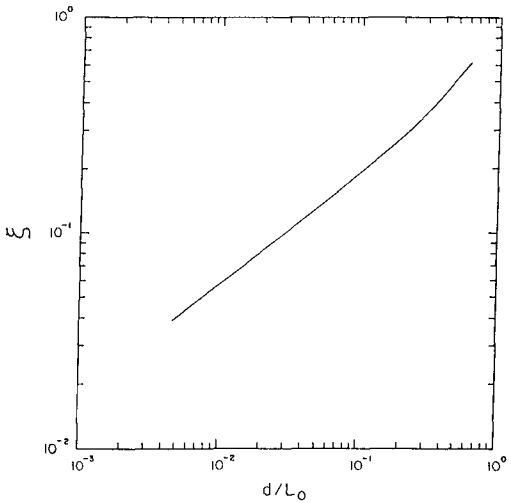

Fig. 6 ξ versus d/L_o.

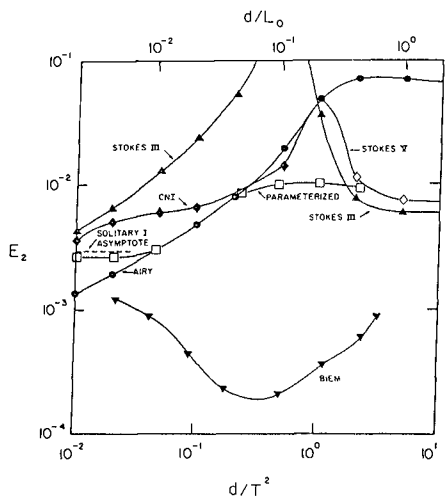

Fig. 7 Comparison of analytic kinematic criterion for limit waves (Dean, 1974)

Schwartz (6), Cokelet (7), and William (10) for three different d/L_b. As is shown in Table 1, the solution obtained by the BIEM technique agrees with the results obtained from these three different limit wave solutions.

$\frac{d}{L_b}$	$\frac{H}{L_b}$ (Schwartz, 1974)	$\frac{H}{L_b}$ (Cokelet, 1977)	$\frac{H}{L_b}$ (Williams, 1981)	$\frac{H}{L_b}$ (BIEM)
0.3665	0.1380	0.1378	0.1378	0.1377
0.0355	-	0.0279	0.0283	0.0279
0.0168	-	0.015	0.0137	0.0139

Table 1: Comparison of limit wave height for various water depths.

CONCLUSION

A numerical solution for periodic nonlinear irrotational surface gravity limit waves is developed by means of the Boundary Integral Equation Method (BIEM). The formulation for limit waves employs Stokes limit criterion.

The BIEM solution theoretically satisfies exactly the Laplace equation, the dynamic surface boundary condition, and Stokes limit criterion, although any numerical solution will contain finite discretization errors. Solution compliance with the kinematic surface condition is forced by iterating the surface until any error is made arbitrarily small. The final surface is taken as the true limit wave. The wave properties including the dimensionless maximum wave height can be determined as functions of a given water depth and wave period. For the cases considered involving 96 boundary elements and iterating to an error $E_2 < 10^{-3}$ one solution requires approximately 45 minutes of CPU time on a UNIVAC 1100/81 system.

ACKNOWLEDGEMENTS

This study was sponsored by the National Science Foundation as part of a study done under Grant No. ENG-11930.

APPENDIX I - REFERENCES

1. Stokes, G.G., 1847. "On the Theory of Oscillatory Waves," Trans. Camb. Phil. Soc. 8, pp 441-455.
2. Boussinesq, J., 1877. "Essai Sur la Theorie des Eaux Courantes," Institu de France, Academie des Sciences, Memories Presents Par Divers Savants, 23.
3. Korteweg, D.J. and De Vries, G., 1895. "On the Change of Form of Long Waves Advancing in a Rectangular Canal on a New Type of Long Stationary Waves," London, Dublin and Edinburgh, Philosophical Magazine, Ser. S. 39, pp 442.
4. Dean, R.G., 1974. "Evaluation and Development of Water Wave Theories for Engineering Application," Vols. I and II U.S. Army, Coastal Eng. Res. Center, Special Report No. 1, Fort Belvoir, VA.

5. Shore Protection Manual, 1984. 2 Volumes, CERC, U.S. Army Corps of Engineers, Ft. Belvoir, VA., Vol. 1.
6. Fenton, J.D. and Rienecker, M.M., 1980. "Accurate Numerical Solutions for Nonlinear Waves," Proc. Coastal Engineering Vol. I, pp 50-69.
7. Rienecker, M.M. and Fenton, J.D., 1981. "A Fourier Approximation Method for Steady Water Waves," JFM, Vol. 104, pp 119-137.
8. Le Mehaute, B., Lu, C.C., and Ulmer, E.W., 1984. "A Parameterized Solution to the Nonlinear Wave Problem," J. of Waterway Harbor and Coastal Engineering Division, Vol. 110, No. 3, Aug. pp 309-320.
9. Stokes, G.G., 1880. "Supplement to a Paper on the Theory of Oscillatory Waves," mathematical and Physical Paper 1: pp 314-326. Cambridge, England.
10. Williams, J.M., 1981. "Limiting Gravity Waves in Water of Finite Depth," Phys. Tran. Roy. Soc., Ser. A. Vol. 302, pp 139-187.
11. Cruse, T.A. and Rizzo, F.J., (ed) 1975. "Boundary-Integral Equation Method: Computational Applications in Applied Mechanics," AMD Vol. II, ASME.
12. Benjamin, T.B. and Feir, J.E., 1967. "The Disintegration of Wave Trains on Deep Water," Part I. Theory, JFM, Vol. 27, pp 417-430.
13. Lu, C.C., 1985. "A Numerical Solution to a Nonlinear Wave Problem Using Boundary Integral Equation Method with Analysis of Limit Cases," Ph.D. Dissertation. Rosenstiel School of Marine and Atmospheric Science, University of Miami, Miami, Florida, USA.
14. Jonsson, I.G. and Wang, J.D., 1978. "Current-Depth Refraction of Water Waves," Institute of Hydrodynamics and Hydraulic Engineering, Technical University of Denmark, Ser. 18.
15. Brebbia, C.A. and Wrobel, L., 1982. "Some Applications of the Boundary Element Method for Potential Problems," Proc. of the 4th Inter. Conf. Hannover, Germany, June 1982, 19-3, pp. 219-28.
16. Liggett, J.A. and Liu, P.L-F., 1983. "The Boundary Integral Equation Method for Porous Media Flow," George Allen and Unwin.
17. Michell, J.H., 1985. "On the Highest Waves in Water," Phil. Mag., Vol. 36, pp. 430-435.
18. Miche, R., 1944. "Mouvements Ondulatorires des Mers en Profondeur Constante on Decroisante," Annales des Ponts et Chausees, pp. 25-78, 1311-164, 270-292, 369-406.

CHAPTER 42

AN EFFICIENT STATISTICAL METHOD OF ESTIMATION OF EXTREME MARITIME EVENTS USING TWO SETS OF RELATED INFORMATION

by

B. MANOHA, J. BERNIER and M. GRAFF *

ABSTRACT

The construction of marine works necessitates a good knowledge of the extreme events which can affect it, such as the storm waves or the water levels. A statistical method of estimation of these extreme events has been developped at L.N.H. The principle of this method, based on the theory of renewal processes, is presented hereafter, as well as the results that it can provide. Some applications of the method are described in the paper ; in particular the application to a site where the available data are insufficient, and where the method enables to precise the results by using complementary numerous data on a neighbouring site, is presented.

1. INTRODUCTION

The important nuclear program developped by Electricité de France since many years, has necessitated, for reasons of safety and reliability, to develop efficient statistical methods enabling to estimate, on the basis of necessarily limited information, extreme natural phenomena such as :

- extreme storm surges (coastal plants) or extreme river flows (river plants), as to fix the highest possible water levels and consequently the corresponding platform levels, thus preventing from flood problems

- extreme low water levels in order to secure a continuous feeding of the intake pumping stations

- extreme waves as to define correct protections of the breakwaters.

The extreme events need to satisfy safety criteria related to return periods associated to these events : for coastal nuclear plants, these return periods are usually 100 years for waves and water level setdowns, 1000 years for water level setups and for river floods (river plants).

* Laboratoire National d'Hydraulique, Electricité de France, Chatou, FRANCE

The method presented hereafter is based on statistical methods previously developped at L.N.H. for problems of floods in rivers ; these methods, derived from the theory of renewal processes, have been adapted to the study of extreme waves, setups and setdowns. It enables a large variety of developments by comparison with the classical method of annual maxima ; in particular this method enables to precise the results by taking into account the complementary information available on a neighbouring site.

We shall only present here examples concerning extreme waves. After a short recall of the notion of return period and of the main other method used, we shall describe the principle of the "partial duration series" method, its practical use, its particular application to the use of two sets of related information, and we shall end with some examples of other applications which can prove useful.

2. THE NOTION OF RETURN PERIOD

It is certainly not useless to recall the important notion of return period and its practical meaning :

The return period T associated with the value H_T of a random variable H (wave height) is defined as the average number of years between two successive occurrencies of the event : $H > H_T$. This definition implicitly assumes a given time unit, the year, at which scale the variable H is defined, for example :

. annual maximum wave height

. significant wave height, for 20 minutes recordings, over-topped every year during 1 day, 2 days, ...

This definition does not imply any regularity of the occurrencies $H > H_T$. The basic assumptions concerning the annual successive occurrencies are :

a/ their independance

b/ the stationarity : invariance of their probabilities of occurrency during the time.

The number of years N separating two successive occurrencies of the studied event is a random variable such as :

$$\text{Prob}\left[N \leqslant n\right] = 1 - (1 - \frac{1}{T})^n \simeq 1 - e^{-\frac{n}{T}}$$

(valid for T big enough)

In practice, this formula gives, for a project whose lifetime is n, the probability of occurrence of an event whose return period is T (figure 1) :

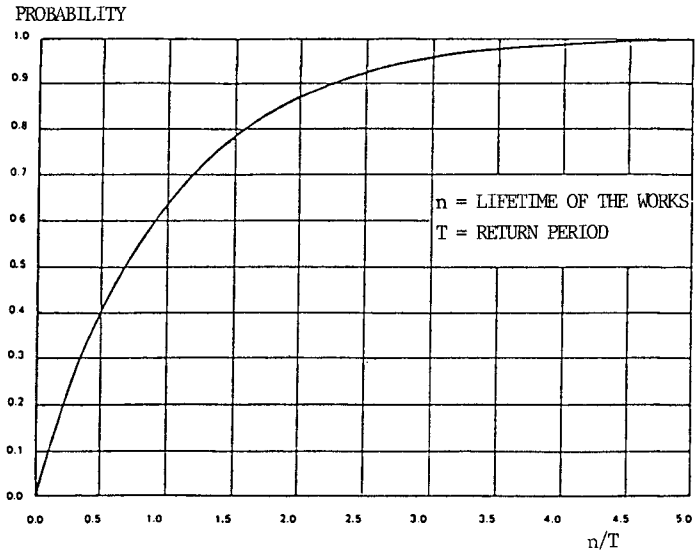

- Figure 1 -

For example, a plant whose lifetime is 50 years (n = 50) has approximately 10% chances to see, at least once in its life, an event associated with a return period of 500 years (T = 500) ; this occurrency reaches 40% for T = 100 years, and 63% for T = 50 years, which is far from negligible.

This emphasizes the point that the return period of a given project must be chosen equal to several times the lifetime of the works in order to limit the risk of damages to an acceptable level.

3. THE STATISTICAL METHODS

The classical method of estimation of the risks associated to extreme geophysical events uses the notion of annual random variable : maximum annual wave height, maximum annual rainfalls or floods, ... : it is known as the method of annual maximas.

Considering that the risk is based on an annual time scale, it seems logical to base the estimation on series of annual maximum values derived from complete sets of data.

This method, widely used in many geophysical problems, can be applied only if the number of years of available data is sufficiant to make a reasonnable extrapolation to extreme events.

In fact, very often, the available data for marine phenomena are related to short periods of measurements, and this method of annual maxima gives information which can lead to a very important uncertainty.

Another approach enables to use a more complete information : not necessarily the complete set of basic data, which would lead to a too complex probabilistic structure, but the most "significant" information constituted of the maximum values of each storm (for sea states), these values being chosen higher than a given threshold Ho as to eliminate small and non significant values.

This approach, based on the theory of renewal processes (by analogy with probabilistic models used in problems of reliability of components in plants), is called the "partial duration series" method.

As we shall see hereafter, this method, compared to other classical methods, enables to use a more complete set of information (bigger than a given threshold), and is then much more efficient in the very frequent case of short periods of available data. Moreover, the method enables to provide a "confidence interval" giving the range of reliability of the obtained results.

4. THE PARTIAL DURATION SERIES METHOD

4.1. Principle of the method

Given a chronological series of wave height data (figure 2), one can define significant independant events Hj higher than a given threshold Ho as follows :

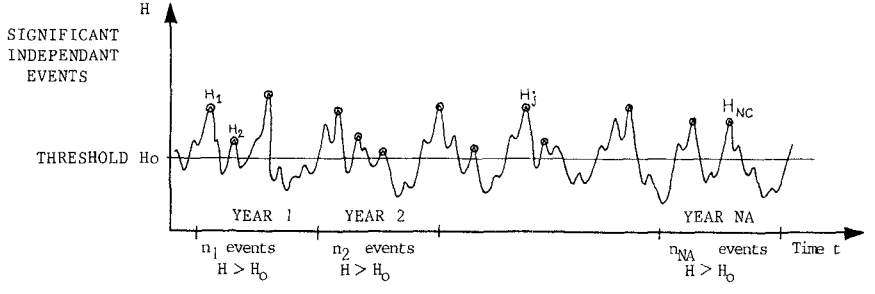

- Figure 2 - Chronology of waves

The notion of significant events, related to the threshold Ho, means that the small values corresponding to weak storms do not need to be considered in this kind of problems where we are in fact only interested in strong storms and their associated probabilistic laws enabling to extrapolate to extreme events.

The other notion of independant storms is very important and corresponds to an assumption of the method. Various definitions can be used : the simplest one consists in considering that two successive storms, characterized by their maximum wave heights Hj, are independant if the wave height between those two storms comes lower than the threshold Ho (figure 2) ; other more sophisticated, and more adapted, definitions use different thresholds (one H_1 for defining significant storms, another lower one Ho, related to H_1 as a percentage of it, defining the end of the storm), or integrate the notion of duration of calm (H < Ho) between two successive storms. In fact this notion of independance is rather difficult to appreciate automatically and must be considered very carefully and cautiously.

From this chronology of significant independant events measured during NA years, one can then define two series :

- Series $\{ n_i \}$ i = 1, NA

  where n_i is the number of events H > Ho during year i

  and P (k) is the associated probability of trespassing k times Ho during year i

- Series $\{ H_j \}$ j = 1, NC

  series of independant wave heights H_j > Ho (NC values)

  with F^k (H) associated probability that H > height > Ho during the year.

The selected storms are then interpreted as the combination of two stochastic processes : one of occurrencies (n_i , P (k)), the other of distribution of selected wave heights (H_j , F^k (H)).

For annual risks, the two processes must be combined to obtain the distribution of the annual maximum wave (same kind of procedure for decennial, centennial or other return periods) :

$$\text{Prob } (H_{max} > H) = 1 - \sum_{k=o}^{\infty} P(k).F^k(H)$$

4.2. Statistical laws

. Series of occurrencies $\{ n_i \}$:

In practice, when the selection of independant storms has been correctly made and the threshold Ho chosen high enough, the series of occurrencies most of the time follows a Poisson process of intensity

$$P(k) = e^{-\lambda}\frac{\lambda^k}{k!}$$

Generally, one assumes that the storm phenomenon is stationary, i.e. its statistical characteristics are independant of the season, which means λ = constant.

However it happens sometimes that this Poisson law does not appear realistic ; the computer program developped at LNH enables then to use also the binomial negative law for the series of occurrencies :

$$P(k) = \frac{\Gamma(\gamma + k)}{k!\,\Gamma(k)}\, p^{\gamma}(1+p)^{k}$$

$$\text{with } \Gamma(\alpha) = \int_0^{\infty} e^{-x}\, x^{\alpha-1}\, dx$$

. Series of wave heights $\{H_j\}$:

The series of wave heights can follow various statistical laws which have also to be adjusted in the method. The computer program tests automatically 4 different laws which, from experience, proved generally to be the best fitted with the wave data :

- Exponential : $\text{Prob}(h < H) = 1 - e^{-\varphi(H-Ho)}$
- Weibull : $\text{Prob}(h < H) = 1 - e^{-\varphi(H-Ho)^p}$
- Log-exponential : $\text{Prob}(h < H) = 1 - e^{-\varphi(\text{Log } H - \text{Log } Ho)}$
- Squares : $\text{Prob}(h < H) = 1 - e^{-\varphi(H^2-Ho^2)}$

In practice, for estimate of extreme wave heights, the Weibull law proved, on the french coasts, to be generally the best fitting law. It has to be noted that the exponential law is a particular application of Weibull law with p = 1.

4.3. Adjustment of the statistical laws :

For all the statistical laws tested for the series of occurrencies and heights, the various parameters characterizing the theoretical expressions (λ, φ, p in particular) are estimated through the classical statistical method of Maximum Likelihood, except for the binomial negative law (series $\{n_i\}$) where the Momentum method is used.

4.4. Validation tests

The validation of the assumptions of the model and of the adjusted distribution laws (occurrencies and wave heights series) is performed through statistical tests which are systematically applied for various thresholds Ho. These tests are :

- Serial independance test of the successive selected maximum wave

heights higher than a given threshold Ho. This test uses the classical transformation $T = \frac{\sqrt{V}\,R}{1-R^2}$, approximatively distributed according to a Student law with V degrees of freddom, where R is the autocorrelation coefficient and V the number minus 2 of couples of storms used for the calculation of R. The calculated value T is then compared with the threshold of probabilistic significance equal to 0.95.

- Classical X^2 test. The determination of the K classes necessary to the calculation of :

$$X^2 = \sum_{i=1}^{K} \frac{(n_i - v_i)^2}{v_i}$$

is made so that the theoritical absolute frequencies v_i, to be compared with the observed frequencies n_i, are equal to the constant value n/K (n is the size of the studied sample).

4.5. Confidence intervals

On the contrary of semi-empirical methods, the partial duration series method, which uses a rigorous modelisation of the probabilistic properties of the wave heights process, enables to calculate confidence intervals associated to wave heights H_T corresponding to a given return period T.

The confidence interval, associated to a confidence threshold $1-\alpha$ (70%, 90%, ...), covers the real, but unknown, value of the extreme wave height H_T with a probability equal to $1-\alpha$.

The amplitude of this confidence interval enables to measure the uncertainties on H_T related to the sampling. It is of course all the bigger as the size of the sample is smaller. The interval is calculated for each fixed statistical law, and then it does not take into account the uncertainty related to the choice of the law, this choice being made through the validation tests previously described (cf. 4.4), and through graphical adjustments (see hereafter).

The method of calculation of these confidence intervals, automatically integrated to the computer program which calculates the 70% confidence interval, uses the approximate properties of the estimations of the maximum likelikoods.

5. PRACTICAL USE OF THE METHOD

Given a sample of wave heights during a certain period of recordings, the use of the method implies different steps before leading to the final result, i.e. decennial, centennial, ... wave height with its corresponding confidence interval :

- Choice of the series of independant significant storms whose maximum wave heights H are bigger than a given threshold Ho.

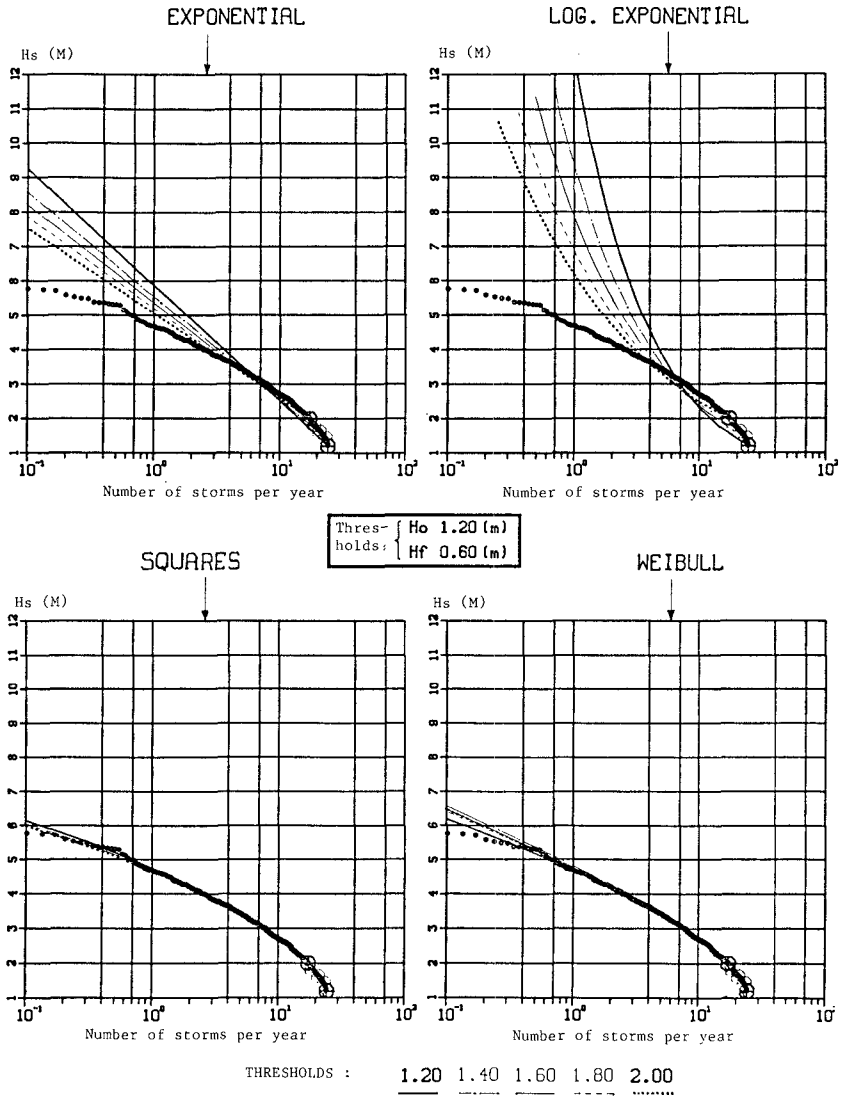

- Figure 3 - Adjustment to the different laws

These wave heights can correspond to mean, or significant H 1/3, or maximum Hmax wave heights derived from the recordings, depending on the problem which is considered. As mentionned previously, different definitions of "independant" events can be chosen.

- From this sample H>Ho, the adjustments to the 4 statistical laws are tested automatically : exponential, Weibull, Log-exponential and squares law (see example of results on figure 3).

- For each statistical law, different thresholds H'o over a basic threshold Ho are tested. As a matter of fact, the threshold which will be finally chosen will have to be :

  . not too low as to represent sufficiently well the impact of the extreme observed events (we are interested here in extreme events corresponding to big return periods)

  . not too high in order to keep a sufficiently large number of events as to be able to make correct statistics on a big enough sample.

- The final choice (statistical law and threshold to be finally considered) will then be made on the basis of the three main following criteria (example of final result on figure 4) :

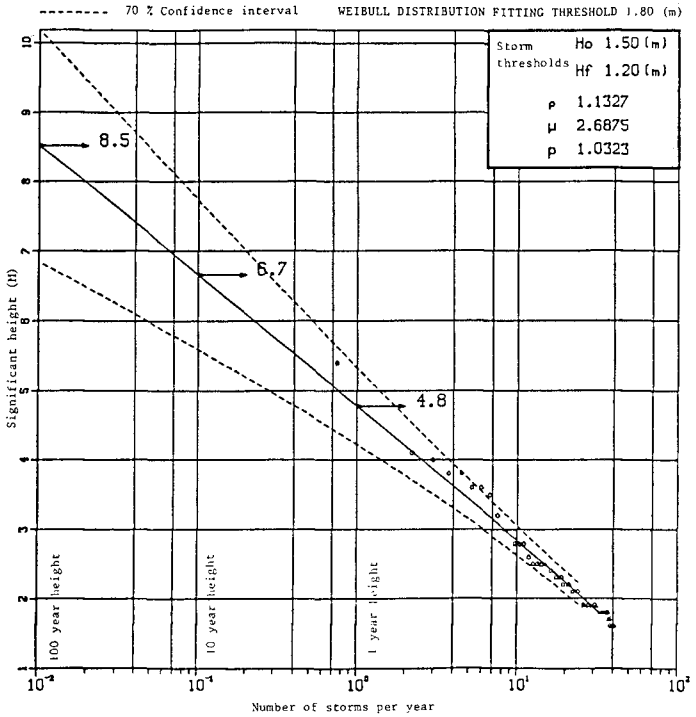

Fig.4 - Annual, decennial and centennial significant waves at BIARRITZ

. graphic adjustment : for each law and threshold, one can see visually if the theoretical adjustment fits or not with the observed values : for the example on figure 3 one can see that the squares law gives the best adjustment with the observations

. X^2 statistical tests : the method provides automatically the X^2 value for each law and threshold and gives an advice, based on statistical criteria, on wheter the adjustment should be accepted or not.

. stability with the threshold : usually, if the adjustment is good, the results on the extreme events do not depend very much on the choice of the threshold H'o.

On the basis of these criteria, one can then make his choice, which is not always very easy, especially for short periods of measurements. An example of final choice is given on figure 4 : on the site of Biarritz, south of France, where some measurements where available from may 1972 to february 1977, the Weibull law was finally chosen with a threshold H'o = 1.80 m (basic threshold Ho = 1.50 m for the definition of independant storms) ; the centennial significant H1/3 wave height (return period of 100 years) was found to be 8.5 m with a 70% confidence interval between 6.8 m and 10.2 m, showing that in this case the uncertainty on the results remains rather large (many holes in the period of measurements).

The method has been used systematically up to now, for 10 sites on the French coast (about 20 more applications are currently under progress), and shows in particular that we need, if we want to get sufficiently reliable results on a site for return periods of at least 10 years, an average period of wave measurements of about 4 years minimum, taking into account the fact that, for many reasons, on average only half of this period (about 2 complete cumulated years) will really provide reliable and useful data.

6. USE OF TWO SETS OF RELATED DATA

6.1. Principle

One of the interests of the method is that it is easy to take into account complementary information (punctual historical data, or information on a neighbouring site) in order to precise the results.

A fresent case concerning the wave recordings is that of a site where only a short series of data X is available, which can lead to a big uncertainty on the estimation of extreme events.

If there exists, on a neighbouring site, a longer series of available data Y, this complementary information can be used to precise the results on site X if there exists a good correlation between the data recorded during the concomitant period (figure 5) :

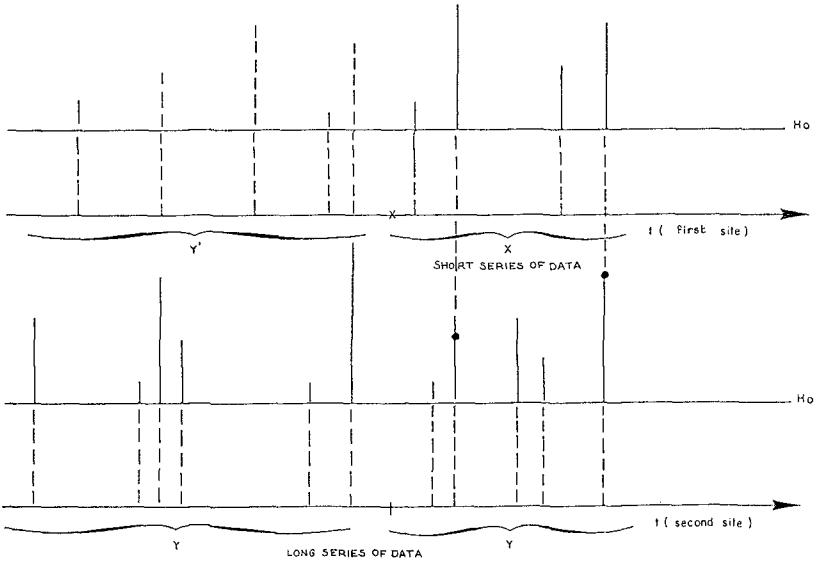

- Figure 5 - Example of concomitant and non concomitant data on the two sites

The idea is then, in this case, to complete the existing information X, Y on the two sites by a fictive information Y' corresponding to missing data on the first site.

The problem is now to estimate this missing information Y' $(Y,\lambda,\varphi, p, r)$; as a matter of fact this estimation depends, not only on the complementary existing information Y, but also on the parameters of the partial duration series (λ,φ, p), and on the correlation parameter r between the two sites.

The calibration of the model will then consist in estimating the parameters λ,φ, p and r on the basis of the real observations X completed by the rebuilt complementary fictive data Y' $(Y,\lambda,\varphi, p, r)$, which necessitates a certain preliminary knowledge of these parameters : this approach is then necessarily based on an iterative process. The E.M. algorithm (E : expectation, M : maximization) developped by Dempster and al-1977 was adopted to solve the problem.

6.2 Example

An example of application of this method is presented on figure 6 on the case of Paluel, where 5 years are available, completed by the 10 years of available data on the neighbouring site of Antifer. It shows the estimation, at Paluel, of annual, decennial and centennial significant wave heights obtained without and with the complementary Antifer information. One can see that with the exponential law chosen as the best adjustment, the decennial wave height changes from 5 m to

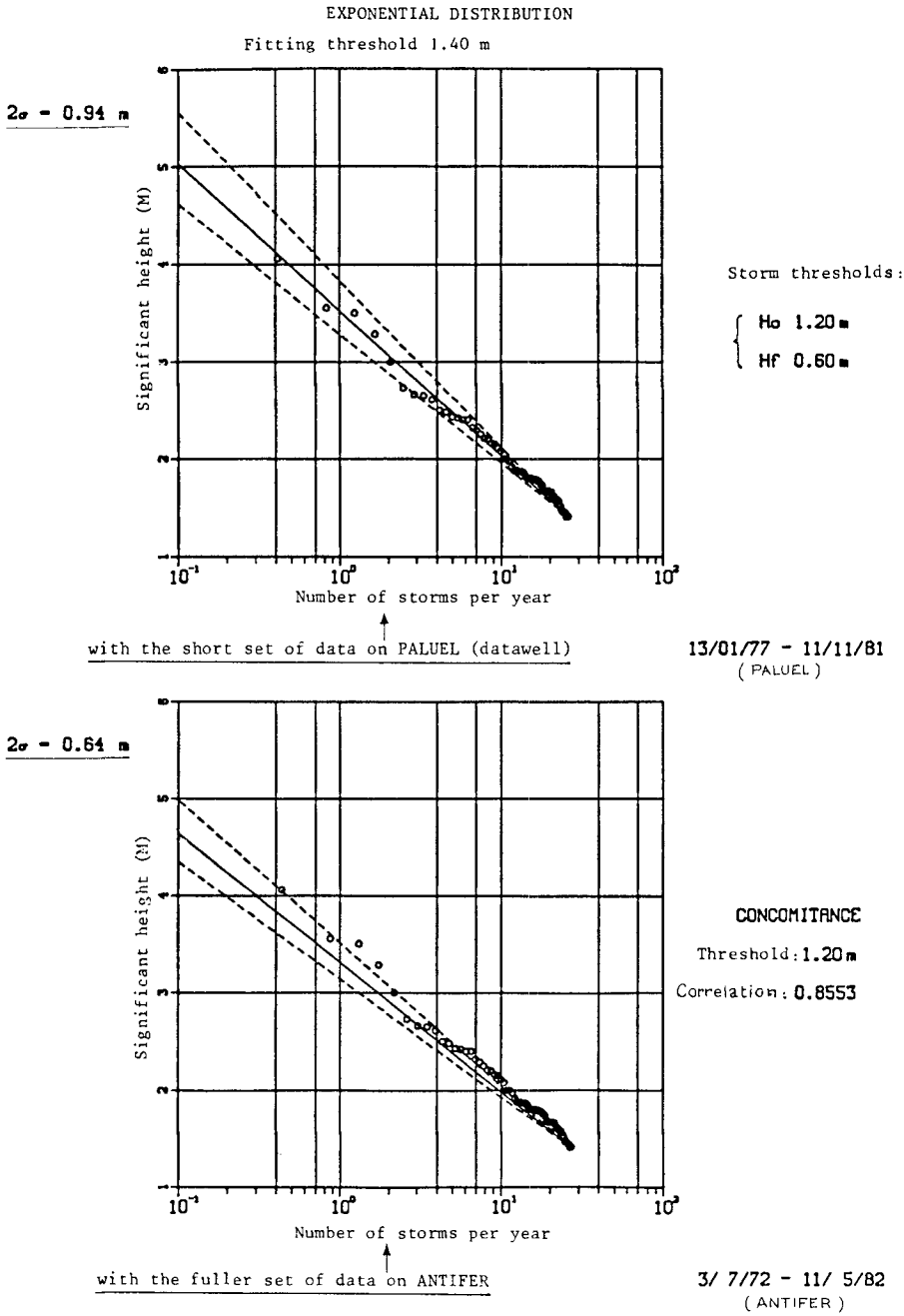

- Figure 6 - Estimation of the design wave at PALUEL

4.6 m with this complementary information, the confidence interval being moreover reduced from 0.94 m to 0.64 m. In this case the correlation coefficient corresponding to the concomitant data was 0.86.

6.3. Further developments

The general problems to be thought about now are to try to determine which is the minimum duration of the short series, and wich is the minimum value of the correlation in order to be sure to obtain good results.

These problems are linked and depend very much on the quality and homogeneity of the data, and on the proximity of the site where the complementary data are available, considering that we are only interested here in extreme events corresponding to strong storms which, if the neighbouring site is not too far, should reasonnably occur rather similarily on both sites.

Up to now, only the application to Paluel - Antifer has been made and no general rule (if any can be found...) can be deduced from the results. Moreoever the method was applied with various lengths of the measuring period at Paluel (6, 9, 12, 21 and 24 months), showing that, in this case, at least 21 months of cumulated available data were necessary, the correlation coefficient varying from 0.61 (with 6 months) to 0.84 (21 months).

Some applications to other sites are planned and should provide interesting information on these particular points. It seems nevertheless that the degree of correlation between the two sites should be at least 0.8 as to be able to get reliable results on the first site.

7. OTHER POSSIBLE APPLICATIONS

Without going into detail in the various applications which have been made with the partial duration series method, we can mention some of them and some further developments associated with the method :

- Integration of historical data : the same kind of methodology as described for two sets of related data can be used in the case where punctual historical data are available. This is often the case for setups or river floods, and can also, but less often, happen for waves ; this complementary information can be introduced in the data in order to precise the results concerning extreme events.

- Duration of the storms : for a given sample of wave recordings H>Ho, one can associate a complementary third series of data $\{ Dj \}$ corresponding to the durations of the storms. Then a statistical analysis of these durations, being made for various increasing thresholds H'o through the partial duration series method, can be

performed in order to associate to a given return period, a series of wave heights with their corresponding durations ; this gives then a much more complete information than only the classical extreme wave height associated to a "zero" duration. This has been made for different sites on the french coast and gives very interesting results which can be used for many purposes (example of height - duration diagram at Antifer on figure 7).

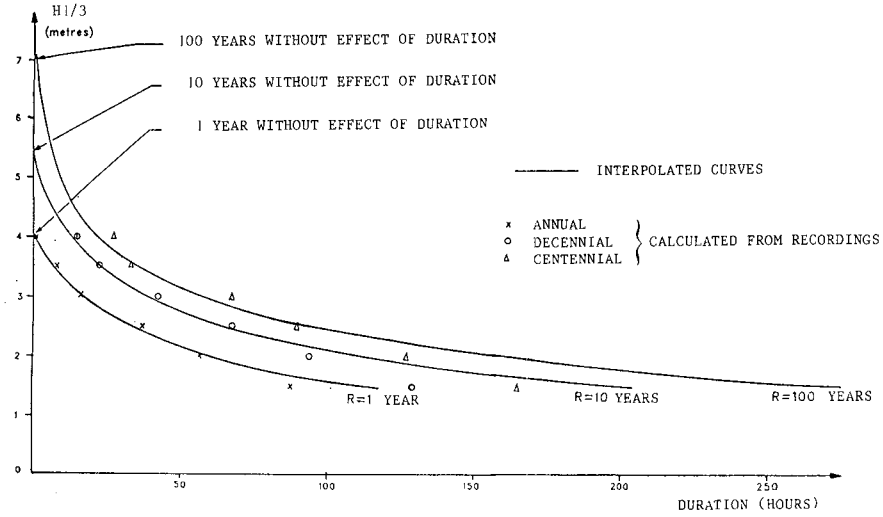

- Figure 7 - Height - duration diagram at ANTIFER

- Effect of the sampling interval : very often wave measurements are made every 2 or 3 hours, sometimes rather continuously (every 20 or 40 minutes for example). Then a study has been made to see the effect of the chosen sampling interval on the results ; this study is in fact very connected with the previous one on the durations of storms.

- Effect of the definition of independant storms : different definitions, more or less sophisticated, have also been tested and gave some interested information which, as for the other applications hereabove mentionned, cannot unfortunately be described here in detail.

8. CONCLUSIONS

The partial duration series method has been systematically applied to extreme wave heights on a certain number of sites on the french coast, through an automatic procedure developped in a computer program. Similar versions applied to setups, setdowns and river floods have been used for the setting of nuclear platforms along the coast or rivers. The basic philosophy of elaboration of the method

was to develop practical tools enabling a complete calculation of extreme waves, from the preparation of data, the determination of analysed events, the statistical validation of the assumptions, the adjustments of the laws, to the final presentation (graphic in particular) of the results.

The need of promoting methods adapted to the most common applications encountered in practice led to develop also procedures and methods enabling in particular the treatment of various types of incomplete information.

Further useful developments can be envisaged concerning in particular the adjustment of a non-stationnary model (effect of the seasons in particular) and of a model of treatment of the missing data.

REFERENCES

J.BERNIER, M.GRAFF - Méthodes d'estimations de la houle de projet avec données incomplètes - Rapport EDF-DER HE/42/83.34.

A.R.DEMPSTER, N.M.LAIRD, D.B.RUBIN - Maximum likelihood from incomplete data via the E.M. algorithm. J.R Stat. Soc - B - n° 39-1-1977.

J.FEUILLET, J.BERNIER, Y.COEFFE, B.CHALOIN - Le dimensionnement des digues à talus - Eyrolles - 1985.

M.GRAFF, Y.COEFFE, J.BERNIER, B.DELANNOY - Notice d'utilisation du programme EVENAL - Estimations d'évènements extrêmes (houle) par la méthode du renouvellement - Rapport EDF-DER HE/42/84.35.

M.G.KENDALL, A.STUART - Advanced theory of statistics - Vol 2 - Griffin - 1961.

J.MIQUEL, J.BERNIER - Sûreté des centrales et états de la mer - Bulletin EDF-DER série A n° 2 - 1981 - pp 73-78.

J.MIQUEL - Guide pratique d'estimation des probabilités de crue - Eyrolles - Collection EDF-DER n° 53 - 1984.

CHAPTER 43

WAVE GROUP PROPERTY OF WIND WAVES FROM MODULATIONAL INSTABILITY

Hajime Mase* and Yuichi Iwagaki, M.ASCE**

ABSTRACT

This paper discusses wave grouping of wind waves from the physical viewpoint of wave modulational instability. Amplitude modulation periods obtained from the smoothed instantaneous wave energy history (SIWEH) of the observed data are compared with the predicted values by the modulational instability theory using the Zakharov equation for a finite constant water depth derived by Stiassnie and Shemer(1984). The modulation period normalized by the typical wave period corresponds to the length of total run. It is shown that the amplitude modulation periods of the observed data agree satisfactorily with the predicted values. Thus we conclude that the modulational instability is a hydrodynamical cause of grouping of high waves.

INTRODUCTION

In recent years wave grouping has been recognized by coastal engineers as an important factor for the stability of rubble mound breakwaters, the fluctuation of wave overtopping quantity of seawalls, the slow drift oscillation of moored vessels and floating structures, the surf beat and so on. Johnson, Mansard and Ploeg(1978) have found by laboratory experiments that even if power spectra of random waves are the same, the degree of damage of a rubble mound breakwater is not the same but depends on the degree of wave grouping; that is, grouped waves cause more severe damage of the breakwater than non-grouped waves.

There are three kinds of theoretical approaches to the statistical properties of run length and total run length of wave heights. One is the theory by Goda(1970) for waves of which successive wave heights are independent, the second is the wave envelope theory by Nolte and Hsu(1973) and Ewing(1973) for waves with narrow-banded spectra, and the third is the Markov process theory by Kimura(1980) for waves of which successive wave heights are mutually correlated with the property of the Markov chain. Elgar, Guza and Seymour(1984)

* Research Associate, ** Professor, Department of Civil Engineering, Kyoto University, Kyoto, 606, Japan

reviewed these existing theories and showed that the theories have internal inconsistencies in their assumptions and treatments.

Studies on statistical properties of wave groups of ocean waves have been carried out by Wilson and Baird(1972), Rye(1974), Chakrabarti and Snider(1974), Goda(1976), Burcharth(1980), Goda(1983), Elgar et al.(1984), Mase and Iwagaki(1984) and Battjes and van Vledder(1984). In these studies, observations of wave group statistics have been compared with the theoretical predictions or with the numerical simulation data. It seems from these studies that among the theories of run length Kimura's theory is most applicable to waves with not only narrow-banded but also wide-banded spectra if the correlation parameter which appears in the two-dimensional Rayleigh distribution and is related to the correlation coefficient of successive wave heights is chosen adequately. However, when the correlation coefficient is larger than 0.4, the mean length predicted by the theory of Kimura is always shorter than the observed one (Mase and Iwagaki, 1984).

Most of the studies concerning wave groups including theories are based on a statistical viewpoint. The existing theories are not based on hydrodynamics of wave motion but consider only statistical wave properties, such as the wave energy spectrum or the wave height distribution. Wave groups are also significant in coastal engineering from a viewpoint of hydrodynamics. One is the modulational instability and the evolution of finite amplitude surface waves. The other is a new model of wind waves such as the envelope soliton model proposed by Mollo-Christensen and Ramamonjiarisoa(1978) (wind wave fields are not composed of linear component waves but composed of envelope solitons which are formed by Stokes waves) and the modulated nonlinear wave model shown by Lake and Yuen(1978) (wind wave fields are considered as a modulated nonlinear wave train with a single carrier wave).

The grouping of high waves can be explained by two different viewpoints. One is the statistical viewpoint in which wave group statistics are discussed in a framework that wave fields are thought to be the superposition of independent linear component waves. The other is the hydrodynamical viewpoint such as the modulational instability. Benjamin and Feir(1967) have made it clear that a uniform wave train in deep water is unstable and that it evolves into a modulated wave train. Lake and Yuen(1978) compared the theoretical modulation frequency by Benjamin and Feir(1967) with the observed one of laboratory wind waves. It was found that both agree qualitatively.

Even if a parameter representing wave groups is a statistical quantity, the characteristic dominated by hydrodynamics is probably contained in the statistical quantity. The objective of this paper is to discuss the wave group property of natural wind waves from the hydrodynamical viewpoint. Concretely, we compare the observed amplitude modulation periods (or repetition periods of groups of high waves) with the predicted ones from the modulational instability theory using the Zakharov equation. The modulation periods normalized by the typical wave period correspond to the lengths of total runs.

ANALYZED WAVE DATA

Wave data used in this paper were collected at Hikone-Aisei of

Lake Biwa in Shiga Prefecture, Japan, where eleven wave gauges of capacitance type were installed. Wave observations at Hikone-Aisei Wave Observatory and Nagahama Wave Observatory were started by Iwagaki et al.(1976) in March, 1975, for the duration of a year to examine properties of fetch-limited wind waves.

Wave data analyzed for amplitude modulation periods are four continuous records of storm waves for five hours from 11:27, 18:00, and 23:00 on October 5, and from 18:30 on December 16, 1975, recorded by the wave gauge N-9 installed in water depth of 4m. The first two have been analyzed in the previous paper (Mase and Iwagaki, 1984) from the statistical viewpoint. The predominant wave direction was NW when the waves analyzed here were recorded, which was nearly perpendicular to the shoreline. The slope of the beach was nearly uniform and approximately 1/50.

The records were digitized at a sampling interval of 0.04 s and recorded on a magnetic tape. These continuous wave records were divided into fourteen segments of twenty minutes long. Fig.1 shows the time series of the significant wave height, $H_{1/3}$, the significant wave period, $T_{1/3}$, the mean wave height, $\overline{H}$, and the mean wave period, $\overline{T}$. The numbers of individual waves contained in each wave record were about 300 to 600.

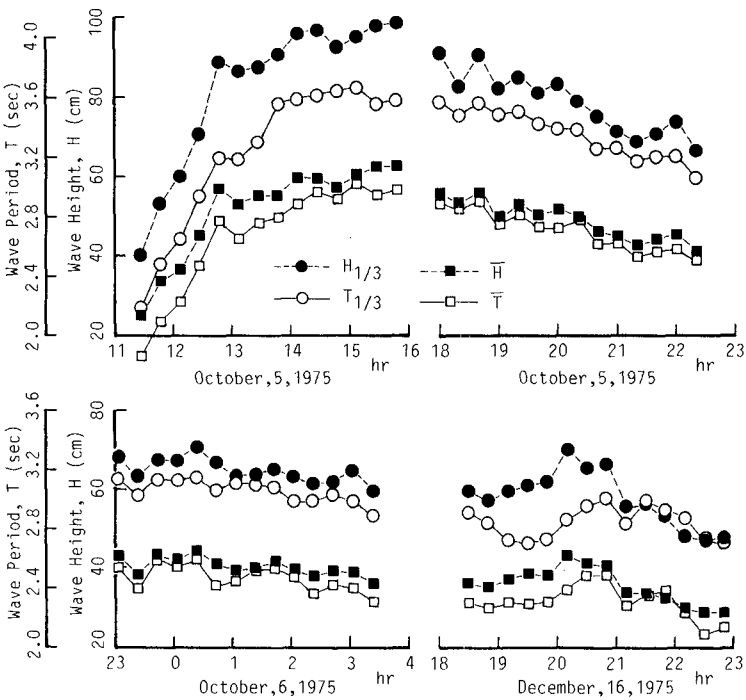

Fig.1. Time series of significant wave height, significant wave period, mean wave height and mean wave period.

AMPLITUDE MODULATION PERIOD BY MODULATIONAL INSTABILITY THEORY

As for the analysis of modulational instability of waves, it has been shown by Crawford, Lake, Saffman and Yuen(1981) that the Zakharov equation first derived by Zakharov(1968) is a useful equation which can consider the effect of finite amplitude. In this section, we describe the theory of modulational instability using the Zakharov equation according to Crawford et al.(1981) and Stiassnie and Shemer(1984), and later we compare the amplitude modulation period predicted by the theory with the observed one. Crawford et al.(1981) used the third order Zakharov equation for infinite deep water, and Stiassnie and Shemer(1984) derived the Zakharov equation to the fourth order for constant (finite or infinite) water depth and investigated the Class I and Class II instabilities by using the modified Zakharov equation. In this study, we use the Zakharov equation up to the third order for finite water depth derived by Stiassnie and Shemer(1984).

Let $B(\boldsymbol{k},t)$ be a kind of amplitude spectrum. The Zakharov equation to the third order is expressed as follows (Crawford et al. and Stiassnie et al.):

$$i\frac{\partial B(\boldsymbol{k},t)}{\partial t} = \iiint_{-\infty}^{\infty} T(\boldsymbol{k},\boldsymbol{k}_1,\boldsymbol{k}_2,\boldsymbol{k}_3)B^*(\boldsymbol{k}_1,t)B(\boldsymbol{k}_2,t)B(\boldsymbol{k}_3,t) \times \delta(\boldsymbol{k}+\boldsymbol{k}_1-\boldsymbol{k}_2-\boldsymbol{k}_3)\exp\{i\{\omega(\boldsymbol{k})+\omega(\boldsymbol{k}_1)-\omega(\boldsymbol{k}_2) - \omega(\boldsymbol{k}_3)\}t\}\,d\boldsymbol{k}_1 d\boldsymbol{k}_2 d\boldsymbol{k}_3, \quad (1)$$

where $*$ denotes the complex conjugate, $\boldsymbol{k}=(k_x,k_y)$ is the wavenumber vector, ω is the angular frequency related to the wavenumber as $\omega(\boldsymbol{k})=(g|\boldsymbol{k}|\tanh|\boldsymbol{k}|h)^{1/2}$, and δ denotes the delta function. Eq.(1) represents the interaction of amplitude spectra or the slow evolution of the dominant components of waves. The kernel $T(\boldsymbol{k},\boldsymbol{k}_1,\boldsymbol{k}_2,\boldsymbol{k}_3)$ (abbreviated as $T_{0,1,2,3}$ hereafter) is shown in the paper of Stiassnie and Shemer(1984). Since there are some misprints in the expression of the kernel, we used the correct expression informed directly by Dr. Stiassnie. The kernel $T_{0,1,2,3}$ is seen in Mase and Iwagaki(1986).

In the case of a uniform wave train with the wavenumber vector $\boldsymbol{k}_0=(k_0,0)$, the solution of Eq.(1) is

$$B_0(\boldsymbol{k}_0,t) = b_0\exp(-iT_{0,0,0,0}b_0^2 t), \quad (2)$$

where $T_{0,0,0,0}b_0^2$ is the Stokes corrected frequency due to the nonlinearity and b_0 is related to the actual amplitude a_0 as follows:

$$b_0 = \pi\left(\frac{2g}{\omega_0}\right)^{1/2}a_0. \quad (3)$$

When disturbances with the wavenumber vectors $\boldsymbol{k}_1=\boldsymbol{k}_0-\boldsymbol{K}$ and $\boldsymbol{k}_2=\boldsymbol{k}_0+\boldsymbol{K}$ with the amplitudes $B_1(\boldsymbol{k}_1,t)$ and $B_2(\boldsymbol{k}_2,t)$ ($|B_1|, |B_2| \ll |B_0|$) are imposed on the uniform wave train, the time evolutions of B_1 and B_2 are

written from Eq.(1) neglecting the squares of small quantities by

$$i\frac{dB_1}{dt} = 2\,T_{1,0,1,0}b_0^2B_1 + T_{1,2,0,0}B_2\,b_0^2\exp(-i\tilde{\omega}t), \tag{4}$$

$$i\frac{dB_2}{dt} = 2\,T_{2,0,2,0}b_0^2B_2 + T_{2,1,0,0}B_1\,b_0^2\exp(-i\tilde{\omega}t), \tag{5}$$

here, $\tilde{\omega} = (2\,\omega_0 - \omega_1 - \omega_2) + 2\,T_{0,0,0,0}b_0^2$. Assuming a solution of the form

$$B_1 = b_1\exp\{-i(0.5\,\tilde{\omega} - \Omega)t\}, \tag{6}$$

$$B_2 = b_2\exp\{-i(0.5\,\tilde{\omega} + \Omega)t\}, \tag{7}$$

the following equation is obtained using the condition that the non-trivial solutions of b_1 and b_2 exist:

$$\Omega = (T_{2,0,2,0} - T_{1,0,1,0})b_0^2 \pm\sqrt{\{0.5\,\tilde{\omega} - (T_{1,0,1,0} + T_{2,0,2,0})b_0^2\}^2 - T_{1,2,0,0}T_{2,1,0,0}b_0^4}. \tag{8}$$

When Ω is not real, disturbances grow exponentially with time and amplitude modulations occur, which means the instability of waves.

For the two-dimensional case such as $K=(K_x,0)$, the non-dimensional perturbation wavenumber κ is defined by K_x/k_0. Fig.2 shows the non-dimensional growth rate $\mathrm{Im}(\Omega)/(\omega_0k_0^2a_0^2/2)$ as a function of $\kappa/2k_0a_0$ for various values of k_0a_0 and for five values of k_0h. Fig.2(a) is the same result as given by Crawford et al.(1981). In experiments with deep water waves by Lake, Yuen, Rungaldier and Ferguson(1977), it was found that even if a uniform wave train is generated by a wave-making paddle the wave train modulates with increase in the propagation distance due to the growth of the most unstable mode which corresponds to the peak of each curve in Fig.2. For example, when waves are generated for which $k_0a_0=0.1$, disturbances with $\kappa/2k_0a_0=0.87$ grow in the case of deep water, see Fig.2(a). It is seen from Fig.2 that the domain of the non-dimensional wavenumber $\kappa/2k_0a_0$ becomes narrow and the non-dimensional growth rate of disturbances $\mathrm{Im}(\Omega)/(\omega_0k_0^2a_0^2/2)$ decreases with decrease in k_0h for the same value of k_0a_0, when $k_0a_0\leqq0.3$. The modulational instability cannot occur if the non-dimensional water depth k_0h is smaller than 1.36.

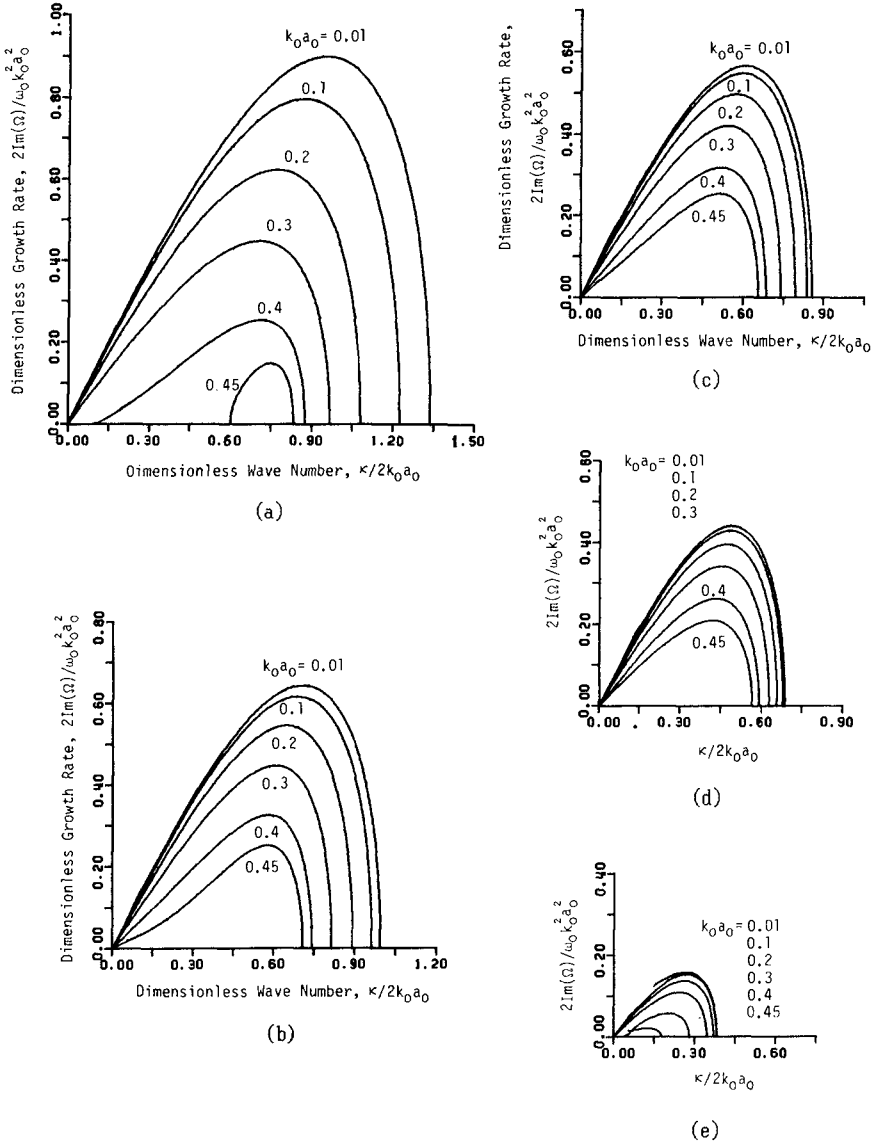

Fig.2. Wave instability diagram. (a) k_0h=10.0; (b) 3.0; (c) 2.5; (d) 2.0; (e) 1.5.

The amplitude modulation period to be compared with the observed modulation period is calculated as follows. For given values of k_0a_0 and k_0h, the value of κ corresponding to the most unstable mode is found. The frequencies of disturbances are given as function of κ by

$$\omega_1' = \omega_1 + 0.5\,\tilde{\omega} - \mathrm{Re}(\Omega), \tag{9}$$

$$\omega_2' = \omega_2 + 0.5\,\tilde{\omega} + \mathrm{Re}(\Omega), \tag{10}$$

where $\mathrm{Re}(\Omega)$ denotes the real part of Ω. The frequency of the dominant wave including the Stokes correction is

$$\omega = \omega_0 + T_{0,0,0,0}b_0^2. \tag{11}$$

The non-dimensional difference between frequencies of the dominant wave and disturbances becomes

$$\Delta = (\omega - \omega_1')/\omega = (\omega_2' - \omega)/\omega$$

$$= \{0.5(\omega_2 - \omega_1) + \mathrm{Re}(\Omega)\}/\omega. \tag{12}$$

Finally, the amplitude modulation period is given by

$$T_g = 2\pi/\Delta\omega. \tag{13}$$

Until now we have used the wavenumber k_0 and the amplitude a_0 of a carrier wave. Wave characteristics obtained by experiments and field observations are not a_0 and k_0, but the wave height H and the wave period T. Therefore, we have to estimate a_0 and k_0 by using H and T. In the estimation of a_0 and k_0 from H, T and the water depth h, we can use the third order Stokes wave theory. Since, however, waves observed in fields are not uniform, and it is not known what quantity we should use as the carrier wave. Lake and Yuen(1978) used the average wave steepness in comparing the experimental results of modulation frequencies with the theoretical values of Benjamin and Feir(1967). In this study, we adopt the significant waves or the mean waves as the carrier waves for the time being, and use $H/2$ as a_0 and the wavenumber determined from T and h by the small amplitude wave theory as k_0.

Fig.3 shows the time series of values of ka and kh obtained from the significant wave (designated with subscript '1/3') and from the mean wave (designated with subscript 'm').

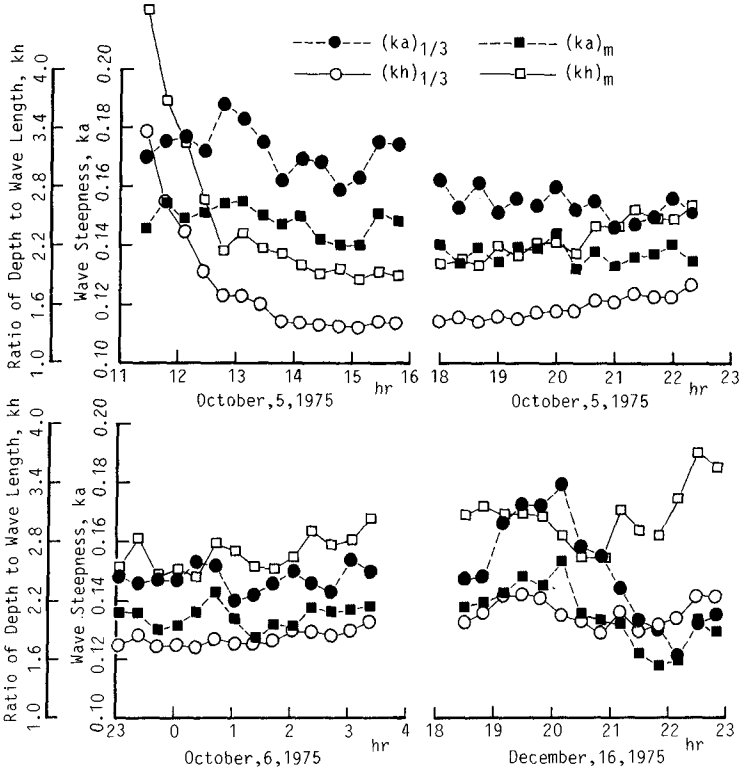

Fig.3. Time series of wave steepness ka and dimensionless water depth kh.

COMPARISON OF OBSERVED AMPLITUDE MODULATION PERIOD WITH PREDICTED ONE BY MODULATION INSTABILITY THEORY

We use the smoothed instantaneous wave energy history (SIWEH) proposed by Funke and Mansard(1979) to calculate the amplitude modulation period of field data. The SIWEH, $E(t)$, is described by

$$E(t) = \frac{1}{T_p} \int_{-\infty}^{\infty} \eta^2(t+\tau) Q(\tau) d\tau, \tag{14}$$

$$Q(\tau) = \begin{cases} 1 - |\tau| / T_p & |\tau| < T_p \\ 0 & |\tau| \geqq T_p \end{cases}, \tag{15}$$

where T_p is the peak period of an energy spectrum, $\eta(t)$ the water surface variation, and τ the time lag.

The amplitude modulation period can be estimated from the SIWEH by various methods. One is to use the peak period of the energy spectrum of SIWEH, $(T_g)_{MP}$. The other is to use the mean value of the zero-up-crossing times of $\{E(t)-\bar{E}\}$, $(T_g)_{MF}$, in which the SIWEH is modified so that the component waves of which frequencies are lower than $0.5/(T_g)_{MP}$ and higher than $1.5/(T_g)_{MP}$ are removed by using the Fast Fourier Transform technique. The amplitude modulation periods $(T_g)_{MP}$ and $(T_g)_{MF}$ almost agree, see Mase and Iwagaki(1986).

Fig.4 shows the comparison of the observed modulation periods $(T_g)_{MP}$ and $(T_g)_{MF}$ with the predicted ones $(T_g)_{CS}$ and $(T_g)_{CM}$ where $(T_g)_{CS}$ is calculated from the significant wave and $(T_g)_{CM}$ from the mean wave by Eq.(13). The predicted values larger than 40.0 s are plotted at 40.5 s in the figure. The values of $(T_g)_{CS}$ are large compared with the observed values except from 11:30 to 12:10 on

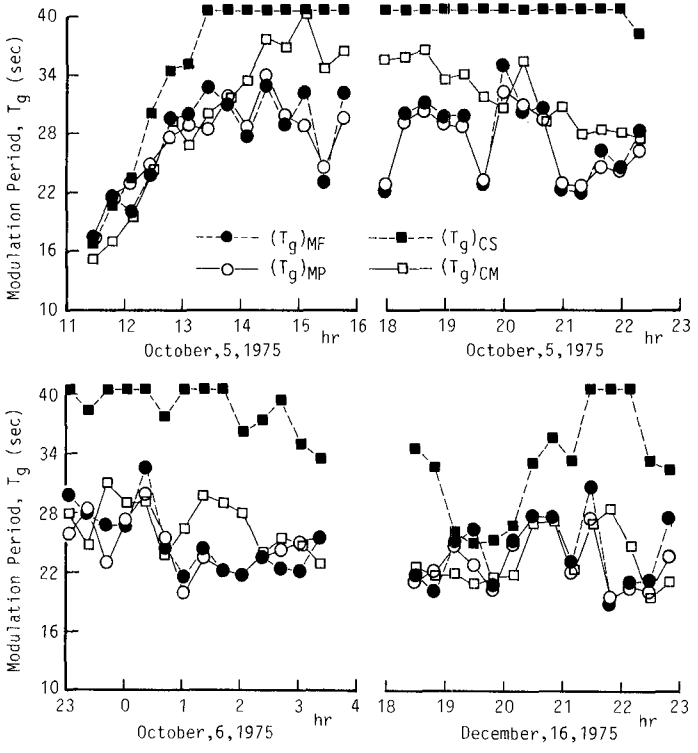

Fig.4. Time series of observed and predicted amplitude modulation periods.

October 5 and from 19:10 to 20:10 on December 16 where the value of $(kh)_{1/3}$ is larger than 2.0. On the other hand, the values of $(T_g)_{CM}$ agree fairly well with the observed data in a wide range. It is seen from the figure that we should better use the mean wave as the carrier wave than the significant wave. However, the values of $(T_g)_{CM}$ are always larger than the observed ones when the value of $(kh)_m$ is smaller than 2.1 (14:30 to 19:30 on October 5).

Fig.5 shows the comparison of $(T_g)_{MF}$ and $(T_g)_{CM}$ in a different form. This figure indicates that the agreement between both values is satisfactory as far as the mean values are concerned. When the non-dimensional water depth $(kh)_m$ is small, the difference between the predicted values and observed ones becomes large the reason is explained in the following discussion.

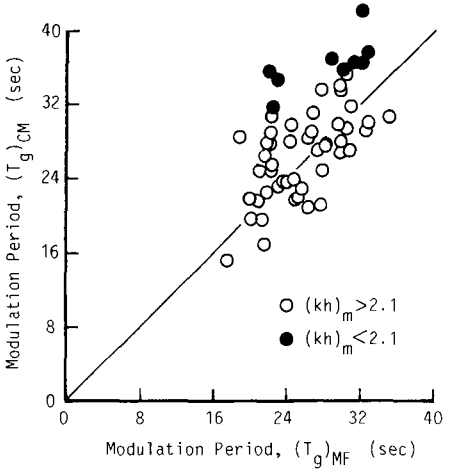

Fig.5. Comparison of observed amplitude modulation period with predicted one.

DISCUSSION

The Zakharov equation derived by Stiassnie and Shemer(1984) was applied to the present study. In spite of the sloping beach of 1/50, the modulational instability theory by the Zakharov equation can predict the amplitude modulation periods of wind waves sufficiently when the non-dimensional water depth is large ($(kh)_m$>2.1 according to the present study). However, there are slight differences between the observed and predicted values of amplitude modulation periods in the case when the water depth is relatively shallow. As shown in Fig.2, the growth rate of disturbances becomes small and the difference between frequencies of the dominant wave and the disturbances becomes

small with decrease in the water depth. Thus, for waves propagating from deep water into a region with small water depth (as $(kh)_m<2.1$), it is considered that amplitude modulations to be formed do not take place sufficiently due to the small growth rate of sideband modes, and that the deep-water amplitude modulation period remains dominant at the shallow-water observation point.

In the experiments of evolutions with the fetch or with the propagation distance of laboratory wind waves by Hatori(1984) and of mechanically generated random waves by Mase, Furumuro and Iwagaki(1984), it was found that there are several significant spikes, or sideband modes around the spectral maximum. The existence of sideband modes indicates that a phenomenon of wave modulational instability occurs in wave fields. Furthermore, Fig.5 in this paper and Fig.13 in the paper of Lake and Yuen(1978) both show that the modulational instability is an important factor in grouping of high waves.

At present, random waves used in experiments are simulated so that their energy spectrum matches a certain target spectrum. However, the sequence of waves, or wave groups, must be considered to simulate the more realistic sea waves. Funke and Mansard(1979) proposed a new technique of random wave simulation which simulates waves to match a target spectrum and a target SIWEH. Mase, Kita and Iwagaki(1983) used the same technique to simulate random waves. From the present study, it is found that the agreement between the amplitude modulation periods obtained from SIWEH of field data and predicted ones by the modulational instability theory is fairly good. This implies that the mean value of repetition periods or the peak period of the target SIWEH used in the random wave simulation must coincide with the theoretical modulation period determined from the wave height and the wave period.

CONCLUSIONS

The grouping of high waves can be explained by two different viewpoints, the statistical and physical viewpoints. Most studies concerning wave groups including run theories depend on the statistical viewpoint. In this paper, we discussed the wave group property of wind waves from the physical viewpoint of wave modulational instability. We chose the amplitude modulation period as a representative factor of the wave group property. The modulation period was calculated from the smoothed instantaneous wave energy history. The theoretical modulation period was calculated by the modulational instability theory using the Zakharov equation.

A comparison of the observed and theoretical modulation periods showed acceptable agreement if the mean wave was chosen as the carrier wave. In particular, when the non-dimensional water depth is as large as $(kh)_m>2.1$, both periods agree well. However, there was a slight difference between both values in the case of shallow water depth, which is attributed to the small growth rate of sideband modes and the effect of the remaining modulation period dominant in the deeper water depth. Thus we conclude that the modulational instability is a hydrodynamical cause of grouping of high waves.

ACKNOWLEDGMENT

We would like to thank Dr. M.Stiassnie, Department of Civil Engineering of Technion (Israel), for his kind suggestion to the Zakharov equation.

REFERENCES

Battjes,J.A. and van Vledder,G.Ph., 1984. Verification of Kimura's theory for wave group statistics. Proc.19th Coastal Eng. Conf., pp.642-648.

Benjamin,T.B. and Feir,J.E., 1967. The disintegration of wave trains on deep water, Part 1. Theory. Jour. Fluid Mech., Vol.27, pp.417-430.

Burcharth,H.F., 1980. A comparison of natural waves and model waves with special reference to wave grouping. Proc.18th Coastal Eng. Conf., pp.303-318.

Chakrabarti,S.H. and Snider,R.H., 1974. Mean length of ocean waves. Jour. Geophys. Res., Vol.79, No.36, pp.5665-5667.

Crawford,D.R., Lake,B.M., Saffman,P.G. and Yuen,H.C., 1981. Stability of weakly nonlinear deep water waves in two and three dimensions. Jour. Fluid Mech., Vol.105, pp.177-191.

Elgar,S., Guza,R.T. and Seymour,R.J., 1984. Groups of waves in shallow water. Jour. Geophys. Res., Vol.89, No.C3, pp.3623-3634.

Ewing,J.A., 1973. Mean length of run of high waves. Jour. Geophys. Res., Vol.78, No.12, pp.1933-1936.

Funke,E.R. and Mansard,E.P.D., 1979. Synthesis of realistic sea states in a laboratory flume. National Res. Council of Canada, Hydraulics Lab. Rept., LTR-HY-66, 54p.

Goda,Y., 1970. Numerical experiments on wave statistics with spectral simulation. Rept. Port and Harbour Res. Inst., Vol.9, No.3, pp.3-57.

Goda,Y., 1976. On wave groups. Proc. Int. Conf. on Behavior of Offshore Structures, pp.115-128.

Goda,Y., 1983. Analysis of wave grouping and spectra of long-travelled swell. Rept. Port and Harbour Res. Inst., Vol.22, No.1, pp.1-41.

Hatori,M., 1984. Nonlinear properties of laboratory wind waves at energy containing frequencies. Jour. Oceanographical Soc. Japan, Vol.40, pp.12-18.

Iwagaki,Y., Tuchiya,Y., Sakai,T., Yamaguchi,M., Shibano,T., Kimura,A., Yasuda,K. and Serizawa,S., 1976. Wave observation in Lake Biwa. Disaster Prevention Res. Inst., Annuals, Vol.19, pp.361-379 (in Japanese).

Johnson,R.R., Mansard,E.P.D. and Ploeg,J., 1978. Effects of wave grouping on breakwater stability. Proc.16th Coastal Eng. Conf., pp.2228-2243.

Kimura,A., 1980. Statistical properties of random wave groups. Proc.17th Coastal Eng. Conf., pp.2955-2973.

Lake,B.M., Yuen,H.C., Rungaldier,H. and Ferguson,W.E.Jr., 1977. Nonlinear deep-water waves: Evolution of a continuous wave train. Jour. Fluid Mech., Vol.83, pp.49-74.

Lake,B.M. and Yuen,H.C., 1978. A new model for nonlinear wind waves. Jour. Fluid Mech., Vol.88, pp.33-62.

Mase,H., Kita,N. and Iwagaki,Y., 1983. Random wave simulation

considering wave groups. Coastal Eng. in Japan, JSCE, Vol.26, pp.61-75.
Mase,H. and Iwagaki,Y., 1984. An analysis of wave data for wave grouping. Coastal Eng. in Japan, JSCE, Vol.27, pp.83-96.
Mase,H., Furumuro,K. and Iwagaki,Y., 1984. The change of characteristics of wave groups with wave traveling. Proc.31th Coastal Eng. Conf., JSCE, pp.158-162 (in Japanese).
Mase,H. and Iwagaki,Y., 1986. Wave group analysis of natural wind waves based on modulational instability theory. Coastal Eng., Vol.10 (in print).
Mollo-Christensen,E. and Ramamonjiarisoa,A., 1978. Modeling the presence of wave groups in a random wave field. Jour. Geophys. Res., Vol.83, pp.4117-4122.
Nolte,K.G. and Hsu,F.H., 1973. Statistics of ocean wave groups. Prepr. 4th OTC, No.1688, pp.139-146.
Rye,H., 1974. Wave group formation among storm waves. Proc.14th Coastal Eng. Conf., pp.164-183.
Stiassnie,M. and Shemer,L., 1984. On modifications of the Zakharov equation for surface gravity waves. Jour. Fluid Mech., Vol.143, pp.47-67.
Wilson,J.R. and Baird,W.F., 1972. A discussion of some measured wave data. Proc.13th Coastal Eng. Conf., pp.113-130.
Zakharov,V.E., 1968. Stability of periodic waves of finite amplitude on the surface of a deep fluid. Jour. Appl. Mech. Tech. Phys. (Engl. Trans.) 2, pp.190-194.

CHAPTER 44

ON THE GROWTH OF WATER WAVES BY TURBULENT WIND

H. Mitsuyasu[1)] and T. Kusaba[1)]
Professor Research Associate

Abstract

The growth of water waves by turbulent wind is studied on the basis of typical results of recent studies. It is shown that the energy input from wind to a spectral component is not much affected by the existence of the other spectral components, and the dimensionless growth rate β/f is uniquely determined by u_*/c if the friction velocity u_* measured over the water surface is used for the analysis. It is also shown that steep monochromatic waves without wind action show very complicated spectrum, but, under the wind action, they tend to be a continuous spectrum which has a spectral peak near the frequency of the lower side band and satisfy the 3/2 power law.

1. Introduction

Since the very famous studies of Miles (1957) and Phillips (1957), great many studies have been made on the growth of water waves by turbulent wind. Particularly many reliable results of field and laboratory measurements have been reported on the growth rate of water waves by turbulent wind (Snyder et al. 1981, Plant 1982, Hsiao & Shemdin 1983).

However, there still remains several fundamental problems that are not fully understood. For example, the following questions are still difficult to answer; Is the growth of dominant wave affected by high frequency waves overlapping on the dominant wave ? Is the energy transfer from wind to a certain spectral component affected by the existence of the other spectral components ? What is the role of wave breaking in the process of wave growth ?

In order to answer these questions and to clarify the fundamental process of wind-induced growth of water waves, discussions are made on the basis of typical results of our recent studies. Although individual studies have been published elsewhere (Mitsuyasu & Honda 1982, Kusaba & Mitsuyasu 1984, Kusaba & Mitsuyasu 1986), important results are combined and discussed in the present paper.

---

1) Research Institute for Applied Mechanics, Kyushu University, Kasuga 816, Japan.

2. Experiments

The following three laboratory experiments have been conducted;

Experiment 1; The wind-induced growth of mechanically-generated monochromatic waves with relatively small steepness has been measured in a wind wave flume both for ordinary tap water and for water containing a surfactant (Mitsuyasu & Honda 1982). In the former water, wind waves are generated and overlap on the mechanically-generated waves, while in the latter water, no wind waves develop on the surface of the mechanically-generated waves. Thus we can measure the wind-induced growth of monochromatic waves with or without the effects of wind waves overlapping on the monochromatic waves. Thirty different waves were used in the experiment; their periods were in a range 0.6 sec $\sim$1.3 sec and their steepness without wind action were in a range 0.01$\sim$0.06. The wind speed was changed successively as 5, 7.5, 10, 12.5 (m/s).

Experiment 2; Similar measurements have been made for mechanically-generated composite waves which have two different frequency components to clarify the effects of other spectral components on the energy transfer from wind to a certain spectral component (Kusaba & Mitsuyasu 1984). As shown in Table-1 two kinds of composite waves were used for the experiment. One has two component waves with much different period, i.e., T =0.6 sec and T =1.2 sec. Another one has two component waves with similar periods, i.e., T =0.6 sec and T =0.7 sec.

Experiment 3; The wind-induced growth of unstable monochromatic waves with relatively large steepness has been measured in the same wind-wave flume for ordinary tap water to clarify the effect of nonlinear instability on the wind-induced growth of water waves (Kusaba & Mitsuyasu 1986). The properties of the waves without wind action are shown in Table-1. The wave (7)(T =0.5 sec, H =1.7 sec, H/L=0.044) is a stable one which is used for the comparison, e.g., to verify the empirical relation derived from the results of the Experiment 1, or to compare its growth properties with those of the unstable waves (8) and (9).

All of the measurements have been done in a wind-wave flume 0.8 m high, 0.6 m wide and with a usual test-section length of 15 m (Fig.1). Waves were measured with resistance type wave gauges at eleven stations (eitht stations for Experiment 3) of 1 m interval. Experimental conditions are summerized in Table-1, where Ur is a reference wind speed measured at the inlet of the test section. Power spectra of every waves were obtained through a FFT method and the spectral energy of the fundamental component was analyzed in the studies. The friction velocity of the wind was

determined from the vertical wind profiles measured above the water surface in the test section. More detailed descriptions of the experiment are referred to the individual papers (Mitsuyasu & Honda 1982, Kusaba & Mitsuyasu 1984, Kusaba & Mitsuyasu 1986).

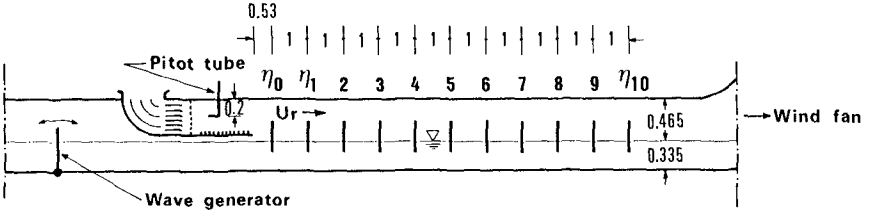

Fig.1 Schematic diagram of wind-wave flume (units in m).

TABLE - 1

EXPERIMENTAL CONDITIONS

Experiment	Water depth d(m)	Wind speed Ur(m/s)	Waves T(sec)	H(cm)	H/L
1	0.335	5, 7.5 10, 12.5	0.6-1.3 thirty different waves	-	0.01 ~0.06
2	0.355	7.7	(1)0.6 (2)1.2 (3)composite waves of (1) and (2) (4)0.6 (5)0.7 (6)composite waves of (4) and (5)	2.0 2.0 1.1 1.5 	0.036 0.011 0.02 0.02
3	0.320	10	(7)0.5 (8)0.5 (9)0.5	1.7 3.2 4.1	0.044 0.082 0.105

3. RESULTS AND DISCUSSIONS

3.1 Wind-induced growth of monochromatic waves with or without overlapping short waves.

Monochromatic waves superimposed by high frequency wind waves grow exponentially with fetch. Their exponential growth rates, β show a quadratic relation to the friction velocity of the wind, u_*,

$$\beta / f = 0.34 \, (u_*/c)^2, \qquad (1)$$

where f is the frequency of the waves and c is the corresponding phase velocity. Almost the same relation holds for the monochromatic waves with smooth surface, i.e., without overlapping wind waves, if the measured friction velocity of the wind is used for the relation (Fig.2).

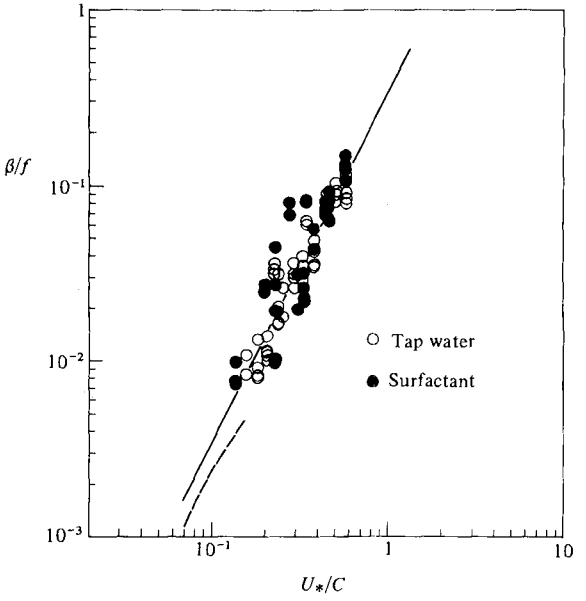

Fig.2 Comparison of β/f for tap water with that for water containing surfactant. The solid line is (1) and the broken line is (2).

For the latter case, the measured growth rate is smaller than that for the former case, but the friction velocity of the wind is also small, and the same relation between β/f

and u_*/c holds for the both cases. A kind of u_*/c similarity is satisfied for the growth of water waves by turbulent wind. We can say, from these results, that the effect of steep short waves overlapping on longer waves are to increase the growth rate of the longer waves through the increase of the downward momentum flux of the wind.

In Fig.2 the broken line corresponds to the empirical relation from Snyder et al. (1981):

$$\beta / f = 0.04 u_*/c - 1.7 \times 10^{-3}, \qquad (2)$$

which is obtained from their original form for the growth-rate parameter $Im\gamma$, $Im\gamma = (0.2 \sim 0.3)(U_5/c-1)$, using the relation $\beta/f = 2\pi(\rho a/\rho w)\, Im\gamma$ and assuming $\rho a/\rho w = 1.2 \times 10^{-3}$ and $U_5 = 23 u_*$. Figure 2 shows that the empirical relation (1) gives slightly larger growth rate than that given by (2) of Snyder et al. (1981) in a region near $u_*/c = 0.1$.

3.2 Wind-induced growth of composite waves.

Figure 3 shows the growth rates of the composite waves, where the growth rates of each component waves alone are also shown with the same symbol. It can be seen that the

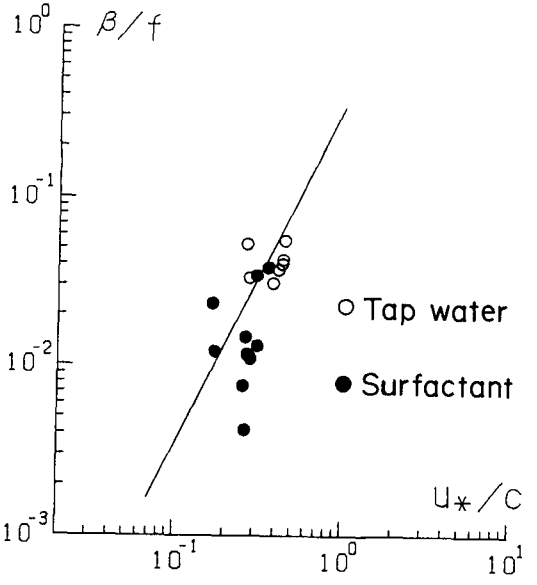

Fig.3 Growth rate of component waves of composite waves which have two frequency components.

growth rates of component waves of the composite waves follow approximately to the empirical relation (1). It should be noted, however, that one of the data for the surfactant water deviate greatly from the empirical relation (1). This data correspond to the wave (5)(T=0.7 sec) co-existing with the wave (4)(T=0.6 sec) for the water containing surfactant*). For this composite wave , since the periods of the component waves are fairly close, the waves show beat structures and their amplitude increase at the loop. Therefore, wave instability or small scale breaking might have happened, which has decreased greatly the growth rate.

Although further studies are needed to clarify the deviation of some data, we can say that the energy transfer from the wind to a certain spectral component is not much affected by the other spectral components if the wave steepness is not large. This is a reason why the empirical relation (1) for monochromatic waves is similar to the relation of Plant (1982), that has been obtained by using various wave data including the waves with contineous spectrum.

3.3 Wind-induced growth of unstable waves

Steep monochromatic waves become gradually unstable even without wind action. Since Benjamine & Fair (1967) made a pioneering study on the nonlinear instability of the Stokes waves, great many studies have been done on this problem; Comprehensive review has been given by Yuen & Lake (1982). However, many of the previous studies are concerned with the instability of steep waves without wind action.

In Fig.4, the left band figure shows the evolution of the spectra of steep unstable waves without wind action and the right hand side shows that of steep unstable waves under wind action. The thin smooth curves in the figure correspond to the wind wave spectra measured independently at each fetch. From the top to the bottom, fetches are 2.51, 4.51, 6.51, 8.61, 10.51 (m) respectively.

The spectra of the steep unstable waves without wind action show many spikes which are attributed to the fundamental frequency component, higher harmonics, and their side bands generated by the wave instability. Under the wind action, however, the higher harmonics and their side band are masked with wind wave spectrum, even the side bands of the fundamental frequency component are obscured, and the wave spectrum tends to be a continuous spectrum which has a

---

*) The similar deviation also happened for the same composite waves on a tap water. This data is out of this figure.

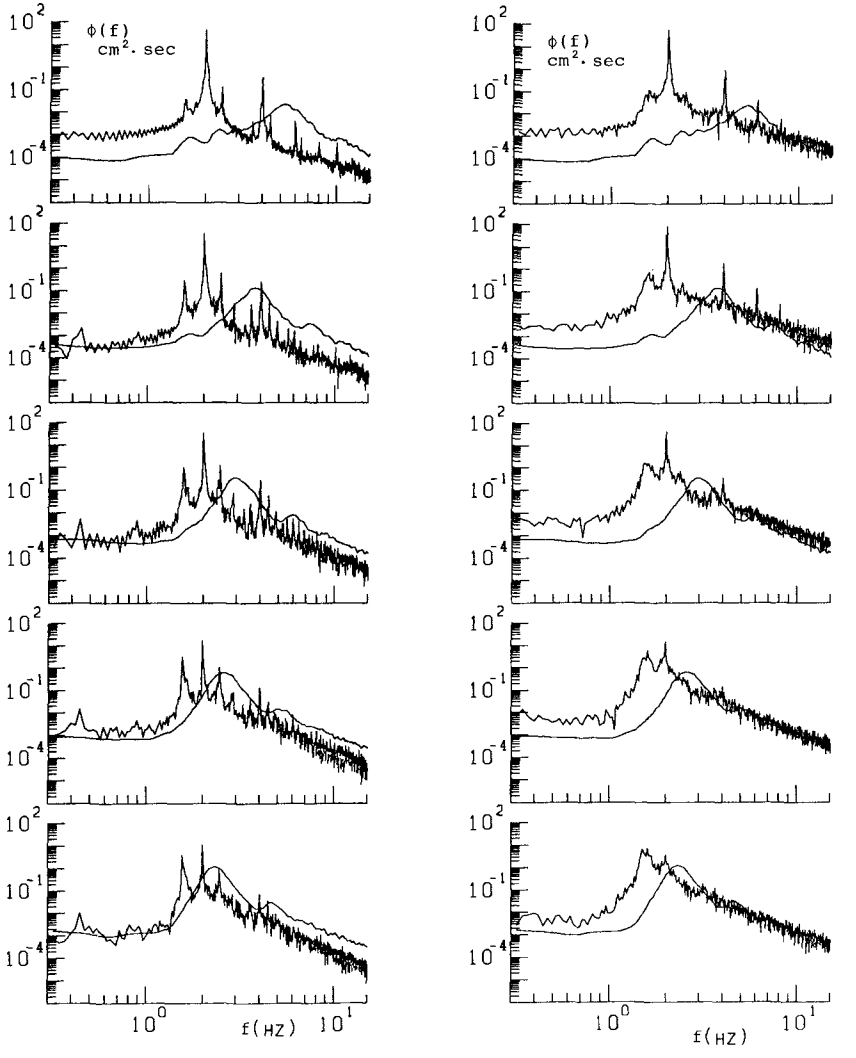

Fig.4 Evolutions of power spectra of steep unstable waves with (right figures) or without (left figures) wind action. Thin smooth curves correspond to the spectra of pure wind waves at each fetch.

spectral peak near the lower side band of the fundamental frequency component. Further development of the wave spectrum is almost the same to that of pure wind waves. These process of the transition to the continuous spectrum are considered to be largely attributed to the effect of wave breaking.

In order to clarify the change of the spectral energy, the wave spectrum was divided into five frequency rigions as shown in Fig. 5, and the spectral energy in each region is studied.

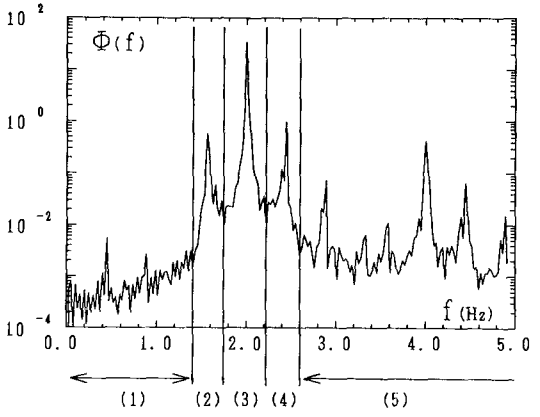

Fig.5 A schematic figure for the characteristic frequency region of the power spectrum of unstable waves.

In Fig. 5, E_1 is the energy in the low frequency region, E_2 the energy of the lower side band, E_3 the energy of the fundamental frequency component, E_4 the energy of the higher side band, and E_5 the energy in the high frequency region.

The change of the spectral energy in each frequency region is shown in Fig. 6. It can be seen that the energy of the fundamental frequency component E_2 decreases gradually with the increase of fetch even under the wind action, while the total wave energy E shows a nearly constant value. At short fetch, E_2 and E_4 are almost the same and increase samely with the fetch. With the increase of fetch, however, E_4 reaches to a saturated value, while E_2 continues to increase with the fetch. The wave energy at the high frequency region, E_5, shows a constant value independent of fetches reflecting a saturation of the high frequency wave spectrum for a fixed wind.

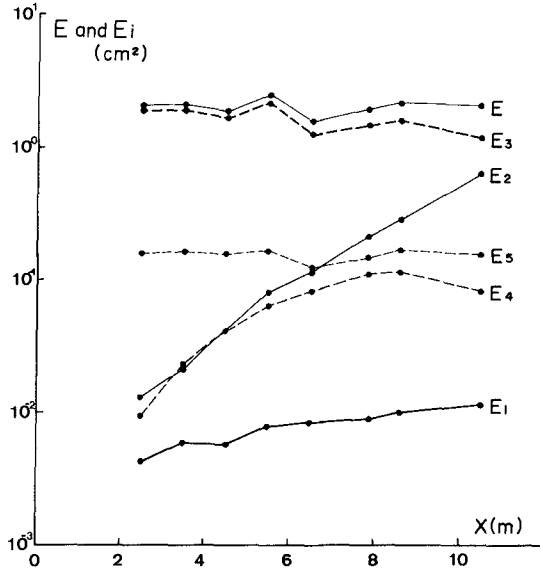

Fig.6 The change of the energy in the characteristic frequency regions of wave spectra under wind action for wave (9), H/L=0.105.

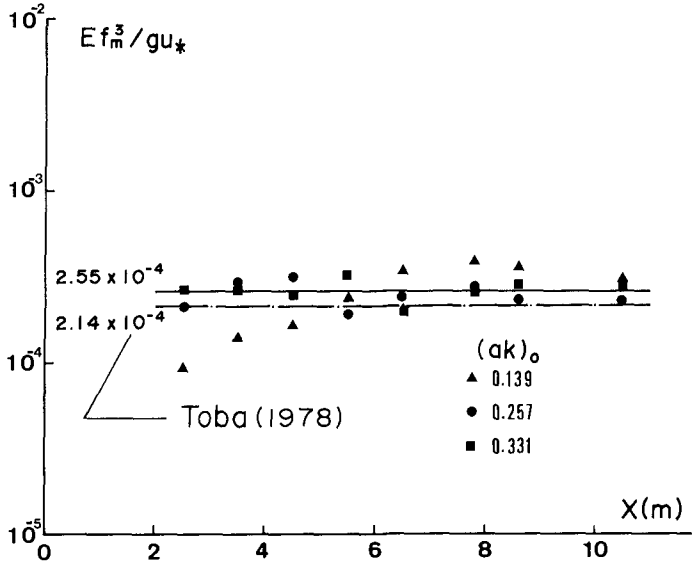

Fig.7 The change of the normalized wave energy.

It is interesting that the total wave energy E shows roughly a constant value within the fetch of the present study. However, it should be noted that this study is concerned with transitional phenomena from monochromatic waves to random waves, which are caused by the wave instability and the wind action. After the transition to the random waves, the waves will develop in the same way as wind waves. Thus, the total wave energy E should increase with fetch, while the dimensionless wave energy Ef^3/gu_* is expected to be constant.

In fact, Fig. 7 shows the saturation of the values of Ef^3/gu_*, and the asymptotic value $Ef^3/gu_* = 2.55\times10^{-4}$ is very close to the value 2.14×10^{-4} which has been obtained by Toba (1978) as the 3/2 power law for developping wind waves.

4. Conclusions

The following conclusions can be drown from the present study;

(i) The growth rate of stable monochromatic waves are given by (1) irrespective of the existence of the high frequency waves, if the measured friction velocity u_* is used in the relation. This is because the high frequency waves overlapping on the monochromatic waves increase both the friction velocity of the wind and the growth rate of the monochromatic waves.

(ii) The growth rate of a component wave of the composite waves is not much different from that of monochromatic waves with the same frequency, if the wave steepness is not large.

(iii) A fundamental frequency component of steep unstable waves decreases with the increase of the fetch even under the wind action, which is considered to be attributed to the wave breaking. However, the lower and higher side bands of the fundamental frequency component increase with the fetch, though the latter tends to be saturated at some fetch.

These properties are quite similar to those of steep unstable waves without wind action. In later stage, however, the spectrum of steep unstable waves under wind action tend to be contineous spectrum which is quite similar to the wind-wave spectrum.

Aknowledgement

The authors are grateful to Mr. K. Marubayashi and Mr. M. Ishibashi for their patient supports during the experiments, and to Miss. M. Hojo for her assistance in preparing the manuscript. This study is a part of Oceanographic Research Project entitled "Measurements and Simulation of Ocean Environment" and supported by the Ministry of Education.

References

Benjamin, T.B. and Feir, J.E. (1967): The disintegration of wave trains on deep water. Part 1, Theory. J. Fluid Mech. 27, 417-430.

Hsiao, S.V. and Shemdin, O.H. (1983): Measurement of wind velocity and pressure with a wave follower during MARSEN. J. Geophys. Res. 88, 9841-9849.

Kusaba, T. and Mitsuyasu, H. (1984): Wind-induced growth of mechanically-generated regular waves with two different frequency components, Bulletin No.60, Research Inst. Appl. Mech., Kyusyu Univ. (in Japanese), 455-466.

Kusaba, T. and Mitsuyasu, H. (1986): Nonlinear instability and evolution of steep water waves under wind action. Reports of Research Inst. Appl. Mech., Kyushu Univ., Vol.XXXIII, 33-64.

Miles, J.W. (1957): On the generation of surface waves by shear flows. J. Fluid Mech. 3, 185-204.

Mitsuyasu, H. and Honda, T. (1982): Wind induced growth of water waves. J. Fluid Mech. 123, 425-442.

Phillips, O.M. (1957): On the generation of waves by turbulent wind. J. Fluid Mech. 2, 417-445.

Plant, W.J. (1982): A relationship between wind stress and wave slope. J. Geophys. Res. 87, 1961-1967.

Snyder, R.L., Dobson, F.W., Elliott, J.A. and Long, R.B. (1981): Array measurements of atmospheric pressure fluctuations above surface gravity waves. J. Fluid Mech. 102, 1-59.

Toba, Y. (1978): Stochastic form of the growth of wind waves in a single-parameter representation with physical implications. J. Phys. Oceanogr. 8, 494-507.

Yuen, H.C. and Lake, B.M. (1982): Nonlinear dynamics of deep-water gravity waves, *Advance in Applied Mechanics*, 22, 67-229.

CHAPTER 45

Experimental study on kinematics and dynamics of wave breaking

Masaru MIZUGUCHI*

1 Introduction

Wave breaking on a slope is one of the most important problems for the coastal engineers to be investigated. However wave breaking is a complex phenomenon which is not yet fully understood, in spite of the fact that many researches have been devoted to that subject. It is well known that waves break in different forms: spilling, plunging and surging. Untill now no theoretical explanation is given for the classification of the breaking pattern. Recently numerical simulation of wave breaking with full nonlinear governing equations based on the irrotational assumption have been developed (Longuet-Higgins & Cokelet, 1976 and so on). The simulation results show that the spilling breaker exhibit a small scale plunging jet as Miller (1976) observed in a laboratory experiment.

Most of the research works on the wave breaking are based on the laboratory experiments, in particular visual observation. Basco(1985) is the latest one on this line. Description of wave breaking based on visual observations provide limited information. Hedge & Kirkgöz(1981) report an experimental work in which the photographic approach was supplemented by the velocity measurement by Laser- Doppler Velocimeter. They found that the water particle velocity at the crest is smaller than the wave crest propagation velocity especially on steep slope beaches, and suggest that the plunging jet is not necessary formed at the crest. It is normally accepted that the flow field is irrotational before waves break. Therefore generation of vorticity as well as turbulence can be considered as eminent features of the wave breaking. Few studies are reported where velocity are measured in a fine grid of points so that the vorticity can be evaluated (Okayasu et al., 1986). There are several papers which pay an attention mainly on the structure of turbulence induced by wave breaking (Peregrine & Svendsen, 1978, Stive, 1980 and so on.)

Our aims are to provide a set of experimental data of a wave breaking of plunging type on a slope, in which the velocity field is measured in detail with high accuracy, and to discuss the kinematics and dynamics based on the data set, especially from the inception of breaking through the plunging process. In view of the initiation of wave breaking, forming of the plunging jet or overturning may be essential. Peregrine (1983) gives a comprehensive study of the fluid dynamics of the wave breaking, in which some possiblities of the plunging process are discussed.

2 Experiment

The experiment was conducted in a laboratory wave flume of width 30 cm and of length 20 m. A wave of period 1.22 s and of wave height 4.4 cm at the uniform depth area of 28.2 cm deep was chosen, as it produced a stable plunging breaker of height 6.1 cm at the depth of 6.5 cm on a

*Assoc. Prof., Dept. Civil Eng., Chuo Univ., Bunkyou-ku Tokyo 113 JAPAN

slope of 1/20. The slope is made of painted steel plate.

Wave profiles were measured by a capacitance-type wave gauge at offshore and by a specially designed resistance-type wire gauge (Masatoyo Kogaku) in the breaker zone. The latter gauge detects the top boundary between the air and the water. The wave gauge has higher frequency response (≅50 Hz for the amplitude of 25cm) and is better to detect the rapid change of the breaking wave profiles. First cross-shore (horizontal) and vertical velocities were measured at 126 points by using two-colour Laser-Doppler Velocimeter (DANTEC). Back scattering method was employed. Later second experiment was carried out, adding 132 measuring points mainly in the shallower and the deeper region. Unfortunately the incident waves were a little (4.5 cm of wave height) larger in the second run. The measuring area covers 112 cm horizontally, extending d=2.7 cm to d=8.3 cm, where d denotes the water depth. It covers the area vertically from the near-bottom to the wave crest level. The measuring section was located about 6 cm apart from the nearer

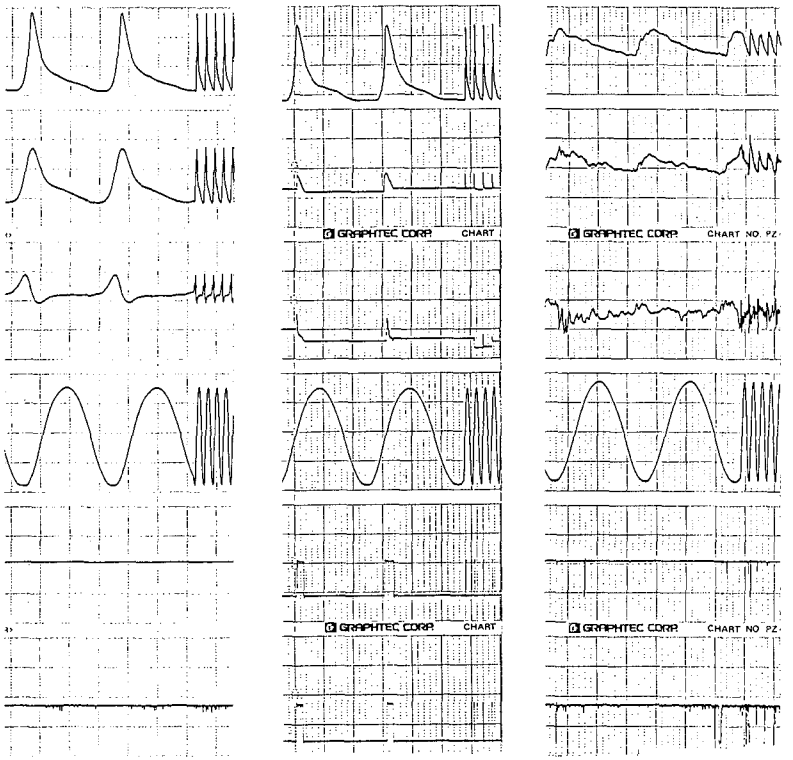

(a) d=7.5cm, z=-2.0cm (b) d=6.6cm, z=2.0cm (c) d=2.7cm, z=-0.8cm

Fig.1 Examples of raw data. Top, surface elevation by the wire gauge, Second, onshore velocity, u, by LDV, third, upward velocity, v, by LDV, fourth, surface elevation by CWG in uniform depth area, fifth, drop-out signal for u, bottom, drop-out signal for v. Vertical axis is not scaled. LDV signals hold the previous values while they drop out.

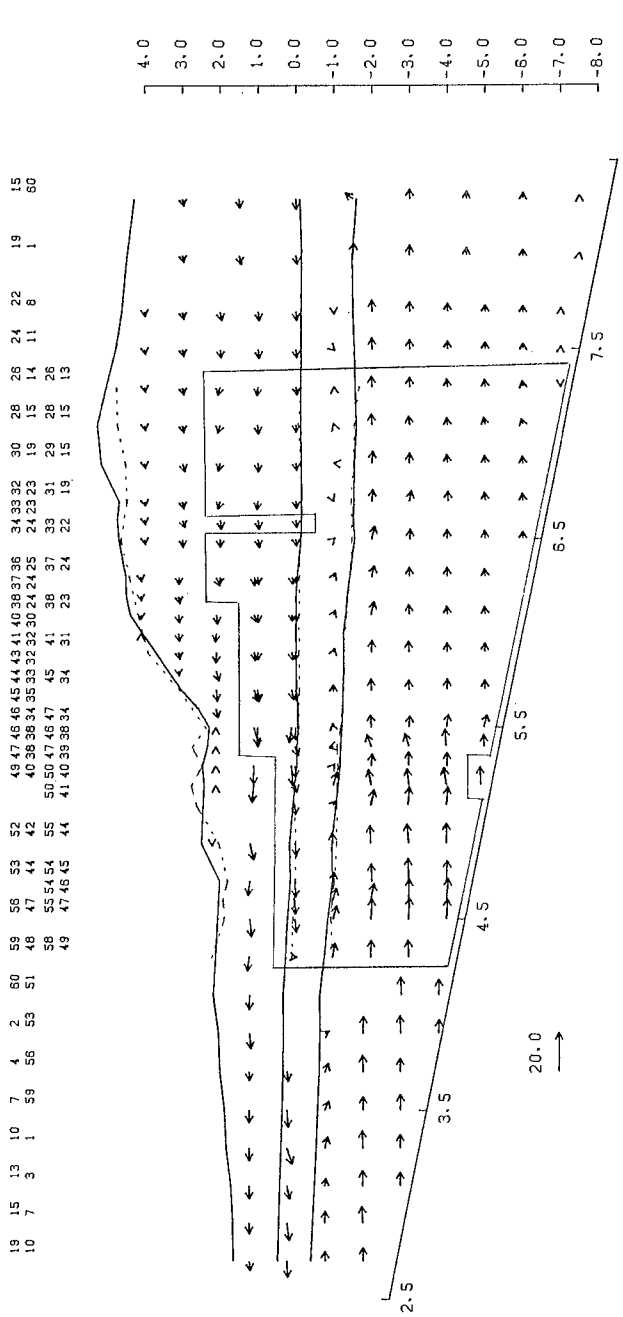

Fig. 2 Measuring points, mean velocities, wave crest level, mean water level and wave trough level. The measuring points within the solid line are for the first run. Some points above the still water level (z=0) were measured in both runs. The number at the top indicate the time by sequence number when the wave crest and trough pass the point. The number of the top two lines are for the second run. The dotted line for wave crest, mean water level and wave trough level are from the first run. The number below the bottom slope indicate the local water depth. Vertical axis is taken upward from the still water level. c.g.s. unit is used throughout the paper.

sidewall, which is made of glass. To prevent the drop-out of LDV signal, it is better to have the section nearer to the wall, although the sidewall effects must be avoided. The experimental data were recorded on a magnetic tape and later digitized with a sampling frequency of 50 Hz.

In Fig. 1 (a)-(c), examples of raw data at various locations are shown. Figure 2 shows the location of measuring points. The mean velocity, mean water level, wave crest level and wave trough level are also plotted in Fig.2. Mean water level, wave crest level and trough level are obtained from the averaged wave profile of those at the points in the same vertical section. It is seen that the total mass flux across a vertical plane may not be zero and directed offshoreward. It is because the LDV signals drop out giving zero velocities when the points, above the trough level, just come into and out of the water as typically shown in Fig. 1-(b). The Eulerian return flow, which compensate the wave mass flux above the wave trough, exhibits uniform vertical distribution after the plunging point. This uniform distribution is attributed to the momentum transfer due to the strong turbulence in that region as shown below. Outside the breaking point the vertical distribution of the return flow show a clear decrease toward the bottom.

Representative temporal profiles of both surface elevation and velocities for one period at each location were obtained by taking the phase average values over the forty waves. In the aerated area and the near-surface area, the signals of LDV drop out frequently as shown in Fig.1-(c). When the signals obtained for no more than ten wave cycles among the forty, the data points for that phase were discarded. Then

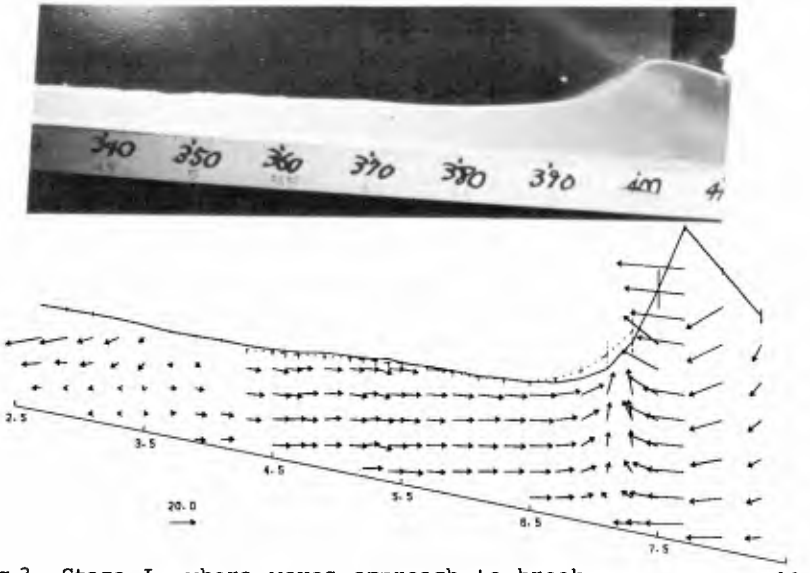

Fig.3 Stage I, where waves approach to break. Photo and (phase averaged) velocity field. (T_i=22) The length of vertical bars on the surface profile denote the standards error of the wave profiles over the points on the same vertical section. It indicates the degree of fluctuation of the waves themselves.

the spatial distribution of the phase-averaged wave profile and velocities are produced by synthesizing the data of all measuring points. The synchronization was done by using the zero crossing point of the wave profiles measured at a fixed point of uniform depth area. Here the error of the order of a sampling time was inevitable. However larger error may occur when the data obtained in a second run and the data in the second run are brought together. These errors may be significant when the spatial derivatives are estimated as done below.

3 Analysis

From the set of spatial distribution of phase averaged velocity, $\underline{u}$, the divergence, $\underline{\nabla}.\underline{u}$ and the rotation, $\underline{\nabla}\times\underline{u}$ of the velocity vector field are calculated. The spatial derivatives of velocities are estimated by fitting a linear plane to the data of the points within an ellipse with a least square error. The ellipse has the horizontal radius $4r_0$ and vertical radius r_0. The value of r_0 is taken to be 1.6 cm. Theoretically the value should be infinitely small. The grid size in our experiments, however, requires a certain finite value. The values of 1.1, 1.3, and 2.1 cm were also tried. Only the results for the values of 2.1 cm produce considerably different distributions of derivatives. The water

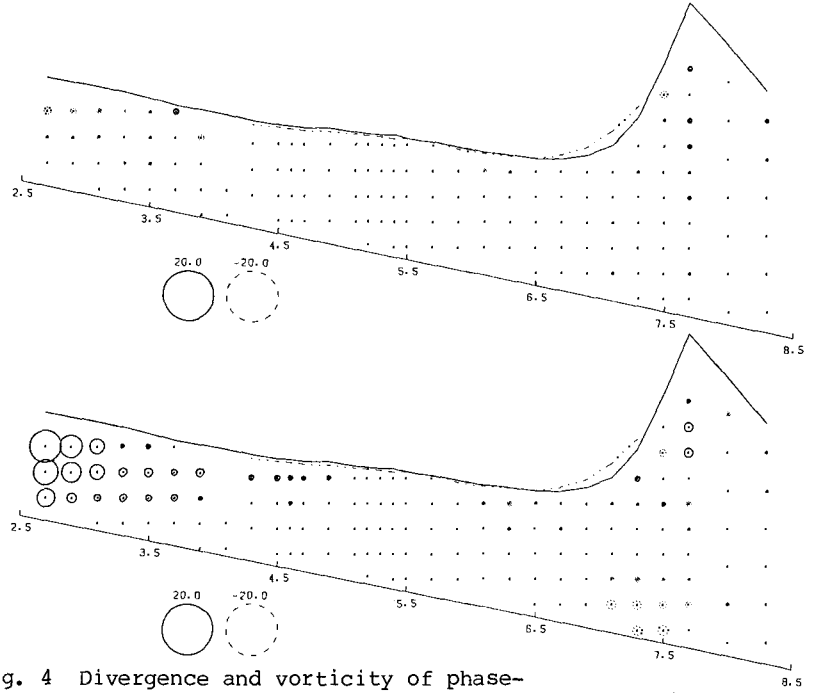

Fig. 4 Divergence and vorticity of phase-averaged velocity field. (T_i=22) The diameters of the circles denote the magnitude. The solid circles indicate positive values while dotted ones do negative values. The positive divergence gives negative gradient of longshore velocity. The positive values of vorticity means anti-clockwise rotation of the water particles.

particle acceleration, $D\bar{u}/Dt$ is evaluated by using the relation $D\bar{u}/Dt = \partial\bar{u}/\partial t+u\partial\bar{u}/\partial x+w\partial\bar{u}/\partial z$. The partial differentiation with respect to time, t, is obtained numerically. Turbulence intensity, $\sqrt{(\bar{u}')^2}$, is also calculated. The turbulence is defined as the difference between the instantaneous velocity and the phase averaged velocity. Thus obtained turbulence include the fluctuation of wave motion and may give overestimation as shown later. From the given spatial distribution of Eulerian velocity field, particle trajectories are traced numerically. Simple forward difference scheme is employed.

4 Results and discussion

Sixty one sequential diagrams of synthesized (phase averaged) velocity field with surface profile are carefully examined. With help of pictures taken during the experiments as well as the quantities $\bar{v}.\bar{u}$, $\bar{v}x\bar{u}$, $D\bar{u}/Dt$ and $\sqrt{(\bar{u}')^2}$, it was revealed that there exist six typical stages in wave breaking, which are qualitatively described as follows.

I) Sharp crested wave, which a little inclines forward, advances in a uniform return flow. This is typically shown in Fig. 3, for the time sequence T_i=22. The initial phase T_i=1 is chosen arbitrary. The uniform return flow under the preceding trough is remarkable. The

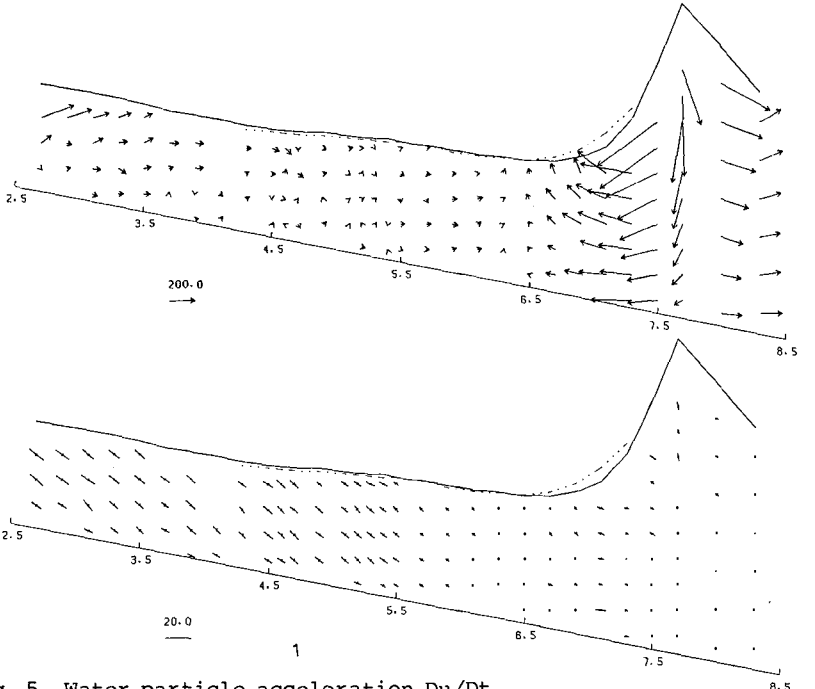

Fig. 5 Water particle acceleration $D\bar{u}/Dt$ and turbulence intensity $\sqrt{(\bar{u}')^2}$. (T_i=22) $D\bar{u}/Dt$ is plotted as a vector. Turbulence intensity is plotted such that the length of the bars has the absolute value of turbulence $\sqrt{(\bar{u}')^2+(\bar{w}')^2}$ and the angle with the onshore horizontal line has the angle $\tan^{-1}(\sqrt{(\bar{w}')^2}/\sqrt{(\bar{u}')^2})$. If the turbulence is isotropic, the angle is 45 deg.

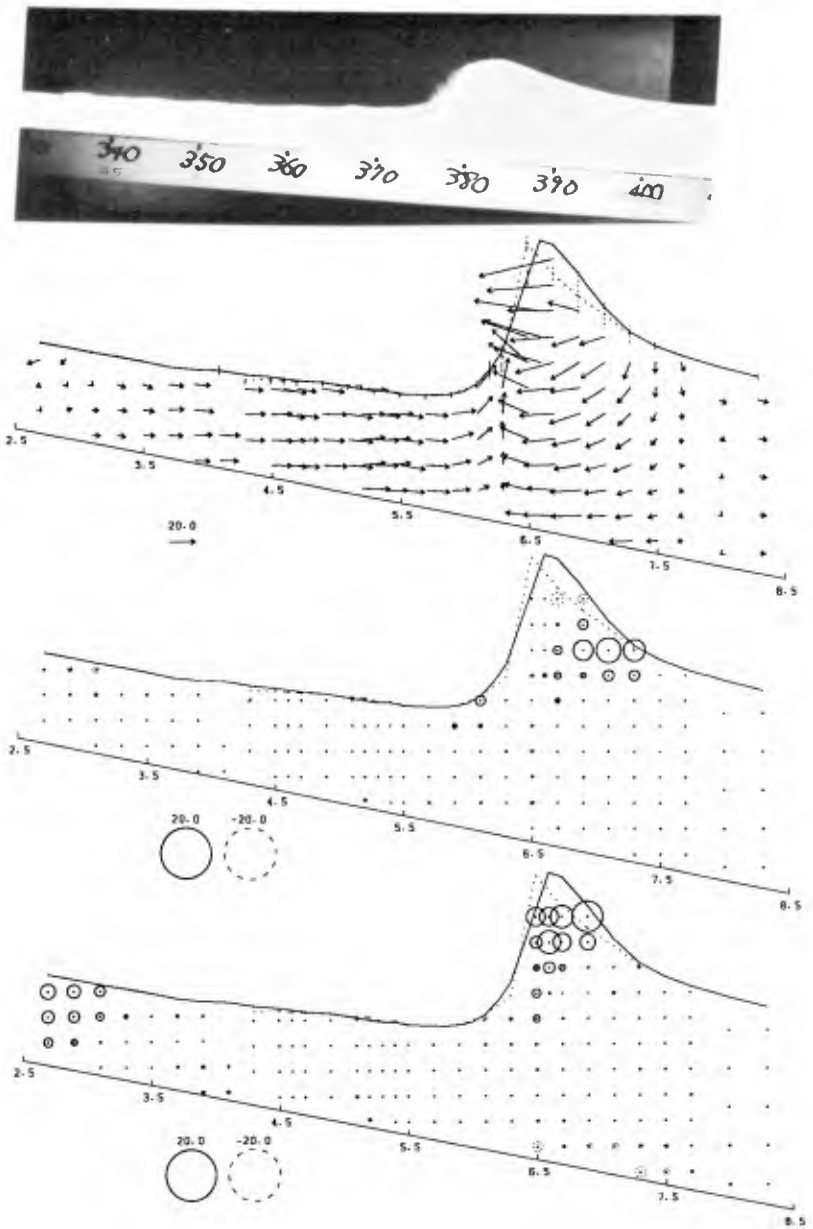

Fig. 6 Stage II, where the wave breaks. (T_i=33) Photo, velocity field, its divergence and vorticity.

foregoing wave has disappeared to the left. In Fig.4, the divergence and rotation are shown for this phase T_i=22. The divergence is nearly zero throughout the measuring area, assuring that the phase averaged flow field is two-dimensional. This may guarantee the reliability of the experiment. The non-zero vorticity, found far left, are the remains of the vorticity generated by the plunging of the foregoing wave. Whether the values of the divergence is negligibly small or not depends on what to compare with. Here the values are compared against the significant values of the vorticity ($\cong 30\ s^{-1}$) observed in this wave breaking process. The vorticity is twice the angular velocity of the rotational motion of a water particle. The indicated values of 20 s^{-1}

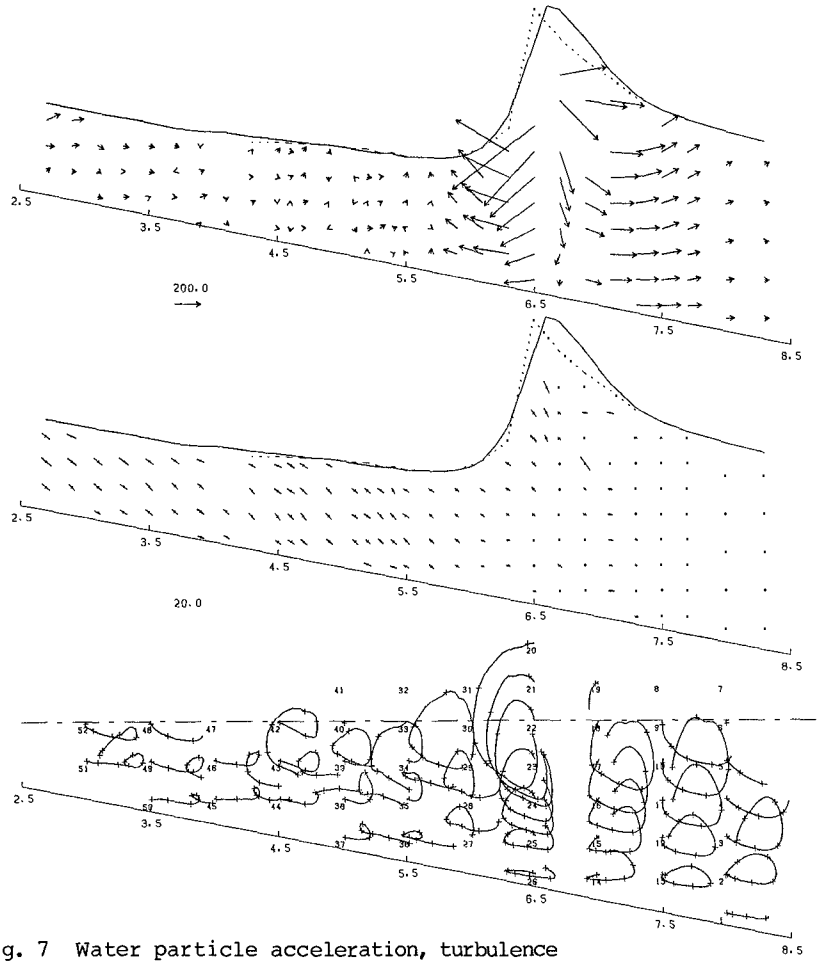

Fig. 7 Water particle acceleration, turbulence intensity and water particle trajectories. (T_i=33) The trajectories are followed for one wave period. The points near the number are the stating positions at this instant.

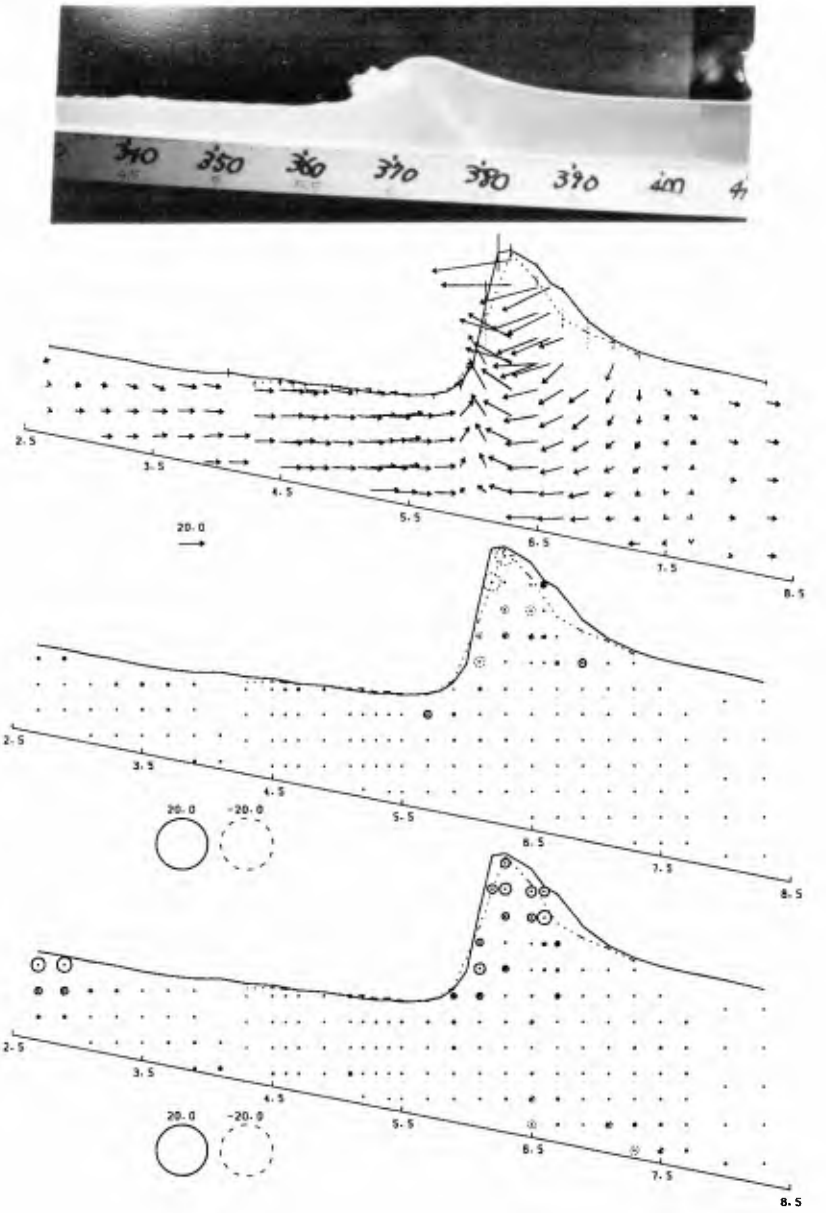

Fig. 8 Stage III, where the breaking (overturning) wave travels. (T_i=36) Photo, velocity field, its divergence and vorticity. The plunging jet does not yet touch down.

in Fig. 4 means that the water particles rotate with the angular velocity 10 s^{-1}. Figure 5 shows the water particle velocity and turbulence intensity for T_i=22. The water particle acceleration shows a reasonable behaviour that particles are accelerated only when the wave crest passes. The dynamics of the breaking wave appears to be quite similar to that of a solitary wave. With respect to the turbulence shown in Fig. 5, significant values are found only after the plunging point. The large values under wave crest are due to the fluctuation of wave motion as is indicated by the vertical bar on the surface profiles in Fig. 3. This stage covers the period of time sequence number (15-32).

II) The crest continues to become sharper and some part of its front face finally becomes vertical. At this breaking moment, horizontally converging and vertically upwelling flow beneath the vertical front face is very remarkable as shown in Fig. 6. Stagnation point is observed at the bottom of the upwelling flow. The maximum value of the velocity measured, which is nearly horizontal, is 67 cm/s. This value is likely to be underestimated as it is the maximum of the phase-averaged ones. From the number plotted in Fig. 2, we have 83 cm/s for wave crest propagation velocity, v_c, near this breaking point. Considering that the point of maximum velocity lies within the fluid, one can imagine that the real maximum velocity is nearly equal to v_c. It is also shown in Fig. 6 that divergence and vorticity take non-zero values around the top of the wave crest. The positive divergence behind the crest results from the fact that the velocity vectors around there do not show a smooth variation. Experimental errors due to very fast

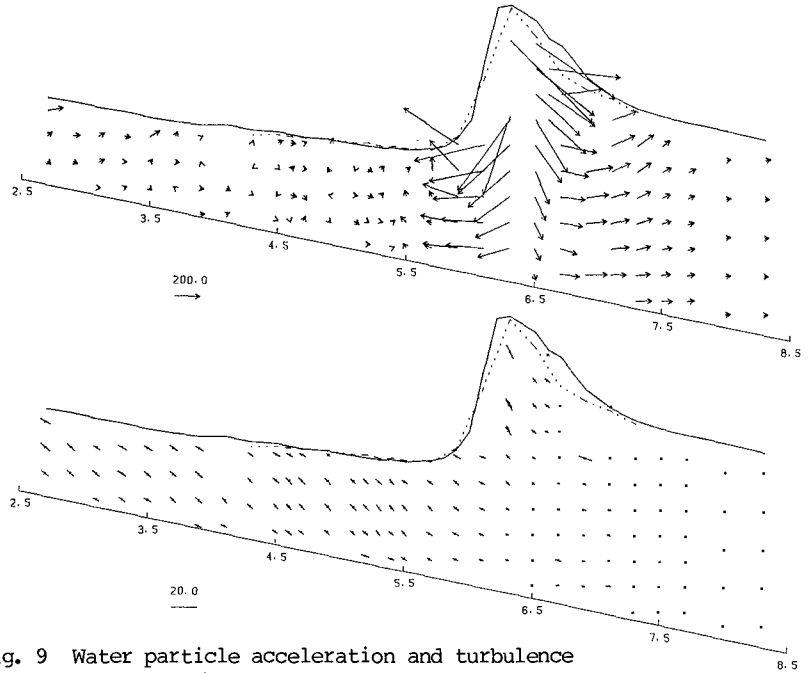

Fig. 9 Water particle acceleration and turbulence intensity for T_i=36.

movement of the breaking wave crest could be responsible for this false (?) three dimensional feature. The positive vorticity at the top of the wave crest is due to the higher nearly-horizontal velocities at the points nearer to the surface. This generation of small vorticity is a token of the breaking inception. Rotational motion at the top of a nearly-breaking wave is also observed for a spilling-type breaker by VanDorn & Pazan(1975). Vorticity far left still remain, decaying. In Fig.7, the observed maximum vertical acceleration is 490 cm/s^2 in the downward direction at the highest point measured beneath the crest. Extaporation up to the surface may give the value of g=980 cm/s^2.

III) The plunging jet is formed from a part of the sharp crest, although the remaining part of the wave continues to propagate independently. As shown in Figs. 8 and 9, the observed features are the same for those of stage II in Figs. 6 to 7, except that the height of wave crest is decreasing. (33-43)

IV) The jet is plunging into the front face of the original wave, hitting the surface as shown in Figs. 10 and 11. In this stage the wave motion still holds its characteristic feature under the plunging jet. This plunging moment is most clearly characterized by the beginning of

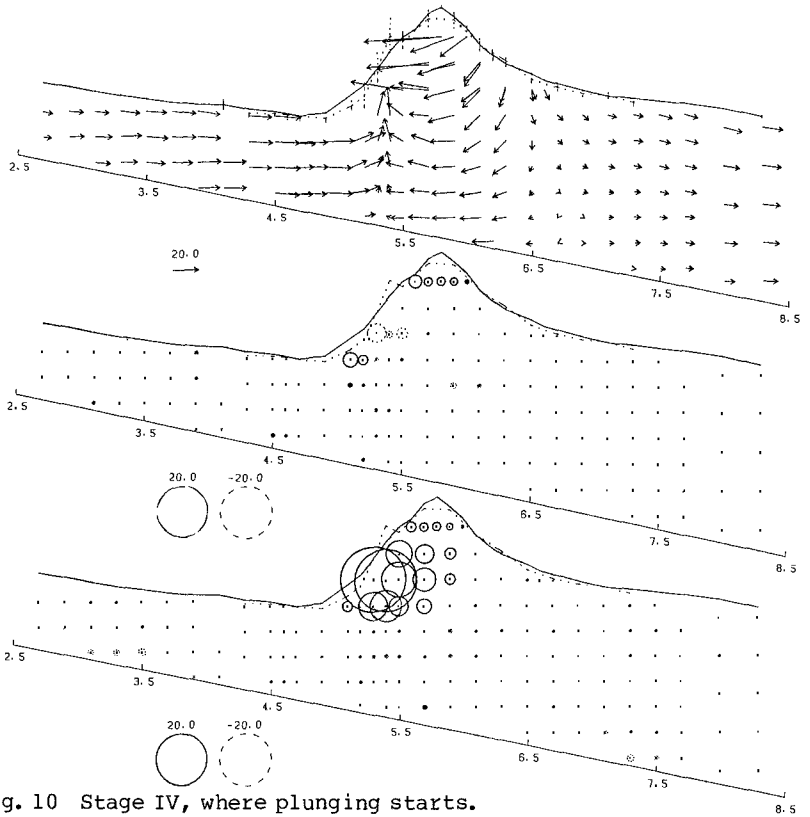

Fig. 10 Stage IV, where plunging starts.
(T_i=44) Velocity field, its divergence and vorticity.

the generation of large vorticity and turbulence near the surface at the plunging point. The vorticity is generated by the strong shear near the surface due to the plunging jet, which appears to flow over the surface. At this stage the vorticity far left produced by the foregoing wave disappears. In Fig. 11 particle trajectories show that the surface particles do not penetrate into water deeply, indicating that the surface generated vorticity and turbulence do not easily reach the bottom. It is noted that the vorticity exists almost only above the wave trough level. On the other hand, the fluctuation of pressure may produce turbulence even near the bottom. (44-50)

V) Then the plunging jet produces a dead water region beneath the plunging point but neither so-called horizontal roller nor offshoreward propagating wave. In Figs. 12 and 13 it appears that the plunging jet bounce up over the dead water region. This process is described by as a jet-splash motion Jannsen(1986) based on visual technique. It is interesting to investigate how this bouncing process changes as the breaking pattern differs. As shown in Fig. 13 and others, turbulence near the surface is likely to be isotropic, but very near the bottom, turbulence in vertical velocity is naturally small. (50-61)

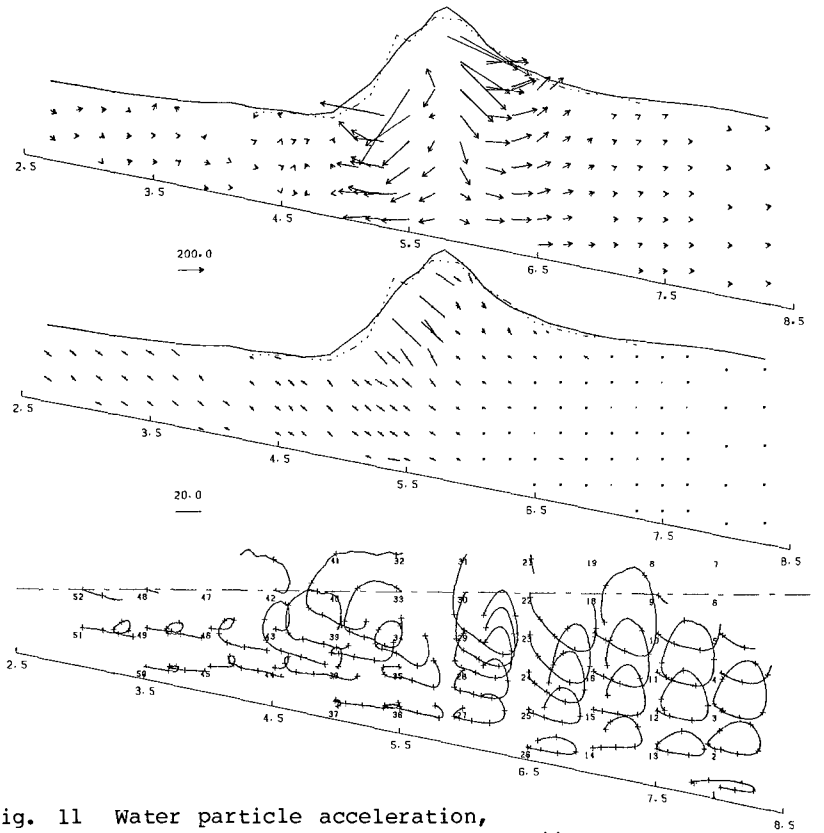

Fig. 11 Water particle acceleration, turbulence intensity, and trajectories for T_i=44.

VI) As shown in Fig. 14, bore-like motion is formed. The flow field at the wave front is similar to that in Stage I as shown in Fig.3. However the vorticity within and behind the bore-like wave exist together with the turbulence. The rotational motion as well as the turbulence is left behind as the crest propagates away. (1-14)

5 Conclusions

It is concluded that wave breaking is a phenomenon in which irreversible motion of the jet-forming with small vorticity stands for its inception and the plunging of the jet into the original wave causes partial destruction of the original wave, resulting with the bore-like motion. However the plunging jet may not penetrate into the interior of water but bounce up over a dead water region and does not form either the roller directly nor the outward-going waves. It also brings about the turbulence together with the rotational motion with vorticity.

Acnowledgements

I would like to give my special thanks to Mr. K. Sakata for his assistance throughout every phase of this study.

Reference

Basco, D.R.(1985), A qualitative description of wave breaking, J. WPCOE, ASCE, 111, No.2, 171-188.

Hedges, T.S. and Kirkgöz, M.S.(1981), An experimental study of the transformation zone of plunging breakers, Coastal Eng., 4, 319-333.

Jansen, P.C.M.(1986), Laboratory observation of the kinematics in the aerated region of breaking waves, Coastal Eng., 9, 453-477.

Longuet-Higgins, M.S. and E.D. Cokelet(1976), The deformation of steep surface waves on water, 1. A numerical method of computation, Proc. Roy. Soc. Lond., A-350, 1-26.

Miller, R.L.(1976), Role of vortices in surf zone prediction: Sedimentation and wave forces, Soc. Econ. Paleontol. Mineralog., Spec. Publ., No.24, 92-114.

Okayasu, A., T. Shibayama and N. Mimura(1986), Velocity field under plunging waves, to be published in this Proceedings.

Peregrine, D.H.(1983), Breaking waves on beaches, Ann. Rev. Fluid Mech., 15,149-178.

Peregrine, D.H. and I.A. Svendsen(1978), Spilling breakers, bores and hydraulic jumps, Proc. 16th Conf. on Coastal Eng., 540-550.

Stive, M.J.F.(1980), Velocity and pressure field of spilling breakers, Proc. 17th Conf. on Coastal Eng., 547-566.

VanDorn, W.G. and S.F. Pazan(1976), Laboratory investigation of wave breaking Part II: deep water waves, AOEL Rep. 71, Scripps Inst. Oceanogr., Univ. Cali., San Diego, 106p.

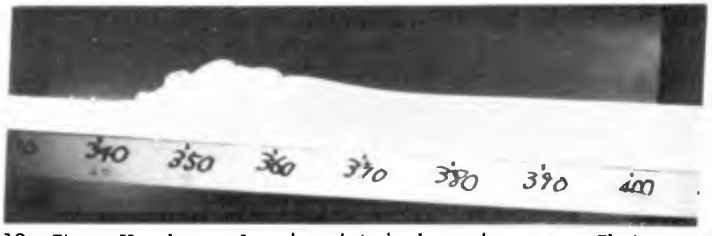

Fig. 12 Stage V, where plunging jet is bouncing up. Photo.

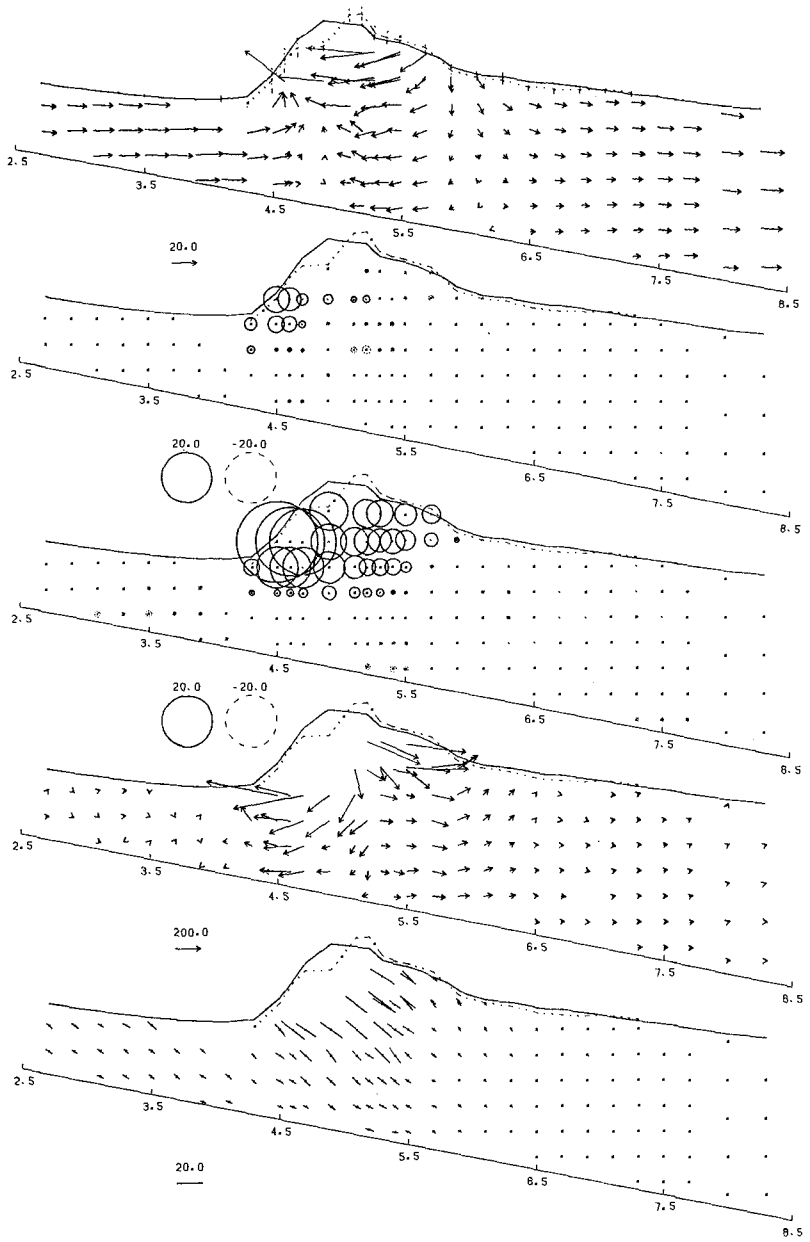

Fig. 13 Velocity field, its divergence and vorticity, water particle acceleration and turbulence intensity. (T_1=51)

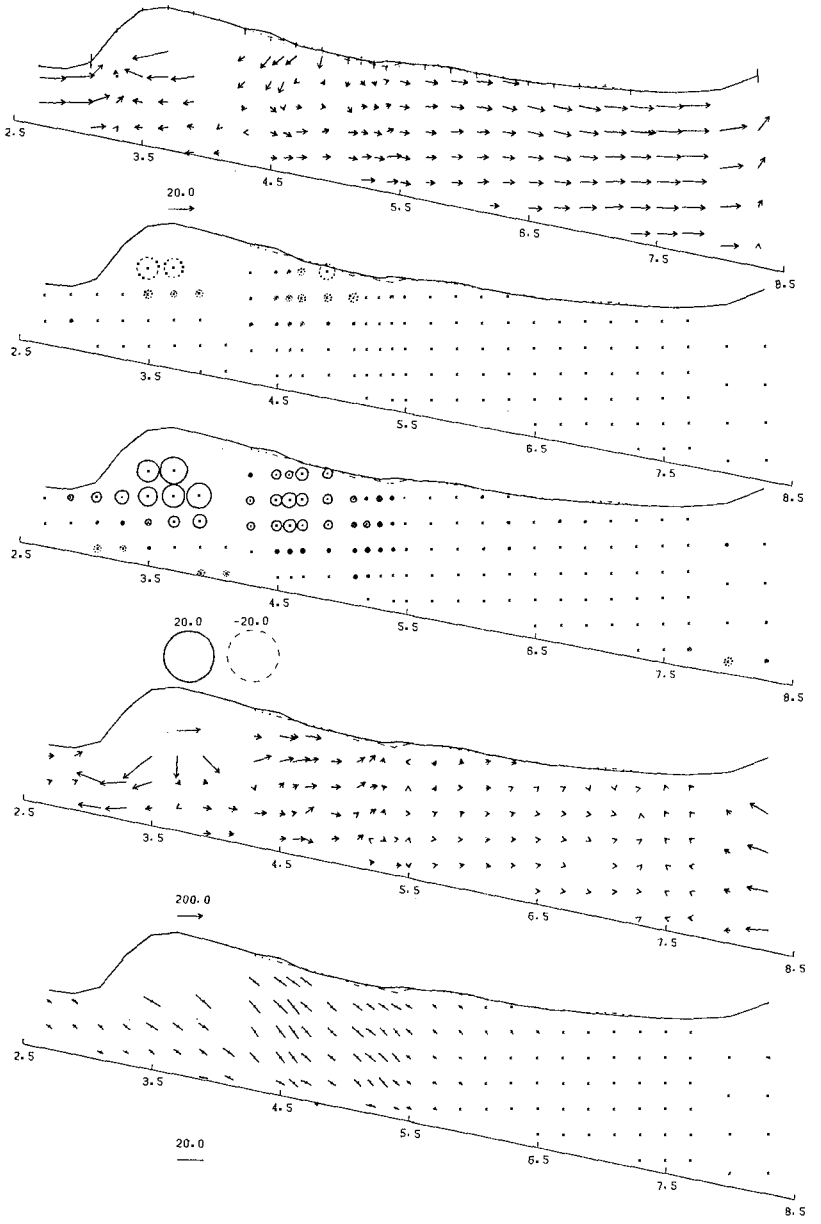

Fig. 14 Stage VI, where bore-like wave is formed. (T_i=6) Velocity field, its divergence and vorticity, water particle acceleration, and turbulence intensity.

CHAPTER 46

FERRY WAVE MEASUREMENTS IN DEEP WATER

Ronald E. Nece, F. ASCE, Michael R. McCaslin,
Derald R. Christensen, and Harry H. Yeh, M. ASCE

ABSTRACT

Data are presented for ship waves generated and measured in deep water. Results show the variation of maximum vessel waves with both vessel speed and distance from the vessel sailing line. Three automobile ferries of different configurations were tested. Field test procedures, limitations, and problems are described.

Introduction

Concerns have been expressed about possible increases in shoreline erosion which might be attributed to waves generated by specific classes of automobile ferries operating fairly close to shore on regular routes in the partially sheltered waters of Puget Sound, Washington, a deep-water estuary on the northern Pacific Coast of the U.S.A. A logical first step in investigating these concerns was to determine whether or not there were indeed significant differences among waves generated by ferries of various vessel classes.

The interest of coastal engineers in ship waves in the past has generally focused on problems associated with operation of ships in confined channels (e.g. Herbich and Schiller, 1984), on shore-mounted or pile-mounted wave gage measurements of waves generated by relatively smaller vessels (e.g., Sorensen, 1967) or on operation of vessels in water of finite depth (exemplified by early laboratory studies such as those reported by Johnson, 1958). The latter concerns arise when the depth Froude number $F_d = V_s / \sqrt{gd}$ (where V_s = vessel speed and d = water depth) becomes greater than about 0.6; the operating conditions for the Puget Sound tests yielded much smaller Froude numbers. Towing tank data were not available on waves generated by the ferries tested. Also, the combination of low Froude numbers and hull configurations placed the ferries out of the range of predictive formulae for wave heights (e.g., Weggel and Sorensen, 1986). Direct field measurements therefore were selected as the best approach. This paper describes the relatively low-cost, single-purpose tests and presents their results.

Department of Civil Engineering, University of Washington, Seattle, Washington, U.S.A.

Objectives

The specific objective was to determine maximum wave heights at various distances from the sailing line for each of three classes of ferries operating over their respective speed ranges in deep water. One representative ferry was tested for each vessel class. The three vessels tested were all double-ended ferries with diesel or diesel-electric propulsion. Characteristics of the vessels at their respective test conditions are listed in Table 1; English units are used.

Table 1
Characteristics of Ferries Tested

Vessel	Displacement[a]	Length[b]	Draft[c]	C_P[d]	C_B[e]
Sealth	2475	314	14.08	0.549	0.345
Yakima	2780	375	17.17	0.528	0.291
Klahowya	1650	301	13.5	0.618	0.310

Notes: a) Long tons, salt water
b) At water line, feet
c) Feet
d) C_P = Prismatic Coefficient = $\frac{\text{Displacement Volume}}{\text{Length x Midship Area}}$
e) C_B = Block Coefficient = $\frac{\text{Displacement Volume}}{\text{Length x Beam x Draft}}$

Test requirements dictated a straight course over which the vessel could be run at a constant speed so the wave pattern was established and non-varying relative to the ship, and so that repetive runs could be made past stationary wave gages. Necessary measurements were of wave height, distance of gage from sailing line, and vessel speed. A calm sea state with minimal tidal currents was desired. The degree to which these requirements were satisfied is discussed for each of the series of tests conducted.

Methodology

Waves were measured by three resistance-type spar buoy staff gages. The three-gage array was deployed in a direction essentially normal to the vessel sailing line along a single mooring line fixed to a permanent buoy at one end and kept in tension and position by being attached to a 9-m sailboat which served as a workboat operating under power at the other end (Figure 1). All electronics are located in the 3.6-m high 75-mm diameter staff portion of the buoys; the 150-mm diameter bottom section provides buoyancy, and the staffs receive their power from a generator on the workboat via a cable attached to the mooring line. The damper plate at the bottom of the spar buoy produces natural periods in heave and roll of 18 and 12 seconds, respectively, both much greater than periods of wind or ship waves at the test sites. Details of the gages have been provided previously (Nelson et al., 1983). The wave staffs were calibrated separately for each series of field experiments.

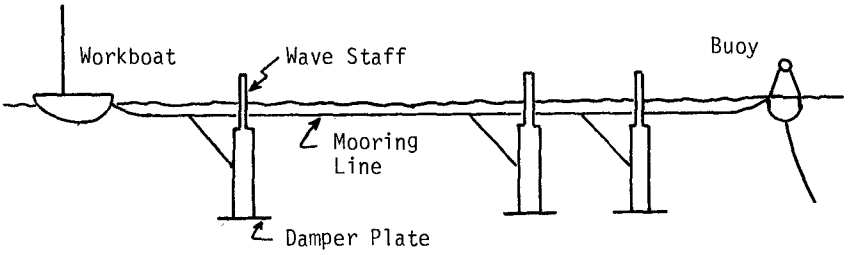

Figure 1. Schematic of wave staff deployment.

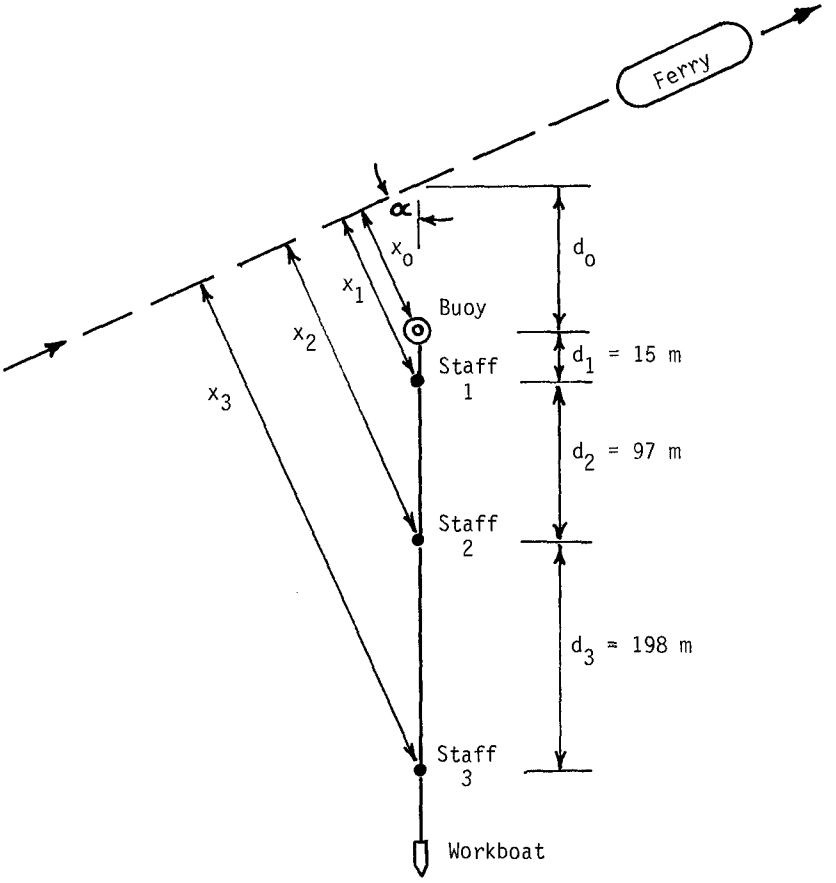

Figure 2. Schematic showing wave staff deployment in relation to ferry sailing line (not to scale).

Four analog recorder channels and one single-channel digital data requisition system were available; the latter could be switched from the output from one wave gage to another so that digital records of the highest ferry waves could be recorded as those diverging waves passed by each staff in turn.

Maximum wave heights were determined by two methods. The unfiltered value presented for each data set listed in Table 2 was obtained by direct visual inspection of the analog trace, using the maximum crest-to-trough reading within the wave train record. Vessel waves had frequencies between 0.25 and 0.5 Hz (2.5 to 4.0-second periods) with maximum wave heights ranging between 0.1 and 0.5 meters. Some coarse filtering was performed on the digital records, using the Fast Fourier Transform technique and a software package described earlier (Christensen, 1984). The filter selected rejected components with frequencies above 1 Hz and below 0.08 Hz. These frequencies are those of typical wind waves on the test dates and of the roll period of the wave staffs; the latter was selected to eliminate any effects of long period motions of the wave staffs caused by tension changes in the mooring line. The filtered data were plotted and the same visual procedure used to determine maximum wave heights. Where gaps occur in the 'filtered' results in Table 2, digital data were not available because of operator error or because the angle between the crests of the ferry-generated waves and the staff array was so small that the ferry waves passed through the array too quickly for more than one channel of digital data to be recorded.

The original project work plan called for both distances and vessel speeds to be obtained via aerial photography. The aerial work was restricted due to bad weather and/or the limitations on the altitudes at which aircraft were allowed to operate; the test sites were within the terminal control area of the Seattle-Tacoma International Airport.

The method used for determining distances for each data set is listed in Table 2. Those particular distances sought were x_1, x_2, and x_3, as identified on Figure 2. Distances d_1, d_2, and d_3 were 'unstretched' mooring line measurements. The six methods are described below:

(1) A photograph was used; the scale was determined by the known length of the ferry. The distance from the buoy to the workboat was measured. This was usually not equal to 310 m, because the mooring line would stretch under tension. Actual values of d_1, d_2, and d_3 were obtained by linear interpolation. The angle α was measured from the photo, also d_0. The "x" distances were determined by trigonometry, with the sailing line determined by extending a straight line back of the ferry. Due to aircraft elevation and/or lighting conditions, the individual wave staffs were not visible in the aerial photos.

(2) Same as (1), except that the distance x_0 was estimated by an observer on the ferry because neither x_0 nor d_0 were obtainable from the photo.

Table 2-a; Summary of Results, Sealth

Dir.	Speed Kt	Dist. m	Staff No. 1 Unfilt. Height m	Staff No. 1 Filt. Height m	Dist. m	Staff No. 2 Unfilt. Height m	Staff No. 2 Filt. Height m	Dist. m	Staff No. 3 Unfilt. Height m	Staff No. 3 Filt. Height m	Method of Finding Dist.
E	10	225	0.23	0.19	335	0.16	0.13	565	0.47	0.42	(1)
W	10	55	0.15	0.16	165	0.15	0.17	390	-	-	(1)
E	10	90	0.23	-	210	0.20		425	0.17	-	(2)
W	10	90	0.19	0.17	200	0.19	0.18	425	-	-	(1)
E	15	100	0.28	0.26	215	0.21	0.20	440	0.19	0.17	(1)
W	15	90	0.24	0.21	200	0.16	0.17	425	0.22	0.17	(3)
E	17	90	0.30	0.32	200	0.29	0.27	425	0.26	0.23	(3)
W	17	90	0.37	0.35	200	0.32	0.28	425	0.32	0.31	(3)
E	18	90	0.46	0.43	200	0.27	0.27	425	0.25	0.26	(3)
W	18	110	0.40	-	210	0.30	-	435	0.30	-	(3)
E	18	110	0.30	0.32	210	0.28	0.26	435	0.27	0.25	(1)
W	18	75	0.38		175	0.34	-	365	0.35	-	(1)
E	17	90	0.25	0.23	175	0.21	0.21	360	0.27	0.26	(3)
W	15	90	0.30	0.30	175	0.20	0.17	350	0.22	0.19	(1)

Table 2-b; Summary of Results, Yakima

Dir.	Speed Kt	Dist. m	Staff No. 1 Unfilt. Height m	Staff No. 1 Filt. Height m	Dist. m	Staff No. 2 Unfilt. Height m	Staff No. 2 Filt. Height m	Dist. m	Staff No. 3 Unfilt. Height m	Staff No. 3 Filt. Height m	Method of Finding Dist.
S	16.3	120	0.22	0.22	230	0.12	0.16	440	0.08	-	(6)
N	16.3	120	0.15	-	230	0.15	-	440	0.13	-	(6)
S	16.3	115	0.19	0.23	225	0.15	-	435	0.13	0.16	(6)
N	14.2	115	0.23	0.22	220	-	-	420	0.10	0.13	(6)
S	14.2	115	0.21	0.20	215	0.27	0.27	410	0.13	0.14	(6)
N	14.2	110	0.25	0.21	210	0.21		400	0.13	-	(6)
S	10.9	110	0.19	0.20	210	0.22	0.21	400	0.09	0.14	(6)

Table 2-c; Summary of Results, KLAHOWYA

Dir.	Speed Kt	Dist. m	Staff No. 1 Unfilt. Height m	Staff No. 1 Filt. Height m	Dist. m	Staff No. 2 Unfilt. Height m	Staff No. 2 Filt. Height m	Dist. m	Staff No. 3 Unfilt. Height m	Staff No. 3 Filt. Height m	Method of Finding Dist.
N	13	110	0.30	0.28	210	0.21	0.27	400	0.08	0.15	(6)
S	13	110	0.21	0.23	210	0.25	0.26	400	0.25	0.20	(6)
N	10	110	0.19	0.22	210	0.11	0.19	400	0.11	0.11	(6)
S	10	150	0.17	0.14	245	0.13	0.14	435	-	-	(6)
N	10	115	0.23	0.20	195	0.13	-	345	0.13	-	(6)
S	10	105	0.30	0.27	140	0.22	0.23	215	0.14	0.13	(6)
N	13	105	0.26	0.25	140	0.16	-	215	0.16	-	(6)
S	<10	45	0.19	-	75	0.26	-	150	-	-	(4)
N	13	75	0.36	0.38	110	0.27	-	185	0.20		(6)
S	13	80	0.30	0.31	125	0.27	0.29	205	0.28	0.29	(4)
N	13	95	0.43	0.45	150	0.32	-	255	0.22	-	(6)
S	10	130	0.23	0.24	175	-	-	260	0.17	0.16	(4)
N	10	95	0.18	0.18	150	0.16	-	255	0.14	-	(6)
S	10	75	0.19	0.19	150	0.26	0.24	305	0.17	0.17	(5)

(3) No photographs were available. The distance x_0 was assumed to be 76 m (250 ft), the 'target' value specified to the ferry pilot, α was assumed to be 90 degrees, and wave staff locations were assumed to be the same as determined from photos for adjoining runs.

(4) A photograph was used; the ferry again provided the scale. The same interpolation scheme was used to get distances between staffs. Because of the low 730 m (2400 ft) aircraft elevation, the larger photograph scale allowed measurements to be taken directly off the photo.

(5) A photograph was used, and the distance x_0 measured directly. As not all of the staff array was included in the photograph, the other distances were assumed and were based on those determined in (4) above for an adjoining (in time) run.

(6) No photographs were available. The distance x_0 and angle α were estimated by an observer on the ferry; wave staff positions were determined by assuming a ten percent stretch of mooring line and using trigonometry.

Although distances in Table 2 are listed to within 5 meters, actual accuracy was not that good. It is believed that the greatest source of error was in the distance x_0. The work boat was too small and too close to the ferry to allow use of the ferry's radar, and sextant readings from the workboat were not feasible. An estimate of the actual distance resolution is 15 meters; consequences are discussed later. All distances and wave heights were initially evaluated in foot units.

Aerial photographs were used to estimate the speed of the Klahowya, as speed pairs of photographs incorporating fixed points on land were obtained for the three engine speeds at which the ferry was operated. These speeds are not considered to be extremely accurate because the time intervals between successive photos and the resolution (± 1 second) of the camera clock visible in the photograph could produce errors as large as ten percent. Consequently, data obtained in previous special sea trials of the Sealth and Yakima were used to determine the speeds of these vessels. These prior data, in the form of propeller shaft rotation rate vs. vessel speed, had been taken very accurately through the use of shore-based radar. Their use was considered acceptable because the vessel drafts on the dates of the present tests were almost identical to those in effect during the sea trials. (At neither time was there a load of automobiles and/or passengers on board).

Field Tests - September 1984

The field tests were initially scheduled for the period 17-19 September, 1984. These dates followed immediately after cessation of the summer schedule for the ferry system so that three vessels could be withdrawn for one day each from regular routes in order to participate in the test program, and were scheduled to maximize daylight hours. Also, predicted tide ranges were small (1.5 m maximum) during daylight hours. The site selected was in deep water (depths in excess of 100 fathoms over most of the vessel path) in central Puget Sound about 15

km north of Seattle. The test ferry was to travel back and forth on the basically east-west path shown in Figure 3, past the wave staff array secured at the southerly end of the string to a permanent navigation buoy dividing the northbound and southbound traffic lanes. The wave staff array was aligned with the direction of current motion. Weather conditions were good and the light, southerly wind did not generate any significant wind waves so that the wave gage signals were uncluttered. There was considerable wave activity at the site which could be attributed to passing vessels. Since these waves has frequencies comparable to those which were to be measured it would be difficult to filter them out of the records obtained. Consequently, ferry runs were delayed until visible waves from larger vessels had cleared the area.

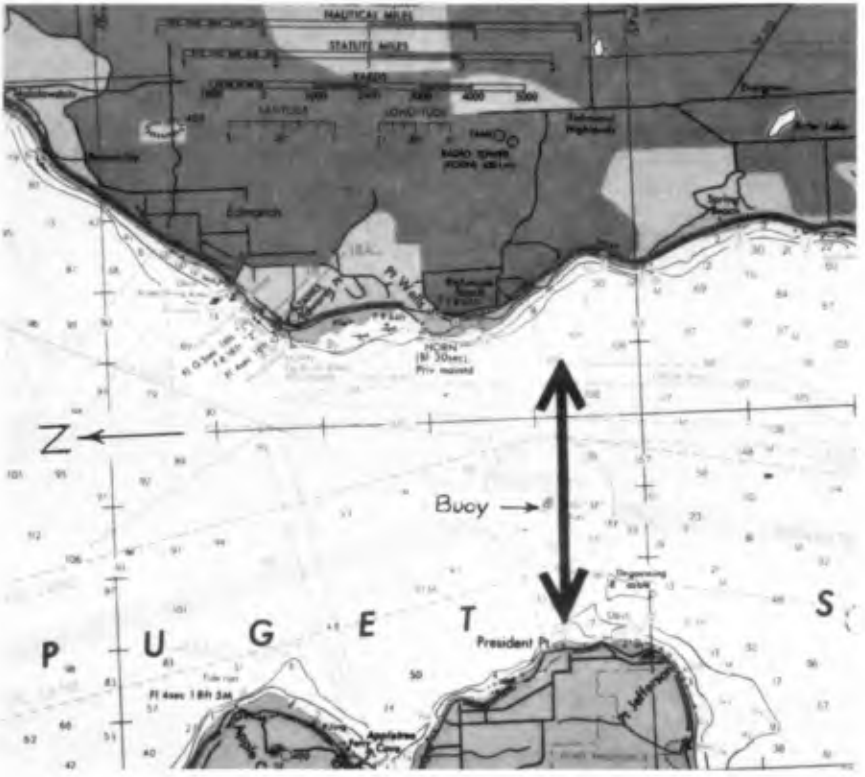

Figure 3. Central Puget Sound site, 17 September tests.

Tests were conducted, using the Sealth, on 17 September. Figure 4, which shows data obtained at the highest speed tested (18 knots) is representative of the results obtained. The values are listed in Table 2. The filtered and unfiltered data are combined on the single plot; it is noted that filtering did not yield any substantial reduction in

the scatter. For the results shown in Figure 4, as with the measurements for the entire program listed in Table 2, errors in measurement of distance will account for only a small amount of the scatter. Even large distance discrepancies would not change the general pattern, especially at larger distances from the sailing line where variations in wave height with distance become smaller. Because ship waves are not entirely regular and repeatable, a number of data sets were obtained for the same ship speed.

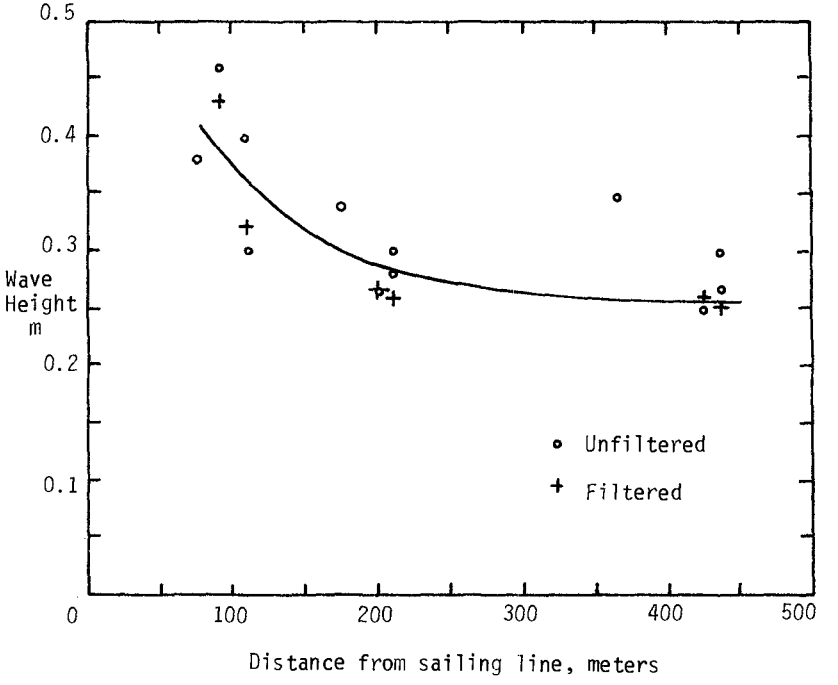

Figure 4. Maximum wave heights, ferry Sealth, 18 knots.

The wave through the plotted points on Figure 4 is strictly a hand-drawn visual fit, as the data were not considered sufficiently numerous to justify use of statistical techniques. The same treatment was applied to all data obtained for the three vessels tested; these curves and further details of the test program have been presented in the project report (Nece et al., 1985).

Mechanical problems experienced by other ferries required rescheduling of ferries, so there was no test vessel available on 18 September. Winds causing wind waves of height about the same as the ferry-generated waves, coupled with electrical problems in the staff array, caused the 19 September tests to be cancelled as well.

Field Tests - October 1984

Anticipated seasonal deterioriation of weather conditions along with uncertainty of availability of ferries for testing led to the selection of a different test location. The site chosen was on the west side of Blake Island, approximately 25 km south of the September site (Figure 5). A fundamental concern was protection from mostly prevalent southerly winds. A permanent mooring buoy provided attachment of the inshore end of the wave staff array which was strung out to the west from shore, so that the workboat was at the end of the string closest to the ferry path. The ferries' path was along a generally north-south line parallel to the west shore of Blake Island. The wave staffs were in depths of 10+ fathoms, and the ferries ran in depths generally of about 20 fathoms, so that deep water conditions prevailed.

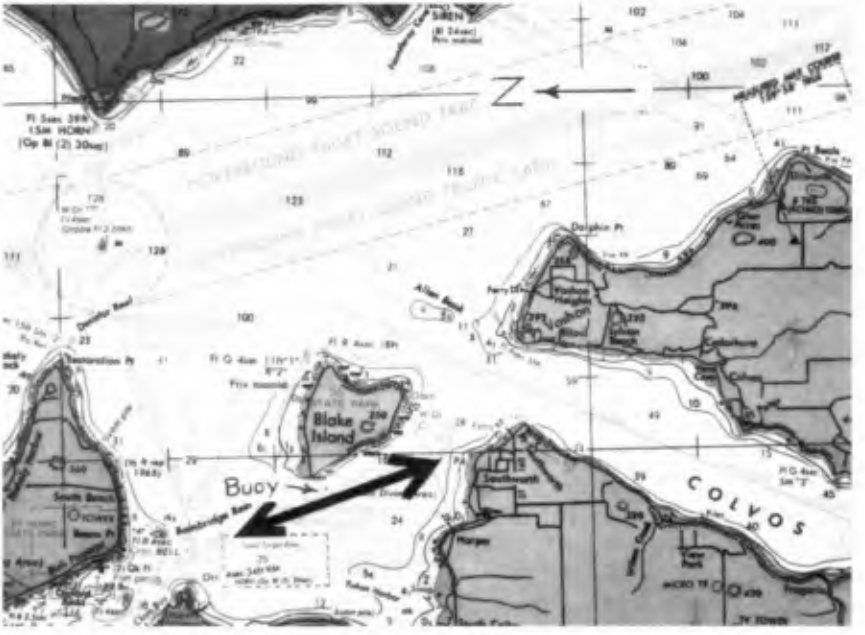

Figure 5. Blake Island site, 23 October tests.

Limited runs were made with the Yakima on the morning of 23 October. Low clouds and rain precluded aerial photography. Unanticipated strong north-flowing tidal currents at the site posed a problem. It was difficult to keep the wave staff array aligned normal to the ferry path. Near the end of the one-hour testing period it was decided to relax the requirement of trying to maintain the angle α at about 90 degrees; for the last runs, α was estimated at 60 degrees.

Maximum wave height vs. distance measurements are shown in Figure 6 for a vessel speed of 14.2 knots. The visual fit solid line curve

through the data reveals apparently anomalous behavior, i.e., increase in wave height with distance from the sailing line. This same anomalous behavior was observed for the one run at a 10.9 knot speed.

Two possibilities were considered to explain this unexpected behavior. One was to consider the direction of ferry movement, and consequently that of its wave pattern as well. The currents could have caused some steepening of the vessel waves. In Figure 6 the dashed line applies to northbound ferry runs only.

Identification of maximum wave heights from the analog records was not clear-cut for the Yakima data. A complex demodulation analysis (see, e.g., Sobey and Liang, 1986, and Bloomfield, 1976) was applied to the 10.9 knot ferry speed data in an attempt to isolate the dominant frequency wave which is the ship wave. Results of this analysis indicated the presence of two dominant frequencies, 0.35 Hz and 0.45 hz. Based on the 10.9 knot vessel speed, the predicted frequency for waves at the boundary of the Kelvin ship-wave wedge was 0.35 Hz. Heights for the 0.35 Hz waves were determined and plotted (dashed curve) on Figure 7; the anomalous behavior indicated by results from the visual inspection of the filtered and unfiltered records (solid line) has been removed.

The complex demodulation analysis was applied to only the one set of data. The procedure holds the potential of isolating bow and stern waves, but was not pursued here because of the pragmatic objectives of the study.

Tests with the ferry Klahowya were conducted in the afternoon of 23 October. The wave staff array was allowed to drift more with the current, so angles α as estimated from the ferry or read from aerial photographs were considerably less than 90 degrees. Distances from the sailing line at which waves were measured then tended to be slightly smaller and more variable. Data for the 10 knot speed are plotted in Figure 8. Again, the curve shown is a visual best-fit line. The trend of decreasing wave height with increased distance from the sailing line is evident, although there is considerable scatter.

Because the currents present during the Klahowya tests were at least as strong as those during the Yakima runs, it is hypothesized that some of the apparently anomalous results obtained with the Yakima were associated with the behavior of the wave staffs when it was attempted to keep the array essentially normal to the direction of the current. Because of uncertainties associated with the Yakima data (all of which are listed in Table 2) they are not included in the summary curves presented in the next section.

Conclusions

Figures 9 and 10 are summary plots of wave height vs. vessel speed at distances of 100 and 300 meters, respectively, from the sailing line. Results are presented for the Sealth and Klahowya only; data for the Yakima are not presented because of the uncertainties discussed previously. The points shown on Figures 9 and 10 do not come from

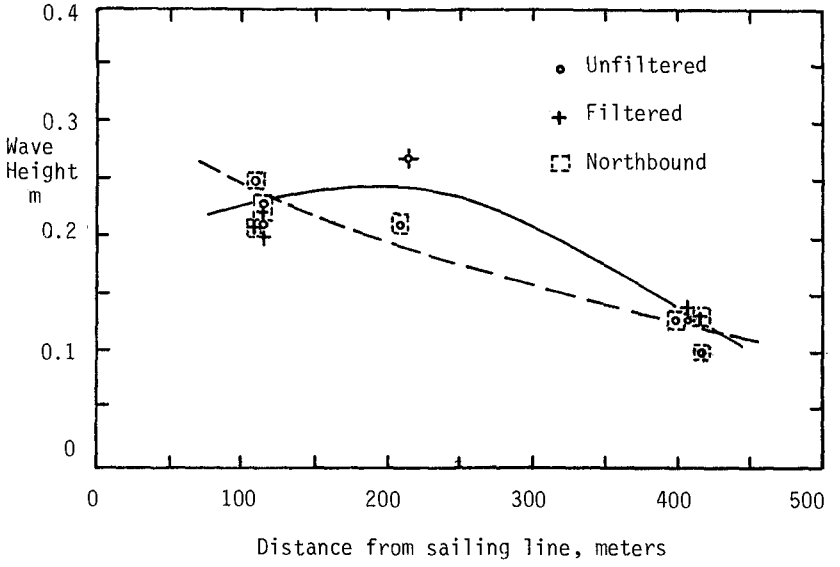

Figure 6. Maximum wave heights, ferry Yakima, 14.2 knots.

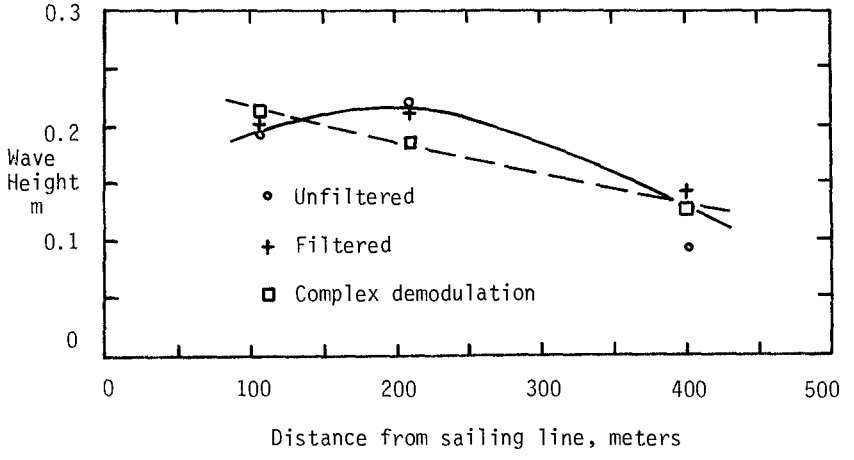

Figure 7. Maximum wave heights, ferry Yakima, 10.9 knots.

Table 2 but have been cross-plotted from the curves such as Figures 4 and 8 and others prepared for the remaining vessel speeds.

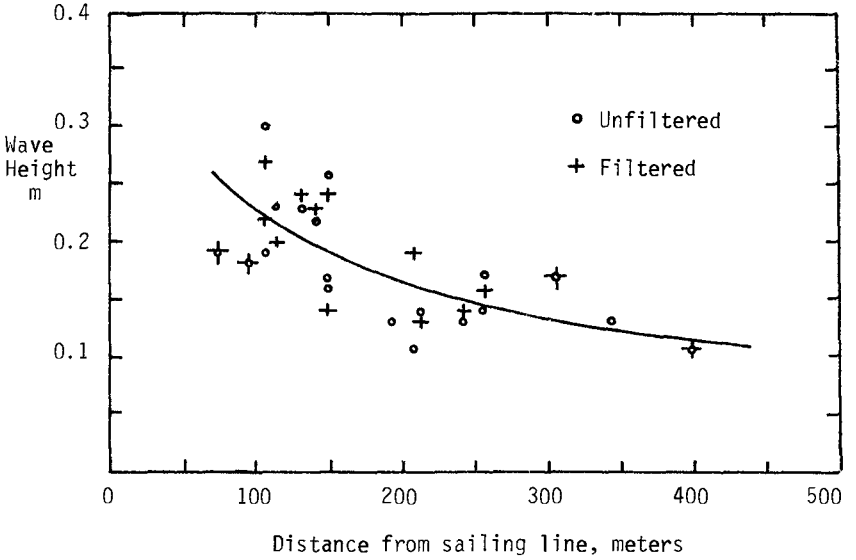

Figure 8. Maximum wave heights, ferry Klahowya, 10 knots.

Results clearly indicate that the different vessel classes do indeed produce waves of different height. Also, despite the uncertainties, it does seem apparent that the Yakima does generate the smallest waves as might be anticipated from comparison of hull geometries in Table 1. The results could also be used as a guide to vessel operation on specific routes in Puget Sound if wave generation is a concern.

Although the waves examined here are smaller than those usually of interest to coastal engineers, given the appropriate conditions the methodology could be applied to measurements of waves from larger vessels.

Acknowledgments

The study was sponsored by the Washington State Department of Transportation, in cooperation with the United States Department of Transportation, Federal Highway Administration. Personnel of the Washington State Ferries participated actively in various phases of the study; the efforts of Frank Vibrans, Captain David Black, and Captain William Haffie in particular are acknowledged. James Walker and Bruce Shaw of the WSDOT Photogrammetric Laboratory were instrumental in the aerial photography work.

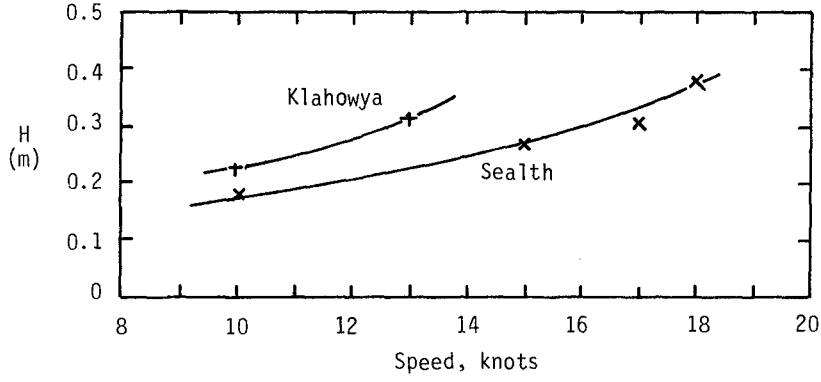

Figure 9. Wave heights at 100-meter distance from sailing line (from wave height vs. distance curves).

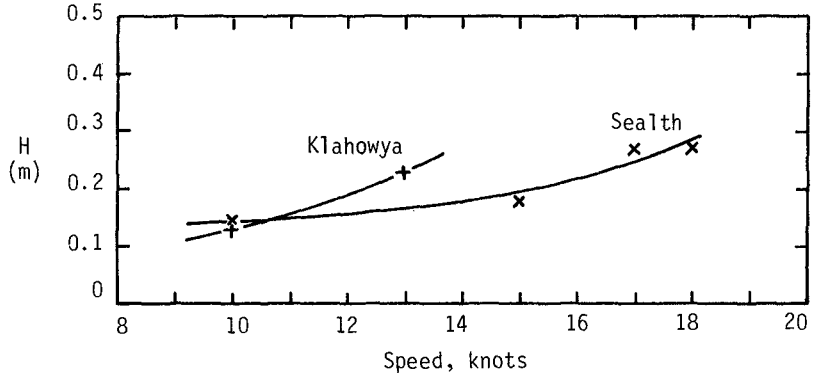

Figure 10. Wave heights at 300-meter distance from sailing line (from wave height vs. distance curves).

References

Bloomfield, P. (1976). "Fourier Analysis of Time Series", John Wiley and Sons, New York, N.Y.

Christensen, D.R. (1984). "Installation, Operation and Maintenance Manuals for Breakwater Data Acquisition and Analysis System", Water Resources Series Technical Report No. 91, Department of Civil Engineering, University of Washington, Seattle, Washington, U.S.A.

Herbich, J.B. and R.E. Schiller, Jr. (1984). "Surges and Waves Generated by Ships in a Constricted Channel", Proceedings of Nineteenth Coastal Engineering Conference, American Society of Civil Engineers, Houston, Texas, U.S.A., pp. 3213-3226.

Johnson, J.W. (1958). "Ship Waves in Navigation Channels", Proceedings of Sixth Conference on Coastal Engineering, Gainesville, Florida, U.S.A., pp. 666-690.

Nece, R.E., M.R. McCaslin and D.R. Christensen (1985). "Ferry Wake Study", Report WA-RD 70.1, Washington State Department of Transportation, Olympia, Washington, U.S.A.

Nelson, E.E., D.R. Christensen and A.D. Schuldt (1983). "Floating Breakwater Prototype Test Program", Proceedings Coastal Structures '83, American Society of Civil Engineers, Arlington, Virginia, U.S.A., pp. 433-446.

Sobey, R.J. and H.-B. Liang (1986). "Complex Envelope Identification of Wave Groups", Proceedings of Twentieth International Conference on Coastal Engineering, American Society of Civil Engineers, Taipei, Taiwan, Republic of China.

Sorensen, R.M. (1967). "Investigation of Ship-Generated Waves", Journal of the Waterways and Harbors Division, American Society of Civil Engineers, Vol. 93, No. WW1, pp. 85-99.

Weggel, R.J. and R.M. Sorensen (1986). "Ship Wave Prediction for Port and Channel Design", Proceedings Ports '86, American Society of Civil Engineers, Oakland, California, U.S.A.

CHAPTER 47

Directional Growth for Numerical Wind Wave Models

W.L. Neu[1]
S.H. Kwon[2]

Abstract

This study is concerned with the operation of spectral wind wave models. Many spectral wind wave models use a growth mechanism which operates on the point spectrum with directionality being introduced after the fact by the use of a spreading function. It is recognized here that this approach leads to errors whenever the wind and wave fields are not aligned. This is demonstrated by comparing the performance of two first generation models under various conditions. One makes use of a point spectral growth mechanism and follows the operation of the Spectral Ocean Wave Model (SOWM). The other uses a directional growth mechanism but is otherwise the same as the first. A large difference between the models is noted for swell corrupted seas.

1. Introduction

A number of operational wave forecasting models exist which perform with varying degrees of accuracy depending largely on the complexity of the situation they are asked to model. Since our understanding of the wave generation process is far from complete, wind wave models must rely heavily on empirical formulas. As long as the conditions a model is asked to simulate correspond with those under which the data for its empirical foundation were obtained, the model performs fairly well. When presented with situations of increased complexity, however, the performance of a model is bound to deteriorate. This was nicely illustrated in the Sea Wave Modeling Project (SWAMP Group, 1985).

In order to improve the performance of a wave model, it seems important to retain in the model as much detail and generality of the physics as possible. A large step in this direction was made by Pierson, et al. (1966) with the development of a model which computed directional wave spectra and allowed for the propagation of wave energy. After undergoing several refinements (Inoue, 1967; Lazanoff and Stevenson, 1975) it has evolved into the Spectral Ocean Wave Model (SOWM) as described by Pierson (1982). The SOWM is an operational wave model in use by the U.S. Navy Fleet Numerical Oceanography Center.

The SOWM is classified as a first generation decoupled propagation model in that the wave growth is dominated by wind energy input as

[1]Assistant Professor, Virginia Polytechnic Institute and State University, Blacksburg, VA 24061, USA
[2]Lecturer, Pusan National University, Pusan, 607, Korea

opposed to nonlinear wave interaction effects and the spectrum is discretized into frequency-direction bands. Each band is allowed to evolve more or less independently and propagate at its own group velocity in its own direction. Other models of this type include those of Barnett (1968) and Ewing (1971).

Second generation discrete models, referred to as coupled discrete models rely heavily on nonlinear interactions in their growth mechanisms. These include the models of Resio (1981) and Golding (1983). The remaining class of models, the coupled hybrid models, are parametric models. These attempt to compute a set of parameters of a point spectrum, typically the JONSWAP spectrum (Hasselmann, et al., 1973), to represent the windsea part of the spectrum and require assumptions as to how the windsea becomes swell and vice versa. Thus they implicitly employ nonlinear energy transfer as the dominant mechanism controlling the spectral shape. An example is the model of Hasselmann, et al. (1976). Several models other than those referred to above and falling in all three classes are described by the SWAMP Group (1985).

The focus of this study is on the directional properties of the wave generation mechanism. By the design of the parametric models, the windsea part of the spectrum at least, must obtain its directionality from a spreading function centered on the wind direction. Some of these models allow the existence of swell whose direction of propagation is independent of the windsea, however, the directionality of any energy generated by the model must still be that of a spreading function.

The discrete models are not inherently so confined. Since they are discretized in direction, they may allow the directionality of the energy growth to be determined by the directionality of the growth mechanism. Further, since the growth rate of the spectrum is strongly dependent on sea state, the directionality (and, in general, magnitude) of the energy growth depends on the directionality of the existing spectrum. However many models, including the SOWM, employ a point spectral growth mechanism and spread the energy growth over direction with a spreading function. This is done presumably due to the lack of a form of the atmospheric energy input as a function of the angle between wind and wave.

In this study, such a function is developed and employed in a fully directional wave growth mechanism. A discrete spectral model using this growth mechanism is assembled following the operation of the SOWM. The performance of this new model under several sets of conditions is compared with that of a version of the SOWM written by the authors.

2. Structure of the Model

The rate of change of the wave spectrum can be described by the energy balance equation proposed by Hasselmann (1960)

$$\frac{\partial E(f,\theta;\vec{x},t)}{\partial t} + \vec{C}_g \cdot \nabla E(f,\theta;\vec{x},t) = S(f,\theta;\vec{x},t) = S_{in} + S_{nl} - S_{ds} \qquad (1)$$

where $E(f,\theta;\vec{x},t)$ is the two-dimensional directional frequency wave spectrum being a function of position $\vec{x}$, time t, wave frequency f, and direction of propagation θ. $\vec{C}_g$ is the group velocity of the spectral component and S represents the sum of individual source functions. S_{in}, S_{nl}, and S_{ds} represent the wind input, nonlinear wave interaction and dissipation source functions respectively. As in the SOWM, nonlinear wave interaction is not explicitly modeled. It is generally accepted that the nonlinear interaction is important for wave growth (SWAMP Group, 1985).

The energy input from the wind S_{in} is represented as

$$S_{in} = A(u,f,\alpha) + B(u^*,f,\alpha)E(f,\theta;\vec{x},t) \qquad (2)$$

where u is the wind velocity, u^* is the friction velocity and α is the angle between the wind and wave directions. The A term represents energy transfer from the turbulent pressure fluctuations to the wave field according to the theory of Phillips (1957) and results in a linear growth of the spectrum. The BE term represents the interaction of an already disturbed surface with the wind.

If we consider an infinite ocean with a homogeneous wind field, the wave spectrum is not a function of position. The numerical model for this case requires only one spacial grid point and no propagation scheme. Without the nonlinear interaction and dissipation terms, equation (1) then becomes

$$\frac{\partial E(f,\theta;t)}{\partial t} = A(u,f,\alpha) + B(u^*,f,\alpha)E(f,\theta;t) \qquad (3)$$

Since equation (3) is linear, each spectral component can grow independently. Also, according to equation (3) the spectral component can grow to an infinite value with time, but in the real situation, dissipation will limit the growth. Wave breaking is thought to be the main mechanism of dissipation. The dissipation function S_{ds} is applied implicitly for wave energy propagating within ±90° of the wind direction in a manner analogous to its implementation in the SOWM. The growth of the spectrum is limited by a fully developed spectrum which will be discussed later.

The directional treatment of the wave growth mechanism is the focus of this study. Before we refer to our model, it is helpful to examine the relation of the energy balance used in the SOWM to equation (3). A directional spectrum can be obtained by multiplying the frequency spectrum by a spreading function:

$$E(f,\theta) = E(f)F(\theta) \tag{4}$$

The spreading function used in the SOWM is that which was derived by the SWOP project (Cote, et al., 1960). It was considered to be a function of wind speed and frequency as well as direction and is given by

$$F(\omega,\alpha,u) = \frac{1}{\pi}\left[1 + (0.5 + 0.82e^{-1/2(\frac{\omega u}{g})^4})\cos 2\alpha + 0.32e^{-1/2(\frac{\omega u}{g})^4}\cos 4\alpha\right]$$

$$\text{for } -\frac{\pi}{2} < \alpha < \frac{\pi}{2} \tag{5}$$

where $\omega = 2\pi f$ and $F(\omega,\alpha,u) = 0$, elsewhere.

Using equation (4), equation (3) can be rewritten as

$$\frac{\partial E(f;t)F(\alpha)}{\partial t} = A(u,f,\alpha) + B(u^*,f,\alpha)E(f;t)F(\alpha) \tag{6}$$

Integrating equation (6) over the parameter α from $-\pi/2$ to $\pi/2$,

$$\int_{-\pi/2}^{+\pi/2} \frac{\partial E(f;t)F(\alpha)}{\partial t}\,d\alpha = \int_{-\pi/2}^{+\pi/2} A(u,f,\alpha)d\alpha + \int_{-\pi/2}^{+\pi/2} B(u^*,f,\alpha)E(f;t)F(\alpha)d\alpha \tag{7}$$

If we let

$$A'(u,f) = \int_{-\pi/2}^{+\pi/2} A(u,f,\alpha)d\alpha \tag{8}$$

$$B'(u,f) = \int_{-\pi/2}^{\pi/2} B(u^*,f,\alpha)F(\alpha)d\alpha \tag{9}$$

and consider that

$$\int_{-\pi/2}^{+\pi/2} F(\theta)d\theta = 1 \tag{10}$$

then we have

$$\frac{\partial E(f;t)}{\partial t} = A'(u,f) + B'(u^*,f)E(f)\ . \tag{11}$$

This directionally integrated energy balance equation, modified to limit spectral values to a fully developed limit, is what is used by

the SOWM. Notice that it assumes that the spectrum is always centered on the wind direction, although the SOWM does not constrain it to be. The directional spectrum is obtained by spreading the growth resulting from this directionally integrated equation at each time step about the wind direction and adding it to the pre-existing directional spectrum, thus forcing the new spectral growth to have the angular distribution of the spreading function.

The model presented in this study solves the energy balance equation in the directional form, equation (3). It does not require the introduction of the artificial angular spreading function and it retains the directionality of the growth. Note that the spectral growth rate is highly dependent on the spectral value through the BE term. The directionality (and magnitude) of the growth will thus depend on the directional properties of the spectrum. This dependence is destroyed if the growth is obtained from equation (11).

3. The A Term

The $A(u,f,\alpha)$ term represents the generation of waves on an initially calm water surface through the turbulent atmospheric pressure fluctuations. It is too weak to explain the major growth of the wave field but it can explain the growth of waves from initially calm water to a certain level where other mechanisms become dominant. Within Phillips' theory, the waves develop most rapidly by means of a resonance mechanism which occurs when a component of the surface pressure distribution moves at the same speed as the free surface wave with the same wave number.

The form of the A function used here is similar to that used by Barnett (1968) and is simply a nonintegrated form of the function used in the SOWM. A summary of the mathematical background is as follows.

Hasselmann (1960) has shown that the A function can be represented in terms of the three-dimensional spectrum of the random atmospheric pressure fluctuations $\Pi(\vec{k},\omega)$. That is

$$A = \frac{4\pi^2 k \omega^3}{\rho_w^2 g^3} \Pi(\vec{k},\omega) \tag{12}$$

where k is the magnitude of the wave number $\vec{k} = (k_1,k_2)$, and ρ_w is the density of sea water. From the experiments of Priestly (1965) and discussion of Snyder and Cox (1966), we find

$$\Pi(\vec{k},\omega) = \frac{1.23A^*}{\pi^2\omega^2} u^4 \frac{0.33k^{1.28}}{0.1089k^{2.56} + (k\cos\alpha - \kappa)^2} \cdot \frac{0.52k^{0.95}}{0.2704k^{1.9} + k^2\sin^2\alpha} \tag{13}$$

where κ is ω/u_c, u_c being the convection velocity of the eddies. The value of the coefficient A^* is determined from the measurements of Snyder and Cox with additional data supplied by Cardone (1969). Since this data was related to the wind velocity at 6.1 m above the sea surface the convection velocity is taken as $u_{6.1}$. Priestly's measurements indicate a modification is appropriate for $\kappa < 0.02$. The form of the A function is then

$$A(f,u_{6.1},\alpha) = \frac{4.793\times10^{-16}\,\omega^4 u_{6.1}^3}{Q_1(\omega,u_{6.1},\alpha)R_1(\omega,u_{6.1},\alpha)} \qquad \frac{\omega}{u_{6.1}} \leq 0.02 \tag{14}$$

$$A(f,u_{6.1},\alpha) = \frac{7.167\times10^{-14}\,\omega^{5.25}\,u_{6.1}^{1.75}}{Q_2(\omega,u_{6.1},\alpha)R_2(\omega,u_{6.1},\alpha)} \qquad \frac{\omega}{u_{6.1}} > 0.02 \tag{15}$$

and

$$Q_1 = Q_2 = 0.2704\left(\frac{\omega}{u_{6.1}}\right)^2 + \left(\frac{\omega^2}{g}\sin\alpha\right)^2 \tag{16}$$

$$R_1 = 4.87\times10^{-6} + \left(\frac{\omega^2}{g}\cos\alpha - \frac{\omega}{u_{6.1}}\right)^2 \tag{17}$$

$$R_2 = 0.1089\left(\frac{\omega^2}{g}\right)^{2.5} + \left(\frac{\omega^2}{g}\cos\alpha - \frac{\omega}{u_{6.1}}\right)^2 \tag{18}$$

A is in m^2/rad, $u_{6.1}$ is in m/sec, and g is in m/sec^2.

It should be noted that the numerical constants appearing in equation (14) and (15) are not those given in Pierson (1982). He gives the form of A used in the computer code where for computational convenience it has been multiplied by the minimum frequency bandwidth (1/180 sec) and the number of seconds in his 3 hour time step. His value for A is also off by a factor of two which was applied separately in the SOWM code.

4. The BE Term

The $B(u^*,f,\alpha)E(f,\theta;t)$ term is the result of the interaction of the air flow with the already disturbed water surface. Miles (1957) considered the perturbation of the mean shear flow in the air by the disturbed water surface, but he neglected the effects of atmospheric turbulence. Phillips (1966) extended the analysis to consider the interaction of the wave induced air flow perturbations with the free stream turbulence. He derived an expression in terms of the mean velocity profile of the wind, U, as follows

$$\frac{B}{f} = \frac{\rho_a}{\rho_w} \frac{1}{c^2 k} \left\{ \frac{M_m N^2 k^4}{\cos^2\alpha} \left(\frac{-U''}{(U')^3} \right)_{z_m} \left(\int_{z_m}^{\infty} [U(z)\cos\alpha - c]^2 e^{-kz} dz \right)^2 \right.$$

$$\left. + M \int_0^{\infty} N^2 (-U'') \cos\alpha \left| U\cos\alpha - c \right| e^{-2kz} dz \right\} \qquad (19)$$

where M, M_m and N are constants and z_m is the matched height where the mean wind speed, $U(z_m)$, is equal to the wave phase speed, c. Phillips suggested $M_m = \pi$, $M = 1.6 \times 10^{-2}$, $N^2 = \frac{1}{3}$ for $z > z_m$ and $N^2 = 1$ for $z < z_m$. Inoue (1967) used these values and assumed a logarithmic velocity profile to evaluate equation (19). He found poor agreement with observational data and abandoned this approach. For his B function he fit a curve to data obtained from wave growth measurements. The function he found and that which is used in the SOWM is

$$\frac{B}{f} = 0.00139 e^{-7000\left[\left(\frac{u_*}{c}\right) - 0.031\right]^2} + 0.725 \left(\frac{u_*}{c}\right)^2 e^{-0.0004\left(\frac{u}{u_*}\right)^2} \qquad (20)$$

We repeated the calculations of Inoue (1967) using a logarithmic velocity profile in equation (19) and found directionally integrated results much larger than given by equation (20). Looking at the integrand of the second term in (19), we found that it became very large for small z since the logarithmic profile has a very large curvature near the surface. Note that the lower limit of this integration is actually the roughness height, z_o, for the logarithmic profile. From these calculations, it appears that the mean velocity must have much less curvature near the surface than is given by the logarithmic profile. Takeda (1963) has measured departures from a logarithmic form very close to the water surface.

In this study, rather than attempting to derive a more appropriate mean velocity profile, Gauss-Laguerre quadrature is used in an effort to avoid the contribution to the integration from this strong peak near the origin. Thus we are integrating a polynomial fit to the integrand which does not follow the peak. In effect, we are assuming a

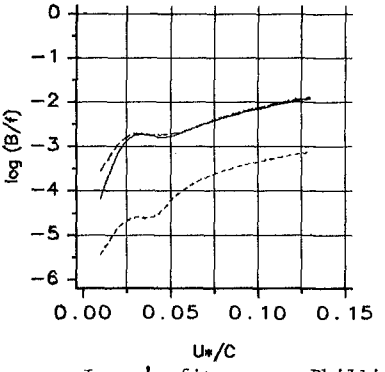

Fig. 1. Evaluation of the B function in directionally integrated form

mean velocity profile which would give us the integrand matching this polynomial fit. The result of evaluating equation (19) in this manner, using the values of the constants suggested by Phillips, and integrating over direction according to equation (9) is shown as the lowest curve in Figure 1. The solid line in this figure is Inoue's curve fit to the observational data, equation (20). The constants M and M_m in equation (19) were adjusted to give agreement with it, requiring the values 1.2 and 12π, respectively. The result using these constants is the remaining curve in Figure 1.

5. Other Details of the Model

As does the SOWM, our model does not explicitly model the dissipation for waves traveling with the wind. A limiting directional wave spectrum is assumed as a function of wind speed. The form used here (and in the SOWM) is the Pierson-Moskowitz spectrum, $E_\infty(\omega,u)$, with the directionality of the SWOP spreading function. The fully developed spectrum is thus

$$E_\infty(\omega,\alpha,u) = E_\infty(\omega,u)F(\omega,\alpha,u) \tag{21}$$

Following Inoue (1967), energy dissipation is assumed to be a function of the ratio of the spectrum to the fully developed spectrum. Then equation (3) can be written as

$$\frac{\partial E(f,\theta;t)}{\partial t} = A(u,f,\alpha) + B(u^*,f,\alpha)E(f,\theta;t) - [A(u,f,\alpha) + B(u^*,f,\alpha)E(f,\theta;t)]\left[\frac{E(f,\theta;t)}{E_\infty(f,\alpha,u)}\right]^2 \tag{22}$$

A closed form solution may be obtained if we multiply A by $[1 - (\frac{E}{E_\infty})^2]^{1/2}$. This has only a small effect on the growth of the spectrum. Equation (23) can then be written as

$$\frac{dE}{dt} = \{A[1 - (\frac{E}{E_\infty})^2]^{1/2} + BE\}[1 - (\frac{E}{E_\infty})^2] \tag{23}$$

with solution

$$E = \frac{A[e^{Bt} - 1]}{B}\{1 + [\frac{A(e^{Bt} - 1)}{BE_\infty}]^2\}^{-1/2} \tag{24}$$

Equation (24) is applied in a directional form in a manner analogous to its directionally integrated application in the SOWM. At each time step, each frequency-direction band that lies within ±90° to the wind direction is allowed to grow if its initial value is less than $0.95E_\infty(f,\theta)$. If $0.95E_\infty \leq E < E_\infty$, E is set equal to its fully developed

value. If the initial value exceeds E_∞, no growth is allowed. Thus under a steady wind, each component will grow until it reaches its fully developed limit. Once all bands have reached saturation, the spectrum reaches a steady state.

If the wind now turns, since the fully developed spectrum is tied to the wind direction, some bands (within ±90° to the wind direction) will exceed their fully developed limit while others will not. If these underdeveloped bands are allowed to grow, the total energy present will exceed that in our fully developed sea. This situation also arises in the SOWM but is given special treatment here. We allow normal growth in those direction bands less than fully developed and attenuate the energy in over developed bands to maintain the same total energy in each frequency band.

Waves traveling at angles greater than ±90° to the wind direction are explicitly dissipated in the same manner as is done in the SOWM. The rate of dissipation depends on the total energy traveling within ±90° to the wind direction and the relative angle between wind and wave. The expression used is

$$E_d(f,\theta,t) = E_o(f,\theta,t)\left[e^{-s\Delta t(E_e(t))^{1/2}f^4}\right]^{r(\theta)} \tag{25}$$

where E_d is the spectral component after dissipation. E_o is the spectral component before dissipation, E_e is the total energy of the wind sea traveling within ±90° to the wind direction. And where $r(\theta) = 0$ for $\theta \leq 90°$, $\theta \geq 270°$. $r(\theta) = 3$ for $90° < \theta \leq 135°$, $225° \leq \theta < 270°$. $r(\theta) = 4.5$ for $135° < \theta \leq 165°$, $195° \leq \theta < 225°$. $r(\theta) = 6$ for $165° < \theta < 195°$. $s = 754.6\ (\frac{\text{sec}^4}{\text{m}})$ and Δt is the time step in hours.

As mentioned in the introduction, two model codes were written. One using the formulation of the SOWM code and one, the directional formulation described above. In the following, the former is referred to as VSOWM while the latter is called VPINK. Both models use 53 frequency bands, each of width 0.005 Hz, from 0.04 Hz to 0.3 Hz and 36 directional bands each 10° wide. In a test of CPU time necessary to complete 14 time steps with the infinite ocean models, VPINK required 2.3 times the time needed to run VSOWM.

6. Computational Results and Discussion

All computations were performed with wind speed at 19.5 m of 40 knots (20.6 m/s) and a time step of three hours. The results are presented in both point spectral form and in polar contour plots of the directional spectra. The point spectra include a dashed curve. This is the Pierson-Moskowitz spectrum which is our fully developed spectrum. The contour plots include an arrow which indicates the wind direction. Contours are drawn at increments of 10% of the maximum spectral value present in each plot.

The first case presented is that of wave growth on an initially calm sea under the influence of a steady wind. Figure 2 shows the evaluation of the frequency spectrum from VSOWM and Figure 3 is the same from VPINK. The VPINK spectra are similar to the VSOWM spectra except that the growth slows as a frequency band approaches the fully developed

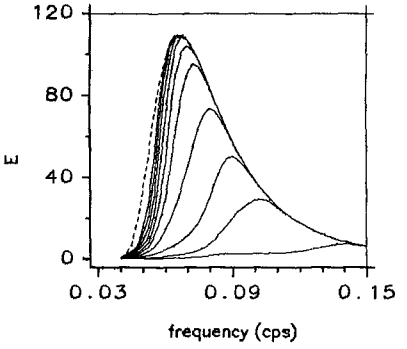

Fig. 2. Point spectrum evolution for a steady wind from VSOWM.

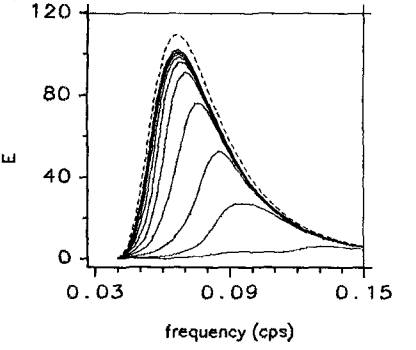

Fig. 3. Point spectrum evolution for a steady wind form VPINK.

limit. The reason for this is that its directional spread is more narrow than the spreading function which we use to define our directional fully developed limit. The direction bands near the wind direction therefore reach saturation first and the more oblique bands continue to grow slowly to fill in the frequency spectrum. This can be seen in the directional spectra of Figures 4 and 5. They are after five time steps from the VSOWM and VPINK respectively. Figure 4, the VSOWM spectrum,

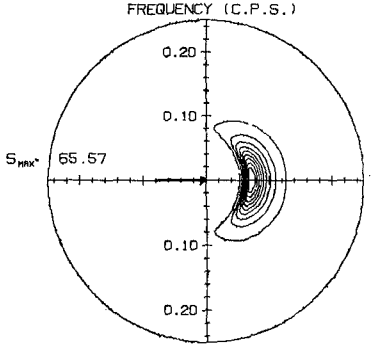

Fig. 4. Directional spectrum at 15 hours from VSOWM - steady wind.

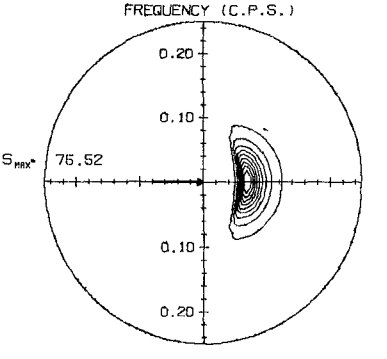

Fig. 5. Directional spectrum at 15 hours from VPINK - steady wind.

has the directionality of the spreading function while the VPINK spectrum in Figure 5 has a narrower spread which was determined by the growth mechanism. The difference in significant wave heights vs. time is small.

For the next case the sea was initially calm and the wind direction was allowed to vary by 10° at each time step, sweeping back and forth between ±20°. This demonstrated two points. First, the frequency spectra agreed more closely; each resembled the VSOWM steady wind case. This suggests that the typical fluctuations of wind direction may have a significant impact on the wave field directionality. The second point is that once the wave energy present within ±90° to the wind direction at a given frequency reaches its saturation level, the evolution of the VSOWM spectrum ceases whereas the directional relaxation mechanism previously discussed becomes active in VPINK. The VSOWM spectrum "freezes" from higher to lower frequencies as each reaches saturation while the VPINK spectrum continues to follow the wind vector (with some time lag). Typical directional spectra are shown in Figures 6 and 7.

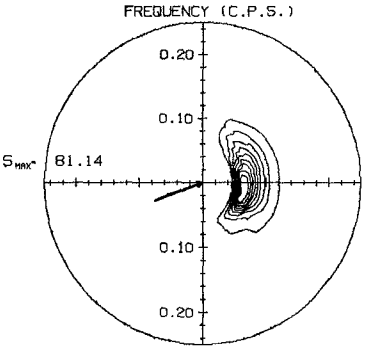

Fig. 6. Directional spectrum at 33 hours from VSOWM - oscillating wind.

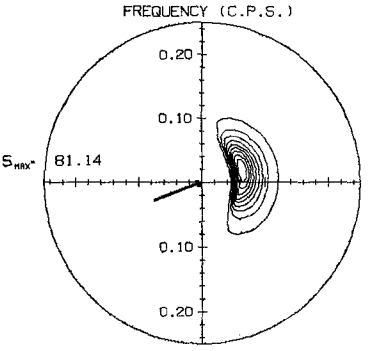

Fig. 7. Directional spectrum at 33 hours from VPINK - oscillating wind.

In the VSOWM spectrum of Figure 6, only those frequencies well below the modal frequency respond to the changing wind direction, quite the opposite of what we would expect to occur naturally. The VPINK spectrum in Figure 7 retains its response to the changing wind direction.

This same problem with VSOWM has even greater consequences when we consider a sudden 90° change of wind direction. We start with a fully developed sea spread about 90° and at $t = 0$ the wind direction changes to 0°. The VSOWM spectrum soon freezes up in a bidirectional form. The wave energy initially travelling in directions $0° < \theta < 90°$ is unchanged, new energy spread about the wind direction quickly grows to saturate each frequency band and thereafter, the only change is the attenuation of the energy initially in the directions $90° < \theta < 180°$. The directional spectrum at $t = 30$ hours is shown in Figure 8. The

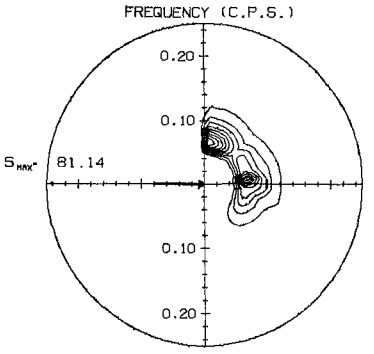

Fig. 8. Directional spectrum at 30 hours from VSOWM - 90° wind direction change.

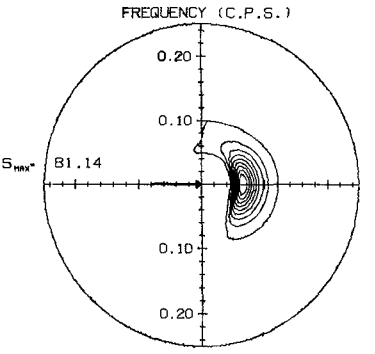

Fig. 9. Directional spectrum at 30 hours from VPINK - 90° wind direction change.

corresponding VPINK spectrum is shown in Figure 9. It evolves more naturally with the gradual growth of waves in the new direction and decay of the other components.

The final, and perhaps most important, comparison case does not involve a freezing up but addresses the fundamental nature of the point spectral growth mechanism. In this case we leave the wind steady but start with an initial low frequency swell on an otherwise calm sea. VPINK is little affected by the swell as can be seen by the point spectral evolution in Figure 10. Directional spectra at t = 3, 9 and 15

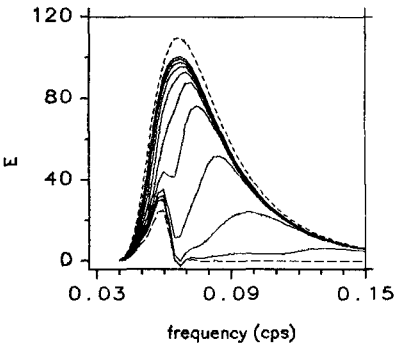

Fig. 10. Point spectrum evolution in the presence of swell from VPINK.

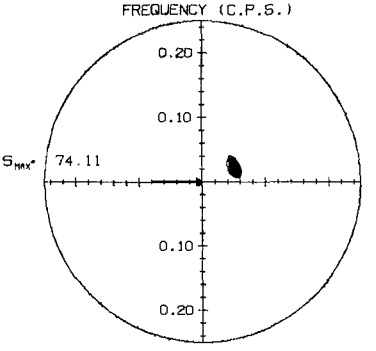

Fig. 11. Directional spectrum at 3 hours from VPINK - initial swell case.

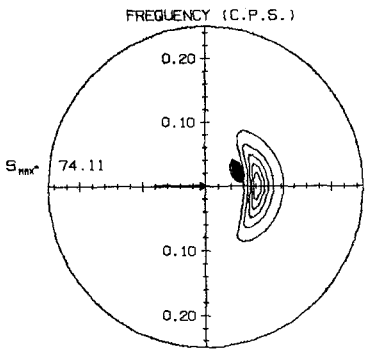

Fig. 12. Directional spectrum at 9 hours from VPINK - initial swell case.

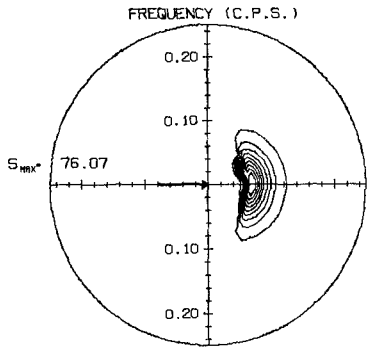

Fig. 13. Directional spectrum at 15 hours from VPINK - initial swell case.

hours are shown in Figures 11, 12 and 13 respectively. Figure 11 is nearly identical to the initial condition. As time proceeds, the wind sea grows to envelope the swell. The point spectral growth mechanism of the VSOWM however assumes that the initial energy present is centered on the wind direction and produces a much larger amount of growth in these frequency bands as can be seen in Figure 14. Figures 15, 16 and 17 are

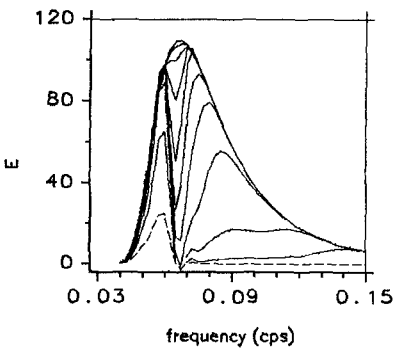

Fig. 14. Point spectrum evolution in the presence of swell from VSOWM.

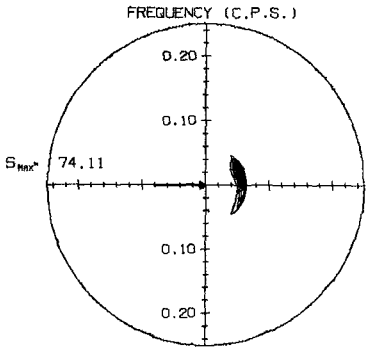

Fig. 15. Directional spectrum at 3 hours from VSOWM - initial swell case.

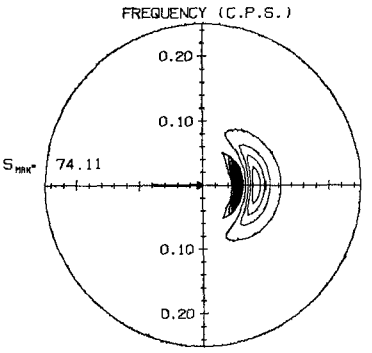

Fig. 16. Directional spectrum at 9 hours from VSOWM - initial swell case.

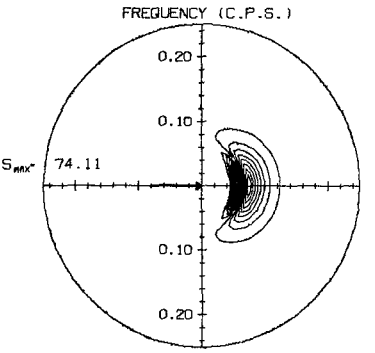

Fig. 17. Directional spectrum at 15 hours from VSOWM - initial swell case.

the directional spectra for t = 3, 9, and 15 hours respectively from VSOWM. From these we see that this new energy is spread widely in direction creating new low frequency components that should take much longer to develop.

These strong low frequency components, spread over ±90° are created due to a swell initially very narrowly spread. If this behavior is coupled with a propagation scheme, as it is in the operational SOWM, and these components are propagated to adjacent grid points, at those points they will act similar to the initial swell here. It is not hard to see that this growth mechanism could quickly corrupt a large area with excess low frequency energy, carried predominantly in the wind direction. Lazanoff and Stevenson (1975) describe several high energy case studies made for verification of the SOWM. Among the inaccuracies noted were the propagation of wave energy in improper directions and frequency shifts of spectral peaks. The problems discussed here may very well be responsible for these discrepancies. It also seems likely that the twenty year hindcast wave climatology produced with the SOWM (Lee, Bales and Sowby, 1985) overestimates both the low frequency wave energy present and its directional spread.

Acknowledgement

This work was supported by the David Taylor Naval Ship Research and Development Center under P.E. 62759N, SF-59-557-695.

References

Barnett, T.P. (1968): On the generation, dissipation, and prediction of ocean wind waves. J. Geophys. Res. 73, 513-529.

Cardone, V.J. (1969): Specification of the wind distribution in the marine boundary layer for wave forecasting. New York University, Department of Meteorology and Oceanography, TR 69-1, 11 pp.

Cote, L.J., J.O. Davis, W. Marks, R.J. McGough, E. Mehr, W.J. Pierson, Jr., F.J. Ropek, G. Stephenson and R.C. Vetter (1960): The directional spectrum of a wind generated sea as determined from data obtained by the Stereo Wave Observation Project. Meteor. Pap., Vol. 2, No. 6, 88 pp., New York University Press, NY.

Ewing, J.A. (1971): A numerical wave predition method for the North Atlantic Ocean: Dtsch. Hydrogr. Z. 24, 241-261.

Golding, B. (1983): A wave prediction system for real-time sea state forecasting. Quart. J.R. Met. Soc., 109, 393-416.

Hasselmann, K. (1960): Grundgleichungen der Seegangsveroussage. Schiffstechnik, 7, 191.

Hasselmann, K., T.P. Barnett, E. Bouws, H. Carlson, D.E. Cartwright, K. Enke, J.A. Ewing, H. Grenopp, D.G. Hasselmann, P. Kruesman, A. Meerburg, P. Muller, D.J. Olbers, K. Richter, W. Sell and H. Walden (1973): Measurements of wind wave growth and swell decay during the joint North Sea Wave Project (JONSWAP). Dtsch. Hydrogr. Z., Suppl. A. 8(12).

Hasselmann, K., D.B. Ross, P. Muller and W. Sell (1976): A parametrical wave prediction model. J. Phys. Oceanogr., 6, 200-228.

Inoue, T. (1967): On the growth of the spectrum of a wind generated sea according to a modified Miles-Phillips mechanism and its application to wave forecasting. TR-67-5, Geophysical Science Laboratory Report, NY University, School of Engineering and Science.

Lazanoff, S.M. and N.M. Stevenson (1975): An evaluation of a hemispheric operational wave spectral model. Tech. Note 75-3, Fleet Numerical Weather Center, Monterey, CA.

Lee, W.T., S.L. Bales and S.E. Sowby (1985): Standardized wind and wave environments for North Pacific Ocean Areas. DTNSRDC/SPO-0919-02.

Miles, J.W. (1957): On the generation of surface waves by shear flow, Part 1, J. Fluid Mech., 185-204.

Phillips, O.M. (1957): On the generation of surface waves by turbulent wind, J. Fluid Mech., 2, 417-445.

Phillips, O.M. (1966): The dynamics of the upper ocean. Cambridge University Press, NY.

Pierson, W.J., L. Tick and L. Baer (1966): Computer based procedures for preparing global wave forecasts and wind field analyses capable of using wave data obtained by a space craft. Proc. 6th Naval Hydrodynamics Symp., Vol. 2, 1.

Pierson, W.J. (1982): The spectral ocean wave model (SOWM), A northern hemisphere computer model for specifying and forecasting ocean wave spectra. DTNSRDC-82/011.

Priestly, J.T. (1965): Correlation studies of pressure fluctuations on the ground beneath a turbulent boundary layer. Natl. Bur. Std. Rpt. 8942.

Resio, D.T. (1981): The estimation of wind-wave generation in a discrete spectral model. J. Geophys. Oceanogr., 11, 510-525.

Snyder, O.H. and C.S. Cox (1966): A field study of the wind generation in a discrete spectral model for specifying and forecasting ocean wave. J. Marine Res., 24(2), 141-178.

SWAMP group (1985): Ocean wave modeling. Plenum Press, NY and London.

Takeda, A. (1963): Wind profiles over sea waves. J. Ocean. Soc., Japan, 19, 16-22.

CHAPTER 48

LOCAL APPROXIMATIONS : A NEW WAY OF DEALING WITH IRREGULAR WAVES

by

Peter Nielsen, Ph.D.*

ABSTRACT

The concept of local approximations via locally defined frequencies is introduced as a tool for dealing with irregular, non linear waves. Practical testing has been performed on the problem of estimating surface elevations from measured bottom pressures. In these tests the new method even in its simplest form proves more accurate than the linear spectral method. With respect to computational effort the new method requires orders of magnitude less than spectral methods, or wave by wave analysis of similar accuracy.

INTRODUCTION

Dealing with irregular waves is one of the major tasks of coastal engineers, and doing it in an appropriate way is often a big problem.

Traditionally, two major approaches have been applied namely spectral analysis and wave-by-wave analysis. Spectral analysis relies on essentially "linear thinking" and has therefore got problems with non linear waves. Wave by wave analysis can be non linear, but there are problems of ambiguity with respect to defining the individual waves.

In order to obtain reasonable accuracy for wave-by-wave analysis of non linear waves one must apply a suitable, high order wave theory. But the complexity of such theories makes it desirable for the practicing engineer to find a different method by which reasonable results can be obtained with a simple wave theory e.g. linear wave theory.

This problem was solved by Daemrich et al (1980) who realised that the long flat trough of a non linear wave might be represented by a correspondingly long flat sine wave, and similarly, the short, strongly curved crest section could be represented by a short, steep sine wave. We may call their method "half-wave-by-half-wave-analysis".

In the following we shall take their idea a bit further and not just apply different frequencies to trough and crest, but apply a locally defined frequency to each point in the wave record.

* Coastal Branch, Public Works Department, N.S.W.,
140 Phillip Street, Sydney 2000. Australia.

Once we have a frequency to work with, there are many wave theories to chose from. It seems however that something simple like linear wave theory with a simple stretching term inbuilt does a good job in most cases. Using the concept of the locally defined frequency, it is in fact possible to devise very simple transfer functions, which are essentially only non linear filters. These semi empirical transfer functions can have very good accuracy and hence be very useful for handling data by hand or by micro processor.

As an example the new idea is applied to the problem of estimating water surface elevations from measured bottom pressures under steep irregular waves. The results are encouraging.

THE CONCEPT OF LOCAL FREQUENCY

A basic assumption to most existing wave theories is that the water motion is periodic and can be described by a suitable combination of the simple harmonic functions.

$$\sum_{0}^{\infty} A_m \cos m\omega t + B_m \sin m\omega t \qquad (1)$$

where A_n and B_n are constants and $\omega = 2\pi/T$. Such combinations can (at least assymptotically) describe the shape of natural waves but in the following we shall take a different approach. We shall deal with slowly curving parts of the wave as if they were parts of long sine waves and with strongly curved parts as if they were part of short sine waves. A step in this direction was taken by Daemrich et al (1980) who applied "half wave by half wave analysis" to irregular waves and thus treated the water motion between two consecutive surface zero crossings as part of a sine wave with a period of twice the interval between the zero crossings.

In the following we shall go a step further and apply a locally defined frequency to each individual point in the time series. The local frequency f is defined as that of the sine curve which matches the wave shape locally. Figure 1 shows measured surface elevations and dynamic bottom pressure under a steep wave and the corresponding variation of the locally defined frequency. We see that the local frequency is well behaved in the crest and trough areas but becomes erratic near the zero crossings. Therefore the concept of local frequency is only really useful in relation to problems where the main interest is on the extreme elevations and/or velocities, but fortunately that is most often the case. Among the meaningful local frequencies the extremes are produced by the surface elevation. In the flat trough, $f(\eta,t)$ falls to just under 0.5/T, and at the crest it reaches 1.7/T. For $f(p,t)$ the range is from 0.6/T to 1.2/T. It is interesting to note that even for the very steep wave in Figure 1 which in the spectral sense contains many high harmonics, the upper limit of $f(\eta,t)$ in the crest area is less than 2/T i.e. lower than the frequency of the second harmonic.

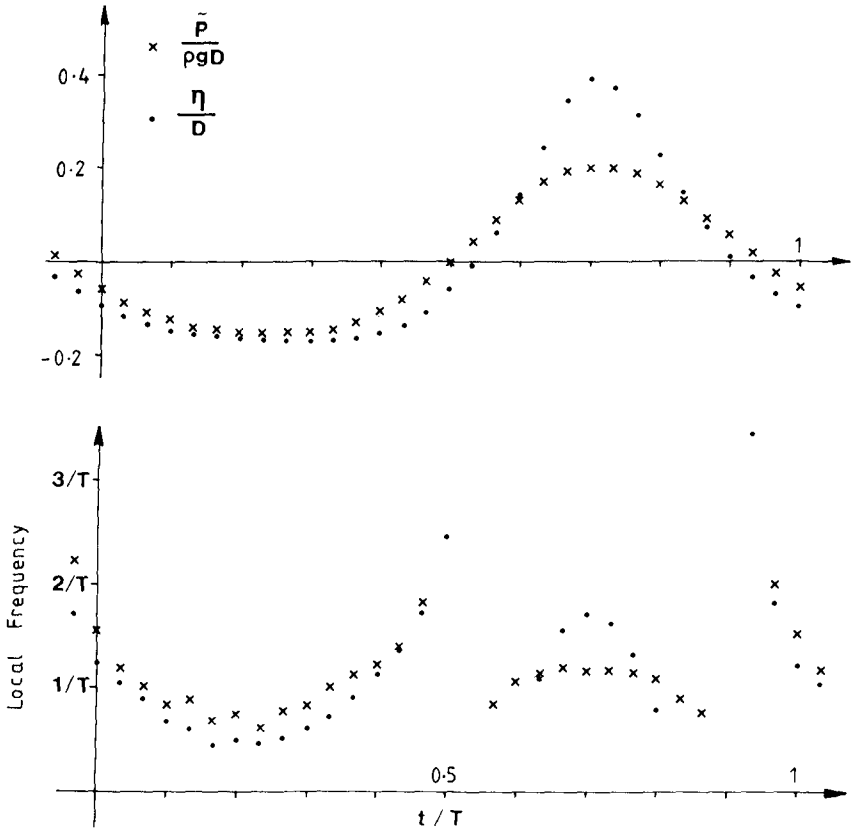

Figure 1 : Top : Measured surface elevations η and dynamic bottom pressures $\tilde{p}$ for a steep 1.8 second wave in 0.4 metres of water. Bottom : local frequencies derived from $\tilde{p}$ and η . The local frequencies $f(\tilde{p},t)$ and $f(\eta,t)$ are well behaved in the crest and trough areas but tend to be erratic near the zero crossings. The well behaved frequencies are typically between half and two times the crest to crest frequency 1/T.

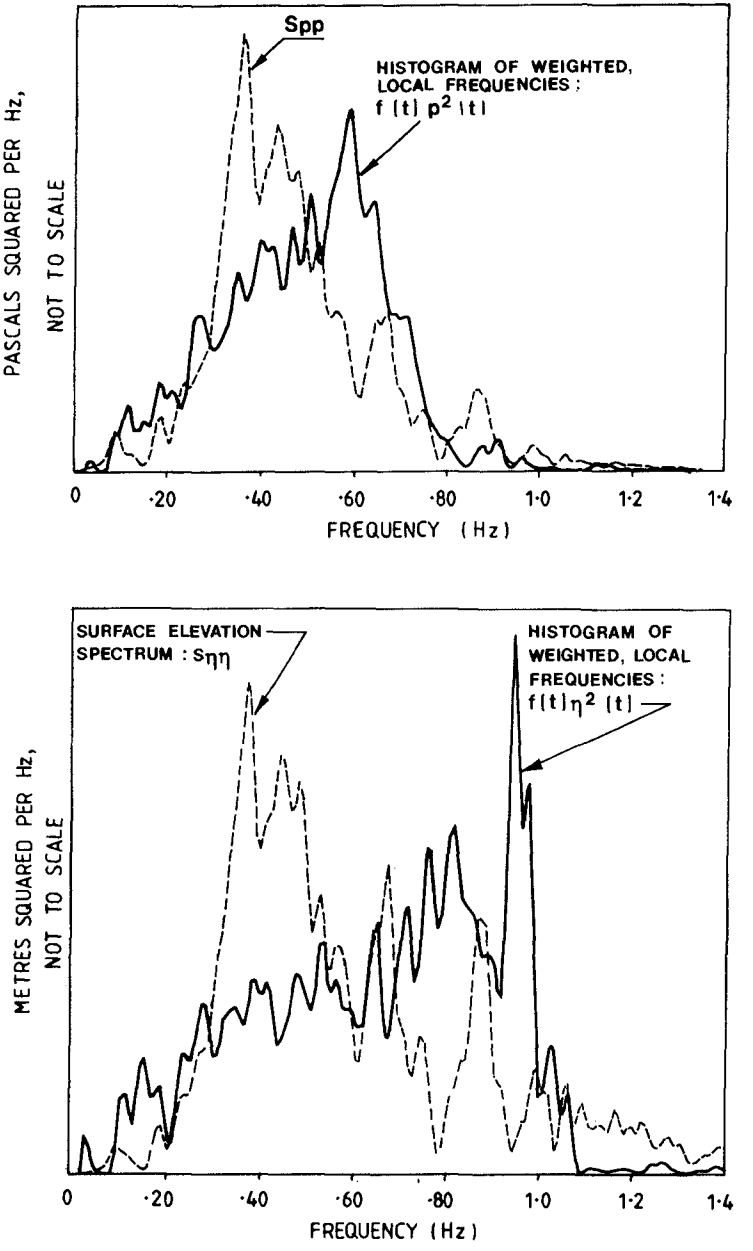

Figure 2 : Histogram of weighted local frequencies and conventional energy spectrum for both $\tilde{p}$ and η from the same irregular wave record.

A histogram of the local frequencies from a wave record weighted with the square of the local amplitude may serve like a spectrum for describing the distribution of wave energy. The meaning of the average frequency is rather obvious but the physical implications of other statistics like the coefficient of variation need further investigation. An example of the histogram of weighted local frequencies is shown in Figure 2 together with the conventional spectrum of the same record. We see that the histogram has a much simpler shape. Possible areas of application for the histogram are break water design where increased attention has been paid to wave shapes recently, see e.g. Bruun et al (1985), and remote sensing of wave climates where the distribution of surface slopes and curvatures influence the surface reflectivity.

CALCULATING THE LOCAL FREQUENCY

A frequency f or radian frequency $\omega = 2\pi f$ can be affixed to any point $x_m = x(t_m)$ in a time series by fitting a cosine curve locally around the point. The simplest fitting proceedure is to pick the uniquely defined curve

$$x(t) = A \cos(\omega t - \varphi) \tag{2}$$

which passes through the point and its neighbour on either side, while more robust estimates may be obtained by least squares fitting to more than three points.

The exact value of ω for a 3-point fit can be found in the following way. Let

$$x_m = A \cos\theta \tag{3}$$

and hence

$$x_{m\pm1} = A \cos(\theta \pm \omega\Delta) \tag{4}$$

where Δ is the time increment between the three points. Then it follows from trigonometric identities that ω can be found from

$$\omega = \frac{1}{\Delta} \cos^{-1}\left(\frac{x_{m+1} + x_{m-1}}{2 x_m}\right) \tag{5}$$

This estimate is always defined if $x_n \neq 0$ but the imaginary values which result if

$$2|x_m| < |x_{m+1} + x_{m-1}| \tag{6}$$

are not immediately interpretable in physical terms. Note that the time interval Δ is not necessarily equal to the sampling interval. Often it is more appropriate to choose Δ a few times larger than the sampling interval.

A slightly simpler estimate, which avoids evaluation of the inverse cosine function in (5) can be obtained via the identity

$$x'' = -\omega^2 x \tag{7}$$

which holds for all functions of the form (2). The second derivative x" is estimated by

$$x'' \approx \frac{x_{m-1} - 2x_m + x_{m+1}}{\Delta^2} \tag{8}$$

Then using (7) we have

$$\omega^2 = -\frac{x''}{x} \approx -\frac{x_{m-1} - 2x_m + x_{m+1}}{\Delta^2 x_m} \tag{9}$$

Again Δ can be a multiple of the sampling interval. The estimate

$$\hat{\omega}^2 = -\frac{x_{m-1} - 2x_m + x_{m+1}}{\Delta^2 x_m} \tag{10}$$

is a biased estimate of ω^2. It under estimates ω in accordance with

$$\hat{\omega}^2 = \omega^2\left[1 - \tfrac{1}{12}(\omega\Delta)^2\right] + O(\Delta\omega)^6 \qquad (11)$$

Hence an improved estimate can be obtained from

$$\omega_1^2 = \hat{\omega}^2\left[1 + \tfrac{1}{12}(\hat{\omega}\Delta)^2\right] \qquad (12)$$

The latter formula is within one percent of error for $\Delta < T/6$ or $\omega\Delta \lesssim 1.0$.

A PRACTICAL APPLICATION

Pressure transducers have several advantages over other field instruments used for wave recordings. They are the most reliable and the easiest to install. It is therefore of interest for practicing engineers to be able to derive other wave properties, such as surface elevations and velocities from measured bottom pressures. We shall now see that local approximations provide a very efficient tool for dealing with this problem.

For a sine wave, the surface elevation $\eta(t)$ is related to the dynamic bottom pressure $\tilde{p}(t)$ by

$$\eta(t) = \frac{\tilde{p}(t)}{\rho g}\cosh kD \qquad (13)$$

where ρ is the fluid density, g the acceleration of gravity and D the water depth. The wave number k is related to the radian frequency through the dispersion relation

$$kD \tanh kD = \frac{\omega^2}{g}D \qquad (14)$$

The traditional way of deriving $\eta(t)$ from $\tilde{p}(t)$ for irregular waves has been by using spectral analysis. The method involves three steps:

1. Find the discrete pressure specturm $S_{pp}(\omega_i)$

2. Transform each spectral estimate in accordance with (13) :

$$S_{\eta\eta}(\omega_i) = S_{pp}(\omega_i) \cosh(k_i D)/\rho g$$

3. Create the $\eta(t)$ time series from $S_{\eta\eta}(\omega_i)$ by the discrete, inverse Fourier transform.

This traditional method is neither fast nor accurate but fortunately we can develop alternative methods involving the use of local approximations which are both faster and more accurate.

The most straight forward approach is to apply the linear-wave formula (13) using a local wave number determined from the local frequency through (14). Such an approach does however systematicly under estimate $\eta(t)$ because linear wave theory, from which (13) is taken, is not geared to handle finite surface elevations. We are free to use any wave theory we like as soon as we have a frequency to work with, but for this purpose it is adequate just to use a modified version of Equation (13)

$$\eta(t) = \frac{\tilde{P}(t)}{\rho g} \cosh k\left(D + \frac{\tilde{P}(t)}{\rho g}\right) \qquad (15)$$

where k is the local wave number determined from the local frequency through (14). Replacing the depth D by $D + \tilde{P}/\rho g$ in the argument of the cosh-function accounts in a way for the fact that the instantaneous water surface can be a finite distance away from the mean water level. Equation (15) based on local frequencies is superior to the traditional spectral method with respect to both speed and accuracy. An example is shown in Figure 3 where estimates from both methods are compared to the actual, measured surface elevations. The local approximations method recovers the crest height a little better and the shape of the troughs is more accurately represented as well. In terms of the normalised deviation dev $(x,y) = \sqrt{\Sigma(x-y)^2/\Sigma y^2}$ based on the full 123 second record, the local approximation estimates gave a deviation of 0.215 while the spectral estimates gave a deviation of 0.242. The fine details of the results depend on the measures applied with each method to overcome noise problems. This aspect will be treated in detail later.

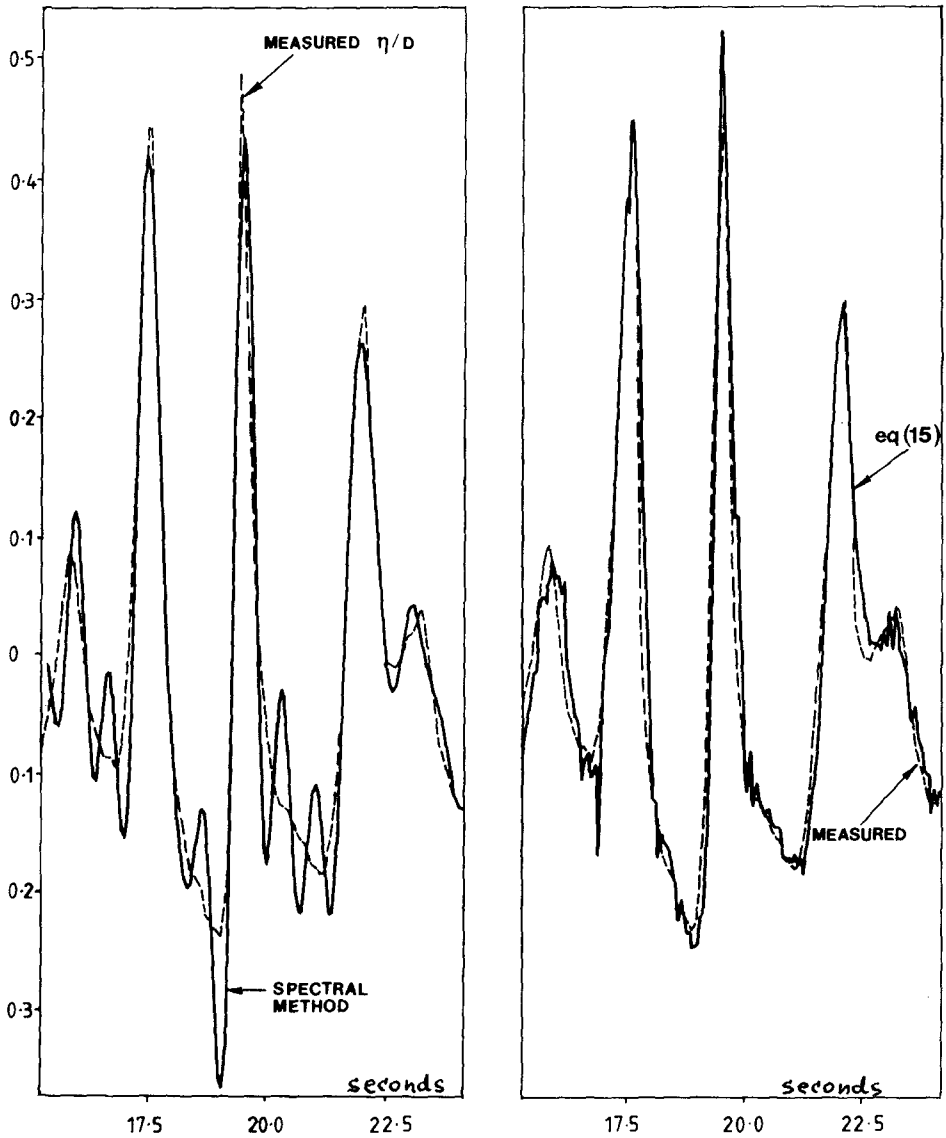

Figure 3 : Estimates of surface elevations from bottom pressures compared to measured surface elevations. The water depth D was 0.38 metres. We see that equation (15) with local frequencies is slightly better at estimating crest heights and much better at estimating depth and shape of the troughs than the spectral method. No smoothing has been applied anywhere in the processing. The cut off frequency of 1.45 Hz applied in the spectral method was deemed optimal.

SEMI EMPIRICAL TRANSFER FUNCTIONS

Semi empirical transfer functions are useful in many practical cases. Also with respect to these can the concept of local frequencies be helpful. Consider again the problem of estimating surface elevations $\eta(t)$ from dynamic bottom pressures $\tilde{p}(t)$ in irregular waves. We want a very simple algorithm for processing data by hand or by micro processor.

From a heuristic physical consideration we may argue that the strength with which a water surface signal is transferred to the bottom depends on the ratio between the radian frequency ω of the signal and the natural frequency of the water column $\sqrt{g/D}$ i.e.

$$\frac{\eta}{\tilde{p}/\rho g} = F\left(\frac{\omega^2}{g} D\right) \tag{16}$$

and here we may replace D by $D + \tilde{p}/\rho g$ in order to account for finite changes in depth hence we have

$$\frac{\eta}{\tilde{p}/\rho g} = F\left[\frac{\omega^2}{g}\left(D + \frac{\tilde{p}}{\rho g}\right)\right] \tag{17}$$

For this purpose we will use the simplest possible estimate of the local frequency, namely

$$\hat{\omega}^2 = -\frac{\tilde{p}_{m-1} - 2\tilde{p}_m + \tilde{p}_{m+1}}{\tilde{p}_m \Delta^2} \tag{18}$$

and hence we have

$$\frac{\eta_m}{\tilde{p}_m/\rho g} = F\left[\frac{-\tilde{p}_{m-1} + 2\tilde{p}_m - \tilde{p}_{m+1}}{\tilde{p}_m \Delta^2 g}\left(D + \frac{\tilde{p}_m}{\rho g}\right)\right] \tag{19}$$

To determine the empirical function F we now plot the left hand side of (19) versus the argument of F for a few accurately known data points, for example taken from Dean's stream function tables (Dean, 1974). That has been done in Figure 4 and we see that F can be adequately represented by a simple exponential, $F(x) = \exp(2x/3)$. Hence the full expression for our transfer function is

$$\eta_m = \frac{\tilde{P}_m}{\rho g} \exp\left[\frac{2}{3} \frac{-\tilde{P}_{m-1} + 2\tilde{P}_m - \tilde{P}_{m+1}}{\tilde{P}_m \Delta^2 g} \left(D + \frac{\tilde{P}_m}{\rho g}\right)\right] \qquad (20)$$

a simple one line expression which compares favourably with the spectral method with respect to accuracy, see Figure 5. The normalised deviation for the eq(20)-estimates was 0.208 while the corresponding value for the spectral estimates was 0.242.

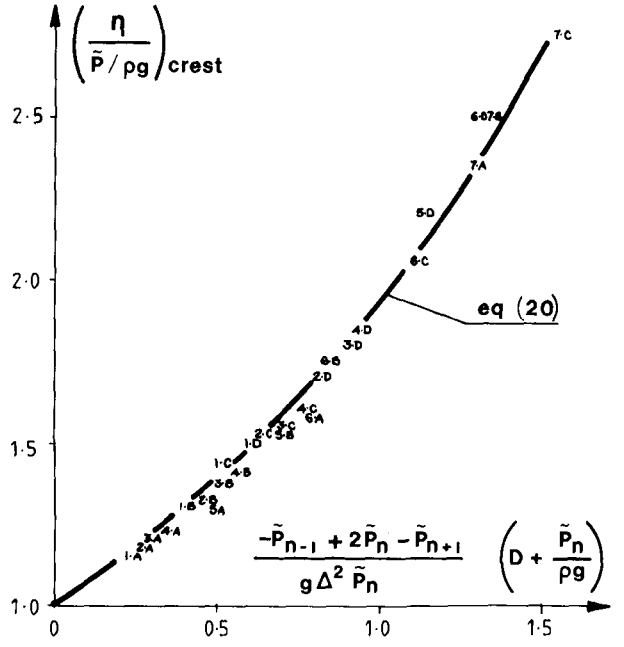

Figure 4 : Data from Dean's stream function tables from which the empirical function in (19) can be determined. We see that equation (20) provides an easy and reliable fit to the data.

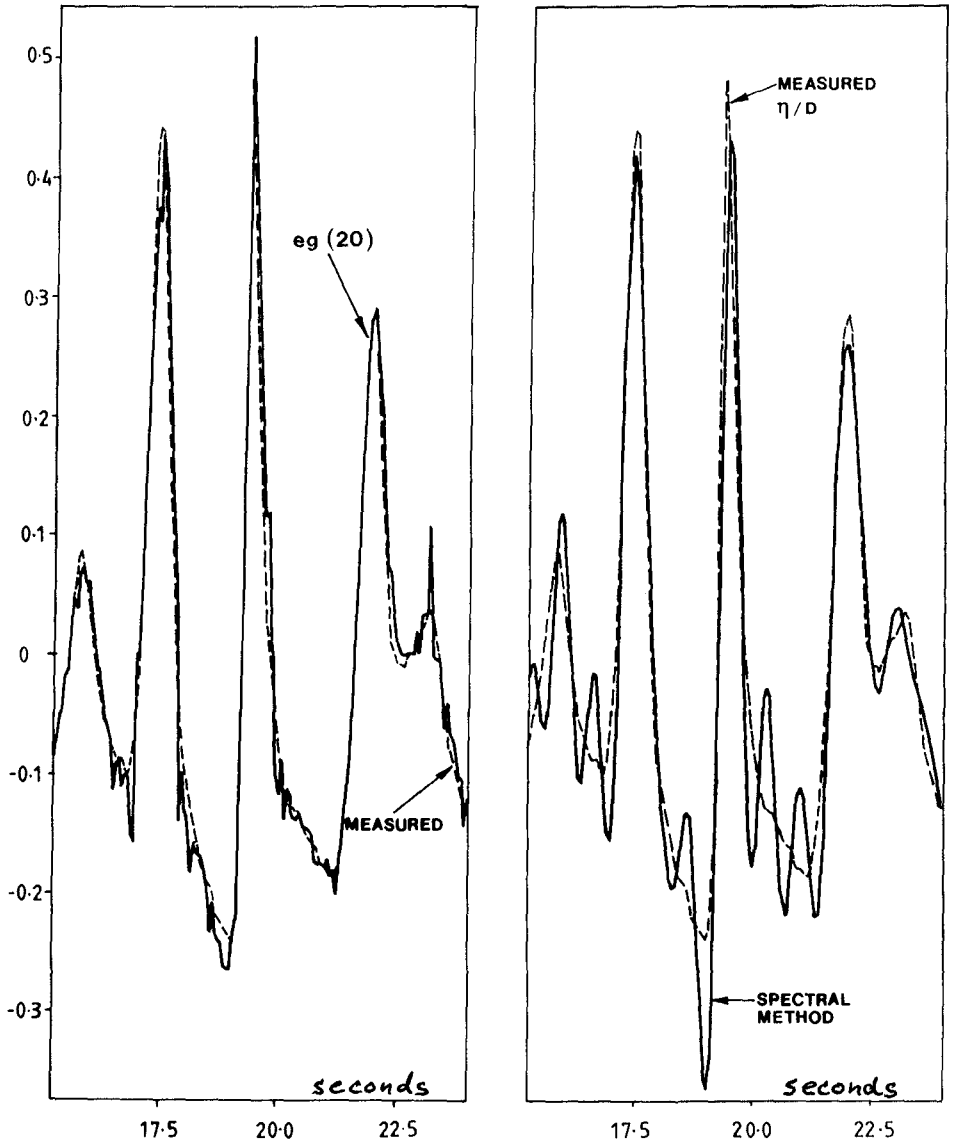

Figure 5 : Surface evaluation estimates by equation (20) and the spectral method compared to actual, measured surface elevations. Equation (20) matches both crests and troughs better than the spectral method and of course it requires much less computational effort.

RESOLUTION VERSUS NOISE

In dealing with real data, there is always a problem of balancing resolution against noise, especially when high frequency signals have to be amplified strongly as is the case when deriving surface elevations from bottom pressures.

The resolution is determined by the time increment Δ. A small Δ gives high resolution while a large Δ overlooks high frequency variations. There is no general rule for the choice of Δ since the optimum must obviously depend on the relative strength and the difference in frequency between signal and noise. However, the following value will generally provide a reasonable first guess.

$$\Delta = \sqrt{D/g} \tag{21}$$

The fact that the meaningful, locally defined frequencies generally occupy a narrower band than all the harmonics needed for a spectral description (see Figure 2) means that it is generally possible to apply a lower cut off frequency when using a local approximations method than with a spectral method.

While the above is true, it must be remembered that there are special problems with defining the local frequency near zero crossings. Unreasonably large or imaginary values of ω may occur. A reasonable upper limit for acceptable local frequencies is $\omega^2 = 1.5\ g/D$, which corresponds to cosh kh = 2.6

When imaginary or unacceptably large values of ω occur it is generally adequate to assign the value zero to ω, at least for those practical problems that have been dealt with so far.

Because the details of the water motion close to zero crossings is generally unimportant, the problem of the local frequency being ill conditioned in this area is of little practical consequence.

DISCUSSION

The use of local approximations via locally defined frequencies is recommended for practical analysis of irregular waves. Firstly because it requires far less computational effort than any other available method, e.g. wave by wave analysis, Fenton's local polinomial method (Fenton 1986) or the previously most popular spectral method. Secondly because it seems to be superior to the spectral method with respect to accuracy.

The strength of local frequency methods such as (15) or (20) relative to the linear spectral method lies first of all in the fact that it is very easy to apply stretching simply by replacing the depth D with $D + \tilde{p}/\rho g$. Secondly, in the fact that the spectral method over

amplifies both signal and noise at high frequencies. This happens because it wrongly assumes that "all waves are free waves" in order to be able to calculate $k(\omega)$ from the disperson relation (14). Talking about the dispersion relation it must be admitted that applying it to a locally defined frequency probably makes very little physical sense. To this one can only reply that the justification for using equation (15) with its reliance on the dispersion relation (14) lies in its proven efficiency.

Semi empirical transfer functions like (20) do not rely on any wave theory but only on a bit of physical intuition and with this somewhat more "unassuming" nature, and their good performance they may turn out to be the most useful area of application for the concept of locally defined frequencies. The conclusions stated in this paper are essentially based on experience with a single practical problem, namely that of deriving water surface elevations from dynamic pressures measured at the bottom. This problem is however a very tough one so it is highly likely that local approximations using locally defined frequencies will prove a useful tool for solving many problems involving irregular, non linear waves.

ACKNOWLEDGEMENTS

Comments and advice from Professor J.D. Fenton has been a great help in the development of this paper. Laboratory data and computor software was kindly made available by Mr I. Varley.

REFERENCES

Bruun, P. (Editor), 1985 : Design and construction of mounds for breakwaters and coastal protection.

Daemrich, K.F., W.D. Eggert and S. Kohlhase (1980) : Investigations of irregular waves in hydraulic models. Proc. 17th Int. Conf. on Coastal Engineering, Sydney.

Dean, R.G. (1974) : Evaluation and development of water wave theories for engineering application. C.E.R.C., Special Report No. 1.

Fenton, J.D. (1986) : Polynomial approximation and water waves. Proc. 20th Int. Conf. on Coastal Engineering, Taipei.

CHAPTER 49

ESTIMATION OF EXTREME SEA SEVERITY FROM MEASURED DAILY MAXIMA

Michel K. Ochi*, David Mesa*, and De-Fu Liu**

ABSTRACT

This paper presents the results of a study to statistically estimate the most severe sea state (significant wave height) expected in 50 and 100 years from analysis of data consisting of the largest significant wave height observed each day by applying the Type III asymptotic extreme value distribution. In applying the Type III asymptotic distribution, the distribution parameters are estimated by three different methods: the maximum likelihood method, the skewness method, and a nonlinear regression method. Since none of these methods estimates values of the parameters which satisfactorily yield a distribution representing well the daily maximum data, a modified Type III asymptotic distribution is newly developed in the present study. The modified distribution yields an excellent fit over the entire range of the cumulative distribution, and the probability density function agrees well with the histogram constructed from the data.

INTRODUCTION

For the design of coastal and ocean structures, it is extremely important to statistically estimate the most severe sea state (the largest significant wave height) expected to occur over a period of time, on the order of 50 to 100 years, sufficiently long to cover the lifetime of the structure. The estimation is usually carried out based on a probability function established from analysis of data accumulated over several years. It should be noted that, in general, the probability distribution derived from an accumulation of significant wave height data is obtained empirically and that there is no theoretical basis for selecting any particular probability distribution to characterize the significant wave height.

However, if the data consist of the largest significant wave height observed every day, and if the number of observations is sufficiently large, then there is a scientific basis to choose particular probability distributions for estimating extreme significant wave

* Coastal and Oceanographic Engineering Department, University of Florida, U.S.A.

** Department of Hydraulic Engineering, Tianjin University, Peoples Republic of China

height. That is, the probability distribution applicable for the significant wave height under this situation must be one of three asymptotic distribution functions developed by Fisher, Tippett, and Frechet -- so called Type I, II, and III asymptotic extreme value distributions.

The Type I asymptotic distribution has been by far the most commonly used method for estimating extreme values from an analysis of data consisting of the daily, weekly, and monthly largest values. The results of the present analysis show that the Type I asymptotic distribution demonstrates reasonably good agreement, in general, with significant wave height data. However, the distribution deviates from the data cumulative distribution for large significant wave heights. This results in substantial overestimation of the 50 and 100 year extreme values if the estimation is made by extending the theoretical cumulative distribution function.

The Type III asymptotic distribution has a unique characteristic in that the distribution is bounded from above. This feature of the distribution appears to be pertinent for analysis of wave data, since the height of waves cannot be unlimited in reality due to breaking. For analysis of data by applying the Type III asymptotic distribution, the distribution parameters are estimated by three different methods: the method of maximum likelihood, the skewness method, and a nonlinear regression method. Unfortunately, none of these methods estimates values of the parameters which satisfactorily yield a Type III asymptotic distribution representing well the daily maximum data.

This paper presents a newly developed modified Type III asymptotic extreme value distribution which yields an excellent fit over the entire range of the cumulative distribution.

DAILY LARGEST SIGNIFICANT WAVE HEIGHT AND ASYMPTOTIC DISTRIBUTIONS

The data used in the present study were obtained by the Coastal Engineering Research Center on the eastern coast of the United States, Duck, North Carolina, at a location 450 m off the shoreline where the water depth is 8.8 m as an average. Observations of significant wave height were made four times daily during a 42 month period from 1979 to 1983. A total of 1,061 observations of largest significant wave height for each day was accumulated as shown in Table 1, and the data (for brevity, they may be called the daily maxima) were analyzed through application of Type I and Type III asymptotic extreme value distributions.

Figure 1 shows the plot of data on Type I extreme value probability paper. If the data points lie on a straight line, it may safely be concluded that the data follow the Type I asymptotic distribution, and contain all statistical characteristics thereof. This allows the extrapolation of the data to higher periods to be made very simply merely by extension of the straight line.

Table 1. Daily maximum significant wave height data

Significant wave height (m)	Number of observations
0.2 - 0.4	11
0.4 - 0.6	151
0.6 - 0.8	158
0.8 - 1.0	175
1.0 - 1.2	109
1.2 - 1.4	116
1.4 - 1.6	91
1.6 - 1.8	63
1.8 - 2.0	47
2.0 - 2.2	40
2.2 - 2.4	27
2.4 - 2.6	19
2.6 - 2.8	21
2.8 - 3.0	12
3.0 - 3.2	6
3.2 - 3.4	7
3.4 - 3.6	6
3.6 - 3.8	2
Total	1,061 in 42 months

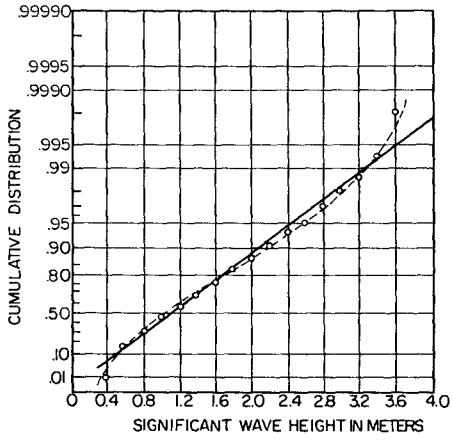

Figure 1. Cumulative distribution function of daily maximum significant wave height plotted on extreme value probability paper

It appears in Figure 1 that the data are represented reasonably well by the Type I asymptotic distribution. However, if we examine the results carefully, the cumulative distribution function of the data (the curved line given in the figure) shows a tendency to slowly deviate with different character from that of the straight line at the higher significant wave heights. Hence, by extrapolating the data and the estimated Type I distribution to comparable return periods, it is seen that the Type I distribution may yield an increasing overestimation of the extreme value prediction. This is a major shortcoming of utilizing the Type I asymptotic distribution for extreme sea state estimation.

Type III asymptotic distribution has three parameters, w, v, and k, as shown in Equations (1) and (2).

Cumulative distribution function

$$F(y) = \exp\left\{ - \left(\frac{w - y}{w - v}\right)^{k} \right\} . \qquad (1)$$

Probability density function

$$f(y) = \frac{k}{w - v} \left(\frac{w - y}{w - v}\right)^{k-1} \exp\left\{ - \left(\frac{w - y}{w - v}\right)^{k} \right\} . \qquad (2)$$

$$-\infty < y < w , \quad 0 < v,k < \infty$$

where, y = random variable, daily largest significant wave height for the present problem.

The distribution is bounded from above by the parameter w. If the parameters w and k become increasingly large, the Type III distribution tends to default to Type I distribution. The Type III distribution has not often been considered for estimating extreme values in engineering problems to the same extent as the Type I distribution. It has a feature, however, that the upper value of the distribution is bounded and thereby the extrapolation of the cumulative distribution function should not overestimate the extreme values.

In order to evaluate the parameters of the distribtuion from the data, the following three different methods are considered in the present study:

(1) Maximum Likelihood Method

The likelihood function of the distribution can be obtained from Eq. (1) as,

$$L(y_i|w,v,k) = \prod_{i=1}^{n} f(y_i) = k^n (w - v)^{-nk}$$

$$x \prod_{i=1}^{n} (w - y_i)^{k-1} \exp\left\{ - \sum_{i=1}^{n} \left(\frac{w - y_i}{w - v}\right)^k \right\} . \qquad (3)$$

Since $L(y_i|w, v, k)$ is a monotonic function, partial differentiation of $\ell n\, L(y_i|w, v, k)$ with respect to the unknown parameters w, v, and k and setting each equal to zero results in

$$\frac{\partial}{\partial w} \ell n\, L = - \frac{nk}{w - v} + \sum_{i=1}^{n} \left[k\left(\frac{w - y_i}{w - v}\right)^k \frac{v - y_i}{(w - y_i)(w - v)} + \frac{k - 1}{w - y_i} \right] = 0$$

$$\frac{\partial}{\partial v} \ell n\, L = \frac{nk}{w - v} + \sum_{i=1}^{n} \frac{-k}{w - v} \left(\frac{w - y_i}{w - v}\right)^k = 0$$

$$\frac{\partial}{\partial k} \ell n\, L = \frac{n}{k} - n\, \ell n(w - v) - \sum_{i=1}^{n} \left[\left(\frac{w - y_i}{w - v}\right)^k \ell n \left(\frac{w - y_i}{w - v}\right)^k - \ell n\left(\frac{w - y_i}{w - v}\right) \right] = 0 . \qquad (4)$$

The three parameters of the distribution can be estimated from the above equations. It is found, however, that the solution cannot be obtained explicitly, but instead involves a lengthy iterative numerical procedure. Furthermore, it is found that the solution is very sensitive to the parameter v. Under these conditions a numerical iterative procedure is developed which initially fixes the parameter v, then determines the corresponding values of the parameters w and k. Since $F(y) = e^{-1}$ for $y = v$ in Eq. (2), the theoretical value of v which satisfies the relationship $F(y = v) = e^{-1}$ is used as a base from which to initiate the iterative algorithm. Graphic and regression analysis indicates a linear relationship exists between the parameters w and k for a given v.

No combination of the w, v, and k parameters determined through the maximum likelihood method, however, represents well the cumulative distribution function obtained from the data as demonstrated in Figure 2. The figure shows a comparison of the data and Type III asymptotic cumulative distribution functions obtained for three values of the parameter v (0.96, 1.00, and 1.04) and the corresponding w and k parameter sets.

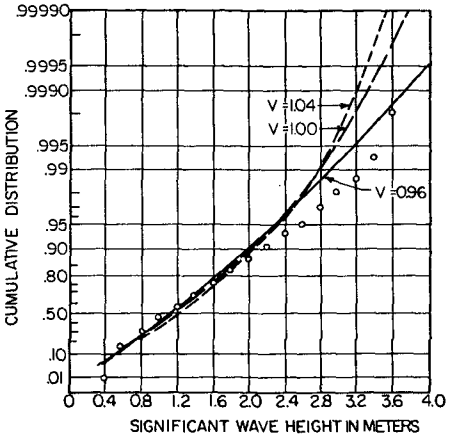

Figure 2. Daily maximum significant wave height and Type III asymptotic cumulative distributions, based on maximum likelihood method

(2) Skewness Method

The principle of the skewness method is based upon the fact that the skewness of the Type III asymptotic distribution can be theoretically expressed solely as a function of the parameter k (Gumbel, 1966). That is,

$$\text{Skewness } \gamma = \{\Gamma(1 - 3/k) - 3\Gamma(1 + 2/k)\,\Gamma(1 + 1/k) + 2\Gamma^3(1 + 1/k)\}\{B(k)\}^3 \qquad (5)$$

where, $B(k) = 1/\{\Gamma(1 + 2/k) - \Gamma^2(1 + 1/k)\}^{1/2}$.

The parameter k therefore can be evaluated from Eq. (5) by calculating the skewness γ from the observed data by

$$\gamma = \frac{E[(y - E[y])^3]}{(\text{Var}[y])^{3/2}} \, . \qquad (6)$$

The parameters w and v are subsequently determined by evaluating the mean and variance with the aid of the following formulae:

$$E[y] = w - (w - v)\,\Gamma(1 + 1/k)$$
$$\mathrm{Var}[y] = (w - v)^2\,\{\Gamma(1 + 2/k) - \Gamma^2(1 + 1/k)\}\,. \tag{7}$$

It should be noted that theoretical background of the skewness method is sound; however, it is sometimes difficult to determine the k-value in practice as is the case for the problem discussed below.

The theoretical skewness expression given in Eq. (5) is shown in Figure 3 as a function of k. The curve is asymptotic at k = 0 and monotonically increases through the zero skewness point (k = 3.602) until reaching its limiting value at 1.139. The skewness increases rapidly up to approximately k = 40, then becomes increasingly insensitive to k as k becomes large. The sample skewness as calculated from Eq. (7) is $\gamma = 1.134$ for the data given in Table 1. This value is very near the limiting value 1.139; hence, a very wide range of k values is possible in this limiting region. For this reason, the skewness method for estimating the parameter k appears to be inappropriate for the present problem.

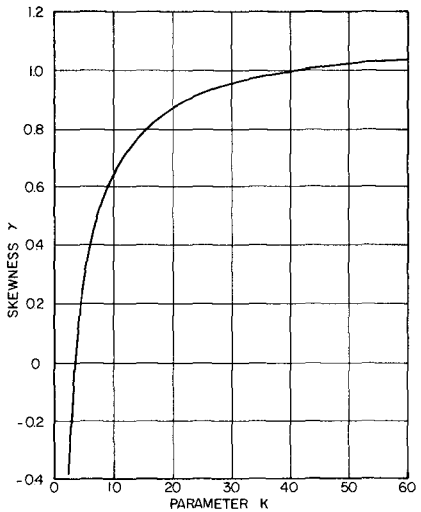

Figure 3. Skewness γ as a function of k

To overcome this difficulty, an alternative method is developed using the skewness approach as a foundation. That is, the parameter v is estimated from the cumulative distribution function constructed from the data such that the parameter v satisfies the condition that the cumulative distribution function $F(y) = e^{-1}$ for $y = v$. The other two parameters are evaluated by using the v-value thusly determined. However, the derived distribution does not well represent the observed data as shown in Figure 4.

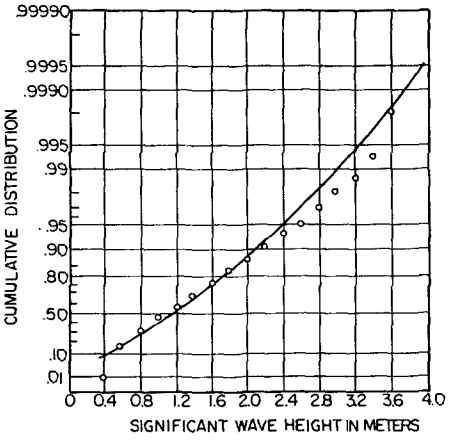

Figure 4. Daily maximum significant wave height and Type III asymptotic cumulative distributions, based on skewness alternative method

(3) Nonlinear Multiple Regression Method

Another method to establish the parameters of the Type III asymptotic extreme value distribution is to apply a nonlinear multiple regression analysis. For this, taking the logarithm of Eq. (1) twice results in

$$\ell n \left[- \ell n F(y) \right] = k \, \ell n \left(\frac{w - y}{w - v} \right) . \qquad (8)$$

The left-hand side of Eq. (8) is determined from the data. The right-hand side is now linear in the parameter k, and monotonic in the parameters w and v. Linearization of the exponent k substantially increases the computational stability in determining the parameter values.

A comparison between the cumulative distribution function obtained by the nonlinear regression method and observed data is shown in Figure 5. Figure 6 shows a comparison between the probability density function and histogram. Although the cumulative distribution function in Figure 5 appears to display a reasonable fit, it is apparent from the probability density function in Figure 6 that the distribution does not well represent the data. The peak does not possess the sharp rapid increase, but instead is much flatter and shifted to the right. Thus, it may be concluded that the Type III asymptotic distribution with the parameters determined by the nonlinear regression method does not well represent.

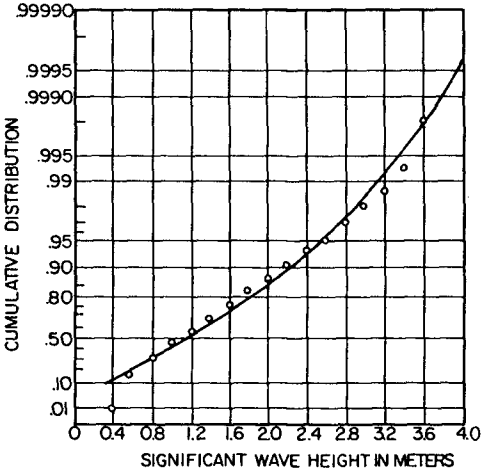

Figure 5. Daily maximum significant wave height and Type III asymptotic cumulative distributions, based on nonlinear regression method

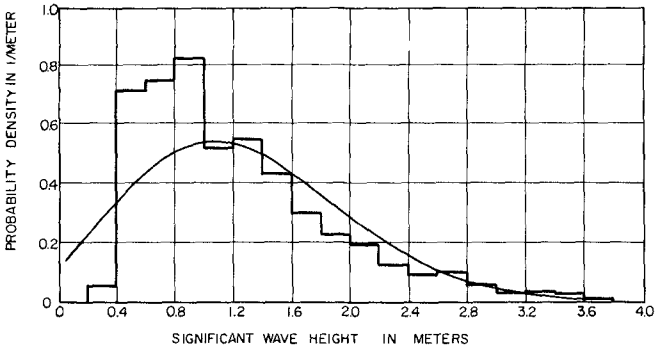

Figure 6. Comparison of daily maximum significant wave height histogram and Type III asymptotic probability density function, based on nonlinear regression method

DERIVATION OF MODIFIED TYPE III ASYMPTOTIC DISTRIBUTION

In order to improve the agreement between the Type III asymptotic extreme value distribution and the observed data, we first examine Eq. (8). Figure 7 shows a comparison between the left-hand side of Eq. (8) presented by using data points, and the right-hand side of the equation expressed using the results of the nonlinear regression method. Writing the difference between the theoretical distribution and the observed data as $\Delta(y)$ results in

$$\ell n\,[-\ell n F(y)] = k\,\ell n\left(\frac{w-y}{w-v}\right) + \Delta(y) \quad . \tag{9}$$

Here, the functional form of $\Delta(y)$ may be expressed in the form of polynomials given by

$$\Delta(y) = a + b(y - y_o) + c(y - y_o)^2 + d(y - y_o)^3 \quad . \tag{10}$$

The values of a, b, c, and y_o are determined again by employing the nonlinear regression procedure. Thus, from Eq. (9), the modified Type III asymptotic extreme value distribution can be written as

$$F(y) = \exp\left\{-\left(\frac{w-y}{w-v}\right)^k e^{\Delta(y)}\right\} \quad . \tag{11}$$

Note that F(y) given in Eq. (11) satisfies the conditions required of the cumulative distribution function. Hence, the addition of $\Delta(y)$ does not affect the basic characteristics of the original Type III asymptotic distribution. If $\Delta(y)$ is zero over the entire variate range, then the modified Type III asymptotic distribution reduces to the original Type III asymptotic distribution.

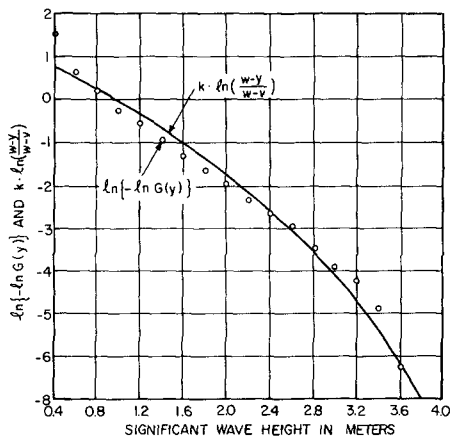

Figure 7. Comparison of cumulative distribution functions of daily maximum significant wave height and Type III asymptotic distribution, based on nonlinear regression method

Figure 8 shows the results of computations using Eq. (10) as applied to the difference $\Delta(y)$ obtained from Figure 6 for which we have $a = -0.314$, $b = 0.513$, $c = 0.464$, $d = -0.171$, and $y_o = 1.687$. The circles in the figure are the differences between the data and the Type III asymptotic distribution obtained from Figure 7.

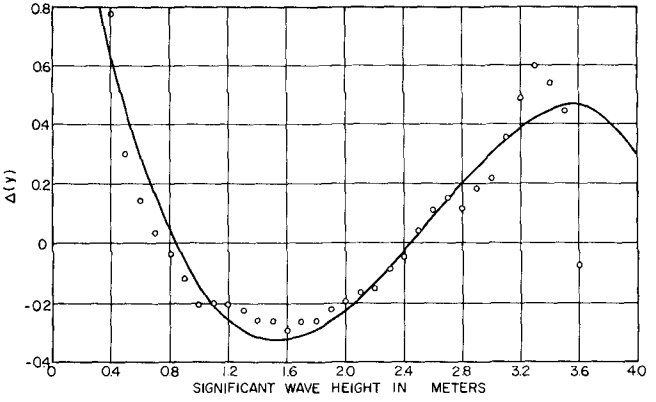

Figure 8. Comparison of $\Delta(y)$ and difference between cumulative distributions of daily maximum significant wave height and Type III asymptotic distribution, based on nonlinear regression method

A comparison between the cumulative distribution function of the modified Type III asymptotic distribution given in Eq. (11) and that obtained from data is shown in Figure 9. Good agreement can be seen between them over the entire data range. The cumulative distribution

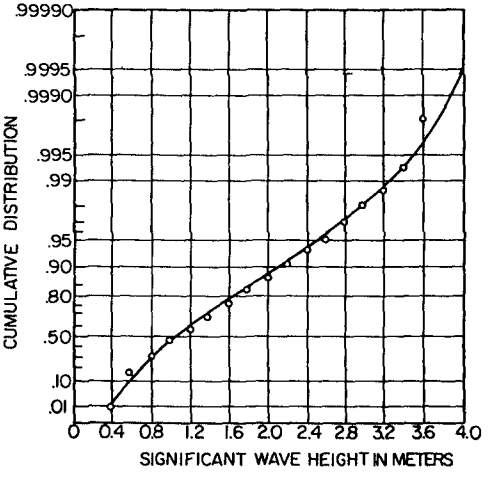

Figure 9. Daily maximum significant wave height and modified Type III asymptotic cumulative distributions

function for large significant wave heights (which is the area of interest) shows asymptotic characteristics as it approaches its limiting value. A comparison between the probability density function of the modified Type III and the histogram is shown in Figure 10 in which a good agreement can be seen over the entire variate range.

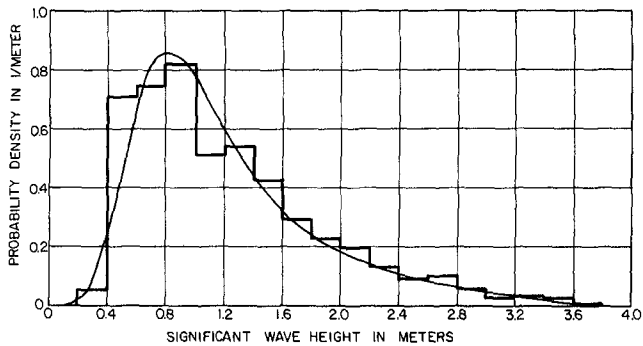

Figure 10. Comparison of daily maximum significant wave height histogram and modified Type III asymptotic probability density function

ESTIMATION OF EXTREME VALUES

The extreme sea severities most likely to occur (modal values of the extreme value distributions) in 50 and 100 years are evaluated from the data given in Table 1 by applying the Type I and the modified Type III asymptotic distributions. The estimated extreme values are tabulated in Table 2.

As can be seen in the table, the extreme significant wave heights estimated by applying the Type I asymptotic distribution are substantially greater than those estimated by applying the modified Type III asymptotic distribution. Since the Type I asymptotic distribution deviates from the data cumulative distribution for large significant wave heights as shown in Figure 1, the distribution yields an increasingly overestimation of the extreme value with increasing variate values.

Table 2 Estimation of 50 and 100 year extreme significant wave heights

Distribution	50 year (m)	100 year (m)
Type I asymptotic distribution	5.8	6.3
Modified Type III asymptotic distribution	4.2	4.3

CONCLUSIONS

This paper presents the results of a study to statistically estimate the extreme sea severity (significant wave height) expected in 50 and 100 years from analysis of data consisting of the largest significant wave heights observed each day. From results of analysis by applying the Type I and Type III asymptotic extreme value distributions, the following conclusions are drawn:

1. The cumulative distribution function of the data shows a tendency to slowly deviate with different character from that of the Type I asymptotic at the higher significant wave heights. Hence, by extrapolating the data and the estimated Type I distribution to comparable return periods, it is expected that the Type I distribution may yield an increasingly overestimation of the extreme value with increasing variate values.

2. The parameters of the Type III asymptotic distribution are estimated by three different methods: the maximum likelihood method, the skewness method, and a nonlinear regression method. None of these methods, however, estimates values of the parameters which satisfactorily yields a distribution representing well the cumulative distribution of the data.

3. The modified Type III asymptotic extreme value distribution newly developed in the present study (Equation 11) yields an excellent fit over the entire range of the cumulative distribution and the probability density function agrees well with the histogram constructed from the data.

4. The extreme significant wave heights in 50 and 100 years estimated by the Type I asymptotic distribution are substantially greater than those estimated by the modified Type III asymptotic distribution.

REFERENCES

Gumbel, E. J.: "Statistics of Extremes", Columbia Univ. Press, 1966.

CHAPTER 50

Velocity Field under Plunging Waves

Akio Okayasu*, Tomoya Shibayama** and Nobuo Mimura***

ABSTRACT

In order to clarify the characteristics of the velocity field in the surf zone, three sets of detailed and precise two dimensional laboratory experiments were performed. Spatial distributions and time histories of velocity were measured by using a hot film velocimeter with a split type probe or a two components laser doppler velocimeter for regular wave conditions. Typical plunging breakers were formed during the experiments. Based on the experimental results, a model was investigated in order to estimate the two dimensional distribution of the on-offshore steady current below the trough level.

1. INTRODUCTION

The velocity field in the surf zone is much concerned with the phenomena there. Therefore, it is a very important technical problem to make it clear. The velocity field there is rather complicated because of its non-uniformities in time and space. However, with the recent development of the velocity measurement techniques, many researches have been carried out to clarify the structure of the turbulent velocity field in the surf zone by measuring the velocity itself [Sakai et al.(1984), Aono and Hattori (1984), Nadaoka et al.(1986) and Mizuguchi (1986)].

Svendsen et al.(1978) separated the surf zone into three regions which were an outer, inner and run-up region. In the outer region, rapid transitions of wave shape occurs, particularly in case of plunging breakers. Sawaragi and Iwata (1974) suggested the existence of a large scale vortex formed just below the wave plunging and it is frequently called "horizontal roller" or "plunging vortex". In the inner region, the breaking wave propagates shoreward with deformation like a bore. Both such bore-like waves and plunging vortexes seem to give strong effect to the generation of turbulence in the surf zone. On the other hand, the existence of "undertow" caused by the mass transport of breaking waves has recognized for many years [see e.g. Hansen and Svendsen (1984)].

* Graduate Student, Dept. of Civil Eng., Univ. of Tokyo, Bunkyo-ku, Tokyo, 113 JAPAN
** Associate Professor, Dept. of Civil Eng., Univ. of Tokyo, Bunkyo-ku, Tokyo, 113 JAPAN
*** Associate Professor, Dept. of Civil Eng., Ibaraki Univ., Hitachi, Ibaraki, 316 JAPAN

Thus we will consider the following factors: (1) plunging breakers, (2) bore-like waves and (3) undertows, which characterize the velocity field in the surf zone in comparison with that in the offshore region. One of the objectives of the present study is to clarify these characteristics of the velocity field through detailed and precise laboratory experiments.

Then, applying the results from these experiments, we will formulate a model to estimate the two dimensional distribution of on-offshore steady current below the trough level.

2. EXPERIMENTS

2.1 Experimental Arrangements and Procedures

Three individual laboratory experiments were performed in a two dimensional wave flume which was 23m long and 0.8m wide and two different beach profiles were used, a step type and a constant slope of 1/20.

For the case 1, the step type beach profile was used for the sake of grasping the behavior of the plunging vortex. The profile consisted of a 1/10 slope and a flat bed. The reasons why we chose this type of beach topography were to fix the breaking point of each wave and to reserve an enough region for the measurement. The beach topography is shown in Fig.1. The measuring area was from 0.5cm to 14.5cm above the bottom and 80cm long in an on-offshore directed vertical plane. The measuring points were arranged to make 2cm grids.

For the case 2 and 3, a constant slope of 1/20 was used to measure the whole area of the surf zone. And it was expected that the effects of the bore-like waves and the undertows would be revealed. The measuring areas were about 250cm long in both cases, but the arrangements of measuring points were different. The 2cm grids arrangement was taken for the case 2. The lowest points were 7mm above the bottom and the detailed arrangement is shown in Fig.2. On the other hand, for the case 3, an arrangement which was rough in the horizontal direction and close in the vertical direction was used for the purpose of detailed measurements of the vertical profiles of the undertow. The measuring points were arranged with 10cm distance in the on-offshore direction and 2.5-10mm distance in the vertical direction. On every measuring line, at least seven measuring points were set below the trough level. The lowest ones were 2mm above the bottom. The arrangement is shown in Fig.3 which is enhanced in the vertical direction.

The x-axis and z-axis were set to be shoreward and vertically upward, respectively. The origin of the coordinates in the case 1 was on the bottom as shown in Fig.1 and in the case 2 and 3, the shorelines at the still water levels were set to be the origins. In the case 3, the breaking point was at x_b=-250cm (indicated by "A" in Fig.3), the plunging point at x_p=-215cm ("B" in Fig.3) in the coordinates. After breaking, the wave propagates shoreward forming successive vortexes on the water surface. And the point where this vortex become a rather stable "surface roller" was around x_i=-170cm ("C" in Fig.3). The point

where the surface roller began to attenuate was at x_d=-80cm ("D"). The mean shoreline was at x_s=50cm in the case 3. In the case 1 and 2, the breaking points were at x_b=10cm, -225cm (indicated by "A" in Fig.1 and 2), and the plunging points at x_p=24cm, -162cm ("B"), respectively.

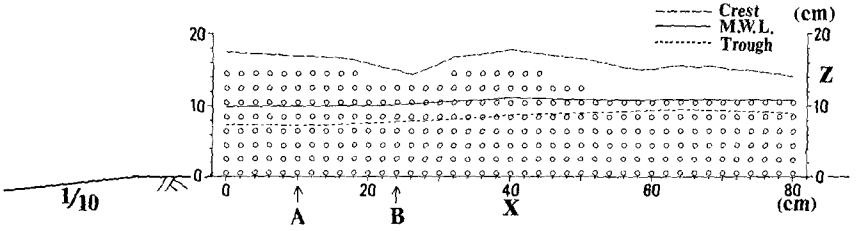

Fig.1 Measuring points arrangement for case 1

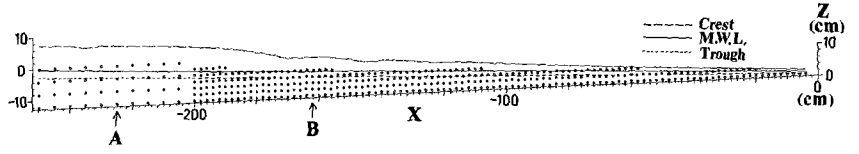

Fig.2 Measuring points arrangement for case 2

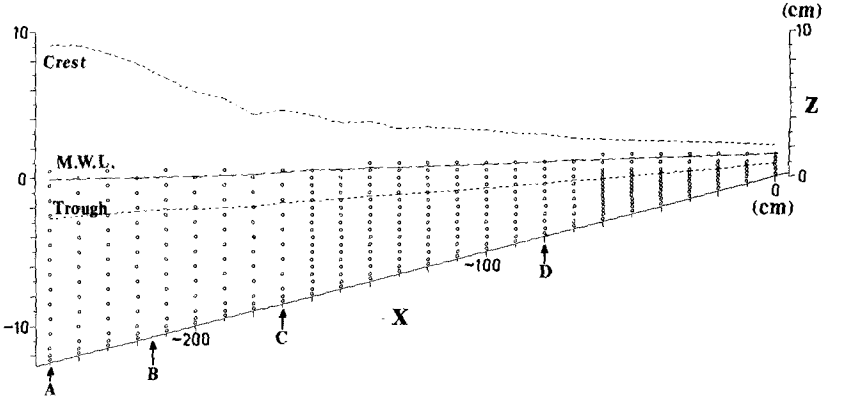

Fig.3 Measuring points arrangement for case 3

The experimental conditions are listed in Table I. In the table, T is the wave period, h_i the water depth in the offshore uniform depth region, H_i the wave height there, H_0/L_0 the deep-water wave steepness, H_b/h_b the depth wave height ratio at the breaking point.

Table I Experimental Conditions

case	beach profile	T(s)	h_i(cm)	H_i(cm)	H_0/L_0	H_b/h_b
1	step	1.55	40.0	6.95	0.0201	1.02
2	const. slope	1.50	40.0	7.36	0.0226	0.901
3	const. slope	1.50	36.4	8.15	0.0249	0.954

2.2 Data Processing and Analysis

A hot film velocimeter with a split film probe (H.F.V.) was used to measure the histories of two dimensional velocity vectors for the case 1 and 2. And a two components laser doppler velocimeter (L.D.V.) was used for the case 3.

By using the H.F.V. we can obtain two components of velocity, which are one component of velocity histories with the plus or minus sign and an absolute value of the other component. Therefore, we cannot get full information about the signs of two components. In the case 1, the sign of the on-offshore component of the velocity was not determined. Therefore, we made an assumption that the surface profile and the on-offshore velocity are in phase. So the sign of the velocity was reversed once in every wave period according to the surface profile. In the case 2, we measured the velocity two times, once for the on-offshore and the other time for the vertical direction to avoid such an uncertainty. In case of using the L.D.V., we can get full information of velocity for two components and there is no problem like that.

The velocity data were sampled every 10ms (for the case 1 and 3) or 12ms (for the case 2) and were converted into digital data. The surface elevation data were also taken simultaneously. The equi-phase-mean values of the velocity over 30 (case 1 and 2) or 100 (case 3) periods were calculated. Each wave period was divided into 150 (or 125 for the case 2) intervals and the equi-phase-mean value was obtained as an average of the velocity values at the same phase of every wave. The turbulence component was determined as the deviation from the equi-phase-mean value.

2.3 Experimental Results

The steady currents, the spatial distributions and time histories of equi-phase-mean velocities, vorticities and turbulent intensities were obtained. Fig.4 gives an example of the results for the case 1. The equi-phase-mean velocity field, the vorticity field and the turbulent intensity field at the time immediately after the wave plunging are shown in the figures. A large scale vortex can be observed obviously by the velocity vectors in the figure. And the high vorticity and turbulent intensity regions are in good agreement with the velocity vectors which suggest the existence of the plunging vortex.

Fig.5 is the successive figures of the equi-phase-mean velocities after plunging. The process that the first plunging pushes up the neighboring water body and the second plunging occurs in a smaller scale is shown. The plunging vortex formed by the first plunging does not move according with the crest and goes downward. The contour maps of the turbulent intensity at the same phases are shown in Fig.6. The high turbulent region goes ahead slowly behind the wave crest and spreads, then dissipates.

Based on these facts, it can be concluded that the generation of the plunging vortex has much influences on the characteristics of the velocity field and is much concerned with the energy dissipation process under plunging waves. Up to now, the velocity field in the surf zone were often described as a form in [steady current] + [wave component (periodic component)] + [turbulence]. This time, however, the measured results point out that the periodic component consists of the irrotational wave component and the organized rotational motion due to

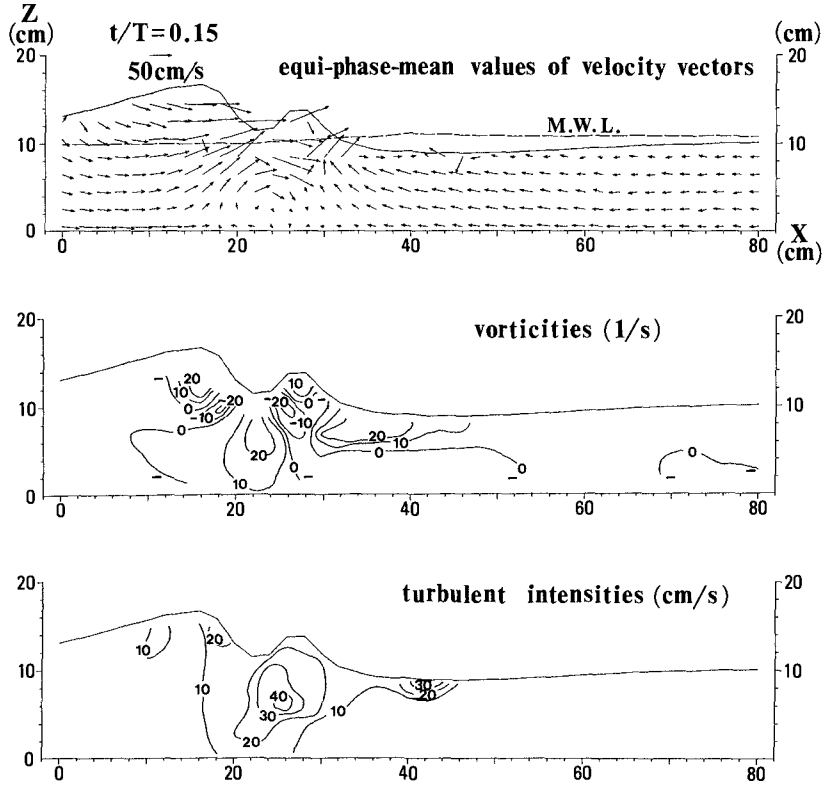

Fig.4 Velocities, vorticities and turbulent intensities immediately after wave plunging

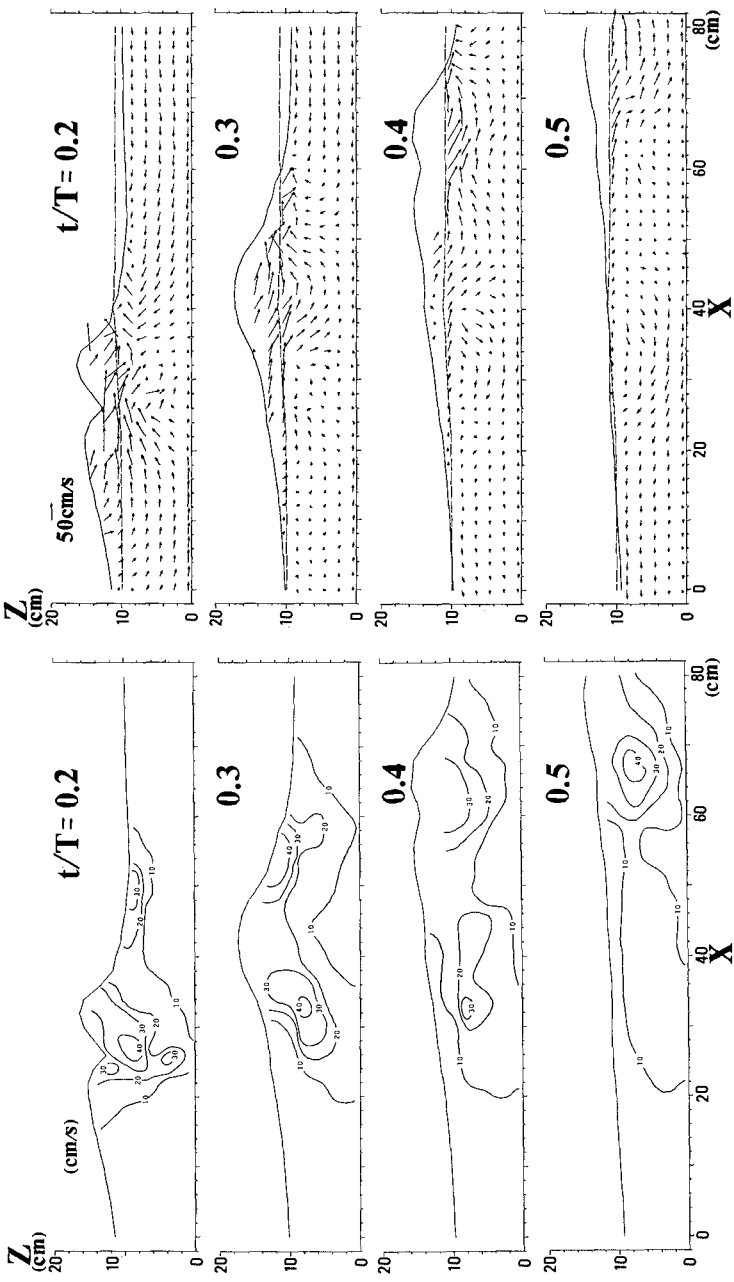

Fig.6 Distributions of turbulent intensities for case 1

Fig.5 Equi-phase-values of velocity vectors for case 1

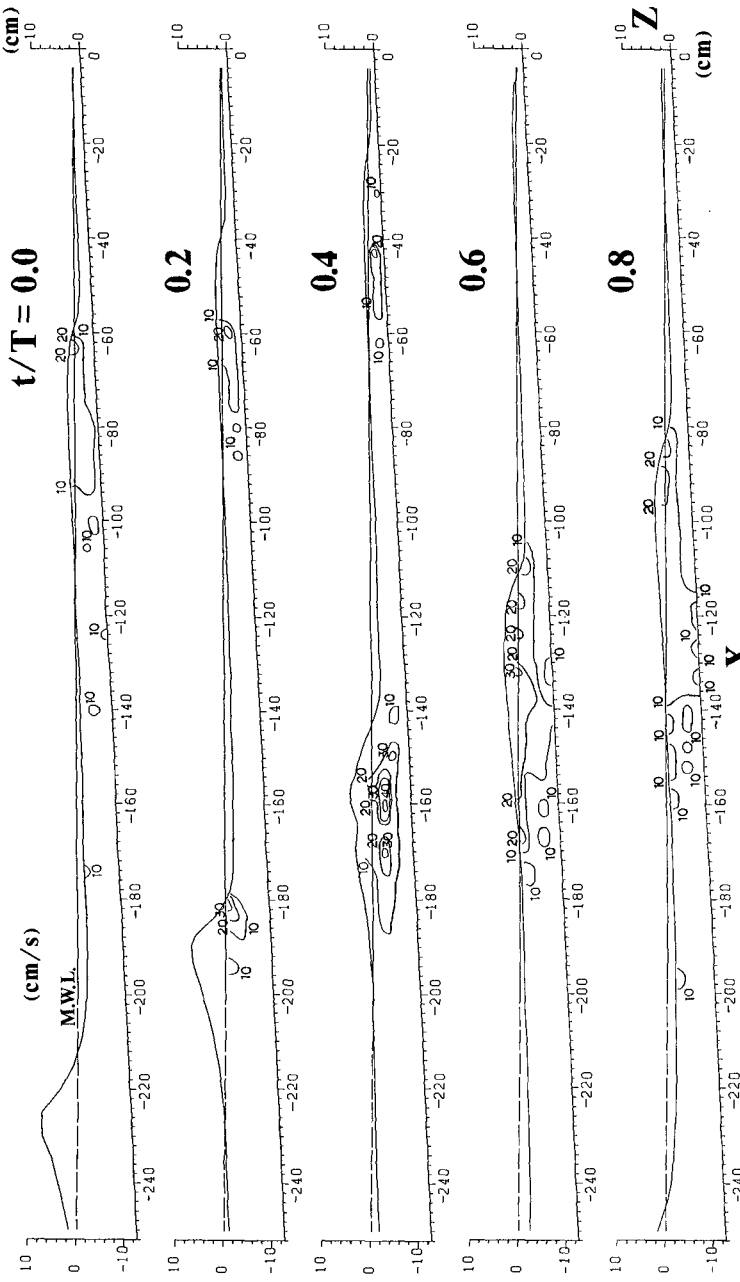

Fig.7 Distributions of turbulent intensities for case 2

the wave plunging. And it can be said that the plunging vortex is an important fluid motion existing between the wave motion and the turbulence or the steady current. Therefore, we propose that the velocity field in the surf zone should be divided into four components as [steady current] + [non-rotating wave motion] + [organized vortex motion] + [turbulence].

Fig.7 gives the successive contour maps of the turbulent intensity for the case 2. The figure shows a high turbulent region in front of the wave crest. It should be noticed that this turbulence is caused by the vortex motion as described by Nadaoka et al.(1986) which is formed there. And in the figure the turbulence spreads downward, so it should influence the turbulent flow field there and the bottom boundary layer. The figure indicates another turbulent region from x=-40cm to x=-80cm at the phases 0.0-0.6. As this high turbulent region stays there after the wave crest passes, it can be said that this turbulence is due to the interaction between the bore-like wave and the return flow from the swash zone. The high turbulent region caused by the wave plunging is also ascertained in this figure.

Fig.8 shows the steady current distribution for the case 3. Observing this figure, we found that the bottom boundary layer develops at the breaking point, but in the region where the bore well develops the bottom boundary layer does not develop any more. And we considered that it is due to the turbulence created by the bore-like waves. The large gradient of the profiles of the undertow shows that large shear stress works at the mean water level.

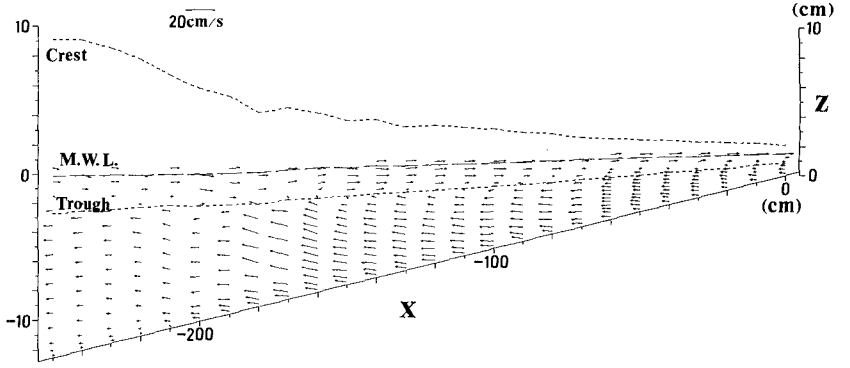

Fig.8 Steady current distribution for case 3

3. MODELING OF UNDERTOW

3.1 On-offshore Variation of Vertically Averaged Undertow

The estimation of the steady current distribution is very important for evaluating such as the convective diffusion of materials or the

sediment transport in the surf zone. However, the steady current distribution in the surf zone is much different from that of any wave theory solved in the invisid condition. The surface roller which is formed just in front of the crest of the bore-like wave propagating in the surf zone affects the mass flux balance and the turbulence generation as shown in the section 2. Now in this section, taking the case 3 as an example, we will try to formulate a model to calculate the profile of the undertow that is the steady current distribution below the trough level.

For the reasons mentioned above, when we consider the mass flux above the trough level which is transported by the bore-like wave, we should take into account both the contribution from the wave component and the contribution from the surface roller. For the wave component, Isobe et al.(1979) reported that the wave component of the velocity in the surf zone fits well to the velocity calculated by the stream function method which is presented by Dean (1965). Accordingly, the stream function method was used for estimating the wave component. We divided the bore-like wave into two parts, the surface roller and the wave component which can be explained by the stream function method. Then as shown in Fig.9, we supposed that the velocity inside the surface roller equals to the wave celerity c in the same manner as Svendsen (1984) did.

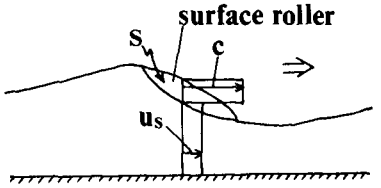

Fig.9 Assumption of velocity distribution of bore-like wave

As the sum of the mass fluxes by the surface roller and the wave component balances to the offshore steady current below the trough, the vertically averaged undertow U_c is calculated by using the projected area S of the surface roller to the xz-plane, the height of the trough d_t and wave length L as

$$U_c = U_S + U_r = U_S + \frac{S}{d_t L} c \quad , \tag{1}$$

where U_S and U_r are the contribution to U_c from the surface roller and the wave component, respectively.

Then we nondimensionalized the projected area S of surface roller by the wave height H and the wave length L. Further more introducing the parameter k,

$$k = \begin{cases} 0 & (x \leqq x_p) , \\ \dfrac{x_p - x}{x_p - x_i} & (x_p < x \leqq x_i) , \\ 1 & (x_i < x \leqq x_d) , \\ \dfrac{x - x_s}{x_d - x_s} & (x_d < x \leqq x_s) , \end{cases} \tag{2}$$

for convenience, as a degree of the development of the surface roller, we presented S as

$$S = kAHL \ . \tag{3}$$

Thus Eq.(1) becomes

$$U_c = U_s + \frac{kAH}{d_t} c \ , \tag{4}$$

where A is a constant and was taken to be 0.06 for the case 3 in order to fit the measured value U_m. And we chose the wave celerity c as

$$c = \sqrt{g (h + H)} \ , \tag{5}$$

based on the solitary wave theory, where g is the gravity acceleration and h the mean water depth.

The comparison between the calculated velocity U_c by Eq.(4) and the measured velocity U_m is shown in Fig.10. As they are in good agreement in the whole area of the surf zone, it can be said that our treatment in which the size of the surface roller is expressed by the parameter k, is adequate.

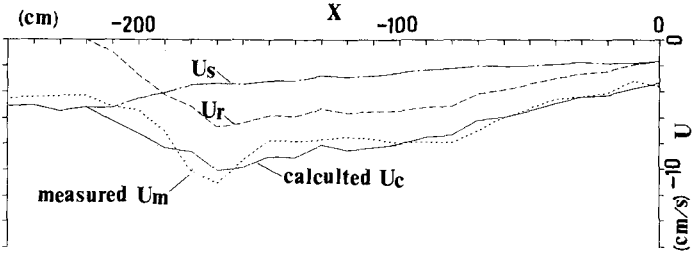

Fig.10 Calculated value of vertically averaged steady current U_c and measured value U_m

3.2 Vertical Variation of Undertow

Svendsen (1984) calculated the vertical variation of the on-offshore steady current by using the eddy viscosity model. But the magnitude of the eddy viscosity was left unknown and the agreement with the measured data near the bottom was not good enough. In the present

study, we will try to estimate the vertical profiles of the undertow with the eddy viscosity ν_t, which is directly calculated from the measured data, the Reynolds stress and the on-offshore velocity.

By using the eddy viscosity model, the relation between the mean shear stress $\bar{\tau}$ acting on the horizontal plane and the steady current U is

$$\bar{\tau} = \rho \nu_t \frac{\partial U}{\partial z} . \tag{6}$$

If the $\partial\bar{\tau}/\partial z$ takes a constant value, Eq.(6) can be written as

$$\frac{\partial \bar{\tau}}{\partial z} = \frac{\partial}{\partial z} \left(\rho \nu_t \frac{\partial U}{\partial z} \right) = \alpha_1 (x) = \text{const.} \tag{7}$$

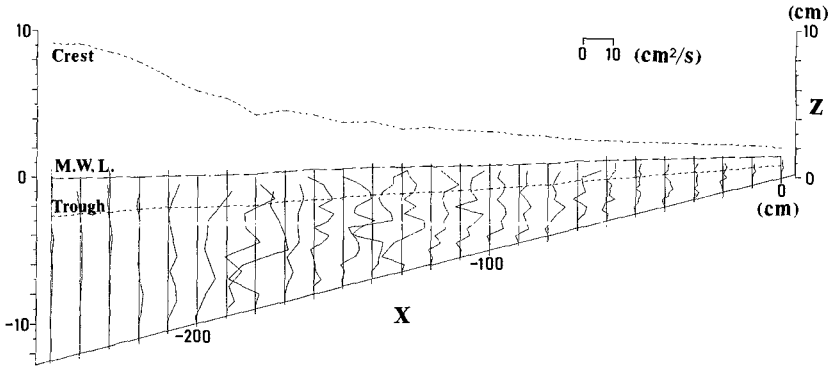

Fig.11 Distribution of mean eddy viscosity averaged over one wave period

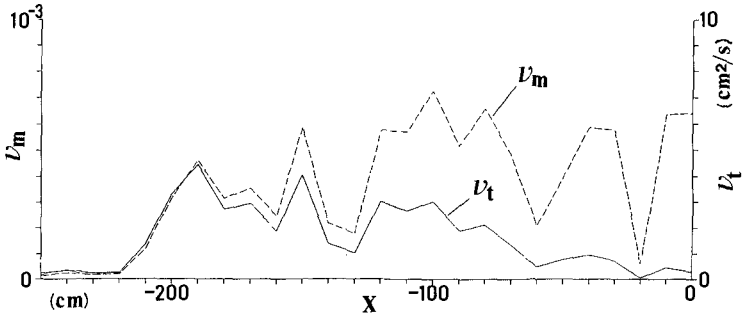

Fig.12 On-offshore distribution of vertically averaged eddy viscosity ν_t and nondimensional value ν_m

Fig.11 shows a distribution of the mean eddy viscosity by averaging the eddy viscosity of each phase over one wave period. In the figure it is possible to take it being constant along a vertical line except close to the bottom. From this reason we made a rather bold assumption that the mean eddy viscosity is constant over the depth. Eq.(7) can be reformed as

$$\frac{\partial \overline{\tau}}{\partial z} = \rho \nu_t \frac{\partial^2 U}{\partial z^2} \ . \tag{8}$$

Furthermore, we obtain

$$\frac{\partial^2 U}{\partial z^2} = \frac{1}{\rho} \frac{\partial \overline{\tau}}{\partial z} \Big/ \nu_t = \alpha(x) \ . \tag{9}$$

The on-offshore variation of the nondimensional value ν_m which is calculated from the vertical average of ν_t below the trough level divided by c and d_t, is shown in Fig.12. It is seen that ν_m progressively increases after the plunging point and then becomes rather stable around 0.005-0.006 in $x>x_i$ (-170cm) except some fluctuations. Therefore, we supposed that

$$\nu_t = 0.005\sim0.006 \ c d_t \ . \tag{10}$$

On the other hand, the nondimensional value obtained from α_1 divided by $\rho c^2/d_t$ can be supposed to be a constant value in $x>x_i$. The value α_1 in Eq.(7) can be expressed as

$$\alpha_1 = 0.0012 \ c^2/d_t \ . \tag{11}$$

Consequently, we denote α in Eq.(9) as

$$\alpha = \frac{1}{\rho} \alpha_1 / \nu_t \simeq 0.2 \ c/d_t^2 \qquad (\ x > x_i \ ) \ . \tag{12}$$

As α is very small in offshore side of the plunging point, it was taken to be 0 in that region. And we linearly interpolated it between the plunging point and the point where a stable surface roller is formed ($x=x_i$). As a result we obtain

$$\alpha = 0.2 \ k' c/d_t^2 \ , \tag{13}$$

where the parameter k' is

$$k' = \begin{cases} 0 & (\ x \leqq x_p \ ) \ , \\ \dfrac{x_p - x}{x_p - x_i} & (\ x_p < x \leqq x_i \ ) \ , \\ 1 & (\ x_i < x \leqq x_s \ ) \ . \end{cases} \tag{14}$$

For the bottom boundary condition, we thought it is appropriate to give it by the slip, i.e., no shear stress condition inside the high turbulent region, because the bottom boundary layer does not develop

there as we mentioned in the section 2. However, the velocity field near the breaking point is not so turbulent that it is better to give 0 to the eulerian steady current on the bottom U_b, as suggested by Isobe (1982). Accordingly, using the bottom steady current U_{b0} which is solved with the slip condition and k in Eq.(2), we calculated U_b as

$$U_b = kU_{b0} \ . \tag{15}$$

Using these three conditions which are, (1) the mean value U_c of the steady current below the trough level, (2) the ratio α of the eddy viscosity ν_t to $\partial\bar{\tau}/\partial z$ and (3) the steady current U_b at the bottom, we can solve Eq.(9). And putting $z'=z+h_0$ where h_0 is the still water level measured from the bottom, we obtain

$$U = \frac{1}{2}\alpha z'^2 + 2(1-k)\ U_{b0}\frac{z'}{d_t} + kU_{b0} \ , \tag{16}$$

where

$$U_{b0} = U_c - \frac{1}{6}\alpha d_t^2 \ .$$

The comparison between the steady current distribution calculated by Eq.(16) and the measured value of it is shown in Fig.13. The calculated and the measured value fit well except in the region between the breaking point and the plunging point. One of the reasons of the discrepancy is that the linear interpolation for α and U_b is not adequate, and another reason is that we neglected the influence of the plunging vortex formed near the plunging point. Anyway we can say that it is difficult to describe the flow field in the outer breaking region where such a violent transition as plunging takes place. And the disagreement near the bottom is due to the assumption of the constant eddy viscosity near the bottom.

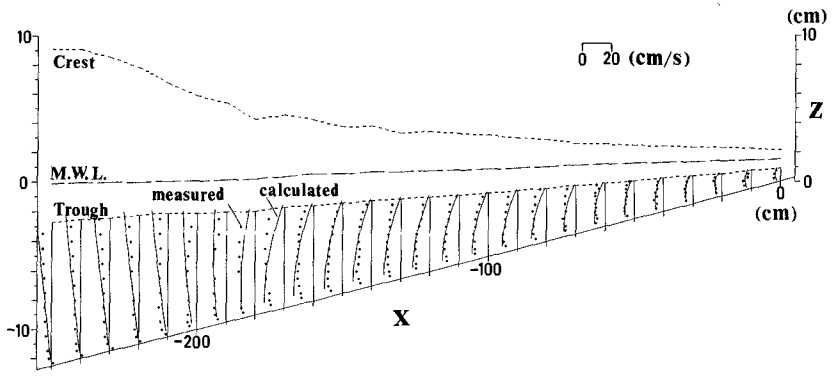

Fig.13 Distribution of calculated steady current and measured value

4. CONCLUDING REMARKS

Through detailed and precise laboratory experiments, we clarified the characteristics of the velocity field in the surf zone with plunging breakers. Then we proposed that the velocity field can be divided into four components, the steady current, wave component, organized vortex motion and turbulence. And this organized vortex motion is an important fluid motion existing between the wave motion and the turbulence.

Based on the laboratory results, we investigated a model for the estimation of the vertical profile of the undertow available in whole the surf zone. We found that the mean steady current over the depth can be divided into the contribution from the wave component and that from the surface roller. The onshore mass flux by the surface roller can be expressed quantitatively by an empirical constant multiplied by the wave length and the wave height and a simple linear interpolation of the constant value. In the region where the surface roller well develops, the vertical variation of the undertow can be estimated by supposing a constant eddy viscosity over the depth and a no shear stress condition on the bottom. On the other hand, the bottom steady current near the breaking point can be taken to be 0. The calculated steady current distribution fits well to that from measured data all over the surf zone, however the agreement is not so good near the bottom and in the outer breaking region.

5. ACKNOWLEDGMENT

The authors thank to Mr. Y. Higuchi who assisted the experiment of the case 2.

6. REFERENCES

Aono, T. and M. Hattori (1984) : Experiments on coherent structures of large scale turbulence under breaking waves, Proc. 31st Japanese Conf. Coastal Eng., pp.6-10. (in Japanese)

Dean, R.G. (1965) : Stream function representation of nonlinear ocean wave, J. Geophysical Res., Vol.70, No.18, pp.4561-4572.

Hansen, J.Buhr and I.A. Svendsen (1984) : A theoretical and experimental study of undertow, Proc. 19th ICCE., pp.2246-2262.

Isobe, M., N. Fukuda and K. Horikawa (1979) : Two dimensional experiment on velocity field in the surf zone, Proc. 26th Japanese Conf. Coastal Eng., pp.41-45. (in Japanese)

Isobe, M. (1982) : Study on drift velocity at the bottom in and near the surf zone, Proc. 29th Japanese Conf. Coastal Eng., pp.140-144. (in Japanese)

Mizuguchi, M. (1986) : Experimental study on kinematics and dynamics of wave breaking, Abstracts 20th ICCE., pp.75-76.

Nadaoka, K., M. Hino and Y. Koyano (1986) : Turbulent flow field structure of breaking waves in the surf zone, Abstracts 20th ICCE., pp.71-72.

Sakai, T., I. Sandanbata and M. Uchida (1984) : Reynolds stress in surf zone, Proc. 19th ICCE., pp.42-53.

Sawaragi, T. and K. Iwata (1974) : Turbulent effect on wave deformation after breaking, Costal Eng. Japan, Vol.17, pp.39-49.

Svendsen, I.A., P.A. Madsen and J.Buhr Hansen (1978) : Wave characteristics in the surf zone, Proc. 16th ICCE., pp.520-539.

Svendsen, I.A. (1984) : Mass flux and undertow in a surf zone, Coastal Eng., Vol.8, pp.347-365

CHAPTER 51

Approximate descriptions of the focussing of water waves

D.H. Peregrine*

Abstract

Underwater shoals and spurs focus water waves that propagate over them. The normal theoretical approach to finding a more accurate solution of the linear equations is to interpret the envelope of crossing rays as a cusp of caustics (see Figure 1) and to use Pearcey's function (Pearcey 1946). In practical cases the ray pattern is rarely sufficiently well defined to enable the cusp parameters to be deduced. An alternative approach is presented in which a length of wave crest heading towards the focussing region is approximated by an arc of a circle or parabola (Figure 2). Corresponding approximate solutions for linear and weakly nonlinear waves are described.

1. Introduction

For calculating the refraction of waves the usual method is to use ray theory. It is a common occurrence to find points in wave ray diagrams where rays cross. The point where rays start to cross is usually a focus at the cusp of two caustics. This is illustrated in figure 1. It is unusual to obtain very clear examples in practice and if only a few rays cross a higher density of rays is needed to clarify the ray structure.

Focussing of rays is an indication that ray theory has become invalid. An improved method of solution including at least some diffraction effects is necessary. One approach is to determine the positions of caustics and use Pearcey's (1946) solution for the cusps of caustics; another approach is to use a parabolic approximation; a third method is to solve a fully elliptic form of the wave equation.

Here two simple approximations for finding the wave amplitude at the focus are presented. Both represent the focus as a single point where an angular spread of waves meet as sketched in figure 2. It is much easier to estimate such an angle than to fit an appropriate caustic cusp. The boundary of the focussing wave is also important. Here we suppose that an initial wave crest is made up of a circular arc of angle 2α, radius R, smoothly joining straight crests representing plane waves as sketched in figure 2. Uniform initial amplitude is assumed.

One approximation is based on an exact linear wave solution and includes diffraction effects. The other is based on an exact solution of a weakly nonlinear parabolic equation for refraction, the nonlinear Schrödinger equation. The approximation includes the major nonlinear

*Reader, School of Mathematics, University of Bristol, University Walk, Bristol BS8 1TW, England.

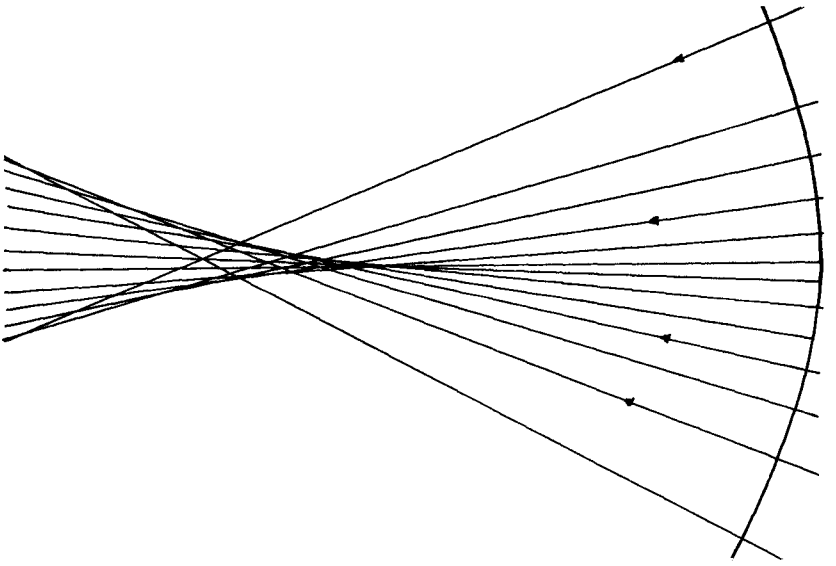

Figure 1. A typical focus.

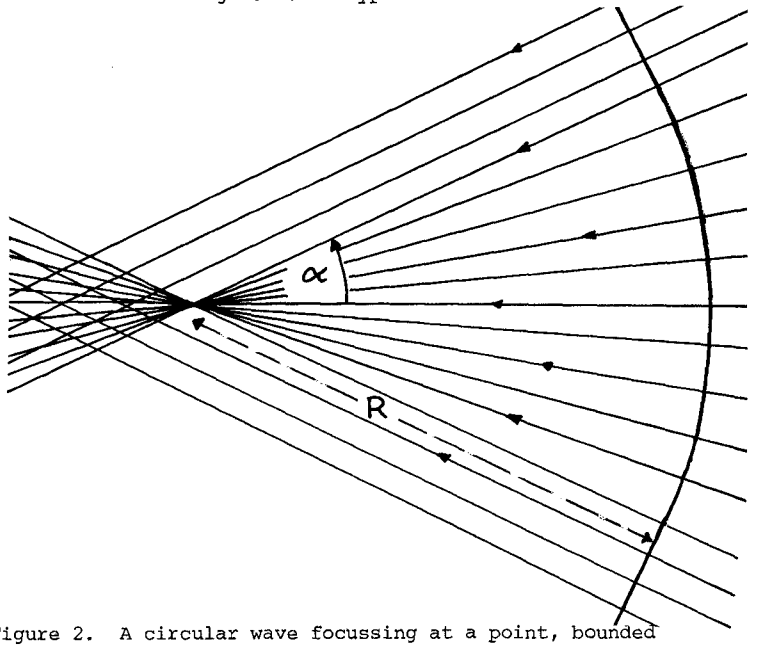

Figure 2. A circular wave focussing at a point, bounded by plane waves.

diffraction effects but neglects some of the linear diffraction. The results are different. It appears that both are likely to give upper bounds on wave amplitude. Both are easy to evaluate once α, R and the initial wave amplitude A_1 are known. The smaller value can be taken as an estimate of wave amplitude at the focus.

2. A linear solution

We consider only water of constant depth, h, and a single Fourier component in time. That is a time variation $e^{-i\omega t}$ is implicit. The wave equation to be solved is then

$$\nabla^2\zeta + k^2\zeta = 0 \tag{1}$$

where k is the wavenumber given by

$$\omega^2 = gk\tanh kh \tag{2}$$

and ζ is the, complex, surface elevation. Introduction of polar coordinates (r,θ) permits expression of the general solution of equation (1) in the form

$$\zeta = \sum_{n=0}^{\infty} (a_n \cos n\theta + b_n \sin n\theta) J_n(kr), \tag{3}$$

where J_n are Bessel functions.

Now take the origin at the focal point of a wave system, and consider a circle of large radius R, such that $kR \gg 1$. Then for all values of n such that $n \ll kR$ the terms of the series (3) can be divided into incoming and outgoing waves by using an asymptotic formula for J_n, for example see Abramowitz and Stegun (1964) equation (9.2.1). In particular:

$$\begin{aligned} J_0(kR) &\simeq (2/\pi kR)^{\frac{1}{2}} \cos(kR - \tfrac{1}{4}\pi) \\ &\simeq (2\pi kR)^{-\frac{1}{2}} \{\exp i(kR - \tfrac{1}{4}\pi) + \exp[-i(kR - \tfrac{1}{4}\pi)]\}. \end{aligned} \tag{4}$$

When combined with $e^{-i\omega t}$ the first exponential term in (4) gives an incoming wave, the second term gives an outgoing wave.

At the origin the only non zero term in the Fourier-Bessel series (3) is the J_0 term, thus we only need to evaluate a_0 to find the wave amplitude there. To evaluate the Fourier coefficients we suppose that on the circle radius R the amplitude and phase of *incoming* waves is known as a complex function of θ, say $A(\theta)$. Then the usual Fourier series evaluation of coefficients and the expression (4) give

$$\int_{-\pi}^{\pi} A(\theta)\, d\theta = 2\pi a_0 (2\pi kR)^{-\frac{1}{2}} \exp i(kR - \tfrac{1}{4}\pi). \tag{5}$$

As an example consider the plane wave

$$\zeta = A_1 e^{ikx} = A_1 e^{ikr\cos\theta}$$

This gives

$$A(\theta) = A_1 e^{ikR\cos\theta} \quad \text{for} \quad -\tfrac{1}{2}\pi < \theta < \tfrac{1}{2}\pi$$
$$= 0 \quad \text{for} \quad |\theta| \geq \tfrac{1}{2}\pi. \tag{6}$$

The integral of equation (5) becomes

$$\int_{-\frac{1}{2}\pi}^{\frac{1}{2}\pi} e^{ikR\cos\theta} d\theta = (2\pi/kR)^{\frac{1}{2}} \exp i(kR - \tfrac{1}{4}\pi), \tag{7}$$

to the same level of approximation as the asymptotic formula (4) for J_o, and thus equation (5) gives $a_o = A_1$ as is expected.

Now consider the wave field sketched in figure 2: that is an arc of a circle of angle 2α of precisely focussed waves bounded smoothly by semi-infinite plane waves. For simplicity let their amplitude at radius R have constant modulus A_1 and continuous phase. The contribution to the integral of equation (5) of the two semi-infinite plane waves is the same as that of a single plane wave, though spread over a different range of angles. The contribution of the focussing arc is simply $2\alpha A_1 \exp(ikR)$ leading to

$$a_o = A_1\{1 + \alpha(2kR/\pi)^{\frac{1}{2}} e^{\frac{1}{4}i\pi}\}. \tag{8}$$

Thus
$$|a_o| = A_1\{1 + 2\alpha(kR/\pi)^{\frac{1}{2}}\} \tag{9}$$

after neglecting terms of an order, k^2R^2, already neglected in the asymptotic result (4).

3. Nonlinear Schrodinger equation

Parabolic approximations are well suited to modelling a focus. A brief derivation for the simple two-dimensional wave equation,

$$\frac{1}{c^2}\frac{\partial^2 u}{\partial t^2} = \frac{\partial^2 u}{\partial x^2} + \frac{\partial^2 u}{\partial y^2}, \tag{10}$$

illustrates the nature of the approximation made. Equation (10) can be rewritten:

$$\left(\frac{\partial}{\partial t} + c\frac{\partial}{\partial x}\right)\left(\frac{\partial}{\partial t} - c\frac{\partial}{\partial x}\right)u = c^2\frac{\partial u}{\partial y^2} \tag{11}$$

The first operator on the left-hand side expresses the fact that waves can propagate in the +x direction, and the second operator relates to propagation in the -x direction.

Near a focus most waves are propagating close to one direction, say the +x direction. Thus

$$u(x,y,t) = a(x,y)e^{i(kx-\omega t)}, \tag{12}$$

where
$$k = \omega/c \tag{13}$$

should be a good first approximation. The exponential describes almost all of the "wavy" behaviour in the x direction. Hence one expects

$$ka >> \frac{\partial a}{\partial x} . \tag{14}$$

Substitution of (12) into (11) gives

$$\left(-i\omega + ick + c\frac{\partial}{\partial x}\right)\left(-i\omega - ick - c\frac{\partial}{\partial x}\right) a = c^2 \frac{\partial^2 a}{\partial y^2} . \tag{15}$$

The inequality (14) implies that the x derivative in the second operator of (15) may be neglected compared with the sum of the other two terms, which is $-2ick$ after using (13). The equation then reduces to

$$\frac{2i}{k}\frac{\partial a}{\partial x} + \frac{1}{k^2}\frac{\partial^2 a}{\partial y^2} = 0 \tag{16}$$

which is the parabolic wave equation (also known as the one-dimensional Schrodinger wave equation). For a derivation directly related to water waves see Radder (1979).

Using the full equations for irrotational water waves Yue and Mei (1980) showed that the appropriate extension of equation (16) for weakly nonlinear water waves (equivalent to third-order Stokes waves) is

$$\frac{2i}{k}\frac{\partial a}{\partial x} + \frac{1}{k^2}\frac{\partial^2 a}{\partial y^2} - Kk^2|a|^2 a = 0. \tag{17}$$

This is a nonlinear Schrödinger equation (NLS equation) in which

$$K = \frac{c}{c_g}\cdot\frac{9 - 12p^2 + 13p^4 - 2p^6}{p - kh(1 - p^2)} \tag{18}$$

where $p = \tanh kh$ and $\frac{c}{c_g} = \frac{2p}{1 + kh(1 - p^2)}$.

Note, $a(x,y)$ is still the complex amplitude of the first approximation

$$a(x,y)e^{i(kx-\omega t)} .$$

A further approximation aids interpretation of solutions of the NLS equation. Substitute

$$a = Ae^{iS} \tag{19}$$

in the NLS equation (17), where A and S are real functions of (x,y). Separate real and imaginary parts. Introduce

$$D = k^2A^2 \quad \text{and} \quad v = \frac{1}{k}\frac{\partial S}{\partial y} . \tag{20}$$

A little algebra and differentiation then gives

$$D_x + (Dv)_y = 0, \tag{21}$$

$$v_x + vv_y + \tfrac{1}{2}KD_y = (A_{yy}/k^2A)_y. \tag{22}$$

The final term in equation (22) includes three y derivatives and is thus only important in rapidly varying parts of a solution. If it is neglected equation (22) becomes

$$v_x + vv_y + \tfrac{1}{2}KD = 0. \tag{23}$$

By substituting a time variation for the x variation in equations (21) and (23), they can be recognized as the nonlinear shallow-water equations with the role of gravity being taken by $\frac{1}{2}K$, and D and v equivalent to the depth and the velocity respectively.

Equations (21) and (23) have two sets of characteristics

$$\frac{dy}{dx} = \pm(\tfrac{1}{2}KD)^{\frac{1}{2}} + v \tag{24}$$

which corresponds to a splitting of the rays in linear theory, see Peregrine (1983).

4. A nonlinear focussing solution

Following the qualitative description of focussing given by Peregrine (1983) numerical solutions of the NLS equation (17) with initial conditions corresponding to the focussing in figure 2, were studied. These solutions all showed that where focussing waves were of a uniform amplitude at the initial value of x the amplitude remained uniform in y varying only with x in a substantial region approaching the focus. An example may be found in figure 3 of Stamnes et al (1983).

A solution corresponding to amplitude being independent of y is easily found. For waves of initial amplitude A_1 at $x = R$, focussing at $x = 0$, it is

$$a(x,y) = A_1(R/x)^{\frac{1}{2}}\exp i\{y^2/2kx - Kk^3A_1^2R\log(x/R)\}. \tag{25}$$

This solution is singular and unrealistic at $x = 0$. However, one effect of nonlinearity is that there is "defocussing", and the effective focus may occur before the geometric focus. This feature can be deduced from the characteristics corresponding to solution (25) which are shown in figure 3. The characteristics also show that the singularity at $x = 0$ is due to wave energy coming in from waves originally at unrealistically large values of $|y|$.

For any initial region of focussing at $x = R$ the corresponding domain of dependence is limited to a region with $x > x_o > 0$. Within this domain of dependence solution (25) is likely to be a good approximation. The characteristics of (25) are given by

$$y = \pm A_1 k(2KRx)^{\frac{1}{2}}\{(x/x_o)^{\frac{1}{2}} - 1\}, \tag{26}$$

where x_o, the position at which $y = 0$, identifies pairs of characteristics. The particular characteristics which bound a domain of depend-

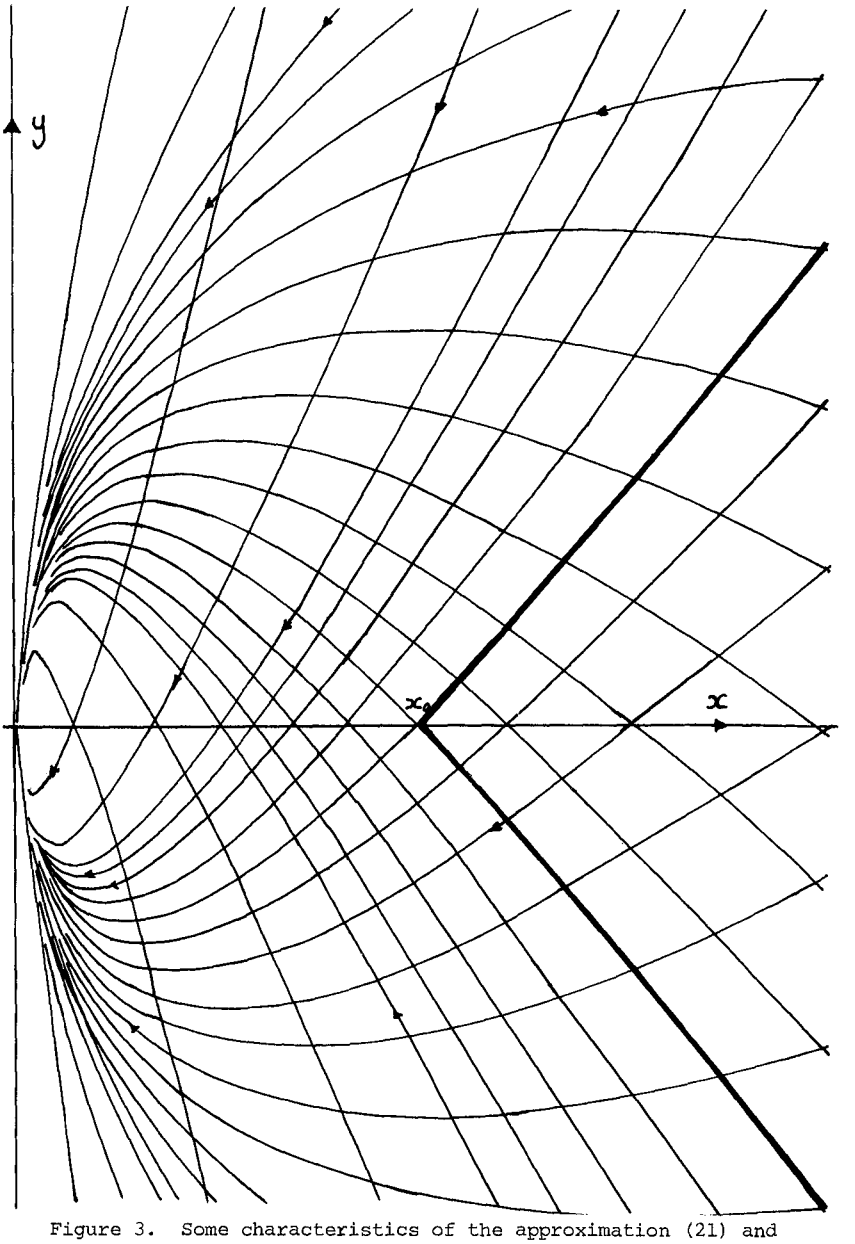

Figure 3. Some characteristics of the approximation (21) and (23) to the nonlinear Schrödinger equation for the solution (25). The boundary of a domain of dependence on initial conditions is outlined.

ence of waves from an angle of 2α at $x = R$, are found by substituting $(x,y) = (R, \alpha R)$ into (26) which gives

$$x_o = \frac{R}{\left\{1 + \frac{\alpha}{kA\ (2K)^{\frac{1}{2}}}\right\}^2}. \tag{27}$$

Unless there are more waves focussing to the same point, $x = x_o$ becomes the effective focussing position, and the corresponding value of amplitude at that point is

$$|a(x_o,0)| = A_1\left\{1 + \frac{\alpha}{kA_1\ (2K)^{\frac{1}{2}}}\right\}. \tag{28}$$

The NLS equation (17) can be scaled to give an identical equation by using the transformation

$$a^* = a/a_o, \quad x^* = a_o^2 x, \quad y^* = a_o y. \tag{29}$$

Thus any one numerical solution can be interpreted in a number of different ways. In particular, some results of computation are shown in figure 4. The amplitude of numerical solutions along $y = 0$ is given for the scaled values $A^* = 1$, $R = 5$, and $\alpha R = 3, 10$ and 20, where k has been set equal to one. Examples of alternative values for these three cases are given in table 1, where L is wavelength and H is wave height.

Table 1.

kA_1	$(H/L)_1$	kR	R/L	α		
0.1	.032	500	80	3.4°	11.5°	22.9°
0.05	.016	2000	318	1.7°	5.7°	11.5°

5. Discussion

Two simple formulae for the maximum amplitude are given. From section 2

$$|a_o| = A\ \{1 + 2\alpha(kR/\pi)^{\frac{1}{2}}\} \tag{30}$$

and from section 4.

$$|a_o| = A_1\left\{1 + \frac{\alpha}{kA_1\ (2K)^{\frac{1}{2}}}\right\} \tag{31}$$

These are different and this difference is due to the different approximations. Expression (30) arises from attempting to include all the linear diffraction effects and is expected to be useful for waves of small steepness, even at the focus. On the other hand expression (31) arises from an approximation which neglects some linear diffraction effects, i.e. the third-order terms in equation (22), but does include

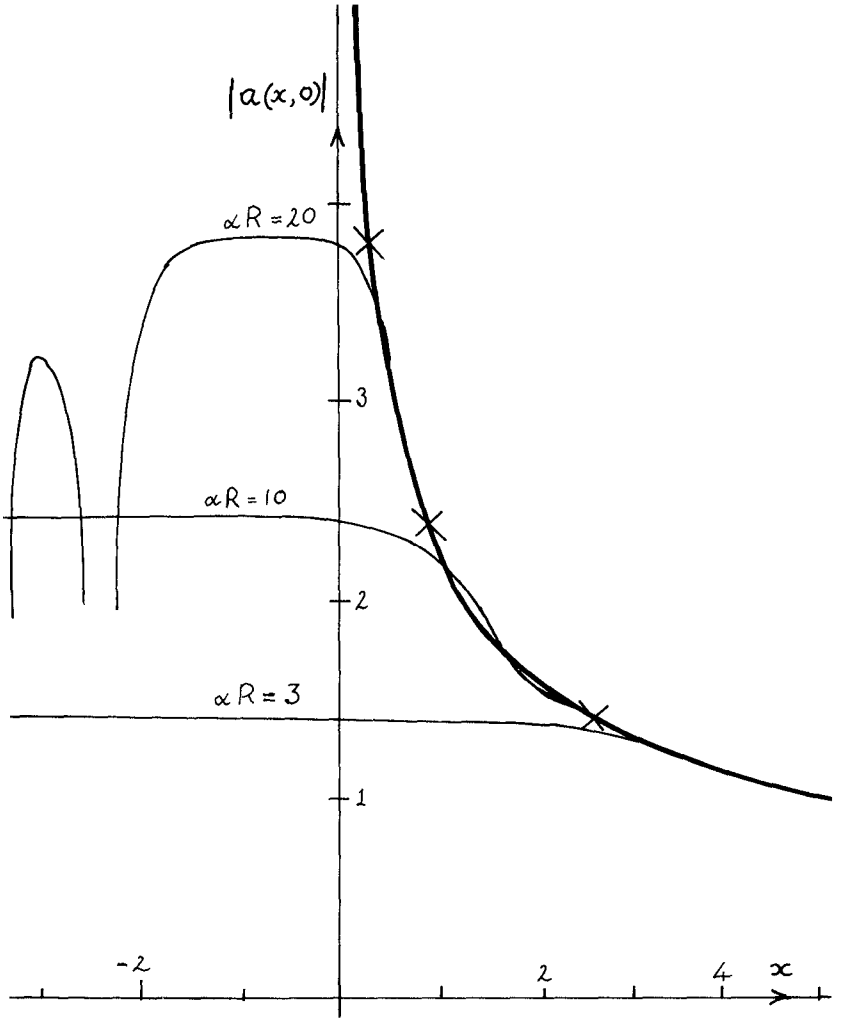

Figure 4. Variation of amplitude of waves along the axis of a focus. Numerical solutions of the NLS equation (17) compared with the solution (25) shown in a heavy curve, with crosses marking the values of x_o, equation (27), corresponding to the numerical examples.

the defocussing effects of nonlinearity.

Both the linear diffraction and nonlinear defocussing spread wave energy so that the singularity at a focus that arises from the ray approximation does not happen in practice. Both expressions (30) and (31) neglect some of the energy spreading so that both of them are likely to be upper bounds on wave energy. To see how they may be used consider a situation where the wave geometry, kR and α, is fixed and the initial steepness is allowed to vary, that is A_1 increases from zero. Initially the linear expression (30) is the lesser value; for zero amplitude waves the nonlinear effects are not relevant, but as steepness increases the two expressions become equal and for steeper waves nonlinear effects are more important and hence expression (31) is the least. This is sketched in figure 5. The initial steepness at which the two expressions are equal is

$$kA_1 = (2\pi/kRK)^{\frac{1}{2}}. \qquad (32)$$

Interestingly, but perhaps in retrospect not surprisingly, this critical steepness is independent of α. As an example, if R is 100 wavelengths and K = 3, i.e. kh = 1.0, then the critical wave steepness kA_1 is 0.06 or $(H/L)_1 = 0.018$.

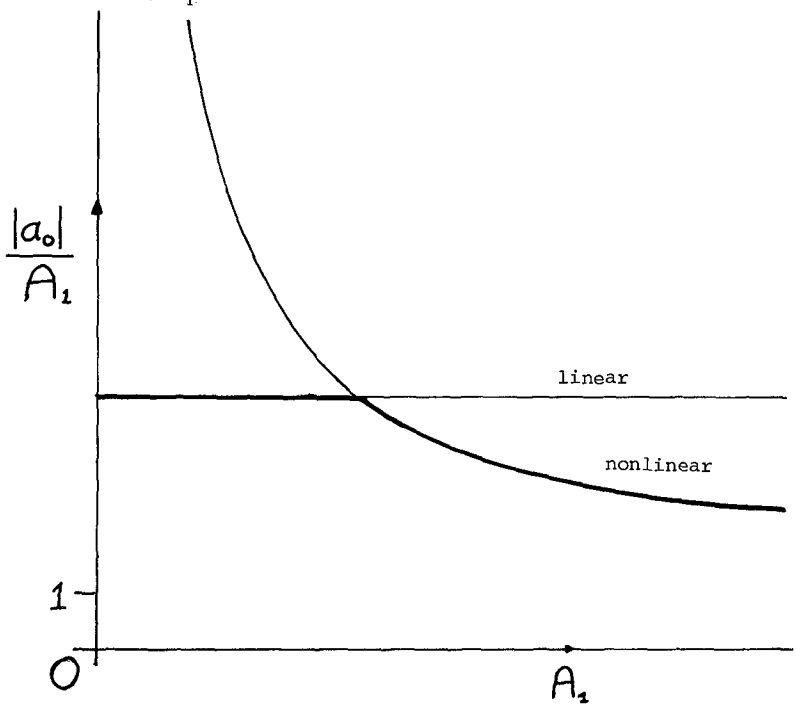

Figure 5. Variation of the linear and nonlinear expressions for amplitude at a focus with the initial wave steepness.

There are limitations in these expressions. They are derived for water of constant depth of initially uniform amplitude. Nonetheless, the author is not aware of any other simple estimates for wave amplitude at a focus and hopes that they may still provide a rough guide in practical situations for assessing the importance, or unimportance, of regions where ray theory shows that waves focus.

6. References

Abramowitz, M. and Stegun, A.I. 1964. "Handbook of Mathematical Functions". Nat. Bur. Standards, Appl. Math. Ser. 55 (also Dover, New York).

Pearcey, T. 1946. The structure of an electromagnetic field in the neighbourhood of a cusp of a caustic. The London, Edinburgh and Dublin Philosophical Magazine and Jour. of Science. 7th Series, Vol.37, pp.311-317.

Peregrine, D.H. 1983. Wave jumps and caustics in the propagation of finite-amplitude water waves. J. Fluid Mech. 136, 435-452.

Radder, A.C. 1979. On the parabolic equation method for water-wave propagation. J. Fluid Mech. 95(1), 159-176.

Stamnes, J.J., Løvhaugen, O., Spjelkavik, B., Mei, C.C., Lo, E. and Yue, D.K.P. 1983. Nonlinear lens focussing of surface waves - theory and experiment. J. Fluid Mech. 135, 71-94.

Yue, D.K.P. and Mei, C.C. 1980. Forward diffraction of Stokes waves by a thin wedge. J. Fluid Mech. 99, 33-52.

CHAPTER 52

WAVE HEIGHT DECAY MODEL WITHIN A SURF ZONE

Shigeki Sakai*, Kouetsu Hiyamizu**, Hiroshi Saeki***

ABSTRACT

A model for wave height decay of a spilling breaker is proposed. The energy dissipation of a breaking wave is approximated by that of a propagating bore. In order to explain the gentle decay of spilling breaker at the initial stage, a development of a foam region, which indicates the amount of foam on the wave profile and determines the rate of energy dissipation, is considered. In addition to this formulation, the energy and momentum balance equations are described by a linear wave theory in shallow water and are simultaneously solved. Comparisons with experimental results show that the model gives a good prediction in both inner and outer regions, and that two coefficients in the present model are related to the deep water wave steepness and the slope of beaches.

1 INTRODUCTION

The height of breaking wave and a rate of its decaying have very important influences on the nearshore wave-induced phenomena, such as the generation of nearshore currents, the transportation of sediments and so on. In order to discuss these phenomena, it is necessary to clarify the characteristics of breaking waves.

Many experimental investigations and several models for breaking wave have been presented. In these models, it is widely used to approximate the energy dissipation of the breaking wave by that of a propagating bore. Originally, this approach was proposed by Le Méhauté(1962). In his study, a conception named "non-saturated breaker" was introduced, and a formulation for the wave energy dissipation of the spilling breaker involving effects of the bottom friction was used to explain the

* Instructor, Civil Engineering Department, Iwate University, Ueda 4-3-5, Morioka 020, Japan
** Graduate Student, Civil Engineering Department, Iwate University, Ueda 4-3-5, Morioka 020, Japan
*** Professor, Civil Engineering Department, Hokkaido University, Kita 13, Nishi 8, Sapporo 060, Japan

wave height index (H=0.78h). Hwang and Divoky(1970) improved this approach by taking a wave set-up into considerations.

Battjes(1978) gave a model using a dissipation function for breaking waves depending on local wave properties and a local breakerheight (γh). This model showed an overall agreement with results of systematic experiments given by Horikawa and Kuo (1966). It was, however, pointed out that in most cases the initial decay was overestimated by this model.

Svendsen, Madsen and Hansen(1978) indicated that the surf zone is divided into inner and outer regions, and Svendsen (1984) showed that "surface roller" has an important role in the wave decay. The results of the model agreed with experiments well in the inner region.

While this approach has been improved by many studies, some problems still remain. The largest difference between calculations by the model and experiments appears in the outer region. Particularly for spilling breakers, models gave the larger energy dissipation than what were experimentally observed.

In the present study, experimental findings of the gentle decay of spilling breaker at the initial stage and a development of turbulent region, called "foam region", during the breaking are first explained. And a new model for the decay of a spilling breaker is proposed. In the model, the energy dissipation of the breaking wave is approximated by that of a propagating bore and the development of the foam region is mathematically expressed based on several assumptions. Energy and momentum equations are also simultaneously applied.

Finally, two coefficients in the model are determined by comparing with the experimental results.

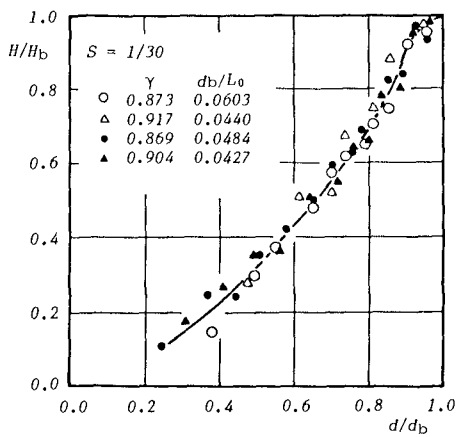

H : wave height, d : mean water depth
$\gamma = Hb/db$, L_0 : deep water wave length
subscript b denotes conditions at breaking point

Figure 1 Wave height decay of spilling breaker

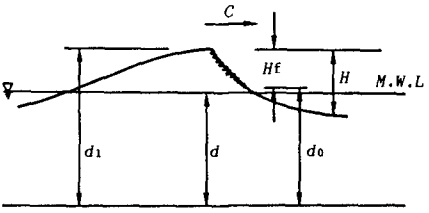

$Hf = d_1 - d_0$: vertical length of foam region
C : wave celerity

(a) spilling breaker

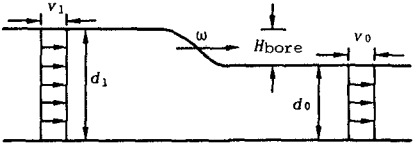

$Hbore = d_1 - d_0$: bore height
ω : propagation velocity of bore
v_0, v_1 : velocity of flow

(b) propagating bore

Figure 2 Comparison between spilling breaker and propagating bore

2 DEVELOPMENT OF FOAM REGION

Examples of wave height decay of spilling breaker in a surf zone are shown in Figure 1. This figure shows that the wave height decay immediately after breaking points is rather gentle, and the change is rapid after the wave propagates some distance. This tendency was found in the experiments given by Horikawa and Kuo(1966), as well as in our experiments. This refers to a fact that a region of turbulence of the spilling breaker is restricted near the wave crest in the outer region and develops as the wave propagates. And the development of the turbulence region increases the rate of the wave energy dissipation.

The turbulence region in spilling breakers is called a "foam region" in this paper, and Hf indicates the vertical length of a foam region, as illustrated in Figure 2 (a). When the energy dissipation of spilling breakers is approximated by that of the propagating bore(Figure 2 (b)), the bore height Hbore corresponds to the length Hf of the spilling breaker, and therefore the change in the size of the foam region has an important influence on calculated results. Since the foam region immediately after breaking is narrower than that of well-developed breaker in the inner region, the increase of the energy dissipation rate of a spilling breaker can be explained by considering the development of the foam region.

3 WAVE HEIGHT DECAY MODEL

3.1 Foam Region

In order to explain the development of the foam region, it is assumed that a water particle is released from the crest of a wave at a breaking point, and the particle again meets the water surface after a very short time Δt, as shown in Figure 3. Now, the lower boundary of the foam region is defined by this point. Then, the water particle jumps again from this point, and consequently the foam region further develops.

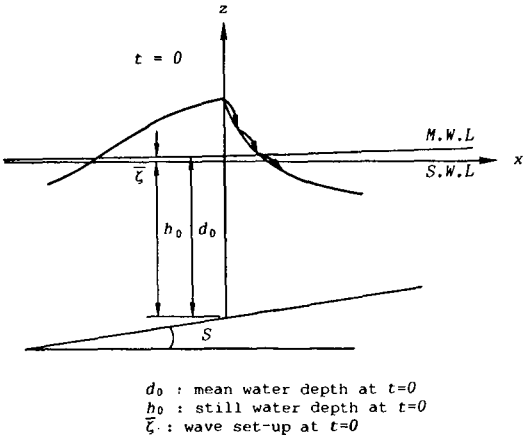

Figure 3 Development of foam region

In the calculations of the time interval and the distance for such action of a water particle, it is assumed that the wave celerity is given by a linear wave theory in shallow water and that the horizontal velocity of the released particle is identical to the wave celerity at the time when it was just released. Thus, the wave celerity C at t=Δt and the horizontal velocity u_0 of the released water particle is given as follows;

$$C = \sqrt{gd_0} - \frac{Sg}{2}\Delta t \quad , \quad u_0 = C_0 = \sqrt{gd_0} \tag{1}$$

where g : the gravitational acceleration, d_0 : a water depth at t=0, and S : a slope of beach.
Therefore, the relative velocities to the wave profile are described as;

$$u' = u_0 - C = \frac{Sg}{2}\Delta t \quad , \quad w' = -g \cdot \Delta t \tag{2}$$

and consequently, the distances measured from the water profile are;

$$\Delta x = \frac{Sg}{4}\Delta t^2 \quad , \quad \Delta z = -\frac{g}{2}\Delta t^2 \tag{3}$$

In addition, the front profile of the wave is approximated as an ellipse. At the time when the released water particle meet again the water surface, the following equation is satisfied.

$$\left(\frac{\Delta z}{R}\right)^2 + \left(\frac{\Delta x - \left(\frac{L}{2} - x_f\right)}{\frac{L}{2} - x_f}\right)^2 = 1 \qquad (4)$$

where notations are explained in Figure 4.
From Equations (3) and (4), the time interval is given, and then the distances are calculated by Equation (3). We further used a coefficient on the time interval, given by Equation (5).

$$\Delta t' = \alpha \cdot \Delta t \qquad (5)$$

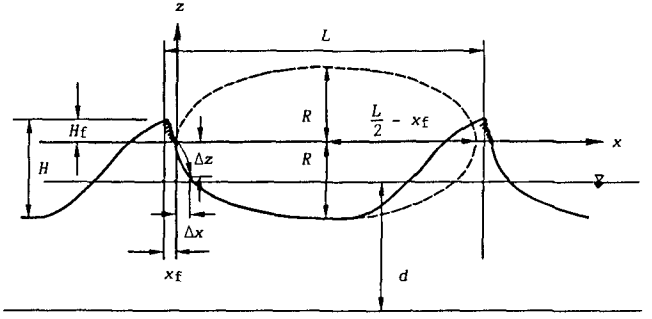

Xf, Hf : horizontal and vertical length of foam region
Δx, Δz : horizontal and vertical increment of foam region
L : wave length, R = H-Hf

Figure 4 Approximation of wave profile by ellipse

3.2 Energy and Momentum Balance

In the present model, the energy dissipation of a spilling breaker is approximated by that of the propagating bore. As widely used in the previous studies, the energy dissipation per a unit length is described as a following equation with a coefficient B.

$$D' = -B\frac{\rho g}{4}\frac{1}{Td}H_f^3 \qquad (6)$$

where ρ is a density of the fluid, T is a wave period.
When the energy flux of the wave is calculated by a linear wave theory in shallow water, the energy balance equation is described as follows;

$$\frac{d}{dx}\left\{\frac{1}{8}\rho g H^2 \left(gd\right)^{\frac{1}{2}}\right\} + B\frac{\rho g}{4}\frac{1}{Td}H_f^3 = 0 \qquad (7)$$

Since the development of the foam region is calculated descretely with the time interval Δt as shown in Figure 5, the energy balance is

also considered within this interval. The time interval is so short that the foam region Hf within the interval can be regarded to be constant. Therefore, Equation(7) is integrated, and the change of wave height from t1 to t2 is given as follows;

$$\left(\frac{H_2}{H_1}\right)^{-1} = \left(1 - \frac{2}{3}K\right)\left(\frac{d_2}{d_1}\right)^{\frac{1}{4}} + \frac{2}{3}K\left(\frac{d_2}{d_1}\right)^{-\frac{1}{2}} \qquad (8)$$

$$K = \frac{2B}{S}\left(\frac{d_1}{gT^2}\right)^{\frac{1}{2}}\frac{H_1}{d_1}$$

In order to calculate correctly the wave height near a shore line, the wave set-up is included in calculations. In the present model, a following relationship given by Longuet-Higgins and Stewart(1964) is used to calculate the mean water depth.

$$\frac{d}{dx}Sxx + \rho g\left(h + \bar{\zeta}\right)\frac{d\bar{\zeta}}{dx} = 0 \qquad (9)$$

Sxx : *radiation stress*

$\bar{\zeta}$: *wave set-up/down*

3.3 Procedure of Calculation

The time interval Δt and the increments of the lower boundary of the foam region Δx_1 and Δz_1, described in Figure 5, are calculated by Equations.(4), (5) and (3). And, the energy and momentum balance equations are simultaneously solved to give Hf2 and $\bar{\zeta}_2$.

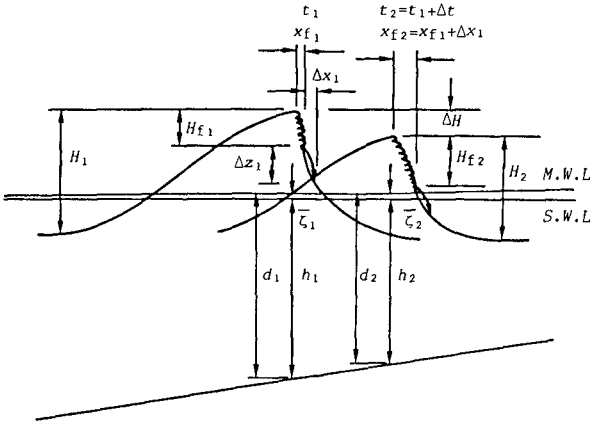

Δt : time interval
ΔH : decrement of wave crest height

Figure 5 Description for development of foam region

Successively, the foam region at the next time step is given as;

$$H_{f2} = H_{f1} + \Delta z_1 - \Delta H$$

$$\fallingdotseq H_{f1} + \Delta z_1 - (H_1 - H_2) \frac{\eta_c}{H} \qquad (10)$$

where η_c is a wave crest height.
However, in order to calculate the decrement of the wave crest height, the relationship between the crest height and the wave height should be considered. Hansen's data quoted by Svendsen(1984) indicated that the ratios of the wave crest height to the wave height vary linearly with the change of the depth, while the magnitude of the ratios is different depending on the deep water wave steepness. This qualitative tendency is adopted to calculate the change of the wave crest height, and a following relationship is assumed.

$$\frac{\eta_c}{H} = 0.55 + 0.2 \frac{d}{d_b} \qquad (11)$$

where db is a breaking water depth.

4 VERIFICATION OF MODEL

Two coefficients α and B are used in the present model, to compensate slight uncertainties of the assumptions. In order to determine these coefficients, some experiments were conducted, and in these experiments the slopes of beaches were 1/15,1/30 and 1/50.

Comparisons between the calculations by the model and experimental results indicate that the optimum value of the coefficient B depends on the slope of beach. B has a larger value when the slope is steeper, and the relationship between the coefficient B and the slope of beach is shown in Figure 6. Experiments on the slope 1/65 given by Horikawa and Kuo(1966) were also explained by the present model with the value on the slope 1/50. This implies that this coefficient is constant on the slopes milder than 1/50.

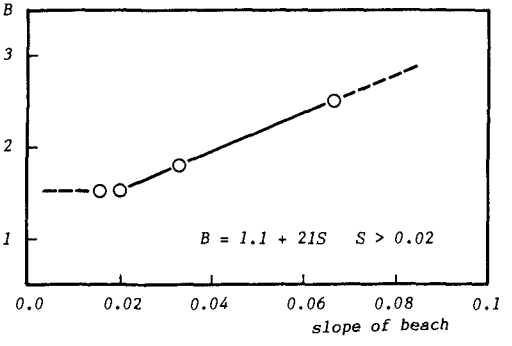

Figure 6 Relationship between coefficient B and slope of beach

For the other coefficient α, the optimum value is 2.5, in the cases where the deep water wave steepness is large and consequently the complete spilling breaker occurs. The decrease of the deep water wave steepness changes the breaker type from spilling to plunging. The spilling breaker with relatively small deep water wave steepness has a somewhat similar properties to plunging breaker. For such breaking waves, the coefficient should be magnified, in order to increase the energy dissipation in the outer region. Within our experiments, a relationship between the coefficient α and the deep water wave steepness is given in Figure 7.

Figure 8 (a),(b) and (c) show comparisons between the calculations by the present model and experimental results on the slope 1/15, 1/30 and 1/50, respectively, in which the deep water wave steepness is large. As shown in these figures, the calculations predict the experimental results fairly well. It is noteworthy that the present model is good, not only in the inner region but also in the outer region.

Figure 9 (a) shows a similar comparison for a spilling breaker on the slope 1/15 with a relatively small deep water wave steepness. The high accuracy of the prediction by the present model still remains. Figure 9 (b) gives a comparison on the slope 1/30. The calculation also agrees with experiments in this case.

Consequently, it was concluded that the present model gives good predictions of the wave height decay of the spilling breaker on the slopes from 1/15 to 1/50.

Figure 10 (a) and (b) show the results with respect to the wave set-up in the surf zone. The earlier models gave rapid increase of the mean water level in the outer region, since the wave energy dissipation was overestimated in this region. While the calculations by the present model still overestimates the wave set-up, the qualitative tendency of the change of the mean water level is explained.

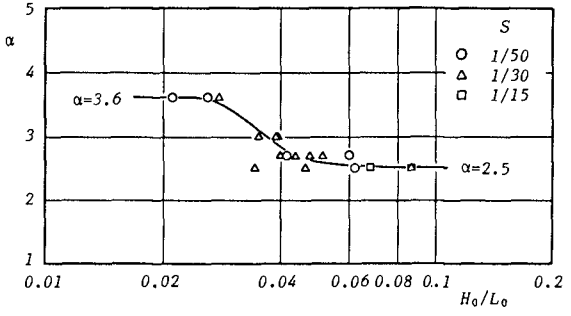

Figure 7 Relationship between coefficient α and deep water wave steepness

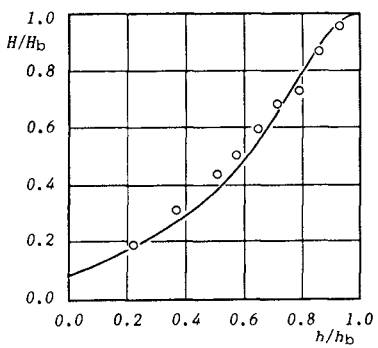

$S = 1/15$ $H_0/L_0 = 0.088$

$(H/h)_b = 0.754$ $h_b/L_0 = 0.112$

$(\bar{\zeta}/h)_b = -0.013$

(a)

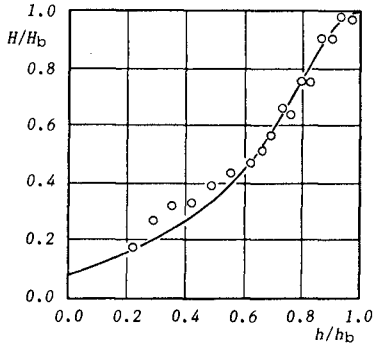

$S = 1/30$ $H_0/L_0 = 0.047$

$(H/h)_b = 0.793$ $h_b/L_0 = 0.065$

$(\bar{\zeta}/h)_b = -0.013$

(b)

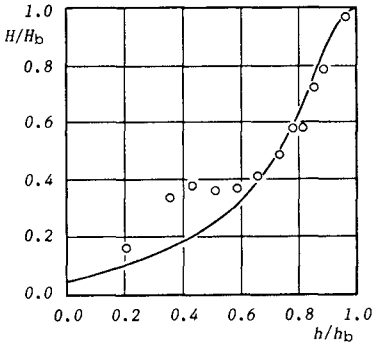

$S = 1/50$ $H_0/L_0 = 0.061$

$(H/h)_b = 0.708$ $h_b/L_0 = 0.085$

$(\bar{\zeta}/h)_b = -0.008$

(c)

Figure 8 Comparisons between calculated and experimental results of wave height decay

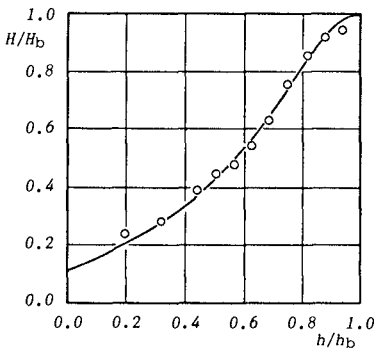

$S = 1/15$ $H_0/L_0 = 0.055$

$(H/h)_b = 0.826$ $h_b/L_0 = 0.072$

$(\bar{\zeta}/h)_b = -0.017$

(a)

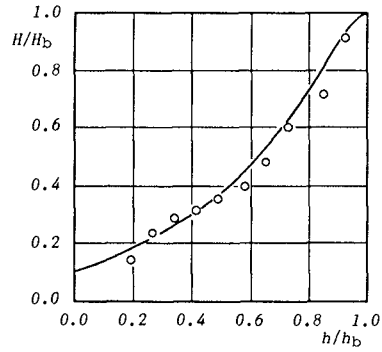

$S = 1/30$ $H_0/L_0 = 0.028$

$(H/h)_b = 0.886$ $h_b/L_0 = 0.042$

$(\bar{\zeta}/h)_b = -0.013$

(b)

Figure 9 Comparisons between calculated and experimental results of wave height decay

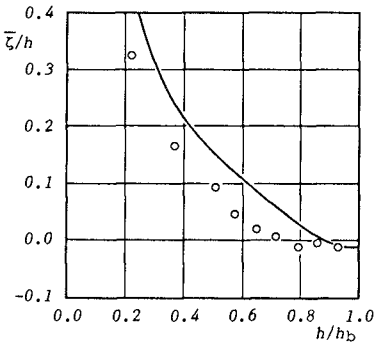

$S = 1/15$ $H_0/L_0 = 0.088$

$(H/h)_b = 0.754$ $h_b/L_0 = 0.112$

$(\bar{\zeta}/h)_b = -0.013$

(a)

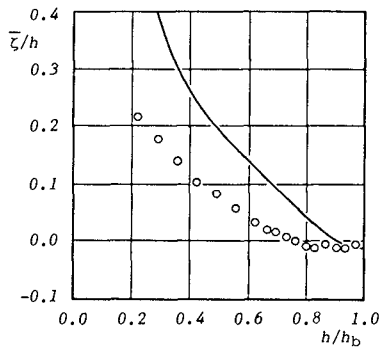

$S = 1/30$ $H_0/L_0 = 0.047$

$(H/h)_b = 0.793$ $h_b/L_0 = 0.065$

$(\bar{\zeta}/h)_b = -0.013$

(b)

Figure 10 Comparisons between calculated and experimental results of wave set-up

5 CONCLUSIONS

Experimental results show that the development of the foam region characterize the wave height decay of the spilling breaker in the outer region. This development and the energy and momentum balances were formulated by a linear wave theory in shallow water. This model explained the characteristics of wave height decay fairly well, even in the outer region. It was found that the coefficients used in the present model are determined by the deep water wave steepness and the slope of beaches.

REFERENCES

Battjes, J.A.(1978). Energy dissipation in breaking solitary and periodic waves. Manus. Delft Univ. of Tech.

Horikawa,K and C. T. Kuo (1964). A study on wave transformation inside surf zone. 10th I.C.C.E.,pp. 217-233.

Hwang, L.S. and D. Divoky (1970). Breaking wave setup and decay on gentle slopes. 12th I.C.C.E., pp. 377-389.

Le Méhauté, B. (1962). On non-saturated breakers and the wave set-up. 8th I.C.C.E., pp. 77-92.

Longuet-Higgins, M.S. and R.W. Stewart (1964). Radiation stresses in water waves; a physical discussion, with applications. Deep-Sea Research, Vol.11, pp. 529-562.

Svendsen, I.A., P.A. Madsen and J.B. Hansen (1978). Wave characteristics in the surf zone. 16th I.C.C.E., pp. 520-539.

Svendsen, I.A.(1984). Wave heights and set-up in a surf zone. Coastal Engineering, 8, pp. 303-329.

CHAPTER 53

IRREGULAR WAVE TRANSFORMATION AFFECTED BY OPPOSING CURRENTS

Shigeki Sakai *, Kouetsu Hiyamizu ** and Hiroshi Saeki ***

ABSTRACT

Transformation of irregular waves affected by opposing currents on a sloping sea bed was discussed, experimentally and theoretically. It was found that representative values of wave height, such as a significant wave height, are larger before breaking and the wave height decaying occurs more promptly in a surf zone as opposing currents become dominant, and that characteristics of a irregular wave transformation are determined by the dimensionless unit width discharge q^* and the deep water wave steepness. This means that the effects of opposing currents on irregular wave transformation are qualitatively identical to that on the regular waves.

A transformation model of irregular waves affected by opposing currents was presented. In the model, formulations for a regular wave transformation, in which the effects of opposing currents were taken into account, were applied to individual waves defined by zero-down-cross-method from irregular wave profiles.

Comparisons between experimental results and the prediction by the model showed that the present model gives a good explanation for wave height distributions and the experimental finding that the surf zone is moved offshore by opposing currents.

1. INTRODUCTION

Many studies on the transformation of irregular waves have been conducted, experimentally and theoretically. Goda(1975), Battjes and Janssen(1978), Thornton and Guza(1983) and Iwagaki, Mase and Furumuro(1983) presented transformation models which deal with irregular waves transformation without currents.

* Instructor, Civil Engineering Department, Iwate University, Ueda 4-3-5, Morioka 020, Japan

** Graduate Student, Civil Engineering Department, Iwate University, Ueda 4-3-5, Morioka 020, Japan

*** Professor, Civil Engineering Department, Hokkaido University, Kita 13, Nishi 8, Sapporo 060, Japan

Authors(1984) presented effects of opposing currents on the transformation of regular waves, and Hedge et.al.(1985) investigated an interaction between irregular waves and currents in the deep water.

However, in order to discuss phenomena caused by waves and currents such as the river mouth blocking, it is necessary to take the effects of opposing currents and the irregularity of waves in the shallow water into account.

In this paper, the effects of opposing currents on the transformation of irregular waves are clarified experimentally. Experiments show that the effects of opposing currents on irregular wave transformation are identical to that on regular wave qualitatively. Next, the transformation model of irregular waves affected by opposing currents are presented. In the model, formulations for the transformation of regular waves are applied to individual waves of irregular waves. And, the applicability of the present model is examined by comparing with experimental results, which shows a satisfactory agreement.

2. EXPERIMENTS AND RESULTS

2-1. Experimental Equipment and Procedure

Our experiments were conducted with an experimental setup as shown in Fig.1, which has a length of 35m, a width of 80cm, a depth of 120cm, and a slope of sea bed is 1/30. The water was circulated by a vacuum pump to produce opposing currents. Uniform currents were obtained on a 5m long flat bed located at an onshore end of wave channel, and flowed onto a sloping sea bed as opposing currents. The water depth on the flat bed was about 10cm.

In these experiments, irregular waves had Bretschneider-Mitsuyasu type spectra. Wave profiles were recorded for about 11 minutes, at 20 points with 90cm intervals.

Wave profiles were digitalized with 0.05 second sampling interval, and frequency components over five times of the peak frequency and under one half of the peak frequency were cut off.

Individual waves were defined by applying zero-down-cross-method to filtered irregular wave profiles.

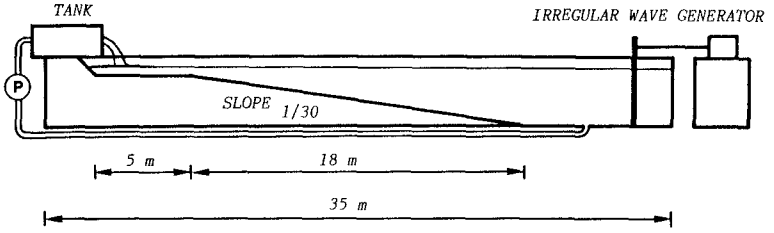

Fig.1 Experimental setup

Table 1 Experimental conditions

Case	q ($cm^3/s/cm$)	Ho' (cm)	To' (s)	Ho'/Lo'	q*
A - 1	0.0	14.9	1.54	0.0402	0.0
A - 2	0.0	14.9	1.55	0.0398	0.0
A - 3	96.4	15.0	1.52	0.0416	2.86×10^{-5}
A - 4	205.5	14.3	1.52	0.0397	6.09×10^{-5}
A - 5	300.0	14.7	1.53	0.0403	8.72×10^{-5}
B - 1	0.0	7.4	1.52	0.0205	0.0
B - 2	0.0	7.4	1.52	0.0204	0.0
B - 3	96.4	7.5	1.51	0.0212	2.92×10^{-5}
B - 4	205.5	6.8	1.51	0.0190	6.21×10^{-5}
B - 5	300.0	7.2	1.48	0.0211	9.64×10^{-5}
C - 1	0.0	11.2	1.30	0.0424	0.0
C - 2	0.0	10.9	1.31	0.0407	0.0
C - 3	96.4	11.3	1.33	0.0411	4.27×10^{-5}
C - 4	205.5	11.3	1.28	0.0443	1.02×10^{-4}
C - 5	300.0	11.0	1.32	0.0406	1.36×10^{-4}

To' : significant wave period in deep water

q* : dimensionless unit width discharge
$q^* = q / g^2 To'^3$

Ho'/Lo' : deep water wave steepness
$Lo' = g\, To'^2 / 2\pi$
(g : gravitational acceleration)

Experimental conditions are shown in Table 1. Capital letters A,B, and C indicate types of irregular wave. Numbers from 1 to 5 mean the condition of opposing currents, and the unit width discharge q was varied from 0 to 300 $cm^3/s/cm$.

Characteristics of irregular waves are defined as follows:
(1) A wave height distribution in the deep water is calculated by adopting a transformation model described in the following section on the individual wave heights at a reference point, which has a largest depth in our experiments. (2) From this wave height distribution, the significant wave height Ho' and period To' are determined.
(3) The deep water wave length Lo' is calculated by To' and the linear wave theory, and the deep water wave steepness is defined as Ho'/Lo'.
(4) q* is a parameter to indicate the magnitude of opposing currents, and is defined by the unit width discharge q and the wave period To'.

Since the deep water wave steepness on Case A is identical to that on Case C, effects of the parameter q* will be examined. And as the deep water wave steepness on Case B is one half of Case A and Case C, the effects of the deep water wave steepness will be able to investigated for cases with a similar value of q*.

2-2. Effects of opposing current on irregular wave transformation

Figure 2 shows a relationship between ratios of the significant wave height to wave height at a reference point and similar ratios with respect to the water depth. Case B has a relatively small deep water wave steepness, and in a region before breaking, wave heights affected by opposing currents are larger than wave heights without currents. It is also seen that the surf zone is moved offshore by opposing currents. In order to examine the effect of currents on wave height decaying in the surf zone, changes of wave heights with a relatively large deep water wave steepness are shown in Fig.3. This figure shows that, in the surf zone, the decaying of wave height with currents takes place more promptly than the decaying without currents.

Therefore it is concluded experimentally that opposing currents increase the shoaling coefficients and cause a prompt wave decaying in the surf zone.

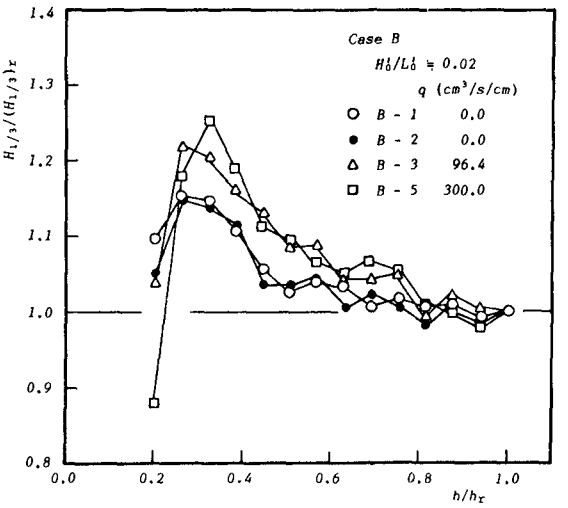

Fig.2 A change of significant wave heights

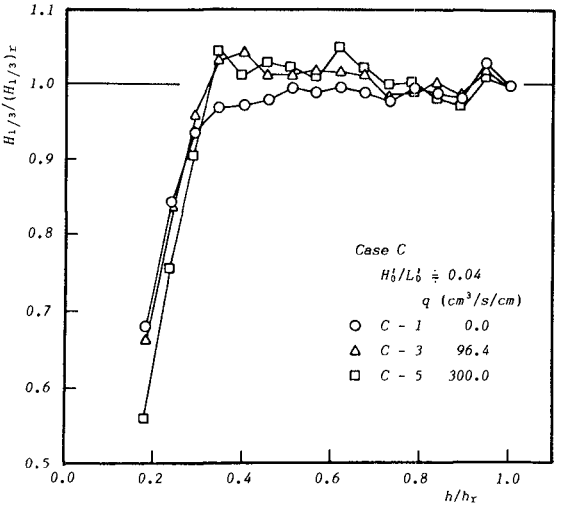

Fig.3 A change of significant wave heights

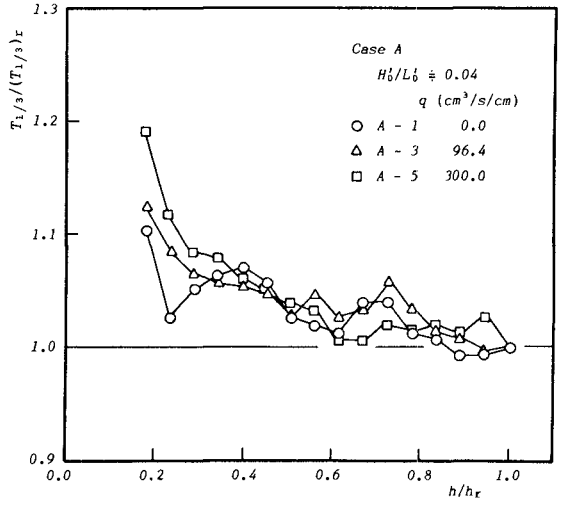

Fig.4 A change of significant wave periods

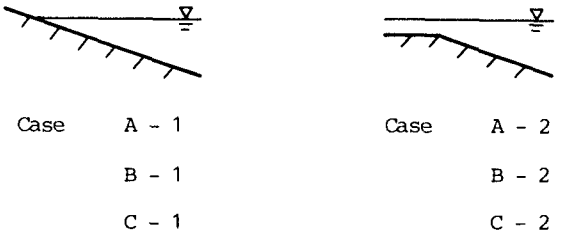

Fig.5 Conditions near the shoreline without currents

Experimental data for the change of the significant wave period, are shown in Fig.4. This figure gives relationships between ratios of the significant wave period to wave period at a reference point and similar ratios with respect to the water depth, and shows that the increase of unit width discharge causes the larger increase rates of the significant wave period especially in the surf zone.

In order to examine the effect of flat bed, which is located onshore of the sloping sea bed, experiments without currents were carried out for two bed configurations. As shown in Fig.5, one condition has a flat bed, and the other condition has an extending slope. The differences due to conditions near the shoreline do not appeared, as shown in Fig.2. Therefore it was regarded that those effects could be ignored in present experiments.

Authors(1984) have indicated the characteristics of regular wave transformation with opposing currents are determined by the dimensionless unit width discharge q^* and the deep water wave steepness, and these parameters will be used to explain the characteristics of irregular wave transformation.

Figure 6 gives a relationship between ratios of significant wave height to the significant wave height in the deep water, and ratios of the water depth to the wave length in the deep water.

If the deep water wave steepness is constant, the shoaling coefficients become larger as the parameter q^* increases.

Further as shown in Fig.7, when q^* is constant, the shoaling coefficient becomes larger and the breaking point is moved offshore as the deep water wave steepness becomes larger.

It was found that the transformation of irregular waves is characterized by q^* and the deep water wave steepness and these two effects are similar to those on regular wave, qualitatively.

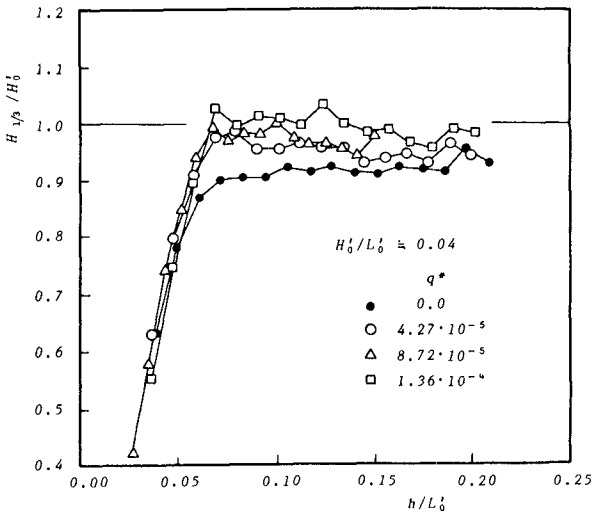

Fig.6 Effects of the dimensionless unit width discharge on irregular wave transformation

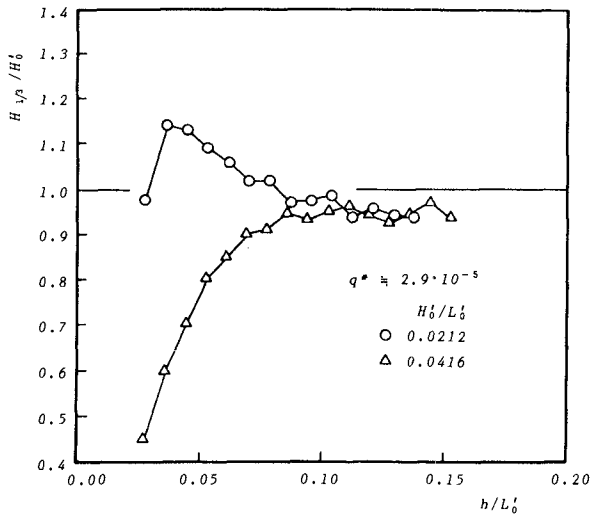

Fig.7 Effects of the deep water wave steepness on irregular wave transformation

3. TRANSFORMATION MODEL FOR IRREGULAR WAVES

In order to examine the effect of opposing currents on transformation of irregular waves quantitatively, a transformation model is proposed. In the present model, to simulate the wave transformation affected by opposing currents, the formulations for a regular wave are applied to individual waves of irregular waves, which have their own wave period and height.

3-1 Shoaling formulation

The formulation for shoaling before breaking is derived from the energy flux conservation law and described, using the linear theory, as follows;

$$E \left(Cg_r - U \right) \left(1 - \frac{U}{Cr} \right) = E_0 \, Cg_{r0} = const. \qquad \text{------- (Eqn.1)}$$

where Cgr indicates a relative group velocity for the water, Cr gives a relative wave celerity, U means the velocity of opposing current, and subscript o indicates a quantities in the deep water.

3-2 Breaking criteria

Miche(1951) indicated that the breaking criteria is expressed by Eqn.2, and the coefficient α without any currents is 0.142.

$$\left(\frac{H}{L} \right)_b = \alpha \tanh \left(\frac{2\pi h}{L} \right)_b \qquad \text{------- (Eqn.2)}$$

Authors(1984) showed that the coefficient with opposing currents is smaller than 0.142. A difference form Miche's coefficient due to the effects of opposing currents is described as $\Delta\alpha$, and a relationship between q* and $\Delta\alpha$ was proposed. However, when the relationship mentioned above was applied to individual waves of irregular wave, the effect of current appeared stronger than what we expected. And after several trials, it was found that the most suitable coefficient α was given by a following equation;

$$\alpha = 0.142 - 0.5 \, \Delta\alpha \qquad \text{------- (Eqn.3)}$$

3-3 Wave height decaying formulation

The wave height decay by the wave breaking is calculated by a bore model with opposing currents. Energy balance equation is given as follows;

$$\frac{d}{dx} \left\{ \frac{1}{8} \rho g H^2 \left(\sqrt{gh} - U \right) \right\} + B \frac{\rho g}{4} \frac{1}{Th} \frac{\sqrt{gh}}{\left(\sqrt{gh} - U \right)} \left(\beta' H \right)^3 = 0 \qquad \text{------- (Eqn.4)}$$

in which the energy flux is calculated by a linear long wave theory and the dissipation of breaking is approximated with the dissipation of propagating bore.

The fraction of turbulence region to the wave height is assumed as follows; (Battjes,J.A. 1978)

$$\beta' = \frac{H}{\gamma h} \qquad \gamma = H_b/h_b \qquad \text{------- (Eqn.5)}$$

After substituting Eqn.5 into Eqn.4, an integration of Eqn.4 results in a following equation;

$$\tilde{H}^{-4} = \frac{1}{(1-A)^2}\left\{1 - \frac{4K}{9(1-A)}\right\}\cdot \frac{(\tilde{h}^{1.5}-A)^2}{\tilde{h}^2} + \frac{4K}{9\tilde{h}^2(\tilde{h}^{1.5}-A)} \qquad \text{------- (Eqn.6)}$$

where,

$$\tilde{H} = H/H_b \quad , \quad \tilde{h} = h/h_b \quad , \quad A = q/h_b \,/\, \sqrt{gh_b}$$

$$K = \frac{2B}{S}\left(\frac{H_b}{h_b}\right)\sqrt{h_b/gT^2} \qquad \text{------- (Eqn.7)}$$

3-4 Procedure of calculation

Wave height is calculated by the shoaling formulation. After a wave height exceeds the breaking criteria, the wave height decay calculation is carried out. These formulations for regular waves are applied to individual waves of the irregular wave. This procedure gives a wave height distribution at each water depth.

4. COMPARISON BETWEEN CALCULATED AND EXPERIMENTAL RESULTS

Figure 8(A) and 8(B) show comparisons between calculated results and experimental results for wave height distributions at a point offshore of the surf zone and in the surf zone, respectively. The horizontal axis indicates the ratio of individual wave height to the significant wave height, and the vertical axis indicates the probability density. In this case, waves have a relatively small deep water wave steepness. Calculations gives a good prediction for wave height distributions. And comparisons for a case where waves have a relatively large deep water wave steepness are shown in Fig.9(A) and 9(B). A good agreement is also obtained.

Figure 10 indicates some examples of comparisons between calculated significant wave height and experimental results with a relatively small deep water wave steepness. The experimental findings that the surf zone is moved offshore by opposing currents is explained well by the present model. In the case with relatively large water wave steepness, calculated results are compared with experimental results in Fig.11. Fig.10 and Fig.11 also confirm the applicability of the present model.

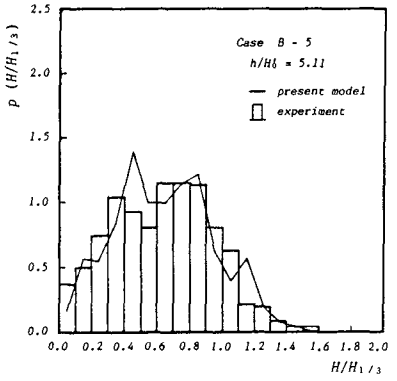

(A) offshore

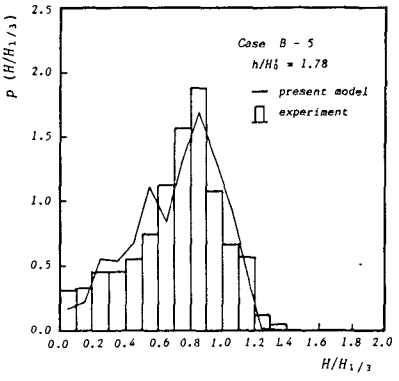

(B) in the surf zone

Fig.8 Comparisons between calculated wave height distribution and experiments (Ho'/Lo' = 0.0211)

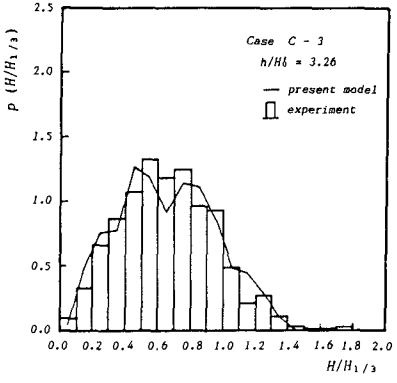

(A) offshore

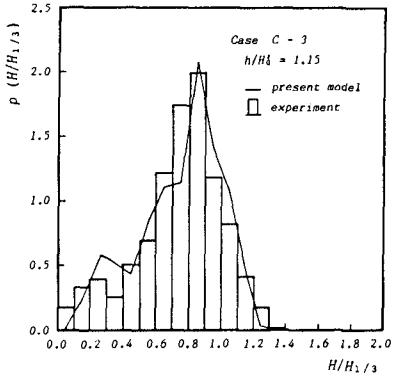

(B) in the surf zone

Fig.9 Comparisons between calculated wave height distribution and experiments (Ho'/Lo' = 0.0411)

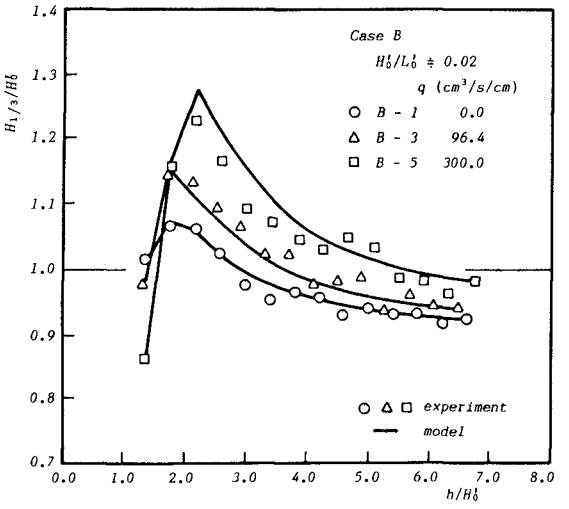

Fig.10 Comparisons between calculated shoaling coefficient and experiments

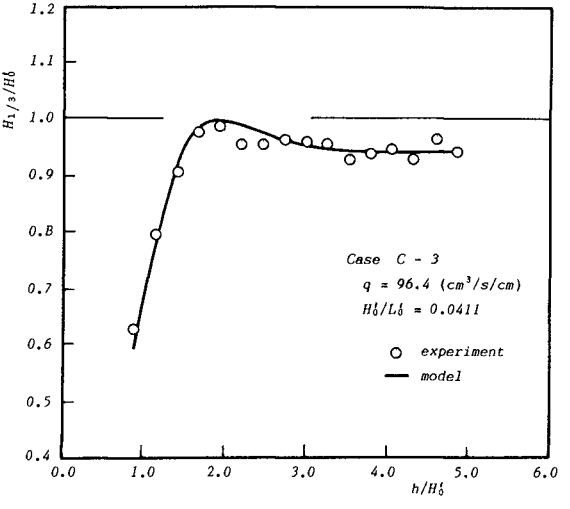

Fig.11 Comparisons between calculated shoaling coefficient and experiments

In order to examine the accuracy of the model for all data, the degree of coincidence between calculated results and experimental results is shown in Fig.12,13 and 14. The horizontal axis indicates calculated results and the vertical axis indicates experimental results, and a 45 degree solid line indicates a perfect coincidence. When the average error is defined by a following equation;

$$E_r = \frac{\sum_{n=1}^{m} \left| \frac{H\ model - H\ exp}{H\ model} \right|}{m} \qquad \text{-------- (Eqn.10)}$$

the average error as shown in Fig.12 is 2.8% of the significant wave height.

The root-mean-square of the wave height is shown in Fig.13, the average error is 2.3%. And even if the one-tenth maximum wave height is examined,the average error is only 3.7% as shown in Fig.14.

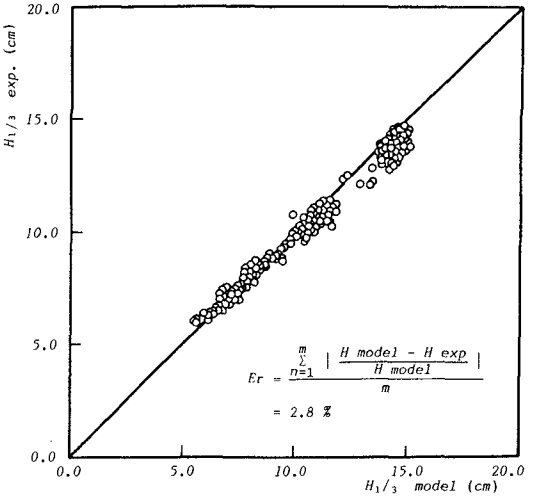

Fig.12 A correlation between calculated $H_{1/3}$ and experimental results

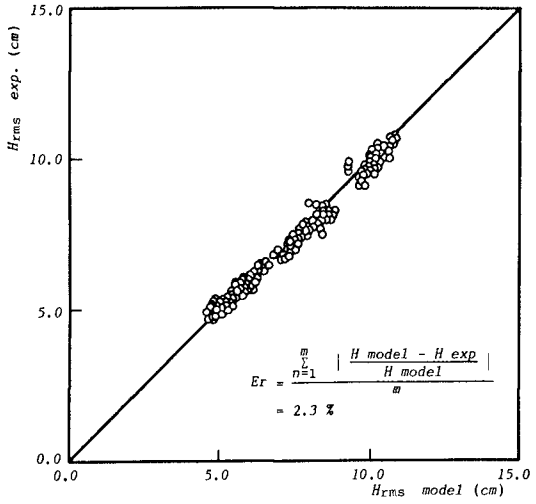

Fig.13 A correlation between calculated Hrms and experimental results

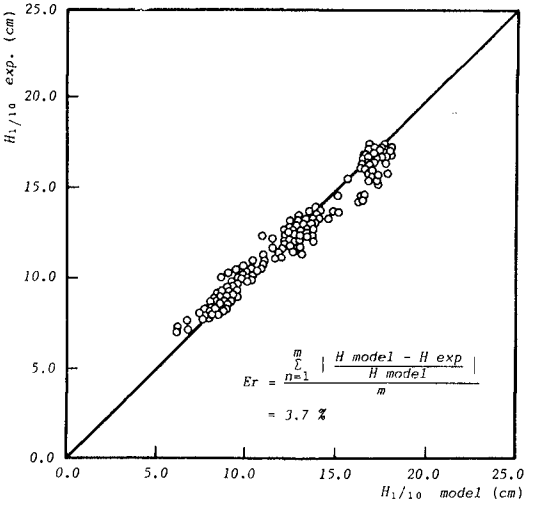

Fig.14 A correlation between calculated $H_{1/10}$ and experimental results

5. CONCLUSIONS

The transformation of irregular waves affected by opposing currents was discussed, experimentally and theoretically. Main conclusions in this paper are as follows:

(1) As opposing currents become dominant, the representative values of wave height, such as the significant wave height, are larger offshore of the surf zone and the wave decaying occurs more promptly after breaking. This tendency is identical to the characteristics of the regular wave affected by opposing currents qualitatively.

(2) The significant wave period also is affected by opposing currents. It was found that the increase of unit width discharge causes the larger increase rates of the significant wave period, and especially this tendency is clear in the surf zone.

(3) The transformation model in which the effects of opposing currents are considered was proposed. In the model, formulations for regular wave affected by opposing currents were applied to individual waves of irregular wave. The comparisons between calculated and experimental results give a satisfactory agreement.

REFERENCES

Battjes, J.A. and J.P.F.M. Janssen(1978)." Energy loss and set-up due to breaking of random waves." 16th I.C.C.E., pp. 569-587

Battjes, J.A.(1978). " Energy dissipation in breaking solitary and periodic waves." Manus. Delft Univ. of Tech.

Goda, Y.(1975). " Irregular wave deformation in the surf zone." Coast. Eng. Jpn., 18, pp. 13-26.

Hedge, T.S., K. Anastasiou and D. Gabriel(1985). " Interaction of random wave and currents." J. of Waterway, Port, Coastal, Ocean Eng., ASCE, vol.111,No.2. pp. 275-288.

Iwagaki, Y., H. Mase and K. Furumuro(1983). " Transformation characteristics of irregular waves including wave breaking (in Japanese)." Disaster Prevention Res. Inst. Annuals, No.26. pp. 559-574.

Miche, M.(1944). " Mouvements ondulatoires de la mer en profondeur constante ou décroissante." Ann. Ponts. et Chausees, 114, pp. 25-78

Sakai, S. and H. Saeki(1984). " Effects of opposing current on wave transformation on sloping sea bed." 19th I.C.C.E., pp. 1132-1148.

Thornton, E.B. and R.T. Guza(1983). " Transformation of wave height distribution." J. Geophys. Res., 88, pp. 5925-5938.

CHAPTER 54

VORTEX FORMATION IN PLUNGING BREAKER

T. Sakai[1], T. Mizutani[2], H. Tanaka[1] and Y. Tada[1]

ABSTRACT

By a flow visualization of a plunging breaker on 1/20 slope beach in a wave tank, an existence of 2nd and 3rd horizontal vortices(Miller, 1976) and slanting vortex(Nadaoka et al., 1986) is confirmed. A MAC method is applied to simulate a violent motion after an impinging of a jet from a crest of a plunging breaker on the trough surface. The calculated maximum water particle velocity in the jet is found to reach three times the linear long wave celerity. Values of circulation of the first four horizontal vortices are calculated and their changes in time are discussed.

INTRODUCTION

Recently the turbulence generated by wave breaking was measured in wave tanks by several researchers (for example, Stive(1980) and Sakai et al.(1982)). Several facts on the turbulence were clarified. The steady current, undertow, was also explained to some extent(Buhr Hansen and Svendsen, 1984). These are useful for our understanding of the so-called inner region of surf zone. In this region, the motion is rather mild.

In the outer region, however, the motion changes very rapidly. The vortex-like motions generated by wave breaking are not yet clarified so much. Especially, the plunging breaker generates large-scale vortex-like motions. This vortex-like motion is important for the sediment movement in the surf zone.

Miller(1976) suggested that several vortices were generated in the shoreward direction. Peregrine(1983) discussed three kinds of possibility for the penetration of plunging water into and the splash from the front trough surface. Nadaoka et al.(1986) pointed out that the vortex having a horizontal axis (horizontal vortex) was unstable and a vortex having a slanting axis (slanting vortex) was developed. Basco(1985) showed a schematical figure of a plunging breaker which contained one horizontal vortex.

In this paper, at first, an existence of the 2nd and 3rd horizontal vortices and the slanting vortex in surf zone suggested by Miller and

---

1) Dept. of Civil Eng., Kyoto Univ., Sakyo-Ku, 606 Kyoto, Japan
2) Res. and Develop. Center, Kawasaki Steel Corp., Naganuma-Cho 351, 281 Chiba, Japan

Nadaoka et al. respectively is examined by a flow visualization on a beach in a wave tank. Secondly, the detail of an impinging of a plunging water upon and a splash from a front face of wave is discussed by using a numerical simulation. The water particle velocity in and around the jet and the circulation of several horizontal vortices are also discussed.

FLOW VISUALIZATION OF HORIZONTAL AND SLANTING VORTICES

A wave tank, 27m long, 50cm wide and 70cm high, in Dept. of Civil Eng., Kyoto Univ., was used. A beach of 1/20 slope was installed in the wave tank.

The experimental conditions are listed in Table 1. i is the beach slope, T the wave period, h_b the still water depth at the breaking point, H_b the breaking wave height, W the width of the surf zone and H_0/L_0 the calculated deepwater wave steepness. The water depth in the uniform depth part was 35cm.

Table 1 Experimental conditions

i	T (sec)	h_b (cm)	H_b (cm)	W (cm)	H_0/L_0
1/20	1.82	15.5	13.5	310	0.021

Pictures of the water motion in the surf zone was taken through the glass side wall of the tank with a video camera and a 35mm still camera. Fig.1 shows the surf zone and the region in which the picture was taken. "b.p." means the breaking point, and "p.p." the plunging point.

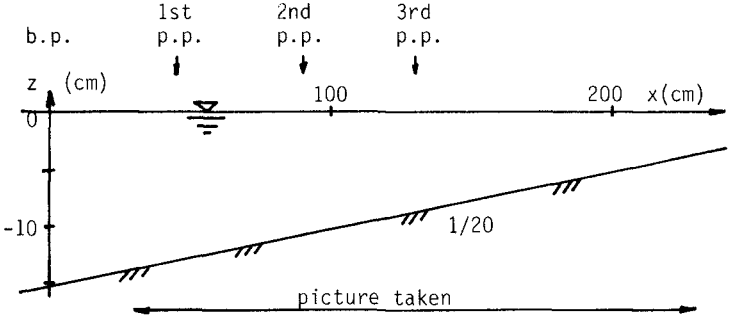

Fig.1 Surf zone and region in which picture was taken

The water motion recorded in a video film was observed carefully by using air bubbles as the tracer. Photo 1 shows a large overturning water mass from the crest. After this overturning mass hits the trough surface, a very violent splash occurs(Photo 2). A part of the overturning mass penetrates into the water body of the trough, and generates a large vortex-like motion having an horizontal axis(Photo 3).

Photo 4 shows a white region in which many air bubbles are contained in the surf zone. The black part is a part of a vertical steel element connecting two neighbouring glass plates of the tank. The upper picture was taken a little bit earlier than the lower one was. The wavy lower edge of this white region indicates an existence of the 2nd and 3rd horizontal vortex-like motions.

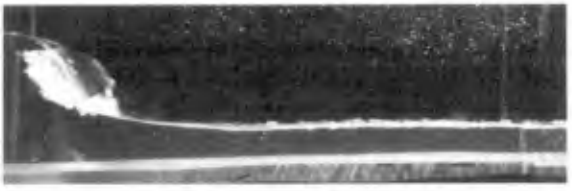

Photo 1 Large overturning mass from crest

Photo 2 Splash from trough surface

Photo 3 Large horizontal vortex

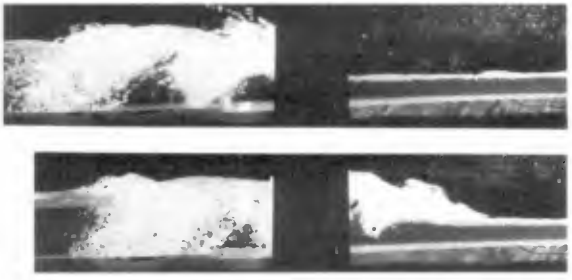

Photo.4 2nd and 3rd horizontal vortices

Photo. 5 shows a picture of a plunging breaker taken from its back. Two or three tails of the white region are seen in the transverse direction of the tank. This indicates an existence of the slanting vortex.

Photo.5 Slanting vortex

MAC METHOD

Physical experimental methods have their limitation for investigating the detail of structure in the outer region, due to the very rapid motion of wave breaking and the entrainment of a lot of air bubbles. An alternative method is numerical experiment.

For the overturning of water mass from wave crest, already many numerical computations have been done. One example is New et al.'s computation(1985)(Fig.2). They calculate a deformation of a overturning water mass, the water particle velocity and acceleration in this water mass, until the tip of overturning mass touches the trough water surface. But after the overturning mass touches the trough water surface, such a calculation fails to simulate the motion. This is because the calculation is based on a potential flow assumption.

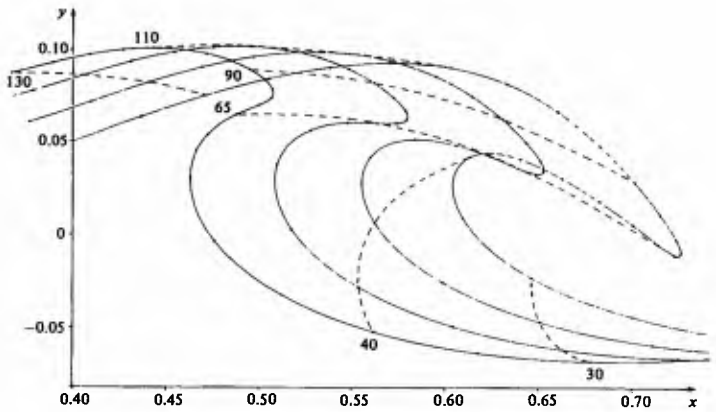

Fig.2 Numerical simulation of overturning mass from crest (New et al., 1985)

Here we used the so-called marker and cell method, "MAC method", to simulate a motion after an overturning mass touches the trough surface. In this method, the full Navier-Stokes equations are calculated. Therefore, the strong shear flow generated by the overturning jet can be calculated. Due to computational limitation, the calculation was done in two dimensional space, a vertical plane. So, the vortex having a slanting axis can not be calculated, because this vortex is generated due to a three-dimensionality of flow. Still, this calculation is expected to simulate the strong shear between the overturning jet and the trough water, the splash and the horizontal vortices.

The used MAC method is the so-called SMAC method(Takemoto et al., 1981). The surface conditions in the numerical model are rather of original type. As the initial conditions, a numerical result computed by Takigawa and Iwagaki(1983) with a finite element method(their figure No.7,(b)) was used(Fig.3). They calculated a propagation on a beach of 1/20 slope of a wave generated by a wave board in a wave tank. The calculation was stopped before the front face of wave becomed steep and the calculation becomed unstable. The conditions of Takigawa et al.'s computation are listed in Table 2. So the breaker type is plunging.

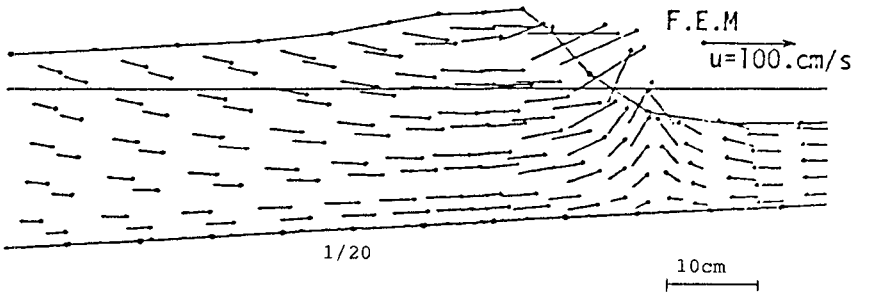

Fig.3 Initial wave profile and water particle velocity of numerical simulation (Takigawa et al., 1983)

Table 2 Conditions of Takigawa et al.'s computation(1983)

i	T (sec)	h_b (cm)	H_b (cm)	H_o/L_o
1/20	2.5	13.5	11.0	0.008

The cell is a rectangle of 1.0cm(Δx) x 0.5cm(Δy)(Fig.4). The time step Δt of the calculation is 0.0025sec. To take into account the existence of beach, the x-axis is taken parallel to the beach face. So the y-axis is not vertical, and the gravity has a x component. The computation region is 92 times 1cm long in x direction and 50 times 0.5cm high in y direction.

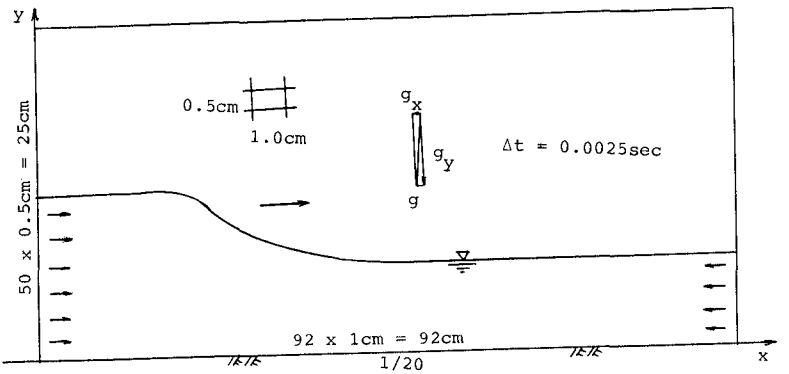

Fig.4 Region and conditions of numerical simulation

RESULTS OF NUMERICAL SIMULATION

Fig.5 shows a result of numerical simulation. The upper figure shows a vector arrow of the water particle velocity and the lower figure shows the location of the markers.

The figure (1) shows the initial condition. The crest height from the bottom is about 22cm. The linear long wave propagation velocity $\sqrt{gh}$ is about 110cm/sec. The maximum velocity in x direction is also about 110cm/sec and equal to the linear propagation velocity.

From the left and right boundaries, uniform currents in x direction flow into the region. This is not the real situation, but it is thought that the difference between the uniform current and the real flow situation does not influence the flow pattern near the plunging point during one run of computation (about 60 time steps).

The figure (2) shows the calculated result of about 0.3sec later. The computation region is shifted 30cm to the right. The uniform inflow current velocity was changed according to the result of calculated velocity at the final time step of the first run. The lower figure shows an existence of the overturning water jet from the crest. The air tube between the overturning jet and the front water surface looks smaller than the real one and the computed result based on potential flow assumption(Fig.2). This can be improved by decreasing the size of cell. Fig.6 is a result in the case of Δx = 0.5cm. The shape of the overturning jet becomes more realistic.

The figure (3) shows the result of 0.4sec later. The jet touches the trough surface, and rebounds. The upper figure shows that the velocity of rebounding and splashing water is very high.

The figure (4) shows the result of about 0.53sec later. The second touching and the second rebound or splash occur. The velocity direction is opposite between the upper jet and the lower trough water. Between these two water bodies, a strong shear exists. Two horizontal vortices

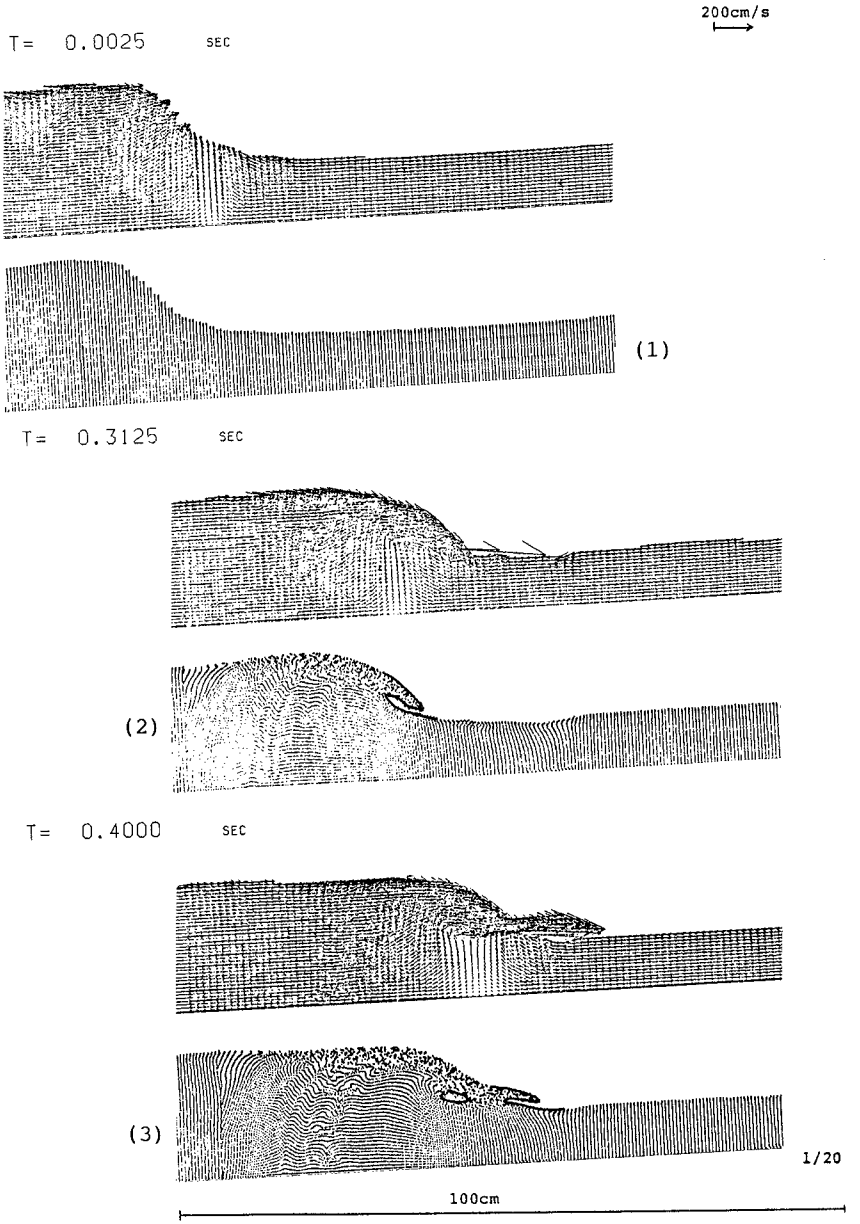

Fig.5,(1)-(3) Result of numerical simulation

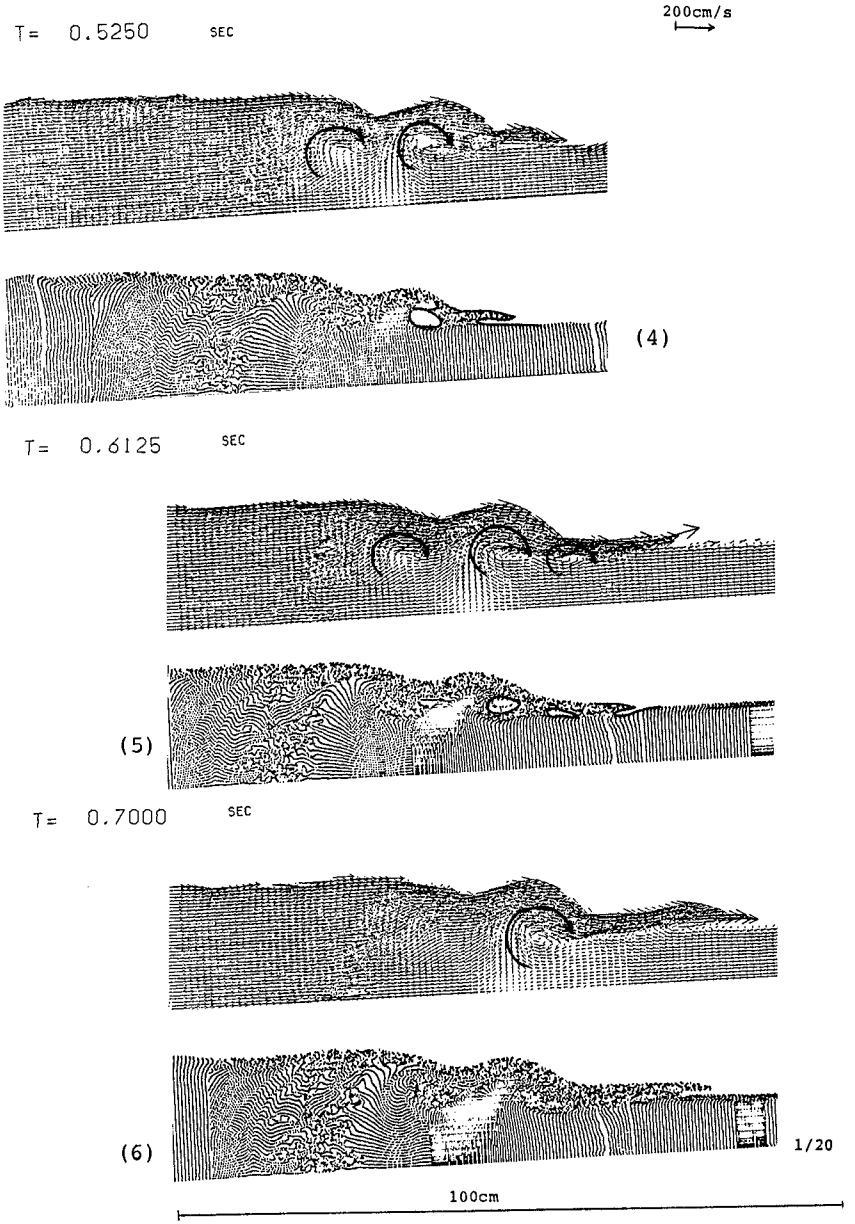

Fig.5,(4)-(6) Result of numerical simulation

are found. They have a horizontal axis rotating clockwise.

The figure (5) shows the result of about 0.61sec later. The computation region is shifted again 25cm to the right. The uniform inflow current velocity was changed again. The third touching and the third splash occur. Totally three horizontal vortices are found.

The figure (6) shows the result of 0.7sec later. Still one large horizontal vortex exists.

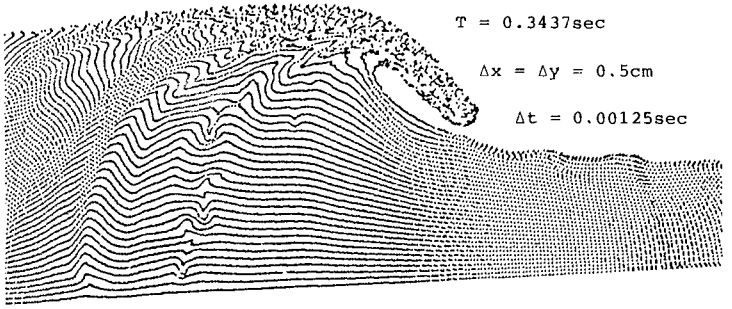

Fig.6 Improvement of shape of overturning jet by decreasing cell size

Photo 3 shows a splash on a 1/20 slope beach in a wave tank, taken from the side of the tank. The wave period is 1.8sec, and the deep-water wave steepness is 0.021(Table 1). So we can not compare this photograph with the calculated results directly. But the splash height in the wave tank is higher than that of the calculated result.

One reason is that the cell size is too large to take into account the existence of small water drop. Also as seen in Photo 3, under the crest, a lot of air bubbles are entrained into the water. The air entrained region reaches near the bottom. This air bubble entrainment is also not reproduced by the numerical calculation.

So, this numerical computation does not simulate the real motion. But, for our understanding of the very rapid motion after wave breaking on beach, these numerical results are useful. In particular, the numerical computation can calculate the instantaneous high speed velocity of water particle. Also the instantaneous value of circulation of the horizontal vortex can be calculated.

DISCUSSIONS

(1) water particle velocity

The maximum water particle velocity in the x direction at the

initial condition(Fig.5,(1)) is about 110cm/sec and occours at the steep front face of the wave. The linear long wave propagation velocity $\sqrt{gh}$ is also about 110cm/sec.

At about 0.15sec later(the result not shown here), it increases to 140cm/sec, and its position is still located at the steep front face. Mizuguchi et al.(1986) measured a velocity field of breaking waves on a beach of 1/20 slope in a wave tank with a laser-doppler velocimeter. A maximum velocity before plunging normallzed by $\sqrt{gh}$ red from their figure is about one. This is comparable with our numerical result.

At 0.29sec later(not shown here), the tip of jet has not yet touches the trough surface. The maximum velocity is about 200cm/sec, and located at the lower surface of the jet. New et al.(1985) said in their paper that the horizontal velocity in the jet are between 1.5 and 2 times the phase speed of the linear wave. In this case, the linear long waves propagation velocity is about 110cm/sec. So our computation result agrees with their result.

Fig.7 shows a contour of water particle velocity in the x direction in and around the jet at 0.33sec later. This instance is just after the first jet touching on the trough surface. Notice that the x direction does not coincide with the horizontal direction. At the tip of the jet, a maximum velocity of more than 300cm/sec occours. It is not easy to find the maximum velocity after plunging from Mizuguchi et al.(1986)'s figure. But the normalized value seems to be still one.

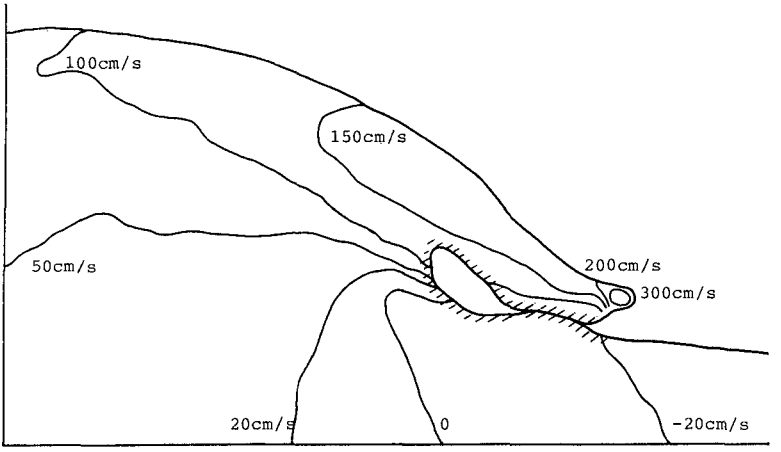

Fig.7 Contour of x component of water particle velocity in and around jet at 0.33sec later(just after 1st jet touching on trough surface)

Jansen(1986) also measured a velocity field in the jet by using fluorescent particles as tracer in a wave tank. From their figure 11, it is found again that the normalized maximum velocity is about one. In our result, the value of $\sqrt{gh}$ is 110cm/sec, and the maximum velocity is more than 300cm/sec. So the normalized value is about 3. It is thought that

the experimentally measured values are underestimated.

Fig.8 shows a similar contour at about 0.47sec later. At this instance the second jet touching on trough surface already finished. The x component of water particle velocity in the jet is still large(about 200cm/sec) in its upper region. But it is small compared with that at the tip at 0.32sec later(Fig.7). It is found that the water particle velocity in the jet decreases gradually in the jet touching and splash process.

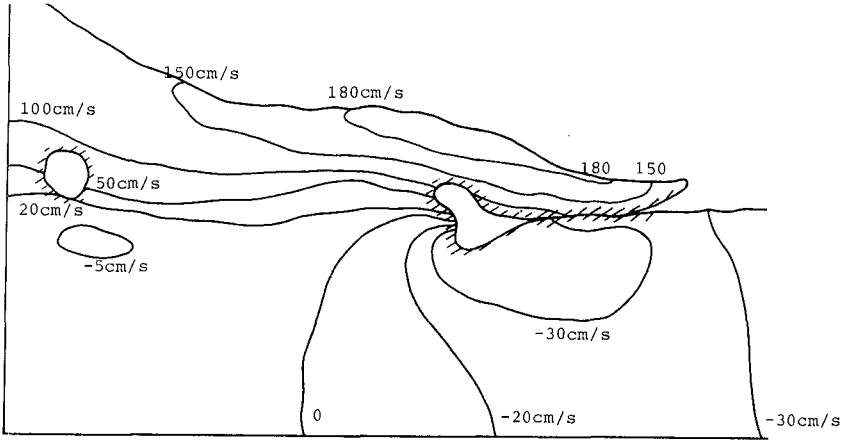

Fig.8 Contour of x component of water particle velocity in and around jet at 0.47sec later(after 2nd jet touching on trough surface)

(2) circulation of horizontal vortices

As seen in Fig.5, several large horizontal vortices are generated between the jet and the lower trough water. Values of circulation of these vortices are calculated. The closed path for the circulation calculation is determined rather arbitrarily.

Fig.9 shows the result. The instance when the vortex is generated is difficult to determine exactly from the figure of marker location. Arrows indicate a possibility that the vortex may be generated earlier. From the figure, it is found that the value of circulation reaches near $2000cm^2/sec$. The circulation of the first vortex decreases gradually, while that of the second vortex grows at first and then decreases. The third and fourth vortices are not so large compared with first two vortices.

Value of circulation of a horizontal vortex was calculated also by Shibayama et al.(1982) using experimental data. The wave period was 1.24sec, deepwater wave height 3.8cm, deepwater wave steepness 0.016, and the initial slope of a movable bed 1/20. They calculated the circulation from a velocity field which was determined from movement of polystyrene particles. From their figure 5, it is found that the

value of circulation is at most 120cm^2/sec. The conditions of their experiment are different from those of our numerical simulation. So a direct comparison is impossible.

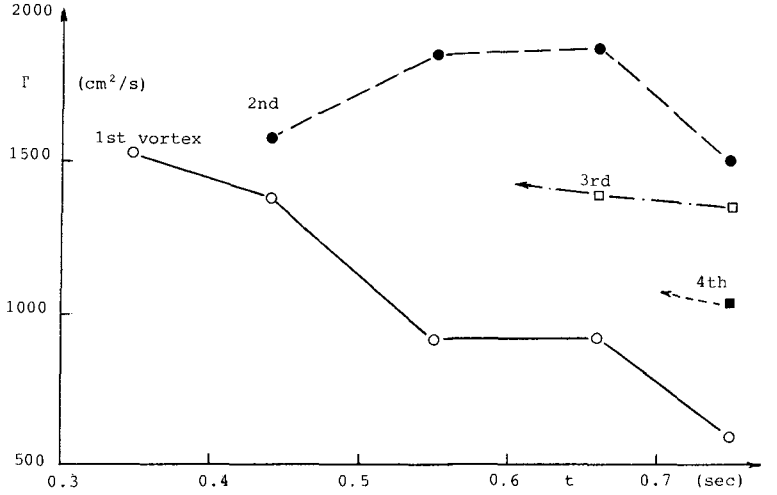

Fig.9 Circulation of four horizontal vortices

CONCLUSIONS

(1) By a flow visualization of a plunging breaker on a 1/20 slope beach in a wave tank, an existence of the 2nd and 3rd vortices suggested by Miller(1976) and the slanting vortex suggested by Nadaoka et al.(1986) is confirmed.
(2) A MAC method is applied to simulate a violent motion after an impinging of a jet from a crest of a plunging breaker on the trough surface. Although the numerical simulation can not reproduce the high splash, the deep air bubble penetration into the trough water and the slanting vortex, it can reproduce the high speed jet on the trough surface and the several horizontal vortices.
(3) The calculated maximum water particle velocity in the jet reaches three times the linear long wave celerity just after the impinging of the jet on the trough surface.
(4) The calculated circulation of the first horizontal vortex decreases gradually. The calculated circulation of the second one is larger than that of 1st one. It increases at first and then decreases. The values of circulation of the third and fourth horizontal vortices are smaller than those of the first and second ones, and become smaller in this order.

ACKNOWLEDGMENT

Part of this study was supported by the Grant-in-Aid for Scientific Research (C)'85-'86 (representative : T. Sakai, Kyoto Univ.)

and the Grant-in-Aid for Research in Disasters '85-'86(representative : Prof. N. Shuto, Tohoku Univ.) of the Ministry of Education, Science and Culture of Japan.

REFERENCES

Basco, D.R., "A qualitative description of wave breaking", *Jour. of Waterway, Port, Coastal and Ocean Eng.*, ASCE, 111(2), 1985, pp.171-188.

Buhr Hansen, J. and SVENDSEN, I.A., "A theoretical and experimental study of undertow", *Proc. of 19th Conf. on Coastal Eng.*, ASCE, 1984, pp.2246-2262.

Jansen, P.C.M., "Laboratory observations of the kinematics in the aerated region of breaking waves", *Jour. of Coastal Eng.*, 9, 1986, pp.453-477.

Miller, R., "Role of vortices in surf zone prediction : sedimentation and wave forces", *Soc. Econ. Paleontol. Mineralog.*, Spec. Publ., 24, 1976, pp.92-114.

Mizuguchi, S. et al., "Experimental study on kinematics and dynamics of wave breaking", *Proc. of 20th Conf. on Coastal Eng.*, 1986(in printing).

Nadaoka, K., et al., "Turbulent flow field structure of breaking waves in the surf zone", *Proc. of 20th Conf. on Coastal Eng.*, ASCE, 1986(in printing).

New, A.L. et al., "Computations of overturning waves", *Jour. of Fluid Mech.*, 150, 1985, pp.233-251.

Peregrine, D.H., "Breaking waves on beaches", *Ann. Rev. Fluid Mech.*, 15, 1983, pp.149-178.

Sakai, T. et al., "Turbulence generated by wave breaking on beach", *Proc. of 18th Conf. on Coastal Eng.*, ASCE, 1982, pp.3-21.

Shibayama, T. and Horikawa K., "Sediment suspension due to breaking waves", *Coastal Eng. in Japan*, JSCE, 25, 1982, pp.163-176.

Stive, M.J.F., "Velocity and pressure field in spilling breakers", *Proc. of 17th Conf. on Coastal Eng.*, ASCE, 1980, pp.547-566.

Takemoto, Y. et al., "Program of numerical solution of incompressible viscous fluid with MAC method", *Bull. of Data Processing Center*, Kyoto Univ., 14(4), 1981, pp.210-225.

Takigawa, K., et al., "Analysis of breaking transformation and inner mechanism of waves on beach using finite element method", *Proc. of 30th Japanese Conf. on Coastal Eng.* JSCE, 1983, pp.20-24 (in Japanese).

CHAPTER 55

Biperiodic Waves in Shallow Water

Norman W. Scheffner*, Member ASCE

Introduction

The propagation of waves in shallow water is a phenomenon of significant practical importance. The ability to realistically predict the complex wave characteristics occurring in shallow water regions has always been an engineering goal which would make the development of solutions to practical engineering problems a reality. The difficulty in making such predictions stems from the fact that the equations governing the complex three-dimensional flow regime can not be solved without linearizing the problem. The linear equations are solvable; however, their solutions do not reflect the nonlinear features of naturally occurring waves. A recent advance (1984) in nonlinear mathematics has resulted in an explicit solution to a nonlinear equation relevant to water waves in shallow water. This solution possesses features found in observed nonlinear three-dimensional wave fields.

The nonlinear mathematical formulation referred to above has never been compared with actual waves, so that its practical value is unknown. The purpose of the present investigation was to physically generate three-dimensional nonlinear waves and compare these with exact mathematical solutions. The goals were successfully completed by first generating the necessary wave patterns with the new U.S. Army Engineer Waterways Experiment Station, Coastal Engineering Research Center's (CERC) directional spectral wave generation facility. The theoretical solutions were then formed through the determination of a unique correspondence between the free parameters of the solution and the physical characteristics of the generated wave.

*Research Hydraulic Engineer, U.S. Army Engineer Waterways Experiment Station, Coastal Engineering Research Center, Vicksburg, Mississippi, USA

Theoretical Background

One of the first mathematical models of nonlinear waves in shallow water with known solutions was presented by Korteweg and deVries in their famous 1895 paper. Their model, known as the KdV equation can be written in the following nondimensional form

$$f_t + 6ff_x + f_{xxx} = 0 \tag{1}$$

in which f represents the water surface displacement, x is the direction of wave propagation and t is time. This equation admits not only solitary wave solutions but also the periodic solutions commonly known as cnoidal waves. These solutions can be written as

$$f(x,t) = 2\sigma^2 k^2 cn^2(\theta;k) - 2\sigma^2\left[\frac{E(k)}{K(k)} - 1 + k^2\right] \tag{2}$$

where each of the terms in the solution are well documented analytic functions which can easily be computed in terms of known wave characteristics such as wave height and wavelength. Unfortunately, cnoidal wave solutions are valid only for long crested waves, e.g., waves which can be described by a single time-dependent one-dimensional surface wave pattern. Natural waves, in contrast, are composed of both long and short crested waves and cannot be adequately described by this theory.

A recent advance in nonlinear mathematics has been reported by Segur and Finkel (1984). They present explicit analytical solutions to a natural three-dimensional extension of the KdV equation proposed by Kadomtsev and Petviashvili (1970), known as the KP equation shown below

$$(f_x + 6ff_x + f_{xxx})_x + 3f_{yy} = 0 \tag{3}$$

where x now represents the primary direction of propagation; however, weak changes in the y-direction are now permitted. When no y-variations occur, the KP equation reverts to the KdV equation.

The KP equation admits an infinitely dimensional family of exact, periodic, solutions (see Dubrovin 1981 and Segur and Finkel 1984) which can be written in the form

$$f(x,y,t) = 2\frac{\partial^2 \ln\theta}{\partial x^2} \tag{4}$$

where θ is a Riemann theta function of genus n. Genus 1 solutions are exactly equivalent to cnoidal waves, they are permanent form, singly periodic, two-dimensional (one vertical and one horizontal) nonlinear waves. Genus 2 waves are biperiodic in that they permit the independent specification of two periodicies in both time and space. The solutions are genuinely three-dimensional, nonlinear, and propagate with permanent form at a constant velocity. Genus 3 and higher order solutions are multi-periodic and cannot be characterized as permanent form with respect to any translating coordinate system as the genus 1 and 2 solutions can. This present investigation is limited to the genus 2 solutions developed by Segur and Finkel.

The construction of a genus 2 solution of the KP equation is based on the specification of the appropriate Riemann theta function. This requires the introduction of a two-component phase variable and a 2 X 2 real-valued Riemann matrix. The first of these, the phase variable, is shown below.

$$\phi_1 = \mu_1 x + \nu_1 y + \omega_1 t + \phi_{10}$$

and (5)

$$\phi_2 = \mu_2 x + \nu_2 y + \omega_2 t + \phi_{20}$$

Where the parameters μ_1, μ_2, ν_1, and ν_2 are wave numbers, ω_1, and ω_2 are angular frequencies, and ϕ_{10} and ϕ_{20} are constants with no dynamical significance. The second ingredient involves the specification of a real-valued, negative definite, symmetric 2 X 2 Riemann matrix as shown below.

$$B = \begin{pmatrix} b & b\lambda \\ b\lambda & b\lambda^2 + d \end{pmatrix} \tag{6}$$

The parameters b, d, and λ represent solution nonlinearity. The genus 2 theta function can now be defined in terms of the above components by the following double Fourier series:

$$\theta(\phi_1,\phi_2,B) = \sum_{m_1=-\infty}^{\infty} \sum_{m_2=-\infty}^{\infty} \exp\left(\frac{1}{2}\, m\cdot B\cdot m + im\cdot\phi\right) \tag{7}$$

The calculation of a general case genus 2 KP solution requires the specification of the 11 parameters shown in Equations 5 and 6. Two of these parameters (ϕ_{10} and ϕ_{20}) have no dynamical significance, their only effect is to shift the origin of the resulting solution. Dubrovin (1981) proved that a genus 2 theta function in

the form of Equation 7 was a solution to the KP equation if, and only if, the solution parameters were related by four additional equations. One of these equations contains a constant of integration. Use of this additional criteria reduces the number of free parameters to 8, representing the minimum number of free parameters required to specify a general case genus 2 solution.

Genus 2 solutions of the KP equation describe a complex two-dimensional surface wave pattern. Similar features were observed by Hammack (1980) to result from the nonlinear interaction of two intersecting waves. The theoretical development by Segur and Finkel was partially prompted, in fact, by these reported waves. The development of an experimental program which would result in the generation of surface wave patterns qualitatively similar to genus 2 solutions was achieved by attempting to experimentally reproduce the conditions reported by Hammack, i.e. intersecting waves. This generation technique can best be described by presenting the analogy of interacting waves. Consider, for example, two periodic waves which intersect and pass through each other as shown in Figure 1. The angles α_1 and α_2 represent the angle of the crest of each wave front with respect to some reference line. The resulting surface wave pattern, according to linear wave theory, would simply be a superposition of the two individual waves. This would produce a diamond shaped surface pattern as indicated in Figure 1. It can be seen that certain of the basic characteristics of the individual waves, wavelength and angle of propagation for example, have been preserved.

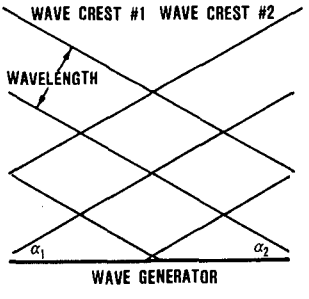

Figure 1. The Linear Intersection of Waves

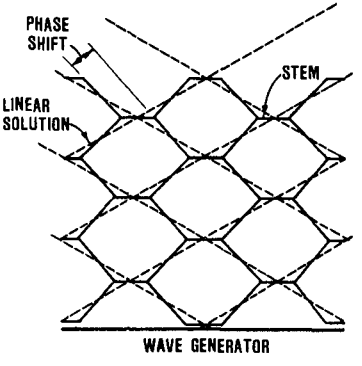

Figure 2. The Nonlinear Intersection of Waves

Now, consider the analagous case in which similarly intersecting waves interact nonlinearily with each other. This scenario is shown schematically in Figure 2. The resulting wave pattern shows that a "stem of interaction" is formed at the point where the two waves

cross each other. The formation of this stem region is a result of a phase shift in the crest line angles of the original waves. This phenomenon is shown in Figure 2 superimposed on the corresponding linear wave solution. The resulting surface wave pattern now assumes a hexagonal pattern in which a third wave crest, separate of the original two, is formed. This phase shift and stem formation are indicative of the nonlinear interaction of the two waves since the exact linear solution does not predict either the phase shift or the new wave crest. Genus 2 solutions of the KP equation predict these features and was tested as a possible model for their description.

Laboratory Facilities and Experimental Procedures

A project was initiated at CERC to generate three-dimensional nonlinear wave fields in the laboratory and then to apply KP theory to the resulting waves in order to determine whether or not the KP equation was a model for these waves and, if so, what was the range of its applicability. This required the use of the CERC directional spectral wave generation facility. This unique wave generator, shown in Figure 3, was designed and constructed for CERC by MTS Systems Corporation of Minneapolis, Minnesota, based on design specifications provided by CERC. The generator is comprised of 60 individually programmable electromechanical wave paddles. Each wave paddle is 1.5 ft wide making the generator a total of 90.0 ft in width. The generator is located in a 98.0 by 184.0-ft wave basin with 2.5 ft high side walls. Computer control of the system is provided by a Digital Equipment Corporation (DEC) VAX 11/750 central processing unit. The above facilities were utilized to generate genus 2 candidate waves in a comprehensive experimental program.

Figure 3. The Directional Spectral Wave Generator

The wave generator was programmed to simultaneously generate intersecting cnoidal wave trains. A variety of wave fields were generated by varying both the wavelength of the individual waves and their angle of intersection. Twelve wave fields, generated in this manner, were used to test the KP equation. The wave fields selected for the experimental program are presented in Table 1. Waves characterized by three wavelengths (7, 11, and 15 ft) were combined with phase shifts between adjacent wavemaker paddles. These phase shifts were approximately equivalent to the angle of the wavecrest with respect to the axis of the wave generator. The angle in the tahle shows the approximate correspondence between the phase lag and the angle of propagation.

Table 1
The Experimental Waves

Test Number	Wavelength (ft)	Phase Shift (deg)	Angle (deg)	Period (sec)
CN1007	7.0	10.0	7.45	1.378
CN1507	7.0	15.0	11.21	1.378
CN2007	7.0	20.0	15.03	1.378
CN3007	7.0	30.0	22.89	1.378
CN4007	7.0	40.0	31.23	1.378
CN1011	11.0	10.0	11.75	1.947
CN1511	11.0	15.0	17.79	1.947
CN2011	11.0	20.0	24.04	1.947
CN3011	11.0	30.0	37.67	1.947
CN1015	15.0	10.0	16.12	2.553
CN1515	15.0	15.0	24.62	2.553
CN2015	15.0	20.0	33.75	2.553

Genus 2 solutions can be visualized as a series of repeating two-dimensional permanent form surface patterns, referred to as period parallelograms. These patterns translate at a constant velocity in a constant direction. The global wave field is represented by a tiling of these basic patterns; therefore, the entire wave pattern can be exactly specified by quantifying just one period parallelogram. The location of a basic period parallelogram within the hexagonal wave field of Figure 2 is shown in Figure 4. The phase variables of Equation 5 define the horizontal limits of these patterns such that each side is uniquely defined by ϕ_1 = constant and ϕ_2 = constant. The components of the Riemann matrix define the vertical and horizontal distribution within the period parallelogram.

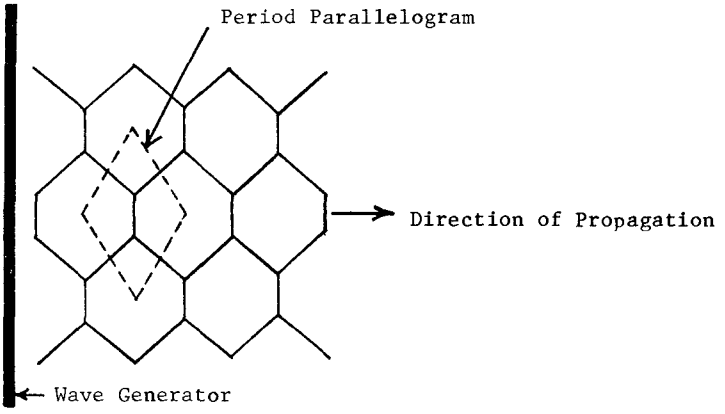

Figure 4. The Period Parallelogram

Detailed measurements of each of the generated wave fields shown in Table 1 were required in order to relate the physical characteristics of the waves to the parameters of the corresponding period parallelogram of the exact solution. This quantification was accomplished by first using overhead photography to determine the dimensions of the period parallelogram and to provide an estimate of the internal features, such as the phase shift and stem length. Knowledge of these horizontal features and their location within the wave tank were then used to locate a linear array of 9 recording wave gages in the wave basin. This approach provided a vertical wave record which could be identified with a known location within the parallelogram.

Comparing Theoretical Solutions To Observed Waves

The experimental program described above generates symmetric cnoidal waves ($\alpha_1 = \alpha_2$ in Figure 1) resulting in a symmetric period parallelogram. This simplification was adopted so that the generated wave patterns would propagate perpendicularly off the face of the wave generator, making it possible to measure all wave forms with a single stationary wave gage array. Symmetry also reduces the number of free parameters which need to be specified, for example, $\mu_1 = \mu_2$, $\nu_1 = -\nu_2$, and $\omega_1 = \omega_2$ from Equation 5. This simplification results in the requirement of only three dynamical parameters and two nondynamical parameters. The parameters chosen were b , μ , and λ along with the phase shift parameters ϕ_{10} and ϕ_{20}. The following sequence of events was used for optimizing these coefficients. Experiment CN3007 will be used to demonstrate the verification process.

Each of the waves of Table 1 were generated in the wave basin. Two overlapping photographs were taken with duel Hasselblad model 500EL/M 70mm cameras equipped with 50mm lenses mounted 23 ft above the floor of the basin. The resulting mosaic photograph, shown in Figure 5, was used to estimate the length and width of the period parallelogram. This resulted in estimates for $\mu_1 = \mu_2$ and $\nu_1 = -\nu_2$. An estimate for the phase shift parameter λ was also determined from the photograph. The accuracy of μ, ν, and λ is a function of the distortions in the photograph. Because of this distortion, their values were considered to be initial estimates. Following the photographing of all waves, a wave gage spacing of 2.5 ft apart and 40.0 ft from and parallel to the generator was selected for use in all tests. The location of each of the gages with respect to wave CN3007 is shown in Figure 5. It can be seen that each gage can be uniquely referenced according to a distance from the center of the parallelogram. Since all parallelograms are identical, wave gages located in an adjacent parallelogram can be referenced to the common center point.

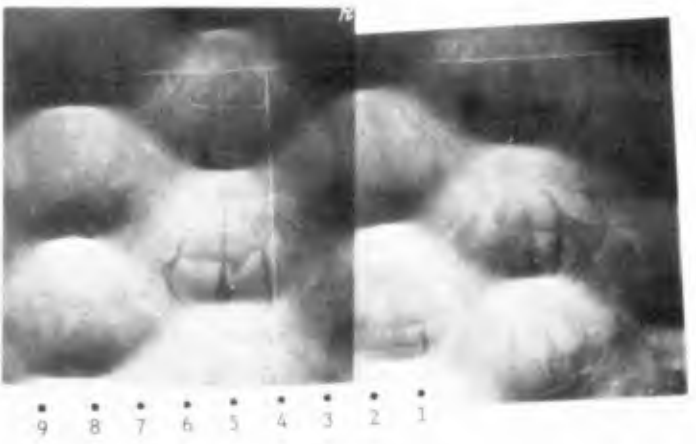

Figure 5. Overhead Mosaic Photograph of Test Wave CN3007

Wave gages were located in the basin and each of the waves of Table 1 were regenerated. Data was sampled for each of the gages at a rate of 50 samples per second for a total of 30.0 seconds. Figure 6 shows the wave traces for one period of wave CN3007. The correspondence between the wave traces and their location within the parallelogram can easily be seen. For example, gage 5 is located on a stem where only one peak per passing of the parallelogram is experienced. Gage 3 is located in the saddle region where two smaller peaks per period are seen. This comparison demonstrates the usefulness of the photographs in interpreting the data since three-dimensional effects are difficult to deduce from two-dimensional data.

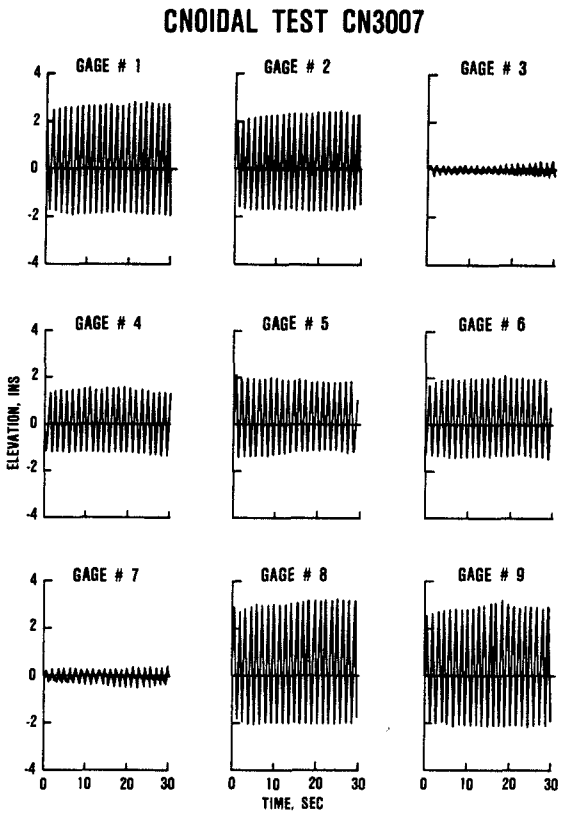

Figure 6. Wave Gage Traces for Test Wave CN3007

The determination of the free coefficients can now be made. Known or estimated data are the period of the wave (determined from the recording wave gages), the length and width of the period parallelogram and an estimate of the phase shift parameter λ determined from the photographs, and a maximum wave height selected from the wave gage data. The following iteration procedure was used to optimize the coefficients:

a. The estimated values for $\mu_1 = \mu_2$ and λ were specified. The nondynamical parameters ϕ_{10} and ϕ_{20} were accounted for by specifying solutions to be computed at location within the period parallelogram corresponding to the location of the wave gages. A value of b was then selected such that the dimensionalized maximum KP solution was within 5.0 percent of the measured value.

b. The value of $\mu_1 = \mu_2$ was adjusted, if necessary, until the dimensionalized period was within 3.0 percent of the measured period.

c. The value of λ was adjusted, if necessary, until the dimensionalized value of $\nu_1 = -\nu_2$ was within 10.0 percent of the estimated value. A 10-percent criteria was used for this iteration since the length of the parallelogram was difficult to determined from the photographs.

d. Because of the nonlinear coupling of the solution coefficients, each adjustment affected all parameters to some extent. If corrections were found to be necessary, steps (a.) through (c.) were repeated until all of the specified tolerances were

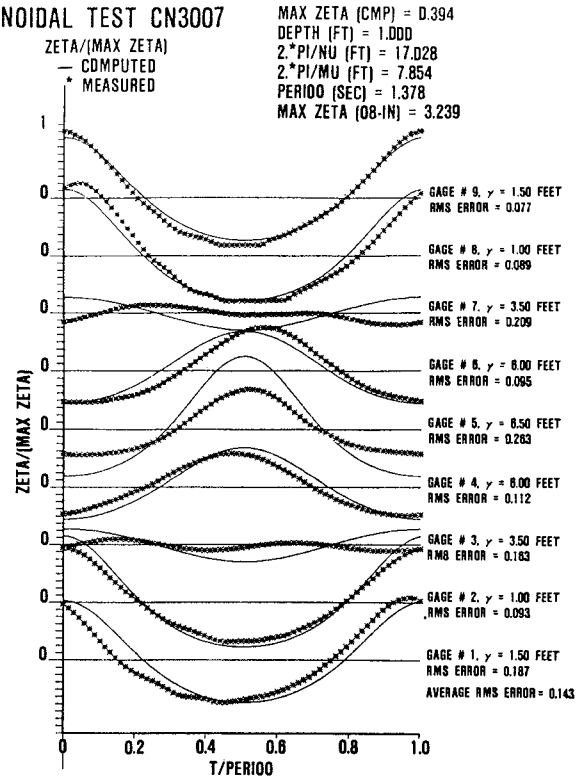

Figure 7. Theoretical and Measured Wave Profiles for Test Wave CN3007

met or exceeded. Possible phasing problems regarding the gage locations within the parallelogram were rectified by adjusting the nondynamical phase parameters.

e. A KP solution corresponding to the location of each of the wave gages was calculated. A normalized plot comparing theory to measurements was made, as shown in Figure 7 for the present example. Included in each plot is the Root Mean Square (RMS) error for each comparison.

f. A normalized contour plot (Figure 8) and a three-dimensional plot (Figure 9) for each wave field was finally prepared as a visual example of the KP solution.

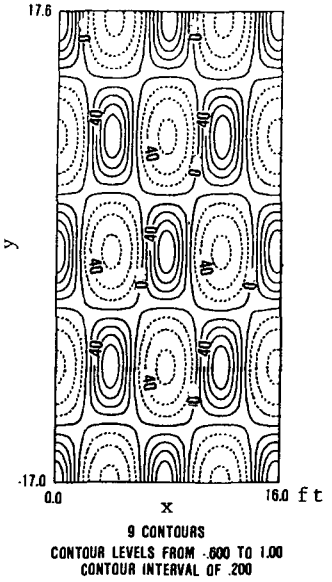

Figure 8. Normalized Contour Plot for Test Wave CN3007

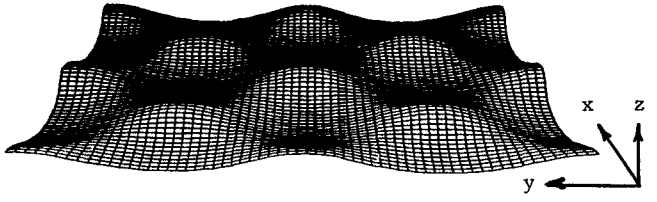

Figure 9. Three-Dimensional Plot of Test Wave CN3007

The above procedures were followed for each of the test wave fields of Table 1. A minimum tolerance of 5.0 percent for waveheight, 3.0 percent for period, and 10.0 percent for the Y-direction wavelength was maintained for all experiments. Table 2 presents those computed results. For each case, an average RMS error is provided which represents a simple average of the 9 RMS values computed for each gage. In no case did this error exceed 20 percent even though variations in the elevation of the basin floor of 10 percent were known to exist. Additionally, the experimental wave fields were generated almost to the point of breaking in order to span the range of solution parameters and investigate the limits of applicability of the genus 2 solutions. In view of these introduced and existing sources of potential error, the degree of fit between the generated wave fields and the exact solutions were found to be very good.

Table 2
Computed wave parameters

Test Number	Max. Height (in)	X-Wavelength (ft)	Y-Wavelength (ft)	Ave. RMS Error
CN1007	2.44	7.0	46.5	0.141
CN1507	3.59	7.2	35.1	0.188
CN2007	3.06	7.5	27.3	0.150
CN3007	3.24	7.9	17.0	0.143
CN4007	3.30	8.7	13.6	0.184
CN1011	2.23	10.7	48.0	0.174
CN1511	2.87	11.1	40.3	0.122
CN2011	3.10	11.6	27.6	0.126
CN3011	2.48	12.6	20.7	0.172
CN1015	2.65	15.0	59.3	0.120
CN1515	2.84	16.1	32.6	0.094
CN2015	2.86	17.1	29.0	0.098

Conclusions

Twelve separate nonlinear wave fields were generated for the purpose of verifying the KP equation to be an accurate model for three-dimensional nonlinear waves. Criteria were developed which provided a unique correspondence between the solution parameters of the KP equation and the physical characteristics of the laboratory generated waves. Results of these experiments showed that both the generated waves and the genus 2 solutions are remarkable robust in that both were stable over a wide range of parameters, including the near breaking of waves. The excellent degree of fit between the observed and computed solutions shows that genus 2 solutions of the KP equation represent a viable model for three-dimensional, nonlinear, shallow water waves.

Acknowledgments

The author is grateful to Drs. Harvey Segur and Joseph Hammack for their help and advice, both of which were necessary for the successful completion of this project. The research results contained in this paper were funded through a Department of the Army In-House Laboratory Independent Research (ILIR) program. The author wishes to acknowledge the Office, Chief of Engineers, U. S. Army Corps of Engineers, for authorizing publication of this paper.

References

Dubrovin, B. A. (1981), "Theta Functions and Non-Linear Equations", Russian Math. Surveys, Vol. 36:2, pp 11-92.

Hammack, J. L. (1980), Unpublished Experiments.

Kadomtsev, B. B. and Petviashvili, V. I. (1970), "On the Stability of Solitary Waves in Weakly Dispersive Media", Soviet Physics - Doklady, Vol. 15, No. 6, pp 539-541.

Korteweg, D. J. and deVries, G. (1895), "On the Change of Form of Long Waves Advancing in a Rectangular Channel, and on a New Type of Long Stationary Waves, Phil. Mag., Ser. 5, Vol. 39, pp 422-443.

Segur, H.. and Finkel, A. (1984), "An Analytical Model of Periodic Waves in Shallow Water", Aeronautical Research Associates of Princeton, Inc., Tech. Memo. 84-12.

CHAPTER 56

TROPICAL CYCLONE GENERATED CURRENTS

by

Y. Peter Sheng, M.ASCE[1], and Sherman S. Chiu[2]

ABSTRACT

AXCP data obtained during Hurricane Josephine in 1984 are analyzed in this paper. In addition, wind-driven currents at several XCP's during Josephine are simulated using a one-dimensional ocean current model.

I. INTRODUCTION

An accurate quantitative determination of design environmental conditions is of great importance for offshore design consideration in oil and gas exploration and production, because of the high costs associated with the construction of deepwater offshore structures. For design consideration in such areas as the Gulf of Mexico, offshore China, and the northwest shelf off Australia, tropical cyclone generated forces in water column have been conventionally used as the major factor. Normally, forces generated by the maximum wave (extreme wave condition) and forces generated by the maximum possible wind-driven currents (extreme current condition) at a particular area are calculated for design consideration. The design criteria resulting from such a consideration may be overly conservative since the extreme wave and extreme current generally do not occur at the same time, at the same location, or in the same direction. Due to difficulties in measuring currents during a storm, however, little is known about the concurrent wind-driven current profiles in the vicinity of the maximum wave zone or the time lag between the maximum wave and maximum current conditions at a given site.

Measured currents at a site may be composed of currents driven by tide, wind, density gradient due to temperature and/or salinity distribution, gravity wave and localized circulation patterns such as internal waves and inertial currents. During a severe storm, the wind-driven

[1] Coastal and Oceanographic Engineering Dept., University of Florida, Gainesville, FL 32611
[2] Standard Oil Production Company, Dallas, Texas

currents become dominant over the other currents. Although a number of current models have been and are being used to calculate the wind-driven currents during severe storms, there is insufficient data available to validate these models. Based on extremely scarce data, however, Gordon (1982) claimed that currents in the ocean surface mixed layer (SML) are very uniform and only "slab model" can represent the current profiles in severe storms.

With the recent development of Air-deployed eXpendable Current Profiler, (Feeney, et al., 1985) or AXCP, "snapshots" of detailed ocean current and temperature profiles within storms can now be measured. It is thus possible to perform a systematic observation and analysis of wind- and wave-induced ocean currents at the ocean surface, surface mixed layer and thermocline. In addition, the wind-driven currents can be used for validation of ocean current models. In 1984, current profiles were measured via the systematic deployment of 31 AXCP's during two hurricanes--Hurricane Norbert in the eastern Pacific, and Hurricane Josephine in the western Atlantic.

This paper presents and discusses, from the point of view of practical engineering application, some ocean current and temperature profiles obtained via AXCP's in Hurricane Josephine during October, 1984. In addition, this paper presents a simulation of the wind-driven currents at several locations in Hurricane Josephine by means of a one-dimensional ocean current model (OCM1D) developed by Sheng (1984a and 1985). The results and understanding obtained from systematic studies such as this one will undoubtedly lead to the ultimate improvement of design criteria for offshore structures.

II. THE OBSERVATION PROGRAM

XCP and AXCP

The expendable current profiler (XCP) was originally developed by Dr. Thomas B. Sanford of Horizon Marine, Inc. It is a free-falling magnetic current meter which can be deployed from either a ship or an aircraft (AXCP). Figure 1 shows the major components involved in the XCP and AXCP deployment (Haustein and Feeney, 1985).

The ocean can be considered as many individual vertical layers with different electric fields which arise because of a process known as motional induction, i.e., electric current is generated as seawater flows through the geomagnetic field of the earth. The AXCP, as it falls through the water column, measures the electric current generated in each of the individual vertical layers via the recorded voltage (in nanovolts) between two horizontally spaced electrodes 5 cm apart. The measured electric currents at all layers yield a vertical profile of relative water velocities or "shears". A compass coil within the spin-stabilized probe measures the direction of current once per revolution as the probe falls with a 16 Hz rotation rate. A continuous temperature profile is measured by a thermistor located within the probe. The regular AXCP has a fall velocity of about 5m/sec and measures the current speed, direction and temperature to a depth of 1500 m. The slow-fall XCP has a fall velocity of about 2m/sec and a 200m depth capacity.

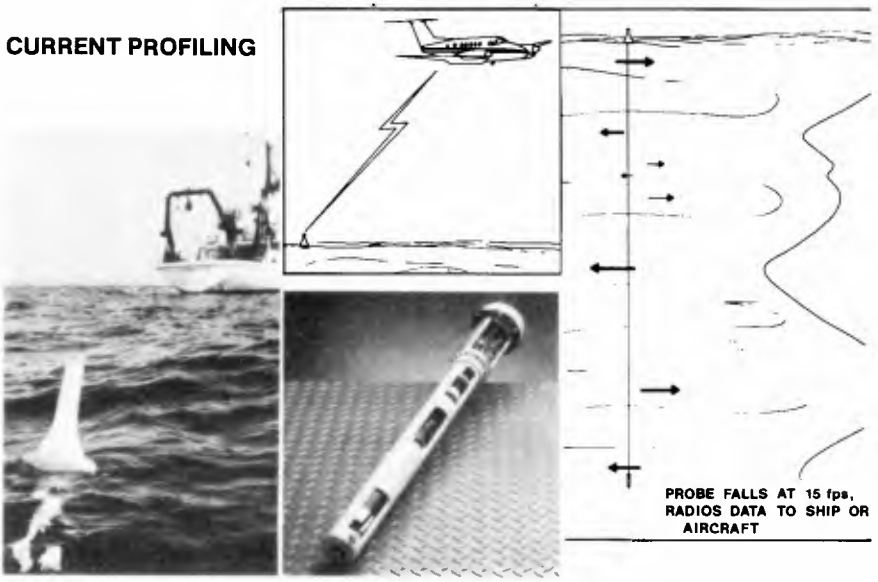

Figure 1 Current profiling using the XCP and AXCP. LEFT: Ship deployment showing attached float bag containing a radio antenna which transmits data back to the ship. CENTER TOP: Aircraft deployment. CENTER BOTTOM: The current profiler, contained within the probe housing. RIGHT: Continuous ocean current profile produced by the descending probe.

Forty seconds after the XCP lands on the water surface, the probe is launched through the bottom of the buoy. Signals measured by the electrodes, compass coils, and thermistor are transmitted from the probe to the surface buoy via a 1500-m or 200-m wire link. The data is then transmitted from the surface buoy, via the RF link, to processing or recording equipment on board a ship or aircraft. However, because the extremely strong winds during storms, the XCP's generally have a rather high failure rate of about 50%.

Ocean Response to a Hurricane

The observation program, "Ocean Response to a Hurricane", was a joint industry program involving nine U.S. oil companies (including Standard Oil, Mobil, Shell, etc.), NOAA's Hurricane Research Division and Office of Aircraft Operations, and Horizon Marine, Inc. (Feeney, et al., 1985). The program was the first systematic effort to measure ocean currents and temperature perturbations under severe meteorological conditions. A total of 31 AXCP's were systematically deployed during two hurricanes in 1984: Hurricane Norbert near Baja Peninsula in the eastern Pacific during September 23-24, and Hurricane Josephine near western Atlantic during October 10-11. While Norbert is relatively stronger, this paper concentrates on the slightly weaker Hurricane Josephine.

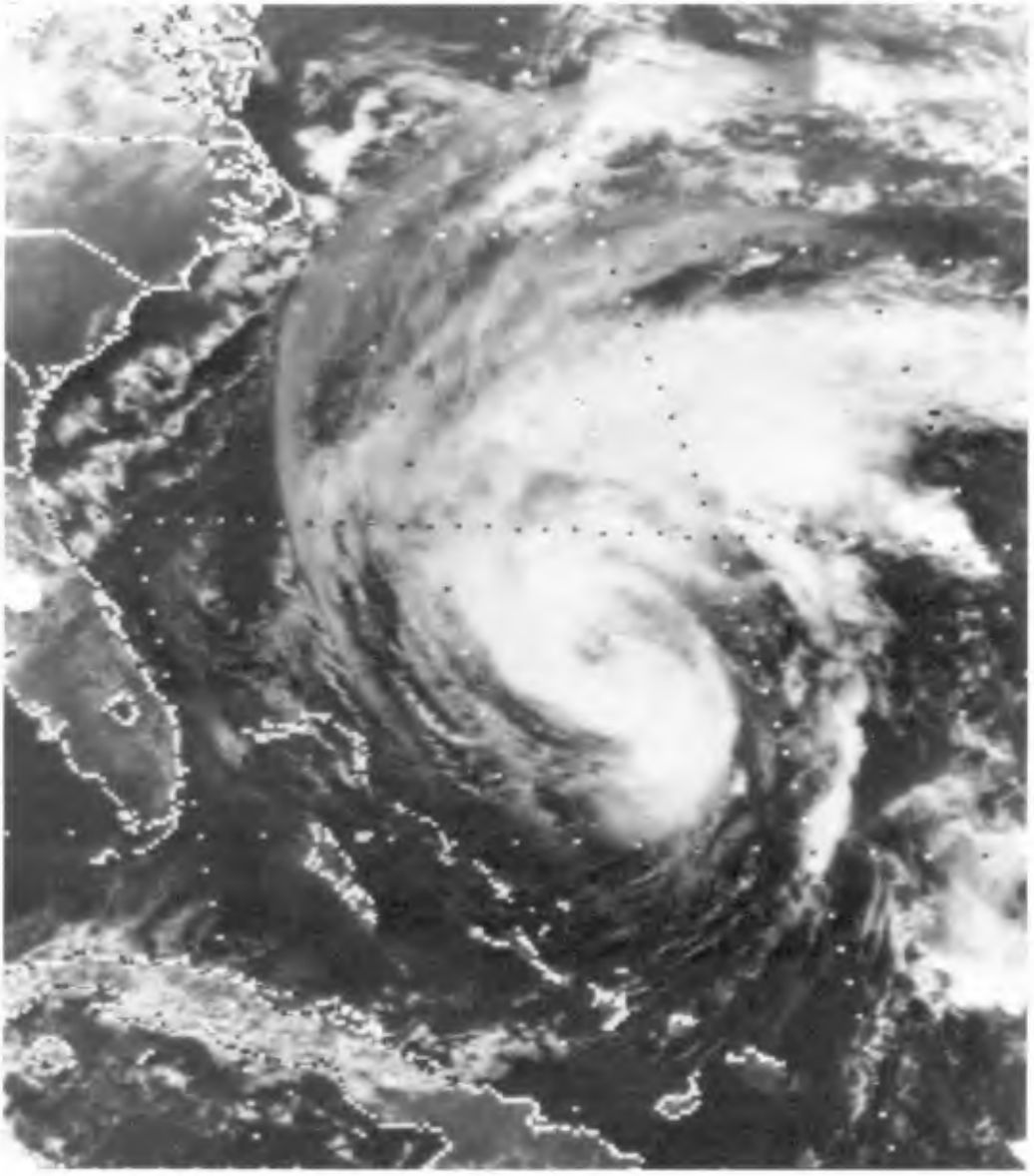

Figure 2 Hurricane Josephine as seen from satellite.

Hurricane Josephine

Flight through Josephine was executed on October 11, 1984, one day after Josephine attained hurricane strength. At that time, Josephine's eye was located near 25.5° N and 72° W with a moderate maximum surface wind of 75 knots and a barometric pressure of about 970 mb. The storm as shown in Figure 2 is located approximately 250 n miles northeast of the Bahama Islands, drifting slowly northward, over waters of approximately 4000 m deep. The survey was conducted with a total of 31 AXCP's which include 17 regular AXCP's with a 1500 m depth capacity and 14 slow-fall AXCP's with a 200 m depth capacity.

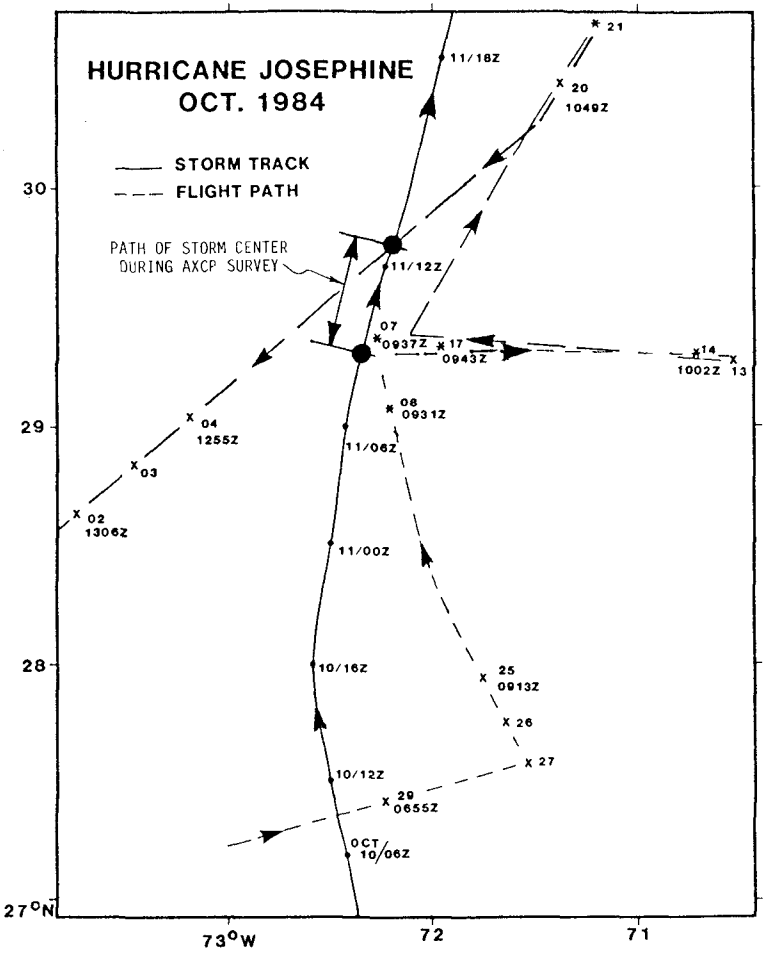

Figure 3 Storm track and AXCP flight path during Hurricane Josephine on October 10-11, 1984.

The flight area of the AXCP survey is shown in Figure 3, where the solid line starting from the south represents the storm track (distance between two adjacent dots represents a 6-hour interval) and the dashed line indicates the flight path between 8:45 AM (Zulu time) and 13:06 PM on October 11, 1984. The highlighted portion in Figure 3 represents the locations of storm center during the flight survey period. During that time, the forward speed of the hurricane was approximately 7 kts and the radius of maximum wind (R) was approximately 35 n miles. The survey covered an area more than 200 n miles (3 degrees) squared. Although a total of 31 AXCP's were deployed, only 50% of the data were usable. Locations with usable XCP data are indicated by the x's in Figure 3. 5 XCP's (XCP07, XCP08, XCP14, XCP17, and XCP21) are of special interest in this paper and are marked by the *'s in Figure 3.

III. XCP DATA DURING HURRICANE JOSEPHINE

All the XCP's were deployed to the right of Hurricane Josephine where the storm effect on current is stronger and where the Gulf Stream has negligible effect, thus allowing easier separation of wind- and wave-induced currents from the background current. Some data are presented in the following.

Current and Temperature Data at XCP17

XCP17 is located at approximately 0.7 R to the east of the storm eye. At the time of the survey, surface wind at XCP17 is about 24 kts toward the north. Several hours before the survey, however, wind exceeded 50 kts at all the XCP's of special interest.

Figure 4 shows the measured current speed, direction, and temperature at XCP17 from surface to 250 m depth. The profiles are plotted from data averaged over every 3 or 4 meters, or approximately 20 raw data points. The current speed (solid line) exceeds 1 m/sec at the surface and decays to about 20 cm/sec below 100 m depth, while the current direction (dotted line) changed form nearly 45^{o} (towards northeast) at surface to about 180^{o} (towards south) below 100 m depth. The effect of surface gravity wave, as is evidenced by the oscillatory velocity profile, is present even below 100 m depth.

Since our primary interest is the wind-driven current, a filtering procedure can be designed to remove the wave-induced orbital velocity from the signal. The filtering procedure makes use of the calculated wave period and the fact that amplitudes of the wave-induced signal decays exponentially with depth. The filtered current speed and direction as shown in Figure 4 are rather smooth and represent the wind-driven current, which will be used for validation of ocean current model. It should be noted that although wave signal can be found even at 100 m depth, the vertical shear associated with the wave orbital velocity is generally rather weak compared to that due to the wind-driven or density-driven currents. Hence, removing the wave-induced signal from current data will have little effect on turbulent mixing in the surface mixed layer.

Figure 4 also shows a thermocline between 70 m and 90 m depths. It is clear that although the temperature is rather uniform within the SML, current profile looks hardly like a "slab". In fact, significant shear

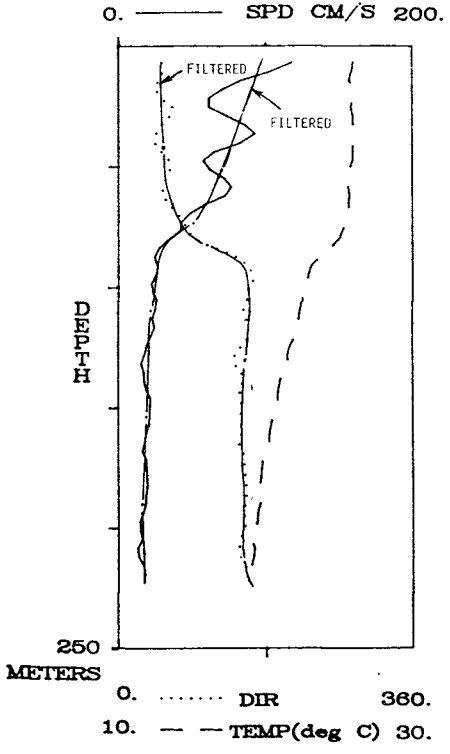

Figure 4 Current speed, current direction, and temperature measured by XCP17 during Hurricane Josephine.

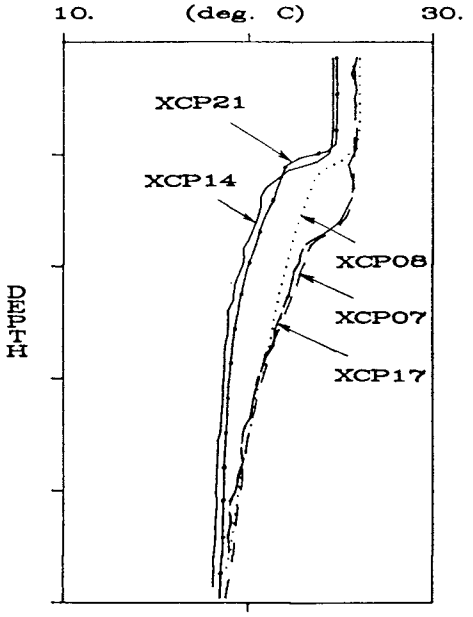

Figure 5 Temperature profiles measured by XCP07, XCP08, XCP14, XCP17 and XCP21.

appears to be present in the mixed layer. It is also noted that the current profile does not quite resemble the classical Ekman layer. Except near the thermocline, little change in current direction is detected.

Temperature Data at XCP07, XCP08, XCP14, XCP17, and XCP21

Temperature profiles at the 5 XCP's are shown in Figure 5. At the three stations within R from storm center (XCP07, XCP08 and XCP17), temperature profiles within the SML are very similar, with XCP07 and XCP17 having almost identical profiles throughout the 250 m depth. At XCP14 and XCP21, more than 2R away from the storm eye, the temperature profiles are similar and relatively undisturbed by the hurricane. The SML temperature at these two XCP's is colder than that at the other three XCP's.

Thermocline at the XCP14 and XCP21 is found at 50 m depth. At XCP07 and XCP17, where winds are 1 kt and 24 kts respectively, but were much stronger several hours before, the thermoclines are found at 80 m depth. At XCP08, where the storm center has passed by about 4 hours ago and the wind is 9 kts, the thermocline is at 50 m depth.

The above data indicate that a time lag on the order of a few hours exists between the occurrences of peak wind and maximum thermocline deepening. As the storm center approaches a location, wind gradually decreases from peak wind to negligible wind when the eye arrives. When the storm center reaches the location, although the wind has decreased substantially, the thermocline continues to be deepened by wind-induced mixing generated during previous hours. At the same time, the positive wind stress curl may produce a positive vertical velocity which tends to move the thermocline upward. This so-called "Ekman suction", however, may also lag behind the arrival of storm center. In addition, lateral pressure gradient within the maximum radius R of the storm eye may also cause geostrophic currents and contribute to the mixing and migration of thermocline. However, the exact manner in which these competing mechanisms operate is not yet clearly understood.

Current Data at XCP07, XCP08, XCP14, and XCP17

Figure 6 shows the unfiltered current and temperature profiles at the 4 XCP's. If one visually removes the wave-induced components from Figure 6, it is apparent that the filtered current profiles in the SML are rather similar. The current decreases gradually with depth in the SML without any resemblance to the so-called "slab".

Current speed in the SML becomes increasingly stronger from XCP08 ($\lesssim$ 50 cm/sec) to XCP07 ($\lesssim$ 75 cm/sec) to XCP17 ($\lesssim$ 1 m/sec). Current direction within much of the SML appears to be at approximately 45° to the right of the wind. Although the wind at XCP14 is the strongest (54 kts) among the 4 XCP's, the wind-driven current is only about 60 to 70 cm/sec. Velocity gradients within the thermoclines are quite different, apparently because of the difference in thermocline shapes. Below the thermocline, there appears to be an anticyclonic gyre around the storm center. Although this could be related to the geostrophic current induced by the pressure gradient, it is unclear as to how

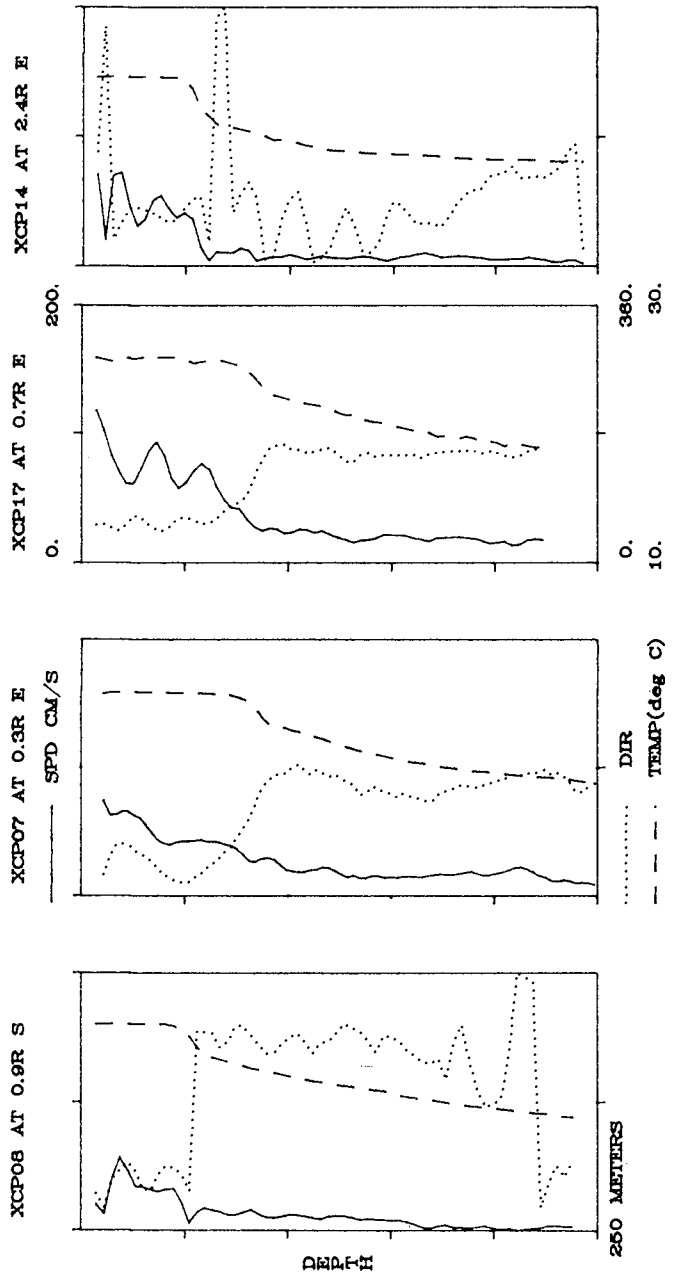

Figure 6 Measured current speed, current direction and temperature at XCP07, XCP08, XCP14 and XCP17.

exactly the pressure gradient and the wind stress interact to cause transient circulation in a hurricane. However, at XCP08, the greater difference (~180°) in current directions below and above the thermocline is consistent with the fact that pressure gradient at XCP08 is stronger than the other XCP's.

TABLE 1

SITE ID: XCP 17 0943Z LOCATION - 29.33N 71.97W
HURRICANE JOSEPHINE (OCT. 7-12,1984)

DATE	TIME	WIND DIR (DEG)	WIND SPEED MPS	WIND SPEED (KT)	WAVE H(SIG) (M)	WAVE H(SIG) (FT)	WAVE H(MAX) (M)	WAVE H(MAX) (FT)	WAVE Tpeak SEC	STORM DIST (NM)	STORM AZM DEG	PRES MBAR
	1300	68	9.6	19	2.13	7.0	4.40	14.4	5.0	224	3	1009
	1400	69	10.2	20	2.37	7.8	4.89	16.1	5.4	214	4	1009
	1500	69	10.9	21	2.62	8.6	5.40	17.7	5.9	203	4	1009
	1600	70	11.9	23	2.96	9.7	6.10	20.0	6.5	192	5	1006
	1700	70	12.5	24	3.32	10.9	6.84	22.5	6.9	183	5	1008
	1800	71	13.4	26	3.68	12.1	7.59	24.9	7.3	175	6	1007
	1900	71	14.1	27	3.98	13.1	8.21	26.9	7.7	168	6	1007
	2000	72	14.7	26	4.22	13.8	8.71	28.8	6.0	163	7	1007
	2100	72	15.1	29	4.38	14.4	9.04	29.7	8.2	159	7	1007
	2200	73	15.4	30	4.53	14.9	9.35	30.7	8.3	155	8	1006
	2300	73	15.8	31	4.69	15.4	9.67	31.7	8.5	151	8	1006
10 10 84	000	74	16.0	31	4.83	15.8	9.97	32.7	8.6	147	9	1006
	100	74	16.3	32	4.97	16.3	10.25	33.6	8.7	144	9	1006
	200	74	16.6	32	5.10	16.7	10.53	34.6	8.9	140	9	1006
	300	75	17.0	33	5.25	17.2	10.84	35.6	9.0	136	10	1005
	400	75	17.5	34	5.42	17.8	11.18	36.7	9.1	132	10	1005
	500	75	17.9	35	5.57	18.3	11.49	37.7	9.3	128	10	1005
	600	76	18.3	36	5.70	18.7	11.76	38.6	9.4	125	11	1005
	700	76	18.5	36	5.73	18.8	11.83	38.8	9.5	123	11	1005
	600	77	18.7	36	5.75	18.9	11.87	38.9	9.5	120	12	1005
	900	77	18.8	36	5.75	18.9	11.87	38.9	9.5	119	12	1005
	1000	78	18.8	37	5.75	18.9	11.86	38.9	9.5	117	13	1005
	1100	79	18.9	37	5.76	18.9	11.88	39.0	9.5	115	14	1005
	1200	79	18.8	36	5.76	18.9	11.88	39.0	9.5	112	14	1005
	1300	80	19.4	38	5.96	19.6	12.30	40.3	9.5	109	15	1004
	1400	81	20.0	39	6.17	20.2	12.74	41.8	9.7	106	16	1004
	1500	82	20.7	40	6.40	21.0	13.21	43.3	9.9	102	17	1003
	1600	84	21.2	41	6.62	21.7	13.65	44.8	10.0	99	19	1003
	1700	85	21.9	42	6.84	22.4	14.12	46.3	10.2	95	20	1002
	1800	86	22.5	44	7.07	23.2	14.80	47.9	10.4	91	21	1001
	1900	87	23.1	45	7.26	23.8	14.98	49.1	10.5	87	22	1001
	2000	88	23.8	46	7.44	24.4	15.35	50.4	10.7	82	23	1000
	2100	88	24.6	48	7.65	25.1	15.79	51.8	10.8	77	23	1000
	2200	89	25.4	49	7.87	25.8	16.22	53.2	11.0	72	24	999
	2300	90	26.3	51	8.09	26.5	16.59	54.4	11.1	67	25	998
10 11 84	000	92	28.9	52	8.29	27.2	16.93	55.5	11.3	63	27	997
	100	94	27.8	54	8.47	27.8	17.19	56.4	11.4	58	29	996
	200	96	28.7	56	8.58	28.1	17.33	56.8	11.5	54	31	995
	300	99	29.5	57	8.68	28.5	17.44	57.2	11.6	49	34	994
	400	103	30.1	59	8.76	28.8	17.42	57.2	11.7	45	38	993
	500	107	30.8	60	8.85	29.0	17.38	57.0	11.7	41	42	991
	600	112	28.6	56	8.56	28.1	16.70	54.8	10.5	36	47	989
	700	118	26.9	52	7.61	25.0	14.61	47.9	10.5	31	53	987
	800	127	21.5	42	6.56	21.5	12.47	40.9	9.4	25	62	983
	900	141	12.4	24	5.52	18.1	10.33	33.9	9.5	20	76	980
	1000	162	7.5	15	4.88	16.0	9.07	29.7	8.5	17	97	977
	1100	188	7.8	15	4.86	15.9	8.98	29.5	8.5	17	123	976
	1200	213	13.1	26	5.65	18.5	10.64	34.9	7.6	20	146	977

II. MODEL SIMULATION OF WIND-DRIVEN CURRENTS IN JOSEPHINE

Wind and Wave Hindcasting

Before simulating the wind-driven currents, the wind and wave field were hindcasted by means of a modified Bretschneider method (1972). With such input values as storm track, central pressure, maximum wind radius R, maximum wind at R, and ambient flows, the model yields the wind and wave conditions. As an example, the hindcast wind and wave data at XCP17 during a 48 hour period prior to the arrival of Josephine are shown in Table 1. At 5:00 AM on October 11, while the storm center is still 41 n m (nautical miles) from XCP17, the wind speed peaked to 60 kts and the significant wave height peaked to 29 feet with a peak period of 11.7 sec. Four hours later at 9:00 AM, the condition has fallen to 24 kts wind speed, 18 feet wave height, and 9.5 sec wave period.

The time-dependent wind fields at all the XCP locations were saved in computer storage and used for simulation of wind-driven currents. Although the pressure was also computed by the hindcast model, it was not used for the present model simulation of wind-driven currents.

A One-Dimensional Ocean Current Model: OCM1D

Sheng (1984a and 1985) developed the OCM1D based on the following mean equations of motion:

$$\frac{\partial u}{\partial t} = fv - \underline{\frac{\partial \overline{u'w'}}{\partial z} - g\frac{\partial \zeta}{\partial x} - \frac{1}{\rho_o}\frac{\partial P_a}{\partial x} + \frac{g}{\rho_o}\int_o^z \frac{\partial \rho}{\partial x}\,dz} \tag{1}$$

$$\frac{\partial v}{\partial t} = -fu - \underline{\frac{\partial \overline{v'w'}}{\partial z} - g\frac{\partial \zeta}{\partial y} - \frac{1}{\rho_o}\frac{\partial P_a}{\partial y} + \frac{g}{\rho_o}\int_o^z \frac{\partial \rho}{\partial y}\,dz} \tag{2}$$

$$\frac{\partial T}{\partial t} = -\frac{\partial \overline{w'T'}}{\partial z} + \underline{\eta(1 - A_s)\frac{\phi_o}{\rho_o C_p}\exp(-\eta z)} \tag{3}$$

$$\frac{\partial S}{\partial t} = -\frac{\partial \overline{w'S'}}{\partial z} \tag{4}$$

$$\rho = \rho(T,S) \tag{5}$$

where (u,v) are the horizontal velocities in (x,y) directions, T is temperature, S is salinity, z is the vertical coordinate pointing upward from z = 0 at the undisturbed ocean surface, ζ is surface displacement, ρ_o is reference density, P_a is atmospheric pressure, ρ is density, (u',v',w') are turbulent fluctuating velocities in (x, y, z) directions, T' and S' are fluctuating temperature and salinity, η is extinction coefficient of solar radiation, A_s is sea surface absorption coefficient, and ϕ_o is solar raditation flux at sea surface. The underlined terms in Eqs. (1) and (2) are non-local terms which can be evaluated if

sea surface slope, atmospheric pressure gradient and density gradient are known (either measured or computed) and specified as input to the model. However, these non-local terms and the solar radiation term in Eq. (3) are not used in the present study.

Turbulent fluxes $\overline{u'w'}$, $\overline{v'w'}$, $\overline{w'T'}$ and $\overline{w'S'}$ are modeled with the so-called "super-equilibrium" version of a second-order closure model of turbulent transport (Sheng, 1984a). The general equations are given in terms of $\overline{u_i'u_j'}$, $\overline{u_i'\rho'}$, and $\overline{\rho'\rho'}$ in tensor notations:

$$0 = -\overline{u_i'u_k'}\frac{\partial u_j}{\partial x_k} - \overline{u_j'u_k'}\frac{\partial u_i}{\partial x_k} - g_i\frac{\overline{u_j'\rho'}}{\rho_o} - g_j\frac{\overline{u_i'\rho'}}{\rho_o}$$
$$- 2E_{ik\ell}\Omega_k\overline{u_\ell'u_j'} - 2E_{jk\ell}\Omega_\ell\overline{u_k'u_i'} \qquad (6)$$
$$- \frac{q}{\Lambda}\left(\overline{u_i'u_j'} - \delta_{ij}\frac{q^2}{3}\right) - \delta_{ij}\frac{q^3}{12\Lambda}$$

$$0 = -\overline{u_i'u_j'}\frac{\partial \rho}{\partial x_j} - \overline{u_j'\rho'}\frac{\partial u_i}{\partial x_j} - \frac{g_i\overline{\rho'\rho'}}{\rho_o}$$
$$- 2E_{ijk}\Omega_j\overline{u_k'\rho'} - 0.75\,q\frac{\overline{u_i'\rho'}}{\Lambda} \qquad (7)$$

$$0 = -2\overline{u_j'\rho'}\frac{\partial \rho}{\partial x_j} - \frac{0.45\,q\,\overline{\rho'\rho'}}{\Lambda} \qquad (8)$$

In addition to the above equations, Λ is computed from three integral constraints, i.e., Λ is bounded by (1) a slope of 0.65, (2) q/Λ, where q is the total turbulent velocity and N is the Brunt-Vaisala frequency, and (3) a fraction of the spread of turbulence. This model was able to successfully simulate the laboratory wind-driven currents (Sheng, 1984a) storm generated currents on continental shelf (Sheng and Szabo, 1986).

A 60 hour model simulation, starting from 60 hours prior to the time of the survey, was performed at all XCP's by assuming XCP21's temperature profile and zero velocity as initial data. The results at XCP17 between hour 42 and hour 57, with a 3-hour interval, are shown in Figure 7. Currents in the SML grow steadily with time in spite of the decrease in wind speed during the last 2 hours. During the 15 hour period, current direction changed from towards NNW to towards NNE as the wind shifted from E to SSE. Thermocline was deepened during the last 6 hours.

Model Results at XCP07, XCP08, XCP14, and XCP17

Model results at the end of 60 hour simulation are shown in Figure 8 for XCP07, XCP08, XCP14 and ACP17. Filtered data are also shown on the same figure. In general, the agreement between model results and data are quite good. The best agreement is at XCP14 which

is at 2.4 times the maximum wind radius from the storm center and hence is not much affected by pressure gradient within the storm center. The current direction at all the XCP's appears to be correctly simulated although current speed at XCP08 seems underestimated. The discrepancy between model results and data at the 3 XCP's within the storm center can be attributed to the following 3 possibilities: (1) uncertainty in the initial condition, (2) pressure gradient not included in the present model simulation, and (3) possible vertical water movement associated with the curl of wind stress was not included in the model simulation.

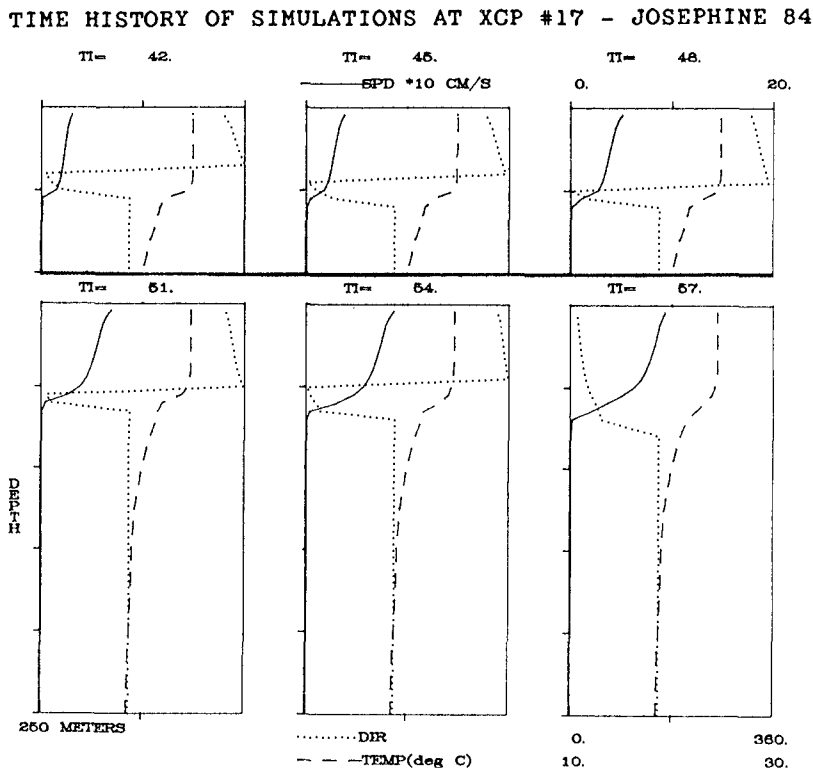

Figure 7 Model simulation of current and temperature at XCP17 during the six 3-hour intervals prior to the arrival of storm center.

V. CONCLUSIONS

During Hurricane Josephine in 1984, a systematic survey of ocean current and temperature within the top 250 m of ocean water was conducted by a joint industry program via the deployment of 31 AXCP's. This paper presents an analysis of the detailed data, which is available

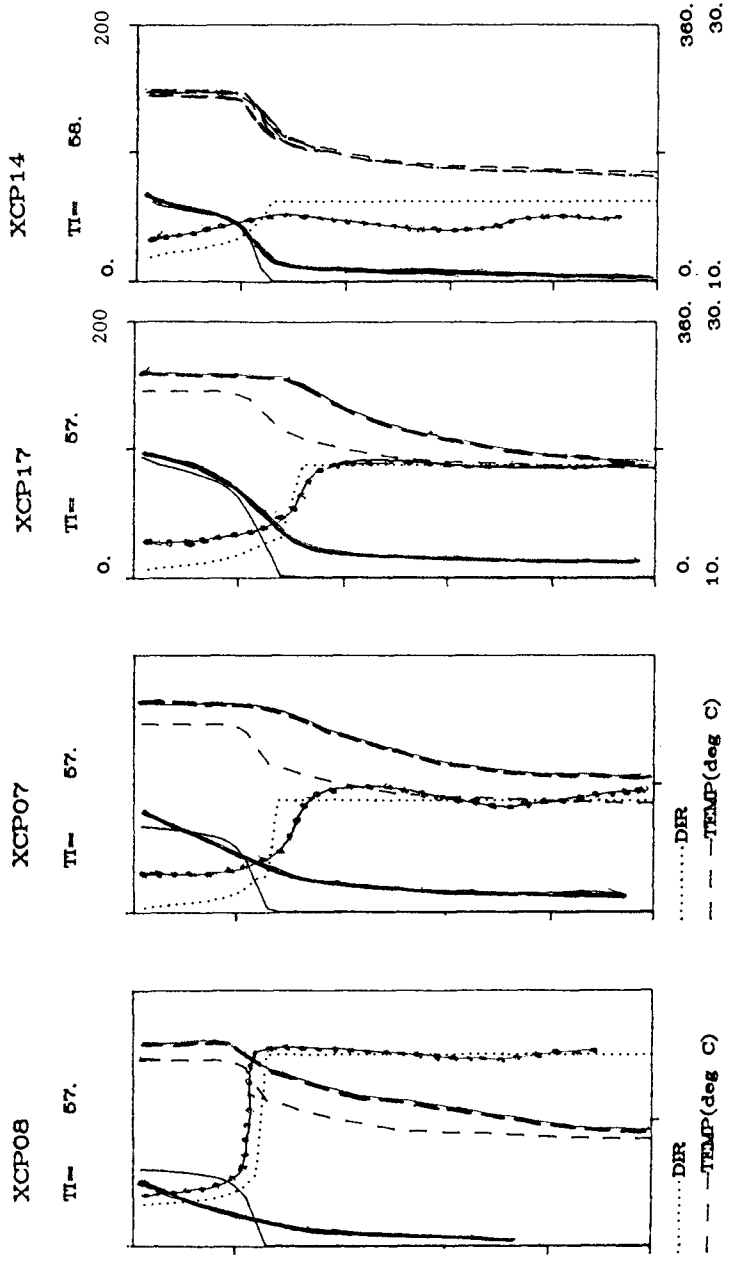

Figure 8. Model simulated and measured current and temperature at XCP07, XCP08, XCP14, and XCP17. Darker lines indicate measured data.

for the first time, and found the data of significant value for further understanding of ocean mixed layer dynamics and for improvement of offshore design criteria.

Model simulation of storm-generated currents at several XCP's was carried out by using the 1-D Ocean Current Model (OCM1D). The results generally are in reasonable agreement with data. It is interesting to note that both XCP data and model results showed significant shear within the surface mixed layer and no "slab"-like current profile was found. Discrepancy between model results and data is attributed to uncertainty in initial condition and neglect of pressure gradient and Ekman-suction in model simulation.

VI. ACKNOWLEDGEMENTS

The first author wishes to acknowledge the support of Standard Oil Production Company and Mobil Research and Development Corporation for the development of the 1-D ocean current model. Sherman Chiu served as the technical monitor for SOPO while David Szabo and Max Sheppard served as technical monitors for MRDC.

VII. REFERENCES

Bretschneider, C. L., 1972: "A Non-Dimensional Stationary Hurricane Wave Model", OTC paper 1517.

Feeney, J. W., T. B. Sanford, and J.R. Haustein, 1985: "Observing Hurricane-Driven Waves and Currents", OTC paper 4934.

Gordon,R. L., 1982: "Coastal Ocean Current Response to Storm Winds", JGR, 87, C3, p. 1939.

Haustein J. R. and J. W. Feeney, 1985: "Gulf of Mexico Deep Water Current Studies for Offshore Oil Exploration and Production", Oceans 85, pp. 1062-1070.

Sheng, Y. P., 1984a: "A Turbulent Transport Model of Coastal Processes", Proc 19th Intl. Conf. Coastal Eng., ASCE, pp. 2380-2396.

Sheng Y. P., 1984b: "A One-Dimensional Ocean Current Model (OCM1D)", A.R.A.P. Report No. 523, prepared for Mobil Research and Development Corporation, A.R.A.P., Princeton, NJ.

Sheng, Y. P., 1985: " A New One-Dimensional Model of Ocean Current", A.R.A.P. Report Prepared for Standard Oil Production Company, Princeton, NJ.

Sheng Y. P. and D. Szabo, 1986: "Validation of Current Model OCM1D in Storm Conditions", A.R.A.P. Report No. 580, Prepared for Mobil Research and Development Corporation, A.R.A.P., Princeton, NJ.

CHAPTER 57

COMPLEX ENVELOPE IDENTIFICATION OF WAVE GROUPS

Rodney J. Sobey[1] and Han-Bin Liang[2]

The complex envelope function is presented as the natural analysis technique for wave records where the identification of wave groups is a dominant interest. Algorithms have been developed and confirmed for separation of the complex envelope function, estimation of the dominant frequency and unwrapping of the phase function. Cross-correlograms and coherence spectra reveal a link between the envelope amplitude and phase traces that appears to be an intrinsic property of wave groups. Nevertheless, the majority of the information in typical wave records can be described as random, accounting for the relative success of the Gaussian random wave model.

INTRODUCTION

There is widespread acceptance of wave grouping in coastal and ocean design and considerable recent research effort has been focussed on the statistics of wave groups and the development of alternative analysis techniques to accommodate wave grouping. There is sufficient evidence from field records that wave grouping does exist but the specific nature and extent of wave grouping remains largely unresolved. It has been suggested, for example, that wave grouping is a direct consequence of the Gaussian random wave model, that it is a consequence of finely-tuned focussing of the phases of linear or non-linear wave trains, and that it is essentially a non-linear phenomenon, such as envelope solitons.

The evidence must be sought initially from field data. Care must be taken, however, that the choice of analysis technique does not predetermine the data interpretation. Spectral analysis and zero-up-crossing identification of individual waves, for example, ignore the phase information in the record and implicitly favor the Gaussian random wave model description. This approach has proved to be useful and reasonably successful. It may ultimately prove appropriate but questions remain regarding the existence of useful phase information in the record.

A natural analysis technique for wave grouping would appear to be the complex envelope function A(t), related to the wave record $\eta(t)$ as

$$\eta(t) = \text{Real}\,[A(t)\,\exp(i\omega_0 t)] \tag{1}$$

where $\omega_0 = 2\pi f_0$ is the dominant frequency. No information is lost from the original record and attention can be focussed on the envelope modulation. For typically narrow-banded sea states, mod $A(t)$ is an excellent approximation to the wave envelope, as recognized by Rice (1943, 1945) and Longuet-Higgins (1951) in the theoretical establishment of the Rayleigh distribution as an estimate of the probability distribution of

[1]Professor, Hydraulic and Coastal Group, Department of Civil Engineering, University of California, Berkeley, California, 94720
[2]Graduate Student, Hydraulic and Coastal Group, Department of Civil Engineering, University of California, Berkeley, California 94720

wave amplitude. Full advantage, however, has rarely been taken of the complete complex envelope function. It is the purpose of the present paper to evaluate its potential in the identification and perhaps quantification of wave groups. Several recent studies of wave grouping have adopted an envelope concept, all based on the application of a low pass moving average filter to $\eta^2(t)$, the square of the wave record. Funke and Mansard (1979) used a filter with half-width $1/(2f_p\Delta t)$ points in defining a smoothed instantaneous wave energy history. f_p is the spectral peak frequency and Δt is the discrete time step of the data record. W.C. Thompson, Nelson and Sedivy (1983) and E. F. Thompson and Seelig (1983) extended the filter half-width to $1/(f_p\Delta t)$ points. These studies have shown the utility of the envelope concept but have not taken advantage of the phase information in the record. In addition, filtering removes potentially valuable information from the record.

COMPLEX DEMODULATION

The potential of complex demodulation in the analysis and interpretation of periodic data has been elucidated by Bingham, Godfrey and Tukey (1966) and Hasan (1982). In principle, complex demodulation is a generalization of harmonic analysis, its objective being to extract the slowly varying amplitude $R(t;\omega)$ and slowly varying phase $\Phi(t;\omega)$ of the signal component at frequency ω. In general, the record will not consist solely of a perturbed sinusoid; it may be represented as

$$\begin{aligned}\eta(t) &= R\cos(\omega t + \Phi) + r(t) \\ &= \frac{1}{2} R\{\exp[i(\omega t + \Phi)] + \exp[-i(\omega t + \Phi)]\} + r(t)\end{aligned} \tag{2}$$

where $r(t;\omega)$ is the residual noise signal. Multiplying Equation 2 by $\exp(-i\omega t)$ gives

$$\eta\exp(-i\omega t) = \frac{1}{2} R\exp(i\Phi) + \frac{1}{2} R\exp[-i(2\omega t + \Phi)] + r\exp(-i\omega t) \tag{3}$$

The second and third items in Equation 3 oscillate at frequencies 2ω and ω respectively, so that the smooth component (and hence R and Φ) can be extracted by linear filtering (Bloomfield 1976). This procedure is appropriate in real time, regardless of the nature of the $\eta(t)$ data series. It will extract the slowly varying amplitude and phase at any nominated frequency ω, and the complete spectrum can be established in this manner.

The value of complex demodulation however is its ability to focus on a single frequency and herein lies its utility in wave record analysis. The spectra of surface gravity waves are consistently narrow-banded, to the extent that some dominant frequency ω_0 can be anticipated. The precise definition of ω_0 requires some further consideration but it is clear that it will be near the spectral peak. The complex demodulate at frequency ω_0 is the complex envelope function $A(t)$. The residual $r(t;\omega_0)$ in Equation 2 is consumed into the definition of $A(t)$, so that $A(t)$ represents the influence of all frequencies other than ω_0. This is Equation 1. A narrow-banded data series is clearly essential to the utility of the complex envelope function, as a wide band width would destroy the essential envelope interpretation of $A(t)$.

The complex envelope function appears to have been introduced by Rice (1944). His interest however was only in the amplitude function $R(t)$, which he termed the envelope. This Rice envelope function formed the basis of his establishment of the Rayleigh distribution as the probability distribution for the amplitudes of narrow-banded random noise. This result was adapted to surface gravity waves by Longuet-Higgins (1951) and has proved remarkably successful. Potential information in the phase function $\Phi(t)$ was not considered.

COMPLEX ENVELOPE FUNCTION

The filtering technique implied above is certainly appropriate but advantage can be taken of the computational efficiency of the FFT algorithm (Sobey & Colman 1983). This requires a specific assumption about the data series, namely that it represents a stationary process. This same assumption is also implicit in traditional spectral analysis of wave records leading to the variance spectrum. That it is a reasonable assumption is well established.

The initial step (Deutsch 1962) is to establish the Hilbert transform $\hat{\eta}(t)$ of the data series $\eta(t)$:

$$\hat{\eta}(t) = \frac{1}{\pi} \int_{-\infty}^{\infty} \frac{\eta(\tau)}{t-\tau} \, d\tau \tag{4}$$

The Fourier transform of $\eta(t)$ is

$$F(\omega) = \int_{-\infty}^{\infty} \eta(t) \exp(-i\omega t) \, dt \tag{5}$$

and it follows from Equation 4 that $\hat{F}(\omega)$, the Fourier transform of $\hat{\eta}(t)$, is

$$\hat{F}(\omega) = \begin{cases} -iF(\omega) & \text{for } \omega > 0 \\ 0 & \text{for } \omega = 0 \\ +iF(\omega) & \text{for } \omega < 0 \end{cases} \tag{6}$$

Computationally, the Hilbert transform can be established from the inverse Fourier transform of $\hat{F}(\omega)$.

The record and the Hilbert transform are combined to establish the pre-envelope function:

$$z(t) = \eta(t) + i\hat{\eta}(t) \tag{7}$$

which in turn can be shown (Deutsch 1962) to be

$$z(t) = R(t;\omega) \exp[i\Phi(t;\omega)] \exp(i\omega t) \tag{8}$$

Multiplying through by $\exp(i\omega t)$ recovers the complex demodulate at frequency ω.

To specifically recover the complex envelope function requires knowledge of the dominant frequency ω_0. Physically, ω_0 must be reasonably close to the peak frequency ω_0, which can be estimated from the variance spectrum (Sobey & Young 1986) as

$$\omega_p = \int \omega \, E^8(\omega) \, d\omega \; / \; \int E^8(\omega) \, d\omega \tag{9}$$

Adopting ω_p as a first guess ω_g at the dominant frequency, the correction of ω_g towards ω_0 follows Bolt and Brillinger (1978). At the dominant frequency, Equation 8 is

$$z(t) = R(t;\omega_0) \exp[i\Phi(t;\omega_0)] \exp(i\omega_0 t) \tag{10}$$

where the complex envelope function is

$$A(t) = R(t;\omega_0)\ \exp[i\Phi(t;\omega_0)] \tag{11}$$

Multiplying both sides of Equation 10 by $\exp(-i\omega_g t)$ gives

$$z(t)\ \exp(-i\omega_g t) = R(t;\omega_0)\ \exp\{i[\Phi(t;\omega_0) + (\omega_0 - \omega_g)t]\} \tag{12}$$

The estimate ω_g may be corrected to ω_0 by estimating and removing any linear trend, identified as $(\omega_0 - \omega_g)t$, in the phase record. In practice, this procedure requires phase unwrapping as an initial step.

UNWRAPPING THE PHASE FUNCTION

Phase unwrapping refers to the modulo 2π operation on phase angles. The phase returned by the FFT and any coded trigonometrical algorithm is in the range $-\pi$ to π and is termed the principal phase $\Phi_p(t)$. Any principal phase angle may in fact be $\Phi_p(t) + 2\ell\pi$, where ℓ is any signed integer, without changing the complex envelope function. The "true" phase is obtained by "unwrapping" the principal phase through addition or subtraction of multiples of 2π; this phase is called the unwrapped phase, $\Phi_u(t)$. The subscript u has been dropped but is implied in the subsequent discussion.

The procedure adopted to determine the signed integer ℓ is closely analogous to that adopted by Read and Sobey (1985) in unwrapping the phase spectrum of $\eta(t)$. From the time derivative of the natural log of Equation 11, it follows that

$$\frac{d\Phi}{dt} = \text{Imag}\left[\ \frac{1}{A}\ \frac{dA}{dt}\ \right] \tag{13}$$

Given the slope of the phase function, numerical integration will provide an estimate of Φ_u at the new time. Integration proceeds by the trapezoidal rule, consistent with its adoption in the definition of the discrete Fourier and inverse Fourier transforms. A raw estimate of the principal phase Φ_p is also available from the Hilbert transform/FFT procedure. In principle, the integer ℓ is

$$\ell = (\Phi_u - \Phi_p)/2\pi \tag{14}$$

In practice, ℓ will not be an integer as Equation 14 utilizes raw estimates of both Φ_u and Φ_p. To retain the same value of principal phase at each time step, ℓ is adjusted to the nearest integer and the raw estimate of the unwrapped phase adjusted to

$$\Phi = \Phi_p + 2\ell\pi \tag{15}$$

It remains to estimate the right hand side of Equation 13. From the definition of the pre-envelope function,

$$A(t)\ \exp(i\omega_0 t) = \frac{1}{2\pi}\int_0^\infty 2\ F(\omega)\ \exp(i\omega t)\ d\omega \tag{16}$$

Differentiating both sides with respect to time leads to

$$\frac{1}{A}\frac{dA}{dt} = \frac{\exp(-i\omega_0 t)}{A(t)}\left[\frac{1}{2\pi}\int_0^\infty 2i\omega F(\omega)\exp(i\omega t)\,d\omega\right] - i\omega_0 \tag{17}$$

The term in square brackets can be computed from the inverse FFT algorithm, noting that the kernel is zero for negative frequencies. The slope $d\Phi/dt$ follows from Equation 13.

The success of this algorithm is demonstrated by Figure 1. The record is a smooth paper wave with a dominant frequency of $2\pi/10.24$ *rad/s* and envelope defined by

$$\text{mod } A(t) = 1.5 + 1.0 \sin \Omega_1 t + 0.75 \sin \Omega_2 t$$

$$\arg A(t) = 2\pi \sin \Omega_3 t + 0.75\pi \sin \Omega_2 t \tag{18}$$

where $\Omega_1 = 24\pi/T$, $\Omega_2 = 40\pi/T$, $\Omega_3 = 10\pi/T$ and $T = 1024$ *s*, the duration of the simulated record. The time step is 0.5 *s*. The paper wave record was established from Equations 1 and 18; it exhibits substantial groupiness. The computed modulus and unwrapped phase records are included in Figure 1. The result is identical with the target envelope, Equation 18.

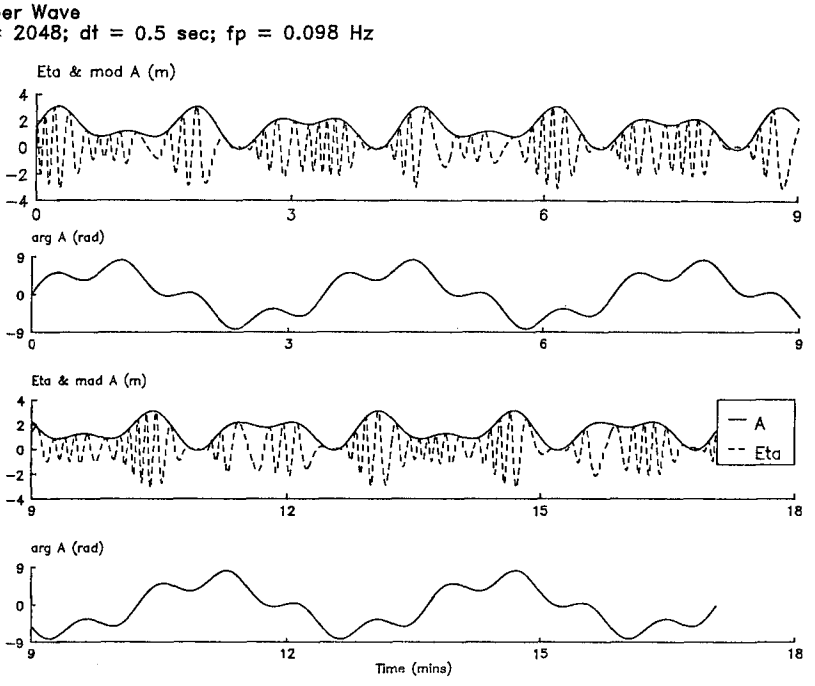

Fig. 1 Complex Envelope for Paper Wave

ALGORITHM EVALUATION

From a purely computational viewpoint, the algorithm described above appeared to be successful. The mod $A(t)$ trace was a consistently good visual representation of the envelope of the record. Visual confirmation of the arg $A(t)$ trace does not seem possible, at least not without considerable experience in complex envelope analysis. One measure of success of the phase unwrapping procedure is the difference $\Delta\ell$ between the real number estimate computed from the right hand side of Equation 14 and the nearest integer ℓ adopted in Equation 15. The differential $\Delta\ell$ was computed at each time step. The mean of the series is closely zero by definition but the standard deviation

$$s = \langle \Delta\ell^2 \rangle^{1/2} \tag{19}$$

is a reasonable measure of the success of the phase unwrapping. For Figure 1, s is zero.

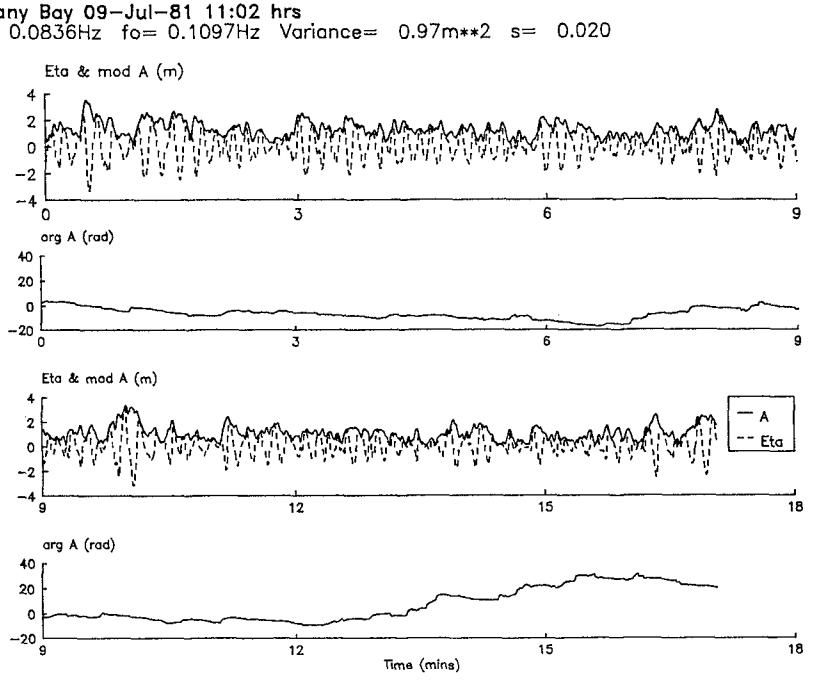

Fig. 2a Complex Envelope for Botany Bay, 9 July 1981, 11:02 hrs.

Figures 2 and 3 are analysis results from field records. The Figure 2 record was measured off Botany Bay on the east coast of Australia in 75 m of water. The record variance is 0.97 m^2, the peak frequency is 0.0836 Hz, the computed dominant frequency is 0.1097 Hz and the standard deviation s is 0.020. The Figure 3 record was measured off Wilson Bluff on the south coast of Australia, the record variance and peak frequency being 1.61 m^2 and 0.0550 Hz respectively. This record is predominantly long period Southern Ocean swell. The computed dominant frequency is 0.0719 Hz and the standard deviation is 0.025. The computed dominant frequencies were typically about thirty percent greater

than the record peak frequencies, but there did not seem to be any apparent physical significance that could be attached to the dominant frequency. The significance of the computed standard deviations might be established by comparison of typical values with expected values if $\Delta\ell$ were a random variable, uniformly distributed in the interval - 0.5 to + 0.5. The theoretical mean and standard deviation of such a distribution would be 0.0 and $12^{-1/2}$ = 0.289, respectively (Ang and Tang 1975). The Figure 2 and 3 results are indeed small with respect to 0.289. These are typical values and clearly demonstrate the relative success of the algorithm.

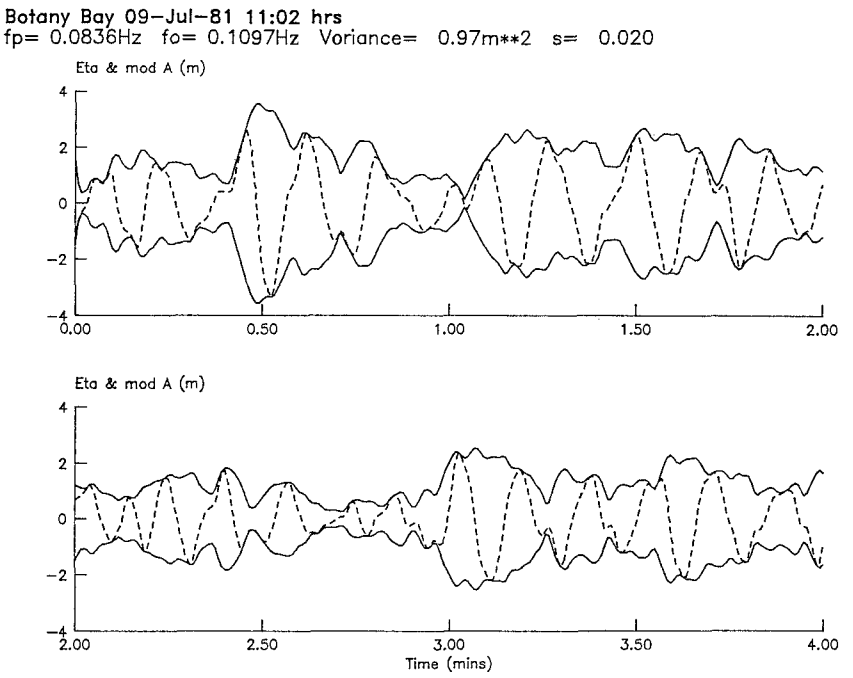

Fig. 2b Expanded Complex Envelope for Botany Bay

An occasional problem was identified in the phase unwrapping procedure where mod $A(t)$ was close to zero. The $d\Phi/dt$ estimate from Equation 13 became very large, resulting in a sudden step change in the $d\Phi/dt$ trace and correspondingly in the Φ trace. This discontinuity could be accommodated by a L'Hospital's rule procedure, as adopted by Read and Sobey (1985) in unwrapping the phase spectrum of the original record, but near zero magnitude points were found to be much less of a probelm for the complex envelope function. A technique suggested by Brillinger (1962) proved to be satisfactory in the vicinity of near-zero $A(t)$ points. This is based on the trigonometrical identity

$$\frac{d\Phi}{dt} = \cos\Phi \frac{d}{dt}(\sin\Phi) - \sin\Phi \frac{d}{dt}(\cos\Phi) \tag{20}$$

A forward difference approximation to the right hand side gave an alternate estimate of

$d\Phi/dt$ that avoided any sudden steps in the $d\Phi/dt$ trace. This procedure was not suitable for general application however as the discrete approximation restricted the estimate of the phase derivative to the range - 1 to + 1.

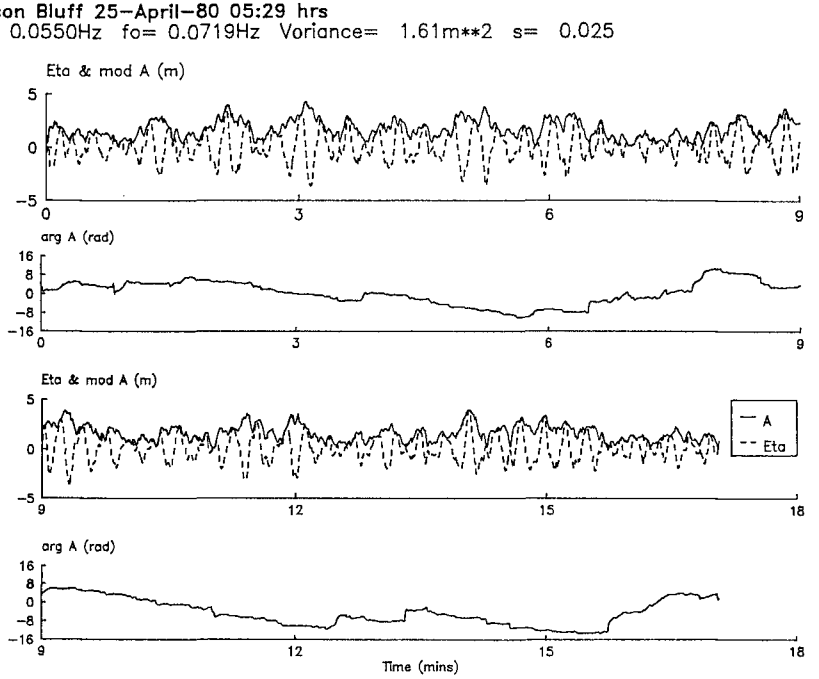

Fig. 3 Complex Envelope for Wilson Bluff, 25 April 1980, 05:29 hrs.

In practice, it was necessary to adopt a rational definition of a near-zero magnitude point. If the envelope amplitudes followed the Rayleigh distribution (Longuet-Higgins 1952), then a characteristic amplitude would be the mean amplitude $(2\sigma^2)^{1/2}$, where σ^2 is the variance of the record. The Equation 20 algorithm was used when mod $A(t)$ was smaller than one-tenth of this value. This tolerance level was not found to be critical.

The value of the mod $A(t)$ traces is clear from Figures 2 and 3, and particularly from Figure 2b which shows only the first four minutes of the Figure 2a results. The removal of the dominant frequency focusses attention quite sharply on the envelope modulations is a very natural manner. Wave grouping is clearly identified, conveniently in a manner that (unlike low pass filtering of $\eta^2(t)$) does not remove potentially valuable information from the record. With only casual experience, the identification of wave grouping in the phase trace alone does not seem possible but some assistance may be forthcoming from the cross-correlation and the cross-spectra between the modulus and argument traces. It is apparent from Figure 2b in particular that there remains potentially significant detail imbedded in the complex envelope amplitude and phase traces.

CORRELATION AND CROSS-CORRELATION

In the time or lag domain, the appropriate statistical summary is the cross-correlogram, plotting the normalized cross-correlation

$$\rho_{R\Phi}(\tau) = C_{R\Phi}(\tau)/\left[C_{RR}(o)C_{\Phi\Phi}(o)\right]^{1/2} \tag{21}$$

against the time lag τ. The cross-correlation $C_{R\Phi}(\tau)$ is the expectation $E[(R(t)-\bar{R})\Phi(t+\tau)]$, where $\bar{R}$ is the average modulus of the envelope. The $C_{RR}(\tau)$ and $C_{\Phi\Phi}(\tau)$ are similarly defined. In practice, the correlograms were computed from the inverse Fourier transform of the variance spectra and cross-spectrum of R and Φ, to take advantage of the FFT algorithm. It is reasonably common in complex demodulation (Hasan 1983) to consider $\ell n\ R(t)$ rather than $R(t)$, as the probability distribution of $\ell n\ R(t)$ is more nearly Gaussian. This practice was considered but not adopted as the range of R in the present problem is relatively small.

Figure 4 shows the correlograms corresponding to the Botany Bay record in Figure 2. The normalized form of the cross-correlation $C_{R\Phi}$ is presented together with the normalized C_{RR} and $C_{\Phi\Phi}$ autocorrelations; $C_{R\Phi}$ is not an odd or even function and there are different traces for positive and negative lags. The correlograms are truncated at $20/f_p$, a typical record length being $100/f_p$.

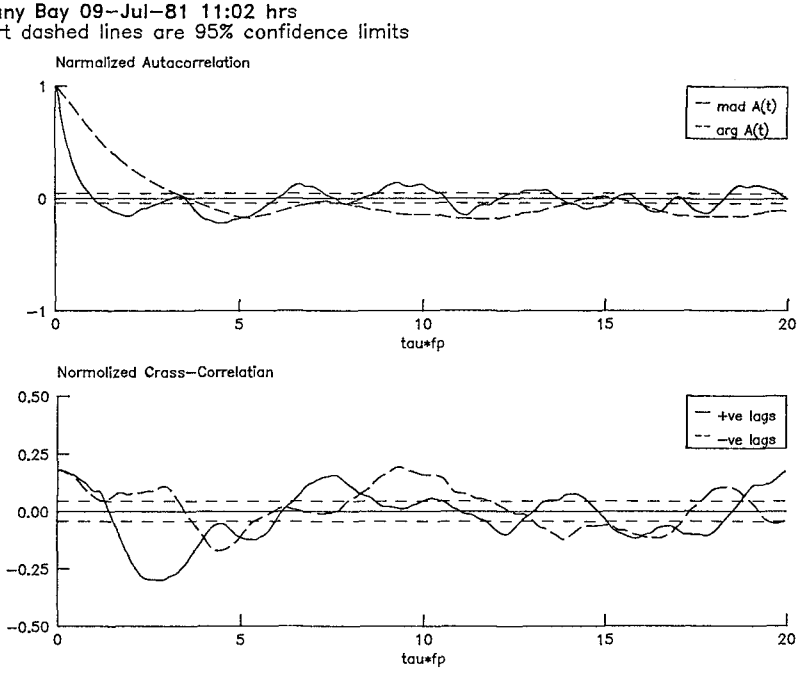

Fig. 4 Correlograms for Botany Bay, 9 July 1981, 11:02 hrs.

The initial part of the C_{RR} trace is typical of random noise. The tail however does not decay but evolves into an irregular long period oscillation with a period of order $4/f_p$. Referring back to the envelope trace in Figure 2, this is the anticipated result, the correlogram oscillation corresponding roughly to the envelope modulations. Similar, but longer period, oscillations are observed in the $C_{\Phi\Phi}$ traces, indicating that the envelope modulations are perhaps a feature of the phase trace as well as the amplitude trace. Periodicity of order $4/f_p$ remains the dominant feature of the cross-correlogram $C_{R\Phi}$, implying some residual coupling between the envelope amplitude and phase. This would appear to impose some qualification on the Gaussian random wave model, which explicitly assumes that the phase trace is completely random. The magnitude and residual periodicity of the cross-correlations imply that the record involves a little order against a lot of background disorder.

The detailed interpretation of correlograms however must acknowledge a number of uncertainties. It is well known (Kendall & Stuart 1966, Jenkins & Watts 1968) that correlograms for short series can be unreliable and may not decay as rapidly as expected; as a rule of thumb, only the first twenty percent might be given any credence. Wave records are moderately long series however, typically 2048 points over seventeen minutes; the maximum lag presented in Figure 4 is $20/f_p$, corresponding typically to less than twenty percent of the record length. These potential uncertainties may be addressed in two ways, the first being the estimation of confidence limits on the correlogram tail. Kendall and Stuart (1965) show that the variance of a normalized auto-correlation estimate is dependent on all autocorrelations in the series, even for large samples with the simplifying assumption of normality. However for a random series where all parent autocorrelations are zero, the expectation of the mean approaches $-1/N$ and the variance $1/N$. The 95 percent confidence limits are accordingly $-1/N \pm 2/(N)^{1/2}$. The width of this confidence band decreases with the length of the series, but is already moderately small at $\pm$ 0.044 for typical 2048 point records. These 95 percent confidence limits are included as the short-dashed lines on Figure 4. Note that rather more than five percent of the autocorrelogram and cross-correlogram tails falls outside this band.

A second approach to these potential uncertainties for moderately small lags is to compute the correlograms from a longer sample, significantly in excess of the typical $100/f_p$. The nominal twenty minute record has become a field measurement standard and longer records are not commonly available. Long records also introduce another problem, in that the record may no longer be statistically stationary. Sea states typically develope at time scales of order hours (Sobey 1986). A record of twenty minutes could reasonably be expected to be stationary, a record of one hour may or may not be stationary according to circumstance, but a record of several hours is unlikely to be stationary. An attempt to solve one problem unfortunately introduces another. Non-stationarity appears as very low frequency trend in the Fourier transform. There is a sharp spectral spike at near-zero frequency, whose magnitude increased substantially with longer records and accordingly finer frequency resolution. This was a particular problem in the phase trace. Jenkins and Watts (1967) recommend removal of such very long period trend prior to analysis by high-pass filtering of the record; this approach was adopted with a cutoff frequency of $0.05\ f_p$. The phase trace was first low-pass filtered by a moving average filter of width equivalent to a $0.05\ f_p$ cutoff. This filtered record was then subtracted from the original phase trace to yield the detrended phase trace. Without detrending, the very low frequency trend completely dominated the Fourier transform and just as completely negated any advantage from a longer record. Detrending was adopted with considerable reservation however, as a developing sea state will likely be accompanied by physical developments in the wave grouping structure which will also negate any advantage from a longer record. An excessively long record (say several hours) is clearly inappropriate. A one hour record might be a reasonable compromise, provided the record is reasonably stationary and due

attention is given to the analysis uncertainties.

The record presented in Figure 2 and again in Figure 4 is the central 2048 points (nominal twenty minutes) of a 8000 point (nominal one hour) record. The variance of this extended record was computed in 1000 point blocks, being 1.40, 0.98, 0.77, 0.99, 0.75, 0.94, 1.06 and 1.18 m^2 for the Botany Bay record. This variation is typical of visually-stationary wave records. Figure 5 is a repetition of the correlogram analyses for the 8000 point record. Record length is of order $400/f_p$ and lags up to $20/f_p$ now represent only five percent of the record length. The confidence band is also somewhat narrower, reflecting the larger sample size. The general trend of the correlogram however remains largely unchanged.

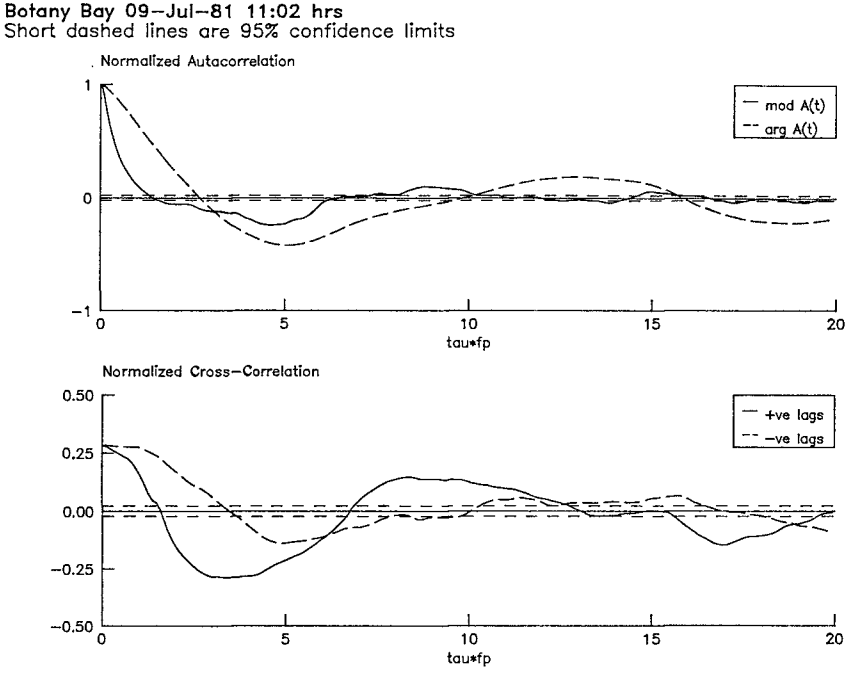

Fig. 5 Correlograms for Botany Bay, 8000 point record.

The Figure 4 correlogram is quite a typical result. It provides a useful perspective on the nature of wave groups in surface gravity waves. A large part of a typical wave record can reasonably be described as random; of order ninety percent of the information can be so described. The residual ten percent or so would appear to be nonrandom, involving long period modulations of the complex wave envelope. The implied low-level correlation between the envelope amplitude and envelope phase traces appears to be an intrinsic property of wave groups.

SPECTRA AND COHERENCE

In the frequency domain, the statistical summary is the cross spectrum

$$E_{R\Phi}(\omega) = \frac{1}{2\pi} \int_{-\infty}^{\infty} C_{R\Phi}(\tau) \exp(-i\omega\tau)\, d\omega \tag{22}$$

$E_{R\Phi}(\omega)$ is a complex function with a real part (the cospectrum) and an imaginary part (the quadspectrum). A useful real function is the coherence

$$\gamma_{R\Phi}(\omega) = \text{mod } E_{R\Phi}(\omega) \,/\, [E_{RR}(\omega) E_{\Phi\Phi}(\omega)]^{1/2} \tag{23}$$

or the squared coherence, the square of Equation 22. The squared coherence approaches unity when the two traces are strongly correlated and it is zero when the traces are uncorrelated. High squared coherence levels suggest some relationship between the phase and amplitude traces, a relationship that is assumed by the Gaussian random wave model to be very small.

The variance spectra $E_{RR}(\omega)$ and $E_{\Phi\Phi}(\omega)$ and the cross-spectrum were estimated directly from the Fourier transforms of the envelope amplitude and phase traces, taking advantage of the FFT algorithm. Raw spectral estimates resulting from the FFT algorithm have only two degrees of freedom and the raw estimate of squared coherence is identically one for all frequencies (Bloomfield 1976). Statistically reliable spectral estimates require a significant increase in the degrees of freedom, achieved by frequency domain smoothing of $E_{RR}(\omega)$, $E_{\Phi\Phi}(\omega)$ and $E_{R\Phi}(\omega)$ prior to estimation of the squared coherence. Frequency domain smoothing (specifically here a moving average filter of half-width L points) increases the degrees of freedom from 2 for the raw FFT estimates to 4L + 2. The widths of 95 percent confidence bands on variance spectral estimates and on squared coherence estimates are accordingly reduced (Jenkins and Watts 1968). A filter half-width L of the nearest integer to $1/(5f_p\Delta t)$ proved to be a suitable compromise between statistical confidence and resolution of detail.

The complex demodulation procedure introduces an immediate problem of frequency resolution in spectral analysis of the complex envelope. A typical 1024 *s* wave record imposes a frequency resolution of 0.000977 Hz, more than adequate to accommodate peak frequencies of order 0.1 Hz. Complex demodulation however removes these frequencies and shifts the spectral peak to frequencies of order 0.01 Hz, where the frequency resolution is distinctly marginal. Frequency resolution is enhanced by a longer record, specifically 8000 points where the frequency resolution is 0.000150 Hz. While this resolution remains marginal, longer record lengths will again introduce problems of non-stationarity.

The frequency domain description for the Botany Bay record is shown in Figure 6, which includes four spectra. Part (*a*) is the variance spectrum for $R - \bar{R}$, the solid line being the raw estimate and the dash-dot line the smoothed spectral estimate, 95 percent confidence bars being shown at selected frequencies for the smoothed spectral estimates. Part (*b*) is an analogous presentation of the variance spectrum for the envelope phase trace. Part (*c*) is the smoothed squared coherence estimate, the dotted line being the 95 percent confidence limit on zero coherence between the amplitude and phase traces. Part (*d*) is arg $E_{R\Phi}(\omega)$, the smoothed phase of the cross spectrum between R and Φ. Variance levels at frequencies above the spectral peak are very small and these presentations are terminated at f_p.

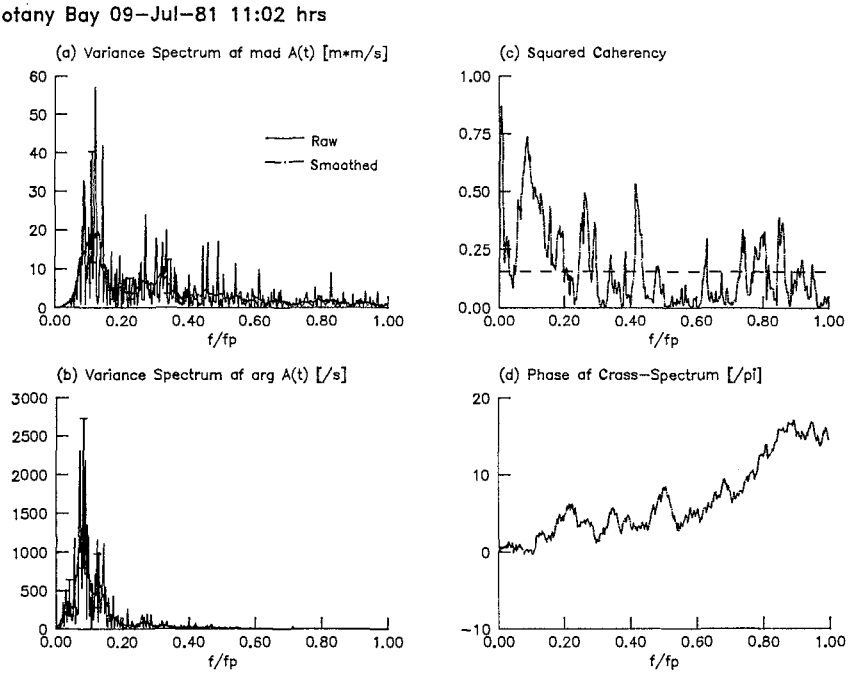

Fig. 6 Spectra for Botany Bay, 8000 point record.

The E_{RR} spectrum for Botany Bay is the result that is anticipated from the correlograms in Figure 4 and 5; it is dominated by short frequencies about an order of magnitude less than the peak frequency. Short frequencies are also clearly dominant in the phase trace in Figure 2 and this is confirmed in Figure 6. The squared coherence spectrum shows moderate coherence in excess of the 95 percent confidence limit on zero coherence at frequencies of order 0.2 f_p to and also 0.8 f_p. The Gaussian random wave model would suggest negligible coherence throughout. Coherence levels are small but not entirely negligible. Analysis of the cross-phase spectrum was not pursued, as marginal frequency resolution and low coherence levels indicated that results would most likely be inconclusive. The higher frequency peak might perhaps be the result of non-linear interactions near the spectral peak. Moderate coherence levels around 0.2 f_p seemed to be a reasonably typical result, at least for waves off Botany Bay.

CONCLUSIONS

The complex envelope function is a very useful analysis technique for wave records where the identification of wave grouping is a relevant interest. The removal of the dominant frequency concentrates attention directly on the envelope modulations without removing potentially useful information from the record. Wave groups are clearly identified against a predominantly random background. An algorithm has been presented for extraction of the complex envelope function, identification of the dominant frequency and unwrapping of the phase trace.

Cross-correlogram and cross-spectral analyses of the simultaneous envelope amplitude and unwrapped phase traces has associated wave grouping with low level phase locking between the amplitude and phase traces. The ordered structure comprises about ten percent of the information contained in a wave record. The balance of the record can reasonably be described as random, as assumed by the Gaussian random wave model. This dominant random component is clearly responsible for the relative success of the Gaussian random wave model.

ACKNOWLEDGMENTS

This work is a result of research sponsored in part by NOAA, National Sea Grant College Program, Department of Commerce, under grant number NA85AA-D-SG140, project number R/CZ-70, through the California Sea Grant College Program, and in part by the California State Resources Agency. The U.S. Government is authorized to reproduce and distribute for governmental purposes. The wave records were provided by the Maritime Services Board of New South Wales and by Esso Australia Ltd. Computations were undertaken on microcomputers provided in part to the University of California, Berkeley, through grants from IBM and from Standard Oil of California (Chevron).

APPENDIX I - REFERENCES

Ang, A. H-S and Tang, W.H. (1974). *Probability Concepts in Engineering Planning and Design*, Wiley, New York.

Bingham, C., Godfrey, M.D. and Tukey, J.W. (1966). "Modern techniques of power spectrum estimation," *IEEE Trans. on Audio and Electroacoustics*, **15**, 56-66.

Bloomfield, P. (1975). *Fourier Analysis of Time Series*, John Wiley & Sons, New York, N.Y.

Bolt, B.A. and Brillinger, D.R. (1978). "Estimation of uncertainties in eigenspectral estimates from decaying geophysical time series," *Geophysical Journal of Royal Astronomical Society*, 59, 593-603.

Brillinger, D.R. (1962). "The practical realization of a Hilbert transformation," Memorandum for File, Bell Telephone Laboratories, unpublished.

Deutsch, R. (1961). *Nonlinear Transformations of Random Processes*, Prentice-Hall, Englewood Cliffs, N.J.

Funke, E.R. and Mansard, E.P.D. (1949). "On the synthesis of realistic sea states," Procs., 17th International Conference on Coastal Engineering, Sydney, ASCE, **3**, 2974-2991.

Hasan, T. (1982). "Complex demodulation: Some theory and applications," in Brillinger, D.R. and Krishnaiah, P.R.(editors), *Handbook of Statistics*, Elsevier, **3**, 125-156.

Jenkins, G.M. and Watts, D.G. (1967). *Spectral Analysis and Its Applications*, Holden-Day, San Frnacisco, CA.

Kendall, M.G. and Stuart, A. (1965). *The Advanced Theory of Statistics*, Hafner Publishing Company, New York, NY.

Longuet-Higgins, M.S. (1951). "On the statistical distribution of the heights of sea waves," *Journal of Marine Research*, 11, 245-266.

Read, W.W. and Sobey, R.J. (1985). "The phase spectrum of surface gravity waves," Manuscript under review.

Rice, S.O. (1943). "Mathematical analysis of random noise," *Bell System Technical Journal*, 23, 282-332.

Rice, S.O. (1944). "Mathematical analysis of random noise," *Bell System Technical Journal*, 24, 46-156.

Sobey, R.J. (1985). "Wind wave prediction," *Annual Review of Fluid Mechanics*, **18**, 149-172.

Sobey, R.J. and Colman, E. (1982). "Scattering analysis and synthesis of wave trains," *Journal of Australian Mathematical Society, Series B*, Special Issue on Waves and Fluids, **25**, 44-63.

Sobey, R.J. and Read, W.W. (1983). "Wave groups in the frequency and time domains," Procs., 19th International Conference on Coastal Engineering, Houston, ASCE, **1**, 695-706.

Sobey, R.J. and Young, I.R. (1985). "Hurricane wind waves - A discrete spectral model," *Journal of Waterway, Port, Coastal and Ocean Engineering*, ASCE, **112**, 370-389.

Thompson, E.F. and Seelig, W.N. (1983). "High wave grouping in shallow water," *Journal of Waterway, Port, Coastal and Ocean Engineering*, ASCE, 110, 139-157.

Thompson, W.C., Nelson, A.R. and Sedivy, D.G. (1983). "Wave group anatomy of ocean wave spectra, " Procs. 19th International Conference on Coastal Engineering, Houston, ASCE, I, 665-677.

CHAPTER 58

Extreme Wave Groups in Storm Seas Near Coastal Water

Ming-Yang Su *

We discuss statistics of wave groups containing the maximal wave height over wave records of 20 minutes. These wave groups are called extreme wave groups (EWGs). The concept of the EWG combines the two previously separately considered design factors of extreme waves and wave groups into a more severe storm seas wave action. The wave data used in this investigation consists of near 540 records of wave staff measurements in the Gulf of Mexico. Specifically, we shall present (a) the dependence of EWG properties on the bandwidth of wave spectra, (b) the mean envelope shape of EWGs, exhibiting distinct differences from the envelope shape of regular basis.

Introduction

The study of wave groupiness has gained increasing attention in the past decade, because of its importance for long-period excitations to marine fixed and/or floating structures. Statistical analyses of ocean waves in storms (Rye, 1974; Goda, 1976; Su, et al., 1982) have firmly established the dependence of wave groupiness, such as its distributions and mean length, on the associated spectral bandwidth. Theoretical analyses (Longuet-Higgins, 1984, Kimura, 1980; Goda, 1976, 1983; Nolte and Hsu, 1972) have further related these properties in terms of either the linear narrow-band Gaussian process, or Markovian process. On the other hand, the most important classical design factor for marine structures is the estimation of extreme waves which are usually assumed to occur singly in nature (see Ochi, 1982 for a review on this subject). It can be convincingly argued, however, that a wave group containing an extremely large wave, if exists, would be an even more appropriate environmental design factor than either the single extreme wave or the "regular" wave group. For the sake of easy reference, we shall call this special type of wave groups, each containing an extremely large wave (to be defined more precisely later) by the name of "extreme wave groups" (EWG) in contrast to the "regular wave group" (RWG) which is normally defined to be a sequence of successive waves whose heights all exceed some prescribed critical value (H_c).

Goda (1976) seems to be the first investigator who made a statistical comparison of these two different types of wave groups. He noted that the mean length of runs for EWG is 2.36 when the critical value $H_c=H_{1/3}$, while the corresponding mean length for RWG is only 1.4. In other words, the highest wave does not appear singly, but is frequently accompanied by two to three high waves. Furthermore, the probability for the highest wave occurring in a group is even higher than regular high waves.

* Naval Ocean Research and Development Activity
NSTL, Mississippi 39529-5004

Wave Data

The first set of wave records used in this investigation was obtained by wave staffs from an offshore platform about 60 miles offshore in the Gulf of Mexico (Ocean Data Gathering Program (OOGP), Station #1) during 1969-1971 under the sponsorship of a consortium of eight oil companies (Ward, 1974). The station is located in South Pass Block 62A, at a depth of about 340 feet. The second set of wave records was measured from a North Sea Platform (Forties Field) at the water depth of 150 ft and was kindly provided to us by UKOOA.

Each wave record is 19.85 minutes long and has been digitized into 4096 data points at the rate of 3.41 samples per second. For this analysis, we selected a total of 533 wave records (from the first set), each with the significant wave height ($H_s=H_{1/3}$)$\geq$2 meters in order to emphasize storm waves. These wave records were measured mostly in winter months, with the exception of during three hurricanes occurring in summer months. The eye of one of the hurricanes, Camille, happened to pass within 10 miles of the measuring platform.

Data Classification

The individual waves with their heights (H_j) and periods (T_j) for j=1,2...N in each wave record are determined by the standard up zero-crossing method. In the set of wave records we used, the value of N lies between 100 and 240 with the average close to 200. The power spectrum E(f) for each wave record is also computed by the Fast Fourier Transform, and is used in turn for computing two parameters indicative of the average bandwidth of the power spectrum. The first parameter was proposed originally by Longuet-Higgins (1984) and called the spectral bandwidth parameter, ν, and defined by

$$\nu = (m_2 m_0/m_1^2 - 1)^{1/2} \tag{1}$$

where m_0, m_1 and m_2 are spectral moments as defined by

$$m_i = \int_0^\infty f^i E(f)df \tag{2}$$

When $\nu^2 << 1$, the power spectrum is said to be narrow. The second parameter was proposed by Goda (1976) and called the spectral peakedness parameter, Q_p, and defined by

$$Q_p = \int_0^\infty 2fE^2(f)df/m_0 \tag{3}$$

The value of Q_p is always greater than unity, and increases with decreasing spectral bandwidth. We have used certain specified ranges of ν and Q_p, independently, to classify the set of wave records into

several subsets in order to see dependence of the statistical characteristics of wave groupiness on the spectral bandwidth.

Definition of Extreme Wave Group (EWG)

For the purpose of our analysis which is constrained by the availability of each wave record being about 20 minutes long, the extreme wave group (EWG) is defined as the wave group containing the largest wave height in the wave record. For convenience of data analyses, we first assume that the EWG may cover up to seven waves and can be expressed as

$$W_{-3}, W_{-2}, W_{-1}, W_0, W_1, W_2, W_3$$

where W_0 is the wave with the largest wave height, the three waves with negative subscripts are waves preceeding W_0, and those with positive subscripts are waves following W_0. The corresponding wave heights, periods, wavelengths, and steepness are denoted by H_i, T_i, L_i and S_i;

$$S_i = a_i k_i = (H_i/2) \times (2\pi/L_i) = \pi H_i/L_i \tag{4}$$

where a_i is the wave amplitude and k_i the wave number (see Figure 1).

Results

We shall present the computed results which show the mean values (denoted with an overbar) of H_i, T_i and S_i for subsets of wave records with prescribed ranges of Q_p or ν. The majority of the wave records had the values of Q_p between 1.3 and 4.0, or has the values of between 0.40 and 1.0. Based on this distribution, we have classified the wave records into the following subsets: (1) for Q_p;

$$\begin{array}{ll} \text{(a)} & 1.0 \leq Q_p \leq 2.0 \\ \text{(b)} & 2.0 \leq Q_p \leq 3.0 \\ \text{(c)} & 3.0 \leq Q_p \leq 4.0 \\ \text{(d)} & 1.0 \leq Q_p \leq 5.0 \text{ (the entire data set)} \end{array} \tag{5}$$

and (2) for ;

$$\begin{array}{ll} \text{(a)} & 0.40 \leq \nu \leq 0.50 \\ \text{(b)} & 0.50 \leq \nu \leq 0.60 \\ \text{(c)} & 0.60 \leq \nu \leq 0.70 \\ \text{(d)} & 0.60 \leq \nu \leq 0.80. \end{array} \tag{6}$$

Table 1 gives the mean values of the wave heights, periods and steepness of the extreme wave groups for each of the three subsets according to the spectral classification of Q_p, plus the entire data set. Note that the wave heights given here have been normalized by the root-mean square of wave surface displacement $(m_0)^{1/2}$ of each corresponding wave record. The wave periods are normalized by the mean wave period of the corresponding wave record.

Table 1. Extreme Wave Group Analysis for Gulf of Mexico Wave Data. $H_{1/3} \geq 2.0$ m. Based on Q_p classification.

	j = -3	-2	-1	0	+1	+2	+3
(a) $\overline{H}_j$	2.335	2.510	3.016	6.284	3.389	2.238	2.322
$\overline{T}_j$	1.093	1.041	1.217	1.369	1.315	1.035	1.003
$\overline{S}_j$	0.152	0.142	0.144	0.186	0.122	0.150	0.143
(b) $\overline{H}_j$	2.491	2.735	3.943	6.335	3.931	2.677	2.361
$\overline{T}_j$	1.024	1.083	1.369	1.289	1.364	1.105	1.014
$\overline{S}_j$	0.154	0.137	0.125	0.195	0.138	0.136	0.146
(c) $\overline{H}_j$	2.667	2.997	4.325	6.352	4.435	3.156	2.704
$\overline{T}_j$	1.085	1.177	1.314	1.233	1.318	1.163	1.059
$\overline{S}_j$	0.122	0.117	0.133	0.208	0.128	0.142	0.136
(d) $\overline{H}_j$	2.506	2.753	3.864	6.325	3.929	2.699	2.418
$\overline{T}_j$	1.047	1.093	1.334	1.291	1.348	1.104	1.022
$\overline{S}_j$	0.153	0.134	0.129	0.196	0.134	0.139	0.143

We shall start with case (d) in Table 1, which includes the entire set of wave records in order to see the overall mean characteristics first, before discussing their dependence on spectral bandwidth. From the mean values of wave heights, H_j, one can see the envelope of the EWG is rather symmetric with respect to the highest wave height, H_0. The mean wave heights for the three central waves are $H_0 = 6.3$ and $(H_{-1}, H_1) = 3.9$, while the mean wave heights for outlying waves; $(H_{-2}, H_2) = 2.7$ and $(H_{-3}, H_3) = 2.5$, are much smaller. Recalling that the mean wave height for a linear narrow band Gaussian process is $H = \sqrt{2\pi} = 2.506$ (Arhan et al., 1976), we can infer, based on the height distribution alone, that (W_{-1}, W_0, W_1) is definitely distinctive from $(W_{-3}, W_{-2}, W_2, W_3)$.

The mean wave periods for the three central waves are $(T_{-1}, T_0, T_1) = 1.3$, while the outlying waves are $(T_{-3}, T_{-2}, T_2, T_3) < 1.1$. Since the expected value of the wave periods for a linear random process would be unity, by definition, we find again that the three central waves (W_{-1}, W_0, W_1) are qualitatively different from the other waves. We also note that $T_0 = 1.29$ is appreciably smaller than $(T_{-1}, T_1) = 1.34$.

The mean wave steepness for the highest wave is $S_0 = a_0 k_0 = 0.2$, while the other waves are about 0.14. (The wave steepness for the highest Stokes waves is 0.443.) So, the highest wave turns out to be also the steepest, in the mean, a very significant feature indeed.

Taking together the above observed properties of both wave heights and wave periods, we may suggest that each extreme wave group, in the mean, contains three waves. Furthermore, if we use a threshold wave height $H_c = H_{1/3} = 4m_0^{1/2}$ for determining a wave group, then the mean (run) group length of the extreme wave group would be slightly less than 2.5. (Since $H_{-1} = 3.86$ and $H_{+1} = 3.93$ are only slightly smaller than the threshold value of 4.0, W_{-1} and W_{+1} will have slightly less than 50% of chance exceeding the prescribed threshold.) This estimated value is thus in good agreement with the value of 2.36 found by Goda (1976). The mean wave group length for EWG is considerably larger than that of regular wave groups ($\approx$1.5) (Goda, 1976; Su and Bergin, 1983).

Next, we shall examine the effects of spectral bandwidth on the above group characteristics by comparing cases (a), (b) and (c) against (d) in Table 1. As the spectral bandwidth becomes narrower, i.e., Q_p increasing from 1.0 to 4.0, or from case (a) to case (c), H_{+1} is found to increase from about 3.2 to 4.4, and H_0 increases from 6.28 to 6.35, and S_0 increases from 0.186 to 0.208, and T_0 decreases from 1.37 to 1.23. Therefore, one may conclude that the specific features noted for the extreme wave group from the entire data set (case d) becomes even more prominent as the wave power spectra becomes narrower as parameterized by Q_p. In other words, for narrower spectral bandwidth, the mean group length will become longer, and the highest waves become steeper, and, increasingly, the wave period of the central waves become shorter than those of the surrounding waves.

It is well known that power spectra have narrower bandwidth in the fetch-limited growth stages than in either the fully saturated stages or in decaying stages. (Here we have excluded the consideration of swells which could have extremely sharp narrow spectra for which the beat phenomenon can be suitably applied.) One thus expects to find most clearly the unique feature of the extreme wave group in the rapidly growing sea.

Table 2 gives the statistics of the extreme wave groups as given in Table 1 with the exception that the wave records are grouped by the spectral bandwidth parameter, ν . We found much the same group characteristics as noted in Table 1 in all three cases, (a), (b) and (c), for ν = 0.4-0.5, 0.5-0.6, and 0.6-0.8, respectively, but the effects of spectral bandwidth based on ν is not as clear as based on Q_p. One possible reason for this relative sensitivity between the classifications of Q_p and ν is as follows: by its definition, Q_p emphasizes the contribution from the peak of the spectrum due to the square of E(f), while ν , by its definition, considers equally the contribution from the higher frequency range due to the factor of f^2 in the m_2 computation. In our determination of individual waves by the zero-crossing method which acts roughly as a low-pass filter, these individual waves thus obtained are primarily energy-containing

Table 2. Extreme Wave Group Analysis for Gulf of Mexico Wave Data. $H_{1/3} \geq 2.0$ m. Based on classification.

	j = -3	-2	-1	0	+1	+2	+3
(a) $\overline{H}_j$	2.586	2.823	3.971	6.320	3.993	2.739	2.404
$\overline{T}_j$	1.046	1.085	1.324	1.228	1.311	1.088	1.029
$\overline{S}_j$	0.131	0.132	0.122	0.213	0.125	0.140	0.129
(b) $\overline{H}_j$	2.537	2.701	3.703	6.233	3.780	2.532	2.429
$\overline{T}_j$	1.068	1.101	1.335	1.316	1.340	1.086	1.012
$\overline{S}_j$	0.148	0.120	0.109	0.169	0.120	0.128	0.140
(c) $\overline{H}_j$	2.310	2.653	3.895	6.347	3.976	2.674	2.478
$\overline{T}_j$	1.018	1.106	1.327	1.389	1.418	1.190	0.972
$\overline{S}_j$	0.140	0.135	0.125	0.177	0.119	0.122	0.159
(d) $\overline{H}_j$	2.557	2.653	3.982	6.420	4.098	2.890	2.429
$\overline{T}_j$	0.965	1.073	1.320	1.359	1.420	1.143	1.000
$\overline{S}_j$	0.139	0.145	0.133	0.193	0.122	0.139	0.156

lower-frequency waves centering around the spectral peak. Hence, Q_p will be a more sensitive parameter than γ in our analysis.

In Table 3(a,b), we show the statistical results of EWG from the wave data from the Forties Field in the North Sea for $H_{1/3} \geq 2.5$ m. Similarly, in Table 4(a,b) we show the results for the same set of wave data, except only for those records with $H_{1/3} \geq 5.0$ m, in order to emphasize the truly extremely large storm waves. Comparing the results from both Table 3 and 4, with those from Table 1, we have found very little difference among them.

Interpretation of Large Waves and Extreme Wave Groups

Several unique features of the extreme wave group, particularly for the case with narrower spectral bandwidth normally expected for growing seas, prompt us to consider a hypothesis that these extreme wave groups may be caused by nonlinear wave instabilities, rather than simply due to the linear beat phenomenon. In this section we shall present some reasoning in support of this hypothesis.

The side-band instability is characterized by two perturbations with the frequencies $f_1 = f_0 - \Delta f$ and $f_2 = f_0 + \Delta f$, where f_0 is the original primary (unperturbed) freqeuncy of a wave train and/or wave

Table 3(a). Extreme Wave Group Analysis for North Sea Wave Data. $H_{1/3} \geq 2.5$ m.

1.00 <= QP <= 2.00

LARGEST WAVE ONLY	(TOTAL NUMBER OF WAVE GROUPS = 33)						
	WAVES						
	-3	-2	-1	0	1	2	3
AVG HEIGHT	2.105	2.204	3.065	6.363	3.277	2.391	2.282
STD DEV	1.042	1.105	1.213	1.069	1.018	1.265	1.324
AVG PERIOD	0.911	0.994	1.272	1.383	1.361	1.039	1.080
STD DEV	0.348	0.414	0.472	0.424	0.460	0.419	0.498
AVG SLOPE	0.036	0.032	0.028	0.047	0.026	0.030	0.032
STD DEV	0.019	0.018	0.017	0.019	0.016	0.015	0.027
AVG STEEPNESS	0.112	0.102	0.087	0.149	0.083	0.094	0.100
STD DEV	0.060	0.056	0.053	0.059	0.051	0.048	0.080

2.00 <= QP <= 3.00

LARGEST WAVE ONLY	(TOTAL NUMBER OF WAVE GROUPS = 511)						
	WAVES						
	-3	-2	-1	0	1	2	3
AVG HEIGHT	2.321	2.464	3.469	6.011	3.443	2.563	2.448
STD DEV	1.180	1.237	1.149	0.578	1.215	1.291	1.255
AVG PERIOD	0.991	1.027	1.265	1.247	1.243	1.059	1.036
STD DEV	0.395	0.385	0.340	0.200	0.343	0.386	0.382
AVG SLOPE	0.035	0.034	0.032	0.053	0.032	0.032	0.032
STD DEV	0.021	0.020	0.026	0.023	0.019	0.017	0.017
AVG STEEPNESS	0.111	0.108	0.099	0.165	0.100	0.101	0.101
STD DEV	0.064	0.063	0.056	0.059	0.054	0.055	0.054

3.00 <= QP <= 4.00

LARGEST WAVE ONLY	(TOTAL NUMBER OF WAVE GROUPS = 415)						
	WAVES						
	-3	-2	-1	0	1	2	3
AVG HEIGHT	2.452	2.883	3.918	6.054	3.836	2.859	2.569
STD DEV	1.240	1.332	1.252	0.563	1.131	1.267	1.284
AVG PERIOD	1.017	1.104	1.286	1.216	1.299	1.118	1.046
STD DEV	0.358	0.356	0.271	0.130	0.249	0.345	0.333
AVG SLOPE	0.037	0.036	0.036	0.058	0.034	0.035	0.035
STD DEV	0.023	0.018	0.020	0.015	0.018	0.019	0.018
AVG STEEPNESS	0.117	0.113	0.113	0.183	0.107	0.110	0.112
STD DEV	0.068	0.057	0.058	0.047	0.048	0.058	0.058

Table 3(b). Continuation of Table 3(a).

4.00 <= GP <= 5.00

LARGEST WAVE ONLY (TOTAL NUMBER OF WAVE GROUPS = 107)

	WAVES -3	-2	-1	0	1	2	3
AVG HEIGHT	2.496	3.040	3.980	5.972	3.902	3.103	2.689
STD DEV	1.180	1.169	1.077	0.515	1.111	1.405	1.279
AVG PERIOD	1.046	1.148	1.273	1.181	1.284	1.123	1.117
STD DEV	0.329	0.282	0.216	0.101	0.176	0.312	0.288
AVG SLOPE	0.034	0.035	0.036	0.061	0.035	0.036	0.032
STD DEV	0.016	0.018	0.014	0.015	0.015	0.016	0.016
AVG STEEPNESS	0.107	0.110	0.114	0.191	0.109	0.112	0.100
STD DEV	0.051	0.058	0.045	0.048	0.046	0.051	0.051

5.00 <= GP <= 6.00

LARGEST WAVE ONLY (TOTAL NUMBER OF WAVE GROUPS = 24)

	WAVES -3	-2	-1	0	1	2	3
AVG HEIGHT	3.112	3.279	4.525	5.962	4.314	3.219	2.699
STD DEV	1.250	1.236	0.959	0.532	0.781	1.339	1.235
AVG PERIOD	1.106	1.191	1.249	1.195	1.308	1.198	1.184
STD DEV	0.288	0.217	0.151	0.092	0.111	0.300	0.257
AVG SLOPE	0.037	0.033	0.042	0.059	0.036	0.033	0.028
STD DEV	0.016	0.013	0.013	0.013	0.011	0.015	0.013
AVG STEEPNESS	0.117	0.104	0.131	0.184	0.113	0.103	0.087
STD DEV	0.051	0.042	0.041	0.039	0.034	0.048	0.042

1.00 <= GP <= 6.00

LARGEST WAVE ONLY (TOTAL NUMBER OF WAVE GROUPS = 1090)

	WAVES -3	-2	-1	0	1	2	3
AVG HEIGHT	2.399	2.690	3.701	6.033	3.652	2.738	2.518
STD DEV	1.208	1.289	1.214	0.590	1.182	1.310	1.273
AVG PERIOD	1.007	1.071	1.273	1.232	1.273	1.090	1.052
STD DEV	0.373	0.366	0.307	0.182	0.299	0.365	0.359
AVG SLOPE	0.036	0.035	0.034	0.056	0.033	0.034	0.033
STD DEV	0.021	0.019	0.022	0.020	0.018	0.018	0.018
AVG STEEPNESS	0.113	0.110	0.106	0.174	0.103	0.105	0.105
STD DEV	0.064	0.060	0.056	0.054	0.051	0.056	0.056

Table 4(a). Extreme Wave Group Analysis for North Sea Wave Data. $H_{1/3} \geq 5$ m.

1.00 <= GP <= 2.00

LARGEST WAVE ONLY (TOTAL NUMBER OF WAVE GROUPS = 27)

	-3	-2	-1	0 WAVES	1	2	3
AVG HEIGHT	2.609	2.728	3.119	6.236	3.310	2.159	2.338
STD DEV	1.420	1.382	1.850	1.176	1.494	1.170	1.192
AVG PERIOD	1.134	1.145	1.179	1.377	1.143	1.015	1.031
STD DEV	0.590	0.723	0.510	0.303	0.494	0.493	0.519
AVG SLOPE	0.039	0.041	0.062	0.073	0.050	0.039	0.039
STD DEV	0.025	0.024	0.117	0.120	0.043	0.027	0.019
AVG STEEPNESS	0.121	0.129	0.122	0.156	0.148	0.121	0.123
STD DEV	0.080	0.075	0.106	0.090	0.106	0.083	0.060

2.00 <= GP <= 3.00

LARGEST WAVE ONLY (TOTAL NUMBER OF WAVE GROUPS = 203)

	-3	-2	-1	0 WAVES	1	2	3
AVG HEIGHT	2.311	2.567	3.400	6.064	3.187	2.578	2.487
STD DEV	1.193	1.296	1.418	0.714	1.260	1.176	1.249
AVG PERIOD	1.018	1.045	1.242	1.286	1.211	1.076	1.044
STD DEV	0.400	0.386	0.387	0.221	0.360	0.378	0.388
AVG SLOPE	0.037	0.039	0.040	0.077	0.038	0.039	0.041
STD DEV	0.021	0.022	0.048	0.196	0.031	0.032	0.073
AVG STEEPNESS	0.115	0.121	0.115	0.172	0.114	0.118	0.113
STD DEV	0.066	0.069	0.073	0.066	0.072	0.072	0.064

3.00 <= GP <= 4.00

LARGEST WAVE ONLY (TOTAL NUMBER OF WAVE GROUPS = 133)

	-3	-2	-1	0 WAVES	1	2	3
AVG HEIGHT	2.528	2.903	3.738	6.035	3.789	2.924	2.502
STD DEV	1.235	1.224	1.207	0.608	1.182	1.177	1.317
AVG PERIOD	1.058	1.090	1.246	1.230	1.259	1.166	1.029
STD DEV	0.346	0.321	0.275	0.134	0.268	0.320	0.411
AVG SLOPE	0.036	0.040	0.038	0.065	0.038	0.049	0.051
STD DEV	0.018	0.023	0.018	0.065	0.017	0.171	0.138
AVG STEEPNESS	0.115	0.125	0.120	0.188	0.119	0.109	0.125
STD DEV	0.057	0.064	0.057	0.045	0.052	0.057	0.074

Table 4(b). Continuation of Table 4(a).

4.00 <= GP <= 5.00

LARGEST WAVE ONLY	(TOTAL NUMBER OF WAVE GROUPS = 40)						
	WAVES						
	-3	-2	-1	0	1	2	3
AVG HEIGHT	2.730	3.107	3.695	5.923	3.840	3.006	2.524
STD DEV	1.066	1.281	1.202	0.722	1.196	1.172	1.125
AVG PERIOD	1.137	1.168	1.328	1.235	1.277	1.148	1.086
STD DEV	0.316	0.320	0.210	0.115	0.199	0.298	0.273
AVG SLOPE	0.037	0.037	0.034	0.061	0.037	0.038	0.033
STD DEV	0.024	0.017	0.015	0.015	0.013	0.018	0.013
AVG STEEPNESS	0.117	0.115	0.107	0.191	0.115	0.120	0.102
STD DEV	0.074	0.053	0.047	0.047	0.041	0.058	0.040

5.00 <= GP <= 6.00

LARGEST WAVE ONLY	(TOTAL NUMBER OF WAVE GROUPS = 11)						
	WAVES						
	-3	-2	-1	0	1	2	3
AVG HEIGHT	2.987	3.311	3.658	5.870	3.591	3.051	2.386
STD DEV	0.972	1.405	1.139	0.433	0.854	0.907	0.858
AVG PERIOD	1.194	1.185	1.265	1.183	1.283	1.245	1.113
STD DEV	0.258	0.140	0.090	0.073	0.075	0.153	0.283
AVG SLOPE	0.035	0.037	0.036	0.068	0.035	0.034	0.035
STD DEV	0.012	0.015	0.012	0.010	0.010	0.016	0.019
AVG STEEPNESS	0.111	0.116	0.115	0.214	0.111	0.108	0.111
STD DEV	0.037	0.048	0.036	0.032	0.031	0.051	0.059

1.00 <= GP <= 6.00

LARGEST WAVE ONLY	(TOTAL NUMBER OF WAVE GROUPS = 414)						
	WAVES						
	-3	-2	-1	0	1	2	3
AVG HEIGHT	2.458	2.757	3.525	6.047	3.462	2.716	2.483
STD DEV	1.217	1.298	1.374	0.720	1.272	1.192	1.248
AVG PERIOD	1.055	1.081	1.248	1.266	1.230	1.112	1.044
STD DEV	0.391	0.391	0.347	0.197	0.328	0.362	0.394
AVG SLOPE	0.037	0.039	0.040	0.071	0.038	0.042	0.043
STD DEV	0.020	0.022	0.047	0.146	0.027	0.100	0.094
AVG STEEPNESS	0.115	0.122	0.116	0.179	0.118	0.115	0.117
STD DEV	0.064	0.066	0.068	0.061	0.066	0.066	0.065

packet under consideration. Furthermore, the Δf is related to the wave steepness, a_0k_0, of the original primary waves by

$$\Delta f = a_0k_0f_0. \tag{8}$$

Experimental observation under laboratory-controlled conditions (Su, 1982 and 1984) showed that at the maximum modulation due to the side-band instability the amplitudes for the two side-band components, a_1 and a_2, are approximately equal to each other, and further related to the amplitude, a_0, of the primary wave at the particular moment by

$$a_1^2 = a_2^2 = 1/2a_0^2. \tag{9}$$

Hence, the time series of the surface displacement, $\zeta(t)$, of the wave train under the maximum modulation of the side-band instability can be expressed as

$$\begin{aligned}\zeta(t) &= a_0 \sin(2\pi f_0 t) + a_1 \sin(2\pi f_1 t) + \\ &\qquad a_2 \sin(2\pi f_2 t) \\ &= a_0 \sin(2\pi f_0 t) \\ &\quad + \sqrt{1/2}\, a_0 \sin[2\pi(1-a_0k_0)f_0 t] \\ &\quad \sin[2\,(1+a_0k_0)f_0 t] \\ &= a_0\,[1+\sqrt{2}\cos(2\pi a_0k_0f_0t)]\sin(2\pi f_0 t).\end{aligned} \tag{10}$$

Note that the expression in the square bracket is the slower varying envelope of the wave group, which have a repitition period equal to $(a_0k_0)^{-1}$ number of primary wave periods. Now, the mean wave steepness for the case (c) with $3.0 < 4.0$ in Table 1 is equal to $S = 1/3\ (0.133 + 0.208 + 0.128) = 0.156$. If we take the average $S = 0.16$, then the repetition length of the wave group is nearly 6 waves. The corresponding wave heights for the seven waves centering around the maximum of the wave envelope are then given by

$$\begin{aligned}H_0 &= a_0(1+\sqrt{2}\cos 0^0) = 2.41\, a_0 = H_0 \\ H_{-1}, H_1 &= a_0(1+\sqrt{2}\cos 60^0) = 1.707\, a_0 = 0.7\, H_0 \\ H_{-2}, H_2 &= a_0\,(1+\sqrt{2}\cos 120^0) = 0.293\, a_0 = 0.121\, H_0 \\ H_{-3}, H_3 &= a_0\,(1+\sqrt{2}\cos 180^0) = 0.41\, a_0 = 0.170\, H_0\end{aligned} \tag{11}$$

The most significant feature of the distribution of the above wave heights is the considerable smallness of $(H_{-3}, H_{-2}, H_2, H_3)$ in comparison to (H_{-1}, H_0, H_1). This feature agrees remarkably well with the observation of the extreme wave group consisting of three high waves, in the mean, as presented in the last section. The ratio $(H_{-1},$

$H_1)/H_0 = 4.435/6.352 = 0.698 = 0.7$ for case (d) in Table 1 agrees almost exactly with the $(H_{-1}, H_1) = 0.7\ H_0$ of the nonlinear model. The observed fact that $T_0 < (T_{-1}, T_1)$ in Table 1 is also consistent with the experimental observation in the side-band instability.

On the other hand, let's consider a wave train consisting of two sine waves with equal amplitudes but with a difference in frequencies by an amount of $f = a_0 k_0 f_0$ the same as in the side-band instability. The time series of the corresponding surface displacement for the beat phenomenon will be

$$(t) = a_0 \sin (2\pi f_1 t) + a_0 \sin (2\pi f_2 t)$$

with $f_1 = f_0 - 1/2\Delta f$, and $f_2 = f_0 + 1/2\Delta f$. Hence,

$$(t) = a_0[2 \cos (\pi\, a_0 k_0\, f_0 t)] \sin (2\pi f_0 t). \qquad (12)$$

The envelope for the beat phenomenon is a simple cosine shape with a repetition period twice longer than the period for the side-band modulation. With the same value of $a_0 k_0 = 0.16$, the seven waves centering around the maximum of the envelope are, approximately,

$$\begin{aligned} H_0 &= 2a_0 \cos 0^0 = 2a_0 = H_0 \\ (H_{-1}, H_1) &= 2a_0 \cos 30^0 = 1.732a_0 = 0.866\ H_0 \\ (H_{-2}, H_2) &= 2a_0 \cos 60^0 = a_0 = 0.5\ H_0 \\ (H_{-3}, H_3) &= 2a_0 \cos 90^0 = 0 \end{aligned} \qquad (13)$$

Note that $(H_{-2}, H_2) = 0.5\ H_0$ in this case is much larger than the corresponding values for the side-band instability. Of course, when Δf used smaller than the $a_0 k_0 f_0$, the value of H_{+2} will increase, and vice versa.

Conclusions

We have analyzed two large sets of ocean wave records collected in storm conditions for the structure of wave groups each containing the highest wave height in that wave record, called the extreme wave groups. We found that the extreme wave group predominantly consists of three high waves with heights greater than the significant wave height, and with the mean periods equal about 1.3 times the average period for the entire collection of individual waves determined by the standard up zero-crossing method, and with the mean wave steepness for the highest wave equal to about 0.20. Furthermore, as the spectral bandwidth becomes narrower, these features of the extreme wave groups become more prominent. Based on a previous knowledge of experimental studies on nonlinear side-band instability of finite-amplitude waves, the extreme wave groups are found to be explainable better as the manifestation of

the maximum modulation under this type of nonlinear instability, than as the simple linear beat phenomenon.

The experimental results, statistical analyses of field data and theoretical findings, led to suggest that spilling wave breaking for large energy-containing waves near the peak frequency can occur due to nonlinear coupling of instabilities for average wave steepness near 0.14 to 0.18.

In summary, large giant waves, wave groups and wave breaking are most likely the different aspects of the same dynamical process due to the intrinsic instabilities of nonlinear steep waves.

References

Goda, Y. 1976. On wave groups. BOSS '76, pp. 115-128.

Goda, Y. 1983. Analysis of wave grouping and spectra of long-travelled swell. Rep. the Port and Harbour Research Institute, Japan.

Kimura, A. 1980. Statistical properties of random wave groups. Proc. 17th Int. Conf. on Coastal Eng. pp. 2955-2973.

Longuet-Higgins, M.S. 1984. Statistical properties of wave groups in a random sea state. Phil. Trans. R. Soc. Lond. A 312, pp. 219-250.

Nolte, K.G. and F.H. Hsu. 1972. Statistics of ocean wave groups. Proc. 4th Offshore Tech. Conf., pp. 139-146.

Ochi, M.K. 1982. Stochastic analysis and probabilistic prediction of random seas. In Advances in Hydroscience, ed. V.E. Chow, Vol. 13, pp. 217-375.

Rye, H. 1974. Wave group formation among storm waves. Proc. 14th Coastal Engineering Conf., Vol. 1, pp. 164-183.

Su, M.Y. 1982. Evolution of groups of gravity waves with moderate to high steepness. Phys. Fluids, 25, pp. 2167-2174.

Su, M.Y. 1982. Three-dimensional deep-water waves. Part 1. Experimental measurement of skew and symmetric wave patterns. J. Fluid Mech., 124, 73-108.

Su, M.Y., M. Bergin and S. Bales. 1982. Characteristics of wave groups in storm seas. Proc. Ocean Structural Dynamics Symposium '82. Corvallis, Oregon, pp. 118-132.

Su, M.Y. and A.W. Green. 1984. Coupled two- and three-dimensional instabilities of surface gravity waves. Phys. Fluids 27(11), pp. 2595-2597.

Ward, E.G. 1974. Ocean Data Gathering Program - An Overview. Offshore Tech. Conf., pp. 771-780.

CHAPTER 59

Practical Method For Evaluating Directional Spectra After Shoaling and Refraction

Frederick L.W. Tang* and C.F. Lin**

ABSTRACT

Different Methods have been developd to calculate the deformation of spectrum as waves advance to the shallow water. Wave ray method is a traditional way to compute the change of wave ray after refraction. It is restricted to the regular wave. After slicing the linear spectrum, a lot of components of spectrum can be gained, and each component can be considered as a monochromatic wave. And then after the deformed components are worked out at the same point in sea, a deformed spectrum in shallow water is gained by summing up them. Therefore the wave ray method could be extended to the irregular wave in ocean. In real bathymetry, the difficulty in applying such method is to solve the wave ray which must pass through the assigned point. In this paper, calculation approach as well as computer program are contrived to adopted in real bathymetry. The results of computation reveal some significant characteristics of directional spectra in shallow water. Furthermore, the statistical features of waves at the point of interest are to be evaluated.

Introduction

For design of offshore structures on continential shelf or shallow water area, it is necessary to evaluate the design spectrum at the location of construction. As waves propagate from deep water into shallow water, they are modified by their interaction with the bottom topography. Provided that the directional wave spectrum in deep water region is known by forcast or measurement, it can be sliced to rectangular columns of finite number as linear spectrum is assumed. Every column represents small amplitude monochromatic wave, its shoaling and refraction are to be calculated by traditional procedures, then the columns are changing their height, and shifting their directions. Summing up the new columns, a wave spectrum at the point of interest is worked out.

With a straight uniform parallel bottom contour model, such method has been used by others (Nagai, 1972, etc). In real bathymatry, more effort must be paid due to the unexpected wave direction as wave advanced into shallow water. A try and error method is adopted in this calculation.

Deformation of spectrum

* Professor, Dr. Eng., Department of Hydraulics & Ocean Eng.,National Cheng Kung University, Tainan, Taiwan, 70101, R.O.C.

** Dr. Eng., Department of Hydraulics & Ocean Eng., National Cheng Kung University, Tainan, Taiwan, 70101, R.O.C.

The basic assumptions needed in this computation are:
(1) Waves are generated in deep sea and diminished on shoreline.
(2) Waves are in steady state, in which the time dependency which may result from wind generation is negligible.
(3) Energy dissipation is disregarded due to wave-seafloor interaction, white cap and breakers.
(4) The mathematical model implies no transfer of energy across orthogonals.

Ocean waves are composed of different frequency component waves in all direction. Its spectral density function can be defined as:

$$D(f,\theta)=S(f)\ F(f,\theta) \qquad \cdots\cdots(1)$$

where S(f): frequency spectrum
$F(f,\theta)$: directional function

in which the directional function is such that

$$\int_{-\pi}^{\pi} F(f,\theta)\,d\theta = 1 \qquad \cdots\cdots(2)$$

therefore, the one-dimensional frequency density function S(f) results from the integration of:

$$s(f) = \int_{-\pi}^{\pi} F(f,\theta)\,d\theta \qquad \cdots\cdots(3)$$

Linear spectrum can be sliced to numerous components. Each component has its representative frequency and can be considered as a regular wave. In practice, we divide the spectrum into finite components which depend on the accurancy of calculation and consumption of computer time.

There are three methods used in slicing the spectrum: (1) equal frequency interval method (2) equal energy interval method (3) combination of those mentioned above. Report indicated that over ninety percentage of spectrum energy concentrated in neighborhood of peak frequency fop, bounded in 0.7 fop $\sim$ 1.6 fop, see Mitsuyasu, 1984. For this reason, it seems more desirable to adopt method(3), but it will take much computer time. In this calculation, we apply the equal energy interval method.

The sketch of sliced spectrum is shown on Fig.1. The representative frequency of every component can be calculated with its second moment as following:

$$f_{en}^2 \cdot \Delta E = \int_{f_{n-1}}^{f_n} f^2\, s(f)\,df \qquad \cdots\cdots(4)$$

where f_{cn}: representative frequency of component spectrum
f_{n-1}, f_n: Lower, upper bounded frequency of component spectrum
spectral energy of component

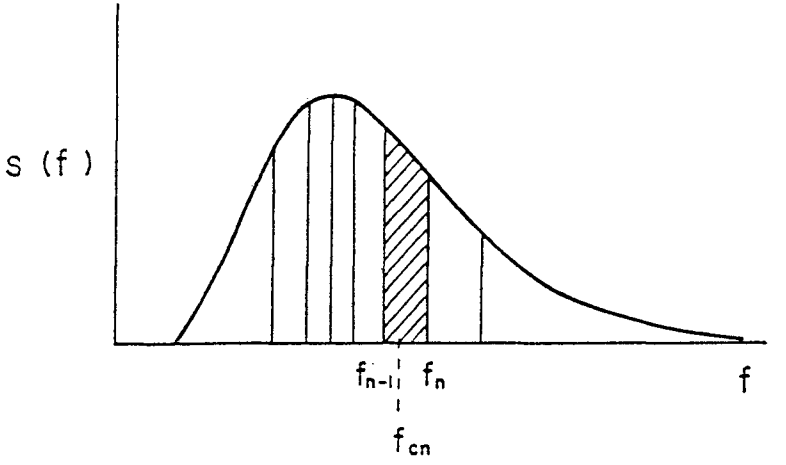

Fig.1 Sketch of sliced spectrum

Directional function can be divided by equal small angle $\Delta\theta$, as shown on Fig.2, then

$$\Delta\theta = \frac{|\theta_{max}| + |\theta_{min}|}{N} \qquad \cdots\cdots(5)$$

N: total dividing number
$\theta_{max}, \theta_{min}$: Max, Min. distribution angle with principal direction respectively.

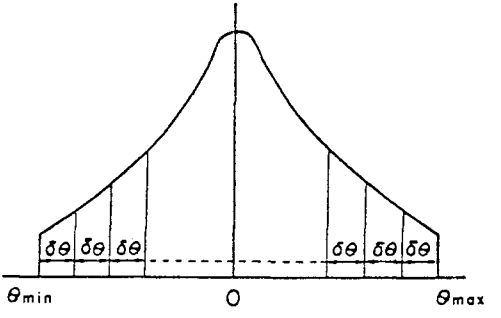

Fig.2 Sketch of sliced directional function

After slicing the known spectrum and directional function in deep sea, we can gain finite numbers of component spectrum with different incident directions and frequcies. Each component is a monochromatic wave, then the traditional wave ray method can be available for computing the deformation of component spectrum at the interesting point.

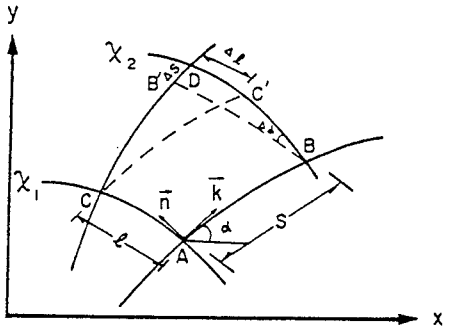

Fig.3 Sketch of wave ray and front

Fig.3 shows the sketch of wave ray and wave front, then the wave ray equation and wave intensity equation are given:

$$\left.\begin{aligned} \frac{d\alpha}{ds} &= \frac{1}{c}\left[\sin\alpha\frac{\partial c}{\partial x}-\cos\alpha\frac{\partial c}{\partial y}\right] \\ \frac{d^2\ell}{ds^2} &- p(s)\frac{d\ell}{ds}+q(s)\ell=0 \end{aligned}\right\} \qquad \cdots\cdots(6)$$

where

$$\left.\begin{aligned} p(s) &= \frac{1}{c}\left[\cos\alpha\frac{\partial c}{\partial x}+\sin\alpha\frac{\partial c}{\partial y}\right] \\ q(s) &= \frac{1}{c}\left[\sin^2\alpha\frac{\partial^2 c}{\partial x^2}-\sin 2\alpha\frac{\partial^2 c}{\partial x\partial y}\right. \\ &\quad \left.+\cos^2\alpha\frac{\partial^2 c}{\partial y^2}\right] \end{aligned}\right\} \qquad \cdots\cdots(7)$$

C: wave celerity
ds: increment along wave ray
$d\ell$: increment along wave front

By solving equation (6), we can find width between two rays, ℓ, refracting angle α. Then the shoaling coefficient, refraction coefficient of component wave are calculated by definition:

$$\left.\begin{aligned} K_s &= \sqrt{\frac{C_o}{2nc}} \\ K_r &= \sqrt{\frac{\ell_o}{\ell}} \end{aligned}\right\} \qquad \cdots\cdots(8)$$

where ℓ_o : initial value of width of two adjacent rays
C_o : wave celerity in deep sea.

$$n: \text{ factor} = \frac{1}{2}\left[1 + \frac{2kd}{\sinh(2kd)}\right]$$

The shoaling coeff., K_s , and refraction coeff., K_r , of deformed spectra can be solved as following:
For unidirectional spectrum:

$$\left.\begin{aligned} K_s &= \sqrt{\sum_{i=1}^{M} (K_s^2 \cdot S_o^*(f^*) \cdot \Delta f_n^*)_i / E_o^*} \\ K_r &= \sqrt{\frac{\sum_{i=1}^{M} (K_s^2 K_r^2 \cdot S_o^*(f^*) \cdot \Delta f_n^*)_i}{\sum_{i=1}^{M} (K_s^2 \cdot S_o^*(f^*) \cdot \Delta f_n^*)_i}} \end{aligned}\right\} \qquad \cdots\cdots(9)$$

For directional spectrum:

$$\left.\begin{aligned} K_s &= \sqrt{\sum_{i=1}^{M}\sum_{j=1}^{N} (K_s^2)_{ij} \cdot (\Delta E_o^*)_i / \sum_{i=1}^{M} (\Delta E_o^*)_i} \\ K_s K_r &= \sqrt{\sum_{i=1}^{M}\sum_{j=1}^{N} (K_s^2 K_r^2)_{ij} \cdot (\Delta E_o^*)_i / \sum_{i=1}^{M} (\Delta E_o^*)_i} \end{aligned}\right\} \qquad \cdots(10)$$

Dimensionless analysis of spectrum

JONSWAP spectrum:

$$S(f) = \frac{\alpha'}{(2\pi)^4} \frac{g^2}{f^5} \exp\left[-\frac{5}{4}\left(\frac{f}{f_{op}}\right)^{-4}\right] \times \gamma^{\exp\left[-\frac{1}{2\sigma_0^2}(f/f_{op}-1)^2\right]} \quad \cdots\cdots(11)$$

SWOP directional function:

$$F(f,\theta) = \begin{cases} \frac{1}{\pi}\{1+(0.5+0.82\exp[-\frac{1}{2}(\frac{2\pi f}{\omega'})^4]\cos 2\theta) \\ +0.32\exp[-\frac{1}{2}(\frac{2\pi f}{\omega'})^4]\cos 4\theta\} & |\theta| \le \frac{\pi}{2} \cdots(12) \\ 0 & |\theta| > \frac{\pi}{2} \end{cases}$$

where $\omega' = g / U_{5.0}$

$U_{5.0}$: wind velocity at 5.0m above sea surface

For the convenience of calculation, we introduce a dimensionless analysis to the known spectrum and directional function. If significant wave height ($H_{1/3}$) and siginificant wave period ($T_{1/3}$) are choosen as parameters, then the dimensionless spectrum S*(f*) is:

$$S^*(f^*) = \frac{S(f)}{H_{1/3}^2 T_{1/3}}$$

For JONSWAP spectrum, Wang et al (1976) derived an approximate value of zero-order moment of spectrum is:

$$m_o \simeq 0.305 \cdot k_1 \cdot f_{op}^{-4} \quad \cdots\cdots(13)$$

$$k_1 = \frac{\alpha' g^2}{(2\pi)^4} \qquad (\alpha' = 0.0081)$$

Introducing coefficients D_1, D_2, then we can establish following expressions:

$$\left.\begin{aligned} H_{1/3} &= D_1 \sqrt{m_0} \\ f_{op} &= \frac{1}{D_2 T_{1/3}} \end{aligned}\right\} \qquad \cdots\cdots(14)$$

From equation (11),(13) and (14), we can gain the dimensionless form:

$$S^*(f^*) = \frac{1}{0.305 \cdot D_1^2 \cdot D_2^4} \cdot f^{*-5} \cdot \exp\left[-1.25 (D_2 \cdot f^*)^{-4}\right] \times \gamma^{\exp\left[-\frac{1}{2\sigma_0^2}(D_2 f^* - 1)^2\right]} \qquad \cdots\cdots(15)$$

In West Taiwan Strait, Ou (1977) analyzed the measured data and deduced the spectrum of a JONSWAP type, those coefficients of spectrum are:

$$\left.\begin{aligned} H_{1/3} &= 3.8 \sqrt{m_0} \\ f_{op} &= \frac{1}{1.13 T_{1/3}} \\ \gamma &= 2.08 \\ \sigma_0 &= \begin{cases} 0.07 & f \le f_{op} \\ 0.09 & f > f_{op} \end{cases} \end{aligned}\right\} \qquad \cdots\cdots(16)$$

A dimensionless from of SWOP directional function is given by Nagai (1972):

$$F(f^*,\theta)=\frac{1}{\pi}\cdot\{1+[0.5+0.82\cdot\exp(-0.4416f^{*-4})]\times\cos 2\theta+0.32\cdot\exp(-0.4416f^{*-4})\cdot\cos 4\theta\} \quad \ldots(17)$$

Numerical computation

Finite difference method is used in solving wave ray equatio and intensity equation. Adopting central-difference method, hence

$$\left.\begin{aligned}\frac{d\ell}{ds}&=\frac{\ell_{n+1}-\ell_{n-1}}{2\Delta s}\\ \frac{d^2\ell}{ds^2}&=\frac{\ell_{n-1}-2\ell_n+\ell_{n+1}}{(\Delta s)^2}\end{aligned}\right\} \quad \ldots\ldots(18)$$

And equation (6) yields:

$$\ell_{n+1}=\frac{4-2(\Delta s)^2 q_n}{2-(\Delta s)p_n}\ell_n-\frac{2+(\Delta s)p_n}{2-(\Delta s)p_n}\ell_{n-1} \quad \ldots\ldots(19)$$

In regular wave, the relationship among wave length, period and water depth is:

$$L=\frac{gT^2}{2\pi}\tanh\left(\frac{2\pi d}{L}\right)$$

Wave celerity C=L/T angular frequency $\omega=\frac{2\pi}{T}$
Then,

$$C=\frac{g}{\omega}\tanh\frac{\omega d}{C} \quad \ldots\ldots(20)$$

From which, following partial derivatives can be establish:

$$\left.\begin{aligned}
&\frac{\partial C}{\partial x} = H(C)\,\frac{\partial d}{\partial x}\\
&\frac{\partial C}{\partial y} = H(C)\,\frac{\partial d}{\partial y}\\
&\frac{\partial^2 C}{\partial x^2} = H(C)\left[\frac{\partial^2 d}{\partial x^2} + \left(\frac{\partial d}{\partial x}\right)^2 \frac{dH(C)}{dC}\right]\\
&\frac{\partial^2 C}{\partial x\,\partial y} = H(C)\left[\frac{\partial^2 d}{\partial x\,\partial y} + \frac{\partial d}{\partial x}\frac{\partial d}{\partial y}\frac{dH(C)}{dC}\right]\\
&\frac{\partial^2 C}{\partial y^2} = H(C)\left[\frac{\partial^2 d}{\partial y^2} + \left(\frac{\partial d}{\partial y}\right)^2 \frac{dH(C)}{dC}\right]
\end{aligned}\right\} \quad \cdots\cdots(21)$$

in which:

$$k_1 = \frac{1}{2\omega} \qquad k_2 = \frac{\omega}{g}$$

$$H(C) = \left[\,2k_1 C\,\frac{k_2}{1-(k_2 C)^2} + 2k_1 \tanh^{-1}(k_2 C)\right]^{-1}$$

$$\frac{dH(C)}{dC} = \frac{-4k_1 k_2 [H(C)]^3}{[1-(k_2 C)^2]^2}$$

With step-by-step procedure, the width of wave ray ℓ_n, refracting angle α_n can be solved. The wave ray and Ks, Kr of component spectrum will be traced and calculated. In uniform slope or parallel straight topography, all the deformed wave on contour line is the same. Therefore, the computation is rather simplified and shallow spectrum of interesting point can be solved easily. In real bathymetry, the deformation varies from point to point, a try and error technique is adopted ingeneuously. Fig.4 shows the schematic grid points of topography, in which COMX, COMY represents X-, y-axis of interesting point respectively. 1~No, 1~Mo are node numbers.

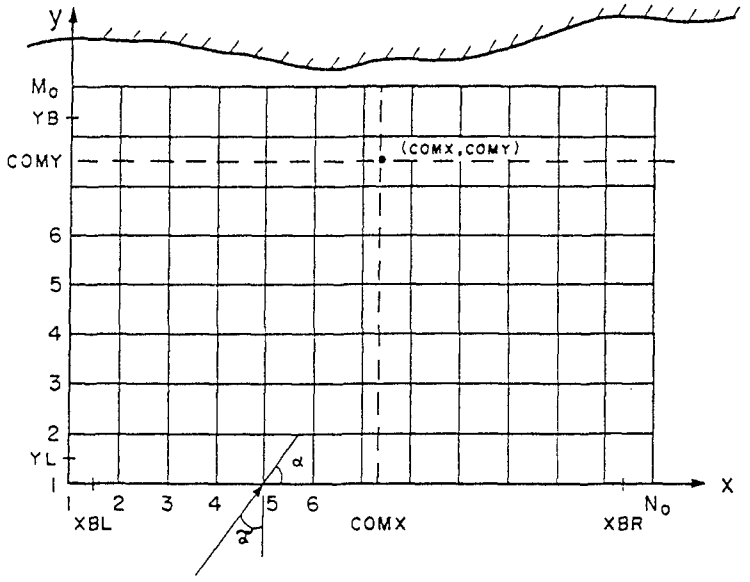

Fig.4 Schematic representations of coordinate

Try and error procedure:

First, setting the initial coordinate $(X_o)_1$ as starting point of computation in deep sea as following:

$$(X_o)_1 = X_o' \pm \left(\frac{90^\circ}{\alpha} - 1 \right)$$

where Xo' is a initial coordinate based on the assumption of no refraction of wave. Last term in above equation is a revised term of refraction, "+" is taken as Xo'<COMX, "-" as Xo'>COMX. When the computation comes to the neighborhood of y=COMY, the Lagrangian interpolation method is applied to abtain the Ks, Kr and α on y=COMY, then the corresponding WXN(1) in X-axis is also obtained. If (COMX-WXN(1))<0.1, it is considered that the wave ray goes pass through the interesting point and the computation of the component is completed. if not, revised the initial point for next step by:

$$(X_o)_2 = (X_o)_1 + (COMX - WXN)\, K_r^2$$

As repeating the same procedure only few times, the results could be gained. In few cases, a least square curve fitting may be avail-

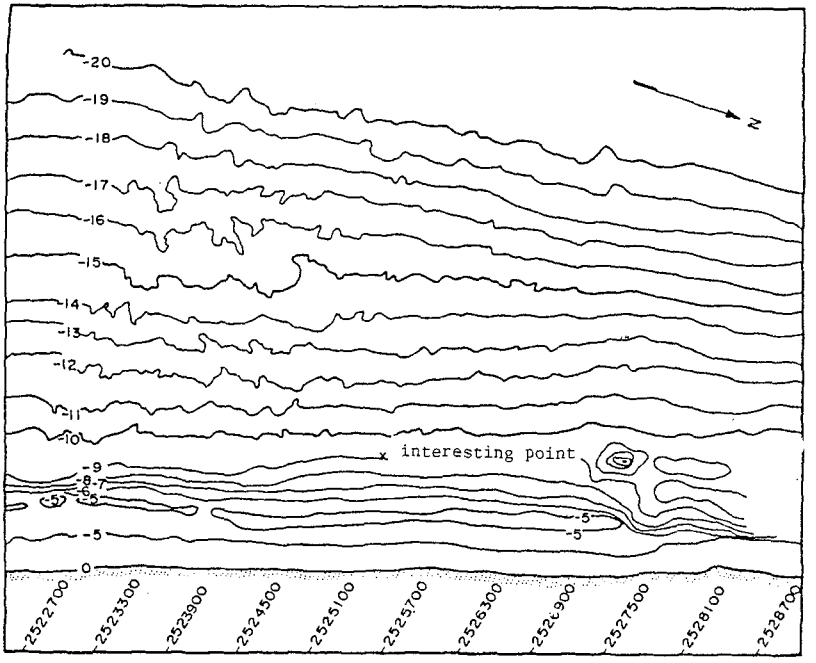

Fig.5 Topography off Hsing-Ta Harbour in West Taiwan Strait

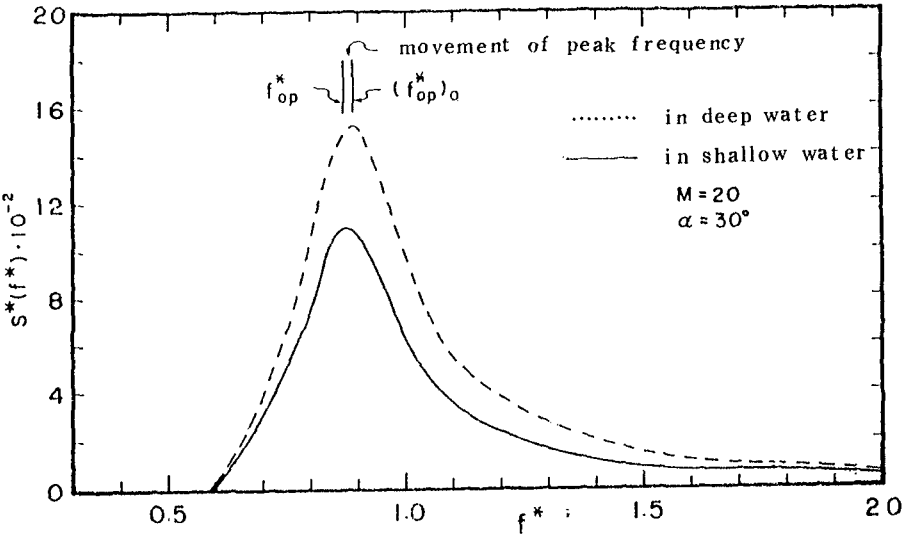

Fig.6 JONSWAP spectrum and its deformed spectrum in West Taiwa starait

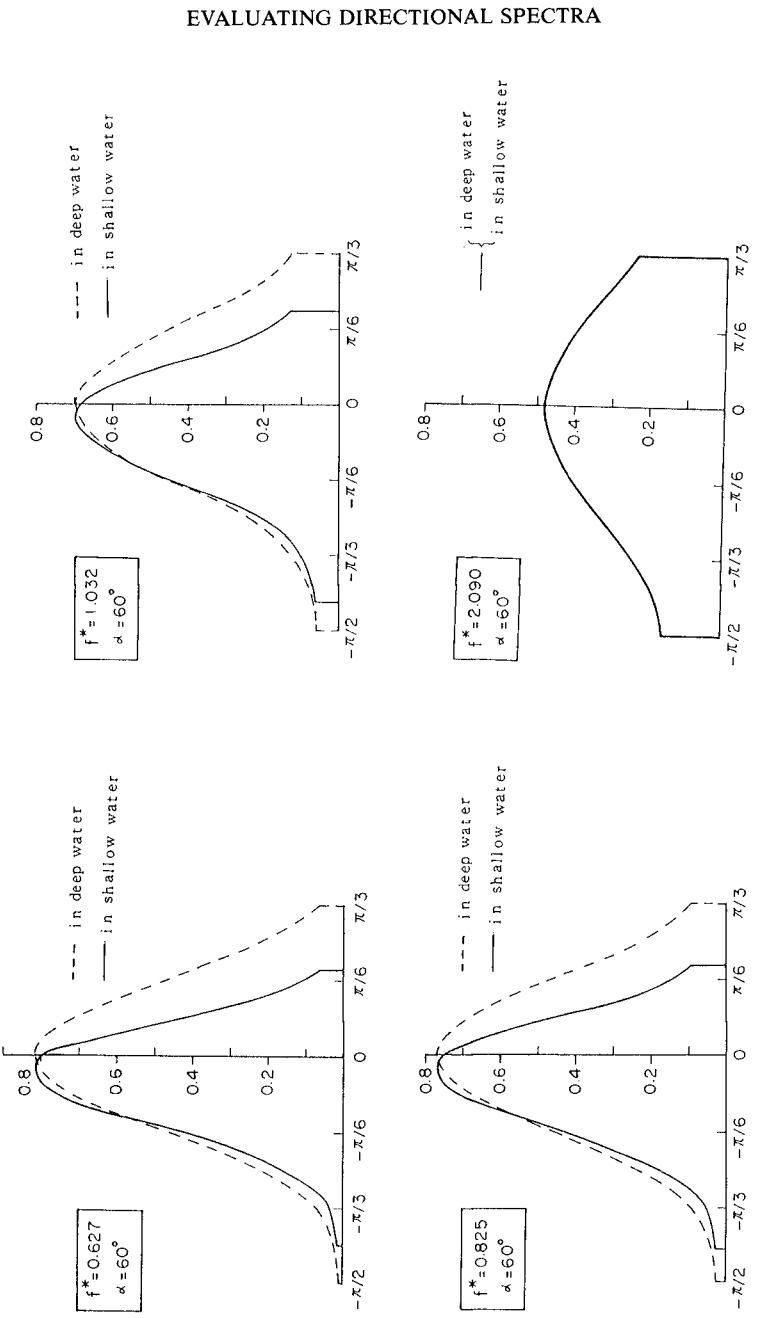

Fig.7 SWOP direction function and its deformed shape

Table 1 Comparison of results with regular wave and directional wave

(H = 7 m , T = 10 sec)

incid. ang. (with X-axis)	sine wave		* P-M		*Bretschneider		* JONSWAP	
	H	T	$H_{1/3}$	$T_{1/3}$	$H_{1/3}$	$T_{1/3}$	$H_{1/3}$	$T_{1/3}$
0°	6.8	10	4.5	10.0	4.4	9.7	4.4	9.9
30°	5.7	10	5.9	10.3	5.6	10.0	5.8	10.2
60°	7.1	10	6.7	10.4	6.4	10.1	6.6	10.3
90°	7.2	10	7.1	10.4	6.8	10.1	7.0	10.3
120°	6.4	10	6.7	10.4	6.4	10.0	6.5	10.2
150°	5.6	10	6.0	10.4	5.8	10.1	5.9	10.2
180°	5.9	10	4.6	10.3	4.5	10.0	4.5	10.2

* SWOP directional function

able to solve the problems.

Due to the local drastic variation of topography or other reasons, there may occur the crossing of wave orthogonals. In such case, topographical smoothing is always used. However, A different way is adopted to treat this situation in this paper. It is by shifting the initial point several times to avoid or by-pass where the crossing is occurred, and a numerical approach is applied to get the solution at the interesting point with those results from different initial point.

Results and Conclusions

This model is applied to the slowly varying topography which ray theory is valid. A computer program is developd to fit this approach. As the coordinate of interesting point and wave spectrum in deep sea are given, the deformed spectrum at interesting point could be gained.

Fig.5 shows the topography off Hsing-Ta Harbour in West Taiwan Strait used in this calculation.

Considering the one-dimensional spectrum in deep sea, where incident angle of waves is 30 degree, and twenty dividing numbers are adopted, the deformed spectrum of interesting point as well as the original spectrum in deep sea is shown on Fig.6. It shows clearly that the peak frequency is different. SWOP directional is a distribution function related to frequency. Fig.7 shows the deformed directional function at various frequencies. The shapes of function in shallow water are more sharp. The energy of component spectrum is more concentrated to principle wave direction as waves advance to the shallow water when directional distribution of wave energy is considered. Table 1 is the comparison of results by applying regular wave and directional spectrum (SWOP directional function) There has a large difference at 0° and 180° between regular wave and directional spectrum. It is partly due to the effective income of energy when directional function is considered.

Reference

1. Mitsuyasu, H. "Recent Studies on Ocean Wave Spectra" Int. Congress of Theoretical and Applied Mechanics, Lyngby, Denmark, 1984.
2. Nagai, K. "Computation of Refraction and Diffraction of Irregular Sea" Report of the Port and Harbour Research Institute, Vol.11, No.2, June 1972.(in Japanese)
3. Ou, S. H. "Parametric Determination of Wave Statistics and Wave Spectrum of Gravity Waves" Doctor Dissertation, NCKU, 1977.
4. Wang, J. and Liang, N.K. "A Note on the Significant Wave derived from JONSWAP Spectrum" Acta Oceanogr. Taiwanica, N.T.U., 1976.
5. Bretschneider, C.L. "significant Waves and Wave Spectrum" Ocean Industry, pp.40-46, Feb. 1968.
6. Rice, S.O. "Mathematical Analysis of Random Noise" in Noise and Stochastic Process, N. Wax, ed., Dover Pblication, New York, pp.133-294, 1954.

CHAPTER 60

Shoaling and Reflection of Nonlinear Shallow Water Waves

Padmaraj Vengayil[1] and James T. Kirby[2]

The formulation for shallow water wave shoaling and refraction-diffraction given by Liu et al (1985) is extended to include reflected waves. The model is given in the form of coupled K-P equations for forward and backward propagation. Shoaling on a plane beach is studied using the forward-propagating model alone. Non-resonant reflection of a solitary wave from a slope and resonant reflection of periodic waves by sinusoidal bars are then studied.

Introduction

Recently, Liu et al (1985) have developed a set of coupled parabolic equations to study the combined refraction and diffraction of time-periodic waves in shallow water over two-dimensional topography. Derivations in that study were based both on the Boussinesq equations for variable depth (Peregrine, 1972) and a variable depth form of the equation of Kadomtsev and Petviashvili (1970) (K-P), leading to similar results. The resulting equations model only the incident wave and neglect the reflected wave component. The problem of the neglected reflected wave component is important, both to the prediction of shoaled wave heights over gentle slopes and to the prediction of waves propagated over undular nearshore topography, which can lead to significant reflection by means of a resonance mechanism.

In this study, we address several questions of accuracy of predictions of the forward-scattered parabolic approximation which were not addressed in the previous study. In particular, we study the shoaling of a normally incident wave on a plane beach and analyze results both in terms of wave-height and wave form prediction in comparison with laboratory data. We then formulate coupled equations for incident and reflected waves and study wave reflection in several situations.

Model Formulation

Following a usual procedure for obtaining coupled parabolic equations for strictly monochromatic waves, we instead study the linear

[1]Graduate Student, Coastal and Oceanographic Engineering Department, University of Florida, Gainesville, FL (presently, Department of Civil Engineering, Massachusetts Institute of Technology, Cambridge, MA)

[2]Assistant Professor, Coastal and Oceanographic Engineering Department University of Florida, Gainesville, FL

nondispersive wave equation for arbitrary surface displacement $\eta(x,y,t)$. Letting $\eta = \eta^+ + \eta^-$, with $\eta^{+(-)}$ denoting forward (backward) propagating components of the wave field (with respect to direction x), we obtain a set of equations which are coupled through the local bottom variations. The equations are extended to include weakly dispersive and weakly nonlinear effects, yielding model equations of the form

$$\frac{1}{c}\eta_t^+ + \eta_x^+ + \frac{h_x}{4h}(\eta^+ - \eta^-) + \frac{3}{2h}\eta^+\eta_x^+ + \frac{h^2}{6}\eta_{xxx}^+ - \int_x^\infty \frac{1}{2h}(h\eta_y^+)_y dx = 0 \quad (1a)$$

$$\frac{1}{c}\eta_t^- - \eta_x^- + \frac{h_x}{4h}(\eta^+ - \eta^-) - \frac{3}{2h}\eta^-\eta_x^- - \frac{h^2}{6}\eta_{xxx}^- + \int_x^\infty \frac{1}{2h}(h\eta_y^-)_y dx = 0 \quad (1b)$$

where $h(x,y)$ is the local water depth and $c(x,y) = (gh)^{1/2}$. We subsequently neglect y-variations and study x-direction propagation alone for the remainder of this study. Details of the derivation may be found in the report by Vengayil and Kirby (1986). For the case of time-aperiodic motions, equations (1) are altered to RLW form and solved conveniently using a variation of the three time level scheme of Eilbeck and McGuire (1977). For the case of wave forms η^+, η^- which vanish as $|x| \to \infty$, it is further possible to show that equations (1) lead to the mass conservation law

$$\frac{d}{dt}\int_{x_0}^\infty (\eta^\pm)dx = \pm \tilde{Q}^\pm \pm \int_{x_0}^\infty c_x \eta dx \quad (2)$$

where x_0 is some arbitrary station and

$$\tilde{Q}^\pm(x_0) = \left\{c\eta^\pm + \frac{3c\eta^{\pm 2}}{4h} + \frac{ch^2}{6}\eta_{xx}^\pm\right\}\Big|_{x_0} \quad (3)$$

represents the flux of mass across station x_0. Taking the limit $x_0 \to -\infty$ then gives

$$\frac{d}{dt}\int_{-\infty}^\infty \eta^+ dx = -\frac{d}{dt}\int_{-\infty}^\infty \eta^- dx = \int_{-\infty}^\infty c_x \eta dx$$

or

$$\int_{-\infty}^\infty \eta dx = \text{constant} \quad (4)$$

indicating exact mass conservation. For the case of weak reflection with $O(|\eta^-|)\sim O(h_x)\cdot O(|\eta^+|)$, the source (sink) term is altered to

$$\int_{-\infty}^{\infty} c_x \eta dx = \int_{-\infty}^{\infty} c_x \eta^+ dx + O(|c_x|^2) \tag{5}$$

and the conclusions on mass balance in the variable coefficient KdV equation given by Miles (1979) are recovered.

For the case of time-periodic motions, the surface displacements η^+, η^- may be expanded in Fourier series with slowly-varying modal amplitudes; we then solve the coupled O.D.E. evolution equations for the amplitudes.

Shoaling of Regular Waves

We first study the shoaling of a regular wave on a plane beach as a means of further testing the accuracy of the model developed by Liu et al (1985). Data for the height and wave-form of shoaling waves were obtained from the results presented by Buhr Hansen and Svendsen (1979) and further described by Svendsen and Buhr Hansen (1978) and Buhr Hansen (1980). Figure 1 shows the configuration of the wave flume used in the tests. The five longest wave conditions were chosen for study; parameters for the chosen tests are shown in Table 1.

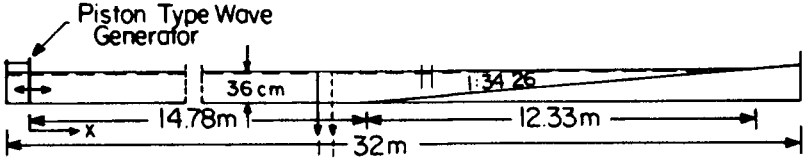

Figure 1. Experimental set-up of Buhr Hansen and Svendsen (1979).

Table 1 Wave parameters at the wavemaker for the test considered from Buhr Hansen and Svendsen (1979).

Buhr Hansen & Svendsen Test No.	H_0(m) (actual)	$\varepsilon = \frac{H_o}{2h_0}$	T(sec)	$\mu^2 = \frac{\omega^2 h_0}{g}$	U_{r_0}
051071	0.067	0.090	2.0	0.362	0.248
051041	0.037	0.051	2.0	0.362	0.140
041071	0.070	0.097	2.5	0.232	0.418
041041	0.040	0.056	2.5	0.232	0.242
031041	0.040	0.056	3.33	0.130	0.445

The model equations were developed by neglecting the wave reflected from the slope, which has been shown to be small (Vengayil and Kirby, 1986). The incident wave η^+ is represented by the Fourier series

$$\eta^+(x,t) = \sum_{n=1}^{N} A_n(x) e^{in(\int k dx - \omega t)} + c.c. \quad ; \quad \omega = ck \tag{6}$$

The series is substituted in equation (1a) (neglecting η^-) to give

$$A_{n_x} + \frac{h_x}{4h} A_n - \frac{in^3 k (kh)^2}{12} A_n +$$

$$+ \frac{3ink}{8h} \left\{ \sum_{\ell=1}^{n-1} A_\ell A_{n-\ell} + 2 \sum_{\ell=1}^{N-n} A_\ell^* A_{n+\ell} \right\} = 0$$

$$n=1,\ldots,N \tag{7}$$

The model equation may be extended to include laminar frictional damping due to bottom and sidewalls by the addition of the term

$$\frac{(1+i)}{2h} n^2 k^2 \left(\frac{2\nu}{n\omega}\right)^{1/2} \left\{1 + \frac{2h}{b}\right\} A_n \tag{8}$$

to equation (7). Here, ν is the kinematic viscosity and b is the channel width.

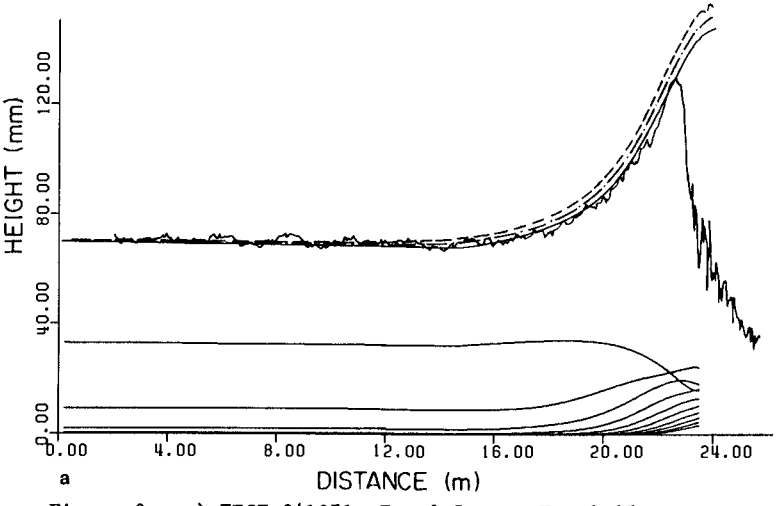

a

Figure 2. a) TEST 041071, T = 2.5 sec, H = 0.07 m.

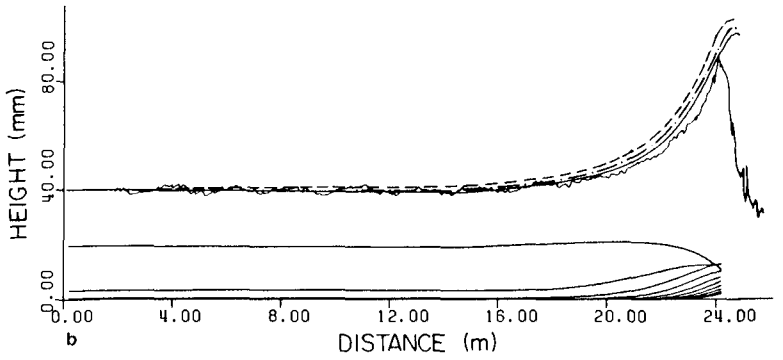

b) TEST 041041, T = 2.5 sec, H = 0.04 m.

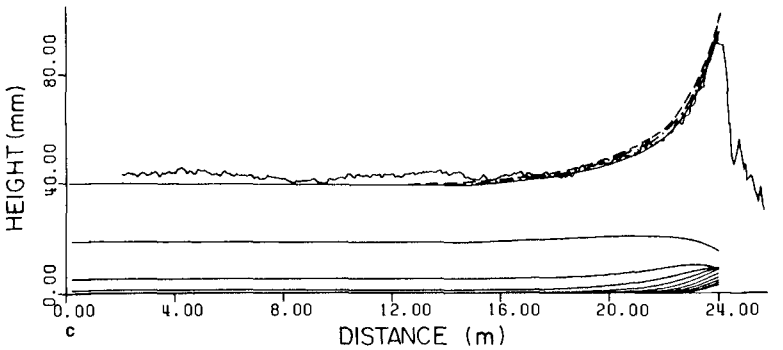

c) TEST 031041, T = 3.33 sec, H = 0.04 m.

Figure 2. Numerical results of shoaled wave height, (----, inviscid theory; —•—•—, bottom friction included ——, bottom and side wall friction included) compared to experimental results of Buhr Hansen and Svendsen (1979). Also shown are the component amplitudes $|A_1|$ - $|A_{10}|$ for flow with bottom and side wall friction.

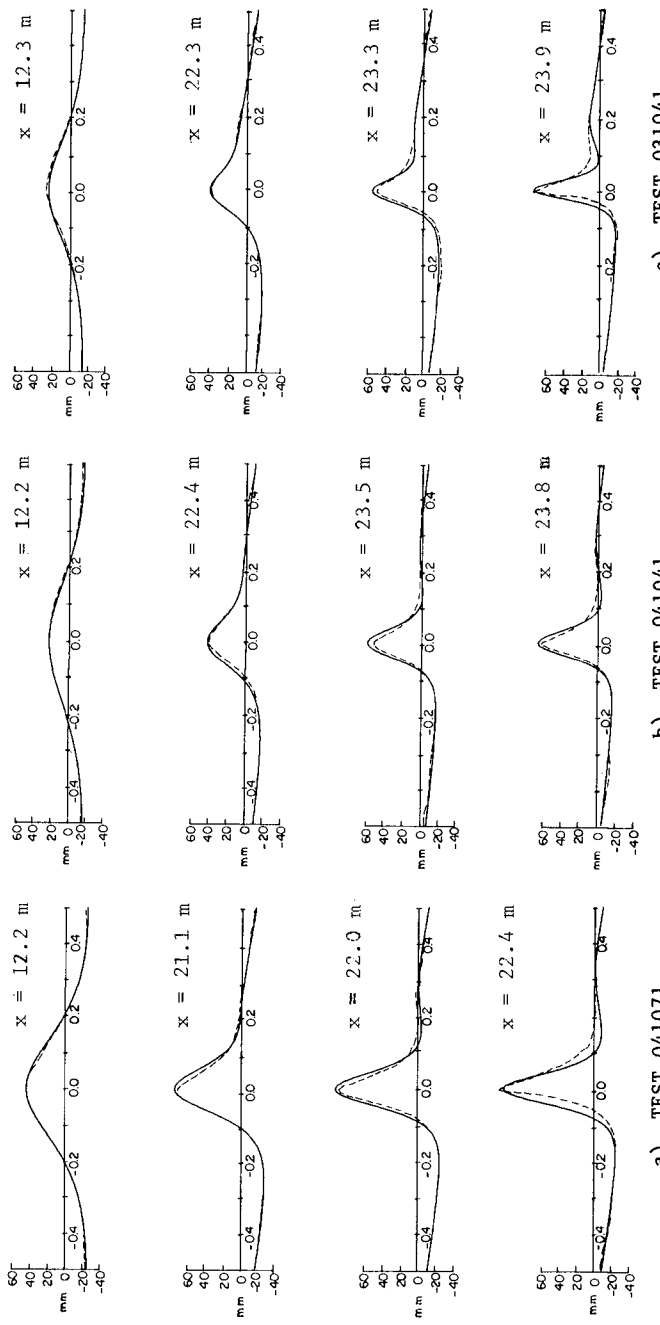

a) TEST 041071 b) TEST 041041 c) TEST 031041

Figure 3. Comparison of wave profiles predicted by the numerical model including bottom and side wall friction effects with the experimental results of Buhr Hansen and Svendsen (1979). —— numerical, ---- experimental. Distances are from wavemaker in Figure 1.

Results for shoaled wave heights are shown in Figure 2a-c for the three longest waves studied. Results are shown for undamped waves, damping due to bottom friction alone, and damping due to bottom and sidewalls. Also included are plots of component amplitudes $|A_1|-|A_{10}|$ for the case with sidewall damping. The reproduction of shoaling wave height is good for the damped cases.

Figure 3 shows computed wave forms in comparison to experimentally measured waves for the cases with bottom and sidewall damping. Reproduction of measured wave form is quite good except in regions close to wave breaking. In these regions the forward face of the wave tilts towards a vertical position and vertical accelerations become quite large, thus invalidating the Boussinesq approximation locally. However, the model has no apparent difficulty in predicting shoaled wave height up to the breaking limit. An investigation of the higher order skewness and asymmetry properties of the shoaled waves is presently underway and will be reported subsequently.

Gradual Reflection of Solitary Waves

A test of the coupled equations was performed by comparing results for reflection of a solitary wave by an underwater slope with experimental data obtained by Goring (1978). Goring also computed theoretical results for reflection coefficients based on numerical

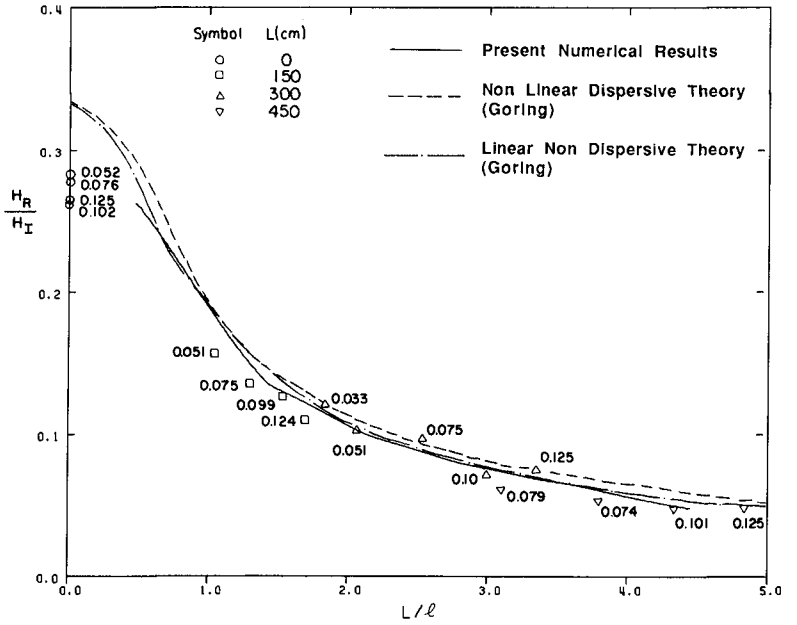

Figure 4. Reflection coefficients for solitary waves propagating over a submerged slope. Data from Goring (1978).

solution of the Boussinesq equations (weakly nonlinear-weakly dispersive case) and on the Bessel function solution of the linear-nondispersive shallow water equation. Figure 4 gives results of reflection coefficient based on the ratio of height of reflected wave to height of incident wave for varying values of slope length L to incident wavelength ℓ, for a particular case of a depth reduction $h_1/h_2 = 4$. The incident wave length is estimated here according to

$$\ell = 1.5\ (H_I/h_1)^{-1/2} h_1 \tag{9}$$

Results of the present study agree most closely with the linear nondispersive theory, indicating the overall dominance of the slope effect in the scattering process. The present theory and Goring's linear theory each deviate slightly from Goring's nonlinear theory, indicating that there is some effect due to nonlinear coupling between the incident and reflected wave. This discrepancy is presently being investigated using a version of the present theory which retains nonlinear coupling between the opposite-going waves.

An example of the time history of a solitary wave reflection for a particular case of a fairly abrupt slope is given in Figure 5. The development of the reflected wave, moving to the left with increasing time, is apparent, as is the nonlinear evolution of the incident wave after it moves onto the shelf. This evolution involves the generation of three soliton modes which are rank-ordered in height and subsequently disperse due to the nonlinear evolution. The reflected wave is seen to have about the same width as the incident wave (as would be expected for a short slope) and evolves only slowly due to its low initial amplitude (scale on right). The presence of a high frequency tail following each wave train is just becoming apparent on the top trace of the picture.

Resonant Reflection by Sand Bars

Recently, Mei (1985) has investigated the resonant interaction which occurs between an incident wave of wavenumber k, a synchronous reflected wave with wavenumber -k and a bar field with dominant wavenumber $\lambda = 2k$. Mei's investigation was for the case of linearized, intermediate depth theory. Here, we have extended the investigation to the case of nonlinear, weakly-dispersive waves. The topography studied had the form

$$h(x) = \begin{cases} h_0 & x<0 \ ; \ x>L \\ h_0 + D\sin \lambda x & 0\leq x\leq L \end{cases} \tag{10}$$

where D is the bar amplitude and $\lambda = 2\pi/\ell_b$ is the bar wavenumber. Results are presented here for $L = 4\ell_b$ (four bars in the patch). The relevant governing equations are developed by using equation (6) for the incident wave η^+ and

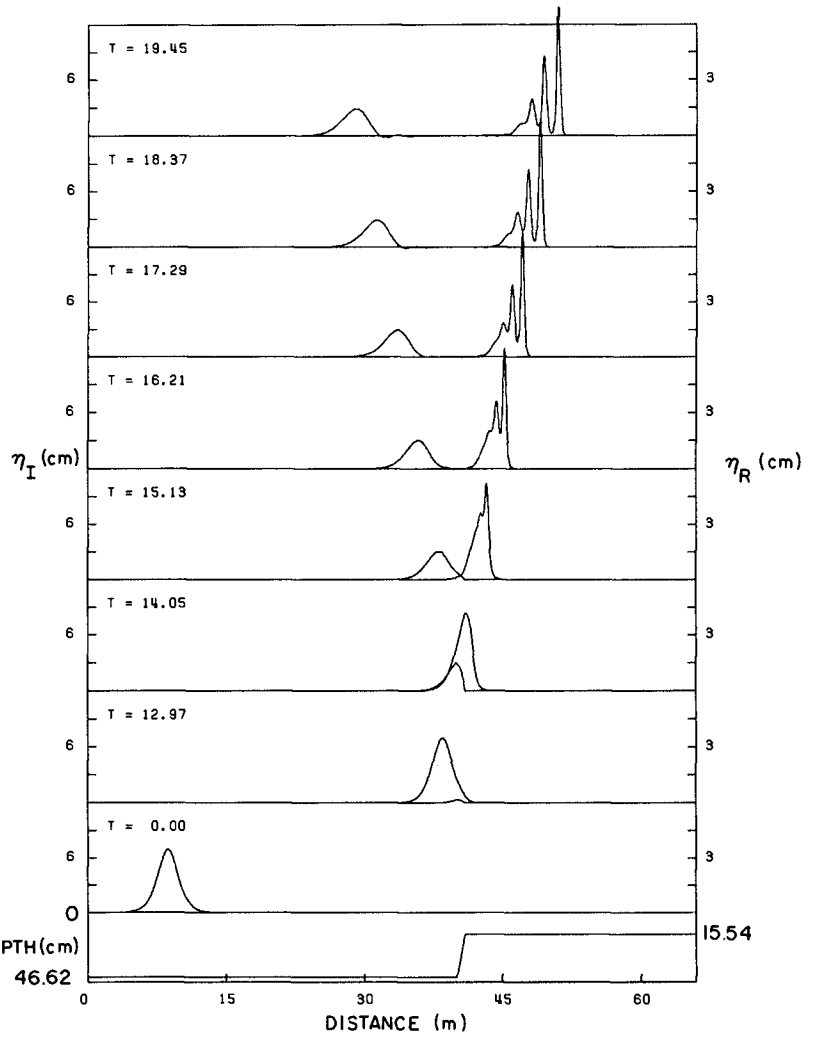

Figure 5. Evolution of a solitary wave. Incident wave propagates to the right.

$$\eta^{-}(x,t) = \sum_{n=1}^{N} B_n(x)\, e^{-in(\int kdx - \omega t)} + c.c. \qquad (11)$$

for the reflected wave. Substitution of (6) and (11) in the governing model equation (1) leads to the coupled system of evolution equations

$$A_{n_x} + \frac{h_x}{4h}\left(A_n - B_n e^{-2in\int kdx}\right) - \frac{in^3k^3h^2}{12} A_n + \frac{3ink}{8h}\left[\sum_{\ell=1}^{n-1} A_\ell A_{n-\ell} + 2\sum_{\ell=1}^{N-n} A_\ell^* A_{n+\ell}\right] = 0 \qquad (12)$$

and

$$B_{n_x} + \frac{h_x}{4h}\left(B_n - A_n e^{2in\int kdx}\right) + \frac{in^3k^3h^2}{12} B_n - \frac{3ink}{8h}\left[\sum_{\ell=1}^{n-1} B_\ell B_{n-\ell} + 2\sum_{\ell=1}^{N-n} B_\ell^* B_{n+\ell}\right] = 0 \qquad (13)$$

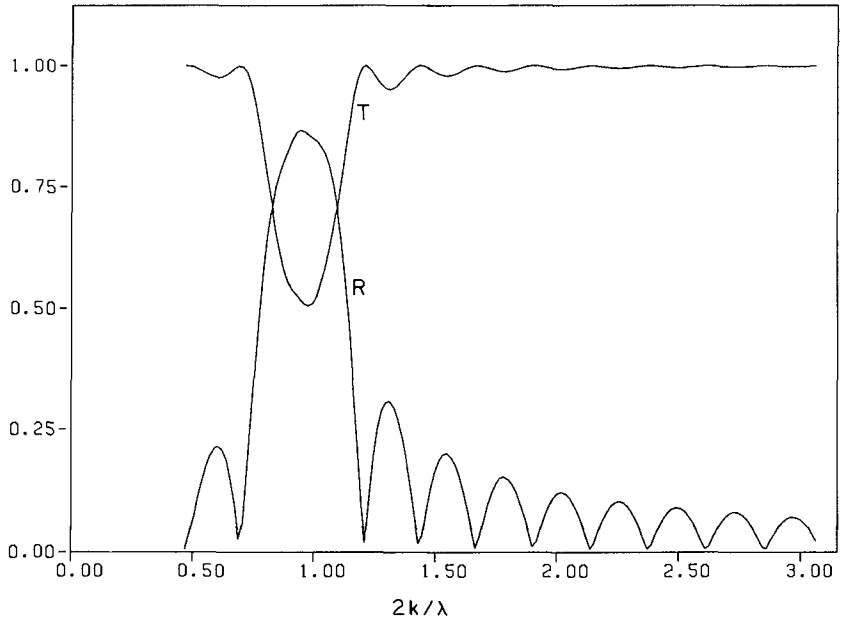

Figure 6. a) linear theory

The incident wave $A_n(0)$ is specified according to a spectral solution for permanent waves in the RLW equation (Vengayil and Kirby, 1986). The $B_n(L)$ are set equal to zero, representing the case of no waves arriving at the patch from large positive x.

Figure 6 shows results for $D/h_0 = 0.4$ and n=4 for a range of bar lengths relative to a fixed wavelength. The plots give calculated reflection coefficient $R_1 = |B_1(0)/A_1(0)|$ and transmission coefficient $T_1 = |A_1(L)/A_1(0)|$ as solid lines. This represents the complete solution for linear theory (Figure 6a). The presence of the resonant peak at $2k/\lambda = 1$ is apparent. In Figure 6b (nonlinear theory), the results for the reflection coefficient R_1, which now represents only one component of the wave field, does not differ greatly from the linear result. This result may be of some importance since it indicates that the linear scattering process dominates the nonlinear effects over the relatively short bar field, which would allow the application of the linear scattering theory in a nearshore, nonlinear wave field.

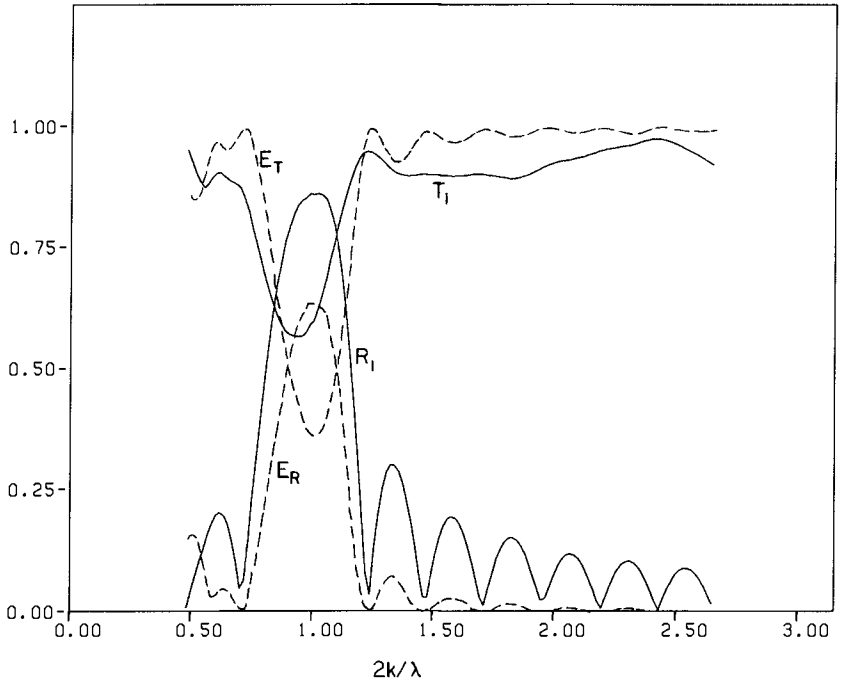

Figure 6. Reflection and transmission of waves by a sinusoidal bar patch. n=4, D/h = 0.4.
b) nonlinear theory.

Also shown in Figure 6b are traces of the total transmitted energy E_T and reflected energy E_R normalized by the total incident energy. The numerical scheme was found to satisfy the requirement

$$E_R + E_T = 1 \tag{14}$$

to several decimal places for suitably fine discretizations of the physical domain. The only effect due to nonlinearity which is readily apparent in the results in Figure 6b is the drop in T_1 below one for $2k/\lambda > 1$. This effect represents a transfer of energy to higher harmonics following from destabilization of the incident wave during its shoaling over the bar crests.

Finally, Figure 7 shows the evolution of the spectral amplitude components during nonlinear evolution at the resonant condition in Figure 6. Only the growth $|B_1|$ is strongly forced by the reflection process; the growth of $|B_2|$ and $|B_3|$ may be partially due to reflection but also is influenced strongly by the nonlinear transfer of energy from $|B_1|$ as it grows. Likewise, $|A_1|$ may gain energy from its harmonics as the incident wave loses energy over the bar field, which would tend to increase the apparent reflection. These two nonlinear effects thus compete in the overall reflection process, and their possible near-cancellation may contribute to the relatively small change in reflection coefficients noted in shifting from linear to nonlinear theory. This effect is presently being investigated in the context of resonantly-reflected solitary waves.

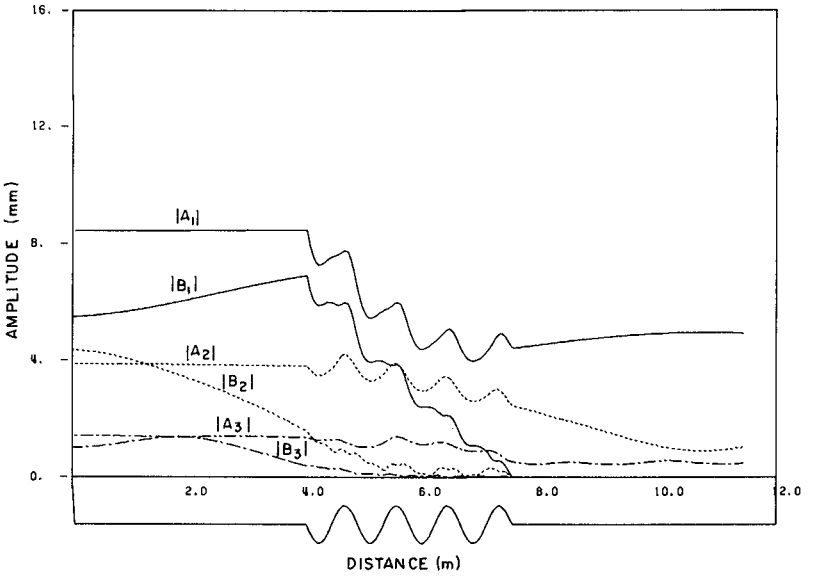

Figure 7. Evolution of component amplitudes $|A_1|-|A_3|$ and $|B_1|-|B_3|$ for the resonant peak of Figure 6. Nonlinear theory.

References

Buhr Hansen, J., 1980, "Experimental investigations of periodic waves near breaking", Proc. 17th Intl. Conf. Coast. Eng., ASCE, 260-277.

Buhr Hansen, J. and Svendsen, I.A., 1979, "Regular waves in shoaling water, experimental data", Series paper 21, Institute Hydro. and Hydraulic Eng., Tech. Univ. Denmark.

Eilbeck, J.C. and McGuire, G.R., 1977, "Numerical study of the regularized long wave equation 1: numerical methods", J. Comp. Phys. 19, 43-57.

Freilich, M.H. and Guza, R.T., 1984, "Nonlinear effects on shoaling surface gravity waves", Phil. Trans. Roy. Soc. A311, 1-41.

Goring, D.G., 1978, "Tsunamis - the propagation of long waves onto a shelf", Report KH-R-38, W.M. Keck Lab. Hydr. and Water Res., California Inst. Tech., Pasadena.

Kadomtsev, B.B. and Petviashvili, V.I., 1970, "On the stability of solitary waves in weakly dispersive media", Sov. Phys. Dokl. 15, 539-541.

Liu, P.L.-F., Yoon, S.B. and Kirby, J.T., 1985, "Nonlinear refraction-diffraction of waves in shallow water", J. Fluid Mech. 153, 185-201.

Mei, C.C., 1985, "Resonant reflection of surface water waves by periodic sand bars", J. Fluid Mech. 152, 315-335.

Miles, J.W., 1979, "On the Korteweg-deVries equation for a gradually varying channel", J. Fluid Mech., 91, 181-190.

Peregrine, D.H., 1972, "Equations for water waves and the approximations behind them", in Waves on Beaches R.E. Meyer (ed.), Academic Press, 95-121.

Svendsen, I.A. and Buhr Hansen, J., 1978, "On the deformation of periodic long waves over a gently sloping bottom", J. Fluid Mech. 87, 433-448.

Vengayil, P. and Kirby, J.T., 1986, "Shoaling and reflection of nonlinear shallow water waves", Tech. Rept. UFL/COEL-TR/062, Coastal and Oceanographic Eng. Dept., Univ. of Florida, Gainesville.

CHAPTER 61

WAVE BASIN EXPERIMENTS ON BOTTOM FRICTION DUE TO CURRENT AND WAVES

Paul J. Visser*

ABSTRACT

Results are presented of experiments in a wave basin on the increase of the mean bottom frictional stress in a flow when a wave field is superimposed on a current. The bottom friction was derived from the mean water level measured at various places. Measurements of wave orbital and mean current velocities were done both with a micro-propeller and with a new type immersible Laser Doppler Anemometer.

The data indicate an increase of the mean bottom shear stress due to the presence of the waves, but less than predicted by Bijker (1967). A suggestion is made to improve the accuracy of this theory. The bottom stresses as predicted by Fredsøe (1984) are somewhat larger than the experimental results.

1. INTRODUCTION

Since many years it is known that when a wave field is superimposed on a current (see fig. 1), the mean bottom friction will increase.

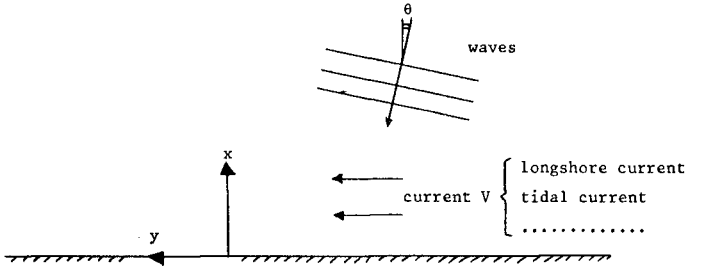

Fig. 1 - Combination of a current and a wave field; θ = angle of incidence, x = coordinate normal to the coast, y = coordinate in longshore direction.

* Scientific Officer, Department of Civil Engineering, Delft University of Technology, P.O. Box 5048, 2600 GA Delft, The Netherlands.

In the pioneering work of Bijker (1967), this phenomenon was investigated both theoretically and experimentally. Since then many investigators have attacked the problem, both theoretically: Lundgren (1973), Bakker and van Doorn (1979), Grant and Madsen (1979), Fredsøe (1984), Tanaka and Shuto (1984) and van Kesteren and Bakker (1985), and experimentally: Bakker and van Doorn (1979) and Kemp and Simmons (1982, 1983). The studies of the wave boundary layer in case of waves alone have much contributed to the present achievements. In this respect the theories of Kajiura (1968), Jonsson and Carlsen (1976) and Brevik (1981), the experiments and analysis of Jonsson (1963, 1967, 1980), Kalkanis (1964), Horikawa and Watanabe (1969), Kamphuis (1975), Jonsson and Carlsen (1976), Sleath (1982) and van Doorn (1982, 1983) and the empirical analysis of Nielsen (1985) should be mentioned.

The most accurate descriptions of the bottom friction due to current and waves are the models of Fredsøe (1984) and van Kesteren and Bakker (1985). These models also allow an arbitrary angle between the directions of the current and the wave field. Van Kesteren and Bakker assume Prandtl's mixing length hypothesis. Nielsen (1985), however, shows that this hypothesis fails in case of oscillatory flow. The model of van Kesteren and Bakker is also rather complicated. Therefore Fredsøe's model is preferable.

For engineering practice the Bijker (1967) model is often used because of the simplicity and handiness of its solution. Applications of Bijker's description to laboratory data of longshore currents, see Visser (1984, 1985), and to field observations by the Delft Hydraulics Laboratory have, however, indicated that this model overestimates the influence of the waves on the bottom frictional stress.

The present paper describes wave basin experiments on the mean bottom friction due to current and waves. The (effect of the) bottom shear stress was measured by determining the mean water level slope from mean water level observations:

$$\rho g h \frac{\partial h}{\partial y} + \bar{\tau}_{by} = 0 \quad \text{in y-direction} , \tag{1}$$

where ρ = density of water, g = acceleration of gravity, h = mean water depth, τ_{by} = mean bottom frictional stress in y-direction (= direction of mean current velocity). Equation (1) assumes uniformity along the coast and zero gradients of radiation and Reynolds shear stresses.

The investigation has been restricted to $\theta = 0^{o}$ in order to prevent recirculation flows on the constant depth part of the wave basin, see Visser (1982). These recirculation flows may disturb the mean water level slope measurements significantly. A further restriction is the application of regular waves.

Actually the investigation is a continuation of Bijker's work. The most important motivations for this study have been: 1. the above mentioned failure of the Bijker model, and 2. the shortage of detailed experimental data in case of small values of θ, in particular for the direct verification via equation (1). The investigation has been carried out within the framework of the Applied Coastal Research programme of the Dutch Public Works Department.

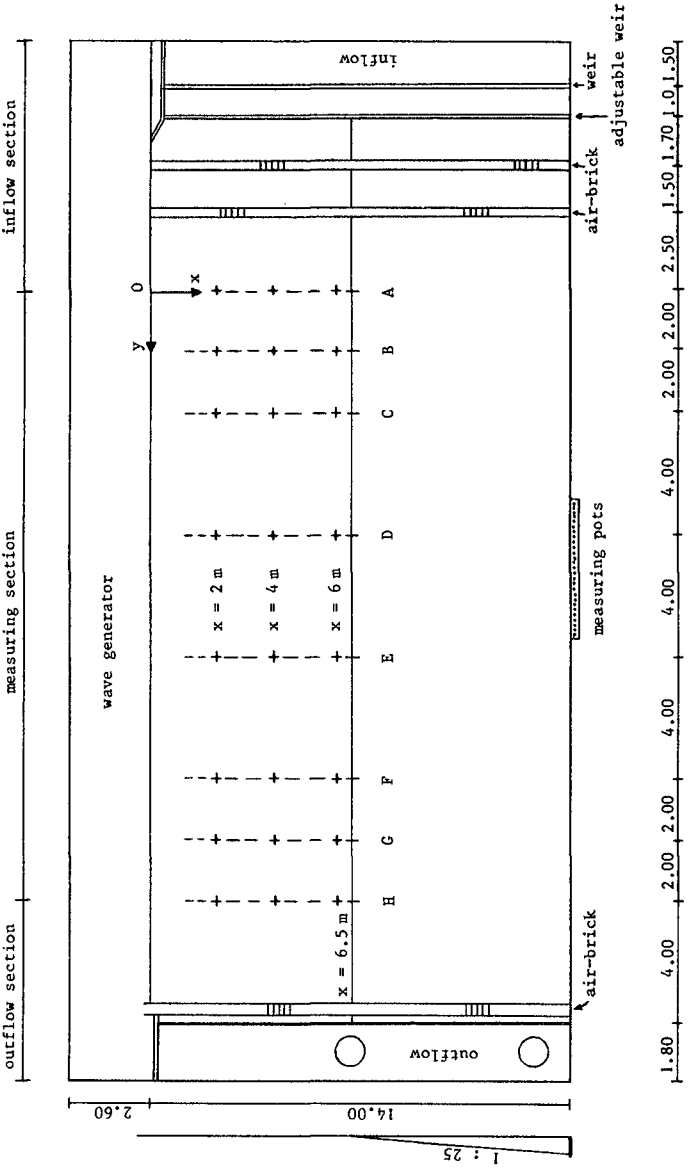

Fig. 2 - Plan view of wave basin (measures in meters, + = tapping for mean water level measurement).

2. DESCRIPTION OF THE EXPERIMENTS

The experiments were performed in the 16.60 * 34.00 m^2 wave basin of the Civil Engineering Department of the Delft University of Technology, see fig. 2. A concrete 1 : 25 beach was built opposite to the wave board in order to minimize reflection of the waves.

A mean current was established in the basin flowing parallel to the shore and the wave board. Much attention was given to the in- and outflow conditions in order to obtain uniformity of this current in the horizontal plane (on the constant depth part of the basin). The details of the experimental set-up are shown in fig. 2. The inflow section of the wave basin consisted of:

- two supply-pipes with a maximum flow rate of 0.8 m^3/s,
- two weirs to distribute the flow over the width of the basin,
- two rows of air-bricks to reduce the turbulence in the current caused by the inflow from the supply-pipes,
- small-mesh wire-netting against one row of air-bricks to adjust the proper vertical velocity distribution at the upstream end of the measuring section.

The outflow section consisted of one row of air-bricks, a small weir and two wells.

The details of the measuring techniques are summarized in table 1. Measurements of orbital and mean current velocity were done with a micro-propeller current meter (in situations with current or waves alone) and with a new type immersible Laser-Doppler Anemometer (LDA),

measurements of	measuring method	sections	number of measuring points per section	number of measuring points per vertical
mean current velocities (current alone)	micro-propeller	D, F(1)	6 ~ 12	10
	LDA	F	2	14
orbital velocities (waves alone)	micro-propeller	D, E(2)	4 ~ 7	1(3)
	LDA	F	2	8 ~ 14
vertical velocity profiles (current and waves)	LDA	D, F	2 ~ 6	8 ~ 14
mean water levels	static head in pots connected with tappings in the bottom	A, B, C, D, E, F, G, H	3	measured 5 times
wave heights	resistance wave probes	D, E	4 ~ 7	

(1) in exp. 1 also in sections C, E and H

(2) in exp. 1 also in sections C, F and G

(3) about 3 cm above the bottom (measurement of u_m, see sketch)

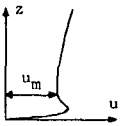

Table 1 - Experimental procedure.

developed by the Delft Hydraulics Laboratory, see Godefroy and Vegter (1984).

This LDA is a very useful tool for velocity measurements in wave basins. A micro-propeller, for instance, fails if there is an angle between mean current direction and wave propagation direction. A disadvantage compared with LDA-measurements through glass side-walls of flumes is the inevitable small disturbance of the flow. An accurate calibration of the instrument, however, can reduce this problem.

The LDA and the probes of the micro-propeller current meter and wave height meter were installed on the measuring carriage of the wave basin.

Six pits were made in the wave basin bottom in sections D and F to be able to measure velocities with the immersible LDA near the bottom, see fig. 3. The pits were covered with perspex plates in order to prevent disturbances on the flow. The perspex plates allowed an exact positioning of the measuring point above it (the contact of the measuring point with the surface of the perspex plate gave a 100% Laser-Doppler signal; in water this was 50 - 60%).

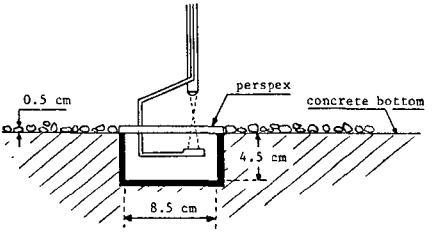

Fig. 3 - Pit in the gravel bottom for the LDA- measurements near the bottom.

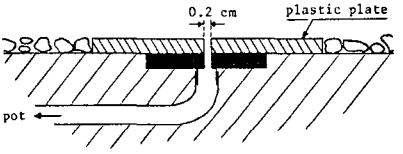

Fig. 4 - Tapping for the mean water level measurement on the gravel bottom.

The mean water level measurements were done in 24 points (see fig. 2) in order to achieve a high accuracy. These observations were made at least five times, since the water level differences were very small and the measuring results showed some scatter.

Experiments were done with a smooth concrete bottom and with a gravel (d_{90} = 8 mm) bottom. Fig. 4 shows a cross-section over a tapping in the gravel bottom. Plastic plates, 10 * 10 cm^2 and 0.6 cm thick were fixed on the concrete bottom in order to obtain horizontal velocities at the tappings (so to prevent dynamic pressures by vertical velocities).

Wave height measurements were only done on the constant depth part of the basin. The observational time was 100 seconds for each measurement.

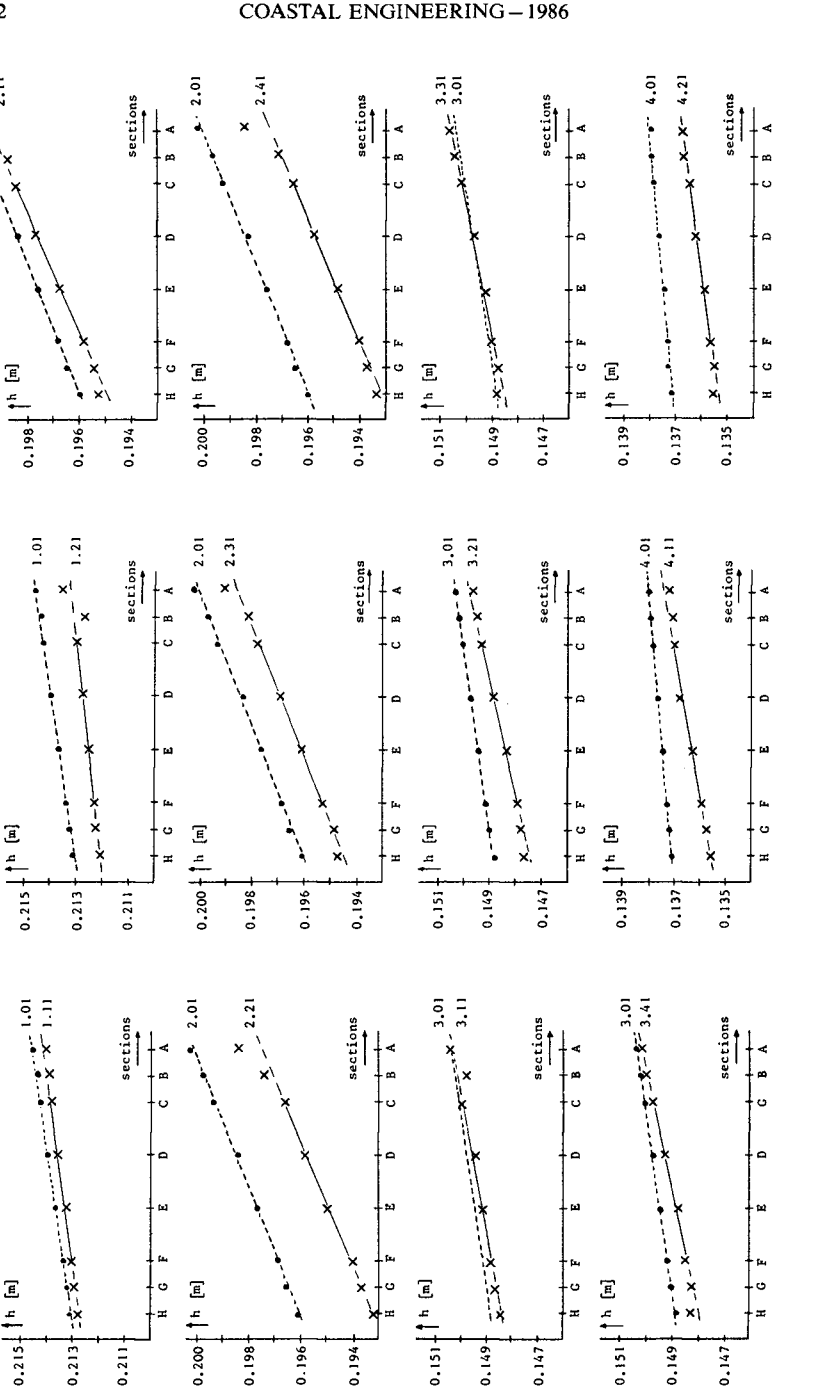

Fig. 5 - Averaged (over width of wave basin) results of mean water level measurements.

3. EXPERIMENTAL RESULTS

The experimental conditions and the main results of the measurements on the constant depth part of the basin regarding averaged wave heights H, mean water depths h, depth-averaged mean current velocities V (V_c in case of current alone, V_{cw} in case of current and waves) and averaged amplitudes of orbital velocities near the bottom u_m are given in table 2. A current alone was present in the experiments 1.01, 2.01, 3.01 and 4.01. The other experimental data of table 2 represent situations of current and waves. V_{cw} was not measured in all experiments. The data (H, u_m) of the experiments with waves alone correspond with those of current and waves. By averaging these data have been incorporated in table 2.

Fig. 5 shows the averaged (three points per section, in time observed at least five times) results of most of the mean water level measurements. The mean water level slopes i (i_c or i_{cw}) in table 2 were calculated by linear regression from the mean water level observations in the sections C, D, E and F. Upstream of section C and downstream of section F the mean water level measurements were influenced by the inflow and outflow conditions, respectively, see fig. 5.

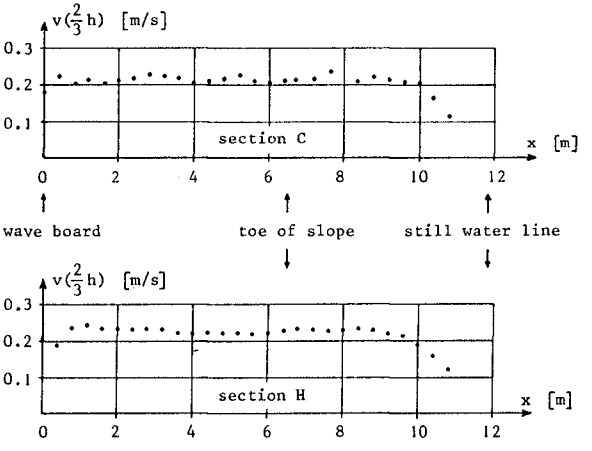

Fig. 6 - Distribution of mean current velocity v at a height of z = 2h/3 in sections C and H in exp. 1.01 (current alone).

Fig. 6 shows the distribution of the mean current velocity v in x-direction at a height of 2h/3 above the bottom in exp. 1.01, measured with the micro-propeller in sections C and H. On the constant depth part of the basin the uniformity of this velocity in x-direction is satisfactory, especially in section H.

Fig. 7 gives examples of the width-averaged results of the

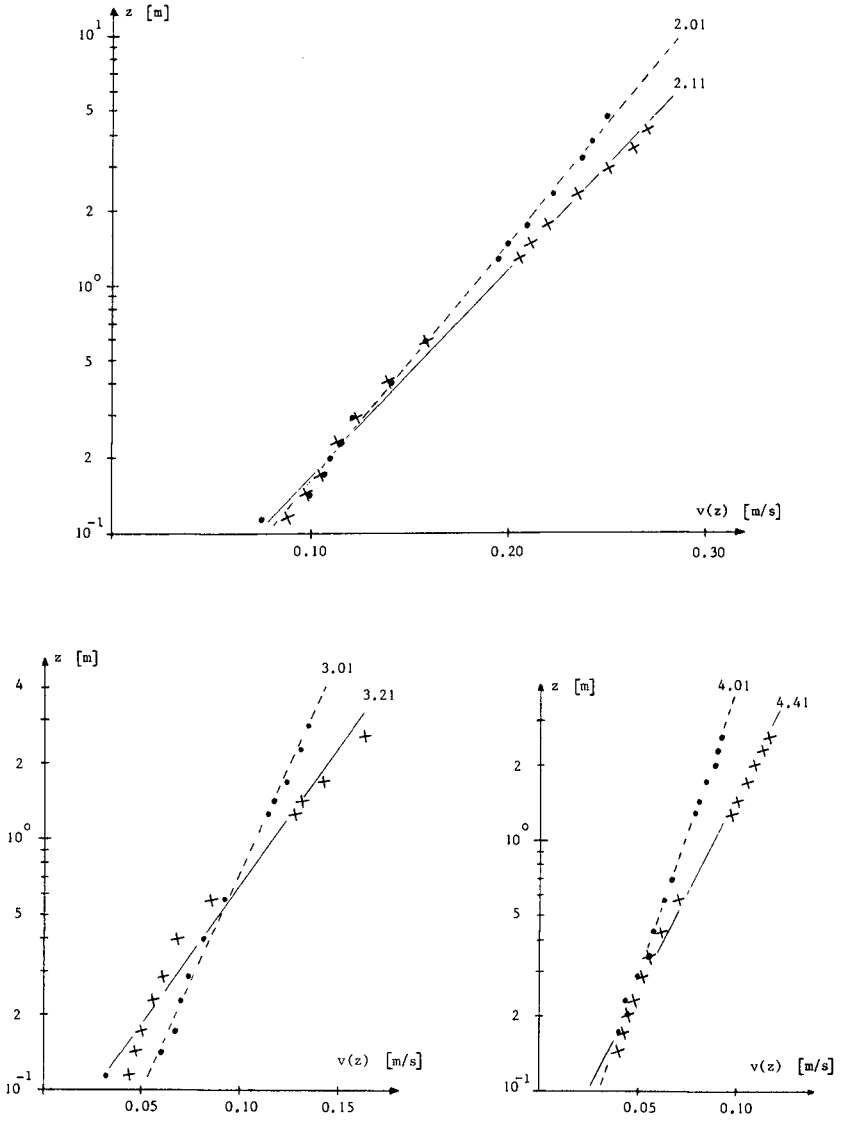

Fig. 7 - Mean current velocities v(z) in section F, averaged over two measuring points x = 3.0 m and x = 5.0 m; z = vertical coordinate, z = 0 at surface of perspex plate (see fig. 3), • • • = current alone, X X X = current and waves.

measurements (in the points x = 3.0 m and x = 5.0 m in section F) of mean current velocity profiles with the immersible LDA.

Fig. 7 reveals also a problem with the mean current velocity data of the experiments on the rough bottom: the velocities on the constant depth part of the basin were larger in the situation with current and waves than in case of current alone, especially at the downstream end of the basin. As such this was not unexpected. Due to the waves the bottom friction on the slope increased more than on the constant depth part of the basin (see also chapter 4). The flow rate Q was the same as in the current alone case and so this gave rise to this larger velocities. But the resulting non-uniformities of the mean current were hard to suppress and therefore the experimental data of V_{cw} (see table 2) are less accurate.

These non-uniformities have also unfluenced the mean water level slope observations. The maximum relative error occurs in exp. 4.21 (see table 2) and is estimated at

$$\frac{V\frac{\partial V}{\partial y}}{g\frac{\partial h}{\partial y}} \simeq \frac{0.09\,(\frac{0.096 - 0.083}{20})}{10 * 0.69 * 10^{-4}} \simeq 0.085 ,$$

which is, fortunately, not extremely large.

A suggestion to avoid this problem in further research is given in chapter 5.

4. COMPARISON WITH THEORETICAL RESULTS

For the combination of a mean current in longshore direction and a wave field (fig. 1), Bijker (1967) has proposed to combine the horizontal mean current and orbital velocity vector in the hypothetical boundary layer (viscous sublayer) at a height z' = e r/33 (r = Nikuradse bottom roughness parameter) above the bottom. Bijker determined the mean current velocity at this height with Prandtl's mixing length theory and put the horizontal orbital velocity at the height z' equal to $p\,u_m \cos \omega t$, with ω = angular frequency and p ≃ 0.4, both theoretically and experimentally. In this way Bijker has derived for the mean bottom frictional stress in y-direction τ_{by}:

$$\tau_{by} = C\,\rho\,V^2\,f(\theta, \xi\frac{u_m}{V}) , \qquad (2)$$

where

$$f(\theta, \xi\frac{u_m}{V}) = \frac{1}{T}\int_0^T \{1 + 2\,\xi\frac{u_m}{V}\sin\theta\cos\omega t + (\xi\frac{u_m}{V})^2\cos^2\omega t\}^{\frac{1}{2}} * \\ * (1 + \xi\frac{u_m}{V}\sin\theta\cos\omega t)\,dt , \qquad (3)$$

$$\xi_B = \frac{p\kappa}{\sqrt{C}} \simeq \frac{0.16}{\sqrt{C}} , \qquad (4)$$

$$C = \left(\frac{\kappa}{\ln\frac{12\,h}{r}}\right)^2 \quad , \tag{5}$$

t = time, T = wave period, C = dimensionless bottom friction coefficient.

The parameter ξ can be condidered as a dimensionless factor depending on how the mean current and orbital velocty near the bottom are combined. If the depth-averaged mean current velocity V and the amplitude of orbital velocity near the bottom u_m are combined, see Visser (1984), then: $\xi = 1$.

Swart (1974) modified Bijker's model to Jonsson's (1963, 1967) experimental results for waves alone and arrived at (2) with (3), (5) and

$$\xi_S = \sqrt{\frac{f_w}{2C}} \quad , \tag{6}$$

in which

$$f_w = \exp\{-5.977 + 5.213\left(\frac{r}{a_b}\right)^{0.194}\} \qquad \text{for} \quad \frac{a_b}{r} > 1.57 \quad , \tag{7}$$

$$f_w = 0.30 \qquad \text{for} \quad \frac{a_b}{r} < 1.57 \quad , \tag{8}$$

where f_w = Jonsson's wave friction factor and a_b = amplitude of orbital particle excursion near the bottom.

The elliptic integral $f(\theta, \xi u_m/V)$ represents the increase of the bottom friction due to the presence of a wave field. Its dependence on θ and $\xi u_m/V$ is shown in fig. 8. The dashed line in fig. 8 represents an analytical expression with which the elliptic integral can be approximated with an error smaller than 3 %, see Visser (1984).

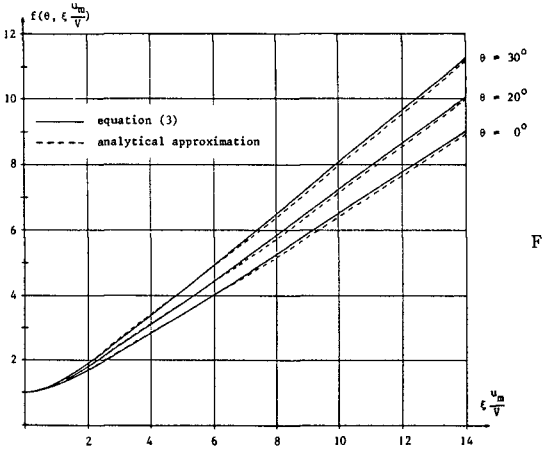

Fig. 8 – $f(\theta, \xi\frac{u_m}{V})$

exp nr	bottom	Q (1/s)	T (s)	H (m)	h (m)	V_c, V_{cw} (m/s)	u_m (m/s)	$i\,10^4$ (-)	$\frac{i_{cw}}{i_c}$ (-)	$\frac{u_m}{V_c}$ (-)	ξ_B (-)	ξ_S (-)	$f(\theta, \xi \frac{u_m}{V_c})$ $\xi=1$	$\xi=\xi_B$	$\xi=\xi_S$	$\frac{C_{cw}}{C}$
1.01	smooth concrete r ≈ 0.0023 m	400	-	-	0.214	0.216	-	0.72	-	-	-	-	-	-	-	-
1.11			1.0	0.046	0.213	0.216	0.119	0.67	0.93	0.55	2.8	3.6	1.07	1.43	1.66	1.2
1.21			1.0	0.070	0.213	0.219	0.179	0.60	0.83	0.83	2.8	3.1	1.15	1.85	2.00	1.3
1.31			1.8	0.043	0.214		0.125	0.68	0.94	0.58	2.8	2.9	1.08	1.48	1.50	1.2
1.41			1.8	0.076	0.213	0.218	0.188	0.71	0.99	0.87	2.8	2.6	1.16	1.93	1.81	1.3
2.01	gravel r ≈ 0.024 m	350	-	-	0.198	0.218	-	2.06	-	-	-	-	-	-	-	-
2.11			1.0	0.056	0.197		0.152	2.18	1.06	0.70	1.8	4.4	1.11	1.31	2.29	1.4
2.21			1.0	0.100	0.195		0.213	2.10	1.02	0.98	1.8	4.4	1.21	1.62	3.05	1.5
2.31			2.0	0.049	0.197		0.177	2.06	1.00	0.81	1.8	3.8	1.14	1.36	2.34	1.4
2.41			2.0	0.106	0.195		0.258	2.17	1.05	1.18	1.8	3.3	1.28	1.68	2.80	1.6
3.01		135	-	-	0.149	0.120	-	0.75	-	-	-	-	-	-	-	-
3.11			1.0	0.049	0.149		0.154	0.96	1.28	1.28	1.7	4.1	1.31	1.76	3.62	1.6
3.21			1.0	0.080	0.149	0.130	0.201	1.18	1.57	1.67	1.7	4.1	1.49	2.15	4.50	1.8
3.31			2.0	0.045	0.149		0.168	0.95	1.27	1.40	1.7	4.1	1.37	1.88	3.90	1.7
3.41			2.0	0.081	0.149	0.134	0.220	1.09	1.45	1.83	1.7	4.1	1.57	2.32	4.84	1.9
4.01		85	-	-	0.137	0.083	-	0.47	-	-	-	-	-	-	-	-
4.11			1.0	0.066	0.137	0.093	0.200	0.93	1.98	2.41	1.7	4.0	1.90	2.88	6.12	2.1
4.21			2.0	0.068	0.136	0.096	0.207	0.69	1.47	2.49	1.7	3.3	1.95	2.96	5.24	2.1

Table 2 - Experimental conditions and results and comparison of i_{cw}/i_c with theoretical predictions.

Assuming a logarithmic velocity distribution inside as well as outside the wave boundary layer (but with different slopes), Fredsøe (1984) has calculated the mean current profile by use of a depth-integrated momentum equation. Fredsøe derived for the mean bottom frictional stress in y-direction τ_{by} (in the notation of the present paper):

$$\tau_{by} = C_{cw} \rho V^2 , \tag{9}$$

where C_{cw} = dimensionless bottom friction coefficient in case of current and waves:

$$C_{cw} = \{ \frac{\kappa}{\ln(\frac{30 h}{r_w}) - 1} \}^2 , \tag{10}$$

in which r_w = apparent bed roughness (which is different from the grain roughness r as the wave boundary layer acts as a larger roughness element). The apparent bed roughness r_w can be determined from fig. 7 in Fredsøe's (1984) paper if V, h, u_m, a_b and r are known. The increase of the bottom friction in a flow due to waves can be expressed from (5) and (10) as:

$$\frac{C_{cw}}{C} = \{ \frac{\ln \frac{12 h}{r}}{\ln(\frac{30 h}{r_w}) - 1} \}^2 . \tag{11}$$

Table 2 gives the comparison of the measured increase of the bottom friction caused by the presence of waves (i_{cw}/i_c) and the theoretical predictions given by equation (3) with $\xi = 1$, $\xi = \xi_B$ and $\xi = \xi_S$, respectively, and those given by Fredsøe (= C_{cw}/C).

The bottom roughnesses r have been calculated from the experiments with current alone using (2) with $f(\theta, \xi u_m/V) = 1$ and (5), see table 2. The value of the diameter of the "roughness elements" of the concrete bottom is estimated at 0.5 - 1.0 mm, d_{90} = 8 mm for the gravel bottom. Thus

$$r/D_{90} \simeq 3, \tag{12}$$

which is in reasonable agreement with Kamphuis' (1975) ratio of 2. With $r/h \simeq 0.01$ and $Re \simeq 5 * 10^4$, the flow on the smooth concrete bottom is practically complete rough turbulent.

Table 2 shows that the measured i_{cw}/i_c are somewhat smaller than predicted by Fredsøe (1984), and lower to much lower than the predictions of Bijker (1967) and Swart (1974). The best agreement is obtained with equations (2) and (3) if $\xi = 1$.

The comparison of theoretical and experimental results for the increase of the bottom friction due to waves has been done using measured V_c in case of current alone. The data of V_{cw} have been ignored for this since these are less accurate (see chapter 3).

Substitution of V_{cw} in $f(\theta, \xi u_m/V)$ and use of it to determine C_{cw}/C will lead to smaller values for both parameters. But these smaller

values should also be compared with corrected values for i_{cw}/i_c:

$$\frac{i_{cw}^*}{i_c} = \frac{h_{cw}}{h_c} \left(\frac{V_c}{V_{cw}}\right)^2 \frac{i_{cw}}{i_c} \quad . \tag{13}$$

5. CONCLUSIONS AND SUGGESTIONS FOR FURTHER RESEARCH

A set of data is presented of wave basin experiments on the increase of the mean bottom frictional stress in a flow when waves are superimposed on a current (angle between directions of current and wave propagation is 90^o). Especially the accuracy of the mean water level slope observations (direct measurement of effect of bottom friction) between sections C and F (fig. 5) is satisfactory. The decrement of the mean current velocities on the slope in case of current and waves has decreased the uniformity of the mean current velocities on the constant depth part of the basin, so also the accuracy of the mean current data (particularly V_{cw}) in this situation.

The following conclusions can be drawn from this investigation:

1. A rather laborious adjustment of the inflow is necessary to obtain uniform mean current velocities.
2. An immersible Laser Doppler Anemometer is a very useful instrument for wave basin experiments. Problems can be expected inside the surf zone caused by air-bubbles in the water.
3. The models of Bijker (1967) and Swart (1974), which are practical for engineering applications, do overestimate the bottom friction in case of current and waves.
4. The equation $\tau_{by} = C \rho V^2 f(\theta, \xi u_m/V)$ with $\xi = 1$ gives rather good agreement with the experimental results. This conclusion has also been followed from a comparison of longshore current data with a mathematical model including this expression, Visser (1984, 1985).
5. The bottom stresses as derived by Fredsøe (1984) are somewhat larger than the experimental results.

The following recommendations for further research are given:

1. The present experimental set-up can be improved by reducing the velocities on the slope significantly (for instance by making the bottom of the slope much more rough than the bottom of the constant depth part of the wave basin).
2. It is recommended to compare the model of van Kesteren and Bakker (1985) with the present experimental data.

ACKNOWLEDGMENT

The author is grateful to J.A. van der Stel, who performed the experiments.

REFERENCES

Bakker, W.T. and van Doorn, Th., 1979. Near bottom velocities in waves with a current. Proc. 16th Coastal Eng. Conf., Hamburg, 1978, pp. 1394 - 1414.

Bijker, E.W., 1967. Some considerations about scales for coastal models with movable bed. Delft Hydraulics Laboratory, Publication no. 50, 142 pp.

Brevik, I., 1981. Oscillatory rough turbulent boundary layers. J. Waterway, Port and Ocean Div., ASCE, vol. 107, pp. 175 - 188.

Doorn, Th. van, 1982. Experimental investigation of the velocity field in the turbulent bottom boundary layer in an oscillating water tunnel. Delft Hydraulics Laboratory, Rep. no. M 1562 part 1 (in Dutch).

Doorn, Th. van, 1983. Computations and comparison with measurements of the turbulent bottom boundary layer in an oscillatory flow. Delft Hydraulics Laboratory, Rep. no. M 1562 part 2.

Fredsøe, J., 1984,. Turbulent boundary layer in wave-current motion. J. Hydr. Eng., ASCE, vol. 110, pp. 1103 - 1120.

Godefroy, H.W.H.E. and Vegter, D., 1984. A new type immersible Laser Doppler Anemometer. Conference papers Transducer Tempcon Conference 84, Harrogate, England, 1984, pp. 384 -403.

Grant, W.D. and Madsen, O.S., 1979. Combined wave and current interaction with a rough bottom. J. Geophys. Res., vol. 84, pp. 1797 - 1808.

Horikawa, K. and Watanabe, A., 1969. Laboratory study on oscillatory boundary layer flow. Proc. 11th Coastal Eng. Conf., London, 1968, pp. 467 - 486.

Jonsson, I.G., 1963. Measurements in the turbulent wave boundary layer. Proc. 10th IAHR Congr., London, 1963, pp. 85 - 92.

Jonsson, I.G., 1967. Wave boundary layers and friction factors. Proc. 10th Coastal Eng. Conf., Tokyo, 1966, pp. 127 - 148.

Jonsson, I.G., 1980. A new approach to oscillatory rough turbulent boundary layers. Ocean Engineering, vol. 7, pp. 109 - 152 and 567 - 570.

Jonsson, I.G. and Carlsen, N.A., 1976. Experimental and theoretical investigations in an oscillatory rough turbulent boundary layer. J. Hydr. Res., vol. 14, pp. 45 - 60.

Kajiura, K., 1968. A model of the bottom boundary layer in water waves. Bull. Earthquake Res. Inst., vol. 46, pp. 75 - 123.

Kalkanis, K., 1964. Transport of bed material due to wave action. U.S. Army Coastal Eng. Res. Center, Techn. Memo No. 2.

Kamphuis, J.W., 1975. Friction factor under oscillatory waves. J. Waterway, Port and Ocean Div., ASCE, vol. 101, pp. 135 -144.

Kemp, P.H. and Simmons, R.R., 1982. The interaction between waves and a turbulent current: waves propagating with the current. J. Fluid Mech., vol. 116, pp. 227 - 250.

Kemp, P.H. and Simmons, R.R., 1983. The interaction between waves and a turbulent current: waves propagating against the current. J. Fluid Mech., vol. 130, pp. 73 - 89.

Kesteren, W.G.M. van and Bakker, W.T., 1985. Near-bottom velocities in waves with a current. Proc. 19th Coastal Eng. Conf., Houston, 1984, pp. 1161 - 1177.

Lundgren, H., 1973. Turbulent currents in the presence of waves. Proc. 13th Coastal Eng. Conf., Vancouver, 1972, pp. 623 - 634.

Nielsen, P., 1985. Om the structure of oscillatory boundary layers. Coastal Engineering, vol. 9, pp. 261 -276.

Sleath, J.F.A., 1982. The effect of jet formation on the velocity distribution in oscillatory flow over flat beds of sand or gravel. Coastal Engineering, vol. 6, pp. 151 - 177.

Swart, D.H., 1974. Offshore sediment transport and equilibrium profiles. Delft Hydraulics Laboratory, Publication no. 131, 217 pp.

Tanaka, H. and Shuto, N., 1984. Friction laws and flow regimes under wave and current motion. J. Hydr. Res., vol. 22, pp. 245 - 261.

Visser, P.J., 1982. The proper longshore current in a wave basin. Comm. on Hydraulics, Dept. of Civil Eng., Delft Univ. of Techn., Rep. no. 82-1, 86 pp.

Visser, P.J., 1984. A mathematical model of uniform longshore currents and the comparison with laboratory data. Comm. on Hydraulics, Dept. of Civil Eng., Delft Univ. of Techn., Rep. no. 84-2, 151 pp.

Visser, P.J., 1985. Uniform longshore current measurements and calculations. Proc. 19th Conf. Coastal Eng., Houston, 1984, pp. 2192 - 2207.

CHAPTER 62

FRICTION IN HURRICANE-INDUCED SURGES

Shang-Yih Wang[1] and B. A. Christensen[2]

ABSTRACT

With the increasing development of coastal areas, it is necessary to have a sound method for predicting hurricane-induced flooding in these areas, especially for studies such as the coastal construction set-back line, flood insurance rate-making and county land use planning. The objective of this study is to develop the capability of describing the friction factor in coastal areas for improved representation in numerical models of storm surges.

Five types of areas are considered: A, ocean bottom with bed forms and some vegetation; B, mangrove fringes and areas; C, forested areas and cypress swamps; D, grassy areas and saltwater marshes; and E, developed residential and commercial areas. The friction factors, which incorporate both the bottom friction coefficient and drag coefficient due to the submerged parts of obstructions were verified by conducting laboratory experiments for mangrove and developed areas, using the typical distribution found in each of these coastal areas. The formulas of the friction factor for the ocean bottom, forested areas and grassy areas are determined by adopting results from previous investigations and discussed with the results of the current study.

INTRODUCTION

Through history flood prone areas in the worlds coastal regions have had an almost magic attraction on man. Today the trend is still towards a more intense utilization of coastal areas with high risk of flooding due to hurricanes than of the safer inland areas. The result is increasing flood losses. Such losses have grown from about $60 million at the turn of the century to more than $1 billion today in the United States alone.

The accurate prediction of local elevations of the 100 year flood plain is therefore more and more important for insurance

[1]Assistant Engineer, Beaches and Shores Resource Center, Florida State University, Tallahassee, Florida, U.S.A.

[2]Professor, Hydraulic Laboratory, Department of Civil Engineering, University of Florida, Gainesville, Florida, U.S.A.

purposes in the coastal zone. In a rapidly developing coastal county a one foot error in the predicted flood elevation may easily result in unnecessary construction and insurance costs in the millions of dollars per year. In an otherwise correct numerical model such an error may be introduced by an erroneous representation of the influence of friction in shallow ocean and overland flows. The present paper addresses itself to this problem.

The first numerical models of storm-induced surges in the ocean did often neglect the influences of bottom friction. While such a simplifying omission of a friction term in the governing equations appears to be acceptable in the parts of the ocean where depths are substantial it does result in errors in the shallow near-cost ocean and, of course, in the even shallower overland flow.

More recently developed models are therefore including this term. For instance, the Tetra-Tech model described by Chen et al. (1977) and widely used in the National Flood Insurance Program, takes bed friction into consideration by using the Manning formula. Other models use the Darcy-Weisbach formula for the bed shear stress τ_b

$$\tau_b = f' \rho \, u_m^2 / 2 \tag{1}$$

where ρ = density of water, u_m = the spatial mean velocity in the local vertical, and f' = the friction factor.

The approach using the Manning formula for evaluation of the bed shear stress leads to the expression

$$\tau_b = \gamma \, n^2 u_m^2 / d^{\frac{1}{3}} \tag{2}$$

using S.I. Units. In Eqn. (2) γ = unit weight of water, n = Manning's n and d = local depth. Elimination of τ_b by combination of Eqns. (1) and (2) shows that the friction factor must be a function of the local depth and, of course, of n that again depends on the equivalent sand roughness of the bed. The method of using a constant value of the friction factor in the ocean, regardless of depth, does therefore not seem satisfactory, although it has given quite decent results in many cases, especially in relatively deep ocean areas.

Using the Manning formula and thereby Eqn. (2) for the bed shear stress may also lead to errors when the apparent sand roughness is not sufficiently small compared to the depth as shown by Christensen (1970). The approach using the Darcy-Weisbach equation for the bottom shear stress is therefore chosen in this paper.

MODEL EQUATIONS

Friction Factor for Surges in Unobstructed Areas

Unobstructed areas include the ocean bottom and grassy areas, the latter of which are assumed to be completely submerged in water during floods. Practically all flow in hurricane-induced surges is in the hydraulically rough flow range. A velocity profile based on a modification of Prandtl's mixing length theory proposed earlier by Christensen (1972) may therefore be applied

$$\frac{\bar{u}}{u_f} = 2.5 \ln \left(\frac{29.73z}{k} + 1\right) \tag{3}$$

where $\bar{u}$ = time-mean velocity in the direction of flow at a distance z from the bed, u_f = friction velocity, and k = Nikurades's equivalent sand roughness. This modification provides a velocity profile that satisfies the no slip condition at the bed where the classic profile yields unrealistic negative velocities approaching minus infinity.

For practical purposes, the time-mean velocity profile is transformed to a depth averaged velocity profile using the fact that the mean velocity (depth averaged), u_m, occurs theoretically at a distance z = 0.368d from the bed also for the modified logarithmic vertical velocity profile, where d/k is larger than 1. Therefore at z = 0.368d Eqn. (3) yields

$$\frac{u_m}{u_f} = 2.5 \ln \left(\frac{10.94d}{k} + 1\right) \tag{4}$$

The friction factor may in general be related to the velocity profile by introducing the Darcy-Weisbach formula into the definition of the friction velocity by

$$\frac{u_m}{u_f} = \left(\frac{2}{f'}\right)^{\frac{1}{2}} \tag{5}$$

Solving Eqn. (5) for f' and introducing Eqn. (4) gives the following expression for the friction factor

$$f' = \frac{0.32}{\left[\ln \left(\frac{10.94d}{k} + 1\right)\right]^2} \tag{6}$$

Friction Factor for Surges in Obstructed Areas

Obstructions in these areas, e.g. mangroves, woods and buildings, are defined as roughness elements with significant heights which either protrude through the water layer or consist of relatively rigid elements with height that are sufficient to cause a form drag that is much larger than surface friction on the same area. The equation presented here is based on the assumption of steady or quasi-steady flow in the rough flow range.

Consider a design flow that passes over an obstructed area where the density is M per unit area, average diameter of the obstruction in the projected plane normal to the flow is D, and average drag coefficient is C_D. The head loss per unit weight of fluid over a bed length of L, ΔH, may be written as

$$\Delta H = f'_e \frac{u_m^2}{2g} \frac{L}{R} = f' \frac{u_m^2}{2g} \frac{L}{R} (1-\varepsilon) + MC_D dD \frac{u_m^2}{2g} \frac{L}{R} \tag{7}$$

in which R = hydraulic radius, ε = fraction of total area occupied by obstructions. An equivalent friction factor, f'_e, which includes the effects of bottom friction and form drag in the form of the Darcy-Weisbach formula is introduced. From Eqn. (7) it is seen that

$$f'_e = f' (1-\varepsilon) + MC_D dD \tag{8}$$

where, according to Eqn. (6),

$$f'_e = \frac{0.32}{\left[\ln \left(\frac{10.94d}{k} + 1\right)\right]^2}$$

EXPERIMENTAL VERIFICATION OF FRICTION FACTOR

According to the principle of conservation of energy, the total energy head at an upstream section 1 should be equal to the total energy head at the corresponding downstream section 2 plus the head loss between the two sections, i.e.,

$$d_1 + \frac{u_{m1}^2}{2g} = d_2 + \frac{u_{m2}^2}{2g} + \Delta H \tag{9}$$

where subscripts 1 and 2 refer to sections 1 and 2, respectively. Relating the measured results of head loss to the Darcy-Weisbach equation

$$\Delta H = f'_e \frac{u_a^2}{2g} \frac{L}{R_a} \qquad (10)$$

in which $u_a = (u_{m1}+u_{m2}) / 2$ and $R_a = (R_1 + R_2) / 2$, the equivalent friction factor f'_e can be determined for the designed roughness elements. To measure the velocities, a Novonic-Nixon type velocity meter was employed. The range of this velocity meter is from 3 to 150 cms^{-1} with an accuracy of $\pm$ 1 % of true velocity. A siphon type depth measuring device is designed to measure the water surface elevations to an accuracy of one millimeter. All the model tests were conducted in the hydraulic laboratory flume of the Civil Engineering Department at the University of Florida. The main channel of this flume is 36.6 meters long, 2.44 meters wide, and 0.81 meter deep.

Model Setup

Mangroves

Based on the average parameters obtained from eleven sampling areas in San Carlos Bay on the southwest coast of Florida, patterns of red and black mangroves were designed as shown in Figures 1 and 2. The dimensions of all stems and roots, including height and diameter of the prototype, are reduced to 1/10 for the model based on the undistorted Froude Law. The legends listed in these figures were the actual dimensions used in the model setup.

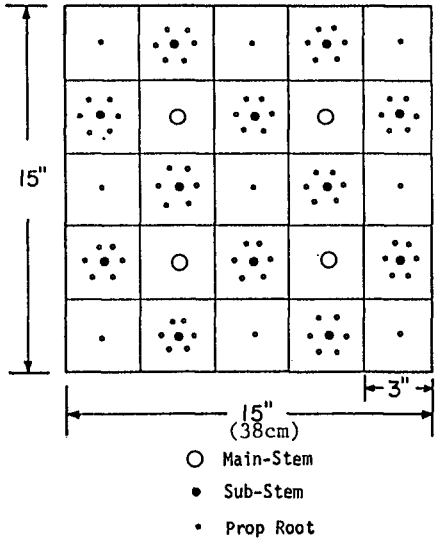

Figure 1: Model Setup for Red Mangroves

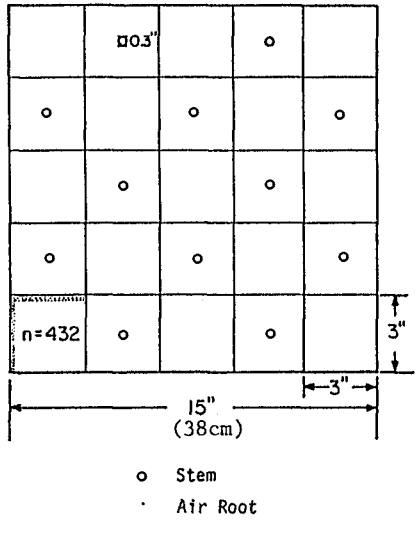

Figure 2: Model Setup for black Mangroves

The stems of red and black mangroves were simulated by dowels of the specified diameters and heights. The substems and prop roots were simulated by galvanized nails with heads removed. A manufactured nylon door mat whose strings have the same height (1.5 cm) and the same thickness (0.06 cm) as the design model dimensions of air roots was used. These dowels, nails and mats were fixed on three 2.4 meters by 1.2 meters marine plywood sheets, which covers half the flume width.

Buildings

Prototype data for the three kinds of buildings: high-rise, medium-rise and residential buildings, were taken and analyzed from aerial photographs of Broward and Dade counties, Florida. Table 1 shows a summary of the average parameters for these three categories. In this case a distorted madel with depth scale N_d and horizontal scale N_ℓ was used.

Table 1: Average parameters of Prototype and Model for Building Areas

Type of Buildings	PROTOTYPE			MODEL (N_d = 10)			
	Approximate Dimension (m)		Density	N_ℓ	Dimension (cm)		Density
	length	width	no. / 46452 m^2		length	width	no. / 2.1 m^2
High-Rise	69	33	7.19	174	39.4	19.1	10
Medium-Rise	31	15	23.62	80	39.4	19.1	7
Residential	19	9	68.87	48	39.4	19.1	7

Since the vertical dimension scale cannot follow the horizontal dimension scale in building models as the flow depth would be much too small for measurements to be made, or the viscous force would become important and cannot be neglected for the small flow depth. Therefore, a model with different vertical scale than horizontal scale is used to keep the model Reynolds numbers in the turbulent flow range. The concrete blocks with dimensions 19.1 cm x 19.1 cm x 39.4 cm were used to simulate the buildings. Figure 3 shows 21 patterns to be tested in which Nos. 1 to 13 were designed to simulate high-rise buildings, while Nos. 14 to 21 were for medium-rise buildings and residential areas. The design densities are started from low to high and cover at least the average densities obtained from the prototype. The whole width of the flume was used in this part of the experiments.

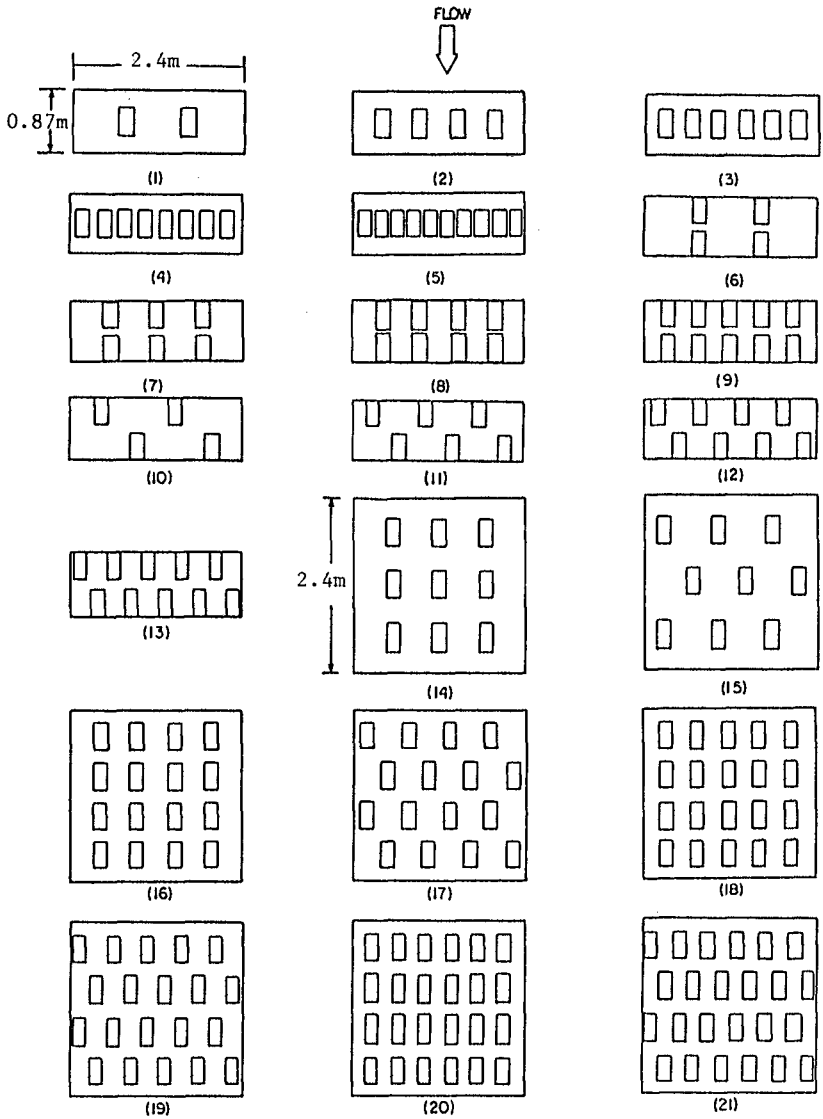

Figure 3: Building Patterns Designed for the Tests

Experimental Runs and Results

Mangrove Areas

During the first part of the experiments, 7 runs were conducted for the air roots of the black mangrove area to determine its apparent roughness height and friction factor. In the second part of the experiments, 38 runs were performed for the red mangrove area and black mangrove area by adjusting the discharge valve and changing the still water depths so that the flow Reynolds numbers covered a range from 20,000 to 55,000 while the Froude numbers varied from 0.14 to 0.44. Table 2 lists the mean values of the results and their corresponding standard deviations for the equivalent friction factors, drag coefficients and apparent roughnesses, k_a.

Table 2: Statistical Values of Experimental Results for Mangrove Areas

Mangroves	Statistical Values	f'_e	C_D	k_a (cm)	
				Model	Prototype
Red	Mean	0.129	0.732	42.69	426.9
	Standard Deviation	0.013	0.077	6.14	61.4
Black Stems	Mean	0.132	1.001	38.53	385.3
	Standard Deviation	0.020	0.090	9.72	97.2
Black Air Roots	Mean	0.028		5.26	52.6
	Standard Deviation	0.003		0.65	6.5

Building Areas

At least 10 runs were conducted for each of the 21 patterns shown in Figure 3. These runs for each pattern were controlled by adjusting the flume discharge valve and the tail gate so that they covered a range of Reynolds numbers from 20,000 to 70,000, while the Froude numbers varied from 0.1 to 0.5. The results obtained for medium-rise building areas can be converted using appropriate scaling factors to use in residential areas since these two areas are presumed to have the same relative distributions and have only dimensional differences. The statistical values of the experimental results for 21 patterns are listed in Table 3.

Table 3: Statistical Values of Experimental Results for Building Areas

Pattern No.	f'_e			C_D			Building Area
	Mean	Standard Deviation		Mean	Standard Deviation		
		value	% of mean		value	% of mean	
1	0.0013	0.0003	23	0.788	0.163	21	High-Rise
2	0.0064	0.0006	38	1.965	0.254	13	"
3	0.0180	0.0030	17	3.406	0.181	5	"
4	0.0460	0.0090	20	7.014	1.121	16	"
5	0.1580	0.0260	16	17.813	1.298	7	"
6	0.0036	0.0006	17	1.108	0.123	11	"
7	0.0046	0.0011	24	0.907	0.230	25	"
8	0.0090	0.0010	11	1.346	0.119	9	"
9	0.0130	0.0010	8	1.597	0.189	12	"
10	0.0080	0.0014	18	2.369	0.275	12	"
11	0.0154	0.0029	19	2.965	0.227	8	"
12	0.0230	0.0040	17	3.662	0.221	6	"
13	0.0350	0.0050	14	4.315	0.389	9	"
14	0.0074	0.0011	15	1.232	0.170	14	Medium-Rise
15	0.0127	0.0030	24	2.082	0.173	8	"
16	0.0117	0.0020	17	1.088	0.096	9	"
17	0.0329	0.0067	20	3.040	0.114	4	"
18	0.0158	0.0018	11	1.181	0.097	8	"
19	0.0448	0.0072	16	3.355	0.098	3	"
20	0.0265	0.0038	14	1.586	0.089	6	"
21	0.0631	0.0112	18	3.926	0.120	3	"
14	0.0123	0.0018	15	1.232	0.170	14	Residential
15	0.0211	0.0050	24	2.082	0.173	8	"
16	0.0195	0.0034	17	1.088	0.096	9	"
17	0.0548	0.0112	20	3.040	0.114	4	"
18	0.0264	0.0030	11	1.181	0.097	8	"
19	0.0747	0.0120	16	3.355	0.098	3	"
20	0.0441	0.0063	14	1.586	0.089	6	"
21	0.1052	0.0186	18	3.926	0.120	3	"

Drag Coefficient - Building Density Relations

The data obtained from pattern 1 through 13 were analyzed and plotted in Figure 4, which shows three possible relations between the drag coefficients and densities for high-rise building areas. Figure 5 shows two relations between drag coefficients and densities for the medium-rise building area and residential area, respectively.

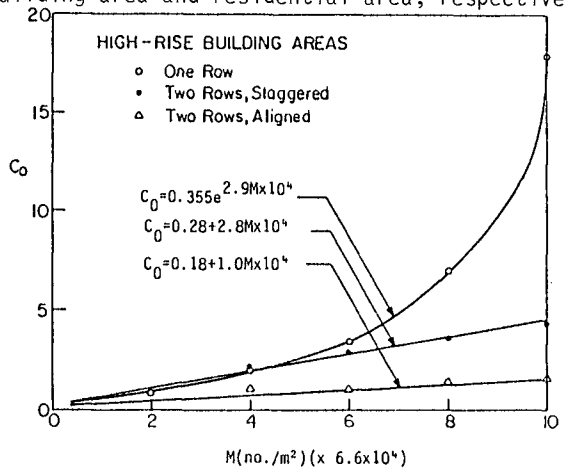

Figure 4: Relation Between C_D and Density M for High-Rise Building Areas

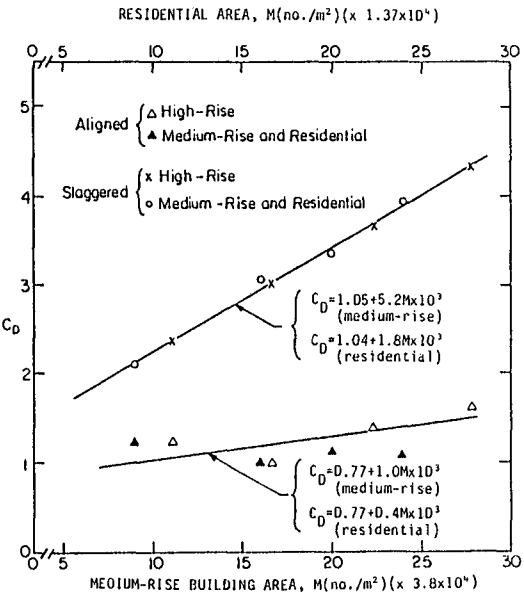

Figure 5: Relation Between C_D and Density M for Medium-Rise Building and Residential Areas

Drag Coefficient - Disposition Parameter Relations

Measuring the diagonal distance between the roughness elements in adjacent transverse rows, S_d, from building pattern 6 to 21, it is found that S_d/D and C_D show a good correlation for both aligned and staggered cases, as shown in Figure 6. This is attributed to the nature of the diagonal spacing, S_d, whose magnitude not only provides a measurement of density but also reveals a difference of disposition for the evenly distributed roughness elements. Therefore, the higher the building density, the smaller the disposition parameter, S_d/D, therefore a larger drag coefficient results. For buildings with the same dimensions and density, the disposition parameter, of the staggered pattern is smaller than that of aligned pattern, which also results in a larger drag coefficient. The same result was also substantiated by Shen (1973) who measured the mean drag coefficient of two cylinder patterns (aligned and staggered) in open channel flow.

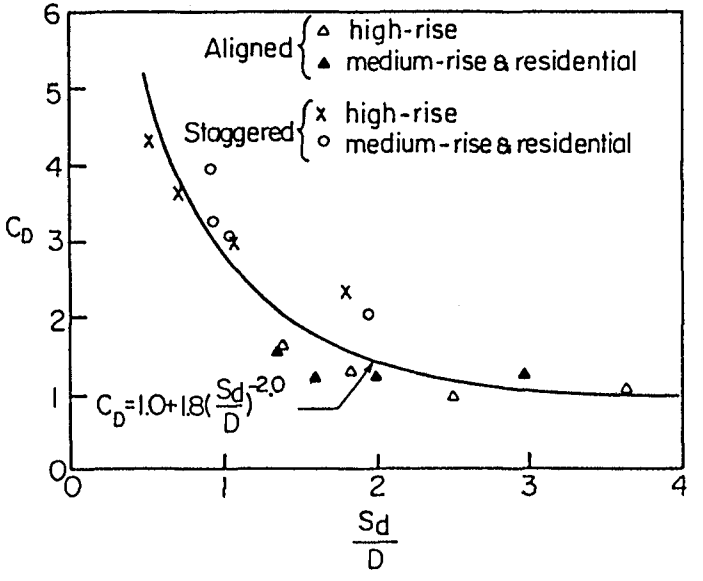

Figure 6: Relation Between C_D and S_d/D

DISCUSSIONS AND CONCLUSIONS

Ocean Bottom

The ocean bottom is mainly composed of different sizes of sands, on which vegetation and sand ripples vary with location. Hydraulic measurements in the field are the best way to determine the friction characteristics, but such measurements of velocity distributions and water depths are nearly impossible during a storm. Therefore, field measurements under normal conditions similar to a storm tide are needed. One possible instance is the flood and ebb flows through a tidal entrance in which the flow is in the fully rough range, and the effect of the temporal acceleration of the flow is generally of a lesser magnitude than the effect due to bed friction; therefore a correspondence between entrance flow and storm flood is expected. Three tidal entrances, John's Pass, Blind Pass and O'Brine's Lagoon Entrance, located on the Gulf coast of Florida were selected for hydraulic measurements to determine the bed friction characteristics (Mehta, 1978).

The values of Manning's n obtained for these three entrances are in the range from 0.020 to 0.026, which corresponds to the following bed morphologic features in open channel flows: clean, straight stream on plain (n = 0.025), gravel uniform excavated channel (n = 0.022), and uniform dredged earth channel with short grass (n = 0.022). This correspondence not only suggests that the values of n in the Manning's n table can be applied to tidal entrance, but that they can also be used for the ocean bottom during storm events. Therefore, for a rough ocean bottom, where the vegetation is significant or other roughnesses such as rocks or reefs exist, the n value is assumed to equal to 0.035, which represents an irregular, rough stream, a clean, winding stream on a plain with some weeds and stones, a dredged channel with light brush on banks, or a flood plain with scattered brush and heavy weeds in open channel flows.

As a results, the k values corresponding to the recommended n values are 0.03 m (n = 0.022) and 0.55 m (n = 0.035) for smooth and rough ocean bottoms, respectively. The friction factors for ocean bottoms can then be estimated using the equations

$$f' = \frac{0.32}{[\ln(365d + 1)]^2} \quad \text{for smooth ocean bottom} \qquad (11)$$

and

$$f' = \frac{0.32}{[\ln(20d + 1)]^2} \quad \text{for rough ocean bottom} \qquad (12)$$

Mangrove Areas

In general, the red mangroves only extend about 15 meters inland

from the shoreline and it is hard to distinguish them from black mangroves on aerial photographs and conventionally used city maps. Examining the case of fine grid system for numerical models whose grid elements are usually chosen to be 1,610 meters square, the average friction for each grid element on the mangrove fringes should be represented by the sum of 1 % of the red mangrove and 99 % of the black mangrove. For engineering applications, therefore, it is not necessary to consider the small difference between red and black mangroves. The equivalent friction factor derived for black mangroves then can be used for all the mangrove areas, i.e.,

$$f'_e = \frac{0.32}{[\ln(21d + 1)]^2} + 0.07d \qquad (13)$$

Forested Areas

Forested areas may consist of many different species, like oaks, magnolia, cedar, palm, pine and cypress, where each species has different representative features. However, for a general view, some typical values of the parameters for evaluating the equivalent friction factor are suggested by Christensen and Walton (1980)

$$k = 0.5 \text{ m} \; ; \; M = 0.1 \text{ m}^{-2} \; ; \; D = 0.6 \text{ m}$$

$$\varepsilon = 0.028 \; ; \; C_D = 0.8$$

It is worthwhile to examine the drag coefficient recommended for forested areas. In Figure 6, it is seen that the drag coefficient has a tendency to become constant and equal to 1.0 when the disposition parameter S_d/D is larger then 4. This relation derived initially for the rectangular roughness elements may also be used for circular roughness elements and can be proved by comparing the measured drag coefficient (1.0) for black mangroves as seen in Table 2. For black mangroves, the disposition parameter is about 17, and the corresponding drag coefficient is 1.0 according to Figure 6, which agrees well with the measured results. Applying the same reasoning to forested areas, whose disposition parameter equals to 12, the drag coefficient can be expected to be approximately 1.0. therefore, the drag coefficient 0.8 proposed by Christensen and Walton is conservative and reasonable. Adopting these values, the equivalent friction factor can be expressed in the form

$$f'_e = \frac{0.31}{[\ln(22d + 1)]^2} + 0.048d \qquad (14)$$

Grassy Areas

Saw grasses are the dominate plant community occurring in the world's coastal zones where water stands all or part of a year. The

results of studies of the flow of water over various grass covers by Palmer (1946) may provide some information to evaluate the roughness characteristics of saw grass. Palmer found that a completely submerged surface of Bermuda grass has a Manning's n of about 0.04, which corresponds to a k-value of about 1.25 m. If it is assumed that there is geometric similitude between Bermuda grass and about three times taller saw grass, Palmer's experiment with Bermuda grass may be considered as a model test of the prototype saw grass. As a results, a k-value of about 4 m for saw grass is expected. Christensen's (1980) indirect observation of the equivalent roughness of grass covered beds of estuaries on Florida's west coast have indicated a k-value ranging from 3 m to 5 m, which is in good agreement with the value derived from palmer's experiments with Bermuda grass. Introducing a k-value of 4 m in the friction factor equation, as suggested by Christensen and Walton (1980), yields

$$f' = \frac{0.32}{[\ln(2.7d + 1)]^2} \tag{15}$$

Developed Areas

The equivalent sand roughness, k, for developed areas cannot be determined by a single value, since the space between the buildings cover many different roughnesses. These roughnesses, in general, consist of pavements, grasses, light brush and trees, whose values of Manning's n are 0.013, 0.025 and 0.040, respectively. Assuming these roughnesses are evenly distributed, then an average value of n equals to 0.026 is assigned for these developed areas which gives k = 0.09 m using the Manning Strickler equation. As a result, the equivalent friction factor for developed areas may be represented as

$$f'_e = \frac{0.32}{[\ln(122d + 1]^2}(1-\varepsilon) + MC_D dD \tag{16}$$

The water depth d should be introduced in meters in all of the above expressions. The mean values of ε, M and D can be determined from the information in Table 2, or from the aerial photographs of the study areas.

The following three drag coefficient equation are suggested for friction factor calculations in developed areas:

$$C_D = 0.355\, e^{2.9M \times 10^4} \quad \text{for the one row high-rise building areas;} \tag{17}$$

$$C_D = 1.05 + 5.2M \times 10^3 \quad \text{for the staggered medium-rise building areas;} \tag{18}$$

and $C_D = 1.04 + 1.8M \times 10^3$ for the staggered residential areas; (19)

in which M is in number per meter square. The particular equation is recommended because on row high-rise buildings are the most predominate type of buildings found in highly developed coastal areas such those in Broward and Dade counties, Florida. For medium-rise buildings and residential areas, most buildings can be assumed to be staggered, since aligned buildings are scarce and the probability that floods will flow normal to the aligned building areas is very small in the field.

REFERENCES

Chen, M., Allen Ashley, David Divoky and Li-San Hwang, "Coastal Flooding Handbook, Part 1 - Methodology, Part 2 - Codes and User's Guide," Tetra-Tech Report, TC-612-10-2, Pasadena, CA, 1977.

Christensen, B.A., Discussion of "Manning n for Cast-in-Place Concrete Pipe," by T.T. Wilson and Edib Kirdar, Journal of the Hydraulics Division, American Society of Civil Engineers, Vol. 96, No. HY3, New York, N.Y., 1970.

Christensen, B.A., "Incipient Motion on Cohesionless Channel Banks," in "Sedimentation" (editor H.W. Shen), Fort Collins, CO, 1972.

Christensen, B.A. and Walton, R., "Friction Factors in Storm Surges over Inland Areas," Journal of Waterways and Harbor Division of ASCE, ww2, pp. 261, May 1980.

Mehta, A.J., "Bed Friction Characteristics of Three Tidal Entrances," Coastal Engineering, Vol. 2, pp. 69-83, Netherlands, 1978.

Palmer, V.J., "Retardance Coefficients for Low Flow in Channels Lined with Vegetation," Transations, American Geophysical Union, Vol. 2, No. II, pp. 187, 1946.

Shen, H.W., "Flow Resistance Over Short Simulated Vegetation and Various Tall Simulated Vegetation Groupings on Flow Resistance and Sediment Yield," Environmental Impact on Rivers, River Mechanics III, Fort Collins, Colorado, 1973.

CHAPTER 63

Real-Time Wave Forecasting with adaptive ARMAX models

H.Wensink* and T. Schilperoort

Abstract

A method is described for improving the accuracy of the wave predictions which are required for the operational guidance of the shipping traffic in approach channels to harbours and to support offshore activities.
The method, as being described here, is based on the assimilation of wave physics and real-time hydrometeorological observations into a statistical time series model called ARMAX.

1 Introduction

In many practical situations operational wave prediction systems are needed, which have an accuracy that cannot be met by the prediction systems generally used in practice.
One way to improve existing methods is to integrate available hydrometeorological data and numerical wave prediction models into one prediction system.
This idea has been worked out by Poulisse and Schilperoort (1983), who investigated the potential of Kalman-filtering and adaptive time series (ARMAX) modelling for wave prediction purposes.

Schilperoort and Strating (1985) have described an adaptive modelling technique based on a correlation of wave observations, measured at different locations along the dominant propagation path of the wave energy.

More insight into the modelling of the wave processes and the development of new measuring instruments as well as the experience in an operational environment necessitated an improvement of the existing (ARMAX) method. These improvements are described by Wensink (1986a, 1986b and 1987).

The purpose of this paper is to describe an improved wave prediction system based on the adaptive time series modelling technique.
In paragraph 2 a short overview is given and the extensions of the wave prediction model are described. Paragraph 3 presents the results of the prediction system in an operational situation.
Finally in paragraph 4 the conclusions and some operational aspects are described.

2. The ARMAX system

The adaptive time series modelling technique as described by Schilperoort and Strating (1985) is a method that can be used for complex physical systems in which diffusion and advection plays an important role.

*Delft Hydrulics Lab, Delft, The Netherlands

The first parameter for which such a system has been developed is the 'low frequency wave energy', E_{10}, a parameter indicating the variance which is present in the wave spectra above the 10 s wave period.

This parameter has been chosen because of its pronounced influence on the motion of large ships and because of its low accuracy of prediction using existing prediction sytems.

The ARMAX prediction system for 'low frequency wave energy' is based on six elements:

- a data pre-processing module, in which, for each individual monitoring station, the raw hydrometeorological observations are transformed using simple wind-wave relationships;
- a data correction module;
  * in which, for each individual monitoring station the hydrometeorological data are reviewed and corrected for missing values
  * which determines the stations in the monitoring network to be coupled by ARMAX models;
- a correlation module, in which the transformed data of two neighbouring monitoring stations are correlated with each other using an ARMAX time series model
- a coupling module, in which a number of correlation modules is coupled, depending on the number of stations in the monitoring network and the quality of the input data;
- an identification module, in which the parameters of the ARMAX models used are estimated using an adaptive modified recursive least squares estimation method;
- a prediction module which generates the E_{10} predictions using the last identified ARMAX models;

2.1 Data pre-processing module

Wave fields not propagating in line with the monitoring stations affect the statistical relations between the observed 'low frequency wave energy' parameter (LFE) at two neighbouring monitoring stations and therefore reduce the maximum possible prediction accuracy.
To account for these secondary wave fields, at each individual monitoring Station i, crude estimates are made of the incoming E_{10} from Station (i-1), the locally generated E_{10} and the outgoing E_{10}, propagating to Station (i + 1).
These estimates are obtained by a direct processing of the online observed wind-velocity, wind-direction and directional wave spectra at that station using simple wind-wave relationships (WWR).
These physical relations include:

i) the calculation of the energy of growing sea, E_s and the growth stage, ξ, from the local wind data using a fetch limited exponential suturating growth curve and assuming a $\cos^2$-distribution function for the wind-sea directions, ϕ_s;

ii) the calculation of the average sea direction, $\bar{\phi}_s$, from the wind data using a directional relaxation function according to Günther et al. (1981);

iii) the calculation of the parameters of an assumed spectrum model (Kruseman model) from the growth stage, using relationships according to Sanders et al. (1980);

iv) the calculation of the locally generated E_{10}, u_1^i, by integrating the spectrum model over the frequency range $0 \leq f \leq 0.1$ Hz;

v) the assumption of an exponential decay of u_1^i in the case of a vanishing or rapidly veering wind, with the decay rate being dependent on the wind and wave direction;

vi) the calculation of incoming E_{10}, u_2 by assuming a $\cos^{2s}\frac{\Theta}{2}$ directional model; the time delay Δ^{i-1}, is calculated by the first and second moment of the directional wave spectra.

vii) the calculation of the modulations of E_{10} generated by the tides in shallow water by using a frequency dependent dissipation function according to Lighthill (1978).

2.2 Data correction module

A prediction system based on real-time hydrometeorlogical observations requires reliable input data. This condition cannot always be fulfilled in an operational situation. Therefore the ARMAX system includes procedures to detect and correct missing data and outlayers.

These wind-wave correction procedures can only be used for missing or bad data over short time intervals. For long time intervals without reliable or without any wind-wave information, the data correction module selects only those stations which posesses reliable input data.

2.3 Correlation module

The ARMAX model structure is based on the assumption that the observed E_{10} at Station i at time k is due to both locally generated E_{10} at time k and the outgoing E_{10} from the preceding Station (i-1) at time $(k - \Delta^{i-1})$ i.e.

$$y^i(k) = u_1^i(k) + u_2^{i-1}(k - \Delta^{i-1}) \tag{1}$$

By introducing the time delay, Δ^{i-1}, in the u_2-contribution, the E_{10} propagation time is taken into account explicitly. However, the model given by equation (1) is much too simple to give an accurate description of the complex phenomena involved. For instance, features like energy dispersion and refraction are not considered.

The simple model equation (1) therefore has been generalized by defining the following ARMAX model

$$y^i(k) = \underbrace{a_1^i y^i(k-1) + \ldots + a_{p_i}^i y^i(k-p_i)}_{\text{autoregressive part}} +$$

$$+ \underbrace{b_o^i u_1^i(k) + \ldots + b_{q_i}^i u_1^i(k-q_i)}_{\text{local sea contribution}} +$$

$$+ \underbrace{c_o^i u_2^{i-1}(k-\Delta^{i-1}) + \ldots + c_{r_i}^i u_2^{i-1}(k-\Delta^{i-1}-r_i)}_{\text{distant swell contribution}} +$$

$$+ d_o^i w^i(k) + \ldots + d_{s_1}^i w^i(k-s_1) + e_1^i \cdot 1 \qquad (2)$$

noise contribution bias term

The autogressive (AR) part acts like a filter for the input signals u_1, u_2 and w, which, for appropriate values of the AR-parameters, $a_1 \ldots a_p$, introduces a certain energy dispersion.
Variable growth rates and small variations in the time delays can be realized if the parameters, $b_o \ldots c_r$, are allowed to be time dependent. Energy dissipation occurs automatically for small values of $c_o \ldots c_r$.
The noise components $w^i(k) \ldots w^i(k-s)$ serve to model the residuals of $y^i(k)$ which cannot be explained by the autoregressive and the exogeneous input. By formulating the noise contribution as a moving average process (MA), residual autocorrelations can be used to improve the model predictions. Finally, the bias term, e_1^i, is added to improve tracking of the E_{10} observations. The combination of autoregressive (AR), moving average (MA) and exogeneous inputs (X) explains the name ARMAX model.

2.4 Coupling module

Because of the structure of the ARMAX models, in which y^i is related explicity to u_2^{i-1}, it is easy to build a sequence of ARMAX models covering all the stations being considered. This is represented schematically in Figure 1, which is explained in more detail in the following sections.

2.5 Parameter estimation module

The ARMAX model (equation 2) can be used to predict the output y^i recursively from known inputs if the model parameters
$a_1^i \ldots e_1^i$ and the model order (p_i, q_i, r_i, s_i) are known.
In the present system the model order has to be specified by the user. The specification of the parameter q_i and r_i requires an understanding of the physical processes involved. The specifications of the parameters p_i and s_i can be obtained from the hydrometeorological observations. Some criteria of best fit for the model order parameters p_i and s_i are described in Haykin (1986).

For a specified model order, the model parameters are estimated using a recursive adaptive estimation algorithm.
Recursive estimation is required because in an operational situation, there is a continuous data stream entering the prediction system, which must be processed on-line in order to avoid unnecessary delays.

In addition, the algorithm must be adaptive because the model (equation 2) is, as yet, too simple to give an accurate description of the E_{10} processes under all hydrometeorological situations. The ARMAX parameters $a_1^i \ldots e_1^i$ are therefore to be adapted to the hydrometeorological situation in order to garantee that the prediction is made with a model which best fit the actual wind and wave conditions.

The performance of a prediction system, which is based on time series modelling depends, to some extent, on the amount of information contained in the input data.

However, a prediction system, operating in real-time situations, must operate under all possible conditions.
Therefore techniques are incorporated to minimize the effect of redundant input data on the performance of the model (Wensink, 1986a). Some of this techniques are described by Goodwin and Sin (1984).

When hydrometeorological observations are used as the input for parameter estimation, the ARMAX system works in the identification mode. In this case there is no through-coupling of the various ARMAX elements. Instead, the model parameters are estimated separately for each individual element.

2.6 Prediction module

The ARMAX model parameters identified from the most recent observations always give the best description of the actual hydrometeorological situation; therefore, these must be used to generate the E_{10} predictions. As a consequence, the prediction system switches constantly from the identification mode to the prediction mode, and vice versa: In the identification mode E_{10} observations are used to estimate the ARMAX model parameter values whereas in the prediction mode these values are used to generate the E_{10} predictions, see Figure 1. In the prediction mode there is a through coupling, of the various elements. The prediction procedure is as follows, see Figure 1.

- Based on the observations from the most remote station, available up to the present time t, the u_2^0 signal is calculated which then serves as an input for the first ARMAX element after a time delay Δ^0;
- the u_1 input for the first ARMAX element should then be known up to time $t + \Delta^0$. Since $t + \Delta^0$ is Δ^0 time steps into the future, the u_1 calculations required are only possible when wind predictions are also available for the second station up to time $t + \Delta^0$;
- the identified first ARMAX element is then used to calculate recursively the E_{10} value y^1 at the second station up to t_1 time steps ahead, where t_1 corresponds to the maximum possible prediction time at the second station, Δ^0.
  The predicted value of E_{10} is subsequently used in the calculation of u_2^1 which serves as an input for the second ARMAX element after a time delay Δ^1;
- the u_1 input for the second ARMAX element should then be known up to the time $t + \Delta^0 + \Delta^1$, etc.

Hence, the maximum possible prediction time $T_p(\max)$ at the final station is determined by the summation of the delays Δ^i.

3. Some results

The ARMAX system is fully in operation and processes the data of four stations in the North Sea Monitoring Network. These stations, AUK, K13, LEG and BG2, are located in line with the dominant swell direction in the southern part of the North Sea, see Fig. 2. A typical performance of the prediction system is illustrated in Figures 4 and 5, which, for the period between 30 december 1984 and 5 january 1985, compare the E_{10} observations and the 5-hours ahead predictions. Figure 3 presents the meteorologic situation on weather charts at that period (Wensink 86a,

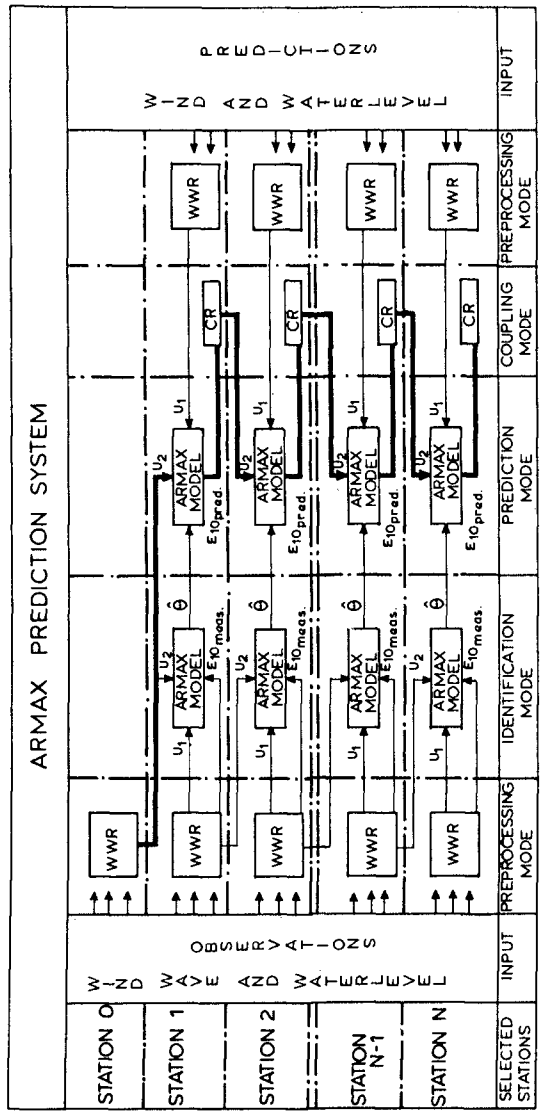

Fig. 1 Schematic representation of the ARMAX prediction system for N monitoring stations

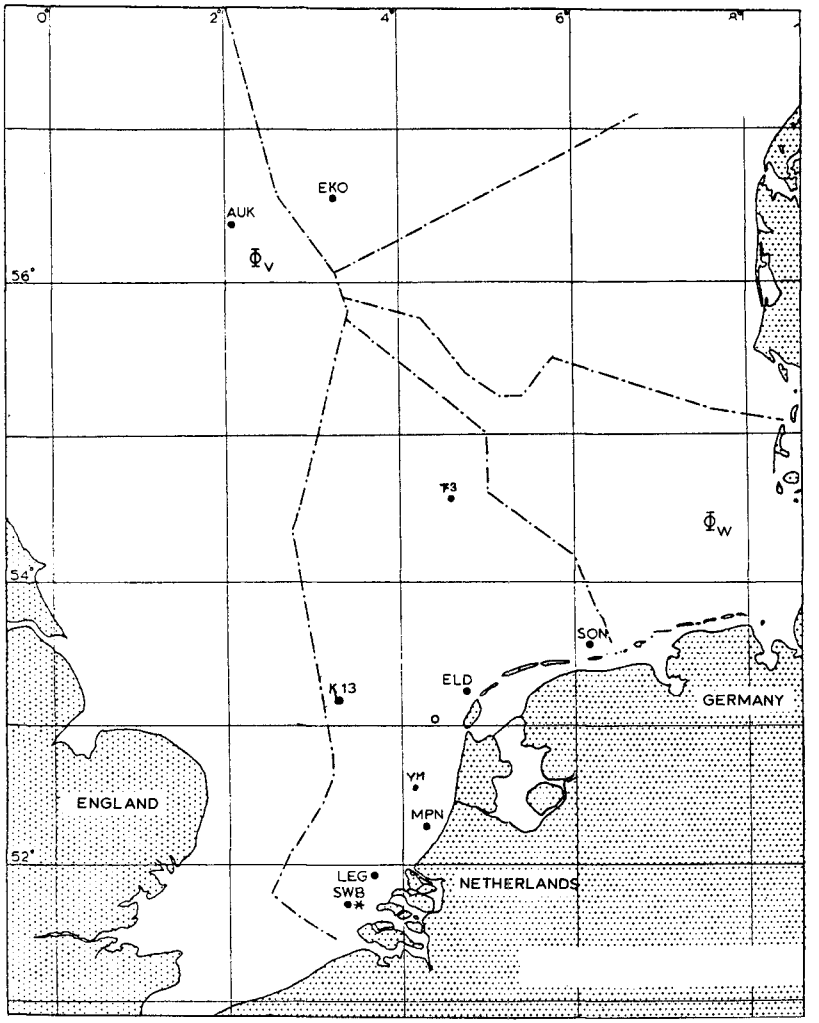

Fig. 2 The North Sea wave monitoring network

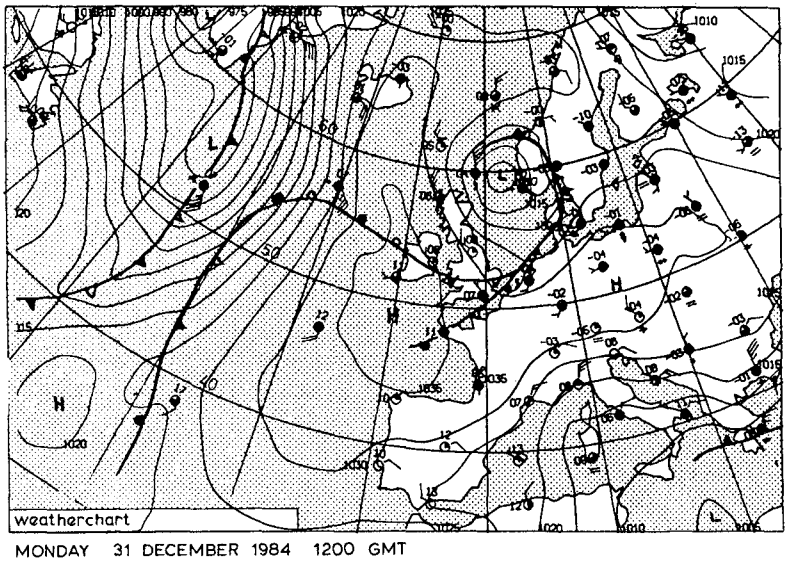

Fig. 3 Meteorological situation

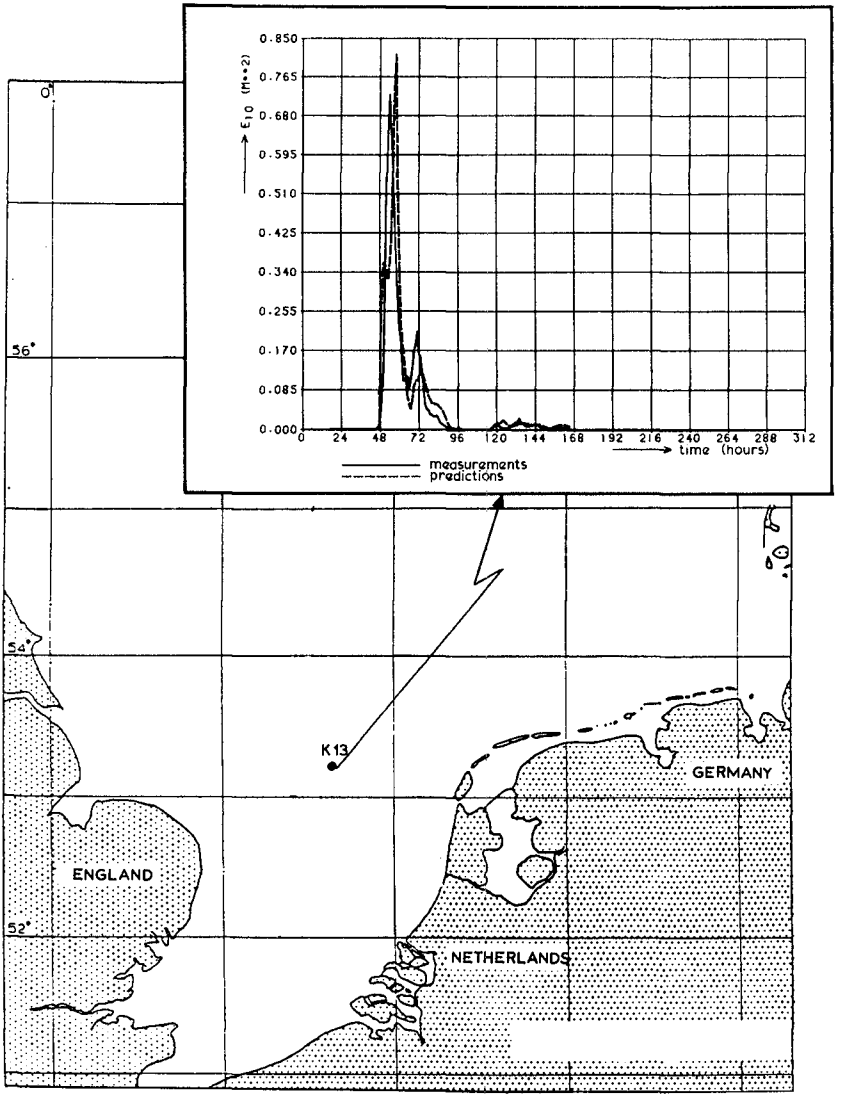

Fig. 4 The North Sea wave monitoring network

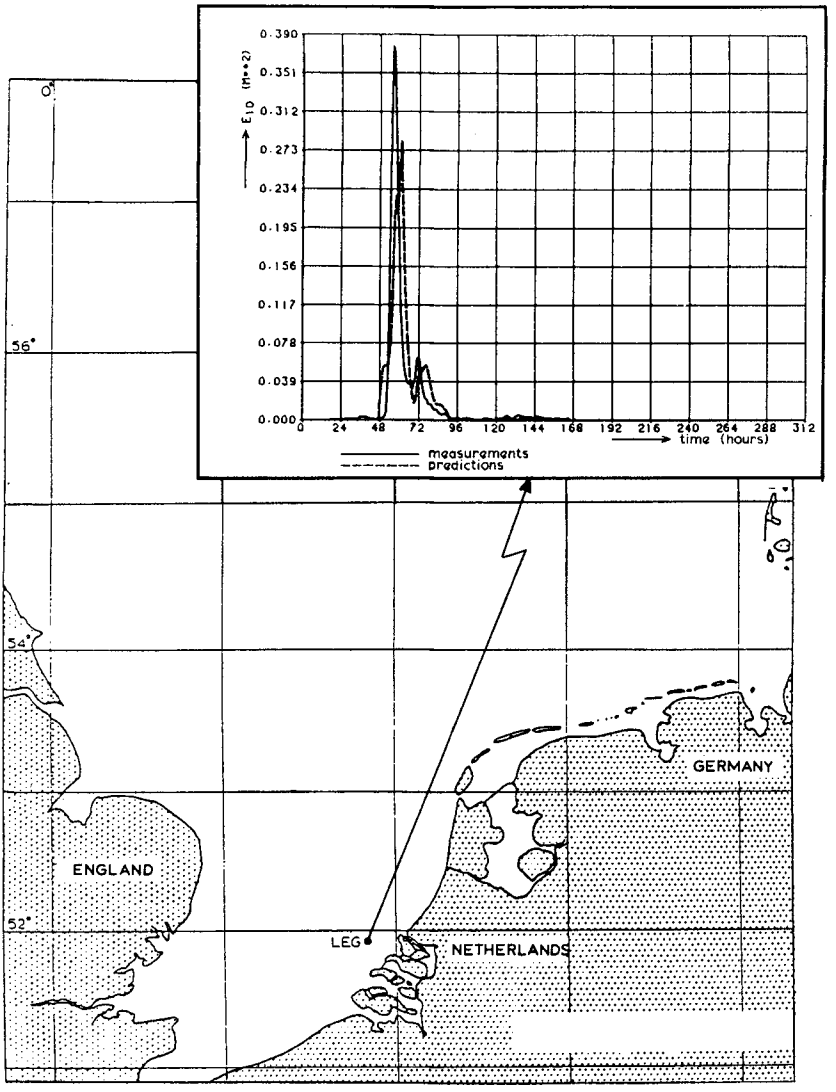

Fig. 5 The North Sea wave monitoring network

86b). Before the Norwegian coast a through of low pressure is moving to the South. On the west side of this through the wind speed increases from 2 m/s to 19 m/s. A combination of sea and swell is propagating into the North Sea. As can be seen in the Figures 4 and 5 the agreement is quite good. The differences between the predictions and observations are caused in part by an incorrect number of dispersion terms (r_1) and by an incomplete modelling of the wave physics.

4. Conclusions

The ARMAX system as described in this paper integrates, to a certain extent, observations and physical knowledge in one system. The system processes point measurements to predict wave energy at pre-selected locations.
Although the physical modelling as applied in the data pre-processing module is rather simple, the predictions are quite good.

The operational aspects of the prediction system can be summarized by:
- because of its size the system can be easily implemented on small computer systems
- because of its recursive parameter estimation algorithm the model has a short computing time
- because of its cascade structure it can be easily extended with more monitoring stations.

Because of its fast processing of new information the advantage of the model, as described here, is that in difficult meteorological conditions the ARMAX system gives immediate insight in the new hydrometeorological situation.

Acknowledgements

The permission of the Ministry of Public Works to publish some results of the ARMAX prediction system study for Rotterdam/Europoort and the Eastern Scheldt is gratefully acknowledged.

This work was supported in the past by the Ministry of Public Works and the Municipality of Rotterdam. The authors would like to thank
Mr. A.J. Kuik, Mr. H. Keyser and Mr. D.M.A. Schaap for their stimulating reponses.

REFERENCES

1. Günther, H., Rosenthal, W., and Dunckel, M., 1981.
The response of surface gravity waves to changing wind direction.
Journal of Physical Oceanography, 11,5, pp,. 718-728.

2. Lighthill, J. Waves in Fluids, Cambridge, 1978.

3. Goodwin and Sin. Adaptive filtering prediction and control, 1984.
Prentice-Hall information and system sciences series 1984.

4. Haykin. Adaptive filtering theory, 1984.
Prentice-Hall information and system sciences series 1986.

5. Sanders, J.W., Voogt, W.J.P. de, and Bruinsma, J., 1980.
Fysisch golfonderzoek Noordzee.
MLTP-report 2, Report Raad van Overleg voor Fysisch Oceanografisch Onderzoek der Noordzee, De Bilt, the Netherlands (in Dutch).

6. Schilperoort, T. and Poulisse, H.N.J., 1983 'Swell prediction using Kalman filters'. Delft Hydraulics Laboratory, Report R1874, the Netherlands (in Dutch)

7. Schilperoort, T., Strating, J.,
An integrated approach towards depth design and operational use of navigation channels, 1985.
International. Shipbuilding progress vol 32, july 1985, nr. 371, p 169-179.

8. Wensink, H.,
Verification and evaluation of the ARMAX prediction model for low frequency wave energy, 1986a,
Report R1231, Delft Hydraulics Laboratory, Delft, the Netherlands (in Dutch).

9 Wensink, H.,
The pre-operational ARMAX prediction model for low frequency wave energy, 1986b,
Report R2260, Delft Hydraulics Laboratory, Delft, the Netherlands (in Dutch).

10 Wensink, H.
The ARMAX prediction system for low frequency wave energy, 1987,
Report H308, Delft Hydraulics Laboratory, Delft, the Netherlands (in Dutch).

CHAPTER 64

A NUMERICAL MODEL OF NEARSHORE CURRENTS BASED ON A FINITE AMPLITUDE WAVE THEORY

by

Masataka Yamaguchi*

ABSTRACT

A numerical model of wave-induced nearshore currents taking into account the finite amplitude effect is developed, with a cnoidal wave theory used for the estimation of wave characteristics. The model is applied to the computation of wave transformation and nearshore currents on uniformly sloping beaches and on two-dimensional model topographies. The comparison with the results obtained by a linear model shows that wave nonlinearity has a strong influence on wave transformation in shoaling water and in the surf zone and on the strength of nearshore circulation, but that it does not have much effect on the longshore current profile. Moreover, the validity of the present model is supported by the quantitative agreement with the experiment for wave height variations, and the qualitative correspondence with the experiment for mean water level variation and longshore currents and the observation for nearshore currents.

1. INTRODUCTION

In most nearshore current models, the small amplitude wave theory has been used for the calculation of wave transformation in shoaling water, the resulting radiation stress which is a driving force of nearshore currents, and the wave-induced bottom shear stress. Since the effect of wave nonlinearity becomes more and more predominant just outside and inside of the surf zone, a nearshore current model taking account of the finite amplitude effect is needed for the purpose of better understanding and description of the coastal phenomena. Nevertheless, there have not been any such numerical models of nearshore currents applicable to an arbitrary bottom topography, although a few analytical models by James(1974) and Tsuchiya et al.(1979) using a finite amplitude wave theory, are available.

Because of the above-mentioned situation, the aim of this study is to develop a numerical model of nearshore currents taking the effect of wave nonlinearity into account, in which cnoidal wave theories derived by both the Stokes first and second definitions for wave celerity are used for the estimation of wave characteristics and to clarify the model behaviour and its applicability by comparison with the results based on a linear numerical model, experiments of wave transformation and longshore currents and observations of nearshore currents.

---

* Prof., Dept. of Ocean Eng., Ehime Univ., Bunkyocho 3, Matsuyama 790, Ehime Pref., Japan

2. MODEL DESCRIPTION

(1) Wave transformation model

When the waves with wave number components (k_x,k_y) propagate on two-dimensional current (U,V), the governing equations of wave number components are derived from the irrotational condition of wave number components, the conservation equations of wave number components and the nonlinear dispersion relation of finite amplitude wave theory as

$$\begin{aligned}
&\frac{\partial k_x}{\partial t}+\frac{\partial}{\partial x}\left\{k_x\left(\frac{\partial \sigma_m}{\partial k}\cos\theta+U\right)\right\}+\frac{\partial}{\partial y}\left\{k_x\left(\frac{\partial \sigma_m}{\partial k}\sin\theta+V\right)\right\}\\
&=k_x\left[\frac{\partial|(\partial\sigma_m/\partial k)\cos\theta|}{\partial x}+\frac{\partial|(\partial\sigma_m/\partial k)\sin\theta|}{\partial y}\right]\\
&\quad+k_x\frac{\partial V}{\partial y}-k_y\frac{\partial V}{\partial x}-\frac{\partial\sigma_m}{\partial D}\frac{\partial D}{\partial x}-\frac{\partial\sigma_m}{\partial H}\frac{\partial H}{\partial x}\\
&\frac{\partial k_y}{\partial t}+\frac{\partial}{\partial x}\left\{k_y\left(\frac{\partial \sigma_m}{\partial k}\cos\theta+U\right)\right\}+\frac{\partial}{\partial y}\left\{k_y\left(\frac{\partial \sigma_m}{\partial k}\sin\theta+V\right)\right\}\\
&=k_y\left[\frac{\partial|(\partial\sigma_m/\partial k)\cos\theta|}{\partial x}+\frac{\partial|(\partial\sigma_m/\partial k)\sin\theta|}{\partial y}\right]\\
&\quad+k_y\frac{\partial U}{\partial x}-k_x\frac{\partial U}{\partial y}-\frac{\partial\sigma_m}{\partial D}\frac{\partial D}{\partial y}-\frac{\partial\sigma_m}{\partial H}\frac{\partial H}{\partial y}
\end{aligned}\tag{1}$$

in which k is the wave number, θ the wave direction, $\partial\sigma_m/\partial k$ the propagation velocity corresponding to the group velocity in the case of small amplitude wave theory, σ_m the relative angular frequency, D(=h+η) the total water depth including the mean water level variation η, h the still water depth and H the wave height. It is seen that the effect of wave nonlinearity is introduced into eq. (1) explicitely through $(\partial\sigma_m/\partial H)\partial H/\partial x$ and $(\partial\sigma_m/\partial H)\partial H/\partial y$ and implicitely through $\partial\sigma_m/\partial k$ and $\partial\sigma_m/\partial D$. The equations are written in the conservative form for the convenience of their numerical integration using a finite difference method.

The energy balance equation with the energy dissipation term due to wave breaking is given by Phillips(1969) as

$$\begin{aligned}
&\frac{\partial}{\partial t}\left(E_n-\frac{M_x^2+M_y^2}{2\rho D}\right)+\frac{\partial}{\partial x}\left(UE_n+F_x-\frac{M_x^2+M_y^2}{2\rho D}\tilde{U}\right)\\
&\quad+\frac{\partial}{\partial y}\left(VE_n+F_y-\frac{M_x^2+M_y^2}{2\rho D}\tilde{V}\right)+S_{xx}\frac{\partial U}{\partial x}+S_{xy}\frac{\partial V}{\partial x}\\
&\quad+S_{yx}\frac{\partial U}{\partial y}+S_{yy}\frac{\partial V}{\partial y}-\frac{M_x}{\rho D}\frac{\partial S_{xx}}{\partial x}-\frac{M_y}{\rho D}\frac{\partial S_{xy}}{\partial x}\\
&\quad-\frac{M_x}{\rho D}\frac{\partial S_{yx}}{\partial y}-\frac{M_y}{\rho D}\frac{\partial S_{yy}}{\partial y}=-E_{bw}
\end{aligned}\tag{2}$$

in which E_n is the wave energy, M_x and M_y the wave-induced mass flux components, $\tilde{U}$ and $\tilde{V}$ the nearshore current components including the effect of mass flux, F_x and F_y the energy flux components, S_{xx}, S_{xy} and S_{yy} the radiation stress tensor including the effect of mass flux and ρ the density of fluid. The nearshore current components and the integral properties are defined by the following expressions.

$$\tilde{U}=U+M_x/\rho D,\ \tilde{V}=V+M_y/\rho D$$

$$M_x=M\cos\theta,\ M_y=M\sin\theta,\ M=\overline{\int_{-D}^{\xi}\rho u dz}$$

$$E_n=E_p+E_k,\ E_p=\rho g\overline{\xi^2}/2,\ E_k=\overline{\int_{-D}^{\xi}\rho(u^2+w^2)dz}/2$$

$$F_x=F\cos\theta,\ F_y=F\sin\theta \tag{3}$$

$$F=\overline{\int_{-D}^{\xi}|\rho(u^2+w^2)/2+p+\rho gz|udz}$$

$$S_{xx}=S_{11}\cos^2\theta+S_{22}\sin^2\theta-M_x^2/\rho D$$

$$S_{xy}=S_{yx}=(S_{11}-S_{22})\cos\theta\sin\theta-M_xM_y/\rho D$$

$$S_{yy}=S_{11}\sin^2\theta+S_{22}\cos^2\theta-M_y^2/\rho D$$

$$S_{11}=\overline{\int_{-D}^{\xi}(\rho u^2+p)dz}-\rho gD^2/2,\quad S_{22}=\overline{\int_{-D}^{\xi}pdz}-\rho gD^2/2$$

in which ξ is the surface displacement, u and w the wave-induced horizontal and vertical water particle velocity components, p the wave pressure, g the acceleration of gravity, E_p the potential energy, E_k the kinetic energy, and the overbar means time average over one wave period.

The estimation of energy dissipation due to wave breaking is done by either of two methods. The first one is to assume that the wave height exceeding the breaking wave height specified by the local characteristics of waves and water depth does not exist in the surf zone, and the breaker index used for the estimation of breaking wave height is

$$\frac{H_{br}}{L_{br}}=a\tanh\frac{2\pi D_{br}}{L_{br}} \tag{4}$$

in which L is the wave length and subscript 'br' means breaking waves. The coefficient in eq. (4) is the constant depending on the beach slope i, and a=0.131 for i=1/50 and a=0.142 for i=1/30 are chosen from the consideration of the Göda breaker index respectively.

The second method is to rely on the bore model proposed by Battjes (1978). The energy dissipation rate due to wave breaking is expressed as

$$E_{bw}=\frac{B}{4\gamma^3}\frac{\rho gH^3\sqrt{gD}}{L}\left(\frac{H}{D}\right)^4,\ \gamma=0.7+5i \tag{5}$$

The coefficient for i<1/20 is given by Iwagaki et al.(1981) as

$$B=\begin{cases}11-10D/D_{br}\ ;\ 0.6\le D/D_{br}\le 1\\ 5\qquad\qquad\ ;\ D/D_{br}\le 0.6\end{cases} \tag{6}$$

In the numerical computation, the beach slope including the water surface slope $\partial D/\partial x$ is used rather than the beach slope itself.

(2) Nearshore current model

The equations used in the computation of nearshore currents are vertically-integrated continuity and momentum equations and they are written as

$$\frac{\partial \rho D}{\partial t}+\frac{\partial \tilde{M}_x}{\partial x}+\frac{\partial \tilde{M}_y}{\partial y}=0$$

$$\frac{\partial \tilde{M}_x}{\partial t}+\frac{\partial}{\partial x}(\tilde{U}\tilde{M}_x)+\frac{\partial}{\partial y}(\tilde{U}\tilde{M}_y)=-\rho g D\frac{\partial \eta}{\partial x}+\frac{\partial}{\partial x}\left(\bar{L}D\frac{\partial \tilde{U}}{\partial x}\right)$$

$$+\frac{\partial}{\partial y}\left(\bar{L}D\frac{\partial \tilde{U}}{\partial y}\right)-\left(\frac{\partial S_{xx}}{\partial x}+\frac{\partial S_{xy}}{\partial y}+\tau_{bx}\right) \tag{7}$$

$$\frac{\partial \tilde{M}_y}{\partial t}+\frac{\partial}{\partial x}(\tilde{V}\tilde{M}_x)+\frac{\partial}{\partial y}(\tilde{V}\tilde{M}_y)=-\rho g D\frac{\partial \eta}{\partial y}+\frac{\partial}{\partial x}\left(\bar{L}D\frac{\partial \tilde{V}}{\partial x}\right)$$

$$+\frac{\partial}{\partial y}\left(\bar{L}D\frac{\partial \tilde{V}}{\partial y}\right)-\left(\frac{\partial S_{yx}}{\partial x}+\frac{\partial S_{yy}}{\partial y}+\tau_{by}\right)$$

in which $\tilde{M}_x=\rho D\tilde{U}$, $\tilde{M}_y=\rho D\tilde{V}$.
The Longuet-Higgins expression(1970) is used as the lateral mixing term.

$$\bar{L}=N_c\rho l_x\sqrt{gD} \tag{8}$$

in which l_x is the distance measured from the shoreline and N_c the lateral mixing coefficient. The bottom shear stress is assumed to be proportional to the squared velocity, taking the wave orbital velocity into account. The definition of bottom shear stress components are given in

$$\tau_{bx}=\rho c_f(u_b\cos\theta+U)\sqrt{(u_b\cos\theta+U)^2+(u_b\sin\theta+V)^2}$$
$$\tau_{by}=\rho c_f(u_b\sin\theta+V)\sqrt{(u_b\cos\theta+U)^2+(u_b\sin\theta+V)^2} \tag{9}$$

in which C_f is the bottom friction coefficient in the wave-current system. Eq. (9) is numerically integrated by the Causs-Legendre formula in each iterative computation. In the actual simulation, the values of N_c and C_f are fixed to be 0.01 and 0.01 respectively.

3. WAVE CHARACTERISTICS AND INTECRAL PROPERTIES OF CNOIDAL WAVES

In the model, the wave characteristics and integral properties of waves are estimated from the second order solutions of the cnoidal wave theories derived using both the Stokes first and second definitions for wave celerity by Chappelear(1962) and by Tsuchiya & Yamaguchi(1972).

The wave characteristics based on the Chappelear theory using the first definition for wave celerity are given for wave celerity c, wave length L and horizontal water particle velocity at the bottom u_b as

$$c/\sqrt{gD}=1+L_2+L_0(1-e)+5L_0L_2(1-e)+L_0^2\{5+4\kappa^2-5(1+\kappa^2)e\}/3$$

$$L/D=4K/\sqrt{3L_0}$$

$$u_b/\sqrt{gD}=L_0(1-e)+L_0^2(5+4\kappa^2)/3-5L_0^2(1+\kappa^2)e/3+5L_0L_2(1-e) \tag{10}$$

$$-\{L_0\kappa^2+L_0^2\kappa^2(1+\kappa^2)+5L_0L_2\kappa^2\}\mathrm{sn}^2\beta x-L_0^2\kappa^4\mathrm{sn}^4\beta x$$

in which κ the modulus of the Jacobian elliptic function, e=E/K, K and E the complete elliptic integrals of the first and second kinds, sn the Jacobian elliptic function and $\beta x=2K(x-ct)/L$. The expansion parameters L_0 and L_3 in the above expressions can be obtained from the following

equations as a function of κ and H/D.

$$L_0\kappa^2\{1+L_0(10+7\kappa^2)/4+6L_2\}=H/D$$
$$2L_2+L_0(\kappa^2+e)+L_0^2\}-(1-6\kappa^2-9\kappa^4)/5+2(1+\kappa^2)e\}+6L_0L_4(\kappa^2+e)+L_2^2=0 \tag{11}$$

Considering the relation that $\sigma_m\sqrt{D/g}=(c/\sqrt{gD})kD$, the partial derivatives in eq. (1) can be computed from

$$\frac{1}{\sqrt{gD}}\frac{\partial\sigma_m}{\partial k}=\frac{-2\pi}{k^2D^2}\frac{\partial\{(c/\sqrt{gD})kD\}}{\partial(L/D)}$$
$$\sqrt{\frac{D^3}{g}}\frac{\partial\sigma_m}{\partial D}=-\frac{1}{2}\frac{c}{\sqrt{gD}}kD-\frac{H}{D}\frac{\partial\{(c/\sqrt{gD})kD\}}{\partial(H/D)}-\frac{L}{D}\frac{\partial\{(c/\sqrt{gD})kD\}}{\partial(L/D)} \tag{12}$$
$$\sqrt{\frac{D^3}{g}}\frac{\partial\sigma_m}{\partial H}=\frac{\partial\{(c/\sqrt{gD})kD\}}{\partial(H/D)}$$

These expressions are estimated by the numerical differentiation of $\sigma_m\sqrt{D/g}$ computed as a function of L/D and H/D.

The integral properties of the cnoidal waves were calculated by Yamaguchi(1977). However, it was found that the results for mass flux and radiation stress are not sufficient in order estimation. Recalculation of these properties was attempted by using the exact relations between the integral properties of finite amplitude waves. For example, the exact relation derived by Crapper(1979) was used in the calculation of radiation stress.

$$S_{11}=4E_k-3E_p+\rho D\overline{u_b^2},\quad S_{22}=E_k-E_p+\rho D\overline{u_b^2}/2 \tag{13}$$

Fig. 1 shows two examples of the wave characteristics and integral properties non-dimensionalized by the results based on the small amplitude wave theory. The dimensionless propagation velocity $\partial\sigma_m/\partial k$ in-

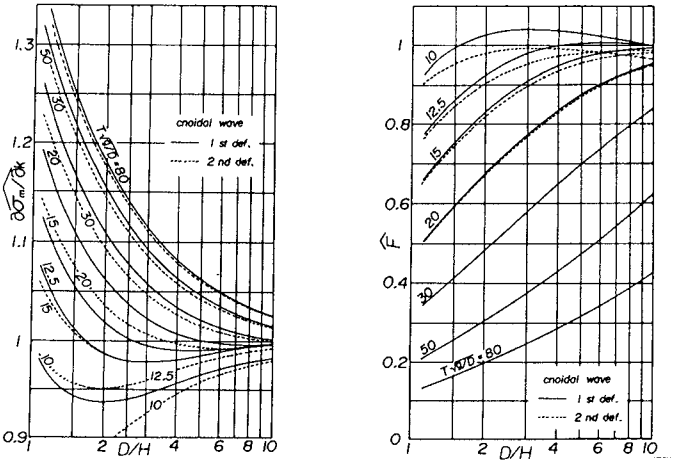

Fig. 1 Examples of wave characteristics and integral properties of cnoidal waves.

creases and the dimensionless energy flux $\hat{F}$ decreases with increasing values of $T\sqrt{g/D}$ and H/D in the case of larger values of $T\sqrt{g/D}$. The effect of the definitions for wave celerity on the wave characteristics and integral properties becomes more significant in the case of smaller values of $T\sqrt{g/D}$ and D/H, and the difference becomes negligible with the increase of these parameters. It is noted that the small amplitude wave theory overestimates or underestimates the wave characteristics including the integral properties of waves and that because of the limitation to practical applicability, the cnoidal wave theory should be used in the range of $T\sqrt{g/D}>12$.

4. NUMERICAL MODEL OF NEARSHORE CURRENTS

(1) Finite difference formulation

A finite difference method is used to solve the governing equations. Fig. 2 is the coordinate system used, in which x axis and y axis are taken in the offshore direction and in the longshore direction respectively. Finite difference approximation for the equations of wave number components and the energy balance equation which constitute the wave transformation model is made by forward difference in time and x direction and by central difference in y direction. The continuity and momentum equations which make up the nearshore current model are discretized by the forward difference with respect to the time variable and by the central difference with respect to the space variables, and finite differencing of these equations is lagged a half step in time. Fig. 3 shows the configuration of variables in the finite difference model. Current components and bottom shear stresses are defined on the grid sides and all other variables are estimated at the grid center.

The initial condition and the conditions for the offshore fixed boundary used in the nearshore current model are the usual ones. In the longshore direction, the periodic boudary condition proposed by E. Noda (1974) is imposed on all the variables relevant to the computation. In

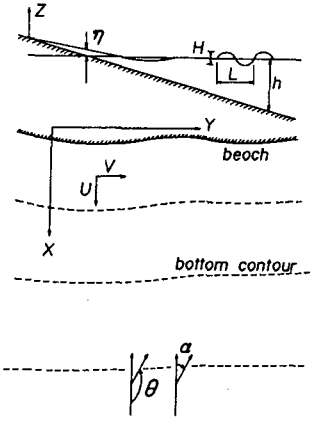

Fig. 2 Coordinate system used in nearshore current model.

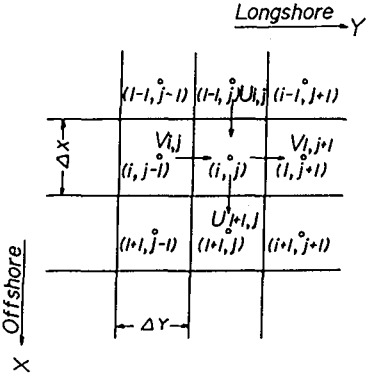

Fig. 3 Configurations of variables in finite difference model.

the wave transformation model, the specified values of wave characteristics are given at the offshore boundary, but any conditions of wave characteristics at an onshore boundary are not required in the case of a straight shoreline because of the property of the finite difference method used.

The computer program starts with determining the spatial distribution of wave characteristics according to the analytical solution of wave transformation on the parallel bottom contour based on the small amplitude wave theory, and the wave characteristics at the first step are computed from the nonlinear wave transformation model. Then, the nearshore current computation is carried out using the radiation stress estimated from the wave transformation model. Thus, one iteration is completed by these computations.

A steady state solution is obtained by 1400 to 2000 iterations of alternating computations between wave transformation and nearshore currents. At an early stage of iterative computation, the input wave height is increased gradually in order to avoid the appearance of numerical instability and to accelerate the convergence to a steady state solution. In the computation of wave transformation, the energy dissipation due to wave breaking is estimated by either the bore model or the breaker index model, when the wave height exceeds the breaking wave height given by eq. (4).

(2) Interpolation of wave characteristics

The wave information obtained directly from each computation of wave transformation is k_x, k_y (L and θ) and E_s ($=E_n - M^2/2\rho D$). When the small amplitude wave theory is used, the effect of mass flux is usually neglected and then the wave height is easily computed from the relation that $E_n=(1/8)\rho g H^2$. On the contrary, when a cnoidal wave theory is used, it is not easy to transform from E_s to H and the numerical computation of the other wave characteristics is also time-consuming, because their expressions are lengthy and contain the elliptic integrals.

In this study, the following method is adopted to save computer processing time. First, the numeric tables of the wave characteristics including the integral properties of waves computed in the range of L/D =5 - 150 every 1 increment and of H/D=0.01 - 1.30 every 0.01 increment are prepared in advance. The wave characteristics tabulated are $c/\sqrt{gD}$, $(\partial\sigma_m/\partial k)/\sqrt{gD}$, $\sqrt{D^3/g}\,\partial\sigma_m/\partial D$, $\sqrt{D^3/g}\,\partial\sigma_m/\partial H$, $E_n/(\rho g D^2/8)$, $E_s/(\rho g D^2/8)$, $M/\rho D\sqrt{gD}$, $S_{11}/\rho g D^2$, $S_{22}/\rho g D^2$, $F/(\rho g D^2\sqrt{gD})$, and κ, L_0, L_3, K and E required in the computation of u_b. Next, a two-dimensional linear interpolation formula is applied to estimate the wave characteristics corresponding to the values of L/D and H/D obtained in each iteration.

$$
\begin{aligned}
&f=a'f_{ij}+b'f_{ij+1}+c'f_{i+1j}+d'f_{i+1j+1}\\
&a'=(1-r)(1-s),b'=r(1-s),c'=(1-r)s,d'=rs\\
&i=[L/D],\ \ j=[100(H/D)]\\
&r=L/D-[L/D],\ \ s=100(H/D)-[100(H/D)]
\end{aligned}
\tag{14}
$$

in which f is the interpolated value, f_{ij} the value of f on the numeric table for the i-th L/D and the j-th H/D and [ ] the Gauss's symbol. The computation of sn function in the expression of u_b is obtained through the theta function in the usual manner, although an approximation such as $\mathrm{sn}\,\beta x \approx \tanh \beta x$ is used in the case of $\kappa > 1-10^{-6}$.

A similar method can be used in the conversion of E_S to H. As $E_S/(\rho g D^2/8)$ is a function of H/D for a fixed L/D, the numeric table of H/D inverted as a function of $E_S/(\rho g D^2/8)$ can be made by applying the linear interpolation formula to the numeric table of $E_S/(\rho g D^2/8)$. Two kinds of tables of H/D given as a function of L/D and $E_S/(\rho g D^2/8)$ are produced to keep the accuracy of interpolated results and to save computer storage memory, in which the range of $E_S/(\rho g D^2/8)$ are 0.001 - 0.15(0.001 increment) and 0.15 - 1.50(0.01 increment) respectively.

After all, the value of H/D corresponding to L/D and $E_S/(\rho g D^2/8)$ computed in each iteration can be interpolated from the H/D-tables, and then the wave characteristics for L/D and H/D can be evaluated by the application of the linear interpolation formula, eq.(14). It is emphasized that since this method is applicable for not only a cnoidal wave theory but also another higher order finite amplitude wave theory, the incorporation of the theory into a nearshore current model is easily possible for its improvement.

5. COMPUTATIONAL RESULTS AND CONSIDERATION

(1) Uniformly sloping beach

The computation is carried out on a plane beach with the slope of 1/30 and constant water depth of h=8 m in the offshore region. The following input conditions are used; the incident wave height H_M=2 m, the wave period T_M=12.5 s and the incident angle of waves $\alpha_M(=\pi-\theta_M)$=30°. Suffix 'M' means the value at the offshore boundary.

In Fig. 4, the results in the nonlinear model are depicted with those in the linear model developed by the authors(1983). Rapid increase of the wave height before wave breaking due to nonlinear shoaling and rapid decay of the wave height due to wave breaking are observed in the nonlinear model using the bore model, and the wave height after wave

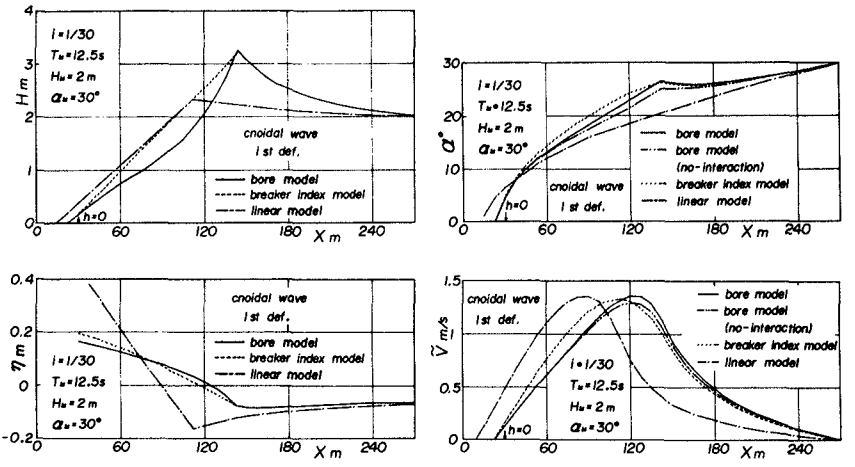

Fig. 4 Change of wave height, wave direction and mean water level variation and longshore current profile on a uniformly sloping beach.

breaking based on the bore model diminishes more rapidly than that based on the breaker index model. While the wave direction in the linear model decreases steadily toward the shore, the wave direction in the nonlinear model slightly increases just before wave breaking and it decreases steadily as well after wave breaking. This is mainly due to the wave-current interaction, because the tendency almost disappears when the effect of the interaction is omitted in the computation.

The wave setup and setdown in the vicinity of the breaking point in the linear model is much greater than those in the nonlinear model, because the small amplitude wave theory overestimates the radiation stress in comparison with a finite amplitude wave theory, as is well known. It is also interesting to note that the current profile and the magnitude in the nonlinear model are similar to those in the linear model, although the peak position of the current profile in the nonlinear model is at a greater water depth.

From the above argument, it is summarized that the wave nonlinearity has a strong influence on the offshore distribution of wave height, wave direction and mean water level variation, and the peak position of longshore currents, but that it does not have much effect on the longshore current profile itself.

Fig. 5 shows the results of wave height variation and the longshore current profile computed on a uniformly sloping beach with a longshore bar. The input conditions are the same as those for a uniformly sloping beach. It is assumed in the computation that the energy dissipation due to wave breaking does not occur on the inversely sloping beach. In the nonlinear model, the waves break after rapid increase of the wave height due to nonlinear shoaling on the offshore regularly sloping beach and propagate with loss of their heights on the inversely sloping beach. Then, the waves again increase their heights due to nonlinear shoaling on the onshore regularly sloping beach and finally dissipate their energy after the second wave breaking. On the other hand, in the linear model, the waves break on the onshore regularly sloping beach after gradual change of the wave height with water depth variation. As a result, the longshore current profile in the nonlinear model has a two peak structure, while the one in the linear model has a single peak structure as well as the result on a uniformly sloping beach.

Thus, it can be said that the correct estimation of the breaking point is of great importance in the longshore current prediction on a bar-trough beach profile.

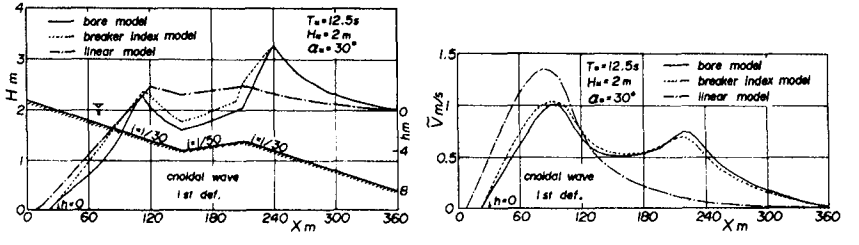

Fig. 5 Change of wave height and longshore current profile on a uniformly sloping beach with a longshore bar.

(2) Two-dimensional bottom topography

The bottom topography model developed by E. Noda(1974) is chosen to the computation of nearshore currents on a two-dimensional topography and it is expressed as

$$h(x,\ y)=ix\left[1+A_0\exp\left\{-3\left(\frac{x}{45}\right)^{1/3}\right\}\sin^2\left\{\frac{\pi}{\lambda}(y-x\tan\varepsilon)\right\}\right] \tag{15}$$

in which i is the mean beach slope of 0.015, λ the longshore beach length of 400 m, A_0 the maximum amplitude of the bottom undulation of 20 m and ε the skewness of the bottom undulation of 0° or 30°. It should be noted that the above expression has different constants from the original one by E. Noda(1974). The model topography with ε=0° and the one with ε=30° are referred to as symmetrical concave topography and asymmetrical concave topography respectively.

Fig. 6 describes the nearshore current pattern on a symmetrical concave topography with normal incidence of waves computed by both the linear and nonlinear models, in which the solid line is the contourline of water depth, and the dotted line indicates an approximate breaker line evaluated from eq. (4). Incident wave height H_M is 1 m and the other conditions are the same as in the case for a uniformly sloping beach. In both the figures, we can see the formation of a pair of dominant nearshore circulation cells centered on a breaking point and a pair of very weak and flat cells near the shoreline. But, the strength of current velocity in the nonlinear model is relatively weaker than that in the linear model and the center of the dominant circulation cell in the nonlinear model also locates in farther offshore region with the movement of the breaking point.

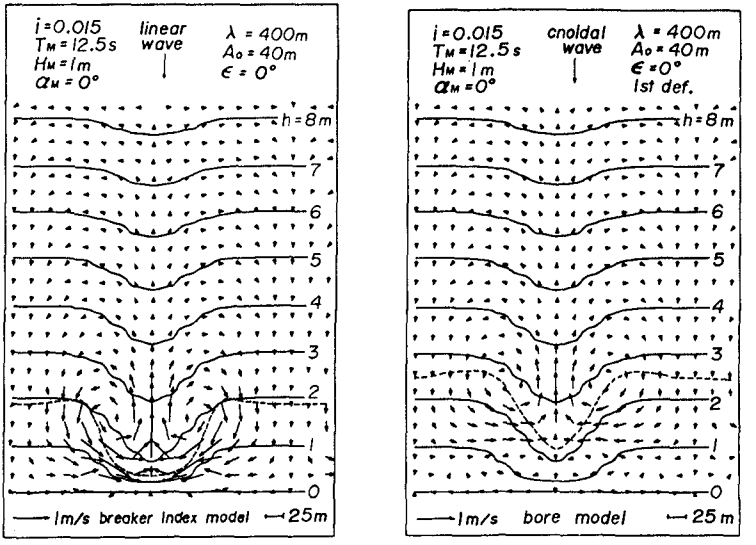

Fig. 6 Nearshore current pattern on symmetrical concave topography.

Fig. 7 is the nearshore current pattern on an asymmetrical concave topography with oblique incidence of waves, in the case where the input wave height H_M is 2 m. It is found in both the figures that the meandering longshore current is predominant and that a counterclockwise circulation cell is formed in the trough region near the shoreline by the effect of concave bottom topography. The scale and strength of a circulation cell in the linear model are greater than those in the nonlinear model.

It can be said from the two examples mentioned above that the wave nonlinearity acts so as to suppress the formation and growth of the nearshore circulation cell.

When a method combining a wave ray technique with a linear interpolation formula is used for the numerical integration of the equations of

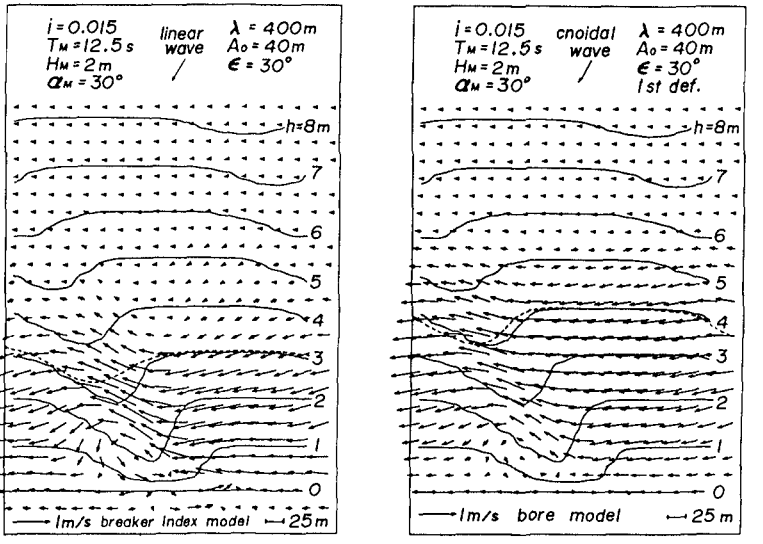

Fig. 7 Nearshore current pattern on asymmetrical concave topography.

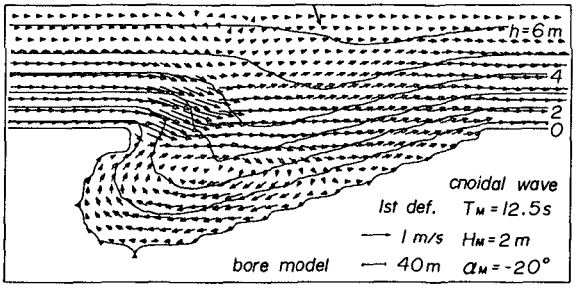

Fig. 8 Nearshore current pattern on curved bay.

wave number components and the energy balance equation, nearshore current pattern on a two-dimensional bottom topography with an arbitrary shoreline can be obtained as shown in Fig. 8, which demonstrates the predominant longshore currents in the outer region and a clockwise nearshore circulation in the inner region.

6. VERIFICATION OF NEARSHORE CURRENT MODEL

(1) Comparison with experiment

Fig. 9 is the comparison of the computed results with the experimental ones for the change of wave height and mean water level variation on a uniformly sloping beach of 1/34.26 conducted by Hansen & Svendsen(1979). As for the wave height variation, the result in the nonlinear model using a cnoidal wave theory of the second definition for wave celerity rather than the first definition for wave celerity gives slightly better agreement with the experiment, and the linear model can not explain rapid increase of wave height before wave breaking.

On the contrary, the nonlinear model underestimates the wave setdown and setup, although it can reproduce the qualitative trend in the experiment. In general, it has been known from experiments that the transition of wave setdown to setup does start from the plunge point rather than the breaking point. However, the present model, as well as the previous models, does not formulate this phenomena. The linear model overestimates the wave setdown in the vicinity of the breaking point and wave setup near the shoreline, although some fraction of the wave setup seems to agree well with the experimental results in appearance.

Fig. 10 indicates the comparison of the computed result with the experimental one for longshore currents on a uniformly sloping beach

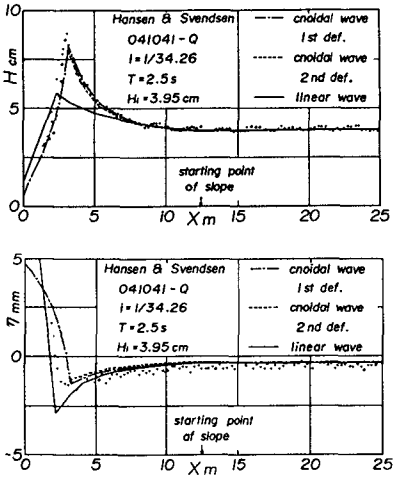

Fig. 9 Comparison between computation and experiment for wave height and mean water level variation.

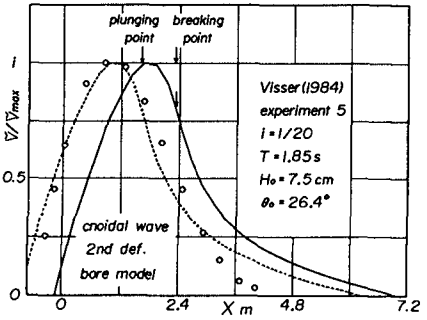

Fig. 10 Comparison between computation and experiment for longshore currents.

with the slope of 0.05 measured by Visser(1984). The current profile itself in the nonlinear model is similar to the experimental profile and the location of the breaking point in the model is in good agreement with that in the experiment. However, in order to get a close agreement with the experiment, the computed result has to be shifted toward the shoreward by approximately the amount of the plunge point distance.

(2) Comparison with observation

Fig. 11 shows the nearshore current pattern re-evaluated from the observation of transport velocity by Sonu(1972) and the corresponding nearshore current pattern computed by the nonlinear model. In the model, the energy dissipation due to wave breaking is estimated by the bore model, and a cnoidal wave theory based on the first definition is used. The input wave conditions given at the offshore boundary are that T_M=5 s, H_M =0.2 m and α_M=0°. The bottom topography used in the computation is slightly modified to be periodic in the longshore direction and to have a straight shoreline. The model reproduces well the qualitative features of the complicated nearshore current pattern found in the observation, such as the onshore currents in both sides of the region and the rip currents in the central part of the region. But, in a quantitative sense, the model appears to give less velocity than the observation.

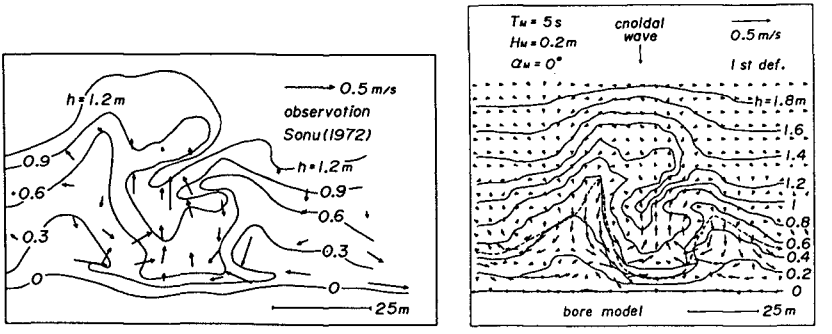

Fig. 11 Nearshore current pattern observed by Sonu(1972) and the corresponding result computed by the nonlinear model.

7. CONCLUSIONS

The main conclusions of this study are summarized as follows.

i) A nonlinear model of nearshore currents was developed, in which the estimation of wave characteristics is based on a cnoidal wave theory.

ii) The wave nonlinearity has a strong influence on the offshore distribution of wave height, wave direction and mean water level variation and the peak position of longshore currents, but it does not have much effect on the longshore current profile itself.

iii) The wave nonlinearity acts so as to suppress the formation and growth of nearshore circulation currents.

iv) The nonlinear model quantitatively predicts the change of wave height in shoaling zone and in the surf zone. It also qualitatively produces the mean water level variation, longshore current profile and nearshore circulation pattern.

v) It is necessary to make allowance for the effect of plunge point distance in the model formulation in order to obtain better agreement with the experimental data on wave setup and longshore currents.

8. ACNOWLEDGEMENT

Thanks are due to Mr. H. Kawahara, Graduate Course student of Ocean Engineering, Ehime University for his valuable help during the study. A part of this study was accomplished with the support of the Science Research Fund of the Ministry of Education, for which the authors express their appreciation.

9. REFERENCES

Battjes, J. A.: Energy dissipation in breaking solitary and periodic waves, Manus., Delft Univ. of Tech., 1978.

Chappelear, J. E.: Shallow-water waves, Jour. Geophys. Res., Vol. 67, No. 12, pp. 4693 - 4704, 1962.

Crapper, G. D.: Energy and momentum integrals for progressive capillary-gravity waves, Jour. Fluid Mech., Vol. 94, pp. 13 - 24, 1979.

Hansen, J. B. and I. A. Svendsen: Regular waves in shoaling water, experimental data, Inst. Hydrodyn. and Hydr. Eng, Series Paper 21, 1979.

Iwagaki, Y., Mase, H. and T. Tanaka: Modeling of irregular wave transformation in shoaling water, Proc. 28th Conf. on Coastal Eng. in Japan, pp. 104 - 108, 1981(in Japanese).

James, I. D.: A non-linear theory of longshore currents, Estuarine and Coastal Marine Sci., Vol. 2, pp. 235 - 249, 1974.

Longuet-Higgins, M. S.: Longshore currents generated by obliquely incident sea waves, 2, Jour. Geophys. Res., No. 33, pp. 6790 - 6801, 1970.

Noda, E. H.: Wave-induced nearshore circulation, Jour. Geophys. Res., Vol. 79, No. 27, pp. 4097 - 4106, 1974.

Phillips, O. M.: The Dynamics of the Upper Ocean, Camb. Univ. Press, p. 261, 1969.

Sonu, C. J.: Field observation of nearshore circulation and meandering currents, Jour. Geophys. Res., Vol. 77, No.18, pp. 3232 - 3246, 1972.

Tsuchiya, Y. and M. Yamaguchi: Some considerations on water particle velocity of finite amplitude wave theory, Coastal Eng. in Japan, Vol. 15, pp. 43 - 57, 1972.

Tsuchiya, Y., Yasuda,T. and K. Tokuda: Theory of rip currents (1) - case of normally incident waves -, Proc. 26th Conf. on Coastal Eng. in Japan, pp. 495 - 499, 1979(in Japanese).

Visser, P. J.: Uniform longshore current measurements and calculations, Proc. 19th International Conf. on Coastal Eng., Vol. III, pp. 2192- 2207,

1984.

Yamaguchi, M.: Some characteristics of finite amplitude waves, Memoirs of the Ehime Univ., Sect III(Eng), Vol.VIII, No. 4, pp. 191 - 202, 1977(in Japanese).

Yamaguchi, M., Tanabe, H. and Y. Nishioka: A numerical solution of nearshore currents taking account of wave-induced mass flux, Proc. 30th Conf. on Coastal Eng. in Japan, pp. 480 - 484, 1983(in Japanese).

CHAPTER 65

Grouping Waves and Their Expression on Asymptotic Envelope Soliton Modes

T. Yasuda[1], M. ASCE , N. Nakashima[2] and Y. Tsuchiya[3], M. ASCE

ABSTRACT

An approach, that treats natural sea states with remarkable groupiness as random sequences of envelope solitons, is suggested here to explain their dynamical and statistical properties from the viewpoint that wave packets contained in the states have their own characteristics and should be regarded as elementary modes. Some examinations are made on its applicability to the temporally observed waves. And the approach is shown to be effective also for waves with a non-zero nonlinearity and finite spectral band-width. Further, a formulation based on envelope solitons is made on the wave drifting force and is shown to be useful for analyzing the time series of drifting forces.

INTRODUCTION

The wave grouping such as runs of consecutive high waves or small waves in nature has been shown to occur more often and to contain more waves than would be expected if waves are completely random. The potential consequences are often quite significant in both offshore and coastal activities. It is well-known, [for example, Spangenberg, 1980] , that many moored offshore structures and floating vessels suffer a great influence of the wave grouping and their responses become maxima when the period of the wave groups is equal to or lies in the vicinity of the natural periods of the moored systems. With the progress of ocean development and coastal activities, the concern on the wave grouping has been grown and various investigations have been made theoretically and experimentally on wave grouping characteristics. However, usual investigations in engineering sides are based on the assumption of a narrow banded Gaussian process and lack the fact that the wave grouping is due to weak but non-zero nonlinearity and should be treated as a nonlinear phenomenon, so that they have limits in evaluating dynamical characteristics of grouping waves.

Wave systems that depend on the band-width and nonlinearity may exhibit component dispersion ranging from that given by the linear dispersion to that of an effectively nondispersive phase-locked system in which wave components propagate essentially with a single speed. This demonstrates that the Fourier spectrum representation and the

1 Associate Professor, Department of Civil Engineering, Gifu University, Gifu 501-11, JAPAN

2 Engr., Nippon Koei Co., Ltd., Chiyoda, Tokyo 102, JAPAN

3 Professor, Disaster Prevention Research Institute, Kyoto University, Uji 611, JAPAN

associated Gaussian random wave theory do not comprise an entirely satisfactory analysis technique forsea states with non-zero nonlinearity. Recent researches on waves with a weak nonlinearity and narrow band-width [for ex. Yuen & Lake, 1982] made clear that the description of grouping waves contained in the wave field provided by the nonlinear Schrödinger(NLS) equation and the Zakharov equation is qualitatively and quantitatively correct and nonlinear effects on the formation of wave groups are significant. It has been already stated [Sobey & Colman, 1982] that the envelpe soliton bears a remarkable resemblance to the common appreciation of wave groups. However, waves in field have spectra with a finite band-width and nonlinear aspects such as peaking of wave crests and flattening of troughs, so that it is difficult to apply directly the NLS equation to them and some trials[for ex. Stiassinie and Shemer, 1984] using the Zakharov equation has not been applied successfully in describing them.

The nature of wave groups in field is a little bit made clear, although their natural occurrence is not in doubt. It is not also clear whether the wave groups are spatially stable or not and they can be regarded as wave packets with soliton properties, that is, envelope solitons or not. However, it is the well-known fact that a nonlinear wave packet, that is, envelope soliton is a stable grouping although linear wave packets are destroyed eventually by dispersion and are spatially unstable. It is, therefore, natural to suppose that waves after having travelled a long distance are generally in a stable state and may have a coherent structure making some stable mode elementary excitation and that the stable wave group contained in the waves can be regarded as a kind of such elementary excitation. This viewpoint is quite different from usual ones interpreting the wave group as a consequence of a mere superposition of some carrier waves and a stochastic sequence of zero-crossing waves. If the wave group has its own characteristics and can be treated as elementary mode of waves with remarkable groupiness, an approach for treating the wave group as elementary mode may become possible for explaining properties of the grouping waves. This approach may be expected to be effective for analyzing the time series of the wave drifting force caused by the existence of wave groups.

In this study, by investigating wave grouping characteristics of waves observed at various locations, we show that they remarkably depend on nonlinear effects and the frequency of carrier waves associated with each wave group is not necessarily identical with the peak frequency of the spectrum and distributes over a finite band-width. Then, all wave groups accompanied with the waves are treated as envelope solitons and their envelope profile is represented as a random train of asymptotic envelope solitons. Some examinations are made on the applicability of the theoretical result to the waves observed temporally at fixed positions and the envelope soliton mode representation is shown to be possible for their envelope profiles. Further, this representation is extended to the formulation of the wave drifting force.

GROUPING CHARACTERISTICS OF OBSERVED WAVES

1. Spectral Band-Width and Nonlinearity

Field data were collected from various observatories locating off Gobo coast (G1-8, Oct. 1979) facing the Pacific ocean, off Ogata coast (O1-12, Mar. 1981) facing the Japan sea, off Caldera Port in Costa Rica (C1-4, May 1981) facing the Pacific ocean and at Lake Biwa (B1-10, Oct. 1975). The data were obtained by the temporal observations of water surface displacements at fixed positions. Table 1 summarizes values of wave parameters calculated from these data. In the table,

Table 1 Wave parameters of observed waves

Data	h(M)	f_p	ν	$\sqrt{\beta_1}$	$k_p h$	Ur	GF	p	$\bar{j}_1$	$\bar{j}_2$
B1	4.0	.293	.991	.037	1.34	2.03	.337	.463	2.47	5.29
B2	4.0	.293	.989	.174	1.34	1.94	.396	.506	2.63	5.27
B3	4.0	.317	.990	.310	1.73	2.01	.398	.481	2.64	5.38
B4	4.0	.305	.990	.260	1.62	2.18	.402	.494	2.49	5.25
B5	4.0	.281	.988	.166	1.43	1.96	.393	.459	2.85	6.28
B6	4.0	.305	.988	.143	1.62	1.61	.374	.447	2.48	5.57
B7	4.0	.322	.987	.070	1.77	1.00	.367	.474	2.49	5.38
B8	4.0	.322	.989	.096	1.77	1.24	.364	.485	2.75	5.57
B9	4.0	.440	.981	.191	3.13	0.27	.371	.518	2.92	5.62
B10	4.0	.440	.982	.136	3.13	0.26	.384	.459	2.49	5.49
G1	28.0	.068	.723	.020	0.80	3.12	.444	.478	4.13	8.29
G2	28.0	.064	.772	.073	0.74	3.12	.468	.456	2.38	5.41
G3	28.0	.072	.765	.069	0.85	3.32	.546	.522	2.77	5.45
G4	28.0	.061	.768	.093	0.70	2.94	.351	.557	3.25	6.50
G5	28.0	.064	.745	.005	0.74	3.68	.471	.457	4.00	7.14
G6	28.0	.064	.720	.124	0.74	2.99	.397	.423	2.73	7.22
G7	28.0	.061	.759	.049	0.70	1.99	.347	.482	2.41	4.33
G8	28.0	.065	.780	1.08	0.75	2.92	.391	.468	3.36	6.70
C1	18.5	.053	.920	.323	0.48	9.09	.411	.492	3.56	7.38
C2	18.6	.057	.910	.252	0.52	9.90	.336	.529	4.27	8.36
C3	18.2	.057	.898	.501	0.51	9.94	.455	.484	3.21	6.94
C4	18.1	.053	.904	.689	0.47	15.5	.446	.492	4.00	7.93
O1	6.2	.107	.981	.393	0.56	8.78	.319	.488	2.05	4.27
O2	6.9	.096	.803	.813	0.53	11.2	.350	.441	3.00	6.67
O3	6.9	.114	.811	.701	0.64	10.1	.367	.493	2.77	5.67
O4	6.9	.175	.977	.489	1.08	4.71	.650	.492	4.80	
O5	6.9	.175	.977	.476	1.08	6.45	.770	.481	4.80	
O6	7.0	.175	.977	.297	1.09	5.69	.700	.485	4.80	
O7	6.2	.096	.803	.968	0.50	5.68	.740			
O8	5.3	.096	.803	1.12	0.46	5.07	.780			
O9	5.3	.096	.803	.845	0.46	4.02	.740			
O10	6.2	.114	.811	.721	0.60	7.64	.720			
O11	5.3	.114	.811	.826	0.55	6.23	.730			
O12	5.3	.114	.811	.618	0.55	7.29	.730			

h denotes the mean water depth, f_p the peak frequency of the power spectra, ν the spectral band-width parameter defined by

$$\nu=[1-m_2^2/(m_0m_4)]^{1/2} \quad , \qquad m_n=\int_0^\infty f^n S(f)df \quad , \tag{1}$$

in which f is the wave frequency, k_p the wave-number corresponding to f_p through the linear dispersion relation, $\sqrt{\beta_1}$ the skewness, U_r the Ursell number, GF the Groupiness Factor defined by Funke and Mansard 1979 , p the probability of the wave-height H of zero-up crossing wave exceeding

the average wave-height $\bar{H}$, and $\bar{j}_1$ the average run length of the zero-up crossing waves exceeding $\bar{H}$. It is easily noticed from this table that all values of ν exceed 0.7 and are near unity rather than zero , that is, observed waves to be used here have not a narrow but finite spectral band-width. The values of skewness $\sqrt{\beta_1}$ of the observed waves except for G5 exceed 0.01 and indicate that their water surface displacements are influenced by nonlinearity. The values of U_r also show that the observed waves have a finite nonlinearity in comparison with a frequency dispersion. Hence, it may be said from these results that the observed waves can not be analyzed on the basis of a narrow-banded Gaussian process.

2. Wave Grouping Characteristics

GF and $q\bar{j}_1$ are used here as the criteria representing wave grouping characteristics. q is the complementary number of p and is defined as 1-p. The value of $q\bar{j}_1$ is unity when the time series of the wave-heights of zero-up crossing waves are completely random. Since a modulational instability occurs when kh>1.36 in the wave field provided by the NLS equation and then envelpoe solitons are formed, kh is used here as the instability criterion relating to the formation of envelope solitons. Figure 1 shows the relation of GF and $q\bar{j}_1$ vs. kh. The value of $q\bar{j}_1$ is slightly inclined to increase with the increasing of the value of 1/kh, although varying remarkably in the region of kh<1.36. While, the value of GF is almost independent of kh. If wave groups possessed in one wave record have the identical carrier frequency with the peak frequency f_p and are governed by the single NLS equation, their envelope profiles shoud be flattened when the value of kh falls below 1.36. That is, as the value of kh gets to be below 1.36 and further decreases, GF should decrease and $q\bar{j}_1$ should increase. However, such a definite trend can not be found out and the outward profile of wave groups is supposed to be still stable even under the value of kh being below 1.36. It, therefore, may be said that wave groups possessed in the waves with a finite nonliearity and finite spectral band-width are still stable in the region, kh<1.36 and that the wave grouping characteristics are almost independent of the value of kh calculated from the peak frequency f_p and

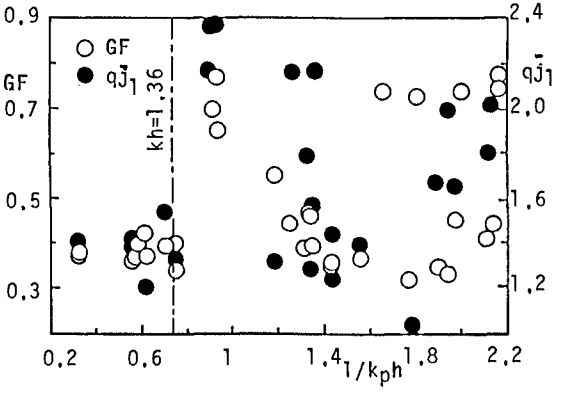

Fig. 1 Relation of kh vs. GF and $q\bar{j}_1$

should be investigated in relation to nonlinearity.

Figure 2 shows the relation of GF and $q\bar{J}_1$ vs. the Ursell number U_r. It is easily noticed from the figure that the wave grouping characteristics evaluated by $q\bar{J}_1$ and GF definitely depends on the ursell number, that is, both values of $q\bar{J}_1$ and GF increase as the value of U_r increases until reaching about 8 and then they suddenly begin to decrease just after the value of U_r exceeds about 8. This states that the degree of groupiness of random waves with a finite nonlinearity and spectral band-width depends on the nonlinearity itself. It, further, is imagined that the wave groups once formed are conserved as stable modes and may be regarded as elementary modes of waves with a non-zero nonlinearity when U_r is less than 5 or 6 and that their associated carrier waves turn to a train of solitons when U_r exceeds about 8 and then are made stable .

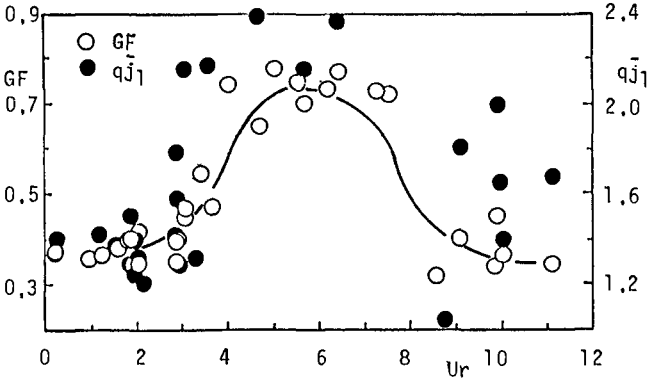

Fig. 2 Relation of U_r vs. GF and $q\bar{J}_1$

Figure 3 shows the relation between the run length j_1 and the ratio $T/\bar{T}$. Where, T is the zero-up crossing period averaged over the consecutive high waves constituting one wave group. $\bar{T}$ is the zero-up crossing period averaged over one record of the observed waves. If all wave groups included in the observed wave can be described by the multi-soliton solution of the single NLS equation, each wave group has the identical carrier frequency with the peak frequency f_p and T agrees with $\bar{T}$. However, it is seen that the ratio $T/\bar{T}$ is not necessarily unity and there is a definite correspondence between j_1 and $T/\bar{T}$. The period of carrier waves associated with one wave group becomes larger as the run length j_1 increases, that

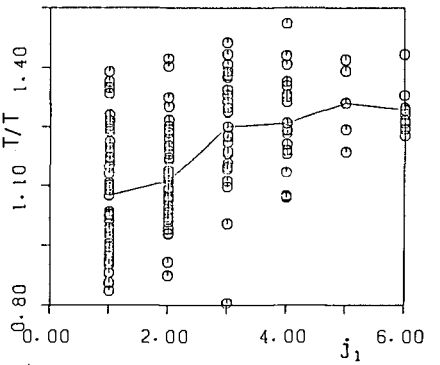

Fig. 3 Relation between the run length and wave period of carrier waves of each wave group

is, the wave group grows up. This says that each wave group accompanies a carrier wave with its own wave period independent of other wave groups.

ASYMPTOTIC ENVELOPE SOLITON MODE REPRESENTATION

1. Fundamental Assumptions

The observed results shown in the preceding chapter revealed that the wave grouping depends on U_r rather than kh and can not be sufficiently explained by the modulational instability under a narrow-band spectrum . This states that the wave groups are formed on the basis of nonlinear dynamics and behave as stable wave packets. Hence, we suggest an approach to treat them as envelope solitons governed by the plural NLS equations, although we can not verify its validity. The motive of this approach is based on the viewpoint that waves with remarkable groupiness have a dynamical structure making envelope soliton elementary excitation. Under the viewpoint, in order to represent them as a sequence of envelope solitons of which amplitudes and phase constants are random variable dependent on an initial probability, the following assumptions are made.

i) All wave groups possessed in observed waves behave as envelope soltons and are composed of the multi-envelope soliton solutions of the plural NLS equations.
ii) The envelope profile of the waves observed temporally at a fixed position can be approximately represented as a random sequence of asymptotic envelope solitons.

A schematic diagram of the sea state corresponding to these assumptions is shown in Fig. 4. The diagram explains that the sea state is governed independently by the L-NLS equations having N_l-envelope soliton solutions ($l=1,2,\ldots L$) and the observed waves are composed of a train of envelope solitons with the number of ΣN_l.

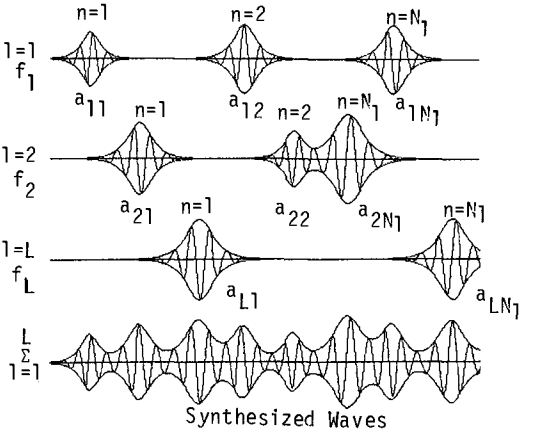

Fig. 4 Schematic diagram of wave field represented as random train of envelope solitons

2. Formulations

Since the wave data are obtained by the temporal observations at fixed positions as mentioned above, the NLS equation of spatial evolution type is required to analyze them and is expressed as follows:

$$-i\partial A/\partial X+\alpha\partial^2 A/\partial\xi^2+\beta|A|^2A=0\cdot\ , \tag{2}$$

where

$$\left.\begin{aligned}
&\alpha=(1/2)[c_g/c-(gh/c^2)\,\mathrm{sech}^2 Kh(1-Kh\tanh Kh)]\ ,\\
&\beta=(\cosh 4Kh+8-\tanh^2 Kh)/(16\sinh^4 Kh)\\
&\quad-(2c\cosh^2 Kh+c_g)^2/[2\sinh^2 2Kh(gh-c_g^2)]\ ,\\
&c=[(g/K)\tanh Kh]^{1/2}\ ,\\
&c_g=(c/2)[1+2Kh/\sinh 2Kh]\ ,\\
&X=\varepsilon^2 Kx\ ,\qquad \xi=\varepsilon 2\pi f(x/c_g-t)\ ,
\end{aligned}\right\} \tag{3}$$

in which K is the wave-number corresponding to the central frequency f of a narrow-band spectrum, εA the amplitude of a carrier wave non-dimensionalized by K, h the mean water depth, c the wave-celerity, c_g the group-velocity, ε the small parameter denoting the degree of nonlinearity, x the horizontal coordinate, t the time and g the acceleration of gravitation.

The asymptotic N_1-soliton solution of eq.(2) is written as

$$\frac{\varepsilon A_l}{K_l}=\sum_{n=1}^{N_l} a_n\,\mathrm{sech}\,[\sqrt{\beta/2\alpha}\cdot a_n(2\pi Kf/c_g)\,\{x-c_g(t-\delta_n)\}]_l\exp(-i\beta_l a_n^2 Kx)\ , \tag{4}$$

where the parameters with the subscript 1 are the quantities related to the envelope soliton with the central frequency f_1, δ_n the phase constant determining the position of the soliton on the temporal coordinate, and a_n the amplitude of the envelope soliton. If all the spacings between two consecutive wave groups are enough wide to make asymptotic approximation possible, the asymptoic expression based on the above assumptions becomes possible. Hence, the leading order profiles η of the observed waves with remarkable groupiness are expressed by using eq.(4) and defining the phase constant σ_1 of carrier waves:

$$\eta=\sum_{l=1}^{L}\frac{|\varepsilon A_l|}{K_l}\cos(K_l x-2\pi f_l t+\sigma_l) \tag{5}$$

Similar expressions of horizontal water particle velocity and water pressure, which are necessary to calculate the wave drift force etc. reflecting wave grouping charqcteristcs, can be easily obtained.

$$u=\sum_{l=1}^{L}|\varepsilon A_l|c_l\left\{\frac{\cosh K_l(h+z)}{\sinh K_l h}\right\}\cos(K_l x-2\pi f_l t+\sigma_l) \tag{6}$$

$$\frac{p}{\rho g}=\sum_{l=1}^{L}\frac{|\varepsilon A_l|}{K_l}\left\{\frac{\cosh K_l(h+z)}{\cosh K_l h}\right\}\cos(K_l x-2\pi f_l t+\sigma_l)-z \tag{7}$$

The envelope profile R(t) of observed waves is expressed as a sequence of M-asymptotic envelope solitons, if eqs.(4) and (5) are used.

$$R(t)=\sum_{m=1}^{M} R_m\,, \qquad R_m=a_m \operatorname{sech}[\gamma_m(t-\delta_m)]\,, \tag{8}$$
$$\gamma_m=2\pi f_m K_m a_m(\sqrt{\beta/2\alpha})_m\,.$$

The above equation states that both the envelope profile and the associated carrier waves are governed by the values of the random variables, a_m, f_m and δ_m. Hence, by investigating statistical characteristics of these random variables, we can make a statistical description both for the envelope profile and carrier waves and a simulation of random waves with a given groupiness. Probability distribution function $F(R_c)$ of the envelope profile R(t) is defined as the probability of R(t) being below the critical value R_c and expressed as

$$F(R_c)=p[R\leq R_c]=\sum_{m=1}^{M}\frac{1}{\gamma_m} \times\int_0^{R_c}\ln\{[1+\sqrt{1-(R_m/a_m)^2}/(R_m/a_m)\}\,dR_m\Big/\sum_{m=1}^{M}(1/\gamma_m) \tag{9}$$

Since the differentiation of $F(R_c)$ by R_c yields the probability density function f(R), a statistical approach becomes possible for runs of consecutive high waves by using f(R). The averaged run length $\bar{j}_1$ making R_c the critical value is expressed as

$$F^*(R_c)=1-\left\{\sum_{m=1}^{M}\frac{2}{\gamma_m}[\ln(1+\sqrt{1-Y_m^2})-\ln Y_m]\right\}\Big/T_0\,, \qquad Y_m=R_c/(2a_m)\,, \tag{10}$$

$$j_1=[(2f_m/\gamma_m)\{\ln(1+\sqrt{1-Y_m^2})-\ln Y_m\}]\,, \tag{11}$$

where brackets [ ] denote the integral representation.

3. Application to observed waves

In order to represent the envelope profile of the observed waves using eq.(8), the values of a_m, δ_m and f_m governing an envelope soliton must be determined from each wave group. Hence, deriving the linear envelope function $R_o(t)$ based on the narrow-band spectrum from the wave record band-pass filtered so as to eliminate both frequencies higher than $1.5f_p$ and lower than $0.5f_p$, we first determine the number of envelope solitons possessed in the record and the values of δ_m from the crest positions expressed by the function $R_o(t)$. And then, we determine both values of a_m and f_m so as to minimize the error energy between the linear envelpe function $R_o(t)$ and the nonlinear envelope function R(t) defined by eq.(8).

$$E=\int_0^T\{R(t)-R_0(t)\}^2 dt \tag{12}$$

That is, both values of a_m and f_m are determined by solving the following simultaneous equation with 2M-dimensions.

$$\partial E/\partial a_m = 0\,, \qquad \partial E/\partial f_m = 0\,. \qquad m = 1, \cdots, M \tag{13}$$

Figure 5 shows some comparisons between the profiles of the observed waves and the envelope profiles represented as a train of the envelope solitons of which parameters were calculated as mentioned above. The comparisons state that the expression based on eq.(8) can be applied to the observed waves with a non-zero nonlinearity and remarkable groupiness instead of the linear envelope function $R_o(t)$ although it utilizes $R_o(t)$ to determine the values of a_m, δ_m and f_m.

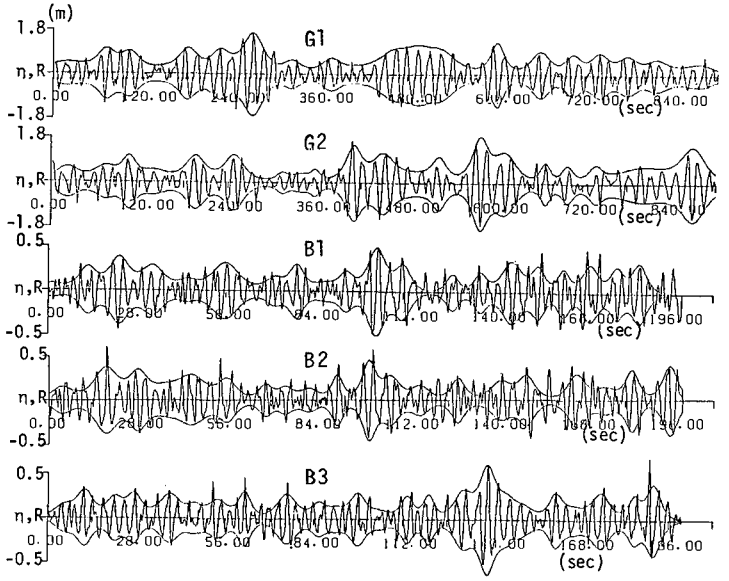

Fig. 5 Comparisons between profiles of the observed waves and the envelope profiles calculated by the present approach

Figure 6 shows comparisons between the envelope profile 2R(t) calculated by eq.(8) and the temporal variations in wave-heights of zero-up crossing waves. It is seen that the properties of the time series of zero-up crossing waves can be easily evaluated on the basis of eq.(8). This states that the statistical approach briefly shown above has a possibility of its application to the observed waves.

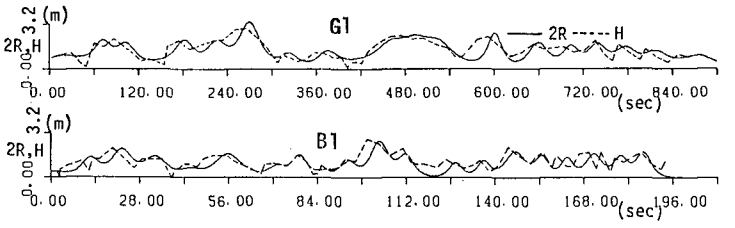

Fig. 6 Comparisons of a train of wave-heights of zero-up crossing waves with the envelope profile represented by the present approach

Figure 7 shows the relation between f_m/f_p and $(\bar{a}/a_m)/k_ph$. Here, f_m is the frequency of carrier waves associated with an envelope soliton corresponding to one wave group and $\bar{a}$ is the averaged amplitude of envelope solitons included in one record of the observed waves. It is noticed that a functional relation equivalent to the regression curve, defined by

$$\left.\begin{aligned} f_m/f_p &= 0.38+2.55x-0.67x^2+0.07x^3, \\ x &= \bar{a}/K_phha_m \end{aligned}\right\} \quad (14)$$

exists between f_m/f_p and $(\bar{a}/a_m)/k_ph$, nevertheless, the values of a_m and f_m are determined only by the conditions shown in eq.(13). This states that grouping waves in field are governed by some dynamics slightly similar to the assumpsions mensioned above and the value of f_m can be estimated using eq.(14).

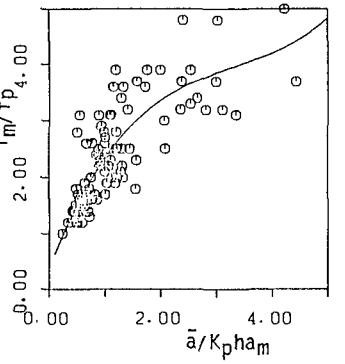

Fig. 7 Relation between peak frequencies of the observed waves and carrier frequencies associated with envelope solitons

As shown above, it is seen that the assumptions i) and ii) hold at least for the observed waves used here and the schematic diagram drawn in Fig.1 reflects partially a correct statement of the physics of the waves with a weak nonlinearity and finite band-width. This states that the approach treating envelope solitons as elementary modes can be applied to the waves with remarkable groupiness. The approach, which may be called as the envelope soliton mode approach, suggests that there is a possibility to explain simply dynamical and statistical properties of the waves and to simulate numerically waves with a expected groupiness. Further, it is expected that the time series of grouping waves can be analyzed by making clear the statistical characteristics of random variables a_m and δ_m, instead of usual approach based on the run theory of zero-crossing waves and the linear envelope function.

DRIFTING FORCE BASED ON ENVELOPE SOLITONS

1. Formulations

It is well-known that the wave grouping is closely related to the slow drift oscillation of moored systems. Pinkster[1975] formulated the wave drifting force under the assumption of a narrow-banded Gaussian process and showed that the slow drift oscillation is due to the resonance between the natural frequency of a moored system and the peak freguency of the spectrum of the drifting force. However, waves with remarkable groupiness have generally a weak nonlinearity and finite spectral band-width and are not suitable for Pinkster's approach based on a narrow-banded Gaussian process. Further, Pinkster's approach is not effective for evaluating the time series characteristics of the drifting force because the spectral analysis itself is not useful for the investigation on time domain. While, the envelope soliton mode approach suggested in the preceding chapter is applicable to such waves and effective for investigating the time series characteristics.

A formulation based on the envelope soliton mode is made on the computations of the wave drifting force based on the direct integration method of pressure acting on the wetted surface of a body with reference to Pinkster's approach. Assuming as well as Pinkster that the envelope profile of the waves slowly varies and using egs.(5), (6), (7) and (8), we can represent the drifting force $F_S(t)$ based on the present approach as

$$F_s(t)=\frac{1}{2}\rho g \sum_m \sum_n a_m a_n C_{FD} \operatorname{sech}[\gamma_m(t-\delta_m)] \operatorname{sech}[\gamma_n(t-\delta_n)] \cos(\omega_m-\omega_n)t \ , \quad (15)$$

where spatial coordinate x is set to be zero for simplicity, and the parameters with the subscript m denote the quantities concerned with m-th envelope soliton with carrier frequency f_m, C_{FD} the drifting force coefficient to be determined experimentally, ω_m the angular frequency $2\pi f_m$, ρ the density of fluid.

If each envelope soliton is independent of others, eq.(15) is further simplified and is rewritten as

$$\left.\begin{aligned} F_s(t)&=(\rho g/2)C_{FD}R(t)^2 \ , \\ R(t)&=\sum_{m=1}^{I} a_m \operatorname{sech}[\gamma_m(t-\delta_m)] \end{aligned}\right\} \quad (16)$$

This expression states that the time series characteristics of the drifting force can be explained in a direct relation with a statistical properties of random variables a_m and δ_m governing dynamically each envelope soliton and that the envelope soliton mode approach is very effective for investigating the properties of the drifting force in a time domain.

2. Characteristics

In order to investigate the properties of the drifting force expressed in eq.(15) and the relation with wave grouping characteristics, comparisons of the drifting force are made among Hsu & Blenkarn's approach[1972], Pinkster's one and authers' one. Figure 8 shows the comparison. Here, the value of the drifting force coefficient C_{FD} is set to be unity commonly for each case. It is found that both results of Pinkster and authors do not suffer the influences of small deviations independent of wave groups and are superior to Hsu and Blenkarn's approach in evaluating the influence due to wave groups themselves. The drifting force by the present approach agrees well with the one by Pinkster's appoach and the former may be used instead of the latter which has been put widely to practical use.

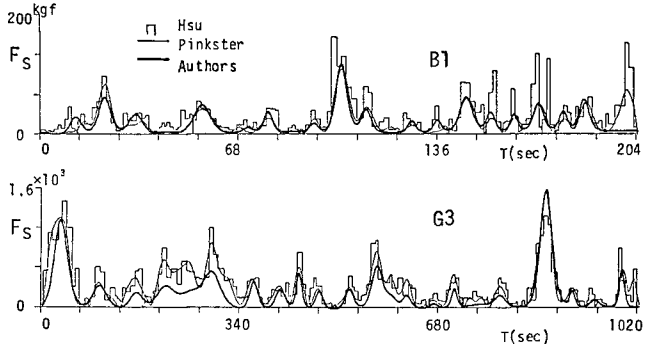

Fig. 8 Comparisons of the wave drifting force calculated by authors approach with the ones by Hsu and Pinkster

CONCLUSION

The approach, regarding an envelope soliton as an elementary mode of grouping waves and representing them as a train of envelope solitons of which amplitudes and phase constants are random variables, is suggested here and is shown to be applicable to the temporally observed waves with a non-zero nonlinearity and finite band-width. It, further, is extended to a formulation of the wave drifting force caused by the existence of wave groups and the fomulation based on the envelope soliton mode is signified to be put to practical use as well as Pinkster's one based on a narrow-banded Gaussian process.

The present study containes some debatable points such that the intutitive picture shown in Fig. 4 is not verified to be a correct statement of the physics of grouping waves and the approach can not describe their propagation process because based on the asymptotic soliton solutions of the plural NLS equations. In order to establish the envelope soliton mode approach, it is required to verify that grouping waves in field have a dynamical structure making an envelope soliton an elementary mode and overcome the above debatable points. However, it should be emphasized that the approach is useful for analyzing the

problems mainly dependent on wave grouping characteristics at a fixed position, such as the slow drift oscillation of moored systems. It, further, is supposed to be effective for evaluating simply statistical properties of grouping waves and simulating numerically waves with an expected groupiness because parameters governing each envelope soliton are random variables expressing directly wave grouping characteristics and statistical quantities concerned with carrier waves and zero-crossing waves can be written as functions of the parameters.

As mentioned above, the approach suggested here remains some points to be examined. But it can be stated at least that the envelope soliton mode approach has a possibility to carry out a new statistical description on waves with a remarkable groupiness.

This research was supported by the Grant-in-Aid for Scientific Research 61550368 from the Ministry of Education, Science and Culture.

REFERENCES

Funke, E. R. and E. P. D. Mansard : Synthesis of realistic sea states in a labratory flume, Nat. Res. Coun. Canada, Hyd. Lab. Rep., LTR-HY-66, 54p., 1979.

Hsu, F. H. and K. A. Blenkarn : Analysis of Peak Mooring Forces Caused by Slow Vessel Drift Oscillations in Random Seas, Soc. Pet. Eng. Jour. (Aug. 1972), pp. 329-344.

Pinkster, J. A. : Low-frequency phenomena associated with vessels moored at sea, Soc. Pet. Eng. Jour. (May 1975), pp. 487-494.

Sobey, R. J. and E. J. Colman : Natural wave trains and scattering transform, Pro. ASCE, Jour. Waterway, Port, Coastal and Ocean Div., Vol. 108, No. WW3, pp. 272-290, 1982.

Spangenberg, S. : The effect of wave grouping on slow drift oscillations of an offshore structure, Danish Ship Res. Lab., Bul. No. 46, 51p., 1980.

Stiassinie, M. and L. Shemer : On modifications of the Zakharov equation for surface gravity waves, Jour. Fluid Mech., Vol. 143, pp. 47-67, 1984.

Yuen, H. C. and B. M. Lake : Nonlinear dynamics of deep-water gravity waves, Advances in Applied. Mech., Vol. 22, pp. 67-229, 1982.

CHAPTER 66

NEARSHORE BEHAVIOR OF BORE ON A UNIFORMLY SLOPING BEACH

Harry H. Yeh and A. Ghazali*

Using the laser-induced fluorescent method, the detailed transition process from bore to run-up mode is clarified experimentally. The transition process is found to be different from the previous predictions, and might provide an explanation for the discrepancies of the run-up height between the theory and laboratory measurements. Turbulence generated in a bore appears to be highly three-dimensional and sporadic. Turbulence generated close to the shore is advected with the bore-front motion and violent turbulent actions result during the transition from bore to run-up mode.

Introduction

A bore and the ensuing run-up on a uniformly sloping beach have been analyzed based on the inviscid theory with the shallow-water approximation; the shallow-water equations are basically depth-integrated conservation equations of mass and momentum with the assumption of a hydrostatic pressure field. The governing equations form a hyperbolic system, which is often solved by the method of characteristics. A bore front is usually treated by the jump conditions, i.e. the conservation of mass and momentum at the methematical discontinuity. (Note that energy across the jump is not conserved.) Using this formulation, Whitham (1958) found that the height of the bore tends to vanish as it approaches the shoreline while the fluid velocity, u, remains finite. Furthermore, Ho and Meyer (1962) found that singularity of the fluid acceleration occurs at the shoreline, while both the fluid and bore velocities approach their common finite value u* in which the value of u* is totally dependent on the offshore boundary condition. This behavior at a shoreline involving rapid conversion of potential to kinetic energy is often called "bore collapse". Shen and Meyer (1963) extended Ho and Meyer's analysis to the wave run-up after the bore collapse. They found that the maximum run-up height, R, is simply, $R = u^{*2}/2g$. Note that the predicted run-up height is independent of the beach slope.

Using the Lax-Wendroff numerical technique, the behavior of a bore on a beach was solved by Hibberd and Peregrine (1979). Because the jump conditions are not used to model a bore front, energy can be dissipated only via numerical dissipation. Their predictions of the maximum run-up heights appeared to be in excellent agreement with the analytical predictions. This indicates that the numerical dissipation involved is comparable to the energy dissipation involved in the jump

*University of Washington, Seattle, Washington, U.S.A.

conditions. Nonetheless, the analytical and numerical predictions of the maximum run-up height are considerably greater than the experimental results measured by Miller (1968). Packwood and Peregrine (1981) extended Hibberd and Peregrine's (1979) numerical model to incorporate viscous effects by using the Chézy friction term. While good agreements with Miller's (1968) experimental results were obtained for the steep beach-slope condition ($\beta = 15°$), for the mild slope condition ($\beta = 2°$) it was found that the friction effects alone cannot be an explanation for the discrepancy of the maximum run-up heights, i.e. the numerical predictions of the viscous model still considerably exceed Miller's experimental results.

The numerical results reported by Hibberd and Peregrine (1979) could not model the complete bore-collapse phenomenon due to the discretization involved in the numerical scheme which limits resolution of the details. In fact, just like the bore front being a discontinuity in the analytical model, Hibberd and Peregrin's numerical model does not provide physical information about the shape and structure of the front itself; the length of the front is artificially determined by the choice of the discretization in the Lax-Wendroff numerical scheme. However, we also conjecture that the complete bore collapse may not take place in a real fluid environment. First, as Hibberd and Peregrine pointed out, a real bore is not a perfect discontinuity but has a finite width which obscures the sharp transition of a predicted bore-collapse phenomenon. Second, a rapid conversion of potential to kinetic energy must involve significant vertical fluid motion; consequently, the applicability of the shallow-water approximation to that local phenomenon is in question. In his extensive experimental study, Miller (1968) reported that there is no complete collapse of a bore but the transition from bore to run-up mode is a rather gradual process. However, because of the measuring technique available to Miller, the detailed transition process was not revealed.

A qualitative description of turbulence involved in a bore in a uniform depth was suggested by Peregrine and Svendsen (1978). According to their description, turbulence is generated at the toe of the bore front and the initial stage of turbulent flow resembles a mixing layer. After the generation, the turbulence spreads and then interacts with the free-surface and, if the water is shallow enough, the bottom boundary. After the interactions, the turbulence behaves like a wake and decays. Applying the k-ε turbulence model to the depth-integrated governing equations, Svendsen and Madsen (1984) attempted to model a turbulent bore on a mildly sloping beach with $\beta = 1.66°$. A similarity profile of the flow velocity in the turbulent region was assumed based on the results for the hydraulic jumps provided by Madsen and Svendsen (1983). (In coordinates moving with the front, a bore in a uniform depth is often considered to be equivalent to a hydraulic jump.)

In this paper, we investigate behaviors of the bore near the shoreline, in particular, the transition from bore to run-up mode. The necessary definitions for this problem are shown in Fig. 1. Here, the x-coordinate points in the inshore direction from the shoreline, $u(x,t)$ is the depth-averaged fluid particle velocity, $h(x,t)$ denotes

the depth of the water and $h_0(x)$ is the quiescent water depth in front of the bore, and g is the acceleration of gravity. Using the laser-induced fluorescence technique (described in the next section), a detailed transition process is revealed experimentally in a precisely controlled laboratory environment. The generation and evolution of turbulence associated with a bore nearshore are also investigated.

Experiment

A series of experiments was performed in a 9.0 m long, 1.2 m wide, and 0.9 m deep wave tank. A schematic view of the experimental setup is shown in Fig. 2. A plane beach is constructed of 1.9 cm thick plexiglass plates bolted on an aluminum frame. This construction assures rigidity of the beach with its precise slope of 7.5 degrees.

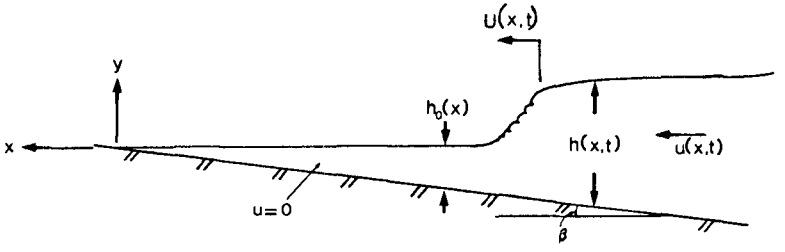

Figure 1. Definition Sketch

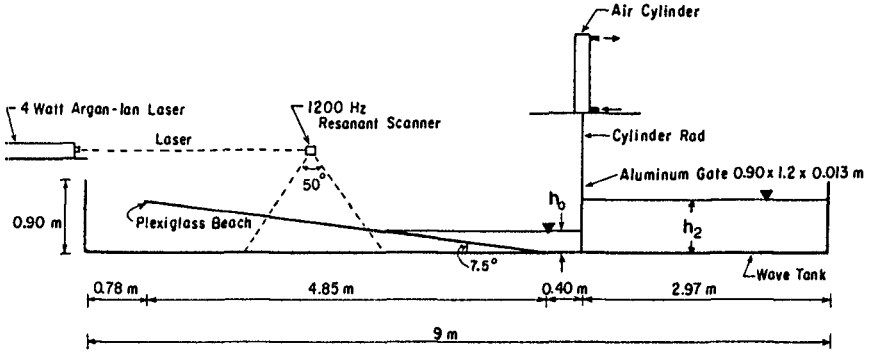

Figure 2. Schematic Drawing of Wave Tank

A single uniform bore is generated by lifting the gate (made of a 12.7 mm thick aluminum plate) which initially separates the quiescent water on the beach from the deeper water behind the gate. This bore-generation scheme has an advantage since the theoretical prediction of the bores can be made without difficulty from the classical dam-break problem. The gate is maintained in a vertical position with the aid of 25.4 mm brass guide channels along the side walls as well as the bottom floor of the tank; the gate itself is sealed against the channel slots by 4.8 mm O-ring rubber embedded in the channels. A pneumatic cylinder with a 10.16 cm bore is used to lift the gate in a controlled manner. The cylinder is electrically activated by a single solenoid valve with the operating air pressure of 650 kPa. It was found that the opening timing is sensitive to bore formation generated at the gate; the faster the opening, the more developed the resulting initial bore. The system is capable of lifting the gate fast enough (the lift-up time of 0.0708 ± 0.0012 sec in 20 cm of travel distance) that developed bores can be generated on the beach.

A 4-watt Argon-ion laser is used for the flow visualization. The emitted laser beam is converted to a thin sheet of laser light through a resonant scanner. The scanner is capable of sweeping the beam at 1200 Hz projected from above in the cross-shore (or longshore) direction and illuminates the vertical longitudinal (or transverse) plane of the water dyed with fluorescein. The fluid motions illuminated with the laser-induced fluorescence were recorded by the 35-mm photo camera. In order to record time directly using photography, a special digital clock was developed; the clock is activated by the initiation of the gate motion with the aid of a photo cell sensor. In addition, an electrical shutter release for the photographic camera was developed; the shutter release is synchronized with a wave sensor in the tank so that the motion at an exact time can be captured by the camera.

Two sets of experiments were performed: experiments for the bore collapse and for the turbulence generation and its development. In the latter experiments, a thin layer (approximately 3 mm thick) of a slightly lighter fluid (diluted ethanol, 0.99 specific gravity) was placed on the water on the beach. Only the upper layer was dyed with fluorescein. When a bore front propagates over the dyed layer, the laser-induced fluorescence indicates the motion of the water engulfed by the toe of the bore. This technique is similar to the one used by Peregrine and Svendsen (1978) who used detergent bubbles as the flow tracer. However, the present laser-induced fluorescence technique can provide the flow visualization in a virtually two-dimensional plane (the laser sheet is approximately 1 mm thick). The flow patterns were recorded by the photographic camera with the motor drive so that evolution of the turbulence can be analyzed. The camera (Nikon F2A Photomic) is capable of taking photographs at the rate of 4 frames per second.

In order to block scattered laser light (mainly at the 488 and 515 nm wave lengths) caused by unwanted particles and, more importantly, air bubbles entrapped in the bore front, the camera was equipped with a high-pass optical glass filter throughout the experiments. Because a relatively fast shutter speed (1/250 and 1/500 sec.) is

required to capture the detailed bore motions, fast-exposure professional photographic films (Fujichrome P1600 D) were used.

Results

The performance of the bore generating system was examined with a variety of the initial conditions. It was found, from visual observations, that developed bores can be generated when $h_2/h_0 \geq 2.0$, where h_2 and h_0 are the initial water depths in front of and behind the gate, respectively. In the case of $h_2/h_0 < 2.0$, linear effects of frequency dispersion become significant, hence bores generated were undular instead (although the leading wave is breaking at its crest when $1.6 < h_2/h_0 < 2.0$). It was also found that when $h_2/h_0 > 2.8$, the behavior of generated bores appears to be too transient for measurements. Perhaps this is due to the limited propagation distance available and the finite time involved in lifting up the gate, i.e. the bore could not have enough time to be developed before it reaches the shore. Nonetheless, qualitative behaviors of bores generated with $2.0 \leq h_2/h_0 \leq 2.6$ appeared to be similar in all aspects investigated in the experiments discussed below. Hence, we concentrate hereafter on the examination of the bore generated with the following initial conditions: $h_0 = 9.75$ cm and $h_2 = 22.5$ cm. With this initial condition, the corresponding initial bore height in the uniform depth, h_1, is predicted to be 15.4 cm and the Froude number, $F = U/\sqrt{gh_0}$, is 1.43, where U is the speed of the bore front. (The values of h_1 and U were computed by solving the dam-break problem.) It is noted that the offshore bore strength characterized by F = 1.43 is comparable to F = 1.45 and 1.37 used in the numerical studies by Hibberd and Peregrine (1979) and Svendsen and Madsen (1984), respectively. Furthermore, $F \simeq 1.4$ seems to be typical of bores on a beach according to the results provided by Svendsen, Madsen, and Hansen (1978).

According to Ho and Meyer (1962), as the bore approaches the shore, the bore height diminishes to zero and the fluid velocity, u_1, behind the front approaches that of the front itself. Note that the values of U and u_1 are finite at the shore although the acceleration becomes singular. This complete bore-collapse phenomenon is thought to be unrealistic since the bore front is not really a discontinuity. To circumvent this difficulty, Hibberd and Peregrine (1979) implemented the Lax-Wendroff numerical scheme without using the jump conditions for the bore front. Their results indicate that the transition from bore to run-up mode is rather smooth and gradual. However, it is emphasized that the detailed shape of the front is determined basically by the discretization of the numerical solution but not by the physical causes. The experimental results of the bore near the shore and the transition from bore to run-up mode are shown in the sequence of photographs in Fig. 3. With repeated experiments, each photograph was taken by shifting the probe location for the electric shutter release at 5 cm intervals from x = -15 cm to x = 15 cm. The experimental results clearly indicate discrepancies from the predictions. The bore front itself never reaches the shoreline, but the small wedge-shaped water body along the shore ahead of the front is suddenly pushed forward. This pushed water mass, involving the violent turbulence, initiates the run-up process. During the transition, the bore

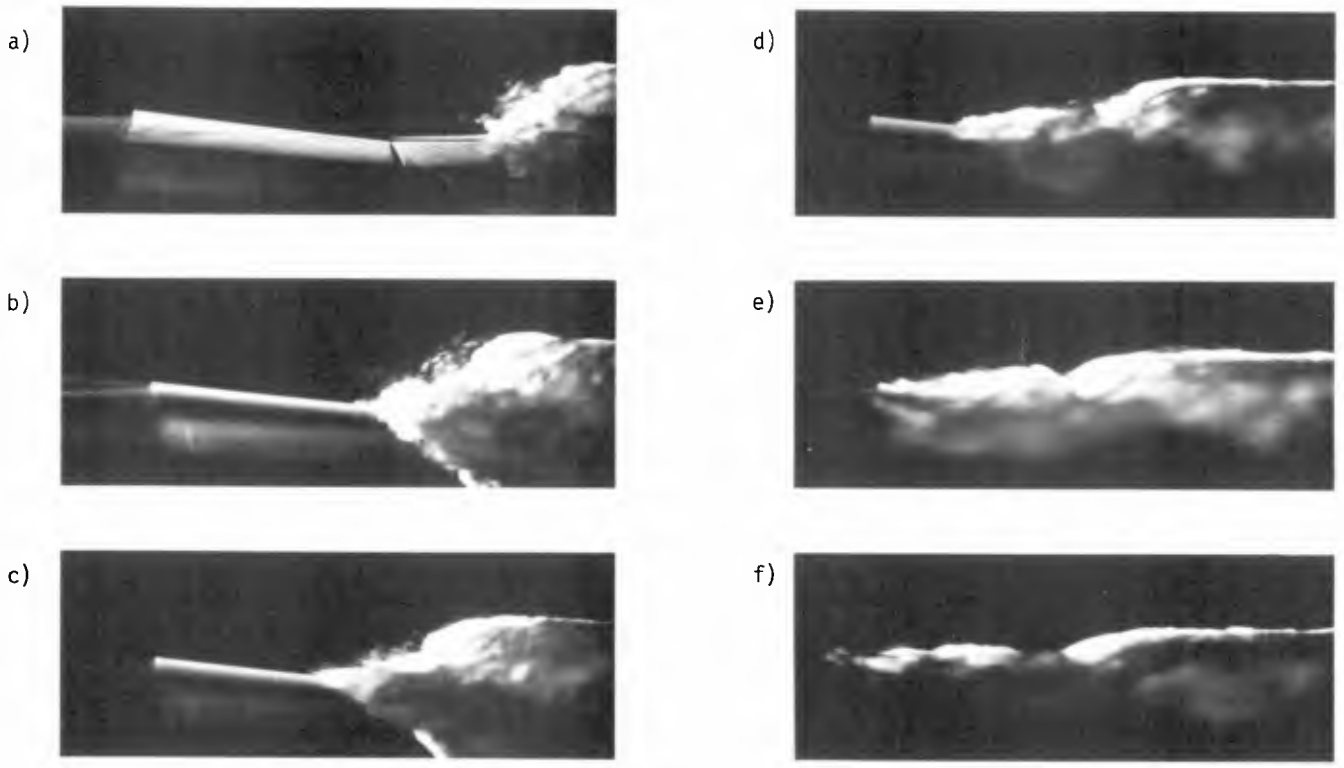

Figure 3. Transition Process from Bore to Run-up Mode. a) x = -15 cm; b) x = -10 cm; c) x = -5 cm; d) x = 0 cm; e) x = +10 cm; f) x = +15 cm

front first steepened and reduces its height. In order to verify this process, we performed another experiment by placing the narrow strip of water dyed with Rhodamine B along the shoreline so that the location of the dyed water can be identified by the red color. It was found that the water along the shore is indeed pushed forward instead of being engulfed by the bore front. By the following argument, this transition process may provide an explanation for the discrepancy on run-up heights between the inviscid theory and experimental measurements as mentioned in the introduction.

Suppose a bore approaching a shore is as shown in Fig. 4. At this instant (t = 0), the water in front of the bore is still quiescent. We assume that, when the ratio h_o/h_1 reaches a certain value, the water in front of the bore is pushed forward with a uniform velocity, u_o. Then, based on the conservation of total energy, the rate of change of kinetic energy of the water in front of the bore is the difference between the energy flux, F, transferred into the control volume through section 1 and the rate of change of energy of the bore, I, i.e.

$$\frac{d}{dt}\left(\frac{1}{2}\rho V_o u_o^2\right) = F - I$$

where ρ is the fluid density, and V_o is the fluid volume of the water pushed forward. Since $V_o = 1/2\ h_o^2/\tan\beta$, integrating the equation yields the maximum value of u_o at $t = t^*$:

$$u_o^{*2} = (2\tan\beta)/(\rho h_o^2)\int_o^{t^*}(F - I)dt.$$

Note that, from the initial and final conditions, $F - I = 0$ at $t = 0$ and t^*. Hence this suggests that u_o^* is dependent on the beach slope, and then the maximum run-up height is also dependent on the beach slope. (u_o^* appears to be proportional to $\tan\beta$, although the real relation remains unknown unless the integration is evaluated.) Together with the viscous effect and the effect of the air-water-beach contact line, this bore collapse process may be an additional explanation for the discrepancy which appeared between Miller's (1968)

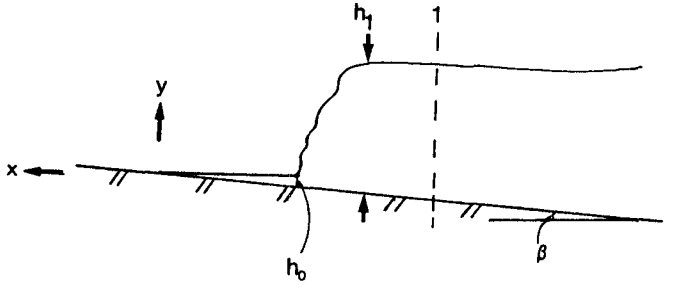

Figure 4. Simplified Model of a Transition from Bore to Run-up Mode.

experimental results and the numerical solutions provided by Hibberd and Peregrine (1979) and Packwood and Peregrine (1981).

It is also noticed in Fig. 3 that the bore front becomes very steep (almost vertical) but smooth (less turbulent), while the water in front of it is extremely turbulent. This suggests that the turbulence generated at the front near the shore is advected forward on the beach instead of being left behind. This conjecture is further supported by the experimental results which follow.

In the experiments for turbulence, a thin dyed layer of diluted ethanol was placed on the water to identify vortices formed at the toe of the bore front. A sequence of photographs for generation and development of bore turbulence are shown in Fig. 5. The first photograph, Fig. 5a, shows that the toe of the front is passing at $x = -20$ cm. The mixing-layer type of turbulence generation cannot be detected in the photograph but the turbulent region is extremely thin and limited near the surface. It appears that the turbulence spreads at a much smaller rate than the change in the water surface. Svendsen and Madsen's results appear to form a thicker turbulent region than that in Fig. 5. However the direct comparison cannot be made because of the different beach slope involved (Svendsen and Madsen used $\beta = 1.66°$ whereas the experiments were performed with $\beta = 7.5°$). The observed turbulence behind the bore front is sporadic rather than forming a distinct turbulent region. A clear spread of turbulence can be observed in Figs. 5b and c at a relatively offshore position; these eddies must be generated when the bore was still propagating in the offshore region. Note that the water-particle velocity offshore is substantialy slower than the bore-propagation velocity. Hence, the generated turbulence is advected behind the front. When the bore reaches the shoreline in Fig. 5b, the turbulence behind the front seems to be weak; turbulent motions appear to be concentrated at the front. These behaviors are not limited to this particular case, but also occurred in the experiments with different initial bore strengths in a range of $1.31 < F < 1.48$. Since the magnitude of u_1 approaches the magnitude of U as the bore approaches the shore, the generated turbulence advected by the fluid velocity also tends to move closer with the front. This indicates that the turbulence generated near the shore is accumulated at the front and then released at the transition from bore to run-up modes. On the other hand, less turbulence is left behind the front and stretched horizontally by the velocity difference, hence relatively calm flow pattern results here.

By following the small turbulent eddy which appeared right behind the front in Fig. 5b, it is observed in the subsequent figure the eddy is stretched in a slanting vertical direction; similar behavior was observed in a broken wave in a uniform depth by Nadaoka et al. (1985).

In order to see more definite behaviors, the flow patterns in a vertical plane perpendicular to the propagation, i.e. in the longshore direction, were examined. (This is achieved by rotating the resonant scanner by 90 degrees.) The results are shown in Figs. 6 and 7. Note that the photographs were taken from the side wall so that the resulting images are somewhat distorted. In Fig. 6, the vertical laser

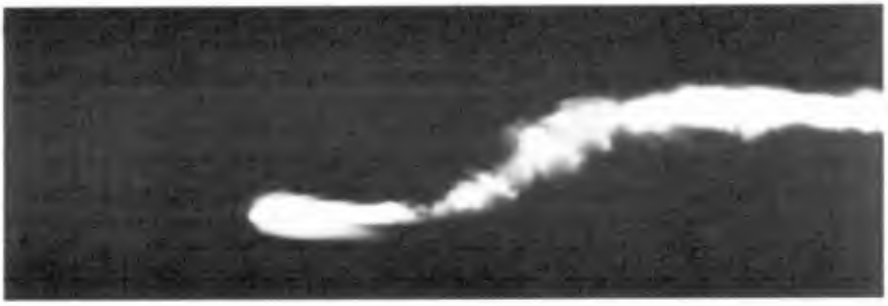

a) t = 0.76 sec

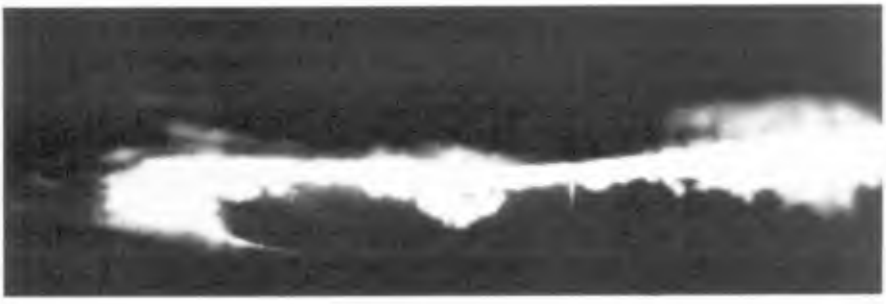

b) t = 1.00 sec

c) t = 1.23 sec

Figure 5. Visualization of Turbulence in a Longitudinal Plane along the Center Line of the Tank. (t = 0 at the gate opening)

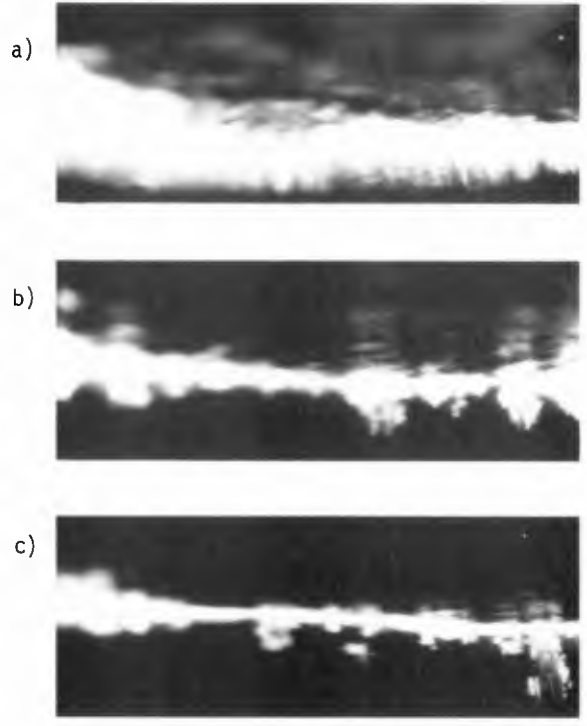

Figure 6. Visualization of Turbulence in a Transverse Plane along x = -12 cm, a) at the front; b), c) 0.25 and 0.50 sec later, respectively

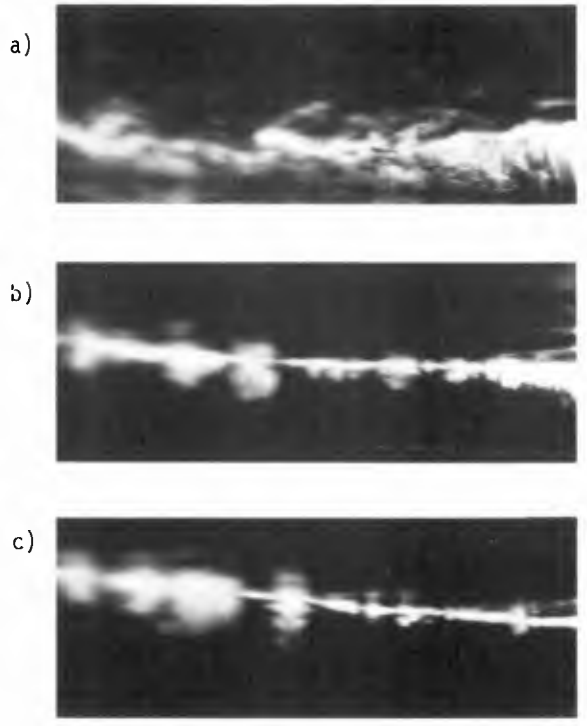

Figure 7. Visualization of Turbulence in a Transverse Plane along x = 0 cm, a) at the front; b), c) 0.25 and 0.50 sec later, respectively

sheet parallel to the shoreline was emitted offshore, x = -12 cm. Three-dimensional and sporadic turbulence structures are evident. In Fig. 7, the vertical laser sheet was emitted along the initial shoreline. Figure 7a shows the flow along the bore front at the shoreline; it is evident that the turbulence there is intense. Nonetheless, once the front passes by, the turbulence left behind the front is surprisingly weak and sporadic as seen in Figs. 7b and c. This confirms the observations made for Fig. 5.

The present results suggest that the turbulence is concentrated in the roller at the surface and the vortical motions generated within the roller are advected sporadically behind the bore front. From this point of view, the generation of the turbulence resembles that involved in a flow separation just as assumed by Longuett-Higgins (1973) for his analysis of steady breaker. This evidently differs from the one suggested by Peregrine and Svendsen (1978). The reason is not clear but it is probably because Peregrine and Svendsen observed the turbulence integrated in the tank width whereas the present observation is that in a virtually two-dimensional plane by the laser-induced fluorescence technique.

Conclusion

The detailed process of the transition from bore to run-up mode, i.e. bore collapse, was revealed. It was found that the bore front itself does not reach the shoreline before the large mass of the bore pushes the small wedge-shaped water body along the shore. During the pushing, the bore height decreases with steepening the front face (to almost vertical). The turbulence located on the front face appears to be advected forward onto the beach. This totally different transition process from the previous predictions may provide an additional explanation for the discrepancies of the resulting maximum run-up height between the theory and measurements. The turbulence generated at the bore front near the shoreline seems to resemble that for a flow separation. The generated turbulence is advected behind the bore; there, the turbulence is weak, three-dimensional, and sporadic. Very close to the shore, the generated turbulence is advected with the front. Hence violent turbulent motion results during the transition from bore to run-up mode, whereas right behind the bore front, a relatively calm motion occurs.

The author wishes to thank Mr. McKay of the University of Washington for his assistance in setting up the experimental facility. The work for this paper was supported by the U.S. National Science Foundation Grant no. ECE-8503436.

References

Hibberd, S. and Peregrine, D.H., 1979. Surf and run-up on a beach: a uniform bore, J. Fluid Mech., 95, 323-345.

Ho, D.V. and Meyer, R.E., 1962. Climb of a bore on a beach. 1: Uniform beach slope, J. Fluid Mech., 14, 305-318.

Longuet-Higgins, M.S., 1973. A model of flow separation at a free surface, J. Fluid Mech., 57, 129-148.

Madsen, P.A., and Svendsen, I.A., 1983. Turbulent bores and hydraulic jumps, J. Fluid Mech., 129, 1-25.

Miller, R.L., 1968. Experimental determination of run-up of undular and fully developed bores, J. of Geophys. Res., 73, 4497-4510.

Nadaoka, K., Hino, M. and Koyano, Y., 1986. Turbulent flow field structure of breaking waves in the surf zone, Proc. Conf. Coastal Eng., 20th.

Packwood, A.R., and Peregrine, D.H., 1981. Surf and run-up on beaches: models of viscous effects. Rep. No. AM-81-07, University of Bristol.

Peregrine, D.H. and Svendsen, I.A., 1978. Spilling breakers, bores and hydraulic jumps, Proc. Conf. Coastal Eng., 16th, 540-550.

Shen, M.C., and Meyer, R.E., 1963, Climb of a bore on a beach. 2: non-uniform beach slope, J. Fluid Mech., 16, 108-112.

Svendsen, I.A., Madsen, P.A. and Hansen, J.B., 1978. Wave characteristics in the surf zone, Proc. Conf. Coastal Eng., 16th, 520-539.

Svendsen, I.A., and Madsen, P.A., 1984. A turbulent bore on a beach, J. Fluid Mech., 148, pp. 73-96.

Whitham, G.B., 1958. On the propagation of shock waves through regions of non-uniform area or flow, J. Fluid. Mech., 4, 337-360.

CHAPTER 67

MAGNITUDE OF THE β-FACTOR UNDER WAVE ACTION

by

J. van de Graaff [1] and

R.C. Steijn [2]

Abstract

The sediment transport due to waves and currents depends on the distribution of sediment concentration and on the distribution of the velocity over the water depth. Our knowledge of both phenomena for practical applications is still rather poor. Some results of wave flume tests concerning the distribution of sediment concentrations due to wave action will be discussed. It turns out that the sediment size of the bottom material has a rather unexpected effect hereupon. With respect to the velocity distribution only some qualitative remarks can be made at the moment.

1. Introduction

The sediment transport (per m) due to waves and currents parallel to the coast can be described in principle with:

$$S = \int_0^h \overline{v(z)}\ \overline{c(z)}\ dz \qquad (1)$$

where:

S	:	sediment transport rate
$\overline{v(z)}$	:	time averaged current velocity (function of z)
z	:	height above the bed (z = 0 being the bottom)
$\overline{c(z)}$	:	time averaged sediment concentration (function of z)
h	:	water depth

[For simplicity reasons the over-bars in $\overline{v(z)}$ and $\overline{c(z)}$ have been omitted further.]

---

[1] Senior Scientific Officer; Delft University of Technology

[2] Student Assistant; Delft University of Technology
(present position: project engineer; Delft Hydraulics)

Eq.(1) is a simplification of the general description according to:

$$S = \frac{1}{t_o} \int_0^{t_o} \int_0^{h} v(z,t)\ c(z,t)\ dzdt \qquad (2)$$

where: t_o : integration time (long with respect to the wave period T)

$v(z,t)$: current velocity (function of z and t)

$c(z,t)$: sediment concentration (function of z and t)

t : time.

For the cross shore sediment transport description Eq.(2) should be applied in principle. The orbital motion affects the parameter $v(z,t)$ continuously and thus in fact the simplifications according to Eq.(1) cannot be made. However, Stive and Battjes (1984) do apply an equation like Eq.(1) also in cross shore transport cases with some success. [The use of Eq.(1) instead of Eq.(2) has great advantages since our knowledge of the parameter $c(z,t)$ on the wave period scale is nearly completely insufficient; see Bosman (1986).]

In longshore sediment transport cases the orbital motion hardly affects (due to refraction) the parameter $v(z,t)$ in Eq.(2), thus the simplification of Eq.(1) seems allowed. Apart from possible applications in cross shore transport cases, we restrict ourselves in the present paper to Eq.(1) (the longshore transport application).

According to Eq.(1) two topics affect the actual rate of sediment transport, viz.:

$v(z)$ - distribution over the water depth

$c(z)$ - distribution over the water depth

(see Fig.1).

In arbitrary coastal engineering applications $v(z)$ as well as $c(z)$ are highly dependent on the boundary conditions like wave height H, wave period T, water depth h, bottom particle size D_{50} and average current velocity v. Although some proposals for possible relationships can be found in literature, general accepted (and soundly proved) formulations are not yet available. That is, in fact, not surprising since many rather simple basic questions cannot be answered up till now. Some examples of these questions are:

- what is the effect of the grading of the bottom material on the c(z) distribution?
- do we understand the behaviour of different particle sizes in a same wave and current generated 'turbulence field' ?

Nielsen (1979) already mentioned the effect of the rate of grading of the bottom material on the apparent diffusion coefficient distribution over the water depth [$\varepsilon_s(z)$ - distribution]. Van de Graaff and Roelvink (1984) showed, with the help of some practical examples, that even in quite normal graded cases ($D_{90} / D_{10} \simeq 2$), completely different

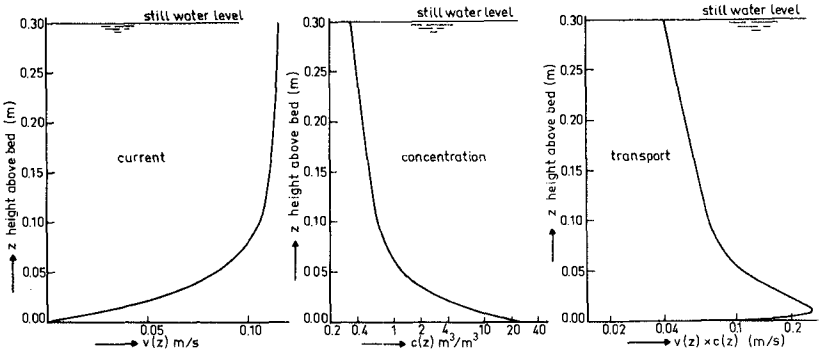

Fig.1 Velocity x concentration = transport

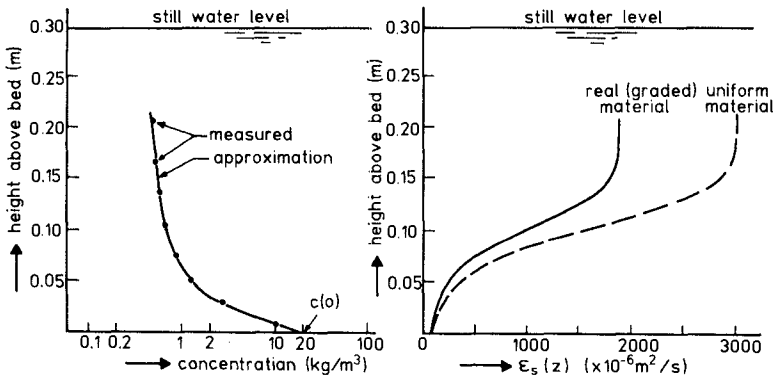

Fig.2 Effect of grading on $\varepsilon_s(z)$ distribution

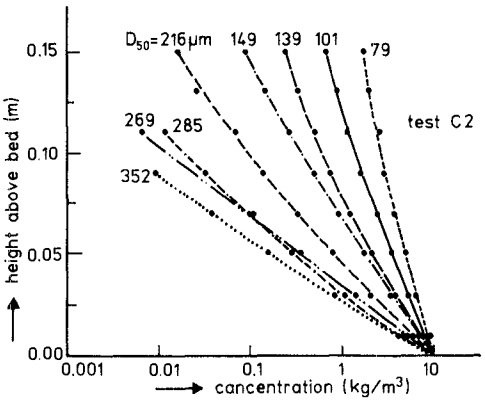

Fig.3 Concentration as function of diameter

$\varepsilon_s(z)$ distributions are found when the actual grading is taken into account in comparison with the $\varepsilon_s(z)$ distribution as calculated under the assumption of uniform bottom material.
Van de Graaff and Roelvink also mentioned a single test result from which it became clear that different particle sizes react quite unexpectedly on the same turbulence field (cf. second question). Since the answer on the second question affects the results arising from the first question, one should know the answer on the second question first.

In the present paper some results, of mainly experimental research in laboratory wave flumes, will be discussed. The tests are aimed to disclose the relationship between the diffusion coefficients holding for the fluid and for the sediment:

$$\varepsilon_s = \beta\, \varepsilon_f \tag{3}$$

where: ε_s : diffusion coefficient for sediment
ε_f : diffusion coefficient for fluid
β : factor.

It will turn out (see Section 2) that β depends (among others) on the sediment size.

Knowledge of the β-factor is important if one likes to know the c(z) distribution as mentioned earlier in the present Section.

In Section 3 some remarks will be made on the possible v(z) distribution for the combination of waves and currents.

2. The β-factor

A uniform flow, a pure horizontal oscillatory flow (e.g. in a wave tunnel), regular waves, irregular waves and a combination of waves and currents, in all cases, together with a sandy bottom, sediment suspensions will be formed in the water column.
When a steady state is considered, convective processes as well as diffusion effects will maintain the concentration distribution. For the time being the concentration distribution, even under wave conditions, will be described by the well-known diffusion equation:

$$w\, c(z) + \varepsilon_s(z)\, \frac{\partial\, c(z)}{\partial\, z} = 0 \tag{4}$$

where: w : fall velocity
c(z) : time averaged concentration at level z above the bed
$\varepsilon_s(z)$: diffusion coefficient for the sediment (function of z)
z : vertical upward directed ordinate; the bottom being z = 0.

It should be stressed that the parameter $\varepsilon_s(z)$ in Eq.(4) is, in fact, an auxiliary parameter in the description of the sediment concentration distribution. It is nearly for sure that not only diffusion processes maintain the concentration distribution.

When one 'knows' the $\varepsilon_s(z)$ distribution and a concentration at a certain level (e.g. the bottom concentration), the entire c(z) distribution can be calculated. However, it is impossible at the moment to predict the $\varepsilon_s(z)$ distribution as a function of the boundary conditions like H, T, h and v. Our knowledge is still completely insufficient to do that.

All over the world a mainly experimental approach is followed to acquire more insight in the concentration distribution. The next sequence is followed in that way:

- Measuring of c(z) distributions
- Find the characteristics of the underlying $\varepsilon_s(z)$ distribution
- Try to relate these characteristics to the boundary conditions
- Try to 'understand' the relationships as have been found.

In Fig.2b the resulting $\varepsilon_s(z)$ distributions are shown belonging to the real measured c(z) distribution as given in Fig.2a. From this example it becomes clear that it is quite important to take the real grading (D_{90} / D_{10} = 2 in this example) into account. Different $\varepsilon_s(z)$ distributions appear whether real graded or uniform material is taken into account. Many problems will undoubtedly arise in relating the boundary conditions with the $\varepsilon_s(z)$ characteristics as found when the real grading is not taken properly into account. [The present example holds for an irregular (non-breaking) wave case in a laboratory wave flume. Notice that even high in the water column apparently rather high diffusion coefficients are present. Straight forward 'theories' predict diffusion coefficients often in a restricted zone close to the bed only.] The diffusion coefficient distributions as found in Fig.2b hold strictly for the bottom sediment as applied. However, the 'fluid' may contain different diffusion coefficients [see Eq.(3)]:

$$\varepsilon_s(z) = \beta\ \varepsilon_f(z) \qquad (3a)$$

where: β : factor.

Depending on the value (or better: the behaviour) of β, one is able to derive the $\varepsilon_f(z)$ distribution from measured concentration distributions. In fact that $\varepsilon_f(z)$ distribution should be related to the boundary conditions. That is more realistic than such a relationship with $\varepsilon_s(z)$, since, depending on the behaviour of β, $\varepsilon_s(z)$ might be dependent on the particle size.

What about β ? If β = 1 (as sometimes is assumed, however, without sound evidence) things become rather simple. The Delft University of Technology has carried out many tests in wave flumes to disclose the β behaviour. In these tests the same mixing activity should be generated by the waves holding for different particle sizes. The dimensions of the bottom ripples (to be formed) will most likely affect the mixing activity. Since these dimensions depend on the particle size, tests with 'natural' sandy bottoms will not fulfill the requirements. In the tests, therefore, artificial roughness elements have been mounted on the flume bottom. During the tests a small amount of sand was maintained on the bottom. The amount was that small that no 'own'

ripples could be formed, but large enough to shape a measurable sediment concentration distribution over the water column. The concentrations have been derived from 'time- and bed averaged' suction samples [see Bosman (1982)]. The suction direction was perpendicular to the orbital plane. In that case the actual concentration differs from the measured one. However, if the intake velocity of the water-sand mixture is large enough compared with the orbital motion, a constant factor is found between measured and actual concentrations [Bosman et al. (1987)]. In the present paper concentration *distribution* aspects are considered rather than *absolute values*, so the application of correction factors is not necessary.

Up till now 3 series of tests have been carried out in several wave flumes (Delft Hydraulics and Delft University of Technology). In Table I the most important parameters of the tests have been summarized.

Test	Wave characteristics			Ripple characteristics			Number of bed materials
	h (m)	H (m)	T (s)	λ (m)	η (m)		
A1 DH	0.30	0.080	2.0	0.07	0.017	*	8
B1 DUT	0.30	0.081	1.5	0.08	0.020	+	5
B2	0.30	0.128	1.5	0.08	0.020	+	5
B3	0.30	0.092	2.5	0.08	0.020	+	5
B4	0.30	0.136	2.5	0.08	0.020	+	5
C1 DUT	0.30	0.064	1.7	0.08	0.020	*	8
C2	0.30	0.125	1.7	0.08	0.020	*	8
C3	0.30	0.044	2.3	0.08	0.020	*	7
C4	0.30	0.072	2.3	0.08	0.020	*	8
C5	0.30	0.142	2.3	0.08	0.020	*	7

Table I Characteristics of tests

Remarks : DH Delft Hydraulics
DUT Delft University of Technology
* triangular shape
+ sinusoidal shape plus steel angle sections
λ ripple length
η ripple height.

Fig.3 shows an example of a set of measured concentration distributions (test C2 of Table I). All test results have been normalized, yielding an (arbitrary) bottom concentration of 10 kg/m^3. The measuring points

have been approximated by a mathematical function according to the method as has been described by Van de Graaff and Roelvink (1984).

Fig.3 shows, as could be expected, a fan-shaped set of concentration distribution lines. The finer material goes 'easier' into suspension than the coarser material. Taking into account the (slight) grading of the bottom material, the apparent $\varepsilon_s(z)$ distributions of each of the bottom materials can be calculated with the help of Eq.(4).
Due to inevitable experimental scatter, quite identical $\varepsilon_s(z)$ curves for the different particle sizes cannot be expected. However, in reality distinct trends could be observed. In Fig.4 some examples of $\varepsilon_s(z)$ values (holding for a constant z level above the bed) are shown as a function of the fall velocity of the bed material. The values of w in Fig.4 correspond with the D_{50} values of the bed materials.

A theoretical basis is still lacking for this, but the measuring points in figures like Fig.4 can be approximated by a straight line. If it is allowed to extrapolate that line to w = 0 m/s, the intersection point can be considered as ε_f, the diffusion coefficient holding for the fluid. This consideration is rather speculative since the diffusion process of water particles will undoubtedly differ from that of very small sediment particles. Density differences between water and particles being a reason.
Lines like drawn in Fig.4 can be represented by (a least square fit procedure):

$$\varepsilon_s = \varepsilon_f + m\, w \tag{4}$$

where: ε_s : diffusion coefficient (sediment)
ε_f : diffusion coefficient (fluid)
m : slope of approximation line
w : fall velocity.

Eq.(4) can be compared with Eq.(3):

$$\varepsilon_s = \beta\, \varepsilon_f \tag{3a}$$

From Eqs.(3a) and (4) follows:

$$\beta = 1 + \alpha\, w \tag{5}$$

where: α : m/ε_f ; non-dimensionless parameter (α in s/m)

It can be seen from Eq.(5) that, depending on the α value (direction of slope m), $\beta > 1$ as well as $\beta < 1$ can be found. Furthermore the actual β value depends on the fall velocity of the bed material.

For many points in a vertical ε_f and α values have been determined for each of the tests. Each $\varepsilon_f - \alpha$ combination has been plotted in Fig.5. A lot of scatter can be seen. It is, however, clear that for relatively small ε_f values positive α values are predominant. For large ε_f values negative α values occur.

Fig.6 shows a typical $\varepsilon_f(z)$ distribution as could be derived for test B2 from Table I. Notice again the relatively large $\varepsilon_f(z)$ values high in the vertical; these values are large in comparison with the $\varepsilon_f(z)$ values close to the bed.

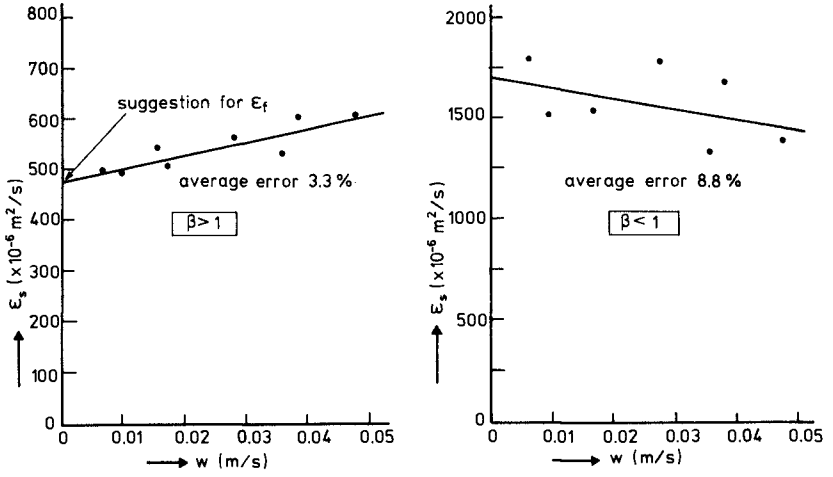

Fig.4 ε_s as function of fall velocity

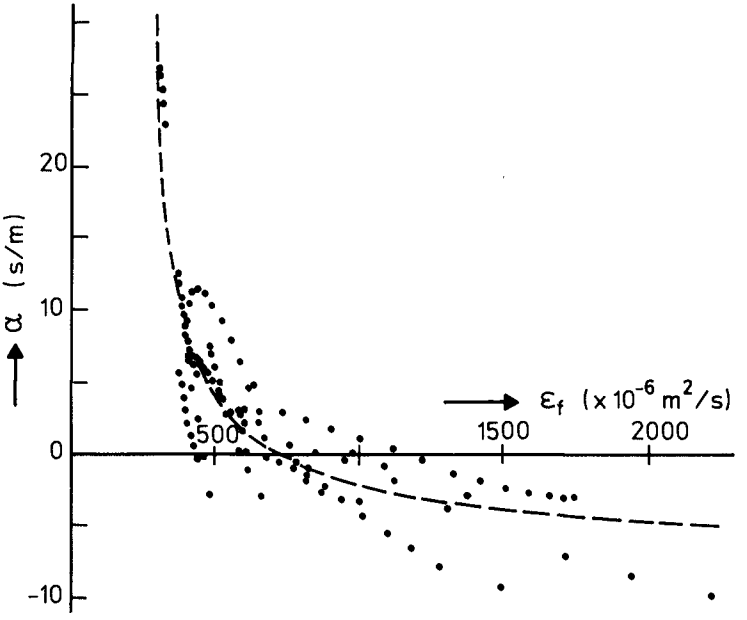

Fig.5 Effect of ε_f on α value

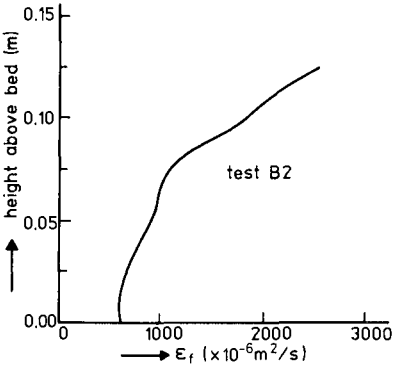

Fig.6 Typical ε_f distribution

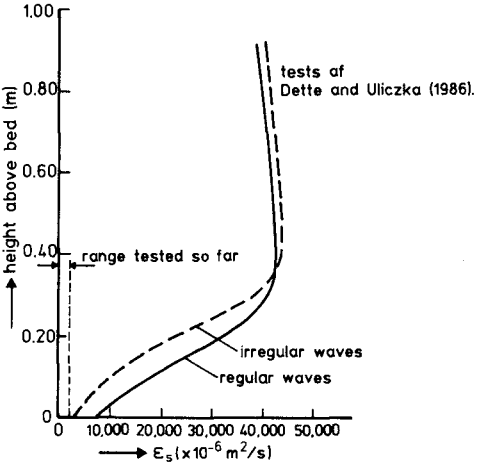

Fig.7 ε_s for large scale tests

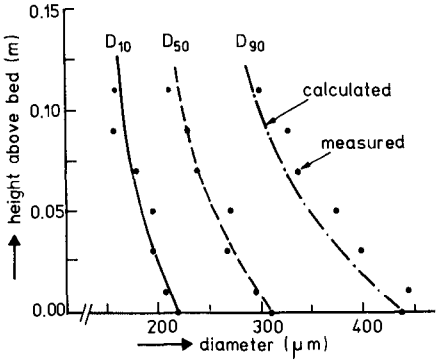

Fig.8 Degradation

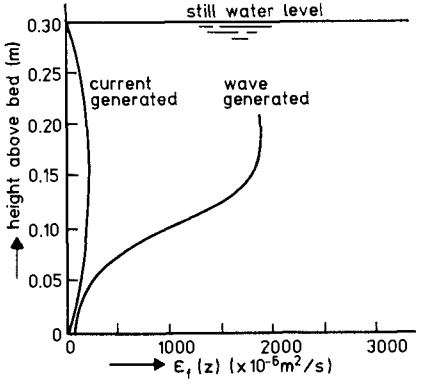

Fig.9 Wave- and current generated ε_f distributions

A convincing explanation for the results of Fig.5 with respect to α (and thus β) cannot yet be given. However, some remarks can be made. Probably the behaviour of α as a function of ε_f is related to the position above the bed. The relatively smaller ε_f values are normally present close to the bed (cf. Fig.6). Due to the 'rippled' bottom, eddies are formed in the bottom layer. These eddies (laden with bottom particles) move as a whole in an upward direction during some phases of the orbital motion. During these phases distinct convective transport processes occur through which, also in the tests with coarse bottom material, the particles can reach rather high levels. Such a process has the same effect as if rather high diffusion coefficients occur for coarse material, thus leading to $\beta > 1$.
Far from the bed (in most cases the zone with relatively large ε_f values) the bottom generated eddies have lost their energy. Probably there occurs a more or less 'normal' diffusion concept according to Eq.(4). In that case $\beta = 1$ could be expected. At this moment the authors cannot formulate a reliable explanation for $\beta < 1$ for these high ε_f values.

The research in the behaviour of β is far from ended. Up till now only some first ideas have been found. The range of ε_f values as have been encountered during the present test series is, in fact, very restricted. For practical applications in future, insight in the behaviour of α for far larger ε_f values should be acquired. That can be demonstrated with the results of some tests by Dette and Uliczka (1986) carried out in the large wave flume of Hannover ($H \simeq 1.5$ m).

Fig.7 shows the ε_s distribution as have been derived from two series of sediment concentration distribution measurements. The analyses have been carried out with the assumption of $\beta = 1$. Fig.7 shows ε_s values in a total different range compared with these found during the tests as discussed so far.

More or less as a by-product of the calculation methods as have been used, the degradation over the water column of the bottom material can be computed. Fig.8 shows a confrontation between computation results and measurements. The rather good fit seems to support to some extent the diffusion-type description of the tests.

3. The v(z) distribution

From the analyses as have been discussed in Section 2 also so-called $\varepsilon_f(z)$ distributions are found (cf. Fig.6 and Fig.7 to some extent). The shape of these distributions is in many cases quite different from 'theoretical' $\varepsilon_f(z)$ distributions as can be found in literature. An $\varepsilon_f(z)$ distribution is frequently used to derive the horizontal velocity distribution over the water depth, viz.:

$$\tau(z) = \rho\ \varepsilon_f(z)\ \frac{\partial\ v(z)}{\partial\ z} \qquad (6)$$

where: $\tau(z)$: shear stress at level z above the bed

ρ : density of the fluid

$\varepsilon_f(z)$: diffusion coefficient (fluid) at level z

$v(z)$: horizontal current velocity at level z

z : vertical upward directed ordinate; the bottom being $z = 0$.

The well-known logarithmic velocity distribution for uniform current is, for instance, found with a triangular $\tau(z)$ distribution [$\tau(z=0)$:maximum; $\tau(z=h)$:zero] and a parabolic $\varepsilon_f(z)$ distribution (ε_f reaches its maximum value for $z = \frac{1}{2} h$).

The test results as have been discussed in Section 2 yield $\varepsilon_s(z)$ [and $\varepsilon_f(z)$] distributions 'generated' by waves only. Waves are obviously able to maintain sediment concentrations at levels rather high above the bed. It can be *assumed* (only an assumption can be made for the time being since a sound proof and verification is still missing) that waves are also very effective in transferring shear stresses in cases of a combination of waves and currents. If that assumption is true, a practical calculation example can clarify the consequences.
The graded material $\varepsilon_s(z)$ distribution of Fig.2b strictly holds for the particular sediment and for waves only. It is, however, assumed that this distribution can be considered as an $\varepsilon_f(z)$ distribution (so taking $\beta = 1$) which holds also for a combination of that wave and a modest current making an arbitrary angle with the wave propagation direction. The distribution of $\varepsilon_s(z)$ in Fig.2b holds for a water depth $h = 0.30$ m and a maximum orbital velocity near the bed, $\hat{u}_o \simeq 0.2$ m/s. The mean velocity of the current is assumed to be $\bar{v} = 0.1$ m/s. Fig.9 shows also the $\varepsilon_f(z)$ distribution which belongs to a mere current situation with $\bar{v} = 0.1$ m/s. It can be seen that the wave generated $\varepsilon_f(z)$ distribution reaches far larger values than the mere current $\varepsilon_f(z)$ distribution. In the further analysis it is assumed that the current contribution can be neglected in comparison with the wave contribution. The resulting $\varepsilon_f(z)$ distribution is not parabolic at all and together with a triangular $\tau(z)$ distribution a non-logarithmic $v(z)$ distribution (with $\bar{v} = 0.1$ m/s) will be found (see Fig.10).

Up till now a physical verification is not yet carried out. Tests are in preparation by the Delft University of Technology. Just to show at least the qualitative agreement, in Fig.11 a comparison has been made between the calculated curve of Fig.10 and actual measurements of Van Doorn (1981) with only roughly comparable boundary conditions. [Same water depth; same average velocity; regular waves with slightly different characteristics; artificial roughness elements instead of natural rippled bed.]

It will be clear that a velocity distribution like Fig.10 has severe consequences for the resulting sediment transport. A quite different transport will be calculated in that case in comparison with a situation where a logarithmic velocity distribution is assumed.

Since only some first thoughts are formulated, all implications cannot be overseen at the moment by the authors.

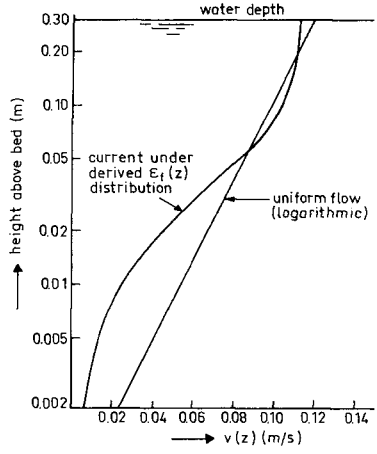

Fig.10 Velocity distributions

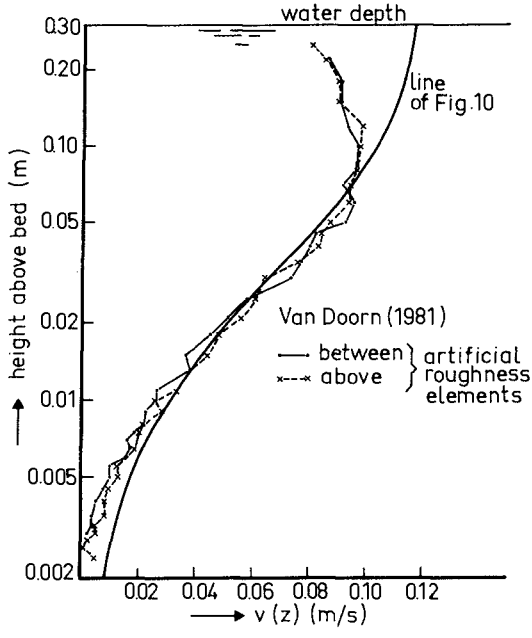

Fig.11 Measured and 'theoretical' distributions

4. Conclusions

- Wave flume tests with artificial roughness elements and different sediment sizes have revealed that the diffusion coefficient distribution for the sediment $\varepsilon_s(z)$ is different for different particle sizes.
- With $\varepsilon_s = \beta \cdot \varepsilon_f$ this means that β differs from unity. Cases with $\beta > 1$ and $\beta < 1$ have been found, probably also depending on the 'level' of ε_f (the diffusion coefficient for the fluid).
- A sound explanation of the behaviour of the β-factor cannot be given at the moment.
- The wave generated diffusion coefficients are far larger than the mere current contribution.
- If a combination of waves and current is considered and the wave generated diffusion activity is also available to transfer shear stresses, a velocity distribution can be calculated which differs totally from a logarithmic distribution. If those ideas are true, te resulting sediment transport will also be affected.
- Verification tests are in preparation by the Delft University of Technology.

Appendix 1 - References

BOSMAN, J.J. (1982)
Concentration measurements under oscillatory water motion.
Delft Hydraulics Laboratory/TOW Report on model investigation.
M 1695 part 2, Delft, February 1982.

BOSMAN, J.J. (1986)
An optical instrument for local concentration measurements in-situ.
Proceedings Int. Symposium on Measuring Techniques in Hydraulic Research (22-24 April 1985).
A.A. Balkema/Rotterdam/Boston 1986.

BOSMAN, J.J., E.T.J.M. van der VELDEN and C.H. HULSBERGEN (1987).
Sediment concentration measurement by transverse suction.
To be published in Elseviers Coastal Engineering.

DETTE, H.H. and K. ULICZKA (1986)
Velocity and sediment concentration field across surf zones.
To be published in Proceedings 20th ICCE, Taipei, Taiwan.

DOORN, Th. van (1981)
Experimental investigation of near-bottom velocities in water waves without and with a current.
Delft Hydraulics Laboratory/TOW Report on model investigation.
M 1423 part 1 and 2, Delft, July 1981.

GRAAFF, J. van de and J.A. ROELVINK (1984)
Grading effects in concentration measurements.
Proceedings 19th ICCE. Part II, Chapter 110, Houston.

NIELSEN, P. (1979)
Some basic concepts of wave sediment transport.
Series paper 20 ISVA. Technical University of Denmark. January 1979.

STIVE, M.J.F. and J.A. BATTJES (1984)
A model for offshore sediment transport.
Proceedings 19th ICCE. Part II, Chapter 97, Houston.

CHAPTER 68

RANDOM BREAKING WAVES - HORIZONTAL SEABED

HANS PETER RIEDEL[1] & ANTHONY PAUL BYRNE[2]

ABSTRACT

According to wave theories the depth limited wave height over a horizontal seabed has a wave height to water depth ratio (H/d) of about 0.8. Flume experiments with monochromatic waves over a horizontal seabed have failed to produce H/d ratios greater than 0.55. However designers still tend to use H/d 0.8 for their design waves. Experiments have been carried out using random wave trains in the flume over a horizontal seabed. These experiments have shown that the limiting H/d ratio of 0.55 applies equally well to random waves.

1. INTRODUCTION

Coastal structures are often located in water depths where the limiting wave height is determined by the maximum water level at the toe of the structure. In Australia there are many regions, particularly those with high tidal ranges, where the approach to a proposed coastal structure site has a slope in the range of 1 in 100 or flatter. Presently the breaking wave height used for design by a large percentage of designers is based on Coastal Engineering Research Centre (1984). For near horizontal seabeds the value of H/d is based on classical theories for wave breaking such as McCowan (1894).

However when monochromatic waves have been propagated over horizontal beds in flume studies, the researchers have typically found that a H/d ratio of 0.78 cannot be obtained. Nelson (1983) reviewed the available literature and presented the results of flume studies on wave breaking on horizontal and near horizontal seabeds. He found that for seabed slopes of 1:250 and flatter the H/d ratio did not exceed 0.55. Published data thus far has been for monochromatic waves.

The difference between a H/d ratio of 0.55 and 0.78 will have an enormous impact on the design wave possible on a coastal structure. In order to start applying these less conservative methods for estimating design waves it is important to ensure that random waves occurring in nature behave in a similar manner to monochromatic waves.

1, 2. Directors of Riedel and Byrne Consulting Engineers P/L
1. 146 Leichhardt Street, Spring Hill, Qld., Australia.
2. 396 Rokeby Road, Subiaco, W.A., Australia.

The study and results presented in this paper provide a start to extending the range of applicability to random waves. A limited number of tests were undertaken, for a horizontal seabed and for a slope of 1:100.

2. EXPERIMENTAL PROCEDURE

The wave flume at the Manly Hydraulics Laboratory of the Public Works Department, N.S.W. was used. Random and monochromatic wave generation is possible. The flume is 30m long, 1m wide and 1.4m deep. The bed is constructed of 1.5m long segments, each segment being supported by a pair of screw jacks. The flume floor can be jacked up to form any desired seabed profile. The slopes used in the test section were a horizontal bed and a 1:100 slope.

Near the paddle, the flume is 2m wide, allowing waves to be generated which will be large enough to retain their height after passing through a wave filter in a transition section.

An aluminium sliding wedge mounted on linear bearings is used as the wave paddle. Driving the paddle is a two sided hydraulic piston, whose position is controlled by a servo valve. The servo system consists of the servo valve, a linear voltage displacement transducer for feed back and the servo electronics, which compare the feedback signal with a drive signal provided by a PDP-11 computer.

Waves were generated in relatively deep water and propagated up an approach ramp to the test section. A beach with a reflection coefficient of less than 10% was used to dissipate the waves.

The floor of the flume was accurately levelled to ensure that the test section was horizontal or had a slope of 1:100 for at least 3 wavelengths (based on the peak period of the spectrum) between the approach ramp and the measurement station. Figure 1 shows a typical test arrangement.

Most of the tests were done with random waves with peak periods of 8 to 12 seconds at a model scale of 1:40. A Pierson - Moskowitz spectral form was adopted and its shape modelled on measured wave spectra during cyclones off the north Australian coast. All results are quoted in prototype dimensions. Some comparative tests with 8 to 14 second monochromatic waves were also completed.

For each test, measurements of wave heights were made by a series of capacitance wave probes along the flume. With random waves it is not possible to pick the section at which the wave is likely to break so the limiting wave heights were obtained by extracting the maximum wave height from a number of sections for each test over a 20 minute sampling period. For monochromatic waves the wave generator was adjusted progressively until the waves first began to break over the test section.

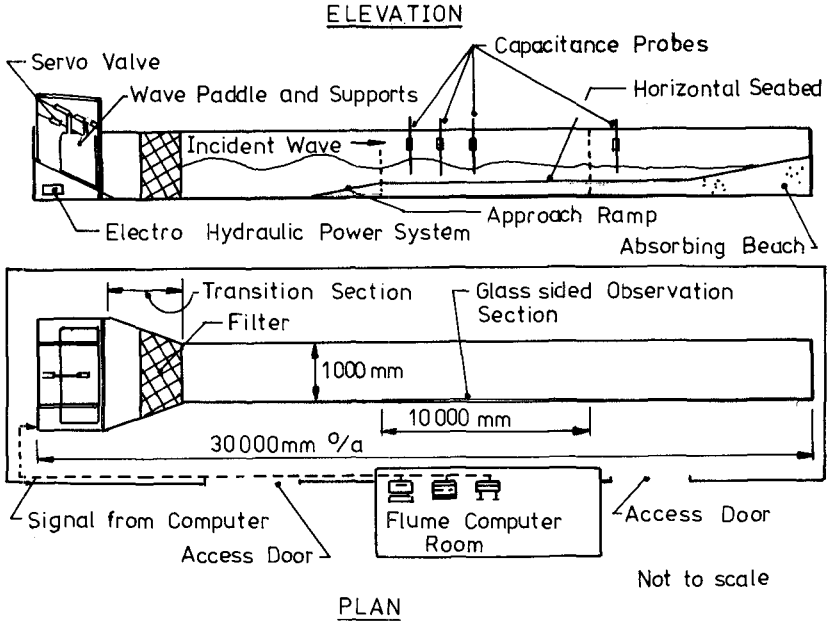

Figure 1. Experimental Setup.

Videotape recordings were made of a number of tests to assist in the interpretation of the results. A measured grid was marked on the side of the flume.

3. EXPERIMENTAL RESULTS

The most convenient method of presenting results in terms of measurable parameters is to use the non-linearity parameter (Fc) of Swart and Loubser (1979). This parameter is a function of T(wave period), d and H.

$$Fc = \left(\frac{H}{d}\right)^{0.5} \left[T\left(\frac{g}{d}\right)^{0.5}\right]^{2.5}$$

Waves of equal Fc have approximately the same relative wave shape.

Table 1 summarizes the results obtained for a horizontal bed. There are 3 data points for each peak period representing three different energy levels in the spectrum. At the lowest energy level only a few waves passed through unbroken. At each higher energy level the proportion of breaking waves increased.

TABLE 1.
TEST RESULTS

Test No.	Wave Type	Peak or Nominal Period	Energy Level	$\frac{Hmax}{d}$	Fc
1	Random	8	Low	0.46	50
2	Random	8	Medium	0.49	52
3	Random	8	High	0.44	49
4	Random	10	Low	0.50	92
5	Random	10	Medium	0.52	93
6	Random	10	High	0.53	94
7	Random	12	Low	0.54	150
8	Random	12	Medium	0.52	147
9	Random	12	High	0.52	148
10	Random	8	Low	0.48	52
11	Random	8	Medium	0.47	51
12	Random	8	High	0.52	54
13	Random	12	Low	0.49	143
14	Random	12	Medium	0.53	148
15	Random	12	High	0.52	148
16	Monochromatic	9	-	0.55	74
17	Monochromatic	10	-	0.56	97
18	Monochromatic	11	-	0.52	118
19	Monochromatic	12	-	0.51	146
20	Monochromatic	13	-	0.55	185

For the random waves the highest value of H/d measured was 0.54 and the values ranged from 0.44 to 0.54. The monochromatic waves had H/d ranging from 0.51 to 0.56 which is in agreement with Nelson's (1983) conclusions.

The tests for random waves over the horizontal seabed show a weak dependent of H/d on Fc. Note that the second sets of test results for each wave period correspond to different cut-off frequencies for the spectrum.

Figure 2 shows our data superimposed on the results presented by Nelson (1983). It is evident that for waves within a random wave train the limiting value of H/d is 0.55. There appears to be slightly less dependence on the non-linearity parameter than shown for experiments with monochromatic waves.

△ Nelson, slope 0.0000, data set 1.
▲ Nelson, slope 0.0000, data set 2.
x Mehaute, slope 0.0000.
■ Keating and Webber, slope 0.0000.
· others, slope 0.0000 (see text and Table 1).
○ Nelson, slope 0.00286.
□ Goda, slope 0.0100.
● Nelson, slope 0.0153.

Limiting Criteria

— — — Shore Protection Manual, slope 0.0100 (based on experimental data).
--------- Shore Protection Manual, slope 0.0000 (based on theory).
———— Nelson, slope 0.0000 (based on experimental data).

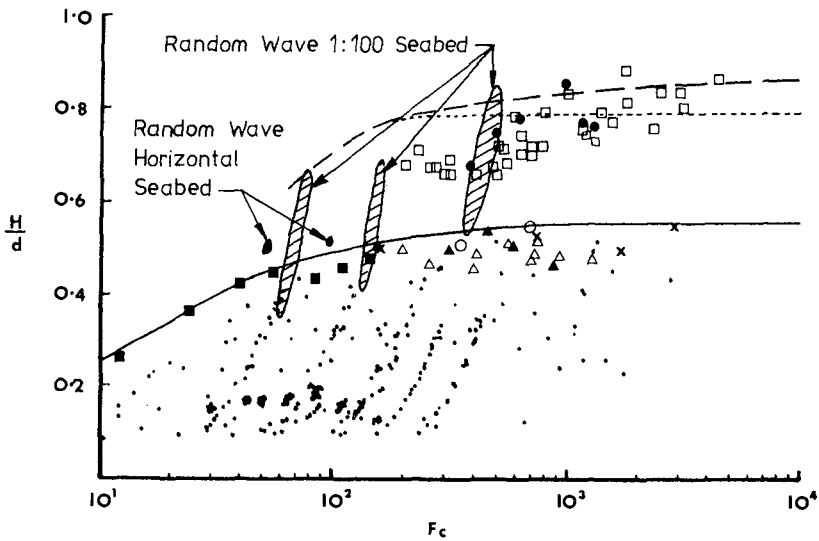

Adapted from Nelson 1983

Figure 2. H/d versus Fc.

In a separate set of tests about a year before the above tests were undertaken, some observations were made of the limiting breaking wave heights on 1:100 slope. The same facility and wave spectra were generated as described above. These tests produced a range of wave height to water depth ratios which showed quite a strong dependence on Fc. These observations were made less rigorously than the test results already discussed. Wave heights and water depth were measured off replays of video tapes.

The results are also shown on Figure 2.

4. DISCUSSION AND CONCLUSIONS

The ratio of limiting wave height to water depth over a horizontal seabed is 0.55 for both monochromatic and random waves. This can be important in the determination of extreme waves in shallow water where the seabed is horizontal or nearly horizontal. These results apply to a unidirectional wave train.

At slopes of 1 in 100 there is already a significant increase in the ratio of H/d and there is also a dependence on the non-linearity parameter Fc.

The extent of testing undertaken was limited and there may be other wave spectral forms that will not produce the same results. The spectra adopted here related to measured spectra in the area where the results were applied.

Most real sea conditions consist of more than one wave train where each wave train has an independent wave direction. It is not clear whether the same limits of H/d would apply. Also superimposed steady currents may have an influence.

There is an urgent need for continued research of depth limiting breaking wave heights

5. REFERENCES

Coastal Engineering Research Centre (CERC) 1984 "Shore Protection Manual", U.S. Army.

McCowan, J. (1894) "On the Highest Waves of a Permanent Type". Philos. Mag. Ser 5, Vol. 38.

Nelson, R. C. (1983). "Wave Heights in Depth Limited Conditions". Civil Engineering Transactions, Inst. of Eng. Australia, Vol. C.E. 27, No. 2.

Swart, D. H. and Loubser, C.C. (1979). "Vocoidal Wave Theory : Vol. 2 : Verification". Coastal Engineering and Hydraulics Division, National Research Institute for Oceanology, Council for Scientific and Industrial Research, Republic of South Africa, Research Report No. 360.

CHAPTER 69

Influence Of Breaker Type On Surf Zone Dynamics

A.S.Arcilla, A.Vidaor and J.L.Monso *

1.Introduction

Two of the most significant variables for surf zone hydrodynamic analyses are the mean rate of wave energy dissipation, D, and the longshore current velocity, Vl . A detailed theoretical model is extremely difficult to establish (definition of bottom and free surface boundaries, stochastic forcing terms, intense turbulent mixing, etc). The type and amount of existing measured values (laboratory and field) also preclude any accurate calibration, particularly for the more complex formulations.

The paper, therefore, presents an average (cross-shore) comparison among state-of-the-art models for D and Vl. This illustrates the dependence of these variables on the surf zone dynamic state (closely related to the beach stage, (Short, 1978)), characterized by Iribarren's parameter, Ir. Well defined relationships with Ir are obtained for these variables. An expansion of the range of validity of certain models is also attained by calibration of their characteristic free parameters as functions of Ir using a large set of field and laboratory data, and by comparing their general expresion with that of (Losada and S.Arcilla, 1985), which does not include any free parameter.

Therefore, theoretical laws for D and Vl as simple functions of beach, wave and dynamic state parameters are presented, together with an improved estimation of the empirical coefficients appearing in the various models, suitable for prediction in all ranges of Ir, even though data on the collapsing-surging range are scarce and should require further calibration.

2.Rate Of Wave Energy Dissipation (D)

No complete theoretical models for the rate of wave energy dissipation (i.e. including bottom friction and percolation, turbulent mixing, front roller, etc.) are nowadays available. Most of them just consider turbulent (mixing) dissipation and have been indirectly calibrated, via the computed longshore current velocity or transport, the corresponding wave attenuation and set-up, etc., as local values of D require accurate local measurements (difficult to encounter).

To get a better insight of the relationship between D and the dynamic state, a cross-shore average value, $\bar{D}$,has been derived from the selected models. It has been obtained assuming stationary and longshore

* A.S.Arcilla, A.Vidaor and J.L.Monso. Harbour and Coastal Eng. Dept., E.T.S.I.C.C.P. Univ. of Catalonia in Barcelona, 31 Jordi Girona Salgado, 08034 Barcelona.

uniform conditions together with a constant bottom slope, m :

$$\bar{D} = \frac{1}{xb} \int_0^{xb} D(x)dx \qquad (1)$$

$\bar{D}$ being the average (cross-shore) value for D , and xb the width of the surf-zone. It is shown that this value is easily related to the dynamic state via the Iribarren's parameter Ir (or Irb when referring to breaking conditions), defined as:

$$Ir = m / (H/Lo)^{1/2} \qquad (2)$$

where m is the bottom slope (assumed to be constant through surf-zone), H wave height and Lo the deepwater wave length.

To get a better insight of the relationship between D and the dynamic state, a non-dimensional value, $\hat{D}$, is defined, refering $\bar{D}$ to an order of magnitude rate of wave energy dissipation Do:

$$Do = \rho g \frac{Hb^2}{T} \qquad (3)$$

where T is the wave period, g is the gravity acceleration and ρ is the water density.

Do may be obtained from dimensional analysis or bore (hydraulic jump) dissipation theory. This reference value can be also obtained via an energetic balance in the surf zone, relating eddy viscosity coefficients to wave energy dissipation:

$$D \; < > \; \text{Stress x velocity} \qquad (4)$$

Characteristic stresses for this problem are, typically, the Reynolds stresses (related to eddy viscosity coefficients):

$$\tau_r = - \rho \overline{u' v'} = - \rho A \frac{dV}{dx} \qquad (5)$$

where A is the eddy viscosity coefficient, and u', v' are the (x,y) components of the turbulent velocity. The eddy viscosity coefficient has the dimension of a typical length times a typical velocity:

$$A \sim l \, . \, V' \qquad (6)$$

Following (Harris et al, 1962) typical scales for length and velocity can be respectively H and H/T . The eddy viscosity coefficient must therefore be of order H^2/T .

The characteristic velocity, V', is assumed to be a typical scale of the turbulent velocity, that can be related, in the surf zone, to the shallow water wave celerity:

$$V' \simeq \hat{B} (g\ hm)^{1/2} \qquad (7)$$

where $\hat{B}$ is a dimensionless constant accounting for breaker type (therefore related to Ir) and hm is an average or characteristic depth through the surfzone.

The energetic balance can be set as in (Battjes, 1975):

$$\frac{\text{Rate of wave energy dissipation}}{\text{Area}} = \frac{\text{Rate of turbulent energy produced}}{\text{Area}} =$$

$$= \frac{\text{Rate of turbulent energy dissipated}}{\text{Area}}$$

(neglecting bottom friction, percolation or any other dissipation phenomena than turbulence).

From this and (5):

$$D < > \text{Stress} \cdot \text{velocity} = \rho A \frac{dV}{dx} \cdot V' \qquad (8)$$

Following the control volume approach presented in (Losada, S.Arcilla and Vidal, 1986) to estimate the partial derivative in (8), the rate of wave energy dissipation can be written as follows:

$$D = \rho A \frac{Vlb}{xb} \cdot \hat{B} (g\ hm)^{1/2} \qquad (9)$$

Vlb being the longshore current velocity at the breaker line, depending on wave, beach and dynamic state parameters.

Assuming (Losada, S.Arcilla and Vidal, 1986) that A , $\hat{B}$, and other parameters involved in the Vlb formulation (γ,Kr,etc.) are Ir functions, it is easy to show that:

$$\frac{D}{\rho g A} = F(Ir) \cdot \cos \Theta b \qquad (10)$$

where Θ is the angle of wave incidence.

In this dimensionless equation F(Ir) is a known function that comes from the formulation used to evaluate Vlb. If we choose (Losada, S.Arcilla and Vidal, 1986), $F(I_r)$ can be written as follows:

Author	$\hat{0}$	Free parameters and order of magnitude or suggested values
Longuet-Higgins, 1970	$\frac{(2\pi)^{1/2}}{8}\gamma^{1/2}\,Irb$	---
Losada, S.Arcilla and Vidal, 1986	$\frac{(2\pi)^{1/2}}{8}\gamma^{1/2}\,(1-Krb^{2})\,\cos\theta b\;Irb$	---
Dally, Dean and Dalrymple, 1984	$\frac{(2\pi)^{1/2}}{8}\gamma^{1/2}\,Irb$	---
Battjes, 1978	$\beta\cdot\frac{B\gamma_B^4}{4\,(0,7+5m)}\;,\beta=0,1134$	$B\sim O(1)$ or $B\gamma_B^4\sim O(1)$
Battjes and Janssen, 1978	$\frac{1}{xb}\int_0^{xb}\left[1-\frac{\alpha}{4}Qb\,.\left(\frac{Hm}{Hrms}\right)^2\right]dx$	$\alpha\sim O(1)$
Stive, 1982	$\beta\cdot\frac{\gamma}{4}\,.\,A_\varepsilon\;Ad$	$A_\varepsilon\sim$ 2tanh (5 Iro) or 2tanh (5 Irb) if Irb < 0,4
Svendsen, 1984	$\beta\cdot\frac{\gamma}{4}\,.\,As\left[1+\gamma\left(\frac{\eta c}{H}\right)\left(1+\gamma\left(\frac{\eta c}{H}-1\right)\right)\right]^{-1}$	$As\sim O(1)$
Guza and Thornton, 1985	$\frac{1}{xb}\int_0^{xb}\left[\frac{3(\pi)^{1/2}}{16}\,.\,B^3\,\gamma\,\left(\frac{Hrms}{Hb}\right)^2\right]dx$	$B\sim O(1)$ or $B^3\sim O(1)$

Table 1. Expressions of non-dimensional average rate of wave energy dissipation, D, as functions of Irb dependant variables, for various analytical models.

$$F(Ir) = \frac{\hat{B} \cdot \tilde{A}}{4 \quad (2)^{1/2}} \cdot \gamma^{1/2} \cdot (1-Kr^2)\, m^2 \qquad (11)$$

where Kr is the reflection coefficient and γ is the breaker index.

Then, assuming that $A \simeq H^2/T$, it follows that:

$$\frac{D}{\rho g H^2/T} = F(Ir) \cdot \cos \theta b \qquad (12)$$

and the reference rate of wave energy dissipation, Do, can be correctly expresed by $\rho g H^2/T$.

Using this reference value, average non-dimensional expressions for the rate of wave energy dissipation can be obtained for all formulations considered, even though some of them require numerical evaluation. These expressions are shown in table 1, together with their free parameters, suggested values for them, and range validity. The dimensionless $\hat{D}$ values are known functions of parameters that depend on Ir. It follows that $\hat{D}$ itself is a function of Ir for all models.

The only formulation including reflection and large angles of wave incidence, without any free parameters, and being valid for the whole range of Ir values, is that of (Losada, S.Arcilla and Vidal, 1986). It will be, therefore, compared to other models to enlarge their range of validity via an estimation of their free parameters as functions of Ir. Values of Kr are taken from (Battjes, 1974). The comparison is made numerically in all cases using laboratory and field data taken from:

Laboratory (Putnam, Munk and Traylor, 1949) (Galvin and Eagleson, 1965) (Mizuguchi et al., 1978) (Kamphuis and Readshaw, 1978) (Vitale, 1981) (Kamphuis and Sayao, 1982)

Field (Komar and Inman, 1970) (Kraus and Sasaki, 1978) (Kraus, Isobe et al, 1982) (Guza and Thornton, 1983)

Results from (Losada, S.Arcilla and Vidal, 1986), (Battjes and Janssen, 1978) and (Guza and Thornton, 1985) are shown in figures 1a to 1c, as an example of the results of some of the models analysed.

To test the models, wave, beach and dynamic state measured parameters are used to estimate the average non-dimensional rate of wave energy dissipation. It is shown that $\hat{D}$ is greater for laboratory than for field data, because viscosity and bottom efects are overestimated in laboratory tests.

The adjustment of free parameters as Ir functions is shown in Table 2. Figures 2a to 2c illustrate the results for (Battjes and Janssen, 1978), (Stive,1982) and (Guza and Thornton, 1985) models, being an example of the fit made for all models.

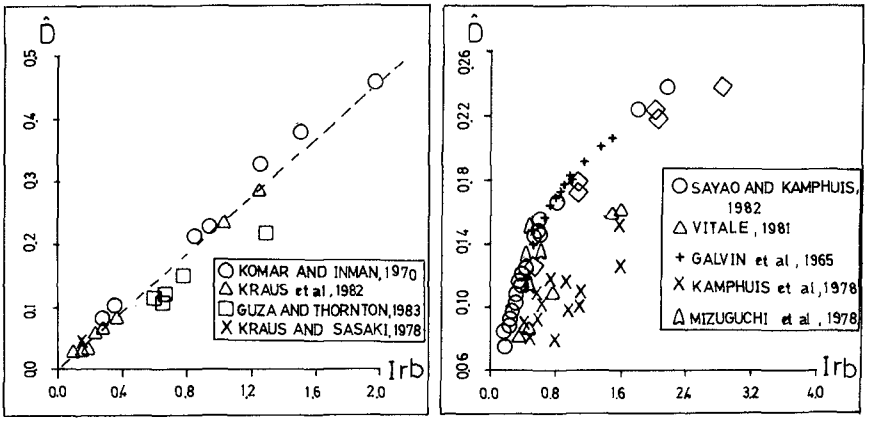

a) b)

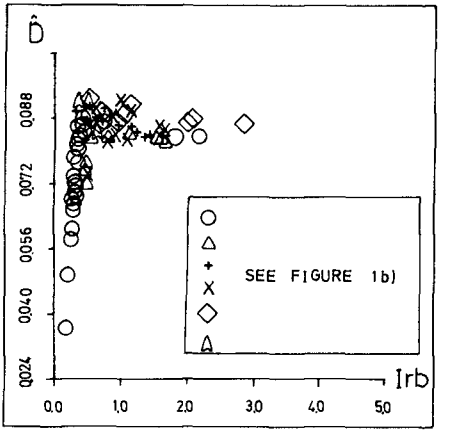

c)

Figure 1. Results of non-dimensional average rate of wave energy dissipation ,$\hat{D}$, for:

a)(Losada,S.Arcilla and Vidal,1986) model.Field data.

b)(Guza and Thornton,1985) model.Laboratory data.

c)(Battjes and Janssen,1978) model.Laboratory data

Author	Free parameter	Initial value of original range of validity	Proposed adjusted value	
			Laboratory	Field
Battjes, 1978	8	1.... 2	5.875 Irb	4.800 Irb
(regular waves)	$8\ \gamma_B^4$	1.... 2	$12.862\ Irb^2$	$7.706\ Irb^2$
8attjes. Janssen,1978	α	0(1)	1.000 Irb ⩽ 0.4	1.100 Irb ⩽ 0.4
(irregular waves)			3.680.Irb Irb > 0.4	2.583.Irb Irb > 0.1
Stive. 1982	A_ε	A_ε = 2 tanh (5Iro)	4.24 Irb	5.000 Iro
Svendsen, 1984	As	1	5.100 Irb	8.000 Irb
Guza , Thornton, 1985	8^3	0(1)	1.875 Irb	2.474 Irb

Table 2. Expressions of free parameter adjustements for all analytical models. obtained by comparison to (Losada and Sanchez-Arcilla and Vidal, 1986) formulation.

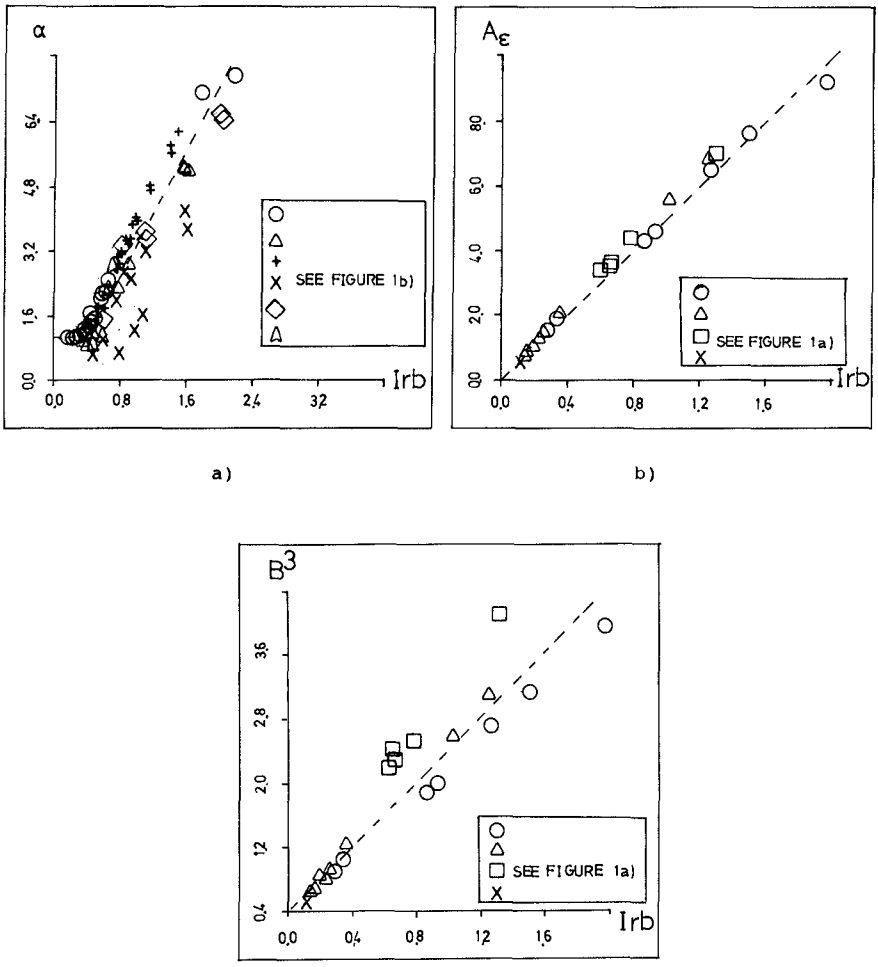

Figure 2. Results of the adjustment of the free parameters:

a) α (Battjes and Janssen,1978),laboratory data

b) A_ε (Stive,1982),field data

c) B (Guza and Thornton,1985),field data

as functions of the Iribarren's parameter Irb

As final remark, a bell-shaped behavior is expected for $\hat{D}$ vs Ir due to:

- incipient spilling breakers, corresponding to low Ir values, produce small dissipation per unit horizontal area (wide surfzone together with a small depth affected by turbulence)

- collapsing-surging breakers, in the higher Ir range, produce small dissipation per unit horizontal area (highly reflecting beach conditions).

- maximum dissipation corresponds to late spilling and plunging breakers, generating maximum turbulence

3. Longshore Current Velocity

Analytical (state-of-the-art) models for the longshore current velocity are based on time and vertically-integrated conservation equations for stationary and longshore uniform conditions with constant beach slope. Most of them also use shallow water linear wave theory.

All formulations depend on two poorly known coefficients, each representing one of the two main retarding terms considered in the momentum balance equation:

- cf, bottom friction coefficient

- M, lateral mixing coefficient, related to eddy viscosity

From the given definition for Iribarren's parameter Ir, (2), an Ir-dependent expression for Vlb may be obtained for each of the selected longshore current velocity models (Table 3). These equations depend on Ir directly or via other parameters related to it (γ, Kr, etc).

From these expressions and order of magnitude considerations, a reference velocity Vo can be defined to obtain a non-dimensional value for Vl:

$$Vo = \frac{Hb}{T} \sin \theta b \qquad (13)$$

$$\hat{V} = Vl / Vo = \frac{Vl}{(Hb/T \cdot \sin \theta b)} \qquad (14)$$

Testing these formulae with the set of data mentioned in section 2, general trends for a relationship between Vlb and Irb may be obtained (an example of them being figure 3):

- lower values of Vlb appear associated to incipient spilling breakers (low range of Irb values)
- stabilized or decreasing values for collapsing-surging breakers (high values of Irb)
- maximum values for Vlb are attained for late spilling and plunging

Author	$\hat{V} = V_{lb} / V_o = V_{lb} / (H_b/T \cdot \sin\theta_b)$	parameters
Longuet-Higgins, 1970	$\frac{(50\pi^3)^{1/2}}{16} \cdot \frac{\gamma^{1/2}}{cf} \cdot \left[P\,(1-P1)(P1-P2)\right]^{-1} \cdot I_{rb}$	$P = \frac{\pi N_m}{\gamma cf}$, $P1 = -3/4 + (9/16+1/P)^{1/2}$, $P2 = -3/4 - (9/16+1/P)^{1/2}$
Losada, S.Arcilla and Vidal, 1985	a) linear bottom friction law: $\frac{3\,(2\pi)^{1/2}}{18} \cdot \gamma^{1/2}\,(1 + 3/5\,\sin^2\theta_b)^{-1} \cos\theta_b\,(1-K_{rb}^2)\,I_{rb}$	
	b) cuadratic bottom friction law: $\frac{(\pi)^{1/2}}{2} \cdot K \cdot \left(\frac{(1-K_{rb}^2)\,\gamma}{m\,cf\,\sin\theta_b \cos\theta_b}\right)^{1/2}$	$K = V_{lb}/V_m = O(1)$, $V_m = V_{mean}$
Liu and Dalrymple, 1978	$\pi \cdot \frac{(\pi)^{1/2}}{2} \cdot \gamma^{1/2} \cdot \frac{1}{m \sin\theta_b} \cdot I_{rb} \cdot f_{11}\left(\frac{\sin\theta_b}{c_b}, g h_b, \gamma\right)$	$V_l \ll U_m$
	$\left(\frac{\pi}{2}\right)^{1/2} \cdot \gamma^{1/2} \cdot \frac{1}{m \sin\theta_b} I_{rb} \cdot f_{12}\left(\frac{\sin\theta_b}{c_b}, g h_b, m, f\right)$	$V_l \gg U_m$
Kraus and Sasaki, 1979	$\frac{(50\pi^3)^{1/2}}{16} \cdot \frac{\gamma^{1/2}}{cf} \cdot f_{ks}(\sin\theta_b, P, Q)\, I_{rb}$	$P = \frac{\pi}{2}\left[\frac{m^*}{cf}\right]$; $Q = \frac{\pi}{2}\left[\frac{m}{cf}\right]$; m^* : modified bottom slope (accounting for set-up)
Madsen, 1978	$\lambda \cdot \frac{(50\,\pi)^{1/2}}{8} \cdot \frac{\gamma^{1/2}}{f} \cdot f_m(P)\, I_{rb}$	$P = \frac{\pi \gamma m^*}{f}$
Komar, 1970	$1.35\,(\pi)^{1/2} \frac{\gamma^{1/2}}{m} \cdot I_{rb}$	
Bijker, 1976	$\frac{(25\,\pi^3)^{1/2}}{8} \cdot \frac{C}{(g\gamma f_w)^{1/2}} I_{rb}$	C : Chezy coefficient
Guza and Thornton, 1985	$\frac{23\,(2)^{1/2}}{20} \frac{\gamma^{1/2}}{cf} \cdot \frac{a^{1/5} h_b^{9/10}}{H_b}\left[1 - h_b^{23/4}\left(\frac{1}{h_o^{23/4}} - \frac{a}{y_o^{5/2}}\right)^{-6/5}\right] I_{rb}$	$a = \left(\frac{23}{15}\right)\left(\frac{g}{\pi}\right)^{1/2} \frac{\gamma^4 m}{B^3}\, T$

Table 3. Non-dimensional longshore current velocity at the breaker line for all models considered.

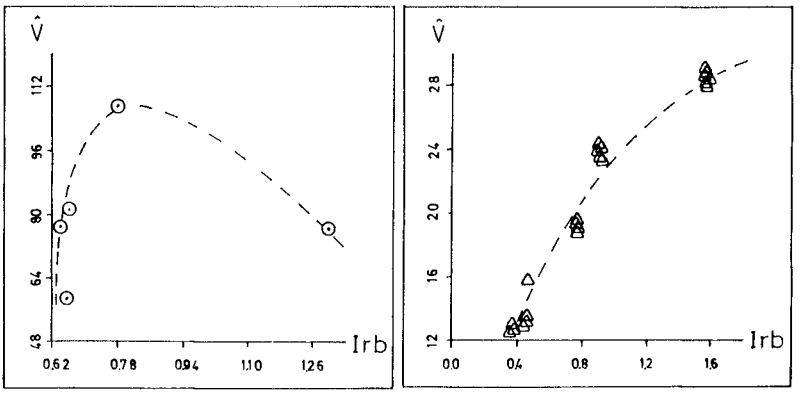

a) b)

Figure 3.

Non dimensional longshore current velocity at the breaker line vs Irb
a) field data taken from (Guza and Thornton,1985)
b) laboratory data taken from (Vitale,1981)

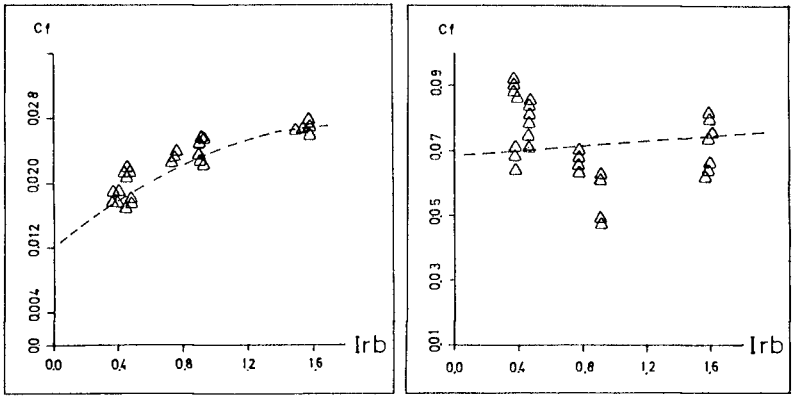

a) b)

Figure 4.

Calibration of bottom friction coefficient , Cf, as a function of Irb
for:
a) (Losada,S.Arcilla and Vidal,1986) model
b) (Guza and Thornton,1985) model
using (Vitale,1981) laboratory data.

breakers (Irb ~ 1)

In the formulations presented, the friction coefficient is shown to be the numerically most significant parameter, defining the order of magnitude for Vl, while lateral mixing, through its caracteristic coefficient, governs the profile shape. Thus, to study the variation of the friction coefficient with the dynamic state, an order of magnitude estimate for the characteristic lateral mixing coefficient is used. With this, the friction coefficient is adjusted by comparing estimated and measured values, taken from the mentioned data set (being figure 4 an example of a good and a bad parameter fit).

In these conditions a general formulation for Vlb can be written as:

$$Vlb = Vo \cdot G(Ir) = \frac{Hb}{T} \sin \theta b \cdot G(Ir) \qquad (15)$$

where G(Ir) is a function of the Iribarren's parameter, to be obtained by calibration with measured data.

4. Conclusions

4.1. Rate of wave energy dissipation, D

A general formulation for $\bar{D}$ can be written as:

$$\bar{D} = Do \cdot Fl(Irb) = \rho g \frac{Hb^2}{T} \cdot Fl(Irb) \qquad (16)$$

where Fl(Irb) is a function of the dynamic state that must be calibrated from laboratory and field data.

The relationship between $\hat{D}$ and Irb appears to be bell-shaped from physical considerations and using the (Losada, S.Arcilla and Vidal, 1986) model, that considers reflection (Kr estimation is critical for the formulation results). Comparing this model to other formulations expands their original range of validity, by obtaining Ir dependent expressions for their free parameters.

The values of $\hat{D}$ estimated for the set of field data are always lower than those obtained from laboratory data, because viscosity and bottom friction effects are overestimated in model tests.

4.2. Longshore Current Velocity, Vl

The driving term in the time-and vertically-integrated momentum conservation equation is well defined using the radiation stress concept. The dependance of this term on Ir is shown through the relationship between D and Ir:

$$\frac{\partial Sxy}{\partial x} = D.\left(\frac{\sin\theta}{C}\right) = D(Ir).\left(\frac{\sin\theta}{C}\right) \qquad (17)$$

where Sxy is the (x,y) component of the radiation stress tensor.

Bottom friction is the (numerically) most significant retarding term in longshore current velocity estimation. Therefore a good estimate of Cf is critical for all model results. No theoretical model is available to obtain this coefficient as a function of Ir, which hinders prediction (only qualitatively through flow conditions which determine bed forms).

Lateral mixing, through not very significant numerically, cannot be neglected. The use of an order of magnitude value appears to provide more accurate results than neglecting lateral mixing.

The bottom friction coefficient determines the order of magnitude of Vl while the lateral mixing coefficient defines the shape of cross-shore profiles. A measured Vl profile can therefore be used for a joint bottom friction and lateral mixing coefficients evaluation, while if there are only two measured values of Vl through the profile, such a joint fitting may have a non-unique solution.

The relationship between $\hat{Vlb}$ and Ir appears to be bell-shaped from: i) physical considerations , ii) obtained formulae and iii) field and laboratory data (figures 3a and 3b). Further measurements are required, particularly for large Ir values (collapsing-surging) to confirm and calibrate the behaviour of $\hat{D}$ and $\hat{Vl}$ vs Ir, as well as to determine a predictive relationship between the bottom friction coefficient, Cf, and Ir (figure 4). Finally a general formulation for Vl is presented:

$$Vlb = \frac{Hb}{T} \sin\theta b.\ G(Irb) \qquad (18)$$

where G(Irb) is a function of the dynamic state to be calibrated from laboratory and field data.

Acknowledgments.

Comments from R.T.Guza on earlier versions of this paper and earlier work are appreciated.

The whole staff of the Harbour and Coastal Eng.Dept. of ETSICCPB helped during the paper's elaboration. Word processing by A.Nisarre is also appreciated.

5. References.

1. Battjes, J.A. (1974) Computation of Set-Up, Longshore Currents, Run-Up and Overtopping Due to Wind Generated Waves. Rep. 74-2, Dep. Civil Engng.Delft University of Technology
2. Battjes, J.A. (1974) Surf Similarity Coastal Engng. Conference, ASCE

3. Battjes, J.A. (1975) Modelling of Turbulence in the Surf Zone Proc. Modelling Techniques, S.F.
4. Battjes, J.A. (1978) Energy Dissipation in Breaking, Solitary and Periodic Waves Manuscript, (Prel)
5. Battjes, J.A. and Janssen, J.P.F.M. (1978) Energy Loss and Set-Up Due to Breaking of Random Waves I.C.C.E. Proc. ASCE
6. Bijker, E.W. (1976) Coastal Engineering Vol.II Coastal Engng. Group, Dep. Civil Engng. Delft Univ. Technology.
7. Dally, W.R., Dean, R.G. and Dalrymple, R.A. (1984) Decay on Beaches I.C.C.E. Proc. ASCE
8. Galvin, C.J. and Eagleson, P.S. (1965) Experimental Study of Longshore Currents of a Plane Beach C.E.R.C. Tech. Mem, 10, 1-80
9. Guza, R.T. and Thornton, E.B. (1985) Surf Zone Longshore Currents and Random Waves: Models and Field Data. Jnl. of Phys. Ocean.
10. Iribarren Cavanilles, R. (1947) Corrientes y Transportes de Arenas Originados por el Oleaje Rev. Obras Públicas. May-June.
11. Kamphuis, J.W. and Readshaw, J.S. (1978) A Model Study of Alongshore Sediment Transport Rate Int. Conf. Coastal Engng. ASCE
12. Komar, P. and Inman, D.L. (1970) Longshore Transport on Beaches Jrnl. Geophys. Res., 75 (30), pp. 5914-5927
13. Kraus, N.C. and Sasaki, T.O. (1979) Influence of Wave Angle and Lateral Mixing on the Longshore Current Mar. Science Comm. Vol. 15
14. Kraus, N.C., Isobe, M. et al. (1982) Field Experiments on Longshore Sand Transport in the Surf Zone I.C.C.E. Proc. ASCE
15. Liu, P. and Dalrymple, R.A. (1978) Bottom Frictional Stresses and Longshore Currents Due to Waves with Large Angles of Incidence. Jrnl. Mar. Res. vol. 36.2
16. Longuet-Higgins, M.S. (1970) Longshore Currents Generated by Obliquely Incident Sea Waves Jrnl. Geophys. Res. 75, 1 and 2
17. Losada, M. and Sánchez-Arcilla, A. (1985) An Alternative Approach to Longshore Current Evaluation Submitted to ASCE Jrnl.
18. Madsen, O.S., Ostendorf, D.W. and Reyman, A.S. (1978) A Longshore Current Model Coastal Zone'78, ASCE
19. Mizuguchi, M., Oshima, Y. and Horikawa, K. (1978) Laboratory Experiments on Longshore Currents Proc. 25th. Conf Coastal Engng. in Japan
20. Putnam, J.A., Munk, W.H. and Traylor, M.A. (1945) The Prediction of Longshore Current Trans. Amer. Geophys. Union, 30 (3), pp. 337-345
21. Sayao, O.S. and Kamphuis, J.W. (1983) Littoral Sand Transport: Model Tests 1977-1982 CE. Res Rep. 79, Dep of Civil Engng. Queen's University, Kingston, Canada.
22. Short, A.D. (1978) Wave Power and Beach Stages: A Global Model Proceedings International Conference on Coastal Ingeneering, 1978.
23. Stive, M.J.F. (1984) Energy Dissipation in Waves Breaking on Gentle Slopes Coastal Engineering, 8
24. Svendsen, I.A. (1984) Wave Attenuation and Set-Up on a Beach I.C.C.E. Proc. ASCE
25. Vitale, P. (1981) Movable-Bed Laboratory Experiments Comparing Radiation Stress and Energy-Flux Factor as Predictors of Longshore Transport Rate Misc. Res. N.81-4. Coastal Engng. Res. Ctr.

SUBJECT INDEX

Page number refers to first page of paper.

AUTHOR INDEX

Page number refers to first page of paper.

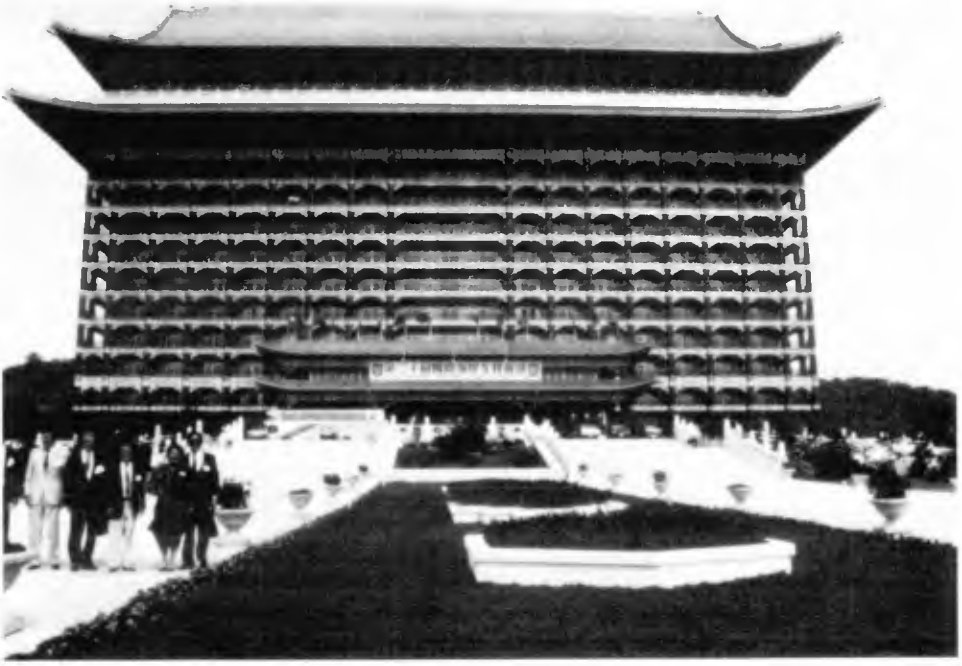

Grand Hotel, Taipei, Taiwan

PART II

COASTAL PROCESSES AND SEDIMENT TRANSPORT

Su-Ao Port—30-ton dolos, Taiwan, ROC—R.L. Wiegel

CHAPTER 70

Changes in Current Properties due to Wave Superimposing

Toshiyuki Asano[1)]

Masahiro Nakagawa[2)]

Yuichi Iwagaki[3)], M. ASCE

ABSTRACT

Changes in current properties due to wave superimposing are investigated experimentally. Variations of the mean water level gradient and the current velocity profile after wave superimposing are examined. Experimental results are discussed in relation to the energy conservation equation including the bottom friction term. It is found that changes in current properties can be well explained by increase in the time averaged bottom shear stress.

1. INTRODUCTION

Compared with studies on wave transformation due to currents, there are few studies which discussed the effect of waves on current properties. In wave-current co-existing fields, there exist mutual energy exchanges between wave and current components, so that current properties do not remain the same as in case of current only after waves are superimposed.

Phillips(1977) derived the momentum and energy conservation equations in the co-existing field; however, he did not consider frictional terms in his analysis. It should be noted that the increase in the time averaged bottom friction due to wave superimposing is the key point to represent the wave-current co-existing field. That is, the current feels larger resistance due to presence of the waves than in the current only field. Lundgren(1972) proposed an approximate theory for the reduction of the current velocity due to wave superimposing. Grant-Madsen(1979) presented an analytical model to represent the velocity field in wave-current co-existing systems.

1) Research Associate, Dept. of Civil Eng., Kyoto Univ.,Yoshida Honmachi, Sakyo-ku, Kyoto, 606, Japan
2) Engineer, Bureau of Port and Harbour Eng., Osaka Municipal Office 2-8-24, Chikuko, Minato-ku, Osaka, 552, Japan
3) Professor, Dept. of Civil Eng., Kyoto Univ., Yoshida Honmachi, Sakyo-ku, Kyoto, 606 Japan

However, the experimental verifications on the model have not been sufficiently yet. Thus, the knowledges on the changes in current properties due to wave superimposing are not enough up to the present.

This paper investigates the water surface gradient and the velocity profile of the current in the co-existing field experimentally, and discusses the results in relation to the energy conservation equation including the bottom frictional term.

2. ENERGY CONSERVATION EQUATIONS

The energy conservation equations including the bottom friction term are obtained after Phillips' derivation. The enery balance equation for waves is given by,

$$\frac{\partial}{\partial t}\{E+\frac{M_\alpha^2}{2\rho(h+\bar{\eta})}\}+\frac{\partial}{\partial x_\alpha}\{U_\alpha E+F_\alpha-\frac{\tilde{U}_\alpha M_\beta^2}{2\rho(h+\bar{\eta})}\}+S_{\alpha\beta}\frac{\partial U_\beta}{\partial x_\alpha}$$

$$=\tilde{U}_\alpha\bar{\tau}_{\alpha,z=-h}-\overline{\int_{-h}^{\eta}\frac{\partial\tau_{\beta\alpha}}{\partial z}u_\alpha^+dz} \qquad (1)$$

in which,
u_α^+ : the composite velocity of the wave and the current components $u_\alpha^+=u_\alpha+U_\alpha$, u_α : the wave velocity component, U_α : the current velocity component,
E : the wave energy density
F_α : the wave energy flux,
M_α : the mass flux due to the wave motion,
$S_{\alpha\beta}$: the radiation stress,
h : the water depth,
$\bar{\eta}$: the displacement of the mean water level due to wave superimposing.

The right hand side of Eq.(1) denotes the energy dissipation due to the time averaged bottom shear stress $\bar{\tau}_{\alpha,z=-h}$ and the internal viscosity and the Reynolds stress component $\tau_{\beta\alpha}$. As the other symbols are the same as those used by Phillips, further explanations on the symbols are omitted.

The energy balance equation for the current is,

$$\frac{\partial}{\partial t}\{\frac{1}{2}\tilde{U}_\alpha\tilde{M}_\alpha+\frac{1}{2}\rho g(\bar{\eta}^2-h^2)\}+\frac{\partial}{\partial x_\alpha}\{\tilde{M}_\alpha(\frac{1}{2}\tilde{U}_\beta^2+g\bar{\eta})\}+U_\beta\frac{\partial S_{\alpha\beta}}{\partial x_\alpha}=-\tilde{U}\bar{\tau}_{\alpha,z=-h} \qquad (2)$$

The second term of the right hand side of Eq.(1) is approximated after Jonsson's(1966) or Brevik-Aas'(1980) simplification.

$$\overline{\int_{-h}^{\eta}\frac{\partial\tau_{\beta\alpha}}{\partial z}u_\alpha^+dz}\approx(\overline{\tau_{\beta\alpha}u_\alpha^+})_{z=-h} \qquad (3)$$

The following consideration is limitted for two dimensional flow. The bottom shear stress τ_b in the streamwise direction is assumed to be presented by the following equation:

$$\tau = \frac{1}{2}\rho f_{cw}(U+\hat{u}\cos\sigma t)|U+\hat{u}\cos\sigma t| \tag{4}$$

in which, U is the depth averaged current velocity, $\hat{u}$ the velocity amplitude of the wave component at the bottom, σ the angular frequency of the waves, ρ the densityof water and f_{cw} the wave-current friction factor.

The following assumptions are introduced for the simplification of Eqs.(1) and (2).
(1) The energy density of the waves, the current velocity and the mean water level are independent of time.
(2) The current is treated as a uniform flow in depth.
(3) The ratio of the wave amplitude a to the spatial averaged mean water depth h_0 is small. This ratio is used as a small parameter in the following consideration.
(4) The spatial variation of the current is small. That is, $dU/dx=O\{(a/h_0)^2\}$.

Ignoring higher terms than $O(a/h_0)^2$, the energy conservation equation for the wave component is obtained as follows:

$$\frac{d}{dx}\{E(U+c_g)\} = -\frac{1}{2}\rho f_{cw}\{\overline{|U+\hat{u}\cos\sigma t|^3} - U\overline{(U+\hat{u}\cos\sigma t)|U+\hat{u}\cos\sigma t|}\} \tag{5}$$

On the otherhand, the equation for the mean current is given by,

$$\frac{d}{dx}\{\frac{\rho}{2}U^3(h+\bar{\eta})\} + \frac{3}{2}U^2\frac{dM}{dx} + \rho ghU\frac{d\bar{\eta}}{dx} + U\frac{dS_{xx}}{dx} = -\frac{1}{2}\rho f_{cw}U\overline{(U+\hat{u}\cos\sigma t)|U+\hat{u}\cos\sigma t|} \tag{6}$$

The right hand side of Eq.(5) means the energy dissipation of the wave component $(E_w)_{cw}$. The ratio of $(E_w)_{cw}$ to that without current $(E_w)_w$ is given by,

$$\frac{(E_w)_{cw}}{(E_w)_w} = \frac{f_{cw}\overline{(|U+\hat{u}\cos\sigma t|^3 - U(U+\hat{u}\cos\sigma t)|U+\hat{u}\cos\sigma t|)}}{f_w\overline{|\hat{u}\cos\sigma t|^3}} = \frac{f_{cw}}{f_w}\frac{(E_w)'_{cw}}{(E_w)'_w} \tag{7}$$

Concerning the current energy dissipation, the similar expression for the ratio of with waves $(E_c)_{cw}$ to without waves $(E_c)_c$ is obtained as follows:

$$\frac{(E_c)_{cw}}{(E_c)_c} = \frac{f_{cw}\overline{U(U+\hat{u}\cos\sigma t)|U+\hat{u}\cos\sigma t|}}{f_c U^3} = \frac{f_{cw}}{f_c}\frac{(E_c)'_{cw}}{(E_c)'_c} \tag{8}$$

The further analytical considerations are possible both for $(E_w)'_{cw}/(E_w)'_w$ and $(E_c)'_{cw}/(E_c)'_c$ by dividing the condition $\hat{u}\geqq|U|$ and $\hat{u}\leqq|U|$. Fig.1 shows the relation between $(E_w)'_{cw}/(E_w)'_w$ and $|U|/\hat{u}$, and Fig.2 the variation of $(E_c)'_{cw}/(E_c)'_c$ with $\hat{u}/|U|$. It is noted from Fig.2 that the current energy dissipation in the co-existing field becomes larger than that in the current only field for the same current velocity. The velocity reduction of the current due to wave superimposing is not considered here.

Next, the similar calculation is performed on the ratio of the wave energy dissipation to the total energy dissipation. Fig.3 shows

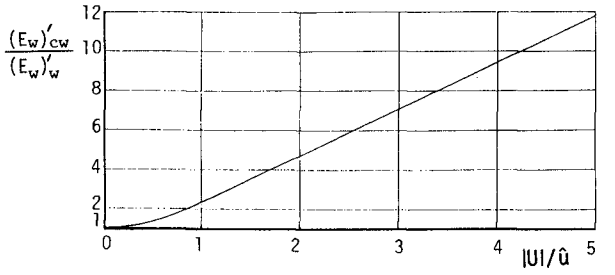

Fig. 1 Energy dissipation ratio for wave component

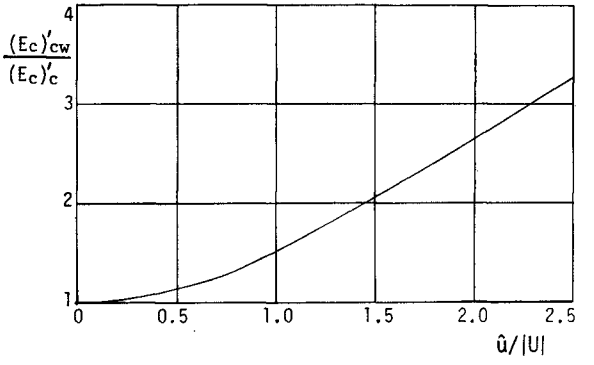

Fig. 2 Energy dissipation ratio for current component

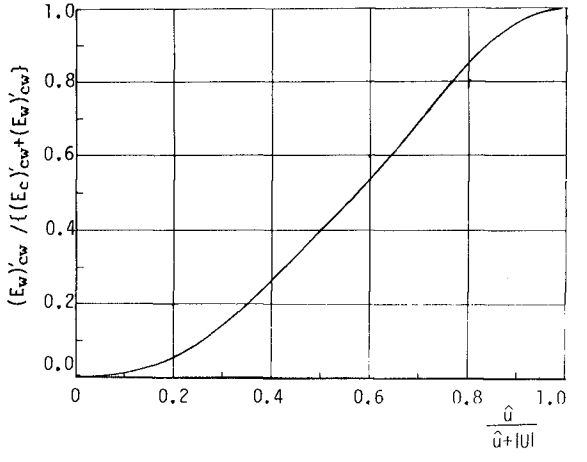

Fig. 3 Composite ratio of wave energy dissipation to total energy dissipation

the relation of the ratio with the wave-current composite ratio $\hat{u}/(\hat{u}+|U|)$. The figure indicates $(E_w)_{cw}/\{(E_w)_{cw}+(E_c)_{cw}\}$ is 0.4 when the wave velocity component is equal to the current one which means that $\hat{u}/(\hat{u}+|U|)=0.5$. It implies that the energy dissipation of the current is 1.5 times of that of the wave component under the condition of $\hat{u}=|U|$.

3. VARIATION OF TIME-AVERAGED WATER SURFACE DUE TO WAVE SUPERIMPOSING

3.1 Experimental apparatus and procedure

The experiment was carried out in a 27m long, 0.5m wide and 0.7m high wave tank(Fig.4), in which circulating flow could be generated by a power pump. In order to produce large energy dissipation in the tank of limited length ,two dimensional artificial roughness elements of 12mm×12mm in cross section and 10cm intervals were added on the bottom over a distance of 16m. Six capacitance type wave gauges were equipped at 2.5m intervals. The water depth is kept 30cm constant for all the cases.

The measurements were conducted for the following three cases; waves without current, current without waves and wave-current combined flow. The signals from the wave gauges were analysed to obtain the wave damping ratio and the gradient of the mean water level. In the experiments, only those waves of a wave train which did not contain reflection effects were used. Since the contamination effect is known to be a cause of wave damping[12], special attention was paid on the cleanness of both water and the surfaces of side walls.

3.2 WAVE-CURRENT CO-EXISTING SYSTEM

Svendsen(1985) has pointed out several difficulties in generating a wave-current system without any disturbance. For example, the ratio of the width of the flume to the water depth should be large enough to avoid the side wall effect on the current component. However, some extent of the water depth is required for wave generating. Therefore, a wide wave tank and a large capasity power pump are needed for both requirements.

The changes in current properties depend on how the wave-current co-existing system is generated. In this experimental facility, the total mass of water in the wave tank and the pipe system is kept constant after wave superimposing; therefore, the increase in the time averaged bottom shear stress due to wave superimposing causes the reduction of the water discharge through the wave tank. Meanwhile, if the discharge is kept constant by a head tank, the increase in the time averaged bottom shear stress changes the water depth and the gradient of the time averaged water surface.

In the present wave-current system, the head raised by the power pump is balanced with the head losses due to the frictions on the

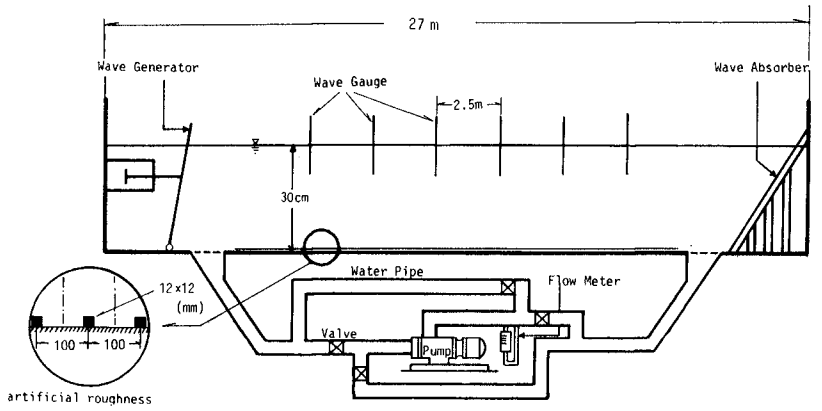

Fig. 4 Experimental apparatus

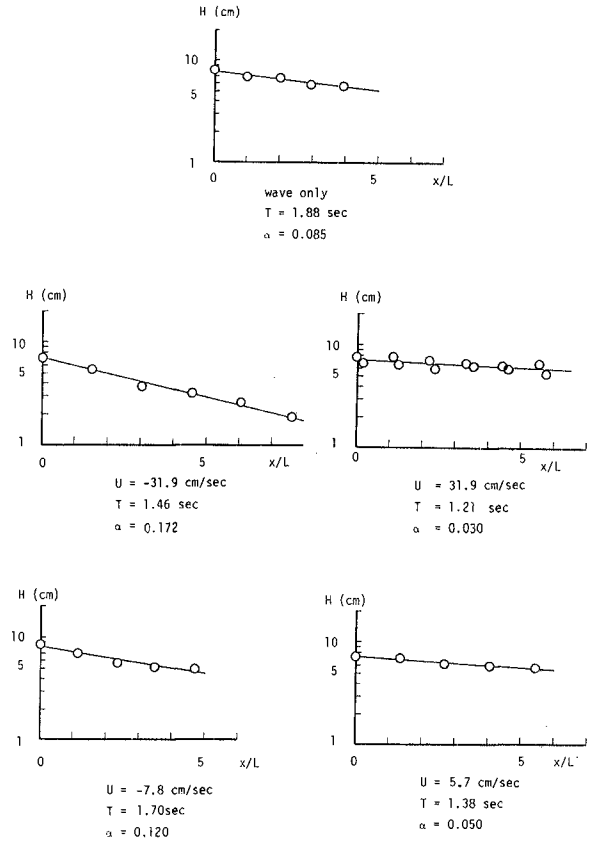

Fig. 5 Wave attenuation profiles

bottom, on the side walls, on the surface of the pipe system, etc. The reason why the large bottom roughness was equipped on the bottom is to make the other losses small compared with the loss by the bottom friction. It is natural to consider that the driving power of the pump is kept constant for both the case of current without waves and the case with waves. Therefore, the both cases are considered to be comparable systems dominated by the same driving power of the pump and the respective properties of the bottom shear stress. Consequently, it is possible to discuss the changes of the current properties due to wave superimposing by comparing the both cases.

3.3 Experimental Results

Preliminary experiments were conducted to investigate the wave damping properties in the fields with and without current. Some examples are shown in Fig.5. It is found that the waves attenuate exponentially even in the wave-current co-existing field, and the damping becomes significant in the opposite current cases. The wave decay modulus α was calculated for the each run by the least square method. The results on α are shown in Fig.6, in which β is defined as $\sqrt{\sigma/2\nu}$ (ν : kinematic viscosity) and L is the wave length. Meanwhile, the water surface variation in the current only field was also measured as a preliminary experiment. The results are shown in Fig.7, in which Δh is the relative water level to that at x=5m. It is noted that the variation of the water surface in the upper stream region than the position x=10m seems to be expressed by a straight line.

The results on the time averaged water surface with and without waves are shown in Fig.8. It is found that the slopes of the water surface become steep after wave superimposing regardless of the current direction. The gradients of the straight lines $d(h+\bar{\eta})/dx$ are determined, then the properties of $d\bar{\eta}/dx$ are discussed as follows. Fig.9 shows the results on $d\bar{\eta}/dx$ with the wave-current composite ratio $\hat{u}/(\hat{u}+|U|)$ as an abscissa. The results indicate that $d\bar{\eta}/dx$ increases with increase in $\hat{u}/(\hat{u}+|U|)$. As shown in Eq.(6), not only the $d\bar{\eta}/dx$ term but also the following terms ; the gradients of the kinematic energy, the radiation stress and the mass flux are related to the energy conservation for the current component. Since dM/dx and dS_{xx}/dx are related to the wave height variation dH/dx , dH/dx becomes one of the factors to contribute to the energy conservation for the current. The ratio of the current energy dissipation in the co-existing field $(E_c)_{cw}$ to that in the current only field $(E_c)_c$ can be calculated on the basis of the left hand side of Eq.(6) from the experimental data of the water surface gradient $d(h+\bar{\eta})/dx$ and the decay modulus α. The results are shown in Fig.10. It is found that the results of $(E_c)_{cw}/(E_c)_c$ are well arranged by the wave-current composite ratio $\hat{u}/|U|$. As the wave component dominates in the composite velocity, $(E_c)_{cw}/(E_c)_c$ becomes large due to the increase in the time averaged bottom friction.

Meanwhile, $(E_c)_{cw}/(E_c)_c$ can be also computed by the right hand side of Eq.(8). The friction factors f_{cw} and f_c are estimated by the

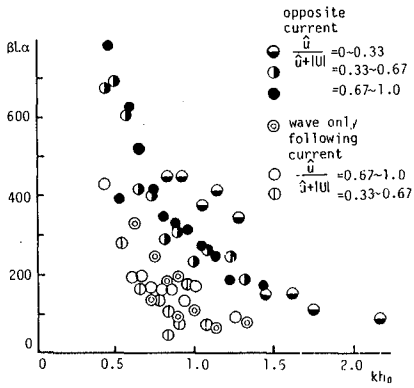

Fig. 6 Wave decay modulus

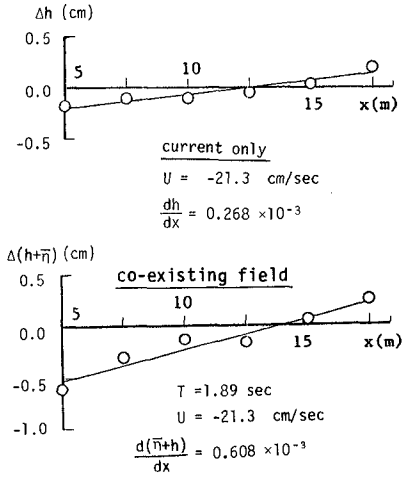

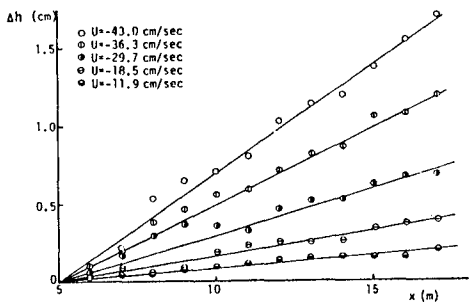

Fig. 7 Water surface profiles without waves

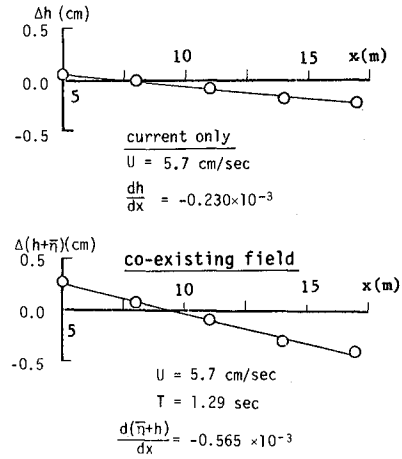

Fig. 8 Mean water level with and without waves

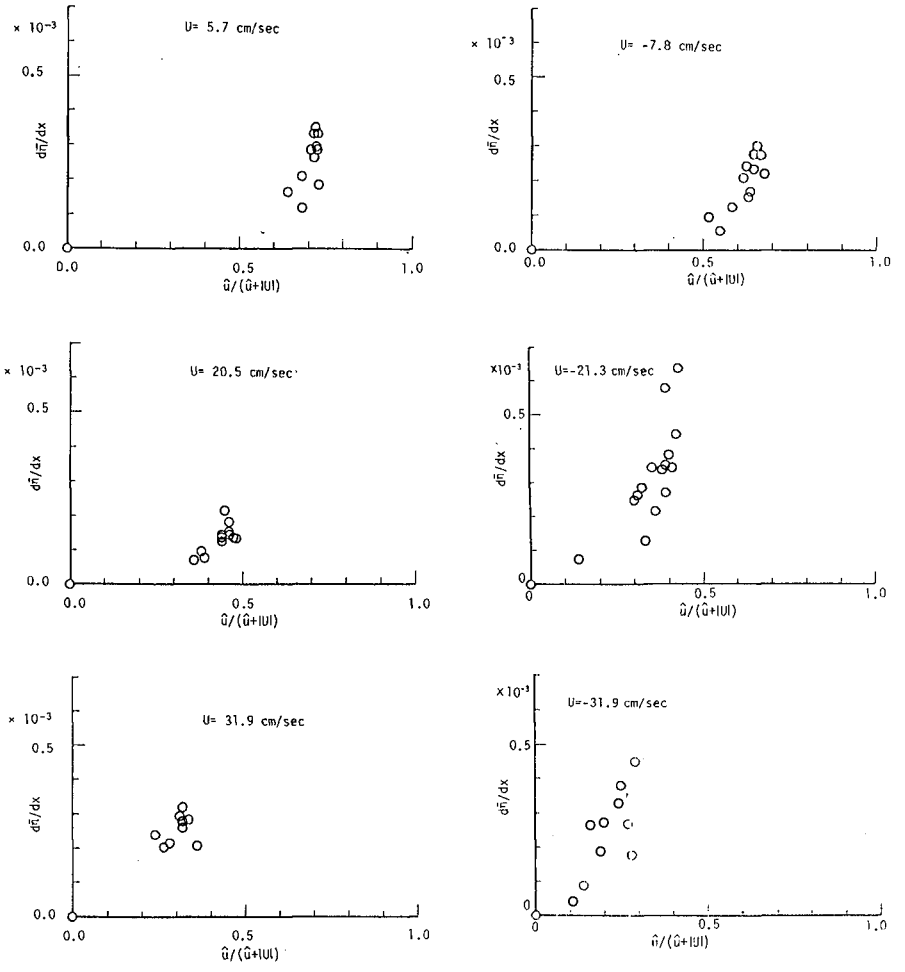

Fig. 9 Variations of gradient of mean water level with wave-current composite ratio

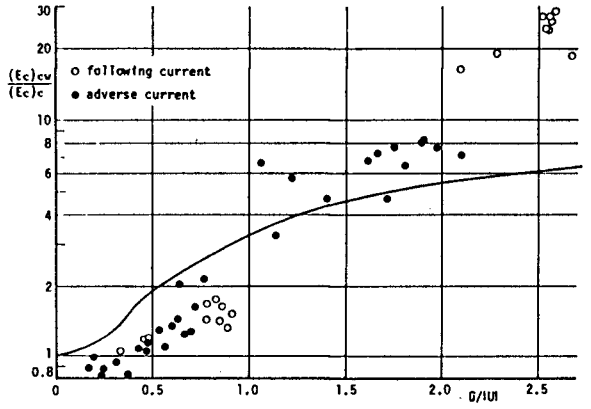

Fig. 10 Energy dissipation ratio for current component

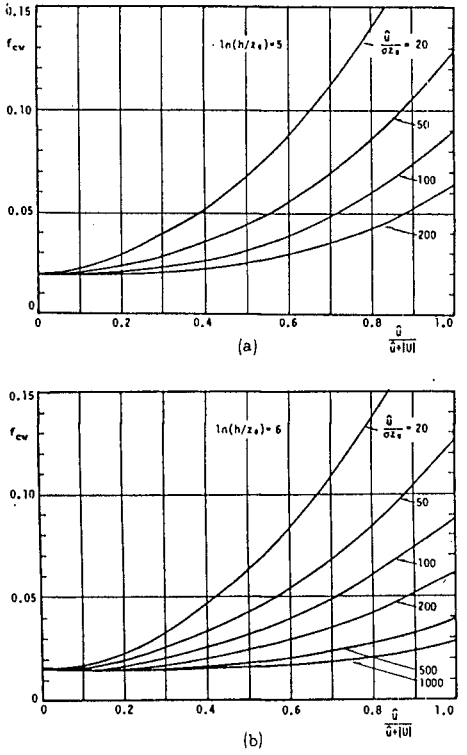

Fig. 11 Friction factors in wave-current co-existing fields

turbulent boundary layer theory in the co-existing field[1]. For fully rough turbulent flow, the friction factor f_{cw} is a function of h/z_0, $\hat{u}/\sigma z_0$ and $\hat{u}/(\hat{u}+|U|)$. Fig.11 shows an example of the properties on the friction factor f_{cw}. The curve in Fig.10 is the calculated result of $(E_c)_{cw}/(E_c)_c$ where f_c and f_{cw} are estimated under the condition of $ln(h/z_0)=4$ and $\hat{u}/\sigma z_0=10$ which are the average values of the present experimental conditions. The current velocity in the numerator of Eq.(8) should be replaced by $\overline{U}_{mod}$ which can be estimated by Eq.(12). Although the present calculation of $(E_c)_{cw}/(E_c)_c$ is only rough estimation, it agrees fairly well with the experimental results for the range of $\hat{u}/|U|\leqq 2$.

4.DEFORMATION OF VERTICAL VELOCITY PROFILE OF CURRENT COMPONENT DUE TO WAVE SUPERIMPOSING

4.1 Experimental procedure

The experiment was carried out in the same wave tank mentioned in 3.1. Two dimensional roughness elements of 2mmx2mm in cross section were added on the bottom at 15mm intervals. A laser-doppler anemometer was used to measure the velocities both in the wave-current co-existing field and in the current only field. All the currents used in the test were in the opposite direction to the wave propagation. The test condition is shown in Table 1.

In addition to the present experimental results, the data by Bakker-van Doorn(1980) and Kemp-Simons(1982) obtained under the similar experimental conditions are used for the analysis.

4.2 Results and Discussion

Fig.12 shows one example of the current profiles measured by authors(1984), and Fig.13 shows that by Bakker-van Doorn(1980). In order to discuss the effect of wave superimposing on current profile quantitatively, several characteristics should be introduced. These characteristics indicated schematically in Fig.12, are defined as follows.

Table 1 Experimental conditions

		$\overline{U}$ (cm/sec)	H (cm)	T (sec)	h (cm)
CASE-I	wave only	0	8.52	1.67	30
	current only	-18.6	——		
	co-existing	-17.4	7.74		
CASE-II	wave only	0	7.99	1.67	30
	current only	-31.6	——		
	co-existing	-25.9	7.49		
CASE-III	wave only	0	8.22	1.67	30
	current only	-42.3	——		
	co-existing	-36.7	6.30		
CASE-IV	current only	-34.9	——	1.67	25
	co-existing	-36.0	7.13		

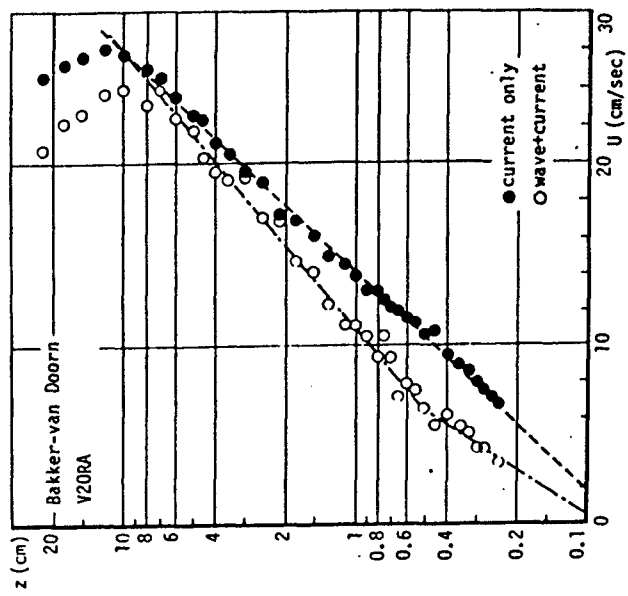

Fig. 13 Velocity profiles of current without and with waves (Bakker-van Doorn; 1980)[2]

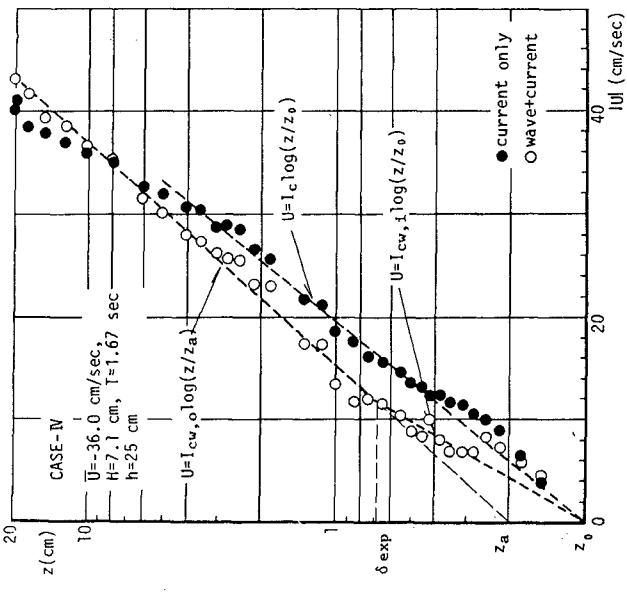

Fig. 12 Velocity profiles of current without and with waves (authors; 1984)[1]

The familiar logarithmic current profile can be found in the current only field. The gradient is defined as I_c and the zero intercept of the logarithmic profile as z_0. Meanwhile, the current velocity in the co-existing field increases more slowly with z in the region of $z \leqq \delta_{exp}$; however, in the range of $z > \delta_{exp}$ the gradient is found to be larger than that of the current only field I_c. The gradients of the current profile in the co-existing field are defined as $I_{cw,i}$ for $z \leqq \delta_{exp}$ and $I_{cw,o}$ for $z \geqq \delta_{exp}$. The zero intercept is obtained by extending the upper velocity profile. The height is named z_a, which means the apparent bottom roughness when waves superimpose on the current.

In the existing analytical model, $I_{cw,o}$ has been treated to be equal to I_c and it has been considered that the gradient of the upper current profile is unchanged and the profile only shifts towards smaller velocity after wave superimposing. However, both of authors' and Bakker-van Doorn's data show that $I_{cw,o}$ is always larger than I_c. This property can be explained by the increase in the time averaged bottom shear stress due to wave superimposing.

In the following, the properties of $I_{cw,i}$, $I_{cw,o}$, δ_{exp} and z_a are discussed. These characteristics are obtained from the Authors', Bakker-van Doorn's and Kemp-Simons' data. Figs. 14, 15, 16 show the relations between these characteristics and the wave current composite ratio $\hat{u}/|U|$. These properties may depend on the other parameters such as $\hat{u}/\sigma z_0$, h/z_0 etc.. However, the dependence on $\hat{u}/|U|$ is only discussed here.

The variation of δ_{exp}/z_0 with $\hat{u}/|U|$ can be expressed by the following equation:

$$\delta_{exp}/z_0 = 1 + 7\,\hat{u}/|U| \tag{9}$$

The following relation between z_a/z_0 and $\hat{u}/|U|$ is found from Fig.15:

$$\frac{z_a}{z_0} = 1 + 1.85\,(\hat{u}/|U|)^2 \tag{10}$$

Meanwhile, the ralation between $I_{cw,o}/I_c$ and $\hat{u}/|U|$ can be expressed in the following equation:

$$I_{cw,o}/I_c = 1 + 0.22\,(\hat{u}/|U|)^{1.4} \tag{11}$$

The reduction of the depth averaged current velocity due to wave superimposing is discussed as follows. Since the velocity in the region $z \leqq \delta_{exp}$ is small enough to be disregarded, the ratio of the depth averaged velocity in the co-existing field $\bar{U}_{mod}$ to that in the current only field $\bar{U}$ is given by,

$$\frac{\bar{U}_{mod}}{\bar{U}} \simeq \frac{I_{cw,o}}{I_c}\,\frac{\ln(\frac{h}{z_a}) - 1}{\ln(\frac{h}{z_0}) - 1} = \frac{I_{cw,o}}{I_c}\left\{1 - \frac{\ln(z_a/z_0)}{\ln(h/z_0) - 1}\right\} \tag{12}$$

Invoking Eqs.(10) and (11), $\bar{U}_{mod}/\bar{U}$ can be calculated as a function of $\hat{u}/|U|$ and h/z_0.

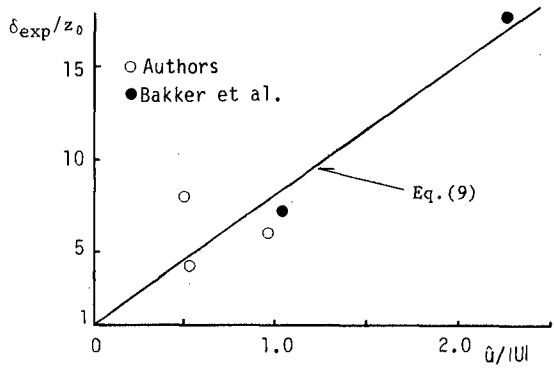

Fig. 14 δ_{exp}/z_0 vs $\hat{u}/|U|$

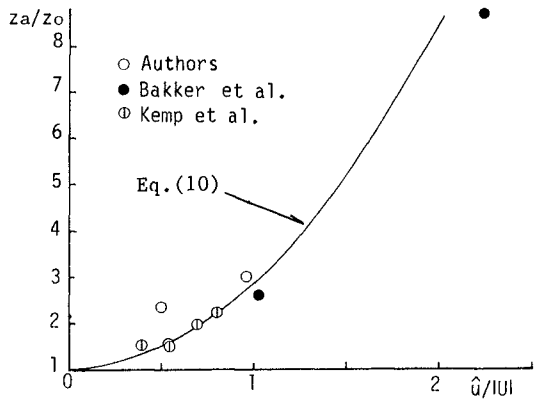

Fig. 15 z_a/z_0 vs $\hat{u}/|U|$

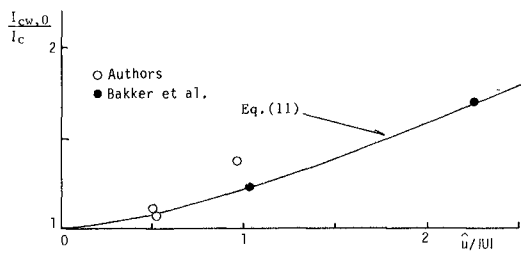

Fig. 16 $I_{cw,o}/I_c$ vs $\hat{u}/|U|$

5. Conclusions

This study investigates changes in current properties due to wave superimposing. The variations of the gradient of the mean water level and the current velocity profile in the co-existing field are examined in relation to the consideration on the energy conservation equation including the bottom stress term. The main results obtained in this study are as follows:

1) The gradient of the time averaged water level becomes steep after wave superimposing due to increase in the time averaged bottom shear stress.
2) The experimental results on the energy dissipation for the current component can be well arranged by the wave-current composite ratio. The estimated energy dissipation based on the energy conservation equation agrees fairly well with the experimental results.
3) Several characteristics representing current profiles with and without waves are introduced. Arranging the existing measurements of the current profiles, the relations between the characteristics and the wave-current composite ratio are obtained. The gradient of current profile after wave superimposing above the wave boundary layer is found to be larger than that without waves.

REFERENCE

1) Asano, T. and Y. Iwagaki : Bottom turbulent boundary layer in wave-current coexisting systems, Proc. of 19th I.C.C.E., pp.2397-2413, 1984.
2) Bakker, W.T. and Th. van Doorn : Near Bottom velocities in waves with a current, Rept. of Delft Hydraulic Lab., Pub. No.208, p.25, 1980.
3) Brevik, I. and B. Aas : Flume experiment on waves and currents, 1. Rippled bed, Coastal Engineering, Vol.3, pp.149-177, 1980.
4) Coffey, F.C. and P.Nielsen : Aspects of wave current boundary layer flows, Proc. of 19th I.C.C.E., pp.2232-2245, 1984
5) Grant, W.D. and O.S. Madsen : Combined wave and current interaction with a rough bottom, J. of Geophy. Res., Vol.84, No.C4, pp.1797-1808, 1979.
6) Jonsson, I.G. : Wave boundary layer and friction factors, Proc. of 10th I.C.C.E., pp.127-148, 1966.
7) Kemp, P.H. and R.R. Simons : The interaction between waves and a turbulent current ; wave propagating with the current, J. Fluid Mech., Vol.116, pp.227-250,1982.
8) Lundgren, H: Turbulent currents in the presence of waves, Proc. of 13th I.C.C.E., pp.623-634, 1972.
9) Phillips, O.M. : The Dynamics of the Upper Ocean, 2nd Edition , Cambridge Univ. Press, p.336, 1977.
10) Sleath, J.F.A. : Sea Bed Mechanics, John Wiley & Sons, pp.50-53, p.335, 1984.
11) Svendsen, I.A. : Physical modelling of water waves, Physical Modelling in Coastal Engineering, Edited by R.A. Dalrymple, A.A. Balkema Press, pp.13-47, 1985.
12) van Dorn, W.G. : Boundary dissipation of oscillatory waves, J. Fluid Mech., Vol.24, pp.769-779, 1966.

CHAPTER 71

THE DYNAMICS OF OSCILLATING SHEETFLOW

by ir. W.T. Bakker [1] and ir. W.G.M. van Kesteren [2].

1.ABSTRACT.
Two mathematical models for the simulation of the dynamics of sheetflow are presented, an analytical and a numerical one.
In the analytical model the theory of Bagnold (1954) is implemented: a constant ratio between shear stress and normal stresses is assumed.
In the numerical model the motion of each layer of grains is considered separately; each layer exists of a rigid rectangular structure of spherical grains. Grain- grain interaction between the successive layers occurs in two ways: on one hand viscous interaction forces, comparable with squeezing forces in lubrication problems and on the other hand direct contact with elastic response when the distance between the grains becomes less than .01 of the grain diameter. When the relative motion of adjacent layers results into compression or dilatation, a resistant force analogous to the Darcy law is assumed.The numerical model has been combined with the turbulent-boundary layer model of Bakker and v. Kesteren (1984).
Results of computations are compared with measurements of Bagnold (1954) and Horikawa et al (1982).
The analytical model predicted the concentration in the sheet flow layer and the intrusion depth rather well, where the numerical model gave reasonable results with respect to the velocity pattern above the sheetflow layer.
It is concluded, that up to now the more sophisticated assumptions of the numerical model do not lead as yet to higher accuracy with respect to the intrusion depth of the sheet flow, probably because the separation between sheet flow and the turbulent boundary layer above has been assumed too smooth.

2. INTRODUCTION.

In this paper two mathematical models for the simulation of the dynamics of sheetflow are presented, an analytical and a numerical one.
Apart from the approach, also the physical schematization of both models is quite different.
In both models it is taken into account, that at high velocities a thicker layer is moving than during the time lapses with lower velocities.
In the analytical model (Ch. 3) the theory of Bagnold (1954) is implemented: a constant ratio between shear stress and normal stresses is assumed.
In the numerical model (ch.4) the motion of each layer of grains is

[1])Scientific Coordinator Coastal Research, Tidal Waters Department Rijkswaterstaat; Principal Scientific Officer Delft University of Technology
[2])Engineer Delft Hydraulics Laboratory

considered separately; each layer exists of a rigid rectangular structure of spherical grains.
Grain- grain interaction between the successive layers occurs in two ways: on one hand viscous interaction forces, comparable with squeezing forces in lubrication problems and on the other hand direct contact with elastic response when the distance between the grains becomes less than .01 times the grain diameter. When the relative motion of adjacent layers results into compression or dilatation, a resistant force analogous to the Darcy law is assumed.
Results of computations are compared with measurements of Bagnold (1954) and Horikawa et al (1982) (ch.4.2). This leads to the conclusions, given in ch 5.

3. ANALYTICAL COMPUTATIONS.

3.1 Assumptions

For the analytical computations the theory of Bagnold (1954),(1956), concerning bed load in a uniform flow, is used. According to this theory it is assumed that a dispersive pressure P proportional to the grain shearstress T is exerted on the grains. In the viscous region Bagnold finds:

$$T = .75\ P \tag{1a}$$

where T is related to the velocity gradient $\frac{du}{dz}$ in the following way:

$$T = 2.2\ \lambda^{3/2} \rho_w \nu \frac{du}{dz} \tag{1b}$$

in which ρ_w=spec. density water, ν=kin. viscosity, u=horizontal velocity, z=vertical coördinate (pos. upwards); λ is the linear concentration as defined by Bagnold (1954):

$$\lambda = [(c_0/c)^{1/3} - 1]^{-1} \tag{1c}$$

Here c is the concentration, having a maximum c_0.This maximum belonging to the maximum packing density, equals .74, assuming a tetrahedral rectangular piling as depicted in fig 1 and 8.
The validity of the viscous region for the sheetflowphenomena can be estimated with the Bagnold-number:

$$N = \frac{\rho_s \sqrt{\lambda}\ D^2}{\rho_w \nu} \frac{du}{dz} < 40 \tag{2}$$

in which D = grain diameter and ρ_s= spec. density sand.
Substitution of ρ_s/ρ_w=2.65, λ=10, D=.2 mm, ν=10^{-6}m^2/s and $\frac{du}{dz}$ =100 s^{-1} yields: N = 34 .
In a first order harmonic solution the shear stress T is given by:

$$T = \hat{T} \sin \omega t \tag{3}$$

Starting with the assumption in eq.(1), eq.(3) yields for the dispersive pressure:

$$P = \hat{P}\ |\sin \omega t| \tag{4}$$

where ω is the angular frequency of the motion and t is the time; the superscript "^" denotes a top value. Furthermore it is assumed, that

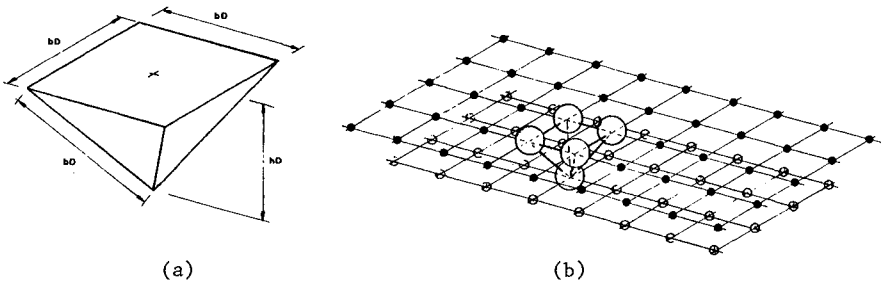

Fig.1 Configuration of moving grain layers.

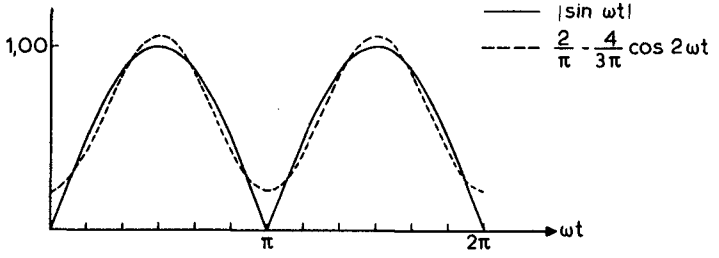

Fig.2 Mean and second harmonic of vertical pressure gradient (p).

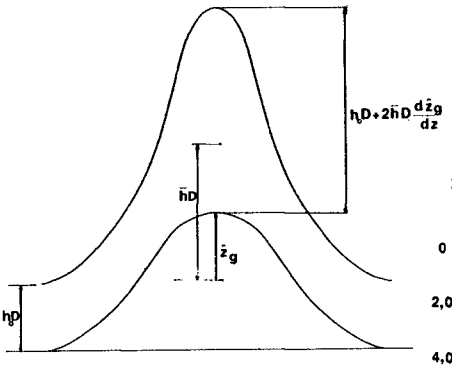

Fig.3 Vertical motion of two adjacent grain layers.

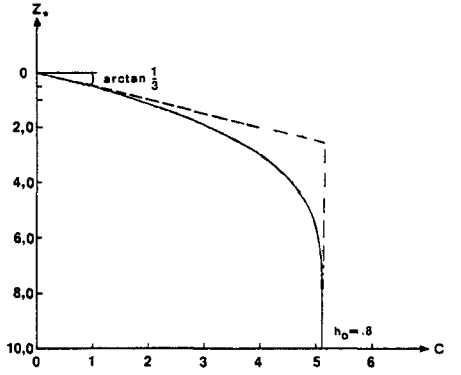

Fig.4 Mean concentration profile in the sheetflow (anal.sol.).

at the moments of rest during the changing of the direction of the oscillation the concentration is constant over the height of the sheet flow layer. The mixture of sand and water in this layer is assumed to be uniformly distributed in horizontal direction and is supposed to oscillate by means of the horizontal pressure gradient and the drag force acting on the grains.

3.2. Analysis.
Where D is the grain diameter, let hD be the mutual vertical distance between the center of two adjacent layers of grains of the sheet flow, when the grains attain their time-averaged vertical position (fig.1a). Then the vertical force p, acting on a layer of grains equals:

$$p = - hD \frac{\partial P}{\partial z} |\sin \omega t| \tag{5}$$

This vertical force can be approximated by its time-average p_0 and its second harmonic, having an amplitude $\hat{p}_2$ (fig 2):

$$p_0 = \frac{2}{\pi} hD \frac{\partial \hat{P}}{\partial z} ; \quad \hat{p}_2 = \frac{4}{3\pi} hD \frac{\partial \hat{P}}{\partial z} \tag{6}$$

Averaged over the wave period, p_0 should balance the weight of one layer of grains.
Furthermore, the second harmonic is counteracted by the vertical drag force $a.\dot{z}_g$, where $\dot{z}_g$ denotes the time-derivative of the vertical position z_g of a grain and "a" denotes a drag coefficient:

$$a = \frac{3\pi \rho_w \nu}{b^2 D (1-c)^3} \tag{7}$$

The drag coefficient is according to Stokes, only hindered settling has been taken into account by means of $(1-c)^3$, where c is the concentration. In (7) bD denotes the horizontal distance between the grains. From the dynamic equation for the second harmonic, $\hat{z}_g$ can be expressed in p_2 and a:

$$\hat{z}_g = \hat{p}_2/(2\omega a) \tag{8}$$

Let the grains in closest packing have a distance $h_0 D$ to each other: $h_0 \cong .8$. This is reached everywhere at the moment of turning of the direction of the orbital velocity. However, $^1/_4$of a wave period later, the porosity is different everywhere, because of the vertical gradient of the vertical motion: the upper grain dances more vigorously than the lower one (fig 3). Therefore, the time-averaged distance between the grains equals:

$$\bar{h}D = h_0 D + \bar{h}D \frac{\partial}{\partial z} (\hat{z}_g) \tag{9}$$

Thus the time-mean vertical spacing between the grains can be expressed in the variation of the vertical pressure p_2. However, this value $\hat{p}_2$ equals $(2/3)p_0$, according to (6), p_0 being equal to the weight of a grain layer. Thus from (8) it shows, that z_g only varies in vertical sense because the concentration varies in vertical sense. One thus understands, that (9) is essentially a differential equation in the concentration, as also h can be expressed in the concentration:

$$h = (1/\sqrt{2})(c_0/c)^{1/3} \tag{10}$$

After some elaboration (cf. Bakker & v.Kesteren (1982)), one finds the dimensionless equation:

$$\frac{\partial c}{\partial z^*} = \{h_0\sqrt{2}.(c/c_0)^{1/3} - 1\}/\{3(1 - c^2)\} \tag{11}$$

$$z^* = z/Z; \quad Z = \frac{1}{54}\,\frac{\rho_s - \rho_w}{\rho_w}\,\frac{g\,D^2}{\omega\,\nu} \tag{12}$$

Eq (11) has been solved, using Simpson's integration method, thus giving c as function of z (fig 4)
A first approximation for the time dependent concentration can be found from the mean concentrationprofile resulting from eq.(11).
Neglecting phase shifts a first order time dependent distance between the grains is given by ($\bar{h}$ denoting the mean value of h):

$$h(t)D = \bar{h}D + (\bar{h}D - h_0D)\sin(2\omega t) \tag{13}$$

Substituting eq.(10) into (13) gives for the timedependent concentration (fig 4) (c_ℓ denoting the limiting value of the concentration in the sheetflow):

$$\frac{c(t)}{c_\ell} = [(\frac{\bar{c}}{c_\ell})^{-1/3} - \{(\frac{\bar{c}}{c_\ell})^{-1/3} - 1\}\sin 2\omega t]^{-3} \tag{14}$$

$$\text{where } c_\ell = \frac{c_a}{(h_0\sqrt{2})^3} \tag{15}$$

Also a first approximation for the intrusiondepth of the sheetflow layer as function of time can be made. Schematizing more rigorously than before, the concentration in the moving sheet layer can be assumed as constant.
As the pressure increases linearly with the depth the grain shear stress also increases linearly and thus (for viscous flow) a parabolic velocity distribution is found (fig 5):

$$u = \hat{U}\,(1 - \frac{z^2}{H^2})\cos\omega t \text{ when } z \leq H \tag{16}$$

$$u = 0 \qquad \text{when } z > H$$

where $\hat{U}$ is the maximum velocity at the top of the sheetflow layer and equals the maximum velocity in the wave boundary layer; H is the time-dependent intrusion depth or thickness of sheetflow layer given by:

$$H = \hat{H}\sqrt{|\cos\omega t|} \tag{17}$$

where $\hat{H}$ is the maximum intrusion depth.
From eq. (1b), (1c) and (16) results for the shear stress:

$$T = 4.4\,\rho_w\nu\,[(\frac{c}{c_0})^{1/3} - 1]^{-3/2}\,\frac{\hat{U}.z}{H^2} \tag{18}$$

This is accompanied by a dispersive pressure gradient given by:

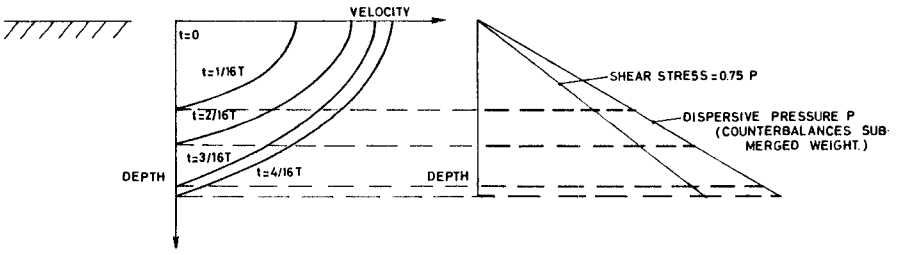

Fig.5 Assumed velocity and stress distribution in the sheetflow (anal.)

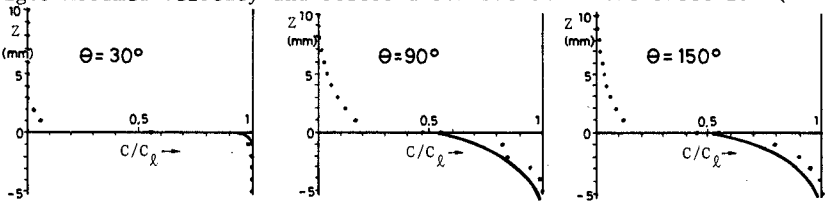

• measurements from Horikawa (1982)
—— analytical theory

Fig.6 Concentration profiles in the sheetflow (anal. comp.).

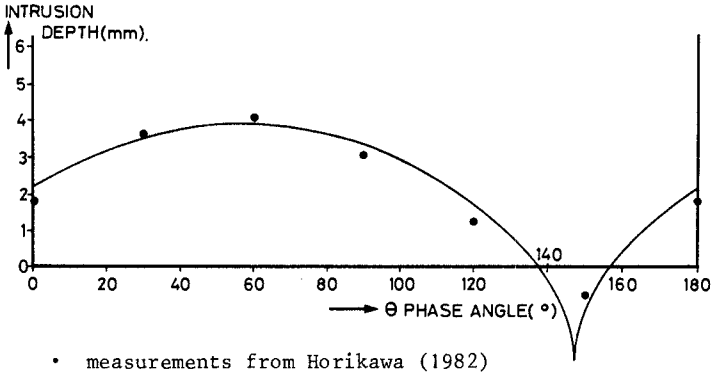

• measurements from Horikawa (1982)
—— analytical theory

Fig.7 Intrusion depth as function of time (anal. comp.).

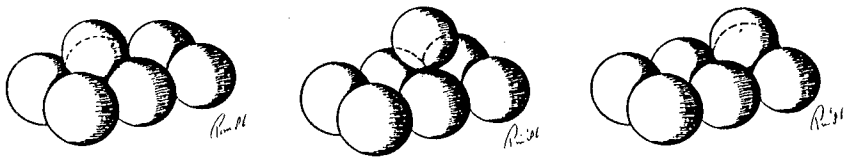

Fig.8 Relative grain motion in two adjacent layers.

$$\frac{\partial P}{\partial z} = 4.4\ \rho_w \nu\ [(\frac{c}{c_0})^{1/3} - 1]^{-3/2}\ \frac{\hat{U}}{H^2}\ \text{cotan}\ \alpha \qquad (19)$$

where α is the angle of internal friction. (tan α = .75; eq (1a))
Because this pressure gradient must counterbalance the gravity forces on the (submerged) grains an expression for H can be found:

$$\hat{H} = \sqrt{4.4\ \frac{\rho_w}{\rho_s - \rho_w}\ \frac{\nu\ \hat{U}}{c\ g}\ [(\frac{c}{c_0})^{1/3} - 1]^{-3/2}\ \text{cotan}\ \alpha} \qquad (20)$$

The time-dependent intrusiondepth H is given by eq.(17).

3.3. Results.
Figure 6 shows some results of the calculated variation (according eq.(14)) of the concentration during half a wave period, compared with the measurements of Horikawa et al (1982). In an oscillating water tunnel Horikawa carried out a series of laboratory experiments under sheet flow condition. The following deals with his experiment 1-1 with a period of 3.6 sec and a maximum orbital velocity of 1.27 m/sec.
Figure 7 gives the intrusion depth (point of zero velocity) of the sheet flow layer as function of time, also compared with the results of Horikawa et al. The depth H has to be taken, starting from a time-averaged bottom level, which is higher than the still bottom level. (The zero-level in the plots of Horikawa). The maximum intrusion depth is assumed to occur at the time of maximum velocity at level z=0 (phase angle $\theta = 60^0$). The theory would predict "still-water-concentration" for $\theta = 15^0$ (60^0 minus a phase shift of 45^0). This tendency also follows from Horikawa's data and from the numerical method treated below (fig 13b).

4. NUMERICAL COMPUTATIONS.

4.1. Grain-grain interactions in the numerical model
In the numerical model the motion of each layer of grains is considered separately; each layer exists of a rigid rectangular structure of spherical grains (Fig 1b). Grain- grain interaction between the successive layers occurs in two ways: on one hand viscous interaction forces, comparable with squeezing forces in lubrication problems and on the other hand direct contact with elastic response when the distance between the grains becomes less than .01 of the grain diameter. When the relative motion of adjacent layers results into compression or dilatation, a resistant force analogous to the Darcy law is assumed The viscous interaction forces are reproduced in the following way.
Let F_s be the Stokes force, exerted on a sphere, moving with velocity u in a fluid:

$$F_s = 6\ \pi\ \rho_w\ \nu\ u\ R \qquad (21)$$

in which R is the radius of the sphere.
Many scientists investigated the increase of this force, when this sphere move to a wall, for instance Lorentz (1907).For the behaviour of the compression force in the immediate vicinity of the wall. Cox and Brenner (1967) find as asymptotic expansion:

$$F/F_s = \varepsilon^{-1} \ (1- .2\varepsilon \ln \varepsilon + .9712 \ \varepsilon \ ) \tag{22}$$

$$\text{where: } \varepsilon = e_1/R \tag{23}$$

and e_1 is the distance between wall and sphere.
Truncating still earlier, one finds a lubrication limit, attributed to Taylor by Ambari et al (1984)

$$F/F_s = 1/\varepsilon \tag{24}$$

In the numerical model, in the contact points between the grains of two successive layers a contact force according to (24) has been assumed, where e_1 is taken as the distance between the spheres.
This force acts on the grains, resulting in a elastic compression, according to Timoshenko and Godier (1951) equal to:

$$\Delta s = A \ F^{2/3} \tag{25}$$

$$\text{in which: } A = \frac{9}{2}\left[\frac{(1 - \nu_c^2)^2}{E^2 \ R}\right]^{1/3} \tag{26}$$

where ν_c is the contraction coefficient
Thus the distance between the centers of two grains becomes $2R - \Delta s$; from the two equations (22) and (25) for F the quantity Δs may be eliminated; F can be related to the distance between the centers of the grains of two successive layers.
In order to demonstrate the resulting way of collision, fig.$9^{a..d}$ shows the motion of the center of gravity y and of the grain surface x when a (smooth) sphere approaches a wall, starting with a certain velocity; this velocity increases in the various figures a..d. In fig. $9^{a..c}$ the sphere comes to rest at a certain distance from the wall, eventually after some elastic rebound. In fig 9^{d} the suction forces between sphere and wall exceed the cavitation limit of the fluid, which liberates the sphere from the wall: an elastic rebound occurs.

Also in the numerical model for the grain piling a tetrahedral piling is assumed.The effect of protuberances is taken into account, with direct contact with elastic response when the distance between the grains becomes less than .01 times the grain diameter. Fig 8 shows the way of motion of the grains. Each grain falls in the hole, shaped by 4 other grains on a lower level. In the equation of motion in horizontal direction sand and water are taken together; in vertical direction sand and water are treated separately, where inertia effects have been taken into account. With respect to friction, a drag coefficient similar to eq. (7) is assumed.
Apart from the friction, resulting from the horizontal components of the pressures in the contact points, viscous friction between the various layers is taken into account

The model of the sheetflow layer disposed here has been combined with the near- bottom velocity model, exposed by Bakker and van Kesteren (1984). In this implicit model, the shear stress τ_b at the top of the sheet flow layer has been determined from the local velocity gradient:

$$\tau_b = \rho_w \kappa^2 z^2 \ \frac{u_2 - u_1}{\Delta z} \ \left|\frac{u_2 - u_1}{\Delta z}\right| \tag{27}$$

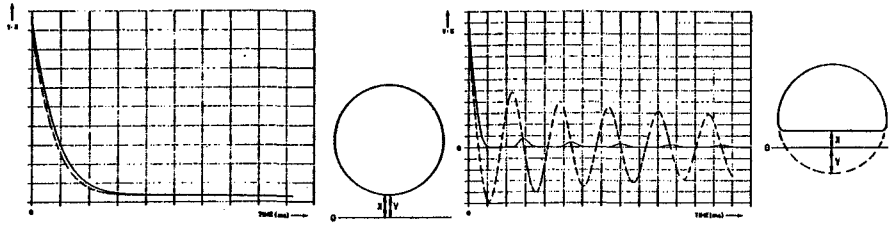

(a) U=.01 m/s

(c) U=.1 m/s

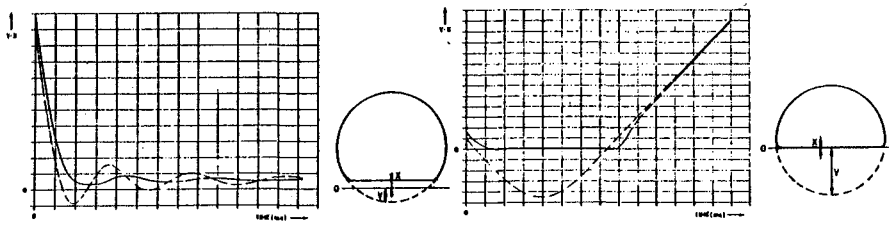

(b) U=.05 m/s
R=.1 mm, E=10 GPa, $\nu=10^{-6}m^2/s$

(d) U=1 m/s

—— x = distance sphere surface to wall
----y = distance sphere centre to wall minus sphere radius

Fig.9 Visco-elastic collision of sphere with wall.

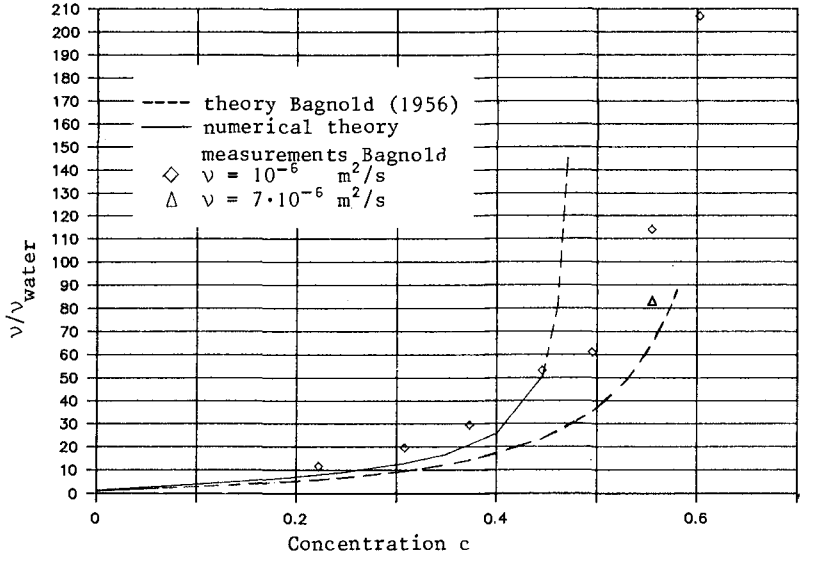

Fig.10 Increase of appearent viscosity as function of the concentration

where u_1 is the velocity of the upper sheet flow layer and u_2 of the first grid point in the (pure) water; the constant κ is the von Karman constant. The level "z=0" has been chosen at the still- sand level, starting from the intuitive feeling that the mixing length κz should be of the order of the vertical motion of the top of the sheetflow layer.

4.2. Results.

In this chapter the results of the numerical model are compared with experiments of Bagnold (1956) and Horikawa (1982)

Fig. 10 shows the results of a numerical simulation of plain shear, applied on grains with the same weight as the surrounding fluid. From this the increase of the concentration on pseudo- viscosity can be investigated. With the assumption of uniform shear between two parallel planes the motion becomes symmetrical, thus giving parallel motion of all the layers. Thus blocking is found when the grains in the layers can not slide between each other without transversal displacement. This occurs for a concentration higher than 48 %. Furthermore the increase in viscosity agrees rather well with Bagnold 's theory and measurements (fig 10).

However, where Bagnold experimentally finds a ratio between normal stress and shear stress equal to .75, the numerical model gives time-averaged normal stresses which are much lower. This is about as could be expected: for concentrations less than 48 % the grains move straight forward without hindering each other too much.

Fig 11 to 14 show the results of an experiment of Horikawa (1982), which has been numerically simulated.

Fig 11^a shows a comparison between measurements and numerical results concerning the velocity profile. Fig 11^b shows the velocities in the various sheetflow layers as function of time; totally 9 layers were mobilized. Layer 1 is the upper one. For the elasticity module a value of 10 MPa has been taken; however, similar computations with soft grains with an elasticity modulus of .1 MPa gave similar results. This indicates, that the effect of the viscous squeezing is much more of importance than the elasticity. Fig 13^a shows the concentration in the grain layers; the numerical model "chooses" its own concentration, depending on the interaction forces between the various layers. In the Horikawa experiment, this concentration is 74 % when the material is in rest (densiest packing) and about 60 % when the material is moving. The same appears from fig 13^b, giving the concentration profiles at various times.

Fig 12 gives the shear stress in the course of time for layer 1 and layer 9. Because in this case gravity takes care for vertical shifting of the layers (different from the Bagnold case), the pattern.is rather irregular. Therefore also the first harmonics are drawn; from this it shows, that the result of the analytical theory, a shear stress , constant per layer and increasing with the depth is too naive. The shear stress as found from the numerical model is not determined by the own weight of the grains, but by the shear stress on the surface. The result of the Bagnold theory of the constant ratio between shear stress and normal stress is checked also in fig 14, giving this ratio as it follows from the mathematical model. In the lower layers, which keep in rest, this ratio decreases gradually (starting from .75)

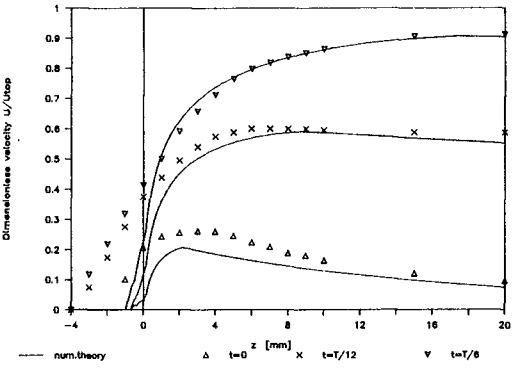

measurements from Horikawa (1982): exp.(1-1)

Fig.11a Velocity profiles at various times (num.comp.).

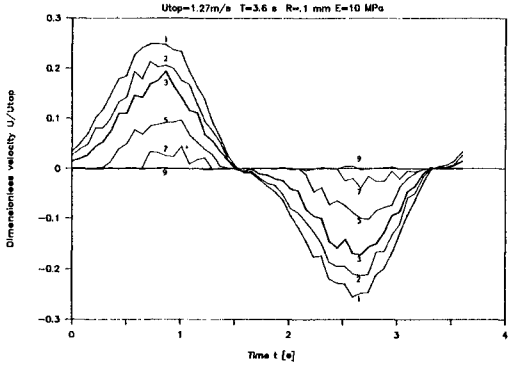

Fig.11b Velocity of the grain layers 1,2,3,5,7 and 9 (num.comp.).

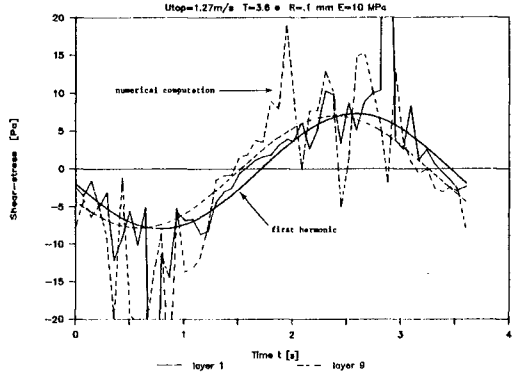

Fig.12 Shear stress in the grain layers 1 and 9 (num.comp.).

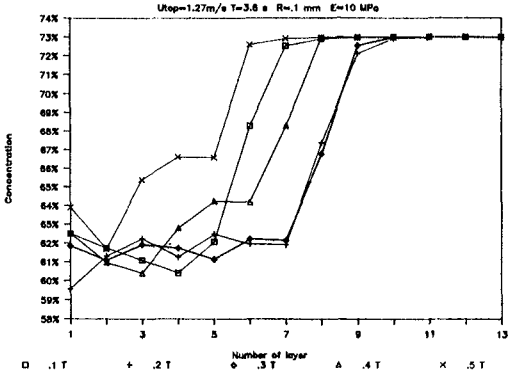

Fig.13a Concentration profiles at various times (num.comp.).

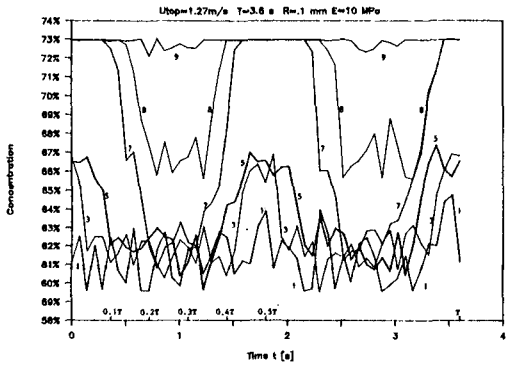

Fig.13b Concentration in the grain layers 1,3,5,7,8 and 9 (num.comp.).

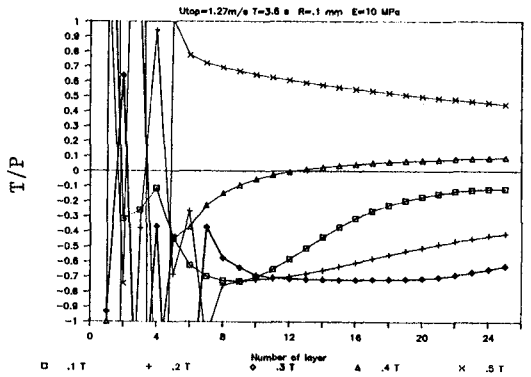

Fig.14 Ratio "shear stress / normal stress" at various times (num.comp).

because of the increasing own weight. In the higher layers, which are in motion, the ratio varies randomly between +10 and -10
It shows, that the numerical model does not tally quite with Bagnold's theory with respect to the dispersive stress.However, the physics of the Bagnold theory is not quite clear.
Indeed, one finds in the viscous region a "transverse pressure analogous to that which occurs in the static arching of grains in contact ", as stated by Bagnold (1954) ("a transverse dispersive tendency of a dense overtaking motor traffic along a one-way road"). However, in the numerical model grains moving from each other after a "collision" tear the layers from each other, by inertia of the grains, combined with viscous forces. This gives tension forces between the grains of the same order as the pressure forces. Where the pressure forces are more vigorous, the tension forces are more persistent, resulting in a very small value of the normal pressure. This appears from calculations with simplified models.
Furthermore dispersive forces are created by the convective terms in the equation of motion for the water in the pores between the grains. In the numerical model, these terms appear to be only a few percent of the shear stress. On one hand this follows from calculations in which the convective terms were left out, on the other hand by simplified calculations in which only this effect was taken into account.
From these calculations one finds a timeaveraged vertical pressure gradient of the order of magnitude of the energy of the vertical motion on the top of the shear flow layer.This vertical motion appears to be in the model only a few mm/sec.
Altogether the impression arises, that the motion on the top of the shear flow layer is too small; the motion is too smooth with as a result, that the shear stresses are too low and therefore the intrusion depth too small: in the numerical model the intrusion depth is 1.5 mm and in the Horikawa experiments 5 mm.
On the other hand Horikawa et al might have overestimated the transport somewhat, although this certainly will not explain the difference in order of magnitude.
Before the grains are able to move the grain structure first has to adopt a somewhat higher porosity. Therefore the highest point with zero amplitude, which determines the lower boundary of the velocity profile of the sheetflow-layer will be higher than the highest point of zero dilatation (cp. fig 11 and 12). This has not been taken into account by Horikawa et al (1982).

5. CONCLUSIONS.

Comparing analytical and numerical model with one of the experimental results of Horikawa et al (1982) leads to the following conclusions:

a. The analytical model reproduces concentration profiles and intrusion depth reasonably well (fig 6 and 7)). Assumptions about velocity profile and shear stress distribution however are too primitive (cp. fig 5 and fig 11 for analytical and numerical computations respectively).

b. Use of the Bagnold theory of constant shear stress ratio in the analytical model leads to better approximation of the intrusion depth than in the numerical model. The numerical model underestimates this depth.
However, the physics of the Bagnold theory is not quite clear.

Indeed, one finds in the viscous region a "transverse pressure analogous to that which occurs in the static arching of grains in contact ", as stated by Bagnold (1954). However, in the numerical model grains moving from each other after a "collision" tear the layers from each other, by inertia of the grains, combined with viscous forces. This gives tension forces between the grains of the same order as the pressure forces. Where the pressure forces are more vigorous, the tension forces are more persistent, resulting in a very small value of the normal pressure.

Furthermore dispersive forces are created by the convective terms in the equation of motion for the water in the pores between the grains. In the numerical model, these terms appear to be only a few percent of the shear stress.

In the numerical model the ratio between pressure and shear stress as found by Bagnold is only a continuous function of depth in the region with no significant motion (fig 14). In the sheetflow layers, the ratio varies at random between +10 and -10.

The increase of viscosity as found by Bagnold reproduces rather well in the numerical model (fig 10). However, simulating numerically the experimental set-up of Bagnold (grains with the same weight as the fluid) in the model a total blocking occurs at a concentration of 48 %, due to a schematization, which is too regular.

c. Of the two possibilities of the numerical model for transferring grain forces from one layer to another: (by "lubrication" or by direct elastic contact), the effect of lubrication appears to be the most important. This appears from comparitive calculations with various values of the elasticity of the grains, which did not have much effect on the intrusion depth of the sheetflow

d. The impression rises, - as well from the velocity distribution as from the intrusion depth - that the present numerical model is too smooth. In this model the transition between sheet flow layer and the uper layer is not yet well reproduced. One might expect here a transition layer with high turbulence, as occurs in density currents. This will give higher shear stress and higher vertical gradients of time- averaged vertical pressures, probably resulting in a higher intrusion depth of the sheetflow.

e. Before the grains are able to move the grain structure first has to adopt a somewhat higher porosity. Therefore the highest point with zero amplitude, which determines the lower boundary of the velocity profile of the sheetflow-layer will be higher than the highest point of zero dilatation (cp. fig 11 and 12). This has not been taken into account by Horikawa et al (1982). This might lead to overestimation of the transport.

f. A more extensive experimental verification of the theory under a broad range of circumstances is needed. For this goal a large pulsating water tunnel is constructed in the Delft Hydraulics Laboratory.

6. ACKNOWLEDGEMENT.

The authors are indebted to prof. K. Horikawa for sending additional information about his experiments. Mr. E. Haak carried out very useful computations. Financial support by the Royal Dutch Society for Sciences and by Rijkswaterstaat is gratefully acknowledged.

7. REFERENCES.

Ambari,A., B. Gauthiar-Manuel and E. Guyon,
Wail effects on a sphare, translating at constant valocity
J. Fluid Mech. 149, pp 235-253 (1984).
Bagnoid, R.A.,
Eperiments on a gravity-frae disparaion of larga soiid
apheres in a Newtonlan fluid under shear.
Proc. Royal Society, Voi. 225, A, p. 49 (1954).
Bagnold, R.A.,
The flow of cohesionlasa grains in fluids,
Proc, Royal Society, Voi. 249, A964, p. 235, Dacembar 18 (1956).
Bakker, W.T.,
Sand concentration in an osciliatory fiow,
Proc. 14th Conf. on Coastai Engng. Copenhagen (i974).
Bakker, W.T. and Van Kesteren, W.G.M.,
Near-bottom velocitiea in wavea with a current:
analyticai and numerical computations
Proc. 19th Conf. on Coastal Engng., Houston (i984).
Cox,R.G. and M.Branner,
The slow motion of a sphera through a viscous fluid towards a plana
surface - II Small gap, including inertial effects.
Chem. Engng. Sci. 22, i753 - i777 (1967).
Morikawa, K., Watanaba, A., and Katori, S.,
Sediment transport under sheet fiow condition.
Proc. 18th Conf. on Coastal Engng. Cape Town (i982).
Lorentz, H.A.,
Abhandl.theor. Physik, Leipzig 1, 23 (1907).
Timoshenko, S.P. and Godier, J.N.,
Theory of elasticity,
Mc Graw Hiil, New York (i951).

8. NOTATION.

a		drag coefficient (eq.(7)).
A	$[m/N^{2/3}]$	stiffness parameter in elastic grain deformation (eq.(25).
b		horizontai distance / grain diametar betwaen grains in tetrahedralrectangular piiing.
c		concentration.
c_0		concentration at maximum density.
c_ℓ		limit concentration in the sheetflow (eq.(15)).
D	[m]	grain diameter.
e	[m]	spacing between spheres.
E	$[N/m^2]$	Youngs moduius of the grains.
F	[N]	grain interaction force.
F_s	[N]	Stokes force (eq.(21)).
g	$[m/s^2]$	acceleration of gravity.
h		vertical distance over grain diameter between centres of adjacent grainiayers.
h_0		value of h in the ciosest packing of grainiayars in tha sheetflow.
H	[m]	intrusion depth.
k	[m/s]	coefficient of permeability.
N		Bagnold-number (eq.(2)).
p	[Pa]	grain force due to vertical diapersive prassura gradient (eq.(5)).
p_0	[Pa]	mean of p (eq.(6)).
p_2	[Pa]	second harmonic of p (eq.(6)).
P	[Pa]	dispersive grain prassure.
R	[m]	grain radius.
Δs	[m]	elastic grain distorsion (eq.(25)).
T	[Pa]	effective grain shear stress.
u	[m/s]	horizontal veiocity
U	[m/s]	horizontai vaiocity at top of tha sheetflow.
z	[m]	vertical coordinata (pos. upwards).
z_g	[m]	vertical coordinate of grainlayer.
Z^g	[m]	verticai length scaie in tha sheatflow (aq.(12)).
α	[deg]	angle of intarnal friction.
ε		spacing between grains over grainradius (aq.(23)).
θ	[deg]	phase angle of osciiiating motion.
κ		Von Karman constant (eq.(27)).
λ		linear concentration (eq.(ic)).
ν	$[m^2/s]$	kinematic viscosity.
ρ_w	$[kg/m^3]$	specific density of water.
ρ_s	$[kg/m^3]$	specific density of sand.
τ_b	[Pa]	shear stress at the top of the sheetfiow.
ω	$[s^{-1}]$	anguiar frequency of the osciliating motion.
$\dot{x}$		time-derivative of x.
$\bar{x}$		mean value of x.
x_*		amplitude of x.
$\hat{x}$		dimensionless value of x.
Δx		increment of x.

CHAPTER 72

Toward A Simple Model of the Wave Breaking Transition Region in Surf Zones

David R. Basco[1] and Takao Yamashita[2]

Abstract

Breaking waves undergo a transition from oscillatory, irrotational motion, to highly rotational (turbulent) motion with some particle translation. On plane or monotonically decreasing beach profiles, this physically takes place in such a way that the mean water level remains essentially constant within the transition region. Further shoreward a rapid set-up takes place within the inner, bore-like region. The new surf zone model of Svendsen (1984) begins at this transition point and the new wave there contains a trapped volume of water within the surface roller moving with the wave speed. This paper describes a simple model over the transition zone designed to match the Svendsen (1984) model at the end of the transition region. It uses a simple, linear growth model for the surface roller area development and semi-empirical model for the variation of the wave shape factor. Breaking wave type can vary from spilling through plunging as given by a surf similarity parameter.

The model calculates the wave height decrease and width of the transition region for all breaker types on plane or monotonically depth decreasing beaches.

1.0 Introduction

A general understanding of the mean flow fields in the transition region of breaking-broken water waves has yet to be achieved. The wave character undergoes a transformation from irrotational, orbital particle motion to rotational, highly turbulent motion with some particle translation. We shall herein define the transition region width from the break point to the point (transition point) where the mean water surface changes from essentially level to an increasing slope (wave set-up). This paper presents relatively simple relationships to calculate the wave height decrease and width of the transition region for plane beaches.

After the transition, the broken wave propagates as a moving bore containing a trapped volume of water in the surface roller moving with the wave speed (Svendsen, 1984). Plunging breakers have an identifiable plunge point where the overturning, falling jet impacts the oncoming trough. Thereafter, a relatively short and violent flow redistribution occurs to develop the bore-like wave character. Spilling breakers have essentially zero plunge distance to begin rotation, but then a relatively long and gradual flow redistribution

[1]Professor Civil Engineering and Director, Coastal Engineering Institute, Old Dominion Univ., Norfolk, VA 23508
[2]Instructor, Diaster Prevention Research Institute, Kyoto University Kyoto 611, Japan.

takes place over the water column. In general, the transition width for spilling breakers is greater than for plunging breakers. We shall tacitly assume that the end of the transition region for both plungers and spillers is also identifiable by the bore-like character of the broken wave within the inner-surf zone region.

Wave height change within and the width of the transition region are not insignificant quantities. Figure 1 shows the wave height, H; celerity, c; and mean water level, $\bar{\eta}$ (set-down, set-up) variations before and through the surf zone (courtesy J. Buhr Hansen) for laboratory scale waves breaking on a plane beach. Zone I is the transition region where $\bar{\eta}$ is (relatively) constant. In this example, roughly one-third of the wave height decrease takes place in a transition distance that is approximately one-quarter of the surf zone width. Galvin (1969) presented a method to estimate the plunge distance from laboratory data on plane beaches. Visser (1984) developed a mathematical model for the wave-induced longshore current which critically hinged on the physical fact that dissipation of wave energy begins at the plunge point and not over the entire surf zone. His laboratory experiments for plunging breakers resulted in plunge distances ranging from 22-43% of the total surf zone width. By definition, the transition width will be an even greater percentage.

We limit this discussion to waves breaking on plane or monotonically (depth) decreasing beaches. In deep water or for waves breaking on bars, the excessive depths after the break point will result in completely different internal physical processes. A fully developed, bore-like wave character may never be achieved, the mean water level may not stay constant and consequently, the transition width may have to be redefined.

2.0 Qualitative Description

A qualitative description of processes and mechanisms within the transition region has been presented by Basco (1985). Both classic spilling and plunging type breakers were found to have similar initial breaking motions, but at vastly different scales. Two primary vortex motions were identified. A plunger vortex is initially created by the overturning jet, which in turn causes a splash-up of trough fluid and subsequent formation of a surface vortex of similar scale. Figure 2 schematically depicts a strong plunging breaker. For plunging breakers, this plunger vortex translates laterally to push up a new surface wave with new wave kinematics that continues propagating into the inner surf zone. For spilling breakers, the small scale plunger vortex creates a small scale disturbance masked by the larger carrier wave. However, the resulting surface roller at the crest slides down and grows in size on the face of the main wave. The end result is also a new wave kinematic structure.

This sequence of events is schematically depicted in Figure 3 for a plunging breaker. Two new key features were introduced for the first time by Basco (1985). The overturning jet is deflected down and to the rear by the onrushing trough to create a rotating fluid mass system (steps 1-5). This plunger vortex translates horizontally much

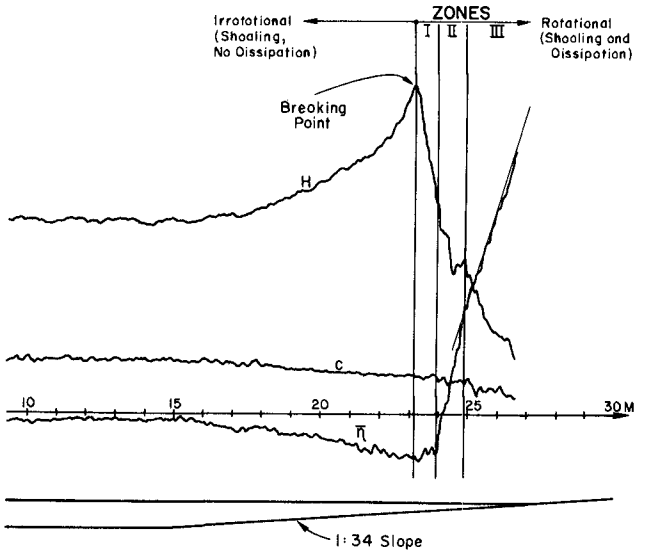

Fig. 1 Example of wave height, celerity and mean water level variations before and after breaking (Test No. 053074 courtesy J. Buhr Hansen, 1982)

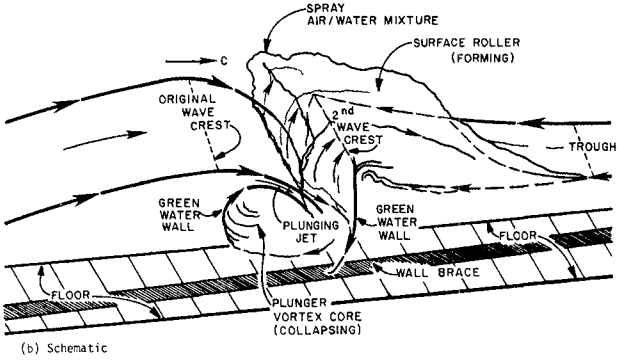

Fig. 2 Schematic of strong plunging breaker

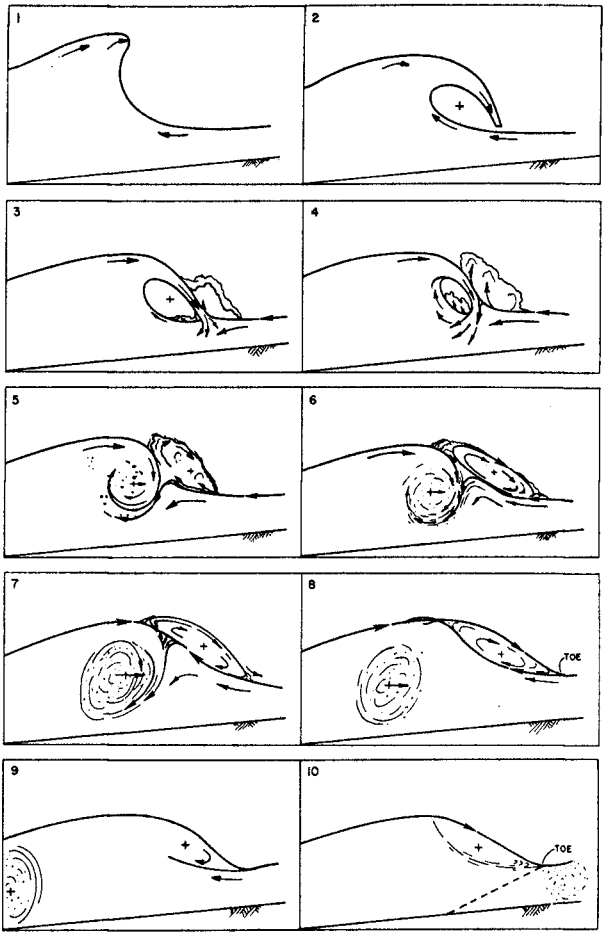

Fig. 3 Schematic sequence of breaking wave events (From Basco, 1985)

like a piston wave board to push up a rising water surface and simultaneously create a new, secondary surface disturbance (5-8). The plunger vortex comes to rest and is left behind which marks the end of the original propagating wave (8-10). The transition point occurs somewhere near step 8.

A new wave has been created (9-10) with kinematic structure that results from mean momentum redistribution and turbulence transport in both vertical and horizontal dimensions. Turbulance production, advection, diffusion and dissipation are locally in a nonequilibrium state. The turbulent redistribution of the mean, internal velocity field results in a trapped, concentration of mass within the surface roller that moves with the wave. Beneath the roller, fluid particles retain their orbital character but in a highly turbulent state.

The transition region can now be viewed as the zone where the original, irrotational, wave like motion comes to rest and simultaneously generates a new, secondary, bore-like wave with completely different wave kinematics as in the Svendsen (1984) model discussed below.

3.0 Recent Theory and Paradoxes

The surf zone model of Svendsen (1984) begins at the transition point. Here, the mean velocity profile relative to a fixed observer is as shown by the dashed line in Figure 4 and area, A. Svendsen found a correlation between A and wave height squared from laboratory data as shown in Figure 4b. The presence of the trapped surface roller was modeled by the simple velocity profile (Figure 4b) and significantly altered both the momentum flux (radiation stress) and energy flux over that determined by linear wave theory. In fact, the radiation stress, S_{xx} increased by 50-100% and the energy flux, E_f essentially doubled.

The resulting conservation equations when solved together permitted calculation of the wave height decrease and mean water surface increase across the inner region. An example comparison of theory (solid line) and laboratory experimental data is reproduced as Figure 5 (from Svendsen, 1984). Note that the theory begins at the transition point, not at the break point. And, that the theory without the surface roller effect (dashed line) gives incorrect results.

Consider the cross-shore momentum balance equation for depth-integrated and time-averaged wave motion

$$\frac{dS_{xx}}{dx} + \rho g h \frac{d\bar{\eta}}{dx} = 0 \qquad (1)$$

where: $h = \bar{\eta} + d$, the mean water depth,
d = the still water depth,
$\bar{\eta}$ = the mean water level change (set-up, set-down),
ρ = the fluid mass density, and
g = the gavitational acceleration.

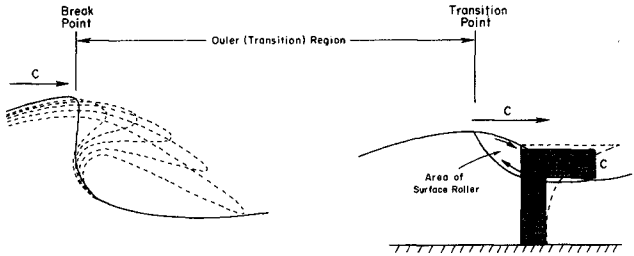

(a) Velocity profile at end of transition (transition point)

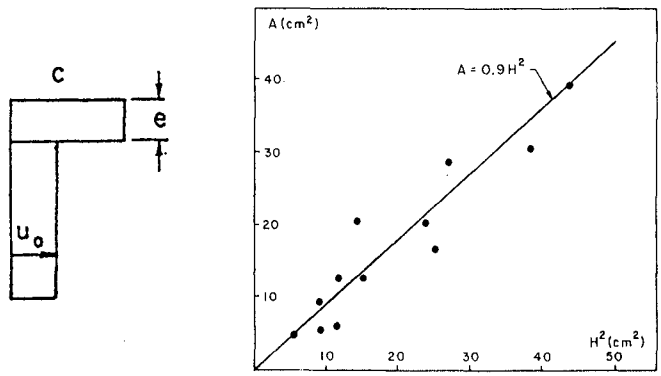

(b) Correlation between surface roller area and wave height, H^2 (from Svendsen, 1984)

Fig. 4 Schematic of wave breaking profiles through transition region

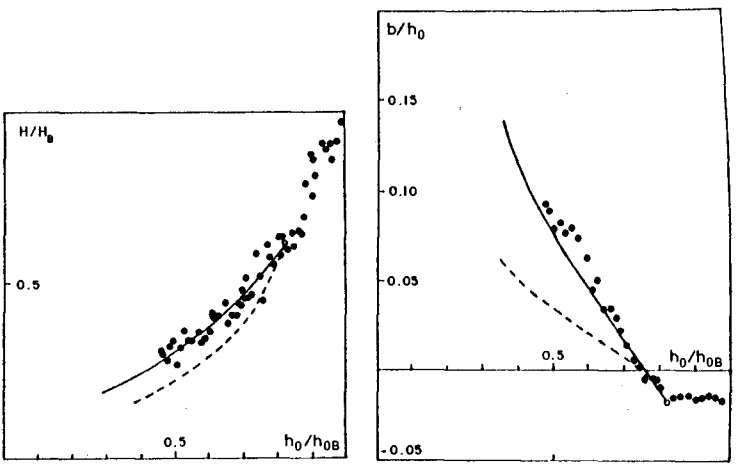

Fig. 5 Wave heights and set-up for a wave with deep water steepness (From Svendsen, 1984, Fig. 13, p. 322)

The data in Figures 1 and 5 reveal that $\bar{\eta}$ is essentially constant across the transition region. This means from Eqn. (1) that S_{xx} is proportional to the wave height squared (e.g. Longuet-Higgins and Stewart, 1964). This presents a paradox. How can $\bar{\eta}$ (i.e. Sxx) remain constant when H decreases rapidly across the transition region? We shall return to this point below.

A second point of emphasis concerns the common misconception that breaking wave height decrease is solely due to energy dissipation through turbulence. Using time-averaged conservation laws of momentum and energy across the transition region considered as one control volume (analogous to the hydraulic jump), Svendsen (1984) demonstrated that about one-third of the energy change due to wave height decrease was actually lost as dissipation. The remaining two-thirds was energy redistribution between potential (pressure) and kinetic (velocity) forms. Thus to continue to view wave breaking as the same wave propagating with some energy dissipation is to miss the fundamental physical transition taking place internally between the velocity and pressure related terms in the momentum and energy balance equations.

4.0 Elements of a Simple Quantified Model

It is instructive to first quantify the momentum flux distribution due to velocity and pressure related components across a steady hydraulic jump.

4.1 Stationary Hydraulic Jump

The total momentum, m (per unit mass density and sectional area) at any section before, within, and after a hydraulic jump can be written

$$m = m_v + m_p \tag{2}$$

or

$$m = \frac{\alpha q^2}{d} + \frac{1}{2} g d^2 \tag{3}$$

where: $q \equiv \int_0^d u\,dz$, the volumetric flowrate,
u = the horizontal velocity component,
d = the local water depth,
z = the vertical coordinate, and
$\alpha \equiv \frac{d}{q^2}\int_0^d u^2\,dz$, the momentum correction coefficient.

Total momentum is the sum of that due to velocity, m_v and that due to an assumed hydrostatic pressure distribution, m_p.

Using the definition of a Froude number, F along with known jump entrance conditions, u_1, d_1, it can be easily show that

$$\frac{m_{v_1}}{m} = \frac{F_1^2}{F_1^2 + \frac{1}{2}} \tag{4}$$

from which it follows that

$$\frac{m_{p_1}}{m} = 1 - \frac{m_{v_1}}{m} \tag{5}$$

From the sequent-depth equation the subcritical downstream depth, d_2, can be determined and similar expressions for m_{v2} and m_{p2} established in terms of F_2. The key fact is that total momentum, m is constant across the hydraulic jump.

Svendsen and Madison (1983) present a new hydraulic jump theory in which the momentum correction coefficient, α is given by the relationship

$$\alpha \equiv \zeta\left[1 + \frac{1}{2F_1^2}(1-\zeta^2)\right] \tag{6}$$

where $$\zeta = \frac{d(x)}{d_1}$$

Using their method, one can calculate d(x) for a given F_1 and consequently, using (6), (3), (4) and (5), in that order, we can also calculate the theoretical partition of m_v and m_p across the jump. Figure 6 presents the results for some representative inlet Froude numbers. For example, when F_1=3 almost 95% of the total momentum at the inlet is due to velocity and only 5% from pressure. Whereas, at the exit, now only 25% is velocity related while nearly 75% is due to pressure. We also see that the jump roller which contains a flow reversal creates $\alpha > 1$ through the jump and is responsible for the nonlinear distributions of m_v and m_p components.

4.2 Broken Waves in Inner Surf Zone Region

Next, consider the time-averaged and depth-integrated excess momentum flux, i.e. the radiation stress for the inner region. For the simplified velocity profile through the trapped surface roller (Fig. 4b), Svendsen (1984) found that

$$\begin{aligned} S_{xx} &= S_v + S_p \\ &= \left[\rho g H^2\left(B_o + \frac{A}{H^2}\frac{h}{L}\right)\right] + \frac{1}{2}\rho g H^2 B_o \end{aligned} \tag{7}$$

where

L = the wave length, and

$$B_o \equiv \frac{1}{T}\int_0^T \frac{\eta^2}{H^2}\,dt \tag{8}$$

with

T = the wave period.

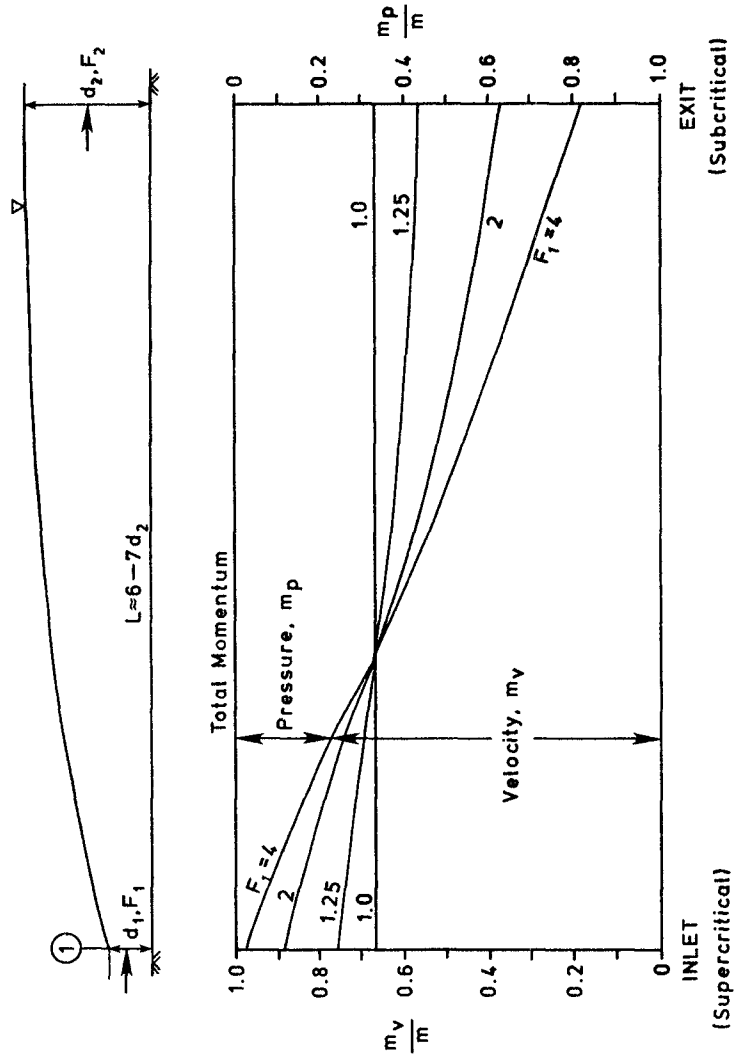

Fig. 6 Partition of velocity and pressure momentum components through a steady, hydraulic jump

B_o is a wave surface shape factor discussed in further detail below. The first part of Equation (7) is that part of S_{xx} due to velocity, S_v and the latter is due to pressure, S_p. Recall that by definition, S_{xx} is the total flux of horizontal momentum across a vertical plane minus the stillwater hydrostatic pressure force. Hence the total force (per unit length) at any section is given by

$$M_{xx} = S_{xx} + \frac{1}{2}\rho g d^2 \tag{9}$$

This results in a total pressure related component, F_p for total momentum given by

$$\begin{aligned} F_p &= S_p + \tfrac{1}{2}\rho g d^2 \\ &= \tfrac{1}{2}\rho g H^2 B_o + \tfrac{1}{2}\rho g d^2 \\ &= \tfrac{1}{2}\rho g (H^2 B_o + d^2) \end{aligned} \tag{10}$$

As an example, consider the partition of a normalized radiation stress, P given by

$$P = P_v \text{ (velocity)} + P_p \text{ (pressure)}$$

$$= \frac{S_{xx}}{\rho g H^2} = \left(B_o + \frac{A}{H^2}\frac{h}{L}\right) + \frac{1}{2} B_o \tag{11}$$

From typical values for plunging breakers, as given by Svendsen (1984) for A/H^2, h/L and B_o, the ratio of P_v/P_p was about 3.5 at the transition point. This means that about 80% of the total excess momentum flux at the transition point is due to velocity. However, when total momentum is considered, the broken waves account for only 20% of the total present.

4.3 Breaking/Broken Waves in Transition Region.

We now return to the first paradox, namely how the mean water level, $\bar{\eta}$ and hence S_{xx} from Equation (1) can remain constant when H decreases rapidly across the transition region. From Equation (7) it becomes apparent that both the A/H^2 ratio and B_o must vary considerably to keep S_{xx} at a constant level. In what follows we tacitly assume that h/L remains essentially constant within the transition region, for a give situation.

Surface Roller Area. For plunging breakers, the surface roller begins forming at the plunge point. For spillers, it grows in size right from the break point. No experimental information is available. We therefore assume a linear growth of the A/H^2 ratio as depicted in Figure 7 from a zero level to a peak of 0.9 at the transition point. Consequently, we match the Svendsen (1984) model at the start of the inner surf zone region.

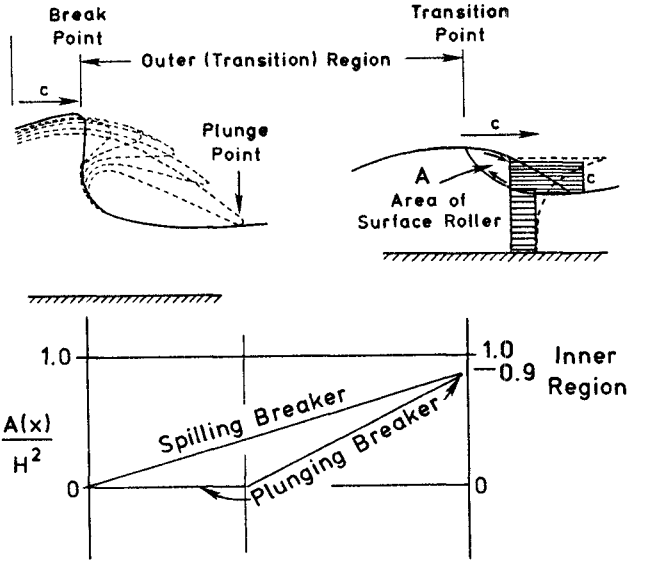

Fig. 7 Empirical $A(x)/H^2$ distribution through transition region for spilling and plunging breakers

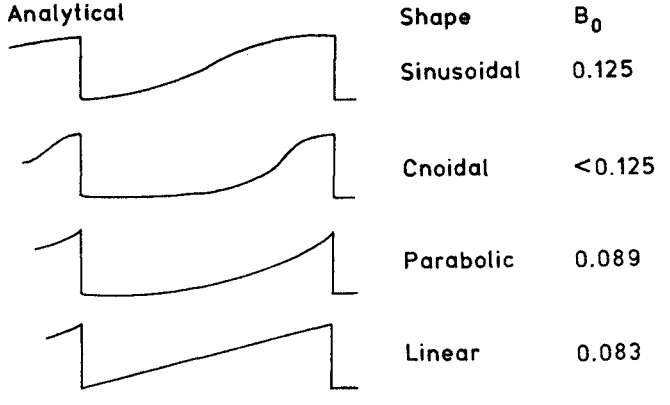

Fig. 8 Theoretical breaking wave shapes and resulting wave shape factor, B_0 as defined by Eqn. (8)

Surface Shape Factor, B_o. Figure 8 depicts some possible breaking wave shapes (sinusoidal, cnoidal, parabolic, linear) that can all be treated analytically within Equation (8) to calculatetheoretical values of B_o at the moment of wave breaking (vertical front face). The resulting B_o values are also shown in Figure 8 and are always less than 0.125.

Using the laboratory measurements of Hansen (1982), values of B_o for various positions across the surf zone were calculated by Svendsen (1984) as reproduced here in Figure 9. For this data, peaky wave profiles produced B_o values as low as 0.035 at the break point (h_o/h_{ob}=1.0). Then, B_o values increased rapidly towards values around 0.06-0.09. Svendsen (1984) noted some variation of B_o with deep water steepness, H_o/L_o.

The surf similarity parameter (i.e., the Iribarren number) defined as

$$\xi \equiv \frac{\text{Bottom Slope}}{(\text{Deep Water Steepness})^{1/2}} = \frac{\tan\beta}{(H_o/L_o)^{1/2}} \qquad (12)$$

is useful to further quantify the possible B_o variations. Figure 10 presents combined theoretical and experimental results (Figure 9) in an heurestic fashion for B_o versus h_o/h_{ob} for spilling (small ξ) through plunging (large ξ) breakers.

In the wave shoaling region ($h_o/h_{ob}>1$) the waves begin with near sinusoidal shape (B_o=0.125) and are transformed in shape to become spilling (relatively high B_o values) or plunging (relatively low B_o values) breakers. Further theoretical results are needed using numerical wave shoaling simulations and experimentally determined data to further quantify this region.

After breaking ($h_o/h_{ob}<1$) the experimentally measured results from Figure 9 have been replotted and smooth curves drawn in Figure 10. Much more experimental data is needed to confirm these trends. Ultimately, the smallest waves running up the beach return to a sinusoidal form. Figure 10 can be used to estimate B_o values for various positions (h_o/h_{ob}) and wave types (ξ) found in surf zones.

Transition Width,W. Figure 10 also shows a curve marking the width of the transition region. At best, this is only a very crude estimate based upon some limited data presented in Svendsen (1984). Spilling transitions are shown to be wider than plunging transition regions. Much further experimental and theoretical research is needed to quantify this estimate. For example, ongoing work is attempting to quantify the partition between momentum flux due to velocity and that due to pressure (wave induced plus static) in a reference frame moving with celerity, c across the transition region. When coupled with a proper energy dissipation model (recall second paradox above), it should be theoretically possible to predict the transition width. The procedure being followed is essentially that used by Madsen and Svendsen (1983) to calculate the length of the stationary hydraulic

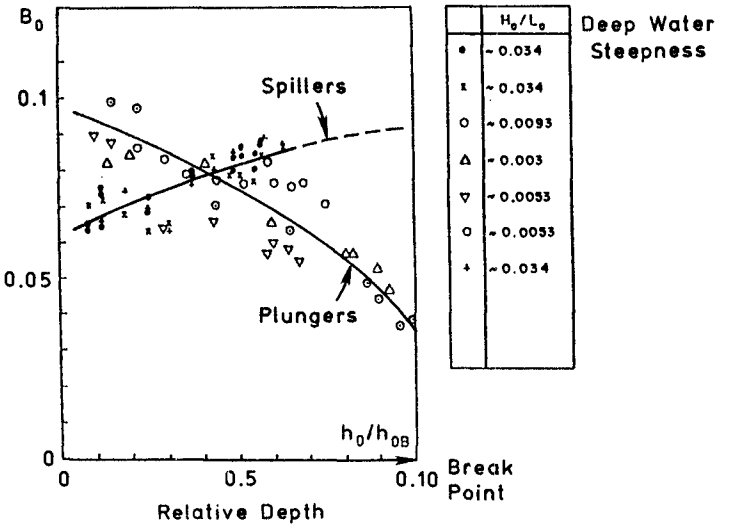

Fig. 9 Measured values of B_0 as defined by Eqn. (8) (From Svendsen, 1984, Fig. 9, p. 316)

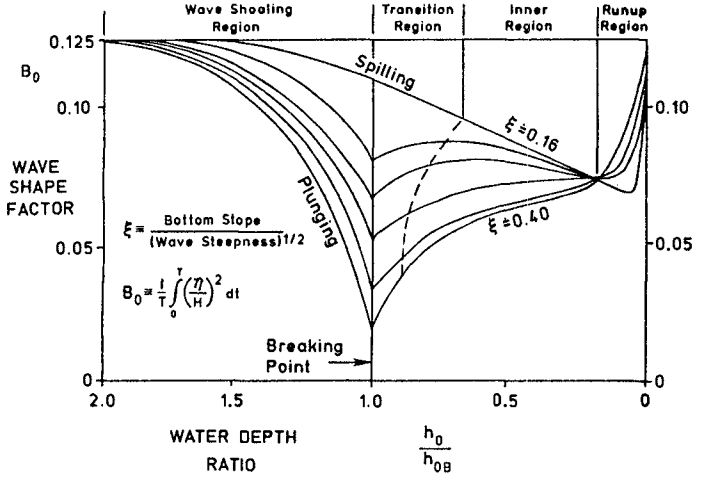

Fig. 10 Variation of wave shape factor, B_0 before and after breaking of spilling through plunging type breakers

jump. Results of numerical model simulations of breaking wave overturning and jet falling up to the plunge point will be employed to calculate the plunge distance.

4.4 An Example Computation

Equation (7) can be rewritten

$$S_{xx} = \rho g H^2 \left(\frac{3}{2} B_o + \frac{A}{H^2}\frac{h}{L}\right) \qquad (13)$$

Given the breaking wave height, H_b, the fluid mass density (fresh or sea water) and the $(h/L)_b$ ratio at breaking, it is now possible to calculate the wave height decrease and width of the transition region. Keeping in mind, of course, these result are only for plane beaches. The key fact is that S_{xx} remains constant across the transition. Figure 7 and 10 are utilized to estimate the $A(x)/H^2$ and $B_o(x)$ variables required.

Plunging Breaker. Assume the deep water steepness (H_o/L_o) and beach slope produce a similarity parameter, ξ equal to 0.35. This is a fairly strong plunging breaker. The computation proceeds as follows (H_b=2.5m, sea water, $(h/L)_b$=0.057):

$$\begin{aligned}
(B_o)_b &= 0.035 \\
A(x) &= 0 \\
(S_{xx})_b &= 0.32 \times 10^4 \text{ N} \\
A/H^2 &= 0.9 \\
(B_o)_T &= 0.045 \\
(S_{xx})_T &= 0.32 * 10^4 \\
&= 10^4 H_T^2 \left[\tfrac{3}{2}(0.045) + 0.9(0.057)\right] \\
H_T &= 1.6 \text{ m} \\
\therefore \quad H_T/H_b &= 0.65
\end{aligned}$$

For all intermediate locations between H_b and H_T, use A equal to zero up to plunge point and Figure 7 beyond linear by interpolation. The resultant H(x) is nonlinear (Eqn. 13).

Spilling Breaker. Now assume the incoming wave gives ξ equal to about 0.2 on the same beach. Using the same values as before (H_b=2.5m, sea water, $(h/L)_b$=0.057 gives:

$$\begin{aligned}
(B_o)_b &= 0.10 \\
A(x) &= 0 \\
(S_{xx})_b &= 0.94 \times 10^4 \text{ N} \\
A/H^2 &= 0.9
\end{aligned}$$

$$(B_o)_T = 0.09$$

$$H_T = 2.2\ m$$

$$\therefore\ H_T/H_b = 0.88$$

Now all intermediate points use linear interpolation for A(x). The resulting H(x) curve is also nonlinear.

These results can now be used as input to the surf zone model of Svendsen (1984) to calculate the H(x) and h(x) distribution over the remainder of the surf zone.

5.0 Summary Conclusions

A simple, quasi-empirical model for the wave breaking transition region of plane and monotonically decreasing beach profiles has been developed. The nonlinear wave height decrease and transition width for various breaker types can be estimated. The key element in the model is the fact that the mean water level is constant. Consequently, the wave ray, radiation stress component is also constant. An empirical, linear formulation is postulated for the surface roller area development. And, a semi-empirical formulation is developed for the wave shape factor. These two variables are taken so that the resulting model matches that developed by Svendsen (1984) at the end of the transition region, i.e. the start of the inner, bore-like wave region. The weakest part of the model is the limited empirical data available to estimate the transition width.

The research effort is ongoing and now focusing on theoretical means to determine the transition width.

The model is limited to plane or monotonoically decreasing beach profiles. But it is seen as a necessary first step to develop similar methods for bar/trough beaches.

References

Basco, D.R. (1980) A Qualitative Description of Wave Breaking, Journal of Waterway, Port, Coastal and Ocean Engineering, Vol. III, No. 2, March, pp. 171-188.

Galvin, C.J. Jr. (1969) Breaker Travel and Choice of Design Wave Height, Journal WW2, Vol. 95, No. 2, May, pp. 175-200.

Hansen, J.B. (1982) personal communication.

Longuet-Higgins, M.S. and R.W. Stewart. (1964) Radiation Stress in Water Waves: A Physical Discussion With Applications, Deep-Sea Research, Vol. II, No. 4, Oxford, England, August, pp. 529-562.

Madsen, P.A. and I.A. Svendsen (1983) Turbulent Bores and Hydraulic Jumps, Journal Fluid Mechanics, Vol. 129, pp. 1-25.

Svendsen, I.A. (1984) Wave Heights and Set-up in a Surf Zone Coastal Engineering, Vol. 8, pp. 303-329.

Visser, P.J. (1984) Uniform Longshore Current Measurements and Calculations, Proceedings, 19th ICCE, (Houston), Vol. III, pp. 2192-2207.

CHAPTER 73

A Numerical Investigation of The Longshore Current Profile for Multiple Bar/Trough Beaches

Steven K. Baum[1] and David R. Basco[2]

Abstract

A numerical model is developed which calculates the longshore current profile for an arbitrary bottom profile. The basis of the model is the use of radiation stress theory in a longshore momentum balance equation which includes a driving stress, a bottom stress, and a lateral mixing stress. Each of the stresses is derived from previously developed formulations, rederiving them to take into account separate cross shore variations in the wave height and the water depth, as well as the wave approach angle. This is done to dispense with the constant wave breaking index assumption used to model wave decay in the surf zone, which is rejected as unrealistic for natural beaches. A numerical model is used to calculate distributions of the wave height and water depth across the surf zone for arbitrary, yet realistic, bottom profiles. A numerical model of the theoretically derived longshore momentum balance equation is developed and solved using the distributions obtained from the wave decay model. The profiles calculated are compared to previous theoretical models and to laboratory and field measurements.

1.0 Introduction

All present-day longshore current models are based on concepts of radiation stress as first introduced by Longuet-Higgins and Stewart (1964). Longuet-Higgins (1970) and others applied these time-averaging principles to the depth-integrated momentum balance equation to obtain the longshore current profile. The component stresses (radiation shear stress, bottom stress and lateral turbulent mixing stress) in the alongshore momentum equation are expressed in terms of three key variables to obtain the current profile as a function of distance from the shoreline. These three variables are the mean water depth, the wave height and the wave angle. More accurately, the gradient of the longshore current across the surf zone is computed using the gradients of water depth, wave height and wave angle across the surf zone.

The original model of Longuet-Higgins (1970) employed many simplifying assumptions regarding these three variables. This permitted an analytical solution to be obtained which facilitated

[1]Ph.D. Candidate, Department of Oceanography, Texas A&M University, College Station, TX

[2]Professor and Director, Coastal Engineering Institute, Department of Civil Engineering, Old Dominion University, Norfolk, VA 23508

physical understanding. For example, Longuet-Higgins (1970) related the wave height to the water depth using a constant wave breaking index model. He also assumed a small incident wave angle and neglected the wave-induced set-up (set-down) effects on the mean water depth which became the sole variable of interest.

Subsequent investigators have relaxed or eliminated many of these assumptions. However, all investigators to date have continued to use the wave breaking index simplification which requires specification of either a linear or monotonically decreasing bathymetric profile. Most natural beaches have single or multiple bar-trough features at sometime during yearly cycles. Multiple wave breaking and reforming regions across these surf zones produce a complex wave height distribution that is clearly not amenable to the use of the wave breaking index to specify the wave height as directly proportional to the water depth.

A mathematical model has been developed that makes no simplifying assumptions regarding the three above mentioned key variables. Water depth, wave height and wave angle can vary separately across the surf zone. Section 2 presents all the theoretical details including the wave height decay (and recovery) model for use across arbitrary, realistic bottom profiles. Because an analytic solution is not possible for realistic bathymetry, Section 3 discusses the computer algorithm based on a finite-difference analog of the governing ordinary differential equation and the solution method. All test results are summarized in Section 4 including those for an artificially devised beach profile with three wave breaking-reforming regions and one final breaker zone on the exposed beach face.

The results are for depth-averaged, longshore current profiles induced by uniform breaking waves on infinite beaches of arbitrary cross-sectional shape. A complete report of this entire study is available (Baum, 1985).

2.0 Theoretical Development

Consider the depth-integrated and time-averaged horizontal momentum balance equation for steady, uniform motion as depicted schematically in Figure 1.

Cross-shore(x)
$$\frac{dS_{xx}}{dx} + \rho g h \frac{d\bar{\eta}}{dx} = 0 \qquad (1)$$

Alongshore(y)
$$\frac{dS_{xy}}{dx} - \bar{\tau}_B + \frac{dT_L}{dx} = 0 \qquad (2)$$

where: S_{xx} = the shorenormal radiation stress component;
S_{xy} = the shear radiation stress component;
$\bar{\eta}$ = the mean water level set-up (set-down);
$\bar{\tau}_B$ = the time-averaged bottom shear stress;
T_L = the lateral, turbulent mixing stress;

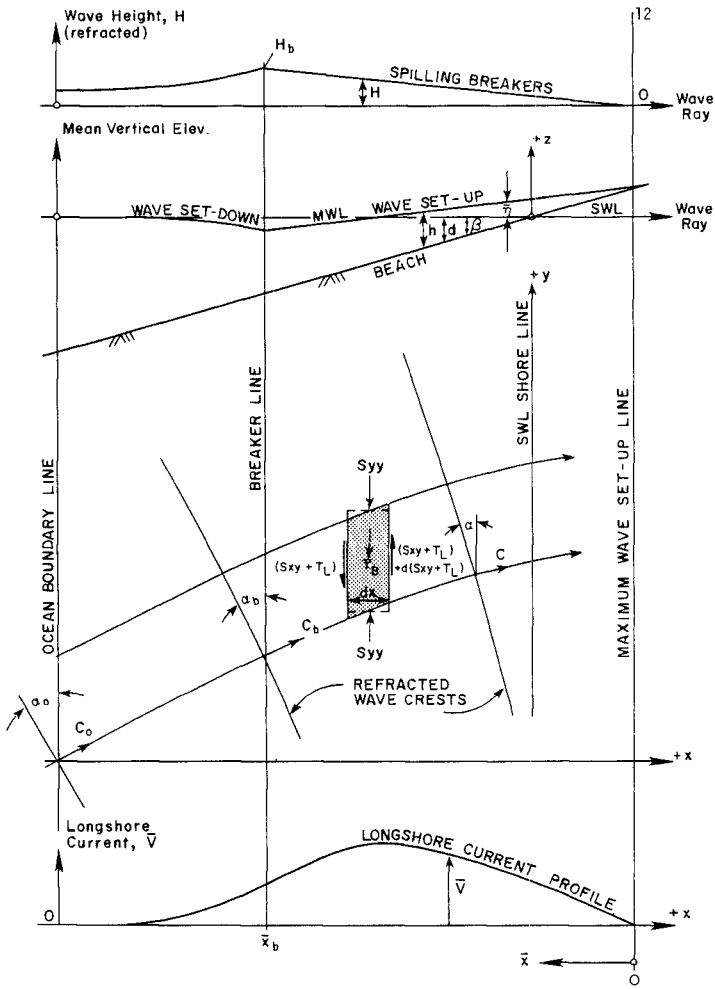

Figure 1. Schematic of surf zone (from Basco, 1982)

ρ = the water mass density; and
g = the acceleration due to gravity.

Equations (1) and (2) are decoupled in the sense that feedback effects of the currents on the wave heights are normally neglected. The cross-shore equation (1) is solved for the wave set-up as part of the method for obtaining the wave height and mean water depth as described below. Equation (2) is then solved for the longshore current profile using the results from (1) and the expressions for the stresses also described below. The complete, unsteady flow, two-dimensional forms of these equations can be found in Basco (1982).

2.1 Wave Energy Decay and Reforming Model

A model is needed to shoal a wave to the breaking point and then calculate the wave energy decay to a point of wave reformation where wave shoaling begins anew to a new break point or the shoreline. For this purpose the newly developed model of Dally et al. (1984) was employed.

The physical idea behind this model is that after a wave breaks it dissipates energy continuously until some stable wave height is reached where breaking stops and wave reforming and shoaling begins. The key assumption in this empirical approach is that the energy dissipation during breaking is proportional to difference between the actual and stable wave energy flux at any point. Using the definition of wave energy density and after integration this gives

$$(H^2 - H_s^2)_2 = (H^2 - H_s^2)_1 \exp\left(\frac{K}{d}\Delta x\right) \qquad (3)$$

where: H_s = the stable wave height
d = the still water depth
Δx = the distance step between points (1) and (2) where evaluation of the new wave height, H takes place, and
K = a wave energy decay factor.

A laboratory investigation conducted by Dally et al. (1984) to calibrate the model obtained best values for K of 0.17 and for H_s to be 0.4h. These coefficients we employed in the present model. Equation (3) reveals this to be an exponential wave energy decay model.

2.2 Cross-Shore Momentum Balance

Using the classical, linear wave theory definition for S_{xx} and wave energy density, E, Equation (1) when rearranged becomes

$$\frac{d\bar{\eta}}{dx} = \frac{2 + \cos 2\theta}{16\, h} \frac{d(H^2)}{dx} \qquad (4)$$

to relate the mean water level set-up to the wave height. The wave

angle distribution across the surf zone was obtained from classic refraction methods using Snell's law.

An iterative procedure was followed in that first Equation (3) using the still water depth was employed to estimate the H(x) distribution. From (4) this gave $\bar{\eta}(x)$ from which a second iteration using $h=d+\bar{\eta}$ in (3) produced convergence to an acceptable tolerance after only 2-3 iterations. At this point, distributions of mean water depth, h(x), wave height, H(x) and wave angle, $\theta(x)$ are completely specified across the surf zone.

2.3 Longshore Momentum Balance

Equation (2) expresses a balance between the driving stress gradient, bottom stress and lateral (turbulent) mixing stress gradient. Previous formulations judged best in each case have been rederived to take into account separate variations of h, H and θ across the surf zone.

Driving Stress. Using classical, linear, shallow water wave theory, the shear radiation stress component can be shown to be (Longuet-Higgins, 1970)

$$S_{xy} = \frac{1}{8}\rho g^{3/2}\left(\frac{\sin\theta}{c}\right) H^2 h^{1/2} \cos\theta \qquad (5)$$

where we now also have c, the wave celerity. Using chain rule differentiation the driving stress gradient becomes

$$\frac{dS_{xy}}{dx} = \frac{1}{8}\rho g^{3/2}\left(\frac{\sin\theta}{c}\right)\left\{h^{1/2}\cos\theta\,\frac{\partial H^2}{\partial x} + H^2\cos\theta\,\frac{\partial h^{1/2}}{\partial x} + H^2 h^{1/2}\,\frac{\partial \cos\theta}{\partial x}\right\} \qquad (6)$$

Bottom Stress. We adopt a bottom stress formulation for large wave approach angles as originally formulated by Liu and Dalrymple (1978) and modified to accommodate separate variations of h and H. The expression employed is

$$\overline{\tau_B} = \frac{\rho f g^{1/2} H (1+\sin^2\theta)}{8\pi h^{1/2}}\, V \qquad (7)$$

where: f = a dimensionless friction coefficient, and
v = the time-averaged, depth-integrated longshore current.

Lateral Mixing Stress. We adopt a lateral mixing stress formulation using a classical, eddy viscosity approach. Following Battjes (1975), we take the water depth as reference length scale and reference velocity related to the local energy dissipation rate, D, where

$$D = \frac{\partial}{\partial x}\left[\frac{1}{8}\rho g^{3/2} H^2 h^{1/2}\cos\theta\right] \qquad (8)$$

Again using chain rule differentiation (8) yields

$$D = \frac{1}{8}\rho g^{3/2} G(x) \tag{9}$$

where

$$G(x) = \left\{ h^{1/2}\cos\theta \frac{\partial H^2}{\partial x} + H^2\cos\theta \frac{\partial h^{1/2}}{\partial x} + H^2 h^{1/2} \frac{\partial \cos\theta}{\partial x} \right\} \tag{10}$$

From the basic relationship

$$T_L = \rho \epsilon h \frac{dv}{dx} = \rho \left(M h \left(\frac{D}{\rho}\right)^{1/3} \right) h \frac{dv}{dx} \tag{11}$$

where: ϵ = the turbulent eddy viscosity, and
M = a turbulent closure coefficient

the gradient of the mixing stress becomes

$$\frac{\partial T_L}{\partial x} = M\rho\left(\frac{1}{8} g^{3/2}\right)^{1/3} \left\{ \frac{\partial h^2}{\partial x} G(x)^{1/3} \frac{dv}{dx} + h^2 \frac{\partial \left[G(x)^{1/3}\right]}{\partial x} \frac{dv}{dx} + h^2 G(x)^{1/3} \frac{d^2 v}{dx^2} \right\} \tag{12}$$

2.4 Longshore Current Profile Equation

Combining equations (2), (6), (7) and (12) gives with $\hat{G}(x)$ given by (10)

$$\frac{d^2 v}{dx^2} + \left[\frac{\beta_1(x)}{\beta_2(x)}\right] \frac{dv}{dx} - \left[\frac{B\beta_3(x)}{A\beta_2(x)}\right] v + \left[\frac{C\, G(x)}{A\beta_2(x)}\right] = 0 \tag{13}$$

where:

$$\beta_1(x) = \frac{\partial h^2}{\partial x} G(x)^{1/3} + h^2 \frac{\partial G(x)^{1/3}}{\partial x} \tag{a}$$

$$\beta_2(x) = h^2 G(x)^{1/3} \tag{b}$$

$$\beta_3(x) = \frac{H\left[1 + \sin^2\theta\right]}{h^{1/2}} \tag{c}$$

$$A = \frac{1}{2}\rho g^{1/2} M \tag{d}$$

$$B = \frac{1}{8}\frac{\rho f g^{1/2}}{\pi} \tag{e}$$

$$C = \frac{1}{8}\rho g^{3/2}\left(\frac{\sin\theta}{c}\right) \tag{f}$$

Equation (13) is a nonhomogeneous, ordinary, second-order differential equation inside the breaker line. It becomes homogenous outside the breaker line because the group of coefficients given by CG(x) is zero there.

The boundary conditions are identical to those employed by Longuet-Higgins (1970) in the original theory. This means taking zero velocity at the new (set-up) shoreline, matching both velocity and its gradient at the breaker line for inner and outer solutions and letting the velocity approach zero far outside the breaker line.

3.0 Numerical Solution

Equation (13) can be written

$$\frac{d^2V}{dx^2} + C_1\frac{dV}{dx} - C_2V + C_3 = 0 \qquad (15)$$

and must be solved numerically because the coefficients, C_1, C_2 and C_3 are nonconstant in x. The numerical method employed falls in a general class called "shooting" methods whereby the slope at a known value of the dependent variable (v=0 at x=0) is first assumed thereby creating an initial value problem which is solved by the fourth-order, Runge-Kutta method. This procedure is repeated until the calculated value at the second boundary point is within a specified tolerance of the actual function value at this location. An estimate of the initial slope was made using the original, analytical solution of Longuet-Higgins (1970) from which two bracketing guesses permit a linear interpolation to accelerate convergence. Because of the two internal, boundary conditions at the breaker line, the numerical algorithm adopted utilized two "shooting" methods, one for the region inside and a second for the zone outside the breaker line. For practical reasons, a distance of approximately three surf zone widths proved reasonable for the limit of the outer region where the current velocity returned to nearly zero values.

4.0 Test Results

4.1 Basic Tests

A series of basic tests were initially conducted to compare numerical model results with those previously published for simple cases using a constant wave breaker index.

Plane Beach. An initial comparison was made to the original analytical results of Longuet-Higgins (1970) for a plane beach. This required making the same simplifying assumptions (constant breaker index, neglect of wave set-up and refraction effects) and conversion of the bottom friction and lateral mixing coefficients to those employed by Longuet-Higgins. In the original model, the mixing parameter, P is defined as

$$P = \frac{N\pi \tan\beta}{c_f\gamma} \qquad (16)$$

where: $\tan\beta$ = m, the beach slope;
$c_f = \frac{1}{8} f$, the bottom friction coefficient;
$N = M\left(\frac{5}{16}\right)^{1/3} \gamma (\tan\beta)^{4/3}$ the lateral mixing coefficient
and $\gamma = \frac{H}{h}$, the wave breaking index.

The curves for both the analytical model of Longuet-Higgins (1970) and the present numerical model for identical data sets are shown in Figure 2. The chosen data results in P = 0.106 for this case. Both curves are identical in shape and size inside the breaker line (dimensionless distance of unity) but slightly different outside. The difference in the results outside the breaker line is simply due to different wave transformation models being used to shoal the wave so that equivalence is theoretically not possible. In Figure 2 and subsequent plots, all velocities are normalized by the breaker line, longshore current with no mixing as first used by Longuet-Higgins (1970).

Large Wave Angle. The model of Liu and Dalrymple (1978) included wave set-up and refraction effects on the velocity profile because their main intent was to study the effects of large incident wave angles. Consequently, they neglected lateral mixing but revised the bottom friction stress formulation to account for strong longshore currents. Figure 3 presents numerical model results from this study (P=0.106) and reveals a decrease in velocity with increasing wave angle, as expected. No comparison with the published results of Liu and Dalrymple (1978) was possible since it was learned that their values are incorrect by some factor (Vemulakonda, 1986). However, both models for very small incidence angle gave nearly identical results compared to the reference velocity profile (triangular with no mixing) of Longuet-Higgins (1970).

Wave Decay Model. A final base test compared differences due to the specification of the wave decay model. A plane beach, small wave angle and no set-up test was devised with P=0.10 but using a slightly different combination of variables. These specifications assured that the differences in the velocity profile were due only to differences to the wave height field.

Using identical data sets, the current profiles from both the numerical model and the original, analytical model of Longuet-Higgins (1970) are shown in Figure 4. Considerable differences now exist. These can be explained from the fact that the wave height decreases linearly in the analytical model and exponentially in the numerical model. In general, the wave decay model of Dally et al. (1984) flattens the profile inside and steepens it outside the breaker line on a plane beach.

4.2 Laboratory Tests

The present numerical model has been compared to laboratory measurements by Mizuguchi et al. (1978, Case 3) as shown in Figure 5. Coefficients for friction and lateral turbulent mixing as determined to give a "best fit" at the maximum velocity by Kraus and

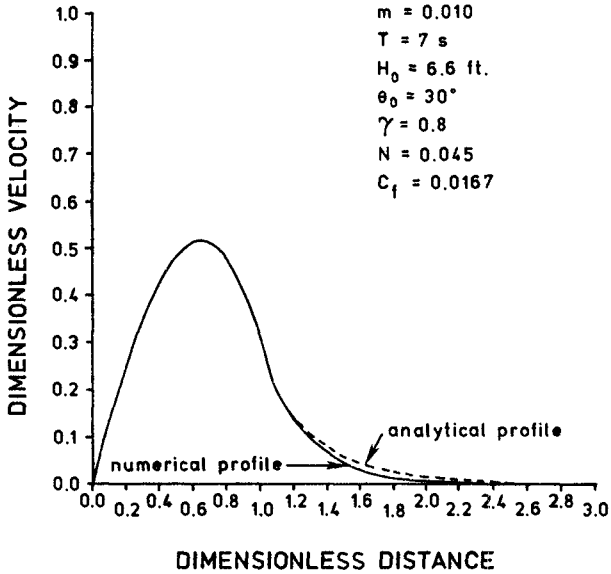

Figure 2. Comparison of numerical model to analytical solution of Longuet-Higgins for identical parameters

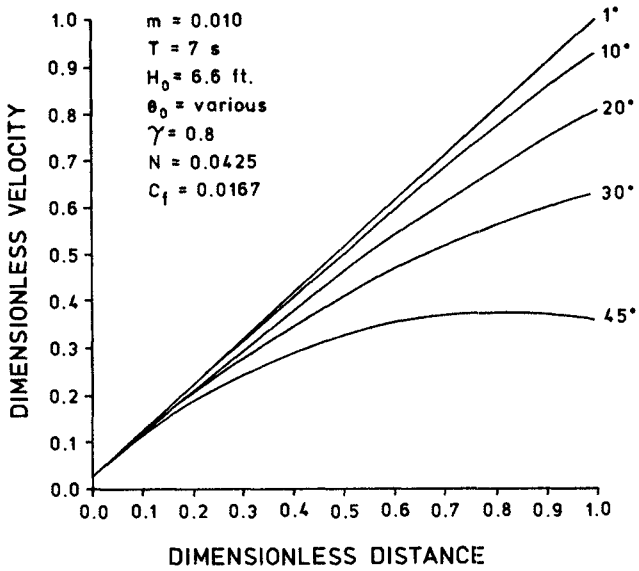

Figure 3. Numerical model results for large angle effects without lateral mixing

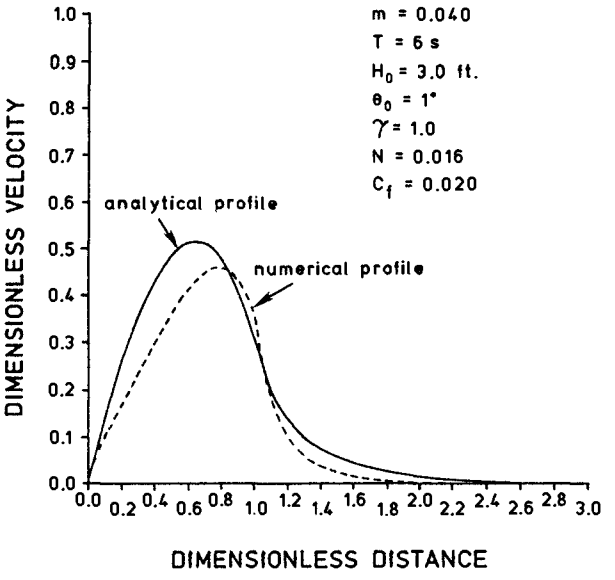

Figure 4. Comparison of differences in velocity profiles due to wave decay specification

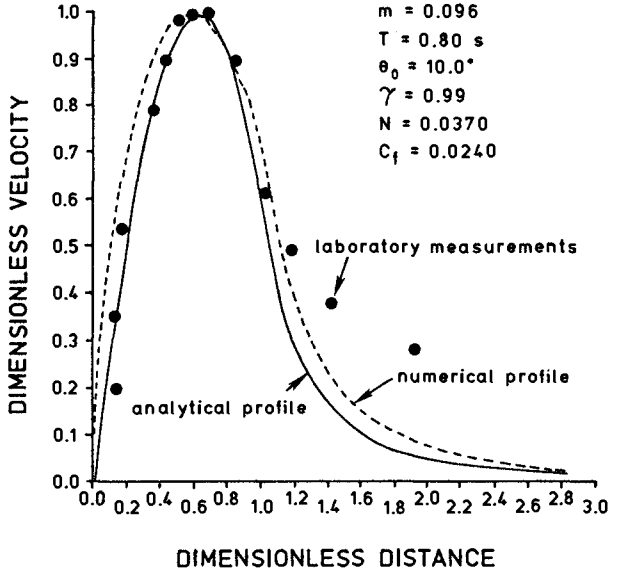

Figure 5. Comparison of predicted velocity profile with laboratory measurements of Mizuguchi et al. (1978 Case 3)

Sasaki (1979) for their model were employed. The analytical solution of Longuet-Higgins (1970) is also shown (P=0.47). The results of the Kraus and Sasaki (1979) model fall somewhere between those shown on Figure 5 and all three give good agreement with measured values inside the breaker line.

The discrepancies outside are primarily due to laboratory-scale effects as discussed by Basco (1982), Battjes (1978) and Kraus and Sasaki (1979) in their use of this data set to test their model. Additional laboratory-scale data sets are now available for plane beaches to test numerical models (e.g. Visser, 1984). No laboratory data is available for a bar-trough beach profile.

4.3 Field Tests

Field measurements of wave-induced longshore currents under uniform and steady wave conditions are difficult to obtain. Because of continuously varying field conditions including local winds not modeled and scales of velocity traces recorded by modern instruments, a standard, universally accepted averaging time to define the longshore current has yet to be determined. We show one comparison here of the numerical model with the field measurements performed by Kraus and Sasaki (1979) in a surf zone with two observed wave breaking lines. Their measured velocity and bottom profiles are displayed in Figure 6. Figure 7 displays the numerically predicted longshore profile using bottom friction and lateral mixing parameters as specified by these same investigators (Kraus and Sasaki, 1979) for use in their model. Both numerical and field plots show a secondary velocity maximum near the shoreline. It is evident that a "best fit" profile could be obtained for the present model by appropriate manipulation of the friction and mixing parameters to values different than those suggested by Kraus and Sasaki (1979) for their model. This has not been done since the objective was simply to simulate a multiple-peaked, longshore current profile.

4.4 Multiple Bar-Trough Beaches

In the absence of a laboratory data-set under controlled conditions for a bar-trough beach profile with multiple breaker and reforming regions, no definitive answer is yet possible as to the adequacy of the present numerical model. Never-the-less, an artifical yet realistic profile was constructed with three offshore bars as depicted in Figure 8. The average slope is 0.048. This profile is typical of those found on lower energy, Gulf of Mexico beaches. Waves broke over the three bars and within the inner slope to give four breaker lines and theoretically, four peaks in the longshore current profile.

The current profile predicted by the numerical model for the contrived bathymetry and representative parameters is shown in Figure 9. Also shown is the analytical model profile of Longuet-Higgins (1970) for an average slope of the entire profile. The profile of the multiple breaker case is seen to be similar overall to the profile developed from the analytical solution for a constant slope.

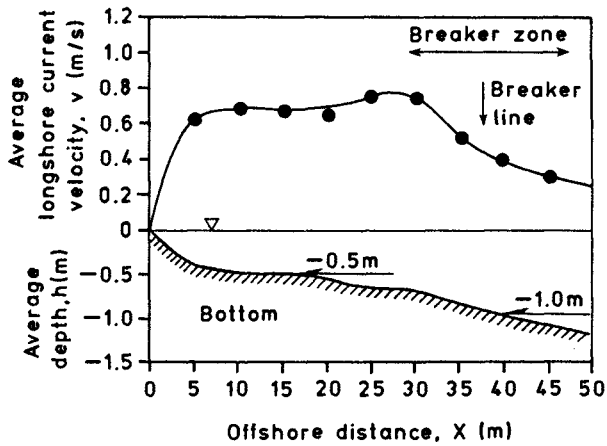

Figure 6. Measured velocity and depth profiles for two breaker Line situation in field (from Kraus and Sasaki, 1979)

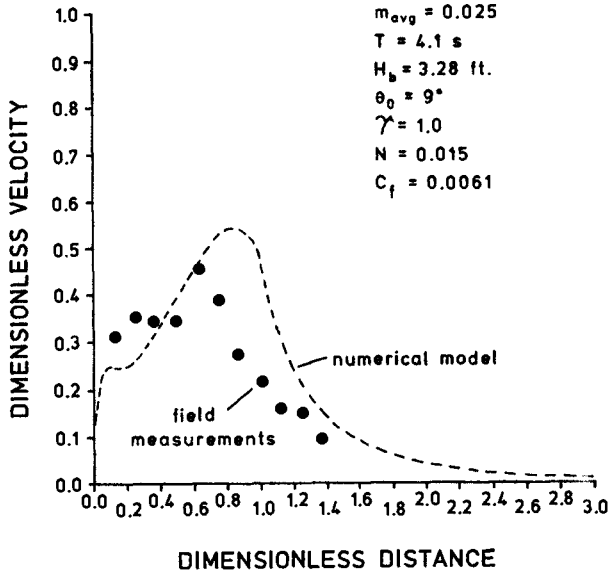

Figure 7. Comparison of predicted velocity profile to measured field profile for two breaker line case.

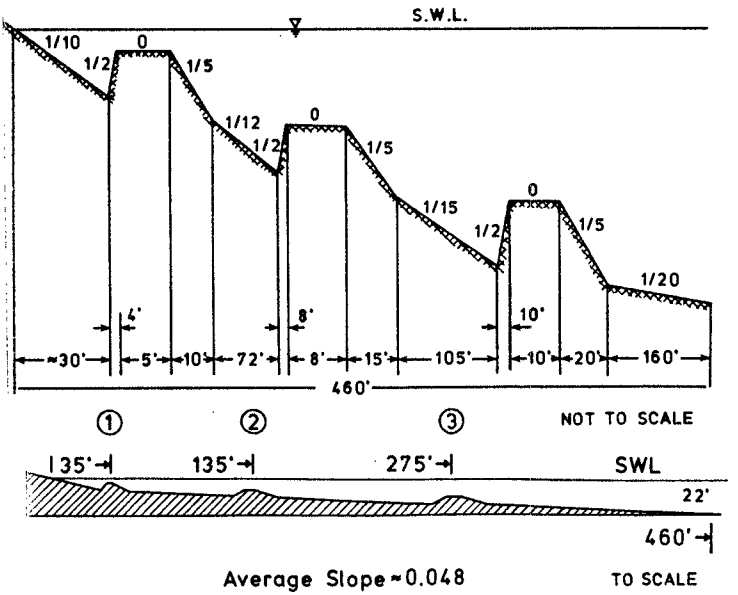

Figure 8. Artificial bottom profile to induce multiple wave breaking

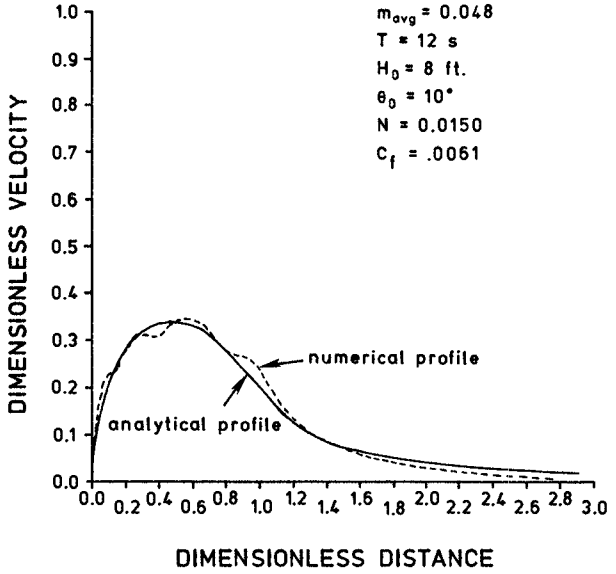

Figure 9. Comparison of velocity profiles due to artificial bathymetry.

The difference is simply four smaller humps present in the overall profile developed by the present model.

The scale of these perturbations is relatively small and similar to the scatter found in field measurements. No attempt was made to make more runs with fewer yet larger bars in lieu of the fact that no laboratory data exists to check the results.

5.0 Summary

A longshore current model for realistic, multiple bar-trough beach profiles has been developed. It permits wave breaking and reforming and this feature in turn produces multiple peaked profiles of the current distribution as found across natural beaches. The model reduces to closed form, analytical solutions for plane beaches. And, it incorporates those components for the stresses that remove the simplifying assumptions made by Longuet-Higgins (1970) in his original model.

It is recommended that more realistic driving stress terms be investigated using radiation stress components derived from nonlinear wave theory outside and broken wave theory inside the surf zone. Svendsen (1984) has shown that the presence of a surface roller in broken surf zone waves increases the radiation stress by 50-100% over that found from linear wave theory. Although limited in scope due to neglect of feedback of currents on the wave field, wind stresses and other natural phenomena, the model is helpful in the development of more general two-dimensional, horizontal models.

References

Basco, D.R., 1982. Surf Zone Currents, Misc. Rept. No. 82-7. US Army, Corps of Engrs., Coastal Engineering Research Center, Vicksburg, MS, Sept. (in two volumes).

Battjes, J.A., 1975. Modeling of Turbulence in the Surf Zone, Proceedings; Symposium of Modeling Techniques, Miami, Florida, Vol. 2, pp.1050-1061.

Battjes, J.A., 1978. A Critical Review of Conventional Models for Some Surf Zone Phenomena; Euromech 102 (Breaking Waves: Surf and Run-Up on Beaches), Univ. of Bristol, Bristol, England, July.

Baum, S.K., 1985. A Numerical Investigation of the Longshore Current Profile, M.S. Thesis, Ocean Engineering, Texas A&M University, College Station, TX, May.

Dally, W.R., Dean, R.G., and Dalrymple, R.A., 1984. Modeling Wave Transformation in the Surf Zone, Misc. Paper CERC-84-8, US Army, Corps of Engrs., Coastal Engineering Research Center, Vicksburg, MS.

Kraus, N.C. and Sasaki, T.O., 1979. Influence of Wave Angle on the Longshore Current, Marine Science Comm., Vol. 5, No. 2, Feb., pp. 91-126.

Liu, P.L.-F., and Dalrymple, R., 1978. Bottom Frictional Stresses and Longshore Currents Due to Waves With Large Angles of Incidence, J. of Marine Research, Vol. 36, No. 2, May, pp. 357-375.

Longuet-Higgins, M.S., 1970. Longshore Currents Generated By Obliquely Incident Sea Waves, Parts 1 and 2, J. Geophys. Res., Vol. 75, pp. 6778-6801.

Longuet-Higgins, M.S., and Stewart, R.W., 1964. Radiation Stress in Water Waves, A Physical Discussion With Applications, Deep-Sea Research, Vol. 11, No. 4, August, pp. 529-562.

Mizuguchi, M., Oshina, Y. and Horikawa, K., 1978. Laboratory Experiments on Longshore Currents, 25th Coastal Engineering Conference of Japan.

Svendsen, I.A., 1984. Wave Heights and Set-up in a Surf Zone, Coastal Engineering, Vol. 8, pp. 303-329.

Vemulakonda, R., 1986, personal communication.

Visser, P.J., 1984. Uniform Longshore Current Measurements and Calculations, Proceedings, 19th Coastal Engineering Conference, Vol. III, pp. 2192-2207.

CHAPTER 74

TIME AND BED AVERAGED CONCENTRATIONS UNDER WAVES

Jan J. Bosman*, research physicist, Delft Hydraulics,
Henk J. Steetzel**, MSc-student, Delft University of Technology,

Abstract:

Four types of sediment concentration under waves are discussed: (a) instantaneous, local, (b) time-averaged, local, (c) instantaneous, bed-averaged and (d) time and bed averaged. The first three mentioned are either hard to interpret or difficult to obtain experimentally. The time and bed averaged concentration is discussed in particular, both its interpretation and its measurement. Two features are discussed: the vertical concentration distribution and the bottom concentration.

1. Introduction

Kennedy and Locher (1972) reviewed the suspension of sediment under waves, and they concluded that the physical understanding is only poor. They specifically paid attention to the vertical distribution of sediment concentration, and they analysed measured concentration profiles relative to theoretical profiles based on different diffusion models. They concluded that the analysis seems to be overwhelmed by success, but that it is more spurious than real. It means that the theoretican can make practically any guess about the distribution or nature of diffusivities. The experimentalist, on the other hand, must achieve extreme precision in his data before they can be used as the basis for selecting one diffusion model over another.

It seems that not much has changed after almost fifteen years. Here the problem is discussed again from an experimental point of view. A simple technique is applied to measure sediment concentrations, which are averaged both over time and over the bed. Without pretending to answer all questions, the present results allow to reconsider the statements of Kennedy and Locher quoted above.

2. The practical relevance of concentrations

2.1 The instantaneous, local concentration

Apart from a cross-flow dependence, the instantaneous, local concentration depends on the longitudinal position (parallel to the water motion), x, on the height above the bottom, z, and on the time, t: $C(x,z,t)$. Several studies have been reported on $C(x,z,t)$ due to wave action. The water motion being partly random (e.g. turbulence) and the bed being a loose boundary, the question rises: 'How large is the random

* presently: head R&D-section, Dept. of Hydro-Instrumentation, Tidal Waters Division-Rijkswaterstaat
** presently: project-engineer, Delft Hydraulics

component in C(x,z,t)?'. Answering the question requires to measure C(x,z,t) under a purely periodic water motion above a so-called 'stable' bed. The deterministic component in C is defined by the periodic part of the concentration. The non-periodic part is the random concentration component.

Wave flumes are not suitable to generate water motions which are exactly periodic. In this respect a wave tunnel is. Only two such experiments are known in which the deterministic and random components of C(x,z,t) have been determined: Nakato et al. (1977) and Bosman (1982) who both performed measurements by an optical probe and in the ripple regime of bed forms under 'equilibrium conditions'. From both experiments it has been concluded that the sediment concentration under waves is largely random (30-100%). The random concentration component contains two contributions:

- from the applied instrument due to the statistical properties of light attenuation;
- from the physical process due to (small) changes in the local water motion and bed geometry.

Nakato et al. (1977) suggested that the large random component is mainly from instrumental origin. Bosman (1982) showed that, although this contribution cannot be neglected, it is almost purely due to changes in the (entrainment) process. Two reasons for this are obvious:

- Ripples are not fixed as they move (slightly) back and forth about their mean positions, viz. the longitudinal position, x, is not a constant relative to the bed geometry. As the concentration (at fixed height) varies strongly along the longitudinal position, see e.g. Nakato et al. (1977), and as the ripple motion is unlikely to be purely periodic, a random concentration component enters through x.
- Even if the ripple positions were fixed, their shapes are not: from one (wave) period to the next one a ripple may be slightly larger or smaller, steeper or smoother. So the water motion (vortices) between the ripples is not purely periodic (even apart from turbulence). Quite likely the amount of entrained sediment is not periodic either. As a result, a random concentration component enters through the time, t.

The instantaneous, local concentrations having such a large random component, its practical relevance is questionable. Under purely periodic waves, the random component can be reduced by ensemble averaging maintaining both the longitudinal and temporal resolution. But what about the relevance? Suppose the ensemble mean concentration is determined above the crest of a selected ripple. As the next ripple is certainly different, the concentration will be different too. Why is the ripple measured more decisive than is another ripple? Anyway, the ensemble mean concentration cannot be determined for natural (irregular) waves.

As the random concentration contribution enters through both t and x, there are three more ways to reduce it:

- Time-averaging of the concentration at a fixed position: $\bar{C}(x,z)$
- Bed-averaging (at fixed height along the longitudinal position) of the concentration at fixed time intervals: C(z,t),
- Time and bed averaging of the concentration at fixed height, z, above the bed: $\bar{\bar{C}}(z)$, where the double overbar indicates the averaging over the two entries, x and t.

2.2 The time-averaged, local concentration $\bar{C}(x,z)$

Such a measurement is easily performed (e.g. by suction at a fixed position). The temporal resolution is lost, but the longitudinal one is kept. As the time-averaged concentration varies with the longitudinal position, see e.g. Nakato et al. (1977), there is still a random contribution to $\bar{C}(x,z)$ due to the bed mobility. This longitudinal influence is often forgotten in the interpretation of $\bar{C}(x,z)$. This will be discussed in Section 3.2.

2.3 The instantaneous, bed-averaged concentration $\bar{C}(z,t)$

To perform such a measurement requires a 'sensitive slit' mounted horizontally at fixed height above the bed and covering several ripples. The slit should respond fast (instantaneously) to the concentration. Such measurements may be useful to study the instantaneous, vertical mixing of sediment, but for the time being there is no method to measure $\bar{C}(z,t)$. (It may be possible by measuring the attenuation/scattering of a horizontal, acoustic beam).

2.4 The time and bed averaged concentration $\bar{\bar{C}}(z)$

For convenience, the time and bed averaged concentration will be abbreviated by TABAC. It can be measured e.g. by a suction system moving horizontally at fixed height above the bed and covering several ripples. With suction at 6 to 8 different heights simultaneously, this is how the present measurements have been carried out. A few details concerning the measuring performance should be emphasized:

- The suction opening is 3 mm $\emptyset$. The suction direction is normal to the ambient water motion. The suction velocity is more than 2.5 times the main flow velocity. Under these conditions the suction calibration is defined well, see Bosman et al. (1987).
- The suction system moves slowly relative to the main flow, but fast relative to the bed form motion: approx. 5 mm/s. The suction system moves back and forth at constant velocity to obtain a fair average over the longitudinal positions.
- Reproduction tests, see Steetzel (1984), showed that (in order to reduce the relative random concentration error under 10%):
  * the averaging time interval should cover at least 100 waves,
  * the averaging bed length should cover at least 3 ripples.

3. Vertical mixing of sediment under waves

3.1 Theoretical approach

The vertical mixing of sediment is usually described by the steady state diffusion equation for the time-averaged concentration, $\bar{C}$:

$$\varepsilon(z) \frac{d\bar{C}}{dz} + w.\bar{C} = 0, \qquad (1)$$

where

$\varepsilon(z)$ = the sediment diffusion coefficient (under waves) depending on the height above the bed, z, in general,

w = sediment fall velocity, in general (unsorted sediment), depending on z as well.

The equation simply states that sediment goes vertically upwards by turbulent diffusion, the first term in Eq. (1), which is compensated by the downward flux due to gravity, the second term. Under definite assumptions for ε (constant, linear, parabolic) and usually with w not depending on z, Eq. (1) can be solved resulting to the concentration profile, $\bar{C}(z)$.
The diffusion equation can be understood quite simply. Let the steady state concentration at level z be denoted by $\bar{C}$, and that at level z+dz by $\bar{C}-d\bar{C}$ (the minus sign indicates that the concentration decreases with increasing height). For small values of dz it may be assumed that the concentration decay ($-d\bar{C}$) is proportional to:
- $\bar{C}$ itself (the larger the concentration, the larger the difference in concentrations is between the levels z and z+dz),
- dz (the larger the distance between the two levels, the larger the difference in concentrations is).

This can be expressed as $d\bar{C} = -\gamma \cdot \bar{C} \cdot dz$, where γ is a positive proportionality factor. Considering an other level, the same expression still holds, although γ may be different, viz. γ depends on the height: $\gamma(z)$. Letting dz diminish, Eq. (1) is obtained with $\gamma(z) = w(z)/\varepsilon(z)$. So Eq. (1) can be established without making any assumption on the suspension mechanism (either turbulent diffusion, or convection by vortices or orbital motion; or both).

The 'classical' theoretical approach has been reconsidered by Kennedy and Locher (1972) under a few assumptions, ending up with a modified diffusion equation. They compared concentration profiles measured to those calculated through their diffusion equation for various 'diffusion models'. They found good agreement between the profiles measured and the ones predicted, no matter on which diffusion model the prediction is based (see Introduction).
Considering this problem, two questions are raised here:
* What is the concentration meant in the diffusion equation? (Section 3.2).
* How is a diffusion model tested in comparing concentration profiles predicted to the ones measured? (Section 3.3).

3.2 The concentration in the diffusion equation

In general, the concentration $\bar{C}$ in a diffusion equation is defined simply by a time-averaged concentration as a steady state is assumed. Recalling Chapter 2, it means that $\bar{C}$ denotes either the time-averaged, local concentration, $\bar{C}(x,z)$, or the time and bed averaged one, the TABAC $\bar{\bar{C}}(z)$. When testing a diffusion concept, the concentration measured is usually a time-averaged one obtained at a fixed longitudinal position, viz. $\bar{C}(x,z)$ which depends definitely on x, see e.g. Nakato et al. (1977). The question should be raised whether this is the concentration meant in the diffusion equation. In the equation, it is not accounted for any longitudinal influence, viz. it is assumed that $\varepsilon(z)$ is identical 'everywhere' along the bed. Stated alternatively: the diffusion equation relates the concentrations at different heights, no matter where the sediment comes from. This concept is often illustrated by the (turbulent) exchange of a water parcel (level z) with some sediment content and an upper parcel (level $z+\Delta z$) with smaller sediment content, see Fig. 1a (the magnitude of the sediment concentration in a parcel is indicated by the cross section of a bold circle).

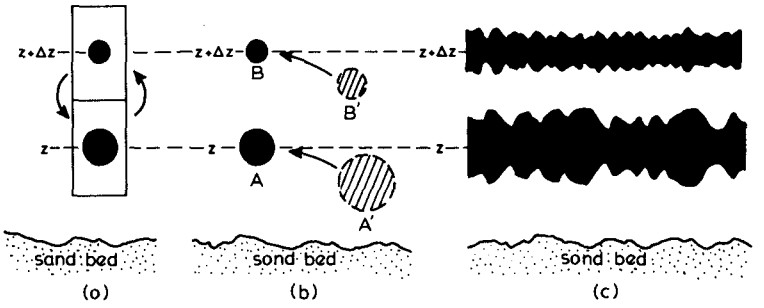

Fig. 1 Sediment exchange due to diffusion (a), motion of sediment concentration under waves (b), and time-averaged local concentrations at levels z and z+Δz (c).

To demonstrate that $\bar{C}(x,z)$ conflicts with this concept, consider Fig. 1b showing the concentrations at positions A and B (levels z and z+Δz) at some instant t. The concentration C_A at time t originates from the concentration $C_{A'}$ (partly dispersed) at time t−Δt. Similarly C_B originates from $C_{B'}$. Near the bed the upward motion of sediment is mainly due to vortices between the ripples. Far from the bed the upward sediment motion is due to the wave orbital velocity (and due to turbulence, if any). Considering the concentrations C_A and C_B (measured at the same longitudinal position), the relationship is determined by $C_{A'}$ and $C_{B'}$ (A' and B' not necessarily at the same longitudinal position), viz. the relationship depends on vertical and longitudinal concentration gradients. (At other moments C_A and C_B may originate from quite different positions A' and B').

To eliminate the longitudinal influence, the concentration must be averaged over all longitudinal positions (at fixed level). These concentrations are the TABAC-s as defined before. So Eq. (1) describes the relationship between TABAC-s at different levels. The time-averaged local concentrations are illustrated in Fig. 1c, where the magnitude of the time-averaged concentration at level z is presented by a vertical bar for all longitudinal positions. The result is a 'cloud' at level z. By averaging over the longitudinal positions it is eliminated from the sediment transfer between two levels, no matter where and when the sediment comes from. So after bed-averaging Fig. 1c is essentially identical to Fig. 1a.

It should be noted that the situation close to the bed under unidirectional flow is not essentially different. But measuring time-averaged concentrations, a bed-averaging is more or less carried out simultaneously (without the experimentalist being aware of it) since 'other longitudinal positions' are passing along the measuring position both due to the nett flow and due to the moving bed.

3.3 Testing concentration profiles

When concentration profiles are compared to an analytical model, the conclusion is usually drawn in terms of 'good or bad fit', whatever it means. Here a general criterion is defined to establish whether a model

is 'realistic' or not. The test on descriptions of concentration profiles can be formulated, in general, by

$$C(z) = f(z) + \Delta C(z), \tag{2}$$

where
$C(z)$ = measured TABAC at level z (dropping the double overbar),
$f(z)$ = some analytical concentration profile,
$\Delta C(z)$ = random measurement error of $C(z)$.

The error ΔC is often forgotten in such tests. However, it represents the realistic scatter of $C(z)$-values measured around the profile $f(z)$ (measured if the analytical profile were exact and the measurements were infinitely precise). This scatter must be reflected properly when comparing $C(z)$ (measured) and $f(z)$ (predicted). Only then the model $f(z)$ is realistic. A realistic model is not necessarily the 'best fit' model. This is easily illustrated by considering an 8-points profile. The best fit is a seventh order polynomial in z, as it passes exactly through all data-points, leaving no scatter. As a result, ΔC is zero which is not realistic.
This acceptance demand for a model requires ΔC to be known in advance.

Concentrations under waves vary over a wide range and the concentration measurement accuracy varies over a wide range too. It is reasonable to assume that large concentrations carry a large random measurement error and that small concentrations have a small one (when there is not much sediment, the absolute error cannot be large). Hence it will be assumed that the relative concentration error, $\Delta C/C$, is of the same magnitude for both small and large concentrations. With this assumption, it is sensible to replace Eq. (2) by a test-equation of the form
$\ln C(z) = g(z) + \Delta(\ln C)$, where $g(z) = \ln f(z)$ and $\Delta(\ln C)$ = random error in $\ln C = \Delta C/C$, since $d(\ln C)/dC = 1/C$.

To simplify the notations, the data $\ln C_i$ obtained at level z_i will be denoted by y_i. Also, the test-equation will be linearized by replacing $g(z)$ by a linear function $\beta_o + \beta_1 x$. If the model tested, $g(z)$, is linear in z, it is obvious to define $x = z$. If the model tested is non-linear, x must be defined by a proper transformation. For example, for the Rouse-distribution (see section 4.3) $x = \ln (h/z-1)$ is a proper transformation, where h is the local water depth. With these definitions the test-equation becomes

$$y(x) = \beta_o + \beta_1 x + \Delta y, \tag{3}$$

As $\Delta y = \Delta C/C$ is assumed to be approximately constant, all measurement results y are equally weighted when testing a model in the form of Eq. (3), which simplifies the testing procedure. Usually concentration profiles are fitted in the form of Eq. (3) without weighing for practical reasons. Thus without being aware of it, the common procedure assumes implicity that $\Delta C/C$ is constant.
The standard procedure to fit the model to the data is the least squares method, viz. to minimize the sum of squared deviations of the data-points y_i form the prediction $\hat{y}_i$, that is $S_E = \sum(y_i - \hat{y}_i)^2$, where the summation is over all data i(i=1, ..., N). The prediction $\hat{y}(x)$ is defined by choosing β_o and β_1 in the model such that S_E is minimum, viz. $\hat{y}$

is the fitted line. Quantitative tests on the goodness of fit can be carried out by regression analysis. A discussion of regression analysis is beyond the scope of the present work, so the reader is referred to one of the handbooks on that topic, e.g. Draper and Smith (1966). Two important quantitative measures are the percentage of explained variation, R^2 (R is the correlation coefficient) and the F-parameter.
The parameter R^2 should be near to 100% for a close fit. However, it is a relative measure, since there is no reason to select a model yielding R^2 = 96% over a model yielding R^2 = 94%.
The F-parameter measures the significance of a regression obtained (with a chosen probability). Thus F-tests can detect a false model, but they do not verify a true model. So in a sense, such tests are relative too.

Under the assumptions that:
- the distribution of y_i is normal for each level z_i,
- the values of Δy_i at different levels are uncorrelated,
- and the variance of y_i does not depend on the level z_i (remember that $\Delta y = \Delta C/C$ does not depend on C, viz. it does not depend on z),

it can be shown that the sum of squares about regression, S_E, is a fair (unbiased) estimator for $(N-2)(\Delta C/C)^2$, see Draper and Smith (1966). Thus $\Delta C/C$ can be estimated from a concentration profile measured, and it can be compared to the value expected. This provides a mean to classify a model to be realistic or not. When testing a two-layer model (see section 4.3) the total sum of squares about regression is an unbiased estimator for $(N-4)(\Delta C/C)^2$.

4. TABAC-results from a wave flume

4.1 Experimental conditions

Time and bed averaged concentrations have been measured in a laboratory wave flume (length x width x depth = 50m x 1m x 1m) for a single bed material (unsorted sand, D_{50} = 0.1 mm) with different bottom slopes (horizontal, 1:80, 1:25) and with local water depths between 0.1 m and 0.6 m. The irregular waves (two different spectra) in the experiments were either non-breaking or breaking (plunging or spilling) at or near the measuring location. Wave heights (significant) were typically in the range 0.1 m - 0.4 m and the averaged zero-crossing wave period was near 2 sec. The experiments have been performed for waves without nett current, for nett current without waves and for waves combined with a nett current. In the wave/current combinations the nett flow velocities were near $\pm$ 0.2 m/s and $\pm$ 0.4 m/s, the plus-minus signs indicating that wave direction and nett flow were both parallel and antiparallel.

The averaging time interval in each measurement was 6 min. and the averaging bed length was 0.3 m. Except for locations in or near breaking waves, the bed was covered with ripples with lengths in the range 0.08 m - 0.12 m. The averaging time interval (approx. 180 wave periods) and the averaging bed length (3 to 4 ripple lengths) are slightly too short to reduce the relative random concentration error under 10%. Nevertheless, the accuracy obtained is sufficient for the present purposes.

The concentration profiles have been obtained by continuous suction at eight levels (see Section 2.4). The distances (in mm) between the suction openings are from bottom to top: 20, 20, 25, 30, 30, 30 and 40.

The lowest measuring height is either 10 or 20 mm above the mean bed level. The total number of concentration profiles measured amounts 134.

4.2 Estimation of concentration accuracy

The acceptance of a 'theoretical' concentration model requires (see Section 3.3) that it yields a realistic value for the relative random concentration error, $\Delta C/C$. As it cannot be measured directly, it must be estimated in advance. For this purpose, four concentration profiles have been chosen arbitrarily out of 134, see Fig. 2. (To separate the profiles the horizontal axis is logarithmic without absolute values.) As the concentrations over the height are related somehow, 'smooth curves' (of arbitrary shape) have been sketched through the data-points. For the moment, these curves are believed to represent the 'true concentration profiles'. Thus the averaged scatter of the data-points around the curves represents the relative random concentration error, $\Delta C/C$ (as the horizontal scale is logarithmic).

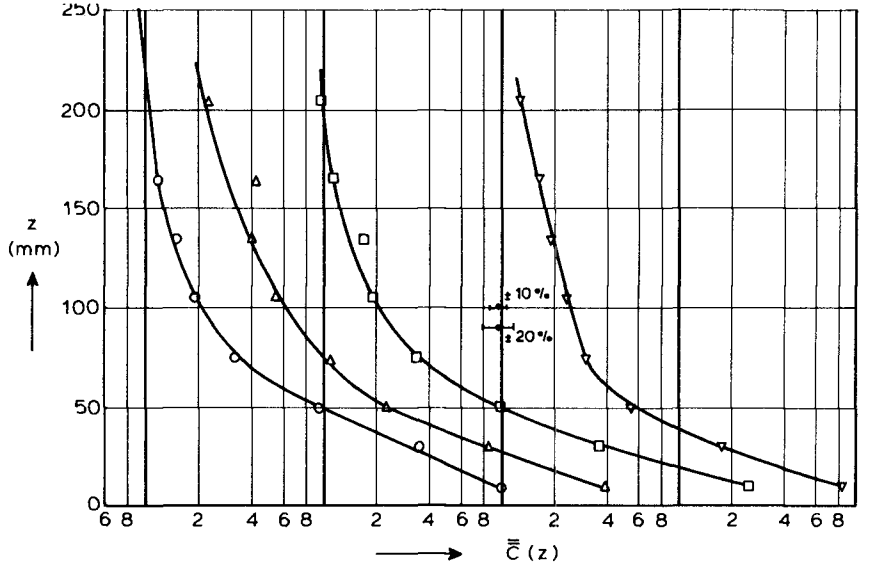

Fig. 2 Four TABAC-profiles 'fitted' by smooth curves

To give some impression, it is indicated in the figure how much scatter on the average corresponds with $\Delta C/C$ = 10% and 20 %. Considering the figure, it is estimated that $\Delta C/C$ is certainly less than 20%, and that it is close to (or probably even less than) 10%. This is the estimate made for $\Delta C/C$ in advance.

4.3 Models tested

Two curved concentration distributions are known from literature:
- The well-known Rouse-distribution:

$$C(z) = C(a)\ \left[\frac{h-z}{z}\ \frac{a}{h-a}\right]^{w/\varepsilon_m}, \qquad (4)$$

where w = sediment fall velocity, h = local water depth, ε_m = maximum diffusion coefficient (at half the water depth) and a = reference level.

- The Bhattacharya-distribution, see Kennedy and Locher (1972):

$$C(z) = C(a)\ \left(\frac{a}{z}\right)^{w/\varepsilon_m}, \qquad (5)$$

where ε_m = maximum diffusion coefficient (at the surface).

In addition a simple two-layer model is considered, which is mainly a guess and which is based only partly on common sense (Section 4.5):

$$C(z) = C(0)\ \exp\ (-z/r_l)\ \text{for } z < A$$
$$C(z) = C(A)\ \exp\ (-z/r_u)\ \text{for } z > A \qquad (6)$$

where A = transition level of the two layers which is defined by the continuity of C(z) for z = A,

r_l, r_u = concentration decay length for the lower and upper layer, respectively. In terms of a diffusion concept, r_i (i = l or u) can be interpreted as $r_i = \varepsilon_i / w_i$ with ε_i being constant and w_i denoting the fall velocity in the specific layer.

These three models have been tested on the TABAC-profiles.

4.4 Results of model tests

From visual comparison of the data-points to the least squares fits, it is concluded that all models fit quite well, except for 2 profiles measured (out of 134). As these profiles may be due to some experimental failure they will be omitted furtheron.

Considering the explained variations, R^2, it is found:

- for the Rouse-distribution: (92 ± 8)%,
- for the Bhattacharya-distribution: (96 ± 5)%,
- for the two-layer distribution: (97 ± 4)%.

Considering, the F-tests it is found that all models provide significant regression except for one to three profiles.

Thus far no model can be selected over another, as stated before by Kennedy and Locher (1972).

The test on the prediction of ΔC/C yields quite remarkable differences as illustrated in Fig. 3. It shows for each profile measured (measurement number) what ΔC/C should be if the specific model were true.

Obviously, ΔC/C (and its scatter) is largest for the Rouse-distribution, and smallest for the two-layer distribution. Averaging over 132 measurements yields for ΔC/C from:

- the Rouse-distribution: (31 ± 15)%,
- the Bhattacharya-distribution: (23 ± 11)%,
- the two-layer-distribution: (13 ± 6)%.

Recalling that ΔC/C has been estimated in advance to be near 10%, it is concluded that the two-layer model describes the concentration profiles in the most realistic way.

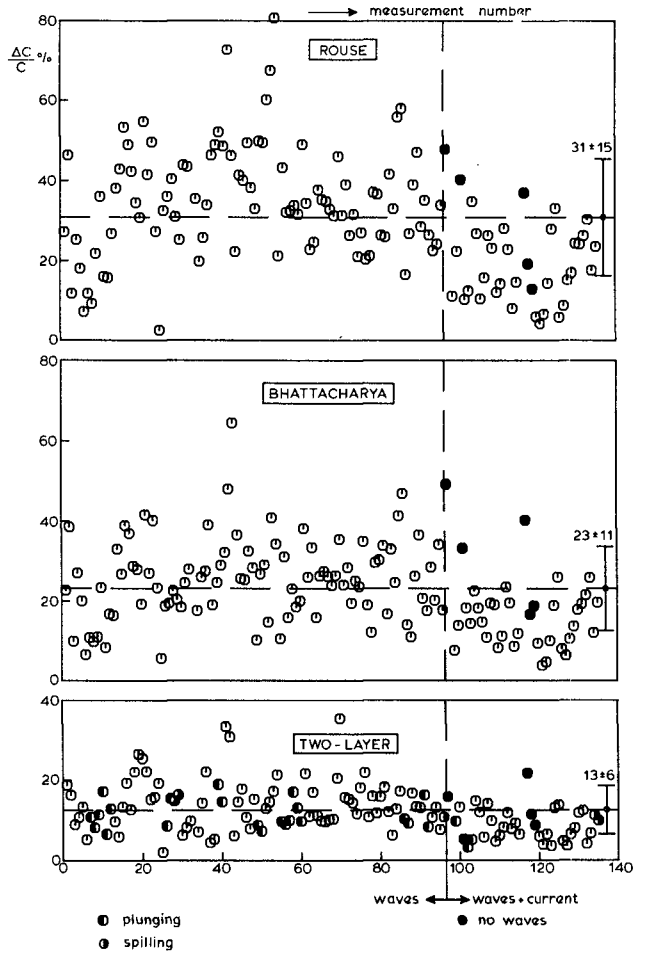

Fig. 3 Results for ΔC/C for the various models

In the two-layer approach the averaged values for ΔC/C for the lower and upper layer yield (7 ± 5)% and (9 ± 5)%, respectively. Since the concentrations in the two layers often differ by two orders of magnitude, the result seems to confirm the assumption that ΔC/C does not depend on C itself.

4.5 The realistic concentration profile

In the former section it has been concluded that the two-layer model provides a 'realistic' description of the concentration profile under widely varying conditions. It means that it fits to the data in a 'natu-

ral way', generating the random concentration error as it should be approximately. It is not the 'best fit', see Section 3.3.
Neither is it the 'true profile', since it yields a concentration gradient which is not continuous, and such gradients occur rarely in nature.
The results show that the two-layer model approaches the truth closely. Therefore it is called 'realistic', viz. it provides a simple mathematical description which is close to the more complicated truth.

The two-layer concentration model states that two layers must be distinguished in the suspension mechanism. This corresponds to the statements by Kennedy and Locher (1972) that two different mechanisms determine the sediment suspension by waves, viz. the turbulence production at the bed and the wave induced orbital velocities, and that the relative importance of the two mechanisms varies with depth. In view of the present results these statements are slightly adjusted: sediment suspension under waves is determined by vortices (and turbulence) near the bed, and by the orbital velocities (and some turbulence) at higher levels. The transition level A indicates a rather abrupt change in the relative importance of the two mechanisms.

5. TABAC-results from a wave tunnel

5.1 Experimental conditions

In order to study near-bottom concentrations in more detail, TABAC-profiles have been measured in a wave tunnel, see Hulsbergen and Bosman (1980). The test results have been described extensively by Steetzel (1984). Here only a few important characteristics will be given. For sinusoidal water motions the periods have been varied over the range 1-7 s and the (maximum) horizontal orbital velocities over the range 0.2-0.6 m/s. The bed (unsorted sand; D_{50} = 0.21 mm) was covered with ripples up to velocities of 0.5 m/s. At larger velocities the ripples changed into bumps: irregular with large heights and lengths. For each condition the experiment started with a flat bed and the height of the suction device was adjusted relative to the flat bed level. The lowest measuring height was chosen such that the lowest suction line did not touch the ripple crests after the suction system had started to move once the bed had reached the equilibrium stage. Only then the actual measurement was started. The averaging time interval in the concentration measurements was 6.5 min. and the averaging bed length was 0.6 m. More than 275 TABAC-profiles have been measured.

5.2 Concentration profiles

In a wave tunnel only the near-bed water motion under waves is simulated. Hence the attention is focussed to this region. Some examples of near-bed TABAC-profiles are shown in Fig. 4. The profiles were found to be exponential (over the height) explaining typically over 99.5% ($=R^2$) of the variation. The relative random concentration errors found were typically less than 5%.

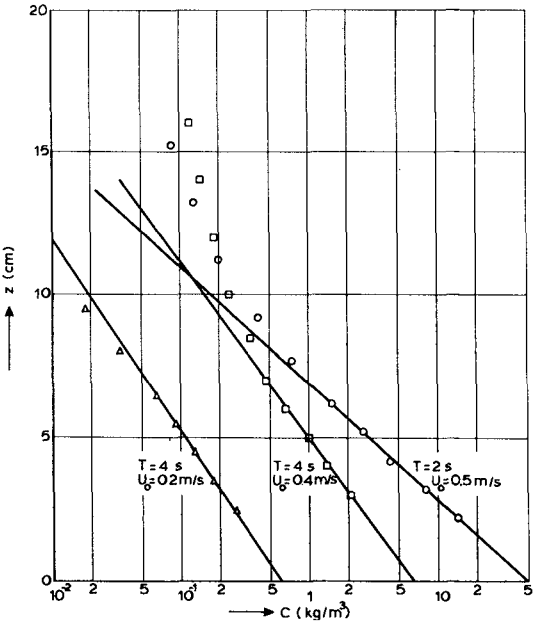

Fig. 4 Some examples of TABAC-profiles near the bed (T = wave period; u_o = peak orbital velocity)

5.3 Bottom concentrations

Analytical descriptions for the concentration profile are only relative, viz. they describe the height dependence of the profile and the magnitude of the concentration is determined by the concentration at some reference level, see for example Section 4.3. Usually the reference concentration is hard to obtain experimentally, also because the choice of the reference level is rather arbitrary (a few grain diameters, or the ripple crest level). The exponential decay of TABAC-s near the bed (if generally valid) permits a good definition of the reference concentration. The measuring heights in TABAC-s are defined relative to the mean bed level (z=0) which can be measured rather easily. Exponential extrapolation (to z=0) of the near-bed TABAC-profile as measured yields a well defined 'bottom-concentration', C(0). This definition of bottom-concentration is a mathematical one rather than a physical one, viz. it determines the magnitude of the concentration, and it is not important whether or not it represents the true TABAC at the mean bed level (defined partly by sediment in suspension and partly by settled sediment). With this unique definition C(0) is expected to be consistently related to the physical process i.e. to the hydraulic conditions. Hence, it has been investigated how C(0) depends on the peak orbital velocity and on the wave period for the conditions described in Section 5.1. It has been found that (over almost 4 orders of magnitude) C(0) can be described well by:

$$C(0) = G.u_o^{3.5}/T^2, \tag{7}$$

where u_o is the peak orbital velocity for purely sinusoidal water motion, and T is the wave period. To be complete, the velocity exponent was found to be 3.5 ± 0.1 and that for the wave period 2.0 ± 0.1. The proportionality factor G, depends on the sediment grain size. For the single sediment type in the measurements (see Section 5.1) it was found that 97% of the variation in C(0) is explained by choosing

$$G = (3000 \pm 8)\ kg.m^{-6\frac{1}{2}}.s^{5\frac{1}{2}} \tag{8}$$

In Fig. 5 the values of C(0) as measured for given u_o and T are related to the values of C(0) as calculated through Eqs. (7-8). The drawn line represents the measured and calculated values being identical. Some of the data in the figure are placed between brackets to indicate that the measured values are somehow suspected since one of more other parameters (e.g. concentration gradient, ripple height or length) showed a discontinuity occurring at larger velocities ($u. \gtrsim 0.5$ m/s). Without going into further detail, this is thought to be due to the limited height (0.4 m) of the wave tunnel which may be troublesome when the ripples grow.

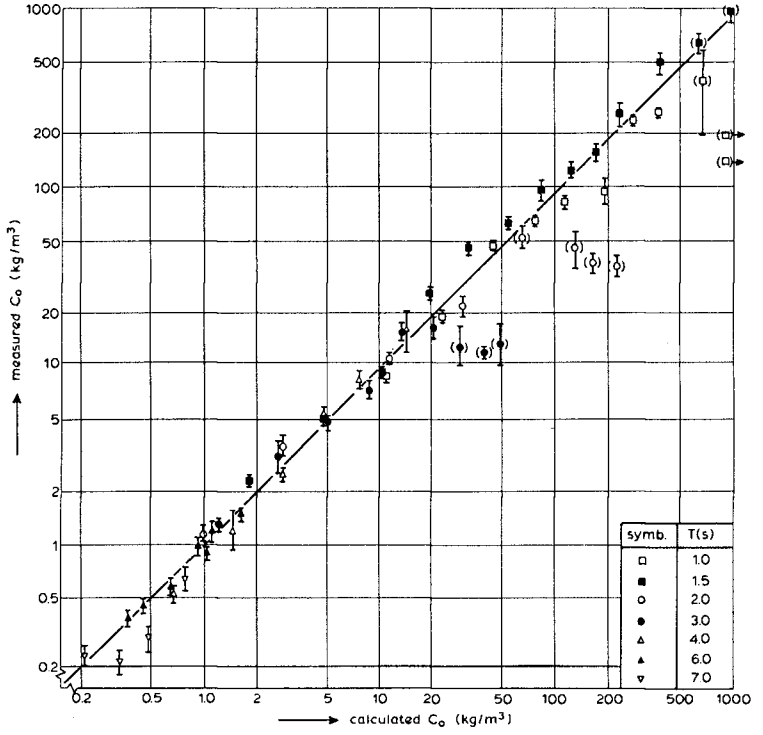

Fig. 5 C(0) measured vs. C(0) calculated

It is hoped for that Eq. (7) is more generally valid, viz. that the influence of the water motion on C(0) can be described fully by $U_0^{3.5}/T^2$ and that the grain size dependence can be fully accounted for through G. So the tests have been continued for other grain sizes. The results are still to be reported.

6. Conclusions/Recommendations

From the present work it is concluded that
- care should be taken in measuring the proper parameter (concentration here) when comparison is made to theory,
- tests on the goodness of fit should be defined well to enable qualification of the goodness of test.

It is concluded more tentatively (because only a few conditions have been examined yet) that
- time and bed averaged concentration profiles under waves/currents look like two-layer distributions with a height-independent relative concentration gradient,
- near the bed, time and bed averaged concentrations under waves/currents depend very consistently on the water motion.

The experiments reported here (wave flume, Chapter 4, and wave tunnel, Chapter 5) are rather limited as they apply to only two (unsorted) sediment types (D_{50} = 0.1 mm and 0.21 mm, resp.) and to mainly rippled beds due to the only moderate orbital velocities. Furthermore, the wave tunnel tests deal with sinusoidal water motions only. Many more tests are required to obtain more evidence. Hence it is recommended to perform similar experiments for
- other grain sizes (sorted/unsorted),
- both regular and irregular water motions,
- higher velocities (with other bed forms).

In principle, the experiments can be carried out easily without requiring sophisticated instruments.

Acknowledgements

The present work is part of the Applied Research Program (T.O.W.) of the Dutch Ministry of Transport and Public Works - Rijkswaterstaat. The wave flume experiments have been carried out in the framework of the project Geomor of Rijkswaterstaat and the cooperation with Messrs. Kohsiek and Misdorp is much appreciated. The authors are grateful to the operators of the Scheldt wave flume at the De Voorst Laboratory (Messrs. Tulp, Pasterkamp, Dokter). Our special gratitude is towards Mr. Th. E. van Maar for his technical assistance in carrying out all TABAC-measurements.

References

Bosman, J.J., 1982
'Concentration measurements under oscillatory water motion',
Report on model investigation, M1695-Part II, Delft Hydrualics Laboratory,

Bosman, J.J., Van der Velden, E.T.J.M. and Hulsbergen, C.H., 1987
'Sediment concentration measurement by transverse suction',
Submitted to Coastal Engineering (Elsevier).
Draper, N. and Smith, H., 1966
'Applied regression analysis', ed. J. Wiley & Sons, New York.

Hulsbergen, C.H. and Bosman, J.J., 1980
'A closely responding, versatile wave tunnel',
Proc. 17th Coast. Eng. Conf., Sydney, pp. 310-317.

Kennedy, J.F. and Locher, F.A., 1972
'Sediment suspension under waves', in "Waves on Beaches",
pp. 249-295, ed. R.E. Meyer, Academic Press, New York.

Nakato, T., Locher, F.A., Glover, J.R. and Kennedy, J.F., 1977
'Wave entrainment of sediment from rippled beds', Proc. ASCE,
J. Waterw., Port, Coast. and Oc. Div., Vol. 103, WW1, pp. 83-89.

Steetzel, H.J., 1984
'Near bottom sediment suspension under oscillatory water motion',
MSc Thesis, Techn. Univ. Delft, Civ. Eng. Dept., Coast. Div. (Dutch text).

CHAPTER 75

Simulation of sandfill building stages with numerical flow models

G.J.Bosselaar *
R.A.H.Thabet **
A.J.G.M.van Roermund ***
L.Bijlsma ****

The paper describes the application of two dimensional vertically integrated models (WAQUA system), the results being used for the calculation of sandlosses during sandfill closure operations.
Investigations with test models, physical scale models as well as numerical models, are presented to prove that the WAQUA system is not only suitable for large scale applications, but also for the simulation of detailed flow patterns.

1. Introduction

A large part of the Netherlands lies below mean sea level. It is protected from floods by dikes and dunes (see figure 1).
In the twentieth century massive construction programs have been carried out to increase the safety of the low lands against storm floods. In former ages the defence merely consisted of building dikes. Only this century projects have been executed to shorten the exposed coast-line. This began in 1932 with the closure of the Zuiderzee, and continued more recently with the Delta Plan in the south-west of the Netherlands.

The rivers Rhine, Meuse and Scheldt formed the Dutch Delta. By its nature the area is flat and low. In the past the Delta was flooded several times. The most recent catastrophic flood disaster happened in 1953 when 150.000 hectares were inundated and more than 1800 people lost their lives (see figure 2).
Immediately after the situation had been restored, the Delta Plan was drawn up to prevent future disasters. According to the plan, all the estuaries had to be closed, except for the entrances to the harbours of Rotterdam and Antwerp.

* Hydraulic Engineer, Data Processing Division, Ministry of Transport and Public Works, P.O.Box 5809, 2280 HV Rijswijk, The Netherlands
** Senior Engineer, Delft Hydraulics Laboratory, P.O.Box 152, 8300 AD Emmeloord, The Netherlands
*** Hydraulic Engineer, Locks and Weirs Division, Ministry of Transport and Public Works, P.O.Box 20000, 3502 LA Utrecht, The Netherlands
**** Senior Engineer, Zeeland Division, Ministry of Transport and Public Works, P.O.Box 5014, 4330 KA Middelburg, The Netherlands

figure 1 The Netherlands without dykes

figure 2 Situation flood 1953, flooded area are shaded

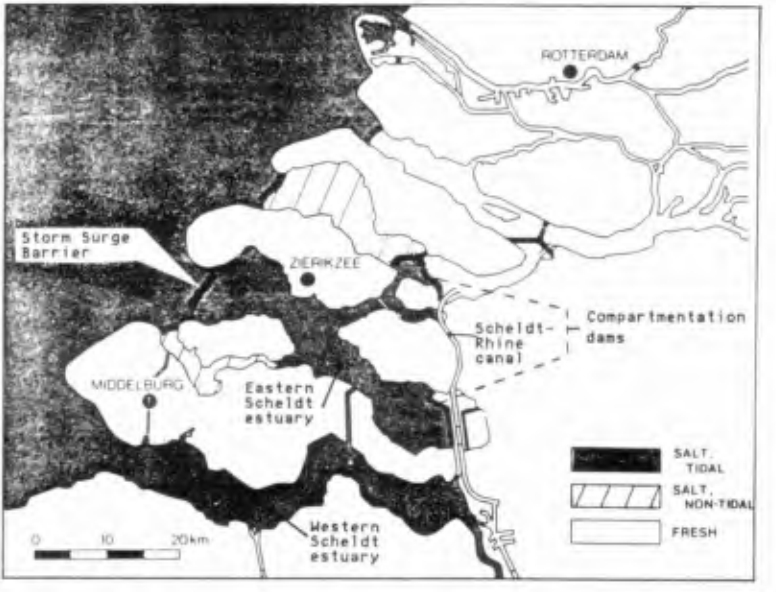

figure 3 The Delta project.

All planned closures but one were executed between 1956 and 1972.

However, contrary to the initial plan, the Government decided in 1976 to build a storm surge barrier in the mouth of the Eastern Scheldt instead of a massive dam. This with the aim to maintain the tide in the estuary under normal conditions, but to eradicate the chance of flooding of the country during storm surges.
The reason for this decision was that it became apparant that the Dutch society in the mean time came to realize that preserving the original environmental conditions in the Eastern Scheldt, with its unique aquatic life and its function as a nursery room for the North Sea, must be considered as a goal, equally important to the safety requirement.

The construction of the storm surge barrier implies the division of the Eastern Scheldt estuary into compartments. In the largest western compartment the tide is maintained, but the eastern part will become a tide-free fresh water lake:
- to prevent salt intrusion into the (agricultural) hinterland
- to provide a tide-free Scheldt-Rhine canal.
The ultimate lay-out of the Delta project is shown in figure 3.

The costs of the projects in the Eastern Scheldt amount to about $4,000,000,000.-. The construction of the storm surge barrier requires the major part of the budget. Related to the compartmentation projects approximately $300,000,000.- are to be spent.

The design and execution of major hydraulic structures is only possible when sufficient data are available.
Until now physical scale models were built to study flow conditions, and in some cases other relevant hydraulic phenomena, during building stages and in the future situation. The past decade, however, numerical flow models developed rapidly.
For the design of the storm surge barrier both physical scale models and numerical models were built. The principles of the applied numerical model based on the WAQUA system will be explained in chapter 2.
The confidence gained in the capability of numerical models to reproduce current patterns nearby the storm surge barrier (Klatter e.a., 1986) led to the decision to investigate whether numerical models can be used to compute current pattern near the planned sandfill closures of the compartmentation dams, without the additional use of tests in physical scale models. The performed tests will be descripbed in chapter 3.
The results of the tests led to the decision to rely entirely on numerical models for the design and execution of the sandfill operations in the closure gaps of the compartmentation dams (see for location figure 3).
Chapter 4 will discuss the results of these investigations.

2. WAQUA system

2.1. Numerical formulation

The model is based upon the so-called vertically integrated semi-momentum equations:

$$u_t + uu_x + vu_y - fv + gz_x + gu(u^2+v^2)^{0.5}/(C^2H) - K(u_{xx}+u_{yy}) = F^{(x)}$$

$$v_t + vv_y + uv_x + fu + gz_y + gv(u^2+v^2)^{0.5}/(C^2H) - K(v_{xx}+v_{yy}) = F^{(y)}$$

$$z_t + (Hu)_x + (Hv)_y = 0$$

in which:

- u = velocity in x direction (vertically integrated)
- v = velocity in y direction (vertically integrated)
- z = water elevation above some plane of reference
- h = water depth below plane of reference
- H = h + z = total water depth
- f = coriolis parameter
- g = acceleration due to grafity
- C = Chezy coefficient for bottom roughness
- $F^{(x,y)}$ = external forcing functions of wind stress or barometric pressure
- K = viscosity coefficient

The computations are made on a staggered rectangular grid system. The equations are solved by means of an Alternating Direction Implicit Method (Leendertse 1967, Stelling 1983).

2.2. Modeling system

For successful model investigations with numerical models a system of interlocking programs is required for data handling, simulation and graphical representation. The system used in this investigation has three major parts, namely, the Input Data Processor, the simulation program and the Simulation Data Display system.
Particularly noteworthy is that the WAQUA system possesses a number of facilities for simulating physical phenomena and the effects of hydraulic structures. The most important are:

- several procedures for the simulation of flooding and drying of intertidal flats (moving boundaries);
- a facility to simulate weirs and sluices whose flow characteristics can be varied with time;
- the possibility to represent narrow dams like groynes and breakwaters;
- the possibility to simulate the discharge of heat and effluents and the intake of cooling water at any location in the computational grid;
- (offline) nesting of models.

The system is designed to be used by civil engineers. Its operation requires no special knowledge of the computer science aspects of data handling and manipulation.

A large number of successful models have already been set-up and operated for tidal regions all over the world (ROOS et.al. 1985, Verboom et.al. 1984, Thabet et.al. 1985).

3. Detail models for sandfill closure gaps

3.1. Theoretical background

Numerical models based on the vertically integrated semi-momentum equations (which are based on the assumption of nearly parallel flow lines and hydrostatic pressure distribution) cannot be straightforward applied in the direct vicinity of hydraulic structures. The flow pattern is basically three dimensional, with flow separation and vertical and horizontal vortices directly downstream of the structure. These three dimensional effects and the additional dissipation of energy in the deceleration zone of the flow are responsible for the pronounced drop in the energy line (or water surface) at the structure. In civil engineering practice, these losses are usually refered to as "form losses", and expressed in terms of weir or gate formulae.
When applying two dimensional models, special measures have to be taken to introduce the energy drop at structure site. This is usually done by expressing "internal boundary conditions" based on the - presumably known - weir or gate formulae. This was the case for the storm surge barrier at the estuary mouth (Klatter et.al. 1986).

The case is different for sandfill closures. Sandfill bodies have flat slopes (1:15 or flater) in all directions. Hence no flow separation and associated "form losses" will take place. Accordingly two dimensional models can in principle be applied for such "structures", provided that the local energy losses not counted for in the semi-momentum equations can be locally incorporated.
These additional local losses are discussed below (see also figure 4).

First the friction losses. This factor dominates the energy drop over the closure gap. Because of the accelerating flow at the closure gap, the boundary layer will become thinner, causing the Chezy factor to drop and hence friction losses to (relatively) increase in the area around the closure gap. Downstream of the gap the change in the friction depends very much on the topography. The corresponding value of C will increase up to its original value over some distance.

Another coefficient which appears to be important is the viscosity factor K. From theoretical approximations we know, that this factor is 0.1 to 10 m2/s, dependant upon the local flow condition. This is only valid, when the numerical viscosity of the system is zero.

A coefficient which is not incorporated in the equations given in section 2.1 is the factor which described the influence of the vertical distribution of the velocity on the advection terms, $B(uu_x+vu_y)$ and $B(vv_y+uv_x)$. Under normal conditions the B value is approximately 1.1. In strongly diverging flows this factor may increase up to a maximum of 1.4. Because the B value is not implemented in the WAQUA system, the resulting energy losses were taken into account by adapting the friction coefficient, see section 3.2.

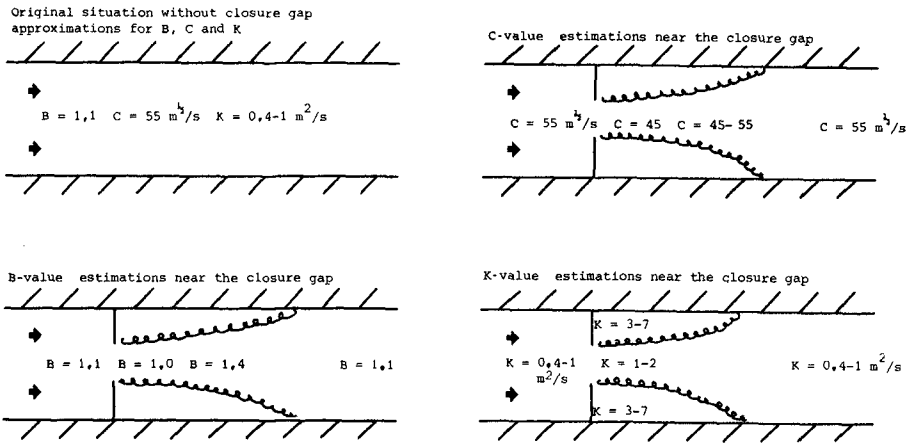

figure 4 Distribution of the values of some coefficients near the closure gap
note: Given C-value corresponds to water depths of the channels at compartmentation dam site

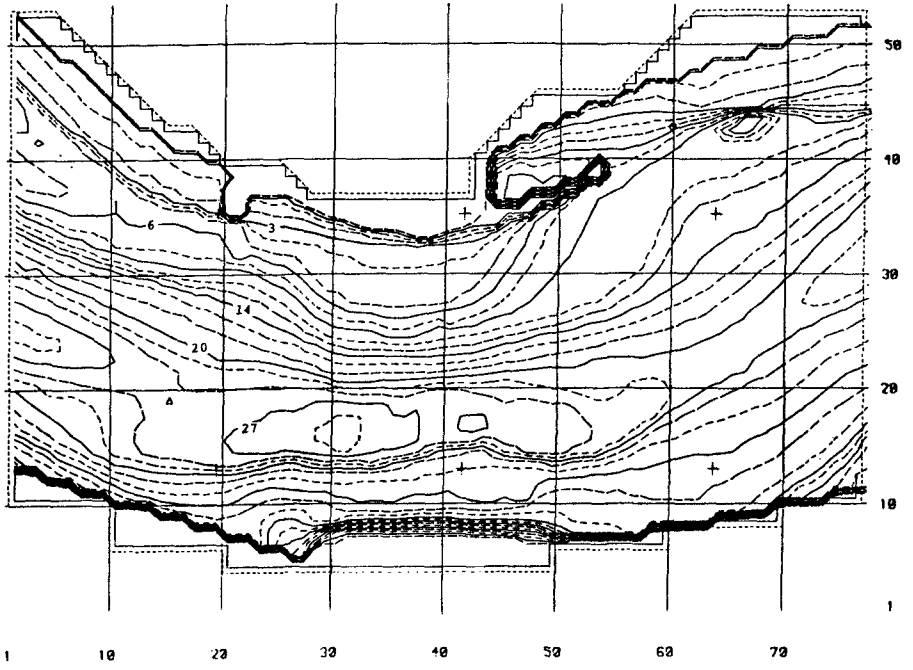

figure 5 Bathymetry of the test model

3.2. Verification tests

The test program

After the decision to investigate whether the WAQUA system is able to compute flow patterns around a sandfill closure, a test program was designed, based upon the comparison between a physical scale model and a numerical model of the same area.
An existing physical scale model was temporaraly changed in order to simulate the characteristics of a sandfill closure gap, see figure 5.
At the same time a numerical model with a grid size of 45 meters of the same area was built, to be able to compare measurements and calculations.
Five representative building stages of a sandfill closure were defined and one after another tested in the physical scale model.
The measured velocity distribution at the upstream and downstream edge of the physical scale model were used as boundary conditions for the numerical model.

Test results

The numerical model proved to be able to reproduce the current pattern fairly accurately.
Figures 6 and 7 show some of the investigated flow patterns. The measured flow pattern as well as the calculated distribution are shown.

As discussed in section 3.1., extra energy losses due to changes in the boundary layer and to the influence of the vertical velocity profile on the advection terms were introduced by increasing the bottom friction of the model.
Experiments proved that the Chezy factor must be decreased to a value of 35-40 to make up for these effects. Note that this value is only valid for geometries and water depths like the ones investigated.

Very low viscosity factors proved to give the best results, as far as the horizontal distribution of the velocity and diversion of the flow downstream of the gap are concerned.
After some tests we decided to use for all the applications a viscosity factor of 1 m2/sec.

The physical scale model is a stationary model. This implies that a changing tidal situation could not be simulated, only max. flood tide and max. eb tide were therefore investigated.

4. Applications

4.1. Tholense Gat model

In 1985 a fine grid model of the final gap in the southern compartmentation dam was built.
The model is situated at the northern edge of the dam, near the coast of the island of Tholen. It has a grid size of 30 meters and a time step of 20 seconds. The number of active grid cells is approximately 3000.
The boundary conditions of the model are generated by a 100 meter grid sized far field model.

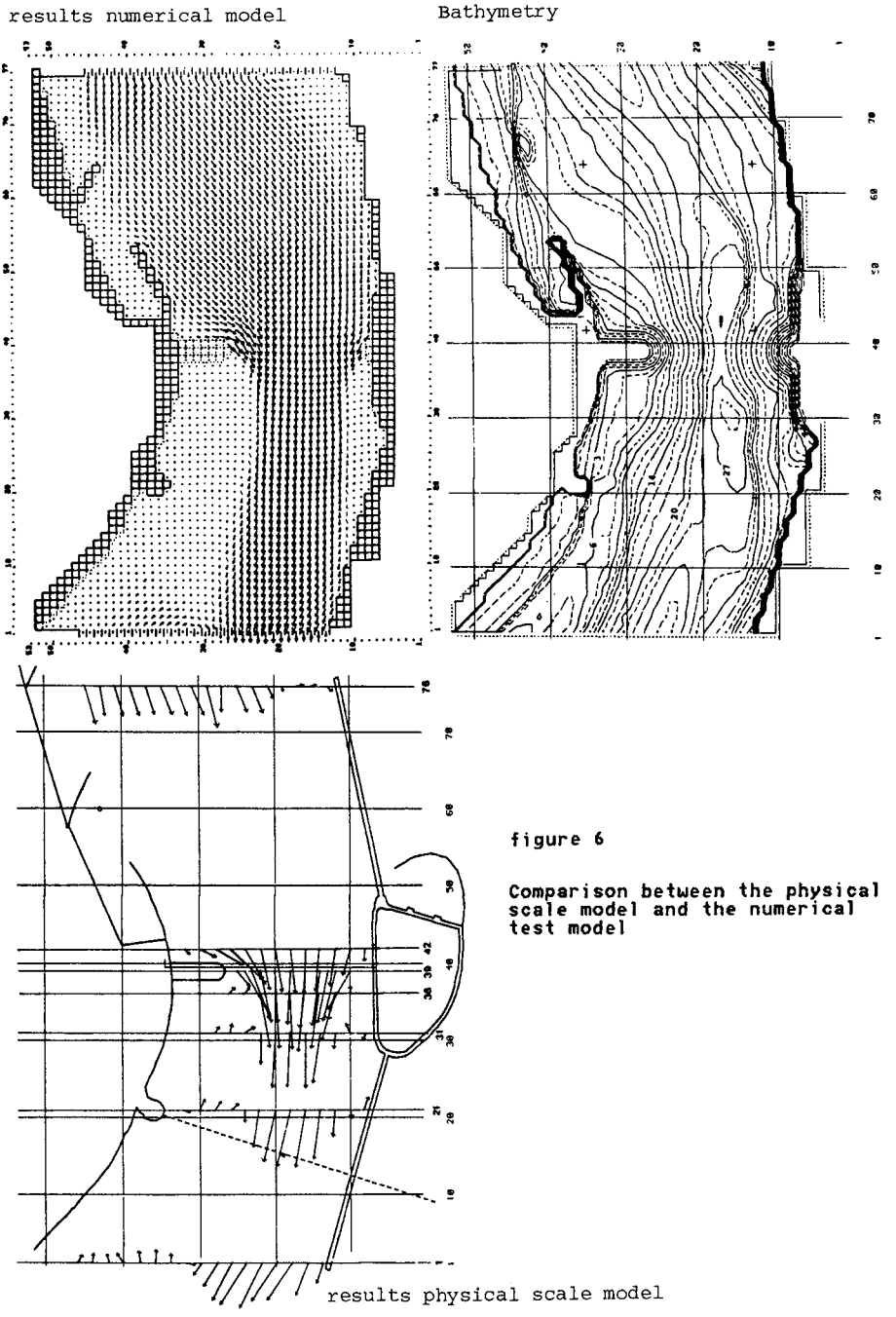

figure 6

Comparison between the physical scale model and the numerical test model

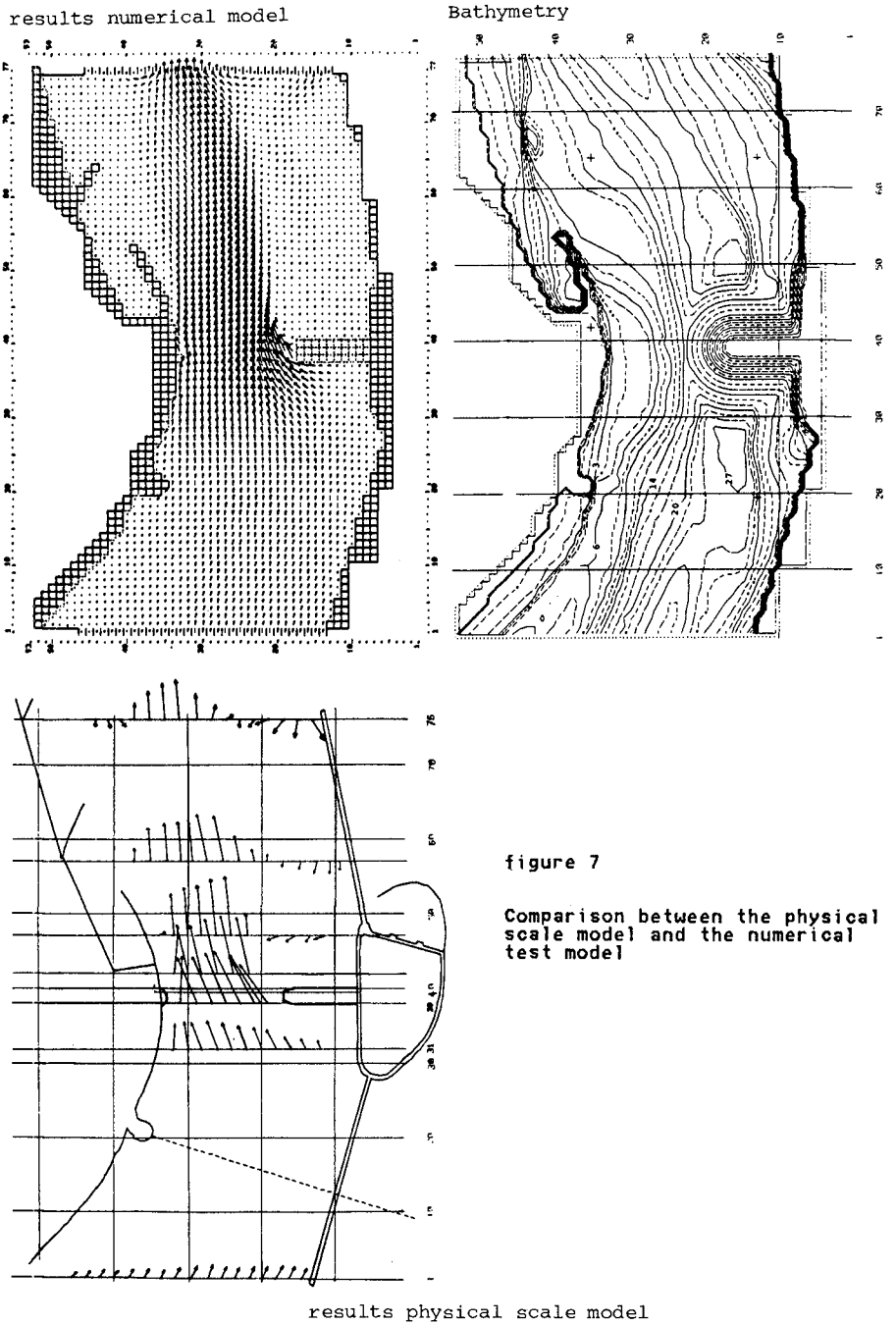

figure 7

Comparison between the physical scale model and the numerical test model

The investigations with the model had two purposes:
- prediction of the flow conditions in the closure gap, the results being used as input for the calculation of sand losses during the sandfill operation and prediction of the flow along the bank of the island of Tholen, in order to prevent possible problems with the existing, rather, weak dykes;
- prediction of the discharge coefficient of the closure gap (as a function of construction stage), such data being used as input for the one dimensional model covering the entire estuary up to the North Sea.

Figure 8 shows one of the investigated building stages.
The closure operation was successfully performed in October 1986.

4.2. Krammer model
Figure 9 shows the situation at the northern compartmentation dam in July 1986. Two gaps are still open.
The model of the area has a grid size of 50 meters, a time step of 30 seconds and some 25000 active grid cells.
The boundary conditions of the model are generated by the overall one dimensional model of the Eastern Scheldt (see also section 4.1.).
In September 1986 the smallest gap in the dam was closed. In figure 10 the flow pattern at the smallest gap, calculated by the model is compared with prototype measurements.
Although the grid size of the model is rather large in relation to the width of the gully, the model was able to simulate the flow pattern quite well.

After the successful closure of this small gap in September 1986 and the completion of the southern compartmentation dam, described in section 4.1., only the gully called the Krammer is still open.
The closure of this gap is planned in April 1987. The planned building stages have been thoroughly investigated. An example of the situation to be expected is shown in figure 11, where the flow pattern is plotted during an average maximum flood tide, when 70% of the gap is closed.
Figure 12 shows the flow pattern during maximum eb tide and maximum flood tide in more detail.
In the remaining cross section of 3000 m2 the average velocity is 2,0 m/sec, but localy 2,75 m/sec will occur.

The described flow pattern with an average velocity of 2,0 m/sec is only possible if the tide in the Eastern Scheldt estuary could be reduced. This is planned to be done by partial closure of the gates of the storm surge barrier.
A large amount of investigation effort has been invested in selecting the tide reducing measures that would reduce the velocities in the closure gap and at the same time would minimise the damage to the ecology of the estuary.
Figure 13 shows the expected (reduced) water elevation in the Eastern Scheldt during the last days of the closure operation of the Krammer Gap.
After completion of the dam, the storm surge barrier will be opened again completely and the tide will be fully admitted to the estuary.

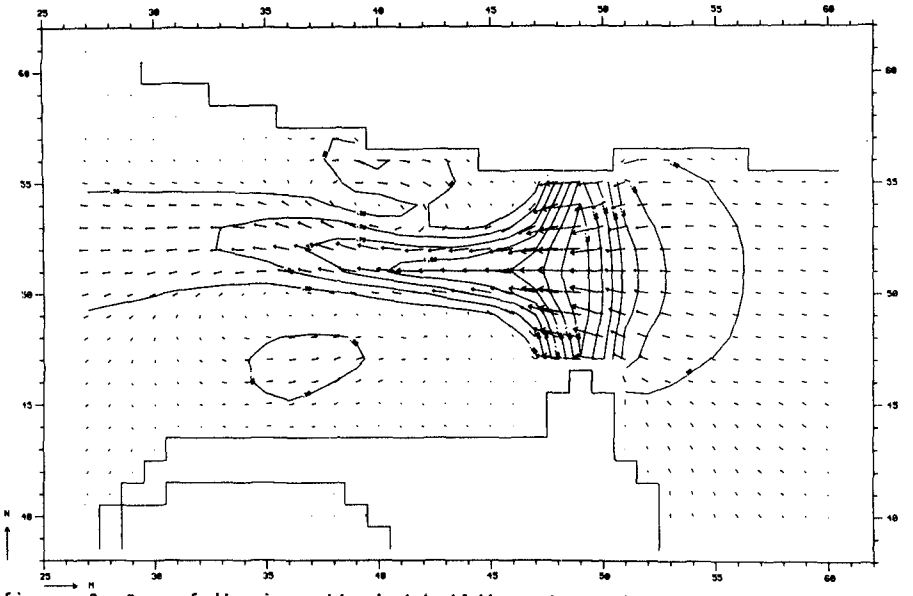

figure 8 One of the investigated building stages in the Tholense Gat model.

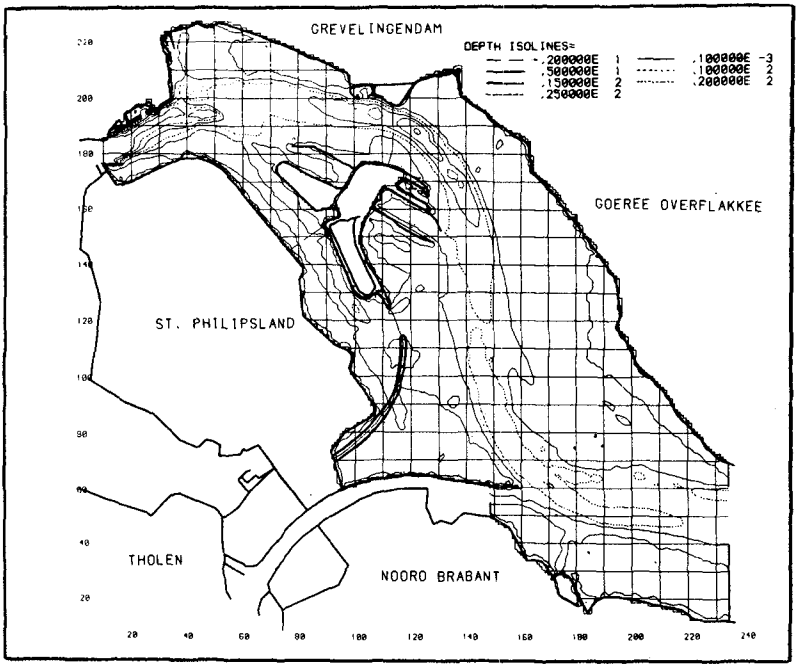

figure 9 Situation at the northern compartmentation dam in July 1986.

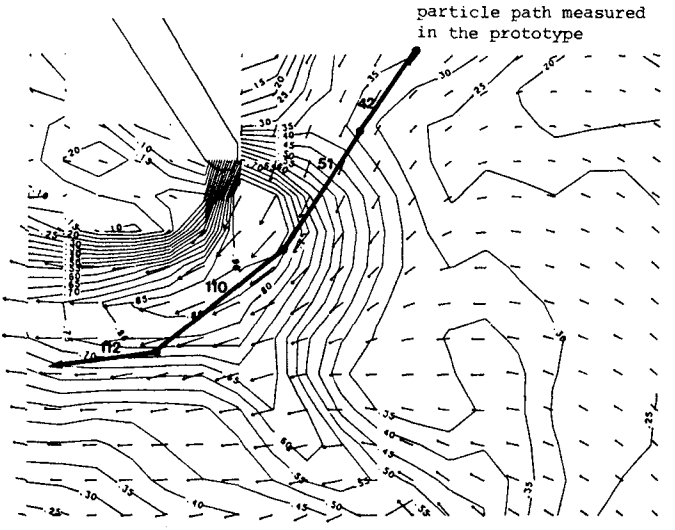

figure 10 Detail of the model of the area round the northern compartmentation dam, showing the comparison between prototype measurements and model calculations for the smallest gap, closed in September 1986.

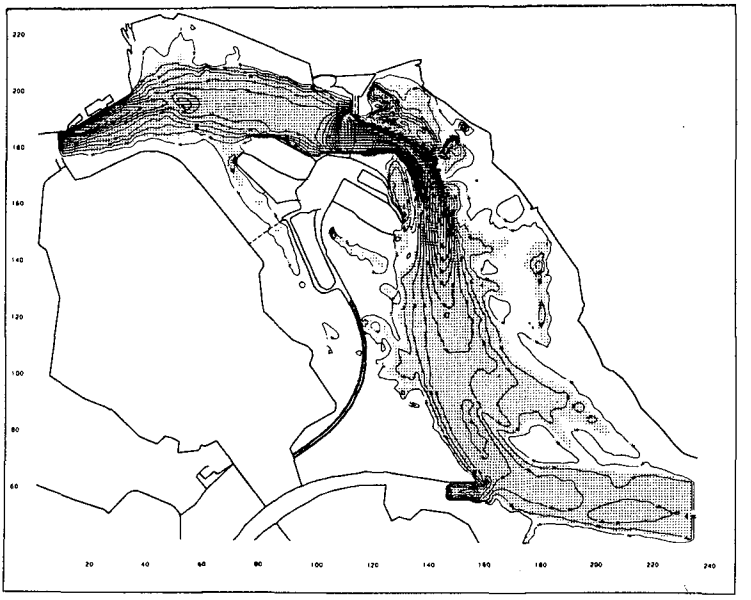

figure 11 One of the investigated building stages of the last gap in the northern compartmentation dam.

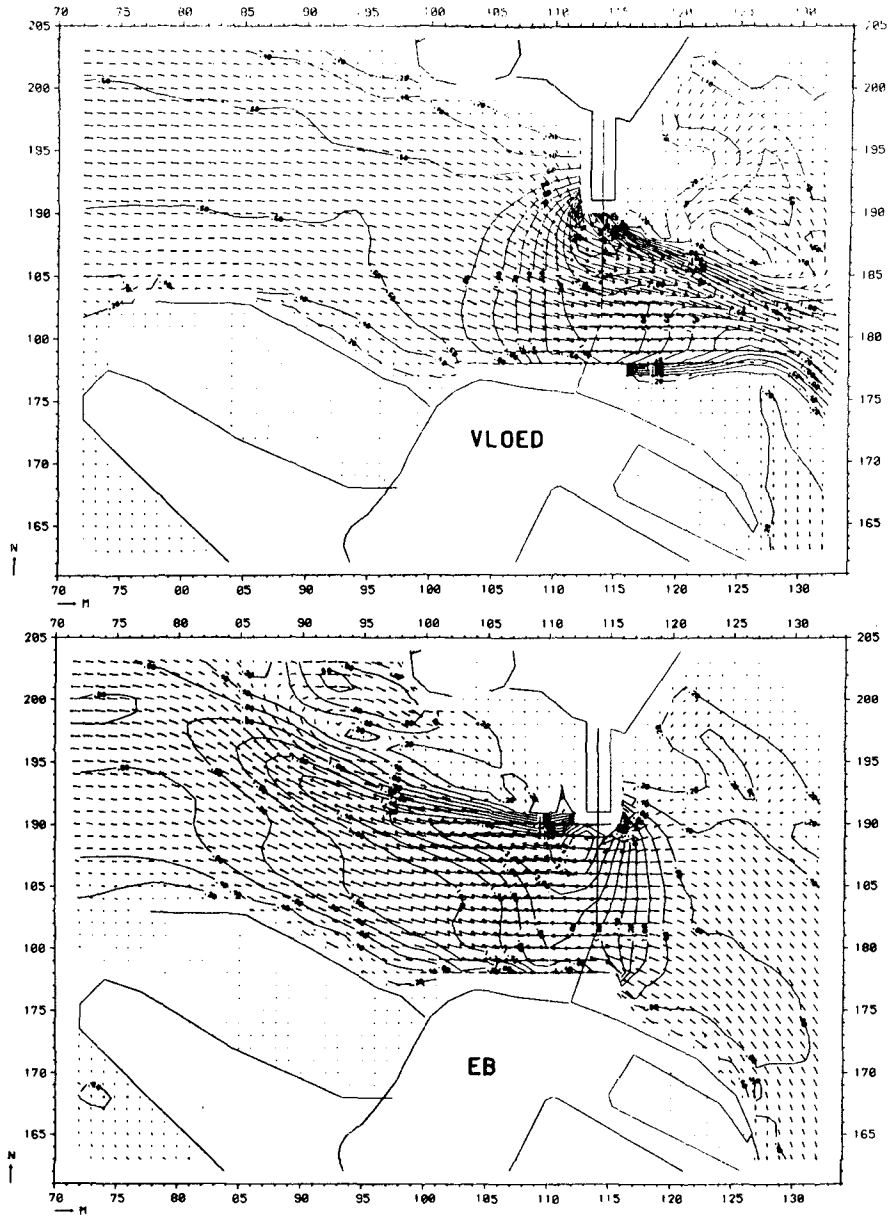

figure 12 Detailed calculated flow patterns during maximum eb tide and maximum flood tide.

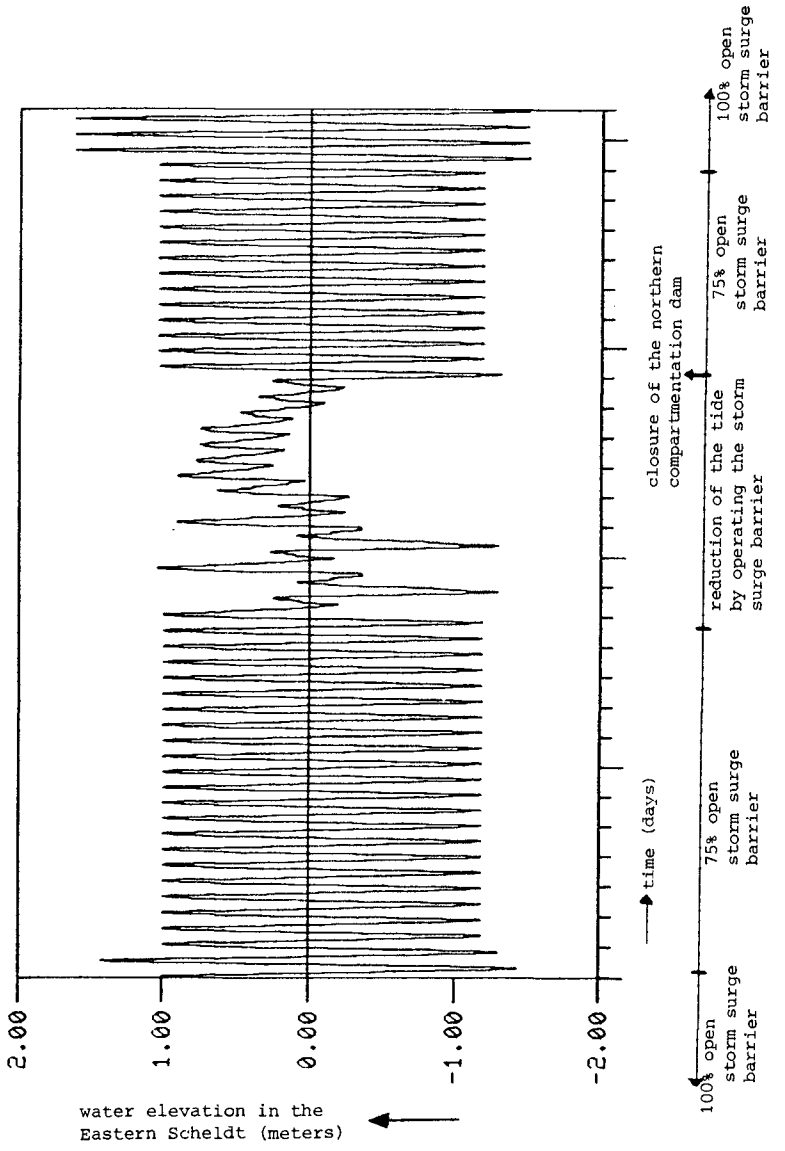

figure 13 Expected (reduced) water elevation in the Eastern Scheldt during the closure of the Krammer gully in the northern compartmentation dam.

5. Conclusions

Extensive tests with the WAQUA system, in comparison with prototype measurements and physical scale model results, have shown that the system is also reliable for small scale applications, provided that governing mechanisms are correctly simulated.
Models of sand closure building stages proved to be able to calculate the flow patterns accurately.
For the first time in the Netherlands, major closure operations were carried out without the use of physical scale models, but entirely based on calculations with numerical flow models.
The system proved to be a very useful engineering tool, accepted by and operated by civil engineers.

References

BOSSELAAR, G.J. (1985). Eindverslag bewijsproef WAQUA, Notitie ddwt 85.298, Delta Department

KLATTER, H.E., DIJKZEUL, J.M.C., HARTSUIKER, G., BIJLSMA, L. (1986). Flow computations nearby a Storm Surge Barrier under construction with Two-Dimensional Numerical Models, 20th ICCE, Taipei

LANGERAK, A., DE RAS, M.A.M. and LEENDERTSE, J.J. (1978). Adjustment and Verification of the Randdelta II Model, 16th ICCE, Hamburg

LEENDERTSE, J.J. (1967). Aspects of a Computational Model for Long-Period Water Wave Propagation, The Rand Corporation, Memorandum RM-5294-PR

ROOS, A., VAN DIJK, R.P. and VINCENT, J. (1985). Overzicht van de bij de Deltadienst en District Kust en Zee in gebruik zijnde WAQUA-modellen d.d. april 1985, Nota wwkz 85.G005, Delta Department

STELLING, G.S. (1983). On the Construction of Computational Methods for Shallow Water Flow Problems, Ph.D.Thesis, Delft Technological University

THABET, R.A.H. and TAAT, J.J. (1985). Twee dimensionaal detailmodel van het sluitgat van het Tholense Gat (THOGAT), Report no. R2103, Delft Hydraulics Laboratory

THABET, R.A.H. and CREBAS, J.I. (1985). Twee dimensionaal detailmodel van het sluitgat van het Krammer, Report no. R2221, Delft Hydraulics Laboratory

THABET, R.A.H. Verboom, G.K. and AKKERMAN, G.J. (1985). Two dimensional modelling of tidal motion for harbour studies, Intern.Conf. on Nunumerical and Hydraulic Modelling of Ports and Harbours, BHRA, Birmingham

VERBOOM, G.K. et al (1984). Nested models: applications to practical problems, 5th Intern.Conf. on Finite Elements in Water Resources, Burlington, U.S.A.

CHAPTER 76

BEACH DEVELOPMENT BETWEEN HEADLAND BREAKWATERS IN A LOW WAVE ENERGY ENVIRONMENT, PASIR RIS, SINGAPORE

S.Y. Chew, M.Eng., FIES, MIEM, MICE, M.ASCE, Manager, Building & Development, Housing and Development Board.
S.K. Ho, FRMIT, M.Eng., FIES, MICE, Senior Principal Civil Engineer, Housing and Development Board.
P.P. Wong, B.A. Hons., M.A. Ph.D.,Senior Lecturer, National University of Singapore.
Y.Y. Leong, B.A. Hons., Trainee Teacher, Institute of Education.

INTRODUCTION

One of the function of the offshore breakwater is to protect the coast from wave action. By dissipating the wave energy along its entire length, the breakwater causes sediments in its lee to deposit and a shore salient is formed. If the offshore breakwater are placed in a series along a coast with a gentle offshore slope and a substantial littoral drift tombolo will form behind the breakwaters between which bays will be sculptured by waves to form stable shapes (1). These attached breakwater would thus form a series of artificial headlands.

In nature, beaches between headlands are influenced by the position of the headlands. Where the headlands are closely spaced and a limited sediment supply exists, small pockets beaches are formed. Where the headlands are far apart and an adequate sediment supply exists, long and wide beaches are formed. Generally, between these two extremes most beaches between natural headlands take a shape that is related to the predominant wave approach; on the downcoast sector is a long and straight beach, while on the upcoast end is curbed beach. Silvester (2) in his model study established a relationship between the logarithmic spiral constant (α) and the angle of predominant wave approach (β). A quasi-permanent shape was reached when waves broke simultaneously around the model bay. As it is difficult to measure the curve sector in nature, Silvester and Ho (3) suggested the use of an indentation ratio to relate the bay's shape to wave approach.

The afore-mentioned concepts of headland breakwaters and beach formation between them were applied in 1968 along the Southeast Coast of Singapore (Fig. 1), where a series of headland breakwater are used to protect about 14 km of the newly reclaimed land (4,5) under the East Coast Reclamation Scheme (Phases I to VII) where 1525 hectares of foreshore was reclaimed at a total cost of $613 million from 1966 to 1985. Rip Rap headland breakwaters of length varies from 55 m to 67 m and spaced at 300 m to 360 m were constructed in series along the edge of the fill. Under wave action, the fines are removed leaving behind sand and gravels to form sandy bay beaches between the headland breakwaters. (see Figs. 2a, 2b and 2c).

The successful implementation of the headland breakwater concept at the Southeast Coast lead to similar technique being used for the reclaimed land at Pasir Ris. Between 1978 and 1980 Housing and Development Board reclaimed 44 hectares of the shallow foreshore at Pasir Ris and Loyang areas in two separate parts on both sides of Sungei Tampines on the northeast coast of Singapore to provide additional land for a park (Figs. 1 and 3). Approximately 2.4 million cu m of earth excavated from existing hills about 6 km away was utilised for the reclamation. The fill material, which is a semi-consolidated mass of gravel, sand and clays, disintegrates rather easily in contact with water. The fines are removed by wave action and coarser material is left behind for beach formation.

PASIR RIS RECLAMATION

The existing coast at Pasir Ris prior to reclamation was a relatively flat muddy coast with pockets of sandy beaches, the entire shallow foreshore up to a distance of 150 m from the existing shore was exposed during low tide.

To provide recreational facilities for residents around the area, it was decided to reclaim the shallow foreshore to creat land for the development of a park. In 1978 Housing and Development Board proceeded with the reclamation of 44 hectares of the foreshore at Pasir Ris and Loyang in two separate parts on both sides of Sungei Tampines and works was completed in 1980 (Fig. 3). The extent of the reclamation was confined mainly to the shallow area which was exposed at low tide. The profile of the reclamation was determined using the existing offshore topography as a guide, ie the edge of the reclaimed area was more or less parallel to the existing offshore contour (see Figs. 4a, 4b and 4c). The concept of rip-rap headland breakwaters which had been successfully implemented at the East Coast Reclamation was adopted for Pasir Ris Reclamation. A series of 10 numbers rip-rap headland breakwater was constructed along the edge of the reclaimed area to creat sandy bay beaches.

The fill material for the reclamation was excavated from existing hills some 6 km away from the reclamation site. The fill material is of Quarternary age and consists of semi-consolidated gravels, sands and clay. Boreholes carried out at the cut site showed that the material was dense to very dense medium to coarse silty clayey sand. Mechanical analysis showed approximately 75% was sand and gravel and 25% was silt and clay.

The material for reclamation was conveyed from the cut site to the reclamation site by lorry. An earth bund of approximately 20 m width was constructed initially along the perimeter of the reclamation site commencing from the existing shoreline and proceeded toward the sea by direct dumping from the lorries. Upon completion of the perimeter bund, filling within the bunded area was then proceeded, an opening in the bund was constructed to facilitate the inflow and outflow of sea water, area around the opening was reclaimed last. The level of the fill was 102.70 m or approximately 4.7 m above the existing seabed level.

Rip rap headland breakwaters constructed dry in the fill material along a near straight edge of fill and subsequently become wet (Fig. 5). The area upon which each rip-rap structure is to be constructed is first overfilled, compacted and thereafter excavated in stages to form an earth mound with a seaward slope of 1:2 and a landward slope of 1:1 1/2. A non-woven filter cloth of thickness 3.5 mm was used as a filtering medium to prevent removal of fill material by wave action was then spread loosely over the entire mound. On top of it were placed 0.1 m of 0.05 to 0.1 m stones, a second 0.25 m layer of 0.1 m to 0.15 m stones and lastly a layer of 0.40 m stone properly pitched. The rip-rap structure extends 1.18 m below LWOST to 1.5 m above HWOST. Subsequent wave action removes the fill materials which was overfilled and exposed the rip-rap breakwater which are spaced at about 200 m. Under wave action, the fines are removed leaving behind sand and gravels for beach formation between the headland breakwaters. The length of the rip rap breakwater is 25 m which has to be such that it would not subsequently become an "offshore island". This can be predetermined using Silvester's relationship between logarithmic spiral constant (α) and the predominant wave approach angle (β). The maximum limit of fill seaward of the rip-rap breakwater was 25 m from the centre of the breakwater. The overfilled material was removed and spread onto the seaward face of the rip-rap headland breakwater upon completion of construction to provide a gentle sloping seaward appearance.

COASTAL ENVIRONMENT

The northeast coast of Singapore is relatively clam as it is located at Johore Strait bound by the southern boundary of Johore and northern boundary of Singapore. Johore Strait is a long and narrow strait with a length of 30 km and an average width of 2 km. Winds from the north during the northeast monsoon do not have a large influence except through refracted swell from South China Sea which enter the Johore Strait from the east. It is essentially a low energy environment throughout the year with refracted waves coming from the northeast quadrant, so that westward littoral drift is present (see figure 3).

WINDS

The wind conditions in Singapore are governed by the two monsoon seasons. The SW-monsoon season prevailing in the months June through Sept. The NE-monsoon season prevailing in the months December through March. Separating these monsoon seasons there are two inter monsoon periods.

Winds were records at the Paya Lebar Airport at a point about 2 km from the sea and 28.0 m above mean sea level and at Changi Airport at a point 1.2 km from the sea and 13.0 m above mean sea level. Sharp contrasts in direction and velocity of winds were recorded for the northeast monsoon (December to March) and the other periods. Long term wind frequency data obtained from Meterological Services Singapore at Paya Lebar Airport from 1956 to 1980 and at Changi Airport from 1972 to 1982 were used to produce the wind rose for the annual average wind speed and direction (Fig. 6a). Southwest monsoon during the period June to September (Fig. 6b) and northeast monsoon during the period December to March (Fig. 6c) for Paya Lebar Airport and the annual average wind speed and direction for Changi Airport (Fig. 6d).

Winds during the northeast monsoon are predominantly from N-NNE and are less than 5.4 m/sec. Wind speed exceeding 10 m/sec only 2 - 3% of the time. Wind during other period are from S-SSE with speeds of less than 3.3 m/sec. The annual wind rose showed a similar pattern to that of the northeast monsoon which indicated that the predominant wind is from the north quadrant.

TIDES

The tides are essentially a combination of diurnal and semi-diurnal (ie a high tide is followed by a not so high tide) with a range of approximately 2.3 m during spring tide, 1.0 m during neap tide and a mean range of 1.7 m. The typical tidal velocity is 0.7 m/sec during spring tide and 0.4 m during neap tide based on information available from Admiralty Chart.

TIDAL CURRENTS

A non-contact current meter manufactured by Koyowa Shoko Co Ltd Japan was installed at the study area at 3 m below surface during the period 7.2.86 to 10.3.86. The current meter is able to measure both the direction and mean current velocity continuously. Current velocity, however, is counted for three minutes at every twenty minutes striped graphically on scratch paper. Measuring range for current velocity is 0.05 - 3 m/sec as mean current velocity with one constant-pitched impeller.

A scatter plot of current speed against direction (Fig. 7a) for all recordings indicated that the current is mainly in the southeast and northwest direction. A cumulative current speed distribution curve (Fig. 7b) showed that 85% or more of the current speed is less than 0.3 m/sec. A plot of west going and east going current together with hourly tide observation for 8.2.86 were shown in Figs. 8a and 8b. From these two figures it can be seen that during ebb tide the current is east going and during flood tide the current is west going. In general, the tidal elevation curve lead the velocity curve by about 3 hours which is approximately one-quarter of the semi-diurnal period. This is an expected observation because it shows that during extremes of tides, ie when the tides are about to change direction, the velocity are almost zero. Also, when the tides are flowing in or ebbing out of the strait, ie at mean sea level, the velocities are maximum.

WAVES AND WAVE REFRACTION

Pasir Ris Reclamation was along a coastline facing north which is subject to refracted swell wave from South China Sea arriving the beach from the north east direction. This results in a net littoral draft from east to west (as indicated by the offshore topography in Fig. 3) whether the waves are generally locally or are swell from South China Sea, they entering the Johore Strait from the east (Figs. 9a and 9b). The wind rose for the area indicates a predominance of winds from NE quadrant. The largest proportion of these are wind of less than 5.4 m/sec. Winds in excess of this velocity from this NE quadrant occur for less than 4% of the time.

The major wave incidence would therefore appear to be swell arriving from South China Sea. The predominance of this wave and current action is indicated by the offshore contour. These clearly indicate an east to west drift of sediment. Considering the general orientation of the bed contour at the study area, a refraction computation indicates a deepwater approach from a north easterly direction, S.Y. Chew (4) measured the waves at Southeast Coast of Singapore, the result indicated that during the northeast monsoon the highest value of H_{max} was 1.1 m and for more than 65% of the time, H_{max} did not exceed 0.6 m. During other period H_{max} exceed 0.6 m for less than 10% of the time. 90% of T_z fell between 2.5 and 4 seconds during northeast monsoon while T_z was predominantly around 3 seconds during other period. A wave period of 4 seconds was used for the plotting of the wave refraction diagram in Figs. 3, 9a and 9b. The wave period is close to that reported in South China Sea of 4 to 7 seconds. Such swell is predominant in the months from December to March when northeast monsoon exist in the area. Figs 10a and 10b showed the wave height exceedence distribution curves and H_s - T_p relations for prevailing system off Changi coast respectively.

IMPLICATION AND EFFECTS OF PROCESSES ON RECLAMATION PROJECT

The northeast coast of Singapore is a sheltered area and local winds do not have a large influence except through refracted swell from South China Sea. It is essentially a low wave energy environment throughout the year with waves coming from the northeast, so that a westward littoral drift is present.

The swell from South China Sea enter the Johore Strait from the east after travelling through the deep water, the waves are refracted toward the reclaimed area, as the offshore topography is almost parallel to the coast, the refracted waves reach the coastline almost perpendicular, this together with the fact that the tidal current is flowing westward during flood tide and eastward during ebb tide with a duration of approximately 15 hours during flood tide and 9 hours during ebb tide, there is a tendency for a net movement toward the westward. In view of the almost perpendicular approach of the wave orthogonal and the weak current, the movement of the sediment is a very slow processes as indicated by the slow beach formation at Pasir Ris Beach. The formation of the beach between the headland breakwaters is slower when it is compared to the coast at East Coast which is more exposed than the beach at Pasir Ris.

GRAIN SIZE DISTRIBUTION OF BEACH MATERIAL

The fill material, which is a semi-consolidated mass of gravels, sand and clays, disintegrates rather easily in contact with water. The fines are removed by wave action and coarser material is left behind for beach formation.

The grain size characteristic of the beach material varied from 0.06 mm to 10 mm. The median size (D50) varied from 0.4 mm to 1.1 mm and the average median size was 0.68 mm (Figs. 11a and 11b). There is a systematic variation of mean grain size normal to the beach, from medium sand at the berm to coarse sand at the step. The average mean grain size is 0.39 m for berm samples, 0.59 m for foreshore samples and 0.88 mm for step samples.

While size variation normal to beach is present, the material is not well sorted. The average berm sample is moderately sorted (0.96) whereas the foreshore and step samples are poorly sorted (1.22 and 1.23 respectively). Poor sorting is attributed to the incomplete process of selective removal of fine grains under low wave energy environment and the short period of beach development (1980 - 84).

There is no systematic alongshore variation of mean grain size and sorting. The lack of alongshore variation in grain size characteristics is due to low wave energy and absence of littoral currents to sort out the beach material.

BEACH PROFILES

The formation of beaches along the reclaimed Pasir Ris coast is essentially similar to a situation where the scarp retreat along the fill will not produce a seaward concave curve until the strip of fill between the headland breakwaters and the sea is removed and the seaward sides of the breakwater are exposed to wave action. The berm is of fairly uniform width along the entire shore in the model proposed for beach formation along reclaimed Southeast Coast of Singapore (8). Basically, a strip of fill material placed seaward of a pair of breakwaters retreats under wave action; as the shoreline retreats in form of a scarp, a sloping abrasion ramp is left behind; the clastic deposits which is derived from the fill covers the abrasion ramp. The extent of development of clastic deposits in form of a beach between a pair of breakwaters varies from cell to cell (See Figure 3 showing cells along Pasir Ris reclaimed coast).

Beach profiles were taken at the upcoast, midcoast and downcoast ends of cells at the Pasir Ris coast (see Figure 12 showing profiles from cells A and F). They are slightly concave and represent profiles of under-nourished beach based on Bruun's (9) classification of beach profiles. The beaches are poorly formed because of an inadequate supply of clastic material from the fill.

The backshore (berm) is present at parts of the cells and is very narrow, averaging 2.4 metres wide. The landward ends of the profiles are marked by active scarp erosion. The foreshore average 7.8 metres wide and consists of a thin layer of clastic material that gets progressively thinner towards the step. The foreshore slope ranges from 4°10' to 8°40'. Exposed abrasion ramps are found mainly in the foreshore zone; generally, they have a sparse cover of pebbles, cobble-sized and boulder-sized pieces of Old Alluvium. The slope of the abrasion ramp is less than that of the foreshore.

Certain features on beach profiles display consistent pattern: the upcoast fill scarp is usually inactive whereas ongoing erosion marks the fill scarps at the midcoast and downcoast sections. The berms are usually located at the upcoast ends and occasionally in the midcoast sections.

BEACH PLANS

With reference to position of the step, most of the beach planforms display a slight seaward concave curvature with an almost straight downcoast sector and a more indented upcoast sector. With development of berms in the upcoast sector, the step at that part of the cell is prograded and straightened.

Active scarps characterized almost the entire length of the cells, with most scarp height between 0.25 and 0.75 metres. The persistence of these active scarps indicates that beaches are still retreating. Small lengths of inactive scarps are found in the upcoast sectors of cells A, C, E, F and G and the downcoast sectors of cells B and C. They occurred at locations where they are protected by berms, bars or mangroves. The height of active scarps tend to increase progressively with distance from monactive scarp until the highest scarp height in the cell is reached (usually in the middle of the cell).

For planning purposes, Silvester's (2) criterion of the logarithmic spiral to determine the maximum position of the beach between the breakwaters was adopted.. These lines of maximum positions are based on a logarithmic spiral of 1.05 with a constant agnel (α) at 72° to a wave approach (β) of 10°. (See Figs 13a and 13b showing lines of maximum positions compared with planform of the scarps of all the cells).

BEACH DEVELOPMENT

Beach platform and changes at cells A and F are shown in Figs 13a and 13b. The profile indicated that there is minor variation of the beach profile between high and low water where a accretion and erosion have occurred. From Fig. 3 it can be seen that the offshore profile is more or less parellel to the edge of the reclamation profile and the wave direction is almost perpendicular to the beach, this together with the weak current resulted in slow erosion and minimum littoral drift which explain the slow formation of the beach development between the rip-rap headland breakwaters. Although the changes is slow, there is still a tendency for westward movement as the duration of the current flowing eastward is generally shorter than the westward movement. For land use purposes, it is necessary to determine the limit of erosion. Silvester (7) has suggested that the relationship between logarithmic spiral constant and the wave obliquity can be used to determine the equilibrium shape of the beaches between headland breakwaters.. The probable shapes based on this criterion of the three bays for wave approach from north are given in Figs 13a and 13b. This assume that the westward drift is reduced or cut off. From Figs 13a and 13b it can be seen that further erosion is expected to take place especially around the curved portion.

DISCUSSION

Even with a longer time period, the beaches at Pasir Ris are unlikely to attain the equilibrium shape according to the logarithmic spiral criterion. This is confirmed by the presence of inactive scarps protected by berms along parts of the cell and the straightening and progradation of the shoreline with berm development. The logarithmic spiral criterion therefore cannot be used to determine beach equilibrium at the Pasir Ris coast because of the low wave energy and a very weak littoral drift. Given the low wave energy and a very gentle offshore gradient, beach type similar to East Coast of Singapore is unlikely to be attained by all the cells at Pasir Ris.

The slow progress in the development of the beach at northeast coast is due to weak current and almost perpendicular approach of the waves. It is most likely that the beach will only reach its anticipated platform after prolong period. Monitoring of the beaches will be carried out to observe the beach development.

ACKNOWLEDGEMENT

The authors wish to thank the Chairman, Hsuan Owyang and the Chief Executive Officer, Mr Liu Thai Ker and the Chief Civil Engineer, Mr Yao Chee Liew of the Housing and Development Board for their encouragement and permission to present this paper.

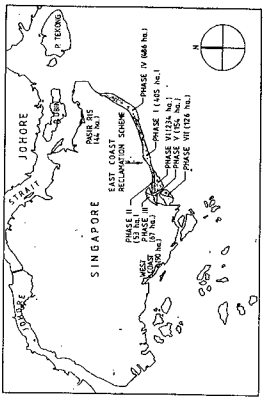

FIG 1 - FORESHORE RECLAMATION BY HOUSING & DEVELOPMENT BOARD

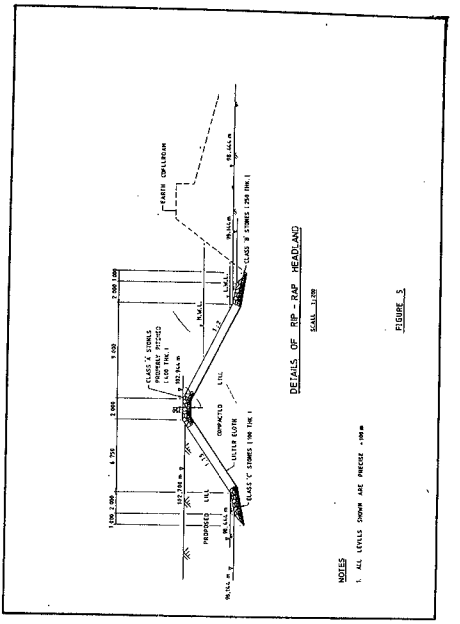

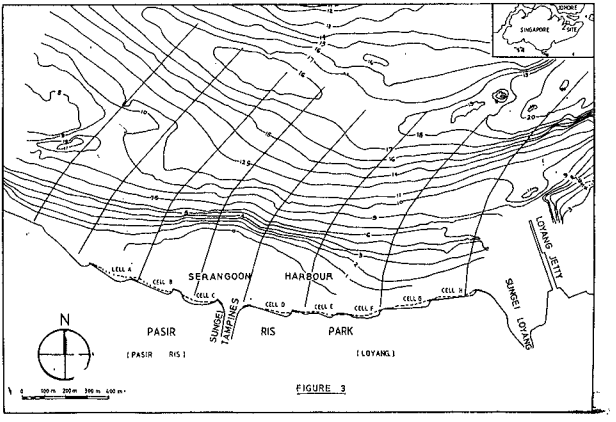

FIGURE 3

FIGURE 2a

FIGURE 2b

FIGURE 2c

FIGURE 4a

FIGURE 4b

FIGURE 4c

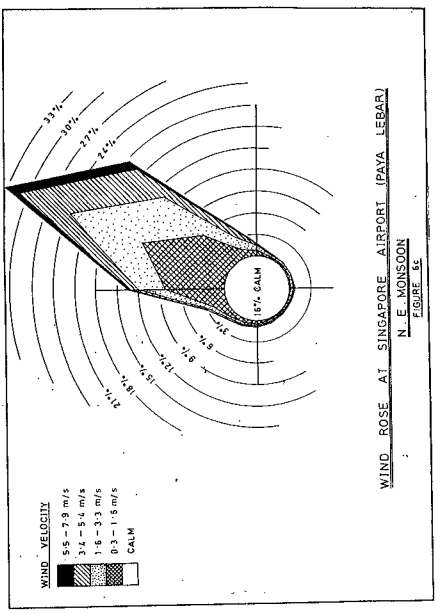

WIND ROSE AT SINGAPORE AIRPORT (PAYA LEBAR)
N. E. MONSOON
FIGURE 6c

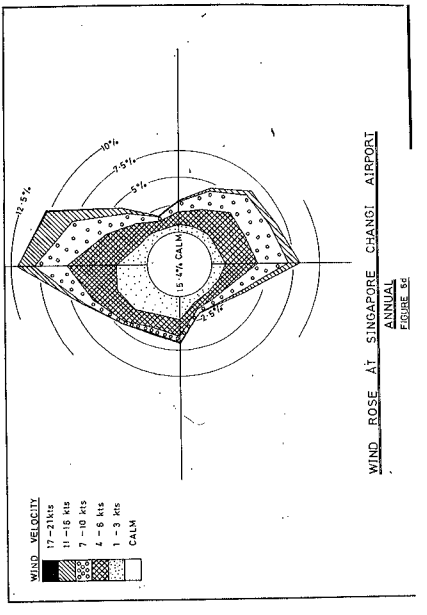

WIND ROSE AT SINGAPORE CHANGI AIRPORT
ANNUAL
FIGURE 6e

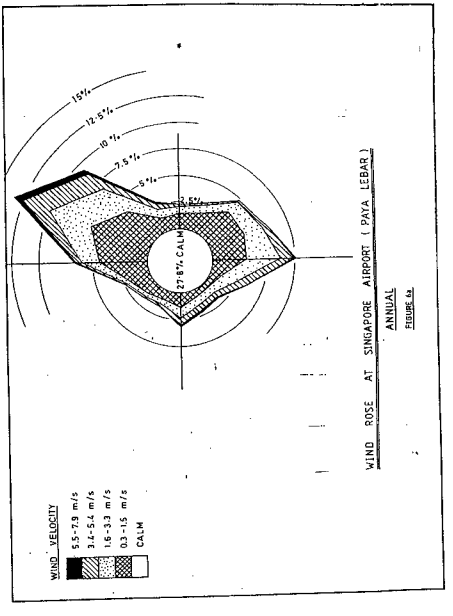

WIND ROSE AT SINGAPORE AIRPORT (PAYA LEBAR)
ANNUAL
FIGURE 6a

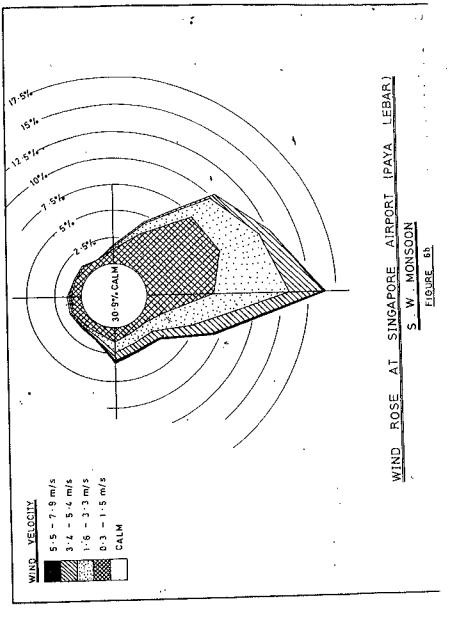

WIND ROSE AT SINGAPORE AIRPORT (PAYA LEBAR)
S. W. MONSOON
FIGURE 6b

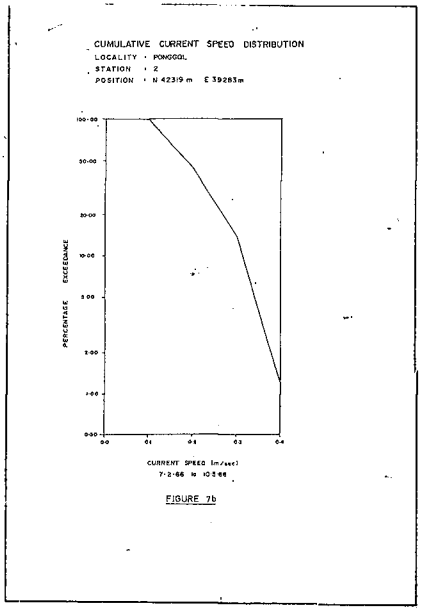

FIGURE 7b

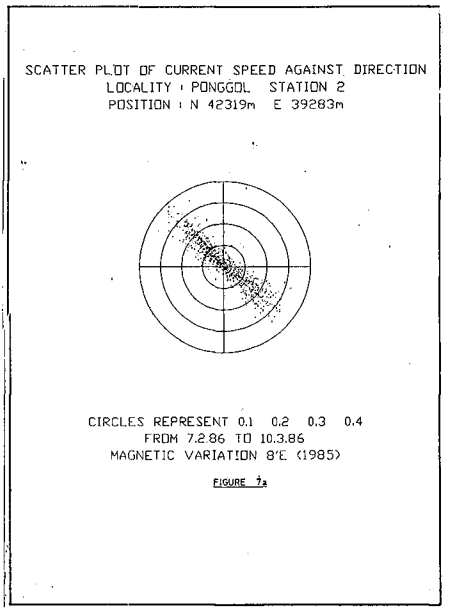

FIGURE 7a

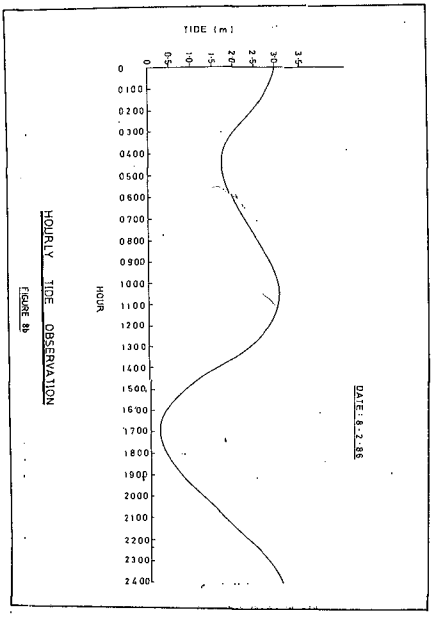

HOURLY TIDE OBSERVATION

FIGURE 8b

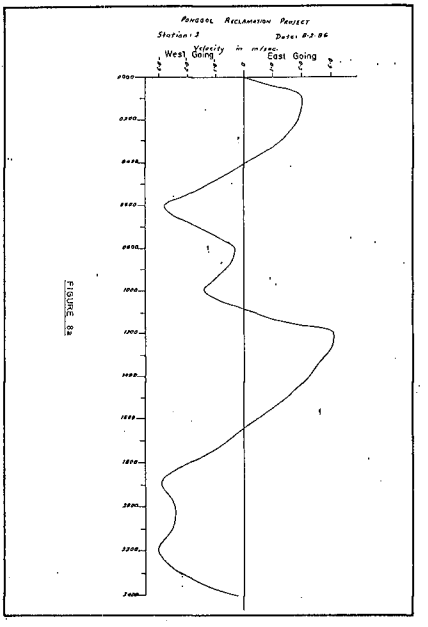

FIGURE 8a

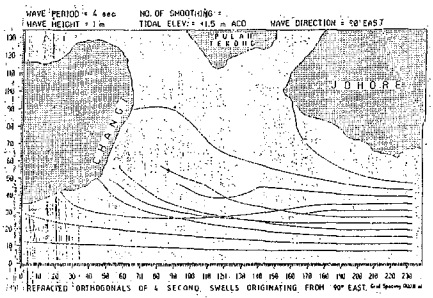

FIGURE 9b

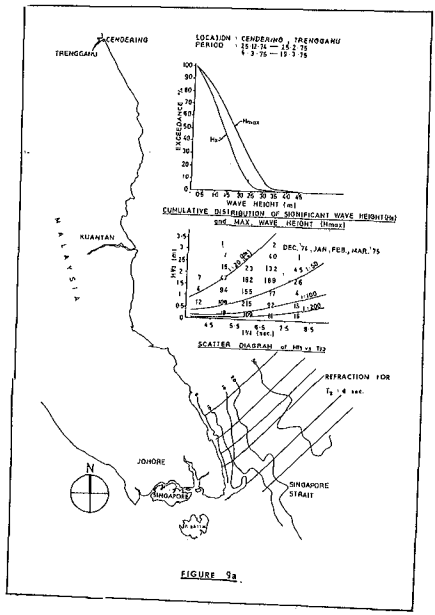

FIGURE 9a

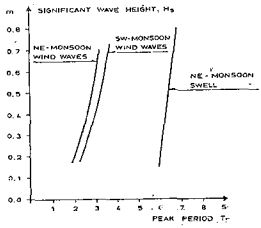

FIGURE 10b

H_s-T_p relations for prevailing wave systems off the Changi Coast.

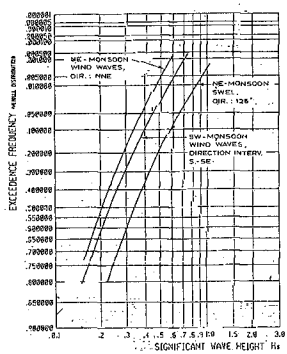

FIGURE 10a

Wave height exceedence distribution curves for the prevailing wave systems off the Changi Coast.

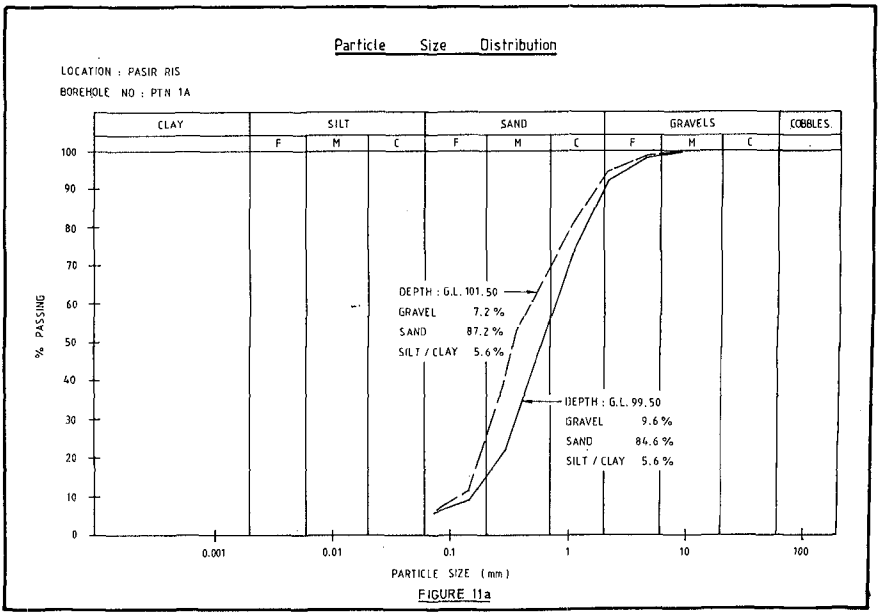

FIGURE 11a

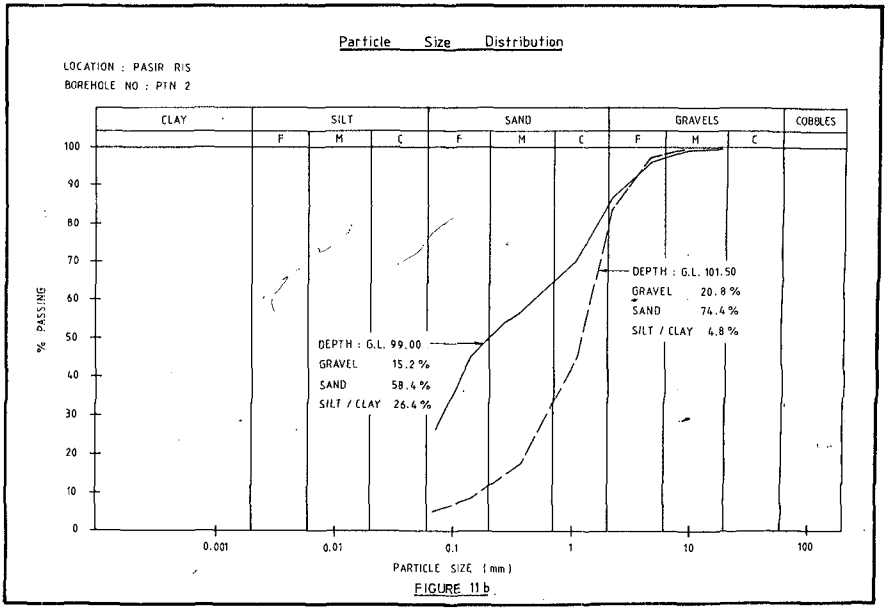

FIGURE 11b

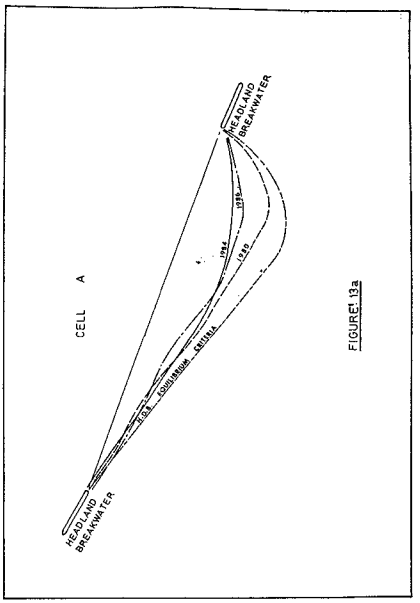
CELL A
HEADLAND BREAKWATER
HEADLAND BREAKWATER
1978
1984
1990
EQUILIBRIUM
CRITERIA
FIGURE 13a

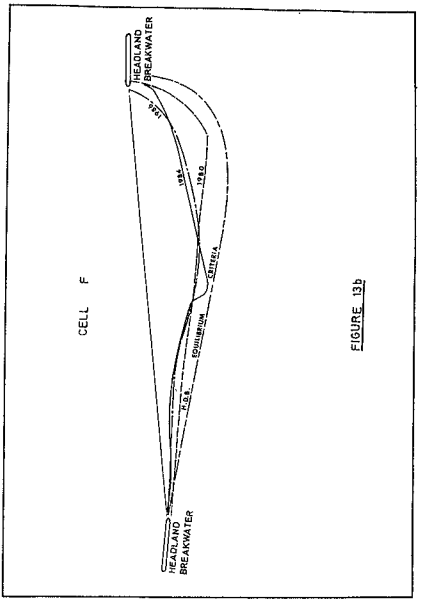
CELL F
HEADLAND BREAKWATER
HEADLAND BREAKWATER
1978
1984
1990
CRITERIA
EQUILIBRIUM
FIGURE 13b

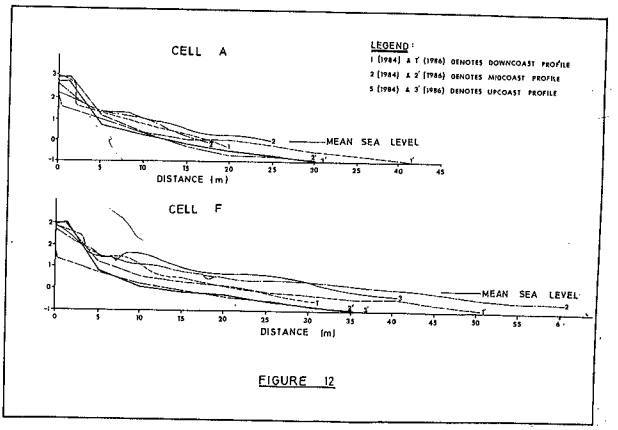
CELL A
LEGEND :
1 (1984) & 1' (1986) DENOTES DOWNCOAST PROFILE
2 (1984) & 2' (1986) DENOTES MIDCOAST PROFILE
3 (1984) & 3' (1986) DENOTES UPCOAST PROFILE
MEAN SEA LEVEL
DISTANCE (m)
CELL F
MEAN SEA LEVEL
DISTANCE (m)
FIGURE 12

REFERENCES

1. U.S. Army Coastal Engineering Research Centre (1973) Shore Protection Manual Vol 1 Page 4 - 141.

2. Silvester, R (1970), "Growth of Crenulate shaped bays to equilibrium" Proceeding of American Society of Civil Engineers, Journal of Waterways and Harbour Division, Vol 96 No WW2 pp 275 - 285.

3. Silvester, R & Ho, SK (1972), "Use of crenulate shaped bays to stabilise coast", Proceedings of the 13th Conference on Coastal Engineering, American Society of Civil Engineers pp 1347 - 1365.

4. Chew, SY, Wong, PP, Chin, KK (1974) "Beach development between headland breakwaters" Proceedings of the 14th Conference on Coastal Engineering, American Society of Civil Engineers pp 1399 - 1418.

5. Chew S.Y., Wei J. (1980), "Major reclamation for Marina City, Singapore". Proceedings of the 17th Coastal Engineering Conference, Sydney, Australia, ASCE.

6. Chew S.Y. (1974), "Waves at Southeast Coast of Singapore" Journal of the Institution of Engineers (Singapore) Vol 14, No. 1 pp. 36 - 40.

7. Silvester, R (1976) "Headland Defence of Coasts", Proceedings of 15th Conference on Coastal Engineering, American Society of Civil Engineers pp 1394 - 1406.

8. Wong, PP (1981) Beach evolution between Headland Breakwaters.

9. Bruun, P. (1963) Longshore currents in one and multi-bar profiles, relating to littoral drift. Proc. 8th Conference Coastal Engineering, pp 211 - 247.

CHAPTER 77

Beach fill at two coasts of different configurations

Ichiro Deguchi[+] and Toru Sawaragi[++]

ABSTRACT

Movements of borrow sand replenished at two coasts of different configurations are investigated by analyzing the topographic data which were surveyed periodically after the beach fill placements. One is a long straight beach and borrow sand was placed behind a submerged breakwater. Another is a pocket beach which has an arc-shoreline with a groyne at one end and a headland at another.

It is found that the amount of borrow sand moved in the long-shore direction surpasses the amount of borrow sand transported in the cross-shore direction regardless of the shape of the coast. A clear correlation is also found between displacements of shoreline and changes of sectional areas. These results imply that the deformation of the artificially nourished beach and the dissipation rate of borrow sand can be predicted by the so-called one-line theory.

1. Introduction

Artificial beach nourishment is a commonly utilized approach for treatment of shore protection problems such as beach erosion, wave over-topping and so on. It is also the direct method to maintain and improve recreational benefits in the coastal zone.

In Japan, there are many coasts where beach fill have been already replenished. At these coasts, structures such as an off-shore submerged breakwater, a detached breakwater and a groyne have been constructed simultaneously in order to prevent beach fill from flowing out from the replenished field.

However because the effective beach fill design involves so many physical factors, the precise degree of beach fill utilization to stabilize a shoreline is not always predictable.

The objective of this study is to investigate behaviors of beach fill replenished at two coasts of different configulations by analyzing successively measured beach profiles to offer informations as to what is the governing factor in the determination of the effctiveness of beach fill.

+ Associate Professor and ++Professor, Department of Civil Engineering, Osaka University, Yamadaoka 2-1, Suita-city, Osaka 565, Japan

2. Configulations of Two Coasts and Location of Beach Fill

Locations of two coasts are shown in Fig.1.

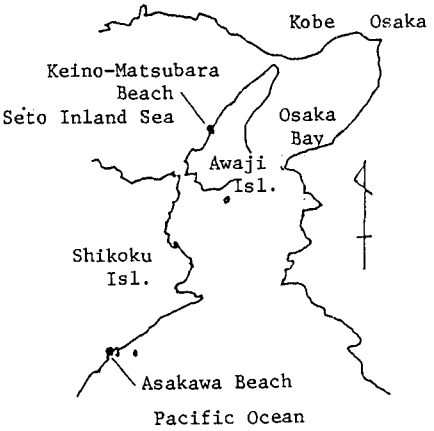

Fig.1 Locations of investigated two beaches

One is Keino-Matsubara-Beach which is on the east side of the Awaji Island facing the Seto Inland Sea and has a long straight beach of about 5km long as shown in Fig.2(a). In this coast, a test offshore submerged breakwater of 80m long and 20m wide was first constructed in 1983 and borrow sand of about 5000m^3 was replenished behind it about one year after the construction of the breakwater.

The upper surface of the submerged breakwater is about 1.5m below D.L.. H.W.L., M.W.L. and L.W.L. correspond to D.L.+1.8m, D.L.+1.2m and D.L.+0.5m. The water depth was measured upward from D.L.. The average beach slpoe is about 1/7 to 1/10 in the shallow water region(shallower than -2m) and about 1/30 in the deeper resion. Mean grain size d_{50} ranges from 0.2mm to 3mm and there is no correlation between d_{50} and water depth. Mean graion size of borrow sand is 1.5mm. These data are summerized in Table 1.

Figure 2(b) indicates a location of the submerged breakwater and the region where beach fill would be placed based on the measured beach profile just after the construction of the submerged breakwater.

Another is Asakawa-Beach which is a so-called pocket beach and has an arc-shoreline of about 400m long and the radius of which is 260m as shown in Fig.3. There is a rockey head land at the south end of the beach and a groyne of 150m long was constructed in 1974 at the other end. A beach slope in a shallow region (shallower than -3m) is about 1/7 to 1/10 and about 1/30 in the deeper region.

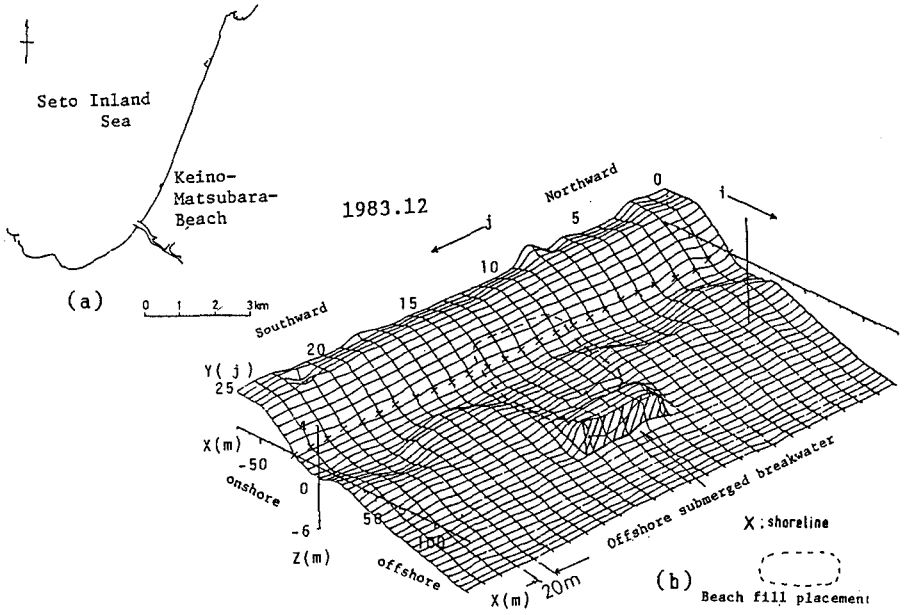

Fig.2 Beach profile of Keino-Matsubara-Beach just after the construction of submerged breakwater

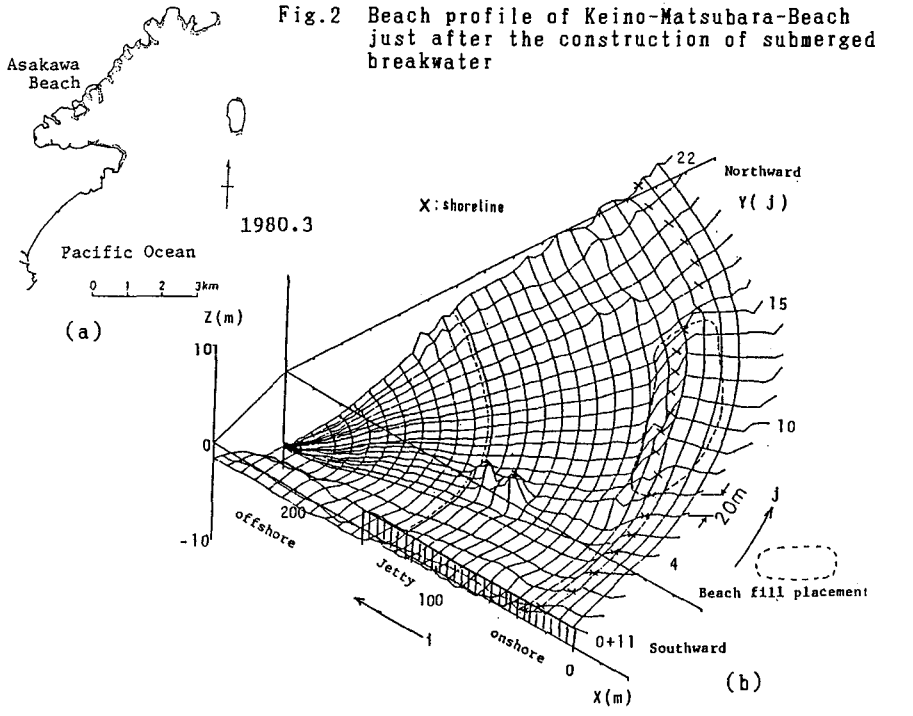

Fig.3 Beach profile of Asakawa-Beach just after the beach fill placement

Table 1 Characteristics of two beaches

	Keino-Matsubara-Beach	Asakawa- Beach
[d_{50}]		
native sand	0.2mm-3mm	0.5mm-3mm
borrow sand	1.5mm	0.4mm and 0.8mm
[Beach slope]		
shallow region	1/7-1/10	1/7-1/10
deep region	1/30	1/30
[waves]		
winter-spring	probability of appearance of waves higher than 1m is 35%.(from W-NW)	large part of waves are less than 40cm
summer-autumn	large part of waves are less than 40cm	waves higher than 1m incidents several times a year in a typhoon seasons.(from SE-E)

Table 2 Progress of beach fill and topographic survey

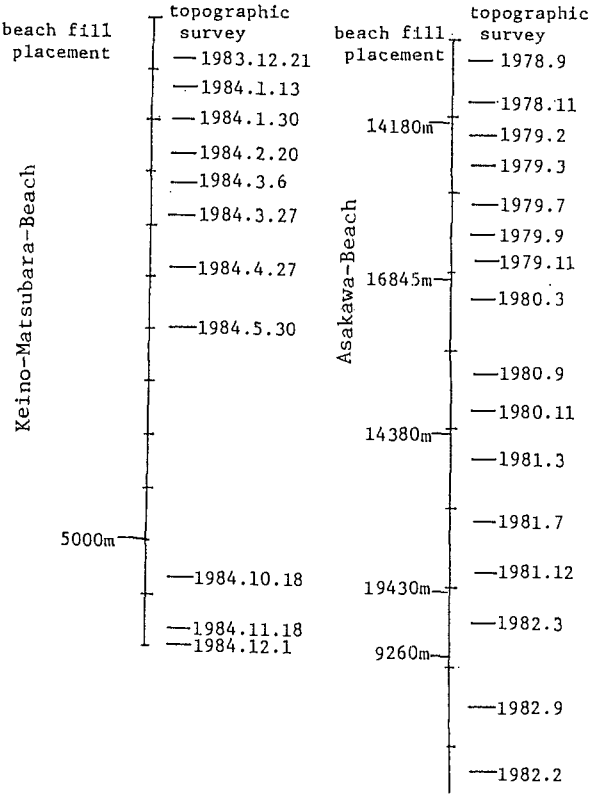

Water depth was measured upward from D.L.. H.W.L. and L.W.L. correspond D.L.+2m and D.L.+0.8m. Mean grain size of native sand d_{50} ranges from 0.5mm to 3mm. These data are also summarized in Table 1.

Figure 3(b) is a bottom topography drawn based on the measured water depth in Sept.1978 just before the continuous sand replenishments began. Since then, beach fill of about 15000m³/year has been continuously placed in the center of the beach. From 1982, a submerged breakwater of 14m width has been constructing along a broken line shown in the figure from the north end of the beach and the construction of total 170m length are finshed in 1984. In this coast, two kinds of barrow sands of which mean grain sizes were 0.4mm and 0.8mm were used.

3. Method of Analysis and Data used

At Keino-Matsubara-Beach, a series of topographic survey have been conducting just after the construction of submerged breakwater. Water depth was measured on 26 surveying lines at the interval of 2.5m. The surveying lines were set at the distance of 20m along the shoreline. Beach profile measured just after the construction of the submerged breakwater in Dec.1983 which is shown in Fig.2(b) is selected as a initial profile in the following analyses.

At Asakawa-Beach, topographic survey has also been conducted periodically from Nov.1977. Water depth was measured on 24 surveying lines at the interval of 5m. Surveying lines were spaced as shown in Fig.3(b) which was drawn based on the water depth measured in March 1980. Beach profile measured in Sept. 1978 is used as a initial profile in the following analyses.

Progresses of the constructions of structutes, beach fill placements and topographic surveys at these beaches are shown in Table 2.

Based on the measured beach profiles, the following are investigated :

a) characteristics of the beach deformation around artificially nourished beach and behaviors of beach fill, and
b) remaining or dissipation rate of beach fill $\alpha(t_n)$ or $1-\alpha(t_n)$.

To investigate these, changes of water depth $\Delta h(i,j,t_n)$ and $\delta h(i,j,t_n)$ were first calculated from the measured water depth $h(i,j,t_n)$ where i indicates the i-th measureing point on the j-th surveying line and n shows the water depth measured at n-th topographic survey. That is,

$$\delta h(i,j,t_n) = h(i,j,t_n) - h(i,j,t_0) \quad (1)$$

$$\Delta h(i,j,t_n) = h(i,j,t_n) - h(i,j,t_{n-1}) \quad (2)$$

where t_o means the initial beach profile.

These topographic changes were also investigated by the empirical eigenfunction method by expanding Δh and δh as linear combinations of products of functions of the distance normal to the shoreline $e_k(i,t_n)$ and those of the distance parallel to the shoreline $c_k(j,t_n)$ as follows;

$$\Delta h(i,j,t_n) \quad \text{or} \quad \delta h(i,j,t_n) = \sum e_k(i,t_n)\, c_k(j,t_n) \qquad (3)$$

Remaining rate of replenished barrow sand $\alpha(t_n)$ is defined in this paper as follows;

$$\alpha(t_n) = \delta V(t_n) / \sum Vb \qquad (4)$$

where $\sum Vb$ is the total volume of replenished borrow sand and $\delta V(t_n)$ is a volumetric change within the analyzing area, that is,

$$\delta V(t_n) = V(t_n) - V(t_o), \quad V(t_n) = \iint h(i,j,t_n)\, dx\, dy. \qquad (5)$$

4. Characteristics of beach deformations around artificially nourished beach and behaviors of beach fill

i) Keino-Matsubara-Beach

Figure 4 shows the topographic change took place during 2-month after the beach fill placement.

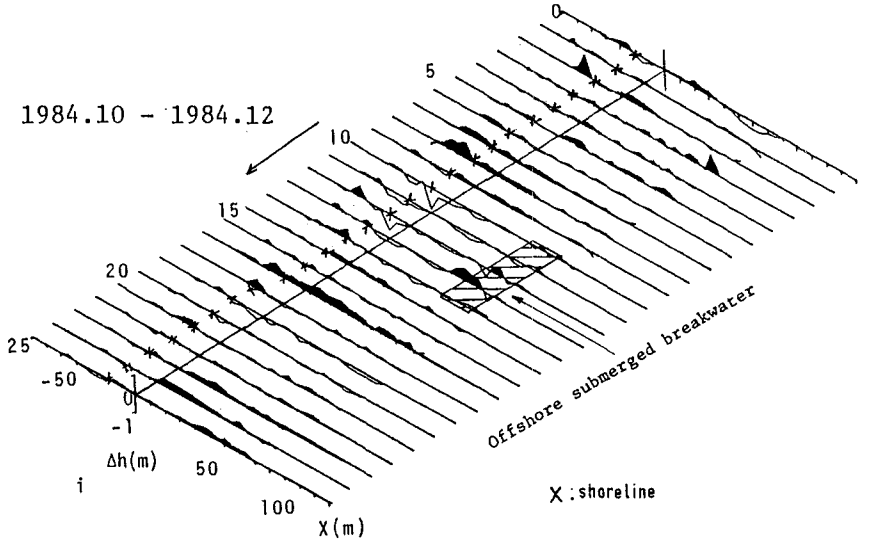

Fig.4 Change of water depth took place during 1-month after beach fill placement at Keino-Matsubara-Beach

In this figure, accreting resions are painted black. At the end of Sept.1984, borrow sand of about 5000m³ was replenished behind the submerged breakwater between the surveying lines No.10 to No.14. Figure 4 indicates that replenished sand mainly moved in the longshore direction and deposited in the landwards of the shoreline and behind the submerged breakwater. However, the amount of those sand is not so large.

Figures 5 and 6 show cross-shore and longshore eigenfunctions $e_1(i,t_n)$ and $c_1(j,t_n)$ calculated from $\Delta h(i,j,t_n)$ which correspond to the largest eigen value.

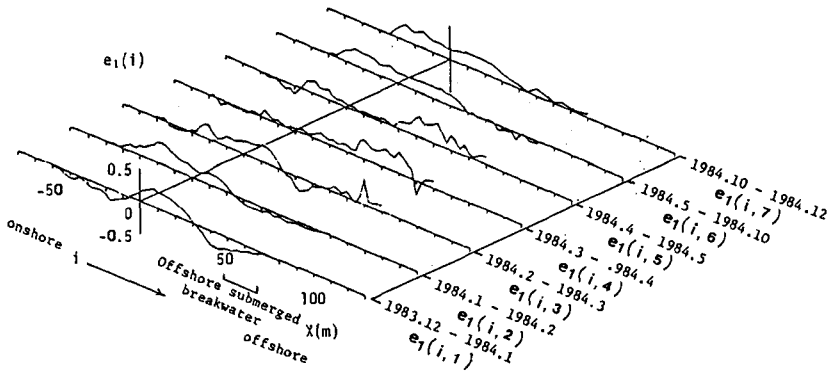

Fig.5 Cross-shore empirical eigenfunction corresponding to the largest eigenvelue

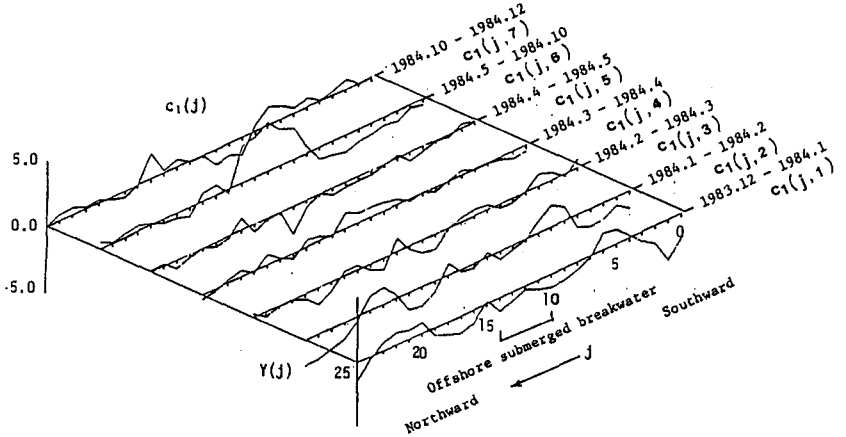

Fig.6 Longshore empirical eigenfunction corresponding to the largest eigenvalue

$e_1(i,1)$ calculated from the topographic changes took place during 1-month after the construction of the submerged breakwater changes its sign negative - positive - negative with the increase of the distance from the shoreline. $c_1(i,1)$ at this duration also alters its sign in the longshore direction. These results imply that both on-offshore and longshore sediment transports took place just after the construction of the submerged breakwater.

As can be seen from $e_1(i,2)$ and $c_1(j,2)$, on-offshore sediment transport became less significasnt and only longshore sediment transport remained when one month passed after the construction of the submerged breakwater. Because $e_1(i,2)$ does not change its sign with increasing the distance from the shoreline.

$e_1(i,6)$ and $c_1(j,6)$ calculated from the topographic change took place before and after the replenishment of beach fill clearly show the effect of beach fill placement.

Finally, $e_1(i,7)$ which corresponds to the topographic change took place during 2-month after the replenishment of beach fill shows positive through the whole cross-shore region and $c_1(j,7)$ is negative behind the submerged breakwater and positive in the out side of the submerged breakwater. This implies again that the replenished borrow sand moved off in the longshore direction from the replenished place and no significant offshore sediment transport beyond the submerged breakwater did not take place.

However, because the ratios of eigenvalues of these eigenfunctions to the trace become 0.4 to 0.5, only 40% to 50% of the whole topographic change can be interpreted by these eigenfunctions.

The authors further conducted numerical simulation concerning wave deformation and wave-induced current around the artificially nourished beach at Keino-Matsubara-Beach. In the simulations, wave direction and height are first calculated using equations of wave kinamatics and wave dynamics based on a linear wave theory at grid points. Then, depth averaged velocities of wave-induced current and displacements of the water level are calculated from the equations for concervations of depth and time averaged momentum and mass fluxes (Sawaragi et al.(1984)).

Some results are illustrated in Fig.7. Wave height H_o and period T used in the similation are 2m and 5sec and wave direction together with the calculated wave breaking points are shown in the figures.

From these figures, it is found that forced wave breaking takes place on the submerged breakwater and strong wave-induced current in the longshore direction is generated behined the submerged breakwater. It seems that replenished borrow sand were easily transported by these current in the longshore direction.

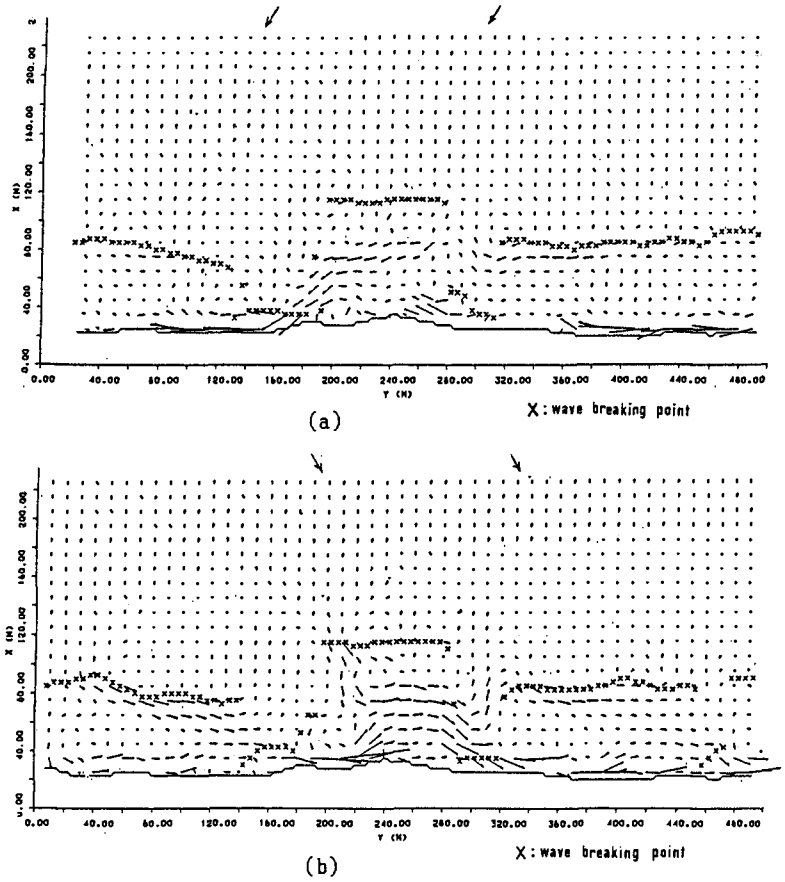

Fig.7 Simulated wave-induced current at Keino-Matsubara-Beach

At this coast, a close correlation between the displacement of shoreline and the change of sectional area at each surveying line is found through out the investigated beach.

ii) Asakawa Beach

As indicated in Table 2, borrow sand of about 15000m³ was placed once a year in winter between the surveying lines No.8 and No.14 above L.W.L.. Figure 8 shows the topographic change took place during Sept.1979 and March 1980 when borrow sand of 16845m³ was placed around the shoreline between surveying lines No.7 and No.15. Figure 9 indicates the topographic change tookplace during 6-month after the beach fill placement.

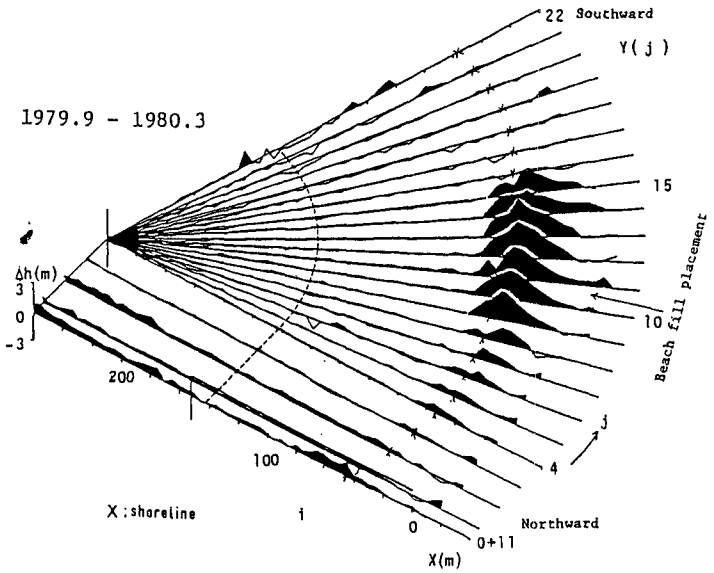

Fig.8 Change of water depth took place during Sept.,1979 and March, 1980 when borrow sand of 16845m^3 was placed around shoreline between surveying lines No.7 and No.15 at Asakawa-Beach

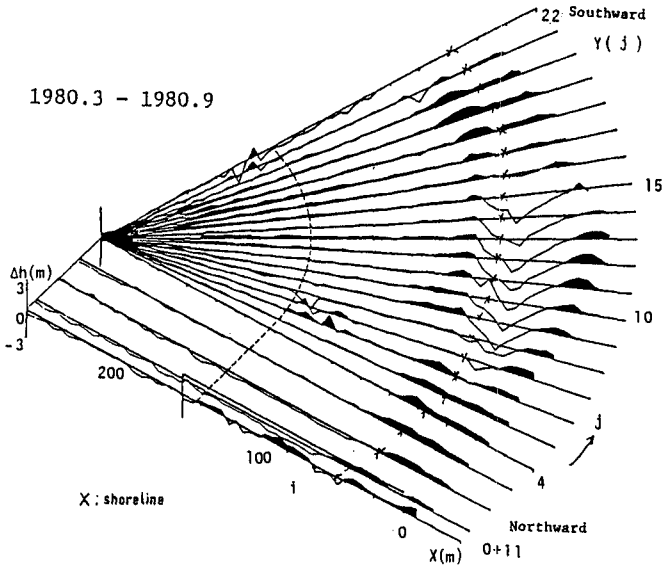

Fig.9 Channge of water depth took place during 6-month after beach fill placement at Asakawa-Beach

From these two figures, it is easily found that the replenished borrow sand moved from the replenished region mainly toward both southward and northward along the shoreline. As is the case of Keino-Matsubara-Beach, a few portion of borrow sand seemed to be transported in onshore and offshore directions.

Figures 10 and 11 show cross-shore and longshore eigenfunctions $e_1(i,t_n)$ and $c_1(j,t_n)$ which correspond to the largest eigenvalues.

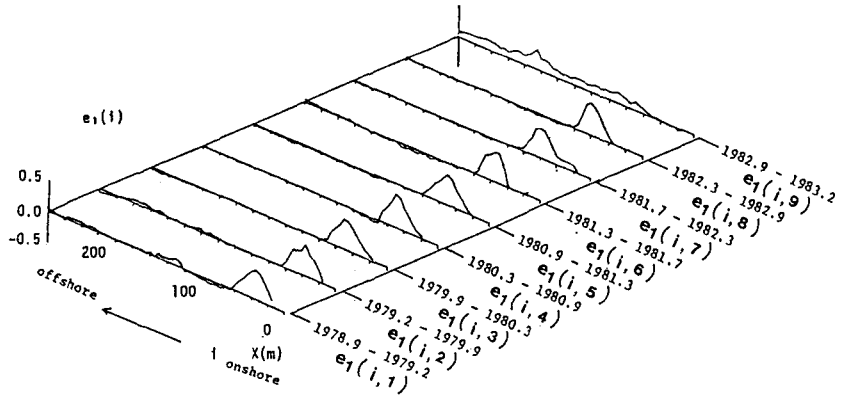

Fig.10 Cross-shore empirical eigenfunction corresponding to the largest eigenvalue.

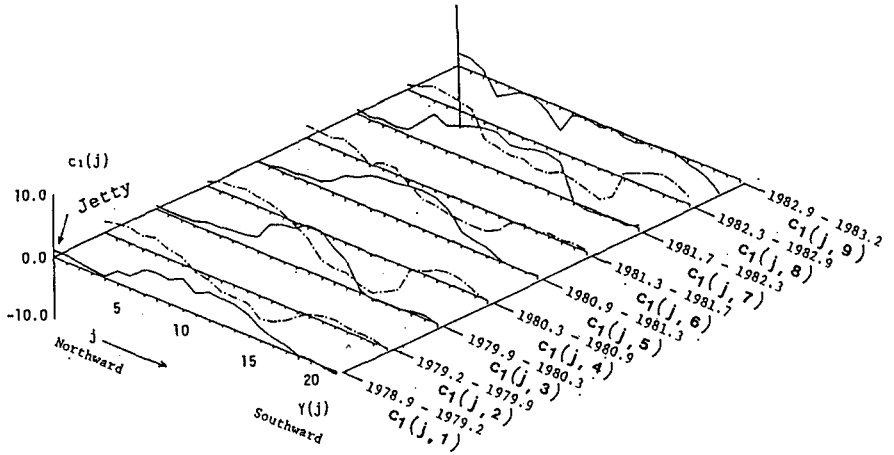

Fig.11 Longshore empirical eigenfunction corresponding to the largest eigenvalue

$e_1(i,t_n)$ has only positive values in narrow regions near the shoreline in all the investigated region and through the whole duration. On the other hand, $c_1(j,t_n)$ calculated from the topographic changes took place during autumn and winter and during spring and summer indicate clear contrast. That is, $c_1(j, t_n)$ in autumn and winter represents the topographic change corresponding to the beach fill placement and $c_1(j,t_n)$ in spring and summer shows the movements of borrow sand towards both ends of the pocket beach along the shoreline.

Further, the positive region of $c_1(j,t_n)$ in spring and summer is larger in the north end of the beach (near the groyne) than that in the south end. This implies that the magnitude of northward sediment transport is larger than that of the southward transport.

It is also found that any significant on-offshore sediment transport took place in the pocket beach.

About 65% to 80% of the total topographic change can be expressed by the product of these cross-shore and longshore eigenfunctions which correspond to the largest eigenfunction.

Fugure 12 illustrates some numerical results of wave-induced currents on a modeled pocket beach with a groyne at one end. Wave height and period used in the simulation are 2m and 5sec and wave diretion is shown in the figure together with the wave breaking points.

As can be seen from these figures, the direction of wave-induced flow near the groyne are always toward the groyne in the pocket beach regardless of the wave directions. This result will be of some help to explane why the magnitude of northward (toward the groyne) sediment transport is larger than that of southward sediment transport.

Again, at this beach, a clear correlation between displacements of shorelines and changes of sectional areas at eachsurveying line can be found.

5. Remaining (or Dissipation) rate of borrow sand

Finally, the remaining rate $\alpha(t_n)$ of replenished borrow sand is investigated in this section.

Figure 13 shows the volumetric change and remaining rate of borrow sand at Keino-Matsubara-Beach. Full and broken lines in the figure indicate the volumetric change δV behind the submerged breakwater between the surveying lines No.10 and No.14 and δV between the surveying lines No.8 and No.16 which appart 40m from region where beach fill was replenished.

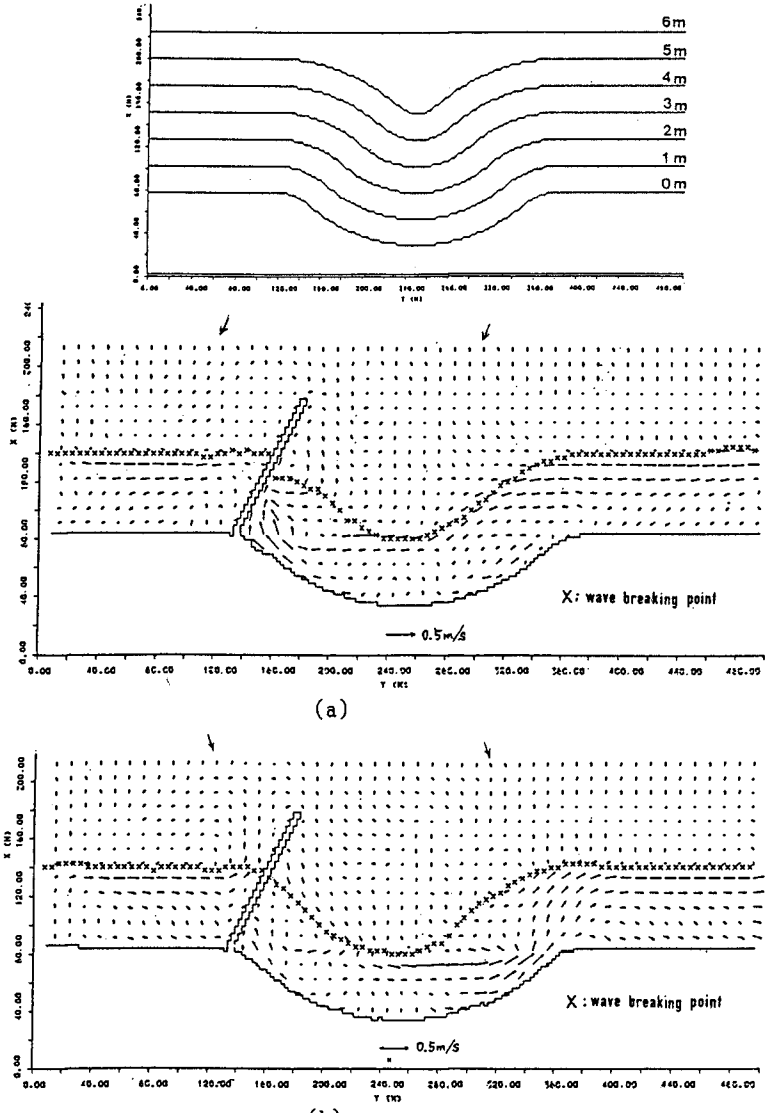

Fig.12 Simulated wave-induced current at Asakawa-Beach

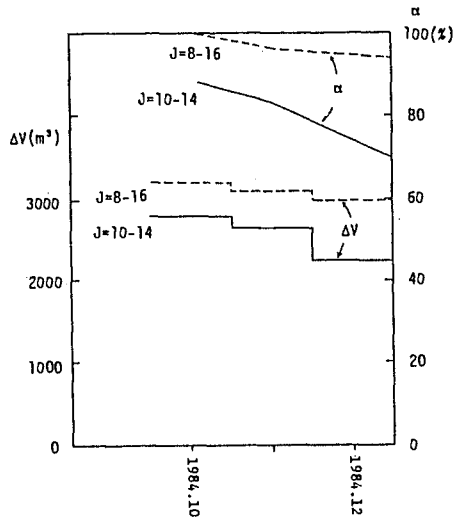

Fig.13 Remaining rate of borrow sand and volumetric change at Keino-Matsubara-Beach

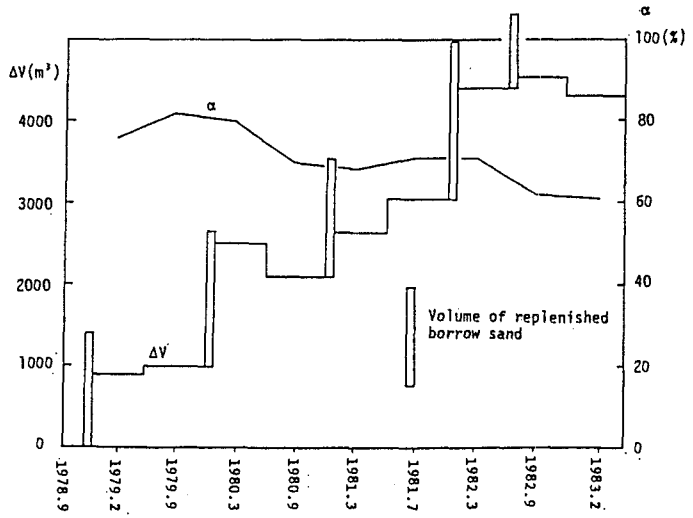

Fig.14 Remaining rate of borrow sand and volumetric change at Asakawa-Beach

Although borrow sand of 5000m³ was placed behind the submerged breakwater, the increase of the sand volume between the surveying lines No.8 and 16 was about 3300m³. Therefore, in the calculation of $\alpha(t_n)$ from eq.(4), we used 3300m³ for Vb.

It is found from this figure that the sand volume just behind the submerged breakwater decreased fast and only 70% remained two month after the beach fill placement. On the other hand, more than 90% of the borrow sand remained between the surveying lines No.8 and No.16. This means that the migration speed of borrow sand is not so fast and only 10% of borrow sand moved off more than 40m from the replenished region.

Figure 14 shows the volumetric changes and remaining rate of borrow sand at Asakawa-Beach. At this beach, the volume of sand in the whole beach increased at every beach fill placement. However, the remaining rate of the total borrow sand replenished in the beach from eq.(4) decreases gradually from 80% and finally reaches 60%. This implies that there is a certain limit to keep sand within a pocket beach which will be determined by the geometrical property of the beach, wave climate and so on.

6. Conclusions

Movements of borrow sand replenished at a long straight beach and a pocket beach which has an arc-shoreline are investigated by analyzing the periodically measured bottom topography after the beach fill placements.

It is found that the amount of borrow sand moved in the longshore direction surpasses the amount of borrow sand transported in the cross-shore direction regardless of the shapes of the shorelines. A clear correlation is also found between the shoreline displacements and the changes of sectional areas.

References

Sawaragi, T., I. Deguchi and J.S. Lee (1985), A new model for a prediction of beach deformation around a river mouth, Proc. Int. Sympo. Ocean Space Utilization '85, 2, pp.229-237.

CHAPTER 78

Offshore Sand Waves

Rolf Deigaard, *) and Jørgen Fredsøe, **)

Abstract

A theoretical model for the equilibrium dimensions of offshore sand waves is presented. The model is an adaptation of the dune model by Fredsøe (1982) to the marine environment, making use of the physical analogies between offshore sand waves and river dunes. The predicted sand wave heights and lengths conform well with the observations of sand wave formation reported in the literature. One of the results from the model is that for a given wave climate sand waves will only be formed under a certain range of mean current velocities. This range becomes narrower for increasing wave height or decreasing water depth and grain size.

1. Introduction

A sea bed on which active sediment transport is taking place will normally not remain plane. Different types of bed forms will be formed depending on the hydrodynamic environment and the characteristics of the bed material.

The dimensions of the bed forms are highly variable. Wave generated ripples may have wave lengths and heights of a few centimetres, while the linear tidal sand banks can have a length of tens of kilometres and a height of up to about 50 m. One of the important bed forms in connection with offshore structures and pipelines is the sand wave, which at the same time can be large enough and migrate fast enough to cause bed level changes around a structure which can give problems during its lifetime.

A comprehensive review of the characteristics of sand waves and other tidal bed forms has been presented by Stride (1982). In the following a brief resume of the conclusions is given, without reference to the original contributions forming the basis for the work by Stride.

Sand waves can be formed in a bed sediment ranging from fine sand to gravel. Sand waves can be symmetrical or asymmetrical depending on the relative strength of the opposing tidal currents. The asymmetric sand waves, generated where the tidal current from one direction is dominant, are the most common and will be treated in the following.

*) Rolf Deigaard, Ph.D., Senior Hydraulic Engineer, Danish Hydraulic Institute, Agern Allé 5, DK - 2970 Hørsholm, Denmark.

**) Jørgen Fredsøe, Ph.D., Dr. Tech., Professor in Marine Hydraulic Engineering, Technical University of Denmark, DK - 2800 Lyngby, Denmark.

An example, taken from Houbolt (1968), of an echo sounding showing a train of sand waves is given in Fig. 1. These asymmetric sand waves have a height of 5-7 m at 25-30 m water depth; the wave length is approx. 200 m.

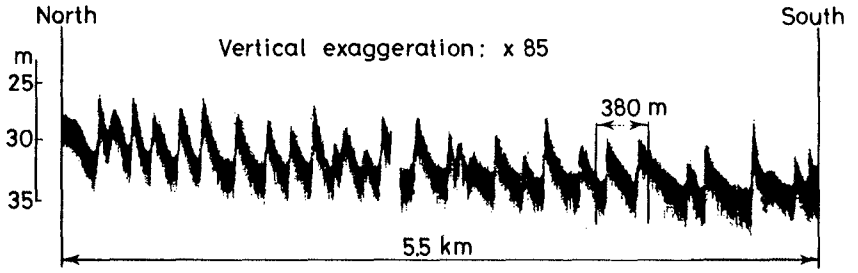

Figure 1. Example of echo sounding showing asymmetric sand waves, West of Imuiden, the Netherlands, from Houbolt (1968).

Sand waves are generally observed to migrate in the direction faced by the steep slopes, which is also the direction of the net sediment transport. The slopes of the steep fronts lie in the range of 5^{o} to 35^{o}, and generally the higher sand waves (> 2 m) have more gentle fronts, less than 20^{o}, and the smaller sand waves have slopes of more than 20^{o}. The gentle slopes lie in the range of 0.5^{o}-4^{o}; generally the more steep slopes are found on the active, migrating sand waves.

The height of the sand waves can vary considerably. It may be only a few centimetres, while the upper limit appears to be determined by the water depth. The highest sand waves are about one third of the water depth.

The sand wave length has also a large variaton, lying between 2 and 20 times the water depth, D, with an average of about 6 D. The ratio between the length and height of a sand wave is generally larger than 15 and may be as high as 100.

The formation and the dimensions of the sand waves will depend on the current velocities and the wave climate. According to Stride (1982) sand waves are not formed at very small current velocities. The lower limit for sand wave formation is given as $\bar{V}_m = 0.65$ m/s, $\bar{V}_m$ being the mean spring tide near surface peak speed. Small sand waves can be formed

at slightly lower speeds, and sand waves formed in gravel require larger flow velocities. It is supposed that a strong current can smooth out the sand waves similarly to the smoothing out of dunes in rivers, but the evidence from field observations is rather weak. The effect of waves is more well documented. The wave action during a storm can reduce the sand wave height at water depths of more than 20 m, and it can be observed that the relative height of the sand waves decreases in the shallower areas, where the near bed wave action increases, Terwindt (1971), Stride (1982). The smoothing out of sand waves by current or by waves is often assumed to be connected with the ratio between the suspended load and the bed load, which increases as the sediment transport rate increases.

The general behaviour of the sand waves, or the physical mechanisms behind the formation of sand waves seems not in any significant way to deviate from the processes associated with dunes formed under unidirectional current. The large sand waves formed by a tidal current can according to Stride (1982) be considered as unidirectional current formed ones, which have been modifed to a lesser or greater extent by the reversing current.

2. The Theory for Dune Dimensions, Current Only

A theory for the dimensions of sand waves (dunes) under steady current conditions has been presented by Fredsøe (1979) and Fredsøe (1982). A key point in this theory is the use of the continuity equation for the sediment :

$$\frac{\partial h}{\partial t} = - \frac{1}{1-n} \frac{\partial q}{\partial x} \qquad (1)$$

where h is the bed level, t is the time, q is the sediment transport rate, x is the coordinate in the transport direction, and n is the porosity of the bed sediment. By applying Eq. (1) to periodic, steadily migrating bed forms, the following relation emerges :

$$q = q_o + a\,(1-n)h \qquad (2)$$

where q_o is the sediment transport passing the trough of the sand waves and a is the migration velocity.

For dunes and sand waves a is determined by the amount af sediment, q_D, which is deposited at the front of the sand wave, Fig. 2 :

$$a = \frac{q_D}{(1-n)A} \qquad (3)$$

where A is the dune height.

The magnitude of q_D depends on the rate of sediment transport at the dune crest and the relative amount of suspended load, q_s, and bed load transport, q_b.

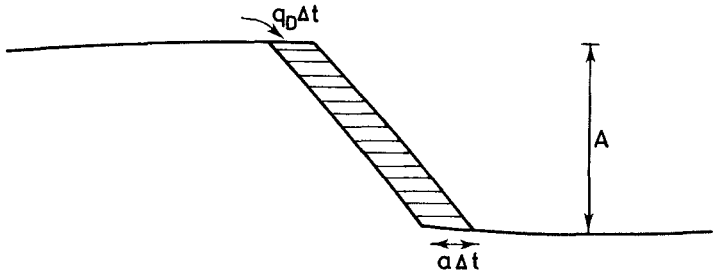

Figure 2. Migration of the dune front.

The bed load transport consists of the grains which move in almost continuous contact with the grains in the bed, and will be deposited at the front where flow separation occurs. The suspended sediment grains move above the bed without contact and will not settle immediately. A suspended grain will contribute to q_D and the dune migration if it by settling or diffusion moves into the separation 'bubble' before it is carried past the separation zone by the flow. Whether the grain is deposited at the front or not will thus depend on its distance from the bed when it passes the dune crest.

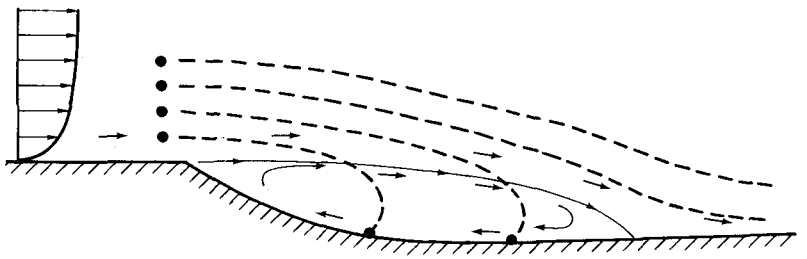

Figure 3. The probability for a suspended grain to settle in the trough depends on its height.

In the model by Fredsøe (1982) the detailed shape of the dune is determined from the requirement that Eq. (2) must fit with the sediment transport rate calculated from the shear stress distribution along the long, gentle upstream slope of the dune. The sediment transport is calculated by the model of Engelund and Fredsøe (1976). This sediment transport model calculates the suspended load and the bed load transport separately. The variation of the bed shear stress along the dune is deter-

mined on basis of flow measurements downstream of a rearward facing step, e.g. Smith (1970). In a recent paper McLean and Smith (1986) presented an analytical treatment of this flow situation.

The length of the separation zone at the steep front is about 6A. The bed shear stress increases gradually in the flow direction from zero at the reattachment point. The bed shear stress attains a local maximum at a distance of 16-20A from the step. Fig. 4 gives an example of the measured shear stress coefficient, $C_f = \tau/\rho V^2$, behind a rearward facing step, and a dune profile calculated by the theory by Fredsøe (1982).

In the following the details concerning determination of the dune shape will not be treated, the emphasis will be put on the main dimensions : the height, A, and the length, λ.

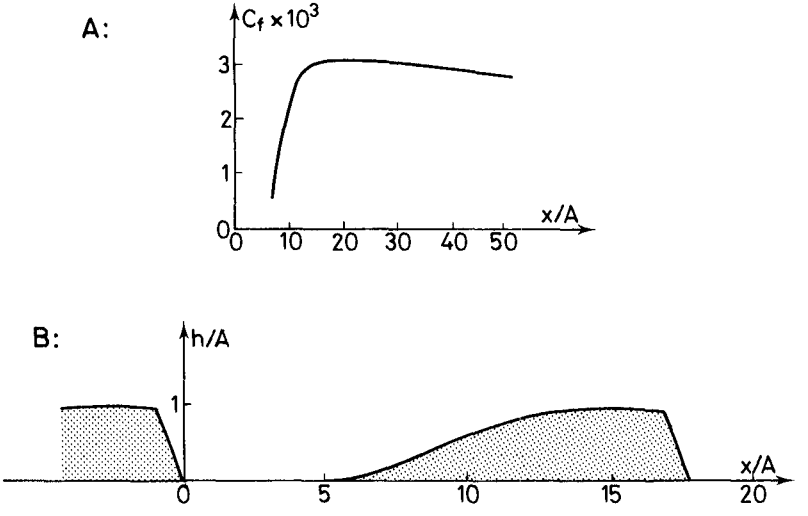

Figure 4. A: Shear stress coefficient downstream of a rearward facing step with the height. B: Example of dune profile calculated from the theory by Fredsøe (1982).

2.1 The Dune Height

Near the dune crest the influence from the preceeding dune is weak and the bed shear stress can be calculated by the logarithmic resistance law :

$$\frac{V}{U_f} = \frac{1}{\kappa}\left(\ln\left(\frac{30\,D}{k}\right) - 1\right) \qquad (3)$$

where V is the local depth averaged flow velocity, U_f the shear velocity: $U_f = \sqrt{\tau_b/\rho}$, κ is V. Karman's constant, D is the local flow depth and k is the bed roughness taken to be 2.5 times d, the grain size of the bed sediment.

The sediment transport model of Engelund and Fredsøe (1976) can for a given bed sediment be expressed in dimensional form :

$$q = q(V, D) \tag{4}$$

The local change in the bed level near the crest can be expressed in two ways :

I) Purely geometrical :

$$\frac{\partial h}{\partial t} = - a \frac{\partial h}{\partial x} = \frac{-q_D}{A(1-n)} \frac{\partial h}{\partial x} \tag{5}$$

II) Through the continuity equation :

$$\frac{\partial h}{\partial t} = \frac{-1}{1-n} \frac{\partial q}{\partial x} = \frac{1}{1-n} \frac{dq}{dD} \frac{\partial h}{\partial x} \tag{6}$$

By combining Eq. (5) and (6) an expression for the dune height is obtained:

$$A = \frac{-q_D}{\frac{dq}{dD}} = \frac{-q_D}{\frac{\partial q}{\partial D} + \frac{\partial V}{\partial D}\frac{\partial q}{\partial V}} = \frac{-q_D}{\frac{\partial q}{\partial D} - \frac{V}{D}\frac{\partial q}{\partial V}} \tag{7}$$

This result for the dune height results in a migration velocity of the dunes given by :

$$a = \frac{1}{1-n} \frac{dq}{dD} \tag{8}$$

2.2 The Dune Length

According to Eq (2) the sediment transport attains a maximum at the top of the dune; immediately after the top the flow separates and the dune ends. At situations with dominant bed load transport the sediment transport is in local equilibrium with the hydraulic conditions, and the point of maximum transport coincides with the maximum in bed shear stress, τ_b. According to the measurements described previously the bed shear stress has a local maximum at a distance of about 16A downstream of the preceeding crest. At dominant bed load transport the dune length, λ, is thus given by :

$$\lambda = 16 A \tag{9}$$

Fredsøe included the effect of gravity in his analysis. The gravity acting on the moving grains will tend to retard the bed load transport moving up the dune, modifying the transport relation which gives a pre-

dicted dune length larger than Eq. (9). The effect of gravity is notable at very low transport intensities.

The suspended load transport cannot be adjusted immediately to changes in the hydraulic conditions, as it takes time for the suspended sand grains to settle out from the concentration profile or be entrained into it. The maximum in the suspended load will therefore have a lag distance, L_s, behind the maximum in the bed shear stress. The dune length in case of both suspended and bed load transport can thus be expressed as :

$$\lambda = 16\ A + \frac{q_s}{q} L_s \qquad (10)$$

3. Sand Wave Dimensions in Wave and Current

3.1 The Sand Wave Height

The physics behind the offshore sand waves are as described in the introduction very similar to the dunes in river, and the relations for dune dimensions can be applied directy if a model for sediment transport under the combined action of waves and current is introduced.

The present calculations are based on the sediment transport model by Fredsøe et al. (1985). This model converges towards the model by Engelund and Fredsøe (1976) for decreasing wave action.

In case of current without waves the first term in the denominator of Eq. (7) can be neglected because the flow resistance, Eq. (3), is insensitive to variation in D. In case of combined waves and current this term can be significant due to the relation between the water depth and the near bed orbital motion induced by waves of given height and period.

Sand wave heights predicted by Eq. (7) using the transport model by Fredsøe et al. (1985) are shown in Fig. 5. The calcualtions have been made for a water depth of 10 m and a bed material grain size of d = 0.20 mm. The direction of the wave motion is normal to the mean current, $\gamma = 90^{\circ}$. Two wave heights are considered : H = 2 m and 4 m with periods of 7.2 s and 10.1 s respectively.

Different assumptions for the settling of suspended sediment at the sand wave front is presented in Fig. 5 A, B and C.

In Fig. 5A it is assumed that all transported sediment is deposited at the sand wave front : $q_D = q_b + q_s$.

In Fig. 5B the sand wave height is calculated, assuming that only the bed load is deposited. For current only, the sand wave height, A, is the same for the lower current velocities because the bed load transport is dominant. For higher current velocities the suspended load transport becomes dominant and the sand wave height decreases if only the bed load is deposited. Under wave action sediment will be suspended in the wave

boundary layer even for small current velocities, and the calculated sand wave heights are different in Fig. 5A and B for all current velocities.

In Fig. 5C the amount of suspended sediment which is deposited at the sand wave front is estimated on basis of the lag distance, L_s, and the length of the separation zone downstream of the front. q_D is calculated as :

$$q_D = q_b + q_s \exp(-L_s/6A) \tag{11}$$

The length scale for the lag of the suspended sediment, compared with the hydraulic conditions can be estimated from the concentration profile as :

$$L_s = \frac{U_c \cdot y_c}{w} \tag{12}$$

where y_c is the height of the centroid of the concentration profile, c(y) :

$$y_c = \frac{\int_a^D cy \, dy}{\int_a^D c \, dy} \tag{13}$$

U_c is the mean current velocity at the height y_c from the bed. w is the settling velocity of the suspended sediment.

For small current velocities L_s is small compared with A, and the calculated sand wave heights correspond to Fig. 5A. For increasing current velocities, L_s increases and the sand wave height converges towards the results in Fig. 5B.

3.2 The Flow Separation at the Sand Wave Front

The key assumption for the theory predicting the sand wave height is that the deposition of sediment at the front and thus the migration rate of the sand wave can be calculated directly on basis of the sediment transport at the crest of the sand wave. The basis for this assumption is that flow separation occurs at the dune front, leading to a vanishing sediment transport capacity at the toe of the dune front.

In case of combined wave and current motion the strong fluctuating pressure gradients associated with the wave motion can under certain circumstances be expected to suppress separation of the mean current.

In the present model a crude approximate criterion is used for the suppression of flow separation by the wave orbital motion. In steady

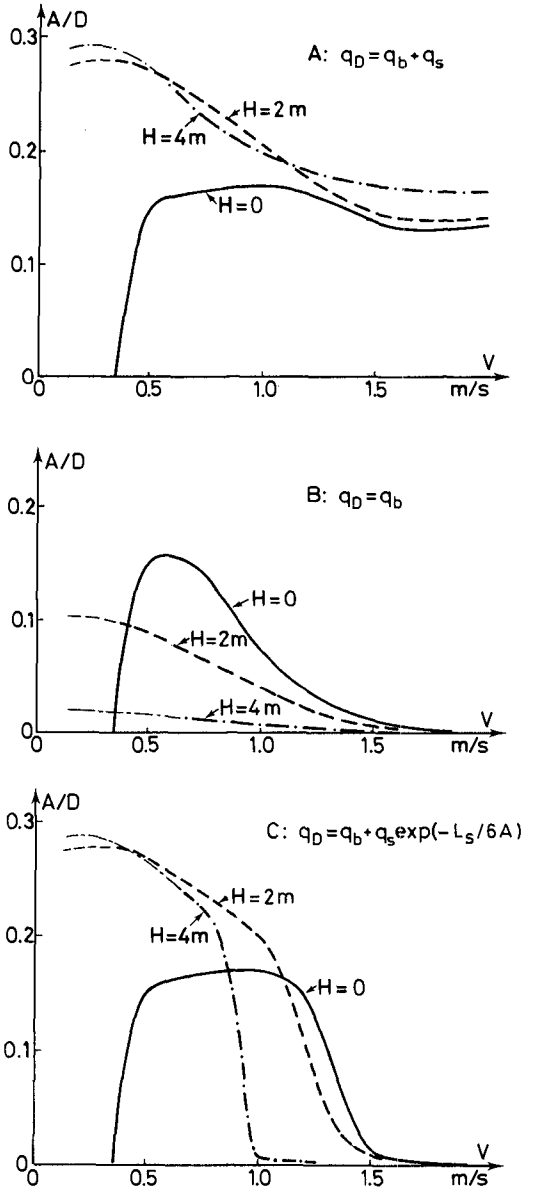

Figure 5. Sand wave height as function of V and H; d = 0.2 mm, D = 10 m, $\gamma = 90^{\circ}$.

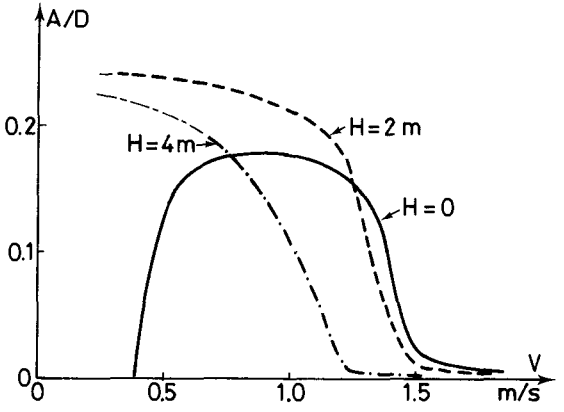

Figure 6. A/D as function of V and H, d = 0.2 mm, D = 20 m, $\gamma = 90^{o}$.

diffusor flow the largest possible diverging half angle without flow separation is about 5^{o}. The sand wave front can be much steeper, close to the angle of repose of the bed material, about 30^{o}.

The effect of the orbital motion is that the near bed water particles move along a much longer path than the straight line of the mean current. The 'effective' angle of divergence will therefore be reduced in combined wave-current motion. If the path travelled by the particle is about 7 times the straight course the average angle of divergence experienced by the water particles on the 30^{o} slope will correspond to the 5^{o} which causes no separation. The criterion for suppression of the flow separation has therefore been taken to be that the oscillating part of the shear velocity, U_{fw}, associated with the wave motion is larger than 7 times the shear velocity, U_{fo}, characterising the mean current in the wave boundary layer.

In the figures showing the results from the model, the part of the curves, where no flow separation is expected to take place due to the wave motion, is shown as thinly drawn lines.

3.3 Sensitivity to Changes in the Parameters

The number of parameters entering the description of the sand waves is too large to allow for the preparation of general dimensionless diagrams for prediction of sand wave heights.

The influence of varying a number of parameters is illustrated in Figs. 6, 7 and 8. In these figures the deposition of suspended sediment has been estimated by Eq. (11).

It can be seen from Fig. 6 that for similar near bed orbital motions the sand waves at 20 m have relative heights close to the sand wave height at 10 m. The transition due to the decrease in settling suspended sediment occurs at a higher current velocity at 20 m water depth because the sand waves are higher, and the ratio L_s/A is smaller for a given transport intensity.

The effect on A/D of changing the angle, γ, between the waves and the current is rather small, Fig. 7.

The most significant changes can be observed when the grain size, d, of the bed material is reduced to 0.15 mm. The range of current velocities, where sand waves are formed become more narrow than for the 0.2 mm sand. For the highest waves considered no sand waves are formed at all, Fig. 8.

For a given wave climate the range of current velocities under which sand waves are formed will gradually become narrower as the water depth decreases, because the near bed orbital motion and the suspended sediment load increase. This is in agreement with the observation that sand waves are decreasing or absent in the shallow parts of the southern North Sea, e.g. McCane and Langhorne (1982), Terwindt (1971) and Houbolt (1968).

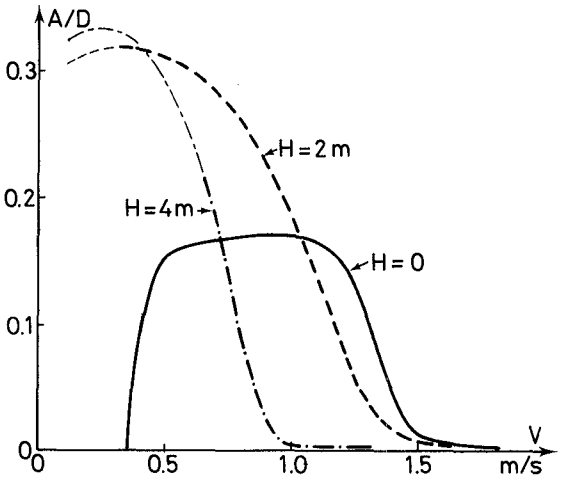

Figure 7. A/D as function of V and H, d = 0.2 mm, D = 10 m, $\gamma = 0^{\circ}$.

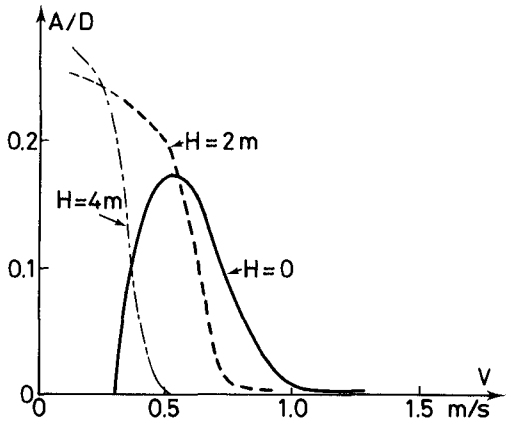

Figure 8. A/D as function of V and H.
d = 0.15 mm, D = 10 m and $\gamma = 90^{o}$.

3.4 The Sand Wave Length

As a first approximation the sand wave length is calculated by Eq. (10). The calculated steepness, A/λ, of the sand waves treated in Fig. 5C are shown in Fig. 9. As the suspended load increases the height decreases and the length increases. The sand wave steepness therefore drops rapidly for increasing current velocity. The effect of gravity on the bed load transport in case of pure current is indicated by the dotted line. In combined waves and current the suspended load is dominant even at small current velocities, and the gravity effect is not expected to be of importance.

Under field conditions the tidal current and the wave conditions will generally vary so fast that the sand waves at a given location reflect a temporal average of the different combinations of waves and current. When estimating this average each combination shall be weighted according to the strength it has in the process of forming the sand waves. A measure which can be used for such a weighting procedure is the quantity : dq/dD, which is proportional to the migration rate, a, of the sand waves. Fig. 10 shows the calculated migration rate for the sand waves treated in Fig. 5.

It can be seen how the wave condition, especially at moderate current velocities have strong influence on the formation of sand waves. It can also be noted that the relation between a and V is non-linear. The asymmetry in the tidal current can therefore be rather small and still produce asymmetric sand waves dominated by the direction of the strongest tidal current.

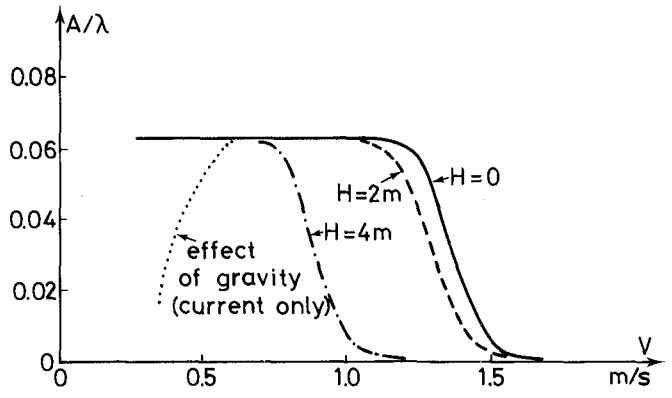

Figure 9. The sand wave steepness as function of V and H, d = 0.2 mm, D = 10 m, $\gamma = 90^{o}$.

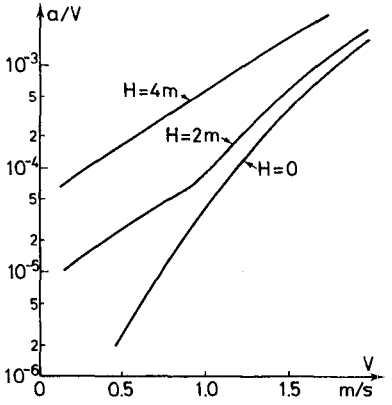

Figure 10. The sand wave migration rate as function of V and H. d = 0.2 mm, D = 10 m, $\gamma = 90^{o}$,

4. Conclusion

A theoretical model for the dimensions of offshore sand waves has been presented. The model is based on a model for dunes in rivers and a sediment transport model for combined waves and current.

At present no data has been published, which are comprehensive enough to allow for a detailed calibration of the different elements in the model. The predicted trends for the sand wave heights and lengths are, however, in general agreement with the observations reported in the literature.

According to the model there will for a given wave condition be a range of current velocities, under which sand waves will be formed. The upper limit for the sand wave formation is caused by the increasing amount of suspended sediment which passes the sand wave without being deposited, and thus does not contribute to the building-up of the sand wave.

For small water waves the lower velocity limit is associated with the initiation of sediment transport.

For large water waves the lower limit is caused by the suppression of flow separation at the front of the sand wave.

For a given wave climate the range of velocities where sand waves are formed become narrower for decreasing water depth or grain size of the bed material and at a certain water depth no sand waves may be formed at any current velocity at all.

5. References

Engelund, F. and Fredsøe, J. : 'A sediment transport model for straight alluvial channels', Nordic Hydrology, Vol. 7, 1976.

Fredsøe, J. : 'Unsteady flow in straight alluvial streams: modification of individual dunes', J. Fluid Mech. 91, pp. 497-512, 1979.

Fredsøe, J. : 'Shape and dimensions of stationary dunes in rivers', J. Hydr. Div., ASCE, Vol. 108, No. Hy 8, 1982.

Fredsøe, J., H. Andersen, O., and Silberg, S. : 'Distribution of suspended sediment in large waves', J.W.W., ASCE, Vol. 111, No. 6, 1985.

Houbolt, J.J.H.C. : 'Recent sediments in the Southern Bight of the North Sea', Geologie en Mijnbouw. Vol. 47, 1968.

McCave, I.N. and Langhorne, D.N. : 'Sand waves and sediment transport around the end of a tidal sand bank', Sedimentology, Vol. 29, 1982.

Mclean, S.R. and Smith, J.D. : 'A model for flow over two-dimensional bed forms', J. Hydraulic Engineering, ASCE, Vol. 112, No. 4, 1986.

Smith, J.D. : 'Stability of a sand bed subjected to a shear flow of low Froude number', J. Geophysical Res. Vol. 75, 1970.

Stride, A.H. (Edt.) : 'Offshore tidal sands', Chapman and Hall, London, New York, 1982.

Terwindt, J.H.J. : 'Sand waves in the Southern Bight of the North Sea', Marine Geology, Vol. 10, 1971.

CHAPTER 79

VELOCITY AND SEDIMENT CONCENTRATION FIELDS ACROSS SURF ZONES

Hans - H. Dette *
Klemens Uliczka **

Abstract

Wave-induced currents and sediment concentrations in suspension across the surf zone were investigated at prototype scale in the BIG WAVE FLUME in Hannover for combined beach and dune profiles as well during the development phase until quasi-equilibrium stage as after beach equilibrium conditions had been reached. The selected initial profiles were partly investigated in repeated tests with regular and irregular waves. Based upon the obtained experimental data a comparison is presented between the measured and calculated landward displacement of sediment volume through a selected point on the beach into seaward areas. The discrepancies in between the results for measured profile change and for calculated sediment transport volume derived from vertical current and suspension distributions are discussed.

Introduction

The description of coastal processes in the surf zone depends upon the understanding of interactions between the beach profile and the breaking waves, the wave-induced currents, and the associated movements of beach material. In order to calculate the net cross-shore sediment transport it is necessary to describe both the horizontal orbital velocity field $u(x, z, t)$ and the sediment concentration field $c(x, z, t)$ in space and time. As it is very difficult to measure these parameters under storm conditions in the field, prototype tests were carried out in the BIG WAVE FLUME in Hannover in order to study these processes at essentially full scale. In the paper first results of measurements on suspended sediment concentrations and wave-induced currents on beaches are presented.

Scope of Investigations

Two test series were carried out in the BIG WAVE FLUME, which is 324 m long, 7 m deep and 5 m wide. The initial profiles - illustrated in Fig. 1 - were called "dune without foreshore" (a) and "dune with foreshore" (b):

* Chief Engineer, Dr.-Ing., Leichtweiss-Institute, Technical University Braunschweig, POB 33 29, M.A.S.C.E.

** Assistant Scientist, Dipl.-Ing., Sonderforschungsbereich 205 "Coastal Engineering", Univ. of Hannover, Fed.Rep. of Germany

(a) + 2 m above still water level (SWL) and 30 m wide dune with a 1 to 4 seaward slope down to channel floor (- 5 m)

(b) + 2 m above SWL and 10 m wide dune with 1 to 4 seaward slope down to 1 m below SWL and following 1 to 20 slope down to channel floor.

Both profiles were subjected to regular wave attack ($\bar{H} = H_{rms} = 1.5$ m, $T = 6$ s, $d = 5.0$ m). The similarity index using the initial profile and $H_o/L_o = 0.04$ yielded $\xi_o = 1.48$ (dune without foreshore) and $\xi_o = 0.29$ (dune with foreshore). Additionally to these tests with regular waves the dune without foreshore experiments were repeated with irregular waves (JONSWAP-Wave-Spectrum, $H_{1/3} = 1.5$m, $T_p = 6$ s, $d = 5.0$ m).

The sand used had a mean diameter $D_{50} = 330$ µm and geometric standard deviation of $\sigma_g = 1.47$.

The experiments were carried out by increments of up to 80 waves as by then the initial wave form became significantly affected by reflection. Therefore, the test series was interrupted and restarted after the water had come to rest; the interval was used for the profile levelling.

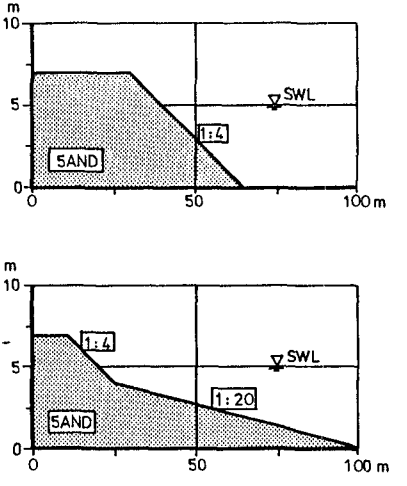

Figure 1. Initial beach profiles: Dune without foreshore (above) and dune with foreshore (below).

The tests with regular waves were stopped whenever the wave height variation reached ± 20 % of the originally generated wave height. Above this limitation it was observed in preceding tests that the breaker-line started to move from its original position. The experi-

ments with the JONSWAP-Wave-Spectrum were interrupted after three repetition intervals totalling nearly 12 minutes.

Sediment Concentration at Equilibrium Profile

Samples of the material suspended due to wave action were extracted by pumps at elevations from 0.02 m to 1.0 m above the bed at selected positions within the surf zone. The prototype of the pumping-system was developed by the DELFT HYDRAULICS LABORATORY (BOSMAN, 1986). The extraction nozzles (diameter: 3 millimeter) were fixed on a vertical pipe and orientated horizontally and perpendicularily to the flow direction of wave-induced currents. The intake-velocity at the nozzle reached about 1.0 m/s which was approximatly equal to the orbital velocities.

The samples were taken during each test increment at one fixed position on the beach profile without taking into consideration the method of bed averaging extraction as suggested by BOSMAN (1986) derived from small scale test in order to eliminate the effects of bed features.

Dune without Foreshore

Results due to Regular Waves

The results presented in the following are thus time-averaged data each from a sequence of about 80 waves (8 minutes). Fig. 2 illustrates suspension distributions over the equilibrium profile (dune without foreshore, Fig. 1 above) at four positions within the breaker zone at different points within the surf zone.

Generally it can be stated from the test results:

- the maximum suspension rate was recorded near the crest of the bar
- in the offshore direction and shoreward of the bar the sediment concentration decreased remarkably
- the breaking-point approximately coincided with the crest of the bar
- the breaker type on the quasi-equilibrium profile, which developed from 1 to 4 slope of the dune without foreshore was the plunging breaker
- the averaged wave heights at the measuring points (A to D) were: $\bar{H}_A$ = 0.8 m, $\bar{H}_B$ = 0.8 m, $\bar{H}_C$ = 1.6 m and $\bar{H}_D$ = 1.9 m
- the water-depths were: d_A = 0.96 m, d_B = 1.48 m, d_C = 1.25 m and d_D = 1.60 m

In Table 1 the sediment concentration data from the investigations at the dune without foreshore with regular waves are summarized.

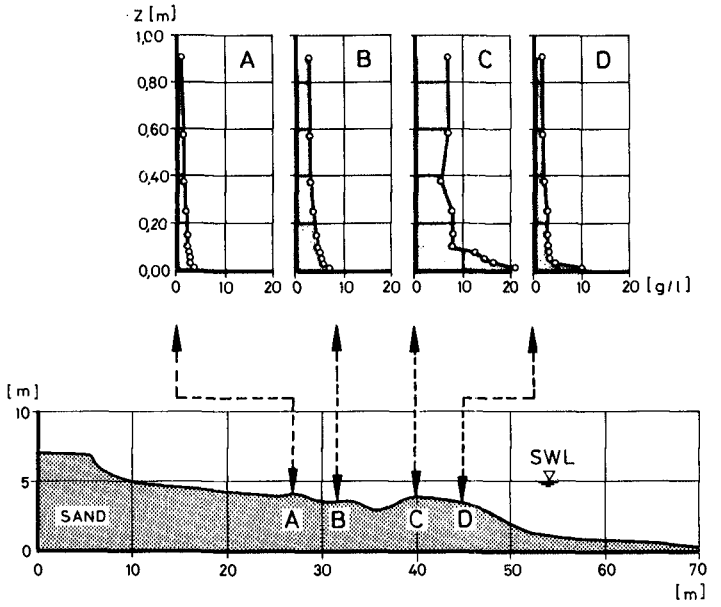

Figure 2. Suspension distributions on the beach at quasi-equilibrium profile conditions due to regular waves for the test series: "dune without foreshore"

Table 1. Sediment concentration data due to regular waves for the test series: "dune without foreshore"

DUNE WITHOUT FORESHORE REGULAR WAVES		H = 1.5 m		T = 6 s
Height above bottom	Sediment Concentration			
	$\bar{c}$	$\bar{c}$	$\bar{c}$	$\bar{c}$
m	g/l	g/l	g/l	g/l
0.02	3.3	7.1	21.0	9.9
0.04	2.9	5.9	16.3	4.6
0.06	2.7	5.5	14.6	3.5
0.085	2.5	5.1	12.6	3.3
0.11	2.2	4.6	7.9	3.1
0.16	2.3	4.7	8.2	3.0
0.26	2.0	3.7	8.0	3.0
0.385	1.6	3.1	5.5	2.3
0.585	1.4	3.1	7.2	1.8
0.91	1.0	2.9	7.0	1.9
Location	A	B	C	D

Results due to JONSWAP-Wave-Spectrum

The sediment concentration data are time-averaged values over three-times the spectrum-repetition-interval (nearly 12 minutes) which is equal to 125 times the peak period T_p = 6 s. Similar to the results for the beach profile due to regular waves, the maximum sediment concentration was observed shoreward of a so-called step in the beach profile (Fig. 3). The breaker zone varied in between 38 m and 15 m from the

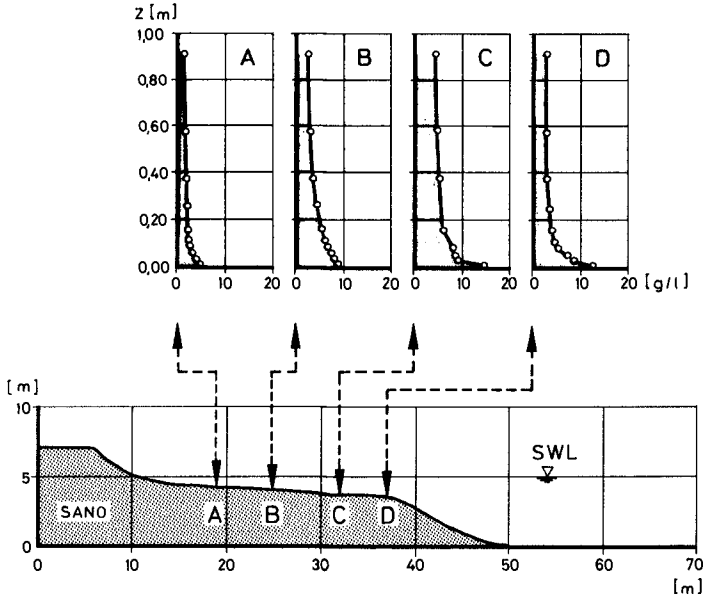

Figure 3. Suspension distributions on the beach at quasi-equilibrium profile conditions due to JONSWAP-Wave-Spectrum for the test series: "dune without foreshore"

shoreline. The significant wave heights at the points A to D were as follows: A: $H_{1/3}$ = 1.0 m, B: $H_{1/3}$ = 1.2 m,
C: $H_{1/3}$ = 1.7 m, D: $H_{1/3}$ = 1.5 m.

The water depths were as follows: d_A = 1.0 m, d_B = 1.15 m, d_C = 1.45 m, d_D = 1.75 m.

Table 2 gives the sediment concentration data associated to the JONSWAP-Wave-Spectrum and the test series "dune without foreshore".

Table 2. Sediment concentration data due to JONSWAP-Wave-Spectrum for the test series: "dune without foreshore"

DUNE WITHOUT FORESHORE JONSWAP-WAVE-SPECTRUM $H_{1/3}$ = 1.5 m T_p = 6 s				
Height above bottom	Sediment Concentration			
	$\bar{c}$	$\bar{c}$	$\bar{c}$	$\bar{c}$
m	g/l	g/l	g/l	g/l
0.02	6.2	9.5	15.4	13.0
0.04	4.6	8.6	9.1	9.0
0.06	3.9	8.0	-	8.0
0.085	3.5	7.1	8.7	6.5
0.11	3.0	6.7	7.3	5.2
0.16	2.8	6.3	6.3	4.8
0.26	2.5	4.2	-	4.3
0.385	2.1	3.6	5.3	3.1
0.585	1.8	3.2	4.9	2.9
0.91	1.3	2.8	4.0	2.7
Location	A	B	C	D

Dune with Foreshore

Results due to Regular Waves

The sediment concentration data obtained over the quasi-equilibrium profile which developed from the dune with foreshore are time-averaged values from a sequence of about 70 waves (7 minutes). The breaker type over the equilibrium profile was the plunging breaker due to the steep seaward slope of the bar. The breaking point was approximately located near the crest of the bar. The averaged wave heights at the points A to C yielded:

$$\bar{H}_A = 1.1 \text{ m}, \bar{H}_B = 1.5 \text{ m}, \bar{H}_C = 2.1 \text{ m}$$

The water depths were: $d_A = 1.95$ m, $d_B = 1.4$ m and $d_C = 2.6$ m.

Fig. 4 illustrates the suspension distribution over the equilibrium profile and in Table 3 the measured data are summarized.

The Accuracy of Concentration Measurements

The accuracy of the measured concentrations depends significantly upon the kind of the selected measuring system and upon the suitablity of system to be used in the laboratory or in the prototype. BOSMAN (1986) recommends on the basis of extensive investigations the TABAC method which means Time-And-Bed-Averaged-Concentration.
BOSMAN (1986) writes:

> The "effect on the local concentration is purely random and can be reduced by averaging either over space or over time".

For the prototype investigations in the BIG WAVE FLUME the time-averaging method was applied by means of a stationary pump system with which suspended sediment samples over 7 to 12 minutes were extracted.

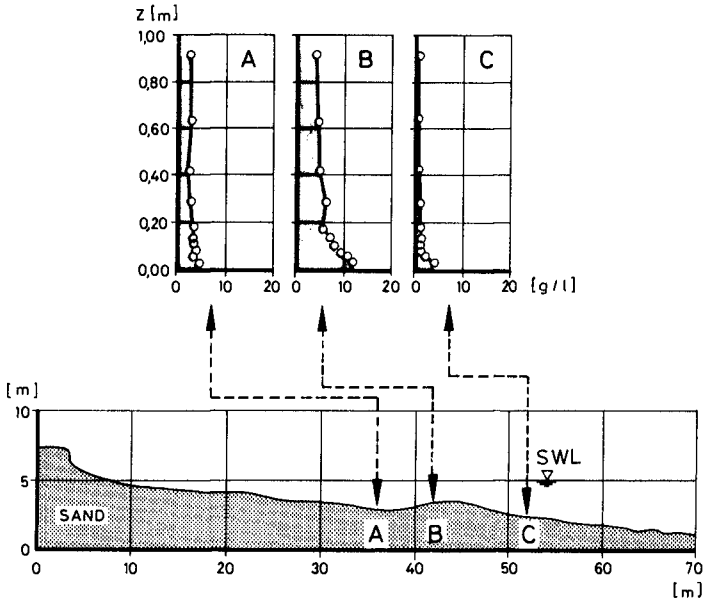

Figure 4. Suspension distributions on the beach at quasi-equilibrium profile conditions due to regular waves for the test series: "dune with foreshore"

Table 3. Sediment concentration date due to regular waves for the test series: "dune with foreshore"

DUNE WITH FORESHORE REGULAR WAVES	H = 1.5 m		T = 6 s
Height above bottom	Sediment Concentration $\bar{c}$	$\bar{c}$	$\bar{c}$
m	g/l	g/l	g/l
0.04	4.7	11.9	4.2
0.06	3.0	10.8	2.1
0.08	4.0	9.4	1.8
0.105	3.6	8.0	1.2
0.13	3.2	7.4	1.4
0.18	3.4	6.0	1.4
0.28	3.1	6.2	0.9
0.405	2.7	5.0	0.9
0.605	2.9	4.7	0.7
0.93	2.7	4.0	0.4
Location	A	B	C

In order to illustrate the range of scattering at one position at quasi-equilibrium condition Fig. 5 shows the results of 4 repeated measurements due to JONSWAP-Wave-Spectrum for the test series "dune without foreshore".

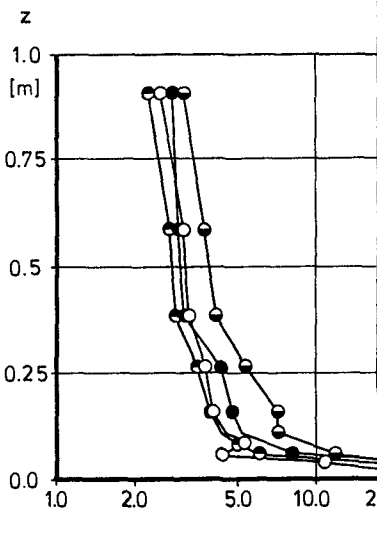

Height above bottom	Sediment Concentration $\bar{c}$	$\bar{c}$	$\bar{c}$	$\bar{c}$
m	g/l	g/l	g/l	g/l
0.02	20.6	43.6	42.4	19.7
0.04	10.7	23.0	16.7	20.8
0.06	4.3	8.0	6.1	11.9
0.085	5.4	6.5	4.9	9.1
0.11	4.5	5.2	4.3	7.1
0.16	4.0	4.8	3.9	7.1
0.26	3.8	4.3	3.5	5.5
0.385	3.2	3.1	2.9	4.1
0.585	3.1	2.9	2.7	3.7
0.91	2.5	2.7	2.2	3.0
WAVE NUMBER	5380 - 5510	5510 - 5640	5640 - 5770	5770 - 5900
SERIES	○	●	◒	◒

Figure 5. Repeated concentration measurements at the same position over the quasi-equilibrium profile developed from the dune without foreshore and JONSWAP-Wave-Spectrum

Near the bed the mean value of concentration from 4 measurements is $\bar{c} = 30 \pm 10$ g/l (approx. $\pm$ 30 %), at a position nearly 1.0 m above the bed the sediment concentration was about $\bar{c} = 3 \pm 1$ g/l (approx. $\pm$ 30 %).

This example of varying suspended sediment concentration may illustrate the problem of "accuracy". Even in laboratory at a prototype scale, i.e., in the BIG WAVE FLUME a stable equilibrium beach profile and constant measuring data cannot be expected. In all tests it was observed that the profile shape fluctuates and that the location of each breaker influences the concentration in a random way and thus the net sediment transport in the surf zone.

Velocity Fields in the Surf Zone

The measurements of wave-induced on-/offshore currents were carried out simultaneously at several fixed positions within the surf zone. Records were obtained from 0.1 m up to 0.6 m above the actual sand bed at the dune without foreshore and up to 1.0 m at the dune with foreshore. The single velocities are time-averaged values obtained from a single test increment (7 to 12 minutes). Fig. 6 shows as an example the distribution of wave-induced on-/offshore currents measured in the surf zone over the equilibrium profile from dune without foreshore and the JONSWAP-Wave-Spectrum. The difference between the averaged seaward and shoreward velocities $\bar{u}$ yields the net velocity u_R.

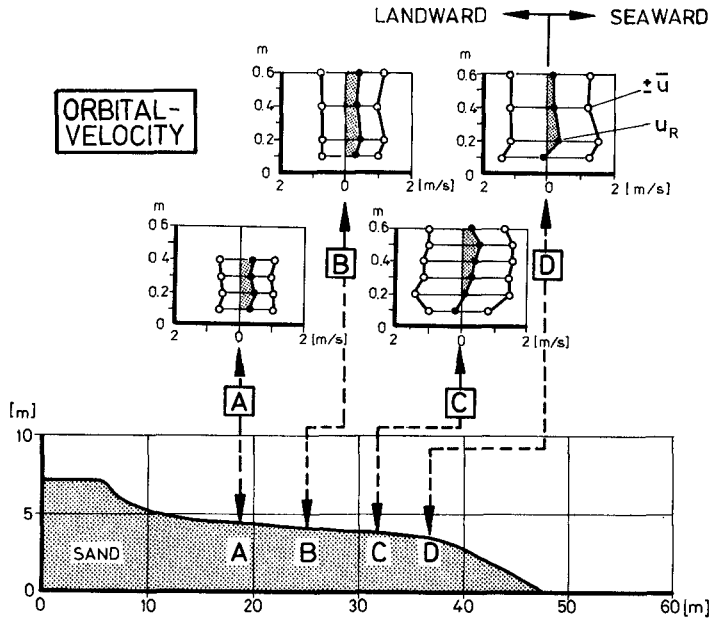

Figure 6. Time-averaged on-/offshore currents due to JONSWAP-Wave-Spectrum over the quasi-equilibrium of the dune without foreshore test series

Table 4 shows the averaged values of the recorded velocities with electromagnetic current meter due to the JONSWAP-Wave-Spectrum. The seaward direction is assumed as positive axis.

Table 4. Time-averaged on-/offshore currents across the surf zone due to JONSWAP-Wave-Spectrum at the dune without foreshore

DUNE WITHOUT FORESHORE
JONSWAP-WAVE-SPECTRUM $H_{1/3}$ = 1.5 m T_p = 6 s

Height above bottom	Time-averaged on-/offshore currents											
	+u	-u	u_R	+u	-u	u_R	+u	-u	u_R	+u	-u	u_R
m	m/s	m/s	m/s	m/s	m/s	m/s	m/s	m/s	m/s	m/s	m/s	m/s
0.1	0.96	0.63	0.33	1.04	0.73	0.31	0.84	1.00	-.16	1.31	1.34	-.03
0.2	0.99	0.57	0.42	1.18	0.70	0.48	1.45	1.27	0.18	1.46	1.13	0.33
0.3	0.96	0.62	0.34	-	-	-	1.48	1.12	0.36	-	-	-
0.4	1.01	0.66	0.35	1.05	0.71	0.34	1.56	1.13	0.43	1.31	1.11	0.20
0.5	-	-	-	-	-	-	1.56	0.97	0.59	-	-	-
0.6	-	-	-	1.14	0.74	0.40	1.31	1.03	0.28	1.29	1.16	0.13
Location	A			B			C			D		

The location of the breaker zone, the significant wave heights and water depths at the points of measurements (A to D) are documented in the previous chapter.

Cross-Shore Sediment Transport Rate

The sediment volume passing at one position of the beach profile which developed from dune with foreshore from shoreward to seaward location is used in the following to compare calculated and measured data to discuss the reliability and to point out the order of magnitude of the sediment transport rates obtainable by means of this method.

Sediment passing a given Location of the Beach

The measurements were carried out after 50 waves had already run on the initial profile of the dune with foreshore. At this stage (after 50 waves) the beach profile was surveyed (= initial profile) and then another 80 waves were run. During this time sediment concentration samples were extracted at a location of x = 26 m from the shoreline and 2.0 m apart from the side wall of the flume. Afterwards the profile was resurveyed in three profiles of the 5 m wide flume, in the centre-line and 1.5 m to either side as basis for the calculation of removed sediments. During the test run the water depth at the point of measurement remained constant with d = 1.9 m. The averaged wave height of the regular waves was $\bar{H}$ = 1.3 m.

Cross-Shore Current

The velocities were measured at the same location (x = 26 m) in the middle of the channel, at elevations between 0.1 m to 1.0 m above the bed. The velocity at one elevation was measured over each increment of 70 waves. It was assumed that during consecutive test increments up to a total of 760 waves the velocities at the selected elevations remained more or less constant. The measured net velocity distribution is illustrated on Fig. 7. It is seen that the seaward column (below 1 m over the bed) is approximately constant at $\bar{u}_R$ = 0.53 m/s. The standard deviation of the measured values was σ = 0.11.

Suspended Sediment

Due to the high turbulence, particulary at macro scale, in the surf zone the sediment moves in whirls and clouds. Therefore no separation of suspended-load and bed-load was made for the following analysis. The measured vertical profile of the suspended sediment was fitted to the exponential function as suggested by v.d.GRAAFF and ROELVINK (1984). Table 5 shows the measured and calculated data together with the computed bottom concentration c_o.

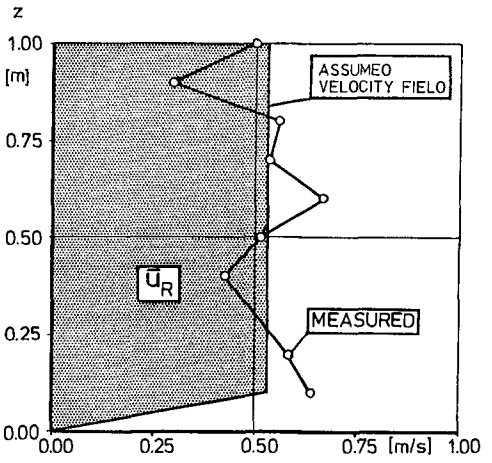

Figure 7. Distribution of the measured data u_R and assumed velocity profile $\bar{u}_R$ for calculation

Table 5. Measured and calculated sediment concentration data

Height above bottom	Sediment Concentration	
	$\bar{c}_{meas.}$	$\bar{c}_{calc.}$
m	g/l	g/l
0.02	(5.93)	8.88
0.04	13.20	8.00
0.06	10.50	7.25
0.085	8.53	6.49
0.11	6.25	5.86
0.16	5.77	4.93
0.26	5.34	3.83
0.385	4.40	3.17
0.585	3.60	2.72
0.91	2.89	2.41
Bottom concentration:		c_0 = 9.95 g/l

Net On-/Off-Shore Transport

The net sediment transport was calculated with the total transport formula:

$$S = \int_0^z c\,(z,t) \cdot u\,(z,t) \cdot dz \qquad (1)$$

which for the present case may be written as

$$\dot{S} = \int_0^z \bar{c}_{cal} \cdot \bar{u}_R \cdot dz \qquad (2)$$

The time-averaged sediment movement seaward past the measuring position during the initial test increment of 80 waves was calculated from the superposition of the beach profiles before and after the test run and referred to 1 m width of beach. The result yielded a volume of $A = 1.14\ m^3/m \pm 30\ \%$. The suspended sediment transport was calculated with the data in Table 5 to $S = 1.57$ kg/s or $S = 0.45\ m^3/m \pm 30\ \%$. From this comparison a difference of 60 percent between measurement and computation is obtained, this is less than one order of magnitude. Fig. 8 illustrates for the point of measurement the relevant data for the analysis.

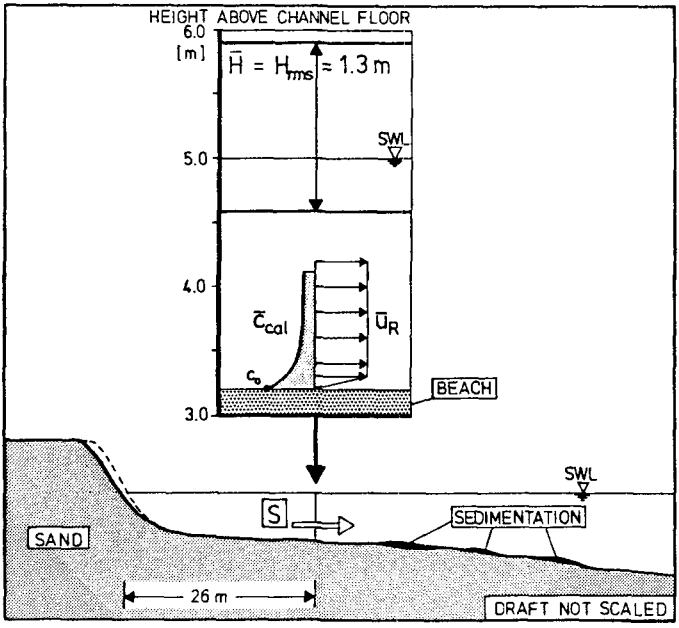

Figure 8. Schematic layout of applied data at the point of measurement for comparison of sediment transport during a test increment of 80 waves

With respect to discrepancies it has to be pointed out that the sediment concentration was measured only up to 0.91 m above the bed which is only 48 percent of the total water depth of d = 1.9 m. From visual observation it was obvious that suspended sediment were moved up to the water surface in the presence of large eddies (Fig. 9 and 10).

Figure 9. Breaker in front of the dune without foreshore initial

Figure 10. Broken wave impinging on backrush water

Sediment Transport during the Development of Beach Profile

Notwithstanding already the difficulties which are connected to the calculation of sediment volume through one point of the beach during first increment of 80 waves this method was also applied for another 10 increments with a total of 760 waves. By this means the variation of sediment volume during the developing phase of the beach profile shall be demonstrated. Fig. 11 shows the comparison of both time-averaged results from the calculation and from the development of the beach profile. The measured and averaged value of sediment transport computed from profile changes over 760 waves yielded $\overline{A}$ = 1.07 m³/m ± 30 % (σ = 0.199) and $\overline{S}$ = 0.3 m³/m ± 30 % (σ = 0.063) for the calculated sediment transport. The difference between the averaged values is Δ = 0.77 m³/m or about 72 % (per increment = 70 waves).
The calculation with the average of instantaneous products of the sediment concentration and the water velocity

$$S = \int_0^t \int_0^z c(z,t) \cdot u(z,t)\, dz\, dt \qquad (3)$$

is not possible, since the data of the sediment concentration are only time-averaged values.

It may be pointed out, that from the averages of instanntaneous products - obtained from 2-dimensional measuring systems - the sediment transport will not be described more accurately than the product of time-averaged sediment concentration and water velocity because measuring errors due to large vortex components have to be taken into account. In the present calculation these errors are compensated.

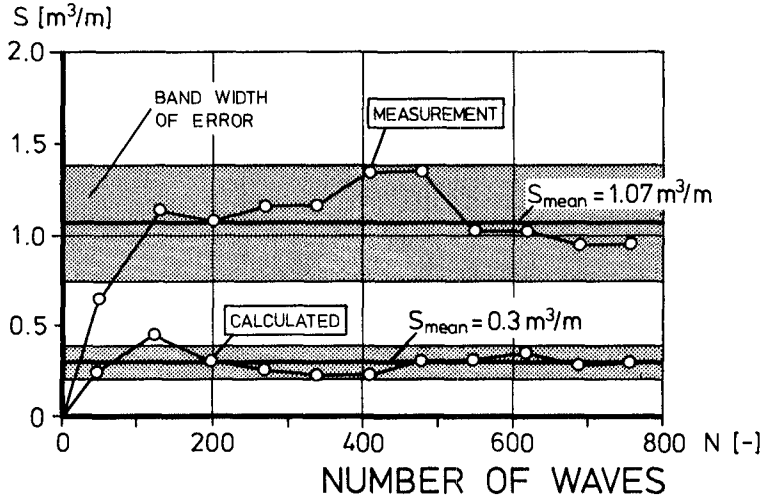

Figure 11. Comparison of sediment transport between the calculated transport and that computed from profile changes during development phase of beach profile (each value represents approx. a sequence of 70 waves)

Conclusion

The BIG WAVE FLUME in Hannover enabled prototype measurements of wave-induced velocities and sediment concentrations across the surf zone during the development phase of beach profile and over the equilibrium profile under regular and irregular waves.

In the paper first results of measurements obtained from two test series: "dune with and without foreshore" are presented.

At one position on the beach the calculated sediment transport was compared with the measured volume changes of the beach profile.

In order to minimize the differences between the calculated and measured values, it is necessary, to study in more detail the sediment transport in the bottom layer and to carry out measurements over the total column of water depth in the surf zone.

Acknowledgment

The "GROSSER WELLENKANAL" GWK (Big Wave Flume) was constructed by the Deutsche Forschungsgemeinschaft (DFG = German Research Association). The DFG also sponsored the investigations described here (Sonderforschungsbereich 205). The authors are very much indebted to the DFG for this support.
The authors like to express their sincere thanks also to Professor

Dr.-Ing. E.h. A. J. RAUDKIVI, University of Auckland, for his generous support and his stimulating remarks during the preparation of this paper.

References

Bosman, J. J., 1986: Some aspects of sediment concentration in the surf zone, Report of investigation, no. M 1695 Part III, Delft Hydraulics Laboratory/TOW Delft, Netherlands

Dette, H. H., 1986: Untersuchungen über Dünenabbrüche und Stranderosionen im GROSSEN WELLENKANAL, Die Küste, Heft 43

Dette, H. H., Uliczka, K., 1986: Prototype and Model Evolution of Beach Profile, Proceedings IAHR Symposium '86 on Scale Effects in Modelling Sediment Transport Phenomena, Toronto, Canada

Graaff, v.d., J., Roelvink, J. A., 1984: Grading Effects in Concentration Measurements, Proceedings 19th Internat. Coastal Engineering Conference Vol II, Chapter 110, Houston, USA

Raudkivi, A. J., 1982: Grundlagen des Sedimenttransports, Springer-Verlag, Heidelberg. Fed. Rep. of Germany

List of Symbols

A	m^3/m	sedimentation
c	kg/m^3	sediment concentration
$\bar{c}$	kg/m^3	time-averaged sediment concentration
c_o	kg/m^3	calculated bottom concentration
D_{50}	μm	mean grain size diameter
$\bar{H}$	m	time-averaged wave height
H_o	m	deep water wave height
$H_{1/3}$	m	significant wave height
H_{rms}	m	root mean square wave height
L_o	m	deep water wave length
N	-	number of waves
S	m^3/m	total sediment transport
T	s	wave period
t	s	time
$\underline{u}$	m/s	wave-induced current
$\bar{u}$	m/s	time-averaged wave-induced current
u_R	m/s	net wave-induced current
x	m	horizontal coordinate
z	m	vertical coordinate
σ	-	standart deviation
ξ_o	-	similarity index
σ_g	-	geometric standard deviation for grain size

CHAPTER 80

A NEW EQUILIBRIUM ANALYSIS FOR NEARSHORE TIDAL BASINS

R. Dieckmann[*1] and H. W. Partenscky[*2]

Abstract

A large tidal flat area of about 40 tidal basins with catchment areas of between 10 and 790 km^2 exists along the coast of the German Bight. Not all of these tidal basins are morphologically stable.

The main parameter necessary for determining the state of equilibrium is the volumetric capacity of the concave portions of the tidal basin. In order to examine the equilibrium state it is necessary to compare the volumetric capacity of the tidal basin determined from hydrographic charts (measured volume) with a theoretical volume given by newly developed stability criteria representing averaged conditions (volume balances). Significant deviations between the theoretical and the measured volumes indicate a state of non-equilibrium.

Using stability criteria it is possible to desribe the state of equilibrium of a tidal basin in a stepwise manner either from the bottom of the tidal basin to the datum plane MHW in order to obtain a cross-sectional stability profile, or from the shore to the seaward boundary of the basin in order to obtain a longitudinal stability profile.

The applicability of the new method for analyzing the equilibrium of a tidal basin will be demonstrated by the example of the Süderau tidal basin in the north of Germany.

1. Introduction

The North Sea is a shallow marginal sea of the Atlantic Ocean. In the south eastern part of the North Sea, known as the German Bight, the coast is formed over a length of 480 km by a tidal flat area of 7500 km^2 consisting of approximately 40 tidal basins with catchment areas of 10 to 790 km^2.

The tidal flats of the German Bight are regions of extensive alluvial activity which has never ceased over many centuries of history. In their composition and form the tidal flats are the result of the constructive and destructive actions of the North Sea. The severe storms surges of the 13th and 14th century, as well as during the 17th and 18th centuries, have caused considerable loss of land along this

*1 Dr.-Ing., Agriculture and Water Resources Office (ALW Husum), Herzog-Adolf-Str. 1, D-2250 Husum, FRG.

*2 Prof. Dr.-Ing. Dr.phys, Director of the FRANZIUS-INSTITUTE for Hydraulic Research and Coastal Engineering, University of Hannover, Nienburger Str. 4, D-3000 Hannover 1, FRG.

coast. Land reclamation measures and offshore dykes have only been able to offset a portion of these erosional losses. Therefore not all of the tidal basins in this area are morphologically stable.

In order to clarify the morphological behaviour of the nearshore zone and to be able to estimate the degree of further erosional losses, sub-regions of the tidal basins have been systematically investigated for about 10 years in relation to their equilibrium state. Further erosional losses must be prevented by appropriate construction works in order to safeguard this unique natural landscape. In addition, the tidal flats are of great importance in the coastal protection system since they considerably reduce the hydrodynamic loading on the coastal dykes.

The initial results of this long-term investigation programme were presented at the Coastal Engineering Conference in Copenhagen, 1984/1/ and in Cape Town, 1982/2/.

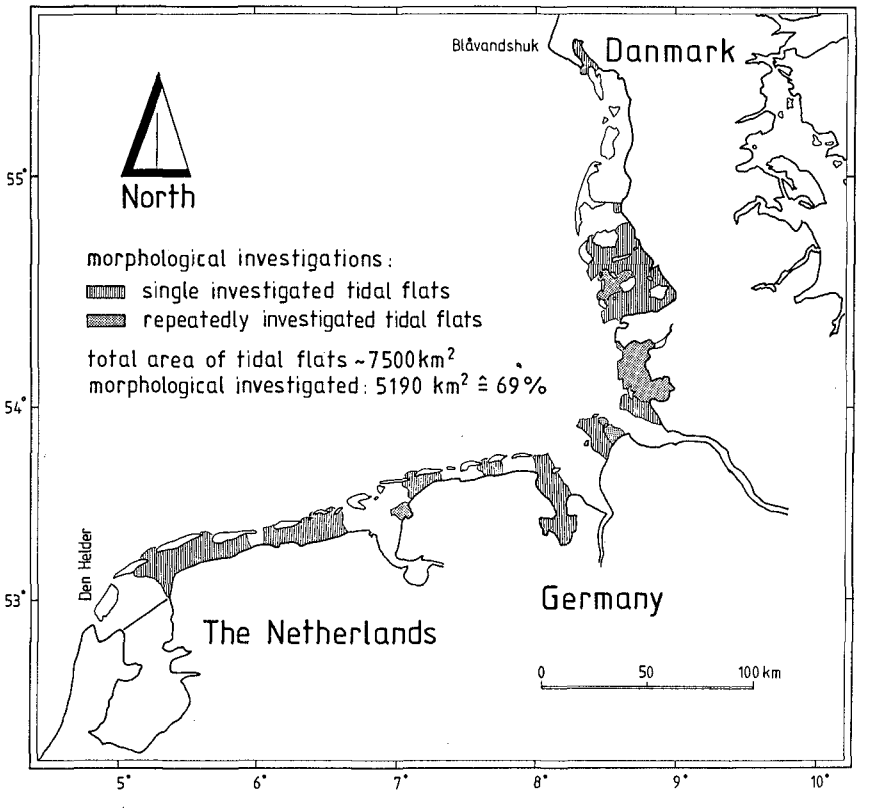

Fig. 1: Morphologically investigated areas along the coast of the German Bight.

2. Concept of the Investigations

2.1 Geomorphological and hydrological Boundary Conditions

The surface shape of a tidal flat area is very complicated. To describe it, the definition of basis units for data collection is necessary. Such basis units are the drainage basins of the tidal creeks and gullies (tidal basins).

Today, the investigated tidal basins of the German Bight represent approximately 69 % of the whole tidal flat area. In addition to this, some tidal basins have been repeatedly investigated. A total data volume from 6250 km^2 of tidal flats is available (see Fig. 1).

The main task of the morphological investigations is to generalize the morphology of the tidal basins by determining the so called constant-level area distribution (CLAD)/3/.

The constant-level area distribution for a tidal basin may be obtained by assigning the included area of a particular closed contour to the geodetic height corresponding to that contour. A distribution function is obtained from a graphical representation of the latter areas which is similar in form for all tidal basins having the same characteristics (see Fig. 2).

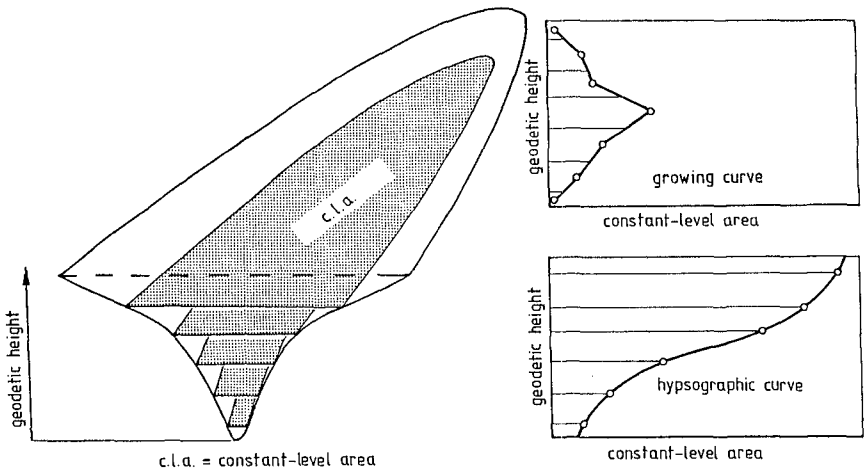

Fig. 2: Determination of the constant-level area distribution (CLAD) of a tidal basin (schematic) /3/.

In order to determine the CLAD, it is necessary to measure the constant-level areas from charts using a planimeter. In the case of larger investigation areas or those having a more complex morphology, the CLAD may be determined for a region as a whole by the summation of the individual contributions of a number of sub-areas.

By numerical integration of the CLAD, the volumetric summation curve (VSC) for a tidal basin may easily be determined (see Fig. 3).

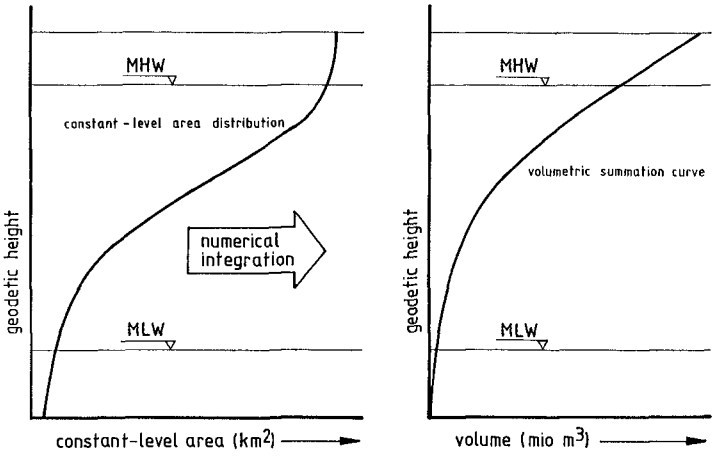

Fig. 3: Constant-level area distribution (CLAD) and volumetric summation curve (VSC) of a tidal basin /3/.

The VSC represents the total volumetric capacity of a hollow-shaped tidal basin with respect to different depths. Values of special importance are the volumetric capacity below the datum planes MLW and MHW /4/.

Applying to HAYES tidal classification /5/, it is possible to subdivide the shallows along the coast of the German Bight into the following 4 classes:

CLASS	TIDAL RANGE
Microtidal coast	< 1 m
Low mesotidal coast	1 - 2 m
High mesotidal coast	2 - 3 m
Low macrotidal coast	3 - 5 m

This classification is of great importance, especially from the geomorphological point of view. On the mesotidal coast, the flats of the German Bight are bordered by barrier islands. In passing from the low mesotidal to the high mesotidal coast the islands of the barrier island chain become smaller. Along the low macrotidal coast no barrier islands are present. This coast is open to the sea (see Fig. 4).

For the comparision of CLAD- or VSC-curves of different tidal basins, the tidal classification mentioned above has to be taken into account.

In Fig. 5, typical CLAD-curves of the 3 types of tidal basins are plotted as a function of the relative surface area (constant level area). When considering the intertidal area between MHW and MLW, the curves clearly show the decrease of this part of the tidal basins with decreasing tidal range. These differences in the morphological structure of several tidal basins can be shown clearly by comparing CLAD- and VSC-curves of the Meldorfer Bucht, which is situated in the low macrotidal range of the West Meep, which represents a tidal basin of the low mesotidal coast. Although both tidal basins have nearly the

same surface area and volumetric capacity at MHW, the CLAD- and VSC-curves are totally different (see Fig. 6).

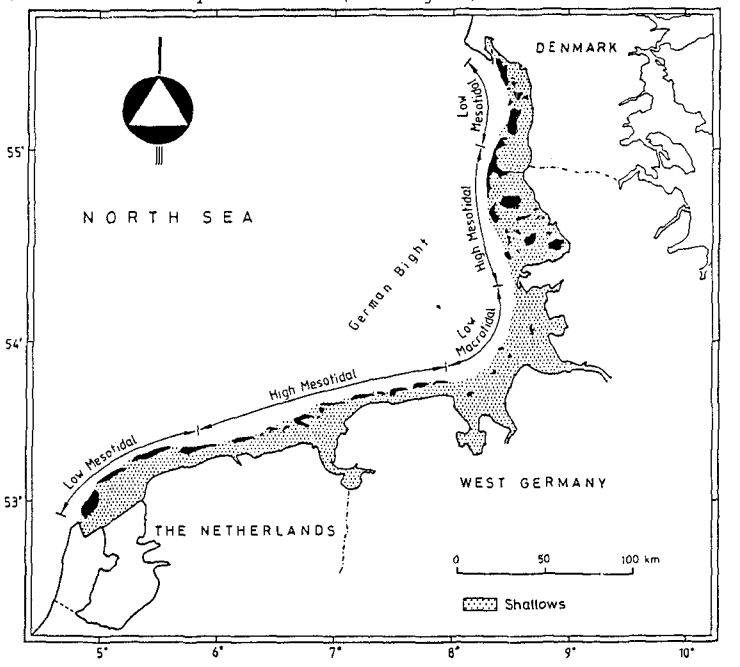

Fig. 4: Map of the German Bight showing the tidal flats /3/.

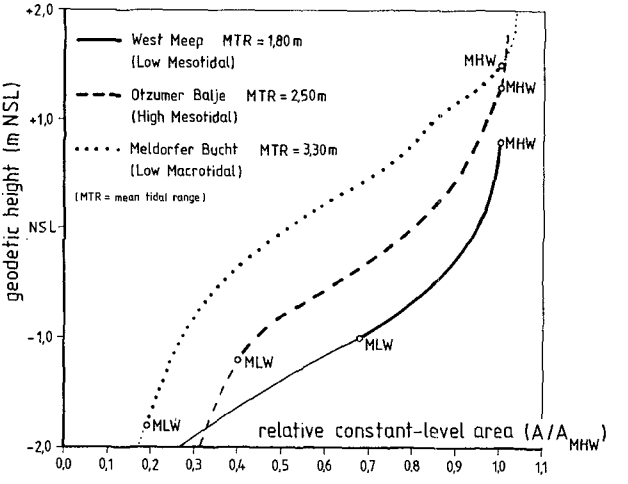

Fig. 5: Comparision of the types of CLAD plotted as a function of the relative surface area /3/.

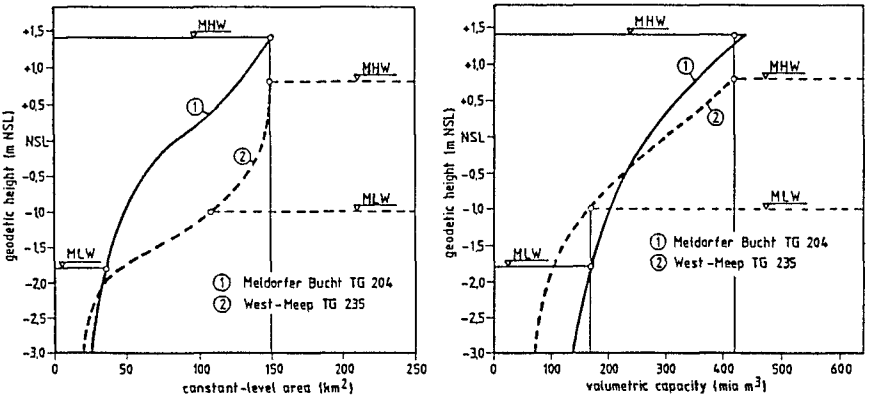

a) Differences in the course of the CLAD - functions

b) Differences in the course of the VSC - functions

Fig. 6: General morphological structure of the Meldorfer Bucht and West Meep tidal basins /3/.

2.2 Regime Theory Basis for the Investigations

River drainage basins or tidal creeks (tidal basins) may be considered as open passive systems (regimes), the states of which may be described by parameters. An open system allows the transport of material and energy across the system boundaries (tidal basin boundaries). Passive systems only change their state when an external disturbance enters the system /6/. Theoretically, such systems are in a time-independent state of equilibrium, which in the case of a tidal basin must satisfy three essential physical conditions:

-- the continuity condition,
-- the relationship between the flow velocity, the depth, the slope and roughness of the channel and
-- the relationship between the flow velocities and the sediment transport.

If external influences disturb the regime of the tidal basin, this must alter to comply with the new boundary conditions and attain a new state of equilibrium within a particular time interval.

Since, however, tidal basins are subjected to many varying boundary conditions and disturbances which have apposing effect, a final state of equilibrium is never reached. Due to the feedback mechanisms between the disturbances and the reactions of the regimes, time delays occur. Self-correcting processes therefore fluctuate about a mean condition representing the modal value, i.e. a dynamic state of equilibrium develops /7/ which corresponds to the mean equilibrium state.

In the case of disturbances, the regime parameters behave in different ways. Only few but important system parameters react very sensitively to disturbances. It is well-known from regime theory, the size of the drainage area is the most important parameter of a channel system.

Accordingly, a strict mathematical relationship (Fig. 7) exists between the drainage area and the volumetric capacity of a tidal basin. The regime of a tidal basin reacts thereby by altering its drainage area by erosion or sedimentation depending upon whether the drainage area has increased or decreased until a new state of equilibrium has been established.

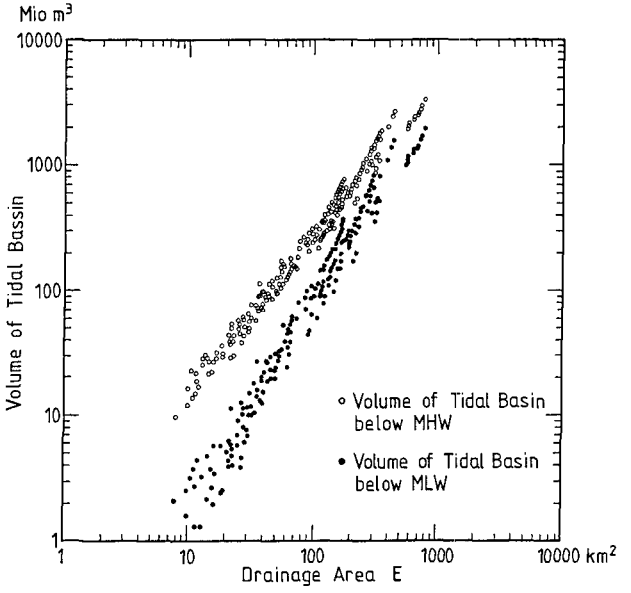

Fig. 7: Relationships between the volumetric capacity below MLW and MHW and the drainage area of tidal basins in the German Bight /3/.

2.3 Approach and Method

The main parameter necessary to determine the state of equilibrium is the volumetric capacity of the concave portions of the tidal basins. The stability criterion for a tidal basin of given dimensions is given by the following equation:

$$V = \alpha^* \cdot (d_z \cdot a_z)^{\beta^*} \qquad (1)$$

where

V = volumetric capacity of the tidal basin for the state of equilibrium,

α^*, β^* = regression coefficients, which are functions of tidal conditions and the tidal section under consideration,

d_z = maximum depth in the tidal basin with respect to the constant level elevation (z) and

a_z = size of the constant level area at the elevation (z).

In order to examine the equilibrium state of a tidal basin and to make predictions of the expected degrees of sedimentation and erosion for a region which may not be in a state of equilibrium, it is necessary to

compare the theoretical volumetric summation curve with a measured curve based upon hydrographic charts.

In the event that significant deviations are revealed through a comparision of the theoretical and measured volumetric summation curves (volumetric balance) for the tidal basin under consideration, this implies that the area concerned is in a non-equilibrium state.

For the case of a volume deficiency, i.e. the measured volume is less than the theoretical volume, the tidal basin is in a state of erosion. In this case, erosion continues until the volume corresponding to the equilibrium state is attained. Conversely, a tidal basin with a volume excess reacts by undergoing gradual sedimentation until a state of equilibrium (theoretical volume) is reached /2/.

As a basis for determining the actual volumetric summation curve, accurate computations of the volumetric capacity are necessary for the channel system under investigation. For this purpose, accurate contour maps of the tidal basins are essential.

3. Stability Criteria for Tidal Basins

3.1 Determination of Regression Coefficients

In order to determine the theoretical volume which characterises the mean equilibrium state of a tidal basin, it is necessary to determine the regression relationship between the actual existing volume (see Section 2.1, Figs. 2 and 3) and the value given by the product $(d_z \cdot a_z)$ from the relationship (1) for all 71 of the tidal basins and sub-regions investigated. The regression coefficients α^* and β^* for the individual tidal basins were determined by the least squares error method of GAUSS from altogether 450,000 data values by means of a special computer program.

In order to obtain a good approximation of the geomorphological boundary conditions, it is necessary to consider the following parameters:

-- the seaward boundary of the tidal basin (see /3/),
-- the differences in the structure of the tidal basin with respect to tidal conditions (Section 2.1),
-- seperate evaluations of the channnel regions and the flat sections of the tidal basin.

The regression coefficients determined for the investigated tidal basins with varying tidal ranges were represented in relation to tidal range under consideration of the height domains channel region (section 1) and flat section (section 2), as shown in Figs. 8a, 8b. From these diagrams, the regression coefficients α and β were determined for an evaluation of the theoretical volume of a tidal basin in relation to the particular mean tidal range (MTR).

The results were as follows:

channel region $\alpha_1 = 0.383 - 0.0133 \text{ MTR}$ (2)

$\beta_1 = 0.883 - 0.004 \text{ MTR}$ (3)

flat section $\alpha_2 = 1.115 - 0.161 \ MTR$ (4)

$\beta_2 = 0.989 - 0.026 \ MTR$ (5)

It is noted that the quality of the approximation for the region 2 (flat section), as expressed by the correlation coefficients, is generally slightly worse. This is not related to errors in the method used but to the "particular morphological characteristics" of the investigated drainage areas which were particularly abundant in the cases considered and which could not be described in terms of the parameter "volumetric capacity".

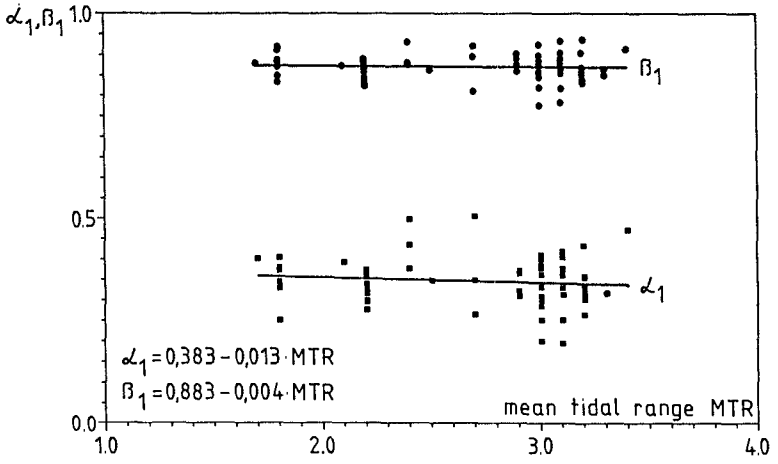

Fig. 8a: Regression coefficients α_1 and β_1.

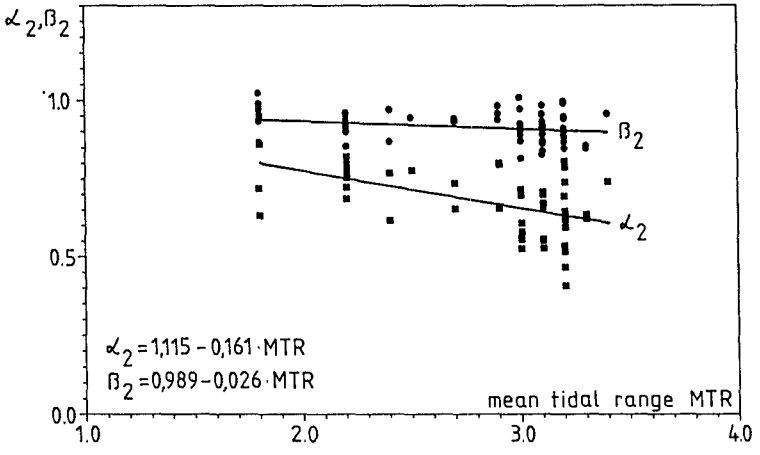

Fig. 8b: Regression coefficients α_2 and β_2.

3.2 Formulation of the stability criteria

The volumetric capacity (nominal volume), which represents mean conditions for the given tidal range, may be regarded as a criterium for the hydrological-morphological stability of a drainage area. This nominal volume may be represented on the basis of the previously described general formula for the region below MLW as follows:

$$V_{z_1} = \alpha_1 \cdot (d_z \cdot a_z)^{\beta_1} \quad \text{(Mio m}^3\text{)} \qquad (6)$$

For the tidal range region, the following holds:

$$V_{z_2} = \alpha_2 \cdot (d_z - d_{MLW})(a_z - a_{MLW})^{\beta_2} \quad \text{(Mio m}^3\text{)} \qquad (7)$$

where

d_{MLW} = depth below MLW (m),

a_{MLW} = constant level area of the reference plane MLW (km^2)

Here, the two sections 1 (channel bed to MLW = channel region) and 2 (MLW to MHW = flat section) must be considered. The coefficients α_i and β_i which should be substituted in the Equations (6) and (7) for the particular case in question may be obtained from Figs. 8a and 8b.

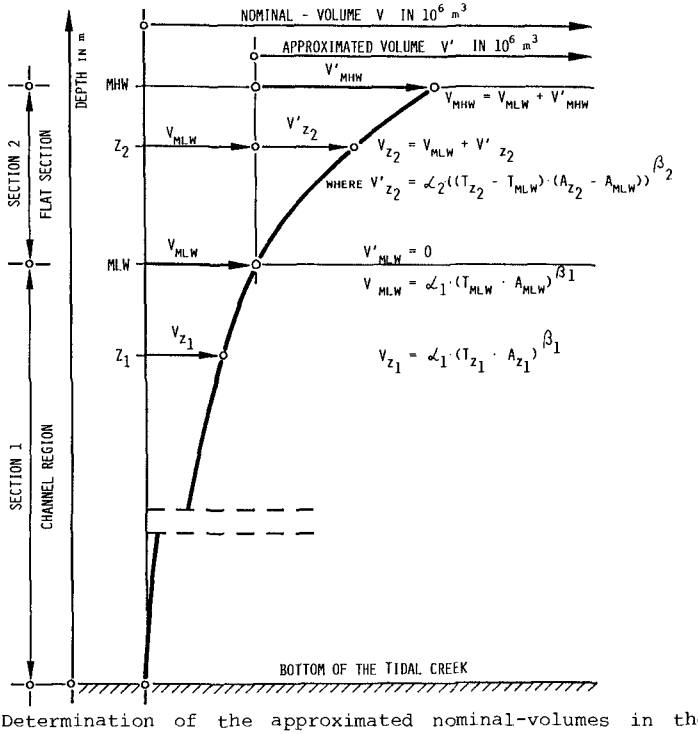

Fig. 9: Determination of the approximated nominal-volumes in the two investigation sections: channel region (section 1) and flat section (section 2) /3/.

Figure 9 shows by way of example the method of determining the approximated nominal volumes in both sections. In section 2 (flat section) a transformed coordinate system based upon the particular value of V_{MLW} is used. By this means, discontinuity in the approximated nominal volumes in the transition zone between sections 1 and 2 is avoided.

Special investigations have shown that the stability criteria not only apply to complete tidal basins, but also to parts thereof (see /8/).

Using the stability criteria, it is possible to describe the state of equilibrium of a tidal basin in a stepwise manner either from the bottom of the channel to the datum plane MHW in order to obtain a cross-sectional stability profile of the basin or from the shore to the seaward boundary of the basin in order to obtain a longitudinal stability profile.

To what extent the composition of bed material influences the stability criteria cannot be stated with any certainty at the present time. In view if this, the given relationship (Equation 6 and 7) can be applied with confidence only for tidal basins of the German Bight.

4. Examples of Application

4.1 General Information

The predictive capability of the stability criteria will be demonstrated by application to the Süderau, which is an approximately 200 km^2 tidal basin on the north coast of the German Bight (Fig. 10).

Along this part of the coast, erosional processes prevail as a result of the geomorphological development of the tidal region since the catastrophic storm surge of 1634. Today this erosion poses a danger to the stability of the tidal areas, the shore protection structures of the mainland, and the entire ecosystem.

Special problems exist in the region of the "Strand", which is a 200 m wide and about 10 m deep channel connecting the two channel systems Norderhever and Süderau (Fig. 10). Due to the tidal conditions in this region, a residual discharge of approximately 50 Mio. m^3 per tide passes through the Strand from the Norderhever into the Süderau. This residual discharge acts as a flushing mechanism in the Süderau. Owing to the large load-carrying capacity of this flushing discharge, the Süderau has been transformed into a very wide and deep tidal basin. At low tide, an additional tidal volume of $10 \cdot 10^6$ m^3 flows to the west from Norderhever into the neighbouring Rummelloch-West (see Fig. 10).

Owing to the historical development and the widening of the Süderau by the flushing discharge, it is to be expected that this tidal basin is in a hydrological-morphological state of non-equilibrium.

4.2 Stability Investigations of the Süderau

The stability criteria make it possible to make predictions of the stability behaviour of a tidal basin from the bed of the channel up to the reference plane MHW. For this purpose, extensive preliminary work was necessary, as given in detail in Section 2.3.

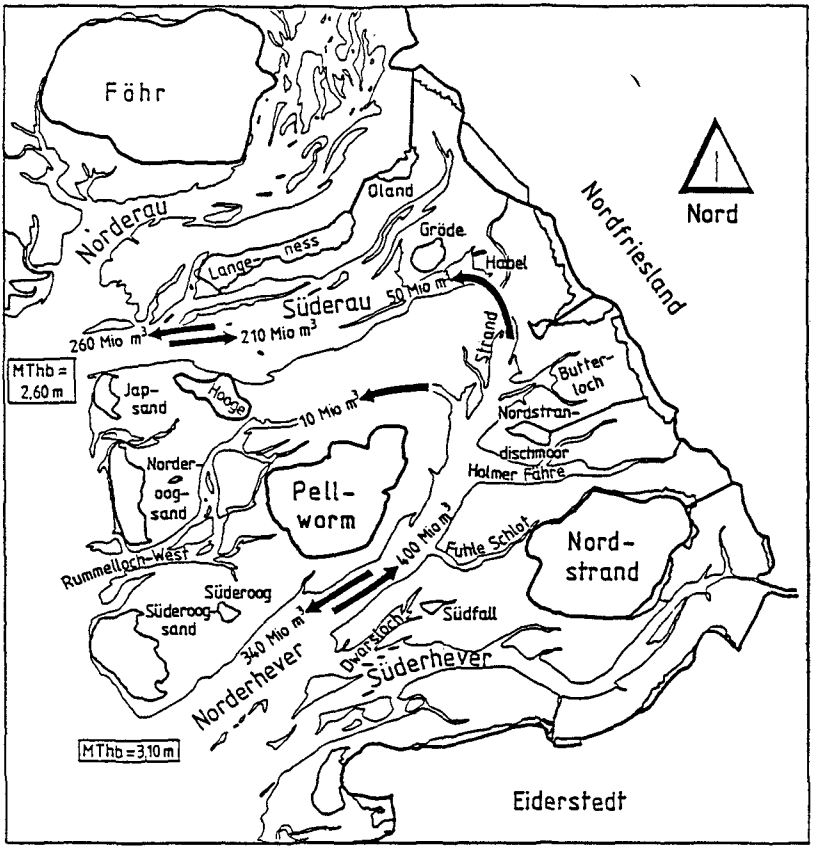

Fig. 10: Balance of tidal discharge in the region of the mudflat channel systems Norderhever-Strand-Süderau and Rummelloch-West.

The results of the evaluations and the subsequent necessary computer analysis are presented in the form of output listings which contain amongst other parameters the theoretical and measured volumes and the volume balances.

With this data, the stability profile of a tidal basin may be represented. The latter shows in the form of a volume balance summation curve the overall degrees of sedimentation or erosion to be expected until an equilibrium state is reached landwards of the profile considered. The stability profile (Fig. 11a) of the Süderau tidal basin indicates a clear volume excess, i.e. the measured volumes are greater than the theoretical ones. On the basis of this, sedimentation in the order of $39 \cdot 10^6$ m^3 is to be expected below MLW (channel region), whilst in the tidal range region (flat section), $(212 - 39) \cdot 10^6$ m^3 = $173 \cdot 10^6$ m^3 is to be expected. The clear non-equilibrium state, particularly above MLW, is mostly due to the flushing capacity of the tidally-induced

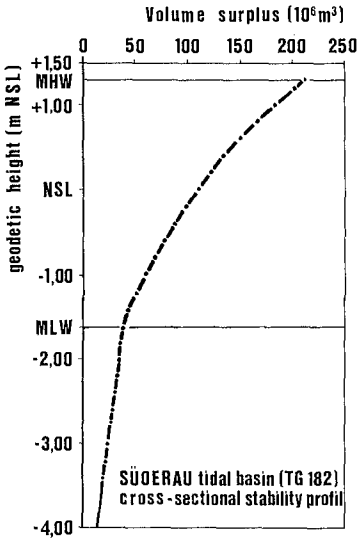

Fig. 11a: Stability profile of the Süderau tidal basin.

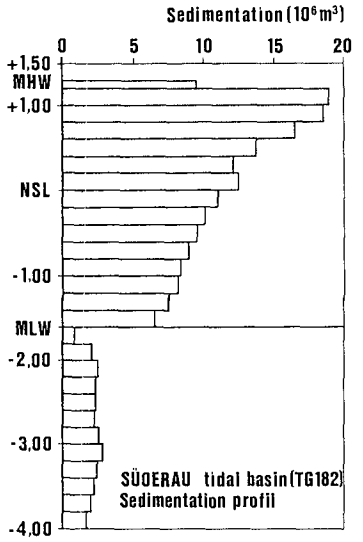

Fig. 11b: Sedimentation profile of the Süderau tidal basin.

flushing discharge from the Norderhever into the Süderau.

The sedimentation profile (Fig. 11b) shows the volume changes (sedimentation) to be expected per height interval. The sedimentation quantities per height interval are determined by simply taking differences from the stability profile summation curve. For sufficiently small height intervals, a functional curve for the sedimentation profile is obtained, which represents the derivative of the stability with respect to the geodetic height.

The stability criteria are also valid for parts of tidal basins. By means of appropriate incremental volume balances in a tidal basin from the coast towards the sea for different reference planes (e.g. MLW or MHW), longitudinal stability profiles are obtained. The latter provide a visual representation of the overall stability behaviour of the entire tidal basin. The longitudinal stability profiles of the Süderau for the reference planes MLW and MHW show that the tidal basin is not only in a state of non-equilibrium at its seaward boundary but also over the entire region, except for several unimportant cases of erosion in the immediate vicinity of the coast (see Fig. 12).

The amount of sedimentation to be expected in the Süderau may be visualized as a cube with a side length of approximately 6 km. It is not expected, however, that the amount of sedimentation predicted on the basis of the volume balances in the present state will actually occur. This will be the case as long as the tidally-induced flushing discharge from the Norderhever (see Fig. 10) continues to be effective. This flushing discharge has produced an artificial state of non-equilibrium which may only be removed when the flushing discharge is

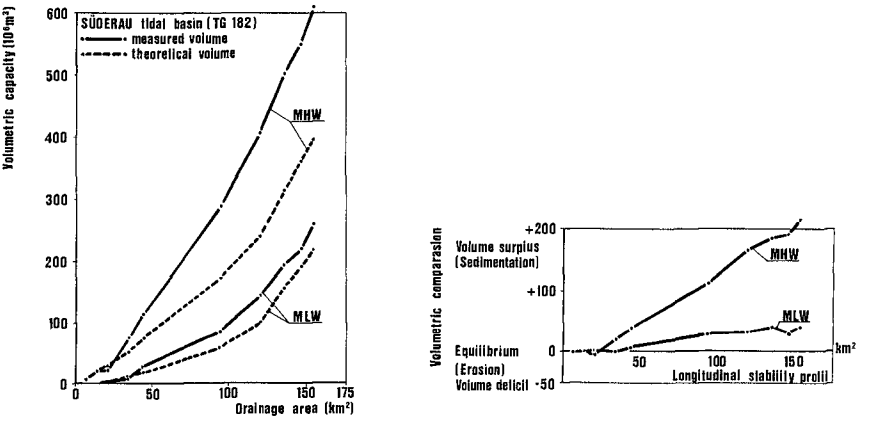

Fig. 12: Longitudinal stability profiles of the Süderau tidal basin.

prevented, as for example by means of an offshore dyke between the mainland and the Island of Pellworm (see Fig. 10). This dyke is being designed at present, and is expected to be constructed sometime after 1990.

5. Conclusion

The investigations described here show that it was possible to obtain a considerable improvement in the stability criteria so far known for tidal basins in the German Bight. This was done by taking into account the differences in the structure of the tidal basins with respect to varying tidal conditions and the separate evaluation of the creek and the flat section of the tidal basin.

The stability analysis for the Süderau tidal basin, that was undertaken as being representative of others, reveals not only the efficacy of the newly developed criteria and of the associated evaluation procedure, but also the possibility of applying it to tidal basins that have special boundary conditions as a result of particular hydrological and morphological developments.

6. References

/1/ RENGER, E.; PARTENSCKY, H.W.: Stability Criteria for Tidal Basins. Proc. 14th Intern. Conf. on Coastal Engineering, Vol II, pp. 1605-1618, Copenhagen (1974).

/2/ DIECKMANN, R.; PARTENSCKY, H.W.; SCHWARZE, H.: Morphological Reactions of Tidal Systems due to Nearshore Construction Works. Proc. 18th Intern. Conf. on Coastal Engineering, Vol. III, pp. 2495-2503, Cape Town (1982).

/3/ DIECKMANN, R.: Geomorphologie, Stabilitäts- und Langzeitverhalten von Watteinzugsgebieten der Deutschen Bucht. Thesis. Mitteilungen des FRANZIUS-INSTITUTS für Wasserbau und Küsteningenieurwewesen der Universität Hannover, Heft 60, (1985).

/4/ DIECKMANN, R.; PARTENSCKY, H.W.: Quantitative Geomorphology of Tidal Flat Areas. Proc. Iceland Coastal and River Symposium, pp. 53-62, Reykjavik, Iceland (1985).

/5/ HAYES, M.O.: Barrier Island Morphology as a Function of Tidal and Wave Regime. In LEATHERMAN, S.P. (Ed.): Barrier Islands, pp. 1-27, Academic Press. Inc. New York (1979).

/6/ HOWARD, A.D.: Geomorphological Systems - Equilibrium and Dynamics. American Journal of Science, Vol. 263 (1965).

/7/ LANGBEIN, W.B.; LEOPOLD, L.B.: Quasi-Equilibrium States in Channel Morphology. American Journal of Science, Vol. 262, (1964).

/8/ PARTENSCKY, H.W.: Neue Erkenntnisse über das Stabilitätsverhalten und den Sedimenttransport in Watt-Priel-Systemen. Mitteilungen des Franzius-Instituts für Wasserbau und Küsteningenieurwesen der Universität Hannover, Heft 50 (1980).

/9/ PARTENSCKY, H.W.; DIECKMANN, R.; OSTERTHUN, M.: A German Multipurpose Offshore Diking Project and its Effects on the Morphology and Ecology of the Adjacent Tidal Flats. Proceedings Coastal Zone 85, ASCE, New York (1985).

CHAPTER 81

DIRECTIONAL NEARSHORE WAVE PROPAGATION AND INDUCED CURRENTS

M.W. Dingemans,[1] M.J.F. Stive,[1] J. Bosma,[1]
H.J. de Vriend[1] and J.A. Vogel[2]

ABSTRACT

Recently, a depth and current refraction model has been developed for the computation of directionally spread, random wave propagation in coastal regions (Booij et al., 1985). For the verification of the performance of this model laboratory measurements in a directional, shallow water wave basin were conducted. Specific attention was given to the verification of the new features of the numerical model, viz. the effects of directional spreading and ambient current field on the wave propagation and transformation process, and the change of characteristic spectral wave frequency due to wave dissipation processes.

1.0 INTRODUCTION

Since the late seventies it has become a policy in the Netherlands to verify the performance of nearshore wave propagation models (see e.g. Dingemans et al., 1984). Recently, the Delft Technical University has devised a depth and current refraction model on a grid including directional characteristics, HISWA, see also Holthuijsen and Booij (1986) in these proceedings. In contrast to the now generally accepted parabolic refraction-diffraction models, for this model it was chosen to disregard the diffraction part in order to include directional spreading of the wave field. Moreover, also the change of characteristic wave period has been modelled. Because from the previous verification studies only scarce information on directional spread is available, a special laboratory experiment has been set up in a new wave basin, equiped to generate directional, shallow water waves (Mynett et al., 1984).

The primary purpose of this study is the verification of the wave heights and the wave periods, including the effect of directional spread on the wave characteristics. A geometry consisting of a semi-cylindrical bank on a horizontal bottom has been chosen, so that these effects may be studied.
In order to separate the two-dimensional effects around the tip of the bank, refraction and diffraction, from the one-dimensional effects due to shoaling and wave breaking, also the case of the fully cylindrical bar has been included. Moreover, to obtain information on the variability of the wave field in the basin, also the case of constant depth is considered.
Here a first, concise report is given of the verification of HISWA against the laboratory measurements. A full report will appear elsewhere.

1) Delft Hydraulics, Delft, the Netherlands
2) Rijkswaterstaat - DGW, den Haag, the Netherlands

2.0 MATHEMATICAL FORMULATION OF HISWA

It is well known that the evolution of random wave fields can be described by

$$\frac{\partial A}{\partial t} + \dot{x}_i \frac{\partial A}{\partial x_i} + \dot{k}_i \frac{\partial A}{\partial k_i} = S, \tag{1}$$

where $A(\vec{k},\vec{x},t)$ denotes the wave action density, $\dot{x}_i \equiv dx_i/dt = \partial\Omega/\partial k_i$ is the group velocity, v_i, and $\dot{k}_i \equiv dk_i/dt = -\partial\Omega/\partial x_i$ is the rate of change of wave number due to refraction. Notice that the summation convention has been used with i = 1,2. The dispersion relation is given as $\omega = \Omega(\vec{k},\vec{x},t)$. When the medium in which the waves propagate does not depend on time explicitly, one has $\omega = \Omega(\vec{k},\vec{x})$, which case is taken here; in that case Ω is a Hamiltonian for the vector field $(\dot{x}_i,\dot{k}_i)$. In the case of an ambient current field $\vec{U}(\vec{x})$ one has

$$\Omega = \omega_r + k_i U_i , \qquad \omega_r = [gk\cdot\tanh kh]^{\frac{1}{2}}, \qquad k = |\vec{k}| ,$$

where $h(\vec{x})$ is the waterdepth. Then one has $v_i = c_{gi} + U_i$ and $c_{gi} = \partial\omega_r/\partial x_i$. Transforming from (k,x) space to the space (x,ω,Θ), with Θ the wave direction, and introducing the absolute energy density $\tilde{E}$ by $\tilde{E} = A\omega$, one obtains for the transport of energy along the vector field defined by the Hamiltonian Ω,

$$\frac{\partial \tilde{E}}{\partial t} + \frac{\partial}{\partial x_i}[\tilde{E} v_i] - \frac{\partial}{\partial \Theta}\left[\tilde{E}\left\{(c_g - \frac{c}{2})\frac{1}{h}\frac{\partial h}{\partial n} + \cos\Theta \frac{\partial U_1}{\partial n} + \sin\Theta \frac{\partial U_2}{\partial n}\right\}\right] = \omega S, \tag{2}$$

where $c = \omega_r/k$ and n is the direction in space normal to Θ.
This equation for the absolute energy becomes, after assuming time-independency ($\partial\tilde{E}/\partial t \equiv 0$, and thus stationary wave fields) and integration over ω between 0 and ∞ :

$$\frac{\partial}{\partial x_i}[\omega^{(A)} \cdot A^{(o)} \cdot \bar{v}_i] + \frac{\partial}{\partial \Theta}[\omega^{(A)} \cdot A^{(o)} \cdot \bar{C}_\Theta] = S_1, \tag{3}$$

where the mean quantities $\omega^{(A)}$, $A^{(o)}$, $\bar{v}_i$ and $\bar{C}_\Theta$ are defined by

$$A^{(o)}(\vec{x},\Theta) = \int_o^\infty A(\vec{x},\omega,\Theta)d\omega , \qquad \omega^{(A)}(\vec{x},\Theta) = A_o^{-1} \int_o^\infty \omega A d\omega$$

$$E^{(o)} = \omega^{(A)} A^{(o)} , \qquad \bar{v}_i = (1/E^{(o)}) \int_o^\infty \tilde{E} v_i \, d\omega,$$

$$\bar{C}_\Theta = -(1/E^{(o)}) \int_o^\infty \tilde{E} \left(c_g - \frac{c}{2}\right)\frac{1}{h}\frac{\partial h}{\partial n} d\omega + \cos\Theta \frac{\partial U_1}{\partial n} + \sin\Theta \frac{\partial U_2}{\partial n} , \qquad S_1 = \int_o^\infty \omega S d\omega.$$

Using Leibniz' rule and rewriting the result, a second equation is obtained:

$$\frac{\partial}{\partial x_i}[A^{(o)} \bar{v}_i] + \frac{\partial}{\partial \Theta}(A^{(o)} \bar{C}_\Theta) = \frac{1}{\omega^{(A)}}\left[S_1 - A^{(o)} \bar{v}_i \frac{\partial \omega^{(A)}}{\partial x_i}\right]. \tag{4}$$

Equations (3) and (4) are the basic equations for HISWA. The source term S_1 is implemented as $(\omega^{(A)}/\sigma^{(A)})S^{(o)}$, where $S^{(o)}$ denotes the change of energy and $\bar{v}_i \partial\omega^{(A)}/\partial x_i$ is interpreted as the change of the frequency

$\omega(A)$ and is prescribed as a function S_ω of the local data. For the inclusion of source terms $S^{(o)}$ and the numerical solution technique is referred to Holthuijsen and Booij (1986).

3.0 EXPERIMENTS

Wave basin

In a wave basin of 26.40 m width and 34 m length a wave generator is available, consisting of 80 flaps which can be driven independently of each other, with a total length of 26.40 m, see Fig. 1. After considering several geometries by numerical investigation, a geometry consisting of a submerged, semi-cylindrical bar on an otherwise horizontal bottom has been chosen, see Fig 1. As a check and for comparison, measurements have also been performed for the case of a submerged, fully cylindrical bar (extending over the whole width of the basin) and for the horizontal bottom situation. The unperturbed water depth is 40 cm. Opposite to the wave generator a wave absorbing gravel beach was made, with a slope of 1:7 and with the waterline at 30 m from the wave board.

Input wave conditions

The input conditions are varied according to the properties of the two-dimensional spectrum $S(f,\theta)$:

- the width of $S(f,\theta)$ in f;
- the width of $S(f,\theta)$ in θ
- the wave height Hm0;
- the incident wave direction, θ_o.

We have :

$$S(f,\theta) = E(f).D(\theta;f),$$

where we took JONSWAP-type spectra E(f) and a $\cos^m(\theta)$-type directional distribution:

$$E(f) = A_o \tilde{S}(\nu) \quad , \quad \tilde{S}(\nu) = \nu^{-5} \exp\left[-\frac{5}{4}\nu^{-4}\right] \gamma(\nu)$$

$$\gamma(\nu) = \gamma_o \exp\left[-\frac{(\nu-1)^2}{2\sigma}\right] \quad , \quad \nu = f/fm,$$

$$A_o = \alpha_o g^2 (2\pi)^{-4} f_m^{-5}; \qquad \sigma = 0.07, \ \nu \leq 1; \qquad \sigma = 0.09, \ \nu > 1$$

and

$$D(\theta;f) = B_2 \cos^m(\theta-\theta_o); \quad -\frac{\pi}{2} \leq \theta-\theta_o \leq \frac{\pi}{2}$$

$$= 0 \quad ; \text{ elsewhere.} \qquad B_2 = \frac{1}{\sqrt{\pi}} \cdot \frac{\Gamma\left(\frac{1}{2}m+1\right)}{\Gamma\left(\frac{1}{2}m+\frac{1}{2}\right)} .$$

Here γ_0 is the peak-enhancement factor and m is the exponent of the $\cos^m\theta$ directional distribution.

The input wave conditions, selected in such a way, that some of them are also useful for testing other wave propagation models, are chosen to be

case	Hs [cm]	Tp [s]	γ_o	m	θ_o [deg]	current meas.
1	5	1.25	7	20	0	-
2	10	1.25	7	20	0	-
3	10	1.25	7	4	0	-
4	10	1.25	1	4	0	-
5	10	1.25	3.3	4	0	+
6	10	1.25	7	20	20	-
7	10	1.25	3.3	4	20	-
8	10	1.25	3.3		0	+

Table 3.1 Input conditions.

Measuring devices

The water surface elevation was measured with a resistance type, temperature corrected wave gauge. The relationship between the depth of immersion of the vertical conductor and the output voltage is approximately linear. The deviation from linearity is less than 1% (relative error).
In order to detect the wave directionality, Delft Hydraulics has developed a wave direction meter in which a wave gauge as described above is combined with point measurement of two orbital velocity components in the horizontal plane. The device is a button-type instrument containing two orthogonal electro-magnetic velocity meters (Fig. 2). The measurement range is from -50 to + 50 cm/s. The stability is approximately 1 cm/s, the noise is better than 1 cm/s and the linearity deviation is less than 1% (relative error). The direction of the two velocity components was +45° and -45° to the orthogonal line from the wave generator.

Measurements

At 26 sites, as depicted in Fig. 3, wave height measurements are taken. At seven of these sites directional information is obtained from measurements of the two horizontal velocity components. Because of the large amount of information, and the fact that only three directional measuring devices were available, two repetitions of each run with a diffe rent lay-out of the instruments were necessary. The instruments at sites 10 and 15 were kept in place so that the reproducibility of the experiments could be assessed.

Current measurements have been performed for the semi-cylindrical bank situation for the cases 5 and 8, at 81 measuring sites located in a square grid pattern at intervals of 3 m. Three wave direction meters have been used for this purpose, which had to be replaced 26 times so as to cover all positions. At all positions the velocities were measured at half water depth. For three positions the velocities were measured at five different levels so as to obtain some information concerning the vertical structure of the velocity field. Moreover, two wave gauges have been used, which remained at the same place during all tests. At the toe

of the wave damping talus the mean water level was measured at ten dif ferent positions by means of a narrow connection tube and gauge-glass.

All cases as given in Table 3.1 have been run for the three different bottom topographies, except the current measurements which have only been performed for the semi-cylindrical bank configuration.

The various measurements are denoted by mexy, where x = 1, 2, or 3 indi cates the geometry (empty basin, cylindrical bank and semi-cylindrical bank respectively) and y gives the measurement condition (1-8) as listed in Table 3.1.

As an example of resulting spectra for me35 the spectra E(f) at site 10, close to the wave board and site 28, behind the bar are shown in Figures 4 and 5, together with the target (JONSWAP) spectra, scaled with the spectral peak and the peak frequency. The principal part of the spectrum closely follows the shape of the target spectrum. It is noted, however, that behind the bar a considerable second harmonic spectral peak in E(f) is observed, due to wave breaking over the bar. The variance of this second harmonic peak in the spectrum has been analyzed for seven sites. To characterize this peak we calculated the variance above the frequency f = 1.4 Hz, m0d2. For the measurements me35, me25 and me15 the rate m0d2/m0 has been given in the next Table, and m0 is the total variance.

$$m0d2 = \int_{1.4}^{3.125} E(f)df, \quad m0 = \int_{0}^{3.125} E(f)df.$$

	site	semi-cyl. me35	cyl. me25	empty basin me15
in front of bank	19	20.8	19.9	18.5
	10	20.0	18.5	17.7
	18	21.2	20.8	20.5
on bank	38	21.2	20.8	20.5
behind bank	39	37.1	51.5	17.6
	29	43.1	52.1	18.3
	28	60.9	51.0	17.8

Table 4.1 Values m0d2/m0 in %.

Inspection of the tabulated results, especially for me15, indicates that the contribution of the second spectral part is approximately 20% in the target spectra, which remains unaffected as the wave field propagates over the horizontal bottom. In the nearly one-dimensional case of wave breaking over the cylindrical bank the second spectral part grows relative to the primary spectral part; the energy densities become approximately equal. In the case of wave breaking over the semi-cylindrical bank the growth of the second spectral part relative to the primary spectral part varies with its position relative to the bank. These results indicate that the concept of one characteristic mean frequency is doubtful in such situations.

5.0 VERIFICATIONS

Boundary conditions and computations

Computations have been performed for all cases in Table 3.1 for both the semi-cylindrical and cylindrical bank geometry. The boundary conditions used as input in the numerical model have been determined from the corresponding measurement series. For the wave height the height Hm0 at site 10 has been taken ($Hm0 = 4\sqrt{m_0}$) and for the wave period T the average wave period, T_{m-10}, has been taken, defined as

$$T_{m-10} = m_{-1}/m_0 , \qquad m_j = \int_0^\infty f^j E(f)\, df$$

The moments m_j have been determined from the measured spectrum.

As the computed wave height behind the bar depends critically on the wave breaking parameter γ, the value for γ has been determined according to the algorithm as given by Battjes and Stive (1985), using T_{m-10} for the wave period. The bottom friction coefficient fw has been set at 0.01, a reasonable standard value.

Because the sidewards boundaries in the mathematical model are dissipative, the wave field close to these boundaries is distorted. Following Dingemans et al. (1984) for the parabolic wave model, a region with an apex of 20 degrees is taken to be a possibly distorted area; this followed also from initial computations with an empty basin. The computational region is now taken to be 50 m wide, instead of 26.40 m, the actual width of the wave basin.

Method of comparison

A relatively large amount of data has been collected, especially since we are dealing with measurements on a grid. The measurement parameters are the wave height Hm0, the wave period T_{m-10}, the main wave direction teta and the directional spread σ_o. In addition to a graphical comparison between measurements and computations, a more objective measure of correspondence was sought. To that end the approach of Willmott (1981, 1984) was adopted, in which a set of statistical measures is used. For all parameters mentioned the following procedure was followed; as an example it is elaborated here for the wave height.

The wave height field as obtained from the measurements mexy is to be compared with that from the corresponding computations; this is done at 26 sites where the wave height is compared with the computed wave height H at that site. In fact, from the computations output is generated in a square of 50 by 50 cm with midpoint the site in question, where 25 wave heights are given (see Sketch 1 below). For the comparison the mean value over the middle 9 points is used; the standard deviations are also computed, but are so low that in fact the wave height at the site alone could equally well have been taken.

```
x  x  x  x  x
x  x  x  x  x
x  x  o  x  x        Sketch 1
x  x  x  x  x
x  x  x  x  x
```

A direct comparison of the HmO and the H values is given by means of a scatter plot, which gives visual information on the correspondence. The statistical parameters recommended by Willmott (1981, 1984) are defined in the following way.

Consider a set of observations $\{O_i\}$ and predictions $\{P_i\}$, i=1,...,n. Then the mean absolute error, mae, and the root mean square error, rmse, are given by, with $\langle\cdot\rangle$ denoting the averaging operator,

$$\text{mae} = \langle|P_i - O_i|\rangle \qquad \text{and} \qquad \text{rmse} = [\langle(P_i - O_i)^2\rangle]^{\frac{1}{2}}.$$

With an ordinary least square regression $\hat{P}_i = a + bO_i$ the systematic and unsystematic part of the rms error, rmses and rmseu, can than be obtained as

$$\text{rmses} = [\langle(\hat{P}_i - O_i)^2\rangle]^{\frac{1}{2}} \qquad \text{and} \qquad \text{rmseu} = [\langle(P_i - \hat{P}_i)^2\rangle]^{\frac{1}{2}}.$$

The potential variance, PE, is given by

$$\text{PE} = \sum_i [\,|P_i - \langle O_i\rangle| + |O_i - \langle O_i\rangle|\,]^2$$

and an index of agreement, d, is given as

$$d = 1 - \frac{n \cdot \text{rmse}^2}{\text{PE}}; \qquad 0 \leq d \leq 1.$$

For d = 1 one has perfect agreement and for d = 0 none at all.

The parameters $\langle O_i\rangle$, $\langle P_i\rangle$, $s(O_i)$, $s(P_i)$, a, b mae, rmse, rmses, rmseu and d form a complete set for comparison purposes. Other variables can be derived from this set, see Willmott (1981, 1984). The bias for instance, is given by $(\langle P_i\rangle - \langle O_i\rangle)/\langle O_i\rangle$. It has to be stressed that a single parameter is in most cases not suited for model validation. Notice that these parameters are not scaled, apart from d.

Due to space limitations in the following the attention is restricted to case 5, for the semi-cylindrical bank. This particular choice is motivated by the fact that the conditions of case 5 come close to situations observed in nature and this case is one of the two primary cases around which the parameters are varied (the other one is case 2).

Wave heights

For case 5 a number of numerical model computations was made. One of the initial computations, ve35b, has been performed with starting values H = 10.42 cm and T = 1.17 s and wave breaking parameter $\gamma = 0.84$. The value of the latter parameter is determined according to the algorithm of Battjes and Stive (1985), so that the model may be considered untuned. The resulting wave heights H at the 26 sites are compared with the corresponding measured HmO values. A scatter plot of these values is given in Figure 6. Notice that the computed wave height values lie mostly below the measured ones; the bias is approximately -7%.

As can be expected in case of the semi-cylindrical bank geometry, a considerable current field is generated by the waves, especially due to wave breaking on the bar. Because the mathematical model also gives the

driving forces (in fact the gradients of the radiation stress components) for subsequent use in current models, such a wave driven current computation has been carried out and the resulting current field has been used in a second computation, ve35bs, in order to account for effects of current refraction on the wave field. The current field of a closely related computation, ve35a, where γ = .80 instead of .84 in ve35b, has been given in Fig. 7 and the stream function is given in Fig. 8. The resulting scatter plot of the pairs of wave heights at the sites is shown in Fig. 9. It is clear upon comparison of Figures 6 and 9 that inclusion of wave driven currents gives a closer correspondence between computed and measured wave heights. The bias has been reduced from approximately -7% to approximately -2%.

Because the wave generated current field has also been measured for case 5 for the semi-cylindrical bank geometry in 81 points 3 m apart, see Fig. 10, the measured current field can also be used for the wave propagation computations. The result of such a computation, ve35s1, has been given in the scatter plot of Fig. 11.

The statistical parameters for the computations ve35b, ve35bs and ve35s1 are given in the Table 5.1 below. For comparison the results for the fully cylindrical bank, computation ve25 (H = 10.23 cm, T = 1.17 s, γ = 0.83), are also included; H_c denotes the computed wave heights.

		ve35b	ve35bs	ve35s1	ve25
<Hm0>	[cm]	8.79	8.79	8.79	6.97
<Hc>	[cm]	8.22	8.65	8.55	6.91
s(Hm0)	[cm]	1.76	1.76	1.76	2.52
s(Hc)	[cm]	2.01	1.76	1.79	2.52
a	[cm]	-1.14	0.48	-0.09	-0.03
b	-	1.06	0.93	0.98	1.00
mae	[cm]	0.72	0.53	0.36	0.22
rmse	[cm]	0.92	0.66	0.50	0.28
rmses	[cm]	0.59	0.19	0.24	0.06
rmseu	[cm]	0.71	0.63	0.43	0.27
d	-	0.94	0.96	0.98	1.00

Table 5.1 Statistical parameters for wave height, over 26 sites.

These figures show that the correspondence between computed and measured wave heights becomes better with increasing accuracy of the current field. Concentrating on the mae and rmse deviation measures a continuous reduction is seen to occur from left to right in the Table. Whereas the accuracy of the wave height prediction in case ve35b (no current refraction) is already satisfactory (bias -6.6% and rmse = 10.5%), a large part of these deviations is due to the neglect of the wave-induced current field.

Taking the measured current field into account in the wave propagation computation, one has bias = -2.8% and rmse = 5.7%; as scaling parameter the value <Hm0> has been used. Considering the systematic part of the rmse deviation, rmses, it is seen that tuning is possible for better correspondence because the contribution to the mean square error due to systematic deviations is still 24% of the total mean square error; in

the optimal case this value should approach zero. It is stressed that the parameter setting has not been tuned to the measurements, only the boundary condition for the wave height and the wave period have been taken from the values at site 10, situated close to the middle of the wave board. Furthermore one single wave height was taken along the boundary, whereas, in the measurements some variation was obtained, primarily due to current refraction. It is noted furthermore that the nearly one-dimensional case, ve25, gives indeed the best results.

Wave periods

In order to be able to compare the computed wave periods, T_c, with the measured ones, it is necessary to derive the wave periods T_{m-10} from the measured wave spectra. This is done only for the 7 sites on which also the wave direction is available. The statistical parameters then become:

		ve35b	ve35bs	ve35s1	ve25
$\langle T_{m-10} \rangle$	[s]	1.11	1.11	1.11	1.12
$\langle T_c \rangle$	[s]	1.07	1.05	1.05	0.95
$s(T_{m-10})$	[s]	0.08	0.08	0.08	0.06
$s(T_c)$	[s]	0.11	0.13	0.13	0.22
a	[s]	-0.31	-0.25	-0.45	-2.41
b	-	1.25	1.17	1.35	2.99
mae	[s]	0.05	0.07	0.07	0.19
rmse	[s]	0.07	0.10	0.10	0.24
rmses	[s]	0.04	0.06	0.07	0.20
rmseu	[s]	0.06	0.08	0.07	0.13
d	-	0.85	0.72	0.76	0.41

Table 5.2 Statistical parameters for wave period, over 7 sites.

Compared with the results of the wave heights, the prediction of the wave periods is not so good. In order to check the deviations more accurately point by point comparisons are made, of which the results are given in the next Table. Here δ is the relative error $\delta = (T_c - T_{m-10})/T_{m-10}$.

	ve35b			ve25		
site	T_c	T_{m-10}	δ %	T_c	T_{m-10}	δ %
19	1.169	1.148	1.8	1.182	1.164	1.55
10	1.169	1.170	-0.10	1.182	1.183	-0.05
18	1.169	1.164	0.42	1.182	1.160	1.94
38	1.021	1.168	-12.25	0.770	1.162	-33.74
39	1.093	1.092	0.12	0.771	1.075	-28.30
29	1.000	1.069	-6.47	0.771	1.054	-26.87
28	0.877	0.966	-9.18	0.772	1.061	-27.24

Table 5.3 Computed (T_c) and measured (T_{m-10}) wave periods at 7 sites.

As wave period changes are best checked with the fully cylindrical bank topography, the result of ve25 is more pertinent to this case than is the result of ve35b. In fact, the change in frequency can be better studied in a wave flume because directional spreading is not of importance

here (higly dissipative waves). It is seen that behind the bar the computed wave periods are about 30% too low. That the figures for ve35b are much better is due to the fact that, because of refraction, a considerable amount of "unbroken" waves reach the region behind the bar; this is especially true for the case ve35b, where no current refraction effects are included.

One should be aware of the simple adjustment of the wave periods, via some similarity approach, taking a very simplified spectral shape. It is clearly necessary to investigate the wave period adjustment further.

Wave directions

The measured values tetam are determined as follows. At each spectral frequency (of a total of 128) the wave direction θ is determined from the Fourier coefficients of the directional function by

$$\theta(f) = b_1(f)/a_1(f)$$

and the directional spread σ_o follows as

$$\sigma_o = \left[2\{1 - (a_1^2 + b_1^2)\}\right]^{\frac{1}{2}}.$$

The values θ_m follow from a simple average of the 10 values around the spectral peak frequency. The inaccuracy of θ_m is estimated to be up to about 4°, due to inaccuracy in the placing of the measuring device and the inaccuracy of the data.

site	me35 θ_m	ve35b θ_c	ve35bs θ_c	ve35s1 θ_c	me25 θ_m	ve25 θ_c
19	-5.6	0	-0.11	0.69	-4.14	0
10	1.34	0	-0.16	-0.06	2.47	0
18	-3.63	0	-0.16	0.15	-0.29	0.01
38	-13.88	-33.10	4.98	-13.18	-4.38	0.22
39	-3.37	-19.16	-4.73	-1.50	-7.54	0.22
29	-9.64	-22.74	0.01	-2.86	-6.35	-0.02
28	2.32	-21.00	-0.19	-7.54	1.06	-0.56

Table 5.4 Measured (θ_m) and computed (θ_c) wave directions.

The site 38 at the tip of the semi-cylindrical bank is the most sensitive one for checking the wave directions (in fact, the point was chosen because of this). It is seen from Table 5.4 that in this situation inclusion of current refraction is of utmost importance to a good prediction of wave directions. This can also be made clear visually from the Figures 12 and 13 where the vector plots of wave heights and directions are shown for the cases ve35a and ve35s1. Total refraction is much reduced when accounting for the wave driven current field. Especially the circulation cell near the head of the bar is important here. In the calculated current field as used in ve35bs this cell was apparently not calculated accurately enough, because the error in the calculated predominant wave direction remained about 20 degrees, but now in the opposite direction.

The values of the statistical parameters for the wave direction θ are:

	ve35b	ve35bs	ve35s1
$\langle\theta_m\rangle$	-4.6	-4.6	-4.6
$\langle\theta_c\rangle$	-13.7	-0.1	-3.5
$s(\theta_m)$	5.7	5.7	5.7
$s(\theta_c)$	13.6	2.8	5.1
a	-7.9	-1.3	-1.6
b	1.3	-0.3	0.4
rmse	14.0	8.5	5.4
rmses	9.2	8.2	3.4
rmseu	10.6	2.2	4.4
d	0.53	0.33	0.69

Table 5.5 Statistical parameters for wave directions.

It is seen from Tables 5.4 and 5.5 that value of the index of agreement d is quite low in all cases, as also follows from the linear regression coefficient b.

6.0 CONCLUSIONS

For wave height prediction the numerical model performs well: without taking the wave-generated current field into account the bias is -6.6% and the rms error is 10.5%. Taking the current field into account these values are -2.8% and 5.7% respectively. Notice that these values are obtained without any tuning of the model, i.e. the parameters are chosen beforehand according to known prescriptions, derived from other model investigations, where, moreover, a fixed frequency was chosen. Especially for the wave breaking parameter γ there are indications, also obtained from other models, that it should be chosen somewhat higher; this would result in a smaller negative, or positive, bias. As the figures are based on all 26 values, and values in front of the bank are of course much better, the accuracy is somewhat less than apparent from the given figures. Taking into account the 17 sites lying on and behind the bank, the result is bias = -7.8 versus -3.2% and rmse = 11.1 versus 5.1%.

For a good prediction of the principal wave direction the inclusion of the wave-generated current field is essential. The prediction of the wave period is less satisfactory, the decrease in T is too fast. The modelling of the change in frequency is too simple; a very schematized spectral shape is assumed and, moreover, the assumed similarity of spectral shapes is seen not to be valid in strong dissipation zones. The effect of wave breaking on the spectral shape is the loss of energy on the low frequency part and the generation of higher harmonics in the spectrum, see Figures 4 and 5. It can also happen that wave breaking is so strong that the wave energy in the original frequency band has totally disappeared and that only the higher harmonic peak in the spectrum remains; an example of this behaviour has been given in Figures 17 and 18 of Dingemans et al. (1984) for field measurements in the Haringvliet region, in the Rhine-Meuse estuary. It is necessary to model the transfer of energy to higher harmonics in the spectrum in order to be able to obtain a good prediction of characteristic wave period due to breaking of waves in shallow water.

The wave-induced current field prediction is quite good. Inclusion of such current fields has been shown to be necessary in some situation so as to obtain more accurate wave height predictions in shallow water regions. The modelling of wave and current fields, possible via an iterative computation procedure, needs further investigation. This may be important for coastal models with waves and tides, especially where the interaction between bottom changes and waves and currents is a very sensative process.

7.0 REFERENCES

Battjes, J.A. and **M.J.F. Stive**, (1985). Calibration and verification of a dissipation model for random breaking waves. J. Geophysical Res. 90 (C5), Sept. 1985 pp. 9159-9167.

Booij, N., L.H. Holthuijsen and **T.H. Herbers**, (1985). A numerical model for wave boundary conditions in port design. Int. Conf. on Numerical and Hydraulic Modelling of Ports and Harbours, Birmingham, England, April 1985, pp. 263-268.

Dingemans, M.W., M.J.F. Stive, A.J. Kuik, A.C. Radder and **N. Booij**, (1984). Field and laboratory verification of the wave propagation model CREDIZ. Proc. 19th Conf. on Coastal Engng, Houston, 1984 pp. 1178-1191.

Holthuijsen, L.H. and **N. Booij**, (1986). A grid model for shallow water waves. Proc. 20th Conf. on Coastal Engng., Taipei 1986.

Mynett, A.E., J. Bosma and **P. van Vliet**, (1984). Effects of directional seas in coastal regions. Symposium on Description and Modelling of Directional Seas, Paper B7, Lyngby, Denmark.

Willmott, C.J., (1981). On the validation of models. Physical Geography 2(2), 1981 pp. 219-232.

Willmott, C.J., (1984). On the evaluation of model performance in physical geography. In: Spatial statistics and models (Eds. G.L. Gaile and C.J. Willmott), pp. 443-460, Reidel 1984.

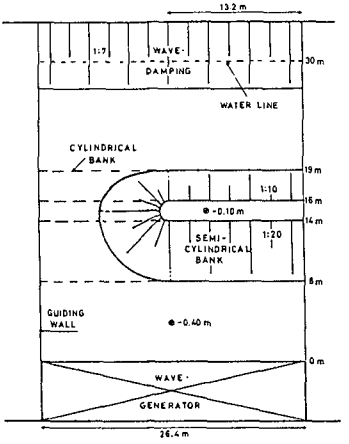

Fig. 1 Wave basin lay out

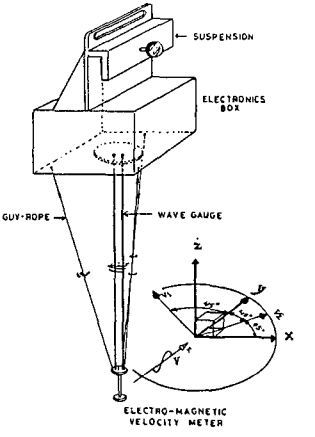

Fig. 2 Wave direction meter

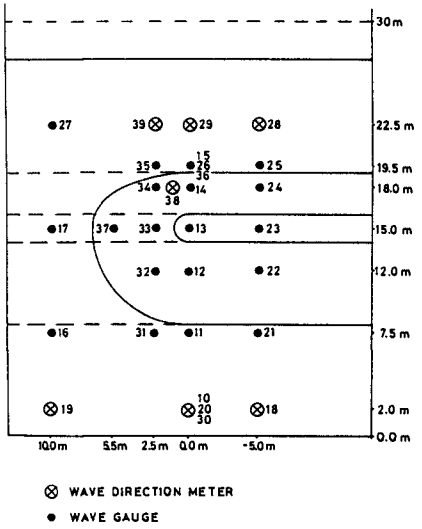

Fig. 3 Measuring positions

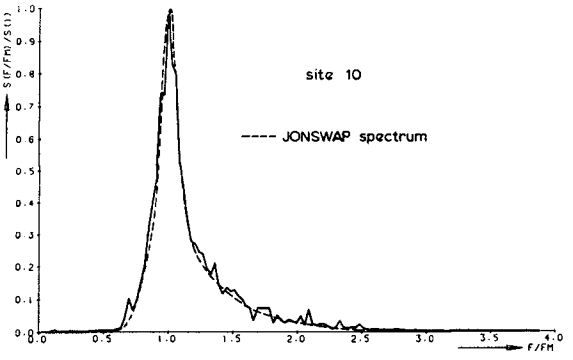

Fig. 4
Spectrum at site 10

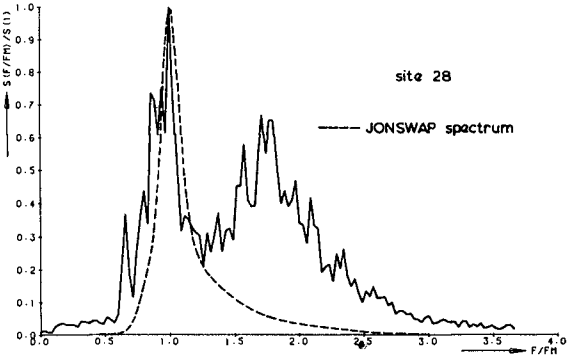

Fig. 5
Spectrum at site 28

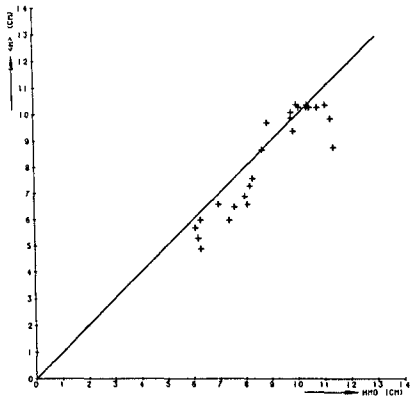

Fig. 6 Scatter plot wave heights, ve35b

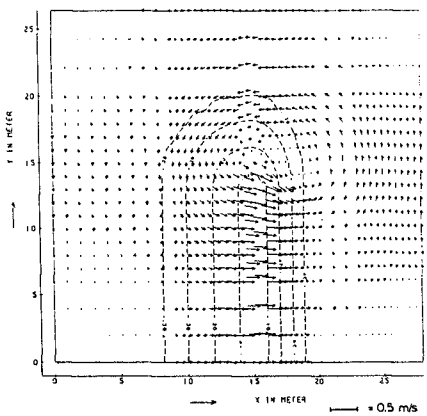

Fig. 7 Current vectors, ve35a

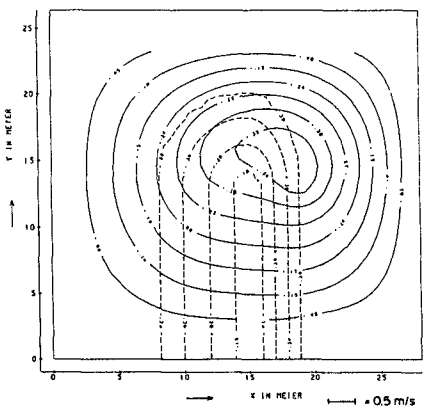

Fig. 8 Stream function, ve35a

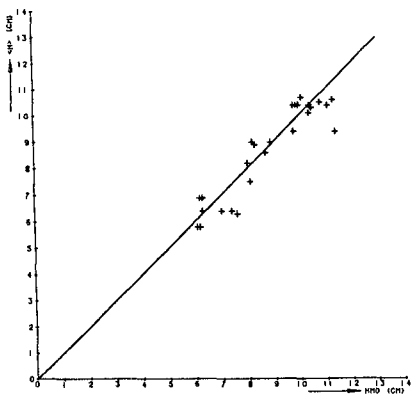

Fig. 9 Scatter plot wave heights, ve35bs

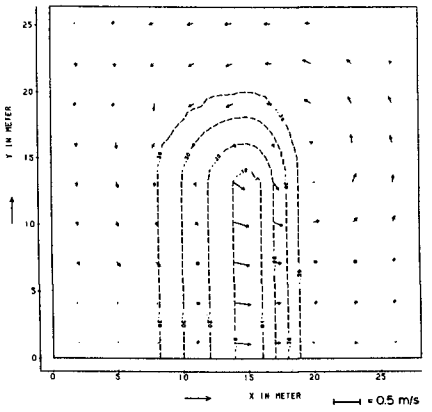

Fig. 10 Measured current vectors, me35

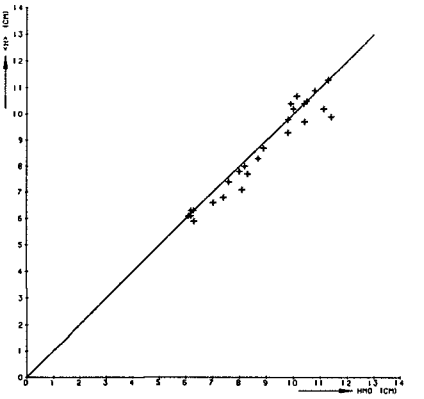

Fig. 11 Scatter plot wave heights, ve35s1

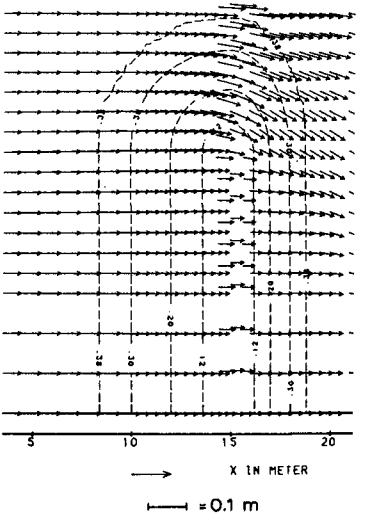

Fig. 12 Vector plot wave heights and directions, ve35a

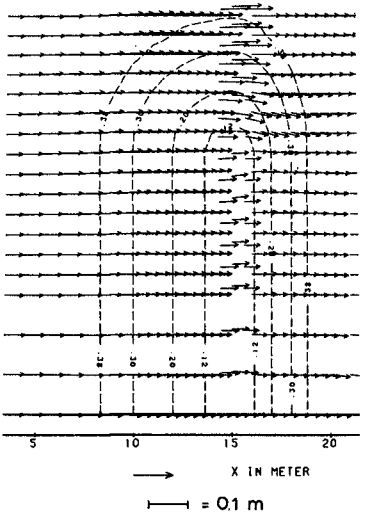

Fig. 13 Vector plot wave heights and directions, ve35s1

CHAPTER 82

FIELD MEASUREMENTS OF DUNE EROSION

J.S. FISHER, M. ASCE*
M.F. OVERTON, Asaoc. M ASCE**
T. CHISHOLM***

ABSTRACT

A series of field experiments was made to evsluate the use of s laboratory derived relationahip between the force in the wave uprush snd the erosion of besch dunes. Mesaurements of the awash velocity snd height st the dune face were used to compute a specific force parameter. This force term was correlated with the specific eroaion of the dune. A linear relationahip aimilsr to that found in the lsborstory waa determined with a R aquared vslue of .87.

INTRODUCTION

The prediction of dune retrest by storms is sn essentisl element of sny besch erosion model. Most of the current models uae some form of an equilibrium besch profile to determine the volume of sand eroded from the dune during s storm. These models have s common basis in the use of the Bruun Rule (Brunn 1954) which states that sa ses level riaes s besch will try to achieve the same profile it had previously. The profile will be ahifted upwards and towards the ahore using the material eroded from the beach to fill the required volume.

In terma of the application of this spproach to the dune, Edleman (1972) and Dean (1976) have both developed methoda which seem to give useful results for extreme events. In this caae the besch can be expected to resch an equilibrium profile. Vellings (1982) and Hughes and Chui (1981) have included phyaicsl model reaults in the application of this spprosch. More recently, Kriebel and Desn (1985) have improved the equilibrium profile model with the use of numericsl methods snd sdditional empirical analysis of storm eroded besches.

An slternstive method for the prediction of dune erosion waa proposed by Fisher and Overton (1984) where the erosion from each

*Prof. of Civil Engineering, North Carolins State University, Raleigh, North Carolina 27695-7908
**Assistant Prof. NCSU
***Grsduate Resesrch Assist., NCSU

individual swssh uprush is used to determine the dune erosion. The total storm erosion is a function of the frequency and intenaity of the awash. Thia spprosch does not require the development of s post-storm equilibrium profile.

Both approsches to the dune eroaion problem have merit. The equilibrium profile method is particularly will suited to long-term plsnning and the prediction of the erosion from extreme events. The wave swash spprosch enables one to estimste the impacts of smsller events for which the equilibrium profile may not be achieved. In order to develop a dune erosion model uaing the swaah characteriatica, it is necesssry to determine the relationahip between the swash and the dune scour. A seriea of laboratory and field experimenta as well as numericsl modeling have been used in this current research. Thia paper presents a portion of our results dealing with the results of the field studiea. Additionsl field resulta sre reported by Chisholm (1986). Young (1986) presents the initial laboratory reaults, and the numerical work is in Overton, Fisher and Fensish (1987).

BACKGROUND FOR FIELD EXPERIMENTS

The basic spprosch of this resesrch is that the total erosion of a dune during a storm can be viewed as the summation of the erosion from ths individual awash uprushes which impact the dune. The uprush is sssumed to behave as a bore characterized by its lesding edge velocity snd s characteristic height. When the bore reaches the toe of the dune, it scours sand and is reflected down the beach. The volume of sand eroded for each swash impact is probably s function of the swash hydraulics, the sediment size, dune geometry snd moisture content. The preaent laboratory reaesrch simplifies ths problem by only considering s single ssnd size snd a limited range of moisture contents.

In order to investigate the relstionship between the swash snd the dune scour, s series of laboratory experiments have been carried out, Young (1986). The experiments focused on the volume of sand eroded for individual bores in a 12 m flume. The bores were generated by releaaing water from a head tank with a quick opening gate. The water then traveled up sn inclined besch to the experimental dune. A number of different initisl head tank elevstions were used, thus generating different bore sizes st the dune.

The analysis of the results for 50 experiments with 10 different head tank levels yielded s linear relationship betwesn the force of the uprush at the dune snd the volume eroded. SVE is defined ss the specific volume eroded, cu m, snd SF is the specific forcs, N/m, exerted by the bore against the dune, defined by the mean of the product of the leading edge velocity squared and the msximum bore height while it is in contact with the dune. Figure 1 illustrstes the linear correlation between SVE snd SF for the laboratory tests. These data have s R squared vslue of .84.

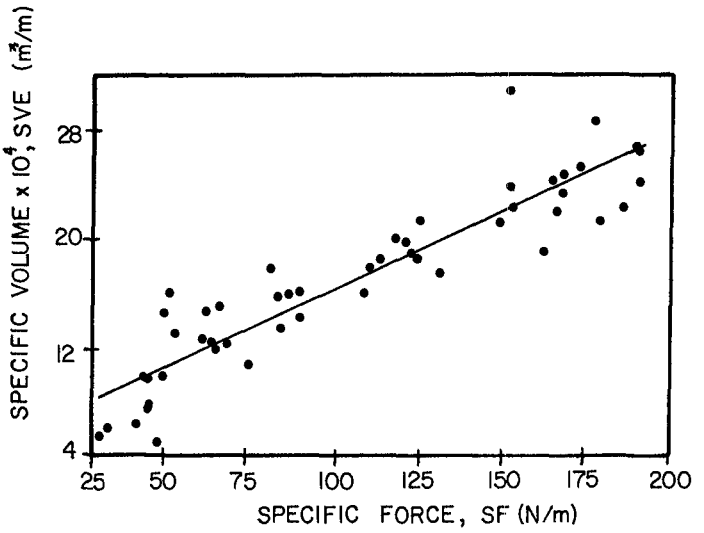

Figure 1. Linear correlation of apecific force and specific volume eroded for laboratory dune.

These results are for a limited number of laboratory experimenta. The dunes were all conatructed with the same size sand. Moiature content was not varied significantly, and the small scale meant that the force on the dune was relatively amall. A aeriea of field experiments waa therefore initiated in order to determine if thia or a similar relationahip could be found at scales more cloaely approximating prototype conditions.

DESCRIPTION OF FIELD EXPERIMENTS

The field experiments were made at the Field Reaearch Facility of the Army Corps of Engineera, Duck, North Carolina. The experiments consisted of the construction of a dune on the beach and the measurement of the rate of erosion by the wave swash as well as the hydraulic characteristics of this awash. Figure 2 is a schematic diagram of the field setup. A detailed description of the experiment is presented in Chisholm (1986).

The test dune is constructed at low tide with its toe at about the position of the mean tide level. No attempt is made to time the dune construction with extreme wave conditions. The experiment proceeds with whatever wave swash is present. The sand for the experimental dune is collected from the local dunes at the research pier. The dune is constructed between two vertical retaining walls. One side is made of a

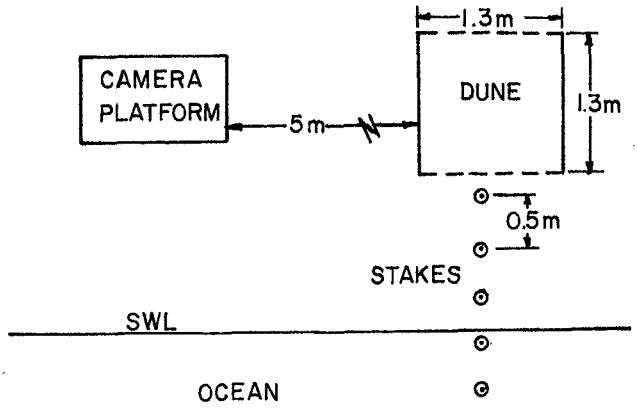

Figure 2. Schematic diagrsm of field aetup.

clesr plsstic (normsl to the shoreline) and the other of plywood. The former side has s grid on it, and both 35mm snd video pictures sre msde of the dune ss it erodes. The walls are 1.3 m spart, snd a typicsl dune is built to an elevstion of about 1 m. The dune is constructed in a series of diacrete stages. New sand ia plsced between the walls, compacted snd saturated by pouring water on it. This ia followed by the sddition of more sand, compaction and water. This process is continued until the desired elevstion is resched.

As the water level rises with the incoming tide the dune begins to be acoured snd eroded by the wave uprush. A video camera records both the changes in the dune (through the clesr plsstic wall) as well sa the swaah. Vertical stakes are placed in a line in front of the dune ss reference points for both the depth snd velocity of the swssh. These data sre also collected by the use of two capacitance wave gagea locsted along this same line in front of the dune. A still camers is used to photogrsph the dune profile sfter every msjor impact. These photographs are then used to calculste both the erosion for each uprush sa well ss the total eroaion for the entire experiment. Additional wave dsta including the significsnt period snd height sre collected ss part of the routine data collection progrsm by the Corps.

A typical experiment consists of the continuoua monitoring of the eroaion of the experimental dune during the time that the swaah reachea the dune, or until the dune is completely destroyed. The output from the capacitance gages is collected during the experiments on a portable computer with an analog to digital conversion system. The computer is powered by a generator, and is located in a truck on the beach. The data from these gages is used to to determine the height of the wave upruah juat prior to the time of impact with the dune. The actual velocity recorded is that of the leading edge of the bore. The volume of erosion for any single awash is determined from a comparison of the aequential still photographs. Theae pictures are digitized and volumes determined with a computer.

RESULTS

The results from four experiments during June 1986 are presented here. While other experiments were completed, these were the most succeasful in terms of the operation of the instrumentation and the construction of the dunea. Table 1 presents a summary of the conditions for each of theae four tests.

TABLE 1

WAVE DATA DURING DUNE EROSION TESTS

DATE	WAVE HEIGHT (M)	WAVE PERIOD (SEC)	TIDAL RANGE (M)
6/11	.33	14.2	.85
6/12	.41	10.6	1.05
6/25	.41	8.8	1.21
6/26	.58	7.2	1.01

The field data waa analyzed to see if a similar relationship exists between the specific force and eroaion for the field dunes. The data shown in Figure 3 for June 12 are typical for all of the tests. As with the laboratory analysis, the specific force is calculated as the product of the square of the leading edge velocity and the maximum bore height while it is in contact with the dune. Unlike the laboratory data, there is conaiderable scatter, and no significant correlation between the force and the erosion. There are several factors which may contribute to this poor correlation. The field data, including both the swaah heights and velocities, are very noisy. An additional factor haa

to do with the difference in the nature in the erosion of the field dune and the one built in the laboratory. In the field the dune continuea to erode with the rising tide. Unlike the laboratory dune, its face is not always vertical, but rather is highly irregular, continuing to change during the experiment. Thia irregular face meana that some uprush hit a vertical wall, othera a curved undercut surface, and still others a recently failed masa of sand. While data are not available to make definitive conclusions, it is probable that the same uprush will erode different volumea of dune sand depending on the nature of dune face.

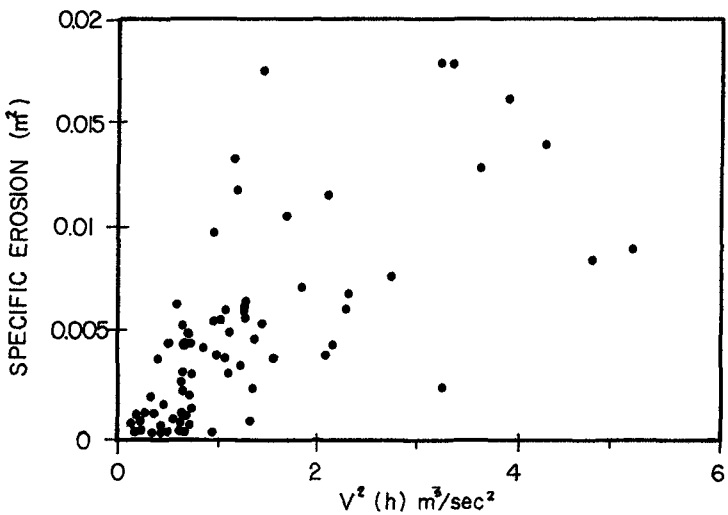

Figure 3. Specific erosion per individual swash force for June 12, 1986.

The scatter shown in Figure 3 was reduced by grouping the data according to intervala of force. Seven intervals were choaen: 0-0.5, 0.5-1, 1-1.5, 1.5-2, 2-3, 3-4, and greater than 4 N/M. For each interval, the average specific erosion was plotted against the average specific force. Figure 4 shows the linear correlation uaing theae intervals for the combined data for three experimenta, June 11, 12, and 26. (Due to a problem with the 35mm camera, the data for June 25 could not be analyzed on an individual swash baais.) There is an improved correlation (R squared equal to .75) between the specific erosion and

the specific force when these data are grouped by these intervals. The intervala obviously smooth out the scatter aaaociated with the individual surges and the irregular dune face. When viewed this way, the field data agree with the laboratory data in that there is a linear relationahip between the erosion and the force on the dune.

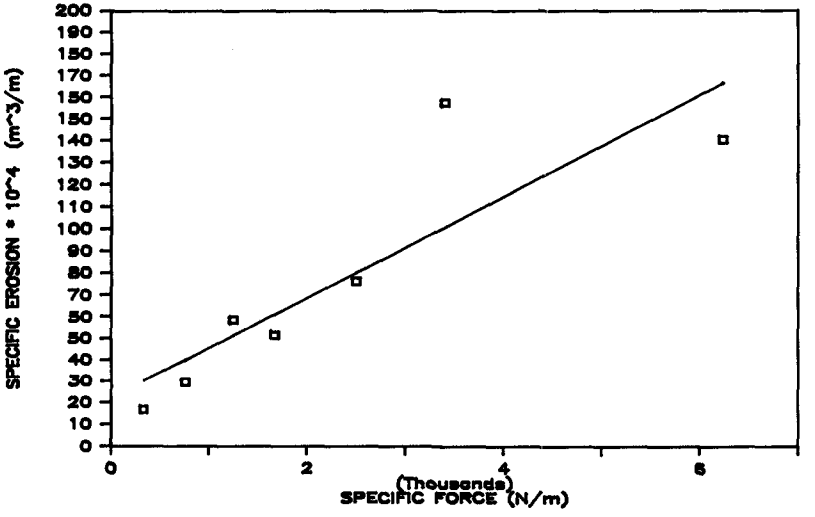

Figure 4. Specific eroaion va. specific force grouped by intervals, combination of June 11, 12, and 26.

From a practical point of view, the prediction of dune erosion based on individual swash bores is unreasonable. A method where the net dune erosion is determined from the cumulative effects of the swash would be more useful. Using the data from the four experimenta, one such method waa evaluated. The total specific erosion during the entire experiment waa plotted against the aummation of the individual specific force valuea, Figure 5. Only four data pairs are plotted, representing the four separate experiments. Aa with the data grouped by the force intervals, these data are also well correlated, R aquared equal to .87.

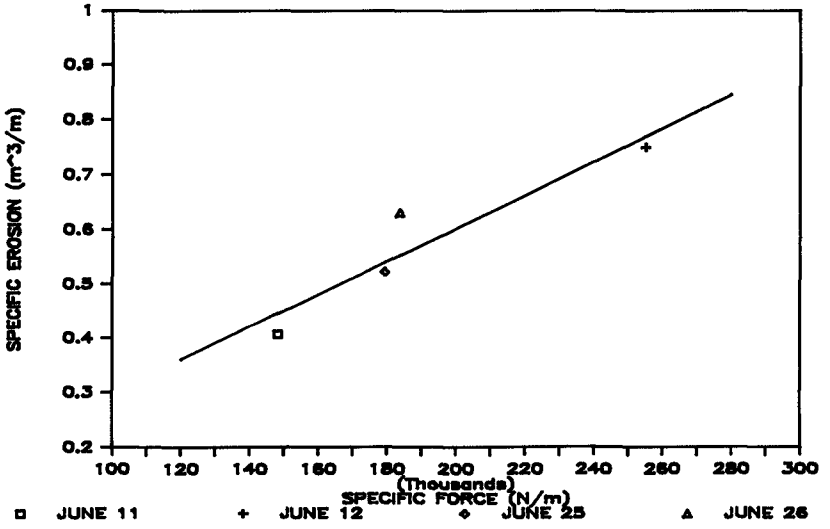

Figure 5. Total specific erosion va. summation of specific force for four experiments.

CONCLUSIONS

The primary objective of theae field experiments was to determine if the relationahip developed in the laboratory is valid for prototype scales. The resulta auggest that the general concept of relating the dune eroaion to the force of the upruah is reasonable. In particular, the good correlation (R aquared equal to .87) for the net dune erosion and the summation of the swash force on the dune provides reason to think that this approach may prove useful in the prediction of dune eroaion. Additional field test are needed for larger dunes and higher levels of awash force. Further resesrch is also needed in the mechanics of erosion, the role of moisture content, and root density from vegetation in the dune erosion process.

ACKNOWLEDGMENTS

This work was sponaored by the National Sea Grant Program, NOAA, U.S. Department of Commerce, under grant number NA85AA-D-SG022, and the North Carolina Department of Administration. Resulta are from Project R/CZS-21. The U.S. Government is authorized to produce and diatribute reprints for government purposes notwithstanding any copyrighta that may appear hereon.

APPENDIX I- REFERENCES

Brunn, Per, "Coast Erosion and the Development of Beach Profiles," Tech. Memo. No. 44, U.S. Army Corpa of Engineers, Beach Erosion Board, June 1954.

Chisholm, Tom, "Field Investigation of the Relationahip of Swash to Dune Erosion," MS Theaia, Department of Civil Engineering, North Carolina State Univeraity, 1986.

Dean, Robert G., "Beach Erosion: Causes, Proceases, and Remedial Measures," CRC Critical Reviews in Environmental Control, Vol. 6, Iasue 3, Sept. 1976.

Edlemen, T., "Dune Eroaion During Storm Conditions," Proceedinga of the 13th Conference on Coastal Engineering, 1972.

Fiaher, J.S., M.F. Overton, "Numerical Model for Dune Erosion Due to Wave Uprush," Proceedings of the 19th Conference on Coastal Engineering, 1984.

Hughea, S. and T. Chiu, "Beach and Dune Erosion During Severe Storms," UFL/COEL TR/043, Univeraity of Florida, 1981.

Kriebel, David, and R.G. Dean, "Numerical Simulation of Time-Dependent Beach and Dune Erosion," Coastal Engineering, Vol. 9, 1985.

Overton, M.F., J.S. Fisher and T. Fenaish, "Numerical Analysia of Swash Forces on Dunes," Coaatal Sediments 87, ASCE, 1987.

Vellinga, P., "Beach and Dune Erosion During Storm Surges," Coastal Engineering, Vol. 6, 1982.

Young, M.A., "Modeling of Storm-Induced Dune Erosion Due to Wave Uprush," MS Thesis, Department of Civil Engineering, North Carolina State Univeraity, 1986.

CHAPTER 83

Evaluation of Models of Nearshore Processes

C A Fleming*, B M Pinchin and R B Nairn**

Summary

The Canadian Coastal Sediment Study, known as C2S2, included numerous activities related to improving the measurement and prediction of sand transport in the nearshore zone. The data was used to evaluate a number of predictive techniques commonly used for coastal zone modelling for both alongshore and onshore/offshore sediment transport modelling. Field experiments were carried out at two sites. This paper is concerned with the first of these sites at Pointe Sapin, New Brunswick. Computed transport rates were compared with volumes of sand that accumulated in a sand trap formed by an offshore breakwater upstream of the mouth of Pointe Sapin harbour. The predictive techniques used were a parametric wave hindcasting model, a spectral wave refraction model, alongshore current predictors, seven of which rely on computed alongshore current distributions.

1 INTRODUCTION

The Canadian Coastal Sediment Study was a multi-departmentally sponsored research programme aimed at improving the knowledge of sand transport on beaches. The original objectives of the study were to develop instrumentation for measuring instantaneous rates of nearshore sand transport, to evaluate existing methods of measuring and predicting nearshore transport, to sponsor co-operative field studies and to encourage the development of new and improved nearshore transport predictors. The authors were contracted to carry out engineering predictions of waves, wave-generated currents and nearshore sediment transport of two sites: Pointe Sapin, New Brunswick and Pointe Deroche, Prince Edward Island. In addition they were contracted to compare these predictions to measurements made at Pointe Sapin between September and November 1983. This whole exercise implicitly involved the extensive application of numerical modelling of nearshore processes including wave hindcasting, wave induced currents and prediction of both alongshore and onshore/offshore sediment transport.

Pointe Sapin, New Brunswick is located at the northern entrance to the Northumberland Strait and that section of the coastline generally faces south-east. The site is exposed to waves generated in the Gulf of St Lawrence (See Figure 1) and is sheltered approximately from east to south by Prince Edward Island. Thus, the wave climate is dominated by waves approaching from the northeast quandrant. The beach at

* Director, Sir William Halcrow & Ptnrs Ltd, Burderop Park, Swindon, SN4 0QD, UK.
** Keith Philpott Consulting Ltd, Thornhill, Ontario, Canada

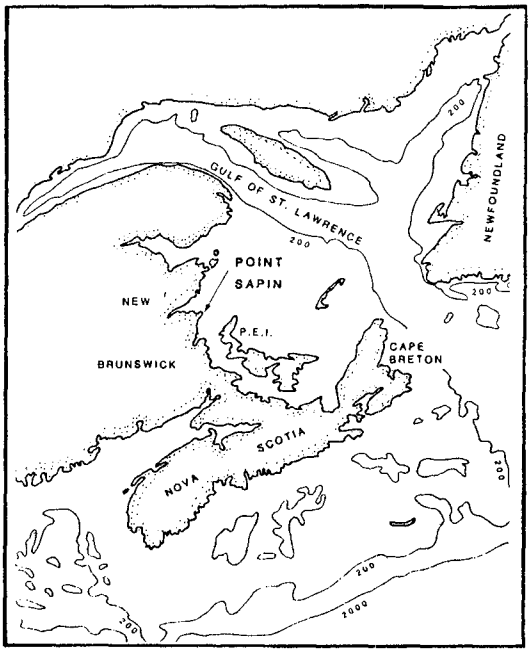

Figure 1: Location of Pointe Sapin

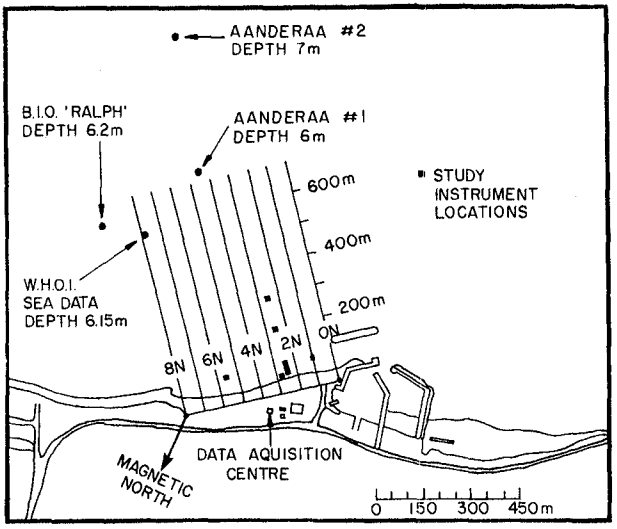

Figure 2: Survey Lines and Instrument Positions

Pointe Sapin is a wedge shaped body of sand between 2 and 3 metres thick on the backshore thinning to nothing between 60 and 75 metres offshore. Thus, the beach overlies a wide rock shelf which is composed of reddish-brown siltstone. The offshore bedrock is covered by a thin layer of gravelly sands. The sediments in the littoral zone are predominantly fine sand sized particles which are well sorted with a mean diameter between 0.18 and 0.25mm. Local deposits of pebbles do occur.

There is a small fishing harbour at Pointe Sapin which has suffered quite severe sedimentation problems in the past. As a result an offshore breakwater was constructed to act as a sand trap and this has been effective in significantly reducing the siltation problem. The offshore breakwater, the layout of which is shown in Figure 2, lies approximately 100 m off the main breakwater of the fishing harbour. It has been estimated that in an average year at least 60% of the littoral drift should be caught in the sand trap. The existence of the sand trap on the south side of the study site was one of the factors that led to the selection of this site. The mean tide range at the site is 0.9 metres and the tidal currents run reversing parallel to the coast with speeds generally less than 0.1 metre/sec.

2 FIELD MEASUREMENTS

The field programme at Pointe Sapin was carried out during the latter part of 1983. Many measurements were made, including offshore wave measurements 8.3km west of the site in 16.5m depth of water (Skafel, 1984), nearshore wave measurements (Aubrey and Spencer, 1984), nearshore current measurements and various sediment concentration devices all of which are summarised by Daniel, 1985.

In addition macro-scale experiments were carried out using a number of different types of bottom drifters as well as radioactive tracers. The sand trap was dredged clear immediately prior to the experiment and profile surveys of the sand trap area and adjacent beaches were carried out at regular intervals throughout the experiment period (Gillie, 1984 a).

3 PREDICTIVE TECHNIQUES

3.1 Wind Hindcasting

A parametric wave hindcasting model was used which included options to use four difference hindcasting models; SMB deep water, SMB shallow water, Derbyshire-Draper and JONSWAP. The wind data required is a time series of wind speed and direction, adjusted if necessary to a standard elevation above mean sea level. For each forward step of the hindcast an effective wave, defined by height, period and direction, is the resultant hindcast wave composed of a generated and a decayed wave train. The larger of the two components was treated as dominant in defining the wave period and direction.

The effective wave for each timestep was computed by examining the wind data and dominant wave conditions for a preceding duration time equal to the selected maximum wave generation sequence. Thus, by backstepping

through the data from the current record every combination of wind speed and duration is examined up to a limiting condition, in this case 2 days, or to a point where the wind direction differs from the average of the preceding sequence by an amount exceeding a defined wave divergence angle eg 22.5 or 45 degrees. The wave decay sequence was initiated either when a calm was encountered or when the wave divergence angle was exceeded. A number of wave decay functions were considered. (See Fleming et al, 1984)

3.2 Wave Transformations

The two principal components of the computational procedure are a wave refraction model and a post-processor that calculates the specteal transfer functions which in turn provide wave height coefficients and direction shifts from deep water to a shallow water point of interest.

The wave refraction model used was based on the highly efficient 'circular arc' technique allowing the high ray density backtracking for several frequencies from each point of interest to be carried out. The seabed was defined by ten digitized depth grids which varied in both overall dimensions and mesh size according to the water depth and proximity to the field investigation site.

The process of refracting a wave spectrum is based on the assumption that the wave energy flux in a frequency band will remain in that band as each component of the wave spectrum is transferred inshore. It is thus possible to discretise a deepwater directional wave spectrum and independently transfer it inshore applying appropriate shoaling coefficients. In this case the JONSWAP model was used. Its applicability to this site was verified by matching computed spectra with offshore spectra measured in 1982 (Fleming et al, 1984).

The direct application of this procedure to the offshore wave measurements led to a substantial over-estimation of inshore wave heights during one of the storms. This led to an investigation into energy dissipation mechanisms and as a result wave spectrum saturation for shallow water were incorporated into the wave spectrum transformation procedure. The shallow water equilibrium spectrum theories used were due to Kitaigorodskii et al, 1975 and Bouws et al, 1981. Comparative results are presented in Section 4.

3.3 Nearshore Sediment Transport

The inshore wave climate defined by the above procedure allowed calculation of alongshore sediment transport rates for the same breaker line, surf zone geometry and hence, alongshore current distribution for up to ten sediment transport models.

A complete description of the theories underlying the models used in these studies has been given (Fleming et al, 1984). This was based on an earlier publication (Fleming and Swart, 1982) in which the theory proposed by Longuet-Higgins was adapted to allow for contribution to the shear term by the longshore current itself and to rationalise the variation of friction coefficient as a function of beach slope and both wave and current friction factors. A similar treatment was carried out

based on Battjes (1974) theoretical approach. This is comparable to Longuet-Higgins approach for regular waves, but considers linear random waves together with the same momentum balance equation.

The friction factor for alongshore currents has been based on roughness length and it is this parameter that is most open to debate. In the absence of bed forms there are a number of different estimates for grain roughness and the one considered in this study has been proposed by Kamphuis (1975) as 2D90 (2D90 refers to the grain size for which 90% of the sediment distribution by weight is smaller). In the presence of ripples the roughness length may simply be taken as some multiple of the ripple height or the expression proposed by Swart (1976a) which includes both the ripple height and the ripple steepness. Whilst this formulation has relatively little data to confirm its validity it seems to have gained quite wide acceptance for lack of any more substantiated work. However, having adopted that expression the problem then shifts to applying a ripple height and length predictor.

Three different ripple models have been considered in this study. They are due to Mogridge and Kamphuis (1972), Swart (1976a) and Nielsen (1978). All three models may be used to determine both ripple height and ripple length as a function of local water depths, wave height, wave period, sediment size and relative density of the material. The formulations are essentially empirical and primarily based on physical models together with some limited field data.

The computational procedures were as follows:

i) The beach profile was divided into a number of representative sections of variable size.

ii) The inshore wave conditions were used to find the breaker position and corresponding properties. These were used in the bulk predictors.

iii) The mean wave height was calculated according to a Rayleigh probability function. The mean wave height was found by integrating the distribution truncated by the maximum possible wave.

iv) Wave and sediment characteristics were used to calculate ripple dimensions. This in turn provided data for the hydraulic bed roughness to be evaluated.

v) The wave and current parameters were used to calculate the alongshore current distribution across the profile.

vi) Wave properties, currents and the various coefficients calculated were used to determine bed shear stresses which in turn are used to drive some of the detailed prediction models.

vii) Each wave condition was taken in turn and running totals of gross and net transport and relative distribution kept as a running total.

Both bulk energy sediment transport predictors as well as detailed predictors were applied as outlined in Table 1.

	MODEL	GENERAL CLASSIFICATION
1	CERC Formula (1977)	Bulk energy model
2	Davies and Kamphius (1985)	Bulk energy model, includes grain size and beach slope
3	Sayao et al (1985)	" " " " " " " "
4	Engelund and Hansen adaptation by Swart (1976)	Based on bed and suspended loan concentrations with a background current, no incipient motion criterion
5	Willis (1978)	Adaptation of Ackers and White (1973), includes an incipient motion criterion
6	van der Graaf and van Overeem (1979)	Adaptation of Ackers and White (1973), includes an incipient motion criterion
7	Nielsen (1979) (for breaking waves)	Based on bed and suspended load concentrations with a background current, includes an incipient motion criterion
8	Nielsen (1979) (for non-breaking waves)	Ditto
9	Fleming (1977)	Ditto
10	Swart (Fleming & Swart, 1982)	Adaptation of Ackers and White (1973), includes an incipient motion criterion derived from a wide range of wave and current conditions

Table 1: General Description of Alongshore Sediment Transport Predictors

4 COMPARISONS OF MEASUREMENTS WITH PREDICTIONS

4.1 Offshore Waves

Figure 3 shows three sets of hindcast and measure wave heights and periods between the 21st and 31st October 1983 for one of the storms that occurred during the experimental period. Set (A) used the SMB deep water parametric hindcast model. It is seen that the hindcast wave heights were in reasonably good agreement with the measurement with the exception of the peak of the storm when the predictions grossly exceeded measurements. The hindcast wave periods were generally in good agreement with measurements throughout the period shown. Set (B) used the

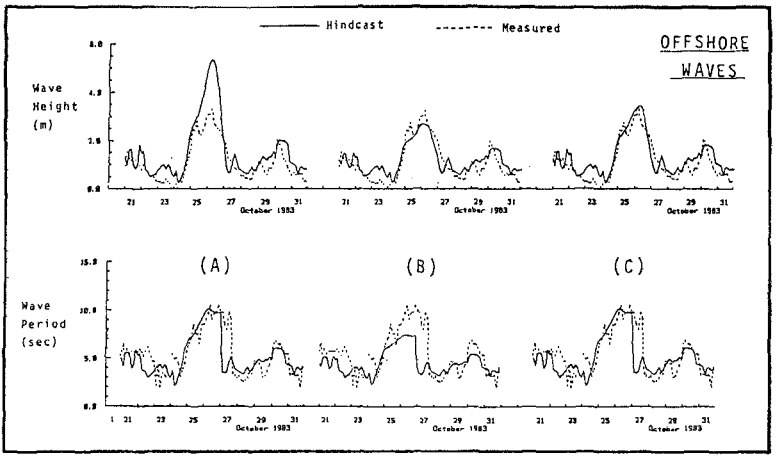

Figure 3: Hindcast and Measured Offshore Wave Data

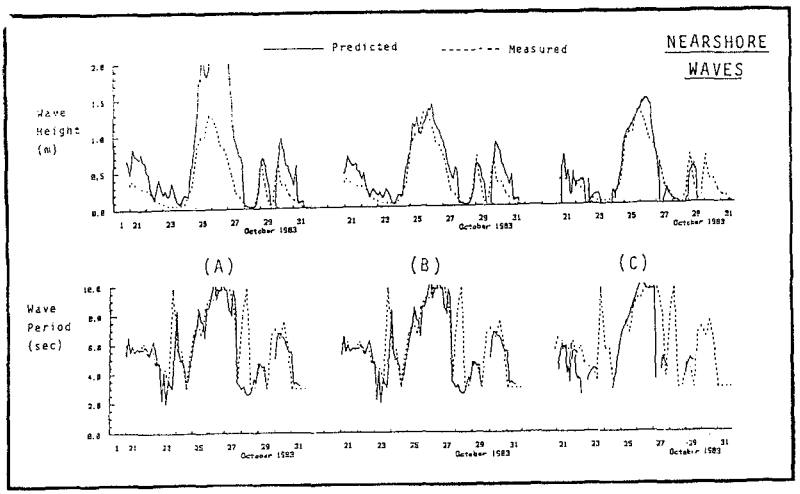

Figure 4: Hindcast and Measured Nearshore Wave Data

SMB shallow water parametric hindcast model. However, instead of using water depths characteristic of the entire fetch the water depth at the wave recording site (16m) has been used. it may be circumstantial, but the hindcast wave heights show much better agreement with measurements during the peak of the storm, but are little changed at other times. In contrast the hindcast wave periods became rather less than the measured particularly through the storm. At this point it might be noted that combination of SMB shallow for wave heights and SMB deep for wave periods would give a reasonably respectable result. The final set (C) was obtained by applying the SMB deep water hindcast model modified for spectral saturation which is a function of depth (Bouws et al, 1985). Here both the hindcast wave height and wave period show excellent agreement with measured values.

4.2 Nearshore Waves

The nearshore wave measurements were made in a little over 6 m mean water depth. Both deep water measured and hindcast wave sets were transferred to this shallow water site by applying the wave height coefficients and directions deduced from the spectral wave refraction model described in Section 3.2.

Figure 4 shows three sets of predicted and measured wave heights and periods between 21st and 31st October 1983 and can thus be compared directly with the previous figure. Set (A) represents the offshore measured waves transferred to shallow water by direct application of the spectral transfer results. It can be seen that the predicted wave heights were largely excessive by up to a factor of two for most of the record length, whilst the wave periods were in reasonably good agreement. Set (B) represents the offshore measured waves transferred to shallow water by application of spectral refraction results modified to include shallow water spectral saturation limits in each frequency band. Here it is seen that the predicted wave heights show excellent agreement with those measured. The wave periods remain largely un- changed and in good agreement with measured values. Set (C) represents the hindcast wave climate offshore which included saturation limits (ie Set (C) in Figure 3) transferred to the shallow water recording site by application of spectral refraction results modified to include shallow water spectral saturation limits as above. The agreement on wave height remains good but the wave period predictions appear to show a slight deterioration.

4.3 Alongshore Currents

The first storm during the experiment occurred between 24 October and 27 October 1983. Two of the current meter records were suitable, but not ideal, for testing purposes. The measured currents were on two

profiles (1.0N and 2.5N) both at a baseline offset of 86 m (see Figure 2). The points lie seawards of the point of maximum alongshore current velocity and there was no information with regard to distribution of current velocity across the profile.

Tests were carried out in a sequence that represents a progression from the simplest assumptions to those which incorporate all the relevant parameters. Only one example of the numerous test is given in Figure 5. In this case the match during the first half of the storm was quite good with the Battjes model. However, none of the model runs managed to predict the large currents at the two separate instruments during the latter part of the first storm. It seems apparent that currents measured after hour 50 were not wave induced and if it possible that this might be the case from as early as hour 25. Other types of currents might be wind-induced, tidal currents and large-scale ocean circulation.

While a quantitative assessment of the contribution of wind stress to longshore currents was not performed, an examination of wind velocities precluded this possibility. Tidal currents at Pointe Sapin are generally less then 0.1 m/sec (Gillie, 1985) and consequently could not have a significant influence on measured values. Large scale circulations were also ruled out as currents of a similar magnitude were not measured at the nearshore wave recorder site in 6 m of water. it was finally concluded that there was most likely some data logger error.

The second storm occurred between 4 and 7 November. In this case the results from two current meters on line 2.5 N at baseline offsets of 71 m and 86 m were compared to predicted results. The wave heights for this storm were rather less so that the measurements were even further down the tail of the cross shore distribution. An example of one of the predictions compared to measurement is shown in Figure 6.

4.4 Alongshore Sand Transport

The volume of sand transported during the two storms that occurred during the experimental period have been estimated by a number of investigators (Kooistra and Kamphuis, 1984, Morse, 1984 and Gillie, 1984) using both the profile surveys of the sand trap and adjacent beach as well as the radioactive sand tracer experiments. The estimate of net volume of sand transported during a particular event is dependent on whether only the sand trap itself is considered as the control volume or whether some part of the beach upstream of the sand trap should also be included. Considering the period of 22nd and 27th October estimated volumes vary from about 5000 cu m to nearly 11000 cu m. These figures do not account for efficiency of the sand trap. A reasonable estimate would increase the range to between 6500 m^3 to 13000 m^3 with an average magnitude of 10,000 m^3.

Less attention has been paid to the second storm which occurred betwen the 4th and 7th November 1983 and during which wave heights were not as large as for Storm 1. In this case estimates of volumes accumulated during the storm have varied between 2,000 m^3 (Gillie, 1984b), 2,600 m^3 $\pm$ 140 m^3 (Morse, 1984) and 3,100 m^3 (Kooistra and Kamphuis, 1984)

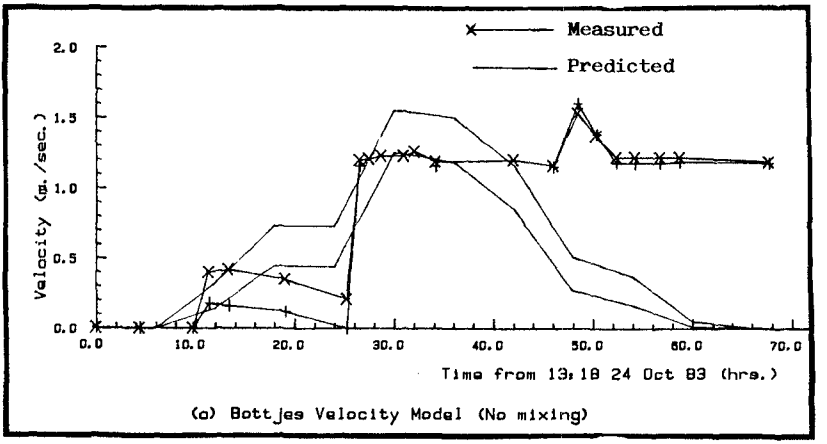

Figure 5: Predicted and Measured Alongshore Currents, Storm 1

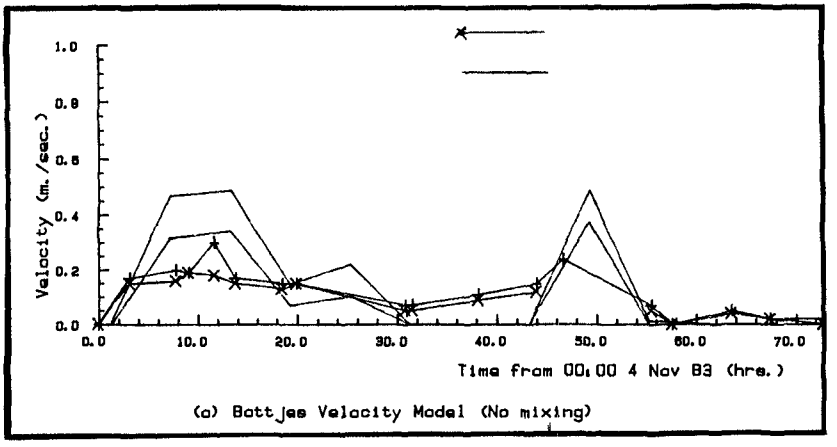

Figure 6: Predicted and Measured Alongshore Currents, Storm 2

A selection of the analyses that were carried out for each storm are given in Table 2. Many more variations and sensitivity tests and details can be found in the Pahse II report (Fleming et al, 1986). In the case of the second storm there were no deep water wave measurements.

Table 2: SELECTION OF ALONGSHORE SAND TRANSPORT PREDICTIONS

STORM 1 October 24 - October 27 1983

	1	2	3	4	5	6
CERC	149,600	63,400	32,610	49,720	27,480	27,480
Queens 1	111,700	31,620	17,630	24,100	24.740	27,740
Queens 2	9,470	26,700	15,100	20,700	21,560	21,560
Bijker	40,740	1,916	96	648	36	8,787
E & H	519,900	95,280	20,570	50,520	11,420	35,040
Willis	530,600	120,500	33,110	70,740	18,450	80,300
V de G et al	580,200	94,380	19,390	46,800	10,480	87,750
Neilson (br)	77,900	24,760	11,100	17,050	8,514	9,508
Neilson (N br)	65,380	18,110	6,609	11,580	4,335	9,589
Fleming	166,100	22,390	5,140	11,900	2,958	16,780
Swart	335,100	47,960	9,067	23,880	4,913	56.360

STORM 2 November 4 - November 7 1983

	1	3	5	6
CERC	6,972	3,749	19,690	19,690
Queens 1	3,162	1,806	15,270	15,560
Queens 2	3,628	2,053	13,500	10,390
Bijker	45	-	42	5,066
E & H	3,719	370	6,588	20,860
Willis	8,455	765	11,110	49,130
V de G et al	2,929	278	5,898	53,460
Neilson (br)	815	391	6,044	3,806
Neilson (N br)	623	132	2,886	5,765
Fleming	961	120	1,752	9,807
Swart	1,186	118	2,698	34,040

Note: All runs use Battjas type alongshore current velocity distribution, variable water level, variable slope and an average sediment grading. Wave climate and ripple models vary as follows:

1 Hindcast using deep water SMB model, refracted inshore without saturation limits, S/L ripple roughness.
2 Measured deep water waves, refracted inshore without saturation limits, S/L ripple roughness.
3 Hindcast using deep water SMB model, refracted inshore with saturation limits, S/L ripple roughness.
4 Measured deepwater waves, refracted inshore with saturation limits, S/L ripple roughness.
5 Measured inshore waves, Swart/Lenhoff ripple roughness.
6 Measured inshore wave, Neilsen ripple roughness.

4.4.1 Storm 1

Referring to Table 2, Run 1 used a hindcast deep water wave climate refracted inshore using standard spectral transfer techniques It has been shown that this will have overestimated the wave heights quite considerably and the estimated transport volumes were correspondingly excessive. Run 2 was similar but used the measured deep water wave climate and hence gave an improved estimate, but still in excess of measured volumes. Run 3 was similar to Run 1 except that spectral saturation was included in the wave transformation to shallow water. Here, the predicted volumes for two of the detailed predictors lie within the range of volumes estimated for measurements. Similarly Run 4 was similar to Run 1 and predicted volumes for three of the detailed predictors fall within the estimated range and in general values for all models were closest.

Run 5 used the measured inshore wave records and generally gave lower predictions than Run 4 due to slightly lower wave heights. All of these runs used the ripple predictor adopted by Swart (1976a). Run 6 is similar to Run 5 except that the Neilsen ripple predictor has been used. Three of the detailed predictors gave reasonable results but others gave quite large over estimates.

Assimilating all of the results from the Storm 1 tests there are a number of observations that can be made:

(i) The Battjes longshore current velocity model used in conjunction with the Fleming and Swart (1982) friction factor gave consistent results.

(ii) For the bulk predictors tested the Queen's 2 predictor gave the closest net volumes transported to those measured in the field in all cases tested but the estimates in these investigations were higher than those made by Kooistra and Kamphuis (1984) for the Queen's 1 model.

(iii) The Nielsen (breaking wave) sediment transport model was the most stable of all of the detailed predictors tested and gave results very close to the measured volume even when the input parameters are varied quite widely.

(iv) The use of different ripple models in conjunction with the Fleming and Swart (1982) friction factor formulation is not strictly valid and will result in higher current velocities for grain roughness or the Nielsen ripple model.

(v) The need to accurately define the nearshore wave climate cannot be over-emphasised, the sensitivity of all predictors having been clearly demonstrated. In the absence of nearshore wave measurements a good wave transformation model is clearly required. In the absence of offshore wave measurements the quality of the result obviously rests almost entirely on the quality of the offshore wave hindcast.

4.4.2 Storm 2

Again referring to Table 2, Run 1,3,5 and 6 were for identical combinations of input parameters as previously described for Storm 1. In this case the inclusion of spectral saturation in the wave transformation to shallow water resulted in an under-estimate of transported volumes for all except the bulk predictors. The 'best' results for the detailed predictors was given for Runs 5 and 6 which correspond to the measured nearshore wave data with different ripple models. However, the bulk predictors gave excessive values for these combinations.

The overall observations relating to Storm 2 results are:

(i) The offshore wave hindcast for Storm 2 did not predict the magnitude and duraction of the waves very well. Consequently both sets of predictions made on this basis significantly underestimate the net volume of sand transported for many of the detailed predictors.

(ii) The bulk predictors overestimated the net transport voumes for all combinations of variables tested except the offshore wave hindcast cases which were known to underestimate the wave conditions. The Queen's 2 predictor gave marginally better results than Queen's 1.

(iii) The results for the detailed predictors are generally much closer to the measured field volumes.

(iv) The Nielsen (breaking wave) model was again the most stable of the detailed predictors under all conditions tested and gave predictions close to measured when nearshore measured wave data is used.

(v) The importance of accurately defining the nearshore wave climate was once again clearly demonstrated.

5 CONCLUSIONS

Wave hindcasts for the offshore measurement site showed that shallow water effects in 16m of water were relatively large. The accuracy of the prediction could apparently be improved significantly by introducing depth dependent energy saturation principles into the hindcast models. Computation of nearshore wave heights and directions on the basis of two dimensional spectral refraction techniques did not provide good estimates for the larger of two storm sequences measured. Again the inclusions of depth-dependent energy saturation modifications to the transformation process improved the predictions considerably. This is not a new application in this context (see for example Resio, 1978). Application of the frequency saturation principles into the wave transformation process can most conveniently be incorporated into the spectral transformation method. As far as the frequency saturation limits are concerned there remain a number of issues that need to be resolved.

The use of the Longuet-Higgins formulation for the distribution of alongshore currents had no advantage or showed no distinctly better fit to the recorded data than the Battjes type model. In fact it suffers one positive disadvantage in that it requires the definition of a mixing coefficient for which there are no real guidelines as to what are appropriate values for different conditions. It may be anticipated that in the case of the existence of offshore bars or beaches with predominantly plunging breakers there will be problems in applying models derived for plane beaches.

It is also abvious that the roughness model used in the sediment transport predictors as well as the alongshore current friction factor empirical relationship plays a very central role in determining the level of shear forces acting on the bed.

Finally turning to the question of the performance of the sediment transport models themselves. Amongst the bulk predictors the Queen's formulations clearly performed better than the CERC formula. For the detailed predictors the Ackers and White derivations appear to be extremely sensitive to current velocities particularly when they exceed a threshold of about 1 m/s. The latest of these derivations reported in Swart and Fleming (1982) appeared to give results closest to the measured values. The Engelund and Hansen adaptation gave results that were quite comparable to the Ackers and White adaptations, but generally overpredicted transport rates, not surprisingly as it does not contain any threshold of movement criterion. Nevertheless it is extremely simple to apply. Results from the Fleming and Nielsen based models were comparable for many conditions, but the latter have proved to be by far the most stable in this application. It is therefore concluded that the Nielsen based models gave the best overall performance of all the detailed predictors tested. That was not without some anomalies related to varying grain sizes and wave heights which appeared to change the bed roughness in the opposite sense to the other models.

To summarise predictions of alongshore transport rates have been made using both bulk energy and detailed predictors which rely on computed alongshore current distributions. A number of comparative estimates have shown (i) the sensitivity of the detailed predictors to the friction factors used which are indirectly dependent upon the ripple roughness model, (ii) the magnitude of error that would have occurred from using an unverified deep water wave hidncast model, (iii) the magnitude of error that would have resulted in using an offshore wave climate transformed by consideration of refraction alone and (iv) a close comparison in results between measured and predicted rates when the improved method of estimating the nearshore wave climate is used. It should also be noted that the best prediction of net volume transported were largely within the range of volumes deduced from various field measurements. However, there is considerable scope for improvement of the sediment transport predictors.

ACKNOWLEOGEMENTS

We gratefully acknowledge the support of Bert Pade and Peter Daniel, C2S2 study managers; Dave Willis, National Research Council; Chris Glodowski, Public Works Canada and other

members of the ACROSES committee. The information gathered by the numerous investigators during the Study has been invaluable in providing the required data. It has been a privilege to have taken part in the C2S2 research programme.

REFERENCES

AUBREY, D G and SPENCER, W D, 1984. "Inner Shelf Sand Transport Wave Measurements Pointe-Sapin, New Brunswick, Canada". National Research Council Canada. Canadian Coastal Sediment Study Report No. C2S2-5.

BATTJES, J A, 1974. "Computation of Set-up, Longshore Currents, Run-Up and Overtopping Due to Wind-Generated Waves". Doctoral Thesis, Technische Hogeschool, Delft. 244pp.

BIJKER, E W, 1971. "Longshore Transport Computations". Journal of Waterways, Harbours and Coastal Engineering Division, ASCE. Vol 97, WW4, pp 687-701.

BOUWS, E, GUNTHER, H, ROSENTHAL, W, and VINCENT, C L, 1985. "Similarity of the Wind Wave Spectrum in Finite Depth Water". Journal of Geophysical Research, Vol 90, No C1, pp 975-986.

CERC, 1984. "Shore Protection Manual". Coastal Engineering Research Centre, US Army Corps of Engineers.

DANIEL, P E, 1985. "Data Summary Index 1983 Pointe Sapin, New Brunswick". National Research Council of Canada, Canadian Coastal Sediment Study Report No C2S2-16.

DAVIES, M H and KAMPHUIS J W, 1985. "Littoral Transport Rate". Proc. Canadian Coastal Conference, St John's pp 223-240.

FLEMING, C A, 1977. "The Development and Application of a Mathematical Sediment Transport Model". PhD Thesis, University of Reading.

FLEMING, C A, PHILPOTT, K L, and PINCHIN, B M, 1984. "Evaluation of Coastal Sediment Transport Techniques Phase I: Implementation of Alongshore Sediment Transport Models and Calibration of Wave Hindcasting Procedure". National Research Council of Canada, Canadian Coastal Sediment Study Report No C2S2-10.

FLEMING, C A, SWART, D H, 1982. "New Framework for Prediction of Longshore Currents". Proc. of the 18th Coastal Engineering Conference, pp. 1640-1658.

GILLIE, R D, 1985. "Evaluation of Field Techniques for Measurements of Longshore Transport". Proc of the Canadian Coastal Conference, St. John's. pp 89-103.

GILLIE, R D, 1984a. "Canadian Coastal Sediment Study Site Maintenance Contract". Report No C2S2-8, 109pp.

GILLIE, R D, 1984b. "Evaluation of Measurement Techniques", Canadian Coastal Sediment Study. Report No C2S2-9.

VAN DE GRAFF, J and van DVEREEM, J, 1979. "Evaluation of Sediment Transport Formulae in Coastal Engineering Practice", Coastal Engineering, Vol 3, pp 1-32.

KAMPHUIS, J W, 1975. "The Coastal Mobile Bed Model", Queen's University of Kingston, Civil Eng Report No 75, 113pp.

KITAIGORODSKII, S A, KRASITSKII, V P, and ZASLAVSKII, M M. "On Phillips Theory of Equilibrium Range in the Spectra of Wind-Generated Gravity Waves". Journal of Physical Oceanography, Vol 5, pp 410-420.

KODISTRA, J and KAMPHUIS, J W, 1984. "Scale Effects in Alongshore Sediment Transport Rates", Canadian Coastal Sediment Study. Report No C2S2-13.

MOGRIDGE, G R and KAMPHUIS, J W, 1972. "Experiments on Ripple Formation Under Wave Action". Proc of the 13th Coastal Engineering Conference, Vancouver. pp 1123-1142.

MORSE, B, 1984. "Volumetric Transport Rates at Pointe-Sapin NB, 1983.". Canadian Coastal Sediment Study. Report No C2S2-11.

NIELSEN, P, 1979. "Some Basic Concepts of Wave Sediment Transport". Institute of Hydrodynamics and Hydraulic Engineering Technical University of Denmark. Series Paper No 20.

RESIO, D T, 1978. "Estimation of Longshore Drift Rates from Numerical Models". Proc Coastal Zone 1978. ASCE pp 2289-2307.

SAYAO, O F S J, NAIRN R B and KAMPHUIS J W, 1985. "Dimensional Analysis of Littoral Transport". Proc Canadian Coastal Conference, St John's, pp 291-255.
SKAFEL, M G, 1984. "Offshore Wind and Wave Data CCIW Wave Direction Buoy". National Research Council of Canada. Canadian Coastal Sediment Study Report No C2S2-14.
SWART, O H, 1976a. "Coastal Sediment Transport: Computation of Longshore Transport". Delft Hydraulics Laboratory Report R968.
SWART, O H, 1976b. "Predictive Equations Regarding Coastal Transport". Proc of the 15th Coastal Engineering Conference, ASCE, Hawaii, pp 1113-1132.
SWART, O H and LENHOFF, L, 1980. "Wave Induced Incipient Motion of Bed Material". CSIR Research Report, NR10, Stellenbosch S Africa.

CHAPTER 84

VIRGINIA BEACH SAND SIZE AS BASIS FOR DESIGN OF ON-SHORE DREDGED MATERIAL DISPOSAL

Cyril Galvin*, M. ASCE, James W. Holton, Jr.**, M. ASCE, Ronald G. Vann***

ABSTRACT

Analyses of sand samples collected along and across the Atlantic Ocean shore of Virginia Beach, Virginia, suggest that sand placed on the shore should have a minimum median diameter of 0.20 mm to efficiently benefit the beach. Size analyses and shoreline change data show that the existing long-term beach replenishment by mechanical bypassing across Rudee Inlet and by truck-hauled sand from land sources is effective and necessary to maintain the shore along the commercial segment of Virginia Beach. The data also indicate that the northern segment of Virginia Beach shore, occupying more than half the distance between Rudee Inlet and Fort Story, is gaining sand. About two million cubic meters of sand to be dredged from the Atlantic Ocean Channel offshore of Virginia Beach will be suitable for placement on the beach.

INTRODUCTION

Background. Channel depths at the entrance to the Harbor of Hampton Roads, Virginia, are insufficient to accommodate modern, fully-laden colliers outbound from the harbor's large coal terminals at Norfolk and Newport News. Achieving sufficient depths will require dredging large volumes of sediment, including dredging the Atlantic Ocean Channel which extends southeasterly from the mouth of Chesapeake Bay (U.S. Army Corps of Engineers, 1985). Ordinarily, the most economical disposal of these dredged sediments is dumping at sea, but sand in the dredged material is a resource that might usefully be placed on nearby beaches of the City of Virginia Beach, Virginia.

At the time this work started, it was not known how much sand would be available from dredging the Atlantic Ocean Channel, and what characteristics were required to make its disposal on the beach a useful operation. The investigation under discussion differs from a typical beach fill project in that dredging will produce sand as a byproduct, and we determine if it would be beneficial to dispose of this sand on

* Principal Coastal Engineer, Box 623, Springfield, Virginia 22150.
** President, Waterway Surveys & Engineering, Ltd.
*** Chief, Dredging Management Branch, Norfolk District, U.S. Army Corps of Engineers.

the beach. The costs of such disposal are not treated here, but it is anticipated that the benefiting beach would bear the differential in cost (if any), compared to the cost of dumping at sea.

This particular investigation is the fourth of five similar investigations on the feasibility of disposing sand on beaches near two Hampton Roads entrance channels. These five investigations, performed under contract by Waterway Surveys & Engineering, Ltd (WS&E) with the Corps of Engineers, Norfolk District, include disposal from Thimble Shoal Channel on Fort Story beaches (WS&E, 1984a), on West Ocean View beaches (WS&E, 1984b), and on East Ocean View beaches (WS&E, 1984c), and disposal from Atlantic Ocean Channel on Virginia Beach (WS&E, 1986a), and on Sandbridge Beach (WS&E, 1986b). Previous technical reports on this study area include the beach profile study of Goldsmith, et al. (1977), four CERC papers by Harrison and associates all dated 1964, and engineering reports related to the Virginia Beach Erosion Commission work.

Purpose. This paper analyzes sand size along and across a ten-kilometer segment of the shore at Virginia Beach, Virginia. The analysis is used to understand how coastal processes affect the beach and, given this understanding, to judge whether sand to be dredged from the Atlantic Ocean Channel may be suitably placed there. The emphasis is on beach sand from Virginia Beach. Additional details on both the beach and Atlantic Ocean Channel sediments are in WS&E (1986a).

Location. The study beach is on the Atlantic coast of Virginia, south of the entrance to Chesapeake Bay (Figure 1). It extends from the south boundary of Fort Story, southward past the residential and commercial segments of Virginia Beach, across Rudee Inlet, to Croatan Beach (Figure 2). This shore trends about 10 degrees to 15 degrees west of north and is partially sheltered by the Virginia Barrier Islands to the north-northeast (Figure 1) and shoals at the Bay entrance. The effects of this shelter on the wave climate, along with the westerly trend of the shoreline, produce a net northward longshore transport at the study beach (opposite the regional southward trend of more exposed Atlantic sites). Mean annual breaker height is less than 0.6 meters and tide range is about 1.0 meters (Table 1). The Atlantic Ocean Channel is 6 to 12 kilometers offshore of the study beach (Figure 2).

Units. Metric units are used for distances, wave heights, and sand volumes (1 km = 0.6 miles; 1 meter = 3.3 feet; 1 cubic meter = 1.3 cubic yards). Since authorized project depths are given in feet, depths are identified first in feet, and then in meters. Two vertical datums are used: Mean Low Water (MLW) for channel depths and National Geodetic Vertical Datum (NGVD) for the beach and nearshore surveys. Sand sizes are given in millimeters (mm). The conversion from mm to phi units needed to design beach fills can be found in the Shore Protection Manual (U.S. Army Corps of Engineers, 1984). The Shore Protection Manual will be indicated hereafter as SPM.

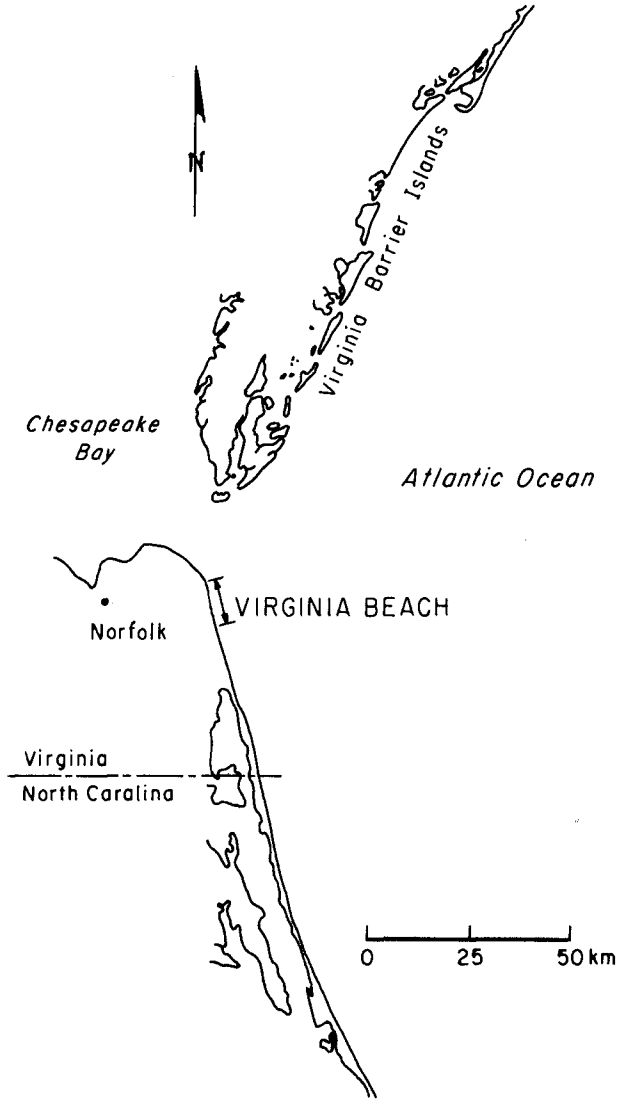

Figure 1. REGIONAL SETTING OF VIRGINIA BEACH STUDY AREA

Table 1. WAVE AND TIDE CHARACTERISTICS AT VIRGINIA BEACH*

Average Height	0.60 m	Mean Tide Range	1.0 m
Average Period	8.32 s	Spring Tide Range	1.2 m
Extreme Height (0.2%)	2.7 m	Tidal Currents (Flood)	0.26 m/s 350°
Extreme Period**	8 s	Tidal Currents (Ebb)	0.21 m/s 170°

* At 36°51'N, 75°58'W for waves (Thompson, 1977) and tide range (NOAA, 1985a); at 36°33', 75°52.1' for tidal currents (NOAA, 1985b)

** Extreme period is the wave period characteristic of the extreme height.

ATLANTIC OCEAN CHANNEL

Project depth in Norfolk Harbor Channel is -55 feet MLW (-16.8 m MLW), but due to sea conditions in the ocean, greater depths will be required in Atlantic Ocean Channel. The Corps of Engineers determined that, for the purpose of this investigation, it is assumed that the Atlantic Ocean Channel will be dredged to a depth of -62 feet MLW (-18.9 m MLW), including an allowance of 2 feet (0.6 m) for advance maintenance dredging. Channel width is taken as 305 meters.

For those design conditions, and the existing bathymetry, about 11.3 million cubic meters of sediment will be dredged from the Atlantic Ocean Channel (WS&E, 1986a).

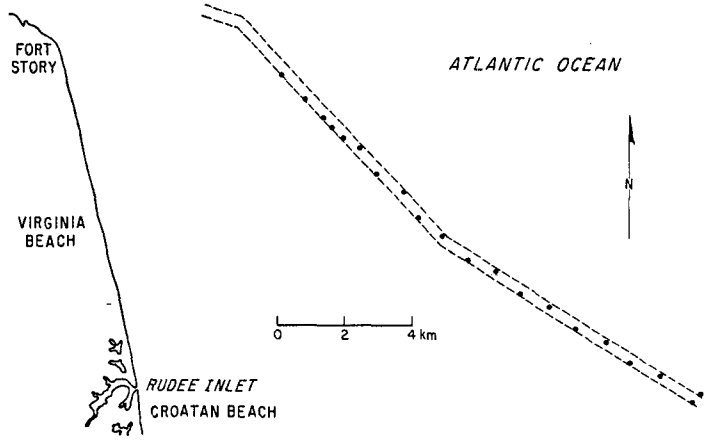

Figure 2. POSITION OF ATLANTIC OCEAN CHANNEL OFF VIRGINIA BEACH

To identify what types of material will be dredged, 21 cores were taken from the Atlantic Ocean Channel (Figure 2). Each core was logged and selected samples of the cores were sieved. These data were made available to WS&E for use in this investigation. Analysis of the logs indicates that about 54% of the material to be dredged is silty sand and sandy silt, 15% is sand and gravelly sand, 11% is a mixture of sand and silty sand, and the remainder is clay or other material.

Detailed examination of the logs and the sieve analyses indicates that about a third of the material to be dredged is sand with a median size of 0.20 mm or coarser, but at least a third of this 0.20 mm sand occurs in thin or isolated deposits that probably would not be economical to exploit, so that slightly less than 2 million cubic meters would be available for placement.

VIRGINIA BEACH

Because of the net northward longshore transport, the south end of the study beach is taken as the origin. The study beach begins at Croatan Beach, south of Rudee Inlet, even though the potential disposal area is north of Rudee Inlet (Figure 3), because Rudee Inlet interrupts northbound longshore transport. Inclusion of Croatan Beach permits an evaluation of the effect of that interruption on the reach needing the sand.

Rudee Inlet is a navigable inlet with a controlling depth of about -3 meters MLW under typical conditions. The inlet is bounded on the south by a jetty which serves as a breakwater and wier, providing shelter for a small hydraulic dredge to bypass sand coming over the wier section. A jet pump is also located north of the wier as a separate bypassing operation. The dredge and the jet pump are estimated cumulatively to bypass about 132,000 cubic meters per year (from Virginia Beach Erosion Commission, quoted in Langley McDonald, 1985). These estimates are based on hours of pumping time and an assumed concentration of sediment, rather than on direct measurement of the bypassed sand. The dredge does most of the bypassing.

North of Rudee Inlet is the highly developed 4-km commercial segment of the Virginia Beach shore where the beach is backed by a bulkhead or a seawall topped by a boardwalk. North of the boardwalk, the shore is backed by residential development and an increasingly broad strip of dunes.

The Virginia Beach shore has high value to the regional and state economy because of beach-related recreation. To maintain the beach, local and federal authorities have been replenishing the sand on a regular basis since 1951, at a long-term average rate from all sources of 190,000 cubic meters of sand per year. Sources include sand pits and stockpiles via truck hauls, and the littoral zone via dredging and the jet pump in Rudee Inlet. In the five years, 1981 through 1985, the average replenishment increased to about 260,000 cubic meters per year

(replenishment rates calculated from Langley McDonald, 1985). Placement by truck haul is usually done in the spring, and was done in April and May 1985, five months before the surveys and samples of this investigation. The dredge and jet pump operate intermittently all year.

The replenishment has had a marked effect on the condition of the beach, as can be seen by analyzing the shoreline change data of Everts, et al. (1983). Results of this analysis are shown in Figure 4 where the horizontal axis is distance north of Croatan Beach and the vertical axis represents accretion or erosion rates (erosion is negative). The long-term rate of change (1859-1980) is determined largely by conditions

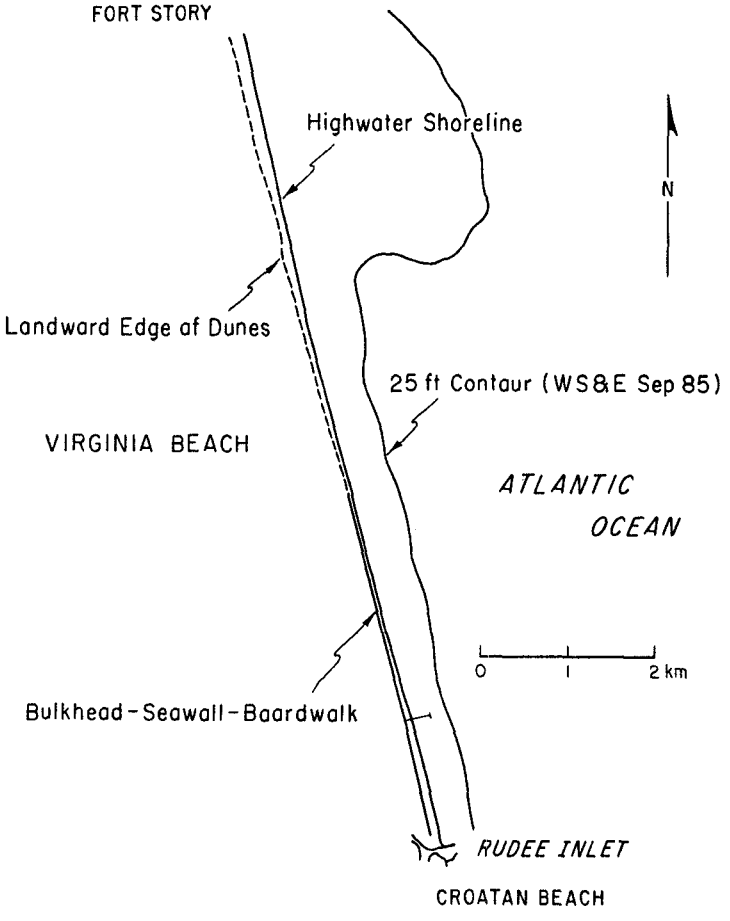

Figure 3. BOUNDARIES OF STUDY AREA

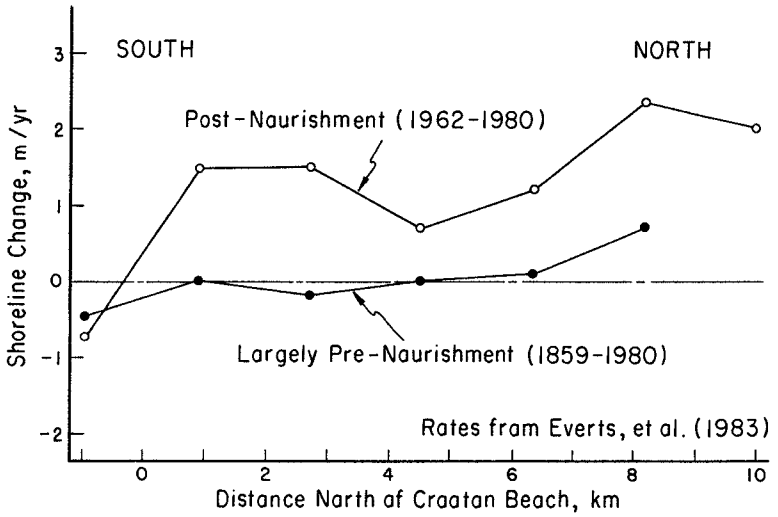

Figure 4. LONG-TERM RATES OF SHORELINE CHANGE

predating the beach replenishment, and the recent rate (1962-1980) is determined by conditions since the start of replenishment. The replenishment period clearly coincides with the onset of significant accretion (Figure 4).

The bathymetry offshore of Virginia Beach has a relatively normal slope from the shoreline to a depth of about -8 meters MLW (-25 feet MLW, Figure 3). At and seaward of this depth, the slope becomes unusually flat, typically 1 in 2000 for distances of at least 3 km. At the north end of the study area, there is a wide shoal (Figure 3) marked by the 25-foot depth contour. The origin of this shoal is probably related to the northward net longshore transport at Virginia Beach interacting with the tidal regime at the entrance to Chesapeake Bay. Whatever its origin, the shoal tends to shelter the study area from the full extreme of the Atlantic Ocean wave climate. This shoal may be responsible for the higher rates of accretion to the north of the study area in Figure 4.

The dimensions of the beach and the nearshore bathymetry are summarized on Figure 5, which is derived from surveys of profile lines performed by WS&E in late September and early October 1985. The horizontal axes of the figure indicates the relative south-to-north position of the surveyed profile lines, with tick marks indicating the even-numbered profile lines. The vertical axis of Figure 5 varies with the symbol, as discussed below.

Backshore width is indicated by open triangles on Figure 5, with each tick mark on the vertical axis equal to 50 feet (15.3 m). As

shown, backshore is widest at the north and south ends of the study area, but is absent over much of the central and southern half of the shore, in agreement with the history of erosion there.

Berm elevation is indicated by the filled triangles, with each tick mark equal to 5 feet (1.5 m) elevation above NGVD datum. The majority of the surveyed berms are at an elevation of about 2.0 to 2.2 meters (NGVD), with a tendency to be somewhat lower in the south and higher in the north.

Foreshore slope is indicated by open squares, with each tick mark on the vertical axis equal to 0.05. The range in slope is from about 0.05 in the south to between 0.10 and 0.18 in the northern half of the study area.

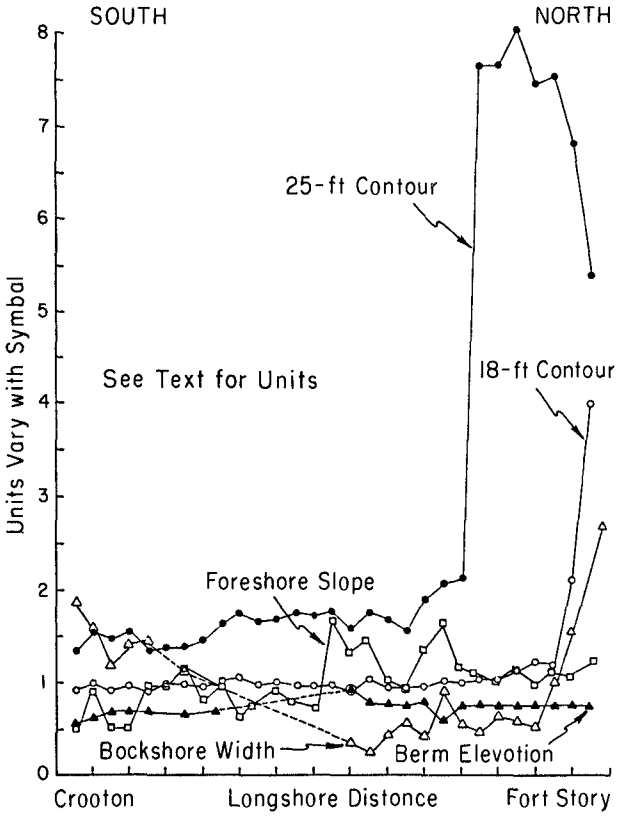

Figure 5. PROFILE CHARACTERISTICS AT VIRGINIA BEACH

The open and filled circles indicate distance to the -18 and -25 foot NGVD depth contours (-5.5 and -7.6 m), with each tick mark equal to 500 feet (153 m) from the shoreline. The abrupt seaward displacement of the contours off the north end of the study area indicates a relatively flat bottom where small changes in vertical elevation produce large changes in position of the contour.

SAND SIZE DISTRIBUTION

Experience with this and related sites (Ramsey and Galvin, 1977) suggests that sand on the typical beach profile can be adequately sampled from locations indicated on Figure 6 by surface grab samples taken during surveying. All 29 profile lines were sampled at the foreshore, and 11 of the 29 profile lines were sampled at the six sites indicated on Figure 6. A total of 86 surveyed samples were obtained in this way and sieved. Their median sand size is summarized in Table 2. A qualitative visual description of each sample is given in Appendix B of WS&E (1986a).

Figures 7 through 12 show longshore distributions of sand size for each of the six sample locations on Figure 6, beginning with the offshore sample (Figure 7) and moving landward to the foredune sample (Figure 12). The axes of these six figures are identical. The horizontal axis is distance north from Croatan Beach, in km. The vertical axis is sand size, in mm. Each figure shows three lines. The middle line is the D_{50}, or median, grain size of the sample; the top line is the size at which 16 percent of the sample is coarser; and the bottom line is the size at which 84 percent of the sample is coarser. The 16 and 84 percent sizes are shown because they are required for SPM beach fill design (in phi units).

Examination of the six figures shows similarities and differences in size from the different sample locations. The samples from offshore (-10 feet or -3 meters) are the most uniform in the longshore direction, have the lowest median size (about 0.18 mm), and the narrowest spread between D_{16} and D_{84}. The samples from the low tide terrace (Figure 8) and just seaward of the foreshore (Figure 9) tend to be more variable in the longshore direction, and show somewhat greater median sizes than the offshore samples, with a greater spread between D_{50} and D_{16} than between D_{50} and D_{84}, perhaps due to shell fragments and pebbles.

For nearly eight kilometers of the 10-km study beach, the foreshore samples (Figure 10) increase northward in median size. This is somewhat unusual in that size usually decreases in the downdrift direction. Several of the foreshore samples have the D_{50} size closer to the D_{16} size than to the D_{84}, a condition which is relatively uncommon in the population of sand samples. The mid-berm (Figure 11) and backshore (Figure 12) size distributions are similar to each other in overall shape, and differ from the foreshore size distribution (Figure 10). The similarities between mid-berm and backshore are shown by their relatively constant D_{50} and D_{84} sizes in the longshore direction and by the variation in D_{16} sizes (both have relatively high values of D_{16} between kilometers 1 and 4 and at kilometers 9 and 10). The dune samples tend

Table 2. SUMMARY OF MEDIAN SAND SIZE

Distance North of Croatan Beach, km	Median Size, D_{50}, mm					
	Foredune	Mid-Berm	Foreshore	Seaward of Foreshore	Low Tide Terrace	10-Ft Depth
0.0	0.34	0.32	0.38	0.57		
0.2						0.19
0.3	0.23	0.25	0.22	0.18	0.27	0.20
0.7			0.25			
1.0			0.22			
1.2			0.37			
1.5	0.30	0.33	0.22	0.16	0.17	0.17
1.6			0.22			
1.7	0.32		0.21			
1.8		0.30	0.22	0.17	0.21	0.16
2.0			0.24			
2.2			0.25			
2.5			0.31			
2.8			0.27			
3.0	0.25	0.38	0.26	0.35	0.30	0.17
3.3			0.33			
3.6			0.39			
3.8			0.34			
4.1	0.42	0.36	0.37	0.26	0.35	0.19
4.4			0.39			
4.8			0.39			
5.1			0.45			
5.5	0.25	0.35	0.48	0.47	0.18	0.18
5.8			0.45			
6.2			0.84			
6.6			0.70			
7.0	0.30	0.30	0.50	0.26	0.20	0.16
7.3			0.80			
7.5			0.28			
7.8			0.38			
8.2	0.25	0.27	0.36	0.35	0.34	0.15
8.8	0.38	0.44	0.43	0.20	0.24	0.16
9.5	0.30	0.48	0.27	0.53	0.17	0.16

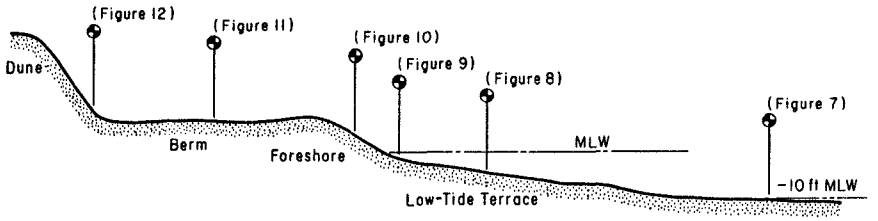

Figure 6. SAND SAMPLE LOCATIONS ON IDEALIZED PROFILE

to have slightly finer D_{50} sizes than the mid-berm samples, being finer in seven of the ten samples north of Rudee Inlet (Table 2), which is consistent with a slight amount of wind sorting.

The overall trends in D_{50} are compared in Figure 13 for the offshore, foreshore, and mid-berm samples. This figure shows clearly the relatively low and constant values of D_{50} found offshore, the higher and relatively constant values of D_{50} on the berm, and the unexpected northward increase of D_{50} on the foreshore.

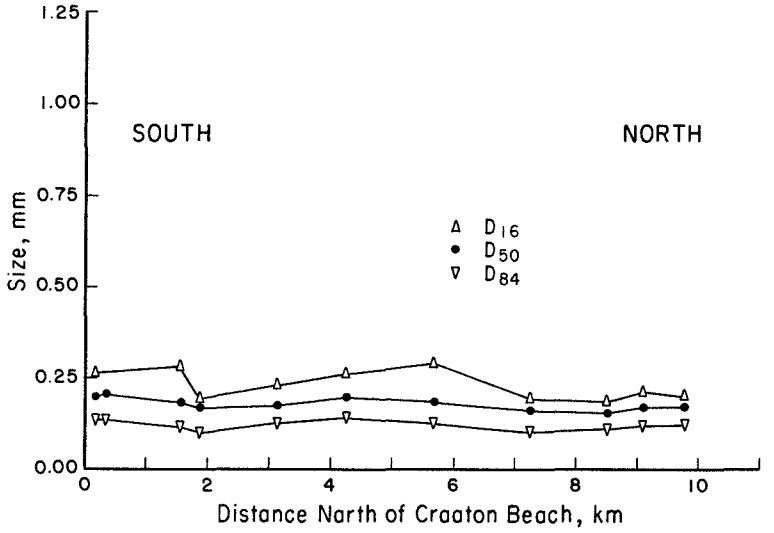

Figure 7. SAND SIZE AT 10-FOOT DEPTH

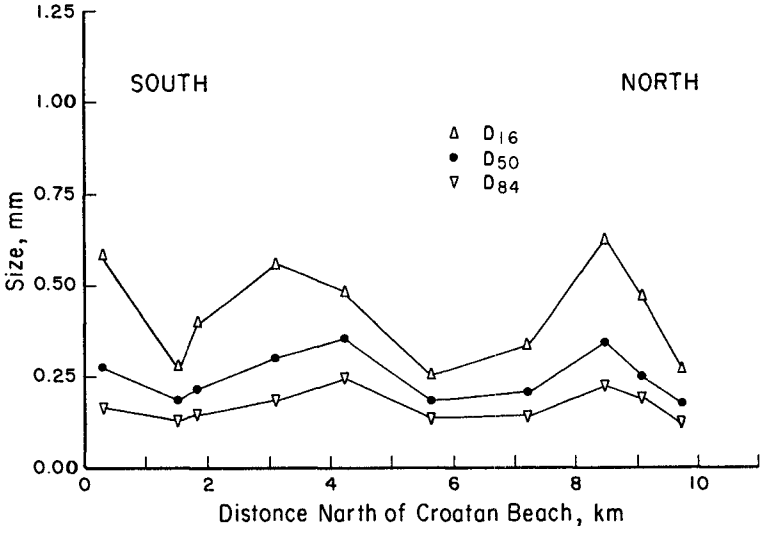

Figure 8. SAND SIZE ON LOW TIDE TERRACE

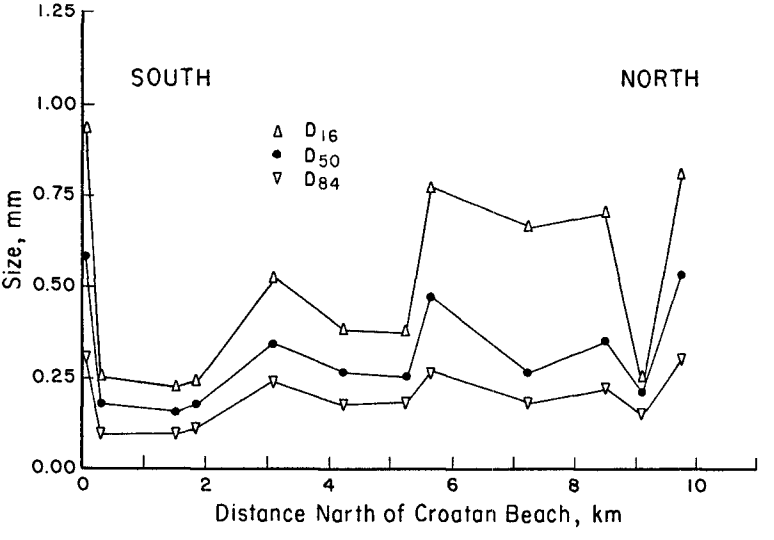

Figure 9. SAND SIZE JUST SEAWARD OF FORESHORE

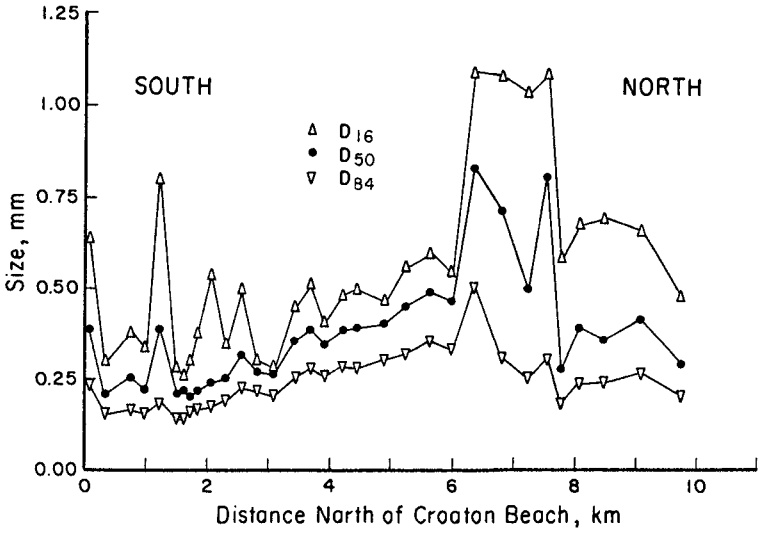

Figure 10. SAND SIZE ALONG FORESHORE

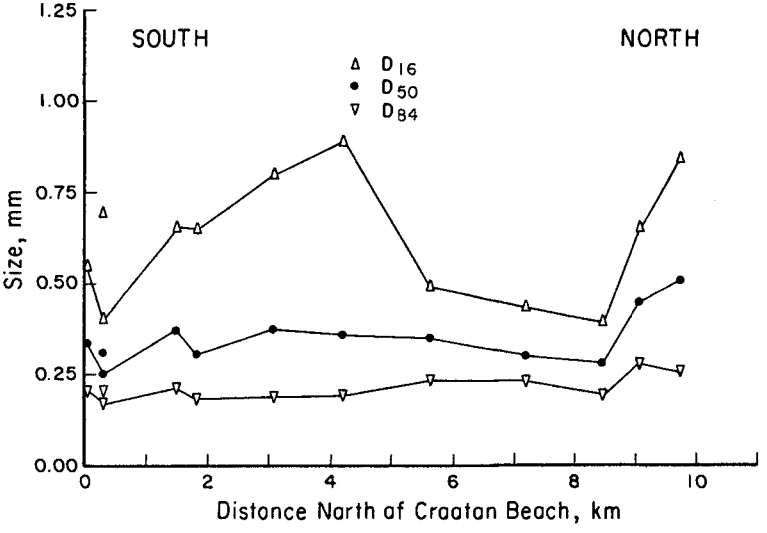

Figure 11. SAND SIZE AT MID-BERM

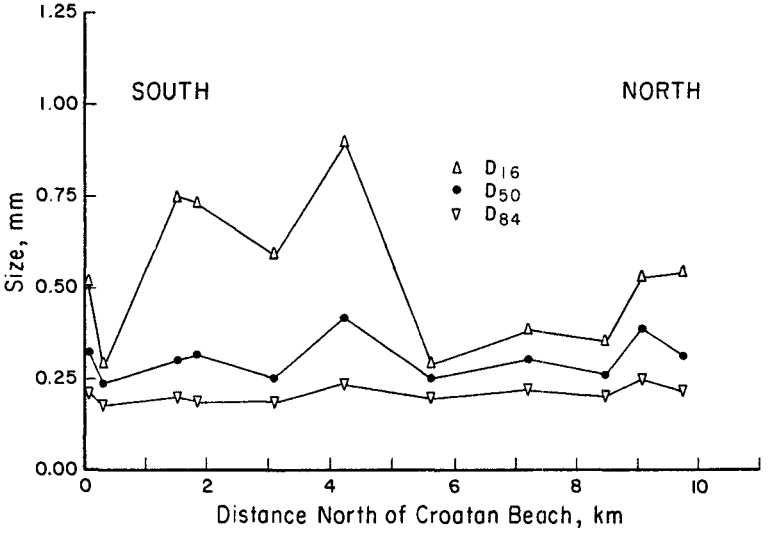

Figure 12. SAND SIZE AT BACKSHORE (TOE OF FOREDUNE OR IN FRONT OF BOARDWALK)

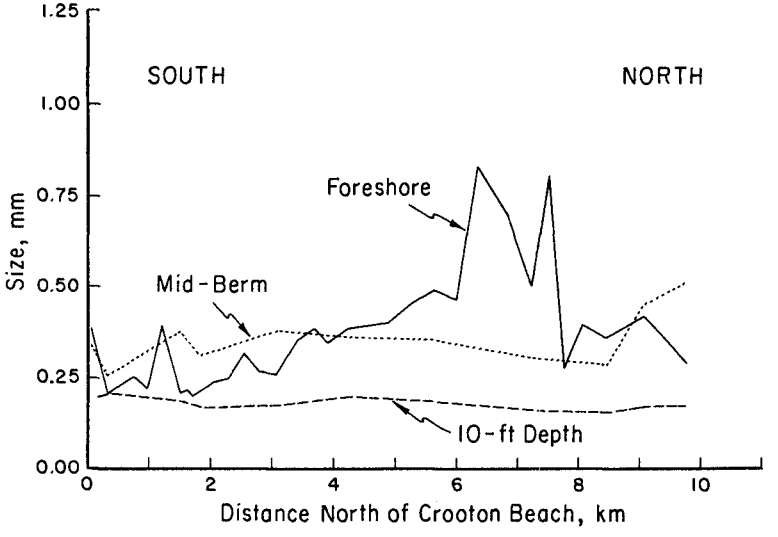

Figure 13. ACROSS-SHORE VARIATION IN SAND SIZE

INTERPRETATION

There are four classes of data which should be integrated for a consistent interpretation of how coastal processes will affect disposal of Atlantic Ocean Channel sand on the study beach. These four include the shoreline change rates (Figure 4), beach replenishment amounts and dates (Langley McDonald, 1985), the profile characteristics (Figure 5), and the sand size distribution along and across the beach (Table 2, Figures 6 through 13).

Bypassing experience clearly indicates net longshore transport is from south to north. Thus, a south placement will get most use from the sand. The shoreline change data indicate erosion has (historically) been greater in the south, which also suggests disposal in the south. The existence of Rudee Inlet at the south end of the study beach suggests that placement should be north of its immediate zone of influence, to avoid shoaling in the inlet.

None of 54 sand samples from the subaerial beach had a D_{50} size less than 0.21 mm (see backshore, berm, and foreshore in Table 2). Only 6 of 21 samples from immediately seaward of the beach had a D_{50} size less than 0.20 mm (see seaward of the foreshore and low tide terrace in Table 2). In contrast, at the ten-foot depth, the highest D_{50} in eleven samples was 0.20 mm (one sample), and the average of the eleven samples was 0.17 mm.

These size data are interpreted to mean that, under prevailing conditions at Virginia Beach, sand must have a D_{50} of at least 0.20 to remain on the subaerial beach, i.e., to add to that part of the beach used in calculating economic benefits. This interpretation is supported by closer analysis of the foreshore size distribution on Figure 10. The foreshore at Croatan Beach, which is the first sample plotted on the left end of Figure 10, has a D_{50} of 0.38 mm and is the only sample south of Rudee Inlet. Of the first ten foreshore samples north of Rudee Inlet, only one is coarser than 0.25 mm. This abrupt drop in foreshore sand size from one side of the inlet to another is interpreted as an effect of the bypassing by dredge and jet pump; these bypassing operations withdraw sand from below water in the inlet (the inlet sand size is the first point on Figure 7) and discharge it on the foreshore north of Rudee Inlet. Since the below-water sand is shown to be fine, the sand discharged on the foreshore will be relatively fine. The distribution on Figure 10 shows this. This interpretation is relatively consistent with profile characteristics on Figure 5, where both foreshore slope and berm elevation are lower in the south end of the study area, as expected from finer sand beaches.

The position of the 25-foot contour (Figure 3 and Figure 5) coincides with the higher long-term accretion rates at the north end of the study area (Figure 4). It is somewhat puzzling that the subaerial beach at this site also has the coarsest sand (Table 2). However, the data are consistent if the offshore shoal represents the finer fraction winnowed from the sand carried northward by longshore transport and the

subaerial beach is the residual coarse material. At any rate, it is clear that the north half of the study beach is not in need of replenishment.

CONCLUSIONS

a. The best location to place suitable sand from the Atlantic Ocean Channel is in the south half of the study area, approximately in the segment from kilometer 1 to kilometer 4 on the horizontal scale used for Figures 7 through 13.

b. Efficient beach replenishment will require sand that has a median (D_{50}) size of at least 0.20 mm, when placed on the beach.

c. Design berm heights should be about 2.1 m above NGVD and expected foreshore slopes will be about 0.05 to 0.10, depending on the coarseness of the sand placed there.

d. Size analyses of surface grab samples from along and across the study beach provide simple but strong constraints on beach disposal design.

Acknowledgements. This paper is based on work done under contract DACW65-85-D-0037 with the Norfolk District, U.S. Army Corps of Engineers (see WS&E, 1985a, in References). The Project Manager for the earlier work was Richard Klein, Waterways and Harbors Section, Norfolk District. Data collection and analysis were assisted by James L. Overton, Mark Ricketts, Robert Taliaferro and Naren Tayal. Greg Hamadock, Law Engineering (McLean Branch), supervised the analysis of the beach sand. Herbert J. Bruder prepared all illustrations and Sheila Zukor typed several versions of the manuscript. Preparation of this report was paid for by the firms of Cyril Galvin, Coastal Engineer and Waterway Surveys & Engineering, Ltd.

REFERENCES

Everts, C.H., J.P. Battley, Jr., and P.N. Gibson, 1983. "Shoreline movements; Report 1: Cape Henry, Virginia to Cape Hatteras, North Carolina, 1849-1980," Technical Report CERC-83-1, U.S. Army Engineer Waterways Experiment Station, Vicksburg, Mississippi.

Goldsmith, V., Sturm, W.C., and George R. Thomas, 1977. "Beach Erosion and Accretion at Virginia Beach, Virginia and Vicinity," M.R. 77-12. U.S. Army Corps of Engineers, Coastal Engineering Research Center, Fort Belvoir, Virginia, 185pp.

Harrison, W., Morris L. Brehmer, and Richard B. Stone, 1964. "Nearshore Tidal and Nontidal Currents, Virginia Beach, Virginia," Technical Memorandum No. 5, U.S. Army Coastal Engineering Research Center, Washington, D.C., 20pp.

Harrison, W., and W.C. Krumbein, 1964. "Interactions of the Beach-Ocean-Atmosphere System at Virginia Beach, Virginia," Technical Memorandum No. 7, U.S. Army Coastal Engineering Research Center, Washington, D.C., 102pp.

Harrison, W., W.C. Krumbein, and W. Wilson, 1964. "Sedimentation at an Inlet Entrance (Rudee Inlet, Virginia Beach, Virginia)," Technical Memorandum No. 8, U.S. Army Coastal Engineering Research Center, Washington, D.C., 42pp.

Harrison, W., R. Morales-Alamo, 1964. "Dynamic Properties of Immersed Sand at Virginia Beach, Virginia," Technical Memorandum No. 9, U.S. Army Coastal Engineering Research Center, Washington, D.C., 52pp.

Langley and McDonald, 1985 (Sept). "Plan of Beach Nourishment for One Year Period, October 1, 1985 to September 30, 1986," Prepared for Virginia Beach Erosion Commission, Virginia Beach, Virginia, 27pp. + Appendices.

National Ocean Survey, 1985. "Tidal Current Tables 1986 - Atlantic Coast of North America," 241pp.

National Ocean Survey, 1985. "Tide Tables 1986 - East Coast of North and South America including Greenland," 288pp.

Ramsey, M.D., and Galvin, C.J., Jr., 1977 (Mar). "Size Analysis of Sand Samples from Southern New Jersey Beaches," Miscellaneous Report No. 77-3, U.S. Army Corps of Engineers Research Center, Fort Belvoir, Virginia, 55pp.

U.S. Army Coastal Engineering Research Center, 1977. "Shore Protection Manual," 3rd edition, U.S. Government Printing Office, Washington, D.C., pp. 4-1 thru 4-180.

U.S. Army Corps of Engineers, 1985 (May). Norfolk Harbor and Channels, Virginia Deepening and Disposal, Final Supplement 1 to the Final Environmental Impact Statement and Appendix: Dam Neck Ocean Disposal Site, Site Evaluation Study, U.S. Army Corps of Engineers, District, Norfolk, Virginia, 104pp. + Appendices.

Waterway Surveys and Engineering, Ltd., 1984 (June). Feasibility Study for Disposal of Dredged Material from Norfolk Harbor Channel Deepening on Fort Story Beaches at Cape Henry, Virginia Beach, Virginia, 50pp. + Appendices.

Waterway Surveys and Engineering, Ltd., 1984 (July). Preliminary Design for Disposal of Dredged Material from Thimble Shoal Channel on East Ocean View Beaches, Norfolk, Virginia, 49pp.

Waterway Surveys and Engineering, Ltd., 1984 (June). Preliminary Design for Disposal of Dredged Material from Thimble Shoal Channel on West Ocean View Beach, Norfolk, Virginia, 76pp.

Waterway Surveys and Engineering, Ltd., 1986 (March). Engineering Study for Disposal of Dredged Material from Atlantic Ocean Channel on Virginia Beach Between Rudee Inlet and Fort Story, Norfolk, Virginia, 83pp.

Waterway Surveys and Engineering, Ltd., 1986 (April). Engineering Study for Disposal of Dredged Material from Atlantic Ocean Channel on Sandbridge Beach Between Back Bay and Dam Neck, Norfolk, Virginia, 79pp.

Thompson, Edward, F., 1977. "Wave Climate at Selected Locations Along U.S. Coasts," U.S. Army Coastal Engineering Research Center, Fort Belvoir, Virginia, Technical Report 77-1, 364pp.

CHAPTER 85

Federal Jetty and Sand Dike at the Entrance to Fire Island Inlet, New York

Cyril Galvin*, M. ASCE, Charles, J. Rooney**
and Gilbert K. Nersesian***, M. ASCE

ABSTRACT

Prior to construction at Fire Island Inlet, Fire Island was moving westward at more than 200 feet per year, the north shore of the inlet was eroding severely, and navigation in the inlet was difficult. The Federal Jetty, completed in 1941, and the sand dike, built in 1959, have halted the westward migration, eliminated the severe erosion, and partially improved navigation, with minimal maintenance or repair to the structures. There has been a large net accretion of sand east of the jetty and west of the dike, an unknown part of which is at the expense of shores to the west of the inlet. At the State Park on the south side of the inlet interior, erosion accelerated, probably because of the dike.

The middle and ocean segments of the 4750-foot Federal Jetty are now (1987) in good condition, although the design implies a stability coefficient for the quarrystone jetty head at time of construction that would now be considered risky. Stability has been promoted by a stone blanket under and east of the jetty, a thick stone apron seaward of the jetty, a low (8 feet MLW) crest, and armor stone that has been partially keyed in place. Damage due to scour, common at other single-jetty inlets, is absent here because longshore transport, which easily overtops the low crest, keeps the inlet channel away from the jetty. Although the two seaward segments of the jetty remain in good condition, the inshore segment of the jetty is in poor condition, despite its apparently sheltered location. The cumulative effects of waves, possibly channeled to the site along recurved spits during storms, have damaged 1200 feet, and tidal scour has destroyed about 230 feet. The damaged segment has a design cross section which is one-fifth and one-twelfth the cross sections of the jetty trunk and head.

The dike was constructed with sand dredged from the inlet, and its seaward shore was later armored by dumped riprap. The dike moved the tidal channel away from the north shore, shifted the ocean entrance of the inlet eastward (against the direction of longshore transport), and shortened the distance to the ocean.

* Principal Coastal Engineer, Box 623, Springfield, Virginia 22150.
** Chief, Project Management Branch, Engineering Division, New York District, U.S. Army Corps of Engineers.
*** District Coastal Engineer, New York District, U.S. Army Corps of Engineers.

INTRODUCTION

Background. Fire Island Inlet is a large permanent tidal inlet on the south shore of Long Island, New York, which connects Great South Bay with the Atlantic Ocean through an unusually long, shore-parallel channel (Figure 1). The entrance to the inlet is the site of two large coastal structures: the Federal Jetty constructed in 1939-1941 and the sand dike, known locally as The Thumb, constructed in 1959. Saville (1960) reviewed the history of these structures up to that time, based on personal experience. See also Gofseyeff (1953). An excellent recent view of both structures is the cover photo of the July 1986 issue of Shore & Beach, taken immediately after Hurricane Gloria made landfall in the vicinity (Terchunian, 1986).

The jetty fixed the position of the western end of Fire Island after that island had moved westward at a rate in excess of 200 feet per year for more than a century. The sand dike has alleviated severe tidal scour along the residential shore of the community of Oak Beach. Together, these structures have forced the inlet entrance into a relatively stable position. Neither structure has had major maintenance, despite the relatively exposed site. Perhaps because they have functioned well and almost without maintenance, these structures are not well known, either to the general public or to the coastal engineering profession.

Purpose. This paper identifies features in the design of the Federal Jetty and the sand dike that have made them functionally and structurally useful over a relatively long time. This knowledge is used to derive lessons which may be applied to coastal engineering projects elsewhere. Conclusions are based on historical information at the New York District, Army Corps of Engineers, and a knowledge of local coastal processes and existing conditions (Galvin, 1985).

Location. The south shore of Long Island, New York, is the northern part of the mid-Atlantic states in the United States. Long Island measures approximately 120 miles (192 km) from the entrance to New York Harbor on the west to Montauk Point on the east. Fire Island Inlet is at the western third of this shore, approximately 36 miles (58 km) east of the entrance to New York Harbor.

Units. Design data are taken from contract documents which use customary English units. Distances are in feet (1 foot = 0.305 meters) and rock weights are in pounds and (short) tons (1 pound = 2.2 kilograms; 1 ton = 0.907 metric tonnes). Locations are identified by surveyor's stations along the jetty centerline, so that Station 33+10, for instance, is 3310 feet measured along the curved jetty centerline from the inlet end of the jetty.

FEDERAL JETTY

Background. Construction of the Federal Jetty was a Depression-era project. The authorized jetty has the stated purpose of checking the westward littoral drift of sand and providing a greatly improved

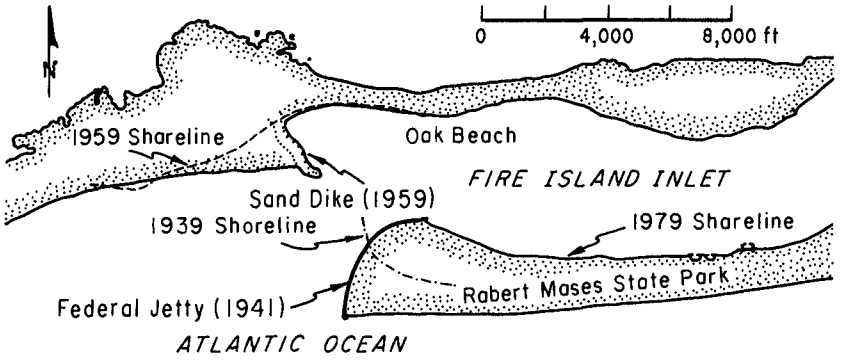

Figure 1. LOCATION OF FEDERAL JETTY AND SAND DIKE AT FIRE ISLAND INLET

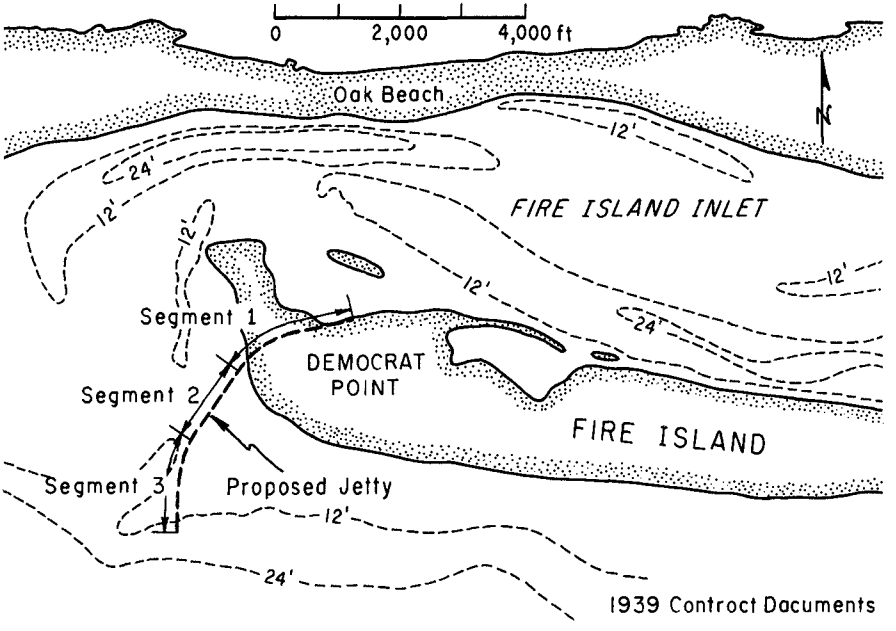

Figure 2. PLAN OF FEDERAL JETTY WITH 1939 SHORELINE AND BATHYMETRY

navigation channel (House Document 33, 75th Congress, 1st Session, Chief of Engineers to Chairman, Committee on Rivers and Harbors, paragraph 4, 13 May 1937). Apparently, appropriations took another year. On 28 September 1938, Robert Moses, President of the Long Island State Park Commission, announced that a jetty would be built at Fire Island Inlet by the Corps of Engineers for an estimated cost of $759,000 (New York Times, 29 Sep 38). (This estimated cost is the same as that in House Document 33.) The Moses announcement came only one week after the 1938 Hurricane, which remains the storm of record for much of Long Island, and it seems probable that the timing of the announcement was affected by that storm. As announced, construction was to be done during the next eight months, but after eight months, only the construction contract was ready. The contract was won by the firm of Spearin, Preston & Burrows, Inc. of New York and signed on 13 June 1939. Work began on 26 June 1939 and was completed on 15 April 1941, for a price that was approximately $75,000 less than the figure announced by Moses (District Engineer's Report, House Document 762, 22 Dec 48).

Design. Figure 2 shows the location of the jetty with respect to the preconstruction shoreline, redrawn from the 1939 contract documents. Total crest length was 4750 feet, and a submerged stone apron extended seaward for an additional 200 feet. The jetty was divided into three segments in plan. Segment 1 covered 2000 feet, crossing land that was exposed at low tide. Segment 2 covered 1350 feet, going from near the then existing shoreline out to a depth of about 8 feet. Segment 3 covered 1600 feet, including the 200 feet of submerged stone apron. Segments 1 and 3 are curved in plan, so that Segment 3 at the ocean is north-south, and Segment 1 at the inlet is almost east-west.

Depths are plotted from the plane of Mean Low Water (MLW), which was taken as 1.8 feet below the plane of mean sea level at the Sandy Hook, New Jersey, tide gage. Mean tide range is 4.1 feet at the ocean end of the jetty.

The design of the jetty is shown in longitudinal section in Figure 3 and in cross section in Figure 4. Noteworthy features of the longitudinal section (Figure 3) include the relatively low crest elevation (8 feet above MLW), and the stone blanket and apron at the seaward end. A stone blanket from 1 to 3 feet thick underlies the entire Segment 3 and extends landward to the 1939 -6 foot MLW contour, about 350 feet into Segment 2. Along the outermost 500 feet of the jetty, this blanket extended 50 feet east of the toe of the jetty side slope. For 200 feet along the centerline (extended) of the jetty, there was a stone apron 3 feet thick and approximately 90 feet wide.

Table 1 summarizes the stone weights and side slopes of the jetty.

Construction. We assume that the jetty was built according to contract plans, since the writers have not seen any as-built modifications of the contract drawings. Photos show that the contractor built

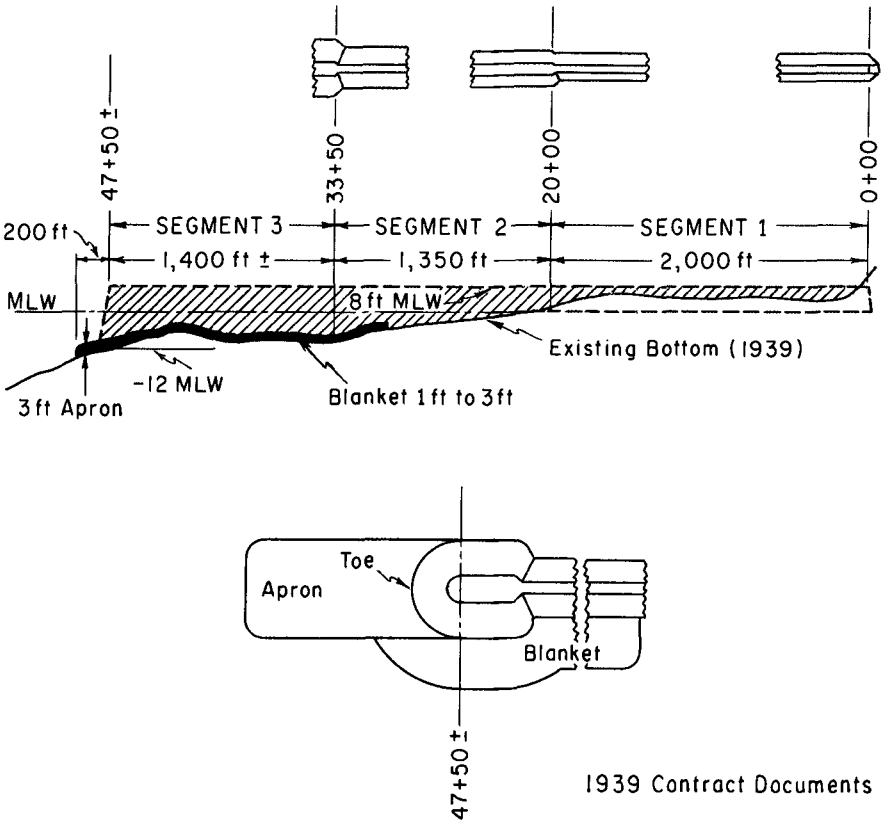

Figure 3. LONGITUDINAL SECTION ALONG JETTY CENTERLINE, WITH PLAN VIEWS OF SEGMENT TRANSITIONS AND SEAWARD END.

a pier at the inlet side of the western tip of Fire Island for unloading materials. A railroad was built on a wooden trestle along the line of the jetty. Stone was barged to the pier, loaded on flat bed rail cars, and taken to the active construction site. The core stone was tipped from the cars. Cap stone (armor stone) appears to have been removed and placed by crane.

Dated photos in the Corps of Engineers' records show that by 3 January 1940, core stone was being dumped at station 3+00 from the pile-supported railroad trestle. The core stone was being dumped into water beside the tracks, which is in agreement with the design (Figure 4) which calls for Section 1 to be excavated to MLW. The same photo shows what appear to be cap stone stockpiled along the route of the trestle. Later photos on 1 February 1940 show cap stone in place at Stations 1+60 and 0+15. At least at 0+15, the cap stone is immediately below the trestle beams, with only a few inches clearance.

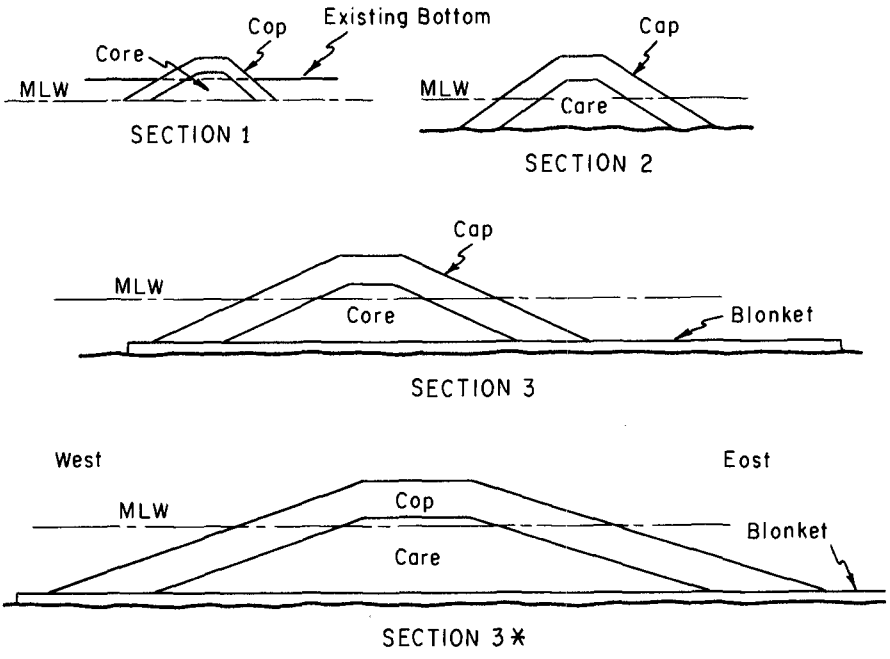

For Detoils of Sections See Toble 1

1939 Contract Documents

Figure 4. DESIGN CROSS-SECTIONS OF JETTY.

Table 1. FEATURES OF JETTY CROSS-SECTION

Section	Side Slopes West	Side Slopes East	Crest Width ft.	Cap Stone	Core Stone	Blanket Stone
1	1:1.5	1:1	6	3-4 tons	15 lbs-3 tons	
2	1:1.5	1:1.5	8	3-4 tons	15 lbs-3 tons	
3	1:2	1:2	12	> 6 tons	15 lbs-6 tons	15 lbs-500 lbs
3*	1:3	1:3	20	$\underline{>}$ 6 tons	15 lbs-6 tons	15 lbs-500 lbs

*(outer 50 feet of Segment 3)

Aerial photos taken on 4 June 1940, 3 October 1940, 8 November 1940, and 10 April 1941 are included here as Figures 5, 6, 7, and 8. These photos were found in the records of the New York District Corps of Engineers (reprinted by permission of the New York Daily News). The photos were taken from the same relative position, and provide a good record of the advancing construction.

Figure 5 suggests that Segment 1 of the jetty (Figure 2) was essentially complete by June 1940, approximately a year after the contract was signed. At this time, the trestle was constructed to Station 33+00, which is approximately the seaward end of Segment 2, and core stone had been placed for about half of Segment 2. The trestle bents in Segment 2 are more than double the width of the railroad. The rails are confined to the west half of the bents. It is evident from close inspection of Figures 5 and 7 that temporary timber platforms were laid on the pile caps east of the track to support cranes that placed the cap rock.

Figures 6 and 7 show the trestle to dogleg to the right at the seaward end, and the track moves from the west side of the trestle to the east side of the trestle after passing the change in direction. Isolated piles in the water along the pre-dogleg line of track suggest that the dogleg replaces a wave-damaged section of trestle.

The survey included in the 1939 contract shows that the three-foot thick stone apron would be placed in depths of 12 to 14 feet. However, after placement of the apron, a December 1940 survey (with probings) in the New York District files shows depths from 15 to 20 feet above the stone apron for at least the outer 100 feet of the apron. Probably, the advancing jetty constricted the preconstruction pattern of tidal flow feeding the marginal flood tide channel (Figure 2), causing scour seaward of the tip of the jetty prior to placement of the apron.

The four photos show rapid accretion of the shore east of the jetty and some erosion immediately to the west. By the end of construction, sand freely overtopped the jetty (Figure 8), as it does today. Even at the start of construction, there was a large sand spit west of the jetty, and a recurved sand spit along the inlet which reattaches near Segment 1 (see top of Figure 5). A recurved spit such as shown in Figure 5 is common today after severe storms.

Present Conditions. The present condition of the jetty varies from remarkably good along Segments 2 and 3 to severe damage along Segment 1. Although it was anticipated that maintenance would cost about $25,000 annually (House Document 33, 75th Congress, 1st Session), little maintenance has actually been done. The District Engineer's report in House Document 672 (printed December 1948) states that repairs up to March 1947 totaled $600.00 (six hundred dollars), and that a total of $50,000 was to be spent on rock repair in 1948. Files in the Navigation Branch, Operations Division, state that 165 tons of rock were placed on the jetty in 1948. Notations on plans indicate that repairs were made at Station 20+00 and between 23+00 and

Figure 5. SEGMENT 1 OF JETTY COMPLETE AND TRESTLE CONSTRUCTED FOR SEGMENT 2 ON 4 JUNE 1940.

New York Daily News Copyright, with Permission

Figure 6. SEGMENT 3 UNDER CONSTRUCTION ON 3 OCTOBER 1940.

New York Daily News Copyright, with Permission

Figure 7. CRANES WORKING ON SEGMENT 3 DURING STRONG WEST WINDS ON 8 NOVEMBER 1940.

New York Daily News Copyright, with Permission

Figure 8. COMPLETED STONE JETTY ON 10 APRIL 1941.

24+00. These locations are in Segment 2, not at the seaward end. No other repairs are known, either from the files or from the memory of knowledgeable persons. The 165 tons is a relatively small amount, occupying, for example, a little more than six feet of the Section 2 shown on Figure 4.

When constructed, Segment 1 was on land (Figure 2), and had a weak cross section (Figure 4 and Table 1). Segment 1 now shows damage both by waves and by tidal currents. Waves have damaged and penetrated behind the jetty for at least 1200 feet, eroding significantly into the dunes east of the jetty (Figure 9). This damage occurs in a relatively sheltered position within the inlet, but the recurved spits, pointing at or terminating at Segment 1, may provide a wave channel which can concentrate ocean waves on the jetty. (During storms, the recurved spits may be submerged, and refraction would concentrate wave energy above the spit, delivering the waves to the jetty.) Recurved spits on the inlet side of the jetty have been a common feature through time. These spits appear across the top of photos in Figures 5, 6, 7, and 8, with shapes and relative positions identical to those observed in recent years. A recurved spit intersecting the damaged length of Segment 1 was especially well developed after the severe northeast storm of 29 March 1984 (Galvin, 1984). Figure 9, based on a June 1984 photo, shows a remnant of this March 1984 spit. However, such a spit was not well developed after Hurricane Gloria (Terchunian, 1986).

Tidal scour from the ebb current flowing out of Great South Bay impinges on the inlet shore of Robert Moses State Park (Figure 1). Scour from this ebb current has severely eroded the shore of the park, and along with the shore, removed about 230 feet of the jetty, i.e. Station 0+00 to about Station 2+30. Since the design section is relatively light and no lower than 0 feet MLW elevation, Segment 1 has no resistance to undermining by the tidal current in a channel that is 20 feet deep or more.

It is worth noting that the east jetty at Shinnecock Inlet (two inlets east of Fire Island Inlet) shows similar damage (Dean and Maurmeyer, 1977) at the same relative positions as the wave and scour damage to Segment 1 of the Federal Jetty. At Shinnecock, however, there are no recurved spits.

At the ocean shore east of the jetty, there has been a large accretion of sand since the jetty was constructed. This is made evident by comparing the 1939 shoreline and bathymetry on Figure 2 with the recent shoreline (June 1984) on Figure 9. The present accreted condition was reached rapidly, probably by 1950, according to Saville (1960).

The area of sand in the spit west of the jetty is, surprisingly, relatively unchanged between the 1939 design condition (Figure 2) and the 1984 photo traced on Figure 9. However, this spit has shifted seaward, from a position adjacent to Segment 1 in 1939 to a position adjacent to Segment 3 in 1984 (compare Figures 2 and 9).

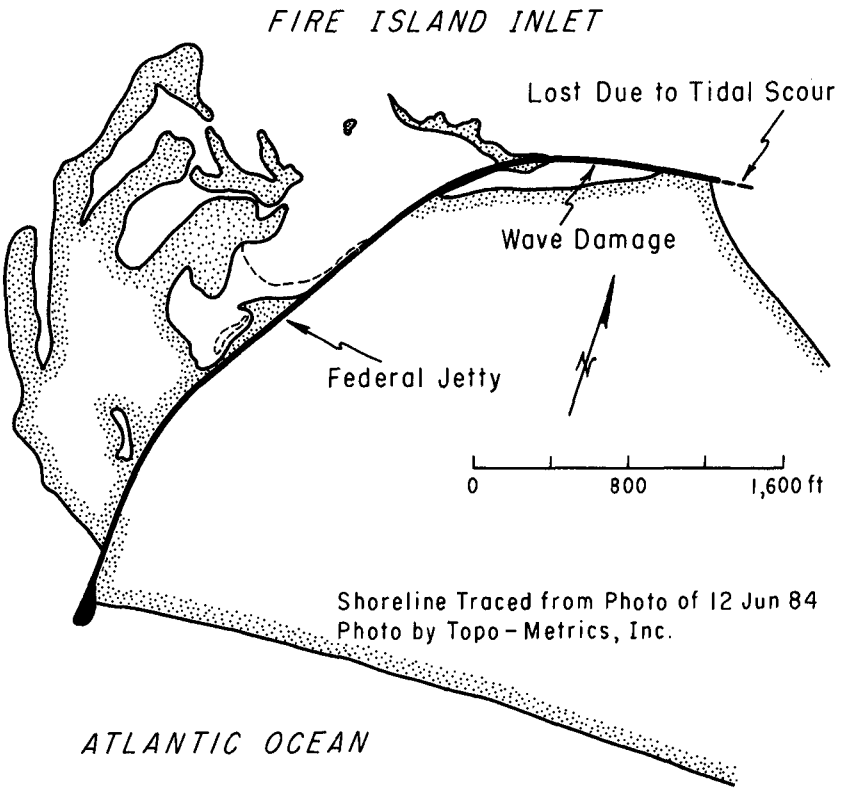

Figure 9. RECENT (1984) SHORELINE IN VICINITY OF FEDERAL JETTY

SAND DIKE

Erosion at Oak Beach. The community of Oak Beach, along the north shore of Fire Island Inlet, had a long history of erosion, mainly due to the deep tidal channel that existed along the shore (see the bathmetry on Figure 2). This erosion predated the construction of the jetty, and is one of the concerns addressed in House Document 33 (1937). The Town, County, and State had each attempted a solution to this problem prior to construction of the jetty, without success.

According to Saville (1960), proposed solutions were developed by the New York District in 1957, and these were reviewed by the Beach Erosion Board. At the time, Saville was himself one of the three civilian members of the Board (and consultant to the Long Island State Park Commission). The Board's review emphasized the need to deal with the tidal currents, ahead of anything else, including a model study.

Construction of Sand Dike. The adopted project required dredging sand from the inlet and placing part of it along the Oak Beach shore. After the project was approved (and apparently after the work had started), the Long Island State Park Commission in the fall of 1959 requested a change, to place the dredged material in a "closure dike" crossing the tidal channel. The Corps of Engineers approved this change on 16 November 1959, and the contractor placed 1,235,300 cubic yards of sand (pay quantity) in a dike (crest elevation 12 to 15 feet MLW) which closed off the channel (letter from New York District to North Atlantic Division, 2 May 61). Construction went from the seaward end of the dike landward (see Figure 1), and closure was complete on 3 and 4 December 1959 (Saville, 1960). This is remarkably swift movement on a major project without prior engineering or model studies. The changes are graphically shown by air photos identified as Figures 3 and 4 in the report of Kassner and Black (1983).

Subsequent History. The changes to this dike are indicated in part by the shorelines on Figure 10. Shortly after construction, local interests placed stone around the dike to armor it (mentioned in the 2 May 1961 letter, but not directly referred to by Saville, 1960). The dike initially had a boot-like shape, but most of the "foot" to the boot was eroded by 1965. The sequence of shorelines on Figure 10 suggest at least another effort at riprap revetment, after 1961. Since then the dike itself has been relatively stable, and its west side has been subject to much accretion (Galvin, 1985).

The effect of the dike on the channel is indicated by the shape and depth of the deepest part of the channel passing around the end of the dike (Figure 10). For most of the first decade after dike construction, the deepest part of the channel trended to the northwest. Gradually, however, the channel reoriented until now it has a northeast trend, and in the process, the old channel west of the dike was abandoned. The abandoned channel became the site of accretion as the ebb channel, forced eastward by the dike, bypassed a large part of the ebb tidal delta, which then accreted to shore. Analysis of the downdrift accretion is given in detail by Galvin (1985). The general bypassing process under natural conditions is discussed by FitzGerald (1983). The location of the ebb tidal delta and the shifting of the shoals in the inlet are shown in air photos by Barwis, et al. (1977).

DESIGN LESSONS

Stone Blanket and Apron. The one to three-foot layer of stone under the jetty provides both a foundation and a filter for the structure. The extension of the blanket east of the jetty probably prevented scour and reduced breaking waves during the time immediately after construction, before beach accretion. The extension of the stone apron seaward of the jetty also prevented scour immediately after construction, and probably still provides a floor for erosion during storms. The stone blanket seems a prudent requirement and the stone apron a necessary requirement for this structure. The data reinforce experience at other projects that scour must be expected

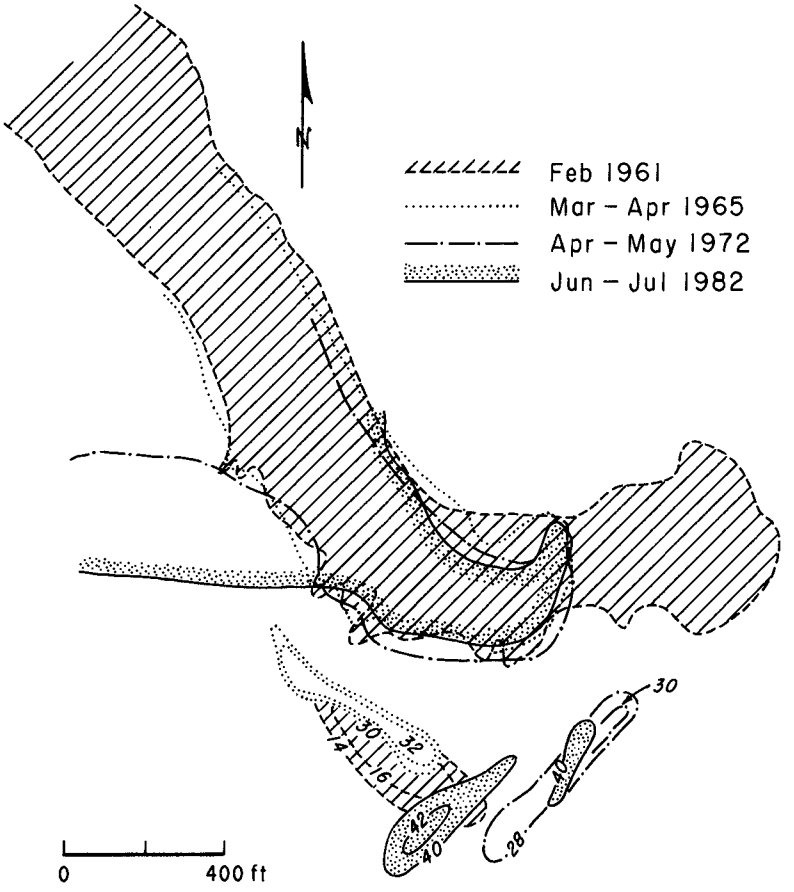

Figure 10. **SHORELINE CHANGES AND THE DEEPENING AND REALIGNMENT OF CHANNEL AT THE SAND DIKE.**

during construction, in front of the advancing jetty, prior to placement of the stone apron.

Design Wave Height. Using presently accepted practice in jetty design (U.S. Army Corps of Engineers, 1984, Shore Protection Manual, referred to hereafter as SPM), the jetty head at the Federal Jetty (as described in Table 1) would now be considered to have a questionable design. The most exposed direction is to the southeast. A profile to the southeast based on the December 1940 survey, after placement of

the stone apron, shows the toe of the jetty in a depth of 15 feet (MLW). Seaward of this depth, the mean slope is nearly flat for 100 feet or more (not steeper than 0.020).

If the 1940 profile governs during storms, breaker travel considerations (Galvin, 1969; SPM, page 7-10) indicate a breaker height of 19 feet may reach the jetty at high tide. (Given the low crest elevations, severe storm surges would submerge the jetty, reducing the potential damage.) Using this height in Hudson's equation, along with the design parameters in Table 1, suggests that WK_D is 42.5 tons. Since the design requires W to be at least six tons (Table 1), and the contractor is not likely to exceed this requirement by much, but is likely to save larger stones for the jetty head, it is estimated that the actual W in the jetty head is eight tons. This implies K_D equal to 5.3, a value which is relatively high for the head of a stone structure (Table 7-8, SPM). This high K_D may have developed due to partial fitting of the cap stone in place, and the practice of grading the core so that the larger core stone is on top. But the armor stone is only a single layer, according to the design. Alternatively, it is possible that, seaward of the jetty head, shoals filter out the very large waves, before they reach the jetty.

The design lesson from this analysis is that care in construction and a long-term shoaling trend may permit a stable jetty head built with nominally underdesigned armor stone.

Single-Jetty Design. It is well known that single jetties at tidal inlets often have scour problems (Kieslich, 1981), but these problems have been absent at the Federal Jetty. Experience at Fire Island Inlet suggests that single-jetty inlets are feasible if there is nearly unidirectional longshore transport, combined with a low crest that permits overtopping (Figure 8). The unidirectional transport at Fire Island is the result of the position of the New Jersey coast, west of Fire Island, which reduces the maximum fetch from the west. The effect of this limited fetch is well illustrated in Figure 7, where the west winds are strong enough to produce foam streaks through the jetty, but these winds have not been able to produce large waves. The long-term effect of this unidirectional westward transport is reflected in the overlapping planform of Fire Island Inlet (Galvin, 1970).

Sand Accretion. The Federal Jetty and the sand dike are both aligned perpendicular to shore. Present knowledge would anticipate the large accretion of sand on the ocean shore east of the jetty (Figure 1), but the major accretion west of the sand dike (Figure 10), on the downdrift side, would perhaps still be unanticipated today. The large volume of sand in the ebb tidal delta is the source of this accretion, and the eastward shift of the channel freed this sand to move ashore.

Shore Erosion. In the two decades after the sand dike was constructed, the inlet shore of Robert Moses State Park (Figure 1) eroded severely (Galvin, 1985). This erosion is probably a reaction of the

inlet system to construction of the Thumb. The large accretion west of the Thumb is not necessarily withdrawn from the littoral system, but may be shifted from the ebb tidal delta to shore. It is believed that sand now crosses the existing inlet channel by natural bypassing (Galvin, 1983), but how much of this sand reaches the downdrift shore of Jones Beach after passing the channel is not known. Thus, the sand dike has an undetermined responsibility for erosion of the recreational beaches to the west.

Role of Engineering Studies. The two major structures discussed in this paper were built without model studies or any of the environmental impact studies now necessary. A model study was subsequently made (Bobb and Boland, 1969), and this did not anticipate the major shoaling west of the sand dike that has since developed (Terchunian, 1986). The Federal Jetty has now (1987) endured without major repair for 46 years and the sand dike for 26 years. The sand dike was constructed on the basis of a major field change to a beachfill project already started.

The present paper, based on field inspection, knowledge of the local coastal processes, and a historical review of events leading to construction has yielded insight on coastal engineering design. Such retrospective studies would be useful on other projects. Considerably more technical detail on erosion, accretion, and dredging at Fire Island Inlet is given by Galvin (1985).

Acknowledgements. This paper is based on knowledge derived from earlier work completed under Contract DACW51-83-C-0005 with the New York District, Army Corps of Engineers. James R. Hill and Robert J. Hallermeier contributed significantly to the writing of the final report on that contract. G.K. Nersesian obtained valuable historical information from the files of the New York District, including the photos in Figures 5, 6, 7, and 8. We thank Eugene Ferrara of the New York Daily News for permission to reprint the photos, and Robert J. Hallermeier, John G. Housley, D. D. Davidson, Thorndike Saville, Jr., and Michael J. Piszker for comments on an earlier version of this manuscript. Herbert J. Bruder prepared all figures, and Sheila Zukor typed several versions of the paper. The preparation of this paper has been paid for by the senior author's consulting firm.

REFERENCES

Barwis, J.H., Perry, F.C., and LaGarde, V.E., "A Computer Aided Aerial Photographic Analysis of Fire Island Inlet Geomorphology," Miscellaneous Paper H-77-12, U.S. Army Engineer Waterways Experiment Station, Vicksburg, MS., 1977.

Bobb, W.H., and Boland, Jr., R.A., "Channel Improvement, Fire Island Inlet, New York; Hydraulic Model Investigation," Technical Report H-69-16, U.S. Army Engineer Waterways Experiment Station, Vicksburg, MS., 1969.

Dean, R.G., and Maurmeyer, E.M., "Predictability of Characteristics of Two Embayments," Coastal Sediments '77, American Society of Civil Engineers, 1977.

FitzGerald, D.M., "Sediment Bypassing at Mixed Energy Tidal Inlets," Proceedings, 18th Coastal Engineering Conference, Vol. II, 1983, pp. 1094-1118.

Galvin, Cyril, Coastal Engineer, "Fire Island Inlet Post-Storm Inspection, Saturday, 31 March 1984," letter report to M[illegible]. Rooney, New York District, Corps of Engineers, dated 2 April 1984.

Galvin, Cyril, "Review of General Design Memorandum for Project Works at Fire Island Inlet," Final report on Contract DACW51-83-C-0005 with New York District Corps of Engineers, 1985, 198 pp.

Galvin, Cyril, "Shoaling with Bypassing at Tidal Inlet," Proceedings, 18th Coastal Engineering Conference, ASCE, Vol. II, 1983, pp. 1496-1513.

Galvin, C.J., "Wave Climate and Coastal Processes," Water Environments and Human Needs, A.T. Ippen, ed., M.I.T. Parsons Laboratory for Water Resources & Hydrodynamics, Cambridge, MA., 1970, pp. 48-78.

Galvin, Jr., C.J. "Breaker Travel and Choice of Design Wave Height," Journal of Waterways and Harbors Division, ASCE, Vol. 95, No. WW2, 1969, pp. 175-200.

Gofseyeff, S., "Case History of Fire Island Inlet, New York:" Council of Wave Research, Engr. Foundation Proc., 3rd Annual Conf. on Coastal Engr., 1953, p. 272-305.

Kassner, J., and Black, J.A., "Fire Island Inlet, New York, Management of a Complex Inlet," Shore and Beach, 1983, pp. 3-8.

Kieslich, J.M., "Tidal Inlet Response to Jetty Construction," GITI Report 19, U.S. Army Coastal Engineering Research Center, Fort Belvoir, VA., 1981.

Saville, T., "Sand Transfer, Beach Control, and Inlet Improvements, Fire Island Inlet to Jones Beach, New York," Proceedings, 7th Coastal Engineering Conference, 1960, pp. 785-806.

Terchunian, Aram, "View Eastward of Fire Island Inlet, Long Island, New York," Shore and Beach, 1986, July Cover Photo.

U.S. Army Corps of Engineers, "Shore Protection Manual," Volumes 1 and 2, Coastal Engineering Research Center, U.S. Army Engineer Waterways Experiment Station, Vicksburg, MS., 1984.

CHAPTER 86

Experimental investigation of the wave and current motion over a longshore bar.

J. Buhr Hansen[1] & Ib. A. Svendsen[1]

Abstract

The results presented in this paper are from a series of experiments in a wave flume modelling the onshore-offshore water motions over a bar bottom profile.

In a true 3-dimensional natural situation the flow of water over the bar varies along the coast. In the experiments the flow of water over the bar is simulated by a controlled discharge through the flume.

1. INTRODUCTION

On a beach with a longshore bar there will in general be a net flow of water over the bar profile caused by the incident waves. The longshore discharge in the trough behind the bar will increase along the coast in the flow direction until it is finally released as a rip current. This study concentrates on the analysis of the on shore wave and current motion over the bar with changing net flow of water into the trough behind the bar.

In Hansen and Svendsen (1984) and Svendsen (1984) the undertow caused by waves on a plane beach with no longshore current and consequently no net on shore flow of water has been investigated. A more detailed literature review may be found in these papers and in Dally & Dean (1986) and Svendsen (1986). For completeness may be added that recently the authors have come across a note by Iwata (1970) in which some of the aspects of undertow has been discussed.

The present study shall be viewed as the first step towards a description and understanding of the full 3-dimensional water motion inside the breaker line on coasts with a longshore bar. The paper concentrates on the results of laboratory experiments aiming at an experimental verification of the theoretical model presented in Svendsen & Hansen (1986) included in these proceedings of the 20th ICCE (in the following referred to as I).

The situation studied is indicated in Fig. 1. The waves are assumed to be perpendicular to the bar and the shoreline. It is so far uncertain how the net flow of water over the bar varies along the coast. In our wave flume experiments the wave and current motion in a cross section is analysed subject to changing net flow of water over the bar simulating the varying conditions along the coast.

[1]Institute of Hydrodynamics and Hydraulic Engineering, Technical University of Denmark, Bygning 115, DK-2800 Lyngby, Denmark

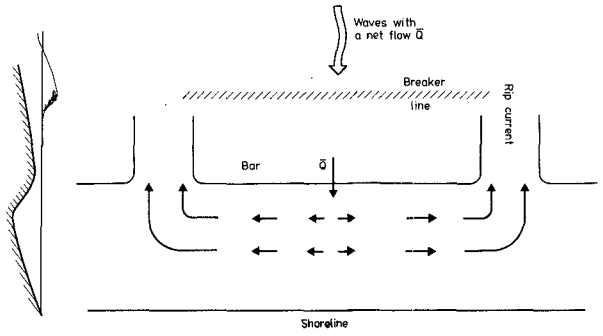

Fig. 1 The natural situation studied

2. EXPERIMENTAL SET-UP

The experiments were carried out in a 60 cm wide wave flume with a bar bottom profile, Fig. 2. The still water depth over the top of the bar is chosen to be approximately 0.6 • H, H being the wave height in relatively deep water. The net flow of water is generated artificially by a closed circuit circulation of water in the flume. The water is pumped from the trough shorewards of the bar - through the wave absorber - and fed back to the flume in front of the piston type wave generator. The water is sprayed onto the surface through 60 5 mm$^{\emptyset}$ holes in a 2 m long diffuser pipe placed above the water surface. The waves used through-out the experiments were generated as H = 12 cm, T = 2s using a non-sinusoidal time variation of the wave generator that yields a minimum of free harmonic disturbances. The still water depth in front of the wave generator was accurately adjusted to h_o = 340 mm in a situation with no waves but with the actual discharge being pumped through the flume[1].

The pumped discharge, Q, is in the series of experiments performed within the range 0 to 8 l/s. (The pumped discharge will be used as indicator of the net flow in the different tests.) The mean discharge per unit length of the coast is $\bar{Q} = 0.6 \cdot Q$. In Table 1 the actual mean current velocities $\bar{Q}/h$ in the different tests are given relative to

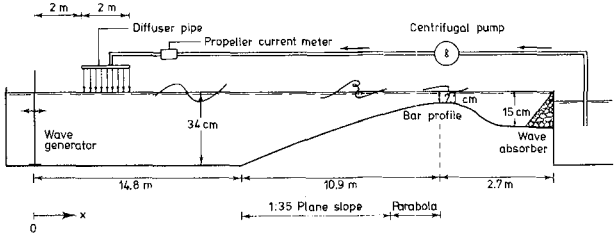

Fig. 2 Experimental set-up.

[1] During the tests the actual mean water depth in front of the wave-generator with both waves and current was 335 mm for the pumped discharges 0; 2.5 and 8.0 l/s but 329 mm for the discharge 5.0 l/s.

$\sqrt{gh}$ at different water depths, and relative to the measured wave particle velocity amplitude, $1/2(u_{w,c} - u_{w,t})$, at the bar crest. $u_{w,c}$ and $u_{w,t}$ are the wave particle velocities under the crest and through, respectively.

Q l/s	$\frac{\bar{Q}}{h\sqrt{gh}}$ at			$\frac{\bar{Q}}{h1/2(u_{w,c}-u_{w,t})}$ at
	'h=34omm'	breaking	bar crest	bar crest
0	0	0	0	0
2.5	o.0069	o.014	0.056	0.40
5	o.0141	o.03o	o.128	o.85
8	o.0219	o.050	o.181	1.36

Table 1. Wave and current combinations

The chosen system for flow generation in the flume has proven to be very succesfull since wave recording 1 m after the diffuser pipe has given heights $\bar{H}$ = 129 mm with a standard deviation of only 2 %. There is found no significant change due to changing discharge. The recorded wave height is 8 % greater than the wave height anticipated from the wave generator motion. This is due to the fact that the wave generator motion is calculated assuming a Stokes 2. order theory, while the Stokes parameter $UR = HL^2/h^3 \simeq 36$ indicates that a higher order theory ought to be applied.

3. EXPERIMENTAL TECHNIQUE AND DATA AQUISITION

For each discharge two independent sets of experiments were performed.

Initially a 'continuous' recording of the wave height H, the mean water surface MWS of set-up, b, and the wave celerity, c, was performed using the slowly travelling carriage technique described in Hansen and Svendsen (1979). In each of the test runs approximately 500 waves were recorded from 1 m after the diffuser pipe (x = 5 m) to 0.6 m after the bar crest (x = 26,3 m).

Subsequently a series of particle velocity measurements were made at selected vertical sections, and at a number of points between the bottom and the wave trough. In each of these tests simultaneous recordings were made by three wave gauges; One gauge at a fixed position 1 m in front of the diffuser pipe and two gauges 20 cm apart over the point of velocity measurement as indicated in Fig. 3. The velocities were recorded by a one component Laser Doppler Anemometer type DANTEC LDA04 with a 60 cm focussing distance which enabled the recordings to be taken in the middle of the wave flume.

The LDA analog output and the analog output from the three wave gauges were sampled by a computer based datalogging system every 15 ms, equivalent to 133 samples per wave period. A total of 30 waves were recorded in each test.

Particle velocity recordings are performed at 7 x-positions in the flume with one x-position (x = 18.81 m) before and 6 after breaking, the last one over the bar crest (x = 25,70 m). At each x-position the velocities are measured at 10-15 different levels, ζ, from 5 mm above

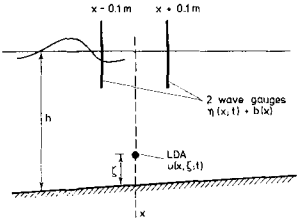

Fig. 3 Positioning of wave gauges and LDA measuring point.

the bottom to the wave through and in some cases to the MWS. Only horizontal particle velocities are recorded.

While the wave gauges are virtually unaffected by the presence of air bubbles in the water after wave breaking, bubbles may cause drop outs in the LDA signal. As the analog signal from the LDA system may be erroneous in case of drop outs, an electronic switch operated by the LDA lock detector output is installed between the LDA analog output and the datalogging system. This gives an easily detectable value (negative overflow in the ADC) in the sampled time series in case of drop out of the LDA signal. The drop outs may then be dealt with in the subsequent data analysis.

4. DATA ANALYSIS PROCEDURES

4.1 LDA drop outs, correction of erroneous data

The data analysis programme constructed to deal with the LDA drop outs and eventually other erroneous data operates on a three step basis

Step 1: The time series is scanned and all drop outs are detected. Single drop out data in otherwise valid series of data are replaced by the mean value of the two neighbour values.

Step 2: Of the remaining drop outs groups of min. 6 consecutive data (~ 0.1 s in time) are analysed for length and periodicity of occurence. In case of a reasonably well defined period of occurence and a reasonably constant drop out length these data are assumed to be recorded above the actual water surface and the velocities are set to zero.

Step 3: The remaining drop outs are replaced by the ensemble average figure calculated from the remaining data in the series. Further in this step all the time series are checked for obviously erroneous data due to neighbouring drop outs or electric noise. These are replaced by the ensemble average figures.

For the wave gauge recordings never more than 1 or 2 data within a series of 4090 are detected in step 3. For the velocity recordings well below the wave trough level a maximum of 2 % of the data are detected during the checking procedures, mainly in step 1.

When the velocity measuring point is above the wave trough level the number of erroneous data may be very high. Fig. 4 shows the first 4 periods of the processed velocity time series recorded 9 mm above trough

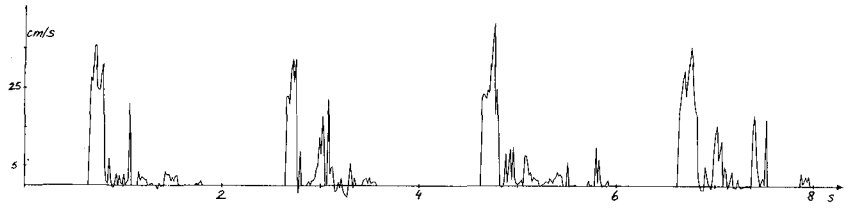

Fig. 4 Velocities recorded above the wave trough.

level at the crest of the bar where the wave height is 30 mm. In this whole series of 4090 data covering 30 wave periods 80 data are changed in step 1, 1900 set zero in step 2 and an additional 160 of the data are changed in step 3.

4.2 Main results from time series

All time series are analysed over an integer number of wave periods and the following figures determined:

1) The zero-up-crossing mean wave period: T = 2.00 s usually with a standard deviation below 0.03 s;
2) The mean value, $\bar{u}$ and b for the velocity and wave gauge recordings respectively;
3) The mean of the maximum values ($u_{w,c}$ and η_c) and minimum values ($u_{w,t}$ and η_t) relative to the mean value;
4) The RMS values relative to the mean (RMS(u_w) and RMS(η));
5) The mean 'wave heights'; and
6) The phase shift, or time lag Δt, between the signals from the two wave gauges used to determine the absolute wave celerity, $c_a = \Delta x/\Delta t$, with Δx = 0.2 m, cf. Fig. 3.

4.3 Separation of wave and turbulent components.

Although the waves are generated with a strictly constant wave period small and inevitable variations in the breaking may create appreciable variations in the period of each individual wave event, no matter how the period is defined. This implies difficulties in separating the turbulent part of the recorded signals from the (ordered) wave component. In fact the irregularities of both surface variation and particle motion makes it a non-trivial problem (even for strictly periodic waves) to decide what rightly is turbulence and what belongs to the wave motion (see also Svendsen, 1987).

In the present investigation we have used an ensemble average procedure to separate the turbulent part of the signal from the wave motion. This was found reasonable because the small variations in the wave periods mentioned above.

The ensemble wave component, $\tilde{\eta}$ and $\tilde{u}_w$ for surface elevation and velocity respectively, are then determined as the mean value of all 30 samples at the same phase of the wave. The standard deviation around each of the mean values represent the surface fluctuations, η', and velocity fluctuations (turbulence), u', respectively.

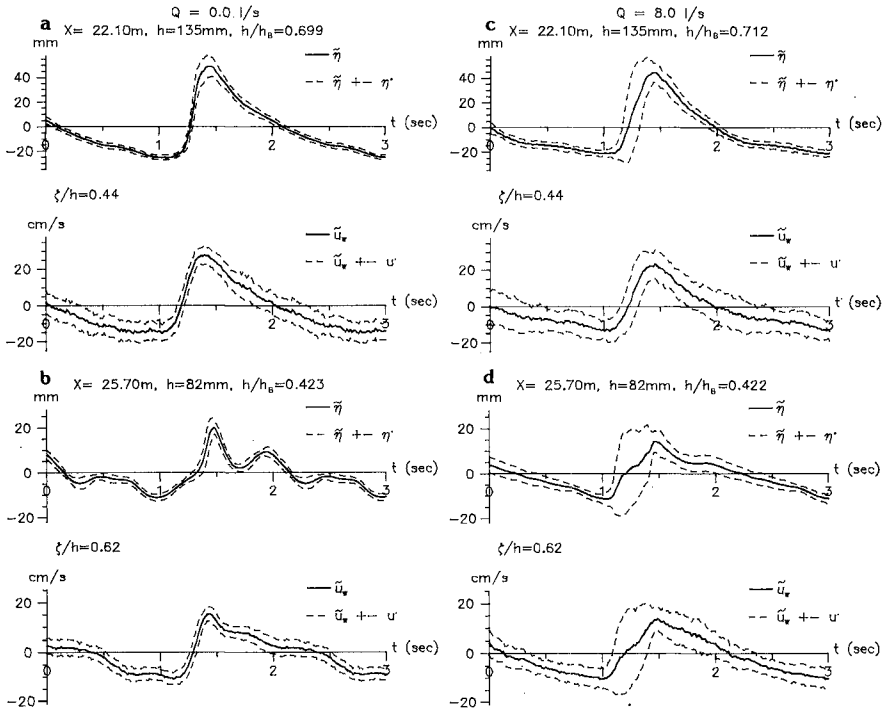

Fig. 5 Ensemble mean profiles for surface elevation, $\tilde{\eta}$, and wave particle velocities, $\tilde{u}_w$, at 2 positions for Q = 0 and 8 l/s.

In Fig. 5 are given the ensemble mean profiles for $\tilde{\eta}$ and $\tilde{u}_w$ from four different tests ($\tilde{\eta} \equiv 0$; $\tilde{u}_w \equiv 0$). The figure 5 further shows the surface fluctuations, η', and u'. In the cases a), b) and c) these are seen to be almost constant over the wave period. In Fig. 5 d), however, the level of fluctuations is considerably higher around the front of the wave than over the remaining part of the wave period. This tendency is observed only in the Q = 8 l/s case and only for measuring points with $h/h_B < 0.5$, where h_B is the breaker depth. For these points with $(\bar{Q}/h)/1/2(u_{w,c} - u_{w,t}) > .88$ the measured velocities are positive over the entire wave period, and the standard deviations on T is as large as 0.2•T. Consequently, in that case, the u' cannot be viewed as turbulence around the wave front, but over the remaining part of the profile the u' level is virtually unaffected by the variations of the wave period.

The chosen ensemble averaging procedure will always yield signal amplitudes smaller than the mean of the individual 'heights'. In the surf zone the height of the ensemble profile is in general 0.91 times the mean of the individual heights. However, in the tests with large variations of the wave periods the ratio is as small as 0.76.

4.4 Accuracy of experimental results

From experiments using the slowly travelling carriage technique reported by Hansen & Svendsen (1979) it is established that the recorded wave heights and water level changes is very accurate. This is also the case for the measured wave celerities up to the point of breaking. In the surf zone, however, the surface fluctuations may cause widely scattered c values. As the second type of experiments performed in this study determines the wave celerity from 30 consecutive waves instead of one wave these results show much smaller scattering and will be used throughout the study.

The wave height and water level changes from the two types of experiments are in Fig. 6 seen to be in close agreement. In figure 6 the 'continuous' wave recordings are compared with the mean values from all individual waves, $\bar{H}$ and b, recorded in the time series. The standard deviation on $\bar{H}$ is less than 2 mm and on the set-up's less than 0.3 mm in all positions but one (x = 21.23) which is the first measuring

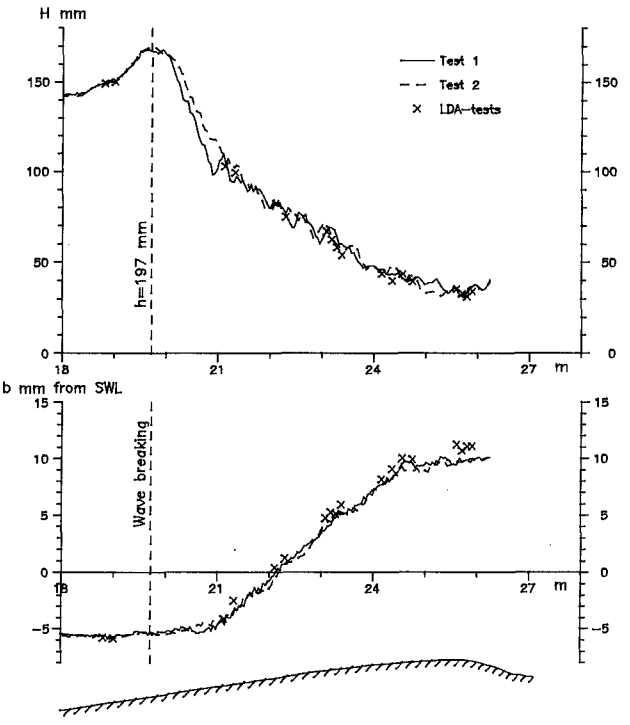

Fig. 6 Reproducibility of wave heights and water level changes for Q = 0. Test 1 and test 2 from 'continuous' wave recordings; LDA-tests are $\bar{H}$ and b from time series.

position after breaking. Fig. 6 is for the Q = 0 case, but the same tendency is clearly observed for other Q values.

Also the velocity measurements show a larger variation near the breaking point than elsewhere. The largest scattering obtained from repeating the same measurement several times is found at x = 21.23 m. Fig. 7 shows the results for the mean velocity, $\bar{u}$, (undertow) from a total of 7 test series. The large variation on the mean values indicates that the 30 waves used in each test is a too small number for a proper averaging at this point. At all other points the variance is much smaller and 30 waves define the mean sufficiently accurately. The results presented in the following chapter of this paper are taken as the mean value of all tests at any particular position and height.

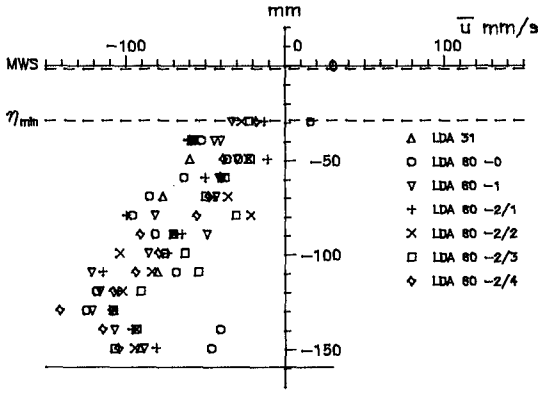

Fig. 7 Repeated measurements of undertow (Q = 0) at x = 21.23 m; h/h_B = 0,80

5. DISCUSSION OF RESULTS

5.1 Surface elevations

As the waves in front of the sloping bed are seen to be virtually unaffected by the superimposed currents this may be expected also to be the case about wave breaking where $(\bar{Q}/h)/\sqrt{gh} \leq 0.05$, see Tables 1 and 2. The point of wave breaking is defined as the point with $(H/h)_{max}$ in the 'continuous' wave recordings; the position varies from x = 19.34 m for Q = 2.5 l/s (h = 205 mm) to x = 19.82 m for Q = 8 l/s (h = 194 mm). When considering that small irregularities in the recorded waves may easily shift the position of $(H/h)_{max}$ point ± 20 cm (see Fig. 6) it is reasonable to conclude that the wave breaking is not significantly influenced by the current.

From the wave data at the bar crest included in Table 2 it appears that the decay of the waves over the surf zone and the set-up, b, are not significantly influenced by the current either. However, the H/h value at the bar crest seems to be increasing with increasing current, which might indicate that the intensity of the wave breaking is reduced with increasing flow velocity. These mechanisms are discussed more detailled in I.

All time series measurements in the surf zone are assumed to be within the inner region of the surf zone as defined in Svendsen et al (1978). This is analysed further in I.

Q	At breaking (from 'continuous' wave recording)				At bar crest (from time series)			
l/s	H_B mm	$\Delta b^{2)}$ mm	h_B mm	H_B/h_B	$\bar{H}^{1)}$ mm	$\Delta b^{2)}$ mm	h mm	$\bar{H}/h$
0	170	-0,6	197	o.87	33.o	16.5	82	o.41
2.5	163	-0,8	205	o.79	37.6	17.6	83	o.45
5	162	-0,5	198	o.82	33.4	15.3	76[3]	o.44
8	156	-0,8	194	o.80	38.5	15.6	82	o.47

1) $\sigma_{H/\bar{H}} \sim 0.1$ in all tests. 2) Relative to MWS at h_o = 340 mm
3) See footnote p. 2

Table 2 Wave characteristics at breaking and at the bar crest

The dimensionless wave energy flux, B_o, is from Fig. 8 seen also to be unaffected by Q, but is, on the other hand, seen to vary considerable over the surf zone with a maximum at $h/h_B \sim 0.6$ and $H/H_B \sim 0.45$. Fig. 8 and Fig. 9 are both included for later comparisons with the velocity measurements.

The absolute wave celerity, c_a, is significantly increasing for increasing discharge through the wave flume. As should be expected, however, the relative celerity c_r given by $c_r = c_a - U$ (where U is the current velocity averaged over the depth) is in Fig. 10 seen to be independent of the pumped discharge.

U is determined from the results given in Fig. 11 as the mean value of $\bar{u}$ from the bottom to MWS, where values above trough level have in most cases been obtained by extrapolation.

A possible interpretation of the results for c_r is that $c_r = \alpha\sqrt{gh}$. This has been used in I with an assumed constant α value. The measured c_r can also be said to agree well with the bore celerity, c_{bore}, as given by

$$\frac{c_{bore}^2}{gh} = 1/2 \frac{d_t \cdot d_c}{h^3} \left(d_t + d_c\right)$$

(eq. 44 in Svendsen et al (1978), where d_t and d_c are the water depth under wave trough and crest, respectively.

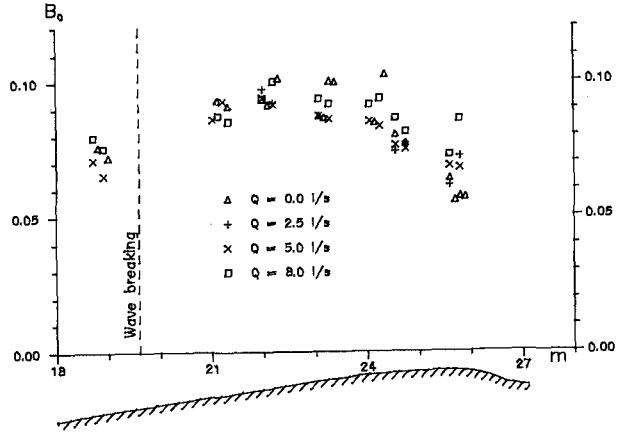

Fig. 8 $B_o = \overline{\tilde{\eta}^2}/H^2$ for the ensemble mean surface profiles .

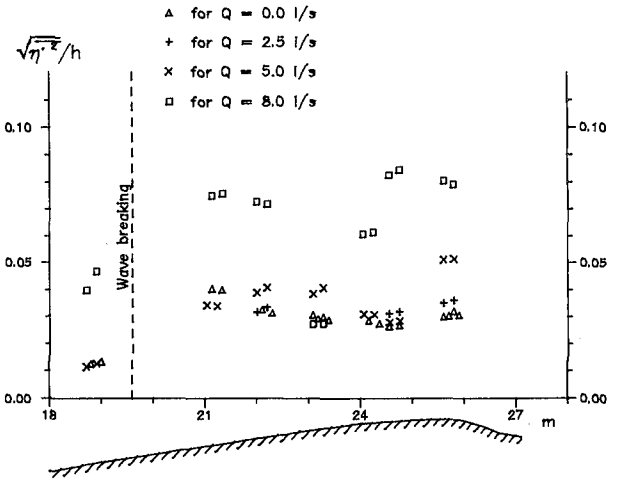

Fig. 9 Surface fluctuations η'.

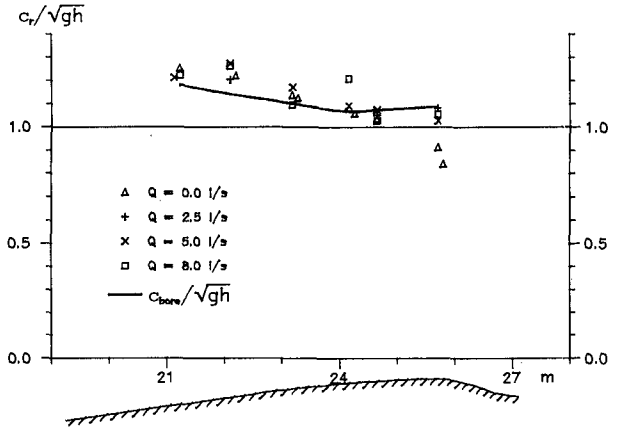

Fig. 10 Relative wave celerity

5.2 Particle velocities

Mean velocities are calculated from the time series as $\bar{u}$ over the total number of periods. The results are compiled in Fig. 11 for all horizontal and vertical positions and for the four different discharges through the flume. The mean velocities for different discharges all show similar depth variations. Only at the two positions closest to breaking (x = 21.23 m and 22.10 m) do the big scatter in the individual results obviously distort the general trend. As previously pointed out (see Fig. 7) the vigorous breaking and associated large variations from wave to wave in this regiuon causes a considerable scatter in the results when averaged over -only- 30 consecutive waves.

The volume flux, Q_s, due to the waves may also be determined from

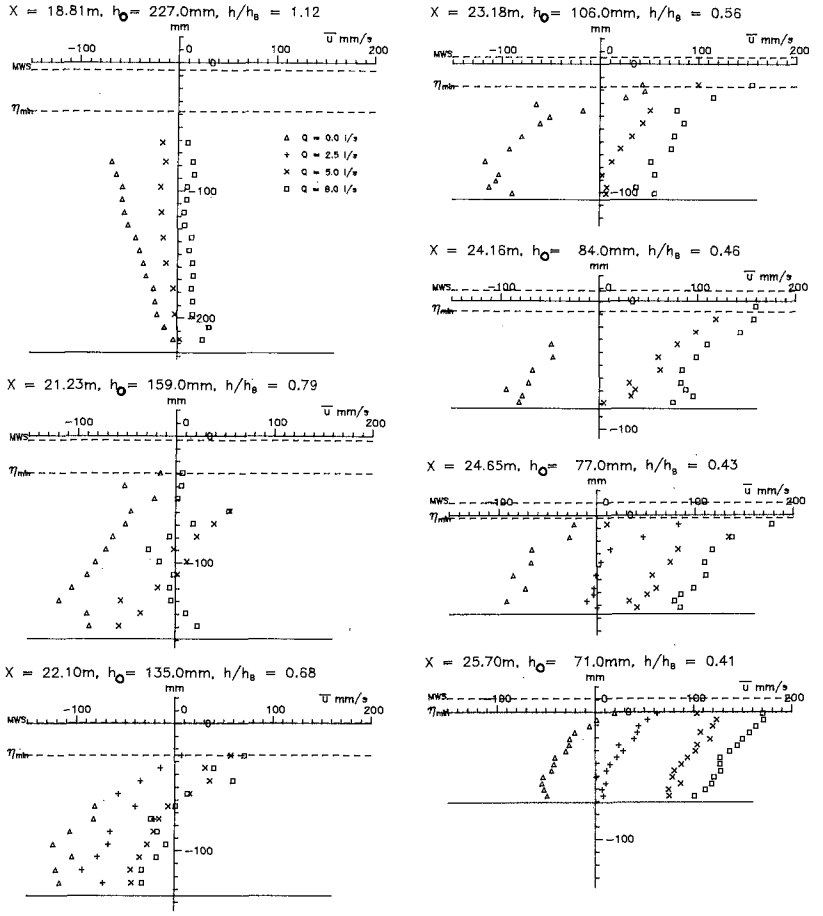

Fig. 11 Mean Eulerian velocities at 7 positions for four different Q values.

the measurements. The depth integrated, time averaged continuity equation reads $\bar{Q} = Q_c + Q_s$. Here Q_c is the mean discharge from bottom to MWS, $Q_c = U \cdot h$. As $\bar{Q}$ is known from the pumped discharge, Q_s can be determined and the results are given in Fig. 12. They show a considerable scatter indicating how delicate these calculations are and how sensitive they are to the accuracy of the recorded $\bar{u}$ or U values. This particularly applies to situations where U is primarily due to $\bar{Q}$ so that Q_s is determined as the difference between two large numbers.

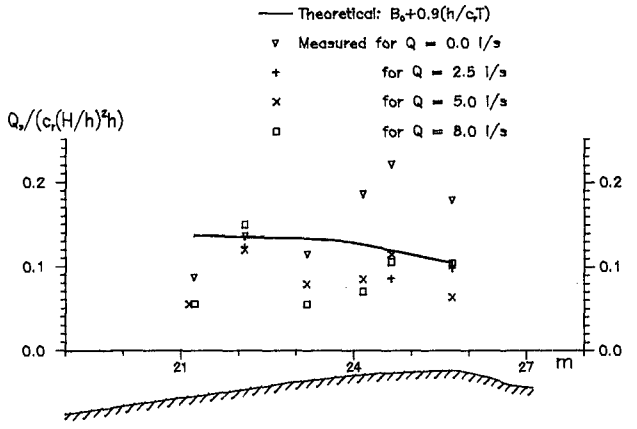

Fig. 12 Theoretical and 'measured' mass flux Q_s due to waves.

Fig. 12 also shows the values of Q_s used in I but calculated from the measured c_r and H as given in Fig. 8 and 10. The 'theoretical' Q_s values are generally higher than the measured values.

The wave particle velocities, $\tilde{u}_w$, for Q = 0 l/s and Q = 8 l/s are shown in Fig. 13. For the 2.5 and 5 l/s cases the picture is exactly the same.

The relation between the surface elevations η and the particle velocities u_w are to the lowest order of approximation

$$u_w = \sqrt{gh} \cdot \frac{\eta}{h}$$

or, when averaged over the period

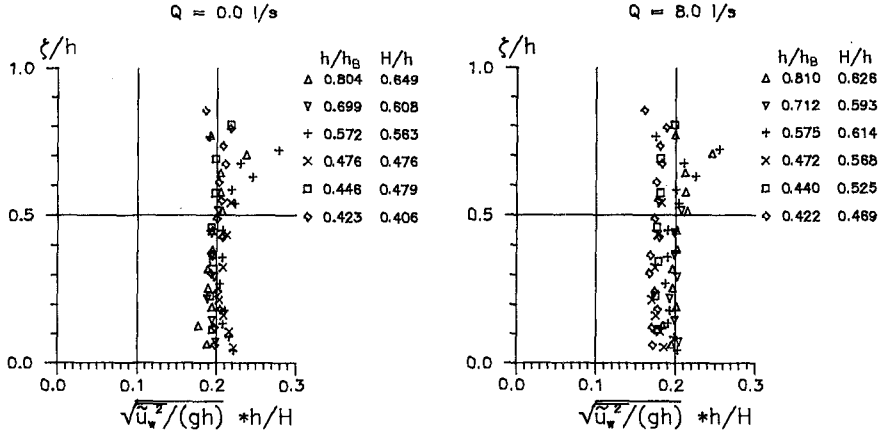

Fig. 13 Kinetic energy in ensemble mean wave particle motions.

$$\sqrt{\frac{\tilde{u}^2}{\frac{w}{gh}}} \cdot \frac{h}{H} \approx \sqrt{B_o}$$

When the velocities are calculated from the surface recordings using this relation (Fig. 8 shows $\sqrt{B_o}$ values ranging from 0.25 to 0.31) they are significantly overestimated.

The implication of this is that in the theoretical results in I B_o should only represent $\overline{\eta^2}$. Where B_o represents $\overline{u^2}$ contributions a smaller value than B_o should be used. A closer analysis is left for future studies.

The velocity fluctuations (turbulence) are shown in Fig. 14 for the two cases Q = 0 l/s and 8 l/s. The significant decrease in turbulence level for decreasing water depth found in the Q = 0 l/s case does not appear in any of the three other current situations.

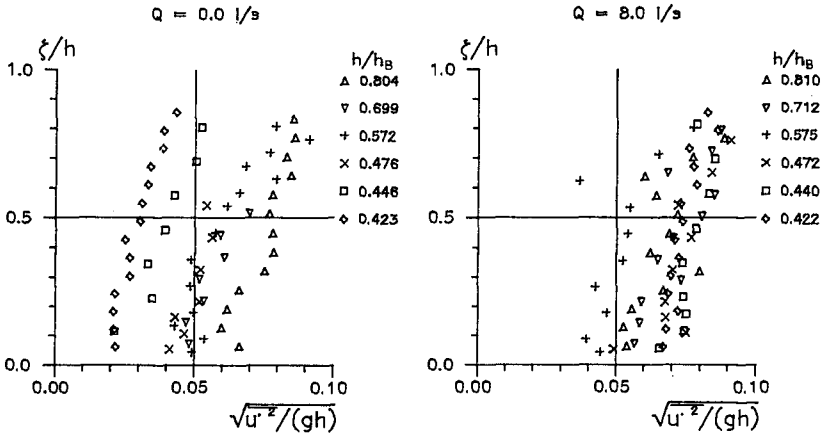

Fig. 14 Turbulent energy in recorded particle motions.

Svendsen (1987) has analysed other available data on surf zone turbulence. The total turbulent kinetic energy, k, may be estimated from u' component as

$$k = \frac{1}{2} \cdot \frac{1}{0.43} \overline{u'^2} = 1.08^2 \overline{u'^2}$$

(Svendsen (1987) eq. 3.1). The results given in Fig. 14 are from this seen to be in close agreement with the results of Stive & Wind's test No. 1 as analysed in Svendsen (1987). It is interesting to notice, that the level of surface fluctuations, $\overline{\eta'^2}/h^2$, as given in Fig. 9 are of the same order of magnitude as the $\overline{u'^2}/gh$ given in Fig. 14. The implication of this and other aspects of the turbulence will be analysed further.

The analysis of the results continues. The theoretical model given in I and the experiments reported here are used interactively to gain further insight into the problem studied.

6 REFERENCES

Dally, W.R. & R.G. Dean (1986) Discussion on: Mass flux and underflow in a surf zone, by I.A. Svendsen Coastal Engineering, 10, 289-299

Hansen, J. Buhr & I.A. Svendsen (1979) 'Regular waves in shoaling water-Experimental data', Series paper 21, Inst. Hydrodyn. and Hydraul. Eng. (ISVA), Techn. Univ. Denmark

Hansen, J. Buhr & I.A. Svendsen (1984) 'A theoretical and experimental study of undertow', Proc 19. International Conf. Coastal Eng., Houston, ch. 151, 2246-2262

Iwata, N. (1970) A note on wave set-up, longshore currents and undertows, J. Oceanogr. Soc. Jap., 26, 4, 233-236

Svendsen, I.A., P.Å. Madsen and J. Buhr Hansen (1978) 'Wave Characteristics in the Surf Zone, Proc. 16th Int. Conf. Coastal Eng., Hamburh, Vol I, chap. 29, 520-539

Svendsen, I.A. (1984) 'Mass flux and undertow in a surf zone', Coastal Engineering 8, 4, 347-365

Svendsen, I.A. (1986) Reply to Dally & Dean (1986) Coastal Engineering 10, 299-307

Svendsen I.A. & J. Buhr Hansen (1986) 'The interaction of waves and currents over a longshore bar', Proc. 20. International Conf. Coastal Eng., Taipei (Denoted I in text)

Svendsen, I.A. (1987) 'Analysis of surf zone turbulence' To be published in Journ. of Geoph. Res. (Also Danish Center for Applied Mathematics and Mechanics, Report No. 330, July 1986)

CHAPTER 87

TWO-DIMENSIONAL EMPIRICAL EIGENFUNCTION MODEL FOR THE ANALYSIS AND PREDICTION OF BEACH PROFILE CHANGES

T.-W. Hsu[1], S.-R. Liaw[2], S.-K. Wang[2] and S.-H. Ou[3]

ABSTRACT

A two-dimensional empirical eigenfunction model is proposed for the analysis and the prediction of beach profile change due to longshore and cross-shore sediment transports. Beach profile data from Redhill coast, Taiwan, measured every two months at 150 meters interval along the detached breakwaters are analyzed and the relative importance from two directions is investigated. Furthermore, by employing the method of Markov process and linear regression, a prediction model is formulated which takes into account the effect of breaking waves, bottom sediment and radiation stress of waves. This 2-D model is shown to be effective in the analysis and the prediction of beach changes near the coastal structures.

INTRODUCTION

The movement of coastal sediment can be decomposed into longshore component and cross-shore component. Longshore transport is defined as sediment transport parallel to the beach, while cross-shore transport is defined as transport perpendicular to the beach. These components are both significant in response to seasonal variations in the forcing parameters such as waves, tides, winds and currents. Therefore, beach profile changes due to longshore and cross-shore transport should be separated and represented as a time series in order to obtain a detailed understanding.

Winant et al.(1975) proposed a method to describe beach changes in terms of empirical eigenfunctions. The usefulness of the eigenfunctional representation was confirmed as a concise method of representing beach profile changes

1 Graduate student, MS. Eng.
2 MS. Eng., former graduate student
3 Dr. Eng., Professor and Chairman
Department of Hydraulics and Ocean Engineering
National Cheng Kung University, Tainan, Taiwan 70101
Republic of China

(Aubrey, 1978; Aranuvachapun and Johnson, 1979). Uda and Hashimoto (1982) proposed a new model to analyze the beach changes due to longshore and cross-shore sediment transports. They used longshore eigenfunctions and cross-shore eigenfunctions to describe temporal variations of beach profile changes. However, the cross-shore eigenfunctions were taken as a time average in their analysis and only the longshore eigenfunctions changing with time. This implies that the beach profile change is independent of cross-shore sediment transport.

The aim of this paper is to extend Uda and Hashimoto's concept and proposes a 2-D empirical eigenfunction model for the analysis and the prediction of beach profile changes for temporal and spatial variation where both longshore and cross-shore sediment transport are significant. Field observation of beach profiles obtained from Redhill, Taiwan, are examined and the relative importance of beach changes from two orthogonal modes is also given. In addition, a prediction model is formulated by employing the method of Markov process and linear regression. The results of prediction model are compared with the existing models and measured data.

THEORETICAL FORMULATION

One-Dimensional Empirical Eigenfunction Method

The method has been described by Winant et al. (1975). In brief, an eigenfunction is expressed in the form of

$$h_{xt} = \sum_n e_{nx} C^*_{nt} \tag{1}$$

where the h_{xt} are the beach profile data, e_{nx} represent the spatial eigenfunctions, C^*_{nt} represent temporal eigenfunctions, and n represent the variation modes.

The spatial eigenfunctions form an orthogonal set as

$$\sum_n e_{nx}\, e_{mx} = \delta_{nm} \tag{2}$$

where δ_{nm} is Kronecker delta.

The spatial correlation matrix A is expressed as

$$A = \begin{bmatrix} a_{11} & a_{12} & a_{13} & \cdots & a_{1n} \\ a_{21} & a_{22} & a_{23} & \cdots & a_{2n} \\ \vdots & \vdots & \vdots & & \vdots \\ \vdots & \vdots & a_{ij} & & \vdots \\ \vdots & \vdots & \vdots & & \vdots \\ a_{n1} & a_{n2} & a_{nj} & \cdots & a_{nn} \end{bmatrix} \tag{3}$$

In which, the elements of matrix A are defined by

$$a_{ij} = \frac{1}{N_x N_t} \sum_t h_{it}\, h_{jt} \tag{4}$$

where N_x is the number of data points per profile, N_t is the

number of measured times. The matrix A possesses a set of eigenvalues λ_n and a set of corresponding eigenfunctions e_{nx} which are defined by matrix equation

$$A\, e_{nx} = \lambda_n\, e_{nx} \tag{5}$$

The temporal eigenfunctions are calculated with

$$C^*_{nt} = \sum_x h_{xt}\, e_{nx} \tag{6}$$

By defining $C_{nt}=C^*_{nt}/(\lambda_n N_x N_t)^{1/2}$, it can be shown that C_{nt} form an orthogonal set, and eq.(1) is rewritten as

$$h_{xt} = \sum_n (\lambda_n N_x N_t)^{1/2}\, e_{nx}\, C_{nt} \tag{7}$$

Analysis of 2-D Empirical Eigenfunction Method

Following Uda and Hashimoto (1982), we extend the 1-D empirical eigenfunction method to the 2-D bed elevation h(x,y,t), which is a function of offshore distance x, and longshore distance y at a certain time t. The expression of h(x,y,t) is as follow

$$h(x,y,t) = \sum_k e_k(x,t)\, e_k(y,t) \tag{8}$$

In this expression, $e_k(x,t)$ are the cross-shore eigenfunctions, $e_k(y,t)$ the longshore eigenfunctions, k the variation modes. Eq.(8), obviously, represents the variation of the beach profile configuration in terms of longshore and cross-shore distances at the specific time t. In some cases, such as the profile configuration around a coastal structure or a rhythmic topography, it is desirable to use the data of all profiles for the analysis of spatial characteristic beach changes instead of the single beach profile.

The cross-shore eigenfunctions form an orthogonal set as

$$\sum_x e_n(x,t)\, e_m(x,t) = \delta_{nm} \tag{9}$$

In order to generate the cross-shore eigenfunctions, like the correlation matrix A, a symmetric matrix B is formed with elements of

$$b_{ij} = \frac{1}{N_x N_y} \sum_y h(i,y,t)\, h(j,y,t) \tag{10}$$

where N_y denotes the total number of measured points alongshore. The matrix B are real matrix with a set of eigenvalues λ_k and a set of corresponding eigenfunctions $e_k(x,t)$

$$B\, e_k(x,t) = \lambda_k\, e_k(x,t) \tag{11}$$

The longshore eigenfunctions $e_k(y,t)$ which define the longshore changes of beach profile are evaluated as

$$e_k(y,t) = \sum_x h(x,y,t)\, e_k(x,t) \qquad (12)$$

In the analysis of beach profile changes due to longshore and cross-shore sediment transports, Uda and Hashimoto (1982) took the cross-shore eigenfunctions $e_k(x,t)$ to be independent of time and only let the longshore eigenfunctions $e_k(y,t)$ changing with time. This means that the nature of variations doesn't depend on cross-shore sediment transport. This paper allows $e_k(x,t)$ and $e_k(y,t)$ to vary with distance and time respectively. The expressions of $e_k(x,t)$ and $e_k(y,t)$ are given as follows,

$$e_k(x,t) = \sum_n (\lambda_n N_x N_t)^{1/2}\ e_k^n(x)\ C_{kx}^n(t) \qquad (13)$$

$$e_k(y,t) = \sum_m (\lambda_m N_x N_t)^{1/2}\ e_k^m(y)\ C_{ky}^m(t) \qquad (14)$$

where $e_k^n(x)$: cross-shore spatial eigenfunctions
$C_{kx}^n(t)$: cross-shore temporal eigenfunctions
$e_k^m(y)$: longshore spatial eigenfunctions
$C_{ky}^m(t)$: longshore temporal eigenfunctions

Formulation of the Prediction Model

In order to relieve forecast errors, the variation of beach profile subtracted the mean beach profile from the original data is used. By this method, the set $h(x,y,t)$ is expressed as

$$h(x,y,t) = \bar{h}(x,y) + \sum_k e_k'(x,t)\, e_k'(y,t) \qquad (15)$$

where $\bar{h}(x,y)$ is the temporal mean of the beach profile. A prime on the eigenfunctions indicates that these eigenfunctions are similar in data sets where the mean profile has not been removed. According to eqs.(13) and (14), $e_k'(x,t)$ and $e_k'(y,t)$ can be expressed, respectively, in the form of

$$e_k'(x,t) = \sum_n (\lambda_{nx} N_x N_t)^{1/2}\ e_k^{n'}(x)\ C_{kx}^{n'}(t) \qquad (16)$$

$$e_k'(y,t) = \sum_m (\lambda_{my} N_x N_t)^{1/2}\ e_k^{m'}(y)\ C_{ky}^{m'}(t) \qquad (17)$$

The fluctuations of beach profile are calculated as

$$h'(x,y,t) = h(x,y,t) - \bar{h}(x,y) \qquad (18)$$

$h'(x,y,t)$ was used to generate eqs.(16) and (17) by processing the procedure of the analysis of 2-D empirical eigenfunction method.

The predictands for prediction model always consist of a representation of the beach profile time series. Accordingly, it is necessary to forecast the next time step eigenfunctions $C_{n(j+1)}$ and let the spatial eigenfunctions $e_k(x)$ and $e_k(y)$ to be constants.

The Markov process based on Sonu (1973) and three forcing parameters were used here to estimate the temporal eigenfunctions $C'_{n(i+1)}$ in the prediction model. The simplest linear equations can be described as

$$\begin{aligned} C'_{1(i+1)} &= \overline{a_{11}}C'_{1i} + \overline{a_{12}}C'_{2i} + \ldots + \overline{a_{1n}}C'_{ni} + \overline{a_{1(n+1)}}F_{i+1} \\ C'_{2(i+1)} &= \overline{a_{21}}C'_{1i} + \overline{a_{22}}C'_{2i} + \ldots + \overline{a_{2n}}C'_{ni} + \overline{a_{2(n+1)}}F_{i+1} \\ &\vdots \\ C'_{n(i+1)} &= \overline{a_{n1}}C'_{1i} + \overline{a_{n2}}C'_{2i} + \ldots + \overline{a_{nn}}C'_{ni} + \overline{a_{n(n+1)}}F_{i+1} \end{aligned} \tag{19}$$

or

$$\begin{bmatrix} C'_{1(i+1)} \\ C'_{2(i+1)} \\ \vdots \\ C'_{n(i+1)} \end{bmatrix} = \begin{bmatrix} \overline{a_{11}} & \overline{a_{12}} & \ldots & \overline{a_{1n}} & \overline{a_{1(n+1)}} \\ \overline{a_{21}} & \overline{a_{22}} & \ldots & \overline{a_{2n}} & \overline{a_{2(n+1)}} \\ \vdots & \vdots & & \vdots & \vdots \\ \overline{a_{n1}} & \overline{a_{n2}} & \ldots & \overline{a_{nn}} & \overline{a_{n(n+1)}} \end{bmatrix} \begin{bmatrix} C'_{1i} \\ C'_{2i} \\ \vdots \\ F_{i+1} \end{bmatrix} \tag{20}$$

where $\overline{a_{11}} \ldots \overline{a_{n(n+1)}}$ are constant coefficients, F_{i+1} are the dimensionless forcing parameters for the next time step.

Three forcing parameters corresponding to breaking waves, features of bottom sediment transport and radiation stresses of waves were taken into account in the present method. The reason why these three parameters are chosen is that they have been used in the past with degrees of success to describe nearshore process. Based on Battjes (1974), the characteristics of breaking waves can be described by surf similarity parameter ζ defined by

$$\zeta = \tan\beta \; / \; (H/L_0)^{1/2} \tag{21}$$

where $\tan\beta$ is the bottom slope, H wave height, L_0 wave length in deep water. The features of bottom sediment transport can be classified by the parameter C proposed by Gourlay (1968)

$$C = H_0 \; / \; wT \tag{22}$$

where w is the fall velocity of sediment determined by the characteristics of sand and kinematic viscosity of the fluid and T is the wave period. The radiation stresses of inclined waves are written as (Bowen,1969)

$$S = \begin{bmatrix} S_{xx} & S_{xy} \\ S_{yx} & S_{yy} \end{bmatrix} = \begin{bmatrix} S_{rr}\cos^2\alpha + S_{ss}\sin^2\alpha & (S_{rr}-S_{ss})\sin\alpha\cos\alpha \\ (S_{ss}-S_{rr})\sin\alpha\cos\alpha & S_{rr}\sin^2\alpha + S_{ss}\cos^2\alpha \end{bmatrix} \tag{23}$$

with

$$S_{rr} = E(2n-1/2) \;, \quad S_{ss} = E(n-1/2) \;, \quad E = 1/8\,\rho g H^2$$

where r is the direction of wave propagation, s is the direction normal to the wave propagation, x is cross-shore coordinate, y is longshore coordinate, α is the angle be-

tween wave crest and beach, n is the ratio of wave group velocity to wave celerity, E is wave energy, ρ is density and g is gravity acceleration. A dimensionless wave energy was introduced for the consistent dimension of forcing parameters

$$E_0 = (1/8\ \rho g H^2) \ / \ (1/8\ \rho g H_0^2) \tag{24}$$

It is convenient to write eq.(19) in general matrix notation as

$$P = \overline{A} \cdot D \tag{25}$$

where P is the (m•N) matrix of m quantities to be predicted, D is the (n•N) matrix of n data parameters and $\overline{A}$ is an (m•n) coefficient matrix, N is the total number of observations of these quantities which are to be used in the prediction. The optimal form of the coefficient matrix $\overline{A}$ was determined by using the linear regression:

$$\overline{A} = C_{PD}\ C_{DD}^{-1} = (P \cdot D^T)\ (D \cdot D^T)^{-1} \tag{26}$$

where C_{PD} denotes the covariance matrix between the predict-and and data, C_{DD} is the auto-covariance matrix of the data, and T is the transpose operator.

The estimator of matrix P is used for both hindcast and forecast models. A hindcast model is defined as the estimate made from the same data and the predictand which are used to form the covariance matrix, whenas a forecast model is defined as the estimate made from the covariances formed from other data and predictand samples. According to Davis (1976), the hindcast skill can be represented by a predictability index S_H:

$$S_H = 1 - \frac{E(P-\hat{P})\ (P-\hat{P})^T}{E(PP^T)} \tag{27}$$

in which E represents the expected value operator, $\hat{P}$ denotes the estimated value. The hindcast skill increases with the higher value of S_H. On the other hand, the forecast ability was described by the mean-square-forecast error S_F:

$$S_F = \frac{E[h(x,y,t) - \hat{h}(x,y,t)][h(x,y,t)-\hat{h}(x,y,t)]^T}{E[h(x,y,t)][h(x,y,t)]^T} \tag{28}$$

where $\hat{h}(x,y,t)$ is the estimated bed elevation. A model is predictable with lower mean-square-forecast error.

FIELD DATA

Beach Profile Data

As shown in Fig.1, Redhill coast is located in the southern part of Taiwan and consists of eroding sandy bluffs ranging from 6 to 10 meters high. Fig.2 shows the detached breakwaters built on the shoreline to prevent waves from reaching the eroding shore.

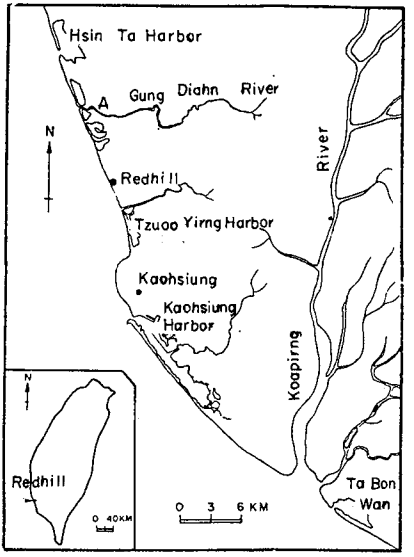

Fig. 1 Location of Redhill coast

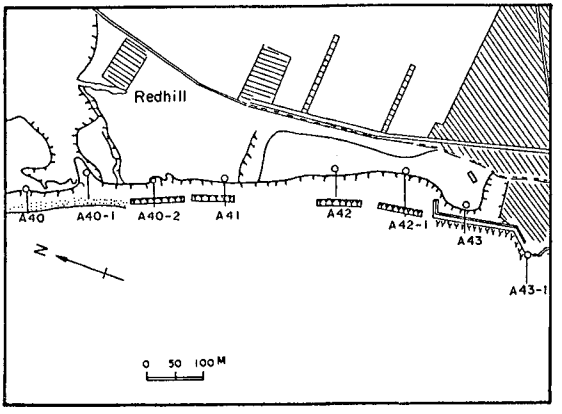

Fig. 2 Alignment of detached breakwaters and observed positions

The beach sand has median grain size of 0.28mm and submerged specific gravity of 1.6 Surveys of the beach profile have been conducted at every two months from 1982 to 1984. Each profile was measured at some intervals over a distance about 600m offshore. A detailed measurement was done on the foreshore part by using standard surveying method, while depth measurements on the offshore part were taken by cable lead.

Wave Climate of Redhill Coast

There are no wave data available at Redhill coast. The wave data observed at Ta Bon Wan located about 48km south of Redhill coast (Fig.1) have been used. The wave height at Ta Bon Wan was measured at the depth of 12.5 meters using a pressure wave gage. In winter, the prevailing direction of incoming wave at Ta Bon Wan is NNE, and waves from various directions were partly sheltered by land. The cumulative relative energy $P_E(\theta)$ is given by

$$P_E(\theta) = \frac{1}{m_0} \int_{-\pi/2}^{\theta} \int_0^{\infty} S(f,\theta)\, df\, d\theta \qquad (29)$$

where $S(f,\theta)$ is directional wave spectrum, f is angular frequency, θ is the azimuth measured counterclockwise, and m_0 is the total wave energy expressed as

$$m_0 = \int_{-\pi/2}^{\pi/2} \int_0^{\infty} S(f,\theta)\, df\, d\theta \qquad (30)$$

For NNE directional waves, the azimuths θ_1 and θ_2 were taken as -45° and 31° for Redhill coast and for Ta Bon Wan, respectively. The wave height ratio k_d between Redhill coast and Ta Bon Wan is determined by using SWOP directional spectrum

$$k_d = \sqrt{P_E(\theta_1) / P_E(\theta_2)} = 3.15 \qquad (31)$$

In summer, since the SW directional incoming wave is almost perpendicular to the coast, wave data from Ta Bon Wan can be directly applied to Redhill coast without any modification.

Based on Sawaragi (1982), the response of the beach to the various kinds of incident waves can be expressed in terms of a representative wave calculated by the following formulas:

representative wave period: $$T_S = \sum_i T_i\, p_i / P_T \qquad (32)$$

representative wave height: $$H_S^2 C_{gS} P_T = \sum_i C_{gi} H_i^2 p_i \qquad (33)$$

representative wave direction:
$$H_S^2 C_{gS} \sin\alpha_S \cos\alpha_S\, P_T = \sum_i H_i^2 C_{gi} \sin\alpha_i \cos\alpha_i\, p_i \qquad (34)$$

where H_i: component wave height
H_S: representative wave height
T_i: component wave period

T_s: representative wave period
α_i: component wave direction
α_s: representative wave direction
C_{gi}: representative wave group velocity
p_i: component probability
$P_T = \sum_i p_i$=total probability

RESULTS AND DISCUSSION

Results of Beach Profile Analysis

The 2-D empirical eigenfunction analysis was conducted by using the beach profile data collected at Redhill coast from December, 1982 to December, 1984. The total number of recording times is N_t=13 and that of calculating points N_x=20, N_y=8.

Fig.3(a) shows the cross-shore profiles of section A40-2 of the first three spatial eigenfunctions e_1^1(solid line), e_1^2 (dash-dot line) and e_1^3 (dash line). The temporal eigenfunctions are given by C_{1x}^1(solid line), C_{1x}^2(dash-dot line) and C_{1x}^3(dash line) as shown in Fig.3(b). The first spatial eigenfunction is interpreted as the mean beach function according to Winant et al.(1975). The time dependence of the mean beach function is almost constant, indicating a stable beach for Redhill coast. The second spatial eigenfunction has a minimum at the location of summer berm and a maximum in the area of winter bar. The negative value of the second temporal eigenfunction accounts for the sand migration up to the level of the summer berm, while the positive value indicates the movement of sand down beach to the winter bar and hence represents erosion on the beach. The third spatial eigenfunction has positive value in the broad region from shoreline to about 400m and negative value in the offshore region. The corresponding temporal eigenfunction is found to have positive values before December, 1983 and negative values after December, 1983.

The 2-D empirical eigenfunction method is also employed for the analysis of shoreline changes due to the construction of detached breakwaters. Based on Uda and Hashimoto (1982), the shoreline changes can be described in terms of the second longshore eigenfunctions $e_2(y,t)$. From Fig.4, we note that the second longshore eigenfunction changes with seaward advancement at the central side on which the detached breakwaters were constructed. The corresponding cross-shore eigenfunction $e_2(x,t)$ is shown in Fig.5, in which the cross-section of a detached breakwater is located about 30m in the x direction. Depositions of sand behind the detached breakwater is also found. Results of analysis reveal that the design and the construction of detached breakwaters are successful for beach preservation measures.

Fig.6(a) presents the first three longshore spatial eigenfunctions e_1^1(solid line), e_1^2(dash-dot line) and e_1^3 (dash line). The time variations of these functions as shown in Fig.6(b) are C_{1y}^1(solid line), C_{1y}^2(dash-dot line)

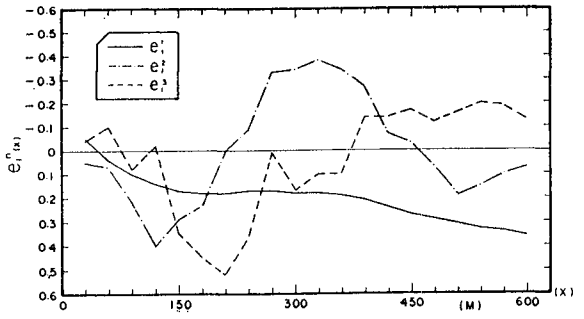

(a) Spatial eigenfunction

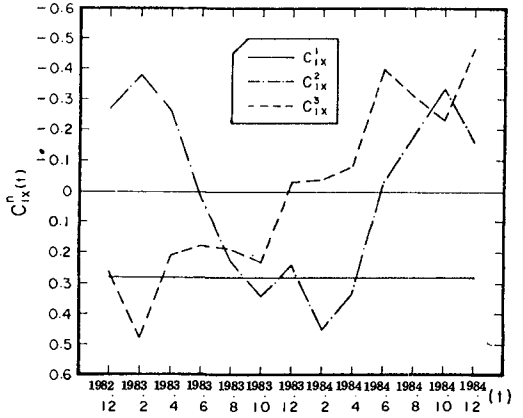

(b) Temporal eigenfunction

Fig. 3 The first three crossshore eigenfunctions (section A40-2)

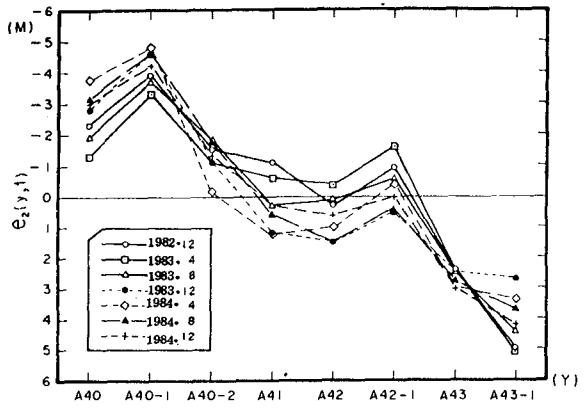

Fig. 4 The second longshore eigenfunctions $e_2(y,t)$

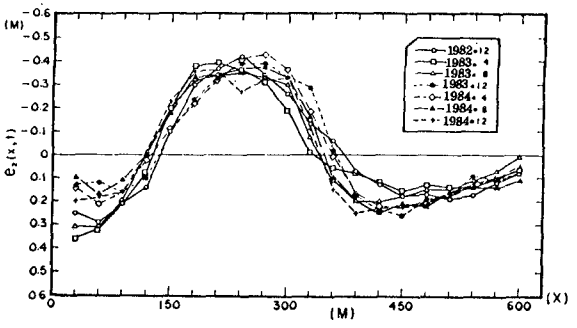

Fig. 5 The second cross-shore eigenfunctions $e_2(x,t)$

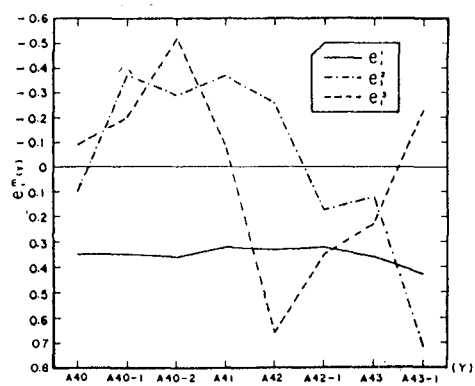

(a) Spatial eigenfunctions

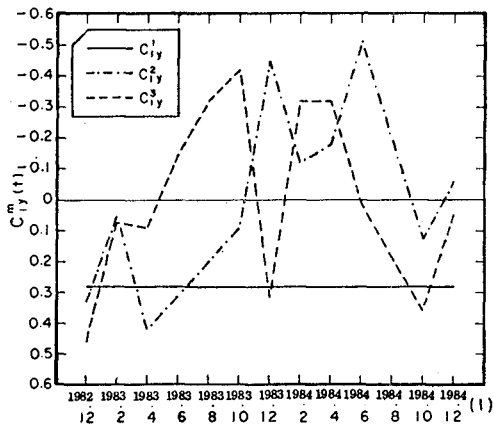

(b) Temporal eigenfunctions

Fig. 6 The first three longshore eigenfunctions

and C_{iy}^{3} (dash line). The temporal function C_{iy}^{1} shows almost no chang over the recording time. The other two eigenfunctions show no clear tendency. Perhaps more data are required for the analysis.

On the other hand, Winant et al. (1975) pointed out that each eigenvalue is representative of certain percentage of the mean square value of the data. Table 1 shows that the eigenvalues of longshore eigenfunctions are larger that those of cross-shore eigenfunctions, indicating that the longshore sediment transport has more effect on beach profile change than the cross-shore sediment transport does.

Prediction of Beach Profile Changes

It has been shown that the stability is an important consideration in the prediction of empirical eigenfunction method (Aubrey,1978). In this paper, two data sets of different sample lengths (N_t=10 and 12) were examined. The results of analysis show that the eigenfunctions are stable with respect to the length of the data (Wang, 1985).

Uda and Hashimoto (1982) calculated the shoreline change by one-line theory, and then the longshore eigenfunction $e_2(y,t)$ was calculated from shoreline changes. Since the nearshore zone is characterized by complex flow fields and fluid-sediment interactions, it is difficult to estimate quantitative shoreline changes by one-line simulation. The correlation between $e_2(y,t)$ and shoreline changes is not significant in present analysis as shown in Fig.7. In this paper, three parameters and computed beach configuration at each time step are used to predict temporal eigenfunctions, because they are easily to obtain from available wave data and beach profile data without any mathematical simulation.

Table 2 shows the mean square value of forecast error S_F for different models. The forecast skill of present analysis is better than 1-D model and Uda and Hashimoto's model, although its predictability S_B was lower as listed in Table 3.

Fig.8(a) and (b) depict two profiles of A40-2 and A41 and their estimates from three different models. It is seen that the prediction of 2-D model yields a better result than 1-D model and Uda and Hashimoto's model as compare to the measured profiles.

Table 1 A comparison of eigenvalues between longshore and cross-shore eigenfunctions

component / mode	longshore eigenfunctions			cross-shore eigenfunctions		
	一	二	三	一	二	三
1	0.124871	0.093681	0.092341	0.049939	0.038738	0.038335
2	0.000050	0.029298	0.029826	0.000029	0.009608	0.009192
3	0.000034	0.000861	0.001430	0.000022	0.001074	0.001438
4	0.000024	0.000702	0.000705	0.000005	0.000191	0.000453
5	0.000011	0.000277	0.000510	0.000002	0.000138	0.000168

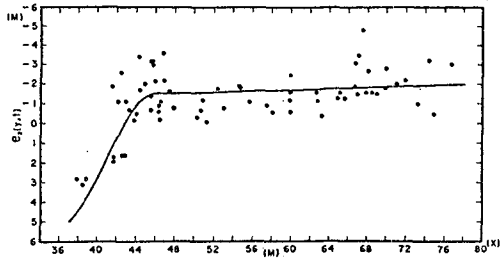

Fig. 7 A relationship between longshore eigenfunction $e_2(y,t)$ and shoreline changes

Table 2 Mean square error S_F for three different models

Sec. No.	1 − D	2 − D	Hashimoto and Uda
A 40	0.0193	0.0083	0.0215
A 40 − 1	0.0194	0.0200	0.0294
A 40 − 2	0.0151	0.0137	0.0147
A 41	0.0107	0.0071	0.0137
A 42	0.0224	0.0153	0.0233
A 42 − 1	0.0262	0.0093	0.1122
A 43	0.0107	0.0105	0.0215
A 43 − 1	0.0068	0.0142	0.0291

Table 3 Predictability index S_H for 1-D and 2-D model

	Sec. No.	S_H	Sec. No.	S_H
1-D	A 40	0.8282	A 42	0.8545
	A 40−1	0.8409	A 42−1	0.8550
	A 40−2	0.8669	A 43	0.8130
	A 41	0.9021	A 43−1	0.8005
2-D	cross-shore	0.7857	longshore	0.6089

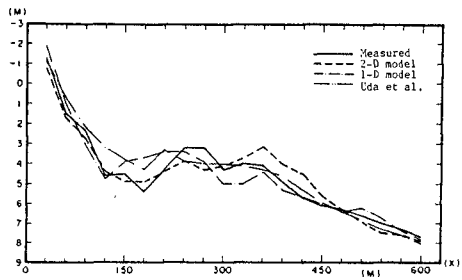

(a) section A 40-2

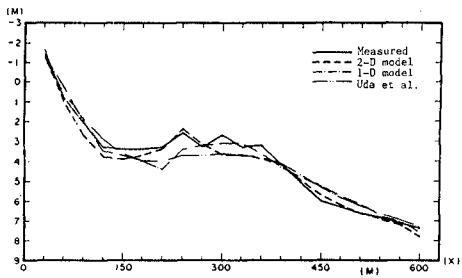

(b) section A 41

Fig. 8 Comparison of predicted results

CONCLUSION

Field data of beach profiles taken over two years at Redhill coast were analyzed by employing the 2-D empirical eigenfunction method. The results indicate that beach profile changes due to longshore and cross-shore sediment transports are separable. A successful detached breakwater as beach erosion countermeasure is also verified. The prediction of 2-D model shows that the beach profile changes are predictable. It is also concluded that this 2-D model is shown to be effective in the analysis and the prediction of beach changes near coastal structures.

REFERENCES

(1) Aranuvachapun, S. and J.A. Johnson: Beach profiles at Gorleston and Great Yarmouth, Coastal Eng., pp.201-203, 1979.
(2) Aubrey, D.G.: Statistical and dynamical prediction of changes in natural sand beaches, Ph.D. dissertation, Univ. of Calif., San Diego, 194pp. 1978.
(3) Battjes, J.A.: Surf similarity, Proc. 14th ICCE, ASCE, pp.466-480, 1974.
(4) Bowen, A.J.: The generation of longshore currents on a plane beach, J. Fluid Mech., pp.206-215, 1969.
(5) Davis, R.E.: Predictability of sea surface temperature and sea level pressure anomalies over the North Pacific Ocean, J. Phys. Oceanogr., vol.6, no.3, pp.249-266,1976.
(6) Gourlay, M.S.,: Beach and dune erosion tests, Delft Hydraulics Laboratory, Report no. M935/M936, 1968.
(7) Sawaragi, T.: Sediment and beach erosion, Morikata Publication Company, Japan, 195pp., 1982.
(8) Sonu, C.J.: A Markov model for beach change, J. Geophys. Res., vol.78, no.9, pp.1462-1471, 1973.
(9) Uda, T. and H. Hashimoto: Description of beach changes using an empirical predictive model of beach profile changes, Proc. 18th ICCE, ASCE, Cape Town, pp.1405-1418, 1982.
(10) Wang, S.K.: On the analysis and the prediction of the two-dimensional beach topographical changes, M.S. thesis, National Cheng Kung Univ., Tainan, Taiwan, 51pp., 1985.
(11) Winant, C.D., D.L. Inman and C.E. Nordstrom: Description of seasonal beach changes using empirical eigenfunctions, J. Geophys. Res., vol.8, no.15, pp.1979-1986, 1975.

CHAPTER 88

TIME SCALE FOR MODELING BEACH CHANGE

by

Masahiro Ito[1] and Yoshito Tsuchiya[2]

1. ABSTRACT

A time scale in the similarity of beach change between model and prototype in transitional beach processes from an initial even slope to an equilibrium is developed using a series of small- and large-scale experiments in which the experimental conditions were set up with the scale-model relationship by the authors (1984). The time scale is obtained empirically as a function of experimental scale. Applied the proposed time scale and the scale-model relationship to model experiments, similarity of morphological beach change such as shoreline change and relative breaker point was well reproduced within the allowable range of experimental error. A semi-theoretical time scale is obtained from the continuity equation, the sediment transport rate, and the scale-model relationship of equilibrium beach profile in two-dimensional beach change. The relation between experimental and semi-theoretical time scale is discussed.

2. INTRODUCTION

Experimental technique for reproducing beach changes during time-dependent storm waves is desirable for beach erosion control and design of coastal structures. Some investigators have attempted to find the scale-model relationship and the time scale for beach change, however, scale-model relationship and time scale in transitional beach processes are not established well. Most of those studies had developed scale-model relationships by using major parameters which govern effectively beach changes. Noda (1972) discussed how the scale-distortion in vertical and horizontal scales and properties of beach material in models influence on the scale-model relationship. Vellinga (1982) carried out a number of small- and large-scale model tests for the dune erosion in Duch coast, Netherland caused during huge waves, and proposed a scale-model relationship with distortion and time scale by summarizing its results. Also, by applying the dynamic similarity condition and the dimensionless fall velocity parameter demonstrated by Dean (1973), Hughes (1983) studied the

1 Associate Professor, Department of Civil Engineering, Meijo University, Nagoya, 468 Japan.
2 Professor, Disaster Prevention Research Institute, Kyoto University, Kyoto, 611 Japan.

scale-model and time scale relationship. He examined the applicability of the proposed relationship to distorted model tests of coastal dune erosion in Panahadle, Florida due to a hurricane. As the result of the tests, the beach profile nearby the shoreline was only reproduced. Hallermeir (1985) proposed a distorted scale-model relationship which was introduced using the parameter composed of sediment and the fluid characteristics, and also discussed it including the scale-model relationships by Hughes and Vellinga. He was examined his relationship using two-dimensional large-scale models which were conducted at the Coastal Engineering Research Center, US Army. The scale-model relationships by Noda, Vellinga and Hughes include an effect of distortion in vertical and horizontal scales. These scale-model relationships have not been examined by verification tests.

The authors (1984) proposed an empirical scale-model relationship by considering the degree of experimental error which appears in model experiments. This scale-model relationship is that gives the relation between experimental scales such as wave properties, water depth in a wave tank which can be determined by the Froude law, and the grain-size scale of beach sand. By using the authors' scale-model relationship, we can be similar the beach profiles and breaking wave properties in the only equilibrium of model and prototype. Then the time scale which can hold the similarity between model and prototype during the transitional beach processes from an initial even slope to an equilibrium must be found.

3. SCALE-MODEL RELATIONSHIP FOR EQUILIBRIUM BEACH PROFILE

To find the scale-model relationship for two-dimensional equilibrium beach profile a series of small- and large-scale experiments was carried out in the following conditions:
(1) The vertical and horizontal length scales, such as scales for beach profile and water depth in a wave tank were taken the same (i. e., undistorted or geometric similarity). Both the vertical and horizontal length scales are subjected to Froude law.
(2) Wave characteristics such as wave height in deep water and period also are determined by the Froude law.
(3) The beach sediment in small-scale models was used sand or silica-sand with the same specific gravity as the sand used in the large-scale models. The grain-size scale $\lambda_d = (d)_m / (d)_p$, is chosen independently of the experimental scale, $\lambda_l = 1/n$, as mentioned in (1) and (2).

In accordance with the abovementioned (1), (2) and (3) small- and large-scale model experimental conditions are given. These experiments were carried out using the large two-dimensional wave tank (78m long, 1m wide and 1. 2m deep) and the medium one (28m long, 0. 5m wide and 1m deep). By arranging results of small- and large-scale model experiments, the similitude zone which indicates a good agreement between the model and prototype beach profiles at equilibrium was found as shown in Fig. 1. The scale-model relationship in Fig. 1 was rearranged for the conditions of $(d/H_0)_p < 0.01$ and $H_0/L_0 = 0.007 \sim 0.042$. We have also reported that the scale-model relationship shown by the dot-dashed line as the central

trend curve of the similitude zone can be expressed by the following empirical relationship

$$\frac{1}{\lambda_d} = 1.7^{a} \left(\frac{1}{\lambda_l}\right)^{b} \qquad (1)$$

where a=1, b=0.83 for the range of experimental scale $1 \geq \lambda_l \geq 1/2.2$, and a=0, b=0.2 for $\lambda_l > 1/2.2$.

4. EXPERIMENTS OF TRANSITIONAL BEACH CHANGES FROM INITIAL TO EQUILIBRIUM STATE

If we set up the experimental conditions of model and prototype so that the both relationships enter into the similitude zone shown in Fig. 1 {i.e., by Eq. (1)}, we are possible to similar the only equilibrium beach profiles between the two, but impossible to similar the beach change between the two in case of the transitional beach process from an initial even slope to an equilibrium. we find out experimentally the time scale relationship so that the prototype beach profile at the specified operation time can similar to the model beach profile which was selected up among experimental results in gradually increasingly wave operation time.

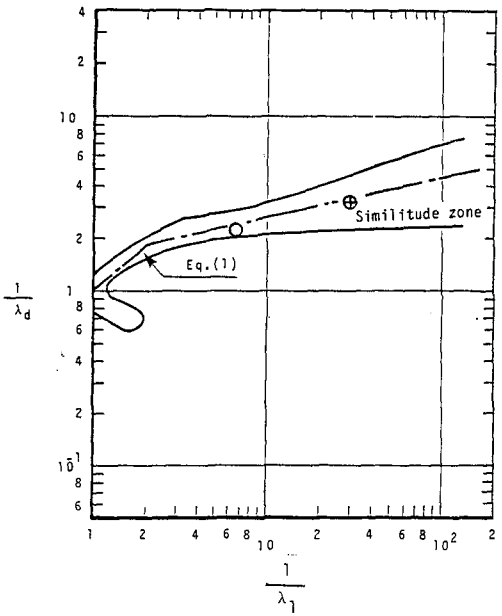

Fig. 1 Scale-model relationship by Ito & Tsuchiya for equilibrium beach changes with time scale relationship obtained by laboratory experiment.

By use of steady and regular waves in the two-dimensional large wave tank, beach changes as large-scale models (prototype) were measured intermittently until they reach from the initial even slope to an equilibrium state The experimental result and condition which Saville (1957) carried out a long time ago using a large wave tank, also is taken to be the prototype. In small-scale models, the vertical and horizontal lengths (experimental scale) such as wave properties and water depth in the wave tank were determined by the Froude law as mentioned in 3. (1) and (2). The sand and silica-sand to be used in the model were chosen according to Eq. (1) so that the grain-size scale enters within the similitude zone in Fig. 1. Model experiments were carried out until the beach profiles reach their equilibrium state for longer time, and beach changes and wave breaking properties during the experiments were measured intermittently. Model beaches in the medium wave tank were made initially the same beach slope with

Table 1 An Example of the experimental conditions in models and prototypes.

Run No.	Experimental scale λ_t	Wave height in deep water Ho (cm)	Period T (sec)	Wave steepness in deep water Ho/Lo	Water depth h (cm)	Initial beach slope i_o	Grain-size scale size λ_d	Sand grain in d_{50} (mm)	Mark shown in Fig.1
3	Proto.	20.6	3.00	0.015	100.0	1/30	Proto.	0.94	○
3M-25	1/6.7	3.5	1.16	0.017	15.0	1/30	1/2.24	0.42	
T-56	Proto.	171.2	5.6	0.035	442.0	1/15	Proto.	0.46	⊕
T-59	1/30	5.8	1.02	0.036	14.7	1/15	1/3.07	0.15	

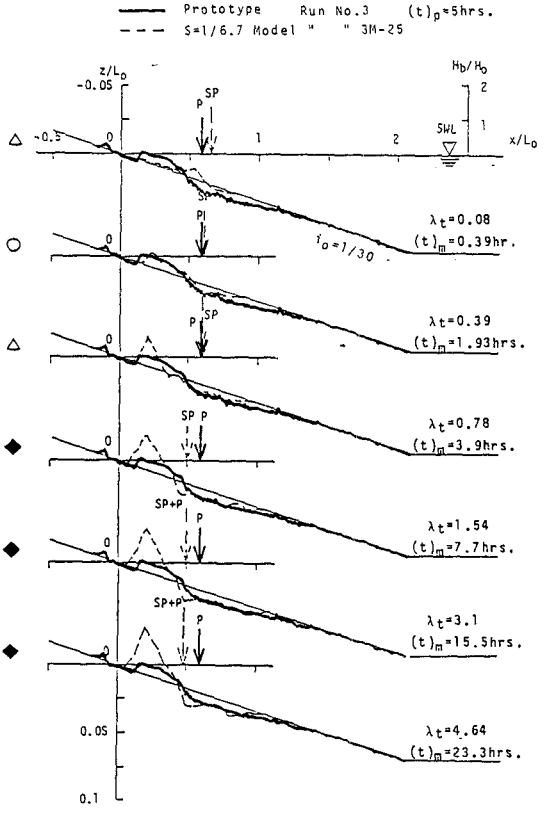

(a) Transitional beach change in model and prototype.

Fig. 2 Similarity comparison of the prototype beach profiles at the given time with temporarily varying model beach profiles (to be continued).

the corresponding prototype. An example of the experimental conditions determined by the manner mentioned is shown in Table 1.

As is seen in Fig. 1, these experiments are satisfied the similarity condition as indicated by the open circle for Run No. 3M-25 to Run No. 3 and the cross-circle for Run No. T-59 to Run No. T-56 (by Saville (1957)). Therefore, the only equilibrium beach profile between the two will become similar, but the similarity in transitional processes is uncertain. To define the similarity in transitional processes, prototype beach profile and breaking wave properties at the time, $(t)_p$=5hr, are compared with those in scale models during the times, $(t)_m$=0.39~23.3hr, as shown in Fig. (2). The position and the length

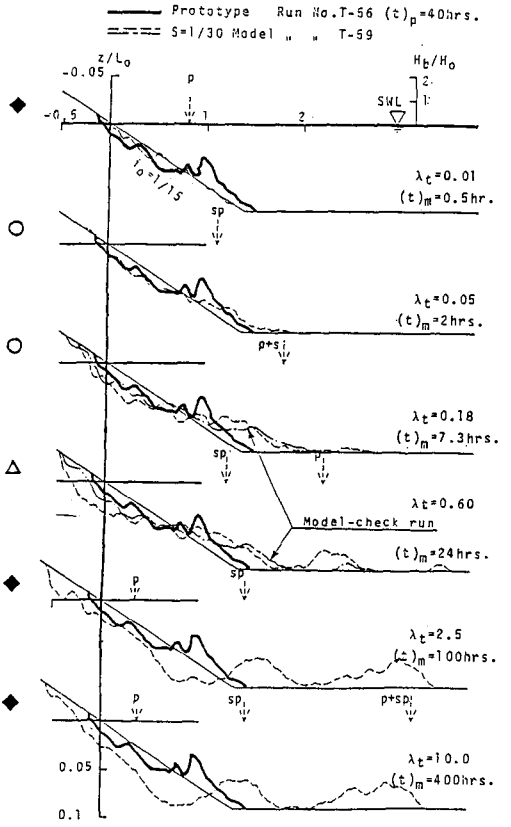

(b) Equilibrium beach profile in prototype.

Fig. 2 Similarity comparison of the beach profile of prototype at the specialized wave operation time with temporarily varying model beach profiles.

of allows in this figure indicate the breaking position and relative breaker height, H_b/H_0, and "P", "SP" and "SP+P" symbols indicate breaker types, plunging, spilling and intermediate between them, respectively. By considering the characteristics of experimental error, similarity of beach profiles and wave breaking properties are classified into three categories, *similitude* ("○"-mark), *quasi-similitude* ("△") and *dissimilitude* ("◆"). It is clearly recognized from Fig. 2 (a) that the judgement for similarity depends on the time scale, $\lambda_t=(t)_m/(t)_p$, and that the arrange of experiments which satisfy the relationship for the time-dependent similarity can easily be found. Also, Fig. 2 (b) shows the similarity comparison of the time-dependent beach profiles of the model, Run No. T-59 in Table 1 with Saville's prototype, Run No. T-56, in which the beach change is almost in equilibrium. By this way, in the case where the beach change of prototype is in transitional stage, non-equilibrium, the judgement results for similarity including the other experimental results are rearranged by λ_t^{-1} and λ_l^{-1} as shown in Fig. 3 (a). Furthermore, in

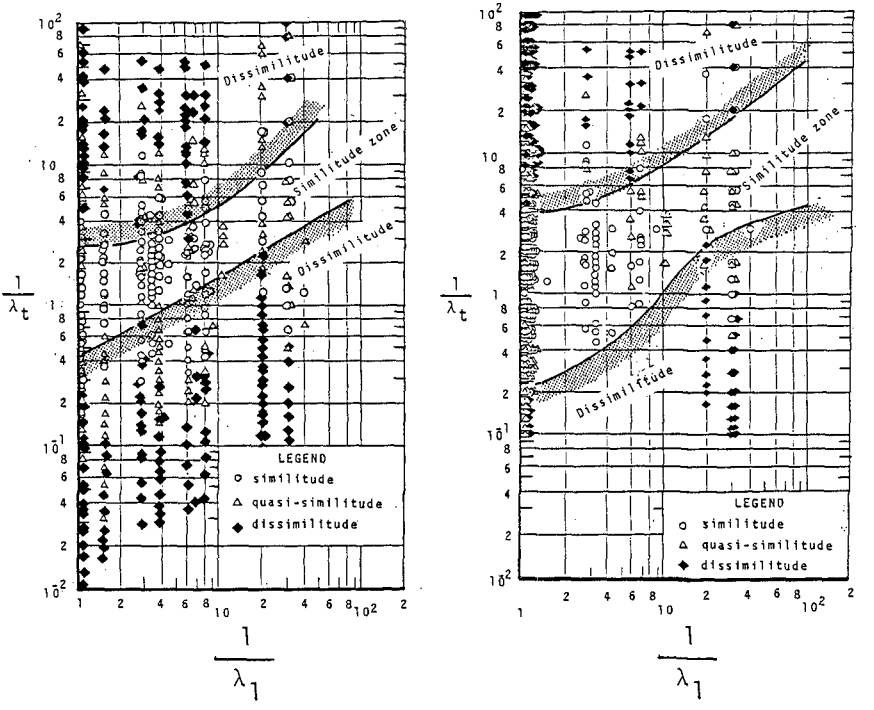

(a) Time scale for beach changes of model and prototype in transitional process.

(b) Time scale for beach changes of prototype only in equilibrium.

Fig. 3 Relationship between the time scale λ_t and the experimental scale λ_l for similarity in beach changes of model and prototype.

the case where the beach change of prototype is in equilibrium, the similarity comparison between the prototype (Run No. 56 in Table 1) and the time-dependent beach change of model (Run No. T-59) is shown in Fig. 3 (b), in which the results of other experimental results are also included. Median grain sizes of the sand and the silica-sand used in the model and prototype range of $(d)_m$=0.15~0.42mm and $(d)_p$=0.15~1.62 mm, respectively. The similitude /dissimilitude zones where the time scale relationship is/not achieved, are shown in Fig. 3 (a) and (b). The similitude zones are in Fig. 3 (a) and 3 (b) are not same, but a overlapped similitude zone can be found in Fig. 4. The similitude zone in Fig. 4 may be expressed by

$$\frac{1}{1.6\sqrt{\lambda_l}} \leq \lambda_t \leq \frac{1}{0.65\sqrt{\lambda_l}} \qquad (2)$$

It is noted in the figure that the dotted line which indicates the average tendency of Eq. (2) agrees closely with the Froude time scale

$$\lambda_t=\sqrt{\lambda_l}=\frac{1}{\sqrt{n}} \qquad (3)$$

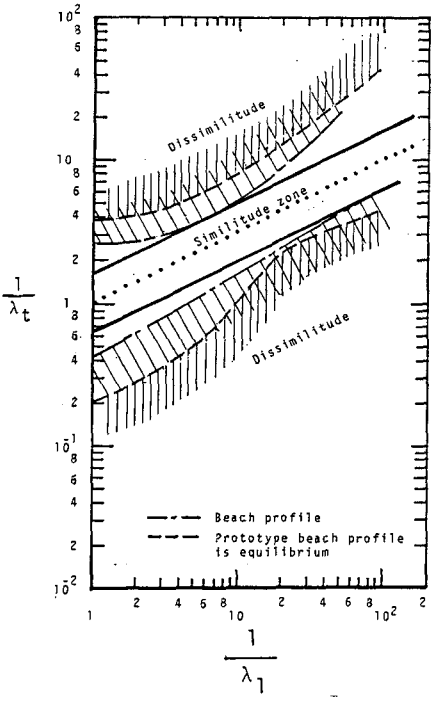

Fig. 4 Empirical time scale for modeling beach change.

5. APPLICABILITY OF THE TIME SCALE RELATIONSHIP PROPOSED

We set the experimental scale and grain-size scale of model for prototype by Eq. (1), and determine the wave duration operation time between the two by Eq. (3) which indicates the average tendency of similitude zone in Fig. (4). In case of this experimental manner, the relationship of the wave duration time in the model, $(t)_m$, and prototype, $(t)_p$, is given by

$$(t)_m=\frac{(t)_p}{\sqrt{n}} \qquad (4)$$

and the relationship of wave periods is

$$(T)_m=\frac{(T)_p}{\sqrt{n}} \qquad (5)$$

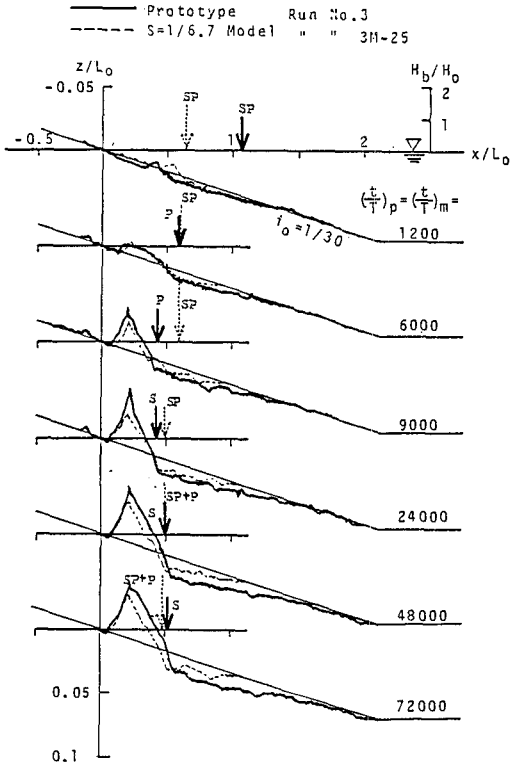

Fig. 5 Similarity of model and prototype beach changes reproduced by applying the time scale relationship.

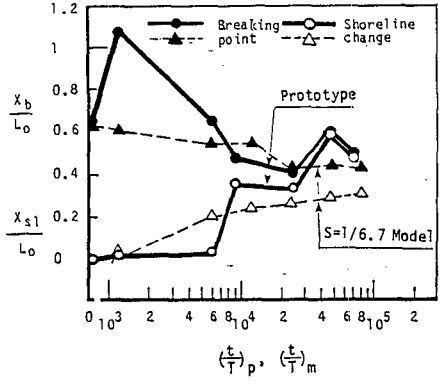

Fig. 6 Time changes of shoreline change and relative breaking position in the similarity experiments.

From Eqs. (4) and (5), we obtain

$$\left(\frac{t}{T}\right)_m = \left(\frac{t}{T}\right)_p \tag{6}$$

An example of the comparison between the beach change reproduced by model and prototype is shown in Fig. 5. At the same dimensionless times by Eq. (6), this figure illustrates changes of the beach profile and the breaking wave properties from an initial even slope to an equilibrium. Fig. 6 also shows in detail the reproduction of the shoreline change, X_{sl}/L_o, and the movement of breaking point, X_b/L_o in dimensionless form. The discrepancy between the two shown in the figure is less than the range of experimental error. From Figs. 5 and 6, it is recognized that the time scale relationship of Eq. (2) is available for the laboratory model for reproducing the transitional beach change in prototype.

6. TIME SCALE BY SEMI-THEORETICAL METHOD

We can introduce the time scale in beach change processes using the three relationships for two-dimensional beach change; 1) the continuity equation of beach change

$$\frac{\partial z}{\partial t} + \frac{1}{1-\Lambda}\frac{\partial q_x}{\partial x} = 0 \tag{7}$$

where q_x is the sand transport rate in the offshore direction, t the time, Λ the bottom sediment porosity, and z and x the vertical and horizontal coordinates, respectively; 2) the sand transport rate; and 3) the the scale-model relationship of equilibrium beach profile expressed by Eq. (1).

From Eq. (7), the time scale ratio in beach change between model and prototype is expressed by

$$\frac{t_m}{t_p} = \frac{\Lambda_m}{\Lambda_p}\frac{(q_x)_p}{(q_x)_m}\frac{z_m}{z_p}\frac{x_m}{x_p} \tag{8}$$

Denoting the scale ratio of model parameter to prototype parameter by $\lambda_{parameter}$, the experimental conditions mentioned in 3. (1) ~ (3) can be presented as

$$\left.\begin{aligned}
&\lambda_l = \lambda_x = \lambda_z = \lambda_{l_0} && \text{(Geometrical similitude)}\\
&\lambda_H = \lambda_{L_o} \\
&\lambda_T = \lambda_x^{1/2} && \text{(Froude law)}\\
&\lambda_S = 1 && \text{(Specific gravity of beach material is assumed to be the same in model and prototype)}\\
&\lambda_\nu = \lambda_\rho = 1 && \text{(Properties of fluid are the same in model and prototype)}
\end{aligned}\right\} \tag{9}$$

$$\left.\begin{aligned} \lambda_A &= 1 \\ \lambda_g &= 1 \end{aligned}\right\}$$

Rearranging Eq. (8) with Eq. (9), the following relationship is yielded

$$\lambda_t = \lambda_{qx}^{-1} \lambda_l^2 \tag{10}$$

For introducing the time scale using Eq. (10), the relationship which specifies exactly the on-offshore sand transport rate in beach change is necessary. Such a formulation of sand transport has not been obtained completely, but empirical relationships of sand transport in a bed load were proposed by Madsen and Grant (1976) and Tsuchiya et al. (1984) from experimental results. These relationships are only applicable in the offshore zone, not surf zone. Tsuchiya et al. proposed the relationship of Kalinske- Brown type

$$\frac{q_x}{U^* d} = K (\tau^* - \tau^*_c)^2 \tag{11}$$

where

$$\tau^* = \frac{U^{*2}}{sgd} \qquad \text{(Shields parameter)} \tag{12. a}$$

$$\tau^*_c = \frac{U^*_c{}^2}{sgd} \sim 0.05 \qquad \text{(Threshold Shields number)} \tag{12. b}$$

$$K = 1.7 \left(1 + \frac{300d}{2a_w}\right) \qquad \text{for} \frac{2a_w}{d} > 100 \tag{12. c}$$

where U^* is the shear velocity at the bed, U^*_c the critical shear velocity, a_w the orbital radius of water particle, and K the constant depending on the ratio of orbital diameter to grain size, $2a_w/d$. The shear velocity at the bed is expressed by

$$U^* = \sqrt{\frac{f_w}{2}}\, Ub_{max} \tag{13}$$

where f_w is the wave friction factor, Ub_{max} the one half of the maximum horizontal velocity of water particle in the vicinity of the bed $\{\pi H/(2T\sinh 2\pi h/L)\}$. By Swart (1976), the friction factor, f_w, is expressed by

$$\left.\begin{aligned} f_w &= 0.0025 \exp\left\{5.21 \left(\frac{a_w}{k_s}\right)^{-0.19}\right\} && \text{for} \quad \frac{a_w}{k_s} > 1.57 \\ f_w &= 0.3 && \text{for} \quad \frac{a_w}{k_s} < 1.57 \end{aligned}\right\} \tag{14}$$

where k_s is the roughness length of the bed which is nearly equal to the sand size. Consequently, the sand transport rate in a bed load by

Eq. (11) becomes

$$q_x = K U^{*5} s^{-2} g^2 d^{-1} - 0.08 K U^{*3} s^{-1} g^{-1} + 0.04^2 K U^* d \tag{15}$$

Substituting Eq. (13) into Eq. (15) and taking the scale ratio of the sand transport rate, we obtain

$$\left.\begin{aligned}
\lambda_{q_x} &= \lambda_K \quad \lambda_{f_w}^{5/2} \quad \lambda_d^{-1} \quad \lambda_H^{5} \quad \lambda_T^{-5} \quad \lambda_{\sinh\frac{2\pi h}{L}} \\
\lambda_{q_x} &= \lambda_K \quad \lambda_{f_w}^{3/2} \quad \lambda_H^{3} \quad \lambda_T^{-3} \quad \lambda_{\sinh\frac{2\pi h}{L}}^{-3} \\
\lambda_{q_x} &= \lambda_K \quad \lambda_{f_w}^{1/2} \quad \lambda_d \quad \lambda_H \quad \lambda_T^{-1} \quad \lambda_{\sinh\frac{2\pi h}{L}}^{-1}
\end{aligned}\right\} \tag{16}$$

Furthermore, combining Eqs. (10) and (16), and arranging those by Eq. (9), the time scale relationship can be given as

$$\left.\begin{aligned}
\lambda_t &= \lambda_K^{-1} \quad \lambda_{f_w}^{-5/2} \quad \lambda_d \quad \lambda_l^{-1/2} \\
\lambda_t &= \lambda_K^{-1} \quad \lambda_{f_w}^{-3/2} \quad \lambda_l^{1/2} \\
\lambda_t &= \lambda_K^{-1} \quad \lambda_{f_w}^{-1/2} \quad \lambda_d^{-1} \quad \lambda_l^{3/2}
\end{aligned}\right\} \tag{17}$$

It is clear from Eq. (17) that the time scale is subjected to the scale effect of $2a_w/d$ (λ_K), the scale effect of wave friction factor, λ_{f_w}, and the grain size scale, λ_d. Using the sand transport rate by Eq. (11), the time scale may be given by the condition which is satisfied simultaneously the three equations in Eq. (17).

On the other hand, Madsen and Grant proposed the dimensionless bedload sand transport rate in the half wave cycle, q_x/wd, using the Shields number, $\tau_{0m}/\rho sgd$, as

$$\frac{q_x}{wd} = 12.5\left(\frac{\tau_{0m}}{\rho sgd}\right)^3 \tag{18}$$

where w is the sediment fall velocity, ρ the fluid density, s the specific gravity of the sediment in water, and τ_{0m} the maximum bottom shear stress by

$$\tau_{0m} = \frac{1}{2} f_w \rho U_{bmax}^2 \tag{19}$$

Combining Eqs. (13) and (19), the scale ratio becomes as

$$\lambda_{q_x} = \lambda_{f_w}^{3} \quad \lambda_w \quad \lambda_d^{-2} \quad \lambda_s^{-3} \quad \lambda_H^{6} \quad \lambda_T^{-6} \quad \lambda_{\sinh\frac{2\pi h}{L}}^{-6} \quad \lambda_g^{-3} \tag{20}$$

The similarity relationship of the sediment fall velocity , as the authors (1984) considered already, may generally be expressed

$$\lambda_w = \lambda_d^{n_w} \tag{21}$$

where n_w=2, 1, 2/3, and 1/2 for Stokes', Allen's, Karman's, and Newton's formulas of sediment fall velocity, respectively. Combining Eqs. (10), (20) and (21), and arranging it with Eq. (9), the time scale can be reduce to

$$\lambda_t = \lambda_{f_w}^{-3} \lambda_d^{2-n_w} \lambda_l^{-1} \tag{22}$$

It is recognized from Eq. (22) that the time scale relationship is influenced by the scale effects of the wave friction factor and grain size.

Now consider how the grain-size scale and the ratio of the orbital diameter of water particles to the grain size influence on the time scale. Eq. (1) may be expressed in a generalized form as

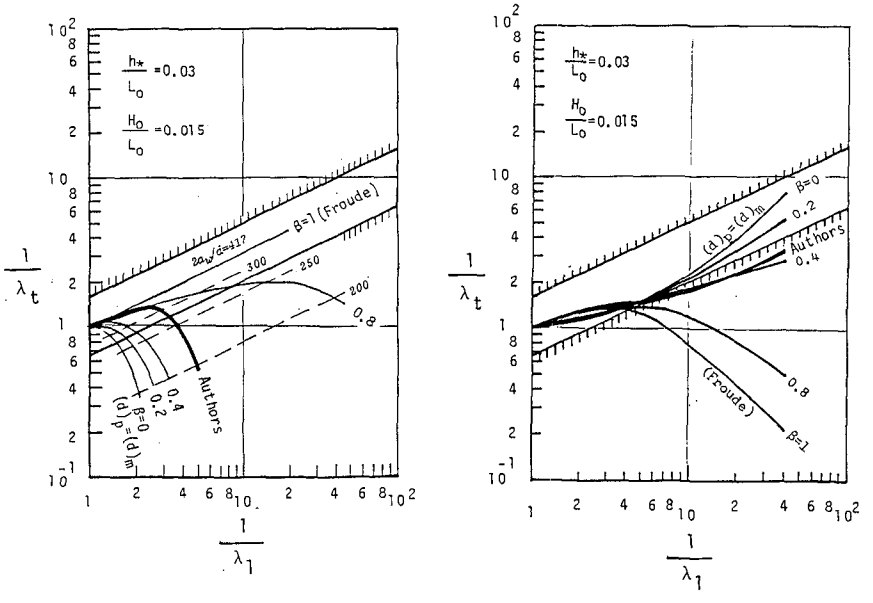

(a) Time scale calculated by using the sand transport rate by Tsuchiya et al.

(b) Time scale calculated by using the sand transport rate by Madsen and Grant.

Fig. 7 Comparison of the time scale obtained experimentally with the semi-theoretical time scale.

$$\lambda_d = \alpha \lambda_l^{\beta} \tag{23}$$

where

$$\left.\begin{aligned} \alpha &= \left(\frac{1}{1.7}\right)^a \\ \beta &= b \end{aligned}\right\} \tag{24}$$

Fig. 7 (a) shows the relationship between the time scale and the experimental scale which was calculated numerically using Eqs. (10), (11) and (23) in the experimental conditions of Run No. 3 in Table 1 and of the beach change at the dimensionless position of $h_*/L_0=0.03$. To understand the influence of grain-size scale on the time scale, the coefficient and exponent of Eq. (23) are changed in steps as $\beta=0$ {$(d)_m=(d)_p$}, 0.2, 0.4, 0.8, and 1.0 when $\alpha=1$; and $\beta=b$ when $\alpha=(1/1.7)^a$ {same to Eq. (1)} From Fig. 7 (a) the influence of grain-size scale for on the time scale can therefore be understood easily. Additionally, the effect of $2a_w/d$ is shown by the broken lines in the figure. The result calculated numerically using the sand transport rate by Madsen and Grant is shown in Fig. 7 (b) taking β as parameter. It is indicated from Fig. 7 that the grain-size scale influences considerably on the time scale.

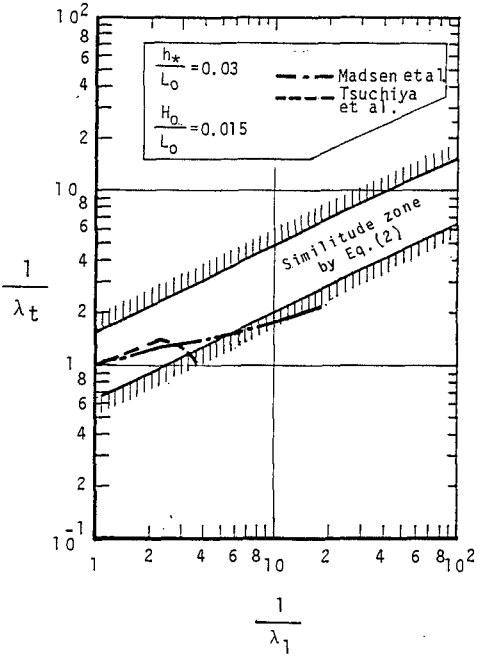

Fig. 8 Comparison of empirical time scale with semi-theoretical time scales.

Comparisons of the time scale relationship by Eq. (2) with the two semi-theoretical time scales mentioned in 6 are shown in Figs. 7 (a) and 7 (b). As is seen in these figures, there exists a quite difference between the two by the relationship of sand transport rate used in calculation. The difference in the time scale relationships is subjected to change in the exponent β in Eq. (23). The comparison of the time scale relationship by Eq. (2) with the semi-theoretical time scales which were obtained using the scale-model relationship of Eq. (1) is shown in Fig. 8. In the experimental scale range of $1 \geq \lambda_l > 1/4$, the semi-theoretical time scales agree well with the empirical time scale relationship proposed.

7. CONCLUSIONS

The main conclusions in this paper are summarized as;
(1) Based on the results of experiments which were conducted by applying the authors' scale-model relationship of Eq. (1), the empirical time scale relationship, which is held the similarity between the model and prototype in transitional beach change processes from an initial even slope to an equilibrium, was proposed by Eq. (2). The average tendency in the similitude zone for the time scale coincides nearly with the Froude time scale.
(2) The model beach processes which was set up using Eqs. (1) and (3) can well reproduce beach changes and breaking wave properties in prototype.
(3) The semi-theoretical time scale introduced by the continuity equation of beach change, the sand transport rate and the generalized scale-model relationship is not only subjected the grain size scale but the effect due to the wave friction factor and the ratio of orbital diameter of water particle to grain size of the bed material.
(4) Two semi-theoretical scales which were obtained by using the authors' scale-model relationship are a little different from those by formulas of sand transport rates, but agree well with the empirical time scale within the range of experimental scale, $1 \geq \lambda_t > 1/4$.

8. REFERENCES

1) DEAN, R. G. (1973) Heuristic models of sand transport in the surf zone, Proc. Eng. Dyn. in Surfzone, Institution of Engineers, Australia, pp. 208-214.

2) HUGHES, S. A. (1983) Movable-bed modeling law for coastal dune erosion, Jour. Water. Port Coast. and Ocean Eng., ASCE, pp. 164-179.

3) HALLERMEIER, R. J. (1985) Unified modeling guidance based on a sedimentation parameter for beach changes, Coastal Eng., Vol. 9, No. 1, pp. 37-70.

4) ITO, M. and TSUCHIYA, Y. (1984) Scale-model relationship of beach profile, Proc. 19th ICCE, ASCE, pp. 1386-1402.

5) MADSEN, O. S. and GRANT, W. G. (1976) Quantitative description of sediment transport, Proc. 15th ICCE, ASCE, pp. 1093-1112.

6) NODA, E. K. (1972) Equilibrium beach profile scale-model relationship, Jour. Water. Harb. and Coast. Eng., ASCE, pp. 511-528.

7) SAVILLE, T. Jr. (1957) Scale effects in two dimensional beach studies, Proc., 7th IAHR, pp. A3-1 - A3-10.

8) TSUCHIYA, Y., UEDA, Y. and OOSHITA, T. (1984) Theory on the threshold of bed load in oscillatory flow, Proc. 31th Japanese Conf. Coastal Eng., pp. 272-276, (Japanese).

9) VELLINGA, P. (1982) Beach and dune erosion during storm surges, Coastal Eng., Vol. 6, No. 4, pp. 361-387.

CHAPTER 89

LENGTHS OF RUNS OF JUST BREAKING AND BROKEN WAVES IN IRREGULAR WAVE TRAIN ON GENTLE SLOPES

Koichiro IWATA*
and
Shunji ITOH**

ABSTRACT

This paper is aimed to investigate theoretically and experimentally the variations of the probability distribution and mean values of the run length and total run length of just breaking and broken waves in an irregular wave train on gentle slopes. The theoretical model developed here is shown to be valid for evaluating the lengths of runs of just and broken waves from deep water up to the shoreline.

1. INTRODUCTION

Different from regular waves, the individual waves in an irregular wave train do not break at one specific location, but break at many different locations on sloping bottom, since their wave height and wavelength are different each other, in general. The estimation of the probability of successive breaking waves and its mean value is basically very important for coastal engineering problems. Although many theoretical models[1)-5)] have been proposed to estimate variations of the probability of wave breaking and wave statistics such as the mean, one-third and one-tenth largest wave heights, there has been no literature dealing with lengths of runs of just breaking and broken waves in an irregular wave train on sloping bottom.

With this background in mind, this paper is to discuss the variations of the probability of wave breaking and lengths of runs of successive just breaking and broken waves from deep

* Dr. Eng., Professor, Department of Civil Engineering, Nagoya University, Nagoya, Aichi 464, JAPAN.

** M. Eng., Civil Engineer, Nitsuken-Design Co.,Ltd.,Civil Engineering Design Office, Osaka, Osaka 541, JAPAN.

water up to the shoreline on gentle slopes. First of all, the theoretical model is described to estimate the probability distribution and mean value of the lengths of runs of just breaking and broken waves for a given probability of occurrence of just breaking and broken waves. Next, a theoretical model is presented to estimate the probability of occurrence of just breaking and broken waves on gentle slopes. The numerical method combining the two theoretical models is proposed to evaluate the variation of the probability distribution and mean values of the lengths of runs of just breaking and broken waves for various kinds of waves on gentle slopes. Secondly, laboratory experiments are carried out to investigate the variation of the probability distribution and mean values of the run and total run lengths of just breaking and broken waves as well as to examine the validity of the numerical method on gentle slopes. The validity of the method proposed here is verified by the laboratory experiments. Using the method, the diagrams are presented to evaluate the variation of the mean run length and mean total run length of broken waves of 6 kinds of irregular waves on gentle slopes of 1/10,1/20,1/30 and 1/50.

2. DEFINITION OF RUN LENGTH AND TOTAL RUN LENGTH OF JUST BREAKING AND BROKEN WAVES

A run length of just breaking wave is defined by the sequence of a just breaking wave. A total run length of just breaking wave is defined by the number of waves between a group of just breaking waves and the next occurrence of a just breaking wave by the succeeding group of waves. The same definition is made to the run length and total run length of broken wave. *The just breaking wave* defined in this paper is an critical wave just at the inception of breaking and has little air bubble. *The broken wave* defined here includes waves in the transformation process immediately after the inception of breaking as well as air-entrained waves with a turbulent water surface. We permit here, however, for the sake of convenience of treatment that the broken wave includes the just breaking wave.

The run length (J_1) and the total run length (E_1) of the just breaking wave, in the case shown in Fig.1, are $J_1=3$ and $E_1=6$. On the other hand, the run length (J_2) and total run length (E_2) of the broken wave are $J_2=4$ and $E_2=6$, as indicated in Fig.1. It should be noted that the broken wave includes the just breaking wave, as stated above.

3. NUMERICAL METHOD

3.1 Estimation of run length and total run length

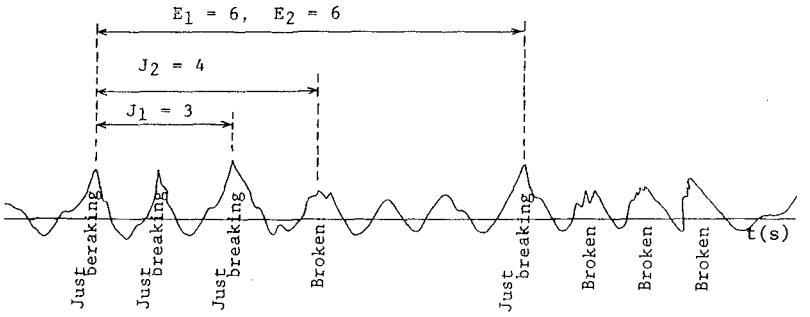

Fig.1 Schematic illustration of definition of run length and total run length of just breaking and broken waves.

Based on the random process which successive waves are uncorrelated, the probability distributions of run lenghts, J_1 and J_2 and total run lengths, E_1 and E_2 of just breaking and broken waves and their mean values, $\bar{J}_1$, $\bar{J}_2$, $\bar{E}_1$ and $\bar{E}_2$ are expressed by[6),7)]

$$\left.\begin{aligned} &P_1(J_1) = P_{JB}^{J_1-1} \cdot Q_{NB}\ ,\quad Q_1(E_1) = \left(\frac{P_{JB}\cdot Q_{NB}}{P_{JB}-Q_{NB}}\right)\left(P_{JB}^{E_1-1} - Q_{NB}^{E_1-1}\right) \\ &\bar{J}_1 = 1/(1-P_{JB}),\quad \bar{E}_1 = 1/P_{JB}(1-P_{JB}) \\ &P_{JB} + Q_{NB} = 1 \end{aligned}\right\}, \tag{1}$$

$$\left.\begin{aligned} &P_2(J_2) = P_B^{J_2-1} \cdot Q_N\ ,\quad Q_2(E_2) = \left(\frac{P_B\cdot Q_N}{P_B-Q_N}\right)\left(P_B^{E_2-1} - Q_N^{E_2-1}\right) \\ &\bar{J}_2 = 1/(1-P_B)\ ,\quad \bar{E}_2 = 1/P_B(1-P_B) \\ &P_B + Q_N = 1 \end{aligned}\right\}. \tag{2}$$

In Eqs.(1) and (2), $P(J_i)$ is the probability of occurrence of the run length J_i, $Q(E_i)$ the probability of occurrence of the total run length E_i, $\bar{J}_i$ the mean run length and $\bar{E}_i$ the mean total run length, where subsuffix i is either 1 or 2 and i=1 and i=2 mean respectively the quantity regarding the just breaking and broken waves. P_{JB} in Eq.(1) is the probability of occurrence of the just breaking wave, and Q_{NB} in Eq.(1) is the probability of non-occurrence of the just breaking wave. P_B and Q_N in Eq.(2) are the probability of occurrence and non-occurrence of the broken wave, respectively. Therefore, given P_{JB} and Q_{NB}, the probability distributions of run length and total run length of the just breaking wave, $P(J_1)$ and $Q(E_1)$, and their mean values, $\bar{J}_1$ and $\bar{E}_1$ are calculated with Eq.(1). Similarly, given P_B and Q_N, the probability distributions and mean values of run length and total run length of the broken wave are evaluated with Eq.(2).

3.2 Estimation of probability of occurrence of just breaking and broken waves

The theoretical model developed here to obtain P_{JB}, Q_{NB}, P_B and Q_N follows basically that of Sawaragi and Iwata[3]. Individual waves in an irregular wave train are assumed to be uncorrelated each other and to experience independently shoaling and breaking. In addition, once an individual wave breaks, the wave is assumed to keep broken up to the shoreline on gentle slopes.

(1) Shoaling condition:
The shoaling condition presented for regular waves, which is based on the linear wave theory, is employed,

$$\left.\begin{aligned} H_S &= K_S H_O \\ K_S &= \left(\tanh kh + kh(1-\tanh^2 kh)\right)^{1/2} \end{aligned}\right\} \qquad (3)$$

where K_S is the shoaling factor, Ho the equivalent wave height in deep water, H_S the wave height at the depth of h and k the wave number ($=2\pi/L$; L the wavelength at the depth of h).

(2) Breaking limit:
Modifying the breaking limit presented by Goda[2] for regular waves, the following equation is used for the 1st approximation,

$$H_b/Lo = 0.15(1-\exp(1.5\pi(h_b/Lo)(1-15S^{4/3}))) \qquad (4)$$

where H_b is the wave height at breaking point, h_b the still-water depth at breaking point, Lo the wavelength in deep water and S the bottom slope. Eq.(4) has been shown to provide a good approximation for the breaking limit of individual waves in an irregular wave train[8),9)].

(3) Mean water level variation from stillwater level:
The mean water level $\bar{\eta}$ at the depth of h is calculated by[10)],

$$\frac{d\bar{\eta}}{dx} = -\frac{1}{(\bar{\eta}+h)}\frac{d}{dx}\left(\frac{1}{8}\bar{H}^2\left(\frac{1}{2}+\frac{2kh}{\sinh 2kh}\right)\right) \qquad (5)$$

where $\bar{H}^2$ is the mean square wave height, x the horizontal distance and $\bar{\eta}$ the mean water level height from the stillwater level. In the numerical calculation, the following equation is employed in place of Eq.(5),

$$\left.\begin{aligned} \bar{\eta}_{j+1} &= \bar{\eta}_j - \frac{D_k}{(h+\bar{\eta})_{j+1/2}}\left(\bar{H}^2_{j+1} - \bar{H}^2_j\right), \\ (h+\bar{\eta})_{j+1/2} &= \left((h+\bar{\eta})_j+(h+\bar{\eta})_{j+1}\right)/2 \\ D_k &= \frac{1}{8}\left(\frac{1}{2}+\frac{2kh_j}{\sinh 2kh_j}\right) \end{aligned}\right\} \qquad (6)$$

where subsuffix j indicates the location of calculation.

(4) Probability of occurrence of just breaking and broken waves, P_{JB} and P_B:

As stated in Section 2, the broken wave includes the just breaking wave. Therefore, the probability of occurrence of the broken wave, P_B at the depth of h^* can be obtained by integrating the probability of occurrence of just breaking waves, P_{JB} from deep water to the water depth, h^*;

$$P_B(h^*) = \int_{h^*}^{\infty} P_{JB}(h)\, dh \quad . \tag{7}$$

The probability of occurrence of the just breaking wave, $P_{JB}(h)$ at the depth of h is determined by the ratio of the number of waves which satisfy the breaking limit to the total number of waves at the depth. Using Eq.(7), the probability of occurrence of just breaking waves, $(P_{JB}(h))_j$ between the depths, h_{j-1} and h_j can be described by

$$(P_{JB}(h))_j = ((P_B)_j - (P_B)_{j-1})/(h_{j-1} - h_j) \tag{8}$$

where h_{j-1} is larger than h_j, and $(P_B)_j$ and $(P_B)_{j-1}$ are the probability of occurrence of broken waves at the depth of h_j and h_{j-1}.

3.3 Procedure of calculation

Based on the previous studies[2),3)], the stillwater depth, h on the sloping bottom was divided into many numbers of portion, as illustrated in Fig.2. The non-dimensional variation of the stillwater depth, $\Delta h/Ho$ in the portion was varied according to the change of dimensionless stillwater depth, h/Ho. That is, $\Delta h/Ho$ =1.0, 0.25 and 0.1 were chosen for h/Ho=5-30, h/Ho=2-5 and h/Ho≤2, respectively. The calculation was done by the step-by-step method[2),3),7)], using the waves given at deep water as an input wave condition. Two kinds of waves such as the waves generated in a wave tank which will be mentioned later and the theoretically proposed waves expressed by Eq.(12) in Section 5.

The outline of calculation method in case of the experimental waves is described in this section. Assuming that the wave period and total number of individual waves are constant from deep water up to the shoreline, the variation of the wave height due to shoaling was calculated with Eq.(4) until the wave arrived at the shoreline. The wave which exceeded the breaking limit of Eq.(4) was treated as the broken wave. The probability

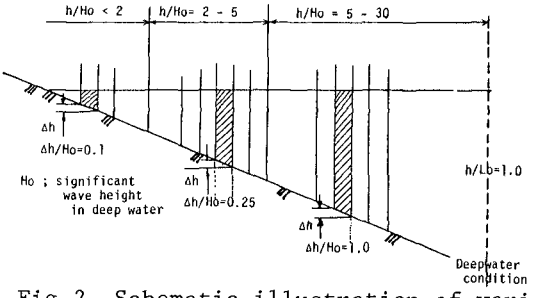

Fig.2 Schematic illustration of variation of Δh due to change of stillwater depth, h.

density corresponding to the broken waves was re-distributed, in proportion to that of non-broken waves, to the probability density of non-broken waves in order to determine $\bar{H}2$ and $\bar{\eta}$ with Eq.(6). The detailed calculation technique is referred to the references 2),3),7) and 9).

The probability of occurrence of broken waves, $P_B(h)$ at the water depth of h is obtained by the ratio of the total number of broken waves from deep water up to the depth, h to the total number of waves at the depth of h. The probability of occurrence of just breaking waves, $P_{JB}(h)$ between the depths, $h+\Delta h/2$ and $h-\Delta h/2$ can be calculated with Eq.(8),where Δh is a small quantity. In the calculation,Δh given by the following equation was employed to evaluate $P_{JB}(h)$,

$$\Delta h/Ho = (\Delta x/Ho)\ S = 1.5\ S$$

where Δx is a small increment of horizontal distance and Δx is taken 1.5 times the one-third largest wave height, Ho in deep water. The reason of this is that the width of coastal and offshore structures is around 1.5 times the design wave height. Using $P_B(h)$ and $P_{JB}(h)$ thus calculated, the probability distribution and mean value of lengths of runs of just breaking and broken waves are easily determined with Eqs.(1) and (2).

4. LABORATORY EXPERIMENT

4.1 Equipment and procedure

In the experiment, an indoor wave tank in 0.95m height, 0.7m width and 25m length at Nagoya University was used. The experimental set-up is illustrated in Fig.3. A flap-type wave generator controlled by Oil-Pressure Servo was installed at one end of wave tank. The water is perfectly shut out from the area behind the wave board. Therefore, the input electrical signal is smoothly converted to the wave motion. At the other end of wave tank, the wooden uniform slope was installed. Two kinds of slopes such as 1/15 and 1/30 were used. Three kinds of irregular waves (W.-2,W-3 and W.-4 in Table 1) were generated to have a Bretschneider spectrum as an expected spectrum. One irregular wave (W.-1 in Table 1)

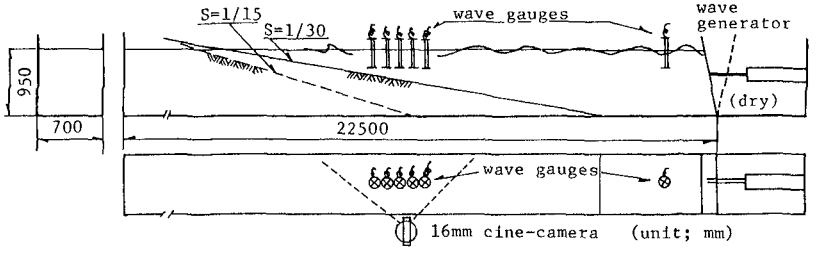

Fig.3 Schematic view of experimental set-up.

Table 1 Experimental waves

Bottom Slope	Case	$\bar{H}$ (cm)	$\bar{T}$ (s)	$H_{1/3}$(cm)	$T_{1/3}$(s)	Ho (cm)	Q_p	f_c (Hz)	Wave
1/15	Case 1	11.2	1.4	13.8	1.3	14.9	7.03	0.45	W.- 1
	Case 2	6.1	1.0	9.3	1.1	9.8	1.97	0.30	W.- 2
1/30	Case 3	8.4	1.0	12.5	1.1	13.4	1.80	0.35	W.- 3
	Case 4	3.9	0.9	6.0	1.1	6.4	1.52	0.30	W.- 4

$\bar{H}$; mean wave height, $\bar{T}$; mean wave period, $H_{1/3}$; significant wave height $T_{1/3}$; significant wave period, Ho; significant wave height in deep water Q_p; spectral peakedness, f_c; peak frequency of power spectrum

was generated to have double peaks on its power spectrum. Some of their spectral and statistic values are given in Table 1.

The water surface profiles were not only measured by capacitance-type wave gauges, but also simultaneously filmed, through glass side wall,by a 16mm high speed cine-camera (50 frames/s) in order to obtain the one-to-one correspondence between the waves in time domain and those in spatial one. This enabled us to omit noise-like small waves frequently observed in the surf zone as well as to classify clearly the waves into the just breaking, broken and unbroken waves. The measuring time of waves was about 12 minutes. Water surface profiles measured by the wave gauges were recorded on magnetic tapes. The irregular waves (W-1,W-2,W-3 and W-4) were generated 5 or 6 times so that the waves at 25 different points located from h=63cm up to near the shoreline were possible to be measured.

4.2 Data analysis

The irregular wave was analyzed by both the wave-by-wave and spectral analyses. The individual wave in an irregular wave train was defined by the zero-downcrossing method. The water surface profile was sampled at every 0.1 s. The wave power spectrum was calculated by B-T[11] method with data of 4800 points. The maximum lag number and degree of freedom were 80 and 120, respectively.

Anlayzing 16mm motion films by means of a film motion analyzer, all the individual waves were carefully classified into the just breaking, broken and non-broken waves. Special care was paid to determine the just breaking wave, since the just breaking wave is defined, as stated already, as the critical wave with little air at the inception of breaking. The breaking point and wave height at the breaking point were all determined by analyzing the 16mm motion films with help of wave data taken by the wave gauges. The high pass filter was used to eliminate the surf beat from wave profiles near the shoreline so as to definitely obtain the individual waves. The number of individual waves generated at the wave board in experiments was 420, 520, 595 and 550, for the waves of W.-1, W.-2, W.-3 and W.-4, respectively.

4.3 Results and discussion

Figure 4 shows one example of time series of successive 206 individual waves in the case of wave, W.-1, where symboles

□ and ■ indicate, respectively, the just breaking and broken waves. The wave without the symboles is non-broken wave. Therefore,most of individual waves at the depth of h/Ho=2.11 in Fig.4 are the non-broken wave. With the irrgular wave approaches to the shoreline, the number of the just breaking wave increases to a maximum and then decreases. The maximum occurrence of just breaking waves in Fig.4 is around h/Ho = 1.01. On the other hand, the number of the broken wave increases continuously as the irregular wave train propagates to the shoreline and most of the individual waves become the broken wave, as indicated in Fig.4.

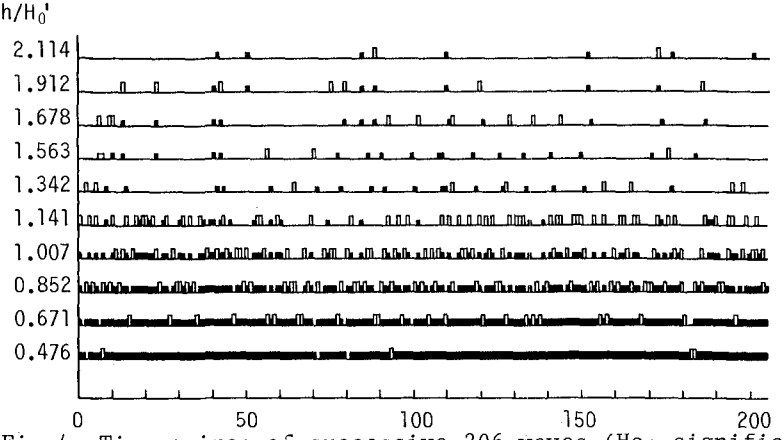

Fig.4 Time seires of successive 206 waves (Ho; significant wave height in deep water).

(1) P_{JB} and P_B

As shown in Fig.5, P_{JB} increases to a maximum and then decreases as the irregular wave approaches to the shoreline. The experiments showed that the maximum value of P_{JB} is 0.29 at h/Ho=1.14, 0.24 at h/Ho=1.00, 0.11 at h/Ho=0.83 and 0.14 at h/Ho=1.1, respectively, for the wave, W.-1,W.-2,W.-3 and W.-4. $P_{JB}(h)$ is given here by $P_B(h-\Delta h/2)-P_B(h+\Delta h/2)$,and $\Delta h=1.3H_o$, as in Eq.(10). The theoretical values estimated with Eqs.(3)-(10) are shown in Fig.5. At the same time, the theoretical values estimated with Eqs.(4)-(10) and Eq.(11) in place of Eq.(3) are shown for comparison. Eq.(11) was proposed as the shoaling condition for finite amplitude regular

$$\left.\begin{array}{ll} H/H_o = K_s & ; \quad gHT^2/h^2 \leq 30 \\ Hh^{2/7} = \text{const.} & ; 30 < gHT^2/h^2 \leq 50 \\ Hh^{5/2}(\sqrt{gHT^2/h^2} - 2\sqrt{3}) = \text{const.} & ; \quad gHT^2/h^2 > 50 \end{array}\right\} \quad (11)$$

waves by Shuto[12]. In Eq.(11), g is the gravitational acceleration, T the wave period. The theoretically estimated values agree quantitatively well with experimental ones. There are, however, some discrepancies about a maximum value of P_{JB} between the calculations and experimental values. The main reasons of this may be (i) Eq.(4) is not a better equation,

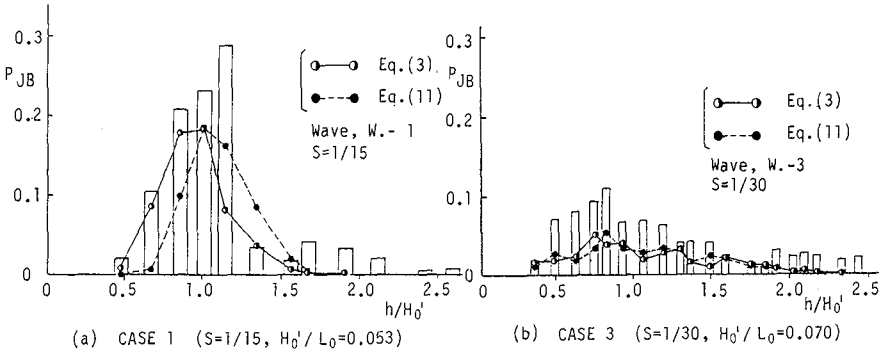

Fig.5 Variation of P_{JB} with decreasing of water depth.

and (ii) number of waves in the surf zone decreases, in the worst case, to 90% of the number of waves generated at the wave board in the experiment.

The probability of occurrence of broken waves, P_B becomes continuously large, as shown in Fig.6, as the wave approaches the shoreline. The agreement of calculated values with experimental ones is much better than the case of P_{JB}. It can be said that P_B is well predicted by the numerical model proposed in this paper. Figure 6 shows that 98% of the wave,W.-1 and about 80% of the wave, W.-3 are broken waves at the non-dimensional water depth h/Ho=0.5.

Figures 5 and 6 show that theoretical values estimated with Eq.(3) as shoaling condition seem to be in better agreement with experimental values more than ones estimated with Eq.(11) as shoaling condition.

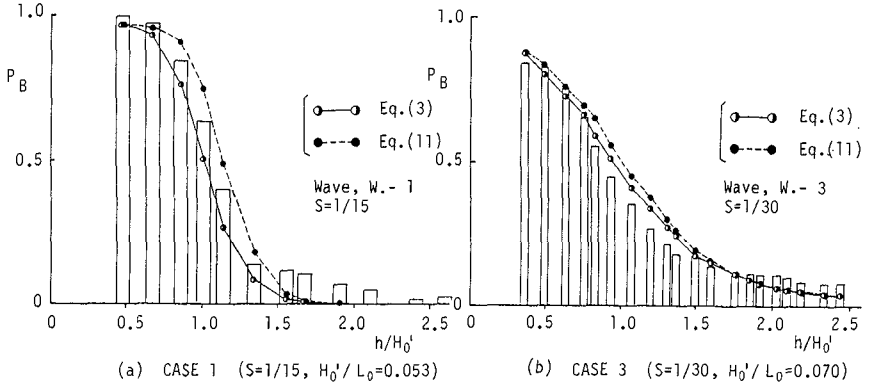

Fig.6 Variation of P_B with decreasing of water depth

(2) $P_1(J_1)$, $P_2(J_2)$, $Q_1(E_1)$ and $Q_2(E_2)$

Figures 7 and 8 show some examples of $P_1(J_1)$ and $Q_1(E_1)$, and $P_2(J_2)$ and $Q_2(E_2)$, respectively. Concerning $P_1(J_1)$, the probability of run length $J_1=1$, $P_1(1)$ is predominantly large, compared with $P_1(2)$ and $P_1(3)$. $P_1(3)$ is negligibly small even at h/Ho=1.066 where P_{JB} becomes maximal. On the other hand, the probabilities of total run lengths, $Q_1(1)$, $Q_1(2)$,$Q_1(3)$, $Q_1(4)$ and $Q_1(5)$ are the same order, although $Q_1(E_1)$ tends to decrease as E_1 becomes large.

The probability distribution of run length of broken waves, $P_2(J_2)$ differs from that of $P_1(J_1)$. $P_2(2)$,$P_2(3)$,$P_2(4)$ and $P_2(5)$ are comparatively large, compared with $P_2(1)$. In case of $P_1(J_1)$, $P_1(1)$ decreases to a minimum and then increases, and $P_1(2)$ and $P_1(3)$ increase to a maximum and then decrease as the waves advance to the shoreline (see Fig.9). In contrast, $P_2(1)$ decreases almost monotonously. The location where $P_1(1)$ becomes a minimum and $P_1(2)$, $P_2(2)$ and $P_2(3)$ take a maximum value correspond to the location at which P_{JB} becomes maximal. The theoretically estimated values are in good agreement with experimental values. The calculation method which employs Eq.(3) as the shoaling condition seems better than one using Eq.(11) to evaluate $P_1(J_1)$,$Q_1(E_1)$,$P_2(J_2)$ and $Q_2(E_2)$.

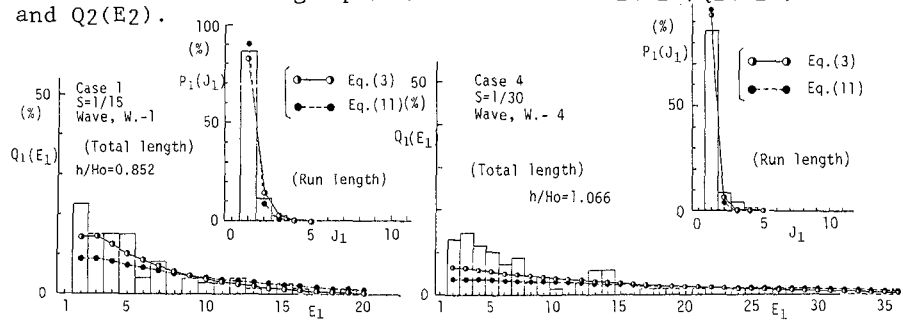

Fig.7 Probability distributions of J_1 and E_1.

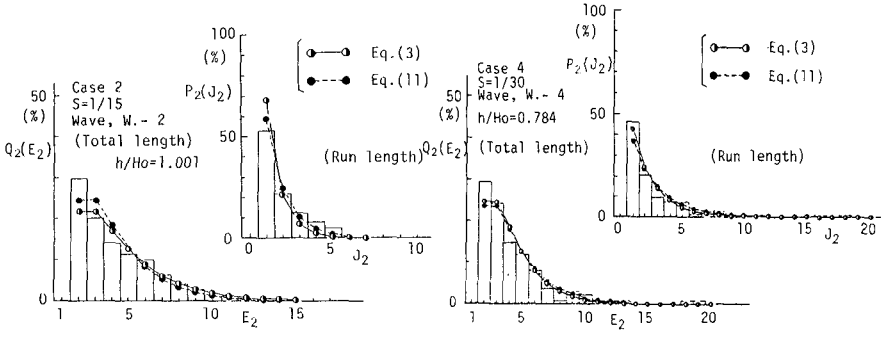

Fig.8 Probability distributions of J_2 and E_2.

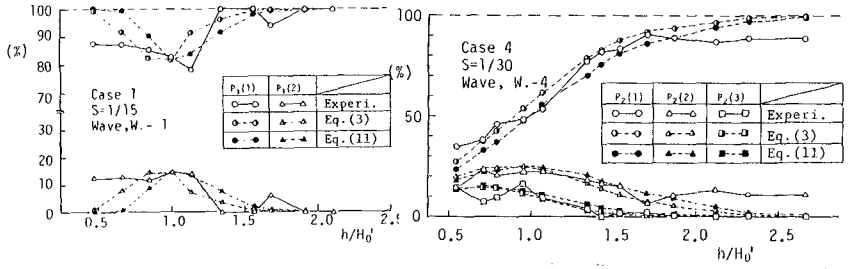

Fig.9 Variation of $P_1(1)$, $P_1(2)$, $P_2(1)$, $P_2(2)$, $P_2(3)$ with h/Ho.

(3) $\bar{J}_1$, $\bar{J}_2$, $\bar{E}_1$ and $\bar{E}_2$

The mean run length of just breaking wave, $\bar{J}_1$ never exceeds 2.0 from deep water up the shoreline, as shown in Fig.10. The maximum value of $\bar{J}_1$ was 1.33, as given in Table 2. This fact means that two waves never break successively on average. There is discrepancy between experimental and calculated values, especially around h/Ho≅1 at which PJB becomes maximal. This reason is that the theoretical model cannot estimate well PJB around h/Ho≅1 at which waves break most frequently.

The mean total run length of just breaking wave, $\bar{E}_1$ decreases to a minimum and then increases as increase of h/Ho, as shown in Fig.11. $\bar{E}_1$ is strongly related to PJB and $\bar{E}_1$ increases with decreasing of PJB. The difference between experiments and calculations is due to the reason that the theoretical model cannot estimate very well PJB, as stated above.

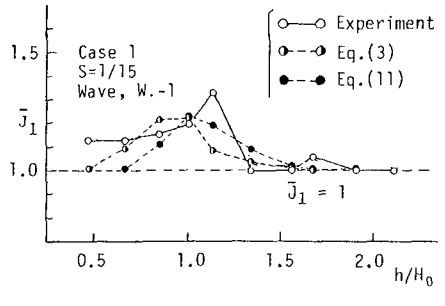

Fig.10 Variation of $\bar{J}_1$ with h/Ho.

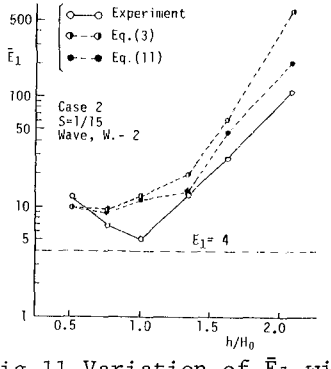

Fig.11 Variation of $\bar{E}_1$ with h/Ho.

Table 2 Experimental values of $\bar{J}_{1max}$, $\bar{E}_{1min}$ and $\bar{E}_{2min}$.

Bottom Slope	Case	Ho/Lo	$\bar{J}_{1max}$	$\bar{E}_{1min}$	$\bar{E}_{2min}$	Wave
1/15	Case-1	0.053	1.33	4.26	3.92	W.- 1
1/15	Case-2	0.050	1.25	5.07	4.14	W.- 2
1/30	Case-3	0.070	1.09	8.93	4.68	W.- 3
1/30	Case-4	0.031	1.24	8.12	3.89	W.- 4

Figures 12 and 13 show variations of $\bar{J}_2$ and $\bar{E}_2$ with h/Ho. The mean run length of broken waves, $\bar{J}_2$ increases continuously from 1 with h/Ho decreases. The variation of $\bar{J}_2$ with h/Ho is very similar to that of P_B. Since the theoretical model estimates very well P_B, the agreement between calculated and experimental values is very good. The variation of $\bar{E}_2$ with h/Ho is very similar to that of $\bar{E}_1$. $\bar{E}_2$ becomes minimal at the location where P_{JB} becomes maximal. According to Eqs.(1) and (2), the minimum value of $\bar{E}_1$ and $\bar{E}_2$ is 4. The minimum values obtained in the experiments was, as given in Table 2, more than 3.9, which is very close to 4. Therefore, it may safely be said that the random process model which considers no correlation between waves is a good model to evaluate accurately the lengths of runs of broken waves.

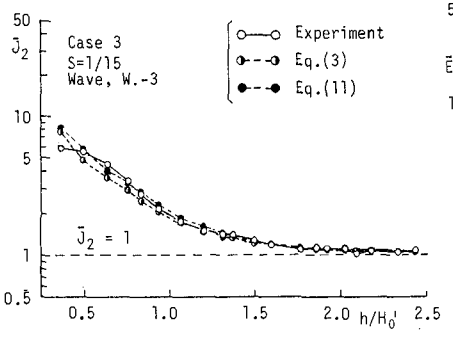

Fig.12 Variation of $\bar{J}_2$ with h/Ho.

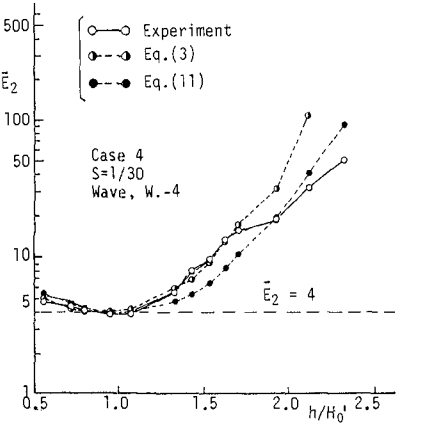

Fig.13 Variation of $\bar{E}_2$ with h/Ho.

5. DIAGRAMS OF $\bar{J}_2$ and $\bar{E}_2$

The theoretical model proposed in this study has been shown to evaluate well the lengths of runs of broken waves. Therefore, we try here to calculate the variation of the mean run and total run lengths, $\bar{J}_2$ and $\bar{E}_2$ with wave propagation from deep water to the shoreline on gentle slopes.

5.1 Calculation method

In the numerical calculations, 4 kinds of bottom slopes such as 1/10,1/20,1/30 and 1/50 and 6 kinds of waves such as Ho/Lo=0.002,0.005,0.01,0.02,0.04 and 0.08 were employed. The irregualr wave given by the following equation was employed as the deep water wave in order to obtain the diagram of $\bar{J}_2$ and $\bar{E}_2$.

$$P(H^*,T^*)=1.35H^*\cdot T^{*3}\exp\left(-\left(\frac{1}{4}H^{*2}+0.675T^{*4}\right)\right) \quad (12)$$

Here, $H^*=H/\bar{H}$, $T^*=T/\bar{T}$, and $\bar{H}$ and $\bar{T}$ are the mean wave height and period, respectively. The wave given by Eq.(12) was divided into 14400 rectangular meshes, i.e., 14400 individual

waves, as indicated in Fig.14. The wave in each grid,i.e., the individual wave is treated to experience shoaling and breaking. Once the wave breaks, the wave was assumed to keep broken up to the shoreline, and no correlation between waves was considered. The calculation method adopted was the same as that described in Section 3-1, and Eq.(3) was employed as the shoaling condition, since Eq.(3) was judged to be better than Eq.(11) as the shoaling condition, as stated in Section 4.

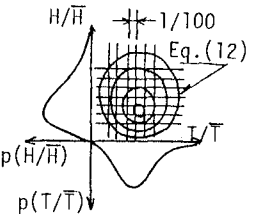

Fig.14 Joint probability distribution function of wave height and period.

5.2 Results and discussion

Figures 15 and 16 show variations of the mean run length, $\bar{J}_2$ and total run length, $\bar{E}_2$ with h/Ho on gentle slopes such as 1/10,1/20,1/30 and 1/50. $\bar{J}_2$ increases rapidly as h/Ho becomes small, as indicated in Fig.15. In addition, Fig.15 shows that the smaller the wave steepness,Ho/Lo and the gentler the bottom slope, the larger becomes h/Ho at which $\bar{J}_2$ grows up rapidly. Concerning to $\bar{E}_2$, $\bar{E}_2$ decreases to the minimum value of 4 and then increases as shown in Fig.16. The dimensionless water depth h/Ho at which $\bar{E}_2$ is minimal becomes larger as the wave steepness becomes smaller and bottom slope becomes gentler.

6. CONCLUDING REMARKS

In this paper, the variations of probability distribution, mean run and total run lengths of just breaking and broken waves on gentle slopes have been discussed, based on laboratory experiments and theoretical calculations. The theoretical model proposed here is shown to be valid and the random process model is powerful, especially for evaluating the characteristics of the probability distribution, mean run and total run lengths of broken waves.

ACKNOWLEDGEMENTS

We are grateful to Mr.Kataoka, formerly graduate student, for his help in laboratory experiments. This study was subsidized by a Grand-in-Aid for Scientific Research, Project No.60550360, from the Ministry of Education, Science and Culture of Japan.

REFERENCES

1) Battjes,J.A.: Set-up due to irregular waves, Proc.13th ICCE, 1972, pp.1993-2004.
2) Goda,Y.: Deformation of irregular waves due to depth-controlled wave breaking, Rept. Port and Harbour Res.Inst., Vol.14,No.3, 1975, pp.60-105 (in Japanese).
3) Sawaragi,T. and K.Iwata: Experimental study on irregular

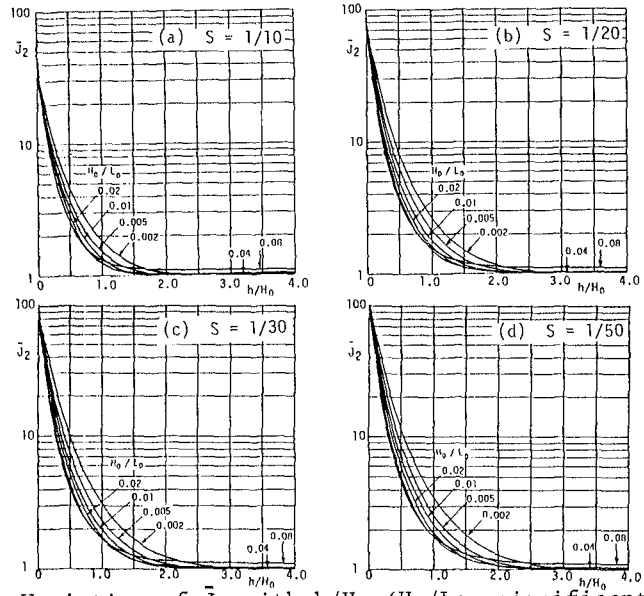

Fig.15 Variation of $\bar{J}_2$ with h/Ho (Ho/Lo; significant wave steepness).

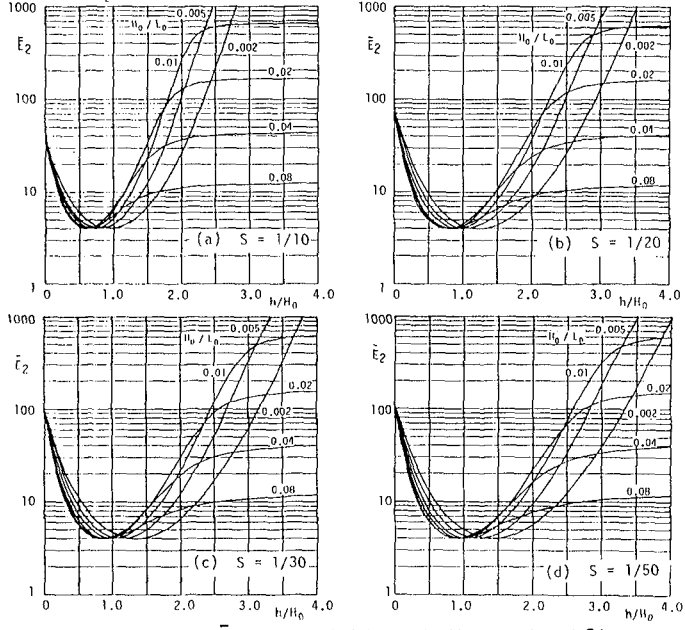

Fig.16 Variation of $\bar{E}_2$ with h/Ho (Ho/Lo; significant wave steepness).

wave deformation due to depth-controlled wave breaking, Proc.Hydrodynamics in Ocean Engineering, 1981,pp.166-182.
4) Sugawara, T. and M.Yamamoto: Calculation model of wave shoaling, Proc.25th Japanese Conf.on Coastal Eng., 1978, pp.80-84 (in Japanese).
5) Iwagaki,Y., Mase,H. and G.Tanaka: Wave height change of random waves in shallow water, Annual Rept.Disaster Prevention Res. Inst. of Kyoto University, No.24, B-2, 1981, pp. 1-15 (in Japanese).
6) Goda,Y.: On the statistics of wave groups, Rept. Port and Harbour Res. Inst.,Ministry of Transportation, Vol.15, No.3, 1976, pp.4-19 (in Japanese).
7) Iwata,K., Kataoka,S. and S.Itoh: Lengths of run of breaking waves in an irregular wave on gentle slopes, Proc. 31st Japanese Conf. on Coastal Eng., 1984, pp.163-167 (in Japanese).
8) Iwagaki,Y.,Kimura,A. and T.Kishida: Breaking of random waves on a sloping beach, Proc. 24th Japanese Conf. on Coastal Eng., 1977, pp.102-106 (in Japanese).
9) Sawaragi,T., Iwata,K. and T.Ishii: Experimental study on irregular wave breaking, Proc. 27th Japanese Conf. on Coastal Eng., 1980, pp.143-147 (in Japanese).
10) Longuet-Higgins,M.S. and Stewart,R.W.: Radiation stress and mass transport in gravity waves, with application to `surf beat´, Jour. Fluid Mech., Vol.13, 1962, pp.481-504.
11) Blackman,R.B. and J.W.Tukey: The measurement of power spectra, Dover, 1985, 190p.
12) Shuto,N.: Nonlinear long waves in a channel of variable section, Coastal Engineering in Japan, Vol.17, 1974, pp. 1-12.

CHAPTER 90

THE BOTTLENECK PROBLEM FOR TURBULENCE IN RELATION TO SUSPENDED SEDIMENT IN THE SURF ZONE

Peter Justesen[1], Jørgen Fredsøe[2] and Rolf Deigaard[3]

ABSTRACT

In the present paper the vertical distribution of turbulent kinetic energy k under broken waves is calculated by application of a one-equation turbulence model. The contributions to the energy level originate partly from the production in the wave boundary layer, partly from the production in the roller. Further on, the findings for k are used to calculate the vertical distribution of suspended sediment in broken waves.

INTRODUCTION

The vertical distribution of suspended sediment in the surf zone is of major importance for the evaluation of the rate of the longshore as well as the on-offshore sediment transport.

Outside the point of breaking, see Fig. 1, the presence of suspended sediment is restricted to the thin wave boundary layer. Models to describe this have been developed among others by Bakker (1974), Grant and Glenn (1983) and Fredsøe, Andersen and Silberg (1985).

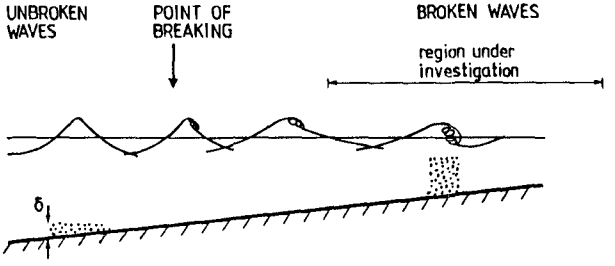

Fig. 1. Development of spilling breaker in the surf zone.

[1] M.Sc., Institute of Hydrodynamics and Hydraulic Engineering (ISVA), Technical University of Denmark, Building 115, DK-2800 Lyngby, Denmark.

[2] Ph.D., Dr. Techn., Professor in Marine Hydraulic Engineering, ISVA, Technical University of Denmark.

[3] Ph.D., Senior Hydraulic Engineer, Danish Hydraulic Institute, Agern Alle 5, DK-2970 Hørsholm, Denmark.

Inside the point of breaking, the surface generated turbulence results in a much higher level of turbulent kinetic energy, especially close to the water surface, where the production of turbulence takes place around the surface roller. This leads to a significant increase in the amount of suspended sediment compared to unbroken waves of same height and period on the same water depth.

In the present paper, we consider the conditions for fully developed broken waves, where the energy loss can be approximated by that in a hydraulic jump. (Turbulent bore).

The transition region from breaking to fully developed broken waves is not included in the present analysis. In case of a plunging breaker, the turbulence may be extremely violent at the location where the breaking wave splashes through the water surface. Until now, this flow has not been satisfactorily described. In case of a spilling breaker, the present theory may be modified to describe also the region between breaking and fully broken waves. This will however require a more detailed description of the development of the surface roller during the initial stages of breaking.

SCOPE OF PRESENT WORK

The main purpose of the present paper is to include a detailed description of the distribution of turbulence in the analysis of the suspended sediment, especially in the overlap region close to the bottom where contributions to the turbulence level originate from the surface roller as well as from the near-bed wave boundary layer.

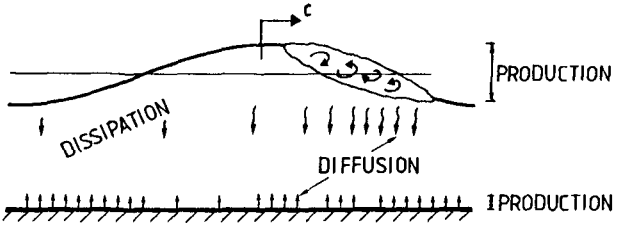

Fig. 2. Sketch of the location of production, diffusion, and dissipation of turbulent kinetic energy.

A first approach to solve this problem by application of a one-equation turbulence model for turbulent kinetic energy was proposed by Deigaard et al. (1986). In their model only the production of turbulence originating from wave breaking was included. Because this term is relatively well defined, the equation of motion could be avoided in the evaluation of the production term. As a result, the bottom generated turbulence was not directly included in the description, and Deigaard et

al. calculated the turbulence in the wave boundary layer independently using a simple model by Fredsøe (1984), in which the memory in turbulence is not included.

Because of the small thickness of the wave boundary layer, this might be a plausible approximation. However, the problem is how to combine the two contributions to get the total eddy viscosity. In Deigaard et al. (1986), the total eddy viscosity ε was estimated by

$$\varepsilon^2 = \varepsilon_b^2 + \varepsilon_t^2 \qquad (1)$$

where ε_b = eddy viscosity formed by production of energy in the wave boundary layer and ε_t = eddy viscosity formed by the production of energy in the water surface. Eq. 1 corresponds to summation of turbulent kinetic energy from the wall and the surface, respectively.

Especially in the overlap region where the level of turbulent kinetic energy is determined by both the surface and bed-generated turbulence a refined modelling of the level of k is needed. We refer to this region as the "bottleneck" region, because the level at this position is of extreme importance for how much sediment will be carried upwards to levels with higher turbulence. In the present theory, we use the transport equation for k to determine the distribution of k over the total depth. This analysis renders Eq. 1 redundant.

The advantage of the model by Fredsøe (1984) is that it is able to in a straightforward way to include the contribution of ε_b from a coexisting current in a three-dimensional motion. In this paper, the existence of such a current is disregarded. However, the present model can be extended to cover the combined wave current motion as long as this motion is restricted to a two-dimensional motion, see Deigaard, Justesen and Fredsøe (1986).

In the following description of the hydrodynamics and behaviour of suspended sediment, the bed is assumed to be plane and hydraulically rough. This restricts the present analysis to high values of the Shields parameter $\theta(> 1)$, according to Nielsen (1979). However, under storm conditions, where major parts of sediment transport takes place, this requirement is normally fulfilled.

HYDRODYNAMIC DESCRIPTION

Several attempts have been made in the past to describe the turbulence in the surf zone. Battjes (1975) has made a depth-integrated model for the turbulent kinetic energy and the eddy viscosity by assuming local equilibrium between the loss of energy from the waves and the dissipation of the turbulent energy. Svendsen and Madsen (1984) and Madsen and Svendsen (1983) applied the transport equation for turbulent kinetic energy to describe the longitudinal variation of the turbulence in a hydraulic jump or a bore. In this paper we shall calculate the eddy viscosity needed for the sediment calculations by use of the flow equation coupled with the transport equation for turbulent kinetic energy.

The flow kinematics are described by the equation of motion, which, neglecting convective terms, reads:

$$\frac{\partial U}{\partial t} = -\frac{1}{\rho}\frac{\partial p}{\partial x} + \frac{1}{\rho}\frac{\partial \tau}{\partial y} \tag{2}$$

U is the horizontal velocity, p is the pressure, and τ is the shear stress. The eddy viscosity ε is defined by

$$\frac{\tau}{\rho} = \varepsilon \frac{\partial U}{\partial y} \tag{3}$$

The turbulence is described by a one-equation turbulence model using the transport equation for the turbulent kinetic energy, k:

$$\frac{\partial k}{\partial t} = \frac{\partial}{\partial y}\left(\frac{\varepsilon}{\sigma_k}\frac{\partial k}{\partial y}\right) + \frac{PROD}{\rho} - C_1 \frac{k^{3/2}}{\ell} \tag{4}$$

According to Launder and Spalding (1972), the Prandtl number σ_k and the dissipation coefficient C_1 are taken to be $\sigma_k = 1$ and $C_1 = 0.08$. The length scale of the turbulence is to be prescribed. In the present model we have used ℓ given by:

$$\ell = \begin{cases} \sqrt[4]{C_1}\kappa y & \text{for } y < 0.07\,\dfrac{D}{\sqrt[4]{C_1}\kappa} \\ 0.07D & \text{for } y > 0.07\,\dfrac{D}{\sqrt[4]{C_1}\kappa} \end{cases} \tag{5}$$

κ is von Karman's constant ($\kappa = 0.40$). Close to the bed, ℓ has the variation normally used for boundary layer modelling, whereas it attains a constant value away from the bed to describe the conditions of free turbulence.

The coefficient of momentum diffusion, the eddy viscosity ε, is determined by the turbulent energy and the length scale:

$$\varepsilon = \ell \sqrt{k} \tag{6}$$

The production term, PROD, in the transport equation has two contributions. The first one is the production derived from the flow equation:

$$PROD = \tau \frac{\partial U}{\partial y} \tag{7}$$

This part of the turbulent production is most important in the wave boundary layer.

The second contribution is from the wave breaking. The details of the flow pattern in the surface roller is not modelled by the hydrodynamic model, and the production of turbulence in the surface roller is included in the transport equation by an analytical approximation introduced by Deigaard et al. (1986). The total energy dissipation due to the wave breaking is estimated from the energy loss in a hydraulic jump with the same height as the waves. The location of the production of turbulence is prescribed in the model on the basis of turbulence measurements in hydraulic jumps presented by Rouse et al. (1958). The turbulence originating from the wave breaking is dominant in the main part of the flow outside the wave boundary layer.

The boundary conditions for the k-equation are the no-flux condition at the surface:

$$\frac{\partial k}{\partial y}\Big|_{y=D} = 0 \tag{8}$$

and

$$k(z_0,t) = \frac{1}{\sqrt{C_1}}\,\varepsilon\,\left|\frac{\partial U}{\partial y}\right|,\quad z_0 = \frac{k_N}{30} \tag{9}$$

which expresses local equilibrium near the bed between production and dissipation of turbulent energy. k_N = bed roughness in Eq. 9. In addition, periodicity in the solution is required.

The pressure gradient in the flow equation is given by the free stream velocity, U_0:

$$\frac{1}{\rho}\frac{\partial p}{\partial x} = -\frac{\partial U_0}{\partial t} \tag{10}$$

The free stream velocity is estimated from linear shallow water theory:

$$U_0 = U_{1m}\sin\left(\frac{2\pi}{T}t\right) \tag{11}$$

By introducing these relations the following equation of motion is obtained:

$$\frac{\partial(U-U_0)}{\partial t} = \frac{\partial}{\partial y}\left(\varepsilon\frac{\partial U}{\partial y}\right) \tag{12}$$

The boundary conditions are (i) the no-slip condition at the bed

$$U(z_0,t) = 0 \tag{13}$$

and (ii) vanishing shear stress at the surface

$$\frac{\partial U}{\partial y}\Big|_{y=D} = 0 \tag{14}$$

Furthermore, periodicity in time is required.

THEORETICAL FLOW RESULTS

Two examples of the calculated instantaneous picture of the turbulent kinetic energy level for $a/k_N = 10^2$ and $a/k_N = 10^4$ are shown on the left hand side of Figs. 3 and 4, respectively. The production of surface generated turbulence has been set to zero in Figs. 3A and 4A in order to study the bed generated turbulence in the wave boundary layer alone. a = is the free stream amplitude and k_N the bed roughness. The variation in the x-direction (the direction of wave propagation) is obtained from the time variation by use of the relation

$$\frac{\partial}{\partial x} = -\frac{1}{c}\frac{\partial}{\partial t} \tag{15}$$

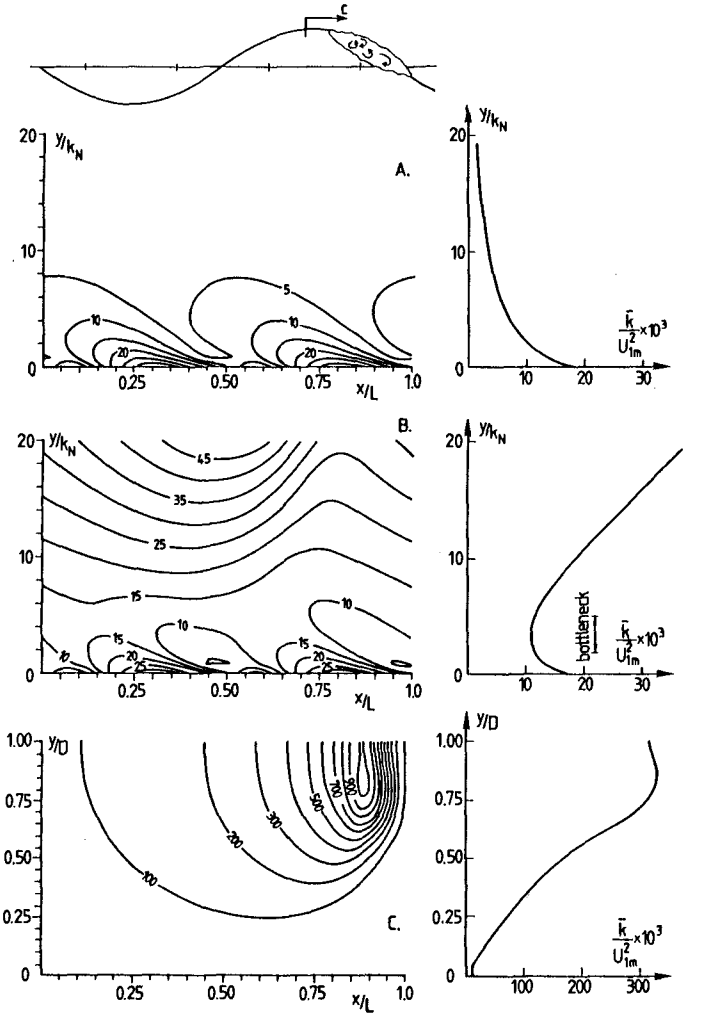

Fig. 3. Calculated distribution of turbulent kinetic energy (TKE) in unbroken and broken waves. Contour plots show the temporal variation of TKE, and the corresponding time-averaged levels of TKE are depicted on the right. A: Unbroken wave only with bottom-generated TKE; B: Near-bed region in broken wave; C: Total depth in broken wave. $a/k_N = 10^2$, $gT^2/D = 300$, $H/D = 0.5$. Levels of TKE indicated on contours are $\frac{\bar{k}}{U_{1m}^2} \times 10^3$.

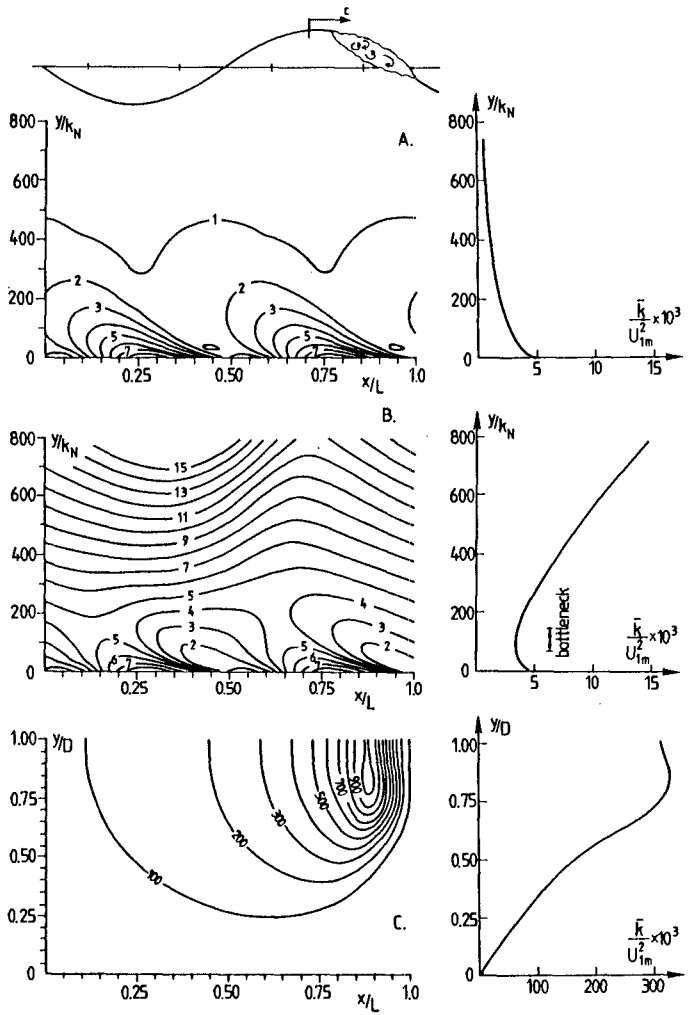

Fig. 4. Same as Fig. 3, but for $a/k_N = 10^4$, $gT^2/D = 300$, $H/D = 0.5$

It is seen that k has a maximum at the bottom, where the main production takes place. The shape of the contour plot is skew because it takes some time for the eddies to decay after being formed (mainly at the large outer flow velocities). The skewness is especially pronounced for small values of a/k_N, where the flow reverses rapidly. The pictures shown in Figs. 3A and 4A are experimentally verified by Hino et al. (1983) in case of a hydraulically smooth bottom.

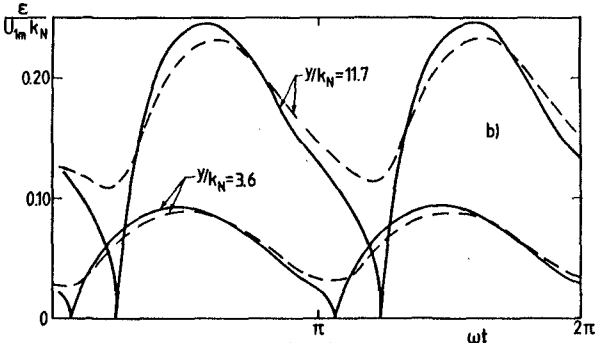

Fig. 5. Calculated temporal variation of eddy viscosity during one wave cycle in unbroken wave. - - - : one-equation model; —— : mixing-length theory. $a/k_N = 10^3$.

Fig. 5 shows the variation in the eddy viscosity during a wave cycle. The eddy viscosity is found from Eq. 6, and the importance of including a description of the behaviour of k is illustrated in Fig. 5 by comparing the predictions of a one-equation model with those of a mixing-length model, Bakker and van Doorn (1978). The implications of including a one equation model in the description of k are twofold: A: the time variation in ε is now predicted to be much smaller, because it takes time for the turbulent kinetic energy to decay, and B: the turbulence intensity increases further away from the bed at small values of a/k_N, because the turbulence level can now be built up with time.

In Figs. 3B, 3C and 4B and 4C contour plots of the instantaneous level of k, including the effect of turbulence formed around the roller, are shown. While the bottom turbulence has two peaks during one wave cycle (due to maximum flow velocity back and forth, respectively) the top generated surface has only one peak, just below the roller. In Fig. B, the detailed contour plots close to the bottom are depicted, while Fig. C shows the conditions over the entire depth. It is seen that the turbulence level is much higher far away from the bed than close to the bed.

On the right hand side of Figs. 3 and 4, the corresponding time-averaged values of k are shown. It is quite clear that a minimum (bottleneck) in k is present very close to the bottom, inside the wave boundary layer. This minimum in k is especially pronounced just below the roller, because it takes some time for the turbulence to penetrate downwards from the roller.

DESCRIPTION OF SUSPENDED SEDIMENT

The description of the vertical distribution of suspended sediment is based on the diffusion concept, for which the governing equation is the well-known

$$\frac{\partial c}{\partial t} = w \frac{\partial c}{\partial y} + \frac{\partial}{\partial y}\left(\varepsilon_s \frac{\partial c}{\partial y}\right) \tag{16}$$

where c = concentration by volume, t = time, w = fall velocity of suspended sediment, and ε_s = turbulent exchange factor for suspended sediment. In Eq. 16 the lateral diffusion term is neglected because the vertical gradient is much larger than the horizontal. ε_s is usually correlated to the eddy viscosity ε by

$$\varepsilon_s = \beta\varepsilon \tag{17}$$

where β is a constant of proportionality. Quite often, β is set equal to unity. Some experimental findings by van der Graaff and Roelvink (1984) suggest, however, that β is a function of the sediment properties: β increases with increasing grain size, and is normally somewhat larger than unity.

In the following calculations we have applied $\beta = 1$, so

$$\varepsilon_s = \varepsilon \tag{18}$$

If another value of β in Eq. 18 is adopted, the present results can still be applied by introducing a new fictive fall velocity

$$w_n = w\beta \tag{19}$$

because the vertical distribution depends only on the relative ratio w/ε_s.

Boundary condition at the bed: One of the major problems in steady current as well as in wave motion is to determine the bottom concentration c_b of suspended sediment. Here c_b is defined as the concentration of sediment a distance of about one to two grain diameters above the bed. Einstein (1950) suggested a kinematic approach, where the concentration of suspended sediment just above the bottom is directly related to the rate of the bed load transport.

Engelund and Fredsøe (1976) developed a model for c_b based on dynamic principles, describing how the fluid shear stress is transferred to the immobile part of the bed through the dispersive stress of the grains in suspension. An experimental result for the dispersive stress obtained by Bagnold (1954) was applied to calculate c_b.

The variation in c_b is obtained as a function of the Shields parameter, defined by

$$\theta = \frac{U_f^2}{(s-1)gd} = \frac{\tau_b}{\rho(s-1)gd} \tag{20}$$

s = relative density (2.65 for sand), g = acceleration due to gravity, d = mean grain diameter), cf. [8].

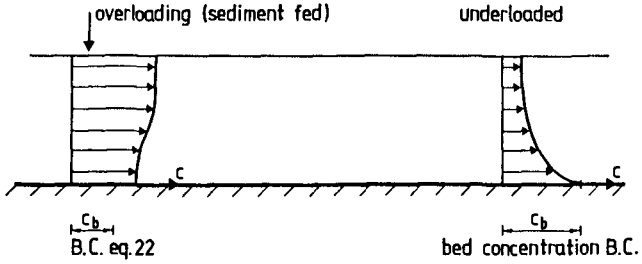

Fig. 6. Definition sketch of boundary condition for sediment concentration.

In two recent papers on suspended sediment in waves by Fredsøe et al. (1985) and Deigaard et al. (1986) the above mentioned method was applied to calculate the instantaneous value of c_b, based on the instantaneous value of θ

$$c_b = c_b(\theta) \tag{21}$$

The application of Eq. 21 seems reasonable from a physical point of view, since the theory behind the estimate of c_b is based on the assumption that c_b must have a certain value in order to transfer the fluid shear to the bed. However, in connection with a related topic, namely non-uniform river flow, Parker [16] discussed the above boundary condition, which he denotes the concentration boundary condition. In case of non-zero flux conditions, (i.e. erosion or deposition occurs in the bed) Parker instead applied a gradient boundary condition. This boundary condition was introduced because Eq. 21 gives physically unrealistic results in the case of overloading.

Let us consider the hypothetic case, in which the flow velocity is suddenly reduced from a certain steady value where $\theta = \theta_0$ to zero: in this case, Eq. 21 gives the result that c_b drops from $c_b(\theta_0)$ to zero instantaneously. However, all the sediment which is in suspension before the change in flow velocity occurs cannot settle faster than the settling velocity w. This means that in the still water, the time evolution in c_b is determined by

$$c_b(a,t) = c(a + \Delta y, t - \Delta t) \tag{22}$$

in which $\Delta y = w\Delta t$.

This equation simply states that the suspended sediment settles without changing its shape of the profile.

The example described above corresponds to the overloaded case. The underloaded case corresponds on the other hand to the flow situation where the fluid velocity is suddenly increased from zero to a certain flow velocity where $\theta = \theta_0$: here, it is possible for the bed concentration to adapt the new value $c_b(\theta_0)$ (disregarding inertia effects, which for sand are negligible)

because the suspended sediment just has to be transported a very small distance of the order of one grain diameter away from the bed. In this case, the sediment is not transported by diffusion, but by grain-grain interaction.

If we apply these considerations to the unsteady case under waves, an alternative boundary condition to the boundary condition Eq. 21 is

Underloading: Eq. 21

Overloading: Eq. 22

so the resulting boundary conditions become

$$c_b = \max \{c_b(\theta),\ c(a + w\Delta t,\ t - wt\} \tag{23}$$

In the wave case where the changes in flow velocity are continuous, Eq. 23 is still applied, as it describes the two extreme limits (for very fast varying flow) correctly.

Boundary condition at the surface: at the free surface, the flux of sediment is zero, or

$$\epsilon \frac{\partial c}{\partial y} + wc = 0 \quad \text{at } y = D \tag{24}$$

Periodicity in concentration: the time variation in c must be periodic, so

$$c(t,y) = c(t + T,\ y) \tag{25}$$

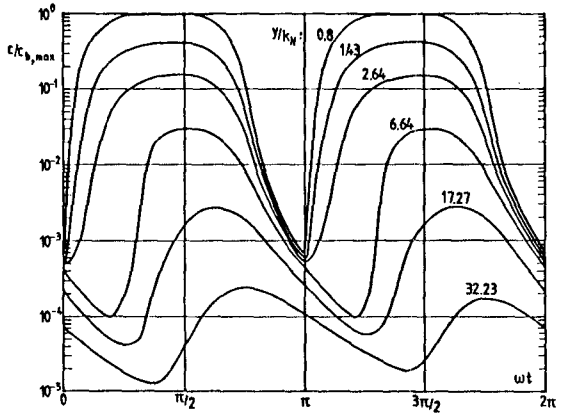

Fig. 7. Sediment concentration in different levels in a broken wave calculated as a function of time. $a/k_N = 10^3$, $gT^2/D = 300$, $H/D = 0.5$, $d = 0.2$ mm, $w/U_{1m} = 0.038$.

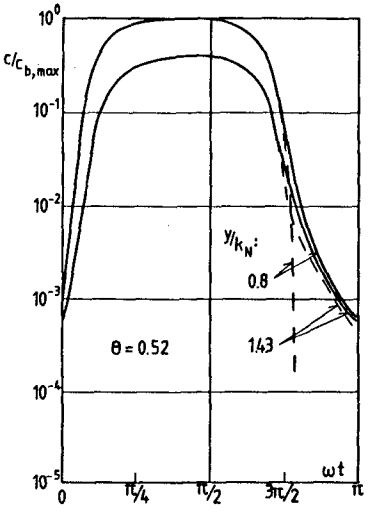

Fig. 8. Effect of choice of boundary condition for the sediment concentration. Solid lines indicate the same results as in Fig. 7 obtained using Eq. 23, whereas the dashed lines show results by using the bed concentration B.C.

THEORETICAL RESULTS FOR SUSPENDED SEDIMENT

Figs. 7 and 8 show the time-variation in the instantaneous value of concentration c of suspended sediment. It is noted from Fig. 7 that the concentration at a specific level is not totally identical in each wave half period. This can be explained by the former hydrodynamic calculations.

Fig. 8 shows the effect of the boundary condition selected: the dashed line in Fig. 8 is the result obtained by applying the bed concentration boundary condition, while the full drawn line is that obtained from Eq. 23. It is seen that the effect from different boundary conditions can be felt only a few grain sizes away from the bed.

Figs. 9 - 11 are related to the predicted vertical mean distribution c: in Fig. 9 the variation in c with a/k_N is depicted. The dashed line shows the results without wave breaking. In Figs. 10 and 11, the variation with gT^2/D and w/U_{1m}, respectively, are depicted.

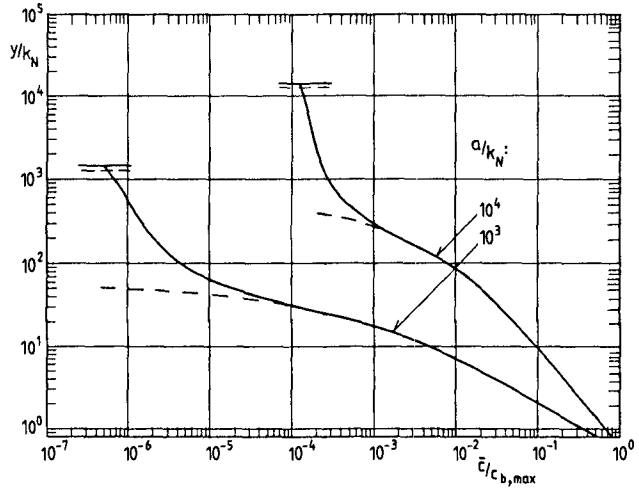

Fig. 9. Time-averaged concentration of suspended sediment as a function of depth for different values of a/k_N. GT^2/D = 300, H/D = 0.5, d = 0.2 mm, w = 0.025 m/s. Dashed lines indicate results for unbroken waves.

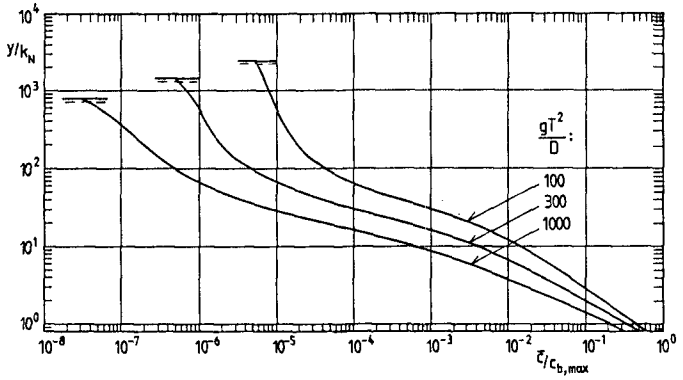

Fig. 10. Time-averaged concentration of suspended sediment as a function of depth for different values of gT^2/D. a/k_N = 10^3, H/D = 0.5, d = 0.2 mm, w = 0.025 m/s.

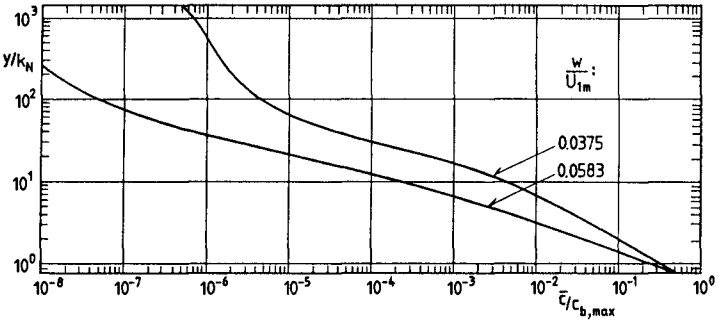

Fig. 11. Time-averaged concentration of suspended sediment as a function of depth for different values of w/U_{1m}. $a/k_N = 10^3$, $gT^2/D = 300$.

REFERENCES

[1] Bagnold, R.A.: "Experiments on a gravity-free dispersion of large solid spheres in a Newtonian fluid under shear". Proceedings, Royal Society, London, England, Ser. A., 225, p. 49, 1954.

[2] Bakker, W.T.:" Sand concentration in an oscillatory flow". Coastal Engineering Conference, pp. 1129-1148, 1974.

[3] Bakker, W.T. and van Doorn, Th.: "Near-bottom velocities in waves with a current". Coastal Engineering Conference, pp. 1394-1413, 1978.

[4] Battjes, J.A.: "Modeling of turbulence in the surfzone". Proc. Symposium on modeling Techniques. ASCE, San Francisco, California, 1975.

[5] Deigaard, R., Fredsøe, J. and Hedegaard, I.B.: "Suspended sediment in the surf zone". J. Waterway, Port, Coastal and Ocean Engineering. Vol. 112, No. 1, pp. 115-128, 1986.

[6] Deigaard, R., Justesen, P. and Fredsøe, J.: "Two-dimensional circulation in the surf zone". Submitted for possible publication. 1986.

[7] Einstein, H.A.: "The bed load function for sediment transportation in open channels". U.S. Dept. Agriculture, Technical Report, p. 1026, 1950.

[8] Engelund, F. and Fredsøe, J.: "A sediment transport model for straight alluvial channels". Nordic Hydrology, Vol. 7, pp. 293-306, 1976.

[9] Fredsøe, J.: "Turbulent boundary layer in wave and current motion". J. Hydraulic Engineering, ASCE, Vol. 110, No. 8, pp. 1103-1120, 1984.

[10] Fredsøe, J., Andersen, O.H. and Silberg, S.: "Distribution of suspended sediment in large waves". J. Waterway, Port, Coastal and Ocean Engineering, ASCE, Vol. 111, No. 6, pp. 1041-1059, 1985.

[11] Grant, W.G. and Glenn, S.M.: "Continental shelf bottom boundary layer model, Vol. I: Theoretical model development". Woods Hole Oceanographic Institution, Ocean Engineering Dept., 1983.

[12] Hino, M., Kashiwayanagi, M.O.B.S., Nakayama, A. and Hara, T.: "Experiments on the turbulence statistics and the structure of a reciprocating oscillatory flow". J. Fluid Mech., Vol 131, pp. 363-400, 1983.

[13] Launder, B.E. and Spalding, D.B.: "Mathematical models of turbulence". Academic Press, London and New York, 1972.

[14] Madsen, P.Å and Svendsen, I.A.: "Turbulent bores and hydraulic jumps". J. Fluid Mech., Vol. 129, pp. 1-25, 1983.

[15] Nielsen, P.: "Some basic concepts of wave sediment transport". Institute of Hydrodynamic and Hydraulic Engineering, Technical University of Denmark, Series Paper 20, 1979.

[16] Parker, G.: "Self-formed straight rivers with equilibrium banks and mobile bed. Part 1: The sand river." J. Fluid Mech., Vol. 89, 1, pp. 109-126, 1978.

[17] Rouse, H., Siao, T.T. and Nagaratnam, S.: "Turbulence characteristics of the hydraulic jump". Proceedings, ASCE, Vol. 84, No. HY1, pp. 1-30, 1958.

[18] Svendsen, I.A. and Madsen, P.: "A turbulent bore on a beach". J. Fluid Mech., Vol. 148, pp. 73-96, 1984.

[19] Van de Graaff, J. and Roelvink, J.A.: "Grading effects in concentration measurements". Coastal Engineering Conference, pp. 1618-1631, 1984.

CHAPTER 91

Local Movements of Sand in the Surf Zone

Kazumasa KATOH[1] and Norio TANAKA[2]

Abstract

The fluorescent sand tracers are injected in a point in the surf zone. Core samples are taken from the sixteen points on the circumference with the time intervals of fifteen minutes for about five hours. At the same time, the horizontal two components of fluid velocities are measured at the injection point by using an electromagnetic currentmeter. The field observations have been carried out three times on two beaches facing to the Pacific Ocean. The relations between the local sand movements and the fluid dynamics are examined on the basis of the data obtained.

1. Introduction

The study on the local sand transport in the surf zone is regarded as one of the very important themes in the coastal engineerings, and it is earnestly hoped to make clear the actual conditions of sediment dynamics in the surf zone. There is, however, a major obstacle to further understanding of the local sand transport, or nearshore sediment dynamics, that is to say, the lack of instruments which can directly measure the sediment transport.

Nadaoka, Tanaka and Katoh (1981) developed the technique to use the fluorescent sand tracer for measuring the local sand movements in the surf zone, and examined its capability by applying it to the field, Ajigaura Beach in Japan. The result proved the technique quite promising, and we decided to explore its possibility further. The field observations with the fluorescent sand tracer have been carried on two beaches facing to the Pacific Ocean - Oarai Beach in 1981 and Sudahama Beach in 1982 and 1983, in Japan.

In this report, based on the data obtained by this method on these beaches, we examine the local sand movements such as the advection speed of sand tracer , the mixing depth into the sea bottom, the local sand transport rate, and so on.

---

1) Chief of Littoral Drift Laboratory, Hydraulic Engineering Division, Port and Harbour Research Institute, 1-1, 3-chome, Nagase, Yokosuka, Japan. 2) Nippon Tetrapod Co., LTD., Japan (Former Director of Marine Hydrodynamics Division, PHRI)

2. Field Observations

2.1 Observation procedure

An outline of the observation procedure employed in the field using fluorescent sand tracer is as follows. First of all, a circle with the radius of 8.75 meters is established in the surf zone at an observation site. In practice, one pipe is set at the center of circle and sixteen pipes are set at the points which divide the circumference into sixteen arcs. An electromagnetic currentmeter is also set near the center of circle to measure the two horizontal components of the current velocity.

Three different colors of the fluorescent sand tracers, red, blue and yellow-green, are prepared in advance by utilizing the sand which have been previously removed from the beach face at the observation site. The observation starts at the time when one of the three colors of the tracers is injected at the center of circle. The remaining two colors of tracers are injected at the center at the time of one and two hours after the first injection, respectively. The volume of each sand tracer injected is 5 kilograms at a time. A sampling of the sand tracer at the sixteen points on the circumference is started 5 minutes after the first injection and is repeated with the time interval of 15 minutes, being 21 times for the typical case.

Core samples are taken at all the sixteen points as shown in Fig.1. The sampling procedure done by frogmen is as follows. (a) A transparent acrylic pipe of about 130 centimeters in length, 3.4 centimeters in inner diameter and 3 milimeters in thickness is brought to the sampling point by a frogman. (b) The acrylic pipe is pushed into the sea bottom by 20 to 30 centimeters. (c) The upper end of pipe is sealed with a rubber stopper. (d) The pipe is pulled out with the core sample inside it. (e) Immediately after it, the lower end of pipe is sealed with another rubber stopper, and the pipe is brought to the shore.

After removing the sea water, the core sample is slowly pushed out from the pipe onto a flat plate by using a piston. In almost all cases, the core sample was able to be taken out in a cylindrical shape without

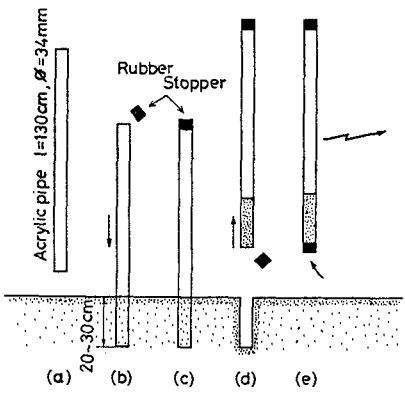

Fig. 1 Method of taking core sample.

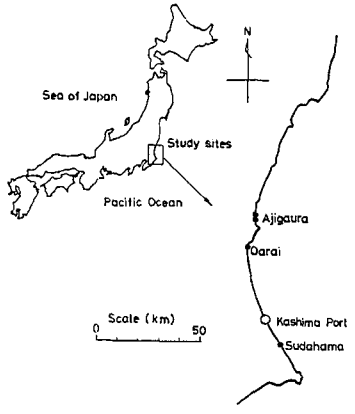

Fig.2 Location of study site.

Table 1 Summary of experiment conditions

Site	Experiment number	H_0 (m)	T_0 (s)	Tide level (m)	Tide level (m)	Clearance (cm)	Sediment d_{50}(mm) S_0, S_k
Oarai	8/31/81	0.52	6.0	0.16	0.77	12, 15	0.24
	9/ 2/81	0.38	5.7	0.36	1.07	8, 8	1.34, 1.12
Sudahama	7/28/82	1.50	8.5	1.03	0.78	12, 20	0.16
	7/29/82	1.20	8.8	0.86	0.90	17, 25	1.17, 0.99
	7/30/82	1.00	8.4	0.75	1.00	20	
Sudahama	8/24/83	1.02	5.7	0.26	1.31		
	8/25/83	0.85	7.5	0.32	1.13	13, 17	

being disturbed. The core sample is then sliced into 2 centimeters segments from the sea bottom to the depth of 12 centimeters. Each segment is well mixed, and about 40 % of its quantity is spread out in the shape of a circular plate having the diameter of 8 centimeters and the thickness of 0.15 centimeter on a flat plate in a pitch-dark room. Then, the number of the sand grains with each tracer color on the surface of the circular plate is counted ocularly under an ultraviolet light.

2.2 Sites of field observations

The tracer experiments were carried out three times on two beaches on the east coast of Japan - Oarai (autumn 1981) and Sudahama (summer 1982, summer 1983). These beaches are classified as micro-tidal beaches, because their tide ranges are about 1 meter. They are exposed to the full wave energy of the Pacific Ocean. The locations of these beaches are shown in Fig.2. An outline of each beach can be found elsewhere (Katoh et al., 1985). In total the tracer experiments were carried out for seven days. In this report, each experiment will be referred to by year, month and day.

General conditions of the sea during the field observations are listed in Table 1. The fifth and sixth columns give the tidal levels at the times of start and end of the observations above the datum line. A clearance listed in the seventh column is the vertical distance of the sensor of currentmeter from the sea bottom. The clearance was measured by using a scale or a palm and fingers of a frogman, repeating twice in almost all cases. The last column gives the medium diameter of sand (d_{50}), the sorting coefficient (S_0) and the skewness parameter (S_k) of the beach materials (quartz sand).

The observation was carried out at the ground elevation around the datum level, 0 meter, in each case. This is because of the fact that we could not help deciding the locations of almost the same water depth for the sampling works by the frogmen. The observation points were usually located inside the surf zone in all cases.

3. Characteristics of Waves and Currents

The two horizontal components of current velocities measured at the injection point were digitized at the interval of 0.1 second. Every two consecutive digital data are averaged to yield the smoothed data with the time interval of 0.2 second, which are utilized for analyses.

The representative values of currents, that is to say, the mean velocity, the principal direction of the incident waves (Nagata,1964), the skewness, the root-mean-square value of velocity fluctuation and a velocity atiltness in the principal wave direction, are calculated for every fifteen minutes.

A principal direction of the waves, θ_p, is defined as

$$\tan 2\theta_p = 2\overline{uv}/(\overline{u^2} + \overline{v^2}), \tag{1}$$

where u and v are the horizontal components of wave motions only, which are obtained by removing the steady state currents from the original data.

The velocity component in the principal wave direction U_p, being defined positive in the direction of wave propagation, can be obtained by the coordinate transformation with the angle of θ_p. The skewness is defined for U_p as

$$\sqrt{\beta_1} = \frac{1}{N}\sum (U_p)_i^3 / (U_p)_{rms}^3. \tag{2}$$

The velocity atiltness which is a new parameter originally proposed by Goda (1985) for the forward tilting of wave profile is calculated. The velocity profile of the forward tilting, when it is differentiated with respect to time, yields the up-and-down asymmetry in the acceleration profile, the magnitude of which can be evaluated by the similar way as the skewness as follow:

$$\sqrt{\gamma_1} = \frac{1}{N}\sum (\dot{U}_p)_i^3 / (\dot{U}_p)_{rms}^3, \tag{3}$$

where the overdot in the expression denotes the differentiation with respect to time.

For every observation, the arithmetic means of the representative characteristics of waves and the vectorial means of mean current velocities are calculated for the period from the time of injection to the end of observation, and the resultant values are listed in Table 2.

According to Table 2, the values of skewness in 7/28/82 and 7/30/82 are negative. As the velocity fluctuation due to waves U_p is defined as positive in the direction of wave propagations in these data analyses, the values of the skewness of U_p in the surf zone would be thought positive and large from the analogy of surface wave profiles. Therefore, It is a quite curious fact that the mean values of skewness are negative on Sudahama Beach. Their cause is examined here.

Figures 3 shows typical records of current variations in the case of negative skewness. The direction of the Y-component is almost the same as the direction of the incident wave propagation and that of the X-component is nearly parallel to the shoreline. The current velocity in the Y-component is featured with the existence of long-period fluctuations which have the period of about 80 to 100 seconds and the amplitude much greater than that of the short-period fluctuations corresponding to the motions of incident waves.

Table 2 Representative value of currents and waves

		$\overline{V}$ (cm/s)	$\sqrt{\overline{U_p^2}}$ (cm/s)	velocity skewness	$\sqrt{\overline{\dot{U}_p^2}}$ (cm/s*s)	velocity atiltness
8/31/81	1	2.27	32.20	0.273	48.95	0.206
	2	2.90	31.20	0.316	47.45	0.177
	3	5.37	30.66	0.354	44.85	0.101
9/ 2/81	1	27.48	28.93	0.719	60.45	0.954
	2	26.23	28.70	0.709	61.20	0.874
	3	22.94	27.92	0.677	63.30	0.725
7/28/82	1	22.88	41.96	-0.266	58.00	0.408
	2	27.15	42.31	-0.289	58.20	0.406
	3	30.14	45.97	-0.131	56.90	0.434
7/29/82	1	49.53	40.97	0.101	44.55	1.040
	2	62.82	43.00	0.195	44.40	1.068
	3	61.17	43.91	0.138	43.80	1.069
7/30/82	1	55.39	53.40	-0.069	43.50	1.075
	2	58.94	53.60	-0.102	44.60	1.002
	3	63.01	52.88	-0.086	45.95	0.951
8/24/83	3	15.97	33.99	0.190	55.30	0.506
8/25/83	3	36.11	45.00	0.049	46.20	0.930

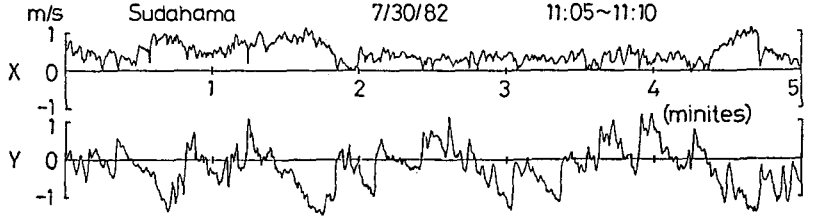

Fig.3 Typical segment of current records

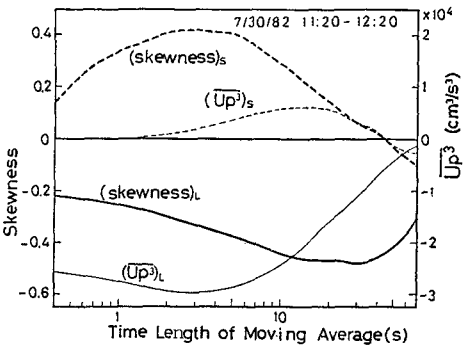

Fig.4 The values of skewness for the long period component and the short one.

By inspecting Fig.3 in detail, we can notice that the long-period components do not fluctuate sinusoidally but in the way that the velocity profile is flattened with longer duration in the positive side (onshore) and is sharpened with shorter duration in the negative side (offshore). Then, two analyses have been attempted for calculating the values of skewness. One analysis is to calculate the value of skewness, which is denoted by $(\text{skewness})_L$, for the smoothed velocity profile which is obtained by the application of the moving average technique; the averaging time length is

varied from 0.45 s to 70 s. Another is to calculate the skewness for the profile with removal of the smoothed profile, which corresponds to that of the relatively short-period components, and the resultant value is denoted by $(\text{skewness})_S$. These analyses have been done for the time series data of one hour. The result of analyses is shown in Fig.4, where the abscissa denotes the averaging time length. According to this figure, the values of skewness for the long-period components is always negative. Therefore, it is considered that the values of skewness for the long-period fluctuation are negative which make the values of skewness for the velocities combined of short and long-period components to be negative.

4. Characteristics of tracer movements

4.1 Advection speed and its direction

In order to estimate the advection speed and its direction of sand tracer, the following equations which have been derived by Nadaoka et al. (1981) are employed here.

Let $C(\omega,t)$ be the number of tracer particles in a core at the time t after the injection of tracer at a point of the direction ω on the circumference having a radius R (see Fig.5). Up to this time, tracer particles of $C(\omega,t)$ in number are considered to have moved from the center of circle to the circumference. It does not matter how tracer particles were transported there, whether in suspension or not, what happened with them on the way, and which way did they pass through. We are only concerned with the fact that they have moved there with the travelling time of t. Then the components of apparent travelling speed of tracer particles in the directions of η and ξ are given by $(R\cos\omega)/t$ and $(R\sin\omega)/t$, respectively. Furthermore, the mean advection velocity of tracer during the experiment can be defined by the following two components, u_m and v_m:

$$u_m = \frac{\int_0^\infty \int_0^{2\pi} C(\omega,t)\frac{R}{t}\cos\omega\, d\omega dt}{\int_0^\infty \int_0^{2\pi} C(\omega,t)\, d\omega dt}, \qquad (4)$$

$$v_m = \frac{\int_0^\infty \int_0^{2\pi} C(\omega,t)\frac{R}{t}\sin\omega\, d\omega dt}{\int_0^\infty \int_0^{2\pi} C(\omega,t)\, d\omega dt}. \qquad (5)$$

By using Eqs. (4) and (5), we have

$$V_t = (u_m^2 + v_m^2)^{1/2}, \qquad (6)$$

$$\theta_t = \tan^{-1}(v_m/u_m), \qquad (7)$$

where V_t is the mean advection speed of fluorescent sand tracer and θ_t is its direction.

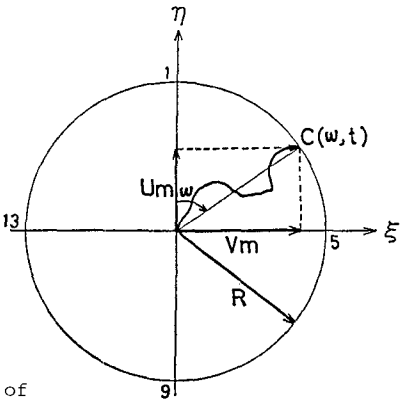

Fig. 5 Coordinate system.

In order to observe clear relations between the tracer advection and the characteristics of waves and currents, an oblique coordinate system which has been introduced by Nadaoka et al. (1981) will be used again. That is to say, the η axis is taken in the principal wave direction and the ξ axis is taken in the mean current direction, as shown in Fig.6. As these two axes generally intersect at an oblique angle, let the angle measured from the η axis to the ξ axis in the clockwise direction be ϕ_s.

Let us assume that the sand advection speed is V_t with the angle ϕ_t, which is defined in the same way as ϕ_s. Furthermore its two components in the directions of the mean current and the wave propagation are denoted by V_s and D, respectively, as shown in Fig.6. Then we have two equations as follows:

$$V_s = V_t \cdot \sin \phi_t / \sin \phi_s, \tag{8}$$

$$D = V_t \cdot \cos \phi_t \cdot (1 - \tan \phi_t / \tan \phi_s). \tag{9}$$

As all of physical quantities in the right-hand sides in Eqs. (8) and (9) can be estimated by Eqs.(1), (6) and (7) by utilizing the data measured, the values of V_s and D have been calculated and are listed in the first and the second columns in Table 3.

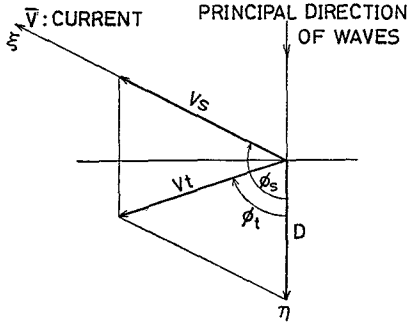

Fig. 6 Oblique coordinate system and definition of symbols.

Table 3 Tracer advection speed and mixing depth

		V_s (cm/s)	D (cm/s)	Mixing depth (cm)
8/31/81	1	-0.224	-0.063	4.08
	2	-0.100	0.151	3.37
	3	0.019	0.209	3.64
9/ 2/81	1	0.151	0.050	4.09
	2	0.158	0.056	3.96
	3	0.208	0.053	3.60
7/28/82	1	0.516	0.145	4.89
	2	0.183	-0.086	4.89
	3	1.054	0.271	3.77
7/29/82	1	0.188	-1.393	3.59
	2	0.319	-0.806	3.16
	3	0.360	-0.334	3.13
7/30/82	1	0.269	0.070	4.32
	2	0.498	0.150	3.60
	3	0.717	0.281	3.67
8/24/83	3	-0.073	-0.255	4.02
8/25/83	3	-0.182	-0.299	6.53

4.2 Mixing depth of fluorescent sand tracer in the sea bottom

As pointed out by Komar and Inman (1970), Nadaoka et al.(1981) and Kraus (1985), a phenomenon of sand mixing in a layer from the sea bottom surface to some depth exists in the surf zone. The vertical distributions of fluorescent sand tracer are calculated for each tracer with all of the data, and the average mixing depth of 80% cut-off are also calculated and listed in the last column in Table 3. In this report the mixing depth is defined as the depth containing 80% of the

total tracer in a core, in the same manner as Nadaoka et al. (1981) and Kraus (1985).

5. Relations between Local Sand Transport and Fluid Dynamics

5.1 Advection speed of sand movement in the direction of mean currents

Nadaoka et al. (1981) obtained a semi-theoretical relationship of

$$\bar{V}_s = 0.01 * \overline{V_l}. \qquad (10)$$

where $\bar{V}_s$ is the mean advection speed of longshore transport and $\overline{V_l}$ is the average longshore current velocity, and they said with some field data that Eq.(10) is valid for the local sand transport.

The values of the advection speed of tracer in the direction of mean currents V_s and mean current velocity $\bar{V}$, which are listed in Table 3, are plotted in Fig.7. As seen in Fig.7, the data points, except one point which have relatively larger values of V_s, scatter around a straight line of

$$V_s = 0.01 * \overline{V}. \qquad (11)$$

Therefore the relation of Eq.(11) is considered to be reconfirmed here.

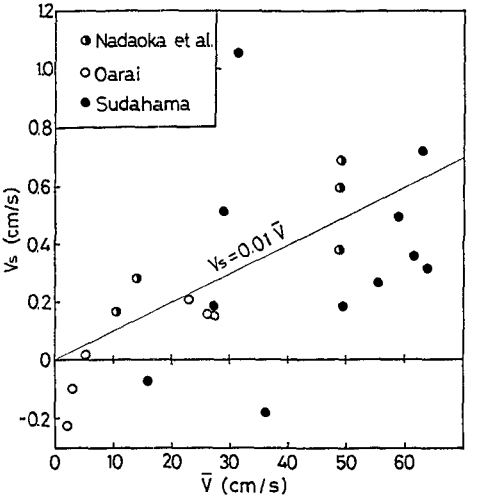

Fig. 7 V_s compared with $\bar{V}$.

5.2 Advection speed of sand movement in the principal wave direction

Nadaoka et al. (1981) showed that the dimensionless advection speed in the principal wave direction , $D/\sqrt{\overline{u^2}_p}$, can be explained by using the skewness parameter, which represents the feature of up-and-down asymmetry of velocity profile. Then, we tried to plot it against the skewness. The dimensionless advection speed, however, can be explained partially but not wholly by using only the skewness parameter (see Katoh et al., 1985), we need to take another parameter into account.

It might be said that the analysis in Nadaoka et al.(1981) has been done for one aspect of sand transport, i.e., bed load transport. Another approach for the explanation of the suspended load transport is thus necessary. Based on the data obtained in the surf zone, Sternberg, Shi, and Dowing (1984) reported that the frequency and duration of individual suspension events were strongly correlated with incident wave conditions, and the events of suspensions were in phase with bores propagating across the surf zone. Therefore, it is better to use a parameter representing the characteristic of the bores which have distinct features of the forward tilting both in the surface profile and in the velocity profile. Then, by using the velocity atiltness parameter (Eq.3), let us assume that the dimensionless advection speed

in the principal direction can be approximately expressed as follow:

$$D/\sqrt{\overline{U_p^2}} = a\cdot\sqrt{\beta_1} + b\cdot\sqrt{\gamma_1}\cdot(\dot{U}_p)^3_{rms} / g^3, \qquad (12)$$

where a and b are the coefficients and the second term in the right-hand side is normalized with the third power of the acceleration of gravity.

The transport direction of suspended load should be taken care, because the newly defined parameter is considered to be related to the concentration of the suspended load alone. According to the Shore Protection Manual, Coastal Engineering Research Center (1977), when the ratio of the deepwater wave height to the fall velocity of the beach sediment, H_0/w, is greater than wave period, T, the significant concentration of suspended load are expected to diffuse offshore and deposit in the offshore side. In the cases of the observations reported here, the fall velocity is of about 1.8 cm/s to 3.2 cm/s. If the period of incident waves, about 8 seconds (see Table 1), is taken for T, and 1.0 meter is taken for H_0, the value of H_0/w is apparently greater than T. Therefore, the suspended load is thought to be transported in the offshore direction.

The above consideration is applicable for the velocity fields due to the incident waves alone, but it is not so for the case in which the predominant long-period components coexist. In the latter case, the direction of the combined velocity depends almost on that of the long-period components. As seen in Fig.3, for example, when the long-period velocity components have a large positive value, the velocity combined with those of incident waves fluctuate mainly in the positive side. Under these conditions, a practice of taking the period of the incident waves as T is not appropriate, because the suspended load due to the passing of bores will be transported in the direction of the velocity of long-period components.

The direction of the net suspended load transport in the velocity fields containing the predominant long-period components will be inferred as follows. The values of skewness for the long-period velocity components are negative, which means that the total duration of the time when the direction of velocity is onshore is longer than that of offshore. The high concentration of suspended load occurs when the bores pass through. If the time interval between two arriving bores is constant, the frequency of the bores passing through a fixed point becomes larger during the time periods of onshore velocities than those of offshore ones, because the duration of the former is longer than that of the latter. This situation can be recognized in Fig.3. Therefore, the larger amount of sand is transported to the onshore direction in suspension, which yields the net onshore transport.

The sign of the coefficient b should be changed based on whether the predominant long-period components coexist or not with the incident waves. For this purpose, the values of skewness or U_p^3 can be utilized as a first step, because it is positive when the incident wave components are relatively large and is negative when the long-period components are relatively large. Thus, Eq.(12) is rewritten as

$$D/\sqrt{\overline{U_p^2}} = a\cdot\sqrt{\beta_1} + b\cdot \mathrm{sgn}(\sqrt{\beta_1})\cdot\sqrt{\gamma_1}\cdot(\dot{U}_p)^3_{rms} / g^3, \quad (13)$$

where $\mathrm{sgn}(\sqrt{\beta_1})$ takes the value of +1 or -1 depending on whether the skewness is positive or negative, and the value of redefined coefficient b should be a negative.

The value of $\overline{\dot{U}_p^3}$ can be obtained by multiplying the third power of $\sqrt{\overline{U_p^2}}$ by the skewness of the acceleration profile which are listed in Table 2. Using a regression analysis for Eq.(13) with the data listed in Table 2, we get the values of 0.024 and -85.1 for a and b, respectively. In turn, the value of the quantity in the right-hand side of Eq.(13) for each sand tracer has been calculated with the values of coefficients obtained, and it is plotted on the abscissa with the corresponding dimensionless advection speed on the ordinate in Fig.8.

Except three data points, the data are gathered around a straight line having the inclination of 0.85. The straight line is decided by applying the least squares method to the data excluding the three distant points so that the line should pass through the origin. By multiplying the coefficients a and b with the value of 0.85 we have the following relation:

$$D/\sqrt{\overline{U_p^2}} = 0.02\sqrt{\beta_1} - 72.4\cdot \mathrm{sgn}(\sqrt{\beta_1})\cdot \overline{\dot{U}_p^3} / g^3. \quad (14)$$

The first term in the right-hand side of Eq.(14) is considered to correspond to the bed load transport, while the second one to the suspended load transport. Equation (14) indicates that the directions of bed and suspended load transports are opposite each other, because $\overline{\dot{U}_p^3}$ usually takes a positive value.

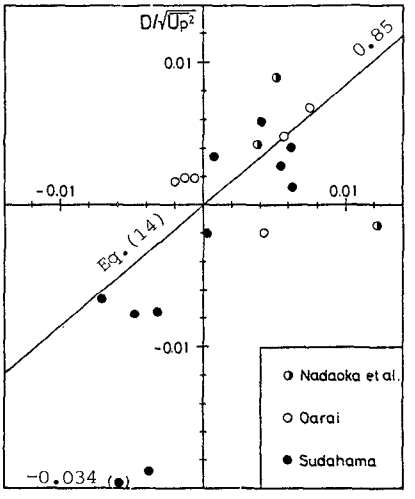

Fig.8 $D/\sqrt{\overline{U_p^2}}$ compared with the skewness and magnitude of forward inclination of velocity profile.

5.3 Mixing depth of sand tracer

Sunamura and Kraus (1985) presented the shear stress model to predict the average depth of wave-induced sediment mixing in the surf zone. The model shows that the mixing depth normalized with the sediment grain diameter is linearly related to the Shields parameter, which is proportional to the square of the velocity of the breaking waves. Then, let us examine whether this relation can be applied to the local mixing depth and the local velocities or not. The mixing depths listed in Table 3 are plotted against the mean-square values of velocities divided by the gravity of acceleration, $\overline{U_p^2}/g$, in Fig.9. Although some scatter is observed in the data points, the straight line drawn through the origin gives the result of

$$b = 2.5 * \overline{U_p^2}/g. \qquad (15)$$

Equation (15) can be rewritten with the local wave height by using the some assumptions as

$$b = 0.10 * H_{1/3}. \qquad (16)$$

This result is nearly same as that of Nadaoka et al. (1981) for the data obtained at Ajigaura Beach, in which the value of coefficient is about 0.08.

Furthermore, by asumming a constant sloping beach, h = x tanβ, and $\gamma = H_{1/3}/h = 0.6\text{-}0.65$ in the case of irregular waves in the surf zone, the average mixing depth in the surf zone can be estimated as follow:

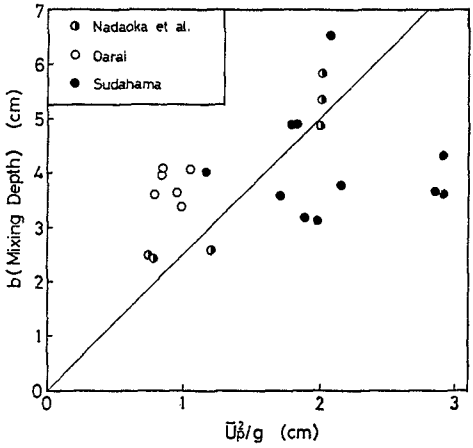

Fig. 9 Local mixing depth compared with $\overline{U_p^2}$.

$$\bar{b} = \frac{1}{X_b}\int_0^{X_b} b\,dx = \frac{1}{X_b}\int_0^{X_b} 0.10\cdot\gamma\cdot x\tan\beta\cdot dx = 0.05\cdot H_b, \qquad (17)$$

where X_b is the width of the surf zone and H_b is the significant wave height at the wave breaking point. The value of coefficient in Eq.(17) is of the same order as that in Sunamura and Kraus (1985), that is to say 0.027, but the former is about twice as large as the latter. At least in this report, the mixing depth should be expressed in terms of the velocity fluctuations as in Eq.(15), because the local wave height have not been measured in our observations.

5.4 Local sand transport rate

In much the same way as the bulk volume of longshore sand transport rate (Komar and Inman, 1970), a bulk volume of local sand transport rate per unit width Q_t is given by the equation

$$Q_t = b * V_t. \qquad (18)$$

The local advection velocity of the sediment V_t has been decomposed into the two components V_s and D in the directions of mean currents and the incident waves, respectively. The local sand transport rate is also decomposed into such two directions as follows:

$$Q_s = b * V_s, \qquad (19)$$

$$Q_D = b * D. \qquad (20)$$

By substituting Eqs.(11), (14) and (15) into Eqs.(19) and (20) respectively, we have

$$Q_s = \frac{0.0025}{g} * \overline{u_p^2} * \overline{v}, \tag{21}$$

$$Q_D = \frac{1}{g}[\ 0.05 \cdot \overline{u_p^3} - 181 \cdot \mathrm{sgn}(\overline{u_p^3}) \cdot (\overline{u_p^2})^{3/2} \cdot \overline{\dot{u}_p^3} / g^3\ ]. \tag{22}$$

The first term in the right-hand side of Eq.(22) mainly corresponds to the bed load transport, while the second one to the suspended load transport. Based on Eq.(22), further interesting discussions can be made. The mixing depth b is multiplied by the second term in the right-hand side of Eq.(14) to yield the contribution of suspended load to the total sand transport rate in Eq.(22). This operation looks strange because the mixing process is a phenomenon in the sea bottom, whereas the suspension of the bed material is that above the sea bottom. This apparent strangeness, however, may serve to understand the mechanics of sand transport in suspension in the surf zone.

For simplicity, let us pay our attention to one sand particle which has the same diameter as the others. The particle pausing on the sea bottom surface at first is suspended when the bore passes over it. Subsequently it is transported in suspension to some distance with the same velocity as the fluid one and deposit after several seconds on the sea bottom. Next, it is buried into the sea bottom due to the some mixing process of bed material. Then it losses an opportunity to be suspended again for a while. The time required for the particle to emerge again on the sea bottom surface becomes longer with increase in the mixing depth of the bed material. The elongation of the reappearance time reduces the apparent advection speed. This effect is already contained in the empirically obtained advection speed D (the second term of the right-hand side of Eq.14). While it is being buried in the sea bottom, the other particles which have been buried in the sea bottom to some depth initially at that point are successively suspended and transported to other points, of course with the same apparent advection speed as that of the particle we pay our attention to. The number of these particles suspended, or bulk volume of the particles, becomes large with increase in the reappearing time of our particle which is inferred to depend on the mixing depth b. Therefore, in order to obtain the total bulk volume of sand transport rate in suspension, the mixing depth b should be multiplied by the advection speed such as the second term in the right-hand side of Eq.(22).

Discussions have actively been held concerning whether the suspended load or the bed load transport is more important in the surf zone. For examples, Komar (1978) concluded that the suspended load is much less significant than the bed load transport, while Sternberg, Shi and Downing (1984) reported that all of the longshore transport at Leadbetter Beach could be accounted for by the suspended load transport. Let q_b and q_s be the absolute values of bed load and suspended load transport rate in the principal wave direction, respectively. They can be expressed from Eq.(23) as follows:

$$q_b = |0.05 \cdot \overline{u_p^3}| / g\ , \tag{23}$$

$$q_s = |181 \cdot (\overline{u_p^2})^{3/2} \cdot \overline{\dot{u}_p^3}| / g^4\ , \tag{24}$$

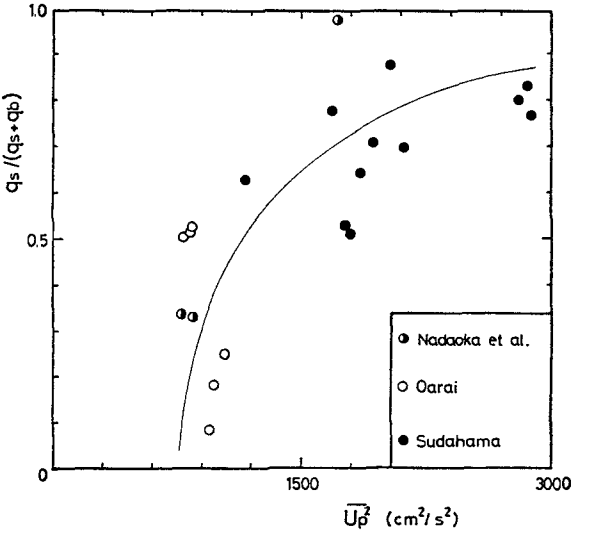

Fig. 10 Rate of suspended load transport compared with $\overline{U_p^2}$.

where sgn($\overline{U_p^3}$) is neglected because it has the absolute value of unity. Utilizing the values listed in Table 2, we can calculate the values of $q_s/(q_s + q_b)$ on the basis of Eqs.(23) and (24). The obtained values are plotted on the ordinate against the values of $\overline{U_p^2}$ on the abscissa in Fig.10. According to Fig.10, the ratio of the absolute suspended load transport to the total transport varies among the values of less than 0.1 to nearly 1.0 with a tendency of increase with the mean-square value of the velocity in the principal wave direction. From this tendency of increase, it can be inferred that the suspended load transport will become more significant under the high wave conditions.

6. Summary

The major conclusions in this report are as follows:

(1) It is reconfirmed that the advection speed of sand tracer in the mean current direction is about 1 % of the mean current velocity.

(2) The advection speed of sand tracer in the principal wave direction depends on not only the up-and-down asymmetry but also the before-and-behind asymmetry in the velocity profiles. The former asymmetry is considered to be related to the bed-load transport and the latter one to the suspended load transport. The magnitude of the before-and-behind asymmetry is evaluated by calculating the skewness for the acceleration profiles.

(3) The local mixing depth of the bed material is approximately proportional to the mean-square value of fluid velocities, which suggests the linear relationship with the local wave height.

(4) For the first approximation, the equations for the local sand transport rate are proposed which are restricted to the field conditions under which the observations have been carried out.

(5) The transporting conditions of suspended load are inferred so that the bed material may be transmittently transported in suspension in relatively short durations and be buried in the sea bottom due to the process of mixing of bed material during the remaining periods.

(6) The suspended load transport will become more significant under the high wave conditions.

The local sand transport rate equations empirically obtained in this study are not necessarily enough, because the local bottom slope, sediment characteristics, the critical velocity of the onset of sand movement and other factors are not taken into account and the assumption in the form of Eq.(13) is for the first approximation. Furthermore, it is a question whether the fluid velocities at the point of about 20 cm above the sea bottom is appropriate or not to be related with the sand transport rate. It is, however, clear for the local sand transport in the onshore-offshore direction that both the up-and-down and the before-and-behind asymmetry in the velocity profiles are important factors.

Acknowledgements

The authors should like to express their heartfelt thanks to Dr.Kazuo Nadaoka, Tokyo Institute of Technology, for his contributions on the field observations when he was a member of the Littoral Drift Laboratory, the Port and Harbour Research Institute.

References

Coastal Engineering Research Center, U.S.Army (1977): Shore protection manual, U.S.Government Printing Office, Vol.1, pp.4-81 to 4-84.

Goda,Y. (1985): Numerical examination of several statistical parameters of sea waves, Report of the Port and Harbour Research Institute, Ministry of Transport, Japan, Vol.24, No.4 (in Japanese).

Katoh, K., N. Tanaka, T. Kondoh, M. Akaishi and K. Terasaki (1985):Field observation of local sand movements in the surf zone using fluorescent sand tracer, Report of Port and Harbour Research Institute, Vol.24, No.4, pp.3-63.

Komar,P.D. and D.L.Inman(1970):Longshore sand transport on beaches, J.G.R., Vol.75, No.30,pp.5914-5927.

Komar,P.D. (1978): Relative quantities of suspension versus bed-load transport on beaches, J. of Sedimentary Petrology, Vol.48, pp.921-932.

Kraus,N.C.(1985):Field observations on vertical mixing of sand in the surf zone, Jour. of Sedimentary Petrology, Vol.55, No.1, pp.3-14.

Nadaoka,K., N.Tanaka and K.Katoh(1981): Field observation of local sand movements in the surf zone using fluorescent sand tracer, Port and Harbour Research Institute, Vol.20, No.2, pp.75-126(in Japanese).

Nagata,Y.(1964):The statistical properties of orbital wave motions and their applications for the measurement of directional wave

spectra, Jour. of Oceanographical Soc. of Japan, Vol.19, No.4, pp.169-181.

Sternberg,R.W., N.C.Shi and J.P.Dowing (1984): Field investigations of suspended transport in the nearshore zone, Proc. 19th Int. Conf. on Coastal Eng., pp.1782-1798.

Sunamura,T. and **N.C.Kraus**(1985):Prediction of average mixing depth of sediment in the surf zone, Marine Geology, 62, pp.1-12.

CHAPTER 92

APPLICABILITY OF SUB-SAND SYSTEM TO BEACH EROSION CONTROL

Yoshiaki KAWATA, M. ASCE* and Yoshito TSUCHIYA, M ASCE**

ABSTRACT

We performed experiments in the laboratory under controlled conditions in order to determine the applicability of a sub-sand filter system to the beach erosion control work. The filter system is used to control a flow condition at the sediment-fluid boundary. In the foreshore, it increases the inflowing velocity into the beach and thus results in increasing the threshold of beach sediment movement. The sub-sand filter system accelerates accretion of much beach sediment in the foreshore through the development of a berm under normal wave conditions. When wave conditions change from normal to stormy , it is also applicable to stabilize the beach profile, and thus decrease loss of beach sediment from the foreshore to the offshore.

INTRODUCTION

As Duncan(1964) pointed out, during flood tide the water level rises faster than the water table within the beach, so that the seaward edge of the water table slopes shoreward. Because of this, most of the sediment transported up the beach face by the swash during flood tide is deposited at the top of the swash limit. During ebb tide the enhanced backwash removes the sediment and deposits it on the shoreward side, where the backwash collides with the incoming surf and loses its transporting capacity. This mechanism has been investigated by many researchers in the field of coastal geomorphology. In the foreshore, the thin and wedge shaped layer of water in the wave uprush /backrush moves the sediment up and down the beach face. The depth of the beach sediment layer over the water table can control the rate of infiltration of sea water accompanied with wave run-up. This leads to changes of swash movement of sediment along the beach. The sub-sediment filter system is used to control the flow condition at the sediment-fluid boundary. In the foreshore, the system increases the inflowing velocity into the beach and thus results in increasing the

* Associate Professor, Disaster Prevention Research Institute, Kyoto University, Kyoto, Japan
** Professor, Disaster Prevention Research Institute, Kyoto University, Kyoto, Japan

threshold of beach sediment movement. In the case of the laminar boundary layer, theoretical expression of the threshold of a sand under suction velocity is given by the authors (1984).

This protection technique has been developed by Chappell(1975) and Machemehl et al.(1976). In order to establish the sub-sand filter system as a means of beach erosion control, it is necessary to perform systematic experiments of beach changes under controlled conditions and to study increment of the threshold of sediment movement by the system. The objectives of this study are to investigate the effects of the system on the stability of beach profiles in the foreshore and to establish the applicability of the system to beach erosion control work.

EXPERIMENTS OF SUB-SAND FILTER SYSTEM

(1) Experimental apparatus

a) Solitary waves

The solitary wave tank shown in Fig. 1 is 21.6m long, 0.75m wide and 1.2m deep and has six trays in permeable slope to construct the sub-sand filter system. Suction pipes are connected to every tray and discharge rate is controlled by valves. Waves are generated automatically by a plunger with an eiectromagnetic cluch at intervals of 5 minutes 50 seconds. All experiments were run at a depth of 43.1cm. The permeable and impermeable beaches of slope 1/10 are constructed with sediment of mean diameter 0.350 mm. The experimental conditions are listed in Table 1, in which H is the wave height and u_s the suction velocity.

b) Monochromatic waves

Beach erosion control tests were carried out in a large wave tank (78m long, 1m wide and 1.5m deep) as shown in Fig. 2. A double hinged flatter type wave generator was used to generate regular waves. The wave period was varied by changing the running speed of the variable-speed drive unit thus enabling a continuous range from 0.5 s to 5 s. The wave height was changed with the eccentricity of the rod connecting the driving disk equipped at the generator. The test beach was 56m in length and was inclined at a slope of 1/30. The mean sediment diameter was 0.940mm. Sixteen pipes of diameter 5cm were used to construct the sub-sand filter system. They had a slit width of 1.5cm covered with fine mesh to prevent the passage of sediment. The header-pipe, of diameter 10cm, was coupled to the intake of a pump. The experimental conditions are listed in Table 2. Each run was further divided into two cases; a filtered experiment (hereafter referred to as A) and an unfiltered one (hereafter referred to as B).

(2) Measuring system

A capacitance type wave gauge and an ultrasonic depth sounder were attached to a movable carriage on the tank. This carriage moved at a speed of 10cm/s. The former was used to survey the bottom topography and the latter to determine the wave breaking point. The beach profile above still water level was obtained by using an improved point gauge.

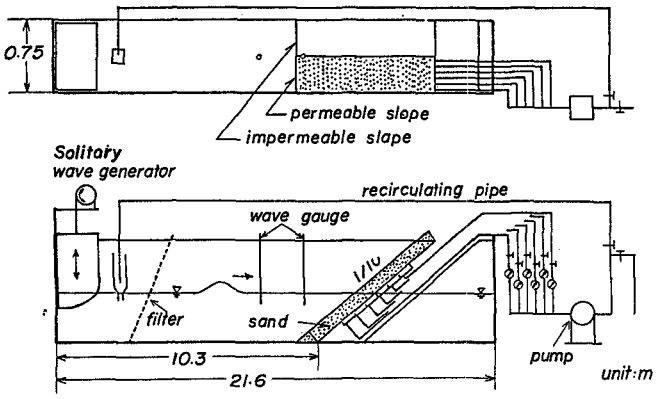

Fig. 1 Solitary wave tank and sub-sand filter system.

Table 1 Experimental conditions by solitary waves.

Run No.	H (cm)	u_s (cm/sec)
1—1	7.18	1.79×10^{-3}
1—2	7.18	1.12
1—3	7.18	2.63
1—4	7.18	1.50
2—1	8.75	2.63
2—2	8.75	1.08

Run No.	H (cm)	u_s (cm/sec)
2—3	8.75	1.79×10^{-3}
3—1	10.8	2.63
3—2	10.8	2.38
3—3	10.8	1.95
3—4	10.8	1.08
4	11.3	2.63

(3) Procedures

To estimate the effects of the sub-sand filter system on the stability of a beach profile, it is necessary to compare the changes in the profile of an unfiltered beach with those in the profile of a filtered beach.

Each run was conducted in the following manner. First, the desired wave characteristics were established. Secondly, the beach was raked into its initial profile (1:10 for solitary waves and 1:30 for monochromatic waves) and the beach profiles were recorded. The pump for the filter system was operated at a constant flow rate during all tests.

CHARACTERISTICS OF BEACH CHANGES

(1) Beach Profile Changes by Solitary Waves

Some examples of the beach changes with respect to the number of solitary waves when equalling 200, 400 and 600 are shown in Fig. 3, in which a solid line and a dotted one are the beach profiles with and without filter operation respectively. The processes of the beach changes by solitary waves are as follows. At the beginning of the experiments, the shoreline retreated rapidly. A berm was formed in the foreshore and a step was formed in the inshore. In the case of

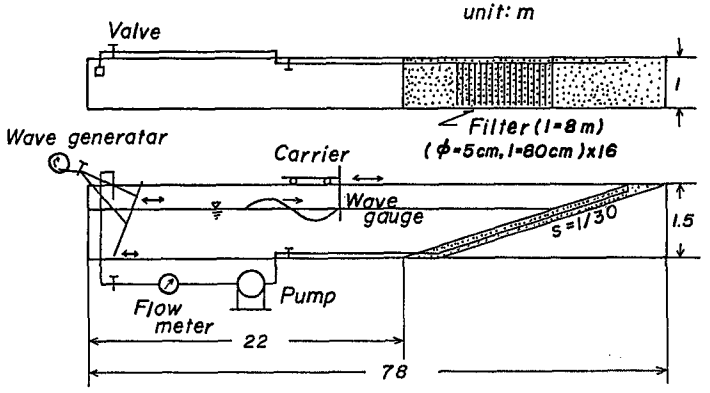

Fig. 2 Regular wave tank and sub-sand filter system.

Table 2 Experimental conditions by monochromatic waves.

Run No.		H (cm)	T (sec)	h (cm)	H_0/L_0	u_* (cm/sec)
5	A	29.8	1.77	90.0	0.0699	0.0231
	B	28.9	1.80	90.0	0.0630	
6	A	21.0	2.99	100	0.0155	0.0986
	B	20.1	3.00	100	0.0150	
7	A	27.0	1.99	100	0.0481	0.0932
	B	26.8	2.00	100	0.0470	
8	A	12.4	2.97	100	0.00932	0.0961
	B	11.8	2.96	100	0.00893	
9	A	29.3	2.03	100	0.0481	0.0932
	B	29.3	2.03	100	0.0481	

A: Suction, B: No suction

the larger wave heights such as in Run Nos. 3 and 4, ripples were generated on the step. Due to the sub-sand filter operation, the growth rate of the berm area with increment of the number of solitary waves was large in comparison with that under natural conditions. Therefore, the seaward slope of the berm with the filter became steep, and then the breaker scour formed at the onshore end of the step enlarged. Consequently, by the sub-sand filter operation, the deposition of sediment in the foreshore was developed, but the characteristics of the beach changes, such as shoreline recession and formation of a berm and a step, were not changed due to the filter operation.

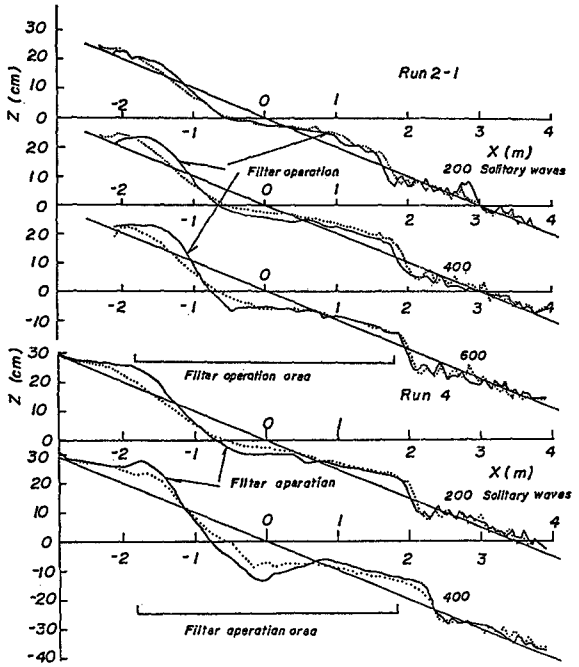

Fig. 3 Beach changes by solitary waves.

(2) Beach Profile Changes by Monochromatic Waves

Typical changes of beach profiles with time are shown in Fig. 4. From the experimental profiles in the nearshore zone in Run 7 (stormy wave condition), it was found that the beach profiles under filter operation are different to those under natural conditions. In the case of (B) (no filter operation), the small bar which was in the nearshore at t=5hr moved shoreward and developed, and changed to a large berm in the foreshore at t=10 hr. Finally, this berm came up to the beach crest and had two peaks. In the case of (A) (filter operation), the beach sediment movement in this area was not as simple as that in (B). Two small bars developed with time and moved shoreward, but the sizes and the moving speeds were very small in comparison with the former case. It was recognized that the sub-sand filter system reduces the sediment movement and stabilizes the beach changes in the nearshore zone.

In Run 8 (normal wave condition), from the view point of processes of berm development in the nearshore zone, existence of the sub-sediment filter system made no distinguishable difference to beach profile changes at t=7hr under natural conditions. After this time, the height of the berm in (A) was larger than that in (B), and then the shoreline advanced in the former case. From a budget of beach

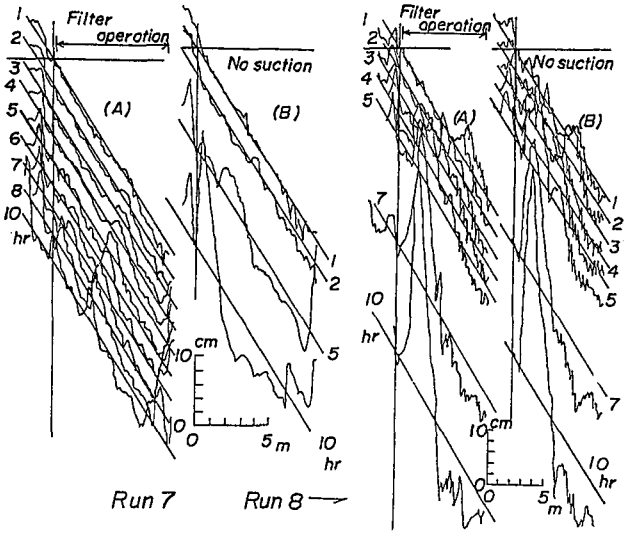

Fig. 4 Beach changes by monochromatic waves.

sediment in the nearshore zone, much sediment moved seaward in the offshore side of the berm and beach erosion occurred in the case of (B). Under the sub-sand filter operation, on the contrary, the accretion of beach sediment in the foreshore was found, because the seaward sediment movement was very controlled in the nearshore zone. It was also pointed out that under the filter operation, the beach profiles in the foreshore have a smooth surface due to the disappearance of ripples.

It is necessary to discuss whether the system is applicable or not when normal wave conditions change to stormy, because bottom roughness formed under the filter operation is very small. Under this bottom condition, incoming wave energy does not quickly dissipate and beach erosion will occur in the foreshore. Fig. 5 shows the results of the beach profile changes under the conditions mentioned above. The initial beach profile in Run 9 (stormy wave conditions) was the profile in which the filter was operated for ten hours in Run 8 (normal wave conditions). The changes of the beach profiles without the filter were very large in the foreshore, especially at the seaward slope of the berm, and much sediment moved seaward from this area. In contrast, the sub-sand filter system could stabilize the sediment movement, so that the changes of the beach profiles were smaller than those without the filter. It was found that the system is also effective, even if the wave conditions change to stormy.

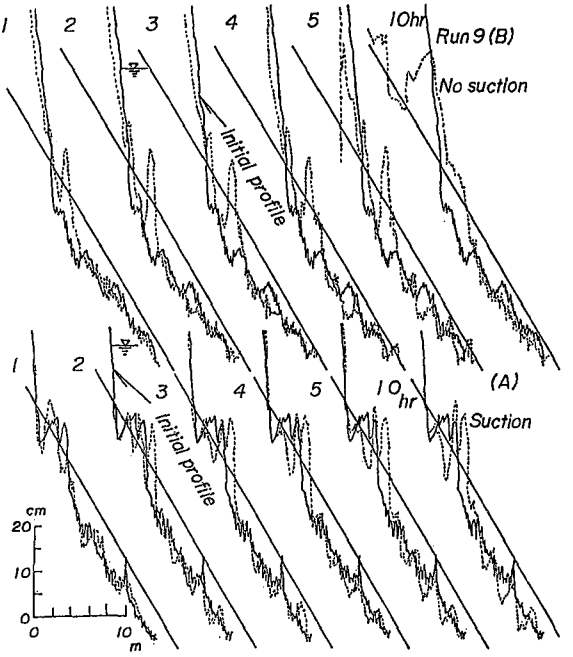

Fig. 5 Beach changes with changes of wave conditions from normal to stormy ones.

EFFECT OF SUB-SAND FILTER SYSTEM ON BEACH CHANGES

The development of a berm by solitary waves is shown as normalized beach profile A/A_a vs. H/h in Fig. 6, with the value of suction velocity u_s as a parameter. The symbol A is the area of the berm and A_a is the area of a right-angle triangle in which the length of the hypotenuse is the distance from a shoreline to a point of maximum runup height. It was found that in the range of the suction velocity, the effect of H/h on the berm size under the filter operation is about twice to four times greater than that under normal conditions. However, the growth rate of the berm with the increment of H/h is unaffected by any suction velocity in our experiments. The suction velocity which gives the largest value of A/A_a in the case of the experiments with 200 solitary waves does not coincide with the maximum velocity in any value of H/h.

The relationship between A/A_a and a dimensionless suction velocity u_s/w_f is shown in Fig. 7 with the value of H/h as a parameter. The symbol w_f is the settling velocity estimated by Rubey equation. In the case of H/h=0.250, the largest value of A/A_o is found at a moderate value of u_s/w_f both in 200 and 400 solitary waves. In other words, there is a most effective suction velocity in the growth of an underdeveloping berm. In the cases of H/h=0.167 and 0.203, the ratio A/A_a becomes nearly constant in the range of u_s/w_f of more than 0.25×10^{-3}. Under small wave conditions, the runup height and the rate of swash sediment transport are small, so that it is very difficult to make clear the effect of the filter. Consequently, the effect of the filter operation on the berm development depends on the runup height. Therefore, the most effective suction velocity will change with time.

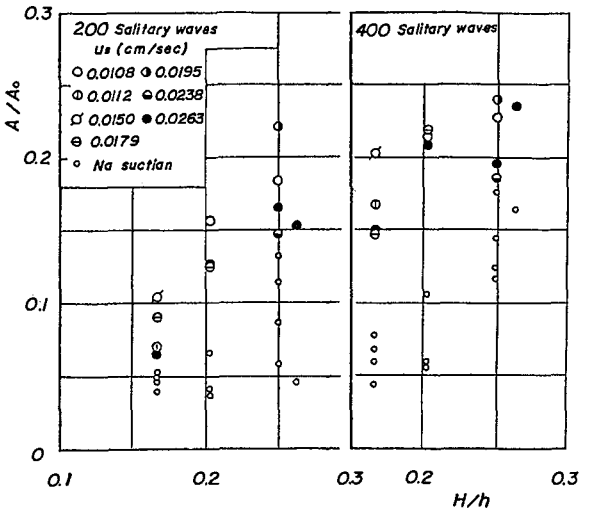

Fig. 6 Relationship between area of berm and ratio of wave height to water depth.

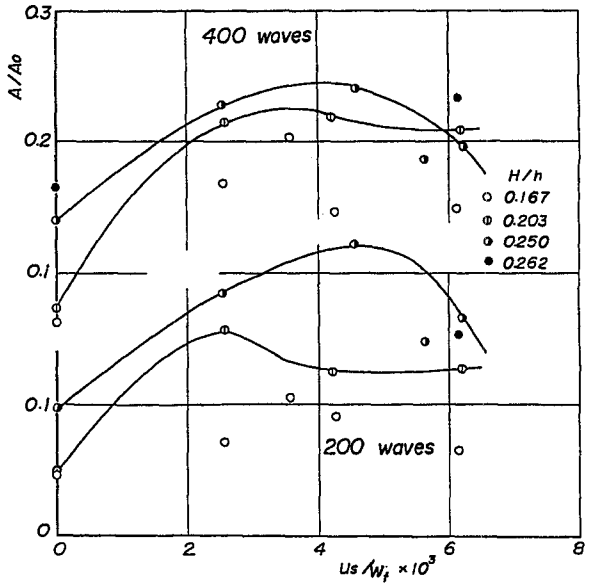

Fig. 7 Relationship between area of berm and suction velocity.

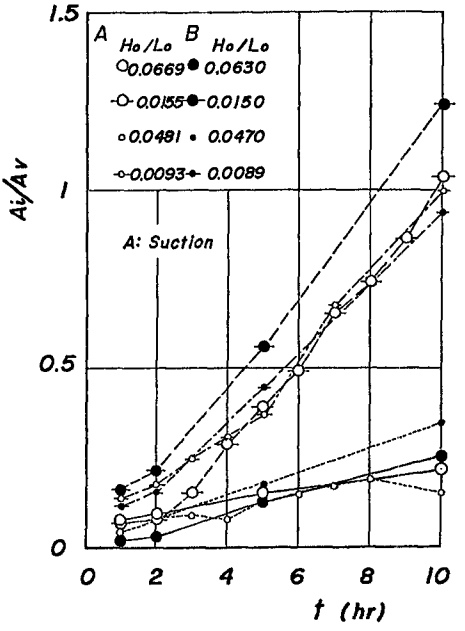

Fig. 8 Changes of budget of beach sediment in the foreshore with time.

The time development of the deviations of the dimensionless area A_i/A_v by monochromatic waves is shown in Fig. 8 with the wave steepness as a parameter. The symbol A_i is the amount of accretion and erosion areas (their absolute values) from the initial beach profile on the sub-sand filter system, and A_v is the area of a right-angle triangle in which the length of the hypotenuse is equal to that of the sub-sand filtered system. In our experiments with monochromatic waves, A_v is constant, because the length of sub-sand filter is 8m and the slope is 1/30, and so this value is 1.065 m^2. It is recognized that the changes of A_i/A_v with time in Run Nos. 6 and 8 (normal wave condition) are very large in comparison with those in Run Nos. 5 and 7 (stormy wave conditions), and this tendency continues until t=10hr. The values of A_i/A_v under the filter operation are smaller than those under natural conditions. This result is similar to that found by Machemehl(1976), though he defined the saturated and partially saturated zones (their boundary is a shoreline, and the area above still water level is defined as the saturated zone and the area below one is the partially saturated zone).

Fig. 9 shows the changes in the amount of accretion and erosion areas from the initial beach profile with time in Run 9. In this experiment, the initial profile was formed by the waves with a wave steepness of 0.0155. Even if the wave steepness changes from 0.0155 to 0.0481, the sub-sand filter reduces areas of accretion and erosion. The smaller value of A_i/A_v indicated that during the filter operation, the beach profile was more stable.

Fig. 10 shows the relationship between A_i/A_v and the wave steepness, with the duration of experiments as a parameter. As mentioned before, A_o in Machemehl's data is the saturated zone which is the area influenced with the filter below the still water level. It is found that the effect of the sub-sand filter system on the stabilization of the beach profile becomes very clear with the increment of the dura-

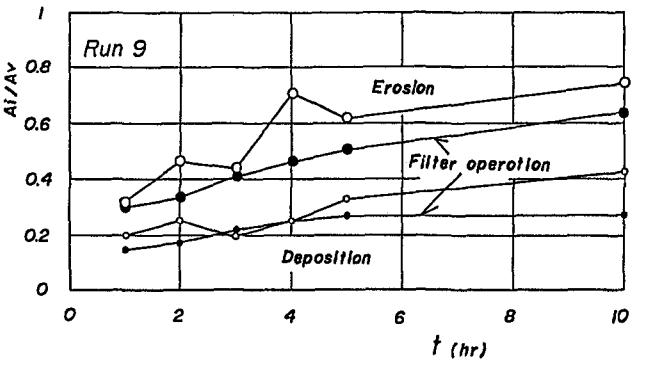

Fig. 9 Changes of budget of beach sediment in accompany with changes of wave characteristics

tion of the operation. Furthermore, the changes of A/A_o with time reduce and come to constant concomitantly with the increment of the wave steepness.

Above all, through our experiments concerning the effect of a sub-sand filter system on the stabilization of the beach profile, it is pointed out as follows: In cases of solitary waves and monochromatic waves with small wave steepness (swell wave conditions), the accretion in the foreshore grows very rapidly and leads to the formation of a berm under the filter operation. As the accretion area enlarged, the filter was not as effective so that a backrush did occur at the end of all our experiments. When the beach changes are caused by the waves with large wave steepness, the effect of the sub-sand filter system on the changes of accretion and erosion areas is not so

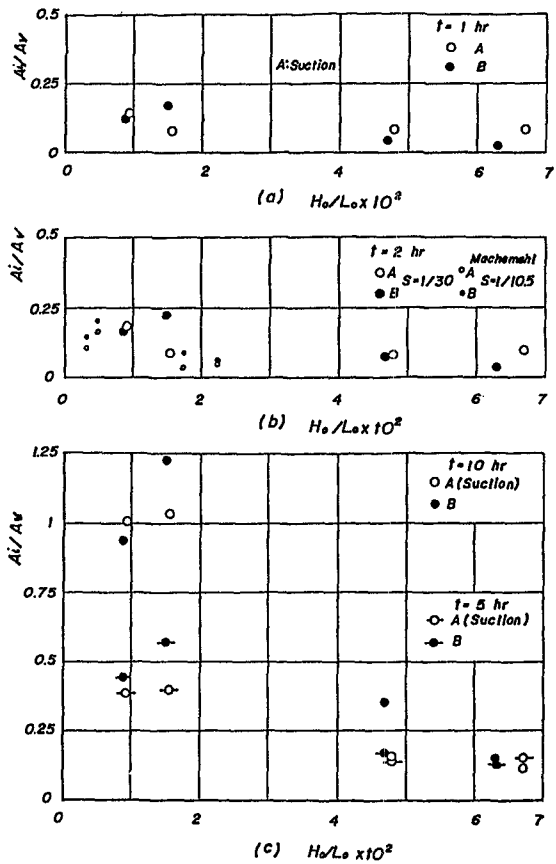

Fig. 10 Relationship between budget of beach sediment and wave steepness.

clear, but the filter did minimize the sediment movement in the area influenced by the filter in the nearshore zone. According to the experimental results of the beach changes under the filter operation, the roughness height become very small and it is very difficult to find ripples in the nearshore zone. In addition, the characteristics of beach profiles such as a stormy beach and a normal one do not change with the filter operation.

APPLICABILITY OF SUB-SAND FILTER SYSTEM

The most important point of the sub-sand filter systems in beach erosion control work is, of course, that the control work has high applicability to prevent or to mitigate beach erosion under any wave conditions. We discuss the applicability of the filter based on our experimental results. From Figs. 6, 7 and 8, the sub-sand filter system can accelerate accretion of much sediment in the foreshore through the development of the berm, so that it is accompanied by a shoreline advance. This characteristic shows the typical beach changes under normal wave conditions, so that this system encourages furthermore the beach changes with the duration of the wave action.

As is a well-known fact, the wave runup height become large with the decrease of the wave steepness. The swash movement of the beach sediment up and down the beach face can be largely controlled by the permeability of the beach, because the increased effective drag force creates a higher threshold for the sediment movement.

When wave conditions change from normal (swell wave) to stormy, the sediment of the berm in the foreshore moves seaward as the sediment in the offshore moves shoreward, and forms longshore bars, as shown in Fig. 4. Under the filter operation, the former sediment movement becomes inactive by the increment of the threshold. Therefore, the offshore sediment is greatly contributes to the formation of a longshore bar. In other words, loss of the sediment from the foreshore decreases. At the same time, the surface roughness mitigated by the filter operation in the foreshore does not lead to the enlargement of the beach erosion as shown in Fig. 9.

Our experiments were two dimensional in relation to cross-shore sediment transport, but saw-tooth movement of beach sediment due to waves with arbitrary wave angle will certainly be controlled by the system, so that the rate of longshore sediment transport is expected to reduce. As the results clearly show, the sub-sand filter system has high applicability to beach erosion control work.

CONCLUSIONS

We have developed the sub-sand filter system for beach erosion control work. The system has high applicability for stabilizing beach profiles in the foreshore, and consequently it is useful to reduce the offshore movement of beach sediment under any wave conditions.

REFERENCES

Chappell, J. (1975). New technique for beach erosion control work, Jour. of the JSCE, Vol. 60, No. 11, 85p.(in Japanese).
DUNCAN, J. R. (1964). The effect of water table and tidal cycle on swash-backwash sediment distribution and beach profile development, Marine Geology, Vol. 2, pp. 186-197.
KAWATA, Y. AND LARSEN, L. R. (1984). Thew effect of suction on the thereshold of a sand movement by waves, Proc. 31st Japanese Coastal Eng. Conference, JSCE, pp. 267-271(in Japanese).
MACHEMEHL, J. L., FRENCH, T. J. and HUANG, N. E. (1976). New method of beach erosion control, Civil Engg. in the Oceans, ASCE, pp. 142-160.

CHAPTER 93

EVALUATION OF INCIDENT WAVE ENERGY IN FLUME TESTS

Eliezer Kit [1], Oded Gottlieb [2] and Dov S. Rosen [3], M. ASCE

ABSTRACT

A two dimensional model study, carried out for a structure in a flume using irregular waves, presents the problem of determining the relationship between the total incident wave energy attacking the structure and its response to that attack (displacements, forces, etc.) in various sea states. The total incident wave energy can be evaluated indirectly only, because the wave energy measured in the flume contains an extent of residual wave energy in addition to that generated by the wave machine. This residual energy consists of the re-reflected wave energy from the paddle of the wave machine, assuming the existence of quasi-stationary wave conditions in the flume. A method originally presented by Gravesen et al. (1974), was applied in this study to evaluate the total incident wave energy. In view of the results obtained by this method, a physically more sound refinement is proposed for the evaluation of the total incident wave energy (and characteristic wave height). Results of model tests were analyzed by the CAMERI refinement and compared with the Gravesen method and with a cross-spectral least squares method, separating incident and reflected wave spectra from wave spectra measured in the flume. Good agreement was found between the results obtained employing the CAMERI refinement and the cross-spectral least squares method. Advantages and drawbacks of these methods are indicated.

INTRODUCTION

The study of wave effects on structures in flumes using irregular waves, for example two dimensional breakwater stabilitiy studies, requires the determination of the incident wave energy in order to relate resulting wave effects (forces, displacements, overtopping, etc.) to the waves and by them to their probability of encounter.

Assuming quasi-stationary wave conditions in the wave flume, the incident wave energy (and the characteristic wave height) can be evaluated indirectly only, because the waves generated by the wave machine are partially reflected by the structure tested, then re-ref-

---

1 Senior Scientist, CAMERI - Coastal and Marine Engineering Research Institute, Technion City, Haifa 32000, Israel.
2 Graduate Student, Faculty of Civil Engrg., Technion - Israel Institute of Technology, Technion City, Haifa 32000, Israel.
3 Senior Research Engineer, CAMERI - Coastal and Marine Engineering Research Institute, Technion City, Haifa 32000, Israel.

lected by the paddle of the wave machine back towards the structure and so on. Thus, a residual incident wave energy is added to the incident wave energy originally generated, resulting in a new total incident wave energy (and characteristic wave height).

Nowadays the most popular methods used for the determination of the incident wave energy in flume tests are as follows:
a) Division of the flume longitudinally into two (or more) sections of which one is used for the structural test, while the other is equipped with a mild sloping - wave absorbing beach and is used to measure the "incident" wave energy.
b) Two points cross spectral analysis, originally proposed by Goda and Suzuki (1976).
c) Three points least squares cross spectral analysis, proposed by Mansard and Funke (1980).
d) Preliminary determination of the coefficient of wave energy re-reflection using the method proposed by Gravesen et al. (1974), hereafter referred as the Gravesen method, or a refinement to it proposed by the authors in this article, referred as the CAMERI refinement.

The two points cross spectral method is based on the main assumption that irregular waves may be described as a linear superposition of an infinite number of discrete components, each with its own frequency, amplitude and phase. Another important assumption is that these components travel at their own individual phase velocity, described by the dispersion relationship. The method consists of measuring simultaneously the co-existing wave trains moving in opposite directions at two wave gauges located in constant water depth, close to each other and aligned parallel to the direction of wave propagation in the flume and cross spectral analysis to evaluate the incident and reflected spectra.

The third method attempts to overcome certain limitations of the two points cross spectral method such as limited frequency range, critical wave gauge spacing and high sensitivity to errors in the measurement of waves. It uses the two points method to measure the co-exsting wave trains moving in opposite directions at three or more locations of constant water depth (to prevent wave shoaling effects) and aligned on a line parallel to the direction of wave propagation in the flume. Spectral analysis of the signals at each wave gauge and cross spectral analysis between the signals of each pair of wave gauges by means of Fourier transform is done to express the wave activity at each wave gauge location in terms of an incident wave, a reflected wave and a noise signal. A least squares method is applied to resolve the Fourier expressions of the signals at each wave gauge in order to minimize the noise for all wave gauges.

The Gravesen method to determine the total incident wave energy is based on the preliminary determination of the re-reflection coefficient of wave energy from the paddle of the wave machine and on the evaluation of the coefficient of reflection of wave energy from the structure afterwards. This method and the proposed CAMERI refinement are described in detail in the following lines.

GRAVESEN METHOD

The evaluation of the coefficient of wave energy re-reflection is accomplished by preliminarily carrying out two separate series of tests in absence of the model structure investigated, but on the same bathymetry and for the same sea states to be generated on the model structure. The first series is performed with a non-reflective beach, while the second series is carried out with a reflecting vertical (rigid) wall, located at the position at which the model structure will be placed in the flume. Finally, the third series of tests is carried out with the model structure, under identical sea states as generated in the two preliminary test series.

For each sea state of any series of tests the assumptions of the cross spectral methods are also accepted. Consequently, the following expresions can be written by measuring the variance of the water elevation at a fixed position in any test:

$$Hm^2 = Hi^2 + Hr^2 \qquad (1)$$

where: Hm is the measured characteristic wave height,
Hi is the total incident characteristic wave height and
Hr is the reflected characteristic wave height.

The reflected energy coefficient Br and the re-reflection coefficient of wave energy Brr are derived from expressions (2) and (3) given below:

$$Hr^2 = Br * Hi^2 \qquad (2)$$

$$Hi^2 = Hg^2 + Brr * Hr^2 \qquad (3)$$

where: Hg represents the wave energy generated by the wave machine.

By inserting (2) in (3) and extracting Hi and then introducing the result in (1), the resulting expressions obtained are:

$$Hi^2 = Hg^2 * [\, 1 / (1 - Br * Brr) \,] \qquad (4)$$

$$Hm^2 = Hg^2 * [\, 1 / (1 - Br * Brr) \,] * (1 + Br) \qquad (5)$$

To determine the unknown values of the coefficient of re-reflection of wave energy from the wave machine paddle (Brr) and the incident wave energy generated by the wave machine (Hg), the Gravesen method assumes a Br value of zero (0) for the tests with a spending beach, which means that in the first series of tests it is assumed that Hm = Hg. In the second series of tests with the vertical wall, it assumes that Br takes the value of one (1). Hence, for each sea state it is possible to determine Brr since Hm remains the same as in the previous series of tests. Finally, in the third series of tests with the model structure, the reflection coefficient of wave energy (Br) from the structure and the total incident characteristic wave height (Hi) can be determined (see schematization in Figure 1).

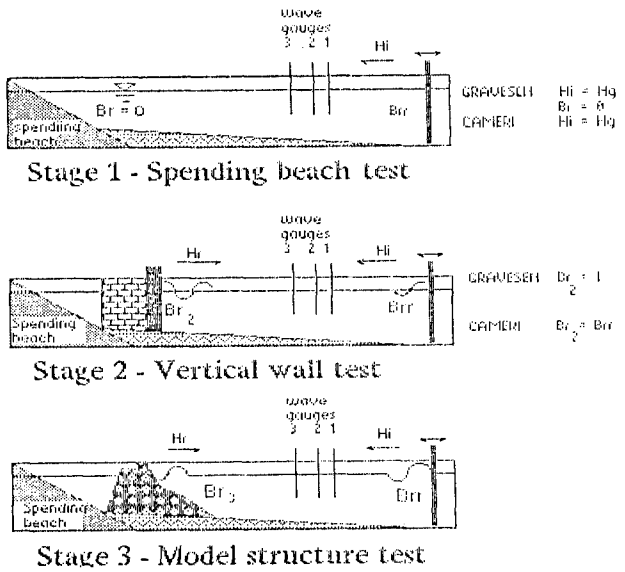

Figure No. 1 - Schematization of Gravesen method and of CAMERI refinement for evaluation of incident energy

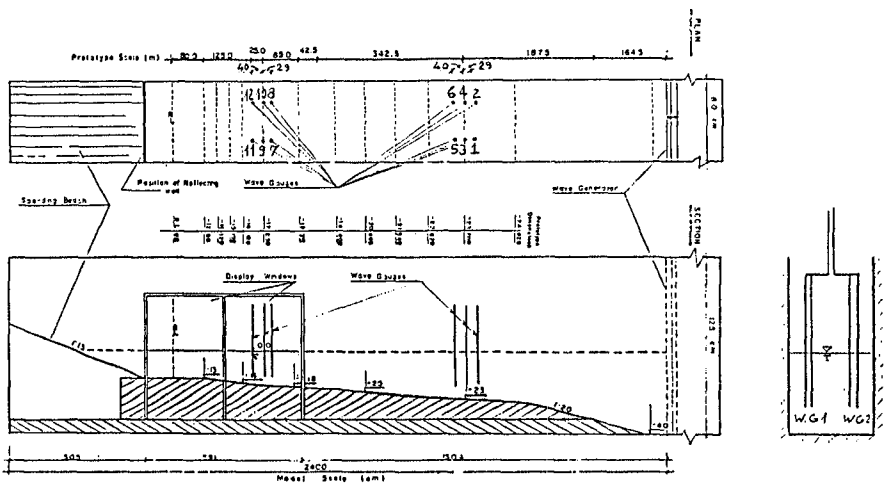

Figure No. 2 - Testing set-up in preliminary testing series (Geometric model scale 1:65)

CAMERI REFINEMENT

The methods described above were considered for use in a two dimensional stability model study for the rehabilitation of the main breakwater of Ashdod Port (Rosen and Gottlieb - 1985). The design storm for this study included various sea states of increasing characteristic wave height. The higher sea states included a large fraction of waves which were expected to break or to be at near breaking point. Under such conditions non-linear effects may be strong and affect the reliability of cross spectral methods based on linear assumptions regarding wave profile and wave transformation. Therefore, the Gravesen method was considered an appropriate alternative. However, this method's assumption of Br = 1.0 from the vertical wall and the expectation of a different value for Brr from the paddle of the wave machine, did not seem physically justified. Consequently, two refinements were introduced to the Gravesen method:

a) In the testing series with a vertical wall, Br would be approximately equal to Brr, especially if a piston type wave machine is used.

b) The value of Brr to be used in the tests with the model structure, should be the average of the values of Brr obtained in the vertical wall testing series with low sea states only.

EXPERIMENTAL SETUP

A preliminary experimental study was conducted to investigate the applicability of the Gravesen method, the CAMERI refinement and the cross spectral least squares method in order to choose the most reliable method for the evaluation of the incident wave energy and characteristic height on the model breakwater.

The investigation was performed in one of CAMERI's wave flumes. Twelve resistance type wave gauges were used to measure the waves in the flume (two groups of three pairs located at two sites). The locations of the wave gauges were in two regions of mild bottom slopes of about 1:80 near the -17m and about 1:100 near the -23m contour lines. The wave generator was located in relatively deep water (-40m) and in the first series of tests a spending beach of rubberized coir material enclosed in wire mesh (slope 1:13) was placed at the end of the flume (see Figure No.2).

The shape of the spectral variance distribution of the synthetic time series was of a JONSWAP type with slightly modified values of the parameters (see Figure No.3). The duration of the sea states was varied (see Figure No. 4) to simulate storm development pattern from low to extreme conditions. The structure used in the preliminary investigation consisted of a smooth slope of 1:5, while the model study consisted of a tetrapod breakwater cross section with an initial slope of 1:1.33 (see Figure No.5).

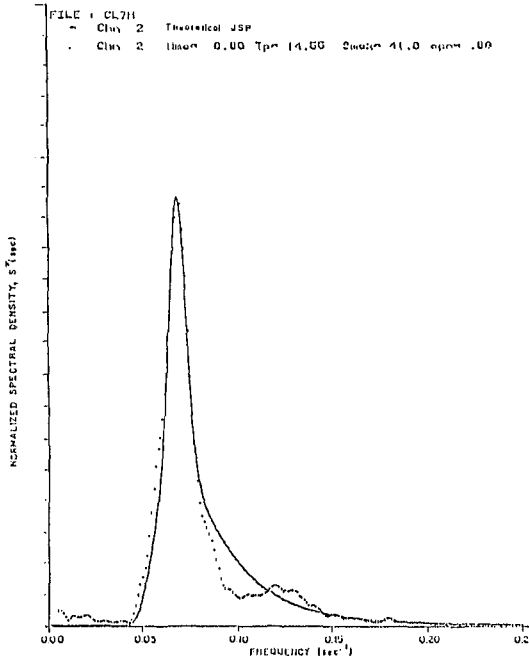

Figure No. 3 - Spectral distribution of modified JONSWAP used in the tests

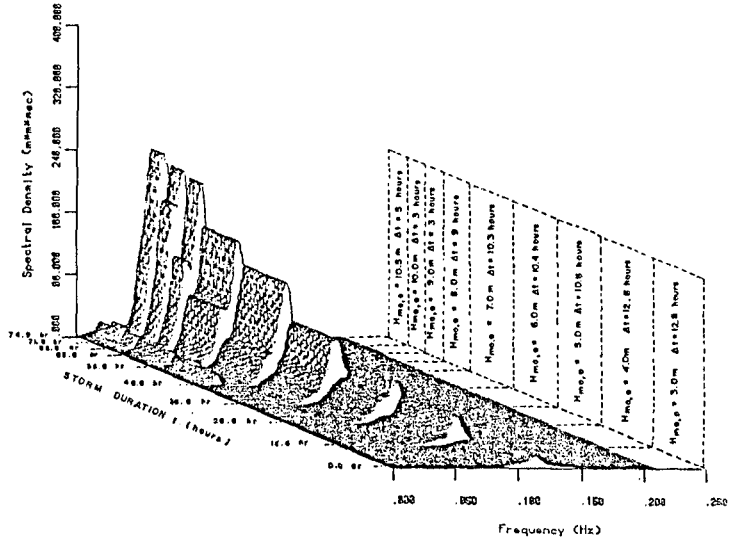

Figure No. 4 - Combined storm growth and decay simulation by sea state steps of varying duration

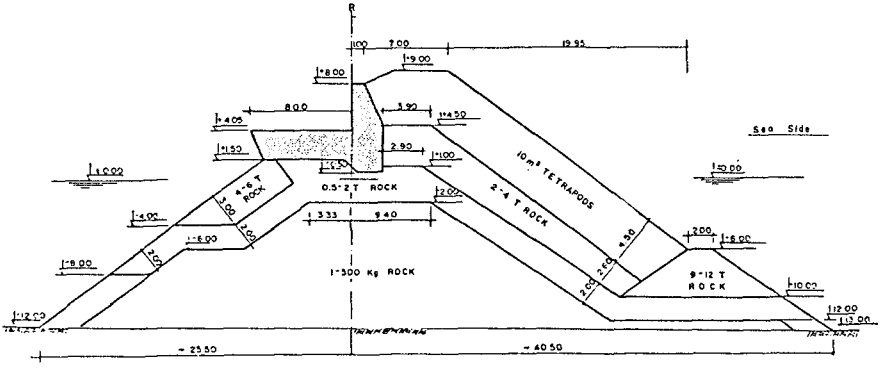

Figure No. 5 - Cross section of the tetrapod breakwater

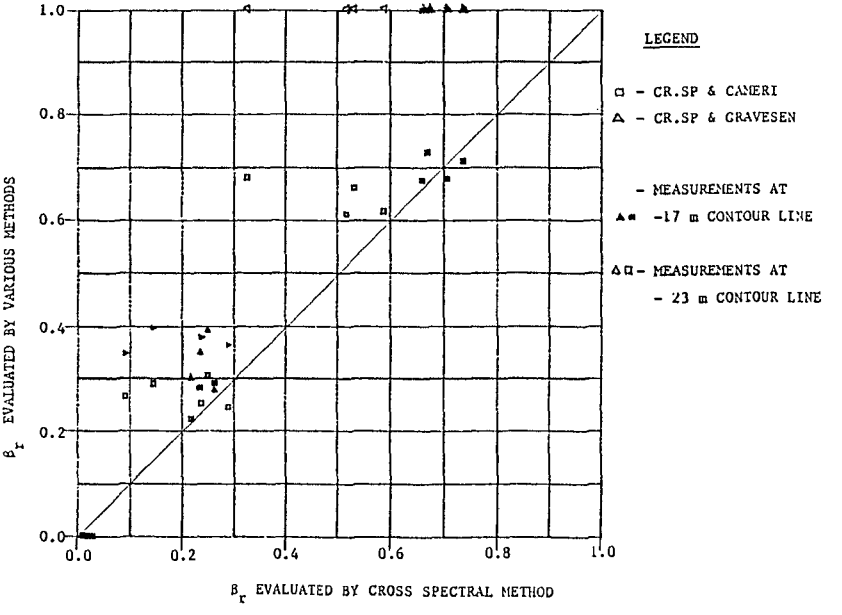

Figure No. 6 - Comparison of coefficients of wave energy reflection obtained for all tests (spending beach, vertical wall, smooth slope 1:5)

DISCUSSION OF EXPERIMENTAL RESULTS

A set of typical results for the preliminary investigation is presented in Tables 1 and 2 based on the wave gauges located on the -17m and -23m contour lines respectively.

It should be noted that in the testing series with the vertical wall, the wave energy reflection coefficients (Br) obtained by the CAMERI refinement are in good agreement with the corresponding values evaluated by the cross spectral least squares method. Both methods give Br values between 0.65 to 0.70, while the Gravesen method assumes a Br value of 1.0. Furthermore, inspite of the fact that a vertical paddle piston type wave machine was used, re-reflection coefficients (Brr) of about 0.3 were obtained using the Gravesen method. These values were significantly different from 1.0, which was the value assumed for the reflection coefficient (Br) from the vertical wall.

The results obtained in the test series with the spending beach by the cross spectral method, confirm the prerequisite assumption of complete energy absorption by the spending beach for both Gravesen method and CAMERI refinement.

The wave energy reflection coefficients (Br) obtained for the 1:5 smooth slope structure, show that the values evaluated by the CAMERI refinement are in better correspondence with the cross spectral method than those evaluated by the Gravesen method.

Similar results from the actual stability model study with the tetrapod breakwater are given in Table 3.

The Br values evaluated by the various methods are plotted against the values determined by the cross spectral least squares method in Figure No.6.

Comparisons of the values of the characteristic incident wave heights evaluated using the various methods are presented in Figures No. 7 through 12 against the characteristic incident wave height values determined by the cross spectral least squares method.

Improved estimates of the total incident wave energy are obtained by the CAMERI refinement using more realistic reflection coefficients, for relatively low to moderate sea states.

It should be mentioned that the accuracy of the cross spectral method is limited in high sea states because the wave profile and the wave length are no longer well described by the linear theory , even if breaking does not occur. On the other hand some minor differences between the results are due to the fact that the wave gauges were not located in a constant depth zone.

The results indicate that better estimates are obtained for the high sea states with breaking waves, employing an average re-reflection coefficient obtained for the low sea states.

Type of reflecting structure	Measured data		Cross-spectral method			CAMERI			Gravesen et al		Incident wave heights		
	Hm (m)	T (sec)	Hi (m)	Hr (m)	β_r	β_r	β_{rr}		β_r	β_{rr}	Cross-spectral	CAMERI method	Gravesen method
Spending beach	2.63	9.49	2.58	0.25	0.009	0.000	-		0.000	-	2.58	2.63	2.63
	3.49	10.90	3.46	0.37	0.012	0.000	-		0.000	-	3.46	3.49	3.49
	4.66	12.53	4.59	0.57	0.015	0.000	-		0.000	-	4.59	4.66	4.66
	5.59	13.31	5.55	0.85	0.024	0.000	-		0.000	-	5.55	5.59	5.59
	6.53	14.55				0.000	-		0.000	-		6.53	6.53
Vertical wall	4.99	10.86	3.75	3.07	0.671	0.722	0.722		1.000	0.444	3.75	3.80	3.53
	6.43	12.22	5.06	4.35	0.741	0.705	0.705		1.000	0.411	5.06	4.92	4.55
	8.14	13.48	7.33	6.00	0.708	0.672	0.672		1.000	0.345	7.33	6.29	5.76
	9.71	17.72	8.86	7.20	0.661	0.669	0.669		1.000	0.337	8.86	7.52	6.87
Model Structure (Slope 1:5)	3.32	9.98	2.95	1.41	0.230	0.281	0.700		0.348	0.444	2.95	2.93	2.86
	4.49	10.86	4.10	2.03	0.245	0.304	0.700		0.390	0.411	4.10	3.93	3.81
	5.61	11.79	5.17	2.38	0.212	0.223	0.700		0.300	0.345	5.17	5.07	4.92
	7.11	13.3	6.30	3.20	0.258	0.290	0.700		0.277	0.337	6.30	6.26	5.87
	8.04	17.74				0.250	0.700					7.19	

Table 1 - Preliminary testing series results (wave gauges located on the -17m contour line)

Type of reflecting structure	Measured data		Cross-spectral method			CAMERI			Gravesen et al		Incident wave heights		
	Hm (m)	T (sec)	Hi (m)	Hr (m)	β_r	β_r	β_{rr}		β_r	β_{rr}	Cross-spectral	CAMERI method	Gravesen method
Spending beach	2.76	9.46	2.68	0.19	0.005	0.000	-		0.000	-	2.68	2.76	2.76
	3.58	10.79	3.47	0.25	0.005	0.000	-		0.000	-	3.47	3.58	3.58
	4.76	12.14	4.60	0.44	0.009	0.000	-		0.000	-	4.60	4.76	4.76
	5.74	13.31	5.53	0.56	0.010	0.000	-		0.000	-	5.53	5.74	5.74
	6.59	14.42				0.000	-		0.000	-		6.59	6.59
Vertical wall	4.83	10.40	4.01	2.28	0.323	0.673	0.673		1.000	0.347	4.01	3.74	3.42
	6.09	12.63	5.02	3.66	0.531	0.654	0.654		1.000	0.309	5.02	4.73	4.31
	7.58	12.44	7.40	5.32	0.516	0.606	0.606		1.000	0.211	7.40	5.98	5.56
	9.21	12.70	10.07	7.72	0.588	0.612	0.612		1.000	0.223	10.07	7.26	6.51
Model Structure (Slope 1:5)	3.41	9.58	3.16	0.93	0.086	0.264	0.650		0.344	0.347	3.16	3.03	2.94
	4.51	10.86	4.28	1.61	0.141	0.289	0.650		0.394	0.309	4.28	3.97	3.82
	5.82	12.46	5.61	2.70	0.233	0.251	0.650		0.376	0.211	5.61	5.20	4.96
	6.98	13.20	6.78	3.63	0.286	0.244	0.650		0.360	0.223	6.78	6.26	5.99
	8.07	14.46				0.253	0.650					7.21	

Table 2 - Preliminary testing series results (wave gauges located on the -23m contour line)

Type of reflecting structure	Measured data		Cross-spectral method			CAMERI			Gravesen et al		Incident wave heights		
	Hm (m)	T (sec)	Hi (m)	Hr (m)	β_r	β_r	β_{rr}		β_r	β_{rr}	Cross-spectral	CAMERI method	Gravesen method
Spending beach	2.89	9.35	2.89	0.25	0.008	0.000			0.000		2.89	2.89	2.89
	3.89	11.27	3.89	0.99	0.058	0.000			0.000		3.89	3.89	3.89
	5.25	12.15	5.18	1.28	0.046	0.000			0.000		5.18	5.25	5.25
	6.26	13.69	6.05	1.71	0.030	0.000			0.000		6.05	6.26	6.26
	7.34	14.68	7.12	2.02	0.024	0.000			0.000		7.12	7.34	7.34
	8.40	16.64	8.13	2.41	0.022	0.000			0.000		8.13	8.40	8.40
Vertical wall	5.15	10.06	3.96	3.10	0.540	0.690	0.690		1.000	0.370	3.96	3.99	3.64
	7.76	11.42	5.45	4.49	0.630	0.750	0.750		1.000	0.500	5.45	5.88	5.50
	9.65	13.07	7.41	5.42	0.640	0.700	0.700		1.000	0.410	7.41	7.35	6.83
	10.63	16.18	8.48	6.11	0.620	0.650	0.650		1.000	0.310	8.48	8.24	7.54
	12.00	17.04	8.92	6.24	0.420	0.630	0.630		1.000	0.250	8.92	9.45	8.48
	13.15	18.79	9.80	6.53	0.440	0.590	0.590		1.000	0.180	9.80	10.40	9.28
Tetrapods breakwater	3.18	9.56	2.88	0.98	0.114	0.114	0.700		0.146	0.370	2.88	3.00	2.97
	4.43	11.69	4.19	1.96	0.202	0.156	0.700		0.181	0.500	4.19	4.12	4.08
	5.39	13.16	5.05	2.46	0.217	0.031	0.700		0.038	0.410	5.05	5.31	5.29
	6.92	12.89	6.58	3.32	0.430	0.120	0.700		0.162	0.310	6.58	6.54	6.42
	8.33	17.85	7.98	4.10	0.141	0.151	0.700		0.217	0.250	7.98	7.76	7.54
	10.03	17.76	9.05	4.97	0.176	0.213	0.700		0.337	0.180	9.05	9.10	8.67

Table 3 - Breakwater tests (wave gauges on -17m contour line)

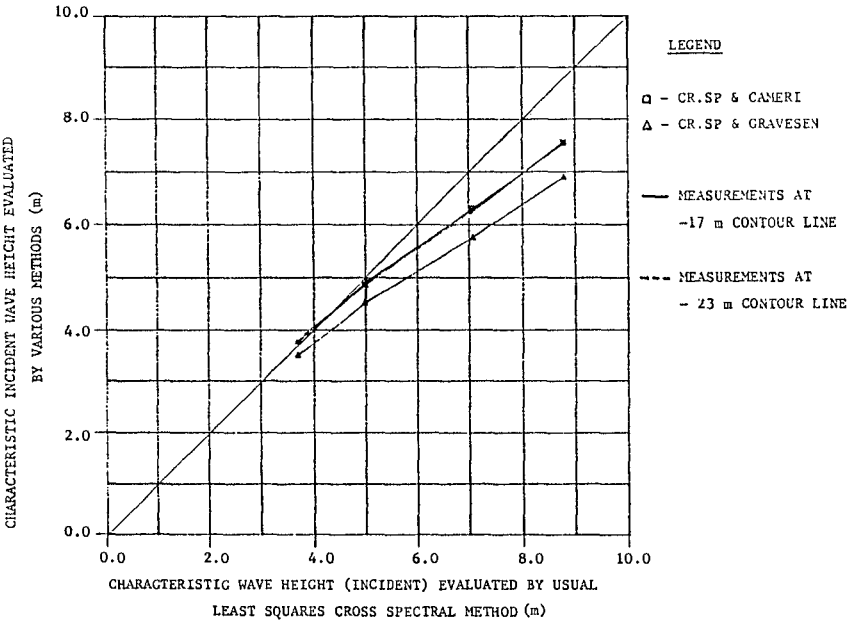

Figure No. 7 - Comparison of incident characteristic wave heights (vertical wall, wave gauges on -17m contour line)

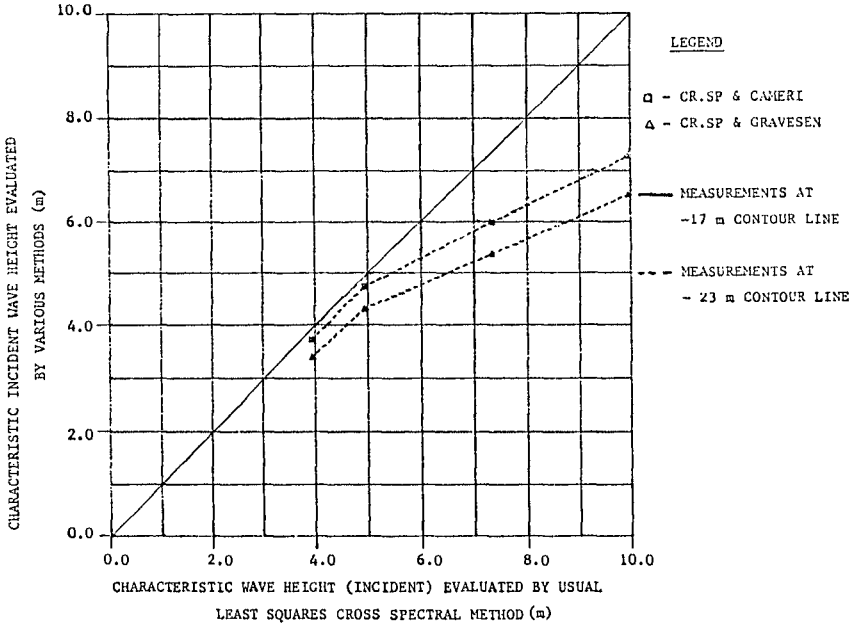

Figure No. 8 - Comparison of incident characteristic wave heights (vertical wall, wave gauges on -23m contour line)

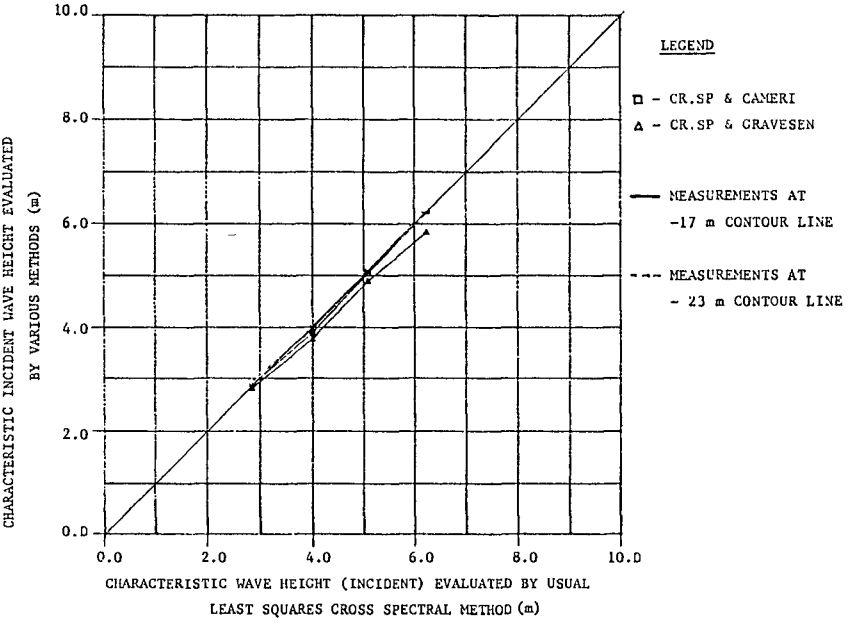

Figure No. 9 - Comparison of incident characteristic wave heights (spending beach, wave gauges on -17m contour line)

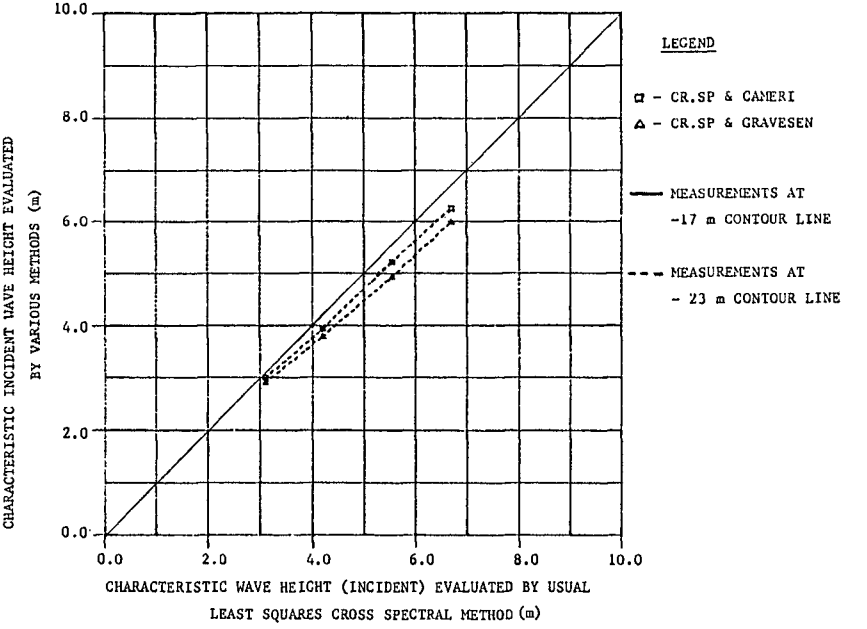

Figure No.10 - Comparison of incident characteristic wave heights (spending beach, wave gauges on -23m contour line)

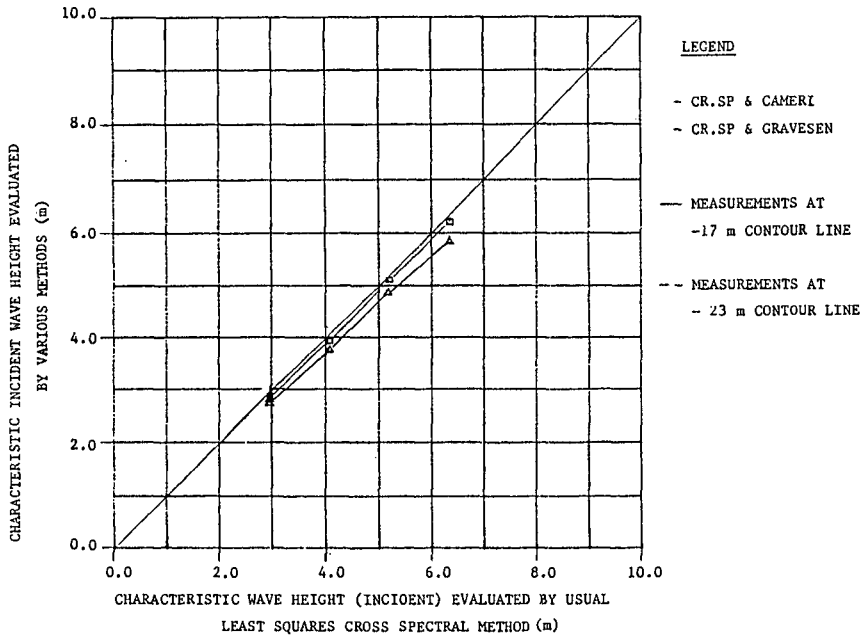

Figure No.11 - Comparison of incident characteristic wave heights (smooth slope 1:5, wave gauges on -17m contour line)

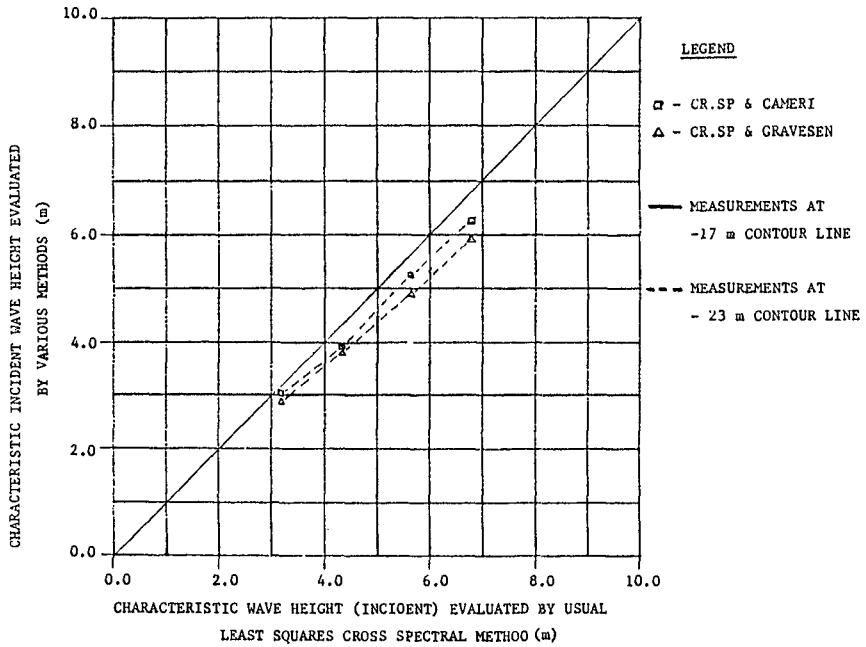

Figure No.12 - Same as Figure No.11, but gauges on -23m line

CONCLUSIVE REMARKS

The CAMERI refinement enables the evaluation of total incident wave energy (characteristic wave height) with almost no dependance on the bathymetry, easily providing real-time results, without any requirements for sophisticated software and comprehensive computer hardware. Its advantages versus the Gravesen method, result from a physically more sound approach, as proven by the analysis performed. Although the Gravesen method leads to lower estimates of the values of the total incident characteristic wave heights which might be considered to lead to conservative designs, the costs related to such conservative estimates, especially those of high sea states can not be reasonably justified.

The cross spectral least squares method provides off-line spectral distributions for incident and reflected waves, unavailable by the former approach, but it requires extensive computer resources and is of limited accuracy in the evaluation of high sea states with near breaking and breaking waves. Its use is also limited to horizontal or mild sloping sea bottoms. The results obtained using the CAMERI refinement can be used to verify results obtained by the cross spectral least squares method, increasing the reliability of the results of any flume study.

ACKNOWLEDGMENTS

The authors express their gratitude to E. Funke and J. Ploeg, Hydraulics Laboratory - National Research Council of Canada, for providing the cross spectral analysis computer programs.

The permission of Port Authority - Israel, to use and publish test results of wave data related to the Ashdod Port main breakwater rehabilitation model study, is gratefully acknowledged.

REFERENCES

GODA, Y. and SUZUKI Y., (1976), "Estimation of Incident and Reflected Waves in Random Wave Experiments", Proc. 15th Coastal Engrg. Conf., Honolulu, Hawaii, ASCE, Vol. I, pp. 828-845.

GOTTLIEB, O. and ROSEN, D.S., (1986), "Repair of the Main Breakwater Trunk at Ashdod Port - Final Report", Coastal and Marine Engrg. Research Inst., Report No. 170/86.

GRAVESEN, H., FREDERIKSEN, E. and KIRKEGAARD, J., (1974), "Model Tests with Directly Reproduced Nature Wave Trains", Proc. 14th I.C.C.E., Vol. I, A.S.C.E. Publ., pp. 372-385.

MANSARD, E.P.D. and FUNKE, E.R., (1980), "The Measurement of Incident and Reflected Spectra Using Least Squares Method", Proc. 17th I.C.C.E., Vol. I, A.S.C.E. Publ., pp. 154-172.

ROSEN, D.S. and GOTTLIEB, O., (1985), "Ashdod Port Breakwater Repairs - A Two Dimensional Stability Model Study : Calibration of the Model", Coastal and Marine Engineering Research Institute, Technical Note Ref.No. 5728, pp. 1-37.

CHAPTER 94

Impact of Offshore Dredging on Beaches along the Genkai Sea, Japan

Haruyuki Kojima, Takeshi Ijima and Tadaaki Nakamuta*

ABSTRACT

Offshore dredging has been taking place in the coast of the Genkai Sea, Japan, since the early 1970's, which totaled more than 20 million cubic meters. In order to evaluate the impact of offshore dredging on shorelines as well as the adjacent sea bed, comprehensive coastal engineering studies were carried out over the last four years. The results obtained are not sufficient to establish a direct cause-and-effect relationship between offshore dredging and beach erosion; however, the correlation is sufficient to serve as a warning of a potentially serious problem. Moreover, the dredged holes above 30 meter depth are found to trap the sand from the neighboring bed, and considerable movement of sediment by wave action was observed above 35 meter depth. Thus, offshore mining that would minimize interruption of beach littoral system should be operated below 35 meter depth in the study area.

I. INTRODUCTION

A series of concave beaches separated by headlands forms the coast of the Genkai Sea in the northern part of Kyushu, Japan, as shown in Figure 1. These beaches have been considered to be stable because of the fact that they exist as sandy beaches without much supply of sediment from rivers. Since the early 1970's, owing to the increase in the demand for aggregate and restriction in the mining of gravel from rivers, sea bed at water depth of 15 to 40 meters has been dredged for the extraction of gravel and sand for use as aggregate in concrete. Recently, it was pointed out that beach erosion has been occurring and the cause is thought to be the possible effects of offshore dredging. Due to the possibility of a man-made cause, this erosion problem became an important issue in conserving valuable beaches in the study area and the impact of offshore mining on coastal morphology became public concern.

The objectives of this study are as follows:

(1) to identify historical shoreline changes and to evaluate characteristics of shoreline changes,

* Department of Civil Engineering Hydraulics, Kyushu University, 6-10-1 Hakozaki, Higashi-ku, Fukuoka 812, Japan

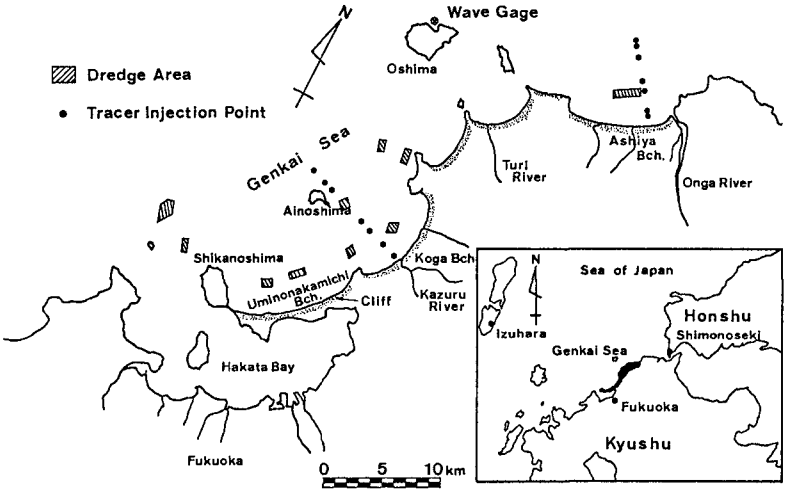

Figure 1 Vicinity Map of the Study Area

(2) to investigate causes of significant beach erosions and accretions through considering wave and climatic characteristics of the study area as well as data pertinent to human activities like offshore dredging and construction of coastal structures,
(3) to assess the link between beach erosion and offshore dredging and the effects of the present offshore dredging activities on the ambient beaches,
(4) to propose guidelines on how offshore mining should be conducted.

II. DATA COLLECTION

Several studies were carried out over four years 1981 to 1985 to obtain pertinent information on morphological changes and offshore dredging effects. They are:
(1) Meteorological surveys including compilation of wind data since 1896 and the number of typhoon attacks.
(2) Compilation of offshore wave data from 1975 to 1984 .
(3) Compilation of allowed volume of sand extraction from the sea bed between 1972 and 1983.
(4) Analysis of aerial photographs to determine historical shoreline changes.
(5) Hydrographic surveys over four years from 1981 to 1985 to obtain profile changes in beach and dredged holes.
(6) Fluorescent tracer studies and sea bed level measurements to acquire data on sediment movement.

III. DESCRIPTION OF THE STUDY AREA

3.1 Description of the Coastal Area

The study area is located in the northern part of Kyushu Island, one of the four main islands forming Japan, and bounded by Onga River to the east and Hakata Bay to the west. One of the major morphological characteristics of the coastline in this area is a series of concave beaches, divided by rocky promontories, resulting from formation of small valleys or basins due to submergence and emergence of land. These beaches stretches from 1 km to 15 km. Because of these headlands, movement of littoral sediment is confined at each concave beach; the supply of sediment from the neighboring beaches is considered to be insignificant.

Major sources of sediment supply in the study area are river and sea cliff. Using annual sediment yield per unit area of drainage basin, obtained from surveys of sediment trapped by reservoirs, and drainage area of each river basin, the total sediment production of each of the rivers was estimated. From this estimation Onga River may at maximum produce about 220,000m^3/year; sediment production of other rivers is considered to be negligible, being less than 10,000m^3/year(1). Sea cliff, another sediment source, is located at the east end of Uminonakamichi Beach, as shown in Figure 1. The cliff is 15 to 20 meters high and stretches about 1.5km along the shoreline.

3.2 Wind and Wave Characteristics

Wind and wave data compiled at Oshima between 1976 and 1980 were used to determine their characteristics. Wind velocity and direction frequencies are shown in Figure 2. The prevailing winds in the study area are from northwest during the winter season and out of the south-southeast during summer months. A dominant direction of strong winds with the velocity of over 10 meters/sec. (hereafter referred to as storm winds) is northwest at any season.

Figure 3 indicates seasonal occurrence frequencies of significant wave height and period. Severe waves with destructive energy occur during winter season. Taking into consideration the direction of storm winds, it is inferred that the prevailing high energy waves in the Genkai Sea are from northwest during winter months.

IV. SHORELINE CHANGES AND THEIR CAUSES

4.1 Historical Shoreline Changes

To quantitatively evaluate long-term shoreline alterations, numerous aerial photographs, taken from 1947 through 1982, were used, together with a digitizer which read positions of the water line on the aerials. After scale and tidal level were corrected, positions of the mean water shoreline were compared at every 50 or 100 meter interval in a consecutive yearly order. Rates of shoreline retreats or advances over three time periods were delineated for each

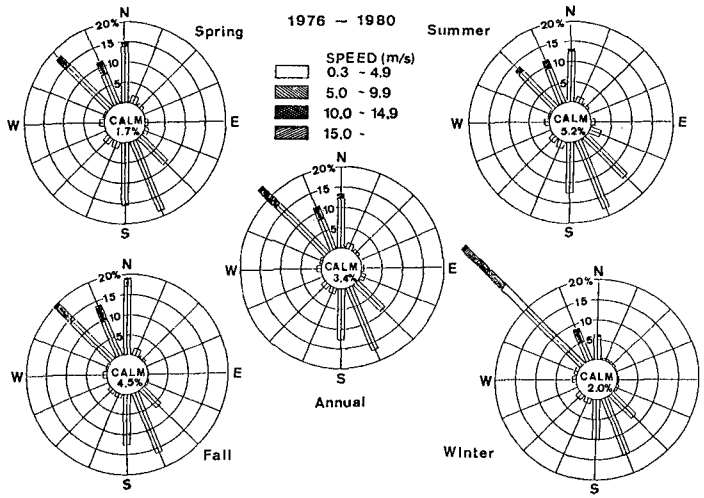

Figure 2 Seasonal Wind Roses

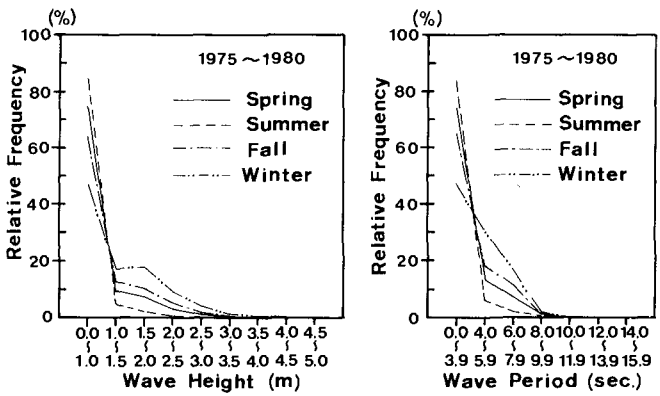

Figure 3 Seasonal Occurrence Frequencies of Significant Wave Heigh and Period

of the concave beaches (called Regions) in Figures 4 and 5. By averaging distances of the shoreline retreats or advances over small portions of each Region (called Areas) which were divided by considerations of spacial distribution patterns of the shoreline change rates plus the location of offshore dredging areas and coastal structures, yearly variations in average shoreline positions were acquired and are shown in Figure 6. Main results drawn from these changes are as follows:

(1) Between 1947 and 1961, a marked beach erosion with an average retreat of 45 meters occurred at the beaches in Region 5, the maximum shoreline recession being 85 meters, which took place in Area 3 of Region 5. For the same period

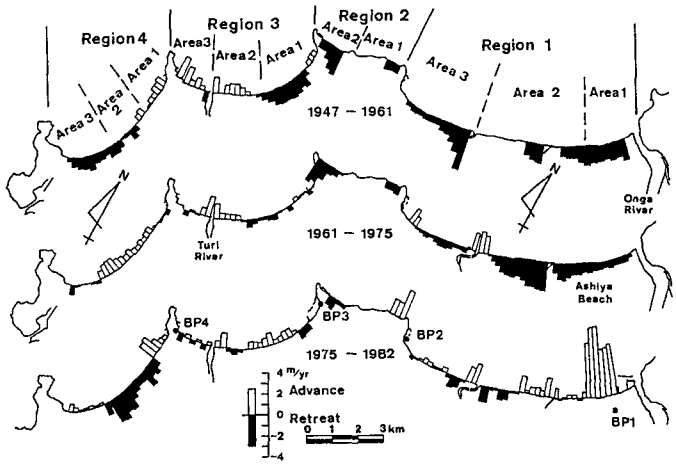

Figure 4 Distribution of Shoreline Change Rates in Regions 1 to 4

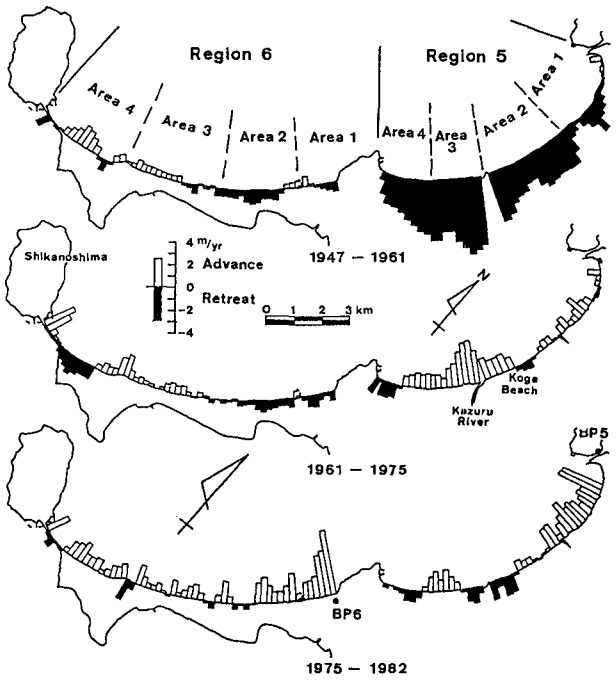

Figure 5 Distribution of Shoreline Change Rates in Regions 5 and 6

other beaches in Regions 1, 2 and 4 also had shoreline retreat ranging from 10 to 30 meters.
(2) Since 1961, most of the beaches have experienced a moderate erosion or stable condition, except for some of the beaches in Region 6 where shoreline receded sharply between 1966 and 1975.
(3) In Region 1, the beaches of Areas 2 and 3 had an erosional trend over 35 years from 1947 to 1982, whereas the beach of Area 1 showed a significant shoreline advance of 38 meters since 1975.
(4) The beaches in Regions 3 and 4, where the curvature of the concave beaches is rather big and an island called Oshima serves as an offshore barrier against the prevailing northwest waves (see Figure 7), indicated small shoreline variations being less than 20 meters over 35 years.

4.2 Causes of Significant Shoreline Changes

Possible causes of the significant shoreline changes identified above, especially beach erosion, are conceived of as follows:
(1) Exceptional intensity of wave impact
(2) Offshore dredging
(3) Construction of coastal structures.

In order to evaluate these factors, we performed extensive wave and weather surveys to determine an offshore wave condition which is regarded as the primary force altering beach configurations, and also collected information on the construction of coastal structures and volumes of the offshore dredgings. Because of the significance of storm-generated winds and typhoons in the overall scheme of coastal processes and erosion, the weather survey consists of two phases: (1) a compilation of data of storm winds with the speed of more than 10 meters/sec. and (2) an investigation of typhoon attacks experienced in the study area. These data were obtained from daily weather reports of the National Weather Service. Wave data measured at the depth of 20 meters offshore of Oshima(see Figure 1) were compiled from 1975 to 1981 for seven years.

Exceptional Intensity of Wave Impact

An attempt was made to correlate yearly fluctuations in the occurrence of both storm winds and severe waves with the trend of the beach erosion. Figure 8 shows occurrence frequencies of onshore storm winds with daily average speed of 5 meters/sec., high waves with significant height of over 3 meters and typhoon attacks which brought onshore storm winds in the study area. A tendency of the storm winds agrees quite well with that of the destructive waves; a remarkably high frequency of the storm winds between 1949 and 1959, thereby suggesting that abnormally strong wave energy may have exerted on the beaches. This period coincides with the occurrence of the severe beach erosion mentioned above.

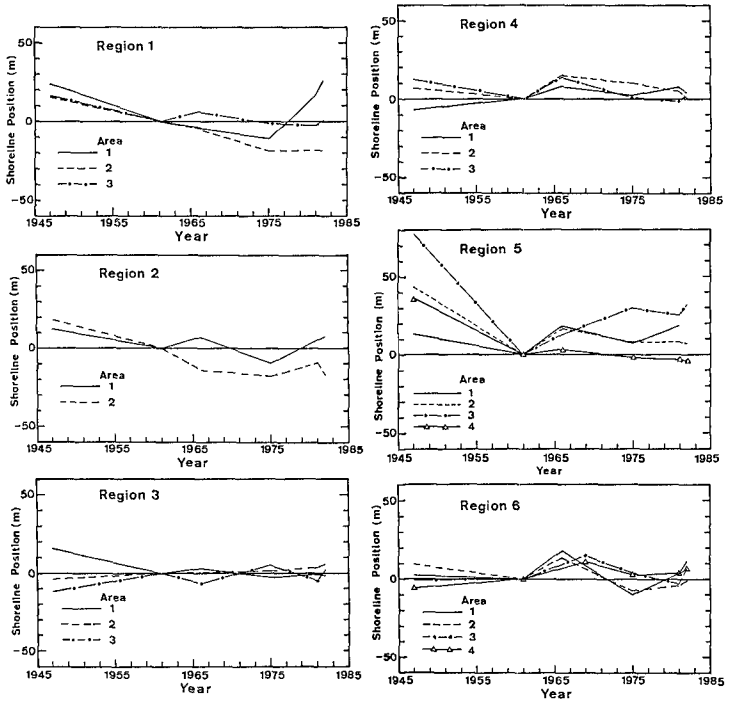

Figure 6 Shoreline Changes for Each Area versus Time

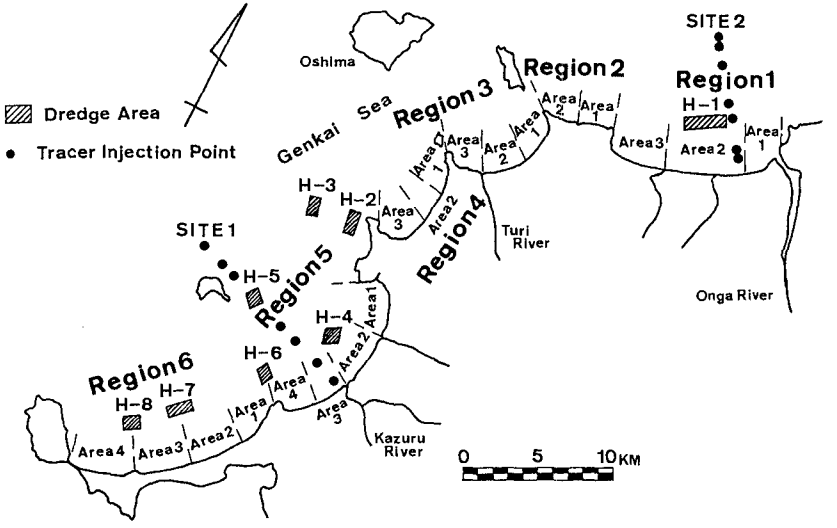

Figure 7 Locations of Areas, Dredging Sites and Fluorescent Tracer Injection Points

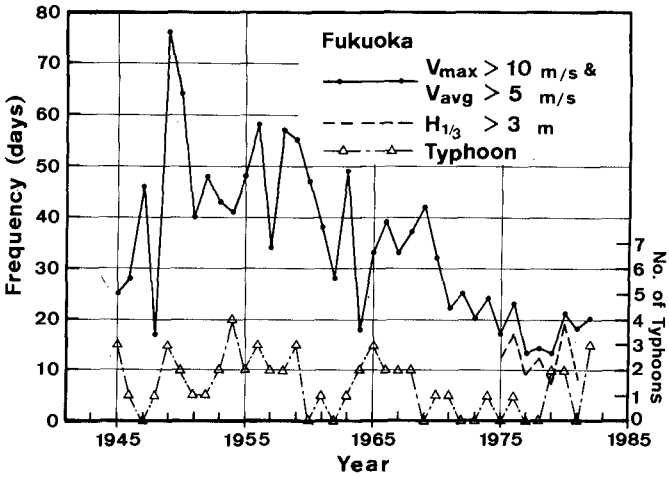

Figure 8 Frequencies of Storm winds, Waves and Typhoons

Thus, this beach erosion would most likely be caused by the exceptional intensity of wave impact.

Offshore Dredging

Annual variations in the dredging volumes were compared with the erosion trends to see if the possible effects of the offshore extraction on the beaches may be evaluated. Location of offshore dredging sites is delineated, in Figure 7, with respect to Areas where yearly shoreline changes were obtained for each Region. There are five Areas, offshore of which gravel and sand have been extracted at the depth of 15 to 20 meters; however, the mining site H-1 was excluded from this analysis because dredging started since 1982 and enough data have not been acquired yet. The average water depth of these four dredged holes are 18 meters for H-4, 25 meters for H-6, 16 meters for both H-7 and H-8.

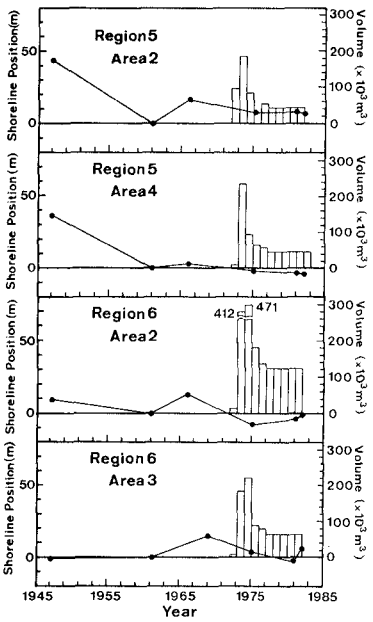

Figure 9 Relation between Shoreline Changes and Dredged Volumes

Figure 9 indicates a relation between annual Varia-

tions in dredged volumes and shoreline changes. Although the beaches in Region 5 had experienced an erosion trend before the gravel extraction, as seen in Figure 9, the beaches in Region 6 suffered a sharp shoreline recession after the offshore dredging started. Between 1966 and 1975 a shoreline recession rate for Area 2 of Region 6 was one of the severest in the study area over the nine year period, during which more than 0.8 million cubic meters of sand was dredged from the bed at 13 to 20 meters. This result therefore suggests the erosive effect of the dredging on the shorelines.

Coastal Structures

There are no data indicating severe shoreline retreat which may be attributed to the construction of coastal structures. However, drastic recovery from an erosion trend which took place on the beach of Area 1 in Region 1 may be a possible effect of the construction of six detached breakwaters in 1979.

V. ASSESSMENT OF THE PRESENT MINING ACTIVITIES

5.1 Profile Changes at the Dredged Holes

We conducted hydrographic surveys over four years from 1981 to 1985 to investigate profile changes at the dredged holes. In the surveys, an electronic positioning system and a sonic depth finder were used. Figure 10 shows typical beach profiles of four different holes dredged at several water depths. Beach profiles at and around dredge holes situated above the water depth of about 30 meters change substantially by piling up the holes with sediment. Profile changes at the dredged hole H-1 clearly illustrate infilling of the hole from the onshore side. Although profiles at greater depth and far offshore might involve considerable horizontal and vertical errors, changes in beach profiles at 35 to 40 meters seem to be insignificant and dredged holes there remain their shapes. Thus, the dredged trenches above, say, 30 meter depth in the study area may interrupt beach littoral system in that they serve as a trap to littoral sediment that would travel either onshore or alongshore. This depth is about twice as deep as the one obtained by Price, et al.(7) or much greater than the active zone of on-offshore movement which extends to about 10 meters, observed off La Jolla, California, by Inman and Rusnak(4). Although active on-offshore sediment movement in the study area would hardly be considered to extend to 30 meter depth, a considerable infilling of the holes with sand from the ambient bed does occur at that depth, which contributes to interception of the sediment supply to the upper portion of the beach and to steepening of a beach slope in the long run.

5.2 Sediment Movement

Fluorescent tracer experiments and observations of sea

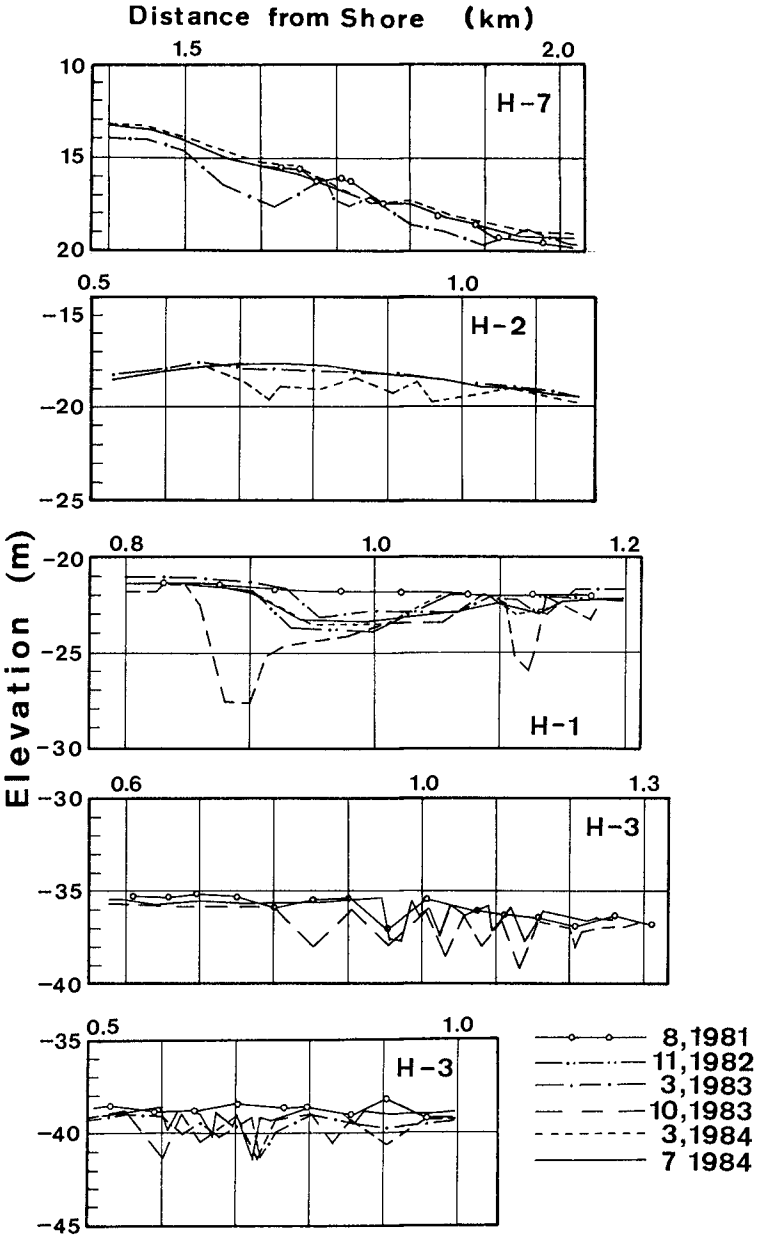

Figure 10 Profile Changes at Dredged Holes

bed levels were carried out to determine critical depth where general movement of sediment may occur. As shown in Figure 7, two locations were chosen for the experiments and fluorescent tracer and a series of graduated rods were placed at every 5 meter depth from the water depth of 10 to 40 meters. Beach profiles and median grain sizes at each 5 meter depth for two sites are shown in Figure 11. We observed tracer movement through taking underwater photographs and measured changes in bed level at the reference rods over three months during the winters of 1984 for SITE 1 and 1985 for SITE 2, the severest season with high waves. Wave data, taken off Oshima during the period of the 1984 measurement, is shown in Figure 12; there are no data for the 1985 measurement due to malfunction of a wave gage.

Figures 13 and 14 show movement of fluorescent tracers and changes in sea bed levels, respectively. Both results indicate that bottom sediment movement above 35 meter depth could be significant, whereas below that depth the movement minimum. This elaborates the result of profile changes at the dredged holes, as mentioned above. At all the observation points were seen sand ripples which form more symmetric shape than asymmetric one, and sea bed levels below 25 meter depth at SITE 1 changes noticeably between 38 and 53 days, during which the highest wave energy was exerted on the bed. These results imply that movement of sediment is more likely activated by wave action rather than unidirectional flow.

There are numerous equations describing sand motion initiation by wave action. It is of great interest for a coastal engineer to know which equations give a representative critical water depth at which sediment movement is considered to be negligible, so that offshore mining at that depth would have minimum adverse effects on the ambient sea bed. The generalized form of expression for critical water depth proposed by many researchers are written as :

$$\frac{H_0}{L_0} = \alpha \left(\frac{d_{50}}{L_0} \right)^m \sinh \frac{2\pi h}{L} \cdot \left(\frac{H_0}{H} \right)$$

where H and L are wave height and length, respectively, h is water depth, d_{50} is median grain diameter, α and m are constant, and subscript 0 indicates offshore condition. Ishihara and Sawaragi(5) proposed α=0.171 and m=0.25 for initial movement; Sato, Ijima and Tanaka(8) suggested α=1.35 and m=1/3 for general movement. Horikawa and Watanabe(3) introduced a more complex expression, based on conditions of bottom surface and boundary layer. In order to determine a critical depth, these three expressions plus recent works on threshold of sediment motion, done by Komar & Miller(6) and Hallermeier(2), were utilized together with the bottom orbital velocity computed from the linear wave theory.

Input parameters for calculation and computed results are shown in Table 1. Wave height and period are those with

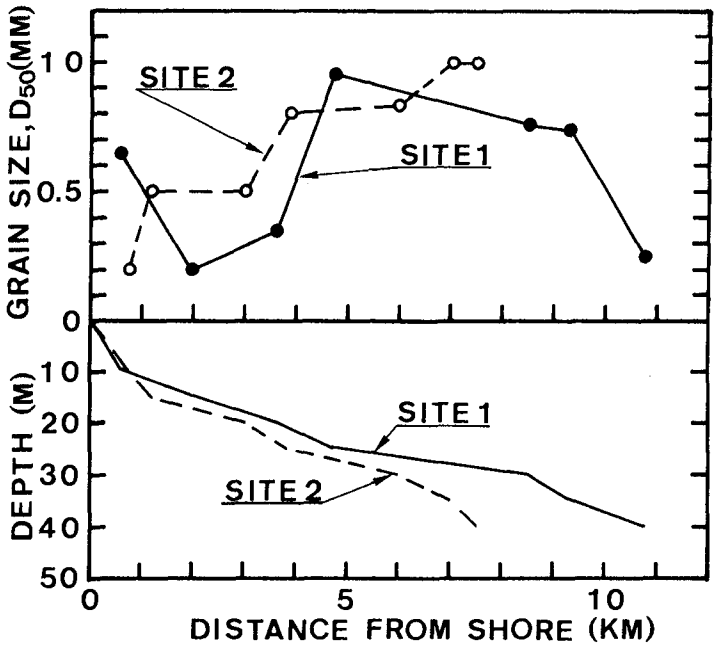

Figure 11 Beach Profiles and Median Grain Size Distribution at SITE 1 and SITE 2

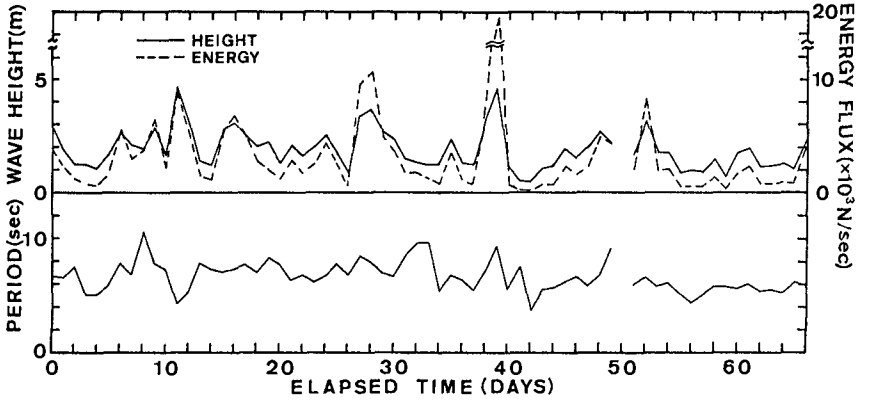

Figure 12 Measured Wave Height, Period and Energy, January 10, 1984 to March 16, 1984

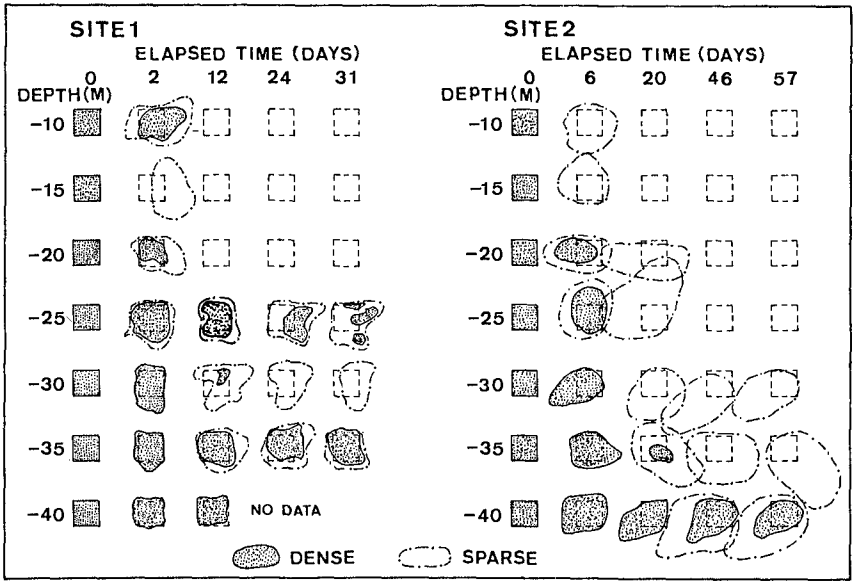

Figure 13 Movement of Fluorescent Tracer at Several Depths

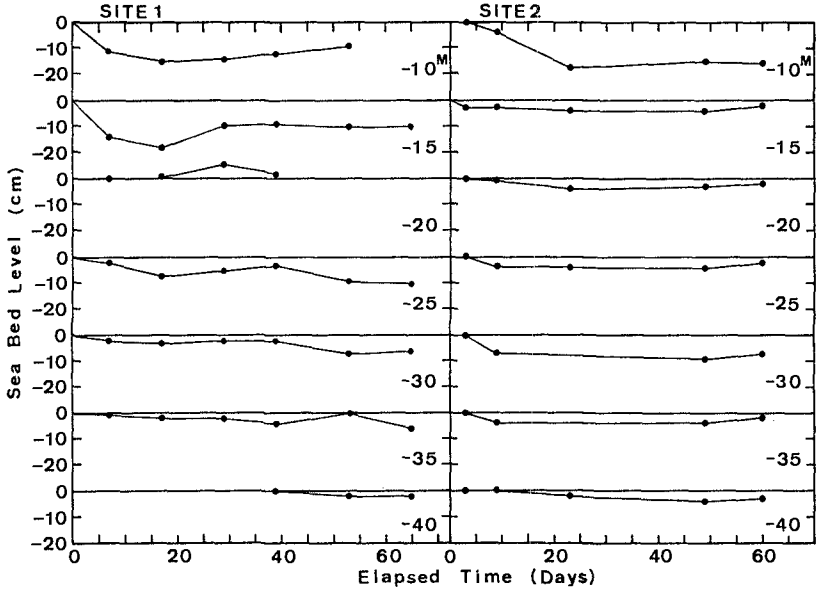

Figure 14 Changes in Sea Bed Levels at SITE 1 and SITE 2

the highest wave energy in Figure 12. The grain diameter was taken as an average value of median sediment grain diameters between 25 and 40 meter depth at SITE 1, as shown in Figure 11. In comparison with the actual measurement indicating a critical depth of 35 to 40 meters, the second and forth values in Table 1 show somewhat smaller and greater depth, respectively. The rest of equations give reasonable estimated depths for this case.

Table 1 Computation of Critical Water Depth

Input Parameters :

Wave Height = 4.58 m, Wave Period = 9.20 sec., d_{50} = 0.58 mm
Specific Weight of Sand = 2.64, Angle of Repose = 45 degree
Kinematic Viscosity = 0.0101 cm^2/sec.

Equation Proposed by	Critical Water Depth(m)
1. Ishihara & Sawaragi	39
2. Sato, Ijima & Tanaka	20
3. Horikawa & Watanabe	37
4. Komar & Miller	49
5. Hallermeier	43

VI. CONCLUSIONS

Although the major cause of the severe beach erosions in the study area would most likely be the abnormally high frequency of destructive wave attacks inferred from the storm-wind data, the offshore dredgings do seem to result in a shoreline recession to some degree. Moreover, dredged holes above the water depth of about 30 meters are found to be refilled with sand which would be mainly transported from the onshore side, thereby interrupting beach littoral system by trapping sand which may travel in the on-offshore or alongshore direction and causing a steeper beach slope in the long run.

The data presented indicates a possible relationship between sand mining and the shoreline changes. Although the available data are not sufficient to establish a direct cause-and-effect relationship between offshore mining and beach instability, the correlation is sufficient to serve as a warning of a potentially serious problem. It is advisable, therefore, that the indiscriminate removal of sand from sea bed be avoided at such water depth that drastic beach profile changes occur. For the study area, it would be above the water depth of 35 meters.

ACKNOWLEDGEMENTS

The authors wish to thank engineers at the Harbor Division, the Prefecture of Fukuoka Department of Civil Engineering, for valuable cooperation and assistance in obtaining pertinent data and for permission to use some of the data. We also appreciated considerable contributions from each member of the Genkai-Hibiki Sea Beach Preservation Advisory Committee chaired by Professor Emeritus T. Ijima, Kyushu University.

REFERENCES

(1) Reports of the Genkai-Hibiki Sea Beach Preservation Advisory Committee, the Prefecture of Fukuoka Department of Civil Engineering, 1985 (in Japanese)

(2) R. J. Hallermeier, "Sand motion initiation by water waves: two asymptotes," Journal of the Waterway, Port, Coastal and Ocean Division, ASCE, Vol. 106, No. WW3, August 1980, pp.299-318

(3) K. Horikawa and A. Watanabe, "A study on sand movement due to wave action," Coastal Engineering in Japan, Vol. 10, 1967, pp. 39-57

(4) D. L. Inman and G. S. Rusnak, "Changes in sand level on the beach and shelf at La Jolla, California," US Army, Corps of Engineers, Beach Erosion Board, Technical Memorandum No. 82, 1956

(5) T. Ishihara and T. Sawaragi, "On the critical velocity and critical water depth of sand movement under wave action," Proceeding of 7th Conference on Coastal Engineering in Japan, 1960 (in Japanese)

(6) P. D. Komar and M. C. Miller, "Sediment threshold under oscillatory waves," Proceedings of 14th Conference on Coastal Engineering, 1974, pp. 756-775

(7) W. A. Price, J. M. Motyka and L. J. Jafferey, "The effect of offshore dredging on coastlines," Proceedings of 16th Conference on Coastal Engineering, 1978, pp. 1347-1358

(8) S. Sato, T. Ijima and N. Tanaka, "A study of critical depth and mode of sand movement using radioactive glass sand," Proceedings of 8th Conference on Coastal Engineering, 1963, pp. 304-323

CHAPTER 95

Undistorted Froude Model for Surf Zone Sediment Transport

by

D. L. Kriebel[1], W. R. Dally[1] and R. G. Dean[2]

Abstract

Small scale movable bed wave tank experiments were carried out according to undistorted Froude model laws with the sediment fall time, H/wT, as the governing parameter for scaling the model sediment. Four questions addressed in this study included: (a) the ability to reproduce larger scale model results for both erosional and accretive conditions, (b) the effects of more realistic concave upward initial beach profiles instead of the more usual planar initial slopes, (c) the criterion for onshore-offshore sediment transport, and (d) the capability of the model to simulate post-storm recovery.

Based on a comparison with large scale results of Saville (1957), it was found that the model provided good agreement for erosive conditions. For accretive conditions, the results were less conclusive although the general patterns of profile change were similar. The final beach profiles resulting from concave upward initial profiles were found to be substantially different from those for an initially planar profile. It appears that the initially planar profile unrealistically affects the breaker type and results in a more pronounced longshore bar and offshore slopes that are steeper than found in nature. Tests conducted to evaluate the criterion separating onshore-offshore transport suggested a higher value of the fall time parameter, H/wT, than was originally proposed by Dean (1973); this is interpreted to be due to scale effects in most of the model data used in the original development. Tests to simulate post-storm recovery were affected by the presence of "reflection bars" associated with a partial standing wave system. The reflection bars appear to strongly affect the sediment transport limiting the post-storm profile recovery. The most effective recovery was induced by continually changing wave conditions to maintain the wave breakpoint slightly landward of the bar crest.

[1]Graduate Research Assistant, Coastal and Oceanographic Engineering Department, University of Florida, Gainesville, FL 32611

[2]Graduate Research Professor, Coastal and Oceanographic Engineering Department, University of Florida, Gainesville, FL 32611 and Director, Division of Beaches and Shores, Department of Natural Resources Tallahassee, FL 32303

Introduction

Simple and direct movable bed modeling laws are applied in a series of small-scale laboratory experiments on beach profile evolution. The basic criteria proposed by Dean (1985) and adopted in this study for modeling of surf zone processes are:

1) the model should be undistorted,

2) the model should be large enough to preserve the character of wave breaking processes and to avoid surface tension and viscous effects,

3) the scaling of hydrodynamic properties should be based on the accepted Froude criterion, such that the prototype to model length ratio, N_ℓ, and time ratio, N_t, are related as:

$$N_t = \sqrt{N_\ell} \tag{1}$$

4) The scaling of sediment properties should be based on preserving the fall time parameter, H/wT, where w is the sediment fall velocity, H is the wave height, and T is the wave period, such that the required fall velocity ratio, N_w, is given by:

$$N_w = \sqrt{N_\ell} \tag{2}$$

The proposed requirements are not new and are not universally applicable since many prototype situations cannot be practically replicated at small scale with an undistorted model. The criteria attempt, instead, to build upon what concensus may exist among modeling laboratories, primarily through reliance on the fundamental Froude model laws and the fall time parameter. In the recently proposed scaling laws for coastal movable bed models of Vellinga (1978) and Hughes (1983), preserving H/wT has resulted in successful duplication of prototype events during highly erosive storm conditions. Noda (1978) has found that preserving H/wT produces closer similarity than when the ratio H/d is preserved. Kamphuis (1982) also concluded that modeling based on the fall time parameter eliminates most of the scale effects associated with attempting to geometrically scale quartz sand grain diameters. By further specifying that the model should be undistorted, ambiguous definitions of length and time scales are eliminated, unrealistic augmentation of gravity forces are avoided, and interpretation of all physical quantities are clarified.

Objectives and Procedures

The overall goal of the study is to evaluate the usefulness of the undistorted Froude model, with sediment scaled according to the fall time parameter, for simulating beach profile evolution under specific erosive and accretive wave conditions. In order to test the proposed model laws, several sets of experiments were conducted to address specific objectives.

The first objective is to examine the ability of the model law to reproduce actual prototype-scale beach profile evolution. For this purpose, two experiments were conducted to simulate full-scale experiments by Saville (1957). The second objective is to examine the evolution of concave initial beach profiles compared to profiles with linear initial slopes for the same erosive and accretive wave conditions. The third objective is to examine the criterion for onshore-offshore sediment transport determined by Dean (1973) based upon the fall time parameter, or equivalently, the wave steepness, H_o/L_o, and a fall velocity parameter, $\pi w/gT$. Ten experiments were performed and the results compared to Dean's criterion as well as to results of prototype-scale experiments of Saville (1957) and Kajima et al. (1982). The fourth objective is to simulate conditions of post-storm beach recovery. A reference storm-barred profile was generated by elevated water levels and erosive wave conditions, then five experiments were conducted by lowering the water and subjecting the storm-generated breakpoint bar to accretive wave conditions.

The laboratory experiments were conducted in the Air-Sea flume at the University of Florida Coastal and Oceanographic Engineering Laboratory. The flume is 37 m long, 1.2 m deep, and 0.86 m wide. The wavemaker can generate regular or random waves; however, all experiments were performed using regular waves. A motorized cart that runs along rails mounted to the top of the tank carries a capacitance-sensing bottom profiler that is capable of resolving sand bed changes to within 2 mm. The sediment used in the experiments was a fine quartz sand with a median diameter of 0.15 mm. The mean fall velocity of the sand was found to be 1.8 cm/sec as obtained from a settling tube analysis.

Due to length restrictions, only a sampling of the figures can be presented in this paper. Much greater detail is available in Kriebel, Dally and Dean (1986).

Results and Analysis

a. Model Verification

The first series of experiments was designed to verify that the undistorted Froude model could reproduce prototype-scale events. Prototype conditions were taken to be two full-scale experiments conducted by Saville (1957) in a large wave tank 193.5 m long, 6.1 m deep, and 4.6 m wide. Saville's experiments were conducted using a linear 1:15 beach slope with 0.4 mm sand having an approximate fall velocity of 5.6 cm/sec. Based on the undistorted Froude model laws, the prototype to model fall velocity and time ratios are 3.1 while the length ratio is 9.6.

Two experiments were conducted, one under erosive wave conditions, the other under accretive conditions. In the erosion test, Saville's wave period was 5.6 seconds while the wave height in the flat section of the wave tank was 1.6 m. In the small-scale model, the wave period and the wave height in the flat portion of the tank were 1.8 seconds and 0.167 m respectively. The model surf zone was on the order of 4 m wide and seemed large enough to permit realistic wave breaking and transformation free of noticeable surface tension or viscous effects.

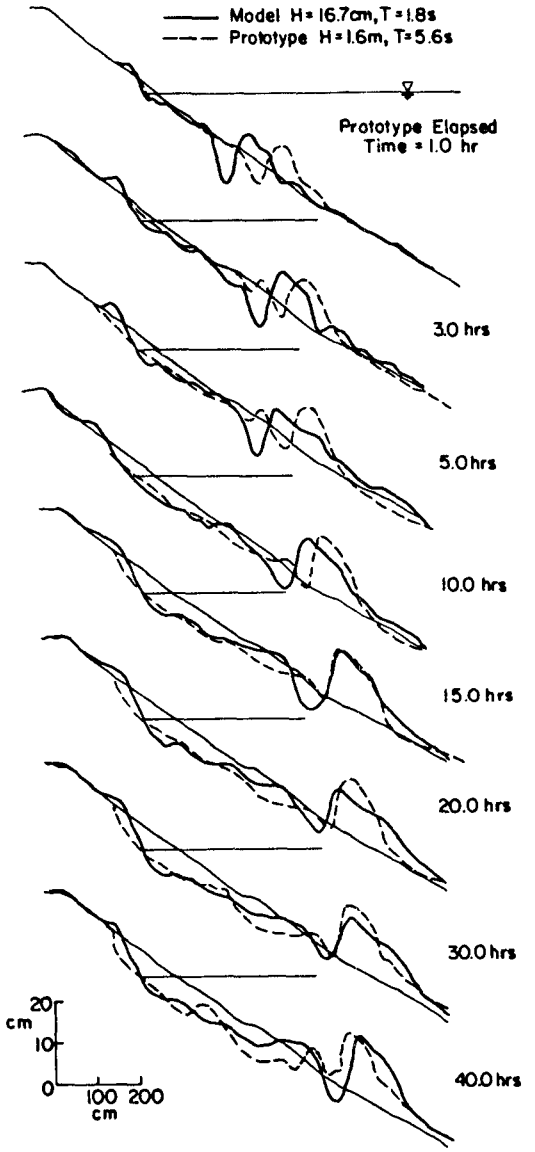

Figure 1. Beach Profile Evolution for Erosive Wave Conditions. Prototype Results Refer to Saville's (1957) Large-Scale Wave Tank Tests. Initial Planar Profile of 1:15 Slope.

In Figure 1, Saville's results are scaled according to the length scale and are compared to small-scale results. In general, the initial differences between the small- and large-scale model results are greater than at later times as equilibrium is approached. The final results at 40 hours are in good agreement and there is general similarity of the beach face slopes, the inner third of the surf zone, bar-trough geometries, and the offshore slopes. Offshore slopes in both model and prototype are approximately 1:5, and appear to be far steeper than natural offshore slopes.

In the second experiment, one of Saville's tests with constructive wave conditions was simulated. Saville's wave period and wave height in the flat section of the tank were 11.33 seconds and 1.28 m repectively. The required model parameters were T = 3.67 s and H = 0.13 m. Unfortunately, the wave generator in the model was not capable of generating a 13 cm wave at the required period, therefore, the maximum possible wave height of 8.5 cm was used. Results between model and prototype may then be compared in a qualitative sense only.

Figure 2 compares the profile evolution of the model and prototype. Despite the lack of similarity of wave heights, both profiles show the same general features with the building of a sizable berm and net onshore sediment transport. A problem encountered in the constructive wave test was severe wave reflection from the beach and re-reflection from the wave paddle. The reflection caused undulations or "reflection bars" in the outer profile, with bar crests located distinctly at the antinodes of the partial standing wave system. In Figure 2, three of these bars are noticeable over the offshore portion of the profile. The offshore bars seem to "lock up" sand and prevent effective onshore sediment migration from the toe of the slope to the berm as in the prototype.

b. Comparison of Results Using Concave Versus Linear Profiles

In an effort to achieve more realistic wave shoaling, wave breaking, and profile evolution, the 1:15 linear beach slope was abandoned in favor of a concave initial profile. As shown by Dean (1977), a profile shape which realistically represents non-barred profiles found in nature is:

$$h = Ax^{2/3} \tag{3}$$

where h is the depth at a distance x offshore and A is a slope parameter related to sediment fall velocity. Based on the initial experiments offshore slopes out to the breakpoint were fitted by an $Ax^{2/3}$ curve to establish a best-fit value of $A = 0.075\ m^{1/3}$. . The stable beach face slope was observed to be approximately 1:5. The new initial profile was therefore established with a 1:5 beach face slope to a point of tangency with the $Ax^{2/3}$ profile just below the still water level, beyond which the $Ax^{2/3}$ form was adopted.

For this initial profile, the same erosive and accretive wave conditions were repeated from the first experiments. The results corresponding to various elapsed times for the erosive case are shown in

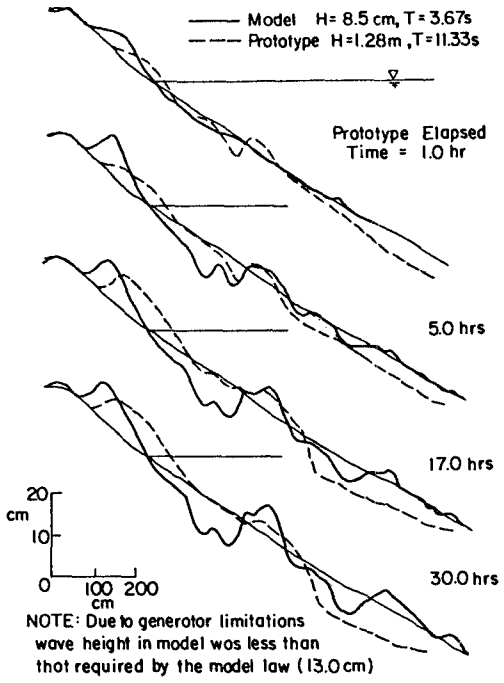

Figure 2. Beach Profile Evolution for Accretive Wave Conditions. Prototype Results Refer to Saville's (1957) Large-Scale Wave Tank Tests. Initial Planar Profile of 1:15 Slope.

Figure 3. Because of the mild offshore slope, waves broke in a spilling fashion during the first few hours of the test, in contrast to the plunging breakers observed in the 1:15 slope test. After 3 to 4 hours, waves began to plunge and a breakpoint bar became fully developed. From the beginning of the test, a broad symmetrical outer shoal grew steadily at a position well seaward of the breakpoint, seemingly due to increased sediment suspension over the rippled bed. As this bar grew, it began tripping waves in a spilling fashion between 10 and 11 hours. Waves then reformed before plunging on the inner bar, which moved shoreward due to the smaller reformed wave heights. Remarkably, the inner surf zone and beach face exhibited minor variation with only slight erosion over the test. It is noted that this offshore bar seems peculiar to this specific set of wave conditions and did not form under other erosive wave conditions.

In the case of low steepness waves beginning with an $Ax^{2/3}$ profile form, wave breaking was altered from surging-collapsing in the 1:15 test

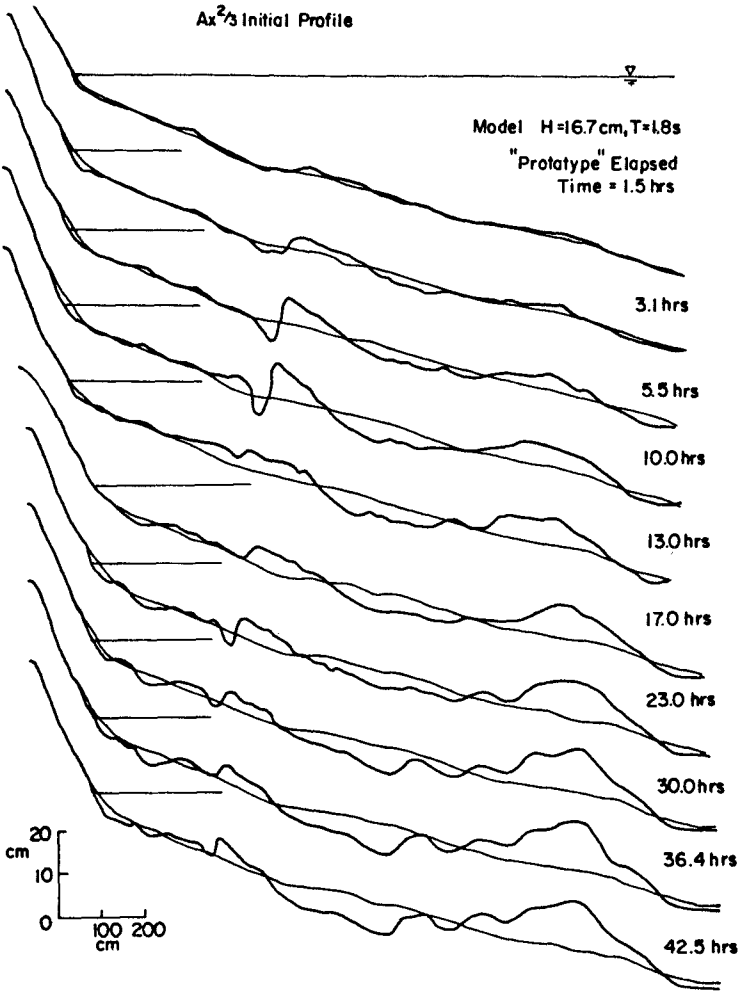

Figure 3. Evolution of Erosive Profile for $Ax^{2/3}$ Initial Profile.

to plunging. Only slight beach face accretion occurred but runup was nearly identical to the 1:15 test. The profile was dominated by multiple reflection bars and some cross-tank variations were present; however, little net onshore-offshore sediment transport occurred.

The effects of the initial profile form can be observed directly by superimposing the final profiles of the 1:15 and $Ax^{2/3}$ tests as shown in Figure 4. The most striking feature of the comparisons are the nearly identical beach face and inner surf zones despite the differences in initial profile forms and breaker type. Over the offshore regions the profiles are quite dissimilar, which may be attributed to different wave shoaling and breaking characteristics. To investigate further the role of bottom shape in wave transformation across the outer part of the profile, the breaker model by Dally, et al. (1985) was applied. Under erosive conditions for the initial profile of 1/15 slope, the model indicates rapid shoaling to an incipient breaker height of 19.8 cm at a mean water depth of 15.6 cm, i.e. $(H/h_b) = 1.27$, in accordance with the observed plunging breaker conditions. On the $Ax^{2/3}$ profile, the wave shoals very gradually until a height of 18.6 cm is reached in a mean water depth of 21.6 cm, $(H/h)_b = 0.86$, indicating a spilling breaker as observed at the beginning of the test. The same behavior is evident under accretive conditions. In general, wave shoaling and incipient breaking seem much more realistic on the $Ax^{2/3}$ profile as compared to the linear initial profile.

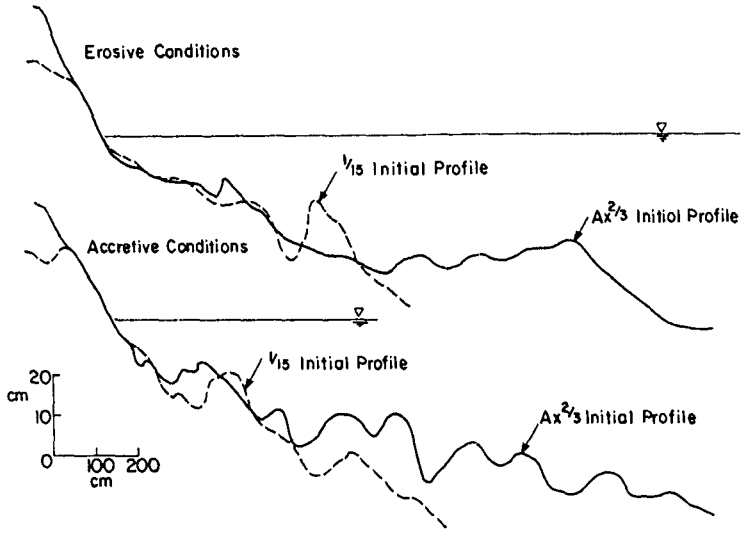

Figure 4. Comparison of Final Profiles Resulting from Planar (Slope 1:15) and $Ax^{2/3}$ Initial Profiles. (a) Erosive Conditions, (b) Accretive Conditions.

c. Model Experiments for Onshore-Offshore Transport

The major series of experiments was concerned with evaluating the undistorted Froude model against full-scale models for determining the criterion for the formation of storm or normal profile forms. Since the Froude model violates the Reynolds criteria, it was a priori expected that results of storm-normal profile tests would be skewed toward the formation of storm profiles, as it was found that onshore motion during constructive conditions is hindered by reflection problems while offshore motion under erosive conditions is enhanced by ripple-dominated suspension.

The framework adopted for the experiments was Dean's (1973) criterion for onshore-offshore transport:

$$\frac{H_o}{L_o} \begin{matrix} > \\ < \end{matrix} 1.7 \frac{\pi w}{gT} \qquad \begin{matrix} > \text{ offshore (storm profile)} \\ < \text{ onshore (normal profile)} \end{matrix}$$

or

$$\frac{H_o}{wT} \begin{matrix} > \\ < \end{matrix} 0.85 \qquad \begin{matrix} > \text{ offshore (storm profile)} \\ < \text{ onshore (normal profile)} \end{matrix}$$

Ten combinations of deepwater steepness and the fall velocity parameter, $\pi w/gT$, were selected. Starting with the $Ax^{2/3}$ initial profile, wave conditions were run for the prototype equivalent of 6 to 12 hours. Profiles were found to exhibit three forms, characterized by net onshore transport, net offshore transport, or a mixed response with simultaneous formation of a berm and offshore bar.

The initial and final profiles from individual tests are shown in Figure 5 and the results for direction of transport are given in Table 1. In general, profile changes are not as dramatic as typically observed on linear initial profiles, presumably since the initial concave profile is in quasi-equilibrium. In Figure 6, the small-scale results are augmented by available full-scale experimental results of Saville (1957) and Kajima, et al. (1982) and plotted in the same format as Dean's original criterion. As found by Dean (1973), a line with a 45° slope seems to reasonably separate storm and normal profiles and is given by:

$$\frac{H_o}{L_o} = c_1 \frac{\pi w}{gT}$$

or:

$$\frac{H_o}{wT} = c_2$$

where c_1 is found to be 4.0 to 5.0 and c_2, the critical value of the fall time parameter H/wT, is therefore 2.0 to 2.5. As expected, the undistorted Froude model exhibits slightly lower critical values than

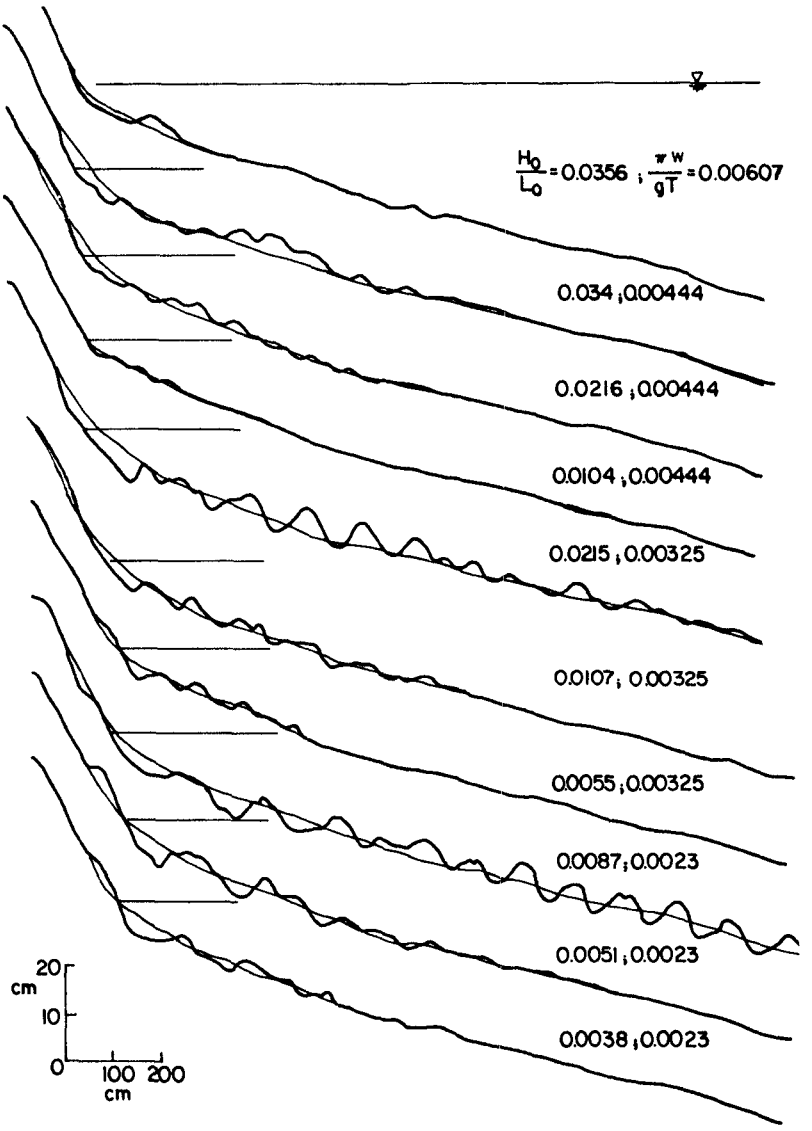

Figure 5. Final Beach Profiles for Test Series to Establish Criterion Separating Onshore and Offshore Sediment Transport. Initial $Ax^{2/3}$ Profile.

the full-scale experiments. The lower number in each range seems to represent the small-scale criterion while the upper number represents the approximate full-scale criterion, although more data is required to establish the criteria more exactly.

Table 1
Test Conditions and Results for Experiments of Onshore-Offshore Criterion

H(cm)	T(s)	L_o(cm)	h/L_o	H_o	H_o/L_o	$\pi w/gT$	Profile Type
4.8	0.95	140.8	0.3268	5.01	0.0356	0.00607	storm
8.1	1.3	263.6	0.1745	8.86	0.0340	0.00444	storm
5.2	1.3	263.6	0.1745	5.69	0.0216	0.00444	mixed
2.5	1.3	263.6	0.1745	2.74	0.0104	0.00444	no change
10.3	1.8	505.4	0.091	10.94	0.0215	0.00325	storm
5.1	1.8	505.4	0.091	5.42	0.0107	0.00325	mixed
2.6	1.8	505.4	0.091	2.76	0.0055	0.00325	normal
8.8	2.5	974.8	0.0472	8.5	0.0087	0.0023	storm
5.2	2.5	974.8	0.0472	5.02	0.0051	0.0023	normal
3.9	2.5	974.8	0.0472	3.77	0.0038	0.0023	normal

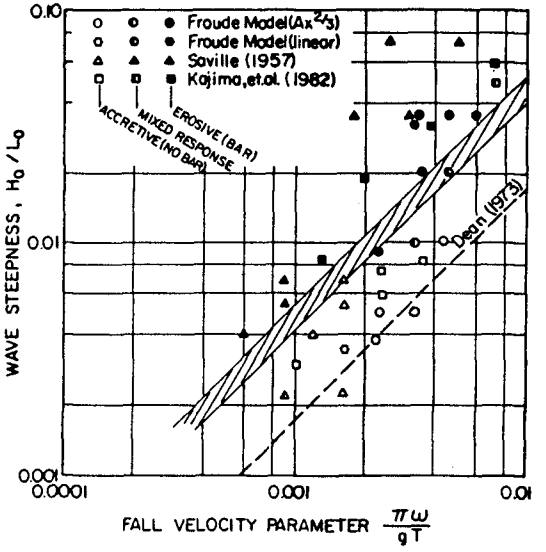

Figure 6. Conditions Separating Onshore and Offshore Sediment Transport Including Results of this Study, as well as Results of Prototype Scale Experiments of Saville (1957) and Kajima, et.al. (1982).

Reasons for the differences between the present criterion and Dean's original criterion are difficult to determine precisely but seem to be due to scale effects incorporated into Dean's original criterion. Other criteria for onshore-offshore transport also exhibit apparent scale effects from small to full scale. Kamphuis (1982) addresses possible scale-effects in small scale mobile bed models and attributes the greatest scale effects to the ratio of a characteristic length scale to the grain diameter, which governs bed roughness and bed geometry. He concludes, however, that it is impossible to determine the magnitude or source of scale effects with certainty. Despite the scale effects in the undistorted Froude model, results seem to agree reasonably with large scale results and are in much better agreement than other small-scale results with either unscaled sediment or unknown distortion effects.

d. Storm Bar Behavior Under Recovery Conditions

A final series of five experiments was designed to directly simulate the behavior of a profile, generated under storm wave conditions and an elevated water level, after the water level had returned to normal and lower steepness waves prevail. The storm profile was generated starting from the same $Ax^{2/3}$ profile used as the initial condition in the previous tests, except the water level was increased by 10 cm. The wave conditions of Saville's erosion test were then maintained for 3.87 hours to form a large breakpoint bar.

In this first test, the wave generator was set to maintain the erosive conditions with the water level returned to normal to see if any recovery would occur simply due to the drop in water level stranding the storm bar inside the new breakpoint. At the end of the test, nearly all traces of the storm bar had been eradicated and a new bar had formed offshore at the new plunge point that was identical to the initial bar. However, only a small berm has been constructed; and, on the whole, the beach face had not shown any signs of recovery and the inner surf zone had remained remarkably inactive.

The second test reduced the wave height so that the deepwater wave steepness was 0.01, while $\pi w/gT$ remained equal to 0.00325. This placed conditions in the recovery regime, according to Figure 6. This resulted in profile changes dominated by the formation of small scale reflection bars. For the first 3 hours the storm profile and bar retained their identity, with the reflection bars superposed on top. Ultimately, some material from the storm-generated bar moved landward to fill the trough and a small berm developed.

In the third recovery test, the deepwater steepness was reduced to 0.005, moving conditions further into the recovery regime. This produced a surging "breaker" at the toe of the beach face and substantial reflection. Energy conditions were so low that even after 8 hours, the original storm bar was still present. Except for a small transfer of material from the bar crest to trough, the storm bar was maintained much like a relict feature. A berm formed due to local onshore transport in the swash region.

In the fourth test, the deepwater wave steepness was returned to 0.01 while $\pi w/gT$ was reduced to 0.0023. According to Figure 6, this placed conditions in the transition between erosion and recovery. Wave conditions were such that the storm bar also caused breaking of the recovery waves, and as a result, much of the profile evolution consisted of a reworking of the bar material seaward. However, a substantial berm was constructed and fully developed within 3 hours.

In the fifth recovery test the deepwater steepness was reduced to 0.005, placing conditions within the recovery regime. The storm bar migrated landward over the first hour of the test and eventually stabilized at the breakpoint of the recovery waves. The berm grew until it stabilized at approximately 5 hours elapsed time, simultaneously with the appearance of reflection bars.

In a related experiment, using a linear initial profile, wave conditions were changed every 30 to 45 minutes to consistently maintain the breakpoint a few centimeters landward of the evolving bar. This test, shown in Figure 7, was the only test in which anything resembling complete shoreward bar migration onto the beach face was achieved. Apparently, under monochromatic wave conditions, complete bar migration requires "tuning" of the wave conditions toward smaller wave heights in order to continually promote the establishment of the bar landward of its previous position while ensuring that the previous bar is the source of sediment for the new bar.

Summary and Conclusions

Several sets of experiments were conducted to: 1) test a simple physical model scaling law for beach profile evolution, 2) investigate the effects of initial profile shape on profile evolution, 3) test the criterion of Dean (1973) for the formation of a storm profile versus normal profile, and 4) study the general behavior of a barred profile under recovery conditions. Only monochromatic waves were used in the experiments.

The model scaling law, based on Froude similarity and using sediment fall velocity as the controlling parameter, was found to reproduce beach profile evolution quite well under erosive conditions. Under constructive wave conditions simulation for portions of the profile seaward of the breakpoint is only moderately successful due to the improperly scaled boundary layer features and due to the persistent formation of fairly stable multiple bars associated with wave reflection.

For the same wave conditions, initial profile shapes of 1/15 planar slopes and $Ax^{2/3}$ produced dramatically different profile evolution and equilibrium shapes, especially offshore from the breakpoint. These differences are attributed to the different breaking behavior governed by different bottom slopes near the breakpoint. However, because depth limited breaking causes all waves to approach the same height regardless of incipient conditions, the inner surf zone and beachface showed remarkable similitude between the two tests. The concave profile was found to have more realistic wave shoaling and breaking characteristics and, on that basis, appears most useful for physical modeling.

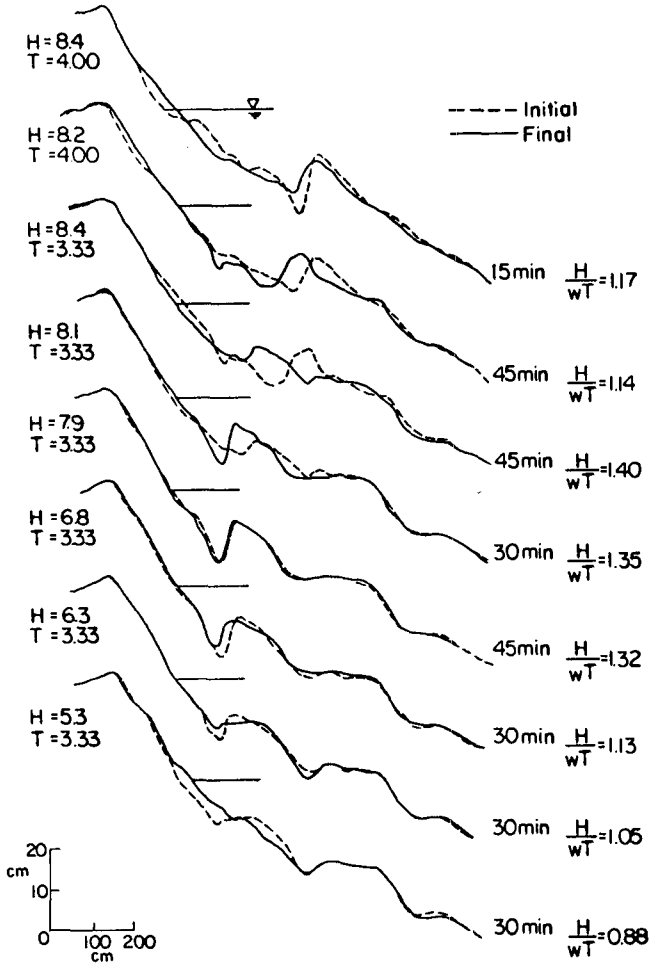

Figure 7. Beach Profile Recovery Resulting from Adjusting Wave Breakpoint to be Located just Landward of Bar Crest.

Model tests of the onshore-offshore criterion, when coupled with the prototype scale results of Saville (1957) and Kajima, et al (1982), resulted in a different criterion than that found by Dean (1973) based mostly on unscaled small-scale experiments. This criterion is more physically realistic, and the agreement of the undistorted Froude Model with prototype-scale experiments is satisfying but needs much additional model verification.

Direct simulation of a storm-barred profile with lowered water levels and constructive wave conditions indicates that onshore bar migration does not occur easily. Bar migration under monochromatic waves seems to require a specific set of finely tuned wave conditions such that the recovery breakpoint is always maintained just landward of the migrating bar. This can only occur due to a gradual reduction in wave height or due to changes in water depth due to tides.

Based on the undistorted Froude model, with monchromatic waves, beach recovery in qualitative or quantitative agreement with nature was difficult to attain. This is due to the aforementioned reflection problems, and scale effects in the bottom boundary layer and ripple formation. Preliminary tests with irregular waves were performed and seem useful for reducing wave reflection effects and for smoothing bottom ripples.

Acknowledgements

This study was supported by the Sea Grant College Program of the National Oceanic and Atmospheric Administration.

References

Dally, W.R., Dean, R.G., and Dalrymple, R.A., "Wave Height Variation Across Beaches of Arbitrary Profile," J. Geophys. Res., Vol. 90;C6, 1985.

Dean, R.G., "Heuristic Models of Sand Transport in the Surf Zone," Proc. Conf.on Eng.Dynamics in the Surf Zone, Sydney, Australia, May, 1973.

Dean, R.G., "Equilibrium Beach Profiles: U.S. Atlantic and Gulf Coasts," Ocean Eng. Rep. 12, Dep. of Civ. Eng., Univ. of Del., Newark, 1977.

Dean, R.G., "Physical Modelling of Littoral Processes," In: R.A. Dalrymple, Physical Modelling in Coastal Eng., 1985.

Hughes, S.A., "Movable-bed Modeling Law for Coastal Dune Erosion," J. of Waterways, Port, Coastal and Ocean Eng., Vol. 109, No. 2, 1983.

Kajima, R., Shimizu, T., Maruyama, K., and Saito, S., "Experiments on Beach Profile Change with a Large Wave Flume," Proc. 18th Conf. Coastal Eng., 1982.

Kamphuis, J.W., "Coastal Mobile Bed Modelling from a 1982 Perspective," Queens Univ., C. E. Research Rpt. 76, May 1982.

Kriebel, D.L., Dally, W.R., and Dean, R.G., "Beach Profile Response Following Severe Erosion Events," Report No. UFL/COEL-86/016, Coastal and Oceanographic Engineering Department, University of Florida, Gainesville, FL, December 1986.

Noda, H., "Scale Relations for Equilibrium Beach Profiles," Proc. 16th Conf. Coastal Eng., 1978.

Saville, T., "Scale Effects in Two-Dimensional Beach Studies," Int. Assoc. of Hydraulic Research, 1957.

Vellinga, P., "Movable Bed Model Tests on Dune Erosion," Proc. 16th Conf. Coastal Eng., 1978.

CHAPTER 96

Experimental study on on-offshore sediment transport of Accretive Beach

CHING-TON KUO* CHING-HER HWANG** I-CHOU TSENG***

1. INTRODUCTION

In treating coastal proceses, sediment transport is usually divided into along-shore and on-offshore components. It is believed that the on-offshore component has a prominant connection with short-term profile changes, observed during storm wave climates. Obviously its shift of sand plays a very vital role in shoreline migration. In other words, the beach profile has great bearing on coastal phenomena related to on-offshore sediment transport. As we know, there have been many studies on this kind of sediment transport rate, and considerable amount of knowledge on this problem has been accumulated so far. Yet it seems that we are still far from a reliable formulus to estimate the beach profile changes. The reason why is due to the complexity of mechanics of sediment transport. Therefore, the aim of this study is to examine experimentally the mechanism between on-offshore sediment transport and the deformation processes of two-dimensional beach profile. Then , a predictive model of the temporal and spatial distribution of net on-offshore sediment transport based on two-dimensional beach profiles and an equation of continuity of sediment transport is proposed. Various parameters of net on-offshore sediment transport in this model are discussed also.

* B.E., M.E., ph.D., Professor of Hydraulic and Ocean Engineering Graduate School, National Cheng Kung University, Taiwan, R.O.C.

** B.E., M.E., Associate Researcher, Institute of Harbor and Marine Technology, Wuchi, Taichung District, Taiwan, R.O.C.

*** B.E., M.E., Graduate of Hydraulic and Ocean Engineering Graduate School, National Cheng Kung University, TAIWAN, R.O.C.

2. THE CONTINUITTY EQUATION OF SEDIMENT TRANSPORT

The evaluation of net sediment transport in this study was on the the basis of continuity equation of sediment transport, assume the transport mode of sediment was just bed-load and there is no suspended sediment occurred. Therefore a coaser sand of 0.57^{mm} ϕ was used as a bed material in order to satisfy this theoritical consideration. Usually, sediment transport rate was measured directly by a sand trap during the last few decades. But due to such apparatus would cause severe disturbance to the fluid motion and the sediment movement. Instead the net rates of sediment transport were estimated by the continuity equation from the beach deformation data comparing with the initial profile. Attemp to find temporal and spatial the relationship between the net transport rate and wave condition were then made. Suppose a beach profile changes as given in Figure 1. By virtue of the conservation of bed material amount, the local net transport rate $q(x,t)$ per unit width is related to the bed elevation $h(x,t)$ measured from a certain datum as :

$$\frac{\partial h}{\partial t} = \frac{1}{1-\varepsilon} \frac{\partial q}{\partial x} \qquad \text{.....(1)}$$

in which ε is the sediment porosity. Therefore the effective net transport rate $Q(x)$ averaged over a time duration Δt of wave action is evaluated from the bed elevation change $\Delta h(x)$ by

$$Q = \frac{\bar{q}}{1-\varepsilon} = \int_{X_R}^{X'} \frac{\Delta h}{\Delta t} X' \qquad \text{.....(2)}$$

where X' is positively seaward and X_R means shoreward limit of beach deformation. Parameter definition is shown as Figure 2.

3. EXPERIMENTAL PROCEDURES

Experiments were carried out in a two-dimensional wave tank, 1 m wide, 1 m deep, 80 m long with a glass wall on one side of 30 m length at the end of tank. Figure 3 shows the general arrangement of the test equipment.

The experiments were performed using monochromatic waves generated by a flap-type wave maker installed at another end of the tank.

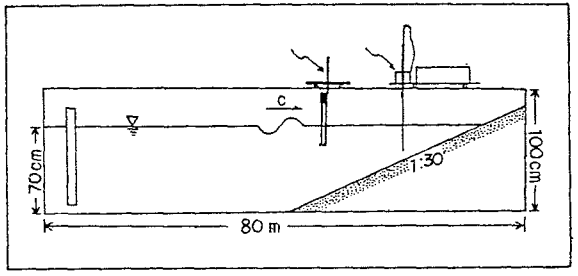

Fig.3 General arrangement of test equipment

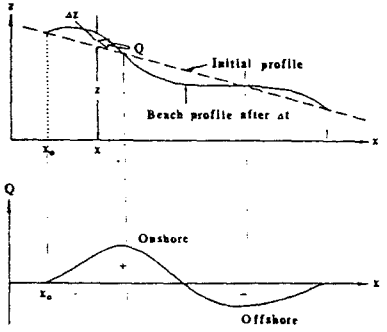

Fig.1 Evaluation of net sediment transport rate

Table-1 Experimental Conditions

	T (sec)	H_i (cm)	H_o/L_o
A1	1.2	8.4	0.039
A2	1.2	6.7	0.031
A3	1.2	5.1	0.024
B1	1.5	12.4	0.038
B2	1.5	8.3	0.026
B3	1.5	6.1	0.019
C1	2.0	12.1	0.021
C2	2.0	8.4	0.015
C3	2.0	6.3	0.011

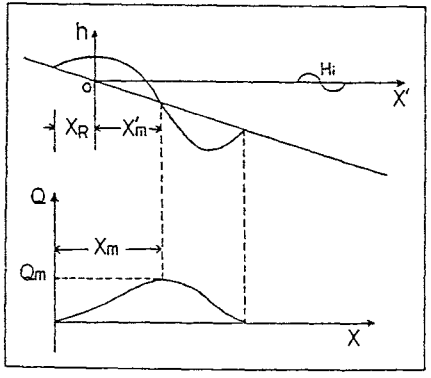

Fig.2 Coordinate system and notation

The incident wave height was measured by a capacitance type wave gage placed just offshore from the toe of the model beach. In order to make simply the experiments, tests were limited to a uniform initial beach profile of 1/30 and one coarse sand of 0.57^{mm} ϕ was used as a bed material mentioned above. Beach profile changes were measured by an electronic profile sensor to record the continuous profile data for every two hours within the testing duration of 18 ~ 20 hrs totally. Then, the temporal and spatial net rate of on-offshore sediment transport was evaluated from the beach profile changes.

Table 1 is a list of experimental cases. Various kinds of wave conditions were investigated for this test. Both the breaker height and local wave heights were also measured by a capacitance type wave gage mounted on a carriage capable of moving with constant speed along the centerline of the tank at the locations of 50 cm interval along the model beach in the middle of wave action. The horizontal distance from a base line on the model beach to the breaking position and the limited shoreward position of run-up were measured by ruler attached on grass wall.

4. EXPERIMENTAL RESULTS & DISCUSSION

Figure 4 (a)~(i) show the beach profiles at the end of wave action for all the cases listed in Table 1. It should be noted that profile changes are belong to the accretive type i.e. a shoreline progresses and no sand deposition takes place offshore. (Sunamura and Horikawa, 1974). The locations of breaking points are indicated by arrow symbols; dot line arrows for the initial stage and solid line arrows for the final stage. Experimental results indicate that the locations of breaking point progress shoreward as the accumulated time of wave increased, i.e. the breaker zone become narrowed gradually as shown in Fig 5 (a) ~(h) and its breaker type changed gradually also from spilling one to plunging breaker. Results also indicate that the maximum sediment transport rate take place arround the breaking point. Figure 6 (a) ~ (b) show some examples of the spatial and temporal distribution of the effective non-dimencsonal net transport rate Q/Qm evaluated from beach profiles mentioned above. It's seen that the

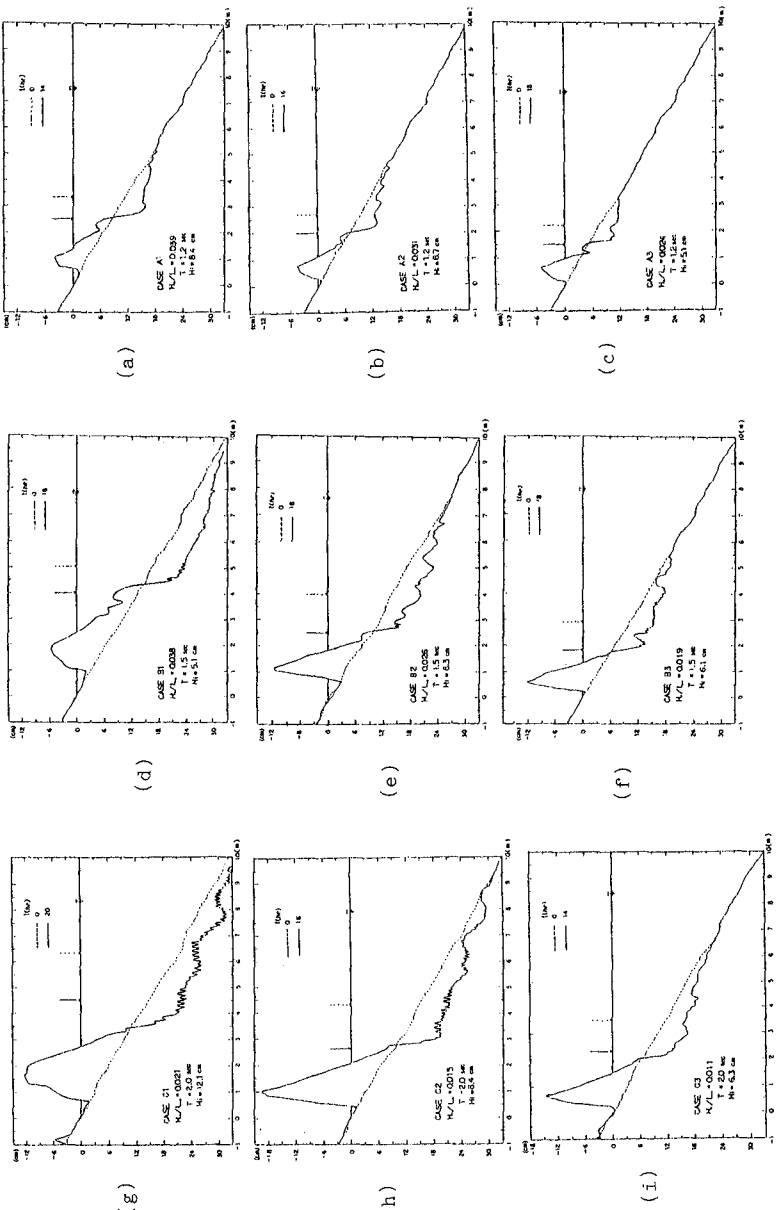

Fig.4 Beach profile after wave action

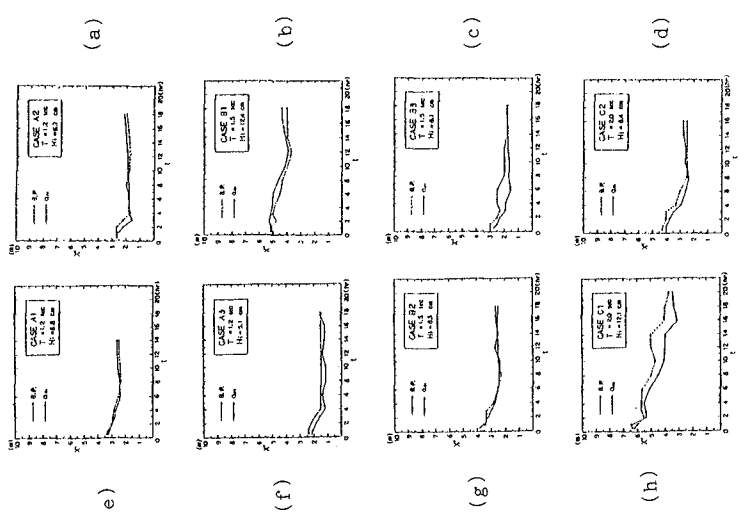

Fig.5 Spatial and temporal relationship between B.P. and Q_m

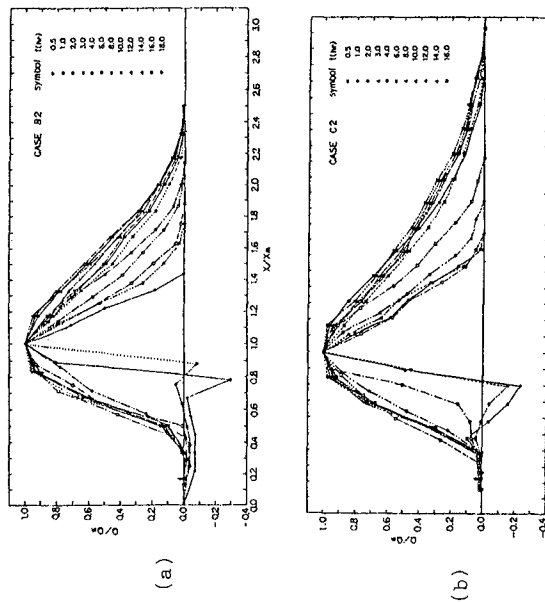

Fig.6 Spatial and temporal distribution of Q/Q_m

dimensionless distribution curves of sediment transport rate tend to steady after $t/T = 1.44 \times 10^4$, in which t is accumulated time of wave action and T is the incident wave period. Based on these data of each case an optimum curve was obtained to represent its characteristics as shown in Figure 7 (a)~(c). Then, a dimensionless sediment transport rate shown as Figure 8 for accretive beach were analyzed and relationship of parameters were shown also as figures 9~13. These experimental formulus were established ae follows:

$$Q/Qm = AM\bar{X}^{M-1} e^{-A\bar{X}^{M-1}} \quad ; \bar{X} > 1 \quad \ldots\ldots\ldots\ldots(3)$$

$$Q/Qm = C_6\bar{X}^6 + C_5\bar{X}^5 + C_4\bar{X}^4 + C_3\bar{X}^3 + C_2\bar{X}^2 + C_1\bar{X} + C_0 \quad ; \bar{X} < 1$$

and

$$C_6 = 32.31 \ , \ C_5 = -87.96 \ , \ C_4 = 79.23 \ , \ C_3 = -25.38$$

$$C_2 = 2.81 \ , \ C_1 = 0.01 \ , \ C_0 = 0.00$$

$$A = 15.16 \left(H_o/L_o\right) + 0.89 \quad \ldots\ldots\ldots\ldots\ldots\ldots(4)$$

$$M = 13.55 \left(H_o/L_o\right) + 2.52$$

in which

$$\bar{X} = X/X_m$$

$$Q_m/Q_o = 478.6 \left(t/T\right)^{-0.64} \ ; \ t/T \geq 1.44 \times 10^4 \ldots\ldots(5)$$

$$Q_o/Wod_{50} = 0.16 \, Ns^{1.51} \quad \ldots\ldots\ldots\ldots\ldots\ldots\ldots(6)$$

$$Ns = H/T \ / \sqrt{(s-1)gd_{50}} \quad \ldots\ldots\ldots\ldots\ldots\ldots\ldots(7)$$

$$Xm'/H_o = 141.3 \left(t/T\right)^{-0.16} \ ; \ t/T \geq 1.44 \times 10^4 \ldots(8)$$

$$X_R/H_o = 0.771 \left(H_o/L_o\right)^{-0.537} \quad \ldots\ldots\ldots\ldots\ldots(9)$$

Where

Q, Qm = local and maximum accumulated sediment transport rate

X, Xm = corresponding position of local maximum accumulated sediment transport rate

Cn = constant

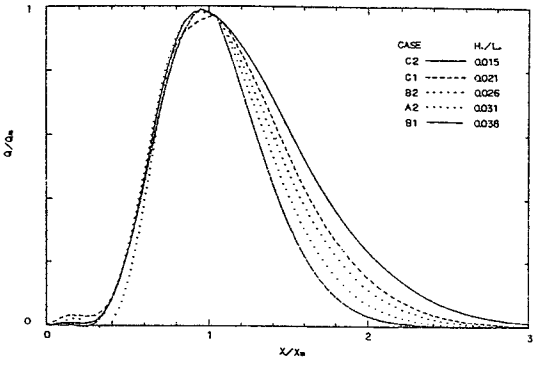

Fig.8 Spatial distribution of non-dimensional Q/Q_m

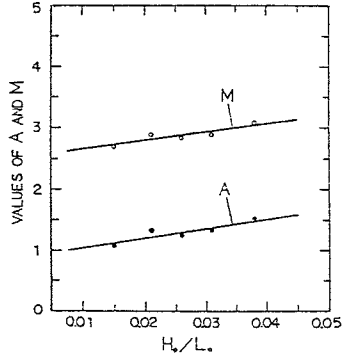

Fig.9 Relationship between H_O/L_O and A, M

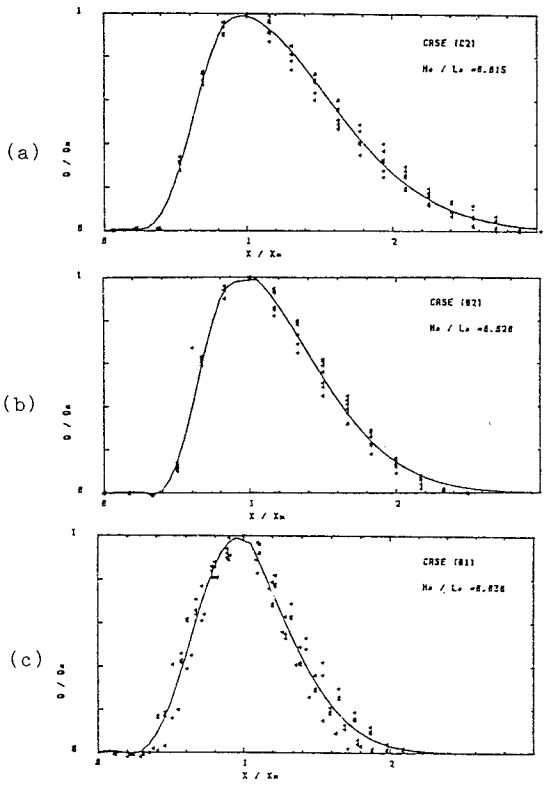

Fig.7 Optimum curve between Q/Q_m and X/X_m

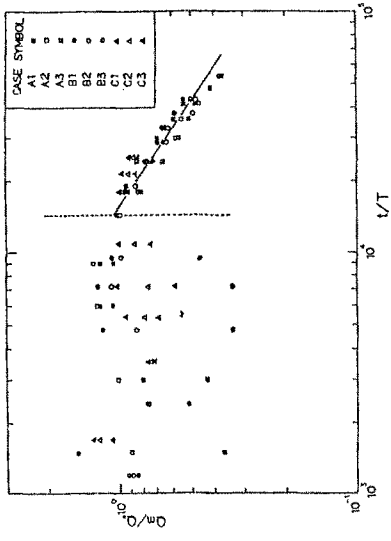

Fig.10 Relationship between Q_m/Q_o and t/T

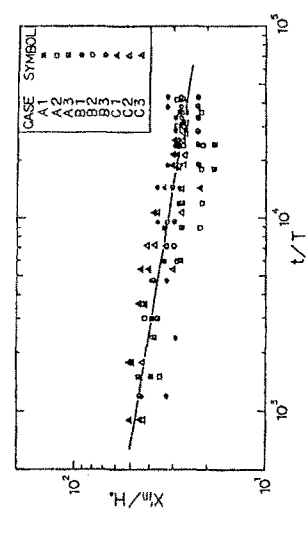

Fig.11 Relationship between X'_m/H_o and t/T

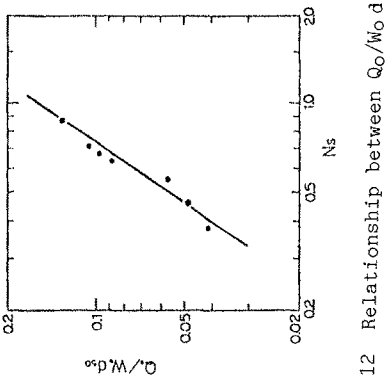

Fig.12 Relationship between $Q_o/W_o d_{50}$ and N_s

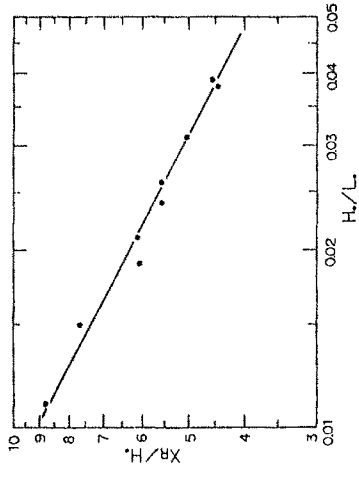

Fig.13 Relationship between X_R/H_o and H_o/L_o

Ns = dimensionless parameter

5. APPLICATION OF THE NUMERICAL MODEL

Based on These experimental formulus mentioned above, then, a numerical model of two-dimensional accretive beach profile changes is presented. Figure 14 (a)$\sim$(c) are the examples of the comparison between this predictive numerical model and experimental results; solid line represents the numerical computational values and dot line represents the experimental results after 20 hours of wave action. Results indicate that the numerical model could be used to describe adequately on-offshore beach profile changes for the accretive beach.

6. CONCLUSIONS

The main conclusions of this study are summarized as follows:

(1) Experimental results indicate that final beach profile changes after 14 $\sim$ 20 hrs wave action respectively for all the cases are belong to the accretive type, i.e. a shoreline will progresses seaward and no sand deposition takes place offshore and predominant mode of sediment transport is the bed-load.

(2) When the time of wave action was increaed, the breaker zone width will become narrower and narrower and its breaker type will change gradually also from spilling one to plunging breaker.

(3) Results indicate that the position of maximum sediment transport rate will take place around the breaking point.

(4) On-offshore sediment transport rate is the function of Ns and t/T , and could be expressed as equation (3) to equation (9). When the acaumulated time of wave action are greater than $t/T = 1.44 \times 10^4$, its normalized non-dimensional spatial distribution of sediment transport rate could tend to be steady.

(5) Based on the experimental results, a predictive numerical model is presented and shown that this model could be used to describe adequately the on-offshore beach profile changes for accretive beach.

7. ACKNOWLEDGEMENTS

The authers wish to expressed their gratitude to all of them who carried out this study. And thanks to the national scientific

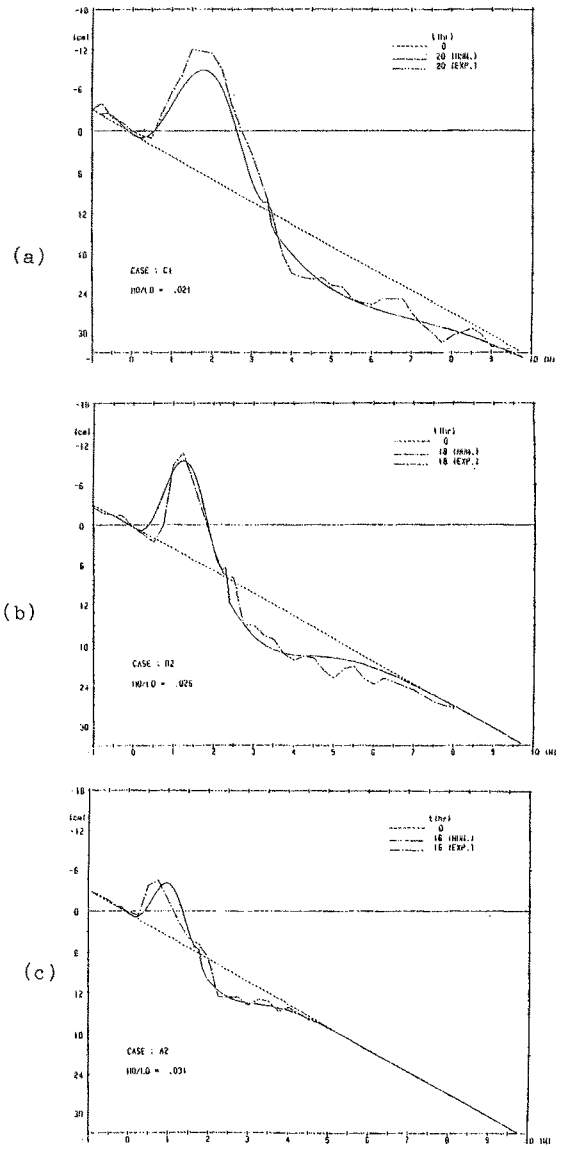

Fig.14 Comparison between numerical model and experimental results

council to support funds under the contact NSC 74-0410-E006-02. Authers would also like to thank Miss Joanna Chang IHMT to type.

8.REFERENCES

SAWARAKI T. & DEGUCHI I. (1980). On-offshore sediment transport rate in the surf zone., Proc of the 17th Conference on Coastal Engineering, Chapter 73, pp. 1194-1214.

WATANABE, RIHO & HORIKAWA(1980). Beach profiles and on-offshore sediment transport., Proc of the 17th Conference on Coastal Engineering, Chapter 68 , pp. 1106-1121.

HATTORI M. & KAWAMATA R. (1980). On-offshore transport and aeach profile changes., Proc. of the 17th Conference on Coastal Engineering, Chapter 72, pp. 175-1192.

HATTORI M. (1982). Field study on On-offshore sediment transport., Proc. of the 18th Conference on Coastal Engineering pp. 923-939.

BAILARD J.A. (1982). Modelling On-offshore sediment transport in the surf zone. Proc. of 18th Conference on Coastal Engineering, PP. 1419-1438.

SHIBAYAMA T. & HORIKAWA K. (1982). Sediment Transport and beach transformation., Proc of 18th Conference on Coastal Engineering, pp. 1439-1458.

CHAPTER 97

NUMERICAL MODEL OF BREAKING WAVE AROUND A RIVER MOUTH

Jong-Sup Lee[+], Toru Sawaragi[++] and Ichiro Deguchi[+++]

ABSTRACT

Equations for wave kinematics and wave dynamics based on small amplitude wave theory have been used in the prediction of wave deformations and wave-indused currents. However, the applicability of the linear wave theory is questionable in a river mouth where forced wave breaking and strong wave-current interaction take place.

A numerical model based on the non-linear dispersive wave theory has been developed, the results by this model was compared with the values of the experiments and the linear theory. Wave transformations including shoaling, wave-current interaction and wave breaking by the model showed a good agreement with the experimental result. In the prediction of wave-induced currents, the excess momentum flux (Pxx) computed by the model has more reasonable value than the radiation stress (Sxx) calculated by the small amplitude wave theory.

1. INTRODUCTION

To predict wave deformation and wave-induced currents in a shallow water region is an important problem not only for a design of coastal structures but also for a prediction of beach deformations in near shore regions. In general, equations for wave kinematics and dynamics based on linear wave theory have been used to solve these problems. However, the applicability of the linear wave theory is questionable in a river mouth where forced breaking and strong wave-current interaction take place. Recentry, Boussinesq type equations have been often used in numerical modelling of short waves in shallow water regions (Abbott et al. (1978), Haugel(1980) and Haugel et al.(1982)) and the accuracy of these equations was discussed by Abbott et al.(1978) and McCowan (1982).

+ Assistant professor, Dept. of Ocean Eng., National Fisheries Univ. of Pusan, Korea.
++ Professor, Dept. of Civil Eng., Osaka Univ., Japan
+++ Assistant professor, Dept. of Civil Eng., Osaka Univ., Japan

In this paper, the applicability of Boussinesq type equations in surf zone dynamics was studied in the problems of wave transformations and wave-induced flows around a river mouth. Results by this model were compared with those of the experiments as well as the results calculated by linear model developed by Sawaragi et al.(1984).

2. BASIC EQUATIONS

Boussinesq equation derived by Peregrine (1967) in a variable water depth are written as follows, where we introduce the viscous term. Fig.1 shows the definition sketch of the coordinate system.

$$\frac{\partial \eta}{\partial t} + \frac{\partial M_i}{\partial x_i} = 0 \tag{1}$$

$$\frac{\partial M_j}{\partial t} + \frac{\partial}{\partial x_i}\left(\frac{M_i M_j}{h+\eta}\right) + g(h+\eta)\frac{\partial}{\partial x_j}\eta\delta_{ij} - \frac{\partial}{\partial x_i}\left(\nu\frac{\partial M_j}{\partial x_i}\right) + \tau_{bj}$$

$$= \frac{h^2}{3}\left[\frac{\partial}{\partial x_j}\left(\frac{\partial^2 M_i}{\partial x_i \partial t}\right) - \frac{M_i}{h+\eta}\frac{\partial}{\partial x_i}\left(\frac{\partial^2 \eta}{\partial x_j \partial t}\right)\right] \tag{2}$$

where $i,j = 1$ or 2
δ_{ij} = Kronecker's δ function
g = gravitational acceleration
ν = kinematic eddy viscosity
τ_{bj} = bottom friction
$M_i = U_i(h+\eta)$: depth integrated velocity, ie, mass flux per unit width

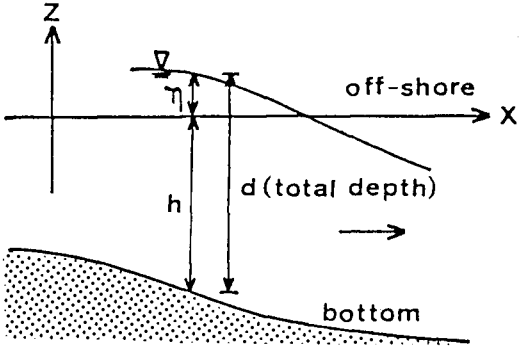

Fig.1 Definition sketch of coordinate system

Now, we define the mass flux per unit width M as a sum of staedy component M_o , phase averaged component of waves M' and turbulent component M''.

$$M_i = M_{oi} + M_i' + M_i'' \tag{3}$$

By using the above expression in eq.(1) and (2), the following equations for mean currents and waves are derived by the time averaging minipulation.

1) For mean currents

$$\frac{\partial \bar{\eta}}{\partial t} + \frac{\partial M_{oi}}{\partial x_i} = 0 \tag{4}$$

$$\frac{\partial M_{oj}}{\partial t} + \frac{\partial}{\partial x_i}\left(\frac{M_{oi}M_{oj}}{h+\bar{\eta}}\right) + g(h+\bar{\eta})\frac{\partial}{\partial x_j}\bar{\eta}\delta_{ij} + \overline{\tau_{bj}} + \frac{\partial p_{ij}}{\partial x_i}$$

$$- L_i = \frac{h^2}{3}\left[\frac{\partial}{\partial x_j}\left(\frac{\partial^2 M_{oi}}{\partial x_i \partial t}\right) - \frac{M_{oi}}{d}\frac{\partial}{\partial x_i}\left(\frac{\partial^2 \bar{\eta}}{\partial x_j \partial t}\right)\right] \tag{5}$$

where "$\overline{\quad}$" denotes the time averaged value, d is a total depth $h+\eta$, P_{ij} is a excess momentum flux by the wave motion, L_i is a lateral mixing term of momentum.

$$p_{ij} = \overline{M_i' M_j'}/(h+\eta) \tag{6}$$

$$L_i = \frac{\partial}{\partial x_i}\left(\frac{\partial M_{oi}}{\partial x_i}\nu - \frac{1}{h+\bar{\eta}}\overline{M_i'' M_j''}\right) \simeq \frac{\partial}{\partial x_i}\left(K_i \frac{\partial M_{oi}}{\partial x_i}\right) \tag{7}$$

where, τ_{bj} is a time averaged bottom friction term by waves and currents.

$$\overline{\tau_{bj}} = f_w\left(\frac{1}{2}\frac{M_{oj}}{h+\bar{\eta}} + \frac{M_j'}{h+\eta}\right)\left|\frac{1}{2}\frac{M_{oj}}{h+\bar{\eta}} + \frac{M_j'}{h+\eta}\right| \tag{8}$$

where, f_w is a bottom friction coefficient on the bottom.

2) For waves

$$\frac{\partial \eta'}{\partial t} + \frac{\partial M_i'}{\partial x_i} = 0 \tag{9}$$

$$\frac{\partial M_j'}{\partial t} + \frac{\partial}{\partial x_i}\left(\frac{M_i' M_j'}{h+\eta'}\right) + g(h+\eta')\frac{\partial}{\partial x_j}\eta'\delta_{ij} + (\tau_{bj} - \overline{\tau_{bj}})$$

$$+\frac{\partial}{\partial x_i}\left(\frac{M_{oi}M_j'}{h+\eta'}\right) + \frac{\partial}{\partial x_i}\left(\frac{M_i' M_{oj}}{h+\eta'}\right) + DM_j \tag{10}$$

$$= \frac{h^2}{3}\left[\frac{\partial}{\partial x_j}\left(\frac{\partial^2 M_i'}{\partial x_i \partial t}\right) - \frac{M_i'}{h+\eta'}\frac{\partial}{\partial x_i}\left(\frac{\partial^2 \eta'}{\partial x_j \partial t}\right)\right]$$

where, DM_j is the momentum dissipation term after wave breaking, it is expressed as :

$$DM_j = \frac{\partial}{\partial x_i}\left[-\nu\frac{\partial M_i'}{\partial x_i} + \frac{-\overline{M_i' M_j'} + \overline{M_i'' M_j''} - \overline{M_i'' M_j''}}{h+\eta'}\right] \tag{11}$$

From eq.(11), we see that the momentum dissipation after wave breaking and the Reynolds stress generated by wave breaking become a governing factor in wave-induced currents because the right hand side of eq.(11) includes the same term which appears in driving force and lateral mixing terms for mean currents. DM_j is evaluated by eq.(12) after Sawaragi et al.(1974).

$$DM_j=\frac{\partial}{\partial x_i}\left[K_i^*\frac{\overline{M_i'M_j'}}{(h+\eta')^2}\cdot(h+\eta')\right] \tag{12}$$

where, the momentum dissipation coefficient K_i has a value of 0.4 ~ 0.6, the 5th and 6th term in the left hand side of the eq.(10) indicates the effects of wave-induced interaction. The effect of the bottom friction is neglected in the wave equation.

3. NUMERICAL MODEL

The implicit method was used, then each time and space were taken as 2-level and central difference scheme respectively. The solution was obtained effectively by the Gauss Seidel interaction method with the A.D.I. double sweep algorithm.

To obtain the numerical solution of waves, the following linear offshore and onshore boundary condition are applied.
At offshore :

$$\eta_t'=a\cdot\sin[\sigma\cdot\Delta t\cdot n+k\cdot\Delta s(i-iE)] \tag{13}$$

where, **a** = amplitude of waves
$\sigma = 2\pi/T$
n = time step
k = wave number
ΔS = interval of grid

and

$$M_t'=-[\sqrt{g/h}\cdot\eta_t']\cdot h=-\sqrt{g\cdot h}\cdot\eta_t' \tag{14}$$

At onshore :

$$M'=(1-r)\sqrt{gh}\cdot\eta'$$
$$\eta'=-M'/\sqrt{gh} \tag{15}$$

where, r is a reflection coefficient. In order to determine the breaking point, the applicabirity of breaking criteria proposed by some investigators to the river mouth where strong wave-current interaction takes place are examined experimentally. Then we used the most adequate criteria in the calculations.

In the computation of mean currents, open boundary conditions at the river mouth(iS) and offshore(iE) are applied. They are given as follows :

$$\text{Open Boundary} \quad \begin{cases} M_{o\,is-1,j} = \text{River discharge}, & M_{o\,iE+1,j} = M_{o\,iE,j} \\ \bar{\eta}_{is-1,j} = \bar{\eta}_{is,j}\ , & \bar{\eta}_{iE+1,j} = 0 \end{cases} \tag{16}$$

As mentioned above, by calculating the waves and currents alternately,the effect of wave-current interaction is considered in waves and currents.

4. 2-D EXRERIMENTS AND NUMERICAL CALCULATION ON WAVE-CURRENT INTERACTION.

Littoral currents and water level around a river mouth are mainly affected by the relative strength of incident waves and river discharges. To investigate the effect of river mouth depth and run off on wave transformations and water levels we performed hydraulic experiments for wave-current interaction in a two dimensional wave tank. Then the results obtained by the experiments were compared with numerical results.

1) Experimental procedure and condition

The experiment was performed in the 2-D wave basin which has a 1/20 slope connected to river channel, 65cm in width and 23m in length, and the river discharge was supplied from the weir tank located in the upper part of the river channel. Fig.2 shows the experimental wave basin.

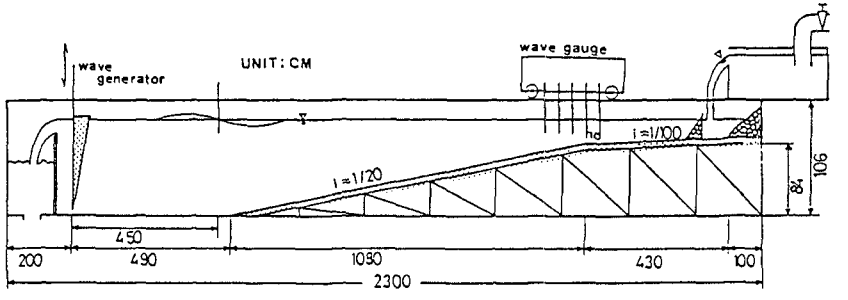

Fig.2 Wave tank and experimental set up

The wave height was measured at the intervals of 10cm by the capacitance type wave gauges equipped on platform car. Data were recorded by a data recorder with analog signals, and the data was analysed by the digital computer after the A-D conversion in 1/1000 sec interval.

We determined the experimental conditions by using a dimensional analysis. The experimental parameters are given as eq.(17).

$$\phi_3(h_o/H_o, q/(h_o\cdot\sqrt{gh_o}), i, H_o/L_o, x/L_o) = 0 \qquad (17)$$

where h_o : water depth in river mouth
H_o : wave height in offshore
T : wave period
i : slope
q : discharge per unit width
L_o : wave length in offshore
x : distance from the river mouth

Table 1 shows the experimental condition

Table 1 Experimental conditions

CASE		q_o	h_o' cm	h_o cm	H_o cm	T sec	h_o/H_o	H_o/L_o
A W	1	0	10.7	10.7	8.2	1.39	1.67	0.02
	1S	0.041	9.0					
	1L	0.069	7.7					
	2	0	6.7	6.7	6.6	1.40	1.00	
	2S	0.037	5.7					
	2L	0.062	5.1					
	3	0	6.7	6.7	8.3	1.66	0.83	
	3S	0.037	5.9					
	3L	0.062	5.4					
B W	1	0	10.7	10.7	5.6	0.89	2.00	0.05
	1S	0.041	9.0					
	1L	0.069	8.5					
	2	0	10.7	10.7	10.5	1.11	1.00	
	2S	0.041	9.0					
	2L	0.069	7.6					
	3	0	10.7	10.7	13.8	1.35	0.77	
	3S	0.041	9.1					
	3L	0.069	7.6					

$q_0 = q/(h_0'\sqrt{gh_0'})$, h_0': water depth at the river mouth from S.W.L.

2) Influence of the depth at river mouth affecting on wave transformation

Fig.3 shows the relationship between wave breaking depth and break height. In the figure, NATU-A and NATU-B are the results in the uniform slope beach which have not river channel.

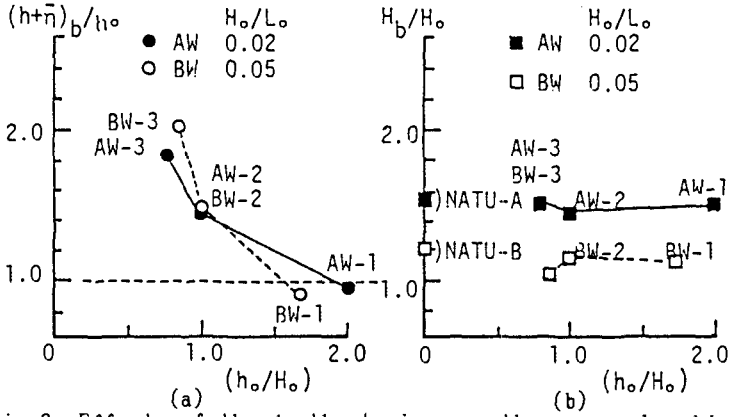

Fig.3 Effects of the depth at river mouth on wave breaking conditions

In Fig.3(b), we see that the break height is not affected by the depth at river mouth. The cases AW-1 and BW-1 of Fig.3(a) show that forced wave breaking took place in the river channel.

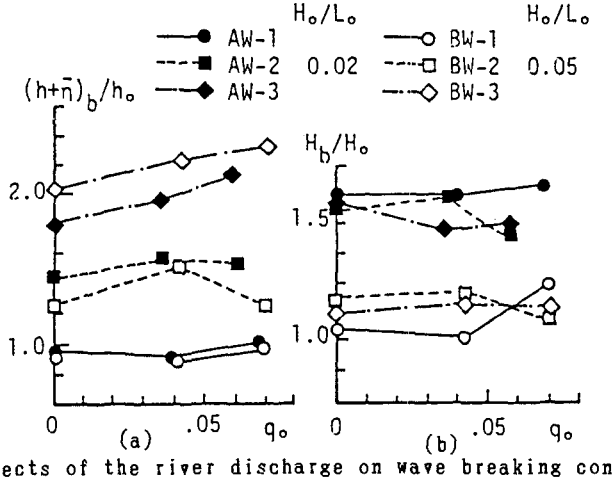

Fig.4 Effects of the river discharge on wave breaking conditions

3) Influence of currents on wave tranformation

Fig.4 shows the relation between the river discharge(q_o) and breaking condition. The results shown in Fig.4(a) show a tendency that the breaking point moves to offshore with increasing river discharge. However, in Fig.4(b), we see that the break height is not affected by the river discharge.

We also examined the applicability of wave breaking criteria to the coexistence field of waves and currents. Fig.5 illustrates the comparison of breaking heights measured by the experiment and the breaking criteria by Miche(eq.(18)) and Goda(eq.(19)).

$$H_b/L_b=0.142\ \tanh(2\pi h_b/L_b) \tag{18}$$

$$H_b/L_o=0.17\{1-\exp[-1.5\ \frac{\pi h_b}{L_o}(1+15\ \tan^{4/3}\beta)]\} \tag{19}$$

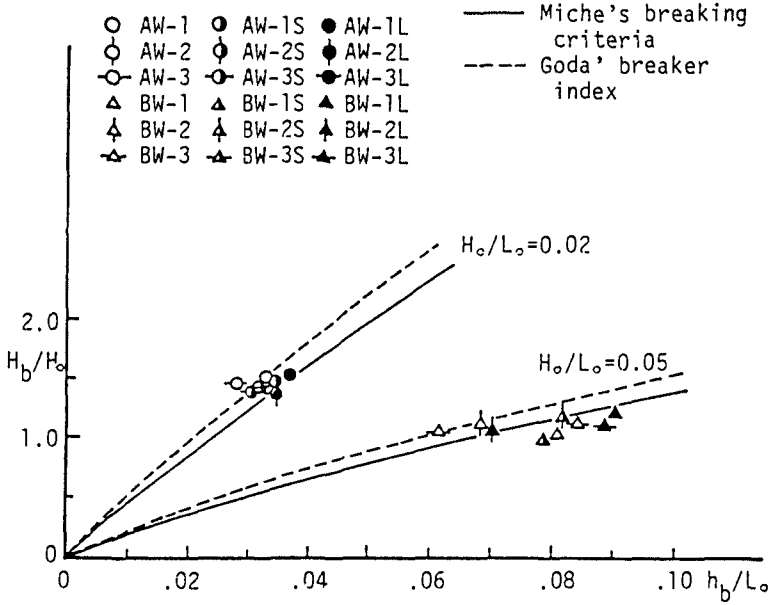

Fig.5 Comparisons between measured and predicted wave breaking conditions

From this figure, experimental results coincide well with both criteria regardless of the wave steepness.

4) Comparisons of numerical and experimental results.

In the preliminary calculations, it is found that the attenuation coefficient of the momentum after wave breaking K_1 in eq.(12) of 0.6 seems to be the most adequate for the prediction of wave transformation on a natural beach. So, we use this value together

with the Goda's breaking criterion in the following calculations.

Fig.6 shows the comparisons of measured and calculated wave heights and mean water levels in the cases where incident waves broke outside the river mouth (Cases AW-3 and AW-3L). Calculated results are shown by thick lines and measured results are indicated by circles. In the figure, calculated results based on the linear model (Sawaragi et al.(1984)) are also shown by thin lines. x = 0 at the horizontal axis corresponds to the location of the river mouth.

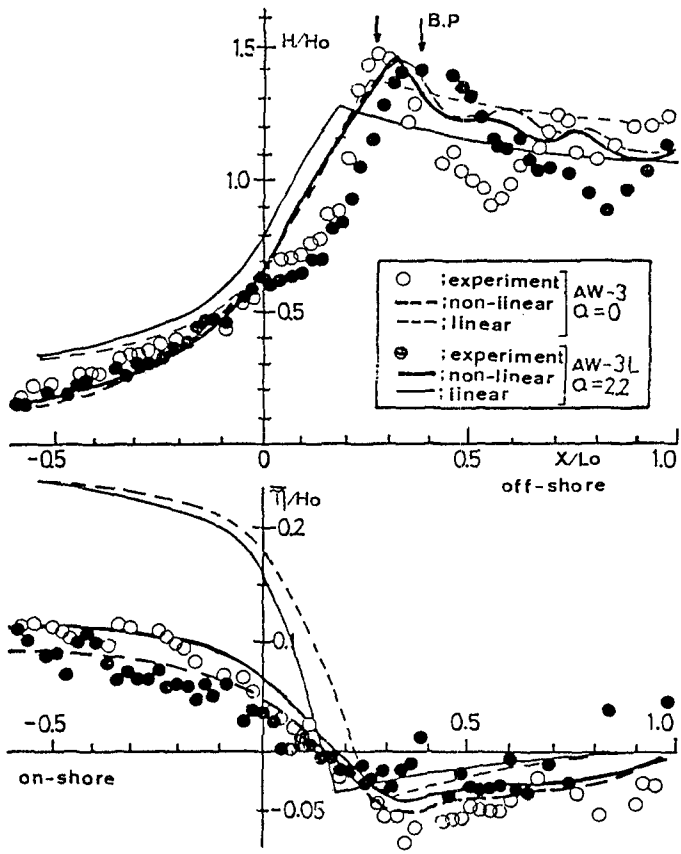

Fig.6 Comparisons between calculated and measured wave heights and mean water levels in the cases where waves broke outside the river mouth

It can be seen that although there are some discrepancies between the calculated and measured wave heights in the region of $0<x/L_o<0.3$, the calculated wave heights and mean water levels by the present model show good agreements with the experimental results regardless of the river discharge when compered with the predicted results by the linear model. Especially, the calculated mean water levels by the linear model give about two times larger estimetes of the experimental results.

Fig.7 illustrates time series of the surface displacements calculated 40cm outside and inside of the river mouth in the case of AW-3. From this figure, it is found that almost steady uniform waves are calculated after the generation of 6th wave.

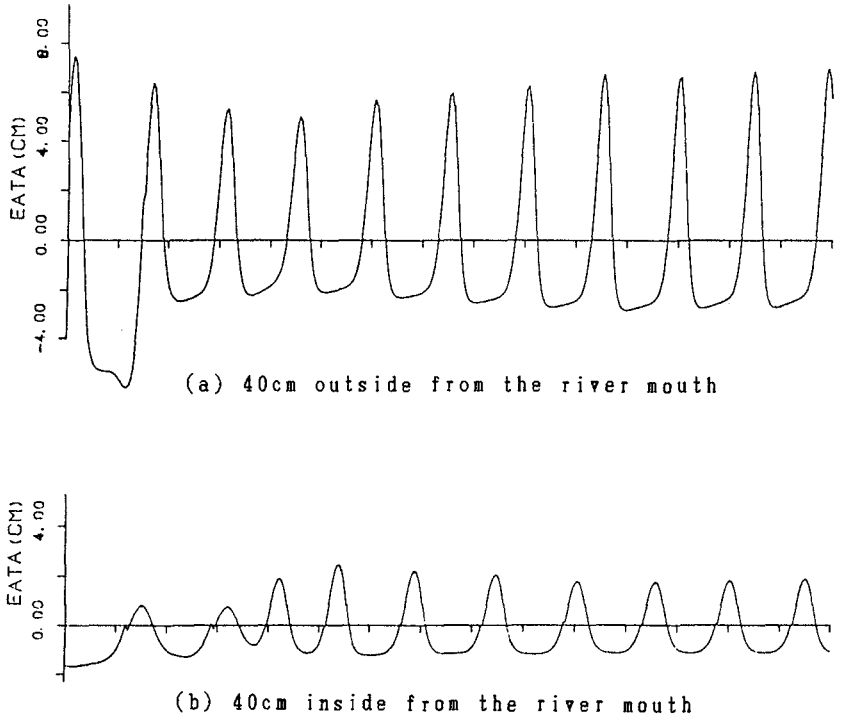

Fig.7 Simulated time series of surface elevation incide and outside of the river mouth

Fig.8 shows the comparisons of measured and calculated wave heights and mean water levels in the cases where the forced wave breaking took place in a river channel (AW-1 and AW-1L).

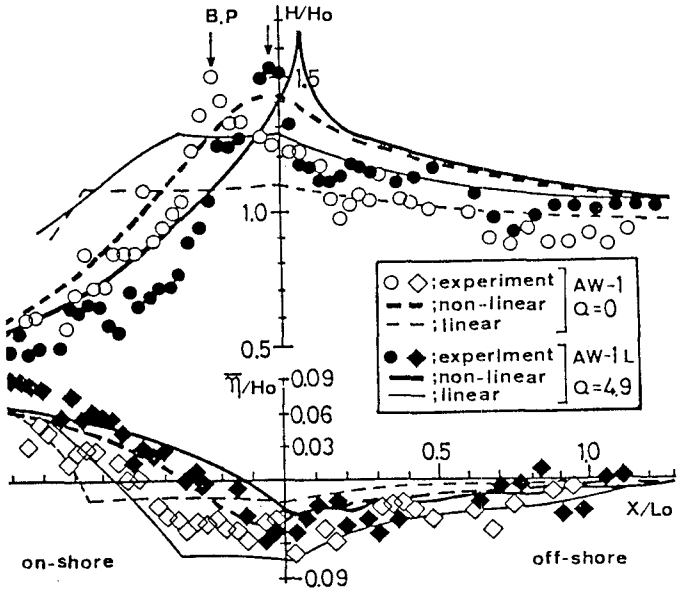

Fig.8 Comparisons between calculated and measured wave heights and mean water levels in the cases where waves broke in the river channel

In these cases, calculated wave heights by the present model no longer show good agreement with the experimental results. This disagreement comes from the difficulty in the determination of wave breaking condition in the river channel where the bottom slope is quite gentle. However, we can predict the closer experimental wave heights and mean water level by the present model than by the linear model.

As mentioned above, the linear model based on the linear wave theory overestimates the dis-placement of mean water level. On the contrary, the present model based on the non-linear wave theory offers good estimates of mean water level.

Fig.9 indicates the comparison between the excess monentum fluxes in the linear model S_{xx} and in the present model P_{xx} in thje case of AW-3. From this figure, the ratio of P_{xx}/S_{xx} becomes about 0.6 at around the break point and this results coincides with the results reported by Sawaragi et al.(1985).

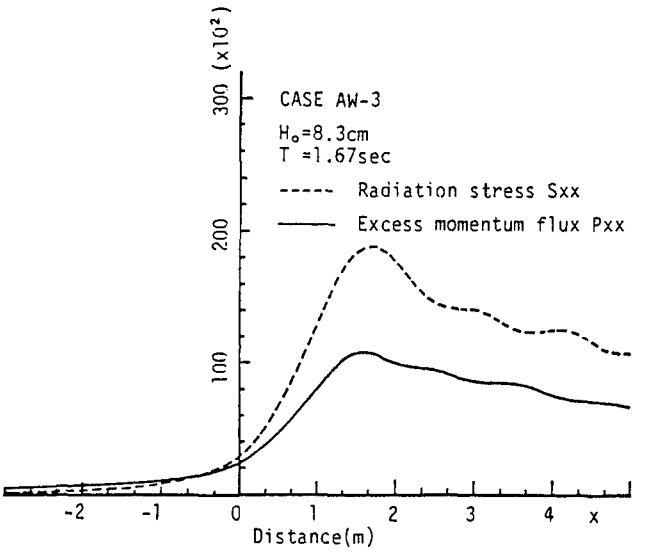

Fig.9 Comparison of P_{xx} and S_{xx}

6. CONCLUSION

In this paper, the authors applied Boussinesq type equations to simulate the wave field including wave breaking and wave-current interaction around a rivermouth.

The results simulated by the numerical model based on non-linear dispersive wave theory show good agreements with the experimental results in shoaling and wave-current interaction, and also in the prediction of wave breaking points and breaking heights it exhibits an improved results than those predicted by the linear model based on the linear wave theory.

REFERENCES

Abbott, M.B., H.M. Petersen and O. Skovgaard (1978) : On the numerical modelling of short waves in shallow water, J. Hyd. Res., Vol.16, No.3, pp.173-204.

Haugel, A. (1980) : A numerical model of storm waves in shallow water, Proc. 17th Conf. Coastal Eng., pp.1057-1072.

Haugel, A. and Ph. Pechon (1982) : Applications of a numerical shallow water wave model, Proc. 12th Conf. Coastal Eng., pp.846-861.

McCowan, A.D. (1982) : Numerical short wave modelling - an evaluation, Abstructs 18th Conf. Coastal Eng., CapeTown, pp.411-412.

Peregrine, D.H. (1967) : Long waves on beach, J.Fluid Mech., Vol.27, Part 4, pp.815-827.

Sawaragi, T. and K. Iwata (1974) : On wave deformation after breaking, Proc. 14th Conf. Coastal Eng., pp.481-497.

Sawaragi, T., J.S. Lee and I. Deguchi (1984) : Numerical models about littoral currents and three-dimensional topographical changes around a river mouth, Proc. 31th Japanese Conf. on Coastal Eng., pp.411-415.(in Japanese)

Sawaragi, T., I. Deguchi and K.H. Kim (1985) : Energy loss and wave set-up due to breaking waves, Tech. Rep. Osaka Univ., Vol.34, No.1779, pp.329-338.

CHAPTER 98

TURBIDITY - SEDIMENTATION IN CLOSED-END CHANNELS

Chung-Po Lin[1], Jonathan W. Lott[2] and Ashish J. Mehta[3]

ABSTRACT: In order to investigate the mechanism by which turbidity currents cause sedimentation in closed-end channels such as pier slips or residential canals, a laboratory investigation using fine-grained sediments was carried out. Two similar flume systems were used, each consisting of a main channel carrying sediment-laden flow and an orthogonally placed closed-end channel with a gate at the entrance. Characteristics of the turbidity current and sediment deposition in the closed-end channel were investigated following gate opening. Behavioral similarities between turbidity current and non-settling gravity currents were observed. Several properties, e.g. suspension concentration, showed exponential-type decay with distance. The ratio of sediment settling velocity to the densimetric velocity was found to be a useful parameter for comparing different test results. A relationship for estimating the sediment influx through the entrance is presented.

INTRODUCTION

Sedimentation problems in closed-end channels such as pier slips, tidal docks and residential canals have been reported extensively (Lin, 1987). In a detailed investigation carried out in pier slips at the Mare Island Naval Shipyard, San Francisco Bay area, Jenkins et al. (1982) showed in quantitative terms that the rate of sedimentation in the slips was measurably higher than that in the main channel to which the slips were connected. In general, mass transport associated with the tidal prism, wind-driven circulation and density-induced currents are mechanisms by which sediment enters the slip. Turbidity current is essentially driven by the difference in density between the sediment-laden outside waters and the relatively quiescent and sediment-free waters in the slip. The contribution to the total rate of sedimentation from this mechanism varies with the physical conditions; where tides are weak or when the sediment concentration outside is high, turbidity current becomes important as the source of sediment in the slip.

[1]Ph.D. Candidate, Coastal and Oceanographic Engineering Department, University of Florida, Gainesville, FL 32611.

[2]Research Engineer, Laboratoire National d'Hydraulique, Electricité de France, Chatou, France.

[3]Associate Professor, Coastal and Oceanographic Engineering Department, University of Florida, Gainesville, FL 32611.

In the presently described laboratory study, only fine-grained sediments were used. The transport of such sediments, particularly where the tides are weak, as in much of Florida, is predominantly episodically controlled. There, fair weather suspended sediment concentrations are typically quite low, on the order of 5-20 mg/L. Therefore the major contribution to slip sedimentation occurs mainly during storms, when concentrations increase by one or two orders of magnitude. Flume experiments were therefore designed with this characteristic of sediment transport in mind. Two conceptually similar flume systems were used, one at the Waterways Experiment Station (WES) of the U.S. Army Corps of Engineers, Vicksburg, Mississippi, and the other at the University of Florida's Coastal Engineering Laboratory (COEL).

A closed-end channel of length L and width B, orthogonally connected to the main channel, is shown in Figs. 1a,b. A turbidity front of instantaneous length x_f measured from the entrance (x=0) occurs. The mean depth of water is H above the horizontal bottom (z=0). The sediment-laden main channel flow is fully turbulent and vertically well-mixed. The fluid density there is $\rho_w + \Delta\rho_o$, where ρ_w is the clear water density and $\Delta\rho_o$ is the density increment due to suspended sediment. Immediately inside the entrance a gyre zone occurs in which circulation is driven by lateral flow shear at the entrance. The vertically mixed flow is weakly turbulent there, and the distance of influence of the gyre is limited, being of the same order as channel width B. Almost immediately inside the entrance, deposition of sediment commences and the suspension density is lower than that in the main channel. The density difference, $\Delta\rho_1$, is therefore characteristically lower than $\Delta\rho_o$. It was found that for most of the front-related phenomena observed, $\Delta\rho_1$ was better representative of the driving force than $\Delta\rho_o$. Beyond the gyre the flow is predominantly viscous and stratified, with a clearly identifiable interface (z=η). Three characteristic features of the forward portion of the front are the nose ($z=h_1$), head (h_2) and neck (h_3).

Initially the gate was closed with equal water levels on both sides, but without sediment in the closed-end channel. The objective was to investigate both the behavior of the front and the characteristics of sediment deposition. Opening the gate to allow the turbidity current to move in is, in a sense, analogous to the generation of a relatively high concentration front during a storm, over very low concentration ambient conditions representing fair weather. In examining the physical phenomena, the focus was on understanding the basic transport mechanisms, without explicit consideration for prototype to model scaling. For the sake of reference, however, it may be noted that, given typical prototype pier slips or residential canals, the selected flume dimensions (noted later) could be considered to represent a prototype to model ratio on the order of 1:20 to 1:40.

A characteristic feature of the turbidity front is that given a sufficiently long channel, front motion generally slows down, and is ultimately arrested at a distance where the finest particles in suspension (at the entrance) settle out. The fluid density decreases up to the nose, where it almost equals that of clear water. A steady state exists, and there is an overall balance of forces involving the

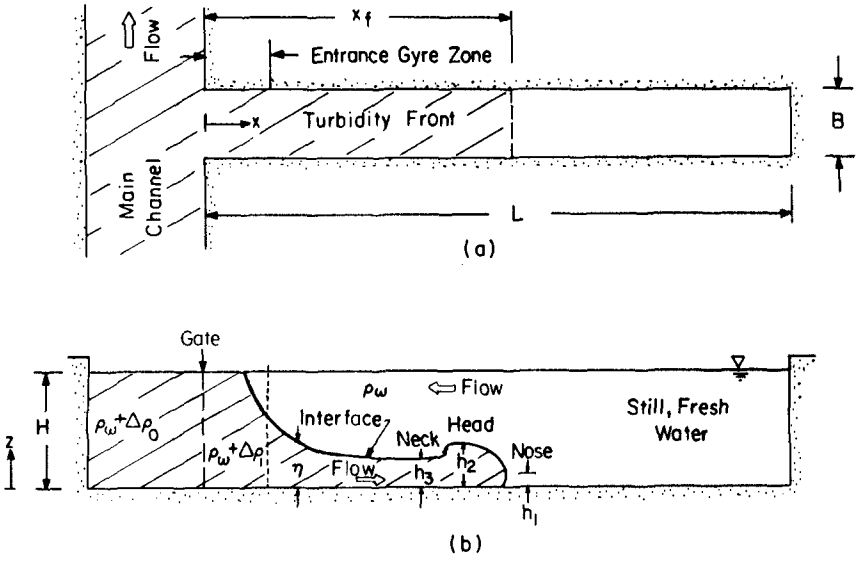

Fig. 1. Turbidity Front in a Closed-End Channel: a) Plan, b) Side View.

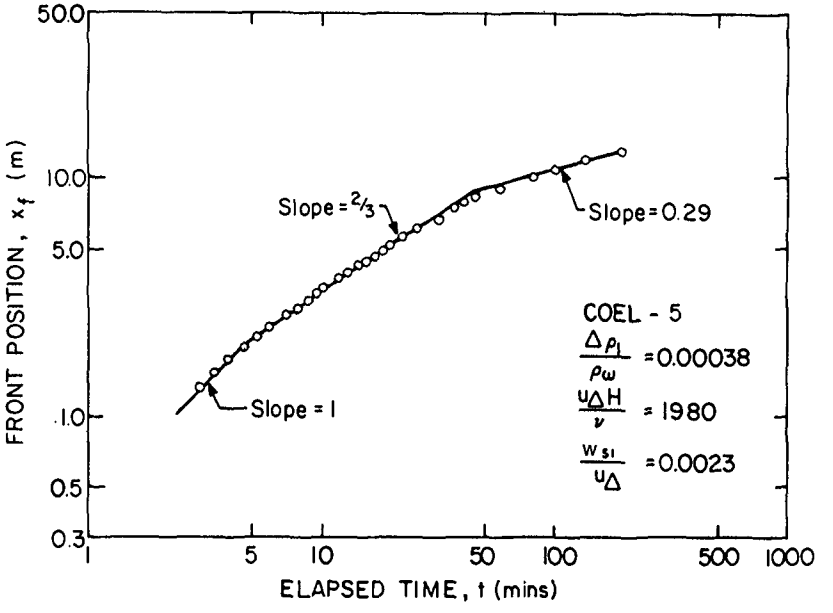

Fig. 2. Front Position with Elapsed Time after Gate Opening, Test COEL-5.

total density difference, water level set up in the channel and bottom friction. However, due to local force imbalance at different elevations above the bottom, sediment-laden water continues to enter through the lower half of the water column at the entrance, while an equal volume per unit time of almost sediment-free water leaves from the upper half.

METHODOLOGY

The three significant aspects of the phenomenon examined were: 1) the transient behavior of the propagating front after gate opening, 2) characteristics of the stationary front at steady state, and 3) rate of sedimentation. The scope of this paper permits only a brief presentation; details have been provided elsewhere (Lin and Mehta, 1986; Lott, 1986; Lin, 1987). In order to facilitate the investigation, three approaches were selected: 1) dimensional analysis for organizing the presentation of data, 2) numerical modeling to examine the transient and stationary front behaviors, and 3) simple analytic approaches to elucidate the stationary front behavior. Salient aspects are summarized below.

Dimensional Analysis

Dimensionless groups were developed for treating data for a number of different characteristics for the propagating as well as stationary fronts (Lin, 1987). One example will illustrate the point. The front speed, u_f, can be expressed as

$$\frac{u_f}{u_\Delta} = f\left(\frac{x}{H}, \frac{B}{H}, \frac{u_\Delta H}{\nu}, \frac{w_s}{u_\Delta}\right) \tag{1}$$

where ν is the kinematic viscosity of the fluid, and w_s is the sediment settling velocity. Furthermore, $u_\Delta = (g\ H\ \Delta\rho_1/\rho_w)^{1/2}$, where g is acceleration due gravity, is recognized as the densimetric velocity. Equation 1 indicates that the dimensionless front speed should depend on the front position, x/H, channel aspect ratio, B/H, densimetric Reynolds number, $Re_\Delta = u_\Delta H/\nu$, and the relative settling velocity, w_s/u_Δ. This relationship is analogous to the result for the speed of the saline front advancing against river flow having a velocity, u_r. In that case, w_s is replaced by u_r (Keulegan, 1966).

Numerical Modeling

A two-dimensional (x,z) time-varying mathematical model was developed to predict the vertical and longitudinal suspension concentration fields, based upon a solution of the equation of flow momentum, continuity and sediment mass conservation. Unlike the case of salinity intrusion which depends, amongst other factors, on the imposed river flow velocity, flow circulation in the present case is due solely to the imposed density difference between the main channel and the closed-end channel. The equation of momentum is therefore inherently coupled with that of sediment mass conservation; hence these equations, together with that of continuity, must be solved simultaneously. This was done using a finite-difference scheme with

appropriate fluid mechanical and sediment-related surface, interface and bottom boundary conditions, as well as no-flow condition at the closed-end, and constant suspension concentration at the entrance.

The coefficients in the model requiring specification were: 1) longitudinal and vertical momentum and mass diffusion coefficients e_x, e_z and ε_x, ε_z, respectively, and Manning's n for bottom roughness. In addition, two deposition-related parameters, the settling velocity, w_s, and the critical stress for deposition, τ_{cd} were required. The latter is equal to the bed shear stress, τ_b, below which all initially suspended sediment (having uniform properties) eventually deposits, while for all τ_b greater than τ_{cd} no deposition occurs. Resuspension of the deposit did not occur, hence was not considered.

The model was tested for stability and convergence. Spatial increments Δx = 0.5 m and Δz = 1 cm, and time-step Δt = 0.15 sec were selected for all test simulations. Data from test COEL-4 were used for model calibration. Some model applications are presented here. By invoking the Reynolds analogy, $e_x = \varepsilon_x$ and $e_z = \varepsilon_z$ were assumed. Since the relatively low concentration flow was laminar everywhere except in the small gyre zone near the entrance, e_z was selected to be equal to the kinematic viscosity of water, 10^{-6} m^2/sec. A value of 5 x 10^{-3} m^2/sec was found to be adequate for e_x. These values of the coefficients, applicable to homogeneous flows, were modified in the model for representing stratified flows, through appropriate formulations involving the gradient Richardson number (Lin, 1987). Manning's n was selected to be 0.030, which was close to that obtained from the Moody diagram. The median (by weight) settling velocity, w_s, of fine-grained sediments varies with sediment concentration; hence its value in the channel is space and time-dependent. Thus, for example, within the concentration range of interest it was found that $w_s = 0.000001C^{0.78}$ for kaolinite, where w_s is in m/sec and concentration, C, is in mg/L. This empirical relationship was derived from an independent set of tests in a settling column (Lott, 1986). It was found practical to select a constant value of w_s for each test, for simulation purposes. The value, w_{s1}, representing the condition of the entrance, was chosen. An evaluation of kaolinite deposition data in the channel yielded a value of 0.13 N/m^2 for the critical stress, τ_{cd}.

Analytic Development

The occurrence of a stationary front permits, for that purpose, a simplification of the governing equations, which can be solved to yield approximate results. An advantage these offer over numerical results is that they demonstrate, via comparison with data, the significance of the more important forces in explaining observations related to the flow field and the suspension concentration field. Space does not permit presentation of the relevant derivations which are given elsewhere (Lin, 1987). Illustrative results are given here.

Flow Velocity: A stationary front occurs under a balance between gravity and viscous forces. The length of the stationary front can be assumed to be considerably greater than the still water depth, H. The water layer above the front is considered to be sediment-free; all the

sediment being confined to the lower layer, with a uniform concentration. Under these conditions, momentum diffusion can be shown to be much more important in the vertical than in the horizontal direction. The closed-end causes a water surface slope to be set up, with the hydrostatic head balancing the excess pressure due to the density gradiant and the flow-induced bottom shear stress. In addition, inflow is balanced by outflow at every flow cross-section. Given the outflow velocity, u_s, at the surface, the following equations for the vertical profiles of the horizontal velocity, u, are obtained in the two layers:

$\xi < \zeta < 1$:

$$\frac{u}{u_s} = \frac{(1.5 - 0.375\xi)\,\zeta^2 - (3 - 0.75\xi)\,\zeta + 1}{-0.5 + 0.375\xi} \tag{2}$$

$0 < \zeta < \xi$:

$$\frac{u}{u_s} = \frac{(\zeta/\xi)^3 + (-3+1.5\xi^2-0.375\xi^3)(\zeta/\xi)^2 + (3-3\xi+0.75\xi^2)(\zeta/\xi)}{-0.5 + 0.375\xi} \tag{3}$$

where $\zeta = z/H$ and $\xi = \eta/H$.

Concentration Below Interface: The longitudinal variation of the depth-mean concentration in the lower layer, $\bar{C}_b$, can be examined by solving the steady state sediment mass transport equation. As a first order approximation only two terms need be considered: $u\partial C_b/\partial x$ and $w_s \partial C_b/\partial z$. Equating these terms amounts to balancing advective transport with gravitational settling. Experimental observations indicated an exponential-type decay for u and for w_s with distance (Lin, 1987). Therefore, $w_s = w_{s1} \exp(-\beta_1 x)$ and $u = u_1 \exp(-\beta_2 x)$ may be assumed, where subscript 1 for w_s and u refers to conditions at the entrance, and β_1, β_2 are empirical coefficients. Without presenting further details, it suffices to state the following resultant relationship for $\bar{C}_b$:

$$\frac{\bar{C}_b}{\bar{C}_{b1}} = \exp\left[-\beta \left(\frac{w_{s1}}{u_\Delta}\right)\left(\frac{x}{H}\right)\right] \tag{4}$$

where β depends on sediment properties. Investigations of lock exchange flows involving salinity-induced gravity currents suggest $\beta > 4$ (Lin, 1987).

Sediment Influx: The sediment influx rate at the entrance, $S = u_1 \bar{C}_1$, where $\bar{C}_1$ is the depth-mean concentration at the entrance. Experimental observations indicate that shortly after gate opening the flow velocity, u_1, approaches a constant value (Gole *et al.*, 1973; Lin, 1987). Furthermore, both the initial front speed, u_{f1}, and u_1 depend on u_Δ. Thus, increasing u_Δ implies increasing u_{f1} and u_1; in fact observations indicate $u_{f1} \simeq 0.5\, u_\Delta$. Likewise, $u_1 = \alpha u_\Delta$ may be assumed, where α is a proportionality constant. Therefore $S = \alpha u_\Delta \bar{C}_1$. Expressing $\Delta\rho_1$ in terms of $\bar{C}_1$, it can therefore be shown that

$$S = \alpha\left[\frac{gH}{\rho_w}\left(1 - \frac{1}{G_s}\right)\right]^{1/2} \bar{C}_1^{\,3/2} \qquad (5)$$

where G_s is the specific gravity of the sediment. It is interesting to note that given the sediment-type and water depth, S is proportional uniquely to the 2/3 power of sediment concentration at the entrance.

EXPERIMENTS

The dimensions of the closed-end channels at WES and COEL are given in Table 1. Also included are the imposed depth-mean concentration, C_o, in the main channel and the corresponding fluid density difference, $\Delta\rho_o$. Hydraulic arrangements were made to run each test for comparatively long durations (Lin, 1987). A total of 13 tests were carried out at WES and 14 at COEL. The longest test duration was 276 min in WES-13. Some difficulties were encountered in the WES tests in maintaining a constant water temperature during a test, owing to changes in the ambient air temperature. At COEL the flume was placed in a temperature-controlled environment. The test-mean temperature at WES ranged from 15.1 to 22.4°C, and at COEL from 18.9 to 26.7°C. In some tests, minor oscillations in otherwise steady flow speed and in suspension concentration in the main channel unavoidably resulted in data scatter.

Table 1. Summary of Experimental Conditions at WES and COEL

Flume	L (m)	B (m)	H (cm)	C_o (g/L)	$\Delta\rho_o \times 10^{-5}$ (g/cm^3)
WES	9.1	0.23	5.0-12.7	58-1878	3.4-114.7
COEL	14.7	0.10	8.0-10.6	250-3746	14.0-229.0

Seven fine-grained sediments together covering a wide range of physical and physico-chemical properties, were used; some cohesive and others nearly non-cohesive. The cohesive materials were flocculated, at fairly low salt concentrations in the fluid (Lin, 1987). Cohesive materials included kaolinite (median grain size 1 μm) and Cedar Key mud (2 μm). The others were flyash I (14 μm), flyash II (10 μm), flyash III (14 μm), Silica flour (7 μm) and Vicksburg loess (18 μm).

RESULTS

Front Characteristics

As in the case of the propagating front, for instance, of a salinity-induced gravity current, three distinct phases are found to occur during the movement of a turbidity front. These are the initial adjustment phase, the inertial phase and the viscous phase. These are

shown for COEL-5 (using kaolinite) in Fig. 2, in which the front position, x_f, is plotted against elapsed time after gate opening. The three phases are marked by lines of different slopes. During the first phase, of unit line slope, the front propagated at a constant speed, being motivated by the initial density gradient between the main and closed-end channels. During the second phase (line slope 2/3) inertia and gravity forces dominate, with the front speed, dx_f/dt, being proportional to -1/3 power of the elapsed time. For gravity currents, this -1/3 power dependence has been demonstrated both theoretically and experimentally (Rottman and Simpson, 1983). In the final phase, gravity and viscous forces entirely control front movement. The slope of 0.29 is slightly higher than 1/5 observed in the case of a gravity current, partly because of the effects of thermal gradients during this test (Lin, 1987).

In several tests, the first phase was too short to be recorded. Furthermore, the point of transition from the second to the third phase was found to be strongly dependent upon the dimensionless settling velocity, w_{s1}/u_Δ. Thus, for example in COEL-5, characterized by $w_{s1}/u_\Delta = 0.0023$, transition occurred at about 400 min. after gate opening, while in COEL-8 (using flyash III), with $w_{s1}/u_\Delta = 0.0208$, transition occurred at about 50 min. Thus, in the latter case, the relatively large particles settled out rapidly, leaving behind a slow moving, very fine particle suspension influenced by viscous drag.

Dimensional analysis suggested that the dimensionless initial front speed u_{f1}/u_Δ, would possibly depend upon the densimetric Reynolds number, Re_Δ, and the channel aspect ratio, B/H. Data plotted in Fig. 3 from all WES and COEL tests show a fair degree of scatter, but no clear trend of dependence of u_{f1}/u_Δ on either Re_Δ or B/H. Part of the reason for the scatter is believed to be the influence of the entrance gyre zone on front propagation. The gyre length in the x-direction was in the range of 0.2-0.4 m in WES tests and 0.1-0.2 m in COEL tests. Therefore, the speed at x=1 m in WES tests and 0.75 m in COEL tests, rather than at x=0, was conveniently selected as the initial front speed. Notwithstanding the data scatter problem, the mean value of u_{f1}/u_Δ is observed to be 0.43, which is fairly close to the value 0.46 obtained by Keulegan (1957) for salinity currents. A value of 0.50 is obtained theoretically (Yih, 1965). Since the effect of sediment settling is much less significant than that of the density gradient at the beginning, the correspondence between gravity and turbidity currents in this respect is not surprising.

In Fig. 4, the ratio of front nose height to head height, h_1/h_2 is plotted against the local head Reynolds number, $Re_h = u_f h_2/\nu$, for COEL tests (no data were collected at WES for this purpose). A trend of increasing h_1/h_2 with decreasing Re_h is evident. In other words, as might be expected, with increasing viscous drag relative to inertia, the nose becomes blunt, and nose height becomes greater relative to that of the head. In addition to COEL data, those on different types of gravity currents obtained from five other investigations have been included in Fig. 4 (Lin, 1987). The data of Lawson (1971) are shown by dashed lines indicating upper and lower bounds. These data, including those of Lawson's which are for gravity current in air, are observed to be entirely consistent with those from the present tests.

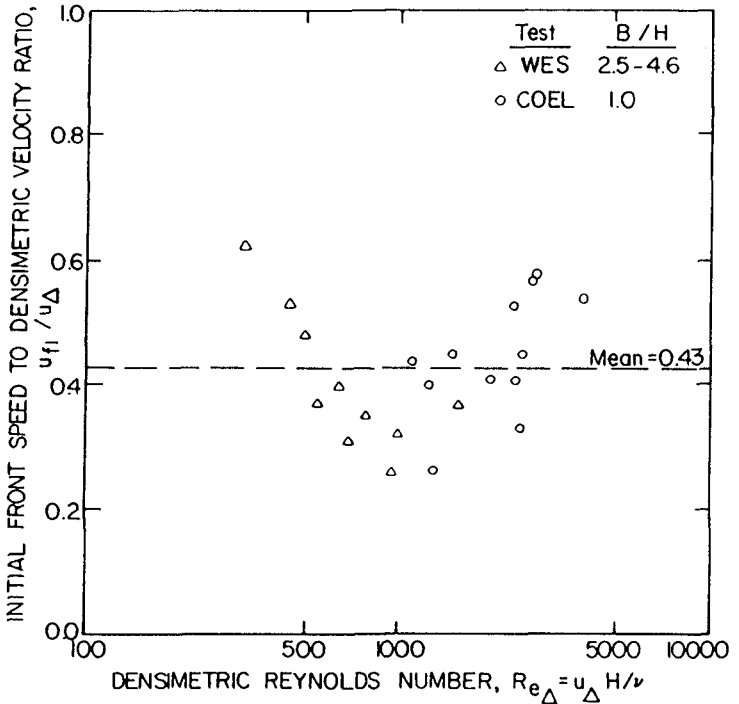

Fig. 3. Dimensionless Initial Front Speed against Densimetric Reynolds Number.

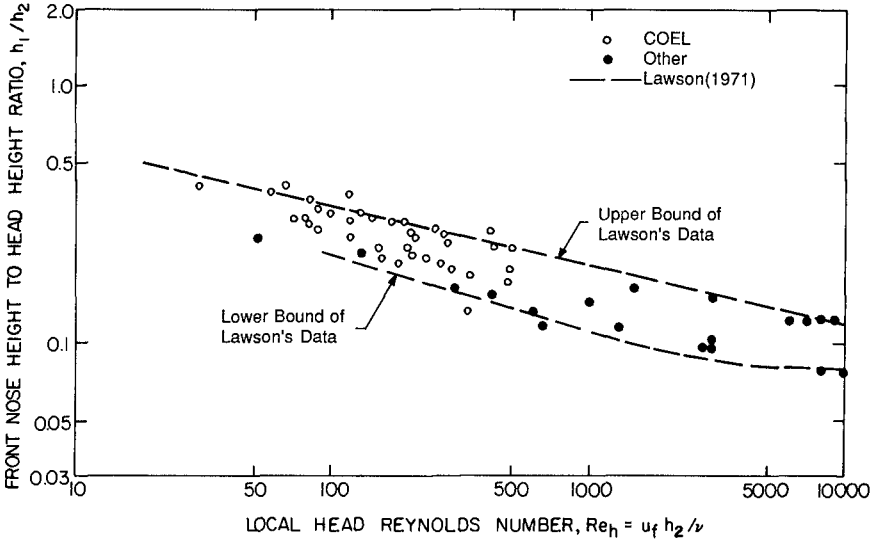

Fig. 4. Front Nose Height to Head Ratio against Local Head Reynolds Number.

Results presented by Lin (1987) indicate that the ratio of front head height to neck height, h_2/h_3, independent of the local neck Reynolds number, $Re_n = u_f h_3/\nu$, with a mean of 1.30. For salinity data at somewhat higher Reynolds numbers, Keulegan (1958) obtained a similar result with a mean of 2.08.

Velocity Profiles

For illustration, only results on the vertical velocity profiles at steady state, corresponding to a stationary front, are presented here. In Fig. 5, the dimensionless horizontal velocity, $u/|u_s|$ is plotted against the corresponding dimensionless elevation, $\zeta = z/H$. The data are for COEL-6 at x=1.8 m. Comparison has been made with numerical results as well as with analytically derived Eqs. 2 and 3. The numerical result is not affected by the boundary layer effects associated with the side walls of the channel. The data were obtained via a dye injection procedure such that the results were influenced both by the wall boundary and by lateral secondary currents. Limitations of the analytic solutions were noted previously. Inspite of these evident differences, the agreement between measured data, numerical and analytic results may be considered to be acceptable. The numerical and analytic results satisfy the steady state continuity requirement of equal discharge both ways. Experimental data are inaccurate in this respect.

Concentration Profiles

In Fig. 6, suspension concentration at elevation z=0.7 cm at five horizontal locations in COEL-5 are plotted as a function of time. At each location this elevation was below the corresponding elevation of the front interface. At each location, the concentration rises from nil ahead of the front to an eventual steady state value. Numerical results compare reasonably well with the data.

In Fig. 7, vertical concentration profiles for COEL-5 are plotted at 67 and 90 min. after gate opening. Five horizontal locations have been included. Agreement between data and numerical results (at 130 min) appears to be acceptable. The total height of each profile corresponds to the thickness of the turbid lower layer at that position and time.

Both the exponential nature of concentration decay with distance and the influence of the dimensionless settling velocity, w_{s1}/u_Δ, on the concentration profile is apparent in Fig. 8, in which the concentration ratio, $\overline{C}_b/C_{b1}$ at steady state is plotted against x/H on semi-logarithmic coordinates. Data from seven tests using kaolinite have been included. The exponential nature of the profiles is apparent. Three lines represented by different values of w_{s1}/u_Δ have been shown. Line slope is observed to increase with increasing w_{s1}/u_Δ, as would be expected since, for a given u_Δ, increasing w_{s1} implies increasing rate of deposition of sediment from suspension. These w_{s1}/u_Δ values (indicated on the lines) were obtained by best fitting Eq. 4 to data using β=7. It can be shown that this value of β corresponds to the ratio $u_1/u_{f1} = 0.57$, which is close to the value, 0.70, obtained experimentally by Gole *et al.* (1973). These w_{s1}/u_Δ

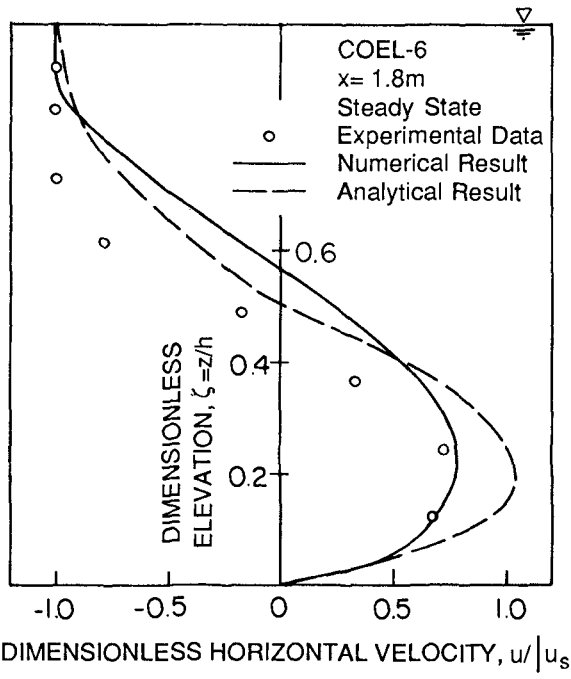

Fig. 5. Dimensionless Horizontal Velocity Profiles, Test COEL-6 at x=1.8 m.

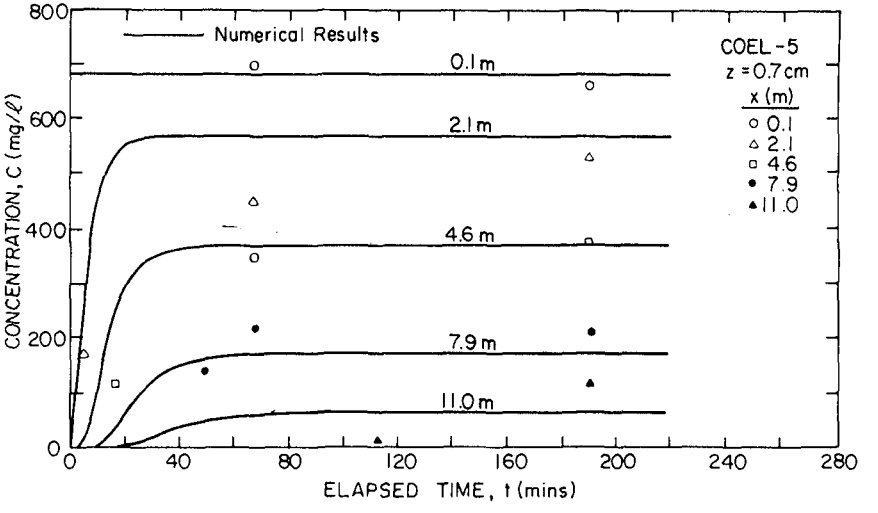

Fig. 6. Suspension Concentration at 0.7 cm Elevation for Five Locations as a Function of Elapsed Time after Gate Opening, Test COEL-5.

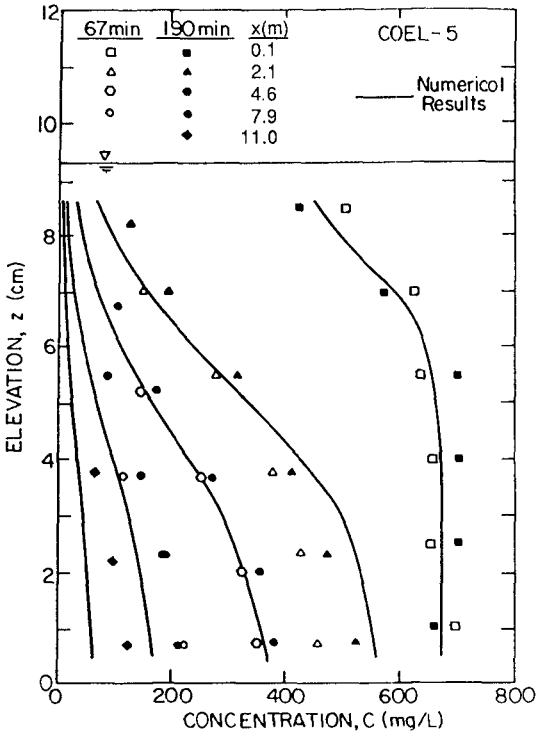

Fig. 7. Concentration Profiles at Steady State at Five Locations, COEL-5

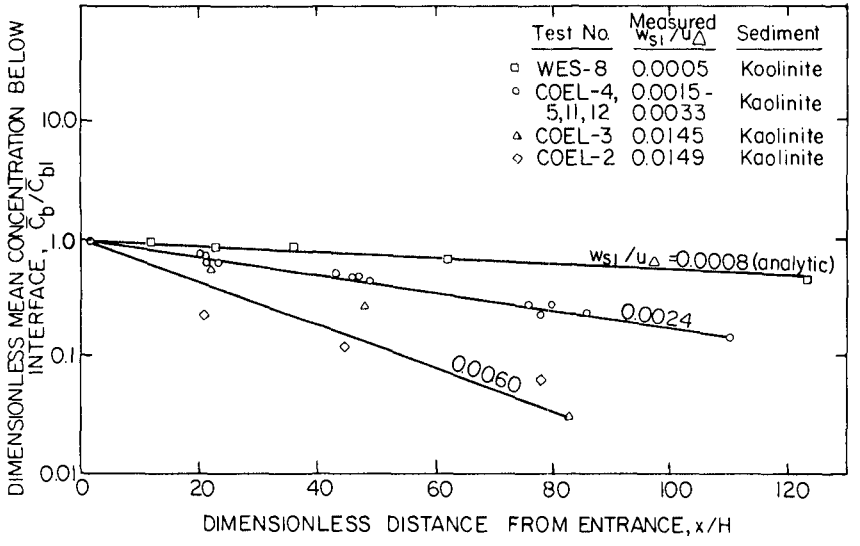

Fig. 8. Dimensionless Mean Conc.below Interface against Dist., Kaolinite

values differ from those based on measurement as given within the figure. The discrepancy increases with increasing w_{s1}/u_{Δ}, as a result of inherent limitation in applying Eq. 4 to data on sediment with a relatively large settling velocity. In such an event, for instance, the vertical concentration gradient becomes pronounced; hence the assumption of a uniform concentration, inherent in Eq. 4, is no longer reasonable.

Sediment Deposition and Influx

Sorting of sediment was characteristically observed in all tests in which relevant data were collected, with the grain size generally decreasing with distance from the entrance. Qualitatively, the same trend has been reported in prototype canals (Wanless, 1975). For nearly cohesionless sediment such as flyash, sorting measurably increased with increasing w_{s1}/u_{Δ}.

In Fig. 9, the rate of deposition, δ, is plotted against distance from the entrance for COEL-5. As would be expected, δ is observed to decrease rapidly with distance, once again suggesting an exponential decay. Agreement between measurement and numerical prediction is acceptable, except that there is a slight over-prediction.

Based upon the concept presented earlier, the rate of sediment influx, S, is plotted against entrance concentration, $\overline{C}_1$ in Fig. 10. A 3/2 power dependence of S on $\overline{C}_1$ is clearly evident in accordance with Eq. 5. Note that S represents a mean value, which was calculated by dividing the total deposited sediment mass in the channel by the test duration and the area of the lower half of the flow cross-section at the entrance. Since the turbidity front moved in fairly slowly during most of test duration except at the very beginning, S can be practically considered to represent the sediment influx rate as would occur at steady state. The coefficient 0.015 was calculated by selecting mean values of H = 8.8 cm and G_s = 2.55, for the twelve selected tests. The value α = 0.35 was empirically chosen, but this value can be shown to be consistent with the observations of Gole et al. (1973) that at steady state, the surface outflow velocity at the entrance is about 30% lower than the initial front speed (Lin, 1987).

CONCLUDING REMARKS

It is worthwhile noting in summary, that the turbidity current behaves generally in the same manner as a gravity current induced, for instance, by salinity, although there are evident differences, principally characterized by the ratio w_{s1}/u_{Δ}, a conveniently measurable parameter related to the turbidity current.

Although no attempt could be made in discussing model to prototype scaling problems because of evident reasons, it is noteworthy that by giving consideration to the basic fluid mechanical laws relating to the observed phenomena, a framework for future prototype investigation of a comprehensive nature is believed to have been established. Comparison may be made here between the present study and similar, very useful, previous investigations in laboratories on salinity-driven gravity currents.

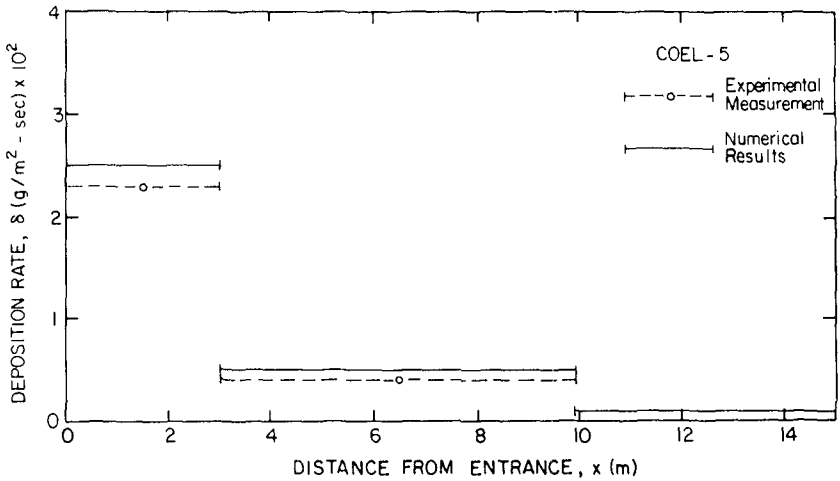

Fig. 9. Variation of Rate of Deposition with Distance, Test COEL-5.

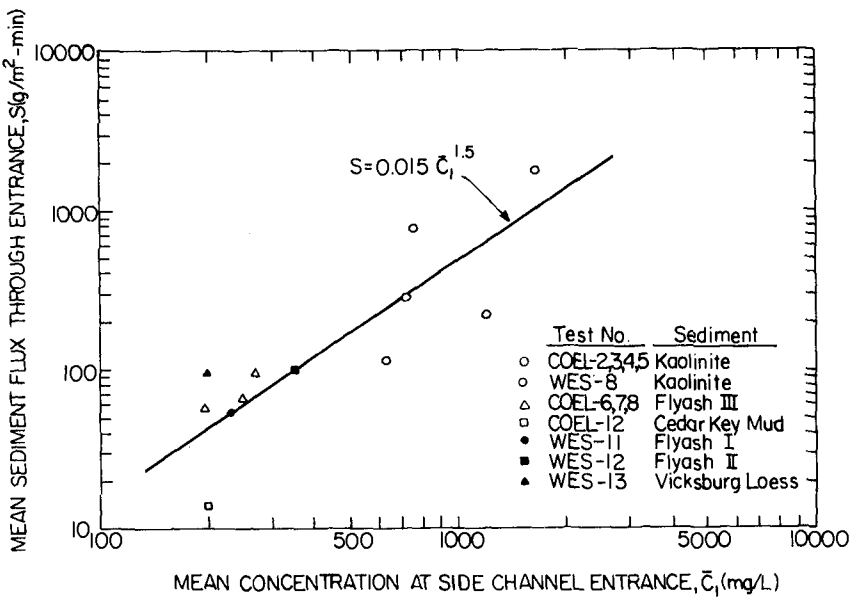

Fig. 10. Mean Sediment Flux as a Function of Depth-Mean Entrance Concentration.

From an engineering application viewpoint, Eq. 5 and its confirmation through Fig. 10 provide a simple means for computing the rate of sedimentation in closed-end channels. Its application to prototype canals seems highly promising, and deserves further consideration in that context.

ACKNOWLEDGEMENT

Support of the National Science Foundation (Grant No. CEE-84-01490), and the Hydraulics Laboratory of the Waterways Experiment Station, Vicksburg, Mississippi, is sincerely acknowledged.

REFERENCES

Gole, C.V., Tarapore, Z.S., and Gadre, M.R., "Siltation in Tidal Docks due to Density Currents," Proceedings of the Fifteenth Congress of I.A.H.R., Vol. 1, Istambul, Turkey, 1973, pp. 335-340.

Jenkins, S.A., Inman, D.L., and Bailard, J.A., "Opening and Maintaining Tidal Lagoons and Estuaries," Proceedings of the Seventeenth Coastal Engineering Conference, ASCE, Vol. II, Sydney, Australia, 1980, pp. 1528-1547.

Keulegan, G.H., "An Experimental Study of the Motion of Saline Water from Locks into Fresh Water Channels," Report No. 5168, National Bureau of Standards, Washington, DC, March, 1957.

Keulegan, G.H., "The Motion of Saline Fronts in Still Water," Report No. 5831, National Bureau of Standards, Washington, DC, April, 1958.

Keulegan, G.H., "The Mechanism of an Arrested Saline Wedge," Estuary and Coastline Hydrodynamics, A.T. Ippen Editor, Ch. 11, McGraw-Hill, New York, 1966, pp. 546-574.

Lawson, T.J., "Haboob Structure at Khartoum," Weather, Vol. 26, 1971, pp. 105-112.

Lin, C.P., "Turbidity Currents and Sedimentation in Closed-End Channels," Ph.D. Dissertation, University of Florida, Gainesville, 1987.

Lin, C.P., and Mehta, A.J., "Sediment-driven Density Fronts in Closed End Canals," Physics of Shallow Estuaries and Bays, Lecture Notes on Coastal and Estuarine Studies Series, Vol. 16, J. van de Kreeke Editor, Springer-Verlag, Berlin, 1986, pp. 259-276.

Lott, J.W., "Laboratory Study on the Behavior of Turbidity Current in a Closed-End Channel," M.S. Thesis, University of Florida, Gainesville, 1986.

Rottman, J.W., and Simpson, J.E., "Gravity Currents Produced by Instantaneous Releases of a Heavy Fluid in a Rectangular Channel," Journal of Fluid Mechanics, Vol. 135, 1983, pp. 95-110.

Wanless, H.R., "Sedimentation in Canals," Report, Division of Marine Geology and Geophysics, Rosenstiel School of Marine and Atmospheric Science, University of Miami, Miami, Florida, 1975.

Yih, C.S., Dynamics of Nonhomogeneous Fluids, Macmillan, New York, 1965.

CHAPTER 99

Closure of Tidal Channel in Land Reclamation

Chin-I Liu *

Ruey-Shyong Chang *

Abstract

The land reclamation of Lunwei subdistrict A in the development of Changhua Industrial Estate Project was commenced in May 1980. Fill sand was dredged by suction dredgers from borrow area and placed in the south and central parts of this subdistrict. Bamboo fence was used as sand retaining structure. In November, a new tidal channel occurred between two fill sand islands and across the head of seawall, it caused the increase of materials and the difficulty of construction of the seawall.

Closure of the tidal channel was completed by constructed a sand embankment dike with low cost materials such as; bamboo piles, bamboo mattress and sand bags.

1. Introduction

The Changhua Industrial Estate Project, located on the west coast of Central Taiwan on a stretch of tidal land, has a total area of about 6,292 hectares divided into six districts, namely, Shingkang, Yupu, Lunwei, Lukang, Fushin and Hanpao (Figure 1). The Yupu, Lunwei and Lukang districts with a total area of about 3,780 hectares were planned for phase 1 development to accommodate heavy industries such as machinery, steel, power and petrochemical.

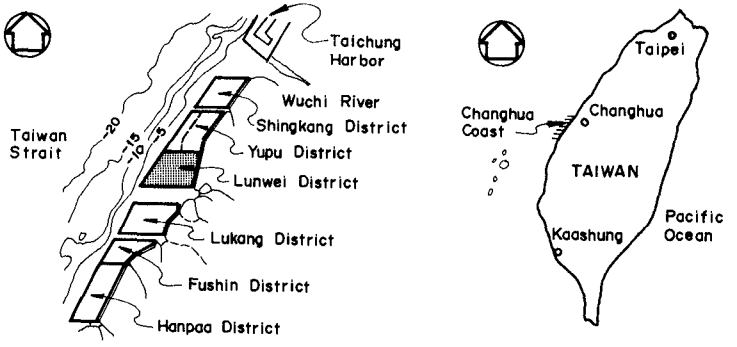

Figure 1 Key Plan of Changhua Industrial Estate

* Engineer, Sinotech Engineering Consultants Inc. No. 171, Sec. 5, Nanking East Road, Taipei, Taiwan, R.O.C.

The 406-hectare subdistrict A of the Lunwei district in the west has now been partially completed. Its development called for the construction of a 3,800 m long seawall and hydraulic fill of 18,800,000 m^3. A tidal channel runs southward through the center of this subdistrict and a sand bar lies west of the channel.

The development work commenced in May 1980. The rubblemound seawall was constructed from north to south along a planned line. Hydraulic fill was placed in the south and central parts of the subdistrict by using five suction dredgers positioned in borrow areas. By November 1980, a 2,700 m length of the seawall had been completed and the sand fill totaled about 4,000,000 m^3. In that month, a new tidal channel occurred between two fill sand islands and it flowed west through the head of the seawall. The original sea bed was scoured down to El.-8.0 m. As a result, the development work was slowed down and the quantities of seawall construction materials had had to be increased. Because the reclamation work must be completed in time to supply the future demand for land, closure of the tidal channel was considered the best solution, and a sand-made embankment dike was selected for this purpose. The dike was constructed within one tide cycle, involving 6 bulldozers and 100 workmen and using steel pipe piles, bamboo piles, mattress and sand bags as retaining structures.

This paper describes the formation and closure of the new tidal channel, the morphological variation and the low cost materials used.

2. Topography and Geology of Lunwei District

Figure 2 shows the boundary line and topography of the Lunwei district. On the north, the boundary is formed by the existing south seawall of the Yupu district, extending west for about 1 km; on the west by a 3.8 km long seawall which has been completed; on the south by a planned 4.8 km long revetment; and on the east by a planned inner dike, separated from an existing seawall by a proposed 200m wide waterway. The total area of the Lunwei district is 1,251 hectares.

A tidal channel runs NE-SW through the center of this district. The width of this 5.5 km long channel below El.-1.0 m ranges from 220 m to 550 m. The channel bed, with a 0.001 slope, has an elevation of -5.5 m at its deepest part, and the side slope is 1:10 below mean water level and 1:5 above mean water level.

The elevation of land on the east side of this tidal channel is +1.8 m, which dips gently on a 1:800 slope westward to the zero line of the channel.

A sandbar lies in a N-S direction along the west side of the tidal channel. Its highest elevation is +1.8 m in the northern part, sloping at 1:1,200 eastward to the tidal channel, and at 1:100 westward to El.-2.00 m. The slope to the south along the seawall line is 1:1,400, and that to the north is nearly flat.

The average elevation of the Lunwei district is about +0.3 m.

The geology of this district is divided into three zones. (1). The first zone is between the existing seawall and a line about 2.5 km to the seashore, which is an area of river deposit composed of yellowish gray fine sand and medium-grain sand in the top layer and fairly fine sand in the bottom layer. The grain size is from 0.2 mm to 0.5 mm. The second zone lies west of the first zone up to the low tide line. Coarser sand is found all over the place. The third zone is located at the river mouth, where the soil consists of silty-sand with a thin clay layer.

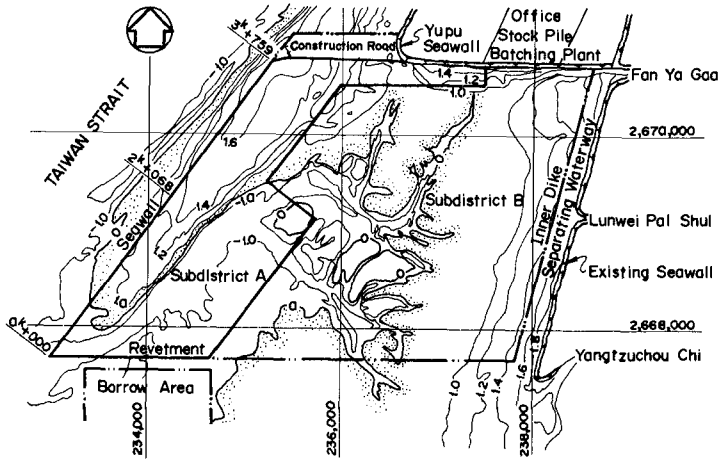

Figure 2 Topography of Lunwei District

3. Main Engineering Works

3.1 Land Reclamation

The Lunwei district is divided into two parts; subdistrict A and subdistrict B. Subdistrict A, with an area of 406 hectares, is planned to be filled to elevation +5.5 m, which will required about 18,800,000 m^3 of fill sand and 540,000 m^3 of cover material. For subdistrict B, which has an area of 845 hectares to be filled to elevation +4.2 m, about 32,000,000 m^3 of fill sand and 1,200,000 m^3 of cover material will be needed.

The reclamation work for subdistrict A started first. Fill sand is dredged from the proposed harbor basin and waterway to the south and east of this district respectively.

3.2 Seawall

The seawall line was set on the sandbar for easy construction

and to get the land needed. Typical section of the seawall are shown in Figure 3. Type A which has a sand core was adopted for the 1,691 m long northern section, while type B with a cobble core was used for the 2,068 m long sourthern section. The access road for the seawall was connected to the existing south seawall of the Yupu district. Bamboo fence was used as sand retaining structure for the sand core of type A seawall. Toe elevation was at El.+0 m, and synthetic mattress was placed between sand and cobble as filter to prevent sand from being sucked away by wave. Five-ton wave dissipation blocks were used to protect the seawall against storm wave.

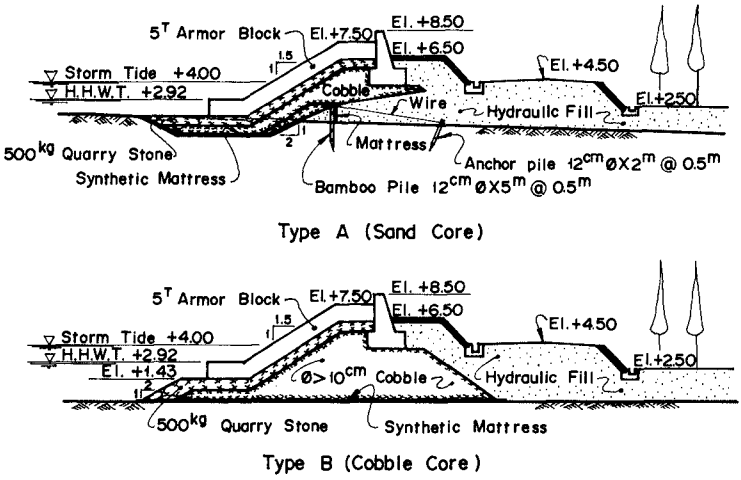

Figure 3 Typical Section of Seawall

4. Land Reclamation for Lunwei Subdistrict A

4.1 Distribution of Fill Sand

The total amount of fill sand required for Lunwei subdistrict A is about 18,800,000 m^3, which is supplied from borrow areas. Of this, about 17,200,000 m^3 is dredged from the south borrow area and the remaining 1,600,000 m^3 from the relocated tidal channel. The material for a 15 cm thick cover, totaling 540,000 m^3 in volume, comes from the Tatu mountain about 20 km away. (2).

4.2 Dredgers

Five suction dredgers with capacities as shown in Table 1 were used for the rclamation work. The arrangement of dredgers is shown in Figure 4.

Table 1 Characteristics of Dredgers

Name	Dimension (m)				Engine Power		Dia. of PiPe (")	Dredging Capacity (m^3/hr.)	Discharge Distance (Km)	Dredging Depth (m)
	Length	Width	Depth	Draft	Type	(HP)				
Taichun 1	34	11	3	1.8	Diesel	3,600	24	300-600	2.5	16
Taichun 2	58	18	3	2.1	Diesel	8,000	32	500-1000	5.5	20
Taichun 3	35	11	3	1.8	Diesel	3,000	24	300-600	2.0	16
Taichun 6	36	11.5	3	2.0	Diesel	3,000	24	300-600	2.0	20
Taichun 7	34	11	3	1.5	Diesel	3,000	24	300-600	1.8	16

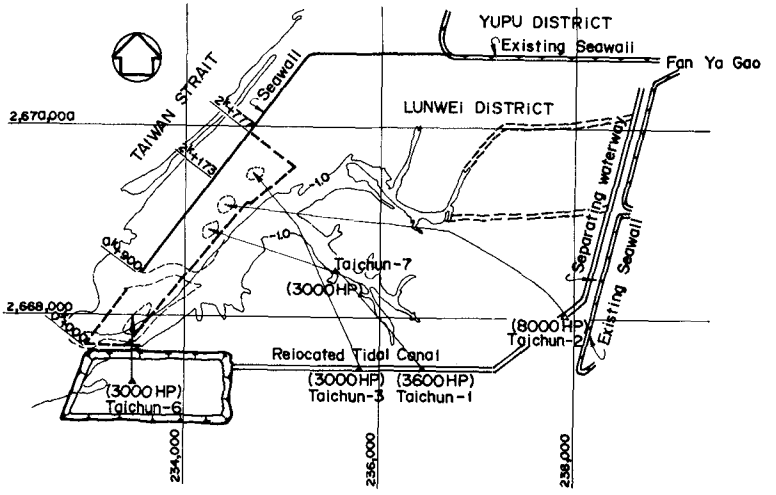

Figure 4 Arrangement of Dredgers for Land Reclamation

4.3 Sand Retaining Structure

Because construction of the seawall was from north to south, while the sand filling work proceeded from south to north. Bamboo fence of a simple type as shown in Figure 5 was used to retain the sand along the west and south boundaries. Bamboo fence consisted of bamboo pile, iron wire, anchor pile, bamboo mattress, etc. Two rows of bamboo fence were erected to prevent swell invasion.

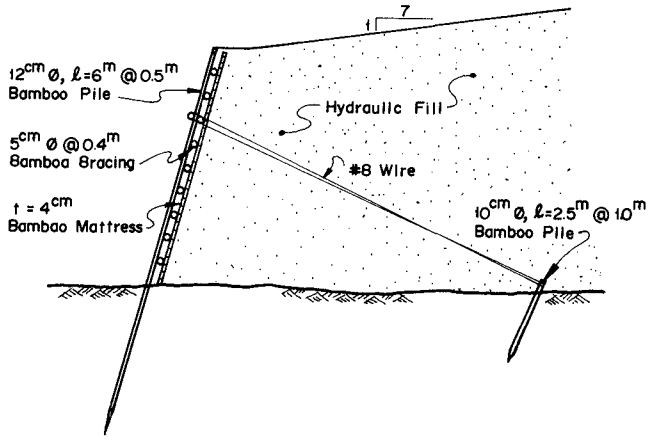

Figure 5 Typical Section of Sand Retaining Structure

5. Formation of Tidal Channel

The reclamation work for Lunwei subdistrict A was started in May 1980. Three 3,000 hp suction dredgers positioned in the south borrow area placed the fill sand in the southern part of this subdistrict. In July, one 3,600 hp and one 8,000 hp dredger positioned in the proposed relocation site for the tidal canal and the east waterway respectively placed sand in the middle part of the subdistrict. In October, two 3,000 hp dredgers in the south borrow area moved to the tidal canal to accelerate the dredging work, placing sand also in the middle part. Bulldozers were used for the earth moving work, which ran between the two sand islands at low tide, but in November the bulldozers could walk no more. The original sea bed was scoured, as even at low tide water still existed. The occurrence of the new tidal channel could be attributed to: (1) The bamboo fence used as retaining structure was partially destroyed by typhoon waves, so sand entered the original tide channel and reduced its flow section; (2) The two fill sand islands approached each other gradually and increased the tidal current velocity to scour the sea bed.

6. Morphological Variation

Figure 6 and Figure 7 show the morphological variation of the proposed closure section of the channel and the head of seawall. The deepest elevation was -6.0 m in the channel, and -8.0 m in the head of seawall.

The current velocity in the closure section was also measured under different tidal conditions. The maximum velocity was 2.25 m S^{-1} at the center during high tide. (3).

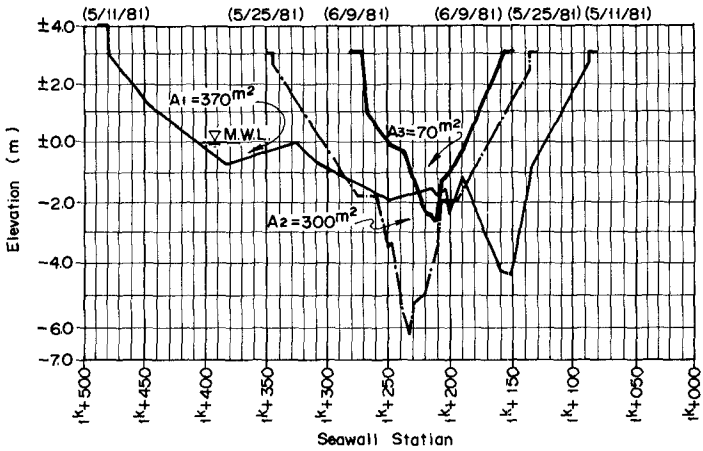

Figure 6 Morphological Variation of the Closure Section of the Tidal Channel

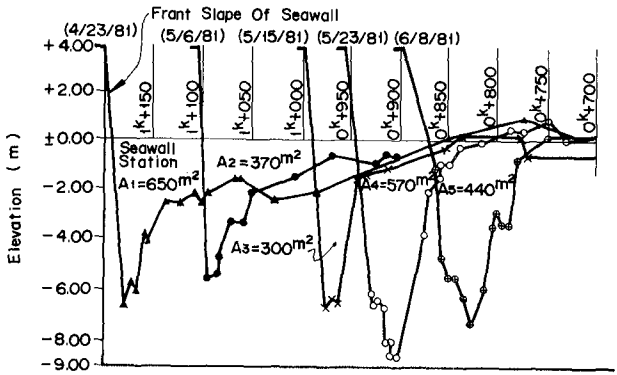

Figure 7 Morphological Variation of the Head of Seawall

7. Closure of Tidal Channel

7.1 Reasons for Closure of Tidal Channel

The scouring phenomenon occurred in November 1980, but land reclamation and seawall construction proceeded until May 1981. Due to the following reasons the closure of the tidal channel was decided.

(1) The scouring of seawall head resulted in construction diffi-

culty and the need for increased use of the construction materials.

(2) A large amount of the fill sand was washed away by tidal current.

(3) The typhoon season would come soon, so the finished part of the work must be preserved.

(4) The development work must be completed as soon as possible.

7.2 Construction of Closure Dike

Several field surveys were made to study the closure location and estimate the work quantity. After considering the construction feasibility, an upstream location was selected where the channel width was the narrowest, due to continued supply of sand. The selected closure date was June 10, 1981, the lowest tide time. Three alternative construction methods for the sand embankment dike were considered: (4).

(1) Use of steel sheet piles as temporary retaining structure and fill sand.

(2) Use of cobbles dumped from truck or barge.

(3) Use of bamboo piles and steel pipe piles as retaining structure and fill sand.

The last method was selected after comparing the material available, degree of difficulty of construction, and haul road condition. When the new channel occurred, about 78 sets of bamboo spurs were constructed along either bank for retaining sand and along the east side slope for reducing current velocity. Three 3,000 hp dredgers continuously supplied sand from each side to raise the channel bed from El.-6.0 m to El.-2.8 m. Prior to the closure date, about 10,000 m^3 of sand, 12,000 sand bags, 8"ϕ steel pipe piles, bamboo piles, mattresses, etc., were stocked on the banks for dike construction. At 10:00 p.m., June 9, 1981, the piling work started with the use of water jet during ebb tide, and bulldozers moved the sand from both banks to fill the dike until 5:00 a.m., June 10, 1981 when the dike was closed. Spurs made of bamboo piles and sand bags were constructed on the east slope to prevent scouring by the original tidal channel.

Eventually, the dike was completed, which has a top width of 10 m with top elevation at +3.0 m as shown in Figure 8.

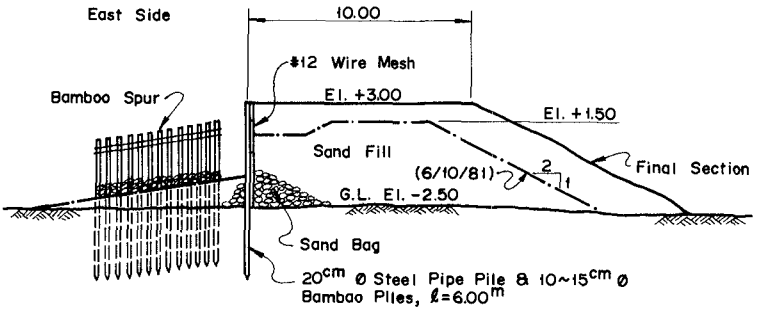

Figure 8 Typical Section of Embankment Dike

8. Conclusion

From our experience with this closure work the following conclusions can be drawn:

(1) Land reclamation from the south in this project has the advantages of higher dredging efficiency and ease of construction of the sand retaining structures, but this decision was risky, as it resulted in the need for closure of a new tidal channel.

(2) The success of the closure work was due to the dredgers' large capacity for supplying sand to reduce the channel depth, and to the use of spurs constructed of bamboo piles and sand bags to retain the fill sand and reduce the channel width so that the dike could be completed within one tidal cycle.

(3) The reclamation sequence must be carefully arranged. If the work started from inshore to offshore or proceeded simultaneously with seawall construction, the new tidal channel might not have occurred.

9. Acknowledgements

The anthours wish to extend their thanks to the field engineers of BES Engineering Corporation for their supply of the field data.

10. References

(1) TAIWAN LAND CONSERVATION COMMITTEE (1966). Report on Development of Changhua Tidal Land.

(2) SINOTECH ENGINEERING CONSULTANTS. INC. (1979). Report on Development of Changhua Industrial Estate - Land Reclamation.

(3) LIU, C. I. (1984). The Influence of Tidal Land Development on Coastal Morphological Variation. Proc. 2nd Conf. Hydraulic Engineering.

(4) HWANG, T. F. (1979). Study Report on Closure Techniques for Tidal Land Sea Dike.

CHAPTER 100

Another approach to longshore current evaluation

M.A. Losada, A. Sánchez-Arcilla and C. Vidal

A simple model to predict the longshore current velocity at the breaker line on a beach with oblique wave incidence, is presented. The model balances driving and resistance terms (gradients of radiation and turbulent Reynolds stresses and bottom friction) to get a general expression for the velocity. This equation shows explicitely the influence of Iribarren's parameter on longshore current generation. It has been tested with field and laboratory data, obtaining a reasonable fit to measured values. The resulting (predictive) model is expected to be valid for any type of breakers though the calibration has been mainly done for spilling and plunging types, due to the scarcity of results for other breakers.

1.- INTRODUCTION

Longshore currents in the surf zone have been acceptably modelled using the radiation stress concept (Longuet-Higgins,1970). The longshore-trust (Nw/m^2) due to an oblique wave approach, given by the gradient of the radiation stress, is balanced (in stationary and longshore-uniform conditions) by bottom friction and horizontal mixing (Bowen, 1969), (Longuet-Higgins, 1970).

The gradient of the radiation stress is evaluated using sinusoidal theory (as a first approximation for slowly varying depths) and turns out to be proportional to the local rate of energy dissipation, D (Joules/(m^2 x sec)), regardless of its origin. Inside the surf zone a significant fraction of D comes from wave breaking because the turbulence associated to the breaking process is responsible for most of the dissipated energy. Bottom friction plays a minor role in this context, being important only in special cases (e.g. very steep and reflective profiles).

This means that turbulent horizontal mixing must be one of the most important factors in longshore-current generation because it accounts for a large part of the dissipated energy which controls the driving term.

Bottom friction turns out to be the main retardating term for the mean flow (e.g. Longuet-Higgins, 1970, Kraus & Sasaki, 1979). It depends on the type of granular material and resulting bed forms but also in the properties of the flow field defined in the fluid. These are, in turn, related to the bed geometry. It is, therefore, reasonable to expect a variation of the frictional stress with the existing level of turbulence (Fleming et al. (9)), defined (albeit simplistically) by the breaker type.

Turbulents horizontal mixing, the remaining retarding term in longshore-uniform conditions, is numerically less significant than bottom friction. This latter effect controls the magnitude of the resulting velocities while lateral mixing determines the profile (shore-normal) distribution.

All these points suggest that breaker type is closely related to longshore current generation. This implies that Iribarren's number, Ir, so far considered a parameter for definition of breaker characteristics, also plays an important role in longshore-current evaluation. A modified parameter, Ir θ, similar to the one used for oblique incidence in mound breakwaters (Losada et al., 1982), must be employed to include the effect of the angle of wave approach:

$$Ir_\theta = Ir \cos\theta = \left(\frac{g}{2\pi}\right)^{1/2} \cdot \frac{T \cdot \tan\beta}{(H_b)^{1/2}} \cdot \cos\theta \qquad (1)$$

in which:

H_b : wave height at the breaker line
T : wave period
$\tan\beta$: bottom slope
g : acceleration due to gravity.

The paper proposes an average evaluation of driving and resistance terms using the surf zone as a control volume and including the influence of breaker type througs Ir_θ. Turbulent stresses are calculated as proposed by Battjes (1975) while bottom friction is estimated with a linear law, based on the equations derived by Liu and Dalrymple (1978). The model has been tested with field and laboratory data from Putnam et al. (1945), Vitale (1981), Komar and Inman (1970) and Wu et al. (1985). The fit between predicted and measured velocities is satisfactory for usual values of the friction coefficient. The derived solution is shown to be valid for any type of breakers, therefore being more general than most of the previously published formulae, even though its field of application is restricted to planar beaches.

2.- LONGSHORE CURRENT FORMULATION

Longshore flow will be formulated using the vertically integrated, time-averaged mass and momentum conservation equations together with the simplifying assumptions of stationary and longshore-uniform conditions. With this approach, similar to the one used by Bowen (1969), the resulting longshore momentum equation is (Mei, 1983):

$$\frac{\partial S_{xy}}{\partial x} + \frac{\partial S'_{xy}}{\partial x} + R_{yb} = 0 \qquad (2)$$

in which:

S_{xy} = Excess momentum flux tensor due to wave fluctuations.
S'^{xy} = Excess momentum flux tensor due to turbulent fluctuations.
R^{xy}_{yb} = y-component of the horizontal shear stress on the bottom.

To obtain equation (2) from the momentum conservation law it has also been assumed that viscosity, bottom slope and wave slope were small (Mei, 1983). The coordinate system used is shown in figure 1. The x axis

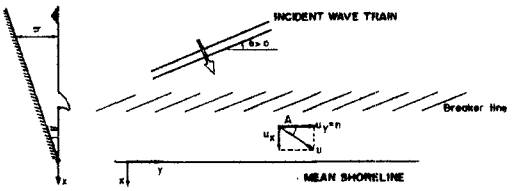

FIGURE 1.- DEFINITION SVETCH OF THE SURF ZONE IN A BEACH WITH LONGSHORE UNIFORM CONDITIONS. FOR A NEGATIVE ANGLE OF WAVE INCIDENCE θ, THE LONGSTORE CURRENT WILL BE ALONG THE NEGATIVE Y-AXIS

is normal to the shoreline and positive shorewards. The y axis is directed alongshore and is positive towards the right. The origin is situated at the mean-level shoreline.

The retarding terms inside the surf zone are, therefore, due to bottom friction and turbulent horizontal mixing (the equations are vertically integrated) with free surface stresses being neglected. It should also be remarked that equation (2) has been time averaged and, therefore, does not consider first order wave induced oscillatory motions with time scales comparable to the wave period.

The lateral mixing retarding term, $\partial S'_{xy}/\partial x$, is usually evaluated by means of the "eddy viscosity" aproximation of Boussinesq, von Schwind (24):

$$\frac{\partial S'_{xy}}{\partial x} = - \frac{\partial}{\partial x} \left(\rho \varepsilon \frac{\partial}{\partial x} (h + \bar{\eta}) V_1 \right) \qquad (3)$$

in which:

ρ = mass-density of sea water.
ε = horizontal eddy viscosity coefficient.
h = water-depth from the still water level.
$\bar{\eta}$ = mean water-level variation due to the waves.
V_1 = longshore component of the current velocity at the surf zone induced by breaking waves.

The resultant equation, (3), is entirely analogous to the ones obtained by Bowen (1969) and Longuet-Higgins (1964).

The radiation stress (associated to the wave induced oscillatory motion), S_{xy}, may be easily expressed as (Longuet-Higgins, 1964):

$$S_{xy} = F_x \frac{\sin\theta}{C} \qquad (4)$$

in which:

θ = angle between wave crests and bottom contours (figure 1).
C = phase speed of the waves.
F_x = energy flux normal to the shoreline, given by

$$F_x = E C_g \cos\theta = (1/8)\rho g H^2 C_g \cos\theta \quad (5)$$

in which:

H = sinusoidal wave-height (when considering irregular waves an equivalent H giving the same energy density, E, must be used).
C_g = group velocity of the waves.

Assuming, as first approximation, that Snell's law is valid throughout the surf zone, the driving term of the momentum equation may be written as:

$$\frac{\partial (S_{xy})}{\partial x} = \frac{\sin\theta_b}{C_b} \frac{\partial F_x}{\partial x} \quad (6)$$

in which b denotes values estimated at the breaker line.

The local average tangential stress (in the y-direction) exerted by the longshore flow in the bottom, R_{yb}, may be expressed by:

$$R_{yb} = \rho C_f < U_{ty} |\vec{Ut}| > \quad (7)$$

in which:

C_f = dimensionless bottom friction coefficient.
$|\vec{Ut}|$ = absolute value of the (total) current velocity vector at the surf zone
U_{ty} = y-component of the velocity vector.
$<>_{ty}$ = time-average operator.

Similar expressions for R_{yb} have been proposed in Liu and Dalrymple (1978) and Kraus and Sasaki (1979). The total velocity vector, $\vec{Ut}$, is composed of a steady part, associated to the current, and an oscillatory part due to the waves.

Using this decomposition and assuming that the oscillatory (wave induced) velocity is large when compared to the steady currents (wave induced or not) it is easy to obtain R_{yb} as, Liu and Dalrymple (1978):

$$R_{yb} = \rho C_f (\gamma/\pi) \sqrt{g(h+\bar{\eta})}\, V_1 (1 + \sin^2\theta) \quad (8)$$

in which:

γ = parameter varying (approximately) between 0.70 and 1.20 as a function of Ir (Battjes, 1974). It may be defined by:

$$\gamma = H_b/h_b$$

This expression, proposed by Liu and Dalrymple for weak currents, coincides with that used by Kraus and Sasaki (1979). It is also a

generalization of the one employed by Longuet-Higgins (1970) in which it was assumed that $\sin\theta << 1$. It seems advisable to retain the more general formulation (8), since, according to published results, significant changes in the final longshore-current value may appear even for moderate angles of wave incidence, θ_b.

The resulting longshore momentum equation is obtained substituting (8), (6) and (3) into (2):

$$\frac{\sin\theta_b}{C_b}\frac{\partial F_x}{\partial x} = -\rho C_f \frac{\gamma}{\pi}\sqrt{g(h+\bar{\eta})}\,V_1(1+\sin^2\theta) + \frac{\partial}{\partial x}\left(\rho\varepsilon\frac{\partial}{\partial x}((h+\bar{\eta})\,V_1)\right) \tag{9}$$

The two retarding terms on the right hand side of the equation are expressed in terms of very poorly known coefficients (C_f and ε respectively) often assumed constant through-out the surf zone. It, therefore, seems adequate to evaluate partial derivatives in an average sense, using a control volume extending from the breaker-to the shore line. With this approach ($\partial F_x/\partial x$), for example, is given by:

$$\frac{\partial F_x}{\partial x} = \frac{\theta - F_{xb}}{x_b} = \frac{F_{xb}}{x_b} \tag{10}$$

in which x_b is the width of the surf zone.

The eddy viscosity coefficient, ε, may be expressed as (Battjes, 1975):

$$\varepsilon = M.h^*\,(D/\rho)^{1/3} \tag{11}$$

in which:

M = dimensionless parameter expected to be of order one. Huntley (1976), obtained values for M in the range 0.3-2.0 for beaches of slope 0.1.

h^*= depth through which the turbulence extends. If $h^* = \delta h$, may be seen that for plunging breakers δ is near one while for other breaker type $0 < \delta < 1$. It is thus, clear that δ depends on $Ir\theta$.

D = mean rate of wave energy dissipation per unit area, given by

$$D = -(\partial F_x/\partial x) \tag{12}$$

Using average (integrated accross the surf zone) values for ε (ε_{ave}) and the bottom tangential stress and evaluating shore-normal gradients with the control volume approach it is easy to write (9) as:

$$-\frac{\sin\theta_b}{C_b}\frac{F_{xb}}{x_b} - 2\rho\varepsilon_{ave}\frac{V_{lb}}{x_b}\tan\beta\frac{6\gamma^2+8}{3\gamma^2+8} - \rho C_f\frac{\gamma}{\pi}(gh_b)^{1/2}\cdot (V_{lb}/\,)\,(1+(3/5)\sin^2\theta_b)) \tag{13}$$

in which:

tang β : bottom slope

$$\varepsilon_{ave} : M h^*_{ave} (F_{xb}/\rho_{xb})^{1/3} \simeq M\delta (h_b/2) (F_{xb}/\rho_{xb})^{1/3} \quad (14)$$

To obtain equation (13) sinusoidal theory (shallow water limit) and Snell's law have been used and $\bar{\eta}$, h and V_1 habe been assumed to vary linearly with x. For planar beaches (h = mx) $\bar{\eta}$ is usually considered to depend linearly on x (e.g. Longuet-Higgins and Stewart, 1964) while the linear profile for V_1 has also been proposed by several authors and seems adequate in this context in which the surf zone is considered as a whole in an average sense.

The available energy density at the breaker line (prior to dissipation) is:

$$E_b = E_{incident} - E_{reflected} = (1/8)\rho g H_b (1-K_r^2) \quad (15)$$

in which:

K_R : reflection coefficient, shown to be a function of Ir by Battjes (1974) for impermeable, rigid slopes.

It should also be remarked that the proposed value for the average bottom friction term coincides with the average tangential stress obtained from Longuet-Higgins formulation when $\sin^2\theta_b << 1$.

The longshore current velocity may be easily calculated from equation (13) which is linear in V_{lb}. Using (14) and (15) it is easy to obtain:

$$V_{lb} = \frac{V^*}{M \phi_M + C_f \phi_C} \quad (16)$$

in which:

V* : reference velocity given by:

$$V^* = \frac{(gH_b)^{1/2}}{4} \frac{\sin\theta_b (\cos\theta_b)^{2/3}}{\tan\beta^{4/3}} \quad (17)$$

ϕ_M : function given by:

$$\phi_M = \frac{8 + 6\gamma^2}{8 + 3\gamma^2} \frac{\delta}{\phi^{5/6}} \frac{1}{(1 + K_R^2)^{2/3}} \quad (18)$$

ϕ_C : function given by:

$$\phi_C = \frac{2}{3\pi} \frac{1 + (3/5)(\sin\theta_b)^2}{(1-K_R^2)(\cos\theta_b)^{1/3} (\tan\beta)^{7/3} \gamma^{1/2}} \quad (19)$$

Considering that γ, δ, K_R and $\tan\beta$ depend on $Ir\theta$ and assuming θ_b to be (numerically) slowly verying it may be written:

$$\phi_M = \phi_m(Ir\theta)$$
$$\phi_C \quad \phi_C(Ir\theta)$$

The structure of expression (16) for V_{lb} is, thus, similar to the formulae proposed by Thornton (1970), Bowen and Inman (1969), Bowen (1969), (1969), Longuet-Higgins (1970) and other authors, cf. Basco (1982). All these equations show a dependence on $(g H_b)^{1/2}$ which is maintained in the proposed model, in which the influence of $Ir\theta$ is clearly shown through V^*, ϕ_M and ϕ_C.

The obtained formulation should then be valid for any type of breakers, provided ϕ_M and ϕ_C as functions of $Ir\theta$, are known. However it would be convenient, from the point of view of calibration and practical applications, to derive a simpler expression. To do it consider that the orders of magnitude in (16) are (after substitution of standard, typical values for K_R, θ_b, γ and δ):

$$\phi_M = O(1)$$

$$\phi_C = O(\tan\beta^{-7/3}) = O(10^2) \quad \text{to} \quad O(10^4)$$

in which $\tan\beta$ has been assumed to be of order $O(10^{-1})$ to $O(10^{-2})$.

Assuming that M is $O(1)$ and C_f is $O(10^{-1})$ to $O(10^{-2})$ the order of magnitude of V_{lb} as given by (16) is:

$$O\left(\frac{V_{lb}}{V^*}\right) = \frac{1}{O(1) + C}$$

with:

$$C = O(C_f \phi_C) = O(1) \text{ to } O(10^3)$$

The samller values of C require large values of β with small values of C_f. This would correspond in Nature to a very steep beach with flat bottom of fine sand and will, therefore, not be found very often.

It seems, thus, reasonable to approximate V_{lb} by:

$$V_{lb} = \frac{V^*}{C_f \phi_{NC}} \tag{20}$$

in which ϕ_{NC} is a new function of $Ir\theta$, numerically similar to ϕ_C, but including the effect of horizontal mixing (i.e., the $M\phi_M$ term). In this final expression for V_{lb} the dependence on turbulent horizontal mixing is included through the $Ir\theta$ parameter which controls ϕ_{NC}. It seems a convenient result due to the difficulty in estimating eddy viscosity coefficients. The aim of the calibration process, developped in next section, will then be to determine ϕ_{NC} as a function of $Ir\theta$.

3.- CALIBRATION WITH FIELD AND LABORATORY DATA

The function ϕ_{NC} must include the lateral mixing effect while remaining of the same order of magnitude as ϕ_C. It may be obtained from equation (19) by retaining only the numerically most significant factors:

$$\phi_{NC} = \frac{1}{A\,(1 + K_R^2)\,(\tan\beta)^{7/3}} \qquad (21)$$

in which:

A : parameter expected to be of order O(1) representing the effect of turbulent mixing.

The final expression for V_{lb} is obtained from (20) and (21):

$$V_{lb} = (A/C_f)\; V^*\; (\tan\beta)^{7/3}\; (1-K_R^2) \qquad (22)$$

Substitution of V* from equation (17) gives:

$$V_{lb} = \frac{A}{C_f}\;\frac{(gH_b)^{1/2}}{4}\;\sin\theta_b\;(\cos\theta_b)^{2/3}\;(1-K_R^2)\;\tan\beta \qquad (23)$$

This formula is entirely analogous to the equivalent expression of Kraus & Sasaki (1979). The weak angular dependence mentioned by these authors (in addition to the factor $\sin\theta_b$) is here estimated as $(\cos\theta_b)^{2/3}$ while their slow variation with the mixing parameter P implies here a slowly varying A coefficient.

The proposed formule is also very similar to Komar's (1975) model. The 2.7 factor in the latter includes the $(A/C_f)\tan\beta$ term of the former, apart from some minor terms of scarce numerical significance ($\gamma^{1/2}$, $\cos\theta_b^{1/3}$, etc.). This implies a nearly constant value of A, in accordance with the results of Kraus et al. (1979), and a slow variation of the ratio $(C_f/\tan\beta)$. This point, also supported by Fleming and Stwart (9), can be explained considering that, for spilling breakers, ocurring on mild slopes with tanβ of order $O(10^{-2})$, the bottom will be rippled or flat with low sediment load and a value of C_f of order $O(10^{-2})$. Plunging breakers, on the other hand, will be move likely found on intermediate slopes ($\tan\beta$ of order $O(10^{-1})$) with and increased sediment load and C_f of order $O(10^{-1})$.

The constancy of the ratio $\tan\beta/C_f$, proposed by Komar (1975), is here reinterpreted as an Ir θ dependence of the C_f coefficient. This can be physically understood considering that the bottom friction coefficient depends on bed material and forms which are closely related to the flow properties in the area. These, in turn, vary with the breaker type and, thus, with Ir θ. Furthermore, when trying to evaluate the ratio $\tan\beta/C_f$ due attention must be paid to the fact than tanβ is distorted in hydraulic models, in which either it is kept artificially fixed (rigid-beds tests) or it is out of scale (mobile-bed tests). This point, together with possible variations of the ratio $\tan\beta/C_f$ for breakers other than spilling and plunging, suggests the convenience of including tanβ in the function of Ir θ

to be calibrated. This function, $X(Ir\theta)$, contains all unknown $Ir\theta$-dependent parameters appearing in equation (23). It may be, thus, written as:

$$X(Ir\theta) = (A/C_f)\ (1 - K_R^2)\ \tan\beta \cos\theta_b \qquad (24)$$

in which the factor $\cos\theta_b$ has been incorporated to reproduce the slope encountered by the obliquely incident waves.

The final expression for V_{lb} is obtained from (23) and (24):

$$V_{lb} = X(Ir\theta)\ ((gH_b)^{1/2})/4)\ \sin\theta_b\ (\cos\theta_b)^{-1/3} \qquad (25)$$

The average (accross the surf zone) longshore current velocity, V_{lave}, can then be estimated from (25) and the assumed linear (weak curvature) V_l profile:

$$V_{l\,ave} = 0.6 \times (Ir\theta)\ ((gH_b)^{1/2})/4)\ \sin\theta_b\ (\cos\theta_b)^{-1/3} \qquad (26)$$

The function $X(Ir\theta)$ has been calibrated with measured (field and laboratory data. It is proportional according to equation (24), to a ratio of lateral mixing to bottom friction effects. The former are related to the parameter A while the latter depend on the C_f coefficient. It is, therefore, reasonable to expect a family of $X(Ir\theta)$ curves varying with a mixing parameter defined here as A/C_f. Figures 2, 3 and 4 show the best-fit curves for laboratory (rigid and mobile-bed) and field data, respectively. These curves estimate $X(Ir\theta)$ from equation (26). The obtained bell shape (to be discussed in next section) is adequately reproduced using a linear times exponential equation, with two degrees of freedom, a, b:

$$X(Ir\theta) = a\,Ir\theta \exp(b\,Ir\theta) \qquad (27)$$

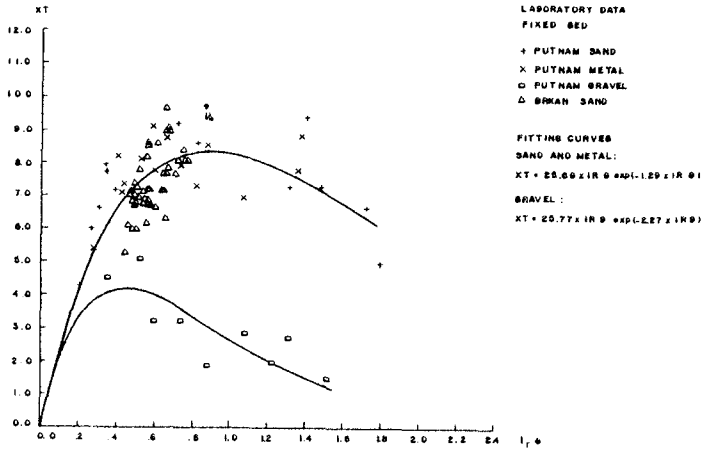

FIGURE 2.- BEST FIT $X(I_r\,\theta)$ CURVE FOR RIGID-BED (LABORATORY) DATA

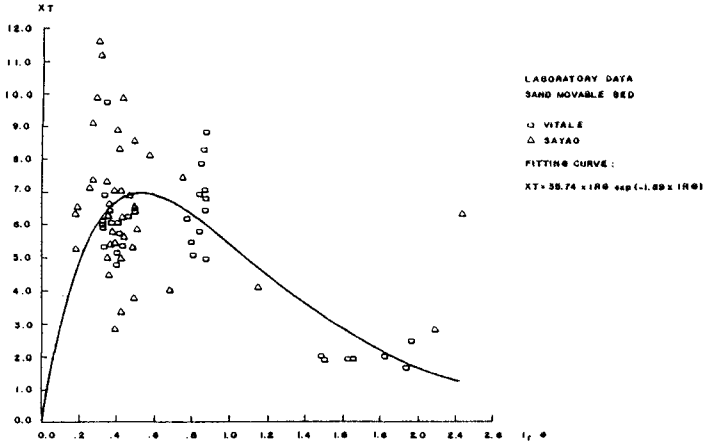

FIGURE 3.- BEST FIT X (I_r θ) CURVE FOR MOBILE - BED (LABORATORY) DATA

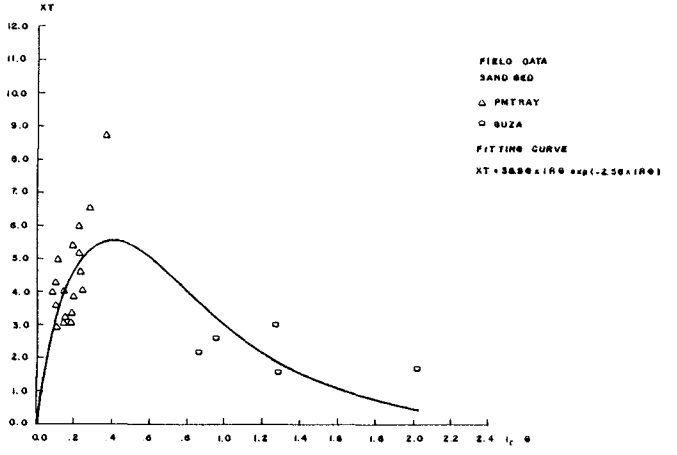

FIGURE 4.- BEST FIT X (I_r θ) CURVE FOR FIELD DATA

Theoretical predictions obtained with this family of $X(Ir\theta)$ curves and equation (26) appear in figures 5a,b and 6 corresponding, respectively, to rigid-bed, mobile-bed and field values. It is important to mention that only average longshore current velocities have been used in the calibration process. The reason was that most of the reported data were explicitely or implicitely defined as mean (accross the surf zone) velocities. Registered maximum values have been, thus, transformed to average velocities using a ratio, based on Longuet-Higgins (1970) profile distribution: $V_{l\,ave}/V_{l\,max}$ = 0.6.

In Vitale's data only tests with measured breaking wave heights have been used. Each velocity was calculated by averaging our sets of data, as presented in the original paper. Slope angle was measured directly from the original figures. The slope in Wu's data was that of the inner surf zone as obtained from the figures in the paper.

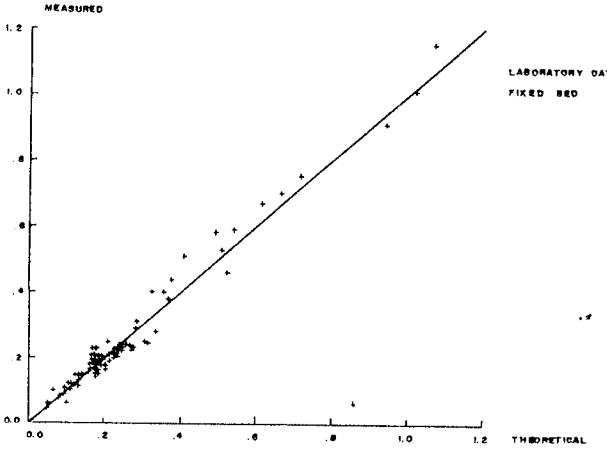

FIGURE 5 a.-LONGSTORE CURRENT MEASURED VERSUS CALCULATED (THEORETICAL) VELOCITIES FOR RIGID-BED (a) AND MOBILE-BED (b) LABORATORY DATA

The correlation coefficient, evaluated for the whole set of field and laboratory data (points), was found to be r^2 =

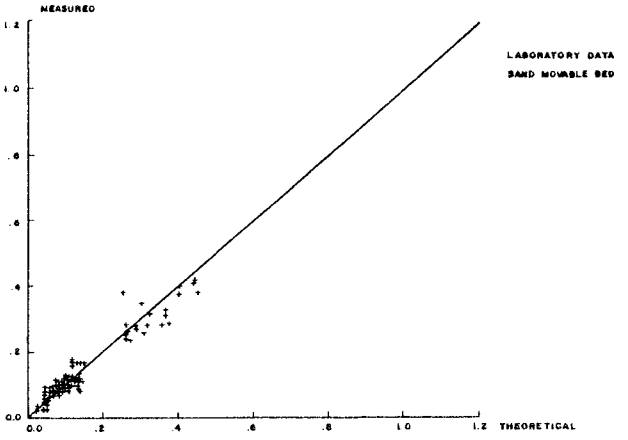

FIG. 5b .- LONGSTORE CURRENT MEASURED VERSUS CALCULATED (THEORETICAL) VELOCITIES FOR RIGID-BED (a) AND MOBILE-BED (b) LABORATORY DATA

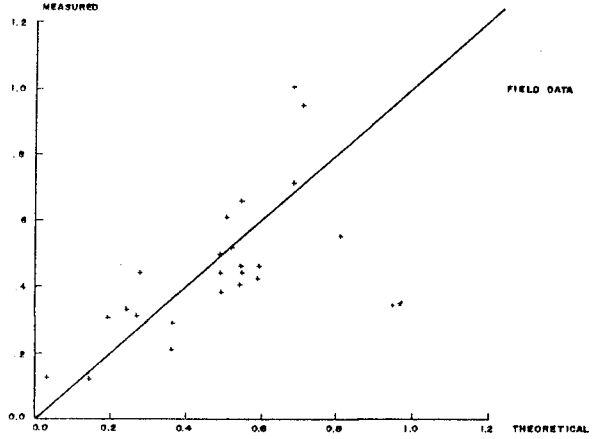

FIGURE 6.-LONGSSORE CURRENT MEASURED VERSUS CALCULATED (THEORETICAL VELOCITIES FOR FIELD DATA)

4.- DISCUSSION

The satisfactory fit of theoretically predicted values to experimental data illustrated the validity of the obtained expressions and the dependence of the longshore current on the Ir_θ parameter.

The control volume approach used to evaluate partial derivatives is consistent with the state-of-the-art knowdledge available for the C_f and M coefficients. The latter is generally accepted to be poorly known, while values used for the former, though sometimes not explicitely stated, are also rough estimates. Bottom friction in the surf zone is, in fact, a highly complex problem. The slope of the beach changes with wave and flow conditions; bed forms appear due, mainly, to wave action, changing the drag caused by surface roughness and introducing form drag as well as producing energy losses due to secondary currents; wave and current interactions cannot be often neglected which requires the evaluation of C_f for combined waves and currents in fully rough turbulent flow (Grant and Madsen (1979). The problem is further complicated by the sediment motion, because the mixture of water and sediment may not behave as clear water, which makes even more difficult and accurate determination of the boundary layer characteristics in this problem.

The changes in C_f with bed forms and material, sediment load and related parameters (Grant and Madsen, 1979, 1982) together with the uncertainties associated to many experimental values (arising from dificulties of measurement in the surf zone, ambiguous definition of velocities and wave heights, etc.) introduce significant errors in the data. This precludes any accurate fitting process which must, thus, be interpreted in a trend-like sense.

The behaviour of V_1 with Ir_θ may be obtained from equation (23). For high values of Ir_θ (corresponding to surging breakers) the amount of reflected energy increases with Ir_θ. This means that less energy is available to generate a longshore current and, thus, low values of V_1 should be expected for the uppermost range of Ir_θ. The other tail of the $V_1=V_1(Ir_\theta)$ curve corresponds to low values of Ir_θ and spilling breakers. Considering that the driving term is proportional to D (mean rate of wave energy dissipation per unit area) it is easy to understand that for very low values of Ir_θ the amount of energy to be dissipated (proportional to H^2) increases more slowly than the area for dissipation (proportional to the width of the surf zone). This means a slightly decreasing D which, in turn, implies a decreasing V_1 (after taking into account the effect of the retarding terms) for (low) decreasing values of Ir_θ.

The obtained bell slope for $V_e(Ir_\theta)$ applies to both mean and maximum longshore current velocities. The particulars of the curve will depend on bed and flow properties (figure 7). This behaviour also determines the bell-like sharpe of $X(Ir_\theta)$ which may be easily obtained from equation (25) or (26) introducing the known variation of V_1 and H_b with Ir_θ. This same trend for $X(Ir_\theta)$ can also be derived from equation (24) considering (A/C_f) as a mixing parameter with a maximum for spilling/plunging breakers and introducing the expected evolution of K_R and $\tan\beta$ with Ir_θ (figure 8).

The calibration process confirmed these results providing a family of $X(Ir_\theta)$

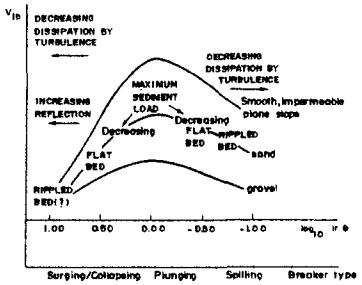

FIGURE 7.- SCHEMATIC VARIATION OF THE LONGSHORE CURRENT VELOCITY AT THE BREAKER LINE, V_{eb}, VERSUS THE TYPE OF BREAKER GIVEN BY $I_r\theta$

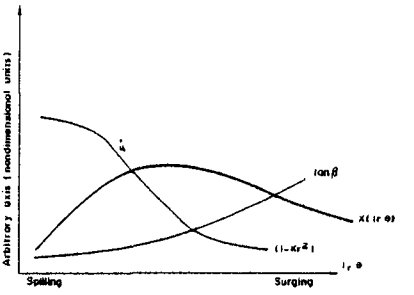

FIGURE 8.- SCHEMATIZATION OF THE EVOLUTION OF $\tan\beta$, $(1-K_R^2)$ AND $X(I_r\theta)$ WITH $I_r\theta$ (FOR DEFINITION OF SYMBOLS SEE TEXT)

curves depending on the mixing parameter, A/C_f. A good fit and low X values should, therefore, be expected for rigid-bed laboratory tests in which scales effects and reduced depths imply an overestimation of C_f and an underestimation of A. The obtained curves also show the increase in C_f (decrease in X) for gravel and coarse sand with respect to fine sand of smooth slopes (figure 2). Mobile-bed tests display larger dispersions due to difficulties associated to the control and adjustment of bed forms and slope for these models. The distorsion due to scale effects and out-of-scale bottom topography should also be considered when assessing the velocity of mobile-bed results (figure 3).

The same trend was found for field data in which the observed deviations of X for the lower range of $Ir\theta$ were attributed to the somewhat erratic behaviour of the A/C_f parameter in this range. This was attributed to the increasing degree of interaction among the various mechanisms acting on longshore current generation in field problems, which multiplied the difficulties associated to the control and estimation of parameters.

5.- CONCLUSIONS

A simple model to predict the longshore current velocity at the breaker line on a beach with oblique wave incidence is presented. From the proposed formulation the following conclusions may be drawn:

1.- The bell shaped dependence of the longshore current velocity on the amount energy dissipated, given by Iribarren's parameter, $Ir\theta$, is shown, even though the usual (spilling breaking) hypothesis, $\gamma = H_b/h_b$, is assumed to hold for all types of breakers. This suggests that $Ir\theta$ so far considered a parameter for definition of breaker characteristics, plays also an important role in longshore current generation.

2.- The structure of the obtained expression for the longshore current velocity is similar to the formulae proposed by other authors but includes (simultaneously) the effects of oblique incidence, bottom

friction, horizontal mixing and type of breakers. The final formula is, however, quite simple and can be reasonably used to predict velocities associated to any type of breakers. More experimental data are nevertheless required for calibration with collapsing and surging breakers.

3.- The $X(Ir_\theta)$ family of curves depend on a mixing parameter defined here by A/C_f. This ratio varies with bottom friction and the existing level of turbulence generated mainly at the free-surface but also including the contribution of the bottom boundary (bed forms, etc.).

This explains the greater dispersion of results obtained in mobile-bed tests and field measurements, corresponding to non-planar beaches. These cases do not fulfill the rather stringent hypotheses used to derive the model which should be, thus, applied with caution to these problems.

4.- The fit of theoretically predicted values to measured data is satisfactory, illustrating the validity of the obtained expressions. In particular, the ratio $\tan\beta/C_f$ appears to be weakly varying with Ir_θ, at least for spilling and plunging breakers. This suggests that C_f partially reflects the degree of turbulent mixing and gives more sense to the A/C_f parameter.

APPENDIX I.- REFERENCES

1. Basco, D.R., Surf zone currents. State of knowledge, Vol. I, Misc. Rep. No. 82-7. CERC, 1982.

2. Battjes, J.A., Surf similarity. Coastal Engineering Conference, ASCE, Vol. 1, 1974, pp. 466-480.

3. Battjes, J.A., Modelling of turbulence in the surf zone. Proceedings modeling techniques, San Francisco, 1975, pp. 1050-1061.

4. Bowen, A.J. The generation of longshore current on a plane beach. Jour. Mar. Res., 27, 1969, pp. 206-215.

5. Bowen, A.J., Rip Currents. 1. Theoretical Investigations. Jour. Geophys. Res. 74, 23, 1969, pp. 5467-5478.

6. Bowen, A.J. and Inman, D.I., Rip Currents. 2. Laboratory and field observations. Jour. of Geophys. Res. Vol. 74, No. 23, 1969, pp. 5479-5490.

7. Brebner, A. and Kamphuis, J.W., Model tests on relationship between deep water wave characteristics and longshore currents. Queen's Univ. Civil Eng. Res. Rep. 31, 1963, 25 p.

8. Bruun, P. et al., Design and Construction of mounds for breakwaters and coastal protection. Elsevier, 1985.

9. Fleming, C.A. and Stewart, D.H., New framework for prediction of longshore currents. Int. Conf. Coastal Eng., ASCE, pp. 1640-1658.

10. Grant, W.D. and Madsen, O.S., Combined wave and current interaction with a rough bottom. Jour. Geophys. Res. 84, 64, 1979, pp. 1797-1808.

11. Grant, W.D. and Madsen, O.S. Movable bed roughness in unsteady oscillatory flow. Jour. Geophys. Res. 87, C1, 1982, pp. 469-481.

12. Huntley, D.A., Lateral and bottom forces on longshore currents. Coastal Engineering Conference ASCE, Chapter 37, 1976, pp. 645-659.

13. Komar, P. and Inman, D.I., Longshore sand transport on beaches. Jour. Geophys. Res. 75 (30) 1970, pp. 5914-5927.

14. Komar, P.D., Nearshore currents: generation by obliquely incident waves and longshore variations in breaker height. Proc. Symp. on nearshore sediment dynamics. Ed. J.R. Hails and A. Carr, Wiley, London, 1975, pp. 17-45.

15. Kraus, N.C. and Sasaki, T.O., Influence of wave angle and lateral mixing on the longshore currents. Mar. Sci. Comm. Vol. 15(2), 1979, pp. 91-126.

16. Liu, P. and Dalrymple, R.A., Bottom frictional stresses and longshore currents due to waves with large angles of incidence. Jour. Mar. Res. Vol. 36, 2. 1978, pp. 357-375.

17. Longuet-Higgins, M.S. and Stewart, R.W., Radiation stresses in water waves. Deep-sea Research, Vol. II, 1964, pp. 529-562.

18. Longuet-Higgins, M.S., Longshore current generated by obliquelly incident sea waves. 1-2. Jour. Geophys. Res. 75, 1970, pp. 6778-6801.

19. Longuet-Higgins, M.A., Recent progress in the study of longshore currents, in waves on beaches. R.E. Meyer Ed. Academic Press, 1972.

20. Losada, M.A. and Giménez-Curto, L.A. Mound breakwaters under oblique wave attack; a working hypothesis. Coastal Engineering, 6. 1982, pp. 83-92.

21. Mei, C.C., The applied dynamics of ocean surface waves. John Wiley & Sons, 1983.

22. Putnam, J.A., Munk, W.H. and Taylor, M.A., The prediction of longshore current. Trans. Amer. Geophys. Union 30(3), 1945, pp. 337-345.

23. Thornton, E.B., Variation of longshore current across the surf zone. Coastal Engineering Conference. ASCE, 1970, pp. 291-308.

24. Vitale, P., Movable-bed laboratory experiments comparing radiation stress and energy flux factor as predictors of longshore transport rate. Misc. Ref. No. 81-4, Coastal Eng. Res. Ctr., 1981.

25. Von Schwind, J.J., Geophysical fluid dynamics for oceanographers. Prentice Hall Inc., 1980.

26. Wang, H. and Yang, W.C., A similarity model in the surf zone. Coastal Eng. Conference. ASCE, 1980, pp. 529-546.

27. Wu, C., Thornton, E.B. and Guza, R.T., Waves and longshore currents: comparison of a numerical model with field data. Jour. Geophys. Res. 90, No. C3, 1985, pp. 4951-4958.

CHAPTER 101

Prediction of Properties of Marine Sand by In-Situ Measurement of Wave Induced Pore Pressure

Yoshihiko MAENO* and Takashi HASEGAWA**

ABSTRACT

The purpose of this paper is to predict the physical and mechanical properties of deposits near the surface of the seabed by in-situ measurements of the wave-induced pore pressure.

First, the wave-induced pressure both at the surface of the seabed and inside the seabed are examined by frequency analysis, to clarify the propagation characteristics of pressure in the seabed.

Secondly, a theoretical equation which gives the relationship between pore pressure fluctuation and wave pressure fluctuation is proposed.

Thirdly, the porosity of the seabed is predicted by the propagating characteristics of the pore pressure within the seabed based on the results of both the model tests by wave tank and the field measurements of the wave-induced pore pressure.

Finally, by fitting the theoretical equation to the spectral ratio of the in-situ measured pore pressure fluctuation to wave pressure fluctuation, the bulk modulus of the seabed and the degree of saturation are predicted.

INTRODUCTION

Wave-induced instabilities near the surface of the seabed, in which the deposit is confined at low pressure, is an interesting theme in coastal engineering. These instabilities are observed in many configurations, e.g., seabed slide, liquefaction of the seabed, moving of soil mass, shore process and so on. To analyze the stability of the seabed based on the theory of effective stress, knowledge of both the properties of the deposit and the wave-induced pore pressure developed in the seabed are needed. Many authors (e.g. Madsen, 1978; Yamamoto, 1977) have investigated the theory of predicting wave-induced pore pressure in a seabed by both theoretical considerations and in-situ measurements. The authors (1985a,1985b) also proposed an empirical equation evaluated by wave steepness to predict the wave induced pore pressure in the seabed. However, it is difficult to clarify the properties of the deposit near the surface of the seabed by element tests because of its low confined condition. Investigation through the in-situ measurement, therefore, is more desirable.

In this study, the physical and mechanical properties of the deposit are investigated by in-situ measurements of the wave-induced

* Assistant Professor, Dept. of Civil Eng., Maizuru College of Technology, 234 Shiraya Maizuru, Kyoto, 625.
** Professor, Dept. of Agricultural Eng., Kyoto University, Oiwake-cho Sakyo-ku, Kyoto, 606.

pore pressure. The wave pressure at the seabed surface and the wave-induced pore pressure in the sand layer were measured at Nabae Beach in Wakasa Bay which is in the Sea of Japan off of Fukui Prefecture, Japan. The propagation characteristics of the wave-induced pore pressure were examined by the frequency analysis (Maeno and Hasegawa, 1985c). In particular, the spectral ratio of the measured wave-induced pore pressure fluctuation to the measured wave-induced pressure fluctuation at the seabed surface is noted as a powerful tool in examining the properties of the seabed deposit. Furthermore, the authors propose a theoretical equation which gives the relationship between the wave-induced pore pressure and the wave-induced pressure. The equation, which is a function of frequency, is compared with the spectral ratio. This equation is based on the assumptions that the seabed consists of fully saturated porous media and that the wave-induced pressure fluctuates at a frequency low enough to disregard the effects of viscous fluid.

THEORETICAL CORRELATION BETWEEN WAVE PRESSURE AND PORE PRESSURE

Correlation between Pore Pressure and Volumetric Strain

Many of the first order features in the relation between pore pressure and ground motion can be explained by the theory of elastic wave propagation (Mavko and Harp, 1984). As the saturated porous media consists of both solids and liquids, if it is assumed that the saturated sediments behave as a linear elastic solid and that the frequency of wave excitation is low enough that viscous fluid effects are negligible, the elastic wave-induced pore pressure is predicted to be proportional to the solid volumetric strain by the reciprocity theorem (Jaeger and Cook, 1969) of saturated porous media.

Therefore, the wave-induced pore pressure is related to the volumetric strain of the solid skeleton as given in Equation (1) (Jaeger and Cook, 1969).

$$p = \{ Kf(Ks-Kc)/[n(Ks-Kf)]\} \varepsilon \qquad (1)$$

where p is the pore pressure, is the volumetric strain of the solid skeleton, Ks is the bulk modulus of mineral grains costituting the solid skeleton, Kf is the bulk modulus of fluids, Kc is the bulk modulus of composites and n is the porosity.

Motion of Fluids in Porous Media

Biot(1956a,b) considered the motion of fluids in porous media and classified fluid motion into two mechanisms as follows. One is the motion induced by the relative acceleration between the solid phase and liquid phase; the other is induced by the pressure gradient caused by uneven compaction, and dissipated through the porous media according to Darcy's law. Both of them possess special individual features.

For example, the former is induced by both the compressional wave of the first kind and the shear wave and accelerates the solid skeleton. The force of inertia influences the phase lag between the fluid motion and the solid motion. The latter, called the local squirt

flow, is induced by the greater pressure gradient caused by the friction force between the liquid and the pore face when elastic waves are transmitted through the porous media. This pressure gradient depends on both the shape and the sinuosity of the pores.

Effects of Pore Shape on Fluid Motion

Biot(1956a,b) also considered the effects of the pore shape on frequency, depending on the force of friction. He examined pore shapes for the slit model and the round model. These models are understood by the aspect ratio of the section of pores. This ratio is assumed to be less than unity for the slit model and unity for the round model. These two pore shapes are extreme cases in the two poles. Although the pore shape in sediments is usually in the region between round and slit, it is reasonable to assume that round and slit models can be used to characterize the fluid motion.

Therefore, his elastic wave propagation theory is taken into account as the structure factor consists of both the shape and sinuosity of pores. However, this treatment of pore shape for wave propagation theory does not take into account the local fluid motion but, rather, takes into account the effects of pore shape on the local fluid motion by varying the value of the structure factor.

Biot(1962) also considered the squirt flow in porous media and investigated the effects of the shape and sinuosity of pores on the spectral ratio of the pore pressure to the volumetric strain. For the compressional wave of the first kind, the slit pore shape induces higher pore pressure than the round pore shape. For the first fluid motion, the spectral ratio of pore pressure to the volumetric strain increases with frequency. For the second fluid motion, that is a local squirt flow, the spectral ratio of pore pressure to the volumetric strain decreases for the round shape and increases for the slit shape as the frequency increases.

Correlation between Pore Pressure and Acceleration for Earthquakes

Mavko and Harp(1984) investigated theoretically the correlation between the pore pressure and the acceleration at the surface of the ground by relating both the horizontal and vertical acceleration to the volumetric strain during an S-wave train and a P-wave train respectively. For example, the spectral ratio of the pore pressure to the vertical acceleration at the surface of the ground during a P-wave train is defined in Equation (2).

$$P = \{zKf(Ks-Kc)/[nVp^2(Ks-Kf)]\}\,Ap \qquad (2)$$

where Vp is the velocity of the compressional wave of the first kind, Ap is the vertical component of the acceleration at the surface of the ground and z is the depth under the ground surface.

They analyzed both wave-induced pore pressure and the acceleration recorded during the 1980 Mammoth Lakes, California, earthquake sequence. Also they showed the spectral ratios of the pore pressure to the vertical acceleration and the horizontal acceleration during a P-wave train and an S-wave train, respectively.
During P-wave arrivals, there is a negative linear correlation between

the spectral ratio and the frequency. During S-wave arrivals, there is no linear correlation between the spectral ratio and the frequency. The spectral ratio decreases exponentially with the frequency. Assuming that P-waves consist mainly of the compressional wave of the first kind, since the spectral ratio of pore pressure induced by the compressional wave of the first kind to the vertical acceleration is shown to decrease linearly with the frequency, the pore shape is round and the fluid motion in the pores dominates the second model of fluid motion, that is the local squirt flow.

Theoretical Equation between Pore Pressure and Wave Pressure

The authors considered the spectral ratio which is defined as the ratio of the power spectrum of the wave-induced pore pressure fluctuation within the seabed to the spectrum of the wave-induced pressure fluctuation at the surface of the seabed. The correlation between the wave-induced pore pressure fluctuation within the seabed and the wave pressure fluctuation at the surface of the seabed under the plane strain condition is derived as follows.

The displacements of the seabed under the wave action are evaluated by Biot's elastic wave propagation theory (Yamamoto, 1981). However, the wave-induced motion of the seabed is a slow phenomenon according to Zienkiewicz's(1980) classification of Biot's dynamic and quasi-static formulation, because the seabed is composed of a sand layer and the period of the gravity wave is less than 1.0 Hz. The accelerations of both the solid and liquid phases are negligible for the formulation of this phenomenon. Then this formulation corresponds to formulations by the quasi-static consolidation theory. Therefore, the displacements are derived according to Biot's(1941) consolidation theory (Yamamoto, 1977).

Equations (4) and (5) give the displacements of the seabed (Yamamoto, 1977). The harmonic load is given in Equation (3).

$$T = P_0 \exp[i(Nx+\omega t)] \tag{3}$$

$$U = i\{m[i(1-2\nu)\omega''-1-2(1-\nu)N'']\exp(-Nz)/[-N''+i(1+m)\omega''] - [1-mN''/[-N''+i(1+m)\omega'']]Nz\exp(-Nz)+m\exp(-N'z)/ [-N''+i(1+m)\omega'']\}(P_0/2NG)\exp[i(Nx+\omega t)] \tag{4}$$

$$W = \{[1+m[1+(1-2\nu)(i\omega''-N'')]/[-N''+i(1+m)\omega'']\exp(-Nz) - [1-mN''/[-N''+i(1+m)\omega'']]Nz\exp(-Nz)-m(1+N'')\exp(-N'z)/ [-N''+i(1+m)\omega'']\}(P_0/2NG)\exp[i(Nx+\omega t)] \tag{5}$$

where

$$N'^2 = N^2+i\omega' \tag{6}$$

$$\beta = (1-\nu)/(1-2\nu) \tag{7}$$

$$\omega' = \omega/c \tag{8}$$

$$\omega'' = (\omega'/N^2) \tag{9}$$

$$c = (k/\gamma)/\{n/Kf'+(1-2\nu)/[2G(1-\nu)]\} \tag{10}$$

$$m = nG/[Kf'(1-2\nu)] \tag{11}$$

$$N'' = (N'-N)/N \tag{12}$$

$$1/Kf' = 1/Kf+(1-Sr)/Pa \tag{13}$$

and Kf' is the apparatus bulk modulus of the pore fluid, G is the shear modulus, ν is Poisson's ratio, ω is the angular frequency, k is the permeability, Sr is the degree of saturation, Pa is the absolute pore pressure, and U and W are the displacements in the x- and z-directions respectively.

The dilatational strain is given in Equation (14).

$$\begin{aligned}\varepsilon &= \partial U/\partial x + \partial W/\partial z \\ &= \{-[(1-Nz)(1+m)+m(1-2\nu)](-N''+i\omega'')\exp(-Nz) \\ &\quad +mN''\exp(-N'z)\}P_0\exp[i(Nx+\omega t)]/G[-N''+i(1+m)\omega'']\end{aligned} \tag{14}$$

The term of $P_0\exp[i(Nx+\omega t)]$ in Equation (14) is the harmonic fluctuation of the wave pressure at the surface of the seabed. Thus, Equation (14) shows the relationship between the volumetric strain and the harmonic fluctuation of the wave pressure at the seabed surface. Therefore, the relationship between pore pressure and harmonic fluctuation of the wave pressure at the seabed surface is obtained from Equations (1) and (14).

$$\begin{aligned}P &= Kf(Ks-Kc)\{-[(1-Nz)(1+m)+m(1-2\nu)](-N''+i\omega')\exp(-Nz) \\ &\quad +mN''\exp(-Nz)\}T/\{nG(Ks-Kf)[-N''+i(1+m)\omega'']\}\end{aligned} \tag{15}$$

METHOD OF FIELD EXPERIMENTS

In-situ measurements of wave-induced pore pressure were conducted at Nabae beach in Wakasa Bay, Fukui Prefecture, Japan, because the physical properties of the deposit and the seasonal change of the shore profile have been already measured at this site. Table 1 shows the properties of Nabae sand. Since the uniformity coefficient is 1.53, Nabae sand is fairly uniform. The grain size distribution of Nabae sand is uniform wherever samples are extracted.

Table 1. - Properties of Nabae Sand.

Specific gravity	2.70
Uniformity coefficient	1.53
Effective grain size	0.114 mm
Average grain size	0.160 mm
Permeability	0.023 cm/s

Figure 1 shows the system for measurements. In our preliminary experiments, pressure transducers were placed on the surface of the seabed and buried in the seabed on one straight line. The wave-induced pressure was measured simultaneously at both the surface of the seabed and at two different depths within the seabed. The wave pressure fluctuation was measured at the surface of the seabed, and the pore pressure fluctuation was measured in the seabed. In this

study, the wave-induced pore pressure was measured with a probe as follows. A pressure transducer with porous cap is fixed inside the probe at a point 15 cm from its tip. The probe has a length and diameter of 250.0 cm and 26.0 mm, respectively, and is tipped with a cone with a 30 degree angle. To clarify the properties of the deposit near the surface of the seabed where the confining pressure is fairly low, the wave-induced pore pressure was measured at a depth of 33 cm on August 9, 1985 and at a depth of 37 cm on August 10, 1985, below the mudline.

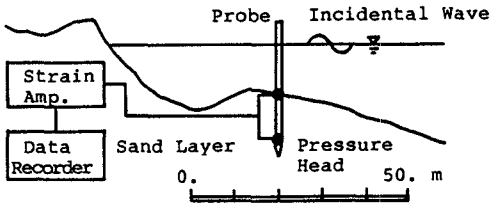

Figure 1. Experimental Set-Up of Field Measurements.

EXPERIMENTAL RESULTS AND DISCUSSIONS

Frequency Analysis of In-Situ Measurement

Figures 2(a) and 2(b) show the fluctuations of the wave-induced pressure at the surface of the seabed and the wave-induced pore pressure within the seabed. It can be seen from these figures that both the wave pressure and the pore pressure fluctuate similarly without any great difference, and that the high frequency component is significantly damped. This fact is made clearer when compared with the power spectrum in Figures 3(a) and 3(b).

The power spectrum decreases as the frequency increases. The conditions for Fourier fast transform(FFT) analysis are as follows: the sampling interval is 0.15 s; the number of sampling points is 1024; the Nyquist number is 3.33 Hz. There are no problems in examining a frequency component below 1.0 Hz.

Figures 4 and 5 show the coherence and the phase between the wave-induced pore pressure fluctuation within the seabed and the wave pressure fluctuation at the surface of the seabed, respectively. Figures 4(a) and 4(b) show that the coherence is unity in the frequency range less than 0.6 Hz and as the frequency increases to over 0.6 Hz the fluctuation increases. This fact suggests that the propagation characteristics of wave-induced pressure vary at a frequency of 0.6 Hz.

Figure 5(a) and 5(b) show that the phase is nearly constant, that is 0.5π in the frequency range less than 0.6 Hz, and as the frequency increases to over 0.6 Hz the fluctuation also increases. Since the phase represents the lag time multiplied by the angular frequency, the lag time between the two fluctuations increases as the frequency decreases. This fact indicates that longer periodic waves propagate easily into the seabed and affect the wave-induced instabilities of the seabed as previously mentioned.

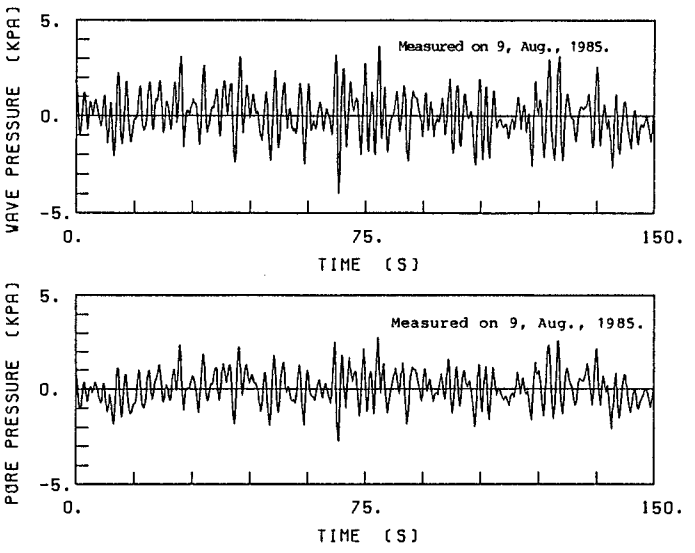

(a) Measured on August 9, 1985.

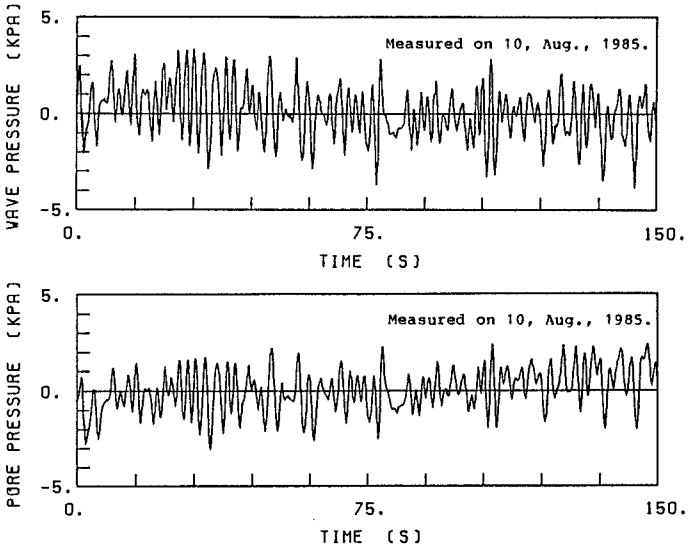

(b) Measured on August 10, 1985.

Figure 2. Comparison between Wave Pressure and Pore Pressure Fluctuations.

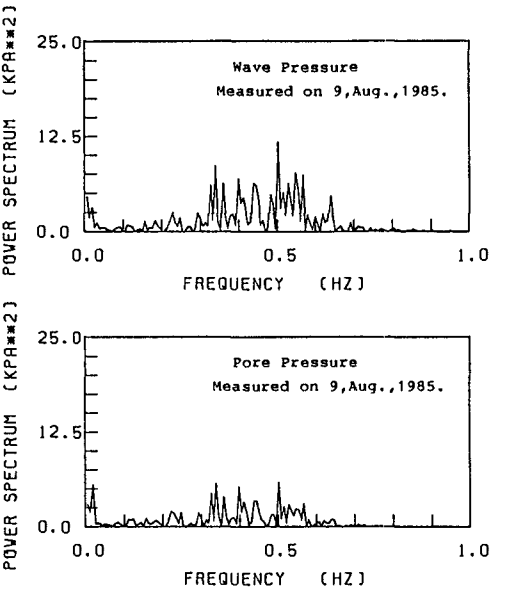

(a) Measured on August 9, 1985.

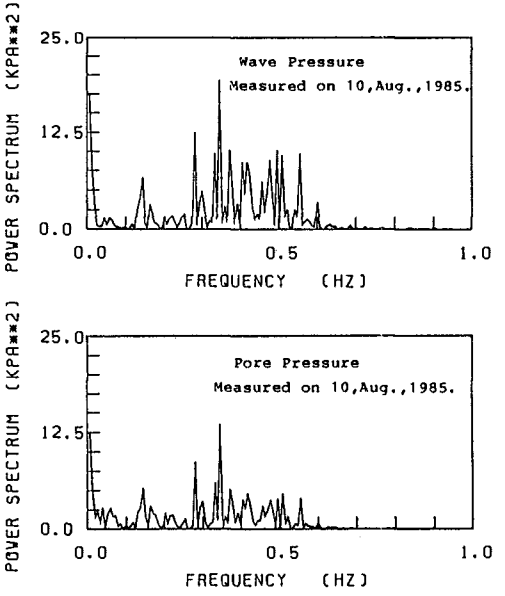

(b) Measured on August 10, 1985.

Figure 3. Power Spectra between Wave Pressure and Pore Pressure.

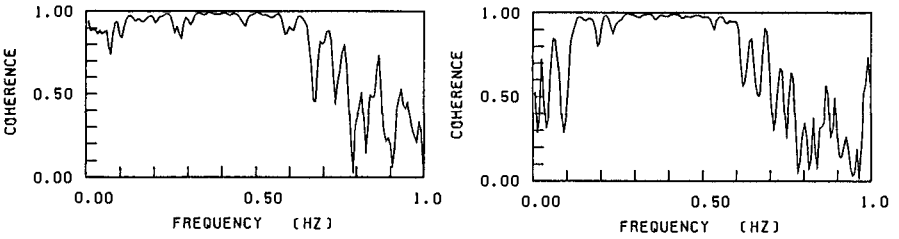

(a) Measured on August 9, 1985. (b) Measured on August 10, 1985.

Figure 4. Coherence between Wave Pressure and Pore Pressure

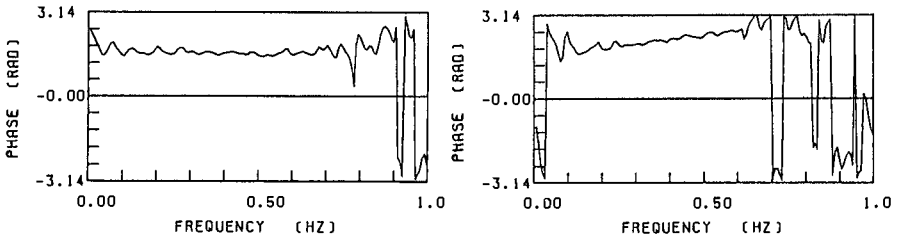

(a) Measured on August 9, 1985. (b) Measured on August 10, 1985.

Figure 5. Phase between Wave Pressure and Pore Pressure.

Figure 6(a) and 6(b) show the frequency response. This figure demonstrates that the frequency response decreases linearly as the frequency increases with the greater fluctuation in the frequency range more than 0.6 Hz. This fact indicates that the low frequency component of the wave pressure fluctuation easily propagates into the seabed.

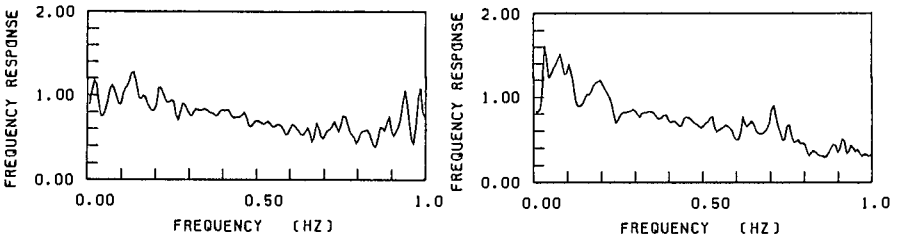

(a) Measured on August 9, 1985. (b) Measured on August 10, 1985.

Figure 6. Frequency Response between Wave Pressure and Pore Pressure.

Prediction of Porosity of Sediments

Many difficulties accompany the measurement of the seabed deposits. For example, the density logs used on land have problems in

performing the experiments in submarine, the method using sampling has disturbances of remolding and swelling, and the method using the radioactive log is now being developed to reduce the costs and the difficulty of operation. The simple method of the density log is proposed based on the propagating characteristics of the wave pressure into the seabed.

Stoll(1977) indicated that the attenuation of pressure within the seabed is understood by the mechanics both of the intergranular friction in the frame of the soil skeleton and the viscosity of the pore fluid moves in relation to the motion of the soil skeleton.

Since the frequency of the waves is less than 1.0 Hz and the seabed is composed of sand, the intergranular friction is predominant and the damping of the viscosity of pore fluid can be neglected.

The intergranular friction depends on the constitution of the soil skeleton. The density of the sand bed is chosen as the tool to decide this constitution. Therefore, the correlation between the damping and the density of the sand bed enables the prediction of the density of the sand bed.

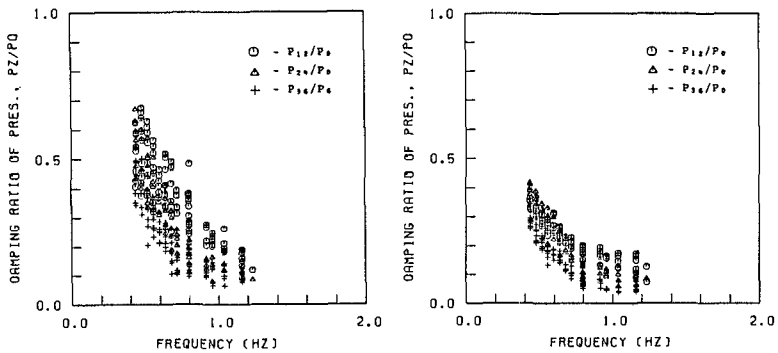

(a) ρ_d = 1.55 tm^{-3} (b) ρ_d = 1.57 tm^{-3}

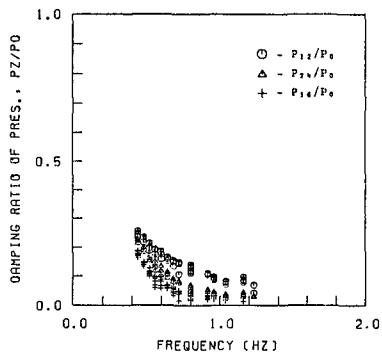

(c) ρ_d = 1.62 tm^{-3}

Figure 7. Effect of Frequency on Damping Ratio of Pore Pressure.

Figures 7(a) through 7(c) show the relationship between the frequency of the waves and the damping ratio, which is defined as the ratio of the measured pore pressure to the measured wave pressure at the surface of the bed, based on the results of our previous works (Maeno and Hasegawa, 1985b). In these figures, the subscript of P denotes the depth downward from the bed surface.

These figures show that the damping ratio decreases quadratically as the frequency increases. Since the damping ratio for the tide is infered to be unity, the damping ratio is unity at the frequency zero, and decreases with decreasing velocity as the frequency increases. This tendency is unique for a dense sand bed. However, the linear correlation between the damping ratio and the frequency can be assumed within the region of our experimental results.

Thus, Figure 8 shows the relationship between the gradient of this linear correlation and the density of the sand bed. In this figure, the gradient decreases with decreasing velocity as the density increases. This correlation can be drawn as the monotonous curve. This correlation is examined for the regular wave for various frequencies between 0.6Hz and 2.27Hz generated by the wave tank in laboratory experiments. However, the ocean waves are irregular. The damping of the non-linear waves must be defined. For the irregular waves, assuming that the damping ratio is defined as the spectral ratio of the pore pressure fluctuation within the seabed to the wave pressure fluctuation at the surface of the seabed, the correlation between the damping ratio and the density of the seabed is examined.

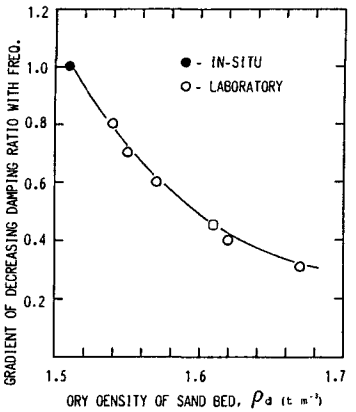

Figure 8. Relationship between Reduction Gradient of Damping Ratio and Dry Density of Sand Bed.

Figures 9(a) and 9(b) show the spectral ratio of the pore pressure to the wave pressure, which were measured at Nabae Beach in Wakasa Bay, Fukui Prefecture. In this figure, the spectral ratio decreases quadratically as the frequency increases. The linear correlation between the spectral ratio and the frequency can be assumed in the region less than 1.0 Hz. In this case, the gradient of this linear correlation is almost unity. The value of this gradient of in-

situ measurements, 1.0 is plotted on the approximate curve in Figure 8. The point determined on this curve indicates the density, 1.51 tm^{-3}. This value is infered to be the density of the seabed deposits.

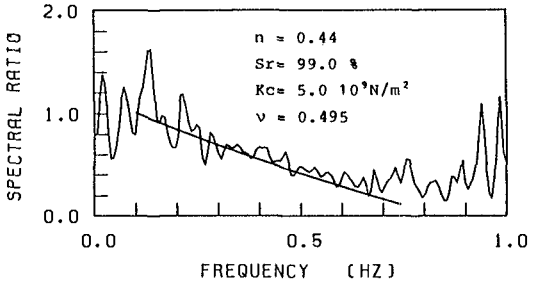

(a) Measured on August 9, 1985.

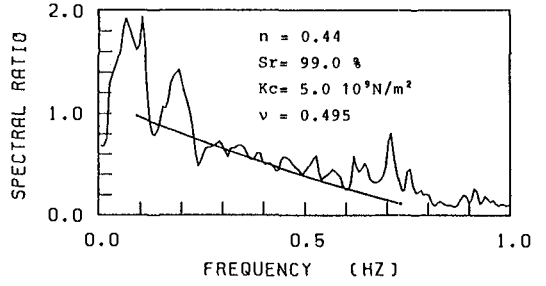

(b) Measured on August 10, 1985.

Figure 9. Spectral Ratio between Wave Pressure and Pore Pressure.

Since the specific gravity of this sand is 2.70 as shown in Table 1, the porosity of the seabed deposits is obtained as 0.44. Based on Komura's(1961) study on the relationship between the porosity and the average grain size, the average grain size of Nabae sand, 0.160 mm indicates that the porosity of the bed is infered to be distributed between 0.35 and 0.45. Hamilton(1972) also indicates that the deposits of the mean grain size, 0.160 mm, has a porosity of almost 0.45. The predicted porosity, 0.44 is reasonable, because the seabed near the surface is loosest.

Therefore, assuming that the spectral ratio is equivalent to the damping ratio, the density of the seabed deposits can be obtained based on the experimental correlation between the damping ratio and the density of the bed.

Further field measurements for various sites make the verification of this prediction possible.

Comparison of Theoretical Equation with Spectral Ratio

Figures 9(a) and 9(b) show the spectral ratio of the pore water pressure fluctuation within the sand layer and the wave pressure

fluctuation at the surface of the sand layer. The spectral ratio decreases as the square of the frequency increases, because the frequency response between the pore pressure fluctuation and the wave pressure fluctuation decreases linearly as the frequency increases. The theoretical equation of the correlation between pore pressure and wave pressure is simulated using the parameters in Table 2.

Table 2. - Physical Parameters of Soils Used in Analysis

Bulk modulus of fluid, Kf	2.0 GPa
Bulk modulus of Mineral grains, Ks	36.0 GPa
Bulk modulus of composite, Kc	4.9-5.4 GPa
Poisson's ratio	0.495
Porosity, n	0.44

By fitting the theoretical Equation (15) to the spectral ratio, the properties of the seabed are examined, that is, the bulk modulus of composite, the porosity of the sand bed, the degree of saturation, the shear modulus and Poisson's ratio. The values of the porosity of the sand bed and Poisson's ratio can be assumed experimentally because they vary within a narrow range under the conditions in this investigation. The porosity is predicted to be 0.44 based on the considerations of the damping ratio of pore pressure as described in the previous section. Poisson's ratio of the saturated soil is in the region of 0.49 to 0.50 for the case of the shear modulus less than 1000 $kgfcm^{-2}$ (Ishihara,1970). And Poisson's ratio is predicted by Hamilton's(1979) Equation (16) consisting of the velocities of the compressional wave of the first kind and the shear wave measured in-situ in the seabed. In this case, Poisson's ratio is assumed to be 0.495.

$$\nu = \{(Vp/Vs)^2-2\}/2\{(Vp/Vs)^2-1\} \quad (16)$$

The shear modulus is derived by the bulk modulus of the composite and Poisson's ratio. The bulk modulus of the fluid and solid are assumed to have typical values as shown in Table 2.

Therefore, the values of the bulk modulus of composite and the degree of saturation can be determined by the theoretical equation which fits the spectral ratio.

In the low frequency range of less than 0.5 Hz, the theoretical value estimated by Equation (15) is in good agreement with those of the spectral ratio of in-situ measured wave-induced pore pressure fluctuation to the wave-induced pressure fluctuation at the surface of the seabed.

In this case, it is predicted that the bulk modulus of composite is between 4.9 GPa and 5.0 GPa and that the degree of saturation is between 97% and 99%. These values are compatible with Esrig and Kirby's(1977) results and those of other considerations.

Discussions

Since Nabae sand is a quite uniform marine sand, as shown in Table 1, the aspect ratio of the pore shape is predicted to be approx-

imately unity and the round model is chosen for the pore shape of this sand. Thus, the fluid motion includes the effects of the local squirt flow with the condition of high permeability.

The propagation characteristics of the wave pressure depend on both the compressional wave and the the shear wave based on Biot's consideration of pore shape. As the spectral ratio of the wave-induced pore pressure to the wave-induced pressure is consistent with the theoretical value predicted by the proposed Equation (15), which takes into account the effects of both the dilatational wave and the shear wave, the wave-induced effects are examined not only for the compressional wave but also the shear wave.

Many authors have investigated the mechanical and physical properties of the deposits in the seabed as described above. There are many difficulties in obtaining the properties of the deposits, for example the remolding and swelling of the samples caused by extraction from the seabed. By the in-situ measuring of the pore water pressure fluctuation within the seabed, information concerning seabed mechanics was derived from this study. Examination of the spectral ratio makes it possible to predict the properties of the deposits based on the theory of wave-induced pore pressure in porous media. Moreover, spectral ratio of the wave-induced pore pressure is similar to that of the earthquake induced pore pressure and both the spectral ratios can be related to each other. It is useful, therefore, to predict the propagation characteristics of earthquake induced pore pressure by the spectral ratio of wave-induced pore pressure.

CONCLUSIONS

The following conclusions were obtained :

1. The low frequency component of wave-induced pressure fluctuation propagates into the seabed as wave-induced pore pressure more easily than does the high frequency component.
2. The phase lag between the wave-induced pressure at the seabed surface and the wave-induced pore pressure within the seabed increases as the frequency decreases.
3. The theoretical equation which gives the relationship between pore pressure and wave pressure fluctuations is proposed.
4. The porosity of the seabed deposit is predicted by the damping ratio of pressure inside the seabed.
5. By fitting the theoretical equation to the spectral ratio between the wave-induced pore pressure and the wave-induced pressure at the seabed surface, the bulk modulus of composite and the degree of saturation can be determined. These values are compatible with those of theoretical and empirical considerations.

APPENDIX I.- REFERENCES

Biot,M.A., "General theory of three-dimensional consolidation," J. of Applied Physics, Vol.26, 1941, pp.182-185.

Biot,M.A., "Theory of elastic waves in a fluid saturated porous solid," I-low frequency range, J. of the Acoust. Soc. of Am., Vol.28, 1956a, pp.168-178.

Biot,M.A., "Theory of elastic waves in a fluid saturated porous sol-

id," II-higher frequency range, J. of the Acoust. Soc. of Am., Vol.28, 1956b, pp.179-191.
Biot,M.A., "Generalized theory of acoustic propagation in porous dissipative media," J. of Acoust. Soc. of Am., Vol.34, 1962, pp.1254-1264.
Esrig,M.I., and Kirby,R.C., "Implications of gas content for predicting the stability of submarine slopes," Marine Geotechnology, Vol.2, 1977, pp.81-100.
Hamilton,E.L., "Compressional-Wave Attenuation in Marine Sediments," Geophysics, Vol.37, 1972, pp.620-646.
Hamilton,E.L., "Vp/Vs and Poisson's ratio in marine sediments and rock," J. of Acoust. Soc. of Am., Vol.66, 1979, pp.1093-1101.
Ishihara,K., "Approximate forms of wave equations for water saturated porous materials and related dynamic modulus," Soils and Foundations, Vol.10, No.4, 1970, pp.10-38.
Jaeger,J.C. and Cook,N.G.W., "Fundamentals of Rock Mechanics," Methuen, London, England, 1969.
Komura,S., "Bulk properties of river bed sediments and its applications to sediment hydraulics," Proc. of Jap. Nat. Cong. for Appl. Mech., 1961.
Madsen,O.S., "Wave-Induced Pore Pressures and Effective Stresses in a Porous Bed," Geotechnique, Vol.28, No.4, 1978, pp.377-393.
Maeno,Y. and Hasegawa,T., "Characteristics of wave-induced pore water pressure in sand layer," Proc. of Int. Symposium on Ocean Space Utilization, Ocean Space'85, 1985a, pp.475-484, Springer-Verlag.
Maeno,Y. and Hasegawa,T., "Evaluation of wave-induced pore pressure in sand layer by wave steepness," Coastal Engineering in Japan, Vol.28, Japanese Soc. of Civil Eng., 1985b, pp.123-136.
Maeno,Y. and Hasegawa,T., "Propagation characteristics of pore water pressure in seabed under wave loading," Proc. of 32th Conference on Coastal Eng., JSCE, 1985c, pp.75-79,(in Japanese).
Mavko,G.M., and Harp,E., "Analysis of wave-induced pore pressure change recorded during the Mammoth Lakes, Calif. earthquake sequence," Bull. of the Seismological Soc. of Am., Vol.74, No.4, 1984, pp.1395-1407 .
Stoll,O.R., "Acoustic Waves in Ocean Sediments," Geophysics, Vol.42, 1977, pp.715-725.
Yamamoto,T., "Wave induced instability in seabeds," Proc. of ASCE Special Conf. Coastal Sediments'77, 1977, pp.898-913.
Yamamoto,T., "Wave-induced pore pressures and effective stresses in inhomogeneous seabed foundations," Ocean Engng., Vol.8, 1981, pp.1-16.
Zienkiewicz,O.C., Chang,C.T. and Bettess,P., "Drained, undrained consolidating and dynamic behavior assumptions in soils," Geotechnique, Vol.30, No.4, 1980, pp.385-395.

CHAPTER 102

LABORATORY STUDY ON TWO-DIMENSIONAL BEACH TRANSFORMATION DUE TO IRREGULAR WAVES

Nobuo MIMURA[1], Yukinori OTSUKA[2] and Akira WATANABE[3]

ABSTRACT

In the present study, effects of irregular waves on two-dimensional beach transformation and related phenomena were investigated through a series of laboratory experiments. Attempts were made to determine a representative wave of irregular wave trains which controlled individual phenomenon related to the two-dimensional beach profile change. It was found that the representative wave is different for each phenomenon. For the macroscopic beach profile change, it is the mean wave which represents whole incident waves. On the other hand, some of microscopic phenomena, such as initiation of sand movement and sand ripple formation, are controlled by larger waves in the wave train selectively, of which representative wave is the significant wave.

1. INTRODUCTION

There have been many studies on two-dimensional beach transformation and cross-shore sediment transport in and out of the surf zone. While a number of laboratory studies were performed on this subject, phenomena in real beaches could not be necessarily reproduced in wave flumes. The difference of phenomena in real beaches and laboratories is caused by several factors such as scale effect of physical model, three-dimensional effect of real topographic change, irregularity of real waves, etc. Among them, the effects of wave irregularity on the beach profile change have scarecely examined, since most of laboratory experiments were carried out by regular waves. While there are a few attempts to investigate bar formation and sediment transport rate under irregular waves such as by Tsuchiya and Inada(1974), and Wang and Liang(1975), complete understanding of this subject is beyond us. In order to connect the knowledge accumulated by historical laboratory studies with real phenomena, it is fundamentally important to determine the effects of wave irregularity on two-dimensional beach transformation.

1 Associate Professor, Department of Civil Engineering, Ibaraki University, Hitachi, Ibaraki 316, Japan
2 Kagoshima Prefectural Government, Kagoshima 892, Japan
3 Professor, Department of Civil Engineering, University of Tokyo, Tokyo 113, Japan

In the present study, a series of laboratory experiments were performed under the action of irregular waves. Beach profiles were measured at several time steps of wave action in an experiment. On the basis of these measurements of beach profiles, macroscopic profile change, threshold of sand movement, characteristics of sand ripples and net rate of cross-shore sediment transport were investigated. In order to examine the effects of irregular waves on these phenomena, results of the present study were compared with those from previous investigations of regular waves. While there are several ways to express the characteristics of irregular waves, the concept of representative wave was employed. As the representative wave, significant wave and mean wave were taken. It is a main objective to determine the representative wave for each phenomenon, which plays an almost same role as a train of irregular waves in generating the target phenomenon.

2. EXPERIMENTAL PROCEDURE

Laboratory experiments were performed in a wave flume, 19m long, 1m deep, and 0.8m wide, as shown in Fig. 1. A sandy beach was placed at one end of the flume. Two kinds of well-sorted quartz sand were used as bed materials: one is fine sand (Toyoura sand) with mean diameter, d_{50}, of 0.18mm, and the other coarse sand with d_{50} of 0.75mm. The wave flume was devided into two parts so that two tests with different bed materials could be carried out simultaneously. In order to make it easy to compare the results of the present experiments with those of regular wave studies, tests were limited to a uniform initial beach slopes of 1/10 or 1/20.

The wave generator used can produce irregular waves with any spectrum. In the present study, the Bretschneider-Mitsuyasu spectrum (Bretschneider 1968, Mitsuyasu 1970) was employed for incident waves. The general form of this spectrum, S, is

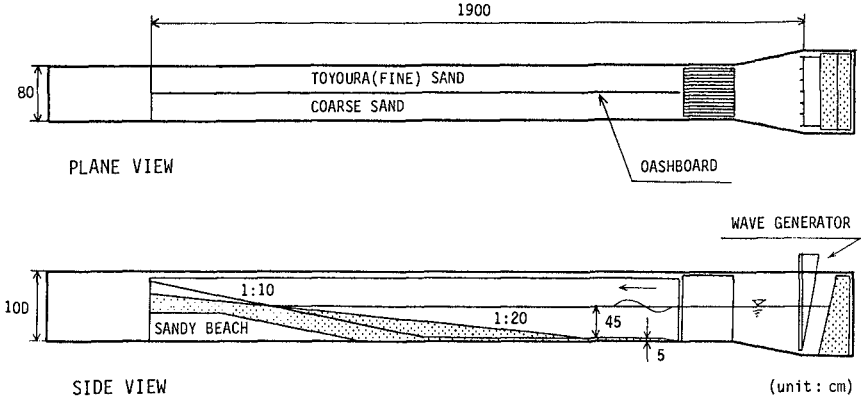

Fig. 1 Wave flume

Table 1 Experimental conditions

Ser. A (TOYOURA SAND, d_{50}=0.18mm)						Ser. B (COARSE SAND, d_{50}=0.75mm)					
Case	Initial Slope	Significant Wave		Mean Wave		Case	Initial Slope	Significant Wave		Mean Wave	
		$(H_{1/3})_o$ (cm)	$T_{1/3}$ (s)	$(H_m)_o$ (cm)	T_m (s)			$(H_{1/3})_o$ (cm)	$T_{1/3}$ (s)	$(H_m)_o$ (cm)	T_m (s)
A-1	1/20	5.3	1.9	3.5	1.5	B-1	1/20	5.4	1.8	3.5	1.6
2		6.2	1.3	4.0	1.1	2		6.1	1.4	4.0	1.2
3		3.4	0.9	2.2	0.8	3		3.4	0.9	2.2	0.8
4		8.7	1.3	5.3	1.1	4		8.7	1.3	5.3	1.1
5		11.9	1.4	7.7	1.2	5		11.9	1.4	7.8	1.2
6		9.5	1.8	6.5	1.7	6		9.5	1.8	6.5	1.7
7	1/10	6.0	1.9	4.1	1.6	7	1/10	5.9	1.9	4.0	1.6
8		6.2	1.4	4.0	1.2	8		6.2	1.4	4.0	1.2
9		3.5	0.9	2.3	0.8	9		3.5	0.9	2.3	0.8
10		9.7	1.3	6.0	1.2	10		9.7	1.3	5.9	1.2
11		9.3	1.8	6.3	1.6	11		9.2	1.9	6.3	1.6
12		11.0	1.4	7.3	1.3	12		10.9	1.4	7.2	1.2

Subscript $_o$ indicates the deep water wave.

$$S(f) = 0.257 H_{1/3}^{2} T_{1/3}^{-4} f^{-5} \exp(-1.03(T_{1/3} f^{-4})) \quad (1)$$

where f is frequency, and $H_{1/3}$ and $T_{1/3}$ are significant wave height and period. Keeping the spectrum of incident waves same, significant wave height and period were changed for each experiment. Consequently, twenty four experimental cases were chosen with combinations of two grain sizes, two initial slopes, and several ranges of representative wave height and period. Experimental conditions are summerized in Table 1.

In the course of each experiment, wave motion, sand movement, and beach profile were measured systematically. In order to measure beach profiles continuously and accurately, bottom profilers of electromagnetic type were used. The region coverd by this measurement is from a sufficient high point on the backshore where wave uprush could not reach to the offshore end of the sandy beach. Beach profiles were measured three times in a case, namely just before the start of wave action (0 hour), 3 and 9 hours after it. Net rate of cross-shore sediment transport was calculated from the data of beach profiles in a similar way developed by Watanabe et al.(1980). In the middle of wave action, wave profiles and near-bottom velocities were measured with intervals of 25 or 50 cm along the beach as well as an offshore point. Moreover, states of wave breaking and sediment motion were observed and recorded by using a video-tape recorder.

3. EXPERIMENTAL RESULTS AND DISCUSSIONS

3.1 Macroscopic Beach Profile Change

As the first topic of experimental results, macroscopic beach profile change will be discussed. Figures 2 (a) to (d) show the beach profiles and distributions of the net rate of cross-shore sediment transport for all the cases listed in Table 1. Beach profiles were obtained after 9 hour wave action and the net rate of sediment transport rate was evaluated from the difference of two successive beach profiles measured at 0 and 3 hours after wave action. Positive values of sediment transport rate indicates onshore transport and negative values are for offshore transport. In Figs. 2 (a) to (d), results are ranged as a parameter C increases, which was suggested by Sunamura and Horikawa(1974) for the classification of beach profiles. As the parameter C is closely correlated with the wave steepness, it can be said that the order of the results corresponds to that of wave steepness.

For the regular wave experiments, it has been reported that sandy beach transforms systematically into some equilibrium profile according to the conditions of incident waves. From Figs. 2, it is seen that beach profile shows a systematic change even under the conditions of irregular waves.

In cases of fine sand (Ser.A), beach profiles vary from accreting type to eroding type. Under the conditions of smaller C, therefore smaller wave steepness, berm forms on the foreshore for both cases with

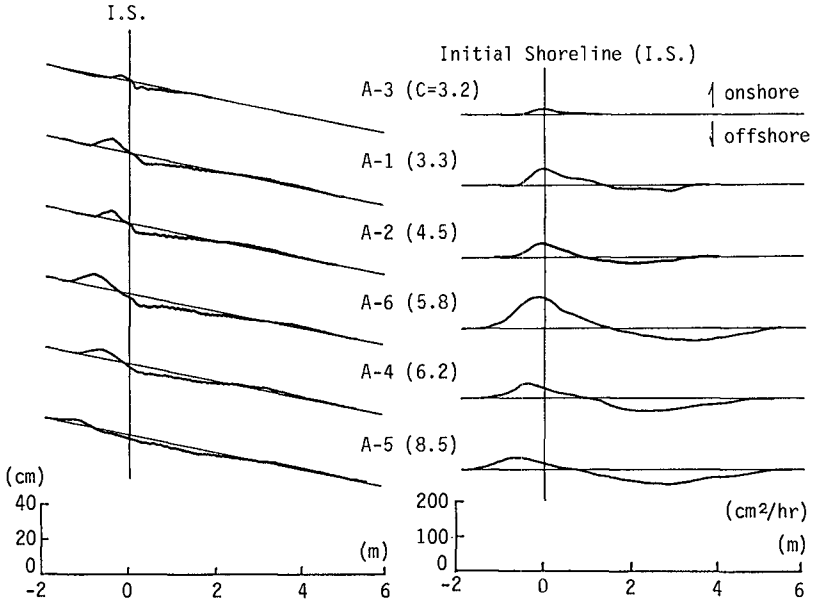

Fig.2 (a) Beach profiles and cross-shore sediment transport rate (initial slope=1/20, d_{50}=0.18mm)

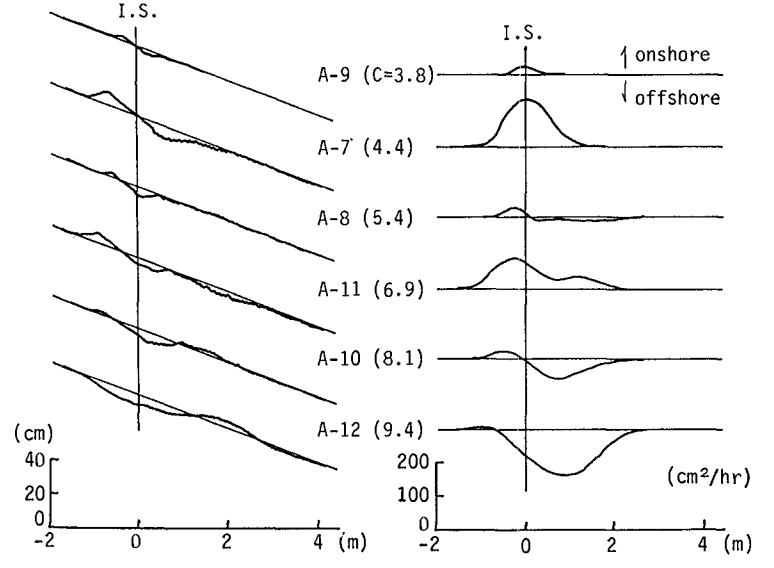

Fig.2 (b) Beach profiles and cross-shore sediment transport rate (initial slope=1/10, d_{50}=0.18mm)

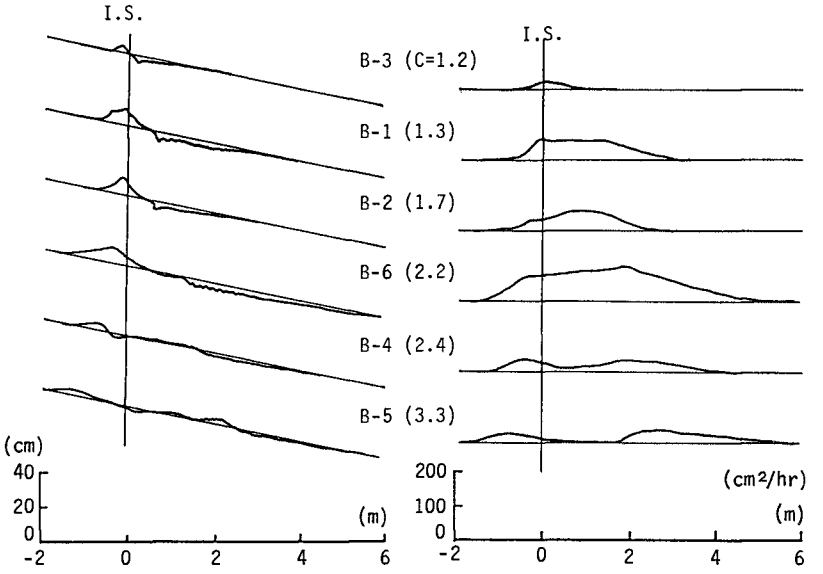

Fig.2 (c) Beach profiles and cross-shore sediment transport rate (initial slope=1/20, d_{50}=0.75mm)

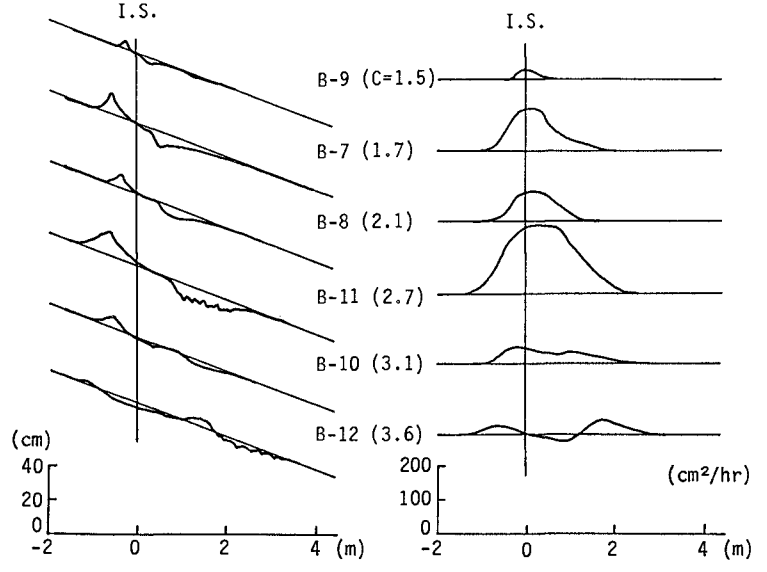

Fig.2 (d) Beach profiles and cross-shore sediment transport rate (initial slope=1/10, d_{50}=0.75mm)

initial slope of 1/10 and 1/20, and the direction of sediment transport is onshore in the whole region. As the value of C increases (wave steepness also increases), erosion of the foreshore begins and a bar becomes noticable. The sediment transport turns offshore. A complete eroding beach formed in Case A-12, of which incident waves were severest among the cases with initial slope of 1/10. In cases of coarse sand (Ser. B), eroding type of beaches did not appear because of the limitation of wave height and steepness. However, it can be seen that beach profiles and distributions of sediment transport rate vary in a systematic manner depending on the value of C.

It was observed that the progress of beach transformation was considerably slow in the present experiments comparing with regular wave cases. This tendency seems to be caused by wave irregularity. Namely, under the incidence of irregular waves, some waves may erode the beach, while other may act toward accretion. Coexistence of waves with conflicting actions yields the slow transformation of beaches. On the other hand, all waves have the same action under the regular wave conditions. Therefore, it should be noted that the beach transformation are accelerated in regular wave experiments.

3.2 Classification of Beach Profiles

It is well known that there are two typical types of natural beaches, that is bar (eroding) and step (accreting) type beaches. Many investigations have been performed to determine parameters classifying beach profiles, such as by Johnson (1949), Iwagaki and Noda (1962),

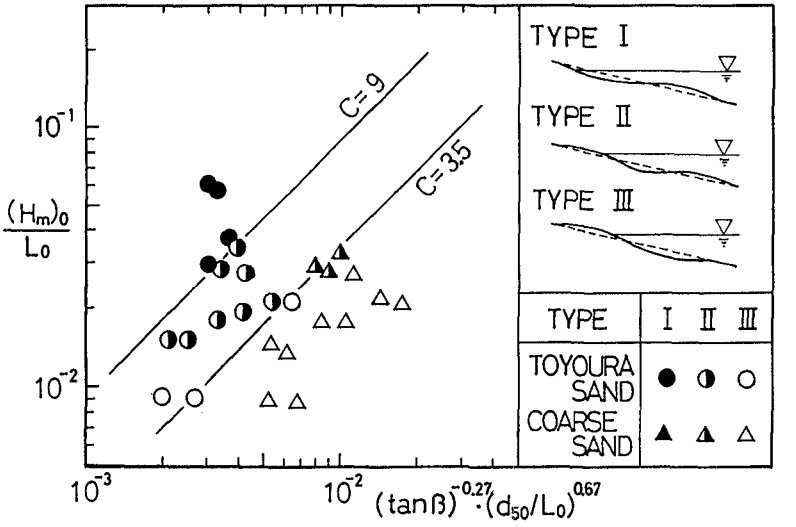

Fig. 3 Classification of beach profiles

Nayak (1970), Dean (1973), Sunamura and Horikawa (1974), and Hattori and Kawamata (1980). In the present study, adaptability of the classification of beach profile suggested by Sunamura and Horikawa is examined.

They classified beach profiles into three types based on the displacement of topography from the initial beach slope: Type I = a shoreline retrogresses and sand accumulates in offshore zone (eroding type), Type II = a shoreline advances and sand piles up offshore (intermediate type), and Type III = a shoreline progresses and no sand deposition takes place offshore (accreting type).

These three types are distinguished by a nondimensional parameter,

$$C = (H_0/L_0)\ (\tan\beta)^{0.27}\ (d/L_0)^{-0.67} \qquad (2)$$

where H_0 and L_0 are deep water wave height and length, $\tan\beta$ is initial beach slope, and d is grain diameter. Horikawa et al.(1975) determined the range of C parameter for each type on the basis of experimental results of regular waves as follows.

Type I: $10 < C$, Type II: $3 < C < 10$, Type III: $C < 3$.

Figure 3 shows the result of application of this classification to the present data given in Figs. 2. Figure 3 also includes the data of additional experiments performed in the same wave flume (Irie et al. 1985). For this application, mean waves were taken as the representative incident wave, that is, the values of ordinate and abcissa of Fig. 3 were calculated based on the wave height and length of the mean wave. It can be seen that this classification is effective for irregular wave cases, and that the mean wave gives considerably close criteria of classification as those for regular waves.

When the significant wave was used as the representative wave, the critical values of C moved from 3.5 to 5 and from 9 to 15 respectively. Therefore, it is concluded that the representative wave for the macroscopic beach profile change is the mean wave. This means that the macroscopic beach profile change is not controlled by a paticular group of waves, but by the whole incident waves.

3.3 Threshold of Sand Movement

As the threshold of sand movement, critical water depth was examined. It was determined based on a measured beach profile for each case, by judging the initiation point for the topographic change of the offshore region. Therefore, the critical water depth in the present study is for the general movement of sand particles, not for the initial movement.

The reference material were taken from the previous study by Horikawa and Watanabe (1967). Their method is certified to correspond with the results of laboratory experiments of regular waves.

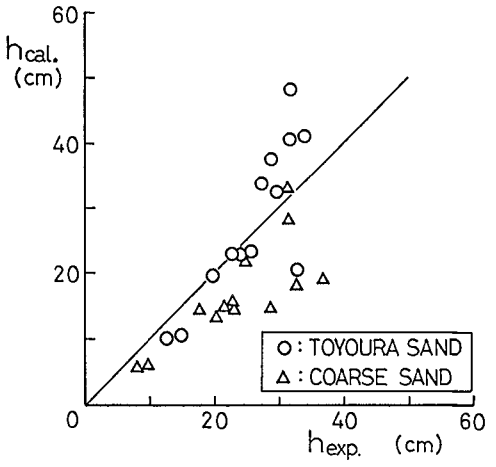

Fig. 4

Comparison of critical water depth between experiments and calculations

Figure 4 shows a comparison of the critical water depths obtained in the present experiments ($h_{exp.}$) and those of calculation by Horikawa and Watanabe's method ($h_{cal.}$). For this calculation, the quantities of significant wave were used. The agreement is considerably good in the region of small water depth, though the measured values tend to scatter as the water depth increases.

On the other hand, the mean wave gave forty percent smaller values of calculated critical depths, resulting in large disagreement with the measured values. Therefore, it is concluded that the representative wave for the threshold of sand movement is the significant wave. This conclusion seems to be as a matter of course, because sand grains cannot feel the influence of small waves in a deep area.

3.4 Characteristics of Sand Ripples

It has been certified that sand ripples play an important role in transporting sediment mainly through regular wave experiments. In the present experiments of irregular waves, sand ripples were observed in all cases of fine sand and a few cases of coarse sand. The most distinguishing feature is that the position and shape of sand ripples were considerably stable in spite that various waves passed over them one after another. Cloud of suspended sediment were often generated above the sand ripples, as seen in the regular wave experiments. It is recognized, therefore, that sand ripples are important for sediment transport also under the action of irregular waves.

In the present study, the initiation of formation and scales of sand ripples are investigated quantitatively. Among many studies on these subjects, the reference materials of regular wave experiments

were taken from the study by Riho et al.(1981).

In the regular wave study, Riho et al. determined the critical conditions of the ripple formation on the basis of two physical quantities: one is the ratio of orbital diameter of water particle at the bottom (d_0) to the median diameter of sand particles (d_{50}),and the other the Shields parameter. The orbital diameter, d_0, was evaluated from the wave profile based on the small ampritude theory. Moreover, in order to take the asymmetry of wave profile into account, they introduced a corrected orbital diameter, d_0', as:

$$d_0' = 4\alpha(1 - \alpha)d_0, \qquad \alpha = \eta_c/H \tag{3}$$

where η_c is amplitude of wave crest and H is wave height. The magnitude of Shields parameter, was calculated from the maximum velocity of water particle at the bottom.

Figure 5 shows the critical conditions of ripple formation. The left-hand side figure is for the significant wave and right-hand side figure is for the mean wave. In these figures, real lines indicate boundaries of ripple formation obtained in the present experiments and dashed lines are those given by Riho et al. for the regular wave experiments. It is seen that the significant wave gives closer values of both boundaries to those for the regular waves.

Figure 6 shows the relationship between the wave length of ripple (λ) and the orbital diameter of water particle (d_0') given by Fig. (3). Again, the left-hand side and right-hand side figures are for irregular wave and regular wave experiments respectively. In these figures, empirical relationships of λ with d_0' are shown: real lines are for irregular waves, and dashed lines are for regular waves. Refering to these figures, it is found that the orbital diameter calculated from the quantities of significant wave gives a considerably close relationship to that for regular waves. On the other hand, the agreement becomes bad, when the mean wave is used for the calculation of d_0'. Consequently, it can be concluded that the representative wave which controls the characteristics of sand ripples is the significant wave.

3.5 Cross-shore Sediment Transport Rate

Watanabe (1981) has proposed a formula for cross-shore sediment transport based on the concept of so-called power model.

$$\Phi = A(\Psi - \Psi_c)\Psi^{\frac{1}{2}} \tag{4}$$

where $\Phi = q/w_0 d$ is dimensionless transport rate, q is net rate of cross-shore sediment transport, w_0 is the settling velocity of sand particle, d is the grain diameter, $\Psi_c$is the critical Shields number for general movement of sands, and A is constant. This formula is based on an assumption that the amount of sand set in motion are considered to be propotional to the excess of Ψ over its critical value, Ψ_c. It was certified that Eq. (4) gives good agreement with the data of regular wave experiments with Toyoura sand, when A is 7 and Ψ_c is 0.11.

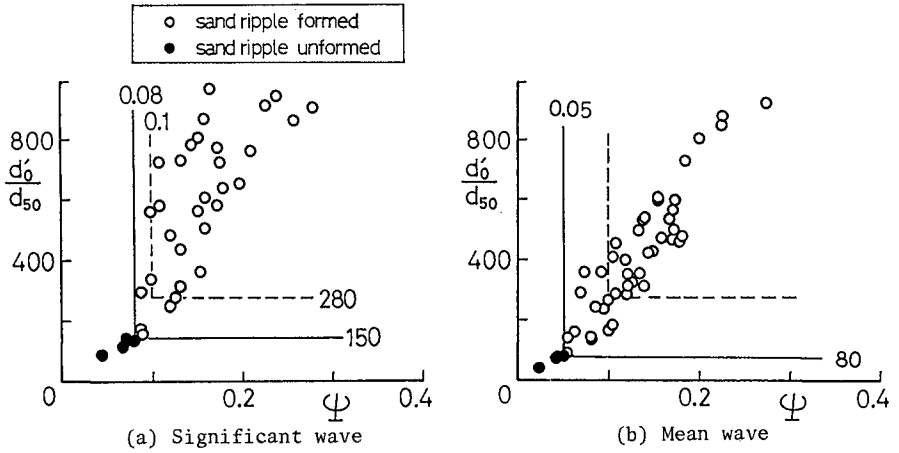

Fig. 5 Critical conditions for sand ripple formation

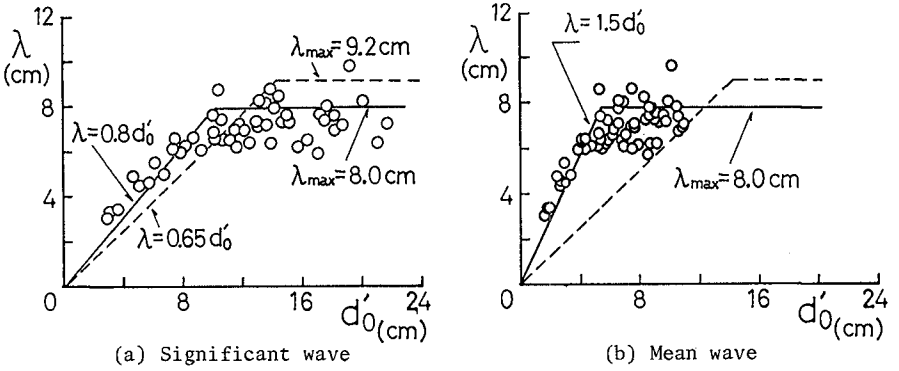

Fig. 6 Relationship between wave length of sand ripples and orbital diameter of water particle

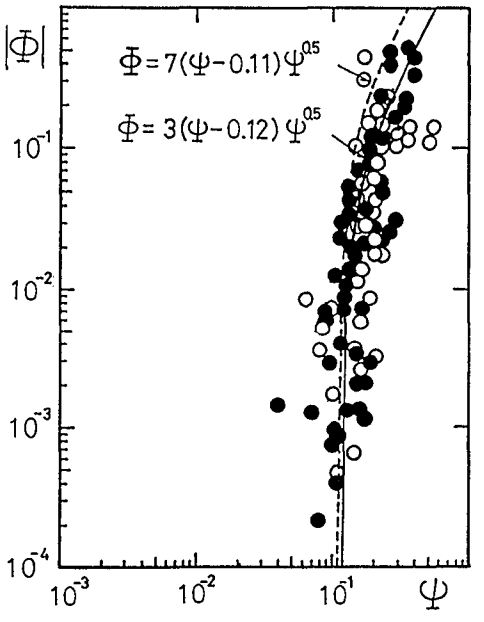

Fig. 7
Net rate of cross-shore sediment transport (Toyoura sand, d_{50} = 0.18mm)

Figure 7 shows the relationship between the non-dimensional sediment transport rate and the Shields parameter for the cases of fine (Toyoura) sand in the present experiments. In the figure, open and closed symbols indicate onshore and offshore transport respectively.

Experimental data do not so scatter, showing the same tendency as seen for regular wave experiments: namely, the value of Φ increases rapidly with the Ψ value while the latter is small, but its increase rate gradually diminishes as Ψ increases. It is very interesting that the Shields parameter is effective in expressing the sediment transport rate even under the irregular wave conditions. Eq. (4) again gives a good expression for the experimental data. However, the magnitude of the coefficient A seems to be somewhat smaller for irregular wave cases than for regular wave ones. This may indicate that the efficiency of wave power to set sand grains in motion reduces under the irregular wave conditions. This tendency corresponds to the slow speed of the beach transformation as mentioned before.

As for the representative wave, two of them gave very similar results. Therefore, the representative wave could not be specified for the sediment transport rate.

4. CONCLUSIONS

Through the present study, the effects of irregular waves on two-dimensional beach transformation were investigated. The examined subjects are macroscopic beach profile change and its classification, threshold of sand movement, characteristics of sand ripples and cross-shore sediment transport rate. The representative wave for each phenomenon were determined by comparing the results of the present experiments of irregular waves with those from regular wave studies. It is very interesting that there are two kinds of phenomena related to the two-dimensional beach transformation, which are controlled by whole incident waves or a group of large waves in a irregular wave train. These understandings are the important step to obtain a general view of beach transformation in real coasts.

REFERENCES

Bretshneider, C.L. (1968): Significant waves and wave spectrum, Ocean Industry, Feb., pp.40-46.

Dean, R.G. (1973): Heuristic models of sand transport in the surf zone, Proc. Conf. Eng. Dynamics in the Surf Zone, pp.208-214.

Hattori, M. and R. Kawamata (1980): Onshore-offshore transport and beach profile change. Summaries of 17th Conf. Coastal Eng., pp.254-255.

Horikawa, K. and A. Watanabe (1967): A study on sand movement due to wave action, Coastal Eng. in Japan, Vol. 10, pp.39-57.

Horikawa, K., T. Sunamura, H. Kondo and S, Okada (1975): On two-dimensional shoreline change due to waves, Proc. 22nd Japanese Conf. Coastal Eng., pp.329-334. (in Japanese)

Irie, Y., T. Shibayama and A. Watanabe (1985): Beach profile and cross-shore sediment transport rate due to irregular waves, Proc. 32nd Japanese Conf. Coastal Eng., pp.316-320. (in Japanese)

Iwagaki, Y. and H. Noda (1962): Laboratory study of scale effects in two-dimensional beach processes, Proc. 12th Conf. Coastal Eng., pp.194-210.

Johnson, J.W. (1949): Scale effect in hydraulic model involving wave motion, Trans. AGU, Vol. 30, pp.517-525.

Mitsuyasu, H. (1970): Development of spectrum of wind waves (2), Proc. 17th Japanese Conf. Coastal Eng., pp.1-7. (in Japanese)

Nayak, I.V. (1970): Equilibrium profiles of model beaches, Proc. 12th Conf. Coastal Eng., pp.1321-1340.

Riho, Y., A. Watanabe and K. Horikawa (1981): Two-dimensional beach transformation and on-offshore sand transport, Proc. 28th

Japanese Conf. on Coastal Eng., pp.217-221. (in Japanese)

Sunamura, T. and K. Horikawa (1974): Two-dimensional beach transformation due to waves, Proc. 14th Conf. Coastal Eng., pp.920-938.

Tsuchiya, Y. and K. Inada (1974): Experimental study on beach profile change due to wind waves —critical conditions for bar formation—, Proc. 21st Japanese Conf. Coastal Eng., pp.219-224. (in Japanese)

Wang, H. and S.S. Liang (1975): Mechanics of suspended sediment in random waves, JGR, Vol. 80, No.24, pp.3488-3494.

Watanabe, A., Y. Riho and K. Horikawa (1980): Beach profiles and on-offshore sediment transport, Proc. 17th Conf. Coastal Eng., pp.1106-1121.

Watanabe, A. (1981): Numerical simulation of nearshore current and beach transformation, Proc. 28th Japanese Conf. Coastal Eng., pp.285-289.

CHAPTER 103

Coastal engineering studies for inshore mining of diamonds at Oranjemund

J P Möller*, K C Owen** and D H Swart*

ABSTRACT

This paper describes a diamond mining operation on the west coast of Africa in Namibia (South West Africa, see Figures 1a and 1b), where a sea-wall of normal beach sand has been built out to a distance of more than 300 m seawards of the original coastline. The wall which runs alongshore is maintained in the high energy environment, which is characterized by northbound longshore transport rates, by means of artificial suppletion at a rate of up to and more than 300 000 m^3/ month. Before embarking on the project the company had to be assured of the sand on the sand-wall; to allow completion of the project free of severe damage by wave action. This implied being able to predict the erosion rate of the sea-wall by the waves. The data set used consisted of wave measurements by Waverider and wave observations obtained from voluntary observing ships; aerial photographs at monthly intervals of the waterline in the study area; and soundings of the beach, sea-wall and nearshore topography by using a helicopter as a platform. Various methods of prediction and projection were used to quantify sediment movement

1. BACKGROUND

The diamonds have been deposited in a number of beaches on a narrow wave cut bedrock shelf. This series of beaches, itself formed by alternating transgressions and regressions of the sea, is covered by varying depths (up to 20 m) of marine sand overburden. The diamond deposits are continuous seawards and this paper addresses particularly the coastal engineering aspects of the mining methods used in this area adjoining the sea. In the 1970's various types of beach protection against wave attack were used to make mining of the beach area in the dry possible. These included interlocking concrete blocks and sheet-piles. Due to economic constraints and the requirement only being for temporary protection attention turned to using the sand overburden, which has to be excavated and dumped to expose the diamond gravels, to build the sea-wall. This structure has a crest width of 25 m, about 10 m above MSL and is progressively developed seawards.

* Sediment Dynamics Division, Coastal Engineering and Hydraulics, National Research Institute for Oceanology, CSIR, P.O. Box 320, Stellenbosch, 7600, Republic of South Africa.

** Assistant General Manager, Consolidated Diamond Mines (Pty) Ltd, P.O. Box 35, Oranjemund, 9000, Namibia.

The mining sequence becomes rather critical in as far as it relates to the distance over which excavated material is to be transported, this being one of the major expense items in the project. This implies that the area to be excavated and the length of sea-wall to be constructed or maintained should always be in close proximity.

The increase in beach slope causes increased offshore losses of material and the stability and construction of such a structure require close monitoring to ensure the safety of personnel and equipment and to make such a capital-intensive undertaking economical. An extensive monitoring programme which includes inshore bathymetric surveys, aerial photography, the analysis of sea-wall volumes and regular site visits by personnel and consultants was incorporated at an early stage.

At present the mine is at its maximum planned offshore limit and the mining programme is now even more strictly governed by the effect of the harsh littoral processes in the area. The regular monitoring of progress and changes in the nearshore coastal area ensures that the project proceeds optimally.

2. OVERVIEW OF AVAILABLE DATA

Wave Data

Oranjemund lies on a desolate part of the coast far from any major harbours and wave data from the area, before the project was started, were rather sparse. A Waverider station was set up in 1978 in 17 m of water depth to gather information for the design of a piled jetty in the surf zone in the mining area. In 1981 the station was moved to a water depth of 106 m and the CSIR has analysed the data from this station by standard methods.

As the Waverider does not record wave direction use had to be made of available Voluntary Observing Ship's (VOS) records that were collected between 1960 and 1979. Figure 1a shows the $1^{\circ} \times 1^{\circ}$ squares in which the VOS data available along the Southern African coast were grouped for the analysis. In Swart and Serdyn (1981) annual, seasonal and monthly analyses are shown for height, period and direction combinations. It was also possible to collect raw VOS data during the project by utilizing Cape Town based coasters that operated on the west coast.

The aim was to use Waverider and VOS data collected during a specific period and correlate these with the beach behaviour during the corresponding period.

Figure 2 contains a wave-height exceedance curve for the 106 m Waverider station at Oranjemund. It can be seen that the wave climate is fairly severe, with a once/year significant wave height of 5,6 m. Figures 3 and 4 show the wave height and period histograms for all data. On the basis of the VOS wave data a swell rose was compiled, as shown in Figure 5. The swell waves exhibit a strong south-easterly tendency, whereas the local wind field is more predominantly south-east (see Figure 6), which is alongshore.

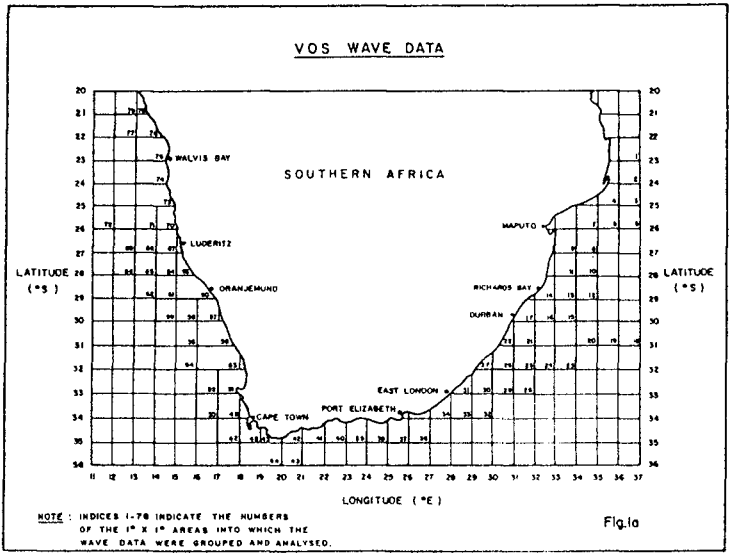

Fig.1a

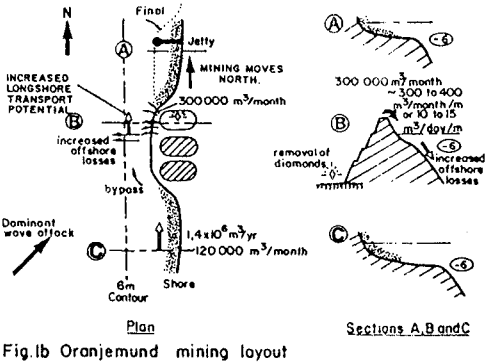

Fig.1b Oranjemund mining layout

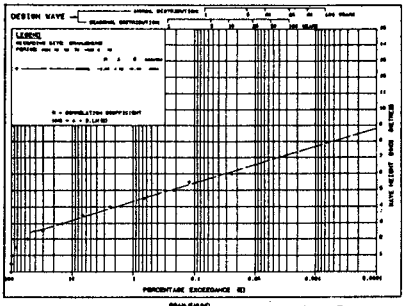

Fig. 2

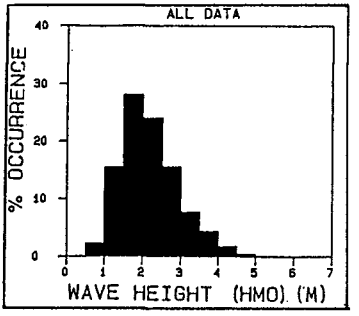

Fig.3

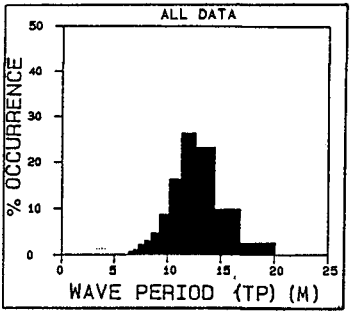

Fig.4

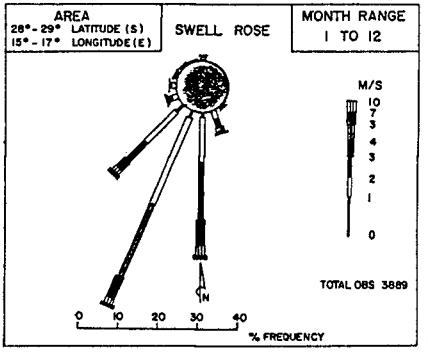

Fig.5

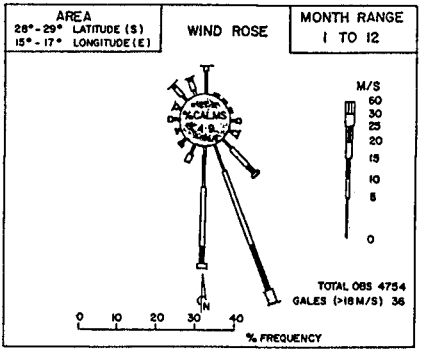

Fig.6

Surveys

The highly dynamic littoral zone along the mining area requires close topographical monitoring, especially in front of the sea-wall where substantial offshore losses could occur during stormy events.

A helicopter is used for the surveying, which is done with a lead-line and 3 theodolites. Beach and nearshore surveys have been carried out routinely at 3-monthly intervals for 10 years. Each survey, which includes a set of 7 lines for which records are available since the beginning of the project, consists of 23 lines that extend from the top of the sea-wall to ± 15 m below MSL.

Profiles, contour maps (Figure 7a) and difference maps (Figure 7b), which relate each survey to the preceding survey, are drawn for each survey. The difference maps clearly show areas of erosion or accretion between surveys which is of great help when trends in the coastal processes are to be studied.

Aerial Photography

Aerial photo mosaics are taken monthly and display beach form characteristics and operational features of importance to the design. The photography is done from a helicopter and a set of ground beacons is used for proper alignment while the camera is horizontal. This allows fairly accurate measurements to be made on the mosaics. Figure 8 shows, for example, the northward advance of the leading edge of the sea-wall in time.

Sand Samples

For the calculation of on/offshore and longshore transport capacities knowledge of the grain size distribution of the beach material is required. Initial sampling along the coastline over 35 km during 1979 indicated that the median grain size decreases towards the north. The median grain size typically varied from about 600 microns at the Orange River in the south to 350 microns 35 km north of the Orange River (see Figure 9). This has been verified by subsequent annual re-sampling.

Artificially Dumped Volumes

Up to 5 million cubic metres of overburden are excavated annually for sea-wall construction and maintenance. Diesel-driven dozers and scrapers are used for this work. It is essential that the schedule at which material is required for the construction and maintenance of the sea-wall matches the scheduled programme for overburden stripping. Figure 10 gives as an example the dumped volume during a 19-month period in 1985/86. During this period the average monthly dump rate was 300 000 m^3, which amounts to nearly 3 times the average northbound drift rate.

It is specifically relevant that due cognizance be taken of the fact that the natural net longshore transport capacity in the area is about 1,3 million cubic metres per year towards the north (see Chapter 3 below). The mining procedure is therefore directed to benefit

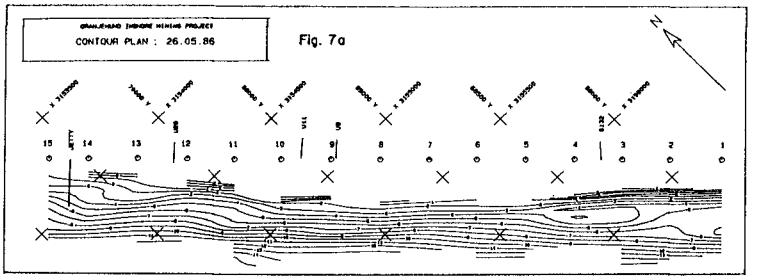

Fig. 7a

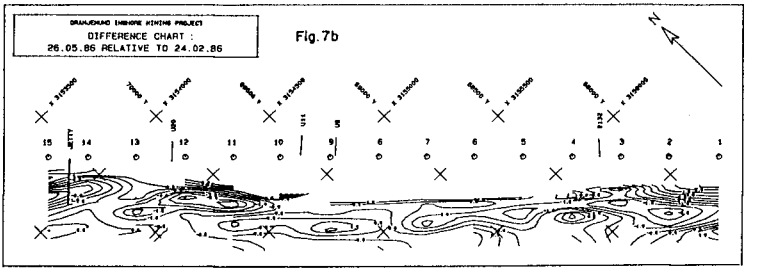

Fig. 7b

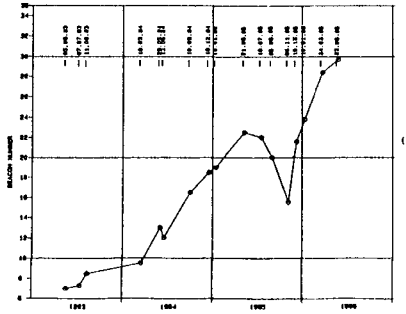

Fig. 8 BEACH BUILDING NORTHWARDS OF THE SEAWALL

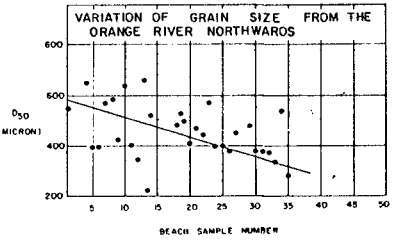

Fig. 9

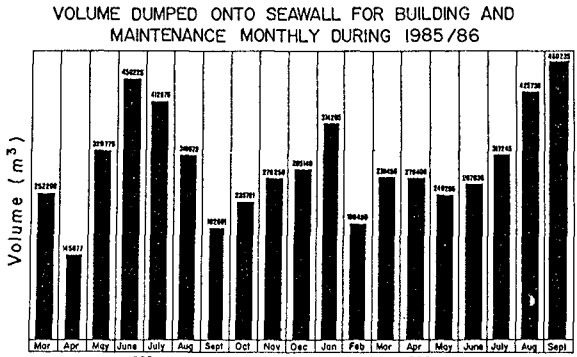

Fig. 10

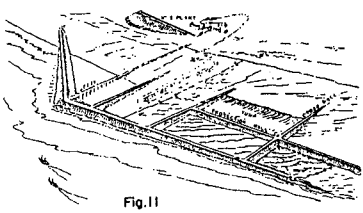

Fig. 11

Fig. 12

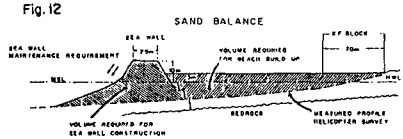

Fig. 13

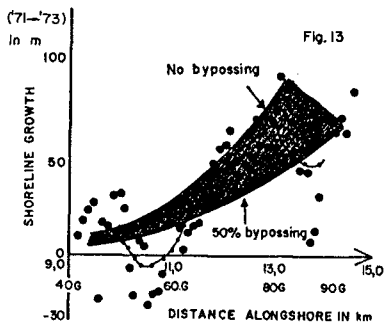

maximally from this natural mechanism of moving material.

3. INTERPRETATION OF PHYSICAL PROCESSES OPERATIVE IN THE COASTAL AREA

In order to assess the behaviour of a sea-wall such as that shown schematically in Figures 11, 12 and 1b, it is necessary to quantify the littoral processes in three different areas, namely,

- the area to the south of the sea-wall proper, which will be shown below to be the updrift area;
- the area in front of the sea-wall proper, and
- the area to the north (downdrift) of the sea-wall proper.

Updrift Area

The available wave data for the area clearly show a strong predominance of waves with a high angle of incidence from the south-southwesterly sector. As a result the littoral drift in the area is predominantly northbound. Swart in CSIR (1979) found on the basis of predictions with the SPM littoral drift predictor (SPM, 1973) that the gross longshore transport in the area is about 1,9 million cubic metres per year, with a net of 1,3 million cubic metres per year northbound. These extremely high values, which are the result of the high angles of incidence referred to above, have been verified by comparison with the rate of updrift infill at the first sea-wall, which was constructed in 1971. Figure 13 shows this verification in the form of a comparison between actual shoreline changes and the shoreline changes predicted with the assumption of a littoral drift rate as given above.

Figure 13 indicates that up to 50 per cent of the littoral drift arriving from the south bypasses into the area in front of the sea-wall proper. Obviously the magnitude (percentage) of the bypassed quantity depends on the degree of build-out of the sea-wall relative to the original waterline and the degree of change in the coastline orientation.

Area Seawards of Sea-wall

Prior to the initiation of inshore mining the sea-bed in the sea-wall area was characterized by a typically concave beach profile which shelved out at 6 m below mean sea level (MSL). The 6 m contour typically was situated about 300 to 400 m seawards of the mean waterline. Swart in CSIR (1979) showed that the plateau referred to here can be physically explained as the lower limit of the active profile development in the area where combined bed-load and suspended load takes place (Swart, 1974). Between the 6 m and 16 m contours the underwater slope was relatively steep at 1 in 30.

The foregoing means that any plans to build out a sea-wall into the nearshore area would be bounded on the seaward side by the sharp change in profile. In practice this meant that the maximum distance over which the mean water line could be shifted seawards was of the order of 200 to 300 m, just by considering the geometry of typical beach profiles found in the area. Obviously this would only be possible if artificial nourishment were to be added at the top of the profile to compensate for additional wave-driven seaward losses due to the

steepening of the beach profile. The studies described in this paper were aimed largely at quantifying these processes and determining practical limits for the beach build-out.

Figures 14 and 15 show examples of hydrographic profiles taken over a 4-year period across the beach in front of the sea-wall. Figure 14 was taken in the southern section of the sea-wall while it was still being built out to its maximum protrusion. Figure 15 depicts profiles in the area of maximum protrusion. The dramatic recent build-up of 180 m can be seen clearly. Prior to 1982 about 10 m of build-up had already taken place in this area, making the total build-up of the order of 300 m. As a reference Figure 16 contains beach profiles about 8 km north (downdrift) of any inshore mining activities. Reference to Figure 12 shows schematically how the sand balance is made up.

Downdrift Area

In the classical case of an obstruction to longshore drift one would expect downdrift erosion. However, in the case of the sea-wall, the processes operative in the area are completely different and merits special discussion. As a result of the artificial nourishment in the area of the sea-wall proper the magnitude of the northbound longshore drift is increased sharply in relation to the initial pre-sea-wall condition. Swart showed in CSIR (1979) that the extent of the increase in the longshore transport rate is a function of the degree of build-out from the original waterline, which is logical. For an offshore build-out of 200 m relative to the already partially built-out shoreline he predicted an increase in the amount of longshore transport of 250 per cent, which sounds very high.

Because the longshore drift potential returns to normal towards the north, as the effects of the inshore mining activities become less, it means that the excess material arriving from the sea-wall area in the south will deposit, thereby creating an area of substantial accretion to the north (downdrift) of the sea-wall proper. Figure 17 contains an example of the seaward growth in the shoreline during 1977 to 1982 at a location about 3 to 5 km to the north of the sea-wall position at that time. Simulations of downdrift shoreline change, performed with the one-line shoreline model of Pelnard-Considère (1954), modified to include longshore variations in wave height and beach profile and location, verified the longshore transport increase by 250 per cent, which was quoted above.

The sedimentation to the north of the sea-wall proper takes place in the form of a low washover fan at the level of a maximum wave run-up, which typically is about 2 to 4 m above MSL. One of the main outcomes of the study reported in this paper was to optimize the northward sea-wall advance such that the sedimentation to the north of the sea-wall can be used to maximum benefit as a platform for the building out of the sea-wall in that area.

4. MINING SEQUENCE AS RELATED TO COASTAL PROCESSES

On the basis of a detailed modelling of the physical coastal processes in the area, it was possible to optimize various aspects related

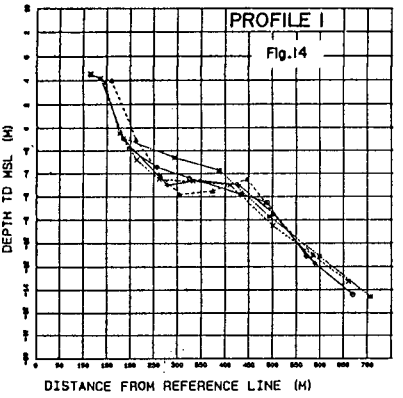
PROFILE I
Fig.14
DEPTH TO MSL (M)
DISTANCE FROM REFERENCE LINE (M)

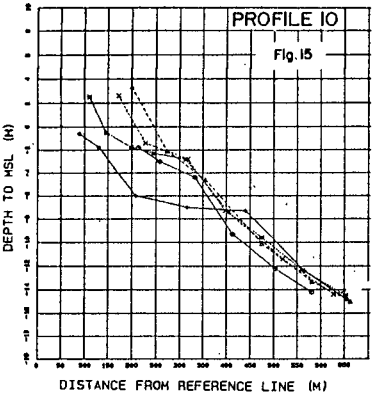
PROFILE 10
Fig.15
DEPTH TO MSL (M)
DISTANCE FROM REFERENCE LINE (M)

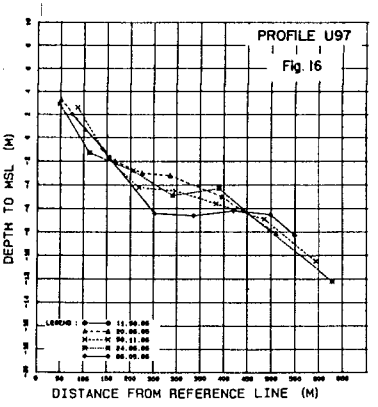
PROFILE U97
Fig. 16
DEPTH TO MSL (M)
DISTANCE FROM REFERENCE LINE (M)

Fig.17

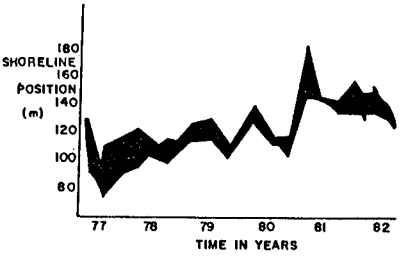
SHORELINE POSITION (m)
180
160
140
120
100
80
77
78
79
80
81
82
TIME IN YEARS

to the sea-wall (CSIR, 1983).

Mathematical models based on the onshore-offshore model developed by Swart (1974), the shoreline evolution theory of Pelnard-Considère (1954) and topographical changes have been and are still being used to predict the littoral response. The model on topographical changes referred to is similar to that developed by Perlin and Dean (1983) but it uses the Swart (1974) method for the prediction of onshore-offshore transport, which is well tried. The wealth of survey data allows for the easy calibration of the above-mentioned mathematical models and also supplies a unique data set showing how very steep and very much flatter beach profiles in close proximity react to the same incident waves.

Calculations were made to determine the extent of maintenance feeding which would be required for different sea-wall offset distances from the original shore. It was concluded that it would be possible to maintain a sea-wall in a position more than 300 m seawards of the original shoreline.

Typical components of a mining sequence strategy developed on the basis of the research are the following:

- the sea-wall should be actively maintained over a 600 m length, which is advanced northwards at 800 m per year;

- the volume of material required annually for sea-wall building and maintenance was theoretically predicted to have a minimum value of 2,7 million cubic metres, which contains 2 million for sea-wall building alone. The maximum predicted sea-wall maintenance is much higher than the minimum value of 0,7 million cubic metres and could be as high as 3 million cubic metres, making the total volume required 5 million cubic metres per year. Actual dumped figures to date fall within these bracketing values.

- The sea-wall is particularly vulnerable during spring high-tide and arrangements must be made to cope with an increased maintenance load during periods of spring tide.

5. SUMMARY AND CONCLUSIONS

In summary, it can be stated that a sea-wall which is maintained at Oranjemund at a distance of more than 300 m seawards of the original waterline, causes updrift accretion of between 50 and 100 per cent of the strong, net littoral drift of about 1,3 million cubic metres per year, which arrives from the south. In front of the sea-wall a beach profile steeper than the initial one is maintained by artificial nourishment. As a result the longshore drift rate in this area is increased more than twofold by the increased suspended load in the water column. To the north (downdrift) of the sea-wall proper the reduction of the drift rate back to normal leads to an area of sedimentation advancing northwards with the sea-wall.

On the basis of the understanding of the processes involved and the mathematical modelling of these processes an optimum mining strate-

gy was developed.

Apart from recommendations regarding the broad strategy for inshore mining, this ongoing study has regularly supplied inputs on the basis of the gathered data and model results which allowed an essentially non-marine project team to optimize their activities to cope with changes in the littoral environment.

In addition, the project can serve as a one-to-one scale beachfill test and could prove extremely useful to evaluate techniques for the design of beachfills.

REFERENCES

CSIR (1979). Oranjemund beach study. CSIR Report C/SEA 7935, Stellenbosch, RSA.

CSIR (1983). Oranjemund sea mining project. CSIR Report C/SEA 8379, Stellenbosch, RSA.

PELNARD-CONSIDèRE, R. (1954). "Essai de théorie de l'évolution des formes di rivages en plages de sable et de galets". Quatriéme Journèes de l'Hydraulique, Paris, 13-15 Juin 1954.

PERLIN, M. and DEAN, R.G. (1983). A numerical model to simulate sediment transport in the vicinity of coastal structures. Miscellaneous Report No. 83-10, US Army Corps of Engineers.

SPM (1973). Shore Protection Manual, US Army Corps of Engineers.

SWART, D.H. (1974). Offshore sediment transport and equilibrium beach profiles. Doctoral thesis, Technische Hogeschool, Delft, 302 pp.

SWART, D.H. and SERDYN, J.de V. (1981). Statistical analysis of visually observed wave data from voluntary observing ships for South African coast. Unpublished CSIR Report, 80 volumes, Stellenbosch, RSA.

CHAPTER 104

An Automated Measuring System to Registrate and Balance Suspended Sediment and Associated Parameters

Lothar J.R.Neumann *

The automated measuring system Oortkaten (AMO) was established in order to determine the balance of suspended sediment and associated parameters. Morphological and velocity weighted averaged samples are taken using the newly developed MOSTRA-Method. This results in a cross-sectional average value.

Introduction

Suspended sediments in rivers and estuaries are a nature phenomenen, but since one knows that this suspension is the carrier of heavy metals and other aggressive material, the answer to the question of its origin and behaviour becomes more and more important. In the beginning, measurements of suspended material and the estimation of transport rates were conducted by single measurements or by monitoring a river-section for a few days. Today we know that this kind of measuring cannot yield the results we need to estimate loads of suspended matter over long periods or even offers insights into the relations between suspended matter and associated parameters, such as temperature, oxygen, river discharge or current velocity.

The main problems for measurements in navigable waterways and the interpretation of data, in the past and even nowadays, are aggreviated by interuptions of passing ships, high costs for staff and material, especially for ship capacities, a lack of data to interpolate between single measurements and last not least inhomogeneities for example in the current velocity profiles or in other distributions in the river-cross-section.

In line with a KFKI-Projekt** permanent measurements of suspended matter should make it possible, to compute transport rates through a cross-section of an estuary. At the same time parallel measurements of associated parameters should answer the question as to their influence on changes in the suspended matter concentration data. Because no instrumentation was available to perform this tasks, an own system was developed, the Automated Measurement Station

* Oceanographer, Strom-und Hafenbau, Hamburg,(Port-Authority) Dalmannstr. 1-3, D-2000 Hamburg 11. Abt.SB 412

** KFKI -Coastal Engineering Board of West-Germany

Oortkaten (AMO). Figure 1 shows the station during ebb.

Figure 1. Automated Measurement Station Oortkaten (AMO)

Location and Boundary Conditions

The operation position of the measurement device AMO is in the river ELBE near the village Oortkaten at streamkilometer 607.5. This location is on the West-German part of the river shortly before the splitt of the river into two river arms with the most important West-German harbour, The Hamburg Harbour, in between. (Figure 2). Here the river has a width of 525 m and a maximal depth of about 10 m.

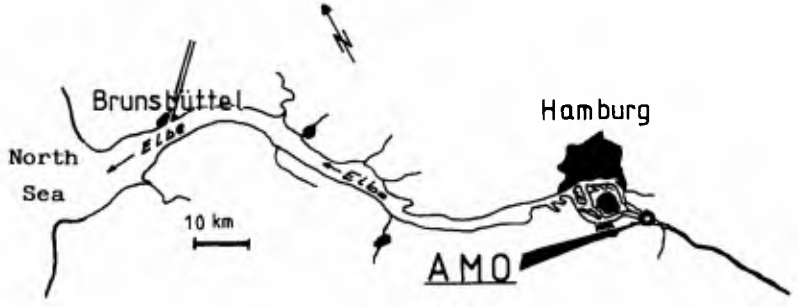

Figure 2. Location of the AMO.

The boundary conditions are important by using automatically working systems. For the location of the AMO the boundary condition are the following ones :

The M 2-tide is dominant, but the tide is influenced by the river-discharge. This leads to a mean duration of ebb for eight hours and four hours for flood. The mean tidal range is 3 m. The ebb current velocity in on an average of 0.9 m/sec with extrem values of 1.5 m/sec. During flood these values are 0.4 and 0.9 m/sec. The mean annual value for the river discharge is 700 m^3/sec, but in times of high water, values up to 3900 m^3/sec were measured. The water temperature is 0 to 25 degree Celsius, depending on the season, and normally there is ice on the river from January until the end of February. The concentration of oxygen varies from 5 - 11 g/m^3 and the suspended sediment concentration range is 15 - 35 g/m^3 with a part of ignition loss, which is with 35 %(+/-5 %) a very constant value.

Measurement Method

Besides waterlevel, current velocity and current direction, concentration of oxygen, pH-value, conductivity, optical attenuation and temperature, the system computes the discharge through the cross-section of the estuary. Watersamples are taken and analyzed seperately in a laboratory on suspended sediment concentration, grainsize distribution and ignition loss. These parameters respectively samples, are measured or collected by a new method called MOSTRA which stands for morphological and current velocity adequated measurement method.

By this method the measuring data of the parameter respectivly the samples are related to the water volume that passes through those parts of the river-cross-section, for which the measurement should be representative (Figure 3).

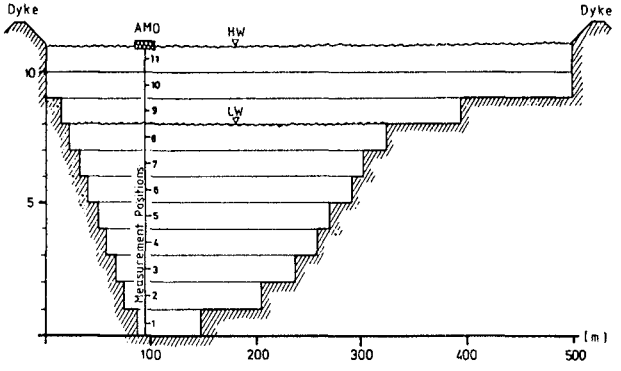

Figure 3. Schematical cross-section of an estuary.

The smaller the cross-section-part, for which the measurement should be representative, the better the dataone measure. If the distributions of the hydrographical parameters in the cross-section are very heterogenous, than it is necessary to measure in more than one profile. In any case representative measurements are necessary. These controls have to be conducted as often as possible with multi-point-measurements.

The knowledge of the cross-section-plane as a function of the water depth, as well as the current velocity for each single measurement position, are necessary requirements for the computation of the measured data. The function for the schematic cross-section (Fig.3) is shown in Figure 4.

For each single measurement position the measured data of the parameters are weighted by the relevant cross-section-plane (Fig.3) and the current velocity. In this way the measured data are related to the water volume, that passes through the relevant river-cross-section part during the measurement.

After having completed measurements at all positions of the profile, the data for each parameter are added and computed to mean values. The result are averaged data vertically integrated and related to the actually transported water volume.

The taking of samples must be related to the cross-section-plane only, because the sampling, depending on the current velocity -so called isokinetic sampling of water- is carried out by a system unit itself. The taking of samples according to the measurements of parameters is being achieved at every measurement position of the profile by the duration of the sample time (Fig.5). Figure 5 shows the extrem differences to an unweighted kind of taking water samples. The greater the gradient of a parameter in the vertical profile, the greater are the differences between the results of the different measurement methods. The complete mathematical background of this method is published by NEUMANN (1985).

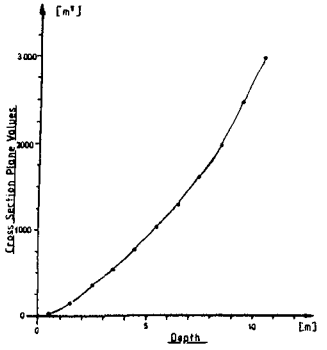

Figure 4. Cross-section-plane, function of waterdepth.

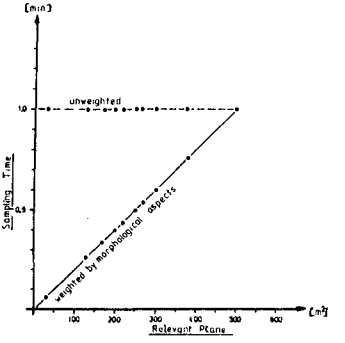

Figure 5. Sample time as a function of the relevant plane

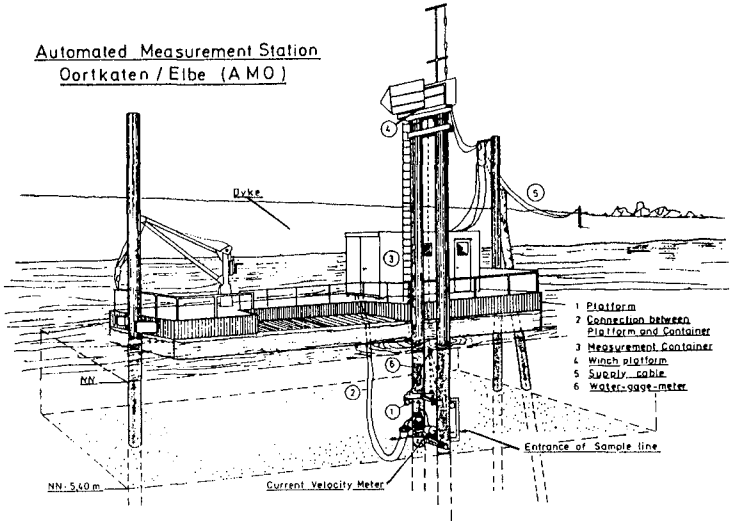

Figure 6. Principle view of the AMO.

Technical System

The Automated Measurement Station Oortkaten consists of several units (Fig.6). The sampling unit is placed on a platform, which is held between two piles and moves, operated by a winch up and down between surface and ground. From here a supply cable and two tubes cimbine the sampling unit through a pontoon with a container. This connection has a length of 18 m. Inside the container all other system are integrated. These are the units to store the samples, measure the parameters and a process-computer-system for operation control and data processing. The 20-feet-container is linked to the shore, which is 50 m away by supply cable for fresh water, electricity and telefon.

The sampling unit on the platform was developed to take the samples isokinetically, measure the current velocity and current direction. The entrances of the sample tube are fixed in the main directions of the river currents. This ensures the position of the AMO, where only alternating current directions occur. For measurements in regions with unsteady directions, a self-directing platform construction is necessary.

To reach the same current velocity at the entrances of the sampling tube as in the river, it is necessary to pump isokinetically. This is important, because flow behaviour of water is different from that of suspended particles. The water velocity is measured with an accoustic current velocity meter, type ME -SM 125, which controls a pump. At the AMO

a NETZSCH- mono-pump type 3-NU/10 is installed, which has an almost linear pumping characteristic between the pumping volume of 0 - 1000 cm^3 per minute. Based on this pattern a linear relation between the pumped water volumes and the current velocities are achieved.

Unit No.2, the sample collection-unit is installed insite the container. All mechanic equipment, as well as tanks and sample bottles are installed in one big box. The interior of this box is cooled down to 4 degrees Celsius to stop biological acticities in the samples. Inside the box several valves direct the water either to one of the collection tanks or back into the river. Two tanks are available and each of them has a capacity of 180000 cm^3. To seperate the suspendion of water and solid material a centrifuge is used. This ceperator type ALFA LAVAL LAPX 202 has a seperation-degree of 0.45 µm grainsize by 6000 rotations per minute. Beneath the tank and the centrifuge an assembly line, with 750 cm^3-sample-bottles is installed. It has a capacity of 64 bottles which garantuees a one-week-working-period of the AMO, because 2 bottles are filled after every half-tide.

The measurement of the parameters temperature, conductivity and pH-value occurs inside the container. The sensors of a multi-parameter-measurement-unit are provided with river water by one of the tubes, coming from a seperate pump, fixed on the moving platform.

The operation control of the single units of the AMO and their working together is aided by an integrated process-computer-system. The computer is in line with a telefon modem which gives the opportunity to control and change the working processes, or have a look at the measured data from a terminal at any place, where a telefon is available.

Sampling Process

Water sampling and measurement of associated parameters are taken every 20 cm between surface and ground of the river. These are done under the use of the MOSTRA-Method. From the platform, schematically shown on the left hand side in the figures 7a,b,c, river water is continuously pumped into the container. If the plateform reaches a measurement position, it stops and the water flow is being directed through an overflowtank or bypass back into the river, until the platform reaches the next position. According to the current velocity, the tank will be filled during a half-tide with 100 - 180 dm^3 river water.

When the current direction changes, the river flow is being directed to tank No.2 in the same way then before into No.1 (Fig.7a). Shortly before and after slack water it is possible that both velocity directions occur in different water depths. In this case the water flow is directed either into tank No.1 or No.2, according to the direction of the current.

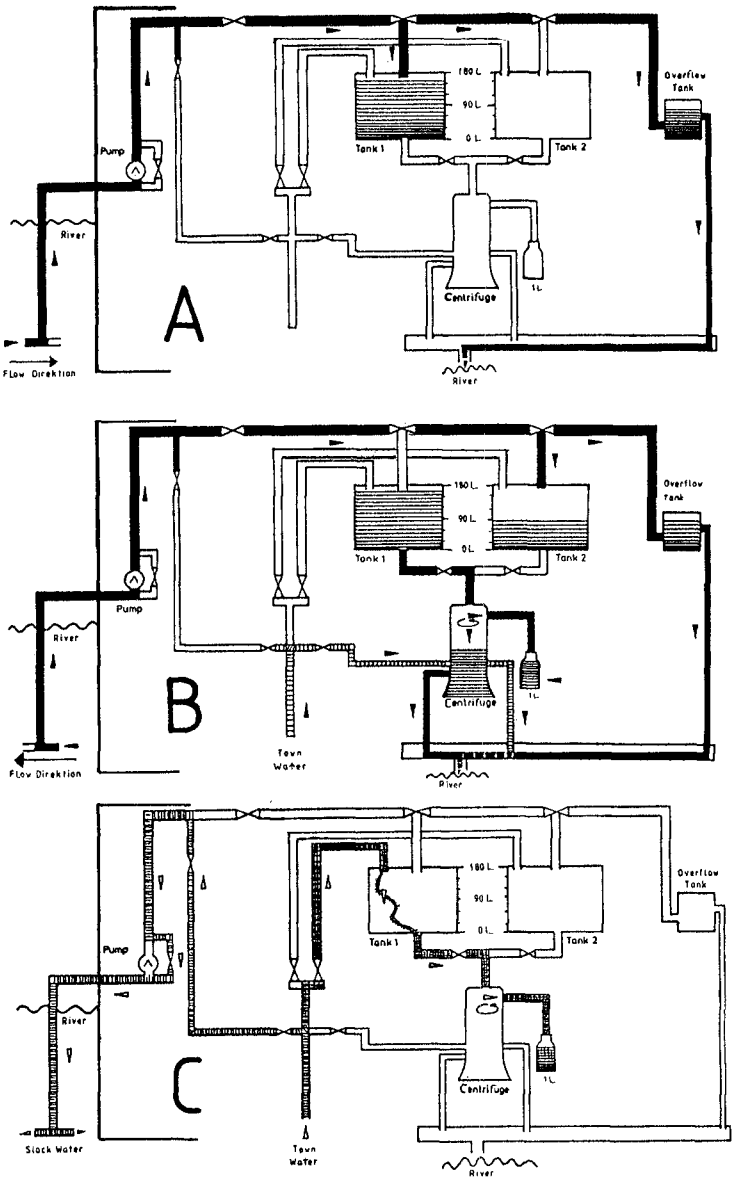

Figure 7. Sampling process of the AMO
a. Sampling of water
b. Centrifugation of sampled water
c. Washing and cleaning of the system

This interplay continuous until the new direction is measured at all measurement positions. Now the water flow is only being directed to tank No.2 and the bypass. Tank No.1 is now ready to be emtied.

In this moment, the centrifuge is started by the computer and the tank outlet-valve is opened. After the tank is completely emptied, the centrifuge content (a substratum of 0.5 dm^3) is filled into a sample bottle. An engine now starts the assembly line and a new bottle is placed beneath the outflow of the centrifuge (Fig.7b).

Tank No.1 and the centrifuge will now be washed with town water (Fig.7c) and the rinsing water is filled into the second sample bottle. After a new bottle has been brought into position, the cetrifuge will be switched off, and the tank outlet-valve be closed.

The whole process last 30 minutes, depending on the content in the tank. Parallel to the tanks the sample tube down to the platform in the river will be washed against the pumping direction to avoid obstructions.

All single phases of the process are computer aided and may be changed in every manner, so that shorter times for taking samples or other interferences are possible.

Recommendation

In line with a KFKI-projekt (CHRISTIANSEN, 1985) an automated measuring system (AMO) was established in order to determine the balance of suspended sediment and associated parameters. Morphological and velocity weighted averaged samples are taken using the newly developed MOSTRA-Method. This results in a cross-sectional average value.

The data of the system afford better answers about transport rates through the cross-section of a river, because the system even works in extrem situations, such as high water, stormy weather and heavy traffic.

References

CHRISTIANSEN, H. (1985). Das Forschungsvorhaben Schlick/ Schwebstoffe in Ästuaren. DIE KÜSTE 42, :115-123.

NEUMANN, L.J.R. (1985). MOSTRA-ein Verfahren zur strömungs- und morphologieadäquaten Bilanzierung von suspendierten Feststoffen und Begleitparametern in geschichteten Ästuaren. DIE KÜSTE 42.:151-163.

CHAPTER 105

Changing of wave climate due to breaking on a tidal inlet bar

Hanz Dieter Niemeyer[+]

ABSTRACT

Changes of wave climate due to breaking on a tidal inlet bar are investigated by analysis of field measurements prosecuted offshore and onshore of the bar. Quantitative results for wave height reduction, period and length transformation and energy dissipation are presented as well as a study considering the dominating breaking criterion.

1. INTRODUCTION

The prevailing longshore drift along the East Frisian islands is eastward directionalized. The sand by passing the inlets leads to the configuration of the typical tidal delta: a number of shoals separated by channels leading from the updrift to the downdrift island like a chain. The landfall area of the sand on the downdrift island divides its beaches into an eroding and accretionary part. A very impressive example are the beaches of the island of Norderney (Fig. 1): Downdrift of the sand's landfall there are broad accretionary beaches while updrift the continuous erosion has forced man to build revetments and groynes, because the sand needed for supply is passing seaward. The only comforting thing is that the shoals act like a submerged breakwater on incident waves and attenuate especially the higher ones. In order to get quantitative information about this effect field measurements were carried out in the offshore area, on the island foreshore and in the tidal inlet of the island of Norderney (Fig. 2). The results gained up to now from these investigations are presented here.

[+]Department for Coastal Research, Norderney, F.R.o.GERMANY

Fig. 1:
Tidal delta with bar of the tidal inlet Norderneyer Seegat
(right side: island of Norderney)

Fig. 2: Map of the investigation area with measuring stations
(I: offshore, II: island foreshore, III: tidal inlet)

2. BOUNDARY CONDITIONS OF THE FIELD MEASUREMENTS

The tidal inlet Norderneyer Seegat is ebbdominated with mixed energy with reference to the classification of HAYES (1979). The mean tidal range is about 2.4 m changing on the average up to 0.7 m due to spring and neap tide. Set-up occuring during storm tides has until now reached the measure of some 3 m. The water depth due to MHWL at the three measuring stations is 12.1 m (offshore), 4.8 m (island foreshore) and 3.2 m (tidal inlet). The measurements were carried out with ultrasonic wave gages, which unfortunately do not always guarantee undisturbed data registration, because this measuring principle is very sensitive due to air

bubbles in the water. Further details considering the investigation area and especially its morphological boundary conditions have been published earlier (LUCK 1978; FITZGERALD, PENLAND + NUMMEDAL 1984).

3. WAVE HEIGHT REDUCTION

Comparing significant wave heights measured offshore and onshore of the tidal inlet bar makes their attenuation due to the crossing of the shoals evident, on the average there is a reduction of 42 % on the island foreshore and of 70 % in the inlet area in relation to offshore significant wave height (Fig. 3 + 4). But this general tendency is superimposed by a scattering of values due to variations of onshore parameters corresponding to offshore significant wave heights which nearly do not differ from each other.

Fig. 3

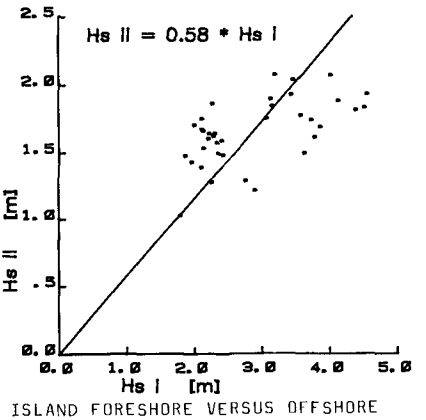

ISLAND FORESHORE VERSUS OFFSHORE SIGNIFICANT WAVE HEIGHT

Fig. 4

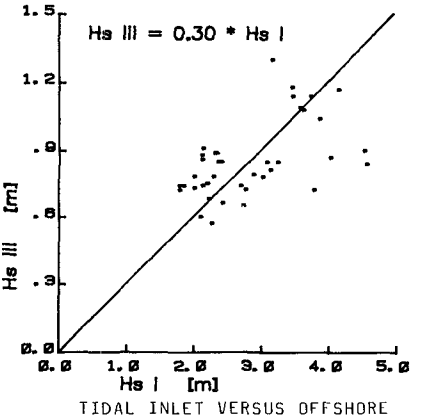

TIDAL INLET VERSUS OFFSHORE SIGNIFIKANT WAVE HEIGHT

The onshore wave heights also generally depend on the water level fluctuations in the investigation area: There is basically a tendency of bigger onshore significant wave heights for increasing water depths. But this relation is also characterized by a scattering of onshore wave heights occuring in coincidence with water depth, which have the some order of magnitude (Fig. 5 + 6). This process corresponds with the paradox of wave breaking on bars: For the same water depth an increase of offshore wave heights does not always effect an increase of those correspondently arriving onshore, but sometimes there is a decrease.

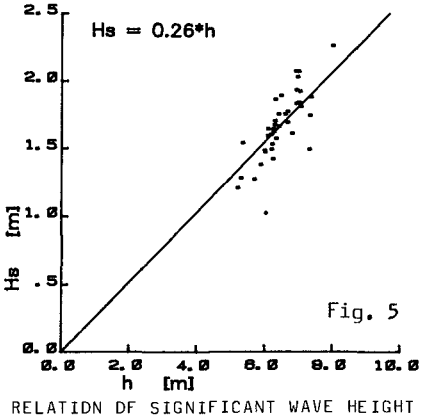

Fig. 5

RELATIDN DF SIGNIFICANT WAVE HEIGHT AND WATER DEPTH (ISLAND FDRESHDRE)

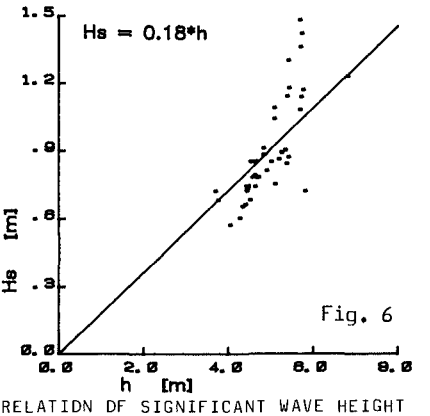

Fig. 6

RELATIDN DF SIGNIFICANT WAVE HEIGHT AND WATER DEPTH (TIDAL INLET)

This first interpretation of data leads to the conclusion that it is impossible to analyse the damping effect of a bar on wave height by taking into account only single related parameters. The interaction of the most important hydrodynamical and morphological boundary conditions governing this process, must be taken into consideration. As the shoals of a tidal inlet bar act on crossing waves like a submerged breakwater, the idea comes up to make use of the analytical formulation of boundary conditions, which was developped in previous research on this subject (ABDUHL KHADER + RAI 1980; JOHNSON, FUCHS + MORISON 1950). Additionally the investigations of DIEPHUIS (1957) on scale effects due the reproduction of wave breaking on bar in hydraulic models of small size were taken into account.

Transferring these results a statistical appromination has been developped considering the following boundary conditions: Wave height/water depth relation in the offshore region and additionally as well relative length shortening due to shoaling, wave steepness and relative water depth in the offshore area as the relations of the bar crest height to offshore water depth and shoal width to offshore wave length.

$$\frac{H_i}{H_a} = a_1\left(\frac{H_a}{h_a}\right)^{b_1} + a_2\left(\frac{H_a}{L_a}\right)^{b_2} + a_3\left(\frac{h_a}{L_a}\right)^{b_3} + a_4\left(\frac{g \cdot T_a^2}{L_a}\right)^{b_4} + a_5\left(\frac{h_a - h_R}{h_a}\right)^{b_5} + a_6\left(\frac{B_R}{L_a}\right)^{b_6}$$

First the regression analysis is carried out particularly for each boundary condition in order to differentiate their importance for wave height transmission across the bar by means of correlation coefficients (Table 1).

Table 1: Partial correlation coefficients for single boundary conditions of wave height transmission

AREA	WAVE HEIGHT	BOUNDARY CONDITION					
		H_a/h_a	H_a/L_a	h_a/L_a	$g \cdot T_a^2 \cdot L_a^{-1}$	$(h_a-h_R)/h_a$	B_R/L_a
ISLAND FORE-SHORE	H_{max}	0,773	0,138	0,530	0,280	0,421	0,578
	H_s	0,859	0,475	0,399	0,663	0,303	0,447
	H_m	0,851	0,263	0,628	0,621	0,258	0,653
TIDAL INLET	H_{max}	0,717	0,256	0,340	0,010	0,252	0,367
	H_s	0,764	0,347	0,464	0,192	0,146	0,481
	H_m	0,708	0,223	0,507	0,583	0,135	0,503

It is evident that offshore wave height/water depth ratio is the dominating boundary condition. All others are in comparison of less importance.

The results of this nonlinear multiple regression analysis are only demonstrated due to limited space for the significant wave heights: Measured and computed data show a rather good agreement (Fig. 7). In or-

Fig. 7

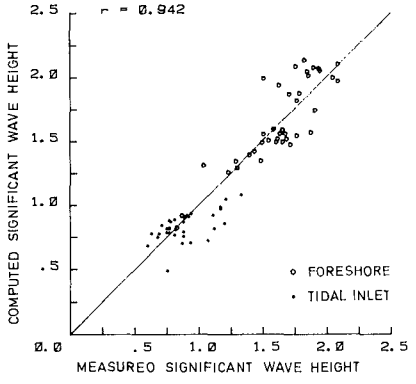

Fig. 8

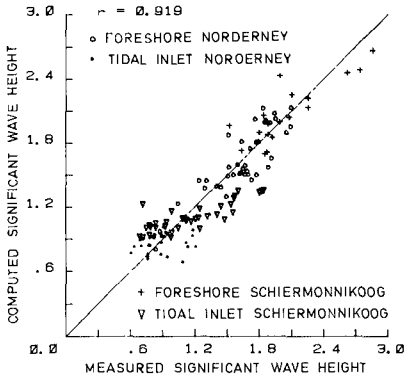

der to check, if this method is also useful for other areas with similar boundary conditions, a second wave data set from the region of the tidal inlet of the West Frisian island of Schiermonnikoog (MAD DELFZIJL 1983) is additionally taken into consideration. The function gained from the regression analysis does also fit the composited data of both areas (Fig. 8).

Summarizing these results it becomes obvious that the formulation of boundary conditions for wave breaking on tidal inlet bars and their functional relationship as developped here are not only applicable to these processes in the investigation area itself but also in other regions with similar morphological boundary conditions.

4. PERIOD AND LENGTH TRANSFORMATION

The breaking of waves on the bar does not only create a damping of their heights but also a transformation of their periods and length. Data analysis for these parameters was carried out in the same manner as for wave heights. The partial correlation coefficients for significant wave period and length are summarized in table 2, separately for the island foreshore and the tidal inlet:

Table 2: Partial correlation coefficients for single boundary conditions

AREA	PARAMETER	BOUNDARY CONDITION					
		H_a/h_a	H_a/L_a	h_a/L_a	$g \cdot T_a^2 \cdot L_a^{-1}$	$(h_a-h_R)/h_a$	$8_R/L_a$
ISLAND FORE-SHORE	T_{Hs}	0,708	0,365	0,707	0,683	0,275	0,336
	L_{Hs}	0,754	0,471	0,754	0,717	0,400	0,435
TIDAL INLET	T_{Hs}	0,536	0,030	0,275	0,536	0,275	0,336
	L_{Hs}	0,582	0,047	0,582	0,554	0,400	0,435

Obviously period and length transformation due to breaking on the tidal inlet bar does not depend primarily on a single boundary condition as wave height transmission by the offshore wave height/water depth ratio. It is also evident that wave breaking on the bar is different on its parts which separate the island foreshore and the tidal inlet itself

from the offshore area. The transformation of periods and lengths do not depend to a similar extent on the same boundary conditions, which is apparently clear for offshore wave steepness.

A direct comparison of periods and lengths measured offshore and onshore of the bar (Fig. 9 + 10), shows that wave breaking on the bar leads to a decay of bigger offshore waves to shorter solitons (GALVIN 1972) or secondary waves (HULSBERGEN 1974).

Fig. 9a

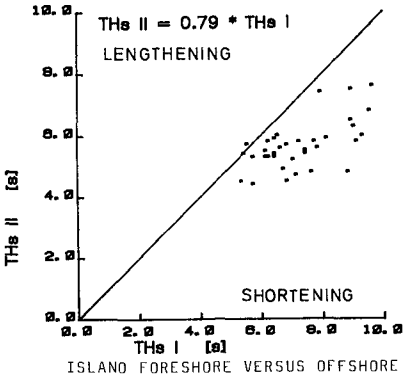

ISLAND FORESHORE VERSUS OFFSHORE SIGNIFICANT WAVE PERIOD

Fig. 9b

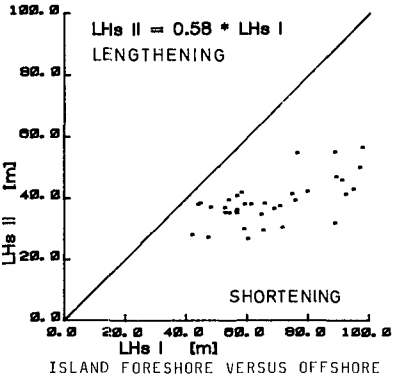

ISLAND FORESHORE VERSUS OFFSHORE SIGNIFICANT WAVE LENGTH

Fig. 10a

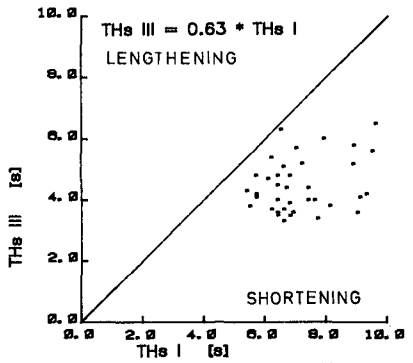

TIDAL INLET VERSUS OFFSHORE SIGNIFICANT WAVE PERIOD

Fig. 10b

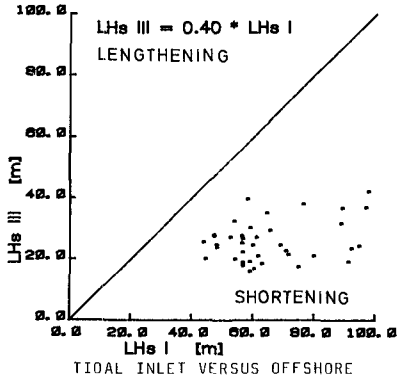

TIDAL INLET VERSUS OFFSHORE SIGNIFICANT WAVE LENGTH

In analogy to wave heights the nonlinear multiple regression analysis was not only carried out for the data measured in the investigation area itself but additionally in connection with those from the region of the West Frisian Island of Schiermonnikoog. Due to limited space only the results of the last are quoted here (Fig. 11 + 12). The data fitting to the treated function is of less accuracy than for wave heights, especially for those from the tidal inlet of the Norderney Seegat. This result agrees well with the order of magnitude of partial correlation coefficients (Table 2). Probably this lack of accuracy is partly created by disturbances in data sampling due to failures of the measuring devices as mentioned before.

Fig. 11

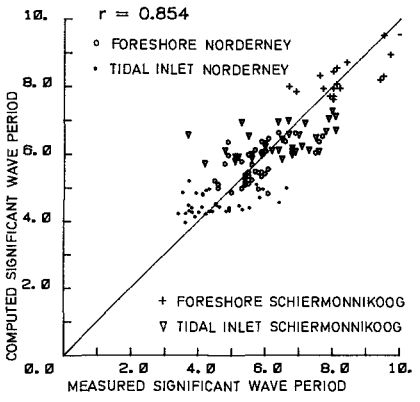

Fig. 12

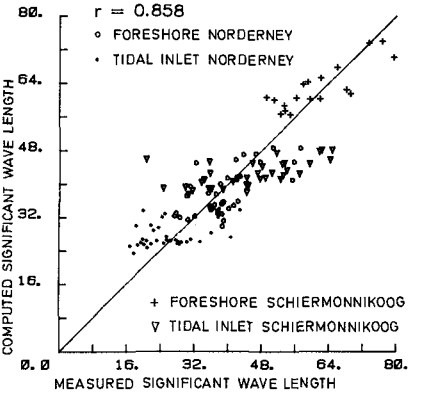

5. ENERGY DISSIPATION

5.1 ENERGETICALLY REPRESENTATIVE WAVES

The energy of a wave is defined as follows:

$$E = \frac{1}{8} \cdot \rho \cdot g \cdot H^2 \cdot L$$

FÜHRBÖTER (1974) suggested determining the power of a wave in terms of electricity:

$$N = 1{,}225 \cdot \rho \cdot g \cdot H^2 \cdot \frac{L}{T} \ (kw)$$

In order to compute the power of an energetically representative wave for measured time series in the offshore area of the German North Sea coast DETTE and FÜHRBÖTER (1977) made the following substitution:

$$\frac{L}{T} = c = \sqrt{g \cdot h}$$

Additionally they introduced the significant wave height H_s for the computation of wave power:

$$N = 1{,}225 \cdot \rho \cdot g \cdot H_s^2 \cdot g \cdot h \quad (kw)$$

But this solution includes two basic faults. Firstly the energetically representative wave height of a time series is in accordance with LONGUETT-HIGGINS (1953) H_{rms} and not H_s. Secondly the use of the approximation for shallow water wave celerity is restricted to values of relative water depth of

$$h/L_o \leq 0{,}05 \quad .$$

As well in the investigation area of DETTE and FÜHRBÖTER (1977) as at the measuring station in the offshore area of Norderney this assumption is not satisfied. Furthermore it seems to be convenient to consider the energy flux, represented by the ratio of wave group and phase velocity. Therefore the power of the energetically representative waves of all measured time series is computed in the following manner:

$$N = 1{,}225 \cdot n \cdot \rho \cdot g \cdot H_{rms}^2 \cdot c$$

$$c = \frac{g}{2\pi} \cdot T_m \cdot \tanh (k \cdot h)$$

A comparison of the results for data from the offshore area of Norderney with the computation method suggested by DETTE and FÜHRBÖTER (1977) shows, that their statement leads to an overestimation of wave power with hyperbolical character of about 400 % on the average (NIEMEYER 1983).

The determination of energy dissipation due to wave breaking is carried

out by comparing the power of the energetically representative waves of all time series measured correspondently offshore and onshore of the tidal inlet bar. In order to avoid an overestimation of longer waves the wave power is summarized per hour considering the possible number of waves which can occur during this unit of time due to their period.

Fig. 13

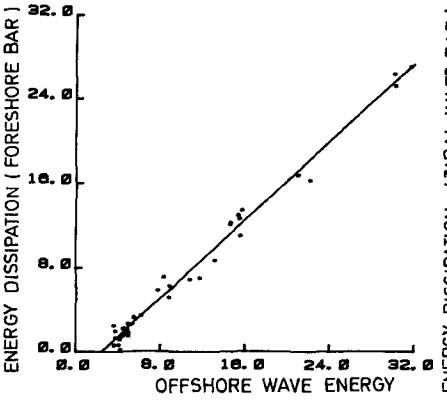

Fig. 14

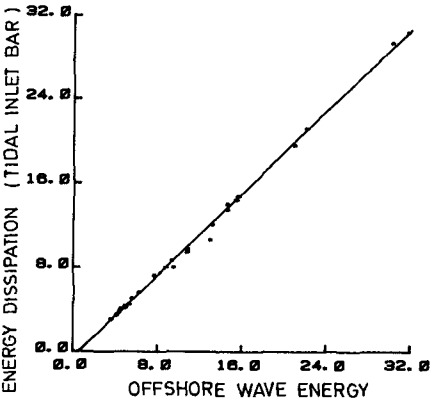

The numerical results of these computations indicate the enormous sheltering effect of the bar for its onshore areas against wave action. There is a strong linear relationship between offshore wave energy and energy dissipation due to breaking on the bar (Fig. 13 + 19): On the average 92 % of wave energy in the offshore area dissipates on the bar's shoals seaward of the tidal inlet and 70 % on those separating the island foreshore from the open sea. These differences in dissipative efficiency of the two parts of the bar, which correspond with wave height damping, could be easily explained by the distinction of its morphological features: The shoals seaward of the bar are higher, have a larger aerial extension and are closer to each other than those surrounding the island foreshore (Fig. 1 + 15). It seems furthermore noteworthy that energy dissipation on both parts of the bar increases with the same tendency as offshore wave energy.

Though there is a strong linear relationship between offshore wave energy and its dissipation on the bar, it is not similarly succesful to

Fig. 15:
Tidal inlet bar (foreground: tidal inlet; background: island foreshore)

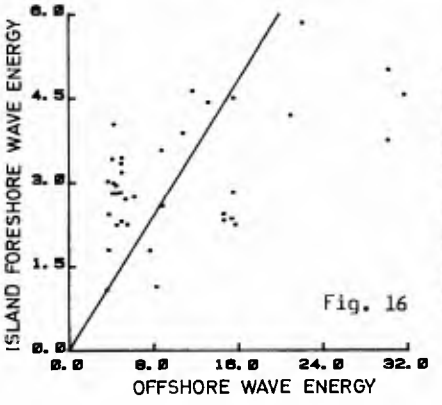

Fig. 16

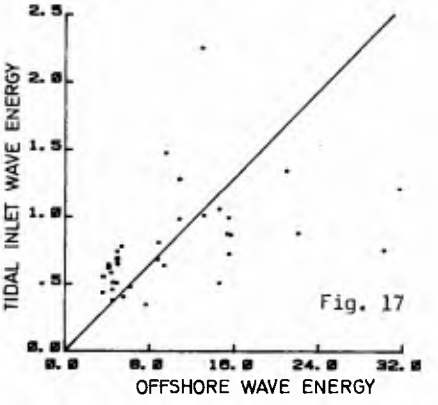

Fig. 17

use it for the derivation of the residual wave energy in the onshore areas (Fig. 16 + 17). There is a remarkable scattering of values due to divergence from the functional average. The reason might be that the residual wave energy is much smaller than both the offshore wave energy and its rate of dissipation due to breaking. So probably the derivation leads to small differences of large numbers. But it is noteworthy that the functional average is well in accordance with the average rate of dissipation derivated above.

5.2 ENERGY SPECTRA

As well as for energetically representative waves of measured time

series, investigations of energy dissipation due to wave breaking have been carried out by comparison of spectra, which have been measured correspondently offshore and onshore of the bar. The intention was to get not only information about energy dissipation but also about energy shifting to other frequencies.

The spectra of two runs are used here for such an exemplary comparison. One is representative for high the other for very high offshore wave conditions (Table 3). Corresponding to the meteorological boundary conditions the energy of spectrum No. 51 is five times greater than that of No. 24 and the relation of peak energy density is even ten to one (Fig. 18 + 19, Table 3). Comparing the spectra onshore of the bar these differences have become remarkably smaller. This result also proves the already established fact that an increase of wave energy in the offshore area leads always to a higher dissipation due to breaking on the bar. The dissipation is not only characterized by a decrease of total energy

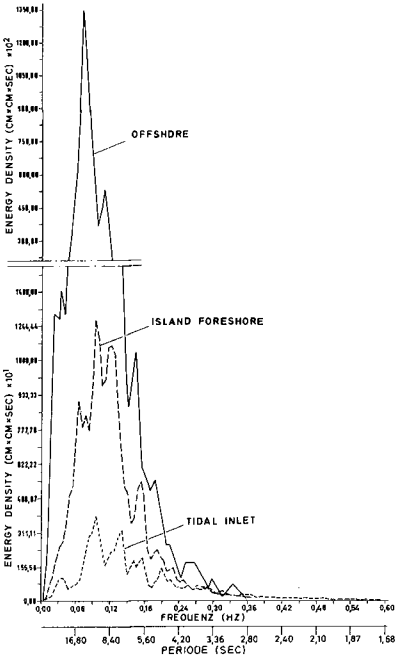

Fig. 18: Spectrum No. 51

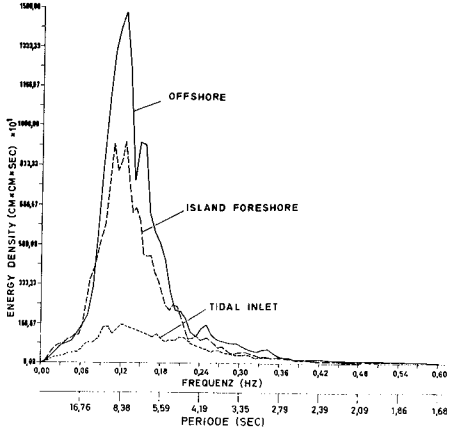

Fig. 19: Spectrum No. 24

Table 3: Comparison of Spectral Parameters

PARAMETER	RUN 24			Run 51		
	OFF-SHORE	ISLAND FORESHORE	TIDAL INLET	OFF-SHORE	ISLAND FORESHORE	TIDAL INLET
$E_{ges}(cm^2)$	5 616	3 654	1 150	25 644	5 182	1 602
$E_{fmax}(cm^2\ s)$	12 900	9 302	1 642	139 200	12 660	3 864
f_{max} (Hz)	0,128	0,127	0,122	0,080	0,093	0,087
T_p (s)	7,8	7,9	8,2	12,5	10,8	11,5
H_s (m)	2,11	1,71	0,95	4,53	2,04	1,19
T_{m02}(s)	5,5	5,7	4,3	7,2	6,3	5,1
ε	0,95	0,93	0,93	0,98	0,96	0,91
Q_p	1,44	1,40	1,01	1,71	1,16	1,08

but also and to a larger extent of the energy peak concentration leading to multi-peak spectra in the onshore areas. The decay of peak concentration intensifies the more firstly the higher the spectral peak concentration in the offshore area and secondly the higher the dissipative efficiency of the shoals. So for both spectra the dissipation of energy is in comparison on the shoals offshore of the tidal inlet itself much larger than on those seaward of the island foreshore. Also the change of the spectral shape due to the decay of the single peak to a number of peaks of similar order of magnitude occur on the island foreshore only significantly for spectrum No. 51 with its very high energy peak concentration.

Analogous high energy dissipation due to the same boundary conditions - high shoals with large areal extension close to each other and high energy concentration in the offshore wave spectrum - effects an energy shifting to higher frequencies (Fig. 20). Considering this result and the correspondent change of spectral shape it is remarkable that there is even nearly no change in peak frequency from the single peak offshore spectrum to the corresponding ones in the onshore areas of the bar with a multi-peak shape. Therefore it seems necessary to reconsider the interpretation of multi-peak spectra by only one peak frequency.

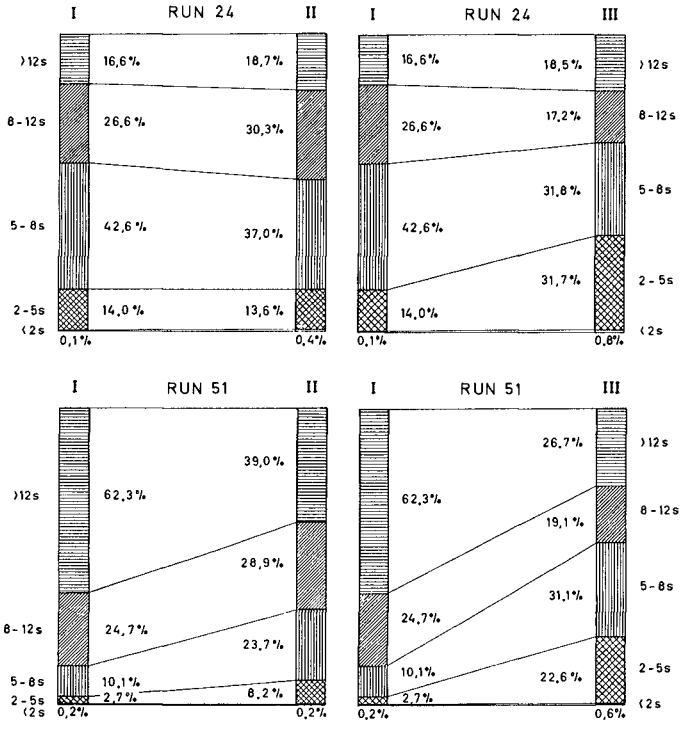

Fig. 20: Spectral energy shifting due to wave breaking on the bar

I: Offshore II: Island foreshore III: Tidal inlet

6. HYDRODYNAMICAL CAUSES FOR WAVE BREAKING

In order to evaluate the hydrodynamical causes for wave breaking on the bar, the two breaking criteria for shallow water were correspondently taken into account. Firstly the limit of wave height/water depth ratio for North Sea conditions (FÜHRBÖTER 1974; SIEFERT 1974) and secondly the critical wave steepness (MICHE 1944) were computed for the measured offshore wave data. Additionally their transformation due to shoaling was considered. The investigations are based on a fictitious water depth on the bar corresponding to the highest areas of the shoals.

Even for this water depth, which is rather small with respect to site conditions a large number of significant wave heights calculated due to shoaling would not break on the bar (Fig. 21 + 22). On the contrary many more of these fictitious significant wave heights would break taking the critical steepness limit (MICHE 1944) into consideration

(Fig. 23 + 24). This result leads to the conclusion that the dissipative efficiency of the bar does not only base on the restricted water depth on the highest part of its shoals but also and probably to a larger extent on shoaling water depth from the offshore area to the bar.

Fig. 21

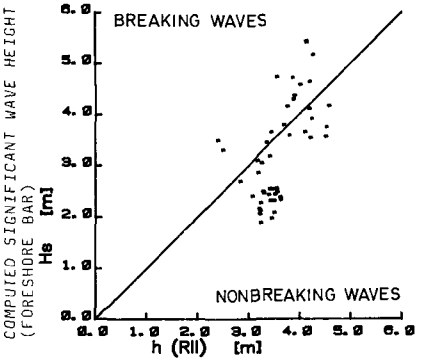

Fig. 22

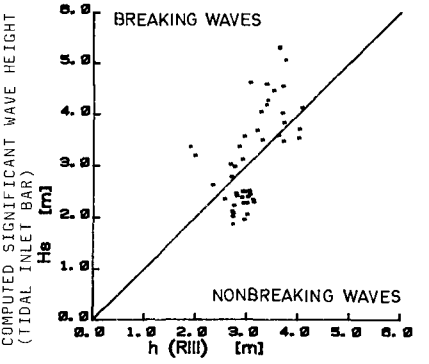

Fig. 23

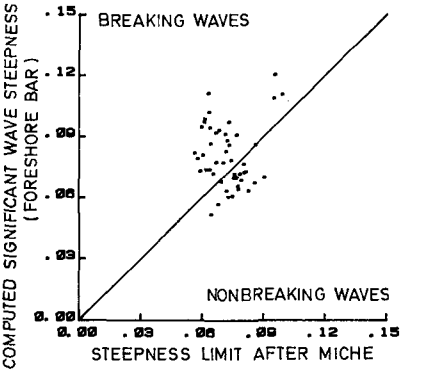

Fig. 24

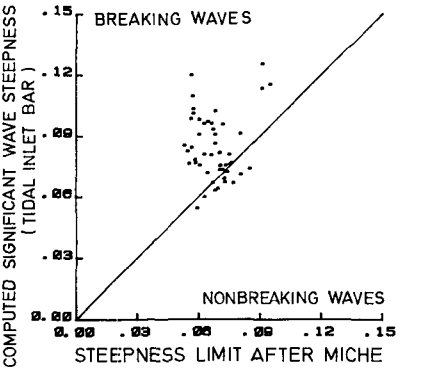

7. FINAL REMARKS AND ACKNOWLEDGEMENTS

These results presented here are part of a more detailed study (NIEMEYER 1986) which was already published ealier in German. The investigation were sponsored as well by the GERMAN FEDERAL MINISTRY FOR RESEARCH AND TECHNOLOGY (BMFT) through the GERMAN COUNCIL ON COASTAL ENGINEERING RESEARCH (KFKI) as by the LOWER SAXONIAN STATE GOVERMENT-MINISTRY FOR THE ENVIRONMENT.

B. REFERENCES

ABDUHL KHADER, M.H. + RAI, S.P. (1980): A Study of Submerged Breakwaters. Journ. o. Hydraul. Res., Vol. 18, No. 2

BATTJES, J.A. + JANSSEN, J.P.M.F. (1979): Energy Loss and Set-up Due to Breaking of Ramdom Waves. Proc. 16th Intern. Conf. o. Coast. Eng. ASCE, New York

DETTE, H.H. + FÜHRBÖTER, A. (1977): Wave Climate Analysis for Engineering Purpose. Proc. 16th Intern. Conf. o. Coast. Eng., ASCE, New York

DIEPHUIS, J.G.H.R. (1957): Scale Effects Involving the Breaking of Waves. Proc. 6th Conf. o. Coast. Eng., Gainesville/Fl.

FÜHRBÖTER, A. (1974): Einige Ergebnisse aus Naturuntersuchungen in Brandungszonen. Mitt. Leichtweiß-Inst., H. 40

FITZGERALD, D.M., PENLAND, S. + NUMMEDAL, D. (1984): Control of Barrier Island Shape by Inlet Sediment Bypassing: East Frisian Islands West-Germany. In: Greenwood, B. + Davis, R.A. (ed.), Hydrodynamics und Sedimentation in Wave-Dominated Coastal Enveronments. Developments in Sedimentology 39, Elsevier, Amsterdam - Oxford - New York - Tokyo

GALVIN, C.H. (1972): Wave Breaking in Shallow Water. In: Meyer, R.E. (ed.): Waves on Beaches and Resulting Sediment Transport. Academic Press, New York

HAYES, M.O. (1979): Barrier Island Morphology as a Function of Tidal and Wave Regime. In: Leatherman, S.P. (ed.), Barrier Islands: From the Gulf of St. Lawrence to the Gulf of Mexiko. Academic Press, New York

HULSBERGEN, C.H. (1974): Origin, Effect and Suppression of Secondary Waves. Delft Hydr. Lab. Publ., No. 132

JOHNSON, J.W., FUCHS, R.A. + MORISON, J.R. (1951): The Damping Action of Submerged Breakwaters. Trans. Am. Geophys. Union, Vol. 32, 5

LONGUETT-HIGGINS, M.S. (1953): On the Statistical Distribution of the Heights of Sea Waves. Journ. o. Marine Res., Vol. XI, Nr. 3

LUCK, G. (1978): Islands in Front of the Southern North Sea Coast. Die Küste, H. 31

MAD DELFZIJL (1983): Parameters van Golfmetingen in het Oostelijke Waddenzee. Meet. en Adviesdienst Delfzijl - Rijkswaterstaat, Directie Groningen

MICHE, R. (1944): Mouvement ondulatoires de la mer en profondeur constante ou décroissante. Ann. d. Ponts et Chauss., 114, Nr.2,7,13,19

NIEMEYER, H.D. (1983): Über den Seegang an einer inselgeschützten Wattküste. BMFT-Forschungsber. MF 0203

NIEMEYER, H.D. (1986): Ausbreitung und Dämpfung des Seegangs im See- und Wattengebiet von Norderney. Jber. 1985, Forsch.-Stelle Küste, Bd. 37

SIEFERT, W. (1974): Über den Seegang in Flachwassergebieten. Mitt. d. Leichtweiß-Inst., H. 40

9. SYMBOLS

B_R : Representative shoal width
E : Wave energy
E_F : Wave energy flux
E_{fmax} : Energy density peak
E_{ges} : Total spectral energy
f : Frequency
f_{max} : Peak frequency
g : Gravitational acceleration
h : Water depth
h_a : Offshore water depth
h_b : Water depth at breakpoint
h_R : Fictitious water depth above the bar
H : Wave height
H_a : Offshore wave height
H_b : Breaker height
H_i : Onshore wave height
H_s : Significant wave height
H_{rms} : Root-mean-square wave height
k : Wave number: $2\pi/L$
L_a : Offshore wave length
L_i : Onshore wave length
L_o : Deep water wave length
L_{Hs} : Significant wave length
MHWL : Mean high tide water level
n : Ratio of wave group and phase velocity
N : Wave power
Q_p : Spectral peakednessparameter
T_a : Offahore wave period
T_{Hs} : Significant wave period
T_i : Onshore wave period
T_p : Spectral peakperiod
ε : Spectral width
ρ : Specific density of seawater
T_{m02} : Mean spectral period

CHAPTER 106

NUMERICAL SIMULATION OF BEACH PROFILE CHANGES

Hitoshi Nishimura*
Tsuguo Sunamura**

ABSTRACT

This paper presents an overall numerical model for predicting beach profile changes due to waves. The local rate of net on/offshore sediment transport is empirically formulated as a function of the Ursell number and Hallermeier parameter. A sub-model of two-dimensional wave transformation includes the wave shoaling, breaking and damping in a surf zone. It is combined with another sub-model of beach profile change for the analyses of wave-profile interaction. The validity of the model is examined through hindcasting of profile changes observed in ordinary and prototype-scale flumes.

1. INTRODUCTION

In planning countermeasures against beach erosion, which is raising serious problems at many coast in the world, it is indispensable to understand the interaction between waves and beach profiles. This paper deals with a numerical model for the prediction of beach profile changes under given conditions of incident waves, bed material and initial profile. The process of profile change is simulated through repetitive calculation of two-dimensional wave transformation and net sediment transport due to waves. Similar trials were made also by Mizuguchi and Mori (1981) and Shibayama (1984).

For these years, trials have been made to establish a more advanced numerical model for analyzing three-dimensional beach processes. Nevertheless, studies on two-dimensional models such as beach profile models and shoreline models are meaningful particularly from the engineering point of view, since it seems to be impossible for the time being to apply a three-dimensional model to the analyses of long-term and/or wide-range beach transformations.

2. MODELING OF TWO-DIMENSIONAL WAVE TRANSFORMATION

Several methods are available for the numerical simulation of wave transformation in a shallow region. Among them, the simplest method based on the law of wave energy conservation will be most relevant here, since the calculation of local wave heights only is required in

* Associate Professor, Institute of Engineering Mechanics, University of Tsukuba, Sakura, Niihari, Ibaraki 305, Japan.
** Associate Professor, Institute of Geoscience, ditto.

modeling of this type. It is also to be borne in mind that the present model involves a net sediment transport rate formula, whose accuracy cannot be so high as yet.

For a steady field of uni-directional waves, the equation governing the variation of wave energy density is written as

$$\frac{\partial EC_g}{\partial x}+\Gamma=0 \tag{1}$$

where x is the shoreward coordinate, E is the wave energy density ($E=\rho gH^2/8$, ρ is the density of water, g is the gravitational acceleration and H is the wave height), C_g is the group velocity of waves, and Γ represents the wave damping mainly associated with breaking. Nishimura (1982) suggested that the wave height attenuation after breaking is well simulated, if the wave energy dissipation is assumed to be proportional to the energy density ($\Gamma=\alpha E$) with α regarded as a function of the water depth. Izumiya and Horikawa (1984) investigated the damping of waves more precisely to evaluate separately the effects of bottom friction and internal turbulence produced by breaking:

$$\Gamma=[\sqrt{2}(2n-1)C_f+C_t]\sqrt{\frac{2n-1}{\rho}\left(\frac{E}{d}\right)^3} \tag{2}$$

where n is the ratio of group velocity to phase velocity of waves, and d is the substantial water depth including wave setup.

The frictional coefficient C_f is normally assumed to take a value of the order 0.01. Another coefficient C_t, which represents the effect of turbulence in the surf zone, is given as

$$C_t=\beta_0\sqrt{nE/\rho gd^2-0.09} \tag{3}$$

where the value of β_0 is about 1.8, although it is affected by the bottom slope to a certain extent. The coefficient C_t is set to be zero before breaking or when $nE/\rho gd^2 < 0.09$. The breaking point is judged by use of the breaker indices given by Goda (1970).

For the numerical integration of Eq. (1), the variables are discretized and the equation is rewritten into a finite difference form. Computation points are uniformly distributed along the x-axis. Then, the wave energy (and, therefore, the wave height) at each point can be determined successively from the offshore to the shore, if the incident wave height and period are given.

Radiation stress accompanying monochromatic waves is easily evaluated from the energy density. Since the gradient of the stress balances with gravitational component of water surface slope,

$$\frac{\partial\zeta}{\partial x}+\frac{1}{\rho gd}\frac{\partial}{\partial x}\left[\left(2n-\frac{1}{2}\right)E\right]=0 \tag{4}$$

The surface elevation due to wave setup is given through the numerical integration of the above equation. In this case, Eqs. (1) and (4) have to be solved simultaneously, because the substantial water depth is the sum of ζ and the still water depth h. The amount of wave setup is actually very small except in a swash zone and it is sufficient to revise the values of ζ only when effective changes appears in d.

3. FORMULATION OF SEDIMENT TRANSPORT RATE

In order to measure a net sediment transport rate in a wave flume,

a tray method (Sunamura,1982) was employed. A rectangular tray, the width of which is equal to that of the flume, is divided into two equivalent compartments by a thin metal splitter having the tray width. The compartments are filled with equal mass of sediment to be tested. The surface of sediment is manually smoothed and the splitter is removed. Then waves are allowed to act for a certain period of time. After completion of wave action, the splitter is returned to the original position. The sediment is separately taken out from each compartment and weighed after complete drying. From the difference in sediment mass, the direction and rate of net sediment transport are determined at a fair level of accuracy.

A wave flume 12 m long, 40 cm high, and 20 cm wide was used. A plunger-type wave generator was equipped at one end of the flume, and a mortar-made uniform slope of 1/20 was installed at the other end. In this experiment, a tray (60 cm long and 2 cm deep) was fixed on the slope after removal of a part of the bottom. The tray was always exposed to the action of broken waves with heights ranging from 1.8 to 3.2 cm and periods from 0.8 to 2.4 s. Five kinds of well sorted sediment with approximately the same specific gravity (about 2.6) but different diameters (0.23, 0.41, 0.79, 1.3, and 2.9 mm) were used. The amount of sediment tested was 1500 g for each compartment. The surf zone data available were incorporated to form a sound base for establishing a transport rate formula which is applicable to the whole range of the nearshore zone.

The data were analyzed with the Ursell number U_r representing the skewness of water particle velocity profile and the Hallermeier (1982) parameter Φ indicating the intensity of sediment movement, where

$$U_r = HL^2/d^3 \quad \text{and} \quad \Phi = (a_0\omega)^2/\gamma' g D$$

in which L is the wave length, a_0 is the near-bottom orbital diameter, ω is the wave angular frequency of waves, D is the grain size of the sediment, and γ' is the specific gravity of immersed sediment.

Figure 1 is a plot of net sediment transport directions on the U_r - Φ plane, showing that

(1) net sediment transport takes place if $U_r > 230$,

(2) onshore transport occurs if $7000/U_r < \Phi < 0.13\,U_r$,

and (3) offshore transport occurs if $\Phi > 0.13\,U_r$.

A quantitative examination of the data plotted in the figure indicated that the normalized sediment transport rate Q/wD can be expressed as a function of Φ for a fixed U_r, where Q is the volume (with void) rate of net onshore sediment transport per unit shoreline length, and w is the fall velocity of the sediment. In order to determine the functional form, the values of Q/wD were plotted against Φ for each range of U_r values, as shown in Fig. 2. Although the critical parameter value for net sediment transport is given by $\Phi_c = 7000/U_r$, data analysis on a quantitative basis suggests that an approximation of $\Phi_c = 0$ is reasonable.

Thus, the following functional form was assumed:

$$\frac{Q}{wD} = -A\Phi(\Phi - 0.13U_r) \tag{5}$$

where A is a function of U_r. The curves were drawn in Fig. 2 as a result of the best fit of Eq. (5) to the data. In spite of considerable data scatter, it is observed that general trends can be described by

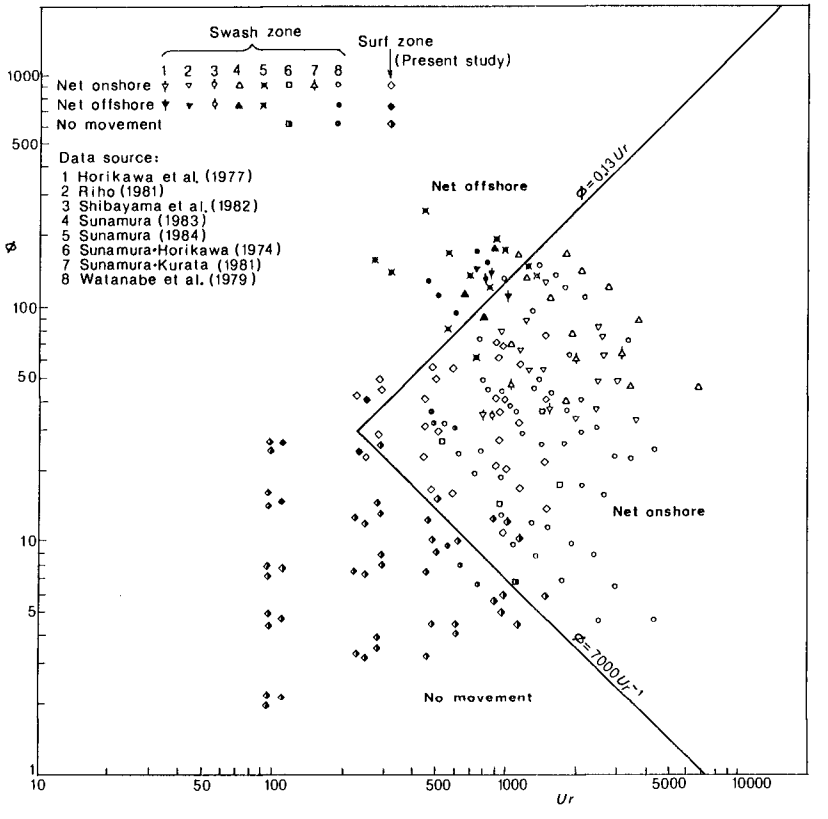

Fig. 1 Demarcation of net sediment transport directions.

this equation. A further plot showed that $A \sim U_r^{0.2}$, so that the following transport rate formula yields:

$$\frac{Q}{wD} = -BU_r^{0.2}\Phi(\Phi - 0.13U_r) \tag{6}$$

where B is a constant of the order 10^{-7} for laboratory tests of ordinary scale, and Q vanishes when $U_r < 230$.

Another set of data was obtained through prototype-scale experiments at the Central Research Institute of Electric Power Industry, Japan, and an investigation on these data indicated that B takes a value of the order 10^{-5} (Sunamura, 1984). As to this scale effect, however, a contradictive conclusion is derived from applications of the above formula as will be shown in Section 5. More studies are needed to fix the value of the coefficient.

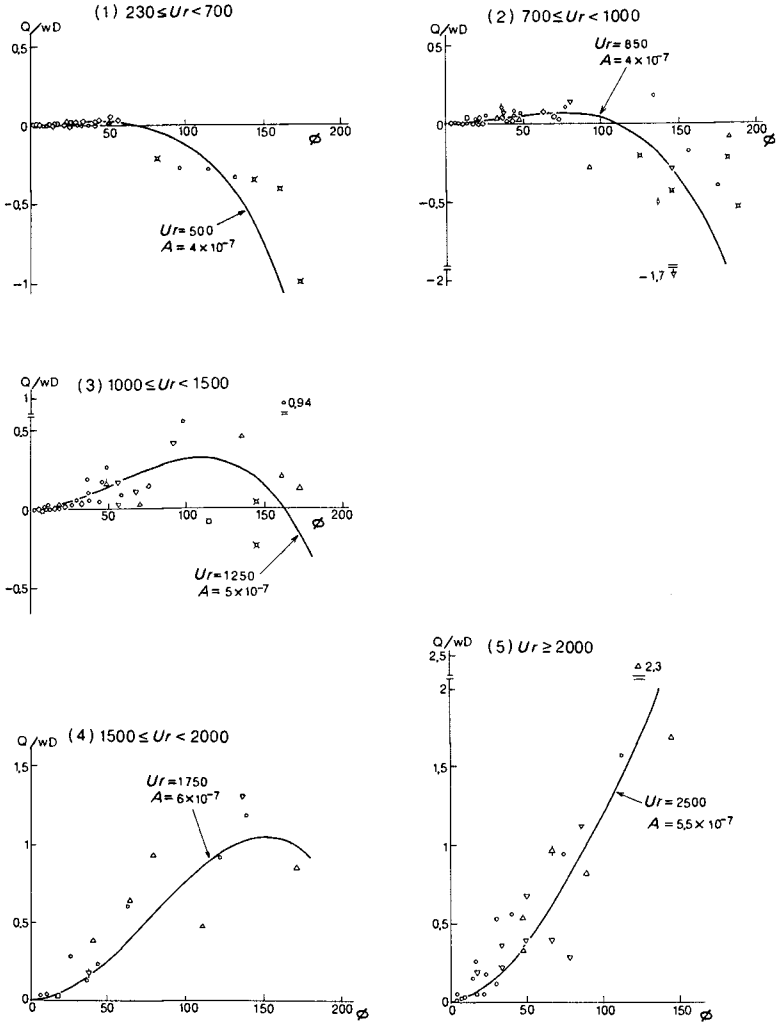

Fig. 2 Relationship between the normalized sediment transport rate Q/wD and the Hallermeier parameter Φ. (See the legend in Fig. 1 for symbols)

4. MODELING OF BEACH PROFILE CHANGES

The formula (6) gives the rate of net sediment transport as a function of local wave height and water depth, including no factor to represent the effect of bottom slope. As a consequence, a model simply based on the above formula may allow the generation of unrealistic local irregularities in the bottom topography. It is also impossible for the model to describe the reduction of net sediment transport which is normally observed as the beach profile approaches to an equilibrium slope.

On the basis of the above discussion, a term proportional to the excess bottom slope is introduced to give the effective sediment transport rate Q':

$$Q'=Q\mp\left(\left|\frac{\partial z}{\partial x}\right|-\beta_*\right)Q_* \tag{7}$$

where z is the bottom surface level and the modification is performed only when the absolute bottom slope exceeds the critical slope β_*. The scale of the modification Q_* is determined empirically as well as β_*. In the above expression, the inverse sign to that of $\partial z/\partial x$ is to be selected. Similar expression was used by Watanabe (1982) in his three-dimensional model.

Now, the continuity equation for bed material is written as follows:

$$\frac{\partial z}{\partial t}+\frac{\partial Q'}{\partial x}=0 \tag{8}$$

where t is the time.

Let the values of the wave height and the water and bottom surface levels be defined at computation points $x=i\Delta x$ $(i=0, 1, 2, \cdots)$ except those of the sediment transport rate which are defined at intermediate points $x=(i+1/2)\Delta x$. Then, the rise of bottom surface Δz_i during the time interval Δt at the i-th point is given as

$$\Delta z_i=-(Q'_{i+1/2}-Q'_{i-1/2})\Delta t/\Delta x \tag{9}$$

in which the values of variables at the intermediate points required for the calculation of Q' are obtained through interpolation from those at neighboring definition points.

Simulation of the beach profile change is achieved by repetitive computations of the wave height, sediment transport rate and bottom surface level. It is recommended to adjust the time interval Δt at each time step of computation so that the resultant maximum change in the bottom surface level may not exceed a given limit. In order to save the computer execution time, variation of the wave height is calculated only when effective changes appeared in the beach profile.

5. EXAMPLE COMPUTATIONS

First, the result of a movable bed experiment of ordinary-scale is used for the examination of the numerical model. The bed material was well sorted sand with the grain size of 0.18 mm and the specific gravity of 2.7. The fall velocity of the material is estimated from Ruby's formula at 2.4 cm/s for the temperature of 15°C. A uniform slope of 1/10 was installed in a wave flume 17 m long, 60 cm high, and 40 cm wide. The bed was fixed and horizontal in the offshore range, where the

water depth was 35 cm.

The slope was exposed to the continuous action of regular waves for 2 hours, and the profiles were measured several times after switching the wave generator off. A touch sensor was used for the measurement of the bottom level at every 5 cm along a longitudinal line. A representative profile was obtained through averaging profiles along 5 measuring lines at maximum, since the bottom topography was not necessarily uniform over the flume width. A typical bar was formed under the incident wave condition of 0.8 s in period and 6.7 cm in height.

Figures 3 show calculated wave height variations before and after the bar formation in comparison with experimental data. Calculated variations of the mean surface elevation are also shown by broken lines in the figures. The spacing of computation points Δx was fixed at 5 cm over the entire range of computation. A notable difference between the calculated and measured wave heights is found at their peaks near the breaking point. This is rather reasonable because the present model simulates the effective wave height which is proportional to the square root of wave energy density. Owing to the shoaling effect, a wave crest becomes steeper as it approaches to the breaking point, and a rapid increase in the apparent wave height is observed when it breaks.

Partial reflection of waves at the front slope of the bar causes a considerable undulation of wave height in the offshore range, as shown in the lower figure. A corresponding undulation also appears in the beach profile. Note that the wave reflection is not taken into account here in the computation. A more realistic results can be obtained through numerical integration of the decomposed mild slope equation with a dissipation term (Nishimura et al., 1983), although much more computational labor is required.

Figure 4 shows the beach profiles observed in the flume, whereas the results of numerical modeling is shown in Fig. 5. The profiles in Fig. 4 describe the very early stage of the observed process, involving already the major part of the profile changes. In the numerical computation, the parameter values such as $\beta_* = 0.1$ and $Q_* = 10^{-5}$ m^3/s were used, and the time interval Δt was adjusted in the range from 60 to 150 s. In spite of the comment in Section 3, the coefficient B was given the value of 10^{-5} here for the best fit to the measured profiles. The generation and development of a bar are well simulated by the numerical model, while the location of the bar is not correctly estimated.

As shown in Fig. 6, the rapid changes in the wave height and water depth result in the complicated variations of U_r and Φ values. The corresponding sediment transport rate is denoted by the broken line in Fig. 7. The solid line in the same figure shows the rate deduced from the observed profile changes. The peak of the former appears at the breaking point, whereas the peak of the latter is located on the back slope of the bar. In the numerical model, the predominant flushing effect appearing at the bar crest causes offshore shift of the bar and, consequently, that of the breaking point. Thus, the continuous and rather rapid move of the bar takes place. Such interactive deformations of waves and beach profile are often observed in a flume and in a field as well, although the speed of bar move is much lower.

The above-discussed defect of the model implies an inadequateness of the basic assumption that the rate of net sediment transport can be evaluated solely from local wave and topographic conditions. In fact,

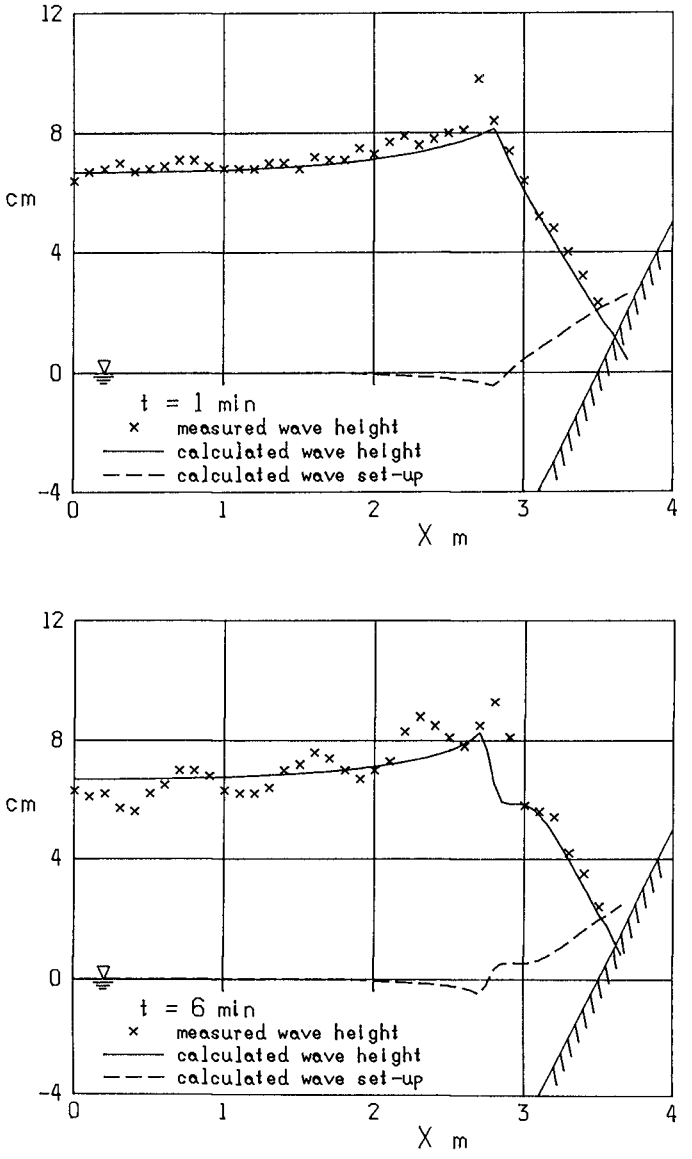

Fig. 3 Variation of the wave height and wave setup.

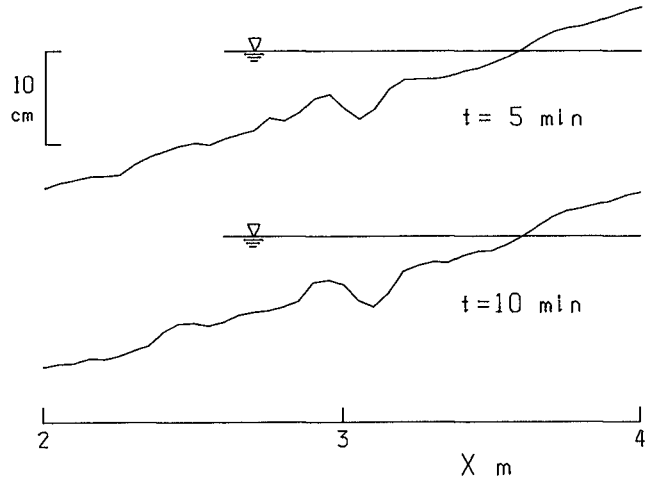

Fig. 4 Beach profiles observed in an ordinary-scale flume.

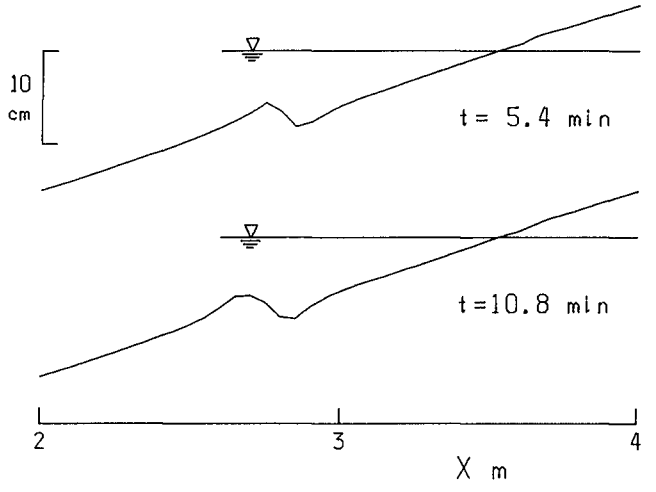

Fig. 5 Calculated beach profiles.

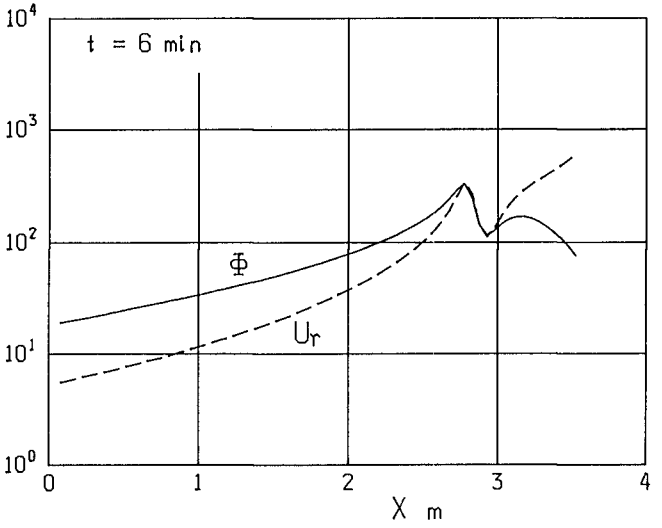

Fig. 6 Variations of the Ursell number U_r and the Hallelmeier parameter Φ.

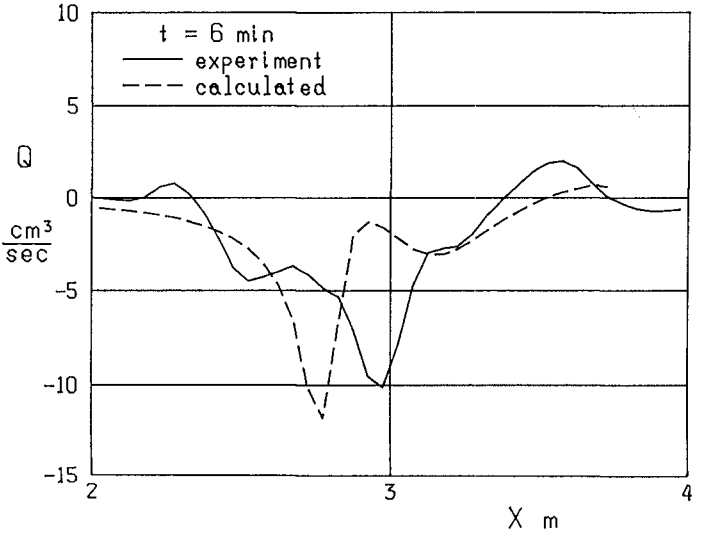

Fig. 7 Variation of the sediment transport rate.

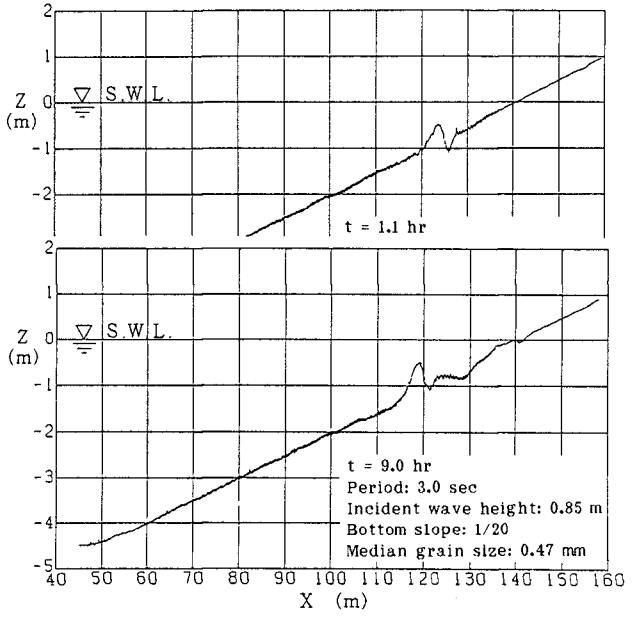

Fig. 8 Beach profiles observed in a prototype-scale flume.

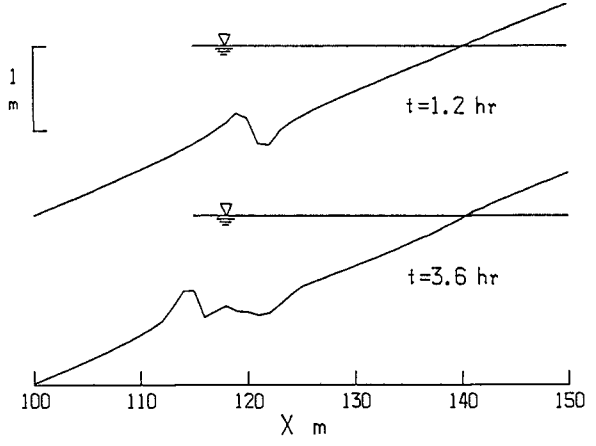

Fig. 9 Calculated beach profiles.

the intense near-bottom flows induced by plunging waves largely contribute to the bar and trough formation.

Figure 8 presents another example of beach transformation observed in the prototype-scale wave flume by Shimizu et al. (1985); experimental conditions are specified in the figure. The corresponding result of numerical hindcasting is shown in Fig. 9, which exhibits the similar tendencies to the preceding example. It is, however, interesting to point out that the numerical model well explain the generation of a secondary bar in the trough behind a main bar. In this example, the spacing Δx and the time interval Δt were expanded to 1 m and 10 ~ 30 min, and Q_* also proportionally to the maximum rate of net sediment transport. A note is that the value of coefficient B in the formula (6) was kept unchanged at 10^{-5} . It is thus concluded through these applications that the significant scale effect does not appear on this coefficient.

ACKNOWLEDGEMENTS

The authors are grateful to the Central Research Institute of Electric Power Industry, Japan, who kindly offered the experimental data for this study. The study was financially supported by the Science Research Fund of the Ministry of Education, Science and Culture, Japan, and also by the Project Research Fund of the University of Tsukuba.

REFERENCES

Goda, Y. (1970): A synthesis of breaker indices, Proc. Japan Soc. Civil Engrs., No.180, pp.39-49.
Hallermeier, R. J. (1982): Oscillatory bedload transport: Data review and simple formulation, Continental Shelf Res., Vol.1, pp.159-190.
Izumiya, T. and Horikawa, K. (1984): Wave energy equation applicable in and outside the surf zone, Coastal Eng. in Japan, Vol.27, pp.119-137.
Mizuguchi, M. and Mori, M. (1981): Modeling of two-dimensional beach transformation due to waves, Coastal Eng. in Japan, Vol.24, pp.155-170.
Nishimura, H. (1982): Numerical simulation of nearshore circulations, Proc. 29th Japan. Conf. on Coastal Eng., pp.333-337. (in Japanese)
Nishimura, H., Maruyama, K. and Hiraguchi, H. (1983): Wave field analysis by Finite Difference method, Proc. 30th Japan. Conf. on Coastal Eng., pp.123-127. (in Japanese)
Shibayama, T. (1984): Sediment Transport Mechanism and Two-Dimensional Beach Transformation Due to Waves, Doctoral Diss., Univ. Tokyo, 159p.
Shimizu, T., Saito, S., Maruyama, K., Hasegawa, H. and Kajima, R. (1985): Modeling of Onshore-Offshore Sand Transport Rate Distribution Based on the Large Wave Flume Experiment, Central Res. Inst. of Electric Power Industry, Civil Eng. Lab. Rep. No. 385050, 60p. (in Japanese)
Sunamura, T. (1982): Laboratory study of on/offshore sediment transport rate in shallow water region, Proc. 29th Japan. Conf. on Coastal Eng., pp.239-243. (in Japanese)
Sunamura, T. (1984): Prediction of on/offshore sediment transport rate in the surf zone including swash zone, Proc.31st Japan. Conf. on Coastal Eng., pp.316-320. (in Japanese)
Watanabe, A. (1982): Numerical models of nearshore currents and beach deformation, Coastal Eng. in Japan, Vol.27, pp.147-161.

CHAPTER 107

Design of beach nourishment scheme

K.W. Pilarczyk*, J. van Overeem**, W.T. Bakker***

1 Introduction

An artificial beach nourishment used to replenish an eroding part of a coast may seem expensive and the need for repetition may discourage coastal managers. However, careful considerations of capital and maintenance cost frequently prove that it may be, in fact, the optimum solution. An added advantage is that the recreational function of the beach is preserved.
In spite of a great number of research-reports and publications on coastal processes and beach nourishment, the practical applicability of this knowledge is still in an initial stage, i.e. formulating the general concepts and trying to test their validity and practical applicability.
On the other hand, the solution of many practical coastal engineering problems cannot wait until complete understanding of these processes and the existing knowledge on this subject (though limited) should be made available for designers and managers involved in coastal engineering.
This was the main reason for the Rijkswaterstaat (Dutch Public Works Department) to prepare a manual on artificial beach nourishment.

In 1983, this Department established the task-group 'Profile Formation of Beaches', with the aim to study the relevant aspects of beach nourishment. These aspects concern among other things the influence of a beach fill on the coastal morphology and the environment, and the design and execution of a beach nourishment scheme.
The members of the task-group originate from various governmental departments, research institutes (Delft Hydraulics) and private organisations (Volker Stevin Dredging, Zanen Verstoep Dredging Contractors). In addition to the members of the working-group some other persons and organizations (also outside the Netherlands) have contributed to the final report.
The results of the studies have been described in a Manual on Beach Nourishment (Manual, 1986). This manual contains both theoretical and practical information, and is intended for persons and organisations who are involved in the prevention of beach erosion. Nearly all available and relevant literature to this subject has been incorporated.
The actual paper reviews part of the contents of the Manual and summarizes aspects related to the aim, the different types and the design process of beach nourishment schemes.

* Rijkswaterstaat, Road and Hydraulic Engineering Division, The Netherlands
** Delft Hydraulics, The Netherlands
*** Rijkswaterstaat, Tidal Waters Division, The Netherlands

2 Contents of the Manual

The Manual presents a comprehensive overview of matters related to shoreline protection by artificial beach nourishment and has been written for any authority, organization or person responsible for assessment of measures to protect, maintain or extend coastal areas. Government bodies, planners, designers and contractors will find the basic information they need. The various aspects to develop a strategy of artificial beach nourishment will pass in review: background information on coastal processes and shoreline evolution, design requirements and parameters, design methods, execution methods, and environmental aspects are the major elements presented in this manual. Furthermore, a number of implemented schemes are evaluated to indicate the applicability and accuracy of present design methods and the gaps in knowledge of this moment. In addition inventories have been made of artificial nourishment projects both in and outside The Netherlands.

The final document consists of two separate reports. The Manual (1986) comprises basically the findings of the working group, whereas the Background Report (1986) is a compilation of relevant information gathered in the scope of this project. Thus the Manual can be used separately without the need to consult the Background Report.

"Manual on Artificial Beach Nourishment" deals with the basic information for planning and design of a scheme of artificial beach nourishment. Coastal processes, computational methods, design parameters and execution methods are discussed here. General conclusions and recommendations for the future are presented in the report.

"Background Information on Artificial Beach Nourishment" comprises the information and detailed data collected, and computations carried out during the study. Literature abstracts, questionnaires on past artificial nourishment projects, model descriptions, hindcast computations and the specific Dutch situation with respect to artificial beach nourishment are comprised by the report.

3 Type in view of the aim of beach nourishment

Artificial beach nourishment schemes are generally executed with the aim to protect the coastline against beach erosion and/or to enlarge the beach for recreational purposes.
The following examples of causes of beach erosion can be mentioned:

- interruption of longshore transport by coastal structures;
- reduction of sediment supply by rivers;
- dune and beach erosion by storm surges;
- shifting of tidal channels;
- alongshore migration of large sand waves;
- relative sea level rise;
- beach mining.

The different types of beach nourishment can be characterized by the location where the sand is placed in the coastal zone, viz.:

(a) position in cross-shore direction (at the back, on top or at the face of dunes, on the beach or on the offshore zone);
(b) position in alongshore direction (placed along the beach, a stock pile of sand, or a continuous supply of sand).

Which specific type to select, depends on the aim of the beach nourishment and/or the cause of beach erosion.

4 Design process of beach nourishment scheme

The design process for an artificial beach nourishment scheme is schematically given in Figure 1. For a proper definition of the type and scale of the beach erosion problem, an assessment should be made concerning the causes of beach erosion and the interests of the actual beach with respect to safety, recreation, environment and economy.

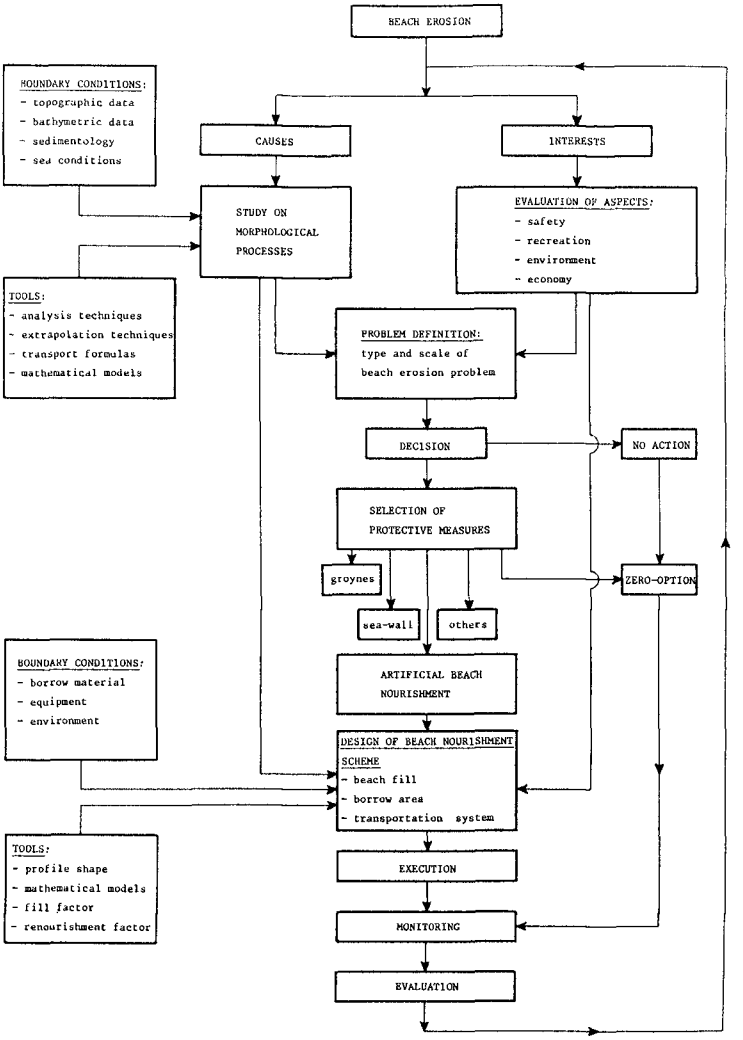

Figure 1 Process of design, execution and evaluation

The causes of beach erosion are determined in a study on morphologic processes, including the analysis of hydro-sedimentological data and the hind- and forecast of the coastal development by means of extrapolation techniques and mathematical models.
Once the problems have been defined, like short-term or long-term erosion (Figure 2), a decision can be made whether or not protective measures should be taken, and if so, which type of measures should be applied (beach nourishment, groynes, detached breakwaters, seawalls, revetments, etc.).

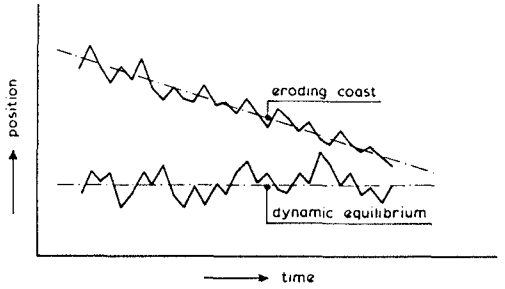

Figure 2 Short-term and long-term coastline variations

Aspects such as effectiveness, flexibility, spreading of cost, executi-on, harmony with nature, environment, etc., should be considered before selecting the protective measure (Figure 3).

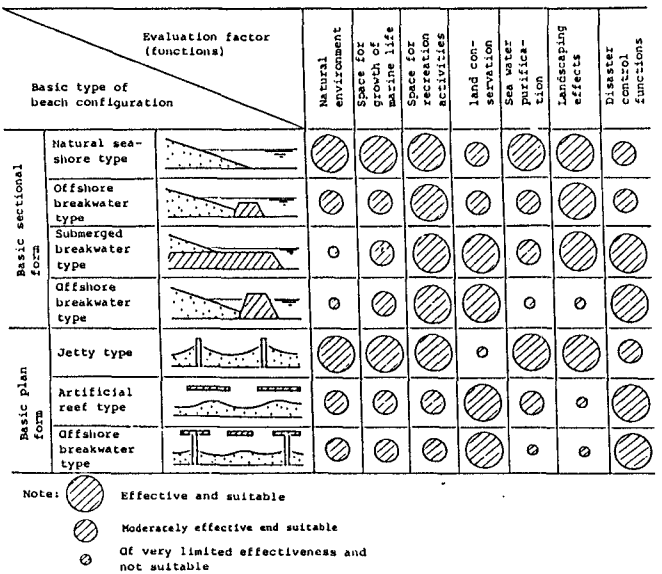

Figure 3 Selection of beach protection measure for project at Yokohama. (Kobayashi et al., 1985)

In this paper only attention is paid to the design of artificial beach nourishment schemes, for which three design elements can be distinguished, viz. the beach fill, the borrow area and the transportation system. The dimensions of the fill should be such that the effectiveness as a coastal protection is guaranteed during a pre-defined period of time. Different tools are available to determine the deformation of the fill as a function of the hydraulic boundary conditions and the applied borrow material (mathematical coastal morphology models, adjusted SPM fill factor and renourishment factor, see Manual (1986) and Shore Protection Manual (1984)).
The selection of the borrow area and the transportation system depends among other things on the available fill material, the influence of the borrow area on the coastline, the local conditions and regulations, the available equipment and the execution method.
It is recommended, that after execution of the beach nourishment, regular surveys are executed to monitor the behaviour of the beach fill and borrow area.

5 Design of beach fill

5.1 Introduction

A major question concerning the design of a beach nourishment is the determination of the required volume of sand, such that the beach fill satisfies the specified requirements during a specified time. As a result of the sand transport in the coastal zone, the beach fill will be reshaped, and possibly sand is leaving the area to be protected. In particular a sand fill placed on an eroding beach, which is the usual case, has a restricted lifetime.
For the design of a beach fill it seems convenient to make a distinction between cross-shore transport and longshore transport. The cross-shore transport is responsible for the shaping of the coastal profile till more or less an equilibrium form is attained. Due to this profile development a retreat of the shoreline may occur. Usually the longshore transport is the main agent in the reshaping of the planform of the beach fill. As a result of this reshaping of the planform sand may leave the coastal area to be protected, while on the other hand sand may also enter the protected coastal area.

5.2 Coastal profile of beach fill

The required volume of sand for a beach fill is to a large extent determined by the development of the coastal profile. In this connection different aspects can be considered, viz. the shape of the active profile as a result of the prevailing hydraulic forces, and the depth to which this profile will develop. Below this depth usually a transition zone has to be defined which meets the original profile.

Shape of active profile:

Many researches have studied the development of coastal profiles under wave attack in order to derive relations between profile shape, wave motion and sediment characteristics. Most of the derived relations are based on the results of small-scale tests in wave-channels. However, the inevitable scale effects and the strong schematization of the conditions in the model do not permit an exact extrapolation of the data to nature. The schematization applies to both the sedimentologic and the hydraulic conditions. In models mostly one type of sand is used as bed material,

whereas in nature the sediment characteristics vary often strongly along the profile. In addition the results of model testing have usually been obtained by applying fixed wave conditions, while in nature the wave conditions are quite variable. As a matter of fact the whole wave climate is responsible for the shape of the coastal profile, while also other factors play a role, like tides, surf beats, coastal currents, etc. Obviously the complexity of the factors has also caused that the analyses of measurements in nature have not led to applicable relations for predicting the shape of coastal profiles.

In case a former situation of the beach should be restored it is obvious to start from the coastal profile at that time, if available. The difference between this former coastal profile and the present profile then equals the volume of sand to be supplied per unit length of beach, provided that the borrow sand is similar to the native sand. If the former profile is not known it can be assumed that the coastal profile will develop according to the present profile up to a certain depth.

The native profile and its dynamics are important to estimate the eventual shape of the beach fill. From curve-fitting on numerous profiles Dean (1983) and Moore (1982) developed an usable relation representing the effect of the particle diameter on the beach shape (see Figure 4):

$$h(y) = Ay^m \approx By^{2/3} D^{1/3} \qquad (1)$$

where h is water depth, A is a constant roughly proportional to $D^{1/3}$ and should be determined for each particular case, D is particle diameter, y is distance from water line, m is exponent (usually assumed equal to about 2/3), B is an unknown factor which has to be determined for each specific case.

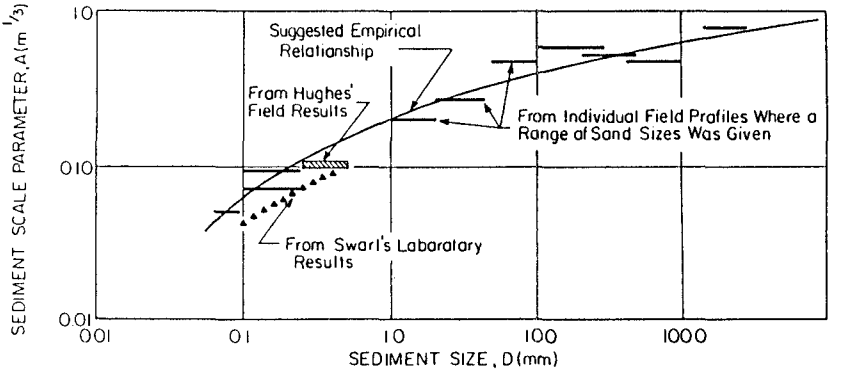

Figure 4 Value of A in $h = Ay^m$ versus sediment size (Dean, 1973, modified from Moore, 1982)

Generally the profile adapts itself rather quickly to the actual wave impact. Erosive profiles occur under severe wave conditions and lead to so-called bar profiles. Accretive profiles are characterized by moderate wave impact and are referred to as step-profiles. Graphs of Dalrymple and Thompson (1976) give a rather illustrative picture of the influence of the wave-grain size parameters on the slope of the profile, both for model and prototype conditions (see Figure 5).

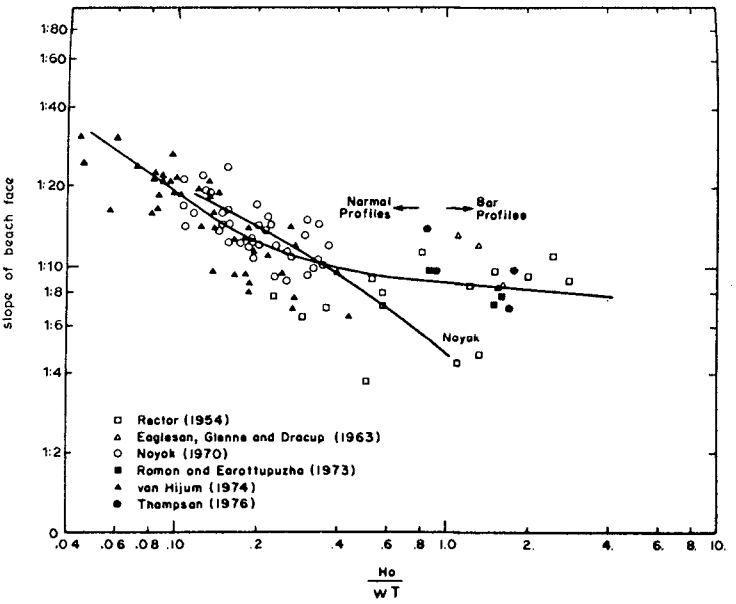

Figure 5 Beach slope versus fall velocity parameter (Dalrymple and Thompson, 1976)

Quite often the borrow sand will not be similar to the native sand, and then it is to be expected that the ultimate profile will differ from the present one. For an estimate of the new profile use can made of the scale relationship for the profile steepness as derived from extensive tests of dune erosion at different scales (Figure 6, see Vellinga (1982)). This relation is as follows:

$$\frac{n_l}{n_d} = \left(\frac{n_d}{n_w^2}\right)^{0.28} \tag{2}$$

in which n_l is the horizontal scale, n_d is the vertical scale, n_w is the scale of the fall velocity of the sand, which is related to the median grain diameter D_{50}.

Now the coastal profile of the replenished beach can be considered as a model of the present profile. The vertical scale n_d is directly related to the scale of the wave height thus $n_d = n_H$. Since the beach fill is subject to the same wave conditions as the present beach, it is clear that $n_d = 1$. Consequently:

$$n_l = n_w^{-0.56} \tag{3}$$

This relation should be read as follows. Suppose that the fall velocity of the native sand is w_1 and that of the borrow sand is w_2. If in the present profile the depth contour d is situated at a distance l_1 from

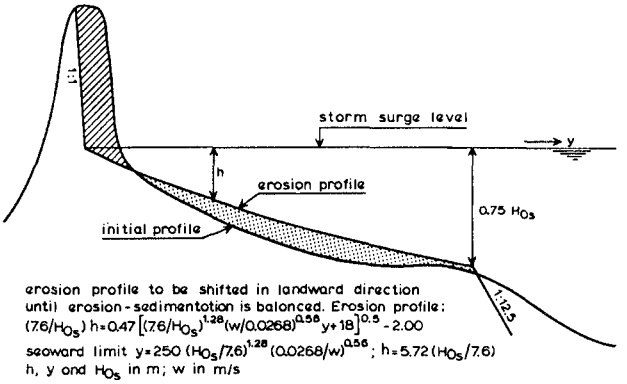

Figure 6 Erosion profile after storm surge (Vellinga, 1984)

the shoreline, then the distance of the same depth contour to the new shoreline of the replenished beach is determined by the relation:

$$\frac{l_1}{l_2} = \left(\frac{w_1}{w_2}\right)^{-0.56} \qquad \text{or} \qquad l_2 = \left(\frac{w_1}{w_2}\right)^{0.56} l_1 \tag{4}$$

The effect of this relation is illustrated in Figure 7. If the borrow sand is coarser than the native sand, thus $w_2 > w_1$, then the profile of the replenished beach is steeper than the original profile, and conversely. It is clearly shown that the use of coarse sand is profitable in view of the required volume of sand to obtain a certain widening of the beach.

It is observed that the method described above provides a fair estimate of the profile shape of the replenished beach. A condition, however, is that representative values for the fall velocity of the native sand and of the borrow sand are applied. This means that, because of the sorting effect of the waves, a large number of samples of the native sand has to be collected and analysed, and this may also apply for the borrow sand. Moreover, because of the handling of the borrow sand, finer parts may be washed out so that the median grain size increases. Because of these reasons an exact prediction of the equilibrium profile of the replenished beach is not possible.

Depth of active profile:

From Figure 7 it can be concluded that it is important to know to which depth the coastal profile will develop. This holds, in particular if the borrow sand is similar or finer than the native sand. In case the profile should develop unlimitedly in seaward direction enormous amounts of sand are needed to obtain a widening of the beach.

It should be stated beforehand that the seaward limit of the profile that is shaped by the action of the waves cannot be ascertained. In first instance the profile will extend rapidly by which sand is removed from the upper part of the profile to deeper water. If the lower limit

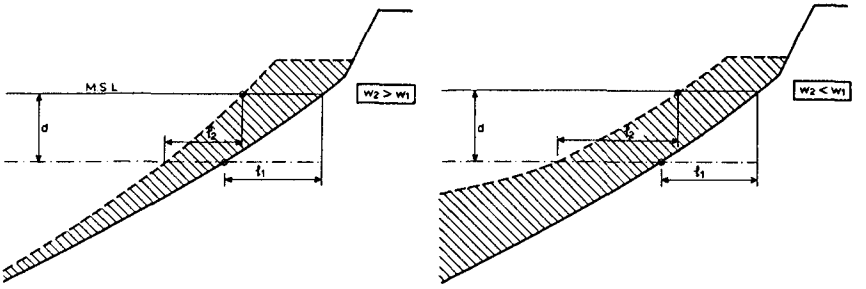

Figure 7 Effect of grain-size on profile steepness

of the developing profile has reached deep water only the infrequent higher waves are able to create offshore transport at that depth. So the development of the profile in seaward direction is slowing down with time, but it is not possible to determine when this process will stop. Nevertheless for the assessment of the quantity of sand needed for a specified widening of the beach, an idea should be achieved of the depth up to which the profile will develop. In case the fill sand is coarser than the native sand, the uncertainty in this depth does not play a prominent role in the determination of the required volume of sand, but it does if the borrow sand is finer.

For an estimation of the lower limit of the active coastal profile use can be made of the relations derived by Hallermeier (1978). He divides the coastal profile into three zones (see Figure 8):

- littoral zone up to depth d_1 with significant alongshore transport and intensive on/offshore transport throughout a typical year;
- shoal zone with significant on/offshore transport up to depth d_I, at which depth expected surface waves are likely to cause little sand transport;
- offshore zone where the surface wave effects on the bed are usually negligible.

In view of the definition mentioned above it is recommended to assume that the active coastal profile will develop up to a depth d_1 by wave action, although below this depth still significant cross-shore transport will occur.

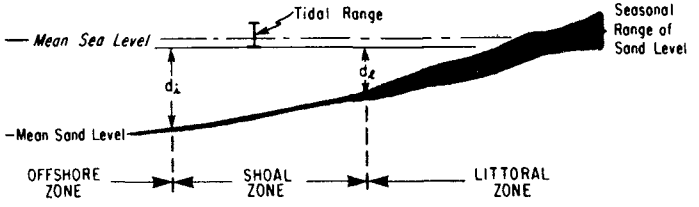

Figure 8 Zonation of seasonal beach profile (Hallermeier, 1978)

On basis of an analysis of available data Hallermeier arrives at the following relation for the lower limit of the littoral zone:

$$d_l = 2.28\ H_s - 68.5\ (H_s^2/gT_s^2) \tag{5a}$$

where d_l is water depth below low water level, H_s is the local significant wave height with a frequency of occurrence of 0.137% (12 hours per year) and T_s is the associated significant wave period.

Birkemeier (1985) has evaluated Hallermeier's method and on the basis of field measurements at the CERC's Field Research Facility in North Carolina. He suggests the relation:

$$d_l = 1.75\ H_s - 57.9\ (H_s^2/gT_s^2) \tag{5b}$$

For a Jonswap spectrum the relation $(H_s/gT_s^2)^{0.5} = 7.1 \times 10^{-2}$ holds good by approximation and for a Pierson-Moskovitz spectrum the relation $(H_s/gT_s^2)^{0.5} = 6.4 \times 10^{-2}$ can be assumed. By substituting these relations into Eq. (5a) it is found that $d_l = 1.93$ or $2.00\ H_s$ and into Eq. (5b) $d_l = 1.46$ or $1.51\ H_s$.
Unless the wave spectrum deviates significantly from the above mentioned spectra, it can be assumed for practical purposes that:

$$d_l = 1.75\ H_{s\ 0.137} \tag{6}$$

It is stressed that H_s pertains to the nearshore wave condition. In case wave condition are only known far offshore, computations are to be done for transferring these data to the nearshore zone.

Transition zone:

If the borrow sand is coarser than the native sand, then the profile of the beach fill may intersect the original profile at a level that is above the profile depth as defined above. In that case the coastal profile is completely fixed. However, in many cases the required intersection between the new and original coastal profile takes place at a lower level. In order to obtain this intersection a transition zone should be defined.
In first instance it seems reasonable to assume that the lower limit of this transition zone is located at the depth d_i so that the boundaries of the transition zone coincide with the boundaries of the shoal zone as defined by Hallermeier (see Figure 8). Hallermeier arrives at the following critical condition for the lower limit of the shoal zone:

$$\phi_c = (U_o^2/\Delta gD) = 8 \tag{7}$$

where U_o is maximum orbital velocity at the bed, Δ is specific density of sand in seawater (= 1.6), g is gravitational acceleration and D is median sand particle diameter.

In Equation (7) the value of U_o is computed according to the linear wave theory:

$$U_o = \pi H/T \sinh (2\pi d_i/L) \tag{8}$$

in which H is annual median significant wave height, T is average wave period associated with the median wave height and L is wave length.

From Equations (7) and (8) it follows that:

$$\frac{2\pi d_i}{L} = \text{arc sinh } \left(\frac{\pi H}{T\sqrt{8\Delta g D}}\right) \tag{9}$$

For known values of H, T and D the value of $2\pi d_i/L$ can be computed.

Measurements seaward of the mouth of the Haringvliet in the Netherlands at a depth of MSL-6 m yield an annual median significant wave height H = 0.55 m with a period T = 3.5 s. Thus for D_{50} = 200 μm the value of d_i = 5.8 m and for D_{50} = 100 μm the value is d_i = 7.1 m. However, the same measurements show that $H_{s\ 0.137}$ = 3.0 m, which means that d_1 = 6.0 m. So d_i and d_1 have virtually the same value in this case, which does not seem realistic. Obviously the relation between d_i, which is the lower limit of the shoal zone in deep water, and the annual median significant wave height does not hold for the observed wave climate in the mouth of the Haringvliet. The relations of Hallermeier are based mainly on wave observations along the U.S. coasts with low wave steepnesses.

Because the relation for the lower limit of the shoal zone, as derived by Hallermeier, cannot be generally applied for defining the lower limit of the transition zone, it is suggested that this lower limit is defined as:

$$d_i = (1.5 \text{ to } 2)\ d_1 \approx 3\ H_{s\ 0.137} \tag{10}$$

The thickness of the beach fill between the depths d_1 and d_i can be assumed to decrease linearly with distance (see Figure 9).

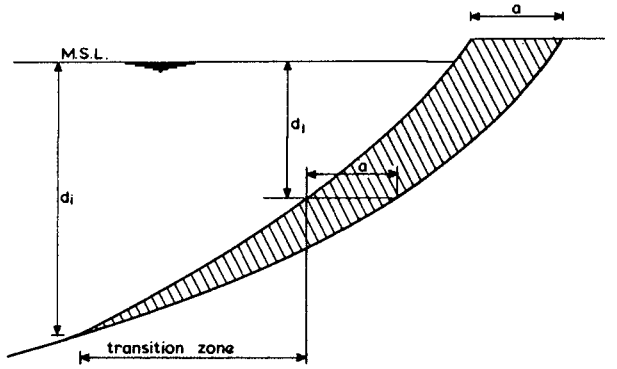

Figure 9 Profile of beach fill, borrow sand equal to native sand

5.3 Adjusted SPM fill factor and renourishment factor

In the Shore Protection Manual (1984) two models are recommended as design tools for beach fills. These models have been developed for the

condition that the textural properties of the borrow sand differ from those of the native sand. The aims of the two models can be defined as follows:

a. The adjusted SPM fill factor (R_A) is used to determine how much overage of borrow sand may be required.
b. The renourishment factor (R_J) is used to determine the relative frequency of renourishment.

Both beach fill models use the mean and sorting values of the composite grain size distributions of the native and the borrow sediments as basic input. This means that careful attention should be paid to the design of sediment sampling plans, since the quality of any beach fill calculation is, at best, only as good as the native beach and borrow composites have been determined. The number of samples to be analyzed for determining the composite grain size distribution depends on the variation of the materials and their individual properties.

Further it is observed that the models only take into account the effect of a possible difference between the properties of the native sand and the borrow sand. Consequently for the application of the models first other aspects of the design of a beach nourishment scheme should be determined, in particular the required volume of sand and the frequency of renourishment in case the properties of the borrow sand and the native sand are similar. For more information regarding the use of the factors reference is made to the Shore Protection Manual (1984).

5.4 Planform of beach fill and mathematical coastal morphology models

During and some time after the placement of a beach fill the reshaping of the coastal profile by onshore/offshore transport is usually the most noticeable phenomenon. However, at the same time the longshore transport will start to reshape the planform of the beach fill, which process may continue for a long period. The effect of the longshore transport on the planform of the beach fill is in particular perceptible at the transition between the replenished beach and the adjacent non-replenished beach. In Figure 11 the morphologic process at the end of a beach fill has been reflected schematically. Because of the replenishment the coastline has moved seaward and a transition zone develops where the direction of the coastline differs from the original direction. In case of a longshore transport from left to right, as drawn in the figure, this longshore transport will be larger in the transition zone due to this difference in coastline direction. The result is that erosion occurs along the left part of the transition zone and accretion along the right part. Because of these processes the transition zone will expand in both directions. If the longshore transport is from right to left, then the coastal development is the same as drawn in Figure 10.

An important question is to predict the dimensions of the initial beach fill, which are required to protect a coastal area during a desired guarantee period. Different methods are available, ranging from simple analytical to sophisticated mathematical, for the prediction of the morphological behaviour of the fill. In the simplest analytical theory, the coast is schematized by one line (Bakker, 1970).

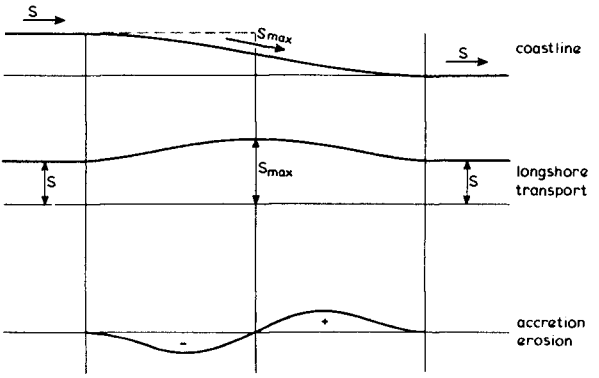

Figure 10 Schematic view of coastal processes at end of beach fill

An example of the one-line theory has been illustrated in Figure 11 for a beach fill with initially a rectangular shape (LxB). This figure shows the parameters B/b (ratio between the initial width B and the minimum required width b), A/a (ratio between the initial area A and the minimum area a) and x_o/L_o as a function of the dimensionless length ℓ/L_o, where ℓ is the length of beach to be preserved and $L_o = \sqrt{4(s/h)t}$, (s is the variation of the longshore transport per radian of coastline rotation, h is the schematized thickness of the active profile and t is time). It will be clear that the coastal stretch where the sand is supplied has to be larger than the area to be protected, in order to account for losses along the sides.

For instance, if the beach area (ℓxb) to be protected during 5 years is 5000 x 50 m^2, while the coastal constant s is 300,000 m^3/rad/yr and the height of the profile is 6 m, then the dimensionless length ℓ/L_o is 5000/1000 = 5. From Figure 12 it can be seen that the initial width of the area should be 1.1 x 50 = 55 m and the extra length at both sides of the fill (x_o) should be 1.2 x 1000 = 1200 m. Consequently the fill should have an area which is about 50% larger than the area to be protected (A/a ≈ 1.5).

This one-line method is rather a strong schematization of reality and the results should therefore be interpreted with care. More sophisticated models give the opportunity for more "taylor made" solutions, as presented in the Manual (1986).

6 Conclusions and recommendations

Generally, artificial nourishment turns out to be a feasible and attractive method to restore, protect, extend and maintain beaches. The essence of the reported advantages are flexibility and harmony with nature. This is concluded after review of literature on about 60 artificial nourishment projects (Manual, 1986).

Inevitably artificial beach nourishment will be applied in the future more and more as standard method for coastal protection and extension of recreational facilities. Whenever technically possible and economically feasible, it is recommended to accomplish the remedy on artificial supply rather than by fixed structures.

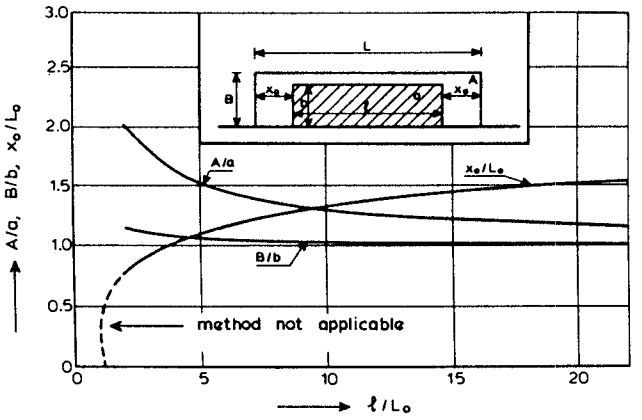

Figure 11 Optimal dimensions of sand supply according to one-line theory

An integral design method for artificial beach nourishment, including all relevant parameters, is not yet available. However, for separate aspects of the design of the beach nourishment various design tools are available, such as models for the prediction of the morphological behaviour of the fill and methods for the determination of the effect of different grain size characteristics.

The performance and deformation of artificial beach fills, which significantly affect the coastal geometry, can be predicted with different tools, ranging from simple to complicated, depending on the boundary conditions of the actual situation. It is foreseen that in future use will be made of two-dimensional horizontal and (quasi) three-dimensional coastal morphological computer models to evaluate the effect of artificial beach fills and to select via comparative computations the optimum location and shape. At the same time it must be stressed that the presently available techniques (long-term coastal monitoring, fill- and renourishment models, profile shape formulations and one- and multi-line models) certainly suffice in the proper cases.

Conclusions about the performance of a fill are often based upon observed changes of only a restricted section of the profile above a certain elevation. Although profile development may extend to greater depths than surveyed, in many cases a reasonable idea is obtained of the performance of the fill. However, it is stressed that surveying of only the subaerial section certainly is insufficient.
Both gradients in longshore transport and severe wave impact generally cause the reported losses. The quantity of sand loss depends on the surveyed profile lengths; therefore care should be taken with the definition of beach loss, since material which is transported further offshore is not necessarily lost for the beach development. Gradients in longshore transport are mostly responsible for "real" losses. It should be stressed that no strict guide-lines can be presented regarding the measurements to be carried out for the evaluation of a beach replenishment project.

Official procedures to attune different projects are still tiresome. In future it will become more necessary to try to use the sand, which comes available from other planned or ongoing dredging projects, for artificial beach nourishment. Material from maintenance dredging should be used after a close examination of its characteristics. Maintenance dredging is normally the removal of siltation which is most of the time odorous and contains a large percentage of fines, which makes it unsuitable for beach nourishment schemes. However, granular material from capital dredging work should well be suitable and could reduce the total coast of a planned nourishment scheme. Therefore it makes sense to enhance the cooperation between the various governmental agencies, who are in charge of such civil engineering projects.

The results of this study underline once again the statement that "still, the more is learned about coastal processes, the more it is realized how little is known yet". Because of the complexity of the problem and its world wide importance, close international co-operation in this field is strongly recommended.

7 Acknowledgements

Apart from the contributions to the Manual (1986) by the members of the working group, many other sources were used in the form of oral or written information, publications or other written documents. The substantiated input of any public or private organization and any person or author who readily made information available for use in the preparation of the report is highly acknowledged.

References

Bakker, W.T., 1970. Littoral drift in the surfzone. Report WWK 70-16, Dutch Public Works Department.

Birkemeier, A.W., 1985. Field data of seaward limit of profile change. ASCE, Journal of Waterway, Port, Coastal and Ocean Engineering, Vol. 111, No. 3.

Dalrymple, R.A./Thompson, W.W., 1976. Study of equilibrium beach profiles. Proc. 15th Coastal Engineering Conference.

Dean, R.G., 1983. Principles of beach nourishment. In "CRC Handbook of Coastal Processes and Erosion", editor Paul D. Komar.

Hallermeier, R.J., 1978. Uses for a calculated limit depth to beach erosion. Proc. 16th Coastal Engineering Conference.

Kobayashi, H./Tanaka, T./Shoyama, S., 1985. Beach nourishment in Yokohama Marine Park. PIANC, 26th International Navigation Congress, Brussels.

Manual, 1986. Manual on Artificial Beach Nourishment. **Background report**, 1986. Report on Background information on Artificial Beach Nourishment. Rijkswaterstaat, Centre for Civil Engineering, Research, Codes and Specifications, Delft Hydraulics Laboratory, The Netherlands.

Moore, B., 1982. Beach profile evolution in response to changes in water level and water height. Master of Science Thesis, University of Delaware, Newark.

Shore Protection Manual, 1984. C.E.R.C., US Army Corps of Engineers.

Vellinga, P., 1982. Beach and dune erosion during storm surges. Coastal Engineering, Vol. 6, No. 4.

Vellinga, P., 1984. A tentative description of a universal erosion profile for sandy beaches and rock beaches. Coastal Engineering, Vol. 8, No. 2.

CHAPTER 108

Analysis of a Beach Quality Problem

Gordon K. Prestedge*, M.ASCE and
Christopher A. Fleming**

A study was recently undertaken to investigate sediment transport on a section of coastline where recreational beaches have experienced periodic erosion. Alongshore, onshore/offshore and aeolian sediment transport processes were investigated and quantitative transports predicted with the aid of calibration using surveys and aerial photographs. This paper describes the study and the recommendations proposed for beach quality improvements.

Introduction

Recreational Beaches at Port Elizabeth, South Africa, consist of small sandy areas on an otherwise rocky section of the Algoa Bay coastline (Figures 1 and 2). The natural beaches, Pollok, Hobie and Humewood (shown on Figure 2) have been plagued by loss of sand and exposure of cobbles and rock sub-strata at times. Poor quality of the beaches particular during peak summer periods has become a matter of considerable public concern. A study was initiated to investigate the macro sediment regime on this coastline, understand the root cause of the problem and put forward proposals for beach improvement measures. The possibility that stabilisation of the headland bypass dunefield in 1968 at Cape Recife has aggravated the problem as well as the impact that a proposed boat launching facility would have on the adjacent beaches was also considered.

Nearshore Wave Data

To be able to determine the wave conditions at the nearshore sites of interest it was first of all necessary to select appropriate offshore wave data. Offshore wave data was obtained from measurements at the site of oil exploration platforms that had been operating for several years in an area south-west of Algoa Bay. Significant wave heights and peak energy wave periods obtained from the Waverider records were combined with concurrent visual observations of wave direction taken from the rig. The deep sea wave rose is shown in Figure 1. The data set of wave height, period and direction for the deep ocean conditions obtained in this way provided an excellent definition of deep ocean wave conditions which were refracted on a record-by-record basis to thirteen nearshore calculation positions along the study coastline. Wave refraction was undertaken using wave ray back-tracking and three-dimensional spectral transfer techniques (Abernethy et al, 1975).

* Associate, Watermeyer, Legge, Pièsold & Uhlmann, Cape Town, Republic of South Africa
** Director, Sir William Halcrow & Partners, Swindon, United Kingdom.

In view of the shape of Algoa Bay and the fact that the majority of energy in the deep ocean was contained in the south-west quadrant, it was important to ensure that a pure refraction model would correctly represent the nearshore wave conditions on the study coastline. An investigation using a combined refraction/diffraction model (Southgate, 1981) as well as pure diffraction (Sommerfeld, 1896) was investigated. It was found that pure diffracted energy would be small in the area of interest for waves with deep ocean directions from the south-west quadrant and for predominant wave periods. Owing to the gently shelving nature of the seabed at Cape Recife, the majority of wave energy would reach the area of interest during south-westerly conditions by refraction alone.

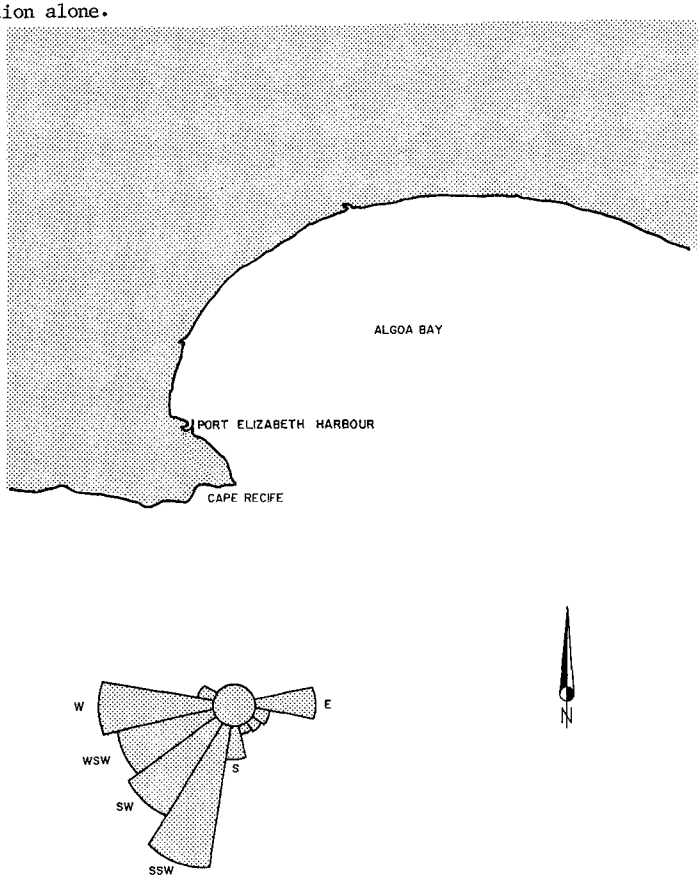

Figure 1. Locality Map and Deep Ocen Wave Energy Rose

Figure 2. Aerial Photograph of Study Coastline

The study coastline is exposed to locally generated wind waves from the easterly sector. A check was therefore carried out using a parametric wind wave hindcasting model to ensure that the locally generated wind wave components were adequately represented in the deep ocean wave data.

Nearshore wave energy roses on the study coastline are shown on Figure 3.

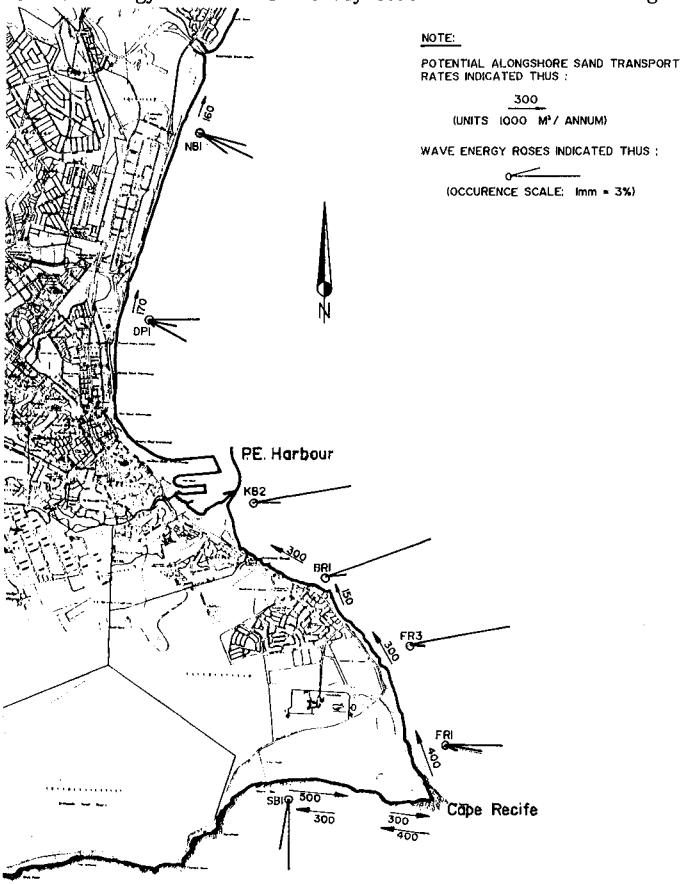

Figure 3. Nearshore Wave Energy Roses and Potential Alongshore Transport Rates

Alongshore Sediment Transport

Alongshore sediment transport was evaluated using three alongshore sediment transport theories after thirteen theories, both bulk and detail predictors had been investigated. The three detailed predictor theories used were as follows:

- Engelund and Hansen as adapted by Swart
- Neilsen
- Swart and Lenhoff (Swart, 1980)

The wave data was arranged in statistical groups of 15° directional increments, 0,5m wave increments and period increments ranging from 1 to 3 seconds. The wave data used represented an average year based on all available deep ocean data. For the detailed predictor type transport models each profile was divided into a number of sand transport zones. From each transport zone local wave conditions were determined from the nearshore wave statistics at the nearshore calculation positions and from refraction and shoaling between the calculation positions and the transport zones. The location of the breaker line was determined by considering refraction and shoaling in relation to input data.

Transport rates obtained from the theories were compared with historical information on the rate of accretion at Kings Beach, the location of which is shown in Figure 2. Port Elizabeth harbour was constructed in 1931 and has formed a total barrier to alongshore transport in this area. Various surveys of the area have been carried out over the years and this has permitted the volume of sand trapped south of the harbour to be quantified. The results are shown in Figure 4. From this information and harbour records (which indicated that a certain amount of sand has permeated the breakwater and has been removed by dredging from the harbour side of the breakwater), a best estimate of the average alongshore sand transport rate at King's Beach of 180 000 cubic metres per annum was established.

The headland bypass dunefield at Cape Recife was stabilised in 1968. It had been suggested that that may have been the cause of beach erosion problems. However dune stabilisation does not appear to have signficantly affected the rate of accretion of sand at King's Beach in recent years. An aeolian transport analysis (Swart, 1985) of the rate at which sand was likely to have been transported across the headland bypass dunefield to the study coastline prior to stabilisation, was undertaken. It was found that the rate of supply of sand from such sources was likely to have been of the order of about 30 000 cubic metres per annum.

It appears therefore that approximately 150 000 cubic metres of sand is at present still being fed to the study coastline from the area west of Cape Recife by wave-induced transport around the gently shelving seabed area in the vicinity of the Cape.

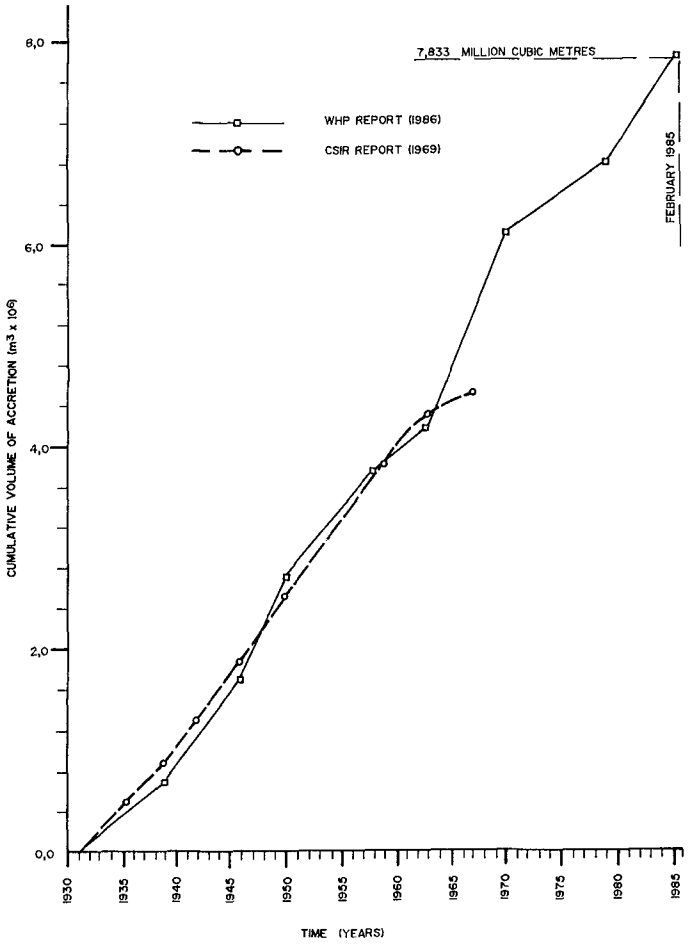

Figure 4. Cumulative volume of Accretion at King's Beach

Theoretically predicted transport rates were calibrated with the aid of data obtained from accretion at King's Beach and it was found that in order to match measured alongshore transport rates, consideration had to be given to saturated wave spectra effects in shallow water after Bouws et al 1985 who developed the TMA spectrum by applying the Kitaigorodskii et al 1975 depth dependant term to the Jonswap spectrum. In this case a nominal nearshore water depth of 6m was used. Considerations of similar analyses for all the shoreline sections led to the derivation of a sand budget based on the variation in alongshore transport obtained from the model. Alongshore sand transport rates are shown in Figure 3.

A large portion of the study coastline is rocky so that it is important to distinguish between the "potential" alongshore sand transport rate and the actual alongshore sand transprot rate. Sand can only be transported at the calculated potential transport rate if sufficient sand exists on the coastline. If insufficient sand exists such as on a rocky coastline, then the actual transport rate would be less than the potential rate and limited to the rate of supply of sand to the coastline from further updrift. The rate of supply is currently estimated to be 150 000 cubic metres per annum despite the stabilisation of the headland bypass dunefield at Cape Recife. Potential transport rates of up to 450 000 cubic metres per annum were calculated.

The apparent net transport rate from east to west in the area immediately west of Cape Recife, is hypothetical since during conditions that produce transport to the east, sand is carried past the headland and northwards along the study coastline and that sand is not available to be moved westwards under westerly transporting conditions.

It was found that for all conditions alongshore transport was northwards on the study coastline between Cape Recife and the harbour.

Onshore/Offshore Sediment Transport

Onshore/offshore sediment transport (Swart, 1985) was used in a qualitative application to examine the response of the beach to storm waves. Calibration required in order to obtain quantitative results was not possible in this case in view of the presence of cobbles and bedrock close to the beach surface which at present prevents full development of the equilibrium profiles. Observations of the beaches after recent major storms were however useful for comparison with theoretical predictions and for evaluating the depth of sand cover required to accommodate beach profile fluctuations without exposing rocky and sub-strata cobble layers.

The beach quality problem accordingly appeared to be the result of a lack of retention of sand on the beaches and not the result of a lack of supply of sand to the coastline.

Beach Processes

It is concluded that the only reason why Pollok Beach, Hobie Beach and Humewood Beach exist is that each is formed by a rocky headland behind which sand is trapped (pocket beaches). If these headlands did not exist there would be no beaches. The rocky headlands are not large enough to trap sufficient sand to ensure sandy beaches under all normal weather conditions. During locally generated wind waves from the east and south-east, the steep storm waves move sand offshore and expose the bedrock and cobbles frequently.

The object of the proposed recommendations are therefore to extend the natural rocky headlands responsible for the creation of the beaches and thereby trap a larger reservoir of sand and in turn enable the beaches to respond to the cyclic onshore/offshore movement of sand under normal storm conditions. This solution would be one of emulating the natural processes and simply trapping larger volumes of sand on the beaches and reducing the occurrence of stony beaches to rare occasions after very stormy seas.

Proposals had also been made previously for the construction of a small boat harbour on this section of coastline and these proposals were investigated in relation to the observed nearshore beach processes. It was advised that a large harbour should not be constructed as this would tend to cut off the alongshore sand transport to beaches downdrift. Furthermore all beach structures should be of minimal length and care should be taken that structures did not divert sand offshore particularly in areas where the seabed dips steeply seawards.

Proposed beach improvements at Pollok Beach, Hobie Beach and Humewood Beach are shown in Figures 5, 6 and 7 respectively. Improvements proposed at Hobie Beach were augmented with an offshore breakwater to improve the launching of small sailing boats from that beach.

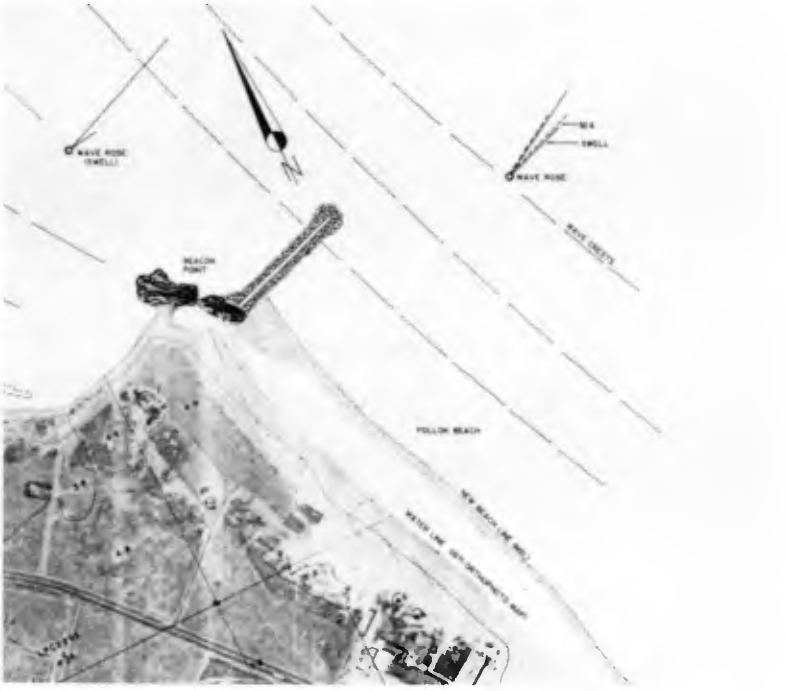

Figure 5. Proposed Headland Extension at Pollok Beach

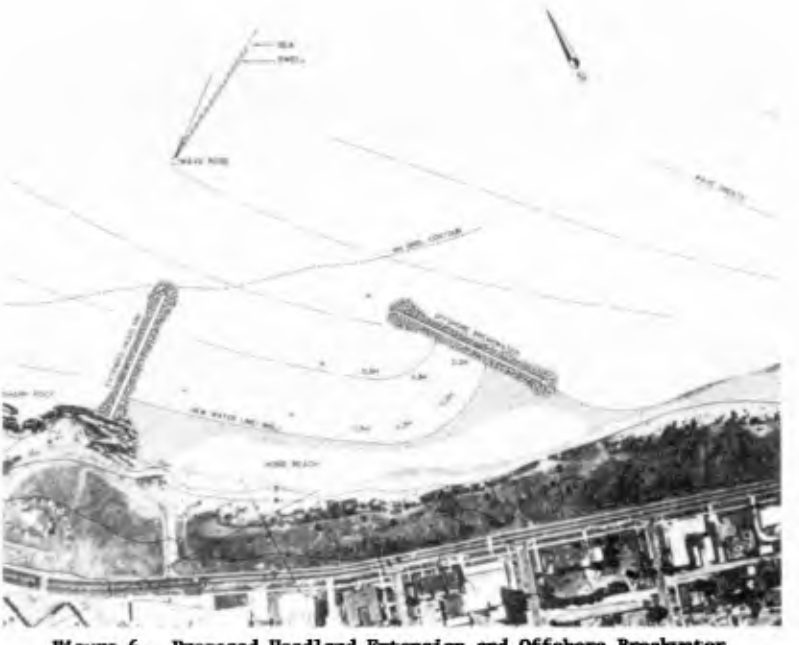

Figure 6. Proposed Headland Extension and Offshore Breakwater at Hobie Beach

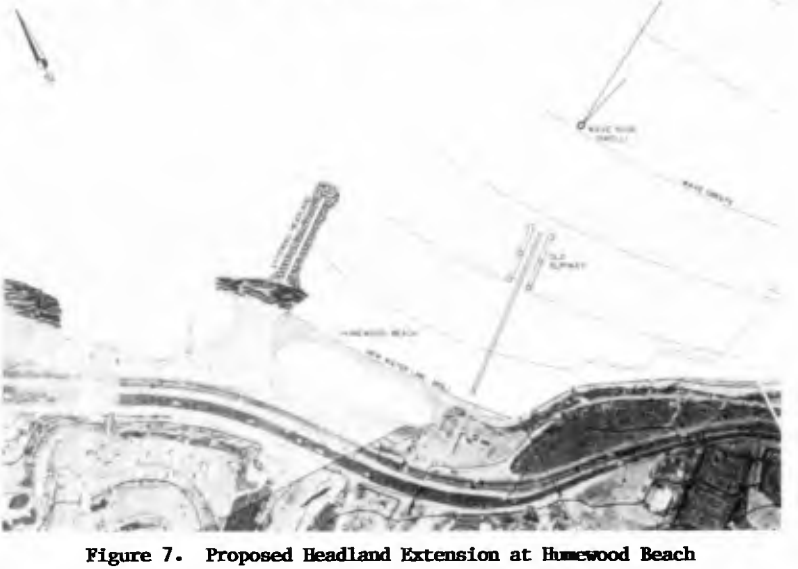

Figure 7. Proposed Headland Extension at Homewood Beach

Conclusions

Beach erosion problems on the southern beaches of Port Elizabeth were found to be caused by an inadequate reservoir of sand on the beaches. The existing reservoir was found to be unable to accommodate the natural beach changes which occur in response to variations in the wave climate. Extensions of the rocky headlands at these beaches would result in more sand being held on the beaches. It was found that an adequate supply of sand is supplied to the study coastline and transported along the coast by wave action to fill and maintain the beaches after the headland structures are built.

Acknowledgements

The City Council of Port Elizabeth is gratefully acknowledged for their permission to publish this paper which is based on a study commissioned by the City Council.

References

1. Abernethy C.L. and Gilbert C. (1975), "Refraction of Wave Spectra" Hydraulics Research Station, Report No. INT 117.

2. Bouws E., Gunther H., Rosenthal W. and Vincent C.L. (1985), "Similarity of the Wind Wave Spectrum in Finite Depth Water". Journal of Geophysical Research, Vol 90, No C1, pp 975-986.

3. Kitaigorodskii S.A., Krasitskii V.P. and Zaslavskii M.M. (1975), "On Phillips Theory of Equilibrium Range in the Spectra of Wind-Generated Gravity Waves". Journal of Physical Oceanography, Vol 5, pp 410-420.

4. Swart D.H. and Fleming C.A. (1980), "Longshore Water and Sediment Movement". Proc. 17th Coastal Engineering Conference. A.S.C.E. Sydney.

5. Swart D.H. (1974), "Offshore Sediment Transport and Equilibrium Beach Profiles". Ph.D Thesis, Delft Hydraulics Laboratory.

6. Swart D.H. (1985), "Prediction of Wind Blown Sediment Transport Rates". C.S.I.R. Research Report.

CHAPTER 109

LABORATORY STUDY ON SAND TRANSPORT OVER RIPPLES DUE TO ASYMMETRIC OSCILLATORY FLOWS

Shinji Sato* and Kiyoshi Horikawa**

ABSTRACT

Mechanism of sand movement due to asymmetric oscillatory flows was investigated through experiments. Measurements of bed forms, suspended sand concentration and net sand transport rate were carried out by using an oscillatory flow tunnel. The process of entrainment and suspension of sand above asymmetric ripples was quantitatively described. The geometry of ripples and the net sand transport rate in regular and irregular flows were expressed in terms of hydraulic parameters characterizing the oscillatory flow. Two-dimensionality of ripples was found to be an important factor in the estimation of the net sand transport rate.

1. INTRODUCTION

In order to predict sediment transport and wave attenuation over a sand bottom, it is of great importance to understand the geometry of bed forms and the mechanism of sand suspension. Sand ripples are frequently observed to be asymmetric in shallow water region where velocity histories near bottom become asymmetric owing to the nonlinearity of surface waves and superimposed currents. The asymmetry of flows and ripples is considered to exert crucial influences on the direction and the net rate of sand transport in the on-offshore direction. Although several models have been proposed for the sand transport rate over ripples on the basis of experimental results [*e.g.* Sunamura(1980)], the validity of these models is not fully verified owing to the lack of reliable data of the sand transport rate.

The present study attempts to investigate the sand movement over ripples due to asymmetric oscillatory flows. A series of experiments are conducted under the conditions of regular and irregular asymmetric oscillations by using an oscillatory flow tunnel. Detailed measurements of bed forms are carried out for each run of the experiments to elucidate characteristics of the sand ripple geometry and the net sand transport rate. The influences of the asymmetry and the irregularity of velocity histories on the shape of ripples as well as the resultant net sand transport rate are discussed for a wide range of conditions. The process of sand suspension under asymmetric oscillations is also described through the measurements of the suspended sand concentration.

2. EXPERIMENTAL PROCEDURES

2.1. FACILITIES AND CONDITIONS OF EXPERIMENTS

Experiments were performed in an oscillatory flow tunnel which consisted of a loop of closed conduits and a hydraulically-driven piston whose motion was arbitrarily controlled by input voltage signals. A section of the tunnel was covered with glass side walls and removable acrylic ceilings. The beds in this section were composed of wooden plates as

* Research Associate, Dept. of Civil Eng., Univ. of Tokyo, Bunkyo-ku, Tokyo, 113 JAPAN.

** Professor, ditto.

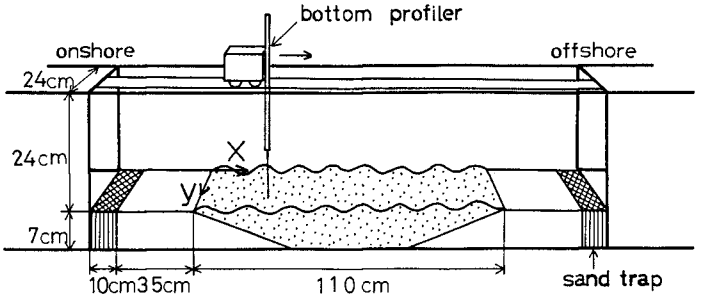

Fig. 1 Experimental set-up.

illustrated in Fig. 1. The central region of the beds was lowered with mild slopes at both ends, in which well-sorted sand with median diameter 0.18 *mm* was filled to make initially flat test bed. Sand traps were installed at both ends in order to trap the sand that would otherwise move out of the test section.

Experiments were carried out for regular and irregular oscillations. The input signals were simulated by using a digital computer, in which time histories of the displacement of water particles under waves were calculated on the basis of linear and nonlinear wave theories. Velocity histories of regular oscillations were simulated on the basis of the fifth-order Stokes or the third-order cnoidal wave theory. Six signals involving various degrees of nonlinearity were created, in which three signals were simulated by using the Stokes wave theory and the other three signals were simulated by the cnoidal wave theory. Figure 2 shows a typical velocity history calculated by the cnoidal wave theory, in which u_c is the maximum onshore velocity, $\hat{u}$ is the total amplitude of the velocity variation and ω is the angular frequency of the oscillation.

It is also of importance to understand the sand movement under irregular oscillations. However, it is not easy to calculate the velocity variations due to nonlinear irregular waves. In order to incorporate the effect of the nonlinearity in a simple manner, wave-by-wave approach was attempted in the present study. Since each wave crest propagates like an independent wave in the very shallow water region, velocity variations can approximately be calculated by applying the regular wave theory to each wave. On assuming the Bretschneider-Mitsuyasu spectrum, variations of the surface elevation were numerically simulated. Each wave was defined by means of zero-up-crossing method and a series of couples of wave heights and periods were obtained. Velocity histories of each wave were then calculated by using the Stokes or the cnoidal wave theory on the assumption that each wave was an independent regular wave. Velocities of each wave were connected at zero-up-crossing points to produce a continuous velocity history as shown in Fig. 3.

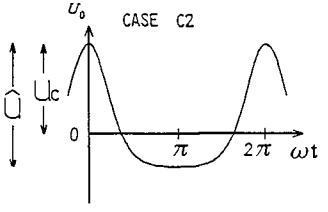

Fig. 2 Velocity history of regular asymmetric oscillations.

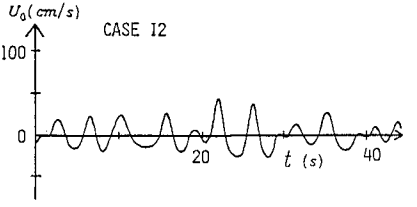

Fig. 3 Velocity history of irregular asymmetric oscillations.

Experimental conditions are listed in Table 1, in which T is the mean period of the oscillatory flows and d_0 is the mean total displacement of the oscillations. The total number of experimental cases is 50 cases for regular oscillations and 25 cases for irregular oscillations.

2.2. NET SAND TRANSPORT RATE

Measurements of bed forms and the net sand transport rate are of practical importance in connection with the calculation of beach profile change. In order to estimate the net sand transport rate over large-scale steady-state ripples in a high accuracy, the following procedures were developed in the present study by combining sand traps and detailed measurements of the bed topography.

(1) Initially flat test bed is exposed to the action of oscillatory flows until steady-state bed forms develop.

(2) Bottom profiles of the test bed are measured in detail and sand transported out of the test bed is removed.

(3) The action of the oscillatory flow is continued for an additional duration Δt.

(4) Bottom profiles are measured again and the sand transported out of the test bed is collected, which is dried for 24 hours in a drying kiln.

The difference of sand surface level $\Delta h(x,y)$ (positive accretion) and the dry mass of sand collected at onshore and offshore ends, m_{on} and m_{off}, are evaluated through the procedures described in the above. Mass conservation of sand leads to

$$(1-\lambda_v)\int_0^B\int_0^L \Delta h dx dy + (m_{on}+m_{off})/\rho_s = 0 \tag{1}$$

where (x,y) indicate the coordinates as in Fig. 1, B and L are the width and the length of the test bed respectively, $\lambda_v(=0.4)$ is the porosity of the sand and ρ_s $(=2.64g/cm^3)$ is the density of sand. The net sand transport rate q_x at x (positive onshore) is evaluated by

$$q_x(x) = \left(\int_0^B\int_0^x (1-\lambda_v)\Delta h dx dy + m_{on}/\rho_s\right)/(B\Delta t) \tag{2}$$

Table 1 Experimental conditions.

Regular oscillations

	$u_c/\hat{u}$	T(s)	d_o(cm)	
RL	0.5	1 - 7	5 - 65	sinusoidal oscillations
S1	0.555	3 - 5	17 - 51	simulated by the Stokes wave theory
S2	0.570			
S3	0.626			
C1	0.639			simulated by the cnoidal wave theory
C2	0.722			
C3	0.831			

Irregular oscillations

	$u_c/\hat{u}$	T(s)	d_o(cm)	
IL	0.5	3.90	16 - 51	symmetric oscillations
I1	0.52	3.68	27 - 51	asymmetric oscillations
I2	0.60			
I3	0.68			

The net sand transport rate free from the disturbances created at the both ends of the test bed was estimated by means of these procedures. In order to make accurate evaluation of sand volume change, bottom profiles were measured in detail along ten measuring lines with a bottom profiler installed on a self-moving carriage. It was found that the ratio of the residue of Eq. (1) to the evaluated net sand transport rate was about 10 % even for a case in which three-dimensional ripples were developed. The error of the evaluation of the net sand transport rate in the present experiments was therefore considered to be less than 10 %, which was excellent compared with other methods attempted in the previous studies.

2.3. CONCENTRATION OF SUSPENDED SAND

In order to understand the process of sand suspension, the concentration of suspended sand was measured for a case in which typical two-dimensional ripples were developed. The measurements were carried out under asymmetric oscillation of signal C2 with the period and the total displacement of the oscillation being 3 *s* and 24.1 *cm* respectively. Variations of sand concentration were measured at about 100 points above an asymmetric ripple with a light-absorption-type probe whose diameter was 0.3 *cm* at the end of the sensor. Measuring points were arranged in a grid whose spacings were 1 *cm* in x direction and 0.5 to 2 *cm* in z direction. The measuring points closest to the bed were set at 0.5 *cm* above the bed, which was found critical in order not to cause the local scour. Variations of the concentration and the displacement of the piston were simultaneously recorded for 40 *s* and were then converted to digital values with an interval of 0.04 *s*.

3. THE GEOMETRY OF RIPPLES

Sand ripples developed in asymmetric oscillatory flows are generally asymmetric as illustrated in Fig. 4; the flank of a ripple facing onshore being steeper than the other. Since the formation of sand ripples plays an essential role in the sand transport, it is firstly of significance to understand characteristics of sand ripples.

Small scale ripples were developed at the beginning of the ripple formation from initially flat bed. It required 5 to 40 minutes under regular oscillations and 15 to 90 minutes under irregular oscillations until steady-state ripples were developed. The irregularity of waves thus tended to delay the formation of steady-state ripples. This is because the action of each wave is not always effective for the formation of the resultant ripple geometry since the size and the intensity of lee vortices were not uniform under irregular waves.

Two-dimensional ripples as shown in Fig. 4 were developed in 45 cases. Three-dimensional ripples were observed in the other 30 cases in the flow with large Reynolds numbers. Since mechanics of sand movement changes drastically over two- and three-dimensional ripples, it is firstly of importance to understand the condition for the occurrence of two- and three-dimensional ripples.

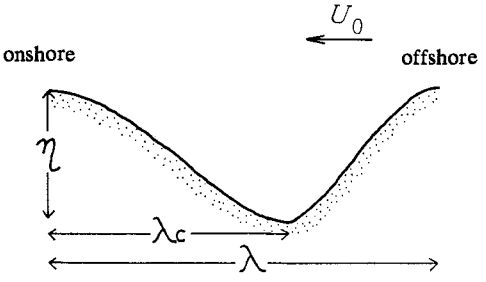

Fig. 4 Schematic diagram of an asymmetric ripple.

Two-dimensionality of wave-generated ripples was systematically discussed by Carstens *et al.*(1969), in which the range of two-dimensional ripples was found to be

$$d_0/D < 1550 \tag{3}$$

where D is the sand diameter. Lofquist(1978) undertook further experiments using an oscillatory flow tunnel and suggested that the two-dimensionality of ripples was dependent on two parameters, d_0/D and $U_0^2/[(\rho_s/\rho-1)gD]$, in which U_0 was the amplitude of velocity histories, ρ was the density of water, and g was the gravity acceleration. Kaneko(1981) classified characteristics of ripples by using $U_0^2/[(\rho_s/\rho-1)gD]$ and D/δ, in which δ was the thickness of the Stokes layer. Transition from two- to three-dimensional ripples was also discussed by Vongvisessomjai(1984), in which relationships for the geometry of ripples in oscillatory flows were proposed in terms of a parameter $U_0/\sqrt{(\rho_s/\rho-1)gD}\cdot d_0/(2D)$.

Relationships between characteristics of ripples and various hydraulic parameters were examined, including new data obtained under the conditions of asymmetric and irregular oscillations [Sato(1986)]. It was found that the most essential parameters to describe characteristics of ripples were d_0/D and the Shields parameter Ψ defined by,

$$\Psi = \frac{1}{2} f_w \frac{U_0^2}{(\rho_s/\rho-1)gD} \tag{4}$$

in which f_w was the friction factor proposed by Jonsson(1966) which was evaluated on the assumption that the bottom roughness was equal to the sand grain diameter.

Figure 5 shows the classification of ripples developed in sinusoidal oscillations in terms of d_0/D and Ψ. Three-dimensional ripples are developed under conditions with large values of d_0/D and Ψ. The boundaries between two- and three-dimensional ripples are well described by the broken lines.

The classification of ripples in asymmetric flows is also made by using d_0/D and Ψ. Figure 6 shows the classification of ripples in asymmetric flows, in which the Shields parameter is evaluated by the following equation:

$$\Psi_{rms} = \frac{1}{2} f_w \frac{(\sqrt{2}u_{rms})^2}{(\rho_s/\rho-1)gD} \tag{5}$$

where u_{rms} indicates the root mean square value of the velocity history.

The wavelength and the wave height of ripples are also formulated in terms of d_0/D and Ψ. Sato(1986) analysed data of ripples obtained in wave flumes, in oscillatory flow tunnels and on natural beaches, in which functional relationships between the ripple geometry and hydraulic parameters were derived as

$$\lambda/d_0 = 1.4(d_0/D\cdot\Psi^{1/2})^{-0.146} \tag{6}$$

$$\eta/\lambda = 0.191(1-(\Psi/0.6)^2) \tag{7}$$

for two-dimensional ripples in regular oscillations and

$$\lambda/d_0 = 350(d_0/D\cdot\Psi^{1/2})^{-1} \tag{8}$$

$$\eta/\lambda = 0.158(1-(\Psi/0.6)^2) \tag{9}$$

for three-dimensional ripples in regular oscillations. Relationships for the conditions of irregular oscillatory flows were expressed by

$$\lambda/d_0 = 3.55(d_0/D\cdot\Psi^{1/2})^{-0.292} \tag{10}$$

for $d_0/D\cdot\Psi^{1/2}<650$ and Eq. (8) for $d_0/D\cdot\Psi^{1/2}>650$, and

$$\eta/\lambda = 0.191(1-\Psi/0.6) \tag{11}$$

where values of d_0 and Ψ were evaluated using significant waves.

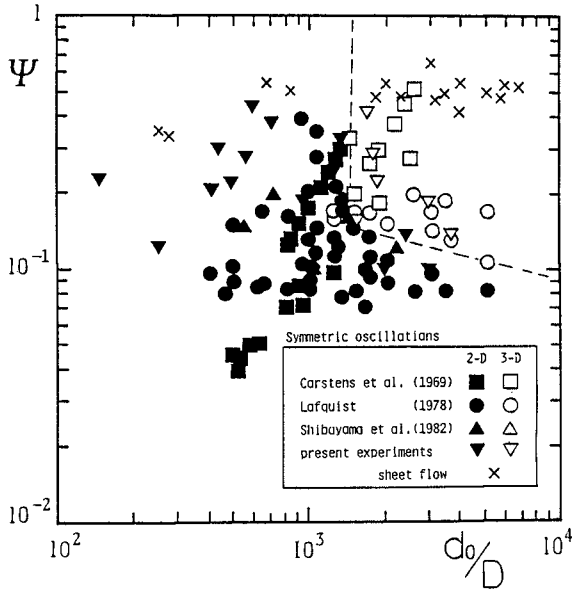

Fig. 5 Occurrence of two- and three-dimensional ripples in sinusoidal flows.

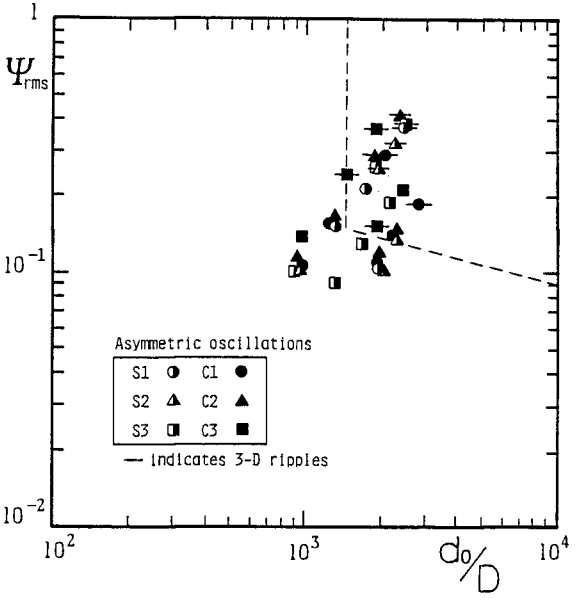

Fig. 6 Occurrence of two- and three-dimensional ripples in regular asymmetric flows.

Figure 7 shows the relationship between λ/d_0 and $d_0/D \cdot \Psi_{rms}^{1/2}$ for the data obtained in the present experiments by using sinusoidal and regular asymmetric oscillations together with existing data in sinusoidal oscillatory flows with sand whose diameter was about 0.2 *mm*. Values of λ/d_0 for two- and three-dimensional ripples are well expressed by Eqs. (6) to (9) with no significant deviations between data in sinusoidal flows and data in asymmetric oscillations.

Figure 8 shows the relationship between the ripple steepness η/λ and the Shields parameter. Values of η/λ are almost constant for both sinusoidal and asymmetric oscillations

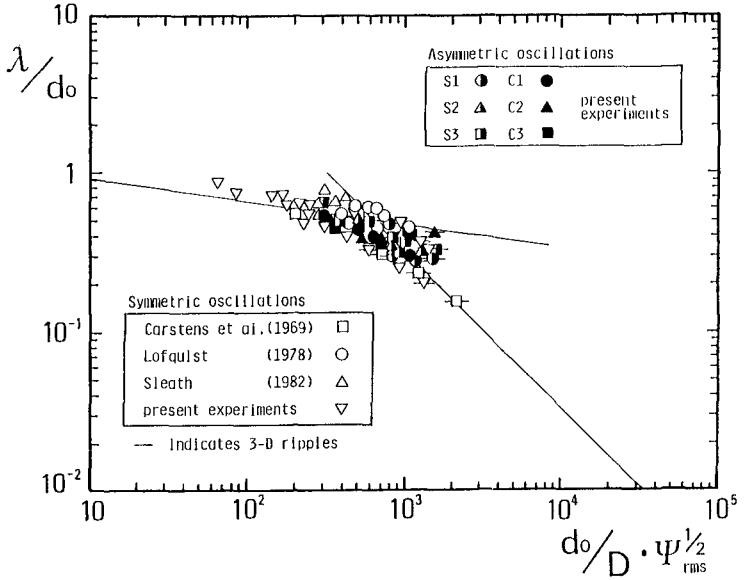

Fig. 7 Relationships between λ/d_0 and $d_0/D \cdot \Psi^{1/2}$ for ripples in regular oscillations.

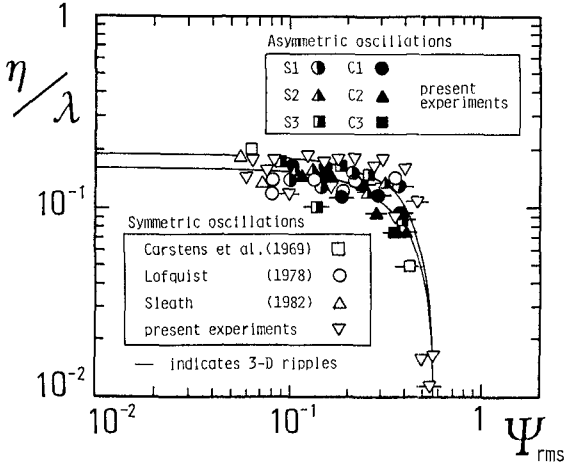

Fig. 8 Relationships between η/λ and Ψ for ripples in regular oscillations.

except in the transition region to the sheet flow. It is confirmed that the ripple steepness in asymmetric oscillatory flows can be consistently predicted by using the Shields parameter.

Figures 9 and 10 show the geometry of ripples in irregular oscillations. It is noticed that the geometry of ripples in irregular flows are also analysed consistently by using two parameters d_0/D and Ψ when these parameters are evaluated by using significant waves. It is found that the wavelength of ripples developed in irregular oscillations is almost the same with that in regular oscillations but the ripple steepness reduces considerably in irregular oscillations, which is consistent with the analysis made by Nielsen(1981).

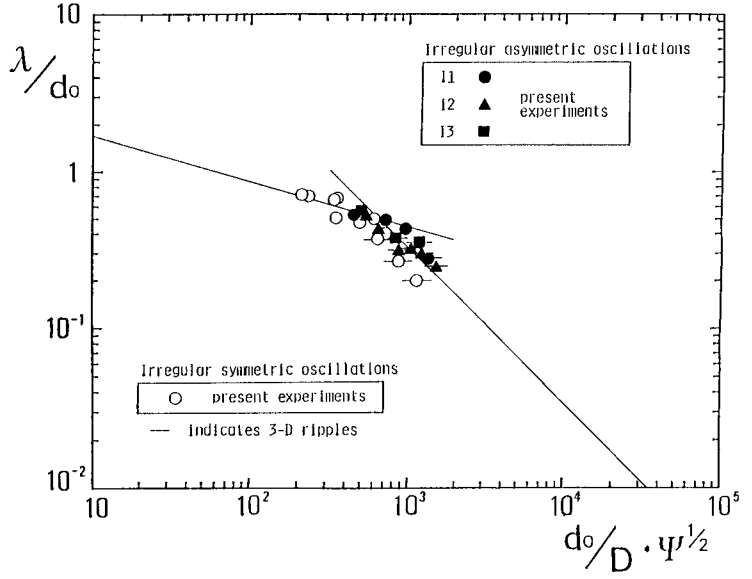

Fig. 9 Relationships between λ/d_0 and $d_0/D \cdot \Psi^{1/2}$ for ripples in irregular oscillations.

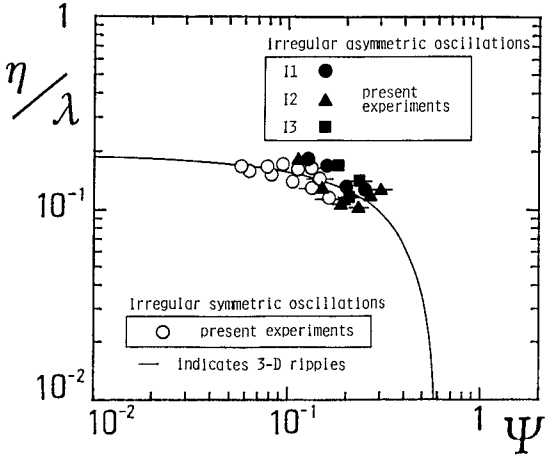

Fig. 10 Relationships between η/λ and Ψ for ripples in irregular oscillations.

The asymmetry of ripples is also of great importance since it exerts strong influences on the formation of lee vortices and in turn on the amount of the net sand transport. Figure 11 shows the relationship between the asymmetry of ripples and that of velocity histories. Data of ripples obtained in the previous experiments by using the same facilities are plotted together. The asymmetry of ripples increases linearly with the asymmetry of velocity histories until it reaches a critical value. On the assumption that the curve of the onshore-facing flank of a ripple is a sinusoidal curve whose maximum slope angle is equal to the repose angle of the sediment ϕ_r, the maximum of the ripple asymmetry is expressed by

$$\left(\frac{\lambda_c}{\lambda}\right)_{max} = 1 - \frac{\pi}{2}\frac{\eta/\lambda}{\tan\phi_r} \tag{12}$$

If values of η/λ and ϕ_r are approximated by the mean values of data in the present experiments, 0.16 and 33 ° respectively, the maximum asymmetry of ripples is estimated as

$$\left(\frac{\lambda_c}{\lambda}\right)_{max} = 0.61 \tag{13}$$

The above relation appears to explain the trend of the experimental data in strongly asymmetric oscillatory flows.

4. DISTRIBUTION OF SUSPENDED SAND CONCENTRATION

It was observed in the experiments that suspended sand clouds of high concentration were formed above two-dimensional ripples and that the sand transport in suspension appeared to contribute as the essential portion of sand movement. In order to predict the sand transport rate over ripples, it is of great concern to estimate the magnitude and the distribution of suspended sand concentration.

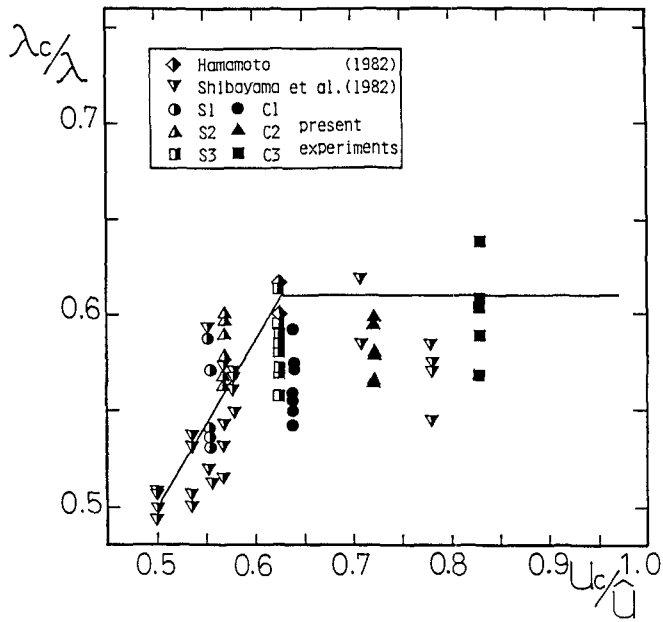

Fig. 11 Relationships between the asymmetry of ripples and the asymmetry of velocity histories.

Distributions of the equi-phase mean concentration were evaluated in order to understand the spatial and temporal variations of suspended sand concentration. Figure 12 illustrates distributions of the equi-phase mean concentration during one period. A suspended sand cloud is formed above the steeper flank of a ripple ($\omega t=\pi/5$) when the direction of the flow is onshore. The cloud is then thrown up over the ripple crest after the flow direction changes ($\omega t=3\pi/5$) and transported offshore. The formation of a sand cloud is not appreciable during the period when the direction of the flow is offshore. The resultant net sand transport therefore becomes to the offshore direction in asymmetric oscillatory flows. It is concluded that the essential portion of sand suspension occurs during the period when the flow direction is onshore. Sand suspension by the strong onshore flow is therefore considered to be of importance in the estimation of the net sand transport rate under asymmetric oscillations.

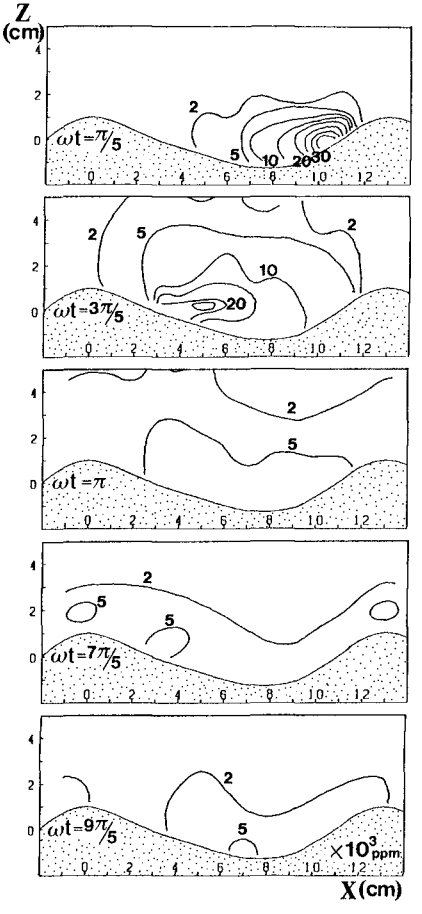

Fig. 12 Distributions of equi-phase mean concentration of suspended sand.

5. NET SAND TRANSPORT RATE

Figure 13 illustrates measured profiles of steady-state ripples developed in a case in which the oscillation was produced by a signal C2. The figure on the bottom indicates the spatial variation of the net sand transport rate q_x evaluated by Eq. (2). The arrows at both ends, $x=0\ cm$ and $x=110\ cm$, represent the volume of trapped sand. Values of q_x are regarded to be almost constant in the central region of the test bed, in which the net sand transport rate free from the disturbance produced at both ends can be estimated. The periodic variations in q_x are considered to be due to the movement of sand ripples. The net sand transport rate Q was therefore evaluated as a mean value of q_x over a region of one wavelength of a ripple at the center of the test bed.

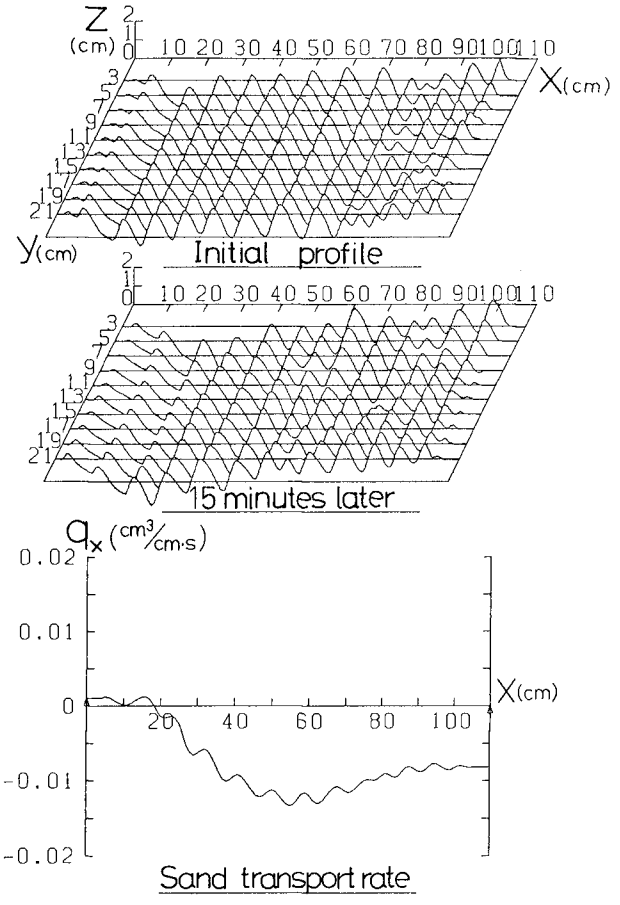

Fig. 13 Measured profiles of bed forms and the net sand transport rate.

Figure 14 shows the variation of the net sand transport rate at various stages in the development of ripples from initially flat bed. Measurements of bottom profiles and collections of trapped sand were conducted at $t/T=150$, 450, 750 and 1050. The net sand transport rate Q was small but positive at the initial stage of ripple formation in which the sand was observed to move dominantly as bed load. The direction of the net sand transport gradually tended to be in the offshore direction with the increase of sand suspension enhanced by the development of ripples until it reached a steady state at $t/T=600$. Since the time required for the development of steady-state ripples is generally considered to be small compared with the duration of steady-state waves on natural beaches, it is practically of significance to elucidate the net sand transport rate over steady-state ripples.

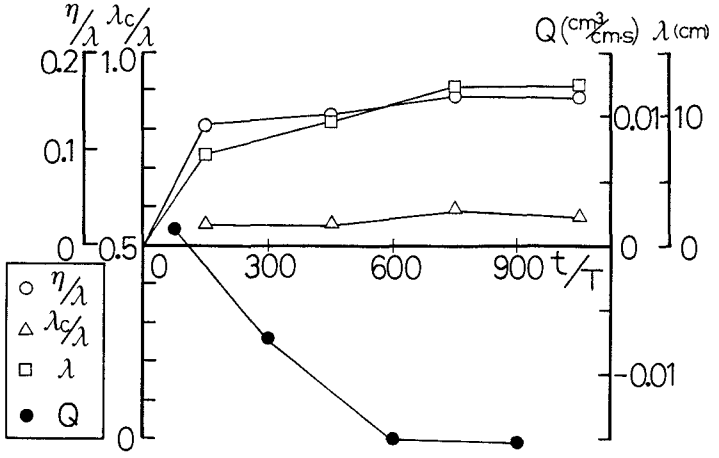

Fig. 14 Variations of the ripple geometry and the net sand transport rate with the development of ripples.

The net sand transport rate over steady-state ripples was in the offshore direction for all the cases in the present experiments. Since sand suspension occurred dominantly above the steeper flank of ripples when the flow direction was onshore, the resultant net sand transport rate was considered to be strongly dependent on the maximum onshore velocity u_c. Figure 15 shows the relationship between the following dimensionless net sand transport rate Φ and the Shields parameter Ψ_{on} evaluated by using u_c:

$$\Phi = \frac{Q}{w_s D} \tag{14}$$

$$\Psi_{on} = \frac{1}{2} f_w \frac{u_c^2}{(\rho_s/\rho - 1) g D} \tag{15}$$

The solid line represents the following empirical relation proposed by Watanabe(1982) on the basis of laboratory experiments of two-dimensional beach deformation

$$|\Phi| = 7(\Psi - \Psi_c)\Psi^{1/2} \tag{16}$$

where $\Psi_c(=0.11)$ represents the threshold of the Shields parameter for the general movement of sand particles. The relation proposed by Madsen and Grant(1976) for the sand transport rate during a half period is also depicted by the broken line,

$$|\Phi| = 12.5\Psi^3 \tag{17}$$

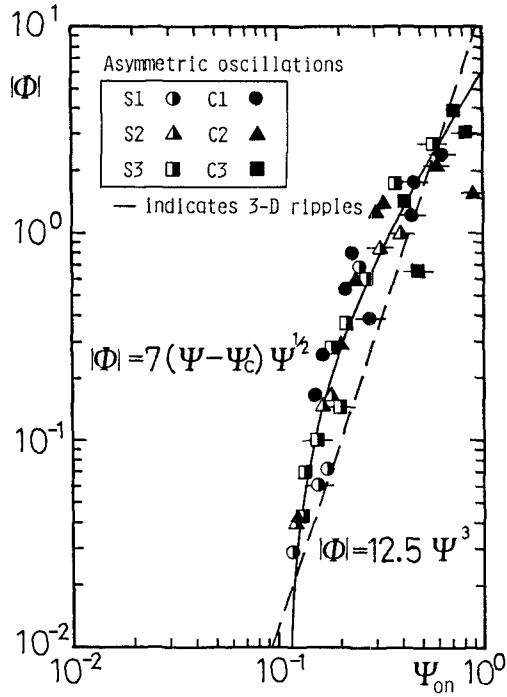

Fig. 15 Relationships between the net sand transport rate and the Shields parameter.

It is found that measured transport rates are expressed well by Eq. (16) for a wide range of conditions. The differences due to the degree of the asymmetry of velocity histories are not recognized but two-dimensionality of ripples appears to be an important factor.

Figure 16 is a comparison between measured net sand transport rates $|\Phi_m|$ and transport rates $|\Phi_c|$ calculated by Eq. (16). The transport rate over two-dimensional ripples exceeds the calculation a little, while the transport rate is found to decrease considerably over three-dimensional ripples. This is considered to be consistent with the observation that sand suspension by coherent vortices is not significant when three-dimensional ripples are developed.

The net sand transport rate under irregular oscillations can be estimated by considering the contributions of each wave in a similar manner with that for the cases of regular oscillations. The net sand transport rate is calculated by

$$\Phi = (\sum_i \Phi_i T_i)/(\sum_i T_i) \tag{18}$$

where T_i represents the period of each wave and Φ_i is the calculated transport rate for each wave calculated by Eq. (16). Figure 17 shows the comparison of measured net sand transport rate $|\Phi_m|$ and the transport rate $|\Phi_c|$ calculated by Eq. (18). Calculated values agree fairly well with measured values for the cases in which two-dimensional ripples were developed. Transport rate decreases considerably under the conditions of three-dimensional ripples.

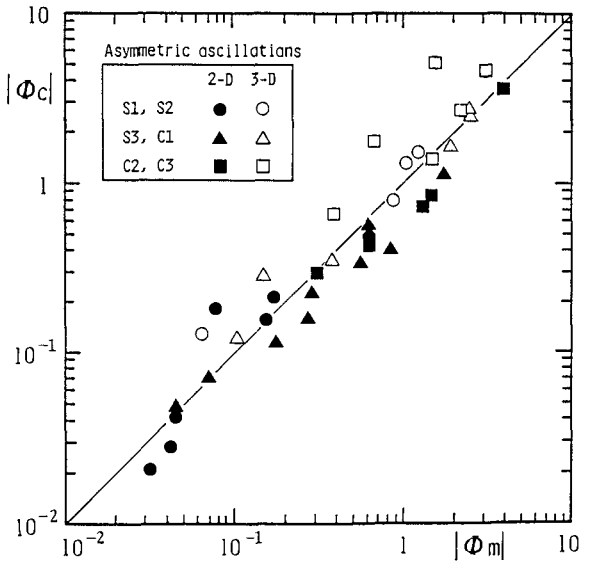

Fig. 16 Comparison of the measured and the calculated net sand transport rate (regular oscillations).

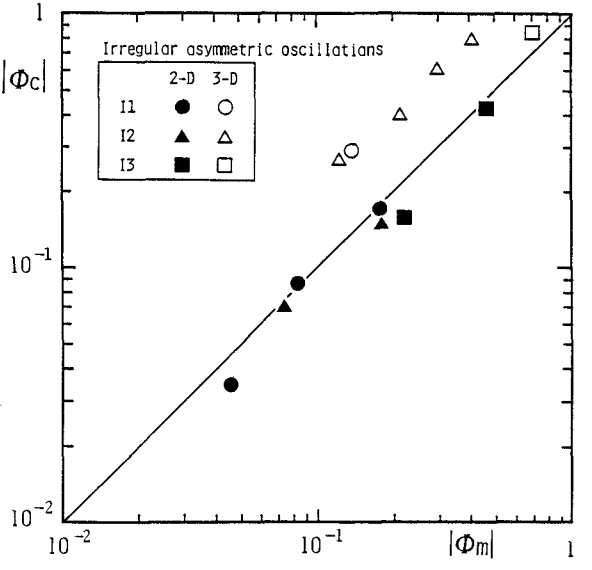

Fig. 17 Comparison of the measured and the calculated net sand transport rate (irregular oscillations).

6. CONCLUSIONS

The mechanism of sand movement due to asymmetric oscillatory flows was investigated on the basis of laboratory measurements. Characteristics of the ripple geometry and the net sand transport rate were discussed in terms of hydraulic parameters characterizing the oscillatory flow. The geometry of ripples in asymmetric oscillations was described by two parameters d_0/D and Ψ for both regular and irregular oscillations. The asymmetry of ripples was found to be dependent on the asymmetry of velocity histories and the repose angle of the sand. The measurements of suspended sand concentration revealed that the asymmetry of flows and ripples exerted strong influences on the formation of sand clouds and that the entrainment of sand by the strong onshore flow was important in the estimation of the sand transport. The net sand transport rate over steady-state ripples was expressed by the Shields parameter based on the maximum onshore velocity. It was found that the net sand transport rate decreased considerably over three-dimensional ripples. Further studies are expected on the measurements under the conditions of much larger bottom shear stresses and the simulation of the nonlinear velocity variation under irregular waves.

REFERENCES

Carstens, M. R., F. M. Neilson and H. D. Altinbilek: Bed forms generated in the laboratory flow, *CERC Tech. Memo.*, No. 28, 39p., 1969.

Jonsson, I. G.: Wave boundary layers and friction factors, *Proc. 10th Coastal Eng. Conf.*, pp. 127-148, 1966.

Kaneko, A.: Oscillation sand ripples in viscous fluid, *Proc. JSCE*, No. 307, pp. 113-124, 1981.

Lofquist, K. E. B.: Sand ripple growth in an oscillatory-flow water tunnel, *CERC Tech. Paper*, No. 75-5, 101p., 1978.

Madsen, O. S. and W. D. Grant: Quantitative description of sediment transport by waves, *Proc. 15th Coastal Eng. Conf.*, pp. 1093-1112, 1976.

Nielsen, P.: Dynamics and geometry of wave-generated ripples, *J. Geophys. Res.*, Vol. 80, No. C7, pp. 6467-6472, 1981.

Sato, S.: Oscillatory boundary layer flow and sand movement over ripples, Doctoral dissertation, the University of Tokyo, 135p., 1986.

Sunamura, T.: A laboratory study of offshore transport of sediment and a model for eroding beaches, *Proc. 17th Coastal Eng. Conf.*, pp. 1051-1070, 1980.

Vongvisessomjai, S.: Oscillatory ripple geometry, *J. Hydraulic Eng.*, Vol. 110, No. 3, pp. 247-266, 1984.

Watanabe, A.: Numerical models of nearshore currents and beach deformation, *Coastal Eng. in Japan*, Vol. 25, pp. 147-161, 1982.

CHAPTER 110

MODELING TURBULENT BOTTOM BOUNDARY LAYER DYNAMICS

Y. P. Sheng*, Member ASCE

ABSTRACT

This paper presents a modeling approach aimed at soving a complete hierarchy of turbulent bottom boundary layers which are often encountered in practical coastal and oceanographic engineering problems. The practical problem is extremely complex due to the presence and interaction of competing processes. A comprehensive model is thus needed to first provide fundamental understanding of a variety of turbulent bottom boundary layers before any simple model for the complex problem can be meaningfully constructed. This paper presents a comprehensive second-order closure model of turbulent transport and in addition, discusses some applications of the model to wave boundary layer, wave-current boundary layer, sediment-laden boundary layer and two-dimensional boundary layer. Example is provided to show how such a comprehensive model may be used to guide the development of a simple model.

I. INTRODUCTION

Flow in coastal waters is generally turbulent. A thorough understanding of the dynamics of turbulent bottom boundary layers is of paramount importance in the field of coastal and oceanographic engineering. For quantitative estimation of sediment transport rate and optimal design of structures in coastal waters, it is essential to first estimate the hydrodynamic forces acting on the ocean bottom which may be flat or complicated by the presence of bedforms or structures such as pipelines (Figure 1). The hydrodynamic forces can be produced by slowly varying currents (due to wind or tide) or short-period oscillatory currents (due to linear or nonlinear short-period waves) or a combination of both. When hydrodynamic forces exceed certain critical values, bottom sediments may be eroded and carried into the water column and, consequently, significant suspended sediment concentration and vertical concentration gradient may be produced thus leading to modification of the flow.

Simple Models or Comprehensive Models?

Dynamics of turbulent bottom boundary layers in coastal waters is extremely complex because of the coexistence of many competing mechanisms in turbulent flows: short-period wave, stratification, wave-

*Coastal & Oceanographic Engr. Dept, Univ. of Fla., Gainesville, 32611

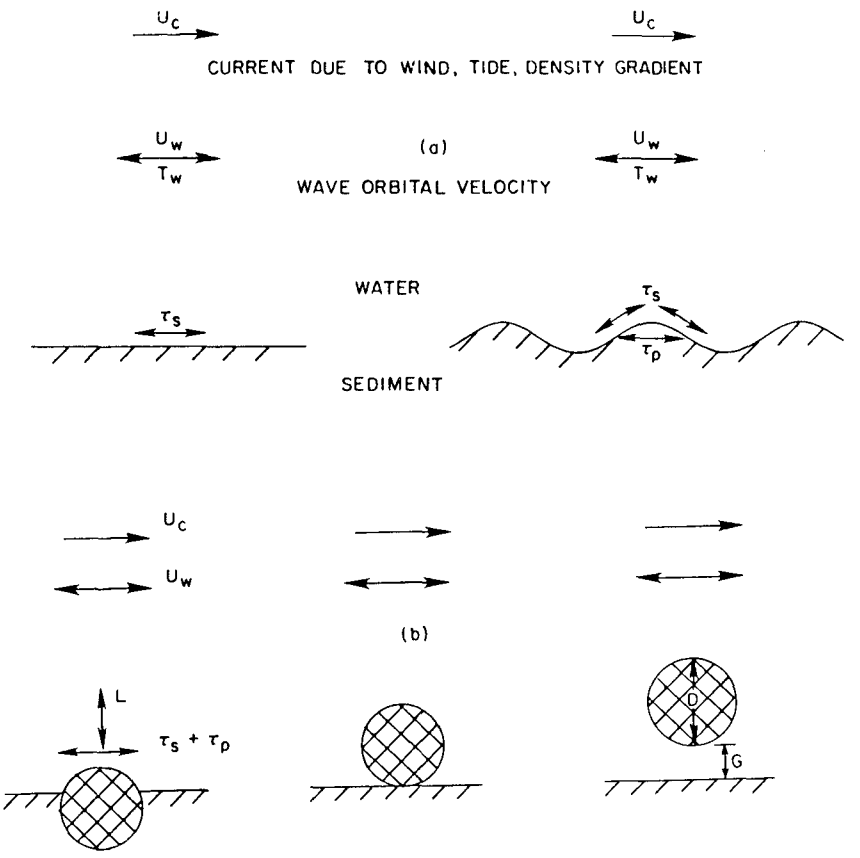

Figure 1 Bottom boundary layer flow over (a) flat and wavy bottom, and (b) flat bottom with pipelines.

current interaction, nonlinearity, and two-dimensional and even three-dimensional effects due to the presence of complex structures or bedforms. A comprehensive model capable of accurately resolving the complex turbulent boundary layer dynamics is urgently needed to provide physical insight and to solve practical engineering problems. Such a model must contain the proper physics of the major competing mechanisms and hence, cannot be necessarily "simple". Despite this fact, however, engineers faced with the complex practical problems in coastal sediment transport and structural design have generally favored the development and use of the so-called "simple" analytical or numerical models which, unfortunately, are often developed at the expense of compromising physics. Indeed, the literature is abound with such "simple" analytical and numerical models for some of the processes described above. For example, since the early eddy-viscosity model of Kajiura (1968), numerous similar eddy-viscosity

models have been developed to simulate turbulent wave boundary layers. Eddy-viscosity models for wave-current interaction (e.g., Bakker and Van Doorn, 1978; Grant and Madsen, 1979) and stratified flow (e.g., Long, 1981) have also been attempted. While these models for individual processes could be calibrated to produce "good" results when sufficient data exist and under limiting conditions, these models generally fail to work when two or more of the competing mechanisms coexist or when little data exist and "prediction" is required. This is primarily due to the grossly simplified turbulence parameterization contained in these simple models, where the turbulence is typically assumed to be always in equilibrium with the mean flow and hence the turbulent transport is modeled as a local diffusive process only. Moreover, simple eddy-viscosity models developed for different processes cannot be readily superimposed for application to complex problems. Nevertheless, simple models continue to be developed and used. For example, forces on bottom pipelines have generally been estimated by using the simple but empirical Morison's equation (Sarpkaya and Isaacsen, 1981), which largely ignores the physics.

Modeling Approach

In order to develop meaningful simple analytical or numerical models for turbulent boundary layers and coastal sediment transport, one must start from comprehensive models which do not make ad-hoc assumptions about the processes described above. This paper describes such a comprehensive second-order closure model of turbulent transport which has been previously applied to simulate wave boundary layer (Sheng, 1982 and 1984) and wave-current interaction (Sheng, 1984). Such a comprehensive model, because of the added physics it contains, can simulate the individual processes without ad-hoc parameter tuning, and hence, is useful for understanding and predicting the complex turbulent boundary layer dynamics when many competing mechanisms coexist or when little data exist. In the long run, we can use the physical insight gained from these comprehensive models to provide guidelines for development of meaningful simple analytical or numerical models.

Model Validation

Previous eddy-viscosity models for wave boundary layers and current-wave boundary layers could only be calibrated against mean flow quantities. On the other hand, Sheng (1984) compared the results of a second-order closure model with both the mean and turbulent quantities within turbulent bottom boundary layers. This is a very important point—when modeling complex turbulent flow phenomena, model results must be compared with turbulence data. Comparison of model results against mean flow data alone and/or quantities of second-order importance (e.g., mass transport) is insufficient to judge the quality of the model. While the second-order mass transport may have some meaning in wave theory or laboratory study of wave boundary layer (Sleath, 1984), in practical situations the negligible mass transport velocity is easily overwhelmed by the tidal currents or wind-driven currents, hence, it is extremely hard to discern and is of questionable practical importance.

This Work

In addition to a brief review of the complete second-order closure model, this work also discusses two simplified versions of the model which are useful under certain conditions. Some recent applications of the second-order closure model to simulate wave boundary layers, wave-current boundary layers, sediment-laden bottom boundary layers, and two-dimensional effects are discussed.

II. MODELS OF TURBULENT FLOWS

Instead of presenting model equations which are only valid for a particular process of interest, this work will present the following general equations which are valid for turbulent flows where more than one of the processes (e.g., stratification, wave-current interaction, nonlineartiy, stratification, and 2-D or 3-D effects) are present. Anticipating applications to 1-D, 2-D, axisymmetric and even 3-D flow situations, the model equations are given in tensor notation.

Mean Equation

Reynolds-averaged equations for the mean flow quantities in an imcompressible fluid in the presence of rotation are:

$$\frac{\partial U_i}{\partial x_i} = 0 \tag{1}$$

$$\frac{\partial U_i}{\partial t} + \frac{\partial U_i U_j}{\partial x_j} = -\frac{\partial \overline{u_i u_j}}{\partial x_j} - \frac{1}{\rho_o}\frac{\partial p}{\partial x_j} - g_i\frac{\tilde{\rho}}{\rho_o} - 2E_{ijk}\Omega_j U_k + \frac{\partial}{\partial x_j}\left(\nu\frac{\partial U_i}{\partial x_j}\right) \tag{2}$$

$$\frac{\partial \phi}{\partial t} + \frac{\partial U_j \phi}{\partial x_j} = -\frac{\partial \overline{u_j \phi}}{\partial x_j} + \frac{\partial}{\partial x_j}\left(\kappa\frac{\partial \phi}{\partial x_j}\right) \tag{3}$$

where U_i and u_i are the mean and fluctuating velocity components, $\tilde{\rho}$ and ρ are the mean and fluctuating components of density, E is permutation tensor, Ω is earth's rotational speed, ν is the kinematic viscosity, κ is the kinematic diffusivity, and Φ and ϕ are the mean and fluctuating temperature (or salinity). An equation of state is needed to relate $\tilde{\rho}$ and Φ.

It is apparent that the above equations are not closed unless additional information is given for the second-order correlations $\overline{u_i u_j}$ and $\overline{u_j \phi}$. Models which provide information on $\overline{u_i u_j}$ and $\overline{u_j \phi}$ are called turbulence models.

Existing models for turbulent transport can be grouped into two categories: those which employ the turbulent (or eddy) viscosity/diffusivity concept, and those which do not.

Eddy-Viscosity Models

The eddy-viscosity/diffusivity concept assumes that, in analogy to the viscous stresses and fluxes in laminar flow, the turbulent stresses and heat or mass fluxes are proportional to the mean velocity and temperature or concentration gradients, respectively. In tensor notation, the concept is:

$$-\overline{u_i u_j} = \nu_t\left(\frac{\partial U_i}{\partial x_j} + \frac{\partial U_j}{\partial x_i}\right) - \frac{q^2}{3}\delta_{ij} \tag{4}$$

$$-\overline{u_i \phi} = K_t \frac{\partial \Phi}{\partial x_i} \tag{5}$$

where ν_t and K_t are respectively the eddy viscosity and diffusivity, and $q^2 = \overline{u_i u_i}$ is twice the turbulent kinetic energy (k). Unfortunately, ν_t and K_t are not fluid properties but depend strongly on the state of turbulence and may vary considerably across the flow, from time to time, and from one flow to another. Despite the simplicity of its concept, however, the precise value/formula for the eddy viscosity is not necessarily simple to determine. One often hears such remarks in a technical paper or presentation: "What kind of eddy viscosity is needed in order that the model results agree with data?" Thus, eddy viscosity is essentially a convenient "tuning parameter" for many people who do not wish to deal with turbulence in a rigorous fashion. One is cautioned that a "well tuned" eddy viscosity formula for one process/problem cannot be readily applied to another process/problem. In addition, the concept breaks down completely in flow regions where the flux is against the gradient of the transported quantity. Such counter-gradient-flux regions occur quite frequently in turbulent flows.

Second-Order Closure Models

This type of turbulence model uses transport equations for the turbulence stresses $\overline{u_i u_j}$ and fluxes $\overline{u_j \phi}$ such that the eddy-viscosity concept does not have to be introduced. The transport equations for a second-order closure model (e.g., Sheng, 1982), following a procedure outlined by Donaldson (1973), are presented in the following in terms of $\overline{u_i u_j}$, $\overline{u_i \rho}$ and $\overline{\rho\rho}$:

$$\frac{\partial \overline{u_i u_j}}{\partial t} + U_k \frac{\partial \overline{u_i u_j}}{\partial x_k} = -\overline{u_i u_j}\frac{\partial U_j}{\partial x_k} - \overline{u_j u_k}\frac{\partial U_i}{\partial x_k} - g_i \frac{\overline{u_j \rho}}{\rho_o} - g_j \frac{\overline{u_i \rho}}{\rho_o} \tag{6}$$

$$- 2E_{ikm}\Omega_k \overline{u_m u_j} - 2E_{jmk}\Omega_m \overline{u_k u_i}$$

$$+ v_c \frac{\partial}{\partial x_k}\left(q\Lambda \frac{\partial \overline{u_i u_j}}{\partial x_k}\right) - \frac{q}{\Lambda}\left(\overline{u_i u_j} - \delta_{ij}\frac{q^3}{3}\right) - \delta_{ij}\frac{2bq^3}{3\Lambda} + \nu\frac{\partial^2 \overline{u_i u_j}}{\partial x_k^2} - \frac{2a\nu\overline{u_i u_j}}{\Lambda^2}$$

$$\frac{\partial \overline{u_i \rho}}{\partial t} + U_j \frac{\partial \overline{u_i \rho}}{\partial x_j} = -\overline{u_i u_j}\frac{\partial \tilde{\rho}}{\partial x_j} - \overline{u_j \rho}\frac{\partial U_i}{\partial x_j} - \frac{g_i \overline{\rho\rho}}{\rho_o} - 2E_{ijk}\Omega_j \overline{u_k \rho} \qquad (7)$$

$$+ v_c \frac{\partial}{\partial x_j}\left(q\Lambda \frac{\partial \overline{u_i \rho}}{\partial x_j}\right) - \frac{Aq}{\Lambda}\overline{u_i \rho} + \kappa\frac{\partial^2 \overline{u_i \rho}}{\partial x_j^2} + \frac{a\kappa\overline{u_i \rho}}{\Lambda^2}$$

$$\frac{\partial \overline{\rho\rho}}{\partial t} + U_j \frac{\partial \overline{\rho\rho}}{\partial x_j} = 2\overline{u_j \rho}\frac{\partial \tilde{\rho}}{\partial x_j} + v_c \frac{\partial}{\partial x_j}\left(q\Lambda \frac{\partial \overline{\rho\rho}}{\partial x_j}\right) + \kappa\frac{\partial^2 \overline{\rho\rho}}{\partial x_j^2} - \frac{2bsq\overline{\rho\rho}}{\Lambda} \qquad (8)$$

where the last 5 terms in Eq. (6), the last 4 terms in Eq. (7), and the last 3 terms in Eq. (8) are "modeled" terms. For example, in Eq. (6), the term containing v_c is a diffusion term, the term containing q/Λ is a tendency-toward-isotropy term, while the last 3 terms are dissipation terms with the last 2 terms vanishing at high Reynolds number. The model constants, $v_c = 0.3$, $b = 0.125$, $a = 3$, $A = 0.75$, and $s = 2.8$, are determined by comparing model simulations with a wide variety of critical laboratory experiments where only one or two of the modeled terms is dominant, and remain fixed for any new model application (Sheng, 1986a). Thus the model is sometimes termed an invariant model.

An equation for the turbulence macroscale Λ is needed to close the system of equations (1) through (8):

$$\frac{D\Lambda}{Dt} = 0.35\frac{\Lambda}{q^2}\overline{u_i u_j}\frac{\partial U_i}{\partial x_j} + 0.6bq + 0.3\frac{\partial}{\partial x_i}\left(q\Lambda\frac{\partial \Lambda}{\partial x_i}\right) - \frac{0.375}{q}\left(\frac{\partial q\Lambda}{\partial x_i}\right)^2 - \frac{0.8\Lambda}{q^2}g_i\overline{u_i \rho} \qquad (9)$$

It is useful to derive an equation for q^2 from Eq. (6):

$$\frac{\partial q^2}{\partial t} + U_k\frac{\partial q^2}{\partial x_k} = -2\overline{u_i u_k}\frac{\partial U_i}{\partial x_k} - 2g_i\frac{\overline{u_i \rho}}{\rho_o} + v_c\frac{\partial}{\partial x_k}\left(q\Lambda\frac{\partial q^2}{\partial x_k}\right) - \frac{bq^3}{\Lambda} + \frac{\partial^2 q^2}{\partial x_k^2} - \frac{2a\nu q^2}{\Lambda^2} \qquad (10)$$

Simplified Second-Order Closure Models

Equations (6), (7), (8) and (9) constitute the so-called "Reynolds stress model" and is the most complete second-order closure model. These dynamic equations contain much more physics of the turbulent flow than the eddy-viscosity model, or first-order closure

model. Although the solution of these equations requires considerable computational effort, simplifications of the equations can sometimes be introduced in practical applications to reduce the computational effort. For example, if the time scale of mean flow is large compared to that of turbulence, "quasi-equilibrium" approximation may be introduced such that only Eqs. (9) and (10) are needed to represent the dynamics of turbulence, while Eqs. (6), (7) and (8) are replaced by a set of algebraic equations where the total derivative and diffusion terms are neglected. If, in addition, the turbulence does not change significantly over Λ, the "super-equilibrium" approximation is valid such that Eqs. (6), (7) (8) (9) are replaced by a number of algebraic equations. Such simplified second-order closure models are used to represent the vertical turbulence in the three-dimensional hydrodynamic model of coastal and estuarine circulation (Sheng, 1986b).

III. SECOND-ORDER CLOSURE MODELING OF WAVE BOUNDARY LAYERS

Wave Boundary Layer

The Reynolds stress model as presented above has been applied to simulate the wave boundary layer of Jonsson and Carlsen (1976). The one-dimensional version of the model was used and hence the equations become considerably simplified, since only vertical gradients appear in the equations. Boundary layer approximation was invoked and the free-stream oscillatory currents are balanced by a lateral pressure gradient which is imposed throughout the boundary layer. Results shown in Sheng (1982) and Sheng (1984) demonstrated that the Reynolds stress model was able to faithfully simulate the mean velocities at various phase angles and the phase lag of mean velocities at different vertical levels. In addition, comparison of the model results vs. computed Reynolds stress data indicated the lack of temporal resolution of mean velocity measurements.

Logarithmic Layer

Perhaps one of the most important model results is the explicit computation of the instantaneous logarithmic layer. It is a well known fact that the velocity distribution within a homogeneous and steady-state bottom boundary layer follows the logarithmic variation:

$$u = \frac{u_*}{k} \ln\left(\frac{z}{z_o}\right) \tag{11}$$

where k is the von-Karmen constant, u_* is the friction velocity and z_o is the roughness height, while the turbulent fluxes are more or less uniform within the layer. In the presence ot density stratification due to variation in temperature, salinity and/or suspended sediment concentration, the thickness of the logarithmic layer (or constant flux layer) may be significantly modified. In addition, the presence of a body force such as pressure gradient may also significantly alter the thickness of the logarithmic layer. Jonsson and Carlsen (1976) could not measure their turbulence directly and hence assumed a fixed logarithmic layer thickness of 6.3 cm. Results of the Reynolds stress

model clearly indicate a much thinner logarithmic layer, as shown in Figure 2, which is modulated by the pressure gradient associated with the free-stream oscillatory flow. The instantaneous Reynolds stress at three levels (0.5 cm, 1 cm and 4 cm above the bottom) and two phase angles as shown agree well with model results.

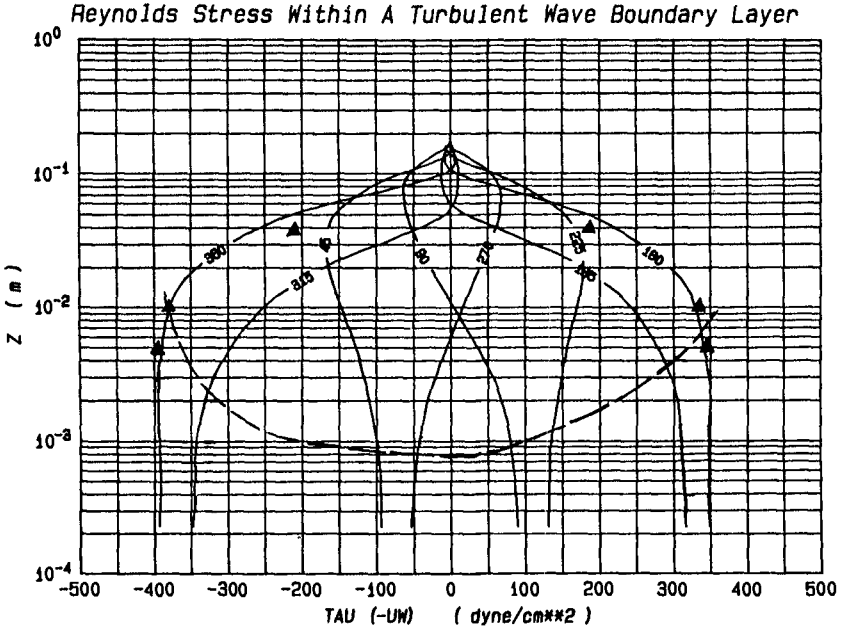

Figure 2 Reynolds stress within Jonsson and Carlsen's wave boundary layer. ——— : model; ▲'s: data; ----- indicates the approximate edge of the logarithmic layer.

Eddy Viscosity

The presence of the logarithmic layer is validated by the model, thus the eddy viscosity near the bottom can be found to scale with ku_*z, where z is the distance above the bottom:

$$\nu_t = \frac{\tau}{\partial u/\partial z} = \frac{\rho u_*^2}{u_*/kz} = \rho u_* kz \qquad (12)$$

Since u_* is a function of time, ν_t must be a function of time and space. This explains why almost all of the previous eddy-viscosity models, which use either spatially varying or temporally varying eddy viscosity, fail to faithfully reproduce Jonsson and Carlsen's wave boundary layer data (Sheng, 1986a). However, Eq. (12) is not valid outside the logarithmic layer.

Another reason why eddy viscosity is a poor concept for studying turbulent boundary layers is visualized in Figure 3 which shows the eddy viscosity calculated from Jonsson and Carlsen's data via $\nu_t = \tau/(\Delta u/\Delta z)$. It is apparent that the eddy viscosity is often scattered and may become negative which is physically meaningless. The solid lines represent the eddy viscosity computed from the results of the Reynolds stress model via $\nu_t = \overline{ww}\,\Lambda/q$.

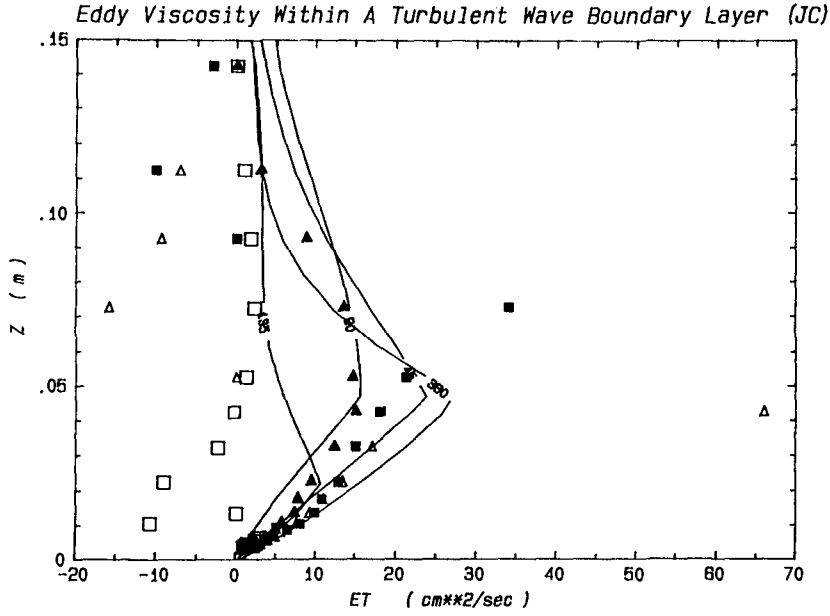

Figure 3 Eddy viscosity computed from Jonsson and Carlsen's data (Δ, , Δ,) and computed from the model results via $\overline{ww}\,\Lambda/q$.

Simplified Second-Order Closure Models for Wave Boundary Layer

Recently, the "quasi-equilibrium" and "super-equilibrium" versions of the second-order closure model were applied to simulate Jonsson and Carlsen's wave boundary layer (Sheng, 1987). The "quasi-equilibrium" results compared very well with data while the "super-equilibrium" results did not do as well. However, this in no way implies that the simplified second-order closure models are sufficient for simulating all turbulent wave boundary layers, since the state of turbulence may vary from one boundary layer to another and from one problem to another.

Other Wave Boundary Layers

Sheng (1984) simulated the turbulent bottom boundary layer underneath a cnoidal wave and found strong asymmetric behavior in the predicted mean velocities and Reynold stresses. The maximum Reynolds stress was found to be 50% higher than that produced by a simple sinusoidal wave boundary layer.

Another interesting wave boundary layer experiment was conducted by Hino, et al. (1983). It was reported that the measured turbulent intensities increased substantially while the flow changes from the acceleration stage to deceleration stage. Again, results of the Reynolds stress model agree well with data (Sheng, 1987).

IV. WAVE-CURRENT BOTTOM BOUNDARY LAYER

Kemp and Simons (1982) measured the mean and turbulent quantities within the turbulent bottom boundary layer underneath a wave propagating with the current. They found that for smooth bed, the turbulent stresses produced by the wave alone and the current alone can be superimposed to give the total stress for the wave-current case. For rough bed, however, the wave-current interaction is highly nonlinear and the turbulent stressed due to current and wave cannot be linearly superimposed. Although their experiments appear to contain 2-D and 3-D effects in the vicinity of the roughness elements (due to the relatively small ratio between particle displacement and roughness A_{bm}/k_s), it is interesting to compare the results of a 1-D Reynolds stress model against their data. As an example, comparison in terms of the maximum vertical varinace is shown in Figure 4, where the model results were for the case of WCR5. Notice the generally good agreement between data and model results, except in the vicinity of the roughness elements where 2-D effect is important.

V. SEDIMENT-LADEN BOTTOM BOUNDARY LAYER

The second-order closure model has been recently applied to simulate the effect of suspended sediment concentration on the boundary layer flow structure and to improve the determination of erosion/deposition relationships from laboratory experiments (Sheng, 1987).

VI. TWO-DIMENSIONAL EFFECT

Most bottom boundary layer models, including those cited above, are one-dimensional and hence cannot be expected to work when two dimensional effect due to bedforms or structures is present. DuToit and Sleath (1981) measured velocity measurements close to rippled beds in oscillatory flow and compared their data with three 1-D models (Kalkanis, 1964; Kajiura, 1968; Bakker, 1974). The agreement between data and model results was found to be rather poor. In 2-D flows, profile drag becomes important in addition to the skin friction drag. Vortex generation and shedding play an important role in the two-dimensional bottom boundary layer dynamics, but are simply not resolved in the one-dimensional models.

As an example, the 2-D version of the second-order closure model was used to simulate the flow and separation behind a backward facing step. As shown in Figure 5, the computed mean velocity and Reynolds stress distribution compare well with data at various downstream distances X behind the step with height H. The Reynolds stress distribution shown is in the vicinity of the flow reattachment point. It should be pointed out that for such a complex problem, a "simple" eddy-viscosity model simply does not exist.

The 2-D version of the Reynolds stress model can be applied to simulate the wave boundary layer or wave-current boundary layer over a wavy bottom. It should be pointed out that such model will be able to correctly resolve the nonlinear inertia terms, without treating it as "second-order" effect as in the 1-D model.

VII. CONCLUSIONS

The dynamics of turbulent bottom boundary layers in coastal waters is extremely complex because of the simultaneous presence of such competing processes as stratification, short-period wave, wave-current interaction, nonlinearity, and two-dimensional effects. Numerous "simple" (from the point of view of computational effort) models for individual processes (e.g., a pure wave boundary layer) have been developed in the past. Unfortunately, many of these models were developed with ad-hoc empiricism and hence one cannot superimpose the simple models for application to complex problems. In order to ultimately derive simple analytical or numerical models of the complex overall problem, a comprehensive model must be first constructed and used to gain physical insight and to provide guidance for formulating simpler models.

A comprehensive second-order closure model of turbulent transport is presented here. Model applications to a variety of bottom boundary layers (wave boundary layer, wave-current boundary layer, sediment-laden boundary layer, and two-dimensional boundary layers) are discussed. The model is capable of simulating the measured mean and turbulent quantities. Simplified versions of the second-order closure model are available and can be applied to some problems. An example was provided to demonstrate the fact that an eddy-viscosity model is meaningful only if it is derived based on sound understanding of turbulent flow.

For meaningful model validation, model results must be compared with measured turbulence data instead of mean flow data only.

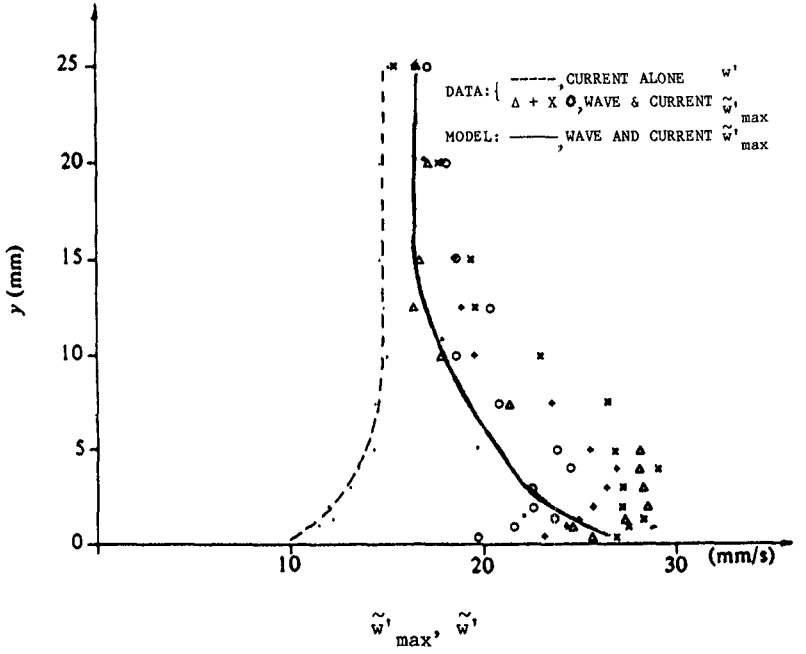

Figure 4 Vertical variance within 25 mm of bed-roughness apex in Kemp and Simons' 1982 wave-current experiment and computed by the Reynolds stress model.

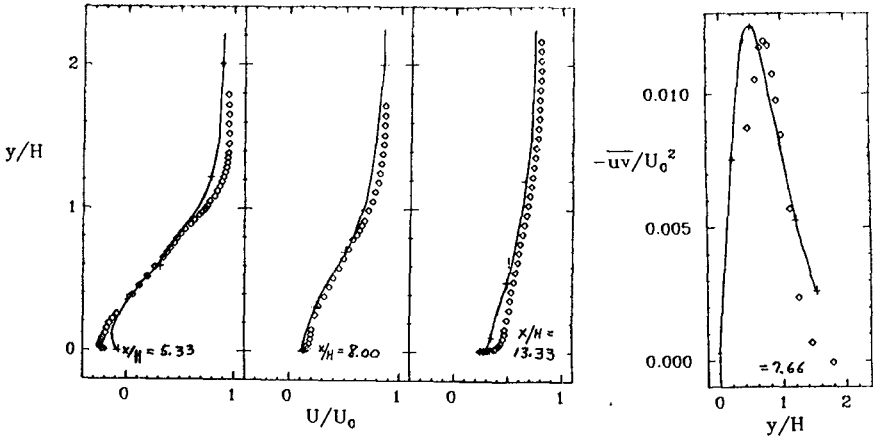

Figure 5 Mean velocity and Reynolds stress at several locations behind a backward facing step. His step height, U_0, is free stream velocity, and x and y are horizontal and vertical distances.

References

Donaldson, C. duP., 1973: "Atmospheric Turbulence and the Dispersal of Atmospheric Pollutants", in AMS Workshop on Micrometeorology, (D. A. Haugen, ed.), Science Press, Boston, pp. 313-390.

DuToit, C. G. and J. F. A. Sleath, 1981: "Velocity Measurements Close to Rippled Beds in Oscillarory Flow", JFM, 112, pp. 71-96.

Grant, W. D. and O. S. Madsen, 1979: "Combined Wave and Current Interaction with a Rough Bottom", J. Geophys. Res., 84, pp. 1797-1808.

Hino, M., M. Kashiwayanagi, a. Nakoyama, and t. Hara, 1983: "Experiments on the Turbulence Statistics and the Structure of a Reciprocating Oscillatroy Flow", JFM, 131, pp. 363-400.

Jonsson, I. G., and N. A. Carlsen, 1976: "Experimental and Theoretical Investigations in an Oscillatory Rough Turbulent Boundary Layer", J. Hydr. Res., 14, pp. 45-60.

Kajiura, K., 1968: "A Model of the Bottom Boundary Layer in Water Waves", Bull Earthq. Res. Inst., 46, pp. 75-123.

Kemp, P. H. and R. R. Simons, 1982: "The Interaction Between Waves and a Turbulent Current: Waves Propagating with the Current", J. Fluid Mech., vol. 116, pp. 227-250.

Sarpkaya, T., and M. Isaacson, 1981: "Mechanics of Wave Forces on Offshore Structures", Van Nostrand Reinhold Co., 651 pp.

Sheng, Y. P., 1982: "Hydraulic Applications of a Second-Order Closure Model of Turbulent Transport", in Applying Research to Hydraulic Practice, (P. Smith, ed.), ASCE, pp. 106-119.

Sheng, Y. P., 1984: "A Turbulent Transport Model of Coastal Processes", Proc. 19th Int. Conf. Coastal Eng., ASCE, pp. 2380-2396.

Sheng, Y. P., 1986a: "Finite-Difference Models for Hydrodynamics of Lakes and Shallow Seas", in Physics-Based Modeling of Lakes Reservoirs, and Impoundments, (W. G. Gray, ed.), ASCE, New York, pp. 146-228.

Sheng, Y. P., 1986b: "On Modeling Three-Dimensional Estuarine and Marine Hydrodynamics", in Three-Dimensional Models of Marine and Estuarine Dynamics, (J. C. J. Nihoul and B. M. Jamart, eds.), Elsevier, In Press.

Sheng, Y. P., 1987: In preparation.

Sleath, J. F. A., 1984: "Measurements of Mass Transport Over a Rough Bed", Proc. 19th Intl. Conf. Coastal Eng., ASCE, pp. 1149-1160.

CHAPTER 111

SEDIMENT TRANSPORT DUE TO BREAKING WAVES

Tomoya Shibayama, A.M. ASCE *
Akihiko Higuchi ** and
Kiyoshi Horikawa, M.ASCE***

ABSTRACT

In the surf zone, the agitation of the bed materials by breaking waves is strong and the suspended sand concentration in the vicinity of the wave plunging point is extremely high. Sand movement in this region was observed and sand concentration was measured in a wave flume. The sand movement in the region was divided into the following two categories: 1) sand suspension due to the large vortex which is created by wave plunging, and 2) sand deposition under turbulent flow. The condition for exciting this suspension process was considered and the result was well explained by the two parameters which are the deep water wave steepness and the bottom slope. Then a numerical model of the sediment suspension process was formulated and the process was well simulated by the model.

1. INTRODUCTION

In recent years, many attempts have been made to formulate cross-shore sand transport and resultant beach transformation. However many of these treatments are based of oscillatory wave motion and the resultant bed shear stress. In order to analyze sand transport within the surf zone more precisely, the dynamics of breaking waves must be understood more clearly. In the surf zone, agitation due to wave breaking lifts the bed material and places it into suspension and the suspended sand concentration in the vicinity of the breaking point is extremely high. Fig. 1 shows the schematic view of the sand movement process in this region. The purpose of the present paper is to describe the nature of sand movement under breaking waves.

The present work was stimulated by the following two studies. Dean (1973) treated the problem of sand suspension at the wave breaking point and gave critical values of two parameters which govern the sand

* Associate Professor, Dept. of Civil Engineering, University of Tokyo, Bunkyo-ku Tokyo 113 Japan
** Engineer, Penta-Ocean Construction Co., Ltd.
***Professor, Dept. of Civil Engineering, University of Tokyo

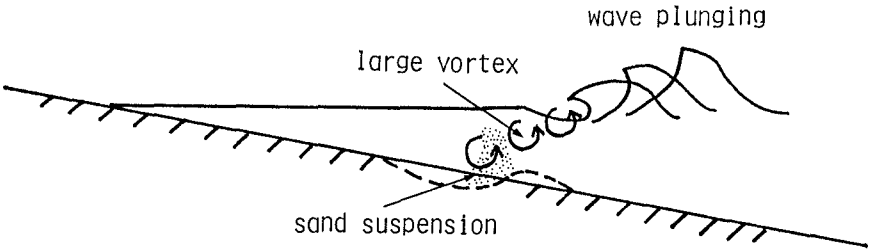

Figure 1: Schematic View for Sand Suspension due to Wave Plunging.

transport direction at the wave breaking point. The two parameters are the wave steepness and the ratio of fall velocity to wave period. Sawaragi and Iwata (1974) investigated the mechanism of wave breaking and reported the nature of plunging waves. They described the physical mechanism of the "horizontal roller" which is the large vortex created by the wave plunging. In the present study, the sand suspension process will be explained in relation to the action of the large vortex.

2. CONDITIONS FOR SEDIMENT SUSPENSION

Wave breaking over a movable bed sometimes results in sand suspension due to agitation caused by the wave plunging. In order to determine the condition when this kind of sand suspension occurs, laboratory experiments were performed for a wide range of flow conditions. In the experiment, two wave flumes, termed A and B, were used. Flume A was 11 m long, 0.2 m wide and 0.3 m deep. Flume B was 25 m long, 0.8 m wide and 1.5 m deep. Sand with median diameter 0.2 mm was used for bed material. In both flumes, sand was placed to form an initial beach profile of uniform slope. The conditions of the experiments performed are summarized in Table 1 together with the conditions of Shibayama and Horikawa (1982).

In order to investigate the water particle movement, polystyrene of diameter 1 mm or 2 mm and specific gravity 1.02 were injected into the water. The motion of sand particles and polystyrene particles in the vicinity of the breaking point was recorded using a 16 mm movie camera. By analyzing the film, the motion of sand particles and the characteristics of the large vortex could be examined.

From the observation, the effect of large vortex itself to sediment suspension, not the small scale turbulence, was found to be the main mechanism to cause the sand suspension at the wave plunging area. Fig. 2 shows the critical values of the bottom slope and deep water wave

Table 1: Experimental Conditions.

Case	Wave Period T(s)	Deep Water Wave Height H_0 (cm)	Deep Water Wave Steepness H_0/L_0	Initial Slope i_0
(a) Present Work				
A-1	0.65	5.33	0.081	0.05
A-2	0.73	5.22	0.063	0.05
A-3	0.80	4.81	0.048	0.05
A-4	0.60	5.35	0.095	0.067
A-5	0.61	5.37	0.093	0.067
A-6	0.65	5.33	0.081	0.067
A-7	0.71	5.19	0.066	0.067
A-8	0.82	4.82	0.046	0.067
A-9	0.60	5.35	0.095	0.1
A-10	0.61	5.12	0.088	0.1
B-1	3.00	4.50	0.0032	0.05
(b) Shibayama and Horikawa (1982)				
A-11	1.62	3.0	0.0073	0.05
A-12	1.42	3.4	0.011	0.05
A-13	1.24	3.8	0.016	0.05
A-14	1.00	2.8	0.018	0.05
A-15	1.00	4.4	0.028	0.05
A-16	0.87	4.0	0.034	0.05
A-17	0.78	6.6	0.069	0.05
A-18	0.67	7.6	0.11	0.05
B-2	1.52	8.7	0.024	0.1
B-3	1.51	10.9	0.031	0.1
B-4	1.50	12.5	0.036	0.1
B-5	1.50	15.7	0.045	0.1

steepness for the creation of a large vortex due to wave plunging. The result of Sawaragi and Iwata (1974) are also shown in the figure. The solid line in the figure defines the boundary between the large vortex and no-large vortex region. The dashed line in the figure shows values of the similarity parameter, I_r, (Battjes, 1975) defining the transition between spilling and plunging breakers, given by $I_r = i_0/(H_0/L_0)^{1/2} = 0.5$ (dashed line in the figure) where i_0 is the initial bottom slope and H_0/L_0 is the deep water wave steepness. As seen from the figure, the two boundaries are different. The customary definition of wave breaking type was based on surface profile appearance at the point of breaking. However from the view point of sediment suspension, it is more important whether a breaking wave produces a large vortex or not. The solid line is more important than the dashed line for describing sand movement in the wave breaking area.

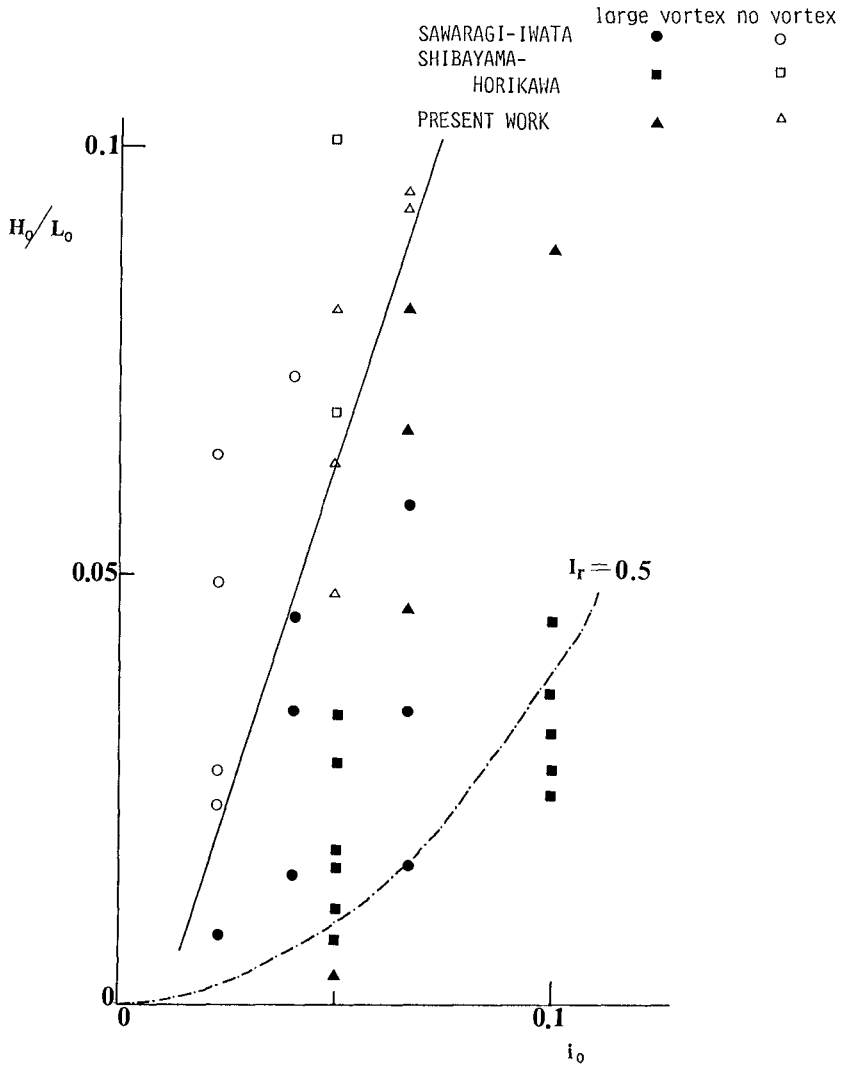

Figure 2: Conditions for Creation of Large Vortex.

From the figure, the necessary wave condition for producing sand suspension due to the mechanism described in the present paper can be determined. This condition is necessary but not sufficient to produce suspended sand. For sand suspension, another condition is required: sand particles must be small, or light enough to be moved or suspended by the velocity field created by the large vortex. However, this condition has not yet been described in a quantitative manner.

3. SAND MOVEMENT AND CONCENTRATION DISTRIBUTION

In experiment B-1, a 35-mm camera utilizing a shutter speed of 1/30 s was used and sand particle pathlines were obtained by tracing the film. The reason why we chose this condition was to minimize the effect of air bubbles. If the wave period is long, air bubbles created by wave plunging go up to the surface in early wave phase, and therefore we can measure sand concentration without the effect of air bubbles thereafter. Figures 3 (a-1) to (a-6) show the experimental results. In this figure, the formation process of the suspended sand cloud can be seen. The arrows indicate the velocity vector of the sand particle movement, the dotted region denotes the cross-sectional area of sand cloud, with one dot representing one sand particles in the photographs.

The sand movement process can be described as follows: (a) Immediately after the wave crest passes the inspection section in the flume, the large vortex created by wave plunging touches bottom. Sand particles on the bottom start into suspension due to the arrival of the vortex (Phase a-1); (b) The suspended sand cloud increases in size and a high concentration area is formed (Phase a-2); (c) Suspended sand particles diverge and some of them are deposited on the bottom (Phase a-3); (d) Suspended sand grains move offshore and some particles are deposited on the bottom (Phases a-4 and a-5); and (e) The next wave crest arrives and a portion of the previously suspended sand particles move onshore (Phase a-6). Figure 3—(A) shows the time history of water surface elevation measured at Point x (observation point indicated in Fig. 3, a-1). The numbers in Fig. (A) indicate the wave phase at the time of each measurement.

Figure 3(b-1) to (b-6) shows the time series of the sand concentration distribution for the the same experimental run. The sand concentration was measured with a Iowa type concentration meter (Nakato et al.,1977), which optically measures the concentration. The probe consists of a 6 mm diameter emitter and detector, separated by a distance of 10 mm. The concentration was obtained at 71 points in the wave breaking area and the equi-phase-mean value over 15 waves were obtained. The equi-phase-mean value should be used because the suspension process fluctuates somewhat from one wave period to the next. In order to calculate equi-phase-mean value of the concentration, each

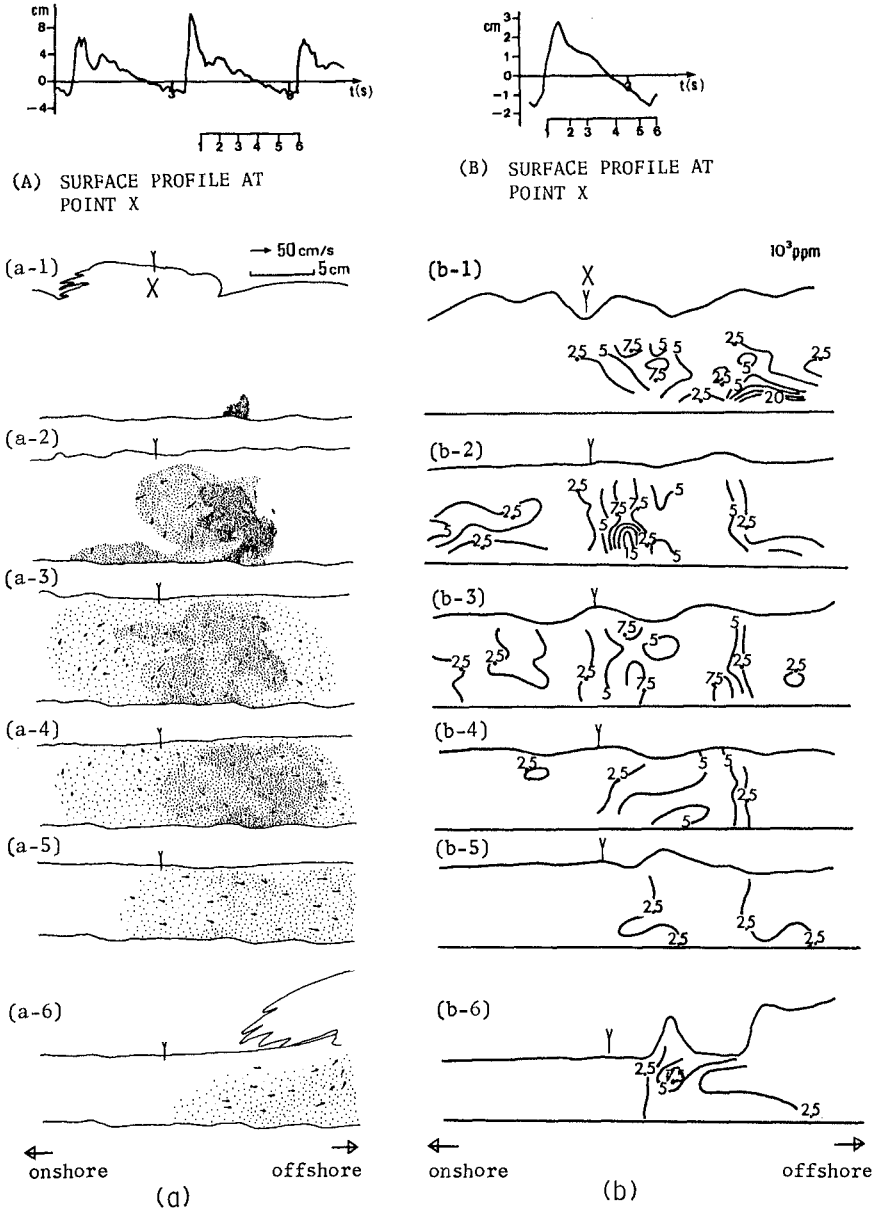

Figure 3: Suspended Sand Movement and Corresponding Sand Concentration.

wave period was divided into 90 intervals. The equi-phase-mean values was obtained by averaging the concentration over 15 waves for each phase. For the wave phase i,

$$\bar{c}(\theta_i) = \frac{1}{N}\sum_{n=1}^{N} c_n\ (\theta_i) \qquad (1)$$

where $\bar{c}$:equi-phase-mean concentration, i:wave phase, $\theta_i = 2\pi i/90$, $i=1,\cdots 90$, n:number of the wave, $n=1,\cdots 15$. From this figure, we can see a high concentration area which corresponds to the location of the suspended sand cloud. The equi-phase-mean value of the water surface are also displayed.

It should be mentioned that the laboratory results discussed here are limited to the case of regular waves traveling onto a beach of initial constant slope. Although the experiment was started with a constant sloping beach, a bottom trough formed due to the action of the plunging waves and the water depth at the wave plunging point became greater as time went on. The result was that the agitation of the bottom material due to wave breaking diminished as time went on. For the present experiments, the initial beach profile was set to form a uniformly sloping beach. Each experiment was allowed to proceed until the bottom becomes somewhat deformed, i.e., less than 100 waves for the present case, then the experiment was stopped and the bottom was smoothed to a uniform slope again. Thus the interaction between the profile change and wave transformation is believed to be negligibly small.

The gradient of wave pressure in the horizontal direction (cross-shore distance) in the breaking area might be considered to play a role in sand movement. Madsen (1974) analyzed this effect and concluded that the pressure gradient alone may affect bed stability but is not great enough to remove sand particles from the bed. Therefore, the pressure gradient appears to be only a secondary factor to control the amount of sand set in motion during the sand suspension process.

4. A SIMULATION MODEL

In order to formulate a simulation model of the sand movement, the following two processes should be evaluated. The first one is the sand suspension process due to a large vortex and the second one is the process of sand transport in turbulent motion. We first consider suspension rate due to a large vortex.

(1) A model for sand suspension rate

The total amount of suspended sand in the sand cloud can be calculated for each phase by integrating the concentration for the area of the sand cloud. Figure 4 shows the result indicating sand mass per one centi-meter width for the same experimental run with Figure 3. In the figure, surface profile history is also indicated. From the figure, we can observe that the total amount of suspended sand rapidly increases after passage of the wave crest and subsequently decreases gradually as part of the sand cloud is deposited on the bottom. If we neglect the rate of sand falling to bed in the sand suspension process, we can estimate the rate of sand suspension from the gradient of sand mass curve. Then a pick up rate is modeled as

$$f(t) = A \sin(2\omega t + \varphi) \qquad (2)$$

where A is the constant, ω is angular frequency and φ is the phase shift. And we will consider the range $f(t) > 0$ and $0 < \omega t + \varphi/2) < \pi$ only. Here the empirical constant A was determined by the previously described sand mass curve of Figure 4 as the gradient of the curve for the first suspension period.

(2) A model for sand movement and velocity measurement in wave breaking region

Next we will consider suspended sand movement in the turbulent field. Here, sand velocity was modeled as the sum of water particle velocity including turbulence and the sediment particle fall velocity. This assumption was called "zero order solution" by Nielsen (1984) and he discussed the validity of the assumption. Then sand movement was simulated by means of the Monte Carlo method. The motions of sand particles were calculated by integrating the velocity of sand particles.

In order to evaluate sand movement, the information of velocity field is required in the wave breaking area. In general, the velocity can be divided into the following three components (Okayasu et al., 1986), which are (1) steady flow, (2) periodic motion (which include wave motion and large vortex), and (3)turbulence. A laboratory experiment was performed by using a wave flume which was 23 m long, 0.8 m wide and a step type beach profile was used. The profile consisted of a 1/10 slope and a flat bed. The reason why we chose this type of beach topography was to fix the breaking point of each wave. Figure 5 shows the beach profile used and the arrangement of measuring points. The measuring area was from 0.5 cm to 14.5 cm above the bottom and 80 cm long in an on-offshore directed vertical plane. The measuring points were arranged to make 2 cm grids. In total, 328 measuring points were set in the test section.

A hot film velocimeter with a split type probe was used to measure

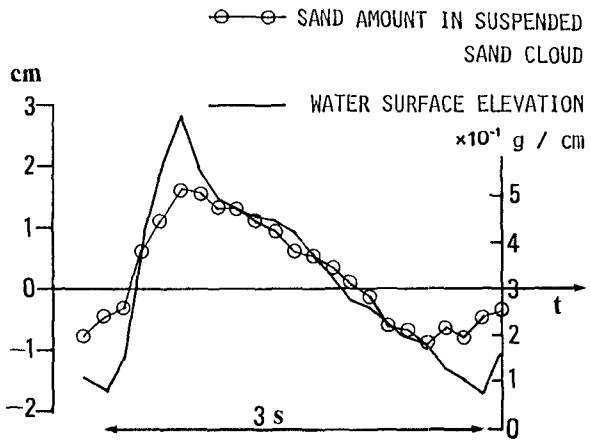

Figure 4: Phase Change of Sand Amount in Suspended Sand Cloud.

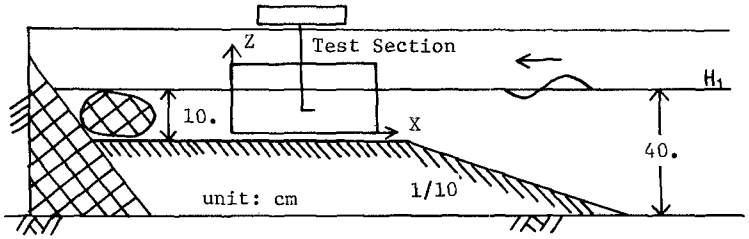

$T = 1.55$ s $H_0/L_0 = 0.020$ $H_1 = 6.95$ cm

Figure 5: Experimental Set-Up and Condition for Velocity Measurement.

the time history of two-dimensional velocity vector. By using the velocimeter, we can obtain two components of velocity data, which are one component of velocity histories with plus or minus sign and an absolute value of the other component. Therefore we cannot get full information about the signs of two components. In the present case, the sign of the on-offshore component velocity was not determined. It was reversed once in every wave period according to the surface profile. The velocity data were sampled every 10 ms and were converted into digital data. The equi-phase-mean values of velocity over 30 periods were calculated. Each wave period was divided into 150 intervals and the equi-phase-mean value was obtained as an average of the velocity value at the same phase of every wave. The turbulence component was determined as the deviation from the equi-phase-mean value.

Figure 6 shows the resultant measured velocity field, which are steady flow, periodic component and turbulent intensity of vertical velocity component at the phase immediately after the wave plunging. The turbulent intensity of horizontal velocity component was also obtained but not illustrated in the figure. From the figure, we can obviously observe a large scale vortex by velocity vectors. The high turbulent region is in good agreement with the vortex region indicated by velocity vectors.

(3) Simulation results

Figure 7 shows an example of simulation result of sand particle distributions. First, sands were suspended from the initial suspension area which is shown in the figure, according to the time history of pick-up function. The initial suspension area was supposed to locate 4 cm above the bottom for the present case. Sands diverged according to velocity field which include turbulence. Here, the velocity characteristics such as the steady flow, the equi-phase-mean velocity and the turbulent intensities between the grid points were determined by means of linear interpolation between the grid points. Sands formed suspended sand cloud and moved to offshore. Sands which fell down to the level of 2.5 cm above the bottom were considered to fall on the bed and they are not indicated in the figure. Figure 8 shows example of sand particle pathlines. Here also we can identify the location of suspended sand cloud area. The sand particle pathlines exhibit the same tendency to the laboratory phenomena which is the formation and the movement of suspended sand cloud under the function of the organized motion in turbulence.

The present model is elementary one and was done as the first trial. It can be concluded that the present model is promising for the future development. For further improvements, precise modeling of pick up rate and velocity field is required.

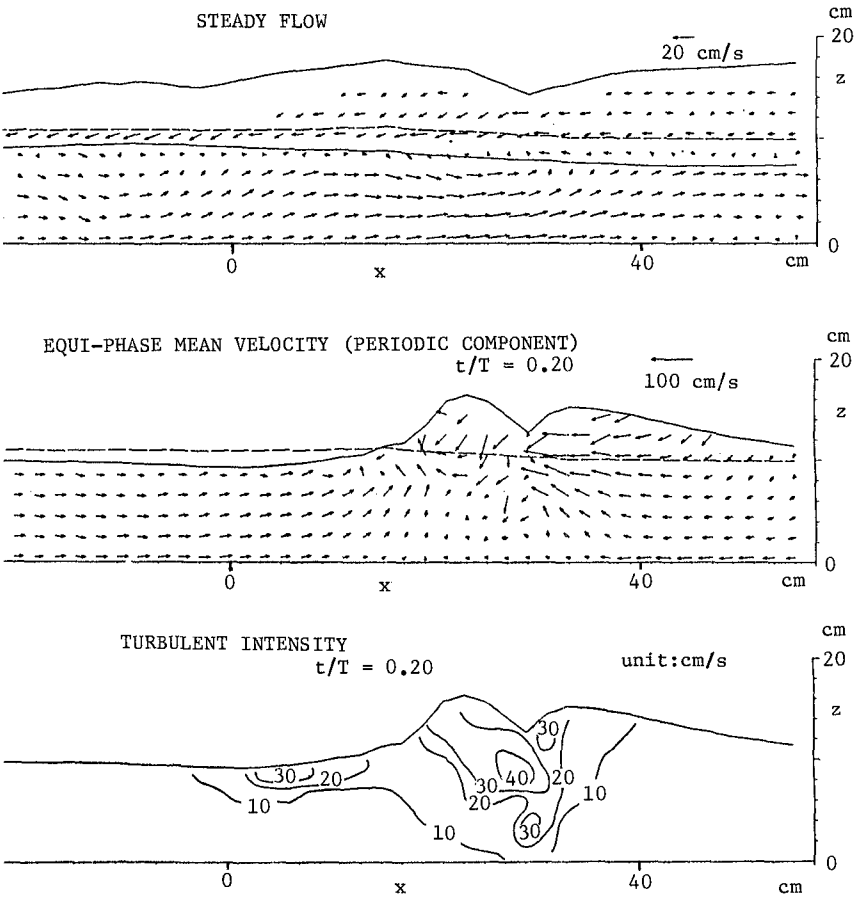

Figure 6: Measured Velocity Field.

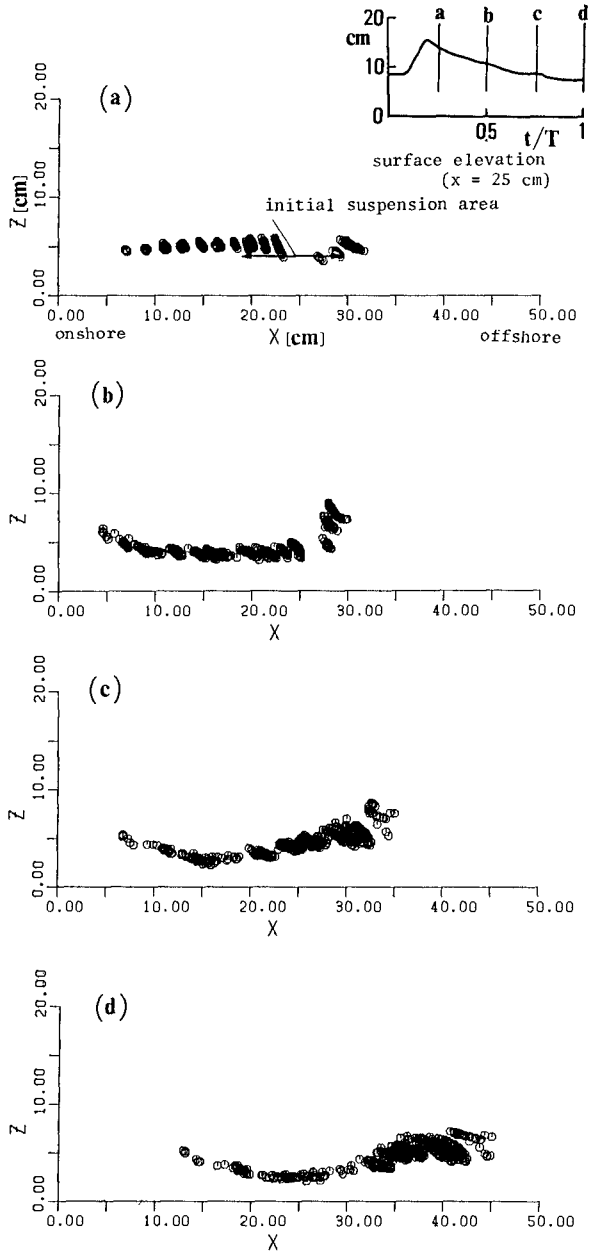

Figure 7: Examples of Sand Particle Distribution.

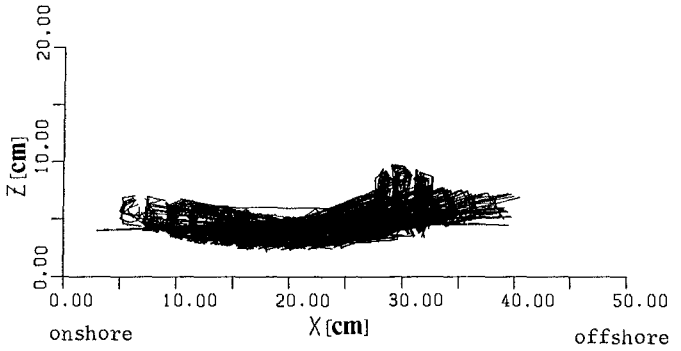

Figure 8: Examples of Sand Particle Pathlines.

The air bubbles have possibility to give an important effect to formation of suspended sand cloud (personal communication with Dr. P. Nielsen). The air bubbles which are created by wave plunging produce upward flow in wave breaking area when they go up to the water surface after the large scale vortex disappears. The upward flow produced by the bubbles transports sand particles upward and therefore diverges sands to upward directions. This effect should be examined more precisely by laboratory experiments as a next step.

5. CONCLUSIONS

The formation of a large vortex induced by plunging waves was found to be one of the necessary conditions for sand suspension caused by breaking waves. The condition for the vortex formation is determined by deep water wave steepness and bottom slope. The movement of suspended sand was divided into two processes; (1) suspension due to the large vortex and (2) sand transport in the turbulent flow. An appropriate modeling of the two processes was performed and simulation results were obtained. The results are not satisfactory but judged to be promising for the further improvement.

ACKNOWLEDGMENTS

The authors thank to Dr. N. Mimura of Ibaraki University, and Mr. A. Okayasu of the University of Tokyo for their co-operations in performing the experiment of Section 4-(2). This study was financially supported by a grant in aid for scientific research, No. 59750405, Ministry of Education, Science and Culture, Japanese Government, which is granted for the first author.

REFERENCES

1. Battjes, J.A., "Surf Similarity," Proc. 14th Coastal Eng. Conf., pp.466-480, 1974.

2. Dean, R.G., "Heuristic Model of Sand Transport in the Surf Zone," Proc. Conf. on Engineering Dynamics in the Surf Zone, pp.208-214, 1973.

3. Madsen, O.S., "Stability of a sand bed under breaking waves," Proc. 14th Coastal Eng. Conf., pp.776-794, 1974.

4. Nakato, T., Locher, F.A., Glover, J.R. and Kennedy, J.F., "Wave Entrainment of Sediment from Rippled Beds," Proc. of ASCE, vol. 103, no. WW1, pp.82-99, 1977.

5. Nielsen, P., "On the Motion of Suspended Sand Particles," J.G.R., vol. 89, no. C1, pp.616-626, 1984.

6. Okayasu, A., Shibayama, T. and Mimura, N., "Velocity Field under Plunging Waves," Proc. 20th Coastal Eng. Conf., 1986.

7. Sawaragi, T. and Iwata, K., "On Wave Deformation after Breaking," Proc. 14th Coastal Eng. Conf., pp.481-499, 1974.

8. Shibayama, T. and Horikawa, K. "Sediment Suspension due to Breaking Waves," Coastal Eng. in Japan, vol. 23, pp. 183-176, 1982.

CHAPTER 112

SHORE PROCESS ALONG THE COAST OF IWO-JIMA

Toshiyuki Shigemura*,M.ASCE

Abstract

Iwo-jima is a small isolated volcanic island located in the Pacific Ocean. Due to the continuous upheaval of the island, foreshore area of this island has been increasing since 1911.

Investigation is made to clarify the variation of the foreshore area of this island by analyzing the various field data obtained during the past three years.

Analyses reveal that the foreshore area is currently increasing at an approximate rate of 180,000 square meters per year due to the unusual upheaval of the island exceeding 45 centimeters per year although seasonal variation of the foreshore area reaches 300,000 square meters.

1. Introduction

Iwo-jima is a small volcanic island located in the Pacific Ocean about 1250 kilometers south of Tokyo (24°45' to 24°49'N, 141°17' to 141°21'E). This island is situated at the southern tip of the Izu-Ogasawara volcanic arc which runs almost parallel to the longitude of 140°E.

Figure 1 shows the present topography of Iwo-jima. To show the beach evolution occurred during the past seven decades, shoreline in 1911 is shown in this figure as a reference. Surface area and shoreline length of this island are currently 23.2 square kilometers and 24.3 kilometers, respectively.

The island is relatively flat with an average of 110 meters except for the area around the Mt. Suribachi. The surface is mostly covered with thick vegetation and there are no rivers on

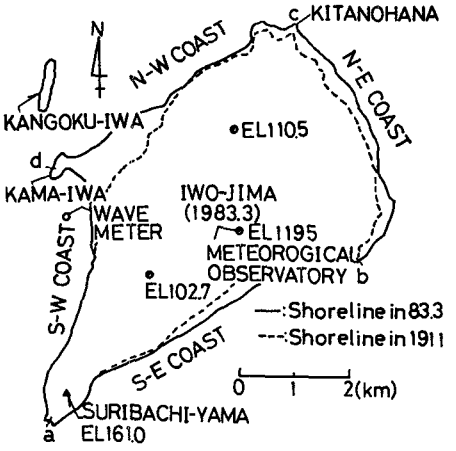

Figure 1. Present topography of Iwo-jima

*Professor, Dept. of Civil Eng., National Defense Academy, 1-10-20 Hashirimizu, Yokosuka, Kanagawa 239, Japan

this island. Thus, few sources of sediments seem to exist in and around the island. However, most of the coast is rimmed by sandy beach, approximately 200 meters wide. Further, quite surprisingly, the shoreline has been advancing seaward year by year since 1911. The author and his colleagues have analyzed old maps, charts and aerial photographs of Iwo-jima, and found that the shore area has increased roughly 3.2 square kilometers during the past seven decades. They also found that this increase was caused by the unusual upheaval of this island, approximately 30 centimeters per year(Shigemura et al, 1984). These are the characteristics of so called a long term variation of the shore area in Iwo-jima. However, the shore area is varying continuously within shorter period, which is important to know from the engineering point of view.

This paper intends to clarify the characteristics of the short term variation of shore area in Iwo-jima by analyzing various field data obtained during the past three years since 1982.

2. Field measurements

To investigate the short term variation of the shore, the following field surveys have been made during the past three years since 1982:

(1) Photographing of the shoreline by a helicopter
(2) Traversing and levelling surveys of the shore
(3) Measuring of the waves by a supersonic wave meter
(4) Collection of wind and tidal data

Details of these field surveys will be described in the following sections.

2-1. Photographing of the shoreline by a helicopter

To get the data of the shoreline variation, aerial photographs of entire shoreline have been taken since November 1982, using a helicopter of JMSDF (Japan Maritime Self Defense Force) stationed there. By the end of September 1985, 19 sets of photographs were taken in total, which were taken at an altitude of 2000 meters except for one set of photographs.

2-2. Traversing and levelling of the shore

To get the data of upheaval and variation of the foreshore area of the island, traversing and levelling surveys have been done on the entire shore of the island since August 1982. These surveys were made at least twice a year, using the 53 measuring points located on the backshore at intervals of roughly 300 meters (figure 2).

2-3. Measurement of the waves by a supersonic wave meter

Wave data has been measured since May 1982 by a supersonic wave meter installed about 450 meters off the west coast

of Iwo-jima at a depth of 12 meters (see figure 1). These data were recorded for 10 minutes every two hours until November 7, 1983 when the typhoon #17 washed the meter away. Thus, waves were measured for 19 months.

2-4. Collection of wind and tidal data

Both wind and tidal data were not measured in each of the field surveys since meteorological data has been measured at the central part of this island since 1968 by JMSDF and tidal data has been recorded at the foot of the Mt. Suribachi since December 1980 by the Japan National Research Center for Disaster Prevention (JNRCDP). These wind data will be used to produce the seasonal wind diagrams covering the period of the field surveys.

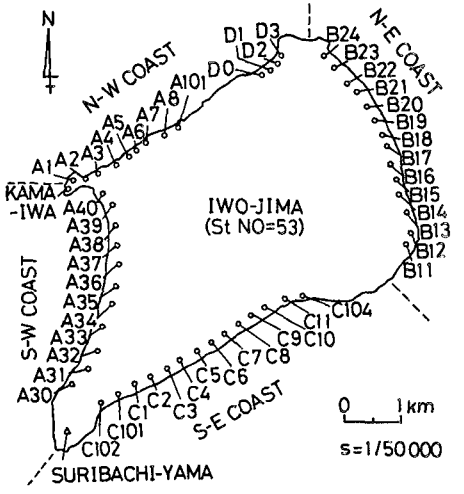

Figure 2. Mesuring points on the backshore of Iwo-jima

Further, the tidal data will be used to refer the elevation of bench mark placed at the foot of the Mt.Suribachi for the levelling survey.

3. Analyses of field data

3-1. Variation of the surface area of Iwo-jima

As mentioned previously, 19 sets of aerial photographs have been taken by a helicoter during the past three years. Table 1 summarizies the details of the photographing.

Unfortunately, most of these photographs were taken with some inclination. Thus, the following procedures were taken to determine the shorelines in each photographed date from these photographs:

(1) Each set of the film was processed into a series of slides.

(2) Five reference maps with a scale of 1/4000 were reproduced from the aerial photographs taken in March 10, 1983 (figure 3).

(3) Each of the reference maps was placed on a special table designed so that it may rotate around three axes, and slides were projected onto it.

(4) After rotating the table until several points on the map fitted with the corresponding points on the projected slide, the shoreline was drawn successively on the reference map.

Table 1. Details of the photographing of the shoreline

No.	Data	Time	Altitude	Tide	Remarks
1	Nov.25,'82	13:35-14:35	2000 m	84.0 cm	inclined photos
2	Feb.16,'83	13:40-14:40	2000 m	42.0 cm	inclined photos
3	Mar.10,'83	10:00-11:00	6000 m	62.0 cm	vertical photos
4	Apr.08,'83	10:25-11:25	2000 m	59.0 cm	inclined photos
5	Jun.07,'83	10:00-11:00	2000 m	40.0 cm	inclined photos
6	Aug.01,'83	09:10-10:10	2000 m	66.0 cm	inclined photos
7	Oct.01,'83	10:00-11:00	2000 m	50.0 cm	inclined photos
8	Dec.14,'83	09:00-10:00	2000 m	54.0 cm	inclined photos
9	Feb.14,'84	09:00-10:00	2000 m	72.0 cm	inclined photos
10	May 16,'84	13:30-14:30	2000 m	06.0 cm	inclined photos
11	Jun.12,'84	11:00-12:00	2000 m	16.0 cm	inclined photos
12	Jul.11,'84	11:00-12:00	2000 m	20.0 cm	inclined photos
13	Sep.05,'84	09:15-10:15	2000 m	40.0 cm	inclined photos
14	Oct.07,'84	15:30-16:30	2000 m	70.0 cm	inclined photos
15	Nov.16,'84	09:30-10:30	2000 m	56.0 cm	inclined photos
16	Mar.01,'85	09:00-10:00	2000 m	75.0 cm	inclined photos
17	May 27,'85	09:00-10:00	2000 m	76.0 cm	inclined photos
18	Jul.12,'85	09:00-10:00	2000 m	46.0 cm	inclined photos
19	Sep.04,'85	14:30-15:30	2000 m	48.0 cm	inclined photos

Shorelines determined in this way, were processed by a special AD convertor and the position of each shoreline was digitalized every 2 millimeters or 8 meters on the actual spot. Based on this data, the surface area of the island on each photographed date was calculated.

Figure 4 shows the variation of the surface area of Iwo-jima during the past three years.

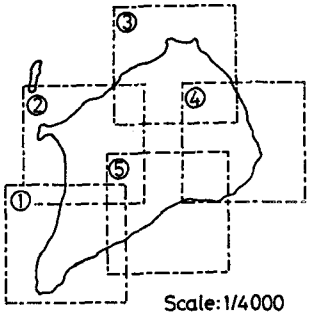

Figure 3. Reference map of Iwo-jima

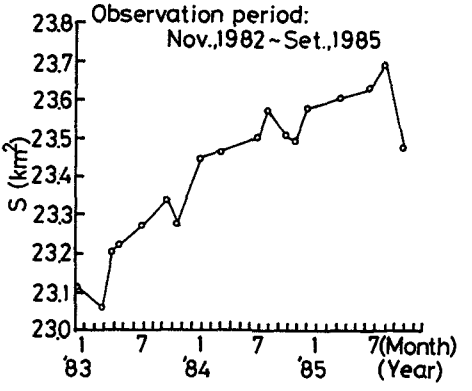

Figure 4. Variation of the surface area of Iwo-jima

Figure 5 shows the current variation of the surface area together with the one occurred before 1982(Shigemura et al, 1984).

From figure 4 and 5, the folloing facts can be seen:
(1) The surface area of Iwo-jima has kept increasing since 1911, although the increasing rate is not constant but varies with time.
(2) Surface area began to increase drastcally in 1952 and kept increasing until 1968 at an approximate rate of 140,000 square meters per year. By the end of 1981, the surface area increased roughly 3.2 square kilometers as compared with the surface area in 1911.
(3) Surfce area is currently increasing at an approximate rate of 180,000 square meters although there is a considerable variation in its magnitude.

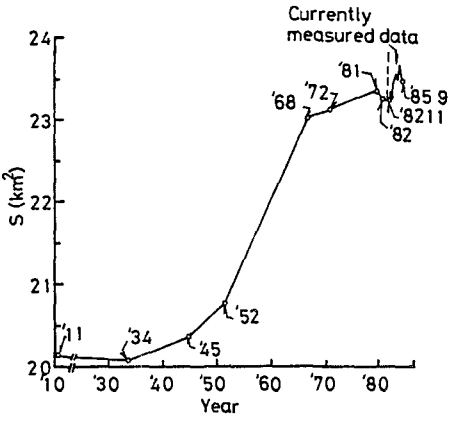

Figure 5. Variation of the surface area of Iwo-jima since 1911

3-2. Upheaval of Iwo-jima

Since August 1982, both traversing and levelling surveys have been made six times along the entire bachshore of the island. Table 2 summarizes the periods in which the surveys have been made.

Table 2. Periods in which surveying has been made

No.	Period
1	Jul.23,'82 to Aug.09,'82
2	Jun.08,'83 to Jun.28,'83
3	Feb.09,'84 to Feb.20,'84
4	Nov.16,'84 to Dec.05,'84
5	Mar.09,'85 to Mar.28,'85
6	May 14,'85 to May 31,'85

All of these surveys have been made with the aid of the 101 Topographic Battalion of the Japan Ground Self Defense Force (JGSDF).

Figure 6 shows the variation of the relative upheaval height, ΔH of each measuring point shown in figure 2, which was determined on the basis of its elevation measured in the first survey (August,1982).

Figure 7 shows the cumulative upheaval height of the backshore of Iwo-jima in the same period which was determined by simply averaging the elevations of the 53 measuring points shown in figure 2. Further, figure 8 shows the cumulative upheaval height of Iwo-jima presented by Kosaka and

his colleagues(Kosaka et al,1979). They determined the upheaval height by comparing the elevations of several points shown in old maps and charts and by analyzing their own data of levelling which was performed four times during the period between 1968 and 1978.

From figure 6, 7 and 8, the following facts can be observed:

(1) Upheaval of Iwo-jima is not uniform along the coast but varies considerably in both time and location.

(2) Iwo-jima upheaved drastically during the period between February 1984 and November 1984 at the rate exceeding 1 meter per year.

(3) Iwo-jima is currently upheaving at an approximate rate of 45 centimeters per year, which is greater than that observed during the period between 1952 and 1968.

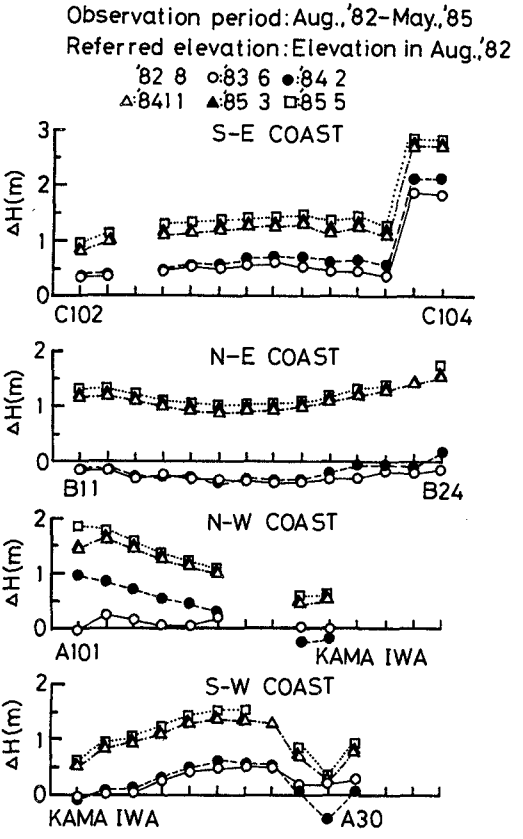

Figure 6. Variation of the relative upheaval height, Δ H of each mesuring point

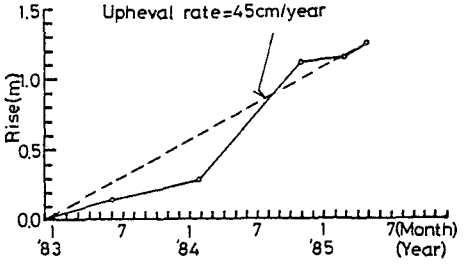

Figure 7. Cumulative upheaval height of Iwo-jima

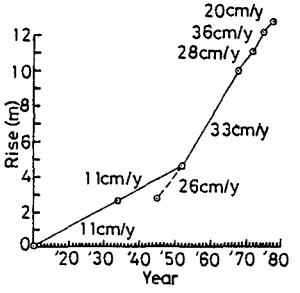

Figure 8. Cumulative upheaval height (After Kosaka et al, 1979)

3-3. Wave characteristics in Iwo-jima

As mentioned in section 2-3, waves were recorded for 19 months after May, 1982. These records were processed at a sampling interval of 0.5 second by an A-D convertor, and wave height and period were determined by applying the zero up crossing method on these processed data.

Table 3 summariges the seasonal distribution rate of significant waves whose height and period are in the given ranges of their magnitudes.

Table 3. Seasonal distribution rate of the significant waves in Iwo-jima

Season	H 1/3(m) 0-1	1-2	2-3	<3	T 1/3(s) <6	6-8	8-10	<10
Spring	62	36	1	1	29	51	16	4
Summer	70	20	4	6	21	42	21	16
Fall	73	14	7	6	8	43	27	22
Winter	59	35	6	0	31	49	16	4

Table 4 summarizes the maximum height and the significant period of the waves recorded while the typhoons were hitting Iwo-jima.

Table 4. Values of H max and T 1/3 of the waves recorded while typhoons were hitting Iwo-jima

No.	Date	Time	Hmax	T 1/3	Pres.	Location	V	θ
#4	May 23,'82	0200	8.4m	18.5s	980mb	NNW 150km	27.5m/s	ENE
#5	Jun.26,'82	1000	5.4m	11.1s	975mb	NW 250km	32.5m/s	N
#10	Jul.31,'82	0800	9.2m	19.0s	940mb	WNW 350km	50.0m/s	NNW
#13	Aug.24,'82	2100	lack of data		940mb	W 850km	45.0m/s	NNW
#15	Aug.30,'82	0900	lack of data		945mb	W 300km	45.0m/s	NW
#18	Sep.11,'82	1000	5.3m	12.0s	965mb	WNW 600km	35.0m/s	NW
#19	Sep.19,'82	0000	5.2m	8.3s	940mb	WSW1400km	45.0m/s	WNW
#21	Oct. 7,'82	1600	9.8m	11.5s	920mb	WSW 600km	50.0m/s	NNW
#5	Aug.13,'83	0600	9.8m	13.3s	915mb	WSW1040km	55.5m/s	NNE
#13	Oct.11,'83	1000	2.5m	10.1s	980mb	NNW1050km	25.3m/s	ENE
#17	Nov. 2,'83	0200	lack of data		985mb	NNE1030km	30.0m/s	NNW

In this table, figures in the column of No. indicate the names of tyhoons, and the information in the column of location indicates direction and distance to the center of a typhoon from the island. Further, does the letters in column of θ indicates the advancing direction of each typhoon.

From these tables, the following facts can be seen:

(1) Dominant waves in Iwo-jima are those whose significant heights are less than 1 meter and whose significant periods are less than 8 seconds through the year.

(2) High waves whose significant height is greater than 3.0 meters and whose significant period is greater than 10 seconds appear in summer and fall.

(3) Huge swell whose maximum height is roughly 10 meters and whose significant period is greater than 12 seconds will hit Iwo-jima when a typhoon with a central pressure less than 940 millibars pass within a region of 600km far from Iwo-jima.

Huge swells of this size usually hit Iwo-jima several times per year. Characteristics of these waves were also reported at the 19th ICCE(Shigemura et al, 1984)

3-4. Wind characteristics in Iwo-jima

As mentioned in section 2-4, JMSDF has been recording the wind data every three hours, since 1968.

By analyzing the wind data recorded in 1983, 84 and 85, seasonal wind diagrams were produced.

Figure 9 shows the seasonal wind diagrams. From this figure, the following wind characteristics can be observed:

(1) East winds are dominant in spring, summer and fall. South winds are the secondarily dominant in spring and summer.

(2) N-E winds are dominant in fall and winds ranging from NE to N are dominant in winter.

(3) Approximately 3% of the total winds analyzed are the high winds whose veloities exceed 10 meters per second. These winds blow from the direction ranging from SE to SSE in summer although they blow from the direction ranging from NNW to NE in fall and winter.

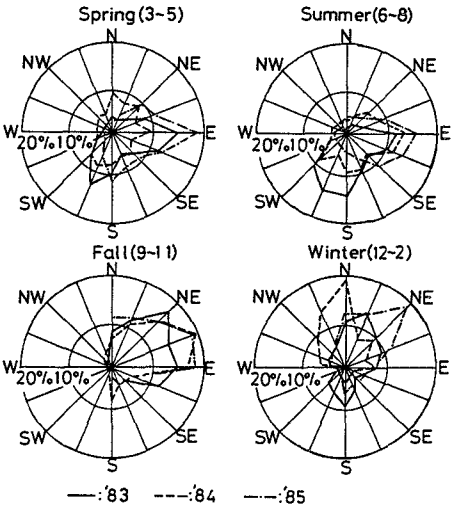

Figure 9. Seasonal wind diagrams in Iwo-jima

These results agreed well with the ones obtained by analyzing the wind data recorded in Iwo-jima during the period between 1968 and 1977(Shigemura et al,1984).

4. Variation of the foreshore area in Iwo-jima

Through the primary analyses, it was found that Iwo-jima was currently increasing its surface area at a rate greater than that occurred before 1982. Further, it was proved that this increase was surely caused by an unusual upheaval of this island.

To see the variation of the surface area more clearly, relative values of the surface area on each photographed date was determined on the basis of the surfase area on March 10, 1983. These values will be called ΔS in the following discussion. ΔS may indicate the increase of the foreshore area if the increase of the surface area is caused

by a continuous upheaval of the island.

Regression analysis was made on the data of ΔS over time. Figure 10 shows the variation of ΔS during the past three years. In this figure, the straight line indicates the regression line of ΔS over time and the symbol of square indicates a deviation of ΔS from its corresponding value predicted by the regression line, which will be referred to as dS in the following discussion. Further, the symbol of black circle shows the relative upheaval height, ΔH.

Regression analysis revealed that the foreshore area was currently increasing at an approximate rate of 180,000 square meters per year although dS scatters considerably along the regression line.

Suppose the increasing rate of 180,000 square meters per year was brought by the current upheaval of the island, dS may indicate the variation of the foreshore area caused by the other factors besides upheaval, namely waves and currents. It is difficult to find a definite trend in the variation pattern of dS. However, the following facts can be observed from this figure:

(1) dS tends to increase from spring to summer and from fall to winter, but to decrease from summer to fall and from winter to spring, respectively.

(2) The range of the variation of dS is approximately 250,000 square meters per year at most.

These findings are the characteristics of the short term or the seasonal variation at least, of the entire foreshore area of Iwo-jima.

Analysis was further proceeded to examine the local effect on the short term variation of dS. To see the local effect, the coast was divided into four sections as shown in figure 11. These sections were designated S-E coast, N-E coast, N-W coast and S-W coast, respectively.

Similar analysis was made on the data of ΔS in each section. Figure 12 shows the analytical results. In this figure, straight lines indicate the regression lines of ΔS over the time in each coast. Further, the symbol of square indicates the relative upheaval height, ΔH and the symbol of white circle represents ΔS. This figure clearly shows that there is a certain analogy among the variation

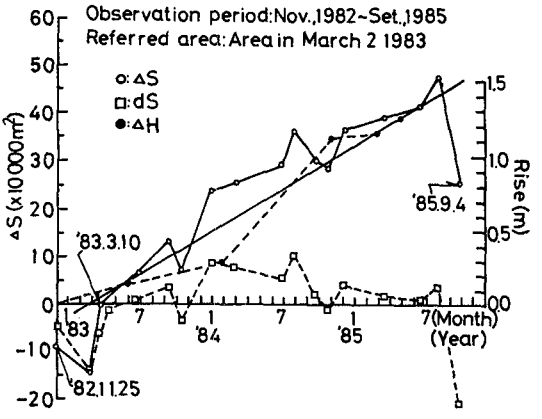

Figure 10. Variation of relative surface area, ΔS in each coast

patterns of ΔS in each coast.

To see this more precisely, variation of dS was checked similarly. Figure 13 shows the short term variation of dS in each coast. From this figure, the following facts were observed:

(1) Variation of dS is generally much greater in both the S-E and N-W coasts compared with that in both the N-E and S-W coasts. Namely, that reaches approximately 300,000 square meters in the former coasts during the period from spring to fall. However, that is usually 150,000 square meters at most in the latter coasts throughout the year.

(2) dS in both the S-E and S-W coasts shows quite similar and rhythmical patterns seasonally. dS in both the N-E and N-W coasts also shows quite similar variation patterns. However, these patterns are not as rhythmical seasonally as they are in the S-E and S-W coasts.

(3) There exist a certain phase lag between the variation patterns of dS in the S-E coast and that in the S-W coast. Similar phase lag is found between the variation patterns of dS in the N-E coast and that in the N-W coast, too.

(4) Variation pattern of dS in the S-E coast is almost opposite to that in the N-W coast.

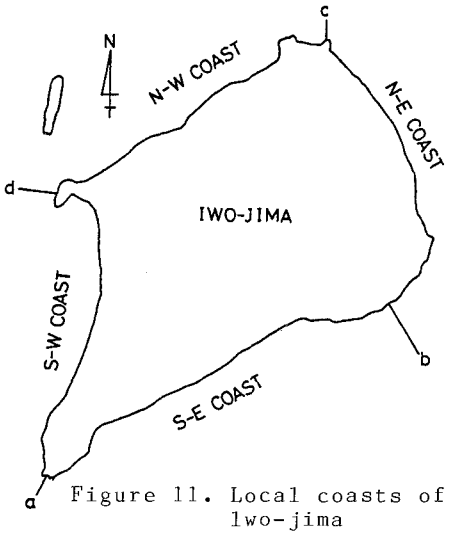

Figure 11. Local coasts of Iwo-jima

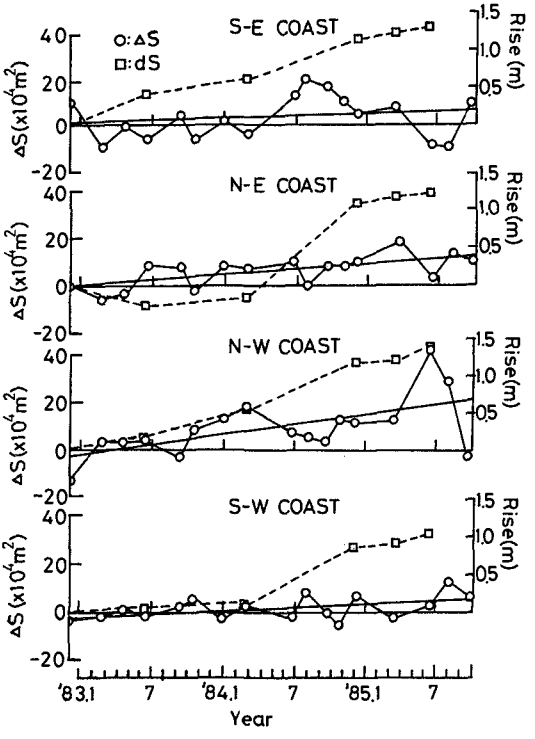

Figure 12. Variation of ΔS in each coast of Iwo-jima

Similarly, variation pattern in the N-E coast is almost opposite to that in the S-E coast.

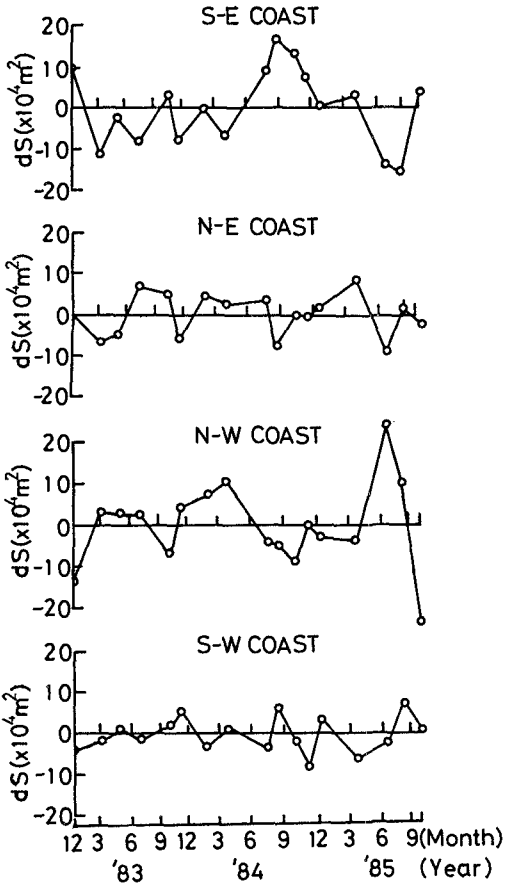

Figure 13. Variation of dS in each coast of Iwo-jima

5. Conclusions

Variation of the foreshore area in Iwo-jima was investigated by analyzing the 19 aerial photographs of the shoreline, land surveying data and wind and wave data which were all obtained through the field surveys performed during the past three years.

As a result, it was found that the foreshore area was currently increasing at an approximate rate of 180,000 square meters per year as a whole, due to the continuous

upheaval of the island exceeding 45 centimeters per year. Further, it was found that two different patterns appeared locally in the variation of the foreshore area and that in S-E and N-W coasts, variation of the foreshore area reached 300,000 square meters seasonally.

Acknowledgement

The author is indebted greatly to the 4th Aviation Group of JMSDF and to the 101 Topographic Battalion of JGSDF for their devoted aids and cooperation which were given in various stages of the field surveys.

References

Kosaka, J. et al(1979). Investigation report of the volcanic action in Ogasawara-Iwo-jima. Santama Office for isolated islands, Tokyo Metropolitan Government, No.3, pp.1-89.

Shigemura, T et al(1984). Formation of tombolo at the west coast of Iwo-jima. Proc. of the 19th ICCE, Chapter 96, pp.1403-1419.

CHAPTER 113

REDUCTION PROCESS OF CROSS-SECTIONAL AREA AT RIVER MOUTH

Takuzo Shimizu*, Kosuke Kondo** and Ryoichi Kajima***

ABSTRACT

Reduction processes of the cross-sectional area at a river mouth were investigated on the basis of numerical simulations and field measurements, in order to predict the possibility of closing of the mouth of the Samegawa River, Fukushima, Japan. As a result, it was found that the decrease in tidal prism, induced by a reduction of the cross-sectional area, had an important effect on the closing of the river mouth. By considering this effect and estimating the sediment transport rate properly, a practical prediction model was successfully established for simulating the reduction processes of the cross-sectional area at the river mouth.

1. INTRODUCTION

A jetty was constructed on the northeastern side at the mouth of the Samegawa River, Fukushima, Japan, in order to prevent increased heated water from the Nakoso Thermal Power Station from affecting the river's fishery. After the jetty construction, the heated water is separately and directly discharged into the Pacific Ocean through an open channel excavated about 500 m northeast of the river mouth through the sand spit which extends along the shore in front of the power station (Figure 1).

One of the most important influences of the jetty construction is the reduction of the cross-sectional area at the river mouth, induced by the decreased discharge passing through it. However, since many factors, such as waves, nearshore currents, tidal flows, inherent river flows, and heated water discharge are involved in complicated sediment transport around the river mouth, beach changes or closing processes near the river mouth are not yet completely predictable.

This study aims to elucidate the mechanism of the interaction between hydraulic factors, especially tidal change and topographical changes at the river mouth, and to establish a prediction model of the reduction processes of the cross-sectional area.

* Engineer, Design and Engineering Department, Penta-Ocean Construction Co., Ltd., 2-2-8 Koraku, Bunkyo-ku, Tokyo 112, Japan.
** Principal Engineer, Design and Engineering Department, Penta-Ocean Construction Co., Ltd., 2-2-8 Koraku, Bunkyo-ku, Tokyo 112, Japan.
*** Chief Engineer, Central Research Institute of Electric Power Industry, 1646 Abiko, Abiko City, Chiba 270-11, Japan.

2. OUTLINE OF FIELD INVESTIGATION

2.1 Study Area

Field investigations were carried out around the mouth of the Samegawa River, located on the Pacific coast in the southern part of Fukushima Prefecture (Figure 1). The sandy beach stretches from southwest to northeast in front of the river mouth. A rocky shoal exists only near the Ryugu Headland at the northeast end of the shore. The bottom contours are parallel to the shoreline and the bottom slope is as gentle as 1/70. The Samegawa River is a small and rapid river having a catchment area of 600.9 km^2 and an average bottom slope of 1/50 to 1/70. The river surface area influenced by tides was about 73,400 m^2 before the jetty construction and now is about 53,600 m^2.

According to the wave climate data observed by the Ministry of Transport over a five-year period from 1981 to 1985 off the Onahama Harbour, about 9 km northeast of the study area, the mean significant wave height is 1.0 m, the mean significant wave period is 8.1 s, and the occurrence frequency of wave heights beyond 2.0 m is less than 6 %. Wave directions, obtained by visual observations twice daily with a transit from the roof of the Power Station, are limited from ESE to SSE. The dominant direction is SE, normal to the shore, and its frequency reaches about 81 %.

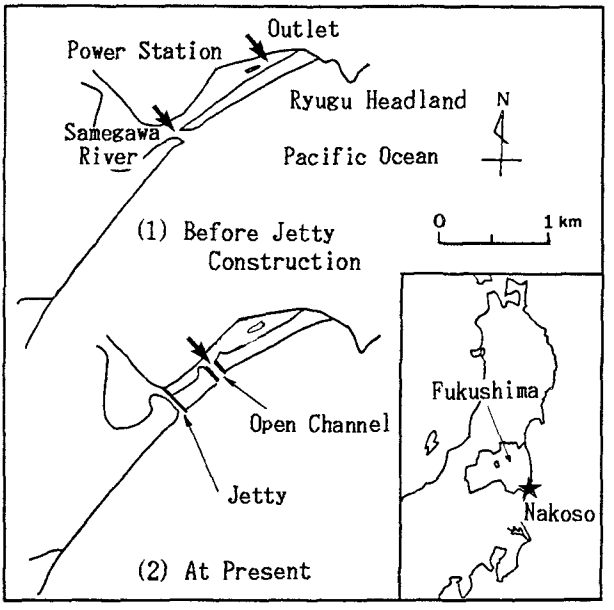

Figure 1 Study Area Location Map.

2.2 Field Investigation Program

The jetty construction was undertaken in August 1982 and completed in May 1985. Field investigations were carried out over a period of approximately five years, beginning in October 1980. The field investigation program consisted of:

(1) coastal topography surveys (about 4 times/year),
(2) cross-sectional area surveys at the river mouth (about once a month),
(3) 25-hour continuous readings of current and water level, during which water temperature and salinity were measured twice (16 times/5 yeras),
(4) nearshore current observations (occasional), and
(5) fluorescent sand tracer experiments (3 times/5 years).

Topographical changes and hydraulic characteristics were studied mainly using the data obtained in (2) and (3) above.

3. TOPOGRAPHICAL CHANGES AT RIVER MOUTH

3.1 Position of River Mouth

Figure 2 shows aerial photographs of the past and the present around the mouth of the Samegawa River. The position of the mouth before the jetty construction had a tendency to shift toward the northeast. Before the extreme flood event in September 1977, it had been located at the Ryugu Headland about 1.5 km northeast from the present position. This shift of the river mouth location is because the most effective wave energy arrives from the southeast direction, driving the net littoral sediment transport northeastward.

In the fluorescent sand tracer experiments carried out twice on the southeastern shore, most of the tagged grains were found along the shoreline extending from the injection points to the river mouth, although longshore currents were not always directed to the northeast. This is attributed to many complicated influences of the incident wave direction, the tidal elevation, the sea-bed topography, the river discharge and so on. This result suggests that not only the longshore currents but also the sediment transport in the swash zone play important roles in the sand spit extension around the river mouth.

3.2 Change of Cross-sectional Area

Figure 3 shows time histories of the cross-sectional area A from October 1980 to March 1985, together with variations of wave energy flux P, inherent river discharge Qr, and heated water discharge Qp. The solid curves in the corss-sectional area diagram are the results of simulations mentioned later.

It is seen in this figure that the cross-sectional area was forcibly and abruptly enlarged by every extreme flood event. After that it was gradually reduced and finally came to a state of dynamic equilibrium. This kind of variation pattern is common and repeated.

(1) 1980.9.30

(2) 1986.5.27

Figure 2 Aerial Photographs of Study Area.

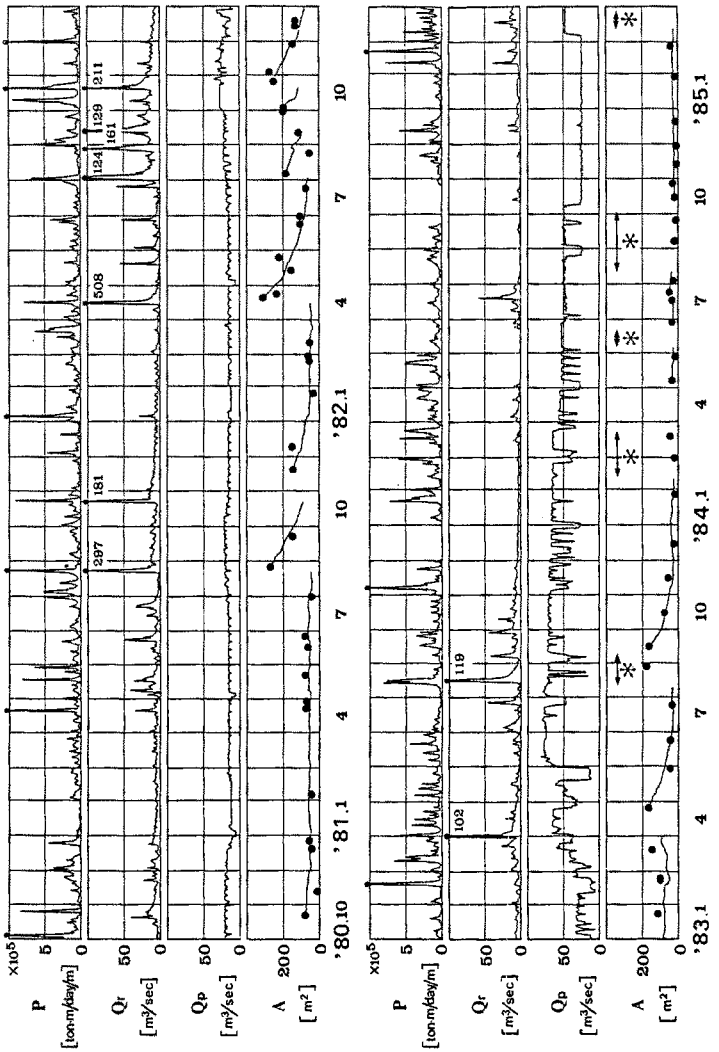

Figure 3 Time Series of Wave Energy Flux P, Inherent River Discharge Qr, Heated Water Discharge Qp and Cross-sectional Area A.
(● : Observation, —— : Calculation, * : Under Dredging)

The equilibrium area was about 50 m^2 before the jetty construction but after then decreased to about 20 m^2 because of the decrease in the total discharge passing through the river mouth caused by the separation of the heated water. Recently, maintenance dredgings have been carried out a few times a year, but not during fishing seasons for sweetfish in spring and salmon in autumn. The cross-sectional area was at the minimum of 11.8 m^2 with a width of 12.7 m in November 1984. This is partly because it was during the salmon fishing season and, importantly, because there were no extreme flood events throughout the year.

Next we investigate shape characteristics of the cross-section. The relationship between the area and the width of the minimum cross-section is close to that of a triangular cross-section rather than that of rectangular one (as Ogawa et al. (1984) has already pointed out). We however assume that the cross-section is rectangular, in order to make easy the use of the relationship between the width and the mean depth in numerical simulations.

The relationships between the cross-sectional area A and the width B or the mean depth h were calculated on the basis of the field surveys by regression analysis. The results are shown as follows:

$$B = 1.83\ A^{0.8} \quad \text{(correlation coefficient 0.91)} \tag{1}$$

$$h = 0.55\ A^{0.2} \quad \text{(correlation coefficient 0.48)} \tag{2}$$

The width shows a fairly good correlation with the area. On the other hand, the mean depth data observed after the jetty construction scatter around the above relationship. This is because the increased river discharge causes scouring adjacent to the jetty instead of enlarging the width.

4. HYDRAULICS AT RIVER MOUTH

4.1 Water Level and Discharge at River Mouth

The water level and the discharge at the river mouth are affected mainly by tidal flows and inherent river flows, aside from the wave set-up. Especially the tidal flow was supposed to be predominant under ordinary conditions but not during extreme flood events. To examine this, sixteen field observations were carried out, in which both the water level and the horizontal velocities were measured for 25 hours running, mainly during spring tide. In this section we report results of the above measurements.

Two or three two-component electro-magnetic current meters were placed about 1 m above the bottom on the minimum cross-section of the river mouth. In order to determine the ratio of the mean velocity at the measurement points to the cross-sectionally averaged velocity, another way of measurement using a propeller-type flowmeter was carried out at about 20 to 30 points spaced on the same cross-section once during flood tide and once during ebb tide. In every case there was no evidence of much spatial asymmetry in the flow, and therefore it can be

considered that data obtained by the electro-magnetic current meters were representative of the cross-sectionally averaged velocities. The water level variations were measured every 30 or 60 minutes by visual observation using poles installed near the electro-magnetic current meter.

Figure 4 shows an example of time series of the water level and the discharge at the river mouth. The highest water level is approximately equal to the coean's high tide level, whereas the lowest does not fall to the ocean's low tide level. Although the ocean tide changes nearly sinusoidally, the water level at the river mouth changes asymmetrically with the ebb period being longer than the flood period.

Figure 5 shows the relationship between the measured high and low water levels at the river mouth and those calculated by the Meteorological Agency at Onahama Harbour. Figure 5 indicates that the above-mentioned tendency becomes apparent when the width of the river mouth is less than approximately 60 m.

Tidal prism is defined, in general, as the gross volume of water entering or exiting an inlet during ebh or flood tides. According to the results of the field observations, it has been confirmed that tidal prism can be estimated by multiplying the difference of water level change at the river mouth by the river surface area under the influence of tides. Therefore, the decrease in tidal range results in a substantial decrease in tidal prism.

Table 1 lists mean annual values of inherent river discharge, heated water discharge, tidal discharge, and total discharge passing through the river mouth. The total discharge was calculated at the sum of the former three. Since the jetty construction in 1983, there has been no heated water discharge through the river. The tidal discharge was estimated by the following method:

(1) The lowest water level at the mouth is estimated by using the two different relations, equation (a) and (b), according to the width beyond or below 60 m as shown in Figure 5.
(2) The tidal prism during a half tidal cycle is calculated by multiplying the difference between the highest and the lowest water levels by the river surface area.
(3) The tidal discharge is then obtained by averaging the tidal prism over the half tidal cycle.

The tidal discharge thus calculated is not strictly true becuase the ebb and flood periods are assumed to be equal, ignoring the actual difference between the two.

The total flow rate passing through the river mouth decreased from a yearly average value of 50 to 60 m^3/s before the jetty construction to about 20 m^3/s after the construction. This is not only because the heated water was separated, but also because the decrease in the river surface area induced the decrease in tidal prism.

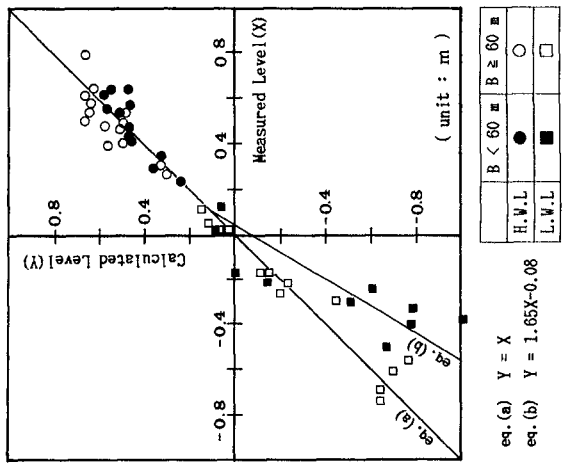

Figure 5 Relationship between Measured High or Low Water Levels and Those Calculated.

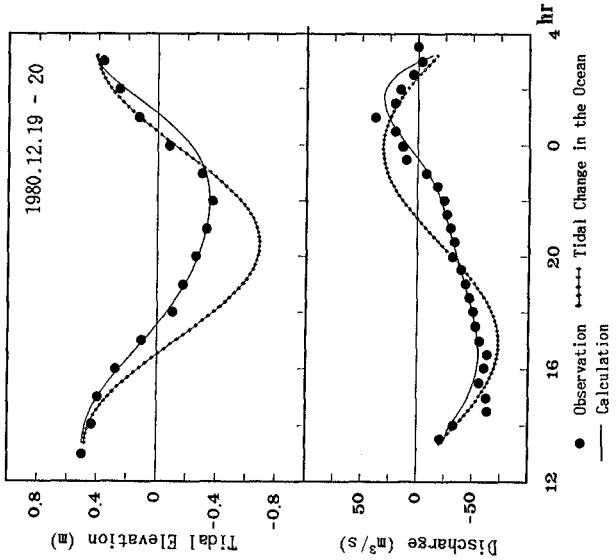

Figure 4 An Example of Time Series of Water Level and Discharge at River Mouth.

Table 1 Mean Annual Values of Inherent River Discharge, Heated Water Discharge, Tidal Discharge and Total Discharge Passing through the River Mouth.

	1980.10 -1981.3	1981.4 -1982.3	1982.4 -1983.3	1983.4 -1984.3	1984.4 -1985.3
Inherent River Discharge	7.6	9.6	15.1	7.2	3.9
Heated Water Discharge	16.0	15.7	21.2	(60.6)*	(37.6)*
Tidal Discharge	25.9	23.3	22.3	16.3	15.4
Total Discharge	49.5	48.6	58.6	23.5	19.3

(unit: m3/s)

* heated water discharge through the new open channel

4.2 Numerical Model

As discussed in the preceeding section 4.1, the water level at the river mouth does not fall as low as the sea water level during ebb tide. As a result the tidal prism decreases so that the width of the river mouth is reduced to less than about 60 m. In the Samegawa River the inherent river discharge is small and the tidal prism shares 70 to 80 % of the total flow rate.

In this section we estimate the decrease in tidal prism by taking into account head losses due to friction and at the entry, exit and bend.

The numerical model developed in this study is essentially similar to that used in the analysis of a sea-inlet-bay system (e.g. see Bruun (1978)). Consider such a model of the river mouth as the tidal-influenced water surface area connected with the sea through a channel with uniform rectangular cross-section. Assuming that the velocity in the channel is constant and that the tidal wavelength is much larger than the channel length, the one-dimensional equation of motion along the channel axis can be expressed as:

$$du/dt + gd\eta/dx + I_f + I_\ell = 0 \tag{3}$$

$$d\eta/dx = (\eta - \eta s)/\ 2\ell \tag{4}$$

$$I_f + I_\ell = g\, n^2 |u|u\ /\ R^{4/3} + fc|u|u\ /\ 2\ell \tag{5}$$

where u is the average velocity (positive into the upstream direction), g is the acceleration of gravity, η is the water level at the river mouth, ηs is the sea water level, ℓ is the channel length, A is the cross-sectional area, I_f is the bottom friction term, I_ℓ is the term of head losses except frictional loss, R is the hydraulic radius, n is Manning's friction coefficient, and fc is the head loss coefficient at the entry, exit and bend.

The continuity equation can be used as expressed in equation (6), assuming that the river water level rises and falls uniformly at any time.

$$A\,u + Qr = S\,d\eta/dt \tag{6}$$

where A is the cross-sectional area, Qr the inherent river discharge, and S the river water surface area taken as independent of the water level. The validity of equation (6) has been verified in the practical sense by field measurements.

Relating equations (4), (5) and (6) to (3) and eliminating the velocity u, the following ordinary differential equation of the second order with respect to η can be obtained.

$$\frac{d^2\eta}{dt^2} + \left\{\left(\frac{fc}{2\ell} - \frac{g\,n^2}{R^{4/3}}\right)\frac{S}{A}\left|\frac{d\eta}{dt} - \frac{Qr}{S}\right| - \frac{B}{A}\frac{d\eta}{dt}\right\}\left(\frac{d\eta}{dt} - \frac{Qr}{S}\right) + \frac{Ag}{S\ell}(\eta - \eta s) = 0 \tag{7}$$

in which the time variation of Qr is assumed to be slow enough to ignore. Equation (7) can easily be solved numerically by using the Runge-Kutta-Gill method. The stationary solution can be obtained by calculating repeatedly for several tidal cycles from certain initial conditions. The initial conditions used in this model are $\eta = \eta s + \Delta\eta$, $d\eta/dt = Qr/A$, at $t = 0$, where $\Delta\eta$ is the displacement of backwater given by the result of non-uniform flow calculation. The sea tide is assumed to be sinusoidal.

Calculation of the variation of the water surface elevation by the above method leads to the result that the high water in the river becomes lower than that in the ocean and the time of high water in the river lags behind that in the ocean. These are natural results caused by nonlinear head losses and are observed in a general sea-inlet-bay system. However, these results are inconsistent with those of the field measurements, which indicate that both the high water level and its time in the river are approximately equal to those in the ocean. Probably, this is because the depth of the channel and the depth of the river surface area influenced by the tide are not large enough as compared with the ocean tidal range. Therefore, the variation of the water level at the river mouth from the time of the ocean's high tide elevation is calculated under the initial conditions, as mentioned previously, whereas it is approximated using an appropriate fifth-order function, from the time when the calculated level becomes lowest or equal to the ocean's tide, to the time of the next high water level.

An example of the result of the numerical simulation is shown in Figure 4. The solid curves show the calculated time series of water level and discharge at the river mouth. In spite of simplicity of the model presented here, the calculated values correlate well with the observed ones. In the other cases, the decrease in tidal prism can be estimated within ±10 % error by properly choosing the head loss coefficient fc and the channel length ℓ.

4.3 Effect of Decrease in Tidal Prism

This section presents effects of the width variation on the total discharge and the sediment transport rate at the river mouth by using the numerical model discussed in section 4.2.

First the variation of the absolute flow volume during a tidal cycle (12.5 hours) as caused by the change in the width is investigated. The relationship between the width and the mean depth obtained in section 3.2 is used.

Figure 6 shows the results of three cases of tidal ranges:(1) 1.45 m of the mean spring tidal range, (2) 0.91 m of the range between the mean higher high and the lower low water levels, and (3) 0.33 m of the mean neap tidal rnage, with no inherent river discharge. The discharge passing through the river mouth decreases exponentially as the width decreases. For example, at spring tide when the width is 5 m, the discharge decreases to about one third that for conditions of 100 m width, in which the water level at the river mouth changes simultaneously with that in the ocean.

Next, the effect of the width variation on the gross volume of sediment transport rate for a tidal cycle is shown in Figure 7, in which comparison is made with that in the cases of the same tidal change at the river mouth as that in the ocean. A Bagnold-type formula, equation (8), proposed by Watanabe (1982) was used to calculate the transport rate.

$$q_r = K_r (u_*^2 - u_{*c}^2) |u| / g \tag{8}$$

in which q_r is the volume transport rate including the sediment porosity, u_* is the friction velocity, u is the flow velocity, and K_r is the dimensionless coefficient. The assumptions used in this calculation are (1) the critical Shields parameter is 0.06, (2) the grain diameter is 0.25 mm, (3) the dimensionless coefficient K_r is 1.0, and (4) the friction velocity is estimated using the turbulent logarithmic velocity profile law.

It is generally seen that the sediment transport rate increases rapidly as the width decreases, because the flow becomes fast. However, when the width becomes narrower to some extent, the sediment transport rate is forced to become much smaller than that in the case of the same tidal change as in the ocean. For example, it becomes 1/10 to 1/100 at spring tide when the width is less than 20 m.

5. NUMERICAL SIMULATION OF REDUCTION PROCESS OF CROSS-SECTION

5.1 Prediction Model

Shuto and Aota (1980) originally proposed a numerical model predicting the time variation of the cross-sectional area at a river mouth and Ogawa et al. (1984) further developed the model. In these models the cross-sectional area was assumed to change owing to sediment

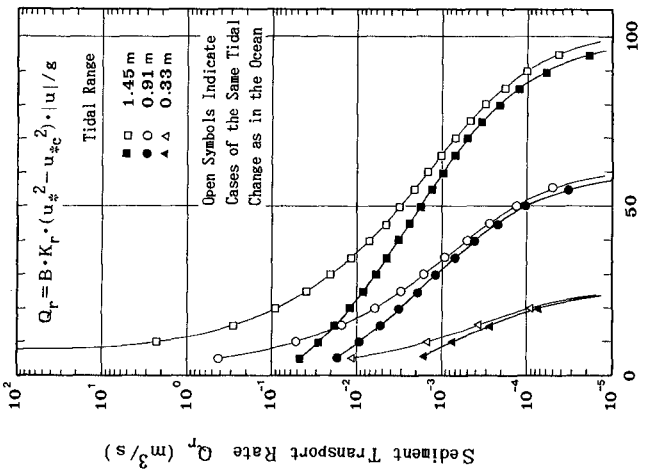

Figure 7 Effect of Width Variation on Sediment Transport Rate.

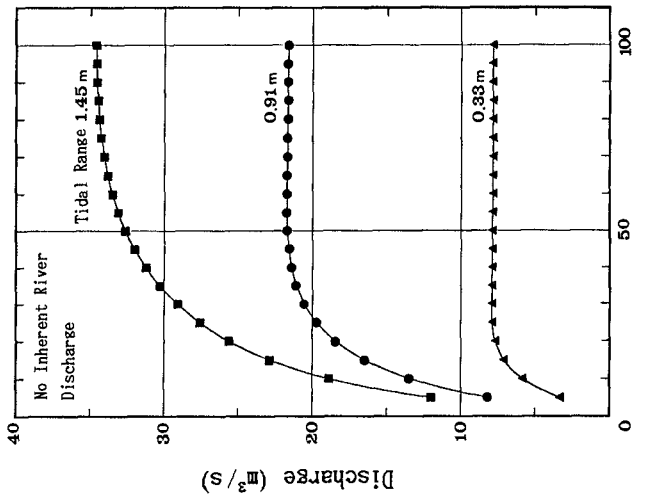

Figure 6 Effect of Width Variation on Discharge.

outflow caused by the river flow and sediment inflow caused by waves (as shown in Figure 8). However, vagueness remains in the physical meaning of the two coefficients involved in the sediment transport formulas; i.e. values of the coefficients suitable for the observed changes are different for different periods at the same place.

We now introduce the effect of the decrease in tidal prism, induced by a reduction of the cross-sectional area at the river mouth, into the prediction model. In this model the instantaneous sediment outflow caused by the river flow is calculated using the water level and velocity estimated by the numerical hydraulic model (discussed in section 4.2) and the total volume of sediment outflow over a tidal cycle from the high tide to the next high tide is evaluated. On the other hand, the volume of sediment inflow is estimated using the wave conditions at the breaking point. Then the variation of the cross-sectional area is simulated for every tidal cycle on the basis of the balance of the two kinds of sediment transport.

The governing equation for sediment mass conservation at the river mouth is expressed as

$$L\, dA/dt = q_r\, B - q_w\, B \tag{9}$$

in which q_r, q_w are the volume transport rates of sediment outflow and inflow, L is the width of the sand spit, A is the cross-sectional area, and B is the width of the river mouth.

The sediment outflow is given by equation (8), and assumed to act so as to maintain the cross-section independently of the flow direction.

The sediment inflow is simply expressed by equation (10), because it is difficult to estimate it quantitatively by taking account of the mechanism of sand motion.

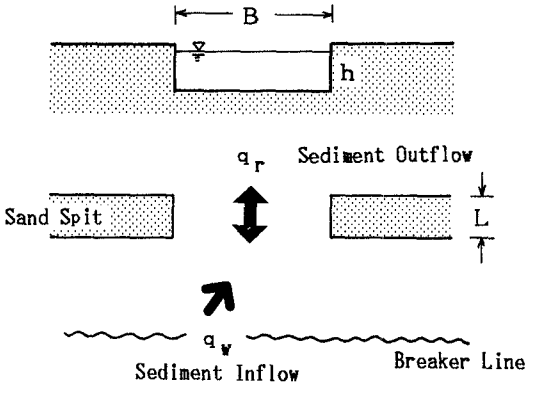

Figure 8 Schematic Diagram of Sediment Transport at River Mouth.

$$q_w = K_w H_b^{1.5} \tag{10}$$

in which H_b is the significant wave height at the breaking points, and K_w is a dimensional coefficient. This expression is obtained by considering that the sediment transport rate in the surf zone is proportional to the wave energy flux at the breaker line and dividing it by the width of the surf zone. The breaker height H_b is estimated using the following formula proposed by Sunamura (1983),

$$H_b/H_o = (\tan\beta)^{0.2} (H_o/L_o)^{-0.25} \tag{11}$$

where H_o is the significant wave height in deepwater, L_o is the wavelength in deepwater, and $\tan\beta$ is the bottom slope.

According to the results of the previous studies and the fluorescent sand tracer experiments, the coefficients K_r and K_w are expected to be of the order of magnitude of 10^0 and 10^{-5} respectively.

The reults of the simulation are shown in Figure 3. Calculation was terminated during extreme flood events causing the abrupt enlargement of the cross-section, and during dredging. With constant values of the coefficients, $K_r = 1.0$ and $K_w = 2.5 \times 10^{-5}$ ($m^{0.5}/s$), the results show a good agreement with the observed changes in the reduction processes at the river mouth. These values of the coefficients used in the simulation are the same order of magnitude with those mentioned above.

5.2 Possibility of River Mouth Closing

In order to examine the possibility of closing, the relationship between the significant wave height in deepwater and the width of the river mouth in a state of dynamic equilibrim ($dA/dt = 0$) is investigated. Figure 9 shows the results obtained under three conditions of tidal ranges with no inherent river discharge. When the wave height is placed above the curve of a reference tidal range at a reference width, the cross-sectional area becomes smaller and in the opposite case it becomes larger.

Since the width of the Samegawa River is now 10 to 30 m, it can be seen that the mouth of the river expands and contracts repeatedly in response to waves and tides. Therefore, it can be concluded that the present cross-section reaches an approximate equilibrium and that complete closure will not occur.

6. CONCLUDING REMARKS

As a result of this study based on the field measurements as well as numerical simulations, it has been found that the closing process has the following mechanism: a cycle that commences with a reduction of the cross-sectional area induces a decrease in tidal prism resulting in a substantial decrease in sediment outflow, and this decreased sediment outflow causes a further reduction of the cross-sectional area as the last phase before another cycle begins again. By considering this

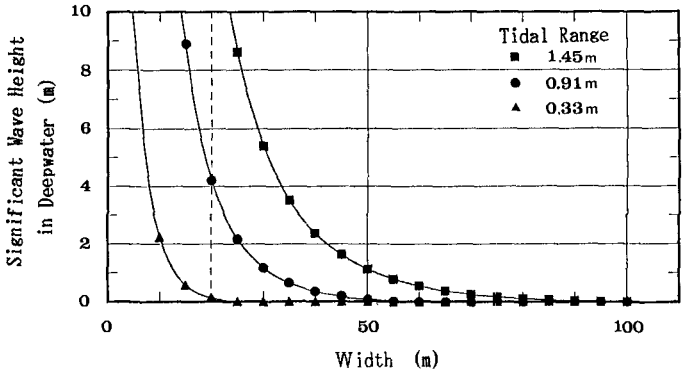

Figure 9 Relationship between Significant Wave Height in Deepwater and Width of River Mouth in a State of Dynamic Equilibrium.

mechanism, it has become possible to reasonably simulate the topographical changes of the river mouth.

However, the prediction model of the reduction process presented here is a simple one-dimensional model and it is impossible to simulate the variation of the sand spit width. Therefore, it is important to properly choose such parameters as to represent the plane configuration of the sand spit and the cross-sectional shape of the channel, on the basis of topographical surveys.

ACKNOWLEDGEMENTS

We would like to express our deep appreciation to H. Kaburagi and Y. Matsubara of the Joban Joint Power Co., Ltd. for the support they lent to this study and for their permission to publish this paper. We would also thank Prof. A. Watanabe of University of Tokyo for his useful suggestion in preparing the manuscript.

REFERENCES

Bruun, P. (1978) : Stability of Tidal Inlets, Theory and Engineering, Elsevier Scientific Publishing Company, pp.83-108.

Ogawa, Y., Y. Fujita and N. Shuto (1984) : Change in the Cross-sectional Area and Topography at River Mouth, Coastal Engineering in Japan, Vol.27, pp.233-247.

Shuto, N. and S. Aota (1980) : Numerical Simulation of the Seasonal Variation in the Cross-sectional Area at River Mouth, Coastal Engineering in Japan, Vol.23, pp.205-217.

Sunamura, T. (1983) : Determination of Breaker Height and Depth in the Field, Annual Report, Institute of Geoscience, University of Tsukuba, No.8, pp.53-54.

Watanabe, A. (1982) : Numerical Models of Nearshore Currents and Beach Deformation, Coastal Engineering in Japan, Vol.25, pp.147-161.

CHAPTER 114

A MODEL FOR CROSS-SHORE SEDIMENT TRANSPORT

M.J.F. Stive*

ABSTRACT

A model for cross-shore sediment transport due to random waves is described which adopts a vertically integrated transport description for sheetflow situations. The formulation of the transport as a function of the instantaneous velocity field is based on the approach of Bailard (1981). This approach assumes in essence that the instantaneous transport is proportional to some power of the instantaneous near-bottom velocity. Implementation of this transport description in a time-dependent model requires a formulation of the time-mean and some low order moments of the near-bottom velocity field. An initial formulation based on a monochromatic, second order Stokes wave representation is presented. The model is checked on the basis of both field and laboratory data. Some consequences for further study are indicated.

1. INTRODUCTION

Observation of sediment transport due to random waves on a two-dimensional beach indicates that one of the more important mechanisms under active surf conditions may be the transport of sediment by the time mean, seawards directed flow near the bottom induced by the breaking of waves. It was shown (Stive and Battjes, 1984) that this mechanism is so dominant that a vertically integrated model incorporating this mechanism alone describes the bottom variations in an active surf zone to a satisfactory, first approximation. Extension of this model with other transport mechanisms is a logical step towards a more complete cross-shore sediment transport model. Here some first suggestions are made to extend the model with transport due to the asymmetry of the wave motion, so that also a mechanism for onshore transport is included.

2. TRANSPORT FORMULATION

Since we are interested in a transport formulation which takes also the effects of wave asymmetry into account, it is essential to adopt a formulation describing the instantaneous transport. A simple approach would be to assume that the instantaneous sediment transport rate, q, is proportional to some power of the local relative velocity between the bed and the fluid outside the boundary layer. For example,

$$q(t) = A\, u(t) |u(t)|^n \qquad (1)$$

where $u(t) = u_b \cos\omega t$ + higher harmonic terms, with u_b the orbital velocity amplitude just outside the boundary layer and ω the angular frequency.

* Senior Researcher, Delft Hydraulics, P.O. Box 152, 8300 AD Emmeloord, The Netherlands.

The latter approach has been elaborated consistently for surf zones on a plane sloping beach by Bailard (1981), who extended the work of Bailard and Inman (1981). Based on Bagnold's (1963) energetics concept these authors use as a starting point a description of the instantaneous sediment transport basically in the form of Equation (1), extended with the effect of a bottom slope. Bailard (1981) distinguishes between bedload transport in a granular-fluid shear layer of a thickness in the order of the wave boundary layer and suspended transport in a layer of greater thickness, typically in the order of several centimeters. For the bedload transport the power n as introduced by equation (1) is given as 2, while for the suspended transport it is given as 3. Here the formulation is reduced for application in the cross-shore direction which yields the instantaneous total load sediment transport equation (see also Bailard, 1982):

$$i(t) = i_B(t) + i_S(t) = \rho c_f \frac{\varepsilon_B}{\tan\phi}\left[|u(t)|^2 u(t) - \frac{\tan\beta}{\tan\phi}|u(t)|^3\right] + \rho c_f \frac{\varepsilon_S}{w}\left[|u(t)|^3 u(t) - \frac{\varepsilon_S}{w}\tan\beta\,|u(t)|^5\right] \quad (2)$$

where i is the total cross-shore immersed weight sediment transport rate (composed of the bedload transport rate, i_B, and the suspended load transport rate, i_S), ρ is the water density, c_f is the drag coefficient for the bed, $\tan\beta$ is the slope of the bed, ϕ is the internal angle of friction of the sediment, w is the sediment's fall velocity and ε_B and ε_S are bedload and suspended load efficiencies, respectively. The efficiency factors ε_B and ε_S denote those (constant) fractions of the total power produced by the fluid motion which are expended in transporting. The immersed weight sediment transport rate is linked to the volumetric transport rate q by

$$q = \frac{i}{(\rho_s - \rho)gN} \quad (3)$$

where ρ_s is the sediment density, g the gravitational acceleration and N the local volume concentration of solids.

The above sediment transport formulation uses vertically integrated equations. As a consequence, the sediment transports are assumed to respond to the near bottom water velocity in an instantaneous, quasi-steady manner. This assumption is probably valid for most natural beaches with prevailing sheet flow conditions and incident wave periods in excess of 5 seconds approximately.

Another uncertainty in the transport formulation concerns the use of bedload and suspended load efficiency factors. Although constant values have been found adequate for certain types of flow, the estimation of their optimal values, and their possible variations with the type of flow considered leaves at least some quantitative uncertainty.

3. WAVE INDUCED CROSS-SHORE FLOWS

Given the variation of the cross-shore velocity field the mean cross-shore sediment transport rate may in principle be calculated from the time averaged Equation (2):

$$\langle i \rangle = \rho\, c_f \frac{\varepsilon_B}{\tan\phi}\left[\langle |u|^2 u\rangle - \frac{\tan\beta}{\tan\phi}\langle |u|^3\rangle\right] +$$

$$+ \rho\, c_f \frac{\varepsilon_S}{w}\left[\langle |u|^3 u\rangle - \frac{\varepsilon_S}{w}\tan\beta\,\langle |u|^5\rangle\right] \qquad (4)$$

The total velocity u is decomposed into a near-bottom, mean (overbar) and an oscillatory (tilde) flow component,

$$u = \bar{u} + \tilde{u} \qquad (5)$$

Conceptual simplifications follow by assuming that the oscillatory velocity is due to a single plane wave of frequency ω and some small nonlinear harmonics:

$$\tilde{u} = u_m \cos\omega t + u_{2m}\cos 2\omega t + \ldots \qquad (6)$$

in which $u_m > u_{2m} > \ldots$

Using Equations (5) and (6) in Equation (4) yields:

$$\langle i \rangle = \rho c_f u_m^3 \frac{\varepsilon_B}{\tan\phi}\left[\psi_1 + \frac{3}{2}\delta_u - \frac{\tan\beta}{\tan\phi}(u3)^*\right] +$$

$$+ \rho c_f u_m^4 \frac{\varepsilon_S}{w}\left[\psi_2 + \delta_u (u3)^* - \frac{u_m}{w}\varepsilon_S \tan\beta\,(u5)^*\right] \qquad (7)$$

in which the relative current strength, δ_u, is

$$\delta_u = \bar{u}/u_m \qquad (8)$$

and ψ_1 and ψ_2, represent non-dimensional velocity moments, defined as

$$\psi_1 = \langle \tilde{u}^3\rangle / u_m^3 \qquad (9a)$$

$$\psi_2 = \langle |u|^3\, \tilde{u}\rangle / u_m^4 \qquad (9a)$$

The even velocity moments $(u3)^*$ and $(u5)^*$ are defined as:

$$(u3)^* = \langle |u|^3\rangle / u_m^3 \qquad (10a)$$

$$(u5)^* = \langle |u|^5\rangle / u_m^5 \qquad (10b)$$

Retaining first order in the relative current strength and odd moments only three velocity moments may be simplified further, i.e.

$$u_m^4\, \psi_2 \simeq \langle |\tilde{u}|^3\, \tilde{u}\rangle + 3\bar{u}\langle |\tilde{u}|^3\rangle \qquad (11)$$

$$\text{and } u_m^3 (u3)^* \simeq \langle |\tilde{u}|^3\rangle + 3\bar{u}\langle |\tilde{u}|\tilde{u}\rangle \qquad (12a)$$

$$u_m^5 (u5)^* \simeq \langle |\tilde{u}|^5\rangle + 5\bar{u}\langle |\tilde{u}|^3\tilde{u}\rangle \qquad (12b)$$

Inspection of the above expressions indicates that we need to evaluate the mean return flow and the oscillatory velocity moments.

Mean return flow

It has been hypothesized by Dyhr-Nielsen and Sørensen (1970) that the seaward directed returnflow or undertow in the surf zone -which compensates for the shoreward directed mass flux above wave trough level- is driven by the imbalance between the vertically non-uniform wave momentum flux on the one hand and the vertically uniform pressure gradient on the other hand. Quantitative evaluations of these ideas leading to models for the circulation have been presented by e.g. Dally (1980), Svendsen (1984), and more recently by Stive and Wind (1986). These cross-shore flow models are all based on a periodic wave formulation. To apply these models in the case of random waves Stive and Battjes (1984) have shown that satisfactory results are obtained, by simply applying the periodic formulation to that fraction of the waves that are breaking.
An evaluation applying this idea to Stive and Wind's model and a generalization to the case of quasi-3D current models has recently been made by De Vriend and Stive (1987). The formulation for the purely 2DV (two-dimensionally vertical) case has been adopted here. It is described below leaving out the rather large number of analytic expressions for which the reader is referred to the paper.

In order to derive the wave-mean cross-shore current, the water column is divided into three layers, viz. a surface layer above the wave trough level, a middle layer and a bottom layer. Stive and Wind (1986) propose to consider only the area below the wave trough level, and to take account of the surface layer effects via an effective shear stress at the trough level, compensating for the momentum decay above it, and via the condition that the net undertow must compensate for the mass flux in the surface layer. This means that the surface layer model is reduced to the formulation of the effective shear stress and the mass flux. The bottom layer velocity due to non-breaking waves is assumed to be similar to Longuet-Higgins' (1953) "conduction solution" for progressive waves. For breaking waves, Stive and Wind (1986) show that assuming a zero bottom shear stress leads to acceptable predictions of the current outside the wave boundary layer. This means that for this part of the current the bottom layer as such can be left out of consideration. Thus the problem has been reduced to solving the velocity in the middle layer from the horizontal momentum balance, both for the case of breaking and of non-breaking waves. In both cases the prescribed shear stress at the wave trough level provides an upper boundary condition, whereas the lower boundary condition follows from the zero shear stress approximation (breaking waves) or from matching with with bottom layer solution (non-breaking waves). The integral condition of continuity can be used to determine the remaining unknown constant (the bottom shear stress for non-breaking waves, the mean return current velocity for breaking waves).

In De Vriend and Stive (1986) these middle-layer solutions are considered in detail, for non-breaking waves, for breaking waves and for a random breaking wave field, respectively. In the latter case part of the waves are breaking, say a fraction $\tilde{Q}_b$ ($0 \leq \tilde{Q}_b \leq 1$). If mutual interaction between the waves is left out of consideration, this means that the secondary current velocities for the breaking and the non-breaking waves have to be added with appropriate weight factors.

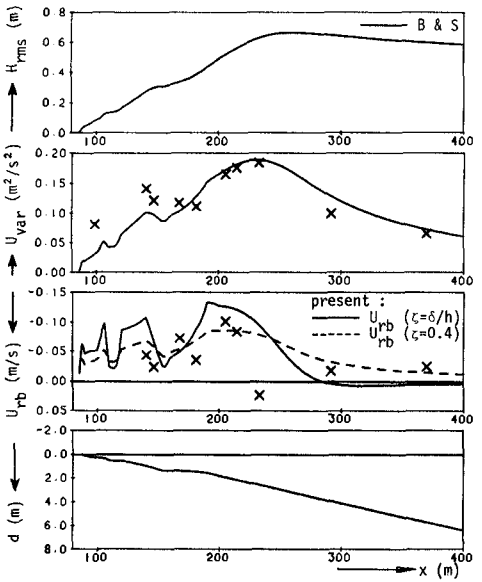

Fig. 1 Wave-induced undertow: comparison with NSTS measurements Nov. 20, 1978 at Torrey Pines beach (after Guza & Thornton, 1985); profile of bottom elevation below MSL (d), cross-shore undertow velocity (U_{rb}), variance of horizontal orbital velocity (U_{var}), and rms wave height (H_{rms}) versus distance normal to shore (x). Data points: measured values. Curves: computation with the models, see legend; B & S is Battjes and Stive (1985), present is present model, where U_{rb} ($\zeta = \delta/h$) is the undertow on top of the bottom boundary layer and U_{rb} ($\zeta = 0.4$) is that at 0.4 times the water depth.

To conclude this section a comparison is made with a field data and laboratory data. The field data are from the NSTS campaign at Torrey Pines Beach (Guza and Thornton, 1985). The wave energy decay prediction model (Battjes and Stive, 1985) was calibrated ($\alpha = 5.0$ and $\gamma = 0.5$) on the basis of the measured orbital velocity variance in the frequency range $0.05 < f < 0.5$ Hz. The velocity measurements were conducted at elevations of 0.4 m to 1.0 m above the bed. Taking account of the inherent inaccuracy of the measured, mean cross-shore velocities, the agreement is good, for the magnitude as well as for the cross-shore distribution of the velocity.

The laboratory data concern a more complicated depth profile (with two bars) under random wave attack. The wave energy decay prediction is again after the above mentioned model, but now according to the suggested parameterization The velocity measurements were conducted at an elevation of 0.05 m above the bed. Assuming that the accuracy of the measured, mean cross-shore velocities is relatively high the agreement in this case is less good. It is expected that the observed discrepancy is mostly due to the difficulty in predicting the breaking wave fraction on a barred beach (see the comparison between measurements and computations of $\tilde{Q}_b$).

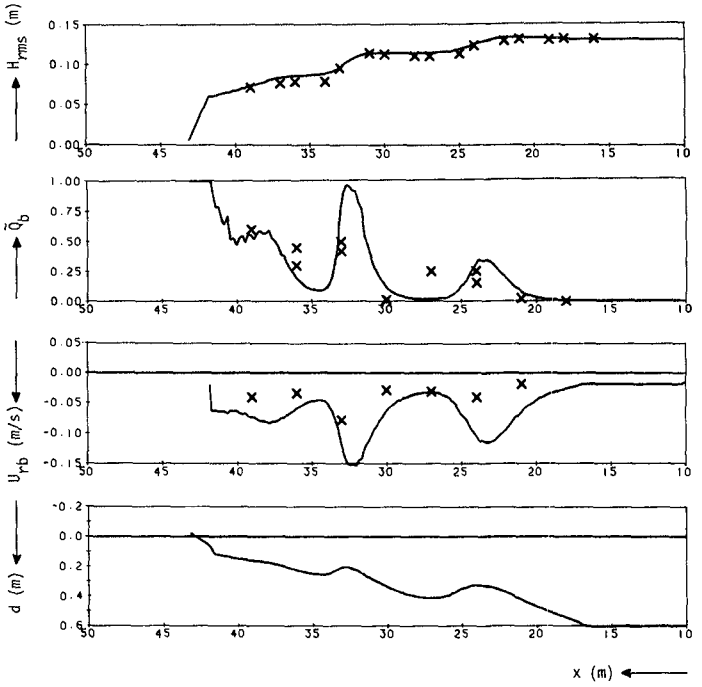

Fig. 2 Wave-induced undertow: comparison with flume measurements: profile of bottom elevation below MWL(d), cross-shore undertow velocity (U_{rb}), fraction of breaking waves ($\tilde{Q}_b$) and rms wave heights (H_{rms}) versus distance normal to shore (x).
Data points: measured values. Curves: computation with the model, where U_{rb} is the undertow at 0.05 m above the bottom.

Oscillatory velocity moments

From the evaluation of the present transport formulation it appears that the following low order oscillatory velocity moments are of importance:
- the four lowest even moments $\langle\tilde{u}^2\rangle$, $\langle|\tilde{u}|^3\rangle$, $\langle\tilde{u}^4\rangle$, $\langle|\tilde{u}|^5\rangle$, which are non zero for symmetric velocities,
- the two lowest odd moments $\langle\tilde{u}^3\rangle$, $\langle|\tilde{u}|^3\,\tilde{u}\rangle$, which are zero for symmetric velocities.

The latter moments are the most difficult to estimate: they are nonzero only for nonlinear waves such as actually occur nearshore. The shoreward velocities in such waves are typically stronger and of shorter duration than the offshore flows, leading to nonzero values for the odd moments.

A theoretical evaluation of the even moments for a random, linear sea (Gaussian model) is given by Guza and Thornton (1985). The theoretical moments are compared to field observations from the NSTS study. Their results indicate that even moments do not critically depend on cross-shore velocity asymmetry. This is due to the fact that also for symme-

tric velocities these terms are nonzero. At the present stage we will therefore rely on the Gaussian estimates for the even moments.

The odd moments are zero for a symmetric velocity field, but can be nonzero for asymmetric (nonlinear) motions. A relevant nonlinear property is the asymmetry of the wave surface about the horizontal axis. For nonbreaking waves this asymmetry may to a first approximation well be predicted on the basis of a horizontal bottom, nonlinear wave theory, assuming that due to gradual bottom variations the waves locally behave as on a horizontal bottom (see Flick et al, 1981). However, in the horizontal bottom, nonlinear wave theories the phases of the harmonics are locked to zero and there is no vertical wave profile asymmetry possible. This asymmetry about the vertical plane is an essential property of the sawtooth shaped breaking waves in the surf zone. These theories are deficient in this respect and thus unsuitable for calculations of odd velocity moments which depend critically on phase. To illustrate this we calculate the two lowest order odd moments assuming that the velocity fluctuation is described by a second order approximation with a locked but nonzero phase between the two components:

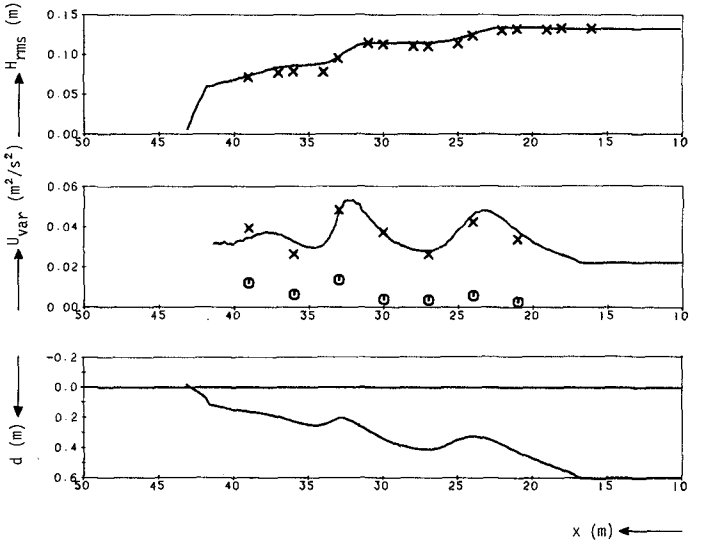

Fig. 3 Wave-induced near-bed velocity variance: comparison with flume measurements; profile of bottom elevation below MWL(d), oscillatory horizontal velocity variance (U_{var}) and rms wave height (H_{rms}) versus distance to shore (x).
Data points: measured values, the circles indicate U_{var} in the frequency range 0-0.25 Hz. Curves: computations with the model.

$$\tilde{u} = u_m \cos \omega t + u_{2m} \cos (2\omega t + \phi_2) \qquad (14)$$

in which $u_m > u_{2m}$. After some algebraic manipulation it may be show that to lowest order the two odd velocity moments are given by:

$$\langle \tilde{u}^3 \rangle = \frac{3}{4} u_m^2 u_{2m} \cos \phi_2 \tag{15a}$$

$$\langle |\tilde{u}|^3 \tilde{u} \rangle = \frac{12}{5\pi} u_m^3 u_{2m} \cos \phi_2 \tag{15b}$$

An interesting perspective now arises when we combine these results with the following observations. In the inner surf zone where the breaking waves are quasi-steady the relative phase of the second harmonic increases smoothly toward the asymptotic value (see Flick et al, 1981):

$$\phi_2 \to \pi/2 \tag{16}$$

Thus, according to Eq. 15a, 15b, the odd velocity moments for breaking waves vanish ultimately.

At this point we may specify our wave decay model which predicts linear and nonlinear properties necessary to derive the velocity moments. As a starting point Battjes and Stive's (1985) wave decay prediction model is adopted to yield the cross-shore variation of the variance of the wave elevation. Given the wave variance, linear theory may be applied to provide the near-bottom velocity variance and thus the even velocity moments based on the Gaussian model. The odd velocity moments are estimated from the nonbreaking fraction of waves only, assuming that the contribution of the breaking waves is negligible in view of the above conclusions. To provide results from this model we use the second order Stokes expansion with

$$\tilde{u} = u_m \cos \omega_p t + \frac{3}{4} \frac{u_m^2}{c} \sinh^{-2}(k_p h) \cos 2\omega_p t \tag{17}$$

and choose $u_m = u_{rms}$ from the consideration that the monochromatic representation of the random wave field should have to same variance.

We conclude with a comparison between the above theory and the same laboratory measurements used earlier in the undertow comparison. Firstly, the velocity variance prediction may be checked from Fig. 3. It appears that the linear, Gaussian estimate is quite accurate. Secondly, the prediction of the remaining low order velocity moments may be checked from Fig. 4. It is noted that all moments are normalized by the variance, that the even moments are based on the linear, Gaussian estimate and that the odd moments are based on the nonlinear, monochromatic estimate. Here it appears that the prediction of the lowest order moments are reasonable given all assumptions made but that the discrepancies increase with increasing order of the moments as could be expected.

4. COMPUTATION OF TRANSPORT AND BOTTOM CHANGES

In the present model the local mean, volumetric cross-shore sediment transport rate, $\langle q \rangle$, is calculated according to the following expressions, where use has been made of expressions (4) and (8)...(12):

$$\langle q \rangle = B_{as} \langle q_{as} \rangle + B_{un} \langle q_{un} \rangle - B_{sl} \langle q_{sl} \rangle \tag{18a}$$

$$\langle q_{as} \rangle = F_B \psi_1 + F_S \psi_2 \tag{18b}$$

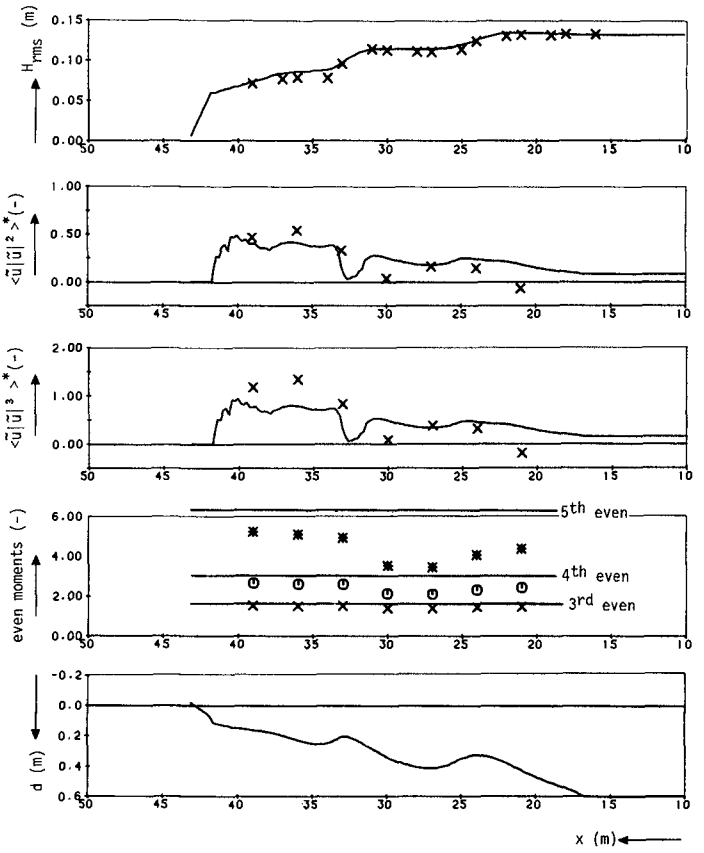

Fig. 4 Wave-induced near-bed velocity moments: comparison with flume measurements; profile of bottom elevation below MWL (d), normalized odd and even moments and rms wave height (H_{rms}) versus distance to shore (x).
Data points: measured values. Curves: computations with the model, where the even moments are according to the linear, Gaussian model.

$$\langle q_{un} \rangle = F_B \frac{3}{2} \delta_u + F_S \, 4\delta_u \, (u3)^* \tag{18c}$$

$$\langle q_{sl} \rangle = F_B \frac{\tan\beta}{\tan\phi} (u3)^* + F_S \frac{u_m}{w} \varepsilon_S \tan\beta \, (u5)^* \tag{18d}$$

$$F_B = \frac{c_f u_{rms}^3 \varepsilon_B}{\Delta g N \tan\phi} \tag{18e}$$

$$F_S = \frac{c_f u_{rms}^4 \varepsilon_S}{\Delta \, g \, N \, w} \tag{18f}$$

Here c_f is the drag coefficient equal to $\frac{1}{2}f_w$ with f_w the friction factor as defined in Stive and Battjes (1984) and B_{as}, B_{un} and B_{sl} are proportionality constants which should be O(1) if the description is right. The free parameters in the above expressions are ϵ_B and ϵ_S which for cross-shore transport are given by Bailard (1982) on the basis of field observations as 0.10 and 0.02 respectively. These values are adopted here.

The cross-shore variation of the local, mean sediment transport may now be calculated with the above expressions (18a...f) given the results of the wave height decay and kinematics model. Through application of the mass balance for the sediment (of which the properties are assumed constant) the bottom changes may be calculated. This procedure may be repeated for the new beach profile. In the numerical evaluation a second order Runge-Kutta algorithm is used in the wave decay model and a modified Lax scheme in the bottom change calculations. As a boundary condition on the waterline the present formulation yields $\langle q \rangle = 0$.

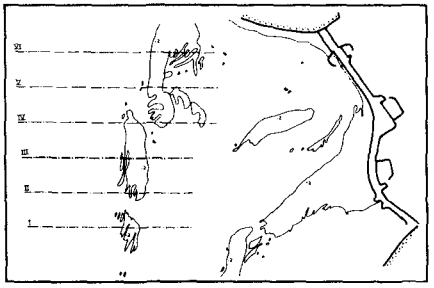

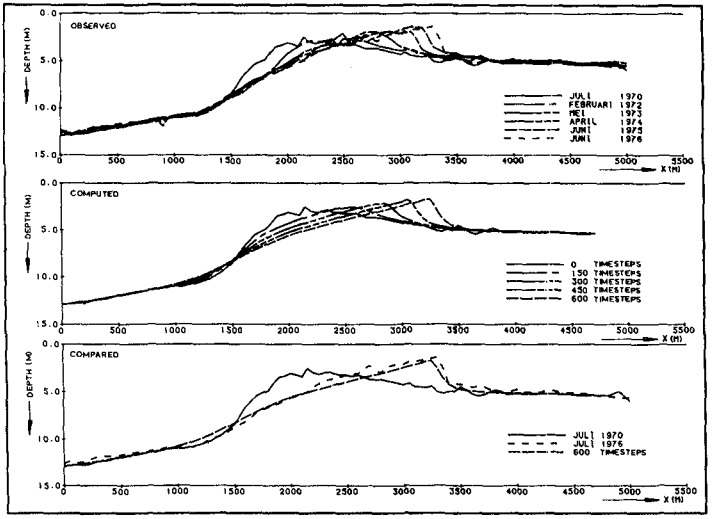

Fig. 5 Profile evolution of the underwater delta in the former mouth of the Grevelingen estuary. Top: situation in 1976. Bottom: results of model hindcast for section III.

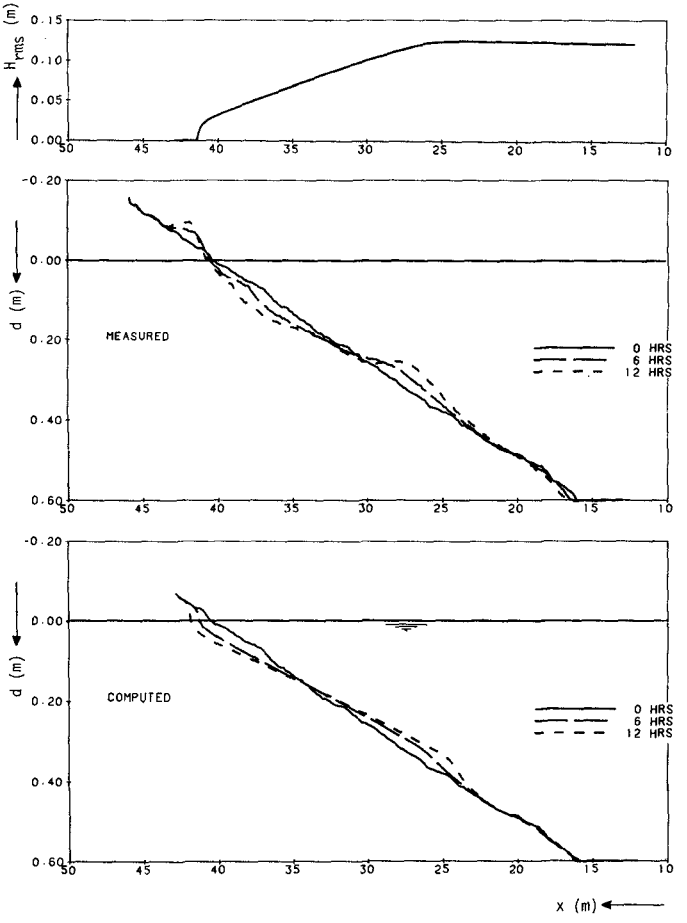

Fig. 6 Deformation of initially plane beach due to random waves: comparison with flume measurements; profiles of bottom elevation below MWL (d) and rms wave height (H_{rms}) versus distance to shore (x).

5. MODEL VERIFICATION

For the purpose of verification of the present model, a comparison was made with available field data, and laboratory measurements were carried out. The field data set concerns observed bar formation and deformation in an estuary region in the South of the Netherlands, the socalled Voordelta, which occurred after closure of one of the Southern Dutch estuaries. The profile deformation in cross-shore direction is appreciable (see Figure 5). The comparison between the hindcast results and the measurements is satisfactory, despite the fact that the wave climate and

hydraulic conditions were schematized to one value for the incident wave characteristics and a fixed waterlevel. The proportionality constants B_{as}, B_{un} and B_{sl} were set at 1.0. Some characteristic parameters of this case are collected in Table 1 below.

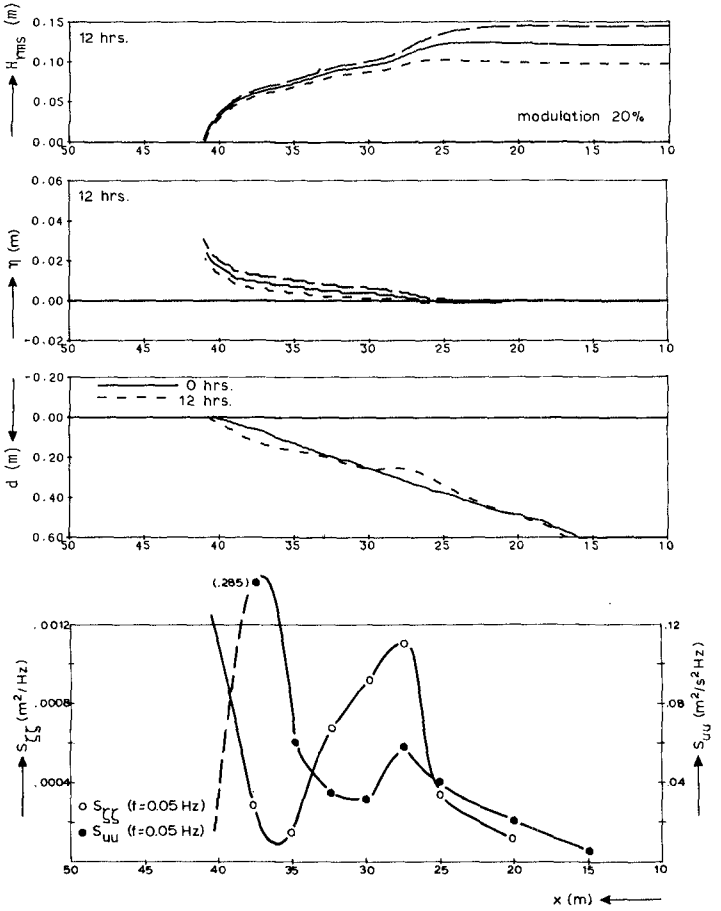

Fig. 7 Low frequency energy on the initially plane beach: computed wave height and set-up modulation and measuerd, resonant 1/2 long wave mode between surf zone's outer region and the shore.

The laboratory measurement programme involved the collection of surface elevation, near-bottom velocity and profile deformation data on two beach profiles -one initially plane and the other barred- under random wave attack (see Table 1 for some characteristic parameters). The velocity data on the barred beach were used in the earlier presented comparisons with the theoretical wave-induced cross-shore flows. The resulting beach profile deformations - restricted to the plane beach case due to space limitations - are compared with the model predictions here.

Fig. 6 gives the measured and computed profile deformation after 6 hrs and 12 hrs on the initially plane beach. It appears that the main erosion and sedimentation patterns agree, also quantitatively (the proportionality constants were all set on 2.0). Here we ignore the small sedimentation in the swash zone above the waterline, a process which is not included in the present model. An important discrepancy, however, is found in the horizontal and vertical development of the sedimentation in the surf zone's outer region. The measurements indicate a more pronounced development of an offshore bar, eventually with a negative shoreside slope. Similar indications of the absence of these developments in the model are found by the results for the profile deformations of the initially single-barred beach. The present model is unable to predict the development of the bar's shore side.

case	profile	grain diameter (μm)	$H_{rms,incident}$ (m)	f_p (Hz)
field	deltaic bar	225	1.50	0.17
laboratory	plane	90	.123	0.50
laboratory	single bar	90	.081/.133	0.50/0.50

Table 1 Characteristic parameters field and laboratory cases

Analysis of the discrepancies has resulted in strong indications that resonant surf beat modes may be the cause of the shoreside bar developments. Some results in support of this are given furtheron. First, we discuss possible surf beat sources. An inventory of the literature on this topic yields two "natural" sources (1, 2) and two "laboratory" sources (3, 4), viz.

(1) the release of or forcing by group-bound long waves due to wave breaking (Longuet-Higgins and Stewart, 1964);
(2) forcing by the time variation of the initial breaking region due to wave-grouping (Symonds and Bowen, 1984);
(3) wave paddle reflection of flume bound long waves;
(4) parasitic, wave paddle generated free long waves.

The third of these sources can be eliminated in the present measurements since the method of active wave absorption was adopted (Kostense, 1984). Discrimination between the other sources is very difficult: in all cases amplitudes and frequencies are closely related and proportional to the wave group characteristics. Whichever source is responsible, the following observation is of importance. On the initially plane beach a resonant ½ wave surf beat mode develops (see Fig. 7) between the water line and the outer surf zone, at which latter position the undertow deposits sand. The interesting, yet not well understood fact is that this mode is resonant. This is not expected by any theory, but the results in Fig. 7 for the modulated wave height indicate that both first two mentioned surfbeat sources can explain a forcing. Also, for the barred beach similar -although more complicated- observations were made.

Obviously, this is a relevant mechanism which should be included in a model. It is noted though that compared to a natural situation the relevance of this development may be somewhat overemphasized, i.e. with the timescale being approximately 4 the above storm wave conditions with fixed water level would have to be strictly constant for two days.

6. DISCUSSION AND CONCLUSION

In this paper a first suggestion is made to extend the earlier formulated model for offshore sediment transport due to undertow (Stive and Battjes, 1984) with the effects due to horizontal asymmetry in the wave motion. To arrive at these results it was necessary to model some low order odd moments of the near-bottom velocity field. An initial formulation based on a monochromatic, second order Stokes wave representation is shown to give a reasonable, first approximation to the odd velocity moments, but obviously the formulation needs improvement.

The odd velocity moments were readily used in the transport formulation of Bailard (1981). This concerns a vertically integrated description of the sediment transport in sheetflow conditions, which assumes that the instantaneous transport is proportional with some power of the instantaneous near-bottom velocity. The validity of this approach for natural surf zones needs further investigation.

A check was made of the ability of the model to predict beach profile deformations. Reasonable agreement was found in the general patterns. However, it appears that in an erosive situation only the onset of the bar formation in the outer surf zone is indicated by the model, whereas subsequent bar growth is not well predicted. The growth is believed to be associated with resonance of particular long wave modes forced by wave grouping effects. This phenomenon needs further investigation, before it can be included in a dynamic cross-shore sediment transport model.

It is finally noted that analysis of this model for several realistic cases has resulted in the following conclusions. There are two main contributions to the sediment transport, viz. that induced by the undertow yielding offshore transport and that induced by the wave-asymmetry yielding onshore transport. In low-frequency or swell conditions the latter dominates and in high-frequency or storm conditions the former dominates. These conclusions coincide with the common suggestions that low-frequency waves build up a coast and that high-frequency waves erode it.

ACKNOWLEDGEMENT

This work was done as a part of the TOW Coastal Research Programme of the Ministry of Transport and Public Works (Rijkswaterstaat) of the Netherlands. The author wishes to thank Dr. H.J. De Vriend for the many helpful discussions and Dr. J.A. Battjes for his critical review of the manuscript.

REFERENCES

Bagnold, R.A. (1963). "Mechanics of marine sedimentation", The Sea: Ideas and observations, vol. 3, New York, Interscience Publishers, 1963, pp. 507-526.

Bailard, J.A. (1981). An energetics total load sediment transport model for a plane sloping beach. Journal of Geophysical Research, vol. 86, no. C11, 1981, pp. 10938-10954.

Bailard, J.A. (1982). Modeling on-offshore sediment transport in the surf zone. Proc. 18th Int. Conf. Coastal Eng., 1982, pp. 1419-1438.

Bailard, J.A. and D.L. Inman (1981). An energetics bedload transport model for a plane sloping beach; local transport. Journal of Geophysical Research, vol. 86, no. C3, 1981, pp. 2035-2043.

Battjes, J.A. and M.J.F. Stive (1985). Calibration and verification of a dissipation model for random breaking waves. Journal of Geophysical Research, Vol. 90, no. C5, 1985, pp. 9159-9167.

Dally, W.R. (1980). A numerical model for beach profile evolution. M.Sc. Thesis, University of Delaware, 1980.

De Vriend, H.J. and M.J.F. Stive (1987). Quasi-3D modelling of nearshore currents. To be published in Coastal Engineering, 1987.

Dyhr-Nielsen, M. and T. Sørensen (1970). Some sand transport phenomena on coasts with bars. Proc. 12th Int. Conf. Coastal Eng., 1970, pp. 855-865.

Flick, R.E., R.T. Guza and D.L. Inman (1981). Elevation and velocity measurements of laboratory shoaling waves. Journal of Geophysical Research, vol. 86, no. C5, 1981, pp. 4149-4160.

Guza, R.T. and E.B. Thornton (1985). Velocity moments in nearshore Journal of Waterway, Port, Coastal and Ocean Engineering, Vol. 111, No. 2, 1985, pp. 235-256.

Kostense, J.K. (1984). Measurements of surf beat and set-down beneath wave groups. Proc. 19th Int. Conf. Coastal Eng., 1984, pp. 724-740.

Longuet-Higgins, M.S., (1953). Mass transport in water waves. Phil. Trans. Royal Soc., A254, 1953, p.p. 535-581.

Longuet-Higgins, M.S. and R.W. Stewart (1964). Radiation stresses in water waves; a physical discussion, with applications. Deep-Sea Res., Vol. 11, 1964, pp. 529-562.

Stive, M.J.F. and J.A. Battjes (1984). A model for offshore sediment transport. Proc. 19th Int. Conf. Coastal Eng., 1984, pp. 1420-1436.

Stive, M.J.F., and H.G. Wind (1986). Cross-shore mean flow in the surf zone. Coastal Engineering, 10, 1986, pp. 325-340

Svendsen, I.A. (1984). Mass flux and undertow in a surf zone. Coastal Engineering, 8, 1984, pp. 303-329.

Symonds, G. and A.J. Bowen (1984). Interactions of nearshore bars with incoming wave groups. Journal of Geophysical Research, Vol. 89, No. C2, 1984, pp. 1953-1959.

CHAPTER 115

BEACH CHANGE AROUND DETACHED BREAKWATERS DUE TO ARTIFICIAL NOURISHMENT OF BYPASSED SAND

SUYAMA, H*., T. UDA** and T. YOSHIMURA***

ABSTRACT

Field experiment of sand bypassing was conducted on the Shimoni–ikawa Coast in Toyama Bay. The materials of 5900m^3 dredged on the updrift coast of the harbor were thrown into behind the detached breakwater. After the nourishment detailed surveys of the bottom topography around the breakwaters, wave observations and tracer tests using colored concrete blocks were carried out in order to investigate the movement of the nourished sand. Temporal and spatial changes of the shoreline positions and the sectional area of the beach in the shoreward zone of the detached breakwater are examined. It is found through the field experiment that the materials nourished behind the detached breakwater were carried slowly in the longshore direction by the westward littoral drift, dominating on the coast, without the outflow of sand through the openings of the breakwaters. It is concluded that the detached breakwater is useful to control the on–offshore sand movement and to retain the sand behind the detached breakwater.

I. INTRODUCTION

The Shimoni–ikawa Coast, located in Toyama Bay and formed by the fluvial sediment supply of the Kurobe River for an alluvial fan, has experienced severe beach erosion for a long time. On the east end of the coast Miyazaki Fishery Harbor has been constructed since 1947, and the balance of littoral transport directing westward was lost due to the presence of the breakwater. The shoreline advanced on the updrift side of the breakwater and the shoaling in the harbor entrance was caused by the sand movement around the tip of the breakwater, whereas the downdrift beach was eroded. In foreign countries sand bypassing method is frequently used to solve the beach erosion and accretion simultaneously, but in Japan the applied cases of the method are rather few.

Ministry of Construction and Fishery Agency performed a cooperative field study on the method to solve these problems, including sand bypassing system, in 1983 and 1984, taking the case of the Shimoni–ikawa Coast into a characteristic example.

This paper mainly summarizes the result of the field investigations conducted by Ministry of Construction. The aim of the study is to investigate the effectiveness of

* Head, Kurobe Work Office, Hokuriku Regional Constuction Bureau, Ministry of Construction, Toyama 938 Japan.

** Dr. Eng., Head, Coastal Eng. Div., Public Works Research Institute, Ministry of Construction, Ibaraki 305 Japan.

*** Kurobe Work Office.

sand bypassing for a way which can solve the problems of the beach erosion and accretion near the harbor simultaneously through the field experiment. The second is to examine the function of the detached breakwater for a structure which can control the abrupt diffusion of the nourished sand by the field experiment.

Ⅱ. FIELD EXPERIMENT OF SAND BYPASSING

The field experiment was carried out on the Shimoni－ikawa Coast located in Toyama Bay (Fig. 1). The coast is one of the famous coasts eroded severely in Japan, and various countermeasure works against beach erosion have been conducted. In recent years the beach has still been eroded, and the settlement of the concrete armour units of the detached breakwaters and the scouring of the sea bottom in front of the sea wall are considerably large. Bottom contours around Miyazaki Fishery Harbor is shown in Fig. 2. Sandy beach extends on the east coast of the harbor, and to the contrary there is no sandy beach on the west coast. Instead, coastal revetments and many detached breakwaters are placed along the coastline to protect the coast. The coastlines east of Miyazaki Fishery Harbor and west of the river mouth of the Sasa River run almost in the east－west direction. Both coastlines have the discrepancy of the shoreline position of around 1km in the on－offshore direction at the downcoast of Miyazaki Fishery Harbor. The discrepancy of the shoreline positions is considered to be formed by the beach erosion. First, the position of the mouth of the Kurobe River historically moved westward and the sand supply of the river decreased on the coast, and hence the beach was eroded by westward littoral drift with the lack of the sand supply. Secondly, westward littoral drift was obstructed by the presence of the breakwater of Miyazaki Fishery Harbor.

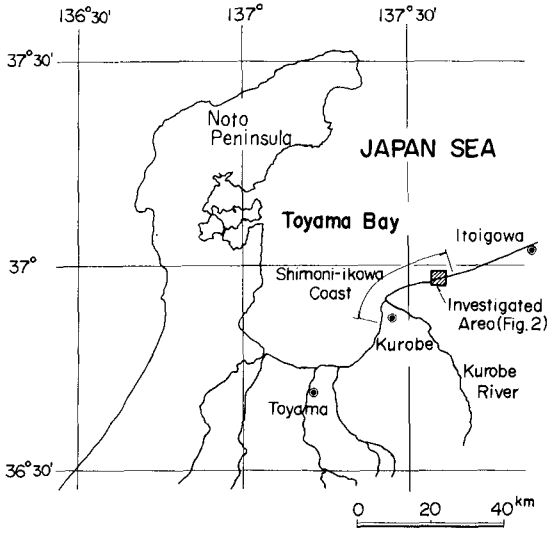

Fig.1 Location of Shimoni－ikawa Coast.

The transportation of sand was conducted by the following method. First, beach materials were dredged on the updrift site of the breakwater of Miyazaki Fishery Harbor, and were carried to 2 . 5 km downdrift location from the harbor by land (Fig. 2). The materials of 5900m³ were thrown into behind the detached breakwater. For the transportation method, dump trucks of 11 tons were used, since the materials mainly consist of gravels and the transportation by sea is thought to be difficult because of high waves in winter, although various methods were examined at first. The transportation were carried out for 34 days from October 13 to December 7 in 1983. Artificial nourishments behind the detached breakwater were conducted 6 times dividedly between November 4 and December 7 in 1983 as summarized in Table 1 .

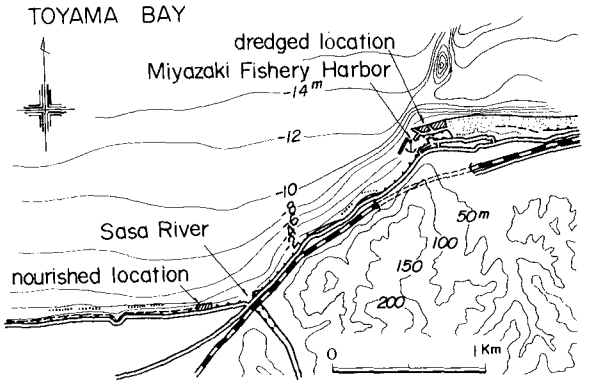

Fig.2 Bottom contours around Miyazaki Fishery Harbor.

Table 1 Nourished amount of sand.

Date	Nov. 4	Nov.10	Nov.16	Nov.17	Nov.29	Dec. 7
nourishd volume	1,050m³	1,100	1,100	530	1,060	1,060
accumulated volume	1,050m³	2,150	3,250	3,780	4,840	5,900

The location of the artificial nourishment was planned at the downdrift coast next to the fishery harbor at first, because of the short transportation distance. However, the nourishment was finally conducted behind the detached breakwater located about 2.5 km west of the harbor, considering the following two reasons. First, the nourishment at the location next to the harbor was anxious about the influence to the fishery, since the coast is a good fishing ground of production of the kelp. Second, the combined method of the construction of the detached breakwater and the artificial nourishment is considered to be effective in order to control the movement of the

The direction of the coastline is taken for the reference line of the figure. It is found that waves are frequently incident from clockwise direction to the normal of the shoreline. Under these conditions, westward longshore sediment transport should prevail.

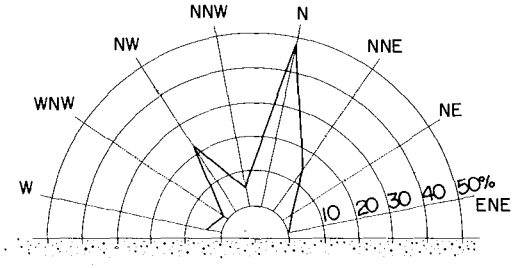

Fig.4 Wave direction measured during November 4 through April 13, 1984 off the nourished location.

Ⅳ. FIELD TEST OF ARTIFICIAL NOURISHMENT

Here, the changes of the shoreline positions, beach profiles and sand volumes obtained by the field experiment of the artificial nourishment are described. First, the alignment of the survey lines of the sounding around the nourished location is shown in Fig. 5. The soundings of wide region were conducted at 40m intervals along 26 survey lines between a and z placed alongshore. The artificial nourishment was carried out behind the detached breakwater located at No.174. The sounding was carried out widely westward from the nourished location instead of ones centered at the nourished breakwater, because the predominant direction of littoral drift is westward and large beach change was expected in the west region. On the other hand, 40–m–interval of the sounding is considered to be too wide near the nourished location, because large beach change might be observed and therefore the soundings of 10 m intervals behind the nourished breakwater and 20 m intervals behind the adjacent breakwaters were selected.

Regarding the beach changes due to the artificial nourishment, bottom contours around the detached breakwaters are compared first. Figure 6 shows the bottom contours measured between October 13, 1983 and January 21, 1984 after the nourishment. The maximum depth behind the breakwaters was about 2 m below the mean sea level before the nourishment. The shoreline behind the detached breakwater protruded remarkably as shown in the bottom contours of December 7 after the completion of the nourishment, and at the same time it began to accrete behind the adjacent breakwater. Furthermore, it is found from the bottom contours until January 21 that the beach change at the openings is small and the tombolo behind the nourished breakwater began to be eroded. To the contrary behind the adjacent breakwater sand accumulated and the scale of the tombolo became large with time.

nourished sand and to prevent the outflow of sand toward the offshore zone, so that the field investigation of the system is valuable for the test of the future measure against beach erosion.

Calculating the actual cost of the transportation of the materials by the price in 1983, the total cost of the transportation and the nourishment was about 10 dollars/m^3 (1 \$≒162¥). The rate of the transportation of the materials was 244m^3/d, since 11-ton dump trucks ran between two locations 40 times a day. More frequent transportation between two locations was difficult because of the environmental influence produced by the passage of the dump trucks in a small town.

Ⅲ. WAVE CONDITIONS DURING FIELD INVESTIGATIONS

Wave conditions during the field investigation of the artificial nourishment were observed at Tanaka Observatory located 5.6km west of the nourished location. Visual observation of wave direction off the nourished detached breakwater was also done. Temporal change of the daily mean of the significant wave height and wave period measured by an ultrasonic wave gauge placed at 15 m deep position off the coast is shown in Fig. 3. During the nourishment between November 4 and December 7, fairly high wave ($\bar{H}_{1/3}$=2.5m and $\bar{T}_{1/3}$=12.9s) attacked the coast on November 20. Besides, several high waves were observed after December 7 when the artificial nourishment was completed. For example, $\bar{H}_{1/3}$=2.30m ($\bar{T}_{1/3}$=5.8s) on December 12 in 1983, $\bar{H}_{1/3}$=3.2m ($\bar{T}_{1/3}$=9.0) on January 17 and $\bar{H}_{1/3}$=2.8 m ($\bar{T}_{1/3}$=11.6s) on January 18 in 1984. Regarding the seasonal change of wave conditions, wave height is high during November through April due to winter storms and calm between May and the midst of August, that is, the wave height becomes smaller than 0.5 m. Wave height and wave period show distinctive seasonal changes. Long-period high waves and short-period low waves appear in winter and summer, respectively.

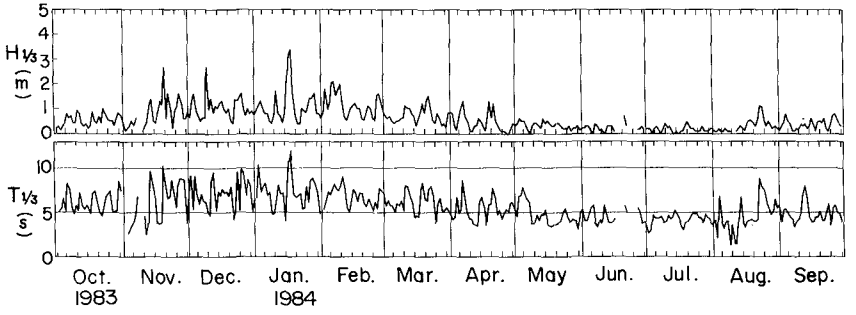

Fig.3 Temporal change of the daily mean of significant wave height and wave period measured at Tanaka Observatory.

Wave direction off the nourished location was visually measured during November 4, 1983 through April 13, 1984 from top of the coastal revetment (Fig. 4).

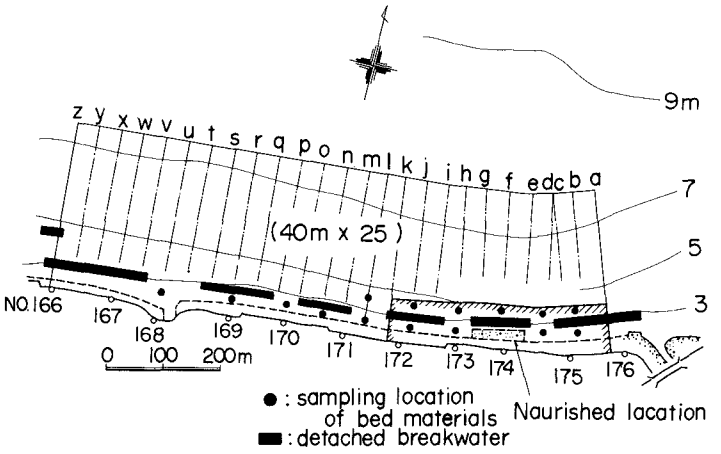

(a) Sounding of wide region

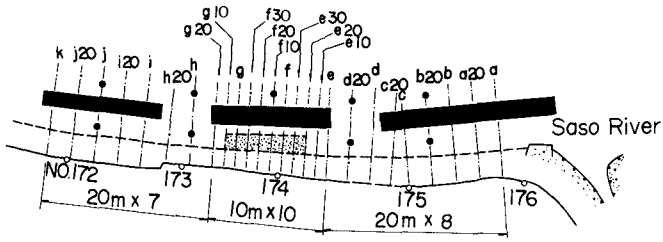

(b) Sounding of narrow region

Fig.5 Scope of the soundings around detached breakwaters.

Figure 7 expresses the longshore changes of the shoreline positions and the sectional area of the beach at some survey lines near the nourished location. The reference date of these changes is selected on October 13, 1983 before the nourishment. The change of the sectional area, $\triangle A$, is calculated in the shoreward zone of the detached breakwater. Besides, the porosity inside the wave breaking works placed along the shoreline was assumed to be 50% in the calculation of the sectional area. The shoreline retreated at the nourished location, although once there was a large projection of sand, and the shoreline behind the adjacent detached breakwater advanced. It is found that the shoreline change is abrupt in the beginning of change, but soon it began to slow down with time. The change of the sectional area corresponds with that of the shoreline positions very well, so that it is understood that the shoreline position becomes a good parameter in expressing the change of the sectional area. However, some small differences are noted at survey lines located at

the openings of the breakwaters (for example at survey line h). The region where △A is small is restricted to a narrow zone between the survey line i and h, although the region of small shoreline change is considerably wide. This means that sand can accumulate in a shallow zone in the openings of the detached breakwaters, even if the shoreline does not advance.

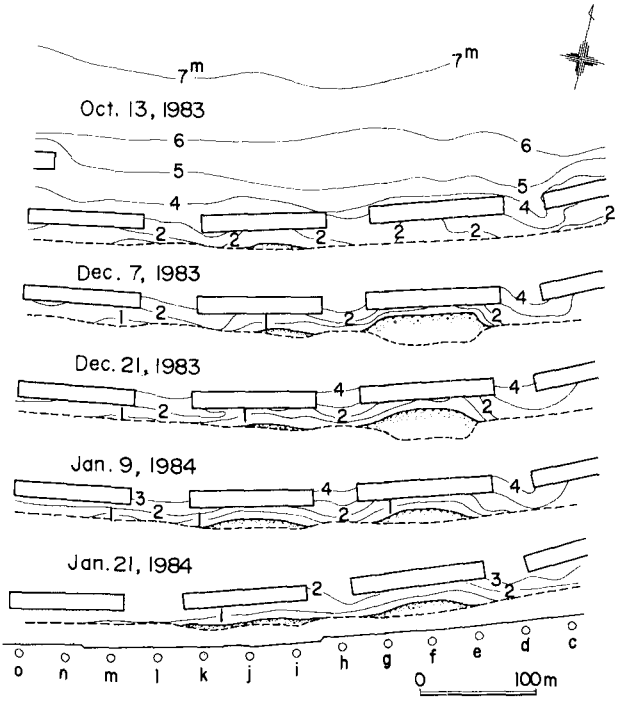

Fig.6 Comparison of bottom contours around detached breakwaters.

The characteristic change of the beach profiles corresponding to the changes of the shoreline positions and sectional area as described above is expressed in Fig. 8. The profies of survey line f, located behind the nourished detached breakwater, is shown. In the profile of December 21, 1983, expressing the beach topography of 14 days after the nourishment, a large amount of sand accumulate in front of the wave breaking works to the onshore end of the detached breakwater, keeping mild slope. Then the beach, of which elevation is between 1.8 m and −1.5 m above the mean sea level, was eroded at this location. It is found that the maximum depth of the eroded beach was restricted within the shallow water zone behind the detached breakwater.

A good correlation is observed between the change of the shoreline positions, △y, and that of the sectional area, △A, as shown in Fig. 7, so that the relationship between △y and △A is examined as in Fig. 9. The solid and open circles are the data obtained in the eroded region behind the nourished breakwater and the accreted

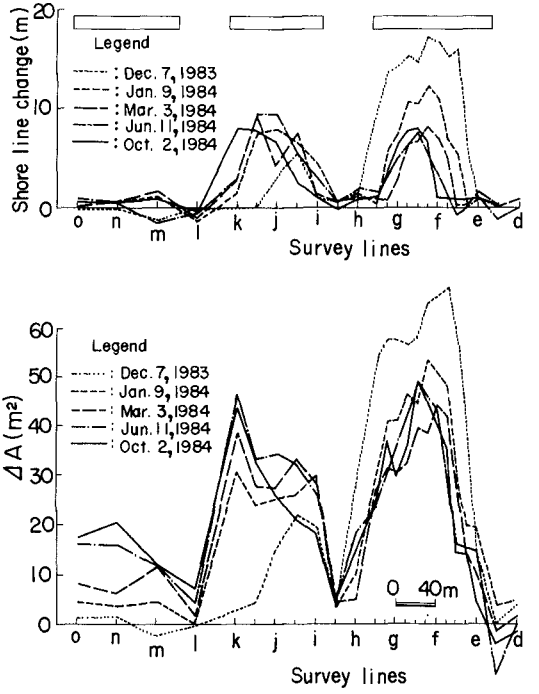

Fig.7 Longshore distributions of shoreline change, △y, and change of sectional area, △A.

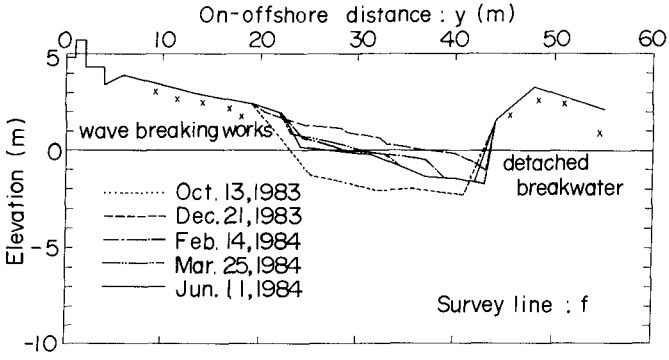

Fig.8 Change of cross section of the beach behind the breakwater (survey line : f) .

region next to the breakwater, respectively. A relation stands between $\triangle A$ and $\triangle y$ with the correlation coefficient of 0.97.

$$\triangle A = 2.6\ \triangle y + 3.5 \qquad (1)$$

where $\triangle A$ and $\triangle y$ have m^2 and m unit, respectively. The regression coefficient of $\triangle A$ and $\triangle y$ is equal to the characteristic height of the beach changes due to littoral transport.[1] Equation (1) shows that the areal change of a section of the beach can be expressed in terms of the change of the shoreline position, and that the characteristic height is equal to 2.6 m. The value is small compared with the one obtained on the other coast. For example, it is around 8 m on the Suruga Coast in Suruga Bay facing the Pacific Ocean.[1] The reason is such that the beach changes are confined within the shallow water zone behind the breakwater in this field experiment.

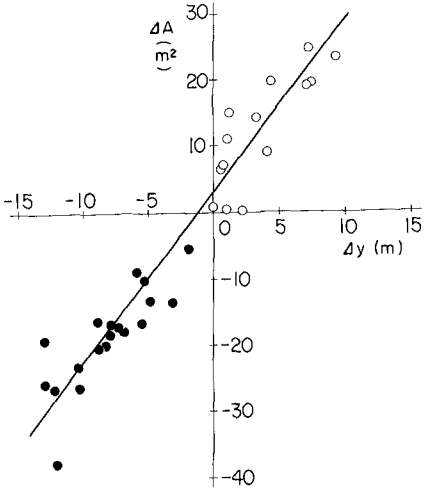

Fig.9 Correlation between the change of the sectional area, $\triangle A$, and that of the shoreline position, $\triangle y$.

Next, temporal changes of the shoreline positions and the sectional areas will be discussed in detail as shown in Fig. 10, since the overall relationship between these variables has already known. The abscissa shows the date of the sounding, and the ordinates are the change of the shoreline position in m-unit and that of the sectional area in m^2-unit, respectively. Changes at 26 survey lines between c and o are shown in the figure. Survey lines between e through g_{20} are located just on the nourished breakwater, and survey lines between i through k are located on the adjacent detached breakwater. The shoreline advanced abruptly between e_{10} and g_{20} during October 13 through December 7 due to the nourishment. At the same time the shoreline at i_{20} and j behind the adjacent detached breakwater advanced without the

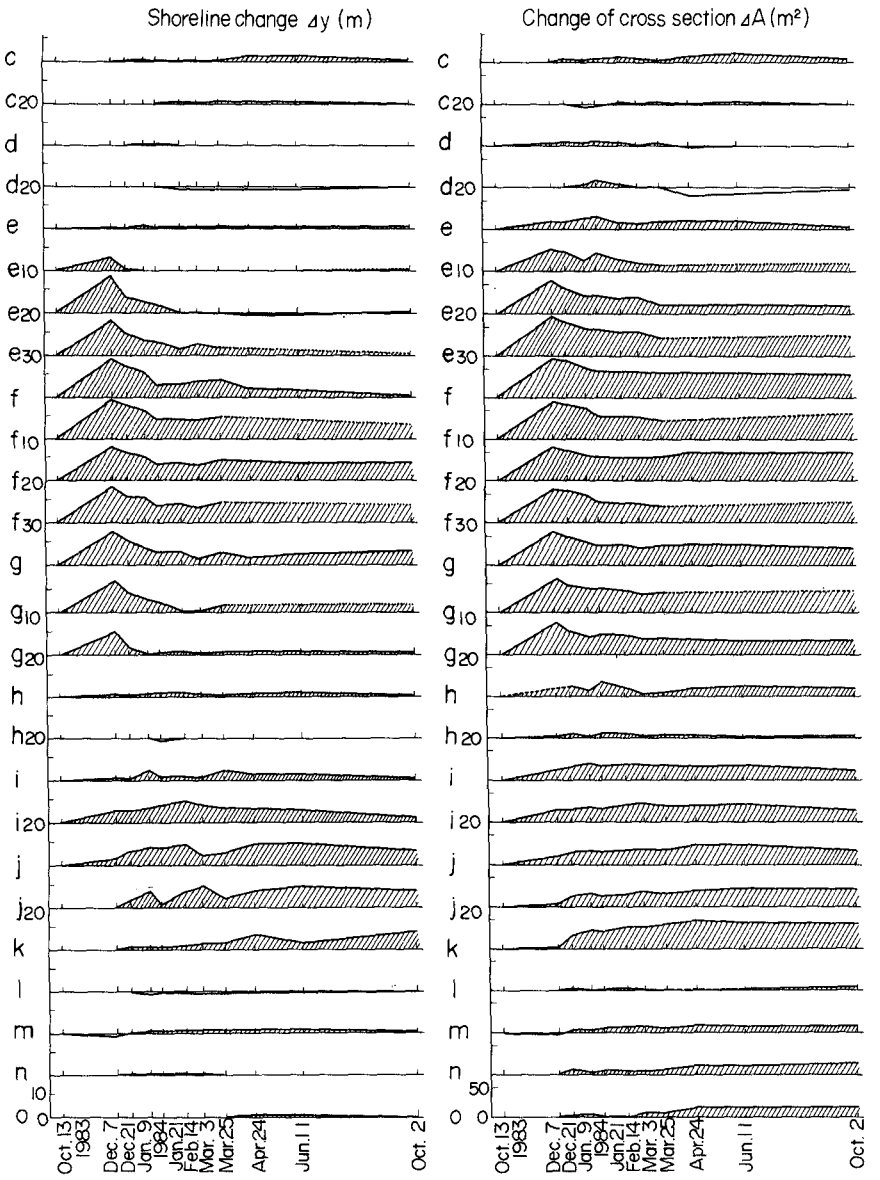

Fig.10 Temporal and spatial change of the shoreline position.

shoreline changes in the opening between the breakwaters. This means that part of the nourished sand were carried quickly westward by the longshore transport with the initiation of the artificial nourishment, and deposited behind the adjacent detached breakwater. Besides, it should be noted that the shoreline did not advance behind the detached breakwater located east of the nourished location, e.g. survey line c and c_{20}. The shoreline change agrees well with the change of the sectional area, and the sectionl area increases with the advance of the shoreline position. In the vicinity of the openings of the breakwaters, for instance at survey lines e, e_{10}, g_{10}, g_{20}, i and i_{20}, the sectional area is considerably large, although the shoreline change is comparatively small. It is found that sand accumulate below the sea surface without the advance of the shoreline. Moreover, the changes of the shoreline position and the sectional area since December 7 were rapid at first, and then the rate of changes decreased with time. Two reasons are considered. First, high waves attacked the beach under the winter storm condition at first, but gradually it became calm wave condition as shown in Fig. 3. Secondly, the rate of change of the nourished form was rapid in the beginning, since nourished sand had a projecting form, even if the artificial nourishment was conducted behind the breakwater.

V. RELATION BETWEEN VOLUME CHANGE AND LONGSHORE COMPONENT OF ENERGY FLUX OF WAVES

In the planning of the beach nourishment behind the detached breakwater, it is important from the technical point of view to know whether there is a possibility of outflow of sand through the openings of the detached breakwater toward the offshore zone or not. Because the sand amount to be needed for the creation of tombolo depends upon both the sand retained behind the breakwater and the loss of sand due to the on–offshore sand movement. Therefore the volume changes in various regions were calculated from the survey data and were summed up as in Fig. 11. In the figure the volume change in each period were normalized by the total volume change, 8152m^3, between October 13, 1983 before the nourishment and December 7 right after the nourishment. In order to obtain the volume change the volume of the materials deposited inside the wave breaking works has to be counted, and for the purpose the porosity inside the wave breaking works was assumed to be 50%. The volume change until December 7 is 2252m^3 greater than the nourished volume of 5900m^3, although both volumes should coincide each other. As for the reasons of the difference, several posibilities are considered such that the assumption of the porosity of 50% was not appropriate, the sounding on October 13 had some error, or the calculation of the total volume of the nourished sand had also some error. However, it is difficult to investigate the problem in detail, so that the volume change of sand is compared by the relative ratio with respect to the total volume change between October 13 and December 7.

Regarding the volume change of sand until October 2 , 1984, it is understood that almost all amount of the nourished sand were retained behind the detached breakwaters and the loss of sand into offshore zone was small, taking account of the

total volume of sand from the nourished location to the second detached breakwater. Comparing the volume changes of sand in each region, the volume behind the nourished detached breakwater had about 80 percent of the total volume in the beginning, but soon it decreased with time. The rate of the volume change was large at first, and then became small. To the contrary the sand volume behind the adjacent breakwater increased rapidly. These changes are considered to be due to the cause that the sand were carried alongshore by the longshore sand transport directing westward in a shallow region behind the detached breakwater. Finally it is concluded that the nourished sand were retained behind the detached breakwater and were useful for the formation of tombolo.

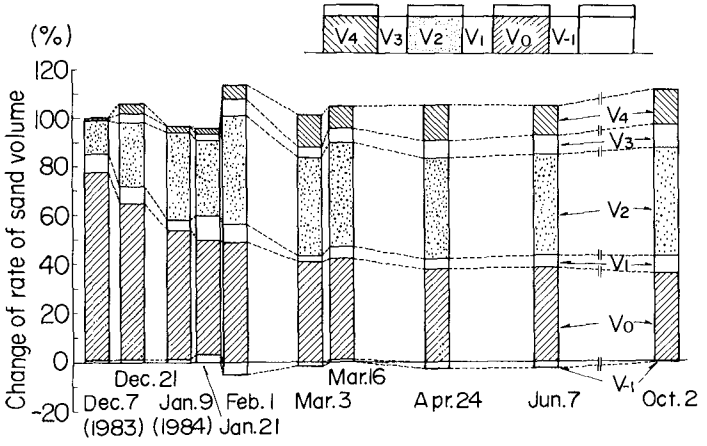

Fig.11 Temporal change of rate of nourished sand volume.

Next, the relationship between the longshore component of the energy flux of waves and the volume change of sand behind the nourished and west detached breakwaters are investigated as shown in Fig. 12. The energy flux of waves are evaluated at a depth of 5 m off the detached breakwater. The energy flux was obtained by the following method. First, wave height at the position of 15 m deep off the nourished location is calculated from the observed data of Tanaka Observatory, considering wave refraction due to the change of the bottom topography. Regarding the wave direction data, the results of the visual observation are assumed to be the input data at the same position, although the accuracy of the visual measurement may not be so high. If the visual observation data are lacking due to the difficulty of the observation under the storm wave conditions, the wave direction at the nourished location was estimated from the data of the visual observation of the wave direction at Tanaka Observatory. Due to the charcteristics of wind velocity and the restricted fetch at Tanaka Observatory, the possibility of the generation of waves having longer period than about 5 seconds in Toyama Bay is very rare, so that waves, having

longer period than 5 seconds and being incident from the west of point of Noto Peninsula are assumed to be incident from the direction connecting Tanaka Observatory with the point of Peninsula. After the incident waves at a depth of 15 m were decided, wave shoaling between 15 m and 5 m off the nourished location was calculated, and finally the energy flux of waves was obtained.

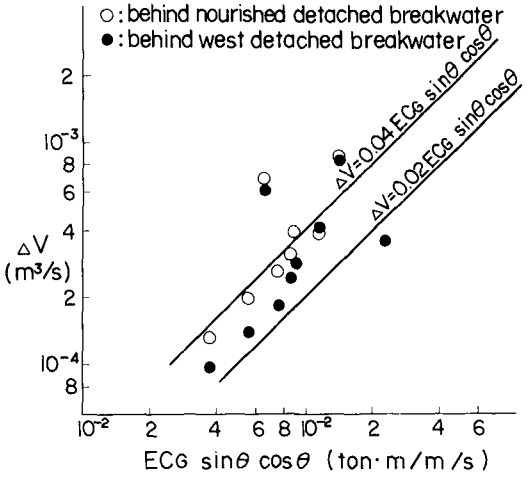

Fig.12 Relation between the longshore component of the energy flux of waves and volume change of sand.

In Fig. 12 the coefficient between the volume change of sand and the longshore component of the energy flux of waves was found to be 0.02-0.04, although it is difficult to compare the value with the past results of the coefficient directly because the longshore component of the energy flux of waves in Fig. 12 is not estimated at the breaking point. The value is one order smaller than the Savage coefficient. In the field experiment the beach changes were mainly confined within behind the detached breakwater, and the wave height behind the breakwaters is small compared with the exposed beach, so that the movement of the bed materials is restricted under the wave conditions and the coefficient is thought to become small.

Ⅵ. RESULTS OF TRACER TEST

In order to examine the direction of the littoral drift around the detached breakwater, tracer test using colored concrete blocks was conducted on December 7 in 1983 after the beach nourishment had just finished. Colored concrete blocks of around 30m³ were placed on the surface of the nourished sand, and the movement was examined by the sampling test of 11 times until October 2 , 1984. The number of the colored concrete blocks was counted directly along the shoreline. For the colored concrete, high strength concrete mixed with the red pigment was used in order to

confirm the easiness of the distinction of colored blocks along the shore and the abrasion resistence. The colored concrete blocks were broken into fine pieces of about 15 cm diameter. The compresive strength of these concrete was around 900kg/cm² at the field test.

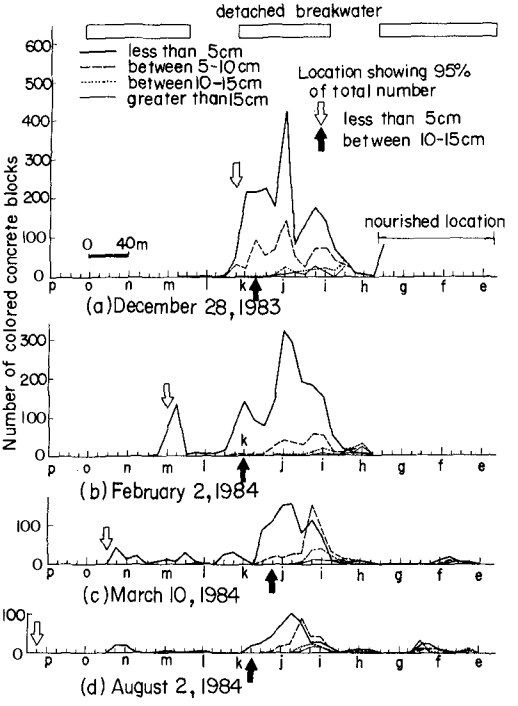

Fig.13 Longshore distribution of number of colored concrete blocks.

Longshore distribution of number of the colored concrete blocks is shown in Fig. 13 with the classification of each grain size of the recovered samples. The number is counted every 10 m intervals alongshore. The arrows in the figure designate the location showing 95% of the total number counted from the west end of the nourished position. Tracers of the grain size less than 5 cm moved westward definitely with time, and they reached to the point P distant about 350m from the nourished location. On the other hand the movement of tracers of larger grain size is slower compared with the case of the smaller grain size. The region where the tracers of the grain size smaller than 5 cm were recovered coincides with the one where large beach changes were observed, so that it is found that the maximum distance of the movement of the nourished sand during the observation period is about 350m.

Ⅶ. CONCLUSIONS

In this study the field experiment of sand bypassing was done on the Shimoni–ikawa Coast in Toyama Bay. Finally the following conclusions were obtained.

(1) In the field experiment the sand nourished behind the detached breakwater were carried slowly in the longshore direction without the outflow of sand through the openings of the detached breakwaters. It is concluded that the detached breakwater is useful to control the on–offshore sand movement and to retain the sand behind the detached breakwater.

(2) On the Shimoni–ikawa Coast tombolos were not formed behind the detached breakwaters, because after the severe erosion of the coast the sand supply to the coast was small. It is found that they can be formed by the nourishment of sand bypassed from the updrift coast. The formation of tombolo is considered to be useful for the prevention of wave overtopping, because the depth near the shore becomes smaller due to the presence of tombolo.

(3) The coefficient between the volume change of sand and the longshore component of the energy flux of waves was found to be 0.02-0.04.

(4) The direction of littoral transport was confirmed to be westward due to the tracer test using colored concrete on the coast. It was also found that the fine tracer were carried more rapidly than coarser tracer.

ACKNOWLEDGEMENT

This study was conducted under the commitee's guidance, of which members consist of Prof. Y. Tsuchiya, Disaster Prevension Research Institute, Kyoto University for the chairman, Prof. N. Shuto, Tohoku University, Prof. H. Noda, Tottori University and the delegates of the government offices. Authors would like to thank Prof. Y. Tsuchiya, Prof. N. Shuto and Prof. H. Noda for many useful discussions.

REFERENCES

1) Uda, T. and T. Takeuchi : An Analysis of Beach Erosion on Suruga Coast, Coastal Eng. in Japan, Vol. 28, pp.161-172, 1985.

CHAPTER 116

The Interaction of Waves and Currents over a Longshore Bar

I.A. Svendsen & J. Buhr Hansen *

Abstract

A two-dimensional model for waves and steady currents in the surf zone is developed. It is based on a depth integrated and time averaged version of the equations for the conservation of mass, momentum, and wave energy. A numerical solution is described based on a fourth order Runge-Kutta method. The solution yields the variation of wave height, set-up, and current in the surf zone, taking into account the mass flux in the waves.

In its general form any wave theory can be used for the wave properties. Specific results are given using the description for surf zone waves suggested by Svendsen (1984a), and in this form the model is used for the wave motion with a current on a beach with a longshore bar. Results for wave height and set-up are compared with measurements by Hansen & Svendsen (1986).

1. Introduction

On a beach with a longshore bar the wave breaking over the bar is usually combined with a net shoreward mass flux which, in a three-dimensional flow situation, feeds longshore currents.

Both field observations and experiments indicate that the longshore current is much stronger in the shore-parallel channel or "trough" behind the bar than on the bar itself. Thus for almost shore-normal waves the motion over the bar can be nearly two-dimensional, at least till a point somewhere around or after the bar crest.

The net flow over the bar and in the trough behind was studied theoretically by Bruun (1963) and later by Dalrymple (1978), who was able to determine the largest possible distance between two successive rip currents. A similar analysis was made by Deigaard (1986). These considerations, however, apply to the creation of the rip over an, in principle, uniform and unbroken bar. Once the rip current has established an opening in the bar the position of the rip is locked to this opening, at least over times long enough for the flow pattern to be considered quasi-steady. Thus the question becomes: how much water flows over the bar with the waves, and how does the net flux influence waves, set-up, etc.?

* Institute of Hydrodynamics and Hydraulic Engineering, Technical University of Denmark, DK-2800 Lyngby, Denmark.

In the present paper we approach these problems theoretically by considering the above-mentioned two-dimensional situation of shore-normal incident waves and a shore-normal current with discharge $\overline{Q}$. In an accompanying paper by Hansen & Svendsen (1986) (denoted by I in the following) this situation is modelled experimentally. The net discharge $\overline{Q}$ is added to the waves well offshore of the slope and runs out through the permeable wave absorber which replaces the actual beach. Thus in this experiment the longshore flow in the trough is not represented.

In choosing this arrangement we implicitly assume that in a prototype situation the magnitude of $\overline{Q}$ will be determined by the distance between the rips and by the position of our two-dimensional flow section relative to the position of the rip currents.

The mathematical numerical model developed is based on the depth integrated, time averaged equations of continuity, momentum, and energy as derived by, e.g., Phillips (1977). These equations apply for a very general combination of waves and currents. In the model, the wave properties, such as radiation stress, mass flux, and energy flux are represented by dimensionless coefficients chosen in a way which makes them depend only weakly on water depth, wave height, and wave period.

The general form of the model allows these coefficients to be determined by any chosen wave theory. In the present application, however, the coefficients are developed using the description of breaking waves suggested by Svendsen (1984a). In that paper, and in Svendsen (1984b) and Hansen & Svendsen (1984), wave height, set-up, and undertow were analysed for breaking waves with no net flow. This is now generalized to include the effect of currents following (or opposing) the waves. This also implies including the effect of the undertow in the wave-current interaction, although in the present form of the model it is only done in a depth-averaged sense.

Finally is presented a comparison with the experimental results for wave heights and set-up over a barred profile described in more detail in I. This is combined with a discussion of the inaccuracies in the theoretical approach as revealed by the comparison.

2. The Basic Equations

The type of model in question belongs to the group of models which consider only the depth integrated equations averaged over a wave period. Thus the effect of the waves on the conservation equations is represented by depth integrated, time averaged quantities, such as (in the continuity equation) the mass (or volume) flux created by the waves, the radiation stress, and (in the energy equation) by the energy flux and the mean energy dissipation per unit of time and area of the bottom.

2.1. Conservation of Mass

Following Phillips (1977) (although with a different notation) we use the definitions shown in Fig. 1. An x,z-coordinate system has its origin in the undisturbed water surface SWL, and the instantaneous water surface elevation $\eta(x,t)$ is measured from the local mean water surface MWS so that the temporal mean of η is zero.

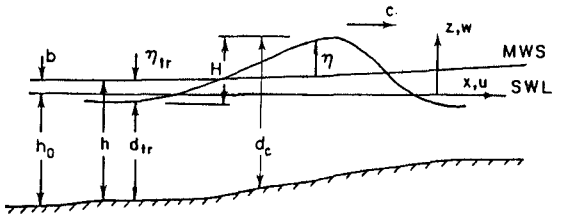

Figure 1. Definitions used.

The horizontal particle velocity u(x,z,t) is divided into two parts u_w (wave) and U (current) defined so that

$$u = u_w(x,z,t) + U(z) \quad ; \quad \overline{u}_w = 0 \tag{2.1}$$

where $\overline{\ }$ means average over a wave period.

We define a depth mean value of U(z) by

$$U = \overline{\frac{1}{h}\int_{-h_0}^{b+\eta} U(z)dz} \tag{2.2}$$

and the volume flux due to the wave part u_w of the motion then becomes

$$Q_s = \overline{\int_{-h_0}^{b+\eta} u_w \, dz} = \overline{\int_{\eta_t}^{b+\eta} u_w \, dz} \quad *) \tag{2.3}$$

where η_t is the (negative) surface elevation in the wave trough. The total mean volume flux $\overline{Q}$ can then be written

$$\overline{Q} = \overline{\int_{-h_0}^{b+\eta} u \, dz} = Q_s + Uh \tag{2.4}$$

Eq. (2.4) is the equation for the conservation of mass.

2.2. Conservation of Momentum

In the present study we will consider only the quasisteady problem of a time-independent current. We also assume that in the depth-integrated and time-averaged momentum and energy equations U(z) can be replaced by U. We can then use the momentum and energy equations given by Phillips (1977).

Following Phillips we define the radiation stress by

*) Notice that this definition of Q_s differs slightly from that by Svendsen (1984b), who used u instead of u_w in (2.3).

$$S'_{xx} = \overline{\int_{-h_0}^{b+\eta} \rho(u_w^2 - w^2)dz} + \frac{1}{2}\rho g\overline{\eta^2} - \frac{\rho Q_s^2}{h} \tag{2.5}$$

where w is the vertical velocity, and ' in S'_{xx} indicates the inclusion of the Q_s-term. This term is actually $O(H^4)$, which is small in ordinary Stokes waves, and it was omitted by Mei (1983). I turns out even in surf zone waves, where H/h = 0.6, to be rather unimportant.

With these definitions and simplifications the horizontal momentum equation can then be written in the following form

$$\frac{d}{dx}\left\{\rho\frac{\overline{Q}^2}{h} + S'_{xx}\right\} + \rho gh\frac{db}{dx} + \overline{\tau}_b = 0 \tag{2.6}$$

which, except for the $\overline{\tau}_b$-term, is the same as Phillips' expression (3.6.11).

2.3. Conservation of Energy

We define the energy flux E_f due to the waves only by

$$E_f = \overline{\int_{-h_0}^{b+\eta} \left\{p_D + \frac{1}{2}\rho(u_w^2 + w^2)\right\} u_w \, dz} \tag{2.7}$$

where p_D is the dynamic pressure defined as

$$p_D = p + \rho g(z - b) \tag{2.8}$$

The energy density E in the waves is

$$E = \overline{\int_{-h_0}^{b+\eta} \frac{1}{2}\rho(u_w^2 + w^2)dz} + \frac{1}{2}\rho g\overline{\eta^2} \tag{2.9}$$

and the total mean dissipation per m^2 bottom and per second is termed $\mathcal{D}$.

The energy equation for the wave motion then becomes

$$\frac{d}{dx}\left\{E_f + UE - \frac{1}{2}\rho\overline{Q}\left(\frac{Q_s}{h}\right)^2\right\} + S'_{xx}\frac{dU}{dx} - \overline{\tau}_b U = \mathcal{D} \tag{2.10}$$

This form also corresponds to Phillips' Eq. (3.6.19) except for the term $\overline{\tau}_b U$, which is the dissipation at the bottom due to the current*). In the surf zone, however, this contribution is very small relative to the total dissipation $\mathcal{D}$, and hence we shall omit it in the numerical computations. $\mathcal{D}$ also includes the dissipation in the bottom boundary layer due to the oscillatory motion, and also that contribution will be ignored in this paper. This implies that $\mathcal{D}$ simply is assumed to equal the breaker disspation.

The two equations (2.6) and (2.10) may be considered generalised versions of the momentum and energy equations often considered in the surf zone

$$\frac{dS_{xx}}{dx} = -\rho gh\frac{db}{dx} - \overline{\tau}_b \quad , \qquad \frac{dE_f}{dx} = \mathcal{D} \tag{2.11}$$

*) See Christoffersen & Jonsson (1980).

Like these two equations, (2.6) and (2.10) can be solved for b and H^2 provided the wave properties are described in terms of h, b, and H^2. Notice, however, that since

$$h = h_0 + b \tag{2.12}$$

even Eqs. (2.11) are complicated.

3. Dimensionless Wave Quantities

As mentioned in the introduction the wave quantities Q_s, S'_{xx}, E_f, and E must all be determined by some wave theory. This also applies to the energy dissipation $\mathcal{D}$ and the mean bottom shear stress $\overline{\tau}_b$. To facilitate a rational approach to this problem we define dimensionless forms of these quantities.

For Q_s, S'_{xx}, E_f, and E we introduce the following dimensionless quantities

$$B_Q = Q_s h/c_r H^2 \tag{3.1}$$

$$P' = S'_{xx}/\rho g H^2 \tag{3.2}$$

$$B = E_f/\rho g c H^2 \tag{3.3}$$

$$B_E = E/\rho g H^2 \tag{3.4}$$

We see that for linear theory these four quantities would depend only on h/L (L being local wave length defined as cT). In nonlinear waves, and particularly breaking waves, the dimensionless quantities will depend also on the wave height, but only weakly so.

The energy dissipation $\mathcal{D}$ is non-dimensionalized by defining D as

$$D = 4\ hT_a/\rho g H^3 \tag{3.5}$$

which is inspired by the idea that the dissipation in breaking waves resembles that in a bore.

The same definitions (except B_Q) were used by Svendsen (1984a), who suggested simple expressions for their form for surf zone waves. Before actually limiting the computations to a particular way of describing the breaking waves we first develop the numerical scheme used for the solution. Thus in the following we simply assume that

$$(B_Q,\ P',\ B,\ B_E,\ D) = f(x) \tag{3.6}$$

where f(x) includes dependence on wave height H, set-up b, and more detailed wave properties such as shape of surface profile, velocity, and pressure distributions, etc. Hence also results for linear theory could be used (although it may not be expected to represent the wave details well).

In the present formulation of the problem we consider $\overline{Q}$ as known (equal to the discharge supplied by the pump). Hence the net current velocity U can be determined from the continuity equation (2.4) as

$$U = \frac{\bar{Q}-Q_s}{h} \tag{3.7}$$

The mean bottom shear stress $\bar{\tau}_b$ will be discussed in Sect. 6.

4. The Numerical Procedure

Christoffersen & Jonsson (1980) showed that for Stokes waves the energy equation for the wave motion corresponding to (2.10) can be written as an equation for conservation of wave action, namely for the steady case considered here as

$$\frac{d}{dx}\left(\frac{E}{\omega_r}(U + c_{gr})\right) + \frac{\mathcal{D} - \bar{\tau}_b U}{\omega_r} = 0 \tag{4.1}$$

where c_{gr} is the Stokes group velocity. This version of the energy equation, however, was derived utilizing the special properties of linear waves and hence cannot be used for the general nonlinear waves considered in this paper. We therefore choose to solve (2.6) and (2.10) directly for b and H^2 respectively.

The numerical solution is obtained by a fourth order Runge-Kutta method. This requires that the two differential equations (2.6) and (2.10) with (3.1) through (3.5) substituted are written on the form

$$\frac{db}{dx} = f_b(x,b,H^2) \quad ; \quad \frac{dH^2}{dx} = f_H(x,b,H^2) \tag{4.2}$$

Since, however, the dimensionless coefficients in general are unknown functions of b and H^2 the form (4.2) cannot be obtained in a strict manner.

We therefore utilize the assumption that the dimensionless coefficient depends only weakly on H. To further simplify the problem we also assume that the additional terms in (2.6) and (2.10) due to the current are small too. For the numerical computations we therefore isolate db/dx and dH^2/dx from the main terms in (2.6) and (2.10), that is the terms included in (2.11). We then accept that derivatives of the dimensionless coefficients, the current, and the Q_s-terms contain db/dx and dH^2/dx. In the computations these db/dx and dH^2/dx are then evaluated only at each grid point, not at intermediate points in each integration interval as the Runge-Kutta method prescribes.

The equations for db/dx and dH^2/dx derived according to these assumptions may be described by introducing the following definitions

$$\alpha = c_r/\sqrt{gh} \tag{4.3}$$

$$D' = D\,\frac{H^2}{h}\,\frac{H}{h}\,\frac{1}{4T_a\alpha\sqrt{g/h}\,B} = \frac{\mathcal{D}}{\rho g c B} \tag{4.4}$$

$$f_1 = \left[\frac{\bar{Q}^2}{gh^3}h_x - \frac{\bar{\tau}_b}{\rho g h}\right] \Big/ \left(1 - \frac{1}{2}P\left(\frac{h}{h}\right)^2\right) \tag{4.5}$$

$$g_1 = \frac{H^2}{E_f}\left[\frac{1}{2}\rho\bar{Q}\,\frac{d}{dx}\left(\frac{Q_s}{h}\right)^2 - S'_{xx}\frac{dU}{dx} - \frac{d}{dx}(EU)\right] \tag{4.6}$$

We then get:

$$\frac{db}{dx} = F_b \tag{4.7}$$

$$\frac{dH^2}{dx} = F_H \tag{4.8}$$

where

$$F_b = -\frac{P'}{h}\frac{D' + H^2\left(\frac{P'_x}{P} - \frac{B_x}{B} - \frac{1}{2}\frac{h_{ox}}{h}\right) + g_1}{1 - \frac{1}{2}P'\left(\frac{H}{h}\right)^2} + f_1 \tag{4.9}$$

$$F_H = D' - \left(\frac{1}{2}\left(\frac{h_{ox}}{h} + \frac{F_b}{h}\right) + \frac{B_x}{B}\right)H^2 + g_1 \tag{4.10}$$

f_1 and g_1 represent the small terms mentioned above. We see that, in addition to contributions that vanish with the net flow $\bar{Q}$, there are terms associated with $\bar{\tau}_b$ or U which for $\bar{Q} = 0$ represents the undertow. Except for the $\bar{\tau}_b$-term all these terms are calculated by differentiating analytically the expressions given in the following Section 5. In the computations we assume that $dB_0/dx = d\alpha/dx = 0$ (see I), and for computation of b_{n+1} and H^2_{n+1} at points x_{n+1}, f_1 and g_1 are evaluated only at x_n.

The fourth order Runge-Kutta scheme for two simultaneous equations is given in, e.g. Hildebrand (1974, 2nd ed.) p. 291.

5. Determination of the Wave Quantities

The mathematical-numerical description presented so far does not presume anything about how the wave properties Q_s, S'_{xx}, E_f, E, and $\mathcal{D}$ are determined. As mentioned a description of the phase motion of the waves must be involved, and most often sinusoidal waves have been used to determine the radiation stress and the energy flux for a wave with a given height and period. Examples are Huang & Wang (1980), Dally et al. (1984), Izumiya & Horikawa (1984). But also solitary waves and cnoidal wave theory have been used.

For the present applications we determine Q_s, S'_{xx}, E_f, and E by using the model for surf zone waves suggested by Svendsen (1984a).

The basic assumption is that the actual horizontal particle velocity in the oscillatory motion shown in Fig. 2a can be approximated by a constant velocity u_0 everywhere except in the surface roller (Fig. 2b). Here the velocity is assumed to be equal to the phase velocity c, since the roller represents a body of water which is carried with the wave. It is furthermore assumed that the pressure is hydrostatic.

Following Svendsen (1984a) we also assume that u_w can be approximated by

$$u_w \simeq c_r \eta/h \tag{5.1}$$

where c_r is the wave speed relative to the water.

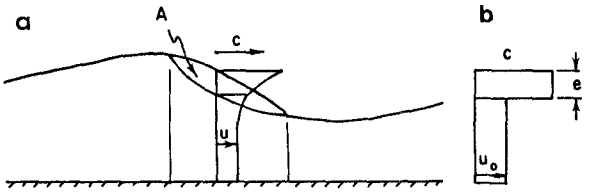

Figure 2. Actual and assumed velocity profiles.

The inaccuracies this leads to are analysed in some detail in I.

c_r, U, and the wave speed c_a observed from a fixed point are related by

$$c_a = c_r + U \tag{5.2}$$

From the definition (2.3) for the volume flux Q_s due to the waves we then get the following for B_Q (defined by (3.1))

$$B_Q = B_0 + B_r \frac{gh}{c_r^2} \tag{5.3}$$

where

$$B_0 \equiv \overline{\left(\frac{\eta}{H}\right)^2} \tag{5.4}$$

$$B_r = \frac{A}{H^2} \frac{c_r}{gT_r} \tag{5.5}$$

Here A is the vertical cross-sectional area of the roller. Svendsen (1984a) found $A/H^2 \sim 0.9$. T_r is the relative wave period which is related to the absolute period T_a through (5.2) by $L \simeq c_r T_r = c_a T_a$. (Notice that owing to the different definition of Q_s, the result for Q_s differs by a factor h/d_t from the result given by Svendsen (1984b). d_t is the water depth under the wave trough, Fig. 1.)

Similarly, we get from the definition (2.5)

$$P' = B_0\left(\frac{1}{2} + \frac{c_r^2}{gh}\right) + B_r - \frac{c_r^2}{gh}\left(\frac{H}{h}\right)^2 B_Q \tag{5.6}$$

(2.7) yields for B

$$B = B_0 + \frac{1}{2} B_r \tag{5.7}$$

and finally, (2.9) yields

$$B_E = \frac{1}{2}\left\{B_0\left(1 + \frac{c_r^2}{gh}\right) + B_r\right\} \tag{5.8}$$

Equations (5.3) - (5.8) together with (3.1) - (3.4) determine Q_s, S'_{xx}, E_f, and E in the momentum and energy equations ((2.6 and (2.10) respectively) for a wave of given height H and phase velocity c_r at depth h.

As in Svendsen (1984a) we will assume that α in (4.3) is constant throughout the surf zone. This is further discussed in I. An alternative - and perhaps more natural - choice would be to assume that c_r equals the speed of a bore with height H. However, in I it is found that the difference is small, and α constant is much simpler to use in the derivations.

Following Svendsen (1984a) we assume that the energy dissipation can be determined as the dissipation in a bore of the same height as the wave. This results in

$$\mathcal{D} = - \rho g \frac{c_r}{L} h \frac{H^3}{4 d_t d_c} \tag{5.9}$$

where d_t and d_c are instantaneous water depths below the wave trough and the wave crest respectively. In establishing this analogy to the bore it is assumed that adding a uniform current to the wave or the bore does not change the breaking process. Therefore, the phase velocity in (5.9) is the relative velocity c_r.

Eq. (5.9) is substituted into the definition (3.5) and we utilize that (5.2) implies

$$T_r = T_a (1 + U/c_c)^{-1} \tag{5.10}$$

This then yields

$$D = - \frac{h^2}{d_t d_c} \frac{1}{1 + U/c_r} \tag{5.11}$$

This expression illustrates that for a current U > 0 following the wave the dissipation decreases relative to a wave of the same absolute period T_a and vice versa for a wave on an opposing current, as one would expect from the corresponding change in wave steepness.

6. The Mean Bottom Shear Stress

The mean bottom shear stress $\overline{\tau}_b$ occurs in the time-averaged momentum equation (2.11). Svendsen et al. (1987) showed how $\overline{\tau}_b$ can be determined from the undertow, which is patched to the flow in the (oscillatory) bottom boundary layer to satisfy the no-slip condition at the bottom. This implies that to determine $\overline{\tau}_b$ we must first determine the velocity distribution over depth of the undertow (which here means the current velocity profile U(z)). Their results for $\overline{\tau}_b$ are equivalent to

$$\overline{\tau}_b = \frac{1}{2} \rho f_w u_{wbm} U_b \tag{6.1}$$

where f_w is the wave friction factor, u_{wbm} is the particle velocity amplitude at the bottom, and U_b the current velocity at the bottom (i.e. outside the boundary layer).

In the present version of the model we will approximate (6.1) by

$$\bar{\tau}_b = \frac{1}{2} \rho f_w u_{wbm} U \tag{6.2}$$

(U given by (2.2)). As the measurements in I show, this is not always a good approximation and may for small U even lead to (small) $\bar{\tau}_b$ values of the wrong sign. The total error on b, however, is estimated not to exceed 20% of this already very small contribution (in numbers less than 0.2•1.2 mm of a total set-up of ~15 mm for the experiments in I).

For u_{wbm} we have used the forward velocity amplitude

$$u_{wbm} = c \frac{\eta_c}{H} \frac{H}{h} \tag{6.3}$$

and f_w is found from Jonssons's diagrams to be $\sim 2 \cdot 10^{-2}$.

7. Comparison with Experimental Results for Waves and Currents Over a Longshore Bar

Numerical experiments have been carried out with the model for the wave-current flow over the longshore barred profile investigated experimentally in I.

In these experiments the still-water depth h_0 is given by (all units in m)

$x < 14.78$ $\qquad h_0 = 0.340$

$14.78 < x < 22.96$ $\qquad h_0 = 0.340 - (x - 14.78) \cdot 0.0280$

$22.96 < x$ $\qquad h_0 = 0.0705 + (x - 25.70)^2 \cdot 5.53 \cdot 10^{-3}$

This corresponds to a plane bottom with slope $h_x = 0.0280 = 1 : 35.7$ between $x = 14.78$ and $x = 22.96$, succeeded by a parabola with summit (bar crest) at $x = 25.70$.

The numerical experiments described here were made with the following (fixed) parameter values (see I):

$A/H^2 = 0.9$; $B_0 = 0.090$

$\eta_c/H = 0.60$; $\alpha = 1.0$

$\Delta x = 0.1$;

Formally, A/H^2 represents the roller, and the value of 0.9 was obtained from deep water measurements (see Svendsen, 1984a).

The choice of B_0 constant and $\alpha = 1$ may be refined on the basis of the experimental results in I. The formulas for the coefficients show that changes in B_0 or α will effect results in much the same way.

The discussion is mainly restricted to the wave height and the set-up variations. Fig. 3 shows a comparison of wave heights for the four $\bar{Q}$-values for which measurements are reported in I, and Fig. 4 shows the set-up. Two sets of computations are shown:

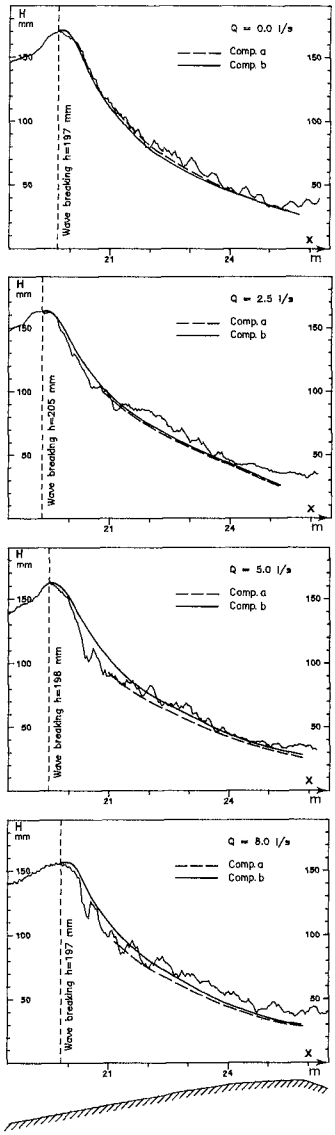

Figure 3. Comparison of measured and computed wave heights.

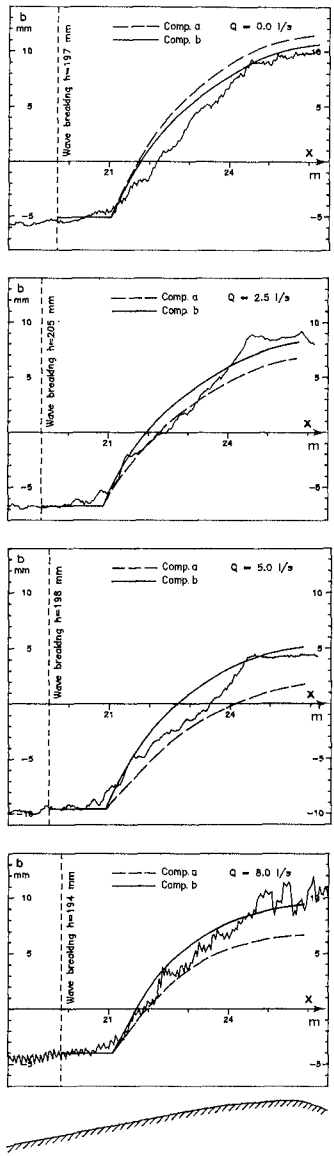

Figure 4. Comparison of measured and computed set-up values.

a) Computations starting at $h_o = 0.8\ h_{oB}$. This point was found by Svendsen (1984a) to correspond to the end of the transition region, in which the collapse of the wave creates an almost constant S_{xx} in spite of the decrease in wave height.

b) Computations starting from the breaking point. In this case the dissipation has artificially been made to grow gradually from 0 at the breaking point and asymptotically approach the value given by (5.9). The expression used is

$$\mathcal{D} := \tanh\left(0.4\ \frac{x - x_B}{h_{oB}}\right)\mathcal{D} \tag{7.1}$$

which implies that at a distance of five times h_{oB} $\mathcal{D}$ has reached 96% of the full value. This modification does not model the simultaneous transitions in S'_{xx} and E_f, and hence (7.1) is combined with the assumption $b_x = 0$ in $x_B < x < x_t$ (x_t representing the transition point). For a more detailed discussion of the transition region reference is made to Basco (1986).

7.1. General Comparison

It is seen from Fig. 3 that the wave height variation is quite accurately predicted by the model with a slight tendency to too low values. It may also be noted that, in spite of the fact that computation a) starts at the transition point with a wave height which is somewhat different from the height obtained by computation scheme b) at that point, the wave heights obtained near the bar crest by the two schemes are nearly the same.

Also the set-up values over the bar crest are in reasonable agreement with the measurements, whereas there is a general tendency to too high b-values in the region between the transition point and the bar crest. In particular, it is noticed that immediately after the transition point the computations have db_x/dx significantly larger than the measurements.

As should be expected, the set-up variation depends strongly on the wave heights. This can be seen by comparing the set-up variations from a) and b) in the four cases and noting that in some cases the wave heights from computation b) are larger than those from a), in some not: the computed set-up variations follow the same pattern. The coupling from set-up to wave height is simply represented by the fact that the set-up represents an increase in depth, which for sufficiently small h_0 may be appreciable.

7.2. The Influence of the Currents

The computations all use measured values of H and b as initial values, and it is seen that in the experiments there are small differences in the mean water level at the breaking point for the four cases. These are caused by small variations in the total amount of water in the flume required to obtain the same mean water depth with the current only.

Computations with the model show that these small differences in the mean water depth do not influence the wave heights and the set-up in the region studied. Therefore, we may get an estimate of the actual effect the current has on the set-up by comparing the set-up variations relative to a common starting point. This is done in Fig. 5, which also shows the wave height variations (see also I, Table 2).

Both wave height and set-up are seen to be almost unaffected by the current.

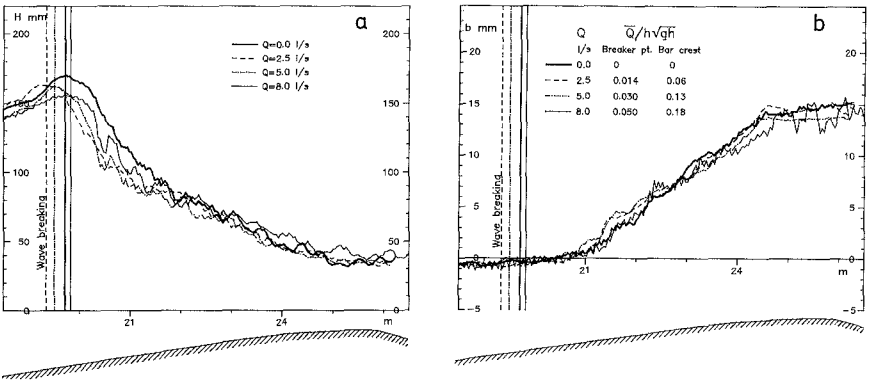

Figure 5. Wave heights (a) and set-up (b) measured for four different values of $\overline{Q}$.

From these results one might jump to the conclusion that the currents have only a negligible effect on the wave conditions. A closer inspection and numerical experiments show that this is too much of a simplification. The extra terms in the equations are important. They just happen nearly to balance each other for the conditions studied.

For the wave heights the behaviour is quite different from a situation with non-breaking waves. The mechanism seems to be that an increase in wave height will also cause an increase in the dissipation and in the energy flux. Hence there is a strong conservatism built into the system at this point, as computations a) and b) also indicated.

For the set-up the mechanism is different: There is no stabilizing effect which parallels that of the dissipation. It is found that the interaction terms in the momentum equation decrease the set-up slightly for all $\overline{Q}$-values, and the bottom shear stress amplifies this by causing a similar decrease in the set-up (up to about 1.2 mm for $\overline{Q} = 8$ ℓ/s). A somewhat stronger effect, however, of the current is caused by the (seemingly) small changes of the wave height described above. That this is the case can be verified in the numerical model by running experiments with the current effect suppressed in one equation and not in the other.

It is particularly interesting to notice that the total set-up Δb at the bar crest measured relative to the water level at the breaking point varies only slightly with the current condition. The measured and computed values are shown in Table 1 below. Considering the many approxima-

tions which the model represents, the very good agreement with the measured values for Δb must be considered fortuitous, as is also suggested by the deviations for the set-up at other x-values.

Notice that the integrated effect of $\overline{\tau}_b$ changes sign when the current increases. This is because shortly after breaking the undertow dominates the (nearbottom) flow ($\overline{\tau}_b < 0$). For large values of $\overline{Q}$ this situation is reversed further shorewards for continuity reasons.

Table 1. Total difference Δb between water level at breaking and over the bar crest.

Discharge $\overline{Q}$ (ℓ/s)	Computation b), $\overline{\tau}_b = 0$	Computation b), $\overline{\tau}_b$ from (6.2)	Measured
0	1.52 cm	1.57 cm	1.55 cm
2.5	1.52 cm	1.51 cm	1.61 cm
5	1.49 cm	1.43 cm	1.42 cm
8	1.39 cm	1.27 cm	1.45 cm

7.3. Inaccuracies in the Predicted Set-Up

The set-up is a direct measure of the variation in shore-normal radiation stress, and the variation of the radiation stress in general is closely associated with the generation of surf zone currents (also in the 3D case). It must therefore be considered an essential condition for a surf zone model that it is able accurately to predict the set-up. At the same time, the set-up is fairly easy to measure and hence a convenient quantity to test models against.

As mentioned earlier Fig. 5 shows that for all $\overline{Q}$-values there is a tendency that the model overestimates the growth rate of the set-up immediately after the transition point (where the momentum equation is switched on in the computations). This inaccuracy was not observed when a model based on the same principles (but without a current) was applied to waves on a plane slope (Svendsen, 1984a). Although the general agreement with measurements might be considered acceptable, and better than other surf zone models, the deviation in db/dx is important. It will cause rather significant discrepancies when db/dx is applied as input for determination of the vertical velocity distribution for the current (see, e.g. Svendsen et al., 1987).

A closer analysis of the situation in the region around the transition point indicates that a major reason for the deviations is related to the abrupt switch between S'_{xx} constant in the transition zone and the rapidly changing S'_{xx} following from the bore description for the inner region. In real waves this transition will of course be gradual.

8. Conclusions

A two-dimensional model for the wave-current interaction in the surf zone has been established. It is based on depth-integrated time-averaged equations of continuity, momentum, and energy. As a description of the

breaking waves is used a generalized form of the method developed by Svendsen (1984a). In principle, however, any wave theory can be used for determination of the coefficients describing the wave properties in the model. The effect of the bottom shear stress is included.

Numerical results for wave heights and set-up are compared with measurements for a bar-type profile. In general, the agreement is found to be quite good although there is a region shortly after the transition point with less accuracy for the set-up.

Finally, the effects of the different elements of the model are discussed.

References

Basco, D.R. (1986), Toward a simple model of the wave breaking transition region in surf zones. Proc. 20th Int. Conf. Coast. Engrg., Taipei.

Bruun, P. (1963), Longshore currents and longshore troughs. J. Geophys. Res. 68, 1065-1078.

Christoffersen, J.B. & I.G. Jonsson (1980), A note on wave action conservation in a dissipative current wave motion. Applied Ocean Res., 2, 4, 179-182.

Dally, W.R., R.G. Dean & R.A. Dalrymple (1984), A model for breaker decay on beaches. Proc. 19th Conf. Coast. Engrg., Houston, 82-98.

Dalrymple, R.A. (1978), Rip currents and their causes. Proc. 16th Int. Conf. Coast. Engrg., Hamburg.

Deigaard, R. (1986), Longshore current behind bars. Inst. Hydrodyn. and Hydr. Engrg., Progr. Rep. 64, 25-29.

Hansen, J.B. & I.A. Svendsen (1984), A theoretical and experimental study of undertow. Proc. 19th Int. Conf. Coast. Engrg., Houston, Ch. 151, 2246-2262.

Hansen, J.B. & I.A. Svendsen (1986) (I) Experimental investigation of the wave and current motion over a longshore bar. Proc. 20th Int. Conf. Coast. Engrg., Taipei.

Hildebrand, F.B. (1974, 2nd ed.), Introduction to numerical analysis. McGraw-Hill, 669 pp.

Izumiya, T. & K. Horikawa (1984), Wave energy equation applicable in and outside the surf zone. Coast. Engrg. Jap., 27, 119-137.

Mei, C.C. (1983), The applied dynamics of ocean surface waves. John Wiley & Sons, 740 pp.

Phillips, O.M. (1977), The dynamics of the upper ocean. Cambridge Univ. Press (2nd ed.), 336 pp.

Stive, M.J.F. & H.G. Wind (1982), A study of radiation stress and set-up in the nearshore region. Coastal Engrg. 6, 1-25.

Svendsen, I.A. (1984a), Wave heights and set-up in a surf zone. Coastal Engrg. 8, 303-329.

Svendsen, I.A. (1984b), Mass flux and undertow in a surf zone. Coastal Engrg. 8, 4, 347-365.

Svendsen, I.A. & P. Justesen (1984), Forces on slender cylinders from very high waves and spilling breakers. Symp. on Description and Modelling of Directional Seas, Techn. Univ., Denmark, June 1984.

Svendsen, I.A., H.A. Schäffer & J. Buhr Hansen (1987), The interaction between the undertow and the boundary layer flow on a beach. Subm. for publ.

Wang, H. & W.-C. Yang (1980), A similarity model in the surf zone. Proc. 17th Int. Conf. Coast. Engrg., I, Ch. 33, 529-546.

CHAPTER 117

Prediction of wind-driven transport rates

D H Swart*

ABSTRACT

The rate of wind-driven sand movement in a dune field is an important parameter needed to establish management strategies for sand dune fields. Until recently not much attention has been given in engineering circles to the possible effect of wind-blown sand transport. However, there is a wealth of literature on the subject which goes back as far as 1936. A study of literature reveals that there are at least 16 formulae for the prediction of the aeolian transport rates which are readily available. This paper describes a technique which utilizes these 16 formulae in the most effective manner for predicting the best estimate of the **potential** wind-blown transport rate. Restrictions on the applicability of the method are discussed and fields for further research are recommended.

1. BACKGROUND

Sediment pathways and sediment budgets in the coastal zone often depend on the balance between wave- and current-driven sediment movement in the nearshore region and wind-driven transport of sand through driftsand areas connecting adjacent bays or embayments. The management of these areas often relies on knowledge of the relative magnitude of the transport in the underwater and driftsand areas.

Evaluation of the merit of stabilizing a driftsand area is a case in point. On the one hand the stabilization may be essential to prevent inundation of townships or valuable agricultural land by driftsands. On the other hand this same driftsand field may be a vital source of sand supply for the beaches downwind of the driftsands. A proper decision about the extent and method of stabilization can then only be made once a reliable estimate has been made of the amount of wind-driven sand movement that could potentially take place annually.

However, the prediction of the aeolian sand transport can only be as good as the wind data. This is frequently a problem. Data of sufficient quality and of long enough duration are needed. A recording period of at least one year and preferably longer is required. Usually such data are only available at focal points for development along the coast with the result that in the case of remote sites one frequently has to resort to the use of visual estimates of wind statistics gathered by lighthouse keepers or to measured data from sites which may be totally unsuitable for application to the site under consideration.

* Head, Sediment Dynamics Division, National Research Institute for Oceanology, CSIR, P.O. Box 320, Stellenbosch, 7600, Republic of South Africa.

Visual estimates of wind characteristics have been made regularly by Voluntary Observing Ships (VOS) since 1960. The estimates are incorporated in six-hourly weather observations of these ships and relayed to the major weather forecasting bureau. Because the deck officers who compile the weather observations are mostly experienced seamen the quality of their estimates is usually good. A vast number of the VOS wind observations for the period from 1960 are available and these cover the entire South African coastline. On the basis of a comparison between VOS wind data and anemometer recordings from shore-based stations Swart (1986) concluded that VOS wind data can be transformed into representative wind statistics on land in the coastal zone.

This paper summarizes the available techniques for the prediction of wind-driven transport, which are based on plane-bed transport situations, and investigates means of applying these techniques to the turbulent wind field situations encountered in driftsand areas.

2. AEOLIAN TRANSPORT PREDICTORS

2.1 General

The predictors for the magnitude of potential aeolian sand transport which have traditionally been used most extensively are those of Bagnold (1941), Kawamura (1951) and O'Brien (1936). More recently Hsu (1971a) and Mossa (1980), amongst others, developed modified predictors. Notwithstanding the large time span between the development of the various formulae, they are all very similar in appearance and in the wind transport rates which are predicted.

The reason for the similarity of appearance of the different formulae is that the mechanism which causes the wind-blown transport of sand is well understood. As soon as the shear stress exerted by the wind field on the sand surface exceeds a critical value, grains start to move. Although certain researchers neglect the critical shear stress in their formulation, all formulae equate the potential aeolian sand transport to some function of the shear stress.

The predicted wind transport rates are similar because the empirical coefficients in the different formulae were updated as more data became available.

This section contains a summary of the equations developed by the researchers mentioned above. To facilitate their easy application all these formulae were transformed into metric units and the transport rates expressed in cubic metres per metre per second, by assuming a porosity of 0.7 in the sand body before transport takes place. The limitations of the predictors will be given here to the extent it is given in the original publications. A more in-depth discussion of each of the 16 formulae can be found in Swart (1987a).

These formulae all relate to the situation where the wind is blowing over a **dry** sand surface, whereas this is obviously not always the case in nature. Therefore, the effect of moisture in the sand on the transport is discussed briefly in Section 2.3. More details can again be found in Swart (1987a).

The following symbols are used extensively in the eguations:

S_a = potential aeolian sand transport rate, expressed in $m^3/m/s$;
u_{*w} = the shear velocity at the sand surface due to wind action, expressed in m/s, which is equal to $(\tau_o/\rho_a)^{1/2}$;
u_{*wc} = critical value of shear velocity above which movement takes place, in m/s;
τ_o = total shear stress at the sand surface due to wind action;
ρ_a = mass density of air in kg/m^3 (1.29 kg/m^3);
ρ_s = mass density of sand in kg/m^3 (2 650 kg/m^3);
g = gravitational acceleration in m/s^2 (9.8 m/s^2);
D_{50} = median grain diameter of sand, in m.

The shear velocity u_{*w} can be determined from the wind velocity profile above the sand surface. The way in which this is done for cases in which the velocity profile is not specifically measured, such as would be the case when predictions are being done, is open to discussion. This aspect will be dealt with in Section 3.

In most of the original publications the potential aeolian sand transport rate is denoted by q and is expressed in g/cm/s. The shear velocities u_{*w} and u_{*wc}, where subscript w incidentally refers to wind, are called u_* and u_{*c} in the original publications and are given in cm/s. The mass densities are given in g/cc in the original papers and the gravitational acceleration is expressed in cm/s^2. All these cgs units have been transformed into metric units for this paper, as indicated above. Symbols used only occasionally will be defined in the text.

2.2 Predictive Formulae

Bagnold (1941) found a formulation for the potential aeolian transport on the assumption that grains move downwind with a bouncing motion near the sand surface. By using data presented by Bagnold (1954), Iwagaki (1958) and Kubota et al. (1982) regarding the empirical constant, the following formula (in metric units) is found:

$$S_a = 0.052\, D_{50}^{0.5} \left(\frac{\rho_a}{g}\right) u_{*w}^3 \quad \text{(in } m^3/m/s\text{)} \qquad \ldots(1)$$

It appears that the data on which the coefficient in equation (1) is based can be summarized as follows:

Range of D_{50} : 0.20×10^{-3} m to 0.40×10^{-3} m
Range of u : 0.14 m/s to 2.85 m/s.

Kawamura (1951) assumed that the shear stress at the sand surface is composed of two components, namely, that caused by the wind and that caused by the impact of saltating and moving sand particles. By using the incipient motion criterion of Bagnold (1941) and experimental data of Kawamura (1951), Horikawa and Shen (1965) and Kubota et al. (1982) the original Kawamura formula can be written as:

$$S_a = 8.24 \times 10^{-4} \left(\frac{\rho_a}{g}\right) (u_{*c} - u_{*wc}) (u_{*w} + u_{*wc})^2 \quad \ldots(2a)$$

(in $m^3/m/s$)

where

$$u_{*wc} = 0.1\left[\left(\frac{\rho_s - \rho_a}{\rho_a}\right) g D_{50}\right]^{1/2} \quad \ldots(2b)$$

The range of conditions for which this formula is valid is the same as that for the Bagnold formula, namely:

Range of D_{50} : 0.20×10^{-3} m to 0.40×10^{-3} m
Range of u_{*w} : 0.14 m/s to 2.85 m/s.

O'Brien and Rindlaub (1936) developed an empirical formula on the basis of field experiments which was transformed by Horikawa (1981) and the present author to

$$S_a = 5.473 \times 10^{-5} (u_{*w} + 0.108)^3 \quad \ldots(3)$$

for $u_{*w} > 0.20$ m.

The range of conditions for which this formula is valid, is as follows:

Range of D_{50} : $D_{50} = 0.20 \times 10^{-3}$ m
Range of u_{*w} : ~ 0.20 m/s to 0.60 m/s.

Hsu (1971a, 1971b, 1972, 1973, 1974a, 1974b) developed on the basis of field measurements a relationship between a shear Froude number and the potential aeolian sediment transport. Empirical coefficients were determined by using laboratory and field data of Bagnold (1941), O'Brien and Rindlaub (1936), Zingg (1952), Kawamura (1951), Horikawa (1960), Belly (1962) and Kadib (1964, 1965).

It can be written in metric units as:

$$S_a = 3.434 \times 10^{-9} \exp(4\,970\, D_{50}) \left[\frac{u_{*w}}{(g D_{50})^{1/2}}\right]^3 \quad \ldots(4)$$

(in $m^3/m/s$).

The range of conditions for which this formula is valid, is as follows:

Range of D_{50} : 0.15×10^{-3} m $\leq D_{50} \leq 1.0 \times 10^{-3}$ m
Range of u_{*w} : 0.18 m/s $\leq u_{*w} \leq$ 2.85 m/s.

Hsu (1974a) only shows a range of u_{*w} extending to 1.0 m/s, but the tests with high wind shear velocities, performed by Kubota et al. (1982), provided another data point which is in agreement with equation

(4), which in effect extends the range of u_{*w} to the value shown above.

Mossa (1980), working under the guidance of Hsu, reanalysed the data which led to equation (4) and found a slightly modified formulation, which is given below although it does not really add any new information over and above that already reported:

$$S_a = 3.475 \times 10^{-9} \exp(4\,910\, D_{50}) \left[\frac{u_{*w}}{(g\, D_{50})^{1/2}}\right]^3 \qquad ...(5)$$

(in $m^3/m/s$).

The range of variables is the same as that for the original Hsu formula.

Chiu (1970) used measurements of wind-driven transport rates at different levels above the sand surface, which he integrated over depth, to obtain an expression for the total wind-driven transport rate. He then used data by Bagnold (1941), Zingg (1952), Horikawa (1960), Belly (1962) and Kadib (1964) to generalize his results to include a range of grain sizes and values of the sorting coefficient s (where $s^2 = D_{75}/D_{25}$). In metric form his results finally lead to:

$$S_a = 5.5 \times 10^{-4} f(s,D_{50}) (2.13 + 0.39\, u_{*w}) \left(\frac{\rho_a}{g}\right) u_{*w}^3 \qquad ...(6a)$$

$f(s,D_{50})$ is for one formulation of Chiu taken as unity and in the other as

$$f(s,D_{50}) = \exp\left(-1.78 \times 10^{-3} (s^2 - 1)^{1/2}\, i\left[\frac{s^3}{D_{50}} (1.6641 - s^2)^2\right]^{1.1}\right) \qquad ...(6b)$$

with $i = 1$ for $s < 1.29$ and $i = -1$ for $s \geq 1.29$.

The range of values of the variables to which these expressions apply is:

Range of D_{50} : 0.145×10^{-3} m $\leq D_{50} \leq 1.0 \times 10^{-3}$ m
Range of u_{*w} : 0.24 m/s $\leq u_{*w} \leq$ 1.35 m/s
Range of s : $1.01 \leq s \leq 1.41$.

Kadib (1964, 1965, 1966) investigated the concepts developed by Einstein (1950, 1953) for the description of sediment motions by flowing rates, and concluded that turbulence, "particle hiding" and flow variation are also important parameters in aeolian transport, as well as in addition also the effect of saltating sand grains on the threshold of particle motion. Kadib assumed that the relationship between the dimensional sediment load intensity Φ and a dimensionless parameter ψ_* which related the submerged particle weight and the lift force on the particle, derived by Einstein for water flow, is also valid for air flow. In addition, he expressed both the particle hiding and the effects of particle impact on the force balance as a correction to the

lift force. He used his own data as well as that of O'Brien and Rindlaub (1936), Zingg (1952), Horikawa (1960) and Belly (1962) to determine this correction factor. His results are given graphically in Kadib (1965). In order to make the method more widely applicable, Swart (1987b) evaluated the high shear data of Kubota et al. (1982) in the same manner described above and performed curve-fitting to the combined graphical results. The final result was obtained:

$$S_a = 8.25 \times 10^{-4} \rho_s \Phi \left(\frac{\rho_s - \rho_a}{\rho_a}\right)^{1/2} (gD_{50}^3)^{1/2} \qquad ...(7a)$$

(in $m^3/m/s$).

where

$$\Phi = \begin{cases} 0 & \text{for } \psi_* \geq 25 \\ 29[\psi_*^{-2.66} - 1.912 \times 10^{-4}] & \text{for } 10 \leq \psi_* < 25 \\ 6.497\ \psi_*^{-2.05} & \text{for } \psi_* < 10 \end{cases} \qquad ...(7b)$$

$$\psi = \left(\frac{\rho_s - \rho_a}{\rho_a}\right) \left(\frac{gD_{50}}{u_{*w}^2}\right) \qquad ...(7c)$$

$$\psi_* = \frac{\xi}{I} \psi \qquad ...(7d)$$

$$\frac{\xi}{I} = \begin{cases} 2.5 - 0.125\psi & \text{for } \psi \leq 10 \\ 6.265\ \psi^{-0.7} & \text{for } \psi > 10 \end{cases} \qquad ...(7e)$$

More details of the above formulations can be found in Swart (1987a, 1987b).

On the basis of the data included in Kadib (1965) and those on high shear velocities added in this study, the range of application of the Kadib method is as follows:

Range of D_{50} : 0.145×10^{-3} m $\leq D_{50} \leq 1.0 \times 10^{-3}$ m
Range of u_{*w} : 0.24 m/s $\leq u_{*w} \leq$ 2.89 m/s.

Nakashima (1979) studied, with reference to the control of blown sand under field conditions, wind-driven sand transport, with specific reference to the threshold shear velocity and its dependence on grain size, particle shape parameter and the water content of the sand surface. Some very interesting aspects of Nakashima's work are referred to in Sections 2.3 and 2.4 and are discussed in more detail in Swart (1987a). The potential transport over a dry sand surface, as given Nakashima and expressed in metric units, is given by:

$$S_a = 1.79 \times 10^{-3} D_{50} u_{*w} \rho_s \left[\left(\frac{u_{*w}^2 \rho_a}{gD_{50}\rho_s}\right)^{0.8} - 0.03\right] \qquad ...(8)$$

On the basis of the data contained in Nakashima (1979), the range of application of equation (8), is as follows:

Range of D_{50} : 0.22×10^{-3} m $\leq D_{50} \leq 1.61 \times 10^{-3}$ m
Range of u_{*w} : 0.2 m/s $\leq u_{*w} \leq$ 1.6 m/s
Range of $s_1 = (D_{84}/D_{16})^{1/2}$: $1.246 \leq s_1 \leq 1.802$.

Tsuchiya and Kawata (1972, 1975) performed a rigorous, theoretical treatment of all aspects related to saltation of sand grains. In the 1972 paper the various elements of the theory were compared to data, and good agreement was found. In the 1975 paper three different theories were derived on the basis of the various saltation processes described in the original paper, which can in metric units be written as:

$$(1) \quad S_a = 0.5\, u_{*w}\, D_{50}\, (\lambda)^{1/2}\, a_r\, a_1\, F_1\, (\tau_* - \tau_{*c}) \qquad \ldots(9a)$$

$$(2) \quad S_a = u_{*w}\, D_{50}\, F_2\, (\tau_* - \tau_{*c}) \qquad \ldots(9b)$$

$$(3) \quad S_a = u_{*w}\, D_{50}\, F_3\, (\tau_* - \tau_{*c}) \qquad \ldots(9c)$$

In the above F_1, F_2 and F_3 and λ, a_r and a_1 are parameters defined in the original publication by Tsuchiya and Kawata (1975). Furthermore, τ_* is the bed shear defined as:

$$\tau_* = \frac{u_{*w}^2}{(\rho_s/\rho_a - 1)\, g\, D_{50}} \qquad \ldots(9d)$$

and τ_{*c} is the critical shear stress assumed equal to 0.01, which corresponds exactly with equation (2b).

The expressions (9a) to (9c) were derived from first principles in the 1975 paper and as such place no restrictions on the range of applicability, although saltation must of course take place for the theory to be valid. However, the various elements of the theory have been compared in the two papers referred to above with data covering the following range of variables:

Range of D_{50} : 0.144×10^{-3} m $\leq D_{50} \leq 0.715 \times 10^{-3}$ m
Range of u_{*w} : 0.054 m/s $\leq u_{*w} \leq$ 1.22 m/s.

Zingg (1952) did wind tunnel experiments to investigate the relationships between wind speed and shear velocity at the sand surface on the one hand and between shear velocity and sediment transport. He obtained a modification of the original formula by Bagnold (1941);

$$S_a = 0.023\, D_{50}^{0.75}\, (\rho_a/g)\, u_{*w}^3 \qquad \ldots(10)$$

The range of variables on which this expression is based, is as follows:

Range of D_{50} : 0.20×10^{-3} m $\leq D_{50} \leq 0.715 \times 10^{-3}$ m
Range of u_{*w} : 0.3 m/s $\leq u_{*w} \leq$ 1.82 m/s.

Zanke (1978) separated bed-load q_b and suspended load and q_s from each other and demonstrated that an earlier theory for the prediction of sediment transport under uniform current flow (Zanke, 1978) is

valid for air flow as well. In the latter case he calibrated the theoretical expressions against field data gathered on the German North Sea coast, and then checked the resulting formulae against data of Exner (1928), O'Brien and Rindlaub (1936) and Kadib (1965).

Zanke (1980) proposes that the total transport is given by one of the following two versions:

$$S_a = \begin{cases} q_b + q_s \\ q_b \end{cases} \qquad \ldots(11a)$$

where the expressions for bed load and suspended load are as follows:

$$q_b = 1.5 \times 10^{-6} \left(\frac{v_1^2 - v_{c1}^2}{w^2}\right)^2 D_*^4 \, \nu \frac{1}{p} \qquad \ldots(11b)$$

and $$q_s = 1.5 \times 10^{-6} \left(\frac{(v_1^2 - v_{c1}^2)(v_1^2 - v_{l1}^2)}{w^4}\right) D_*^4 \, \nu \frac{1}{p} \qquad \ldots(11c)$$

where ν is the kinematic viscosity of air, p is the porosity, taken to be equal to 0.7 by Zanke, and v_1 is the wind velocity at 1 cm above the sand surface, obtained from measurements of wind speed 10 m above the surface by assuming a logarithmic velocity profile.

D_* is a dimensionless grain diameter;

$$D_* = \left\{\frac{(\rho_s/\rho_s - 1)g}{\nu^2}\right\}^{1/3} D_{50} \qquad \ldots(11d)$$

The range of variables used to establish equations (11) is:

Range of D_{50} : $D_{50} = 0.24 \times 10^{-3}$ m.

The theory was, however, tested against data collected by O'Brien (1936), Kadib (1965) and Exner (1928). This extends the range to:

0.145×10^{-3} m $\leq D_{50} \leq 1.0 \times 10^{-3}$ m

Range of v_{10_m} (velocity at 10 m) $v_{10} \leq 20$ m/s.

The range of u_{*_w} in the measurements of O'Brien, Kadib and Exner referred to above is 0.2 m/s to 2.89 m/s.

Horikawa et al. (1983), in a useful summary of available formulae for the prediction of wind-blown sand transport, concluded that most formulae failed to predict accurately transport rates in the case of sands with a wide grain size distribution, characterized by a sorting coefficient u_c (= D_{60}/D_{10}) >> 1. Swart (1987b) used the first tentative results of Horikawa et al. (1983) to reanalise the original data used to establish all the formulae given herein and obtained the following:

$$S_a = K_{MBKS} \left(\frac{\rho_a}{g}\right) (u_{*w} - u_{*wc}) (u_{*w} + u_{*wc})^2 \quad ...(12a)$$

This Modified-Bagnold-Kawamura-Swart formula is identical to the Kawamura formula (equation (2)) except for the coefficient, which is given by:

$$K_{MBKS} = 5.49 \times 10^{-4} \; u_{ca}^4 \left(\frac{D_{50a}}{D_{50}}\right)^{-0.5} \left(0.02 \left(\frac{D_{50}}{D_{50_r}}\right) + 0.08\right) (u_c - 1)^{-2/3} \quad ...(12b)$$

where D_{50_r} = reference grain size = 0.2×10^{-3} m

$$D_{50a} = \beta u_* + 2.4 \times 10^{-3} \quad ...(12c)$$

If $D_{50a} > D_{50}$ then $D_{50a} = D_{50}$

$$\beta = 1.5 \times 10^{-4} (1 - \sigma_u) \quad ...(12d)$$

$$\sigma_u = \frac{D_{60}}{D_{90}}$$

$$u_{ca} = \alpha u_* + 1.5 \quad ...(12e)$$

If $u_{ca} > u_c$ then $u_{ca} = u_c$

$$\alpha = 1 - \sigma_u$$

The range of variables on which this formulation is based, is as follows:

Range of D_{50} : 0.145×10^{-3} m $\leq D_{50} \leq 1.0 \times 10^{-3}$ m
Range of u_{*w} : 0.054 m/s $\leq u_{*w} \leq$ 2.89 m/s
Range of D_{60}/D_{10} : $1.02 \leq D_{60}/D_{10} \leq 1.988$
Range of D_{60}/D_{90} : $0.662 \leq D_{60}/D_{90} \leq 0.988$

2.3 Transportation of moist sand

It is not the purpose of this paper to review the transportation of moist sand by wind action. However, because the sand is frequently moist when wind speeds capable of moving dry sand occurs, it is necessary to study this phenomenon. Horikawa, Hotta and Kubota (1982b) presented an excellent review of work done to date on blown sand on wetted sand surfaces. From this review it is clear that:

(1) The problem of blown sand on wetted sand surfaces has not been conclusively studied yet and a number of problem areas still remain to be solved.

(2) Wind-driven sand transport depends, amongst other things, on the water content of the sand layer, humidity, air temperature and solar radiation. It will be very difficult ever to use these

parameters on a routine basis for the prediction of wind-driven transport rates because of the scarcity (non-existence) of parallel statistics on the various variables. It is nonetheless important to quantify the effect on the transport rate of these variables.

(3) In trying to predict the mechanism of blown sand on wet sand surfaces it will be necessary to know to what depth the sand is wetted by a rainfall of known intensity and duration as well as the manner in which the sand bed will dry out again. The rôle of sand characteristics, humidity, wind speed, air temperature and solar radiation needs to be addressed in this respect.

(4) It would appear that the main differences between blown sand on wet and dry sand surfaces is that the critical wind speed when sand movement starts is increased on a wetted sand surface and that the variation of sediment concentration is different. It would, however, appear that as a first estimate the Kawamura type formula could be used for blown wet sand, provided that a modified incipient motion criterion is used. The results given by Horikawa et al. (1982a,b), Hotta et al. (1984) and Nakashima (1979) in this regard indicate that there is a wide divergency in the available data, perhaps because of the difficulty of accurately defining and measuring the moisture content in the sand bed.

(5) More controlled measurements under laboratory conditions as well as field experiments are required to address the points raised above.

2.5 Discussion

This chapter has reviewed the available formulations for the prediction of blown sand on dry and wet surfaces. At present the best that can be done is to predict the transport of blown sand on a dry surface which, for ease of reference, is termed the **potential** sand transport. Apart from the problem of wet sand surfaces which was addressed in Section 2.3, there are a few other aspects which are particularly relevant to field application of the techniques, which will require systematic study. The two most important of these are:

(1) The effect of the topography of the sand surface over which the wind blows on the shear velocity and the magnitude of the blown sand volume. To date little work has been done in this respect, but reference can be made to Nakashima (1979), Svasek and Terwindt (1974) and Harmse (1985).

(2) The effect of vegetation cover has not been addressed quantitatively. Particularly in the case of blown-sand control or dune management this aspect, coupled with the previous point on topography, is of major importance. In this respect reference can be made to Fryberger et al. (1984), Illenberger (1986) and Swart and Reyneke (1987).

3. DETERMINATION OF SHEAR VELOCITY

Most of the formulae given in the previous chapter relate sand transport to the shear velocity at the bed. Mostly the shear velocity has to be computed on the basis of wind speed measurements at some distance above the sand surface. It is assumed that a logarithmic velocity profile exists, although this aspect still has to be addressed in the case of sand transport through dune fields where the dune height may be higher than 50 m. A number of different formulations, all of an empirical nature, exist in the body of literature referred to in Chapter 2. For the purpose of uniformity all the data used to determine these different relationships were plotted together in the form of a graph relating shear velocity with the wind speed at 2 m above the sand surface. This graph is shown here as Figure 1.

The best fit through the data points is given by

$$u*_w = 0.0275\ u_2^{1.25} \qquad \ldots(13)$$

where u_2 is the wind speed at 2 m above the sand surface.

The scatter in the data is encompassed by an upper and a lower envelope at a distance of plus or minus 20 per cent from the line defined by equation (13). This expression is used together with the logarithmic velocity law for all work reported on in this paper.

4. COMPARISON BETWEEN VOS WIND DATA AND SHORE-BASED ANEMOMETER RECORDS

In the determination of a sand budget as part of some preliminary engineering design it is often necessary to establish the contribution of the wind-driven component of sand transport to the overall budget. Under such circumstances the situation frequently arises that reliable wind statistics are not available in the close proximity of the area under consideration. It has been found quite useful then to rely, as a first approximation, on anemometer data recorded by Voluntary Observing Ships (VOS) in the coastal waters off the study site.

Swart (1987c) has shown that a reasonable similarity exists between the wind direction variation offshore and at the coast (see Figure 2). Obviously major topographic features modify the offshore wind climate but as a first estimate this is a reasonable assumption. In addition, he showed that the VOS wind speed is generally higher than that recorded at land-based anemometer stations. However, a comparison of all available shore-based anemometer wind speed data with corresponding VOS data showed that a good first estimate of wind speed can be obtained by

$$v_2 = 0.6\ v_{VOS} \qquad \ldots(14)$$

(see Figure 3).

The purpose of the foregoing is not to suggest that there is no need for shore-based anemometer data, but only to provide first estima-

tes in the case of feasibility studies. In the final instance the variability of the wind field along the coast in sympathy with topographical variations is such that the only reliable results on aeolian transport will be those based on long-term wind data gathered on site.

5. SUMMARY OF PROCEDURES

The problem to be addressed is that 16 different formulae for the prediction of wind-driven sand transport on a dry sand surface were given in Chapter 2. Each of these have a different field of applicability. It has not been possible to demonstrate conclusively that any one of these formulations is clearly superior or inferior to the rest. The method described below gives a technique which allows the establishing of a good best estimate of the wind-blown transport rate.

For any given value of wind speed the wind speed is converted via the logarithmic law to a representative height above the ground of 2 m. The potential sediment transport rate is predicted for each of the 16 formulae and the answers ordered from the highest to the lowest. The highest 3 values and the lowest 3 are then rejected and the average of the central 10 estimates is then used as the predicted potential wind-blown transport rate according to the technique. Figure 4 gives an idea of the scatter involved for the case of D_{50} = 300 μm and v = 15 m/s.

For normal application wind statistics from an anemometer of given height above the ground would serve as input data along with grain size details. It has been shown that data obtained from Voluntary Observing Ships can be used to obtain a good first estimate of the coastal wind climate. The results obtained from the analysis are represented in a creep diagram which is really an inverted rose.

Figure 5 gives an example of the aeolian creep diagram. It is possible to quantify the aeolian sand budget either on the basis of such a diagram or by using a tabular representation of the results.

6. FIELD VERIFICATION OF TECHNIQUE

The formulae given in Section 2, with the exception of those by Tsuchiya and Kawata (1975), were derived empirically. The empirical coefficients in the various formulations are therefore based on laboratory results or individual field experiments. This does not, however, give any indication of how any of these techniques will behave when applied to long-term wind statistics. For this purpose the method of application outlined in Chapter 5 was tested against long-term wind-data in situations where the sand drift was also known.

The method has been applied to a number of sites around the South African coast, amongst others the dune fields around Port Elizabeth and the dune fields on the South West African coast in the vicinity of Walvis Bay (see Figure 7). Measurements of dune advance rates at both these sites have been used to verify the technique. **Port Elizabeth** data indicate gross eastbound transport rates of 68 $m^3/m/yr$ at Cape Recife (McLachlan, pers. com.), whereas Prestedge (pers. com.) estimates the net eastward movement in the area at 45 $m^3/m/yr$ for the

period 1972 to 1981. East of the Sondags mouth McLachlan estimates, on the basis of dune advancement, a net eastbound transport rate of 35 to 42 $m^3/m/yr$ and a shoreward movement of about 30 $m^3/m/yr$. The latter figure was revised by Illenberger (1986) to 22 to 30 $m^3/m/yr$. Predictions with the technique described herein show the following potential rates:

Northbound:	gross	27 $m^3/m/yr$
	net	18 $m^3/m/yr$
Eastbound :	gross	78 $m^3/m/yr$
	net	45 $m^3/m/yr$

Calculations by Swart (1986) show variations in the predicted annual drift rate of a factor 3 on a year-to-year basis over an eleven-year period due to the variability of the wind field (Figure 6).

Walvis Bay data by Le Roux show northward volumetric dune advance rates of 120 $m^3/m/yr$ in the lower Kuiseb valley. Calculations with two different sources of wind data show northward aeolian transport rates of 109 and 122 $m^3/m/yr$ respectively. The good correspondence is shown in Figure 8.

7. CONCLUSIONS

This paper reviews the quantitative techniques for the prediction of windblown sand transport. The main conclusions reached are the following:

(1) Sixteen different techniques were identified which can be used to predict potential wind transport rates over dry, unvegetated sand surfaces.

(2) None of these is clearly superior or inferior to the others. Therefore a computational scheme was developed which utilizes the central ten predictions out of an ordered (high to low) set of 16 predictions for a given set of boundary conditions.

(3) By application to two prototype examples where long-term data are available, it was shown that the method can be used to give accurate predictions of aeolian transport rates, provided that reliable wind statistics are available.

(4) It was shown that Voluntary Observing Ships' wind data provide a good, first estimate of the uncontaminated wind field on the coast, provided that there are no major topographical features such as mountains to deflect the wind patterns locally.

(5) The method described in this paper supplies potential windblown transport rates and neglects the effect on the transport of air temperature, the humidity, the moisture content of the soil, which is related to the amount and intensity of the rainfall, the salt content of the sand, the percentage of vegetation cover of the sand and the topography of the ground over which the wind is blowing.

8. RECOMMENDATIONS

It should be clear from the above that although the technique described supplies a reliable estimate of the potential windblown transport rate, there are still a number of factors which need to be researched further in detail before it will allow the prediction of prototype transport rates under variable prototype conditions. Much of this research is already underway. Factors which demand particularly urgent attention are those listed under item (5) in Chapter 7. Every effort should be made to co-ordinate the activities in this respect of the various researchers actively working toward understanding the effect of these parameters on the windblown transport rate.

REFERENCES

Bagnold, R.A. (1941, new edition 1954). The physics of blown sand and desert dunes. Methuen and Co. Ltd, London.

Belly, P.Y. (1962). Sand movement by wind. Tech. Rep. of Univ. of Calif., Inst. Eng. Science, 102(3), pp. 143-146.

Chepil, W.S. (1945). Dynamics of wind erosion III, The transport capacity of the wind. Soil Science, Vol. 60, No. 6.

Chiu, T.Y. (1970). Sand transport by wind. Tech. Rep. No. 1, Dept. of Coastal and Oceanographic Eng., College of Eng., Univ. of Florida, Gainesville, Florida.

Einstein, H.A. (1950). The bed load function for sediment transportation in open channel flows. Technical Bulletin No. 1026, US Dept. of Agric., Washington, D.C.

Einstein, H.A. and N. Chien (1953). Transport of sediment mixtures with large sizes. Missouri River Div., Sediment Series No. 2, Inst. of Eng. Research, Univ. of California, Berkeley, California.

Exner, F.M. (1928). Dünenstudien auf der Kunishen Nehrung, Vienna.

Fryberger, S.G., A.L. Al-Sari, T.J. Clisham, S.A.R. Rizvi and K.G. Al-Hinai (1984). Sedimentology, Vol. 31, pp. 413-431.

Harmse, J.T. (1985). Trend surface analysis of aeolian sand movement on the Southwest African coastline. South African Geographical Journal, Vol. 67, No. 1, pp. 31-39.

Horikawa, K. (1978). Coastal Engineering. An introduction to ocean engineering. University of Tokyo Press, Tokyo.

Horikawa, K., S. Hotta, S. Kubota and S. Harikai (1981). Blown sand on beaches. Proc. 28th Japanese Coastal Eng. Conf., pp. 574-578 (in Japanese).

Horikawa, K. and H.W. Shen (1960). Sand movement by wind action. BEB Tech. Memo No. 119, 51 pp.

Horikawa, K., S. Hotta and S. Kubota (1982a). Field observation of blown sand distribution across a beach. Proc. 29th Japanese Coastal Eng. Conf., pp. 269-273 (in Japanese).

Horikawa, K., S. Hotta and S. Kubota (1982b). Experimental study of blown sand on a wetted sand surface. Coastal Engineering in Japan, Vol. 25.

Hotta, S., S. Kubota, S. Katori and K. Horikawa (1984). Sand transport by wind on a wet sand surface. Proc. 19th ICCE, Houston, pp. 1265-1281.

Hsu, S.A. (1971a). Wind stress criteria in aeolian sand transport. J. Geophys. Res., Vol. 76.

Hsu, S.A. (1971b). Measurement of shear stress and roughness length on a beach. J. Geophys. Res., Vol. 76.

Hsu, S.A. (1972). Boundary-layer trade-wind profile and stress on a tropical windward coast. Boundary layer Meteorology, Vol. 2, pp. 284-289.

Hsu, S.A. (1973). Computing aeolian sand transport from shear velocity measurements. J. Geology, Vol. 81, pp. 739-743.

Hsu, S.A. (1974a). A dynamic roughness equation and its application to wind stress determination at the air-sea interface. J. Phys. Oceanogr., Vol. 4, pp. 116-120.

Hsu, S.A. (1974b). On the log-linear wind profile and the relationship between shear stress and stability characteristics over the sea. Boundary layer Meteorology, Vol. 6, pp 509-514.

Hsu, S.A. (1977). Boundary-layer meteorological research in the coastal zone. Geoscience and Man, H.J. Walker (ed.), Baton Rouge, The School of Geoscience, LSAU, Vol. 18, pp. 99-111.

Illenberger, W. (1986). The Alexandria Coastal dunefield: morphology, sand budget and history. MSc Thesis, University of Port Elizabeth, RSA.

Iwagaki, Y. (1950). On the effect of the sand-drift on the coast by wind for sand deposition in Ajiro Harbor. J. JSCE, Vol. 36, No. 6, pp. 19-25 (in Japanese).

Kadib, A.L. (1964). Sand movement by wind. Tech. Memo, No. 1, US Army Corps of Engineers, Addendum II.

Kadib, A.L. (1965). A function of sand movement by wind. Univ. California, Berkeley, Tech. Report HEL2-12, 91 pp.

Kadib, A.L. (1966). Mechanics of sand movement on coastal dunes. J. Waterways and Harbors Division ASCE, No. WW 2, pp. 27-44.

Kawamura, R. (1951). Study of sand movement by wind. Rep. of the Inst. of Science and Technology, Univ. of Tokyo, Vol. 5, No. 3/4, pp. 95-112 (in Japanese).

Kubota, S., K. Horikawa and S. Hotta (1982). Blown sand on beaches. Proc. 18th Coastal Eng. Conf., ASCE, Vol. II, pp. 1181-1198..

Mossa, J. and S.A. Hsu (1980). A modified aeolian sand transport equation. Unpublished LSU Report.

Nakashima, Y. (1979). A fundamental study on the blown sand control. Bulletin of the Kyushu University, Forests, No. 51, pp. 125-183.

O'Brien, M.P. and 8.D. Rindlaub (1936). The transportation of sand by wind. Civil. Eng., Vol. 6, No. 5, pp. 325-327.

Svasek, J.N. and J.H.J. Terwindt (1974). Measurements of sand transport by wind on a natural beach. Sedimentology, Vol. 21, pp. 311-322.

Swart, D.H. (1985). Physical processes at Schelmhoek, Sundays River. CSIR Research Report 557, National Research Institute for Oceanology, Stellenbosch, RSA.

SWART, D.H. (1987a). Formulations for potential aeolian drift rates. In preparation.

SWART, D.H. (1987b). In-depth review of formulation and prediction of aeolian drift rates. CSIR Research Report, in preparation.

Swart, D.H. (1987c). Correlation between ships' wind data and land based anemometer data. CSIR Research Report (in preparation), National Research Institute for Oceanology, Stellenbosch, RSA.

Swart, D.H. and P. Reyneke (1986). The beaches at Waenhuiskrans. Joint information pamphlet by the CSIR and the Directorate of Forestry, Department of Environment Affairs, RSA.

Tsuchiya, Y. and Y. Kawata (1972). Characteristics of saltation of sand grain by wind. Proc. 13th Conf. on Coastal Eng., Vol. II, pp. 1617-1625.

Tsuchiya, Y. and Y. Kawata (1975). The sand transport rate by wind on basis of saltation of sand grain. Proc. 19th Japanese Conf. on Hydraulics, JSCE, pp. 7-12.

Zanke, U. (1978). Zusammenhänge zwischen Strömung und Sedimenttransport, Teil 1. Mitteilungen des Franzuis-Instituts der Universität Hannover, Heft 47.

Zanke, U (1980). Sand transport under the action of wind. Proc. 17th Conf. on Coastal Engineering, ASCE, Vol. II, pp. 1576-1583.

Zingg, A.W. (1952). Wind tunnel studies of the movement of sedimentary material. Proc. 5th Hydraulics Conf., pp. 111-135.

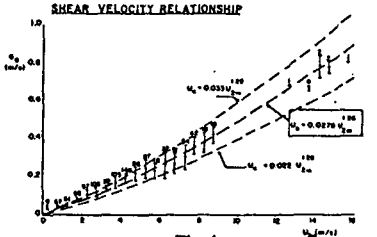

Fig.1

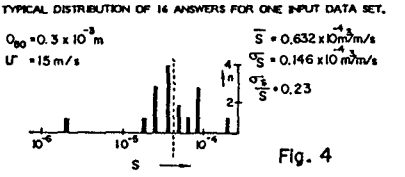

Fig. 4

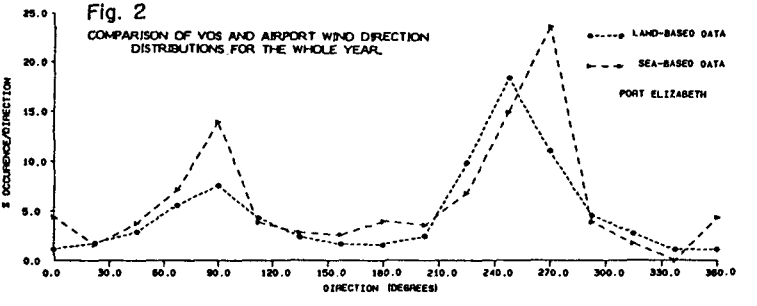

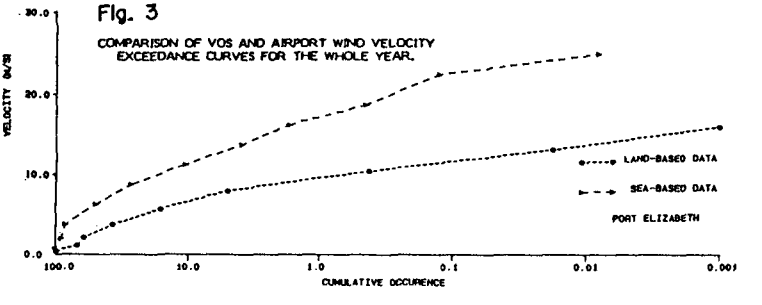

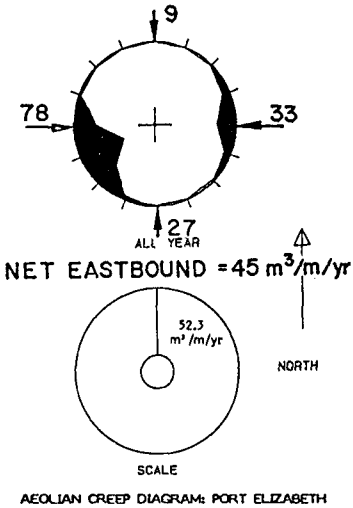

Fig. 5

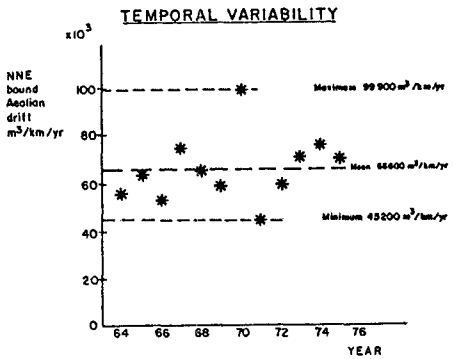

Fig. 6

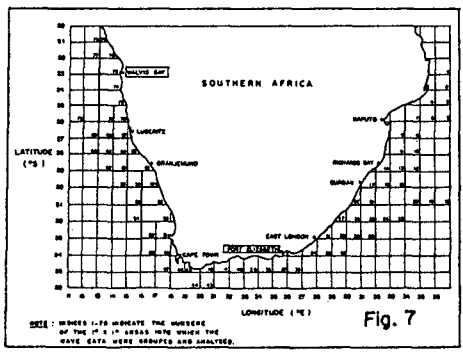

Fig. 7

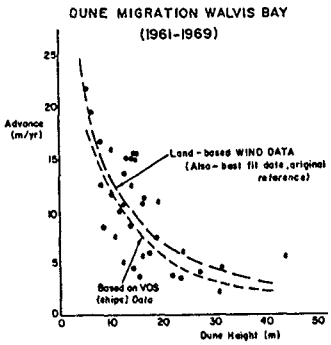

Fig. 8

CHAPTER 118

BEACH CHANGES BY STORM WAVES

Ichirou Takeda* and Tsuguo Sunamura*

ABSTRACT

Monitoring of beach profiles was carried out during one-year period at two sites located 3 km apart along a Pacific beach, Japan. These two sites are composed of beach sand with different grain size: 0.76 mm and 0.26 mm. It was found that the shoreline did not move even in storm wave events at the site with 0.76-mm sand, where the "seesaw mode" profile change took place in the subaerial portion of the beach. It was also found that the shoreline was not always retreated by storm waves at the 0.26-mm sand site, where the "parallel mode" profile change dominated, at the time of presence of bars working as a submerged breakwater to protect the beach from erosion.

INTRODUCTION

It is generally considered that storm waves erode beach material and transport offshore causing shoreline recession on a coast with dominant cross-shore sediment transport. In some cases, however, no shoreline retreat occurs even in the event of storm waves. There have been few systematic studies on such a phenomenon. The present study purposes to investigate this problem based on one-year consecutive monitoring of beach changes and incident wave characteristics.

STUDY AREA AND DATA ACQUISITION

Beach monitoring was carried out at Naka Beach, Ibaraki Prefecture, Japan (Fig. 1). The beach, facing the Pacific Ocean, is an approximately straight coast with a north-south oriented shoreline 5 km long. The beach sediment is

*Institute of Geoscience, University of Tsukuba, Ibaraki 305, Japan.

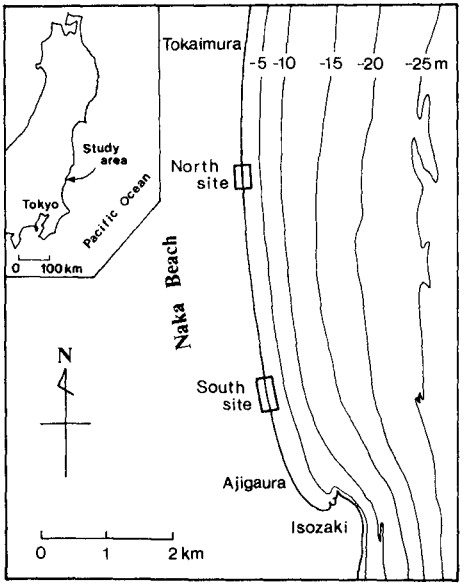

Fig. 1 Study area and two monitoring sites.

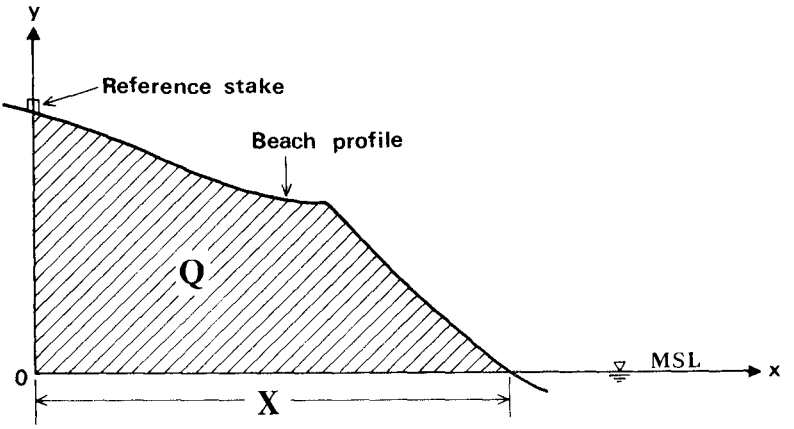

Fig. 2 Schematic diagram showing beach width and subaerial beach sediment volume

composed of coarse sand in the northern part of the beach and fine sand in the southern part (Takeda, 1984). The shoreline of the study area is stable on a long-term basis (Tanaka et al., 1973). The direction of long-term longshore sediment transport would be southward, but cross-shore sediment transport dominates for short-term beach changes. No man-made coastal structures have been constructed on the beach.

An outer bar is always located nearly parallel to the shoreline, and an inner bar only develops under certain physical conditions. The average bottom slope is 0.011 to a water depth of 20 m, and is almost constant along the beach. No significant alongshore difference in incident wave characteristics has been observed. The beach is in a microtidal environment, a maximum tidal range is 1.4 m and a mean is about 1 m.

Two monitoring sites, 3 km apart, were established along this beach (Fig. 1). They are called North Site and South Site. North Site has an alongshore length of 300 m and South Site has a 500 m length. The mean grain size of the beach material was 0.76 mm at North Site and 0.26 mm at South Site. Reference stakes were installed along the shoreline on the highest part of the beach. Sixteen stakes were set up at an interval of 20 m at North Site and eleven stakes were installed at 50-m interval at South Site.

Beach profiles were surveyed perpendicular to the general shoreline trend from each stake to the surf zone using a telescopic level, a surveyor's rod, and a tape. The survey was conducted at an interval of once or twice per week for a period of one year beginning August 28, 1980.

Based on the beach survcy results, the beach width and the subaerial beach sediment volume, defined in Fig. 2, were calculated. In this figure, the x-axis extends offshore on mean sea level from the origin which is located at the intersection with the y-axis extending upwards through a reference stake. The beach width, X, is the horizontal distance between the origin and the point at which the beach profile meets the x-axis. The subaerial beach sediment volume, Q, is the cross-sectional area (hatched area) bounded by the beach profile, the x-axis, and the y-axis. Averaged values of X and Q over 16 survey lines for North Site and 11 lines for South Site were obtained, and they were denoted by $\bar{X}$ and $\bar{Q}$, respectively.

The two quantities, $\bar{X}_*$ and $\bar{Q}_*$, are defined as:

$$\bar{X}_* = \bar{X} - \bar{X}_0 \quad (1)$$

$$\bar{Q}_* = \bar{Q} - \bar{Q}_0 \quad (2)$$

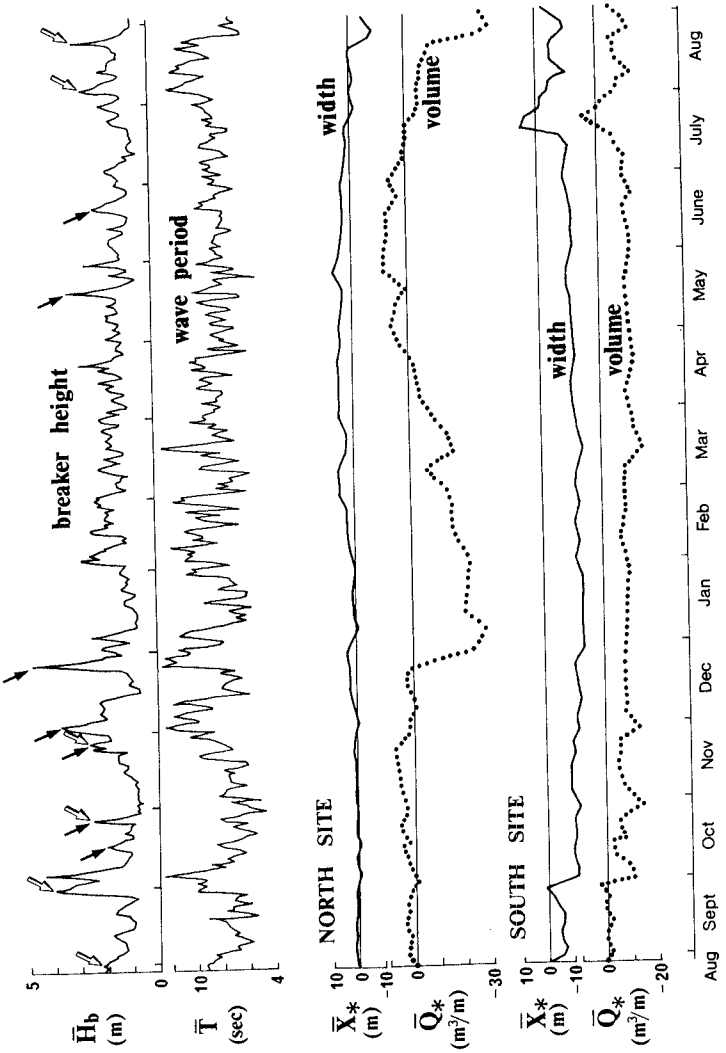

Fig. 3 Time-series data of waves and beach characteristics.

where $\bar{X}_0$ and $\bar{Q}_0$ are values of $\bar{X}$ and $\bar{Q}$ of August 28, 1980, the first day of the investigation, respectively.

Waves were measured by an ultrasonic-type wave gage installed about 10 km south of the study area at a water depth of 21 m. Continual wave records obtained over 20 minutes for every two hours were available. Based on the wave records, daily averages of deepwater significant wave height and period were obtained. Daily averages of significant breaker height, $\bar{H}_b$, were calculated using the following relationship (Sunamura, 1982):

$$\frac{H_b}{H_0} = (\tan \beta)^{0.2} \left(\frac{H_0}{L_0}\right)^{-0.25} \quad (3)$$

where H_b is the breaker height, H_0 and L_0 are the deepwater wave height and length, respectively, and $\tan\beta$ is an average nearshore bottom slope.

Time-series data of $\bar{X}_*$, $\bar{Q}_*$, $\bar{H}_b$, and daily averages of significant wave period, $\bar{T}$, are shown in Fig. 3.

RESULTS AND DISCUSSION

Beach Erosion Pattern

The time-series data of $\bar{X}_*$, $\bar{Q}_*$, and incident waves (Fig. 3) illustrate that the characteristics of subaerial beach change in the event of storm waves is different between the two sites. Namely, the pattern of change in $\bar{X}_*$ is the same as that in $\bar{Q}_*$ at South Site, while the change pattern of $\bar{X}_*$ is different from that in $\bar{Q}_*$ at North Site.

At South Site, storm waves simultaneously decreased both $\bar{Q}_*$ and $\bar{X}_*$. This change pattern was observed at storm events shown by open allows in Fig. 3, i.e., storms in late September, 1980; late October, 1980; late November, 1980; early and late August, 1981. Such a subaerial beach change is schematically shown in Fig. 4-(A); that is, storm waves decrease the beach width and the subaerial beach sediment volume at the same time, and the "parallel mode" profile change takes place.

A typical example of this type of profile change actually observed at South Site is shown in Fig. 5. The solid line indicates the profile before the storm waves (with a maximum of $\bar{H}_b$ = 2.7 m) in late November, 1980. The step had a height of about 0.3 m. The dashed line shows the after-storm profile. As shown in Fig. 5, the storm wave action decreased both the subaerial beach sediment volume as well as the beach width.

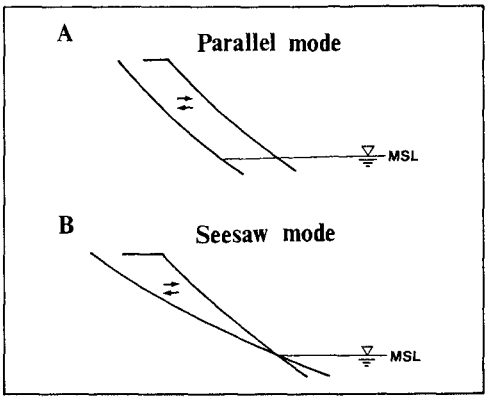

Fig. 4 Schematic diagram showing subaerial beach changes.

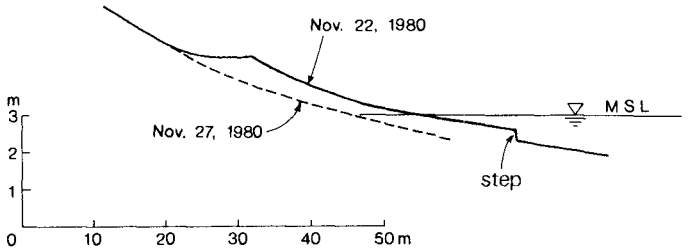

Fig. 5 Typical beach erosion pattern observed at South Site.

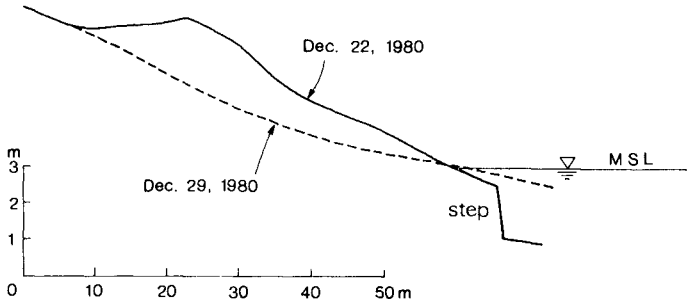

Fig. 6 Typical beach erosion pattern observed at North Site.

On the other hand, storm waves decreased $\bar{Q}_*$ but they did not decrease $\bar{X}_*$ at North Site. This change pattern was observed at storm events shown by solid allows in Fig. 3, i.e., storms in middle and late October, 1980; late November, 1980; early and late December, 1980; middle May, 1981; and late June, 1981. This subaerial beach change is shown in Fig. 4-(B). In spite of that subaerial beach material is eroded away by storm waves, the shoreline advances or does not change, and the "seesaw mode" profile change occurs in the subaerial portion of the beach.

Figure 6 shows an actual example of the seesaw mode profile change occurred at North Site due to the storm waves with $(\bar{H}_b)_{max}$ = 4.8 m on December 25, 1980. The pre-storm profile (solid line in Fig. 6) had a step with a height of about 1.5 m. The storm waves markedly decreased the subaerial beach sediment volume, whereas the shoreline position did not retreat but advanced. The surf zone could not be surveyed due to high waves, but it was observed through wading that the eroded subaerial beach material deposited near the shoreline.

The difference in the two patterns of beach profile changes are due to the scale of a step formed under calm-sea conditions before the attack of storm waves. Larger steps usually developed at North Site, where beach material eroded by storm waves was not transported offshore but deposited just in front of the step, and no shoreline retreat occurred as schematically shown in Fig. 7-(B). The height of steps formed at South Site was much smaller. Eroded material was not deposited near the shoreline, but transported seaward to build up an inner bar in the surf zone, and the shoreline retreated [Fig. 7-(A)].

Beach Response of South Site to Storm Waves

It was often observed that the South Site beach also was not always eroded by large storm waves. For example, the beach was severely eroded by the action of storm waves in late September, 1980, but the beach was not significantly eroded by the storm in late December, 1980, which was the highest storm waves during the one-year survey period (Fig. 3). A similar phenomenon could also be recognized at the storm events in early February, late April, and middle May, 1981. Figure 3 shows that this phenomenon always occurred when the beach had a low $\bar{Q}_*$-value, that is, the beach was poor in the subaerial beach sediment volume. Beach material eroded from the subaerial portion of the beach had been transported offshore and formed an inner bar in the surf zone as schematically shown in Fig. 7-(A). It can be considered that such an inner bar is closely related to the condition for beach erosion.

Moreover, if the inner bar effects the condition for beach erosion, the outer bar also probably affects beach erosion. Because energy of waves arriving at the beach is greatly influenced by the position and water depth of a bar (Carter and Balsillie, 1983). The position of the outer bar in this study area was greatly changed by the action of the largest storm waves on December 25, 1980. The bar, located 70 to 120 m offshore before this day, was moved further offshore and thereafter its location was kept between 150 to 250 m in offshore distance. The time-series data (Fig. 3) were split into two parts on this day for the purpose of examining the critical condition for beach erosion.

In order to express the existence or nonexistence of inner bar, a dimensionless parameter, Q_R, is introduced, which is defined as:

$$Q_R = \frac{\bar{Q}_* - Q_{min}}{Q_{max} - Q_{min}} \tag{4}$$

where Q_{max} and Q_{min} are the maximum and minimum values of $\bar{Q}_*$ during the one-year investigation period, respectively. The parameter Q_R, which shows a relative subaerial beach sediment volume, is a value ranging from 0 to 1. A berm-developing beach state (fully accretionary state) has larger Q_R-values compared with an inner-bar forming beach state (erosional state), and a bar-welding beach state takes intermediate values.

The magnitude of storm waves can be expressed by a dimensionless coefficient, k, in the following equation (Sunamura, 1984; Takeda, 1984):

$$\frac{H_b}{gT^2} = k\frac{D}{H_b} \tag{5}$$

where D is the grain size of beach material, and g is the gravitational acceleration.

Because (1) wave climate changes in time and (2) beach change is most sensitive to larger waves during one interval of two consecutive beach profiling, $(\bar{H}_b)_{max}$ and $\bar{T}_{max}$ were substituted for H_b and T in equation (5), respectively:

$$\frac{(\bar{H}_b)_{max}}{g\bar{T}_{max}^2} = K\frac{D}{(\bar{H}_b)_{max}} \tag{6}$$

where $(\bar{H}_b)_{max}$ is the maximum value of daily average breaker height during one interval between surveys, $\bar{T}_{max}$ is the average wave period of the day giving $(\bar{H}_b)_{max}$, and K is a dimensionless coefficient. The larger value of K means the

higher wave-intensity resulting in net offshore sand transport in the surf zone (Sunamura, 1984).

Using two parameters, Q_R and K, the critical condition for beach erosion was examined. Figure 8 is a plot of data obtained before December 25, 1980 (the outer bar was located near the shoreline). Beach accretion or erosion is determined by the change in subaerial beach sediment volume $\bar{Q}_*$ during one survey interval, i.e., an increase in $\bar{Q}_*$ is defined as accretion, while a decrease in $\bar{Q}_*$ is defined as erosion. In Fig. 8, the open symbol indicates accretion and the solid symbol denotes erosion. Data showing small change in $\bar{Q}_*$ less than 1.0 m^3/m were excluded from the plot. Although some overlapping of the data points is seen, the erosion-accretion demarcation can be described by the solid curve. The figure shows that no erosion takes place even for the case of larger K-value when the beach has lower Q_R-value. Namely, the beach is not likely to be eroded even by the large storm waves when an inner bar develops. This suggests that the inner bar protects the beach acting as a submerged breakwater.

Figure 9 is a plot of data obtained during the period when the outer bar was located further offshore. A similar tendency to the former case is found. These two results show that the existence or nonexistence of an inner bar is closely related to the critical condition for beach erosion.

Comparison of Figs. 8 and 9 indicates the influence of the outer bar on beach erosion. The demarcation curve in Fig. 9, compared with Fig. 8, is plotted in the lower-left area. This suggests that less severe storm waves can erode the beach when the outer bar is located offshore. The water depth of bars increases with increasing offshore distance (Keulegan, 1948). Because the outer bar located closer to the shoreline has smaller water depth, such an bar is likely to protect the beach acting as a submerged breakwater like the above-mentioned inner-bar case. On the other hand, the outer bar located offshore can not effectively work as a submerged breakwater to protect the beach from erosion.

CONCLUSIONS

The data of beach monitoring shows that the seesaw mode profile change dominates at the coarse sand beach (North Site) and the parallel mode profile change takes place at the fine sand beach (South Site). In the case of seesaw mode profile change, little significant shoreline retreat occurs in the event of storm waves. It is found that the presence of inner bar and the location of outer bar greatly influence the subaerial beach change occurring on the fine sand beach.

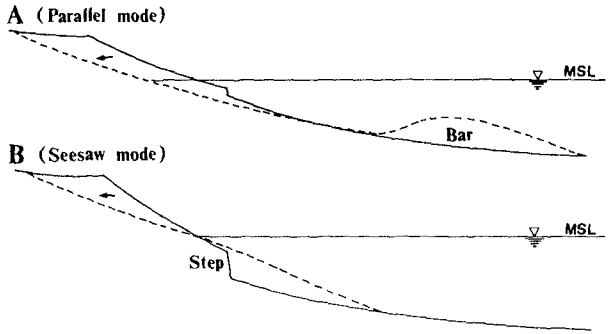

Fig. 7 Schematic diagram showing beach erosion patterns.

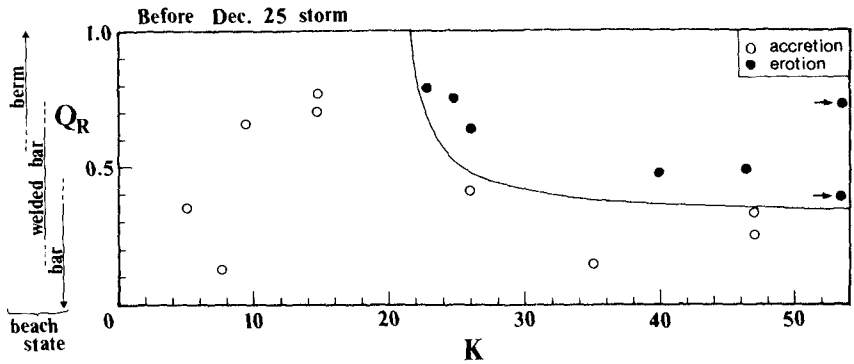

Fig. 8 Critical condition for beach erosion at South Site (Aug. 28, 1980 - Dec. 24, 1980).

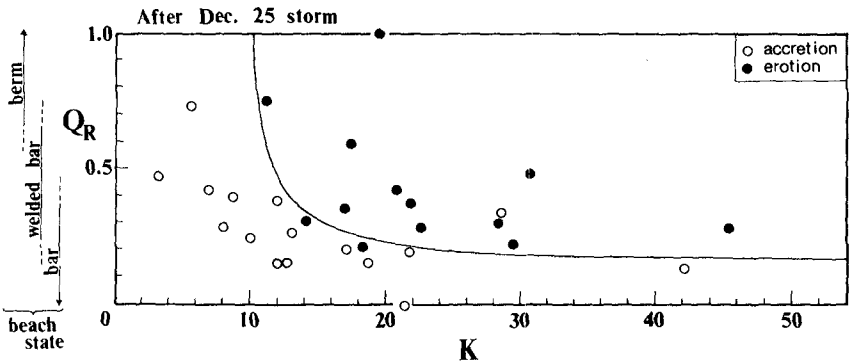

Fig. 9 Critical condition for beach erosion at South Site (Dec. 25, 1980 - Sept. 1, 1981).

REFERENCES

Carter, R. W. G. and Balsillie, J. H. (1983): A note on the amount of wave energy transmitted over nearshore sand bars. Earth Surface Processes Landforms, vol. 8, p.213-222.

Keulegan, G. H. (1948): An experimental study of submarine sand bars. U. S. Army Beach Erosion Board, Tech. Rept., No. 3, 40p.

Sunamura,T. (1982): Determination of breaker height and depth in the field. Ann. Rep., Inst. Geosci., Univ. Tsukuba, No. 8, p.53-54.

Sunamura, T. (1984): Prediction of on/offshore sediment transport rate in the surf zone including swash zone. Proc. 31st Japan. Conf. Coastal Eng., p.316-320 (in Japanese).

Takeda, I. (1984): Beach changes by waves. Sci. Rep., Inst. Geosci., Univ. Tsukuba, Sec. A, Vol. 5, p.29-63.

Tanaka, N., Ozasa, H. and Ogasawara, A. (1973): Note of the investigations on changes of shorelines in Japan, Part 1. Port Harbour Res. Inst., Ministry Transport, Japan, Tech. Note, No. 163, 95p. (in Japanese).

CHAPTER 119

NUMERICAL SIMULATION OF TURBULENT WAVE BOUNDARY LAYERS

J. H. Trowbridge[1], A.M.ASCE, C. N. Kanetkar[2] and N. T. Wu[3]

ABSTRACT: This paper reports numerical computations of fully rough turbulent boundary layers produced by first and second order Stokes waves. The computations are based on a mixing length turbulence closure and on a slightly more sophisticated turbulent kinetic energy closure. The first order results compare well with existing laboratory results. Reversal of the second order steady streaming under relatively long waves, which has been predicted analytically, is also predicted in the numerical results. The steady second order velocity field is found to become fully established only after a development time on the order of a few hundred wave periods. Both the first and second order results indicate that advection and diffusion of turbulent kinetic energy play a minor role in determining the Reynolds averaged velocity field.

INTRODUCTION

A quantitative understanding of turbulent wave boundary layers is necessary for coastal engineers concerned with dissipation of wave energy, wave-induced sediment transport, and the effect of waves on large-scale, slowly varying currents. This study is confined to the case of fully turbulent boundary layers produced by weakly nonlinear waves near fixed hydrodynamically rough boundaries. The boundary roughness elements are assumed to be small compared to the boundary layer thickness.

Previous analytical studies (Kajiura, 1968; Grant and Madsen, 1979; Brevik, 1981; Myrhaug, 1982; Trowbridge and Madsen, 1984a), numerical studies (Bakker, 1974; Johns, 1975; Bakker and van Doorn, 1978), experimental studies (Jonsson, 1966; Jonsson and Carlsen, 1976; Bakker and van Doorn, 1978; Kamphuis, 1975) and semi-empirical analyses (Jonsson, 1966) have clarified the physics of the first-order problem. This is the purely oscillatory case corresponding to linear wave theory. By using relatively simple analytical solutions based on eddy-viscosity models, or numerical results based on Prandtl's mixing-length theory, one can predict with confidence the Reynolds-averaged velocity field, boundary shear stress and energy dissipation for the first-order case.

---

[1]Assistant Professor, Dept. of Civil Engrg., University of Delaware, Newark, DE 19716.
[2]Central Water and Power Research Station, Pune, India.
[3]Graduate Student, Dept. of Civil Engrg., University of Delaware, Newark, DE 19716.

The second-order solution, which incorporates the effect of wave nonlinearity, is not as well established. The quantity of particular interest in the second-order problem is the steady streaming, or steady current which is generated in the boundary layer due to frictional dissipation of energy and nonlinearity. The asymmetry in the velocity field and bottom shear stress are also of interest in transport problems. Longuet-Higgins (1958) assumed that the effective viscosity is constant from the point of view of a moving fluid particle, although he allowed it to vary with mean particle position. He was able to show that under this restriction, the steady streaming just outside the wave boundary layer has the same value as in laminar flow. This value is independent of the molecular viscosity, and it is always in the direction of wave propagation. A later similar study, based on a time-invariant viscosity with a particular vertical structure, was reported by Johns (1970) with similar results. Later Johns (1977) reported a study based on a more realistic turbulent kinetic energy closure, but he neglected the second-order properties of the pressure field outside the boundary layer. In addition, he found that the steady streaming outside the boundary layer was zero. This result contradicts the laminar solution and existing analytical solutions, and will be discussed below in more detail. Trowbridge and Madsen (1984b) reported an analytical study based on a detailed, physically based eddy viscosity model, and found that the steady streaming produced by Stokes waves is in the direction opposite that of wave propagation for relatively long waves. Jacobs (1984) obtained a similar result by using an analysis based on Saffman's turbulence model.

Trowbridge and Madsen (1984b) found that their predictions of the steady streaming were sensitive to the eddy viscosity model. They used two models: one in which time variation of the viscosity extended throughout the boundary layer, and one in which the time variation of the viscosity was confined to a thin layer near the boundary. Example results are shown in Figure 1, indicating that predictions of the steady streaming are quite sensitive to the model used. The two models produced nearly indistinguishable results in the first order problem, and hence could not be judged on this basis.

Observations of the second-order properties of wave boundary layers are scarce. Bakker and Van Doorn (1978) reported a study carried out in a laboratory wave basin, in which the horizontal velocity was measured inside the boundary layer. In order to obtain turbulent flow at relatively small laboratory scales, Bakker and van Doorn had to use roughness elements which were quite large compared to the boundary layer thickness, and therefore the relevance for comparison with the theoretical studies quoted above is limited.

This paper reports a numerical study of turbulent wave boundary layers, based on Prandtl's mixing-length model and on a slightly more sophisticated turbulent kinetic energy closure, which was originally suggested by Prandtl (e.g., Schlichting, 1979), developed by several researchers, and summarized, for example, by Reynolds (1976). The purposes of this study are the following: (1) to clarify the physics of the second-order turbulent wave boundary layer; and (2) to give insight for developing a simpler analytical model which can be used as

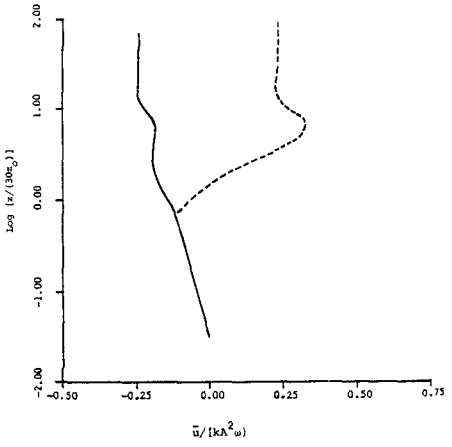

Figure 1. Mean velocity $\bar{u}$ as a function of vertical coordinate z based on the analyses reported by Trowbridge and Madsen (1984b). Solid line, first model; dashed line, second model. $kh = 0.50$, $A/(30z_o) = 179$.

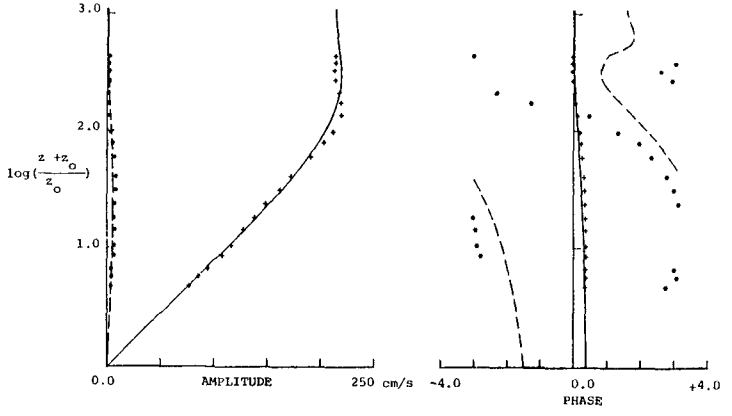

Figure 2. Computed amplitude and phase of the first and third harmonics of the horizontal velocity based on the mixing length model, compared with measurements reported by Jonsson and Carlsen (Test 1). Solid line, first harmonic; dashed line, third harmonic; asterisk, measurement. $30\ z_o = 1.59$ cm.

the basis for future studies involving more complicated processes.

GOVERNING EQUATIONS

The flow to be considered is produced by a regular train of plane waves which is described locally by Stokes' second-order solution. The governing equations are the boundary layer approximation to the 2-D Reynolds-averaged mass and momentum equations. These are

$$\frac{\partial u}{\partial x} + \frac{\partial w}{\partial z} = 0 \tag{1a}$$

$$\frac{\partial u}{\partial t} + u\frac{\partial u}{\partial x} + w\frac{\partial u}{\partial z} = \frac{\partial U}{\partial t} + U\frac{\partial U}{\partial x} + \frac{\partial}{\partial z}\frac{\tau}{\rho} \tag{1b}$$

(e.g., Tennekes and Lumley, 1972) where x is the horizontal coordinate, positive in the direction of wave propagation, z is the vertical coordinate, positive upward with z equal to zero at the fixed bed, t is time, (u,w) is the Reynolds-averaged velocity vector inside the boundary layer, U is the horizontal velocity outside the boundary layer, τ is the Reynolds shear stress, and ρ is the fluid density. The corresponding boundary conditions are the no-slip conditions at the bed and the no-stress condition far away from the bed:

$$u = w = 0 \qquad \text{at } z = 0 \tag{2a}$$

$$\tau \to 0 \qquad \text{as } z \to \infty \tag{2b}$$

The unsteady component of U is determined by Stokes' second-order solution, which is

$$U - \bar{U} = A\omega\cos(\omega t - kx) + \frac{3}{4}\frac{kA^2\omega}{\sinh^2(kh)}\cos[2(\omega t - kx)] \tag{3}$$

(e.g., Dean and Dalrymple, 1984). Here an overbar denotes a time-averaged quantity, A is the near-bottom excursion amplitude, ω is the radian frequency, k is the wave number, and h is the water depth. The steady component of U is determined by the mechanics of the boundary layer, and hence is not known initially.

An additional equation necessary for the turbulence closure is the boundary layer approximation to the turbulent kinetic energy equation, which is

$$\frac{\partial}{\partial t}\left(\frac{1}{2}q^2\right) + u\frac{\partial}{\partial x}\left(\frac{1}{2}q^2\right) + w\frac{\partial}{\partial z}\left(\frac{1}{2}q^2\right) = \frac{\tau}{\rho}\frac{\partial u}{\partial z} + \frac{\partial D}{\partial z} - \epsilon \tag{4}$$

(e.g., Tennekes and Lumley, 1972) where $(1/2)\,q^2$ is the Reynolds averaged turbulent kinetic energy per unit mass, D is the vertical flux of kinetic energy due to turbulent "diffusion," and ϵ is the Reynolds averaged dissipation per unit mass.

The leading terms in (1b) are the temporal acceleration terms and the stress term, and the leading terms in (4) are the time deriva-

tive term and the three terms on the right side (production, diffusion and dissipation). In both equations, the advective terms are order kA compared to the leading terms, and the neglected terms are order $k\delta$ compared to the leading terms, where δ is the boundary layer thickness. The viscous terms are neglected in both equations because they are small everywhere compared to the other terms for the case of hydrodynamically rough bed.

An important simplification is achieved by using the condition of periodicity in space and time. By using this condition together with the mass conservation equation to determine the vertical velocity, one can write equations (1b) and (4) as follows:

$$\frac{\partial u}{\partial t} - \frac{u}{c}\frac{\partial u}{\partial t} + \frac{1}{c}\frac{\partial u}{\partial z}\int_0^z \frac{\partial u}{\partial t}\,dz = \frac{\partial U}{\partial t} - \frac{U}{c}\frac{\partial U}{\partial t} + \frac{\partial}{\partial z}\left(\frac{\tau}{\rho}\right) \tag{5a}$$

$$\frac{\partial}{\partial t}\left(\frac{q^2}{2}\right) - \frac{u}{c}\frac{\partial}{\partial t}\left(\frac{q^2}{2}\right) + \frac{1}{c}\frac{\partial}{\partial z}\left(\frac{q^2}{2}\right)\int_0^z \frac{\partial u}{\partial t}\,dz = \frac{\tau}{\rho}\frac{\partial u}{\partial z} + \frac{\partial D}{\partial z} - \epsilon \tag{5b}$$

where c is the wave speed. Equations (5) involve derivatives with respect to z and t only, rather than x, z and t.

TURBULENCE CLOSURES

We shall discuss results based on two turbulence closures. The first is Prandtl's mixing length model, which is

$$\tau = \rho\, \ell^2(z)\, \left|\frac{\partial u}{\partial z}\right| \frac{\partial u}{\partial z} \tag{6}$$

Here $\ell(z)$ is a vertical length scale which must by specified. We shall use simply

$$\ell = \kappa(z + z_o) \tag{7}$$

where κ is the Karman constant and z_o is the bed roughness scale. The turbulent kinetic energy equation is not needed for this closure, and the governing equations are simply (5a) and (6).

The second closure is a slightly more sophisticated turbulent kinetic energy closure. In this closure, the stress is written

$$\tau = c_2\, q\, \ell \tag{8}$$

where c_2 is an empirically determined constant, and the length scale $\ell(z)$ must be specified. As before, we shall use (7). The diffusion and dissipation terms are modeled by

$$D = c_2\, c_3\, q\, \ell\, \frac{\partial}{\partial z}\left(\frac{q^2}{2}\right) \quad ; \quad \epsilon = c_1\, q^3/\ell \tag{9a}$$

where c_1 and c_3 are constants. The boundary conditions for q are

$$q \to 0 \quad \text{as} \quad z \to \infty \quad ; \quad q^2 = c_4\, |\tau/\rho| \quad \text{at } z = 0 \tag{9b}$$

where c_4 is an empirical constant. The constants have been determined by other researchers by comparison with observations made in steady flows. We shall use the following values: $c_1 = 0.054$, $c_2 = 0.38$, $c_3 = 0.59$, $C_4 = 7$ (Reynolds, 1976).

It can easily be shown that the turbulent kinetic energy closure reduces to the mixing length model if temporal rate of change, advection, and diffusion of turbulent kinetic energy are neglected. The mixing length model can therefore be regarded as being based on a simplified turbulent kinetic energy balance in which production balances dissipation.

SOLUTION METHOD

As noted above, the advective terms on the left and right sides of (5a) and the left side of (5b) are order kA compared to the leading terms. In Stokes waves, kA is a small quantity, and the advective terms may be neglected for the purpose of a first approximation, yielding

$$\frac{\partial u}{\partial t} - \frac{\partial}{\partial z}\left(\frac{\tau}{\rho}\right) = \frac{\partial U}{\partial t} \tag{10a}$$

$$\frac{\partial}{\partial t}\left(\frac{q^2}{2}\right) - \frac{\partial D}{\partial z} - \frac{\tau}{\rho}\frac{\partial u}{\partial z} + \epsilon = 0 \tag{10b}$$

These equations are consistent with Stokes first order solution (linear waves). With the use of one of the turbulence closures discussed above, these equations may in principle be solved subject to the appropriate boundary conditions, with $\partial U/\partial t$ determined from the first term in (3). This solution is purely oscillatory and contains only odd harmonics of the fundamental Fourier component, i.e., terms with periods of T, T/3, T/5,etc., where T is the fundamental wave period.

Once a first-order solution is obtained from (10), the small advective terms in (5) may be estimated from the first-order solution. Equations (5)can be written

$$\frac{\partial u}{\partial t} - \frac{\partial}{\partial z}\left(\frac{\tau}{\rho}\right) = \frac{\partial U}{\partial t} - \frac{U}{c}\frac{\partial U}{\partial t} + \frac{u}{c}\frac{\partial u}{\partial t} - \frac{1}{c}\frac{\partial u}{\partial z}\int_0^z \frac{\partial u}{\partial t}\, dz \tag{11a}$$

$$\frac{\partial}{\partial t}\left(\frac{q^2}{2}\right) - D - \frac{\tau}{\rho}\frac{\partial u}{\partial z} + \epsilon = \frac{u}{c}\frac{\partial}{\partial t}\left(\frac{q^2}{2}\right) - \frac{1}{c}\frac{\partial}{\partial z}\left(\frac{q^2}{2}\right)\int_0^z \frac{\partial u}{\partial t}\, dz \tag{11b}$$

With the advective terms determined by the first order solution, and with the terms involving U determined by both terms in (3), the right sides of equations (11) are known. By using one of the turbulence closures discussed above, one may in principle solve equations (11) subject to the appropriate boundary conditions. This procedure yields a solution consistent with Stokes' second order solution for the wave field. To this level of approximation, the boundary layer solution consists of a large, purely oscillatory, first order part, containing only odd harmonics of the fundamental Fourier component, and a smaller second order part, containing even harmonics of the fundamental Fourier component, as well as a steady component.

Equations (10) and (11) resemble coupled heat equations, each containing an unsteady term, a diffusion term, and various source and sink terms. These equations can be solved subject to the appropriate boundary conditions by means of a fully implicit, finite control volume procedure described in detail by Patankar (1980). In deriving this procedure, one integrates the governing equations across a small control volume of height Δz and considers the fluxes of momentum and turbulent kinetic energy across the interfaces of each control volume. The scheme leads to a numerical time-stepping procedure in which one solves iteratively for the spatial distribution of velocity and kinetic energy at each time step.

In the computations described below, we used a vertical grid with a spacing varying as the cube of the distance above the solid boundary, and we applied the conditions at infinity at a finite distance above the boundary equal to A. In most computations we used 360 time steps per wave period and 51 grid points, and our convergence criterion was that the last iteration must yield values within approximately one part in 10^4 of the previous iteration. We found that computations carried out on this basis yielded results which were nearly identical to results obtained with larger numbers of grid points and time steps, and with a stronger convergence criterion. We began the computations from rest, and we found that the first order solution reached a periodic state after roughly six to ten periods. The second order solution required a much larger time to reach a periodic state, as discussed below.

FIRST ORDER RESULTS

As discussed in the Introduction, the first order solution for the case of a fixed bed with roughness elements small compared to the excursion amplitude is fairly well established on the basis of existing experimental, theoretical and semi-empirical studies. The purposes of presenting additional first order results here are to show that the numerical solutions reproduce available observations, and to compare the results produced by the two different turbulence closures.

Figure 2 shows vertical distributions of amplitude and phase of the first two nonzero Fourier components in the first-order velocity field. The Figure also shows observations reported by Jonsson and Carlsen (1976, Test 1). The computations in Figure 1 are based on the mixing length closure. Figure 3 shows a comparison of results based

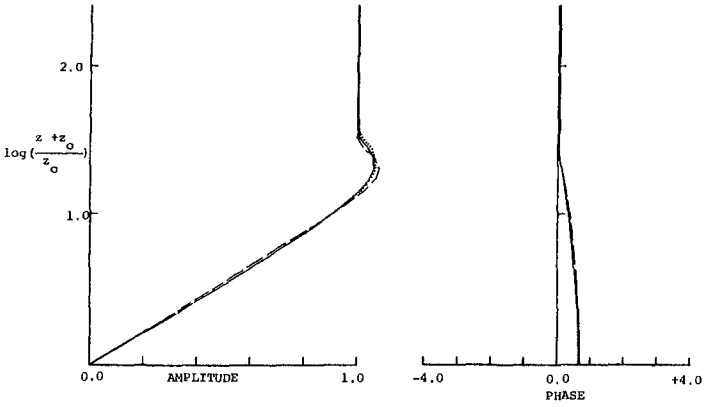

Figure 3. Computed dimensionless amplitude and phase of the first harmonic of the horizontal velocity. Solid line, mixing length model; dashed line, time rate of change of turbulent kinetic energy equal to production minus dissipation; dotted line, turbulent kinetic energy closure. $z_o/A = 0.004$.

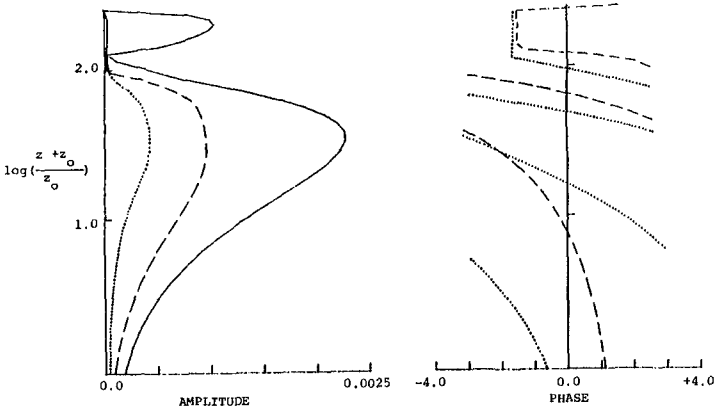

Figure 4. Computed amplitude and phases of the first three nonzero Fourier components of the first order eddy viscosity, normalized by A and ω, based on the mixing length model. Solid line, mean component; dashed line, second harmonic; dotted line, fourth harmonic. $z_o/A = 0.004$.

on the mixing length model and on the turbulent kinetic energy closure. Both closures reproduce the experimental observations well, and the results based on the two closures are nearly indistinguishable from each other. A small improvement in the agreement between computations and observations is possible if one uses a more physically reasonable length scale than that given by (7). This point is well understood based on previous theoretical studies (Kajiura, 1968; Brevik, 1981; Trowbridge and Madsen, 1984a) and will not be pursued here.

We thought initially that because wave boundary layers are an unsteady phenomenon, the most important parts of the first-order turbulent kinetic energy balance might be unsteadiness, production and dissipation, because diffusion is known to be relatively small in steady turbulent flows near solid surfaces (e.g., Tennekes and Lumley, 1972). Neglect of the diffusion term in the turbulent kinetic energy balance leads to a simplified solution, because in this case no boundary conditions are necessary for the turbulent kinetic energy. We found, however, that computations based on a simplified model without the diffusion term are only slightly different, but slightly worse from the point of view of comparison with experiments, than computations based on either the mixing length or kinetic energy closures. We therefore abandoned this approach.

Figures 4 and 5 show computations of the eddy viscosity, ν_T, which is defined by

$$\tau = \rho \, \nu_T \frac{\partial u}{\partial z} \tag{12}$$

In the mixing length closure,

$$\nu_T = \kappa^2 \, z^2 \left|\frac{\partial u}{\partial z}\right| \tag{13a}$$

and in the kinetic energy closure

$$\nu_T = c_2 \, q \, \ell \tag{13b}$$

The results in Figures 4 and 5 are very close. This is a convincing demonstration that the mixing length and kinetic energy closures give nearly identical results in the first order problem, because computations of eddy viscosity are more sensitive to the closure model than are computations of velocity.

The conclusions based on the first order results presented here are the following: (1) both turbulence closures reproduce the observations quite well; and (2) advection and diffusion of turbulent kinetic energy, which are the processes neglected in the mixing length model, have no significant effect on the Reynolds averaged motion.

SECOND ORDER RESULTS

Existing analytical models (Trowbridge and Madsen, 1984b) indicate that predictions of the second order boundary shear stress and the

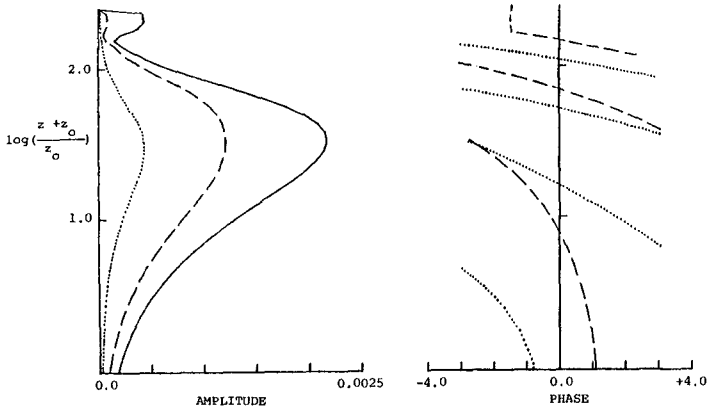

Figure 5. Computations as in Figure 4 based on the turbulent kinetic energy closure.

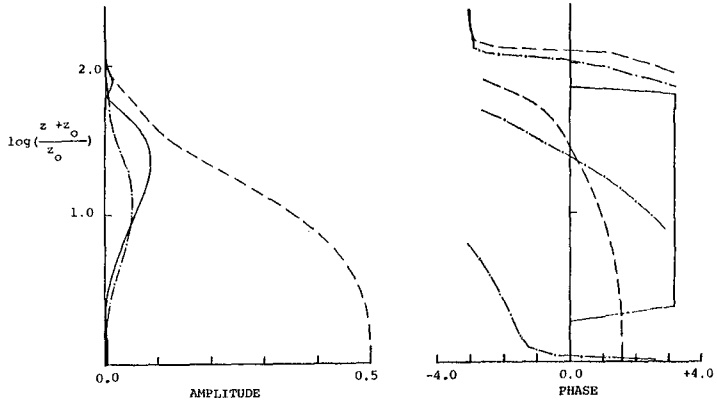

Figure 6. Computed amplitudes and phases of minus the second order forcing term on the right side of (11a), normalized by $kA^2\omega^2$, based on the mixing length model. Solid line, mean component; dashed line, second harmonic; dashed-dotted line, fourth harmonic. $z_o/A = 0.004$, $kA = 0.2$, $kh = 1.0$.

unsteady component of the velocity inside the boundary layer are relatively insensitive to the particular eddy viscosity model used. In discussing the second order results, we shall therefore concentrate on the steady streaming. Because there is no significant mean pressure gradient in an oscillatory wave field, the steady motion is forced solely by the nonlinear advective terms on the right side of equation (11a). In general, these terms contain a mean component plus components at even harmonics of the fundamental frequency. Figure 6 shows the vertical distribution of the amplitudes and phases of the forcing function on the right side of (11a). The dominant forcing occurs at twice the frequency of the first order wave field, but the mean forcing is clearly evident. Throughout most of the boundary layer, the mean forcing is in the direction of wave propagation, but near the outer edge of the boundary layer the mean forcing is in the opposite direction. Outside the boundary layer, of course, the mean forcing is zero.

In carrying out the second order solution, we began the computations from rest, as in the first order solution. The solution for the velocity profile appeared to become nearly periodic after approximately six to ten periods. For those short times, we found mean velocity profiles which approached zero outside the boundary layer, similar in this respect to Johns' (1977) computations. Computations carried out over larger times, however, showed that the mean velocity inside the boundary layer continues to evolve for a long period, gradually reaching a steady state only after a few hundred periods. Figure 7 shows the mean velocity at several different times after the start of the motion, indicating the gradual approach to a positive, steady profile at very large times. At small times, the velocity outside the boundary layer is in the direction opposite that of wave propagation. This behavior is explained by the fact that the mean forcing is negative near the outer edge of the boundary layer. Initially, the boundary layer thickness is small, and the vertical transport of momentum due to Reynolds stresses is small compared to the mean forcing. Consequently, at small times the fluid at the outer edge of the boundary layer acts like a frictionless fluid under the action of a mean, negative, distributed body force. The resulting velocity is negative until the effect of the solid boundary diffuses outward far enough to begin moving the fluid forward. The results in Figure 7 are believed to be qualitatively correct with possible quantitative discrepancies due to recovery from initial conditions and the finite computational domain.

The velocities shown in Figure 7 correspond to kh equal to 1.0, or waves in water of intermediate depth. In this case, the mean velocity at large times is in the direction of wave propagation. Figure 8 shows similar mean velocity profiles for kh equal to 0.5, corresponding to relatively long waves. As in Figure 7, the gradual approach of the mean velocity to a steady state is evident. In Figure 8, however, the mean velocity is in the direction opposite that of wave propagation. This figure confirms qualitatively the reversal of the steady streaming under long waves which was found analytically by Jacobs (1984) and Trowbridge and Madsen (1984b).

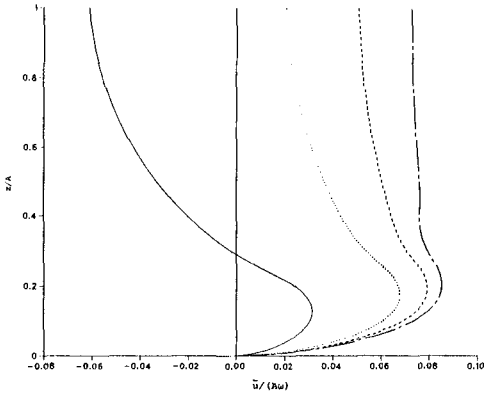

Figure 7. Computed mean velocities at several different times after the start of the motion. From left to right, the curves correspond to t/T = 10, 30, 50, 100. z_o/A = 0.004, kA = 0.2, kh = 1.0.

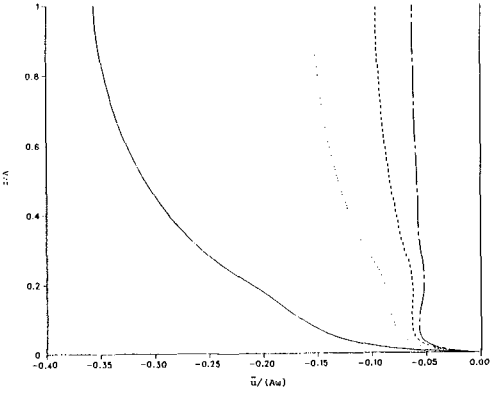

Figure 8. Computations as in Figure 7 for kh = 0.5.

Because of the long time periods required for the mean velocity to reach a steady state, numerical simulations of the second order problem based on implicit time-stepping procedures are very time-consuming. Our present results indicate, however, that computations based on the mixing length closure are nearly identical to computations based on the turbulent kinetic energy closure. Figures 7 and 8 are based on the mixing length model, and at relatively short times (of order ten wave periods) there is no significant difference between these results and the computations based on the turbulent kinetic energy closure.

The conclusions based on the second order computations are the following: (1) reversal of the steady streaming produced by relatively long waves is confirmed qualitatively; (2) the two turbulence closures give very similar results, indicating that processes in the turbulent kinetic energy equation other than production and dissipation have no significant effect on the Reynolds averaged velocity and stress; and (3) the time-averaged motion requires a very long time to reach a steady state. Conclusion (3) implies that the averaged motion may not become steady during time periods over which a natural wave field can be considered stationary. Consequently, it may be necessary to consider the history of the wave field when considering low frequency boundary layer motions produced by natural waves. In laboratory basins, where controlled, stationary conditions are possible for long times, the mean motion might have time to reach a steady state, if experiments are carried out for long enough periods.

A SIMPLE ANALYTICAL MODEL

For the purposes of studying more complicated processes, such as sediment transport, a simple analytical model which captures the main features of the flow is preferable to a more complicated, although possibly more consistent, numerical solution. One of the purposes of the numerical study reported here is therefore to guide development of realistic analytical models. The following very simple analysis is essentially the argument of Jacobs (1984) in a slightly more straightforward form. It is based on a mean momentum balance derived by Longuet-Higgins (1958) and on the assumption of a constant friction factor.

The mean momentum balance derived by Longuet-Higgins (1958) is, to second order,

$$\bar{\tau}_b = -(\overline{uw})_{z=\infty} \tag{14}$$

where τ_b is the boundary shear stress. Use of the mass equation and the condition of periodicity in space and time shows that the vertical velocity may be written

$$w = \frac{1}{c} \int_0^z \frac{\partial u}{\partial t} \, dz \tag{15}$$

Substitution of the first order momentum balance (10a) yields

$$w = \frac{z}{c} \frac{\partial U}{\partial t} + \frac{1}{\rho c} (\tau - \tau_b) \tag{16}$$

to first order. Substitution of (16) into (14) and use of the boundary conditions (2) gives

$$\overline{\tau_b} = \frac{1}{c} \overline{\tau_b U} \tag{17}$$

correct to second order. If we assume that a constant wave friction factor f gives an adequate representation of the boundary shear stress, we have

$$\tau_b = \frac{1}{2} f \rho U|U| \tag{18}$$

Substitution of (3) and (18) into (17) yields, after straightforward algebra, the following result for the steady streaming just outside the boundary layer:

$$\bar{U} = \frac{2}{3} \frac{\overline{U^2}}{c} \left[1 - \frac{3}{4} \frac{1}{\sinh^2(kh)} \right] \tag{19}$$

correct to second order. Equation (19) is the result obtained by Jacobs (1984). This result agrees fairly well with the present numerical computations, and it indicates a reversal of the steady streaming produced by long waves. It is noteworthy that (19) is independent of the boundary roughness.

The above analysis may be used to calculate the time-varying boundary shear stress in a manner which incorporates the presence of the steady streaming consistently, although approximately.

ACKNOWLEDGMENT

This work was supported in part by the National Science Foundation (NSF Award Number CEE-8404258).

REFERENCES

Bakker, W.T. 1974. Proceedings of the 14th International Conference on Coastal Engineering, ASCE.

Bakker, W.T. and van Doorn, Th. 1978. Proceedings of the 16th International Conference on Coastal Engineering, ASCE.

Brevik, I. 1981. Journal of Waterway, Port, Coastal and Ocean Engineering, 107: 175-188.

Dean, R.G. and Dalrymple, R.A. 1984. Water Wave Mechanics for Engineers and Scientists, Prentice-Hall.

Grant, W.D. and Madsen, O.S. 1979. Journal of Geophysical Research, 84: 1797-1808.

Jacobs, S.J. 1984. Journal of Fluid Mechanics, 146: 303-312.

Johns, B. 1970. Journal of Fluid Mechanics, 43: 177-186.

Johns, B. 1975. Journal of Geophysical Research, 80: 5109-5112.

Johns, B. 1977. Journal of Physical Oceanography, 7: 733-738.

Jonsson, I.G. 1966. Proceedings of the 10th International Conference on Coastal Engineering, ASCE.

Jonsson, I.G. and Carlsen, N.A. 1976. Journal of Hydraulic Research. 14: 45-60.

Kajiura, K. 1968. Bulletin of the Earthquake Research Institute. 46: 75-123.

Kamphuis, J.W. 1975. Journal of the Waterways, Harbors and Coastal Engineering Division, ASCE. 101: 135-144.

Longuet-Higgins, M.S. 1958. Proceedings of the 6th International Conference on Coastal Engineering, ASCE.

Myrhaug, D. 1982. Ocean Engineering, 9: 547-565.

Patankar, S.V. 1980. Numerical Heat Transfer and Fluid Flow. McGraw-Hill.

Reynolds, W.C. 1976. Annual Review of Fluid Mechanics. 8: 183-208.

Schlichting, H. 1979. Boundary Layer Theory. McGraw-Hill.

Tennekes H. and Lumley, J.L. 1972. A First Course in Turbulence. MIT Press.

Trowbridge, J.H. and Madsen, O.S. 1984a. Journal of Geophysical Research. 89: 7989-7997.

Trowbridge, J.H. and Madsen, O.S. 1984b. Journal of Geophysical Research. 89: 7999-8007.

CHAPTER 120

TRANSIENT RIPPLE FORMATION AND SEDIMENT TRANSPORT

By Suphat Vongvisessomjai,[1] M. ASCE, L.C.J. Munasinghe,[2] and P.P. Gunaratna[2]

ABSTRACT

A knowledge of sediment transport rates due to wave action is essential for an understanding of various coastal engineering problems. Many problems have to be resolved before successful measurement can be made for sediment transport rates due to waves.

Since gradients of sediment transport cause changes of beach morphology, the sediment transport rate outside breaker can be determined from measured beach changes. Measurements of ripple growth and migration yield their mathematical descriptions in the same manner as those of surface waves. Expressions of sediment transport rates are then derived.

It is found from the study that the sediment transport rates are strongly controlled by the rates of growth and migration of ripples.

INTRODUCTION

Passage of water waves over an erodible bed of sands produces an oscillatory sediment transport. Due to wave action, the initially straight bed is deformed into wavy undulations known as ripples. These ripples will grow in height and length until they attain in equilibrium geometry for a set of wave-beach characteristics. The phenomenon of ripple formation due to wave action is of considerable interest due to a resulting contribution to sediment transport. In addition, the ripples on the bed significantly affect wave attenuation, wave induced current and beach profile. Not much data on transient ripple formation and migration are presently available despite the fact that they are needed to determine the sediment transport rate due to ripple migration.

The objectives of this study are to quantify the growth and migration of ripples due to wave action normal to beaches outside breaker lines from experimental results in a wave flume, and to determine the resulting rate of sediment transport. Since the offshore sediment transport does not yield a well defined ripple migration, only the onshore ripple migration and sediment transport are presented. This report is prepared from two master theses of Gunaratna (1984) and Munasinghe (1985).

SURVEY OF EARLIER WORK

Reviews will first be made on geometries of stable, not transient, ripples generated by oscillatory flows and followed by rates of sediment transport generated by oscillatory flows.

---

[1] Professor and [2] Graduate Students, Div. of Water Resources Engrg., Asian Inst. of Tech., P.O. Box 2754, Bangkok 10501, Thailand.

Ripple Geometry.- Ripple geometries generated by oscillating bed were first tested by Bagnold (1946) and Manohar (1955). Prototype ripples were measured by Inman (1957) and Dingler (1974). Extensive laboratory tests on ripple geometries were made by Mogridge and Kamphuis (1972). Analysis was made on ripple geometries by Vongvisessomjai (1984) using published and supplementary data tested by the author. These studies reveal that, when the bed shear stress of an oscillatory fluid exceeds the critical value required for initial motion on a flat sediment bed, rolling grain ripples will slowly form; as the shear stress increases, the height and length of ripples will also increase accordingly. The growing ripples continue to enlarge as the bed shear stresses reach higher values until optimum condition is reached. Beyond this stage, the ripple height will decay, while its length remains practically constant or decays slowly.

Empirical Rate of Sediment Transport.- Almost all empirical formulae of sediment transport rates were developed from oscillating bed data, only that proposed by Vongvisessomjai (1986) was developed from wave flume data.

Manohar (1955) employed an oscillating bed of sediment to study regimes of sediment transport, ripple geometries and rates of sediment transport. He found the governing parameter of all the phenomena to be

$$\psi_1 = \frac{U_{1m}}{[(s-1)g]^{0.4} (\nu D)^{0.2}} \quad \text{.....(1)}$$

in which U_{1m} = maximum orbital velocity of fluid just outside boundary layer; s = relative density of sediment; g = gravitational acceleration; ν = kinematic viscosity of fluid; and D = mean or median diameter of sediment.

In order to obtain rates of sediment transport, he generated asymmetrical motion by changing the angular frequencies of a flywheel driving the oscillating bed when it was at its extreme positions, while he held the amplitudes of the excursions constant. These asymmetrical motions yield a net sediment transport, the sediment being collected in a tray set into the sediment bed.

Kalkanis (1964) and Abou-Seida (1965) developed a relationship between the flow intensity ψ_2 and the bed load intensity ϕ_*, using the principle of Einstein's theory (1950) for sediment transport in open channels and introducing the effect of wave motion on the bed sediment. Their experimental data were obtained on oscillating beds. They found that Einstein's bed load equation for sediment transport in open channels was the same as that describing sediment transport induced by oscillating beds. This was so when the mean fluid velocity in open channels, used in defining ψ_2, was replaced by the amplitude of the oscillating bed velocity U_a, calculated at a distance 0.35D from the mean level of the bed.

$$\psi_2 = \frac{1}{\frac{U_a^2}{(s-1)gD}} \quad \text{.....(2)}$$

and

$$\phi_* = \frac{q_s'/\gamma_s}{D\sqrt{(s-1)gD}} \quad \text{.....(3)}$$

in which q_s' = the dry weight rate of the gross sediment transport per

unit width; and γ_s = the sepcific weight of the bed sediment. When U_a is correlated with U_{1m}, their relationship is $U_a \doteq 0.625U_{1m}$.

Madsen and Grant (1976) re-analyzed data of Manohar (1955) Kalkanis (1964) and Abou-Seida (1965) and expressed the volumetric rate of gross sediment transport, mornalized by the settling velocity and the diameter of the sediment, as function of the Shields parameter. They stated that in Kalkanis (1964) and in Abou-Seida (1965) ripples might have been present, and for Manohar (1955), ripples were present. However, the Shields parameter was computed using Jonsson's friction factor (1966) and based on grain diameter.

Sleath (1978) used a motion picture camera to determine the instantaneous and mean sediment transport rates averaged over a half cycle induced by an oscillating bed on flat sediment beds. From his data and those of Kalkanis (1964) and Abou-Seida (1965) he obtained an expression for the mean volumetric rate of the gross sediment transport per unit width q_v' from his data and those of Kalkanis (1964) and Abou-Seida (1965):

$$\frac{q_v'}{\omega D^2} = 47(\psi_* - \psi_{*c})^{3/2} \quad \text{.....(4)}$$

in which ψ_{*c} = the critical value of Shields parameter ψ_* for initial motion; $\omega = 2\pi/T$ = angular velocity; and T = period of oscillation. His expression of the friction factor was the same as that obtained by Jonsson (1966) and his equivalent sand roughness was taken to be the sediment grain size. Note that Grant and Madsen (1982) found a remarkable difference between friction factors of immobile and mobile beds with sediment suspension.

Sleath's instantaneous sediment transport rate $q_v(t)$ for sand and gravel was

$$q_v'(t) = \frac{8}{3} q_v' \cos^3(\omega t + \alpha) \left|\cos(\omega t + \alpha)\right| \quad \text{.....(5)}$$

in which t = the time; $q_s^* = (1-\beta)\gamma_s q_v^*$; β = porosity of bed sediment; and α = the phase lag of the local velocity behind the water surface

$$\alpha = 0.15 + 0.000018 \frac{q_v'}{\omega D^2} \left(\frac{a_{1m}}{D}\right) \frac{U_{1m}}{(\omega\nu)^{1/2}} \quad \text{.....(6)}$$

in which $a_{1m} = U_{1m}/\omega$ = nearbed amplitude of water particle excursion.

Kobayashi (1982) derived a criterion for the initiation of sediment movement on a gentle slope by balancing the forces acting on a sediment particle lying on the slope. A relationship for the instantaneous rate of the bed load transport on a gentle slope, which was quite similar in form to that of Madsen and Grant (1976), was then derived from a simple and quasi-steady analysis of the motion of sediment particles. His theory was in reasonable agreement with experiments, conducted on horizontal beds by Kalkanis (1964), Abou-Seida (1965) and Sleath (1978).

Vongvisessomjai (1986) found from analyses of sediment transport data from oscillating beds and wave flumes that they were different. The sediment transport rate developed from wave flume data was as follows:

For bed load transport ($Fd_* < 4$)

$$\phi_* = \frac{q_s'/\gamma_s}{D\sqrt{(s-1)gD}} = 0.0002\, Fd_*^3 \quad \text{.....(7)}$$

For total load transport ($Fd_* > 4$)

$$\phi_* = \frac{q_s'/\gamma_s}{D\sqrt{(s-1)gD}} = 0.0015\, Fd_*^{3/2} \quad \text{.....(8)}$$

in which the densimetric sediment Froude number $Fd_* = U_{1m}^2/[(s-1)gD]$.

METHODOLOGY

Basing on a theoretical model to explain the formation of wave-generated sediment ripples presented by Kennedy and Faclon (1965) in which a profile of ripple bed $z(x,t)$ was represented by a moving sinusoid of varying amplitude $\eta(t)$ and a constant ripple length, a time dependent ripple length $\lambda(t)$ is used in this study as follows:

$$z(x,t) = s_o x + \eta(t) \sin\left\{\frac{2\pi}{\lambda(t)}\left[x - \int_o^t C_r(t)dt\right]\right\} \quad \text{.....(9)}$$

in which x is the horizontal coordinate; t is time; s_o = beach slope; $C_r(t)$ is the celerity of ripple.

The growth rates of ripple height $\eta(t)$ and ripple length $\lambda(t)$ of Equation (9) are found from experimental results in a wave flume to be the same as

$$\eta(t) = \eta_{max}\{1 - \exp[-B^*(\frac{t}{T})]\} \quad \text{.....(10)}$$

and

$$\lambda(t) = \lambda_{max}\{1 - \exp[-B^*(\frac{t}{T})]\} \quad \text{.....(11)}$$

in which η_{max} is the maximum height of ripple; λ_{max} is the maximum length of ripple; B^* is the dimensionless growth of ripple; and T is the wave period. Information of geometry of equilibrium ripples has been provided by Vongvisessomjai (1984).

Sediment Transport Rate Due to Ripple Growth.- A simple rate of sediment transport q_r is determined only from ripple geometry developed from an initially straight bed excluding the information on ripple migration as

$$q_r = \frac{d}{dt}\left[(1-\beta)\gamma_s \int_o^{\lambda/2} z(x,t)dt\right]$$

$$= \frac{2}{\pi}\gamma_s(1-\beta)\frac{B^*}{T}\eta_{max}\lambda_{max}\exp[-B^*(\frac{t}{T})]\{1-\exp[B^*(\frac{t}{T})]\} \quad \text{.....(12)}$$

in which β is the porosity of sand on the bed. The maximum value of the above rate of sediment transport at time $t_{max} = 0.693T/B^*$ is

$$q_{rmax} = \frac{0.5}{\pi T}\gamma_s(1-\beta)B^*\eta_{max}\lambda_{max} \quad \text{.....(13)}$$

Figure 1 shows an example of transient growth of ripple height, Eq. 10, and its corresponding sediment transport rate due to ripple growth, Eq. 12. Sediment transport rate due to ripple growth and migration will be presented as follows.

The celerity of ripple $C_r(t)$ of Equation (9) is found from experiments to follow several patterns:

(a) a similar pattern to the growth rate of ripple as

$$C_r(t) = C_{rmax}\{1-\exp[-C^*(\frac{t}{T})]\} \quad \text{.....(14a)}$$

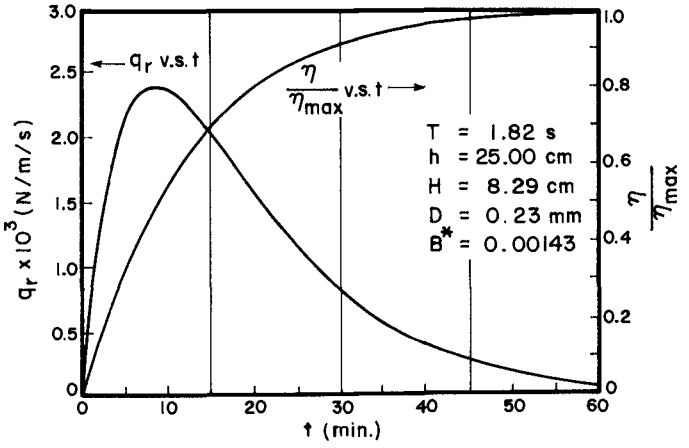

Figure 1. Transient Growth of Ripple Height and Its Sediment Transport Rate

in which C_{rmax} is the maximum celerity of ripple and C^* is the dimensionless migration rate of ripple.

(b) a growing-decaying pattern as

$$C_r(t) = At^m \exp(-Bt^n) \quad \text{.....(14b)}$$

in which A, B, m and n are empirical constants.

(c) a constant celerity as

$$C_r(t) = \bar{C}_r \quad \text{.....(14c)}$$

The rate of sediment transport per unit width $q_s(x,t)$ can be expressed in terms of the ripple bed profile $z(x,t)$ of Equation (9) as

$$\frac{\partial q_s(x,t)}{\partial x} + \gamma_s \frac{\partial z(x,t)}{\partial t} = 0 \quad \text{.....(15)}$$

The rate of sediment transport per unit width $q_s(x,t)$ can then be determined from the above equation using the measured bed profile $z(x,t)$ i.e. Equations 10 11 and 14a and a boundary condition of the instantaneous rate of sediment transport per unit width $q_s(t)$. These analytical solutions will be presented as follows.

Sediment Transport Rate Due to Ripple Growth and Migration.- Solving for $q_s(x,t)$ by integrating Eq. 15 with respect to x where the bed profile $z(x,t)$ is described by Eq. 9 yields

$$q_s(x,t) = \gamma_s \left[\frac{\lambda}{2\pi} \left(\frac{\eta}{\lambda} \frac{d\lambda}{dt} + \frac{d\eta}{dt} \right) \cos\left\{ \frac{2\pi}{\lambda} \left(x - \int_o^t C_r \, dt \right) \right\} + \left(\eta C_r + \frac{\eta}{\lambda} \frac{d\lambda}{dt} x - \frac{\eta}{\lambda} \frac{d\lambda}{dt} \int_o^t C_r \, dt \right) \sin\left\{ \frac{2\pi}{\lambda} \left(x - \int_o^t C_r \, dt \right) \right\} \right]$$

$$+ f(t) \qquad \ldots\ldots\ldots\ldots\ldots\ldots\ldots\ldots (16)$$

The unknown function f(t) in the above equation has to be determine from a suitable boundary condition, i.e. at x = 0

$$q_s(o,t) = q_s(t) \qquad \ldots\ldots\ldots\ldots\ldots\ldots\ldots\ldots (17)$$

Using the above boundary condition, Eq. 16 is

$$q_s(x,t) = \gamma_s \left[\frac{\lambda}{2\pi} \left(\frac{\eta}{\lambda} \frac{d\lambda}{dt} + \frac{d\eta}{dt} \right) \left(\cos \left\{ \frac{2\pi}{\lambda} (x - \int_o^t C_r \, dt) \right\} - \cos \left\{ \frac{2\pi}{\lambda} (\int_o^t C_r \, dt) \right\} \right) \right.$$

$$+ \left(\eta \, C_r - \frac{\eta}{\lambda} \frac{d\lambda}{dt} \int_o^t C_r \, dt \right) \left(\sin \left\{ \frac{2\pi}{\lambda} (x - \int_o^t C_r \, dt) \right\} + \sin \left\{ \frac{2\pi}{\lambda} (\int_o^t C_r \, dt) \right\} \right)$$

$$\left. + \frac{\eta}{\lambda} \frac{d\lambda}{dt} \, x \sin \left\{ \frac{2\pi}{\lambda} (x - \int_o^t C_r \, dt) \right\} \right] + q_s(t) \qquad \ldots\ldots\ldots\ldots (18)$$

The above $q_s(x,t)$ depends on $C_r(t)$ and $\int_o^t C_r(t)dt$ which are assumed as the following four cases:

Case	$C_r(t)$	$\int_o^t C_r(t)dt$
I	0	0
II	$C_{rmax}\{1-\exp[-C^*(\frac{t}{T})]\}$	$C_{rmax}(t - \frac{T}{C^*}\{1-\exp[-C^*(\frac{t}{T})]\})$
III	$-C_{rmax}\{1-\exp[-C^*(\frac{t}{T})]\}$	$-C_{rmax}(t - \frac{T}{C^*}\{1-\exp[-C^*(\frac{t}{T})]\})$
IV	$C_{rmax} \sin(\frac{2\pi t}{\tau})$	$\frac{\tau C_{rmax}}{2\pi}\left[1 - \cos(\frac{2\pi t}{\tau})\right]$

The resulting expressions of $q_s(x,t)$ were present by Gunaratna (1984).

The above four $C_r(t)$ and $\int_o^t C_r(t)dt$ are plotted as a function of time t in Figure 2, and their resulting sediment transport rates $q_s(x,t)$ at times t = 15, 30 45 and 60 minutes are plotted in Figures 3a, 3b, 3c and 3d respectively using Sleath's Eq. 5 as boundary condition, $q_s(t)$ of Eq. 17 or 18. The sediment transport rates due to ripple growth and migration, $q_s(x,t)$ shown in Figures 3a, 3b, 3c and 3d used the same ripple growth of Figure 1, therefore, their rates of sediment transport can be compared.

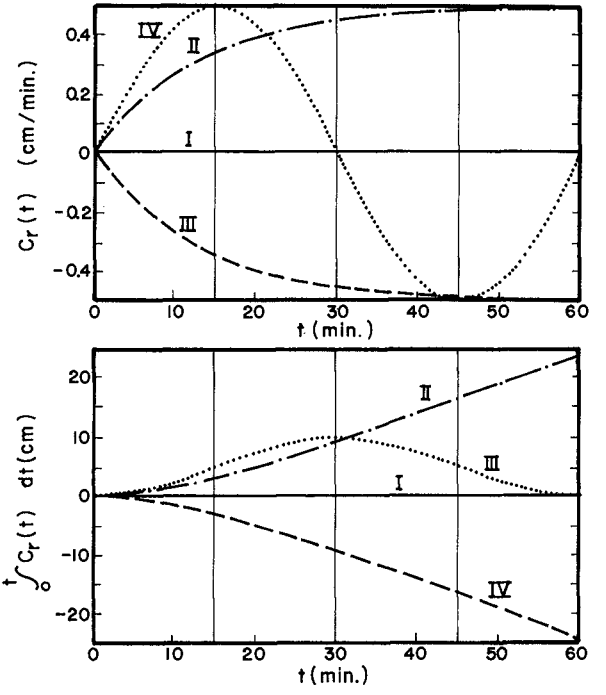

Figure 2. Four Cases of Ripple Celerities and Their Integration

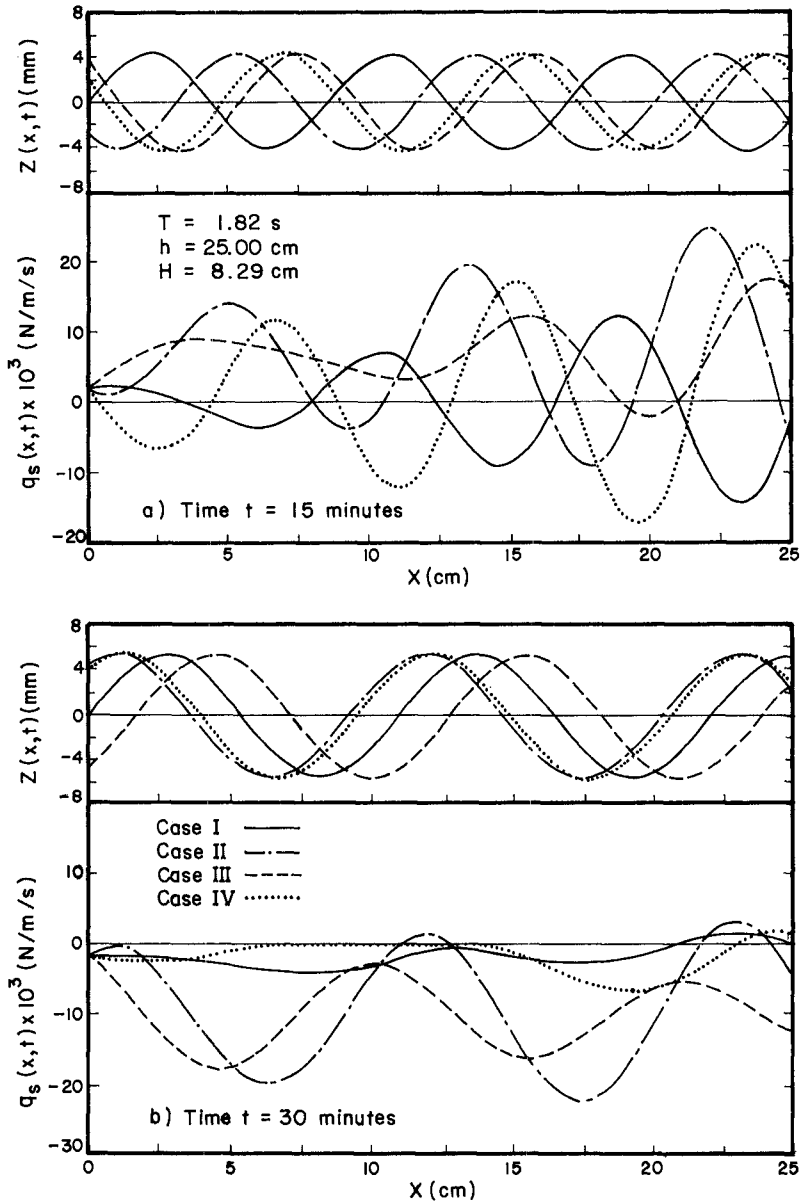

Figure 3. Spatial Variations of Bed Form and Sediment Transport Rate

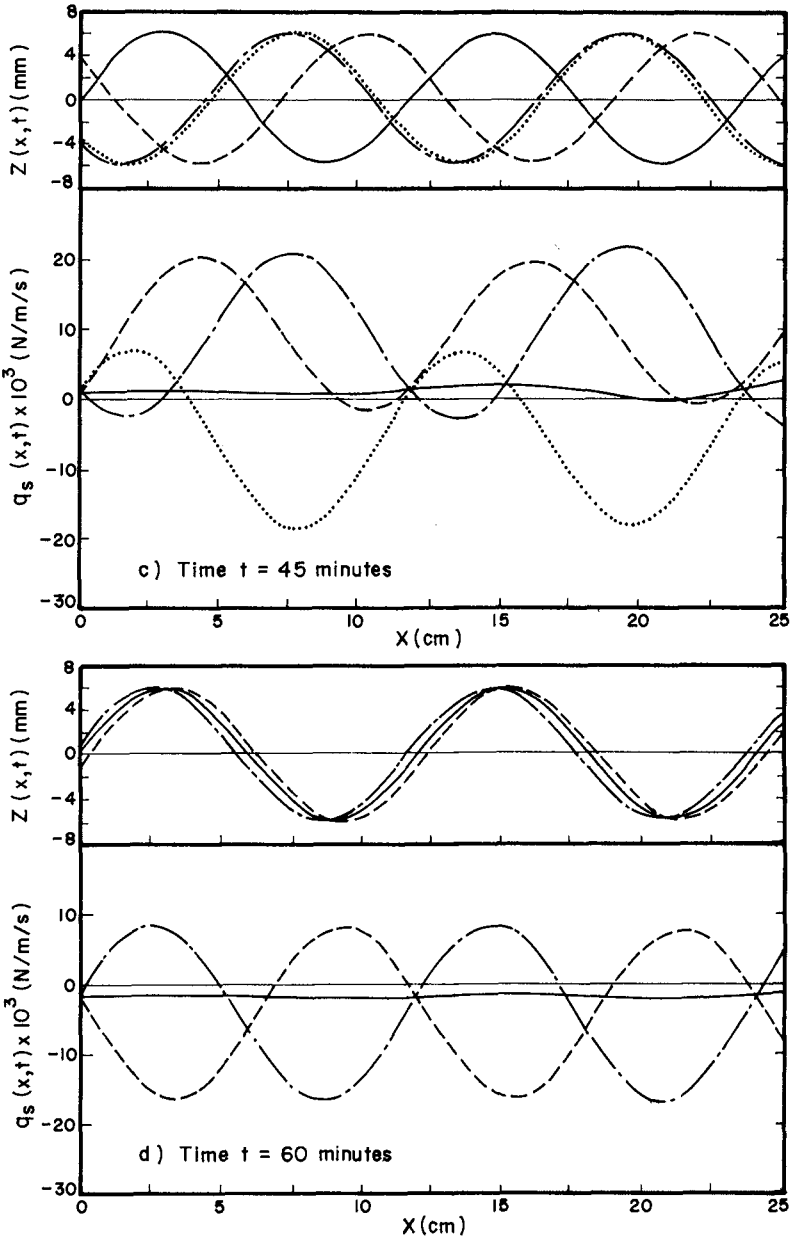

Figure 3. Continued

EXPERIMENTATION AND RESULTS

Experimentation.- Experiments were conducted in the Hydraulic Laboratory of the Asian Institute of Technology. The major apparatus consisted of a wave flume (1m x 1m x 40m) with a flap-type wave generator, capacitance wave gauges connected to an amplifier and a chart recorder.

Various wave characteristics were tested on 1:20 and 1:10 slopes of medium sand (D_{50} = 0.41 mm) and on 1:20 slope of finer sand (D_{50} = 0.23 mm). Wave profiles along the flume were recorded at the start, middle and end of each run while reading of sand accummulation in sand trap were made at 5 minutes, 15 minutes, 25 minutes, etc. Observations of ripples and bed profile changes were made at various locations along sloping beds at mean water depths h = 17, 27, 32, 37, and 42 cm at various time intervals. Table 1 lists the experimental condition which was plotted in Figure 4 as compared with the onshore-offshore criterion of Sunamura and Horikawa (1974) confirmed that most of the runs were onshore transports.

TABLE 1.-Experimental Condition

Run No. (1)	Period T (s) (2)	Excentricity (mm) (3)	Steepness H_o/L_o (4)	D_{50} (mm) (5)	Slope S_o or tanα (6)	$q'_{yexp} \times 10^{-6}$ ($m^3/s/m$) (7)
1	2.70	150	0.0075	0.41	1:20	8.98
2	2.46	150	0.0110			4.44
3	2.04	150	0.0167			6.42
4	2.95	175	0.0062			10.63
5	2.43	175	0.0124			6.29
6	2.07	175	0.0197			9.43
7	2.96	200	0.0074			12.64
8	2.66	200	0.0096			9.76
9	2.44	200	0.0139			6.19
10	2.63	150	0.0075	0.41	1:10	4.47
11	2.29	150	0.0105			3.66
12	2.09	150	0.0130			0.75
13	2.90	175	0.0069			-0.49
14	2.40	175	0.0100			1.82
15	2.01	125	0.0165			1.46
16	3.00	150	0.0148			3.34
17	2.75	200	0.0086			1.85
18	2.47	200	0.0107			-0.36
19	2.03	125	0.0143	0.23	1:20	-0.58
20	2.98	125	0.0044			3.21
21	2.02	117	0.0134			-0.11
22	1.92	115	0.0127			-0.32
23	1.87	110	0.0122			-0.33
24	1.85	100	0.0020			0.00
25	1.86	90	0.0086			-0.08
26	2.06	120	0.0119			2.27
27	2.04	130	0.0132			1.18

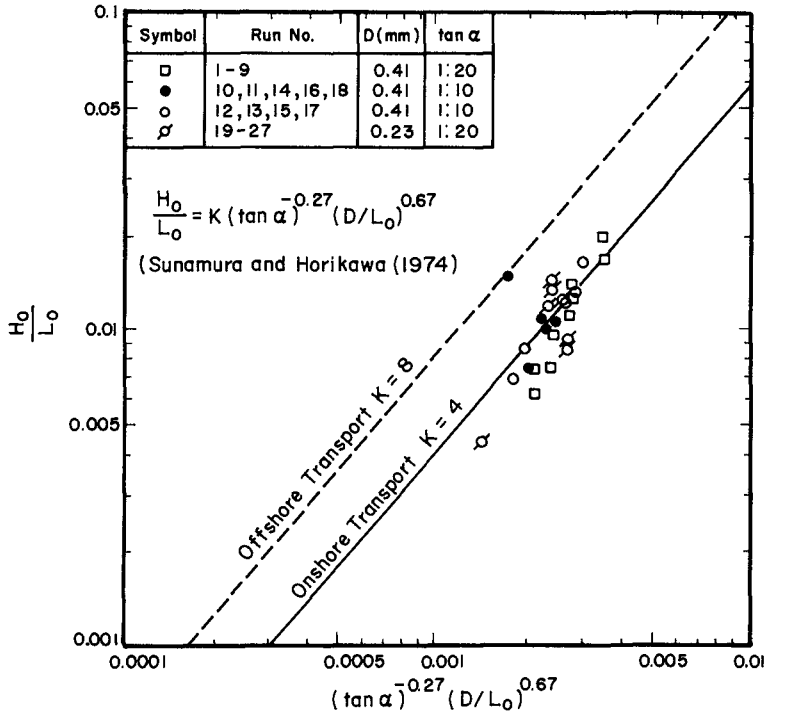

Figure 4. Experimental Condition

Experimental Results.- Experimental data were then used to determine the growth rate of ripples B^*, the geometry of the maximum ripples, η_{max} and λ_{max}, and the celerity of ripples. Since a systematic pattern of ripple migration could not be obtained, the time average celerity $\bar{C}_r$ and the maximum celerity C'_{max} of ripple migration were presented. These obtained empirical results were found to correlate well with the densimetric sediment Froude number $Fd_* = U_{1m}^2/[(s-1)gD]$ and the relative bed smoothness $a_* = a_{1m}/D$, in which $U_{1m} = \pi H/[T \sinh(2\pi h/L)]$ = nearbed water particle velocity; H = wave height; h = mean water depth; L = wave length; $a_{1m} = U_{1m}/\omega$ = nearbed amplitude of water particle excursion; $\omega = 2\pi/T$ = wave angular velocity; T = wave period; s = relative density of sand with respect to water; g = gravitational acceleration; D = median diameter of sand. Denoting the obtained results (B^*, η_{max}/a_{1m}, λ_{max}/a_{1m}, $\bar{C}_r/C$ and C'_{max}/C where C = celerity of the surface wave) by Y, their relations with Fd_* and a_* are

$$Y = k\, Fd_*^i\, a_*^j \quad \text{..... (19)}$$

Table 2 summarizes the empirical constants k, i and j obtained from regression analyses. Most of j for medium sand equal zero implies that the obtained results are independent on a_* but dependent on Fd_* only. Examples of these relationships for medium sand are shown in Figures 5-7 respectively for B^*, η_{max}/a_{1m} and λ_{max}/a_{1m}, $\bar{C}_r/C$ and C'_{max}/C.

TABLE 2.-Empirical Constants k, i and j of Eq. 19

Parameter Y	Medium Sand (D = 0.41 mm)			Finer Sand (D = 0.23 mm)		
(1)	k (2)	i (3)	j (4)	k (5)	i (6)	j (7)
B^*	1.77×10^{-6}	-0.394	1.68	1.82×10^{-4}	0.432	0.366
η_{max}/a_{1m}	0.464	-0.324	0	16.0	0.325	-0.951
λ_{max}/a_{1m}	2.79	-0.328	0	60.6	0.183	-0.800
$\bar{C}_r/C$	3.16×10^{-6}	1.25	0	1.40×10^{-6}	0.271	1.22
C'_{rmax}/C	6.20×10^{-6}	1.25	0	5.34×10^{-7}	0.717	0.500

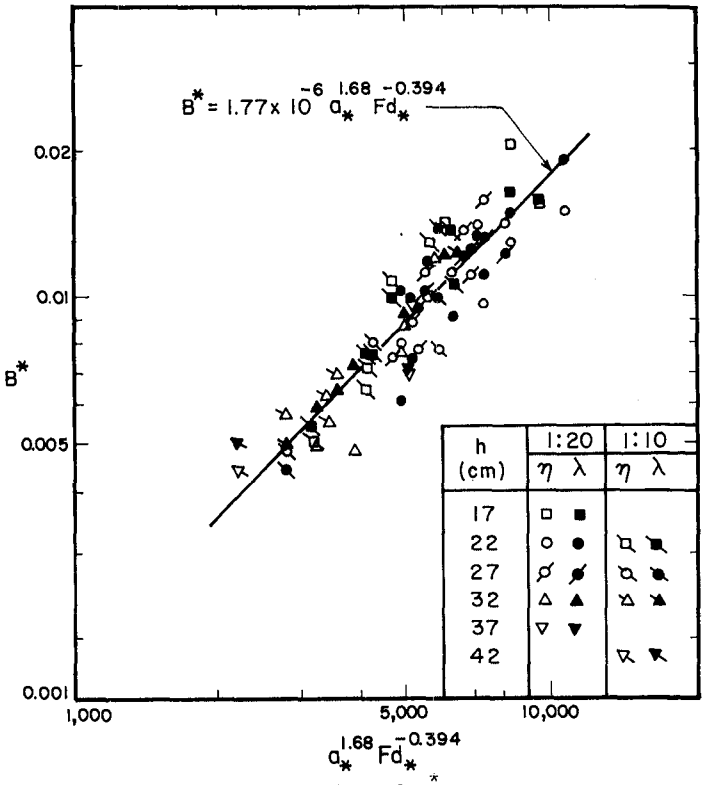

Figure 5. Correlation of B^* Versus $a^{1.68} Fd_*^{-0.394}$ for Medium Sand

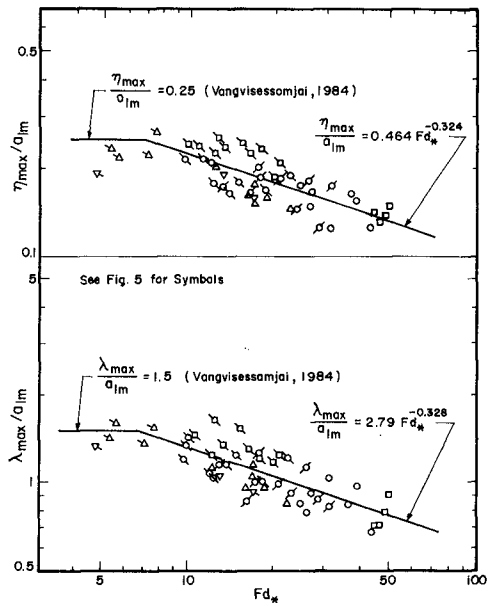

Figure 6. Correlation of Maximum Ripple Geometry Versus Fd_*

Sediment Transport Rate.- The averaged net sediment transport rates $\bar{q}'_{vexp}$ measured in the trap at 5, 15 and 25 minutes as listed in Table 1 were found to be of the same magnitudes of those computed from ripple growth and migration. These measured transport rates were found to be about 30 to 60 per cent of the empirical rate, Eq. 8, for medium sand of Run Nos. 1-18 while they were about 5 to 30 per cent of Eq. 8 for finer sand of Run Nos. 19-27 which were in the ranges of transition and offshore transport shown in Figure 1.

Basing on the same growth rate of ripple, the sediment transport rate due to ripple growth, $q_{rmax} = 2.4$ N/m/s as shown in Figure 1, was much smaller than that due to ripple growth and migration, $q_s(x,t) \doteq \pm 20$ N/m/s for Cases II to IV and about equal to that of Case I with $C_r = 0$ as shown in Figures 3a to 3d.

CONCLUSIONS

From this study of the trasient formation and migration of ripples, and the resulting sediment transport; the following conclusions could be drawn:

1. Growth rates of ripple height and length were found to follow the exponential form of Equations 10 and 11 respectively.
2. Celerities of ripple migration were found to have several patterns, Equations 14a, 14b and 14c, only the time averaged and maximum values were presented. More experiments would be required to quantify this phenomenon.
3. Empirical rate of sediment transport due to waves should be used with great care. Characteristics of ripple growth on a horizontal bed were rather uniform along the bed with negligible ripple celerity, therefore, the sediment transport rate should be negligible. However, a tray set into sediment bed would cause non-uniformity and thus traps a gross sediment transport forward and backward at either edge of the tray; this rate of transport of the mobile sediment could be calculated from expression for sediment transport rate due to ripple growth, Eq. 12.
4. On a sloping beach, characteristics of fluid, ripples and sediment transport rate were nonuniform and varied along the slope. Outside the breaker, the turbulence was smaller than that inside with less suspended sediment, the onshore transport rate here could be computed from the expression of sediment transport rate due to ripple growth and migration, Eq. 18.

APPENDIX I.-REFERENCES

1. Abou-Seida, M.M., "Bed Load Function Due to Wave Action," Report HEL-2-11, Hydraulic Engineering Lab., University of California, Berkeley, Calif., 1965.
2. Bagnold, R.A., "Motion of Waves in Shallow Water, Interaction between Waves and Sand Bottom," Proceedings of the Royal Society of London, Series A, Vol. 187, 1946, pp. 1-15.
3. Dingler, J.R., "Wave Formed Ripples in Nearshore Sands," thesis presented to the University of California, at San Diego, Calif., in 1974, in partial fulfillment of the requirements for the degree of Doctor of Philosophy.

4. Einstein, H.A., "Bed-Load Function for Sediment Transportation in Open Channel Flows," U.S. Dept. Agric. S.C.S. Technical Bulletin No. 1026, 1950.
5. Grant, W.D. and Madsen, O.S., "Movable Bed Roughness in Unsteady Oscillatory Flow," Journal of Geophysical Research, Vol. 87, No. C1, 1982.
6. Gunartna, P.P., "An Analytical Model in Ripple Formation," thesis presented to Asian Inst. of Tech., Bangkok, Thailand, in 1984 in partial fulfillment of the requirements for the degree of Master of Engineering.
7. Inman, D.L., "Wave-Generated Ripples in Nearshore Sands," Technical Memo No. 100, U.S. Army Corps of Engineers, Beach Erosion Board, 1957.
8. Jonsson, I.G., Wave Boundary Layers and Friction Factors, Proceedings of the Tenth International Conference on Coastal Engineering, Vol. 1, 1966.
9. Kalkanis, G., "Transportation of Bed Meterial Due to Wave Action, Technical Memo. No. 2, U.S. Army, Corps of Engineers, Coastal Engineering Research Center, 1964.
10. Kennedy, J.F., and Falcon, M., "Wave Generated Sediment Ripples," Report No. 186, Hydrodynamics Laboratory, Massachusetts Institute of Technology, 1965.
11. Kobayashi, N., "Sediment Transport on a Gentle Slope Due to Waves," Proc. ASCE, Journal of the Waterway, Port, Coastal and Ocean Division, Vol. 108, No. WW3, 1982.
12. Madsen, O.S. and Grant, W.D., "Sediment Transport in the Coastal Environment," Report No. 209, Ralph M. Parsons Laboratory for Water Resources and Hydrodynamics, Massachusetts Institute of Technology, 1976.
13. Manohar, M., "Mechanics of Bottom Sediment Movement Due to Wave Action," Technical Memo. No. 75, U.S. Army, Corps of Engineers, Beach Erosion Boards, 1955.
14. Mogridge, G.R., and Kamphuis, J.W., "Experiments on Bed Form Generation by Wave Action," Proceedings of the Thirteenth International Conference on Coastal Engineering, Vol. 2, 1972, pp. 1223-1142.
15. Munasinghe, L.C.J., "Transient Ripple Formation and Resulting Sediment Transport," thesis presented to Asian Inst. of Tech., Bangkok, Thailand, in 1985, in partial fulfillment of the requirements for the degree of Master of Engineering.
16. Sleath, J.F.A., "Measurements of Bed Load in Oscillatory Flow," Proc. ASCE, Journal of the Waterway, Port, Coastal and Ocean Division, Vol. 104, no. WW3, 1978.
17. Sunamura, T. and Horikawa, K., "Two-Dimensional Beach Transformation Due to Waves," Proceedings of the Fourteenth Conference on Coastal Engineering, Vol. 2, 1974, pp. 920-938.
18. Vongvisessomjai, S., "Oscillatory Ripple Geometry," Journal of Hydraulic Engineering, ASCE, Vol. 110, No. 3, 1984.
19. Vongvisessomjai, S., "Sediment Transport under Oscillatory Flow," Proceedings of the Fifth Congress of Asian and Pacific Regional Division, Int. Assoc. for Hyd. Research, Seoul, Korea, 1986.

CHAPTER 121

Analytical Research of Littoral Transport Rate and Wave Energy Along the Putai Harbor site

T. J. WANG
Chia-Yi County Government, Republic of China
C. S. LIN
Chia-Yi County Government, Republic of China
H.-S. HOU
Institute of Transportation, Minisrty of Communications, Pepublic of China

ABSTRACT

Oue to the sheltering effect of the Wai-San-Ding Sand Barrier, the hydraulic condition of the putia harbor site is quite favorable. Since the relatively well-protected location of the Putai harbor area with regard to both waves and wind, no special navigational problems have to be envisaged.

The wave energy of the Putai harbor site is computed from the measured waves by considering the refraction effect down to breaking line. As the lack of wave records, the wind speed is used by applying the regression equations among the wave height, period and wind speeds, and then compute the wave height and period for obtaining the breaking wave energy. Therefore the total breaking wave energy (P_l) of the whole year along the Putai harbor coast is summated.

The littoral transport rate (I_l) is calculated from the mesh method by comparing the echo-sounding maps of two continuous different years. Therefore, the relationship of P_l and I_l is correlated in the Putai harbor site.

1. Introduction :

Pu-Tai harbor site area is located along the coast of Chia-Yi county, it faces to the Taiwan Strait, the bay area is about 900 hectoare. There is an large scale sand barrier 22 km long, 3-km wide, located on the NW of Pu-Tai bay, and then the barrier forms good wave sheltering effect to the bay.

The field records of wind condition at Pu-Tai from Nov., 1982 to Oct., 1983 show that the winter monsoon in December mainly blows the wind from NNE,N and NNW directions, etc., and with the stronger wind speed. In January, the prevailing wind directions are the same as those in December and totally 90% of occured frequency. The strongest wind occurs in N direction, and then in NNE direction also in February, wind overwhelmingly occurs in NNE, N, NNW directions which are in total 80% of occurred frequency. Wind in N direction occurs very frequently, but wind velocity of N and NNW directions is stronger. In March, wind comes more often from WNW, NW and NNW directions which totally reach up to 60%. Wind speed is highly reduced such that the occurrence of wind with speed stronger than 5 m/sec is only 17%. The wind in April occurs often from northerly direction, while in May, it comes from

southern direction. From the long-term data, summer monsoon blows from April to August, the direction is from south, while wind speed is quite small. The prevailing wind direction is NNE to NNW blows during Winter monsoon from September to Next March.

From the wave measurement, the maximum wave height reaches 1.8 m, commonly wave height locates between 20 cm to 80 cm: while wave period is between 4 sec to 8 sec. Wave Rider is installed in the NW direction of the offshore area near-15 m deep; while KSK cassette type wave meter installed at the proposed harbor mouth. The measurement shows that wave height decays obviously from offshore toward harbor mouth; especially for the big wave, it decays almost 50%; while wave period becomes longer when wave reaches harbor area.

The distribution of significant wave heights and significant wave periods in June, 1983 indicates wave height appearing from 25 cm toward 1.25 cm; while wave period is from 2 sec to 8 sec; they are located in the lower value. They show during summer time, navigational condition is quite well in the Pu-Tai harbor area.

The measured wave distribution in December at the Pu-Tai Offshore (-15m) which locates the South-West of the promontory delta. Even in December, the significant wave height is in the range of 30 cm to 80 cm, the corresponding significant wave period is between 3 sec to 8 sec. In such case, the NE winter monsoon waves decay rapidly due to the sheltering promontory delta area. The measured results show that there is perfectly calm sea surface for ship anchoring in the Pu-Tai bay area.

The winter monsoon waves recorded at the proposed harbor area becomes smaller compared to the offshore zone; while period shows a little longer due to the scan from KSK cassette recorder has the tendency to collect significant wave and neglect the smaller wave, therefore, commonly two waves scan to record as one wave such that period becomes longer.

Pu-Tai proposed harbor entrance is located in the SW direction of Ueng Tau, and there is a wide natural sheltering Wai-Shan-Ding Barrier Island in the NW direction, therefore, it has a good condition for wave prevention from northerly direction. According to the records of the winds at Au-Ku meteorological station, the winds occur most frequent in the direction of NNE (40.2%) and then ENE (22.2%). The hurricane waves in SSW to W directions affect the site most significantly and therefore they are selected as the design waves of the proposed harbor which are 7 m of height and 12-15 sec of period. As the results from computer processing show, the waves in SSW direction diverge mostly (and with K=0.45) as they approach the vicinity of the proposed harbor site. Otherwise, the waves (with T 1/3=14.5 sec) in SW direction converge lightly at the same position. Generally speaking, the waves in other directions diverge as they approach the proposed site, therefore, the proposed site is convenient and suitable. Fig. 1-1 shows the wave refraction drawing of Pu-Tai harbor site with wave direction of SSW and wave period T 1/3=14.5 sec. It has the same decaying tendency with that of the field measured waves.

Figure 1-1 The wave refraction drawing of Pu-Tai site

ID : SSW T : 14.5 Sec

2. The calculation of the alongshore breaking wave energy: The wave data are recorded by the wave gauge at the depth -15m per 2 hours in 1983 at Putai offshore area.

The wave is affected by the effects of shoaling, refraction, bottom friction and percolation. By neglecting the effects of bottom friction and percolation.as wave is propagating toward the surf zone,therefore the breaking wave height is equal to H = HoKrKs where Kr and Ks are refraction coefficient and shoaling coefficient respectively. The mathematical representation is as follows

$$Kr = (Bo / B)^{1/2} \tag{2.1}$$

$$Ks = (Cgo / Cg)^{1/2} \tag{2.2}$$

where B is the separation of the wave rays and prefix "o" represents the characters of deep water. As the bottom slope is smaller than 1/10 then Kr and Ks could be calculated from the four equations derived by Chao,Y.Y.(1970) as follows

$$C^2 = \left(\frac{G}{K}\right) \tanh kh \tag{2.3}$$

$$\frac{dB}{ds} = \frac{1}{c}\left(\sin\theta \frac{\partial c}{\partial x} - \cos\theta \frac{\partial c}{\partial y}\right) = -\frac{1}{c}\frac{dc}{dB} \tag{2.4}$$

$$H_o (C_g)_o B_o = H\ C_g B = \text{constant} \tag{2.5}$$

$$\frac{dB}{ds} - P^{(1)} \frac{dB}{ds} + P^{(2)} B = 0 \tag{2.6}$$

$$P^{(1)} = \frac{1}{c}\left(\cos\theta \frac{\partial c}{\partial x} + \sin\theta \frac{\partial c}{\partial y}\right) \tag{2.7}$$

$$P^{(2)} = \frac{1}{c}\left(\sin^2\theta \frac{\partial^2 c}{\partial x^2} - 2\sin\theta\cos\theta \frac{\partial^2 c}{\partial x \partial y} + \cos^2\theta \frac{\partial^2 c}{\partial y^2}\right) \tag{2.8}$$

where D is water depth, θ is the angle between X axis and wave direction, S is the distance along wave ray and C is the phase velocity. Use numerical method to get

$$D_{n+1} = D_n + \left(\frac{\partial D}{\partial x}\right)_n dx + \left(\frac{\partial D}{\partial y}\right)_n dy + \frac{1}{2}\left(\frac{\partial^2 D}{\partial x \partial y}\right)_n dx dx + \left(\frac{\partial^2 D}{\partial x \partial y}\right)_n dx dy + \frac{1}{2}\left(\frac{\partial^2 D}{\partial x \partial y}\right)_n dy dy \quad (2.9)$$

$$P_{n+1} = (4-2P_n^{(1)}\Delta S^2)/(2-P_n^{(1)}\Delta S)\ \theta_n - (2+P_n^{(1)}\Delta S)/(2-P_n^{(1)}\Delta S)\ B_{n-1} \quad (2.10)$$

The subscript "n" represents the value of the nth calculation, as shown in Fig.2.1, where X axis is taken parallel to the shoreline. Developing these numerical calculations to get "THE WAVE CHARACTER COMPUTING PROGRAM", (Hou etc., 1980) the wave characters such as Kr, Ks, H, Cg and θ could be found out at any water depth h=D. Since $\theta = \frac{\pi}{2} - \alpha$ as shown in Fig.2.1 then $(P_1)_b = \frac{1}{8}\rho g H_b^2 (c_g)_b \cos\theta_b \sin\theta_b$ is the alongshore breaking wave energy.

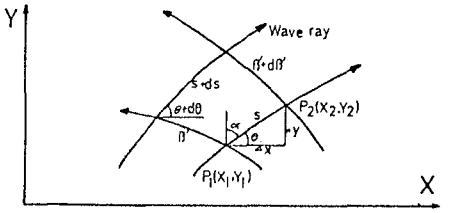

Figure 2.1 The diagram of the wave refraction.

Since there is no records of wave direction at -15m depth, the incident wave direction is found out by the above program using the deep water incident wave direction which is the wind direction as the wave gauge serves.

Consider only the waves which are moving onshore could cause littoral transporting. The waves which have the same incident direction are summed up. The root mean square value of their heights and the mean value of their periods are found out. Therefore, the total onshore acting waves are compiled to θ equivalent waves which have the "rms" wave height Hrm , mean wave period T. This is because

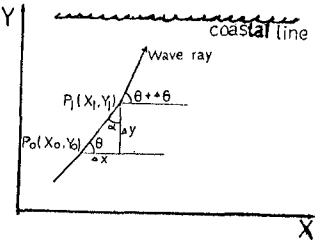

Figure 2.2. The diagram of the wave refraction.

$$(P_l)_b \propto H^2 \cos\theta\sin\theta \propto H^2 \sin 2\theta$$

$$\sum_{i=1}^{M} (P_l)_{bi} \propto \left(\sum_{i=1}^{M} H_i^2\right)\sin 2\theta = M H_{rms}^2 \sin 2\theta \quad (2.11)$$

Where M is the number of the waves which have the same wave direction , and H_{rm} is represented as

$$H_{rms}^2 = \frac{1}{M}\sum_{i=1}^{M} H_i^2 \quad (2.12)$$

To compute the alongshore breaking wave energy, the input data including the water depths of the grid points, the water depths and the coordinates of the incident points, the Hrm values and the T values of the equivalent waves with the incident wave direction at the depth -15m of the Putai offshore area, are all considered.

3. Computation Model between Wind and Waves

The paper is based on the winds and measured waves record, and then obtain their relationships. By using the 2nd order polynomial regression equation to work as the model for wind speed to compute wave height and wave period. From the above model and the measured wind records of the Pu-Tai Coast, the insufficient data could be supplied.

The computation procedure is described as follows.

1) To find out the statistical relationship between waves and winds for each month. By applying the records of wind speeds and wind directions, and the measured wave data from February to May., the relations among the wind speeds vs wave heights and wave periods correspondently at the same time could be reduced.

The wind speeds below 5 m/sec are neglected, since they have not significant effect to produce wave. To get rid of the small values of wind speeds and then compute the mean value, variance and correlation coefficient of each month. The statistical value is listed as the Table 3.1.

Table 3.1. Statistical Analysis of V, H & T.

	Wind Speed V(m/sec)		Wave Height Hrms(cm)		Correlation Coefficient of H vs T
month	Mean μ_V	Variance	Mean μ	Variance	TH
February	7.60	1.72	17.38	4.80	0.20
March	7.76	2.45	17.10	5.31	0.55
April	6.85	1.61	21.24	11.11	0.01
May	6.34	1.15	14.33	4.47	-0.20

In the Table 3.1, the mean is expressed as

$$U_X = \frac{1}{N}\sum_{i=1}^{N} X_i \qquad (3.1)$$

The variance is expressed as

$$\delta_x = \frac{1}{N}\sum_{i=1}^{N} (X_i - \mu_x)^2 \qquad (3.2)$$

and the correlation coefficient is expressed as

$$S_{xy} = \frac{\sum_{i=1}^{N} [(X_i - \mu_X)(Y_i - \mu_y)]}{\sqrt{\sum_{i=1}^{N} (X_i - \mu_X)^2 \sum_{i=1}^{N} (Y_i - \mu_y)^2}} \qquad (3.3)$$

From the above table, it is known that the correlation between wind and waves is so so perfect, the better one is in March, those of February and May are the next, the value in April is not so good correlation. The reason for fair correlation is due to the coastal geomorphological effect by the large Wai-San-Ding Sand Barrier, therefore winds and waves intrude into the Pu-Tai Bay area and show obvious refraction and energy diffusion. The effect of wave sheltering and shoaling is much complicated; while, in March, April and May, due to monsoon transitiond zone, the wind directions are changeable. For the avobe reasons, they cause the correlation coefficient be not so large. Except that, the time delay between wind and wave has some negative effect.

2) To find out the polynomial regression equations of wind speed vs wave height, and wind speed vs wave period. The correlations between winds and waves in February and in May are much better, and their wind directions are quite stable, therefore, February is considered as the base for computing the winter monsoon waves., while May is taken as the base for computing the summer monsoon waves. By using the least square method, and then the polynomial regression equations are obtained.

Let $X_1, X_2, X_3, \ldots, X_n$ as the n units of wind speed value.

$Y_1, Y_2, Y_3, \ldots, Y_n$ as the n units of corresponding wave height and wave period values.

as the constants of the m^{th} order polynomial regression equation.

$$X = \begin{bmatrix} 1 & X_1 & X_1^2 & X_1^3 & \cdots & X_1^m \\ 1 & X_2 & X_2^2 & X_2^3 & \cdots & X_2^m \\ \vdots & & & & & \vdots \\ \vdots & & & & & \vdots \\ 1 & X_n & X_n^2 & X_n^3 & \cdots & X_n^m \end{bmatrix}$$

$$Y = \begin{bmatrix} Y_1 \\ Y_2 \\ \vdots \\ \vdots \\ Y_n \end{bmatrix} \qquad A = \begin{bmatrix} A_o \\ A_1 \\ A_2 \\ \vdots \\ A_m \end{bmatrix}$$

The following relationship is obtained

$$X^T X A = X^T Y \qquad (3.4)$$

where X^T is the Transposed Matrix of X.

Solving "A" from EQ.(4), then the constants of the m^{th} order regression eguations of wave height vs wind speed, and of wave period vs wind speed correspondingly of each month are attained.

Wave period and wave height could be calculated by Eg.(5) and Eg.(6).

$$H = a_o + a_1V + a_2V^2 + \ldots \ldots + a_mV^m \quad (3.5)$$

$$T = b_o + b_1V + b_2V^2 + \ldots \ldots + b_mV^m \quad (3.6)$$

where V is the wind speed.

From wind and waves data of February and May, by using the above method, the following regression eguations are obtained.

1. In February
   a. For the 1^{st} order regression equation (i.e. m=1)
      $H = 13.08 + 0.57V$ (3.7)
      $T = 11.12 + 0.10V$ (3.8)
   b. For the 2^{nd} order regression equation (i.e. m=2)
      $H + -3.73 + 4.95V - 0.27V$ (3.9)
      $T = 12.00 - 0.39V + 0.014V$ (3.10)
   c. For the 3^{rd} order regression equation (i.e. m=3)
      $H = -29.87 + 14.93V - 1.48V + 0.047V$ (3.11)
      $T = 11.34 + 0.14V - 0.016V + 0.0012V$ (3.12)
2. In May
   a. For the 1^{st} order regression equation (i.e. m=1)
      $H = 11.15 - 0.76V$ (3.13)
      $T = 0.11 + 0.55V$ (3.14)
   b. For the 2^{nd} order regression equation (i.e. m=2)
      $H = 52.53 - 11.00V + 0.75V$ (3.15)
      $T = -2.87 + 3.31V - 0.20V$ (3.16)
   c. For the 3^{rd} order regression equation (i.e. m=3)
      $H = 75.02 - 21.22V + 2.27V - 0.073V$ (3.17)
      $T = -18.31 + 10.33V - 1.24V + 0.050V$ (3.18)
      Units H : cm, T : sec, V : m/sec
      After comparing with each other, the 2^{nd} order regression eguations are suitable and selected as the computation model.

Analytical Results

To compute the other month's wind speed and convert to wave height and wave period, data are wind records of November and December of 1982, July and August of 1983 from Putai meteorology station and records of September and October of 1983 from Ao-Ku coastal station. By using the winter computation model, wind records of September, November, December and January are converted into wave heights and wave periods. While wind records of September, November, December and January are converted into wave heights and wave periods. Similarly, wind records of July and August are applied by using the summer computation model to get waves correspondently. After all waves are acquired, by using

computation model of wave energy (Hou etc., 1984), then monthly wave energy are obtained and the results are shown in Table 3.2.

Table 3.2. Wave Energy monthly and daily in Putai Harbor Site

month / Wave Energy	July	August	Sept.	Oct.	Nov.	Dec.	Jan.	Unit
Monthly Wave Energy	14,960	14,530	12,670	13,380	13,470	18,250	16,830	$\frac{\text{ton-m}}{\text{m-month}}$
Daily Mean wave Energy	483	469	422	448	449	589	543	$\frac{\text{ton-m}}{\text{m-day}}$

To reduce wave energy of twelve months of the whole year, then they are shown in Fig.3.1 and Fig.3.2 and June shows heavy wave energy, since hurricane waves attacking, during this month, along the Putai coast.

4. Relationship between total Wave Energy and Littoral Transport Rate

Based on the analyzed result, it is found out the alongshore wave energy is 287,000 ton-m/m-yr, the corresponding littoral transport rate is 1.3×10^3 m^3/m-yr. The profile change of the Putai Bay area are shown from Fig4.1 to Fig.4.8. From the equation $I_l = K(P_l)_b$, the value of K is then become 3.5×10^{-3}. Therefore, the equation $I_l = 3.5 \times 10^{-3}(P_l)_b$ is applied to the Putai harbor site area. From the profile change of 1963, 1967 and 1980 they show that scour occurring along the Wai-San-Ding sand barrier due to supply of river sediment becomes less.

5. Conclusion and Suggestion

1) Applying the energy approach for unidirectional steady flow (Bagnold, 1963), derive out the relationship between the alongshore breaking wave energy and the littoral immered weight transport rate as $I_l = K(P_l)_b$. K is function of wave height, bottom slope, the grain size and the sediment transport pattern. It increases as the grain size decreases or it does either there exists are ocean current in the predominant littoral transport direction or under the action of the bigger waves. This reveals that the larger part of wave energy is supplied to transport sediment as the wave energy becomeslarger. This is shown by the empirical relationship $I_l = 0.154(P_l)_b$. But for a coast, such as the Taichung coast, where the oceanographic condition is so steady that the alongshore breading wave energy fluctuates slightly, the relationship between I_l and $(P_l)_b$ could be written as $I_l = K(P_l)_b$, where K is constant. Then the Putai coast has the relation of $I_l = 0.0035(P_l)_b$. This eguation could be applied for the coast of similar oceanographic conditions and beach characteristics to estimate the littoral transport rate. Such that the harbor planning and the shore protection could be based on.

2) Littoral transport study along the upstream and downstream of the Wai-San-Ding sand barrier (Hou, 1985) and the wave decaying and refracting of the Putai new port (Hou etc, 1984), has been deeply discussed. However, this paper deals with the measured data of wind speed, wind

direction and waves, then detail analyses are made to obtain the whole yearly alongshore wave energy. The littoral transport rate is obtained from the data of hydrographic survey. Therefore, the formula of $l_{\ell}=3.5 \times 10^{-3}(P_{\ell})_b$ is very appropriate for computing the littoral transport rate. The field measured data is very precious, since coastal area is widely surveyed, and very delicate, accurate instrument is used.

3) The model of wave height and wave period is deduced from wind speed. It's really a convenient and effective predict model for wind wave. Therefore, it could be applied and referred to ocean and coastal engineering use. However, the applicability of different wind conditions under different seasons need to be carefully considered.

4) The coefficient of littoral transport rate, K value, could be furtherly reconfirmed by comparing with the yearly dredging quantity of the Pu-Tai New Port. and then be modified.

5) As the shelf wind waves entering into the offshore due to the effect of Wai-San-Ding sand barrier, and then wave diffraction is shown, waves will turn around their direction, especially during winter season. Therefore, waves come from NNE and N directions will turn into NNW direction and then dissipate over the beach. It's really the features of local wind wave in the Putai harbor site. Therefore, the computation of wave energy along Putai coast, the offshore wave direction should be thoroughly considered.

6) Based on the calculation of wave energy along the Taichung harbor coast (Hou, etc, 1980) her yearly wave energy is sheltered by than that of the Putai harbor site. Since, the wave sheltering due to the Wai-San-Oing Sand Barrier, the offshore wave energy decays and decreases largely as it reaches the Putai harbor site.

References

1) Hou, Ho-Shong, Lee, C.P., Weng, G.H. and Lin, L.H. "Research Report of planning and Oesign of Pu-Tai New Harbor Master Plan". Graduate Institute of Harbor and Ocean Engineering, Keelung, Taiwan, R.O.C. Oct., 1980.

2) Hou, Ho-Shong, Lee, C.P. and Lin, L.H. "Relationship Between Alongshore Wave Energy and Littoral Orift in the Mid-West Coast at Taiwan". Proceedings of the Seventeenth International Coastal Engineering Conference, March 23 to 28, 1980, Sydney, Australia.

3) Hou, Ho-Shong, "Researches of Harbor Site Investigation, Planning and Oesign of Coastal Shipping System in Taiwan, R.O.C.". Special Report No.7, Institute of Harbor and Marine Technology, Wuchi, Taichung Oistrict, Taiwan, R.O.C. November, 1982.

4) Oceanographic Environmental Investigation of the Northern Coast of Taiwan, R.O.C." Preliminary Report, Institute of Harbor and Marine Technology, Oecember, 1983.

5) "Research of the Wave Decaying of Pu-Tai proposed Harbor". The 10th Annual Conference of the Chinese Institute of Civil and Hydraulic Engineering, Taipei, R.O.C. November, 1983. Hou, Ho-Shong, Tseng, Z-M and Weng, G-H.

6) Hou, Ho-Shong, "The Survey and Design of the Proposed Harbor of the Coastal Shipping System in Taiwan, R.O.C." Tech. Rept. 75-2-201, Institute of Transportation, Ministry of Communications, Taipei, Taiwan, R.O.C., December, 1985.

7) Hou, Ho-Shong, "Littoral Drift Model Investigation along the Taiwan Coast and Research of the Related Problems of Inlet planning (II)" NTU-INA-Tech, Rept. 216. Institute of Naval Architecture, National Taiwan University, December, 1985.

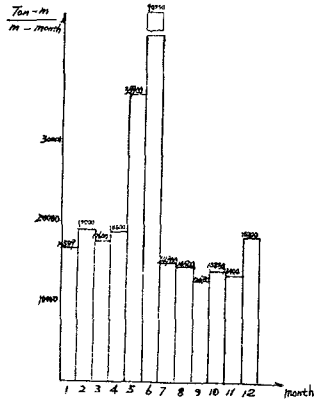

Fig.3.1 Monthly Mean Wave Energy of Putai Harbor (1983)

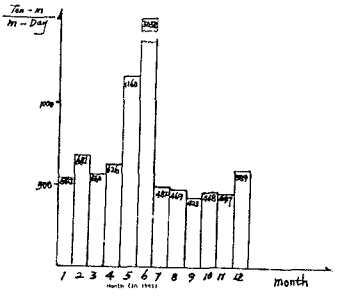

Fig.3.2 Daily Mean Wave Energy of Putai Harbor (1983)

Fig. 4.1. PROFILE LINE No.: 1

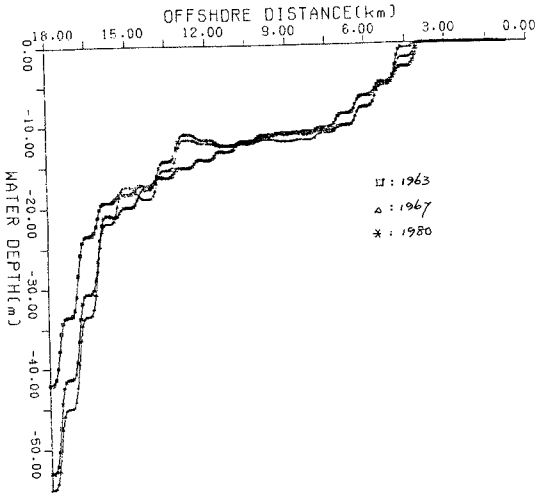

Fig. 4.2. PROFILE LINE No.: 6

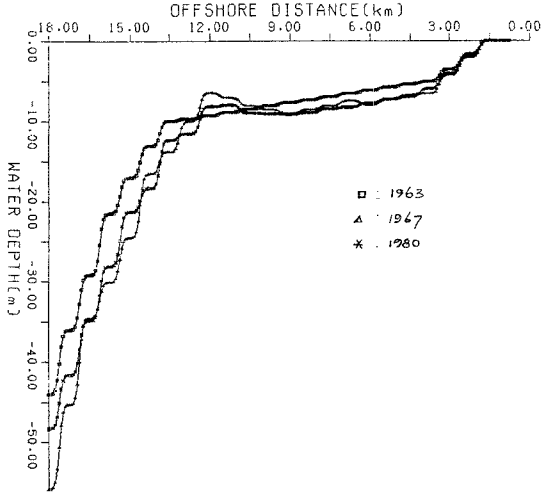

Fig. 4.3. PROFILE LINE No.: 11

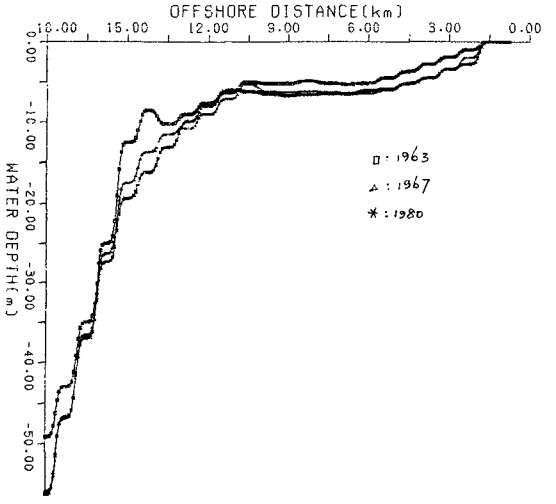

Fig. 4.4. PROFILE LINE No.: 16

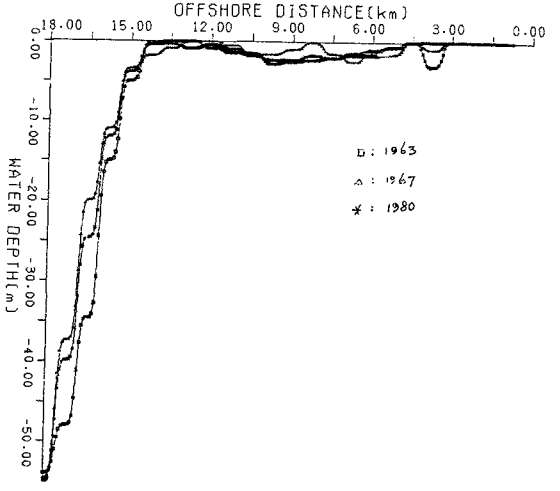

Fig. 4.5. PROFILE LINE No.: 21

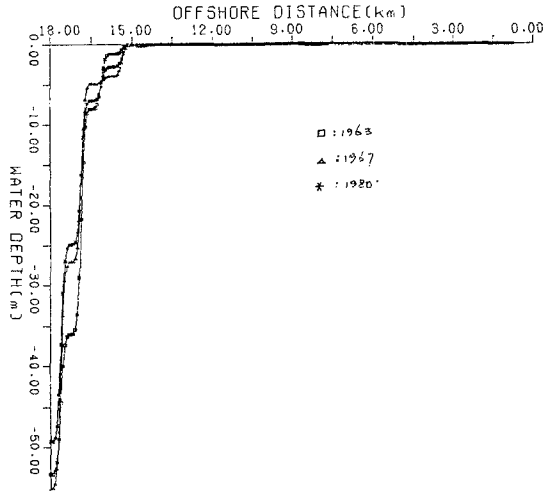

Fig. 4.6. PROFILE LINE No.: 26

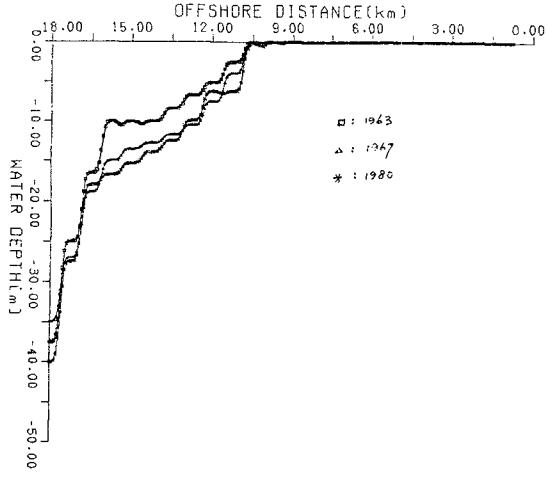

Fig.4.7. PROFILE LINE No.: 30

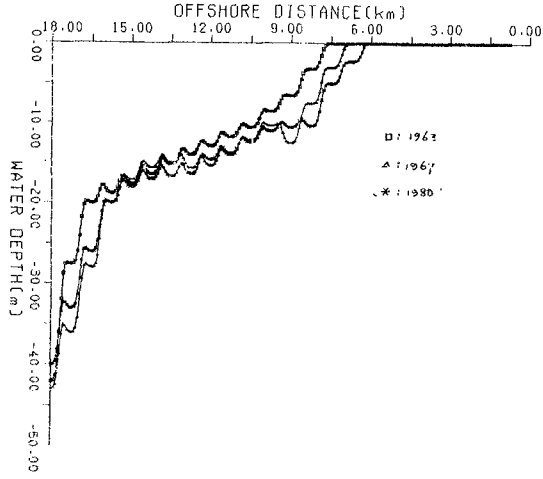

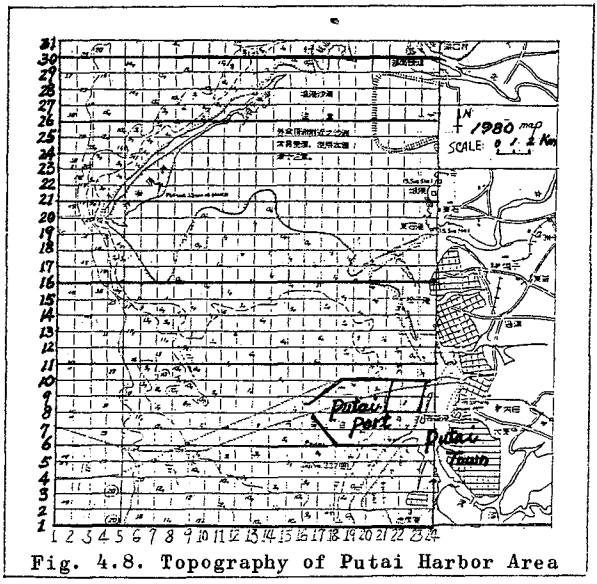

Fig. 4.8. Topography of Putai Harbor Area

CHAPTER 122

MATHEMATICAL MODELLING OF WAVE-INDUCED NEARSHORE CIRCULATIONS

DONGHOON YOO[1] and BRIAN A. O'CONNOR[2]

The paper presents a mathematical model for describing wave climate and wave-induced nearshore circulations. The model accounts for current-depth refraction, diffraction, wave-induced currents, set-up and set-down, mixing processes and bottom friction effects on both waves and currents. The present model was tested against published experimental data on wave conditions within a model harbour and shown to give very good results for both wave and current fields. The importance of including processes such as advection, flooding and current-interaction in coastal models was demonstrated by comparing the numerical results without each process to the results from the complete scheme.

1. INTRODUCTION

Wave-induced nearshore circulations are the result of complex processes driven by gravity water waves. When waves approach either the shoreline or man-made coastal structures, processes of shoaling, refraction, diffraction, dissipation and wave-current interaction occur. When waves propagate closer to the shoreline or diffract behind a breakwater, nearshore currents are produced by the excess momentum flux of the waves (radiation stresses). The nearshore currents are then modified by bottom friction and mixing processes, particularly in the surf zone. An additional effect produced by the presence of the waves is a change in mean water level, called set-up and set-down.

The last two decades have seen tremendous developments in the study of nearshore circulations induced by waves, with the establishment of various wave models and the use of more realistic closure models of bottom friction and mixing processes. Although recent numerical models have enabled a mathematical formulation of many of the nearshore processes to be made, a comprehensive model, which is able to describe all engineering situations, has yet to be developed. The model presented in the present paper is an attempt by the authors to improve the engineering modelling of complex nearshore processes.

In the present paper, an attempt is made to refine the classical ray model including the effects of diffraction and current-interaction, see also Yoo and O'Connor[13]. Thus, the new ray model is able to deal with large or small scale areas involving caustic zones and/or

---

[1]Research Associate, Dept. of Civil Eng., University of Liverpool.
[2]Professor, Dept. of Civil Eng., University of Liverpool, P.O. Box 147, Liverpool, L69 3BX, U.K.

diffraction in the lee of coastal structures. The wave field is defined at regular grid points, and hence any interpolation procedure often required for ray tracking method is avoided.

2. KINEMATICS OF REFRACTIVE AND DIFFRACTIVE WAVES IN SLOWLY VARYING CURRENT FIELD

For a plane wave, the wave number vector K_i and the wave frequency σ are given, respectively, by the spatial gradient and the time derivative of the phase function D. The local values of the slowly varying wave number vector and the frequency of the nearly plane wave may also be described by the same definitions, and the kinematic conservation is obtained from the definitions:-

$$\frac{\partial K_i}{\partial t} + \frac{\partial \sigma}{\partial x_i} = 0 \tag{1}$$

along with the zero-vorticity equation:-

$$\frac{\partial K_i}{\partial x_j} = \frac{\partial K_j}{\partial x_i} \tag{2}$$

where t is time, x is the cartesian coordinate and i,j=1,2 as in conventional tensor notation.

When the waves propagate on a current we also have the Doppler relation:-

$$\sigma = \sigma_0 + K_i U_i \tag{3}$$

where σ is the apparent or observed angular frequency, σ_0 is the intrinsic or Doppler-shifted angular frequency and U is the current velocity.

Waves generally appear to be propagating on still water in the moving frame of reference. All the relevant equations for the wave field are valid, therefore, on the moving frame of reference and the dispersion relation can be used in the form:-

$$\sigma_0^2 = gk \tanh kd \tag{4}$$

where g is the acceleration due to gravity, d is the water depth and k is the separation factor, which is the same as the wave number K (eiconal) for non-diffractive waves.

Battjes[1] discovered that the wave number K is not eiconal to k when diffraction occurs and produced the following relation:-

$$K^2 = k^2 + \delta^* = (1 + \delta)k^2 \tag{5}$$

where

$$\delta^* = \frac{1}{a} \frac{\partial^2 a}{\partial x_i^2} \tag{6}$$

$\delta = \delta^*/k^2$ and a is the wave amplitude. The wave number vector is not affected by a translation of coordinates. Thus equation (5) will be valid without modification for waves on a current.

It is then realised that

$$\sigma = \sigma\{\sigma_0(k,d),\ K_i(k,\delta^*),U_i\} \tag{7}$$

where the variables in the brackets are independent of each other. Differentiating equation (7) with respect to x_i using the chain rule and inserting it into equation (1) with the zero vorticity equation (2) produces the kinematic conservation equation for the wave number vector K_i:-

$$\frac{\partial K_i}{\partial t} + (R_j + U_j)\frac{\partial K_i}{\partial x_j} + S\frac{\partial d}{\partial x_i} + K_j\frac{\partial U_j}{\partial x_i} - \frac{R}{2ka}\frac{\partial^3 a}{\partial x_i \partial x_j^2} = 0 \tag{8}$$

where R_j are the intrinsic group velocity components given by

$$R_j = \frac{K_j}{k} R \tag{9}$$

$$R = \frac{1}{2}(1 + G)\frac{\sigma_\theta}{k} \tag{10}$$

$$S = \frac{G}{2}\frac{\sigma_\theta}{d} \tag{11}$$

$$G = \frac{2kd}{\sinh 2kd} \tag{12}$$

Here the second order derivatives of amplitude curvature are ignored. The last term of equation (8) expresses the diffraction effect on the transformation of kinematic wave properties. It further corrects the number of waves per unit length, depending on the gradient of amplitude curvature. Existing ray theories lack this term, and hence such methods fail to ensure kinematic conservation when diffraction occurs.

3. DYNAMICS OF WAVES AND TURBULENT CURRENTS

The major equations governing the dynamic motion of waves and turbulent currents derive from the conservation equations of motion. The wave-period and depth-averaged forms of the governing equations are as follows (see Yoo[12] for details):-

$$\frac{\partial \eta}{\partial t} + \frac{\partial}{\partial x_i}(d\,U_i) = 0 \tag{13}$$

$$\frac{\partial U_i}{\partial t} + U_j\frac{\partial U_i}{\partial x_j} + \frac{1}{\rho d}\frac{\partial S_{ij}}{\partial x_j} + g\frac{\partial \eta}{\partial x_i} + \frac{|U|}{d}C^{U_i}U_i = \frac{\partial}{\partial x_j}\epsilon_j\frac{\partial U_i}{\partial x_j} \tag{14}$$

$$\frac{\partial a}{\partial t} + \frac{1}{2a}\frac{\partial}{\partial x_i}\{(R_i + U_i)a^2\} + \frac{S_{ij}}{\rho g a}\frac{\partial U_j}{\partial x_i} + C^a a^2 = 0 \tag{15}$$

where η is the wave-period-average surface elevation, ρ is the water density, ϵ_j are eddy mixing coefficients, C^U is the bottom friction coefficients associated with U_i, C^a is the bottom friction coefficient associated with a, and S_{ij} are the radiation stresses given by

$$S_{ij} = < \int_{-h}^{\zeta} (\rho \tilde{u}_i \tilde{u}_j + p \delta_{ij}) dz - \int_{-h}^{\eta} p_0 \delta_{ij} dz > \quad (16)$$

where ζ is the instantaneous surface elevation, h is the bottom elevation, $\tilde{u}$ is the wave particle velocity, p is the dynamic pressure, p_0 is the hydrostatic pressure and δ_{ij} is the Kronecker delta.

If it is assumed that the wave field is independent of the turbulent current field in such a way that any input or output of wave energy due to turbulent motion is made in an indirect way, the wave motion may be described by a potential formulation.

If we define the wave velocity potential by the equation:-

$$\tilde{u}_\alpha = - \frac{\partial \varphi}{\partial x_\alpha} \quad (17)$$

where $\alpha = 1,2,3$, from the Laplace and Bernoulli equations for the linear sinusoidal waves we have:-

$$\varphi = \frac{ga}{\sigma_0} \frac{\cosh k(h+z)}{\cosh kd} \cos D \quad (18)$$

where z is the water elevation. Substituting Equation (17) with Equation (18) into Equation (16) yields:-

$$S_{ij} = \frac{1}{2}\{(1 + \delta)(1 + G) \frac{K_i}{K} \frac{K_j}{K} + G \delta_{ij}\}(\frac{1}{2} \rho g a^2) \quad (19)$$

Equation (19) is the general expression for the radiation stresses of refractive and diffractive waves.

The four depth and wave-period averaged equations (8, 13, 14 and 15) form the basis of the present model and describe the wave and current fields in interacted flow. Equations (13) and (14) describe the current field, while equation (15) describes the wave field, when considered along with equation (8). It is also clear from the above equations that any solution of the proposed model requires proper estimation of the coefficients C^U, C^a and ϵ_j. In the surf zone, wave heights are eventually controlled by breaking, and a breaking criterion has commonly been used to limit wave height. In the present investigation, improved closure sub-models for evaluating such parameters are used. They are outlined in the following section.

4. CLOSURE SUBMODELS

MIXING PROCESS

Though many researchers seem to have realised that the mixing process in the surf zone should be related to the amount of wave energy dissipated by breaking, only Battjes[2] derived the velocity scale of turbulence from any sort of parameter directly related to the wave breaking. He found the cube root of the energy dissipation rate to be a proper measure of the velocity scale for turbulent eddy viscosity. He also suggested that the characteristic size of eddies would be primarily restricted by their vertical extent rather than their horizontal extent. This fact is well known in the field of river engineering. Many experimental and field measurements have indicated the strong depth-dependency of both horizontal and vertical eddy viscosity (see Fisher, et al. [5]).

Since the present wave amplitude equation (15) is of a transient form, the dissipation rate induced by wave breaking can easily be evaluated by checking to see if breaking has occurred, using a breaking criterion. If the wave amplitude given by equation (15) exceeds the breaking limit, the excess energy is considered to contribute to mixing processes. Otherwise, mixing processes would not be directly influenced by wave breaking.

The cube root of the energy dissipation rate, divided by fluid density, might be called the 'dissipation speed', since the square root of the bottom shear stress, divided by fluid density, is called the '(bottom) frictional velocity'. This concept is useful for considering the eddy motion of pure oscillatory flow or combined wave and current flow. Since significant amount of eddy motion is expected from bottom friction, even in the surf zone, a velocity scale for the eddy viscosity should also be related to the bottom friction. However, while a frictional velocity has been successfully used for modelling mixing process in uni-directional channel flows, it is of no use for oscillatory flow since the wave-period-average bottom friction of oscillatory flow vanishes.

In the present surf zone studies, the contribution of the bottom friction on the eddy motion is taken into account by regarding the combined breaking and frictional dissipation speed as the proposed velocity scale for the eddy viscosity. The inclusion of the bottom friction improves the Battjes' eddy viscosity model, which displays a sharp discontinuity at the breaking point.

The turbulent motion is also assumed to be anisotropic, and hence some allowance for directional preference is made in the model when describing the eddy viscosity. It has been assumed that the eddy viscosity has an ellipsoid form, of which the semi-major axes is determined by 60% of the total energy dissipation and the minor axes by 20%. The details are found in the recent work of Yoo[12].

BOTTOM FRICTION

Bottom friction has been recognised as one of the most important factors balancing the forces driven by radiation stresses in the nearshore circulation system. Due to this recognition, several numerical modellers have made efforts to evaluate more precisely the period-average bottom friction of the combined flow. However, in their approaches the friction factor was kept constant over the whole domain and its value seems to have been determined somewhat arbitrarily by the modeller's own personal view of the problem.

Fortunately, several detailed models now exist for evaluating the bottom shear stress of combined interacting wave and current flows. However, the majority of these models are too complex or involve time-consuming computer methods which are unsuitable for use in an engineering model of coastal circulations where many calculations have to be performed at a large number of grid points. The present authors have, therefore, taken one of the simpler "detailed models", that due to Bijker[4], and have modified it to include the effects of the reduction in mean current speed due to the presence of the waves. The modification also enabled expressions to be produced for the total energy dissipation rate and enhanced wave energy dissipation rate and the coefficients C^U and C^a.

The improved Bijker approach, see Yoo[12] and O'Connor and Yoo[9] for further details, was tested against results from other detailed models. It was shown to be as good as the more complex models and to be better than the existing simpler models but to take up little computation time. It was therefore adopted for the present model.

BREAKING CRITERION

The transformation of waves in the surf zone is eventually controlled or limited by wave breaking which results from the loss of stability of wave formation and in turn provides a major contribution to surf zone mixing processes. It has been common practice to describe the breaking process by a simple criterion which allows the wave growth only up to a certain limit.

Miche's criterion[8] has been widely used for numerical computation due to its mathematical reliability and broad coverage from deep to shallow water. In the late 1960's it was realised from experimental evidence that beach slope influenced the breaking mechanism and criterion. To include the slope effect, Miche's criterion was reworked by Battjes & Janssen[3] as follows:-

$$(Ka)_b = \frac{\pi}{7} \tanh (q\ Kd)_b \qquad (20)$$

where $q_b = (7/\pi)\ \gamma_b$ and γ_b is the ratio of wave amplitude to the water depth at the breaking point $(a/d)_b$. In this formulation, they also matched equation (20) with the breaking criterion for solitary waves in very shallow water, i.e., when $kd \to 0$ to find the value for q_b.

The factor q_b or γ_b may also be evaluated by empirical equations related to the bed slope. However, the existing relations do not take into account the current-interaction effect, which can be significant in the nearshore circulation system. Based on a theoretical reasoning, a new surf zone parameter β, applicable to the current-interacted situation, was developed by the authors. The parameter β is the relative intensity of the residual kinematic group velocity to the depth-mean energy propagation velocity. In the combined flow we may replace them by the absolute velocities, i.e.

$$\beta = \frac{R - P}{R + U_w} \tag{21}$$

where R is the relative kinematic group velocity, P is the depth-mean energy propagation velocity and U_w is the current velocity in the wave direction. Using the new parameter, a number of experimental data sets were examined and the following relation found (Yoo[12]):-

$$q_b = 0.8 + \tanh (90\beta) \tag{22}$$

Equation (21) also expresses that waves are liable to be more easily broken when they encounter an opposing current as the surf parameter reaches a higher value than when they propagate with a following current.

5. NUMERICAL MODELLING

The combined wave and current flow in coastal areas has been described by the set of Eulerian conservation equations, that is, equations (8) and (15) for the wave field and equations (13) and (14) for the current field. The bottom friction coefficients C^U and C^a and the mixing coefficients ϵ_j are defined using closure models, while the wave amplitude is given by equation (15), unless the breaking criterion of equation (20) shows a limited wave height at which point excess wave energy is transferred to mixing processes.

Due to several complicated non-linear terms in the equations, the solution of the system is best achieved by using numerical techniques. Finite difference explicit schemes are employed for solving both wave and current equations, since the full interaction between waves and currents is taken into account. It is here emphasised that the long and complex procedure of solving large number of simultaneous equations at each time step negates the large time step allowed by implicit schemes and drastically reduces the efficiency of implicit methods. Therefore, explicit schemes are chosen for the present work.

The angled derivative explicit (ADE) scheme, which was introduced by Flather & Heaps[8] for tide modelling, is used for solving the current momentum equations, while an upstream differencing scheme is used for solving the wave equations. Since waves are assumed to be progressive, the 'upstream' differencing scheme, which controls the direction of differencing by the direction of the progressive motion, was found to be an excellent choice for the wave equations (see Yoo[12] and Yoo & O'Connor[13] for details).

The solutions of finite difference forms of the governing equations are obtained by providing initial and boundary conditions. Tests with the model showed that the best arrangement was a 'cold start' for the current field with a flat water surface and zero current velocity everywhere and a 'hot start' for the wave field, that is, the wave variables over the modelled area were set to be the same as the inflow boundary values. Tests also showed that the initial errors were quickly damped down particularly in the surf zone, by imposing a breaking criterion which prevents excessive build-up of wave energy. No-flow condition was applied to the inflow boundary at the offshore end as well as to the land boundary.

In order to cope with situations involving the 'wetting' and 'drying' of computational grids, the Flather and Heaps' scheme[6] is employed in the present model, which tests the wet condition at each velocity point instead of each elevation point. It can allow the flooding from any direction and generally ensures mass continuity during a transition period from wet to dry or dry to wet. Unrealistically high velocities were found on steep slopes when the condition changed from wet to dry. This was improved by imposing a sensible depth, below which the flow velocity was put to zero, see Yoo[12].

6. MODEL APPLICATION

The present model has been tested against several well-controlled experiments with satisfactory results (Yoo[12]). The present paper presents a set of results obtained on a model breakwater study. The experiments were conducted by Gourlay[7] to study the nearshore circulation produced behind a semi-detached breakwater normal to the direction of wave approach (see Fig. 4 of Gourlay[7]). The beach behind the breakwater was formed of concrete. In the sheltered area behind the breakwater, it was curved with a constant radius centred on the breakwater tip. The water depth offshore of the beach was maintained at 20 cm throughout the tests. The inflow wave conditions were a = 45.5 mm and T = 1.5 seconds with waves propagating normal to the breakwater.

The investigation area was resolved by finite difference meshes of Δx = 0.185 m and Δy = 0.2075 m with 41 meshes in the x direction and 34 meshes in the y direction (see Fig. 1). The left-hand side of the training wall in front of the breakwater was not included in the computation domain and the inflow wave condition was imposed along the line at the offshore end of the training wall. The time step chosen was 0.005 seconds to ensure computational stability.

A value of 0.001m was chosen for the effective roughness height of the concrete in the model. Several trials with the model showed that the dimensionaless mixing coefficients M_b = 2.0 and M_f = 4.0 gave the best solution for the present case. The value of M_b = 2.0 is similar to that (M_b = 3.0) found by Visser[11] using experimental results for a uniform beach.

Fig. 2 shows the time variations of the wave amplitude, current velocity and mean surface elevation at the inshore points A and B (see Fig. 1). While the mean surface elevation still substantially

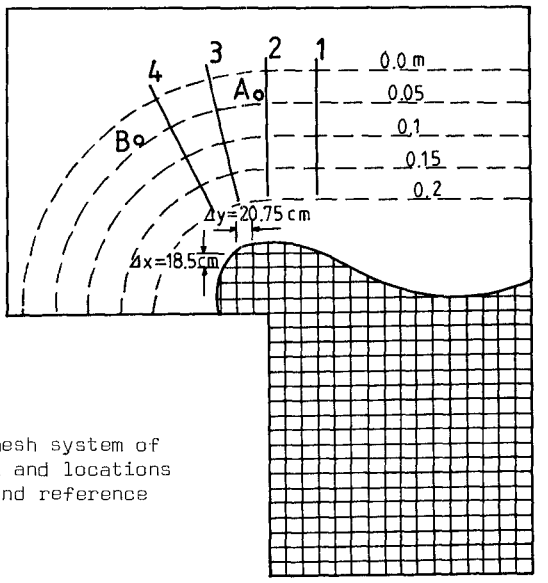

Fig. 1 Finite difference mesh system of Gourlay's wave tank and locations of cross-sections and reference points

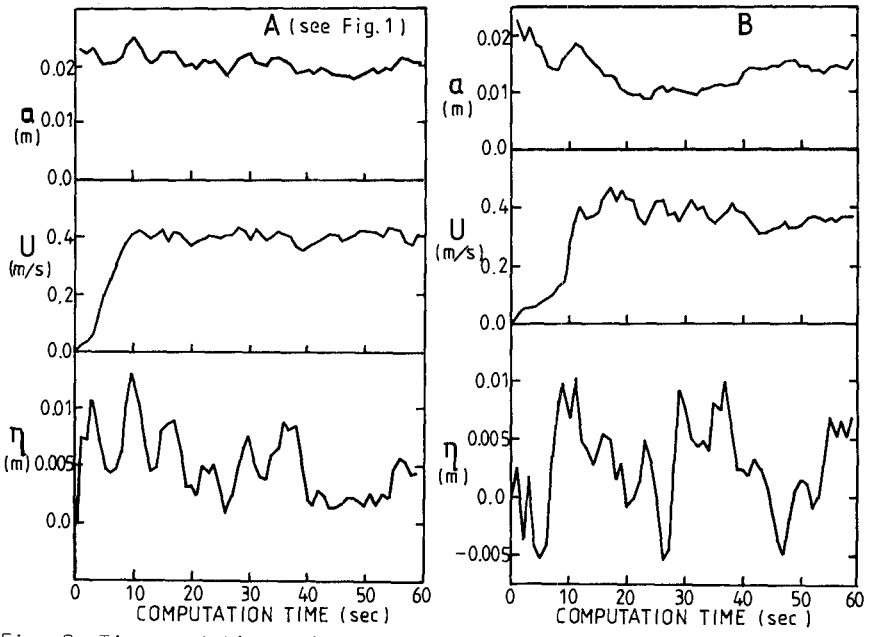

Fig. 2 Time variations of wave amplitude, current velocity and mean surface elevation at locations A and B.

oscillates up to 60 seconds, both wave amplitude and current velocity soon fully develop within a short period. It is interesting to note that at location B the wave amplitude gradually decreases below 0.01m up to 24 seconds, then slowly increases over 0.013m up to 40 seconds and finally remains relatively constant during the rest of the computation period. This changing history of the wave amplitude is certainly caused by the current interaction effects, which seem to alter the wave environment significantly over the whole area.

From Fig. 2, it is believed that the steady state is reached roughly at around 40 seconds. It was, therefore, decided that the result at 50 seconds was likely to be the final solution for the flow field in the present case. The results at time 50 seconds are shown in succeeding figures; wave height distribution in Fig. 3 and wave-induced currents in Fig. 4. The computed results are compared with the experimental data in plan and detailed comparison of the current values is made on several cross sections (refer to Fig. 1 for the details of the location of the cross sections). The agreement between the model and the experiment results is seen to be very good overall.

The computed wave height distribution is seen to be very similar to the experimental one (see Fig. 3). Some minor deviations are found in the middle of the right-hand side of the tank and in the left-hand corner behind the breakwater. Higher values at the left-hand corner in the lee of the breakwater seem to be due to reflection from the beach, while lower values in the middle of the right-hand side may be caused by the non-linear effect of wave transformation near the breaker zone.

The computed current pattern agrees quite well with the experimental one, both qualitatively and quantitatively (see Fig. 4). The computed main gyre behind the breakwater is located at a similar position to the experimental one, being located about 0.5m further inside the breakwater, while even the small eddy motion at the left-hand corner behind the breakwater is well represented by the present model. The detailed comparison of the currents on several cross sections shows the quite good agreement of the model results with the experimental ones in both offshore and inshore regions. In offshore regions, the model slightly over-estimates the current velocity, while inside the surf zone slightly under-estimates it. But the difference is considered acceptable, in view of likely errors in the measurement of conditions in the physical model and the limitation of grid resolution.

The model was finally employed for demonstrating the significance of the role of each term; advection, current-interaction and flooding. This can be best achieved by producing the computational results excluding each term and comparing them with the results from the experiments or the complete scheme. The computation results at 50 seconds are shown in Fig. 5, together with the results from the complete scheme. Problems were found when excluding the advection terms of the momentum equation. The flow developed so rapidly near the coastline that eventually the whole system became unstable at a

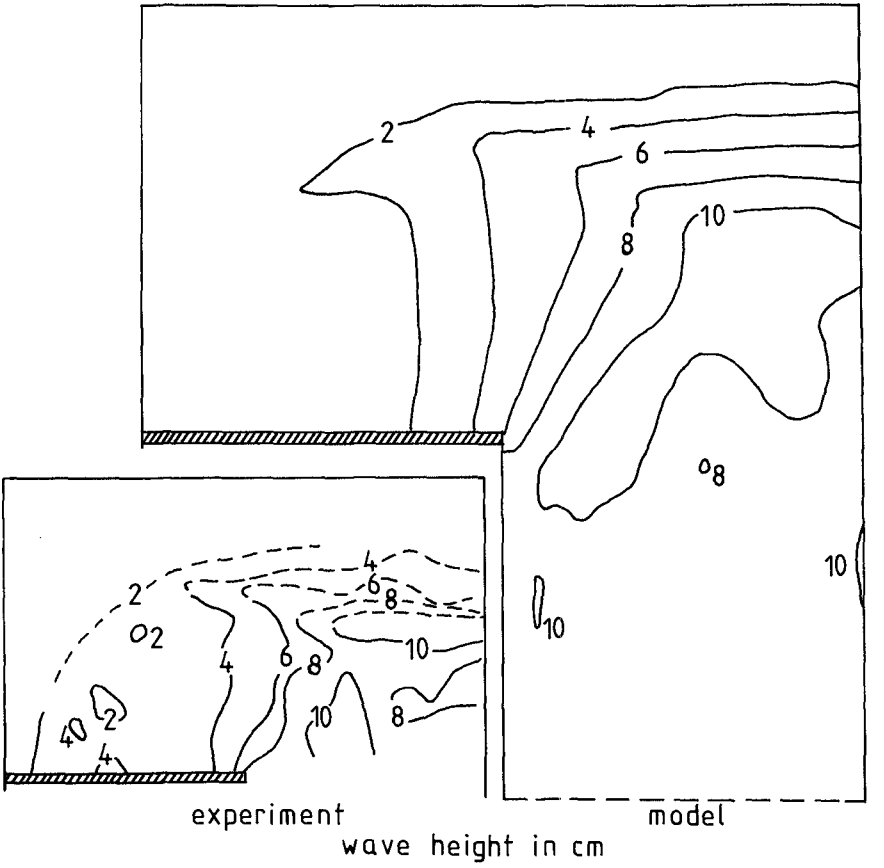

Fig. 3 Comparison of wave height between Gourlay's experiment and the present model

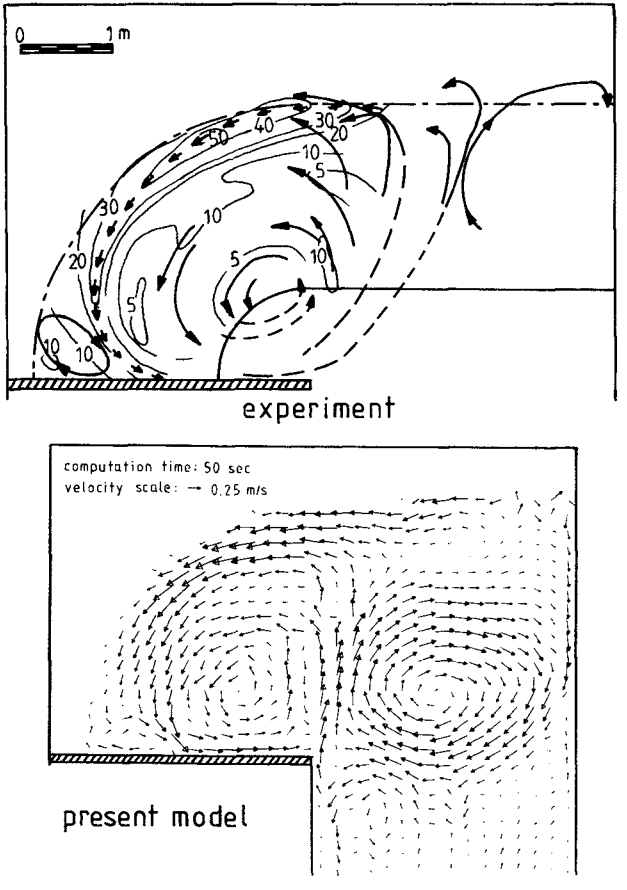

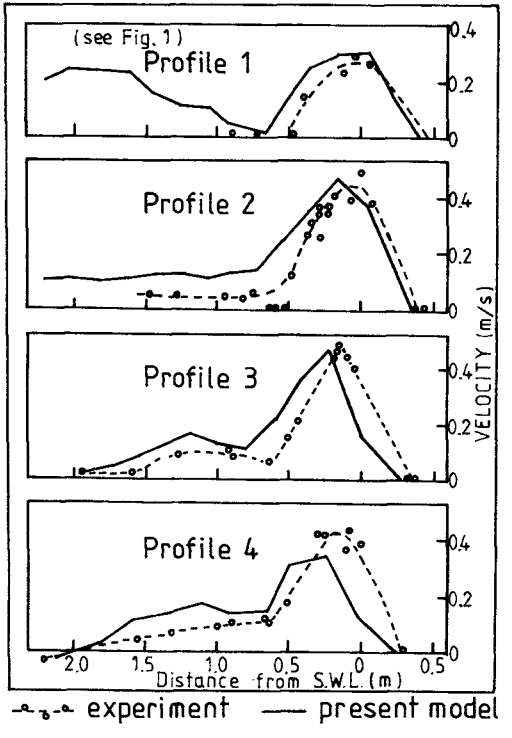

Fig. 4 Comparison of current velocity between Gourlay's experiment and the present model

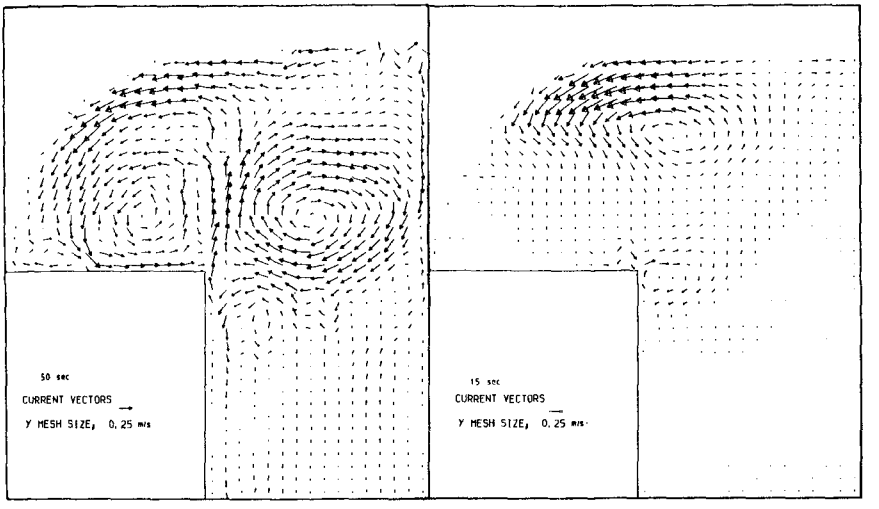

(1) complete (2) no-advection

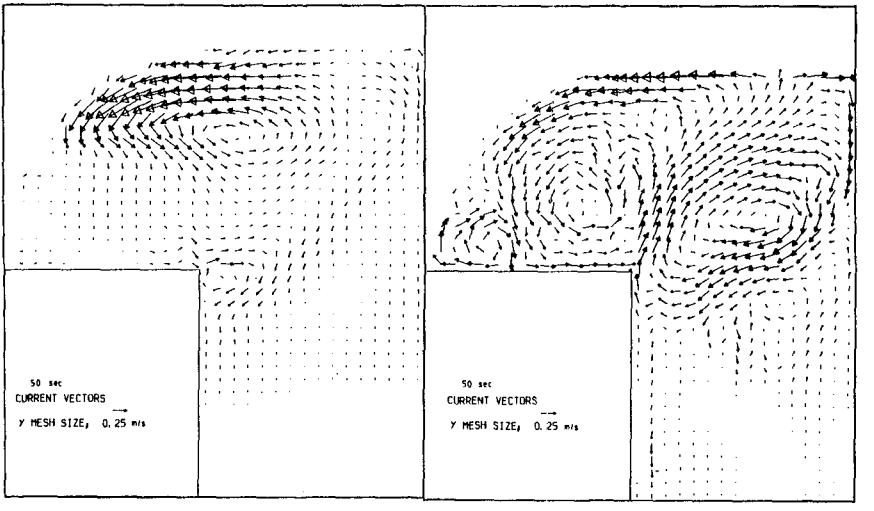

(3) no-current-interaction (4) no-flooding

Fig. 5 Velocity distributions of wave-induced currents from different versions of the present model

run time of about 18 seconds. Therefore, the intermediate result at 15 seconds after the start of the computation is presented for the no-advection case.

Both schemes of no-advection and no-current-interaction are incapable of representing the small eddy motion at the left-hand corner behind the breakwater, while the centre of the main gyre is located a considerable distance from the experimental one. A totally wrong current pattern is thus given by the no-advection and no-current-interaction schemes. By contrast, the no-flooding scheme seems to have described the current pattern nearly as well as the complete interaction one. However, it generally over-estimates the current velocity particularly near the coast; the maximum velocity of the main gyre being predicted at over 65 cm/sec compared with about 50 cm/sec from the experiment, and the maximum velocity of the small gyre at over 25 cm/sec compared with about 10 cm/sec in the experiment. Therefore, if flooding is not included in the model, it is clear that incorrect answers will be obtained for both elevation and current velocity and, indirectly, for mixing coefficients.

7. CONCLUSION

The present work has been concerned with the development of an engineering computer model for evaluating both wave and current fields, particularly when they interact with each other as in the surf zone. The present wave model is fully based on ray theory, which has been extensively used in evaluating wave condition in field situations. The major deficit of existing ray models is that they are incapable of handling caustic or diffractive waves and hence the results are of limited use in areas with complex topography.

The present paper has shown how diffraction effects may be taken into account together with current-interaction effects. The authors' early works[12,13] proved the capability of the present ray model for handling caustic waves, while the present paper demonstrates the model's ability for evaluating the wave-current flow fields in breakwater situation while fully accounting for diffraction and the interaction between waves and current. The model is shown to give very good results for both wave and current fields.

Comparison of model and laboratory tests illustrate the effects of current interaction on wave transformation as well as the current field itself; non-linear advective accelerations on momentum transfer; and flooding of flat zones due to set-up. When any one of the above processes is excluded, the current pattern is shown to be strikingly different from the experimental result or the complete, computer model result.

8. ACKNOWLEDGEMENT

This research is supported by the Science and Engineering Research council through its Marine Technology Directorate and Marinetech North West, U.K.

9. REFERENCES

1. Battjes, J.A., 'Refraction of Water Waves', Journal of Waterways, and Harbors Division, ASCE, Vol. 94, WW4, 1968, pp. 437-451.

2. Battjes, J.A., 'Turbulence in the Surf Zone', Proceedings of the Modelling Techniques, ASCE, 1975, pp. 1050-1061.

3. Battjes, J.A. and Janssen, J.P.F.M., 'Energy Loss and Set-up due to Breaking of Random Waves', Proceedings of the 16th Conference of Coastal Engineering, ASCE, 1978, pp. 569-589.

4. Bijker, E.W., 'The Increase of Bed Shear in a Current due to Wave Motion', Proceedings of the 10th International Conference on Coastal Engineering, ASCE, 1967, pp. 746-765.

5. Fisher, H.B., List, E.J., Koh, R.C.Y., Imberger, J. and Brooks, N.H., 'Mixing in Inland and Coastal Waters, Academic Press, 1979, pp. 104-112.

6. Flather, R.A. and Heaps, N.S., 'Tidal Computations for Morecambe Bay', Geophysical Journal of Royal Astronomical Society, Vol. 42, 1976, pp. 489-517.

7. Gourlay, M.R., 'Wave Set-Up and Wave Generated Currents in the Lee of a Breakwater or Headland', Proceedings of the 14th International Conference on Coastal Engineering, ASCE, 1974, pp. 1976-1995.

8. Miche, M., 'Movements ondulatoires de las mer en profondeur constant ou decroissante', Annales des Ponts et Chaussees, 1944.

9. O'Connor, B.A. and Yoo, D., 'Mean Bed Friction of Combined Wave and Current Flow', Coastal Engineering, (submitted).

10. Swart, D.H., 'Offshore Sediment Transport and Equilibrium Beach Profiles', Delft Hydraulic Laboratory, Publication 131, 1974.

11. Visser, P.J., 'Uniform Longshore Current Measurements and Calculations', Proceedings of the 19th International Conference on Coastal Engineering, ASCE, 1984, pp. 2192-2207.

12. Yoo, D., 'Mathematical Modelling of Wave-Current Interacted Flow in Shallow Waters', Ph.D. Thesis, University of Manchester, 1986.

13. Yoo, D. and O'Connor, B.A., 'Ray Model for Caustic Gravity Waves', Proceedings of the 5th Congress of Asian and Pacific Division, International Association of Hydraulic Research, Vol. 3, 1986, pp. 1-13.

CHAPTER 123

Wave and Current Interactions in Shallow Water

By Sung B. Yoon[1] and Philip L-F. Liu[2]

1. Introduction

Interactions between waves and currents are common and important phenomena in the coastal zone. Coastal currents, such as longshore currents, rip currents, and river flows, can significantly change wave heights and directions of wave propagation. Consequently, the design for shoreline protection measures must be adjusted accordingly.

Various theories for wave-current interactions exist and have been reviewed by Peregrine and Jonsson (1983). Most of these theories are developed for large-scale currents where the length-scale for the current variation is much greater than the typical wavelength. These theories cannot be applied to the coastal currents which are small-scale currents.

In this paper, the interactions between currents and nonlinear shallow water waves are investigated. Boussinesq equations are used to derive evolution equations for spectral wave components. The current intensity is assumed to be larger than the leading wave orbital velocity and smaller than the group velocity. The length-scale of the current is much shorter than those assumed in the existing large-scale theories.

To facilitate numerical computations, the parabolic approximation is applied and a simplified model is developed. A numerical example is given for the refraction and diffraction of cnoidal waves over a rip current on a sloping topography. Both normal and oblique incident cases are examined.

2. Boussinesq Equations

In the present study, the current velocity is assumed to be stronger than the leading order wave orbital velocity. Using ω as the characteristic wave frequency, a_0 as the characteristic wave amplitude and h_0 as the characteristic water depth, the following dimensionless variables are introduced:

[1]Graduate Research Assistant, [2]Professor and Associate Dean of Engineering College

Joseph DeFrees Hydraulics Laboratory, School of Civil and Environmental Engineering, Cornell University, Ithaca, NY 14853

$$t = \omega t \quad , \quad (x, y) = \frac{\omega}{\sqrt{gh_o}} (x , y) \quad , \quad h = h / h_o \quad ,$$

$$\xi_w = \xi_w/(\epsilon h_o) \quad , \quad \vec{u}_w = \vec{u}_w/(\epsilon \sqrt{gh_o}) \quad ,$$

$$\xi_c = \xi_c/(\mu^2 h_o) \quad , \quad \vec{u}_c = \vec{u}_c/(\mu \sqrt{gh_o}) \quad , \tag{1}$$

where

$$\epsilon = a_o/h_o \ll 1 \quad , \quad \text{and } \mu^2 = \omega^2 h_o/g \ll 1 \quad , \tag{2}$$

are small parameters and are assumed to be in the same order of magnitude. In equation (1) $\vec{u}_w$ denotes the depth-averaged horizontal wave velocity vector, while $\vec{u}_c$ represents the current velocity vector. ξ_w and ξ_c represent the free surface displacements associated with wave and current field, respectively. The Boussinesq equations can be written in the following dimensionless form:

$$\frac{\mu^2}{\epsilon} \vec{u}_c \cdot \nabla \vec{u}_c + \frac{\mu^2}{\epsilon} \nabla \xi_c + \frac{1}{2} \frac{\mu^4}{\epsilon} \nabla [\nabla \cdot (h \vec{u}_c)]^2 + \frac{\partial \vec{u}_w}{\partial t} +$$

$$\epsilon \vec{u}_w \cdot \nabla \vec{u}_w + \mu (\vec{u}_c \cdot \nabla \vec{u}_w + \vec{u}_w \cdot \nabla \vec{u}_c) + \nabla \xi_w -$$

$$\mu^2 \frac{\partial}{\partial t} \{\frac{h}{2} [\nabla \cdot (h \vec{u}_w)] - \frac{h^2}{6} \nabla (\nabla \cdot \vec{u}_w)\} = 0(\mu^4) \quad , \tag{3}$$

$$\frac{\mu}{\epsilon} \nabla \cdot [(h + \mu^2 \xi_c) \vec{u}_c] + \frac{\partial \xi_w}{\partial t} + \mu \nabla \cdot (\xi_w \vec{u}_c) +$$

$$\nabla \cdot [(h + \epsilon \xi_w + \mu^2 \xi_c) \vec{u}_w] = 0(\mu^4) \quad . \tag{4}$$

Note that in equations (3) and (4) the length scales for the wave field, current field and the topographical variation are all in the same order of magnitude, namely the typical wavelength. If the water depth is assumed to vary slowly, i.e. $\nabla h \sim 0(\mu)$, the momentum equation (3) can be simplified to be

$$\frac{\mu^2}{\epsilon} \vec{u}_c \cdot \nabla \vec{u}_c + \frac{\mu^2}{\epsilon} \nabla \xi_c + \frac{\partial \vec{u}_w}{\partial t} + \epsilon \vec{u}_w \cdot \nabla \vec{u}_w +$$

$$\mu (\vec{u}_c \cdot \nabla \vec{u}_w + \vec{u}_w \cdot \nabla \vec{u}_c) + \nabla \xi_w - \frac{\mu^2 h^2}{3} \nabla (\nabla \cdot \frac{\partial \vec{u}_w}{\partial t})$$

$$= 0(\mu^3) \quad . \tag{5}$$

We assume that the free surface displacement and the velocity vector for the wave field can be written as a Fourier series with the fundamental frequency ω, i.e.,

$$\xi_w = \frac{1}{2} \sum_n \xi_n \, e^{-int} \quad ,$$

$$\vec{u}_w = \frac{1}{2} \sum_n \vec{u}_n \, e^{-int} \quad , \tag{6}$$

where $n = \pm 1, \pm 2, \cdots$ and $(\xi_{-n}, \vec{u}_{-n})$ are the complex conjugates of $(\xi_n, \vec{u}_n)$. Substitutions of equation (6) into equations (4) and (5) and collections of terms for different Fourier harmonics yield:

$$\nabla \xi_c + \vec{u}_c \cdot \nabla \vec{u}_c + \frac{\epsilon^2}{4\mu^2} \sum_s \vec{u}_s \cdot \nabla \vec{u}_{-s} = 0(\mu^3) \quad , \tag{7}$$

$$\nabla \cdot [(h + \mu^2 \xi_c) \vec{u}_c] = 0(\mu^3) \quad , \tag{8}$$

where $s = \pm 1, \pm 2, \cdots$, and

$$-i n \vec{u}_n + \nabla \xi_n + \mu (\vec{u}_c \cdot \nabla \vec{u}_n + \vec{u}_n \cdot \nabla \vec{u}_c) + \frac{\epsilon}{2} \sum_s \vec{u}_s \cdot \nabla \vec{u}_{n-s} + i n \mu^2 \frac{h^2}{3} \nabla (\nabla \cdot \vec{u}_n) = 0 \ (\mu^3), \tag{9}$$

$$-i n \xi_n + \nabla \cdot [(h + \mu^2 \xi_c) \vec{u}_n] + \mu \nabla \cdot (\xi_n \vec{u}_c) + \frac{\epsilon}{2} \sum_s \nabla \cdot (\xi_s \vec{u}_{n-s}) = 0(\mu^3) \quad . \tag{10}$$

Equations (7) and (8) govern the current velocity $\vec{u}_c$ and the corresponding mean free surface displacement ξ_c with the influences of the wave field. On the other hand, equations (9) and (10) describe the wave field, ξ_n and $\vec{u}_n$ $(n = \pm 1, \pm 2, \cdots)$, which is affected by the current field. The current field can be split into two parts:

$$\vec{u}_c = \vec{q} + \mu^2 \vec{q}_2 \tag{11}$$

$$\xi_c = \eta + \mu^2 \eta_2 \tag{12}$$

where $(\vec{q}, \eta)$ represent the velocity vector and free surface displacement without the influence of waves and $(\vec{q}_2, \eta_2)$ denote the small corrections on currents due to waves. Substituting equations (11) and (12) into equations (7) and (8) yields

$$\nabla \eta + \vec{q} \cdot \nabla \vec{q} = 0 \quad , \tag{13}$$

$$\nabla \cdot (h \vec{q}) = 0 \quad , \tag{14}$$

and

$$\nabla \eta_2 + \vec{q} \cdot \nabla \vec{q}_2 + \vec{q}_2 \cdot \nabla \vec{q} + \frac{\epsilon^2}{4\mu^4} \sum_s \vec{u}_s \cdot \nabla \vec{u}_{-s} = 0 \quad , \tag{15}$$

$$\nabla \cdot (h \vec{q}_2 + \eta \vec{q}) = 0 \tag{16}$$

Substitutions of equations (11) and (12) into equations (9) and (10) yield the following equations

$$-i n \vec{u}_n + \nabla \xi_n + \mu (\vec{q} \cdot \nabla \vec{u}_n + \vec{u}_n \cdot \nabla \vec{q}) + \frac{\epsilon}{2} \sum_s \vec{u}_s \cdot \nabla \vec{u}_{n-s} + i n \mu^2 \frac{D^2}{3} \nabla (\nabla \cdot \vec{u}_n) = 0(\mu^3) \quad , \tag{17}$$

$$-i n \xi_n + \nabla \cdot (D \vec{u}_n) + \mu \nabla \cdot (\xi_n \vec{q}) + \frac{\epsilon}{2} \sum_s \nabla \cdot (\xi_s \vec{u}_{n-s}) = 0(\mu^3) \quad , \tag{18}$$

where

$$D = h + \mu^2 \eta \quad , \tag{19}$$

is the total water depth. The small terms in the current field, η_2 and $\vec{q}_2$, do not affect the accuracy of the wave field.

From equations (17) and (18) the following simple relationships can be found:

$$\vec{u}_n = - \frac{i}{n} \{\nabla \xi_n - \frac{i\mu}{n} [\vec{q} \cdot \nabla (\nabla \xi_n) + \nabla \xi_n \cdot \nabla \vec{q}]\} + 0(\mu^2) \quad , \tag{20}$$

$$\nabla \cdot \vec{u}_n = i n \frac{\xi_n}{D} + 0(\mu) \quad . \tag{21}$$

Multiplying D on the both sides of equation (17) and taking divergence of the resulting equation, we obtain a wave equation for ξ_n:

$$\nabla \cdot (D \nabla \xi_n) + n^2 \xi_n + i n \mu (\nabla \cdot \vec{q}) \xi_n + i n \mu \vec{q} \cdot \nabla \xi_n -$$

$$\frac{\mu^2 n^2 D^2}{3} \nabla^2 \xi_n + \mu \nabla \cdot [D (\vec{q} \cdot \nabla \vec{u}_n + \vec{u}_n \cdot \nabla \vec{q})] +$$

$$\frac{\epsilon}{2} \sum_s [D \nabla \cdot (\vec{u}_s \cdot \nabla \vec{u}_{n-s}) + i n \nabla \cdot (\xi_s \vec{u}_{n-s})] = O(\mu^3), \quad (22)$$

in which equations (18) and (21) have been used.

In summary, solutions for the current velocity $\vec{q}$ and the mean free surface displacement η can be obtained by solving the shallow-water equations (13) and (14). The wave field can be obtained by solving the nonlinear wave equation (22) with appropriate boundary conditions. The effects of the current field on the wave field are included in equation (22). The modification in the current field due to the wave field can be found from equations (15) and (16).

3. Parabolic Approximation

Consider the cases where the dominating wave propagation direction is in the x-direction. The free-surface displacement for the n-th harmonic can be written as

$$\xi_n = \psi_n (x, y) \exp [i n \int \frac{1}{\sqrt{d(x)}} dx] \quad , \quad (23)$$

where $\psi_n (x, y)$ is the amplitude function and d(x) is a reference depth which is a slowly varying function in x. We adopt the usual parabolic approximation that the length-scale of the amplitude function in the wave propagation direction is larger than that in the lateral (y -) direction, i.e.,

$$\frac{\partial \psi_n}{\partial x} \ll \frac{\partial \psi_n}{\partial y} \quad , \quad \frac{\partial^2 \psi_n}{\partial x^2} \ll \frac{\partial \psi_n}{\partial x} \quad . \quad (24)$$

To be more specific, we assume that the current field may be rotational and has a length scale which is slightly longer than the wavelength.

$$O(\frac{\partial U}{\partial y}) \sim O(\frac{\partial V}{\partial x}) \sim O(\alpha) \quad ,$$

$$O(\frac{\partial U}{\partial x}) \sim O(\frac{\partial V}{\partial y}) \sim O(\mu) \quad . \quad (25)$$

where (U, V) are the components of $\vec{q}$ in the x- and y-direction respectively. The small parameter α is assumed to be $O(\mu^{2/3})$.

Furthermore, the topographical variation is assumed to be much weaker than the current variations, i.e.,

$$O(\frac{\partial D}{\partial x}) \sim O(\frac{\partial D}{\partial y}) \sim O(\mu^2) \quad . \tag{26}$$

Consequently, we specify that

$$O(\frac{\partial^2 \psi_n}{\partial x^2}) \sim O(\mu^3) \text{ and } O(\frac{\partial^2 \psi_n}{\partial y^2}) \sim O(\alpha^2) \quad . \tag{27}$$

Substituting equations (20) and (23) into equations (22) and using the order of magnitude estimates, equations (25) - (27), we obtain the following parabolic wave equation for ψ_n:

$$2 i n (\frac{D}{\sqrt{d}} + 2 \mu U) \frac{\partial \psi_n}{\partial x} + D (1 + \mu \frac{U}{\sqrt{D}}) \frac{\partial^2 \psi_n}{\partial y^2} +$$

$$[\frac{\partial D}{\partial y} + 2i \mu n V + 2\mu \sqrt{D} (\frac{\partial V}{\partial x} + \frac{\partial U}{\partial y})] \frac{\partial \psi_n}{\partial y} +$$

$$\{i n \frac{\partial}{\partial x} (\frac{D}{\sqrt{d}} + 2 \mu U) + n^2 [1 - \frac{D}{d} - \mu \frac{U}{\sqrt{d}} (1 + \frac{D}{d}) +$$

$$\frac{\mu^2 n^2 D}{3} - \mu^2 \frac{U^2}{D}] - i n \mu^2 \frac{V}{\sqrt{D}} \frac{\partial U}{\partial y}\} \psi_n =$$

$$\frac{\epsilon}{2D} \sum_s n (n + s) \psi_s \psi_{n-s} + O(\mu^3) \quad , \tag{28}$$

where $D/d = 1 + O(\mu^2)$ is assumed.

4. A Numerical Example

In this section we employ the parabolic equation obtained in the previous section to study the propagation of shallow water waves over rip currents. The current velocity satisfying the shallow water equations (13) and (14) and the corresponding topography can be expressed as:

$$h = (30 - x)/30 \quad ,$$

$$U = -C_2 (30-x) \exp - [(30 - x)^2/C_3^2 + y^2/C_4^2]/2 \quad ,$$

$$V = -\sqrt{\frac{\pi}{2}}\, C_1 \left[2 - \left(\frac{x - 30}{C_3}\right)^2\right] \exp - \left[(30 - x)/\sqrt{2}\, C_3\right]^2 \operatorname{erf}\left[y/(\sqrt{2}\, C_4)\right]. \tag{29}$$

for $\sqrt{2}\, C_3 < (30 - x) < 30$, and

$$h = \sqrt{2}\, C_3/30 \quad ,$$

$$U = -\frac{\sqrt{2}}{e}\, C_2\, C_3 \exp - \left[y/(\sqrt{2}\, C_4)\right]^2 \quad ,$$

$$V = 0 \quad , \tag{30}$$

for $(30 - x) \leq \sqrt{2}\, C_3$, where C_1, C_2, C_3 and C_4 are constants. In the present computations, the following values are used: $C_1 = 0.078$, $C_2 = 0.049$, $C_3 = 7.98$ and $C_4 = 1.596$. The velocity profile is shown in Figure 1. Note that the depth is a constant in the region $x > 18.715$.

The incident wave train contains three harmonics $\psi_1 = 0.9988$, $\psi_2 = 0.0475$ and $\psi_3 = 0.0019$. The small parameters along the initial line are $\epsilon = 0.02$ and $\mu^2 = 0.361$. Thus, initially the incident wave is almost a linear dispersive system.

Using the linear wave ray theory, we plot the ray pattern of a normal incidence over rip currents (Figure 2). Because of wave refraction, caustics occur along the centerline of the rip currents; the ray theory becomes invalid. The present numerical solutions are shown in Figure 3. The linear solutions are obtained by ignoring the nonlinear terms in equation (28). The basic features of the wave height distribution are similar in linear and nonlinear results. However, the detailed free surface profiles are quite different since the nonlinear theory solutions contain higher harmoncis as seen in Figure 3c. A plot of the instantaneous contours of positive free surface displacement is given in Figure 4. The features illustrating the larger amplitudes along the centerline of the rip currents and the wider trough are clearly demonstrated.

Numerical results are also obtained for the case of an oblique incident wave train with the angle of incidence 30° along the initial line. The ray pattern is displayed in Figure 5 which shows oscillatory pattern in caustics. This feature is confirmed by the present numerical solutions as shown in Figure 6. The corresponding free surface profiles using linear and nonlinear theories are given in Figure 7. On the lee side of the rip current the nonlinear results show a faster phase velocity.

Acknowledgement

The research reported here is supported, in part, by the New York Sea Grant Institute.

Appendix

References

Peregrine, D.H. and Jonsson, I.G. 1983 "Interaction of waves and currents" Misc. Rept. No. 83-6, U.S. Army Coastal Engineering Research Center 88p.

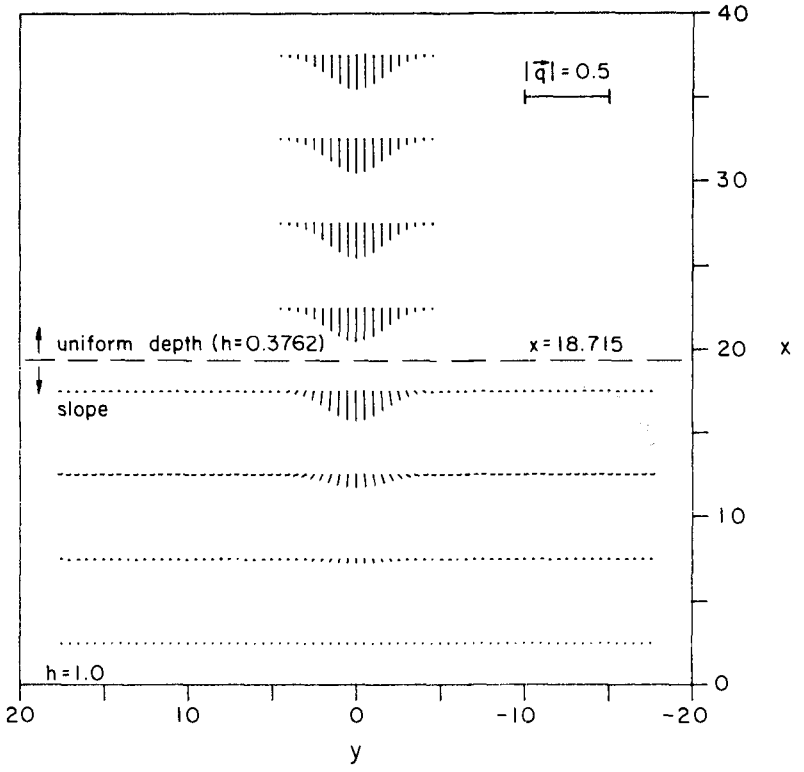

Figure 1 Current field $\vec{q}$.

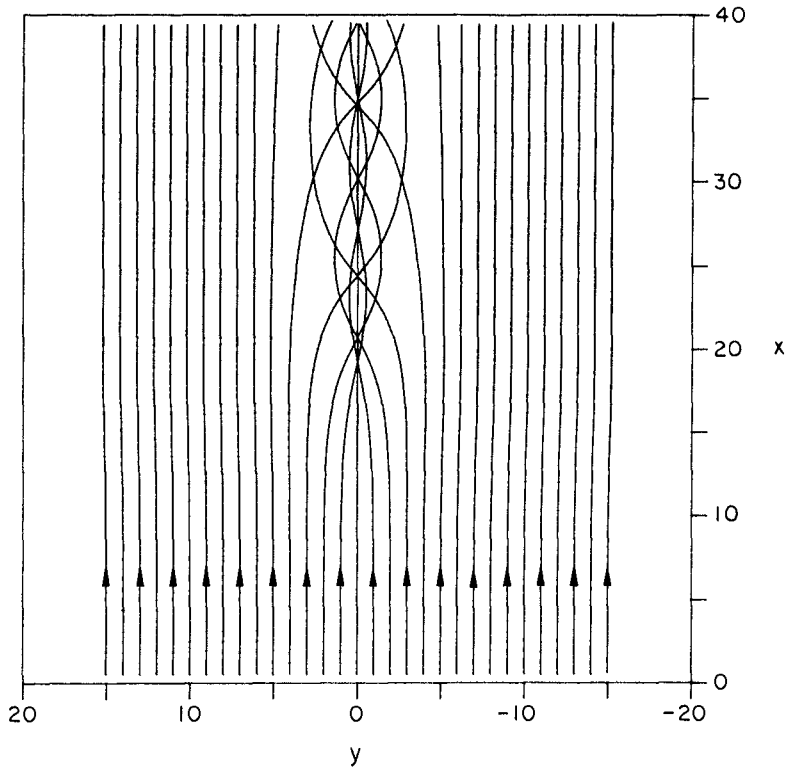

Figure 2 Wave ray pattern over a rip current.

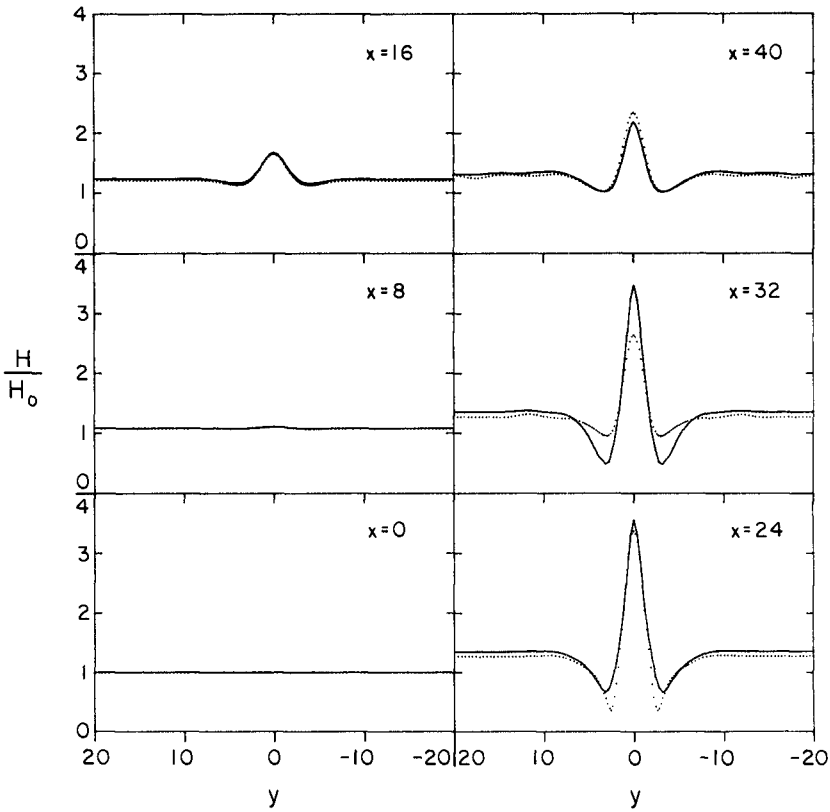

Figure 3a Normalized wave height along x = constants; ——— nonlinear theory, ----- linear theory.

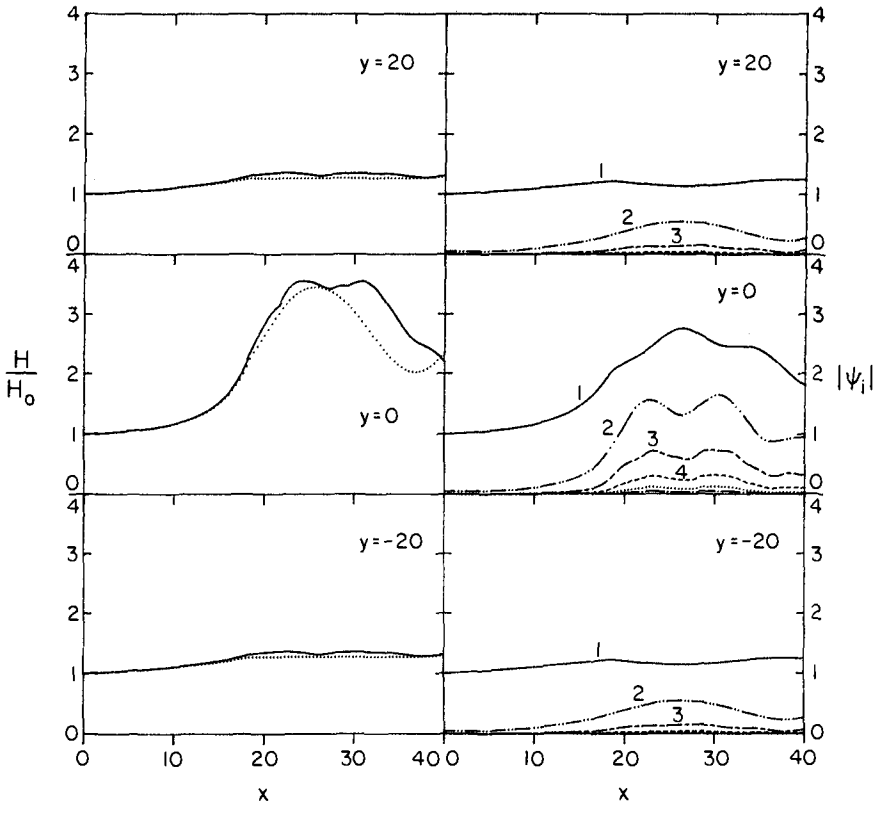

Figure 3b Normalized wave height (left column) and wave amplitude components (right column) along y = constants; for wave heights ——— nonlinear theory, ----- linear theory.

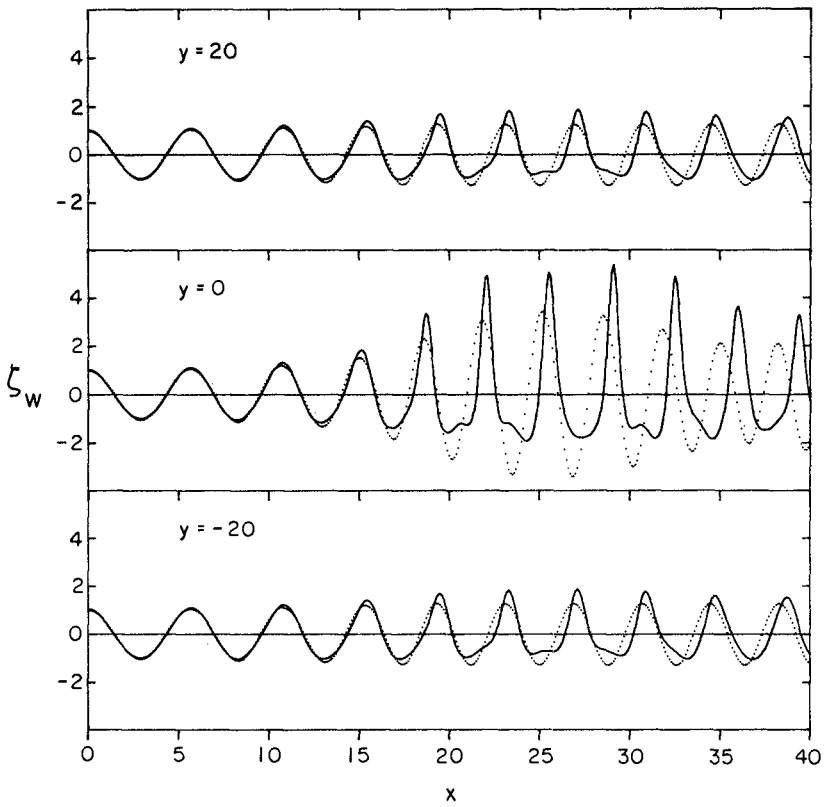

Figure 3c Free surface profiles along y = constants, normal incidence, ——— nonlinear, ----- linear.

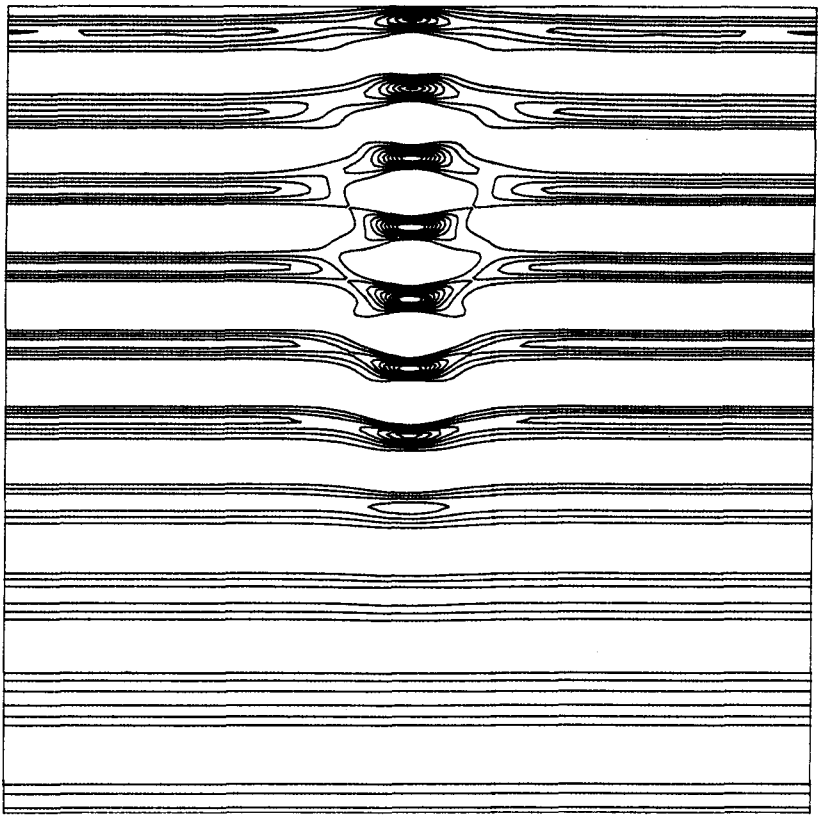

Figure 4 Contours of instantaneous free surface displacement above the mean water level ($\xi \geq 0$); $\Delta\xi = 0.5$.

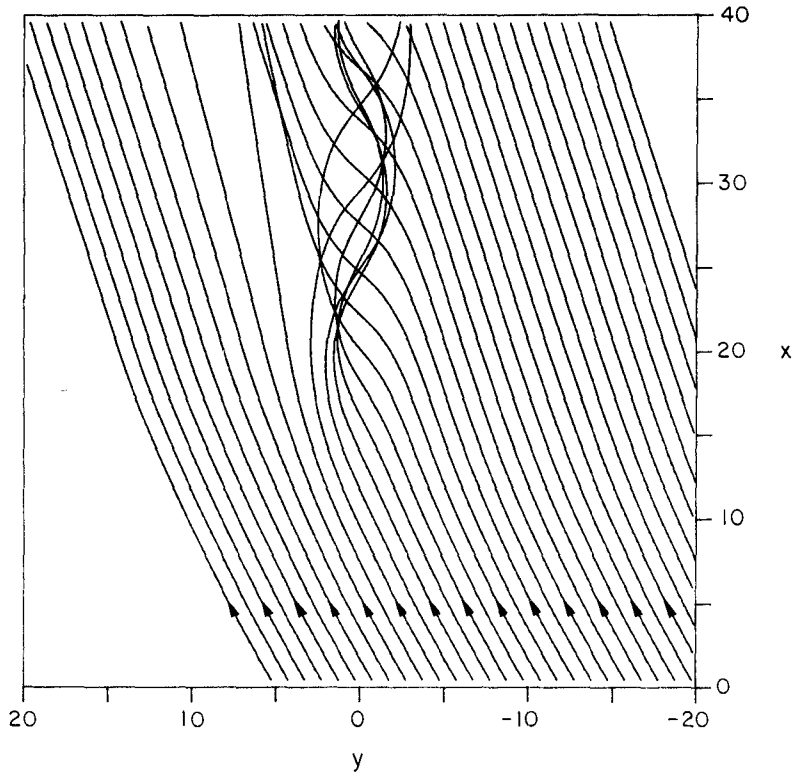

Figure 5 Wave ray pattern for an oblique incident wave over a rip current.

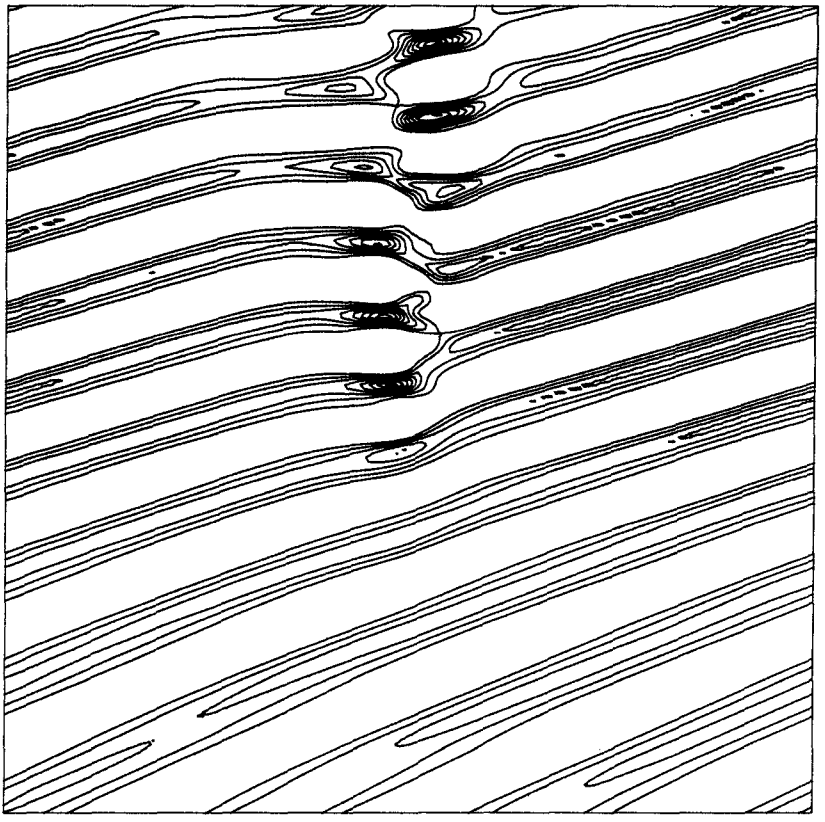

Figure 6 Contours of instantaneous free surface displacement above mean water level ($\xi \geq 0$); $\Delta\xi$ = 0.5.

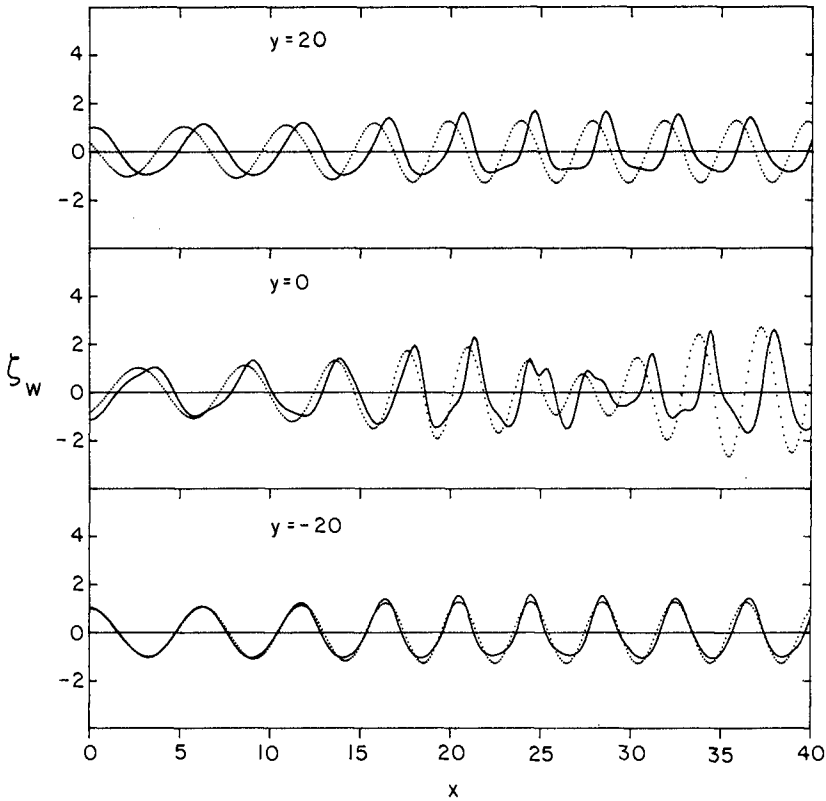

Figure 7 Free surface profiles along y = constants, ——— nonlinear, ----- linear.

CHAPTER 124

2DH COMPUTATION OF TRANSIENT SEA BED EVOLUTIONS

Huib J. de Vriend*

ABSTRACT

The interaction between the constituent models for waves, currents, sediment transport and bottom level changes in a class of compound 2DH mathematical models of transient sea bed evolutions in the coastal zone is investigated mathematically, using the theory of characteristics and a harmonic analysis technique. This leads to contrary indications as to the importance of including diffraction in the wave model and to the unambiguous conclusion that the bottom slope effect on the sediment transport is indespensable for the mathematical system to be inherently stable. This conclusion is shown to imply that depth-integrated current model are insufficient to describe the flow in this type of morphological computations for the nearshore zone or complex coastal areas.

INTRODUCTION

In recent years, the progress in the physical understanding and the mathematical modelling of the water and sediment motion in coastal areas has enabled the numerical simulation of these phenomena to become a widely applied and useful tool in coastal hydraulics and coastal zone management. Besides, they seem to have brought the mathematical modelling of the integrated effect of these phenomena, the 3D morphological evolution of the sea bed, within reach. Various research institutes, all over the world, are making substantial research efforts in this field (see e.g. Fleming et al., 1976; Watanabe, 1982; Coeffé et al., 1982; McAnally et al., 1984; Yamaguchi et al., 1984; De Vriend, 1987a,b).
One of the cornerstones in the development of mathematical models of transient sea bed evolutions is a thorough physical knowledge, of the elementary phenomena tide, waves, currents, sediment motion and sedimentation/erosion, as well as their interactions (also see De Vriend, 1987a). The present paper attempts to contribute to this last field of knowledge, which still exhibits significant lacunae.
After the description and the mathematical formulation of the class of models to be considered, the interaction between the constituent models is analysed mathematically and the sensitivity of the model to some major simplifications in the constituents is assessed. Finally, conclusions are drawn on the applicabitlity.

GENERAL OUTLINE OF THE MODELS

The models concern 3D transient morphological evolutions in coastal areas. Basic elements are depth-integrated wave and current models, local sediment transport formulae and the sediment balance.

*Delft Hydraulic Lab., Delft, The Netherlands

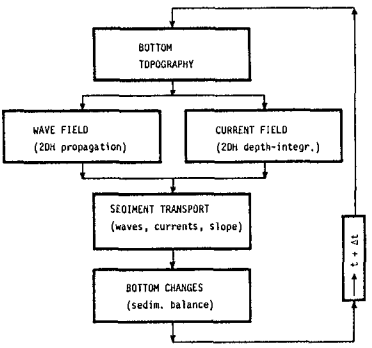

Fig. 1 Flow chart of investigated models

Fig. 1 gives an aggregate flow chart of the interconnection of these elements. Although the present analysis concerns systems of differential equations and the behaviour of their solutions, this flow chart also pertains to their elaboration in a numerical model, so that it can be considered as describing a computational procedure.

Fig. 1 shows that the constituent models are connected in series, with feedback via the bed topography only. This is a simplification of reality, as it ignores other feedback mechanisms, such as current refraction. On the other hand, it focuses attention on the morphological interaction to be investigated.

Another important simplification is the absence of wave dissipation. This means that wave-driven currents are left out of consideration as a mechanism through which the waves can interact with the other components of the system. The principal remaining interaction mechanism for the waves is the stirring of sediment. From a practical point of view, this is a fairly limitative assumption, but on the other hand the interaction analysis should be built up step by step. After the analysis for currents alone (De Vriend, 1987a,b), this is another step on a much longer way to go.

WAVE MODEL

The most general formulation of the wave models to be considered is based on the mild-slope equation for linear monochromatic unidirectional gravity waves (Berkhoff, 1976). Ignoring current refraction and dissipation, this equation can be written as

$$\frac{\partial}{\partial x}\left(cc_g \frac{\partial \Psi}{\partial x}\right) + \frac{\partial}{\partial y}\left(cc_g \frac{\partial \Psi}{\partial y}\right) + k^2 cc_g \Psi = 0 \qquad (1)$$

in which: x, y = cartesian co-ordinates in the horizontal plane,
c = phase celerity of the waves,
c_g = group celerity of the waves,
k = wave number and
Ψ = complex wave potential.

Substitution of the wave-type expression

$$\Psi(x,y) = \mathrm{Re}\left[a(x,y)\exp\left\{i\Phi(x,y)\right\}\right] \qquad (2)$$

in which $i = \sqrt{(-1)}$ and the amplitude and phase functions $a(x,y)$ and $\Phi(x,y)$ are real, leads to the eikonal equation

$$\left(\frac{\partial \Phi}{\partial x}\right)^2 + \left(\frac{\partial \Phi}{\partial y}\right)^2 = k^2 + \frac{1}{cc_g a}\left[\frac{\partial (cc_g)}{\partial x}\frac{\partial a}{\partial x} + \frac{\partial (cc_g)}{\partial y}\frac{\partial a}{\partial y}\right] + \frac{1}{a}\left[\frac{\partial^2 a}{\partial x^2} + \frac{\partial^2 a}{\partial y^2}\right] \qquad (3)$$

and the transport equation

$$\frac{\partial}{\partial x}\left(cc_g a^2 \frac{\partial \Phi}{\partial x}\right) + \frac{\partial}{\partial y}\left(cc_g a^2 \frac{\partial \Phi}{\partial y}\right) = 0 \qquad (4)$$

For purely refracting wave fields (geometric optics approximation), the last two terms of (3) drop out and the equations can be reduced to (also see Appendix I)

$$\frac{\partial}{\partial x}(k \sin\Theta) - \frac{\partial}{\partial y}(k \cos\Theta) = 0 \qquad (5)$$

$$\frac{\partial}{\partial x}(E\, c_g \cos\Theta) + \frac{\partial}{\partial y}(E\, c_g \sin\Theta) = 0 \qquad (6)$$

in which Θ denotes the direction of wave propagation and $E = \frac{1}{2}\rho g a^2$ is the energy density of the wave field.
Both the complete refraction/diffraction equations (3) and (4) and the refraction equations (5) and (6) will be investigated in their interaction with the other components of the model.

CURRENT MODEL

In order to avoid unnecessary complications, the current model includes a number of simplifying assumptions, most of which can be shown to have no essential influence on the interaction (De Vriend, 1985):

- depth-integrated formulation in terms of depth-averaged velocities,
- almost-parallel flow (no secondary currents),
- rigid-lid approximation for the free surface,
- no horizontal diffusion or dispersion of momentum,
- no wave influence on the bottom shear stress,
- bottom shear stress acting in the depth-averaged flow direction,
- no coriolis acceleration,
- no external driving forces, and
- steady flow.

Under these assumption, the flow model can be written as

$$u\frac{\partial u}{\partial x} + v\frac{\partial u}{\partial y} = -\frac{1}{\rho}\frac{\partial p}{\partial x} - \frac{\tau_{bx}}{\rho h} \qquad (7)$$

$$u\frac{\partial v}{\partial x} + v\frac{\partial v}{\partial y} = -\frac{1}{\rho}\frac{\partial p}{\partial y} - \frac{\tau_{by}}{\rho h} \qquad (8)$$

$$\frac{\partial u}{\partial x} + \frac{\partial v}{\partial y} + u\frac{\partial h}{\partial x} + v\frac{\partial h}{\partial y} = 0 \qquad (9)$$

in which: u, v = depth-averaged velocity components
p = total pressure (piezometric head * spec. weight)
ρ = mass density of the fluid
h = water depth
τ_{bx}, τ_{by} = bottom shear stress components.

For the system of equations to be closed, the bottom shear stress has to be related to the other dependent variables in the system. The present analysis requires no further specification than

$$\frac{\tau_{bx}}{\rho h} = ru; \quad \frac{\tau_{by}}{\rho h} = rv \quad \text{with} \quad r = \text{fnct}(u_t, h); \quad u_t = (u^2 + v^2)^{\frac{1}{2}} \qquad (10)$$

The flow model (7) through (10) will only be considered in its complete form, as the effects of simplifications have been investigated before (De Vriend, 1985 and 1987a).

SEDIMENT TRANSPORT MODEL

As was stated before, the sediment transport model is basically restricted to sediment transport formulae. Especially in coastal areas, where a large part of the transported sediment is suspended load, this can be a rather limitative assumption, though not necessarily fatal (c.f. Van Banning et al., 1987). Nevertheless, this type of model is choses, not only from the step-by-step philosophy, but also because transport formulae are widely used in practice. All the same, systems including suspended load models remain to be investigated (cf. Lin et al., 1984).
In addition to this restriction, it is assumed that, apart from the bottom slope effect,

- the magnitude of the transport is a function of the current velocity, the water depth and the wave height (and possibly other quantities that are not figuring as dependent variables in the present system),
- the direction of the transport coincides with the depth-averaged flow direction, and
- the magnitude of the transport is independent of the derivatives of the dependent variables.

This leads to the following mathematical formulation of the transport without bottom slope effect;

$$S'_x = \frac{u}{u_t} S'_t \; ; \; S'_y = \frac{v}{u_t} S'_t \text{ with } S'_t = \text{fnct } (u_t, h, E) \tag{11}$$

in which S'_x and S'_y are the components of the transport vector and S'_t denotes its magnitude.
The near-bottom sediment transport is influenced by the bottom slope, via the downslope gravitational force, acting on the bed load, and via the vertical component of the near-bed velocity, acting on the suspended load. These effects can be incorporated via the following approximative adjustments (cf. Koch et al., 1981 and Bailard, 1981):

$$S_t = S'_t \left(1 - \beta_1 \frac{\partial z_b}{\partial s}\right) \text{ and } \tan\alpha \triangleq \frac{S_y}{S_x} = \tan\delta - \beta_2 \frac{\partial z_b}{\partial n} \tag{12}$$

in which z_b denotes the bottom level, and s and n are stream-oriented and stream-normal horizontal co-ordinates (metric), respectively; δ is the depth-averaged flow direction.
Depending on the transport concept, the factors β_1 and β_2 are equal (Bailard, 1981) or not (Koch et al., 1981) and vary with the wave and current parameters. For simplicity, they are chosen equal and constant, i.e. $\beta_1 = \beta_2 = \beta$, so that (11) and (12) can be elaborated to

$$S_x = S'_t \left(\cos\delta - \beta \frac{\partial z_b}{\partial x}\right) \text{ and } S_y = S'_t \left(\sin\delta - \beta \frac{\partial z_b}{\partial y}\right) \tag{13}$$

provided that the bottom slopes are small compared with β^{-1}.

BOTTOM LEVEL CHANGES

The rate of change of the bottom level follows from the conservation of sediment mass

$$(1 - \varepsilon_p) \frac{\partial z_b}{\partial t} + \frac{\partial S_x}{\partial x} + \frac{\partial S_y}{\partial y} = 0 \tag{14}$$

in which ε_p denotes the porosity of the bottom. This part of the model

is quite unambiguous and, if combined with a transport formula, leaves no room for alternative formulations.

LINEARIZATION OF THE SYSTEM

Equations (3), (4), (7) through (10), (11), (13) and (14) basically from the mathematical model equations, although additional expressions have to be given for c, c_g, k, h, r and S'_t in terms of the dependent variables Φ (or Θ), a (or E), u, v , p and z_b. It is not necessary, however, to have these expressions explicity. The analysis of the system concerns the linearized equations in the vicinity of an arbitrary point in the solution space. If the values of the dependent variables at this point are indicated by the suffix "o", a non-linear relation like the sediment transport formula, for instance, is approximated by

$$S'_t(u_t,h,E) \approx S'_{t_o} + (u_t-u_{t_o})\left.\frac{\partial S'_t}{\partial u_t}\right|_o + (h-h_o)\left.\frac{\partial S'_t}{\partial h}\right|_o + (E-E_o)\left.\frac{\partial S'_t}{\partial E}\right|_o \qquad (15)$$

For each of the non-linear additional expressions, it is sufficient to specify the derivatives with respect to the relevant dependent variables.

After some elaboration of the equations, the most convenient way to specify the necessary quantities of this type turns out to be the specification of

$$T_1 \triangleq \frac{1}{1-\varepsilon_p}\left[\frac{h}{S'_t}\frac{\partial S'_t}{\partial h} - 1\right] \; ; \; T_2 \triangleq \frac{1}{1-\varepsilon_p}\left[\frac{u_t}{S'_t}\frac{\partial S'_t}{\partial u_t} - 1\right] \; ; \; T_3 \triangleq \frac{1}{1-\varepsilon_p}\frac{a}{S'_t}\frac{\partial S_t}{\partial a} \qquad (16a)$$

$$C_h \triangleq \frac{h}{c}\frac{dc}{dh} \; ; \; C_{gh} \triangleq \frac{h}{c_g}\frac{dc_g}{dh} \; ; \; R_u \triangleq \frac{u_t}{r}\frac{\partial r}{\partial u_t} \; ; \; R_h = \frac{h}{r}\frac{\partial r}{\partial h} \qquad (16b)$$

Since the wave number in the present wave models is inversely proportional to the phase celerity c, the relation between k and h is sufficiently characterized by k_o and C_h. Finally, the rigid-lid approximation provides the linear relation

$$h = z_s - z_b \qquad (17)$$

in which z_s is the prescribed elevation of the rigid lid.

Making use of these relations and definitions, and considering T_1, T_2, T_3, C_h, C_{gh}, R_u and R_h as constants in the vicinity of the point "o", the system of equations can be elaborated as described in Appendix I. The resulting system contains two equations describing how the wave field responds to small changes in the bottom topography, three equations describing how the current field responds to such changes and one equation describing how the bottom elevation responds to small changes in the wave and current fields. This last equation reads (also see: De Vriend, 1987b):

$$\frac{\partial z_b}{\partial t} + (T_2 - T_1)\frac{S'_t}{h}\left[\frac{u}{u_t}\frac{\partial z_b}{\partial x} + \frac{v}{u_t}\frac{\partial z_b}{\partial y}\right] - \beta S'_t\left[\frac{\partial^2 z_b}{\partial x^2} + \frac{\partial^2 z_b}{\partial y^2}\right] + T_2\frac{S'_t}{u_t^3} +$$

$$+ \left[-v^2\frac{\partial u}{\partial x} + uv\frac{\partial u}{\partial y} + uv\frac{\partial v}{\partial x} - v^2\frac{\partial v}{\partial y}\right] + T_3\frac{S'_t}{a}\left[\frac{u}{u_t}\frac{\partial a}{\partial x} + \frac{v}{u_t}\frac{\partial a}{\partial y}\right] = 0 \qquad (18)$$

This can be considered as an advection/diffusion equation for the bottom level, in which the last two terms, representing the effects of the wave and current fields, act as source terms. It shows that the bottom evolu-

tion must have a partly propagative, partly diffusive character, the former due to the non-linearity of the transport formula (otherwise the factor T_2-T_1 equals zero), the latter due to the bottom slope effect on the transport.

CHARACTERISTICS ANALYSIS

The system of equations derived in Appendix I can be analyzed with the theory of characteristics (Courant et al., 1961; also see Flokstra, 1981), which provides information on the elementary behaviour of the bottom changes, such as the celerity of bottom disturbances. Application of this technique to the same system without waves revealed (De Vriend, 1987b), that the bottom evolution has a propagative character if the bottom slope effect on the sediment transport is ignored. Even though in that case the transport is directed exactly downstream, bottom disturbances will not only propagate downstream with the well-known 1D celerity derived by De Vries (1969) and also showing up in Eq. (18): like an elementary disturbance in the water surface of a pond, they will also expand in all directions, in a peculiar star-shaped pattern (see Fig. 2).

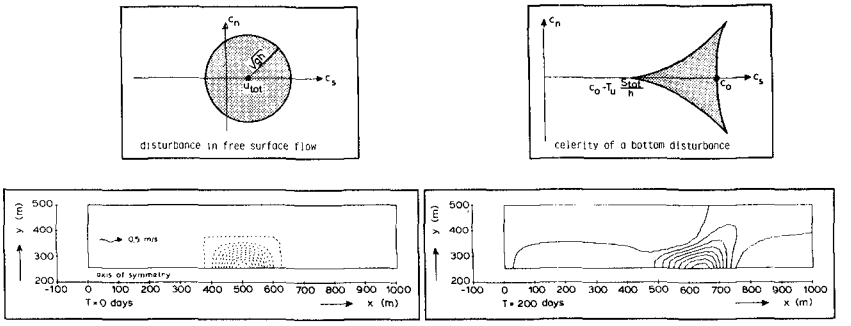

Fig. 2 Celerity patterns in 2DH models. Top left: current and surface wave. Top right: current and alluvial bottom. Bottom: numerical simulation of elementary bottom evolution.

Although formally the propagative character vanishes when the bottom slope effects are included (vide the diffusive character these effects introduce into Eq. (18)), numerical experiments have shown the typical celerity pattern to remain recognizable in the bottom evolution, like it is in the numerical experiment shown in Fig. 2. Therefore, a characteristics analysis with the bottom slope effects disregarded is expected to provide relevant information on the elementary bottom evolution, also in the presence of waves.
Application of the characteristics analysis to the present extensive system is a cumbersome task, which cannot possibly be described here. A detailed description and a discussion of the technique are given in a recent publication by the author (De Vriend, 1987b). Here only some of the results will be given. As the sustaining numerical experiments are awaiting the completion of an appropriate computer program, these results are presented with some reserve.

If the complete mild-slope equation is incorporated in the model, the bottom celerity components with respect to the stream-oriented co-ordinate system are given by

$$c_s = (T_2-T_1)\frac{S_t'}{h} + T_2\frac{S_t'}{h}\xi;\quad c_n = T_2\frac{S_t'}{h}\eta \tag{19}$$

in which the parameters ξ and η are related by

$$\eta^4 + (2\xi^2 - 5\xi - \tfrac{1}{4})\eta^2 + \xi(\xi+1)^3 = 0 \tag{20}$$

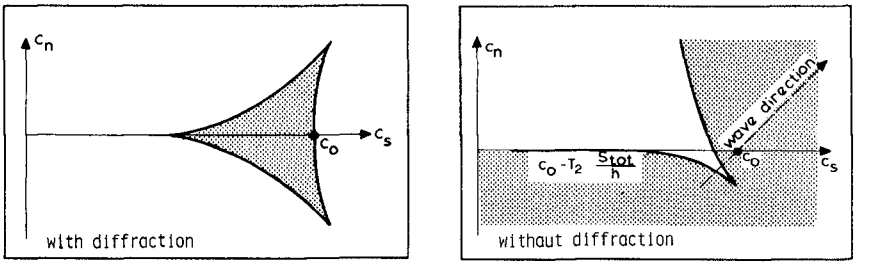

Fig. 3 Influence of wave diffraction on bottom celerities

These expressions, represented graphically in Fig. 3 (left), are exactly the same as for the case without waves. So the celerity is qualitatively independent of the way the sediment transport is influenced by the wave height: T_3 does not figure in (19) or (20). Quantitatively, the celerity does depends on the wave height via S_t'.
If the sediment transport depends on the angle between the wave and current directions the agreement with the case without waves is disturbed. So the conclusion is sensitive to the type of transport formula.

An entirely different celerity pattern can emerge when using simplified wave models. As this pattern is determined by the highest derivatives of the dependent variables in the various equations, disregarding diffraction leads to an essentially different system in this respect.

With the refraction equations (5) and (6), instead of (3) and (4), the expressions for the bottom celerity components read

$$c_s = (T_2-T_1)\frac{S_t'}{h} + T_2\frac{S_t'}{h}\xi + \frac{1}{2}C_{gh}T_3\frac{S_t'}{h} + \frac{1}{2}C_hT_3\frac{S_t'}{h}\xi^* \tag{21}$$

$$c_n = T_2\frac{S_t'}{h}\eta + \frac{1}{2}C_h\,T_3\frac{S_t'}{h}\eta^* \tag{22}$$

with the parameters ξ, η, ξ^* and η^* related by

$$\xi = (1-X)(2X-1) \text{ and } \eta = \pm 2X\left[X(1-X)\right]^{\frac{1}{2}} \tag{23}$$

$$\xi^* = X^4\,\frac{X^3(1-X)^3 - \left[X\xi\sin(\Theta-\delta)\cos(\Theta-\delta) + \eta(1-X)\sin^2(\Theta-\delta)\right]^2}{(1-X)^2\left[X^2\cos(\Theta-\delta) + \tfrac{1}{2}\eta\sin(\Theta-\delta)\right]^4} \tag{24}$$

$$\eta^* = 2X^6\,\frac{X\xi\sin(\Theta-\delta)\cos(\Theta-\delta) + \eta(1-X)\left[\sin^2(\Theta-\delta) - \tfrac{1}{2}\right]}{(1-X)\left[X^2\cos(\Theta-\delta) + \tfrac{1}{2}\eta\sin(\Theta-\delta)\right]^4} \tag{25}$$

in which the parameter X goes through all values between 0 and 1. Note that (23) is equivalent to (20), so that the celerties (21) and (22) consist of two parts, one corresponding with the case without waves and one proportional to T_3, the latter also depending on the angle between

the wave and current directions.
Fig. 3 (right) gives an example of this celerity pattern, for

$T_1 = -2$; $T_2 = 2$; $T_3 = 2$; $C_h = 0.5$; $C_{gh} = 0.375$ and $\Theta - \delta = 45°$

corresponding with the adapted Engelund-Hansen transport formula (Van de Graaff et al., 1979) and the shallow water wave celerities.
The resulting celerity pattern is essentially different from the one with diffraction included: it is no longer a closed curve and, consequently, the area of influence has become semi-infinite. On closer inspection, this behaviour is related to an essential property of purely refracting wave fields: if a wave ray encounters a bottom disturbance, its entire further course is influenced, and so is the wave height along this part of the ray (see. e.g. Dingemans, 1985).
Caution is required when interpreting these results in terms of applicability of types of wave models in the computation of transient morphological evolutions. The results suggest that a refraction model as described by Eqs. (5) and (6) be not applicable. It has to be noted, however, that the characteristics analysis focuses attention on a single aspect of the bottom evolution, viz. the celerity of small disturbances. It is thinkable that this aspect is irrelevant to certain situations. Only numerical experiments for well-selected test cases can show this.

HARMONIC ANALYSIS

In addition to the characteristics analysis, a harmonic analysis can be utilized to investigate the interaction between the constituents of a compound morphological model (cf. Deigaard, 1983 and Tsujimoto et al., 1985). It provides information on the propagation and amplification/damping of harmonic bottom waves. In principle, it can be applied to the transient morphological processes, considering the bottom-wave evolution in time, as well as to the equilibrium bottom topography, considering the variation of harmonic modes in space (cf. Struiksma et al., 1985).

So far, the harmonic analysis of the system including wave effects has only been successful for the transient processes. Like the characteristics analysis, this technique considers the linearized system, for simplicity about the point $(\Theta_o,\ a_o,\ u_o,\ v = 0,\ p_o,\ z_b = 0)$
in the solution space. The resulting system is given in Appendix I.
The technique of the harmonic analysis is well-known: harmonic perturbations of the type

$$z_b = \hat{z}_b \exp\{i(k_t t + k_x x + k_y y)\} \tag{26}$$

with k_t complex and k_x and k_y real, are substituted into the linearized system of equations, to yield a system in $\hat{\Theta}$, $\hat{a}$, $\hat{u}$, $\hat{v}$, $\hat{p}$ and $\hat{z}_b$, with k_t, k_x and k_y as parameters. The condition under which there is a non-trivial solution gives a relation between k_t, k_x and k_y, from which k_t can be solved if k_x and k_y are given.
In order to have a reference for the wave effects, this technique will first be applied to the system without waves. Without going into the algebraic operations, the result reads

$$\mathrm{Re}(\zeta_c) = \sigma\left\{-1 + \frac{4A_c\sigma^2\nu^2(\sigma^2+\nu^2) + 2B_c\nu^2[\sigma^2 + (1+Ru)\nu^2]}{4\sigma^2(\sigma^2+\nu^2)^2 + [\sigma^2 + (1+Ru)\nu^2]^2}\right\} \tag{27}$$

$$\mathrm{Im}(\zeta_c) = D_c(\sigma^2+\nu^2) + \frac{2A_c\sigma^2\nu^2\,[\sigma^2 + (1+Ru)\nu^2] - 4B_c\sigma^2\nu^2(\sigma^2+\nu^2)}{4\sigma^2(\sigma^2+\nu^2)^2 + [\sigma^2 + (1+Ru)\nu^2]^2} \tag{28}$$

$$\text{with:}\quad \zeta_c = \frac{k_t}{2(T_2-T_1)r_o}\ ;\ \sigma = \frac{u_o}{2r_o}k_x;\ \nu = \frac{u_o}{2r_o}k_y \tag{29}$$

$$A_c = \frac{T_2}{T_2-T_1}\ ;\ B_c = \frac{T_2}{T_2-T_1}\,\frac{1+R_u-R_h}{2}\ ;\ D_c = \frac{\beta}{T_2-T_1}\,\frac{2r_o h_o}{u_o} \tag{30}$$

Note that this system contains two important physical length scales (also see Struiksma et al., 1985), viz. the adjustment length of the flow, λ_w, and the adjustment length of the bottom, λ_s, given by

$$\lambda_w = \frac{u_o}{2r_o} \quad \text{and} \quad \lambda_s = \beta h_o \tag{31}$$

The second term in the expression for $\mathrm{Im}(\zeta_c)$ is easily shown to be negative if $A_c > 0$, and $R_h < 0$, as is usually the case. This means,that for $D_c = 0$, i.e. in the system without bottom slope effects, all modes are unstable. So this system has no stable solution (cf. De Vriend, 1985). For $D_c > 0$ (negative values are not realistic), the additional term in (28) is positive, i.e. the bottom slope effect on the sediment transport has a damping effect on bottom disturbances, as it should according to the bottom level equation (18). Besides, the additional term increases with the resultant wave number, so this damping effect will be stronger for shorter waves (which have steeper slopes).
As an example of how this works out quantitatively, Fig. 4 gives a graphical representation of (27) and (28), with and without bottom slope effects. The values of the constants correspond with the Engelund and

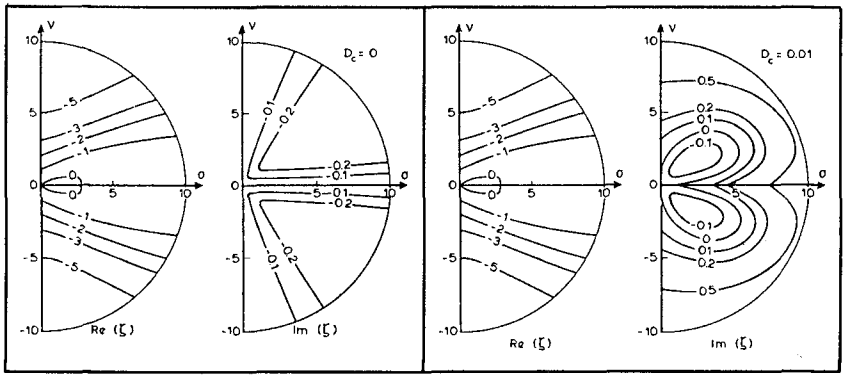

Fig. 4 Initial growth rate of harmonic bottom disturbances (current only)

Hansen transport formula ($T_1 = -1$, $T_2 = 4$) and Chezy's bottom friction law ($R_u = 1$, $R_h = -1$, $r_o = gu_o/[C^2h]$). In the case with bottom slope effects, D_c was chosen 0.01, which corresponds with $\beta \approx 4$. For $D_c = 0$, $\mathrm{Im}(\zeta_c)$ is always negative, indeed, whereas for $D_c \neq 0$, $\mathrm{Im}(\zeta_c)$ is only negative in two relatively small areas, representing fairly long bottom waves. The existence of such unstable modes is not necessarily unrealistic (Deigaard, 1983; also see Struiksma et al., 1985 and De Vriend, 1987a).

When applied to the system including waves, the harmonic analysis yields the following result

$$\mathrm{Re}(\zeta_w) = \sigma\{-1 + \frac{4A_w\sigma^2\nu^2(\sigma^2+\nu^2) + 2B_w\nu^2[\sigma^2+(1+R_u)\nu^2]}{4\sigma^2(\sigma^2+\nu^2)^2 + [\sigma^2+(1+R_u)\nu^2]^2} + \frac{4C_w\gamma^2\chi^2 - E_w(\phi^2+\chi^2)^2}{4\gamma^2\phi^2-(\phi^2+\chi^2)^2}\} \tag{32}$$

$$\mathrm{Im}(\zeta_w) = D_w(\sigma^2+\nu^2) + \frac{2A_w\sigma^2\nu^2[\sigma^2+(1+R_u)\nu^2] - 4B_w\sigma^2\nu^2(\sigma^2+\nu^2)}{4\sigma^2(\sigma^2+\nu^2)^2 + 5\sigma^2 + (1+R_u)\nu^2]^2} \tag{33}$$

with:

$$\zeta_w = \frac{k_t}{2(T_2-T_1+\frac{1}{2}C_{gh}T_3)r_o}\ ;\ \phi=\sigma\cos\theta_o+\nu\sin\theta_o;\ \chi=\sigma\sin\theta_o-\nu\cos\theta_o \tag{34}$$

$$A_w = \frac{T_2}{T_2-T_1+\frac{1}{2}C_{gh}T_3}\ ;\ B_w = A_w\frac{1+R_u-R_h}{2};\ D_w = \frac{\beta}{T_2-T_1+\frac{1}{2}C_{gh}T_3}\frac{2r_o h_o}{u_o} \tag{35}$$

$$C_w = \frac{\frac{1}{2}C_h T_3}{T_2-T_1+\frac{1}{2}C_{gh}T_3};\ E_w = \frac{\frac{1}{2}C_{gh}T_3}{T_2-T_1+\frac{1}{2}C_{gh}T_3};\ \gamma = \frac{u_o}{2r_o}k \tag{36}$$

Apart from the coefficients, these expressions are very much the same as in the case without waves: the only difference is an additional term in the expression for Re(ζ). This implies that the amplification/damping behaviour of the bottom disturbances remains qualitatively the same, with a predominant role for the bottom slope effects.

As a quantitative example, Fig. 5 gives graphical representations of (33) and (34), without and with bottom slope effects ($D_w = 0$ and $D_w = 0.01$, respectively), without and with diffraction ($\gamma = 0$ and $\gamma = 30$, respectively).

The values of the constants are chosen the same as in the example in Fig. 3, viz. $T_1=-2$, $T_2=2$, $T_3=2$, $C_h=0.5$, $C_{gh}=0.375$, but now with $\theta_o=0°$ (waves and current in the same direction) and with $R_u=1$ and $R_h=-1$ (Chezy). Apparently, the diffraction effect on Re(ζ_w) is rather small, especially for the longer modes.

These results suggest that the incorporation of diffraction in the wave model should have a minor effect on the elementary behaviour of bottom disturbances. However, caution should be exercised, again, when interpreting these results in terms of applicability of types of wave models. The analysis focuses attention on the evolution of small harmonic bottom perturbations, starting from the linearized system of equations. Besides, the indication it gives is contrary to the one given by the characteristics analysis. This does not imply that the two analyses yield contradictory results, since they consider different aspects (amplitude behaviour and propagation behaviour, respectively). Which of these aspects is decisive for the sensitivity of the model to diffraction is still not clear. Numerical model tests and further research are needed in order to arrive at definite conclusions.

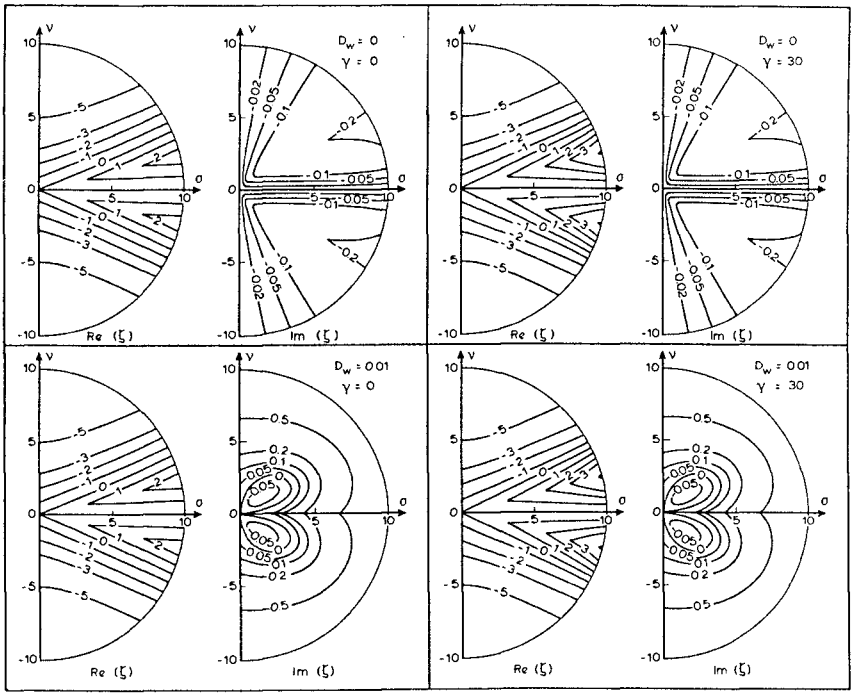

Fig. 5 Influence of wave diffraction on initial growth rate (waves + currents)

DISCUSSION

The investigated system, though including the principal interacting constituents (waves, currents, sediment transport, bottom level changes), is still a highly simplified representation of reality. For instance, the interaction via the response of wave breaking and the induced currents to morphological changes is left out of consideration. Especially in the surf zone, this seems to be an interaction of primary importance.

Nevertheless, the present analyses are practically relevant. If the dissipation of wave energy by breaking is formulated according to Battjes et al., (1978) and the corresponding driving forces per unit area are taken proportional to the dissipation density divided by the phase celerity (Longuet-Higgins, 1970; Dingemans et al., 1987), the relevant terms in the wave and current models are easily shown not to contain the highest derivatives of the dependent variables. Hence this interaction has no effect on the bottom celerity pattern found from the characteristics analysis. The harmonic analysis with this interaction included is still in progress, but is has already become clear that the bottom slope effect on the sediment transport is still a major (if not the only) damping agent in the system.

Another limitation of the present work is, that only linearized systems are considered. When there is a better outlook on the composition and the validity of mathematical models of transient 3D sea bed evolutions, their non-linear behaviour, including the possibility of bifurcations and chaotic behaviour, will have to be investigated.

The harmonic analysis of all variants and extensions of the model that have been investigated so far, clearly indicates that the bottom slope effect on the sediment transport is indispensable in the computation of transient morphological evolutions. If this slope-reducing mechanism is included, however, also the principal slope-generating mechanisms have to be taken into account, if it were only not to wind up with a zero beach slope.
In the nearshore zone, the onshore transport due to the asymmetry of the near-bottom orbital motion is a major slope-generating agent, as appears from investigations of coastal profile evolutions (Stive, 1986; De Vriend, 1986). A fascinating corroboration of this statement, though for edge waves instead of sea or swell, was given by Holman et al. (1982).
On the other hand, the wave-induced undertow in the surf zone causes an off-shore, so usually down-slope transport that is mostly stronger than the asymmetry-induced on-shore transport there (De Vriend et al., 1986). So, once the asymmetry-induced transport is included in a model of near-shore morphological evolutions, the transport due to the undertow, and hence the undertow itself, cannot be left out of consideration. This means that a depth-integrated current model is not sufficient for this kind of situations.
In most of the practical applications, the model area extends beyond the nearshore. Outside the surf zone, the undertow is absent and the waves induce only a much weaker drift current. The asymmetry-induced transport is found wherever the waves "feel" the bottom (so usually in large parts of the model), but it decreases as the water depth increases. This does not imply, that at deeper water the bottom slope effect is the only remaining cross-stream mechanism and that, consequently, a depth-integrated current model suffices. In the complex situations to which 2DH models use to be applied, the flow is curved almost as a matter of course. Besides, sand coasts without strong winds are rare and the coriolis-effect is present almost everywhere. Hence secondary flows due to wind, curvature and the coriolis-effect will occur and exert their influence on the sediment transport and the morphological changes. So in these cases the application of depth-integrated current models is disputable, as well.
This negative conclusion regarding depth-integrated current models does not mean that 2DH flow computation facilities are useless for morphological computations. Experience with river bend modelling (Struiksma et al., 1985) and recent investigations on the modelling of 3D nearshore currents (De Vriend et al., 1986) make clear, that without too limitative assumptions, the flow can be described with a standard depth-integrated model, extended with a simple profile technique for the secondary flow.

CONCLUSIONS

The two methods used to analyse the interaction between the constituents of the present class of compound 2DH mathematical models of transient sea bed evolutions yield contrary indications on the importance of diffraction in the wave model.

The harmonic analysis unambiguously shows, that the bottom slope effect on the sediment transport (via gravitation and via vertical advection) is indispensable for inherent stability of the mathematical system.
The necessity to include this bottom slope effect implies, that the influence of the asymmetry of the wave-induced orbital motion and of secondary flows has to be taken into account, as well. Consequently, depth-integrated current models are insufficient to describe the flow in models of 3D morphological evolutions, in the nearshore zone and in complex coastal areas.
Depth-integrated current models extended with a simple profile technique to describe the secondary flow appear to be suited for this kind of applications.

ACKNOWLEDGEMENTS

The investigations described herein were part of the TOW Coastal Research Programme, financed by the Netherlands Government and conducted jointly by the Ministry of Transport and Public Works (Rijkswaterstaat), Delft Hydraulics and the Technical University Delft. The author gratefully acknowledges Mr. M.W. Dingemans for his lessons in wave-field theory.

REFERENCES

Bailard, J.A., 1981. An energetics total load sediment transport model for a plane sloping beach. J. Geoph. Res., 86, no. C11, p. 10938-10954.
Battjes, J.A. and Janssen, J.P.F.M., 1978. Energy loss and set-up due to breaking of random waves. Proc. 16th ICCE, Hamburg, p.569-587.
Berkhoff, J.C.W., 1976. Mathematical models for simple harmonic linear water waves; wave diffraction and refraction. Delft Univ. of Techn., Doct. thesis, 103 pp. (Also: Delf Hydr. Lab., Publ. no 163.).
Bijker, E.W., 1971. Longshore transport computations. Proc. ASCE, J. of the Waterways, Harbours and Coastal Engineering Division, WW4, p.687-701.
Coeffé, Y., Péchon, Ph., 1982. Modelling of sea-bed evolution under wave action. Proc. 18th ICCE, Capetown, p. 1149-1160.
Courant, R. and Hilbert, D., 1962. Methods of mathematical physics II, Interscience Publishers, New York, 830 pp.
Deigaard, R., 1983. Formation of large bed undulations under waves and current - a stability analysis. Tech. Univ. Denmark, Inst. Hydrodyn. and Hydraulic Engrg., Prog. Rept. 59, p. 3-11.
De Vriend, H.J., 1985. Flow formulation in mathematical models of 2DH morphological changes. Delft Hydr. Lab., TOW-rept. R1747-5, 64 pp.
De Vriend, H.J., 1986. Two and three-dimensional mathematical modelling of coastal morphology. Delft Hydr. Lab., TOW-rept. H284-2, 36 pp. (Also: Delft Hydraulics Comm. no. 377).
De Vriend, H.J., 1987a. 2DH mathematical modelling of morphological evolutions in shallow water. To appear in Coastal Engineering.
De Vriend, H.J., 1987b. Analysis of 2DH morphological evolutions in shallow water. To appear in J. Geoph. Res. (Oceans).
De Vriend, H.J., and Stive, M.J.F., 1986. Quasi-3D modelling of nearshore currents. JONSMOD '86 Colloquium, Delft, The Netherlands (to appear in special JONSMOD-issue of Coastal Engineering).
De Vries, M., 1969. Solving river problems by hydraulic and mathematical models. Conf. on Simulation of Hydrodynamic Phenomena, Jablonna, Poland. (Also: Delft Hydr. Lab., Publ. no. 76-II).

REFERENCES (continued)

Dingemans, M.W., 1985. Surface wave propagation over an uneven bottom; Evaluation of two-dimensional wave propagation models. Delft Hydr. Lab. Rept. no. W301-5, 117 pp.
Dingemans, M.W., Radder, A.C. and De Vriend, H.J., 1987. Computation of the driving forces of wave-induced currents. JONSMOD '86 Colloquium, Delft, The Netherlands (submitted for publication).
Fleming, C.A. and Hunt, J.N., 1976. Application of a sediment transport model. Proc. 15th ICCE, Honolulu, Hawaii, p. 1184-1202.
Flokstra, C., 1981. Numerical aspects of calculating the bed level in river bends, Delft Hydr. Lab., Rept. R657-XII/W308 part II, 34 pp.
Holman, R.A. and Bowen, A.J., 1982. Bars, bumps and holes: models for the generation of complex beach topography, J. Geoph.Res., 87, no. C1, p. 457-468.
Koch, F.G. and Flokstra, C., 1981. Bed level computations for curved alluvial channels, Proc. XIXth IAHR Congress, New Delhi, Vol. 2, p. 357 (also: Delft Hydr. Lab., Publ. no. 240).
Lin, P.N. and Shen, H.W., 1984. Two-D flows with sediment by characteristics method, J. Hydr. Engrg., 110, no. 5, p. 615-625.
Longuet-Higgins, M.S., 1970. Longshore currents generated by obliquely incident sea waves. J. Geophys.Res., 75, p. 6778-6801.
McAnally, W.H., Letter, J.V., Thomas, W.A. and Brogdon, N.J., 1984. Application of Columbia hybrid modelling system. J. Hydr. Engrg., 110, no. 5, p. 627-642.
Stive, M.J.F., 1986. A model for cross-shore sediment transport. Proc. 20th ICCE, Taipei.
Struiksma, N., Olesen, K.W., Flokstra, C. and De Vriend, H.J., 1985. Bed deformation in curved alluvial channels. J. Hydr. Res., 23, no. 1, p. 57-79.
Tsujimoto, T. and Fukushima, T., 1985. Flow over the three-dimensional wavy bed - a linearized theory for bed instability analysis. Memoirs Fac. of Techn., Kanazawa Univ., Japan, 18, no. 2, p. 11-21.
Van Banning, G.K.F.M., De Vriend, H.J. and Boer, S., 1987. Schematization and validation of 2DH mathematical models of coastal morphology. Coastal Sediments '87, New Orleans, Louisiana.
Van de Graaff, J. and Van Overeem, J., 1979. Evaluation of sediment transport formulae in coastal engineering practice. Coastal Engineering, 3, p. 1-32.
Watanabe, A., 1985. Three-dimensional predictive model of beach evolution around a structure. Symp. Water Wave Research, Hannover.
Yamaguchi, M. and Nishioka, Y., 1984. Numerical simulation on the change of bottom topography by the presence of coastal structrues, Proc. 19th ICCE, Houston, Texas, p. 1732-1748.

APPENDIX I - ELABORATION OF THE CONSTITUENT EQUATIONS

If the right-hand member of the eikonal equation (3) is named κ^2, this equation can be replaced by

$$\frac{\partial \Phi}{\partial x} = \kappa \cos\Theta \text{ and } \frac{\partial \Phi}{\partial y} = \kappa \sin\Theta \qquad (37)$$

Then the compatibility conditions for these phase function derivatives and the transport equation (4) can be elaborated to the linearized system

$$L_2(\Theta) - \frac{k^2}{\kappa^2}\frac{C_h}{h} L_1(h) + \frac{1}{2\kappa^2} L_1\left(\frac{\nabla^2 a}{a}\right) + \frac{C_h + C}{2\kappa^2 ha} gh\, L_1\left(\frac{\partial a}{\partial x}\frac{\partial h}{\partial x} + \frac{\partial a}{\partial y}\frac{\partial h}{\partial y}\right) + \text{h.o.t.} = 0 \qquad (38)$$

$$- L_1(\Theta) + \frac{2}{a} L_2(a) + \frac{1}{2\kappa^2} L_2\left(\frac{\nabla^2 a}{a}\right) + \left[\frac{C}{gh} + \left(1 - \frac{k^2}{\kappa^2}\right)\frac{C}{h}\right] L_2(h) + \\ + \frac{C_h + C}{2\kappa^2 ha} L_2\left(\frac{\partial a}{\partial x}\frac{\partial h}{\partial x} + \frac{\partial h}{\partial y}\frac{\partial h}{\partial y}\right) + \text{h.o.t.} = 0 \qquad (39)$$

in which ∇^2 denotes the Lapalician and "h.o.t." indicates higher order terms in the derivatives of a and h. The operators L_1 and L_2 are defined as

$$L_1 = \cos\Theta \frac{\partial}{\partial x} + \sin\Theta \frac{\partial}{\partial y} \quad \text{and} \quad L_2 = \sin\Theta \frac{\partial}{\partial x} - \cos\Theta \frac{\partial}{\partial y} \qquad (40)$$

The flow equations (7) though (10) remain unaltered, except for the linearization of the bottom shear stress

$$\frac{\tau_{bx}}{\rho h} = \left(\frac{\tau_{bx}}{\rho h}\right)_o + (u-u_o)\, r_o + \left(u_t - u_{t_o}\right) \frac{u_o r_o}{u_{t_o}} R_u + (h-h_o) \frac{u_o r_o}{h_o} R_h \qquad (41)$$

and a similar expression for the y-component.

Substitution of the linearized expression for the sediment transport, (15), into (12) and (13) and subsequently into the sediment balance equation (14) yields, after some elaboration and making use of the equation of continuity (9), the advection/diffusion equation (18).

Equations (38) through (41) and (7) through (9) form a representation of the system in which all derivatives refer to the dependent variables Θ, a, u, v, p and z_b (or h).
If this system is linearized about the point $(\Theta_o, a_o, u_o, v=0, p_o, z_b=0)$ in the solution space, i.e. if the x-axis is oriented downstream and the undisturbed bottom is horizontal, it can be written as

$$L_2(\Theta') + \frac{C_h}{h_o} L_1(z_b') + \frac{1}{2a_o k_o^2} L_1(\nabla^2 a') = 0 \qquad (42)$$

$$- L_1(\Theta') - \frac{C}{gh_o} L_2(z_b') + \frac{2}{a_o} L_2(a') + \frac{1}{2a_o k_o^2} L_2(\nabla^2 a') = 0 \qquad (43)$$

$$u_o \frac{\partial u'}{\partial x} = - \frac{1}{\rho}\frac{\partial p'}{\partial x} - (1 + R_u)\, r_o u' - R_h \frac{u_o r_o}{h_o} h' \qquad (44)$$

$$u_o \frac{\partial v'}{\partial x} = - \frac{1}{\rho}\frac{\partial p'}{\partial y} - r_o v' \qquad (45)$$

$$\frac{\partial u'}{\partial x} + \frac{\partial v'}{\partial y} - \frac{u_o}{h_o}\frac{\partial z_b'}{\partial x} = 0 \qquad (46)$$

$$\frac{\partial z_b'}{\partial t} + (T_2 - T_1) \frac{S_{t_o}}{h_o} \frac{\partial z_b'}{\partial x} - \beta S_{t_o} \nabla^2 z_b' - T_2 \frac{S_{t_o}}{u_o} \frac{\partial v'}{\partial y} + T_3 \frac{S_{t_o}}{a_o} \frac{\partial a'}{\partial x} \qquad (47)$$

in which the primes indicate the deviation of the relevant quantity from the solution in point "o" in the solution space. The operators L_1 and L_2 are given by (40), with $\Theta = \Theta_o$.
The system (I.9) through (I.14) is subject to the harmonic analysis.

CHAPTER 125

Dynamic stability of rock slopes and gravel beaches

J.W. van der Meer* and K.W. Pilarczyk**

Abstract

More than 150 tests have been analyzed in order to describe the dynamically stable profiles of rock slopes and gravel beaches under wave attack. Relationships between profile parameters and boundary conditions have been established. These relationships have been used to develop a computer program. This program is able to predict the profiles of slopes with an arbitrary shape under varying wave conditions, such as those found in storm surges and during the tidal period.

Introduction

An extensive research program has been performed on the static and dynamic stability of rubble mound revetments, breakwaters and gravel beaches. The results of the first part of this program, which dealt with static stability, were presented at the 19th International Conference on Coastal Engineering (Van der Meer and Pilarczyk, 1984). New stability formulae were given mainly based on statically stable rubble mound revetments with an impermeable core. Rubble mound breakwaters with a permeable core were subsequently tested and results were presented at the Breakwaters '85 Conference, (Van der Meer, 1985). A complete analysis of this part of the research (the static stability) was given by Van der Meer (1986-1 and 1986-2). Based on more than 250 tests, two practical stability formulae were given which take into account the wave period, storm duration and permeability of the structure.

The second part of the research program, dealing with dynamically stable structures and profile development, forms the subject for the present paper. About 150 tests have been analyzed.

Dynamic stability

Most breakwaters and revetments are designed in such a way that only little damage is allowed for in the design criteria, damage being defined as the displacement of armour units. This criteria demands large and heavy rock or artificial concrete elements for armouring. A more economic solution can be a structure with smaller elements, profile development being allowed in order to reach a stable profile.

The $H_s/\Delta D_{n50}$ parameter can be used to give the relationship between different structures, see Figure 1, where: H_s = significant wave height, Δ = relative mass density and D_{n50} = nominal diameter of average stone mass.

* Delft Hydraulics, P.O. Box 152, 8300 AD Emmeloord, The Netherlands
** Road and Hydraulic Engineering Division, Rijkswaterstaat, P.O. Box 20904, 2500 EX The Hague, The Netherlands

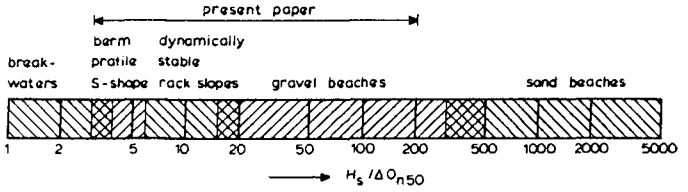

Figure 1 Type of structure as function of $H_s/\Delta D_{n50}$

Small values of $H_s/\Delta D_{n50}$ give structures with large armour units. Large values imply gravel beaches and sand beaches. Figure 1 gives the following rough classification:

- statically stable breakwaters: $H_s/\Delta D_{n50} = 1 - 4$
- berm breakwaters and S-shaped profiles: $H_s/\Delta D_{n50} = 3 - 6$
- dynamically stable rock slopes: $H_s/\Delta D_{n50} = 6 - 20$
- gravel beaches: $H_s/\Delta D_{n50} = 15 - 500$
- sand beaches: $H_s/\Delta D_{n50} > 300$

The area given by $H_s/\Delta D_{n50} = 3 - 200$ will be discussed in the paper.

Governing variables

The object of this paper is to show how the dynamic profile is influenced by the strength and load parameters. The governing strength parameter variables are:

stone size, grading of the stone, shape of the stone, initial slope and shape of the foreshore.

In the paper the size of armour units or gravel is referred to as the average mass of graded rubble or gravel, W_{50}, or the nominal diameter, D_{n50}, where:

$$D_{n50} = (W_{50}/\rho_a)^{1/3} \quad (1)$$

where: D_{n50} = nominal diameter (m)
W_{50} = 50% value of the mass distribution curve (kg)
ρ_a = mass density of stone (kg/m^3)

The relative mass density of the stone in water can be expressed by:

$$\Delta = \rho_a/\rho - 1 \quad (2)$$

where: Δ = relative mass density (-)
ρ = mass density of water (kg/m^3)

The grading of the stone is expressed here by D_{85}/D_{15}, where the subscripts refer to the 85 and 15 percent value of the sieve curve, respectively. The shape of the stone can be angular, rounded or flat. The initial profile can vary from a uniform slope to a berm profile or a structure with a low crest.

The governing load parameter variables are:
significant wave height H_s, average wave period T_z, storm duration given by the number of waves, N, and water level (tide).

Test equipment, materials and procedure

Tests were conducted at Delft Hydraulics in a small scale 1.0 m wide, 1.2 m deep and 50 m long wave flume and in the large Delta flume which is 5.0 m wide, 7.0 m deep and 230 m long. Random wave generators were used equipped with a system for measuring and compensating for waves reflected at the wave board. With this system standing waves and basin resonance were avoided. A surface profiler on a computer controlled carriage was developed for the investigation. This profiler is described in more detail by Van der Meer and Pilarczyk (1984).

Broken stone or gravel was used for the tests. The nominal diameter ranged from 4 mm upto 27 mm and the wave height from 0.13 m up to 1.7 m. Each complete test consisted of a pre-test sounding of the slope, a test of 1000 waves, an intermediate sounding, a test of 2000 more waves and a final sounding.

Test programme

The present research on dynamic stability can be divided into three parts:

- The research of Van Hijum and Pilarczyk (1982) on gravel beaches for which $H_s/\Delta D_{n50}$ was in the range 15 - 30, see Figure 1. The results of this research have been included in the present analysis. The research included also three-dimensional tests, resulting in derivation of a longshore transport formula for gravel.
- $H_s/\Delta D_{n50} \approx 3 - 15$. This range was investigated in the small scale flume. The influence of all the governing parameters mentioned above were investigated in this range.
- $H_s/\Delta D_{n50} \approx 30 - 200$. This range can only be investigated on a large scale since small scale investigations would give unacceptable diameters in the order of 1 mm and smaller, for which the fall velocity of the material becomes more important than the diameter. This range was tested in the Delta flume, by using 19 mm and 4 mm gravel and a wave attack with $H_s = 0.5 - 1.7$ m.

The research of Van Hijum and Pilarczyk (1982) resulted in 43 tests. About 120 dynamically stable tests were conducted in the small scale flume. Nine tests were performed in the Delta flume on dynamic stability.

Results

Each test resulted in two measured profiles in addition to the initial profile, one after a wave attack of 1000 waves and one after 3000 waves. A first analysis was done by comparing profiles for various tests. The conclusions from this analysis were used to develop a model for the dynamic profile. Relationships were subsequently derived to describe this model as a function of the boundary conditions.

Figure 2 shows the profiles measured for three tests. The initial slope was a 1:5 uniform slope, the wave period was $T_z = 1.75$ s and the diameter was $D_{n50} = 0.011$ m for all tests. The significant wave heights were $H_s = 0.129$, 0.188 and 0.237 m respectively; the lowest wave height in fact produced the smallest changes in slope. From Figure 2 it can be concluded that the wave height has a large influence on the profile.

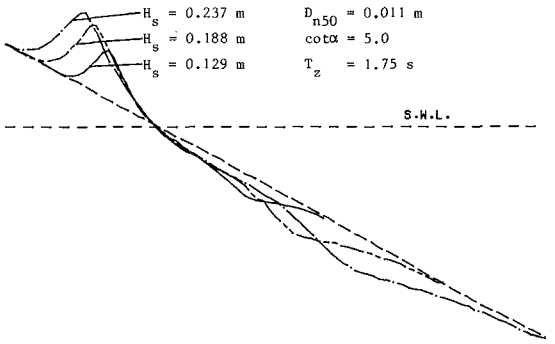

Figure 2 Influence of wave height

Figure 3 shows the influence of the wave period; the initial slope was again a 1:5 uniform slope and the nominal diameter was D_{n50} = 0.011 m. The significant wave height for all three tests was H_s = 0.13 m. The wave periods were T_z = 1.32, 1.77 and 2.52 s; the shortest period in fact produced the smallest changes in slope. A similar conclusion can be drawn as for the wave height namely that the wave period has a large influence on the profile. From Figures 2 and 3 can be seen that the wave height and wave period have the same order of influence on the slope.

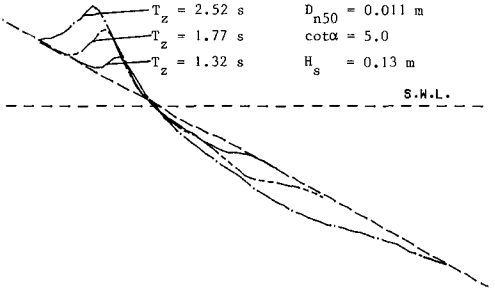

Figure 3 Influence of wave period

By analysis it was shown that the storm duration (the number of waves N) and the diameter (D_{n50}) also had a large influence on the dynamic profile. For small diameters, however, it was concluded that some parts of the profile, for example the crest height, were not influenced by the diameter.

In most tests the initial slope was a 1:3 or 1:5 uniform slope. In other tests a berm breakwater was tested with a 1:3 upper slope, a horizontal berm above, at, or below the still water level, and a 1:1.5 slope for the lower part. Low crested structures were also tested. Figure 4 shows a comparison of two tests with the same boundary conditions, but with different initial slopes. The initial slopes were a 1:3 uniform

slope and a berm breakwater with the berm at the still water level. The wave height was H_s = 0.19 m, the period T_z = 2.5 s and the nominal diameter was D_{n50} = 0.0257 m. The figures are compared by plotting the profiles at the same intersection with the still water level.

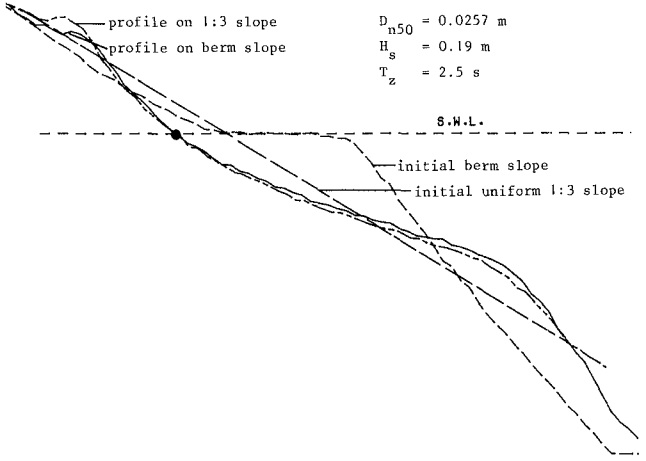

Figure 4 Influence of the shape of the initial slope

The conclusion is clear. In spite of the different initial slopes, the same profile is reached for a large part of the total profile. This part ranges from the crest to the transition to a steep slope (the step) at the deep water end of the profile. Figure 5 gives the same profiles for a 1:5, a 1:3 and a 1:1.5 uniform initial slope. Only the upper and lower parts of the profile are in fact dependent on the initial slope. The direction of transport of material and the position of the profiles is, of course, largely influenced by the initial slope.

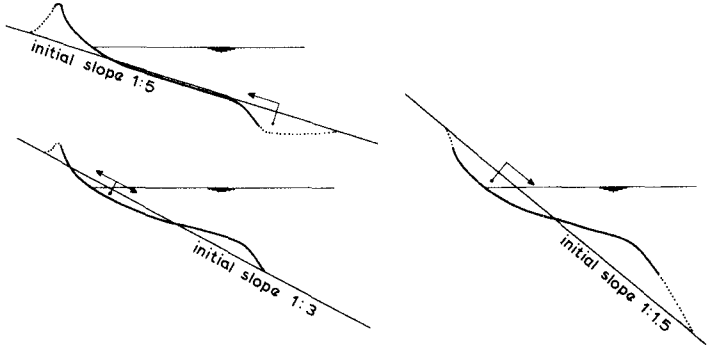

Figure 5 Profile obtained with different initial slopes

The same conclusion can be drawn from the results of the tests in which the influence of tide was investigated. Figure 6 gives the results

of one of these tests. Three profiles were measured during the test, two at high water and one at low. The wave height (H_s = 0.128 m) and period (T_z = 1.73 s) were constant during the test. The final profile in Figure 6, the second high water, is almost the same as the first, the first high water profile. In fact, the profile changed directly with changing water level.

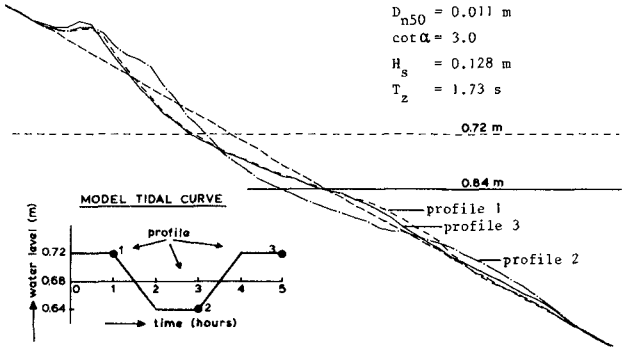

Figure 6 Influence of tide

Static stability is largely dependent on the initial slope, as is clearly expressed by the well known Hudson formula. Of course, for dynamically stable structures which are almost statically stable, the initial slope has also influence on the profile. It can be stated that, for $H_s/\Delta D_{n50} < 10 - 15$ the initial slope has influence on the profile.

From the analysis it could be concluded that the wave spectrum shape had no or only minor influence on the profile, provided that the average wave period was used to compare the tests, and not the peak period. The same conclusion was found for static stability by Van der Meer and Pilarczyk (1984). The grading of the material also has no or only minor influence on the profile, using the nominal diameter, D_{n50}, as a reference.

Summarizing, from the comparison of profiles it was concluded that wave height H_s, wave period T_z, number of waves, N, and nominal diameter D_{n50}, all have influence on the dynamic profile.

The spectrum shape and the grading of the material have no or only minor influence; the initial slope has no influence on a large part of the profile for $H_s/\Delta D_{n50} > 10 - 15$.

Development of a model of a dynamic profile.

On the basis of the conclusions described above a model was developed to describe the dynamic profile. Two points on the profile are very

important. These are shown in Figures 7 and 8, where profiles for a 1:3 and 1:2 uniform slope are illustrated schematically. The first point is the upper point of the beach crest and the second point the transition below SWL from the gentle part to a steeper part. The local origin is chosen at the intersection of the profile and the still water level.

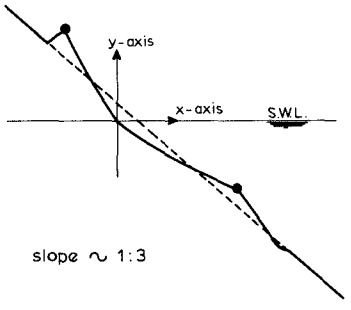

Figure 7 Schematized 1:3 profile

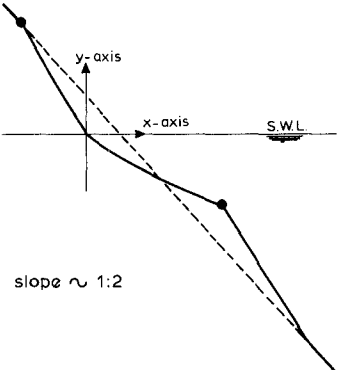

Figure 8 Schematized 1:2 profile

Figure 9 shows the model for a dynamic profile. A 1:5 uniform initial slope is shown with a high beach crest and a step. The profile is schematized by using a number of parameters all of which are related to the local origin or to the water level. The beach crest is described by the height, hc, and the length, lc. The transition to the step is described by the height, hs, and the length, ls. Curves, described by power functions, start at the local origin and go through these two points. The run-up length is described by the length, lr. The step is described by two angles, β and γ. Finally, the transition from β to γ is described by the transition height, ht.

The final analysis must result in relationships which describe the above profile parameters as a function of the boundary conditions. The height and length parameters lr, hc, lc, hs, ls and ht can be related to the nominal diameter, D_{n50}, or to the wave height, H_s, in order to get dimensionless parameters.

Development of relationships

First the influence of the storm duration was analyzed. Long duration tests (up to 25,000 waves) and the ratio of the parameters after 1000 and 3000 waves were used. The influence of the storm duration can be described by:

$$par = aN^b \tag{3}$$

where: par = lr, hc, lc, hs, ls or ht
a and b are curve-fitting coefficients.

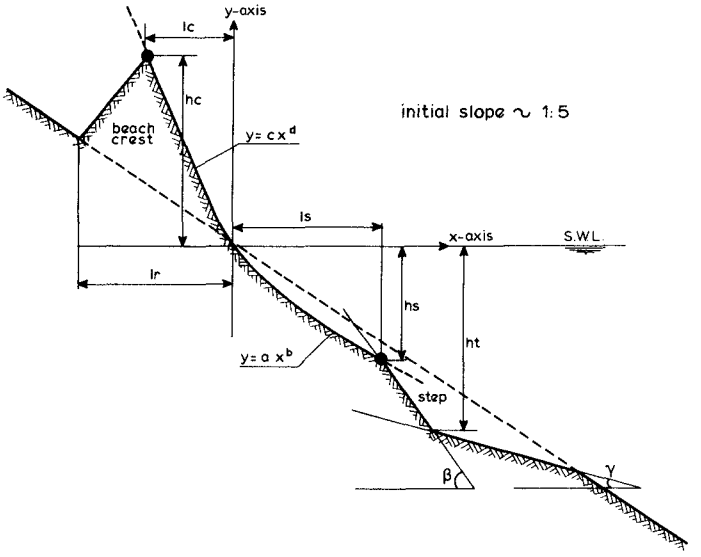

Figure 9 Model for dynamic profile

The coefficient b was established for each parameter. A dimensionless parameter, including the storm duration, can be expressed by:

$$par/D_{n50}N^{b} \quad \text{or} \quad par/H_{s}N^{b}$$

For the height and length parameters this resulted in:

- run-up length : $lr/D_{n50}N^{0.05}$ or $lr/H_{s}N^{0.05}$
- crest height : $hc/D_{n50}N^{0.15}$ or $hc/H_{s}N^{0.15}$
- crest length : $lc/D_{n50}N^{0.12}$ or $lc/H_{s}N^{0.12}$
- step height : $hs/D_{n50}N^{0.07}$ or $hs/H_{s}N^{0.07}$
- step length : $ls/D_{n50}N^{0.07}$ or $ls/H_{s}N^{0.07}$
- transition height: $ht/D_{n50}N^{0.04}$ or $ht/H_{s}N^{0.04}$

The parameter which is most influenced by the storm duration is the crest height hc, where the power coefficient amounts to 0.15. The remaining governing variables are the wave height and wave period. If the height and length parameters are related to the wave height, the remaining variable is only the wave period. This wave period can be described in a dimensionless form by using the wave steepness H_s/L_z, where $L_z = gT_z^2/2\pi$. By doing this the influence of the diameter has been ignored. As already concluded, this might be the case for high $H_s/\Delta D_{n50}$ values (above 15 - 30). One has then to determine the following relationship:

$$par/H_{s}N^{b} = f\ (H_s/L_z) \qquad (4)$$

If the diameter influences the height or length parameter it is reasonable to relate these height and length parameters and also the wave height and period to the nominal diameter. The wave height can be described by the $H_s/\Delta D_{n50}$ or the N_s-number which has also been used for static stability analysis, Van der Meer (1984). The wave period can be related to the nominal diameter by the following expression:

$$\text{dimenionless wave period} = \sqrt{g/D_{n50}}\ T_z \tag{5}$$

From the analysis of the profiles it was concluded that wave height and period had similar effect on the profile. This conclusion results in a combined parameter, HoTo, for the wave height and wave period.

$$\text{HoTo} = H_s/\Delta D_{n50} * \sqrt{g/D_{n50}}\ T_z \tag{6}$$

Using this parameter, HoTo, the following relationship should be established for each length or height parameter:

$$\text{par}/D_{n50}\ N^b = f(\text{HoTo}) \tag{7}$$

Equations (4) and (7) are the basis for the description of the profile parameters. Figure 10 shows Equation (4) for the crest height, hc, for several HoTo values > 1000. Since all the HoTo values lie on the one curve, irrespective of their individual values, this implies that different diameters fit the same relationship which in turn means that indeed the crest height is not influenced by the diameter for these particular HoTo values.

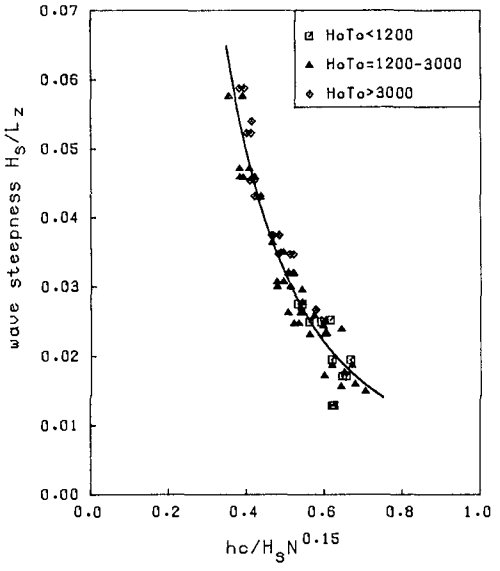

Figure 10 Relationship between crest height, hc, and wave steepness, H_s/L_z

Figure 11 shows the results for the crest length, lc, as a function of the wave steepness. Here different diameters show a different relationship. It is clear that, for this length parameter, the influence of the diameter cannot be ignored, even not for very small grain sizes.

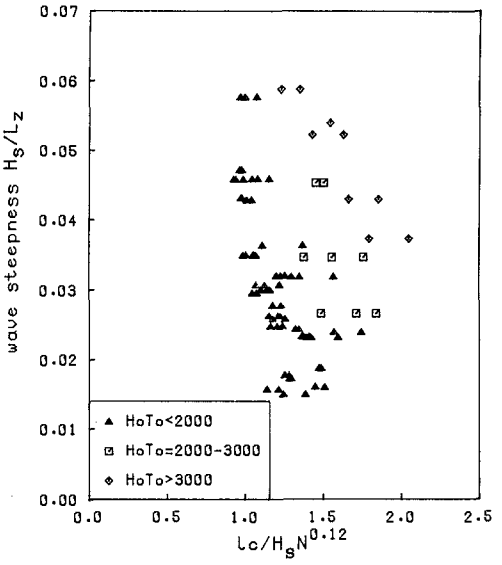

Figure 11 Relationship between crest length, lc, and wave steepness, H_s/L_z

Figure 12 shows again the crest length, lc, but in this case for the complete area for dynamic and static stability; this is achieved by using a logarithmic scale. For HoTo values smaller than 100 the slopes are stable as required in the traditional breakwater design. For HoTo values higher than 100,000 the transition area to sand beaches is entered. The highest point in the figure was found using 4 mm gravel with a wave height of about 2 m. On the horizontal axis the crest length, lc, is now related to the grain diameter instead of the wave height. Figure 12 shows also that for the transition to static stability, the lower part of the figure, the initial slope becomes important. The curves show a small difference between a 1:3 and 1:5 uniform slope.

Figures of the type shown in Figures 10 to 12 where plotted for each parameter. For all height parameters (hc, hs and ht) a relationship such as Equation (4) was established for high HoTo (HoTo > 1000-2000) values:

- crest height : $hc/H_sN^{0.15} = 0.89\ (H_s/L_z)^{-0.5}$ see Figure 10 (8)
- step height : $hs/H_sN^{0.07} = 0.22\ (H_s/L_z)^{-0.3}$ (9)
- transition height: $ht/H_sN^{0.04} = 0.73\ (H_s/L_z)^{-0.2}$ (10)

For the length parameters (lr, lc and ls), relationships for high HoTo values were established according to Equation (7):

- run-up length: $HoTo = 2.9\ (lr/D_{n50}N^{0.05})^{1.3}$ (11)

- crest length : $HoTo = 21\ (lc/D_{n50}N^{0.12})^{1.2}$ see Figure 12 (12)

- step length : $HoTo = 3.8\ (ls/D_{n50}N^{0.07})^{1.3} + 180$ (13)

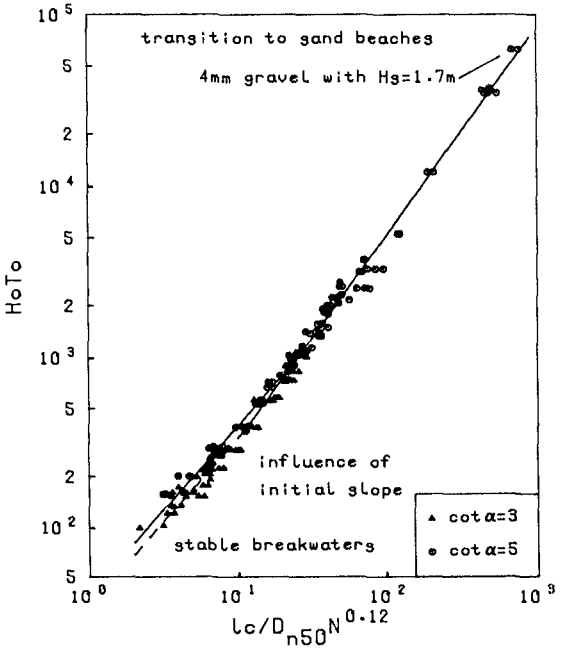

Figure 12 Relationship between crest length, lc, and HoTo

For lower HoTo values (HoTo < 1000 - 2000) an equivalent slope angle was introduced into the equations. To summarize two relationships were established for each length or height parameter, describing the influence in the lower and higher HoTo area. Relationships for the angles β and γ were also established.

Curves described by power functions start at the local origin, and go through the points described by hc and lc and by hs and ls, repectively, see Figure 9. From regression analysis it follows that the curves can be described by:

$y = a\ x^{0.83}$ below SWL, and (14)

$y = a\ (-x)^{1.15}$ above SWL (15)

where the coefficients a are determined by hc, lc and hs and ls.

Verification of the model

All the relationships for the height and length parameters, the power curves, the two angles β and γ and the method used to establish the equivalent slope angles for lower HoTo values were used to develop a computer program. This program can be used to calculate the profile, starting from an arbitrary slope and with varying water levels (tide) and wave conditions.

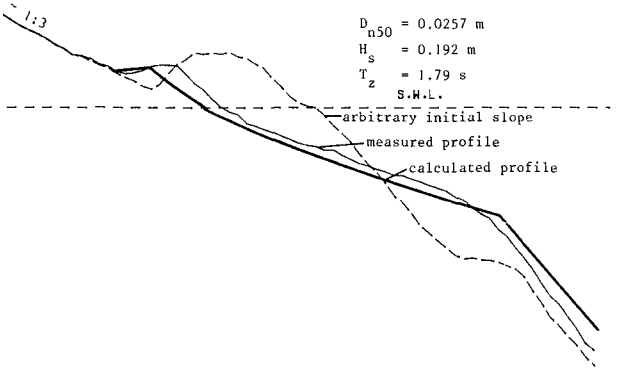

Figure 13 Measured and calculated profile developed from an arbitrary initial slope

In one test the man who constructed all the models was asked to build an arbitrary slope in the way he preferred. Figure 13 shows the slope he constructed and the measured and computed profile. The initial slope had an upper slope of 1 in 3 and a lower slope, with some irregularities, varying between 1 in 1.5 and 1 in 2. Figure 14 shows the calculation procedure and the results of the computer model. First the profile is calculated with the local origin at the intersection of the initial profile with the still water level. It is clear that this is not the right position of the profile, but it shows that the model parameters are independent of the initial slope and that the profile can be drawn anywhere. By means of an iteration process the profile was moved along the still water level untill the mass balance was fulfilled. The profile in the middle of Figure 14 was obtained after the fifth iteration and the profile on the left shows the final position.

Figure 13 shows the comparison between calculation and measurement. Some differences exist, but it can be concluded that the agreement is reasonable.

Figure 15 shows the calculation of the profiles for the same boundary conditions as those described for Figure 6, where the influence of tide was investigated. Here again the calculated profile at the end of the tide, Profile 3, is very similar to that for the first profile, Profile 1. The agreement between measurement (Figure 6) and calculation (Figure 15) is very good.

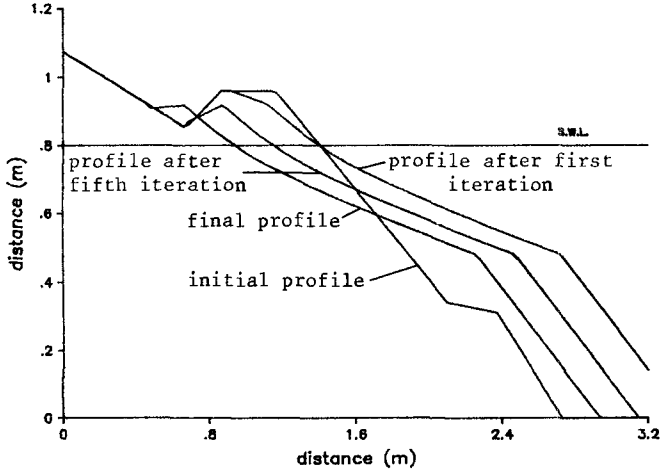

Figure 14 Calculation of dynamic profile

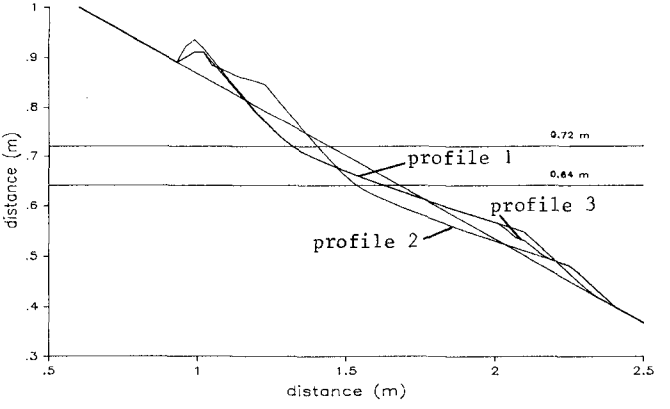

Figure 15 Verification of test shown in Figure 6 (tide)

Applications

The model can be used to describe the behaviour of rock and gravel beaches, including the influence of storm surges and tides. It can also be used to predict the stable profile for a berm type breakwater. The length of the gentle part of a berm type breakwater can be estimated and also the position of this part below the still water level. Another application is the prediction of the behaviour of core and filter layers under construction when a storm hits the incomplete part of a breakwater.

Special attention should be payed to structure with small diameters. The limitation of applicationis determined by the longshore transport under oblique wave attack. Van Hijum and Pilarczyk (1982) have derived a longshore transport formula for gravel. This formula was also described by Pilarczyk and Den Boer (1983).

Conclusions

More than 150 tests have been analysed to develop a computer model which is able to describe dynamically stable profiles. Initially conclusions were drawn by comparing profiles. These conclusions were then used to schematize the profile. The parameters for the schematized profile were then related to the boundary conditions. These relationships were used to develop a computer model and this model was verified using the test results.

References

1. PILARCZYK, K.W., and DEN BOER, K. Stability and profile development of coarse material and their application in coastal Engineering in Developing Countries, Sri Lanka, March, 1983.

2. VAN DER MEER, J.W., PILARCZYK K.W. Stability of rubble mound slopes under random wave attack. 19th International Conference on Coastal Engineering,
September 1984, Houston.

3. VAN DER MEER, J.W., Stability of rubble mound revetments and breakwaters under random wave attack, Breakwaters '85 Conference, October 1985, London.

4. VAN DER MEER, J.W., Stability of breakwater armour layers - design formulae. Submitted for publication to the Journal of Coastal Engineering, June 1986-1, Amsterdam.

5. VAN DER MEER, J.W., Deterministic and probabilistic design of breakwater armour layers. Submitted for publication to the Journal of ASCE, November 1986-2, New York.

6. VAN HYUM, E., PILARCZYK, K.W. Gravel beaches, equilibrium profile and longshore transport of coarse material under regular and irregular wave attack, Delft Hydraulics Laboratory, Publication No. 274, July 1982.

Taichung Harbor, Taiwan, ROC—R.L. Wiegel

PART III

COASTAL STRUCTURES AND RELATED PROBLEMS

Differential movement due to earthquake which occurred during 20th ICCE, Hualien, Taiwan, ROC—R.L. Wiegel

CHAPTER 126

Wave Transmission across Submerged Near-Surface Breakwaters

Clark B. Adams[1] and Choule J. Sonu, Ph.D.,[2] Members, ASCE

Abstract: Wave transmission across a submerged breakwater at Santa Monica, California, is examined through a three-dimensional model test. The results agree with empirical criteria previously proposed by Tanaka (1976).

Introduction

In 1983, El Niño came to California. By the time it left, over 20 piers and breakwaters had been damaged, countless beaches had lost sand, and new records for high tide levels had been set. At Santa Monica, the municipal pier was severely damaged. The seaward 120 meters of the pier were completely destroyed as were 110 meters of the adjoining Newcomb Pier. This occurred despite the fact that a submerged breakwater partially protects the pier from offshore swell.

The submerged breakwater was to figure prominently in repair alternatives considered by the City as they sought a plan most responsive to their needs. A major issue was whether to rebuild the breakwater and utilize its protective ability in developing the pier repair plans or to concentrate the reconstruction effort in strengthening the pier and avoid expending resources on the breakwater. To aid in making this decision, the City's consultant, Daniel, Mann, Johnson, & Mendenhall (DMJM), commissioned a three-dimensional model study of the site to investigate the effect that various breakwater configurations had on the alternative pier designs.

This paper compares the data on wave transmission across the submerged breakwater at Santa Monica obtained from the model study to results of wave transmission studies presented by Tanaka (1976). The Santa Monica data tend to corroborate Tanaka's results, suggesting their use in design application.

Setting

Santa Monica is part of the Los Angeles metropolitan area. Figure 1 shows the location of the site. The breakwater and pier are at the head of Santa Monica Bay, a broad open body of water bounded by the Santa Monica Mountains to the north and the Palos Verdes Peninsula to the

[1]Civil Engineer, Daniel, Mann, Johnson, & Mendenhall, 3250 Wilshire Boulevard, Los Angeles, CA 90010, USA.

[2]President, Tekmarine, Inc., 37 Auburn Avenue, Sierra Madre, CA 91024, USA.

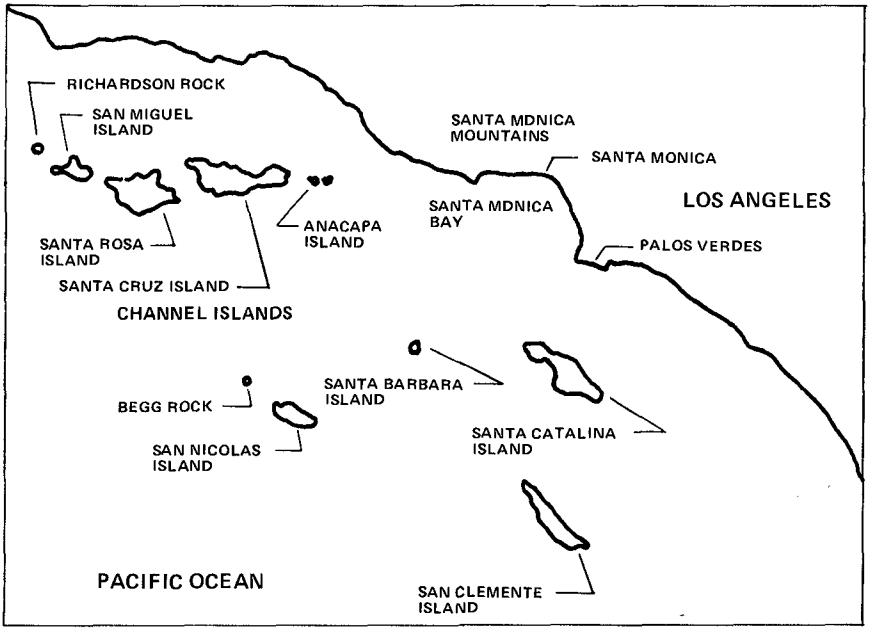

Figure 1. Site Location

south. The site is partially protected from offshore swell by Santa Catalina Island, Santa Barbara Island, San Nicolas Island, the Channel Islands, and Point Conception.

The Santa Monica shoreline is a broad sandy beach at the base of a 9 to 12 meter high bluff. Littoral transport is generally toward the south. Man-made structures such as the Santa Monica breakwater, the Marina del Rey jetties, and the Redondo Harbor breakwater interrupt this flow of sand at several points along the bay until the Redondo submarine canyon finally traps most of the remaining littoral drift at the southerly end of the bay and diverts it offshore.

History

A review of the history surrounding the Santa Monica breakwater will help in understanding several unusual aspects of its configuration. Man-made structures began to be constructed on Santa Monica Beach as early as the 1870s. The first structure on record was a small pier located near the site of the present pier. By 1876, a railroad pier supported by a substantial number of pilings had been built. In 1908, the first municipal pier was built; it failed 12 years later. The present municipal pier was built in 1921.

The Santa Monica breakwater was constructed in 1933 and 1934 by the City to provide a pleasure boat anchorage. The breakwater was

constructed parallel to the shoreline about 610 meters long and was located about 610 meters offshore. Figure 2 illustrates the breakwater configuration as it was constructed. The top elevation was 3 meters

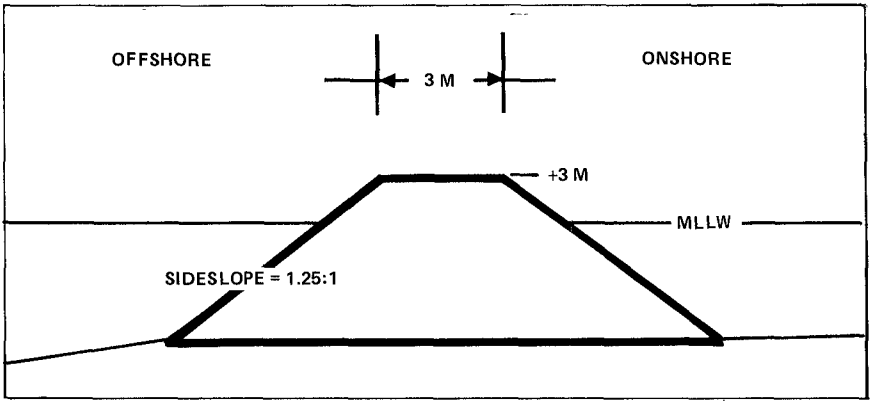

Figure 2. Original Santa Monica Breakwater Configuration

above mean lower low water (MLLW) and had a crest width of 3 meters. It had fairly steep sideslopes of 1.25 horizontal to 1 vertical. A rapid siltation of the anchorage followed the breakwater construction, and the beach behind the breakwater began advancing seaward. By 1937, as many as 245 anchorages had been lost to siltation. At the same time, the breakwater began deteriorating, and there are accounts of wave damage creating a gap in the breakwater as early as August 1934.

Based on survey data of a typical cross-section 30 meters from the northern end contained in the damage survey report of the Federal Emergency Management Agency dated July 21, 1983, the breakwater lost approximately 0.3 meter of its crest height after the first year of construction, another one meter by 1956, and an additional 0.2 meter by 1972. A survey of this breakwater after the 1983 storms showed the crest elevation of this section had lowered another 3 meters since 1972, although it is difficult to determine if the reduction was due to the storm or if it occurred gradually throughout the 11-year period. Figure 3 shows the site in 1975 and 1983 and illustrates the relative position between the pier and the breakwater. The shoreline bulge in the lee of the breakwater seen on the 1975 picture has retreated by 1983, possibly as a result of the deterioration of the breakwater. Figure 3 also illustrates the damage to the pier caused by the 1983 storms.

The 1983 configuration is illustrated in Figure 4. The crest height is -1.6 meters MLLW and the crest width at that level is 13.4 meters. Material from what was the upper portion of the breakwater has fallen down, creating a more stable sideslope of 2 horizontal to 1 vertical.

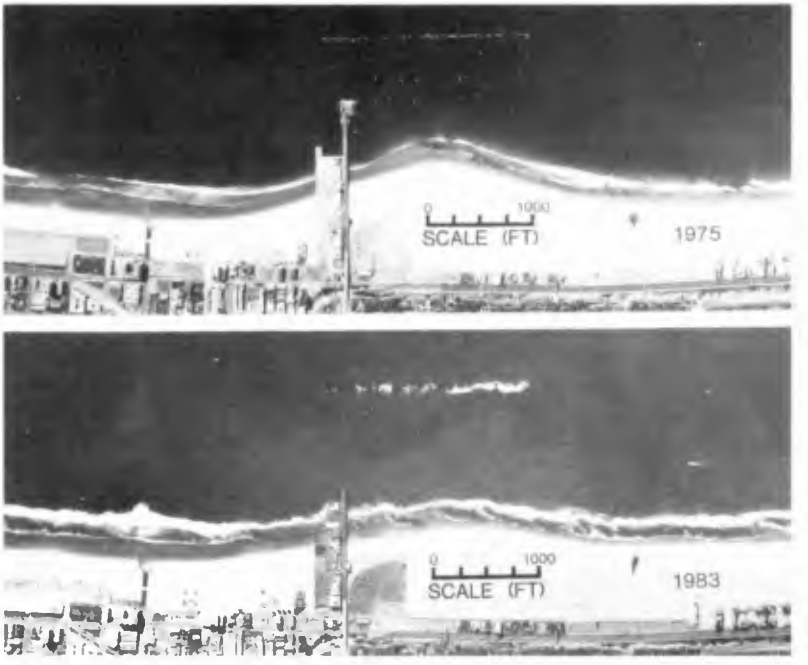

Figure 3. Comparison of Shorelines for 1975 and 1983

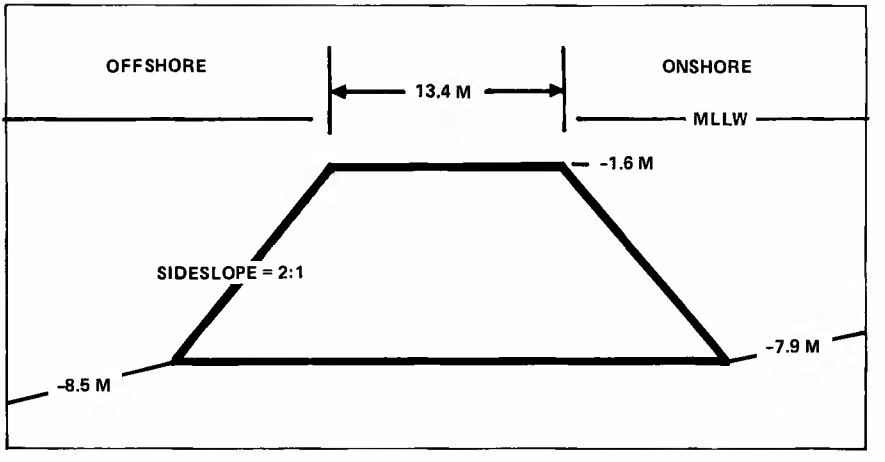

Figure 4. 1983 Breakwater Configuration

This was the condition of the breakwater when DMJM began its analysis. The breakwater was essentially submerged, especially at high tide, although the crest elevation was nonuniform in height and projected above the water surface in several locations. These complications played a role in the decision to utilize a model study in analyzing the wave action on the pier.

Model Study

The three-dimensional hydraulic model study was conducted by the Offshore Technology Corporation to determine the protection provided to the pier by various breakwater configurations. The results of the existing submerged configuration are analyzed in this paper. The model scale was 1 to 50. It covered an area of 37 meters by 24 meters, which represents 1,850 meters by 1,200 meters in prototype. Five breakwater configurations were modeled using rocks approximately scaled from the size specified in the prototype. Waves were directed at the site from three different directions, three different tide levels were studied, and six different significant wave heights were used.

The model bathymetry was constructed to model bathymetric survey data obtained in December 1983. Gravel was used to build up the model floor, and the final 0.025 meter finish layer was made of mortar. The prototype breakwater had a quarry run core, an underlayer of 900 kilogram (1 ton) stone, and an armor layer of 7,800 kilogram (8.6 ton) stone arranged in one and two layers. The model used a pea gravel core, 7 gram concrete aggregate for the underlayer, and 80 gram concrete aggregate for the armor layer. The stone size was modeled correctly, although the model armor was heavier than necessary to model the prototype rock. This was considered acceptable because the tests were conducted primarily to determine wave patterns and wave heights at the pier rather than armor unit stability.

The submerged breakwater had (prototype) crest elevations ranging from -1.8 meters MLLW to +1.8 meters MLLW and crest widths ranging from 11 meters to 24 meters. Waves were directed at the breakwater at an angle 13 degrees north of normal (235° azimuth). Water levels of 3.0 meters and 2.6 meters (prototype) above mean lower water were used in conjunction with tests of significant wave heights of 3.4, 3.9, 3.0, 1.9, 4.1, 3.2, and 1.9 meters. The waves were generated with periods having a frequency distribution matching the spectrum recorded on offshore wave recorders during the storm that damaged the pier.

Wave heights in the model were measured using capacitance-type wave gauges. Wave gauge locations were concentrated in the vicinity of the pier, although a wave gauge immediately behind and another in front of the breakwater are of particular interest in this paper.

Previous Studies

Researchers have conducted investigations of wave transmission across permeable structures for over 30 years. Some of the earliest work may have been studies of wave filters used in front of laboratory wave

generators. Saville (1963) examined a number of structures with crest elevations near the still water level for a proposed breakwater at Point Loma, California. Goda (1969) tested impermeable breakwaters for transmission by overtopping and developed an expirical equation to predict transmission coefficients which was found to be a function of the breakwater freeboard. Cross and Sollitt (1971) presented a semiempirical treatment for overtopping of subaerial breakwaters in which transmission coefficients depend on the breakwater freeboard to wave runup ratio. Keulegan (1973) studied vertical faced permeable breakwaters. Sollitt and Cross (1976) developed an analytical-empirical model for transmission through permeable breakwaters. Madsen and White (1976) presented a model of wave transmission and reflection for subaerial rubble-mound breakwaters. Seelig (1980) combined the model for transmission through permeable breakwaters of Madsen and White (1976) with prior work on transmission by overtopping.

Tanaka (1976) found the wave transmission coefficient related to the relative submergence depth and the relative crest width. His work is unique in that it deals with a continuous spectrum of breakwater crests, including both negative and positive clearance, while at the same time considering a broad range of crest widths. The continuous spectrum of crest heights was particularly useful for our purpose because, depending on the restoration scenario, the breakwater might function alternatively as a partially submerged or partially emerged structure at different phases of the tide. The broad range of crest widths was likewise

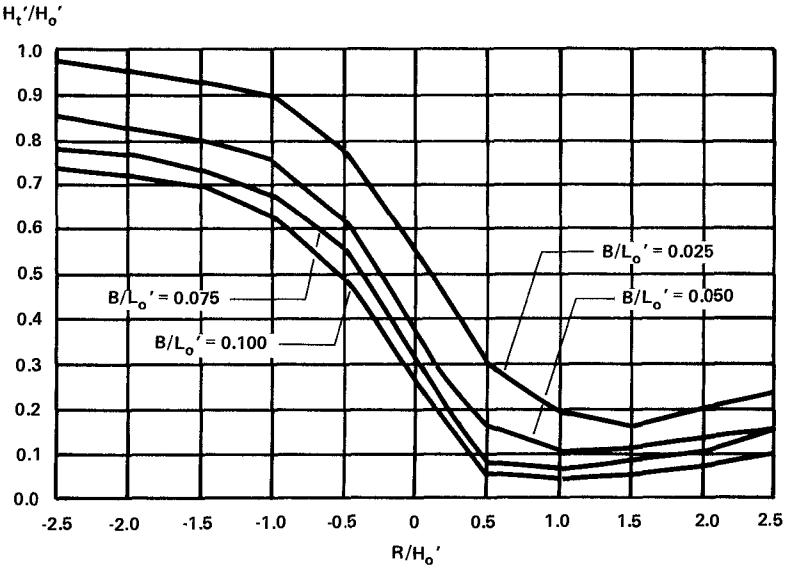

Figure 5. Results of Tanaka Study

appealing because the scenario included both the existing deteriorated broad-crested breakwater and rebuilt highly emerged narrow-crested configurations. The crest width to wave length ratio ranged from 0.025 to 0.8.

As shown in Figure 5, Tanaka's criteria give the transmission coefficients H_t/Ho' as a function of B/Lo and R/Ho', that is, as a function of crest width clearance, wave period, and wave height where B is the crest width, Lo is the deepwater wave length, R is the crest clearance, Ho' is the equivalent deepwater unreflected wave height, and H_t is the transmitted wave height. Tanaka found that for values of R/Ho' less than about -1.0, the breakwater produced little reduction in wave height and the transmission coefficient was not highly dependent on R/Ho'. For values of R/Ho' between -1.0 and +1.0, changes in R/Ho' produce large changes in transmission coefficient. For values of R/Ho' greater than +1.0, the breakwater was effective in reducing the wave height but the transmission coefficient was not highly dependent on R/Ho' and wave reflection was significant.

Comparison of Data

The general approach used in this paper is to compare the results from the Santa Monica model study to the results presented by Tanaka to see if his criteria predict the Santa Monica results. Figure 6 shows the Santa Monica results and the values that were obtained by applying Tanaka's criteria superimposed on the graph shown in Figure 5.

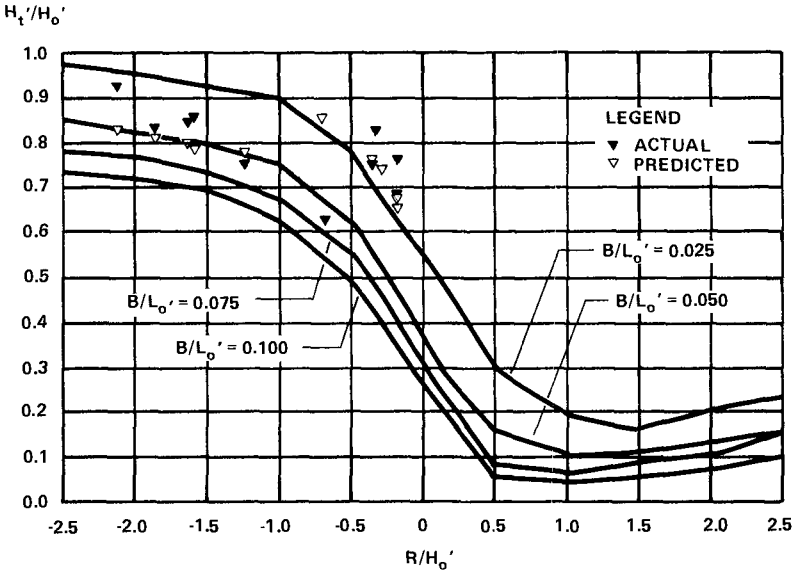

Figure 6. Santa Monica Data Comparison

Because Tanaka's criteria are based on monochromatic waves, our wave data were reduced to comparable parameters. Wave data in the Santa Monica tests were processed by the zero downcrossing method to obtain a frequency spectrum at each gauge. After several trials, it became apparent that parameters consisting of a significant wave height defined by

$$H_s = 4.0\ (m_o)^{1/2}$$

$$\text{where } m_n = \int_0^\infty f^n S(f)\,df$$

$$S(f) = (1/2)\ a^2(f)$$

$$a = \text{amplitude}$$

$$f = \text{circular frequency}$$

and a peak period provided the best agreement with Tanaka's results.

It is interesting to note that with a crest elevation of 1.5 meters below MLLW, the breakwater offers little attenuation for waves under 4.6 meters in height.

Figure 7 shows the predicted values of the transmission coefficient plotted against the values of the transmission coefficient measured in the Santa Monica model study. The figure shows the degree to which

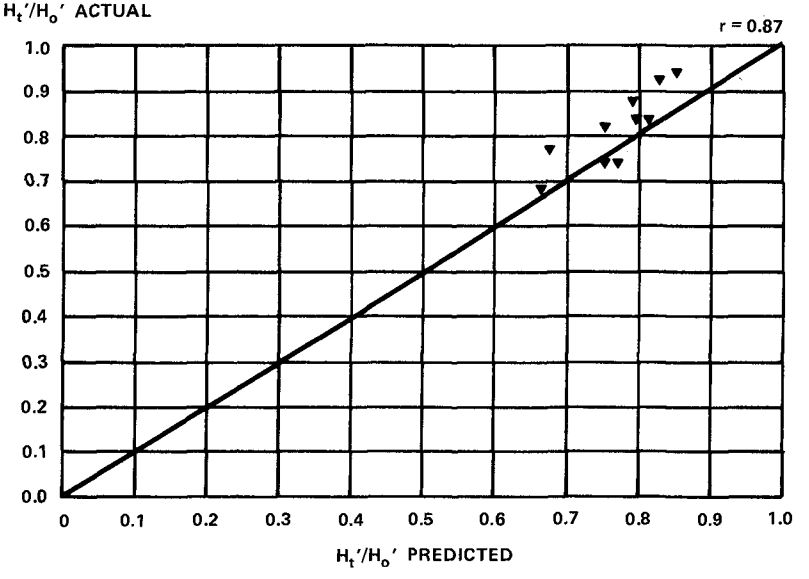

Figure 7. Actual vs Predicted Transmission Coefficients

Tanaka's criteria predict actual results. A perfect correlation would occur if all the data points fell on the diagonal line. Here we found r, the Pearson Product Moment Correlation Coefficient, to be equal to +0.87, essentially corroborating the criteria by Tanaka.

The figure indicates that the predicted transmission coefficients underestimate the actual results observed in the model test. This is demonstrated by the fact that most of the plotted points fall above the 45° diagonal line rather than being distributed evenly on either side. An interesting future study would be to determine if diffraction around the end of the breakwater in the Santa Monica model was the cause of this result.

Conclusions

Our conclusions are that the Santa Monica model data agree with the trend of Tanaka's findings. The correlation coefficient, a measure of this agreement, is +0.87. This conclusion lends credence to the use of Tanaka's curves as design tools when investigating submerged breakwaters. Tanaka's curves underpredict the transmission coefficients found in the Santa Monica model tests, so some care must be used in applying the curves. We also determined that except for very large waves, the existing breakwater at Santa Monica is not effective in attenuating wave height.

ACKNOWLEDGMENTS

The authors would like to acknowledge the City of Santa Monica for its support in making this study possible and the Offshore Technology Corporation for its role in conducting the model study.

APPENDIX I, REFERENCES

Cross, R., and C. Sollitt, "Wave Transmission by Overtopping," Technical Note No. 15, Ralph M. Parsons Laboratory, Massachusetts Instititute of Technology, July 1971.

Federal Emergency Management Agency, Damage Survey Report No. 101070, July 21, 1983.

Goda, Y., "Reanalysis of Laboratory Data on Wave Transmission Over Breakwaters," Report of the Port and Harbor Research Institute, vol. 18, no. 3, September 1969.

Keulegan, G. H., "Wave Transmission through Rock Structures," Research Report No. H-73-1, U.S. Army Engineers Waterways Experiment Station, Vicksburg, Miss., 1973.

Madsen, O. S., and S. M. White, "Reflection and Transmission Characteristics of Porous Rubble Mound Breakwaters," MR 76-5, U.S. Army Corps of Engineers, Coastal Engineering Research Center, 1976.

Saville, J., Jr., "Laboratory Data on Wave Runup and Overtopping on Shore Structures," TM-64, U.S. Army Corps of Engineers, Beach Erosion Board, 1959.

Seelig, W. N., "Two-dimensional Tests of Wave Transmission and Reflection Characteristics of Laboratory Breakwaters," Technical Report No. TR 80-1, U.S. Army Corps of Engineers, Coastal Engineering Research Center, 1980.

Sollitt, C. K., and R. H. Cross, "Wave Reflection and Transmission at Permeable Breakwaters," TP 76-8, U.S. Army Corps of Engineers, Coastal Engineering Research Center, 1976.

Tanaka, N., "Effects of Submerged Rubble-Mound Breakwater on Wave Attenuation and Shoreline Stabilization," Proceedings of 23rd Japanese Coastal Engineering Conference, 1976, pp. 152-157.

CHAPTER 127

A PROCEDURE FOR THE ANALYSIS AND DESIGN OF CONCRETE ARMOR UNITS

W.F. BAIRD*, J.S. READSHAW*, R.D. SCOTT* AND D.J. TURCKE**

ABSTRACT

A rational approach to the design of rubble mound breakwaters that incorporates both the hydraulic stability and the structural integrity of individual concrete armor units is presented. A key element of this improved design procedure is the development of instrumentation to measure loads occurring on armor units in a physical model of a breakwater. Numerical methods have been employed to determine stresses throughout the armor unit once the loads are known and interaction design curves were developed from measured data. These interaction curves provide a useful assessment of the structural integrity of the armor units. The curves clearly demonstrate the overall factor of safety associated with the armor unit and the expected mode of failure. Based on the results of this type of analysis, the cost effectiveness and safety associated with different design alternatives may be explored and a breakwater that is both hydraulically and structurally efficient may be designed.

INTRODUCTION

The use of concrete armor units has become increasingly widespread, especially as rubble mound breakwaters have been constructed at locations where quarried rock of sufficient size was not available. In recent years, however, the armor layers of many breakwaters throughout the world have been severely damaged. This damage has often led to a breach of the breakwater structure rendering it only partially effective; the financial costs of such damage have sometimes totalled into the hundreds of millions of dollars. In certain cases, these breakwater failures have been attributed to the breakage of the individual concrete armor units. These problems have arisen because the research and development of concrete armor units has tended to focus on the hydraulic stability of the units with little or no consideration given to the structural integrity. Guidelines do not exist to aid the engineer in the structural design of armor units as there is a complete lack of knowledge of the nature and magnitude of the forces that may occur on the units in the breakwater environment.

The damage that has occurred on many breakwaters has clearly demonstrated the inadequacy of existing design procedures for

*W.F. Baird & Associates Coastal Engineers Ltd., 38 Antares Dr., Suite 150, Ottawa, Canada, K2E 7V2.
**Department of Civil Engineering, Ellis Hall, Queen's University, Kingston, Canada.

concrete armor units. A rational design procedure for breakwaters must encompass many facets of engineering endeavour including hydraulic, structural, geotechnical and materials engineering. The ultimate goal of an effective design scheme is to improve the hydraulic and structural efficiency of the armor layer, leading to more cost effective breakwater structures.

A comprehensive approach to the design of concrete armor units is presented in this paper. A key component of this design method was the development of instrumentation to determine the structural response of armor units in a physical model when subjected to simulated prototype wave attack. The structural integrity of the armor unit may be assessed once stresses and strains occurring in the unit can be quantified. The design of a unit is facilitated by the development of interaction diagrams which display armor unit structural strength and the unit's load response, and clearly demonstrate the overall factor of safety associated with a selected unit.

THE DESIGN PROCEDURE

Baird and Hall (1983) first suggested an alternate design procedure for concrete armor units that assesses both the hydraulic stability and structural adequacy of the individual units once the forces exerted on the units are defined. This procedure has been adapted in this report and is presented in Figure 1. Such a procedure represents a natural extension of current modelling practice and incorporates the load measuring instrumentation scheme discussed in the next section.

Referring to Figure 1, the first step in the design of any breakwater is to define the environmental conditions to which it will be exposed; the most important factor being the wave climate. An initial design for the breakwater must then be developed on the basis of experience or with the use of design formulas such as Hudson's equation. The selection of the armor unit will depend on a number of variables such as performance data reported in the technical literature, costs, and construction considerations.

The design is then tested using a physical model and modified until the selected armor units are hydraulically stable under the design wave conditions. At this stage, all of the units are assumed to remain structurally sound.

The next step in the design sequence is to determine the forces and/or the structural response of the armor units in the breakwater model. The response to both static and quasi-static loads can now be measured by a specially instrumented armor unit, which is discussed in the next section of this paper. The instrumentation system measures the internal bending and torsional moments at one location in the armor unit. The present investigation focuses on the dolos unit but the application of such techniques is not limited to this particular form of armor

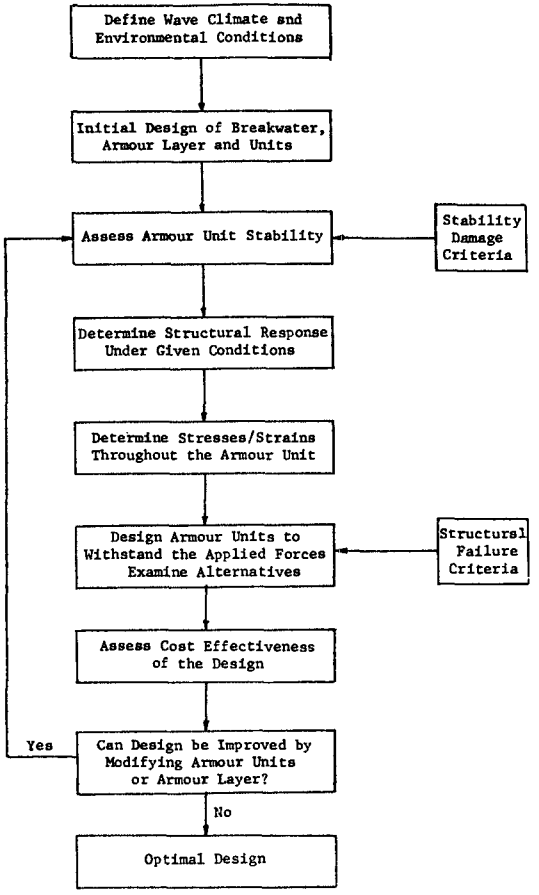

Figure 1 The Design Procedure

unit but to many units where bending and torque may be induced. As well, other similar types of instrumented units can be easily developed. Several instrumented units are placed at various locations in the armor layer and a series of tests conducted with the measured forces/stresses continually monitored.

The measured data are scaled to prototype and the individual armor units must then be analyzed with respect to the scaled forces or stresses. Generally, the armor unit's structural response can only be determined at a specific location on the unit. These stresses must be examined statistically and are then extrapolated to other locations to determine extreme stresses in the most critical regions within the armor unit. This may be achieved most easily by numerical analysis techniques such as the finite element method.

Once the critical stresses are known, the armor unit is designed to resist the applied extreme loading conditions. This entails the adoption of structural failure criteria and safety factors as is done with all structural design. Several alternatives can be examined, including alterations in the geometry and materials of the unit. Different means of increasing the strength of armor units that may be explored include the use of reinforcing, prestressing, fibre-reinforcing and high strength concretes. The effects of such changes on the structural strength of individual armor units may be readily assessed using standard analytic procedures in structural engineering. A sufficient margin of strength should be retained in the unit so that any potential dynamic loads may be resisted, such as may occur during handling and placement, and due to impacts caused by direct wave action, by inter-unit impact and by projectiles.

An important stage in the design procedure is to assess the design and its various alternatives in terms of cost effectiveness. In current design procedures, the economic benefits of altering the structural strength of armor units could only be assessed qualitatively as there was, up until now, no means of evaluating just how strong the units should be.

Finally, the overall breakwater design must be examined in terms of possible modification to either the armor unit or armor layer design. For example, altering the breakwater geometry or modifying the shape of the armor units themselves may be more cost effective than increasing the strength of the individual units.

The design process for concrete armor units outlined above will result in an optimum breakwater design that is both hydraulically and structurally sound under the given wave conditions. This design procedure is analogous to conventional structural engineering practice whereby the loads on a structure are initially defined, stresses throughout the structure determined, and the structure designed to resist the applied loadings.

THE ARMOR UNIT LOAD CELL

The key element in the design procedure discussed above is the load cell or load measuring system. The basis of this system is a thin-walled aluminum tube, which is instrumented with strain gauges and then inserted at the mid-shank location of a model armor unit (in this case a dolos) constructed of a steel-fibre reinforced epoxy, as shown in Figure 2. Strain gauges mounted on the tube measure all of the surface strains due to bending and torsion. Since dolosse primarily experience stresses due to bending and torsion, as exhibited by prototype testing and by the nature of their shape, the axial and shear stresses are considered to be of secondary importance. Details of the design, calibration and evaluation of the instrumentation scheme may be

Figure 2 The Armor Unit Load Cell

found in Scott, Turcke and Baird (1986) and Scott (1986).

The tubes which are inserted are of a different diameter, shape and material than the dolos shank, thereby violating complete similitude, but were designed such that the bending and torsional rigidity of the section were properly scaled from prototype. Such techniques have previously been suggested for structural models by Le Mehaute (1965) and Murphy (1950). Thus, bending and torsional strains were properly scaled but axial and shear strains were distorted. This technique allowed the measurement of strains under even the smallest loads. The output voltages of the strain gauge circuits that measure the bending moments and torques are calibrated against known loading conditions. Thus, two orthogonal moments and torques are measured directly by the system. This creates, in effect, an armor unit "load cell". The net result is that bending moments and torques can be established with a high degree of accuracy at one section in the armor unit under different load conditions.

Two dolosse having overall lengths of 203 mm and 106 mm were constructed using this force measurement scheme. The model units were made of a steel-fibre reinforced epoxy material, Devcon Plastic Steel, modified by the addition of lead pellets to make the density equivalent to that of concrete. This epoxy was utilized because it could be easily cast and then machined and worked in similar manner to any soft metal. Other materials could have been employed if they had a density similar to that of the prototype concrete.

The two dolos load cells were calibrated by the application of static point loads at various locations on the armor units and the strain gauge output measured; this procedure is employed in the calibration of any load transducer. A linear relationship was established between gauge output and the bending or torsional moments.

The calibrations were repeated prior to each test series to ensure that the load cells' characteristics had not changed in time. The calibrations were also performed prior to and subsequent to the application of the waterproofing, and showed that the water protection system had no effect on the load measurements.

An extensive series of tests were designed to fully evaluate the performance of the measurement system in both a dry environment and in the dry/wet environment of a hydraulic flume. Specific objectives of the test program were to examine both the sensitivity and accuracy of the load cell for measurement of forces in a model breakwater. The tests were divided into three categories: (1) static tests under self-weight loading; (2) static tests in a model breakwater; and (3) tests in a hydraulic flume. The results of the tests in the first category were compared against theoretical computations of moments and torques to determine the accuracy of the load cells.

The second set of tests examined the static forces on an amour unit due to placement and settlement in a breakwater. It was noted from the preliminary results that up to 25% of the structural capacity of the dolos unit can be utilized to resist these static loads. Such information is important for the proper design of armor units and may be readily extracted from physical models for different breakwater configurations.

The final set of evaluation tests employed a single instrumented unit rigidly mounted on a smooth slope. These tests were conducted to determine the effect of changes in wave height and location on armor unit response under controlled experimental conditions where the fluid flow was not as complex as which occurs in the breakwater environment.

The evaluation tests demonstrated the viability of the load measurement scheme for determining the structural response of armor units in the breakwater environment. This system had numerous advantages:

i) proper distribution of mass throughout the model,
ii) extremely high sensitivity levels with good accuracy in small scale models,
iii) excellent protection from environmental influences,
iv) flexibility of use: the same instrumentation could be employed in different types and sizes of armor units.

ANALYSIS AND DESIGN OF A BREAKWATER

A typical breakwater of conventional design was selected for the model investigation. The breakwater model was constructed in a two-dimensional hydraulic flume at a length scale of 1:40 as shown in Figure 3.

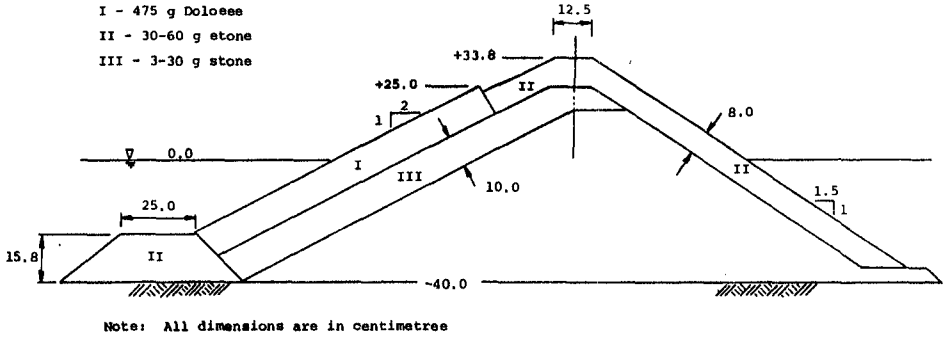

Figure 3 The Breakwater Model

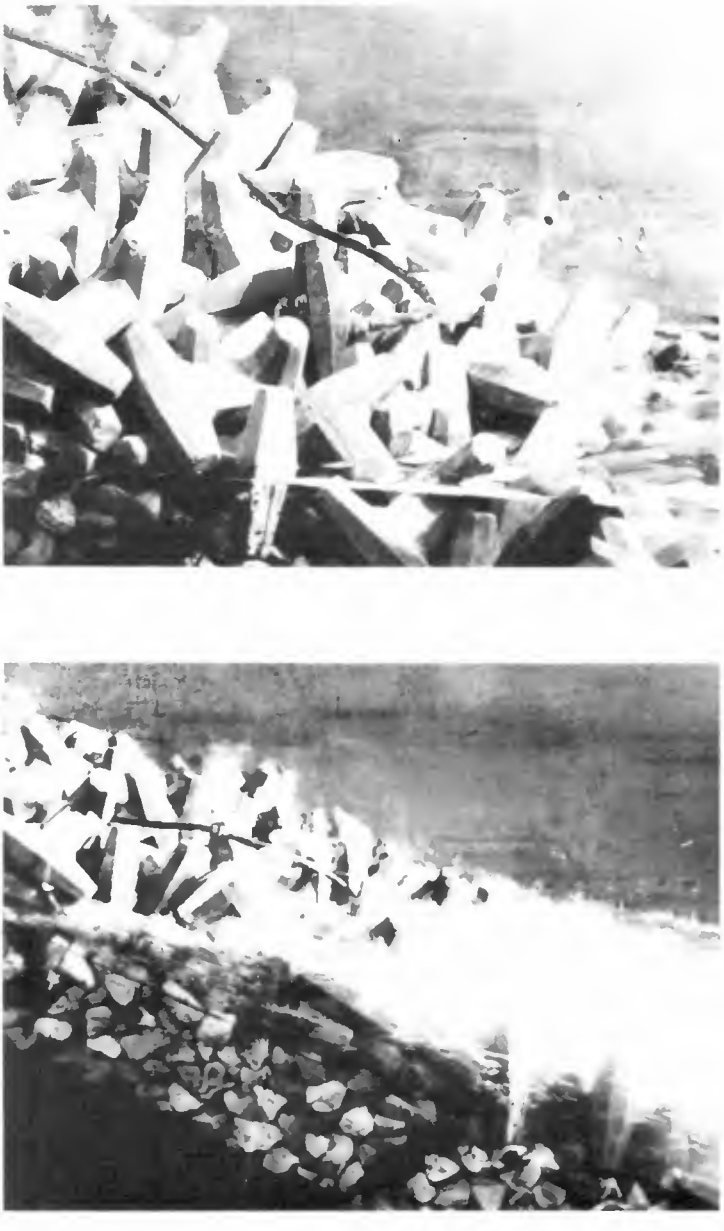

Figure 4 Photographs of the Breakwater Test

The primary armor layer was formed of 475 gram dolosse placed in two layers. At the specified scale, these units corresponded to 30 tonne units in prototype. During the test program, the structure was subjected to regular waves of height 24 cm and a period of 1.75 seconds, corresponding to a wave height of 9.6 metres and a period of 11.1 seconds in prototype. Assuming a K_d value of 15.9 (i.e. two layers of randomly placed dolosse, non-breaking waves, less than 2% damage (no rocking)), Hudson's formula yields a dolos weight of 24.3 tonnes for the given wave conditions [U.S. Corps of Engineers (1984)]. Thus, the 30 tonne units used in the model were hydraulically stable. This was supported by observations during the breakwater tests, in which little or no rocking of the dolos units was observed. The photographs of Figure 4 show the instrumented unit positioned in the armor layer and the breakwater being subjected to wave action.

Tests were conducted at twelve different locations in the armor layer; six were in the top layer and the remainder in the bottom layer. Prior to each test, the instrumentation was zeroed and calibrated. The unit was then placed in the armor layer and the static load response measured. The internal forces were monitored and graphically displayed when the model breakwater was subjected to wave action. Both the nature and magnitude of the forces were examined. These forces are created by both the inertial and drag forces of the water during wave breaking, uprush and downrush. A typical response of the armor unit to wave attack is shown in Figure 5 where the measured response for the two orthogonal bending moments and torque have been plotted against time. The repeatability of the peak signals with the wave period was excellent in all tests and the levels of the static forces may be noted on the plot. There was also excellent correlation of the peak signals from test to test at any one location.

Figure 6 displays some of the results of the test series. Here, torque has been plotted against the vector sum of the orthogonal bending moments for the maximum response recorded in each test as obtained from the time history plots of the internal forces.

Throughout the test series, the load cell performed with a high degree of reliability, and the waterproofing protected the instrumentation even under the severe environmental conditions of the model breakwater. The load cell exhibited high sensitivity levels and was able to measure even the small induced forces of static loading. The presence of lead wires to the instrumented unit did not pose any difficulties in the tests and did not affect the stability of adjacent units.

The next step in the design procedure, once the structural response is known in the model, is to assess whether structural failure will occur and how the armor units may best be designed to resist the induced forces in prototype. Several activities

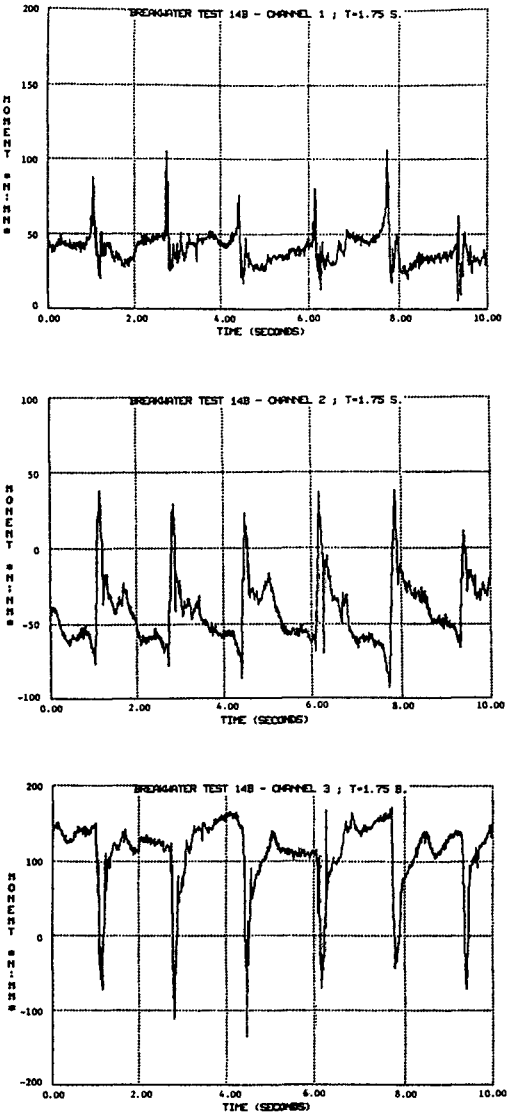

Figure 5 Typical Response of the Local Cell to Wave Attack

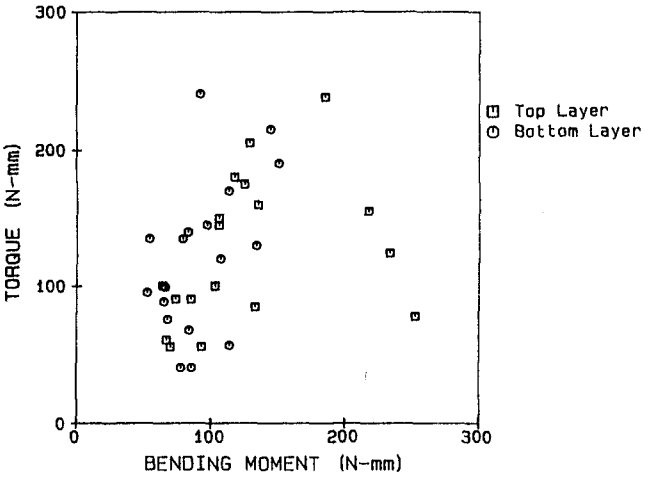

Figure 6 The Peak Internal Forces Measured

are essential to achieving this goal. First, the model forces/stresses must be scaled to prototype using the appropriate scale factors. Second, certain failure criteria for the designed armor unit must be identified and compared to the scaled data. Third, as the forces/stresses cannot be measured at all locations within the armor unit, approximate stress distributions must be determined throughout the unit.

Using the appropriate scaling relationship, the moment and torque levels in the prototype were computed. In order to determine if the combined effect of the moment and torque would cause a section to fail, a failure criteria had to be established. This led to the development of an interaction equation, based on the concrete failure theory of Cowan (1953, 1955), relating failure in the dolos shank composed of plain concrete under the combined actions of bending and tension:

$$\left(\frac{M}{M_{cr}}\right) + \left(\frac{T}{T_{cr}}\right)^2 = 1$$

where:

$$M_{cr} = 0.1597\ (Rh)^3\ f'_t$$

$$T_{cr} = 0.2140\ (Rh)^3\ f'_t$$

M_{cr} and T_{cr} are the pure bending moment and pure torque that would induce cracking in the dolos shank, R is the waist ratio, h is the dolos size and f'_t is the direct tensile strength of the concrete. The above expression is valid within the dolos shank; however, many dolos failures have been known to occur at the fluke-shank interface of the unit. Therefore, it was necessary to extrapolate the measured response to other regions in the

armor unit. This was achieved by means of numerical analysis using the finite element method where the stress increase at the fluke-shank interface was examined under different extreme loading and boundary conditions. The finite element grid used for the dolos unit is shown in Figure 7.

A typical result is displayed in Figure 8 where the peak moments and torques at the fluke/shank interface are plotted along with the failure curve for concrete strengths of 30 MPa and 40 MPa. It can be seen very clearly that the results for some of the units lie outside the safe region and, therefore, these units would have failed. These test results showed that despite using armor units which were hydraulically stable under the incident wave conditions, structural failure would occur, consequently demonstrating the inadequacy of the dolos armor unit as designed for this particular application. Fatigue has not been considered, though it can be a very likely source of problems in the breakwater environment.

The next stage in the analysis was to redesign the armor units to withstand the applied forces. This could be achieved by either altering the geometric shape of the unit, increasing the size of the unit or increasing the structural strength of the unit. The strength of concrete may be augmented by numerous means, such as by the use of reinforcing, prestressing, high strength concrete or fibre-reinforcing. These are just a few examples of the different design alternatives and does not by any means represent a comprehensive examination into the various design possibilities. An example of the effect of using reinforcing steel to increase the structural capacity of the dolos unit is shown in Figure 9.

The cost effectiveness of the various alternatives may now be truly examined because the structural requirements can be quantified. Such information is essential to the development of different design alternatives.

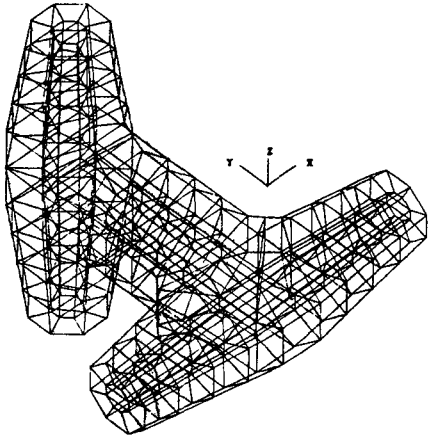

Figure 7 The Dolos Finite Element Method

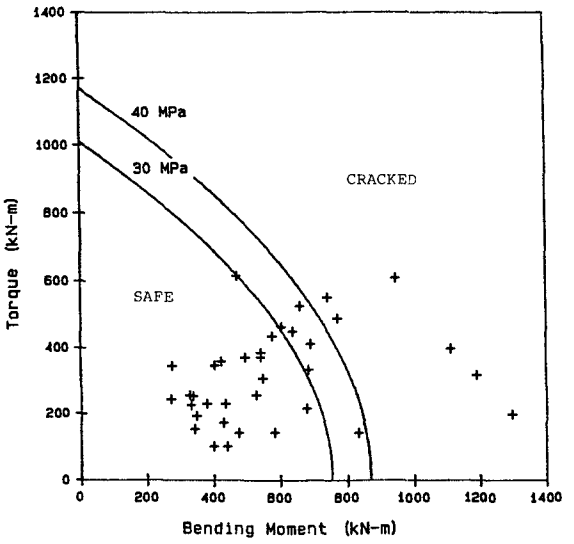

Figure 8 Peak Forces at the Fluke/Shank Interface

CONCLUSIONS

A rational procedure for the design of concrete armor units has been presented. A unique "load cell" was developed which measures the structural response of armor units in a standard breakwater model. This permits the structural integrity of the armor units to be assessed through the use of interaction curves, thus clearly demonstrating the overall factor of safety associated with the armor unit and the expected mode of failure.

Such a procedure represents the application of existing technologies and a comprehensive engineering approach to the design of rubble mound breakwaters. Some features of the design method are:

1) Methods of standard structural engineering practice are followed where first the loading conditions are assessed and the structure designed to resist the applied loads.
2) Numerical analysis techniques such as the finite element method are employed.
3) It is an extension of current design practice where physical models are utilized.
4) Materials technology and failure criteria are examined.

Consequently, an effective design scheme is available which incorporates both the hydraulic and structural considerations of a breakwater structure and , thus, can provide more cost effective solutions.

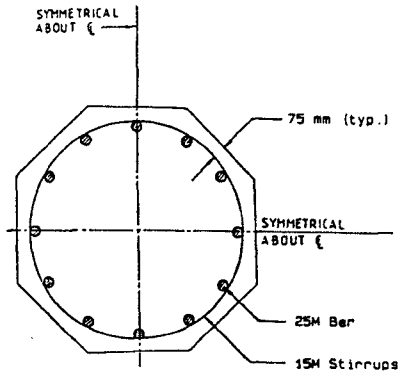

(a) Reinforcing Arrangement

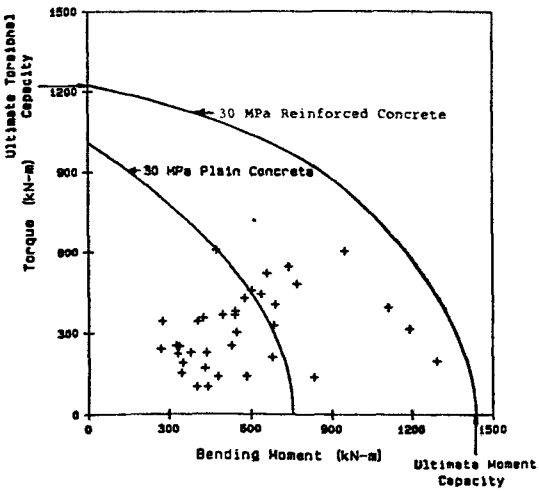

Figure 9 The Effect of a Reinforced Dolos Shank

REFERENCES

Baird, W.F. and Hall, K.R., "The Design of Armour Systems for the Protection of Rubble Mound Breakwaters", Conference on Breakwaters - Design and Construction, Institution of Civil Engineers, London, May, 1983.

Cowan, H.J., "The Strength of Plain, Reinforced and Prestressed Concrete Under the Action of Combined Stresses with Particular Reference to the Combined Bending and Torsion of Rectangular Sections", Magazine of Concrete Research, Volume 5, No. 14, pp. 75-86, December, 1953.

Cowan, H.J. and Armstrong, S., "Experiments on the Strength of Reinforced and Prestressed Concrete Beams and of Concrete-encased Steel Joists in Combined Bending and Torsion", Magazine of Concrete Research, Vol. 7, No. 19, March, pp. 3-20, 1955.

LeMehaute, B., "On Froude-Cauchy Similitude", Proceedings of the ASCE Conference on Coastal Engineering, Santa Barbara, pp.327-346, 1965.

Murphy, G., "Similitude in Engineering", The Ronald Press Co., New York, 1950.

Scott, R.D., Turcke, D.J., and Baird, W.F., "The Analysis and Design of Concrete Armour Units", Proceedings of the West Coast Regional Coastal Design Conference, Oakland, California, November 7-8, pp. 339-342, 1985.

Scott, R.D., "The Analysis of Concrete Armour Units in a Breakwater", Ph.D. Thesis, Queen's University, Kingston, Ontario, 1986.

Scott, R.D., Turcke, D.J., and Baird, W.F., "A Unique Instrumentation Scheme for Measuring Loads in Model Dolos Units", Proceedings of the Twentieth International Coastal Engineering Conference, Taipei, November 10-15, 1986.

U.S. Army Corps of Engineers, Waterways Experiment Station, Coastal Engineering Research Centre, Shore Protection Manual, 4th Edition, 2 Volumes, U.S. Government Printing Office, Washington, D.C., 1984.

CHAPTER 128

SCOUR AROUND STRUCTURES

ECO W. BIJKER*, Member ASCE

Abstract

The physics of scour around structures and especially underneath pipelines is discussed. It is demonstrated that a combination of current and waves with an equal bottom shear stress as a uniform current gives lower scour rates than a single current with the same bottom shear stress.

The principle of the performance of scale series is discussed and it is shown that this method has still some weak points.

1. Introduction

When a structure is placed in water on an erodable bottom and is subject to a current or wave field, scour will most likely occur around the structure. It is difficult to predict this scour because the scour process is even more complicated than the normal transport process. In this paper the various processes and prediction methods will be discussed for pipelines on a sandy bottom because a lot of data is available from an extensive research carried out within the framework of the Dutch Marine Technology Research (MaTS).

At present it is possible to predict the current pattern around a structure, c.q. the pipeline, by numerical models. These models can also calculate the rate of turbulence and the bottom shear stress. Modelling of transport processes is, however, still very difficult [Leeuwestein and Wind (1984) and Leeuwestein et al. (1985)]. Good progress is made in obtaining a reliable description of the transport and scour phenomena.

As long as the final goal is not yet reached, physical model tests can offer a solution, not only for predicting scour values but also for obtaining a better insight in the physical processes. However, with physical modelling serious and well known scaling problems will arise. A method to cope to some extent at any rate with that problem, is the application of scale series. In this procedure a set of models with varying scales is applied and the results, for instance measured values of the scour, are extrapolated to values for scale 1:1.

---

* Professor of Coastal Engineering, Delft University of Technology, P.O. Box 5048, 2600 GA Delft, The Netherlands

This should give the correct answer. Since this extrapolation is rather difficult, often an attempt is made to determine for each test the best possible scale factor for the scour. In the ideal case all predicted scour values should give then the same value. Even in the case this ideal is not reached, the extrapolation of these 'up-scaled' values is much more easy than of the observed test values. This principle is demonstrated in Figure 1.

In this paper this procedure is worked out for the scour around pipelines and the possible deficiencies which are still inherent to this method are discussed.

2. Physics of scour

A basic difference exists between the scour caused by current and waves.

i. In a current field, normally a continuous transport exists. In this case the basic condition for the equilibrium situation in the immediate vicinity of the structure, so for the equilibrium scour hole configuration, is that the transport gradient, $dS(x)/dx = 0$. When the current is so low that in the undisturbed current field no transport occurs, the scour around the structure, c.q. underneath the pipeline, will develop until also in the vicinity of the structure the transport is zero. So again $dS(x)/dx = 0$. (See Figure 2.)

ii. Under the influence of an orbital wave motion hardly any continuous transport occurs. In this case the scour process is determined by the excursion distance of the sediment particles through the orbital motion. The amplitude of the sediment motion is closely related and even almost equal to the amplitude of the orbital motion of the water at the bottom. (See Figure 3.)

Moreover, another difference exists between the development of scour by only current or by waves. This is caused by the fact that in the case of only current, the scour will take place by an accelerated current which has subsequently a relatively low rate of turbulence. The bottom shear will be, however, higher than in the case of a uniform flow, since the boundary layer is not yet adjusted. This effect, of the adjustment of the boundary layer, does not occur for the situation with only waves, since the boundary layer under waves must be adjusted continuously. This effect is almost equal for the undisturbed wave motion and for the wave motion in the scour area.

For the combination of waves and current this effect is also noticeable. The bottom shear stress of the combined effect of waves and current can be written as

$$\tau_{cw} = \tau_c + \tfrac{1}{2}\hat{\tau}_w = \tau_c \left(1 + \frac{\hat{\tau}_w}{2\tau_c}\right) \qquad (1)$$

in which τ_c = bottom shear stress by current; $\hat{\tau}_w$ = amplitude of bottom shear stress by waves; τ_{cw} = combined bottom shear stress [Bijker (1966 and 1971)].

Since in the scour area τ_c increases relatively more than $\hat{\tau}_w$, the

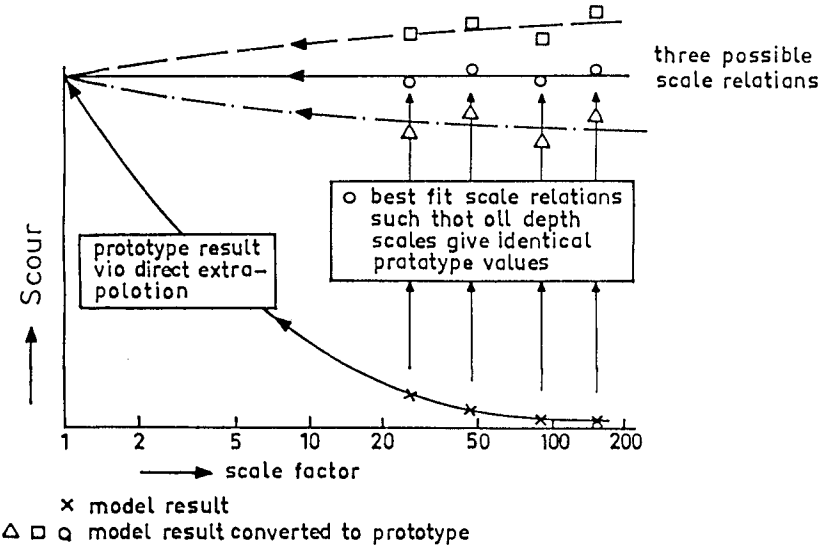

Fig. 1 Philosophy of a scale series

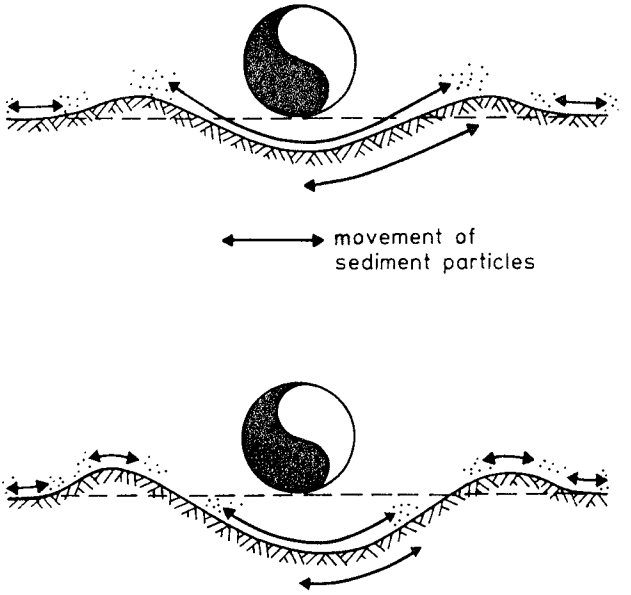

Fig.3 SCOUR DUE TO WAVES.

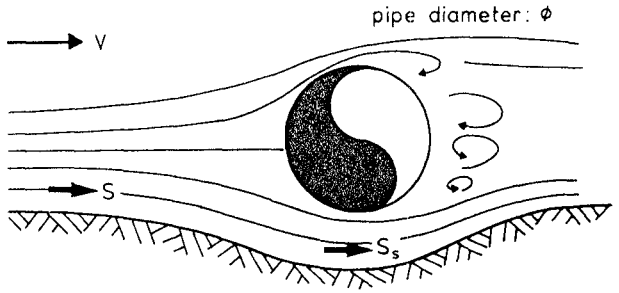

Fig. 2 SCOUR AS RESULT OF CURRENT

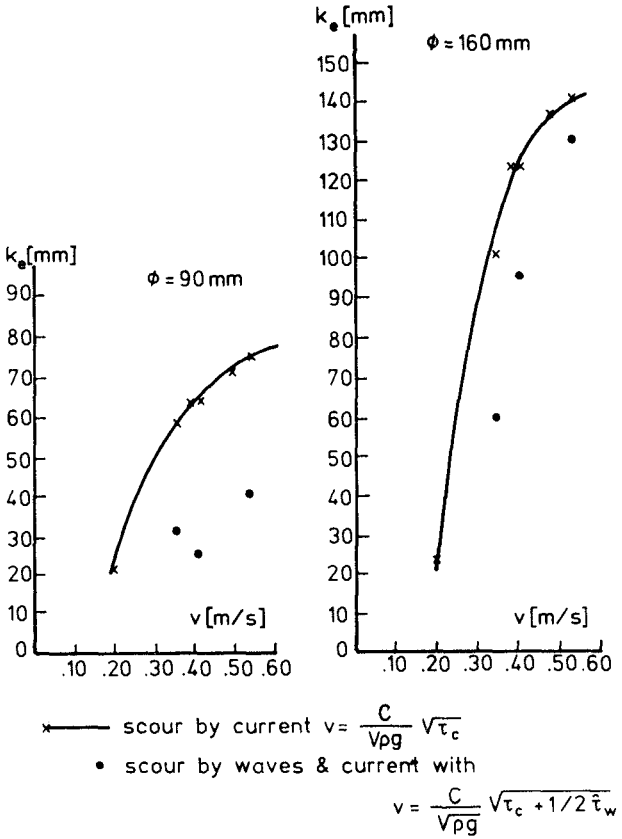

Figure 4. SCOUR FOR CURRENT AND CURRENT + WAVES.

factor by which the transport due to current is increased by wave motion is in the scour area less than in the undisturbed area.

The scour will be, therefore, less and this is demonstrated by tests in which scour has been subjected to a current and to a combination of current and waves with an equal bottom shear stress in the undisturbed area.

The velocity in the case of only current should be

$$v_1 = C\sqrt{\frac{\tau_{c,1}}{\rho g}} \qquad (2)$$

in which C = the Chezy bed resistance factor.

In the case of the combination of a current and waves, the current should be less, resulting in a bed shear $\tau_{c,2}$, so that

$$\tau_{c,w} = \tau_{c,1} = \tau_{c,2} + \tfrac{1}{2}\hat{\tau}_w \,. \qquad (3)$$

The scour occurring under these conditions should be compared with scour $k_{e,1}$ occurring by the velocity

$$v_1 = C\sqrt{\frac{\tau_{c,2} + \frac{1}{2}\hat{\tau}_w}{\rho g}} \,. \qquad (4)$$

The results are shown in Table 1 which gives the observed scour values for various combinations of waves and currents. The values v_1 of a single current giving the same resulting shear stress as the combination of waves and current are given with the corresponding scour values.

The results are also presented in Figure 4. Apart from the test with $v_2 = 0.40$ m/s and $\hat{u}_b = 0.15$ m/s, the scour underneath a pipeline subjected to a combination of waves and currents is less than the scour when the pipeline is subjected to a single current v_1 with the same bottom shear stress as v_2 and $\hat{u}_b$.

For a continuous transport the bottom changes can be described by

$$\frac{\partial}{\partial t}\left[\int_{z_b}^{z_s} c(x,z,t)\cdot dz\right] + \frac{\partial S(x,t)}{\partial x} + (1-p)\frac{\partial z_b(t)}{\partial t} = 0 \qquad (5)$$

in which $c(x,z,t)$ is the sediment concentration at place x, height z and time t, z_b is the height of the bottom, z_s = height of the water level, or any level above which $\frac{\partial}{\partial t}\left(c(x,z,t)\right) = 0$; $S(x,t)$ is the total sediment transport per unit of width at place x and time t, and p = the porosity of bottom material.

Equation 5 demonstrates that scour will not only occur as a result of $\partial S/\partial x$, but also because more sediment can go into suspension. This is especially important in those cases where the material brought into suspension can be transported outside the area of expected scour. This is of great importance for the scour around structures when locally material can be brought into suspension and then can be

transported by a continuous current.

This phenomenon also explains the difference in scour patterns in front of a vertical wall with coarse and fine bottom material [de Best et al. (1971), Irie and Nadaoka (1984)] .

3. Formulation of sediment transport

Sediment transport formulae can be written in the following general form:

$$\phi = f(\psi), \tag{6}$$

$$\text{in which } \phi = \frac{S}{\sqrt{g\Delta D^3}}, \tag{7}$$

with S = transport per unit width; g = acceleration of earth gravity; D = grain size of sediment and Δ = relative density of sediment;

$$\text{and } \psi = \frac{\tau}{\rho g \Delta D}, \tag{8}$$

with τ = bottom shear stress.

$$\text{For current } \psi_c = \frac{\kappa\, v_t^2}{g\Delta D} = \frac{\bar{v}^2}{C^2 \Delta D}, \tag{9}$$

with v_t = velocity just above laminar sublayer at er/33 and $\bar{v}$ = mean velocity, averaged over the depth

$$\text{and for waves } \psi_w = \frac{f_w \hat{u}_b^2}{2g\Delta D}, \tag{10}$$

with $\hat{u}_b$ = amplitude of the orbital velocity at the bottom and f_w = bottom friction factor of Jonsson [Jonsson (1966)] .

For the case of a combination of current and waves, ψ_c should be replaced by ψ_{cw}, which can be written as

$$\psi_{cw} = \psi_c + \tfrac{1}{2}\psi_w \tag{11}$$

[Bijker (1966, 1971)] .

Some sediment transport formulae are:

Meyer-Peter, Mueller

$$\phi = 13.3\,(\psi_c - 0.047)^{1.5} \tag{12}$$

Kalinske-Frijlink

$$\phi = 5\sqrt{\psi_c}\, e^{-0.27/\psi_c} \tag{13}$$

Paintal

$$\phi = 10.9\; 10^{18}\, \psi_c^{16} \quad \text{for } \psi_c < 0.05 \tag{14}$$

$$\phi = 21.7\, \psi_c^{2.5} \quad \text{for } \psi_c > 0.05 \tag{15}$$

Engelund and Hansen

$$\phi = \frac{C}{g} \psi^{5/2} . \qquad (16)$$

All above descriptions can, over a limited velocity range, be simplified to

$$S = \alpha v^{\beta} , \qquad (17)$$

in which α is a non-dimensionless coefficient. This simplification is used for the derivation of simple scale relations used in the scale series. A close analysis of the above quoted formulae shows that α is mainly determined by D and that the influence of the velocity and the type of transport, viz. : mainly bed load or mainly suspended load, or a combination of these two, are represented by the value of β .

For low transport rates, mainly in the form of bed load, β is larger, 0 (6), than for high transport rates with a large ratio of suspended load over bed load, 0 (2 or 3).

4. Prediction of scour by current through a scale series

In Chapter 1 it has been stated that, in order to be able to extrapolate the measured scour values for the various model pipes, c.q. structures to scale 1:1 , an as accurate as possible scale for the scour should be found. This requires a good choice for the velocity scale belonging to the various scales of the structure. The correct value of this scale is, moreover, at any rate necessary for a good performance of the model test. In the ideal case the transport scale is constant over the entire area, that is upstream and downstream and around the structure.

So, $$n_S = n_{S_s} , \qquad (18)$$

in which n_S = transport scale factor = prototype value over model value and the subscript s denotes the value at the place of maximum scour. This leads in this case through Equation (17) to

$$n_{(\alpha\, v^{\beta})} = n_{(\alpha_s\, v_s^{\beta_s})} . \qquad (19)$$

Equation (19) leads to a value of n_v and in some cases also to a relation of n_v to n_l .

From the discussion in Chapter 3 , α proves to be determined mainly by the grain size of the sediment. Since the material in the scour area will not differ much from that in the undisturbed area; $n_\alpha = n_{\alpha_s}$.

In order to make the computations not too complicated, n_β and n_{β_s} are assumed to be 1 . This is only so when the type of transport in the model is equal to that in the prototype. Since this is not completely true, the derived scale relation will not be the 'ideal' one. However, when the relation is consistent, extrapolation through a continuous curve to the prototype condition, $n_l = 1$, will be possible.

Equation (19) in this case can be written as

$$n_v^{\beta} = n_{v_s}^{\beta_s} \qquad (20)$$

Normally the relation between v_s and v is known. For a vertical pile $v_s = 2\,v$, which would lead to

$$n_v^{\beta} = 2^{\beta_s}\, n_v^{\beta_s} \quad . \tag{21}$$

For the tests with pipelines the situation differs somewhat since a pipeline with a larger diameter will force more water through the gap underneath the pipeline. The ratio between the velocity underneath the pipeline and the undisturbed velocity is, therefore, a function of the pipeline diameter ϕ.

Tests have shown that this ratio can be described by

$$v_s/v = \phi^{0.2} \quad . \tag{22}$$

In this case Equation (20) [Leeuwestein (1986)] can be written as

$$n_v^{\beta} = n\left(v\,\phi^{0.2}\right)^{\beta_s} = n_v^{\beta_s}\, n_\phi^{0.2\,\beta_s} \quad , \tag{23}$$

$$\text{or} \quad n_\phi = n_v^{p} \quad , \tag{24}$$

$$\text{with} \quad p = \frac{\beta - \beta_s}{0.2\,\beta_s} \quad . \tag{25}$$

Reasonable values for β and β_s are 5 and 3 respectively. The value of β_s is chosen lower than β because a numerical analysis by the Delft Hydraulics Laboratory revealed that underneath the pipeline a greater ratio of suspended load over bed load exists than in front of the pipe [Leeuwestein and Wind (1984)].

In that case $p = 3.3$ and subsequently

$$n_\phi = n_v^{3.3} \quad . \tag{26}$$

Another possible scale relation is based on Froude modelling of the flow pattern, so

$$n_\phi = n_v^{2} \quad . \tag{27}$$

The procedure to determine the scour underneath a pipeline of ϕ = 500 mm for an undisturbed current velocity of 0.7 m/s is as follows.

For various pipe diameters ϕ, ranging from 10 to 100 mm, the scour is measured for velocities of 0.2 , 0.3 , 0.35 and 0.4 m/s. The results are shown in Figure 5. For each value of the velocity, the velocity scale (with respect to v = 0.7 m/s) is determined and from that velocity scale the scale for the pipeline n_ϕ is calculated through Equation (24). When this exercise is performed for $p = 2$ and $p = 3.5$, a velocity in the test of $v = 0.35$ m/s, leading to $n_v = 2$, gives values of $n_\phi = 4$ and 11.3 respectively. In this way a set of scour values under pipelines with varying scales with regard to the pipeline of 500 mm and 'realistic' values of the tests-velocities is obtained. These points form the lower line of Figure 6. Exrapolation

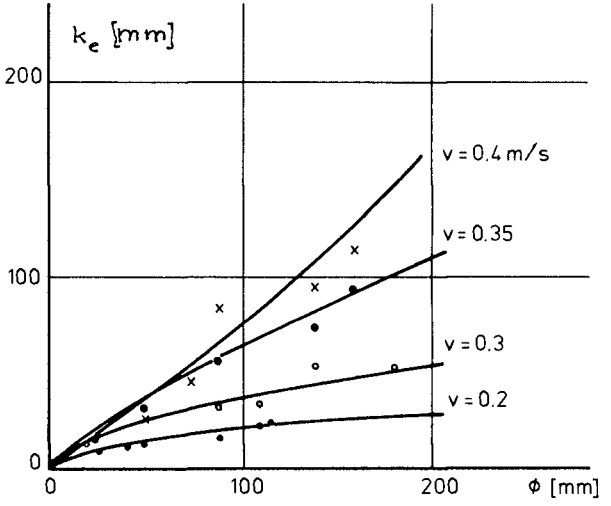

Figure 5. MEASURED SCOUR DEPTHS (CURRENT).

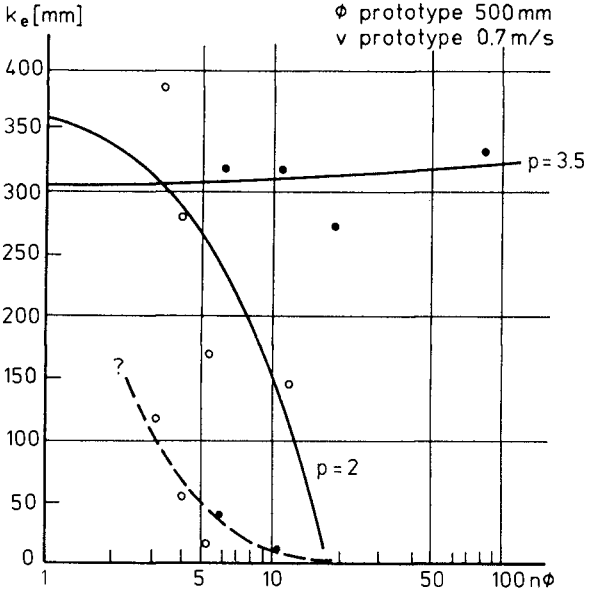

Figure 6. SCOUR BY CURRENT (MATS DATA).

of this line to $n_\phi = 1$ would give the expected scour for a pipe of 500 mm and a velocity of 0.7 m/s. This extrapolation is, however, easier when the observed scour values are multiplied with the expected scale factor of the scour. For the 'ideal' velocity scale this factor will be equal to n_ϕ . The lines obtained in this way for p = 2 and 3.5 are also given in Figure 6. Extrapolation is done by a linear regression analysis. In Chapter 6 the results will be discussed more in detail.

The same exercise has been done for the data of Kjeldsen, which are summarized in Figure 7. The final result is shown in Figure 8.

5. Prediction of scour by means of scale series for waves

In principle the same procedure as for a current is followed. However, in order to make a first estimate for p in $n_\phi = n_v^p$, a somewhat different procedure has to be followed, since the principle of scour around a structure by waves is basically different from that by current (see Chapter 2).

In the case of scour by waves no continuous transport of any importance exists. The criterium that $\partial S/\partial x = 0$ and, therefore, the requirement that n_S in front of the structure should be equal to n_{S_s} in the scour hole is irrelevant.

In the ideal situation $n_{k_e} = n_\phi$ and since the current pattern around the structure is determined to a great extent by the pressure around the structure, c.q. underneath the pipe, $n_\phi = n_{\hat{u}}^2$.

According to the physics of the scour underneath a pipeline as discussed in Chapter 2 , the amplitude of the orbital motion should be reproduced on the scale of the pipeline; n_ϕ . When the wave period is reproduced on $n_\phi^{\frac{1}{2}}$, this requirement also leads to $n_{\hat{u}} = n_\phi^{\frac{1}{2}}$.

The scale series have been performed with values of p = 1 , 1.5 and 2 . The original test results for scour by waves are given in Figure 9 and the final results for the scale series in Figure 10. The scour for the prototype pipeline of ϕ 500 mm and $\hat{u}_{b,pr} = 1$ m/s then is 187 , 205 and 210 mm which is reasonable close together. These values are, as could be expected, much less than the values obtained for a steady current of comparable value.

6. Discussion

For the pipeline of 500 mm in a steady current of 0.7 m/s, data are available from full scale tests in the large flume of the Delft Hydraulics Laboratory. The MaTS data give for p = 2 a value of k_e = 355 mm and for p = 3.5 a value of k_e = 302 mm. As a matter of fact, these two values should have been equal. Moreover, the full scale test gives a value of only 220 mm.

One of the reasons for this 'low' value of 220 mm probably is that the tests in the large flume have not been run long enough. In Figure 11 the results of these tests are shown. These results indeed give the impression that extension of the test with v = 0.7 m/s would have given somewhat larger values for the scour.

Another reason could be the layout of the test as shown in Figure 12. The feeding of the sand by controlled dumping in the flume some 50 m upstream of the pipe, could have led to a too high suspended load and,

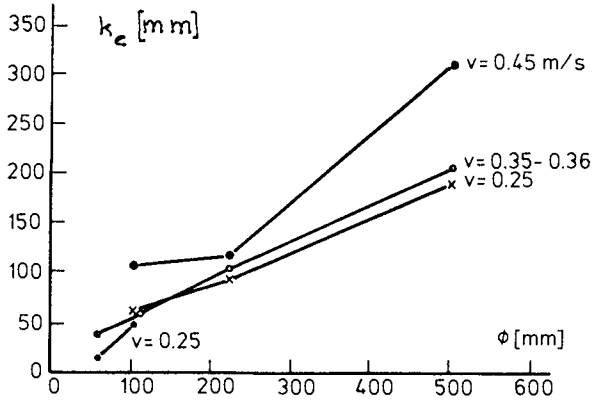

Figure 7. KJELDSEN SCOUR DATA.

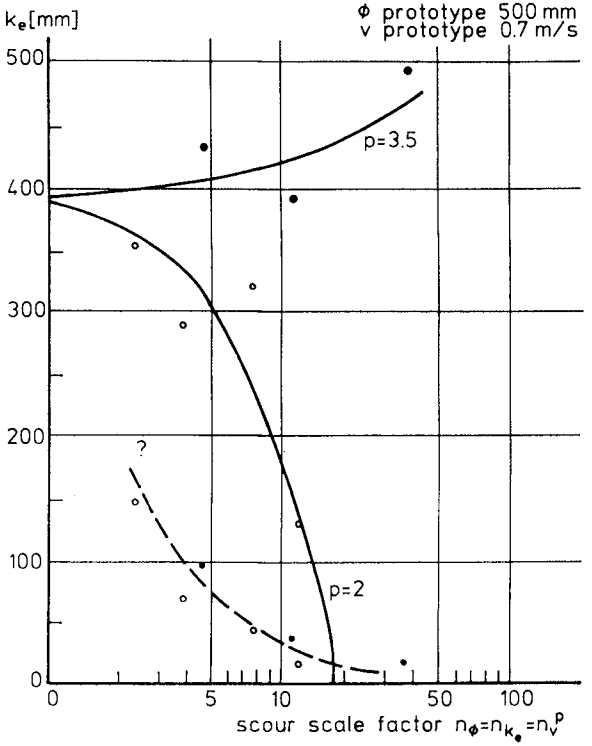

Figure 8. SCOUR BY CURRENT (KJELDSEN DATA).

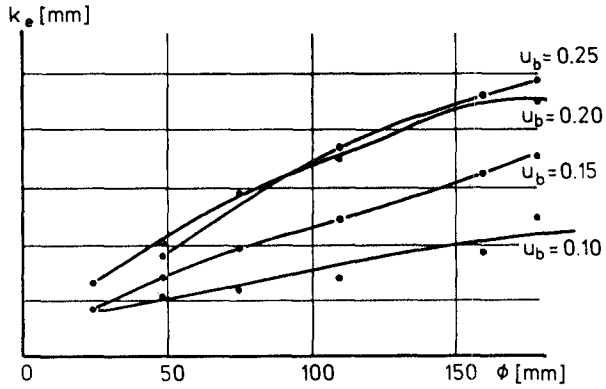

Figure 9. MEASURED SCOUR DEPTHS (WAVES).

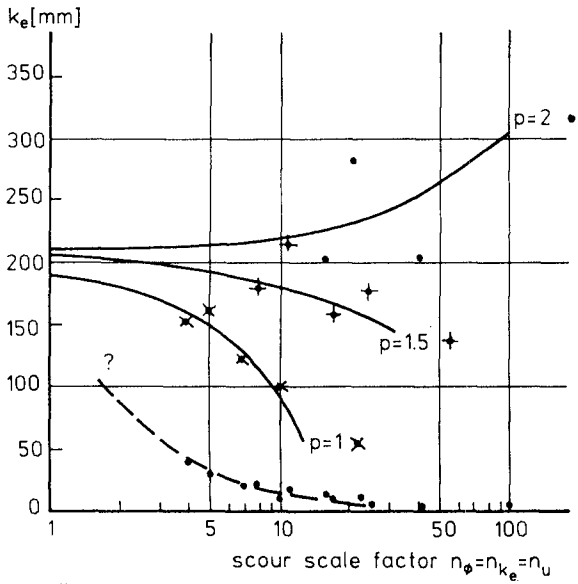

Figure 10. SCOUR BY WAVES.

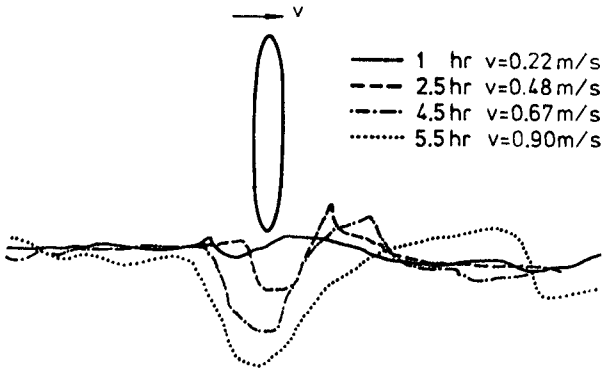

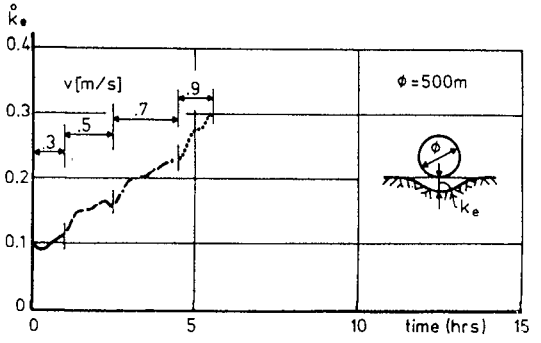

Figure 11. SCOUR MEASUREMENTS IN LARGE FLUME of D.H.L. (de Voorst).

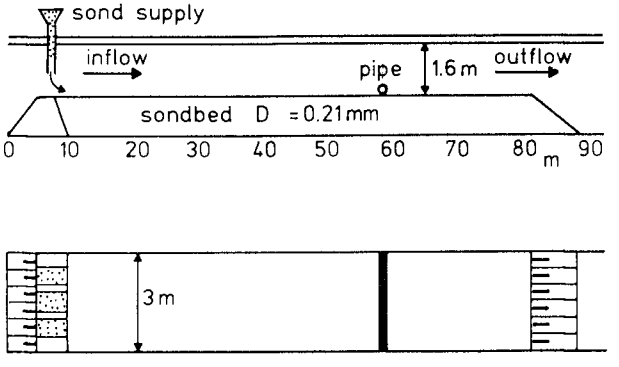

Figure 12. LARGE FLUME D.H.L. (de Voorst).

therefore, to too high sand supply to the scour hole. This also led in some cases to the formation of very large dunes.

Also the Kjeldsen data lead to values of the scour of the order of 390 mm, which is higher than predicted by the formula of Kjeldsen,

$$k_e = 0.97 \left[\frac{v^2}{2g}\right]^{0.2} \phi^{0.8} \qquad (28)$$

This would give $k_e = 266$ mm .

Of course, this value corresponds rather well with the direct extrapolation of the Kjeldsen data. However, it is not sure that this extrapolation is allowed, because the transport mechanism is changing when the velocity is increased so much from the values of the Kjeldsen data.

This also demonstrates the weak point of every scale series. It is well possible that extrapolation to the required prototype value will change the transport mechanism so fundamentally that extrapolation by a continuous curve is not allowed any more. Therefore, utmost care in the application of scale series is still necessary.

The ultimate procedure for scour prediction will be, therefore, in the nearby future the use of numerical models based on a description of the transport and scour processes through basic physical research.

		Measured values of $k_{e,2}$ [mm], for		$\tau_{c.w}$ [N/m^2]	v_1 [m/s]	Scour values $k_{e,1}$ [mm], for	
v_2 [m/s]	$\hat{u}_b$ [m/s]	ϕ=90 mm	ϕ=160 mm			ϕ=90 mm	ϕ=160mm
.20	0	20	24	.13			
.20	.15	32	60	.43	.36	58	100
.20	.20	25	90	.60	.42	63	124
.40	0	63	124	.52			
.40	.15	90	140	.82	.50	70	136
.40	.20	40	130	.97	.55	75	140

Table 1 Scour values for only current and a combination of waves and currents

Appendix I - References

BEST, A. de, E.W. BIJKER and J.E.W. WICHERS
Scouring of a sand bed in front of a vertical breakwater.
Proc. 1st Int. Conf. on Port and Ocean under Arctic Conditions (POAC), Trondheim, 1971, Vol. II, pp. 1077-1086.

BIJKER, E.W.
The increase of bed shear in a current due to wave action.
Proc. 10th Int. Conf. on Coastal Engineering, Tokyo, 1966, Vol. I, pp. 746-765.

BIJKER, E.W.
Longshore transport computations.
Proc. ASCE, Journal of the Waterways, Harbors and Coastal Engineering Division, WW 4, November 1971.

IRIE, I. and K. NADAOKA
Laboratory reproduction of seabed scour in front of breakwaters.
Proc. 19th Int. Conf. on Coastal Engineering, Houston, 1984, Vol. II, pp. 1715-1731.

JONSSON, I.B.
Wave boundary layer and friction forces.
Proc. 10th Int. Conf. on Coastal Engineering, Tokyo, 1966, Vol. I, pp. 127-148.

KJELDSEN, S.P.
Experiments with local scour around submarine pipelines in a uniform current.
Technical University of Norway, Trondheim, 1974.

LEEUWESTEIN, W. and H.C. WIND
The computation of bed shear in a numerical model.
Proc. 19th Int. Conf. on Coastal Engineering, Houston, 1984, Vol. II, pp. 1685-1700.

LEEUWESTEIN, W., E.W. BIJKER, E.B. PEERBOLTE and H.C. WIND
The natural self burial of submarine pipelines.
Proc. 4th Int. Conf. on Behaviour of Offshore Structures (BOSS'85), Delft, 1985, pp. 717-728.

LEEUWESTEIN, W.
The natural self burial of submarine pipelines.
MaTS Stability of pipelines, scour and sedimentation.
PL4-2 DD, 1986.

CHAPTER 129

Durability of Rock Armour on Coastal Structures

A P Bradbury BSc *
N W H Allsop BSc MICE +

Abstract

This paper summarises many of the recent advances in the testing of rock quality for coastal structures. Advanced work on armour profile and armour unit shape descriptors is identified. A set of assessment methods for monitoring armoured slopes in the field are described, with examples drawn from recent monitoring exercises. The paper concludes by describing future directions of research in this field.

1 Introduction

Rock of mean unit weight within the range 2 to 20t is frequently used to protect or armour coastal structures such as breakwaters and sea walls. These structures are usually designed to dissipate much of the incident wave energy in flow over and through the rough and porous armour layer. Within such armour layers, each individual armour unit must therefore be capable of resisting the forces due to wave action, and must withstand mechanisms of chemical and physical deterioration operating in the marine environment. Historically the design of such armour layers required the use of rock judged to be "hard and durable", although few engineering tests were established to quantify the potential durability of the rock from any particular source. In this context durability may be defined as the capability of remaining useful for the original purpose. A more limiting definition, and that used in this paper, might require the material to remain at or above a defined level of usefulness, as given by armour layer performance and stability, over the full design life of the structure.

Recently a series of simple engineering tests have been developed to help quantify the potential durability of rock armour to be used on coastal structures, see Fookes & Poole (Ref 1). Appropriate acceptance values for each test have been advanced, based upon measurements of performance both in service and in the laboratory, see Poole et al, and Allsop et al (Refs 2, 3).

In most design work it has usually been assumed that the armour layer will remain at its original performance and stability levels throughout its design life, often about 30 to 50 years. However, it has been noted that rock armour on some structures has often not been as durable as had been hoped or anticipated. Many examples of early

* Scientific Officer, Coastal Structures Section
+ Principal Scientific Officer, Coastal Structures Section, Maritime Engineering Department, Hydraulics Research, OX10 8BA, UK.

deterioration reducing the stability and effectiveness of the armour have been identified (Ref 1). At some sites the rock available may be of inferior quality and will therefore be more likely to deteriorate under the action of waves, tides and other environmental factors. Alternatively, the design of the armour layer may itself allow significant levels of armour movement, giving rise in turn to impact and abrasion damage. Such movement might be envisaged at the design stage, as on rock berm breakwaters, see Baird & Hall (Ref 4), or on dynamically stable rock slopes, see Van der Meer & Pilarczyk (Refs 5, 6). On more conventional structures these high levels of armour movement may not however be expected, and will consequently not have been allowed for in the design. This may occur if the wave climate has been under-estimated, or if the structure is otherwise under-designed. A few design methods do envisage some armour movement, and the extent and rate of armour unit removal may be calculated, see Allsop et al (Ref 7) and Thompson & Shuttler (Ref 8). None, however, allow the deterioration of the armour layer performance or stability to be predicted.

Similarly, all design methods for rock, or concrete, armouring assume implicitly that the armour unit size and shape will remain constant throughout the structure life. To compound the problem, the methods used for monitoring completed structures offer relatively little assistance in quantifying the performance in service of an armour layer, or of its constituent armour units.

A number of techniques are presently being developed in the UK to assist the designer of rock armoured coastal structures to predict the likely deterioration of the armour over the design life of the structure. These techniques include rock quality testing, hydraulic model studies, and field monitoring methods. It is hoped that these techniques will allow the designer to adopt either of two different strategies, depending upon the client's administrative and financial position.

In situations where little or no maintenance will be possible, the designer may choose to use an over-size armour calculated to remain within acceptable stability levels throughout the structure design life. The initial size of the armour will be specified allowing for a possible level of deterioration. Such a design approach will allow the benefits and costs of importing a hard and more durable rock to be compared with the alternative use of less durable local material. Long-term consequences of different construction and armour placement techniques might also be assessed.

Where low initial cost is required, but provision may be made either for maintenance or refurbishment, the designer may choose an alternative strategy. In this situation the structure may be armoured using the best material locally available. Measurements of the rock quality using engineering tests, together with estimates of the severity of local degradation processes, possibly derived from monitoring other local structures, will then allow predictions to be made of the rate of armour layer deterioration. From this, the designer may then estimate the frequency of maintenance or

refurbishment requirements. Such estimates may be somewhat uncertain initially. Advanced monitoring techniques are therefore being developed to allow the degree, and hence rate, of deterioration to be quantified.

In any review of the technical literature it may be noted that the terms "damage" and "armour layer damage" are used by various authors with somewhat different meanings. In particular "damage" has often been taken to mean the permanent extraction of an armour unit from its original position in the armour. Such a definition does not, however, permit the quantification of more gradual deterioration, such as the fracture or progressive abrasion of armour units in situ. For this paper, and it is hoped for subsequent work, two definitions of damage are suggested:

(a) armour unit degradation - deterioration/change of armour unit size and/or shape from an original or an idealised size/shape;

(b) armour layer damage - deterioration of an armour layer from an original or idealised state leading to changes in the hydraulic performance and/or stability of the armour layer.

2 Recent Developments

2.1 Rock quality assessment and engineering tests

A wide range of engineering tests are available to quantify material properties such as strength, hardness, abrasion, and chemical resistance. Of these, some tests have been developed by researchers at Queen Mary College (QMC) for the testing of rock, principally intended for use as roadstone or aggregates, but more recently also for use on coastal structures as rock armour. In such applications the rock will be subject to processes of mechanical and chemical deterioration. These processes include impact, abrasion, freeze/thaw, salt crystallisation and leaching, and have been discussed fully by Fookes & Poole, and Poole et al (Refs 1, 2). The use of standard engineering tests is however of little benefit to the designer unless the test results can be related to prototype performance.

In a recent study, a wide range of rock types and prototype structures was studied. Rock from sites in the UK, Arabian Gulf, and east coast of Australia was subjected to a range of engineering tests. The results of these tests were correlated with experience of performance, particularly of rounding, spalling or fracturing. This project yielded a suggested suite of tests with appropriate acceptance values. These studies have been reported fully by Allsop et al (Refs 3, 7). Some aspects of the tests, the acceptance values suggested, their limitations and use, are discussed further with examples in Section 3 below.

It may be noted, however, that the rock available in some circumstances may be of low potential durability. The use of simple accept or reject criteria only for the supply of rock armour may therefore not be particularly helpful. Techniques that allow the in

service life of the available rock to be estimated will be more useful to the designer. A simple example of this approach has been presented recently by Fookes & Thomas (Ref 9). They describe the assessment of locally available rock in the course of a brief site visit. None of the rock easily available would pass the criteria suggested in References 2 and 3, and time was not available for a comprehensive test programme. A set of ad-hoc and qualitative assessment techniques was developed to allow the selection of the best material available. Engineering tests for point load strength, water absorption, and apparent specific gravity were used, together with a comprehensive understanding of the local geology, and of the processes of weathering and hardening. The potential useful life of the rock selected was estimated from the performance in service of various local coastal structures. In particular, assessments of armour stone rounding in service were made using a visually estimated score of relative roundness. In their brief appraisal, Fookes & Thomas demonstrated the potential use of engineering tests for rock quality assessment, together with in service performance monitoring of existing structures, as part of the design process for rock armouring. Since their appraisal, conducted in 1984, there have been further developments in monitoring techniques and in the quantification of the state of rock armour layers, and these are discussed in Sections 2.2 and 4 below.

2.2 Slope and shape monitoring techniques

Classic design methods for rock armouring envisage the construction of armour layers of fixed slope angle(s), thickness and layer porosity. The armour units within the layer are generally described only by the median unit weight, or by upper and lower limiting weights. Such simple descriptors do not, however, allow the hydraulic performance or stability levels of the armour layer to be fully quantified. Nor do they provide a particularly appropriate framework within which to monitor changes to the armour either in the field or in the laboratory.

Recently Latham & Poole (Ref 10) have advanced a set of more sophisticated techniques for the numerical description of the state of an armour layer. They have identified a range of descriptors intended to quantify the armour profile at both macro and micro levels. The descriptors have been tested using experimental profiles formed with glass balls or aggregate particles. Latham & Poole have described the use of high and low pass filters to the data. High pass filtering is clearly useful where particle shape and surface roughness are important. Conversely, low pass filtering may be used to reveal settlement or subsidence of the profile. It is however acknowledged that any relation between the properties of the armour layer profile and its hydraulic performance is as yet unquantified. The data rate required, at around 15-20 points per armour unit, also demands an automated measuring technique. This may be appropriate in the laboratory, but is not yet possible in the field. To accelerate data acquisition, researchers at both QMC and Hydraulics Research (HR) are actively pursuing video image processing techniques, some of which might be capable of digitising armour layer profiles directly.

Further advanced work is also continuing at QMC on the description of particle shape and roughness. Both of these factors considerably influence the hydraulic performance and the stability of the armour layer. Historically relatively little attention has been paid to particle shape. Qualitative terms such as cubic, angular, flat, and rounded, have often been used to describe shape. In some instances ratios of maximum and minimum perpendicular dimensions have been measured, or limiting values suggested. In few instances have the effects of particle shape been quantified. In no example known to the authors has armour unit shape or roughness been quantified and related numerically to armour performance or stability. In an effort to help overcome these problems, Latham and Poole have developed a number of sophisticated descriptors for particle shape and roughness. Preliminary work suggests that a single total roughness parameter might be used to assess many of the effects of armour unit shape on hydraulic performance and stability. A surface texture factor has also been derived for use in quantifying changes in armour unit texture and roughness. Again, automated data collection methods, such as video image analysis, have been investigated.

3 Rock Quality Tests

A suite of engineering tests have been used to assess the durability of the rock fabric, in rock armouring, on coastal structures. The tests have been adapted to analyse the effects of the physical and chemical degradation mechanisms operating in the marine environment; in particular the mechanisms causing abrasion, fracturing and spalling of the armour. The tests selected and the recommended acceptance value for each test are given below.

Recommended Acceptance Values for Quality Control Tests

Test	Recommended Acceptance Value
Aggregate impact value	25 maximum
Franklin point load index	$4MN/m^3$ minimum
Water absorption	2.5% maximum
Specific gravity	2.6 minimum
Magnesium sulphate soundness loss	12% maximum
Fracture toughness	$0.7MN/m^{3/2}$ minimum

The sulphate soundness and water absorption tests are used to assess the effects of salt water on the degradation of the armour. This is particularly important in situations where the rock has a high clay mineral content, such as in clay cemented sandstones or in weathered igneous rocks. Absorption and soundness tests have proved to be particularly useful in assessing the relative performance of various low strength rocks (Ref 9). The sulphate soundness tests induce swelling pressures within the rock fabric, causing accelerated disaggregation of the minerals. The specific test used in this study is a modified version of the ASTM soundness test. Magnesium sulphate is used in preference to sodium sulphate, as it produces more repeatable results, due to the single form into which magnesium sulphate crystallises.

The specific gravity of the rock is also of particular importance, in its stability against wave induced movement. Empirical design formulae for rock armoured structures indicate that more dense rock will be more stable than less dense rock of otherwise similar characteristics (Ref 7).

The Franklin point load test is used as a measure of tensile strength of the rock fabric. This test is particularly useful, since it requires no specimen preparation and can be carried out with portable test apparatus. It should, however, be noted that a fairly wide scatter of results may be obtained from this test. A sufficiently large sample of specimens should therefore be tested, to ensure that the results are statistically valid. Other tests have been considered as a measure of tensile strength; in particular the test for fracture toughness using the single edge notched beam method. This test provides results which correlate well with breakwater armour performance, and with the other engineering tests. Accurate specimen preparation and expensive testing equipment are, however, required for this particular test. Additionally, some difficulties have been experienced in preparing test specimens of coarse grained rocks (such as granites), where the test provides less reliable results. Whilst it is felt that this test does provide useful additional information on the rock quality, the additional costs and time taken tend to mitigate against its use.

The aggregate impact test is used as a measure of the potential for the disaggregation of the rock fabric by rock impact. This type of degradation typically occurs where armour is allowed to rock under wave action, or is subject to impact by suspended materials. Other tests have also been used to examine the wear resistance of the rock, including the Los Angeles abrasion test, an especially developed roller mill test, and the aggregate abrasion test. Whilst none of the tests have yet been fully calibrated against structure performance, general guidelines for the aggregate abrasion test have been drawn from the standards used in roadstone selection and experience drawn from a number of coastal structures.

The acceptance values tabulated above have been suggested on the basis of the in service performance of a range of rock types. In instances where the rock does not meet the specifications, in one or more of the tests, the full range of results should be considered carefully. Additionally, large scale inherent weaknesses in the rock, such as natural joints and bedding planes, which may affect armour unit size should also be considered. Only after careful analysis of the implications of any deficiencies in the rock should a decision be made to accept or reject the material.

In many instances, where the only rock available is of marginal or inferior quality, the tests may be used as a guideline to the performance of such material. Modifications to the design may sometimes be made to allow for the use of inferior quality of materials in the design. Further calibration data is, however, still required to allow the performance of substandard rock to be predicted with any degree of confidence.

The case studies outlined below illustrate some limitations of the durability tests and discuss the implications of results, suggesting appropriate modifications to the designs wherever necessary. A range of test results achieved in recent studies is shown in Table 1.

Two coarse granites from Spain have been examined, both of which exhibit good results in all but the Aggregate Impact Value test (AIV), where values of 30 and 41 were achieved - both above the recommended maximum of 25. These high values are clearly a function of the extremely coarse crystals of which these rocks are composed, and the angular nature of the aggregate size samples tested. The high impact values imply that the rock is less resistant to impact than might be desirable and suggest that abrasion, caused by movement of armour, or attrition by suspended sediment might cause fairly rapid rounding of the rock.

Rock type 4, (Table 1), exhibited an AIV of 41. Whilst the other test results were within acceptable limits, they were not so high as to imply a high level of durability. The shape characteristics of the armour, which was virtually cubic, and the absence of inherent planes of weakness in the armour did, however, allow a tight placement of the armour, thus reducing the likelihood of impacts from rocking movements. Hydraulic model tests conducted previously for a specific use had shown the rock armour to be very stable. The rock could therefore be expected to remain reasonably immobile under most wave conditions, and should therefore only suffer abrasion damage due to attrition by suspended sediments. By allowing a minimal over-design of rock weight, and ensuring that the armour is tightly packed, such rock of otherwise marginal quality should perform to an acceptable level.

The use of rock quality testing, together with hydraulic model tests may be illustrated by an example of a recent study for the rehabilitation of a vertical sea wall using rock armour. Two sources of rock were considered, the properties of which are given in Table 1 (rock types 1 and 2). Both rock types exhibited good results in all of the rock fabric tests. However, the large inherent weaknesses due to jointing in the carboniferous limestone indicated that the rock armour might break into smaller pieces if subjected to movements under wave action. The proposed construction method was considered carefully in the placement of rock in the hydraulic model. During testing, noticeable levels of armour rocking were recorded. The client was advised both on the hydraulic consequences of the design and the proposed construction method, and also on the implications of the anticipated armour movement on the selected rock armour type. As a result of the hydraulic model studies and the rock durability tests, it was possible to give advice on a suitable method of construction, to increase the packing density of the armour and thus reduce potential movement of the inferior quality rock.

4 Monitoring Techniques

Most conventional damage assessment techniques have been concerned solely with the evaluation of the proportion of armour units extracted permanently from the armour, resulting in cavities or voids. This is

Table 1: Rock properties

Rock Type	Location	Apparent Relative Density t/m^3	Water Absorption %	Magnesium Sulphate Soundness %	Franklin Point Load Index	Aggregate Impact Value	Aggregate Abrasion Value
1 Carboniferous Limestone	Westleigh UK	2.70	0.6	0.1	7.4	20	10.2
2 Gritstone (greywacke)	Triscombe UK	2.66	0.1	9.5	13.8	10	4
3 Granite Coarse Biotite	Pico D'Ouro Spain	2.64	0.6	0.2	10.4	30	3.5
4 Granite Coarse Biotite	Porrino Spain	2.64	0.5	0.6	5.9	41	5.4
5 Fine Grained Greywacke	Belfast N Ireland	2.67	0.7	2.1	8.1	11	6.7
6 Kentish Limestone	Offham UK	2.53	2.4	40.0	-	28	19.6
7 Granite	Gothenburg Sweden	2.70	1.0	0.6	-	-	-
8 Granodiorite	Gothenburg Sweden	2.85	0.3	4.1	8.0	19	3.9

perhaps an over simplification of armour layer damage, since a number of significant, but more gradual degradation processes are not considered. The type of damage or degradation may vary according to a number of controlling factors.

(a) Environmental factors; such as waves, tidal range, temperature, salinity.
(b) Armour shape and size.
(c) Armour interlock.
(d) Rock quality.

An inspection method has been developed that allows the simultaneous appraisal of the effects of each of these elements. The methods used in this study are based closely on those developed by researchers at QMC and described by Allsop et al (Ref 3). A number of categories of armour layer damage have been identified, allowing the principle mechanisms of damage to be clearly defined on each structure. A brief description of each of the damage categories is given below.

The most obvious form of armour layer damage is the void or cavity, as considered by more conventional damage assessment methods. Fractures in armourstones may occur when the armour is permitted to move freely under wave action and/or where there are large inherent planes of weakness in the rock. Subsize armour may be defined as armour which is below specification size. This may occur as a result of poor quality control during construction, or may result from fracturing whilst in service. The final damage category used in this method of damage description is unstable armour. This is loosely defined as armour which is visibly mobile under wave action. Unstable armour is often characterised by rounded or abraded edges resulting from rocking movements, and is frequently observed on newly constructed structures, where initial placement may allow the armour to move freely. Such a condition is, however, usually temporary, as unstable armour tends to stabilise or is removed completely from the armour layers by wave action.

These armour layer degradation descriptors have been used in a monitoring method which aims to give a fuller description of armour layer damage than methods used previously. No sophisticated equipment is required to carry out surveys, but the method is, at present, limited to the sections of the structure that are surface emergent. Data is collected within carefully selected, delineated areas, each of which must be of sufficient size to provide a statistically valid sample of the armouring. The size of sample areas is dependent upon armour size and the freeboard of the structure. As a guideline, sample areas should contain a minimum of 100 armourstones. Similarly, the number and location of sample areas needed depends upon the size and exposure of the structure. Where possible, separate sets of measurements should be made for the intertidal and supratidal zones of the structure. Sample areas should be referenced to local fixed points, to allow relocation on subsequent surveys.

Surveys are conducted by counting the number of armour units in each of the damage categories. The most useful expression of damage is given by the total number of armour units in each category, expressed as a percentage of the total number of armour rocks in the study area.

A number of other damage assessment methods have also been considered (Ref 11). Expression of the degree of armour unit interlock may be a useful indicator of the integrity of the armour layers. A descriptor known as co-ordination number has been used to evaluate block interlock. This is simply defined as the average number of armourstones in contact with each individual armourstone in the sample.

Comprehensive monitoring programmes have been instigated using these measurement techniques. Several structures have been surveyed, covering a range of degrees of exposure to wave conditions and structure types. Some important aspects and conclusions drawn from the inspections are given below.

Port Talbot breakwater main arm was chosen for study, as a structure of typical rubble mound construction, exposed to a fairly severe wave climate. The main breakwater is approximately 2km long, changing alignment twice along its length, and is subject to a particularly large tidal range of approximately 8 metres. Sample areas were selected at locations of varying exposure - according to water depth and breakwater alignment, and separate sets of measurements were recorded in the intertidal and supratidal zones. The results of the first survey are shown in Table 2. A marked contrast in armour layer damage occurs between the intertidal and supratidal zones. Certain sections of the structure have degraded more rapidly than others, particularly in the intertidal zone. Sample area 3 (Table 2) has suffered far greater damage than other sections of the structure. This area is in a more exposed location, in deeper water and facing the predominant wave direction. The predominant category of armour layer damage on this structure is cavities. This is largely due to the severe wave conditions to which the structure is exposed. The rock armour is of relatively good quality, as is evidenced by the relatively low proportion of fracture damage. However, degradation by fracturing is significantly greater on the more exposed section of the structure, where more movements are likely to occur.

The revetment at Herne Bay, Eastcliff III is a recently constructed (1986) riprap armoured structure. Armour has a W_{50} of 850kg and the rock armour type is a granodiorite from Sweden. The properties of the rock are given in Table 1. An extremely low level of armour layer damage was measured on the first survey (Table 3). Good quality control during construction is evidenced by the absence of subsize armour. The quality of the rock appears to be very good, with little evidence of abraded or fractured armour. It should, however, be noted that the structure had not been subjected to a winter storm season at the time of the survey. Whilst overall armour layer damage was low, unstable armour figured prominently as a damage type. This might reasonably be expected on a newly constructed structure. Initial

Table 2: Breakwater Damage Assessment - Port Talbot

Sample No	No of Rocks	Fractures (%)	Cavities (%)	Subsize Armour (%)	Unstable Armour (%)	Total (%)	Co-ordination No
1 Supratidal	492	0.4	4.1	0.2	0.4	5.1	4.4
Intertidal	368	0.8	10.6	0.3	5.4	17.1	4.1
2 Supratidal	468	0.9	7.1	0.2	1.3	9.4	4.8
Intertidal	408	1.2	14.0	2.2	0.7	18.1	4.2
3 Supratidal	223	3.6	9.9	0.4	0.9	14.8	3.7
Intertidal	177	4.0	33.3	4.0	2.8	44.1	4.0

Table 3: Breakwater Damage Assessment

Location	No of Rocks	Fractures (%)	Cavities (%)	Subsize Armour (%)	Unstable Armour (%)	Total (%)	Co-ordination No
Port Talbot	2712	1.1	9.4	1.5	0.8	12.8	4.2
Stornoway	693	1.4	1.7	2.2	3.0	8.3	4.6
Herne Bay Eastcliffe III	828	0.2	2.2	0	1.7	4.1	4.9

settlement and removal of any unstable blocks during the first winter may well result in a reduced proportion of damage, in this particular category, on the next survey. The relatively wide grading of rock armour made measurement of the co-ordination number difficult, and where the rock grading was reduced in median size, at the less exposed end of the structure, the rock was too small to make measurement of the co-ordination number practicable. A series of levels were also taken along profile lines running from toe to crest of the structure.

The structure monitored at Stornoway airport is also armoured with riprap. The median rock size is, however, larger than that at Herne Bay, with a W_{50} of 1 tonne. This structure had been in existence for some years prior to the first damage survey, but sections of the structure had been repaired only a few months before the survey took place. The rock type used on this structure is a Lewisean gneiss, which often includes large inherent planes of weakness in the armourstones. This is evidenced in the damage analysis (Table 3) by the proportion of fractured armourstones in the samples. Cavities were infrequent, since most of the damage to the structure had recently been repaired. A relatively high proportion of structure damage occurred either as subsize armour or as unstable armour. This may be explained, to some extent, by the fact that the structure was a little unusual, in that it had undergone recent rehabilitation. Prior to repair the structure had a large number of cavities, due to armour removal. When armourstones are extracted it is quite common for units surrounding the voids to move to new positions, often reducing the size of the voids, and also reducing interlock between armourstones. In some instances the voids are reduced to a size such that the replacement rock cannot be placed in a stable position during repair. Alternatively, armour below the original specification size must be used to fill the voids, thus maintaining a reasonable degree of interlock. Whilst this may explain the reasons for the presence of some subsize armour on the structure, some of the armour has clearly degraded in situ as a result of fracturing along the planes of weakness in the rock.

Data collected in this study can be used to provide a detailed analysis of armour layer damage. By identifying the proportions, quantities and locations of each of the damage types, scheduled maintenance can be planned. If surveys are carried out on a regular basis, problems of gradual degradation that might otherwise go undetected may be identified. As more data becomes available, it should provide a basis for the selection of appropriate materials and construction techniques at the design stage, or allow revised placement techniques or material standards to be adopted during the repair of existing structures.

5 Recommendations

The work described in this paper has identified a number of techniques of use to the designer or owner of rock armoured coastal structures. A set of engineering tests has been developed to allow the identification of durable rock, and to grade available material for potential durability. Field monitoring techniques using a minimum of equipment have been described that quantify changes both to the

armoured slope and to individual armour units. A range of numerical descriptors have been defined and tested for armour profiles, and for armour unit shape and roughness.

Two further areas of research may now be identified. Armour unit shape and surface roughness clearly influence both the hydraulic performance and the stability of an armoured slope. Now that numerical descriptors are available for particle shape and roughness, it should be possible to conduct a series of hydraulic model tests to relate hydraulic performance and stability parameters directly to those for armour unit shape and roughness.

Also of importance to the prediction of armour layer performance is the quantification of changes to armour unit size and shape under the chemical and mechanical deterioration processes of the marine environment. This will require the quantification of rates of deterioration, such as rounding, in relation to the original rock material properties, wave climate and environmental parameters.

6 Acknowledgements

The work on which this paper is based has been funded in part by the Department of the Environment and the Ministry of Agriculture, Fisheries and Food. The authors are also grateful for the assistance of Dr J P Latham and Dr A B Poole of Queen Mary College, and Mr T J Austin of Canterbury City Council, and for the advice of Mr M W Owen, Manager of the Coastal Engineering Group, Hydraulics Research.

7 References

1. Fookes P G and Poole A B. Some preliminary considerations on the selection and durability of rock and concrete materials for breakwaters, and coast protection works. Q J Eng Geol, Vol 14, 1981.

2. Poole A B, Fookes P G, Dibb T E and Hughes D W. Durability of rock in breakwaters. Proc Conf Breakwaters - design and construction, ICE, London, 1983.

3. Allsop N W H, Bradbury A P, Poole A B, Dibb T E and Hughes D W. Rock durability in the marine environment. Report SR 11, Hydraulics Research, Wallingford, March 1985.

4. Baird W F and Hall K R. The design of breakwaters using quarried stone. Proc 19th Coastal Eng Conf, Houston, September 1984.

5. Van der Meer J W and Pilarczyk K W. Dynamic stability of breakwaters, rock slopes and gravel beaches. Proc 20th Coastal Eng Conf, Taipei, November 1986.

6. Van der Meer J W. Stability of rubble mound revetments and breakwaters under random wave attack. Proc Breakwaters 85, ICE, London, October 1985.

7. Allsop N W H, Powell K A and Bradbury A P (editors). Proc Seminar on the use of rock in coastal structures, Hydraulics Research, Wallingford, January 1986.

8. Thompson D M and Shuttler R M. Design of rip-rap slope protection against wind waves. Report No 61, CIRIA, London, 1976.

9. Fookes P G and Thomas R S. Rapid site appraisal of potential breakwater rock at Qeshm, Iran. Proc ICE Pt 1, ICE, London, October 1986.

10. Latham J P and Poole A B. The quantification of breakwater armour profiles for design purposes. Coastal Engineering 10, Elsevier Science Publishers, Amsterdam, 1986.

11. Bradbury A P and Allsop N W H. Monitoring techniques for performance and stability of armoured coastal structures. Report SR 99, Hydraulics Research, Wallingford (to be published 1987).

CHAPTER 130

THE INFLUENCE OF WAIST THICKNESS OF DOLOSSE ON THE HYDRAULIC STABILITY OF DOLOSSE ARMOUR

by
Hans F. Burcharth *
Torben Brejnegaard-Nielsen **

ABSTRACT

The paper presents results from experiments with Dolosse having the same mass and volume but with different waist thickness to height ratios. The armour was exposed to irregular waves simulating one storm with increasing wave heights and the effect of waist to height ratio on the hydraulic stability was studied. A low packing density of approximately 0.65 was used corresponding to a two-layer armour with high porosity.

From the results it is concluded that the hydraulic stability of Dolos armour is not very sensitive to variations in the waist to height ratio. Only for damage levels exceeding displacement of approximately 5% of the armour blocks in the most exposed area there seems to be a significant decrease in hydraulic stability with increasing waist to height ratio. Thus the waist ratio only influences the residual hydraulic stability.

Based on a short discussion of stressed in armour units it is concluded that design criteria solely based on movements of armour units as observed in hydraulic models are not adequate for the assessment of structural integrity of the units.

The paper also presents the results of each stability test as well as the scatter and the distributions. The large scatter found underlines the need for adoption of more restrictive safety factors than generally used in rubble mound breakwater design. It also supports the idea of a probabilistic approach in the design process.

INTRODUCTION

The recent failures of major rubble mound breakwaters have demonstrated the need for developments in breakwater design and construction. The problem is highly complex as the loads on the breakwaters and the response to match are typical stochastic wide-banded processes. On that background all parameters involved in breakwater design certainly have to be considered and their relative importance evaluated. One parameter of great importance is the mechanical strength of concrete armour units.

* Professor of Marine Civil Engineering, University of Aalborg, Denmark.
** Consulting Engineer, London, UK.

It is evident and well documented that the relative strength of concrete armour units decreases with the size of the armour units (Burcharth, 1981a), (Burcharth, 1981b), and (Silva, 1983).

Generally in complex types of armour units the stress level due to flow forces and static (gravity) forces increases linearly with the characteristic length (e. g. the height of the armour unit) while the stress level due to impacting units increases with the square root of the characteristic length. The relative importance of these stresses depends on the geometry of the units and their position on the slope, cf. Fig. 1.

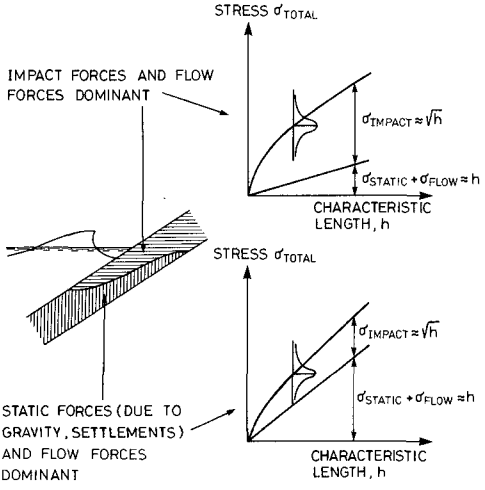

Figure 1. Qualitative representation of stresses in complex armour units as function of the size (length) of the units.

It follows from this that a design criterion solely based on movements of armour units in a hydraulic scale model is not adequate for the assessment of the structural integrity of the armour units.

Because of the size dependent stress level, one must either increase the strength of the units and/or apply a milder design criterion (e. g. a certain degree of rocking instead of displacements) when dealing with larger units.

In the case of complex types of armour units such as Dolosse, one way of increasing the strength is to increase the crosssections, i.e. apply a larger waist thickness to height ratio, r = d/h, see Fig. 3. However, by doing so the hydraulic stability will be changed too, which must be considered in the design. Thus, the relationship between the waist ratio and the hydraulic stability must be known. Scholtz et al. (1982) studied this relationship for Dolosse exposed to regular waves.

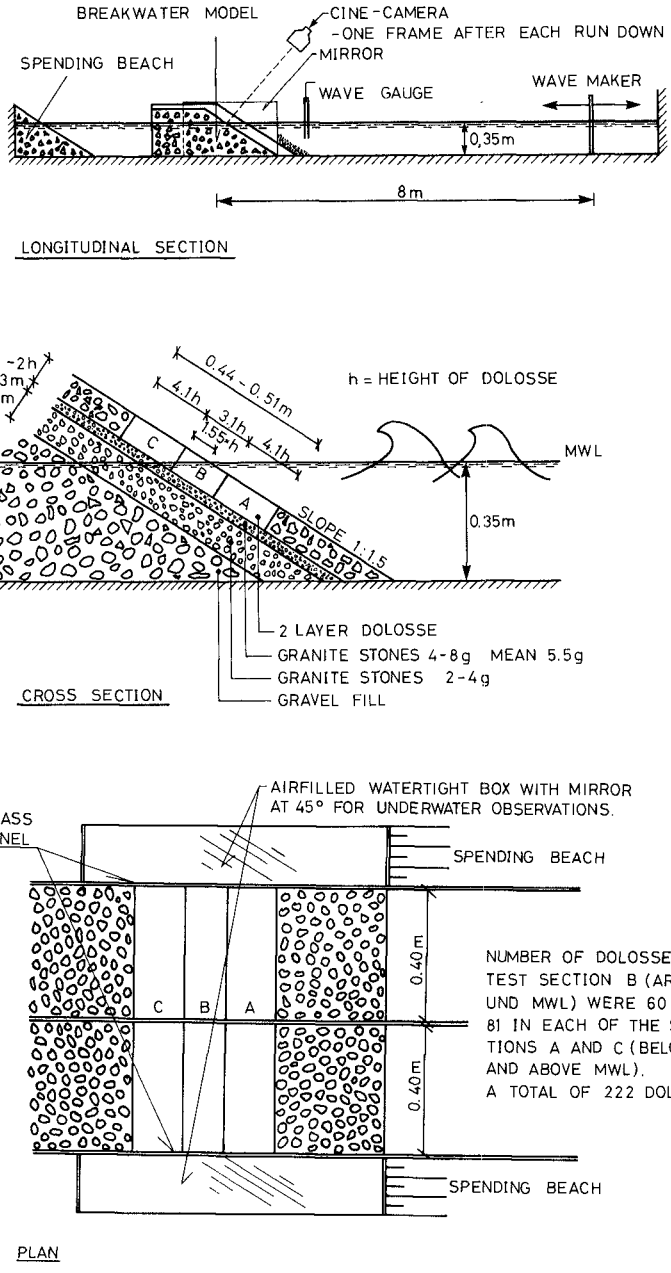

Figure 2. Test set-up.

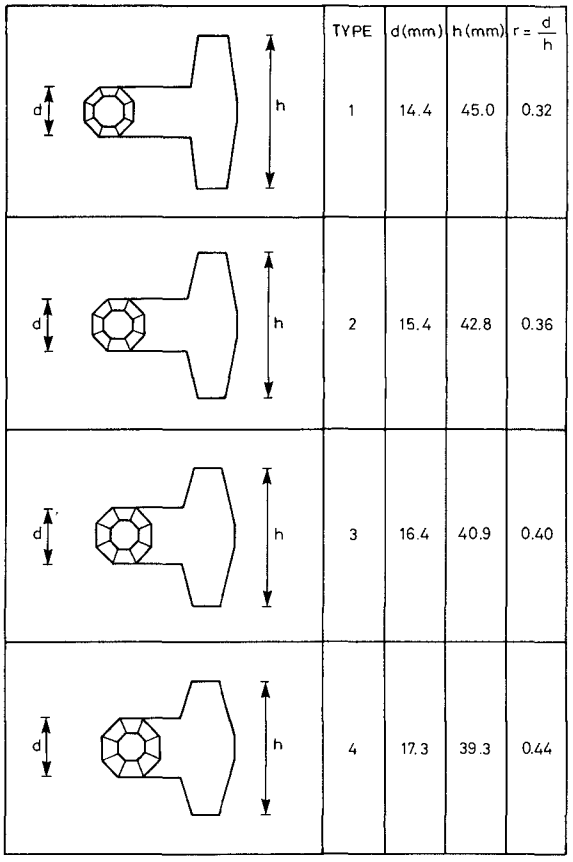

Figure 3. Geometry of model Dolosse.

In the present work the same hydraulic stability dependence is studied in irregular, two-dimensional waves for waist ratios of r = 0.32, 0.36, 0.40, and 0.44.

MODEL LAY-OUT

The tests were carried out in a 5 meter wide wavebasin, equipped with a spending beach, Fig. 2. As the total width of the model was only app. 1.6 meter, the wave reflection from the model was negligible.

The model was built in two separated sections to allow for a comparative study, where one section in all tests was armoured with Dolosse with a waist ratio of 0.32 used as a reference.

Each of the test sections was divided into three sub-sections called above, around and below mean water level. The Dolosse were placed randomly with a loose hand in two layers. For each test a total number of N = 222 Dolosse were applied in each section of 11.3 h x 0.40 m, where h is the height of the Dolos. Four types of Dolosse having the same volume and made of cement mortar with a mass density of ρ_a = 2.24 t/m^3 were tested. The geometry is given in Fig. 3. The theoretical volume of the Dolos is 14.2 cm^3, but pores in the surface made the actual volume V = 13.7 cm^3.

The packing density of the armour, defined as $\varphi = N\, V^{2/3}$, where N is the number of blocks per unit area, was 0.61, 0.64, 0.67, and 0.70 for waist ratios, r = 0.32, 0.36, 0.40, and 0.44, respectively. This corresponds to a two-layer armour with loose packing and high porosity. The increase in φ with r compensates for the otherwise increasing openness (exposure of filter layer stones) with increasing r. This, however, also means increasing amount of concrete per unit area with increasing r.

Generally a larger packing density in the order of 1.0 is recommended, but here the low values were chosen deliberately to represent the worst conditions in a real breakwater situation where uneven distribution of Dolosse on the slope can occur.

Cement mortar was applied in order to represent the prototype surface roughness as closely as possible. The tests were performed with irregular waves generated with a piston type wave maker on basis of a 5 parameters JONSWAP-spectrum.

$$S(f) = \alpha g^2 (2\pi)^{-4}\, f^{-5} \exp\left(-\frac{5}{4}\left(\frac{f}{f_p}\right)^{-4}\right) \cdot \gamma^{\exp\left(-\frac{1}{2}(f-f_p)^2/\sigma^2 f_p^2\right)}$$

with the four parameters;

f_p = 0.83 Hz
σ = 0.07 for $f < f_p$
σ = 0.09 for $f \geq f_p$
γ = 3.3

The fifth parameter α was used as a gainfactor to establish the desired significant wave-height $H_s = 4\sqrt{m_o}$, where m_o is the variance of the surface elevation.

Five values of H_s were chosen such that rocking of single blocks and displacements of several blocks would appear for the smallest and the largest H_s values, respectively. The values of H_s are given in Table 1 together with the parameter $\xi = (H_s/L_{H_s})^{-0.5} \tan\alpha$, where L_{H_s} are the wavelength corresponding to H_s and $\tan\alpha$ the slope.

Table 1. H_s and ζ values applied in the model tests.

Level	1	2	3	4	5
H_s (mm)	43	59	67	83	94
ζ	3.9	3.3	3.1	2.8	2.6

The duration of each test was 20 min. corresponding to approximately 1200 waves.

TEST PROCEDURES

Three series of tests were performed each containing the reference Dolosse (r = 0.32) and one of the other three block types. To evaluate the scatter each series consisted of five repeated (independent) tests, cf. Table 2, in each of which the wave height was increased corresponding to the above mentioned five levels of H_s.

Table 2. Test program.

Serie	1	2	3
Block type	r = 0.32, r = 0.44	r = 0.32, r = 0.40	r = 0.32, r = 0.36
No. of independent tests	5	5	5
No.of wave levels in each test	5	5	5

For each wave level in each test visual observations of the rockings and displacements in each of the sub-sections A, B, and C were made by 2 persons simultaneously by means of a special mirror system (Fig. 2). The mirror system allowed underwater observations throughout the running tests.

As a supplement single frames were taken by a cine-camera, which was activated when the water level during down-rush was approximately at the lowest level.

Two modes of movements were observed namely the rocking of the blocks (moving without translation) and the displacement of the blocks (moving with translation).

It was very clear from the testing that realistic information on the number of units rocking and being displaced cannot be obtained without the possibility of continuous underwater observations.

TEST RESULTS

In the Figures 4 to 7 the observed stability in terms of relative numbers of rocking and displaced units is depicted as functions of H_s, H_s/h and the stability number

$$N = \frac{\rho_a H_s^3}{M(\rho_a/\rho_w - 1)^3} = \frac{H_s^3}{V(\rho_a/\rho_w - 1)^3}$$

where ρ_a and ρ_w are the mass density of the Dolos and the water, respectively, and M and V are the mass and the volume of the Dolos, respectively.

N^3 can be derived from Hudson's formula as $K_D \cot\alpha$, where K_D is the Hudson stability factor. However, K_D should not be used for Dolos because the hydraulic stability is practically independent of the slope angle for $1 < \cot\alpha < 3$, which means that Hudson's formula is not valid for Dolos armour (Brorsen et al., 1974). However, to facilitate comparisons with the many published K_D values for Dolos also a K_D scale is shown in the figures.

To illustrate the scatter in the experimental results also the standard deviation over the mean value is shown for the various wave levels. Moreover, each test result is shown as a dot to visualize the actual distributions of the test results. It might be seen that these distributions can be fitted to the Poisson type distributions. It should be mentioned that these distributions, which represent the movements of the armour units, are different from the still unknown distributions related to the stresses in the units.

The figures illustrate the well known fact that the damage to the Dolosse armour is most severe in area B around the mean water level.

Despite its lack of consideration of the strength of the armour units, a design criterion corresponding to app. 5% of the units being displaced (within the levels SWL $\pm$ H_s) is often used. It is interesting to see that this compares to app. 10% of the units rocking and to H_s/h-values in the range 1.5-1.7 corresponding to K_D-values in the range 6.5-7.5. These K_D-values are lower than generally recommended. The reason for this discrepancy is probably that in many model tests the set-up did not allow underwater inspection of the movements of the armour units, which means that milder degrees of damage were recorded. Another reason might be lack of control of the reflected waves in some flume tests. Also the low packing density used in the present tests might have some influence on the K_D values, cf. the following conclusions.

Figure 8 shows a comparison of the stability of the four types of Dolosse. A decrease in stability with increasing waist ratio r is seen, but only for the more severe wave conditions, say $H_s/h > 1.5$ or $N^3 > 10$. For the smaller values of H_s/h there are only minor, non-systematical differences between the stabilities of the various shapes of Dolosse.

COMPARISONS AND CONCLUSIONS

Tests were performed on the hydraulic stability of Dolosse with waist thickness to height ratios of r = 0.32, 0.36, 0.40, and 0.44 exposed to irregular waves. It can be concluded that the hydraulic stability is decreasing with increasing waist ratios but only for high degrees of damage, i.e. damage levels exceeding displacements of approximately 5% of the blocks in the most exposed area. Thus the waist ratio only influences the residual hydraulic stability of the armour. The reduction in the hydraulic stability is probably due to the relatively quicker loss of effective permeability ("reservoir effect") and interlocking ability for units

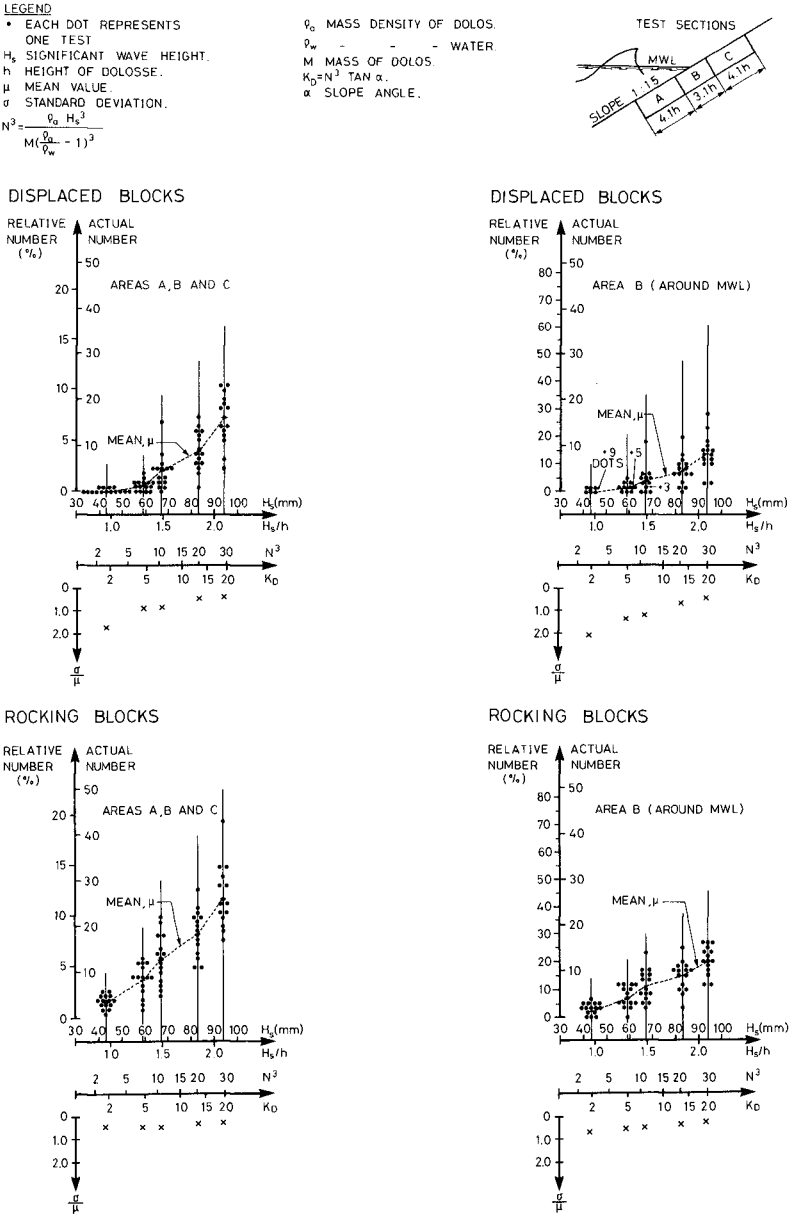

Figure 4. Test results for Dolosse with waist ratio r = 0.32.

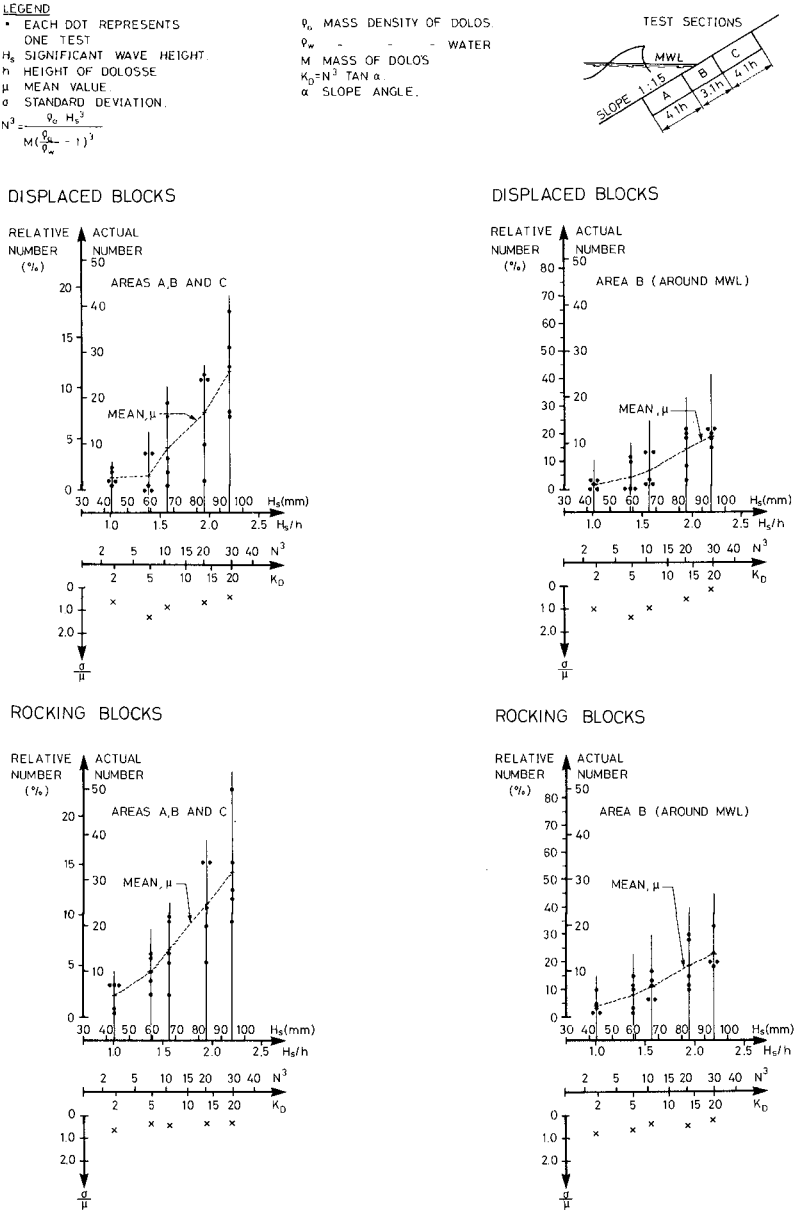

Figure 5. Test results for Dolosse with waist ratio r = 0.36.

LEGEND
- • EACH DOT REPRESENTS ONE TEST.
- H_s SIGNIFICANT WAVE HEIGHT.
- h HEIGHT OF DOLOSSE.
- μ MEAN VALUE.
- σ STANDARD DEVIATION.
- $N^3 = \frac{\rho_a H_s^3}{M(\frac{\rho_a}{\rho_w} - 1)^3}$
- ρ_a MASS DENSITY OF DOLOS.
- ρ_w - - - - WATER.
- M MASS OF DOLOS.
- $K_D = N^3 \tan \alpha$.
- α SLOPE ANGLE.

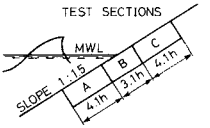

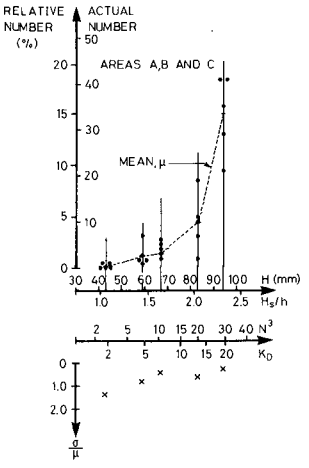

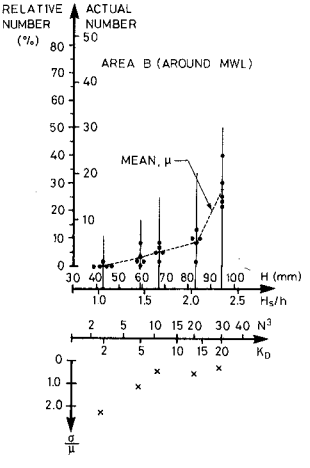

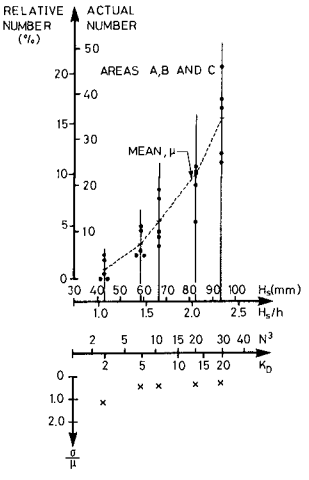

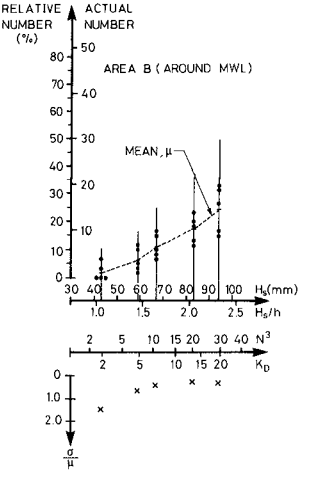

Figure 6. Test results for Dolosse with waist ratio r = 0.40.

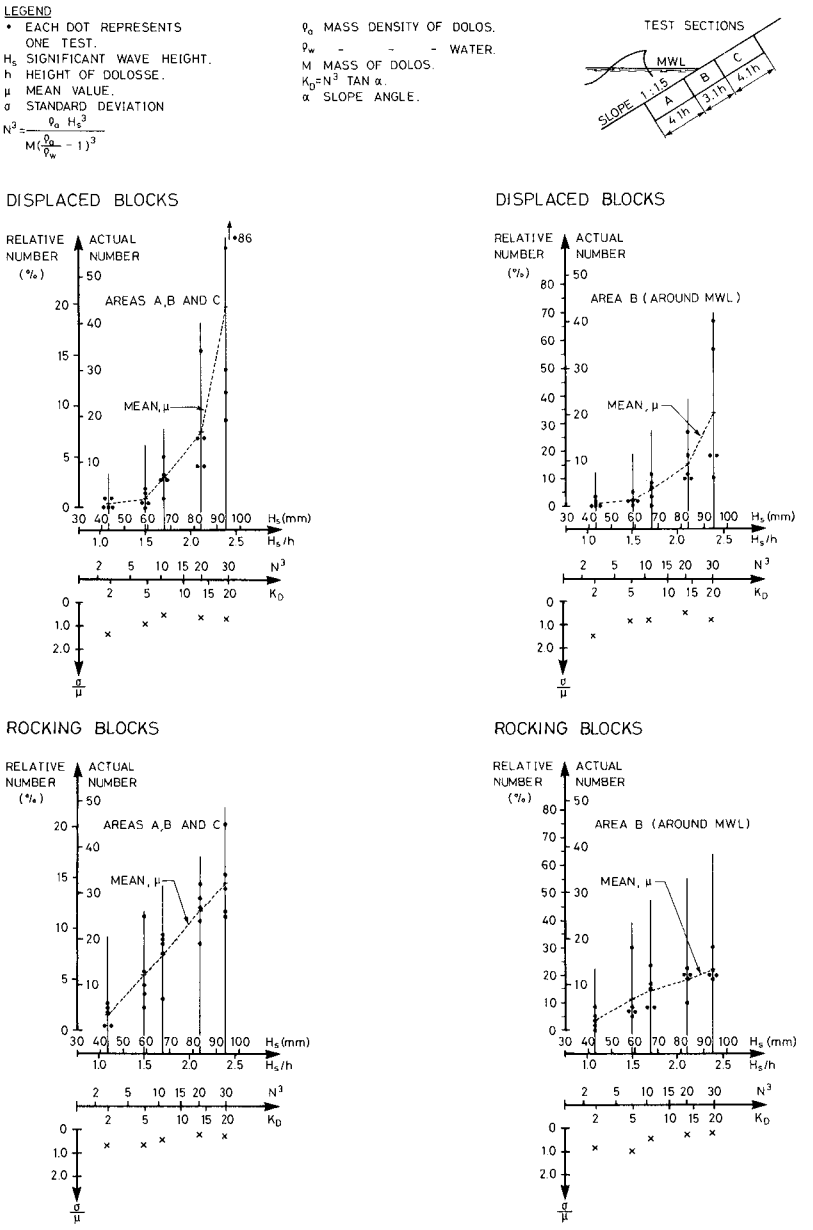

Figure 7. Test results for Dolosse with waist ratio r = 0.44.

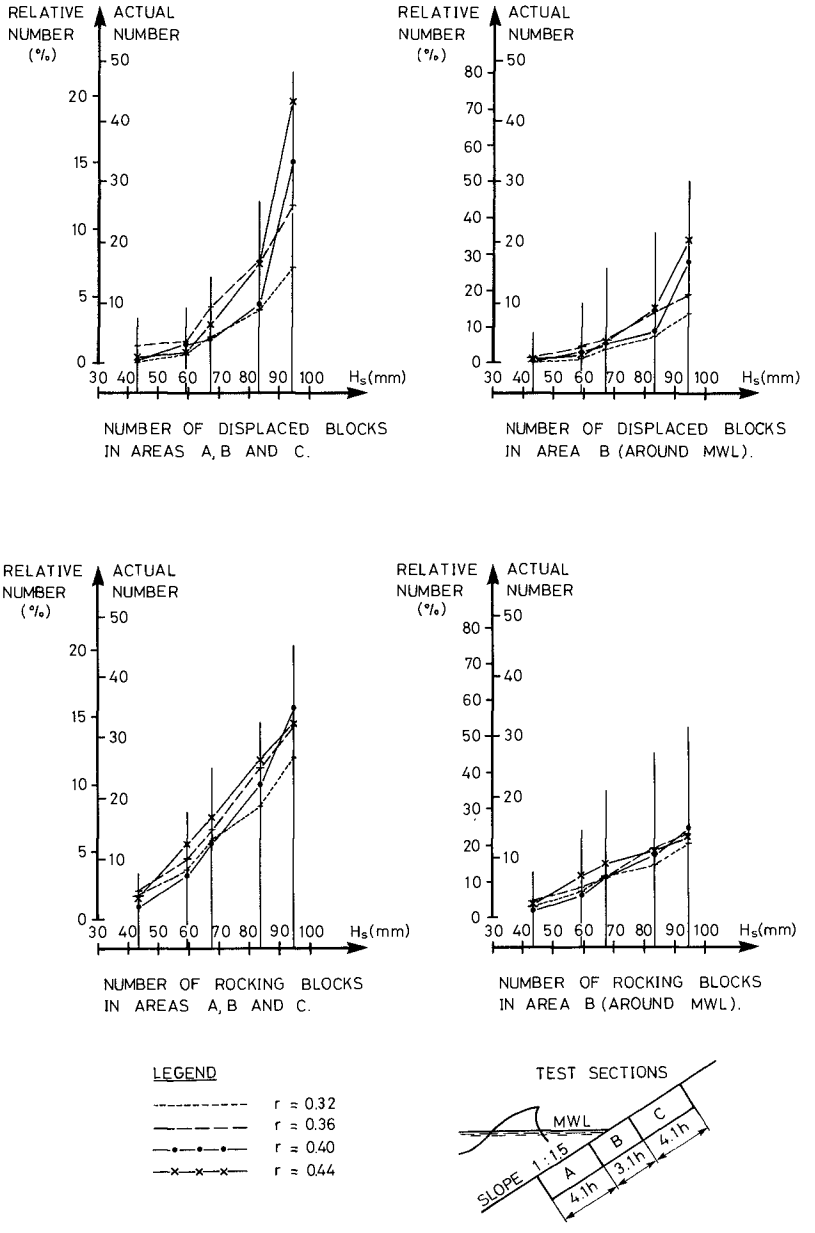

Figure 8. Comparison of hydraulic stability of Dolosse with waist ratios 0.32, 0.36, 0.40, and 0.44.

with large waist thicknesses (Burcharth et al., 1983).

The same trend but more pronounced was found by Scholtz et al. (1982). However, they used regular waves in the experiments such that a comparison cannot be made directly. Brorsen et al. (1974) found that irregular waves of H_s will cause the same degree of damage as regular waves with the height $H \cong 0.8H_s$.

A comparison of the present results with the results of Scholtz et al. gives $H \cong 0.6H_s$ for the same damages. An explanation for a part of this discrepancy is probably that Scholtz et al. did not use a technique which allowed underwater inspection of the movements of the armour units. This means that the present tests certainly will show a larger number of moving units (other things equal) and thus a lower stability of the Dolos armour, because all units are kept under observation during the tests.

Moreover, Scholtz et al. used a packing density of 1.00 for the Dolos armour while a range of 0.61-0.70 was used in the tests presented here. The difference should, according to tests in regular waves by Zwamborn et al. (1982), compare to a reduction in wave height of approximately 6% for the lower packing density.

It should also be noticed that damage levels expressed in terms of the relative number of moving units are dependent on the actual number of units in the section under observation, i.e. dependent on the size of the section and the packing density. For example by increasing the packing density from 0.65 to 1.0 the relative number of moving units will decrease by app. 50% but of course only if the actual number of moving units is independent of the total number of units in the section, which is not the case.

A similar comparison of the present results with the results obtained by Brorsen et al. (1974) and Burcharth (1979) for regular waves and Dolos packing densities of 1.0 shows approximately the same relationship $H \cong 0.6H_s$ as mentioned above. This again is mainly due to the fact that the set-up of these tests did not allow continuous underwater inspections. It is believed that the relationship $H \cong 0.8H_s$ is the more realistic although based on the tests by Brorsen et al. where underwater inspection was impossible. This is because these tests are a comparative study where exactly the same observation technique was used on both regular and irregular waves and because it is reasonable to assume the same proportionality between the total number of moving units and the observed number of moving units for both regular and irregular wave conditions.

The presented results indicate that in areas of the armour layer where impacts are the dominant loads it is possible to obtain a balance between the hydraulic stability and the structural integrity also for the very large Dolosse of say 40 t or more by increasing the waist ratio. However, because stresses due to static (gravity) forces and flow forces increases more rapidly with the size of the units than stresses due to impact forces it might well be that for the armour layer as a whole the structural integrity cannot be obtained.

The large scatter in the experimental results underlines the need for adoption of more restrictive safety factors than generally used in rubble mound breakwater design. It also supports the idea of a probabilistic approach in the design process (Nielsen et al., 1983).

REFERENCES

Brorsen, M., Burcharth, H.F., Larsen, T. (1974): Stability of Dolos slopes. Proc. 14th ICCE, Copenhagen, 1974.

Burcharth, H.F. (1979). The effect of wave grouping on on-shore structures. Coastal Engineering, 2, 1979, p. 189-199.

Burcharth, H.F. (1981a): A design method for impact loaded slender armour units. ASCE Int. Convention, New York 1981. Laboratoriet for Hydraulik og Havnebygning, Bulletin No. 18, University of Aalborg, Denmark, 1981.

Burcharth, H.F. (1981b): Full-scale dynamic testing og Dolosse to destruction. Coastal Engineering, 4, 1981, p. 229-251.

Burcharth, H.F., Thompson, A.C. (1983): Stability of armour units in oscillatory flow. Proc. Coastal Structures '83, Washington, 1983.

Nielsen, S.R.K., Burcharth, H.F. (1983): Stochastic design of rubble mound breakwaters. Proc. 11th IFIP Conf. on System Modelling and Optimazation, Copenhagen, 1983.

Scholtz, D.J.P., Zwamborn, J.A., van Niekerk, V. (1982): Dolos stability, effect of block density and waist thickness. Proc. 18th ICCE, Cape Town, 1982.

Silva, M.G.A. (1983): On the mechanical strength of cubic armour blocks. Proc. Coastal Structures '83, Washington, 1983.

Zwamborn, J.A., van Niekerk, M. (1982): Additional model tests, Dolos packing density and effect of relatively block density. CSIR Research Report 554, Stellenbosch, 1982.

CHAPTER 131

STUDY OF STATISTICAL CHARACTERISTICS OF IRREGULAR WAVE PRESSURE ON A COMPOSITE BREAKWATER

by

Chien-Kee Chang* and Ching-Her Hwang**

ABSTRACT

Wave pressure is the most important external force for the design of breakwater. During recent years, there has been considerable development in the technology of vertical face breakwater; however, there is no reliable method to compute wave forces induced by irregular waves. The purpose of this study is to obtain statistical characteristics of irregular wave pressure distribution from the data of model tests.

The results of this study shown that vertical face breakwater under the action of irregular waves, some waves are reflected, so that the next wave breaks a critical distance resulting in a rapidly rising shock pressure on the breakwater. On the average, the wave pressure increase with incoming wave height, but the maximum wave force does not necessarily occur for the largest wave height. It can be occurred for serval larger wave group in an appropiate phase composition. The irregular wave pressure distribution on the breakwater is quite uniform; the ratio of tested and calculated wave pressures decreases with the reduction of relative crest height of breakwater.

Goda formula can predict the total horizontal force of the upper part of breakwater quite well except exetreme shock pressure occurred by non-breaking waves. Wave forces calculated by Miche-Rundgren and Nagai wave force formula are about 10% cummulated exceeding percentage of wave force obtained from model test.

Introduction

Sainflou (1928) drived a wave pressure formula for standing wave by using trochoidal wave theory. Sainflou formula has been widely used in calculating non-breaking wave forces for the past years. Rundgren (1958) by using Miche higher order wave theory and taking wave reflection into consideration, proposed Miche-Rundgren wave pressure formula for non-breaking waves. Nagai (1968) adopting small amplitude

* Deputy Director, Institute of Harbor and Marine Technology, Taiwan, R.O.C.

** Associate Researcher, Institute of Harbor and Marine Technology, Taiwan, R.O.C.

wave theory and test results suggested wave pressure formula according to three different relative depths. Goda (1974) suggested wave pressure computation method by taking the expected sliding proposed by Ito, into consideration and using the maximum wave height.

Lundgren (1974) studied the vertical face of composite type breakwater to reduce shock pressure by using irregular waves. When shock forces occur, they are functions of the ever varying combinations of wave shape. Hence they must be analyed statistically. The results show that the statistical distribution is often linear in a semilogarithmic diagram.

Katsutoshi (1984) studied random wave forces on upright section of breakwater, the test results show that for non-breaking wave trains, peak pressure can be predicted quite well by Goda formula to the joint distribution of wave height; the respective wave force defined as the same ways for the wave height can be predicted by Goda formula by using the corresponding respective wave. But, in case of breaking waves, the maximum pressure is far exceed the value predicted by Goda formula.

Experiment

A wind flume 100^{m} long, 1.5^{m} wide, 1.5^{m} deep, equipped with irregular wave generator, wind blower and circulation as shown in figure 1. Wave gauges, pressure gauges are interfaced on line with data acquisition system. The sampling rates for stage I and II are 45 samplings/sec. and 200 samplings/sec. respectively. The diameters of pressure transducer used for stage I and II are 8^{mm} and 1.8^{mm}.

Typical cross section is shown in figure 2. Two linear model scales 1/49 and 1/25 are used for stage I and II respectively. For the first stage, water depth range from 33.0^{m} to 37.5^{m}; wave heights are from 8.0^{m} to 16.5^{m}; the corresponding wave periods change from 12.0^{sec} to 14.6^{sec}. At the second stage, water depths vary from 10.5^{m} to 18.5^{m}; wave heights change from 3.0^{m} to 7.0^{m}; and wave periods are from 8.0^{sec} to 12.0^{sec}.

Test Results

Typical form of incident wave spectrum is shown in figure 3; cummulated exceeding percentage of wave height distribution is shown in figure 4. Time series of waves and corresponding pressure density are illustrated in figures 5 and 6 for the first and second stages respectively. Figure 5 shows that incident significant wave height 13.24^{m}, water depth 37.5^{m}, the relative water depth is 2.83. In general, it seems deep enough to prevent shock pressure induced by breaking waves; but, it occurs shock pressure at time 19.4^{sec}, when several larger waves attack the breakwater continually. It should be noted that the wave form is upside down in this figure. In the second stage, figure 6 shows that wave pressures are in phase with water level in front of the breakwater. Although, the relative water depth 2.85 (14.25/5.0) is almost equal to that of the first stage 2.83; but there is no shock pressure occurs in this test run.

The cummulated exceeding percentage of wave force for typical cases are shown in figure 7. Figure 8 shows comparision of wave forces acting on the same cross section for different test conditions. The force distribution on the vertical face breakwater shows quite uniform.

Wave forces calculated by different formula for wave height obtained from model test are plotted against the test results as shown in figure 9. Although, Goda formula can not predict wave pressure at a single point; but it can obtain the total horizontal force of the upper part of the breakwater quite well, except very exetreme shock pressure occurred by non-breaking waves. Wave forces calculated by Miche-Rundgren and Nagai formula is about the maximum one-tenth of the wave force (F10%) obtained from model tests.

From linear fitting curve, F1% and F10% are wave forces which occurred at cummulated exceeding percentage of 1% and 10% respectively. Figure 10 shows the ratio of wave forces between model test and formula computation (F_t/Fc). F_t is either F1% or F10% and Fc represents wave force calculated by Goda formula Fg. Miche-Rundgren formula Fm and Nagai formula Fn. The ratio Ft/Fc decreases with the decreasing of relative crest height d_c/y_c as shown in figure. Figure 10 shows when lower crest height of the breakwater, wave force formula predict larger wave force than those obtained in model tests. When d_c/y_c greater than 0.85, the ratio F_t/F_c varies from 0.9 to 1.0.

Conclusion

1. The maximum wave pressure does not necessarily occur for the largest wave height; the incident and reflected of a group of larger waves may induce the maximum pressure.

2. Under the action of irregular waves the pressure distribution acting on vertical force breakwater is quite uniform.

3. For non-breaking incident waves reflected by vertical wall, shock pressure can be occurred by an appropriate phase composition.

4. The ratio of wave forces obtained from model tests and calculated by different wave force formula decreases with the decreasing of relative crest height of breakwater.

5. Goda wave force formula can predict the maximum wave force in a wave train, except very exetreme shock pressure occurred by non-breaking waves. Wave forces calculated by Miche-Rundgren and Nagai formula are about 10% cummulated exceeding percentage of wave force obtained form model tests.

Reference

1. Nagai, S. (1969). Pressure of standing waves on vertical wall Journal of the Waterways and Harbor Division, ASCE, Vol.95, No.WW1, pp.53-76.

2. Goda Yoshimi (1974). New wave pressure formula for composite breakwaters, Coastal Engineering, Chap. 100, ASCE.

3. H. Lundgren and H. Gravesen (1974). Vertical face. breakwaters, KVIV, Int. Havenknogres.

4. Katsutoshi T., Shigeo T. and Kazuyuki M. (1984). Experimental study of random wave forces on upright section of breakwaters, Report of the Port and Harbor Research Institute, Vol. 23, No.3, Japan.

5. CERC, Shore Protection Manual, 1977.

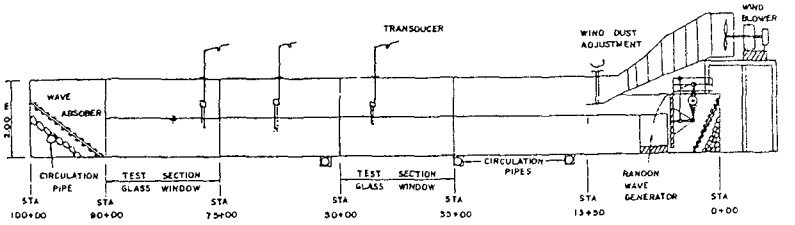

Figure 1 Wind Wave Flume

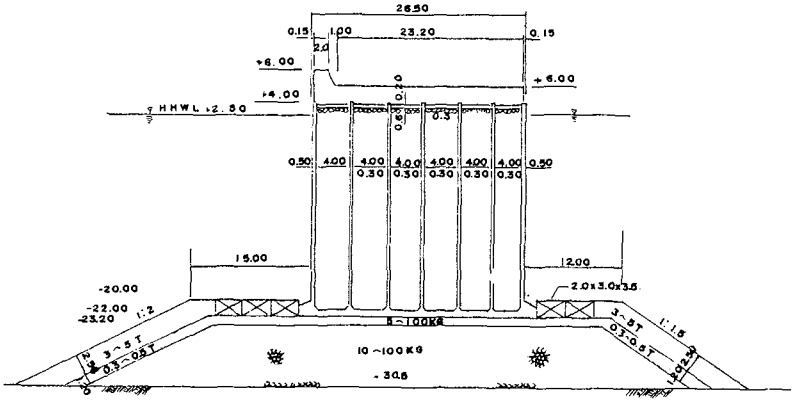

Figure 2 Typical Section of Composite Type Breakwater

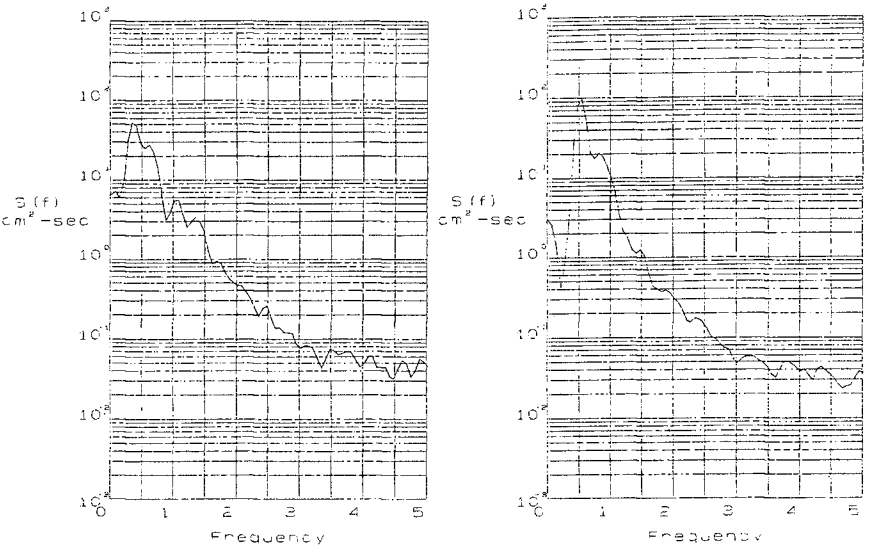

Figure 3 Incident Wave Spectrum

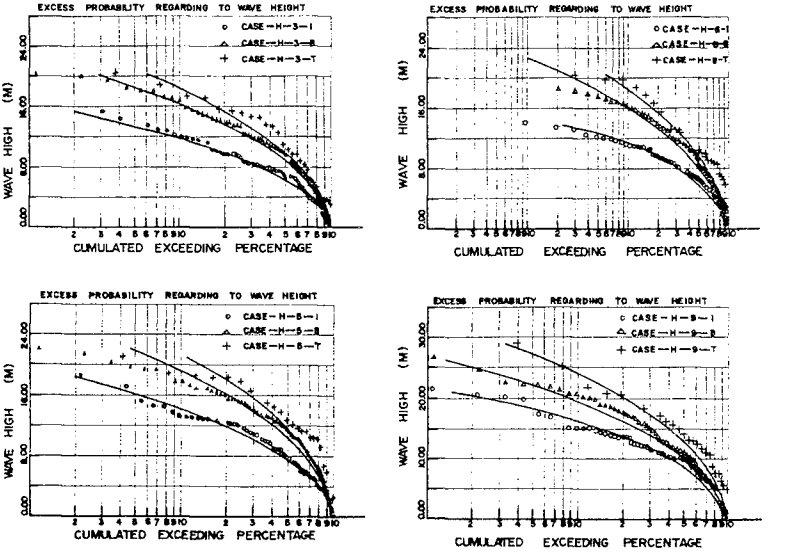

Figure 4 Cummulated Exceeding Percentage of Wave Height Distribution

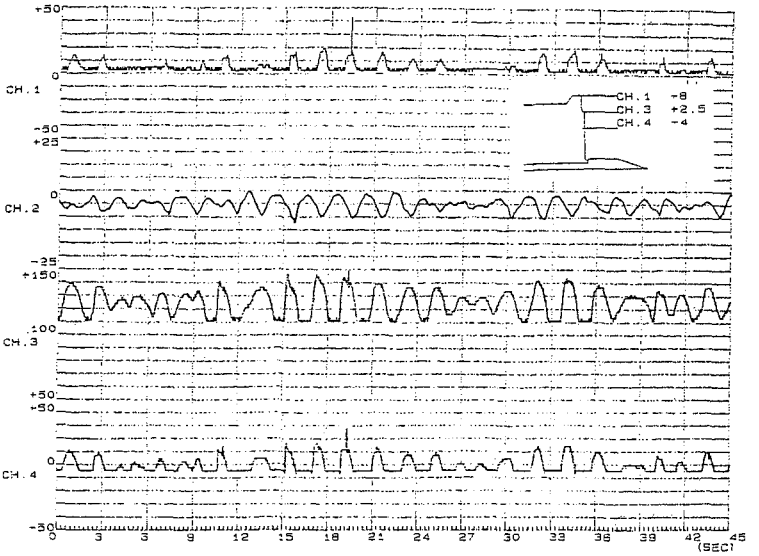

Figure 5 Time Series of Waves and Pressure (Stage I)

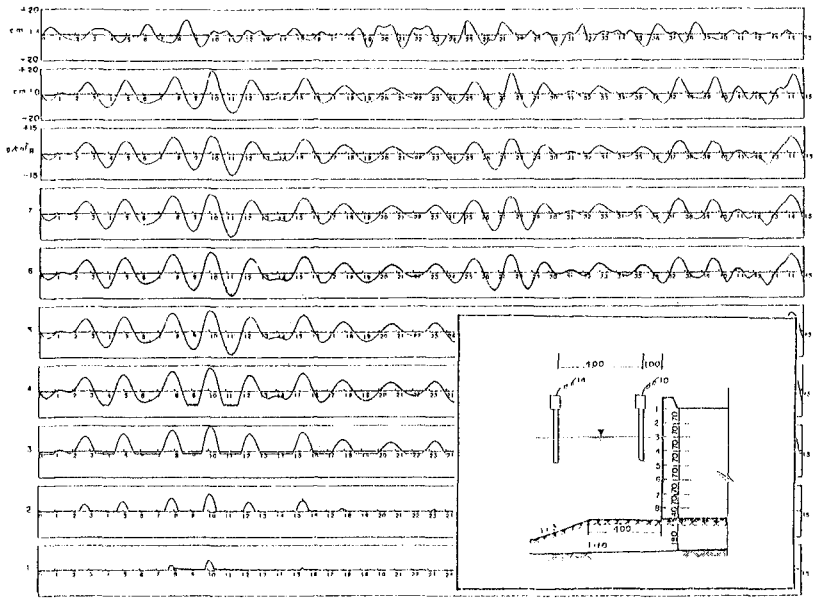

Figure 6 Time Series of Waves and Pressure (Stage II)

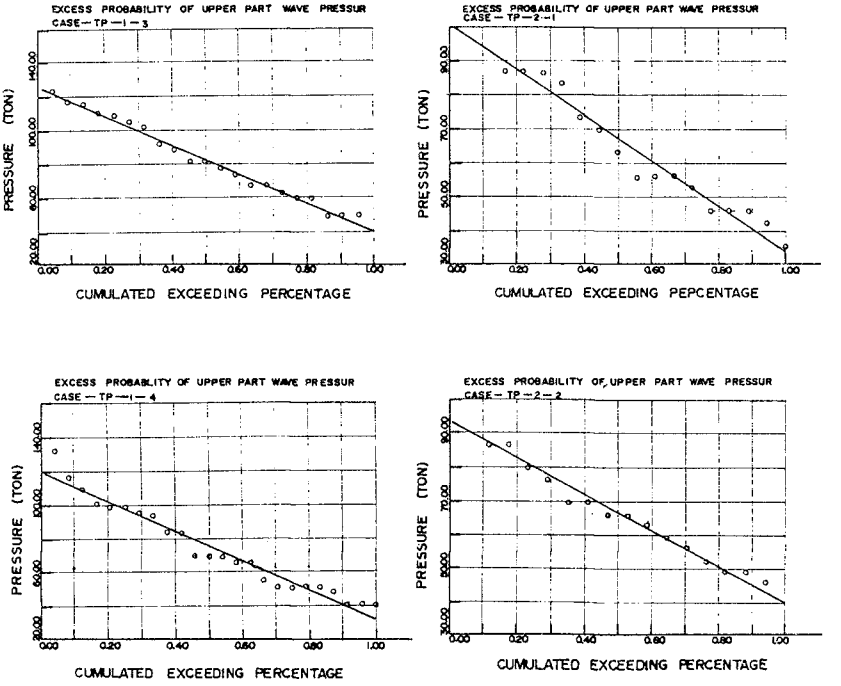

Figure 7 Cummulated Exceeding Percentage of Wave Force Distribution

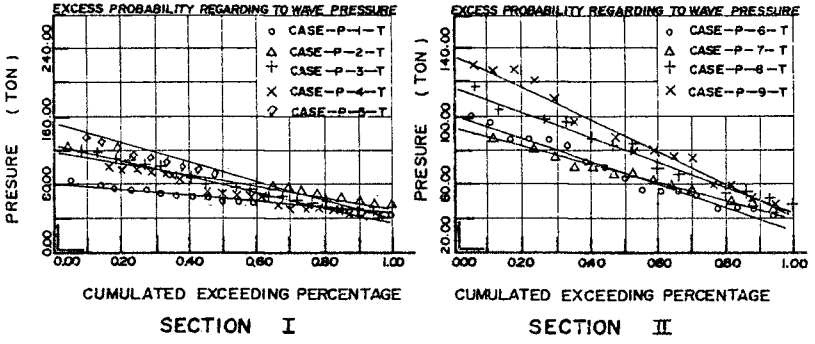

Figure 8 Comparision of Wave Force Distribution for Different Test Conditions

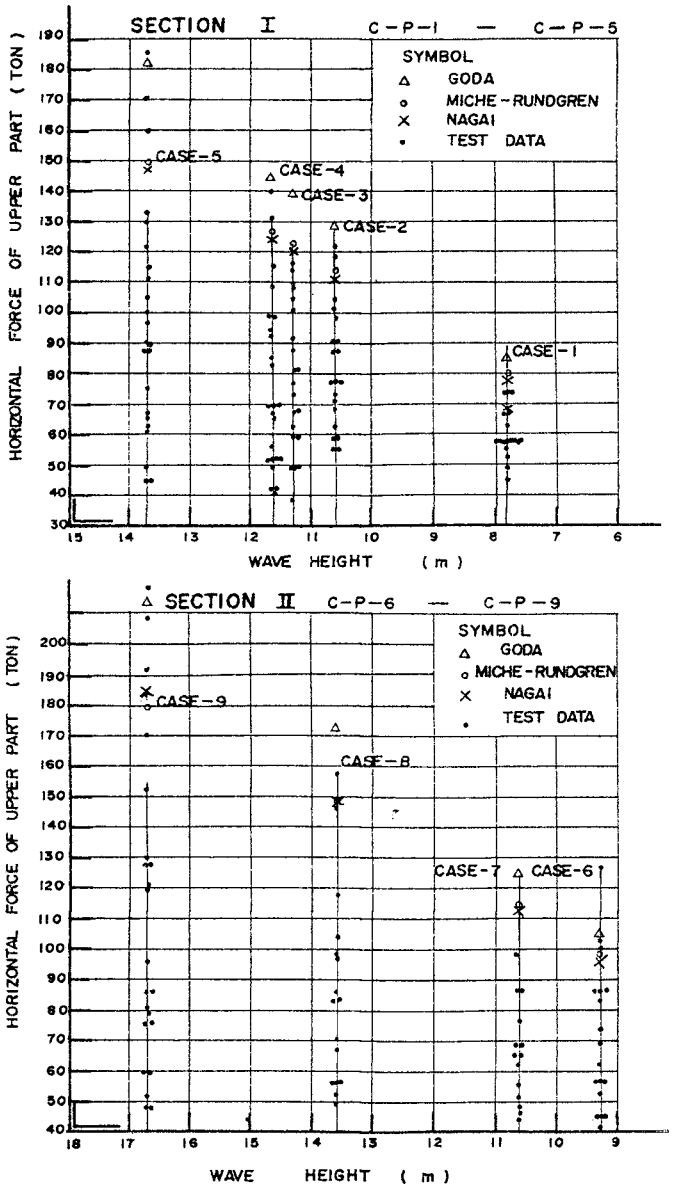

Figure 9 Wave Forces Calculated by Different Formula and Test Data

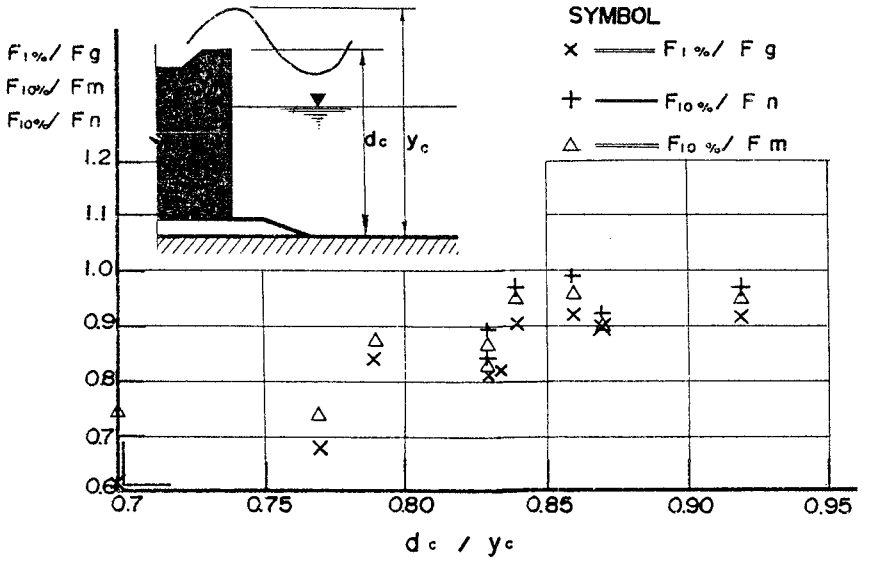

Figure 10 The Ratio of Wave Forces Between Model Test and Formula Computation

CHAPTER 132

THE RELATIONSHIP BETWEEN WAVE LENGTH AND WEIGHT OF ARMOUR BLOCKS

by

Kuo-Quan Chen*, Ruey-Chy Kao**, Frederick L.W.Tang***

ABSTRACT

Every coastal engineer realizes that the weight of armour blocks decided by Hudson's formula is safe enough for short steep waves, however, suffering damage from long period swells, even though the incidental wave height is the same. Several corrections have been made and submitted to ICCE as well as in other occasion. The authors try to explain analytically the influence of wave length on the design weight of armour blocks and justify by much of experiments in order to offer new formula and graphs for practical application.

INTRODUCTION

Armour blocks used as effective protection on seashore or structures, the wave energy absorbed due to its surface roughness, porosity and stability, when wave attacked. While an appropriate design of weight of armour unit, it is difficult to derive from theory because of many factors and conditions which conducted to

* President, China Port & Harbor Engineering Consultants, F7,No.17, LN 135, SEC.1, Fuhsing S. Rd., Taipei 10639, Rep. of China.
** Assistant Researcher, Tainan Hydraulics Laboratory, National Cheng-Kung University, Tainan 70101 Taiwan, Rep. of China.
*** Professor Emeritus, National Cheng-Kung University, Tainan 70101, Taiwan, Rep. of China.

select it. [1]. Generally, the most frequently used formla, today, modified by Hudson(1959) and given by

$$W = \frac{\rho_s \quad g \quad H^3}{K_d \left(\frac{\rho_s}{\rho} - 1 \right)^3 \cot \theta} \qquad (1)$$

Where: W = armour blocks design weight

ρ_s, ρ = mass density of blocks and sea water

K_d = stability number

θ = slope angle of riprap facing offshore.

H = wave height at the location of the breakwater without wave breaking.

Its popularity comes from the limited variable of parameters and convinient to use.

From the viewpoints of safety and economics, design of armour unit used as shore protection, selection of the type, arrangements and its weight are the main consideration factors. Some armour unit, developed with spescial characteristis on its shapes and arrangements, but the weight of armour unit depends on equation (1), though it's safe enough for short waves, the damage occured from long waves occassionally. Especially for the waves caused by Typhoon on the sea area around Taiwan during summer and fall every year.

In accordance with the expiriences abovementioned, the authors try to consider wave period as an important factor as design of appropriate weigut of armour unit. For wave energy is under various influences, such as wave height, wave length, etc, ie, $E = \rho$ (ρ, g, H^2, L). From the point, the authors developed fundamently the

design equation for armour blocks involved the effect of wave period on stability, and justified by experiments for practical applications.

Some papers described armour blocks effected under irregular waves recent time, mostly based on Hudson's formula [8][10], However, Pilarczyk and Boer (1983), [7][11], developed series of stability formula, under random wave attacked, of which the parameters included wave period, number of waves, armour grading, spectrum shap, groupiness of waves and permeability of the core, etc. The abovementioned subjects were rubble mound but not armour unit, especially for artificial armour unit was lacking to make mention of. The authors have performed much expiriences on study and design of coastal and harbor engineering, [2,3,4,5,6,9,12] and realized that it is necessary to develop an application formula from the fundamentally studies.

ANALYSIS

If the weight of armoured block, on slope angle θ, is W, density ρ_s in air, then the vertical component force is $(1 - \frac{\rho}{\rho_s})$ W cos θ, therefore, the drag force (F_1) of aumour block against incoming waves express as follows, if μ as friction coefficient between block and mound. (Fig. 1)

$$F_1 = (1 - \frac{\rho}{\rho_s}) W (\mu\cos \theta - \sin \theta) \text{----------} (2)$$

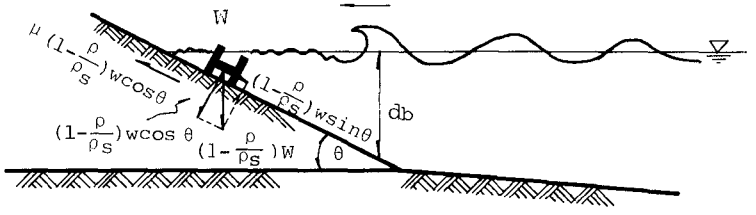

Fig. 1 Definition

The volume of armour block $V = \frac{W}{\rho_s g}$ is direct proportional to the cross sectional area of vertical direction of incoming waves, ie, proportional to $V^{2/3}$. if wave velocity v, then amour block attacked by wave force will be:

$$F_2 = C_D \rho v^2 \left(\frac{W}{\rho_s g}\right)^{2/3} \text{----------(3)}$$

Irribarren derived from velocity of long wave, under the stability conditions of armour block, $F_1 \geq F_2$. ie,

$$\left(1 - \frac{\rho}{\rho_s}\right) W \left(\mu\cos\theta - \sin\theta\right) = \frac{1}{2} C_D \rho g H \left(\frac{W}{\rho_s g}\right)^{2/3} \text{----(4)}$$

Irribarren's formula

$$W = \frac{K' \mu^3 \rho_s g H^3}{\left(\frac{\rho_s}{\rho} - 1\right)^3 \left(\mu\cos\theta - \sin\theta\right)^3} \text{----------(5)}$$

Where, $K' = C_D^3/8\mu^3$, C_D = drag coefficient.

In the case of a definite cross section, μ, ρ_s, ρ, and θ may be regarded as constant but C_D will be different according to the shape of block and velocity.

Let

$$C = \frac{1/8 \ \rho_s g}{\left(\frac{\rho_s}{\rho} - 1\right)^3 \left(\mu\cos\theta - \sin\theta\right)} \text{----------(6)}$$

Consequently

$$W = C C_D^3 H^3 \text{----------(7)}$$

H is to be replaced by H' under water level

$$H' = \frac{\pi H^2}{L_o \left(\sinh \frac{2\pi d}{L} \right)^2} = \frac{2\pi H^2}{L \sinh \left(\frac{4\pi d}{L} \right)} \qquad (8)$$

Substitute (8) to (7)

$$W = C C_D^3 H^6 \frac{\left(2\pi/L \right)^3}{\sinh^3 \left(4\pi d/L \right)} \qquad (9)$$

A non-dimensional expression is worked out as follows

$$\frac{W}{\rho_s g C_2 C_D^3 H^3} = \frac{\left(H/L \right)^3}{\sinh^3 \left(4\pi d/L \right)} \qquad (10)$$

Where

$$C_2 = \left[\frac{\pi}{\left(\frac{\rho_s}{\rho} - 1 \right) \left(\mu \cos \theta - \sin \theta \right)} \right]^3 \qquad (11)$$

This will be a new formula if the coefficients μ and C_D are selected properly which authors will be measured by experiments.

EXPERIMENT INVESTIGATION

In order to verify under the conditions of the armour blocks attacked by incoming waves, equation (10) and (11) in which friction coefficient μ and drag coefficient C_D included.

The values of μ and C_D which is obtained by a series of experiments.

Test on friction coefficient, it measured friction between block and mound under water, due to the block considered as submerged condition when wave attacked. The test layout as Fig.2, the value

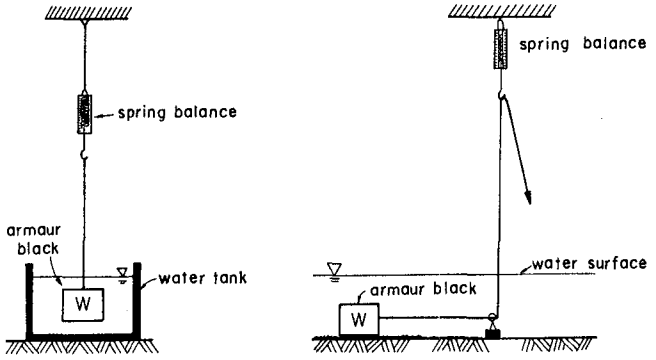

Fig. 2 Test of Friction Coefficient

of μ was obtained in average value of repeated experiments, as table 1.

Table-1 Friction Coefficient

Types	Wa (grf)	Ww (grf)	f (grf)	μ
HOLTRIPOD	74.9	42.5	61.67	1.4511
HEXA-HOLLOW TRI-LEG	46.1	30.1	50.00	1.6667
	67.4	45.0	75.00	1.6667
	84.9	57.5	83.75	1.4565
	110.9	72.5	103.57	1.4286
	137.6	79.1	119.45	1.5101

Another test on drag coefficient C_D, due to C_D related to reynoulds number of flow, authors tried to express volume of block as 2/3 order of characteristic length, using falling velocity experiment to find out the falling velocity, the instrument as Fig.3

and Photo-1, tested blocks namely Holtripod and Hexa-Hollow Tri-leg (Photo-2).

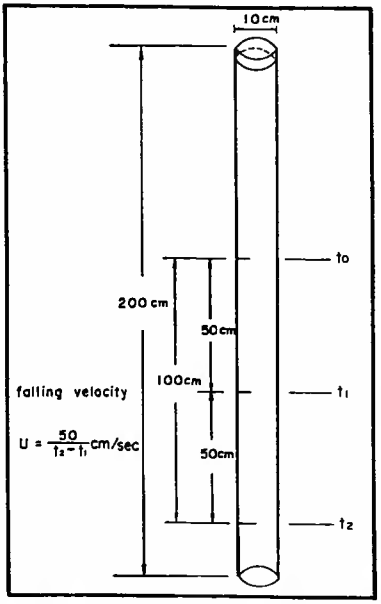

Fig. 3 Test on Falling Velocity

Photo-1 Test Instrument of Falling Velocity

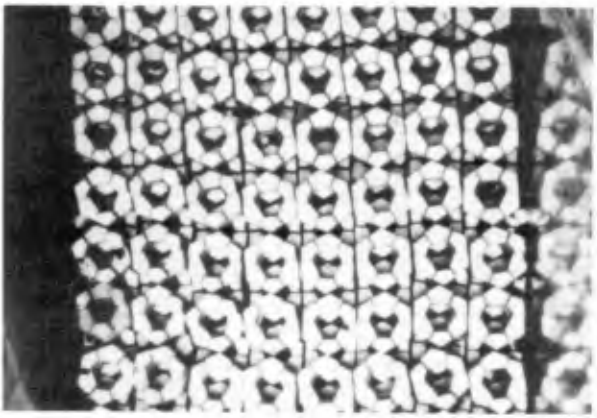

Photo-2 Model Blocks

The value of falling velocity of every model block obtained by measuring average of 30 repeated experiments, defferent weight of 4 blocks to be tested. These value were substitute to equation (13) and obtained C_D as table-2.

$$(\rho_s - \rho) g V = \frac{1}{2} \rho g v^2 C_D v^{2/3} \quad \text{----------(12)}$$

$$\Rightarrow C_D = 2 \left(\frac{\rho_s - \rho}{\rho} \right) g \frac{v^{2/3}}{v^2} \quad \text{----------(13)}$$

Where V = Volume of armour blocks

v = falling velocity

Using value of μ and C_D substitute to equation (10) and (11), it was calculated for varying relative depth d/L and wave steepness H/L and then plotted on theoretical curve in Fig. 4.

Table-2 Test Data of Drag Coefficient

Types	Wa (grf)	Ww (grf)	$\forall$ (cm^3)	γ (grf/cm^3)	U (cm/sec)	C_D
HOLTRIPOD	74.9	42.5	32.56	2.282	59.2445	2.286
HEXA-HOLLOW TRI-LEG	46.1	30.1	20.00	2.310	58.6809	2.024
	67.4	45.0	29.43	2.290	59.8402	2.180
	84.9	57.5	37.00	2.295	60.7334	2.293
	110.9	72.5	48.70	2.277	61.3556	2.428
	137.6	79.1	59.70	2.305	63.9164	2.447

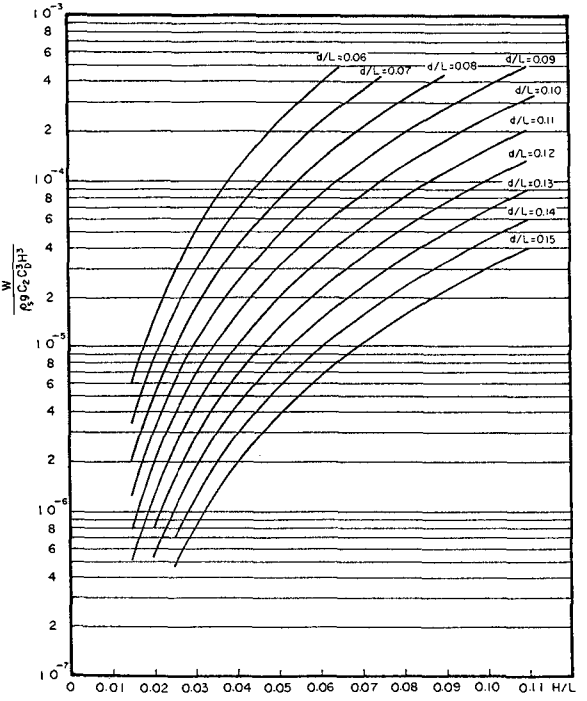

Fig. 4 Theoretical curve from eq. (10),(11)

To examine the results abovementioned, numerous experiments have been carried out in the regular wave flume of Tainan Hydraulics Laboratory, National Cheng-Kung University, Taiwan, as Photo-3. A channel 75 m long, 1.0 m wide and 1.2 m deep was equiped with a hingeplate wave generator near one end, wave height and period were measured with resistance gages, amplifier and recording oscillograph. The cross section of test model as Fig. 5, and test conditions as table-3.

Photo-3 Wave flume

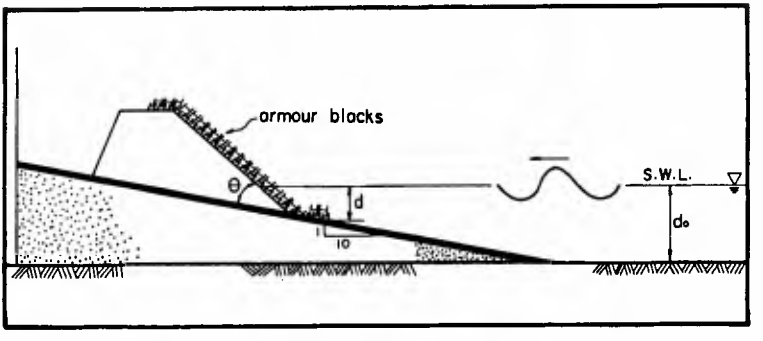

Fig. 5 Dike cross section in the wave flume

Table-3 Testing wave conditions

Testing wave Conditions	Wave Height Ho (cm)	wave periods T (sec)			water depth d (cm)	do
	10 — 26	1.0	1.3	1.6	15.0 cm	50 cm
		1.8	2.0	2.14	25.0 cm	60 cm

Fig. 6 shows the experimental results graphically simultaneously with calculated results of equation (11).

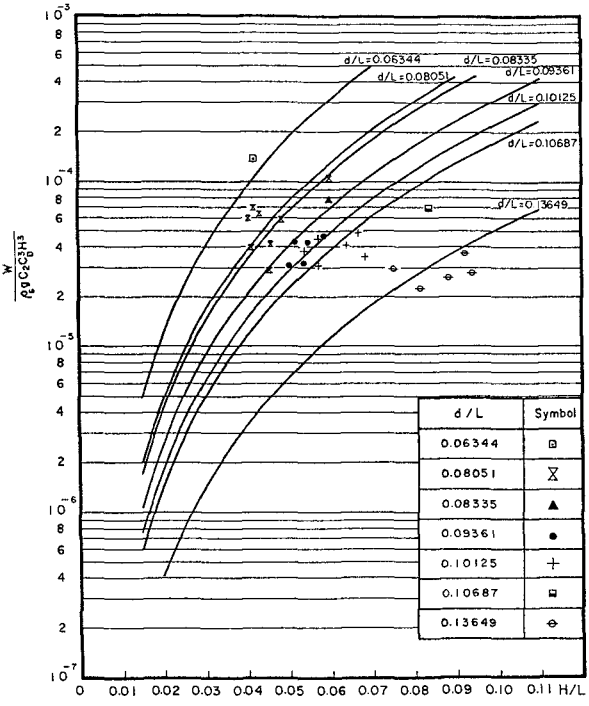

Fig. 6 Experimental result

CONCLUSIONS

1. According to abovementioned analytical calculations and experiments, equation (10) namely

$$W = \rho_s\, g\, C_2\, C_D{}^3\, H^3\, (\, H/L\,)^3 / [\sinh(\, 4\pi d/L\,)]^3$$ is to be applied

in practical design, while C_2 in equeation (11) is known for the same type of blocks and definite design profile, the coefficient μ and C_D should be determined by the experiments having been

performed by the authors.

2. From the outcomes of calculations and experiments, it is obvious that wave length has marked effect on the design weight of armour blocks. In experiments, the influence of relative depth even greater than steepness. This reality reveals the fact that to determine the weight of armour block by wave height only will be deficient.

3. Based on this fundermental results, the authors will try to modify the value of drag coefficient C_D for futher studies, such that measuring flow condition of armour block under the design wave length, for practical application.

NOTE, DEFINITION

W	: armour block design weight	(kgf/m^3)
ρ_s	: mass density of block	(kg/m^3)
ρ	: mass density of sea water	(kg/m^3)
K_d	: stability of Hudson's formula	
θ	: slope engle of riprap facing offshore	
H	: wave height at the location of the breakwater without wave breaking	(m)
K'	: stability coefficient of Irribarren's formula	
C_D	: drag coefficient	
μ	: friction coefficient between blocks and mounds	
g	: acceleration due to gravity	(cm/sec^2)
Wa	: armour block's weight in air	(grf)
Ww	: armour block's weight in water	(grf)
f	: friction force	(grf)
V	: volume of armour block	(cm^3)
U,v	: falling velocity	(cm/sec)
γ	: specific Weight of armour blocks	(grf/cm^3)
H_o	: wave height of testing wave conditions	(cm)
T	: wave period of testing wave conditions	(sec)

d : water depth in the toe of dike (cm)

d_o : deep water depth of testing wave conditions (cm)

REFERENCES

1. Bruun, P. & Johannesson, P., Parameters Affecting Stability of Rubble Mounds. Journal of the Waterways Harbors and Coastal Engineering Division, No. WW2, P.141-164, 1976.
2. Benjamin P.J.Chi, F.L.W.Tang, S.W.Twu, J.S.Hwang, Design and model Studies for the New Types of Concrete Block. Taiwan Hydraulics Laboratory of National Cheng-Kung University, Taiwan, R.O.C. Published Bulletin No. 54, 1982.
3. Kuo-Quan Chen, Design of Coastal Protection for Hsieh-Ho Power Plant, Taiwan, R.O.C., China port & Harbor Engineering Consultants Report of 1972.
4. Kuo-Quan Chen, Planning and Design of Port of Shen-Ao oil Harbor, China Port & Harbor Engineering Consultants, Report of 1977.
5. Kuo-Quan Chen, Design of Breakwater of Port of Kai-Yuan, Taiwan, R.O.C, China Port & Harbor Engineering Consultants, Report of 1980.
6. F.L.W.Tang, S.W.Twu, R.C.Kao, J.M.Leu, The Hydraulic model Tests of Sheltering Effect and Structural Stability of Breakwaters for the Unloading Pier of 4th. Nuclear Power Plant, T.P.C.. Tainan Hydraulics Laboratory of National Cheng-Kung University, Taiwan, R.O.C., Published Bulletin No. 79, 1985.
7. J.W.Van der Meet & K.W. Pilarczyk, Stability of Rubble Mound Slopes under Random Wave Attack. Proc. of 19th. Conf. on Coastal Engineering, ASCE, PP. 2620-2634, 1984.
8. Katsutosh Tanimoto, Tadahiko Yagyu, Yoshimi Goda, Irregular Wave Tests For Composite Breakwater Foundations. Proc. of 18th Conf. on Coastal Engineering, ASCE, P.P. 2214-2162, 1982.
9. Kao, Ruey-Chy, H.H.Hwung, W.T.Hwung, The Studies of Stability and Dissipation Efficiency on the Hexa-Hollow Tri-Leg Concrete Block. Tainan Hydraulics Laboratory of N.C.K.L., Bulletin No.91, 1986.
10. Mol, A, R.L.Groeneveld, A.J.Waanders, Safety and Reliability of Breakwaters. Proc. of 19th Conf. on Coastal Engineering, ASCE, P.P. 2451-2466, 1984.

11. Pilarczyk, K.W. & Boer, K. den, Stability and Profile Development of Coarse Material and Their Application in Coastal Engineering. Delft Hydraulics Laboratory, Publication No.293, 1983.

12. Twu, S.W., Ruey-Chy Kao, C.T.Wen, Model Studies on the Concrete Block of New Patterns. Tainan Hydraulics Laboratory of N.C.K.L., Bulletin No.87, 1986.

CHAPTER 133

Wave Trapping by Breakwaters

by Robert A. Dalrymple[1], M. ASCE, James T. Kirby[2], A.M. ASCE and Daniel J. Seli[3]

ABSTRACT: The refraction of water waves around the heads of breakwaters can lead to large wave heights along the sheltered side of the structure. These waves are shown to be edge waves, trapped on the breakwater, based on the comparison of laboratory data and linear edge wave theory.

Introduction

Water waves experience refraction, diffraction and shoaling on a breakwater. On the seaward side of the structure, wave breaking and reflection, due to the steep sides, often dominate the wave environment along the trunk of the structure. When the angle of incidence is large (with respect to the normal to the breakwater), Mach stem reflection can occur. It is this side of the structure, which receives the most attention by engineers. On the leeward side of the breakwater, the wave climate is supposed to be reduced, and the wave field dominated by diffraction. However, the rounded head of a breakwater can cause a significant amount of wave energy to be refracted onto the leeside of the breakwater, forcing the waves to be trapped there. These trapped waves then propagate along the breakwater into the sheltered region, with wave heights far larger than expected (they can exceed the wave heights on the seaward side of the breakwater). These waves are edge waves and decrease in size only due to frictional and percolation damping along the breakwater. Fortunately the edge motion decreases rapidly away from the breakwater, so that the sheltered area is unchanged, except along the breakwater. These edge waves, with their greatest amplitudes occurring at the waterline, may be large enough to warrant their consideration in design; particularly for large structures.

This paper examines the mechanisms for wave trapping by breakwaters, showing several model predictions of the phenomenon (using both an edge wave model and a parabolic combined refraction/diffraction model) and then laboratory data are presented to show the presence of these trapped waves, verifying that they are edge wave motions.

---

[1]Prof., Dept. of Civil Engrg., U. of Delaware, Newark, DE 19716.
[2]Asst. Prof., Coastal and Oceanog. Dept., Univ. of Florida, Gainesville, FL 31611.
[3]Undergraduate Student, Dept. of Civil Engrg., U. of Delaware, Newark, DE 19716

It has been known for a long time that the head of a breakwater is the location of wave focussing due to refraction of the waves over the submerged rounded portion of the terminus of the breakwater. Waves incident on the head of the breakwater are refracted around the structure in such a way as to create regions of very high waves on the shoulder of the structure. Palmer (1960) cites several breakwaters in the Hawaiian Islands that required repair due to this focussing. For the Nawiliwili breakwater, the extensive submerged head of the structure caused so much focussing of the waves that the waves broke and formed a jet of fluid on the lee side of the breakwater. Magoon (1984) has referred to this as the "Palmer jet". While the intent of this paper is not the discussion of the Palmer jet, it is a manifestation of the wave focussing that creates the trapped wave motion.

Smith (1986), presenting a methodology for breakwater design for the Corps of Engineers, points out that the complicated flow field in the vicinity of the breakwater head creates a design situation which is a "highly subjective and empirical process". Clearly more research into the behavior of waves in this region is important.

Theoretical Considerations

Wave-trapping on the Downwave side of Breakwaters

The simplest method for examining wave trapping by refraction around the head of the breakwater is through the use of Snell's Law. If we consider the trunk of the breakwater as a long steep beach, with parallel contours, then Snell's law applies for the refraction of the waves.

$$\frac{\sin \theta}{C} = \frac{\sin \theta_o}{C_o} \tag{1}$$

Here the subscripts denote offshore conditions. If a wave is reflected from the structure at a large angle and propagates from shallow to deep water, the wave propagation angle increases with depth. If this angle goes to 90°, then the wave is reflected from the deep water back into the shallow water (and back onto the breakwater). Due to the steepness of the breakwater, the waves, as they refract shoreward, once again reflect seaward, and the process continues. (Camfield (1982) has discussed this trapping mechanism with regard to reflective structures on straight shoreline.)

If the waves reach a 90° angle at the toe of the structure, then Snell's law reduces to

$$\sin \theta_c = \frac{C_c}{C_t} \tag{2}$$

where C_t is the wave speed at the toe of the structure and the angle, θ_c, is the critical angle. Therefore for a given depth on the breakwater, if the wave angle exceeds θ_c, then the waves will be trapped. The mechanism for inducing the waves to approach the trunk of the structure with large angles of incidence is of course the refraction at the head of the structure. See Figure 1.

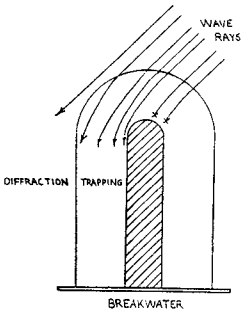

Figure 1. Schematic of Wave Trapping

It is in principle possible to determine the incident angle for wave trapping on a breakwater. Mei (1985) examines the capture of waves by circular islands, which can serve as an analog to the rounded head of a breakwater. For islands with very mild nearshore slopes, Pocinki (1950), all of the waves which cross the submerged bathymetry of the island eventually hit the island's shoreline. For islands with steeper nearshore slopes, less of the incident waves refract into the islands. This would be true for breakwaters. For waves normally incident on a breakwater, some percentage of the waves which pass the head of the structure will be captured; this percentage increasing with decreasing nearshore slope.

The trapped wave motion can be described by edge wave theory, which describes waves, which travel along a beach, rather than incident from offshore. These waves have been studied extensively by Guza (1985), who discussed the state of the art. Recently, Yeh (1986) reports laboratory verification of the edge wave theories to higher order. The dispersion relationship for a small amplitude edge wave on a planar beach of constant slope is

$$\sigma^2 = g \lambda \sin (2n+1)\beta \tag{3}$$

where σ is the angular frequency of the waves, $\sigma = 2 \pi/T$, λ is the wave number of the edge wave, $\lambda = 2 \pi/L$, where L is the wave length, g is the acceleration of gravity and β is the beach slope. Here n is the modal number, which describes how many zero crossings may occur in the wave profile in the offshore direction. Thus for a given breakwater slope and incident wave period the wave length of the edge waves can be determined. The free surface displacement of a zeroth mode standing edge wave can be described by an exponential function in the "offshore" (normal to the breakwater) direction (y):

$$\eta(x,y,t) = A e^{-\lambda y} \sin (\lambda x) \cos (\sigma t) \tag{4}$$

If the water depth at the toe of the structure is not too deep, then the edge waves are affected by the change in slope from the sloping structure to the bottom slope. The above dispersion relationship is no longer valid and therefore another means is necessary to find the wave length. Kirby, Dalrymple and Liu (1981) present a

finite difference procedure for solving the mild-slope equation for edge waves. This procedure was used here to compute wave lengths of laboratory waves, although it was found for the depths and slopes used here that Eq. (3) is quite accurate.

The mild-slope equation for periodic waves on an arbitrary beach profile can be written as

$$p\,\eta_{yy} + p_y\,\eta_y + (\sigma^2 q - \lambda^2\,p)\,\eta = 0 \tag{5}$$

where the subscripts denote derivatives and the water surface displacement is assumed to be

$$\hat{\eta} = \eta(y)\cos(\lambda x)\cos(\sigma t) \tag{6}$$

and $$p = C\,C_g$$

$$q = C/C_g$$

Here C and C_g are determined from linear wave theory, based on the local depth. By introducing the variable, $\zeta = \eta y$, Kirby et al. reduced the problem to an eigenvalue problem, as $\zeta \to 0$ as $y \to 0$ and $\zeta \to 0$ as $y \to \infty$. It then becomes a matter of finding the correct value of λ for the given wave period and beach profile. Holman and Bowen (1979) solved this problem using a shooting method, which involved many iterations for each mode of the edge wave motion. Using a finite difference technique, Kirby et al. were able to obtain all edge wave modes at one time, without iteration.

The solution follows by dividing the offshore distance, x, into a number of discrete intervals, from 0 to a large number representing infinity. Expressing Eq. 5 in finite difference form (using central differences), a tri-diagonal eigenfunction equation results.

$$\{A\}\,\{\zeta_i\} = \lambda^2\,\{\zeta_i\} \tag{7}$$

where {A} is a coefficient matrix and ζ_i are the discretized dependent variable. (This equation is slightly simpler than Kirby et al. as we have divided through by $p_i y_i^2$.) Solving the eigenvalue problem, using standard mathematics libraries (ISML), yields the eigenvalues, λ, which are the alongshore wave length of the edge waves, and the forms of the associated eigenfunction.

Wave Propagation Modelling

A refraction-diffraction model is capable of modelling the behavior of waves in the vicinity of the breakwater. In fact, the presence of the edge wave motion along the breakwater was first observed by the model, developed by Kirby and Dalrymple (1983, 1986). The parabolic model can be described as a solution to the following complex differential equation:

$$A_x - i(k-k_o)A + \frac{1}{2C_g} C_{g,x} A - \frac{i}{2C_g \sigma} (CC_g A_y)_y = 0 \qquad (8)$$

where the water surface displacement, η, is given by

$$\eta = \mathrm{Re}\ \{A(x,y)\ e^{i(k_o x - \sigma t)}\} \qquad (9)$$

and $i = \sqrt{-1}$. Here k_o is a representative wave number for the region of interest. This model is developed in finite difference form and solved by the Crank-Nicolson procedure. The results of the model are the complex amplitude, A, from which the instantaneous water surface or the transmission coefficient can be found. The reader is referred to the above papers and Kirby and Dalrymple (1984) for more details on the model, REF/DIF 1.

Laboratory Experiments

The Ocean Engineering Laboratory of the University of Delaware has a directional wave basin, with dimensions of 20m x 20m x 1.1m and a thirty element wave generator along one wall. The wave paddles, driven by Mavilor 600 servo-motors, can create waves in different directions as they are individually programmable using an HP 1000 computer.

A model breakwater with 2:3 slopes was built in the basin with a rounded head and a trunk length of 2.41m. The width of the breakwater trunk at the bottom was 2.1 m. The water depth of the basin was 0.36m. The angle of incidence of the waves was 37.8°. See figure 2. A reflecting wall was placed at the downwave end of the breakwater to prevent waves from flanking the structure, producing spurious effects, and to enhance the edge waves by reflection. This produced a partial standing edge wave pattern along the trunk of the breakwater on the downwave side.

Wave data was taken at four locations, using resistance wire gages. Gages were calibrated before and after each experiment to ensure accurate conversion of voltage data to elevation data. In front of the breakwater, the incident wave was measured at location A in figure 2. Then three wave gages were located on a transect

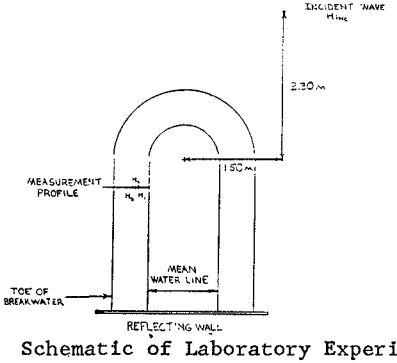

Figure 2. Schematic of Laboratory Experiment

normal to the breakwater axis, spaced 0.155m, 0.22 m, and 0.295 m from the still water line. This transect is also shown on the figure. Four separate wave periods were used for the tests. The wave heights at the wave gages were obtained for a given wave train.

Table 1 contains the wave data for the various tests, where T is the incident wave period and H_i is the incident wave height. In Table 2, the measured wave heights at the three shore-normal gages (with H_1 being the most inshore gage) are shown along with the measured spacing between the crests of the standing wave pattern along the breakwater, Lr. (This distance is one-half of the edge wavelength.)

TABLE 1. INCIDENT WAVE CHARACTERISTICS

TEST	T(s)	H_i(m)	θ(°)
234	1.00	0.068	37.8
227	1.30	0.057	37.8
212	1.35	0.091	37.8
230	1.40	0.068	37.8

TABLE 2. MEASURED WAVE DATA

Test	H_1(m)	H_2(m)	H_3(m)	L_r(m)
234	0.123	0.0860	0.0406	0.44
227	0.218	0.165	0.104	0.77
212	0.145	0.0930	0.0673	0.80
230	0.119	0.0630	0.0343	0.80

Comparing the wave heights at the innermost wave gage (H_1) for the different tests shows that there is a preferential amplification of the wave motion trapped along the breakwater. Dividing the wave height, H_1, by the incident wave heights for the four tests, we obtain the following ratios: 1.8, 3.8, 1.6, 1.7. The amplification of the waves along the trunk of the breakwater is clearly significant, with the 1.3 s. test (#227), showing almost a four-fold increase in wave height. This is thought to be due to the reflection that may occur at the breakwater head. The presence of the reflecting wall at the downwave end of the breakwater forces a partial standing wave system for the trapped waves. If the waves for test 227 are more efficiently

reflected by the change in bathymetry at the head of the structure, then a more resonant situation occurs.

In Table 3, two comparisons are shown with the data and the results from the theoretical edge wave model. The measured spacing of the antinodes of the partial standing edge waves is related to λ by $\lambda = \pi / L_r$. Column 2 and 3 show the comparison of the data and the numerical model, respectively. The average error is 8.3%. The discrepancy is not likely to be attributed to wave nonlinearities, as the nonlinear terms in the dispersion relationship act to increase the wave length (Guza and Bowen, 1976). It should also be noted that for these tests, the effect of the break in slope at the toe of the breakwater is negligible. Calculating the edge wave length using the dispersion relationship for constant slope, Eq. 3, results in a maximum 2% discrepancy with that predicted with the numerical model.

TABLE 3. COMPARISON OF DATA TO NUMERICAL MODEL

TEST	L_r(m)	L_p(m)	E (%)	$\lambda_{m1}(m^{-1})$	$\lambda_{m2}(m^{-1})$	$\lambda_p(m^{-1})$
234	0.44	0.47	−6.8	7.97	7.14	6.63
227	0.77	0.81	−5.2	5.3	3.88	3.87
212	0.80	0.86	−7.5	5.44	3.92	3.64
230	0.80	0.91	−13.8	8.89	3.92	3.43

In columns 5 and 6 of Table 3, the λ determined from the laboratory data is calculated two ways. Column 5 is the wave number calculated by π/Lr. In column 6, the wave number is found by a least squares fit to the three measured wave heights for each test, found by minimizing the total error, E:

$$E = \sum_{i}^{3} (H_i - A\, e^{-\lambda y_i})^2$$

for A and λ. There is a discrepancy between the two measures of λ. In Column 7, the value obtained from the numerical calculation is shown. The A values found by the least squares method for the four tests, which are a measure of the wave height at the shoreline, are 0.448, 0.509, 0.326, 0.464 m in order of increasing wave period.

In figures 3 and 4, the wave heights for four tests are shown on semi-log scale. According to the edge wave theory, the zeroth mode edge wave should decay exponentially, with a slope equal to the wave number, λ. The measured data are shown with a corresponding straight

line, which corresponds to the best fit line found by minimizing E, given above, for A alone, with λ given by the numerical model of Kirby et al. (Col. 7, Table 3). The agreement between the slope of the data and the straight lines in three of the tests (excepting test 230) indicates that the offshore decay of the measured wave motion is well described by an exponential behavior, as occurs with edge waves.

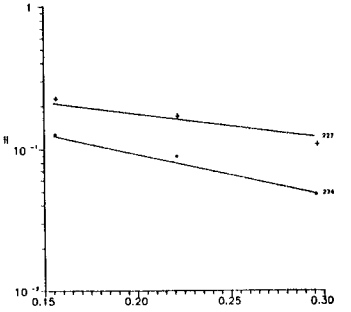

Figure 3. Wave Height Decrease with Offshore Distance for Tests 234 and 227.

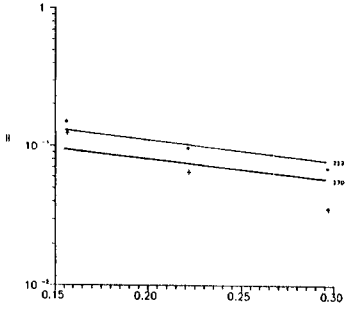

Figure 4. Wave Height Decrease with Offshore Distance for Tests 212 and 230.

In figure 5, the results of the refraction/diffraction calculation are shown. In this case, there is no reflective barrier at the end of the breakwater and thus the edge waves are progressive. For ease in modelling, two breakwaters are used. One situated on the upwave lateral boundary of the model and another on the downwave side. See Fig. 6. This permits the modelling of both the seaward and the downwave sides of the breakwater at the same time; although care must be taken to ensure that the structures are separated far enough so that the reflection from the downwave breakwater does not affect the upwave structure. Further, although the slope of the breakwater remains the same as in the physical model test, a 5 cm wall is assumed to exist along the water line, to ensure no wave breaking. The corresponding bathymetry is shown in figure 6. It should be obvious

from the figure 5 that the edge wave motion becomes trapped onto the downwave side of the breakwater. (Despite appearances, the edge waves do not increase in amplitude with distance along the breakwater. They just become more prominent, as they go deeper into the diffraction zone.)

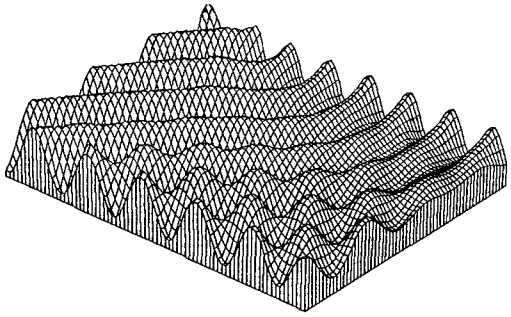

Figure 5. Instantaneous Water Surface Elevation Around Breakwaters.

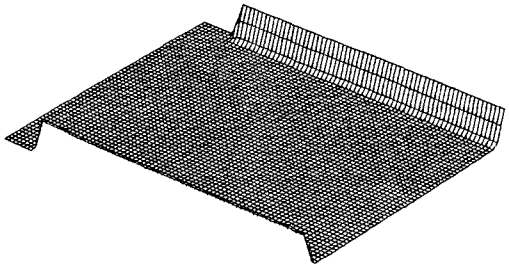

Figure 6. Bathymetry for Figure 5.

It can be presumed that should the edge wave motion on breakwaters become important, there are means to reduce their amplitudes. Clearly artificial roughness reduces their size. Another method of reducing their size is to reduce the amount of trapping that occurs. This can be done by reducing the amount of submerged head to refract the waves. Another possibility is to induce breaking on the head or to make a discontinuity in the breakwater bathymetry. In figures 7 and 8, the breakwater head is altered by adding a circular tip, which extends beyond the trunk width of the breakwater. This change reduces the amount of wave energy which can propagate around the structure.

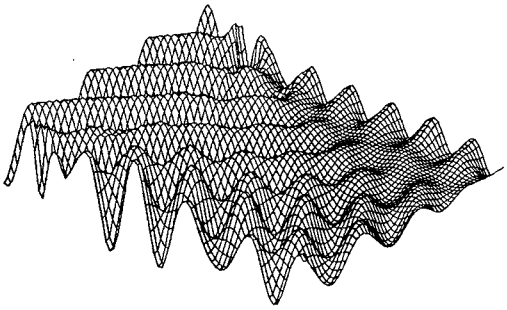

Figure 7. Instantaneous Water Surface Elevation for Rounded Head Breakwater.

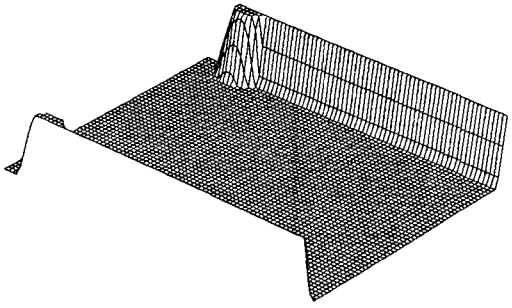

Figure 8. Bathymetry for Figure 7.

Conclusions

Waves, propagating around the head of a breakwater, can be channelled onto the lee side of the structure, where they will propagate, in the absence of friction, as edge waves. The laboratory data, obtained on a model breakwater, show trapped wave motion, which has the wave length and offshore dependency corresponding to edge waves.

Should this motion be of significance in the field (for large breakwaters), there are means to explore to reduce the amount of wave trapping that can occur. Further, by adding damping to the breakwater and reducing its reflectivity, the size of these waves can be reduced.

Acknowlegments

This material was based upon work supported by the National Science Foundation under Grant MSM 8114826. Mr. Douglas W. Coffin's help in the early stages of the laboratory work is gratefully appreciated.

References

Camfield, F.E., "Calculation of Trapped Reflected Waves", J. Waterway, Port, Coastal and Ocean Div., ASCE, 108, 1, 109-111, 1982.

Guza, R.T., "Laboratory Modelling of Edge Waves", in Physical Modelling in Coastal Engineering, A.A. Balkema, Rotterdam, 1985.

Guza, R.T. and A.J. Bowen, "Finite Amplitude Edge Waves", J. Marine Research, 34, 269-293.

Holman, R.A. and A.J. Bowen, "Edge Waves on Complex Beach Profiles", J. Geophys. Res., 84, 6339-6346, 1979.

Kirby, J.T. and R.A. Dalrymple, "A Parabolic Equation for the Combined Refraction-Diffusion of Stokes Waves by Mildly Varying Topography," J. Fluid Mech., Vol. 136, Nov., 1983.

Kirby, J.T. and R.A. Dalrymple, "Modeling Waves in Surfzones and Around Islands," Journal of the Waterway, Port, Coastal and Ocean Division, ASCE, 112, 1, 1986.

Kirby, J.T. and R.A. Dalrymple, "Verification of a Parabolic Equation for Propagation of Weakly-Nonlinear Waves," Coastal Engineering, May 1984.

Kirby, J.T., R.A. Dalrymple, P.L-F. Liu, "Modification of Edge Waves by Barred-Beach Topography," Coastal Engineering, 5, 35-41, 1981.

Magoon, O., personal communication, 19th Int. Coastal Eng. Conf., 1984.

Mei, C.C., The Applied Dynamics of the Ocean Surface Waves, McGraw-Hill

Palmer, R.Q.,"Breakwaters in the Hawaiian Islands", J. Waterways and Harbor Div., ASCE, 86, WW2, 39-67, 1960.

Pocinki, L.S., "The Application of Conformal Transformations to Ocean Wave Refraction Problems", Trans. Amer. Geophys. Un., 31, 6, 856-866, 1950.

Smith, O.P., "Cost-effective Optimization of Rubble-mound Breakwater Cross Sections", U.S. Army Coastal Engineering Research Center, T.R. CERC-86-2, February, 78pp. plus Appendices, 1986.

Yeh, H.H., "Experimental Study of Standing Edge Waves", J. Fluid Mech., 168, 291-304, 1986.

CHAPTER 134

ULTIMATE RESISTANCE OF VERTICAL PLATE ANCHORS IN CLAY

Braja M. Das,[1] M., ASCE, and
Miguel Picornell,[2] A.M., ASCE

Abstract

Laboratory model test results for the ultimate pullout resistance of vertical square anchors embedded in saturated or near saturated clay have been presented. The undrained shear strength of the clay and the embedment ratio of the anchors have been varied. Based on the model test results, an empirical parametric relationship for estimation of the ultimate pullout resistance of shallow and deep square anchors has been presented.

Introduction

Vertical anchor plates (Fig. 1) are generally used for construction and design of waterfront structures such as sheet pile bulkheads. More recently, a number of studies relating to the ultimate pullout resistance of vertical anchor plates embedded in sand have been published (1,4,5,6,8, 9,10). Most of the important findings have been summarized in a paper by Das (1). In contrast, very few attempts have so far been made for evaluation of the ultimate resistance of vertical plate anchors embedded in saturated clay (ϕ=0 concept). The purpose of this paper is to present the results of some laboratory experimental studies for the ultimate pullout resistance of square anchor plates in saturated or near saturated clay soils.

Previous Studies For Ultimate Resistance of Vertical Anchors in Clay (ϕ=0 Concept)

When an anchor plate embedded in a clay soil is being subjected to an ultimate pullout load Q_u (Fig. 1), the failure surface in clay in front of the plate may extend to the ground surface. This will be the case when the embedment ratio H/B (H=depth of embedment of the anchor plate; B= height of the anchor plate) of the anchor plate is small. This type of anchor is referred to as a shallow anchor.

---

[1]Professor of Civil Engineering, The University of Texas at El Paso, El Paso, Texas, 79968, U.S.A.
[2]Assistant Professor in Civil Engineering, The University of Texas at El Paso, El Paso, Texas, 79968, U.S.A.

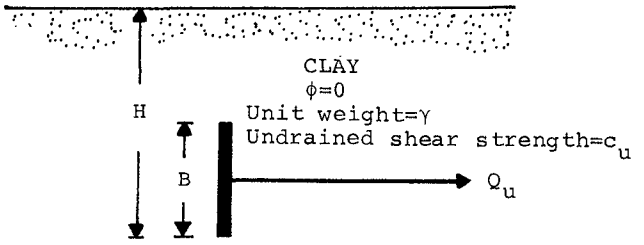

Figure 1. Vertical anchor plate.

However, if H/B is relatively large, local shear failure in the clay around the anchor will take place, and the failure surface in the soil will not extend to the ground surface. This type of anchor is referred to as a deep anchor. For shallow strip anchors with H/B<about 2, Teng (11) has suggested that

$$Q_u = L(P_p - P_a) \tag{1}$$

where L = length of the anchor plate at right angles to the cross section as shown in Fig. 1
P_p, P_a = Rankine passive and active force per unit length of the anchor in the front and the back, respectively

For ϕ=0 condition

$$P_p = \tfrac{1}{2}\gamma H^2 + 2c_u H \tag{2}$$

and

$$P_a = \tfrac{1}{2}\gamma H^2 - 2c_u H \tag{3}$$

where γ = unit weight of the clay
c_u = undrained shear strength

Combining Eqs. (1), (2), and (3)

$$Q_u = 4c_u HL \tag{4}$$

For anchor plates with limited length-to-height ratios (i.e., L/B≤about 5 to 6), the resistance derived from the sides of the plate during pullout needs to be accounted for. For such cases, Teng (11) suggested that

$$Q_u = 4c_u HL + 2c_u H^2 \quad \text{(for H/B<about 2)} \tag{5}$$

Mackenzie (7) conducted a number of laboratory model

tests on strip anchors in two different clay soils. According to this study and Tschebotarioff (12), the ultimate resistance of vertical anchors with dimensions B×L can be conveniently expressed in a nondimensional form as

$$F_c = \frac{Q_u}{BLc_u} \tag{6}$$

where F_c = breakout factor

Figure 2 shows the average variation of F_c with H/B as obtained by Mackenzie (7). It needs to be pointed out that

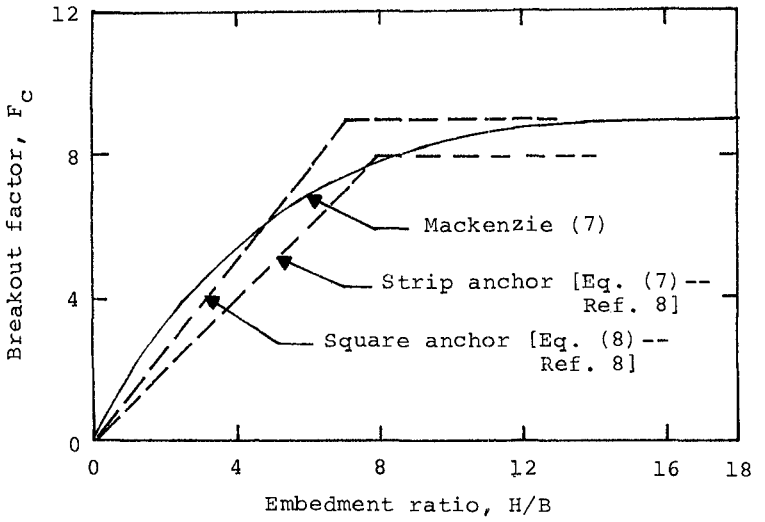

Figure 2. Breakout factor variation with embedment ratio from previous studies.

the magnitude of F_c increases with H/B up to a maximum value ($F_c=F_c^*$) at $H/B=(H/B)_{cr}$. For $H/B>(H/B)_{cr}$, the magnitude of the breakout factor remains practically constant (i.e., F_c^*). So, anchors with H/B less than or equal to $(H/B)_{cr}$ may be referred to as shallow anchors; and when the embedment ratio is greater than $(H/B)_{cr}$, they may be referred to as deep anchors. For Mackenzie's tests, the magnitudes of $(H/B)_{cr}$ and F_c^* are about 12 and 8.5, respectively.

Meyerhof (8) has suggested that conservative estimates of the breakout factor F_c with embedment ratio may be given as

$$F_c = 1.0(H/B) \leq 8 = F_c^* \quad \text{(for strip anchors)} \tag{7}$$

and

$$F_c = 1.2(H/B) \leq 9 = F_c^* \quad \text{(for square anchors)} \tag{8}$$

For comparison purposes, these relations have also been plotted in Fig. 2. The present study relates primarily to the determination of the breakout factor variation of square anchors only.

Laboratory Investigation

Laboratory model tests for determination of the ultimate pullout resistance of vertical square anchors were conducted with two steel model anchor plates measuring 38.1 mm × 38.1 mm and 50.8 mm × 50.8 mm (B×L). Each of the plates had a thickness of 9.5 mm.

The model tests were conducted in a box measuring 0.915 m × 0.508 m × 0.915 m (height). The sides of the box were braced to avoid lateral yielding.

Two clayey soils (referred to as Soil A and Soil B) collected from the field were used for the present tests. Soil A had 78% passing No. 200 U.S. sieve, with liquid and plastic limits of 32 and 19, respectively. Similarly, Soil B had 68% passing No. 200 U.S. sieve. The liquid and plastic limits of Soil B were 39 and 14, respectively. Based on the Unified soil classification system, both soils belonged to the group CL. The soils were initially pulverized in the laboratory, and desired amounts of water were added to them. After thorough mixing, the moist soils were transferred to several plastic bags. The bags were then sealed and kept in a moist curing room for about a week before use.

A schematic diagram of the laboratory test arrangement is shown in Fig. 3. In order to conduct a test, the desired anchor plate was rigidly attached to a steel rod. The rod, in turn, was attached to a steel cable. The cable passed over a pulley attached rigidly to the side of the box. The other side of the cable was attached to a load hanger.

For conducting a test, the moist soil from the plastic bags was poured into the box and compacted in 50.8mm thick layers to the desired height. The compaction was done in sections by using a flat-bottomed rammer. After compaction, step loads were placed on the load hanger, and the corresponding horizontal movements of the anchor were observed by a dial gauge. A time lapse of 5-8 minutes was allowed between the placement of each step load. This time lapse between the step loads was allowed to take primary creep into account. Loading continued until failure occurred.

A total of five series of tests were conducted in the laboratory. Other details of the tests are presented in

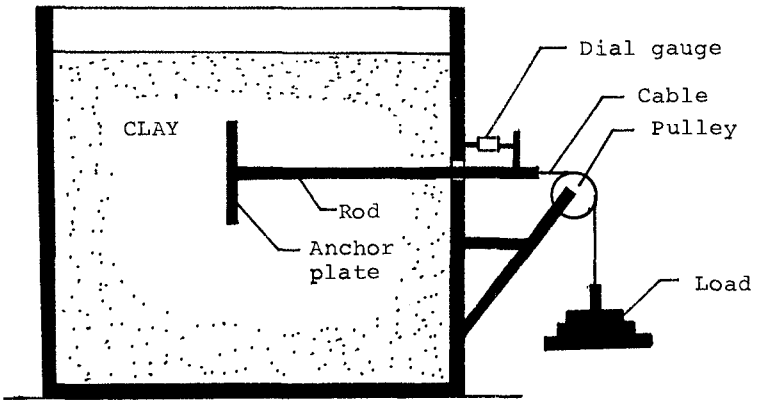

Figure 3. Schematic diagram of the model test arrangement in the laboratory.

Table 1. It may be noticed from this table that the larger model anchor plate measuring 50.8 mm × 50.8 mm was used for tests in softer clays.

Table 1. Model Test Details

Test series	Soil	Plate width, B (mm)	Properties of compacted soil (Average values)			
			Moist unit weight, γ (kN/m^3)	Moisture content (%)	Degree of saturation (%)	Undrained shear strength, c_u (kN/m^2)
1	A	50.8	19.65	24.5	97	20.3
2	A	38.1	20.76	17.6	94	42.4
3	B	50.8	19.03	28.5	98	12.5
4	B	38.1	20.29	18.5	92	28.1
5	B	38.1	20.65	16.2	93	52.0

Typical net load (Q) vs. horizontal displacement of the anchors as obtained from the laboratory tests are shown in Fig. 4. For all tests reported herein (a total of 41), a

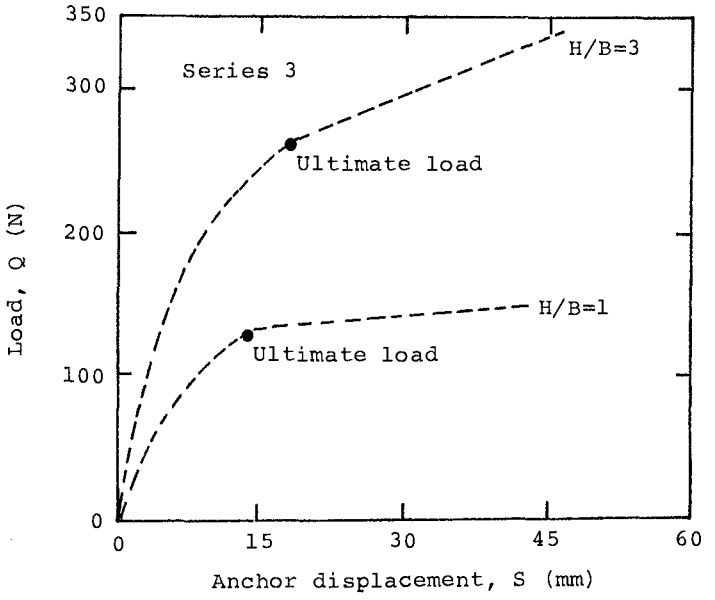

Figure 4. Typical net load vs. anchor displacement diagrams as obtained from the laboratory.

peak failure load was not observed. This is somewhat similar to the load-displacement plots obtained for local shear type of failure in soil in the bearing capacity tests of shallow foundations. The ultimate load for a given anchor pullout test is defined as the net load at which the load-displacement plot became practically linear (i.e., $\Delta Q/\Delta S$ became minimum). The net ultimate pullout loads for all tests conducted under this program are plotted in Fig. 5.

Model Test Results

Critical Embedment Ratio, $(H/B)_{cr}$

The relationship of the breakout factor for a rectangular anchor is given in Eq. (6). For square anchors, B=L; hence, the breakout factor

$$F_c = \frac{Q_u}{B^2 c_u} \tag{9}$$

By substituting the experimental values of the net ultimate load (Q_u), B, and c_u in the right-hand side of Eq. (9), the

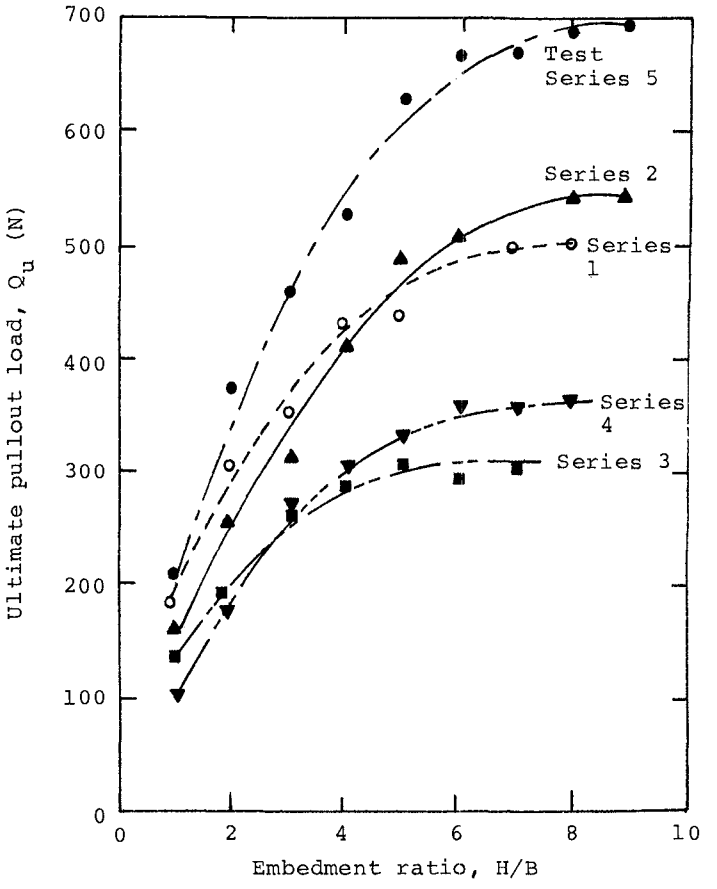

Figure 5. Ultimate pullout load for the model tests.

experimental values of the breakout factor F_c for all tests have been determined and have been plotted in Fig. 6. As expected, for a given test series the magnitude of the breakout factor increases with the embedment ratio H/B up to a maximum value and remains constant thereafter. Based on the average curves, the critical embedment ratios $(H/B)_{cr}$ at which the magnitude of F_c $(=F_c^*)$ becomes constant are also shown in Fig. 6. It can be seen from this figure that, for a given anchor plate, i.e., B/L=constant, $(H/B)_{cr}$ is not a constant. It is a function of the undrained shear strength of the clay in which tests are being conducted. The variation of the critical embedment ratios as determined from Fig. 6 have been plotted in Fig. 7 as a function of the undrained shear strength of the clay. The average plot in

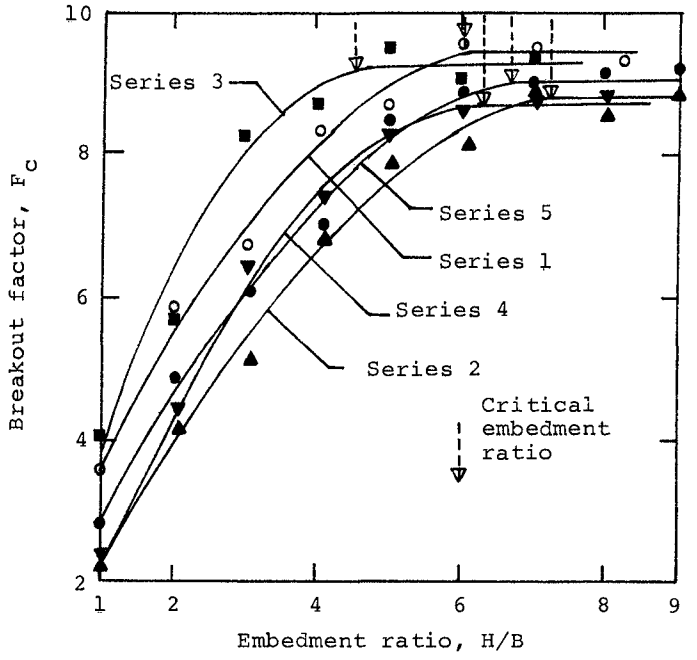

Figure 6. Variation of the experimental breakout factor.

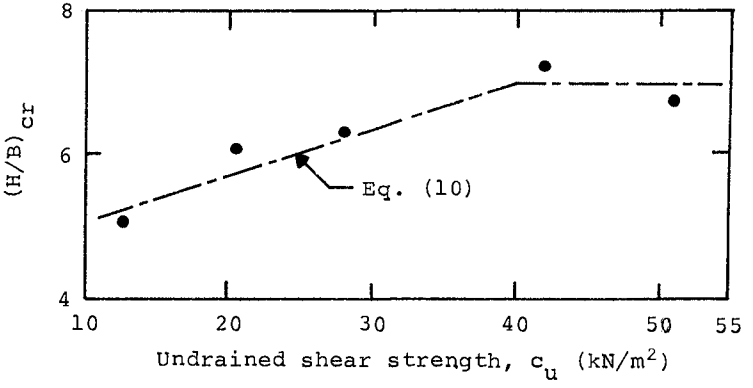

Figure 7. Variation of experimental $(H/B)_{cr}$ with c_u.

this figure can be approximated as

$$(H/B)_{cr} = 4.33 + 0.067c_u \leq 7 \qquad (10)$$

where c_u is in kN/m^2

Variation of Maximum Breakout Factor, F_c^*

As previously mentioned, the breakout factor for deep anchors is a constant, i.e., $F_c=F_c^*=$constant. Figure 8 shows the plot of the experimental variation of F_c^* as obtained

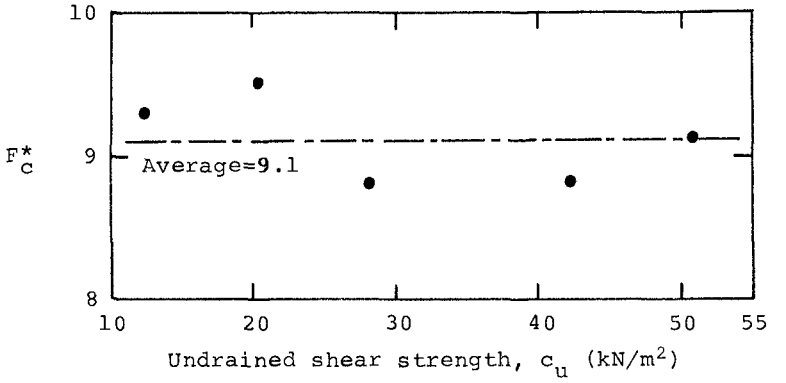

Figure 8. Experimental variation of F_c^* with c_u.

from the present tests with c_u. Based on this figure, it appears that F_c^* varies between 8.8 to 9.5, with an average of about 9.1. This indicates that F_c^* is not a function of the undrained shear strength of the soil and is similar to the magnitude of the bearing capacity factor N_c for square and circular foundations on saturated clay ($\phi=0$ condition). Hence, considering the errors involved in the laboratory tests of this type, the value of F_c^* may be assumed to be equal to 9.

Parametric Relationship for Breakout Factor of Shallow Foundations

In the process of developing a procedure for the estimation of the ultimate uplift capacity of shallow horizontal anchors embedded in saturated clay, Das (2,3) proposed a nondimensional parametric relationship which appears to be useful for the present problem under consideration.

The two parameters under discussion are as follows:

$$\alpha = F_c/F_c^* \tag{11}$$

and

$$\beta = \frac{(H/B)}{(H/B)_{cr}} \tag{12}$$

Using the above definitions, the experimental variation of β/α and β for each average plot of F_c vs. H/B as shown in Fig. 6 have been determined and are shown in Fig. 9. Although there is some scattering, all points in Fig. 9 appear

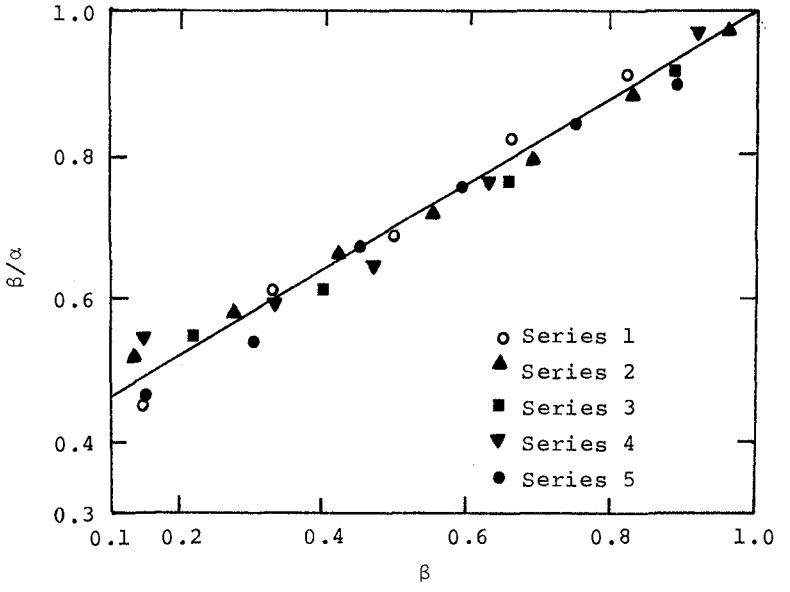

Figure 9. Variation of β/α with β--experimental results.

to fall in a narrow range. The average plot can be expressed in the form

$$\beta/\alpha = 0.4 + 0.6\beta \tag{13}$$

or

$$F_c = F_c^* \left\{ \frac{(H/B)/(H/B)_{cr}}{0.4+0.6[(H/B)/(H/B)_{cr}]} \right\} \leq F_c^* \tag{14}$$

Hence, once $(H/B)_{cr}$ is determined from Eq. (10), the value can be used in the preceding equation to obtain the breakout factor. However, based on previous discussions, if F_c^* is taken as 9, then

$$Q_u \simeq 9c_u B^2 \left\{ \frac{(H/B)/(H/B)_{cr}}{0.4+0.6[(H/B)/(H/B)_{cr}]} \right\} \leq 9c_u B^2 \qquad (15)$$

Conclusions

A number of laboratory model test results on square vertical anchors in clay (ϕ=0 concept) have been presented. Based on the model test results, the following conclusions can be drawn:

1. The ultimate pullout resistance of a vertical anchor can be expressed in the form of a nondimensional breakout factor, F_c.

2. The magnitude of the maximum breakout factor F_c^* is approximately equal to 9 for square anchors.

3. The critical embedment ratio increases with the undrained shear strength of clay; however, for stiff clays the magnitude of $(H/B)_{cr}$ is about 7.

4. The variation of the breakout factor with embedment ratio in clays of various consistencies can be expressed by a single nondimensional parametric equation [Eq. (15)].

References

1. Das, B.M., "Holding Capacity of Vertical Anchor Slabs in Granular Soil," Proceedings, Coastal Structures '83, ASCE, 1983, pp. 379-392.
2. Das, B.M., "A Procedure for Estimation of Ultimate Uplift Capacity of Foundations in Clay," Soils and Foundations, Vol. 20, No. 1, 1980, pp. 77-82.
3. Das, B.M., "Model Tests for Uplift Capacity of Foundations in Clay," Soils and Foundations, Vol. 18, No. 2, 1978, pp. 17-24.
4. Das, B.M., "Pullout Resistance of Vertical Anchors," Journal of the Geotechnical Engineering Division, ASCE, Vol. 101, No. GT1, 1975, pp. 87-91.
5. Das, B.M., and Seeley, G.R., "Load-Displacement Relationship for Vertical Anchor Plates," Journal of the Geotechnical Engineering Division, ASCE, Vol. 101, No. GT7, 1975, pp. 711-715.
6. Das, B.M., Seeley, G.R., and Das, S.K., "Ultimate Resistance of Deep Vertical Anchors in Sand," Soils and Foundations, Vol. 17, No. 2, 1977, pp. 52-56.
7. Mackenzie, T.R., "Strength of Deadman Anchors in Clay," M.S. Thesis, Princeton University, New Jersey, 1955.
8. Meyerhof, G.G., "Uplift Resistance of Inclined Anchors and Piles," Proceedings, VIII International Conference on Soil Mechanics and Foundation Engineering, Vol. 2.1, 1973, pp. 17-24.
9. Neeley, W.J., Stuart, J.G., and Graham, J., "Failure

Loads of Vertical Anchor Plates in Sand," Journal of the Soil Mechanics and Foundations Division, ASCE, Vol. 99, No. SM9, 1973, pp. 669-685.

10. Ovesen, N.K., and Stromann, H., "Design Method for Vertical Anchor Slabs in Sand," Proceedings, Specialty Conference on Performance of Earth and Earth-Supported Structures, ASCE, Vol. 1, Part 2, 1972, pp. 1481-1500.
11. Teng, W.C., Foundation Design, Prentice-Hall, Inc., Englewood Cliffs, New Jersey, 1962.
12. Tschebotarioff, G.P., Foundations, Retaining and Earth Structures, McGraw-Hill, New York, 1973.

SUBJECT INDEX

Page number refers to first page of paper.

AUTHOR INDEX

Page number refers to first page of paper.

CHAPTER 135

COASTAL ARMORING: EFFECTS, PRINCIPLES AND MITIGATION

by

R. G. Dean*

ABSTRACT

An attempt is made to conduct a rational assessment of the potential adverse effects of coastal armoring on adjacent shorelines and to propose methodology for mitigation, where appropriate. Specific attention is directed toward claims that armoring causes: profile steepening, increased longshore sediment transport, intensified local scour, transport of sand to substantial offshore distances, etc. The assessment presented here is based on a combination of sound principles and the availability or lack of laboratory and field data to either support or refute the claims. Although it is found that data relating to coastal armoring effects are sparse, conclusions can be drawn. There seems to be no factual data to support the contentions that armoring causes profile steepening, increased longshore transport, transport of sand to a substantial distance offshore, or significantly delayed profile recovery following a severe erosion event. Armoring does have the potential to cause intensified local scour both in front of and at the ends of an armored segment. Reasons for these effects, based on knowledge of response of a natural profile, are presented. Additionally, armoring which projects into the active surf zone can act as a partial barrier to the net longshore sediment transport, thereby causing downdrift erosion.

Methodology is presented for quantifying the appropriate mitigation for a particular armoring situation. The proposed mitigation is the annual placement of sand in the vicinity of the armoring to offset its potential adverse effects. The two potential adverse effects addressed in the methodology include the reduction of sediment supplied to the system as a result of the armoring and the blockage of longshore sediment transport by a protruding armoring installation.

INTRODUCTION

Coastal armoring in the form of seawalls or revetments is usually designed to be located along sandy shorelines which are either experiencing an erosional trend or which are subject to substantial seasonal

*Graduate Research Professor, University of Florida, Coastal and Oceanographic Engineering Department, Gainesville, FL 32611 and Director, Division of Beaches and Shores, Florida Department of Natural Resources, Tallahassee, FL 32303.

swings and/or storm-induced fluctuations that could conceivably endanger upland structures.

Coastal armoring, once regarded as a relatively desirable means of achieving shoreline stabilization, has recently been the focus of much attention including various concerns over possible adverse effects to the adjacent beach system, see for example Kana and Svetlichny (1982). An analysis of the available literature demonstrates that definitive laboratory or field data are sparse, thereby providing a fertile ground for conjecture and misinformation. Placed along a shoreline with an erosional trend, armoring can perform its intended function of upland stabilization while the adjacent shoreline segments continue to erode. The resulting offset between stabilized and unstabilized segments may be interpreted incorrectly that the armoring has caused the adjacent erosion. Coastal armoring does have the potential of causing adverse effects to the adjacent shoreline. In situations where coastal armoring is contemplated, it is important to recognize, and where possible to quantify and perhaps mitigate for these adverse effects. Specific alleged adverse effects of coastal armoring include: (1) offshore profile steepening, (2) intensified local scour, (3) transport of sand to a substantial distance offshore, (4) adverse downdrift erosion, and (5) delayed post-storm recovery. The coastal engineering profession has a responsibility to develop an improved understanding of the interaction of coastal armoring with the nearshore sand transport system in order to allow jeopardized structures to be protected where warranted without causing adverse effects to adjacent shorelines.

ASSESSMENT

The two possibile bases that can be used to assess the effects of coastal armoring include sound principles and data either from the laboratory or the field. A principle is present below followed by a discussion of processes and available data relevant to various possible armoring effects.

Principle

The strongest principle that can be applied in any discussion of coastal processes is that of sediment conservation. Clearly, coastal armoring neither adds to nor removes sand from the sediment system, but may be responsible for the redistribution of sand and may prevent sand from entering the system. As an obvious and immediate application of this principle, if as has been contended, coastal armoring causes profile steepening through nearshore erosion, then that same volume of sand must be transported to and deposited elsewhere. It is important to keep the principle of sand conservation in mind in reviewing the interaction of coastal armoring with the adjacent shoreline and offshore profile.

Laboratory and/or Field Data Relating to Various Possible Effects

Offshore Profile Steepening - Some have claimed that steeply sloping revetments, vertical seawalls and even steep dunes cause an associated increased wave reflection and sand to be eroded and

transported and deposited so far offshore that it is effectively "lost" to the littoral system. Increased wave reflection can clearly occur as a result of coastal armoring; however, there does not appear to be a mechanism for an associated offshore transport to significant depths nor is there evidence to support such transport.

While wave reflection can cause shore parallel bars in the laboratory, primarily for monochromatic waves, the existence of reflection bars in nature does not appear to be well-documented or at least highly prevalent. Moreover, the hydrodynamics associated with wave reflection does not offer an obvious explanation for offshore sediment transport. It appears that the behavior of a beach in nature is dependent primarily on the amount of sand in the nearshore system as compared to that for the equilibrium profile. Under normal conditions, the profile fronting seawalls and natural beaches will be the same up to the location of the seawall. If waves were completely reflected, it is acknowledged that the onshore and offshore forces on a sediment particle must be completely balanced and for this limiting condition, no tendency for onshore or offshore motion could exist. The equilibrium profile in this case could only be the superposition of barred topography on an otherwise horizontal bottom.

Storm-Induced Intensified Local Scour - Local scour under normal wave conditions has been addressed in the preceding section. During conditions of elevated water levels and high storm waves, the equilibrium profile requires sand to be transported seaward, both along natural and armored shorelines. Some of this material will be deposited as an offshore bar. Consider first a two-dimensional case as would occur in a wave tank. Because the armoring "denies" upland material for bar formation, this material is obtained from as near a location to the natural source as possible, i.e. immediately adjacent to the base of the seawall. This explanation is illustrated in Figure 1. Thus, during storms, it is expected that increased scour would occur at the toe of the vertical seawall. This is consistent with data presented by Kriebel, et.al. (1986) for post-Hurricane Elena profiles in which, relative to natural profiles, accentuated toe scour occurred at the base of seawalls, see Figure 2.

Extending to three dimensions, the above discussion of shoreline response during storms, since immediately in front of armoring there is insufficient sand to satisfy the "demand" of the offshore bar, the shore parallel downward slope to the area immediately seaward of the unarmored segment, combined with the mobilizing effects of breaking waves causes sediment to flow from the region offshore of the natural shoreline to that offshore of the armored segment. The effect of this interaction is to cause an additional "erosional stress" adjacent to the armoring with the magnitude of this stress increasing with the length of the armoring. This interaction is illustrated in Figure 3 and is consistent with post-Hurricane Eloise measurements as reported by Walton and Sensabaugh (1979), see Figure 4.

Projection of Armoring into the Active Surf Zone - If an isolated armored segment is constructed on an eroding shoreline where a substantial longshore sediment transport exists, the armoring will in time project into the surf zone and will act as a groin to block the

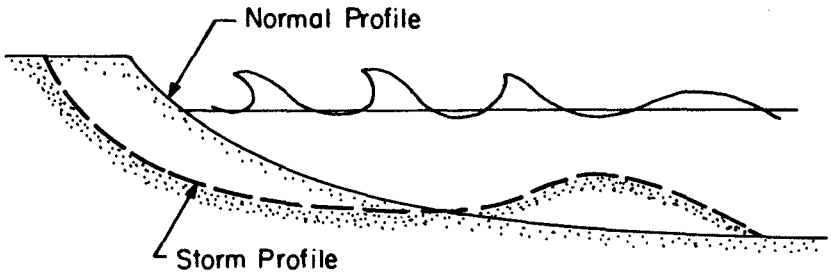

a) Normal and Storm Profiles on a Natural Shoreline

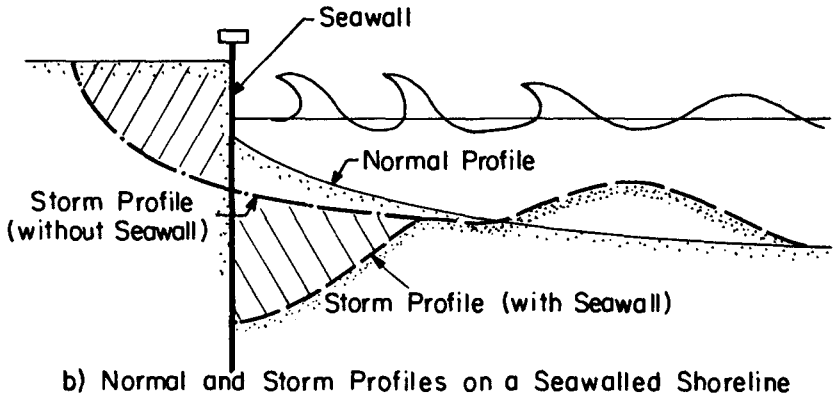

b) Normal and Storm Profiles on a Seawalled Shoreline and Comparison with Profiles on a Natural Shoreline

Figure 1. Additional Scour Immediately in Front of a Seawall Due to Storms.

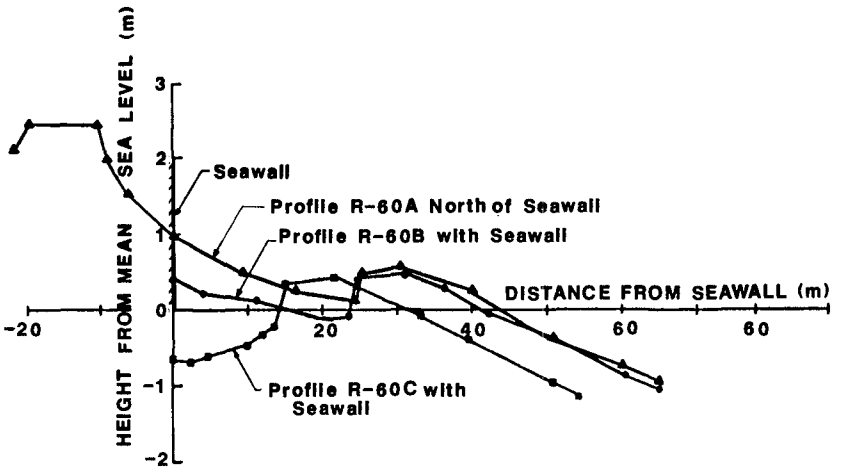

Figure 2. Comparison of Response of Natural and Seawalled Profiles to Hurricane Elena, September, 1985. (From Kriebel, et.al., 1986).

net longshore sediment transport. The annual deficit of sediment downdrift of the armoring will be the sum of that blocked by the projecting armoring and that not yielded by the upland protected by the armoring. The downdrift annual deficit will thus increase with (a) the length of the armoring, and (b) time as a result of increasing projection into the surf zone thereby blocking a greater and greater fraction of the longshore sediment transport. A simple method will be presented later to quantify approximately the downdrift deficit.

Effect of Wave Reflection on Longshore Sediment Transport - It has been argued that wave reflection from a seawall causes greater longshore sediment transport in front of the seawall and thus a local steepening of the profile. As presented in the discussion on "Principle" if this were the case, one would expect this effect to contribute to an equivalent deposition downdrift of the armoring, since greater quantities of sediment would be transported in the longshore direction in front of the armoring, but the transporting capacity of the waves would not be increased downdrift of the armoring. Contrary to the hypothesis that wave reflection causes increased longshore sediment transport, a rational argument can be advanced that the effect of wave reflection is to reduce the longshore sediment transport. Clearly, for an idealized shoreline with straight and parallel bottom contours, the total net longshore thrust, F_L, can be determined from momentum flux considerations as

$$F_L = \frac{\gamma H_o^2}{32} (1 - \kappa_r^2) \sin 2\alpha_o \qquad (1)$$

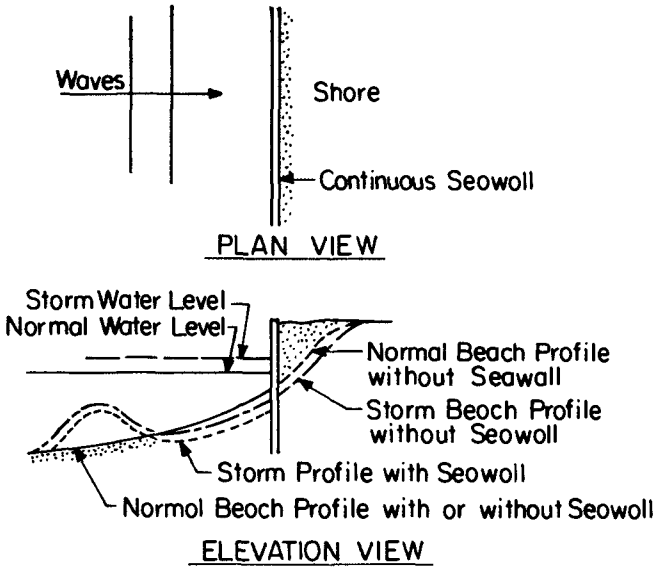

a) Qualitative Effects of Continuous Seawall on Storm Beach Profile.

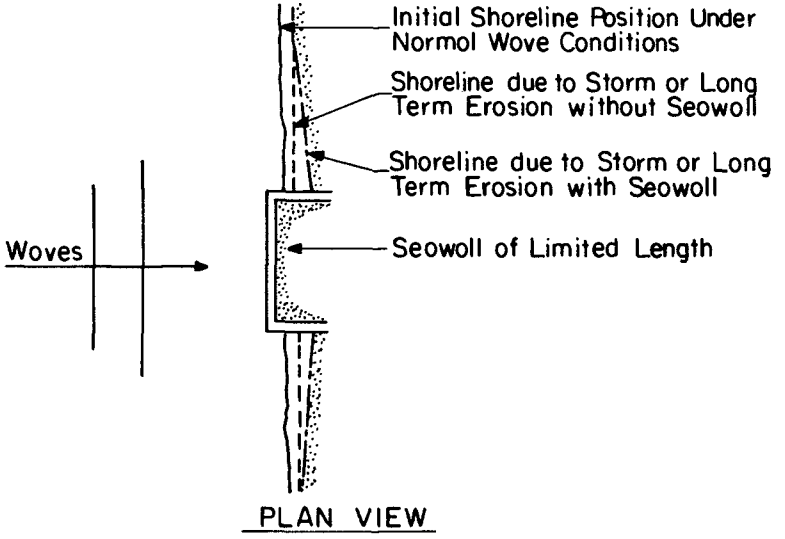

b) Effect of Seawall of Limited Length on Storm or Long-Term Beach Planform.

Figure 3. Two- and Three-Dimensional Effects of a Seawall on Beach System during Storms.

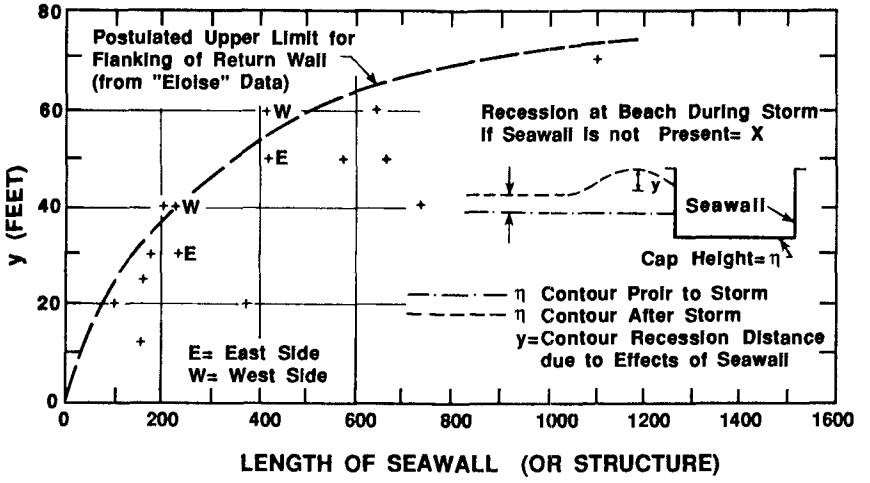

Figure 4. Additional Bluff Recession Due to Seawalls. Based on Post-Hurricane Eloise Field Observations by Walton and Sensabaugh.

in which κ_r represents the reflection coefficient as measured seaward of the surf zone, γ is the specific weight of sea water, and α_o is the deep water wave direction relative to a normal to the bottom contours. Thus for larger reflection coefficients, the total longshore thrust is reduced. Counter arguments are that there is an increase in the longshore current because the very shallow water portion of the profile provides much of the retarding force and that even with a reduced total longshore thrust, the currents and associated sediment transport can be increased. Clearly, this is a complex problem and deserves careful consideration prior to reaching a conclusion.

Interference with Post-Storm Recovery - Wave reflection from coastal armoring could be the cause of a delayed post-storm recovery. Although this hypotheses has been proposed, it is again helpful to look to nature to attempt to address this question. First if the presence of coastal armoring were responsible for a delayed post-storm recovery, there should be ample evidence in the form of deposits remaining seaward of armoring and armored shorelines in front of which the contours are displaced landward relative to the adjacent shorelines. Data presented by Kriebel, et.al. (1986) from Hurricane Elena supports an equally rapid or nearly equally rapid recovery adjacent to coastal armoring. Moreover, observations by Mr. Ralph Clark immediately after Hurricane Elena (September, 1985) and approximately eight months later (May, 1986) indicate that recovery had occurred to at least the pre-storm condition. Figure 5 presents a somewhat representative pair of photographs taken immediately after Elena and eight months later; inspection of these photographs supports natural beach recovery even in front of vertical seawalls.

a) September 9, 1985, within One Week after Hurricane Elena.

b) May 16, 1986, Approximately Eight Months after Hurricane Elena.

Figure 5. Beach Recovery in Front of a Vertical Seawall. Comparison of Photographs Showing Eroded Shoreline after Occurrence of Hurricane Elena and Naturally Recovered Shoreline Eight Months Later (Courtesy of R. R. Clark).

Summary Assessment Based on Principles and Available Data

Based in part on the discussion above, Table I presents a summary assessment and evaluation of some common perceptions concerning the effects of coastal armoring.

PROPOSED APPROXIMATE PRINCIPLES

Based on the foregoing discussion and observations of cases of armoring in nature, the following two approximate principles are proposed:

1. In a two-dimensional situation in nature with wave and sediment conditions not conducive to formation of an offshore bar, the beach profile seaward of an armored segment does not depend on the presence of the armoring, but depends almost entirely on the equilibrium beach profile vis-a-vis the amount of sand available to form this profile.

2. In a two-dimensional situation in nature with wave and sediment conditions conducive to formation of a longshore bar, the additional volumetric scour immediately fronting the armoring will be less than or equal to that volume of material that would have been provided through erosion by that portion of the profile upland of the armoring if the armoring were not present.

MITIGATION

It has been noted that coastal armoring can cause adverse effects to adjacent shorelines, primarily through: (1) depriving the littoral system of material that would have been provided if erosion of the upland had not been prevented by the armoring, (2) blockage of the longshore sediment transport by armoring projecting into the active littoral zone, and (3) during storms due to sediment being drawn from adjacent profiles to replace that prevented from being eroded by the armoring.

In principle, it would appear desirable to assess the potential adverse effects of each armoring considered and to condition the construction on appropriate mitigation to offset these adverse effects. The mitigation would be the annual addition of sand to volumetrically compensate for that denied the adjacent shorelines by the armoring. This concept is illustrated by Figure 6, where installation of armoring without any mitigative sand placement will result in adverse effects to the shoreline, but with increasing annual volumes of sand added, the combination of armoring placed plus mitigative sand added become a benefit. The focus of this section is to recommend methodology for identifying the "neutral" point where the annual mitigative sand placement just offsets any adverse effects of the armoring. Two effects will be considered: (1) the reduction in sand supply through prevention of erosion, and (2) the blockage of sediment transport by a projecting revetment.

Reduction of Upland Sediment Supply by Armoring - Consider the situation presented in Figure 7 in which the erosional trend is, R, in

Table I. ASSESSMENT OF SOME COMMONLY EXPRESSED CONCERNS RELATING TO COASTAL ARMORING

Concern	Assessment	
Coastal armoring placed in an area of existing erosional stress causes increased erosional stress on the beaches adjacent to the armoring.	TRUE	By preventing the upland from eroding, the beaches adjacent to the armoring share a greater portion of the same total erosional stress.
Coastal armoring placed in an area of existing erosional stress will cause the beaches fronting the armoring to diminish.	TRUE	Coastal armoring is designed to protect the upland, but does not prevent erosion of the beach profile waterward of the armoring. Thus an eroding beach will continue to erode. If the armoring had not been placed, the width of the beach would have remained approximately the same, but with increasing time, would have been located progressively landward.
Coastal armoring causes an acceleration of beach erosion seaward of the armoring.	PROBABLY FALSE	No known data or physical arguments support this concern.
An isolated coastal armoring can accelerate downdrift erosion.	TRUE	If an isolated structure is armored on an eroding beach, the structure will eventually protrude into the active beach zone and will act to some degree as a groin, interrupting longshore sediment transport and thereby causing downdrift erosion.
Coastal armoring results in a greatly delayed post-storm recovery.	PROBABLY FALSE	No known data or physical arguments support this concern.
Coastal armoring causes the beach profile to steepen dramatically.	PROBABLY FALSE	No known data or physical arguments support this concern.
Coastal armoring placed well-back from a stable beach is detrimental to the beach and serves no useful purpose.	FALSE	In order to have any substantial effects to the beaches, the armoring must be acted upon by the waves and beaches. Moreover, armoring set well-back from the normally active active shore zone can provide "insurance" for upland structures against severe storms.

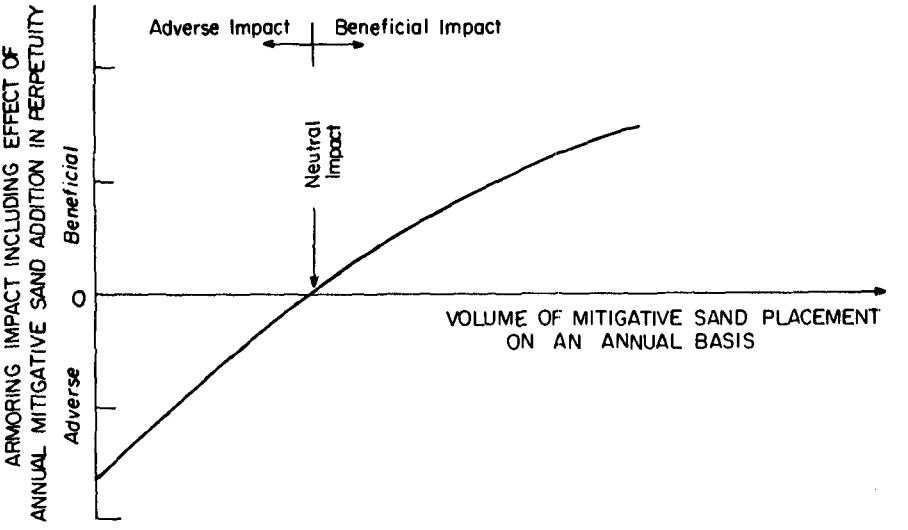

Figure 6. Effect of Annual Mitigative Sand Placement in Reducing the Adverse Impact of a Coastal Armoring Project.

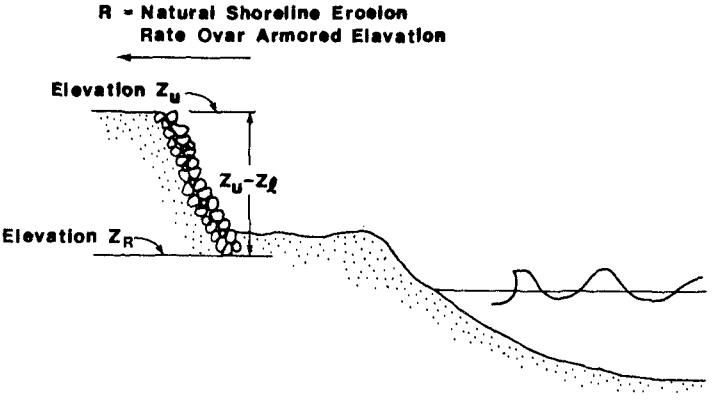

Figure 7. Definition Sketch. Describing Basis for Armoring Mitigation Due to Prevention of Upland Supply by Erosion.

m/yr and the armoring extends from a lower elevation, Z_ℓ, up to Z_u and the length of the armoring is ℓ. For this case, the required annual mitigative sand placement, Ψ_1, to achieve a neutral effect is

$$\Psi_1 = (Z_u - Z_\ell)(R)(\ell) \tag{2}$$

As an example, if the erosional trend rate is 1 m/yr, the length of the armoring is 100 m and the armoring extends from a lower elevation, Z_u, of 0 m to an upper elevation, Z_u, of 5 m, the annual volumetric mitigative requirement

$$\Psi_1 = (5-0)(1)(100) = 500 \text{ m}^3/\text{yr}.$$

Interruption of Longshore Sediment Transport - A coastal armoring constructed on an eroding coastline will eventually protrude into the active surf zone where it will cause a partial blockage of the longshore sediment transport with the familiar pattern of deposition and erosion updrift and downdrift of the armoring, respectively. This problem is complicated as the rate of impoundment will increase annually with the ultimate potential of blocking the entire net longshore sediment transport.

The volume of storage can be estimated by several different approaches. For purposes here, two different bases will be presented and it is recommended that an average of the two be used. For both, it is assumed that the updrift impoundment planform is linear and aligned with the incoming waves, see Figure 8.

The first method considers the profile in the storage area to be the same as that along the unperturbed beach. The additional annual volumetric storage rate, Ψ_{2_a}, can be shown to be

$$\Psi_{2_a} = \frac{(B + h_*)}{\tan\theta} \, b \, R \tag{3}$$

in which B = berm height, h_* = profile closure depth, R = long-term erosion rate, b = projection of armoring beyond unperturbed shoreline, and θ is angle of the wave crest approach relative to the unperturbed beach. Lacking specific information, a value of $\tan\theta = 0.1$ appears reasonable. It is noted that the projection distance b increases with time in accordance with $b = b_o + Rt$, in which b_o is the projection at the initial time and t is the number of years into the future.

The second method assumes that the profile modifications extend only out to the solid oblique line shown in Figure 8. Figure 9 shows profiles of the unaffected and assumed affected profiles for the second method. Clearly the second method represents an underestimate of the impounded volume whereas the first method is an overestimate. The equation for the annual rate of increased volume storage, Ψ_{2_b}, is

$$\Psi_{2_b} = \frac{1}{\tan\theta} \left(B + \frac{3}{5} h'\right) b \, R \tag{4}$$

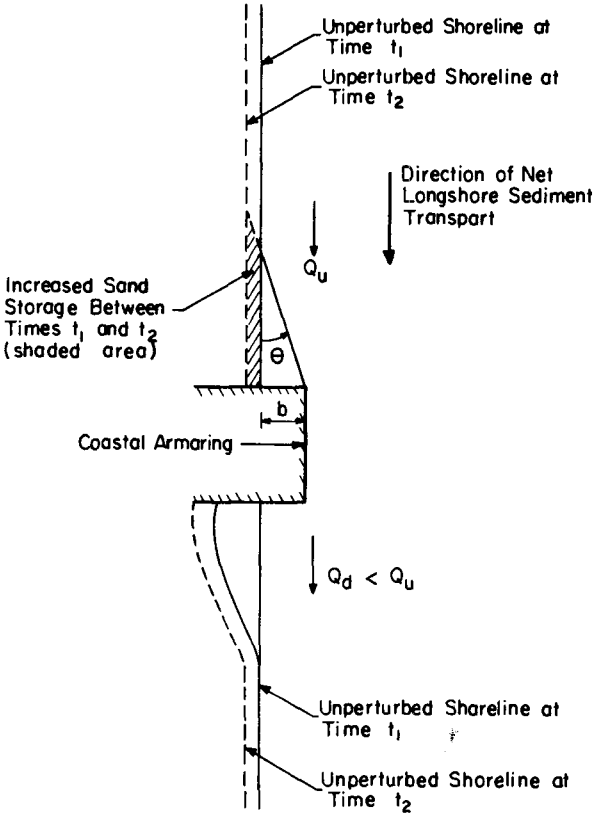

Figure 8. Illustration of Sand Storage by Coastal Armoring Projecting Beyond the Unperturbed Shoreline.

in which h' is the depth that would be present at the toe of the seawall if the seawall were not present. Eq. (4) incorporates the assumption of an equilibrium profile of the form $h = Ax^{2/3}$, in which h is the water depth at a distance x offshore and A is a scale parameter determined for the natural profile of interest. The parameter A has dimensions of $(\text{length})^{1/3}$ and for fine to medium sands is on the order of 0.1 $m^{1/3}$ (0.15 $ft^{1/3}$). Alternatively, h' can be estimated at a distance b along an unperturbed shoreline.

As noted before, recognizing that the first and second methods for estimating Y_2 are too large and too small respectively, it is recommended that an average of the two be used, i.e.

$$Y_2 = \frac{1}{2}\left(Y_{2_a} + Y_{2_b}\right) = \frac{Rb}{\tan\theta}\left[B + \frac{h_* + \frac{3}{5}h'}{2}\right] \qquad (5)$$

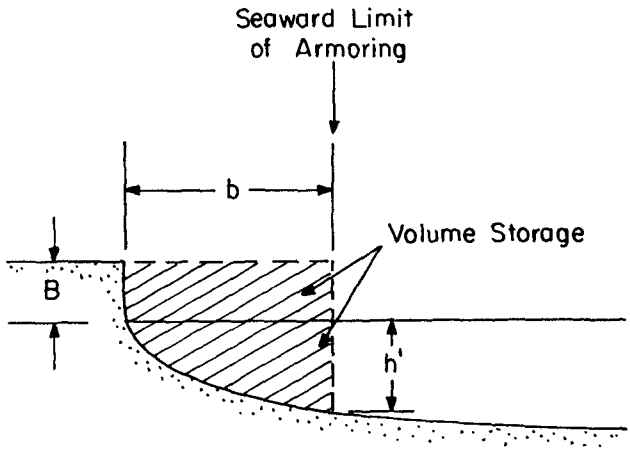

Figure 9. Profile Considerations in Method B.

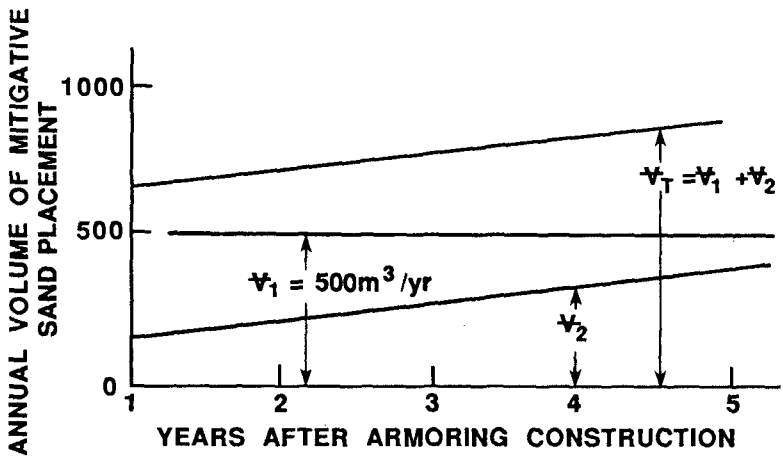

Figure 10. Illustration of Annual Volume of Mitigative Sand Placement for Example Presented in Text.

As an example, suppose that R = 1 m/yr, b_o = 2 m, tanθ = 0.1, B = 2 m, h_* = 7 m and A = 0.1 m $^{1/3}$. The mitigative sand requirement increases with time as presented in Figure 10 where Ψ_1, Ψ_2 and the total annual mitigative sand requirement $\Psi_T = \Psi_1 + \Psi_2$ are presented.

It should be noted that an upper limit to, Ψ_2, should be the net longshore sediment transport and that bypassing around a projecting armoring could be considered as an alternate mitigative strategy.

SUMMARY AND CONCLUSIONS

Uncertainties resulting from a lack of definitive information has led to considerable speculation and claims regarding the adverse effects of coastal armoring on the adjacent shorelines. Employing sound principles and laboratory and field data, an attempt is made to evaluate the potential adverse effects of armoring. It is concluded that:

1. There are no factual data to support claims that armoring causes: profile steepening, increased longshore transport, transport of sand to a substantial distance offshore, or delayed post-storm recovery.

2. The interaction of an armored segment of shoreline with the littoral system is more of a "geometric" or "kinematic" interaction as contrasted to a "dynamic" interaction. The interaction depends on the amount of sand in the system vis-a-vis the equilibrium beach profile for the prevailing tide and wave conditions.

3. Armoring can cause localized additional storm scour, both in front of and at the ends of the armoring. A simple sediment supply-demand argument is proposed to explain the scour.

A methodology is presented to quantify the potential adverse effects of an armoring installation and appropriate periodic sand additions proposed as a means of mitigation to elevate the installation to one of neutral impact on the adjacent shoreline.

REFERENCES

Clark, R.R., Personal Discussion on Recovery Along Armored Coasts Following Hurricane Elena, 1986.

Kana, T.W. and M. Svetlichny, "Artificial Manipulation of Beach Profiles", Proceedings, Eighteenth International Coastal Engineering Conference, 1982, p. 903-922.

Kriebel, D.L., W.R. Dally and R.G. Dean, "Beach Profile Response Following Severe Erosion Events", Report No. UFL/COEL-86-016, Coastal and Oceanographic Engineering Department, University of Florida, Gainesville, FL, 1986.

Walton, T.L. and W.M. Sensabaugh, Seawall Design on the Open Beach, Florida Sea Grant, Report No. 29, 1979.

CHAPTER 136

Scour About a Single, Cylindrical Pile Due to Combined Random Waves and a Current

Robert W. Eadie, IV* and John B. Herbich,** M.ASCE

Introduction

There have been many studies of scour around piles caused by waves, and some studies of scour by waves and currents combined. However, almost all of the studies were conducted with monochromatic waves. The purpose of this investigation was to study what scouring effects various currents and random waves have on a single, cylindrical pile. These results were then compared with the results from previous studies of scour resulting from currents and monochromatic waves at Texas A&M University (Armbrust, 1982 and Wang, 1983).

Experiments were conducted in a two-dimensional wave tank. The pile used in this study had a diameter of 1.5 inches. Two water depths, four currents, one sediment size and four random wave spectra were utilized. Using data obtained from the experiments, an attempt was made to describe scour in terms of relevant dimensionless parameters.

Scour

The scour phenomenon begins with the incipient motion of sediment particles. Incipient sediment motion is defined to be "an instantaneous condition reached when the resultant of all the active forces on the particle intersects the line connecting the bed particle contact points," (Eagleson and Dean, 1961). There are three types of active forces acting on a sediment particle. Two of these forces, the drag and lift forces, are due to the fluid motion. These forces are in turn balanced by the sediment particle mass.

A thorough understanding of these forces is required in order to comprehend fully the processes of incipient motion, bedload transport and bed form development; all of which depend on the collective response of initially stationary bed particles to fluid forces.

In oscillatory flow generated by waves, the scour hole initiates at the side of the cylinder, and sometimes sediment deposition is found to occur against the upstream and downstream sides of the cylinder. Once fully developed, the scour hole is a radially symmetric frustrum of an inverted cone having side slopes at the angle of repose of the sediment (Palmer, 1969).

The mechanics of scour due to waves and currents are quite complicated and this type of scour occurs in almost all ocean environments. The

*Lt, CEC, U.S. Navy, Navy Experimental Diving Unit, Panama City, FL 32401.

**Professor, Civil and Ocean Engineering, Civil Engineering Department, Texas A&M University, College Station, TX 77843-3136.

scale and shape of the scour hole depends on the relative magnitude of the unidirectional velocity and the oscillatory flow velocities.

Experimental Study

Apparatus. Scour experiments were conducted in a 120-foot long (36.6 m), 3-foot deep (0.91 m) and 2-foot (0.61 m) wide, two dimensional, glass-walled wave flume. The test area was located approximately 40 feet (12.2 m) from the wave generator. The entire test area measured 40 feet (12.2 m) in length and was divided into several sections. An 8-foot (2.4 m) long, 5-inch (0.13 m) deep test sediment bed was bordered on each end by an 8-foot long (2.4 m) 10-inch (2.7 m) high false bottom. At the leading edge of the test area, a 16-foot (4.9 m) long ramp was used to gradually bring the wave up to the new depth at the top of the false bottom. A 1.5 inch (0.04 m) diameter aluminum pile was positioned along the centerline of the sediment bed.

Currents were produced using a centrifugal pumping system. The flow rate was monitored using a Fischer and Porter electromagnetic flow meter. The pump discharge entered the wave flume just forward of the wave generator and was diffused using a louvered grate. A Thermo-Systems model 1050 hot film anemometer was used to measure the vertical velocity distribution of the combined waves and currents.

The random wave generator used was a Seasim modular wave making system. This system consisted of a servo control system amplifier, a programmable spectrum random signal generator, an autocompensating wave height gauge and a paddle type sea wave simulation rolling seal modular wave generator.

A capacitance-type wave gauge was used with a Hewlett-Packard model 17403A carrier pre-amplifier to measure wave profile. To determine the significant wave height from the wave profile, a wave digitizer was used.

A wave absorber was positioned in the wave flume at the opposite end of the wave generator to reduce any reflections which might occur.

Scour depth readings were made using a point gauge after each test.

Procedures

A total of 20 experiments were performed. Four runs utilized currents only and the remainder used a combination of waves and currents. All test runs used a 1.5 inch (0.04 m) diameter pile placed in a bed of glass microbeads. The microbeads had a mean diameter (D_{50}) of 0.1 mm and a specific gravity of 2.45. Four different wave spectra were generated: Darbyshire, Pierson-Moskowitz, Jonswap (wave period = 8 secs) and Jonswap (wave period = 10 sec). Two water depths 0.917 ft (0.28 m) and 1.167 ft (0.36 m) and two different currents at each depth were employed, i.e. 0.380 fps (0.116 mps) and 0.650 fps (0.198 mps) at 0.917 ft (0.280 m), and 0.405 fps (0.123 mps) and 0.485 fps (0.148 mps) at 1.167 ft (0.036 m).

At the onset of each test, the sediment bed was leveled to a 5 inch (0.13 m) uniform thickness. After achieving the required water depth, the proper flow rate was established. The desired water level was maintained by regulating a 10-inch discharge valve located at the rear of the tank. The sediment bed was once again leveled as the above variables remained constant. The previously programmed signal generator then started generating the desired wave spectrum. Maximum scour depth was recorded at various intervals throughout each run, the time increment increasing as the test progressed. Each test was completed when equilibrium in the measured maximum scour depth was attained. After draining the tank, the patterns were photographed and sediment elevations, taken in the form of a rectangular grid, were established with the point gauge to determine equilibrium scour depth.

Results

Dimensionless Plots. There are many pertinent variables in a study of scour; the more important are: water depth (h), significant wave height ($H_{1/3}$), acceleration due to gravity (g), combined wave-current velocity (U), pile diameter (D), median sediment diameter (D_{50}), sediment/fluid density difference ($\rho_s - \rho$), density of water (ρ), kinematic viscosity of water (ν), and ultimate scour depth (S_d).

Since random waves were used in the study, and were defined by the significant wave height ($H_{1/3}$), wave period and wave length were omitted from the above list of variables. In the dimensional analysis S_d was chosen as the unit of length, S_d^2/ν as the unit of time and $/S_d^3$ as the unit of mass. The remaining seven variables expressed in these units give the following dimensional numbers:

$$S_d/h,\ S_d/H_{1/3},\ S_d/D,\ S_d/D_{50},\ \rho/(\rho_s-\rho),\ \nu^2/S_d{}^3g,\ \nu/S_d u$$

by rearranging and combining terms:

$$\frac{1}{(S_d/D)(\nu/S_d u)}\ \frac{UD}{\nu} = N_{RP}$$

$$[(S_d/h)(1/(\nu/S_d u)^2)(\nu^2/S_d{}^3g)]^{1/2} = u/\sqrt{gh} = N_F$$

$$[(S_d/D)(1/(\nu/S_d u)^2)(\nu^2/S_d{}^3g)]^{1/2} = u/\sqrt{gD} = N_{FP}$$

$$[(1/2)(\nu 2/S_d{}^3g)(1/(\nu/S_d u)^2)]^{1/2} = u/\sqrt{2S_d g} = N_{ES}$$

$$[(1/(\nu/S_d u)^2)(\nu^2/S_d{}^3g)(S_d/D_{50})(\rho/(\rho_s-\rho))]^{1/2}$$

$$= U/\sqrt{gD_{50}((\rho_s-\rho)/\rho)} = N_S$$

Therefore, the functional relationship for scour is:

$$\frac{S_d}{h} = f(S_d/H_{1/3},\ S_d/D,\ S_d/D_{50},\ N_{RP},\ N_F,\ N_{FP},\ N_{ES},\ N_S).$$

On various dimensionless plots, data from experiments conducted by Armbrust and Wang were used in combination with data obtained from the random wave-current interaction experiments. Regression analysis was performed on the plots in order to construct the appropriate curves. Logarithmic regression analysis was used on the semi-logarithmic plots, and power regression analysis was used on the full logarithmic plots. The "r^2" term adjacent to each curve represents the correlation coefficient for each curve.

It was discovered that a relationship exists between scour depth and sediment number (N_S), (Figures 1 and 2) as well as between scour depth and the pile Reynolds number (N_{RP}), (Figures 3 and 4). However, scour depth is not dependent on N_S, or N_{RP} alone, but is also dependent on pile diameter as well as sediment size.

By plotting the relative scour depth (S_d/h) against the product of the pile Reynolds number and the sediment number (N_{RP})(N_S), all data points collapsed onto a single curve regardless of variance in pile diameter or sediment size (Figure 5). It appears that since all data collapse onto a single curve, the type of wave train used for model studies, either monochromatic or random, is insignificant in the prediction of scour depth about a single cylindrical pile. However, the geometric shape of the scour hole differs with the type of wave train generated. By using a dimensionless plot (Figure 5), it appears as though predictions of scour depth could be made for situations in which the pile diameter or mean sediment size varied without utilizing scaling factors. Before any conclusions can be made, field data are required to evaluate the need, if any, for scale effects.

Scour Patterns. The rate of scour hole development by wave-current interaction was faster than that due to a steady current alone. Scour development is very rapid initially, the scour rate then decreases until the equilibrium scour depth is reached. Figure 6 shows a typical pattern of scour development in its initial stages, approximately the first 2 to 5 minutes of test. Figures 7 and 8 are the typical scour patterns that occur due to wave-current interaction 30 minutes and 2 to 3 hours after test commencement, respectively.

In all cases, the scour hole due to wave-current interaction was similar in shape to the scour hole formed by a steady current. This shape resembles an inverted cone. A typical example of a scour hole formed by a steady current is shown in Figure 9. Figures 10 to 13 depict the scour pattern formed by the same current used in Run 4 (Figure 8), combined with four different random wave spectra. As stated previously, the equilibrium scour hole associated with the wave-current interaction was deeper when compared to the equilibrium scour hole formed by a steady current alone. The size and shape of the equilibrium scour hole associated with wave-current interaction was at times greater than, approximately equal to, or less than the size and shape of the scour hole due to a steady current alone. These results differ from the prediction made by Niedoroda and Dalton in 1982. They stated that the scour hole

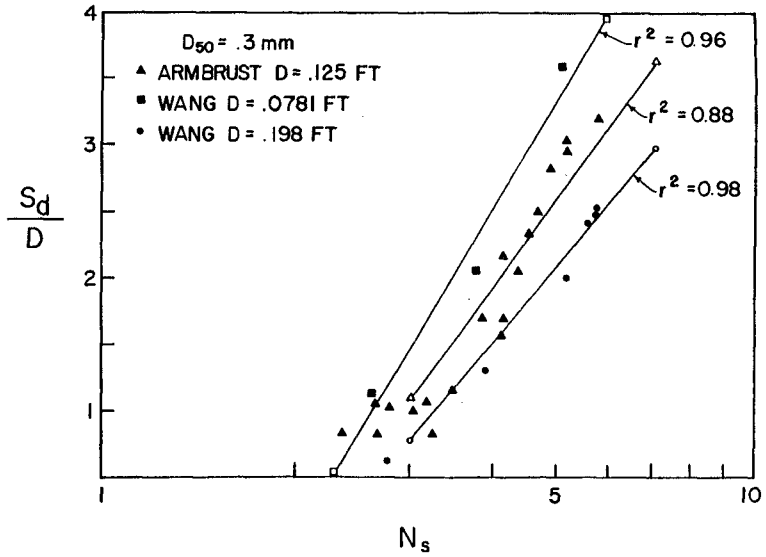

Figure 1. Relative scour depth, S_d/D, vs. sediment number for a constant sediment size and various pile diameters.

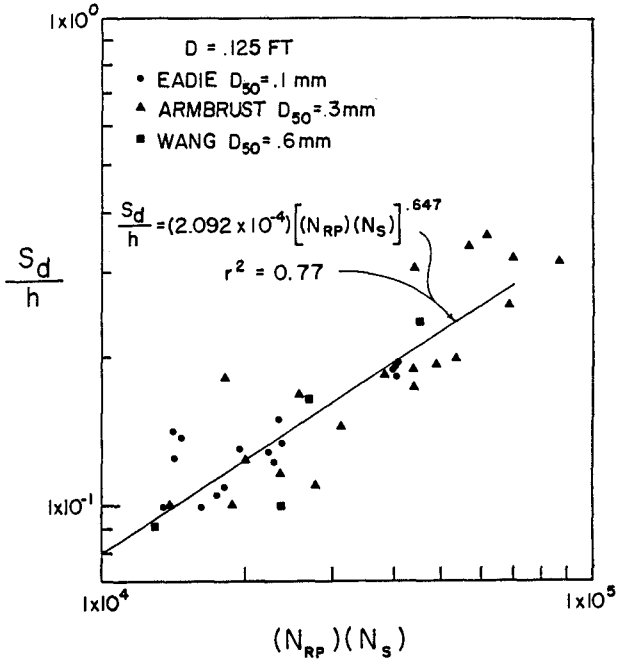

Figure 2. Relative scour depth, S_d/D, vs. sediment number times pile Reynolds number for a constant pile diameter and various sediment sizes.

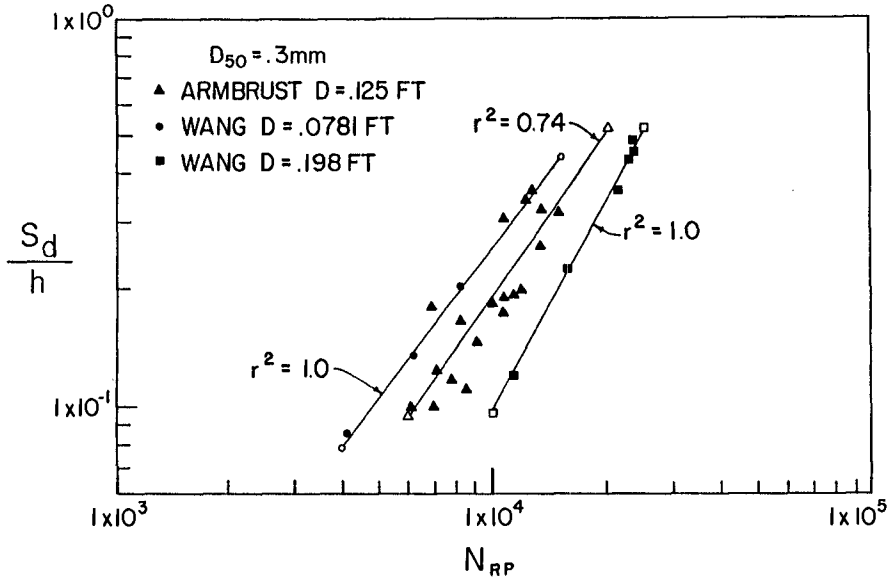

Figure 3. Relative scour depth, S_d/h, vs. sediment number times pile Reynolds number for a constant sediment size and various pile diameters.

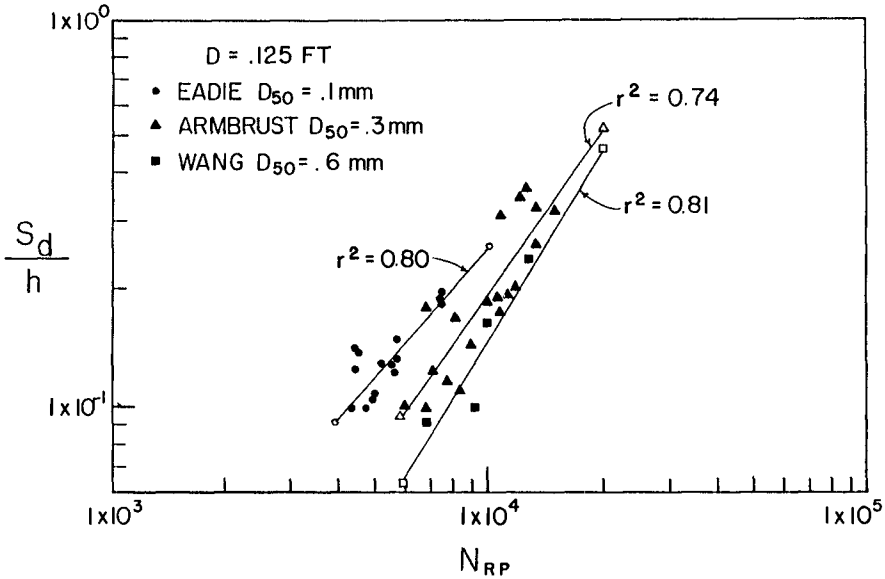

Figure 4. Relative scour depth, S_d/h, vs. pile Reynolds number for a constant pile diameter and various sediment sizes.

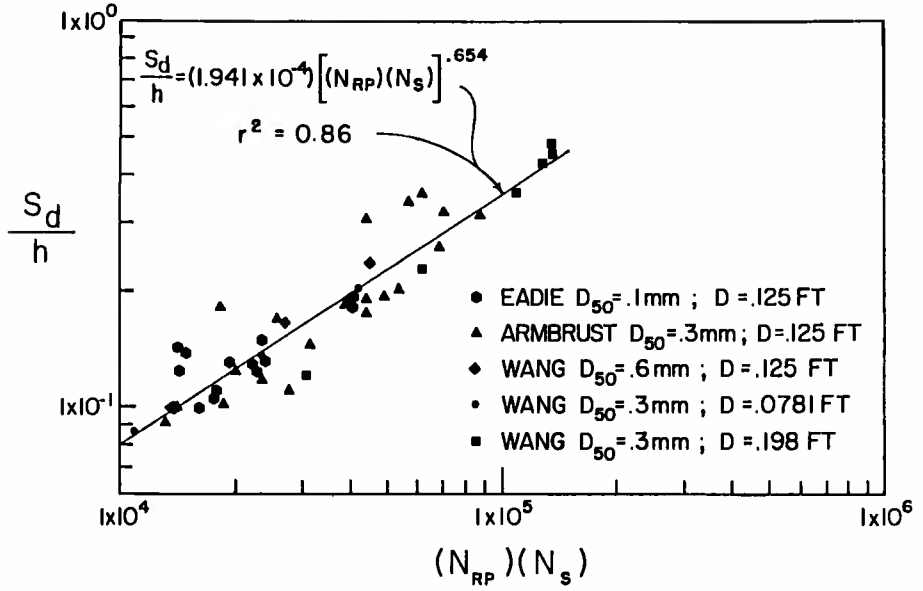

Figure 5. Relative scour depth, S_d/h, vs. sediment number times pile Reynolds number for various sediment sizes and pile diameters.

Figure 6. Initial stages of scour development.

Figure 7. Scour pattern 30 minutes after test commencement.

Figure 8. Scour pattern 2 to 3 hours after test commencement.

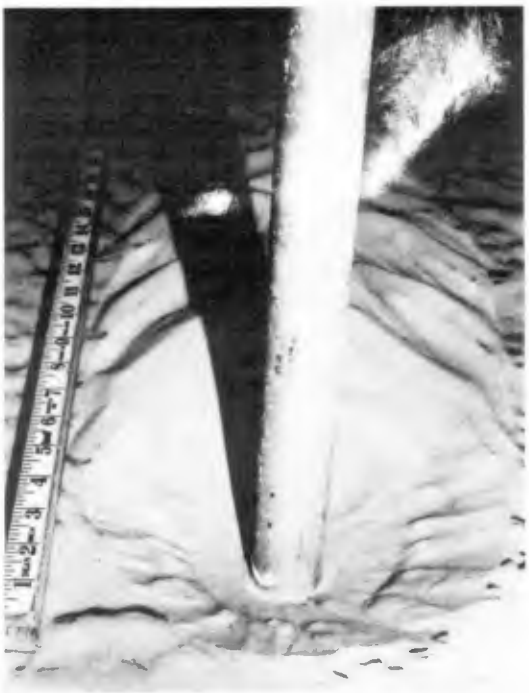

Figure 9. Typical scour cavity due to a steady current.
h=1.167 ft (0.36 m); U_c=.485 fps (0.148 mps); D=.125 ft; S_d=.14 ft (0.043 m)

Figure 10. Scour pattern due to random waves and current - Run 13.
h=1.167 ft (0.36 m); U_c=.485 fps (0.148 mps); U=.498 ft/sec (0.1518 mps); wave spectrum-Darbyshire; $H_{1/3}$=.1724 ft (0.053 m);D=.125 ft (0.038 m); S_d=.143 ft (0.044 m)

Figure 11. Scour pattern due to random waves and current - Run 14.
h=1.167 ft (0.36 m); U_c=.485 ft/sec (0.148 mps); U=.491 ft/sec (0.150 mps); wave spectrum=Pierson-Moskowitz; $H_{1/3}$=.1527 ft (0.047 m); D=.125 ft (0.038 m); S_d=.149 ft (0.045 m)

Figure 12. Scour pattern due to random waves and current - Run 15.
h=1.167 ft (0.36 m); U_c=.485 ft/sec (0.148 mps); U=.504 ft/sec (0.154 mps); wave spectrum=Jonswap (T=8 sec); $H_{1/3}$=.1631 ft (0.050 m); D=.125 ft (0.038 m); S_d=.174 ft (0.053 m)

Figure 13. Scour pattern due to random waves and current - Run 16.
h=1.167 ft (0.36 m); U_c=.485 ft/sec (0.148 mps); U=.508 ft/sec (0.155 mps); wave spectrum=Jonswap (T=10 sec); $H_{1/3}$=.1550 ft (0.047 m); D=.125 ft (0.038 m); S_d=.155 ft (0.047 m)

size and shape for combined waves and currents should not be as great as that developed by a steady current alone.

The general scour pattern was one of localized scour around the pile. A vortex formed around the pile due to disturbed flow and suspended the sediment. The sediment was carried farther downstream under the combined effects of waves and currents than it was with a steady current alone. Initially, the sediment suspension appeared to become greater as the scour hole developed, possibly due to a strengthening of the vortex system surrounding the pile. Because of the disturbance of flow caused by the pile, trailing ripples formed immediately behind the pile extending in the direction of wave propagation as the test progressed.

In all cases, the maximum scour depth occurred downstream of the pile, approximately 1/4 inch from the pile, and at an angle of approximately 40 degrees to the left or right of an imaginary line drawn through the pile and parallel with the wave flume walls.

Summary

1. Scour development was very rapid initially. The scour rate then decreased until an equilibrium scour depth was reached.

2. Scour development due to current and wave action occurred faster than scour due to a steady current alone.

3. The equilibrium scour depth caused by wave-current interaction is approximately 10 percent greater than the scour depth caused by a steady current alone.

4. The shape of the scour hole due to waves and currents and the shape of the hole due to current alone are similar. The shape resembles an inverted cone.

5. A relationship exists between scour depth and sediment number (N_S). However, scour depth is not dependent on N_S alone, but is also dependent on pile diameter and sediment size.

6. A relationship also exists between scour depth and the pile Reynolds number (N_{RP}). Again, scour depth is not dependent on (N_{RP}) alone, but is also dependent on pile diameter, as well as sediment size.

7. By plotting the relative scour depth (S_d/h) against the product of the pile Reynolds number and sediment number, (N_{RP}) (N_S), all data points collapse onto a single curve regardless of variance in pile diameter or sediment size.

Although the amount of data is limited, due to the fact that all data could be collapsed onto one curve when plotting S_d/h versus (N_{RP})(N_S), (Figure 5), it appears as though the type of wave train used for model studies, either mono-chromatic or random, is insignificant in the

prediction of scour depth about a single, cylindrical pile. However, when attempting to predict the geometry of the scour hole, the irregularity of the wave train becomes very significant. Armbrust stated that the pattern of scour for wave-current interaction is no longer conical in shape, but the pattern is irregular due to the wave particle orbital motion. The data in this study clearly indicate a conical scour pattern for random wave-current interaction. Although these results are different from those of Armbrust, they agree with field data, as well as with the predictions of Niedoroda and Dalton. The fact that the geometric shape of the scour hole differs with the type of wave train used, may become important in the prediction of scour depth around multiple pile cases.

The conclusions resulting from this study were found for a flow in which the steady current was greater than the oscillatory flow produced by the waves. If the magnitude of the two flows in relation to one another change, the flow patterns will also change and the geometry of the scour hole may very likely differ from results found in this study.

References

Armbrust, S.F. (1982). Scour about a cylindrical pile due to steady and oscillatory motion. Master's Thesis, Texas A&M University.

Eagleson, P.S. and Dean, R.G. (1961). Wave induced motion of bottom sediment particles. Transactions, ASCE, Vol. 126:1162-1189.

Herbich, J.B., Schiller, R.E., Jr., Watanabe, R.K., Dunlap, W.A. (1984). SeaFloor Scour: Design Guidelines for Ocean-Founded Structures, Marcel Dekker, Inc., New York and Basel.

Niedoroda, A.W. and Dalton, C. (1982). A review of the fluid mechanics of ocean scour. Ocean Engineering, 9(2):159-170.

Wang, R.K. and Herbich, J.B. (1983). Combined current and wave-produced scour around a single pile. COE Report No. 269, Texas A&M University.

List of Notations

Symbol	Quantity	Units	Dimensions
D	pile diameter	ft	L
D_{50}	mean diameter of sediment	ft	L
h	still water depth	ft	L
$H_{1/3}$	significant wave height	ft	L
N_{RP}	pile Reynolds number = UD/ν	-	-
N_s	sediment number = $U/\sqrt{gD_{50}[(\rho_s-\rho)/\rho]}$	-	-
S_d	ultimate scour depth	ft	L
T	wave period	sec	T
U	mean wave-current velocity	ft/sec	L/T
U_c	current velocity	ft/sec	L/T

CHAPTER 137

PIER PROTECTION SYSTEM FOR THE DUWAMISH SHIP CHANNEL IN SEATTLE

Y. Eisenberg[1]; M. ASCE

ABSTRACT

In 1978 an out-of-control ship hit and severely damaged a bascule bridge across the Duwamish West Waterway in Seattle seriously affecting both ship and highway traffic. The high level West Seattle Bridge was subsequently constructed to handle all through-highway traffic. A swing bridge was also designed to handle local traffic over the ship channel. The function of the pier protection system described in this paper is to protect the pivot piers and swing spans of this new bridge from damage by absorbing the part of the tranverse energy component imparted by a colliding ship, which is not absorbed by deformation of the ship's hull.

1. DESIGN

The Duwamish ship channel in the Port of Seattle, Washington will be widened from 150 to 250 feet (46 to 76 meters) and deepened to 43 feet (13 meters) below mean low low water (MLLW), thereby accommodating ships with displacement of up to 100,000 kips (45,000 tons) and a length of 650 feet (200 meters). The pier protection systm to be placed along the edge of the channel shall provide protection for the pivot piers and the open swing span superstructures from ship impact.

1.1 DESIGN ASSUMPTIONS

1.1.1 Design Vessel

The maximum size of vessel which is expected to use the Duwamish waterway has a displacement of 100,000 kips (45,000 tons) and a length of 650 feet (200 meters).

1.1.2 Design Collision

The pier protection was designed to protect the bridge elements from the impact of the assumed design vessel moving at three knots or 5 ft. (1.5 meters)/sec. at an angle of between 0 and 18 degrees to the centerline of the channel. A transverse impact of the stern of the ship was also considered.

Impacts in the longitudinal (head-on) direction were assumed at each end of the pier protection system only.

[1] Parsons Brinckerhoff Quade & Douglas, Inc.
San Francisco, California, U.S.A.

It was further assumed that transverse impacts may occur anywhere along the pier protection system.

1.1.3 Design Energy

1.1.3.1 Longitudinal

The kinetic energy of the ship in the longitudinal direction was taken as:

$KEL = \frac{1}{2} MV^2$ with M = Mass of the ship and V = Velocity of the ship

$KEL = \frac{1}{2} \times \frac{100,000}{32.2} \times 5^2 = 38,000$ ft.-kips, say 40,000 ft.-kips (5,500 meter-tons)

1.1.3.2 Transverse

The transverse component of the 5 ft. (1.5 m)/sec. velocity at an angle of 18 degrees is 1.55 ft. (0.47 m)/sec.

In addition, in the transverse direction, a factor of about 1.0 must be added to account for the hydrodynamic mass of the water behind the vessel.

Therefore, total $KE = \frac{1}{2} \frac{100,000}{32.2} \times 1.55^2 (1+1) =$ 7,500 ft.-kips (1,040 meter-tons).

A vessel trying to correct course may impact the pier protection with its stern. As there are no reliable data available for this type of impact, the use of a somewhat higher transverse design energy seemed prudent. Therefore, a value of 10,000 ft.-kips (1,400 meter-tons) was finally used.

1.1.4 Transverse Clearance

The height of the pier protection system was selected to restrain the ship deck overhangs of the design vessel from damaging the bridge. For purpose of the design of the pier protection, low water was taken as elev. -12 ft. (-3.66 m) and high water was taken as elev. 0.0. All elevations were based on the City of Seattle datum.

1.2 LOAD RESISTANCE FOR DESIGN IMPACTS

A collision of a fully-loaded design vessel at the design speed and angle has a very low probablility of occurring. The normal design safety factors were, therefore, not applied. The total resistance of the pier protection system was utilized, and

the timber protection was considered expendable for anything other than minor impacts.

1.2.1 Longitudinal Design

At each end of the pier protection system, a concrete topped sheet pile cell will protect the bridge from head-on impact. If the full design energy will have to be dissipated, it was assumed that substantial damage to both the pier protection system and the vessel will occur.

1.2.2 Transverse Design

The pier protection system for transverse impacts consists of timber facing, reinforced concrete distribution beam and rubber fenders. This system will be supported by dolphins on piles.

To absorb the full transverse design energy, the plastic deformation of the pier protection system and of the vessel will take place, resulting in damage requiring repair work to both the pier protection and the vessel.

1.3 OTHER COLLISIONS

1.3.1 Usual Collisions

The usual type of collision to be expected is a glancing blow by a vessel. This will require an energy dissipation of a small percentage of the full design energy. Another probable occurrence is that of a ship which may drift sideways and use the pier protection system as a guideway.

A timber facing consisting of rubbing planks (placed from elev. -12 ft. (-3.66 m) to +2 ft. (+0.61 m) and timber piles shall run the full length and extend at least 30 feet beyond the center of each end cell. At this point, the timber protection shall be turned around a pile cluster toward the bank of the waterway.

This timber protection will limit damage to ships at low energy impacts. Damage which may occur to the timber elements will be relatively easy to repair.

1.3.2 Collision Exceeding Design

An effort has been made to provide a reasonable level of protection for the bridge. It must be recognized, however, that it is possible that the waterway may be used by larger vessels or vessels of unusual configuration. It was not deemed to be economical to try to prevent damage to the bridge for all possible impact conditions. Therefore, some risk factors remain.

1.4 DESIGN COMPONENTS

The pier protection system (see Figures 1, 2 and 3 - Plan, Elevation and Section) consists of the following components:

- o Timber piles (with timber facing) driven to 15 to 20 feet (5 to 6 meters) below channel bottom and end cluster dolphins, one at each corner of the pier protection system. (See Figure 2)
- o Small timber and structural steel wale system for transmitting loads from the timber piles and facing to the reinforced concrete distribution beams. (See Figure 3)
- o Reinforced concrete distribution beams. (See Figure 3)
- o Rubber fendering units transmitting horizontal loads from the distribution beams to the reinforced concrete dolphins. (See Figure 4)
- o Reinforced concrete dolphins vertically supporting the distribution beams and resting on batter piles. (See Figure 3)
- o Supporting struts carrying horizontal loads from the distribution beams to the reaction blocks. (See Figure 3)
- o Reinforced concrete reaction blocks. (See Figure 3)
- o Sheet pile cells, one at each corner of the pier protection system. (See Figure 1)

The various components of the pier protection system are described below:

Timber piles with timber facing and end cluster dolphins

The timber piles will be driven to a depth of 15 to 20 feet (5 to 6 meters) below the channel bottom. They are essentially designed to withstand only minor scraping by passing ships and to protect small craft. A blow of any consequence will surely damage or destroy them, but they can be easily replaced.

Timber and structural steel wale system

The wale system consists of 12 inch x 12 inch (0.30 m x 0.30 m) timber wales and structural steel WT members and its function is to tie the timber pile system to the distribution beams and thereby facilitate the transmission of loads from the piles to the beams.

Reinforced concrete distribution beams

The distribution beams are continuous reinforced concrete beams with spans varying from 115 feet to 132 feet (35 to 40 meters).

They are supported vertically on reinforced concrete dolphins and on intermediate 18-inch (450 mm) diameter pipe piles and are restrained laterally by fendering units.

The pipe piles are provided to assist in resisting an instantaneous vertical component from a ship impact at midspan of the distribution beam. Both dolphins and fenders are discussed further below. The distribution beams, whose main function is to transmit lateral ship loads, are approximtely 4 feet (1.25 meters) high and 12 feet (3.65 meters) wide. They are designed to withstand at yield an equivalent horizontal colliding ship load in excess of 2,000 kips (900 tons). Stainless steel plates are embedded in the concrete dolphin surfaces interfacing with the distribution beams to facilitate lateral sliding. The distribution beams are restrained from moving laterally by energy-absorbing rubber fenders that have lateral displacement capacity of almost 5 feet (1.50 meters).

Fendering Units

The function of the fenders is to absorb the colliding ship's energy as they compress and transmit the lateral loads from the distribution beams to the supporting dolphins. The buckling column type fenders are composed of trapezoidally-shaped rubber manufactured by several producers. The corner fenders (1,500L x 2,500H) are over 8 feet (2.5 meters) thick. The intermediate fenders (1,500L x 2,000H) are over 6 feet (2.0 meters) thick. the corner fenders are sized to absorb up to 3,000 foot-kips (415 meter-tons) of energy with a reaction of 2,000 kips (900 tons) at each dolphin. The intermediate fenders are sized to absorb up to 2,000 foot-kips (280 meter-tons) of energy with a reaction of 1,900 kips (800 tons) at each dolphin.

Reinforced Concrete Dolphins

The reinforced concrete dolphins are supported vertically by two 36-inch (915 mm) diameter batter piles. The piles are battered in the longitudinal direction, i.e., in the direction of ship traffic, and provide some resistance to longitudinal impacting ship forces. The dolphins' main function, however, is to transmit the lateral impacting ship forces through the timber piles, wale system, distribution beams and fender units and on to the supporting struts.

Supporting Struts

The supporting struts, which are about 60 to 100 feet (18 to 30 meters) long, are composed of 48-inch (1,220 mm) diameter steel pipes with a compressive ultimate capacity of 2,500-3,000 kips (1,100 to 1,400 tons). The function of the supporting struts is to carry the lateral loads from the reinforced concrete dolphins to the reaction blocks.

Reinforced Concrete Reaction Blocks

The reaction blocks and supporting struts will be placed in sheeted or bentonite slurry trenches. The reaction blocks, which are 20 feet (6 meters) high and 25 feet (7.6 meters) wide are designed to mobilize sufficient ultimate passive soil pressure, at 550 lbs/ft^3 (8800 kg/m^3) equivalent fluid pressure, behind them to withstand a minimum lateral load of 3000 kips (1400 tons) on any strut. In fact, the supporting struts are designed to buckle or yield at below 3,000 kips (1400 tons) load to forestall backward movement and upward heave of the soil behind the reaction blocks.

Sheet Pile Cells

The sheet pile cells are composed of 45-foot (13.7 meters) diameter interlocking sheet piles driven to elev. -75 feet (-23 meters) or about 20 feet (6 meters) below the channel bottom. They are filled with compacted or densified sand and gravel and are capped with 5 feet (1.5 meters) of reinforced concrete to elev. 0. Their function is to act as crash barriers at the four corners of the pier protection system. They are able to withstand a lateral or longitudinal force of about 2,600 kips (1200 tons) by a ship in the channel with 6-inch (0.15 meters) to one-foot (0.3 meters) displacement, and a force of up to about 3200 kips (1,450 tons) while being permanently displaced by no more than 4 to 5 feet (1.2 to 1.5 meters) in the process. While being thus damaged, the sheet pile cells will, in the process, deflect serious damage from the swing bridge and other components of the pier protection system.

Total Pier Protection System

The energy absorption capacity of the total pier protection system, just prior to its collapse is about 10,000 to 12,000 foot-kips (1400 to 1700 meter-tons).

1.5 DESIGN PROCESS

Since it was assumed that a design level impact will be such an infrequent occurrence, structural yielding was permitted as an energy dissipating device, as mentioned before. The pier protection system elements will yield as follows: the timber fendering will crush; the distribution beam will form plastic hinges; some rubber marine fender will be crushed; some struts will develop plastic hinges; some intermediate supports will develop plastic hinges; the colliding ship's hull will be deformed; and some sheet pile cells will deform plastically.

The distribution beams were modeled to reflect the beam spans, size and support conditions including the nonlinear behavior of large rubber marine fenders. The model was loaded either in spans or at supports with a uniform load of a magnitude

corresponding to a yield stress on the ship's hull. This is a maximum unit force that the ship can impart to the distribution beam. The magnitude of the force can increase only by increasing the area of ship yielding, i.e., the contact length. The ship can contact the distribution beam at one area for a given collision; therefore, only single spans or single supports are loaded. The load length is increased until either the energy requirements are met or the beam undergoes structural yielding. When yielding occurs, a plastic hinge is applied to the model and the load is increased. To install a plastic hinge, a member end is released for rotation and equal and opposite hinge capacity movements are applied to the member ends framing into the joint. The load is then increased until energy requirements are met while checking that secondary hinges do not form elsewhere in the structure.

Energy requirements are met when the sum of energy absorbing components equals or exceeds the design energy. The energy absorbing components considered are the ship's hull deformation caused by the beam reaction, the marine fender deformation, the beam elastic strain energy, the sheet pile cell deformation and the hinge rotation from the development of plastic hinges.

Marine fenders were sized to allow adequate displacement to absorb energy, yet minimize beam moments. A combination of two fender sizes was found adequate to meet these requirements.

The distribution beam plastic hinge capacity was determined by selecting reinforcing bars patterns that provide large moment capacities for the section. Although the reinforcing steel percentage is very high it was accepted because of the anticipated infrequency of the collision design loading.

The dolphin structure was modeled to reflect the three-dimensional nature of both the structure and the loadings. Reactions from the distribution beam analysis, both along the channel and normal to the channel as well as gravity loads, were applied to the dolphins. Batter piles and struts were designed for biaxial bending such that yield may occur under imparted design ship energy.

As mentioned before, the timber fendering was designed so that the timber piles are the "weak link". Timber piles are capable of absorbing a relatively small amount of energy before failure, thus the failure loads were used for design of the timber system.

2. CONSTRUCTION

Construction of the pier protection system will be completed in two phases. The first phase will provide protection to the west pier of the swing bridge and minimal protection to the east pier. The second phase will complete the pier protection system at the east pier of the bridge.

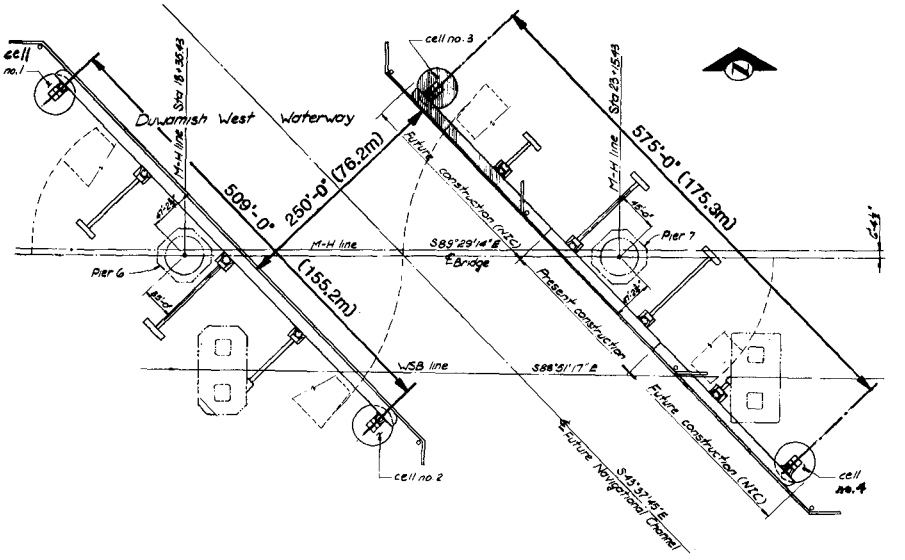

PLAN

Figure 1

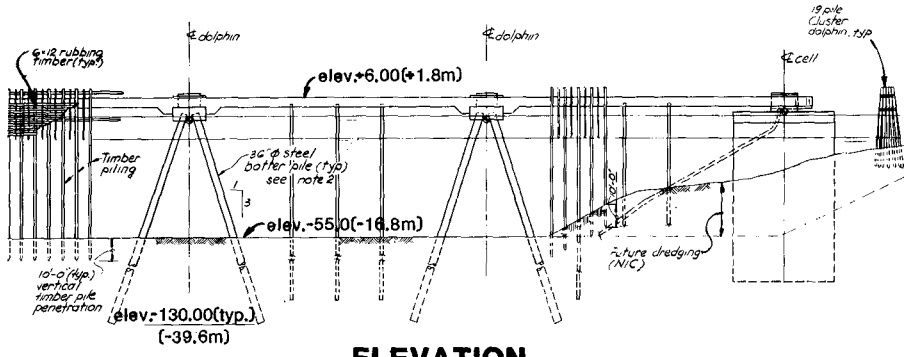

ELEVATION

Figure 2

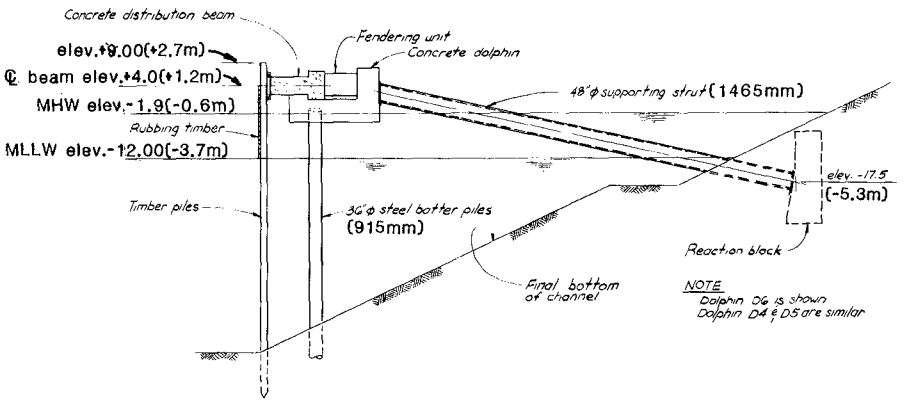

SECTION

Figure 3

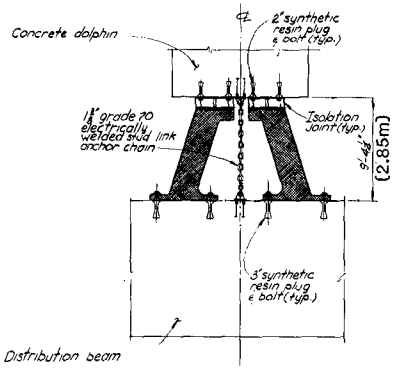

CORNER FENDERING UNIT

Figure 4

3. ACKNOWLEDGEMENTS

Owner of the facility is the City of Seattle. Project Engineer for the City is F. S. Yamagimachi.

Consulting services are provided by a Joint Venture of Anderson-Bjornstad-Kane-Jacobs (ABJK), Parsons Brinckerhoff (PB), and Tudor Engineering Company (TEC).

Project Manager for the Joint Venture is T. A. Kane (ABKJ).
Project Manager for PB is R. J. Berg.
Project Engineer for PB is H. Saxer.

The author was in charge of the design of the pier protection system and T. B. Jackson of PB prepared the detailed structural design calculations.

4. REFERENCES

1. Chapter 7, "Dynamics of Ship Collision" (Figure 7 on Page 46), Published in "Marine Board Report on Ship Collisions with Bridges," November, 1983.

2. Derucher, F.N. and Heins, C.P., Jr., "Bridges and Pier Proective Systems and Devices," [Chapter IV, "Design Parameters," pages 92 and 93 Hydrodynamic Coefficients.] Published by Marcel Dekker, Inc., 1979.

3. Kuesel, T.R., "Newport Bridge Collision," International Association for Bridge and Structural Engineering (IABSE) Colloquium. Copenhagen, 1983.

4. Larsen, J., "Ship Impact in Ferry Berths," IABSE Colloquium. Copenhagen, 1983.

5. Quinn, A. DeF., "Design and Construction of Ports and Marine Structures," (pages 330 to 393). McGraw-Hill, 1972.

CHAPTER 138

THE DESIGN OF A SLOTTED VERTICAL SCREEN BREAKWATER

J D Gardner*, I H Townend* and C A Fleming**

INTRODUCTION

This paper describes the wave studies, model testing and structural design of a 250 metre long slotted vertical screen breakwater for a marina at Plymouth, England.

The marina is being developed by Plymouth City Council to provide a purpose built facility for hosting the major long distance races that start or finish at Plymouth, in addition to the usual marina facilities for private boat owners.

After examining three alternative locations Plymouth Council selected a site in the north-east corner of Plymouth Sound as shown in Figure 1.

The site is confined on two sides by existing shipping channels and by a rocky shore on the land side. Exposure to wave attack is limited to the south west sector.

Because the existing seabed at the marine site was the responsibility of the Duchy of Cornwall, an Act of Parliament was required before Plymouth Council could commence construction. The Act contains clauses regulating the use of the marina and the permissable changes to the wave conditions in the adjacent shipping channels.

DESIGN CRITERIA

The basic maritime criteria governing the design are:-

(i) Wave heights in the marina should not exceed Hs = 0.3 metres for more than 200 hours per year.

(ii) With the exception of a 10 metre carriageway on the SW face of the breakwater wave heights in the adjacent shipping channels should not be increased, as a consequence of the breakwater, by more than 50% above the conditions existing before construction.

(iii) The breakwater should be designed to withstand the 100 year return period storm occurring at any tide level.

---

* Senior Engineer, Sir William Halcrow & Partners Ltd, Burderop Park, UK
** Director, Sir William Halcrow & Partners Ltd, Burderop Park, UK

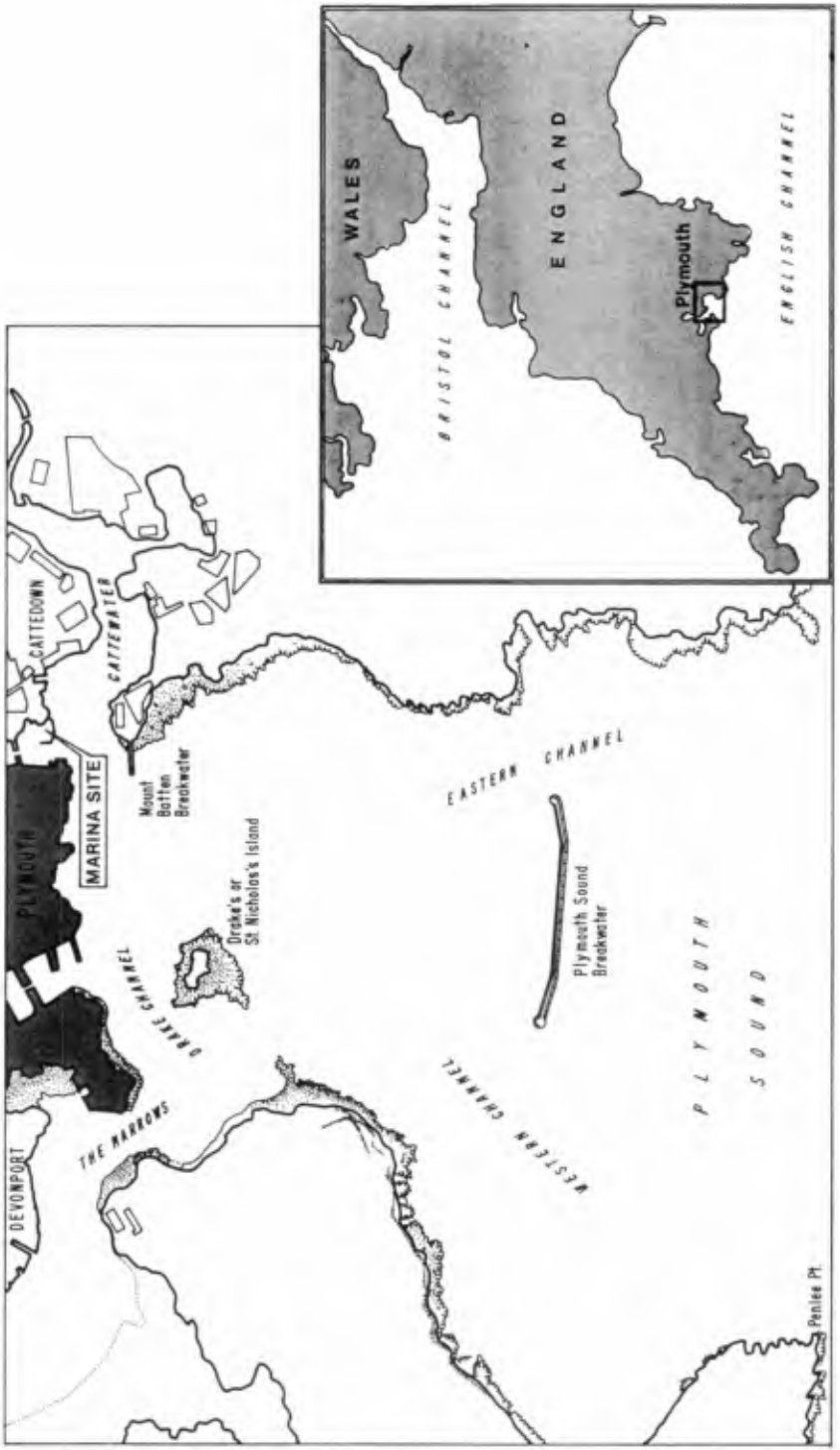

Figure 1: Site Location Plan

The preparation of construction drawings and tender documens was not started until parliamentary approval had been given. This was obtained in April 1985 and Plymouth Council decided that the marina should be ready for hosting the Two Handed Trans Atlantic Race in June 1986. To achieve this programme detailed design, testing and tender documents had to be prepared in the period May to mid-August so that tenders could be received by mid-September to allow construction to commence in November 1985.

EXISTING WAVE CONDITIONS

Deep water swell from the English Channel can only reach the marina area from the south-west. The most severe wave conditions will therefore comprise combined swell waves and locally generated wind waves arriving from this direction.

Data for deep water wave conditions were available from the Institute of Oceanographic Sciences (IOS) in the form of a report on data collected by a Waverider buoy located near the Eddystone Lighthouse. The deepwater wave climate was transferred to the marina site in two stages.

(i) wave refraction backtracking and spectrum transfer from deep water to the Plymouth Sound breakwater.

(ii) diffraction of the resulting wave energy spectrum from the Plymouth Sound breakwater to the marina site.

Wave heights and periods for locally generated waves were calculated using the Carter Equations derived from the Jonswap energy spectrum formulation. Wind speeds calculated from data recorded at Fort Stanford, Plymouth and the equations used for a fetch limited growing sea were:

$$H_s = 0.0163\ X^{0.5}\ U$$
$$T_z = 0.439\ X^{0.3}\ U^{0.4}$$

where X is the effective fetch in kilometres and U is the wind speed in metres per second.

The resulting wave heights at the marina site were as follows:

Return Period	Hs(m) (deepwater)	Hs(m) (local)	Hs(m) (combined)
100	1.5	0.8	1.7
50	1.4	0.75	1.6
10	1.2	0.7	1.4
1	1.1	0.6	1.3

Examination of the Admiralty Charts for Plymouth shows that the approach direction for the swell waves is limited by Penless Point to the west and the Plymouth Sound and Mount Batten Breakwaters to the east. Approach directions for the critical wave condition are therefore limited to the sector between 210° and 220°.

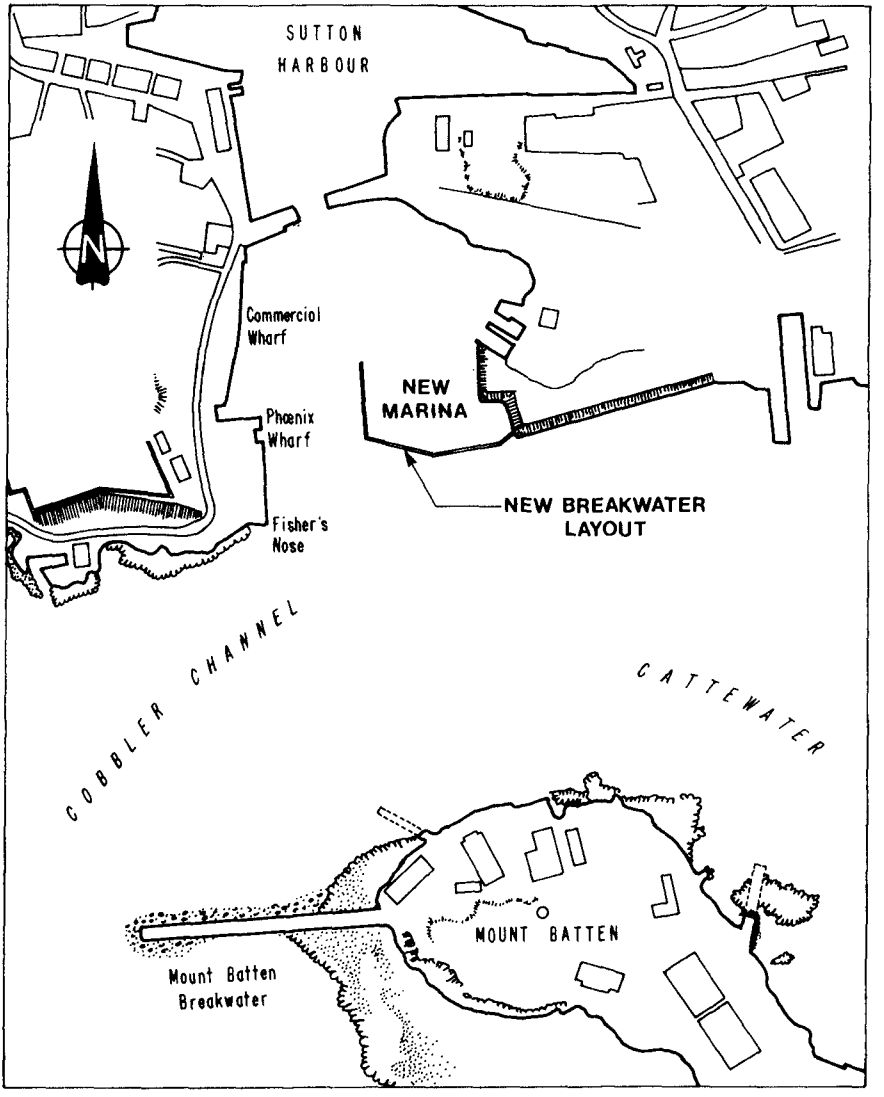

Figure 2: Outline plan for new marina

Under critical wave conditions the wave climate to the west and south of the marina will be influenced by sheltering and diffraction effects caused by the coastline adjacent to Fisher's Nose (see Figure 2).

The treatment of wave diffraction was based on the Sommerfeld solution as presented by Wiegel (1964). A Halcrow computer model was used to evaluate wave height factors at the nodes of a square grid across the area of study. Wave height factors being defined as:

$$\text{wave height factor} = \frac{\text{wave height at node}}{\text{height of incident wave}}$$

The model could be used to evaluate wave conditions in the vicinity of systems of one or two impermeable breakwaters. The breakwaters could also assume any degree of reflection of incident wave energy.

The sheltering effect of Fisher's nose was represented by a breakwater aligned north/south. The resulting wave height factors are given in Figure 3 where the factors are expressed relative to the incident wave height off Fisher's Nose.

WAVE CONDITIONS AFTER CONSTRUCTION OF THE MARINA BREAKWATER

The wave diffraction model was run for each segment of the breakwater and the results were superimposed to provide a composite diffraction solution. Thus a relatively simple program provided a quick and realistic answer. The results for a fully reflecting breakwater are shown in Figure 4.

Comparison of Figure 3 with Figure 4 gives the percentage change in wave height factors resulting from construction of the breakwater. These initial results showed that wave heights would increase to an unacceptable level in the two adjacent shipping channels.

The wave diffraction model was re-run using breakwater reflection coefficients less than unity and it was found that acceptable wave conditions could be achieved with the following reflection coefficients:

Section A - $K_R \leq 0.8$
Section B - $K_R \leq 0.5$
Section C - $K_R = 1$

In this appraisal the consequence of varying the incident wave period was also examined and this was found to alter the area influenced by the reflected waves quite significantly.

CHOICE OF STRUCTURE FOR THE MARINA BREAKWATER

Several types of structure were considered during the feasibility stage of the project. These included: a floating breakwater; a rubble mound breakwater; a blockwork wall and a vertical screen breakwater.

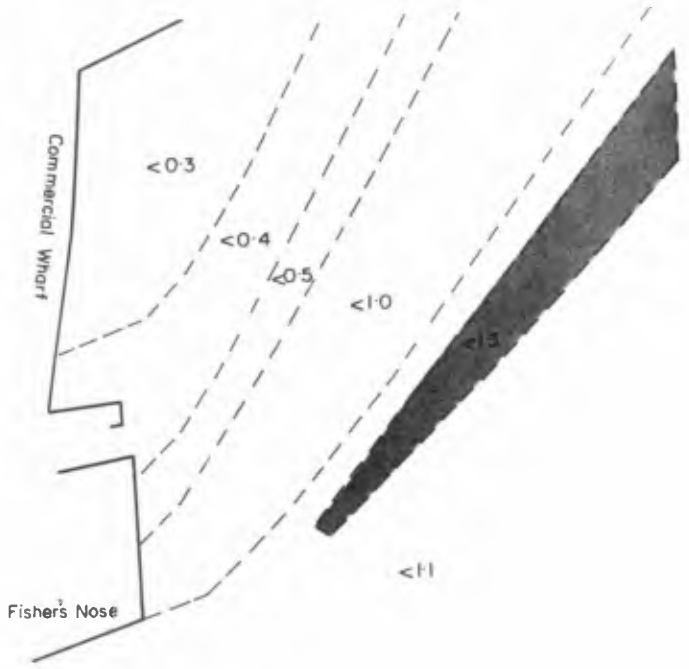

Figure 3: Wave height factors for existing site

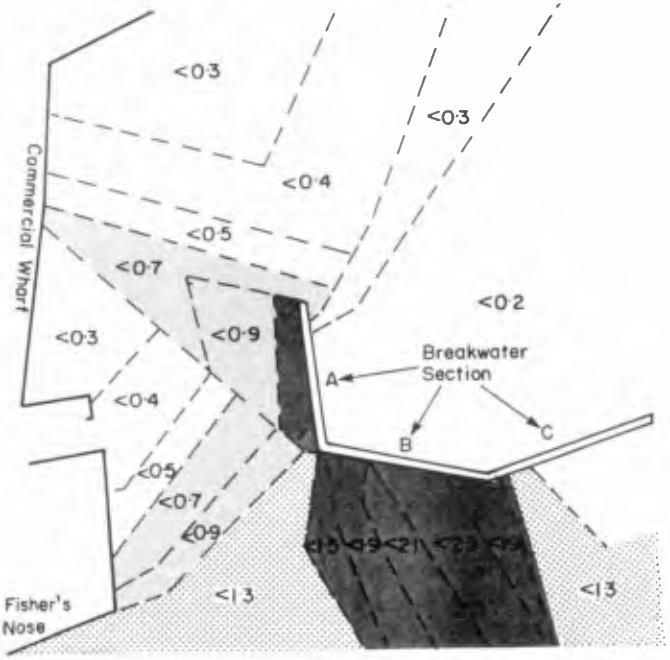

Figure 4: Wave height factors with fully reflecting breakwater

However this site has three major constraints: the seabed consists of soft silt up to 30 metres thick overlying bedrock; the area available for the marina is small; the spring tidal range is 5 metres. A vertical screen supported by piles driven to bedrock was considered to be the most practical and economic solution within these constraints.

Following the initial numerical diffraction and reflection analysis various configurations of perforated screens were examined. Examination of existing literature (refs 1, 3, 4 and 5) indicated that a double screen would be required for Section B whereas a single screen would be sufficient for Section A. The extent of the double screen was a balance between wave reflection, wave transmission into the marina and construction cost.

Although existing case histories were sufficeint to demonstrate that a solution could be found to suit the basic design criteria there was insufficient information to permit detailed design to be carried out. The final configuration of the screens was therefore based on the results of a set of simple flume tests.

MODEL TESTING

To meet the tight design programme, model testing commenced at the start of the detailed design phase. This then enabled the final structural design to take account of the test results.

Model testing was carried out at Hydraulics Research, Wallingford in a 45 metre long wind wave flume. The purpose of the tests was to measure the reflection and transmission coefficients (K_R and K_T) for single and double screens whilst changing the following variables identified during the conceptual design stage:

(i) Wave periods between 3 and 12 seconds
(ii) Screen porosity varying between 8% and 35%
(iii) Space between screens varying between 5 metres and 15 metres
(iv) Slots horizontal or vertical
(v) The gap between the bottom screen and the seabed
(vi) The effect of changing the plank thickness from 300 mm to 150 mm
(vii) Screens tilted or vertical

The model scale was 1:15 and random waves were used. Wave measurements were made using three wave probes and incident and reflected spectra calculated using an analysis program. The method determines the reflection and transmission coefficients for each frequency considered in the incident wave spectrum.

As the model tests progressed some changes were made to the testing sequence taking account of the previous results and the requirements of the structural design, which was proceeding simultaneously, thereby avoiding tests unlikely to yield a useful solution. In all 54 tests were carried out and the results are given by Hydraulics Research Laboratory (1986).

The principal results are summarised in Figures 5, 6 and 7.

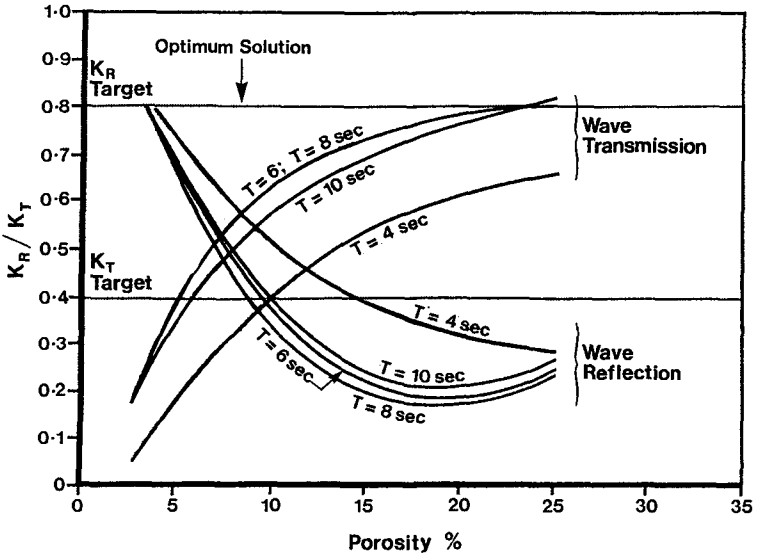

Figure 5: Reflection coefficient (K_R) & Transmission coefficient (K_T) v Porosity for single vertical screen

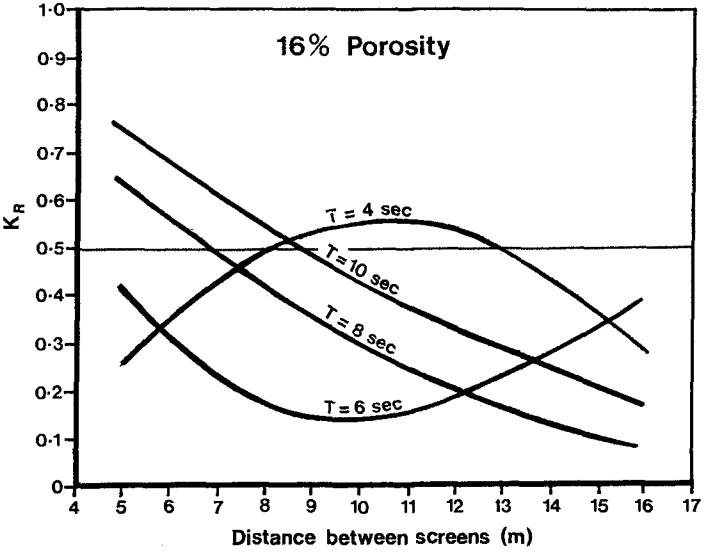

Figure 6: Reflection coefficient v Distance between screens

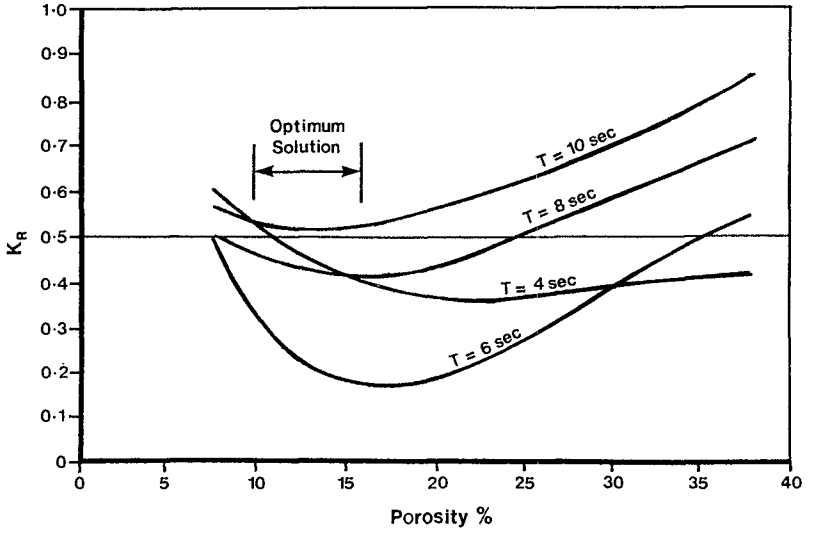

Figure 7: Reflection coefficient v Front screen details for screen spacing of 8m

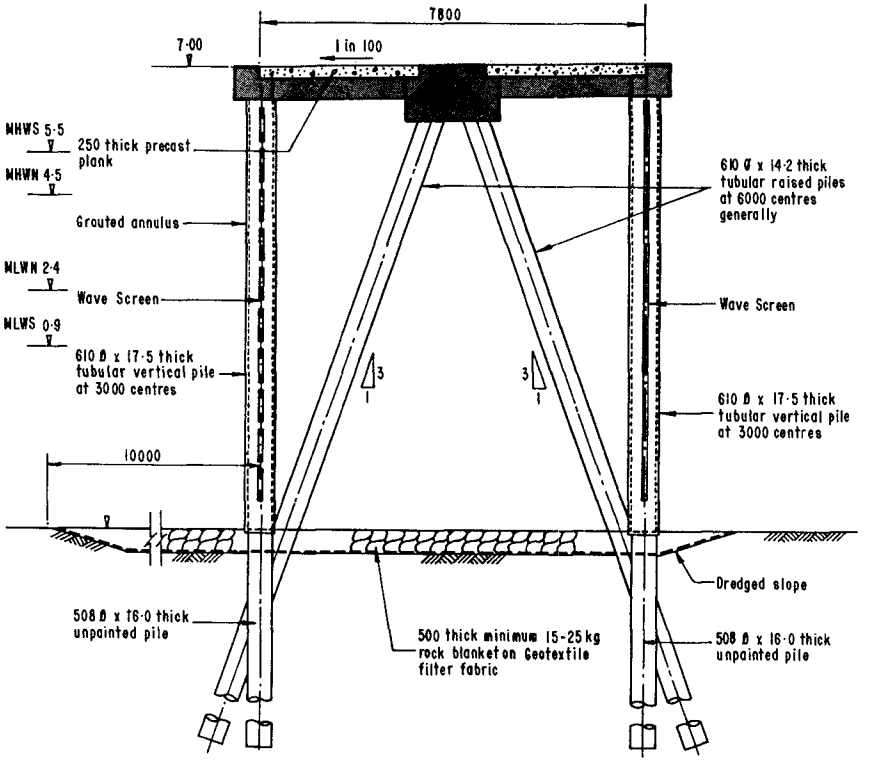

Figure 8: Section through double screen

For the single screen:

(i) a porosity of 8% gave acceptable values of K_R and K_T (see Figure 5)

(ii) the performance of horizontal slots was similar to that of vertical. Horizontal slots were therefore adopted because this orientation suited the proposed construction method

(iii) a 1 metre gap beneath the screen gave unacceptable wave transmission results

(iv) the hydraulic performance of 150 mm planks was similar to that of 300 mm planks.

For the double screen:

(i) a double screen with a front screen with 16% porosity spaced 8 metres from a solid back screen gave suitable reflection coefficients (see Figures 6 and 7)

(ii) the performance of horizontal slots was similar to that of vertical. Horizontal slots were therefore adopted because this orientation suited the proposed construction method

(iii) a 1 metre gap beneath the screens gave unacceptable wave transmission results

(iv) the hydraulic performance of 150 mm planks was similar to that of 300 mm planks

(v) tilting the screens did not show any improvement over vertical screens.

FINAL WAVE STUDIES USING MODEL TEST RESULTS

The numerical diffraction model previously discussed was re-run using the results from the flume test as follows:

Wave Period (secs)	4		6		8	
Breakwater Section	K_R	K_T	K_R	K_T	K_R	K_T
A (single, 8% porosity)	0.6	0.3	0.6	0.4	0.6	0.4
B (double, 16% porosity 8 m space)	0.4	0.0	0.2	0.0	0.4	0.0
C (single, solid)	0.9	0.0	0.9	0.0	0.9	0.0

The results showed that wave heights outside the breakwater were within the required limits except for one small area to the south of the breakwater. It should be noted that the diffraction - reflection - transmission analysis does not take account of wave-wave interaction, wave breaking and the lateral internal diffraction of waves. As these non-linear effects would all lead to a reduction in resultant wave heights it was decided that this small area did not justify any changes in the proposed breakwater.

The results also showed that transmission into the majority of the marina had been retained below the target value of Hs = 0.3 metres. A small area in the south-west corner showing higher contours would be deleted by an additional length of double wave wall.

STRUCTURAL DESIGN

The typical structural details for the double screen are shown in Figure 8. The single screen is similar except that the rear screen and half of the deck is deleted. Typical isometric views of both types of screen are illustrated in Figure 9.

The wave loads on the screen are transmitted to the bedrock by the pairs of raking piles. The maximum compression and tension loads are approximately 2500 kN and 1800 kN respectively. The high compression loads are taken by end bearing on the rock and for this reason the pile toes are plugged with concrete. The tension loads are taken by dead anchors drilled beyond the pile toes and grouted into bed rock.

The vertical pile is a composite pile with the upper section comprising an external sleeve grouted onto the inner pile after the inner pile has been driven to bed rock. The external pile is a prefabricated section with flanges for wave screen plank fixing. The use of the composite pile allowed the inner pile to be designed for the forces below the bed level, with the grouted sleeve above bed level providing the additional stiffness to carry the high moments induced by the wave screen. This arrangement also helped to eliminate alignment problems with the plank fixings.

The screen planking material is greenheart timber and the deck is concrete. Handrails and lights are provided on the deck to provide a public promenade and viewing area.

The cost of the breakwater, excluding pontoons and other marina items, is approximately £1.8 million, of which approximately 65% is the cost of the tubular steel piles.

The Contractor for the project was Dean and Dyball (Western) Ltd from Exeter.

Figure 10 shows the project nearing completion.

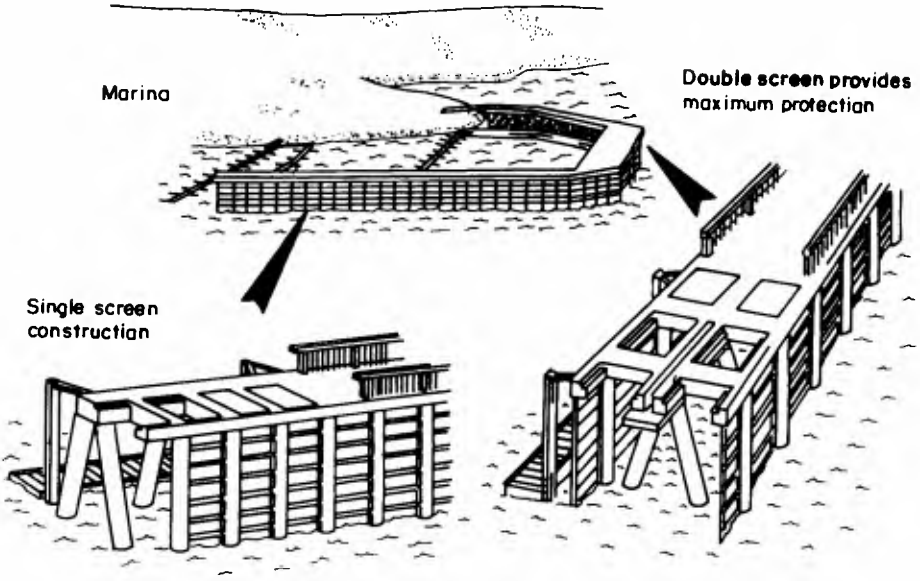

Figure 9: Typical views of single and double screen breakwater

Figure 10: Marina Nearing Completion

CONCLUSION

Based on visual information during the 4 month period since the breakwater was completed wave reflection into the shipping channels appears to be well within the permissible levels.

Without the use of a slotted vertical screen the marina project would not have been allowed to proceed, but using the relatively inexpensive methods of analysis and testing described in this paper a practical and aesthetically acceptable solution has been found.

ACKNOWLEDGEMENT

The authors are indepted to the City Engineer, Plymouth for his permission to publish this paper.

REFERENCES

1. Hutchinson P S, Raudkivi A J, Case history of a spaced pile breakwater at Half Moon Bay Marina, Auckland, New Zealand, Proc Coastal Engineering Conf, ASCE, Houston, Sept 1984.

2. Hydraulics Research, Wallingford, 1985, Plymouth marina events base - perforamnce of wave screens, Report No EX 1327.

3. Kakuno S, 1983, Reflection and transmission of waves through vertical slit type structures, Proc Coastal Structures 83, ASCE, Arlington, March 1983.

4. Kakuno S, 1984, Water-wave reflection and transmission by an infite array of vertical flat plates. Proc 32nd Japan National Congress for Applied Mechanics, University of Tokyo Press.

5. Wekckmann J, Bigham G N, Dixon R O, 1983, Reflection characteristics of a wave-absorbing pier, Proc Coastal Structures 83, ASCE, Arlington, March 1983.

6. Wiegel R L, 1964 - Oceanographical Engineering, Prentice-Hall Inc.

CHAPTER 139

STABILITY ANALYSIS OF OCEAN PIPELINES : A PROBABILISTIC APPROACH

Leon C Geustyn*, Gideon de F Retief**

ABSTRACT

A probabilistic approach to the lateral stability of a pipeline on the sea-bed is considered. The uncertainties involved in the deterministic approach, due to the stochastic nature of variables, inaccuracy of models and statistical error are discussed. Variables representing these uncertainties are identified and their statistical properties investigated. Procedures for computing the probability of stability failure are developed using both analytical and Monte Carlo simulation techniques. Example calculations are presented indicating typical applications. It is concluded that the probabilistic procedure, as presented here, can serve as a valuable tool in the stability analysis of ocean pipelines.

1. INTRODUCTION

An important consideration in the design of pipelines resting on the ocean bottom involves their protection against possible structural instability. Included in the stability design must be a provision for the capacity of the structure to resist forces caused by wave-induced water motion and currents. This is normally achieved through an application of some form of anchorage or weighting down of the pipeline and taking into account the resistance against sliding of the bottom foundation.

Determination of the structural loads and resistances entering the stability design problem is based on theoretical and/or empirical models that consider a variety of influencing factors, such as hydrodynamic forces and soil frictional resistance. Due to uncertainties involved in various aspects of these models (e.g., random variable input parameters, experimentally determined coefficients, etc.), the final design is heavily influenced by the experience and judgement of the designer.

* Engineer, Ocean Engineering, University of Stellenbosch, and Geustyn, Forsyth & Joubert, PO Box 413, Stellenbosch South Africa, 7600

** Professor, Ocean Engineering, University of Stellenbosch Stellenbosch, 7600 South Africa

This has often resulted in conservative attitudes in code directives and design decisions. The latter are commonly based on the concept of a global factor of safety. Recognition of the factor of safety's nonlinear relationship to certain input parameters and inability to distinguish between contributions of parameters separately, have caused designers to propose improvements in the method of expressing safety (Ellinas et al, 1984).

The objectives of the present study are to: (1) identify random variables that are present in the stability analysis; (2) determine their statistical properties and (3) develop a procedure to determine the probability of stability failure. A probabilistic description of the relevant random functions is used. The random variables in the analysis are the wave height and period, force and soil coefficients and variables representing uncertainty in the prediction of wave kinematics. Distribution functions for the variables are either determined from available data or using their commonly accepted representations. Evaluation of the random functions is done through analytical transformation of variables and Monte Carlo simulation.

2. PROBLEM FORMULATION

The case under consideration is that of a straight pipeline situated directly on a flat, rigid, impermeable bottom in the ocean. In terms of structural, lateral stability, the pipeline is considered to be safe if no movement thereof occurs.

For the purpose of this study the demand on the pipeline is considered to be the hydrodynamic forces exerted on it due to it being exposed to wave-induced oscillatory flow and a steady uniform current. The resistance to movement is considered to be provided by either anchorage or frictional resistance of the bottom soil.

The wave and current directions relative to the pipeline, θ_w and θ_c respectively, are assumed to be sufficiently small for the forces along the section of the pipeline which is of interest, to be essentially constant. A unit length of the pipeline is therefore considered to be representative of the section of interest in the design. For the unit length of pipeline the stability criterion requires that the lateral component of the force, F_H, be less than the resisting force, F_R. The stability condition to be investigated can therefore be expressed in terms of a stability parameter, G as

$$G = \frac{F_H}{F_R} < 1 \qquad \text{- - - - (1)}$$

3. DETERMINISTIC ANALYSIS AND IDENTIFICATION OF UNCERTAINTIES

The deterministic (conventional) methods used to evaluate lateral stability of a pipeline can be generally summarised under the following steps:

- Definition of the environmental conditions, with regard to waves and currents, based on specific statistical extreme states.
- Definition of the kinematics at the seabed using appropriate wave theories.
- Definition of the hydrodynamic forces through application of semi-empirical force models.
- Evaluation of the lateral stability using models describing the resistance to movement provided by either anchorage or the bottom soil, for chosen anchorage specifics or pipeline weight.

The specific models normally applied, and uncertainties involved in the procedure, are discussed in the next sections.

3.1 Definition of environmental conditions

The parameters which normally are used to define the environmental conditions are wave height, H, and period, T, and uniform current, U_c. These parameters are, due to their stochastic nature, most often determined in terms of an expected frequency of occurrence, or more practically, in terms of a return period, such as 50 or 100 years. The implication is that for decisions in this respect there has to be relied on extrapolation from statistical models which are based on measured data. The accuracy of results derived through this process depends heavily on the quantity and quality of the basic data. Mol et al (1984) describes inaccuracy in prediction of H due to (1) scatter and inaccuracies of the original data; (2) selection of a probability function and (3) extrapolation outside the observation period, resulting in a coefficient of variation typically in the order or 10% to 15%.

Further uncertainty is also present in the selection of the right design wave height and period combination. Chen et al (1979) e.g., determined distributions for T conditional to H from measurements within a stationary sea state. According to their study the conditional distribution of T is normal with a coefficient of variation which decreases with increasing H from about 18% at H_S to about 8% at H_{max}.

3.2 Definition of the kinematics at the sea-bed

Kinematics at the sea-bed such as horizontal velocity and acceleration are normally determined through use of a wave theory. Although verification of certain wave theories such as the linear, vocoidal and stream function theories, in relation to specific conditions such as water depth, has been done (Swart and Loubser, 1979; Dean and Perlin, 1986), it is only in the average sense.

Results of experimental work, especially such as those obtained by Grace (1976) in real ocean conditions, show large scatter and possible errors in the prediction of the maximum horizontal velocity, u_m, by the linear or stream function theories of up to 60% and 50% respectively. Even larger scatter and possible errors exist in the prediction of the maximum horizontal acceleration, a_m. Substantial uncertainty therefore exists in the prediction of kinematics at the sea-bed by wave theories.

3.3 Definition of the hydrodynamic forces

Application of Morison-type equations to determine the magnitude of hydrodynamic forces on a pipeline, is widely accepted to provide good average values (Karal, 1985; Grace and Zee, 1981).

The maximum hydrodynamic forces per unit length can be expressed as follows (Grace and Zee, 1981):

$$F_{Hm} = 0.5\rho D C_{Hm} u^2_m \quad - - - - \quad (2)$$

and

$$F_{Lm} = 0.5\rho D C_{Lm} u^2_m \quad - - - - \quad (3)$$

where

F_{Lm}, F_{Lm} = maximum horizontal and lift forces in a wave cycle, normal to the pipeline
ρ = water density
D = pipe outside diameter
C_{Hm}, C_{Lm} = maximum force coefficients (horizontal, lift)
u_m, a_m = maximum horizontal particle velocity and acceleration in a wave cycle, normal to the pipeline.

The accuracy of predictions by the above equations relies heavily on the choice of values for the force coefficients used. There is however a substantial degree of uncertainty related to appropriate choices in this respect, due to large scatter in the results of experimental work performed in the laboratory such as reported by Jacobsen and Bryndum (1984), and even more so for results from ocean experiments such as performed by Grace and Zee (1981) and the Hydraulics Research Station (1982).

The type of uncertainty involved in the prediction of the hydrodynamic forces is therefore mainly related to model inaccuracies. A certain degree of measurement error, in the determination of force coefficient values, would however also be present.

3.4 Uncertainties in the evaluation of the lateral stability

If the resistance to movement is provided by the soil frictional resistance the Coulomb friction force model is normally considered appropriate. The resistance force is thus determined as

$$F_R = S(W_S - F_L) \qquad ---- \quad (4)$$

Therefore the stability condition is described by

$$G = \frac{F_H}{S(W_S - F_L)} \qquad ---- \quad (5)$$

where

S = lateral soil resistance coefficient
W_S = submerged weight of the pipeline.

In the application of this model the main source of uncertainty lies in the value of S. Experimental results show considerable scatter in values of S (Anand and Agarwal, 1981) and choices normally has to be made from a range of possible values. Predictions of S, based on experience of soil conditions similar to those occurring in the case under consideration, or theoretical predictions from measurements of soil characteristics, will be subjected to a large degree of uncertainty. Even if this procedure was totally reliable, the possible variation of soil conditions along the pipeline and random results from measurements of values of soil parameters would introduce uncertainty in the prediction of S for a specific pipeline section.

3.5 The effects of uncertainties on the stability design

The effect of having to cope with uncertainties in the stability design of a pipeline, is that of introducing methods which are aimed at producing an overall conservative result. Upper bound values are used for random parameters such as coefficients and environmental parameters, and procedures, such as linear vectorial addition of wave and current kinematics are implemented. In addition to this a safety factor is included in the final analysis.

Although such practices would normally ensure safety, no quantifiable estimate can be made of the real degree of safety since the procedure does not account for the uncertainty related to true parameter values and model predictions. With conservatism being introduced at each step of the design procedure, the cumulative effect of the conservatism is difficult to quantify. Apart from this situation being unsatisfactory from a scientific viewpoint, the risk for unduly conservative design, or even failure in some cases, is present. The effects of over-conservative design could be drastic due to the sensitivity of installation methods to pipeline weight.

4. PROBABILISTIC APPROACH

The objective of the probabilistic approach is to account for the uncertainties involved in an analysis and to provide an improved measure for the reliability of the structure. The procedures followed in this approach are aimed at determining the probability of failure, P_f, for a structure. These procedures can generaly be summarized as:

- Description of the failure function $F = f(x_1,x_2,x_3 \ldots x_n)$ (where $x_1,x_2,x_3 \ldots x_n$ are the n variables in the analysis);
- Identification of the variables representing the uncertainties in the analysis and description of their statistical distributions or properties;
- Determination of the statistical distribution or properties of F and consequently P_f = Probability that $F < 0$, by approximate methods (Level II) or exact methods (Level III).

In the present study the above listed procedures are followed to develop a method through which the probability of stability failure of a pipeline can be determined. The probabilistic modelling is done according to the exact method (Level III) which implies full description of the random variables in terms of their probability density functions. Calculation of P_f is performed by both analytical development of the failure function and Monte Carlo simulation.

4.1 Description of the failure function

Since the stability criterion determines that $G < 1$, as defined in equation (1), it follows that to satisfy this criterion

$$F = F_R - F_H > 0 \qquad \text{- - - -} \quad (6)$$

which is the basic expression for the failure function F.

If maximum forces are considered and the resistance is assumed to be provided by the bottom friction force, equation (6) can be expanded to

$$F = S(W_S - BF_{Lm}) - F_{Hm} \quad ---- \quad (7)$$

where B is a reduction factor on F_{Lm} at the instant when F_{Hm} occurs.

Introducing equations (2) and (3) into (7) gives:

$$F = S(W_S - 0.5\rho DBC_{Lm}u^2_m) - 0,5\rho DC_{Hm}u^2_m \quad --- \quad (8)$$

where u_m is e.g. described by the linear wave theory as

$$u_m = \frac{HgT\cosh[2\pi(z+d)/L]}{2L\cosh(2\pi d/L)} + U_c \quad ---- \quad (9)$$

with
- L = wavelength
- d = waterdepth
- z = - depth below still water level
- U_c = uniform current velocity

4.2 Description of variable statistics

In the description of probability distributions to be used for the variables in the probabilistic analysis, distinction is made between two types of variables. The first type concerns those variables whose distributions will be dependant on the specific conditions of the case under consideration. The variables H, T and S are of this type as their statistical properties will be determined from measured data, only applicable to the relevant conditions. The second type of variable concerns those variables for which distributions can be derived which are generally applicable. It is assumed here that those variables which represent model uncertainty, such as C_{Hm} and C_{Lm} are of this type.

The variables which are treated as random variables in this study are:

Wave parameters, H and T
Soil frictional resistance, S
Wave kinematics model uncertainty parameters,

$$E_u = \frac{u_{wm}\ (\text{true})}{u_{wm}\ (\text{theory})} \qquad E_a = \frac{a_{wm}\ (\text{true})}{a_{wm}\ (\text{theory})}$$

with u_{wm}, a_{wm} = maximum horizontal velocity, acceleration due to wave action in a wave cycle.
Wave force coefficients, C_{Hm} and C_{Lm}.

4.2.1 Wave parameters, H and T

As explained above there is no general distribution function which applies for the description of the distribution of e.g. H. Typical distributions used are the Log-Normal and Extremal Type I, II and III. Similarly there is no general distribution for T which applies. Typically it can be taken to be Normal (Chen et al, 1979). The general models developed in this study allow the use of any distribution function for H and T but for specific examples the Log-Normal and Normal distribution are used for H and T respectively. H and T are taken to be uncorrelated.

4.2.2 Soil frictional resistance parameter, S

Although the distribution of S will in practice ideally be obtained from site specific measurements, it could, due to the lack of such measurements, be necessary to assign to it a distribution from previous knowledge pertaining to similar conditions. For this kind of subjective probabilistic treatment a distribution is chosen and parameters for it determined from existing knowledge concerning the value of S, such as its mean or maximum and minimum. Typical distribution functions which can be used in this fashion are the Rectangular, Triangular and Normal distributions. For example calculations in this study the Normal distribution is used for S with chosen mean value, S, and coefficient of variation, CV_S.

4.2.3 Wave kinematics model uncertainty parameters, E_u and E_a

It is assumed that the true value of e.g. u_{wm} is that of u_{wm} predicted by theory multiplied by a random factor, E_u.

The procedure followed to describe the statistical properties of E_u and E_a was as follows:

Using experimental data from which frequency histograms for E_u and E_a could be obtained, best fit general theoretical distribution functions were determined. It was found that the Log-Normal distribution provides the best fit for both E_u and E_a (see Figure 1). Parameters (mean and coefficient of variation) to be used in this distribution, applicable to both the linear and stream function wave theories, were obtained from appropriate available data

sets. A summary of the results obtained is given in Table 1.

TABLE 1: Summary of statistical properties of E_u and E_a.

Variable	Mean	CV	5% value = 95% exceedance according to Log-Normal distribution
E_u (linear theory)	1.10	0.16	1.42
E_u (stream function)	0.96	0.18	1.26
E_a (linear theory)	1.22	0.39	2.10
E_a (stream theory)	1.07	0.36	1.82

Results based on data from: Grace (1976); Swart and Loubser (1979); Dean and Perlin (1986); Grace and Zee (1981).

4.2.4 Force coefficients, C_{Hm} and C_{Lm}

The force coefficients are assumed to represent the model uncertainties in predicting hydrodynamic forces. In the statistical treatment of C_{Hm} and C_{Lm} their distributions conditional to the dimensionless parameter, $P = u_m^2/Da_m$, were obtained. This was done by fitting distributions to available data for P-interval widths equal to 1. The Log-Normal distribution function was found to provide the best fit in general (an example fit is presented in Figure 2). The parameters required in this distribution are the mean and standard deviation. Least squares regression analysis on the means for each interval of P, provided continuous functions of P for $\bar{C}_{Hm}$ and $\bar{C}_{Lm}$. The values of the standard deviations of C_{Hm} and C_{Lm} can be obtained using the "average" coefficient of variation defined from those calculated for each P-interval. Table 2 contains values for the coefficients A, B, C and D obtained from a least squares fit of the equation $C_{Hm}, C_{Lm} = A + B\exp(-CP) + D/P^2$ to the interval means. The latter expression is similar to that used by Grace and Zee (1981).

Values for A, B, C and D resulting from fitting the same equation to the 95% exceedance values obtained for each P-interval, are also shown.

TABLE 2: Statistical properties of C_{Hm} and C_{Lm}.

Variable		$C_{Hm}, C_{Lm} = A + B\exp(-CP) + D/P^2$ for $P > 1$				CV
		A	B	C	D	
C_{Hm}	Mean	1.37	2.45	0.26	4.24	0.21
	5% value	1.89	3.36	0.26	4.47	
C_{Lm}	Mean	1.24	7.66	0.49	-1.47	0.23
	5% value	1.75	10.83	0.49	-2.07	

5% value = 95% exceedance using Log-Normal distribution.
Results based on data from: Grace and Zee (1981); Jacobsen and Bryndum (1984).

4.3 Development of models to calculate P_f

4.3.1 Analytical model

In order to reduce mathematical complexities in the analytical development of P_f, simplification of the failure function is desirable. This proves to be possible as follows:

For the relative narrow range of P values covered in a specific case the ratio between the mean values of C_{Lm} and C_{Hm} can be taken as constant. Also, the analysis is relatively insensitive to variation in the value of B, the reduction factor on the lift force. By assuming B to be constant, the failure function as expressed in equation (7) can now be rewritten as:

$$F = SW_S - F_{Hm}(cS + 1) \qquad ----(10)$$

where $c = BC_{Lm}/C_{Hm}$

If the kinematics model error factor E_u is introduced into equation (10), the final form of the failure function can be written as:

$$F = SW_S - KC_{Hm}(E_u u_{wm} + U_c)^2(cS + 1) \quad -- (11)$$

where $K = 0.5\rho D$

Following the criterion that $P_f = P_r(F < 0)$, the development of (11) in terms of the probability density function of the random variables S, C_{Hm}, E_u and u_{wm} results in:

$$P_f = \int_{F_{min}}^{0}\int\int\int\int \frac{f_S(q)\, f_{C_{Hm}}(t)\, f_{E_u}(w)\, f_{u_{wm}}\left[\sqrt{\frac{qW_S - r}{Kt(cq+1)}} - U_c\right]_{w}}{2Kt(cq+1)\sqrt{\frac{qW_S - r}{Kt(cq+1)}}} dw\, dt\, dq\, dr \quad (12)$$

where $f_X(X)$ is the probability density function of x evaluated at X,
F_{min} and F_{max} are the realistic lower and upper limits respectively of F,
and q, t, w and r are dummy variables in the integration.

The analytical development of $f_{uwm}(u_{wm})$ in terms of $f_H(H)$ and $f_T(T)$ is not possible with existing wave theories. However, if T is assumed constant the linear wave theory allows the development to be performed.

Closed form solutions of the expression in equation (12) is possible only in the most simple cases. A computer program was developed in this study which performs numerical integration to calculate P_f according to equation (12).

4.3.2 Monte Carlo simulation model

Whereas the analytical model prevents development of $f_{uwm}(u_{wm})$ in terms of $f_H(H)$ and $f_T(T)$, the Monte Carlo simulation technique provides a way to include both these variables. A computer program was developed in this study to perform this task using equation (8) and linear wave theory. This entails random generation of a large number of values for each variable according to its specified distribution function, calculation of the failure function for each set of variables and counting of the number of failures. P_f is then calculated as the ratio of the number of failures to the total number of variable sets evaluated.

In both the analytical model and Monte Carlo procedures the distribution function applicable to each variable can be selected by including the appropriate subroutine in the computer programs. The distribution parameters for C_{Hm} and C_{Lm} are determined by establishing the mean value and using the appropriate coefficient of variation in the Log-Normal distribution function. The mean value is calculated in each case through application of the point estimate method, developed by Rosenblueth (1975), to determine moments of the random functions C_{Hm}, $C_{Lm} = f(P) = f(u_m, a_m) = f(H,T,E_u,E_a)$.

5. APPLICATIONS

Calculations for two different cases were performed to serve as examples of the application of the methods described above.

The first example (Case I) comprises a 0.4 m diameter pipeline of which the lateral stability is to be provided by its own weight. The statistical properties assumed for the wave height, period and bottom frictional resistance are given in Table 3.

TABLE 3: Statistical properties of variables in Case I.

Variable	Distribution	Mean	CV	1% Value
H	Log-Normal	6 m	0.13	8 m
T	Normal	12 s	0.08	14 s
S	Normal	0.6	0.08	0.5

1% value = 99% exceedance according to distribution function chosen.

For the statistical properties of E_u, E_a, C_{Hm} and C_{Lm} the values in Tables 1 and 2 are accepted and the value of B was taken as 0.95. The probability of failure, P_f, was calculated at three waterdepths, d = 80 m, 90, m and 100 m for a range of values of pipeline weight, W_S. The results are presented in Figure 3. Also shown are the W_S values obtained in a deterministic analysis with global factor of safety, FS = 1.5, 2.0 and 2.5, for d = 80 m. The analysis was performed using the 1% values in Table 3 for H, T and S, and the 5% values for E_u, E_a, C_{Hm} and C_{Lm} given in Tables 1 and 2.

The second case (Case II) comprises a 0.6 m diameter pipeline of which the stability is to be provided by anchorage. Exactly the same properties for the variables as used in Case I were applied. The calculations of P_f,

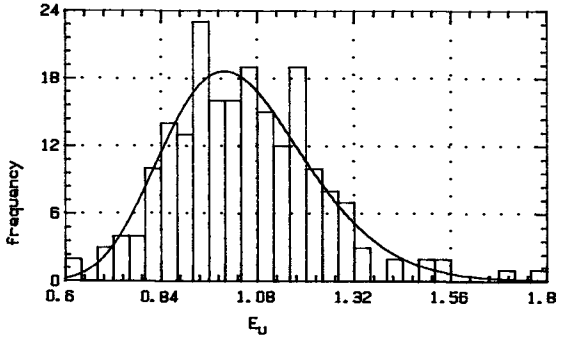

Figure 1: Frequency histogram of E_u with Log-Normal distribution function

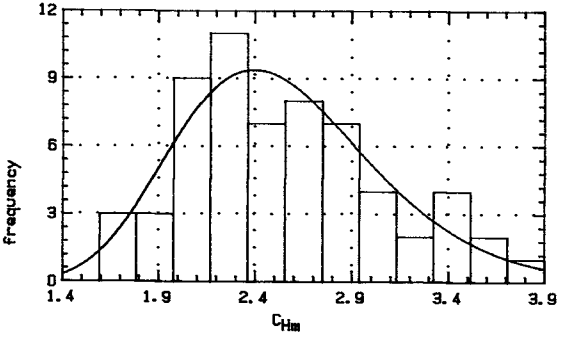

Figure 2: Frequency histogram of C_{Hm} for $3 < P < 4$, with Log Normal distribution function

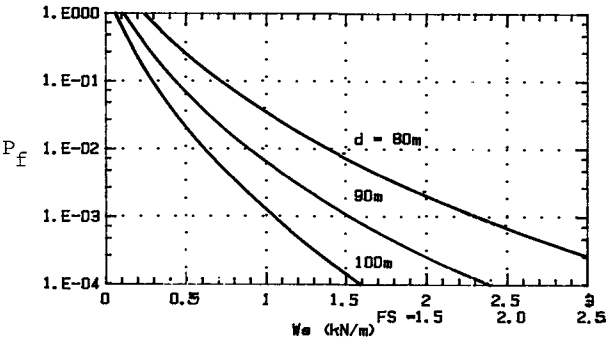

Figure 3: P_f vs W_S for Case I (FS shown for d = 80 m)

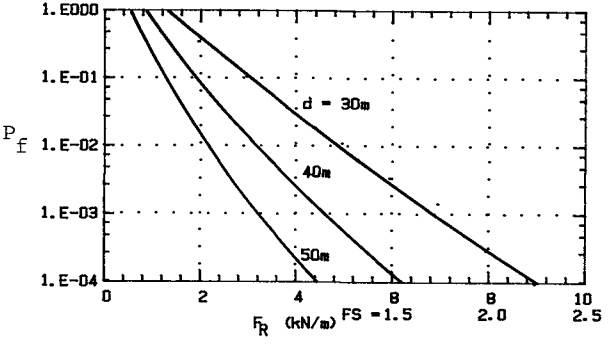

Figure 4: P_f vs F_R for Case II (FS shown for d = 30 m)

for a range of F_R values (F_R = capacity of anchorage), were performed at waterdepth, d = 30 m, 40 m and 50 m. The results are shown in Figure 4. Values for F_R calculated in a deterministic analysis, using the same variable values as in Case I, are also shown for FS = 1.5, 2.0 and 2.5, at d = 30 m.

The almost logarithmic increase in safety, with linear increase in pipeline weight or anchorage capacity, is clearly indicated by the results of the above calculations. In order to utilize these results in the stability design, the important question is that of which P_f value to accept. Meaning can, however, only be attached to such a value in terms of the concept "consequence of failure" incorporated in a risk analysis. Of more immediate practical importance is the evaluation of relative safety between different design options or along a pipeline route, using results such as provided in the examples presented above.

6. CONCLUSIONS

Based on the analyses performed and results obtained in this study the following conclusions can be drawn:

i) The traditional deterministic analysis of ocean pipeline stability involves several uncertainties which are difficult to represent realistically with safety factors alone. It is possible to represent these uncertainties with random variables for which statistical properties can be obtained.

ii) The incorporation of all the random variables representing uncertainties, in terms of their probability density functions, in the probabilistic procedure presented here, provides a more realistic measure of safety than is possible with the application of a safety factor alone.

7. ACKNOWLEDGEMENTS

The authors wish to thank Prof Robert A Grace from the University of Hawaii in Honolulu, and Hydraulics Research in Wallingford, England for making available data from seperate ocean tests on pipelines. Also, valuable advice on the study leading to this paper and comments from Prof Dimitri A Grivas from the Rensselaer Polytechnic Institute in Troy, New York, are sincerely appreciated.

8. REFERENCES

1. Anand, S, Agarwal, S L (1981) Field and laboratory studies for evaluating submarine pipeline frictional resistance. Jnl. of Energy Sources Technology, ASME, Vol 103, September: 250-258.

2. Chen, E, Borgman, L, Yfantis, E (1979) Height and period distribution for hurricane waves. Civil Engineering in the Oceans IV, San Francisco: 321-335.

3. Dean, R G, Perlin, M (1986) Intercomparison of near-bottom kinematics by several wave theories and field and laboratory data. Coastal Engineer, 9: 399-437.

4. Ellinas, C P, Raven, P W J, Walker, A C, Davies, P (1984) Limit state philosophy in pipeline design. Proc. of the 3rd Offshore Mechanics and Arctic Engineering Symposium, New Orleans: 27 pp.

5. Grace, R A (1976) Near-bottom water motion under ocean waves. Proc. of the 15th Intl. Conference on Coastal Engineering, Honolulu: 2371-2386.

6. Grace, R A, Zee, G T Y (1981) Wave forces on rigid pipes using ocean test data. Jnl. of the Waterway, Port, Coastal and Ocean Division, ASCE, Vol 107, No WW2, May: 71-92.

7. Hydraulics Research Station (1982) Wave forces on pipelines. Report No. EX 1056, Wallingford, England.

8. Jacobsen, V, Bryndum, M B (1984) Determination of flow kinematics close to marine pipelines and their use in stability calculations. Preprints of the 16th Offshore Technology Conference, OTC 4833, Houston, Texas: 7 pp.

9. Karal, K (1985) A concept for design of submarine pipelines to resist ocean forces. Jnl. of Energy Resources Technology, ASME, Vol 107, March: 42-47.

10. Mol, A, Groeneveld, R L, Waanders, A J (1984) Safety and reliability of breakwaters. Proc. of the 19th Intl. Conference on Coastal Engineering, Houston: 2451-2466.

11. Rosenblueth, E (1975) Point estimates for probability moments. Proc. of the National Academy for Science, USA, Vol 72, No 10: 3812-3814.

12. Swart, D H, Loubser, C C (1979) Vocoidal waterwave theory, Volume 2: Verification. CSIR Research Report 360, Stellenbosch, South Africa.

CHAPTER 140

Beachwalls for Beach Erosion Protection

Ralph M. Hayashi, P.E.*
Member, American Society of Civil Engineers

Introduction

Many shoreline property owners, in an effort to protect the beaches from erosion, have constructed sea walls. In many situations, these sea walls have caused an increase in beach erosion forcing, by "domino effect", adjoining properties to construct sea walls to protect their shoreline. The construction of a sea wall often causes erosion on the adjacent property. Unfortunately, more often than not, where beaches once existed, the construction of sea walls in addition to causing beach erosion to adjacent property has caused the disappearance of the beaches.

Because of the concern for the eroding beaches and the proliferation of sea walls, the design of a "beachwall" was proposed over four years ago by the author. Several of these beachwalls have been constructed, and the beaches fronting these structures have thus far been preserved or restored.

The design of a beachwall emulates nature's construction of a typical beach profile terminating with a sand dune or berm (figure 1). The design of the beachwall

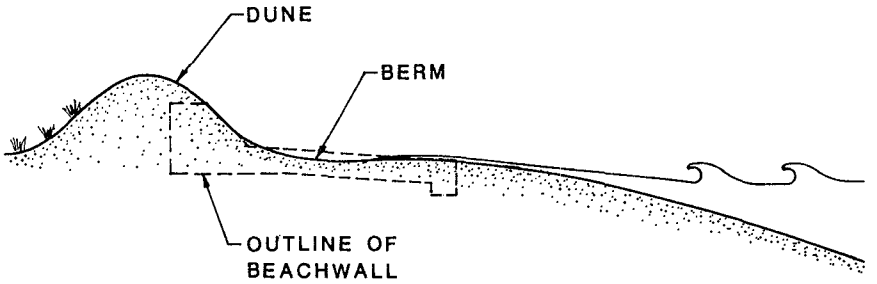

Figure 1. Typical Beach

*Vice-President, M & E (Metcalf & Eddy) Pacific, Inc., 1001 Bishop Street, Suite 500, Honolulu, Hawaii 96813

accommodates the energy forces of waves, minimizes wave rebound and scouring, and allows the deposition of sand, thus encouraging beach build up. The design of the beachwall addresses the problem of erosion at the toe of seawalls.

Protection of Beach Property

In the effort to protect beach property from existing or potential failures, sea walls with vertical or nearly vertical wall faces are often constructed along the property lines. By a "domino effect", property owners adjacent to such sea walls are sometimes forced to construct sea walls for protection of their property. Often, one sea wall causes the construction of another sea wall, which causes the construction of yet another, and so forth.

In many cases, because of the wave energy interaction with sea walls, there is erosion at the toe of the wall ultimately leading to wall failure. Additionally, the wave energy interaction with these walls will not allow beach build up and causes the disappearance of the beach. Thus, although the shoreline and property are saved and preserved by the wall, the beach is lost.

Over four years ago, the author felt a better approach to the then present concept of "protect the shoreline property in spite of losing the beach" would be to "first preserve the beach and in doing so protect the shoreline property". With this in mind, the beachwall design was developed.

Beachwall Design

The design of a beachwall begins with the selection of a design wave and design water level or wave run up as the controlling parameters for the wall design height. Other factors to consider in determining the wall height are the amount of damages that might occur from overtopping of the structure, the littoral drift and amount of sand in suspension in the water, and determination of optimum beachwall slopes, along with seasonal variations of the shoreline and offshore processes.

A practical method for designing the height of a beachwall is to observe wave run up during a high wave action or storm episode. The design high water level may be determined by noting the debris line after the high wave episode. Once the high water level has been determined, a freeboard height is to be selected. The freeboard height is determined to eliminate or minimize overtopping of the structure during extraordinary high wave action, with consideration to property damages that may be suffered by overtopping of the beachwall.

The face of a beachwall (figure 2) is composed of two sections of different slopes. The first section allows for wave run up, and experiences have shown that a slope of twenty percent (20%), 1:5, is satisfactory. The optimum slope for the run up section of the beachwall may be determined by using the slope of the sand existing in the vicinity where the beachwall is to be constructed. The length of the run up section is a function of a) the amount of wave run up (wave energy) to be accommodated by this section of the beachwall, and b) the amount of area available in which the beachwall can be constructed.

The second section is the freeboard portion of the beachwall. Experiences show that this section can have a slope of 1:1 or even steeper as its function, in addition to providing protection, is to eliminate or minimize overtopping. This section must also take care of the wave energy that is not accommodated by the run up section of the beachwall. Experiences show that the wave run up section of the beachwall can be about ten to twelve feet in length. Thus, any wave run up in excess of ten to twelve feet will have to be accommodated by the freeboard section. Of course, the length of the run up section is a function of the wave design height and will vary from one locale to another.

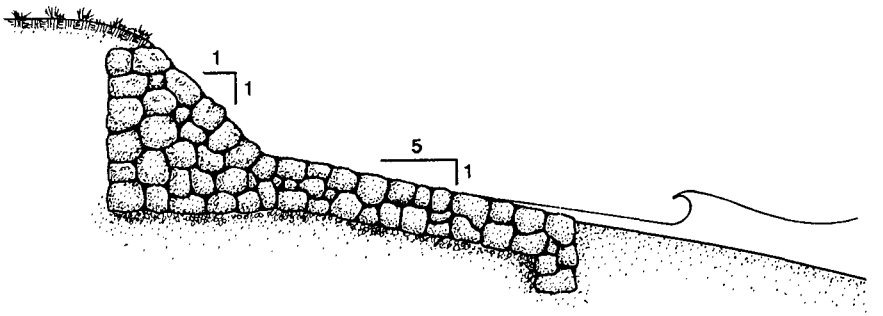

Figure 2. Beachwall

Setting of the beachwall, elevation wise, requires knowing tide levels of the area. Usually historical records of the elevations of high and low tides are available through government sources. In absence of such records, measurements should perhaps be taken through at least one year of seasonal shoreline water level variations. The elevation of the toe of the beachwall is set at or below low water elevation to make certain that

toe erosion will not occur. This elevation, along with the beachwall design accommodating the energy forces of waves, eliminates or minimizes wave rebound and scour thus addressing the problem of toe erosion of the structure.

Wave Energy on Structures

Normally beaches cannot form or reform because of the lack of suspended sand in the water or erosive velocity of the waves. This condition occurs when, following a high wave episode, sand that has been eroded from the beach is, displaced far off shore, trapped behind some reef or seaweed or both, or not allowed to be deposited because of successive high wave episodes. These conditions, especially when successive high wave episodes occur, often lead to the construction of sea walls.

Observations of vertical or nearly vertically faced sea walls and other similar types of structures show that beaches fronting such sea walls often erodes and do not return. The sand beach erodes or cannot form because of the wave forces. This erosion, often noted at the seaward footing of the wall, leads ultimately to wall failure.

When waves approach the shore, most of its energy is in the form of a velocity gradient. If there is sand off shore, the wave may be carrying sand in suspension. When the wave runs up the shore of a beach, its velocity begins to diminish due to slope of the beach and also friction with the shoreline. As the wave's velocity approaches zero, sand held in suspension will drop out because of gravity. This condition causes sandy beaches to form, or in the case of existing beaches, replenishes sand to the beach.

When waves approach a hard structure such as a seawall, it's velocity upon impact with the seawall is directed upward and downward about parallel with the face of the wall. The portion of the wave energy that is directed upward is usually visible as sea spray. The downward portion of the wave energy, often unseen, causes erosion at the base of the seawall. Because of this downward energy force, any sand or loose material at the base of such structures will eventually erode and wash away. This oftentimes leads to structural failure, and also causes the loss of the beach that may have once fronted the structure (figure 3).

Wave Energy on Beachwalls

The design of a beachwall emulates nature's construction of a typical beach profile which is composed of a run up slope section (beach) and terminating with the freeboard section (sand dune). The beachwall by design offers little, if any, wave reflection surfaces and rebound

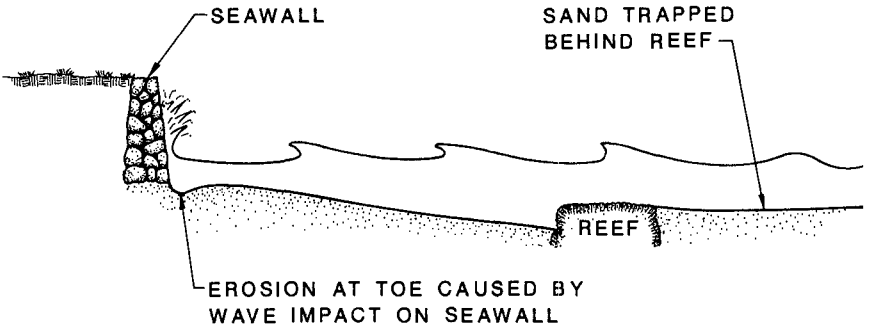

Figure 3. Loss of Beaches

of wave forces. The design effectively emulates a naturally occurring shoreline process. As the approaching wave flows up the run up face of the beachwall, the velocity gradient of the wave diminishes because of friction and slope, similar to the wave run up on a beach. As the velocity gradient approaches zero, sand held in suspension will settle out because of gravity and will be deposited on the beachwall. This action allows sand to accumulate and encourages the build up of a beach in a method similar to that which naturally occurs on sand beaches.

Summary

While it may sometimes be important to protect the shoreline and property from erosion due to wave action, it is equally if not more important to protect the shoreline against the loss of beaches. The task of saving property from erosion is simpler than the task of saving beaches and encouraging the formation of beaches. When the shorelines need to be protected, site conditions both on-shore and off-shore must be assessed before designs and construction of structures are undertaken. Poorly designed and improperly constructed erosion protection devices are oftentimes worse than doing nothing.

There are situations in which erosion control devices such as seawalls, revetments, groins and other hard structural techniques are required. However, erosion control should, whenever possible, begin by considering and utilizing natural shoreline defenses such as encouraging the growth of vegetation. If this is not possible or practical, then softer techniques such as beach fills or perhaps devices such as offshore sandbars should be considered.

Experiences over a three year period have indicated that a beachwall may be considered a soft device. While the beachwall is a "hard" structure, it behaves as a "soft" device by allowing the build up of sand. The beachwall shows promise in preserving and restoring beaches. Keep in mind however, that this beachwall may not necessarily be successful in all applications of preventing beach erosion or encouraging beach restoration.

CHAPTER 141

Studies on fixed rectangular surface barrier against short waves

CHING-HER HWANG* FREDERICK, L.W. TANG**

1. INTRODUCTION

In short waves, the particle motion in deeper region are to be negligible. For rigid vertical breakwaters built in considerable deep water, the lower part of vertical wall does not play the vital role of wave defending. It can be replaced by a frame to support the surface barrier which bears the wave force, and remain vacancy of the lower part of breakwater. Hence the theoretical and experimental characteristics of wave transmission and spectra alternation are investigated respectively here for this kind of the fixed, rigid, rectangular surface barrier in order to obtain an economic section and verify its capable relative depth as the design basis of deep port breakwater.

2. THEORITICAL CONSIDERATIONS

The theoritical considerations in this study are on the basis of the concept of the surface horizontal plate velocity potential theory derived by Dr. IJIMA and extended to this kind of rigid, rectangular surface barrier. Its coordinate scheme is shown as figure 1.

The flow in the fluid region about the breakwater is assumed to be irrotational, the fluid is incompressible and wave of small amplitude. These assumptions imply the existence of a velocity potential $\bar{\Phi}(x,z;t)$

$$\bar{\Phi}(x,z;t) = \phi(x,z) \exp(i\sigma t) \quad \text{.....(1)}$$

* Associate Researcher, Institute of Harbor and Marine Technology, Wuchi, Taichung District, Taiwan, R.O.C.

**Ph.D., Professor of Hydraulic and Ocean Engineering Graduate School, National Cheng Kung University, Tainan, Taiwan, R.O.C.

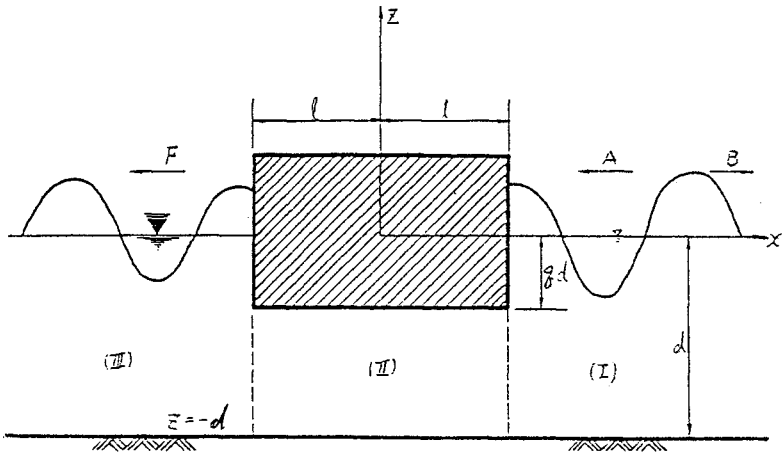

Fig.1 Coordinate system and notation

Table-1 Experimental conditions

	SINUSOIDAL		RANDOM	
RUN	T	H	$T_{1/3}$	$H_{1/3}$
R 1.	0.87	6.00	0.89	5.50
R 2.	1.03	6.24	1.02	5.58
R 3.	1.02	12.40	1.06	9.12
R 4.	1.24	6.19	1.23	6.09
R 5.	1.24	12.36	1.23	12.29
R 6.	1.47	6.38	1.48	6.26
R 7.	1.48	12.81	1.44	12.84
R 8.	1.93	6.63	1.85	5.95
R 9.	1.93	11.75	1.97	11.68

which satisfies the Laplace equation for a scale function $\phi(x,z)$

$$\frac{\partial^2\phi}{\partial x^2} + \frac{\partial^2\phi}{\partial z^2} = 0 \quad \text{.....(2)}$$

In this equation, x is the horizontal coordinate axies, measured positive to the right, z is the vertical coordinate axies,measured positive up from the still water level, and t is the time variable.

A solution is sought for $\phi(x,z)$ which satisfies the fluid equations of motions and the boundary conditions for the fluid and the fixed solid surface breakwater as following
the surface boundary condition

$$\frac{\partial\phi}{\partial z} = \frac{\sigma^2\phi}{g} \quad ; \quad z=0 \quad \text{.....(3)}$$

the rigid body boundary condition at bottom z=-d , -qd

$$\frac{\partial\phi}{\partial z} = 0 \quad ; \quad z = -d\ ,\ -qd \quad \text{.....(4)}$$

In addition to the above boundary conditions, the velocity potential at arbitrary assigned fictitious vertical boundaries on either side of the breakwater must satisfy the radiation conditions, which states that the velocity potential at the boundaries must match the velocity potential for the incident and outgoing waves. Then region I, II and III, the velocity potential are expressed as, respectively

$$\phi_I(x,z)=\left(Ae^{ik(x-\ell)} + Be^{-ik(x-\ell)}\right)\frac{\cosh k(z+d)}{\cosh kd} + \sum_{n=1}^{\infty} C_n e^{-k_n(x-\ell)} \frac{\cos k_n(z+d)}{\cos k_n d} \quad \text{.....(5)}$$

$$\phi_{II}(x,z) = \sum_{r=0}^{\infty} \left(Dr \frac{\cosh \frac{r\pi x}{d-qd}}{\cosh \frac{r\pi\ell}{d-qd}} + Er \frac{\sinh \frac{r\pi x}{d-qd}}{\cosh \frac{r\pi\ell}{d-qd}}\right) \cos \frac{r\pi(z+qd)}{d-qd} \quad \text{...(6)}$$

$$\phi_{III}(x,z) = Fe^{ik(x+\ell)} \frac{\cosh k(z+d)}{\cosh kd} + \sum_{n=1}^{\infty} G_n e^{k_n(x+\ell)} \frac{\cos k_n(z+d)}{\cos k_n d} \quad \text{..... (7)}$$

The coefficients A,B and F are incident, reflective and transmitted wave height respectively. Cn Gn Dr and Er are the unde-

termined coefficients. The symbols k and k_n represent the wave number in which.

$$\frac{\sigma^2 d}{g} = kd \tanh kd = -k_n d \tan k_n d \qquad (n= 1,2,3....)..(8)$$

Then the continuity of mass and energy flux, or similarly the continuation of the velocity and pressure at the fluid-breakwater media interface was considered.

at $x = \ell$

$$\phi_I = \phi_{II}$$

$$\frac{\partial \phi_I}{\partial x} = \frac{\partial \phi_{II}}{\partial x} \quad ; \quad -qd > z > -d \quad .....(9)$$

$$= 0 \quad ; \quad 0 > z > -qd$$

at $x = -\ell$

$$\phi_{II} = \phi_{III}$$

$$\frac{\partial \phi_{II}}{\partial x} = \frac{\partial \phi_{III}}{\partial x} \quad ; \quad -qd > z > -d \quad .....(10)$$

$$= 0 \quad ; \quad 0 > z > -qd$$

we obtain

$$B = \frac{i}{2} \sum_{r=0}^{\infty} \left[I_{or}\, Er + Dr\, I_{or} \tanh \frac{r\pi k\ell}{\bar{\lambda}_o} \right] + A \quad .....(11)$$

$$F = -\frac{i}{2} \sum_{r=0}^{\infty} \left[I_{or}\, Er - Dr\, I_{or} \tanh \frac{r\pi k\ell}{\bar{\lambda}_o} \right] \quad .....(12)$$

$$Cn = -\frac{i}{2} \sum_{r=0}^{\infty} \left[Dr\, I_{nr} \tanh \frac{r\pi k\ell}{\bar{\lambda}_o} + Er\, I_{nr} \right] \quad .....(13)$$

$$Gn = -\frac{i}{2} \sum_{r=0}^{\infty} \left[Dr\, I_{nr} \tanh \frac{r\pi k\ell}{\bar{\lambda}_o} - Er\, I_{nr} \right] \quad .....(14)$$

$$\left.\begin{aligned} Do &= \frac{1}{2} \left[\sum_{n=1}^{\infty} (Cn + Gn)\, R_{nr} + (A+B+F)\, R_{or} \right] \\ Dr &= \sum_{n=1}^{\infty} (Cn + Gn)\, R_{nr} + (A+B+F) R_{or} \end{aligned}\right\} \quad .....(15)$$

$$Er \tanh \frac{r\pi k\ell}{\bar{\lambda}_o} = (A+B-F) R_{or} + \sum_{n=1}^{\infty} (Cn-Gn)\, R_{nr} \quad .....(16)$$

Where

$$R_{nr} = \frac{\sin \bar{\lambda}_n}{\cos \lambda_n} \cdot \frac{1}{\bar{\lambda}_n \left[1-\left(\frac{r\pi}{\bar{\lambda}_n}\right)^2\right]}, \quad \lambda_n = k_n d, \quad \bar{\lambda}_n = k_n(d-qd)$$

$$R_{or} = \frac{\sinh \bar{\lambda}_o}{\cosh \lambda_o} \cdot \frac{1}{\bar{\lambda}_o \left[1+\left(\frac{r\pi}{\bar{\lambda}_o}\right)^2\right]}, \quad \lambda_o = kd, \quad \bar{\lambda}_o = k(d-qd)$$

$$I_{or} = \frac{2\sin\bar{\lambda}_n\cos\lambda_n}{Nn\,\lambda_n} \cdot \frac{r\pi/\bar{\lambda}_n}{[1-(r\pi/\bar{\lambda}_n)^2]}, Nn = \frac{1}{2}\left(1+\frac{\sin 2K_{nd}}{2K_{nd}}\right)$$

$$I_{or} = \frac{2\sinh\bar{\lambda}_o\cosh\lambda_o}{No\,\lambda_o} \cdot \frac{r\pi/\bar{\lambda}_o}{\left[1+\frac{r\pi}{\bar{\lambda}_o}\right]^2}, \quad N_o = \frac{1}{2}\left(1+\frac{\sinh 2kd}{2kd}\right) \ldots(17)$$

After substituting eq (11) ~ eq (14) into eq (15)~(16), we get

$$Dr + \sum_{n=1}^{\infty}\left[\sum_{r=0}^{\infty}\left(Dr\, I_{nr}\tanh\frac{r\pi k\ell}{\bar{\lambda}_o}\right)\right]R_{nr} - i\left[\sum_{r=o}^{\infty}\left(Dr\, I_{or}\tanh\frac{r\pi k\ell}{\lambda_o}\right)\right] R_{or} = 2R_{or} \quad \ldots\ldots(18)$$

$$\left(\tanh\frac{r\pi k\ell}{\bar{\lambda}_o}\right) Er + \sum_{n=1}^{\infty}\left[\sum_{r=0}^{\infty}\left(Er\, I_{nr}\right)\right] R_{nr} - i\left[\sum_{r=0}^{\infty}\left(I_{or}\, Er\right)\right]R_{or} = 2R_{or} \quad \ldots\ldots(19)$$

Then, the water level variations at Region I, the up-lift dynamic pressure distribution of barrier bottom at Region II and the transmitted coefficient at Region III are found respectively

. Water level variations at Region I

$$\eta/A = -\frac{i\sigma}{g}\left\{e^{i[k(x-\ell)+\sigma t]} + (B/A)\, e^{-i[k(x-\ell)-\sigma t]} + \sum_{n=1}^{\infty}(Cn/A)e^{-[K_n(x-\ell)-i\sigma t]}\right\} \quad \ldots\ldots(20)$$

. Up - lift dynamic pressure of barrier bottom at Region II

$$\frac{\rho}{gA} = -\frac{i\sigma}{g}\left\{\sum_{r=o}^{\infty}\left\{\left[(Dr/A)\frac{\cosh\frac{r\pi x}{d-gd}}{\cosh\frac{r\pi\ell}{d-gd}} + (Er/A)\frac{\sinh\frac{r\pi x}{d-gd}}{\cosh\frac{r\pi\ell}{d-gd}}\right]\right.\right.$$

$$\left.\left.\cos\frac{r\pi(z+gd)}{d-gd}\right\}\right\} e^{i\sigma t} \quad \ldots\ldots(21)$$

. Transmitted coefficient of barrier at Region III

$$K_t = |F/A| \quad \ldots\ldots(22)$$

3. EXPERIMENTAL TESTS

Experiments of wave spectra alternation characteristics of this fixed, rigid, rectangular barrier were investigated also in a

$100^m \times 2^m \times 1.5^m$ wind wave flume in Institute of Harbor and Marine Technology. Its arrangement was shown in Figure 2 .

Then, the different immerged depth q ratioes and relative width B/L of barrier were used to investigate its characteristics of the spectra alternation under different relative water depth d/L. Various kind of wave conditions were also carried out in this study as shown in Table 1.

4. RESULTS AND DISCUSSIONS

4-1 Analytical solutions of velocity potential theory

Analytical solution of velocity potential theory were shown in figure 3 to figure 7. Figures 3(a) (b) (c) represent respectively the curves of water level variations before the barrier at region I under relative immerged water depth q=0.3 and different relative width B/L = 0.004 , 0.08 and 0.2 etc. Results indicate the more larger relative water depth d/L and relative width B/L are, the more closed sine curves the water level profiles are. For short waves (ie d/L = 0.5), the minimum η/A ratio value is equal to 1.25 when both q and B/L are equal to 0.3 and 0.2 respectively, and this value is increasing with the relative water depth d/L.

Figure 4~6 show the analytical solutions of the up-lift dynamic pressure distribution at the bottom of barrier at Region II under different relative water depth and relative width. Results indicate that the dynamic pressure distribution has the relationship with B/L , d/L and q etc. respectively. In general, the larger the relative width is, the larger up-lift dynamic pressure difference between both side bottom of the surface barrier is. And its distribution at the bottom of the barrier more uniform if the q value is larger. Moreover, up-lift pressure decreased as the d/L decreased and tend to a horizontal distribution when the relative water depth is equal to 0.2-0.3. For example, as shown in figure 6, the dynamic pressure variations at both sides of the surface barrier bottom are obviously increased with the relative width, comparing with the Figure 4 and 5, under different relative immerged water depth q values. This means that its slope is more

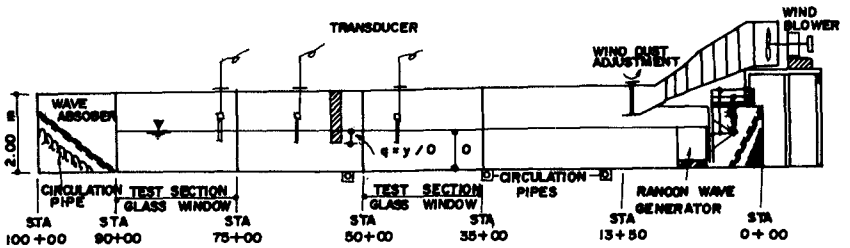

Fig.2 General arrangement

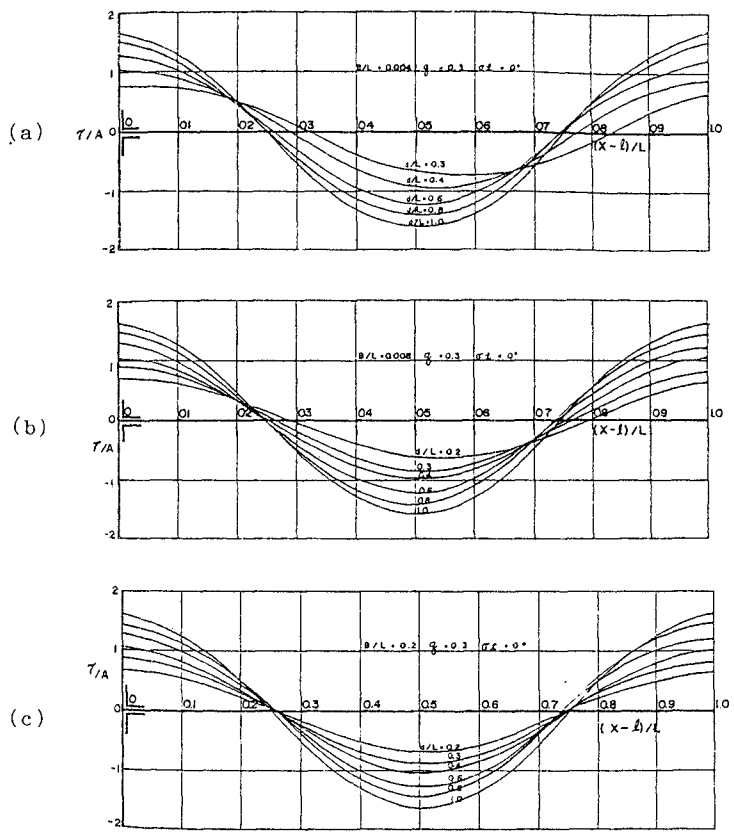

Fig.3 Curves of water level variations before the barrier

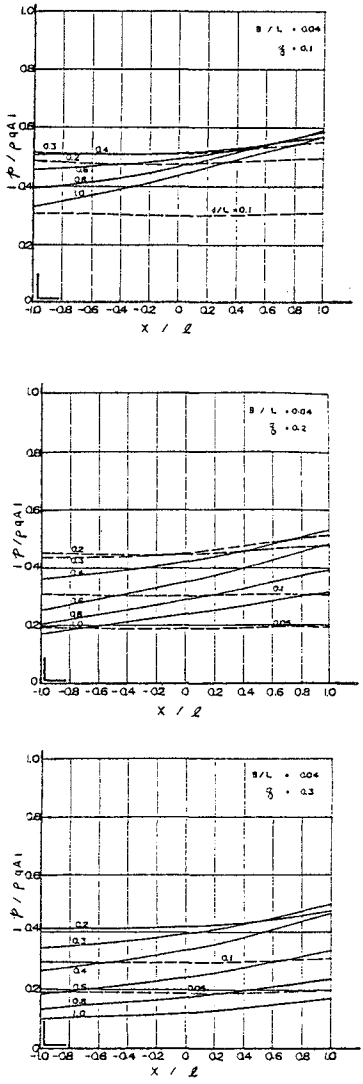

Fig.4 Up-lift dynamic pressure distribution at the bottom of barrier

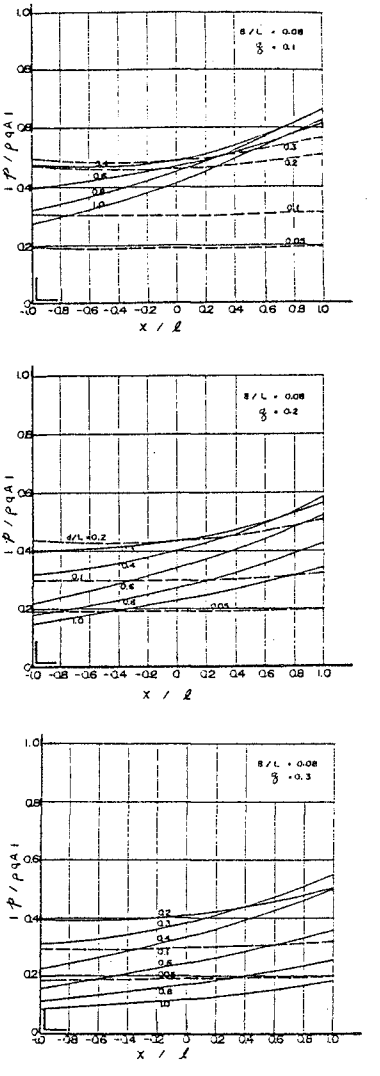

Fig.5 Up-lift dynamic pressure distribution at the bottom of barrier

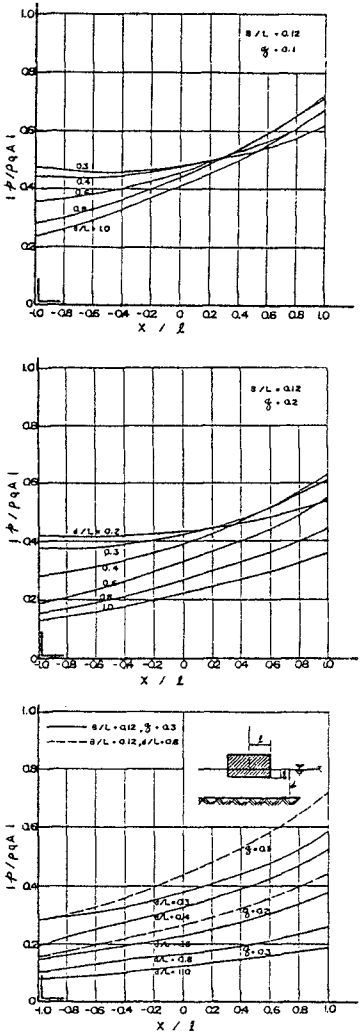

Fig.6 Up-lift dynamic pressure distribution at the bottom of barrier

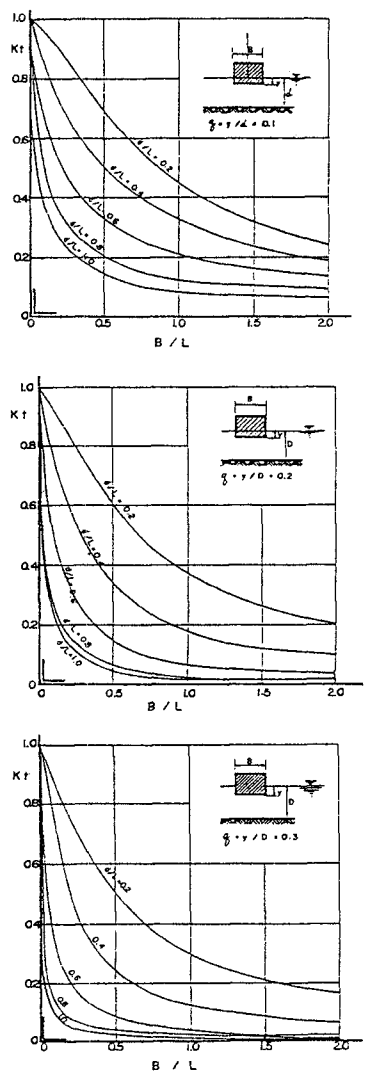

Fig.7 Relationship between K_t and B/L

steepen as the relative width of surface barrier increased.

Figure 7 are results of the analytical relationship between the transmitted coefficient K_t and relative width B/L under various relative water depth d/L at q=0.1,0.2 and 0.3 etc. respectively. Analytical results mean that we can expect to obtain an ideal wave stability behind the barrier when its relative width B/L is equal to 0.2~0.4 and the relative immerged depth q value is equal to 0.3 for the deep water waves i.e. short waves, assume the allowable transmitted coefficient criterion we adopted is equal to 0.2. Therefore, this dimension of barrier is an economic section in theoretical consideration for us to maintain an ideal wave stability at the basin , and can be used as the design section of deep water port breakwater.

4-2 EXPERIMENTAL RESULTS

In order to verify the capability of this type breakwater, laboratory experiments were also carried out under random waves in wind wave flume. Figure 8 and 9 are the results of energy spectrum curves of penestrated wave for various relative width and immerged water depth respectively. Figure 8 (a)~(d) are the experimental results for this breakwater under different immerged water depth q value and various relative water depth d/L. Experimental results show that the energy density peak value decreases above one order if q is equal and greater than 0.3, and relative water depth d/L is greater than 0.5 i.e. for short waves. Figure 9 (a)~(d) are the experimental results for this fixed rectangular surface barrier under different relative water depth d/L relative width B/L at immerged water depth q value is equal to 0.3. Results also indicate that the energy density peak value decreases above one order if relative width B/L is equal to 0.4 at q=0.3 for deep water waves. This means that we can expect again to obtain the same dimension of breakwater used as the section of the deep port breakwater from the experimental viewpoint.

5. CONCLUSIONS AND RECOMMENDATION

Summarize these results mentioned above, we can obtain some conclusions as following :

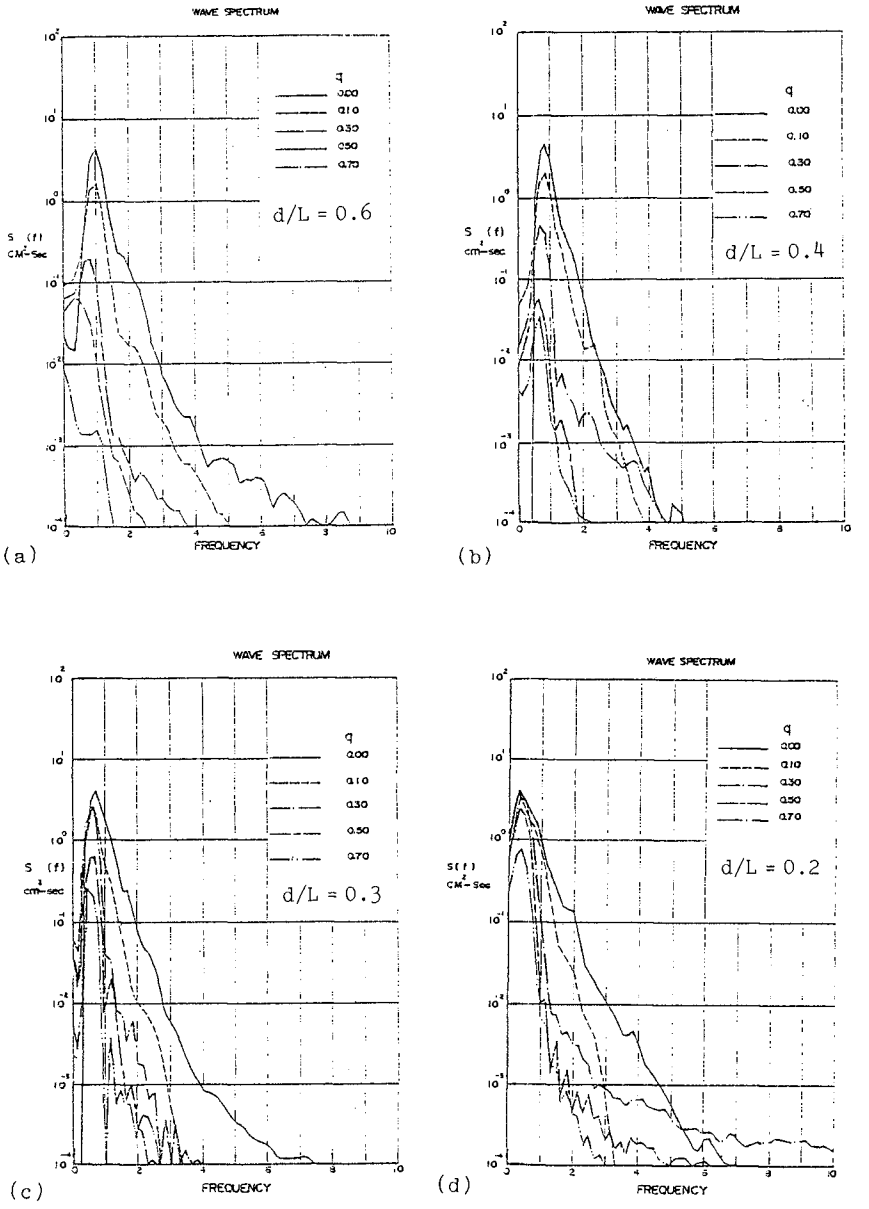

Fig.8 Energy spectrum curves of penetrated wave for various relative width (thin Breakwater)

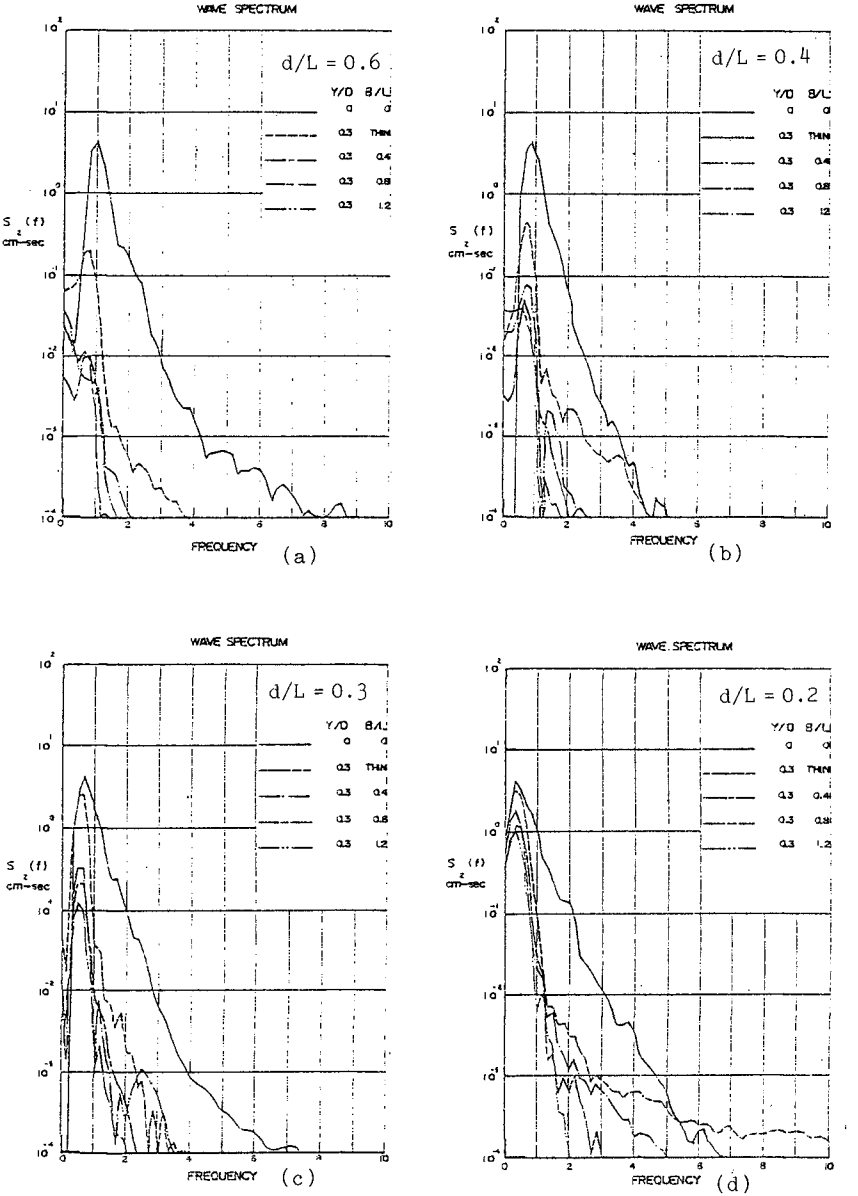

Fig.9 Energy spectrum curves of penetrated wave for various relative width (q = 0.3)

(1) Theoritical results indicate that the up-lift dynamic pressure distribution of barrier has the relationship with B/L, d/L and q etc. respectively. In general, the bigger the relative depth is, the larger the up-lift dynamic pressure difference between both side bottom of the surface barrier is. And its distribution at the bottom of the barrier is more uniform if the q values is larger. Moreover, up-lift pressure decreased as the d/L decreased and tend to a horizontal distribution when the relative depth is equal to 0.2∽0.3.

(2) K_t will decrease as q and d/L decreased for the same B/L value. It verifies that this barrier can defend effectively the short waves when q is equal to 0.3 and B/L is equal to 0.2 ∼ 0.4, and its K_t is less than 0.2.

(3) Energy spectrem curves of penestrated wave for various B/L and q of the surface barrier verify that the peak magnitude of energy spectrum would decrease predominantly above one order and filter many short wave components when the q and B/L of the surface barrier is equal to 0.3 and 0.4 respectively.

(4) This type of breakwater and its economic section mentioned above could be used as the design criterion of the outer breakwater of Yeh-Liu deep port, at the North of TAIWAN, in future if we can solve the engineering problem: "How to fix this kind of surface barrier in deep water region ? ".

6. ACKNOWLEDGEMENTS

The laboratory work in this study was carried out through the sincere cooperation of many people, and authers would like to thank all of them. In particular, I would like to express my appreciation to Mr. C.K. Chang, Deputy Director of IHMT, who affords all possible helps. Authers would also like to thank Miss Joanna Chang to type this manuscript.

7. REFERECES

Ippen , T., (1966). Estuary and coastaline Hydrodynamics, New York Mc Graw-Hill, Inc.

URSELL, F.,(1947). The effect of a vertical barrier on surface waves in deep water, proc. Camb phil Soc, Vol 43.

DEAN, W.R.(1945). On the reflection of surface waves by a sub-merged plane barrier, Proc. camb. phil., Soc., Vol. 41.

WIGEL, R.L.,(1960). Transmission of waves past a rigid vertical thin barrier., J. Waterway and Harbor Division, Proc. of ASCE, 86,

KUO, C.T. etl. (1973). The effect of a barrier on surface waves in shallow water., J. of NSC, Taiwan, No. 6, pp. 415 - 430.

IJIMA T.,(1970). Wave effected on horizontal and vertical wall, proc. of the 17 conference on coastal Eng. in Japan.

CHAPTER 142

WAVE FORCES ON VERTICAL PILES CAUSED BY 2- AND 3-DIMENSIONAL BREAKING WAVES

Søren Peter Kjeldsen [1]
Alf Tørum [2]
Robert G. Dean [3]

ABSTRACT

The present study deals with analysis of results from a new experiment in which local wave forces on a vertical pile penetrating the free surface were measured, both in transient breaking waves and in 2- and 3-dimensional irregular seas, regular waves, and waves and uniform currents superposed. The performance of the entire experimental programme showed that extreme wave load intensities are associated with transient 2- or 3-dimensional breaking waves, of relatively short wave periods, and not with the highest waves in the simulated sea states. The total integrated in-line force and the total overturning moment caused by breaking waves exceeded the values measured in monochromatic regular waves by a factor of 3. Inception of wave breaking was caused by phase superposition, and occurred also for very low values of wave steepness s = 0.05.

1 INTRODUCTION

The study of breaking waves in deep waters was initiated in Norway after a quite large number of capsizings of cargo vessels and fishing trawlers, which had occurred over a few years. Kjeldsen & Myrhaug (1980) analysed field data from 22 gales, and found encounter probabilities for high and steep waves occurring in deep water conditions based on multivariable probability density functions. After this Kjeldsen (1982) developed a non-linear wave generation technique, based on sweep frequency modulation with the ability to produce breaking freak waves with a control of breaker type (spilling, bore, plunging) within a hydrodynamic laboratory. Application of such a technique produces violent plunging breakers at a specified position and time in a wave basin. The plunging breakers occur in deep water and repeat with great accuracy. Further the position of the plunging jet can be shifted horizontally according to rules for non-linear dispersion of transient wave trains. In addition the particle velocities within the crests of these transient plunging breakers in deep waters were measured. This was achieved with a newly developed wave-follower-system, consisting of a carriage with a high-speed cine camera and a current meter that followed one particular wave crest

[1], [2]: MARINTEK, Norwegian Marine Technology Research Institute A/S, P.O. Box 4125, N-7001 Trondheim, Norway.
[3] : University of Florida, College of Engineering, Coastal and Oceanographic Engineering Dept, 336 Weil Hall, Gainesville, Florida, 32611, USA.

until it finally became unstable and developed into a plunging jet, see Kjeldsen (1984a). The very large particle velocities measured in the upper part of the crests suggest that local wave forces in breaking waves close to the free surface should be much higher than predictions of wave forces obtained from application of Stokes' higher order wave theories. Wave forces measured on piles in the Mexican Gulf during Hurricane Carla, were analysed by Dean, Dalrymple and Hudspeth (1981), who found quite a reduction in measured wave forces close to the free surface in the crests of the waves. It was then found that theoretical predictions of wave force, based on higher order Stokes' theories, in general overestimate the local wave force in a local area close to the free surface. Therefore, in order to investigate the intensity of local wave forces very close to the free surface in breaking and non-breaking wave crests, an extensive experimental programme was performed in the large new Ocean Simulating Basin at MARINTEK, Trondheim, Norway. The problem we consider is the following: a vertical pile encounters wave crests, which can be 3-dimensional as Fig. 1 shows, or 2-dimensional swell. The wave crests considered here can be either breaking or non-breaking.

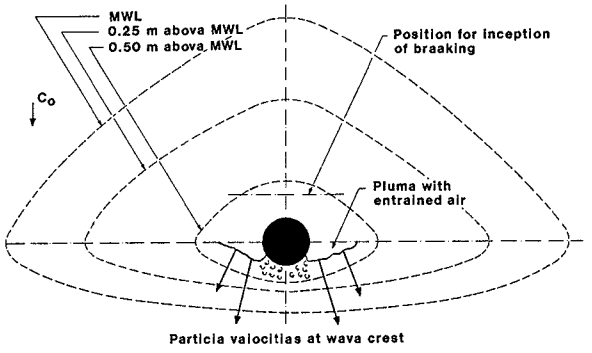

Fig. 1 Definition of problem. Contour lines of a 3-dimensional wave crest near the pile are shown. The wave crest has a very steep front and a less steep rear side. The position for inception of breaking can be controlled. The horizontal particle velocity vectors at the free surface of the upper part of the crest are shown. The ratio between the magnitudes of these vectors and linear phase velocity (shown in upper left corner) is nearly 3.

We focus on force measurements in the upper part of a breaking wave crest. Here the flow is not oscillatory, but it is an accelerating and decellerating flow where the horizontal particle velocity component maintains mainly the same direction. Therefore eddies released behind the pile will not be swept backwards and return in the following wave, as the case is in the fully submerged part of the pile.

Thus the separation points in this upper part of the wave crest will be shifted. In addition air entrainment takes place when the waves break. Thus Morison's equaiton is probably not the best force model to describe such a complicated situation. Emphasis should be given to the 3-dimensional character of the problem. Lift force components of considerable magnitude was found to occur. In the present study in-line forces are defined as force components acting in the main wind direction, which also is assumed to be the main direction for wave propagation in a simulated 3-dimensional sea. These are considered to be mainly drag forces. Lift forces or transverse forces are defined as force components acting perpendicular to the main wave direction.

2 EXPERIMENTAL PROGRAMME

In order to investigate the intensity of local wave forces very close to the free surface in wave crests, an extensive experimental programme was performed in the new Ocean Simulating Basin at MARINTEK, Trondheim, Norway. This basin has the following main dimensions: length - 80 m, width - 50 m. It is equipped with an adjustable bottom that permits water depths in the range 0.1 - 10.0 metres.

Experiments can be carried out with maximum wave heights close to 1.0 m and wave periods in the range 0.5 - 3.6 seconds. It is also possible to superpose waves upon uniform currents with logarithmic profiles. The present experiments were performed with a water depth of 3 metres, corresponding to deep water conditions.

A vertical pile with a diameter of 60 mm (a leg of a steel jacket platform in scale 1 : 25) was installed with 26 shear force transducers mainly located in the zone between the highest wave crest and the lowest wave trough. Each shear force transducer consisted of a 15 mm wide horizontal ring. Force measurements on each ring were obtained by strain gauges. In addition to local measurements of in-line and transverse forces on the pile, sea surface elevations, uniform currents and directional wave spectra were measured. An experimental programme was then performed containing the following test conditions:

SEA SIMULATION	Hydraulic Double Flap Wave Generator	Hydraulic Double Flap Wave Generator with Steady Uniform Current Superposed	Electric Multi Flap Wave Generator with 144 Elements
REGULAR 2-DIMENSIONAL WAVES	20	-	-
2-DIMENSIONAL IRREGULAR SEA WITH PIERSON-MOSKOWITZ SPECTRA	15	-	-
2-DIMENSIONAL TRANSIENT FREAK WAVES, PLUNGING BREAKERS	20	-	-
A UNIFORM CURRENT WITH 2-DIMENSIONAL IRREGULAR SEAS SUPERPOSED (PM-SPECTRA)	-	12	-
3-DIMENSIONAL IRREGULAR SEAS WITH PIERSON-MOSKOWITZ AND JONSWAP SPECTRA	-	-	10
3-DIMENSIONAL SHORT CRESTED BREAKING FREAK WAVES, SPILLING BREAKERS			10
			Total : 87

Fig. 2 shows a vertical section of the pile with the distribution of shear force transducers. The right hand side of this figure shows flow patterns at various horizontal planes behind the pile as functions of Reynolds and Keulegan-Carpenter numbers. In the present investigation Reynolds numbers in a range of 0 - $2.9 \cdot 10^5$ and Keulegan-Carpenter number in a range of 0 - 135 were achieved. Data acquisition took place on 63 channels simultaneously with a sampling frequency of 20 Hz. Data acquisition in the Ocean Basin took place for 5 minutes in each experiment, and for some experiments with irregular seas, data acquisition was extended to 20 minutes.

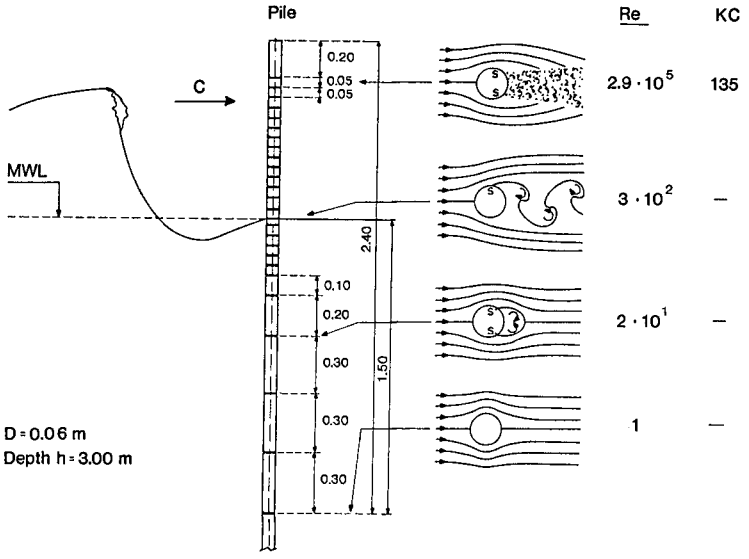

Fig. 2 Left: Experimental arrangement.
Right: Flow patterns and eddy development in horizontal planes behind the pile at various elevations, shown as functions of Reynolds and Keulegan-Carpenter numbers.

3 RESULTS

The main result from the entire programme was that the 2-dimensional breaking waves occurring in deep waters as plunging breakers gave far the largest wave forces. These particular waves were generated as a superposition of 43 frequencies contained in a wave group. By means of a non-linear amplitude-dependent sweep frequency modulation, the breaking waves were obtained right on the structure. Fig. 3 shows an example of the measured surface elevation of such a wave. The wave shown in this particular example had a zero-downcross wave height H_{zd} = 0.504 m, a zero-downcross wave period T_{zd} = 1.385 sec, a horizontal asymmetry factor μ = 0.879 and a crest front steepness ϵ = 0.539. (For definition of μ and ϵ, see Kjeldsen & Myrhaug (1980).)

Fig. 3 also shows the measured in-line and transverse force components in this kind of wave. The lift force component is close to 20 % of the measured drag component and should be taken into consideration in design. The particular shape of the lift force component shown in Fig. 3, indicates that eddy shedding takes place.

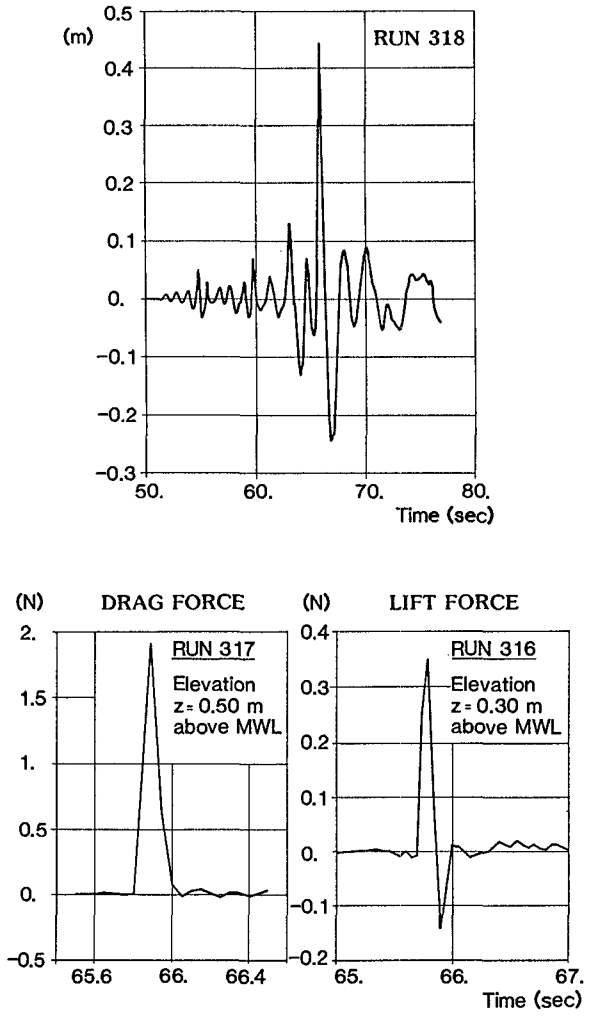

Fig. 3 Above: Surface elevation of a 2-dimensional transient freak wave breaking as a plunging breaker. Below: Drag- and lift force components measured in such waves above mean water level (MWL).

Fig. 4 shows a remarkable result. In this particular example a wave group consisting of 3 waves were obtained at the pile. The upper left corner in Fig. 4 shows the surface elevation of these waves. The first wave is small and unimportant. The second wave A is breaking violently as a plunging breaker. The third wave B is a regular wave very similar in shape to predictions made by Stokes 2-order wave theory. Wave B has a much longer wave period than wave A and we should thus expect that the associated wave kinematics and also the resulting drag force component are higher in wave B than in wave A. However, the measured drag force components shown in Fig. 4 clearly demonstrate that the transient wave A, breaking as a plunging breaker gives rise to much higher drag forces at all levels. This can be explained by the fact that the breaking wave is generated as a phase superposition of many individual waves, and thus contains much more wave energy in the crest, than the higher wave B. This is the case even when wave B has a longer zero-downcross wave period.

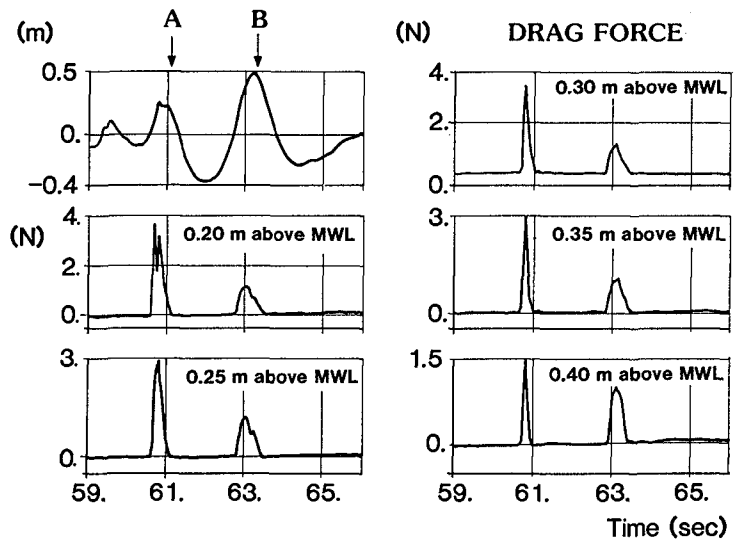

Fig. 4 Upper left: Surface elevation of wave group. Wave A is a plunging breaker. Wave B is a higher more regular wave with a longer wave period. Below and right: Drag force components measured for wave A and wave B above MWL.

Fig. 5 shows a comparison of the vertical profiles of maximum local instantaneous drag forces obtained in a plunging breaker and obtained in a test series with regular monochromatic waves which turned out to have profiles very close to those predicted by Stokes 2. order wave theory. We see in Fig. 5 that the plunging breaker has a maximum local wave force that is close to 5 times larger than the maximum local force obtained in the monochromatic wave.

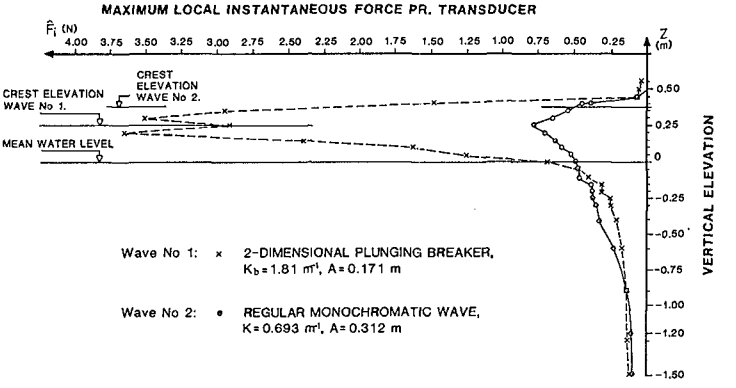

Fig. 5 Comparison between vertical profiles of maximum drag force obtained in plunging breaker and obtained in test series with regular monochromatic waves. (K is the wave number, and A is the wave amplitude H/2.)

Not only the local wave force, but also the total integrated drag force was much higher in the breaking wave than the corresponding drag force in the monochromatic wave. A factor of nearly 3 was found. Fig. 6 shows integrated in-line forces for breaking waves and results for monochromatic waves plotted as a function of wave steepness. Also the envelope for the tests with breaking waves is indicated. It is remarkable that plunging breaking waves were found to occur with steepnesses as low as 0.05. Other breaking wave transients occurred with steepnesses as high as 0.191. Thus it is obvious that the theoretical limiting steepness for monochromatic waves s = 0.141 can not be used to predict inception of breaking in transient or random waves. (See also Kjeldsen (1984b) and Dold and Peregrine (1986).)

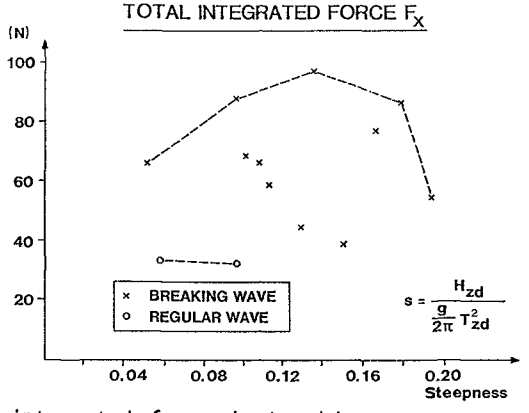

Fig. 6 Total integrated force in breaking waves compared with the total integrated force in regular waves with comparable steepnesses.

Also the total overturning moment was much higher for the breaking waves than for the monochromatic waves. Also here a factor of nearly 3 was found. The contributions from the drag force components near the free surface to the total overturning moment M_y at the seabed become more and more important when structures are developed for deeper waters, see Fig. 7. Results can also be presented in 3-dimensional plots as functions of wave height H_{zd} and wave period T_{zd}.

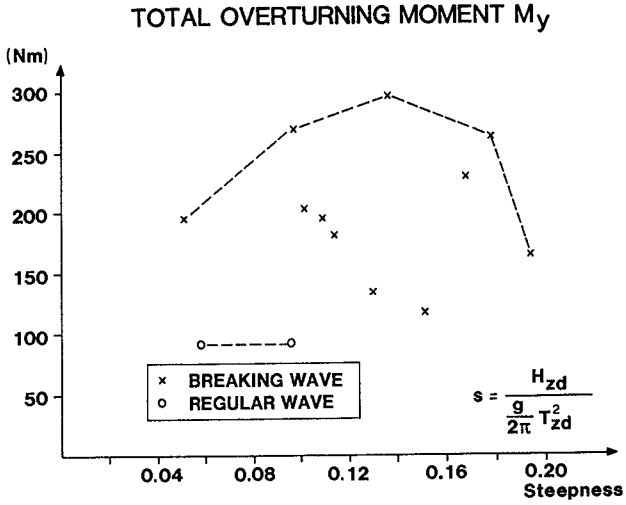

Fig. 7 Total overturning moment in breaking waves compared to total overturning moment in regular waves with comparable steepness.

We now proceed to 3-dimensional short-crested breaking waves occurring in deep water. These waves were focussed over a sector angle nearly 98 degrees. We attempted to model a situation with crossing wave orthogonals in deep water, such as can occur leeward of islands and reefs due to topographic refraction. The short-crested breaking waves were obtained using one frequency and waves approaching from 144 directions towards a focussing point with crossing orthogonals. They were generated with the 144 electrically driven flaps for 3-dimensional sea generation. Fig. 8 shows an example of such a short-crested 3-dimensional breaking wave. (See also Kjeldsen & Åkre (1985).)

Fig. 8 Short-crested 3-dimensional breaking wave with zero-downcross wave height H_{zd} = 0.692 m and zero-downcross wave period T_{zd} = 1.69 sec. The steepness s_{zd} based on these parameters is $2\pi H_{zd}/g \cdot T^2_{zd}$ = 0.155.

Fig. 9 shows an overall non-dimensional comparison of obtained results. Dimensionless local mean pressure Ω is plotted against dimensionless vertical elevation. The mean pressure $\bar{p}_i$ is defined as $\hat{F}_i/D \cdot t'$, where $\hat{F}_i$ is the maximum instantaneous wave force measured in the wave dispersion direction, D is the diameter of the pile, and t' is the width of the shear force transducer.

The wave number K_b at the position where inception of breaking takes place is defined as $K_b = 4\pi^2/g \cdot T^2_{zd}$ where T_{zd} is measured at the position where the wave profile becomes vertical.

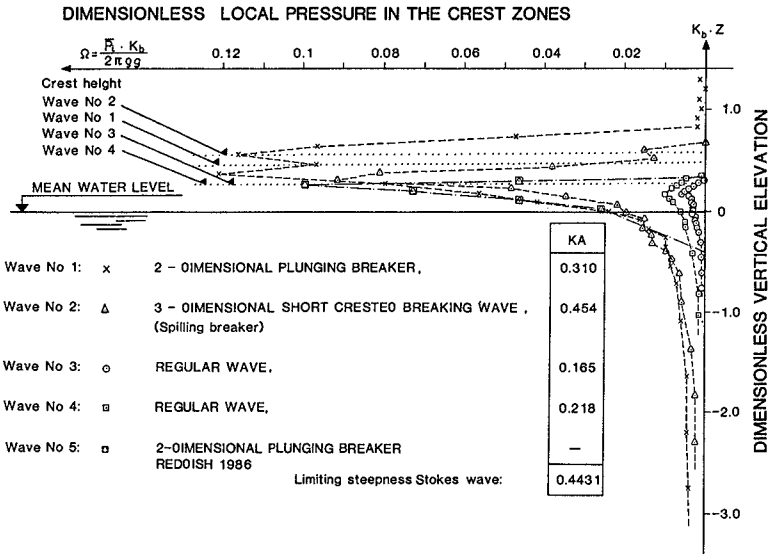

Fig. 9 Comparison between dimensionless local mean pressure in the crest zones measured in 2-dimensional plunging breaker waves, 3-dimensional short crested breaking waves, and 2-dimensional monochromatic waves. (K is wave number, A is wave amplitude H/2.)

The 2-dimensional plunging breakers gave the highest local forces, the highest integrated forces and the highest overturning moments in the entire test programme. The 3-dimensional short-crested breaking waves gave high but somewhat less forces, due to the angular spreading of crest particle velocities. Shown here are also results for a shallow water breaking wave measured by Reddish (1986). Reddish found local wave forces at the same level as the present investigation. However, numerical simulations of kinematics in deep and shallow water waves made by Vinje & Brevig (1981) show that kinematic vectors in breaking wave crests attain larger values in shallow waters than in deep waters. We should therefore expect that also wave forces associated with shallow water breaking waves are higher than the forces associated with deep water breaking waves which are reported here. Tørum (1985) performed an in-depth analysis of measured in-line wave forces associated with regular monochromatic waves. (See also Dean, Tørum, Kjeldsen (1985).)

It is important to be aware of the fact that wave impact or wave slamming is not incorporated in the present investigation. Data was sampled with a frequency 20 Hz. Wave impact forces have durations of the order $1 \cdot 10^{-3}$ sec and that demands much higher sampling frequencies. If wave impact forces occur these forces must be added to the viscous wave forces reported here. A separate investigation of a vertical and tilted plate exposed to impacts from crests of deep water breaking waves was performed by Kjeldsen (1981).

4 WAVE KINEMATICS

The present study is extended to include wave kinematics. Melville (1983) has shown that the Hilbert transform can be used to measure the amplitude, frequency, wave number and phase velocity as continous variables even in a strongly non-linear unsteady wave train. In the present study application of the Hilbert transform is extended to include a continous calculation of the horizontal and vertical particle velocities at the free surface based on measurements of free surface elevation. Fig. 10 presents results of such a calculation. It was found to predict wave kinematics at the free surface, even in very non-linear waves close to inception of breaking. For further details, see Kjeldsen (1986).

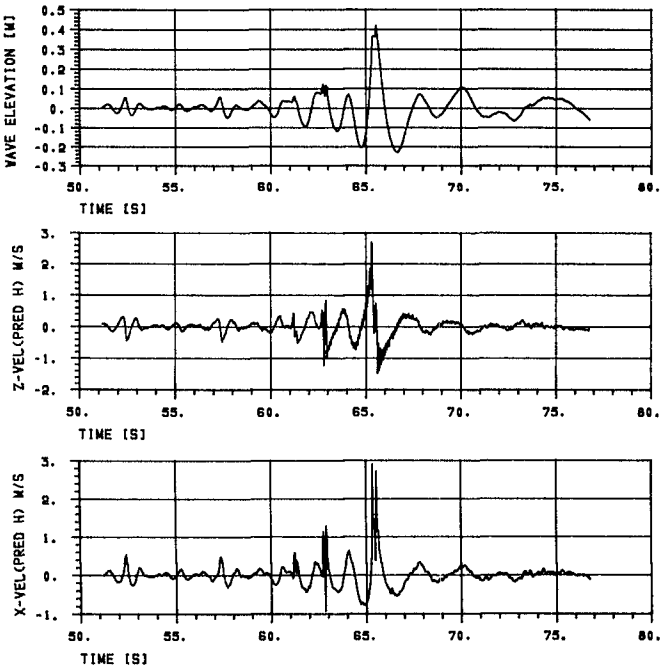

Fig. 10 Surface elevation and predicted horizontal and vertical particle velocities.

5 INSTABILITY OF 3-DIMENSIONAL WAVES

Su, Bergin, Marler and Myrick (1982) found that 3-dimensional subharmonic bifurcation of 2-dimensional wave trains can occur when the wave steepness exceeds $ak \geq 0.25$. As a result 3-dimensional spilling breakers are generated with large crest front steepnesses. During this process, two series of oblique wave groups are formed and radiate symmetrically away from the primary wave direction at a constant angle of about 30 degrees. These spilling breakers are thus examples of a source of directional spreading of wave energy. Such a mechanism can also explain the presence of breaking waves in deep waters. This phenomenon has also been observed in the Ocean Basin.

6 CONCLUSIONS

1) The performance of the entire experimental programme showed that extreme wave load intensities are associated with transient 2- or 3-dimensional breaking waves, of relatively short wave periods, and not with the highest waves in the simulated sea states.

2) Local wave pressures measured close to the free surface in the crests of transient 2-dimensional plunging breakers exceeded local wave pressures in monochromatic regular waves by a factor of 5. The regular waves had surface elevations very close to predictions made from Stokes' second-order wave theory.

3) The total integrated forces and the total overturning moments in breaking waves exceeded those measured in regular monochromatic waves by a factor of 3.

4) Local wave forces measured in 3-dimensional short-crested breaking waves were lower than local wave forces measured in 2-dimensional plunging breakers. This result can be explained by the fact that horizontal crest particle velocities in general are lower in 3-dimensional waves than corresponding horizontal crest particle velocities in 2-dimensional waves.

5) Inception of wave breaking was caused by phase superposition, and occurred also for very low values of wave steepness $s = 0.05$.

6) Our final recommendation is therefore that much more attention should be given to breaking waves, and that experiments of the kind reported here be extended in the future to include breaking waves also in shallow water and breaking waves occurring on beaches.

7 ACKNOWLEDGEMENTS

Acknowledgements are given to the Research Programme for Marine Structures, coordinated by Professor Faltinsen at the Institute of Marine Hydrodynamics, The Norwegian Institute of Technology (NTH). The programme for Marine Structures has the Royal Norwegian Council for Scientific and Industrial Research (NTNF), NORWEGIAN HYDRO and STATOIL as sponsors. The experimental programme on wave forces near the free surface reported here is one of the activities in this research programme. Acknowledgments are also given to Dr. C.T. Stansberg for development of software related to the application of the Hilbert transform.

APPENDIX

1. Dean R.G., Dalrymple R.A., Hudspeth R.T. (1981): "Force Coefficients from Wave Projects I and II. Data including free-surface effects". Society of Petroleum Engineers Journal. December 1981, pp. 777-786.

2. Dean R.G., Tørum A., Kjeldsen S.P. (1985): "Wave Forces on a Pile in the Surface Zone from the Wave Crest to the Wave Trough". Proc. International Symposium on Separated Flow Around Marine Structures. The Norwegian Institute of Technology. Trondheim, Norway. June 1985.

3. Dold J.W. & Peregrine D.H. (1986): "Wave Modulation". Proc. 20th International Conference on Coastal Engineering. Taipei, Taiwan.

4. Kjeldsen S.P. & Myrhaug D. (1980): "Wave-Wave Interactions, Current-Wave Interactions, and Resulting Extreme Waves and Breaking Waves". Proceedings 17th International Conference on Coastal Engineering. Sydney, Australia.

5. Kjeldsen S.P. (1981): "Shock Pressures from Deep Water Breaking Waves". International Symposium on Hydrodynamics in Ocean Engineering. The Norwegian Institute of Technology, Trondheim, Norway.

6. Kjeldsen S.P. (1982): "2- and 3-Dimensional Deterministic Freak Waves". Proc. 18th International Conference on Coastal Engineering. Cape Town, South Africa.

7. Kjeldsen S.P. (1983): "Determination of Severe Wave Conditions for Ocean Systems in a 3-dimensional Irregular Seaway". Proc. from the VIII Congress of the Pan-American Institute of Naval Engineering. Washington D.C., USA. September 12-17, 1983.

8. Kjeldsen S.P. (1984a): "The Experimental Verification of Numerical Models of Breaking Waves". Proc. 19th International Conference on Coastal Engineering. Houston, Texas, USA:

9. Kjeldsen S.P. (1984b): "Dangerous Wave Groups". Norwegian Maritime Research. Vol. 2. 1984, pp. 4-16.

10. Kjeldsen S.P. & Åkre A.B. (1985): "Wave Foces on Vertical Piles Near the Free Surface Caused by 2-Dimensional and 3-Dimensional Breaking Waves". Report No. 1.10. Programme for Marine Structures. MARINTEK. Trondheim, Norway.

11. Kjeldsen S.P. (1986): "Wave Forces and Kinematics in Deep Water Breaking Waves". Report. Programme for Marine Structures. MARINTEK. Trondheim, Norway.

12. Melville W.K. (1983): "Wave Modulation and Breakdown". J. Fluid Mech. Vol. 128.

13. Reddish H.J. (1986): "Laboratory Study of Plunging Breaker Wave Force Distribution on a Slender Pile". Thesis for the degree of Master of Engineering. College of Engineering. Texas A & M University.

14. Su M., Bergin M., Marler P. and Myrick R. (1982): "Experiments on Non-linear Instabilities and Evaluation of Steep Gravity-Wave Trains". J. Fluid Mech., Vol. 124, pp. 45-72.

15. Tørum A. (1985): "Wave Forces on a Pile in the Surface Zone. Regular, Non-breaking Waves". Programme Report No. 1.9. Programme for Marine Structures. MARINTEK. Trondheim, Norway.

16. Vinje T. and Brevig P. (1981): "Breaking Waves on Finite Water Depths - A Numerical Study". N.S.F.I. Rep. No. R-111.81. Trondheim, Norway.

CHAPTER 143

Flow Computations nearby a Storm Surge Barrier under Construction with Two-Dimensional Numerical Models

H.E. Klatter *
J.M.C. Dijkzeul **
G. Hartsuiker ***
L. Bijlsma ****

This paper discusses the application of two-dimensional tidal models to the hydraulic research for the storm surge barrier in the Eastern Scheldt in the Netherlands.
At the site of the barrier local energy losses dominate the flow. Three methods are discussed for dealing with these energy losses in a numerical model based on the long wave equations.
The construction of the storm surge barrier provided extensive field data for various phases of the construction of the barrier and these field data are used as a test case for the computation at methods developed. One method is preferred since it gives good agreement between computations and field data. The two-dimensional flow patterns, the discharge and the head-difference agree well.
The results of scale model tests were also available for comparison. This comparison demonstrated that depth-averaged velocities, computed by a two-dimensional numerical model, are as accurate as values obtained from a large physical scale model. Even compicated flow patterns with local energy losses and sharp velocity gradients compared well.

Introduction

As result of the 1953 storm flood disaster the Dutch government initiated a comprehensive construction program called the Delta Plan. Its purpose is to protect the south western part of the Netherlands against storm surges from the North Sea. In accordance with the Plan most Dutch estuaries have been closed by dams. The final, and by far the largest inlet, the Eastern Scheldt (Figure 1) will not be closed, but safety will be ensured by a storm surge barrier. Under normal weather conditions the barrier gates will be open and the tidal move-

* Hydraulic Engineer, Hydraulic Research Division, Ministry of Transport and Public Works, P.O. Box 5044, 2600 GA Delft, The Netherlands.
** Mathematician, Tidal Water Division, Ministry of Transport and Public Works, Van Alkemadelaan 400, 2597 AT, The Haque, The Netherlands.
*** Poject Engineer, Delft Hydraulics Laboratory, P.O. Box 152, 8300 AD, Emmeloord, The Netherlands.
**** Senior Engineer, Zeeland Division, Ministry of Transport and Public Works, P.O. Box 5014, 4330 KA Middelburg, The Netherlands.

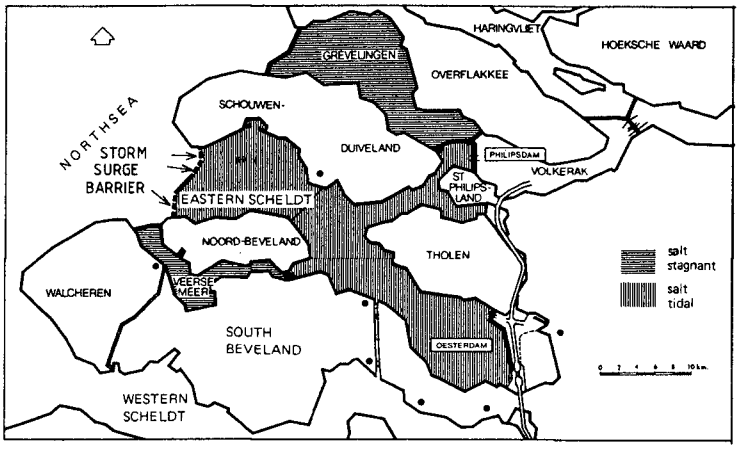

Figure 1. Location of the Storm Surge Barrier.

ment in the estuary will be maintained. This will preserve the unique-Eastern Scheldt environment. During storm surges the 62 gates of the barrier will be closed.

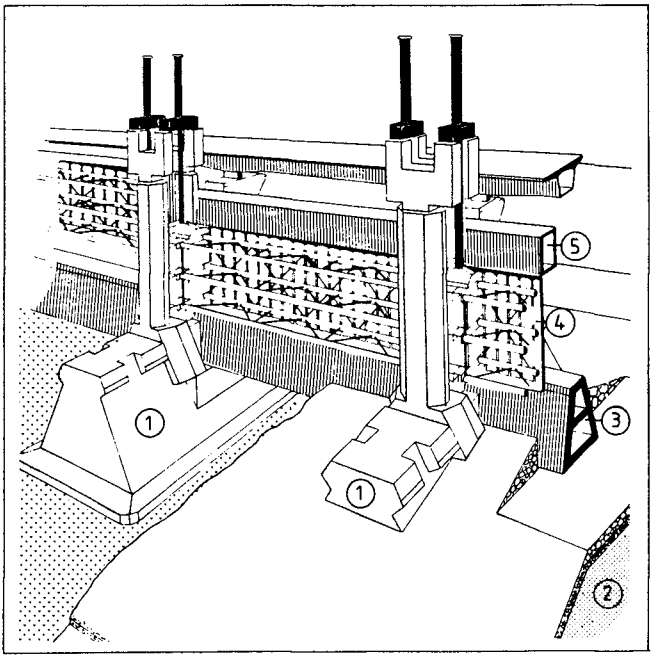

1. pier
2. rubble sill
3. sill beam
4. steel gate
5. upper beam

Figure 2. Storm Surge Barrier.

The barrier, which was completed in October 1986, has been built in the three main tidal channels. The structure comprises prefabricated piers, rubble sills, concrete sill beams and steel gates (Figure 2). Since the structural elements were to be prefabricated and positioned under open sea conditions, using specially constructed floating derricks, an extensive research program concerning the water motion in the vicinity of the barrier was needed. This research program extended over a period of 10 years, both before and during the barrier construction and was aimed at optimizing the design of the structural elements and derricks and achieving better execution management for the construction works.
At the site of the storm surge barrier the tidal range varies between 2.5 and 3.5 m. The continued reduction of the hydraulic cross-section during the barrier construction, caused increases in current velocities up to 5 m/s through the barrier, under normal tidal conditions.
This paper discusses the use of two dimensional numerical models for the prediction of the depth-averaged tidal motion. These computations provide detailed information of for example:
- overall tidal motion, total discharge
- flow patterns in the mouth of the estuary, used in the prediction of morphological effects
- detailed flow patterns in the vicinity of the barrier for computing, for example, local scour near the barrier.

Main Features of the Numerical Solution

For the two-dimensional (horizontal) simulation of tidal motion the WAQUA program system is used. WAQUA is originally developed by the Rand Corporation, USA. In its further development it has been redesigned by the Data Processing Division of the Netherlands Department of Transport and Public Works and the Delft Hydraulics Laboratory.
WAQUA is based on a numerical solution of the two-dimensional long wave equations. These are derived under the following assumptions:
i) vertical velocities and accelerations are negligible relative to the gravitational acceleration; in other words, hydrostatic pressure distribution is assumed (nearly parallel flow).
ii) the water body is well-mixed vertically.
The resulting equations, containing vertically averaged velocity components, are:

$$\frac{\partial U}{\partial t} + U\frac{\partial U}{\partial x} + V\frac{\partial U}{\partial y} - fV + g\frac{\partial \zeta}{\partial x} - \nu_t\left(\frac{\partial^2 U}{\partial x^2} + \frac{\partial^2 U}{\partial y^2}\right) + g\frac{U(U^2+V^2)^{\frac{1}{2}}}{C^2(h+\zeta)} + X = 0 \quad (1)$$

$$\frac{\partial V}{\partial t} + U\frac{\partial V}{\partial x} + V\frac{\partial V}{\partial y} + fU + g\frac{\partial \zeta}{\partial y} - \nu_t\left(\frac{\partial^2 V}{\partial x^2} + \frac{\partial^2 V}{\partial y^2}\right) + g\frac{V(U^2+V^2)^{\frac{1}{2}}}{C^2(h+\zeta)} + Y = 0 \quad (2)$$

$$\frac{\partial \zeta}{\partial t} + \frac{\partial((h+\zeta)U)}{\partial x} + \frac{\partial((h+\zeta)V)}{\partial y} = 0 \quad (3)$$

where:

U = depth-averaged velocity in x direction (m/s)

V	=	depth-averaged velocity in y direction	(m/s)
ζ	=	water elevation relative to the reference plane	(m)
h	=	distance from the bottom to the reference plane	(m)
t	=	time	(s)
X,Y	=	external force components per unit mass	(m/s^2)
f	=	Coriolis parameter	(s^{-1})
g	=	acceleration due to gravity	(m/s^2)
ν_t	=	eddy viscosity coefficient	(m^2/s)
C	=	Chézy coefficient for bottom friction	($m^{\frac{1}{2}}/s$)

Equations 1, 2 and 3 are solved at discrete space increments and discrete time intervals by an implicit finite difference method (References 2,3,4). The model area is schematized by a two-dimensional grid composed of equal square cells. In addition, the system possesses a facility to simulate drying and flooding processes of the tidal flats. The eddy viscosity coefficient ν_t is a constant, the corresponding terms taking care of lateral momentum transfer. At the site of the barrier the flow is dominated by energy losses generated by the rapid acceleration and deceleration of the flow. Local vertical velocities and accelerations are then no longer negligible and the depth-averaged equations, equations 1,2 and 3, are no longer valid. A resistance law is applied here, based on an equation of motion derived from the Bernoulli equation (accelerating flow, see Figure 3):

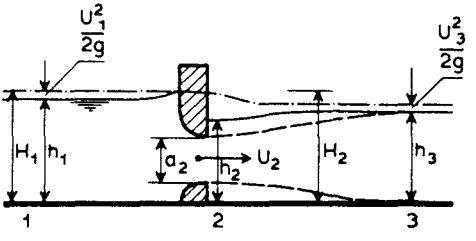

Figure 3. Flow at the Barrier Site.

$$q = a_2\sqrt{2g(H_1 - h_2)} \qquad (4)$$

where:

q	=	discharge per unit length	(m^2/s)
a_2	=	cross section height at Section 2	(m)
g	=	accelaration due to gravity	(m/s^2)
H_1	=	upstream energy level	(m)
h_2	=	waterlevel at Section 2	(m)

In Equation 4, the waterlevel h_2 is replaced by the downstream waterlevel h_3 and a discharge coefficient, μ, is added to compensate

for energy losses caused by the deceleration of the flow. For practical applications the upstream energy level H_1 is replaced by the waterlevel h_1. The inaccuracy of this approximation is small when

$$\frac{U_1^2}{2g} \ll \frac{U_2^2}{2g}$$

U_1 and U_2 are depth-averaged velocities at Section 1 and 2 respectively.

The resulting equation is:

$$q = \mu a_2 \sqrt{2g\,(h_1 - h_3)} \qquad (5)$$

where:

q	= discharge per unit length	(m^2/s)
μ	= discharge coefficient	(-)
a_2	= cross section heigth at section 2	(m)
g	= acceleration due to gravity	(m/s^2)
h_1	= upstream water level	(m)
h_3	= downstream water level	(m)

The discharge coefficient can be obtained from flume tests or from literature. Equation 5 describes a steady state type of flow. For unsteady flow this approach is not precise for the short period around slack water. For most applications this is of minor importance and can be neglected.

Three different methods introducing energy losses at the barrier site into the WAQUA program were applied:

1- Substitution of the long wave eqation by a barrier eqation.
   At the barrier site the long wave equations, Equations 1,2 and 3, are replaced by Equation 5, creating a sort of internal boundary at the barrier site. Both sides of this boundary are coupled by Equation 5.
2- Adapted fixed roughness.
   At the barrier site an adapted fixed value of the Chézy coefficient is calculated by equating the Chézy equation to Equation 5. At the barrier site equations 1, 2 and 3 are solved completely.
3- Dynamically adapted roughness
   This is a mixed version of methods 1 and 2.
   At the barrier site the roughness coefficient is continuously adapted so that the discharge and headloss satisfy Equation 5 for a given value of the discharge coefficient, μ.
   Thus continually a new Chézy value is calculated during the computation.

Methods 1 and 3 make it possible to use different coefficients for different flow directions and different equations for different flow conditions, such as subcritical or supercritical flow.
With Methods 1 and 3 Equation 5 is solved by an explicit method. The solution is found iteratively so that it fits in the results calculated by the implicit WAQUA scheme precisely.

Application of Two-Dimensional Numerical Models to the Storm Surge Barrier in the Eastern Scheldt

In the case of the Eastern Scheldt it is not feasible to use one single model for all purposes. A set of models is therefore used which consists of an overall tidal model and a number of nested detail models (Figure 4).
The main function of the overall model is to provide boundary conditions for the detail models. The overall model covers the entire estuary of the Eastern Scheldt. The model has a length of 65 km and a maximum breadth of 15 km. The grid size is 400 m.
A relatively large detail model describes the mouth of the Eastern Scheldt. This model covers an area 21 km long and 10 km broad. The grid size is 100 m. The model is used to evaluate relatively large scale phenomena such as morphological changes in the tidal channels and on the tidal flats between the main channels (Reference 1).
A set of nested models is used to compute details of the flow pattern in the vicinity of the barrier. This set consists of two models with 90 m grid size and a model area equivalent to 10 x 6 km.One model contains both the northern branches of the estuary, the Hammen and the Schaar, and the other contains the south branch, the Roompot.
Three separate models each with 45 m grid size, are used for the Hammen, the Schaar and the Roompot. The area of these models is equivalent to about 3,5 x 2,5 km. The axis of the 45 m models are orientated so that one axis is parallel to the barrier.
The boundary conditions for the models are a mixture of velocity type and of waterlevel type boundary conditions.

This paper discusses the results of the small detail models, 45 m grid size, in more detail. The parameters used for the calibration of the models are:
v_t, C and μ see Equations 1, 2, 3 and 5. Also the grid size and the timestep are important to the accuracy of the results. The values that were used for these parameters are given below.

- Grid size, $\Delta x = \Delta y$.
  A grid size of 45 m has been selected. 45 m is exactly the distance between the piers of the barrier.
- Time step, Δt
  A time step of 15 s is used to obtain an accurate computed flow pattern.
- Eddy viscosity coefficient, v_t
  For an correct reproduction of the velocity gradients and eddies downstream of the barrier the value of v_t had to be 2 m^2/s has been used. The numercal viscosity is negligible compared with this value of v_t.
- Roughness parameter, C
  A Chézy value is used which corresponds to a fixed value of the Manning coefficient n = 0.0262 $m^{1/3}/s$. The value of the roughness parameters is of minor importance in the small detail models. It determines the overall tidal motion.
- Discharge coefficient, μ
  The discharge coefficients are derived from steady state flume tests

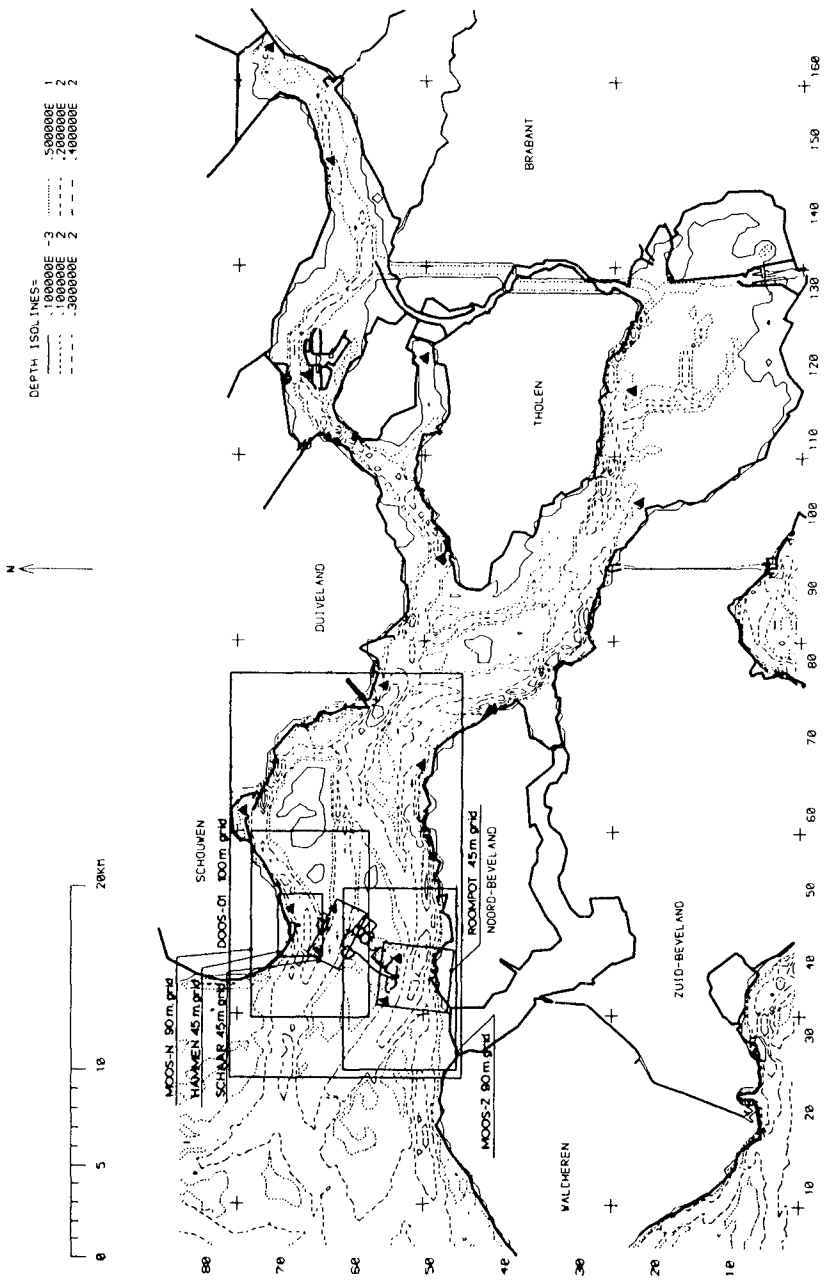

Figure 4. Lay-Out of the Numerical Models

for a 45 m section; 45 m is the distance between the piers.
The coefficients were determined for both flow directions for a number of different construction stages and locations.

Results

The construction of the barrier in the Eastern Scheldt is accompanied by an extensive hydraulic measurement campaign.
The hydraulically most interesting phase is the installation of the sill beams, Figure 2. These beams reduce the flow area between the piers abruptly. This causes an abrupt change of the flow pattern. Installation of the sill beams was a crucial phase for:
- the floating construction equipment
- morphological changes
- the stability of the bed protection near the barrier
- the development of scour holes at the boundaries of the bed protection

For 15 construction stages extensive field data are available. These data consist of waterlevels, head differences, discharges, flow velocities and flow directions upstream, downstream and at the site of the barrier. Special equipment was developed to obtain these field data.
The tidal flow has been computed by the WAQUA system for all these construction stages and was compared with the observed flow.
General conclusions on the three numerical methods used to introduce energy losses at the barrier site are:
- Method 1: Substitution of the long wave equation by a barrier equation.
  The flow pattern downstream the barrier, which is with this method an internal boundary in the model, is disturbed. (compare Figure 11 with Figure 12) The computed total discharge and head difference agree well with observations.
- Method 2: Adapted fixed roughness.
  The downstream flow pattern is correct; the barrier is no longer an internal boundary in the model. A disadvantage is the general approximation of the resistance and, because an averaged roughness is used, it is not possible to account for the influence of different flow directions and different flow conditions. This results in a less accurate reproduction of the discharge and the head difference than Method 1.
- Method 3: Dynamically adapted roughness.
  This proves to be the best solution and the disadvantages of Method 1 as well as of Method 2 are avoided.

For this study the results of a scale model of the mouth of the Eastern Scheldt are available for comparison. This model is an undistorted steady state model with scale 1:80 of approximately the same area as the 45 m grid size numerical detail models.The indications are that the depth-averaged velocities computed with Method 3 agree as well with field data as depth-averaged velocities obtained from the scale model.
The results of the computations are discussed below in more detail for

two situations, see Figure 5:

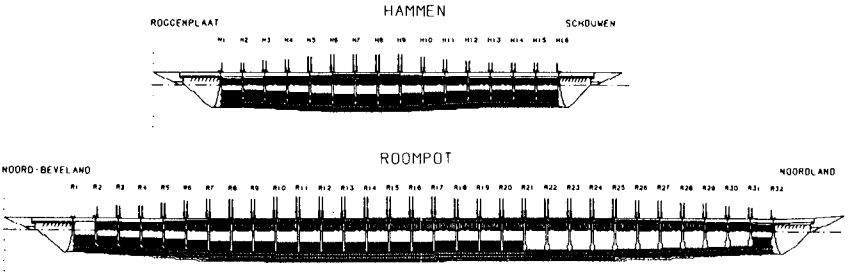

Figure 5. Geometry of the Barrier Under Construction in the Roompot and the Hammen.

- The Roompot: a situation in wchich 21 of the 31 sill beams have been installed. Ebb flow.
- The Hammen: a situation in which all 15 sill beams have been installed. Flood flow.

In these situations the flow is dominated by two-dimensional effects:

- The Roompot: At the transition between the rubble sill and the concrete sill beams there is a sharp discontinuity in the barrier: In the flow opening and in the discharge coefficient. Downstream this discontinuity a mixing zone develops with a sharp velocity gradient.
- The Hammen: Downstream of the barrier a large eddy is formed.

The results presented below have been computed with Method 2: Adapted fixed roughness. Except for one example which shows the effect of Method 1: Substitution of the long wave equation by a barrier equation. On basis of these results it was decided to develop and program Method 3: Dynamically adapted roughness. The initial tests showed that Method 3 is very promising.

The results for both the Roompot and Hammen flow situations are presented in Figures 6 through 13:

- The computed flow pattern in the Roompot has been plotted in Figure 6 for maximum ebb flow.
- In Figure 7 the observed and computed transport rate in the Roompot are given for both ebb flow and flood flow.
- The observed and computed flow velocities and flow directions at 350 m upstream and 630 m downstream of the barrier are presented in Figures 8 and 9 (maximum ebb flow).
  The transport rate per gate opening has also been plotted in Figure 8.
- The transport rate in the Hammen is presented in Figure 10
- In Figure 11 the computed flow pattern in the Hammen during maximum flood flow has been plotted.
- The flow pattern in the Hammen computed with Method 1 (barrier equation substituted) has been plotted in Figure 12; to be compared with Figure 11.

- Figure 13 finally gives the observed and computed velocities at 400 m upstream and 630 m downstream of the barrier and the transport rate per barrier gate (maximum flood flow). Additioned to the field data and computed velocities the observed flow velocities in the scale model are given 630 m downstream of the barrier.

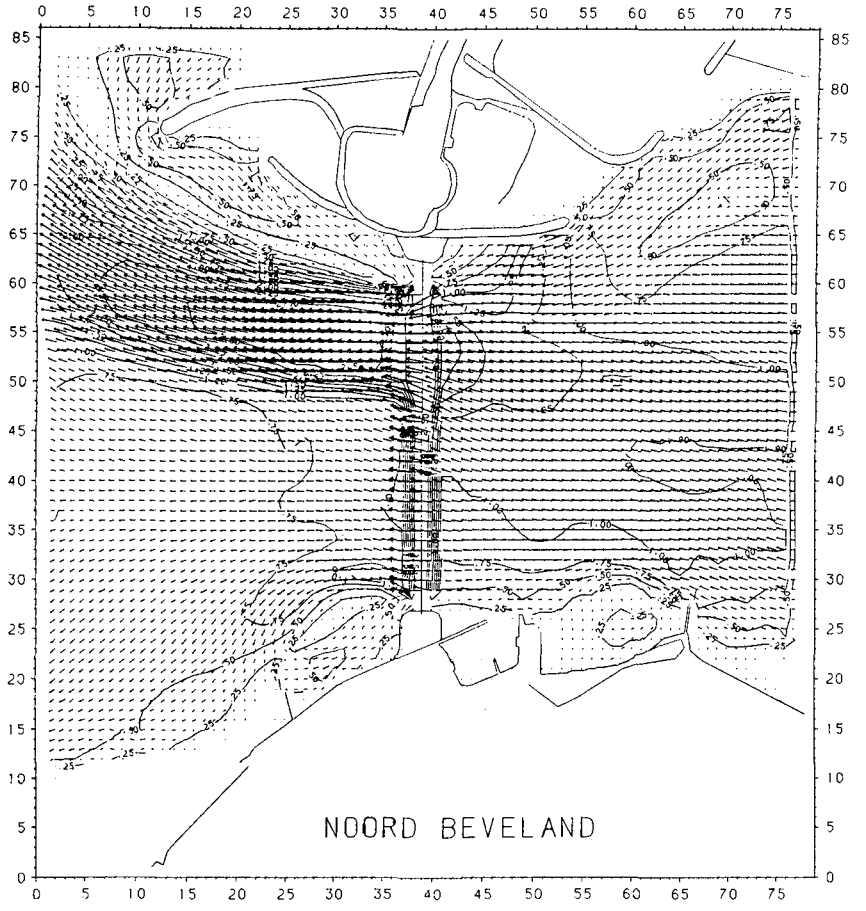

Figure 6. Roompot, Flow Pattern Maximum Ebb Flow.

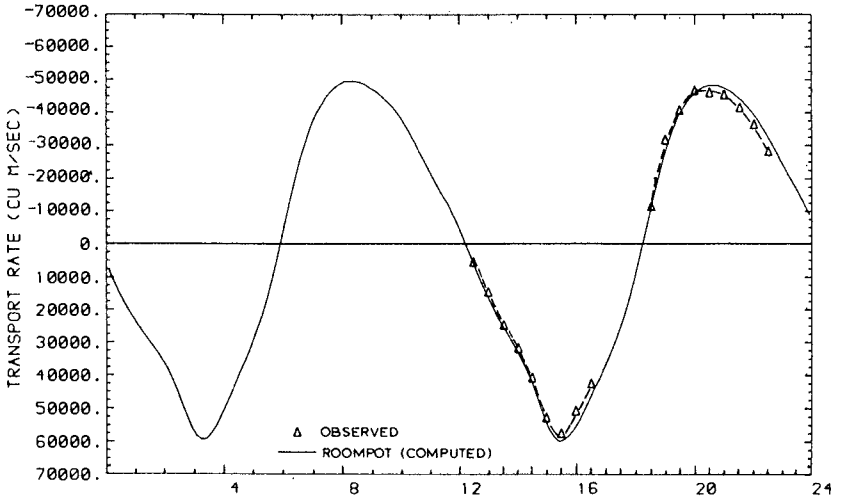

Figure 7. Roompot, Transport Rate.

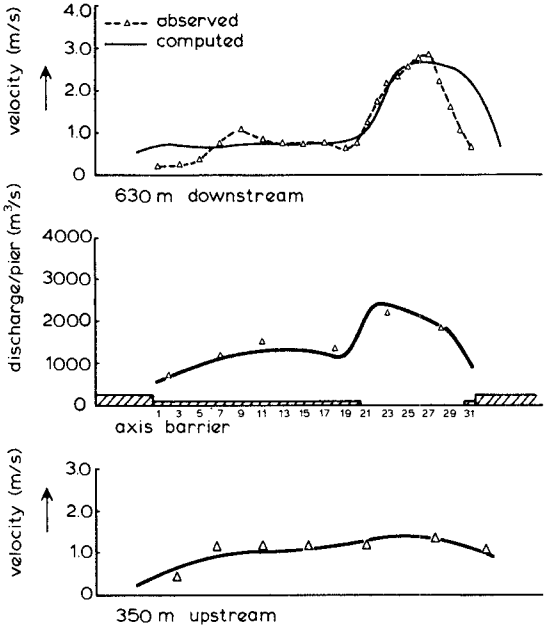

Figure 8. Roompot, Flow Velocities Maximum Ebb Flow.

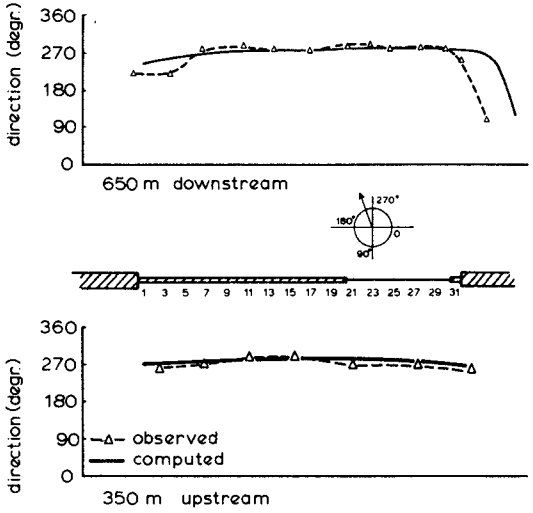

Figure 9. Roompot, Flow Directions Maximum Ebb Flow.

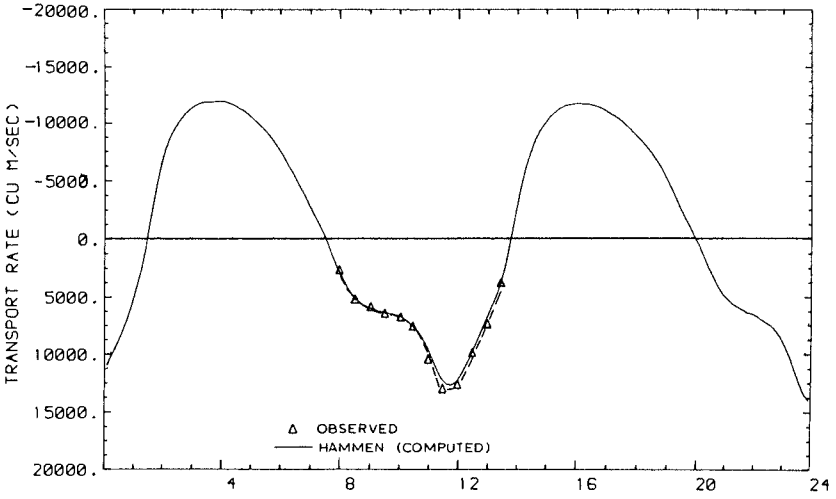

Figure 10. Hammen, Transport Rate.

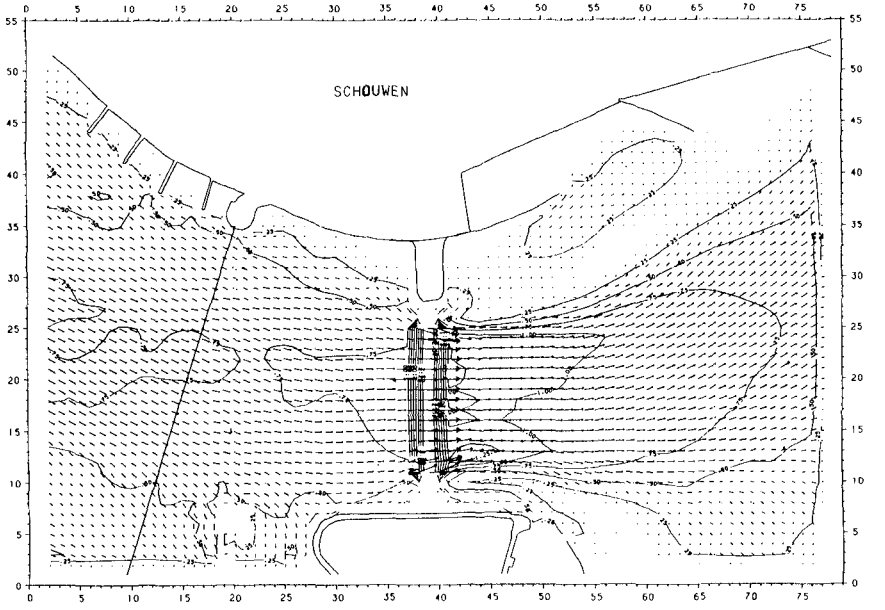

Figure 11. Hammen, Flow Pattern Maximum Flood Flow (Method 2).

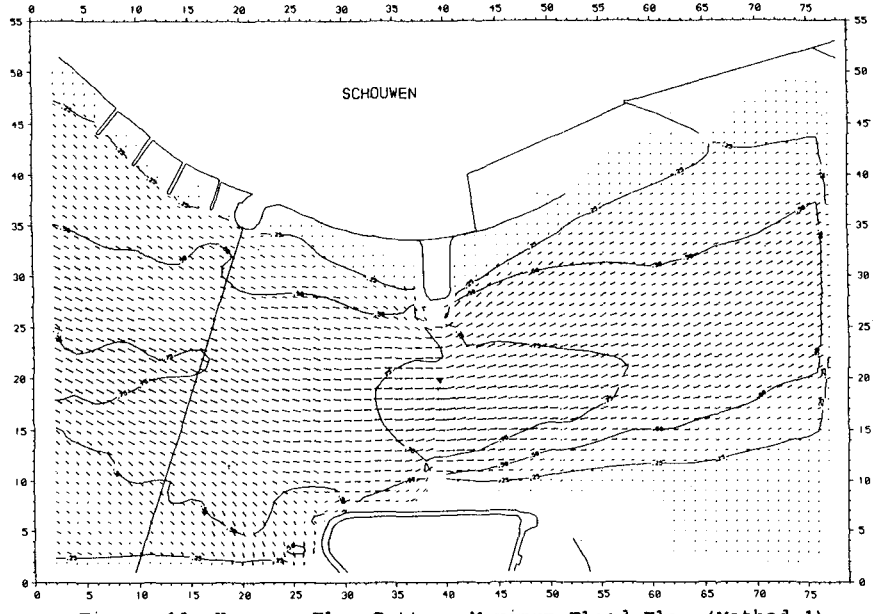

Figure 12. Hammen, Flow Pattern Maximum Flood Flow (Method 1).

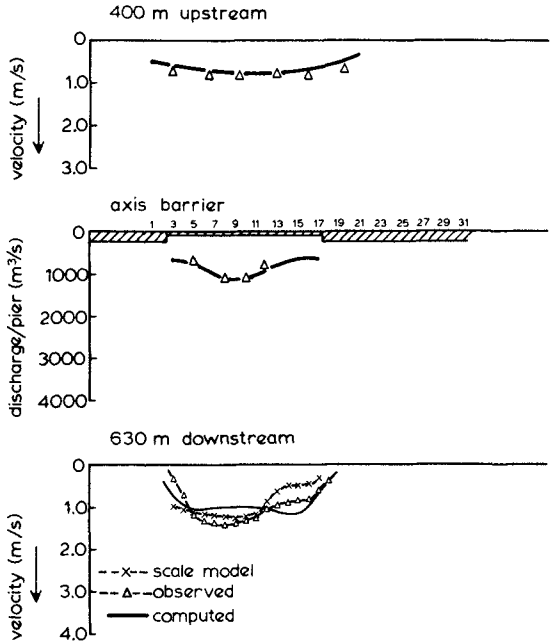

Figure 13. Hammen, Flow Velocities Maximum Flood Flow.

Conclusions

Comparison of the results computed by the WAQUA system with the field data shows that in general the agreement between WAQUA and the field data is good:

- Computed transport rates agree well with field data
- The agreement between the computed flow patterns and the field data is very good upstream of the barrier and at the site of the barrier
- Downstream the barrier the agreement between the computations and field data is acceptable. The computed maximum velocities and the steepness of the velocity gradients are correct. The locations where these occur however are not accurate. For engineering applications, for example calculation of the stability of bed protection or calculations of scour holes, this difference is acceptable.

The quality of the depth-averaged flow pattern computed by WAQUA is as accurate as that obtained from a large physical scale model. The method to deal with the energy losses at the barrier site greatly influenced the quality of the results.
This paper demonstrates that a method based on a local adaptation of the roughness is an accurate way of dealing with these local energy losses.

References

1. Bliek, A.J., Klatter, H.E., Konter, J.L.M., van der Meulen, T. "Short Cut Channels in Tidal Estuaries", proceedings, Third International Symposium on River Sedimentation, Jackson, Mississippi, USA, 1986.
2. Leendertse, J.J. "A Water Quality Simulation Model for Well Mixed Estuaries and Coastal Seas", Principles of Computation, Vol. I, RM-6230-RC, Rand. Corp., Santa Monica, USA, 1970.
3. Stelling, G.S., "On the Construction of Computional Methods for Shallow Water Flow Problems", Ph.D. thesis Delft University of Technology, Delft, The Netherlands, 1983. Also appeared as Rijkswaterstaat Communications, No. 35, The Hague, The Netherlands, 1984.
4. Stelling, G.S., Wiersma, A.K., Willemse, J.B.T.M., "Practical Aspects of Accurate Tidal Computations", Journal of Hydraulic Engineering, Vol 112, No. 9, September 1986.

CHAPTER 144

PREDICTION OF WAVE RUNUP AND RIPRAP STABILITY

By Nobuhisa Kobayashi[1], M.ASCE and Jeffrey H. Greenwald[2], A.M.ASCE

ABSTRACT: A numerical model has been developed to predict the wave motion on a rough impermeable slope and the hydraulic stability and sliding motion of armor units under the action of a specified normally-incident wave train. The developed numerical model has been compared with riprap test results to calibrate and verify the model.

INTRODUCTION

The present design practices of coastal structures protected with armor units such as breakwaters and revetments are based on hydraulic model tests and empirical formulas although our quantitative understanding of the problem has been improving steadily (4,23,26,29,30). Further improvements of the present design practices will require reliable numerical models which can complement hydraulic model tests since large-scale model tests with minimum scale effects are expensive and time-consuming. Furthermore, some of the important quantities such as the spatial variation of the stability of armor units are very difficult to measure in detail.

As a first attempt, Kobayashi and Jacobs (8) developed a simple analytical model to predict the flow characteristics in the downrush of regular waves on a uniform slope and the critical condition for initiation of movement of armor units. This simple model gives a physical insight into the mechanics of armor stability under the action of surging breakers but is not reliable enough to be applied to actual design problems.

In order to improve the analytical model, Kobayashi et al. (12,13, 14) have developed a numerical model to predict the flow characteristics in the uprush and downrush on a rough impermeable slope and the resulting hydraulic stability and sliding motion of armor units under the action of a normally-incident wave train. Comparison with available riprap test data (1,10) has indicated that the numerical model can predict wave runup, rundown and reflection as well as zero-damage wave heights for uniform and composite riprap slopes if some of the input parameters required for the numerical model are calibrated.

In order to calibrate and verify the developed numerical model more

---

[1]Assoc. Prof., Dept. of Civil Engrg., Univ. of Delaware, Newark, DE 19716.

[2]Grad. Student, Dept. of Civil Engrg., Univ. of Delaware, Newark, DE 19716; presently, Research Staff, Center of Naval Analysis, Alexandria, VA 22302.

extensively, Kobayashi and Greenwald (15) have conducted eight test runs in a wave tank using a 1:3 glued gravel slope with an impermeable base. For each run with the specified incident wave train generated in a burst, measurements have been made of the free surface oscillation at the toe of the slope, the waterline oscillation on the slope, the temporal variations of dynamic pressures on the base of the slope and the displacements of loose gravel units placed on the glued gravel slope. The calibrated numerical model has been shown to be capable of predicting the measured temporal variations of the hydrodynamic quantities and the measured spatial variations of the amount of the riprap movement.

In this paper the mathematical and numerical backgrounds of the numerical model developed by Kobayashi et al. (12,13,14) are critically reviewed to indicate possible future improvements of the numerical model. Then, the riprap experiment conducted for calibrating and verifying the numerical model is described together with the test results which have not been presented by Kobayashi and Greenwald (15). Furthermore, additional experiments required for further calibration and verification of the numerical model are discussed in light of the limitations of the experiment conducted by Kobayashi and Greenwald (15).

WAVE MOTION ON A ROUGH SLOPE

Wave uprush and downrush on the seaward slope of a coastal structure protected with armor units are similar to wave motions in the swash zone on a beach although the structural slope is normally steeper than the beach slope. It is noted that the surf similarity parameter (3) is widely used to describe the gross wave characteristics on the structural and beach slopes. Use may hence be made of the hydrodynamic models developed for breaking waves on beaches which have been investigated more extensively as reviewed by Peregrine (21). The finite-amplitude shallow-water equations including the effects of bottom friction are suited for predicting the movement of the waterline on the rough slope of the coastal structure if the slope is relatively mild and impermeable. The waterline movement on the slope determines wave runup and rundown and affects the hydraulic stability of armor units as shown by the simple analytical model developed by Kobayashi et al. (8,11). However, the finite-amplitude, shallow-water equations based on the assumption of hydrostatic pressure are not capable of describing detailed two-dimensional behavior of overturning waves (17).

Limiting to the case of a normally-incident wave train on the rough impermeable slope shown in Fig. 1, the finite-amplitude, shallow-water equations including the effects of bottom friction may be written as

$$\frac{\partial h'}{\partial t'} + \frac{\partial}{\partial x'}(h'u') = 0 \tag{1}$$

$$\frac{\partial}{\partial t'}(h'u') + \frac{\partial}{\partial x'}(h'u'^2) = -gh'\frac{\partial \eta'}{\partial x'} - \frac{\tau_b'}{\rho} \tag{2}$$

in which t' = time, x' = horizontal coordinate at the still water level (SWL) which is taken to be positive in the landward direction

with $x' = 0$ at the toe of the slope, h' = water depth below the free surface, u' = depth-averaged horizontal velocity, g = gravitational acceleration, η' = vertical displacement of the free surface relative to SWL, τ_b' = bottom shear stress, and ρ = fluid density which is assumed constant neglecting the effects of air entrainment (5). The bottom shear stress may be expressed as

$$\tau_b' = \frac{1}{2} \rho f' |u'| u' \tag{3}$$

where f' = friction factor associated with the rough impermeable slope which is simply assumed constant. It should be noted that f' will depend on h' if Manning formula is used to express τ_b' (18,19). The empirical formula proposed by Madsen and White (16) has been found satisfactory in estimating the constant value of f' for riprap slopes although additional calibration may be required (13,15).

If the permeability of the underlayer below armor units is not negligible, the flow over the rough permeable bottom and the flow in the permeable underlayer are coupled through the mass and momentum fluxes between these two flow regions. Kobayashi (11) formulated this coupled problem and performed an order-of-magnitude analysis to evaluate the degree of the effects of the permeable underlayer. On the other hand, Hannoura et al. (5) analyzed the flow inside a permeable breakwater using the measured pressure on the rough permeable slope as input. Because of the assumption of the impermeable underlayer, the present numerical model is not applicable to permeable breakwaters such as reef type breakwaters (2).

Denoting the characteristic period and height associated with the normally-incident wave train by T' and H', respectively, the following dimensionless variables are introduced

$$t = \frac{t'}{T'} \quad , \quad x = \frac{x'}{T'\sqrt{gH'}} \quad , \quad u = \frac{u'}{\sqrt{gH'}} \tag{4}$$

$$z = \frac{z'}{H'} \quad , \quad h = \frac{h'}{H'} \quad , \quad \eta = \frac{\eta'}{H'} \quad , \quad d_t = \frac{d_t'}{H'} \tag{5}$$

in which z' = vertical coordinate which is taken to be positive upward with $z' = 0$ at SWL as shown in Fig. 1, and d_t' = water depth below SWL where the incident wave train may be specified conveniently. Limiting to the case where the incident wave train is well-behaved without any

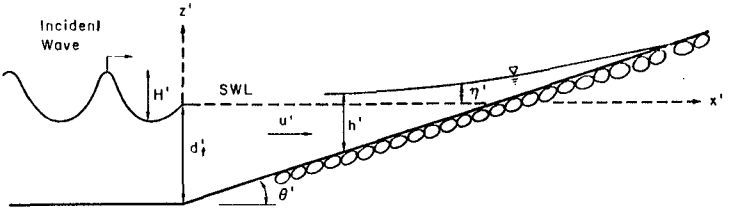

Fig. 1 - Normally-Incident Wave Train on Rough Slope

breaking at the toe of the slope, d'_t is taken to be the water depth below SWL at the toe of the slope as shown in Fig. 1. Substitution of Eqs. 3-5 into Eqs. 1 and 2 yields

$$\frac{\partial h}{\partial t} + \frac{\partial}{\partial x}(hu) = 0 \tag{6}$$

$$\frac{\partial}{\partial t}(hu) + \frac{\partial}{\partial x}\left(hu^2 + \frac{h^2}{2}\right) = -\theta h - f|u|u \tag{7}$$

with

$$f = \frac{1}{2}\sigma f' \quad , \quad \sigma = T'\sqrt{\frac{g}{H'}} \tag{8}$$

$$\theta = \sqrt{2\pi}\,\xi \quad , \quad \xi = \frac{1}{\sqrt{2\pi}}\sigma \tan\theta' \tag{9}$$

in which f = normalized friction factor, σ = dimensionless parameter related to wave steepness, θ = normalized gradient of the slope, and ξ = local surf similarity parameter with θ' = local angle of the slope. For the regular wave incident on a uniform slope of constant θ' as shown in Fig. 1, ξ defined in Eq. 9 reduces to the surf similarity parameter introduced by Battjes (3). The numerical model can easily be applied to examine the effects of the slope geometry on wave runup and armor stability by varying the local slope angle θ' along the slope. Composite slopes approximating the characteristic S-geometry of matured breakwaters have been shown to increase armor stability and reduce wave runup as compared to uniform slopes (4,9,10).

Eqs. 6 and 7 are solved numerically in the time domain to compute h and u as a function of t and x for given θ (i.e., ξ), f, initial and boundary conditions. The initial conditions for h and u are taken such that h = normalized depth below SWL (i.e., η=0) and u=0 at t=0 for the region $x \geq 0$ on the rough slope, corresponding to the conditions before the arrival of the incident wave train at the toe of the slope. In general, the computation in the time domain can incorporate nonlinear effects easily relative to the computation in the frequency domain. However, for the incident regular wave train, the time-domain computation starting from the assumed initial conditions at t=0 needs to be continued until the state of periodicity is reached. For the computation made by Kobayashi et al. (12,13,14) the transient duration has been limited to the relatively short duration $0 \leq t \lesssim 5$ where the normalized period of the incident regular wave train is unity. Furthermore, the time-domain computation will become expensive if the number of individual waves in an incident irregular wave train becomes large.

The landward boundary on the rough slope is located at the moving waterline where the water depth h is essentially zero, assuming that no wave overtopping occurs. However, it is desirable to generalize this boundary condition so as to allow wave overtopping over the specified crest geometry of the structure since some wave overtopping is normally accepted in designing the crest geometry (29). If wave overtopping is to be allowed, it will be necessary to apply a discharge relationship at the point of overflow by assuming the similarity between wave overtopping over the crest of the coastal structure and overflow over

a weir in open channel flow (18).

At the seaward boundary located at x=0 it is normally required for practical applications to specify the incident waves as input and estimate the reflected waves originating from the region x≥0 on the rough slope. This implicitly assumes that the reflected waves will not modify the specified incident waves. In order to derive an appropriate seaward boundary condition, Eqs. 6 and 7 are expressed in the corresponding characteristic forms (13). Then, the equation for the seaward-advancing characteristics originating from the region x≥0 is used to obtain a relationship for the values of u and h at x=0. Since an additional relationship is required to find u and h at x=0, the normalized total water depth at the seaward boundary is expressed as

$$h = d_t + \eta_i(t) + \eta_r(t) \qquad \text{at } x = 0 \tag{10}$$

in which η_i and η_r are the free surface variations normalized by H′ at x=0 due to the incident and reflected waves, respectively. The superposition of η_i and η_r at x=0 implicitly assumes that nonlinear interaction between the incident and reflected waves is negligible in the vicinity of the seaward boundary. The incident wave train at x=0 is specified by prescribing the variation of $\eta_i(t)$ with respect to t≥0. $\eta_r(t)$ may be computed approximately from the value of the seaward advancing characteristic variable at x=0 using the relationship between u and η applicable for linear long waves. This approximation is not crucial as long as wave reflection from the rough slope is small and η_r is negligible in Eq. 10. The practical difficulty associated with the seaward boundary condition is that the design incident waves are normally specified in terms of the wave energy spectrum or the significant wave height and period rather than the temporal variation of the free surface associated with the incident wave train which is directly related to the sequence and group of individual waves in an incident irregular wave train. Furthermore, for the incident regular wave train with given H′ and T′ in the water depth d_t', $\eta_i(t)$ needs to be estimated using an appropriate wave theory. To specify $\eta_i(t)$ at x=0 for given H′, T′ and d_t', Kobayashi et al. (12,13,14) have used cnoidal or Stokes wave theory although these wave theories are not really consistent with the finite-amplitude shallow-water equations. If cnoidal wave theory is applied, it is more consistent to use Boussinesq equations (27). In fact, Pedersen and Gjevik (20) developed a numerical model based on Boussinesq equations for computing runup of a non-breaking solitary wave.

For the specified initial and boundary conditions Eqs. 6 and 7 are solved using an explicit dissipative Lax-Wendroff finite-difference method developed by Peregrine and co-workers (6,7,18,19) for simulating spilling-type breakers and resulting swash oscillations on gentle slopes. In this numerical method, the front of a breaking wave becomes almost vertical without any separate treatment of the wave front but an artificial dissipative term needs to be included to reduce numerical oscillations in the vicinity of the front caused by discretization. Use is made of a finite-difference space and time grid of constant space size Δx and constant time step Δt in which the values of Δx and Δt are determined considering the numerical stability criterion of the

adopted explicit method and the desired spatial and temporal accuracies. Svendsen and Madsen (28) showed that this numerical dissipation would not be required if the effects of turbulence generated by wave breaking were included in the numerical model. Nevertheless, the explicit dissipative Lax-Wendroff finite-difference method has been tested and is relatively easy to apply for simulating the moving waterline on the relatively mild slope where the present computation based on Eqs. 1 and 2 may be appropriate if $(\tan\theta')^2 \ll 1$. The major contribution by Peregrine and co-workers (6,7,18,19) is the development of the predictor-corrector-smoothing procedure dealing with the moving waterline although the details of this procedure are somewhat intuitive and may still be improved (13). As a whole, the adopted numerical method has been found to be very satisfactory although the CPU time for a typical case using 200 nodal points and 2,000 time steps per wave period is approximately 30 sec per wave period (13).

HYDRAULIC STABILITY AND MOVEMENT OF ARMOR UNITS

The finite-difference solution of Eqs. 6 and 7 yields the values of u and h at each of the space grid points along the slope at each time level starting from t=0. In order to compute the normalized horizontal water particle acceleration, du/dt, at each space grid point using the computed values of u and h at given time level, Eq. 7 is rewritten as

$$\frac{du}{dt} = \frac{\partial u}{\partial t} + u\frac{\partial u}{\partial x} = -\frac{\partial h}{\partial x} - \theta - \frac{f|u|u}{h} \tag{11}$$

in which use is made of a central-difference approximation of $\partial h/\partial x$. The computed values of u and du/dt at each space grid point at given time level are then used to estimate the hydrodynamic forces acting on an individual armor unit on the rough slope.

The hydraulic stability analysis of stationary armor units performed by Kobayashi et al. (12,14) is similar to the simplified analysis of Kobayashi and Jacobs (8) which was limited to the downrush period only. Fig. 2 shows the forces acting on a stationary armor unit on the 1:cotθ' slope. Limiting to the case of $(\tan\theta')^2 \ll 1$, it is assumed that the drag force F_D and the inertia force F_I act upward or downward parallel to the slope, whereas the lift force F_L acts upward normal to the slope since the flow tends to be parallel to the slope as shown in Fig. 2. On the other hand, the submerged weight W_S acts

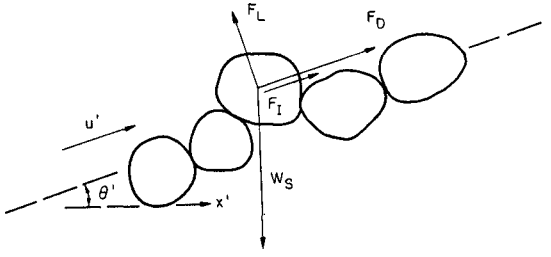

Fig. 2 - Forces Acting on a Stationary Armor Unit

vertically downward. The expressions for F_D, F_I, F_L and W_S are given by Kobayashi and Jacobs (8) except that F_D is proportional to $|u'|u'$ in this analysis for both uprush and downrush periods. The expressions of the hydrodynamic forces F_D, F_I and F_L include the drag, inertia and lift coefficients denoted by C_D, C_M and C_L, respectively. These coefficients need to be determined experimentally on the basis of the simultaneous measurements of the fluid velocity and acceleration and the resulting hydrodynamic forces which will be extremely difficult for an armor unit located on the rough slope under the action of breaking waves. Furthermore, the temporal variations of the hydrodynamic forces can be more complicated than those based on the adopted expressions, judging from the simpler measurements of the lift force on a single sphere near a plane wall in well-behaved oscillatory flow reported by Rosenthal and Sleath (22). Tentatively, Kobayashi et al. (12,14,15) have assumed that for riprap units $C_D \simeq 0.5$, $C_M \simeq 1.5$ and $C_L = 0.18$ -0.4 in which C_L is varied in this range on the basis of available scattered data on C_L summarized by Sleath (25).

The stability condition for a stationary armor unit against downward or upward sliding or rolling are expressed as

$$|F_D + F_I - W_S \sin\theta'| \leq (W_S \cos\theta' - F_L) \tan\phi \tag{12}$$

in which ϕ = frictional angle of the armor units and $\phi \simeq 50°$ for angular riprap units (8,12,14,15). Limiting to the case of $C_D > (C_L \tan\phi)$, Eq. 12 can be rearranged as

$$N_s = \frac{H'}{s-1}\left(\frac{W'}{\rho g s}\right)^{-1/3} \leq N_R\,(t,x) \tag{13}$$

where N_s = stability number, s = specific density of the armor unit, W' = weight of the armor unit, ρ = fluid density, and $N_R(t,x)$ = dimensionless function involving u and du/dt which depends on t and x (12,14). Eq. 11 indicates that du/dt may become very large at the wave front where h decreases rapidly with x. The computed fluid accelerations have been found to be as large as 4g which may not be unrealistic in comparison with the computed accelerations as large as 5g or 6g beneath overturning wave crests obtained by New et al. (17). Nevertheless, it has been found necessary to impose the physical bounds, $a_{min} \leq (du'/dt')/g \leq a_{max}$, which can be rewritten as

$$a_{min}\,\sigma \leq du/dt \leq a_{max}\,\sigma \tag{14}$$

in which the values of the dimensionless parameters a_{min} and a_{max} are chosen such that Eq. 12 is satisfied for u=0 for which $F_D = F_L = 0$. The lower bound in Eq. 14 may not be required since the computed values of du/dt have turned out to be greater than $a_{min}\,\sigma$ in which $a_{min} = -0.8$ has been used (14,15). On the other hand, use has been made of $a_{max} = 1.0$ in the stability computation made by Kobayashi et al. (14,15) on the basis of the experimental results given by Sawaragi et al. (23). This physical upper bound is related to the uncertainty of the computed inertia force using constant C_M at the point of wave breaking as well as to the uncertainty of the response time of an armor unit under the action of the large fluid acceleration of a very short duration.

The stability condition for a stationary armor unit against lifting can be shown to be satisfied as long as Eqs. 13 and 14 are satisfied (14). Consequently, it is sufficient to consider the stability against sliding or rolling for establishing the criterion for initiation of armor movement. For the regular incident wave train specified at x=0, it may be sufficient to consider one wave period after the periodicity of the armor stability is established. The local stability number for initiation of armor movement at given location x along the slope is hence defined as

$$N_{sx}(x) = \min[N_R(t,x) \,|\, t_p \le t \le (t_p + 1)] \qquad (15)$$

in which t_p = normalized time when the periodicity of $N_R(t,x)$ with respect to t is established, and the normalized period of the incident wave is unity. Eq. 15 implies that $N_{sx}(x)$ for given x is the minimum value of $N_R(t,x)$ during one wave period after the establishment of the periodicity. The critical stability number N_{sc} for initiation of armor movement is the minimum value of the local stability number $N_{sx}(x)$ which varies along the slope.

The value of the stability number N_s defined in Eq. 13 can be calculated for specified incident wave and armor unit characteristics. The armor units located in the region of $N_s > N_{sx}(x)$ will slide or roll downwards or upwards along the slope. However, the amount of armor movement needs to be predicted to determine whether a specific moving unit will move in place or be dislodged out of place. Wiberg and Smith (31) developed a detailed theoretical model for saltating sediment particles in uni-directional flow. To simplify the analysis for unsteady flow, moving armor units have been assumed to slide essentially parallel to a rough slope without rolling. The displacement X_a' of a sliding armor unit has then been computed by solving the simplified equation of motion for an individual armor unit identified by its initial location on the slope at time t=0 (14,15). This computation is based on a Lagrangian approach in which each sliding unit of its representative length d' is followed starting from its initial location at t=0 and its subsequent location at each time level is found using the computed normalized displacement $X_a=(X_a'/d')$. As a result, X_a depends on t for each sliding unit identified by its initial location on the slope. The computed normalized displacement may be regarded as a statistical average since the present analysis does not account for the effects of the irregular rough surface on the armor movement explicitly. Moreover, a significant extension of the present analysis will be required to predict the temporal change of the slope profile and the resulting breakwater damage which needs to be considered for the practical design of breakwaters (26). Since the degree of the breakwater damage depends on the wave characteristics during an entire storm such as the number of waves (30), the present numerical model will also need to be simplified to simulate the breakwater behavior during an entire storm.

COMPARISON WITH EXPERIMENTS

Kobayashi et al. (12,13,14) have compared the numerical model with the large-scale riprap tests of Ahrens (1) for uniform slopes with $\cot\theta'$=2.5, 3.5 and 5 in which incident wave trains were generated in a burst and measurements were made of wave runup and zero-damage wave heights. Comparison has also been made with the similar but small-scale riprap tests for composite and 1:3 uniform slopes conducted by Kobayashi and Jacobs (10) who measured wave runup, rundown and zero-damage wave heights. The computed wave runup and rundown using the friction factor f'=0.3 have shown to agree with the visually-measured wave runup and rundown. The numerical model with the adopted seaward boundary condition has also predicted the observed increase of the reflection coefficient with the surf similarity parameter (24). Furthermore, the computed critical stability number for initiation of riprap movement has been shown to be in good agreement with the measured zero-damage stability number if the lift coefficient C_L is calibrated in the range C_L=0.18-0.4 and the upper bound of the computed fluid acceleration is imposed.

Kobayashi and Greenwald (15) have conducted additional riprap tests in a wave tank which is 36 m long, 2.5 m wide and 1.5 m deep. A piston-type wavemaker controlled by a function generator or a computer is used to generate incident regular wave trains in a burst which are measured using resistance wire wave gages with a wave-absorber beach in the tank. The water depth in the tank is kept constant and d'_t=0.4 m in these tests. A 1:3 glued gravel slope with an impermeable base is installed in the tank and exposed to the same incident wave trains. The incident wave conditions considered for eight test runs correspond to plunging, collapsing and surging breakers. For each run with given incident wave train and slope characteristics, measurements are made of the free surface oscillation at the toe of the 1:3 slope, the oscillation of the waterline on the slope, wave pressures on the base of the slope and the displacements of loose gravel units placed on the glued gravel slope. These measured quantities are normalized and compared with the computed normalized quantities for each run. Kobayashi and Greenwald (15) have presented the summary of the comparisons and the detailed results for Runs 2 and 7 which have been selected as typical runs involving plunging and surging breakers, respectively. In the following, the compared results for Run 4 are presented as a typical run for collapsing breakers.

For Run 4 the surf similarity parameter ξ=3.1, the normalized water depth at the toe of the slope d_t=5.6 and the dimensionless parameter related to wave steepness σ=24. Use is made of the friction factor f'=0.1 after comparing the measured oscillation of the waterline with the computed results using f'=0.1 and 0.2. Fig. 3 shows the normalized measured oscillation $\eta_i(t)$ for the incident wave train specified as input for the numerical computation. Fig. 3 also shows the computed oscillation $\eta_r(t)$ at the toe of the slope associated with the normalized reflected wave train. Fig. 4 shows the comparison between the measured and computed free surface oscillation $\eta_t(t)$ at the toe of the 1:3 gravel slope in which the computed oscillation $\eta_t(t)$ is the sum of $\eta_i(t)$ and $\eta_r(t)$ shown in Fig. 3. Fig. 4 indicates

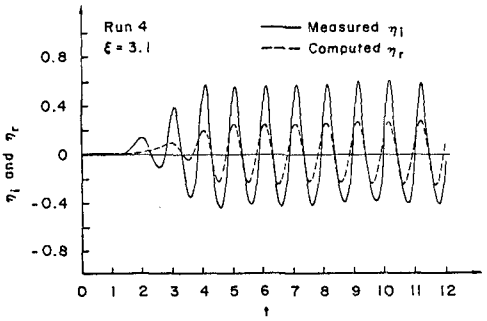

Fig. 3 - Incident and Reflected Wave Trains

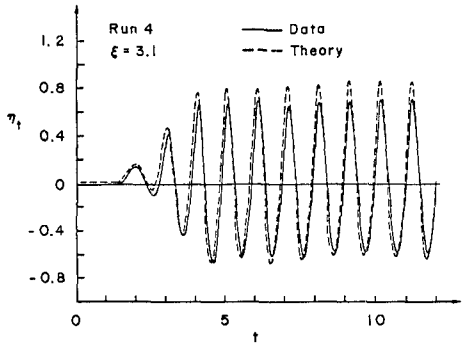

Fig. 4 - Measured and Computed Free Surface Oscillations

appropriateness of the seaward boundary condition used in the numerical model. Fig. 5 shows the comparison of the measured and computed oscillations $z_w(t)$ of the waterline on the 1:3 gravel slope expressed in terms of its vertical elevation relative to SWL normalized by the incident wave height H'. On the other hand, Fig. 6 shows the comparison of the measured and computed dynamic pressure variations at the depth d'=10 cm below SWL expressed in terms of $\eta_p(t) = [p'/(\rho g H')]$ with $p' \approx$ measured dynamic pressure excluding the hydrostatic pressure below SWL. In summary, the agreements between the measured and computed hydrodynamic quantities are similar to those shown in Figs. 4 and 5 but the agreements for η_p are poor for Runs 3 and 4 corresponding to collapsing breakers. The assumption of hydrostatic pressure used in Eq. 2 may not be appropriate at the particular location of the pressure measurement for Runs 3 and 4.

The additional input parameters required for the computation of the hydraulic stability and movement of armor units have been summarized by Kobayashi and Greenwald (15). The lift coefficient C_L alone has been calibrated by trying C_L=0.3 first and then C_L=0.18 or 0.4 if necessary. For Run 4 the lift coefficient C_L=0.3 and the stability number N_s=2.2.

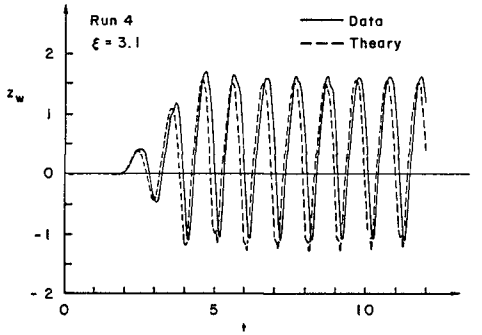

Fig. 5 - Measured and Computed Waterline Oscillations

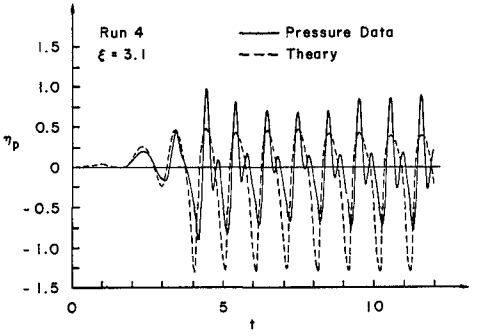

Fig. 6 - Measured and Computed Dynamic Pressure Variations at d'_p = 10 cm

Fig. 7 shows the computed variation of the local stability number N_{sx} defined by Eq. 15 as a function of the normalized vertical location z

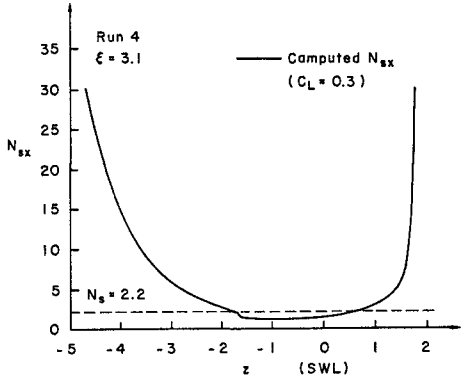

Fig. 7 - Computed Variation of Local Stability Number along 1:3 Slope

relative to SWL along the 1:3 gravel slope. The wave action on the slope is limited in the range $-d_t \leq z \leq R$ where R = computed upper limit reached by the uprushing water above SWL. Loose gravel units placed in the region where $N_s > N_{sx}$ are predicted to move. Fig. 8 shows the comparison between the measured displacements of loose gravel units normalized by the representative length of the units and the computed normalized displacement X_a at the end of the specified incident wave train. The measured and computed values of X_a are plotted as a function of the initial location z on the slope of an individual gravel unit. The negative value of X_a implies the downward movement along the slope. All the measured values of X_a for the eight runs are negative or zero. The data points along the line $X_a=0$ in Fig. 8 correspond to the loose gravel units which are not displaced. On the other hand, the computed points in Fig. 8 include only the displaced units located initially at the finite-difference grid points used for the computation.

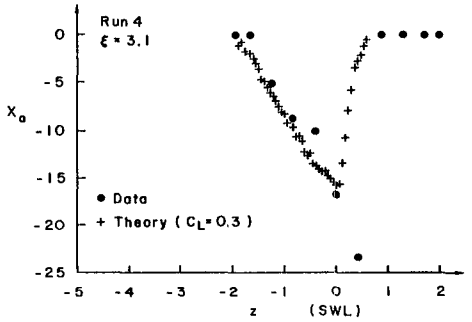

Fig. 8 - Measured and Computed Gravel Unit Displacements

In summary, the agreements between the measured and computed displacements are reasonably good for most of the eight runs.

CONCLUSION

The numerical model developed by Kobayashi et al. (12,13,14) has been show to be capable of predicting the measured quantities related to the wave motion on the riprap slope and the hydraulic stability and movement of riprap units (1,10,15). However, these measurements limited to the quantities which can be measured fairly easily are not sufficient for determining the friction factor f' and the hydrodynamic coefficients C_L, C_D and C_M in a rigorous manner. The fluid velocities and resulting hydrodynamic forces need to be measured so as to better establish these parameters for different armor units. Furthermore, the numerical model needs to be improved and extended to make it as versatile as hydraulic model testing although the present numerical model yields the quantities of practical importance which are difficult to measure.

ACKNOWLEDGMENT

This study has been supported by the National Science Foundation under Grant No. CEE-8408996.

REFERENCES

1. Ahrens, J.P., "Large Wave Tank Tests of Riprap Stability," Tech. Memo. No. 51, U.S. Army Coastal Engineering Research Center, Ft. Belvoir, Va., 1975.
2. Ahrens, J.P., "Reef Type Breakwaters," Proceedings of 19th Coastal Engineering Conference, ASCE, 1984, pp. 2648-2662.
3. Battjes, J.A., "Surf Similarity," Proceedings of 14th Coastal Engineering Conference, ASCE, 1974, pp. 466-480.
4. Bruun, P., Design and Construction of Mounds for Breakwaters and Coastal Protection, Elsevier, New York, 1985.
5. Hannoura, A.A. and McCorquodale, J.A., "Rubble Mounds: Numerical Modeling of Wave Motion," Journal of Waterway, Port, Coastal and Ocean Engineering, Vol. 111, No. 5, 1985, pp. 800-816.
6. Hibberd, S., "Surf and Run-up," presented to the University of Bristol, at Bristol, U.K., in 1977, in partial fulfillment of the requirements for the Ph.D. degree in Mathematics.
7. Hibberd, S. and Peregrine, D.H., "Surf and Runup on a Beach: A Uniform Bore," Journal of Fluid Mechanics, Vol. 95, Part 2, 1979, pp. 323-345.
8. Kobayashi, N. and Jacobs, B.K., "Riprap Stability Under Wave Action," Journal of Waterway, Port, Coastal and Ocean Engineering, ASCE, Vol. 111, No. 3, 1985, pp. 552-566.
9. Kobayashi, N. and Jacobs, B.K., "Experimental Study on Sandbag Stability and Runup," Proceedings of Coastal Zone '85, ASCE, Vol. 2, pp. 1612-1626
10. Kobayashi, N. and Jacobs, B.K., "Stability of Armor Units on Composite Slopes," Journal of Waterway, Port, Coastal and Ocean Engineering, ASCE, Vol. 111, No. 5, 1985, pp. 880-894.
11. Kobayashi, N., "Closure of Riprap Stability Under Wave Action," Journal of Waterway, Port, Coastal and Ocean Engineering, ASCE, Vol. 112, No. 6, 1986, pp. 673-681.
12. Kobayashi, N., Roy, I. and Otta, A.K., "Numerical Simulation of Wave Runup and Armor Stability," OTC Paper 5088, 18th Offshore Technology Conference, Vol. 1, Houston, Texas, 1986, pp. 51-56.
13. Kobayashi, N., Otta, A.K. and Roy, I., "Wave Reflection and Runup on Rough Slopes," to appear in Journal of Waterway, Port, Coastal and Ocean Engineering, ASCE, Vol. 113, 1987.
14. Kobayashi, N. and Otta, A.K., "Hydraulic Stability Analysis of Armor Units," to appear in Journal of Waterway, Port, Coastal and Ocean Engineering, ASCE, Vol. 113, 1987.
15. Kobayashi, N. and Greenwald, J.H., "Waterline Oscillation and Riprap Movement," submitted to Journal of Waterway, Port, Coastal and Ocean Engineering, ASCE, 1987.
16. Madsen, O.S. and White, S.M., "Energy Dissipation on a Rough Slope," Journal of the Waterways, Harbors and Coastal Engineering Division, ASCE, Vol. 102, No. WW1, 1976, pp. 31-48.
17. New, A.L., McIver, P. and Peregrine, D.H., "Computation of Over-

turning Waves," Journal of Fluid Mechanics, Vol. 150, 1985, pp. 233-251.
18. Packwood, A.R., "Surf and Run-up on Beaches," presented to the University of Bristol, at Bristol, U.K., in 1980, in partial fulfillment of the requirements for the Ph.D. degree in Mathematics.
19. Packwood, A.R. and Peregrine, D.H., "Surf and Run-up on Beaches: Models of Viscous Effects," Report No. AM-81-07, School of Mathematics, University of Bristol, Bristol, U.K., 1981.
20. Pedersen, C. and Cjevik, B., "Runup of Solitary Waves," Journal of Fluid Mechanics, Vol. 135, 1983, pp. 283-299.
21. Peregrine, D.H., "Breaking Waves on Beaches," Annual Review of Fluid Mechanics, Vol. 15, pp. 149-178.
22. Rosenthal, C.N. and Sleath, J.F.A., "Measurements of Lift in Oscillatory Flow," Journal of Fluid Mechanics, Vol. 164, 1986, pp. 449-467.
23. Sawaragi, T., Ryu, C. and Iwata, K., "Considerations of the Destruction Mechanism of Rubble Mound Breakwaters Due to the Resonance Phenomenon," Proceedings of 8th International Harbour Congress, Antwerp, Belgium, 1983, pp. 3.197-3.208.
24. Seelig, W.N., "Wave Reflection from Coastal Structures," Proceedings of Coastal Structures '83, ASCE, 1983, pp. 961-973.
25. Sleath, J.F.A., Sea Bed Mechanics, Wiley-Interscience, New York, 1984.
26. Smith, O.P., "Cost-Effective Optimization of Rubble-Mound Breakwater Cross Sections," Tech. Report CERC-86-2, U.S. Army Coastal Engineering Research Center, Vicksburg, Ms. 1986.
27. Svendsen, I.A. and Jonsson, I.G., Hydrodynamics of Coastal Regions, Technical University of Denmark, Lyngby, Denmark, 1980.
28. Svendsen, I.A. and Madsen, P.A., "A Turbulent Bore on a Beach," Journal of Fluid Mechanics, Vol. 148, 1984, pp. 73-96.
29. U.S. Army Coastal Engineering Research Center, Shore Protection Manual, Vol. II, U.S. Government Printing Office, Washington, D.C., 1984.
30. Van der Meer, J.W. and Pilarczyk, K.W., "Stability of Rubble Mound Slopes under Random Wave Attack," Proceedings of 19th Coastal Engineering Conference, ASCE, 1984, pp. 2620-2634.
31. Wiberg, P.L. and Smith, J.D., "A Theoretical Model for Saltating Crains in Water," Journal of Geophysical Research, Vol. 90, No. C4, 1985, pp. 7341-7354.

CHAPTER 145

ON THE SCATTERING OF CONCRETE ARMOUR UNITS OF DETACHED BREAKWATERS DUE TO WAVES

KOHNO, H*., T. UDA** and Y. YABUSAKI***

ABSTRACT

On the Fuji Coast 15 detached breakwaters and 17 wave dissipating breakwaters have been constructed to prevent beach erosion. By virtue of the construction of the breakwaters the retreat rate of the shoreline position has decreased. However a large number of concrete blocks have been scattered due to waves. This study investigates the actual circumstances on the scattering of the concrete armour units of the detached breakwaters through the field observations on the Fuji Coast located in Suruga Bay facing the Pacific Ocean. The change rate of the plane area of the breakwater is examined from the aerial photographs, and the relationships among the parameter, the depth at the offshore foot of the breakwater and the number of the removed concrete armour units are investigated.

I. INTRODUCTION

In recent years beach erosion is severe in Japan. They are caused partly by the construction of dams in rivers, the extraction of sand from rivers, or the influence of the construcion of the harbor structures on the coast. Countermeasure works have been conducted at many locations to improve the condition. The Fuji Coast is one of these coasts, and beach erosion has been caused by the decrease of the fluvial sediment supply from the Fuji River and the interception of longshore sand transport due to the construction of Tagono-ura Port in the middle of the coast. On the coast 15 detached breakwaters and 17 wave dissipating breakwaters, composed of concrete armour units and placed along the shoreline, have been constructed. By virtue of the construction of these breakwaters, the retreat rate of the shoreline position became small. However a large number of concrete blocks have been scattered due to waves, and sometimes fishing nets were damaged by the scattered concrete blocks. The number of the detached breakwaters have been increasing, and hence the stability of the concrete armour units is important for the maintenance of the detached breakwaters or the wave dissipating breakwaters. Nevertheless there are few studies on this kind of problem.

The aim of the study is to investigate the actual circumstances on the scattering of the concrete armour units of the detached breakwaters and the wave dissipating breakwaters by the field investigations on the Fuji Coast. The change rate of the plane area of the breakwater is examined from the aerial photographs, and the relationships

* Head, Numazu Work Office , Chubu Regional Construction Bureau, Ministry of Construction, Shizu-oka 410 Japan.

** Dr. Eng., Head, Coastal Engineering Division, Public Works Research Institute, Ministry of Construction, Ibaraki 305 Japan.

*** Numazu Work Office.

among the parameter, the depth at the offshore foot of the breakwater and the number of the removed concrete armour units are investigated. It is concluded through the study that the change rate of the plane area of the breakwater correlates well with the depth at the offshore foot and it increases with the depth. Furthermore on the detached breakwater the greater the rate of change of the depth at the offshore foot of the breakwater is, the larger the change rate of the plane area becomes. On the wave dissipating breakwater, it is found that the change rate of the plane area correlates well with the total weight of the recovered concrete blocks.

Ⅱ. GEOGRAPHICAL FEATURES OF INVESTIGATED AREA

The Fuji Coast, formed by the fluvial sediment supply of the Fuji River, is located on the bottom of Suruga Bay (Fig. 1). The coast around the river mouth has been eroded since 1960s due to the decrease of the fluvial sediment supply caused by the excavation of sand in the river. Besides, the breakwater of Tagono-ura Port was built between 1959 and 1962, and littoral drift directing eastward was cut due to the presence of the breakwater, so that beach erosion and accretion began on the east and west sides of the breakwater, respectively. On the downdrift coast of the port wave dissipating breakwaters have been placed since 1974 against beach erosion, and detached breakwaters were constructed between the mouth of the Fuji River and the port. By virtue of the construction of the breakwaters, recent retreat rate of the shoreline position became small.

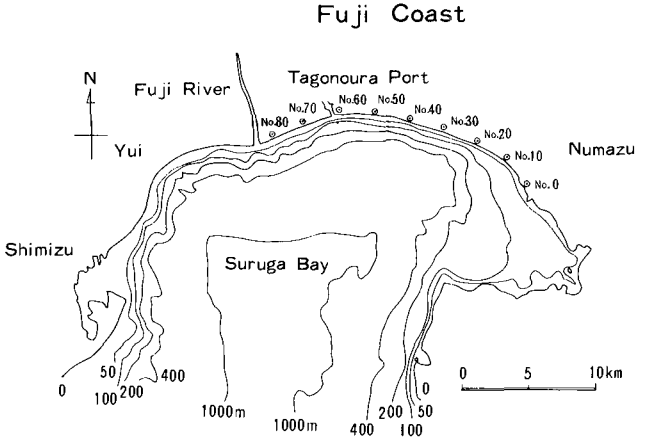

Fig.1 Location of Fuji Coast.

The locations of the detached breakwaters and the wave dissipating breakwaters on the Fuji Coast are shown in Fig. 2. Figure 2 (a) is the arrangement of the detached breakwaters in Fuji region, where is adjacent to the mouth of the Fuji River on the west side and ends by the breakwater of Tagono-ura Port on the east side. The direction of littoral drift in the region is eastward[1),2)], so that the sediment supply

from the Fuji River is carried eastward. The construction of 17 detached breakwaters had been done by using 50-ton concrete armour units (tetrapod) by the order of the number shown in the figure during 1978 through 1984. Similarly Fig. 2 (b) is the arrangement of the wave dissipating breakwaters in Yoshiwara region located on the east side of Tagono－ura Port. On the west side of the region the breakwater of the port was constructed during 1959 through 1962, and littoral transport directing east was obstructed, so that severe beach erosion occurred on the downdrift coast. In order to prevent the shoreline retreat, 17 wave dissipating breakwaters had been constructed by the order of the number shown in Fig. 2 (b) from west to east during 1974 through 1979. These breakwaters were useful for the preservation of the shoreline position, but the scattering of the concrete blocks is severe in recent years. Because of the severity of the scattering of the blocks, the weight of the concrete armour units composing the wave dissipating breakwaters have been increased year by year. At first, 25-ton concrete armour units were used for No. 1 through No. 4 breakwaters built in earlier years. For No. 5 and No. 6 breakwaters, 40-ton concrete armour units were used at offshore part of the breakwater to strengthen the breakwater and to prevent the subsidence of the concrete armour units. Regarding No. 7 through No.17 breakwaters, 25-ton and 40-ton blocks are mixed, and both sides of the breakwaters are strengthened by 50-ton blocks to prevent further scattering of the blocks.

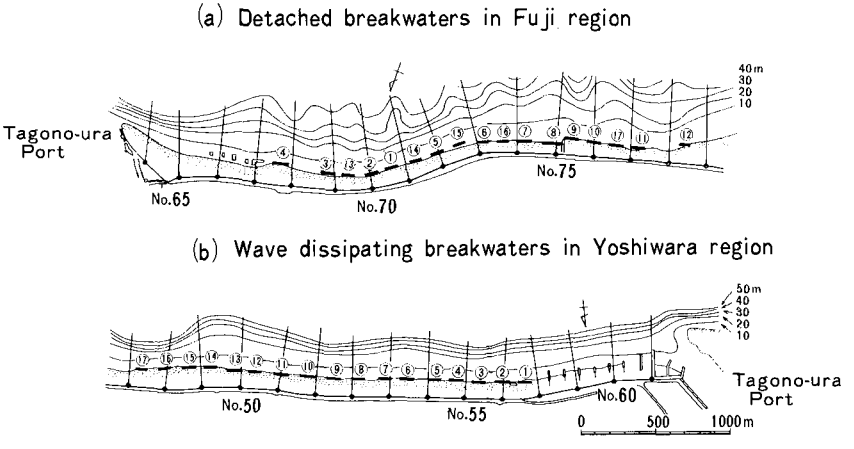

Fig.2 Locations of detached breakwaters and wave dissipating breakwaters on Fuji Coast.

The concrete armour units of the detached breakwaters are set on the sea bed directly without the rock mound in a shallower region than about 6 m, because of the difficulty of the construction of the rock mound on the steep slope beach. Similarly the armour units of the wave dissipating breakwaters are set on the shoreline without the rock mound.

Figure 3 shows the cross section of the beach passing through the center line of No.17 detached breakwater, which is useful to understand the relative location between the coastal dike and the detached breakwater. The distance between the coastal dike and the detached breakwater is around 100m in length, and there are foot protection works and wave breaking works between two structures. Since the beach slope of the Fuji Coast is very steep like as 1/3−1/10, and Suruga Bay, where the Fuji Coast is located, is facing the Pacific Ocean, the incident wave height in the typhoon season becomes so large. For the planned wave condition, significant wave height and wave period are equal to 17m and 20 sec, respectively. Because of frequent attack of high waves, the crown height of the coastal dike is high enough to attain to 17m above the mean sea level. In the sectional view of the beach shown in Fig. 3, the recent beach profiles are also shown. It is found that the sea bed off the detached breakwater was eroded between June, 1985 and February, 1986, and the maximum change of the bed reached to 1.7 m.

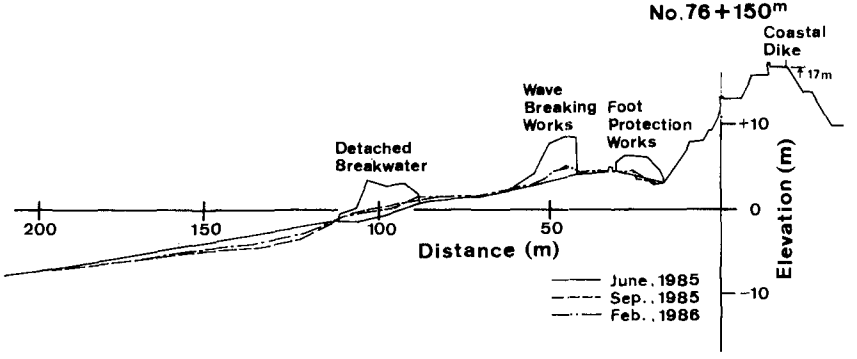

Fig.3 Cross section of the beach passing through the center line of No.17 detached breakwater.

Ⅲ. SCATTERING OF CONCRETE ARMOUR UNITS OF DETACHED BREAKWATERS

For the investigation on the scattering of concrete armour units, the change of the plane area of the breakwater was examined first. The plane shape of the breakwater was traced from the aerial photographs, whose scale is 1/2500, and the change of the shape was determined by the subsequent photographs. Furthermore, the shoreline positions around the breakwaters were also examined, and the relation between the shoreline change and the scattering of the blocks were investigated. The results of the investigation are summarized in Fig. 4. The change of the shape of the detached breakwaters is expressed in an order from east to west. Each breakwater was constructed on the date shown in the figure. Tidal levels in the subsequent photographs differ from each other, but the correction of the shoreline change due to the change of the tide level was not considered, because the beach slope around the

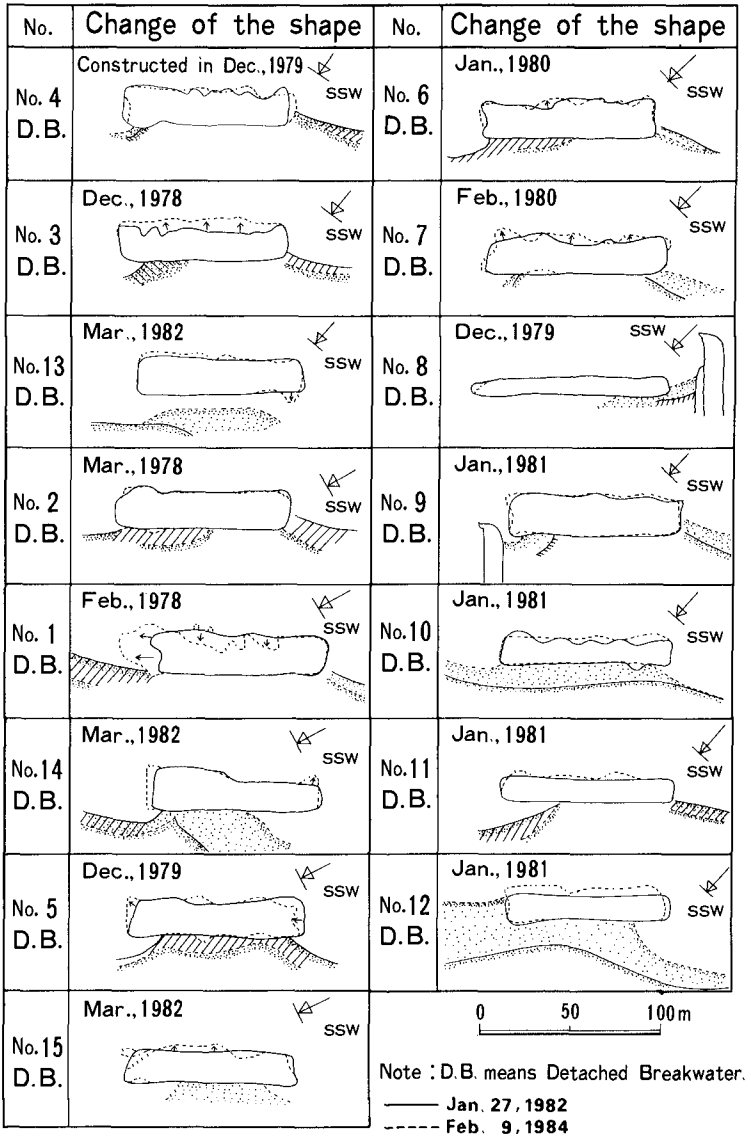

Fig.4 Traces of shapes of detached breakwaters in February, 1982 and February, 1984. Each breakwater was constructed on the dates shown in the figure.

breakwaters is very steep.

During the examination period of change of the form of the detached breakwaters between February, 1982 and February, 1984, high waves of Hmax= 9.85m and H 1/3=7.26m attacked the coast in September, 1982. Large change of the form are observed in No. 3, No. 1, No. 5, No. 15, No. 7 and No. 12 detached breakwaters during the period, and particularly the change of No. 1 breakwater is large. Regarding the general features of the form change of the detached breakwaters, large changes are observed at the offshore side and the east end of the breakwaters. Three causes are considered. First, wave force is large at the offshore side of the breakwater, so that the blocks are apt to be scattered by strong wave force. Second, the east end of the breakwater may be scoured, since the predominant direction of littoral transport is eastward. Thirdly, wave force acts on the blocks obliquely, because wave incidence prevails between S and SSW in storm wave condition on the coast and this wave incidence makes a considerably large angle with the longshore direction of the breakwaters.

The direction of the detached breakwater, θ, measured counterclockwise from South, the offshore distance from the shoreline to some contour lines, ℓ, and the total number, M, and the total weight of recovered concrete blocks, W_T, are expressed in Fig. 5 as well as the arrangement of the detached breakwaters. The abscissa is the number of the survey lines of 250m intervals. The directions of the breakwaters, defined by the angle between the normal of the breakwater and South, at No. 2 through No.15 detached breakwaters differ from those at the other breakwaters over 20 degrees, since the directions of coastline themselves change to a great extent as shown in Fig. 2. The offshore distances from the shoreline to 10, 20 and 30m deep contour lines have such a distinctive feature that they are short between No. 2 through No.15 detached breakwaters. In other words, the bottom slope of the detached breakwater is steep at locations between No. 2 and No.15 breakwaters compared with the other locations. Under such a condition the incident waves are considered to attack the breakwaters without large attenuation of wave energy, so that the scattering of the blocks should be severe at these locations.

On the Fuji Coast the recovery works of the scattered concrete blocks, obstructing the local fishery, have been conducted at offshore zone up to about 10m deep off the detached breakwaters and the wave dissipating breakwaters since 1981. The total number and the total weight of the recovered blocks in Fig. 5 are the summation during the period from October, 1982 to February, 1984. The location where many scattered blocks were recovered agrees well with the one where the normal to the detached breakwater makes a large angle with South, the offshore distances to some contour lines are short, and hence the beach slope is very steep.

Next, the change rate of the plane area of the breakwater (Y), the depth at the offshore foot of the breakwater (h), and the change of the depth ($\triangle$h) from February 1982 to February, 1984 are expressed in Fig. 6. Y is equal to the change of the plane area during the period divided by the area measured in February, 1982. h is obtained in the central section of the breakwater, and in addition $\triangle$h is positive when the water depth increases. In the calculation of the plane area of the breakwaters there are two cases in which the change of the shape of the breakwater protrudes

against the original form and it is depressed to the original one. Here, the change of the plane area is defined by the addition of both changes. The change rate of the plane area of the breakwater, Y, has a fairly large variations alongshore, and its maximum is 0.34 at No. 1 breakwater. It is found that Y is in good correlation with the depth at the offshore foot, h in February, 1984 except the data at No. 12 breakwater, where is close to the river mouth of the Fuji River. Generally the change rate of the plane area, Y increases with the depth at the offshore foot of the breakwaters. To the contrary, it is not in good correlation with h in February, 1982.

On the changes of the depth, $\triangle$h, from February 1982 to February 1984 shown in Fig. 6, the changes are considerably large, that is, maximum increase and decrease of the water depth attain to 2.2m at No. 3 breakwater and −2.2m at No.12 breakwater, respectively. There is a tendency that the depth at the offshore foot of the breakwater having larger number than No. 8, expressing the later construction than No. 8 breakwater, decreases and the depth increases at the older breakwaters than No. 8. This means that sand accumulate not only behind the breakwater, forming a tombolo, but also in the offshore zone of the newly constructed breakwaters,

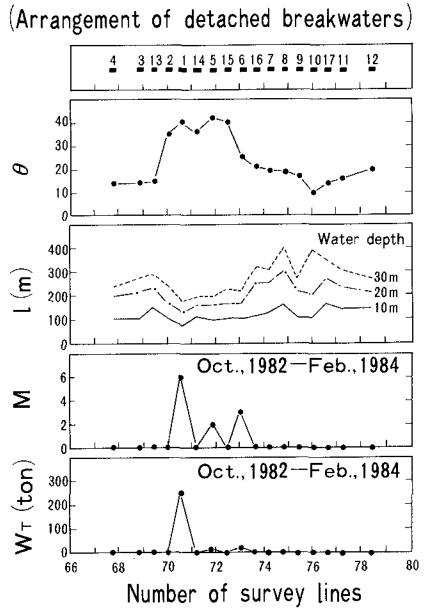

Fig.5 Spatial changes of the direction of the detached breakwater, θ, the offshore distance from the shoreline to some contour lines, ℓ, and the total number, M, and the total weight of recovered concrete blocks, W_T.

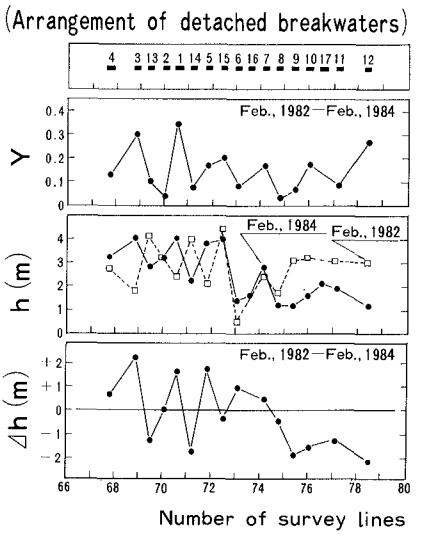

Fig.6 Spatial changes of the change rate of the plane area of the breakwater, Y, the depth at the offshore foot of the breakwater, h, and the change of the depth, $\triangle$h, from February, 1982 to February, 1984.

although the cause is not clearly understood.

Regarding the relation between the change of the depth at the offshore foot of the breakwater, $\triangle h$, and the change rate of the plane area, Y, fairly good correlation can be found. In other words, the change rate tends to increase with the positive change of the depth except No.12 breakwater located close to the river mouth.

The relations among the change rate of the plane area, the depth at the offshore foot and the change of the depth are investigated directly. Figure 7 expresses the relationship between Y and h. The relation is given by the equation

$$Y = 0.019h^2 \qquad (1)$$

where Y is a dimensionless variable and h is the depth in meter unit. The change rate of the plane area increases with the square of the depth at the offshore foot of the breakwater. The relation is considered to be obtained because wave height depends on the water depth strongly near the surf zone where the detached breakwaters are located, and in addition wave force acting on the concrete armour units depends on the wave height at that depth.

The relation between Y and $\triangle h$ is shown in Fig. 8. Two broken lines in the figure are drawn in order to confine almost the lower and upper limits of the data except that at No. 12 breakwater. It is known from the relation that Y also increases as $\triangle h$ becomes large. Namely, this means that the scattering of the concrete blocks becomes severe with the increase of the depth at the offshore foot of the breakwater.

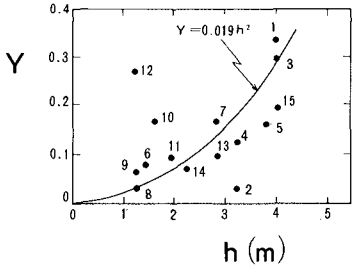

Fig.7 Relationship between the change rate of the plane area of the breakwater, Y, and the depth at the offshore foot of the breakwater, h.

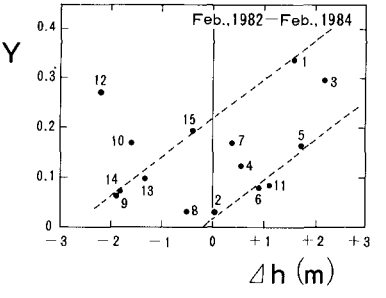

Fig.8 Relationship between the change rate of the plane area of the breakwater, Y, and the change of the depth at the offshore foot, $\triangle h$.

Finally, pictures taken to know the setting condition of the concrete armour units at the offshore foot of the breakwater are shown in Pictures 1 and 2, where No.17 detached breakwater is selected as an example. These underwater photographs were taken at the east end of the breakwater as shown by the circle sign in Fig. 9 on February 20, 1984. The water depth is around 4 m deep. There does not exist the local scouring hole, and bed materials mainly consist of gravels in the vicinity of the

breakwater. Far from the location there extends sandy bed and sand ripples develop. For the reference length for the decision of the ripple scale and diameters of gravels, it can be used that the radius of tip of the leg of 50-ton concrete armour units is equal to 0.455m and in addition the length of the leg is about 1.8 m long. Comparing these scales with the gravels, it is found that the maximum scale of the bed materials are around 10-20 cm.

Picture 1 Underwater picture taken at the offshore foot of No.17 detached breakwater (1).

Picture 2 Underwater picture taken at the offshore foot of No.17 detached breakwater (2).

Owing to the grain size test of the bed materials on the Fuji Coast, generally coarse materials having the median diameter of 10-20 mm are found at the foreshore, and then the diameter of the materials decreases with the water depth. The median diameter in the offshore zone deeper than 6 m becomes less than 1 mm. These features of the grain size distribution of the bed materials agree considerably well with the ones observed in Pictures 1 and 2.

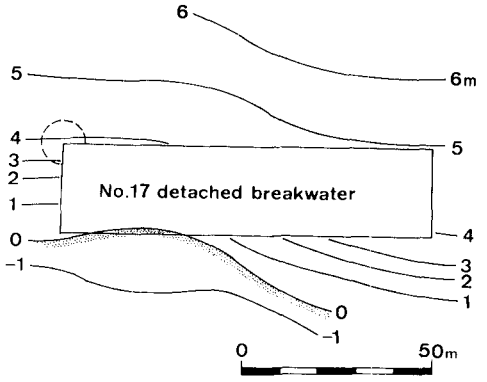

Fig.9 Bottom contours around No.17 detached breakwater measured on February 20, 1984.

V. SCATTERING OF CONCRETE ARMOUR UNITS OF WAVE DISSIPATING BREAKWATERS

Regarding the wave dissipating breakwaters, the same kind of the investigation was carried out as the detached breakwaters by using the aerial photographs. The arrangement of the wave dissipating breakwaters, the direction of the normal to the breakwater, θ, the offshore distance to some contour lines from the shoreline, ℓ, the change rate of the plane area, Y and the depth at the offshore foot of the breakwater, h are expressed in Fig. 10. The total number and the total weight of the concrete blocks recovered between October, 1981 through February, 1984 are also shown. The abscissa is the number of the survey lines of 250 m intervals. The direction of the coastline where the wave dissipating breakwaters were placed is almost uniform as shown in Fig. 2. The direction of the normal to the breakwater, measured counterclockwise from South, does not vary so much alongshore, since the breakwaters are set along the straight shoreline. According to the offshore distances to 10-30m deep contour lines, the bottom slope is steep in the zone deeper than 20m, because the interval of the distances is relatively narrow. The change rate of the plane area, Y, was calculated from the photographs obtained in December, 1979 and February, 1982. The maximum wave height in the period is Hmax=8.6 m, H1/3= 3.5m measured in October, 1981. It is found that Y correlates well with h measured in December, 1979, although its correspondence with the depth in February, 1982 is

not dominant. The depth at the offshore foot, h, was particularly large at four locations of No. 6 , No. 7, No. 10 and No. 11 breakwaters in 1979, but then increased as a whole in February, 1982 because of beach erosion.

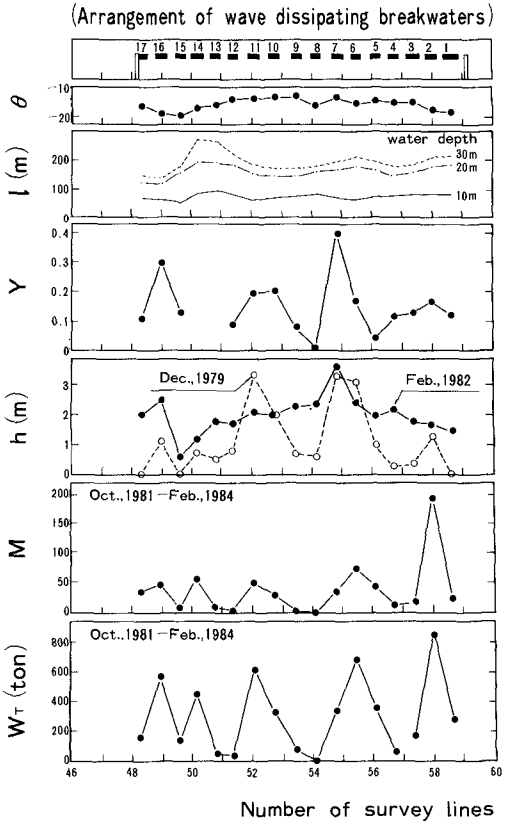

Fig.10 Spatial changes of the direction of the normal to the breakwater, θ, the offshore distance to some contour lines from the shoreline, ℓ, the change rate of the plane area, Y, the depth at the offshore foot of the breakwater, h, the total number, M, and the total weight of the scattered concrete blocks, W_T.

Next, the total number and the total weight of the scattered concrete blocks shown in Fig. 10 are studied. It is understood that there is a good correlation among Y, M and W_T. The total number and the total weight of the scattered blocks increase with Y. The change rate of the plane area of the wave dissipating breakwater determined from the aerial photographs becomes a good parameter for judging the extent of the scattering of the concrete blocks.

Since the longshore distributions of the depth at the offshore foot and the actual

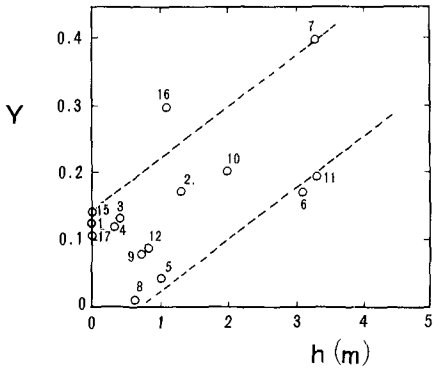

Fig.11 Relationship between the change rate of the plane area of the breakwater,Y, and the depth at the offshore foot of the breakwater,h.

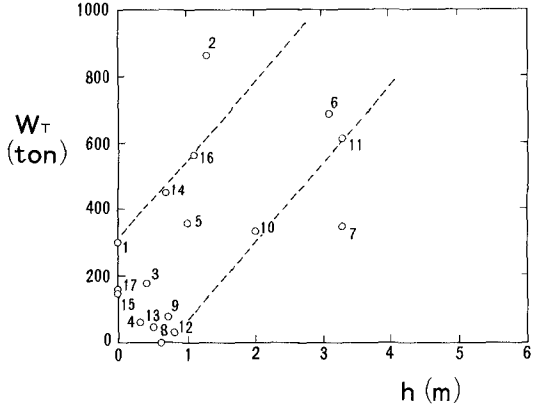

Fig.12 Relation between the total weight of the concrete blocks, W_T, and the depth at the offshore foot, h.

conditions of scattering of the concrete blocks have already been known, the relations among the parameters are studied. The relation between the rate of change of the plane area of the wave dissipating breakwaters, Y, and the depth at the offshore foot of the breakwater, h, measured in December, 1979 is expressed in Fig. 11. There are considerably large scatter in the relation, so that lower and upper limits, enveloping the almost whole data, are shown by the broken lines to decide the mean relation. It is found that a relation stands between the rate of change of the plane area, Y, and the depth at the offshore foot, h, except No.16 wave dissipating breakwater.

$$0.077h - 0.052 < Y < 0.077h + 0.143 \qquad (2)$$

where Y is dimensionless parameter and h is the depth in meter unit. On an average, the change rate of the plane area of the wave dissipating breakwater, Y, is proportional to the depth at the offshore foot of the breakwater, h. Similarly, Figure 12 expresses the relationship between the total weight of the recoverd concrete blocks, W_T, and the depth at the offshore foot of the breakwater, h. There are some scatters in the relation, but almost all data can be confined within two broken lines except No. 2 and No. 7 breakwaters. It should be noted that the total weight of the scattered concrete blocks increases with the greater foot depth.

Finally the weight and the number of the recovered concrete blocks by the sweeping operation of the sea bed are counted at 0.5m deep intervals as shown in Fig.13. In the figure the recovered weight of the detached breakwaters and the wave dissipating breakwaters are shown differently by open and solid circles, respectively. Solid line represents the summed number of the recovered concrete blocks at every 1 m deep interval. It can be concluded from the figure that almost all scattered concrete blocks concentrate on the depths between 6 and 8 m deep. The reason is due to the abrupt change of the beach slope. Taking survey line No.75 for an example, beach slope between the foreshore and 5 m deep contour is steep enough as 1/9, and on the other hand between 5 and 10 m deep contours the slope becomes relatively mild like as 1/25. It may be concluded that it is difficult for the scattered concrete blocks to stop on the steep slope between the foreshore and 5 m deep contour, and that scattered blocks are apt to gather on the bed of relatively mild slope.

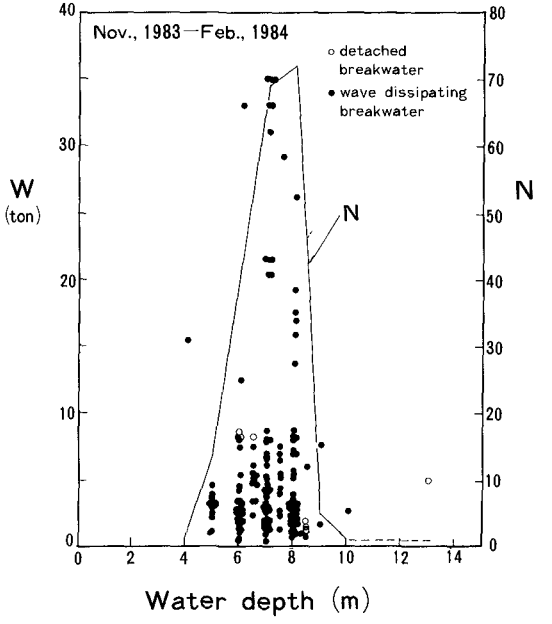

Fig.13 Vertical distributions of the weight and the number of the recovered concrete blocks.

V. SUMMARY OF SCATTERING OF CONCRETE BLOCKS

The relation between the scattering of the concrete blocks and wave conditions is studied based upon the actual results of the recovery of the concrete armour units. Table 1 summarizes the results. The recovery works were carried out during October through February in each fiscal year, and in this study the data from October, 1981 to February, 1983 are summarized. The items of the data summary are the number of the scattered blocks, the total weight of the blocks, the average weight of a scattered block, the maximum weight of the blocks and the average distance of the scattering. Wave conditions observed at Tagono-ura Port or Hara Observatory on the Fuji Coast are also summarized. ΣHmax・t and ΣH1/3・t are the summations of the maximum wave height larger than 5 m and the significant wave height larger than 3 m, respectively, multiplied by the observation period (t= 2 hr) in place of the duration of the waves.

Table 1 Summary of scattering of concrete blocks.

		Oct.1981 −Feb. 1982	Oct. 1982 −Feb. 1983	Nov. 1983 −Feb. 1984
D. B.	M	0	7	4
	Wt (t)	−	254.7	30.7
	$\overline{W}$ (t)	−	36.3	7.7
	Wmax(t)	−	45.1	8.6
	$\overline{X}$ (m)	−	31.6	31.3
	$\overline{W}\cdot\overline{X}$	−	1147	241
W. D. B.	M	43	360	215
	Wt (t)	318.6	3640	1040
	$\overline{W}$ (t)	7.4	10.3	5.1
	Wmax(t)	24.5	46.0	35.0
	$\overline{X}$ (m)	26.1	39.9	41.7
	$\overline{W}\cdot\overline{X}$	193	409	211
	Hmax (m)	6.59	9.85	6.94
	ΣHmax・t	25.5	305.6	78.7
	H⅓ (m)	3.57	7.26	5.0
	ΣH⅓・t	20.3	223.9	46.1

D.B. : Detached breakwater, W.D.B. : Wave dissipating breakwater, M : Number of the scattered blocks, Wt : Total weight of the scattered blocks, $\overline{W}$: Average weight, Wmax : Maximum weight, $\overline{X}$: Average distance of the scattering.

The number of the scattered blocks are less than 10 on the detached breakwater, but on the wave dissipating breakwaters they reach 360 at maximun. The fact that a large number of the concrete armour units are scattered is due to the causes that the beach slope is steep and the beach has been eroded year by year at the sites where the

wave dissipating breakwaters are located, and that the weight of the concrete armour units of the wave dissipating breakwaters is lighter than that of the detached breakwaters. $\overline{W}_B \cdot \overline{X}$, expressing the work done by wave force, is large on the detached breakwaters rather than on the wave dissipating breakwaters. This implies that the wave force acting the blocks of the detached breakwaters is greater than that in a case of the wave dissipating breakwaters. Regarding the comparison of the period, many blocks were scattered from October, 1982 to February, 1983, because maximum significant wave height of about 10 m attacked the breakwater. The average weight of the scattered blocks is less than 10 tons except the data obtained from October, 1982 to February, 1983 on the detached breakwater, although 50-ton blocks are used for the detached breakwaters, and 25, 40 and 50-ton blocks for the wave dissipating breakwaters. It should be noted that almost all scattered concrete blocks are broken ones. Two causes of the damage of the concrete blocks are considered. First, the blocks are damaged directly due to the wave force. Second, the engagement of the blocks is worsen and it is damaged by both dead load of the blocks itself and the wave force.

Ⅵ. CONCLUSIONS

The conclusions obtained through the study are summarized as follows.

(1) The change rate of the plane area of the breakwater calculated by the aerial photographs becomes a good parameter in order to analyse the scattering condition of the concrete armour units of the breakwaters.

(2) There exists a correlation between the change rate of the plane area of the breakwater, Y, and the depth at the offshore foot of the breakwater, h. A relation $Y = 0.019\ h^2$ stands.

(3) Y also becomes large when the rate of increase of the depth h is large.

(4) Concrete armour units of the detached breakwaters were scattered severely at locations where the depth off the breakwater is deeper compared with the average depth and the direction normal to the shoreline makes a large angle with the direction of the incident wave, because of large longshore sand transport.

(5) The change rate of the plane area of the wave dissipating breakwater correlates well with the total weight of the recovered concrete blocks. Due to the actual results of the recovery of the concrete armour units, the average weight of the scattered blocks is less than 10 tons. It is concluded that almost all scattered blocks are broken ones, judging that the initial weight of the blocks is greater than 25 tons.

REFERENCES

1) Noda, H. and H. Hashimoto:Littoral drift and shore protection facilities, Gihodo Press, 1981 (in Japanese) .

2) Kohno, H., T. Uda, Y. Yabusaki and M. Mizuno : Beach erosion on the Fuji Coast and Prediction of 3-D Beach changes, 33th Japanese Conf. on Coastal Eng ., pp.475-479, 1986 (in Japanese) .

CHAPTER 146

MEASUREMENT OF REFLECTION COEFFICIENT OF SEAWALL IN OMURA BAY

by

Kosuke Kondo*, Masayuki Akama** and Masahiko Isobe***

ABSTRACT

Field investigations were performed in order to establish the reflecting characteristics of a steel sheet-piling type seawall and two vertical wave-dissipating type seawalls through directional wave measurements of wave reflection systems. A pre-designed line array of several capacitance-type wave gauges was used to measure the wave field just in front of the seawall, and the MMLM (Modified Maximum Likelifood Method) was applied for the calculation of the directional wave spectrum and the reflection coefficient. The estimated directional spectra demonstrated that the MMLM has high resolution power and can sufficiently separate the incident and the reflected wave energies. As a result , it was found that the reflection coefficient of the vertical steel sheet-piling seawall is about 0.9 and is independent of the incident wave conditions, whereas those of the vertical wave-dissipating type seawalls show considerable change in correlation to the incident wave period or the mean water level.

1. INTRODUCTION

Many types of wave-dissipating vertical seawall structures have recently been constructed in Japan in order to reduce the effect of reflected waves from these structures. In designing and constructing them, it is necessary to estimate the reflective characteristics of these structures.

Laboratory flume tests are often performed using a scale model of a seawall. Actual reflection coefficients are, however, expected to be different from those obtained in laboratory flumes because actual sea waves are directionally spread and so measuring the reflection coefficient of seawalls in the field is of great importance.

* Principal Engineer, Design and Engineering Department, Penta-Ocean Construction Co., Ltd., 2-2-8 Koraku, Bunkyo-ku, Tokyo, 112 Japan.
** Engineer, Design and Engineering Department, Penta-Ocean Construction Co., Ltd., 2-2-8 Koraku, Bunkyo-ku, Tokyo, 112 Japan.
*** Associate Professor, Department of Civil Engineering, Yokohama National University, 156 Tokiwadai, Hodogaya-ku, Yokohama, 240 Japan.

The following methods have been examined in the field to know the reflection coefficient of prototype structures(Goda,1985):

1) simultaneous measurement of the wave height Hs in front of a structure (at a distance more than one wave length from the structure) and the incident wave height Hi at a location free from the effect of reflected waves;
2) measurement of the directional wave spectrum sufficiently far from the reflective structure where the effect of phase-locking of incident and reflected waves becomes negligible; and
3) application of the method for resolving the incident and reflected wave spectra in a wave flume by using the autocorrelation function (Kajima, 1969) or the fast Fourier transform technique (Goda and Suzuki,1976).

These methods have, however, the following problems. By the method 1, the reflection coefficient is affected too much by a slight change of wave height ratio Hs/Hi. For example, 10% error of Hs/Hi changes the reflection coefficient between 0.1 and 0.7 when the actual reflection coefficient is 0.5. In using the method 2, the dispersion of waves reflected from a finite length of reflective structure has to be considered. The method 3 is only applicable when waves incident to a structure with narrow directional spreading and the mean direction is almost perpendicular to the structure.

Recently, Isobe and Kondo (1984) presented a theory named MMLM (Modified Maximum Likelihood Method) to measure the directional wave spectrum in a wave reflection system and to determine the reflection coefficient of a structure in a directional sea. The object of this study is to confirm the applicability of the MMLM to the field data and to establish the reflecting characteristics of three different types of seawalls through directional wave measurements of wave reflection systems in the field.

2. FIELD INVESTIGATIONS

2.1 Site Description

The field investigations were performed on the eastern shore of Omura Bay, Nagasaki Prefecture, Kyushu, Japan in March, 1982 and in January, 1984. A location map of the investigation site is showen in figure 1. Omura Bay is almost entirely separated from the open sea by the surrounding topography. The scale of the bay is about 20 km north to south and about 10 km east to west. The wave climate is very mild throughout most of the year. The exception is winter when the northwest monsoon sometimes blows and wind waves develop.

During the first investigation in 1982, data for a vertical steel sheet-piling type seawall was collected. After this investigation, two vertical wave-dissipating type seawalls (Type A and Type B) were constructed. In 1984, about half a year after the seawalls were constructed, the second investigation were carried out in order to collect the data for the newly constructed seawalls.

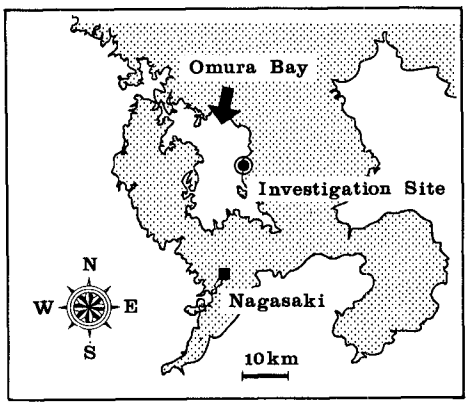

Fig. 1 Location map of the investigation site.

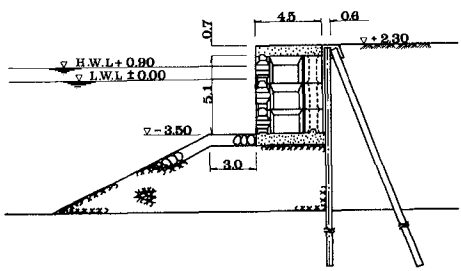

Fig. 2 Schematic profile of the Type A wave-dissipating seawall.

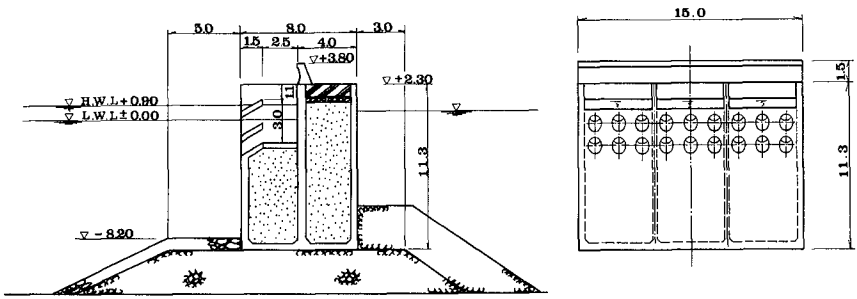

(a) Side view (b) Front view

Fig. 3 Schematic profile of the Type B wave-dissipating seawall.

Schematic profiles of these vertical wave-dissipating type seawalls are given in figures 2 and 3. Type A is a block type. Three concrete blocks with wave chambers are piled up just in front of the steel sheet-piling wall. Type B is a caisson type. As seen in the front view, this type has many sloping holes in its front wall.

2.2 Field Investigation Program

The field investigation program consisted of these three items:

1) measurements of incident and reflected waves in front of the seawall by a line array using three to five capacitance-type wave gauges arranged perpendicular to the wall;
2) measurements of incident waves in the location free from the effect of reflected waves by a line array using two to four capacitance-type wave gauges arranged nearly perpendicular to the wind direction; and
3) measurements of wave height distribution within 1 km of the seawalls using a floating buoy with a twice electronically integrated accelerometer or ultrasonic wave gauges.

In the first investigation, three capacitance-type wave gauges were installed with the distances of 10.0 m, 11.2 m and 13.6 m away from the steel sheet-piling wall respectively, and two capacitance-type wave gauges with an interval of 1.2 m each other were placed about 2 km north of the seawall. The location and arrangement of the wave gauges in the second investigation is explained in figure 4. Five capacitance-type wave gauges were installed just in front of each vertical wave-dissipating type seawall. The incident wave measuring point was located about 2 km north of the seawalls as was in the first investigation, and four capacitance-type wave gauges were arranged with intervals of 2.4 m, 3.6 m and 1.2 m.

A truck-crane was used at the seawalls to support the beam from which wave gauges hung. Several red and white poles were placed at regular intervals between the wave gauges to determine the details of wave height distribution within one wave length of the seawall. This was filmed with a 16 m/m memo-motion camera. At the incident wave measuring point, a small self-elevating platform was used. The wind speed and direction were measured at the level of 10 m over the ground surface at the north cornor of the reclaimed area.

The arrangement of wave gauges just in front of the seawalls in the second investigation was decided by numerical simulation so as to achieve a high resolution power of the directional wave spectrum and high accuracy in estimating the reflection coefficient. Details about the procedure for this numerical simulation will be explained later.

Every analogue record of approximately 5 minutes length was converted to disital record with a sampling interval of 0.1 second. All data were analyzed statistically, including the calculation of significant wave height and period by the zero-up-crossing method. The frequency spectra were computed using the fast Fourier transform technique on records of 2048 samplings with an interval of 0.1 second after the correction of mean water level. The effective number of degree of freedom was about 23.

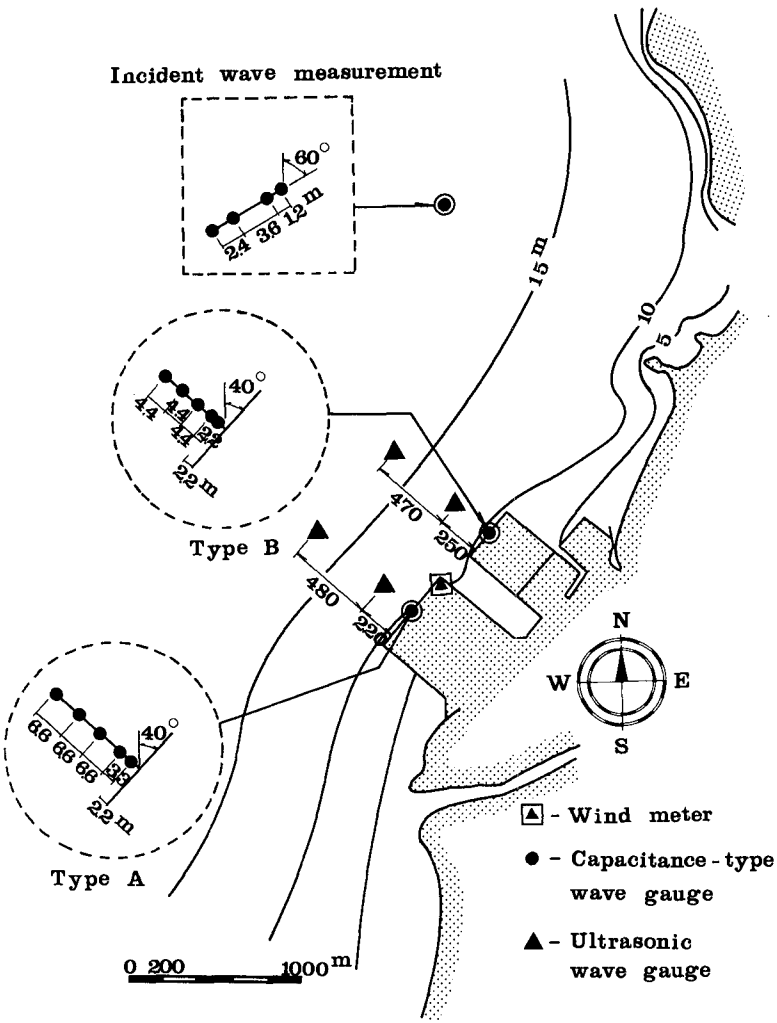

Fig.4 Location and arrangement of the wave gauges in the 2nd investigation.

2.3 Wind and Wave Conditions

The wind and wave conditions during the observation periods are shown in figure 5. From the upper side, wind speed, wind direction, wave height, wave period, wave direction and tidal level are presented. Significant wave height reached 0.5 m to 0.8 m in each observation. Significant wave period was 2.5 seconds to 3 seconds. Most of the observed frequency spectra had the shape that indicated greater part of the energy concentrated around the peak frequency. Wave direction was almost equal to the wind direction, that was north-west, and was nearly perpendicular to the seawalls. The wind conditions in the first investigation changed markedly, whereas in the second investigation rather steady wind conditions prevailed.

Figure 6 compares the height of incident waves and that of waves in front of the seawalls. The incident wave height is indicated by the broken line, and that of waves in front of the seawalls is shown by the black or white circle. The wave height near the seawall is an averaged value of those measured by two or three wave gauges located more than one wave length away from the reflecting surface. In the first investigation, the wave height near the seawall was unexpectedly found to be lower than the incident wave height. This may have been due to the unsteadiness of the wind conditions during the first investigation. Such phenomena were very rare in the second investigation. Comparing the two wave heights in front of the Type A and Type B vertical wave-dissipating seawalls, that of Type A is generally greater, which implys that the reflection coefficient of Type B is smaller than that of Type A.

3. DIRECTIONAL WAVE SPECTRUM

3.1 Basic Formura for Estimating the Directional Spectrum

In the analysis of the directional spectrum with no reflected waves, all the component waves are assumed to be independent, with random and uniformly distributed phase angles. In analyzing the directional wave spectrum in the wave reflection system, however, the fixed phase relation of each pair of incident and reflected wave components should be considered. Therefore, the Modified Maximum Likelihood Method or MMLM was applied for the calculation of the directional wave spectrum and the reflection coefficient. This method is based on the relationship between the directional spectrum and the cross-power spectrum, with extra terms so called phase interaction terms. A directional wave spectrum and a reflection coefficient can be estimated by these two equations.

$$\frac{\alpha}{\hat{S}(\boldsymbol{k},\sigma)} = \sum_m \sum_n \Phi^{-1}_{mn} \exp\{i\boldsymbol{k}(\boldsymbol{x}_n - \boldsymbol{x}_m)\} - \frac{[\sum_m \sum_n \Phi^{-1}_{mn}[\exp\{i\boldsymbol{k}(\boldsymbol{x}_n - \boldsymbol{x}_{mr})\} + \exp\{i\boldsymbol{k}(\boldsymbol{x}_{nr} - \boldsymbol{x}_m)\}]]^2}{4\sum_m \sum_n \Phi^{-1}_{mn} \exp\{i\boldsymbol{k}(\boldsymbol{x}_{nr} - \boldsymbol{x}_{mr})\}} \quad (1)$$

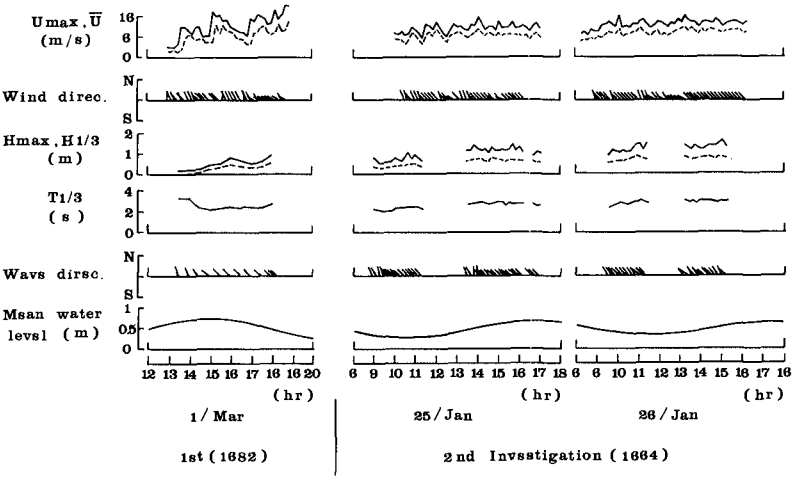

Fig. 5 Wind and wave conditions during the observation period.

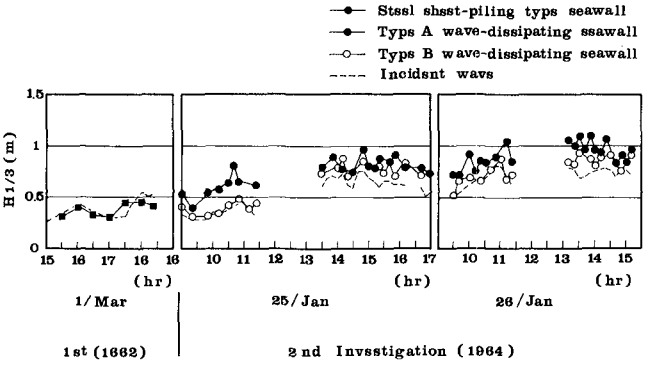

Fig. 6 Comparison between the height of incident waves and that of waves in front of the seawalls.

$$r=-\frac{\sum_m \sum_n \Phi^{-1}_{mn}[\exp\{i\boldsymbol{k}(\boldsymbol{x}_n-\boldsymbol{x}_{mr})\}+\exp\{i\boldsymbol{k}(\boldsymbol{x}_{nr}-\boldsymbol{x}_m)\}]}{2\sum_m \sum_n \Phi^{-1}_{mn}\exp\{i\boldsymbol{k}(\boldsymbol{x}_{nr}-\boldsymbol{x}_{mr})\}} \tag{2}$$

Where $\hat{S}(\boldsymbol{k},\sigma)$ means the estimated wavenumber-frequency spectrum. r denotes the reflection coefficients. $\Phi_{mn}(\sigma)$ is the cross-power spectrum of the water surface variations at point $\boldsymbol{x}_m$ and point $\boldsymbol{x}_n$. And α is a propotionality constant to adjust the power of the spectrum. Without the second term in the right-hand side of equation (1), it completely coincides with that for the standard MLM.

3.2 Design of Wave Gauge Array

The resolution power of a directional wave spectrum of the MMLM depends on the number and the arrangement of wave gauges. Therefore, the design of wave gauge array is one of the most important procedure in planning the measurement of the directional wave spectrum and the reflection coefficient. Numerical simulation was performed prior to the second investigation in order to study adequate arrangements of wave gauges. The procedure for the numerical simulation is as follows:

1) Specify a form for the directional energy distribution $S(\boldsymbol{k},\sigma)$ and the reflection coefficient. Here, the Mitsuyasu-type directional distribution expressed by equation (3) was used. The constant reflection coefficient was assumed for every directional component of waves.

$$S(\boldsymbol{k},\sigma)=\cos^{2s}\{(\theta-\theta_0)/2\} \tag{3}$$

where θ_0 is a principal wave direction and s is a parameter representing the degree of directional energy concentration.

2) Calculate $\Phi_{mn}(\sigma)$ for a given wave gauge array using the relationship between the cross-power spectrum and the directional wave spectrum in an incident and reflected wave field, which is expressed by equation (4).

$$\begin{aligned}\Phi_{mn}(\sigma)=\int_{\boldsymbol{k}} & S(\boldsymbol{k},\sigma)\\ & \times\{\exp(i\boldsymbol{k}\boldsymbol{x}_m)+r\exp(i\boldsymbol{k}\boldsymbol{x}_{mr})\}\\ & \times\{\exp(-i\boldsymbol{k}\boldsymbol{x}_n)+r\exp(-i\boldsymbol{k}\boldsymbol{x}_{nr})\}\,d\boldsymbol{k}\end{aligned} \tag{4}$$

3) Estimate the directional energy distribution from equation (1) and compare to the given one.

A line array with four wave gauges which has a pattern described in figure 7 was analyzed by the numerical simulation, using the values of the parameter s of 5 and 50. In figure 7, Δx is the distance between the first wave gauge and the reflective wall and D is the basic distance between the first and the second wave gauges. The third is located at 2D away from the second and the last is at 4D from the third.

The results indicated that the arrangement, in which Δx is less than 0.5L and D is between 0.2L and 0.3L, is effective for wide range of wave length. In the investigation, one more wave gauge was placed at the middle of the third and the last wave gauges.

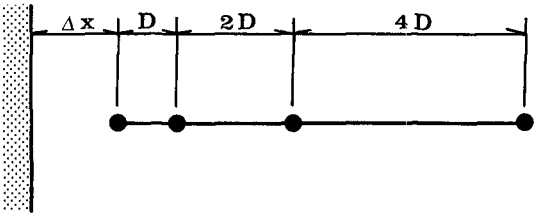

Fig. 7 Definition sketch of wave gauge array

3.3 Analysis of Field Data

Figure 8 shows some examples of the directional wave spectrum estimated from field data with MMLM. These are derived by integrating the wavenumber-frequency spectrum with respect to the frequency. The energy level is normalized by the total wave energy. The directional wave spectra for the incident waves, for the waves in front of the Type A and for the waves in front of the Type B seawall are compared. 0° and 180° are parallel with the line array of wave gauges. These directions are simultaneously perpendicular to the seawall line in figures 8(b) and 8(c).

At the incident wave measuring point, the wave direction is nearly perpendicular to the line array and most of the energy concentrates around the peak direction. The estimated directional wave spectrum in front of a seawall has two peaks in the symmetrical positions of 90°, corresponding to the incident and the reflected waves. The directional peaks of the incident and the reflected waves are sufficiently separated.

An example of the normalized directional energy distribution for each frequency is shown in figure 9. The graphs are arranged from bottom to top and from left to right, as the frequency increases. The peak frequency of wave energy is around 0.32 Hz. The separation of the incident waves and the reflected waves is good enough for each frequency.

4. REFLECTION COEFFICIENT

4.1 Definition of Reflection Coefficient

In estimating the reflection coefficient, the following two methods were compared. Equation (2) gives an estimation of the reflection coefficient for each frequency and for each direction. The first method is to adopt this one at the peak frequency and the peak direction. This reflection coefficient is denoted by r_p. The second

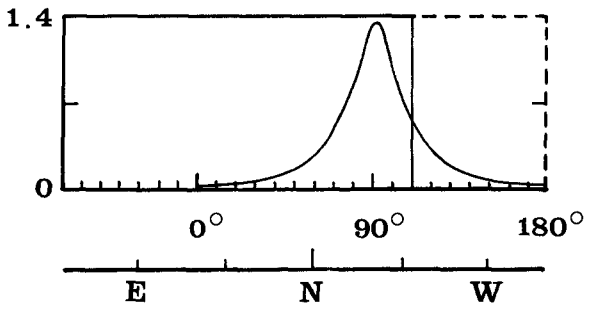

(a) Incident waves

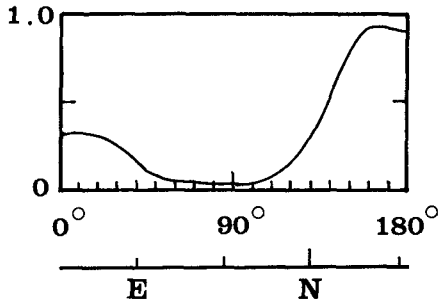

(b) Incident and reflected waves in front of the Type A seawall.

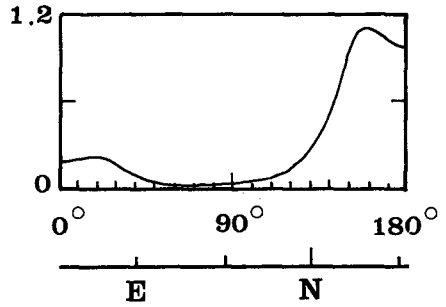

(c) Incident and reflected waves in front of the Type B seawall.

Fig. 8 Examples of estimated directional wave spectrum (1984/1/26, 13:30).

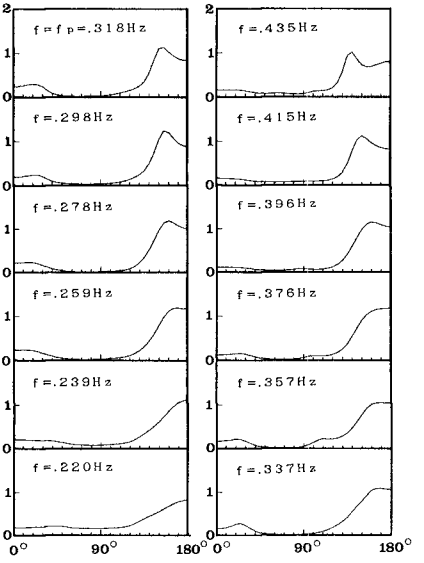

Fig. 9 An example of directional energy distribution for each frequency.

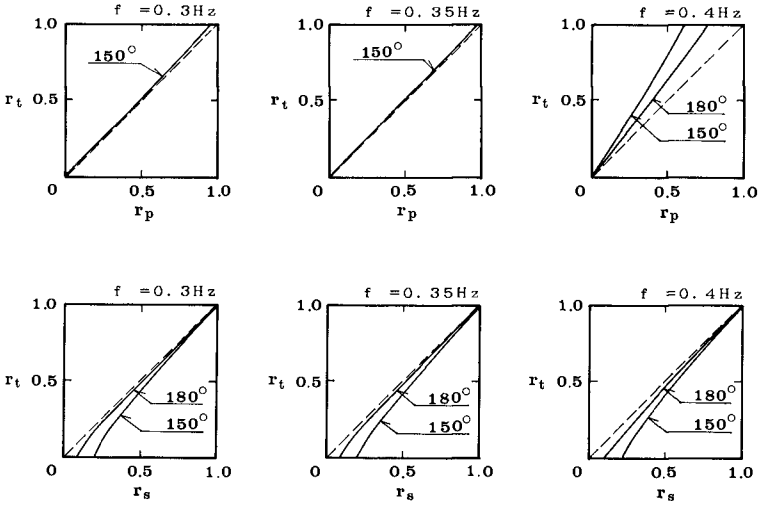

Fig. 10 Comparison between estimated and true reflection coefficients.

method is to adopt the square root of the ratio between the integrated reflected and incident wave energy. This reflection coefficient is denoted by r_s. The correspondence between the true reflection coefficient and the estimated one was analyzed by numerical simulation.

The results are presented in figure 10. In each graph the horizontal axis is an estimated reflection coefficient r_p or r_s and the vertical axis is a true reflection coefficient r_t. Three different frequency cases are shown for both r_p and r_s. The arrangement of wave gauges was assumed as that adopted in front of the Type B seawall. It can be found that r_p gives a fairly accurate value for the full range of the reflection coefficient when the peak frequency is between 0.3 and 0.35. Should the peak frequency be 0.4, r_p tends to underestimate in the high reflection range. When the true reflection coefficient is larger than 0.5, r_s gives a fairly good value for all frequencies.

4.2 Reflecting Characteristics of Seawalls

Tabel 1 shows the reflection coefficients of the vertical steel sheet-piling seawall estimated for twelve occasions of measurement. The incident wave direction, defined as an angle from the normal direction of the seawall line, varied between -20° and 30°. The peak frequency of the incident wave was between 0.34 and 0.44. The reflection coefficient is independent of the direction and the peak frequency of the incident wave and shows rather stable values between 0.85 and 1.0 with a mean value of 0.92.

Figure 11 shows the relationship between the relative width of wave chamber to wave length (l/L) and the reflection coefficient of the Type A wave-dissipating seawall. The wave length was calculated for the peak frequency of the incident wave. The reflection coefficient shows the minimum value of 0.3 at $l/L = 0.25$ and the maximum value of 0.9 at $l/L \approx 0.5$. This is the same tendency as was obtained by Tanimoto and Yoshimoto (1982) in the wave flume experiment for a vertical slit caisson (figure 12).

The reflection coefficient of the Type B wave-dissipating seawall was also plotted against l/L, but there seems to be poor correlation (figure 13). Figure 14 shows the relationship between the mean water level and the reflection coefficient. The reflection coefficient of the Type B doesn't depend on l/L, but has a good correlation to the mean water level. This is considered to be caused by the relative position of the holes through the front wall of the caisson and the water surface level under the condition of rather low wave height compared to the size of the holes.

The tendencies of the reflection coefficient changes stated above was also confirmed by the results of the wave height distribution measurements carried out simultaneously in the front area of the seawalls.

Table 1 Reflection coefficient of vertical steel sheet-piling type seawall.

time (1/Mar)	reflection coefficient		wave direction (deg)	peak frequency (Hz)
	r_p	r_s		
15:30	0.96	0.93	25	0.435
16:00	0.84	0.87	20	0.376
16:30	0.86	0.98	20	0.357
16:50	0.89	(1.06)	20	0.357
17:00	0.72	(1.01)	0	0.376
17:10	0.82	0.93	0	0.337
17:20	0.96	0.96	25	0.357
17:30	0.73	0.89	25	0.376
17:40	0.90	0.89	30	0.357
18:00	0.86	0.87	30	0.337
18:10	0.93	0.98	-20	0.347
18:20	0.78	0.90	-20	0.337
mean	0.85	0.92		

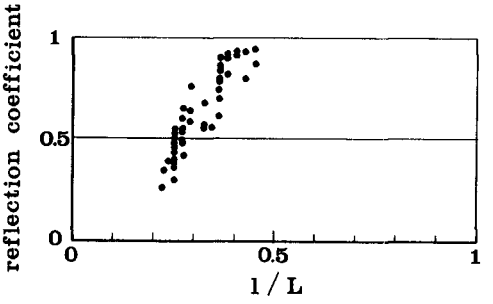

Fig. 11 Relationship between relative width of wave chamber(l) to wave length(L) and reflection coefficient: Type A seawall.

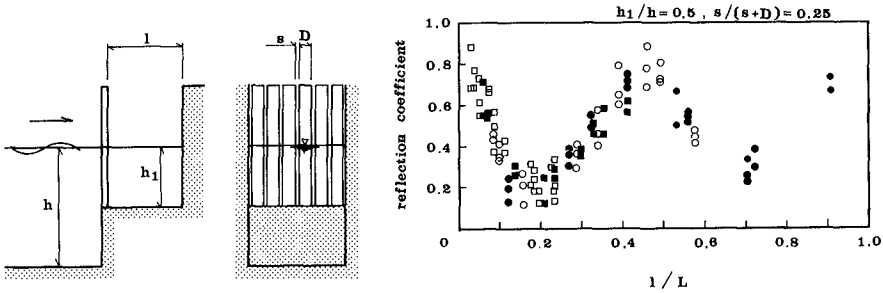

Fig. 12 Relationship between l/L and reflection coefficient in a flume experiment for a vertical slit caisson :after Tanimoto and Yoshimoto (1982)

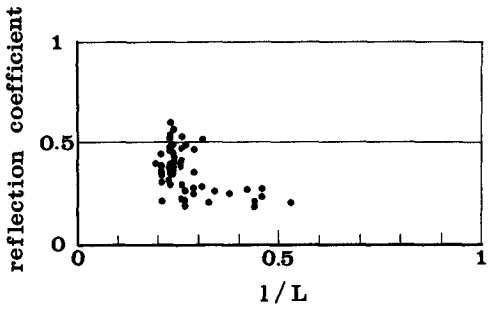

Fig. 13 Relationship between l/L and reflection coefficient: Type B seawall.

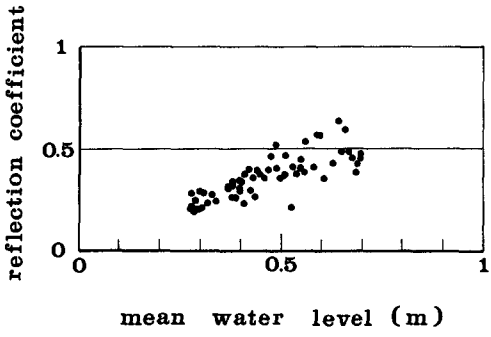

Fig. 14 Relationship between mean water level and reflection coefficient: Type B seawall.

5. CONCLUSIONS

The MMLM was applied to the field data in order to estimate the reflection coefficients of three different types of seawalls. The estimated directional wave spectra demonstrated that the MMLM has high resolusion power and can sufficiently separate the incident and the reflected wave energies.

As a result , it was found that the reflection coefficient of the vertical steel sheet-piling seawall is about 0.9 and is independent of the direction and the period of the incident wave, whereas those of the vertical wave-dissipating seawalls show considerable change in correlation to the incident wave period or the mean water level.

The design of wave gauge array is one of the most important procedure in planning the measurement of the directional wave spectrum and the reflection coefficient. It was possible in this study to determine the arrangement of wave gauges by numerical simulation so as to achieve a high accuracy in estimating the directional spectrum and the reflection coefficient since the dominant wave period and direction at the study area had been known before the investigation. Much more analysis by numerical simulation and understanding of the applicable limit of a wave gauge array used may be necessary in the measurement in an open sea, where the wave condition changes in a wide range of wave period and direction.

ACKNOWLEDGEMENTS

The authors express their appreciation to Mr. R. Kajima of the Central Research Institute of Electric Power Industry for his valuable consultation and advice. We would also like to thank Mr. K. Kaneko and Mr. T. Oku of the Kyushu Electric Power Co., Ltd. for their support to this study and for their permission to publish this paper.

REFERENCES

1) Goda, Y. (1985): Random Seas and Design of Maritime Structures, University of Tokyo Press, 323p.
2) Goda, Y. and Y. Suzuki (1976): Estimation of Incident and Reflected Waves in Random Wave Experiments, Proc. 15th Int. Conf. Coastal Eng., Hawaii, pp.828-845.
3) Isobe, M. and K. Kondo (1984): Method for Estimating Directional Wave Spectrum in Incident and Reflected Wave Field, Proc. 19th Int. Conf. Coastal Eng., Houston, pp.467-483.
4) Kajima, R. (1969): Estimation of Incident Wave Spectrum in the Sea Area Influenced by Reflection, Coastal Engineering in Japan, Vol.12, pp.9 - 16.
5) Mitsuyasu, H. et al. (1975): Observation of the Directional Spectrum of Ocean Waves Using a Clover-leaf Buoy, Jour. Physical Oceanogr., Vol.5, No.4, pp.750 - 760.
6) Tanimoto, K. and Y. Yoshimoto (1982): Factors of Wave Reflection from Vertical Slit Caisson Wall, Proc. 29th Japanese Conf. Coastal Eng., pp.389 - 393.

CHAPTER 147

WAVE ENERGY DISSIPATION IN ARBITRARILY SHAPED HARBOURS OF VARIABLE DEPTH

J.K. Kostense*, K.L. Meijer*, M.W. Dingemans*,
A.E. Mynett* and P. van den Bosch*

ABSTRACT

A finite element model for combined refraction-diffraction problems of linear water waves has been extended to include the effect of various dissipative mechanisms on wave excitation response in harbours of arbitrary shape and variable depth. Especially, the effects of bottom friction, partial absorption along the harbour contours, and transmission through permeable breakwaters have been considered. Although, within the mild slope approximation, the model is valid for arbitrary wave lengths, in this paper its effectiveness for harbour design applications is demonstrated for long wave induced resonance phenomena. For this purpose a realistic harbour geometry has been selected. A hydraulic scale-model of this harbour enabled experimental verification of the computational results.

1. INTRODUCTION

The propagation of linear time-harmonic waves in areas of variable depth can be described by the mild-slope equation, as derived by Berkhoff (1972). He solved the equation using a hybrid finite element method, representing the solution in the exterior by a continuous distribution of sources along the radiating boundary. A more elegant approach, resulting in symmetric matrices, was formulated by Chen and Mei (1974). They used a series expansion in terms of Hankel functions for the radiating waves and included the unknown expansion coefficients in a variational formulation.

After the introduction of a partially reflective boundary condition, Berkhoff (1976) could use his model to compute the wave disturbance in harbours with arbitrary reflective properties. As all absorbing conditions for numerical models, this condition cannot maintain the rate of energy dissipation for waves of different angles of incidence. Behrendt (1985) showed how to approximate the perfect boundary condition to higher order.

Booij (1981) suggested a modification of the mild-slope equation to account for the effect of bottom friction by adding a dissipative term. Dingemans (1985) considered the effect of bottom dissipation for shallow water conditions and shows the analogy between the obtained equations and the modified mild-slope equation. Dalrymple et al. (1984) have given several forms of the extra dissipation term for different energy dissipation mechanisms. Liu et al. (1986) showed that the extra term even can

* Delft Hydraulics, the Netherlands

be used to estimate the effects of reflective and transmissive breakwaters in numerical models based on the parabolic approximation of the mild-slope equation. On the other hand, Behrendt (1985) included the effect of bottom friction in the original mild-slope equation by formulating the energy loss as a flux of complex energy through the bottom.

Especially for very long waves the energy loss at the harbour entrance due to flow separation may be important. The modelling of a quadratic flow separation term can be incorporated in a numerical model by amending the matching conditions for pressure and normal velocity at the harbour entrance, see e.g. Berger (1986), who considered diffraction only.

Dissipation mechanisms may have a considerable influence on the wave disturbance in harbours, either for short period wind waves and swell, or for long period waves (tsunamis etc.), or both. For long waves resulting in harbour resonances the peak amplitudes at resonance are influenced by a number of mechanisms, see e.g. Mei (1983):

- radiation damping, i.e. energy escaping seaward from the harbour entrance,
- partial absorption along harbour boundaries due to wave breaking and frictional losses, including internal losses in permeable breakwaters,
- bottom friction,
- flow separation near the harbour entrance,
- finite-amplitude effects of energy transfer into higher harmonics.

Apart from the finite-amplitude effects, all these mechanisms can be accounted for in a newly developed numerical model solving the mild-slope equation. When finite-amplitude effects are expected to be the dominant mechanism, a model based on the Boussinesq equations for shallow water conditions could be applied, see e.g. Abbott et al. (1978).

The newly developed model solves the modified mild-slope equation accounting for bottom friction, and is equipped with a variety of options for appropriate boundary conditions, including one for combined reflection and transmission. To illustrate the effectiveness of the model for harbour design, a series of long wave computations is discussed for one specific realistic harbour geometry (see Fig. 1). Part of these computations have been compared with hydraulic scale-model experiments.

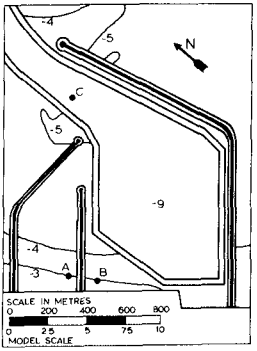

Figure 1 Harbour geometry

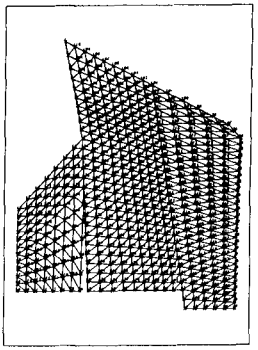

Figure 2 Finite-element grid no. 1

2. MODIFIED MILD SLOPE EQUATION

The mild-slope equation as derived by Berkhoff (1972, 1976) is a two-dimensional depth-integrated elliptic wave equation governing the propagation of linear time-harmonic waves in areas of moderate slope. The modified equation including the dissipation term as suggested by Booij (1981) reads

$$\nabla.(cc_g\nabla\phi) + cc_g(k^2 + ik\gamma)\phi = 0, \tag{1}$$

where $\phi(x,y)$ denotes the two-dimensional velocity potential in the horizontal plane, related to the total potential $\Phi(x,y,z,t)$ according to

$$\Phi(x,y,z,t) = \phi(x,y)\,\frac{\cosh k(h+z)}{\cosh kh}\,e^{-i\omega t}. \tag{2}$$

In Eq. 1, c, c_g and k represent the phase velocity, the group velocity and the wave number, respectively, which can be evaluated from the linear dispersion relation. The funtion γ is defined as W/c_g, where W is the rate of energy dissipation per unit wave energy intensity.

In order to derive Eq. 1, including the effect of energy dissipation due to bottom friction, the principle of virtual work may be employed. Notice in this respect that the original mild-slope equation was obtained by application of a variational principle, and that variational principles are especially suited for conservative systems. However, this approach would be rather intricate and will not be followed here. Instead, Eq. 1 will be made plausible by showing the analogy to the result for shallow water waves. For the case of shallow water, the vertically integrated continuity equation and the horizontal momentum equation read in linearized form

$$\frac{\partial\eta}{\partial t} + \nabla.(\vec{hu}) = 0 \quad , \quad \frac{\partial\vec{u}}{\partial t} + g\nabla\eta + \frac{\vec{\tau}}{\rho h} = 0 \ , \tag{3}$$

where $\vec{\tau}$ is the bottom shear stress vector, for which the friction law

$$\vec{\tau} = \frac{1}{2}\,f_w\,\rho|\vec{u}_b|\vec{u}_b \tag{4}$$

is taken, where $\vec{u}_b$ is the wave velocity just outside the bottom boundary layer. With $\vec{u}_b = \vec{u}/\cosh kh$, according to linear theory, the term $\vec{\tau}/\rho h$ is linearized as $W\vec{u}$, so as to obtain the same amount of dissipation over one wave period. This results in

$$W = \frac{4f_w}{3\pi h}\,\frac{1}{(\cosh kh)^2}\,u_e, \tag{5}$$

where f_w is the wave friction coefficient, and u_e represents the effective amplitude of the horizontal velocity

$$u_e = \frac{3\pi}{8}\int_0^T(\vec{u}.\vec{u})^{3/2}dt \;/\; \int_0^T(\vec{u}.\vec{u})dt \ . \tag{6}$$

The product $(\vec{u}.\vec{u})$ can be written as

$$\vec{u}.\vec{u} = p + q\cos(2\omega t - \alpha), \tag{7}$$

where p and q are functions of the derivatives of the real and imaginary parts of the velocity potential $\phi(x,y)$ with respect to x and y. Substituting Eq. 7 into Eq. 6, one obtains after some algebraic manipulation

$$u_e = \sqrt{p+q}\ \{E(m) - \frac{1}{4}(1 - \frac{q}{p})K(m)\}, \qquad m = \frac{2q}{p+q}\ , \tag{8}$$

in which K(m) and E(m) denote the complete elliptic integrals of the first and second kind, respectively, and m is the elliptic parameter. Notice that for p=q the horizontal velocity components are in phase, and the effective velocity amplitude equals the amplitude of the unidirectional velocity $\hat{u}$. Upon combination of the continuity and the momentum equation, and introducing the velocity potential, one obtains for time-harmonic motion

$$\nabla.(gh\nabla\phi) + gh(k^2 + \frac{ikW}{\sqrt{gh}})\phi = 0\ . \tag{9}$$

Because of the close resemblance between this equation and the unmodified mild-slope equation for shallow water, where $c = c_g = \sqrt{gh}$, it seems reasonable to model wave dissipation in the mild-slope equation according to Eq. 1.

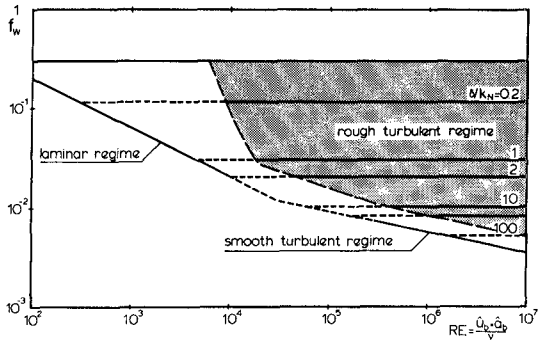

Figure 3 Wave friction coefficient f_w for different boundary layer regimes, see Jonsson (1978)

To determine the wave friction coefficient f_w, as defined in Eq. 4, the relations derived by Jonsson (e.g. 1978) have been used. Jonsson distinguishes three relations for the different types of boundary layers (see Fig. 3):

- laminar regime: $f_{w,l} = 2\ (RE)^{-0.5}$ (10)
- smooth-turbulent regime: $f_{w,s} = 0.09\ (RE)^{-0.2}$ (11)
- rough-turbulent regime: $f_{w,t} = 0.0605/(\log \frac{27\delta}{k_N})^2$. (12)

Moreover, the friction coefficient has a maximum value:

$$f_w \leq 0.30\ . \tag{13}$$

In these relations the amplitude Reynolds number is defined as

$$RE \equiv \frac{\hat{u}_b\ \hat{a}_b}{\nu}\ , \tag{14}$$

where ν denotes the kinematic viscosity, and $\hat{a}_b$ represents the amplitude of the particle excursion at the bed. The thickness of the rough-turbulent boundary layer, δ, can be determined from

$$\delta = 0.072 \, (\hat{a}_b k_N)^{0.25}, \tag{15}$$

where k_N is the well-known Nikuradse roughness parameter. Although the above equations have been derived for unidirectional oscillating flow conditons, $\hat{u}_b$ can be approximated by $u_e/\cosh(kh)$ and $u_e/[\omega\cosh(kh)]$, respectively (see Eq. 6). In nature the boundary layer will always be rough-turbulent. However, as all regimes have been implemented in the numerical model, small-scale hydraulic model conditions can be handled too. This is especially useful for verification studies.

Eq. 1 is solved by means of standard finite element techniques, using triangular elements with linear interpolation functions. The non-linearity, as introduced by the dissipation term, is treated in a straightforward iterative way. If the bottom friction is a predominant dissipation factor, which can be the case for harbour resonance problems, an average number of 3 to 5 iterations appears to be adequate to obtain reliable results. However, if the bottom friction is only a secondary dissipative effect, as for most problems where short wind waves are involved, 2 iterations are already sufficient in most cases.

3. BOUNDARY CONDITIONS

Different types of boundary conditions have been implemented in the finite element model, viz.

- radiation conditions,
- a wave-maker condition,
- a condition for partial reflection, and
- a condition for combined partial reflection and transmission.

Radiation damping can be treated in two ways. Both methods match the finite element region and the outer region, where constant depth is assumed by requiring the continuity of pressure and normal velocity. The first method, applied by Berkhoff (1972, 1976), is to represent the solution in the outer region by a continuous distribution of sources along the open boundary:

$$\phi_s = \int_A u(M) \, \frac{1}{2i} \, H_0^1(kr) \, ds \, , \tag{16}$$

where ϕ_s is the velocity potential of the scattered waves, A is the open boundary, and $H_0^1(kr)$ denotes the Hankel function of the first kind and zero'th order. The unknown source strength $\mu(M)$ at point M must be solved along with the inner region by requiring the two matching conditions. Chen and Mei (1974) succeeded to incorparate the matching conditions as natural boundary conditions in a variational principle by representing the velocity potential of the scattered waves as a series expansion of Hankel functions,

$$\phi_s = \sum_{n=0}^{\infty} H_n^1(kr) \, (\alpha_n \cos n\Theta + \beta_n \sin n\Theta) \, , \tag{17}$$

where r and Θ are polar co-ordinates. Again, the coefficients α_n and β_n are determined by matching with the solution in the inner region. Both methods have been implemented in the numerical model. In general, the second method is to be recommended, as it results in a symmetric matrix. However, as the region to be modelled will generally be larger for this method, sometimes the source method may be preferable, especially for harbours and bays with wide openings.

To be able to compare with hydraulic model experiments, a wave-maker condition is very useful. The implemented condition reads

$$\frac{\partial \phi}{\partial n} + ik\tilde{\phi} = 0 \ , \tag{18}$$

where $\tilde{\phi}$ is the velocity potential of the generated waves, and n is the direction normal to the wave paddle. As can be simply derived, Eq. 18 implies a 100% reflective paddle.

Partially reflective harbour contours are modelled with the well-known equation (see e.g. Berkhoff, 1976)

$$\frac{\partial \phi}{\partial n} - ik(1-r)\phi = 0 \ . \tag{19}$$

This condition will work for all kinds of incident wave systems in regions of variable depth, and for curved boundaries. However, to relate the actual reflection coefficient R to the complex coefficient r, a long-crested wave incident on a straight boundary in constant water depth is assumed, i.e.

$$\phi = \phi_i e^{i(kx\cos\alpha - ky\sin\alpha)} + R\phi_i e^{i(kx\cos\alpha + ky\sin\alpha + \rho)} , \tag{20}$$

where ρ denotes the phase shift at the boundary. Subsitution in Eq. 19 yields

$$Re^{i\rho} = \frac{\sin\alpha - 1 + r}{\sin\alpha + 1 - r} , \tag{21}$$

showing the dependence of R on the angle of incidence α.

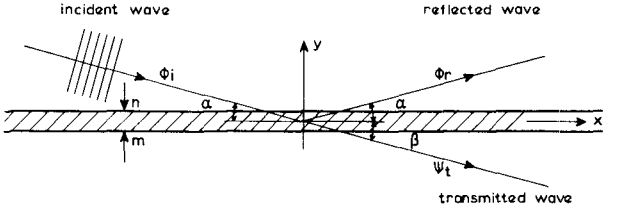

Figure 4 Definition sketch for a transmitting boundary

Analogously to Eq. 19 a boundary condition for combined reflection and transmission has been developed, assuming equal reflection and transmission characteristics in both directions, i.e. symmetrical constructions. The velocity potentials on either side of the transmitting boundary are denoted as ϕ and ψ, where

$$\phi = \phi_o + \phi_t \quad , \quad \psi = \psi_o + \psi_t . \tag{22,23}$$

The subscript t refers to that part of the local potential which originates from transmission, see Fig. 4 for a reference sketch. The general form of the boundary condition consists of the following set of four equations

$$\psi_t = s\phi_o \quad , \qquad \phi_t = s\psi_o \tag{24,25}$$

$$\frac{\partial\phi_t}{\partial m} = -t\frac{\partial\phi_o}{\partial n} \quad , \qquad \frac{\partial\phi_t}{\partial n} = -t\frac{\partial\psi_o}{\partial m} \quad , \tag{26,27}$$

where s and t are complex coefficients. Eq. 19 for ϕ_o and a similar one for ψ_o, Eqs. 22, 23 and similar ones for the normal derivatives of the potential, and Eqs. 24 to 27 constitute a set of 10 equations for 12 unknowns. Elimination yields the following two equations in terms of the potentials ϕ and ψ, and their respective normal derivatives:

$$(1-s^2)\frac{\partial\phi}{\partial n} - ik(1-r)\{(1+st)\phi - (s+t)\psi\} = 0 \tag{28}$$

$$(1-s^2)\frac{\partial\psi}{\partial m} - ik(1-r)\{(1+st)\psi - (s+t)\phi\} = 0 \ . \tag{29}$$

Across the boundary the velocity potential jumps discontinuously, which can be numerically treated by means of line elements with double nodes. To achieve full reflection for r = 1, as well as non-transmission for t = 0, the coefficient s has been taken to be

$$s = (1-r)t \ . \tag{30}$$

Again assuming long-crested waves in constant water depth, the velocity potential on either side of the boundary may be described by Eq. 20 along with

$$\psi = T\phi_i e^{i(kx\cos\beta - ky\sin\beta + \tau)} , \tag{31}$$

where τ denotes the phase shift of the transmitted wave over the barrier, see also Fig. 4 for the reference system. For $\beta = \alpha$, substitution of Eqs. 20 and 31 in Eqs. 28 to 30 yields

$$Re^{i\rho} = \frac{-t^2(1-r)^2(1-\sin\alpha)(1+\sin\alpha) + (1-r+\sin\alpha)(1-r-\sin\alpha)}{+t^2(1-r)^2(1-\sin\alpha)^2 - (1-r+\sin\alpha)^2} \quad \text{and} \tag{32}$$

$$Te^{i\tau} = \frac{-2t(1-r)(2-r)\sin\alpha}{+t^2(1-r)^2(1-\sin\alpha)^2 - (1-r+\sin\alpha)^2} \ . \tag{33}$$

As an example, for t = 1 and $\rho = \tau = 0$ these equations result in

$$R + T = 1 \ , \tag{34}$$

which implies a rate of energy dissipation

$$D = 1 - R^2 - T^2 . \tag{35}$$

Eq. 34 has been derived by Madsen and White (1975) for a permeable breakwater and long waves. Fig. 5 shows the dependency of R and T on the angle of incidence, also for t = 1 and $\rho = \tau = 0$. For normally incident waves Eqs. 32 and 33 reduce to

$$Re^{i\rho} = \frac{r}{2-r} \qquad \text{and} \qquad Te^{i\tau} = \frac{2t(1-r)}{2-r} \ . \tag{36,37}$$

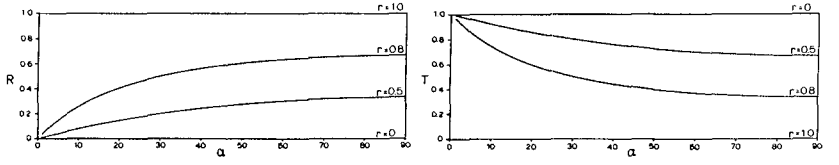

Figure 5 Reflection (R) and transmission (T) coefficients as functions of the angle of incidence (α); $t = 1$, $\rho = \tau \approx 0$

Apart from transmission through permeable breakwaters, the transmission conditions might be also applied to approximate the effect of energy loss due to flow separation at the harbour entrance, and at protruding structures within the harbour. The usual formulation for the energy loss at the harbour entrance is

$$\eta^- - \eta^+ = \frac{f_e}{2g} u|u|, \tag{38}$$

where η^- and η^+ denote the free-surface displacements on either side of the constriction, and u is the velocity component normal to the entrance. In the equation the apparent inertia term has been neglected, which is acceptable for long waves. Unfortunately, direct empirical knowledge of the friction coefficient f_e is hardly available, but generally f_e is assumed to be ≤ 1.5.

4. SOME APPLICATIONS FOR A COMPLEX HARBOUR GEOMETRY

The model has been satisfactorily verified for a variety of simple configurations, permitting a comparison with analytical solutions. The verification programme included the classical Homma island surrounded by a parabolic shoal, a rectangular harbour with constant depth, and obliquely incident waves over a linearly sloping bottom with constant depth at both sides. After these verifications the model has been used in normal laboratory advice practice, mostly to study harbour responses due to wind waves and swell. The model has recently been implemented on a CRAY-XMP supercomputer. Taking full advantage of the vector-processor, the sytem of equations is solved quite efficiently. Until now, the largest system which has been solved, referred to a grid of 37,000 nodal points for a 10 second wave computation without bottom dissipation in an area of about 10 km^2. The CPU time to execute this computation was about 2 minutes.

Hereafter, some results of further research will be shown to illustrate the effectiveness of the numerical model to solve harbour resonance problems. It is well known that harbour oscillations induced by long waves may result in considerable hazards for e.g. moored ships. Although a variety of forcings can be responsible for these oscillations, the most studied forcing is due to incident free long waves (tsumamis etc.). Until now, most numerical models mainly predict the natural frequencies of the harbour and the corresponding oscillation modes. However, there is an increasing need for realistic peak amplitudes at resonance, especially for numerical methods to determine the dynamic behaviour of moored vessels inside a harbour, see e.g. Mynett et al. (1985). To examine whether this model could fulfil this need, a series of computations was

performed for a realistic harbour geometry (see Fig. 1). The choice of this specific lay-out enables the comparison with experiments in a physical model having a length scale of 1:80. The harbour area of about 1 km^2 is divided into two parts by an inner breakwater. The main part has been dredged to -9.0 m; the shallow part accomodates fishing-boats etc. All computations and experiments have been carried out for a water level of Chart Datum + 1.25 m. For the computations three different finite element grids have been used, viz.

- grid no. 1, including the harbour area only, and having scale-model dimensions (see Fig. 2),
- grid no. 2, reproducing the scale-model (see Fig. 9), and
- grid no. 3, reproducing the harbour and surroundings at natural scale (see Fig. 13).

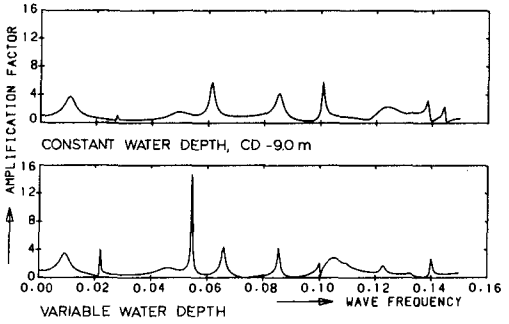

Figure 6 Harbour response at position B for constant and variable depth; radiation damping only, grid no.1

Grid no. 1 was used for some first computations on the effects of the variable depth and the (laminar) bottom friction. The direction of the incident waves was 30° from North (see Fig. 1) and the harbour contours were 100% reflective. Fig. 6 shows for position B (see Fig. 1), that, even for a harbour with constant water depth in its main part, a combined refraction-diffraction model is essential to predict natural frequencies. For the same position, Fig. 7 illustrates the effect of bottom friction, using a Nikuradse roughness of k_N = 0.5 mm, which represents the cemented bottom of a scale model. Even for a very moderate height of the incident waves, H = 1.5 mm, the reduction due to bottom friction can be quite considerable, especially for sharp resonance peaks. For example, the peak at 0.055 Hz, representing a mode with half a wave length between the inner breakwater and the eastern one, is reduced to less than 20% at point B.

A sketch of the lay-out of the physical model is shown in Fig. 8. The long wave experiments have been performed for one wave direction, for which situation the position of the wave generator and two guiding walls have been indicated. Monochromatic waves with a wave height of 3 mm were generated for a series of wave periods between 10 and 40 seconds, excluding the occurrence of wave breaking. Ten wave height gauges were used, including one in the harbour mouth. The measured signals have been Fourier analysed to obtain the wave amplitude in the fundamental frequency. All breakwaters had a 1:2 slope of rough stones and were fully

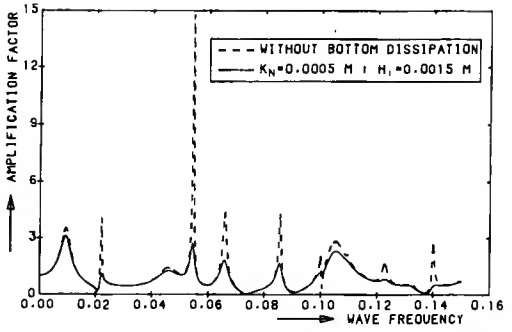

Figure 7 The effect of frictional damping on the harbour response at position B, grid no. 1

impermeable. The boundaries at the south end of the harbour were vertical quays. The finite element grid for the verification study is shown in Fig. 9. The main reason to reproduce the area around the access channel was to be certain of correct wave directions at the harbour mouth. As Fig. 9 shows, the regions behind the guiding walls have not been reproduced. The boundaries at the end of the guiding walls have been supposed to be fully absorbing; all other boundaries were 100% reflective. Earlier computations had revealed that only a marginal absorption rate in the order of 5% can reduce the harbour response at resonance by more than 25%, see also Behrendt (1985). However, such small reductions are hardly measurable in a complex harbour model. Another main reason to expect lower responses in the scale model beforehand, is that the wave generators are not fully reflective, which was assumed in the numerical model, see Eq. 18.

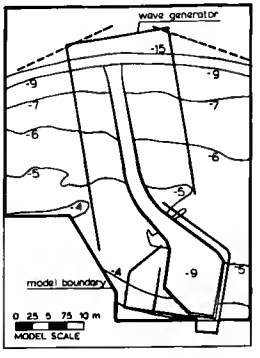

Figure 8 Lay-out of 1:80 scale model

Figure 9 Finite-element grid no. 2

Fig. 10 shows representative examples of the comparison between measurements and computations for two stations. Position A refers to a corner in the shallow basin and position C is situated in the harbour entrance, see Fig. 1. The lowest graph shows the amplification between both stations. Looking at the upper graphs, it is obvious that in general the

computed responses indeed exceed the measured ones. However, especially for two frequencies considerable discrepancies occur, i.e. for f=0.039 Hz and f=0.066 Hz. As shown in Figs. 11 and 12, these specific frequencies induce resonance in the outer area, between the wave generator and the breakwaters. This distance equals one wave length for f = 0.039 Hz and 2.5 wave lengths for f = 0.066 Hz. The discrepancies at these frequencies may be explained by the fact that the wave generator did not reflect the incident wave energy completely, as was assumed in the numerical model. Nevertheless, this hardly explains the large amplification between stations A and C for 0.066 Hz (see Fig. 10). A more thorough examination of this frequency revealed that the amplification was very sensitive for the position of the antinodal line at the harbour entrance. A minor change of this position, due to a slightly different grid in the sharp corner between the western breakwater and the outer boundary, reduced the amplification between stations A and C considerably. Apart from the discussed frequencies, the agreement between measurements and computations is quite satisfactory, especially when considering the amplification between the harbour entrance and positions within the harbour. In general, the computations result in higher responses at resonance frequencies. This may be attributed to the following reasons: minor absorptions along the boundaries, the energy loss due to flow separation at the breakwater ends, and finite-amplitude effects resulting in energy transfer to higher harmonics. The small shifts in the peak frequencies are ascribed to non-linear effects.

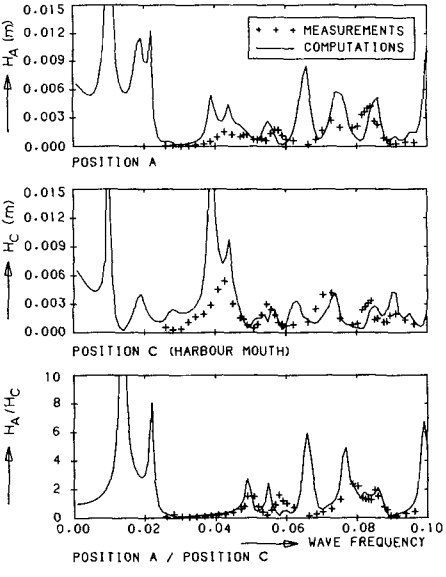

Fig. 10 Comparison between measured and computed harbour response at positions A and C; H_I = 0.003 m, k_N = 0.0005 m

The third set of computations refers to prototype scale, implying turbulent boundary layers. The bathymetry in the grid area is shown in Fig. 13. A constant value of the Nikuradse roughness, k_N = 0.04 m, has been taken for the entire area. Although less dominant than for the laminar case the effect of bottom friction can still be considerable; results will be reported elsewhere. The effects of partial reflection and transmission have been studied for monochromatic waves incident from a direction perpendicular to the main breakwater (70 °), with an incident wave height H = 0.25 m and wave frequencies up to 0.01 Hz. The boundary conditions 28 and 29 have been used for all three breakwaters, whereas the southern boundaries of the harbour have been assumed to be fully reflective for all computations. As an example of the results, the harbour response at position A is compared in Fig. 14 for the following three breakwater characteristics:

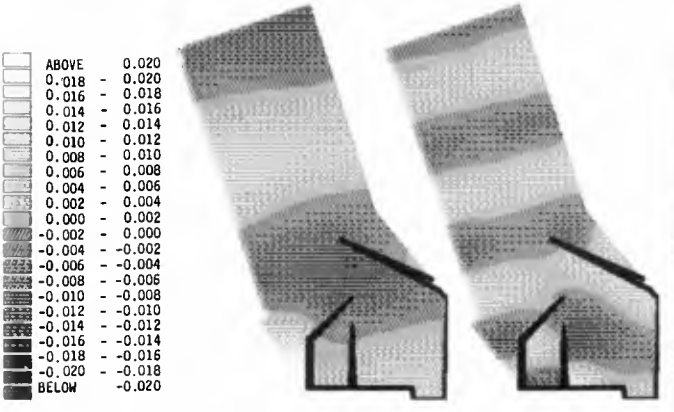

Fig. 11 Free surface contours at the moment of maximum elevation for $f = 0.039$ Hz; $H_I = 0.003$ m, $k_N = 0.0005$ m

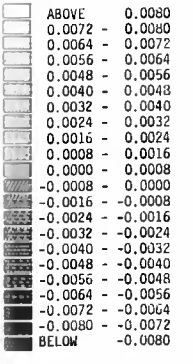

Fig. 12 Free surface contours at the moment of maximum elevation for $f = 0.066$ Hz; $H_I = 0.003$ m; $k_N = 0.0005$ m

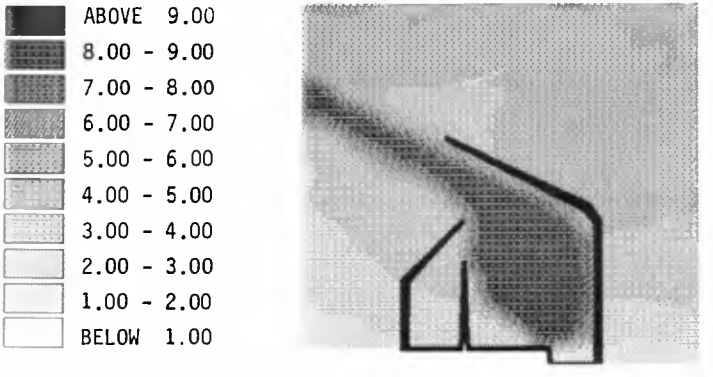

Figure 13 Bathymetry in computational area (grid no.3)

a) full reflection: $R = 1.0$, $T = 0.0$
b) partial reflection: $R = 0.9$, $T = 0.0$ and
c) partial reflection and transmission: $R = 0.9$, $T = 0.1$.

The constants in Eqs. 28 and 29 have been determined from the relations 36 and 37 under condition of no phase shift, i.e. $\rho = \tau = 0$.

A comparison of conditions a) and b), see Fig. 14, shows that a small reduction of R results in a considerable reduction of the amplifications at resonance. The maximum amplification is seen to be about 2, which also holds for other positions within this specific harbour. Although, for impermeable breakwaters a reflection coefficient of $R = 1.0$ is quite

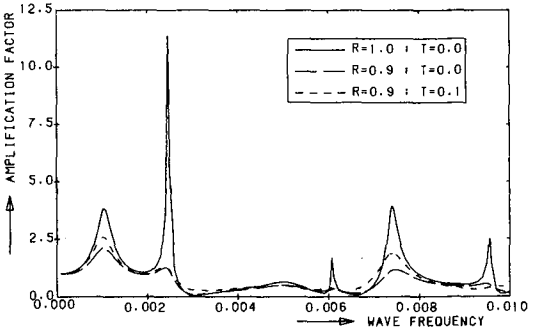

Figure 14 The effect of partial reflection and transmission on the harbour response at position A, grid no. 3

realistic for relatively long waves, condition c) is more appropriate for permeable breakwaters of the rubble mound type, for which T = 0.1 is even a rather low value. As Eq. 35 shows, conditions b) and c) result in almost the same energy loss at the boundaries. However, due to transmission there is an extra inflow of energy through the breakwaters, here primarily through the main breakwater. A comparison of conditions b) and c) in Fig. 14 shows a small increase in amplification due to transmission for all frequencies. It is noted that for other positions the amplifications of c) can also be less than those of b) for parts of the frequency range. The above results suggest that for permeable breakwaters the energy dissipation within the breakwater is of paramount influence on the response characteristics, whille the extra inflow of energy is much less important.

In Fig. 14 the response peak at 0.0246 Hz refers to the Helmholtz mode of the inner shallow basin. The small peak at 0.00608 Hz represents an oscillation mode of the main basin. This mode is shown in Fig 15 for four different conditions, and illustrates again that partially absorbing boundaries may have an enormous effect on peak responses.

5. CONCLUSIONS

A finite element model solving the modified mild-slope equation for waves with arbitrary wave length has been applied to study dissipative effects on harbour resonance phenomena. The effects of bottom friction, partially absorbing boundaries, and also transmission have been considered. To model the effect of combined reflection and transmission, a new boundary condition has been proposed. The following conclusions have been obtained:

- In harbour design studies, it is essential to include the effect of variable depth in the mathematical model to obtain a good prediction of the resonance frequencies.
- Bottom dissipation may be of considerable influence on the harbour response at resonance, both for laminar and turbulent flow regimes.
- Usually, harbour response studies are performed for fully reflective harbour contours. It has been shown that a small reduction of reflection coefficients may result in a drastic decrease of the harbour response at resonance. Such reductions occur in case of permeable rubble mound breakwaters. The effect of the additional inflow of wave

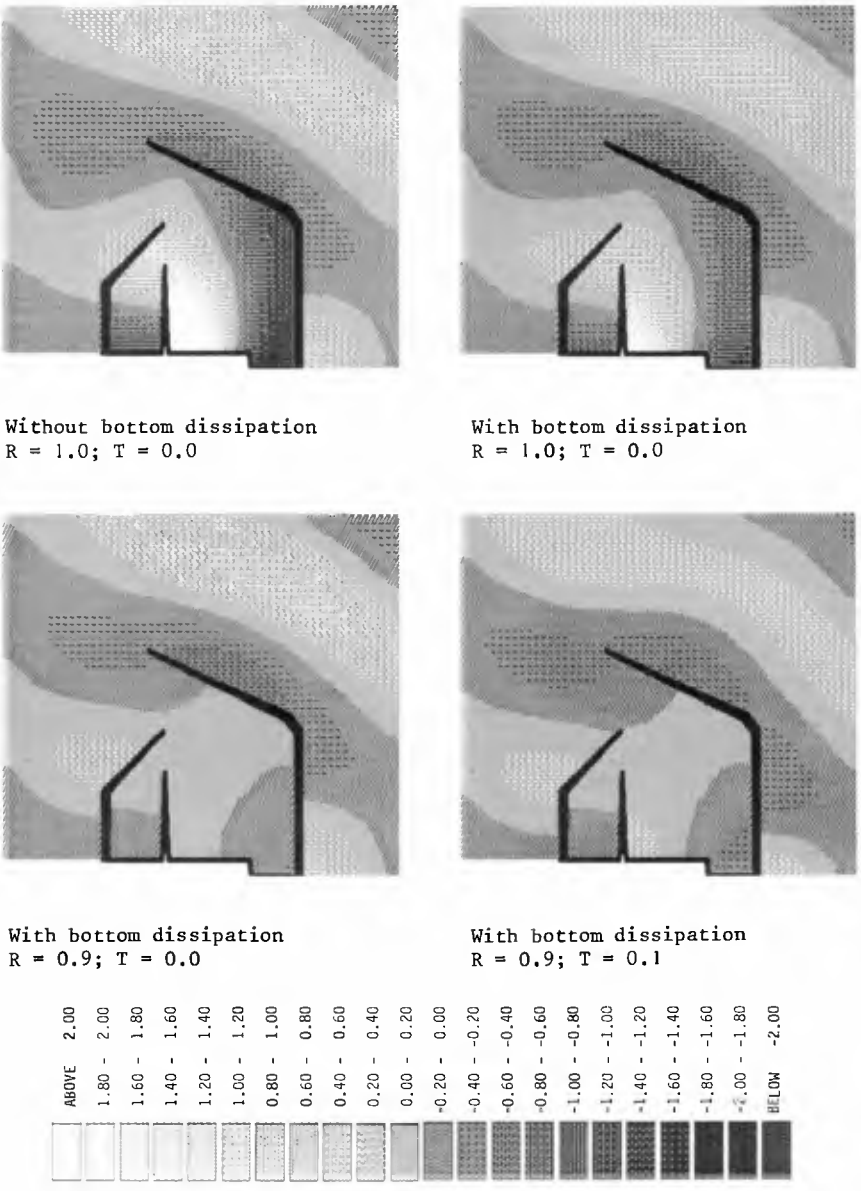

Figure 15 Free surface contours at the moment of maximum elevation for f = 0.00608 Hz; H_I = 0.25 m, k_N = 0.04 m

energy through these breakwaters is found to be less important than the effect of energy dissipation within the breakwater.

- Comparison between measurements in a hydraulic scale model and numerical computations shows a satisfactory agreement in harbour responses. This confirms that, also for long waves, the numerical model is an useful tool for engineering design purposes. The agreement might be even further improved by inclusion of the effect of flow separation in the model. However, for applications it is most essential to represent the appropriate boundary conditions correctly.

REFERENCES

Abbott, M.B., Petersen, H.M. and Skovgaard, O., 1978: On the numerical modelling of short waves in shallow water; J. Hydr. Res., Vol. 16, No. 3, pp. 173-204.

Behrendt, L., 1985: A finite element model for water wave diffraction including boundary absorption and bottom friction; Inst. Hydrodyn. and Hydraulic Engng., Techn. Univ. Denmark, Series Paper no. 37.

Berkhoff. J.C.W., 1972: Computation of combined refraction-diffraction; Proc. 13th Int. Conf. Coastal Engng., ASCE, Vancouver, Vol. 1, Chap. 24, pp. 471-490.

Berkhoff, J.C.W., 1976: Mathematical models for simple harmonic linear water waves, wave diffraction and refraction; Delft Hydraulics Lab., Publ. no. 163.

Booij, N., 1981: Gravity waves on water with non-uniform depth and current; Communications on Hydraulics, Dept. of Civil Engng., Delft Univ. of Techn., Rep. no. 81-1.

Chen, H.S. and Mei, C.C., 1974: Oscillations and wave forces in an offshore harbor; Parsons Lab., Massachusetts Inst. of Techn., Rep. no. 190.

Dalrymple, R.A., Kirby, J.T. and Hwang, P.A., 1984: Wave diffraction due to areas of energy dissipation; J. of Waterway, Port, Coastal and Ocean Engng., ASCE, Vol. 110, No. 1, pp. 67-79.

Dingemans, M.W., 1985: Surface wave propagation over an uneven bottom, evaluation of two-dimensional horizontal wave propagation models; Delft Hydraulics Lab., Rep. no. W310, part 5.

Gerber, M., 1986: Modelling dissipation in harbour resonance; Coastal Engineering, Vol. 10, pp. 211-252.

Jonsson, I.G., 1978: A new approach to oscillatory rough turbulent boundary layers; Inst. Hydrodyn. and Hydraulic Engng., Techn. Univ. Denmark, Series Paper no. 17.

Liu, P.L.-F., Yoon, S.B. and Dalrymple, R.A., 1986: Wave reflection from energy dissipation region; J. of Waterway, Port, Coastal and Ocean Engng., ASCE, Vol. 112, No. 6, pp. 632-644.

Madsen, O.S., and White, S.M., 1975: Reflection and transmission characteristics of porous rubble mound breakwaters; Parsons Lab., Massachusetts Inst. of Techn., Rep. no. 207.

Mei, C.C., 1983: The applied dynamics of ocean surface waves; John Wiley and Sons, New York.

Mynett, A.E., Keuning, P.J. and Vis, F.C., 1985: The dynamic behaviour of moored vessels inside a harbour configuration; Proc. Int. Conf. Numerical and Hydraulic Modelling of Ports and Harbours, IAHR, Birmingham, pp. 211-220.

Skovgaard, O., Behrendt, L. and Jonsson, I.G., 1984: A finite element model for wind wave diffraction, Proc. 19th Int. Conf. Coastal Engng., ASCE, Houston, Vol. 1, Chap. 74, pp. 1090-1102.

CHAPTER 148

On the floating breakwater - a new arrangement

C.H. LEE* and S.W. TWU**

Abstract

A new type of floating breakwater composed of net-tubes and buoy-balls is presented in this paper. A series of model studies have been carried out for several arrangements of this structure. As wave damping effect is concerned, a case that the structure being set vertically is shown to be better than the one being set horizontally, while more than two rows of the structures are set vertically and separately, a case which being connected with ropes between adjoining rows is proved to be better than the case without connecting ropes.

1 INTRODUCTION

Breakwaters have been developed into many practical patterns. Most of them are made of rubble or/and caissions which are effective but expensive. It is known that most wave energy distributes over the upper portion of water depth. Hence it is economical to attenuate wave energy in the vicinity of free surface.

With booming of economics and a rise in population, Republic of China is in urgency searching any available resources to meet the demand of continuous development. Fortunately, Taiwan is situated on the continental shelf where is fit for aquaculture, knowever, the wave conditions make it difficult to run. Consequently a special device of floating breakwater may be the alternative.

In general, most floating breakwaters are designed to be laid over the water surface "horizontally". It is interesting to note what the effect is if a floating breakwater is set "vertically". A structure composed of net-tubes and buoy-balls has been developed by the authors as shown in photo 1, also named wave-fence for convience. This type of floating breakwater may meet the requirements of water-circulation and wave-dissipation effectively as well as economically if designed properly.

2. ANALYSIS OF WAVE DISSIPATION BY THE NEW ARRANGEMENT

It is reasonable that multiple rows of wave-fences will be more effective than single one. If each of them is linked by ropes, the water body within those rows can be regarded as a part of the damping system and the effect of wave damping will be better.

* Engineer, Planning Dept., BES Engineering Corporation, P.O. Box 335, Taipei Taiwan Republic of China.
** Professor Hydraulics & Ocean Engg. Dept., Cheng-Kung University, Tainan, Taiwan, Republic of China.

According to the small amplitude wave theory, it is known that the water particles in the crest and the trough of a wave move in the same magnitude but opposite direction respectively. With this idea, we may set the interval of two rows to be half length of the incident wave and connect them with ropes simultaneously. When the crest and the trough are exactly on the two rows respectively, each of which will incur wave forces in the same magnitude but opposite direction. Then the two rows will stand still like a fixed system for a while and the exerting wave forces will be eliminated each other through such a system.

In fact the waves on the open sea cover a wide range of period. We may pick up some dominant waves, i.e. design waves, of different periods which are to be disposed, say N waves. The required number of wave-fences, M, is related with N by the formula

$$\frac{M(M-1)}{2} = N \qquad \text{where } M > 2$$

For example, when M=4, there are 3 spacing, say S1, S2, S3 in sequence, among these four rows of wave fences. Then the system has six effective intervals, i.e. N=6, they are S1, S2, S3, S1+S2, S2+S3, S1+S2+S3 respectively. If each effective interval coincides half length of a design wave, and the fences are linked with ropes, the damping system will work all the time.

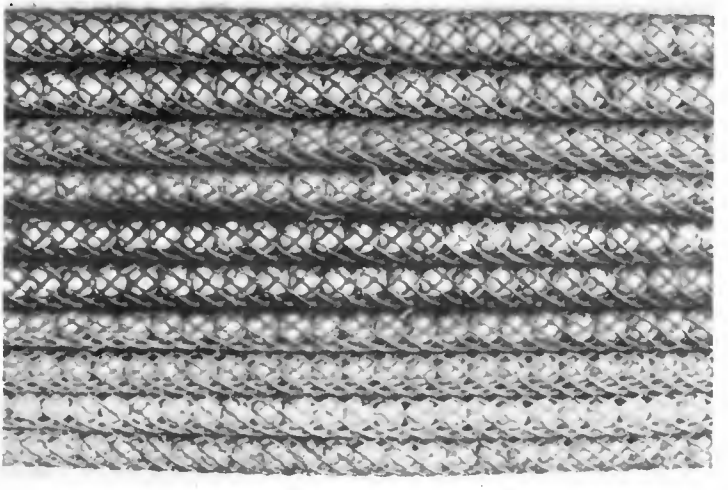

3. EXPERIMENTAL STUDIES

The wave periods ranged from 0.8 sec to 2.0 sec were carried out for the model test. The wave heights varied between 2 cm and 23 cm. The specific gravity of buoy-ball, γ_b, used in the experiments is 0.3.

First, the comparison of damping effect was made between the horizontally moored style, as Fig 1, and the vertically moored style, as Fig 2, of the same floating breakwater. The experimental results are shown in Fig 4-7, where the transmission coefficient K is the ratio of the average wave height behind the floating breakwater to the average incident wave height, and q is the immersing ratio of the draft of wave-fence h to water depth D. The cross-points and the solid lines represent the results of horizontal style, and the dot-points and the dash lines represent the data of vertical style. It is evident that the solid lines are always higher than the dash lines. It goes without saying that the wave-fence will be more effective if moored vertically.

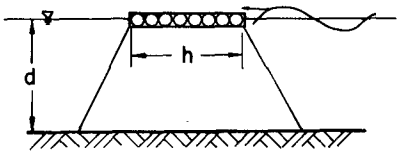

Fig 1. Horizontally moored style of wave-fence

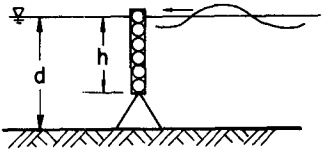

Fig 2. Vertically moored style of wave-fence

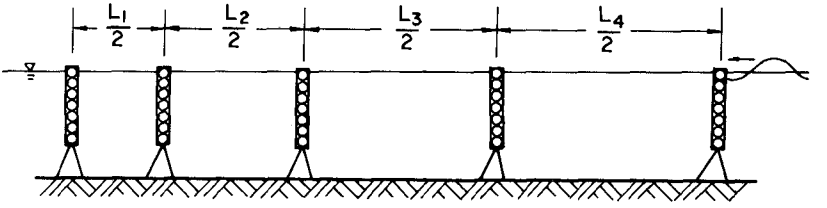

Fig 3. Five rows of wave-fences without/with connection which intervals correspond to half of designed wavelengths respectively

Since the wave-fence is flexible and swinging with the waves that diminishing the function of dissipation. The multiple wave-fences were then arranged to be tested. With the idea stated in previous section. if two rows of wave-fences which interval is equal to half of wave length of a certain wave period, the linking-effect would function only for that kind of waves. Therefore, for practical purpose, a system of more than two wave-fences is needed and set

in to be tested in the wave channel. A system of this structure of five rows with four spacings is chosen for the model test, Four perids of 0.8 sec, 1.2 sec, 1.6 sec, 1.8 sec were chosen as the basic spacings for the experiments. For convenience, five rows of wave-fences were arranged with appropriate intervals matching each half wavelength. A series of model tests with wave periods ranging from 0.8 sec to 2.0 sec were performed. The results are plotted in Fig. 8 The solid line and dash line represent linked and unlinked conditions respectively, which indicates that the former is much better than the latter.

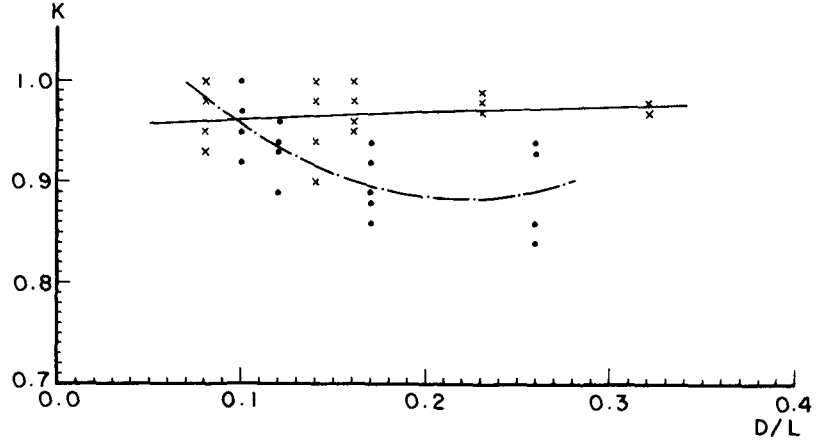

Fig 4. Transmission coefficient VS. relative depth for q=0.3,γ_b=0.3

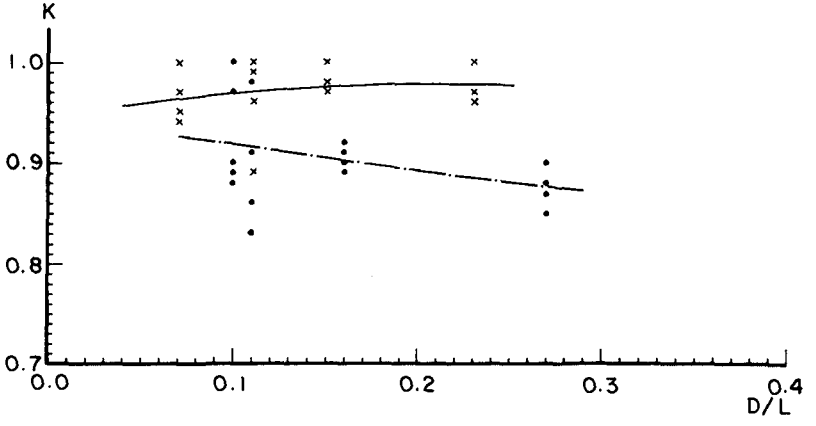

Fig 5. Transmission coefficient VS. relative depth for q=0.4,γ_b=0.3

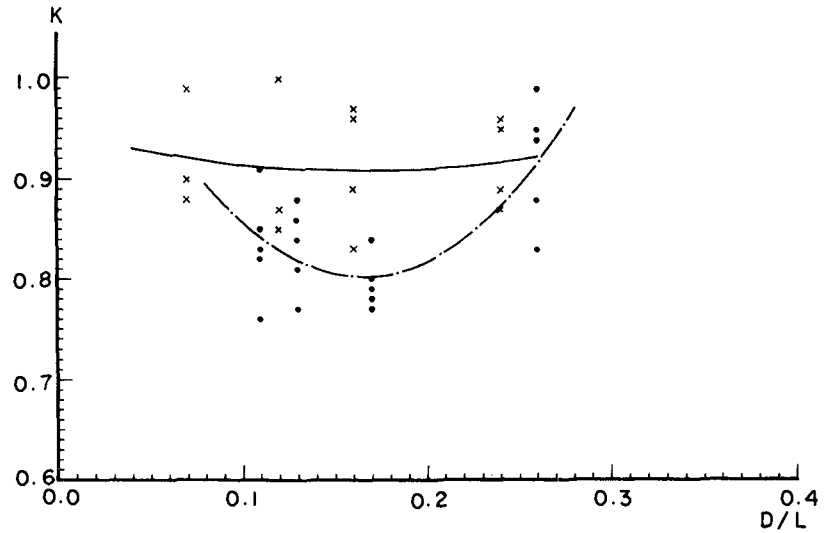

Fig 6. Transmission coefficient VS. relative depth for q=0.5, γ_b=0.3

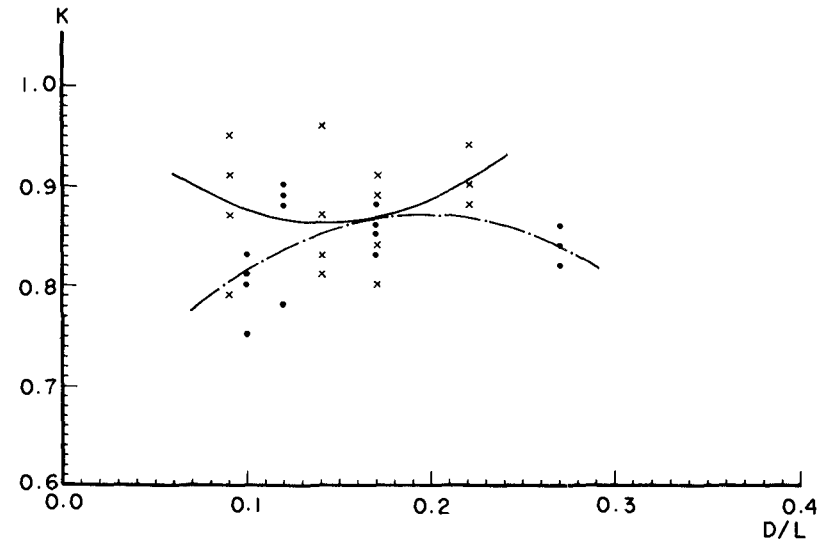

Fig 7. Transmission coefficient VS. relative depth for q=0.6, γ_b=0.3

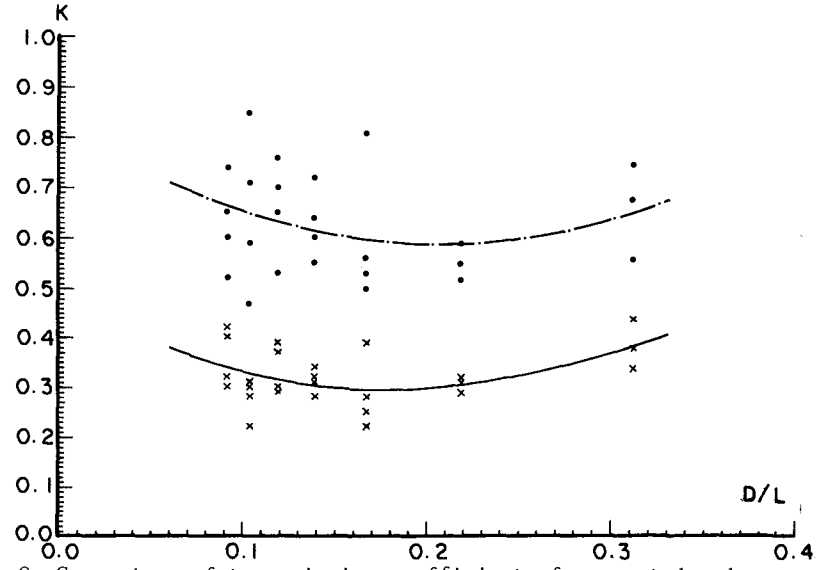

Fig 8. Comparison of transmission coefficient of connected and unconnected conditions for five-row wave-fences

4. CONCLUSION

(1) As wave dissipation is concerned, it is better to lay the wave-fence vertically than horizontally.
(2) The system of more than two rows of wave-fences being connected with ropes is always more effective than that without connection.
(3) If each "effective interval" of the system corresponds to each half length of a number of design waves, and the adjoining rows are linked with ropes, this system will serve as a good wave-fence.

REFERENCE

1. Kennedy, R.J. & Marsalek, J. (1968). Flexible porous floating break-waters. Proc. 11th Conf. on Coastal Engineering, 2, 1095-1103.
2. Marks, W. (1966). A perforated mobile breakwater for fixed and floating applications. Proc. 10th Conf. on Coastal Engineering, 2, 1079-1129.
3. Terrett, F.L. (1966). Model studies of a perforated breakwater. Proc. 11th Conf. on Coastal Engineering, 2, 1104-20.
4. Lee, Cheng-hsiun (1983). "Wave Transmision in Shallow Water under the Arrangements of Net-tubes and Buoy-balls". M.E. Thesis, Cheng-Kung University.
5. Twu, S.W., Kao R.C. & Huwng, H.H. (1986) "On a wave dissipation method for offshore aquaculture areas" J. Aquaculture Engineering. England. pp271-286

Wave Uplift on Platforms or Docks in Variable Depth

Jiin-Jen Lee* and C.P. Lai**

ABSTRACT

Wave uplift forces on two dimensional platforms or docks in a variable depth medium has been studied theoretically and numerically. The incident waves are non-linear waves with maximum amplitude greater than the clearance between the still water surface and the underside of the platforms or docks.

The flow is assumed to be inviscid, irrotational without ambient current. Thus, the theoretical model solves the Laplace equation along with full non-linear free surface conditions. In order to conveniently handle the moving free surface in an irregular bottom topography with the presence of platform or dock an isoparametric mapping technique was used to transfer the fluid domain and its boundaries into a regular geometry. A Galerkin finite element model is developed to model the transformed fluid region. The resulting discrete equations are solved iteratively by using adaptive Line SOR (Successive-Over-Relaxation) technique. Artificial viscosity is included in both the dynamic and kinematic free surface equations to damp out the free surface oscillations in the front region of the platform or dock. The Runge-Kutta method is employed to integrate the time variation in the nonlinear free surface equations.

Results obtained by the numerical method were compared to the available experimental data obtained by others in order to demonstrate the workability of the proposed algorithm.

1. INTRODUCTION

In a storm or in the present of unusual wave activities, marine structures, such as platforms or docks, may be subjected to significant uplift forces even if they are built above the still-water level. These forces occur when large incident wave propagate beneath the structure and make contact with it. If these uplift forces are not properly accounted for in the design, they can ultimately destroy the structure.

* Jiin-Jen Lee, B.S., M.S., Ph.D. Professor of Civil Engineering and Director of the Foundation for Cross-Connection Control and Hydraulic Research, University of Southern California, Los Angeles,CA 90089-0231

** C.P. Lai, B.S., M.S.,Ph.D Research Fellow, W.M. Keck Laboratory of Hydraulics and Water Resources, California Institute of Technology, Pasadena, CA 91125. Formerly, Graduate Research Assistant, University of Southern California, Los Angeles, CA 90089- 0231

When waves approach the coastal region, they are continously modified by the bottom topography and the coastline configuration. The decrease in water depth contributes to the increase in the effect of nonlinearity of the wave. Due to the importance of nonlinearity effect in sloping bottom, finite amplitude wave theories has to be applied. Furthermore, if a platform or dock which is built above the still-water level is present then the problem will be more complex. The problem to be encountered is a combination of nonlinear free surface conditions, upper and bottom rigid boundaries, and shoreward edge rigid boundary (if dock problem is considered). A suitable numerical model must be applied to handle this complex problem.

The major objective of this paper is to present a convenient numerical model to investigate aspects of wave uplift forces on platforms and/or docks either in horizontal or a sloping bottom.

2. MATHEMATICAL AND NUMERICAL FORMULATION

To develop the mathematical model, the flow is assumed to be inviscid, irrotational and without ambient current. The entire physical problem can be illustrated in Fig. 1 and the governing equations for the velocity potential are:

$$\nabla^2\phi = 0$$

$$\phi_y = h_t + \phi_x h_x \tag{1}$$

$$\phi_t + \frac{1}{2}(\phi_x^2 + \phi_y^2) + gh = 0 \qquad on \quad y = h(x,t)$$

Due to the nonlinearity of free surface equations, irregular bottom topography, and the presence of platform or dock, the original physical problem is difficult to solve by ordinary finite element method. To overcome this difficulty, a transformation technique is applied to map the complex physical domain into a regular computational domain.

Two steps are needed to transfer the physical domain into a regular computational domain by using isoparametric mapping. The first step is to transfer the irregular free surface and the bottom boundary into straight line segments by using six-node isoparametric elements. In this stage, the flow field has been transfered into several rectangular cells. The second step is to consider each rectangular cell as being separately mapped by a local bilinear isoparametric mapping to a new isoparametric plane.

The transformed governing differential equations take the following form:

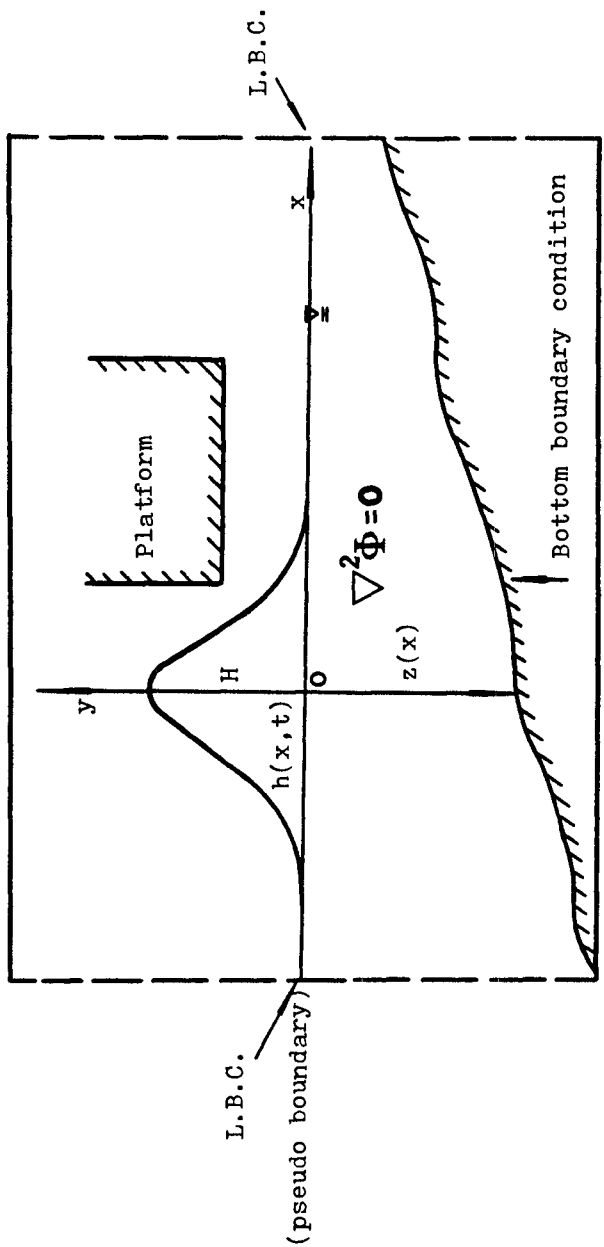

Fig. 1 Conceptual model of a solitary wave hitting a platform or a dock.

$$A_{KM}\phi_{\overline{\xi}\xi} + B_{KM}\phi_{\overline{\eta}\eta} + C_{KM}\phi_{\overline{\xi}\overline{\eta}} + D_{KM}\phi_{\overline{\eta}} = 0$$

$$\phi_t + \frac{1}{2}A_{KM}\phi_{\overline{\xi}}^2 + \frac{1}{2}B_{KM}\phi_{\overline{\eta}}^2 + \frac{1}{2}C_{KM}\phi_{\overline{\xi}}\phi_{\overline{\eta}} + gh = 0 \qquad (2)$$

$$h_t + A_{KM}h_{\overline{\xi}}\phi_{\overline{\xi}} + H_{KM}\phi_{\overline{\eta}}h_{\overline{\xi}} - G_{KM}\phi_{\overline{\eta}} = 0$$

where the following various coefficients are defined

$$A_{KM} = \xi_x^2 \qquad D_{KM} = \eta_{xx}Q$$

$$B_{KM} = (\eta_x^2 + \eta_y^2)Q^2 \qquad G_{KM} = \eta_y Q$$

$$C_{KM} = 2\xi_x\eta_x Q \qquad H_{KM} = \eta_x\xi_x Q$$

$$\text{where } Q = \overline{\eta}_\eta = \frac{2}{\Delta\overline{h}}$$

In the analysis, the approximate solutions of the transformed equations are sought by using the Galerkin's finite element method. The finite element model is advanced in time by integrating the free surface dynamic and kinematic equations. The Runge-Kutta method is employed with mass lumping. A major difficulty in numerical integration of the free surface equations is the nonlinear computational instability. To avoid the instability of numerical integration, artificial viscosity is included in both dynamic and kinematic free surface equations. An adaptive line SOR algorithm is developed and used to speed the repeated solution of linear algebraic equations resulting from finite element discretization of the transformed Laplace equation. It was found the adapted line SOR algorithm could effectively reduce the error norm by several orders of magnitude for the similar number of iteration.

3. NUMERICAL RESULTS

When ocean waves approach the coastal region, the wave shape and the propagation direction would change because of changes in coastal topography. A solitary wave traveling in a uniform depth region would not change its unique shape, however, it will break into a number of solitons when it propagates into a shallower continental shelf. Such "fission" phenomena have been found by many investigators (for example, see Madsen and Mei (1969) and Kim (1977)).

Fig. 2 presents the numerical solution of the development of an initial solitary wave over a shelf of 1:20 slope using the numerical model developed in the present study. The initial wave amplitude is 0.36 in., the water depth at the upstream of the shelf is assumed to be 3 in.; downstream of the shelf is chosen to be 1.5 in.. This bottom configuration has been used by Madsen and

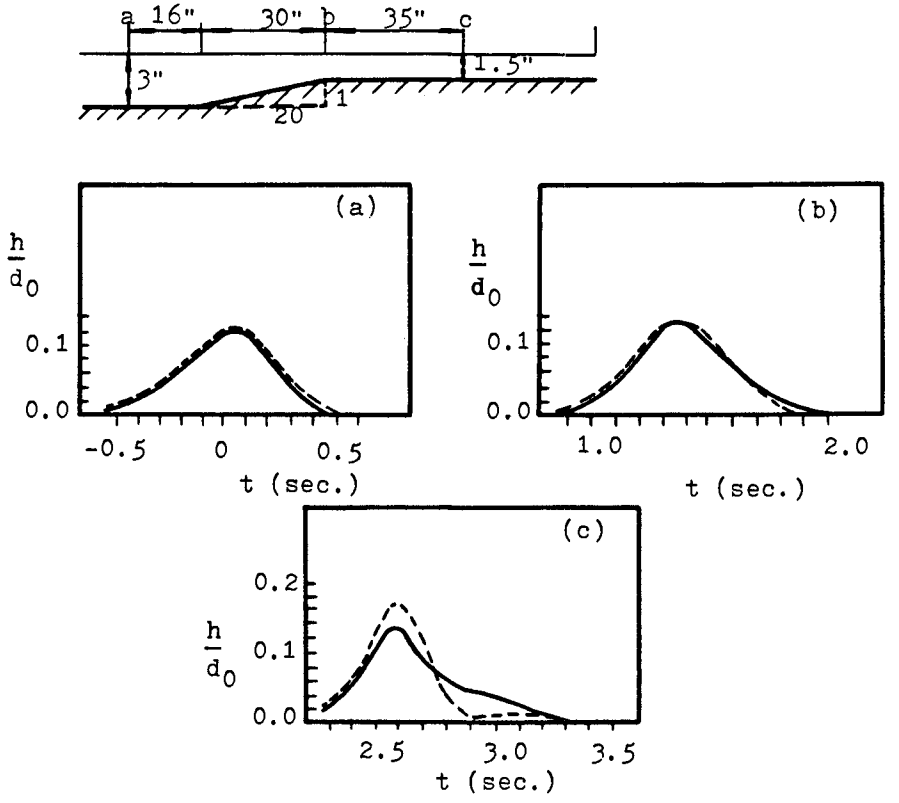

Fig.2 The propagation of solitary wave over an uneven bottom. Comparison of numerical results and experiments. ($H/d_0=0.12, d_0=3.0"$)

Mei (1969) in their numerical and experimental analysis. In our computational model, the time increment is taken to be 0.01 sec., and spatial interval is chosen to be 1.0 in.. The computational time for this case requires about 1 hour and 5 minutes (on VAX-11/780 machine).

The numerical results of wave profile at locations (a) and (b) in Fig.2 agree well with the experimental data obtained by Madsen and Mei (1969). However, by observing the wave profile at location (c) in Fig.2, there is disagreement between numerical and experimental values of wave profile. The maximum amplitude of computed wave profile is higher than that of experimental wave profile. A small hump in the tail of computed wave profile can be seen. This hump in the wave tail will be separated from the leading wave when the wave is propagated further downstream. This result have been found by Madsen and Mei (1969) and Kim (1977) using the same geometrical data and fluid parameters. This example demonstrates that the present numerical model is acceptable for sloping bottom.

Fig.3 shows the hydrodynamic uplift force on a horizontal platform resulting from a solitary wave travelling in a constant water depth. The ratio of the crest amplitude to the water depth is 0.24 which is 20% larger than the platform clearance. The ordinate is the ratio of the total hydrodynamic uplift forces (integrated from the computed uplift pressure over the entire platform) divided by the total hydrostatic force. The total hydrostatic force (Fs) is taken as the integrated weight of the water above the elevation of the platform which is denoted as the shaded area in the inserted sketch. The computed force based on the present numerical procedure is plotted as a function of the normalized time history. The experimental data was obtained by French (1969). The present numerical results are also compared with Iradjpanah's results (1983). It is seen from Fig.3 that the present numerical results agree reasonably well with the experimental data. It shows that when the solitary wave strikes the platform the platform experiences an uplift force followed by a negative force which is substantially larger than the positive uplift.

Fig.4 presents the time-history of normalized total force for a relative amplitude $H/d=0.32$ of wave propagating over a shelf. The platform is situated at the location which is 40 in. away from the beginning point of the slope. The horizontal dimension of the sloping bottom is 200 in.

It can be seen from Fig.4 that the effect of sloping bottom on the normalized total hydrodynamic force is very significant and the normalized total force increases in the sloping bottom. However, the total hydrodynamic force of the steep slope is slightly smaller than that of the mild slope.

If the platform is moved further away from the beginning point of the slope

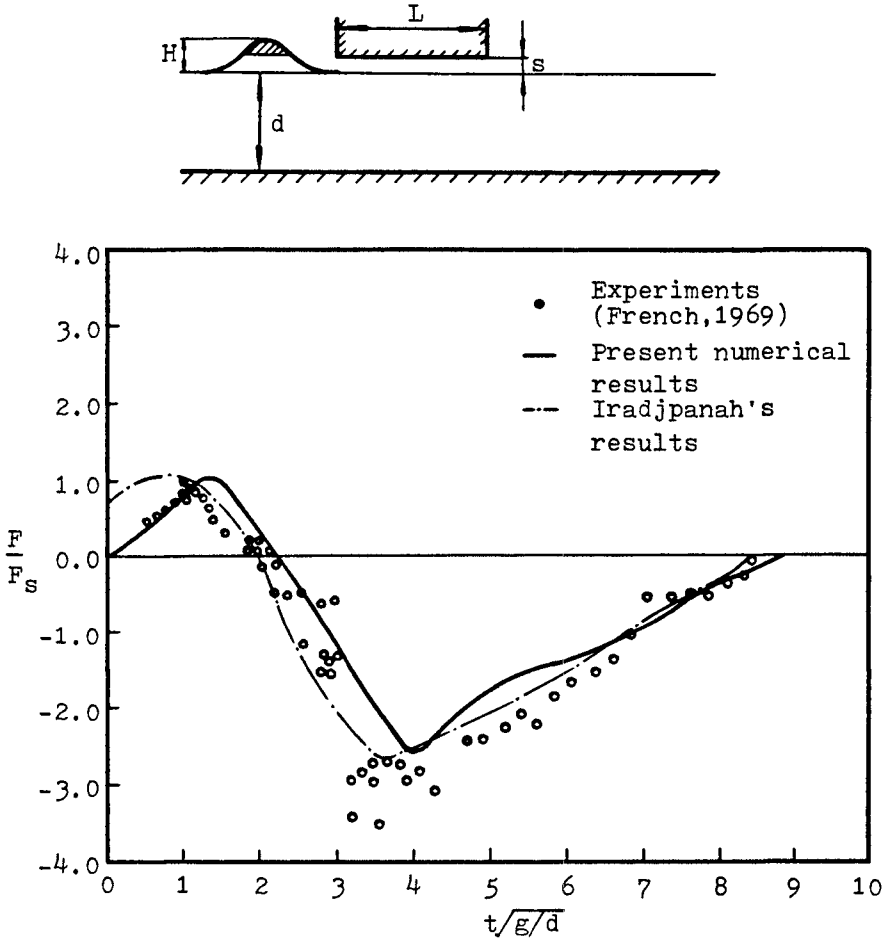

Fig. 3 Normalized total hydrodynamic force per unit width.
(H/d=0.24,s/d=0.2,L/d=4,d=15")

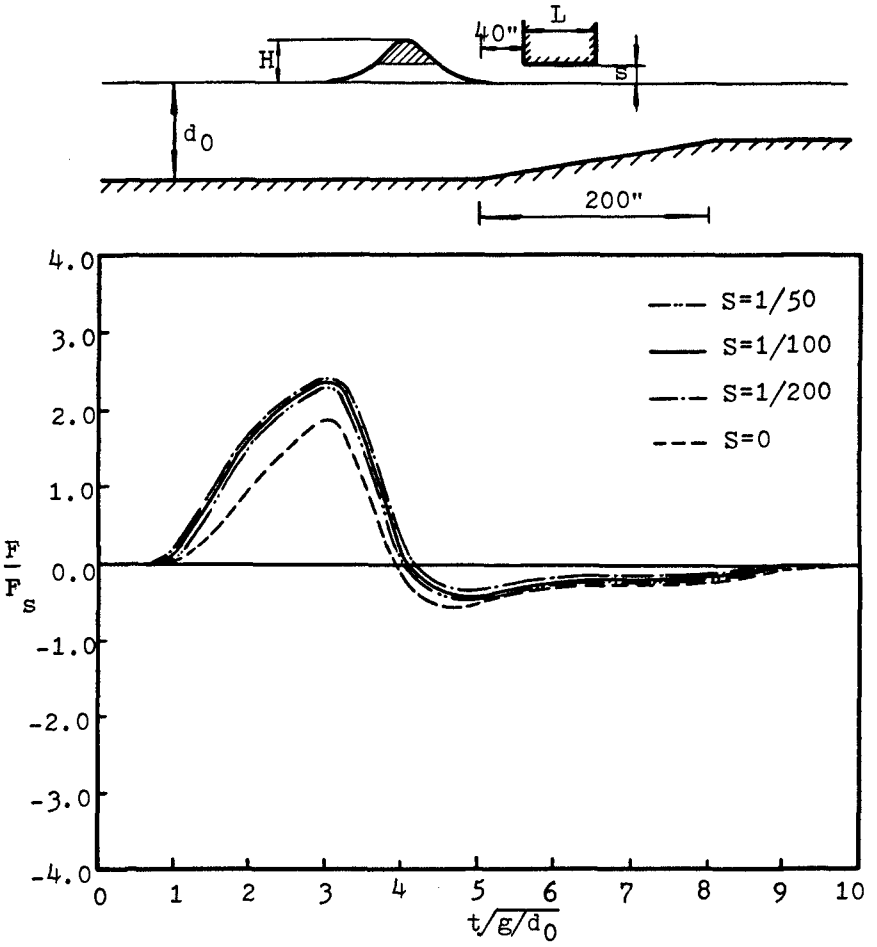

Fig. 4 Normalized total hydrodynamic force per unit width.
(H/d_0=0.32, s/d_0=0.2, L/d_0=4, d_0=15")

as shown in Fig.5, the nonlinearity and reflection effects of sloping bottom are more remarkable than that in Fig.4. The increase in the effect of nonlinearity increases the maximum amplitude of the wave, hence the total hydrodynamic force. This phenomenon is more significant for the mild slope than for the steep slope. A possible reason for this phenomenon is that the reflection effect reduces more nonlinearity effect for the steep slope than for the mild slope such that the amount of the increase of the total hydrodynamic force or the maximum amplitude is not proportionally increased.

Fig.6 shows the resulting uplift force when a reflecting boundary is introduced and the water depth is allowed to vary. This would represent a dock located near a reflecting wall. The ordinate and the abscissa are normalized as that shown in Fig.3. The incident wave height however is 60% greater than the platform clearance. By comparing the general feature of Fig.3 and 6, it is seen that the effects of the sloping bottom and the reflecting boundary significantly increase the positive uplift forces.

4. CONCLUSIONS

The numerical results computed from various incident wave heights in different bottom profile striking platforms and/or docks of varying nature show a consistent picture that the present numerical model works well. The platform experiences a positive uplift followed by a negative uplift force when a wave stikes the platform. The magnitude of this uplift force can be computed using the developed model but can not be generalized by a simple formula because of the complexity of the problem. For a dock problem (reflecting wall placed at the end of the dock) the positive uplift appeared to be significantly increased while the negative uplift is reduced.

5. ACKNOWLEDGMENTS

The authors appreciate the funding supports from the U.S.C. Foundation for Cross-Connection Control and Hydraulic Research (FCCCHR) and the NOAA Sea Grant Program.

6. REFERENCES

1. French, J.A. (1969), "Wave Uplift Pressure on Horizontal Platforms," Report No. KH-R-19, W.M. Keck Laboratory of Hydraulics and Water Resources, California Institute Technology, Pasadena, California.

2. Iradjpanah K. (1983), "Wave Uplift Force on Horizontal Platform," Ph.D. thesis, University of Southern California.

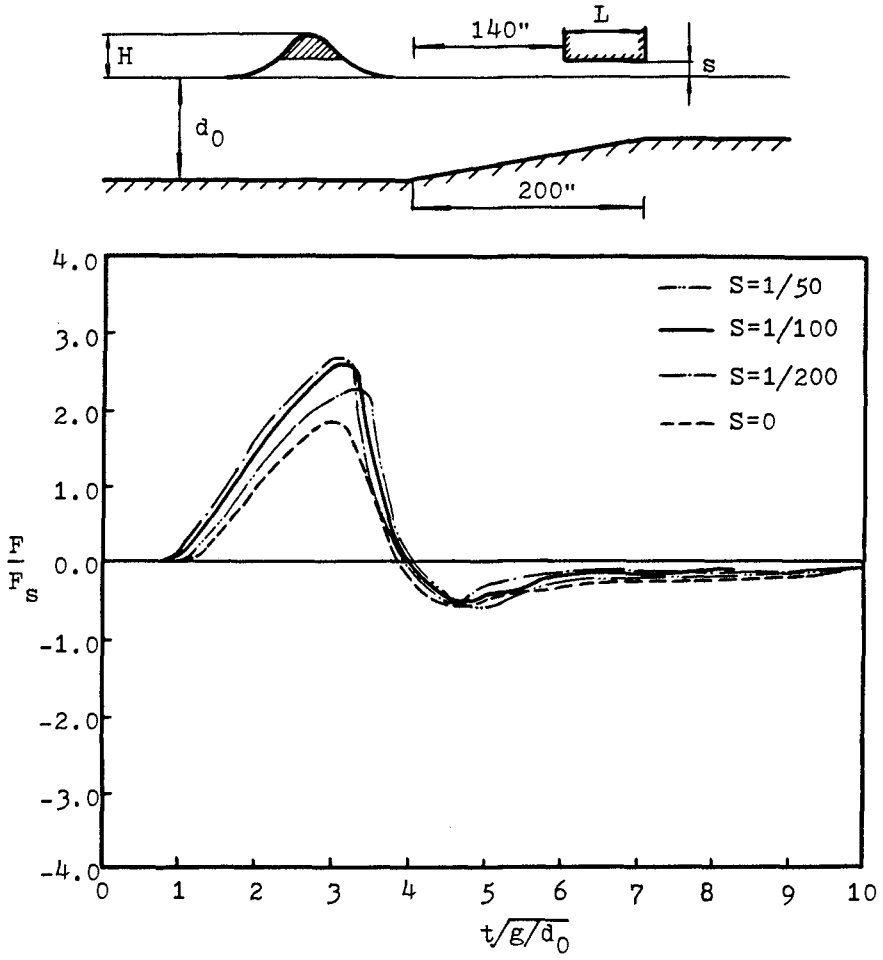

Fig.5 Normalized total hydrodynamic force per unit width.
(H/d_0=0.32, s/d_0=0.2, L/d_0=4, d_0=15")

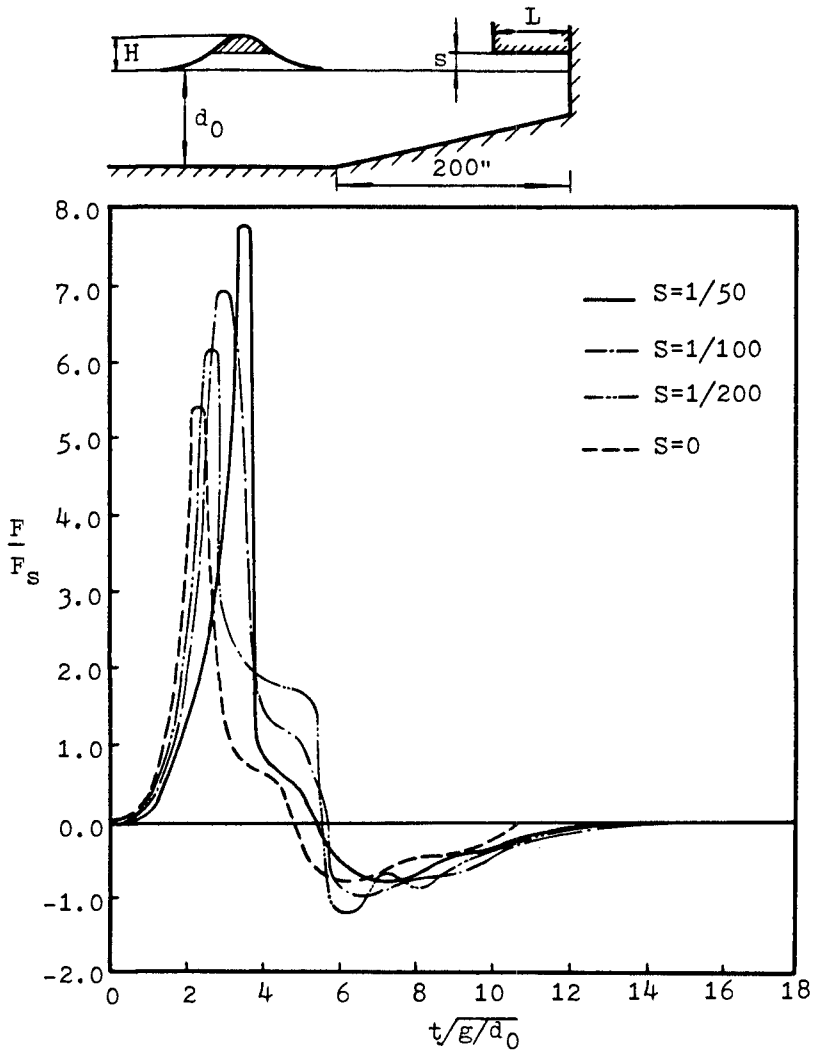

Fig. 6 Normalized total hydrodynamic force per unit width. ($H/d_0=0.32, s/d_0=0.2, L/d_0=4, d_0=15"$)

3. Kim, S.T. (1977), "Effects of Viscous Dissipation on the Propagation of Nonlinear and Dispersive Waves," Ph.D. thesis, University of Southern California.

4. Lai, C.P. (1986), "Wave Interaction with Structure: Hydrodynamic Loading on Platforms and Docks," Ph.D. thesis, University of Southern California.

5. Madsen, O.S. and Mei, C.C. (1969), "The Transformation of a Solitary Wave over an Uneven Bottom," Journal of Fluid Mechanics, Vol. 39, part 4, pp. 781-791.

CHAPTER 150

NEARSHORE CIRCULATIONS DUE TO WAVE INDUCED CURRENTS BY OFFSHORE BREAKWATER IN FINITE ELEMENTS

Shinn-Chung Liang *

1. INTRODUCTION

The objective of the present study is concerned with the numerical prediction of wave patterns and wave induced currents adjacent to a breakwater. The wave theory used is that of Berkhoff's (1972) mild slope wave equation with effects of diffraction, refraction and reflection described as Bettess, Liang and Bettess (1984). A finite element model is applied with appropriate boundary conditions. The singularity in the velocity at the tip of the breakwater is modelled effectively using the technique of Henshell and Shaw (1975), originally developed for elasticity. In the case of waves induced currents a potential representation of velocity in the fluid has been used to derive a set of radiation stress expressions based on the theory of Longuet-Higgins (1964, 1970a,b), which are for an arbitrary wave pattern and the bottom variation. These expressions used account for the mean sea level and satisfy Mei's (1973) static balance of momentum flux.

The radiation stress is applied to obtain forcing terms for use in a shallow water equation in conjunction with limiting ratio wave breaking where wave height, wave period, wave steepness and beach slope may be considered. Finally, an offshore breakwater on a beach for shore protection has been applied in a complete finite element model to predict both wave pattern and nearshore currents. Two angles of wave incidence are chosen. A series result has been produced.

2. THEORIES

2.1. WAVES

The wave equation of Berkhoff (1972,1975) is used as

$$\nabla.(cc_g \nabla\phi_o) + \frac{\omega^2 c}{c} g\phi_o = 0 \qquad (1)$$

with ω : angular frequency,
c : wave celerity and $c = \omega/k$, k is a wave number,
c_g : group velocity by $c_g = nc$ and $n = \frac{1}{2}(1+2kh/\sinh 2kh)$
ϕ_o : velocity potential in deep water.

For shallow water due to kh is small and tanh kh = kh Eq. (1) becomes

$$\nabla.(h\nabla\phi_o) + \frac{\omega^2}{g} \phi_o = 0 \qquad (2)$$

For deep water, kh is large and so tanh kh = 1, this leads to $c = g/\omega$ and n = 1/2, so that

*Visiting Aso. Professor, Department of Hydraulics and Ocean Engineering National Cheng Kung University, Taiwan. Formerly: Department of Civil Engineering, Imperial College, U. K.

$$\nabla^2 \phi_o + \frac{\omega^4}{g^2} \phi_o = 0 \qquad (3)$$

The boundary conditions of Eq. (1) must be satisfied and specified. On a solid boundary the velocity must be zero and hence $\partial\phi / \partial n = 0$, with n : outward normal to the surface. This implies a total reflection of a wave. In a real problem the reflection will be partial as energy absorption will occur on a beach due to wave breaking, or/on a real breakwater where the porous nature of the boundary does not result in a zero boundary velocity. For such a boundary the condition can be written as

$$\frac{\partial \bar{\phi}}{\partial n} = \frac{\alpha}{c} \frac{\partial \bar{\phi}}{\partial t} \qquad (4)$$

where $\bar{\phi}$: velocity potential for periodic wave, and

$\bar{\phi}(x,y,z,t) = \phi(x,y,z) \exp(i\, t)$

: a real dimensionless damping coefficient, as

$\alpha = 0$: total reflection

$\alpha = 1$: total absorption

$0 \leq \alpha \leq 1$: any partial reflection.

Where the energy absorption is due largely to inertia terms, such as occur in wave breaking, α could be given a complex value.

2.2. WAVE BREAKING

Waves break in different ways depending on wave height, wave period, steepness and beach slope. The determination of the initial line of breaking is a purely empirical matter. Breaking criteria are based on three important aspects of the breaking theories which are solidary wave, Airy wave theories and similarity parameter introduced by McCowan (1891) etc., Komar and Gauphan (1972) and Iribarren and Nogales (1949) respectively.

Lacking direct empirical data for waves with varying amplitude, a plausible criterion to waves with longshore modulation is extended as

$$\phi(x,y,t) = -\frac{ig}{\omega} \eta'(x,y,t) \qquad (5)$$

where $\bar{\eta}$ is the local wave amplitude. Approximating for shallow water and invoking along with breakerline

$$\eta'(x,y) = \gamma(\bar{\eta} + h) \qquad (6)$$

with γ is an empirical breaking criterion, obtain from previous ideas.

Inside the surfzone wave energy is dissipated due to the generation of turbulence in wave breaking and bottom friction. The local wave amplitude decreases towards the shore and becomes negligible along the mean shoreline. Using three different breaking criteria to find the waves inside the surfzone, the variations of radiation stresses are obtained in two channel meshes of slope = 1/10 and 1/50, as shown in Figs. (1) and (2). There are no significant differences among three criteria in mild slope case but for the steeper of slope = 1/10, we would prefer to use one of the criteria of Iribarren and Nogales or Komar and Gauphan, which considers more factors, such as bottom slope and wave steepness.

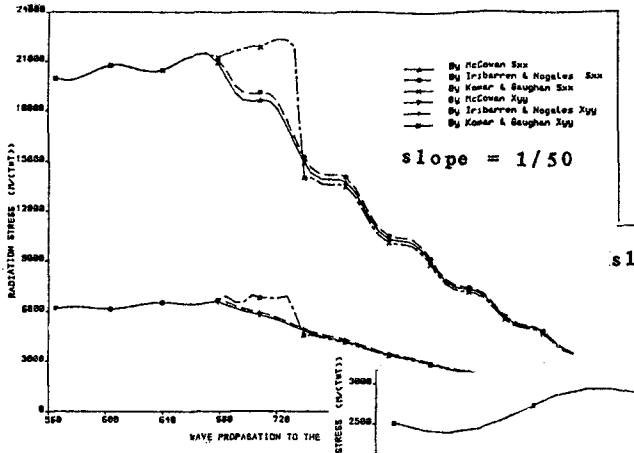

Figure 1.

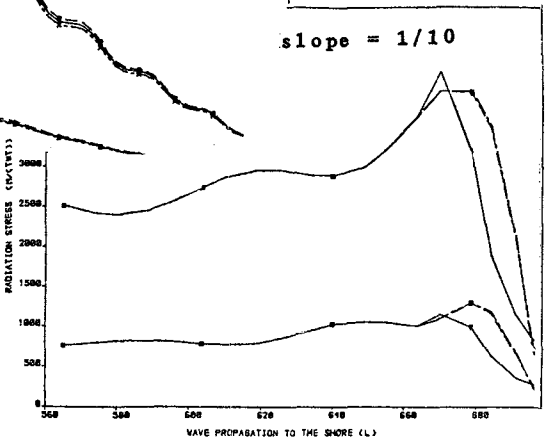

Figure 2.

2.3. RADIATION STRESSES

Based upon Longuet-Higgins and Stewart (1964) and Mei (1973), a finite element model of radiation stress has been developed by Liang (1983) to generalize the radiation stress for arbitrary wave patterns and bottom variations. Mei (1973) mentioned that the equation of a static balance of momemtum is given as

$$\bar{P}_h \frac{\partial h}{\partial x_\alpha} - \rho g h \frac{\partial \bar{\eta}}{\partial x_\alpha} - \frac{\partial S_{\alpha\beta}}{\partial x_\beta} = 0(ka)^3 \tag{8}$$

For constant depth (h = constant) the equation becomes

$$-\rho g h \frac{\partial \bar{\eta}}{\partial x_\alpha} - \frac{\partial S_{\alpha\beta}}{\partial x_\beta} = 0 \tag{9}$$

where $\alpha, \beta = 1,2$, $S_{\alpha\beta}$ is the radiation stress tensor and $\bar{\eta}$ is the time average of mean sea level. For slowly varying depth, due to higher derivatives of h are small comparing with other two terms, therefore the first term is usually insignificant. The static balance is also as Eq. (9) shown.

The next step is to determine the expressions of $S_{\alpha\beta}$ and $\bar{\eta}$ in Eq. (9). The radiation stress tensor is defined as

$$S_{\alpha\beta} = S^{(1)}_{\alpha\beta} + \delta_{\alpha\beta} S^{(2)} \tag{10}$$

where $\delta_{\alpha\beta}$ being the kronecker delta and to the second order of the approximation these expressions are equivalent to

$$S^{(1)}_{\alpha\beta} = \rho\int_{-h}^{\bar{\eta}} \overline{u_\alpha u_\beta}\, dz + O[(ka)^3] \tag{11}$$

$$S^{(2)} = \int_{\bar{\eta}}^{\eta} \bar{p}\,dz + \int_{-h}^{\bar{\eta}} \bar{p}\,dz - \frac{1}{2}\rho g(\bar{\eta}+h)^2 + O[(ka)^3] \tag{12}$$

In the first term of Eq. (12), the pressure is taken as hydrostatic

$$p = \rho g(\eta - z), \qquad 0 < z < \eta(x,y,t). \tag{13}$$

In the second term of the equation, P can be obtained from the time averaged as

$$\bar{p} = \rho g(\bar{\eta} - z) + \rho\int_{-h}^{\bar{\eta}} \frac{\partial}{\partial x_i}(\overline{u_i w})\,dz - \rho(\bar{w})^2 \tag{14}$$

with $x_i = x, y$ and $u_i = u, v$. Therefore components of radiation stress tensor can be written as:

$$S_{xx} = \int_{-h}^{\bar{\eta}} \rho(\overline{u^2} - \bar{w}^2)\,dz + \frac{\partial}{\partial x}\int_{-h}^{\bar{\eta}}\int_{z'}^{\bar{\eta}} \rho\,\overline{uw}\,dz'dz + \frac{\partial}{\partial y}\int_{-h}^{\bar{\eta}}\int_{z'}^{\bar{\eta}} \rho\,\overline{vw}\,dz'dz + \rho g h\bar{\eta} + \int_{\bar{\eta}}^{\eta} \bar{p}\,dz \tag{15}$$

$$S_{xy} = \int_{-h}^{\eta} \rho\,\overline{uv}\,dz \tag{16}$$

S_{yy} and S_{yx} can be found by interchanging x and y everywhere in Eqs. (13) and (14).

The mean sea level of Eq. (9) is derived from Longuet-Higgins (1967) and Mei (1973) as

$$\bar{\eta} = -\frac{1}{g}\overline{\frac{\partial \phi}{\partial t}} - \frac{1}{2g}\overline{\left[\left(\frac{\partial \phi}{\partial x}\right)^2 + \left(\frac{\partial \phi}{\partial y}\right)^2 - \left(\frac{\partial \phi}{\partial z}\right)^2\right]} \qquad z = 0 \tag{17}$$

or

$$\bar{\eta} = -\frac{1}{g}\overline{\frac{\partial \phi}{\partial t}} - \frac{1}{2g}\left[\overline{u^2} + \overline{v^2} - \overline{w^2}\right] \qquad z = 0 \tag{18}$$

If set

$$\phi(x,y) = A(x,y) + iB(x,y) \tag{19}$$

and

$$\phi = \mathrm{Re}\,[\phi(x,y)\cosh k(z+h)\exp(-i\omega t)] \tag{20}$$

Where A and B are real and $i = \sqrt{-1}$, then the velocities, such as u, v and w and their square or time-averaged values etc., are easy to derive in terms of A and B. That means if we can find the values of A and B and their higher order derivatives through velocity potential of wave in the technology of finite element simulations, we can find the tensor straightwards.

The major interest for us is to find the tractive forces which induce currents and set-up. These are

$$\tau_x = -\left(\frac{\partial S_{xx}}{\partial x} + \frac{\partial S_{xy}}{\partial y}\right) \tag{21}$$

$$\tau_y = -\left(\frac{\partial S_{xy}}{\partial x} + \frac{\partial S_{yy}}{\partial y}\right) \tag{22}$$

The gradients can be found in terms of A and B as

$$\begin{aligned}\frac{\partial S_{xx}}{\partial x} = {} & \frac{\rho}{8}\left[\left[2\left(\frac{\partial A}{\partial x}\frac{\partial^2 A}{\partial x^2} + \frac{\partial B}{\partial x}\frac{\partial^2 B}{\partial x^2}\right) - \frac{1}{2}\frac{\partial F}{\partial x}\right]\left(\frac{\sinh 2kh + 2kh}{k}\right)\right. \\ & \left. + \left[\left(\frac{\partial A}{\partial x}\right)^2 + \left(\frac{\partial B}{\partial x}\right)^2 - \frac{F}{2}\right]\frac{\partial}{\partial x}\left(\frac{\sinh 2kh + 2kh}{k}\right)\right] \\ & + \frac{\rho}{4}\left[\frac{\partial F}{\partial x} h \cosh^2 kh + F\frac{\partial h}{\partial x}\cosh^2 kh + Fh\frac{\partial}{\partial x}(\cosh^2 kh)\right. \\ & \left. + (A^2 + B^2)\frac{\partial}{\partial x}(k^2 h) + 2k^2 h\left(A\frac{\partial A}{\partial x} + B\frac{\partial B}{\partial x}\right)\right] \\ & + \frac{\rho}{8g}\left[\left[\left(\frac{\partial A}{\partial x}\right)^2 + \left(\frac{\partial B}{\partial x}\right)^2 + \left(\frac{\partial A}{\partial y}\right)^2 + \left(\frac{\partial B}{\partial y}\right)^2\right]\cosh^2 kh\right. \\ & \left. - k^2(A^2 + B^2)\sinh^2 kh\right]\left[\left[\left(\frac{\partial A}{\partial x}\right)^2 + \left(\frac{\partial B}{\partial x}\right)^2 + \left(\frac{\partial A}{\partial y}\right)^2\right.\right. \\ & \left.\left. + \left(\frac{\partial B}{\partial y}\right)^2 - k^2(A^2 + B^2)\right]\cosh kh \sinh kh \frac{\partial(kh)}{\partial x}\right. \\ & \left. + \left[\left(\frac{\partial A}{\partial x}\frac{\partial^2 A}{\partial x^2} + \frac{\partial B}{\partial x}\frac{\partial^2 B}{\partial x^2}\right) + \left(\frac{\partial A}{\partial y}\frac{\partial^2 A}{\partial x\partial y} + \frac{\partial B}{\partial y}\frac{\partial^2 B}{\partial x\partial y}\right)\right]\cosh^2 kh\right. \\ & \left. - k\left[k\left(A\frac{\partial A}{\partial x} + B\frac{\partial B}{\partial x}\right) + \frac{\partial k}{\partial x}(A^2 + B^2)\right]\sinh^2 kh\right]\end{aligned} \tag{23}$$

$$\begin{aligned}\frac{\partial S_{xy}}{\partial x} = {} & \frac{\rho}{8}\left[\left(\frac{\partial A}{\partial x}\frac{\partial A}{\partial y} + \frac{\partial B}{\partial x}\frac{\partial B}{\partial y}\right)\frac{\partial}{\partial x}\left(\frac{\sinh 2kh + 2kh}{k}\right)\right. \\ & \left. + \left(\frac{\sinh 2kh + 2kh}{k}\right)\left(\frac{\partial A}{\partial x}\frac{\partial^2 A}{\partial x\partial y} + \frac{\partial B}{\partial x}\frac{\partial^2 B}{\partial x\partial y} + \frac{\partial A}{\partial y}\frac{\partial^2 A}{\partial x^2} + \frac{\partial B}{\partial y}\frac{\partial^2 B}{\partial x^2}\right)\right]\end{aligned} \tag{24}$$

$$\begin{aligned}\frac{\partial S_{xy}}{\partial y} = {} & \frac{\rho}{8}\left[\left(\frac{\partial A}{\partial y}\frac{\partial A}{\partial x} + \frac{\partial B}{\partial y}\frac{\partial B}{\partial x}\right)\frac{\partial}{\partial y}\left(\frac{\sinh 2kh + 2kh}{k}\right)\right. \\ & \left. + \left(\frac{\sinh 2kh + 2kh}{k}\right)\left(\frac{\partial A}{\partial y}\frac{\partial^2 A}{\partial x\partial y} + \frac{\partial B}{\partial y}\frac{\partial^2 B}{\partial x\partial y} + \frac{\partial A}{\partial x}\frac{\partial^2 A}{\partial y^2} + \frac{\partial B}{\partial x}\frac{\partial^2 B}{\partial y^2}\right)\right]\end{aligned} \tag{25}$$

where

$$F = -\frac{1}{h}\left[\frac{\partial h}{\partial x}\left(A\frac{\partial A}{\partial x} + B\frac{\partial B}{\partial x}\right) + \frac{\partial h}{\partial y}\left(A\frac{\partial A}{\partial y} + B\frac{\partial B}{\partial y}\right) + (A^2 + B^2)\, k \tanh kh\right]$$

$$+ \left(\frac{\partial A}{\partial x}\right)^2 + \left(\frac{\partial A}{\partial y}\right)^2 + \left(\frac{\partial B}{\partial x}\right)^2 + \left(\frac{\partial B}{\partial y}\right)^2 \tag{26}$$

$$\frac{\partial F}{\partial x} = -\left[\frac{\partial}{\partial x}\left(\frac{A}{h}\frac{\partial h}{\partial x}\frac{\partial A}{\partial x}\right) + \frac{\partial}{\partial x}\left(\frac{B}{h}\frac{\partial h}{\partial x}\frac{\partial B}{\partial x}\right) + \frac{\partial}{\partial x}\left(\frac{A}{h}\frac{\partial h}{\partial y}\frac{\partial A}{\partial y}\right)\right.$$

$$\left. + \frac{\partial}{\partial x}\left(\frac{B}{h}\frac{\partial h}{\partial y}\frac{\partial B}{\partial y}\right) + \frac{\partial}{\partial x}\left(\frac{A^2 k}{h}\tanh kh\right) + \frac{\partial}{\partial x}\left(\frac{B^2 k}{h}\tanh kh\right)\right]$$

$$+ \frac{\partial}{\partial x}\left[\left(\frac{\partial A}{\partial x}\right)^2 + \left(\frac{\partial A}{\partial y}\right)^2 + \left(\frac{\partial B}{\partial x}\right)^2 + \left(\frac{\partial B}{\partial y}\right)^2\right] \tag{27}$$

The expression for $\frac{\partial S_{yy}}{\partial y}$ is analogous to that $\frac{\partial S_{xx}}{\partial x}$ just change x to y everywhere in Eqs. (22) and (26).

2.4. NEARSHORE CURRENTS

The finite element program to be used to calculate currents in the whole nearshore system is based upon the penalty form of shallow water equations of Zienkiewicz (1978) for a steady state which are similar in form to the Navier - Stokes equations for turbulent flow. These are

$$\frac{\partial}{\partial x}(h\bar{u}) + \frac{\partial}{\partial y}(h\bar{v}) = \frac{\eta}{\lambda} \tag{28}$$

$$\rho\left[\bar{u}\frac{\partial \bar{u}}{\partial x} + \bar{v}\frac{\partial \bar{v}}{\partial y} - f\bar{v}\right] - \rho g\lambda\frac{\partial}{\partial x}\left[\frac{\partial}{\partial x}(h\bar{u}) + \frac{\partial}{\partial y}(h\bar{v})\right]$$

$$= 2\frac{\partial}{\partial x}\left[\mu_h\frac{\partial \bar{u}}{\partial x}\right] + \mu_h\frac{\partial}{\partial y}\left(\frac{\partial \bar{u}}{\partial y} + \frac{\partial \bar{v}}{\partial x}\right) + \frac{\tau_x}{h} - \frac{C\bar{u}}{h} \tag{29}$$

$$\rho\left[\bar{u}\frac{\partial \bar{v}}{\partial x} + \bar{v}\frac{\partial \bar{v}}{\partial y} + f\bar{u}\right] - \rho g\lambda\frac{\partial}{\partial y}\left[\frac{\partial}{\partial y}(h\bar{u}) + \frac{\partial}{\partial x}(h\bar{v})\right]$$

$$= 2\frac{\partial}{\partial y}\left[\mu_h\frac{\partial \bar{v}}{\partial y}\right] + \mu_h\frac{\partial}{\partial x}\left(\frac{\partial \bar{u}}{\partial x} + \frac{\partial \bar{v}}{\partial y}\right) + \frac{\tau_y}{h} - \frac{C\bar{v}}{h}. \tag{30}$$

Where μ_h is a horizontal mixing length (eddy) viscosity coefficient and f is an angular rotation of coriolis acceleration and c is a friction coefficient. λ is a very large number called penalty parameter. τ_x and τ_y are wave tractive forces. u and v are represented the mean transport velocity component.

The equations are discretized using the method of weighted residuals. The choice of a penalty parameter, λ is fairly critical although empirical. If it is too large machine error will dominate the results, while if it is too small the condition is not enforced. A value of λ in the order of 10^6 was suggested for this shallow water problems.

Longuet-Higgins (1970a,b) reasoned that the eddy viscosity effects should tend to zero at the shoreline and suggested

$$\mu_h = N\rho |x| (gh)^{1/2} \tag{31}$$

N is a dimensionless constant. μ_h is horizontal viscosity. From studies of the effects of littoral friction on the velocity profile using field data, the range of N was found to be between 0.0024 and 0.0096. Many authors also had introduced their expressions for eddy viscosity. James (1974) summarized some available values of N were between 0.009 and 0.064. N = 0.01 is used in this computation.

Longuet-Higgins assumed a similar quadratic law which similar to standard quadratic law for turbulent river for bottom stress, would apply to the oscillatory flows encountered under waves in the surfzone. He suggested that if there were longshore currents bottom friction under a wave would be given by

$$\tau_b = F_{LH} |u_{orb}| u_{orb} \tag{32}$$

where u_{orb} was the orbital velocity and F_{LH} was the Longuet-Higgins friction coefficient. The coefficient is given as

$$F_{LH} = \frac{g}{C_z^2} \tag{33}$$

where C_z is Chezy's coefficient. If there is a range of Chezy's coefficients of 60 - 100, there is a range of Longuet-Higgins' coefficients of 0.003 - 0.001. Longuet-Higgins' suggested value for F_{LH} = 0.01. Liu and Mei (1976a,b) adopted two values of 0.01 and 0.09 in their nearshore current computations.

Longuet-Higgins etc. supposed that the radiation stress was a crucial driving force in the nearshore current. Inside the surfzone the wave energy decreases shoreward, leading to a decrease in the radiation stress. Outside the surfzone because of no wave energy dissipation the longshore gradient of the radiation stress is always zero, and the flow is therefore driven only inside the surfzone. The radiation stress terms τ_x and τ_y are given as Eqs. (21) and (22).

2.5. LONGSHORE BOUNDARY CONDITIONS

When waves and currents are predicting numerically in a region adjacent to a long coastline, there are four boundaries enclosing the region of interest: the coastline, two roughly normal to the coast and a seaward boundary. When waves are incident from deep water upon the coastline at some angle, θ , due to shoaling effects they refract and diminish the angle of incidence as they travel into the shallow water. In the region, the problem can be complicated by wave reflections leading to partial standing waves, diffraction resonance effects. Incorrect treatment of these artificial boundaries of the model will induce chaos in the problem. some damper and repeatibility boundaries are introduced in the present model.

Shoreline - A finite depth and smoothing the depth profile near shoreline is given to prevent infinite number of elements in the mesh

due to wave number k tending to infinity. Then we apply boundary damper by Sommerfeld's (1896) radiation condition to absorb the incident wave.

Boundary parallel to the shoreline - The model is simply terminated at this boundary.

Boundaries normal to the shoreline - Dampers and Snell's law have been used. The dampers absorb and generate the longshore component of the incoming wave.

In the case of current model it is assumed the flow profile at one artificial boundary is the same as the flow profile at the second boundary and a repeatability condition is applied as

$$u(x,0) = u(x,L)$$
$$v(x,0) = v(x,L) \qquad (34)$$

The condition is restrictive in that the beach slope and water depth need to be identical at each end of the model.

3. GEOMETRY, DATA AND RESULTS

3.1 GEOMETRY

The geometry chosen here is that of an offshore breakwater at Santa Monica, California which has been described by Liu and Mei (1976a,b). These are as Fig. (3) shown,

breakwater
- length : 700 m
- thickness : 0 m
- wall : vertical and perfectly reflective
- position : 350 m from shoreline
- domain : x = 350 m, 350 m $\leq$ y $\leq$ 1050 m parallel to the shore
- depth : 7 m

beach profile
- uniform slope : slope = 1/50 for all y.

3.2 DATA

In order to model the wave accurately four elements per wavelength rule is maintained. Wider spacing is used in y direction, except at the tips of the breakwater where singularities occur. Restricted by the computation time for the fact that the numbers of the element will become enormous for covering all the describing region after the mesh is finer, a little bit longer wave period will be set to match the rule instead of subdividing the mesh in this computation. The wave climates are as

periods	: T = 10 sec and 20 sec
incident wave amplitute	: a = 0.5 m
angular frequency	: ω = 0.62832 and 0.31416 (1/sec)
gravity	: g = 9.81 m/sec^2
mass density of water	: ρ = 1000 kg/m^3
incident angles	: θ = 0 and 10 degrees.

Empirical data are

breaking criterion	: McCowan's value γ = 0.8
eddy viscosity	: μ_h = 10.0 kgf.s/m
friction coefficient	: F_{LH} = 0.0015, 0.01 and 0.09
penalty parameter	: P = 100000 and 1000000
coriolis coefficient	: f = 0.

3.3 RESULTS

3.3.1 DIFFRACTION AND REFRACTION

In Fig. (4) contours of absolute values of wave elevation around offshore breakwater in the case of normal wave incidence of T = 10 sec are shown. It is could be seen that a strong reflection effects has resulted in standing waves in front of the breakwater. The peak of the wave elevation was at 1.2 m, compared with an incident wave amplitude of 0.5 m. Meanwhile some diffracted waves had intruded into the sheltered area of the breakwater. Similar situation is shown in Fig. (5) of T = 20 sec but wave penetrations are more profoundly because of longer wavelength. Fig. (6) is shown an oblique incident wave of 10 degrees attacks on the breakwater. A standing waves were form obliquely in front of the breakwater and more intruded waves In the upstream part.

3.3.2 NEARSHORE CURRENTS

As shown in Figs. (7), (9) and (11) which are in normal wave incidence of T = 10 sec there are two symmetrical counter - rotating cells found behind the breakwater in the case of friction coefficients, F_{LH} = 0.0015, 0.01 and 0.09 respectively. The variations of alongshore mean velocity component, V, through the centres of the circulation cell of constant y are shown in Figs. (8), (10) and (12) respectively. Two features can be seen immediately. First, the values of the velocity are decreasing as friction increasing. The maximum mean alongshore velocity component decrease from 1.911 m/sec, 1.310 m/sec to 0.568 m/sec. Second, the centres of the circulation cells shift outward about 50 m in each case apparently. This show the velocity is strongly affected by the friction which is a very difficult quantity to ascertain in the field. The two cells theoretically should be symmetrical but because of different distances from the boundaries chosen the unsymmetrical are found.

In the cases of a normal wave incidence of T = 20 sec, two more compact circulation cells are induced as shown in Figs. (13). The maximum alongshore mean velocity components, V, is 0.831 m/sec as Fig. (14) shown. In a 10 degree wave incidence of T = 20 sec because the wave force acts obliquely a strong circulation cell is found on the upstream of the surfzone. However on the other end, downstream, it is much weak comparatively. The maximum mean alongshore velocity is 0.845 m/sec on the upstream and much weak on the downstream. These are as Figs. (15) and (16) shown.

3.3.3 COMPARISONS

Because of the restriction of the available values of longshore current in the field or laboratory, only two references can be used for comparison. Firstly, Sauvage etc. (1955) has carried out a laboratory studies with sandy bottoms for an offshore breakwater and current directions. The observed trend of current and particle movement is sketched in Fig. (17). It is consistent with the present results above. Secondly, Liu and Mei (1976a,b) have developed a finite different model based on ray theory and ignoring that of convective inertia and viscosity. The comparisons between Liu and Mei and present results have been made in Fig. (18) and describe as:

Normal wave incidence, F_{LH} = 0.01

1. Position of the circulation centres
   y - direction
   Liu and Mei : y = 1125
   present : y = 1200
   x - direction
   Liu and Mei : x = 60
   present : x = 135
2. Max. mean alongshore velocity components, V
   Liu and Mei : 0.48 m/sec
   present : 1.365 m/sec

The above comparisons show good agreement in the general form of the circulation pattern, although there are some differences of detail.

4. CONCLUSIONS

An offshore breakwater on a beach for shore protection has been considered in the complete finite element model to study the wave variations due to diffraction, refraction and reflection, and nearshore current due to breaking wave inside or near surfzone with the considerations of convective inertia, eddy viscosity and bottom friction. A quite pleased result has been produced in this research.

Figure 3.

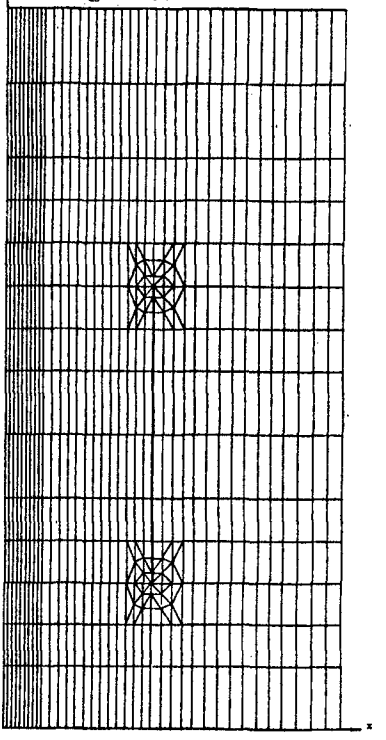

Figure 4.

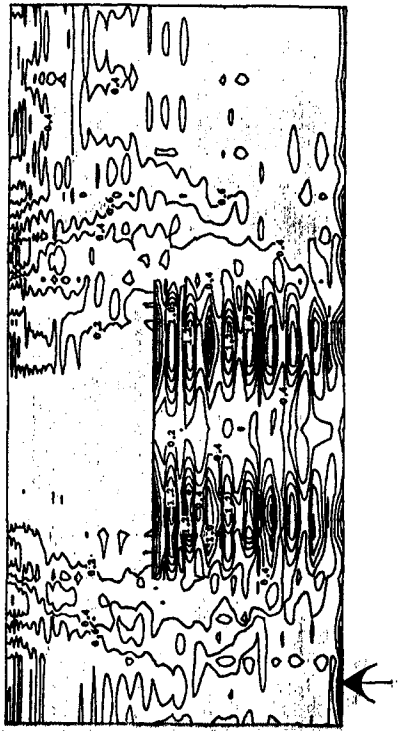

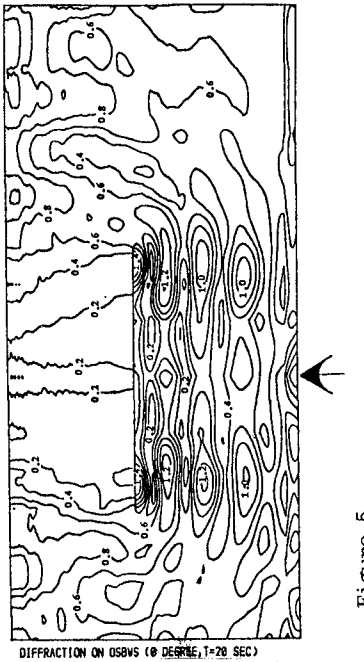

Figure 5.

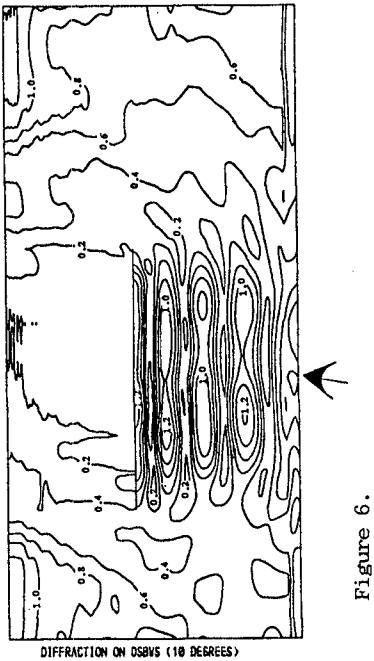

Figure 6.

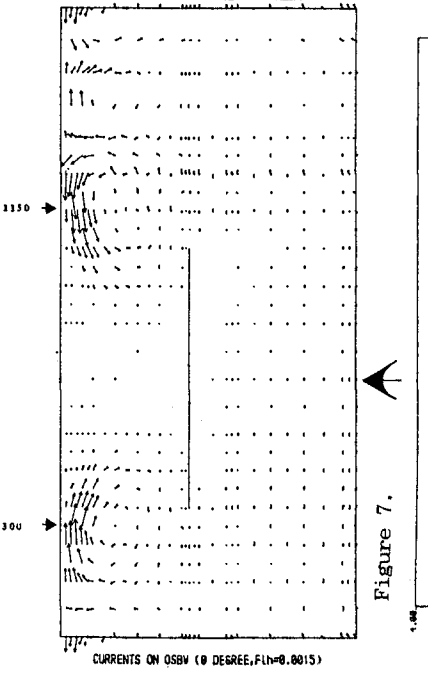

Figure 7.

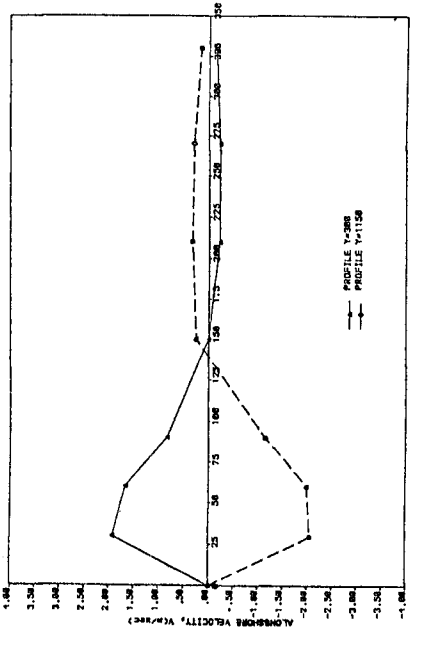

Figure 8.

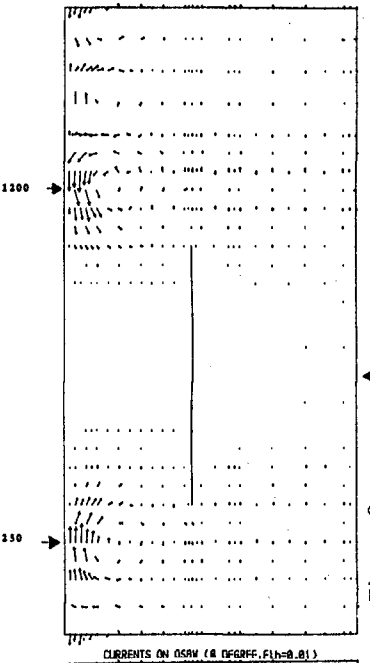

Figure 9.

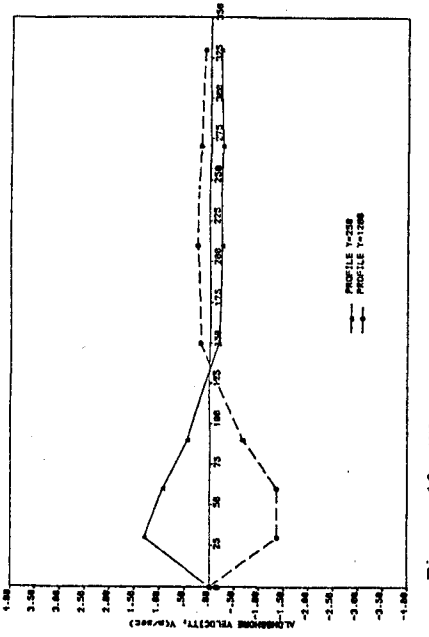

Figure 10.

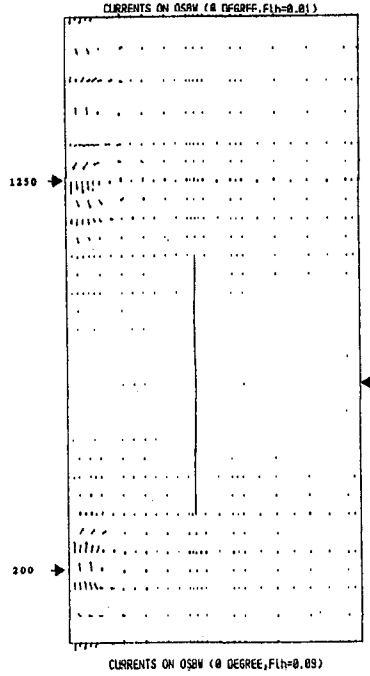

Figure 11.

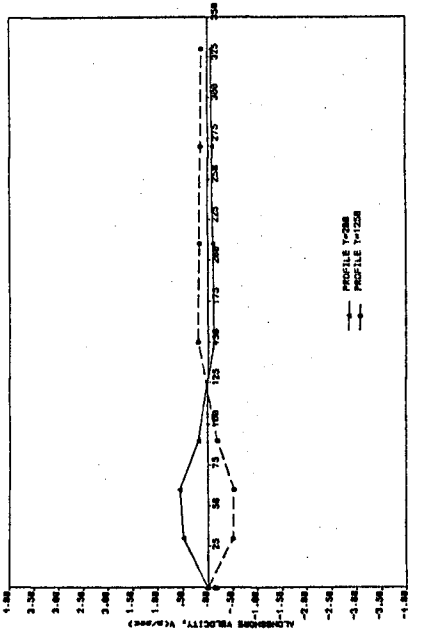

Figure 12.

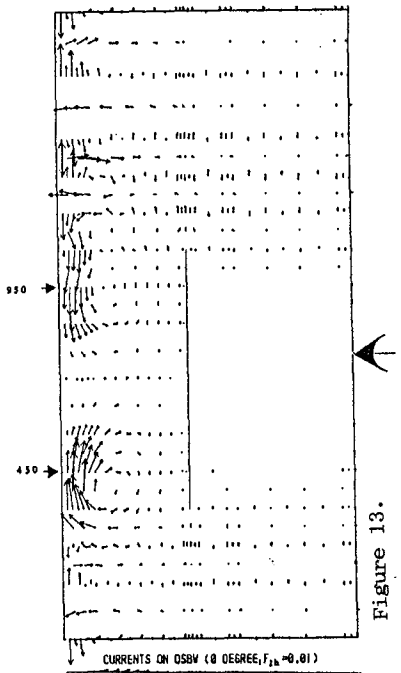

Figure 13.

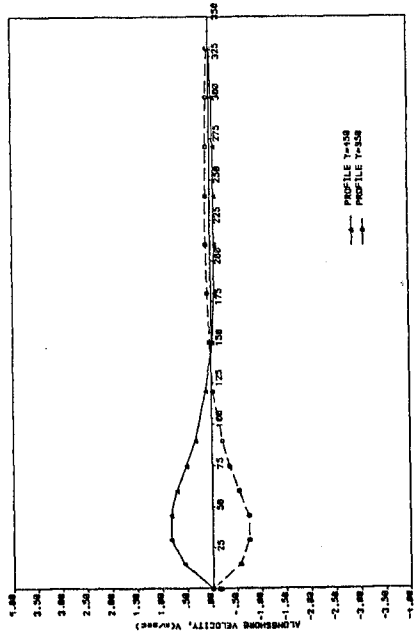

Figure 14.

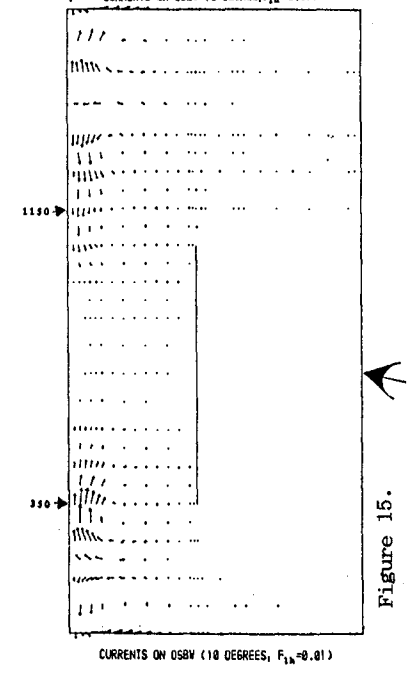

Figure 15.

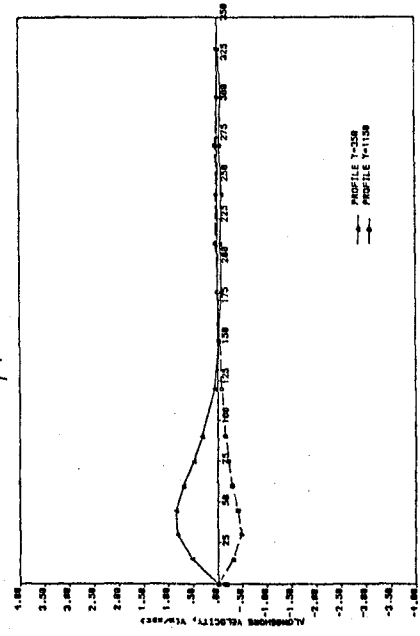

Figure 16.

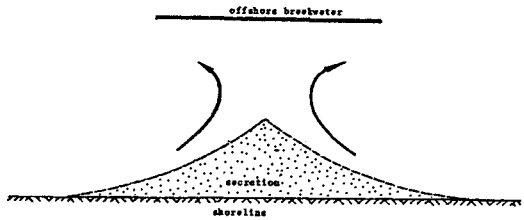

Figure 17.

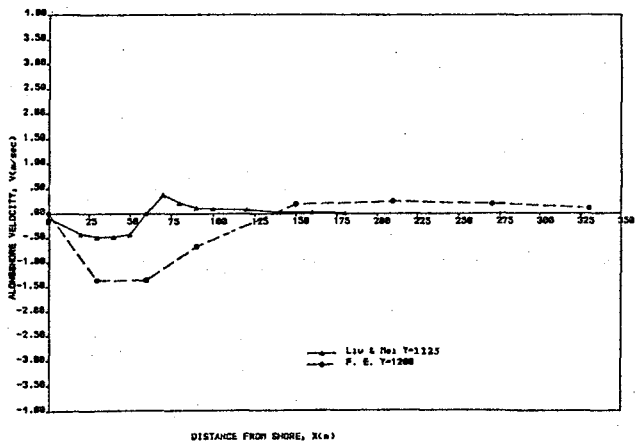

Figure 18.

5. REFERENCES

BERKHOFF, J.W. (1972). 'Computation of combined refraction-diffraction'. 13th Int. Conf. of Coastal Engng., Vancouver.

BERKHOFF, J.W. (1975). 'Linear wave propagation problems and the finite element method'. Finite Element in Fluids, Vol. 1, Chap. 13, John Wiley, London.

BETTESS, P., LIANG, S.C. AND BETTESS, J. (1984). 'Diffraction of waves by semi-infinite breakwater using finite and infinite elements'. Int. J. for Num. Meth. in fluids. Vol. 4.

HENSHELL, R.D. and SHAW, K.G. (1975) 'Crack tip finite elements are unnecessary'. Int. J. Num. Meth. in Engineering, Vol. 9.

IRIBRREN, C.R. and NOGALES, C. (1949). 'Protection des ports'. Section II, Comm. 4, 17th Int. Nav. Congress, Lisbon.

JAMES, I.D. (1974). 'Non - linear waves in the nearshore region : shoaling and set-up'. Est. and Coast. Mar. Sci..

LIANG, S.C. (1983). 'Prediction of wave induced surfzone currents adjacent to breakwaters'. Ph. D. Thesis. Univ. College of Swansea, U.K.

LIU, P.L.F. and MEI, C.C. (1976a). 'Water motion on a beach in the presence of a breakwater, 1, waves'. J. Geophys. Res., 81.

LIU, P.L.F. and MEI, C.C. (1976b). 'Water motion on a beach in the presence of a breakwater, 2, mean currents'. J. Geophys. Res.,81.

KOMAR, P.D. and GAUGHAN, M.K. (1972). 'Airy wave theory and breaker height prediction'. 13th Int. Conf. of Coast Eng., Vancouver.

LONGUET-HIGGINS, M.S. and STEWART, R.W. (1964) 'Radiation stresses in water waves: A physical discussion with application'. Deep Sea Res., 11.

LONGUET-HIGGINS, M.S. (1967). 'On the wave - induced difference in mean sea level between the two sides of a submerged breakwater'. J. on Mar. Res. Vol. 25.

LONGUET-HIGGIHS, M.S. (1970a,b). 'Longshore currents generated by obliquely incident sea waves'. J. Geophys. Res., 75.

McCOWAN, J. (1891). 'On the solitary wave'. Phil. Mag.(5), 32, No. 194.

MEI, C.C. (1973). 'A note on the averaged momentum balance in two - dimensional water waves'. J. of Mar. Res., Vol. 31.

SAUVAGE DE SAINT MARC, M.G. and VINCENT, M.G. (1955). 'Transport littoral formation de fleches et de tomolos'. Proc. of 5th Conf. on Coastal Eng..

SOMMERFELD, A. (1896). 'Theore mathematique de la diffraction'. Math. Ann. Vol. 47.

ZIENKIEWICZ, O.C. and HEINRICH, J.C. (1978) 'The finite element method and convection problems in fluid mechanics'. Finite Element in Fluid Mechanics, Vol. 3, Chap. 1, John Wiley, London.

CHAPTER 151

Effects of Short-crested Waves on the Scouring Around the Breakwater

Ming-Chung Lin* Chi-Tung Wu**
Yen-Chi Lu*** Nai-Kuang Liang****

The aim of this research is to investigate qualitatively the influence of short-crested waves on the scouring around the breakwater through mainly some laboratory studies. At first, we succeed to observe clearly in laboratory some sedimentary bed forms such as troughs, holes, triangle bars and longitudinal bars under short-crested wave actions. Then we elucidate the associstion of their formation mechanism with theory of short-crested waves, also indicate its effect on scouring at the toe of breakwaters. In addition, it is shown that the breaking wave height of short-crested waves is certainly higher than that of two-dimensional standing waves. Finally we demonstrate some facts of failure of breakwater caused by short-crested wave breaking basing on some field results.

1. Introduction

As the breakwater is built in the sand bed region the incident waves and their reflected waves are combined into Short-crested waves system. The vortex motion and maxro-tubulence structure under the wave system can scour deep holes and result in subsidence of the breakwater. This phenomen is well known to the practicing engineers.

A theorietical solution presented by Fuchs (1952), based upon linear theory, had been applied to short-crested wave system. Later, the extensive work by Chappelear (1961) had improved the accurocy of Fuch's approximation, but with the difficulty of immediate application due to very length formulation. A more sophisticated second order theory had been proposed by Hamada (1965) by means of the secondary interactions. A third order approximation to the short-crested waves was derived by Hsu (1978). In addition, that breaking wave height of short-crested waves is certainly higher than that of two dimensional progressive waves was shown by Halliwell and Machen (1981). The breaking wave height obtained from the third approximation of Hsu & Siloverster (1982) matchs well with that result by Halliwall (1981). The aim of this paper is to investigate qualtatively influence of short-crested waves on the scoaning around the breakwater through mainly the movable model tests studies.

* Professor, Dept. of Naval Architecture, National Taiwan University, Taipei , Taiwan, R.O.C.
** Senior Engineer, Taichung Harbor Bureau, Taichung, Taiwan, R.O.C.
*** Professor, Dept. of Civil Eng., National Taiwan University, Taipei Taiwan, R.O.C.
**** Director, Inst. of Harbor and Marine Technology, Wuchi, Taichung, Taiwan, R.O.C.

2. Summary of short-crested wave theory

2.1 Basic properities of short-crested waves

When waves approach and are reflected from vertical breakwater, they creat a surface undulation of a diamond pattern, known as short-crested waves, as shown in Fig. 1. With a coordinate system of x being in the direction of advancing the combined crest, Y tranversally to the celerity vector of the combined wave and Z positive upward from the still water surface, Fuchs (1952) derived the frist order approximation as:

$$\phi = \frac{ag}{m C_s} \frac{\cosh r(d+y)}{\cosh(rd)} \cos m(X - C_s t) \cos nZ \quad \text{(2-1)}$$

$$m = \frac{2\pi}{L} \qquad n = \frac{2\pi}{L'} \qquad r^2 = m^2 + n^2$$

$$Y_s = -\left[\frac{1}{g}\frac{\partial \phi}{\partial t}\right]_{y=0} = a \sin m(X - C_s t) \cos nZ \quad \text{(2-2)}$$

$$C_s^2 = \frac{gr}{m^2} \tanh(r \cdot d)$$

$$= \frac{gL}{2\pi}\sqrt{1 + \left(\frac{L}{L'}\right)^2} \tanh\left[\frac{2\pi d}{L}\sqrt{1 + \left(\frac{L}{L'}\right)^2}\right] \quad \text{(2-3)}$$

where ϕ, Y_s and C_s are velocity potential, surface profile and wave velocity repectively.

$$C_s = \frac{gT}{2\pi}\sqrt{1 + \left(\frac{L}{L'}\right)^2} \tanh\left[\left(\frac{2\pi d}{L}\right)\sqrt{1 + \left(\frac{L}{L'}\right)^2}\right] \quad \text{(2-4)}$$

because $\sqrt{1 + \left(\frac{L}{L'}\right)} \geq 1$ then

$$C_s \geq \left(\frac{gT}{2}\right) \tanh \frac{2\pi d}{L} \quad \text{(2-5)}$$

Eq.(2-5) Show that the combined celerity of short-crested wave is larger than wave celerity of incident waves.

The water partical velocities in X,Y and Z direction under the short-crested waves are as follows:

$$u = \frac{\partial \phi}{\partial X} = \frac{ga}{C_s} \frac{\cosh[r(Y+d)]}{\cosh(rd)} \sin m(X - C_s t) \cos nZ$$

$$v = \frac{\partial \phi}{\partial Y} = -\frac{gar}{mC_s} \frac{\sinh[r(Y+d)]}{\cosh(rd)} \cos m(X - C_s t) \cos nZ$$

$$w = \frac{\partial \phi}{\partial Z} = \frac{gan}{mC_s} \frac{\cosh[r(Y+d)]}{\cosh(rd)} \cos m(X - C_s t) \sin nZ \quad \text{(2-6)}$$

The orbital of water partical is :

$$X = \left(\frac{H}{2}\right) \frac{\cos\left(\frac{2\pi}{L}\right)(Y+d)\sqrt{1+\left(\frac{L}{L'}\right)^2}}{\sqrt{1+\left(\frac{L}{L'}\right)^2}\sinh\left(\frac{2\pi d}{L}\right)\sqrt{1+\left(\frac{L}{L'}\right)^2}} \left[\cos\left(\frac{2\pi Z}{L'}\right)\sin\left(\frac{2\pi X}{L}\right)\right]$$

$$Y = \left(\frac{H}{2}\right) \frac{\sinh\left(\frac{2\pi}{L}\right)(Y+d)\sqrt{1+\left(\frac{L}{L'}\right)^2}}{\sinh\left(\frac{2\pi}{L}\right)\sqrt{1+\left(\frac{L}{L'}\right)^2}} \left[\cos\left(\frac{2\pi Z}{L'}\right)\cos\left(\frac{2\pi X}{L}\right)\right]$$

$$Z = \left(\frac{H}{2}\right)\left(\frac{L}{L'}\right) \frac{\cosh\left(\frac{2\pi}{L}\right)(Y+d)\sqrt{1+\left(\frac{L}{L'}\right)}}{\sqrt{1+\left(\frac{L}{L'}\right)^2}\sinh\left(\frac{2\pi d}{L}\right)\sqrt{1+\left(\frac{L}{L'}\right)^2}} \left[\sin\left(\frac{2\pi Z}{L'}\right)\cos\left(\frac{2\pi X}{L}\right)\right] \quad \ldots(2\text{-}7)$$

The water particles follow elliptical paths which are angled to the horizontal.

$$\tan\beta = \frac{n \tan(nZ)}{r \tanh r(Y+d)} \quad \ldots\ldots\ldots\ldots\ldots\ldots\ldots\ldots\ldots\ldots \quad (2\text{-}8)$$

Furthermore, also derived the free surface profile to the second-order approximetion as follow:

$$\phi = A \cosh r(d+Y) \cos m(X - C_s t) \cos n Z + B \cosh 2r(d+Y) \cdot \sin 2m(X-C_s t) \cos 2nZ + D \cosh 2m(d+Y) \sin 2m(X-C_s t)$$

$$A = \frac{am}{r} \frac{\cosh r(d+Y)}{\sinh r d} \cos n Z$$

$$B = -\frac{3}{16} \frac{A^2 r^2}{C_s m \sinh^2 r d}$$

$$D = \frac{A}{8 m C_s} \frac{4 n^2 \cosh^2 rd - 3r^2}{2 \cosh 2md - (m \sinh 2md/r \tanh rd)} \quad \ldots\ldots\ldots \quad (2\text{-}9)$$

$$Y_s = a \sin m(X-C_s t) \cdot \cos nZ + \frac{a^2 r^2}{4 \sinh 2rd}(2 \sinh^2 rd - 1 + \frac{3 \cosh 2rd}{\sinh^2 rd}) \cdot \cos 2m(X-C_s t) \cdot \cos 2nZ + \frac{a^2(m^2-n^2 \cosh 2rd)}{4r \sinh 2rd} \cdot \cos 2nZ + \frac{a^2}{4r \sinh 2rd} \left[\frac{(3r^2-4n^2\cosh^2 rd)\cosh 2md}{\cosh 2md - (m \sinh 2md/2r \tanh rd)} - m^2 \cosh^2 rd + 3r^2 \sinh^2 rd + n^2 \cosh^2 rd\right] \cdot \cos 2m(X-C_s t) \quad \ldots\ldots\ldots \quad (2\text{-}10)$$

2.2 Water partical motions under the short-crested waves system.

Basing on the Fuths theory, Silvester (1974) sketched the schematic diagram of water particle path under short-crested wave action, as Fig. 2. From this figure, the water particle motions can be described as

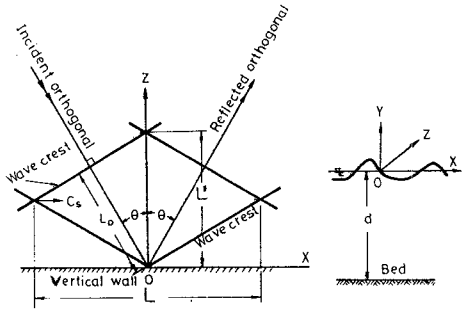

Fig. 1 Short-crested wave formed in front of a vertical wall.

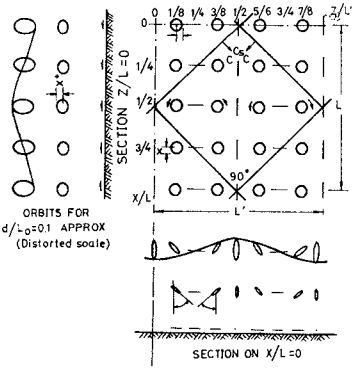

Fig. 2 Water particle orbits and mass transport under the short-crested wave. (Silverster, 1974)

follows.

(1) The wave profile along the centreline of the crests, at Z/L' = o, 1/2 , 1. etc., is more likely to be that of a solitary wave.
(2) Half-way between these crest alignment, at Z/L'=1/4, 3/4, etc., the orbital motion are rectilinear and are transverse to wave propagation.
(3) Between these again, at Z/L' = 1/8, 3/8, 5/8 , etc., the water particles follow elliptical paths which are angled to the horizontal.

The influence of these complex water motions on a sedimentary bed have been examined by. Tanalca and ozasa (1972), and Silvester (1974).

2.3 The breaking wave height wave height of short-crested wave.

There are two different theorm on the breaking wave height of short-crested wave so far. One is solitery wave theorm, another is progressive wave theorm.

(A) Solitary wave theorm:
Halliwell and Machen (1981), basing upon work of Milies (1977) , derived the breaking wave height of short-crested as follows:
when

$$C_S/C_1 \doteqdot \text{Sec } \theta_1$$

$$C = \sqrt{g(\eta+d)} \quad \text{.....(2-11)}$$

$$\frac{d+\eta_3}{d+\eta_1} = \text{Sec } \theta_1 \quad \text{.....(2-12)}$$

$$\frac{\eta_3}{\eta_1} = \left(\frac{d}{\eta_1}+1\right)\sec^2\theta_1 - \frac{d}{\eta_1} \quad \text{..... (2-13)}$$

$$\therefore \ \eta_3 \geq \eta_1 \quad \text{..... (2-14)}$$

Let the breaking wave condition be $U_{max}/C_S = 1$, since $C_S > C$, there are greater Umax than that of incideut progressive wave with celectiy C. That is why the breaking wave height of short-crested wave is higher than that of progressive wave.

(B) The interaction of progressiv wave theorem.
Hsu & Silverster (1982), basing the third order approximation and taking the $U_{max}/C_S=1$ as a condition of breaking wave, got the breaking wave height which is larger than that of progressive wave and depend on the angle of interaction of two progressive wave.

3. Laboratory experiments

In order to investegate the effects of short-crested wave on the scouring around the breakwater, the movable bed model expeniments were performed in a wave basin with 60 m length, 43 m width and 1 m depth. A vertical breakwater was built in wave basin for producing a reflected wave train . The scouring at the toe of the breakweter has been since before one of the serious problems confronting the Taichung engineers. The laboratory studies are therefore based on the model test of Taichung Harbour located in Mid-western Taiwan. Fig. 3 depictes a schematic sketch of the experimental hydraulic model employed.

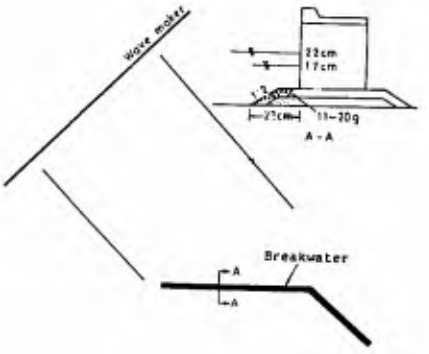

Fig. 3 Schematic diagram of the experimental model.

Fig. 4 Short-crested wave formed in front of the breakwater.

The ratios of model employed were that the breakwater , wave period, wave velocity., and wave pressure were 1/64 and the rock weight was $1/64^3$. The sand used for movable bed was directly taken from the natural beach in the vicinity of Taichung Harbour and its mean median diameter D_{50} was 0.22 mm.

It takes about one hour of time to complete a run of experiaments. Measurements performed were mainly included wave height distribution, breaking wave height and overall bed form. The bed forms were simultaneously obtained by photographing and level measuring. In order to investigete the scouring, when performing the experiments, we paid particularly attention to the situation as the short-crested waves are breaking.

4. Results and discussions

The runs of model test, the results of laboratory studies and the field data survey are shown in Table 1, 2 and 3. The short-crested wave formed in front of the breakwater was shown in Fig. 4 and Fig. 5. A typical result of bed forms under the action of short-crested waves are depicted in Fig 6 and 7. It can be clearly seen from this figure that the sedimentary bed is scoured by the breaking short-crested waves. As shown in Fig. 8 and Fig. 9, concerning the bed form in detail near the breakwater, deep holes and triangle bar are generally formed at the place of wave breaking. In Fig. 10 the sand ripples appear in the front of the breakwater and in Fig 11, the longitudinal bar and trough appear around the corner of the breakwater. If the breaking short-crested wave height is even greater, the impinging wave breaking will produce a large scouring hole just at the toe of the breakwater, as shown in Fig. 12.

(1) The brearking wave height resulting from the short-crested wave is greater than that of incident wave and this result matchs that of Hsu & Silvester. (1982), as shown in Fig. 13 and 14.

(2) The scouring in front of breakwater under the short-crested wave is strong and serious. The characteristics of the scouring as follows.
   (a) at Z/L'=0,1/2 , 1..., the sand hed were scoured and the sediments were transported in the X dinection.
   (b) at Z/L'=1/4, 3/4, ... there are the back and forth motion of water particles along the Z direction. There are no sediment transported in the X direction
   (c) at Z/L'=1/8, 3/8, 5/8, 7/8...etc., the swirling motion of water particles have much contribution in expediting the sediment movement. The moving sediments are transported into the adjoining regions.

(3) The mechanism of various sedimentary bed forms may be explained as follws:
   (a) at Z/L'= 0, 1/2, 1, etc, the sediments are transportad along the short-crested wave progessing. The greater the wave height is, the more the transportation is. Then, in this condition, the trough is formed along these lines (Z/L'=0, 1/2, 1 etc), as shown in fig. 1.
   (b) at Z/L'=0, 1/4, 1, .. only a few sediments are transported along transverive and longitadinal direction. In this characteristic, the longitudinal bar was formed.
   (c) When the breaking waves take place, the sand bed is formed

Table 1: The wave conditions of model test

Run	Wave period (sec)	Incident angle (θ_i)	Water depth (m)	Wave height (m)
1	1.25	35°	0.22	0.098
2	1.25	45°	0.17	0.098
3	1.25	45°	0.22	0.098
4	1.25	45°	0.17	0.124
5	1.25	30°	0.165	0.111
6	1.25	60°	0.21	0.123
7	1.25	45°	0.21	0.075
8	1.00	45°	0.205	0.110

Table 2: The breaking wave heights obtained from the results of experimental tests

Run	Wave period (sec)	Incident angle θ_i	Water depth d_{sb}	Breaking wave height	Wave length	$\frac{d_{sb}}{gT^2}$	$\frac{H_{sb}}{ds}$	$\frac{H_{bs}}{L_1}$	$\frac{d_{sb}}{L_1}$
1	1.25	35°	0.22	0.3093	1.663	0.0144	1.41	0.186	0.132
2	1.25	45°	0.17	0.258	1.495	0.011	1.518	0.173	0.114
3	1.25	45°	0.22	0.3232	1.663	0.0144	1.47	0.194	0.132
4	1.25	45°	0.17	0.297	1.495	0.011	1.74	0.199	0.114
5	1.25	30°	0.165	0.2317	1.476	0.0107	1.404	0.157	0.112
6	1.25	60°	0.21	0.2575	1.632	0.0137	1.226	0.157	0.129
7	1.25	45°	0.21	0.3003	1.632	0.0137	1.43	0.184	0.129
8	1.00	45°	0.205	0.2582	1.222	0.021	1.26	0.211	0.168

Table 3: The breaking wave heights of short-crested wave obtained from the field data survey, Taichung Harbor Bureau, 1973.

Wave period (sec) T	Incident angle θ_i	Water depth d_{sb}	Breaking wave height H_{sb}	Wave length L_1	$\frac{d_{sb}}{gT}$	$\frac{H_{sb}}{ds}$	$\frac{H_{bs}}{L_1}$	$\frac{d_{sb}}{L_1}$
10		13	18	156	0.01	1.38	0.115	0.083

Fig. 5 Short-crested wave breaking in front of the breakwater.

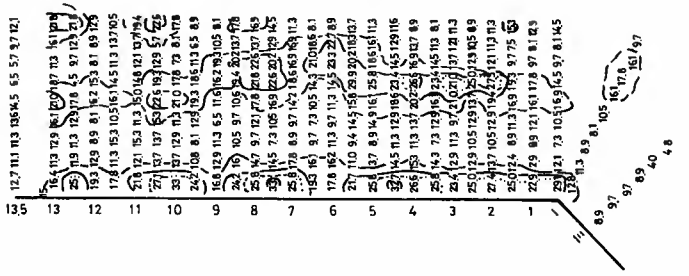

Fig. 6 Short-crested wave height distrobution in front of breakwater. Incident wave period = 1.25 sec, incident angle = 45°, incident wave height = 0.098m, water depth in front of breakwater = 22 cm.

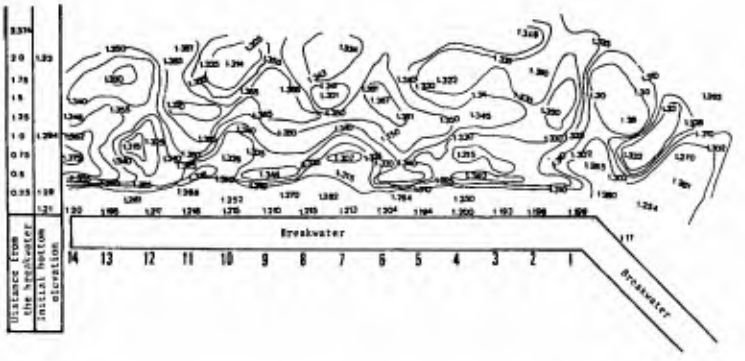

Fig. 7 Contours of bottom topography under short-crested wave actions.
incident wave period=1.25sec., incident angle=45°.
incident wave height=0.098m, water depth at the breakwater= 22cm.

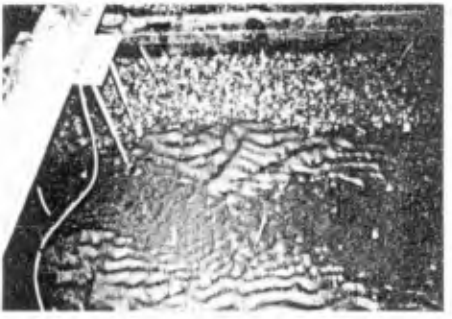

Fig. 8 Triangle sand bar and deep hole in the front of the breakwater.

Fig. 9 Triangle sand bar under the short-crested wave breaking.

Fig. 10 The sand ripples under the short-crested wave which did not break.

Fig. 11 The longitudinal bar and trough around the corner of the breakwater.

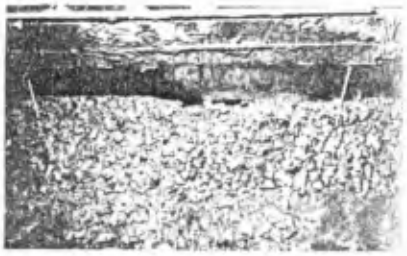

Fig. 12 Scouring hole at the toe of the breakwater.

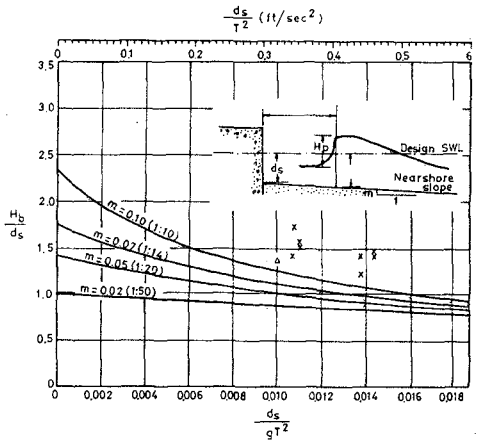

Fig. 13 Compare the breaking wave height of short-crested wave with that from Shore Protection Manual (1977).
-: the results by Weggel
X: the lab results by authors
Δ: the field data

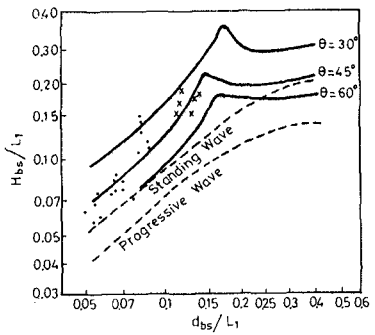

Fig. 14 Compare the breaking wave height of short-crested wave with that of standing wave, progressive wave, the numerical solution by Hsu & Silvester and the lab results by Halliwell.

• : the lab results by Halliwell
- : the numberical solution by Hsu & Silvester
X : the lab results by authors

into deep hole under the breaking waves, and the sand bed, by the deep hole, was formed triangle bar.

(d) Furthermore, for comparision, the sea bottom contours around the corner of the breakwater obtaned from the field data survey is depicted in Fig. 15, revealing the same tendancy as that of leboratory.

5. Conclusions and Remarks

From the laboratory experiments and field observation, the scouring effect, resulted from the short-crested wave system, on the foundation of breakwater can be drawn:

(1) Oblique incident waves and their reflected waves are formed into short-crested waves system in front of the breakwater. This short-crested waves progress along the breakwater and gradually swell up. Swelling up along the breakwater is greater than that of breaking wave height limit, the short-crested wave are broken. The breaking short-crested wave height is larger than that of progressive wave, and belong to plunging breaking wave. This breaking waves result in serious scouring around the breakwater.

(2) The characteristics of water particle motions under the short-crested wave system enforced the sediment transport and form into special bed forms such as troughs, holes, triangle bars and longitadinal bars.

(3) While the breaking waves happen, the vortex motions penetrate to the bed in the vicinity of the breakwater scour the foundation of the breakwater, and result in subsidence of the breakwater.

(4) It's suggested that when the breakwater is designed or built, the influence of short-crested wave should be considered.

(5) However, in this paper, only the qualitative results were reported.

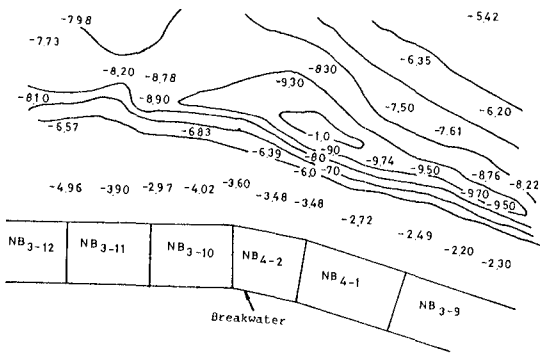

Fig. 15 Bottom contours around the corner of the breakwater for field case.

6. References:

1. Fuchs, R.A. (1952): "On the theory of short-crested oscillatory waves" Grovity waves, U.S. Nat. Bur. Stand. Circular No.521, pp.187-200.
2. Halliwell, A.R. and P.C. Machen (1981): "Short-crested breaking waves in water of limited depth" Proc, Instn Civ, Engrs Part 2, 71. pp.663-674.
3. Hamada, T. (1965): "The secondary interaction of surface waves" Report of port and harbour technical research institute,Japan, Report No. 10.
4. Hsu, J.R.C., Y. Jsuchiya and R. Silvester (1979): "Third-order approximation to short-crested waves". J. Fluid Mech., Vol.90, part 1, pp.179-196.
5. Hsu, J.R.C. and R. Silvester (1982): "Short-crested breaking waves in water of limited depth" Discussion. Proc Instn Civ. Engrs, Part 2, 73, pp.489-491.
6. Miles, J.W. (1977): "Obliquely interaction solitary wave" J. Fluid mech. 79. No. 1 pp.157-169.
7. Silvester, R., (1974): Coastal Engineering, Elsevier Scientific Publishing Co. Amsterdam.
8. Tanaka,D. and H. Ozasa, (1972): "A study of the velocity distribution of mass transport used by diagonal partial standing waves" Port and Harbour research institue (in Japanese) Vol.11, No. 3, pp.122-137.
9. U.S. Coastal Engineering Research Center (1979): "Short Protection Manual" US Coastal Research Center, Fort Belvoir VA.
10. Wiegel, R.L. (1964): Oceanographical Engineering , Prentice Hall, pp.53-58.
11. Taichung Harbor Bureau: Hydrographic data survey of Taichung Harbor, Taichung, Taiwan, 1973. (in chinese)

CHAPTER 152

THE STRUCTURAL RESPONSES OF DOLOS ARMOR UNITS UNDER THE DYNAMIC LOADING

Wei-Ming Lin*, Cheng Rau**, Rea-Lon Su**

ABSTRACT

The "Dolos" is now used widely for harbor and shore protection works in various ports of Taiwan (R.O.C.) and some damage has been noted. The purpose of this research is to understand the major factors which influence dolos breakage. The factors studied include plain or reinforced concrete, rebar arrangement, chamfered or enlarged fillet corner and the fracture behavior by pendulum and drop test.

Site observations and laboratory dynamic tests are included in this paper. The site observation investigated the behavior of the broken dolos at each habor. In the laboratory dynamic tests 42 specimens of 1.5 tons dolos were used for drop tests; frontal and transverse pendulum tests (Fig.1).

The results show that the fracture behavior in the laboratory tests agree with those of site observation, i.e. cracking due to frontal impact is more severe than that of transverse impact. The arrangement of rebar also influences the strength of the dolos. Therefore, it is suggested that the dynamic tests are necessary for dolos tesing.

INTRODUCTION

The sequence of breakwater failures in the late seventies and early eighties raised questions whether there were deficiencies in the design or construction of rubble mound breakwaters. Conclusions from some of the damage investigations were [1]:

- Damage to dolos of more than 15 tons can occur due to rocking, and hydraulic damage criteria are no longer applicable.
- More basic research and full scale monitoring is required to establish proper design guidelines.

A successful desing must ensure both the hydraulic and structural stability of the units. Consequently, problems related to the structural strength of dolos have been discussed. Lillevang[2] used 3D

* Head of Harbor Engineering Material Division, Institute of Harbor & Marine Technology, WuChi, Taichung District, Taiwan, R.O.C.

** Assistant Researcher of Harbor Engineering Material Div. Institute of Harbor & Marine Technology, Taichung, Taiwan, R.O.C.

photoelastic stress analysis to examine the stress distribution of dolos models with various shapes of stem-fluke corner under static loads. Burcharth[3] did drop and pendulum tests using 1.5 tons and 5.4 tons dolos, and proposed a method for a dynamic test, and Terao[4] also carried out drop and static load tests using 0.04 tons, 0.4 tons and 4 tons units.

Dolos have been used in various ports of Taiwan, R.O.C. The dolos have suffered impact loading resulting from rocking/rolling of units and missiles of broken units.

SITE OBSERVATIONS

Fig.2 is key map of the site obscration of dolos destruction in Taiwan and Table 1 shows a summary of detailed information of these dolos projects in Taiwan. The most severe storm damage which occurred at the east breakwater of Hua-Lien Harbor during typhoon Andy was up to 70%. The probable reason was the limited ability for placing 40 tons Dolos, hence the units were unstable on the steep armor slope. Damage of 20% occurred at the west breakwater of Hua-Lien Harbor, while still under construction and before the crown wall had been constructed. Hua-Lien Harbor faces the Pacific ocean and the units suffered from severe wave impact loade. Typical dolos destruction in Taiwan, R.O.C. is shown in Fig. 3.

THEORETICAL CONSIDERATIONS FOR ANALYSIS OF DYNANMIC TESTS

The dynamic testing of dolos to destruction is to simulate the impace force when the units are rocking or struck by broken units. Burcharth[3] derived formulae for the maximum tensile stress in a dolos exposed to impace load in a drop test and a pendulum test (Fig.4) by using impulse moment equations and dimensional analysis as follows:

$$\text{drop test : } \frac{\sigma}{MghC^{-3}} = C_1 \frac{1+r}{r^2}\sqrt{\frac{E}{\rho gh}} \quad , \quad 0.3 \leq 4 \leq 0.4 \quad \ldots\ldots\ldots\ldots \quad (1)$$

$$\text{pendulum test (1) : } \frac{\sigma}{mghC^{-3}} = C_2 \frac{1}{r^3}\sqrt{\frac{E}{\rho gh}} \quad \ldots\ldots\ldots\ldots\ldots\ldots \quad (2)$$

where σ = maximu tensile stress
$M(m)$ = dolos (pendulum) mass
h = fall height of pendulum (or dolos center of gravity)
C = dolos height
g = gravitational acceleration
E = elastic modulus
ρ : mass density of pendulum and dolos
r : waist ratio (0.319 in this test for 1.5 tons dolos)
C_1 and C_2: constant factors to be determined by tests

Since thest formulae were developed for specific test set-ups involving bending and shear stress in the most exposed cross seciton, we developed another test set-up for a transverse pendulum test which creates mainly torque in the stem. A formula were developed similar to the frontal pendulum test as follows:

pendulum test (2) : $$\frac{\tau}{mghC^{-3}} = C_3 \frac{1}{r^3}\sqrt{\frac{E}{\rho gh}} \quad \ldots\ldots\ldots\ldots\ldots\ldots \quad (3)$$

where τ = torsion
C_3= constant to be determined by tests.

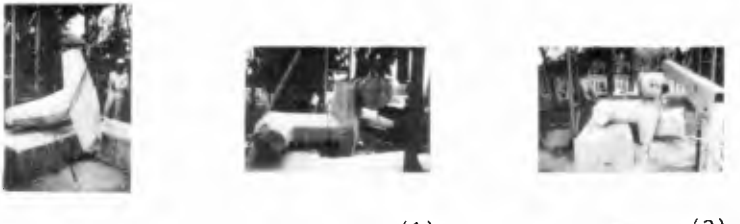

DROP TEST PENDULUM TEST(1) PENDULUM TEST(2)

Fig.1 DYNAMIC TESTING SET UP

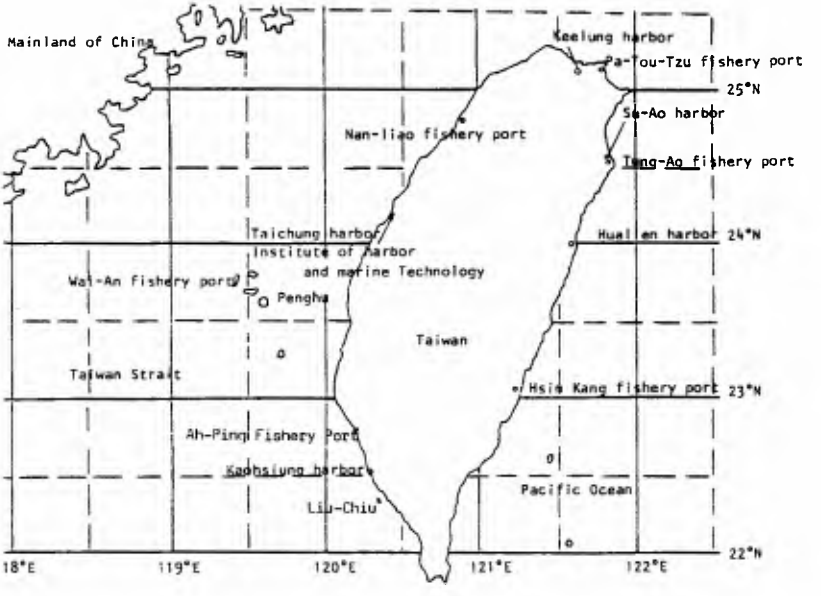

Fig. 2 KEY MAP OF THE SITE OBSERVATIONS OF DOLOS DESTRUCTIOIN IN TAIWAN

KEELUNG HARBOR

SU-AO HARBOR

HALIEN HARBOR

PA-TOU-TZU
FISHING PORT

SU-AO HARBOR

HALIEN HARBOR

KAOHSIUNG HARBOR

TUNG-AO FISHING PORT

HSIN KANG FISHING PORT

Fig. 3 TYPICAL DOLOS DESTRUCTION IN TAIWAN

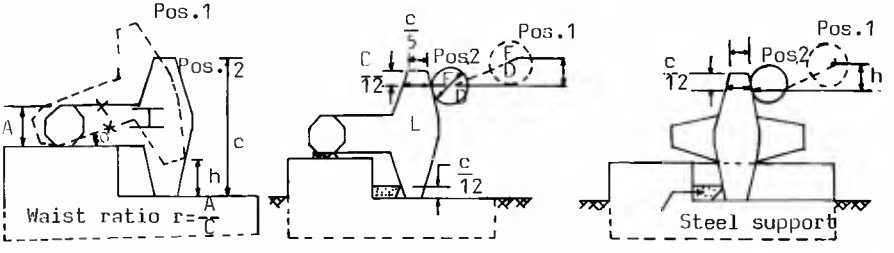

(a) Drop Test (b) Pendulum Test (1) (c) Pendulum Test (2)

Fig 4. SIMULATED DYNAMIC TEST

TABLE 1: SUMMARY OF DETAILED INFORMATION ON KNOWN DOLOS PROJECTS IN TAIWAN

Project & details		Design conditions					Structure geometry				Dolos armouring particulars							Site Experience									
Name and period of construction	Part *	wave height H (m)	wave period T (s)	Angle approach (°)	Recurrence (years)	Design damage (%)	Armour slope (tanα)	Crest height of Dolos(Hc)	Armour depth (m) ±	Water depth (m)	Dolos mass W(tons)	Dolos height (m)	Waist ratio (-)	Density of block tons/m3	Design compressive strength (Mpa)	Packing density	Underlayer mass (tons)	Dolos stripping (days) x	Dolos moving (days)	Dolos placing (days)	28days compr-th (Mpa)	Breakage of Dolose (%) during Manufacture	Breakage of Dolose (%) during placing	Breakage of Dolose (%) during Initial Shake down	Storm wave height (m)	Storm damage (%)	Number of dolos used	Unit cost (US$)
Su - Ao harbour																											
composite caisson breakwater 1974-1979	MBT	10	11		13		0.5	+32	25	25	30	4.3	0.32	2.45	28		2-5	1	5	28	28						5130	1000
Rubble mound breakwater 1974-1979	MBT	10	13		13		0.5	+27	8-20	8-20	10	3	0.32	2.45	28		2-5	1	5	28	28		3.92	0.27			9300	300
Keelung harbour																											
pa-chyy-Men breakwater 1979-1980	MBT						0.33 / 0.5	+11.8 / +14.1	-5.0 / -10.0	-6.0 / -11.0	20 30 40 40	3.76 4.31 4.79 4.79	0.27 0.26 0.26 0.26	2.35	35 24.5 35 24.5	2	3-5 0.5-1 0.5-1 0.5-1	3	7	15	35 24.5 35 24.5	0.3	0.2	0	8-9	0	1320 1093 898 1193	443 747 1076 985
East Breakwater 1976-1981	MBT						0.67	+7.0		Sea side -2 ~ -12 harbor -8 ~ -24	15 20	3.43 3.76	0.27 0.27	2.5 2.35	35 35	2	0.5-1 0.5-1	3	7	15	35	0.3	0.2	0	8-9	0	1962 1383	193 300
Kaohsiung harbour																											
Second harbor breakwater 1977-1984	MBT	6.0	10							13.0	7.5	2.67			20.59			2	7		23.6						3025	200
An-ping breakwater 1977-1978	MBT	6.0	10							8.0	7.5	2.67			20.59			2	7		23.6						5023	200
Chung Shan university breakwater 1983-1984	SP									6.0	7.5	2.67			24			2	7		27.6						3280	200
Hualien harbour																											
Old- east breakwater 1980-1982	MBT						2	+11	8 6	8 6	4 4	4.66 4.66	0.33 0.33	2.4 2.4	28 28	1.49 1.49	>5 NO	3	7	28	30	0	0	1	13.0# (calc)	70§	404	1100
Old- east breakwater 1983-1984	MBT						2	+13	6	6	41 40	4.66 4.66	0.33 0.33	2.4 2.3	28 28	1.49 1.49	NO NO	3	7	28	30	0	0	1			16 465	1100 850
New- west breakwater 1980-1983	MBT	9	12.3	27	25	1	0.5	+16	6.5	6.5	20	3.76	0.34	2.3	28	1.25	3-5	3	7	28	30	0	0	0.5	13.0 # (calc)	20§	2835	450
New- west breakwater 1980-1983	MBT MBH	9	12.3	27 63	25	1	0.5	+16.5~+18.5 +12	7-9	7-9	20	3.76	0.34	2.3	28	1.25	3-5	3	7	28	30	0	0	1			591	450
Fishery Ports:																											
Pa - Tou - Tzu 1980-1982	MBT	7.7~13.0	11.8~13.1	0 12		1	0.5	+2.7	-11	-20	30	4.32	0.32	2.4	20.7	0.76	7										3000	1050
Han - Tzao 1982-1984	MBT1S MBT MBH	3.7 / 7.8	9.3 / 9.7	5 / 45		1	0.67 / 0.5	+4.3 / +4.5	-2.0 / -4	-3.5 / -5.3	4 5	2.5	0.3	2.4	17.2	0.71 0.7	0.2 0.5										3434 6165	120 150
Liu - Chiu 1984	MBT MBH	7	11.7	0		1	0.5	+0 +0.32	-3 -4	-8	10 30	2.99 4.32	0.33 0.33	2.4 2.4	17.2 17.2	0.74 0.74	2 4	2	7	28							450 270	320 900
Hsin - Kang 1978	MBH						0.5	+1.1	-9.5	-9.5	7.5				17.2												428	
Wai - An 1982	MBT	4.1	8.6				0.67	+6.5	-3.5	-3.5	5 10				17.2 17.2												402 1525	
Tung - Ao 1983	MBT										12																100	

* MBT/MBH -Main breakwater Trunk/Head; SP-Shore protection; MBT1S-MBT inner slope.

× All days after casting.

± All depths are to be mean sea level (MSL).

Calculated from Andy Typhoon. (July 28 1982).

§ Damage occured at the section of MBT where crown wall had not built completed; Two Thirds of the damage was caused by Andy Typhoon.

TEST PROGRAMME

Test Specimens

A total of 42 units of 1.5 tons dolos were used in the tests and classified into seven types. Six units of each type were used for drop tests, frontal and transverse pendulum tests. The geometry and specifications of the units are shown in Fig. 5 and Table 2 respectively.

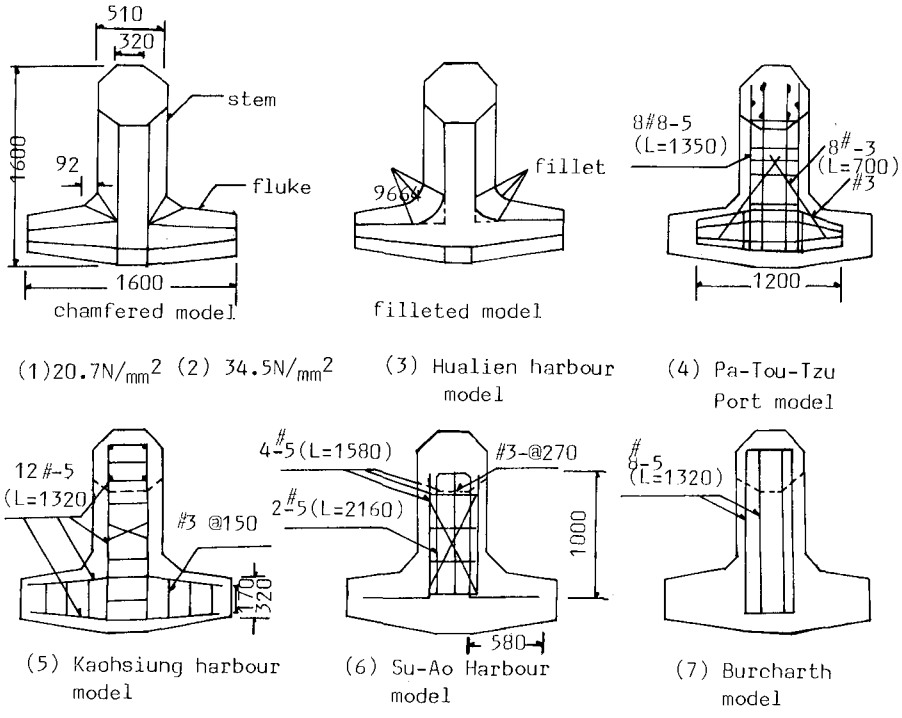

Fig 5. GEOMETRY OF DOLOS UNITS

Fig. 6 shows the preparation of dolos specimens. For quality control, two control specimen (15 cm x 30 cm) for each dolos unit were manufactured and tested by 100 tons universival material testing machine (Fig.7). They were also taken nondestructive tests by using test hammer (Fig.8) and ultra-sonic pulse measuring units (Fig.9). These data were compared to the compressive strength of control specimen's results.

TABLE 2. SPECIFICATIONS OF THE TEST SERIES

Series No.	1	2	3	4	5	6	7
Design compression strength (N/mm^2)	20.7			34.5			
Mass of unit M(Tons)	1.39	1.44	1.44	1.49	1.48	1.47	1.46
Density ρ ($Tons/m^3$)	2.14			2.22			
Height of unit C (mm)	1600	1600	1600	1610	1610	1600	1600
Waist ratio $r=\frac{A}{C}$	0.319			0.329			
Mass of pendulum m(Tons)	0.318			0.323			
Cement content (kg/m^3)	294			417			
Water-Cement ratio	0.68			0.48			
Aggregate	crushed, max. dia 20mm						
Mean static compression strength; 150x300 mm cylinder σc (N/mm^2)	22.7			43			
Mean flexural strength; center point loading test σ_f (N/mm^2)	4.64			8.08			
Mean static tensile strength; cylinder splitting test. σ_T (N/mm^2)	1.85			3.58			
Poisson ratio (%)	24.2			21.8			
Mean dynamic modulus of elasticity; ultrasonic method test E (N/mm^2)	3.6×10^4			4.3×10^4			
Mass of steel (kg)	0	0	0	47	38	25	21
Steel VS. Conc. ratio by weight (%)	0	0	0	3.26	2.64	1.74	1.46
Steel area ratio (%)	0	0	0	1.890	0.945	1.890	1.890

THE BIRD'S EYE VIEW OF DOLOS MANUFACTURE

DOLOS MOLDING

CURING

PLACING

DEMOLDING

DOLOS SPECIMENS

Fig.6 DOLOS SPECIMES PREPARATION

Fig.7 100 TONS UNIVERSIVAL MATERIAL TESTING MACHINE

Fig.8 TEST HAMMER

Fig.9 ULTRA-SONIC PULSE MEASURING UNIT

Experimental Method and Equipment

Three different types of test were used (Fig. 4). The drop test simulates the wave induced rocking of the units. The pendulum tests (1) and (2) simulate the frontal and transverse impact from pieces of broken units that are thrown around by the waves.

The experiment was carried out on a test platform. In the drop test, one end of the dolos is lifted to a predetermined height and then dropped by means of a quick release hook (Fig. 10 & 11). In the pendulum tests (1) and (2), the pendulum is pulled back a certain distance and then released.

The pendulum is a steel cylinder mould with wall thickness of 10 mm, filled with the same type of concrete as used in the dolos. Its weight is 1/5 of the dolos weight. The pendulum is suspended on two wires hanging on a steel gantry.

Before dynamic testing the dolos specimen were tested by using test hammer and ultronic-sonic pulse measuring unit (Fig.12) to be sure of good quality.

In the drop tests, we measured the fall height (the vertical distance from the base to the center of the fluke end); the initial drop of 100mm was gradually increased in increments of 20mm. In the pendulum tests, we measured the draw back distance (the shortest distance between the surface of the pendulum and the impact point on the dolos); and it was gradually increased from 300mm in the first strike, in increments of 20mm.

Because of the rebound, the dolos was jerked back against the steel packing block after each pendulum blow.

The concrete surface was carefully examined after each strike and the width and extent of the cracks were recorded.

With the purpose of examining the fracture, the loading on the plain concrete was continued until the unit broke into two pieces. Failure of the reinforced units was taken as occurring when the crack width exceeded o.15mm which examined by a crack detection microscope (Fig.13).

Fig.10 DROP TEST QUICK RELEASE HOOK

Fig.11 PENDULUM TEST QUICK RELEASE HOOK

Fig.12 ULTRA-SONIC PULSE VELOCITY MEASUREMENT OF DOLOS

Fig.13 CRACK DETECTION MICROSCROPE

TEST RESULTS

Maximum Fall Height

The average maximum fall height of the pendulum (or the dolos center of gravity) was defined as the point at which the plain concrete dolos broke into two pieces and the crack width of reinforced units exceeded 0.15mm.

The test results of average maximum fall height of dolos destruction for the seven types used are shown on Fig.14. It is quite obvious that the Pa-Tou-Tzu fishery port model is the best one. For chamfered corner dolos made of plain concrete, a strength of 34.5 N/mm² (5000 psi) is better than that of 20.7 N/mm² (3000 psi), and for the same strength of 34.5 N/mm² (5000 psi), the chamfered corner type is better than the enlarged fillet corner type.

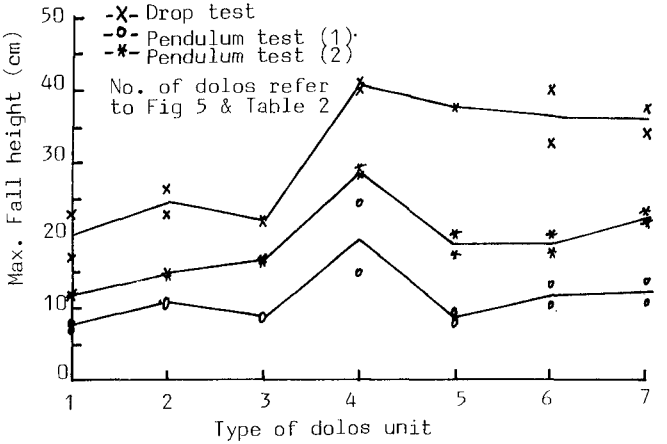

Fig 14 Max. Fall Height of Dolos Destruction

Fracture Types

The fracture types of dolos destruction are shown on Fig.15 and Fig.16 and described as follows:

Drop test: There were two fracture types. In the first type, cracks started at the top of the stem-fluke corner and spread to the bottom of the stem. In the second type, the fractures not only developed in the stem-fluke corner but also in the middle part of the bottom of stem, and spread to the top of the stem.

Pendulum test (1) : In one type, cracks started at the bottom of the stem-fluke corner and spread to the top of the stem. In another, cracks started at the top of stem-fluke corner and spread to the fluke.

KAOHSIUNG HARBOR MODEL
DROP TEST

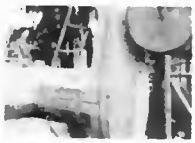

PA-TOU-TZU PORT MODEL
PENDULUM TEST(1)

PLAIN CONC FILLETED
PENDULUM TEST(2)

PLAIN CONC CHAMFERED
DROP TEST

KAOHSIUNG HARBOR MODEL
PENDULUM TEST(1)

SU-AO HARBOR MODEL
PENDULUM TEST(2)

Fig.15 TYPICAL FAILURE TYPES UNDER DYNAMIC TESTS

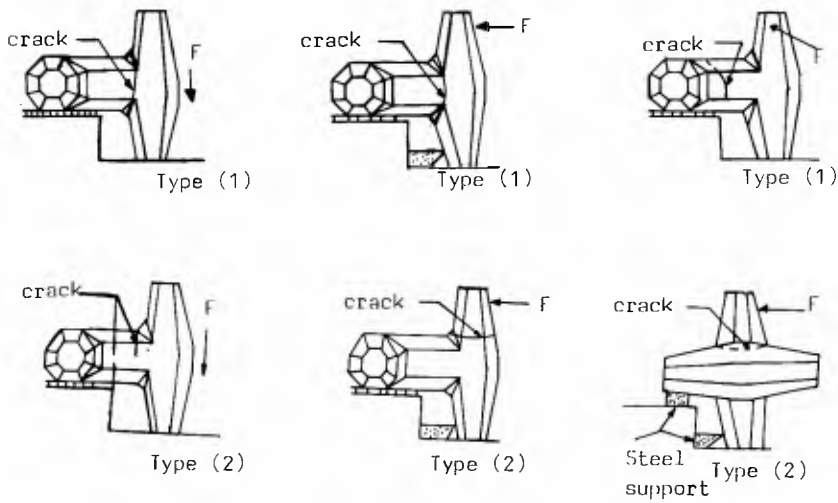

(a) Drop test (b) Pendulum test (1) (c) Pendulum test(2)

Fig 16. Typical cracks and fractures under dynamic tests

Pendulum test (2) : The cracks either started in the middle part of the top of the stem and spread to the bottom of the stem, or started at the top of the stem-fluke corner and spread to the fluke. For reinforced units, the crack spread is fast in the fluke and very slow in the stem.

Maximum Stress vs Fall Height

Test data for the three kinds of plain concrete units were input into eq.(1), eq.(2) and eq(3). The constant factors were determined by test results and are shown in Table 3. The maximum tensile stress on the dolos is proportional to the square root of the average maximum fall height of the pendulum. This relationship is shown in Fig.17. Therefore by comparing with the plain concrete cylinder splitting test data, the mean static tensile strength of each type of dolos model can be obtained and is shown in Table 4.

TABEL 3. FACTORS IN EQ.(1)-(3) DETERMINED BY TEST RESULTS

Test type	Factor	34.5N/mm² Chamfered	34.5N/mm² Filleted	20.7N/mm² Chamfered
Drop	C1	0.116	0.123	0.074
Pendulum(1)	C2	0.333	0.372	0.227
Pendulum(2)	C3	0.286	0.266	0.178

TABLE 4. COMPARISON OF MEAN STATIC TENSILE STRENGTH IN REINFORCED UNITS (N/mm²)

Test type	Pa-Tou-Tzu fishery port	Ksohsiung Harbor	Su-Ao Harbor	Burcharth's paper
Drop	4.628	4.454	4.379	4.349
Pendulum(1)	4.912	3.273	3.829	3.894
Pendulum(2)	4.595	4.132	4.155	4,540

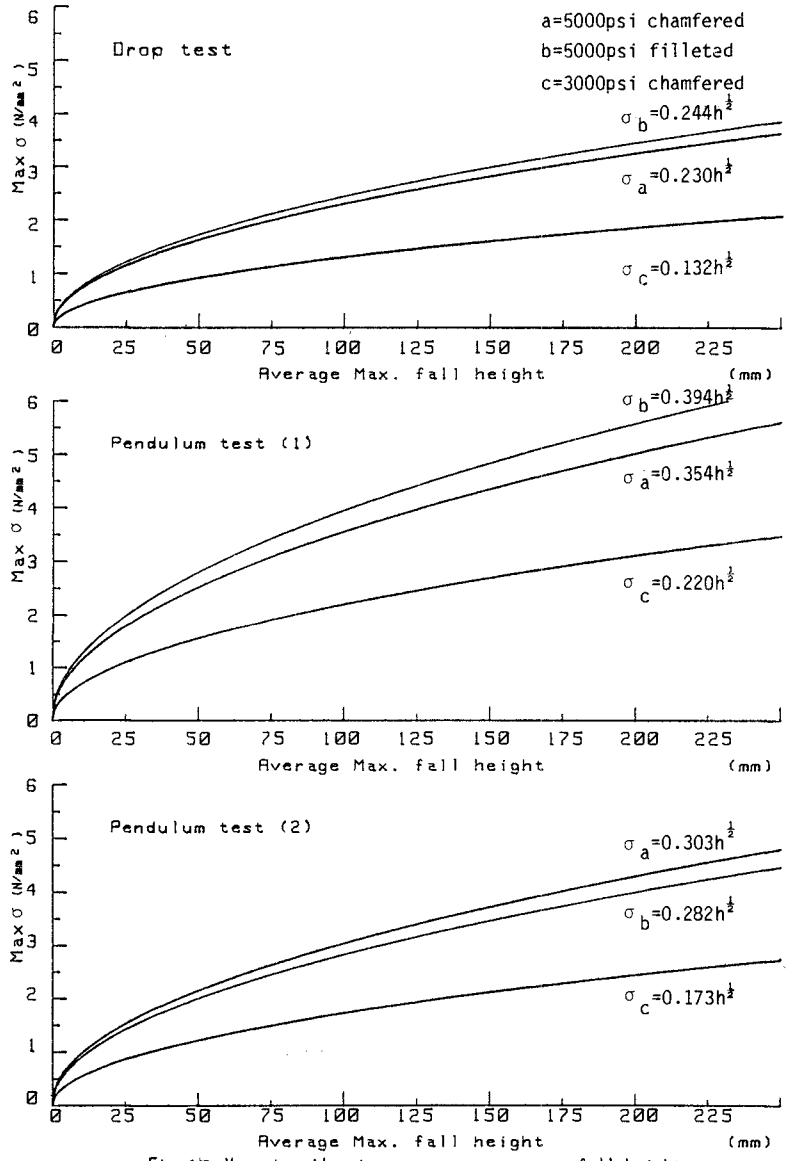

Fig 17 Max. tensile stress vs average max. fall height

DISCUSSION

1. Fig.14 shows that the dynamic strength of reinforced concrete units is better than that of plain concrete, therefore putting suitable rebar into the tension zone will reinforce the tensile strength of dolos.

2. Wave forces are random, therefore the rebar should be distributed throughout the stem and fluke of the dolos. In the Su-Ao Harbor model, the rebar in the fluke deflected to one side, and the dynamic strength was low. In the Kaoshiung harbor model, the quantities of rebar in the stem were inadequate. There is no rebar in the fluke of the Burcharth model, so it is easy to break the fluke. The rebar design in the Pa-Tou-Tzu fishery port model is better, and therefore it shows the best performance in the dynamic tests.

CONCLUSIONS

1. The cracking behavior in dynamic tests coincided with those of site observation. In the design of dolos, the design criteria should consider both the hydraulic and mechanical instability.

2. Comparing the results for units of both reinforced and plain concrete, it is clear that reinforcement of the unit could reduce the magnitude of the stress concentration, but a suitable rebar arrangement must be made to ensure durable behavior, otherwise corrosion of rebar may occur.

3. From the dynamic tests, it was found that cracks start at the corner between the stem and fluke. If the cross section of this corner is increased, then the free length of fluke will be shortened and the probability of dolos fracture will be decreased.

4. Fracture by frontal impact is more severe than that of transverse impact which in turn is more severe than that of the drop test.

REFERENCES

1. LIGTERINGEN, H., HEYDRA, G. Recent progress in breakwater design. The Dock and Harbor Authority, vol. LXV No.761, pp.47-50, July 1984.

2. LILLEVANG, O.J.: NICKOLS, W.E. Experimental studies of stress within the breakwater armor piece-dolos. Proc. 15th Int. Conf. on Coastal Engineering, ASCE, Honolulu, pp.2519-2543, 1976.

3. BURCHARTH, H.F. Full scale dynamic testing of dolosse to destruction. Coastal Engineering, 4, pp.229-251, 1981.

4. TERAO, T., et al. Prototype testing of dolosse to destrution. Proc. 18th Int. Conf. on Coastal Engineering, ASCE, Cape Town, pp.2062-2078, 1982.

CHAPTER 153

PROTOTYPE EXPERIENCE WITH RUBBLE MOUND BREAKWATERS

K.J. MacIntosh* and W.F. Baird*

ABSTRACT

At the 19th ICE Conference in Houston in 1984 an alternative concept for the design of rubble mound breakwaters was introduced. This concept has the objective of providing a least-cost structure by optimizing the use of locally available materials and utilizing simple construction procedures. Contractors' bids demonstrated that significant cost savings could be achieved, when compared to the cost of traditional designs.

Considerable prototype experience has now been obtained with this concept of breakwaters. Breakwaters have been built using the concept in Canada, the United States, and Iceland since 1984 and have been subjected to storms and ice action.

Prototype observations have supported the performance predicted during the design process. In this paper surveys of a breakwater taken after construction and after storm action are presented. In addition to wave action, this breakwater has also been subjected to extensive ice action. The response of the breakwater has been monitored and observed and is discussed.

INTRODUCTION

In 1984, Baird and Hall described an alternative procedure for designing a rubble mound breakwater. The objective of the design procedure is to maximize the use of local materials and to give consideration to construction procedures with the intent of minimizing cost.

It is useful to consider that successful rubble mound breakwater designs, providing protection from extreme storms, may extend from the use of one layer of large stones to sand beaches. Considering this "family" of breakwaters there is, of course, a point where there occurs extensive movement of the "stones" or sand grains that must be considered in the design process. However, stones at least one-fifth the weight of conventional armor stones (placed in two layers) can be used without any continuing movement of stones occurring, even at the head of the breakwater.

* W.F. Baird & Associates Coastal Engineers Ltd., 38 Antares Drive, Suite 150, Ottawa, Canada, K2E 7V2

Baird and Hall (1984) describe breakwater designs where continuing movement of stones does not occur. The designs specify armor stones significantly smaller than armor stones required for two layer conventional armor designs. Stability is achieved by increasing the width of the armor layer and through interlocking of the armor stones at the surface of the breakwater.

This alternate design using smaller armor stones is based on the observation that if the armor layer is built to significantly greater thickness than that of two stones, much smaller stones are required to provide stable protection against wave action. Therefore, the thickness of the armor layer for a specific breakwater is determined based on the gradation of the available armor stones and the incident wave climate.

The relatively high porosity of the mass of armor stones allows the waves to propagate amongst the stones and dissipate their energy over a large area within the wide armor layer. In a conventional two stone armor layer, the flow produced by the incident wave is restricted by the relatively impermeable filter and core and, consequently, there are large velocities produced by the wave uprushing or downrushing within the narrow armor layer. In the berm the flow has a larger area into which it can move and as a result localized velocities are greatly reduced thereby decreasing the external hydrodynamic forces applied to the stones. A considerable increase in stability is achieved as a consequence of this dissipation of wave energy within the permeable mass of armor stones.

The mass of armor stones also increases its stability as a result of wave action. Wave action causes consolidation and a resulting increase in shear strength of the mass of stones. Motion of some stones at the surface results in "nesting" of the surface stones. This nesting process also results in an increase in the frictional restraint on individual stones. Depending on the size of stones available and the design wave conditions, movement of stones on the outer surface may occur to varying degrees during the early stages of exposure to wave action. The stones eventually find a geometrically similar space in the berm surface into which they nest. The result of this process is a natural armoring of the outer layer of the stones.

These designs have allowed the engineer to use the most appropriate stones for the selected location. This has allowed complete utilization of local quarries at some locations, and has allowed the use of material produced as a by-product of an existing quarry operation at another.

The basic design consists of a core, which may consist of the lower fraction of the quarry yield, and the armor, which may consist of the upper fraction of the quarry yield, as shown in Figure 1.

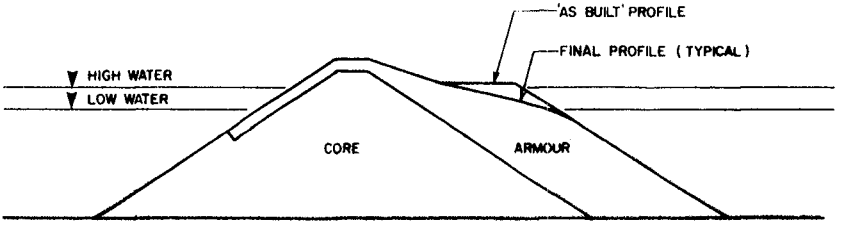

EXAMPLE OF BREAKWATER WITH WIDE ARMOUR LAYER(BERM)

Figure 1

Breakwaters based on this design concept have been built at a number of locations. They are summarized below.

Codroy, Newfoundland.

The breakwater was designed to use the yield of a local quarry with stones ranging from 0.5 to 4.0 tonnes. The depth limited design wave height was 6 m. Construction was completed in the fall of 1984. Although no recorded wave data exists, it is expected that the design wave conditions have occurred on more than one occasion since construction.

Iceland

Seven breakwaters have been designed using this concept, by the Icelandic Harbour Authority, since 1983.

Helguvik Bay, Iceland

The breakwater was designed to use the yield of a local quarry which provided 1.7 to 7 tonne stone. The design significant wave height was 6 m, with depths renging from 25 to 30 m. Construction began in the spring of 1986 and is expected to be completed by the fall of 1987.

Racine, Wisconsin

The breakwater was designed to use the yield of a local limestone quarry. Stone sizes ranged from 0.14 to 2.7 tonnes. The design significant wave height was 4.4 m, with depths ranging up to 7.5 m. Construction was completed in November 1986.

North Bay, Ontario

A stockpile of waste stone from a previous construction project was used as the source of material for the North Bay breakwater. Stones weighing between 4 and 250 kg (the maximum weight available) were used to construct the breakwater. The

structure is located in depths up to 5 m, with a design significant wave height of 1.5 m. Construction was completed in November 1984.

The experience gained by the authors with their involvement with the design, construction and monitoring of these breakwaters is described below.

TRANSPORTATION

Restrictions and cost premiums associated with transportation of armor stones have been found to be important considerations in the design of a breakwater. Trucks and procedures for transportation also vary from location to location depending on the local construction requirements.

In Ontario, Canada, for example, highway trucks will carry stones below a certain size range (approximately 500 kg) without charging a premium. For stones larger than 1 ton, flat-beds are generally used. It is found that 2 to 5 tonne stones represent an ideal weight range where full loads can be obtained. A premium is charged for other sizes.

In Racine, highway trucks with special rock boxes were used that could carry any sized stone up to 2.7 tonnes. In North Bay it was possible to use highway trucks with regular boxes because of the smaller stone size. At other locations such as Helguvik Bay, it was possible to use off road trucks for construction of the breakwater and no restrictions or problems were encountered.

QUARRY OPERATIONS

Generally, there are two situations to consider in the design process. Either a quarry is to be operated specifically for the breakwater construction, or a product of an existing quarry operation will be used.

In either case, the weight gradation of the quarry or available quarried material is estimated and the breakwater is designed to optimize the use of these materials. Each design provides for the simple division of the quarry yield into two fractions, the armor stone and the core material.

During construction, the essential requirement is to verify that the actual gradation being obtained is similar to that assumed in the design process. Monitoring of the gradation of the armor is required with the procedure used depending on the stone weight. For relatively small stones, satisfactory results have been obtained by taking representative samples and establishing the gradation of the sample. For large stones (for example, greater than one tonne), in addition to establishing the gradation of representative samples, it is also useful to count the number of stones in selected trucks and compare this to the total weight of the load (which is measured by a weigh scale).

There will be a unique number of stones to weight ratio for any defined gradation.

Quarry operations are simple because a particular size of stone is not being selected. The armor stones may be produced by a screening process or by removal of all stones above a specified weight. Both processes have been successfully used in prototype situations as discussed below.

The North Bay breakwater design consisted of using all the stones available above 4 kg. The removal of the material less than 4 kg, completed with a grizzly operation, was required to provide sufficient voids for wave energy dissipation in the armor layer. Some difficulties occurred in developing an efficient grizzly operation; however, the problems associated with the removal of the small stones were eventually resolved. Because of the size of the breakwater and amount of stone available it was not necessary to build a core. It was more economical to build the entire breakwater cross-section of one stone gradation.

In Helguvik Bay, a quarry operation was set up on the rock bluff directly adjacent to where the breakwater is under construction. The rock was blasted and then sorted using hydraulic excavators. Then, depending on the stage of construction, the stone was trucked to an armor stock pile or trucked directly to the breakwater for placement. This efficient operation is shown in Figures 2 and 3.

PLACEMENT

Experience with armor placement has been obtained with the use of bulldozers in an essentially "dump-and-push" operation, and with cranes.

Both have been successfully used, although there is a limit to the stone weight that can be effectively moved by a bulldozer during breakwater construction. Bulldozers were used at Codroy, Racine, and North Bay for moving armor stone. With larger armor stones, such as at Helguvik, a crane operation can proceed very quickly because there is no requirement to carefully locate and place each stone in the armor layer. Contractors have found that a crane operation can easily keep up with the truck supply. If a crane operation is implemented then it is important that a well designed grab be used, appropriate for the size of stones to be handled.

Figure 2 Quarry Operation Adjacent to Breakwater Construction

Figure 3 Breakwater Construction

ARMOUR SPECIFICATIONS

The essential specifications for the armor are as follows:

1) The stones must be durable, or the durability must be known and accounted for in the design process,

2) The gradation of stone weights must be the same as that specified,

3) The voids must not be contaminated with undersized material since it is essential that the permeability of the armor be maintained.

The propagation of waves and the dissipation of their energy within the mass of armor stones is very evident and an important test of the correct construction of the armor. The propagation of waves up to the core can be seen and heard provided that the voids have not become filled with undersized material.

CORE SPECIFICATIONS

The core has been specified to contain any material not required for the armor. Filter layers have not been specified. In all of the very extensive model tests that have been completed (with geometric scales varying from 1:25 to 1:50), leaching of core material into the armor was not observed. However, a specification for a maximum percentage of fines, for example the percentage by weight of material less than 1kg, should be developed.

It is proposed that an appropriate percentage of allowable fines would be in the order of 30 per cent, as opposed to the 5 or 10 per cent specified for conventional breakwaters.

MONITORING

As noted in Baird and Hall, 1984, consolidation and change in the profile of the armor will occur when subjected to wave action. Prototype results from the North Bay breakwater reveal an accurate prediction of the expected profile by comparing it to the prototype profile measured after the breakwater was subjected to numerous storms. An example of the cross-section surveyed on the breakwater at North Bay, the as-built profile and the profile predicted from model test results are shown in Figure 4.

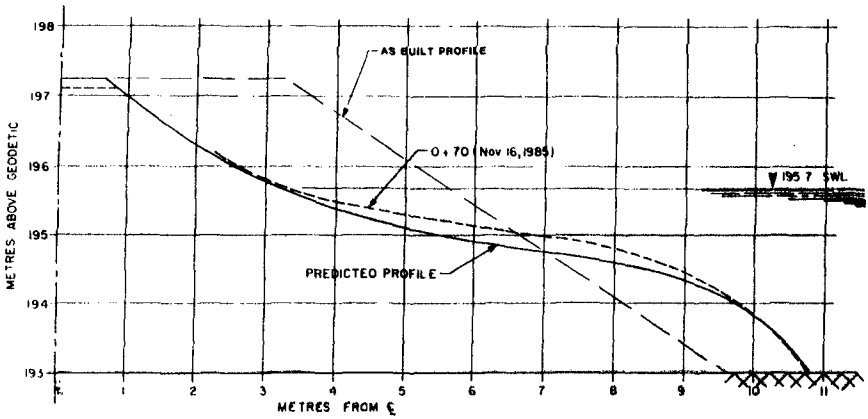

COMPARISON OF PREDICTED & MEASURED PROFILES

Figure 4

ICE

A field monitoring program of ice interaction with the North Bay breakwater was undertaken during the winter of 1984-85.

Because of the small armor stone size on the North Bay breakwater, there was concern about the effects of ice interaction with the structure. Therefore, a detailed field investigation was undertaken during the structure's first winter in service.

The objectives of this study were to:

1) Gather data on ice-breakwater interaction using surveying techniques, photography, and other general observations.

2) Determine the structure and origin of the various ice types present around the breakwater and relate the results to the meteorological data for the site.

3) Study the formation of ice and temperature profiles within the breakwater, by designing and installing an array of thermocouples (temperature sensors) to assess the extent of ice growth within the structure.

4) Analyze the collected data and develop relationships between the various parameters.

5) Provide an assessment of the ability of the breakwater to withstand interaction with ice.

The study program consisted of several measurement and observation techniques including: temperature measurements throughout the horizontal and vertical profile of the breakwater; surveys of the external profile of the breakwater structure and of the surrounding shore and ice profiles; determination of the properties and characteristics of the ice adjacent to the breakwater using crystallographic techniques; and measurement of water column temperature profiles.

In addition to the measurements noted above, visual observations were made of the modes of failure of ice on the breakwater and the relationship of water level changes to failure modes. The visual observations of ice-structure interaction were documented using field notes, photography and video recorders, as presented in MacIntosh (1985).

The investigation provided several interesting results concerning the response of the breakwater to ice action.

1) No significant ice inclusions formed within the berm due to the combination of heat provided by the lake water and insulation from the snow and ice, overlying the breakwater. Consequently, the voids within the breakwater were never filled with ice.

2) Failure and deterioration of the ice surrounding the breakwater occurred in such a manner that the ice did not move any stones from the breakwater either by plucking or by pushing. The buildup of spray ice on the surface of the breakwater was not sufficient to create any substantial loads or influence the stability of the breakwater slope.

3) The profile developed by wave action on this breakwater was advantageous in protecting the breakwater against damage from ice.

Overall, it appears that the berm type breakwater is not significantly affected by the interaction of fresh water ice with the structure. However, additional monitoring of the performance of the berm design under ice loadings, especially at other locations, is recommended. Extreme ice conditions not covered in the North Bay study may occur in the future although the ice conditions of 1984-85 were considered to be above average severity.

CONCLUSIONS

Prototype experience with rubblemound berm breakwaters has supported the performance predicted during the design process and led to the development of more efficient, cost effective construction techniques. Each berm design construction project, completed to date, has had a unique set of construction procedures. Variations in the quarry operations, transportation

methods, placement of armor and core materials, and monitoring of gradations have provided a better understanding of what methods are the most beneficial in each situation. Although each breakwater construction project completed in the future will also be unique, the experience gained during the construction of the breakwaters described in this paper is extremely valuable. The application of this knowledge to both the design and construction aspects of future projects will translate into more efficient and lower cost breakwater construction projects.

REFERENCES

Baird, W.F. and Hall, K.R., "The Design of Breakwaters Using Quarried Stones", Proceedings of Offshore Technology Conference, Houston, Texas, 1984.

MacIntosh, K.J., "Ice Interaction with a Rubble Mound Breakwater - A Case Study", Final report submitted to Fisheries & Oceans Canada, Small Craft Harbours Branch, Ottawa, Ontario, Canada, August 1985.

CHAPTER 154

Verification of the Analytical Model for Ocean Wave-Soil-Caisson Interaction

William G. McDougal[1], Yau-Tang Tsai[2], and Charles K. Sollitt[1]

Abstract

An analytical model for wave-soil-caisson interaction is verified by comparison with a finite element model and large scale experimental results. The analytical and finite element model estimates of the stresses and surface displacements of an elastic layer of finite thickness are in good agreement. The physical model experiments were conducted at the O.H. Hinsdale Wave Research Facility at Oregon State University. A 10-ft high, 8-ft long caisson was constructed on a bedding layer overlying 1 to 3 ft of soil. The caisson was exposed to waves with heights of 0.68 to 4.4 ft with periods of 1.77 to 8.80 sec. Experimental and analytical comparisons for porewater pressure were in agreement but the displacements were quite scattered.

1. Introduction

Caissons on permeable bases have been designed and constructed for a variety of needs in coastal and offshore engineering. An evaluation of the adequacy of the foundation beneath the structure is required for an economic and safe design. Recently, an analytical solution (Tsai et al., 1986) has been developed to model the wave-induced displacements, stresses, and porewater pressure under caissons. Before this solution can be used in engineering practice, it must be verified. Therefore, both a finite element model and a physical model are used to verify this analytical model.

2. Finite Element Model

The finite element model developed by Milovic et al. (1970) predicts the stresses and displacements in an elastic soil of finite thickness. The applied load is inclined and eccentric over a rigid strip. This configuration is shown in Fig. 1, in which F is the applied load, e is the eccentricity, θ is the inclined angle of the load, 2c is the width of the strip, and d is the thickness of the elastic layer. The strip foundation is perfectly rigid and has a rough base. The soil is assumed to be an isotropic, homogeneous, linearly elastic layer bounded by a plane horizontal boundary above and by a rigid base below. This numerical model corresponds to the radiation problem in the analytical model.

[1]Associate Professor, Ocean Engineering Program, Department of Civil Engineering, Oregon State University, Corvallis, Oregon 97331-2302.
[2]Assistant Professor, Ocean Engineering Program, Department of Civil Engineering, Oregon State University, Corvallis, Oregon 97331-2302.

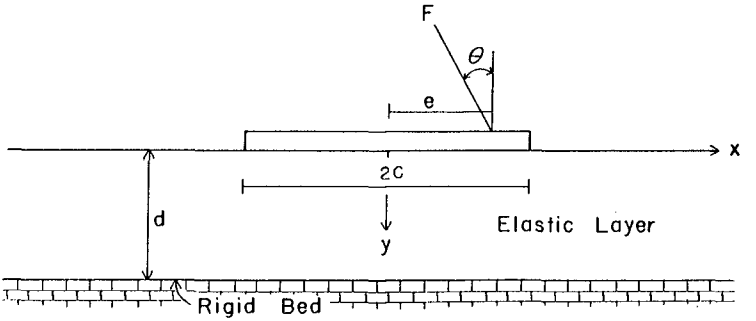

Figure 1. Definition sketch for a loaded infinite long rigid strip overlying an elastic layer

In this comparison the stresses are scaled by the averaged load per unit area and the displacements and thickness of the elastic layer are scaled by the block half-width. The comparison of contact stresses is presented in Fig. 2. The agreement between these two methods is reasonable for dimensionless soil depths of D = 2.0 and D = 6.0. Figure 3 shows the comparison of the vertical stress profiles along the center line of the strip for D = 2.0 and D = 6.0, respectively. Again, the analytical model and numerical model are in good agreement. The comparison of surface displacements in Fig. 4 shows that the analytical model predictions are slightly less than the finite elment model values for all three degrees of freedom. These comparisons also indicate that the soil responses are not particularly sensitive to the thin soil assumption in the development of the analytical model.

In the development of the analytical model, the solution for a contact problem was modified to provide the displacement boundary condition along the entire mudline for the outer region problem. The contact solution is developed under the assumption of a thin elastic layer so that the solution satisfies negligibly small shear stress and vertical normal stress conditions along the exposed upper surface for the radiation problem. The influence of the soil depth on these stresses is examined for various soil depths and locations along the exposed mudline. For this examination, the conditions in Table 1 are assumed.

Figure 5 reveals that at a dimensionless distance of 0.1 from the toe, the normal stress is less than one percent of the peak stress at the caisson toe, even though the dimensionless soil depth is up to 6. At a distance of 0.001, the stress ratio is small (0.15%) only for dimensionless soil depths less than 0.25. A similar result is also obtained for shear stress.

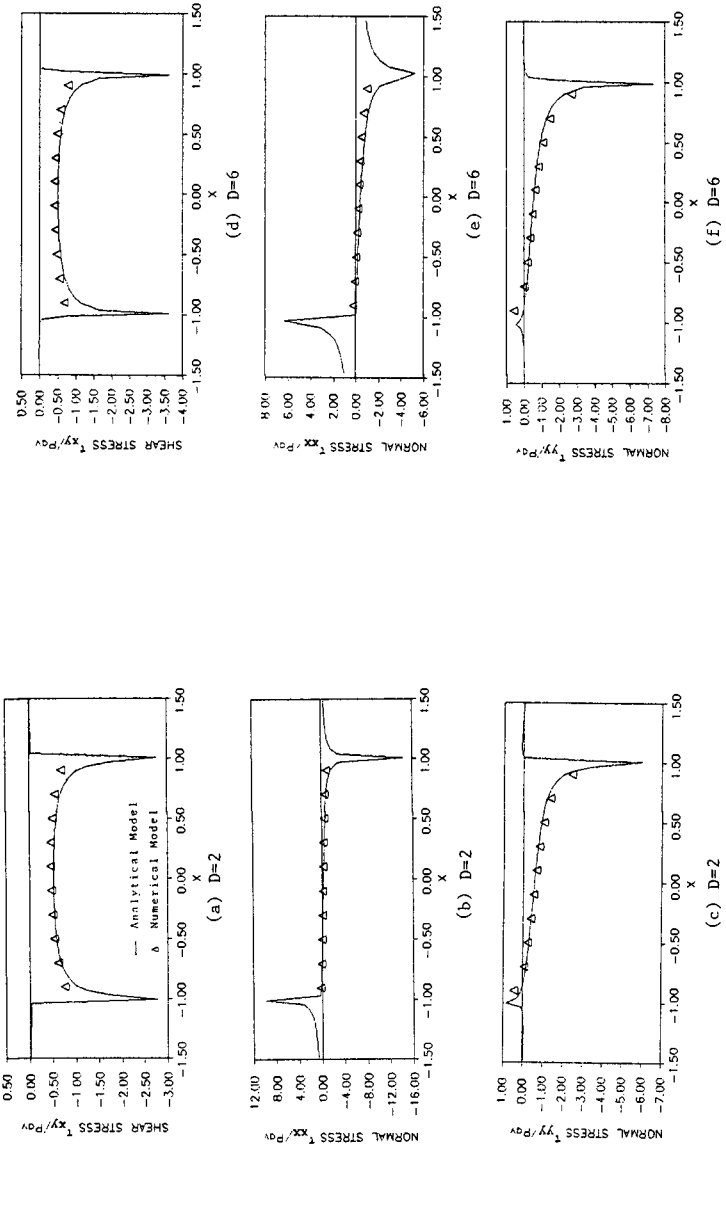

Figure 2. Comparison of the analytical and finite element models for the contact stresses on an elastic layer for Poisson's ratio = 0.3 and eccentricity = 0.5

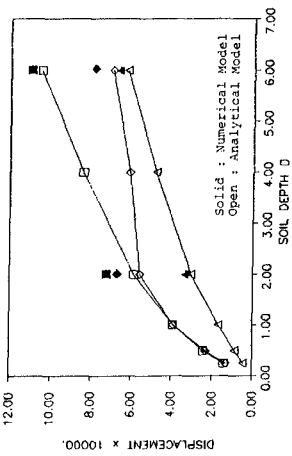

Figure 4. Comparison of the analytical model and finite element model for the surface displacements

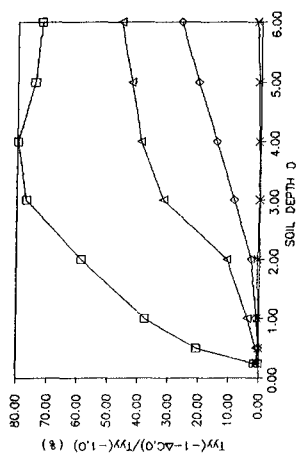

Figure 5. Vertical normal stress ratio along the exposed mudline as a function of soil depth

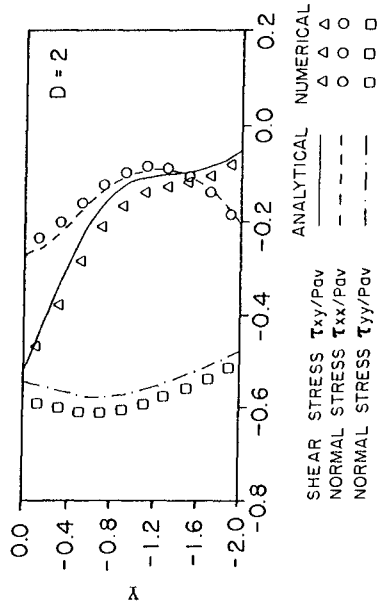

Figure 3. Comparison of the analytical model and finite element model for the vertical stress profiles at the strip center for Poisson's ratio = 0.3 and eccentricity = 0.5

Table 1. Conditions used in the examination of the thin layer assumption

Wave Period	= 4 sec
Wave Height	= 4 ft
Water Depth	= 8 ft
Thickness of the Rubble Bedding Layer	= 1 ft
Caisson Half-Width	= 4 ft
Mass of the Caisson	= 83 slugs
Mass Moment of Inertia of the Caisson	= 3,660 slugs-ft^2
Poisson's Ratio	= 0.3
Shear Modulus	= 80,000 psf

From the above and comparison with the numerical model, the influence of the thin layer assumption on the analytical model may be summarized as:

a) For the soil regions under the caisson and under the exposed mudline greater than 0.1c from the caisson, the analytical model is applicable for all soil depths.

b) For the response in the region (0~0.1)c from the caisson, the model is applicable only for soil depths d/c < 0.25.

These limits on thin layer assumption are illustrated in Fig. 6.

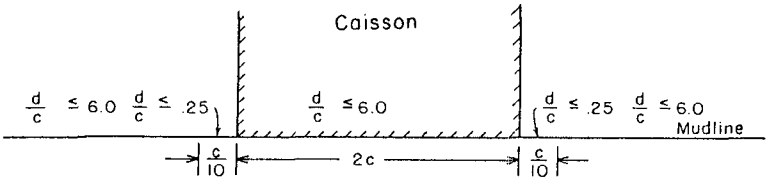

Figure 6. Limits on "thin layer" assumption

3. Physical Model

Two series of experiments of wave-soil-caisson interaction were conducted at the O.H. Hinsdale Wave Research Facility at Oregon State University during the springs of 1984 and 1985. A variety of wave conditions were examined. Incident waves, reflected waves, and transmitted waves were measured. Porewater pressure was monitored in the soil under the caisson. Three degrees of caisson motion, surge, heave, and pitch were measured with sonic transducers. Wave pressures also measured along the front face and bottom of the caisson and along the upstream portion of the mudline.

Experimental Conditions

Wave Tank - The OSU wave flume is 342 ft long, 12 ft wide, and 15 ft deep. The hinged-flap-type wave generator is able to produce solitary, periodic, and random waves. Simple periodic waves up to 8 sec in period and 5 ft in height can be generated. A polyurethane seal around the edges of the wave board confines the water to one side of the board. Precast concrete panels are available to form a false bottom with the desired water depth and slope.

Test Section - A test section, 30 ft long, 5 ft wide, and 4 ft deep, was constructed at the downstream end of the wave flume. A false channel bottom was installed to match the test section elevation. The sides and ends of the test section were fabricated with reinforced plyboard. The entire test section was bolted to the channel bottom and side walls. Figure 7 shows the test section. The side chambers of the test section were filled with highly permeable gravel to provide the extra strength and prevent side wall deflection during

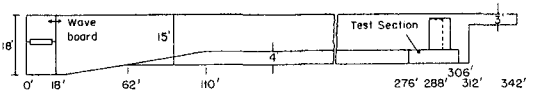

(a) Elevation

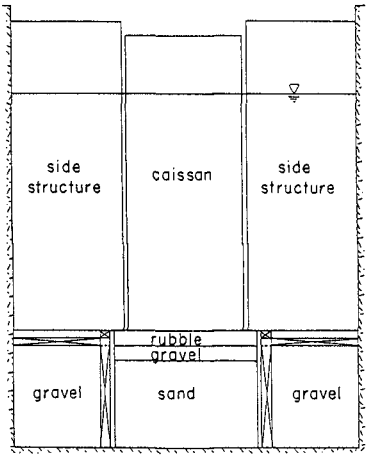

(b) Cross section

Figure 7. Test section

the test. A perforated pipe was laid on the bottom of the channel to facilitate drainage during dewatering. In the middle chamber, a 3-ft layer for sand was used for the 1984 test. In the 1985 test, a 6-inch thick reinforced concrete slab was constructed as an impermeable hard-bed 1.5 ft above the bottom to provide a 1-ft deep sand layer above the concrete slab. These sand beds were fluidized and then reconsolidated back to a homogeneous condition. The fluidization was accomplished by using an inverted T-shaped manifold to inject a high-pressure water jet into the sand (Nath et al., 1977). This procedure prepared a uniform soil layer to ensure the repeatability of the experiments. Soil conditions are given in Table 2. The reconsolidation was induced through an over-burden of 6 to 12 inches of pea gravel separated from the sand by a geotextile. Rubble then was placed over the lift of the pea gravel to form a rubble bedding layer of approximately 1 ft thickness. The rubble had a mean diameter of 4 inches. The test caisson was then placed on the rubblemound foundation. Toe and heel protection were added.

Table 2. Soil properties for the tests

Year	1984	1985
Poisson's Ratio	0.3	0.28
Porosity	0.49	0.5
Shear Modulus	140,000 psf	110,000 psf
Permeability Coefficient	0.00033 ft/sec	0.00040 ft/sec

To provide a continuous caisson face across the width of the flume, fixed dummy side structures were constructed along each side of the caisson. These dummy sections were rigidly attached to the side walls of the wave flume. To allow caisson motion, a 1-inch gap was left between the caisson and side structures. The front of the gap was covered with a rubber strip to provide a watertight seal. The side structures were 3.9 ft wide, 12.3 ft long, and 10.5 ft high. They were constructed of heavily reinforced plyboard and rigidly bolted to the bottom and sides of the wave flume.

Test Caisson - The test caisson was 10 ft high, 8 ft long, and 4 ft wide. It was also made of heavily reinforced plyboard. To obtain the desired mass, the caisson was filled with concrete cylinders and sand bags. For the 1984 test, only the weight of the cylinders and bags was measured. For the 1985 test, the locations of cylinders and bags were also measured. The weight of the empty caisson in air was 1470 pounds. The total weight of the caisson including the ballast was 5640 pounds in the 1984 test. For the 1985 test, three different weights of the caisson in water were tested, as shown in Table 3.

Instrumentation - The wave profiles and caisson motions were measured with sonic transducers. The dynamic pressures were measured with pressure transducers (Druck model PDCR10). Carborundum filter stones covered the transducer housings to prevent soil from clogging the pressure transducers. A small amount of air in the stone may sig-

Table 3. Weight, mass, and mass moment of inertia of the caisson in water for the 1985 tests

Weight (pounds)	Mass (slugs)	Mass Moment of Inertia (slugs-ft^2)
5,280	164	2,765
7,150	222	5,630
10,690	332	14,631

nificantly affect the dynamic response of the transducers. Therefore, the stones were first boiled to remove air and then always kept underwater. The transducers were calibrated by raising and lowering the still water level in the channel before and after each sequence of runs. The instrument locations for the 1984 and 1985 tests are shown Figs. 8 and 9, respectively.

Wave Conditions - The tests were run at a water depth of 8 ft. The periods and heights of the simple periodic waves were selected to span deep to shallow water conditions based on Dean's stream function wave theory (Dean, 1974). The wave case, height, and period employed in the tests are shown in Table 4. In the 1985 experiments, the wave periods were slightly adjusted to provide pure standing waves in the flume.

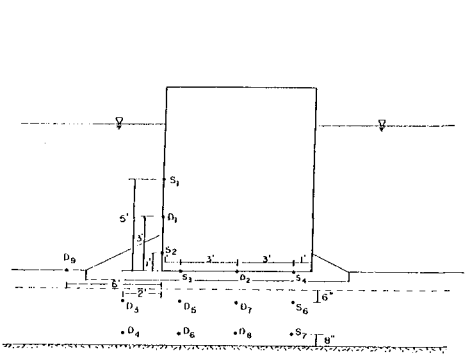

(a) Pressure monitors

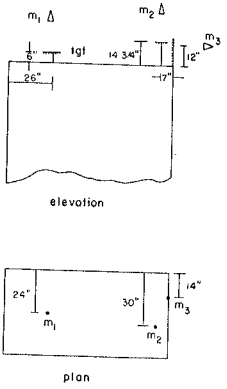

(b) Displacement monitors

Figure 8. Instrumentation for the 1984 test

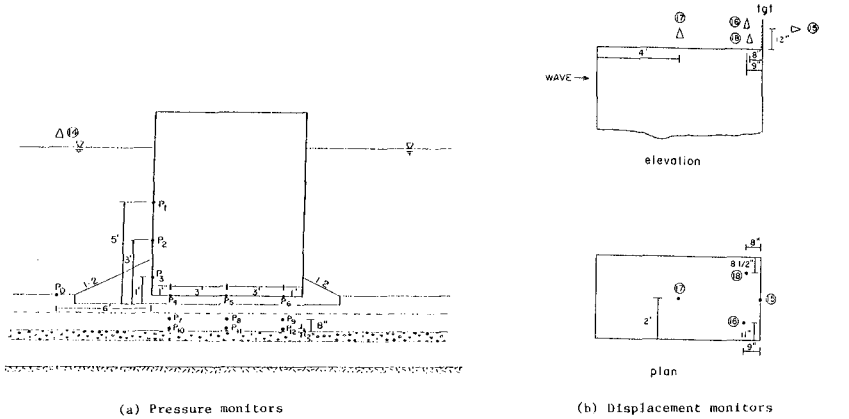

(a) Pressure monitors (b) Displacement monitors

Figure 9. Instrumentation for the 1985 test

Table 4. Wave conditions for the 1984 tests

Wave Case	Wave Period (sec)	Wave Height (ft)
8A	1.77	0.68
8B	1.77	1.36
8C	1.77	2.03
7A	2.80	1.28
7B	2.80	2.52
7C	2.80	3.76
6A	3.95	1.47
6B	3.95	2.92
6C	3.95	4.40
5A	5.59	1.55
5B	5.59	3.07
4A	8.84	1.56

Experimental Results

One of the sonic profilers used to measure the caisson motion malfunctioned in the 1984 experiment. Several of the pressure transducers in the 1985 experiment did not calibrate well. Therefore, only the pore pressure measurements of the 1984 tests and the caisson motion measurements of the 1985 tests were analyzed.

Typical records of pore pressure and displacement are shown in Fig. 10. Significant noise was observed in the displacement measurements. To remove this noise, an eleven-point moving box car (i.e., Δt = 0.076–0.381 sec) was used. This poor signal-to-noise ratio and heavy filtering reduces the confidence in the displacement data.

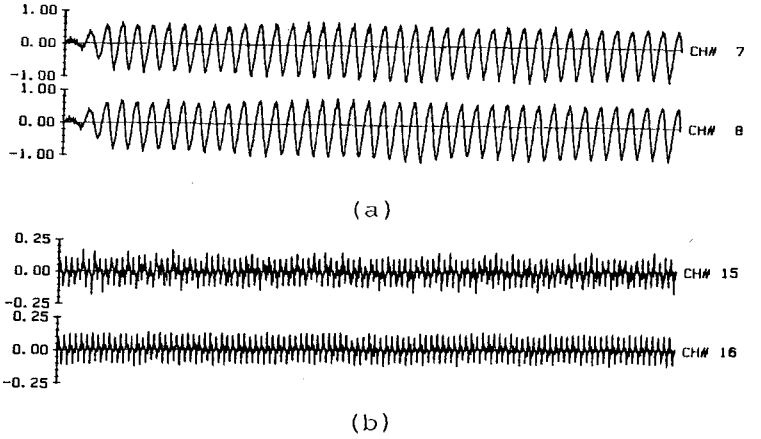

Figure 10. Measurement samples: (a) pore pressure and (b) caisson motion

The dimensionless pore pressure amplitudes are shown as a function of wave period in Fig. 11. The pressure amplitudes were scaled by S2; the pressure on the caisson front face measured one foot above the mudline. A smooth line has been drawn through the data to help iden-

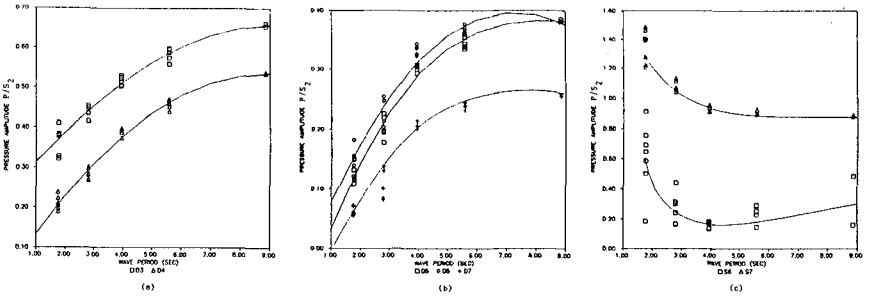

Figure 11. Pore pressure ampltitude of measurements: (a) gages D3 and D4, (b) gages D5, D6, and D7, and (c) gages S6 and S7 as a function of wave period

tify trends. The caisson motion had the least influence on gages D3 and D4 since they were not underneath the caisson. The pressure at these locations decayed with the soil depth. The two pairs, D5-D6 and S6-S7, were obviously affected by the caisson motion because the pore pressure increased with the soil depth. For gages D3, D4, D5, D6, and D7 the dimensionless pressure amplitudes increase with increasing wave period. For gages S6 and S7 the opposite is observed.

The dimensionless mudline displacements are plotted against H/h (wave height to water depth) for various values of h/Lo (depth to deep water wave length) in Fig. 12. Generally, the displacement increases with an increase in water height or wave period. This result is anticipated because the wave force on the caisson is proportional to the wave height and wave period. However, the vertical and rotational displacements are somewhat scattered.

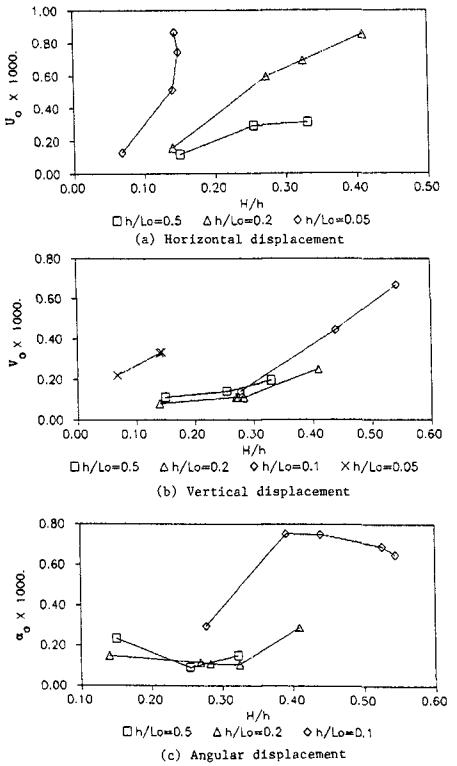

Figure 12. Dimensionless mudline displacements of measurements as a function of wave height for different water depths

Comparison of Theory and Measurements

The measurements of D5, D6, D7, S6, and S7 (cf. Fig. 8) were compared with the analytical model. Figure 13 shows the calculated pressure versus the measured pore pressure. Although the trend is predicted, there is considerable scatter. Figure 14 shows the computed contours of pore pressure and measurements. Again, the trend is in general agreement but there is considerable scatter. The deviation of the predicted porewater pressure from the measured may result from the assumption of a linear wave pressure distribution underneath the caisson. A more accurate pressure model being developed by Ward (1986) may be employed to obtain a more realistic pressure boundary condition. Unfortunately, this model was not completed in time to be used in the present study.

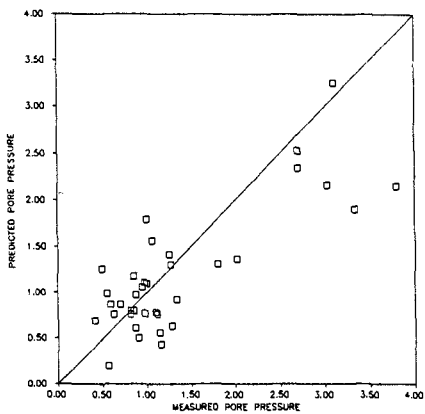

Figure 13. Comparison of theory and measurements for pore pressure

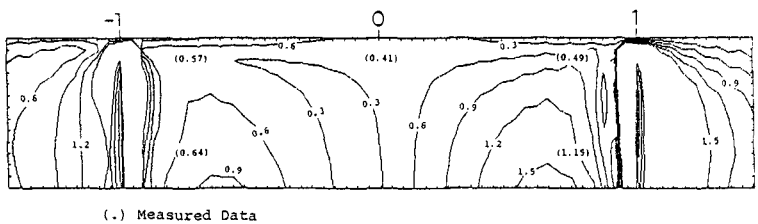

Figure 14. Comparison of the predicted pressure contours and the measured data (T = 5.6 sec and H = 3.2 ft)

The measured and the predicted displacements are shown in Fig. 15. The dimensionless displacements were plotted to the dimensionless calculated horizontal wave force in the caisson F_1/wh^2. The wave force, F_1, was calculated by the method recommended in the Shore Protection Manual (1984). The measured displacements are rather scattered. The horizontal and the vertical displacement data are larger than the predicted. However, the measured rotational displacement data are in reasonably good agreement with the predicted. The predicted angular displacement is in better agreement with the laboratory results than both the horizontal and vertical displacements because the angular motion is the largest among the three degrees of the caisson motion. Thus, the noise effects on the measured angular displacement are less than on the horizontal and vertical displacement measurements.

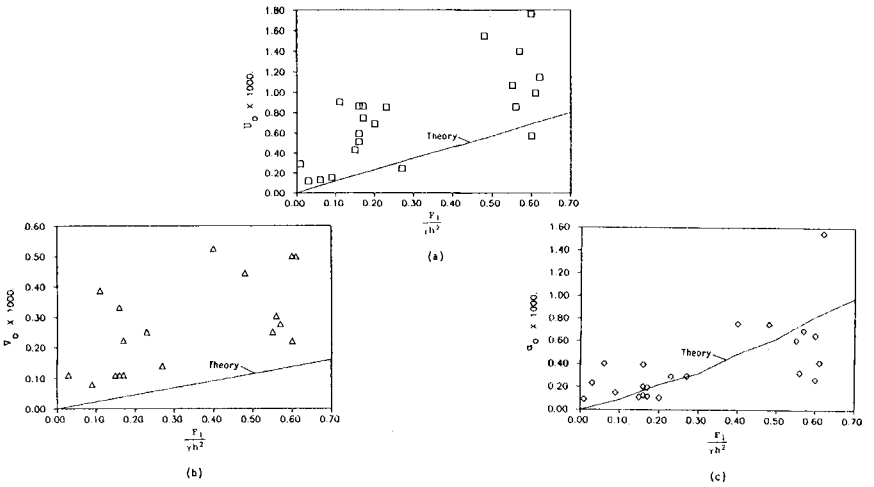

Figure 15. Comparison of the predicted and measured displacements: (a) horizontal, (b) vertical, and (c) angular

4. Conclusions

1. The analytical model agrees well with finite element model for all soils depths examined. This implies that the analytical model is not particularly sensitive to the thin layer assumption for the soil.

2. Under the caisson, the porewater pressure in the soil increases with the depth because of the confining of the impermeable rigid bed below. This is observed in both the analytical and physical models.

3. The predicted porewater pressure is in reasonable agreement with the measured data.

4. Displacement data are unreliable due to the very poor signal-to-noise ratio. Thus, the following modifications to the experimental procedure are recommended:
   a) Using an LVDT for displacement measurements.

   b) Occupying entire wave channel width for caisson to avoid the effects on the measurements from both the side channels and dummy structures.

   c) Making a stiffer caisson, e.g., using concrete.

5. For comparison with data, more accurate methods to estimate the wave pressure on the mudline and forces on the caisson would be useful.

5. Acknowledgment

This research was supported by the Oregon State University Sea Grant College Program, National Oceanic and Atmospheric Administration Office of Sea Grant, Dept. of Commerce, under Grant No. NA81AA-D-00086 (Project No. R/CE-13). The U.S. Government is authorized to produce and distribute reprints for governmental purposes, notwithstanding any copyright notation that may appear hereon.

Appendix I. References

Dean, R.G., (1974), Evaluation and Development of Water Wave Theory for Engineering Application, Vol. I, Special Report No. 1, U.S. Army Corps of Engineers, Coastal Engineering Research Center, 121 pp.

Milovic, D.M., G. Touzot, and J.P. Tournier, (1970), "Stress and Displacements in an Elastic Layer Due to Inclined and Eccentric Load Over a Rigid Strip," Geotechnique, 20:231-252.

Nath, J.H., et al., (1977), Pressures in Sand from Waves and Caisson Motion, Oregon State University Wave Research Facility, Transportation Research Institute, 266 pp.

Shore Protection Manual, (1984), U.S. Armuy Coastal Engineering Research Center, U.S. Government Printing Office, Washington, DC.

Tsai, Y.T., W.G. McDougal, and C.K. Sollitt, (1986), "An Analytical Model for Ocean Wave-Soil-Caisson Interaction," Proc. 20th ICCE, in press.

Ward, D.L., C.K. Sollitt, and W.G. McDougal, (1986), "Wave Interaction with an Caisson Style Structure on a Rubble Foundation," Abstracts 20th ICCE, p. 48.

Appendix II. English/SI Unit Conversions

Area	1 ft^2	= 0.0929 m^2
Density	1 $slug/ft^3$	= 515.4 kg/m^3
Force	1 lb	= 4.4483 N
Length	1 ft	= 0.305 m
Mass	1 slug	= 14.60 kg
Pressure	1 lb/ft^2	= 47.9 N/m^2
Specific Weight	1 lb/ft^3	= 157.1 N/m^3
Stress	1 lb/ft^2	= 47.9 N/m^2
Velocity	1 ft/s	= 0.305 m/s
Volume	1 ft^3	= 0.0283 m^3

CHAPTER 155

Analysis of Permeable Breakwaters

Hitoshi MURAKAMI*, Yoshihiko HOSOI** and Yoshitaka GODA***

Abstract

This paper discusses the characteristics of hydraulic and water exchange due to the wave action against vertical slit-type breakwaters. The theoretical solution of the reflection and the transmission coefficients for the breakwater models is compared with the experimental results. Furthermore, the water exchange discharge and the water concentration change through the gap of the permeable breakwater are examined experimentally. Finally the most effective geometry of the cross section is suggested for the breakwaters used here.

1. Introduction

With increasing pressure to conserve in a clean way the water quality in a harbor, a new breakwater should be devised. That means an effective breakwater for not only the reduction of the reflection and transmission of wave energy but also the increase of the water exchange discharge through a permeable wall.

Since Jarlan(1961) proposed the perforated vertical wall breakwater, many different kinds of permeable wall breakwaters have been designed(Kondoh et al.,1983). The hydraulic characteristics of these breakwaters have been examined experimentally for the most part. The theoretical solutions for the reflection and the transmission coefficients have been obtained only for the breakwaters with a comparatively simple cross section geometry.

Furthermore, the water exchange characteristics due to the wave action through a permeable wall has not been discussed sufficiently.

This study deals with both hydraulic and water exchange characteristics of the vertical slit-type breakwaters with some devised horizontal cross section geometries in a chamber of the breakwater, though they are very simple as shown in Fig.1. The purpose of this study is to obtain the necessary data to make a breakwater with a horizontal cross section geometry effective from those viewpoints mentioned above.

From here on, we shall call the models by their abbreviations S.P, G.C, G.E and so on.

* Professor, Technical College, The University of Tokushima, Minami-jyosanjima, Tokushima, 770, Japan.

** Associate Professor, Technical College, The University of Tokushima.

*** Nikken Gijyutsu Cosultant Co., Ltd., Osaka, Japan.

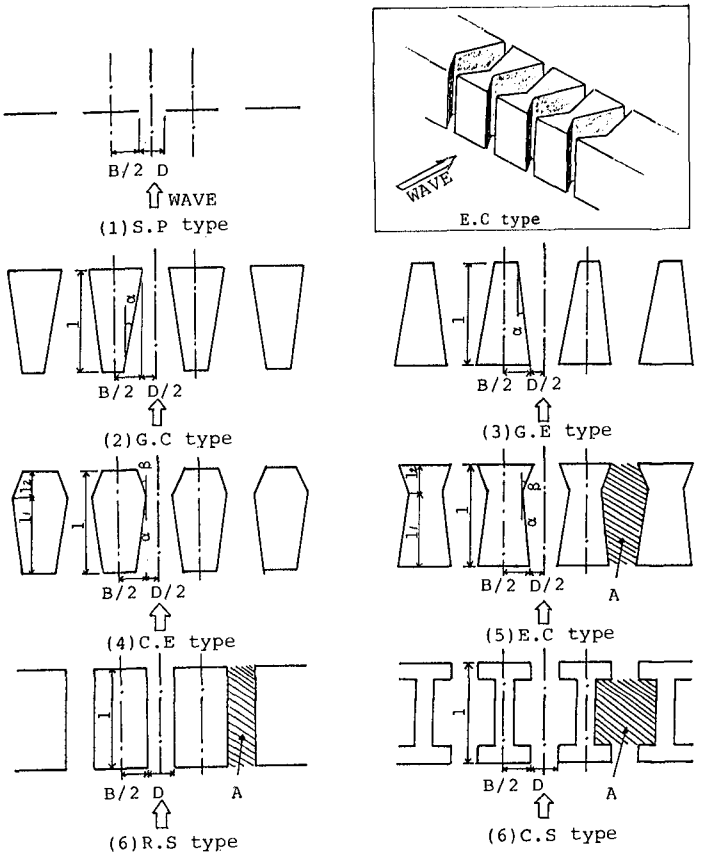

Fig.1 Horizontal cross sections of vertical slit-type breakwaters

2. Theoretical Solution of Reflection and Transmission Coefficients

Let us show as an example how to obtain the result of the reflection and the transmission coefficients for the C.E type breakwater in Fig.1-(4).

Fig.2 shows a coordinate system and a definition of the notation. For analysis, we consider a limited width of the breakwater (D+B) and divide the region into four parts. Then, we assume a small amplitude long wave coming perpendicular to the breakwater, the wave height along the breakwater not varying and the water depth being constant in all the regions.

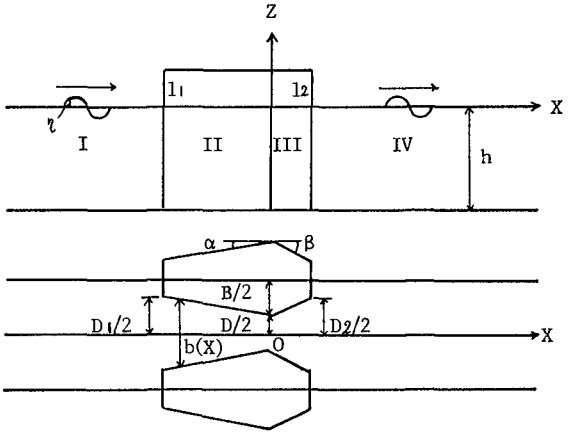

Fig.2 Coordinate system and definition of notations

A momentum and a mass equation at Regions II and III are expressed by eqs (1) and (2), respectively.

$$\partial u/\partial t + g\partial \eta/\partial x = 0 \qquad (1)$$

$$\partial \eta/\partial t + (h/b)\partial(bu)/\partial x = 0 \qquad (2)$$

$$b = D - 2x \tan\alpha , \qquad -l_1 \leq x \leq 0 \qquad (3)$$

$$b = D + 2x \tan\beta , \qquad 0 \leq x \leq l_2 \qquad (4)$$

where, η ,u and g are water elevation from still water, horizontal water particle velocity and gravity acceleration,respectively; b represents the gradually changing width between the wedges.
A mass equation at Regions I and IV are as follow:

$$\partial \eta/\partial t + h(\partial u/\partial x) = 0 \qquad (5)$$

The boundary conditions for each region which are energy and mass conservation laws are represented by eqs (6)-(11).

$$\eta_1 - \eta_2 = (C_A/g)\{(D + B)/D_1 - 1\}u_1|u_1| , \qquad x = -l_1 \qquad (6)$$

$$(D + B)u_1 = D_1 u_2, \qquad x = -l_1 \qquad (7)$$

$$\eta_2 = \eta_3, \qquad x = 0 \qquad (8)$$

$$u_2 = u_3, \qquad x = 0 \qquad (9)$$

$$\eta_3 - \eta_4 = (C_B/g)\{1 - (D + B)/D_2\}u_4|u_4| , \qquad x = l_2 \qquad (10)$$

$$D_2 u_3 = (D + B)u_4, \qquad x = l_2 \qquad (11)$$

In eqs (6) and (10), the energy loss coefficients are given as C_A and C_B, respectively.

By solving the above equations to satisfy the boundary conditions, we can obtain the result of the reflection and the transmission coefficients as eqs (12) and (13), respectively.

$$r_R = \frac{\sqrt{\{-1 + Eo - Gn + (\psi g/c)\}^2 + (Ep + Gm)^2}}{|1 + (\psi g/C)|} \qquad (12)$$

$$r_T = \frac{\sqrt{(E's - G'r)^2 + (E't + G'q')^2}}{|1 + (\phi g/C)|} \qquad (13)$$

where,

$$o = h'm - jn$$

$$p = jm + h'n$$

$$q' = \frac{(Ao - Fn)A'a + (Ap + Fm)(A'b' + F')}{A'^2a^2 + (A'b' + F')^2}$$

$$r = \frac{(Ap + Fm)A'a - (Ao - Fn)(A'b' + F')}{A'^2a^2 + (A'b' + F')^2}$$

$$s = aq - b'r$$

$$t = b'q + ar \qquad (14)$$

$$h' = (fd + eg')/(d^2 + e^2)$$

$$j = (dg' - ef)/(d^2 + e^2)$$

$$m = -2\underline{k}/(\underline{k}^2 + \underline{l}^2)$$

$$n = 2\underline{l}/(\underline{k}^2 + \underline{l}^2)$$

$$\underline{k} = \{1 + (\psi g/C)\}(D_1Ij + D_1M)/p - Eh'$$

$$\underline{l} = -\{1 + (\psi g/C)\}D_1Ih'/p - Ej - G$$

$$d = -H'b'A - L'A - A'b'H - F'H$$

$$e = H'aA + A'aH$$

$$f = H'aF + A'a\underline{L}$$

$$g' = H'b'F + L'F + A'b'\underline{L} + F'\underline{L}$$

$$a = \frac{\{1 + (\phi g/C)\}(D_2 E'M'/p - D_2 G'I'/p)}{\{1 + (\phi g/C)\}^2 D_2^2 I'^2/p^2 + E'^2}$$

$$b' = \frac{-\{1 + (\phi g/C)\}^2 D_2^2 M'I'/p^2 - E'G'}{\{1 + (\phi g/C)\}^2 D_2^2 I'^2/p^2 + E'^2}$$

$$\psi = C_A\{(D + B)/D_1 - 1\}|u_1|/g$$

$$\phi = C_B\{1 - (D + B)/D_2\}|u_4|/g$$

$$C = \sqrt{gh}$$

where,

$$A = J_0[kD/\gamma], \qquad A' = J_0[kD/\gamma']$$

$$E = J_0[k(l_1 + D/\gamma)], \qquad E' = J_0[k(l_2 + D/\gamma')]$$

$$F = N_0[kD/\gamma], \qquad F' = N_0[kD/\gamma']$$

$$G = N_0[k(l_1 + D/\gamma)], \qquad G' = N_0[k(l_2 + D/\gamma')]$$

$$H = J_1[kD/\gamma], \qquad H' = J_1[kD/\gamma'] \qquad (15)$$

$$I = J_1[k(l_1 + D/\gamma)], \qquad I' = J_1[k(l_2 + D/\gamma')]$$

$$L = N_1[kD/\gamma], \qquad L' = N_1[kD/\gamma']$$

$$M = N_1[k(l_1 + D/\gamma)], \qquad M' = N_1[k(l_2 + D/\gamma')]$$

$$\gamma = 2\tan\alpha, \quad \gamma' = 2\tan\beta, \quad k = 2\pi/L$$

where, J_i and N_i are the Bessel and the Neumann functions of i-th order, respectively. L is a wave length.

The energy dissipation factor ε is expressed as follows:

$$\varepsilon = 1 - r_R^2 - r_T^2 \qquad (16)$$

We can obtain the solution for any other breakwater by the same procedure (Murakami (1984,1985,1986)).

3. Experiments for Hydraulic Characteristics

The wave tank with a flap-type wave generator at an end, which is 15 cm long, 20 cm wide and 30 cm deep was used for measuring an incident, reflection and the transmission wave. The models were placed at a distance of 10 cm from the wave generator.

The water depth h and the wave period T were kept 15 cm and 0.75 sec, respectively. Incident wave steepnesses H/L were in the range of 0.01 to 0.05.

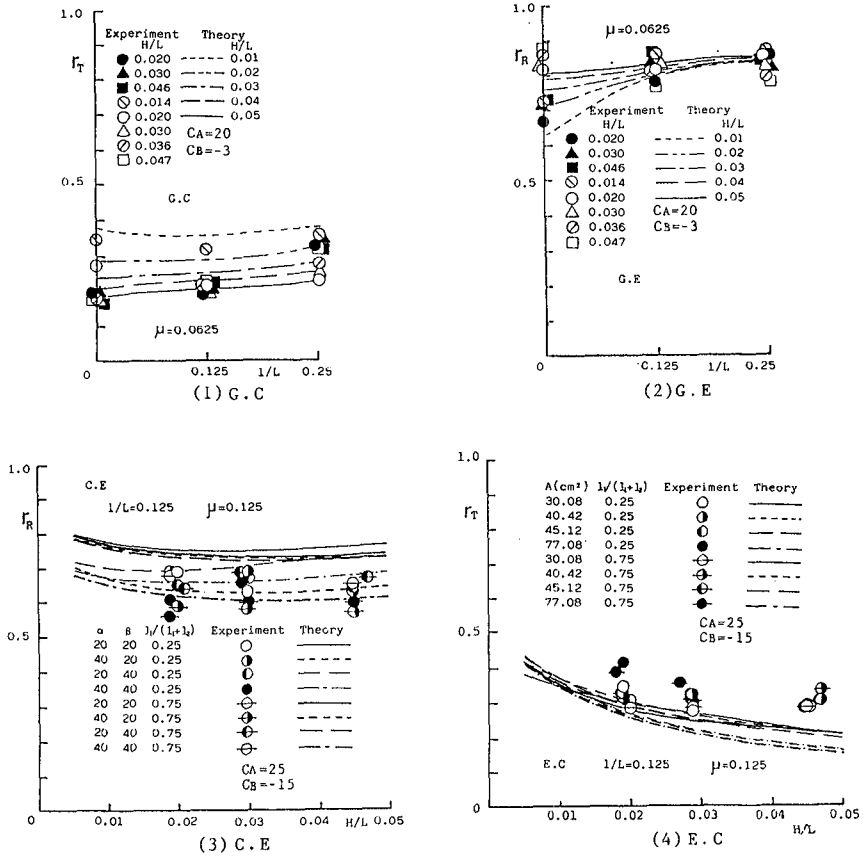

Fig.3 Comparison of theoretical results with experimental data

Fig.3 shows some examples of the transmission and the reflection coefficients comparing theoretical results with experimental data. In figures, μ is the opening ratio D/D+B. It is found that the theoretical results coincide comparatively well with the experimental data, if appropriate values are assumed for the energy loss coefficients C_A and C_B.

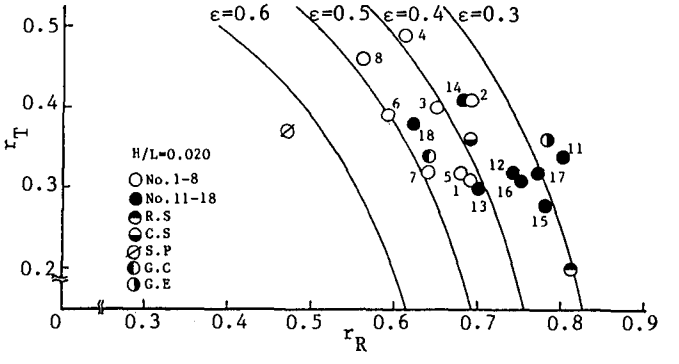

(1) H/L=0.020

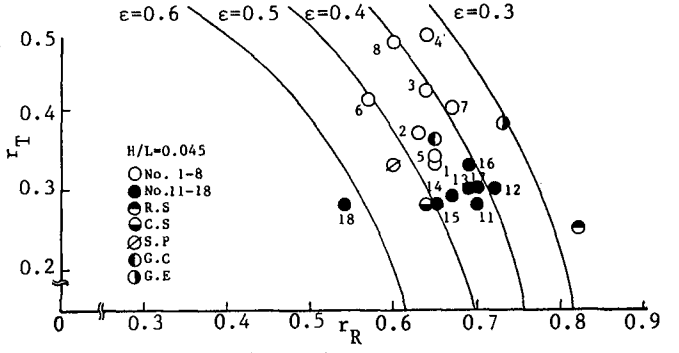

(2) H/L=0.045

Fig.4 Relation between reflection coefficients and transmission coefficients for each breakwater

Fig.4 illustrates, on the basis of the experimental results, the relation among the reflection coefficient r_R, the transmission coefficient r_T and the energy dissipation factor ε.

These experimental data are plotted for the relative breakwater width 1/L = 0.125 and the opening ratio μ = D/D+B = 0.125. In the G.C type, the wedge angle α equals 19 degree. The experimental conditions of other types are shown in Table 1.

Table-1 Experimental Conditions

T=0.75sec, h=15cm, h/L=0.20, H/L=0.01~0.05

NO.	Type	μ=D/(D+B)	$l=l_1+l_2$(cm)	$l_1/(l_1+l_2)$	$\alpha^{(o)}$	$\beta^{(o)}$	A(cm^2)
01	S.P	0.0625	0				
02		0.125	0				
03		0.25	0				
41	G.C	0.0625	9.4		19		
42		0.125					
43		0.25					
44		0.0625	18.8				
45		0.125					
46		0.25					
51	G.E	0.0625	9.4		19		
52		0.125					
53		0.25					
54		0.0625	18.8				
55		0.125					
56		0.25					
1	C.E	0.125	9.4	0.25	20	20	
2					40	20	
3					20	40	
4					40	40	
5				0.75	20	20	
6					40	20	
7					20	40	
8					40	40	
11	E.C	0.125	9.4	0.25	20	7	30.08
12					40	16	40.42
13					46	20	45.12
14					68	40	77.08
15				0.75	7	20	30.08
16					16	40	40.42
17					20	46	45.12
18					40	68	77.08
20	R.S	0.125	9.4				21.62
30	C.S	0.125	9.4				77.08

First, let us compare the values of three simpler types, S.P, G.C and G.E. The transmission coefficients of the three are almost the same, while the reflection coefficient becomes progressively larger from S.P through G.C to G.E.

For the R.S type, the reflection coefficient is largest in all the data, though the transmission coefficient is smallest.

The group of white circles is concerned with the C.E types. When we note the pairs of No.1 and No.2, No.3 and No.4 , No.5 and No.6 in order to discuss the effect of the wedge angle, the transmission coefficient has a larger value for the bigger number of the pair. On the other hand , the reflection coefficient does not change remarkably. This means that it is effective to make the wedge angle small for the breakwater in consideration of the hydraulic aspect. In the C.E type, the wedge angles α and β , the relative wedge length l_1/l_1+l_2 affect mainly the transmission coefficient.

The group of black circles is concerned with the E.C type. They have a chamber in each breakwater. The bigger the number, the larger the chamber area is. It is found that chamber area A and the relative wedge length l_1/l_1+l_2 do not remarkably affect the transmission coefficient, though an exception can be observed in the case of H/L = 0.02. Generally speaking, the transmission coefficients for the E.C type are much smaller than those for the C.E type. On the other hand, the reflection coefficients for the E.C type are nearly equal or a little bit larger than those for the C.E type.

The C.S type in this study has the same chamber area as those for the No.14 and No.18 of the E.C type. The transmission coefficients of both types are almost equal to each other for H/L = 0.045 and they are a little bit smaller in the C.S type for H/L = 0.02.

4. Experiments for Water Exchange Characteristics

4.1 Water exchange discharge

The horizontal water particle velocity at the smallest gap of a breakwater was measured by the propeller type current meter at the point of 7 cm from the water surface. The water exchange discharge per unit breakwater length through a gap caused by the wave action is expressed as follow:

$$q = \frac{4}{T}\int_0^{T/4} \frac{Dh}{D+B} V_{max} \cos\frac{2\pi}{T}t = \frac{2Dh}{\pi(D+B)} V_{max} \qquad (17)$$

where, V_{max} is the average value of maximum water particle velocities of two opposite directional flows at a gap.

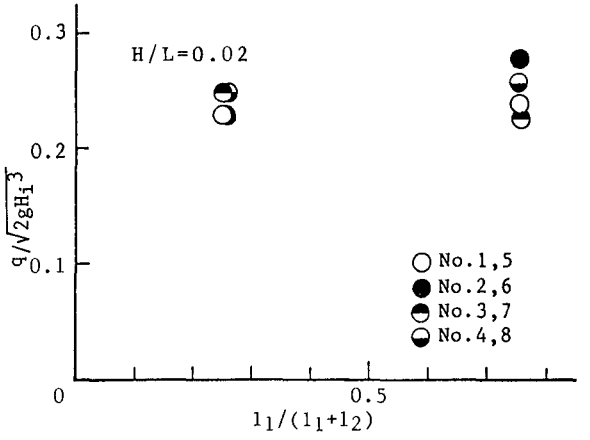

Fig.5 Relation between $q/\sqrt{2gH_i^3}$ and l_1/l_1+l_2

Fig.5 shows the relation between a nondimensional water exchange discharge and the relative wedge length for the C.E type. H_i in the vertical axis expresses an incident wave height. In this type, the water exchange discharge increases slightly with the increase of the relative wedge length l_1/l_1+l_2. However, such a relative wedge length and the wedge angles α and β do not remarkably affect the water exchange discharge.

To cite for reference, the values of $q/\sqrt{2gH_i^3}$ for the S.P, G.C and the G.E types are 0.23, 0.26 and 0.19, respectively. The water exchange discharge for the C.E type is nearly equal or bigger than those for the S.P and G.C types.

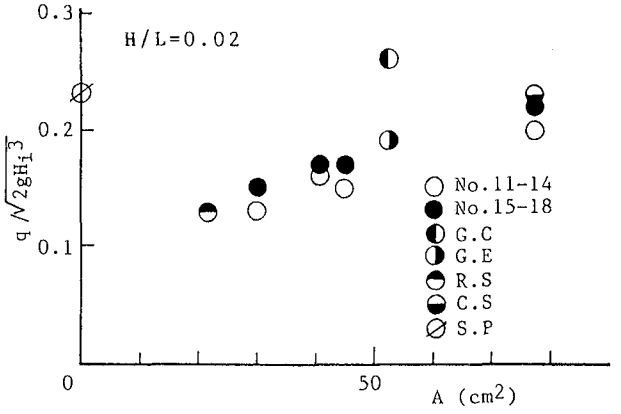

(1) front side

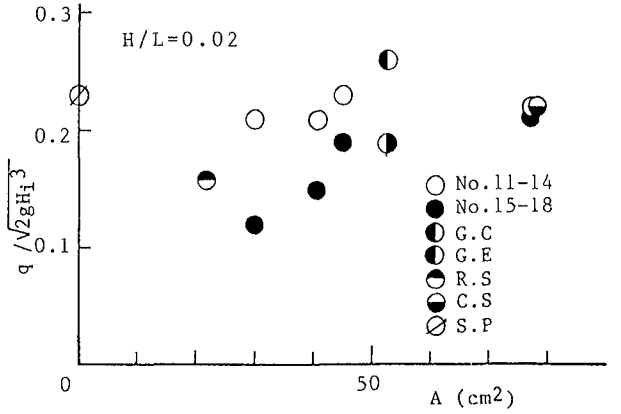

(2) rear side

Fig.6 Relation between $q/\sqrt{2gH_i^3}$ and A

Fig.6 is concerned with the E.C type. This type of breakwater has two gaps at the front and the rear. The abscissa of the figure represents a chamber area as shown by the shadow zone in Fig.1.

The exchange discharge increases slightly with the increase of chamber area A. The discharge at the rear side gap is large when l_1/l_1+l_2 is small, though the tendency is opposite at the front side gap. It seems that both values of discharge for the C.E and C.S types are almost equal, when the two chamber areas are equal. The R.S type breakwater is not effective for water exchange.

As a result of considering the water exchange discharge, we can say that the C.E type breakwater has the most effective cross section in these experiments.

4.2 Diffusion characteristics

Fig.7 shows the experimental equipment. The wave tank was sheltered by two sheets of thin plates from the rear of the breakwater to a distance of about 2 m in front. Salt water with a constant concentration was in this basin. Other regions of the wave tank were filled with fresh water. The sheltering plates were pulled up before an incident wave had just reached the posision of the front side plate. Then concentration changes at the three points of 1 cm, 2.5 cm and 4 cm from the bottom at a distance of 15 cm behind the breakwater were measured by the concentration meters for about 4 minutes.

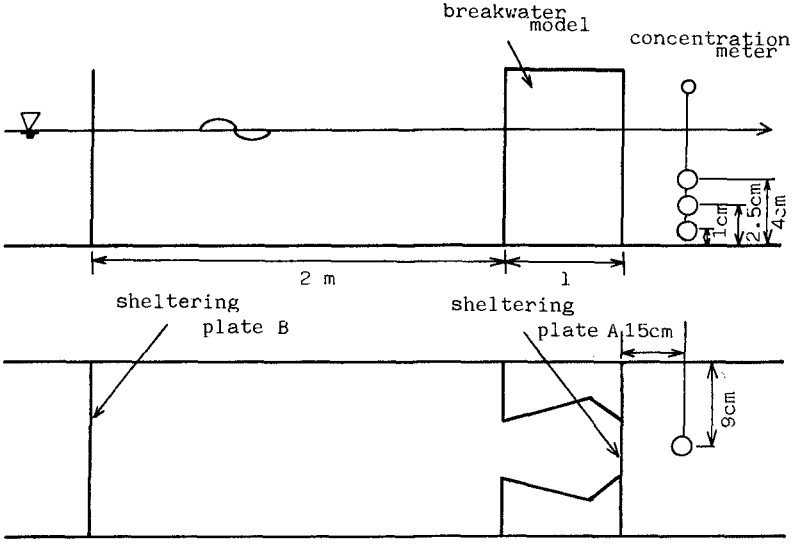

Fig.7 Experimental equipment for water concentration change through gap of breakwater

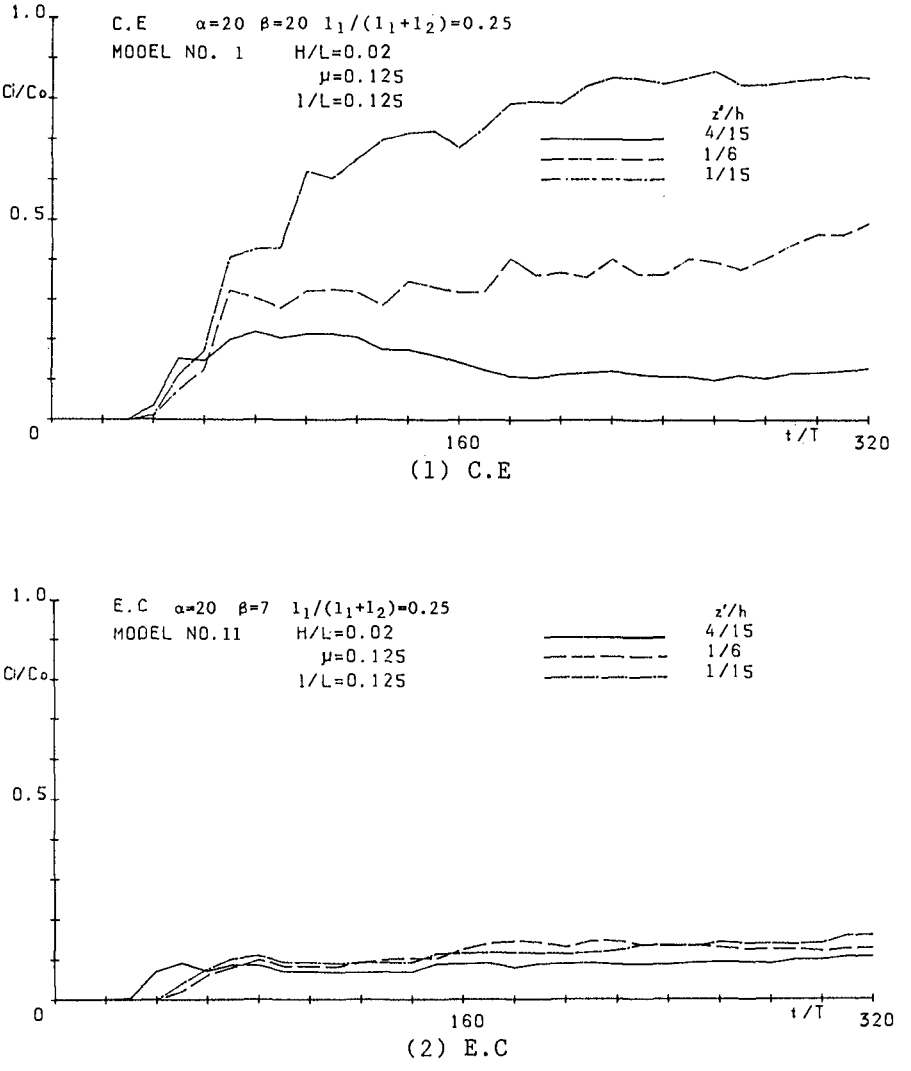

Fig.8 Nondimensional concentration change with time

Fig.8 shows two typical examples of nondimensional concentration changes with time t. C_0 is an initial concentration. T is a wave period. The concentration changes at the measuring points were remarkable for the G.E and R.S types as well as for the C.E type. On the other hand, the concentration did not change at the three points for the S.P, G.C and the C.S types, which are similar to the E.C type.

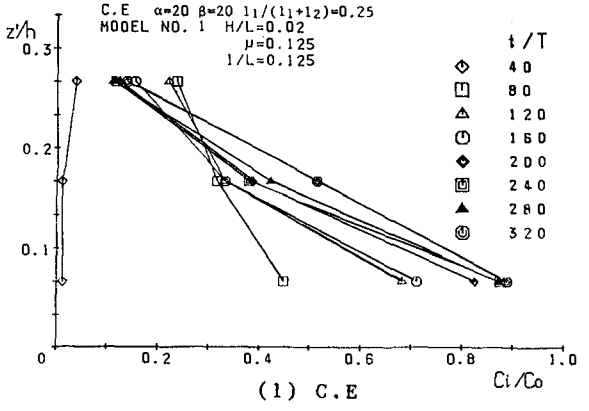

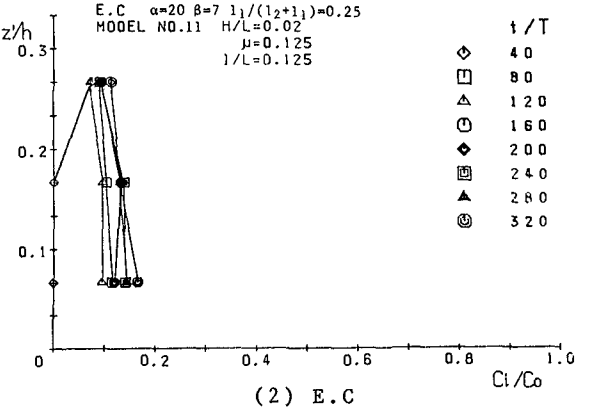

Fig.9 Vertical concentration distribution at regular time intervals

Fig.9 shows the vertical concentration distribution at regular time intervals for the C.E and E.C types. The ordinate z'/h is the nondimensional distance measured from the tank bottom. The parameter t/T represents the number of waves which penetrated through the slit after sheltering plates were pulled out. In the case of the C.E type, the concentration changes at the lower measuring points are more remarkable than at the upper point. The concentration near the bottom becomes almost the same as in the open sea after the 320th wave. In contrast, the vertical concentration distributions do not vary with time. Furthermore, all values of the concentration at each point are smaller than those for the C.E type.

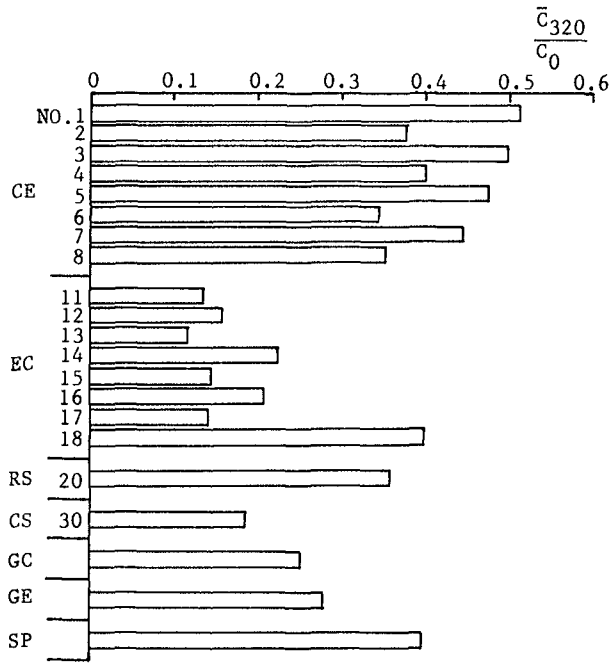

Fig.10 Comparison of average concentration after 320th wave for each breakwater

Fig.10 shows the comparison of the average concentration after the 320th wave for each breakwater. The values of concentration for the C.E type breakwaters are comparatively bigger than those for all other cases. Especially, in comparison of No.1 with No.2 or No.1 with No.5, the water mixes actively between the inside of the breakwater and the outside, when both the wedge angle α and the relative wedge length $1_1/1_1+1_2$ are small.

The nondimensional concentration for the E.C type is smallest in all experiments except the No.18. The value for the R.S type is much bigger, though the water exchange discharge was not bigger, than those for other cases. This means the characteristics of diffusion due to the setting up of the breakwater is not the same as those of the water exchange discharge due to the wave action.

5. Conclusion

The characteristics of the hydraulic and the water exchange due to the wave action against vertical slit-type breakwaters were discussed. Results are summarized as follows.

(1) We can estimate analytically the reflection and the transmission coefficients of the permeable breakwater with composition of the wedge shape parts for the horizontal cross section.

(2) We can find in this study that the C.E type breakwater is most effective as to both the hydraulic and the water exchange characteristics.

Acknowledgement

The study reported here was supported by Grant-in-Aid for Scientific Research from the Ministry of Education, Science and Culture of Japan.

Reference

1) Jarlan,G.E. : A perforated vertical wall breakwater, The Dock and Harbour Authority, No.4, pp.394-398, 1961.

2) Kondoh,H. and H.Takeda : Wave energy dissipating structure, Morikita Publishing Company, 275P, 1983 (in Japanese).

3) Murakami,H.,Hosoi,Y. and Y.Goda : Wave deformation and water exchange due to a vertical slit-type breakwater, Proc. of 31-st Conf. on Coastal Engng, pp.497-501, 1984 (in Japanese).

4) Murakami,H., Hosoi,Y. and Y.Goda : Wave deformation and water exchange due to a permeable breakwater, Proc. of 32-nd Conf. on Coastal Engng., pp.535-539, 1985 (in Japanese).

5) Murakami,H.,Hosoi,Y. and Y.Goda : Hydraudic and water exchange characteristics of slit-type permeable breakwaters, Proc. of 33-rd Conf. on Coastal Engng, pp.412-416, 1986 (in Japanese).

CHAPTER 156

ON STRESS IN TETRAPODS UNDER WAVE ACTION

Wakiro Nishigori*
Taiji Endo**
Atsuyuki Shimada***

ABSTRACT

Recently, as well as hydraulic stability, structural strength of armor blocks has emerged as a major problem in breakwaters. This problem is studied by research organizations in many countries. In Nippon Tetrapod Co., Ltd., a series of hydraulic model tests was conducted to measure the surface strain on Tetrapods under wave action.

In this paper, the results of the hydraulic model test are described. Prior to the hydraulic test, a similitude relation on impact stress and strain between the prototype and model was derived and a drop test was performed to investigate the scale effect on impact strain on Tetrapods. The hydraulic test was conducted to measure the surface strain on 50kg model Tetrapods using strain gages. In addition, impact strain on 50t Tetrapods under wave action was estimated applying the similitude relation.

The strain on Tetrapods under wave action was clarified through this study.

1. INTRODUCTION

In recent years very large armor blocks have been used for many coastal structures especially in rubble mound breakwaters in deep areas. Wave forces hitting structures in these areas are very large. Blocks in an armor layer receive extreme wave forces and some of them are subject to breakage. In one such incident, the breakwater in Sines, Portugal received serious damage.

Armor layers are usually designed by means of Hudson's formula or hydraulic experiments on their stability. Structural damage to individual blocks is not considered, so there is a possibility that the armor blocks are hydraulically stable but structurally unstable

* Research Engineer, Hydraulic Laboratory, Nippon Tetrapod Co., Ltd. , 2-7 Higashi-Nakanuki, Tsuchiura, Ibaraki, 300 Japan.
** Dr. Sc., Director, Hydraulic Laboratory, Nippon Tetrapod Co., Ltd. , 2-7 Higashi-Nakanuki, Tsuchiura, Ibaraki, 300 Japan.
*** Senior Research Engineer, Central Research Institute of Electric Power Industry. , 1646 Abiko, Abiko-shi, Chiba, 270-11 Japan.

as a result of such design methods. Structural damage to individual blocks can escalate into hydraulic damage to the whole armor layer. It is necessary to design coastal structures that take into consideration not only block hydraulic stability but also block structural strength.

In order to study stress occurring in blocks, Terao et al (1982) and Burcharth (1981) carried out drop tests using prototype Dolosse while Delft Hydraulics Laboratory (1983) and Hall et al (1984) measured bending moment in model Tetrapods and stress in model Dolosse respectively, both made of new materials, under wave action using new measuring techniques.

Stress in blocks is not well known under wave action. If the stress in blocks could be monitored and clarified, the results could contribute to the design of better armor layers.

From this view point, a hydraulic model test was conducted to measure the surface strain on blocks under wave action. The block utilized was Tetrapod because it is commonly used for coastal structures in Japan. In the test section, 50kg Tetrapods were placed in two standard layers and surface strain on two instrumented Tetrapods in the vicinity of each other just above the still water level was measured using strain gages.

The behavior of Tetrapods under wave action can be distinguished as follows, (1) Tetrapods rocking slightly, (2) Tetrapods rocking easily and repeatedly and (3) Tetrapods falling down. The test was conducted to examine the strain on Tetrapods for each category of behavior due to waves.

2. LAW OF SIMILITUDE

In the case of block collisions, the impulse induced by the impact force is assumed to be equal to the change in momentum, so the following equation is validated.

$$\int_0^\tau Pd\, dt = m\,(v' - v) \tag{1}$$

where Pd; impact force
v,v'; velocity of the block just before and after collision respectively
m; mass
τ; duration of impulse

From eq. (1),

$$Pd \propto \frac{m v (1+e)}{\tau} \tag{2}$$

where e; coefficient of restitution

is derived. The time it takes for a longitudinal shock wave to travel from the point of impact to a free edge and back again equals

the duration of an impulse, as shown by Burcharth (1981) and Aoyagi (1972). As concrete was used for the model material , the modulus of elasticity, density, coefficient of restitution and the speed of a longitudinal wave in concrete are the same as those of the prototype. Therefore, the impact force is proportional to the speed of collision, and inversely proportional to the distance between the impact point and a free edge of the block.

In this test, the armor blocks are assumed to be moving according to Froude's law,

$$v_m / v_p = \lambda^{1/2} \tag{3}$$

where λ is a linear scale of a model Tetrapod and the subscripts m and p refer to the model and prototype respectively.

From the consideration above, the similitude ratios of the impact and elastic forces are obtained as follows.

$$Pd_m / Pd_p = \lambda^{5/2} \tag{4}$$

$$Pe_m / Pe_p = (\sigma_m / \sigma_p)\lambda^2 = (\varepsilon_m / \varepsilon_p)\lambda^2 \tag{5}$$

where Pe; elastic force
σ; stress
ε; strain

The similitude relations of the stress and strain between the model and prototype under wave action are represented by eq. (6), as eq. (4) is equal to eq. (5).

$$\sigma_m / \sigma_p = \varepsilon_m / \varepsilon_p = \lambda^{1/2} \tag{6}$$

3.TEST EQUIPMENT AND TEST METHOD

3.1.Model of Tetrapod

The following equation should be valid in order for the similitude relation to hold true.

$$\varepsilon = \alpha v \tag{7}$$

where ε; impact strain
v; collision speed
α; a constant factor

The value of α in the model is the same as that in the prototype. A drop test was performed beforehand to confirm the validity of eq. (7) using from 736g to 4t Tetrapods. Fig. 1 shows α values calculated by eq. (7) utilizing measured values of maximum impact compressive strain generated at the top of a leg (on the compressive side) with a linear scale factor based on 40kg Tetrapods. This figure indicates that α became constant when Tetrapods heavier than 40kg were utilized. So if 50kg Tetrapods were used in the test,

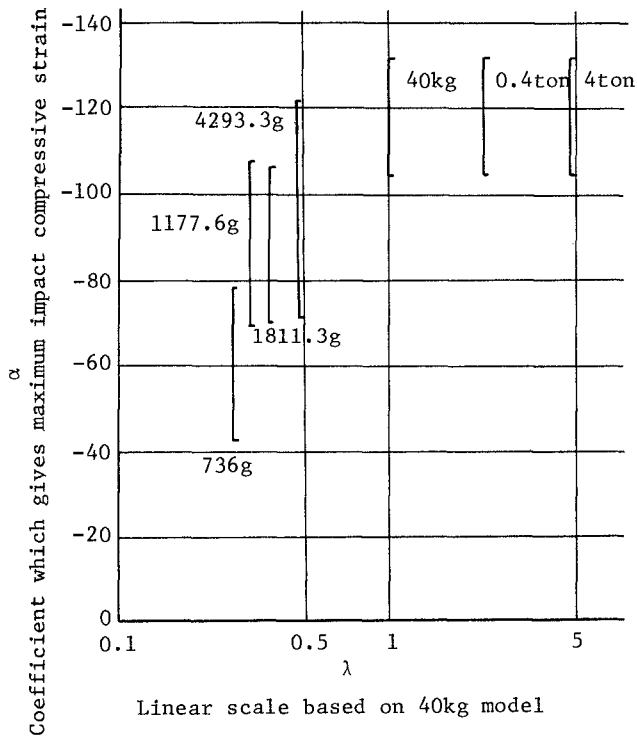

Fig. 1 Scale Effect Concerning Impact Strain on Tetrapod

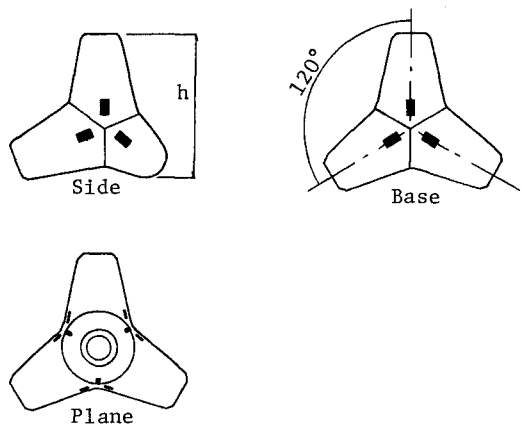

Fig. 2 Locations for Strain Measurement

eq. (6) could be applied. Therefore in the hydraulic experiment, 50kg Tetrapods were used.

Four instrumented Tetrapods of 50kg were made of concrete using gravel of size 25mm. Strain was measured at three locations 120 degrees to each other on the top center of each leg. Totally 12 points per one Tetrapod were examined as shown in Fig. 2. Strain gages (length=10mm) on the surface of the instrumented Tetrapods were covered with waterproofing cement. Photos 1 and 2 show a Tetrapod model completed. Characteristics of the test Tetrapods were measured and tabulated in Table 1. These values were close to standard concrete.

Photo 1 Strain Gages on the Surface of the Test Tetrapod

Photo 2 50kg Tetrapod Model

Table 1 Characteristics of the Test Tetrapods

Characteristics of the test Tetrapods	Moist condition	Air-dried condition
Unit weight (kgf)	50.6	49.7
Specific weight (gf cm^{-3})	2.36	2.31
Static modulus of elasticity (kgf cm^{-2})	3.08x10^5	2.45x10^5
Dynamic modulus of elasticity (kgf cm^{-2})	3.60x10^5	3.68x10^5

3.2.Test Equipment

A large wave channel, 205m long, 3.4m wide and 6.0m deep, at the Central Research Institute of Electric Power Industry was used in order to generate large waves for the 50kg Tetrapods utilized. Fig. 3 shows the diagram of the test section.

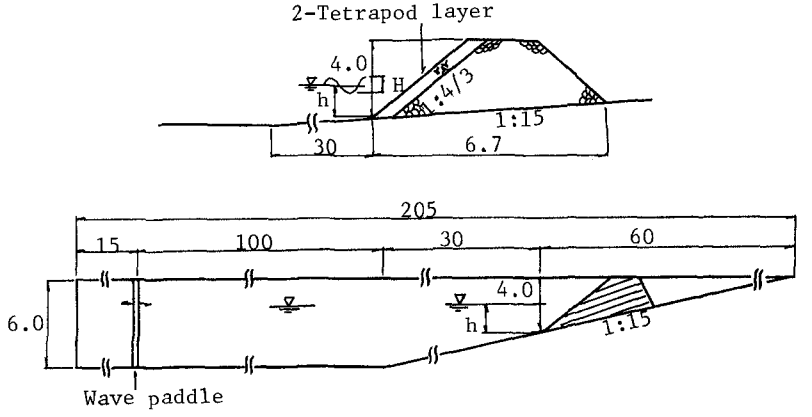

Fig. 3 Sketch of Test Section (unit ; m)

The apparatus for measurement used in the experiment is listed below.

*Dynamic strain amplifier ; This was used for amplifying electric current from strain gages.
*Data recorder ; This was used in order to record analog data through the dynamic strain amplifiers.
*Multi-channel oscillograph ; Strain was reproduced on a multi-channel oscillograph chart.
*Video system ; This was used to record Tetrapod motion.

3.3.Test Method

A test section was constructed at a distance of 130m from the wave paddle in the flume. In the test section, 50kg Tetrapods were set up in two standard layers. The two instrumented Tetrapods were placed in the vicinity of each other just above the still water level so that they received the maximum impact wave force. Photo 3 shows the condition during placement.

Strain was recorded by the data recorder and reproduced on a strip chart at a speed ratio of 1 : 32 that of the recording speed for the duration of the impact strain itself, which was in the order of one millisecond to obtain a clearer result. Strain on the chart was measured by a scale.

Photo 3 The Condition during Placement

3.4.Test Cases

Test cases are summarized in Table 2. In the table,

*h (m) ; water depth at a toe of the Tetrapod slope
*T (sec) ; wave period
*Lo (m) ; wave length in deep water
*Ho' (m) ; equivalent deep water wave height
*H (m) ; wave height at the toe of the Tetrapod slope with the structure not in place
*Ns ; stability number
*Tetrapod Number ; T.P.No.1-4 are the instrumented Tetrapod number.

Experiments were conducted to study the strain on Tetrapods for each category of behavior of Tetrapods due to waves (as mentioned in the introduction).

Table 2 Test Cases

Case No.	h (m)	T (sec)	Lo (m)	Ho' (m)	H (m)	Ns^3	Tetrapod Number
1-1 ~ 1-11	1.7	4.0	24.96	0.96 ~ 1.51	1.04 ~ 1.51	23.6 ~ 72.1	T.P. No.1,4
2-1 ~ 2-9	1.4	6.0	56.15	0.87 ~ 1.17	1.55	78.0	T.P. No.2,3
3-1 ~ 3-8	1.5	6.0	56.15	1.09 ~ 1.31	1.60	85.8	T.P. No.2,3
4-1 ~ 4-4	1.5	4.0	24.96	0.90 ~ 1.33	0.97 ~ 1.35	19.1 ~ 51.5	T.P. No.3,4
5	Drop Test						T.P.No.3

In cases 1-3, tests were carried out after standard placement to measure the impact strain for Tetrapods rocking slightly. In case 4, one of the two instrumented Tetrapods was placed so that it rocked easily and repeatedly, while the other was placed so that it would fall down easily. Waves were generated for 100sec in cases 1 and 4, and 60sec in cases 2 and 3. This was decided after taking effect of re-reflected waves from the wave paddle in the wave tank into consideration. In case 5, one instrumented Tetrapod was pushed down manually from the crown of the dike in the still water condition. Photo 4 shows waves hitting Tetrapods in case 1.

Photo 4 Waves Hitting Tetrapods

4.TEST RESULTS

Test results are classified into three categories according to the behavior of Tetrapods due to waves.

4.1.Category No.1 ; Tetrapods Rocking Slightly

In this category, Tetrapods were placed with sufficient interlocking. Actual motion of test Tetrapods was not visible under wave action in the flume, but was observed by a comparison of the position of Tetrapods just before and after waves hit.

Measured impact strain is tabulated in Table 3. ε tmax and ε cmax are used for the maximum values measured on tensile and compressive side respectively when collisions occurred. Behavior of Tetrapods due to wave attack is shown in Fig. 4.

In case 1, Tetrapods moved gradually according to wave action and Tetrapod No.1 fell down in case 1-11. The impact strain was not measured on Tetrapod No.4, but was measured in case 1-10-3 (during the third wave generation) on Tetrapod No.1. In cases 1-1 - 1-9, impact strain was not measured.

In case 2, a number of waves, of which the wave heights measured 1.55m, hit the Tetrapods. Because both instrumented Tetrapods moved only slightly, the impact strain on them was not measured.

In case 3, impact strain was not measured in cases 3-1 - 3-4, but was measured and found to be $3\text{-}26\text{X}10^{-6}$ on Tetrapod No.2 in cases 3-5 - 3-7-1. Tetrapod No.2 fell down in case 3-7-2, because a number of large waves, of which $Ns^3 = 85.8$ hit them continuously. In this case, impact strain on Tetrapod No.3 was measured after the fall of Tetrapod No.2. When impact tensile strain had just exceeded $25\text{X}10^{-6}$, it decreased gradually even though waves were continuously generated.

4.2.Category No.2 ; Tetrapods Rocking Easily and Repeatedly

In this category, the movements of the instrumented Tetrapod are noted in Fig. 5. Its reactions to waves were as follows ; leg 1 crashed into Tetrapod A due to the waves and returned to its previous location due to gravity. Leg 2 collided with Tetrapod B. The distance which leg 1 moved was approximately 20cm. The measured impact strain is summarized in Table 4.

4.3.Category No.3 ; Tetrapods Falling Down

In this category, the measured values of impact strain are summarized in Table 5.

In cases 1-11 and 3-7-2, Tetrapods rolled down toward the toe of the Tetrapod slope. In these cases, tests were conducted after standard placement with sufficient interlocking. In cases 4-1, 4-2

and 4-3, each instrumented Tetrapod moved down a distance equal to approximately 1/2-1 of the block height. In case 4-4, the instrumented Tetrapod moved down a distance of 1/2 the block height, and continued to roll down toward the toe of the slope. In these cases, tests were performed after each instrumented Tetrapod was placed so that it would fall down easily.

Table 3(a) Measured Impact Strain for Tetrapods Rocking Slightly

Case No.	T (sec)	H (m)	Ns^3	The maximum impact strain ($\times 10^{-6}$)			
				Tetrapod No.1		Tetrapod No.4	
				ε tmax	ε cmax	ε tmax	ε cmax
1-1 ~ 1-10-2	4.0	1.04 ~ 1.51	33.6 ~ 72.1	0	0	0	0
1-10-3	4.0	1.51	72.1	26	-32	0	0
1-11	4.0	1.51	72.1	Falling down		0	0

Table 3(b) Measured Impact Strain for Tetrapods Rocking Slightly

Case No.	T (sec)	H (m)	Ns^3	The maximum impact strain ($\times 10^{-6}$)			
				Tetrapod No.2		Tetrapod No.3	
				ε tmax	ε cmax	ε tmax	ε cmax
3-1 ~ 3-4	6.0	1.60	85.8	0	0	0	0
3-5	6.0	1.60	85.8	3	-4	0	0
3-6-1	6.0	1.60	85.8	12	-19	0	0
3-6-2	6.0	1.60	85.8	26	-25	0	0
3-6-3	6.0	1.60	85.8	9	-10	0	0
3-7-1	6.0	1.60	85.8	10	-13	0	0
3-7-2	6.0	1.60	85.8	Falling down		25	-20
3-7-3	6.0	1.60	85.8	Not measured		19	-30
3-8-1	6.0	1.60	85.8			17	-22
3-8-2	6.0	1.60	85.8			11	-10
3-8-3	6.0	1.60	85.8			20	-27

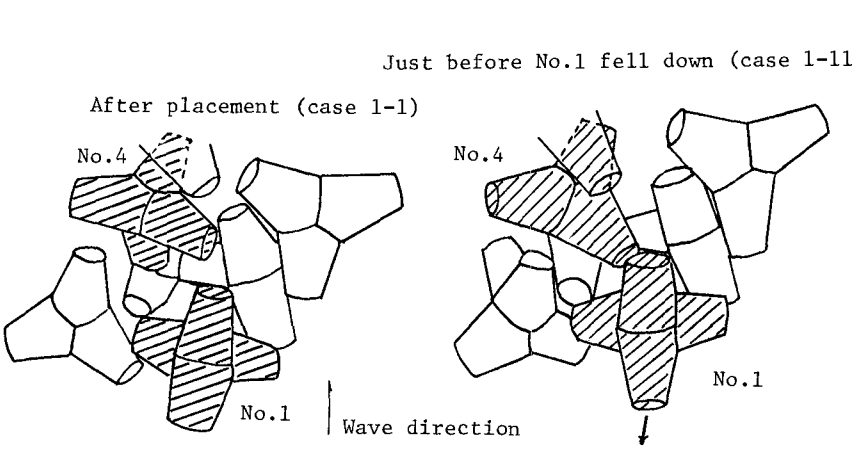

Fig. 4(a) Behavior of Tetrapods in Case 1

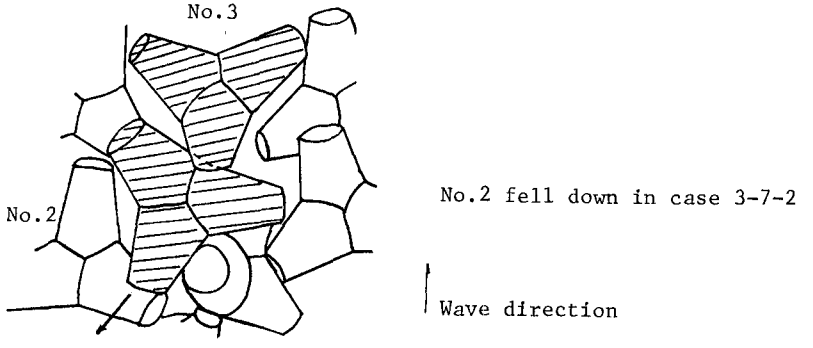

Fig. 4(b) Behavior of Tetrapods in Case 3

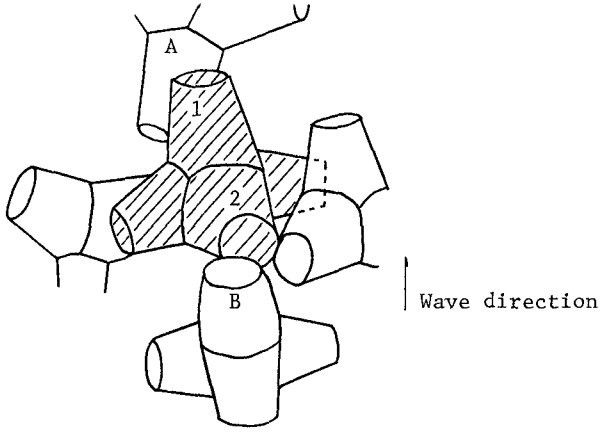

Fig. 5 Behavior of Tetrapod Rocking Easily and Repeatedly in Case 4

Table 4 Measured Impact Strain for Tetrapods Rocking Easily and Repeatedly in Case 4

Case No.	T (sec)	H (m)	Ns^3	The maximum impact strain ($X10^{-6}$)	
				ε tmax	ε cmax
4-1	4.0	0.97	19.1	20	-20
4-2-1	4.0	1.04	23.6	29	-23
4-2-2	4.0	1.04	23.6	30	-30
4-3	4.0	1.18	34.4	19	-20
4-4	4.0	1.35	51.5	27	-30

Table 5 Measured Impact Strain for Tetrapods Falling Down

Case No.	T (sec)	H (m)	Ns^3	The maximum impact strain ($X10^{-6}$)	
				ε tmax	ε cmax
1-11	4.0	1.51	72.1	62	-60
3-7-2	6.0	1.60	85.5	92	-80
4-1	4.0	0.97	19.1	38	-93
4-2-1	4.0	1.04	23.6	58	-61
4-2-2	4.0	1.04	23.6	45	-64
4-3	4.0	1.18	34.4	11	-28
4-4	4.0	1.35	51.5	40	-65
5	Drop test			36	-44

5. DISCUSSION

5.1. Impact Strain and Wave Properties

Because impact strain was significantly influenced by Tetrapod placement, correlations between impact strain and wave properties could not be clarified. After waves began to hit the test Tetrapods placed in standard layers, even when wave heights were large, corresponding to $Ns^3 = 70 - 85$, the impact tensile strain was found to be $3 - 12 \times 10^{-6}$ because interlocking was sufficient. However in the three test cases, impact tensile strain was measured to be approximately 25×10^{-6} prior to the instrumented Tetrapod falling or after adjacent Tetrapods fell down. It can be seen that this value was

almost the same as that obtained in the case where the instrumented Tetrapod was placed without sufficient interlocking. When such strain occurred, the instrumented Tetrapod was not in a condition of interlocking. Therefore, such strain was classified into category No.2. When impact tensile strain had just exceeded 25×10^{-6}, one of two things occurred : i.e. the instrumented Tetrapod fell down or the impact strain decreased gradually again even though waves were continuously generated. The latter indicates that Tetrapods are inclined to move from unstable positions to more stable ones under wave action.

In the case where the instrumented Tetrapod was placed without interlocking, behavior of the Tetrapod followed the wave action repeatedly. The measured impact strain when leg 1 crashed into Tetrapod A was larger than that when leg 2 collided with Tetrapod B (as mentioned in 4.2.). It can be deduced that when incident waves hit the test Tetrapod the block accelerated, and when it returned, its behavior depended mainly on gravity.

The maximum impact strain on one instrumented Tetrapod pushed down manually from the crown of the dike into still water was not so large as that generated by the wave down rush even though the falling distance was long. It was observed that when Tetrapods fell down under wave action, their fall accelerated due to wave run-down. Their collision speed also increased.

5.2.Estimation of Impact Strain on 50t Tetrapods

From the test results, the impact strain in 50t Tetrapods under wave action was estimated applying eq. (6) as follows.

$$\varepsilon_{50t} = 3.12\, \varepsilon_{50kg} \tag{8}$$

where ε_{50t}; impact strain in 50t Tetrapods
ε_{50kg}; impact strain in 50kg Tetrapods

The maximum values of impact tensile strain on 50t Tetrapods $\varepsilon_{50t\,tmax}$ were calculated and tabulated in Table 6.

Table 6 Estimated Maximum Impact Strain on 50t Tetrapods

Behavior of Tetrapods	$\varepsilon_{50ttmax}$
Rocking slightly	37×10^{-6}
Rocking easily	94×10^{-6}
Falling down the distance equal to 1/2-1 their size	181×10^{-6}
Falling down toward the toe of the slope	287×10^{-6}
Falling down in the still water condition	112×10^{-6}

When the maximum impact tensile strain on a 50kg model Tetrapod was found to be 92×10^{-6} as in case 3-7-2, cracks or breakage did not occur. On the other hand, Terao et al (1982) carried out drop tests using prototype Dolosse and showed that the maximum impact tensile strain measured without breakage was larger than 250×10^{-6}. However it could not be verified whether breakage of Tetrapods would occur or not under wave action from only the information mentioned above. It must be considered that occurrence of breakage would be influenced by not only the magnitude of strain but also the distribution of strain. Therefore, it was necessary to perform a series of drop tests using the model and prototype Tetrapods in order to examine in more detail the critical impact tensile strain when Tetrapods break.

6. CONCLUSIONS

The following conclusions were derived through the experiment.

(1) When 50kg Tetrapods are used, the similitude relations on impact stress and strain between the model and prototype are satisfied even under wave action.
(2) In cases where Tetrapods fall down under wave action, impact strain generated is larger than that in the still water condition.
(3) It is necessary to examine in more detail the critical impact tensile strain when Tetrapods break.

REFERENCES

Aoyagi, S. (1972). Matrix methods in analysis of impact phenomena on structures. Proc. of JSCE. No.206, pp.13-22 (In Japanese).

Burcharth, H. F. (1981). Full scale dynamic testing of Dolosse to destruction. Jour. Coastal Engineering, Vol.4, No.3, pp.229-251.

Delft Hydraulics Laboratory (1983). Strength of concrete armor units for breakwaters.

Hall, K. R. et al (1984). Development and evaluation of instrumentation package for measuring strain levels in model breakwater armor units.

Terao, T. et al (1982). Prototype testing of Dolosse to destruction. Proc. of 18th Coastal Engineering Conference, Cape Town, pp.2062-2078.

CHAPTER 157

On the Behavior of Armour Unit in the Coverlayer

Hans Werner Partenscky[1], John Rutte[2] and Reinold Schmidt[3]

1 INTRODUCTION

As a result of the large-scale failure of the rubblemound breakwater at SINES, Portugal in 1978 a number of research programs were begun. At present, however, very little information is available from technical publications regarding new design criteria, recommendations, or test procedures for model tests of rubblemound breakwaters. The need still exists, therefore, for economically practical model tests and standardized test procedures so that more tests can be conducted and reproducible results from different institutions can be compared.

At the same time, a number of factors related to the stability of rubblemound surface elements, and the interrelationships between those factors, have not been adequately examined or explained. Apparently without extensive model tests, for example, it has been suggested that greater stability can be obtained by using elements with greater unit weights (comparing elements of the same absolute weight), either by adding scrap metal or denser materials, such as granite, to the concrete.

Furthermore, susceptibility to breakage is of major importance to the long-term stability of armour layer units, particularly for dolos and similar less massive element types. This aspect has been generally neglected in laboratory tests, however, and attempts to simulate the lower ultimate strength of elements in reduced-scale model tests appear extremely difficult, as well as costly in terms of time and materials.

Several other factors which can significantly affect the stability of an armour layer include the surface roughness of the individual elements, as well as boundary conditions such as the beach slope.

An attempt will be made in this paper to discuss the various factors mentioned above on the basis of extensive testing of rubblemound breakwaters recently conducted at the Franzius Institute for Hydraulics and Coastal Engineering at the University of Hannover. Standardized procedures, which are independent of the type of element, are introduced for conducting model tests as well as for systematically evaluating and quantifying the results. Results will be presented from tests using both concrete and aluminum dolos with different unit weights, in addition to concrete cubes and tetrapods. K_D-values are proposed for these different element types. The

1) Prof. Dr.-Ing. Dr. phys., Director of the Franzius Institute, University of Hannover, Nienburger Str. 4 D-3000 Hannover 1
2) M.E., University of Florida, 1984-85 at the Franzius Institute
3) Dipl.-Ing., Project Engineer, Franzius Institute

characteristic distribution of wave-induced damage over the face of the breakwater and the reasons for this distribution are given. The complex interrelationships between the beach slope, wave period, and water depth, and their influence on the extent and location of damage are also discussed.

2 TEST PROGRAM AND EQUIPMENT

Model tests were carried out in the wave channel at the Franzius Institute (length = 90 m, width = 2.2 m, max. wave height = 0.50 m) with government funding provided by the Federal Republic of Germany. A computer-controlled hydraulic wave generator was used which is capable of generating all types of spectra and third order regular waves.

Tests of rubblemound breakwaters were conducted using three types of armour layer elements (dolos, cubes and tetrapods), all of which are similar in terms of hydraulic stability. Particular emphasis was placed on the investigation of dolos elements.

A model scale as large as practical was chosen in order to minimize scale effects. The wave heights used ranged from about H_s = 10 cm (settlement phase) to H_s = 30 cm. Reynolds Number values varied from $Re = 3.5 * 10^3$ to $Re = 1.1 * 10^5$.

The weights of the various element types used were chosen so as to conform to the equipment and facilities available, with a range of 0.183 - 1.005 kg. The unit weight of the concrete used for all three element types was 2.24 g/cm^3, while the unit weight of the aluminum dolos was 2.7 g/cm^3. The aluminum dolos were purchased from the Waterloopkundig lab in Delft, Holland.

Individual surface elements were not marked with paint so that the test results would not be distorted by the change in surface roughness. Painted elements generally have a smooth surface which can significantly alter test results.

Due to the action of electrolytic corrosion, which attacked the aluminum within a short period of time following its exposure to water, the surface roughness of the aluminum dolos was considered to be comparable to that of the concrete elements.

Breakwaters were built on bed slopes of 1:15 and 1:30 in order to simulate conditions as close to natural as possible. The generated waves broke either on or directly in front of the breakwater. The water depth at the toe of the breakwater varied from 0.05 m to 0.40 m for overall waterdepths of up to 1.20 m in front of the wave generator.

During the construction of the breakwater an attempt was made to closely simulate actual construction practices. As such, elements were randomly placed according to a grid pattern and were allowed to fall into position after initial contact with the surface of the breakwater.

Each test series was begun at 75% of the maximum wave height which the breakwater could theoretically withstand, calculated using the HUDSON equation of C.E.R.C. (1984). This simulates the normal settlement or consolidation phase which normally follows initial

construction. Wave heights were increased in stages until failure in order to monitor damage progression. Each test with a particular wave height was interrupted twice so that photos could be made in order to differentiate between further consolidation and progressive damage.

The wave spectra used included Pierson-Moskowitsch and Jonswap, as well as order regular waves.

3 DEFINITION OF DAMAGE FOR RUBBLEMOUND BREAKWATERS

The following four different methods were used to observe and evaluate the movement of armour layer elements and the extent of damage to the breakwater:

a) direct observations verbally recorded by test personnel equipted with tape recorders;
b) continuous recordings with a high quality video system, also used to support the direct observations of (a);
c) single frame pictures taken using a Super-8 movie camera whenever the receding wave would leave the surface of the breakwater momentarily exposed;
d) positive-negative overlays of photos taken between test runs, with the water drained away.

An addition procedure for defining damage for breakwaters composed of natural stones or rubble was introduced by VAN DER MEER and PILARCZYK (1984). They suggest using the change in the surface profile of the breakwater following a wave attack as a measure of damage to the breakwater. This method is less suitable for breakwaters with concrete armour layers because the comparatively large displacements in the cover layer would lead to breakage of the concrete armour units.

Close analysis of the test results showed that the overlay method of evaluating surface layer movements is considerably better than a system of direct observations supported by video recordings. Even simple movements are easily recognizable in the overlays and at no time were rocking motions observed or recorded which did not also result in some degree of noticeable displacement in the overlays. The theoretical disadvantages that rocking motions and damage progression cannot be recorded with the overlay method therefore appear to be unfounded, particularly when each test is subdivided into three parts so that the damage development sequence associated with a specific wave height can be monitored. Positive-negative overlays therefore still represent the best method - short of installing accelerometers on every element - of recording and evaluating movements in the armour layer.

Each movement visible in the overlay photos was classified as one of 35 different combinations of rotation (7 classes) and displacement (5 classes) in order to establish a distribution diagram (histogram) of all the elements' movements. The system used for dolos to classify a movement in terms of rotation and displacement is shown in Fig. I. The determination of the extent of movement for a single element begins by considering its rotation. The angle (degree) of rotation is estimated after first establishing the point about which an individual element rotates. The second step is then to determine the translation of this point of rotation. Analogous systems were used for the tetrapod and cube elements.

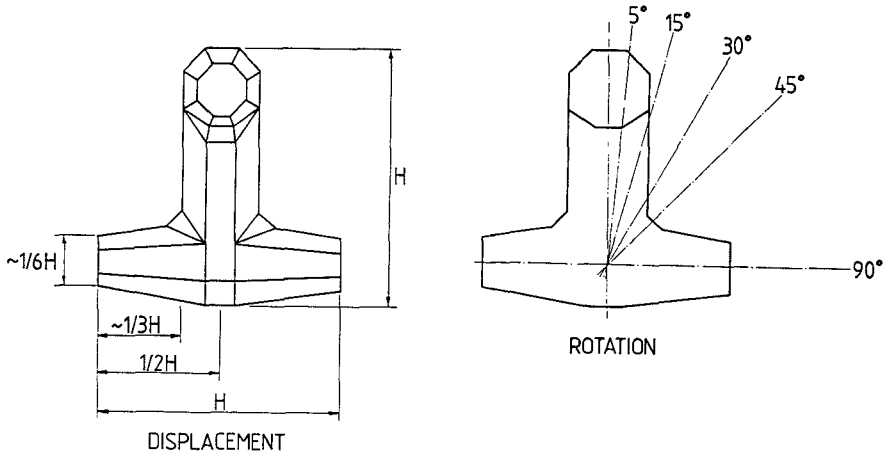

FIGURE I

Classification of Displacement and Rotation for a Dolos Element

A computer was then used to examine various possible groupings of these 35 classes. A meaningful and harmonious distribution was achieved using 6 classes, with the following combinations of rotation : displacement as upper limits:

Class No.	Maximum Rotation	Maximum Displacement	
1	5°	very small	
2	15°	H/6	H = height
3	30°	H/3	of the
4	45°	H/2	element
5	90°	≤ H	
6	90°	roll	

If the rotation and displacement of an element fall into two different classes, only the higher of the two classes is considered. This system is an extension of the method of class division presented by PAUL and BAIRD (1971).

The tests conducted at the Franzius Institut have shown that the damage distributions over large areas were very similar when these 6 general classes were used and the curves normalized, as shown in Fig. II.

This was true for all three types of elements tested, dolos, tetrapod and cube. Likewise, the distribution over a range of loading conditions, from the settlement phase up to the beginning of failure, is almost identical. The number of normalized damage events only first began to increase significantly in classes 4 to 6, with a corresponding decrease in classes 1 to 3, with wave heights which cause greater more progressive damage to the breakwater. This behaviors, which is indicative of unacceptably large damage to the breakwater, was observable in all tests.

A maximum allowable percentage of damage was determined for each of the 6 classes which reflect the susceptibility to breakage of the element type in question. Since the danger of breakage is different for the relatively slender dolos, the more sturdy tetrapods and the rather massive cube elements, these allowable damage limits for each of the 6 classes vary with the type of element. Tests conducted by BURCHARTH (1981) showed that dolos are extremely suspectible to breakage. As such, dolos movements greater than 15° : H/6 should be very strictly limited.

No published information could be found regarding the susceptibility to breakage of cubes or tetrapods. It is known, however, that a relatively high percentage of broken elements have been found in tetrapod breakwaters. The danger of breakage exists even in the case of large concrete cube or block elements as the result of shrinkage cracks caused by temperature changes during curing.

Taking the differing susceptibilities to breakage into consideration, limits on the allowable movements for each of the three types of surface layer elements were set, as shown in Fig. III. As a recommendation, damage curves which exceed these limits in any of the 6 classes should not be considered allowable.

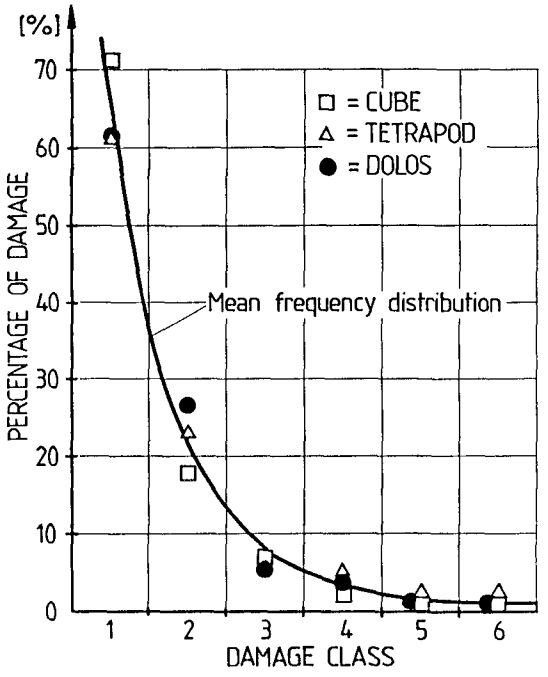

FIGURE II

Normalized Damage Distribution for Dolos, Cube and Tetrapod

(Mean Value)

The percentage of surface layer elements whose movements fall within each of the 6 classes previously described are calculated with reference to the total number of elements within a range extending $1.25 * H_{1/3}$ above and below the still water level (SWL). This is the

region in which almost all of the damage occurs. The percentage of elements experiencing a certain class of movement should always be calculated with reference to the total number of elements within this specified range, not the overall total for the breakwater. Although movements of elements outside of this range were found to be rare, they should also be considered, while still using the same total number of elements as the basis of reference. Only when the breakwater dimensions are smaller than this given range should the total number of surface elements be used.

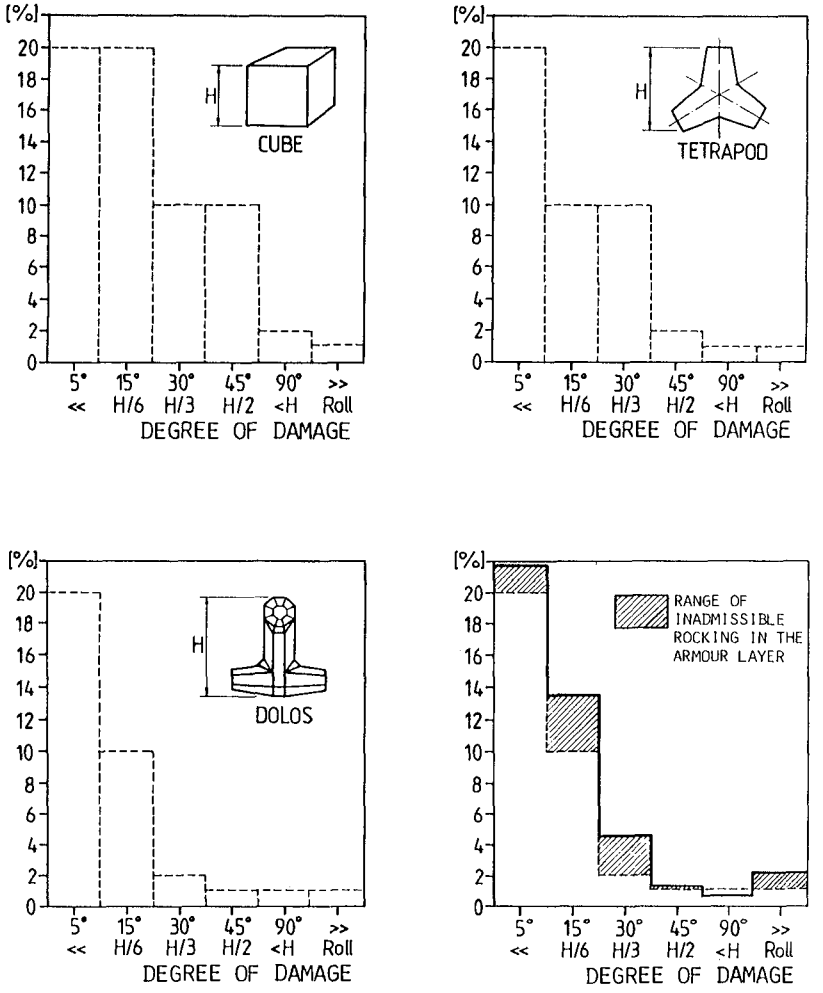

FIGURE III

Allowable Rocking for Individual Damage Classes for Cubes, Tetrapods and Dolos Elements

4 RESULTS

As part of a program of basic research sponsored by the German government's Special Research Department (SFB), extensive model tests of rubblemound breakwaters were conducted using dolos, cube and tetrapod surface layer elements.

Each test was begun using a moderate wave height in order to allow initial consolidation to take place. Following this settlement phase, wave heights were gradually increased until the breakwater failed or a state of progressive damage signaled eminent failure.

Each test at a particular wave height was interrupted twice (ie. subdivided into three parts) so that photographs could be taken. Positive-negative overlays were made from these photos, which were then evaluated using the system previously described. Video recordings of every test were used to confirm the accuracy of the overlays.

The K_D-values determined from these evaluations showed considerable variation in some cases. The influences of the wave period and the offshore slope can be offered as two of the probable reasons for these wide fluctuations.

4.1 INFLUENCE OF THE WAVE PERIOD

Assertions by various authors that wave periods become increasingly critical for breakwaters as they either increase or decrease, depending on the author, were not substantiated. Greater damage was most often associated with a wave period of intermediate length, with the extent of damage decreasing for wave periods both shorter and longer than this critical, intermediate length.

The height of a short (period) wave is limited by its maximum steepness, or breaking limit. Longer waves, on the other hand, roll more slowly over the breakwater. The resulting forces from the up- and downrush of water therefore remain small and the breakwater is not so heavily stressed.

This tendency for more intermediate length wave periods to be more critical was clearly borne out by every series of tests, with all conditions remaining constant except the length of wave period. The actual numerical values of these critical periods varied depending on the type of armour layer element and the form of the foreshore.

4.2 INFLUENCE OF THE SLOPE OF THE FORESHORE

It is obvious that the slope of the foreshore greatly influences the extent of damage. The slope largely controls the form of the wave as well as the interplay between the water rushing up and down the face of the breakwater. The breaking point of a wave, for example, is affected by the extent of the water cushion in front of the breakwater.

At the same time, the dolos elements proved to be extremely sensitive to changes in the foreshore slope and form. The results of different model tests could be characterized as varying from stable to total destruction for a prototype storm duration of 3 hours or less. The wave heights generated and the type of spectra used were identical for these tests, with the only variable being the form of the

foreshore. Statements regarding the reasons for this phenomenon and the various interrelated factors involved, however, would be premature at this point in our continuing study.

The influences of the wave period and foreshore slope were considerably smaller in the case of tetrapods and were hardly noticeable for cube elements, on the basis of these tests.

4.3 INFLUENCE OF THE UNIT WEIGHTS

Test conparisons between two dolos types of different unit weights with the same total block weight, aluminium with 2.7 g/cm^3 (169 lbs/ft^3) and concrete with 2.24 g/cm^3 (140 lbs/ft^3), came out clearly in favor of the less dense (larger) concrete elements. The denser (smaller) elements were similar in terms of stability only in those model tests in which the wave heights were limited by shallow water depths directly in front of the breakwater. The reasons for this can be attributed to the larger stresses exerted on the surface layer when water rushes back down and, at the same time, out of the breakwater; the wave having already broken and lost most of its energy. In such a case a denser element becomes more effective.

On the basis of the model tests, however, the absolute size of the individual elements appears to be the more important factor in those cases where the approaching and breaking waves (plunging and collapsing breakers) exert the principle stresses on the breakwater.

Exactly where the optimum unit weight lies is not yet known. The K_D-values for aluminium dolos determined from these tests were considerably lower than those of the cement elements.

4.4 K_D - VALUES

K_D-values were determined according to the HUDSON formula for the different element types used, as summarized in Table I. These values are valid for the breakerwater trunk and were determined for slopes of between cot = 1.5 - 1.8 (also cot = 1.33 for tetrapods).

Elements Tested	K_D-Values Measured Range	Medium	K_D-Value Recommended
Dolos (aluminum)	5.8 - 10.0	7.9	10.0
Dolos (concrete)	7.6 - 23.1	11.8	
Tetrapod (concrete)	5.9 - 10.6	7.5	7.2
Cube (concrete)	9.5 - 22.0	12.5	7.0

TABLE I

K_D-Values Determined from Tests at the Franzius Institute

In all tests the simple cube showed itself to be surprisingly stable. To be safe, however, the authors hesitate to recommend a drastic increase in the K_D-value for cubes. On the other hand, the K_D-values determined for dolos were so low that hydraulic model tests are strongly recommended as a design check for all larger-scale construction projects involving dolos elements. At the same time, it is very important to incorporate the underwater topography in front of the breakwater to a sufficient extent into the model.

FIGURE IV

Cube Protection at Bari / Italy

5 CONCLUSIONS AND RECOMMENDATIONS

For 25 years now the HUDSON equation has been the principle tool used in the design of rubblemound breakwaters. This despite the fact that the equation is widely known to be less than fully reliable. In his paper "State of the Art" I.W. STICKLAND (1983) determined that considerable damage has occured to 40 rubblemound breakwaters out of a worldwide survey of 148 breakwaters conducted by the P.I.A.N.C. .

This fact is underlined by the recently published book by PER BRUNN, "Design and Construction of Mounds for Breakwaters and Coastal Protection" (1985), in which a great many cases of failure are presented. Despite these serious problems and the obvious shortcomings of the HUDSON equation, research on rubblemound breakwaters has often not gone beyond recommending simple changes in the K_D-values used in the equation.

Completely new breakwater design criteria are not likely to be developed in the foreseeable future. On the contrary, it is more likely that it will become increasingly difficult to make general recommendations as more of the numerous complex factors related to the stability of such structures become better known.

Research conducted on behalf of the Special Research Program of the F.R.G. provided the opportunity to take up and more closly investigate some of these complex factors in hydraulic model tests. Federal support made it possible to conduct this study completely free of constraints on the scope and direction of the research, which are often elements of privately funded work. While these test results are not sufficient to develop a completely new method of designing rubblemound breakwaters, they nevertheless shed new light on several of the more important factors involved.

From the tests conducted thusfar it is clear that the individual components of the design sea state cannot be considered as isolated elements. Rather, the wave height, wave period, and the underwater beach profile, as well as the water depth in front of the structure and the type of surface element used are all closely interrelated factors which determine the effectiveness of the breakwater design. The entire structure can become surprisingly stable or instable as a result of a change in any one of these parameters. As an example, dolos elements are particularly unstable for steep underwater beach profiles with shallow water depths directly in front of the breakwater, while the same conditions have no great negative effect on tetrapods.

A standardized system for evaluating and interpreting test results is urgently needed so that all future work in this field can be better coordinated and compared. The evaluation method presented in the paper, employing positive-negative overlays, is meant to serve as a step in this direction. This method is sufficiently accurate and considerably less costly than installing accellerometers on each and every surface layer element or the use of armour elements of scale-reduced strenght. Furthermore, it is important that additional boundary conditions be made known, such as the actual wave heights used during the test, the water depth at the toe of the breakwater, as well as the inclination and length of the foreslope.

It is the authors' hope that in the near future the present uncertainties surrounding the design of rubblemound breakwaters can be sufficiently clarified so that the need for expensive model tests can be eliminated. For the time being, however, it is highly recommended that design plans be verified by hydraulic model tests. Although such tests can be rather costly, they can protect considerably larger investments in breakwater structures against extremely unpleasant surprises.

6 REFERENCES

PAUL and BAIRD (1971). Discussions on Breakwater Armour Units. Proc. P.O.A.C., Trondheim, Vol. III, pp. 1109-1135.

BURCHARTH, H. F. (1981). Full-scale Dynamic Testing of Dolosse to Destruction. Coastal Engineering 4, pp. 229-251.

STICKLAND, I. W. (1983). State of the Art. Proc. of the conference BREAKWATERS Design & Construction. Th. Telford Ltd., London.

C.E.R.C. (1984). Shore Protection Manual. Waterways Experiment Station, Vicksburg, Missisippi.

VAN DER MEER, J.W. and PILARCZYK, K.W. (1984). Stability of Rubblemound Slopes under Random Wave Attack. Proc. 19th Coastal Engineering Conference, Houston, Vol. III, pp. 2620-2634.

BRUNN, PER (1985). Design and Construction of Mound for Breakwaters and Coastal Protection. Elsevier Publishing, Amsterdam.

CHAPTER 158

DEVELOPMENT OF DESIGN CRITERIA FOR SEGMENTED BREAKWATERS

Joan Pope*
Julie L. Dean**

ABSTRACT

This paper will discuss experience and approaches to the use of segmented breakwaters for beach erosion control in the United States. Several prototype cases are examined and generalizations drawn concerning the resultant beach response. This experience is further evaluated in order to develop a preliminary approach for developing design criteria.

INTRODUCTION

A shore parallel breakwater separated into segments is a viable and proven approach for protecting the shore. Such segmented breakwater projects have been constructed in various areas of the world (Bishop, 1982; Silvester and Ho, 1972; Toyoshima, 1972; Lesnick, 1979). Beach erosion control breakwaters have been designed and constructed as both single and segmented structures. In both cases the breakwater is built approximately parallel to shore with the intent of causing beach accretion. Breakwaters can range from structures that are very close to shore with sufficent elevation to prohibit overtopping, resulting in artifical headlands or tombolos, to those which are offshore submerged structures which cause bulges in the shoreline.

Whereas a single breakwater is usually built to protect a short, local section of beach, a segmented breakwater system has gaps in between and functions as a system to protect large portions of the shore. The purpose of this paper is to discuss the more complex, segmented system. A segmented breakwater system may promote the beach to accrete to the structure resulting in the formation of tombolos. In other situations, a series of sinuous bulges develop in the beach planform, called "salients." A particular system may form both salients and tombolos or evolve back and forth from one form to the other as local wave and water level conditions vary.

BEACH EROSION CONTROL IN THE UNITED STATES

United States shores include eroding sandy beaches, shores which may be innundated by coastal storms, heavily structured shores, eroding cohesive bluffs, and migrating beach forms such as barrier islands. Each beach which has erosion or flooding problems may be worthy of a

* Supervisory Physical Scientist, U.S. Army Engineers, Coastal Engineering Research Center, Waterways Experiment Station, P.O. Box 631, Vicksburg, MS 39180-0631
** Hydraulic Engineer

different solution. Segmented breakwaters are not applicable in all situations. Beach erosion control plans or devices which work well in one place may not work elsewhere. The design intent of a segmented breakwater system may vary. For example, the purpose of the breakwater and the resultant beach response may be to preserve a recreational beach, halt erosion of the backbeach, or reduce storm surge induced flood damages.

Much of the United States shore is developed for recreational, residential, or commerical use. Public interest and shoreline use often dictate the need to design the erosion control solution to minimize downdrift impacts. Expected benefits to the shore to be protected have to be weighed against potential damages to neighboring shores. Beach fill placement is an important means of mitigating these damages, but its behavior is difficult to predict. When designing segmented breakwaters an accurate prediction of the beach response is necessary in selecting the structure configuration. A review of previously constructed segmented breakwater projects provides insite into developing this ability.

SEGMENTED BREAKWATER PROJECTS IN THE UNITED STATES

Experience in the United States with segmented breakwaters has been limited to littoral sediment-poor shores which are characterized by a local fetch-dominated wave climate. Thus these projects typically experience short period, steep waves which tend to approach the shore with only limited refraction, and therefore tend break at a steep angle to the shore. These projects also tend to be in areas which are prone to storm surges and erratic water level fluctuations, particularly the Great Lakes projects.

Table 1 is a summary of the seven breakwater projects in the United States which were assessed in this study. Figure 1 displays the geographic location of each of these projects. Four of these projects are on Lake Erie in the Great Lakes. This does not necessarily mean that these projects are located in "protected waters," as both Presque Isle and Lakeview Park have experienced significant storms accompanied by storm surges in excess of 1 meter. The two projects in the Atlantic coastal area are in relatively protected areas. Only the Holly Beach project can be considered as on the "open" ocean coast.

Most of these projects have been monitored and reported on elsewhere in the literature (Pope and Rowen, 1983; Pope, 1985; Gorecki, 1985; Bender, 1985; Dean, Pope, and Fulford, 1986; Nakashima, et al., 1987). Only the East Harbor and Winthrop Beach projects have not been monitored. The typical monitoring program consists of the acquisition of beach response and some process information for a period of 2 to 5 or more years after initial construction. Full evaluation of the monitoring data is still continuing for most of these projects. However, in all cases, including those projects which have not been subjected to a formal monitoring program, the development of a characteristic equilibrium beach planform and the general impact on the littoral regime can be determined. The brief review which follows on each project will describe the project parameters and beach response.

Table 1. Summary of United States Segmented Breakwater Projects

Table 1
SUMMARY OF U.S. BREAKWATER PROJECTS

Project	Location	Coast	Date of Construction	Number of Segments	Project Length (Lp)	Segment Length (Ls)	Gap Length (Lg)	Distance Offshore Preproject	Distance Offshore Effective (X)	Water* Depth (ds)	Fill Placed	Beach** Response
Winthrop Beach (Low Tide)	Massachussetts	Atlantic	1935	5	625m	91m	30m	unknown	80m	3.0m (mlw)	No	1
Winthrop Beach (High Tide)	Massachussetts	Atlantic	1935	1	625	625	0	305	205	5.7 (mhw)	No	3
Lakeview Park	Ohio	Lake Erie	1977	3	403	62	49	137	85	3.8	Yes	4
Presque Isle (Low Water)	Pennsylvania	Lake Erie	1978	3	440	38	60,91	46	20	1.2	Yes	2-3
Presque Isle (High Water)	Pennsylvania	Lake Erie	1978	3	440	38	60,91	46	30	1.7	Yes	3
Colonial Beach (Central Beach)	Virginia	Atlantic	1982	4	427	61	45	64	20	1.7	Yes	2
Colonial Beach (Castlewood Park)	Virginia	Atlantic	1982	3	335	61,93	26,40	46	20	1.1	Yes	1
Lakeshore Park	Ohio	Lake Erie	1982	3	244	38	60	120	100	2.2	Yes	5
East Harbor	Ohio	Lake Erie	1983	4	550	46	90,105,120	170	170	2.3	No	5
Holly Beach	Louisiana	Gulf of Mexico	1985	6	555	47,53	93,89	64	61	2.5	No	4

* Datum used is local average water depth at structure location during the period of post-construction monitoring (unless otherwise stated).
** Beach response is coded as follows:
1 - permanent tombolos
2 - periodic tombolos
3 - well developed salients
4 - subdued salients
5 - no sinuosity

Local conditions make each project unique and the design nontransferable to another site. However, by reviewing the structure configuation and planform response, a pattern of project effectiveness has been identified which can be used to develop some general design guidance. A more detailed summary of most of these projects appears in Dally and Pope, 1986.

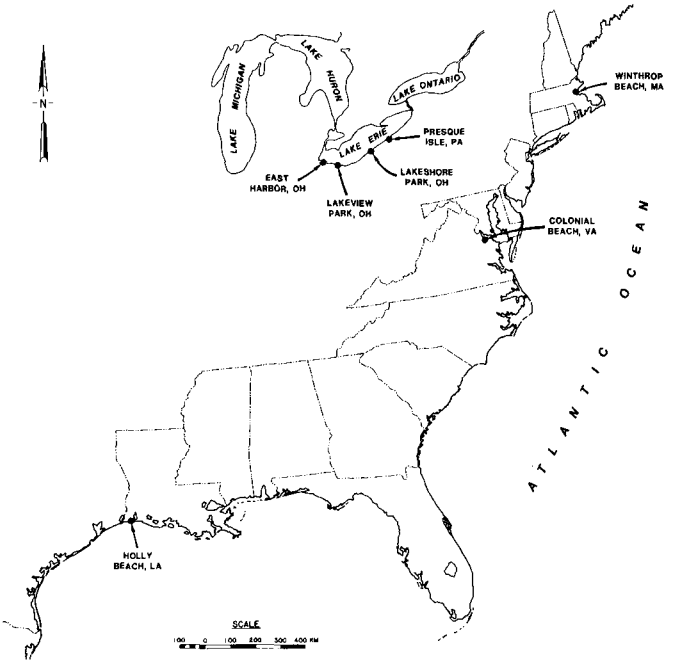

Figure 1. Location Map for United States Segmented Breakwater Projects

Winthrop Beach

The Winthrop Beach project was built in 1935. It consists of five breakwater segments separated by very small gaps. It was built 305 m off of the backbeach seawall and is in an area which experiences an approximately 2.7-m tide range. No beach fill was placed (Magoon, 1976). During high tide the five segments behave as one breakwater, resulting in a single, well developed salient. However, during low tide, individual tombolos are exposed behind several of the segments resulting in low tide headlands (Dally and Pope, 1986). This project has effectively trapped material out of the littoral regime resulting in a stable salient and tombolos along a shore which otherwise lacks a subaerial beach.

Lakeview Park

The Lakeview Park project consists of three breakwater segments, two terminal groins, and a placed beach fill (Walker, Clark, and Pope, 1981). It was constructed in 1977 and formally monitored for 5 years. The monitoring program consisted of semi-annual bathymetric and topographic surveys, three sets of aerial photography each year, annual sediment sampling, Littoral Environment Observations (LEO) made daily by a local volunteer to document the nearshore wave and current conditions, periodic project inspections, and a limited current measurement study and wave gage data collection. The structures have successfully established a stable beach headland along an otherwise sandless coast (Pope and Rowen, 1983). Once the project had established an equilibrium beach planform in response to the structure configuration, the range of wave and water level conditions only caused minor variations in the shoreline. The beach planform at Lakeview Park remained fairly stable within a limited envelope (Figure 2). There is some minor response to seasonal conditions. In particular, during the low water of the fall, the beach tends to exhibit three discernable, although subdued salients. During the high water of the spring, the beach typically will have only two subdued salients and a slight "hip" behind the western-most breakwater. As there is a strong asymmetry to the local wave climate with most of the wave energy out of the west, the west end of the beach retreated. Active transport of the native littoral material continues from west to east, through the project. However, the overall quantity of sand in the lee of the breakwaters has gradually increased through time. Over the five years of monitoring, the project gained approximately 3000 cubic meters of material per year (Pope and Rowen, 1983).

Presque Isle

The Presque Isle segmented breakwater project was built in 1978 as a prototype experiment to determine if breakwaters could be used to retard the erosion of a very large (approximately 10-km long) recurved sand spit which has been the target of various attempts at beach erosion control for over 150 years (Pope and Gorecki, 1978). Three segments were constructed and beach fill was placed. The beach exhibits some seasonal variablity resulting in two characteristic planforms, primarily responding to changes in the water level and the resultant degree of structure overtopping during storm events. During low water levels and low wave energy conditions, a tombolo sometimes forms behind the western-most (updrift) segment with two downdrift salients behind the other segments. However, during high water levels or after significant storms the tombolo is severed from the segment, resulting in three distinctive salients (Figure 3). The amount of sediment behind the breakwaters has remained fairly stable, despite an evolutionary trend toward offshore deepening (Gorecki, 1985).

Colonial Beach

Two segmented breakwater projects were built at Colonial Beach, Virginia on the Potomac River estuary in an attempt to build recreational beaches and protect a public highway which had frequently been

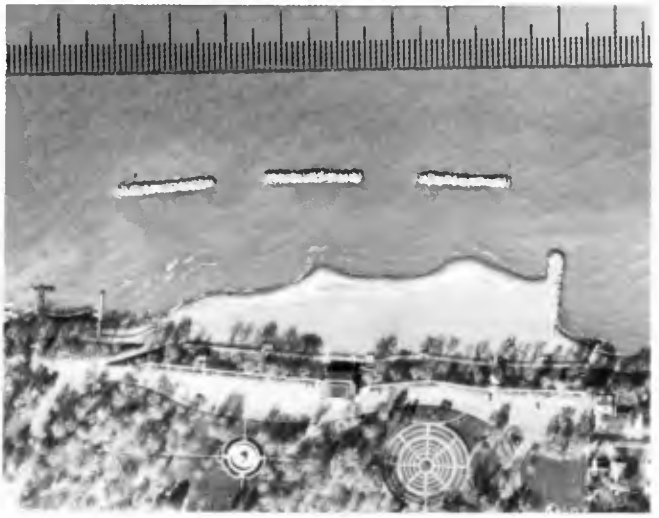

Figure 2 . Aerial Photograph of Subdued Salients at Lakeview Park, Lorain, Ohio

Figure 3. Aerial Photograph of Well-Developed Salients at Presqu Isle, Erie, Pennsylvania During Higher Water Levels

damaged by erosion (Dean, Pope, and Fulford, 1986). Central Beach consists of four segments and Castlewood Park consists of three segments plus a downdrift terminal groin. Beach fill was placed at both locations. The breakwaters in both projects were built fairly close to shore with small gap to segment length ratios (Table 1). Thus the breakwaters functioned as efficient traps which gained material from the littoral system (approximately 2000 cubic meter per year per project). The beach at Castlewood Park has been relatively inactive. Tombolos quickly formed and have remained as stable features. Central Beach is slightly more dynamic with an apparently stable tombolo behind the second segment from the updrift end and well-developed salients behind the other three segments (Figure 4). Between the salients and the breakwater segments there are very narrow channels of open water. The breakwater crest elevation is low enough that moderate storms will cause overtopping of the structure. Dye studies conducted at Central Beach suggest that even this very narrow section of open water behind the segments is important in allowing alongshore transport within the project and in releasing any hydraulic head which may otherwise be created within the compartment during a storm surge.

Lakeshore Park

The Lakeshore Park project is a three-segment structure built in 1982 at Ashtabula, Ohio on Lake Erie (Bender, 1985). Within a very short period of time after construction the placed beach fill shoreline began to retreat. The beach has continued to erode as material is lost alongshore. There is very little suggestion of sinuosity in the beach planform (Figure 5). The tendency for erosion may be partially due to the fine grain size of the beach fill, but the lack of morphological response in the shoreline suggests that the structures are too far offshore to significantly reduce the inshore wave climate and prevent erosion.

East Harbor

Four segments were constructed at East Harbor, Ohio in 1983 to protect and restore a recreational beach. No beach fill was placed and, as this is an area of low sediment supply, the project will mature slowly. High lake levels, poor sediment supply, and a structure location approximately 180 m offshore, have combined to result in the beach planform which is fairly unresponsive to the structures.

Holly Beach

In late 1985, a six-segment breakwater system was built along the erosion and hurricane prone Louisiana coast of the Gulf of Mexico to protect a highway which has frequently been damaged. One segment is rubblemound and the other five segments are built out of various geometries of timber-pile rows with tires stacked over the piles (Nakashima et al., 1987). The tire-and-pile breakwaters tend to have a higher coefficient of wave transmission than the rubblemound structures which have been used at the other project sites reviewed during this study. Salient formation occurred rapidly even though no fill

Figure 4. Aerial Photograph of Periodic Tombolo Formation at Central Beach Colonial Beach, Virginia

Figure 5. Oblique Photograph of Non-sinuous Beach response at Lakeshore Park, Ashtabula, Ohio

had been placed. Initial salient formation occurred at the two ends of the project as sediment was driven into the protected section of shore from either direction. The rubblemound breakwater has created a low-tide tombolo but the tire-and-pile breakwaters exhibit various salient morphologies in response to the wave transmission characteristics of each segment. The higher transmission segments tend to cause more subdued and blunted salients. The lower transmission segments (including the rubblemound) are backed by better defined, more peaked salients.

CLASSIFICATION SCHEME FOR BREAKWATER PROJECTS

In order to develop design criteria for segmented breakwaters, the desired beach response must first be identified (Dally and Pope, 1986). There are specific implications to beach use, degree of protection and effect on the littoral regime associated with tombolo formation. Salient formation may result in a more aesthetic and naturally behaving recreation beach with fewer adverse impacts on the littoral regime, but salients are usually not as stable and therefore tend to be less effective in providing permanent, reliable protection to the backbeach. The amplitude of the salient sinuosity (i.e., well-developed verses subdued) has important implications on the shoreline retreat behind the gaps. In general, the more sinuous the shoreline, the more stable it will be during times of increased wave action.

Beach response characteristics which need to be considered in developing the design are: the resultant beach width and planform (the presence of tombolos or salients); the amount and rate of sediment trapping from the littoral regime including regional impacts; the sinuosity of the beach planform; the beach profile slope and uniformity along the length of the project beach; and stability of the beach despite seasonal changes in wave activity, water level, and storms.

Beach response is a direct result of the amount of wave energy reaching the lee of the breakwater segments. A classification scheme has been developed based on the beach planforms which have been observed in the described projects (Figure 6). The subject projects are ranked relative to a classification scheme where the lowest wave energy in the lee of a breakwater projects results in tombolo formation. Projects in which high wave energy reachs the shore tend to have little or no sinuosity. The five beach response planforms used in this classification scheme follow:

(a) PERMANENT TOMBOLOS - In this case, very little wave energy reaches the shore and the protected beach is stable. There is very little transport along the shore. Littoral transport maybe displaced into deeper water, seaward of the structures. Castlewood Park at Colonial Beach exhibits this planform.

(b) PERIODIC TOMBOLOS - One or more segments are periodically backed by tombolos. This is primarily due to variablity in the wave energy reaching the lee of the individual segments. In the classification scheme developed here, periodic tombolos may be either unstable or stable through time, or the planform maybe variable through the

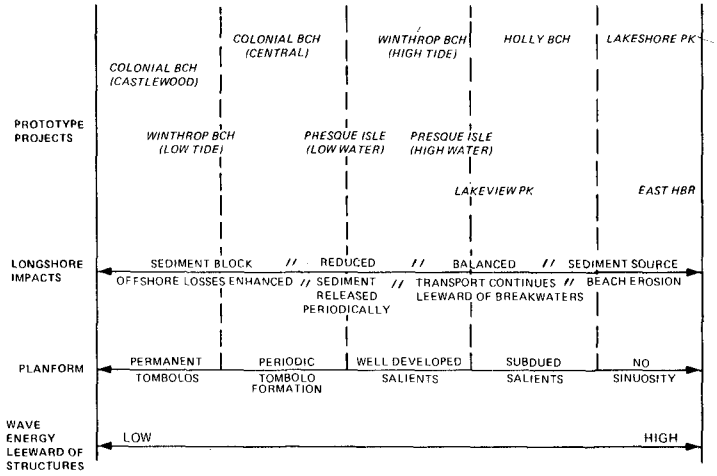

Figure 6. Proposed Classification Scheme for Segmented Breakwaters Based on Beach Response

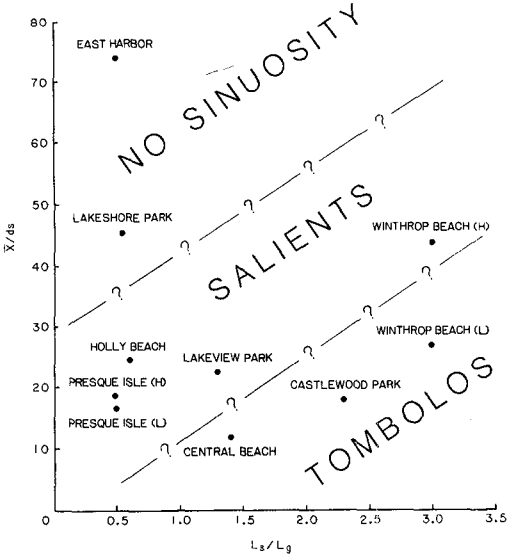

Figure 7. Dimensionless Plot of United States Segmented Breakwater Projects Relative to Structure Configuration.

project length. During high wave energy, tombolo(s) may be severed from the structure resulting in a salients. During low wave energy periods sediment accretes and the tombolo returns. The longshore effect of this type of planform may be periodic trapping of littoral material followed by a release of a "slug" of sediment. Even in a relatively stable project, only some segments may be backed by tombolos, due to alongshore variablity in the amount of energy behind the breakwater system. Presque Isle, during low water, provides an example of periodic tombolos which are unstable. Central Beach at Colonial Beach is an example of periodic tombolos which are stable (Figure 4).

(c) WELL-DEVELOPED SALIENTS - The well-developed salient beach planform occurs when higher wave energy reaches the lee of the structure and is characterized by a balanced sediment budget. Well-developed salients are not apparent until sufficient time has passed for the project shore to stablize relative to the structure configuration. Longshore moving material enters and leaves the project at approximately the same rate. In addition, rip current development within the gaps is unusual and very little material is lost into the offshore. Presque Isle, during high water, exhibits the characteristics of this planform (Figure 3).

(d) SUBDUED SALIENTS - In this case, the shoreline sinuosity is not as obvious, and amplitude of the salient is of lower relief. The project beach may periodically store and release sediment. Although the quantity of material retained in the project may remain generally balanced through time, there will be periods of increased loss or gain and the uniformity of the beach planform is not as assured. Holly Beach and Lakeview Park are examples of this classification (Figure 2).

(e) NO SINUOSITY - If high wave energy reaches the beach, including the area directly behind the segments, the beach planform may not mirror the presence of the segments. Placed beach fill may actually serve as a source of material for downdrift beaches. Although there may be some minor trapping of material from neighboring shores, the characteristic shoreline morphology is missing. Lakeshore Park is an example of a nourished beach and East Harbor is an example of an unnourished beach which illustrate this classification (Figure 5).

PARAMETERS EFFECTING BEACH RESPONSE

The forementioned classification scheme subdivides the observed beach responses into a morphological hierarchy which reflects the level of wave energy which reaches the lee of the structure. The wave energy reaching the lee of the structure (E) may be considered to be a function of the incident wave energy at the structure (W*), the structure configuration or planform (S*), and the wave transmission characteristics of the structure cross section (T*) or;

$$E = f\ (W^*,\ S^*,\ T^*).$$

Incident wave energy, is the wave climate at the structure and the result of transformation of the deepwater wave climate (height, period, and angle) over the nearshore bathymetry. Variability of the wave climate will have a significant effect on stablity of the beach planform. As most segmented breakwater projects are built in shallow water, incident wave energy is frequently directly controlled by the local water depth (ds) and its variablity. The wave climate which drives the characteristic condition of the beach is the "average" wave condition rather than the extreme. A severe storm may erase the beach planform but a structure configuration which is designed for this event will probably not display the desired beach planform on a daily basis.

Structure configuration is the density of protection provided by the structure plan and is defined through several parameters: the segment length (Ls), gap length (Lg), project length (Lp), number of segments, and the distance offshore. The offshore distance is a parameter for which there are several possible definitions. The distance offshore may be described either as the distance off the original pre-project shore or as the distance between the placed beach fill shore and the structures. Neither definition is really a true indicator of the amount of open water over which the transmitted wave energy must be distributed within the lee of the structures. The averaged distance of the structure from the effective shoreline ($\overline{X}$) may be somewhat different due to the artificial advance of the shore by the addition of groins or beachfill.

Transmitted wave characteristics are a result of the amount of incident wave energy which is transmitted into the project lee either through or over the structure crossection. The structure crest elevation controls the amount of overtopping wave energy. The permeablity of the structure cross-section controls the efficiency of the structure in absorbing incident wave energy.

Although a basic assumption of this paper is that wave energy in the lee of the structure controls beach planform, sediment characteristics of the natural littoral regime and the placed fill are also significant in influencing the eventual beach response. The quantity of material available and grain size of the sediment is important in influencing the rate at which the project reaches maturity and the eventual profile slope. Theoretically there is also a relationship between the grain size of the littoral material and the stablity of that material when exposed to various levels of wave energy. However, stablity of various grain sizes under a particular longshore transport potential is here considered as a second-order design factor.

APPROACH FOR DEVELOPING DESIGN CRITERIA

Prototype experience with the described breakwater projects and the relationship between beach response and wave energy in the lee of the structures is used to develop an approach for designing segmented breakwaters. These criteria are based on both experience and an appraisal of coastal processes.

In order to relate the beach response classification scheme to a single measure of the project wave energy, E, each factor which controls E was explored. Although E is a function of three basic parameters, only structure configuration, S*, could be tested using prototype data. The number of prototype projects available to test any approach are very limited as was the data available on each project, particularly regarding incident wave energy, W*. However, a review of the projects suggested that although incident wave climate, W*, was different from project to project, all were located in low to moderate wave environments dominated by steep, local wind fetch generated waves. In each case, the wave transmission characteristics of the structure crossection, T*, did influence the variablity of the shoreline envelope around an average beach planform. However, only the pile-and-tire breakwaters of the Holly Beach project allowed enough wave transmission during non-storm periods, to modify the beach planform from segment to segment.

A number of dimensionless parameters were evaluated in order to test the influence of S* on the beach response characteristics. Figure 7 displays the relationship between all prototype projects relative to two dimensionless parameters. The ratio of segment length to gap length, Ls/Lg, was found to be an excellent parameter for defining the capability of the structure plan to block incident wave energy. The ratio of the average distance of the structures from the effective shoreline to the average water depth at the structures, $\overline{X}/ds$, represents the influence of the structure location in effecting shoaling and diffraction of the incident wave energy. Water depth at the structures, ds, limits the amount of wave energy which can enter through the gaps (i.e., controls the breaking wave height. The distance between the effective shoreline and the structures, $\overline{X}$, implies where the shoreline intersects the diffracted wave pattern.

The projects plotted in Figure 7 display a grouping which may illustrate fields of a predictable beach planform response for low to moderate wave climates. Figure 7 displays, in effect, the inverse of the average post-project slope relative to the segment-to-gap ratio. This is an exploratory effort which may be of interest to the coastal scientist who is selecting a breakwater plan. This is not, however, a final result and much testing of this premise is needed.

FUTURE WORK

Verification and testing of the classification scheme, the relationships discussed, and the fields suggested by Figure 7 are planned. Although additional prototype data will be sought, such data are difficult to attain and are often complicated by site specific parameters. A generalized shoreline response numerical simulation model (Hansen and Kraus, in preparation) will be used to extend the prototype data presently available. Individual prototype cases will be modelled. The dimensionless relationships suggested by Figure 7 and other parameters will be varied to explore the sensitivity of the beach planform to those parameters which affect wave energy in the lee of structures.

SUMMARY

A classification scheme was developed to summarize the stablized, or average, beach planform observed for eight segmented breakwater projects in the United States. Data and monitoring results are presented for each of these projects. An assessment of these projects suggests that beach response is directly related to the wave energy which reaches the lee of the structures. Wave energy in the lee of the structures is a function of the incident wave energy, the structure plan or configuration, and the wave transmission characteristics of the structure crossection. Prototype data is displayed relative to dimensionless parameters which suggest a correlation between the beach slope, segment plan, and beach planform.

This paper attempts to simplify the complexities associated with segmented breakwater design into some generalized design criteria. However, individual projects present a number of site specific limitations which restrict the application of generalized "rules of thumb." The summary presented here is an attempt to translate prototype experience into a form which may help in project planning. The use of physical and numerical models which have been adapted for the specific conditions of the project site are recommended for detailed design.

ACKNOWLEDGEMENTS

Through the various projects and monitoring programs many have contributed to this study. In particular, the work of the United States Army Engineers Districts at Buffalo and Baltimore, the state of Ohio Department of Natural Resources, and the state of Louisiana Geological Survey are recognized for their initiative, not only for using segmented breakwater systems, but also for establishing monitoring programs to learn from these installations. Mr. Clifford L. Truitt, Mr. Thomas W. Richardson, and Dr. Nicholas C. Kraus contributed through helpful discussions during the development of this paper. This study was conducted under the work unit "Evaluation of Navigation and Shore Protection Structures" of the Coastal Structures, Evaluation, and Design Research Program of the United States Army Engineers. Permission was granted by the Chief of Engineers to publish this information.

REFERENCES

Bender, T. A., 1985, "Lakeshore Park, Ashtabula, Ohio, Segmented Offshore Breakwater Project," in Proceedings of 42nd Meeting of the Coastal Engineering Research Board, R. Whalin, editor, U.S. Army Engineer Waterways Experiment Station, p 135-141.

Bishop, C. T., 1982, "A Review of Shore Protection by Headland Control," Study No. 352. National Water Research Institute, Canada Center for Inland Waters.

Dally, W. R. and Pope, J., 1986, "Detached Breakwaters for Shore Protection," Technical Report CERC-86-1, U.S. Army Engineer Waterways Experiment Station, Vicksburg, MS, 62 p.

Dean, J. L., Pope, J., and Fulford, E., 1986, "The Use of Segmented Detached Breakwaters to Protect Cohesive Shores: Colonial Beach, VA." Proceedings, Symposium on Cohesive Shores, May 5-7, 1986, Burlington, Ontario, National Research Council, Ottawa, Canada, p 292-308.

Gorecki, R., 1985, "Evaluation of Presque Isle Offshore Breakwaters for Beach Stabilization," in Proceedings of 42nd Meeting of the Coastal Engineering Research Board, R. Whalin, editor, U.S. Army Engineers Waterways Experiment Station, Vicksburg, MS, p. 83-122.

Hanson, H. and Kraus, N. C. (in preparation), "Generalized Shoreline Simulation Systems - Report 1: GENESIS - A Shoreline Change Numerical Model for Engineering Use." CERC Draft Technical Report, U.S. Army Waterways Experiment Station, Vicksburg, MS.

Lesnick, J. R., 1979, "An Annotated Bibliography on Detached Breakwaters and Artificial Headlands," CERC Miscellaneous Report 79-1, U.S. Army Engineer Waterways Experiment Station, Vicksburg, MS.

Magoon, O. T., 1976, "Offshore Breakwaters at Winthrop Beach, Massachusetts," Shore and Beach, Vol 44, No. 3, Oct 1976, p 34.

Nakashima, L. D., Pope, J., Mossa, J., and Dean, J. L. (in press), "Performance Evaluation of a Segmented Breakwater System, Holly Beach, Louisiana." Coastal Sediments '87, American Society of Civil Engineers.

Pope, J. and Gorecki, R. G., 1982, "Geologic and Engineering History of Presque Isle Penninsula, PA," Field Trip Guidebook for New York State Geological Association 54th Annual Meeting, p 183-216.

Pope, J. and Rowen, D. D., 1983, "Breakwaters for Beach Protection at Lorain, OH," Proceedings of Coastal Structures '83, American Society of Civil Engineers, p 753-768.

Pope, J., 1985, "Segmented Offshore Breakwaters: An Alternative for Beach Erosion Control," Proceedings of the Ninth Annual Conference of the Coastal Society, 14-17 October 1984; The Coastal Society, Bethesda, MD, (also in Shore and Beach, Vol 54, No 4, October 1986, p 3-6.

Silvester, R. and Ho, S., 1972, "Use of Crenulate Shaped Bays to Stabilize Coasts," Proceedings of the Thirteenth Conference on Coastal Engineering, American Society of Civil Engineers, Vol 1, pp 1347-1365.

Toyoshima, O., 1972, Coastal Engineering for Practicing Engineers and Beach Erosion, Morikita Publishing Co., Tokyo, Japan, 320 pp.

Walker, J. R., Clark, D., and Pope, J. 1981, "A Detached Breakwater System for Beach Projection," Proceedings of Seventeenth Coastal Engineering Conference, American Society of Civil Engineers, Vol 2, pp 1968-1987.

CHAPTER 159

WAVE FORCE AND MOVEMENT CALCULATIONS FOR A FLEXIBLE OCEAN OUTFALL PIPELINE

J D POS[1], K S RUSSELL[2] and J A ZWAMBORN[3]

ABSTRACT

The design process for the calculation of wave forces and movements for a flexible (plastic) ocean outfall is described. The design procedure is illustrated using a case study of the design of two High Density Polyethylene (HDPE) pipelines of 0,9 m and 1,0 m OD (4 290 m and 5 450 m long) constructed at Richards Bay, South Africa, to dispose of dense and buoyant effluent respectively.

The pipeline anchor weights are based on the 1 in 1 year wave forces on the pipeline, implying that the pipeline is allowed to move during its design life. Special star anchor weights are used which keep the pipe clear of the bed while maintaining the stability of the pipeline.

Friction tests were undertaken with a section of pipeline and two star weights, above water on concrete and sand and below water on sand, to determine realistic friction coefficients for the pipeline design. The results of these tests are summarised in this paper. It was found that the mean friction coefficient for submerged star weights on sand was 0,75.

The movements of sections of the 0,9 m OD pipeline were calculated using a finite difference computer programme developed by Prof I Larsen and the results are summarised in the paper. It was found that movements of 1 to 2 m could occur under design wave conditions (50 to 100 year waves) and these were considered acceptable provided that the pipeline was not obstructed by rock outcrops.

1. INTRODUCTION

Two High Density Polyethylene (HDPE) pipelines of 0,9 m and 1,0 m OD have been constructed at Richards Bay, South Africa, (160 km North of Durban) to dispose of dense and buoyant effluent respectively. The dense and buoyant effluent pipelines are 4 290 m and 5 450 m long (measured from the pump station) and discharge at depths of 24 m and 29 m respectively. The dense effluent consists primarily of waste gypsum from a fertiliser plant while the waste from a large paper pulp mill accounts for the bulk of the buoyant effluent.

1 Research Engineer, Maritime Structures Division, National Research Institute for Oceanology, CSIR, Stellenbosch, South Africa.

2 Deputy Director, National Research Institute for Oceanology, CSIR, Stellenbosch, South Africa

3 Head, Maritime Structures Division, National Research Institute for Oceanology, CSIR, Stellenbosch, South Africa.

During the initial design phase NRIO was involved with the site investigations and the effluent dilution calculations. When the contract went out to tender, flexible HDPE pipelines were proposed and subsequently constructed. These pipelines were originally designed using the Scandinavian Design Procedure (SDP) for flexible pipelines which was based on a large amount of experience with flexible pipelines in the Scandinavian countries. Since previous pipeline experience in South Africa was with rigid concrete or steel pipelines, NRIO reviewed the flexible pipeline design procedure. NRIO was then commissioned to check the "as built" design of the Richards Bay outfall marine pipelines. To do so, the design wave conditions, wave forces and consequently the required weighting along the pipelines were calculated. Friction tests were carried out to determine realistic friction coefficients and the expected movements of various sections of the pipelines were determined.

2. WAVE FORCE CALCULATIONS

2.1 The Scandinavian Design Procedure (SDP)

The forces on the pipelines and the weights of the anchor blocks were calculated in accordance with the SDP. Firstly, it should be noted that there is no "design code" for flexible pipelines. Present design is based on experience gained in Scandinavia over the past 20 years (Janson, 1974, 1978; Janson and Larsen, 1979; Björkland, 1983).

The "design procedure" should include the following steps:

i) The choice of HDPE or PP (Polypropylene) material type is dependant on the effluent temperature.

ii) Pipe wall thickness is determined to ensure that stresses due to internal pressure do not exceed a given value which depends on material, temperature and service life as well as adequate safety against buckling due to external and internal loads.

iii) **Assuming** a friction factor f = 1 stability against sliding requires:

$$f(W - F_L) \geq F_H \qquad (1)$$

where: W = submerged anchor weights

F_L = lift force

F_H = horizontal force (maximum combined).

Thus for $F_L = 0$ (pipe well clear of the bed) it follows:

$$W \geq F_H$$

or the anchor weight is equal to (or greater than) the horizontal force. If f = 1 and square or star-shaped anchor blocks are used the safety against overturning of loose anchor blocks is the same as the safety against sliding.

iv) It is accepted that the pipe may move once or twice a year. This means that, say, the once-a-year occurring **maximum** wave heights must be used to determine the forces on the pipe, that is,

$H_{max} \simeq 2\ H_{mo}$, where H_{mo} is the characteristic wave height based on six-hourly records with an occurrence of once a year.

v) In determining the wave forces it is assumed that the pipe will always be clear of the bottom (resting on the anchor blocks which protrude usually more than D/4 from the pipe, where D is the pipe diameter). If the anchor blocks were to sink into the sea bottom because of local scour, a lift force would develop which would increase at smaller pipe clearances. If the lift force exceeded the anchor weight, the pipe would become buoyant and would lift off the bottom until the vertical forces found a new equilibrium, re-establishing a clearance. Deposition of sand beneath the pipe is unlikely because of increased water velocity and extra turbulence in the area. If it did happen the same lifting process would occur. If the sea bottom were to be raised in the area by general accretion, the pipe would be buried and the wave forces reduced accordingly.

vi) Pipe force calculations may be based on the simplified formulae and refraction graphs contained in Janson (1974) if more detailed information is not available. However, more reliable results can be obtained by using a higher-order wave theory in the shallower water and local wave conditions or wave conditions converted by actual refraction diagrams to the site, taking into account depth-limiting conditions. This information is then fed into the basic Morison equation.

For the SDP the horizontal (parallel to the bed) wave forces on a pipeline are calculated using the Morison equation. Based on the assumption of minimum (D/4) clearance before horizontal motion can take place, the following force coefficients are used:

$C_M = 2$ (inertial/added mass coefficient)

$C_D = 0,7$ ($C_D = 0,33$ is the original SDP value which has been in use for almost 20 years. In view of the new rules of Norske Veritas for oil and gas pipelines, which may be somewhat conservative, and the tests of Sarpkaya, a value of 0,7 was used in these studies; Larsen, 1984)

$C_L = 0$ (lift coefficient).

vii) Knowing the anchor blocks and the pipe characteristics, it must be ensured that the spacing between the blocks will be such that the permissible bending will not be exceeded (Europlast, 1984). It should then be determined whether, for the design life of the pipe, for example 50 years, the total movement and resulting maximum bending moments and strains will be acceptable, that is, movement should preferably not exceed a few metres, short-term strain should not exceed **1,5 per cent** and long-term deformation after 50 years must not exceed 6 per cent (Janson and Larsen, 1979 and Europlast, 1984). Recent data (private communication Prof Larsen) indicates that short-term strains $\leq$ 2,5 per cent would be acceptable. Further details of the SDP are given by Pos (1986).

For the Richards Bay pipelines star-shaped anchor weights were used. It was hypothesised that these weights would provide greater

resistance against sliding than the more conventional square anchor weights. Figure 1 shows typical star weights as installed on a section of the Richards Bay pipelines.

Figure 1: Typical star weights, Richards Bay HDPE pipeline

2.2 Calculation of Anchor Block Weights

The SDP states that the weighting required at a particular location along a pipeline is equivalent to the maximum horizontal 1:1 year wave force expected to occur at that position. The maximum horizontal wave forces along the 0,9 m and 1,0 m marine pipelines, for 1:1 year design waves were calculated using the programe "PIPE" installed on the CSIR's CDC computer. The above programme uses the Vocoidal wave theory (Swart and Laubser, 1978) to calculate the horizontal velocities and accelerations and the Morison equation to calculate the maximum combined horizontal wave forces on the marine pipelines.

The 1:1 year maximum horizontal wave loadings along the 0,9 m OD Richards Bay outfall marine pipeline are given in Table 1 as a sample of the results*. For each chainage position the following data are given in Table 1:

(a) The water depth, wave height, angle of incidence, maximum crest bottom velocity, maximum trough bottom velocity, maximum absolute bottom acceleration (12 s period waves were used throughout).

(b) The maximum drag and inertial and combined drag and inertial (incorporating phase effects) horizontal force (kN/m).

(c) The above horizontal force expressed as a percentage of the weight of water (per m length) displaced by the pipe.

*Details regarding the design wave conditions used for the force calculations are given in CSIR (1985).

(d) The installed weighting.

Comparison of the last two columns in Table 1 shows that except for the first section of the pipeline, the installed weights are larger than those calculated using the SDP, which requires that the submerged anchor weight be equal to the maximum horizontal force for the 1:1 year wave condition (if it is assumed that for a pipe mounted D/4 above the bed inertial, drag and lift coefficients of 2, 0,7 and 0 respectively apply and a friction coefficient of 1,0 was used for these calculations). In a subsequent study Pos (1986) has suggested that based on the work of Sarpkaya (1977) and DNV (1981) inertial, drag and lift coefficients of 2, 0,8 and 0,4 would be more appropriate. The lift force (in phase with the drag force) particularly will have an effect on the pipeline stability in those regions where the drag and inertial forces are of similar magnitude, such as the diffuser sections.

Table 1: 1:1 Year maximum horizontal wave loading along the 0,9 m OD pipeline

Chainages along the pipe	Water depth (m)	Wave height (m)	Angle of incidence (degrees)	Maximum crest bottom velocity (m/s)	Maximum through bottom velocity (m/s)	Maximum absolute bottom accel. (m/s^2)	Maximum inertial force (kN/m)	Maximum drag force (kN/m)	Max. combined drag and inertial horizontal force (kN/m)	Horizontal force expressed as a percentage of displ. weight	Installed weights expressed as a percentage of displ. weight
Ch 1000	8,5	6,6	48	3,29	-1,23	3,98	3,85	1,93	4,03	63,0	50,0
Ch 1250	12,0	8,9	50	3,61	-1,68	3,83	3,82	2,47	3,99	62,4	50,1
Ch 1500	13,8	8,6	51	3,19	-1,72	2,97	3,01	1,99	3,11	48,7	50,1
Ch 2000	16,7	8,6	52	2,78	-1,86	2,29	2,35	1,55	2,38	37,3	40,1
Ch 2500	18,0	8,6	52	2,64	-1,93	2,08	2,13	1,40	2,15	33,6	40,1
Ch 3000	19,0	8,6	49	2,54	-1,98	1,94	1,91	1,18	1,91	29,9	40,1
Ch 3500	20,0	8,6	49	2,44	-2,04	1,81	1,78	1,10	1,79	27,9	30,8
Ch 4000	21,0	9,3	52	2,53	-2,22	1,89	1,94	1,28	1,95	30,4	30,8
Ch 4290	24,0	10,0	53	2,41	-2,38	1,79	1,86	1,20	1,92	30,0	33,2
Ch 4290 (0,61 m OD)	24,0	10,0	53	2,41	-2,38	1,79	0,91	0,84	1,01	32,1	33,2

Displaced mass of 0,9 m OD pipe = 652,1 kg/m
Displaced mass of 0,61 m OD pipe = 299,6 kg/m

The pipe is assumed to be D/4 m clear of the bed
C_m = 2,0
C_D = 0,7
C_L = 0,0

3. FRICTION TESTS

3.1 Introduction

In order to check the SDP assumption that the friction factor f = 1, it was decided to carry out tests, using a section of the pipeline with associated star weights, to determine realistic friction coefficients for a range of test conditions.

These tests were carried out at Richards Bay on 23 and 24 April 1985 to establish the friction factors associated with the sliding of the concrete star anchor weights, **out of water** over concrete and sand, and **under water** over sand. The above-water friction tests simulated underwater conditions and enabled a range of surfaces from smooth concrete to dry sand to be monitored visually and photographically. Full details regarding the test configurations, procedures and results are given in CSIR (1985), while the main findings are summarised below.

3.2 Test Configurations

The test configuration used for the above-water concrete and sand friction tests is shown in Figure 2. The test rig consisted of a 3 m section of 900 mm OD (40 mm wall thickness) High Density Polyethylene (HDPE) pipe to which was attached two half star weights spaced 1 m apart symmetrical about the centre of the length of pipe. The two half star weights were clamped to the pipe using two steel clamps. The reason for using the half star weight test rig for all the above-water friction tests is that its weight above water is approximately equal to the submerged weight of the whole star weight rig. It was thus proposed that this test arrangement could be used to simulate, above water, the submerged sliding behaviour of a section of the pipeline.

The test configuration used for the underwater friction tests was the same as that used for the above-water tests except that now full star weights were used. For both configurations the pulling force was applied at the level of the pipe axis.

Figure 2: Above-water friction test configuration

3.3 Test Procedures

The above-water friction test procedures both for the concrete and sand friction tests were virtually identical. The ends of the half loop of chain was shackled to the steel clamps of the test configuration as shown in Figure 2. This was then connected to the pulling cable of a mobile crane via a load shackle. A continuous load (in the form of milli-volts from the strain gauges) versus time plot was obtained for each test via a pen recorder interfaced with the load shackle amplifier. The milli-volt versus time plots were converted into load (in kN) versus time plots using a predetermined calibration curve.

To determine the displacement of the star weights with time two survey staffs were placed on the ground, parallel to the pulling cable, with the beginning of each staff adjacent to the toe of a star weight. For

the tests on concrete the staffs were aligned with the front toes (closest to the crane) of the weights (see Figure 2), while for the above-water sand tests the staffs were aligned with the back toes of the weights. A stop-watch was started at the beginning of the test and the time noted at 0,1 m displacement increments as each weight displaced relative to its staff.

For the tests on concrete, consecutive tests were merely started with the test rig in the position corresponding to the end of the previous test. For the tests on sand, however, after each test, the test rig was lifted and positioned on a section of undisturbed sand before the next test was started.

The underwater friction tests were performed in a large flooded pit with a sand bed using the test configuration described previously. The crane cable was connected to the pulling cable of the test configuration via the load shackle. As for the above-water tests, a continuous load versus time plot was obtained for each test via the load shackle and its peripherals. After each test the test rig was lifted and repositioned in an undisturbed section of the basin.

To determine the displacement of the test rig with time a survey staff was placed on the ground, parallel to the pulling cable, with the beginning of the staff adjacent to a chalk mark on the load shackle. A stop-watch was started at the beginning of the test and the time noted at 0,1 m displacement increments, as the load shackle displaced relative to the staff. A note was also made of the time at which the star weights had stopped displacing laterally and were only tilting.

3.4 Friction Coefficient Calculation Procedure

The friction coefficients were calculated using Equation 1. Setting the lift force F_L to zero and assuming that the pipe is on the point of motion, Equation 1 reduces to:

$$Wf = F_H \tag{2}$$

and thus

$$f = \frac{F_H}{W} \tag{3}$$

where, in this case,

F_H = horizontal pulling force

W = weight of test rig

f = friction coefficient

3.5 Above Water Friction Test Results

The friction test results for smooth (surface roughness $\pm$ 1 mm) and rough (surface roughness $\pm$ 5 mm) concrete are summarised in Tables 2 and 3 respectively. The movement of the anchor weights across the concrete consisted of a number of individual sliding events. Each event consisted of a load build-up phase during which the star weights

tilted over slightly and a sliding phase in which the load was released. The mean peak pulling force (associated with the initiation of sliding) of individual sliding events and the corresponding friction coefficients (calculated by means of Equation 3) for these tests are summarized in Tables 2 and 3. The test mean friction coefficients are 0,82 and 0,76 for the smooth and the rough concrete tests respectively.

Table 2: Friction Coefficients for Smooth Concrete

Test No.	Mean peak pulling force of individual sliding events (kN)	Mean friction coefficient
2-1	20,2	0,83
2-2	20,6	0,84
2-3	19,1	0,78
Test mean	20,0	0,82

Table 3: Friction Coefficients for Rough Concrete

Test No.	Mean peak pulling force of individual sliding events (kN)	Mean friction coefficient
3-1	17,9	0,73
3-2	18,8	0,77
3-3	18,7	0,76
Test mean	18,5	0,76

The above-water wet and dry sand friction test results are summarised in Tables 4 and 5 respectively. In each table the mean friction coefficients for initial movement (F_{init}), for the displacement range 0 - 0,2 m ($f_{0-0,2}$), 0,2 - 0,4 m ($f_{0,2-0,4}$), 0,4 - 0,6 m ($f_{0,4-0,6}$), >0,6 m, ($f_{>0,6}$), and for the pure tilting phase (f_{tilt}) are given. It is evident that there are three distinct phases during the movement of the anchor weights across the sand, namely:

(i) an initial pure sliding phase;

(ii) a sliding and tilting phase in which the weights progressively slide less and tilt more;

(iii) a pure tilting phase in which the weights tilt over with little or no further forward displacement.

Table 4: Friction Coefficients for Wet Sand

Test No.	f_{init}	$f_{0-0,2}$	$f_{0,2-0,4}$	$f_{0,4-0,6}$	$f_{>0,6}$	f_{tilt}
4-3	0,24	0,31	0,58	0,71	-	0,84
4-4	0,30	0,45	0,66	0,73	-	0,85
4-5	0,34	0,50	0,70	0,82	-	0,93
Test mean	0,29	0,42	0,65	0,75	-	0,87

Table 5: Friction Coefficients for Dry Sand

Test No.	f_{init}	$f_{0-0,2}$	$f_{0,2-0,4}$	$f_{0,4-0,6}$	$f_{>0,6}$	f_{tilt}
5-1	0,13	0,32	0,59	0,75	0,81	0,86
5-2	0,13	0,34	0,60	0,74	-	0,91
5-3	0,11	0,41	0,68	0,84	0,89	0,94
Test mean	0,12	0,36	0,62	0,78	0,85	0,90

3.6 Underwater friction test results

The underwater friction test results are summarised in Table 6. As for the above water tests on sand, the initial movement and the mean friction coefficients for the previously described displacement ranges are given in this table. A sample force and displacement plot is shown in Figure 3. From this plot it is evident that, as for the above water friction tests on sand, the displacement of the submerged anchor weights over the sand bed again incorporate the three movement phases of pure sliding, combined sliding and tilting and pure tilting.

Table 6: Friction Coefficients for Underwater Tests

Test No.	f_{init}	$f_{0-0,2}$	$f_{0,2-0,4}$	$f_{0,4-0,6}$	$f_{>0,6}$	f_{tilt}
6-1	0,45	0,56	0,72	0,86	0,94	0,87
6-2	0,50	0,51	0,65	0,71	0,76	0,70
6-3	0,37	0,51	0,69	0,79	-	0,80
Test mean	0,44	0,53	0,69	0,79	0,85	0,79

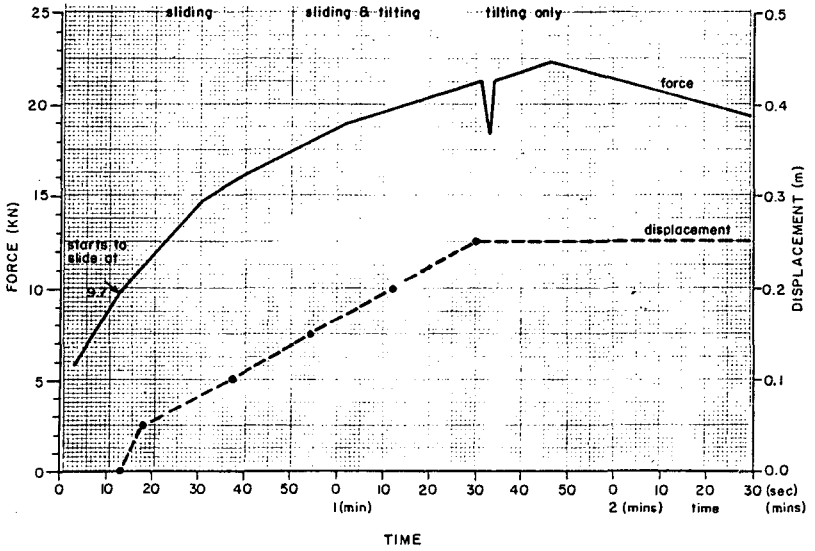

Figure 3: Force and displacement-versus-time plot for underwater friction test No 6-3

3.7 Conclusions

For the smooth and rough concrete tests the mean friction coefficients were 0,82 and 0,76 respectively. The rough concrete friction coefficient of 0,76 would seem the most appropriate for the case for example, of star weights resting on a flat rock reef. This coefficient is significantly less than the SDP assumed friction coefficient of 1. The movement of the anchor weights over such a rock surface will probably consist of a series of sliding events.

The wet sand tests, the dry sand tests and the underwater tests all showed that the movement of the star weights across sand consisted of an initial pure sliding phase, followed by a combined sliding and tilting phase and ended with a pure tilting phase.

Since the pure sliding phase was associated with the digging in of the legs of the star weights, it is thought that the most realistic values to adopt are the $f_{0,2-0,4}$ and $f_{0,4-0,6}$ values. The $f_{>0,6}$ and f_{tilt} values are not thought to be realistic as, due to the high torsional resistance of the pipeline, it is likely that the weights will rotate on the pipe rather than tilt (through any appreciable angle) monolithically with the pipe.

For the above-water tests on sand the wet sand $f_{0,2-0,4}$ and $f_{0,4-0,6}$ values of 0,65 and 0,75 (see Table 4) are thought to be the most representative. For the underwater tests the $f_{0,2-0,4}$ and $f_{0,4-0,6}$ values of 0,69 and 0,79 (Table 6) are thought to be the most appropriate for design purposes.

Based on these data it is suggested that for a sandy sea bottom a value of 0,75 be used, which is significantly lower than the value of 1,0 used when designing the pipeline according to the SDP. It is interesting to note that Lambrakos (1985) also obtained an average maximum friction coefficient of 0,75 for the lateral sliding of a 0,61 m OD steel pipe (with no anchor weights) on a sandy sea bed.

4. PIPELINE MOVEMENT CALCULATIONS

Because the friction tests had shown that friction coefficients could be less than 1, the expected (design wave) movements of the pipelines were calculated for the most critical sections, using a pipeline movement program developed by Prof Larsen (Abbott, Larsen and Verwey, 1977) and modified to incorporate the Vocoidal wave theory (Swart and Laubser, 1978).

For each wave-loading condition investigated a 380 m section of the 0,9 m OD pipeline was modelled using the program. The pipe section was modelled using 39 nodes, that is, with a 10 m spacing between nodes. The time step used throughout was 0,2 s. The relevant design wave data and the results are summarized in Table 7. For each chainage position listed the following data are given:

1. The return period of the design wave conditions used;

2. The MSL water depth, the maximum wave height and the mean angle of incidence of the waves relative to the pipeline axis (12 s period waves were used for all the conditions tested).

3. The pipe OD; for the transition between the pipe and the diffuser runs were done using both 0,9 m and 0,61 m OD pipes;

4. The friction coefficient used (0,5; 0,75 or 1);

5. The installed anchor weighting per metre, expressed as a percentage of the displaced weight;

6. The maximum transient excursion and the maximum residual displacement for one wave cycle (measured in the central 140 m portion of the pipeline). As an example the displacement plot for chainage 4290 for a 1:50 year wave and a relatively low friction factor of 0,5 is shown in Figure 4.

For a friction coefficient of 1 the results showed expected lateral movements of 0,07 to 0,19 m for the 1:1; 0,26 to 0,55 m for the 1:10; 0,65 to 1,09 m for the 1:50 and 0,87 to 1,34 m for the 1:100 year design wave. For a more realistic friction coefficient of 0,75, these movements were approximately double. The total expected movements for design storms can be obtained by accumulating the movements for individual wave heights.

Table 7: Lateral displacements along sections of the 0,9 m OD pipeline

Chainage	Return period (yesrs)	MSL depth (m)	Maximum wave height (m)	Mean angle of incidence (degrees)	Pipe OD (m)	Friction coeffi-cient	Installed weighting expressed as a % of displaced weight	Absolute Displacement	
								Maximum excursion (m)	Maximum residual displace-ment (m)
1 000	1:1	8,5	6,6	48	0,90	1,0	50,0	0,12	0,05
1 250	1:1	12,0	8,9	50	0,90	1,0	50,1	0,19	0,11
1 250	1:10	12,0	9,5	50	0,90	1,0	50,1	0,30	0,18
2 000	1:100	16,7	12,5	52	0,90	1,0	40,1	1,02	0,51
3 500	1:1	20,0	8,6	49	0,90	1,0	30,8	0,07	0,01
3 500	1:10	20,0	10,6	49	0,90	1,0	30,8	0,26	0,05
3 500	1:50	20,0	11,9	49	0,90	1,0	30,8	0,65	0,18
3 500	1:100	20,0	12,5	49	0,90	1,0	30,8	0,87	0,26
4 000	1:1	21,0	9,3	52	0,90	1,0	30,8	0,09	0,02
4 000	1:10	21,0	11,5	52	0,90	1,0	30,8	0,55	0,09
4 000	1:50	21,0	12,9	52	0,90	1,0	30,8	1,09	0,18
4 000	1:50	21,0	12,9	52	0,90	0,75	30,8	1,85	0,20
4 000	1:100	21,0	13,5	52	0,90	1,0	30,8	1,34	0,17
4 290	1:1	24,0	10,0	53	0,61	1,0	33,2	0,07	0,06
4 290	1:10	24,0	12,3	53	0,61	1,0	33,2	0,39	0,35
4 290	1:50	24,0	13,8	53	0,61	1,0	33,2	0,76	0,74
4 290	1:50	24,0	13,8	53	0,61	0,75	33,2	1,30	1,25
4 290	1:50	24,0	13,8	53	0,61	0,5	33,2	2,01	1,84
4 290	1:100	24,0	14,5	53	0,61	1,0	33,2	0,98	0,96

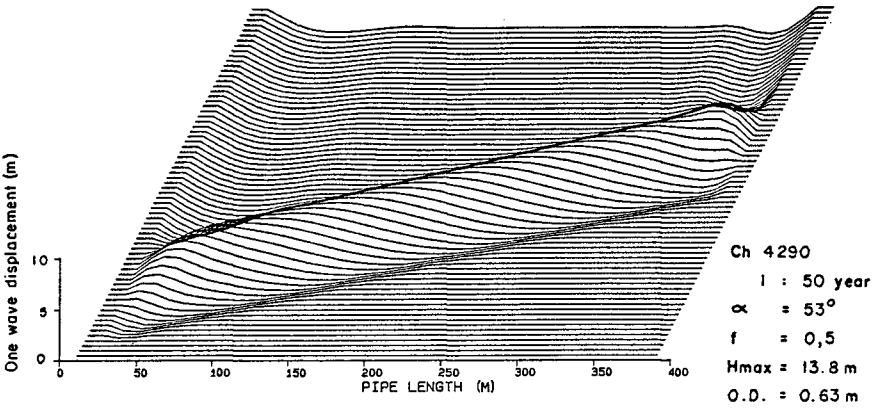

Figure 4: Movement of Pipeline section under Single Design Wave

5. CONCLUSIONS

For a proper pipeline design reliable wave height, period and direction data are needed. For the design of the Richards Bay pipelines a detailed wave refraction analysis was combined with nearshore (Waverider) wave height measurements to determine the design wave conditions along the pipeline route. The choice of the design wave conditions for calculations of the anchor weights depends on the acceptable pipeline movements. For flexible pipelines designed according to the SDP the anchor weighting is based on a 1 in 1 year maximum wave height.

To determine the weighting, the bed kinematics must be calculated using a suitable higher order wave theory and the forces on the pipeline must be calculated using a suitable wave force theory. For the Richards Bay pipelines the bed kinematics were calculated using the Vocoidal wave theory and the wave forces were calculated using the Morison equation.

Pipeline movements should be estimated for the design life of the pipeline using a numerical model. The movements will depend largely on the actual weighting and the resistance of the pipeline with anchors to movement (friction). For the Richards Bay pipelines the movements were calculated using a finite difference model developed by Prof Larsen (Abbot, Larsen and Verwey).

Since no data was available on the friction factors for the Richards Bay pipelines with the star weights and because the assumption of $f = 1$ appeared optimistic, full scale friction tests were done to determine the friction factor for star weights on both hard surfaces ("rock") and on sand. The results showed that the friction factors fell predominantly in the range $f = 0,7$ to $0,8$ and that a value of $f = 0,75$ would seem generally applicable. However, initial friction factors (small movements) on sand can be as low as $f_{0-0,2} = 0,4$ to $0,5$.

Using the Vocoidal wave theory, $f = 0,75$ and the actual weighting, movements were found to range from 1,3 to 1,9 m for 1 in 50 year maximum waves. This movement was considered acceptable except for two rocky reef areas where additional weighting was added to those sections of the pipelines passing throught these reef areas.

It became clear from these studies that if movement of the pipeline has to be limited to small values, eg. 0,1 to 0,2 m, as in the case where an HDPE pipeline traverses rocky areas with pinacles, the required weighting may become so large that the pipeline with the anchor weights attached cannot be floated out during laying, thereby loosing much of the advantages of using HDPE piping. It must therefore be concluded that the flexible pipeline concept, which allows acceptable movements of the pipeline under design wave conditions, is particularly suitable for locations where the sea bed consists predominantly of sand.

ACKNOWLEDGEMENT

We would like to thank the Mhlatuze Water Board and consulting engineers Campbell, Bernstein and Irving for their permission to publish this paper. We would also like to thank Mr J D P Scholtz for his help with the friction tests.

REFERENCES

ABBOTT, M B, LARSEN, I and VERWEY, A (1977). Computer control of pipe laying procedure. Proc, 17th Congress International Association for Hydraulic Research, Vol. 4, pp 501-508.

BJORKLUND, I (1983). Experience of using large-diameter polypropylene pipes for the transport of pulp-mill effluent. Europipe 1983 Conference, Basle, Switzerland, paper 7.

CSIR (1985). Richards Bay Ocean Outfalls, Engineering design aspects, Wave Forces and Movements, CSIR Report C/SEA 8541, November.

DNV (1981). Det Norske Veritas. Rules for Submarine Pipeline Systems, 1981 edition.

EUROPLAST (1984). Buckling calculations for HDPE pipes (etc). W N series, West Germany.

JANSON, L E (1974). Plastic pipe in sanitary engineering, New York.

JANSON, L E and LARSEN, I (1979). Flexible submarine outfall systems. VBB Special Report 07:79.2, Stockholm.

LAMBRAKOS, K F (1985). Marine pipeline soil friction coefficients from in-situ testing. Ocean Engineering, Vol. 12, No. 2, pp 131-150.

LARSEN, I (1984). Wave force calculation and anchorage design for a flexible pipeline installed upon the seabed. Royal Institute of Technology, Stockholm (draft report also included in Pos, 1986).

POS J D (1986). Force calculation and anchorage for a flexible pipeline on the sea-bed; Preliminary reports and discussions. NRIO Memorandum 8610, April.

SARPKAYA, T (1977). In line and traverse forces on cylinders near a wall in oscillatory flow at high Reynolds numbers. Proc. 1977 Offshore Technology Conference, OTC Paper No 2898, Houston.

SWART, D H and LOUBSER, C C (1978). Vocoidal theory for all non-breaking waves. Proc. 16th International conference on Coastal Engineering. Hamburg, 1978, Vol. 1, pp 467-486.

CHAPTER 161

STATISTICAL INVESTIGATIONS ON DIKE FAILURE

Ing. P. Roelse[1] and ir. W.T. Bakker[2]

1. ABSTRACT

For the probabilistic design of dikes it is necessary to know the failure probability of the dike as function of the load of the dike (wave attack).

This paper reports on the statistical analysis of the failure behaviour of the dikes around the Eastern Scheldt after the storm surge on February 1, 1953.

2. INTRODUCTION AND BACKGROUND

In 1975 the political decision was made in The Netherlands to construct a storm-surge barrier in the Eastern Scheldt instead of closing off the area completely (Fig. 1).
This lead to the consequence, that the safety of the surrounding area with respect to storm surges would be attained 5 years later than originally anticipated; this because new designs had to be made and because the construction would be more intricate and time-consuming.
Thus, the additional decision was made, that the dikes around the Scheldt should be partially enheightened, in order to stand a storm surge with a probability of occurrence of 1/500 per year.
To compare: Now the storm-surge barrier is completed (1986) the whole area should be safe with respect to storm surges occurring with a frequency of 1/4000 per year.
As a consequence, in a short time it had to be decided, whether for each dike section along a total stretch of about 140 km the section should be enheightened or not.
Figure 2 shows an example of the kind of dikes; Figure 3 shows examples of cross sections, before and after the enheightening. Many of the dikes originally had retaining walls on top (Fig. 4, 5), sometimes with a road landward of it (Fig. 6). Mostly the dikes consisted of clay. The final construction was a sand dike with a clay cover.
As the advice had to be given rather quickly, the design height was determined in a simple way, described in chapter 4.

This paper gives an analysis of the method, showing as well the advantages as its limitations.
Using the method, it is essential to know: the probability of failure as function of the "lack of crest height", i.e., the difference between the real height of the dike and the design height.

1) Project Engineer, Rijkswaterstaat, Tidal Waters Department, Section Middelburg.
2) Scientific Coördinator Coastal Research, Tidal Waters Department Rijkswaterstaat; Principal Scientific Officer Delft Univ. of Techn.

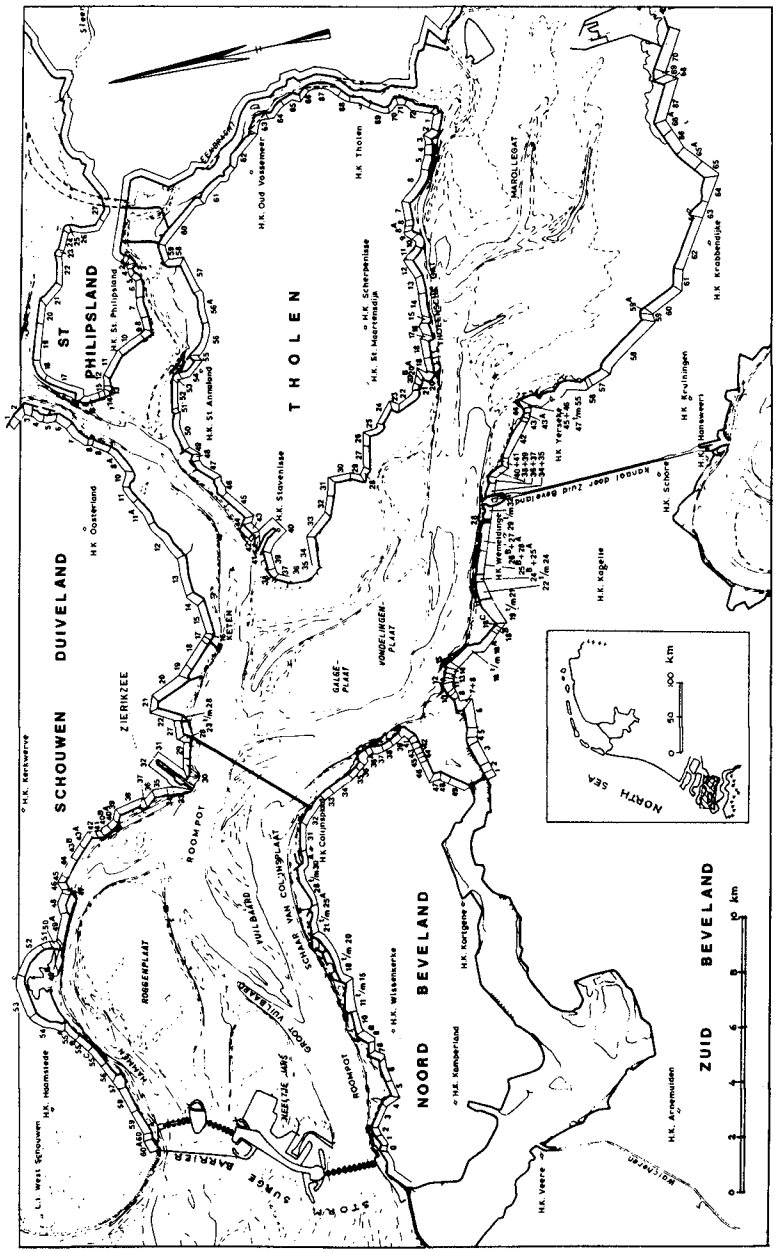

Fig. 1. Situation Eastern Scheldt

In order to get an impression of this function, it has been calculated what should have been (according to the same method) the dike height during the surge of 1953, when many dikes collapsed and 1835 people were killed. The number of dike segments which failed in 1953 was compared with the total number of dike segments having the same crest height deficiency.
In the same way, dikes with different characteristics (with or without return wall, steeper or flatter inner slopes etc.) can be compared.
Of course, the method as used only gives a rough indication.
One might question, whether the lack of crest height (as calculated in the way, given in chapter 4) is decisive for the failure probability.
In the first place, in order to give the failure probability some meaning, the dike considered should be more or less uniform with respect to the construction. Therefore, the dikes have been classified into various categories (chapter 3).
In the second place, dikes with the same lack of crest height should have the same wave attack.
Chapter 6 deals about this matter; it has to be investigated, whether the same lack of crest height implies always the same amount of overtopping. As the design crest height is determined as well by surge level as by wave run-up this is not self-evident.
In 1953, practically all dike failures were caused by wave overtopping, resulting in a failure of the inner slope. Therefore, data as given here only applies for this kind of failure mechanism.

A second question rises, how the extrapolate the results. For Dutch circumstances, one possibly might see the probabilities found as a pessimistic estimate, as the improved dikes have a much flatter inner slope than the former ones; on the other hand, a modern dike is a clay-covered sand dike, where the former dikes consisted of clay.
Therefore, at present a more sophisticated method of probabilistic design is developed in The Netherlands (Bakker & Vrijling, 1980).
How imperfect the present results may be, it is considered useful publishing these data, as these may give an impression of the strength of dikes of a kind which may occur also in other parts of the world.
A warning should be given, that the data refer to the failure probability of dike sections of a length of the order of some hundreds of metres. The failure probability of a dike ring consisting of many sections will be much higher, as a chain is a strong as its weakest link (Bakker & Vrijling, 1980 and Chapter 7).

3. AVAILABLE DATA

Figure 1 shows the investigated area and the various dike sections considered. For 273 dike sections the wave run-up in 1953 could be reproduced in a way described in chapter 4, where the inner slope of the dike in 1953 was known as well. Some (13) dike sections along the area considered had to be omitted because of lack of data.
The dikes were divided into various categories, using the following characteristics:
- with or without return wall;
- with or without road on the crest;
- inner slope flatter than 1:1.5 or not flatter.

Fig. 2 Eastern Scheldt dike (without return wall)

Fig. 4 Eastern Scheldt dike (with return wall)

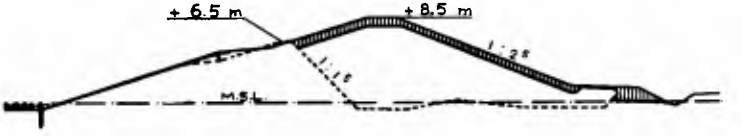

Fig. 3 Cross-section before and after enheightening

Fig. 5 Construction of a returnwall

Fig. 6 Eastern Scheldt dike with return wall and roas behind the crest

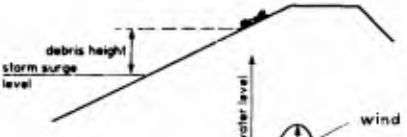

Fig. 7[a] Definition of debris heights

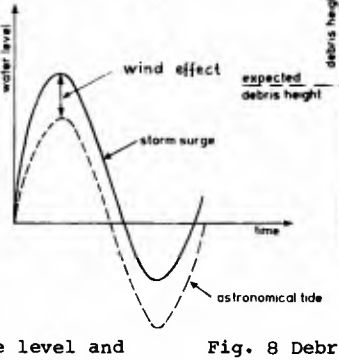

Fig. 7[b] Storm surge level and astronomic tide

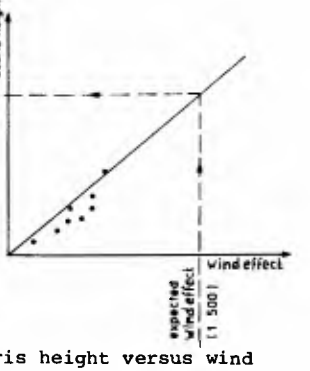

Fig. 8 Debris height versus wind effect

Table 1 shows some characteristics of the dike sections (the dikes mentioned on the second and third line did not have a road on the crest).

Table 1. Characteristics of dike sections.

	without wall		with wall		total	
	total	break-through	total	break-through	total	break-through
road on crest			10	-	10	-
inner slope flatter than 1:1.5	143	17	60	4	203	21
inner slope not flatter than 1:1.5	49	17	11	-	60	17
Total	192	34	81	4	273	38

4. LACK OF CREST HEIGHT

The wave attack, which occurred during the 1953 surge can only be hindcasted by a rough approximation. After many storm surges, before and after 1953, at each dike section along the Eastern Scheldt the level of the debris line has been measured. From extrapolation, the hypothetical height of the debris line after the 1953 storm surge has been derived. This height is hypothetical, since it usually surpasses the crest level of the dike.
The extrapolation has been carried out by plotting for each measured debris height the wave run-up (difference between storm-surge level and debris height) against the wind effect (difference between storm-surge level and astronomical tide)(Fig. 7a, b and 8).

For each dike section, the lack of crest height has been determined, being the difference between the hypothetical debris height in 1953 and the crest level of the dike. Where seawalls were on the dike, the level of the top of the seawall has been taken as crest level (Fig. 9a, b).

In the following, the lack of crest height in 1953 will be denoted by "z".

5. STATISTICAL HANDLING OF DATA

5.1. Dikes without a training wall

The dike sections have been divided into classes with increasing lack of crest height z. The classes have a "band width" of 0.25 m (0 z 0.25 m, 0.25 z 0.50 m, etc.). When x is the number of dike sections in a certain class which break through and n is the number of sections in that class, the probability of break-through x/n has been determined as well as the

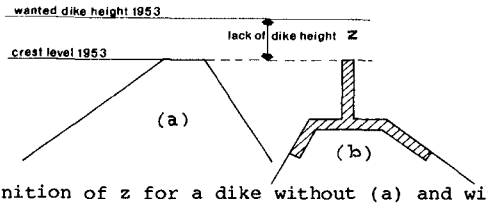

Fig. 9 Definition of z for a dike without (a) and with (b) a return wall

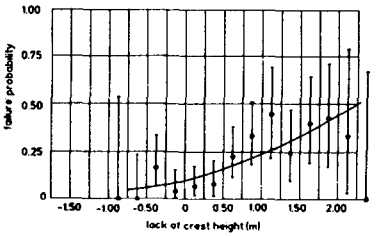

Fig. 10 z versus probability of dike failure (all dikes)

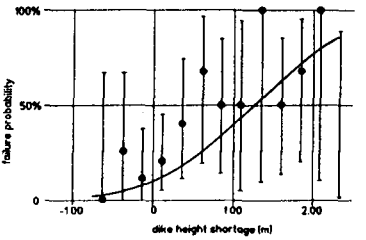

fig. 11 z versus probability of dike failure (dikes with inner slope 1:1.5 or sleeper)

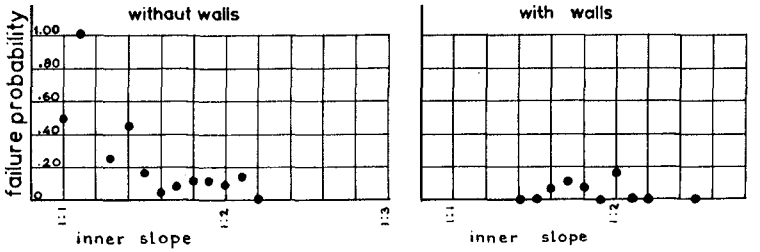

Fig. 12 Effect of slope on failure probability

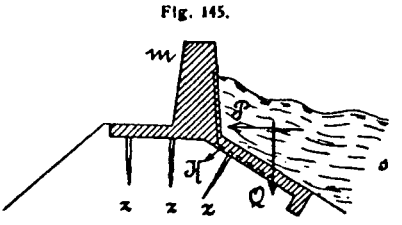

Fig. 13 Performance of return wall according to De Muralt (1913)

confidence interval with a two-sided confidence limit of 20%. Figure 10 shows the relation, valid for all dikes without a training wall. Complete data and elaboration are given by Bakker & Roelse (1981).
The material still offers puzzling results. Even after elimination of a dike section, which collapsed by a second World War gun position, still one finds dike sections with a lack of crest height of 2.25 m which did not collapse. In one of those cases still the dike ring break through at another place (which may have protected the section), but in the other case only a large amount of overflow has been reported. In the cases of break-through with a surplus of crest height either the wave run-up is underestimated, either the crest height overestimated (by reasons, not to be traced after 30 years), either a construction in the dike has been the reason for dike failure. In all cases (a heavy) overtopping has been reported.
Therefore, the results of the following analysis have more the status of "indications" than of "proofs", as correlations found are rather low.
For instance: the correlation between the lack of crest height z and the failure probability appeared to be only 0.35

Where Figure 10 gives z versus probability of dike failure for all dikes, Figure 11 gives the same kind of result for all dikes with an inner slope of 1:15 or steeper.

For the failure probability Pr (failure) a normal distribution has been assumed:

$$\Pr(\text{failure}) = \frac{1}{\sqrt{2\pi}} \int_{-\infty}^{z^*} e^{-u^2} \, du \qquad (1)$$

with

$$z^* = (z - \bar{z})/\sigma \qquad (2)$$

The values of $\bar{z}$ and σ have been determined with an existing statistical analysis, the "probit analysis" (Finney).
The calculations have been carried out by IWIS-TNO (Technical Physical Research).
The following results were found:

Table 2. Magnitude of $\bar{z}$ and σ for dike sections without walls.

Inner slope	$\bar{z}$	σ
1:1.5 or steeper	1.22 m	1.41 m
flatter than 1:1.5	2.69 m	1.73 m
all slopes	2.25 m	1.76 m

From this table it shows, that dikes without walls with a slope of one in 1.5 or steeper react more predictable than dikes with a flatter slope; the probability of failure is much larger. This is also illustrated by Figure 12, which shows the effect of slope on dike failure more into detail.

5.2. Dikes with return walls

Consider now dikes with return walls, of which figure 5 and 6 give a picture. The height of these walls is of the order of 0.5 to 1 m. Figure

13 shows a cross-section and the anticipated action according to the designer de Muralt (1913). The turning moment by the impact of the wave is neutralized by the normal pressure on the basement plate.

No failures were found for the 11 dike sections, having an inner slope of 1:1.5 or steeper; from the 59 dike sections having a slope flatter than 1:1.5, a number of 3 break through.
Now dikes with the same crest height with return walls and without have been compared.

As an example, Table 3 shows the comparison of all dikes (regardless of inner slope) with or without return walls, classified according to crest height deficiency.

Table 3. All dike segments with $z \geq 0$ classified according to crest height deficiency.

class of z		with walls		without walls	
from	to	total	failure	total	failure
0.00	0.25	21	1	29	2
0.25	0.50	13	0	25	2
0.50	0.75	3	0	22	5
0.75	1.00	3	1	18	6
1.00	1.25	2	0	9	4
1.25	1.50	4	1	12	3
1.50	1.75	1	0	10	4
1.75	2.00	1	0	7	3
Total		48	3	132	29

Table 4. All dike segments without roads (inner slope 1:1.5 or steeper) classified according to crest height deficiency.

class of z		with walls		without walls	
from	to	total	failure	total	failure
0.00	0.25	3	0	10	2
0.25	0.50	4	0	5	2
0.50	0.75				
0.75	1.00	1	0	4	2
Total		8	0	19	6

Data at the same line refer to dikes with equal crest height deficiency z, where, as mentioned, in the case of return walls z refers to the upper side of the return wall.

The statement has been tested, whether both groups being compared belong to the same population. Using Cochran's test (cf. Everitt, 1977), a probability of 5.3% was found, that this was the case; therefore with this confidence limit one might conclude that dikes with return walls are significantly stronger.
Using partial datasets (eliminating dikes with roads on the crest and discrimination on inner slopes) it was found with a confidence limit of 3%, that dikes (without roads) with an inner slope 1:1.5 or steeper with a return wall were stronger than dikes with the same value of z without a return wall (Table 4).
However, evaluating these results, one has to keep the low correlation between dike height deficiency and failure probability in mind.

6. RELEVANCE OF THE CREST HEIGHT DEFICIENCY FOR THE LOAD ON THE DIKE

Let H be the mean wave height, surpassed by 50% of the waves. In the case of a Rayleigh distribution of the waves, H equals:

$$H = 0.59\ H_S \tag{3}$$

where H_S is the significant wave height.
From Fig. IV.5.4 from TAW (1972) the following approximating relationship between dimensionless amount of overtopping q_* and dimensionless dike height K_* can be derived (Fig. 14):

$$q_* = 10^{-(K_* - 1{,}5)/5} \tag{4}$$

in which:

$$q_* = 2\pi\sqrt{\frac{\pi}{10}} \cdot \frac{\bar{q}}{\sqrt{gH^3}} \tag{5}$$

Here q is the amount of overtopping per unit of time and per unit of crest width and g the accelaration of gravity.
Furthermore K_* is per definition:

$$K_* = K(\cot\alpha)^{3/2}/H \tag{6}$$

in which K is the crest height above the still water level.

In the range considered the amount of wave overtopping appears to decrease practical negative-exponentially with the crest-level.
Assuming the debris height analogous to the 1%-wave run-up (according to dutch measurements) and assuming the 2% wave run-up equal to 8 $H_S \tan\alpha$, where α is the revetment slope; furthermore assuming the 1% wave run-up 7.5% higher than the 2% wave run-up, from (3) one finds:

$$y_{dh} = N.H \tan\alpha \tag{7}$$

with:

$$N = 14.6 \tag{8}$$

where y_{dh} is the height of the debris above the still-water level.
The dike height deficiency equals:

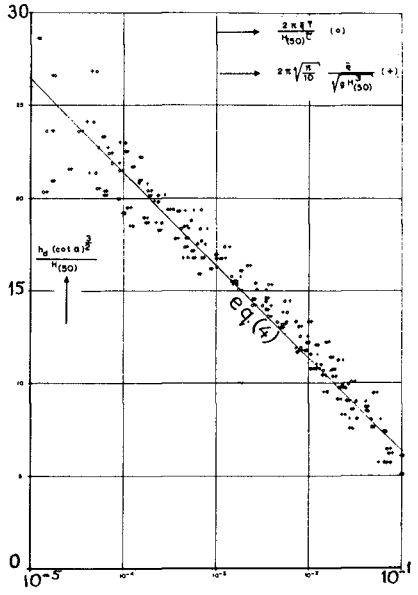

Fig. 14 Exponential relation between demensioless overtopping and dimensionless crestheight. Data from TAW (1972)

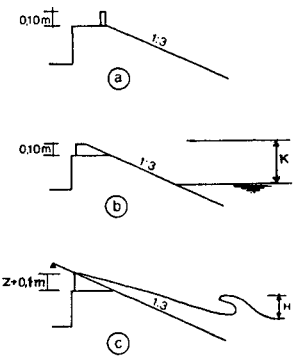

Fig. 16 Experimental set-up Doodeman (1985)

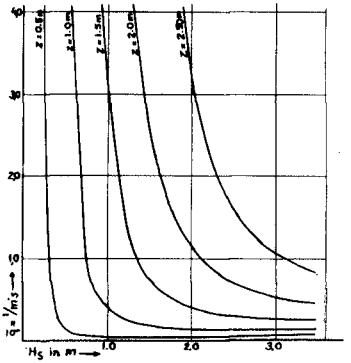

Fig. 15 Relation between dike height deficiency, sign. wave height and wave overtopping

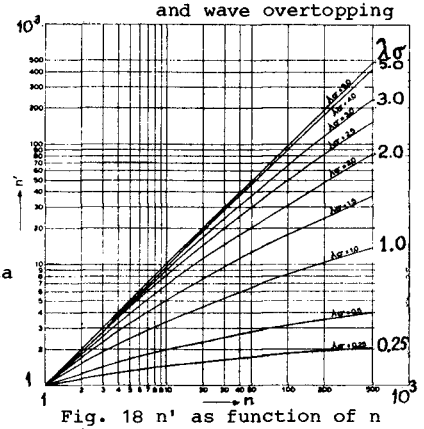

Fig. 18 n' as function of n

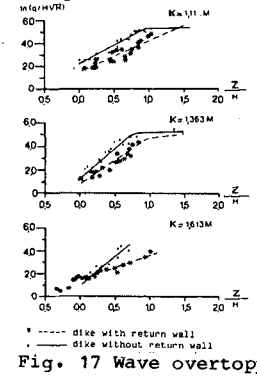

Fig. 17 Wave overtopping with and without return wall according to Doodeman (1985) (exp. scale 1:10)

$$z = y_{dh} - K \tag{9}$$

Using (5), (6), (7) and (9), one may write (4) as:

$$\bar{q} = A \cdot H\sqrt{H} \cdot e^{Bz/H} \tag{10}$$

in which:

$$A = \frac{1}{2\pi}\sqrt{\frac{10g}{\pi}} \cdot 10^{-(N\sqrt{\cot an\alpha}\,-\,1,5)/5} \tag{11}$$

$$B = (\cot an\alpha)^{3/2} \cdot (\ln 10)/5 \tag{12}$$

Thus it shows, that the dike height deficiency z does not determine in its own the amount of overtopping, but that this is also a function of the wave height.
From Figure 15 it shows, that for a large significant wave height and a small deficiency of crest height the deficiency determines the amount of overtopping quite well (it does not depend much on the wave height). However, when the deficiency is of the order of the wave height the lack of crest height gives blurred information on the amount of overtopping. Thus dikes with the same (large) crest height deficiency may have had a quite different amount of overtopping. However, other ways of calculation of amount of overtopping did not give more reliable results.

7. EXPERIMENTS

Because of confined financial means the only experiments with respect to this subject were carried out with regular waves. Therefore, from these experiments only qualitative indications can be derived concerning the amount of overtopping of dikes with a return wall compared to dikes without a wall.
The experiments were carried out by Doodeman (1985) on Delft Technological University.
The experimental set-up, simulating a scale 1:10 with respect to prototype, is shown in Figure 16. In a wave flume with waterdepth (for 3 successive sets of tests) of 0.45 m, 0.425 m and 0.40 m respectively a slope 1:3 was mounted up to a horizontal level of 0.4613 m above the bottom of the flume. Each test was carried out in three options:

a. with a return wall with a height of 10 cm above the original "dike";
b. with an enheightening of the dike with 10 cm, using the same seaward slope;
c. with an extension of the slope in upward direction in order to measure the wave run-up.

For various wave periods, simulating waves of 3 to 5 sec. in prototype, the wave-run up R was determined, resulting in an average value of 1.8 H; here H denotes the wave height.
Furthermore, the amount of overtopping q was measured. In a dimensionless plot, one might display $q/(H\sqrt{gH})$ versus z/H, where z is the crest height deficiency. This has been done in Figure 17, where the constant g has been omitted. H is given in m and q in l/ms. When z is of the order of the wave height one finds a truncation of the exponential increase of the run-up as suggested by (10). This will be clear, as no more discharge as contained in the wave crest will overtop.

Apart from some minor overtopping of the return wall for negative values of z (lowest picture of Fig. 17) Doodeman finds less overtopping for dikes with a return wall than for dikes without for the same value of z. Compare (for dikes without walls) the constants A and B according to (11) and (12) on one hand and according to the experiments on the other hand. It should be kept in mind that in the case of Doodeman the "debris height" would only be at a level of 1.8 H instead of 14.6/3 = 4.87 H for irregular waves (see (7)). Substituting of $N=1.8/\tan\alpha = 5.4$ for N in Doodeman's case one finds from his experiments: $A = 0.00420\sqrt{m/s}$. For B, which should be 2.39 for irregular waves, Doodeman finds 4.38. This means, that eqn (10), thus applied, gives for regular waves too high values for the overtopping discharge when the crest height definciency is small and too small values in the opposite case.

8. FAILURE PROBABILITY OF A DIKE RING

The probability of failure of a dike section differs from the probability of failure of the dike ring, of which the dike section forms a part. Bakker & Vrijling (1980) give an outline of a probabilistic design of sea defences. In order to give an idea of the effect of the length of a dike on the necessary design height, in the following a simple schematization is used.

a. With respect to the water level, an exponential probability distribution is assumed;
b. As the wave run-up is about proportional to the wind velocity for small fetch length and the probability distribution of the wind velocity is negative-exponential, a negative-exponential distribution of the wave run-up is assumed. The above statement is valid in the Eastern Scheldt when hydraulically deep water can be assumed; this is the case where a tidal channel occurs in front of the dike (Fig. 1). However, often shoals at about mean sea level are found in front of the dikes. In that case mostly the waves will be about proportional to the water depth and the probability distribution of waves an wave run-up will be conform the one of the water level, i.e. (again) negative-exponential.
c. Failure could be assumed, when the wave run-up surpasses the crest height; however, several additional inaccuracies are taken into account, as the uncertainty with respect to the strength of the dike (as treated before), the uncertainty with the exact constants in the formula for the negative-exponential distributions mentioned above, uncertaintly with the exact crest level etc.
   With respect to the inaccuracies mentioned ad c, a normal distribution is assumed.
d. In the following it will be assumed that all sections of the dike ring in principal are attacked by the same wave run-up; however, the unaccuracies mentioned ad c can be different for each dike section.

Mathematically, the formulation will be, that it is assumed, that a dike failure occurs when a stochastical quantity $\underline{z}$ (the wave run-up) surpasses a magnitude K (crest height) at one of n sections; here $\underline{z}$ is the sum of a stochastical quantity $\underline{x}$, being the same for all sections and having a negative exponential distribution, and a stochastical quantity $\underline{y}$, having a Gaussian distribution with expectation zero and standard deviation σ:

$$\underline{z} = \underline{x} + \underline{y} \tag{13}$$

$$P_r(\underline{x} > x) = A_o e^{-\lambda x} \quad (x > x_o) \tag{14}$$

$$P_r(\underline{y} > y) = 1-P\ (y/\sigma) \tag{15}$$

in which:

$$P(y) = \frac{1}{\sqrt{2\pi}} \int_{-\infty}^{y} e^{-t^2/2}\, dt \tag{16}$$

In (16), P(y) is the Gaussian probability function with expectation zero and standard deviation 1.

It is assumed, that $\underline{x}$ and $\underline{y}$ are statistically independent.
Then the failure probability can be defined as:

$$P_r(\text{failure}) = P_r\ (\underline{z}_{max} > K) \tag{17}$$

with:

$$\underline{z}_{max} = \underline{x} + \underline{y}_{max} \tag{18}$$

As calculations in the appendix show, taking the number of sections and the inaccuracies y into account increases the failure probability with a factor $n'.\exp(\lambda^2\sigma^2/2)$. Here n' is a number smaller than the number of sections n; the value of n' is a function of n and $\lambda\sigma$; it is displayed in Figure 18. The ratio n'/n decreases, when $\lambda\sigma$ decreases, i.e., when the standard deviation of inaccuracy $\underline{y}$ decreases with respect to the characteristic height $1/\lambda$, of the exponential distribution of $\underline{x}$.
The amount of n' is smaller than n, because also when more sections collapse during one surge, only one dike-ring failure happens.
Now let K be the necessary crest height of a dike, taking only the distribution of $\underline{x}$ and the failure of one dike segment into account. According to (14) this includes a failure probability of $A_o.\exp(-\lambda x)$.
If one does not want to exceed this probability and still take as well the inaccuracy $\underline{y}$ as the number of sections into account, the dike should be enheightened with $\lambda\sigma^2/2 + (\ln n')/\lambda$.

9. CONCLUSIONS

The following indications deal about dikes and return walls with construction and materials as found in the Netherlands in 1953:

a. During the storm surge of 1953 dikes with a steep inner slope (1:1.5 or steeper) with return walls showed a smaller failure probability than dikes without return walls, when the shortage of crest height (as defined in ch. 3) was the same .
b. On the average, the dikes could stand a crest height deficiency of 1 to 2 m dependent of the inner slope. This holds for sections of a length of ca. 0.5 km. For a dike ring the strength of the weakest dike section will be decisive for the strength of the dike. Ch.8 gives a way to bring this effect into account.

ACKNOWLEDGEMENT

The authors gratefully acknowledge the consent of Mr. Doodeman to publish his results. His experiments on the Delft University of Technology were guided by Ir. A. Paape and ir. J.J. van Dijk. Discussions within the Working Group "Probabilistic Design of Sea Defences" of the Technological Advisory Committee on Sea Defences, (which is preparing guide lines on this subject on a more sophisticated basis than presented here) were most fruitful. Photographs presented here are disposed by ing. M.A. van Dijk and by the Center for Research on Sea Defences.

REFERENCES

Bakker, W.T. & J.K. Vrijling. Probabilistic Design of Sea Defences. (Proc. 17th Int. Conf. on Coastal Engng., Sydney, 1980).

Bakker, W.T. De invloed van de onnauwkeurigheid van de voorspelde waterstanden en golfhoogten en van de lengte van een dijk op de in rekening te brengen waakhoogte van de dijk.
(The influence of the inaccuracy of the predicted waterlevels and wave heights and of the lenght of a dike on the projected height of the dike, in dutch).
Rijkswaterstaat, Advisory Dept. at Flushing, Rep. WWKZ-81.V006.

Bakker, W.T. & P. Roelse. Statistisch onderzoek naar de relatie tussen veekmerkhoogten en het bezwijken van de dijken.
(Statistical investigation on the relation between Debris heights and Dike Failure, in dutch).
Rijkswaterstaat, Advisory Dept. at Flushing, Rep. WWKZ-81.V007.

Doodeman, A.M. Proefondervindelijk onderzoek naar het verschil in golfoverslag tussen dijken met en zonder een (Muralt-)muurtje en de invloed van deze golfoverslag op het proces van dijkdoorbraak.
(Experimental investigation on the difference in wave overtopping between dikes with and without a return wall and the effect of this run-up on the proces of dike failure, in dutch).
Delft University on Technology, Coastal Engineering Group, rep. S-85.-018 (1985).

Everitt, B.S. The analysis of contingency tables. Chapman & Hall, London (1977).

Technological Advisory Committee for Sea Defence (TAW), Golfoploop en golfoverslag.
(Wave run-up and wave overtopping, in dutch).
The Hague, 1972.

APPENDIX

Calculation of n' from n

Let the probability of $\underline{x}$ be given by (14).
The probability of failure under the condition that $y<\underline{y}_{max}<y+dy$ equals:

$$P_r(\text{failure}|y<\underline{y}_{max}<y+dy) = P_r(\underline{x}>K-y) \quad (A1)$$

According to (14) this probability equals:

$$P_r(\text{failure}|y<\underline{y}_{max}<y+dy) = A_o e^{-\lambda(K-y)} \quad (A2)$$

Thus the total failure probability is the probability, quoted in (A2), multiplied with the chance on $y<\underline{y}_{max}<y+dy$, integrated over all possibilities of y:

$$P_r(\text{failure}) = \int_{-\infty}^{+\infty} A_o e^{-\lambda(K-y)} . p(y_{max})\, dy \quad (A3)$$

where $p(y_{max})$ is the probability density function of y_{max}:

$$p(y_{max}) = \frac{d}{dy}\,[\,Pr(y_{max}<y)\,] \quad (A4)$$

with:

$$P_r(\underline{y}_{max}<y) = (P(y/\sigma))^n \quad (A5)$$

From (A4) and (16) one finds:

$$p(y_{max}) = \frac{d}{dy}[\,(P(y/\sigma))^n\,] \quad (A6)$$

$$p(y_{max}) = \frac{n}{\sigma}.(P(y/\sigma))^{n-1}.\, Z(y/\sigma) \quad (A7)$$

in which:

$$Z(y) = \frac{1}{2\pi}\, e^{-y^2/2} \quad (A8)$$

Z(y) is the probability density function of the Gaussian distribution.
Substitution of (A6) into (A1) gives:

$$P_r(\text{failure}) = \frac{nA_o}{\sigma}\, e^{-\lambda K} \int_{-\infty}^{+\infty} (P(y/\sigma))^{n-1}.Z(y/\sigma).e^{\lambda y}\, dy \quad (A9)$$

Replacing y/σ by u yields:

$$P_r(\text{failure}) = A_o e^{-\lambda K}.f(n,\lambda\sigma)$$

$$f(n,\lambda\sigma) = n.\int_{-\infty}^{+\infty} (P(u))^{n-1}.Z(u).e^{\lambda\sigma.u}du$$

The function $f(n,\lambda\sigma)$ is calculated numerically and given in Figure 18.
More details are given by Bakker (1981).

CHAPTER 160

A New Design Method of Rubble Mound Structures

Cheong-Ro Ryu[1] and Toru Sawaragi[2]

Abstract

A new design method of rubble mound structures with stability and wave control consideration is proposed, by which the reduction of wave reflection and run-up and increase in rubble stability are assured under the given wave conditions. Wave control and stability increasing functions due to change of the slope shape of rubble mound structures are discussed on the basis of the experimental results for regular and irregular waves.

The new design formula developed here considered the allowable percentage of damage and the wave grouping effects on rubble stability using a new assumption of the mean run-sum as an index of the irregular wave force. The run-sum is defined as the energy sum of a run satisfying a critical wave condition and the mean run-sum is the mean of run-sum for a irregular wave train.

1. Introduction

The selection of statistic design wave height in irregular waves is the most important problem in the design of rubble mound structures using the conventional design formulas. The problem mainly occurs due to the irregularities of ocean waves well known as the spectrum shapes and the grouping characteristics etc.. The effects of irregularity on the stability of rubble monnd structures were pointed out by Johnson et al.(1978) and Sawaragi et al.(1984 and 1985) as an important external force index that should be considered in the design. Furthermore, the stability will depend not only on the wave height but also on the slope controling wave breaking conditions which is greatly affected by the interaction of successive waves and wave period.

The destruction process of rubble mound structures shows a tendency to form a stable equilibrium slope under the given condition. This means that the stability increases due to the formation of equilibrium slope. It is desirable to use a berm type composite slope at the initial design stage for the ease of construction, and is important in a optimal design concept with allowable failure ratio.

Ryu(1984) and Ryu et al.(1986) stressed the reflected wave problems for a calm sea and the reduction of run-up correspond to the necessity

1) Assistant Professor, Department of Ocean Engineering, National Fisheries University of Pusan, Pusan, 608 Korea.
2) Professor, Department of Civil Engineering, Osaka University, Osaka, Japan.

of construction of lower crown-height in the design of coastal structures with an optimal design concept. Considering those irregularity effects on the stability and the reduction of wave reflection and run-up, Sawaragi et al.(1985) and Ryu et al.(1986) developed the design formula introducing the irregular wave force index such as the mean run-sum, but still the formula has a problem that the design rubble weight must be calculated by every design formula for every slope.

In this paper, the characteristics on the reduction of wave reflection and wave run-up, and stability increasing functions by the change of the slope shape are studied through model tests, and new design formulas are developed for the uniform slopes that can apply an universal formula to every slope and for the optimal composite slope considered wave control and stability increasing functions. The new design formulas have considered the allowable failure ratio and the irregularity effects including wave period and wave grouping effects on the stability of rubble mound structures with the conception of the mean run-sum of the conditional run of modified surf-similarity parameter under the condition of significant wave height.

2. Model experiments

A wave tank of 30m long, 70cm wide, and 95cm height was used in the present experiments. An irregular wave generator is installed at an end of the tank. For all experiments, characteristic dimensions of structures with uniform and composite slopes shown as Fig.1 were selected as specified in Table 1. Wave height is initially set at less than 3cm and then it increase until 100% destruction of rubble mound results.

For the test of the sensitivity of rubble mound structures to the wave grouping and other irregularity parameters, an irregular wave simulation technique of the impulse response function method is used. It is basically the same as the method of Kimura(1976) and the spectrum shape of irregular waves can be arbitrarily controlled. The frequency spectrum of ocean waves is normally expressed as:

$$S(f) = S(f_p)\left(\frac{f}{f_p}\right)^{-m} \exp\left[\frac{m}{n}\left\{1 - \left(\frac{f}{f_p}\right)^{-n}\right\}\right] \qquad (1)$$

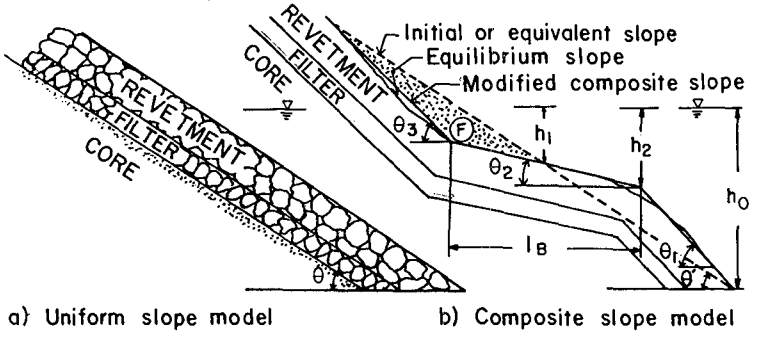

Fig. 1 Schematic diagram of model breakwaters.

Table 1. Experimental conditions

General conditions	Slope conditions							Wave conditions						
	Uniform slopes	Composite slope configurations						Regular wave		Irregular wave				
	θ	h_1(cm)	l_B(cm)	θ_1	θ_2	θ_3	θ'	T(sec)	H(cm)	case	f_p	$S(f_p)$	m	n
W_a : 20g		5	15	1:1.5	0	1:1.5	1:2.0	0.8	3.0	W.1	1.0	5.0	5	4
l_a : 1.96cm	1:1.5	5*	25*	1:1.5*	0*	1:1.5*	1:2.3*	0.9	5.0	W.2	0.9	5.0	5	4
l_f : 1.0cm 1.5cm		5	30	1:1.5	0	1:1.5	1:2.5	1.0	6.0					
	1:2.0	5	35	1:1.5	0	1:1.5	1:2.7	1.1	7.0	W.3	0.6	5.0	5	4
l_c : 0.5cm		10	15	1:1.5	0	1:1.5	1:2.0	1.2	9.0	W.4	1.0	5.0	6	2
		10	25	1:1.5	0	1:1.5	1:2.3	1.4	11.0	W.5	0.8	5.0	6	2
r_a : 2.0 l_a	1:3.0	10	30	1:1.5	0	1:1.5	1:2.5	1.6	13.0					
h_0 : 20cm		10	35	1:1.5	0	1:1.5	1:2.7	1.8	15.0	W.6	0.6	5.0	6	2

W_a : weight of rubble for revetment, l_a : characteristic length of rubble for revetments,
l_f : characteristic length of rubble for filter layer, l_c : characteristic length of rubble for core layer,
r_a : thickness of revetment, h_0 : water depth at the toe of breakwater,
* : the composite slope configuration examined under the irregular waves.

where f_p is the peak frequency; m and n are the constants which specify the spectrum shape. The combinations of peak frequency and shape parameters used in this study are also listed in Table 1. Using these basic irregular waves, 200 cases of stability experiments were carried out, and the destruction process and the wave motions on the slope are pictured and analyzed by 16mm high speed cine camera(50 frame/sec) and analyzer.

For the measurement of the water surface elevation in the presence of the breakwaters, the capacity type wave gauges were located at 2cm intervals along them. The reflection coefficient was estimated by the Healy's method under the regular wave conditions, while the two point measuring method proposed by Goda et al.(1976) was used to obtain the reflection coefficient under the irregular wave conditions. The wave run-up and run-down were measured by a run-up meter set on the slope surface. After digitizing all the data of water surface elevation recorded in an analog data recorder, the individual wave analysis and the spectral analysis methods were applied for the investigation of hydraulic characteristics on the slopes.

3. Characteristics of irregular waves

3.1 Reliability of generated waves

Spectrum shape of all experimental waves were in good agreement with those of expected waves given in Table 1. For the probability distribution of wave heights, periods and surf-similarity parameters, experimental and well-known theoretical results on the statistics of ocean waves coincide fairly well. As for the ascertain of the statistical reliability of generated waves and related discussions, readers are referred to Ryu(1984) or Sawaragi et al.(1985).

Fig.2 shows the occurrence probability of run-length of higher waves $j(\ j=1,2,3,\ldots\ldots,\infty\ )$ for the present data, reported field data and predicted results by the well-known stochastic process. The present data is the mean of 200 experimental cases of irregular waves, and field data are referred from the results analyzed by Burcharth(1980) and Rye(1974). The grouping characteristics of experimental waves in the study satisfied also with that of the field data. From these results, the model irregular waves are judged to be satisfactorily simulated the ocean wave trains.

3.2 Mean run-length and mean run-sum

The effects of grouping waves on the stability of coastal structures were considered with the run-length of higher waves by Johnson et al.(1978). However, the effects of wave period and resonance condition on the stability have been verified as a non-negligible one by Sawaragi et al.(1983), Bruun et al.(1978) and many other researchers. Considering these effects, in the study, a new irregularity parameter is proposed by the comparative study of correlations between the irregularity parameters for various definitions of the run, and its significancy is verified by applying to the representation of the stability of rubble mound structures. The new grouping parameter finally used here is a conditional run of ξ_o^* under the condition of critical wave height H_c same as Sawaragi et al.(1985), where ξ_o^* means the relative surf-similarity parameter

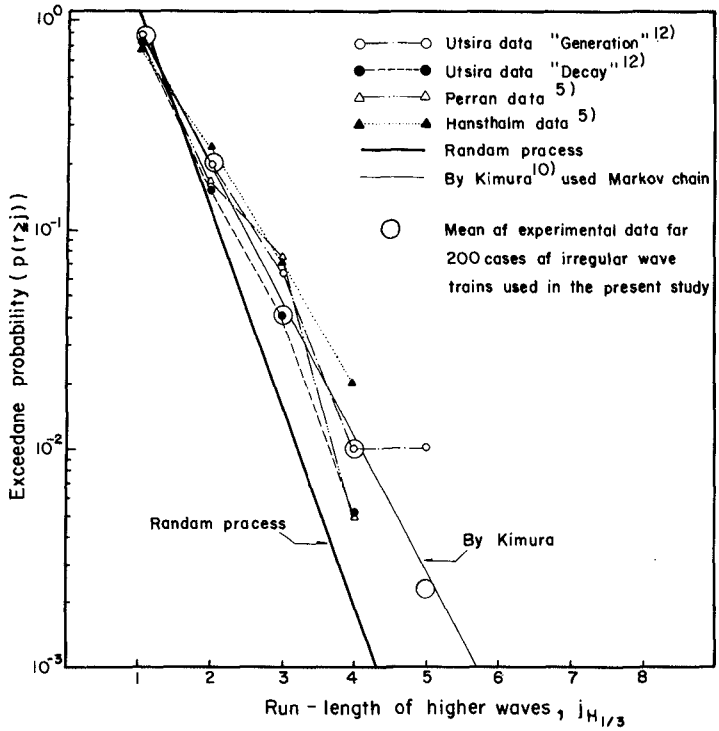

Fig. 2 The occurrence probability of run-length j of higher waves.

such as:

$$\xi_o^* = \frac{\xi}{\xi_o} = \frac{\tan\theta \,/\sqrt{H/L_o}}{\tan\theta \,/\sqrt{(H/L_o)_{max}}} \qquad (2)$$

where θ is the slope of the structures, H the wave height, L_o the deep sea wave length, and subscript max the maximum wave. As for the detail discussions of the run, readers are referred to Sawaragi et al.(1985).

Mean run-length of the run have the linear relationship with the spectrum peakedness parameter Q_p. As the run-length is only the number of group formed waves, it is difficult to introduce the run-length into the design formula as a external force parameter. Hence, a new conception of run-sum is proposed in the study, where the run-sum is defined as the energy-sum of grouped waves. The mean run-sum(E_{sum}) is the mean of run-sum in a irregular wave train expressed as:

$$E_{sum} = \frac{1}{8} \rho_w g \sum_{k=1}^{\infty} H_k \,/ \sum_{j=1}^{\infty} N_j \qquad (3)$$

where N_j is the numbers of run-length j(j=1,2,3,...,∞), H_k(k=1,2,3,..., ∞) denote the k-th wave height of group formed waves in a wave trian, ρ_w is the density of sea water and g is the acceleration of gravity. From the author's another study results on the relations among the mean run-sum, the mean run-length and the spectrum peakedness parameter Q_p , we can estimate the E_{sum} by the following equation(Sawaragi et al.(1985)).

$$E_{sum\ j}(\xi_o^*/H_c) = \rho_w g H_c^3 (0.04Q_p + 0.13), \text{ for } H_c = H_{1/3} \quad (4)$$

$$Q_p = \frac{2}{m_o^2} \int_o^\infty f\ S^2(f)df \quad (5)$$

where, $m_o = \int_o^\infty S(f)df$

4. Effects of the friction coefficient and the slope on the stability

4.1 The effect of friction coefficient

The author(1983,1984), Losada and Gimenez-Gurto(1979), Günbak et al. (1983), Brunn et al.(1976,1978) and Ahrens(1975,1981) pointed out the wave period effects on the stability as a important factor in design. And they reported same tendency of results that the stability number N_s varied with surf-similarity parameter ξ or wave steepness, and the minimum N_s was appeared in the range of $2<\xi<3$. Ryu(1984) suggested the parameter ξ_o^* to present the stability with a universal stability curve for the various slopes instead of ξ because ξ for the minimum point of N_s changed by mainly due to the slope angle.

However, the value of stability number including minimum N_s varies with the change of the initial slope and damage ratio. If this problem can not be improved, the design considering the wave period effects on the stability must be done by using the every stability curve for the every slope. This problem occurs, because the friction coefficient and the slope angle is not included in the stability number indicated as following:

$$N_s = \frac{\gamma_w^{1/3} H_{D(\%)}}{(\gamma_r/\gamma_w - 1) W_a^{1/3}} \quad (6)$$

where γ_r and γ_w are specific weights of rubbles and water, $H_D(\%)$ is the design wave height for the failure ratio in percent, W_a the weight of rubble unit, θ the slope angle, and K_D the stability coefficient in the Hudson's formula(1959).

To estimate the effect of friction coefficient on the stability , the experiments on the variation of friction coefficient was carried out for various armour materials such as quarry stone(W_a=30g, 50g), concrete cube(W_a=100g), and tetrapod(W_a=100g). 50 times of experiments for every materials are repeatedly carried out. The friction coefficient f is

estimated by the relation of

$$f = \tan \phi \tag{7}$$

where ϕ is the repose angle of materials in the water.

As a results, obtained the mean friction coefficients of 1.09, 1.28 and 1.42 for the quarry stone, concrete cube and tetrapod respectively , and the standard deviation was 0.1 for all materials.

On the other hand, when the hydrodynamic force act upon an armour unit, the variance of the destructive force F according tothe change of the slope can estimate by the following equation:

$$F = \left(1 - \frac{\rho_w}{\rho_r} \right) W_a \left(f \cos\theta - \sin\theta \right) \tag{8}$$

From Eq.(8), the calculated results of nondimensional destructive force F/W_a due to the change of relative slope($\tan\theta/\tan\phi$) are shown as Fig.3. In the figure, the correlation between two parameters has almost linear relation regardless the change of the friction coefficient. From the Fig.3, the effects of the friction coefficient and that of slope angle can estimate by using the linear relation.

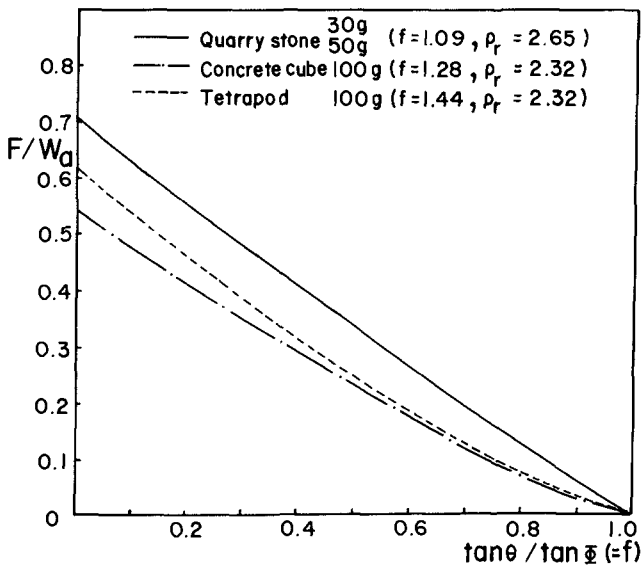

Fig. 3 Variation of the destructive force due to change of slopes.

4.2 The effect of slope angle

The effect of relative slope angle on the stability is considered using the modified stability number N_S' as shown as equation (9) from the linear relation of Fig.3.

$$N_s' = N_s \cdot \frac{\tan\theta}{\tan\phi} \tag{9}$$

Fig.4 corresponds to the correlation between modified stability number and ξ_o^* using the results for regular waves. In the figure, the variation of N_s' by ξ_o^* shows a similar curve regardless the difference of initial slopes for the same ratio of destruction. The minimum N_s' is appeared in the range of $1.5<\xi_o^*<2.5$ and the point of ξ_o^* shown the minimum N_s' is shifted to smaller region according to the progress of destruction. The destruction ratio D(%) is defined as:

$$D = \left(\frac{A_f}{A_o}\right) \times 100 \tag{10}$$

where A_f is the destructed volume of the cover layer and A_o is the destructed volume where the destruction reaches the core layer. The physical meaning of this failure ratio was discussed in the previous work of the author(1983). This shifting of the minimum N_s' is occured caused by the change of the local slope at the destructed area during the formation of equilibrium slope. However, the stability is not correctly presented, the most convenient curves are obtained to consider the wave period effects by using the monochromatic wave conception such as the design wave height and period.

4.3 Equilibrium slope

The characteristics of equilibrium slope formation due to severe waves are important in designing rubble mound structures. For the quantitative discussion of the equilibrium slope, its characteristic length is defined as shown in Fig. 1(b).

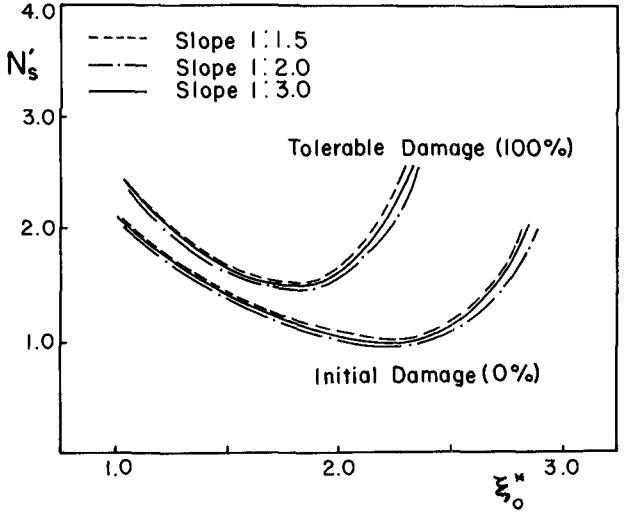

Fig. 4 $N_s' - \xi_o^*$ curves for various slopes.

Since θ_1, θ_2 and θ_3 vary depending on the characteristic depth and width of equilibrium slope, it is necessary first to discuss the width and the depth of berm in an equilibrium slope. Ryu and Sawaragi(1986) discussed these, and as a result, the berm depth and the berm width of equilibrium slopes are formulated as:

$$\left.\begin{aligned} 0.4 \leq h_1/H \leq 0.5 \\ 0.9 \leq h_2/H \leq 1.1 \end{aligned}\right\} \tag{11}$$

$$\frac{l_B}{L_{o\max}} = 2.075 \frac{H_{1/3}}{L_{o1/3}} + 0.04 \tag{12}$$

where h_1 is the minimum water depth of the berm, h_2 the maximum of that, H the incident wave height for the regular wave, l_B the berm width; L_o the deep sea wave length, and the subscripts max and 1/3 denote the maximum wave and the significant wave respectively.

From the Eqs.(11) and (12), rubble mound structures with composite slopes are modelled simulating the characteristics of equilibrium slope under the conditions of regular and irregular waves, and experiments on the stability and the hydraulic characteristics such as reflection and run-up on the slope are carried out under the condition of Table 1 as well as for the uniform slopes.

5. Wave control and stability increasing functions of the composite slope

5.1 Stability increasing function

To applicate the characteristics of Fig. 4 to the presentation of stability for irregular waves, normalized the mean run-sum by the characteristic length of armour unit and relative slope. It is assumed as a index of irregular wave force, and the variation of damage ratio is investigated by the index. Fig. 5 shows the results. In the figure, black circles denote the experimental data for the composite slope and white symbols are that for the uniform slopes.

Although the difference of damage ratio for the same irregular wave force index between the uniform and composite slopes is occured caused by the stability increasing functions on the composite slope. The significant difference is not appeared due to the variation of the slope for the uniform slopes. It means that the index is a very useful and reasonable parameter to present the stability of rubble mound structures under the irregular wave condition as well as the regular wave. From the Fig.5, the stability increasing characteristics of the composite slope is also clarified for the irregular wave. As for the detail discussions of stability increasing mechanism under the regular wave condition, readers are referred to Ryu and Sawaragi(1986).

5.2 Wave control function

If the equilibrium slope is decided and constructed as a shape of rubble mound structures as the initial design stage, the stability is increased more than 50% comparing the stability for the uniform slope, but how is the reflection and the run-up on the slope.

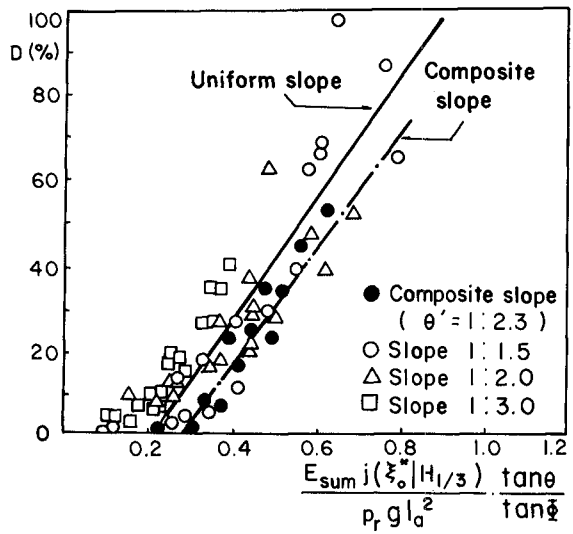

Fig.5 The relations of relative E_{sum} and percentage failure ratio(D%).

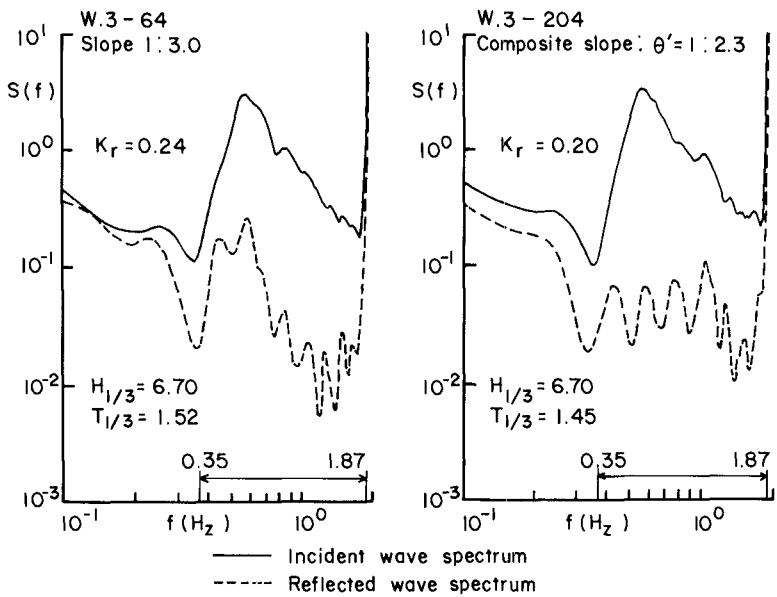

Fig.6 The reflection control function of the composite slope by irregular waves.

The reduction of reflection coefficient and run-up are very important for a calm sea and a low crest height respectively. Ryu and Sawaragi (1986) discussed the wave control functions according to the change of relative depth and width of the berm of composite slope. As a results, it is clarified that the reflection coefficient varies with the berm width l_B and depth h_B, and the minimum value of K_r is always appeared under the condition of $l_B/L_o = 0.2$ and $H/2 < h_B < H$. If the optimum composite slope is selected, the reflection coefficient decreases more than 50%, the run-up height decreases about 10%, and the run-down height decreases about 20-50% comparing the results for the uniform slopes. As for the detail discussion of the reduction mechanisms, readers are referred to Ryu and Sawaragi(1986).

The reflection characteristics of irregular waves on the uniform and composite slopes are now investigated to examine the applicability of the results for regular waves. Fig.6 shows examples of the incident and the reflected wave spectra on an uniform slope and on a composite slope. The reflection coefficient on the composite slope are smaller than that on the uniform slopes. It is noted, however, that the equivalent slope of the composite slope is 1/2.3, which is steeper than the uniform slope 1/3.

As is seen from the spectrum of reflected waves, the predominent frequency can not be identified in case of the composite slope while it appears in case of the uniform slope, being almost the same as that of incident wave spectrum. From the fact that the composite slopes scattered frequency spectral density of reflected waves, it can be stated that the reflection control function of composite slopes for the irregular waves is basically same as for the regular waves.

From the wave control and stability increasing functions of the composite slope, the author emphasize the necessity of composite slope for the constructing of the optimal rubble mound structure.

6. A new design method for the irregular waves

6.1 A new design formula

From the correlation between the mean run-sum and spectrum peakedness parameter and Fig.5, the design rubble weight can be estimated by the following steps. The best fitting line for the variance of destruction ratio due to the irregular wave force from the Fig.5 can be derived empirically as:

$$D(\%) = 153.8\left[\frac{E_{sum}\, j(\xi_o^*|H_{1/3})}{\rho_r\, g\, l_a^2}\,\frac{\tan\theta}{\tan\phi}\right] - 30.1 \qquad (13)$$

for the uniform slopes,

$$D(\%) = 136.4\left[\frac{E_{sum}\, j(\xi_o^*|H_{1/3})}{\rho_r\, g\, l_a^2}\,\frac{\tan\theta'}{\tan\phi}\right] - 36.3 \qquad (14)$$

for the composite slopes.

where θ' is the equivalent slope of the composite slope, and $j(\xi_o^* | H_{1/3})$ denotes the conditional run of ξ_o^* under the condition of significant wave height. To estimate the design weight of a rubble unit, Eq.(13) and (14) can be transformed as;

$$W_a = \rho_r g l_a^3 = \left[\frac{153.8 E_{sum} j(\xi_o^* | H_{1/3})}{(\rho_r g)^{1/3} (D + 30.1)} \frac{\tan\theta}{\tan\phi} \right]^{3/2} \quad (15)$$

for the uniform slopes,

$$W_a = \left[\frac{136.4 E_{sum} j(\xi_o^* | H_{1/3})}{(\rho_r g)^{1/3} (D + 36.3)} \frac{\tan\theta'}{\tan\phi} \right]^{3/2} \quad (16)$$

for the composite slopes.

From the Eqs.(15), (16) and (4), by using the spectrum peakedness parameter Q_p which is calculated directly in the spectrum analysis, we can easily derive the design formula as follows:

$$W_a = \left[\frac{\rho_w g (6.15 Q_p + 20.0)}{(\rho_r g)^{1/3} (D + 30.1)} \frac{\tan\theta}{\tan\phi} \right]^{3/2} H_{1/3}^3 \quad (17)$$

for the uniform slopes,

$$W_a = \left[\frac{\rho_w g (5.46 Q_p + 17.73)}{(\rho_r g)^{1/3} (D + 36.3)} \frac{\tan\theta'}{\tan\phi} \right]^{3/2} H_{1/3}^3 \quad (18)$$

for the composite slopes.

The design formulas Eq.(17) and Eq.(18) reflect the allowable percentage of damage and the wave grouping effects on the rubble stability using a new conception of the mean run-sum as an index of the irregular wave force. For the uniform slopes, the design rubble weight can be calculated by the only a design formula of Eq.(17). It is an epoch-making advantage comparing the author's previous work (Sawaragi et al. (1985)), and only a design formula that introduced or considered directly the irregularity effects of ocean waves and allowable percentage of damage into the design formula until now. Eq.(18) is a design formula for the composite slope, however, this formula can not use to the all type of composite slopes, only can use for the optimal conditions of composite

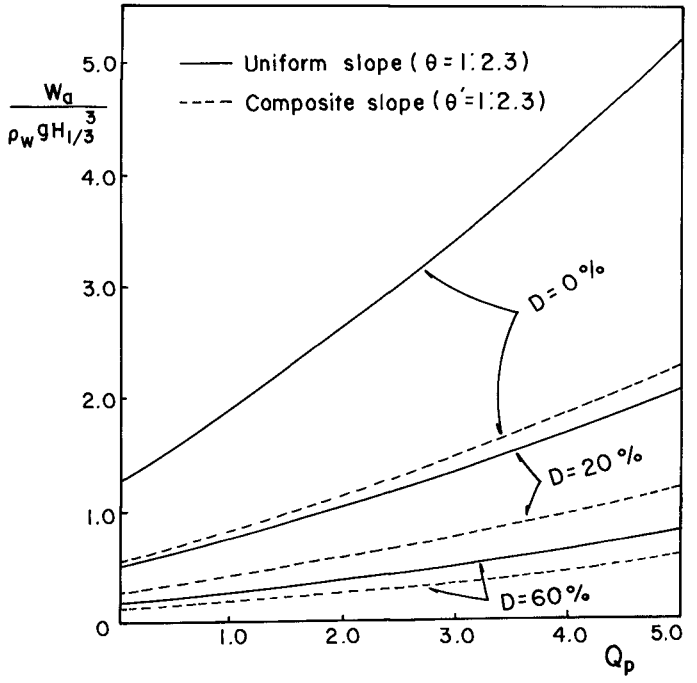

Fig.7 Design example on the variation of ralative design weight according to the spectrum peakedness parameter

slope with stability and wave control consideration such as:

$$\left.\begin{aligned} l_B &= 0.25 L_p \\ 0.4H_{1/3} < h_B &< 0.7H_{1/3} \end{aligned}\right\} \qquad (19)$$

where L_p is the wave length for the peak frequency of the energy spectrum. This condition is a optimal condition of the composite slope in the study of the author(1986).

6.2 Design examples

Using the new design formulas Eqs.(17) and (18), the variation of the relative weight of armour unit is calculated according to the spectrum peakedness parameter considered the allowable damage ratio in percent. Fig. 7 is one example for the uniform slope of 1/2.3 and for the equivalent composite slope of 1/2.3. As can be seen from the fig., the design weight of armour unit becomes heavier due to the increasing of spectrum peakedness parameter and the rubble weight for composite slope becomes more light than that of uniform slope.

Fig. 8 shows the variation of the design weight due to the change of the allowable damage under the design wave conditions of Q_p = 2.5

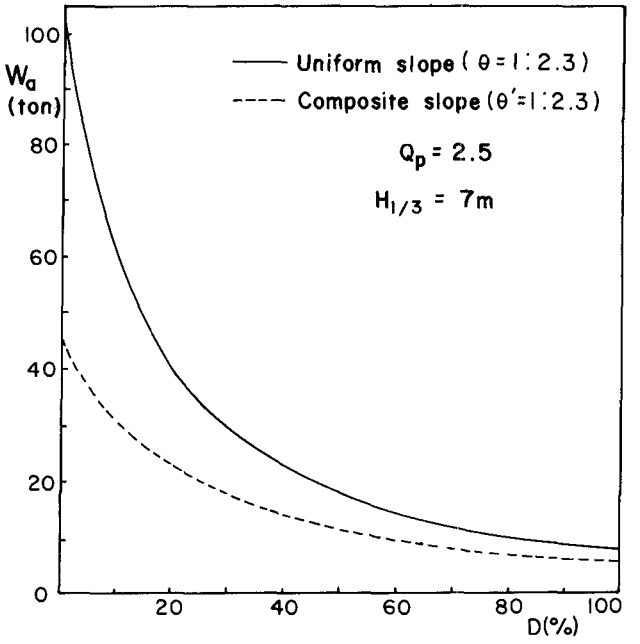

Fig.8 Design example on the variation of design weight according to the allowable failure ratio.

and $H_{1/3}$ =7m for the same slope condition with Fig.7. The design weight becomes heavier according to the decreasing of allowable damage ratio for both slope conditions, and the design weight for the composite slope is half or less of that for the uniform slope in the initial damage(D < 10%). Considering this stability increasing and before mentioned wave control functions, the optimal design concept using the rubble mound with the composite slope should be applied to the design of coastal structures.

7. Conclusions

A new design method is developed based on the results of stability experiments under the regular and irregular wave conditions. The new design formula reflects the effects of spectrum shape, breaking conditions, wave period and wave grouping characteristics on the stability, and can introduce the allowable damage ratio.

The design formula for the uniform slope structure has an advantage comparing the author's previous work, because the present method calculate by a formula for every slope. The importance of the design of composite slope structures is emphasized through the comparative studies of the hydraulic characteristics and the rubble stability on the uniform and composite slopes. A new method of designing composite slope structures with optimum berm width and depth is proposed, by which the reduc-

tion of wave reflection and run-up and increase in rubble stability are assured under the given wave conditions.

Acknowledgements

The financial support of the Korea Science and Engineering Foundation for this research is greatly acknowledged. The authors would like to thank to Mr. H. J. Kim and S. K. Kim for their helpful research assistants.

References

1. Ahrens, J.P. and B.L. McCartney (1975): Wave period effect on the stability of riprap, Proc. of the Special Conference on Civil Eng. in the Ocean/III, ASCE, pp.1019 - 1034.
2. Ahrens, J.P. (1981): Design of riprap revetment for protection against wave attack, U.S. Army, Corps of Engineers, C.E.R.C., TP 81-5.
3. Bruun, P. and A.R. Günbak (1978): Stability of sloping structures in relation to $\xi=\tan\theta/\sqrt{H/L_o}$, Coastal Engineering, 1(4), pp. 287 - 322.
4. Bruun, P. and P. Johannesson (1976): Parameters affecting the stability of rubble mounds, Proc. of ASCE, WW2, pp.141 - 164.
5. Burcharth, H.F. (1980): A comparison of nature waves and model waves with special reference to wave grouping, Proc. of 17th International Conference on Coastal Eng.,2993 - 3009.
6. Goda, Y. and Y. Suzuki (1976): Estimation of incident and reflected waves in random wave experiments, Proc. 15th International Conf. on Coastal Eng., pp. 828 - 845.
7. Günbak, A. and N. Merzi (1983): Effect of wave period on the stability of rubble mound breakwaters, Proc. 8th International Harbor Cong. pp. 3.15 - 3.20.
8. Hudson, T.Y. (1959): Laboratory investigation of rubble mound breakwaters, Proc. of ASCE, WW3, pp. 93 - 121.
10. Kimura, A. (1976): Random wave simulation in a laboratory wave tank, Proc. 15th International Conf. on Coastal Eng., pp.368 -387.
11. Losada, M.A. and L. Cimenez-Curto (1979): The joint effect of the wave height and period on the stability of rubble mound breakwaters using Iribarren's number, Coastal Engineering, 3, pp. 77 -96.
12. Rye, H. (1974): Wave group formation among storm waves, Proc. 14th International Conf. on Coastal Engineering, pp.164 - 183.
13. Ryu, C.R. (1984): A study on the hydraulic optimal design of the rubble mound breakwaters, Thesis of Doctor of Eng., Osaka University, 165p. (in Japaneae)
14. Ryu, C.R. and T. Sawaragi (1986): Wave control functions and design principles of composite slope rubble mound structures, Coastal Eng. in Japan, Vol. 29, (to be published).
15. Sawaragi, T., C.R. Ryu and K. Iwata (1983): Consideration of the destruction mechanism of rubble mound breakwaters due to the resonance phenomena, Proc. 8th I.H.C., pp.3.197 - 3.208.
16. Sawaragi, T., C.R. Ryu and M.kusumi (1984): Destruction characteristics of rubble mound breakwaters by irregular waves, Proc. 31th Japanese Confenence on Coastal Eng., pp.562 - 566 (in Japanese).
17. Sawaragi, T., C.R. Ryu and M. Kusumi (1985): Destruction mechanism and design of rubble mound structures by irregular waves, Coastal Engineering in Japan, Vol. 28, PP. 173 - 189.

CHAPTER 162

REFLECTION OF IRREGULAR WAVES AT PARTIALLY REFLECTING STRUCTURES INCLUDING OBLIQUE WAVE APPROACH

Hans-Joachim Scheffer *

Sören Kohlhase **

1 Introduction and summary

The reflection of irregular seas is increasingly considered in coastal engineering and harbour design as well with respect to wave pattern at the structure and energy dissipation as regarding the dimensioning of structures exposed to waves. It becomes evident that the three-dimensional sea state (oblique wave approach, irregularity of the waves) at partially-reflecting structures of a complex design cannot be described by means of a constant reflection coefficient alone, as is common practice. This is due to the fact that the coefficient is largely frequency-dependent and the physically effective reflection point of the structure cannot be clearly specified.

In the light of this, basic investigations on wave reflection have been performed with different partially-reflecting structures, wave spectra and wave approach angles. In addition to laboratory experiments using both a wave flume and a wave basin, a theoretical solution based on diffraction theory was determined to describe the wave field in the reflection area of various structures. The investigations were restricted to non-breaking wave conditions.

The reflection behaviour of structures is expressed by a complex reflection coefficient, containing two parameters, which have to be determined by model tests.

2 Theory

2.1 Total wave reflection

It has been indicated by BERGER and KOHLHASE (1976) that SOMMERFELD's diffraction theory, which is also applicable to water waves (linear wave motion), describes the wave motion in the reflection area of a totally-reflecting semi-infinite vertical wall for harmonic waves. The theory also explains the so called MACH-effect (local wave height greater than twice of incoming wave height). The modulus of the complex SOMMERFELD solution-function $F(r,\vartheta)$ describes the diffraction coefficient k' as the ratio of the local wave height H_i and the incident wave height H_o

---

* Dr.-Ing., Research Engineer
** Dr.-Ing. habil, Chief Engineer
both FRANZIUS-INSTITUT, University of Hannover, F.R.Germany

$$F(r,\theta,k) = f(\sigma)\, e^{-ikr\cos(\theta-\theta_o)} + f(\sigma')\, e^{-ikr\cos(\theta+\theta_o)} \qquad (1)$$

$$f(\sigma) = \frac{1+i}{2} \int_{-\infty}^{\sigma} e^{-i\pi t^2/2}\, dt \qquad f(\sigma') = \frac{1+i}{2} \int_{-\infty}^{\sigma'} e^{-i\pi t^2/2}\, dt$$

$$\sigma = 2\sqrt{\frac{kr}{\pi}}\, \sin\left(\frac{\theta-\theta_o}{2}\right) \qquad \sigma' = -2\sqrt{\frac{kr}{\pi}}\, \sin\left(\frac{\theta+\theta_o}{2}\right)$$

$$k' = H_i/H_o = |F(r,\theta,k)| \qquad (2)$$

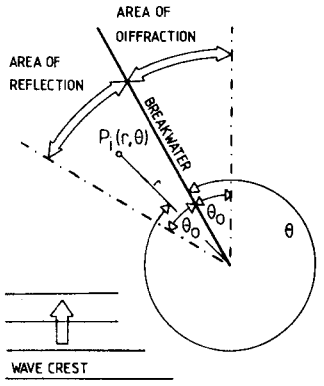

Fig. 1:
Coordinate System of the SOMMERFELD solution

If linear relationships can be assumed (no local wave breaking) and the motion of an irregular wave train can be described as a superposition of harmonic waves of different frequencies and amplitudes (FOURIER representation), this theory can also be applied to the general case of irregular seas.

As described in the literature, the SOMMERFELD solution-function F is a function of the geometrical location r and θ related to the tip of the breakwater (see Figure 1). In general F is dependent upon the relative distance kr (=$2\pi r/L$). Therefore it has a strong frequency characteristic even for constant water depth. The frequency curve for a fixed geometrical location thus describes the transfer function between the local $S_{\eta,i}$ and the uneffected approaching linear wave spectrum $S_{\eta,o}$.

$$F(f) = TF(f) = S_{\eta,i} / S_{\eta,o} \qquad (3)$$

This assumption has been validated by model experiments (GÖTSCHENBERG and SCHEFFER, 1984).

For normal wave approach ($\theta_o = 90°$) and neglecting the contribution of scattered waves ($r \to \infty$) the SOMMERFELD solution gives the k'-values of a standing wave field in which x' represents the distance normal to the structure.

$$k' = |F(\theta_o=90°)| = | e^{ikx'} + e^{-ikx'} | = | 2 \cos (kx') | \qquad (4)$$

2.2 Partial wave reflection

In order to describe the wave motion in front of a partially-reflecting structure the reflection behaviour of the structure is idealized by a two-parametric complex reflection coefficient in a virtual vertical plane trough the seaward base of the structure as shown in Figure 2.

$$K = \kappa e^{-i\phi} \qquad (5)$$

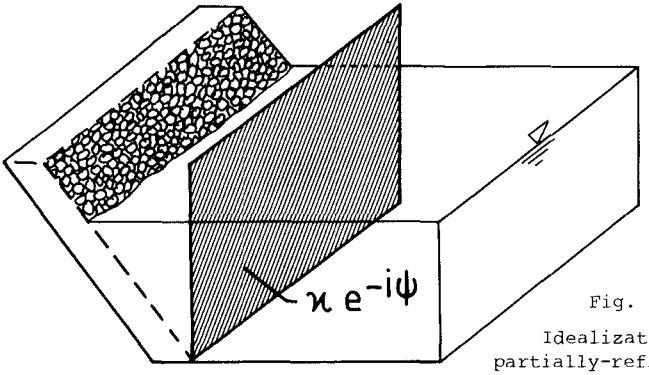

Fig. 2:
Idealization of partially-reflecting structure

In case of normal wave attack (without scattered waves) eq. 4 has to be written

$$k' = | e^{ikx'} + \kappa e^{-i\phi} e^{-ikx'} | \qquad (6)$$

Eq. 6 indicates that the approaching waves leave the seaward region in front of the virtual vertical plane ($x' = 0$) and that waves with reduced amplitudes (κ: amplitude reduction factor) and a phase difference (ϕ: phase angle) enter the region from outside. The phase shift term $e^{-i\phi}$ provides a measure of the distance to the physically effective reflection point.

For the general case of a semi-infinite partially-reflecting structure and oblique wave approach, the wave motion in the reflection region is suggested to be described by an extended SOMMERFELD solution. The terms of the solution (eq. 1) which can be grouped according to the reflected waves, have to be extended by the complex reflection coefficient. In a mathematical sense, the idealization of the structure for calculation of the reflection behaviour as a virtual vertical plane means that the scattered wave term of the incoming waves must be extended with the phase shift term $e^{-i\phi}$. The following solution may be written (SCHEFFER, 1985).

$$
\begin{aligned}
F(r,\theta,k) = \; & e^{-ikr\cos(\theta-\theta_o)} \\
& - e^{-i\phi} f(-\sigma)\, e^{-ikr\cos(\theta-\theta_o)} \\
& + \kappa\, e^{-i\phi}\, e^{-ikr\cos(\theta+\theta_o)} \\
& - \kappa\, e^{-i\phi} f(-\sigma')\, e^{-ikr\cos(\theta+\theta_o)}
\end{aligned}
\qquad (7)
$$

$$
\left.
\begin{aligned}
f(-\sigma') &= 1 - f(\sigma') \\
f(-\sigma) &= 1 - f(\sigma)
\end{aligned}
\right\} \quad \text{see eq. 1}
$$

The frequency characteristic from eq. 7 again represents the transfer function of the linear wave spectrum for a given location and constant water depth.

2.3 Determination of coefficients

Up to now we don't know an adequate theoretical formulation for determining the coefficients of the complex reflection term (eq. 3). For a vertical wave absorber, MADSEN (1983) has presented a theoretical solution for determining the amplitude reduction factor. Similarly to a method applied by MADSEN and WHITE (1976) he linearized the friction term describing the energy loss inside of the absorbing porous front layer using the LORENTZ principle of equivalent work. Both investigations considered only shallow water waves, i.e. the horizontal orbital velocity is independent of the water depth. Furthermore it was not considered by MADSEN (1983) that nearby the structure the vertical water particle velocity is more or less (depending on degree of reflection) predominating. Beyond that, a comparison of his theoretical formulation with model test results shows unneglectable differences.

But according to the results of these investigations, it will be assumed that (for nonbreaking waves) the amplitude reduction factor may be considered to be dependent upon the properties of the structure itself (e.g. porosity, mean stone weight and thickness of the surface layer, revetment slope, water depth and wave length (as a function of wave frequency and water depth)). From the results of our investigations it can be concluded that the amplitude reduction factor is not affected by the wave approach angle. The phase angle ϕ will have the same dependence and will furthermore be strongly affected by the

approach angle.

From extensive model experiments with various partially-reflecting structures (and normal wave attack, GÖTSCHENBERG and SCHEFFER, 1984) it can be concluded that the intersection point between the stillwater level and the impermeable rear slope of the structure can be considered as the physically effective reflection point. From these results SCHEFFER (1985) has set up limiting conditions, which are shown for normal and parallel wave attack in Figure 3. The signed region represents the frequency dependent region of ϕ.

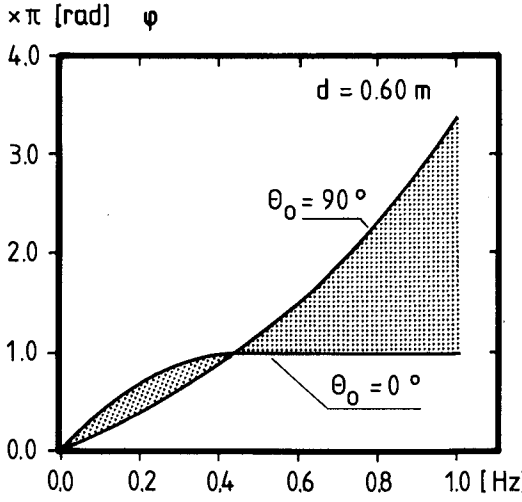

Fig. 3:
Limiting conditions of the phase angle ϕ for oblique wave approach

For the time beeing a determination of both parameters of the complex reflection coefficient by means of hydraulic model tests is recommended. An outline of the conduction of adequate tests is given by GÖTSCHENBERG and SCHEFFER (1984) and SCHEFFER (1985).

3 Model experiments

Within the scope of a basic research programme on the motion of ships at berths, the reflection behaviour of partially-reflecting revetment structures was investigated in a wave flume (length/width/depth = 110/2.0/2.2 m) for normal wave attack and in a wave basin (48/18/1.0 m) for parallel and oblique wave approach. The variation of structural conditions is shown in Figure 4.

The model investigations were carried out comparatively with regular waves and with various theoretically determined wave spectra. Special attention was directed to eliminate the influence of reflected waves and waves re-reflected at the wave maker on the determination of uneffected incident wave spectra. Besides a special arrangement of test performance (see SCHEFFER, 1985), which allows a direct determination of the uneffected approaching wave spectra and the reflection

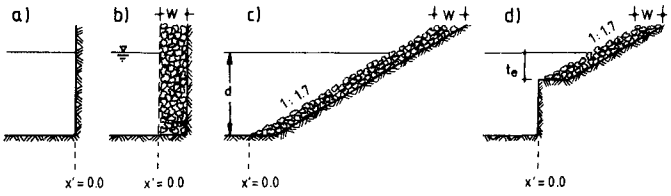

Fig. 4: Reflecting structures investigated

properties by transfer function technique, a 3-wave-gauge-system was installed and the generation technique implied an active absorption control system.

4 Results

4.1 Parameters of reflection coefficient

As a brief summary of the model test results the amplitude reduction factor of a uniform rough slope (see Fig. 4; $t_e = d$) is shown as a function of the wave frequency in Figure 5. The solid line shows the averaged results of tests with different wave spectra. Several tests with regular waves and different wave steepnesses were performed (4-5 wave heights for each frequency). There are no significant differences in the results of regular and irregular wave tests, which confirms the assumed linearity. A slight dependence on the wave steepness can be seen, but there is no clear trend over all wave frequencies within the presented small range of steepnesses, this influence is slight as the influence of the wave length (or for constant water depth the wave frequency).

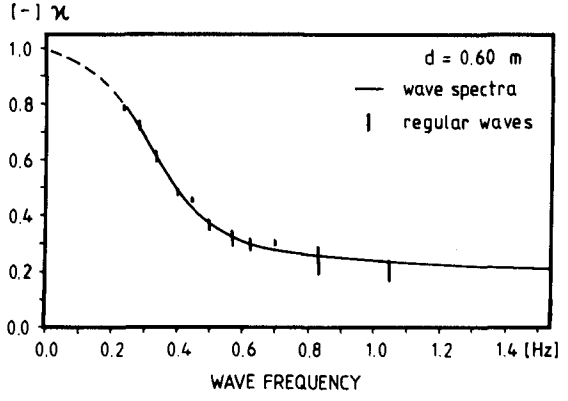

Fig. 5: Amplitude reduction factor κ of the investigated uniform rough slope (Fig. 4c)

The phase angle ϕ of the uniform rough structure is shown in Figure 6 as analyzed from model tests for different wave approach angles. The mentioned limiting conditions shown in Figure 3 are confirmed.

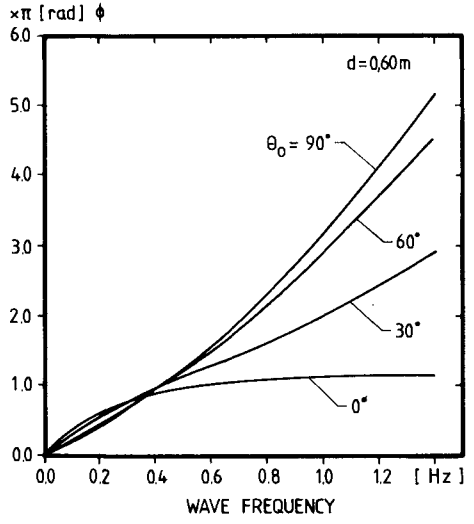

Fig. 6:
Phase angle ϕ of different wave approach directions θ_o

The amplitude reduction factors for all investigated combined structures are shown in Figure 7. The graphs show the interesting effect that in certain frequency range a combined structure will cause a smaller amplitude reduction factor than the continuous slope. This can be explained with the phase shift between the wave proportion reflected at the bottom of the structure at the vertical wall and that one reflected in the upper slope area at the intersection point of stillwater level and impermeable rear slope.

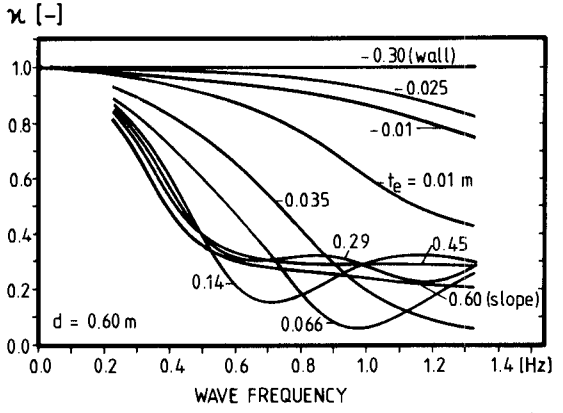

Fig. 7: Measured amplitude reduction factors of various combined structures

4.2 Three-dimensional wave field

As an example of the wide range of experimental results, the transfer function between local linear wave sprectra and uneffected incoming linear wave spectra are shown in Figure 8 for different test alignments. The measured results from different wave spectra and regular waves are presented together with results of theoretical calculations (eq. 7 with measured reflection coefficient, section 4.1).

The results of the investigations show that even the previously inadequate solution to the problem of wave absorption for a wave runnning parallel (θ_o = 0°) to a partially-reflecting revetment can be described. A detailed discussion of this special case may be found by SCHEFFER (1985).

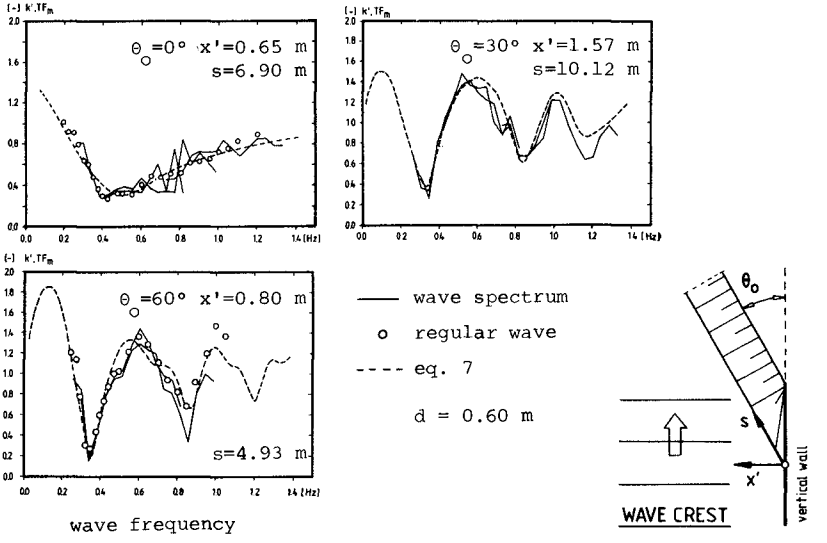

Fig. 8: Measured and calculated k' - values

By way of comparison, Figure 9 shows the wave motion in the reflection area of a totally-reflecting vertical wall (Fig. 9a) and of a partially-reflecting rough slope (t_e = d) (Fig. 9b). In each case, the same time-step of an irregular wave train was calculated. The calculations were carried out in the frequency domain, where the magnitude and the phase of the diffraction coefficient were calculated at each grid point for each component of the 20-frequency component sprectrum adopted here. All components were superimposed true to phase and the inverse FOURIER transfromation gave the wave motion in the time domain as shown in the computer plots.

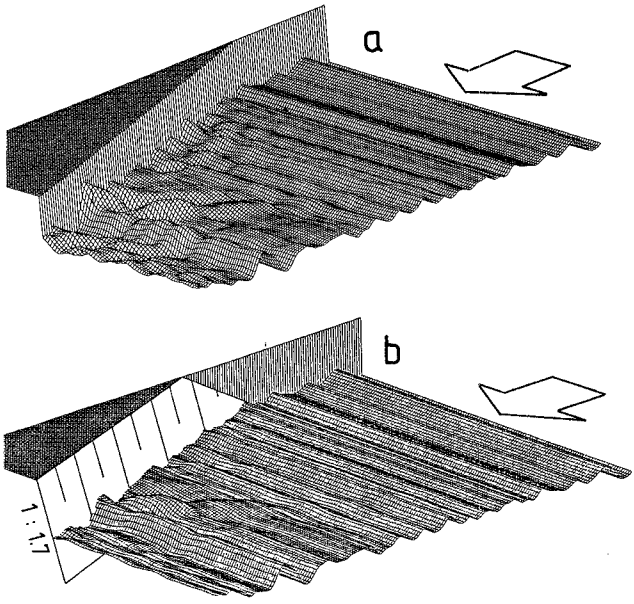

Fig. 9: Wave motion in front of vertical wall and uniform rough slope

5 References

BERGER, U. and KOHLHASE, S.: MACH-reflection as a diffraction problem. Proc. 15th Coastal Eng. Conference, Honolulu 1976.

GÖTSCHENBERG, A. and SCHEFFER, H-J.: Three dimensional investigations on wave relfection including irregular waves. Proc. 4th Congress APD-IAHR, Chiang Mai 1984.

MADSEN, O.S. and WHITE, S.M.: Reflection and transmission characteristics of porous rubble mound breakwaters. R.M. Parson Laboratory, Massachusetts Institute of Technology, 1975.

MADSEN, P.A.: Wave reflection from a vertical permeable wave absorber. Coastal Engineering, Vol. 7, No. 4, 1983.

SCHEFFER, H-J.: Wellenunruhe in Häfen und Schiffsbewegungen. Mitt. des Franzius-Instituts der Universität Hannover, Heft 61, 1985.

CHAPTER 163

A UNIQUE INSTRUMENTATION SCHEME FOR MEASURING LOADS IN MODEL DOLOS UNITS

R.D. SCOTT*, D.J. TURCKE** and W.F. BAIRD***

ABSTRACT

An instrumentation scheme for the measurement of the structural response of dolos units in a physical model due to static and quasi-static forces is presented. This was achieved by the development of a specialized armour unit "load cell". The load cell was tested under a variety of loading conditions ranging from static point loads to the complex forces arising from simulated prototype wave action. In the final stage of testing, a model breakwater was constructed and analyzed. The results of these tests demonstrated the accuracy of the developed instrumentation and the feasibility of its use for measurements conducted in physical models. Knowledge of the structural response of armour units in the breakwater environment may be incorporated into an improved overall design procedure for armour units that considers both the hydraulic stability and the structural integrity of the individual units.

1. INTRODUCTION

Concrete armour units have often been employed to protect rubblemound breakwaters and other similar structures exposed to the marine environment. The use of these units has permitted more economic construction of such structures and, in certain cases, has allowed the construction of rubble structures in locations where natural stone of sufficient size could not be found. In recent years, however, extensive damage has occurred to the armour layers of many breakwaters. This damage has often led to a breach of the breakwater structure rendering it only partially effective with finanancial costs for repairs sometimes totalling into millions of dollars. In certain instances, these failures have been attributed to the breakage of the individual concrete armour units and have clearly illustrated the inadequacies of current design procedures for the armour layers of breakwaters. These breakages have occurred predominately in certain

* Graduate Student, Queen's University, Kingston, Ontario
** Professor of Civil Engineering, Queen's University, Kingston, Ontario
*** W.F. Baird & Associates, Coastal Engineers, Ltd., 38 Antares Drive, Suite 150, Ottawa, Ontario.

types of armour units, such as the dolos or tetrapod units, but structural failure is not limited to such units. Avoiding the utilization of particular units does not avoid the central problem; there is a complete lack of knowledge regarding the nature and magnitude of the forces occurring in the armour layer of breakwaters.

Concrete armour units are subject to a wide variety of mechanical loads in the breakwater environment, ranging in nature from static to quasi-static to dynamic. There forces arise from a number of sources. Thermal loads are caused by concrete curing and by freeze-thaw action in colder climates. Static forces result from the self-weight of the individual unit and of adjacent units as well as by the settlement of the armour layer and ice action. Quasi-static loads are induced under wave action by the drag and inertial forces during fluid uprush and downrush. A number of dynamic forces may occur due to wave slamming and during the construction phase when the armour units are transported and placed. In cases where the units are in motion on a breakwater subjected to wave action, impulse loads due to inter-unit impact and, potentially, projectile impact can occur. An essential step in the design of an armour layer is to design the individual concrete armour units to withstand these applied loadings. Quantification of the environmental forces has an inherent complexity due to the highly variable interaction between fluid and structure as well as due to the randomness of the armour layer with regard to the location and orientation of the individual units. In an effort to determine these loads, procedures have been reported for measuring loads in model armour units. [Hall, Baird and Turcke (1984); Baird, Hall, Turcke and Chadwick (1983)].

The purpose of this paper is to present a unique instrumentation scheme for measuring the structural response of the dolos unit in a physical model. This was achieved by the development of a special armour unit "load cell". Although this study concentrated on one particular armour unit, the dolos unit, the instrumentation could be readily utilized in a number of different armour unit shapes.

2. LOAD CELL DEVELOPMENT

The method of load measurement that was developed was the result of an experimental program carried out on a previously developed instrumentation scheme that employed small scale physical models composed of an epoxy plastic [Hall, Baird and Turcke (1984); Scott et al. (1985); Scott, Turcke and Hall (1985)]. Out of this initial work, a new "load cell" was developed, based on strain gauge technology, that had much superior load sensitivity and instrumentation protection as compared to the previous instrumentation system. [Scott (1986), Scott, Turcke and Baird (1985)].

This dolos "load cell" consisted of a small physical model employing a distorted section at mid-shank where the instrumentation was located. The key element of the load cell was a strain-gauged, thin-walled aluminum tube. This component was inserted in the mid-shank location between the two halves of a dolos unit fabricated from a steel reinforced epoxy plastic. Unassembled and assembled views of the instrumentation are shown in Figures 1 and 2. The aluminum tube

was designed such that it had the equivalent flexual and torsional rigidity to that of a selected prototype unit properly scaled to the model size. It had twelve strain gauges mounted on its surface which were wired into 3 full bridge circuits. Sufficient clearance was maintained between the two halves to ensure that the internal forces in the dolos shank were completely transferred through the instrumented tube. Lead mass was added to the unit in appropriate locations to compensate for loss of material when holes were bored into the unit for tube placement. Waterproofing was applied to the exterior of the dolos shank to maximize strain gauge protection from water intrusion.

The load cell was calibrated to give directly the bending moments in two orthogonal directions and torque by applying known loads to the instrumented unit and measuring the strain gauge output. This type of procedure is followed in the calibration of any load measuring device.

The instrumentation was developed to determine the structural response of the dolos armour unit at the mid-shank location when subjected to static and quasi-static forces. Its applicability to dynamic loadings must be further examined with tests conducted on instrumented prototype units. As well, the use of such instrumentation implies that failure in the dolos unit occurs due to bending and torque. This has been shown by typical structural failures of such units in prototype and in experimental investigations [Terao et al. (1982)].

Figure 1 - The Instrumentation Prior to Assembly

Figure 2 - Assembled Dolos Load Cell

Load cells of two different sizes were constructed. One had an overall length of 106 mm with a material density of 2500 kg/m^3 while a second dolos unit had a length of 203 mm with a density of 2150 kg/m^3. Signals from the load cells were fed directly into an instrument recorder with a frequency response of 9.5 kHz. The recorded signals were replayed into an analogue to digital (A/D) converter and stored on magnetic disk for visual display and manipulation by computer.

3. TEST PROGRAM AND RESULTS

The instrumented units were put through an extensive series of tests to determine both the accuracy of the measurements of the internal forces and the suitability of the units for use in a hydraulic flume. These tests are briefly summarized in the following sub-sections:

a) Static Point Loads

The initial tests were conducted on the units by restraining the units in a test rig and applying point loads of known magnitude at various locations on the dolosse. The measured responses were compared to theoretical calculations of the internal moments and torques at mid-shank. The load cells displayed high levels of accuracy with the measured forces generally being within 5% of their corresponding theoretical values.

b) Loads Under Self-Weight

The next series of tests were conducted by positioning the load cells in various orientations and measuring the internal forces induced by self-weight alone. Again, the measured response was compared with theoretical computations and the accuracy of the load

cells noted. The load cells were even capable of measuring the internal forces induced due to their over self-weight when resting on a flat surface. A typical example of such a test is shown in Figure 3 and the results are displayed in Table 1. The longer (203 mm) armour unit was consistently more accurate than the smaller unit due to greater accuracy in its manufacture and due to the increased load levels for a unit of this size. Errors in measurement can arise from inaccuracies in dolos and tube fabrication and in small mis-alignments of the strain gauges.

c) Simulated Armour Layer

A section of a model armour layer was constructed in the dry by building a filter layer on a rigid platform sloped at 1:2 over which two layers of 203 mm dolosse were placed. The armour layer was rebuilt entirely for each test with the instrumented unit placed at various locations. Measurements were made of the induced moments and torques then the layer was vibrated, to simulate armour layer settlement, and the forces recorded once again.

Some of the test results are shown in Figure 4 where the measured bending moments have been compared with the theoretical values, scaled to the model size, which would cause concrete cracking in the shank of a 30 tonne dolos unit having the indicated concrete compressive strengths. The results appeared reasonable when considering the randomness of the applied loads and boundary conditions and demonstrated the viability of the instrumentation.

Size (mm)	Horizontal Fluke	Measured Moment (N-mm)	Theoretical Moment (N-mm)	Percent Deviation
106	1-2	67.0	72.0	6.9
		63.9	72.0	11.3
		63.9	72.0	11.3
		68.0	72.0	5.6
		73.3	72.0	1.8
		73.3	72.0	1.8
	3-4	66.0	72.0	8.3
		65.1	72.0	9.6
		65.1	72.0	9.6
		74.3	72.0	3.2
		71.1	72.0	1.2
		73.4	72.0	1.9
	Average	68.7	72.0	4.6
203	1-2	838	814	2.9
		832	814	2.2
		836	814	2.7
		836	814	2.7
		836	814	2.7
		834	814	2.4
	3-4	802	814	1.5
		793	814	2.6
		800	814	1.7
		800	814	1.7
		805	814	1.1
		802	814	1.5
	Average	818	814	0.5

Table 1 Results of Self-Weight Load Tests

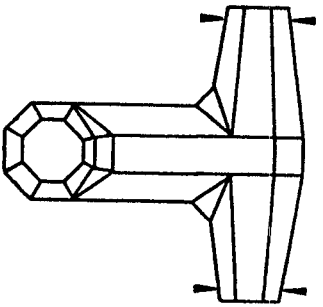

Figure 3 - Dolos Supported in Test Rig

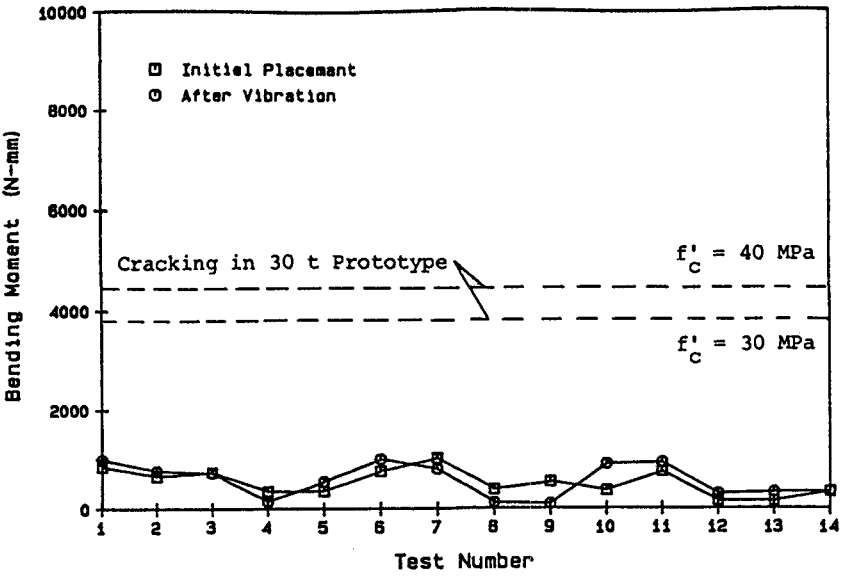

Figure 4 - Typical Results of Simulated Armour Layer

d) Single Dolos in a Hydraulic Flume

The final set of evaluation tests were conducted in a two-dimensional flume using a single instrumented unit rigidly mounted in a specified orientation on a sloped platform, see Figure 5. The purpose of the tests was to examine the change in structural response of the instrumented armour unit due to variations in wave height and dolos location under controlled experimental conditions where the fluid flow was not as complex as which occurs in the armour layer. The dolos unit was placed such that the upper fluke was parallel to the incoming waves and would catch the maximum effect of the wave action.

The load cell was mounted at various locations measured along the slope with respect to the still water level (SWL). Regular waves of three different heights, 15.1 and 19.0 and 24.1 cm, were employed at each test location. The wave period was kept constant at 1.70 seconds for all the tests. At each specified location and wave height, the test was carried out three times.

The typical trace of bending movement versus time displayed in Figure 6 illustrates the excellent correlation of the peak structural response with the wave period. The actual shape of the structural response signal varied depending on the location of the instrumented unit. Placements above and at the SWL gave a response with a strong positive bending movement of short duration. As the unit was placed at lower elevations, the positive movement due to uprush decreased in magnitude while a negative movement due to downrush increased.

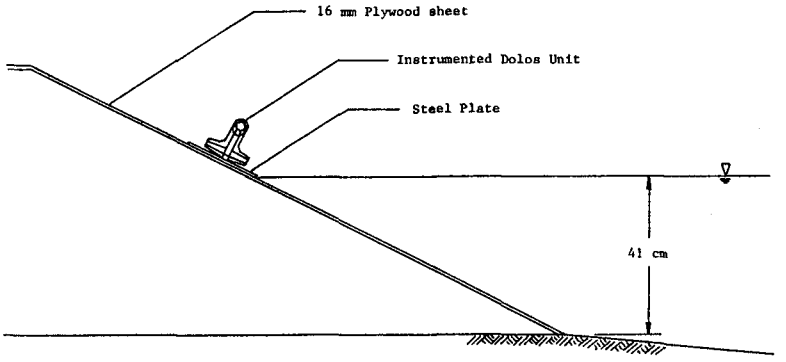

Figure 5 - Single Dolos in Hydraulic Flume

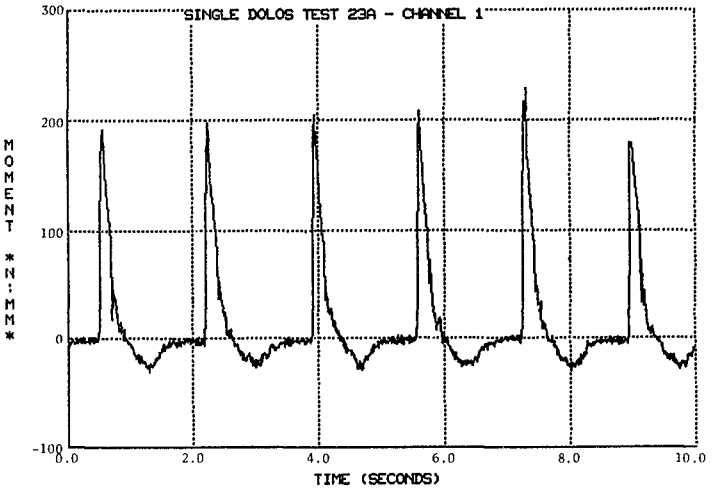

Figure 6 - A Typical Plot of Moment Versus Time

Figure 7 illustrates the variations in peak moment as a function of position for two of the wave heights. It may be noted from the figures that the largest bending moments were measured at positions just below the still water level, a location where many breakwater failures are believed to have been initiated. At any given location, the bending moment increased with increasing wave height.

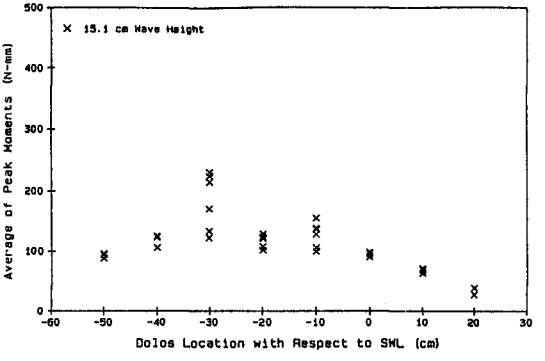

Figure 7 - Effect of Location on Peak Moments - 15.1 cm Wave Height

4. ANALYSIS OF A MODEL BREAKWATER

In the final stage of evaluating the instrumentation system, a model breakwater was constructed and then subjected to simulated prototype wave attack in a two dimensional flume. This exposed the load cell to a wide range of loading conditions ranging from the static loads due to placement in the armour layer to the quasi-static forces created by the fluid motion.

The model breakwater was constructed at a scale of 1:40 in which the model armour units corresponded to 30 tonne dolos units in prototype having a waist ratio of 0.32. The filter layer beneath the dolos armouring consisted of 3 to 30 gram angular stone while the armour layer on the basin side of the breakwater and the toe region was made up of 30 to 60 gram stone. The primary armour layer was formed of 475 gram dolos units of length 106 mm. The dolosse were randomly orientated and dropped into position in an attempt to simulate prototype placement.

Regular waves of height 24 cm and a period of 1.75 seconds were employed in all of the tests, corresponding to waves of 9.5 m height with a period of 11.1 seconds in prototype. The water depth in front of the structure was 40 cm.

The equivalent stability coefficient, K_D, as given by Hudson's formula was approximately 11.0. The armour units did not move under the given conditions.

The instrumented unit was placed at various locations within the armour layer in both the top and bottom layers and both above and below the still water level. A number of waves were allowed to strike the breakwater and the response of the load cell was recorded on an instrument recorder.

A typical response of the instrumented unit to wave action is shown in Figure 8. There was excellent correlation of the peak signal with the wave period and good repeatibility of the results from test to test at any given location. Large stress reversals may occur within the armour unit demonstrating that fatigue may be critical in such units.

Figure 9 displays the static levels of the internal forces as measured prior to wave action in each test. Here, the absolute torque has been plotted against the vector sum of the bending moments. Figure 10 shows a plot of the peak internal forces, which are considerably higher in magnitude than the static forces, as would be expected.

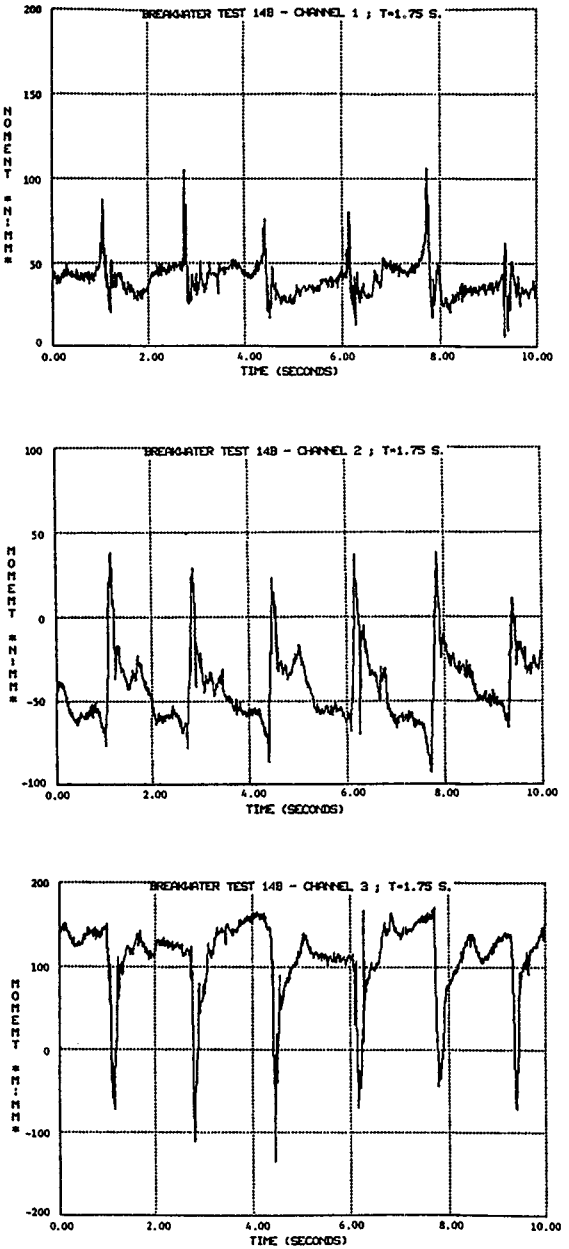

Figure 8 - A Typical Plot of Breakwater Test Results

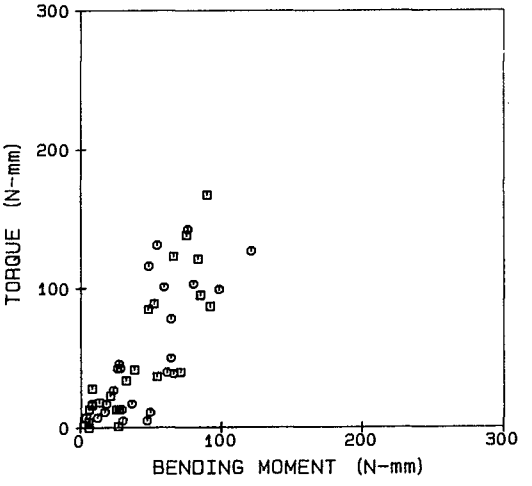

Figure 9 - Static Forces

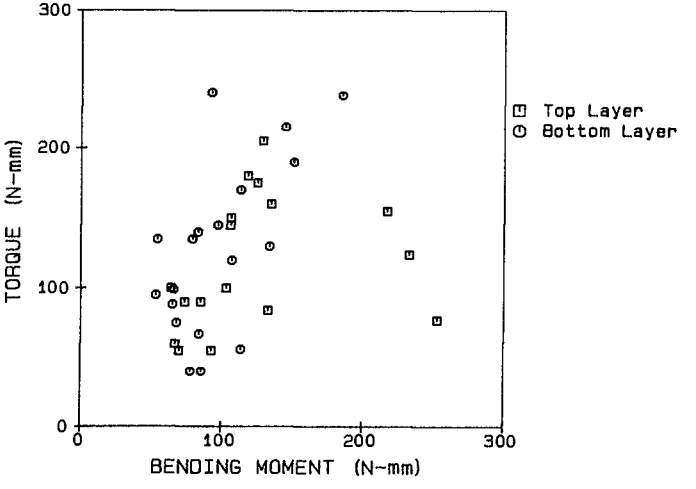

Figure 10 - Peak Internal Forces

CONCLUSIONS

The instrumentation system proved quite capable of measuring the structural response of dolos armour units subjected to static and quasi-static forces in a small scale physical model. The load cell exhibited high sensitivity levels, capable of measuring the response under its own self-weight when resting on a flat surface, but was also quite robust and was able to withstand repeated wave action in a hydraulic flume. The dolos load cells performed with a high degree of reliability and repeatibility throughout the test series.

Various tests were conducted on the instrumented units to evaluate their performance in terms of accuracy of measurement and suitability for use in the hydraulic environment. These tests culminated in the application of the load measurement system to a model rubblemound breakwater armoured with dolosse. Some of the test results were presented but the real value in employing this instrumentation scheme as an analysis or design tool is whether it can determine the structural integrity of armour units in a breakwater. Baird, Scott and Turcke (1986) discusses the incorporation of this instrumentation scheme into an overall design procedure for concrete armour units. Such a procedure must examine scaling of the measured data to prototype and structural failure criteria for the armour units.

REFERENCES

Baird, W.F., Hall, K.R., Turcke, D.J. and Chadwick, D.C., "Development of a Procedure for the Design of Concrete Armour Units for Rubble Mound Breakwaters", Report for Public Works Canada, March 1983.

Baird, W.F., Scott, R.D. and Turcke, D.J., "An Analysis and Design of Armour Units", Proc. of the Twentieth International Coastal Engineering Conference", Taipei, Nov. 10-15, 1986.

Hall, K.R., Baird, W.F. and Turcke, D.J., "Structural Design Procedures for Concrete Armour Units", Proc. of The Nineteenth Coastal Engineering Conference, Houston, Texas, Sept. 3-7, 1984.

Scott, R.D., The Analysis of Concrete Armour Units In a Breakwater, Ph.D. Thesis, Queen's University, December, 1986.

Scott, R.D., Turcke, D.J., Baird, W.F. and Hall, K.R., "The Measurement of Stresses in Model Dolos Units", Presented at the Workshop on Measurement and Analysis of Structural Response in Concrete Armour Units, Vicksburg, Miss., Jan. 23-24, 1985.

Scott, R.D., Turcke, D.J. and Hall, K.R., "Experimental Modelling of Breakwater Units in an Hydraulic Environment", Proc. of the Tenth Canadian Congress of Applied Mechanics, The University of Western Ontario, London, June 2-7, 1985.

CHAPTER 164

CRITICAL RUN-UP HEIGHT ON THE SEA WALL

by Akira Seyama* and Akira Kimura**

ABSTRACT

This study aims at clarifying the difference between irregular and periodic wave run-ups on a slope or a sea wall. Since hydraulic phenomena on a slope are the induced result of an interaction between a running up wave and a back-wash. The run-up height, therefore, has to be investigated in terms of a back-wash properties in addition to run-up wave properties. The experiments which are so designed that waves can run up on a slope without meeting back-wash, were conducted to evaluate the back-wash effects. The relative run-up heights R_r/H_0 of periodic waves in these experiments reached up to about two times as high as those of periodic waves which have the same steepnesses.

The run-up heights of irregular waves on a slope were also investigated experimentally. There are no clear relations between R_r/H_0 and H_0/L_0 as those for periodic waves ordinary observed, and they distributed widely. The upper-most value of R_r/H_0 in the distribution for any H_0/L_0 was almost equal to the value in the above experiment. The uppermost (critical) relative run-up heights R_r/H_0 for the given H_0/L_0 and slope may exist. The differences between the critical and ordinary run-up height of periodic waves on the sea wall were also experimentally investigated. The difference is prominent when a sea wall is set on-shore from the shore-line. It reaches up to about 4 times when a sea wall is set a little on-shore from the shore line.

Some statistical discussion on the probability of the situation in which the critical run-up may be brought about is given at the last part.

* Prof. Dept. of Ocean Civil Engg. Faculty of Engineering, Tottori University, Tottori, Japan.

** Associate Prof. Dept. of Ocean Civil Engg. Faculty of Engineering, Tottori University, Tottori, Japan.

1. INTRODUCTION

Traveling time t_d from the maximum run-up point on a slope to the still water level (SWL) is given by Gunbak(1977) as

$$t_d/T = \sqrt{1/\pi} \cdot 1/\cos\alpha \cdot 1/\sqrt{\xi} \qquad (1)$$

where T is a incident wave period, α is an angle of a slope, ξ is the surf similarity parameter. Run-up time t_u to the maximum point from SWL is also given by him as

$$t_u/T = 0.7\ \xi^{-1/2} \qquad (2)$$

The time left t_l for the down-wash front to retreat down to SWL without meeting the next run-up becomes

$$t_l/T = 1 - t_u/T = 1 - 0.7\ \xi^{-1/2} \qquad (3)$$

In the region $\xi < 1.6$, no interaction between run-up and down-wash takes place above SWL on a slope. Roos and Battjes (1976), however, gave a region, $\xi < 2.5$, for the same situation. Consecutive waves in the region $\xi > 1.6 \sim 2.5$, may interact with each other above SWL on a slope more or less.

Although Saville (1962), Van Oorschot et. al. (1968), Battjes (1971), and Gunbak (1977) showed the validity of the Saville's "hypothesis of equivalency" between periodic and irregular wave run-ups in some degree, these values t_d, t_u and t_l may be different from those of irregular waves which have the same zero-up-cross properties. Because the repetitive effect of the back wash to the next run-up is constant in case of periodic wave run-up. On the contrary, due to the random nature, back-wash effect on the next run-up differs wave by wave in case of irregular wave run-up. In this case, waves with the same properties do not bring about the same run-up height, since a deceleration effect of the back-wash differs wave by wave. This random nature of back-washes must be taken into account when irregular wave run-up on a mild slope is investigated.

In this study, irregular wave run-ups are investigated to show that there are large differences between periodic wave run-ups, firstly. Secondly, experiments which is so designed that an incident wave runs up without meeting the back wash, are conducted and the existence of the critical (upper most) value of R_r/H_0 for H_0/L_0 is shown. Thirdly the same technique is used to investigate the critical run-up heights on the sea walls. Lastly the possibility of the chance in which such critical

run-ups may take place is discussed statistically with the theory of wave groups.

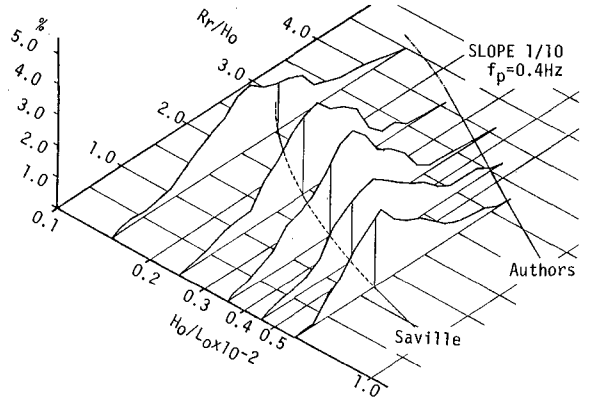

(a) f_p=0.4Hz

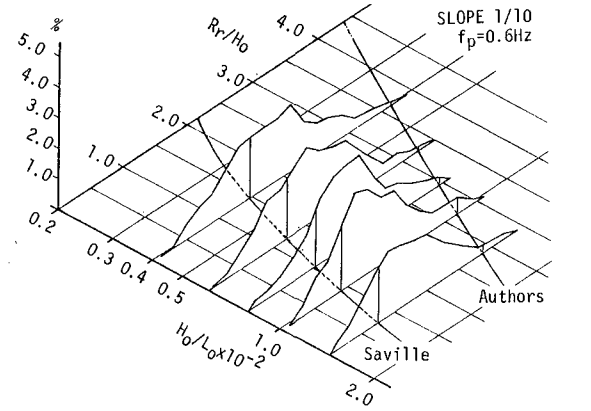

(b) f_p=0.6Hz

Fig.1 Distributions of the relative run-up height of the irregular waves

2. IRREGULAR WAVE RUN-UPS

A wave tank used in the experiments was 27m long, 0.75m deep and 0.5m wide with glass side walls. At one end of the tank, an irregular wave generator was furnished (Kimura et al.,1976) and at the other end, a

smooth slope of 1/10 was installed. A channel section of 2m long, 2cm wide and 1 cm deep was mounted into the center of the slope. The run-up wave gauge of a capacitance wire type was so set in the channel that the wire keeps the equal level to the surface of the slope. Wave gauges were set at h=50cm , 45cm, 20cm, 15cm, 10cm, 5cm and 2cm along the slope in which h is water depth. A water depth at the horizontal bottom was 50cm. Five Pierson-Moskowits type wave spectra, the peak frequencies f_p of which were 0.4Hz, 0.6Hz, 0.8Hz, 1.0Hz and 1.2Hz, were simulated. Since the experiments were conducted to investigate the run-up heights in terms of the incident wave properties, one-to-one correspondence between incident and run-up waves is the necessary condition in the present study. Two cases, f_p=0.4Hz and 0.6Hz, were selected among them, which almost fulfilled the condition. On the average, two or more incident waves formed a single run-up in other cases.

Incident wave properties such as zero-up-cross wave height and period were measured at h=20cm (f_p=0.4Hz) and h=15cm (f_p=0.6Hz) respectively. These two points were almost outside of the breaking zones respectively. Measured wave properties were transformed into those for deep water wave by the linear wave theory, e.g. H_0, L_0. Run-up height R_r was measured vertically from SWL to the maximum run-up point of the wave front.

One typical property of the result is that the relation between measured R_r/H_0 and H_0/L_0 in both cases showed wide scattering. No clear relation between them is estimated as in the periodic wave case (Saville,1953). Figure 1 shows frequency distributions of R_r/H_0 in individual narrow ranks of H_0/L_0. The upper and lower bound of the ranks are listed in Table-1. Transformation of irregular waves due to their dispersive nature from the point h=20cm or 15cm where incident waves were measured to the shore-line was observed to be small. Therefore these wide distributions of R_r/H_0 in the figures may depend on a random characteristics of waves.

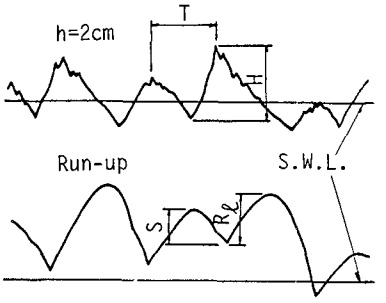

Fig.2 Definition of the properties R_ℓ , S, H and T.

Table-1 Properties of the run-up distributions

f_p=0.4Hz

$H_0/L_0 X10^3$	1-2	2-3	3-4	4-5	5-7
$(H_0/L_0)_i X10^3$	1.52	2.50	3.52	4.48	5.75
R_S/H_0	2.52	1.88	1.58	1.39	1.22
R_r/H_0	2.32	2.13	1.90	1.88	1.77
Prob.$(R_r/H_0>R_S/H_0)$ (%)	38	65	70	72	77

f_p=0.6Hz

$H_0/L_0 X10^3$	3-5	5-7	7-9	9-12	12-20
$(H_0/L_0)_i X10^3$	4.06	6.01	7.94	10.29	14.54
R_S/H_0	1.47	1.20	1.04	0.93	0.74
R_r/H_0	1.94	1.71	1.66	1.54	1.33
Prob.$(R_r/H_0>R_S/H_0)$ (%)	70	77	88	86	87

Another feature is that a significant part of the distribution exceeds the experimental result of periodic waves R_S/H_0 by Saville (i=1/10). The larger H_0/L_0 becomes the higher portion of the data which exceed the Saville's result becomes as listed in Table-1. Nearly 90% of data exceeds the dotted line $R_S/H_0 \sim H_0/L_0$ when $(H_0/L_0)_i$=0.0145 in figure (b).

These wide distributions of R_r/H_0 are presumably brought about by occasionally different effect of back-washes on the next run-up waves.

To investigate the back-wash effects, the relations between the properties in Fig.2 were measured and analyzed. T is an interval of the incident bore crests at h=2cm. This is almost equal to the zero-up-cross wave period measured just outside the breaking zone. H is a height of the bore from its toe to crest. S is a vertical distance from the former crest of the run-up wave to its crossing point with the next run-up. And R_ℓ is a vertical distance from the crossing point to the next run-up wave crest.

Figures in Fig.3 show the averaged relations between measured values. Totally these properties of 1000 waves in the case of f_p=0.4Hz were measured. Measured data were divided into ranks of T and S. The region of the ranks are listed in the figures. Data of H are divided into three groups of the same size in individual ranks of T and S. Symbols in the figures are plotted at the centers of individual ranks. Almost linear relations exist between R_ℓ and H while T is small. And the

slope of their relation increases with decreasing S. Since, the larger S becomes the more back-wash is accelerated on the slope, and the more the next wave which runs up against the back-wash may lose its energy.
The effect of T is indirect on the contrary. The larger T becomes the shorter time interval in which a back-wash acts on the next run-up on the slope reduces. If T is larger than a traveling time of a run-up and -down on the slope, this property gives no effect on the next wave run-up. If T is small, on the contrary, two or more incident waves form a single run-up since the next wave runs up before the former run-up reaches its maximum. In the selected two cases (f_p=0.4Hz and 0.6Hz), these two extreme situations in T were seldom. A run-up wave is, therefore, affected somehow by a back-wash of the former run-up wave. From Fig.3, we may conclude that the smaller the back-wash effect reduces the higher wave runs up. This situations may take place when the former wave height is very small or the time interval of consecutive bores is very large i.e. S is very small or T is very large. The former situation is so called "jump of waves" (Burcharth,1980). Its probability of realization is not negligibly small (Section 5). The latter situation in T is also possible because T has a statistical nature (Longuet-Higgins, 1975, Kimura, 1981 and etc.).

3. CRITICAL RUN-UP HEIGHT

The upper-most (critical) run-up height may take place when run-up wave meets no back-washes on a slope. To investigate the critical run-up height, the facilities shown in Fig.4 was used, which could realize a run-up of waves on a slope with no back-wash effect.

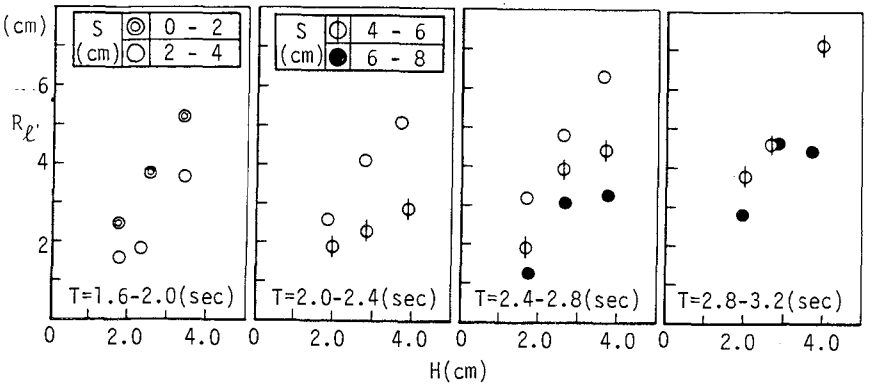

Fig.3 Relation between R_{ℓ} and H.

A water tight wave reflection board which was movable upward, was installed on the slope at h=20cm, (Case-II). A water tight block was put at h=9cm in addition to that for Case-II, and all water shore-side of the block was pumped into the interval between the block and the board, (Case-III). The run-up without these facilities were investigated for comparison, (Case-I). The water depth at the flat bottom was 35cm. Run-up height R was measured vertically from SWL to its maximum run-up point on the slope.

The techniques used in the experiments were as follows. In case-II, the reflection board was removed upward when a water surface of a standing wave just crossed SWL upward at the board. This was the instance when a front of an incident zero-up-cross wave just reached the board. Since shore-side of the board was still water unless the board was removed, the incident zero-up-cross wave propagated and run up on a slope with no effect of the former wave. Although small deformation around wave front was observed, overall deformation due to the discontinuity seemed to be negligibly small within the range of waves used in the present study. In Case-III, a slow oscillation started on the slope when only the shore-side block was removed quickly. The generated wave traveled back and forth within an interval between the slope and the reflection board for a while. The board was removed at the same instance as for Case-II. In addition to the timing in case-II, the timing of the block to remove was so adjusted as a result that the run-up wave just passes

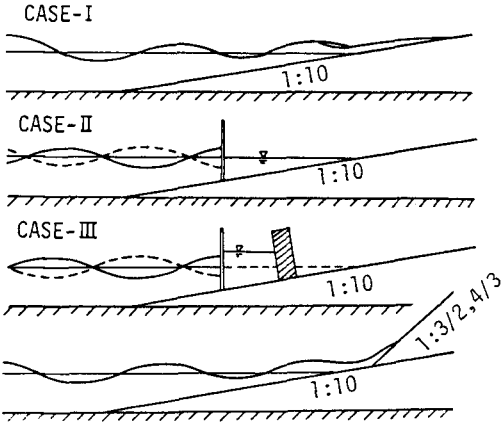

Fig.4 Experimental facilities

over the slow oscillation when it reached the second maximum on the slope. Energy loss of run-up wave due to friction loss on a dry bed might reduce with this technique.

Three different periodic waves T=1.72s, 1.21s and 0.74s were experimented. Wave heights were changed gradually until they started to break in individual cases. Figure 5 shows the relations between experimented values of R/H_0 and H_0/L_0. The solid line shows the result in Case-I. It agrees well with Saville's results.

The broken lines II_1 (T=1.72s), II_2 (T=1.21s) and II_3 (T=0.74s) show the averaged relations between R/H_0 and H_0/L_0 for individual wave periods in Case-11. Individual lines give different relations between R/H_0 and H_0/L_0. R/H_0 keeps an almost constant value where H_0/L_0 is small but decrease quickly when wave starts to break on the slope. In Case-I, plunging or collapsing type break takes place around the shore line. Breaks do not take place, however, when H_0/L_0 is small in Case-II and III. In the larger region of H_0/L_0 than the points where the broken line breaks in individual cases, waves break also and the values of R/H_0 reduce quickly.

Circles in the figure show the relation between R/H_0 and H_0/L_0 for Case-111. The same wave periods and wave heights as in Case-II were used in the experiments. Plotted data form almost the parallel line to those for Case-1. And their values are almost double of those for Case-I for the same H_0/L_0. Incident waves start to break at almost the same value of H_0/L_0 as in Case-II. R/H_0 in the large region of H_0/L_0 also reduces rapidly as in Case-II. The differences between broken lines and circles may not come only from friction loss on the slope. There may be affected

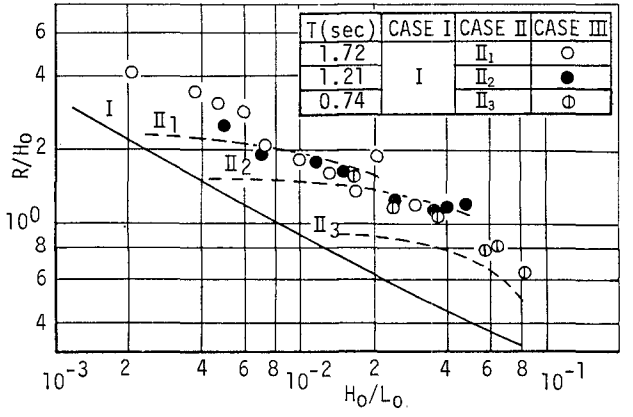

Fig.5 Relation between R/H_0 and H_0/L_0 on the 1/10 slope.

by the slow oscillation in addition, i.e. forward current and apparent water depth induced by this oscillation. These differences may take place in real sea conditions when mean water level changes due to surf beat, for example. Such effects in Case-111 as forward current and apparent water depth change give little change when incident wave properties reach the breaking condition in Case-11 and 1II, since an averaged value of plotted data in Case-III passes through the bends of lines in Case-11. The plotted data in Case-III may give a relation between the upper-most run-up height R/H_0 for H_0/L_0 on the slope of 1/10. The above lines in Fig.1 (a), (b) are the mean relation between R/H_0 and H_0/L_0 for Case-111. These lines almost pass the upper bound of the distributions. Therefore the situations in the Case-I1 and III may take place in irregular wave run-ups. This may be the reason why a large portion of the irregular wave run-ups exceed the values for periodic waves.

4. RUN-UP ON THE SEA WALL

The critical run-up height on a sea wall is investigated in this section using the same techniques in the former section. Two sea walls i=3/2 and 4/3 were used (i is a slope). Run-up height on these sea walls at several locations along the slope (1/10) were measured. Figure 6 shows the relation between relative run-up height R/H_0 of periodic waves on the 4/3 slope and d/L_0 (d is a water depth at toe of the sea wall). The steepness of the incident waves in individual figures are H_0/L_0=0.017 (top), 0.031 (center) and 0.041 (bottom) respectively. Since the wave period (wave length) is constant in each figure, i.e. T=1.72s (top), 1.21s (center) and 0.74s (bottom), d/L_0 practically indicates the water depth at the toe of the sea wall.

Therefore these three figures show practically the change of R/H_0 in terms of water depth. Circles and triangles are the results in Case-1 and 1I respectively. Run-up heights in Case-1 are larger than those for Case-I1 in a offshore region, and gradually decrease with decreasing water depth. The run-up heights for Case-II, on the contrary, keep almost constant value or show a little increasing nature with decreasing water depth unless $d/L_0 < -0.01$. Inequality of plotted values for Case-1 and I1 is reversed a little off the shore-line in individual cases.

Figure 7 shows the relative depth d/L_0 at the reversal points in Fig.6 in terms of H_0/L_0. In the below region of the line, irregular waves may bring about the larger run-up heights than those by periodic waves on the sea wall.

Figure 8 (a),(b) and (c) show the run-up heights on the 3/2 slope. The sea wall was installed (a) at the shore line, (b) 30cm and (c) 50cm on-

shore from the shore line along the slope. The wave periods experimented were 1.72s, 1.21s and 0.74s. In each figure, circles, triangles and circles with an oblique line show that those are the results for Case-I, II and III respectively. The decreasing nature of R/H_0 with respect to H_0/L_0 for Case-I becomes slightly milder than that in Fig.5. Although this tendency reduces with a distance from the shore-line to the sea wall. R/H_0 increases more or less with H_0/L_0 unless waves do not break on the slope in Case-II. When wave start to break, R/H_0 reduce very quickly with H_0/L_0. The upper-most values of R/H_0 are about (a) 2.5, (b) 4.0 and (c) 3.5 times as large as those for Case-I.

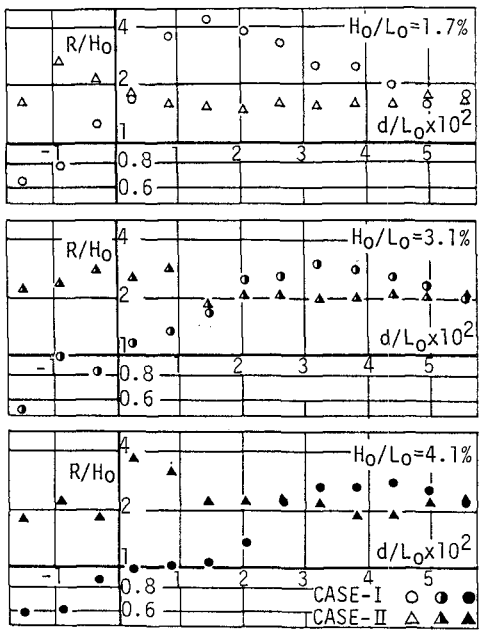

Fig.6 Change in R/H_0 with respect to d/L_0 (sea wall:4/3, slope:1/10)

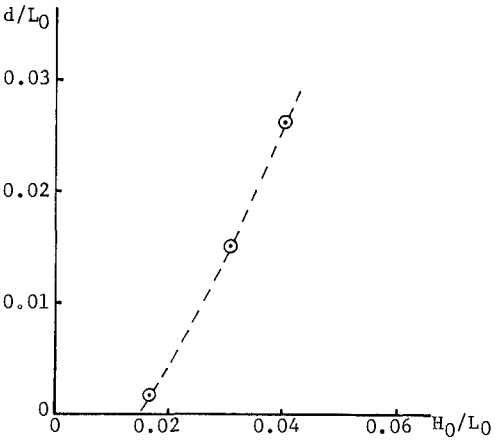

Fig.7 Relative depth at the reversal points of the run-up height.

The relation between R/H_0 and H_0/L_0 for Case-III is different from that for Case-II, however, the maximum R/H_0 value and its H_0/L_0 are almost the same as those for Case-II. The existences of the critical run-up heights shown with the dotted lines in the figures can be presumed.

5. JUMP OF WAVE HEIGHTS

The experiments were so conducted that waves run up without any effects of the back-wash on the slope or sea walls in Sections 3 and 4. And the existences of the critical run-up heights are eventually shown. This situation could practically realize in a real sea condition. For example, when a large wave runs up just after a small wave, i.e. jump of wave heights (Burcharth,1980), the above situation may take place on a slope. Table-2 gives the probability that consecutive wave heights H_1 and H_2 fall in the listed region in the vertical and horizontal column, (Kimura,1980). The correlation coefficient used in the theory is that for the Pierson-Moskowits type irregular waves. Since about 10^4 - 10^5 waves attack on a sea wall within a single storm, mentioned situations may take place with a considerable frequency.

(a)

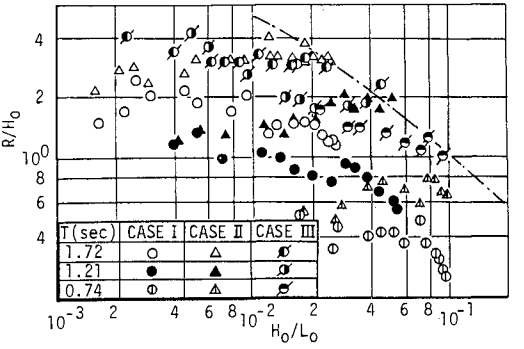

(b)

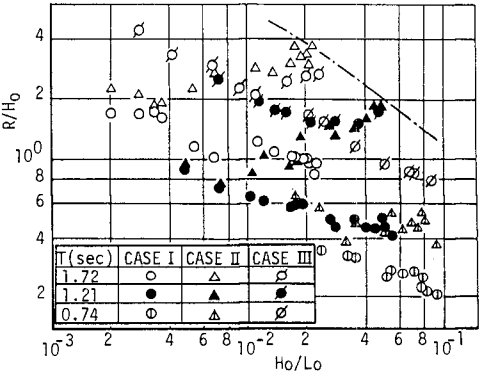

(c)

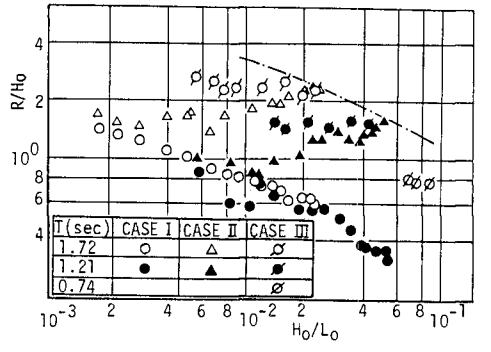

Fig.8 Relations between R/H_0 and H_0/L_0 (sea wall:3/2, slope:1/10)

Table-2 Prob.($H_1<h_1, H_2>h_2$)

		$H_2/H_{1/3}$			
	h_2	1.0	1.25	1.50	1.75
	h_1				
$H_1/H_{1/3}$	0.1	0.0019	0.0005	0.0001	-
	0.2	0.0073	0.0019	0.0004	0.0001
	0.3	0.0157	0.0043	0.0009	0.0001
	0.4	0.0272	0.0074	0.0015	0.0002
	0.5	0.0403	0.0112	0.0023	0.0004

Acknowledgment

The authors wish to express their thanks to Prof. Y.Iwagaki, Kyoto University, for his permission in using facilities, and to Dr. H. Mase, Kyoto University for his help in the experiments and analysis. And acknowledgments are also directed to Mr. M. Tamagawa, K. Sasaki, S. Wakasa and H. Kasuya for their help in experiments.

REFERENCES

Battjes, J.A. (1971): Run-up distribution of waves breaking on slopes, Proc. ASCE, Vol.97, WW1, pp.91-114.

Burcharth, H.F., (1980): Full scale trials of Dolos-blocks to Destruction, Proc. 17th ICCE, pp.1928-1947.

Gunbak, A.R. (1977): See Per Bruun ed. (1985), Design and construction of mounds for breakwaters and coastal protection, Elsevier.

Kimura, A. and Y. Iwagaki (1976): Random wave simulation in a laboratory wave tank, Proc. 15th ICCE, pp.368-387.

Kimura, A. (1980): Statistical properties of random wave groups, Proc. 17th ICCE, pp.2955-2973.

Kimura, A. (1981): Joint distribution of the wave heights and periods of random sea waves, Coastal Engg. in Japan, Vol.24, pp.77-92.

Longuet-Higgins, M.S. (1975): On the joint distribution of the periods and amplitudes of sea waves, Jour. Geophy. Res., Vol.80, No.18, pp.2688-2694.

Roos, A. and J.A. Battjes (1976): Characteristics of flow in run-up of periodic waves, Proc. 15th ICCE, pp.781-795.

Saville, T. (1953): Wave run-up on shore structures, Trans. ASCE, Vol.123.

Saville, T. (1962): An approximation to wave run-up frequency distribution, Proc. 8th ICCE, pp.48-59.

Van Oorschot, J.H. and d'Angremond, K. (1968): The effect of wave energy spectra on wave run-up, Proc. 11th ICCE, pp.888-900.

CHAPTER 165

Scale Effects on Stability and Wave Reflection regarding Armor Units

by

Atsuyuki Shimada[1], Toshimi Fujimoto[2], Syozo Saito[3],

Tsutomu Sakakiyama[4], and Hiromaru Hirakuchi[5]

ABSTRACT

In the studies on stability of the armor units and reflection from those, there are some indications on scale effects which are included in the results of small scale experiments. In this study, the fact has been confirmed with large wave flume test, and estimated the critical Reynolds Number where was no scale effect. And by this result on the stability of urmor units, we can evaluated the results in small and middle scale test, and can correct the minimum weight of armor units. So we can design the breakwaters and seawalls rationaly and economically.

However, it has not been confirmed the critical Reynolds Number where the influence of scale effect on reflection became negligible.

1. INTRODUCTION

In recent years, according to enlargement of thermal and atomic power station sited on coastal regions in Japan, breakwaters and seawalls which protect harbour facilities have been constructed in the areas with water depth of more than twenty meters, so it is necessary to design armor units rationaly and economically.

Especially, the concrete Blocks (urmor units) which are used for decreasing the wave force and reflection waves are main structural materials of breakwaters and seawalls, and in deeper areas, many volume of armor units are necessary and the proportion of their cost to the total construction cost is not few.

To design the armor units which are used for coastal structures, it is important to decide the shapes and weight of armor unit considering following three points of view,

---

1),2),3) Principal Research Engineer Structural Hydraulics Section Hydraulics Department Abiko Research Laboratory Central Research Institute of Electric Power Industry.

4),5) Assistant Research Engineer, Current employments are same as above.

(1) the hydraulic characteristics on stability to the wave force and wave reflection
(2) the relation between the shape of armor units and the strength of concrete
(3) the geological characteristic of sea bed soil in the site.

And in respect to the stability on armor units in (1), hitherto, it have been used to estimate the minimum weight of armor units with Hudson's[1] formula. And in this formula, the coefficient K_D was conducted from the result of small scale tests on rubble mound.

However, since he proposed in 1958, now, from the review of actual damage examples, it has been pointed out that the value of K_D had been conservative a little.

And Thomsen[2] et al. (1972) have investigated about scale effects on stability of rubble mound and some kinds of armor units, and they have pointed out the existence. However, there is almost no study about scale effect on stability of armor units which are widely used in Japan. And in the investigation by Alf Torum[3] et al, they have conducted the model test about the revival of damaged breakwater in site. And they reported that there was no scale effect on the deformation of the cross section.

Thus, it has not been obtained to get a general consensus about this theme. And more data about this investigation are needed[4].

We have already investigated the scale effect on stability and reflection of armor units using model tests in small and middle wave flume.

Now, we are going to clarify the hydraulic characteristic of armor units with large wave flume, and to detect the hydraulic range where indluence of scale effect on stability and reflection ratio become negligible. And if the range or criteria of these scale effect are made to clarify, verious results obtained from small model tests will be more applicable.

2. EXPERIMENTAL METHOD AND DIMENSION

The small wave flume is 20m long, 0.6m high and 0.3m wide, and middle wave flume is 77m long 1m high and 0.9m wide. And we have investigated about scale effect in these wave flumes.

The weights of model armor units used in these tests ranged from 16g to 300g. The large wave flume is 205m long, 6m high and 3.4 wide. And it can generate a maximum of 2m wave height.

Figure-1 shows the profile of this flume.

Figure-2 shows an example of cross section model in the test.

The each dimension of model cross section was decided with the scale in proportion to prototype. Three kinds of the armor units were used in the experiment and these weights range from 2kg to 50kg.

The armor units were put at random with two layers thickness.

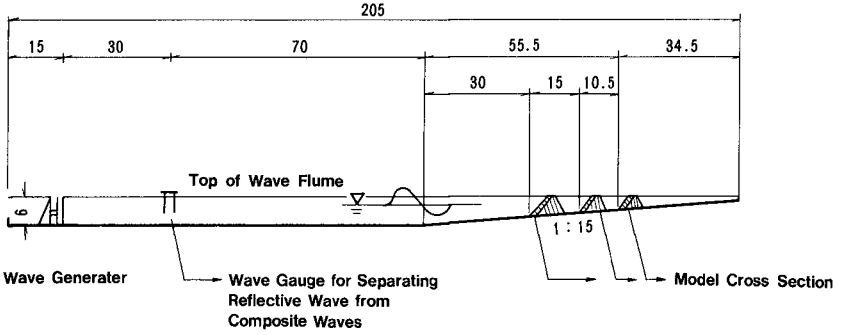

Figure-1 Profile of Large Wave Flume (unit m)

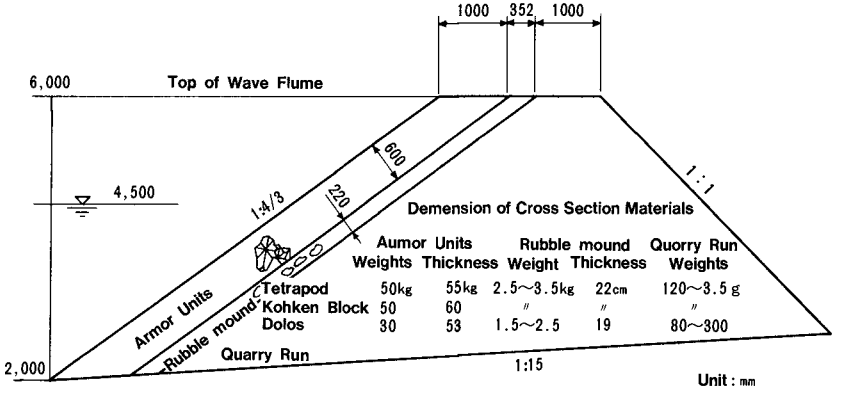

Figure-2 Model Cross Section

Figure-3 shows the shapes of the armor units in the experiment.

The experimental waves are regular waves which are broken at the toe of cross section. To avoid the occurrence of multi-reflection wave in flume, generated waves were stopped in about 2 minutes once a time and were continued to a setting duration. Incident and reflection wave height were measured by the method of separating reflection wave from composite waves at uniform water depth in the flume.

To decide the judgement criteria of the armor units stability, damage percentage was defined as the ratio of removed armor units numbers to the all armor units which were exposed to the wave actions. And the word "removed" means that an armor unit moved over the length of the armor unit height. And using this definition, the removal of up to one armor unit is considered to be zero damage in this experiment. Breaking wave heights Hb which cause 0% and 2% damage were searched in each model cross section.

Table-1 shows conditions of all experiments.
The movements of armor units were observed by video camera and eyes. And run-up heights on surface layer were observed by wave height recorder which was set on the slope.

Test Dimension

Large Wave Flume	**205m (Length) 6m (Height) 3.4m (Width)**
Test Wave	**Wave Height up till Breaking Wave (max 1.85m)**
	Period 2.3sec~6sec

Name of Armor Units

Tetrapod	**2.16kg**	**6.81kg**	**20.85kg**	**49.34kg**
Dolos	**1.99kg**	**9.66kg**	**29.37kg**	
Kohken Block	**2.05kg**	**6.61kg**	**19.65kg**	**49.58kg**

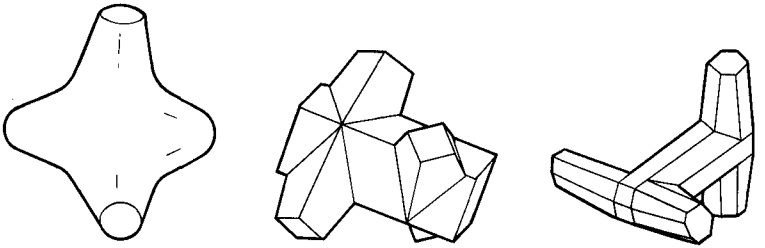

Figure-3 Dimensions in Tests and Shapes of Armor Units used in Large Wave Flume

Table-1 Conditions for large flume tests

Test No.	armor units	Weight(kg)	Section	depth(m)	Period(sec)	Wave Height(m)
1—1	TeTrapod	2.16	I	0.50	2.3	0043 ～0.48
1—2	〃	2.16	〃	0.50	3.0	0.46 ～0.49
1—3	〃	2.16	〃	0.45	4.0	0.49 ～0.51
2—1	Kohken Block	2.05	I	0.50	2.3	0.44 ～0.48
2—2	〃	2.05	〃	0.50	3.0	0.495～0.50
2—3	〃	2.05	〃	0.45	4.0	0.495～0.51
3—1	Dolos	1.99	I	0.65	2.3	0.52 ～0.575
3—2	〃	1.99	〃	0.60	3.0	0.57 ～0.61
3—3	〃	1.99	〃	0.60	4.0	0.62 ～0.66
4—1	Tetrapod	6.81	II	0.80	2.5	0.70 ～0.76
4—2	〃	6.81	〃	0.70	3.5	0.75 ～
4—3	〃	6.81	〃	0.70	4.5	0.80 ～0.84
5—1	Kohken Block	6.61	II	0.80	2.5	0.70 ～0.74
5—2	〃	6.61	〃	0.70	3.5	0.75 ～
5—3	〃	6.61	〃	0.70	4.5	0.83 ～0.85
6—1	Tetrapod	20.85	III	1.30	3.0	1.05 ～1.12
6—2	〃	20.85	〃	1.30	4.0	1.18 ～1.25
6—3	〃	20.85	〃	1.20	5.0	1.17 ～1.26
7—1	Kohken Block	19.65	III	1.30	3.0	1.13 ～1.20
7—2	〃	19.65	〃	1.30	3.5	1.02 ～1.17
7—3	〃	19.65	〃	1.30	4.0	1.25 ～1.30
8—1	Dolos	9.66	III	1.10	3.0	0.84 ～0.90
8—2	〃	9.66	〃	1.00	4.0	0.97 ～1.05
8—3	〃	9.66	〃	1.00	5.0	1.05 ～1.15
9—1	Tetrapod	49.34	IV	1.70	4.0	1.50 ～1.51
9—2	〃	49.34	〃	1.50	6.0	1.60 ～1.63
10—1	Kohken Block	49.58	IV	1.80	4.0	1.50 ～1.59
10—2	〃	49.58	〃	1.50	6.0	1.63 ～
11—1	Dolos	29.37	IV	1.80	4.0	1.39 ～1.58
11—2	〃	29.37	〃	1.70	5.0	1.53 ～1.65
11—3	〃	29.37	〃	1.70	6.0	1.55 ～1.76

3. RESULT AND CONSIDERATION

(1) Characteristics of Experimental Wave

The sea bottom slope below model in large flume is 1:15. Before the stability test, characteristics of generated wave were observed.

Figure-4 shows the relation between breaking wave height Hb and breaking depth hb in the large wave flume.

In figure, curves show outline of progressive waves on each sea bottom slope, obtained from general small and middle flume tests.

And dotted points show experimental values in this large flume.

These values show good coincidence and the ratio of Hb/hb are distributed within 0.8 and 1.2..

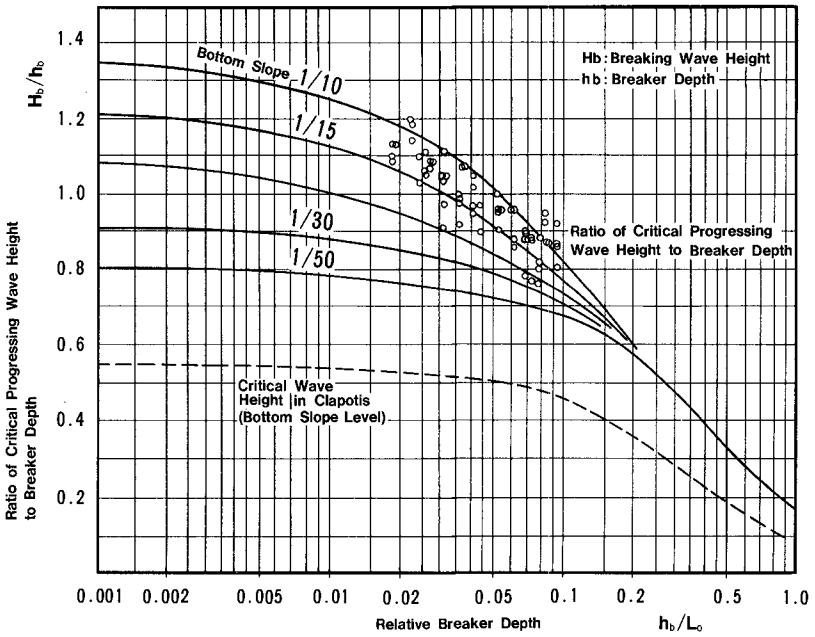

Figure-4 Characteristic of Breaking Wave in the Test

(2) Wave Run Up

Figure-5 shows wave run up heights by which 0% and 2% damages were caused. In figure, curves show the wave run up on smooth surface and the layer covered with armor units at slope of tan θ : 3/4 by the method of the temporary slope which was proposed by T. Saville[6].

Figure-5 shows that the values of wave run up in the experiments are almost below the values in smooth surface but are distributed in fairly higher location than the values in the case of layer covered with armor units. Considering that the curves by Saville's method were obtained from the results in small scale tests, it is recognized that there are scale effects in this behavior.

So it is necessary to consider the relation between the stability of armor units and wave run up.

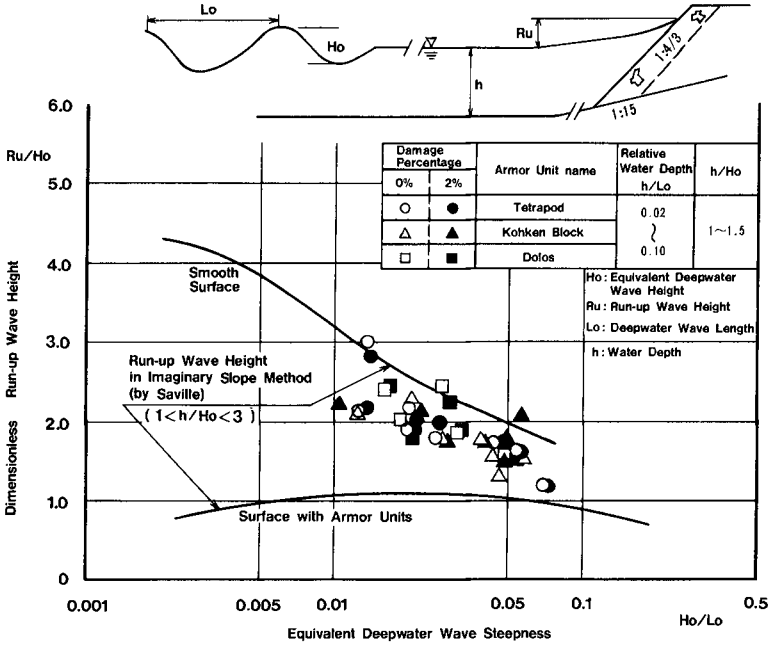

Figure-5 Wave Run-up in the Test Cross Section

(3) Stability of Armor Units

The results of experiments on the scale effect of stability of armor units are shown in Figure-6. The axis of ordinate indicates the stability number Ns. And Ns mean the ratio of wave force which act to

armor units and the resistance force of armor units.

And Ns is difined as following equation.

$$Ns = \frac{Hb \cdot \gamma^{1/3}}{W^{1/3} \cdot (S-1)} \quad \cdots\cdots (1)$$

Where, Hb : breaking wave height at the point where the toe of model section is set after (cm)

γ : the specific weight of the armor units (g/cm^3)

S : the ratio of γ to the specific weight of water

W : the weight of one armor unit (g)

Further, the K_D value in Hudson formula in the case of which cross section slope is θ degree are defined as following equation.

$$K_D = \frac{Ns^3}{\cot \theta} \quad \cdots\cdots (2)$$

The transverse axis indicates the Reynolds Number which show the influence of the force by fluid viscosity around the armor units. In this Reynolds Number, the terms in water particle velocity are estimated first by long wave velocity C: $\sqrt{gh}$, g: gravity acceleration, h: depth, and further, h are displaced by breaking wave height Hb which is nearly equal to h. And the terms of length are estimated by the volume of the armor unit to the one-three power.

So, in this study Reynolds Number are defined as following equation,

$$Re = \left(\frac{\gamma_f}{\mu}\right)\left(\frac{W}{\gamma}\right)^{1/3}\left(\frac{H}{g}\right)^{1/2} \quad \cdots\cdots (3)$$

where, γ_f : the weight in unit volume of water (g/cm^3)

μ : viscosity coefficient of water ($g \cdot sec/cm^2$)

W : the weight of one armor unit (g)

g : gravity acceleration (cm/sec^2)

And wave period T are indicated by nondimensional style, $gT^2/(W/\gamma_f)^{1/3}$. In Figure-6, the results in each kind of armor units which weights range from 16g to 50Kg are ploted.

And the results in smaller than 300g weights have been obtained already from small and middle wave flumes[7].

Figure-6 shows that according to the Reynolds Number increasing, stability Number of each kind of armor units tend upward too, and this feature indicate the scale effect on the stability of armor units. However, where the Reynolds Number take more than nearly 4×10^5, that means the experimental armor unit weights are more than 6.8kg in the case of any armor unit, it is found that the values of Ns approach to a constant value. However, the influence of wave period to the stability of the armor units is not so obvious and as the result, the values of Ns in long waves is smaller rather than in short waves. It is considered that, to this tendency, experimental waves were all limited to the breaking wave at the toe of cross section.

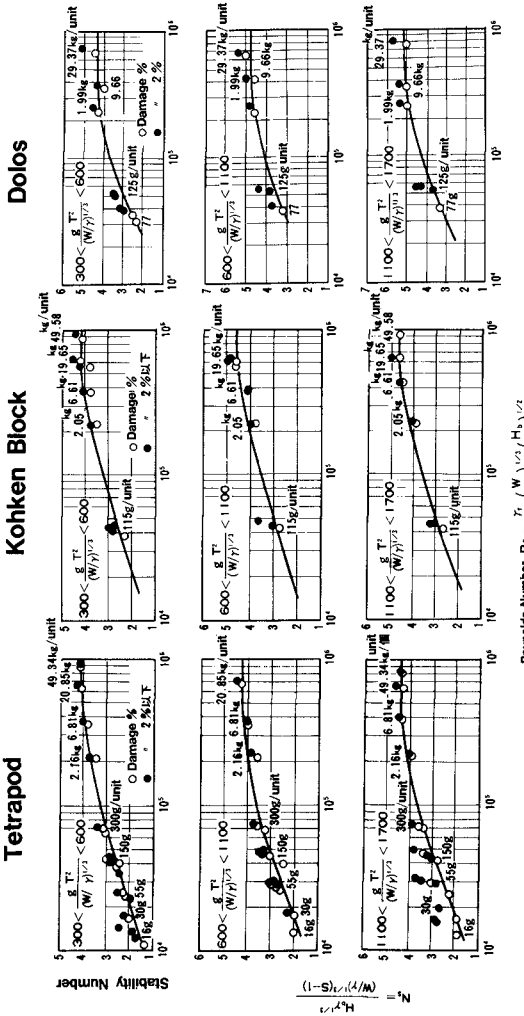

Figure-6 Relation between Stability Number and Reynolds Number

And the long waves breaker at that point are generated in shallower depth than in short period wave breaker. So it is concluded in this study long period wave energy attacking cross section is smaller than short period wave.

Figure-7 shows the stability of each kind of armor units with the expression Hb/D in stead of Stability Number Ns in transverse axis in Figure-6.

Where Hb is breaker height in the stage of stability criteria and D indicates two layers thickness of each armor units. In Figure-7, variable amounts which indicate the scale effect on the each armor units are concentrated on the same curved line.

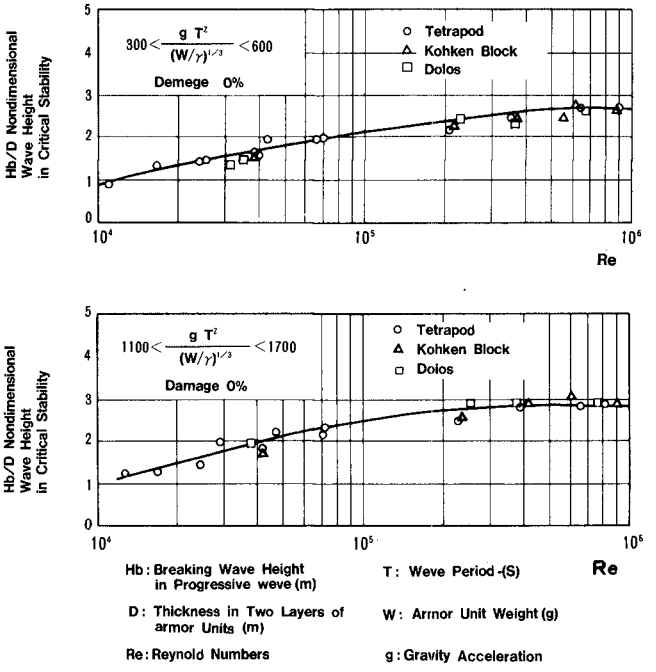

Figure-7 Relation between Reynolds Number and nondimensional wave Height in critical Stability considered Thickness in Two Layers of Armor Units

In this investigation, it was known that the shapes of armor units are connected with the stability of the armor units than that of rubble mound even if interlocking matter were included.

And the value of Hb/D will give the outline in design of the armor units. To give the correct value of Stability Number Ns in prototype from results in small scale experiment.

Figure-8 is presented by rewriting.

Now, Figure-6 and this expression was quoted from Thomsen[2]. For example, if the armor units in weight 100g has been used in test, it will be reasonable in prototype design to take 1.45 times Ns. In Figure-8 the results of rubble mound in CERC are shown, and it's tendency is similar to our results.

And the results of small scale tests will be more applicable by using this result.

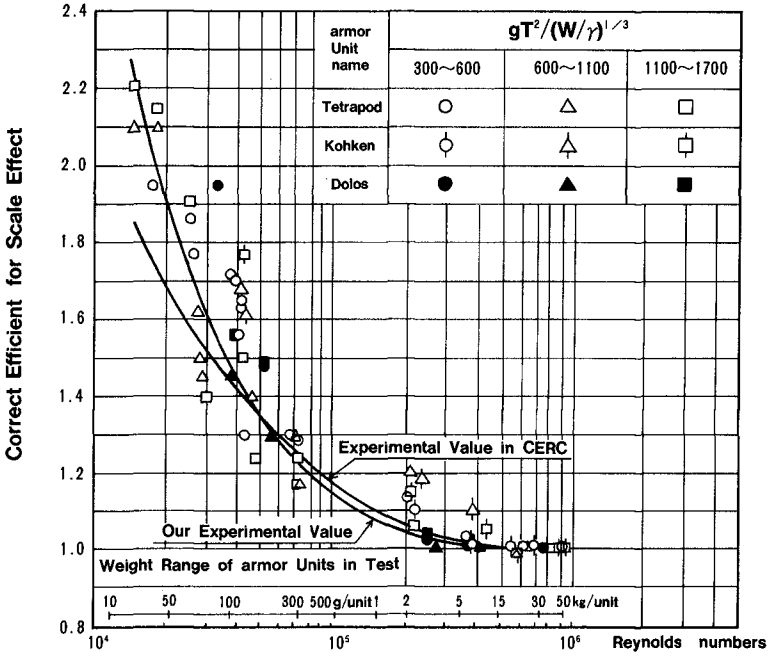

Figure-8 Correct Efficient of Stability number using Re number in no scale Effect

(4) Correction of Coefficient K_D

From experimental investigation on the stability of the armor units by irregular wave[8] which has been conducted by one of authors, it is known that there is a relation shown following equation between regular wave height H and irregular wave significant wave height $H_{1/3}$, which cause the same damage up to several percentage.

that is $H = 1.2\ H_{1/3}$ ..... (4)

And this result is shown in Figure-9.

Now, using this relation, experimental results are revised, and the K_D, coefficient in Hudson Formula (1), are corrected. And the result of correction are shown in Table-2. According to Table-2, it is expected to increase the K_D coefficient to the range of 1.6 ∿ 3.6 times, that is, to lighten the minimum weight of the armor units.

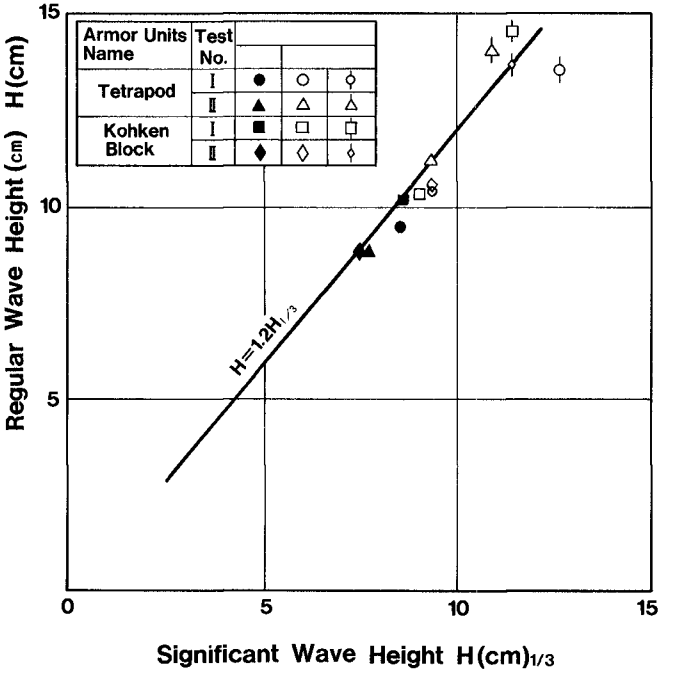

Figure-9 Relation between Regular Wave and Irregular Wave in Same Damage

Table-2 Correct K_D Value with Test Results (0% Damage)

$gT^2/(W/\gamma)^{1/3}$ 300~600

$Re > 4\times10^5$

Armor Unit Name	Hb/D	Ns	K_D	Correct Value by Irregulur Wane	K_D in Present Method
Tetrapod	2.71	4.05	49.8	28.8	8
Kohken Block	2.64	4.05	49.8	28.8	8
Dolos	2.64	4.45	63.9	36.9	22

Ns : Stability Number $Ns = Hb/(W/\gamma)^{1/3}(S-1)$
Hb : Breaking Wave Height
D : Thickness in Two Layers of armor Units

(5) Scale Effect on Reflection Coefficient

It has been conducted to compare the reflection coefficient of the armor units in small and large scale tests likewise as stability test.

Figure-10 shows the results in comparison. The axis of ordinate indicates the reflection coefficient and transverse axis indicate the Reynolds Number Rb which is composed with the long wave velocity, the height of the armor unit and kinematic viscosity also as stability investigation.

The value of Rb is about one and half times of the value of Re in equation (3) in the case of tetrapod and in small wave steepness Rb is larger than Re, because the term gh_t is larger than the term gH_b.

Figure-10 shows the reflection coefficient in same wave steepness and same relative depth.

And if the Reynold's Numbers increase, that mean the case in larger armor units, the reflection coefficients have a little upward tendency.

And the deference is with in 10%. But it is not found to approach to a constant values according as Reynolds Number become high. So it is recognized that there is scale effect on the reflection, but the deference in small and large scale is little.

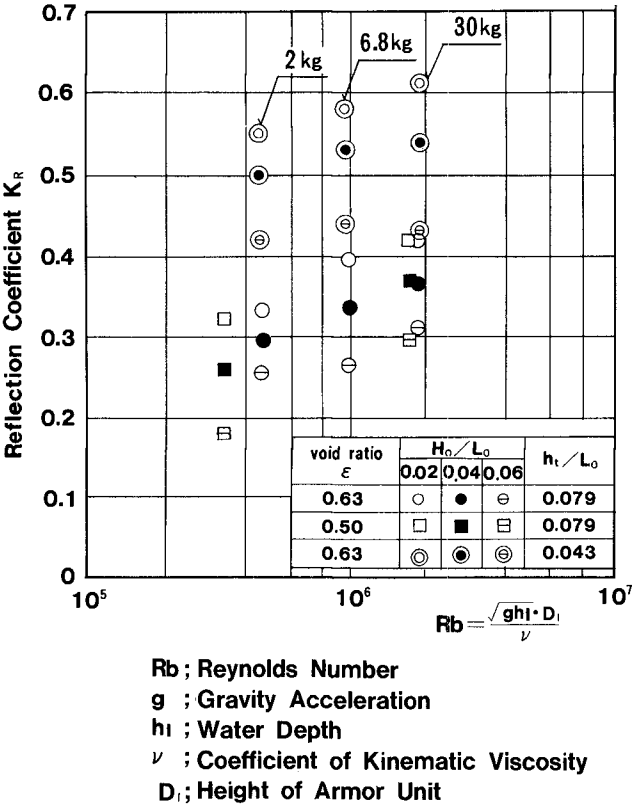

Figure-10 Scale Effect for Reflection Coefficient

4. CONCLUSION

(1) It was recognized from the experiments in small and large wave flumes that there were scale effects on the hydraulic stability and reflection regarding armor units.

(2) The influence of the scale effect on the stability becomes small and will be negligible in more than the Reynolds Number

$$Re : 4 \times 10^5$$

And this Number indicate that the armor unit weights are over than 6.8kg.

(3) It is expected that the minimum weight of armor unit can be calculated under nearly half value as compared with present design method, though irregular wave are considered.

(4) The scale effect on reflection coefficient of the armor unit are recognized in small and large scale tests, however, the deference is smaller than that of stability.

REFERENCES

1) Hudson, R. Y. : Laboratory investigation of rubble mound breakwaters. Proc. of the Amer. Soc. of Civil Eng. Journal of the Waterways and Harbours Division, Vol.85, No.WW3, Sept. 1959.

2) Thomsen, A. L., P. E. Wohnt and A. S. Harrison : Rip-Rap stability on earth enbankment tested in large and small scale Wave tanks. CERC Technical Memorandum No.37, June 1972.

3) Tørum, A., B. Mathiesen and R. Escutia : Scale and Model effects in breakwater model tests. P.O.A.C., 1335pp., 1979.

4) Sorensen, T. and O. J. Jensen : Reliability of hydraulic models of rubble-mound breakwater as proven by proto-type measurements. The Dock & Harbour Authority, Vol.LXV, No.768, 155pp., March 1985.

5) Hydraulic Formulas 510p. 1985, edited by Civil Eng. in Japan.

6) Hydraulic Formulas 530p. 1985, edited by Civil Eng. in Japan.

7) T. Fujimoto, N. Abe, and H. Hasegawa : Experimental Study on hydraulic characteristics of wave dissipating concrete armor units.
Central Research Institute of Electric Power Industry Research Report 382001 1982.

8) T. Fujimoto : Effects of wave Irregularity on Stability of Concrete Armor Units.
Central Research Institute of Electric Power Industry Research Report 385008 1985.

CHAPTER 166

THE INFLUENCE OF OBLIQUE REFLECTION ON BREAKWATERS

by Richard Silvester M. ASCE*

ABSTRACT

The degree of reflection from rubble-mound breakwaters, even those comprising large pre-cast concrete armour units is greater than is usually thought. This is because the bulk of the face consists of smaller stones where water exchange in voids is minimal. Theory and experiment have shown that for 100% reflection of oblique waves the orbital motions are very complex, varying across the crest length of the short-crested system from rectilinear oscillation to circular or vortex motion. Also the influence of these high velocity orbital motions on a sedimentary bed have been shown to have a high scouring capacity. This has been exhibited in hydraulic models and in the field.

1. INTRODUCTION

In most cases of experiments on breakwaters of any form the flume is used to simplify the problem to two dimensions. They assume, therefore, that waves of any consequence are arriving normal to the structure, which often is not the case. For the purpose of discussing sediment transport it is not the short duration storm waves that create the problem but the more persistent swell, even though this varies in height and period continually. Where a structure is angled to the crests of such repetitve waves the scouring can be severe, which is not exhibited in a flume test. In fact, in this case, accretion will occur at the antinode of the standing wave adjacent to the toe (Xie 1981).

As the angle of obliquity increases so the scouring shifts from the nodal area to the antinodal area, next to the structure. Material can be removed until a trough is formed parallel to the face whose profile approaches the angle of repose for the sediment. In any subsequent storm the build-up of pore pressure can cause a slumping of this trough face and concomitant subsidence of the breakwater. It is the author's belief that this could have been the cause of the Sine's breakwater failure, which was sudden over the bulk of its length even with a less than design storm. In any case it behoves the engineer

* University of Western Australia, Nedlands, 6009, Western Australia.

involved in design of these massive structures to conduct 3 dimensional model investigations to observe the scouring that can occur.

2. REFLECTION FROM RUBBLE MOUND BREAKWATERS

Rubble-mound structures, especially those faced with large precast concrete monoliths to just below the water line, appear to dissipate waves very effectively, from observation of the turbulence within the voids of these units. However these larger than normal blocks are not taken down the full depth of the face for economic and constructional reasons. As indicated in the cross-section of the Sines breakwater in Figure 1, the Dolos armour units extended down to only -15 m whereas the bed (which was not rock as indicated in the original figure (Edge et al 1982) but was sand for several metres) ranged down from -30 m to more than -45 m. Thus 5 m thickness of stone was 16-20 ton, another 5 m of 9-20 ton and 20 m of ½ to 6 ton. Hence the lower ½ to ⅔ of the wave action was impacting on rubble material with very small voids. Since the water orbits at these depths are virtually horizontal oscillations little or no energy is dissipated. This is the reason for substantial reflection being experienced.

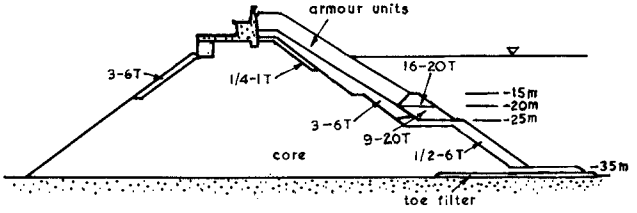

Fig. 1 Cross-section of the Sines breakwater (Edge et al 1982).

Tests have been carried out for normal waves, on breakwaters of differing materials (Gunback 1976, Sollitt & Cross 1972, Hyd. Res. Stn. Wallingford 1970) and summarised by Losada and Giménez-Curto (1981). The reflection coefficient was correlated with the Iribarren No. $Ir = \tan\alpha/\sqrt{H/L_o}$, where α is the face slope, H is the local wave height and L_o is the deep-water wave length. The resulting curves, taking the maxima of the data points rather than the mean, are shown dotted in Figure 2. These data and I_r do not specify the size of the units involved which could make a difference to the degree of reflection. However, it is worthwhile substituting some reasonable values into I_r to see what readings are applicable. Assuming $\tan\alpha = 0.5$, $H = 1$ m (swell), $T = 12$ sec. then $I_r = 7.5$. Hence for rip-rap or dolos the reflection coefficent is 0.8.

It should be noted that Gunback (1976) had armour stone thickness to water depth at 0.18 whilst Sollitt and Cross (1972) used 0.36. Also the former had 0.82 of the depth taken up with these units whilst the latter had 0.57. In a prototype structure, as indicated in Figure

1 these proportions could vary significantly with resulting different reflections.

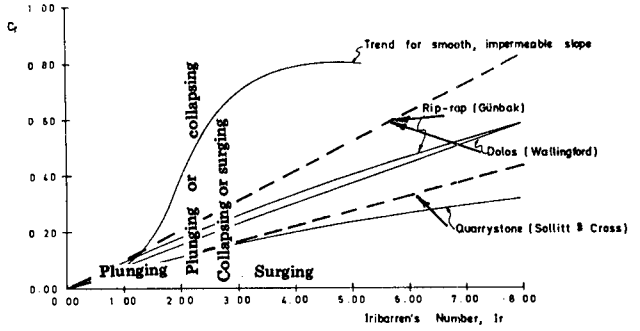

Fig. 2 Reflection coefficient I_r showing the wave type. (Losada and Giménez-Curto 1981).

3. COMPLETE SHORT-CRESTED SYSTEM

The theory of angled waves in which the components are of unequal height is too difficult to solve with the current state of the art. However for two oblique waves of equal height and period, solutions have been found for the kinematics and, also the mass-transport near the bed. (Hsu et al 1979, Hsu et al 1980). This theory to the 3rd order has been verified in a wave basin with a unique window in its bed. (Hsu 1979, Silvester 1977). Such waves might be termed "complete" as for standing waves where this term is used for opposing waves of equal height and period.

But inspite this simplification the orbital motions of the water particles are quite complex as depicted in Figure 3. (Silvester 1972). They vary from rectilinear oscillation to circular across the crest length L', which is finite and not infinite as in a progressive wave. The circular motions on alignments Z/L' = $\frac{1}{8}$, $\frac{3}{8}$, ... are in a constant direction as dictated by their location. Such vortices, even if formed near the surface, as for deep water conditions, will expand along their axes to a boundary, which in this case is the bed. In so doing they exert a strong suction which draws sediment from the floor and throws it out radially into other zones of motion. These whirling bodies of water also generate secondary vortices which make for excessive macro-turbulence which helps keep particles in suspension.

Like any oscillatory motion of wave action short-crested systems have their own specific mass-transport or net motion per wave cycle. This is evident in Figure 4 from tests conductd by Hsu (1979). Even in the alignments (Z/L' = $\frac{1}{4}$, $\frac{3}{4}$, ...), where rectilinear motion is normal to the wall or path of the island crests, there is a net movement along the wall. Theory shows a distribution of mass transport across each quarter crest length as in Figure 5. (Silvester 1985) It is seen that along crest alignments this ratio is maximum

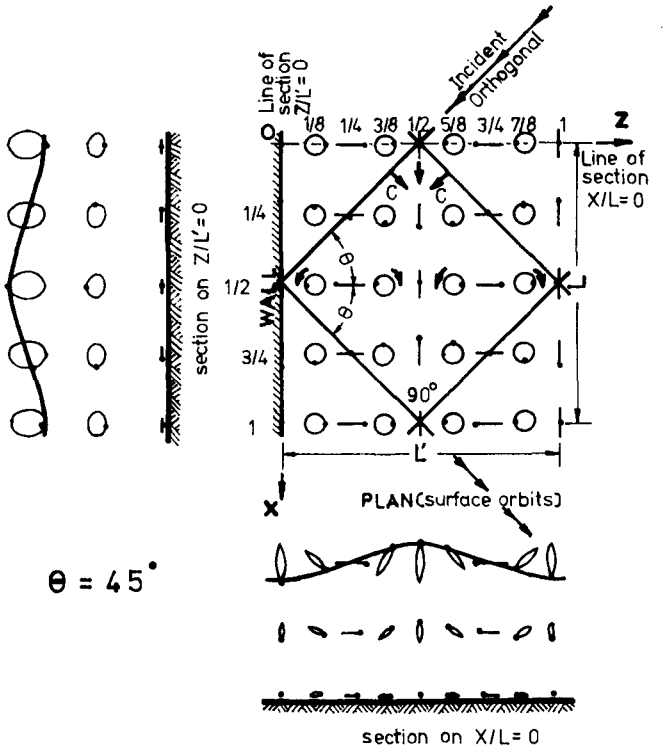

Fig. 3 Water particle motions in a complete short-crested wave system. (Silvester 1972).

and can be 2 or 3 times that of the incident wave. The shearing of material from the floor by the orbital motions at this alignment or half way between (i.e. $Z/L' = \frac{1}{4}, \frac{3}{4}, \ldots$) varies with the wave obliquity. For near standing waves the velocities and hence the scour are greater at $Z/L' = \frac{1}{4}, \frac{3}{4}, \ldots$ but for greater obliquity it is excessive at $Z/L' = \frac{1}{2}, 1, \ldots$.

4. EXPERIMENTAL EVIDENCE OF SCOUR

The movement of sedimentary material on the sea floor can be considered in 3 stages. Firstly, ripples are formed whose orientations and characteristics are dictated by the water particle orbits in the vicinity. (Silvester 1974) Secondly, erosion occurs in alignments parallel to the wall where velocities are excessive. Thirdly the complete region of the ribbon of reflected waves is scoured after accretion has occurred firstly at the downcoast end due to the passage of material from the upcoast end. This last phenomenon requires sufficient duration in model studies for this to be exhibited. Prior to this stage erosion occurs in selected zones for monochromatic waves but is less evident for irregular waves.

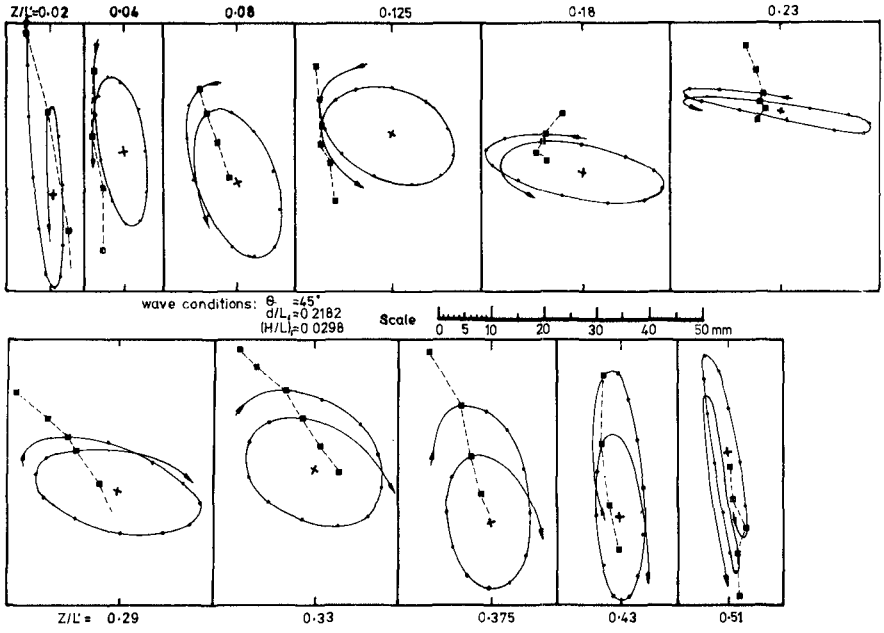

Fig. 4 Orbital motions recorded at the bed for a short-crested system showing the mass transport per wave cycle. (Hsu et al 1979)

Since the persistent swell wave, with its longer periods and good reflection, is the culprit in this removal of sediment, its orbital motions in a short-crested system need to be studied. A factor to be remembered is that such waves are changing in period continually as they travel at different speeds in a dispersal or so-called decay area. (Silvester 1974). These produce variations in orbital amplitudes and hence crest lengths of bed ripples. During such changes more sediment is placed in suspension, which then is subject to the mass-transport of the water in the wave motion.

The crests of any ripple formation will be normal to the water oscillation creating it. Thus those adjacent to the wall and at crest alignments Z/L' = $\frac{1}{2}$, 1, ... will be normal to the wall; whereas those half way between (Z/L' = $\frac{1}{4}$, $\frac{3}{4}$, ...) will be parallel to it. Along alignments between again (Z/L' = $\frac{1}{8}$, $\frac{3}{8}$, ...) the vortices will create circular mounds which make for a snake-like undulation. These are exhibited in Figure 6, where waves have reflected at 45° to the wall on the right of the figure, with the Z/L' distances marked. The slight deviations from these alignments in the figure are due to the partial transport that has occurred which introduced changes in water depth and concomitant refraction.

After some time the zones of high velocity water oscillation causes them to be eroded first which is evident in Figure 7 where

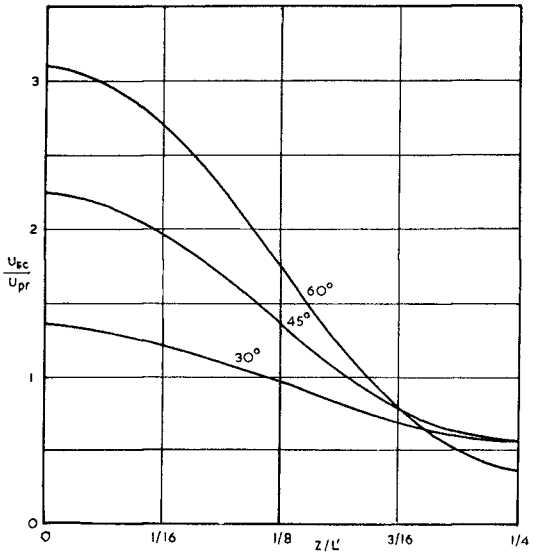

Fig. 5 Ratio of mass-transport in a short-crested wave (U_{sc}) to that in a progressive wave (U_{pr}) for various angles of incident to a reflecting wall. Z is measured normal to the wall across the crest length L'.

removal has occurred at Z/L' = $\frac{1}{4}$, $\frac{3}{4}$, ... where ripple crests are parallel to the wall. It is seen that for this approach angle of 25° scour has taken place for more than 3 crest lengths from the structure. The orthogonal of the reflected wave through the upcoast tip of the reflecting wall is shown. To the right of this these waves are diffracting, so suffering a curved crest pattern and reducing in height. Even so, the short-crested system still exists as exemplified in the scouring that has occurred beyond this ribbon of reflected wave. In other photos a similar expansion occurred from the downcoast limiting orthogonal. (Silvester 1985).

This is not to imply that the reflected wave height remains the same in its propagation from the wall. Its passage can be likened to transmission through a breakwater gap as in Figure 8, the diffraction of which has been determined experimentally for no reflection from adjacent breakwater arms. (Silvester 1981) As the wave travels along multiples of the non-dimensional width B/L its energy is absorbed in diffraction beyond the limiting orthogonals. As seen in Figure 9 the diffraction coefficient reduces so that on the centre-line at R/B = 4 the height has been reduced to half. Thus the incident wave will be double the height of the reflected and will therefore have more effect on the movement of sediment. The water particle orbits will be very complex but still conducive to bed scour.

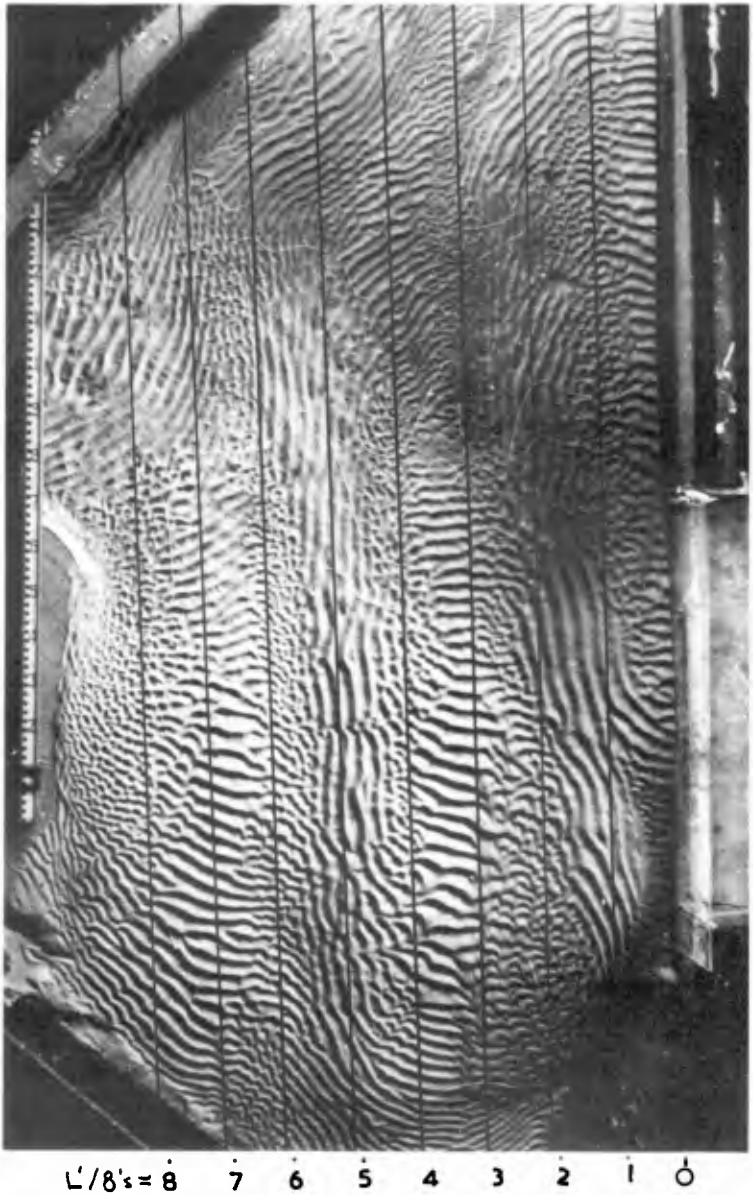

Fig. 6 Bed ripple formations in a short-crested system. (Silvester 1972).

Fig. 7 Differential erosion occurring at quarter crest lengths from the wall.

Tests carried out for 60 hours with waves angled 30° to a wall in water depth of 25 cms, wave period 1.0 sec. and sand bed thickness of 5 cms, resulted in scour as seen in Figure 10. During this limited duration material removed from the RHS is in transit through the area to the left so causing shoaling in that region. Had the experiment been carried out for longer this accretion would ultimately disappear. A similar test has been carried out by Tanaka et al (1972) where sediment 10 cms in thickness and water depth 5.5 cms waves of 2.8 cm height and 0.52 seconds period caused progressive erosion at the upcoast end of a breakwater with approach angle of 30°. As seen in Figure 11 accretion occurred in the downcoast region after 10 hours duration. It is seen, as in Figure 10, that the bed is affected even outside the limiting orthogonal through the upcoast tip of the

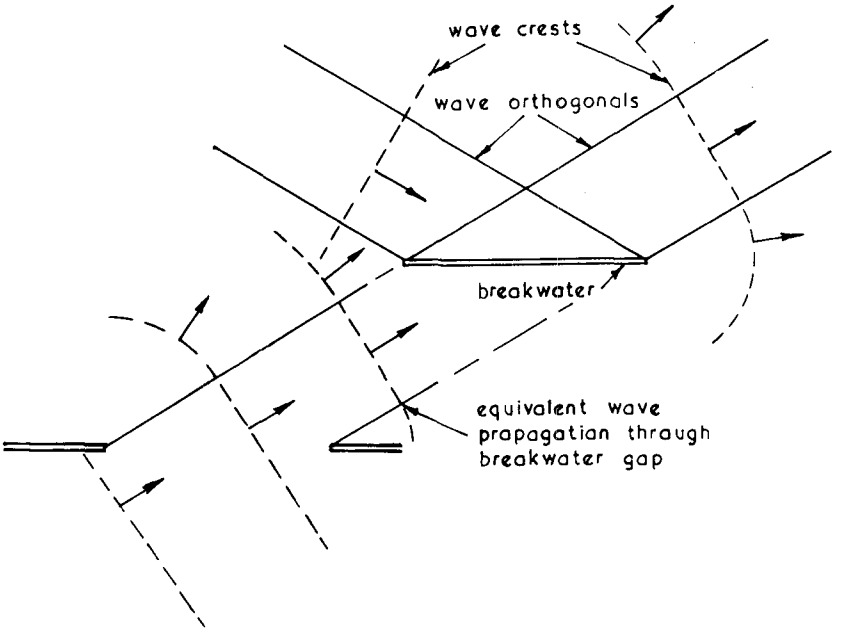

Fig. 8 Comparison of reflected waves to diffraction through a breakwater gap.

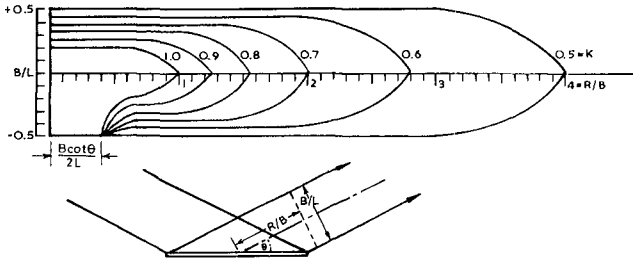

Fig. 9 Diffraction coefficient distribution in front of a reflecting wall.

breakwater. The variations in bed level in the figure are based upon the assumption that a profile recorder had a distance to the original bed of 25 cms in the data provided by the authors. Irie and Nadaoka (1984) have conducted model tests on a breakwater where the bed was sloping upwards towards the downcoast end as seen in Figure 12. The final contours after 11 hours duration are shown from which zones of erosion and accretion can be identified. It is seen that these zones vary across the normal to the breakwater.

More recently Irie et al (1985) have conducted further experiments with angled waves both regular and irregular. The

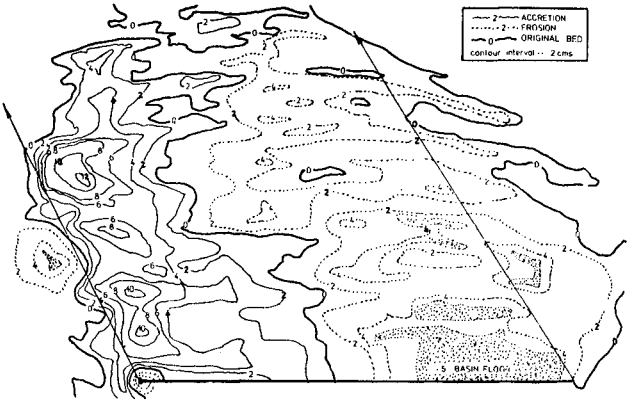

Fig. 10 Scour of bed to concrete floor after 60 hours duration.

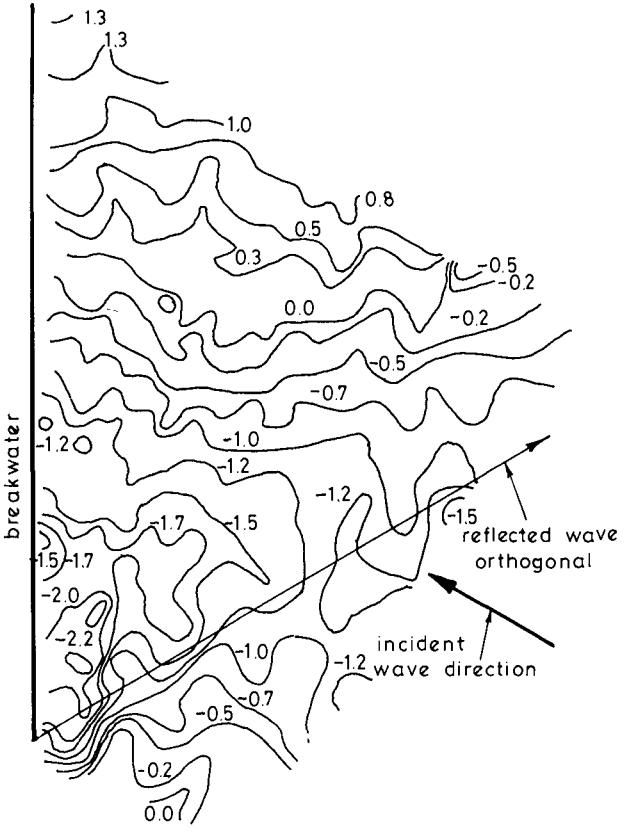

Fig. 11 Contours after 10 hours duration. (Tanaka et al 1972).

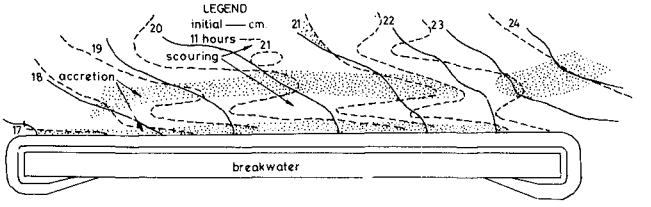

Fig. 12 Tests showing differential erosion and accretion for a duration of 11 hours with irregular waves. (Irie & Nadoaka 1984).

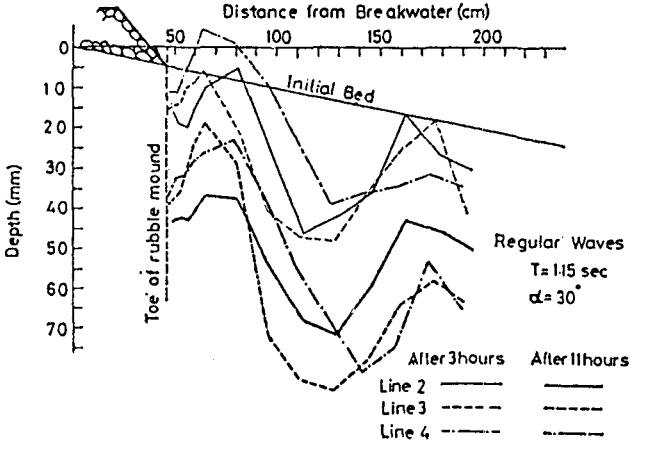

Fig. 13 Profiles normal to the breakwater for regular waves at 30° after specified durations. (Irie et al 1985).

breakwaters were of caisson type with a trapezoidal rock mound on the sea side. Profiles normal to the breakwater at the point of greatest scour were measured after 3 and 11 hours the results of which are reproduced in Figure 13. A significant feature of these profiles is the steep slope of the near side of the major trough which is 1:3.4, even after such a short duration. From tests with irregular waves (Figure 14) the same steep slopes exist near the toe of the rubble mound. In this case the scour is more uniform across the bed. Irie also plotted profiles parallel to the breakwater over certain durations which showed severe erosion at the upcoast end and accretion at the downcast tip. The progressive deepening is illustrated in Figure 15, where it is seen that scouring is rapid over the first hour but slows down with time. An optimum had not been reached for the regular waves after 11 hours duration.

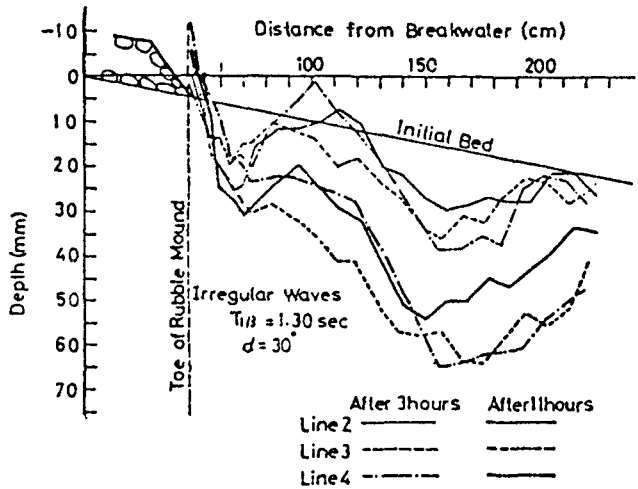

Fig. 14 Profiles normal to the breakwater for irregular waves at 30° after specified durations. (Irie et al 1985).

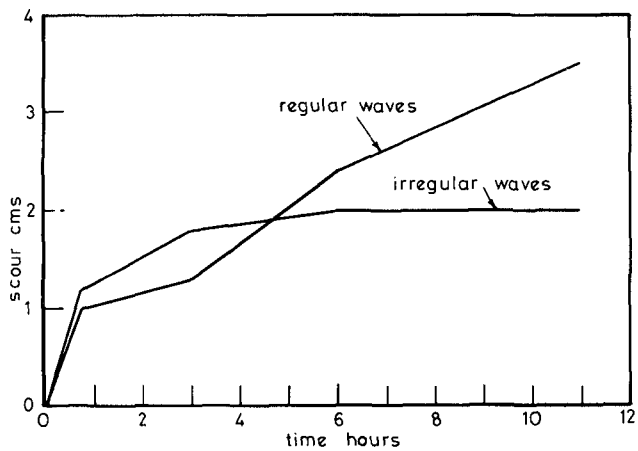

Fig. 15 Progressive scouring at zone of deepest hole for regular and irregular waves. (Irie et al 1985).

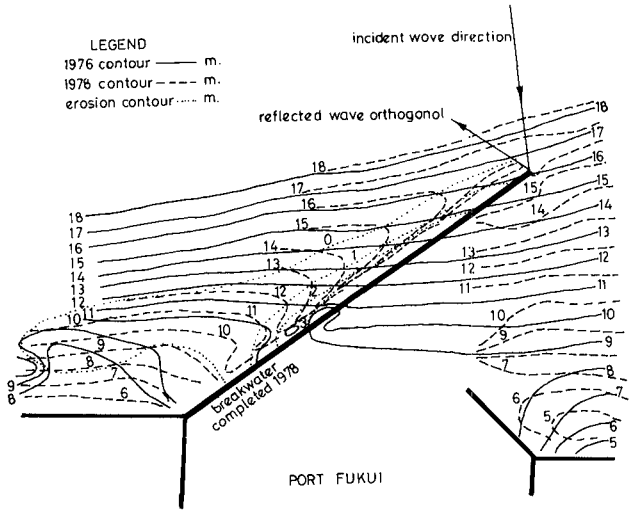

Fig. 16 Contours at the port of Forkui, Japan in 1976 and 1978 showing zones of scour. (Irie & Nadoaka 1984)

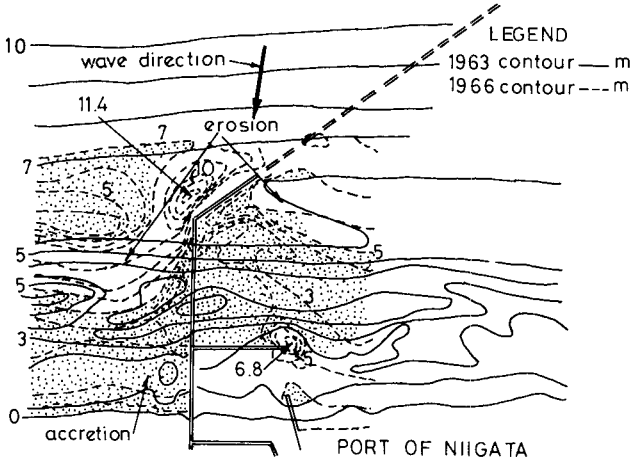

Fig. 17 Erosion and accretion at Niigata between 1963 and 1966. Sato et al 1969, Sato & Irie 1970).

5. FIELD EVIDENCE OF SCOUR

Scouring has been observed by Irie and Nadaoka (1984) in prototype situations. The port of Forkui is angled to the shoreline and to the bulk of the waves arriving. It was completed in 1978 when

a hydrographic survey was conducted, which can be compared to the 1976 contours as in Figure 16, showing the zones of erosion and accretion. Scouring down to 3 metres over a large length of this breakwater took place in a matter of months. It would be interesting to see the contours some eight years later.

Another example of erosion is given by Sato et al (1969) who give contours in 1966 for the port of Niigata, Japan, presumably soon after the completion of the breakwater to this stage. (Figure 17) These bed profiles are compared to those in 1963 provided by Sato and Irie. (1970). Zones of erosion and accretion are hatched and stippled respectively. It is seen that near the corner a depression of 11.4 m has been scoured in an original depth of 6.5 m. In the second reference (Sato & Irie 1970) contours are shown for a slight extension of the breakwater in 1967 and the installation of a rubble mound base for caisson units to the limit shown in Figure 17. These show some accretion in the region previously scoured, probably due to the transmission of sediment along the submerged mound during this short time period. It would be instructive to see hydrographic data for the current situation after some years of completion.

6. CONCLUSIONS

1. The degree of reflection from rubble-mound structures is significant enough in oblique wave approach to generate short-crested wave systems which are conducive to scour.

2. Consultants should not depend solely on flume tests if erosion of a sedimentary bed is possible as these imply normal approach for both storm and swell waves.

3. Theory and experiment have shown that the water particle orbits in a complete short-crested system (equal heights and periods of component waves) to be quite complex and severe in their erosive capacity.

4. Besides high velocity orbital motions the water particles experience a strong mass transport, greatest along the alignment of the island wave crests, which can interact with tidal currents to remove suspended material.

5. Model experiments with obliquely reflected waves have shown their ability to form trenches parallel to a structure that have profiles approaching the angle of repose of the sediment which could cause subsidence if pore pressure is built up during even moderate storm action.

6. Field measurements of scour adjacent to breakwaters have only been carried out soon after construction but even so have exhibited severe erosion which is being blamed on currents rather than waves.

8. REFERENCES

Edge B.L. et al (1982) Failure of the breakwater at Port Sines, Portugal, ASCE, Coastal Eng. Res. Council.

Gunback A.R. (1976) The stability of rubble-mound breakwaters in relation to wave breaking and run-down characteristics and to the $\xi = \tan\alpha\, T/\sqrt{H/L_o}$ number. Divn. Port and Ocean Eng. Norwegian Inst. Tech, Trondheim, Rep. 1-1976.

Hsu J.R.C. (1979) Short-crested water waves. Ph.D Thesis, University of Western Australia.

Hsu J.R.C., Y. Tsuchiya and R. Silvester (1979) Third order approximation to short-crested waves, J. Fluid Mech, 90(1), 179-196.

Hsu J.R.C., R. Silvester and Y. Tsuchiya (1980) Boundary-layer velocities and mass-transport in short-crested waves, J. Fluid Mech. 99(2), 321-342.

Hyd. Res. Stn. (Wallingford) (1970) High island water scheme, Hong Kong, Rep. EX 532.

Irie I. and K. Nadaoka (1984) Laboratory reproduction of seabed scour in front of breakwaters, Proc. 19th Inter. Conf. Coastal Eng. ASCE, Vol. II, 1715-1731.

Irie I. et al (1985) On the protection methods of scour in front of breakwaters, Proc. 32nd Coastal Eng. Conf. of Japan, 445-449 (In Japanese).

Losada M.A. and L.A. Giménez-Curto (1981) Flow characteristics on rough permeable slopes under wave action, Coastal Eng., 4, 187-206.

Losada M.A. and L.A. Giménez-Curto (1982) Mound breakwaters under oblique wave attack; a working hypothesis. Coastal Eng. 6, 83-92.

Sato S., N. Tanaka and I. Irie (1969) Study on scouring at the foot of coastal structures, Coastal Eng. in Japan 12, 83-98.

Sato S. and I Irie (1970) Variation of topography of sea-bed caused by the construction of breakwaters, Proc. 12th Inter. Conf. Coastal Eng. Vol. II, 1301-1319.

Silvester R. (1972) Wave reflection at seawalls and breakwaters, Proc. Instn. Civil Engrs. 51, 123-131.

Silvester R. (1974) Coastal Engineering Vol. 1, Elsevier Publ. Co., Amsterdam.

Silvester R. (1977) The role of wave reflection in coastal processes, Proc. Coastal Sediments Conf. 1977, ASCE, 639-654.

Silvester R. (1981) Diffraction through a breakwater gap, Trans. Instn. Engrs. Aust. CE23(2), 114-117.

Silvester R. (1985) Sediment by-passing across coastal inlets by natural means, Coastal Eng. 9, 327-346.

Sollitt C.K. and R.H. Cross (1972) Wave transmission through permeable breakwaters, Proc. 13th Conf. Coastal Eng., Vol. III, 1827-1846.

Tanaka N., I. Irie and H. Ozasa (1972) Report Port and Harbour Res. Inst. Vol. II, No. 3, 112-140 (In Japanese).

Xie S.L. (1981) Scouring patterns in front of vertical breakwaters and their influence on the stability of the foundations of the breakwaters. Rep. Coastal Eng. Group, Delft Univ, of Tech.

CHAPTER 167

Design and Evaluation of Beach Protection Schemes

D H Swart* and K Horikawa**

ABSTRACT

On the basis of eleven poster presentations on beach protection schemes and/or devices, at the recent 20th International Conference on Coastal Engineering, the various levels involved in the design and evaluation of beach protection schemes are discussed in this paper. These are: (1) the assessment of the problem and processes operative in the area; (2) the establishment of an overall master plan for development; (3) the design stage; (4) the construction phase, and (5) the post-construction phase. It is concluded that it would be useful if some form of international co-operation could be instigated to allow the collation of techniques used at the various levels in one handy location, for dissemination by all contributors.

1. INTRODUCTION

The International Conferences on Coastal Engineering, held every two years at a different venue, have traditionally brought together coastal scientists from more than twenty countries. The 20th such conference, held in Taipei, Republic of China, in November 1986, was attended by about 500 coastal scientists from around the world. During the conference two poster discussion sessions on beach protection devices were held, under the chairmanship of the authors of this paper. On the basis of the contents of the eleven individual poster papers presented in these two sessions, the various aspects related to the design and evaluation of beach protection schemes were discussed at the conference. Significant advances were made in bringing together data on these aspects. This paper contains an overview of the results achieved during the two poster discussion sessions.

It should be pointed out here that the discussions were held in a way which allowed the audience to contribute by filling in any gaps in knowledge that were apparent after the presentation of overviews by the chairmen.

After the discussion of the various levels of evaluation and design a wider perspective is taken in suggesting the comparison of techniques used worldwide. Means of achieving this are discussed.

The eleven papers under discussion can be subdivided as follows:

* Council for Scientific and Industrial Research, P.O. Box 320, Stellenbosch, 7600, Republic of South Africa.
** Department of Civil Engineering, University of Tokyo, Bunkyo-ku, Tokyo 113, Japan.

(1) **those dealing with beachfill**
Möller, Owen and Swart (1986)

(2) **those dealing with offshore breakwaters**
Yeh and Ou (1986)

(3) **those dealing with combinations of beachfill and structures**
Deguchi and Sawaragi (1986); Pui (1986); Kana, Al-Sarawi and Holland (1986); and Suyama, Uda and Yoshimura (1986)

(4) **those dealing with offshore dredging**
Kojima, Ijima and Nakamuta (1986)

(5) **those dealing with river deltas**
Kadib et al. (1986); and Gambardella (1986)

(6) **those dealing with other related topics**
Hayashi (1986); and Kawata and Tsuchiya (1986).

The contributions by the above authors and members of the audience during the discussions helped make these poster discussions very successful and are gratefully acknowledged.

The rest of this section is devoted to a short summary of the key elements of the different papers referred to above, to serve as a basis for the discussion in the further sections of this paper.

Beachfill

Möller et al. (1986) describe a diamond mining operation on the west coast of Africa in Namibia, where a sea-wall of normal beach sand has been built out to a distance of more than 300 m seawards of the original coastline. The wall which runs alongshore (as shown in Figure 1) is maintained in the high energy environment, which is characterized by northbound longshore transport rates, by means of artificial suppletion at a rate of more than 300 000 m^3/month. The question which had to be answered before the project could commence was whether there would be enough overburden sand available on land to allow the completion of the project free of severe damage by wave action. The data set used consisted of wave measurements by Waverider and wave observations obtained from voluntary observing ships; aerial photographs at monthly intervals of the water line in the study area, and soundings of the beach, sea-wall and nearshore topography (using a helicopter as a platform).

The individual survey results were used to establish a sand budget for each survey period. These sand budgets were used as input to a N-line littoral, morphological model. This model was preferred to a one-line coastal model because of the large alongshore differences in profile shape. During the three years that the project has run to date this technique was used to project the required volume of sand to complete the project by the expected completion date of March 1988. The project can serve as a one-to-one scale beachfill test and could prove extremely useful to evaluate techniques for the design of beachfills.

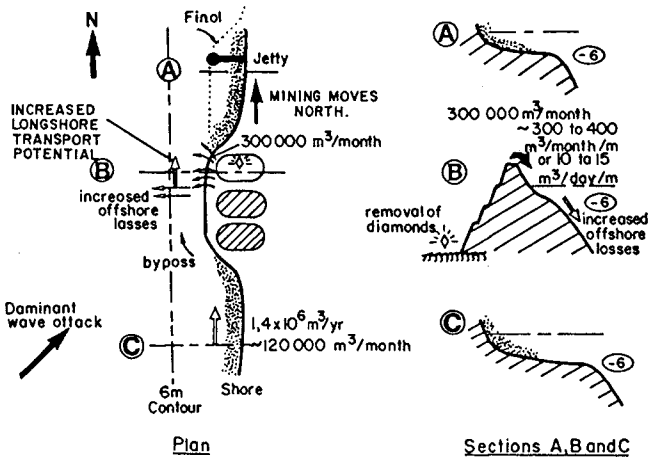

Fig.1 Oranjemund mining layout
(after Möller et al, 1986)

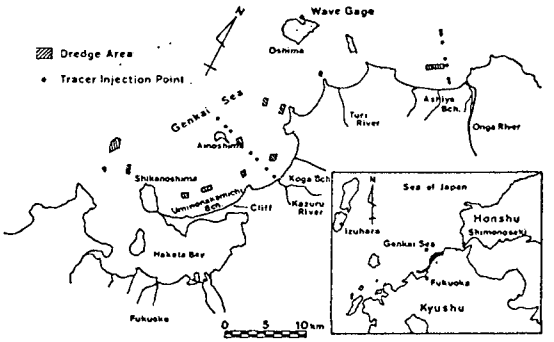

Figure 2 Vicinity map of the study area
(after Kajima et al, 1986)

Offshore breakwaters

This type of structure has found widespread application in the protection of eroding beaches. 8ecause of the formation of cuspate forelands behind such breakwaters and the attractive embayments that are formed between them, bathing conditions are created which are both safe and of a varying nature. The design of offshore breakwaters involves the choice of the breakwater length, distance offshore, crest elevation, the gap/length ratio and the necessity of supplementary beachfill landwards of the breakwaters. The paper by Yeh and Ou (1986) discusses the application of offshore breakwaters to the Redhill coast of Taiwan in the Republic of China. The coastline in the area consists of sandy eroding cliffs 6 to 10 m high and has a limited natural sand supply. In 1978 seven detached, offshore breakwaters with a length of 80 m each and a gap spacing of 30 m were built at mean sea level to protect the beaches. Field observations were done over a period of 3 years covering pre- and post-construction phases. The data were analysed using eigenfunction techniques. In 1985 laboratory tests were done to supply design data for determining gap spacings. Substantial improvement in beach stability has been experienced since the construction of the breakwaters.

Combined beachfill/structures

8eachfill is often used in combination with structures, especially in areas where it is expected that the natural littoral drift will transport sediment out of the area too quickly, thereby reducing the effective life-time of the beachfill. Three of the papers listed above fall in this category. Deguchi and Sawaragi (1986) describes how sand was placed in the lee of a 80 m long offshore breakwater in 1984, one year after construction of the breakwater was completed. Surveys were done 4 to 6 times a year. Immediately after construction of the breakwater both longshore and offshore sediment transport took place as the beach reacted to the changed littoral regime. Thereafter longshore transport dominated until the beachfill was placed. Within two months after placement fifty per cent of the beachfill was lost from the area behind the breakwater, and a further 10 per cent of the initial volume lost in the next two months. This study clearly indicated the benefit of using a mathematical simulation model to help interpret the field results. In the model used, wave deformation, wave-induced currents, sediment movement and associated bottom changes were simulated.

Pui (1986), on the other hand, shows how as a result of land reclamation to meet the increasing needs of the fast-growing Singapore population, the shore was built out to such an extent that the littoral processes were accelerated, thereby necessitating the simultaneous construction in some areas of revetments or headland breakwaters. In a few cases additional measures were not required owing to the favourable alignment of the beachfill. An interesting aspect of the work carried out in Singapore is that it is quite possible that beach protection carried out on Singapore beaches could influence beaches in the adjacent Malaya. This aspect was not formally addressed in the paper and poses the question of how such cases should be handled.

Kana et al. (1986) give a very good example of a combined beach-

fill/structures approach. It is most probably one of the most extensive recreational waterfront projects ever designed. The results of a field-monitoring programme, which started in 1977, were used to draw up a master plan for beachfront improvement as well as a series of design criteria. The scheme includes artificial beaches, promenades, revetments, outfalls which also serve as headland breakwaters for the artificial pocket beaches and an artificial island. On the basis of the wave data longshore transport calculations were done and were used to orientate the pocket beaches to the waves, thereby largely eliminating longshore sediment losses. An interesting aspect of the design of the beachfill is that a berm elevation of 1 m above mean high water springs was used. This allowed washover and as a result the beaches attained a natural appearance soon after construction. Two years of post-construction monitoring has been done to evaluate the behaviour of the artificial beaches. Typically, ten days of recordings are done every three months. Wave energy levels are compared with pre-construction levels, and profile data are used to compute sediment budgets for the various beach compartments. The monitoring shows that the sand losses from the scheme are low and it is not expected that renourishment will be required later.

Suyama et al. (1986) describes a field experiment on the Shimoni-Ikawa coast on Toyama Bay in Japan. Downdrift of Miyazaki fishing harbour the coast is eroding owing to the interruption of littoral drift by the harbour. The purpose of the field experiment was to investigate the effectiveness of sand bypassing as a method of combating beach erosion and to evaluate the degree to which offshore breakwaters in the downdrift area can serve to minimize sediment redistribution after replenishment of the beach. The measuring program included wave measurements (height, period, direction), nearshore bathymetric surveys and a tracer experiment. It was concluded that a slow longshore movement of sand took place without appreciable sand losses through the gaps between the three breakwaters, which were situated about 20 m offshore. The artificial sand infill into the area behind the breakwaters helped to create tombolos, which would not have formed otherwise, and reduced wave overtopping of the structures due to shallower water at the structures.

Offshore dredging

The supply of sand for building and other purposes is posing an ever greater problem in many parts of the world. Offshore sand bodies are frequently exploited. In such cases where offshore dredging is done, it is necessary to establish the best location and dimensions for the borrow pit. Aspects which have to be carefully considered are the following:

- the relation of the location of the borrow pit to the dynamic swept prism and the corresponding effect it has, either directly or indirectly, on the sediment transport processes in the area;

- the effect of the borrow pit on wave propagation patterns and the associated effect on wave focusing and hence on beach erosion at the shore; and

- the potential effect of the dredging operation on the general ecology of the area, and the degree to which recovery of the sub-bottom faunal life will take place.

The paper by Kojima et al. (1986) discusses most of these aspects, with the exception of the ecology. Figure 2 shows the areas on the Genkai coast where offshore dredging has been done. Kojima et al. describe a wide range of measurements done to establish whether or not the offshore dredging has accelerated beach erosion in the area. Typical elements of the data gathering and analysis exercises were the following:

- an analysis of aerial photography in the period 1947 to 1982;

- hydrographic surveys and sediment sampling to establish recent trends;

- fluorescent tracer experiments in which the fate of underwater injection at water depth intervals of 5 m in the area between 10 m and 30 m water depth is investigated with the aid of underwater observations; and

- extensive wave and weather surveys, supplemented by a compilation of available old data dating back to 1945, where, amongst others, it has been shown that the frequency of occurrence of high wind speeds (> 10 m/s) has decreased steadily over the last ten years.

It is concluded that although beach erosion has taken place before dredging started due to mainly high incident storm-energy, it was more than likely that offshore dredging did affect shore processes. It was furthermore concluded that borrow pits situated in water depths shallower than 30-35 m filled in readily from the landward direction, thereby showing that the borrow pits should be situated further offshore in deeper water. This is interesting since it is deeper than is traditionally recommended.

River deltas

When dealing with shore protection schemes on river delta coastlines the general problem is compounded because of the added processes associated with the river delta itself. Here specific attention should be focused on current patterns related to the river delta formation and orientation, decrease in the shore area, relative sea-level rise (relative shore drop) and shoreline protrusion with the associated effect on morphological processes.

The papers by Kadib et al. (1986) and Gambardella (1986) serve as reference. Kadib et al. describe the development of the Nile river delta. Up to the end of the 19th century the supply of sediments to the delta generally exceeded the losses due to wind, current and wave processes in the shore area. After construction of the lower Aswan Dam on the Nile in 1912 beach erosion at a rate of 30 m/year commenced. This increased to more than 170 m/year after 1966, when the Aswan High Dam was built. The Egyptian Government recognized the seriousness of the situation, and instigated an extensive investigation programme. On

the basis of an analysis of the field data gathered as part of this programme, the 350 km coastal area was subdivided into six morphological regions. Various shoreline protection schemes are being evaluated against each other, each taking into account the specific morphological behaviour of the region under consideration. Protection devices which are being considered are shoreline hardening with the use of armour units, sand nourishment, groyne systems or detached breakwaters in conjunction with sand nourishment, "no action" with assessment of the economic consequences and other options.

Gambardella (1986) shows that the shoreline of the Po river delta in Italy receded dramatically since the 1950's. Two main processes can be identified as being causative factors. Natural subsidence of the more than 2 000 m thick, unconsolidated post-Pliocene sediments which is about 1,5 mm/year, increased to about 15 mm/year due to water and gas extraction, reaching a maximum of 3 m/40 years locally. Secondly hydraulic works, industrial installations and extensive reclamation works altered the natural equilibrium of the outer coastal area, thereby giving rise to shoreline recession. It is not always possible to shift back the protective sea-walls because settlements have been established in the coastal area immediately behind the sea-walls. Figure 3 shows the cross-section of the standard dike-breakwater construction which was traditionally used as beach defence. Due to the substantial erosion of the delta beachfront the dike/breakwater systems proved ineffective to prevent beach erosion. The application of 1 m to 1,8 m diameter sand-filled "Longard" tubes in a configuration as shown in Figure 4 has to date proved very effective and is considered the mechanism to combat future erosion.

Other beach protection techniques

Two papers fall in this category. Hayashi (1986) described the use of beach-walls as opposed to sea-walls, to serve as an effective beach erosion protection in the Hawaiian situation. Kawata and Tsuchiya (1986), on the other hand, describe the use of a sub-sand filter system as beach erosion control mechanism. Using the Hawaiian experience as an example, Hayashi shows that by using sea-walls with a nearly-vertical seaward face to protect properties and maintain the certified shoreline, beach erosion is frequently enhanced and extends to the adjacent properties, thereby giving rise to the so-called "domino" effect. The use of beach-walls, a concept developed by Hayashi, however, leads to much more natural beach processes. Experience over two years has shown that beaches are retained more readily in front of beach-walls (see Figure 5 for typical cross-section) than in front of sea-walls or other hard structures.

Kawata and Tsuchiya (1986) discuss both theoretical and experimental studies to investigate the effect of a sub-bottom filtration system whereby water is drawn into the bed. As is to be expected, the increased inflow velocity into the bed causes the threshold velocity of bottom sand to be increased, as can be seen in Figure 6. Although the laboratory experiments showed conclusively the benefit of such a filtration or draw-off system, the main problem that remains is the manner in which such a system can be constructed and maintained on a natural beach.

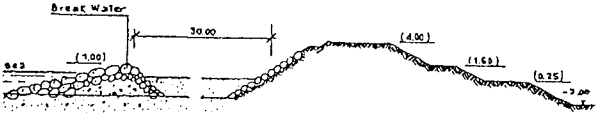

Fig. 3 - Cross-section of a standard dike-breakwater system, in the Po river delta area.

(after Gambardella, 1986)

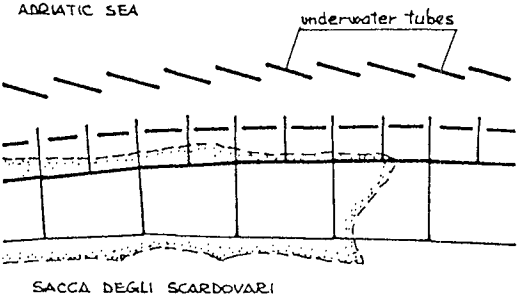

Fig. 4 - Plan of progressive reconstruction of an eroded sand spit, at Sacca degli Scardovari, southern Po river delta, using the 'Longard - tube' system. The dotted line indicates the shoreline prior to the tube installation. Thick and thin lines indicate 1.8 m and 1.0 m tubes, respectively.

(after Gambardella, 1986)

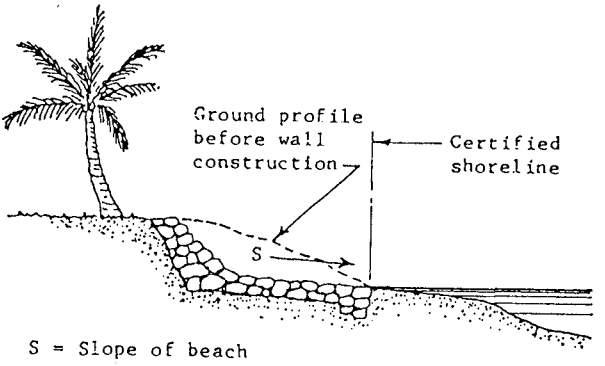

Figure 5 ´ Typical beachwall section

(after Hayashi, 1986)

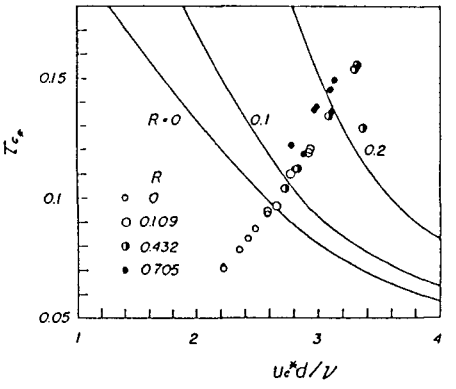

Fig. 6 Comparison between theoretical threshold of sediment movement and experimental one

(after Kawata and Tsuchiya, 1986)

2. PROBLEM/PROCESS ASSESSMENT

The first level at which a beach protection design needs to be addressed is the "problem or process assessment" stage. It is always advisable to know not only what is happening but also how and specifically why it is happening. With this background knowledge it is then possible to proceed with the further steps of the design.

The following types and sources of data can prove useful/essential in acquiring the necessary background knowledge:

- old maps and charts;
- aerial photographs;
- topographic/hydrographic surveys;
- wave/weather data;
- landward needs/problems;
- geomorphology; and
- ecology.

It is always advantageous to review old and/or existing data to gain an idea of the processes/trends operative in the area, before embarking on a new measuring campaign. The same pre-screen of available data also applies to wave data, where observations made by merchant shipping (the so-called VOS wave data) give a good first idea of the wave climate in the area, including seasonal changes, and also helps in designing the measuring exercise. In any beach protection design it is important to make a sediment budget analysis. It is usually possible to make a first stab at such a budget by using the shoreline position on old charts to estimate volumes. With the aid of all the preceding it is possible to design a measuring exercise in relation to old/available data.

Hydrographic data usually play an important rôle in assessing sediment budgets. Because the sediment budget is freguently determined by taking the difference between two large volumes, it is essential that the surveys used for this purpose should be as accurate as possible.

In this respect it is appropriate to examine the closure depth for repetitive surveys carefully, to decide whether the observed closure depth can be explained in terms of physics. Another check for accuracy is to compare elevations in an area of overlap between land-based and sea-bed survey data.

It is important that the coastal engineer should realize that the guality of the project may be vastly improved by close liaison during the problem/process stage with scientists of other disciplines, be they geomorphologists, planners, landscape architects, geographers and/or ecologists. It is also particularly important to the client that he does not get conflicting advice from the various disciplines, but one sensible answer. It is in this respect that the engineer can play an important rôle in bringing together the other disciplines to assess processes and evolve working concepts as a basis for sound coastal engineering design.

3. ESTABLISHMENT OF MASTER PLAN

Having established the exact magnitude and nature of the problem, the next level of attack is to determine an overall master plan which will allow one to foresee future problems in other areas and give one the opportunity of gaining a wider perspective of the beach protection problem. It is important, therefore, never to treat problems in isolation. It is also appropriate to establish future requirements at the site or in the vicinity, and to decide on the optimum manner in which work needs to be phased to best solve the problem in the long run.

Although this may sound rather early to talk about the optimum solution, it is quite foreseeable that there are some specific site problems such as the non-availability of rock, which preclude certain solutions. This may also be the case with the specific culture or requirements of the locals/beach-users.

In all cases it is of the utmost importance to start with a public relations exercise as early as possible to make the public aware of what is at stake and what they can expect from such a beach protection scheme.

In deciding how far to go with the establishment of a master plan, it is important to realise that by deciding on, for example, a long-term policy of beach nourishment, it helps one to phase other activities such as the development of a market, determining dredging capacity, etc.

At this early stage one has to clearly address the question of what the feasible options are for beach protection, with the relative merits of each. One viewpoint expressed during the discussion is that in making this decision one should look to nature to see how it would do it, and what would happen. Dr Silvester, in making this comment, ended up saying that headland embayments are natural features optimizing energy losses in the most efficient manner. However, it is the belief of the authors that this philosophy of looking to nature for the wider clue to the solution is a sound one and may result in different solutions under different circumstances.

4. DESIGN STAGE

The next and most important level in the establishment of a beach protection scheme is the design stage. The following aspects are all relevant in this respect:

- the various elements of the type of solution, and the phasing of the work/needs; which necessitates an evaluation of the alternatives;

- the design technique(s) used, whether involving
  - field data
  - laboratory experiments with fixed and/or movable bed models
  - mathematical/numerical simulations or
  - some (hybrid) combination of the above

- whichever of the above technigues are used, the design approach should include an appropriate calibration condition and a predictive mode/data set;

- it is important to consider the **interaction** between the beach protection scheme and the nearshore environment, that is, the effect of the solution/scheme/structure on the morphology, as well as the effect of the nearshore environment on the solution/scheme/structure, and

- for a proper evaluation of each alternative it is essential that the initial (construction) costs and subsequent maintenance costs should be separated.

The following are some general points related to various types of beach protection device which were discussed in the two sessions:

Filtration systems

The idea of increasing the inflow of water into the bed in order to increase the threshold velocity and reduce the movement of sand is sound and its effectiveness has been demonstrated both numerically and in the laboratory. Before it can be applied in the field, however, the researchers responsible for promoting the idea should collaborate with contractors capable of applying these thoughts in practice, in order to sort out the various problems associated specifically with securing such a system in nature and making it a low-maintenance system.

Beach-walls

With reference to the paper by Hayashi (1986) it would appear that beach-walls would be preferable to sea-walls not only on account of their lesser interference with morphological processes, but also on aesthetic and ecological grounds. The importance of the latter will be appreciated if one recognizes that the ecology reacts to changes in the natural, physical environment. As it is expected that beach-walls will change the natural environment to a lesser extent than sea-walls, the ecology will also be less affected. Although not called beach-walls (a term coined by Hayashi) such structures have been built in numerous locations around the world, with great success. Aspects of beach-walls which need to be addressed further are the optimum crest elevation and the degree of damage which can be tolerated. Obviously the crest elevation will be a function of the application: for example, the Dutch have buried a protective wall in their vulnerable coastal foredunes in areas where the protection afforded by the dunes alone was insufficient. In this case the crest elevation approaches the dune crest elevation. However, for more traditional applications such as those referred to by Hayashi (1986) it should be possible to establish some guidelines for the preferred crest elevation.

Detached breakwaters

Over the last twenty years or so hundreds of detached breakwaters have been constructed in widely different environments. The behaviour of a fair percentage of these has been monitored. Because the design

geometries of these breakwaters, as depicted by breakwater length, gap size, offshore distance, water depth at structure and crest elevation of structure, also vary greatly, it should be possible, and highly profitable, to characterize the behaviour according to design geometry. Rosen and Vajda (1982) and Schoonees in CSIR (1986) have attempted to do so. This does not mean that one can get away without a detailed design stage; it merely allows one to make a very intelligent first guess at a scheme. Aspects of the design of beach protection schemes by means of offshore breakwaters which require specific attention are the following:

- the volume of sediment which needs to be moved by the waves to reshape the beach and, related to this, the time required to do so as well as the extent of possible areas of erosion;

- with the first point in mind, the necessity for artificial nourishment of sand to aid the reshaping process;

- the aesthetic appearance of such offshore structures, with specific reference to the "requirement" of bathers to be able to see the sea, to allow them to feel they are on the beach and not only at some inland water pool, and

- the structural design of these structures, which is frequently neglected and which necessitates either costly maintenance at an early stage or the redesign of the scheme in total.

Groynes

In the first half of this century groynes were mostly seen as the ultimate solution to beach erosion problems. Usually, not enough attention was given to the process assessment stage and the end result was that downdrift beach erosion was enhanced. Groynes are only effective against long-term erosion due to longshore gradients in the longshore transport. Even then they do not prevent erosion but only retard it while the longshore drift fills up the updrift beach before bypassing commences. A major problem with groynes is the extent of the downdrift erosion. Downdrift erosion can be curtailed/minimized by using different types of partially permeable groynes which do not present such an impermeable barrier to the longshore drift. Groynes of this type are low-level groynes which allow part of the drift to pass over the low-level portion of the groyne, which could, for example, be sloped to a desired beach profile, or piled structures which allow part of the drift to pass through the piles, or combinations of these two types, or short groynes which fill quickly and have a shorter offset. In all these uses it is important to assess **quantitatively** beforehand what proportion of the sand will bypass, and when and how, as well as the type of flow field which will be set up updrift of the groyne, for example, an eddy or a rip current, and the extent to which this flow will influence the morphology in the vicinity of the structure.

Another important aspect which needs to be taken into account at the design stage is that if vertical walls (such as closely spaced piles) are to be incorporated in the design, it would be essential to consider the extent of scour which would result on the updrift side of

the structure in the area where increased turbulence results from interactions between reflection off the structure and the updrift rip current, should it occur.

Recently the tendency has been to use permeable groynes of one type or another **in conjunction with** beachfill, to achieve a minimum guaranteed beach width.

Beachfill

Beachfill is perhaps the type of beach protection scheme most-favoured today, mainly because of its natural appearance upon completion. Ecologically this is also preferred because natural habitats can re-establish themselves - although during placement fairly substantial mortalities of sub-bottom communities could occur, mainly as a result of the pumping exercise.

In designing a beachfill it is imperative that the designer understands the processes at work. It is particularly important that he understands the mechanism(s) by which material will be removed out of the fill and where such material will end up.

The traditional techniques advocated for the establishment of the magnitude of the fill required, for example by Krumbein and James (1965), Dean (1974), James (1974) and SPM (1984) do not take the mechanisms of movement into account **and can therefore at best provide a first estimate of the required placement.** In addition, most of these techniques exaggerated the required placement because they depart from the premise that the grain size distributions of native and borrow material must be similar.

Nowadays it is recognized that a more detailed design of a proper beachfill is required, especially as it is now such a popular protective technique and because of the high cost, both in the initial stages and thereafter, if maintenance is required. The Dutch have just published a manual for artificial nourishment (Manual on artificial beach nourishment and coastal processes, 1985) which covers most of the aspects to be considered in a beachfill design very adequately. This document is a must for every designer using beachfill.

The following techniques exist for a more detailed design of beachfills:

- One-line coastline evolution models such as that by Pelnard-Considerè (1954), but modified to include diffraction effects. This type of model will only have limited application because of the nature of the assumptions, that is, transport takes place in one layer, profile shifts as a geometrically undistorted profile, the difficulty of defining the effect of the beachfill on the amount of longshore transport "by-passing" the beachfill and the fact that onshore-offshore transport cannot be accounted for.

- Two-line coastline evolution models such as that by Bakker (1968) are more relevant because of the inclusion of onshore-offshore transport but its application is still limited because the coastal

constants required for predictive purposes with this type of model are functions of the profile geometry, which makes it impossible to use the model in a predictive mode before a series of measurements in the full-scale had been made of the evolution of the beachfill.

- N-line or multi-layer coastline evolution models (N > 4), such as that by Perlin and Dean (1983) may give a very good indication of the reshaping of the coast in the vicinity of the beachfill. Möller et al. (1986) used such a model for Oranjemund with great success. It is essential that good field data are available to calibrate the model. A problem of this and all other predictive models is that it is difficult to cater for the effect of differences in the grain size distribution of the native and borrow materials. It is possible, however, to obtain bracketing answers.

- Longshore transport predictors may have some limited merit to show the extent to which the longshore transport regime in the beachfill area is modified.

- Onshore-offshore predictors such as the method by Swart (1974, 1986) are extremely useful to evaluate the effect of a beachfill geometry that is different to the original beach profile. This technique has been used effectively by Campbell, Macleod and Swart (1985) to bracket the losses from a beach nourishment project in Durban, South Africa.

- Mathematical models which model the nearshore water and sediment movement accurately are better than any of the preceding methods but are very costly to execute and still suffer from the deficiency of not catering adequately for differences in the grain size distribution of the native and borrow materials. References which can be consulted in this regard are Watanabe (1982), Boer et al. (1984), Coeffe and Pechon (1982) and Sheng and Butler (1982).

- Physical models with a movable bed are also a possibility but are expensive to construct and take long (6-18 months) to execute, if one takes into account the construction, calibration and predictive stages. Proper scaling to allow the model to cater for a beachfill of limited geometrical proportions is also a problem.

- Field observations from the area may give a good first indication of the expected behaviour of the beachfill. For all of the above, field data are needed in any case to calibrate the respective techniques.

Experience has shown that in most cases the use of some sort of hybrid technique, that is, a combination of some of the above techniques is the most effective. In this respect a **mathematical or physical model** which will predict only the **water movement** can prove useful in conjunction with some of the above techniques.

Other aspects of beachfill which are important and which were discussed during the poster discussion sessions are:

- How do you define the required volume of sand related to the lifetime of the beach nourishment. In this respect the concept of a beachfill **half-life** was raised. During the design stage one should establish the future behaviour of the beachfill and decide whether it is a once-off exercise, whether it would have to be repeated from time to time (when the so-called half-life principle comes into the picture) or whether it should be maintained continuously. It is also important that these aspects are communicated to the public at an early stage so that they know what to expect.

- The design technique chosen should provide for the evaluation of the actual wave climate, to allow for the inclusion of extreme wave events and the cumulative effect of a number of extreme wave events in a short time span (the El Niño effect reported on by Seymour et al., 1984).

- The choice of a borrow area in relation to the littoral active zone or dynamic swept prism is of extreme importance, particularly as related to possible aggravated beach erosion elsewhere in the vicinity if located too close by. The borrow area also needs to be "designed". From both the physical and the environmental point of view it will be advantageous if the borrow area is a large flat area, that is, if only a thin layer of sand is removed.

5. CONSTRUCTION PHASE

It is not the purpose of this review to discuss the construction phase in detail. The reader is referred to the Dutch beachfill manual mentioned above in the case of beachfill design. Considerations similar to those covered in the manual for the construction phase will apply to other types of beach protection devices. However, the following few items are of particular relevance to the establishment of a good design for a beach protection scheme.

- It is important to decide beforehand on the phasing of the various components of the beach protection scheme, with specific attention to the question of how each completed part of the scheme will influence the rest of the scheme and of the longshore direction in which the scheme should be developed (up- or downdrift) to gain the most benefit from the littoral drift.

- The best construction techniques and their effect on the design should be considered. In this respect it is important for designers and contractors to get together at an early stage to evaluate these aspects and perhaps cater for some predictions in the design stage of construction phases.

- Perhaps the most important aspect related to the construction phase is that of quality assurance. Each element/component of the design/construction phase needs to be evaluated and the risk of failure due to, for example, extreme wave events during construction considered. Alternatives should be provided for. In this way the preparation of the project is more costly but the possible risks are reduced.

6. POST-CONSTRUCTION PHASE

It is necessary in the design stage to address the following aspects and to discuss their importance with the client.

- The necessity for post-construction monitoring should be stressed. Aspects of particular importance are the frequency of monitoring as related to the forcing mechanisms, the nearshore environment and the expected/predicted behaviour of the beach protection scheme, the extent of the monitoring and, last but not least, the body with whom the responsibility rests to pay for the monitoring. It is usually advantageous to include some funds for monitoring in the construction vote, as it is after all this monitoring which is going to determine to what extent the design is successful.

- Linked to the previous point is the need for a re-appraisal of the shoreline stability in the area and again a decision as to whose responsibility it would be.

7. DISCUSSION

From the discussion in the preceding sections it should be clear that although the planning, design and execution of beach protection schemes have come a long way in the past few decades, there are still many areas requiring detailed inputs from scientists and engineers. To allow us as a community to learn from our mistakes, it would be advantageous if we could:

- establish international co-operation and exchange on all the levels mentioned in this review;

- exchange good quality field data suitable for the comparison/verification of different design techniques and beach protection types;

- jointly address the matter of quality assurance and investigate the possibility of using a "half-life" concept as a measure of the effectiveness of any type of beach protection device.

In this respect the Dutch have indicated that they are willing to do the above as far as it relates to beachfill. The discussion at the conference indicated that initially there is no merit in establishing formal working groups, but that this should be done informally.

Let us make it our challenge when we have such a discussion again in the future, to be in a position by having addressed some or all of the points raised herein to say that we have advanced the science of planning, designing and executing beach protection schemes.

8. SUMMARY

With the exception of the paper presented by Kawata et al., all papers related results on the basis of practical experience gained through field works in various parts of the world, namely Eygpt,

Hawaii, Italy, Japan, Kuwait, Singapore, South Africa and Republic of China, Taiwan.

It is true that a lot of case studies have been done during the last decades in various countries, states, counties, prefectures, cities and towns, and extensive data sets have been accumulated. However, only limited data have unfortunately been made available to the relevant scientific and engineering fraternity. At present shore protection problems are the serious concern of not only the inhabitants of the coastal area but also the governmental agencies who have responsibility to maintain or rather improve the coastal environment. Therefore shore protection studies are highly needed world wide in order to understand the coastal phenomena more clearly and then to apply our knowledge to the preservation of beaches as well as the production of a better environment in the coastal zone.

Shore protection studies should cover broad phases in the coastal and nearshore area. These are related not only to the coastal characteristics in the physical sense such as waves, nearshore currents, sediment transport, interaction between coastal structures and natural forces, but also the social circumstances including environmental concern.

Therefore shore protection is one of the important tasks of coastal engineers. At the same time shore protection is a subject of serious debate for other people such as politicians, land owners, property owners, lawyers, bankers, insurers and fishermen. That is to say, shore protection is really a multidisciplinary subject.

From such a view point, coastal engineers should take the heavy responsibility of offering a good service or good guidelines to the people who are seriously concerned with shore protection. Therefore they should always consider the complicated real situations which contain the following two aspects. The first one is the subject related to the natural conditions such as wave climates, beach slope, beach material, and beach width. The second one is that related to the social circumstances such as social demand, economic conditions and environmental impact in the broad sense caused by human activity.

It is natural that these stated conditions are quite different from one location to another. Therefore we should carefully observe the information and data presented here and elsewhere in order to evaluate the adaptability of the measures or the concepts to any given site.

As a conclusion of the present summary paper, we would like to stress the importance of information exchange on shore protection measures not only from the engineering point of view but also from the view point of social demand.

9. REFERENCES

BAKKER, W.T. (1968). The dynamics of a coast with a groyne system. 11 International Conference on Coastal Engineering, ASCE, Volume I, 492-517, London.

BOER, S., DE VRIEND, H.J. and WIND, H.G. (1984). System of mathematical models for the simulation of morphological processes in the coastal area. Proceedings 19th International Conference on Coastal Engineering, Houston, 1437-1453.

CAMPBELL, N.P., MACLEOD, D.C. and SWART, D.H. (19B5). Bypassing and beach nourishment scheme at Durban. 26th International Navigation Congress, PIANC, Section II, Subject 3, 7-18, 8russels, 8elgium.

CDEFFE, Y. and PECHDN, P. Modelling of sea-bed evolution under wave action. Proceedings 18th International Conference on Coastal Engineering, Cape Town, 1149-116D.

CSIR (19B6). False Bay: The hydraulic design of bathing improvement schemes using a sediment model. CSIR Report, National Research Institute for Oceanology, Council for Scientific and Industrial Research, Stellenbosch, South Africa (unpublished report, in Afrikaans).

DEAN, R.G. (1974). Compatibility of borrow material for beachfills. 14th International Conference on Coastal Engineering, ASCE, Volume II, 1319-133D, Copenhagen, Denmark.

GAM8ARDELLA, F. (1986). The Po River delta: erosion and protection of the coast. 2Dth International Conference on Coastal Engineering, ASCE, Taipei, Republic of China.

HAYASHI, R.M. (1986). 8eachwalls for beach erosion protection. 2Dth International Conference on Coastal Engineering, ASCE, Taipei, Republic of China.

JAMES, W.R. (1974). 8orrow material texture and beachfill stability. 14th International Conference on Coastal Engineering, ASCE, Volume II, 1334-1344, Copenhagen, Denmark.

KADI8, A.L., SHAK, A.T. and MAZEEN, A.A. (1986). Shore protection plan for the Nile delta coastline. 2Dth International Conference on Coastal Engineering, ASCE, Taipei, Republic of China.

KANA, T.W. AL-SARAWI, M. and HDLLAND, M. (1986). Design and performance of artificial beaches for the Kuwait waterfront project. 2Dth International Conference on Coastal Engineering, ASCE, Taipei, Republic of China.

KAWATA, Y. and TSUCHIYA, Y. (1986). Applicability of sub-sand filter system to beach erosion control. 2Dth International Conference on Coastal Engineering, ASCE, Taipei, Republic of China.

KOJIMA, H. IJIMA, T. and NAKAMUTA, T. (1986). Impact of offshore dredging on beaches along the Genkai Sea, Japan. 2Dth International Conference on Coastal Engineering, ASCE, Taipei, Republic of China.

KRUM8EIN, W.C. and JAMES, W.R. (1965). A lognormal size distribution model for estimating stability of beachfill material. Technical Memorandum No. 16, US Army, Corps of Engineers, Coastal Engineering Research Centre, Fort 8elvoir, Virginia, USA.

MANUAL ON ARTIFICIAL NOURISHMENT AND COASTAL PROCESSES (1986). Rijkswaterstaat and Delft Hydraulics Laboratory, Netherlands, 2 volumes.

MÖLLER, J.P., OWEN, K.C. and SWART, D.H. (1986). Coastal engineering studies for inshore mining of diamonds at Oranjemund. 20th International Conference on Coastal Engineering, ASCE, Taipei, Republic of China.

PELNARD-CONSIDÉRE, R. (1954). "Essai de théorie de l'évolution des formes di rivages en plages de sable et de galets". Quatriéme Journèes de l'Hydraulique, Paris, 13-15 Juin 1954.

PERLIN, M. and OEAN, R.G. (1983). A numerical model to simulate sediment transport in the vicinity of coastal structures. Miscellaneous Report No. 83-10, US Army, Corps of Engineers, Coastal Engineering Research Center, Fort 8elvoir, Virginia, USA.

PUI, S.K. (1986). 100 years of foreshore reclamation in Singapore. 20th International Conference on Coastal Engineering, ASCE, Taipei, Republic of China.

ROSEN, D.S. and VAJDA, M. (1982). Sedimentological influences of detached breakwaters. 18th International Conference on Coastal Engineering, Volume III, 1930-1949, Cape Town, South Africa.

SEYMOUR, R.J., STRANGE, R.R. (III), CAYAN, D.R. and NATHAN, R.A. (1984). Influence of El Niños on California's wave climate. 19th International Conference on Coastal Engineering, ASCE, Volume I, 577-592, Houston, Texas, USA.

SHENG, Y.P. and 8UTLER, H.L. (1982). Modelling coastal currents and sediment transport. Proceedings 18th International Conference on Coastal Engineering, 1127-1148.

SHORE PROTECTION MANUAL (1984). US Army Corps of Engineers, Coastal Engineering Research Center, Fort 8elvoir, Virginia, USA, 3 volumes.

SUYAMA, H., UDA, T. and YOSHIMURA, T. (1986). 8each change around detached breakwaters due to artificial nourishment of bypassed sand. 20th International Conference on Coastal Engineering, ASCE, Taipei, Republic of China.

SWART, O.H. (1974). Offshore sediment transport and equilibrium beach profiles. Publication No. 131, Delft Hydraulics Laboratory, Netherlands.

SWART, D.H. (1986). Prediction of beach changes and equilibrium beach profiles. Short course, 20th International Conference on Coastal Engineering, Dynamics of sand beaches, Taipei, Republic of China.

WATANA8E, A. (1982). Numerical models of nearshore currents and beach deformation. Coastal Engineering in Japan, Vol. 25, 147-161.

YEH, J.-L. and OU, S.-H. (1986). Detached breakwaters at Redhill coast, Taiwan. 20th International Conference on Coastal Engineering, ASCE, Taipei, Republic of China.

CHAPTER 168

IMPULSIVE BREAKING WAVE FORCES ON AN INCLINED PILE EXERTED BY RANDOM WAVES

by

K. TANIMOTO*, S. TAKAHASHI*, T. KANEKO**, K. SHIOTA**

ABSTRACT

A calculation method of the impulsive breaking wave forces on piles is proposed in this paper. It is derived on the basis of experimental results with some theoretical considerations. Wave forces on a cylinder caused by both regular and irregular trains of waves are measured in a large wave flume. The experimental results are compared with the values predicted by both Wagner and Karman. In the proposed method, it is assumed that the impulsive force acts on the upper half of the pile between the still water level and the wave crest, and that the force distribution along the pile is triangular shape. The peak value in the distribution is expressed by the function of both the breaking force parameter and the inclination angle of the cylinder. The breaking force parameter is the ratio of the bottom slope to wave steepness. The time history of the impact force is given as a triangular pulse with a vertical rise. The duration time is determined as half of the value predicted by Karman's theory.

1. INTRODUCTION

Wave forces which act on cylindrical members supporting coastal and offshore structures are generally predicted as the sum of drag and inertia forces. However, impact forces should be counted in addition to these forces when breaking waves act on a pile.

A prediction method for the impact force is shown in the Shore Protection Manual(1975) on the basis of the experimental studies by Ross(1955,1959) and Hall(1958). According to the method, the total force by a breaking wave can be estimated by Morison's equation with the drag coefficient being 2.5 times the ordinary value. The experiments by Ross and Hall, however, were conducted with a steep bottom slope condition. The impact force is very large if the bottom slope is steep. The value of the impact force estimated by the formula, therefore, may be excessive for a gentle bottom slope condition. The dynamic response of structures resisting such an impact

* Hydraulic Engineering Division, Port and Harbour Research Institute Ministry of Transport, 3-1-1 Nagase, Yokosuka, Japan
** Engineering and Construction Division, Kawasaki Steel Corporation 2-2-3 Uchisaiwai-cho, Chiyoda-ku, Tokyo, Japan

force cannot be predicted, because it provides information only on the peak value of the impact force.

Goda et al. (1966) proposed a calculation method for the impact forces acting on a vertical pile, referring to the virtual fluid mass theory derived by Von Karman(1929). They obtained a diagram for the curling factor, which can evaluate the impact forces for both 1/10 and 1/100 bottom slope conditions. The time history of the impact force can be also predicted by the method.

Many inclined piles are used as the members of sea structures such as sea-berths and jetties. The authors (1986A,B) carried out a series of experiments to investigate the breaking wave force on an inclined pile and proposed a calculation method. The method was an extension of Goda's method.

All of these studies, however, were based on the experiments only by regular waves. Because ocean waves are random, it is important to investigate the wave force exerted by irregular waves. Only Ochi et al. (1984) discussed the statistical characteristics of impact pressure on a pile by random waves.

This paper proposes a calculation method for the impact forces of breaking waves due to random ocean waves. First, some theoretical consideration based on Wagner's theory was given to the impact force which occurs by a collision between the pile and the water surface. Secondly, experiments were conducted to measure the impact forces on the pile due to not only regular waves but also irregular waves. Then, the calculation method was derived. The present method provides information on the impact force including the peak value, the time history, and the distribution along the pile. The method is applicable not only to vertical piles but also to inclined piles.

2. THEORETICAL CONSIDERATION

Wagner (1932) derived a set of equations for the impact pressure due to collision between a rigid body and water surface. Figure 1 shows Wagner's model when the water surface strikes a pile. The water surface "pile-up" along the pile surface can be seen in the figure, which is taken into account in the theory. In this figure, D, R and V are the pile diameter, the pile radius, the uprising velocity of the water surface. An equivalent plate of the width 2b is considered between the two attaching points of the pile surface to the water surface. The axis x is parallel to the plate and the axis y is perpendicular to it. Equations which

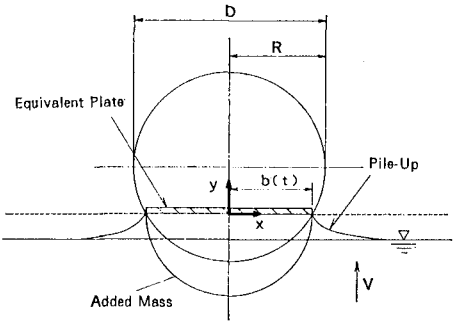

Fig.1 Wagner's model for impact force

determine the water surface profile at time t and the pressure on the pile surface are obtained from the complex potential of the flow around the flat plate.

In the actual calculation of the impact pressure, the pile surface should be expressed as a function of x. Here, the pile surface is approximated by the following equation:

$$\frac{y_1}{R}=\left(\frac{x}{R}\right)^m \qquad (1)$$

where, y_1 is the distance of the water surface from the bottom of the pile. Figure 2 shows the approximated profile of pile surface for several values of the power m in Eq.(1). The broken line, the dot-dash line, the two dots-dash line and the dotted line indicate the cases for m = 1, 2, 3 and 4 respectively. In the case where m =1, the profile by Eq.(1) is actually a wedge with the angle of 45 degrees. The bottom portion of the approximated profile swells as m increases. The profiles for m = 3 and 4 are close to a circle which is drawn by the solid line.

Figure 3 shows the time history of the total impact forces on the pile which are obtained from Wagner's theory. The vertical axis is the non-dimensional force $F/(w_0DV^2/2g)$, where F is the impact force, w_0 is the unit weight of water,and g is the gravity acceleration. The horizontal axis is the nondimensional time t/(R/V). The lines in the figure correspond to the same number of the power m respectively as in Fig.2. The solid line which represents the force on the circular pile based on the Karman's theory is also shown for comparison. Karman's theory neglects the pile-up effect. The followings can be pointed out from the figure:

a) The characteristics of the impact forces change greatly by the change of the pile profile. In the case of the wedge-shape pile (m = 1), the force increases linearly with time. When the pile profile

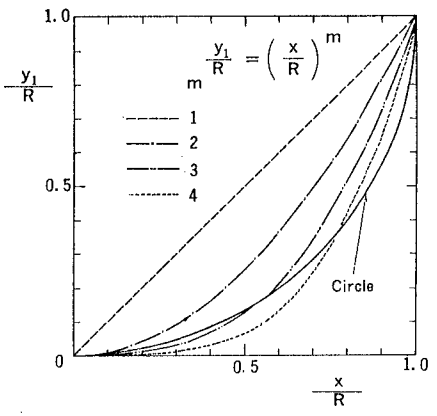

Fig.2 Approximated pile profiles

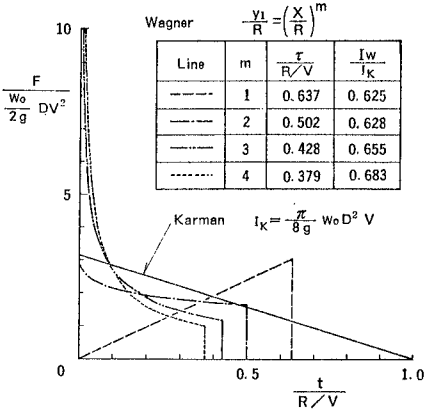

Fig.3 Calculated Impact force

approaches the circular shape (m= 3 and 4), the impact force becomes hyperbolic shape with a steep rise at the instant of collision and a sudden decrease after the peak.

b) The impact force on a circular pile by Wagner's theory is quite different from that by Karman's theory. For example, the peak value when m=3 is 471, which is more than one hundred times the peak value by Karman's theory. This is caused by the fact that the incremental rate of added mass of the equivalent flat plate by Wagner's theory is large because of the pile-up phenomenon, which is not considered in Karman's theory. In the range of $t/(R/V) > 0.09$, however, Wagner's impact force is smaller than Karman's one. This is due to the effect of negative pressure induced by the current along the pile surface. This effect is considered only in Wagner's equations.

c) By the effect of the pile-up, the impact duration time τ by Wagner's theory is shorter than that by Karman's theory. The Wagner's duration time with m = 3 is 0.428 times Karman's one.

d) The impulse of total force by the Wagner's theory is 0.6 - 0.7 times that by Karman' theory. This is also caused by the negative pressure component.

3. EXPERIMENTAL FACILITY AND PROCEDURE

Wave Tank and the Bottom Slope

The experiments were carried out in a large wave tank, which is 105 m long, 3 m wide and 2.5 m deep. The wave tank was divided into 80 and 205 cm wide flumes by a partition wall which was installed 42 m away from the wave generator. The model pile was installed in the 80 cm flume. The piston type wave generator in the wave tank could generate both regular and irregular waves.

The cross sections of the wave flume in the experiments are shown in Fig. 4 (a) and (b). The bottom slope i near the model was fixed at 1/30 or 1/100 as shown in the figure. The model pile was installed 72 m away from the wave generator. The water depth at the pile location h is maintained at 70 cm.

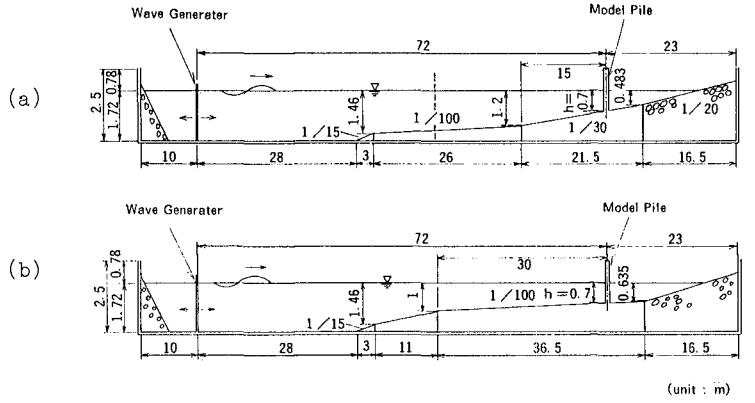

Fig.4 Cross sections of the wave tank

Model Pile and Wave Force Sensors

Figure 5 shows the model pile. The pile inclination was changed at angles $\theta = 0^{\circ}$, $\pm 15^{\circ}$ and $\pm 30^{\circ}$. The bottom end of the pile was fixed on a base plate. The top end was also fixed to the side wall of the wave tank with a steel beam. The pile diameter D was 14 cm. The model pile comprised thirteen wave force sensors (F1-F13) and two dummy pipes.

The details of the wave force sensor are shown in Fig.6. The sensor was an aluminum pipe with 5 mm thickness and 14 mm diameter, which was connected to a rigid steel pillar by 3 mm thick steel plates. When the wave force acted on the pile, the bending strain appeared in the steel plates. The force component perpendicular to the plates was measured with four strain gauges pasted on the plates. The sensitivity of the sensor was $8.7\,\mu$ / Kgf and the natural frequency was 745 Hz in air and 422 Hz in water. The damping factor was 0.026 in air and 0.068 in water.

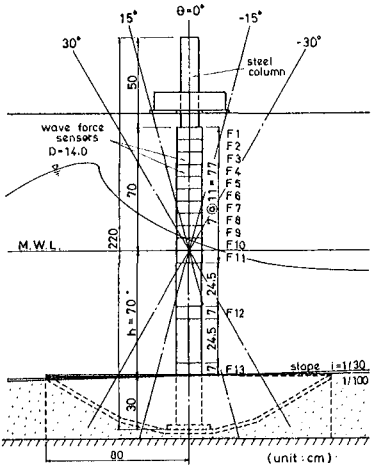

Fig.5 Model pile

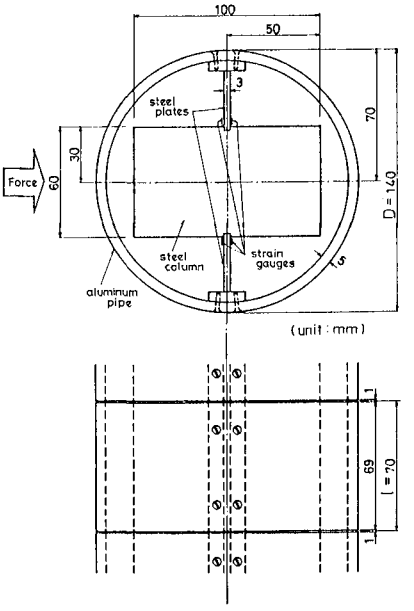

Fig.6 Wave force Sensors

Measurement and Analysis Method

The analogue signal from the wave force sensors was sent to a computer through amplifiers and low-pass filters, and was analysed by the computer. The low-pass filters were used not only to cut off the noise but also to reproduce the correct input force signal eliminating the response effect of the sensors. Although the natural frequency of

the sensors was very high, a dynamic response appeared in the sensors when the impact force is very large. The authors (1983) already investigated a method to obtain the impact force signal from the response data. This method was used in the present experiments. The applicability of the method was examined in the preliminary test. The cut-off frequency was set at 400 Hz for the sensors F1 - F10 , which were installed above the still water level. For the sensors F11 - F13 which were below the still water level, the cut-off frequency was set at 20 Hz since the impact force did not act on them. The sampling time in the analogue-digital conversion in the computer was 0.005 s.

4. CHARACTERISTICS OF WAVES

Regular Waves

The wave period T of regular waves was set at 2, 3 and 4 s. The wave height was fixed at H'/H_b = 0.5, 0.8, 0.9, 1.0, 1.1, 1.2 and 1.7, and the additional values of the wave height were selected near the breaking wave height H_b to obtain the maximum breaking wave force. The term H' is called here " the hypothetical passing wave height",which is the wave height at the measuring point for non-breaking waves but is the breaking wave height at the breaking point for breaking waves. The breaking wave height and the crest elevation η_b were measured in the experiments, which had the values very close to those evaluated by Goda's breaker indices (Goda 1970). The breaking wave velocity C_b measured by 16 mm film agrees very well with the value calculated by

$$C_b=\sqrt{g(h+\eta_b)} \tag{2}$$

Irregular Waves

The irregular waves in the experiments have the Bretschneider-Mituyasu spectrum (see Goda(1985) pp. 23-27). Three wave groups were prepared for the irregular wave tests, namely wave-A, wave-B and wave-C. The significant wave period of the three wave groups $T_{1/3}$ were 2, 3 and 4 s respectively. Each wave group has three wave trains;(A1 - A3), (B1 - B3) and (C1 - C3). Each wave train contains about two hundred waves, and therefore each wave group has about six hundred waves. Three different levels of the significant wave height were employed in the experiments as shown in Table 1. A wave train with the highest level of the significant wave height contains a number of breaking waves, while that of the lowest level has few breaking waves. Six more wave trains were prepared for the wave group B to examine the effect of the number of waves.

Table 1 Significant wave height

Wave Group	$H_{1/3}/h$					
	i = 1/30			i = 1/100		
A	0.307	0.491	0.556	0.311	0.457	0.519
B	0.370	0.601	0.674	0.359	0.539	0.580
C	0.364	0.656	0.766	0.363	0.557	0.623

The relation between the maximum wave height H_{max} and the maximum wave crest height, η_{max} can be expressed as follows from the results of the wave measurement.

$$\eta_{max}/H_{max}=0.5+a\sqrt{H_{max}/h} \tag{3}$$

$$\left.\begin{array}{ll} a\approx 0.247 & : \quad i=1/30 \\ a\approx 0.315 & : \quad i=1/100 \end{array}\right\} \tag{4}$$

5. EXPERIMENTAL RESULTS

Results of Regular Wave Tests

Figure 7 shows profiles of breaking waves striking a pile. This figure was made by tracing the film record for the case of T = 3 s, H' = 55.3 cm, i = 1/30, and θ = 0°. The vertical wave front near the crest is hitting very hardly the sensor F4 in the figure.

Figure 8 shows the time history of the force by the same breaking wave in Fig. 7. F_3 through F_7 indicate the force on the sensors F3 - F7 respectively. F is the total force which is obtained by integration of the forces on the sensors. The forces are presented in non-dimensional form with unit weight of water, w_0, the pile diameter D, the water depth h and the height of the sensor l. Large impact forces are observed in F4 and F5. The time histories of the impact forces are similar to that by Wagner's theory shown in Fig.3. The rising time is about 0.001 s.

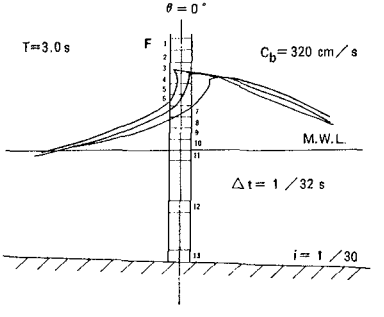

Fig. 7 Profiles of breaking wave striking the pile

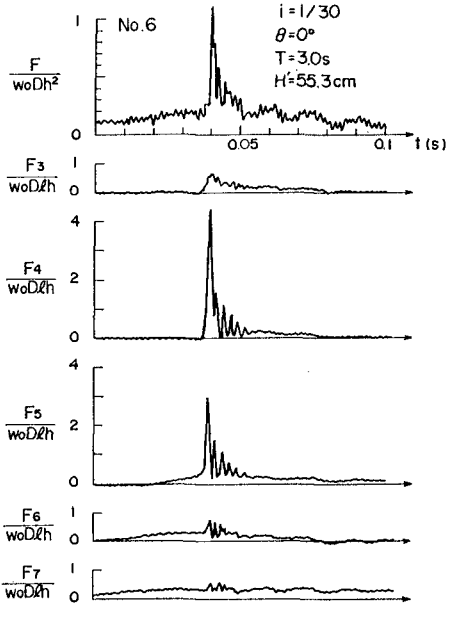

Fig. 8 Time history of impact force by breaking wave

Figure 9 shows the relation between the peak value of the total force F_m and the hypothetical passing wave height H' for the case of i = 1/30, $\theta = 0^\circ$ and T = 3 s. The arrow in the figure indicates the relative breaking wave height H_b/h. When H' approaches H_b, the impact force acts on the pile, and F_m scatters to a great extent. In the range of $H' > H_b$, the impact force decreases because post-breaking waves acts.

Figure 10 shows the relation between the maximum breaking wave force F and the "breaking force parameter" $i/(H_b/L_o)$, where L_o is the wave length in deep water. The breaking force parameter represents the change of the breaker type refering to the results of a series of small scale model tests (Authors 1986) The maximum breaking wave force F increases greatly in the range of $i/(H_b/L_o) = 0.4 \sim 0.7$ where the breaker type changes from spilling to plunging. As the pile inclines seaward, the wave which has a straight and sharp front just before breaking whips the face of the pile, causing a large impact force. When the pile inclines shoreward, however, the impact force is reduced. This is because only a small portion of the curling wave front just after breaking hits the face of the pile, and because the other portion of wave front is disturbed by itself.

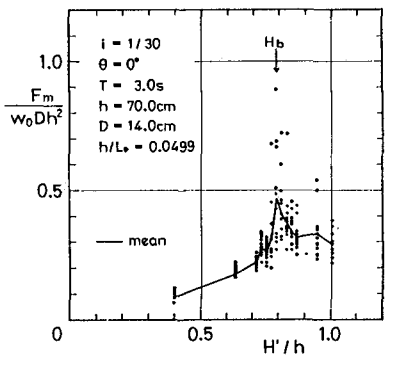

Fig. 9 Wave force vs wave height

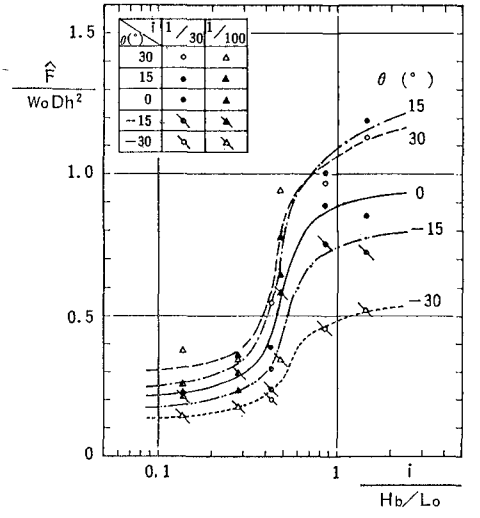

Fig.10 Maximum impact force

Figure 11 shows the breaking wave force distribution for several values of time when i = 1/30, $\theta = 0^\circ$, T = 4 s and H' / h = 0.83. The vertical axis z is the co-ordinate along the pile from the mean water level. When t = 0, a small force acts within the range z = -60 ~ + 20 cm. When t = 0.0825 s, the impact force with a sharp peak is observed just under the crest. The distribution of the impact force is symmetrical and triangular.

Results of Irregular Wave Tests

Figure 12 shows the time history of the water surface elevation

η , the total force F and the force on each wave sensor F_4 - F_{12} for the case of i = 1/30, θ = 0°, wave-B(B5),and $H_{1/3}/h$ = 0.676. Large impact forces are observed when the wave profiles are very steep in the figure. The irregularity of the wave forces is much emphasized compared with the irregularity of the waves.

The individual waves for a train of irregular waves are defined by the zero-upcrossing method. The peak values of the total force F_m for the individual waves were statistically analysed and the representative values of the peaks were obtained. The maximum value of

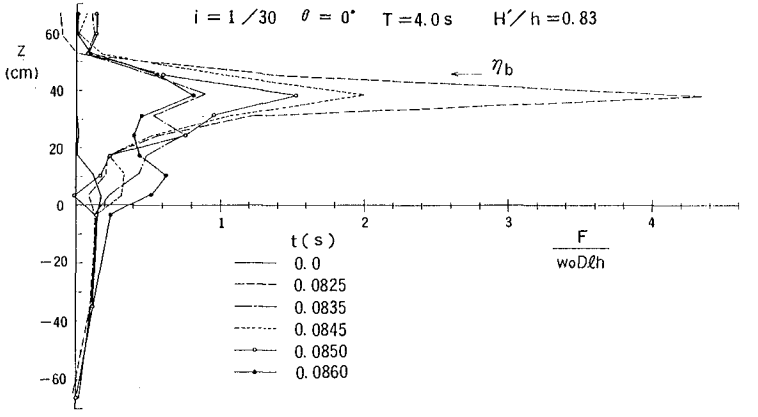

Fig. 11 Distribution of impact force

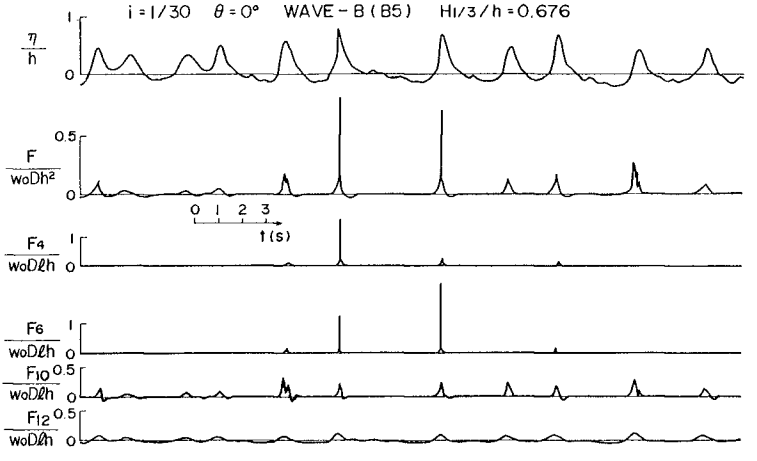

Fig. 12 Wave and wave force profiles by random waves

F_m in a wave train is denoted by F_{max}. The average of F_m from the highest to the 1/10 highest is called the 1/10 largest force $F_{1/10}$. The average of F_m from the highest to the 1/3 highest is called the 1/3 largest force $F_{1/3}$. The average of of all the peak values is denoted by F_{mean} respectively. The average of all the representative values for the different wave trains in the same wave group are expressed by $\bar{F}_{max}$, $\bar{F}_{1/10}$, $\bar{F}_{1/3}$ and $\bar{F}_{mean}$ respectively. The maximum value of F_{max} in a wave group is denoted by $\hat{F}$.

Figure 13 (a) and (b) show the frequency distribution of the peak wave force F_m in the form of probability density for the case of i = 1/30, $\theta = 0^o$ and wave-B(B1-B10). When $H_{1/3}/h$ =0.367 breaking waves were scarcely included, and then maximum value of $F_m/\bar{F}_{mean}$ is 5.3. When $H_{1/3}/h$ = 0.676, a fairly large number of breaking waves were included, and the maximum value of $F_m/\bar{F}_{mean}$ goes up to 7.3. This indicates that the peak values of the impact force vary very widely.

Table 2 shows the mean value and the standard deviation of the maximum force F_{max} to investigate the statistical characteristics of the maximum impact force. This is for the case of $\theta = 0^o$ and wave-B. The ratios between the representative forces are also shown. The mean value of F_{max} increases as the increase of $H_{1/3}$. For the case of $H_{1/3}$ = 0.676 and i = 1/30, the value of $\bar{F}_{max}$ is 0.808 and the standard deviation is 0.172. The columns of B3(Run 1 - 10) show the values when the same wave train B3 was repeated ten times. For the case of $H_{1/3}/h$ = 0.676 and i = 1/30, the values by the B3 wave train are almost the same as the values by the wave trains from B1 to B10.

Figure 14 shows the relation between the maximum force $\hat{F}$ and the breaking force parameter $i/(H_{max}/L_o)$. The maximum wave height instead

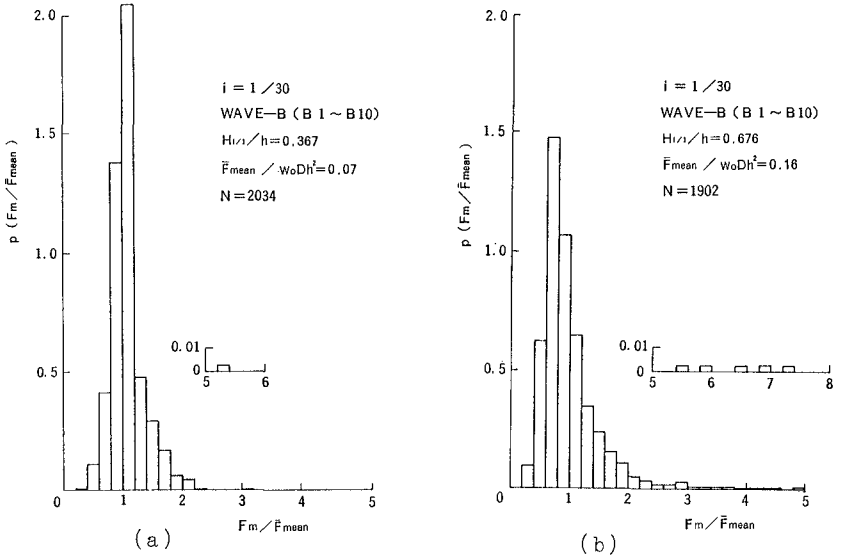

Fig. 13 Frequency of wave forces

Table 2 Statistical characteristics of wave forces

i	wave trains	$H_{1/3}/h$	F_{max}/w_0Dh^2			$\frac{\bar{F}_{max}}{\bar{F}_{1/3}}$	$\frac{\bar{F}_{1/10}}{\bar{F}_{1/3}}$	$\frac{\bar{F}_{mean}}{\bar{F}_{1/3}}$
			$\bar{x}$	σ	$\sigma/\bar{x}$			
1/30	B1～B10	0.367	0.153	0.081	0.529	1.88	1.25	0.752
		0.604	0.599	0.145	0.242	3.16	1.54	0.671
		0.676	0.808	0.172	0.213	3.38	1.51	0.640
	B3 (Run1～10)	0.676	0.834	0.164	0.197	3.39	1.67	0.504
1/100	B1～B10	0.359	0.116	0.028	0.241	2.00	1.17	0.667
		0.549	0.425	0.199	0.468	3.91	1.45	0.636
		0.586	0.468	0.167	0.357	3.62	1.54	0.615
	B3 (Run1～10)	0.586	0.368	0.083	0.226	2.71	1.49	0.610

$\bar{x}$: mean σ : standard deviation

of the breaking wave height is used to evaluate the breaking force parameter for irregular waves, and the maximum wave height in the figure is the maximum wave height in each wave group. Similar to the results in the regular wave tests, $\hat{F}$ increases as the breaking parameter increases and the pile inclines seaward. However, the increasing curves are more straight in the figure than those for regular waves in Fig.10. That is, the wave force increases gradually with the increase of the breaking parameter. This is because various wave profiles can appear due to the combination of wave period and wave height in irregular waves.

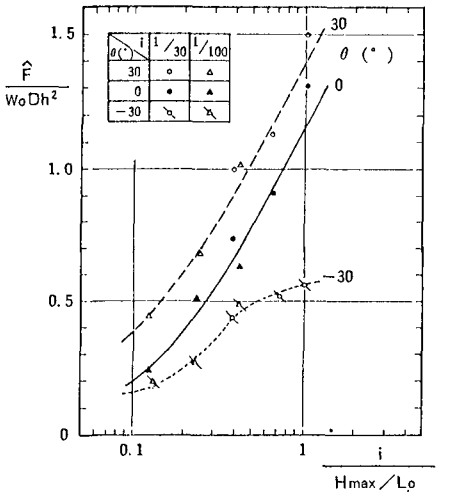

Fig.14 Maximum impact force

6. CALCULATION METHOD

Outline of the Method

The calculation method is proposed in this chapter. The method is based on Karman's and Wagner's theories but is simplified considering the experimental results by regular and irregular waves. As shown in Fig. 15, the impact force is assumed to act on the pile with a triangular distribution. The peak value and the width of the distribution are denoted by f_p and δ. The height of the peak above the still water level is denoted by l_p. The distribution of the impact

force is expressed by

$$f_z=\left\{1-\frac{|l_p-z|}{\delta/2}\right\}f_p \qquad for\ |l_p-z|<\delta/2 \qquad (5)$$

where f_z is the impact force on the pile at the location z .

The impact force is also assumed to vary with respect to time t as a triangular pulse which has a vertical rise. The duration time is denoted by τ . Therefore, the time history of the impact force at the peak location is

$$f_p=f_{pm}\left(1-\frac{t}{\tau}\right) \qquad for\quad 0<t<\tau \qquad (6)$$

where f_{pm} is the peak value of f_p with respect to time. The impact force at a certain point of the pile and at certain time is given by Eqs(5) and (6).The total impact force F_I and the peak value F_{Im} with respect to time in the calculation method are simply expressed by 0.5 δf_p and 0.5 δf_{pm} respectively.

Parameters

The parameters in the calculation method are determined as follows:

a) Peak Value at Peak Location

The peak value at the peak location is assumed to be in the following form:

$$f_{pm}=\nu f_{Km} \qquad (7)$$

where f_{km} is the peak value which is obtained by Karman's theory and ν is the adjustment factor. Karman's peak value is expressed by

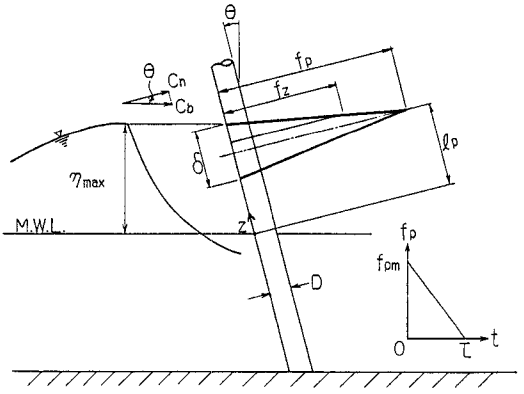

Fig.15 Impact force in the calculation method

$$f_{Km}=\frac{\pi}{2g}w_0 C_n^2 D \qquad (8)$$

where C_n is the wave celerity component perpendicular to the pile, which is

$$C_n=C_b\cos\theta \qquad (9)$$

b) Duration Time

According to Wagner's theory, the duration time and the impulse are about 0.4 and 0.65 times Karman's values respectively. The experimental results agree well with Wagner theory. Therefore, the duration time in the calculation method is assumed to be 0.5 times Karman's one as follows:

$$\tau = 0.25D/C_n \tag{10}$$

c) Height of the Peak Location above the Still Water Level

The height of the peak location above the still water level is averagedly 0.68 times the crest height for irregular waves in the experiments. Therefore, the height in the calculation method is assumed as

$$l_p = 0.75\,\eta_b/\cos\theta \tag{11}$$

d) Distribution Width

The distribution width is averagedly 0.516 times the crest height for irregular waves in the experiments. The distribution width in the calculation method is approximated as

$$\delta = 0.5\eta_b/\cos\theta \tag{12}$$

e) Adjustment Factor

The adjustment factor can be expressed by the following equation if the above relations are considered:

$$\nu = (8g\cos\theta/\pi w_0 C_n^2 D)(F_{Im}/\eta_{max}) \tag{13}$$

The adjustment factor ν was determined by the experimental data of F_{Im} with Eq.(13). It should noted that the value of F_{Im} is the pure impact component which is substracted the ordinary inertia and drag force component from the impact wave force. Two kinds of experimental values of F_{Im} were evaluated which were denoted by $\bar{F}_I$ and $\hat{F}_I$. $\bar{F}_I$ was evaluated by $\bar{F}_{max}$ which is the average of F_{max}, and $\hat{F}_I$ was evaluated by $\hat{F}$ which is the maximum value of F_{max} in each wave group. Two kinds of the adjustment factors denoted by $\bar{\nu}$ and $\hat{\nu}$ are evaluated by $\bar{F}_I$ and $\hat{F}_I$ respectively. The adjustment factor in the calculation method was determined by these two adjustment factors as follows:

$$\nu = (0.8+0.4\sin\theta)\tanh\{2.5\log_{10}\frac{i/(H_{max}/L_0)}{0.25}\}+1.0+1.2\sin\theta \tag{14}$$

Comparison of Results

Figure 16 shows the comparison of the calculated value of the impact force by the above method with the experimental values. In the figure, both $\bar{F}_I$ and $\hat{F}_I$ are shown. The experimental values agree with the calculated values on the average, and the difference between them is regarded to be small if the tendency of the large variation in the impact force is taken into account.

The calculated value by the method can be compared with the

calculated value by the method in the Shore Protection Manual (1975). For example, when h = 8 m, the wave height in deep water H_o = 6 m, $T_{1/3}$ = 10 s, D = 1 m, and i = 1/30 and 1/100, the maximum wave height H_{max} can be obtained as 6.78 m for i = 1/30 and 6.06 m for i = 1/100 by Goda's diagram (see Goda (1985) pp. 71 - 87). The impact forces by the present method are 43.4 tf and 25 tf for i = 1/30 and 1/100 respectively. These values are the pure impact component and the total impact forces become 55.4 tf and 47.3 tf if the ordinary inertia and drag component are evaluated to be 12.0 tf and 10.1 tf respectively. The impact breaking force by the method in Shore Protection Manual are nearly equal to the values by the present method for i = 1/30 but 35 % larger than the value by the method for i = 1/100.

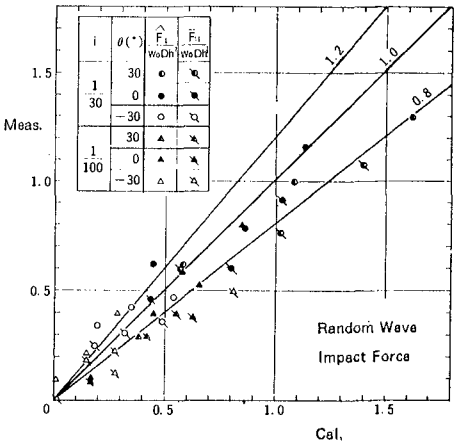

Fig.16 Comparison of the calculated results with experimental results

7. CONCLUSIONS

The major conclusions in the present study are as follows:

1) The peak values of the impact force on a circular pile by Wagner theory is larger than that by Karman's theory. The duration time and the impulse are about 0.4 and 0.65 times Karman's values respectively.
2) As a pile inclined seaward, the impact force increase greatly. As the pile inclined shoreward, the impact force decreases. If the inclination angle is within 30°, the impact force varies 20 ~ 50 % compared with the force on the vertical pile.
3) A new parameter called "the breaking force parameter", which is the ratio of bottom slope to wave steepness, can express the variation of the impact force. For regular waves, the impact force increases suddenly where the parameter is from 0.3 to 0.7. However, the impact force increases gradually with the increase of the parameter for irregular waves.
4) A calculation method of the impact force is proposed. The method is based on Karman's and Wagner's theory, but is simplified considering the experimental results. The distribution shape of the impact force is approximated as a triangle. The impact force is also approximated as a triangular pulse with respect to time. The adjustment factor is introduced in the method which expresses the variation of the impact force due to the breaking parameter and the inclination angle. The calculated results by the method agree with the experimental results as a whole.

ACKNOWLEDGEMENT

The authors wish to thank Dr. Yoshimi Goda, Director General of the Port and Harbour Research Institute for his many precious comments during the course of this work.

REFERENCE

Coastal Engineering Research Center (1975). Shore Protection Manual, U.S.Army Corps. of Engineers, Washington D.C., Vol.II.

Goda, Y., Haranaka, S. and Kitahata, M.(1966) Study of impulsive breaking wave forces on piles, Rept. of Port and Harbour Res. Inst., Vol.5, No.6, pp.1-30 (in Japanese)

Goda, Y. (1970). A synthesis of Breaker Indices, Trans, JSCE, Vol.2,pt 2, (in Japanese)

Goda, Y. (1985). Random Seas and Design of Maritime Structures, Univ. of Tokyo Press, 323 p.

Hall, M.A.(1958). Laboratory study of breaking wave force on piles, U.S. Army Corps of Engineers, Beach Erosion Board, Washington D.C, TM 106.

Honda, J. and Mitsuyasu, H. (1974). Experimental Study of breaking wave force on a vertical circular cylinder, Coastal Engineering in Japan, Vol.17, pp.59-70.

Ochi, M.K. and Tsai, C.H. (1984), Prediction of impact pressure induced by breaking waves on vertical cylinders in random seas, Applied Ocean Research, Vol.6, No.3, pp. 157-165.

Ross, C.W. (1955). Laboratory study of shock pressures of breaking waves, U.S. Army Corps of Engineers, Beach Erosion Board, Washington D.C., TM 59.

Ross, C.W.(1959). Large-scale tests of wave forces on piling, U.S. Army Corps of Engineers, Beach Erosion Board, Washington D.C., TM 111.

Sawaragi, T. and Nochino, M. (1984) Impact forces of nearly breaking waves on a vertical circular cylinder, Coastal Engineering in Japan, Vol.27, pp.249-263.

Tanimoto, K., Takahashi, S., Yoshimoto, Y.(1983). Estimation method of exciting shock force from a linear damped vibration system, Technical Note of the Port and Harbour Res. Inst., No.474, 24p. (in Japanese)

Tanimoto, K., Takahashi, S., Kaneko, T. and Shiota, K. (1986A). Impulsive pressure of breaking wave on piles, Proc. 6th Offshore South East Asia, pp.492 -496.

Tanimoto, K., Takahashi, S., Kaneko, T. and Shiota, K. (1986B), Impact force of breaking waves on an inclined pile, Proc. 5th Offshore Mechanics and Arctic Engineering Symposium., Vol.1, pp.235-241.

Von Karman, Th. (1929). The impact on seaplane float during landing, NACA, TN321.

Wagner, H. (1932) Über stoss-und gleitvorgänge an der oberfläche von flüssigkeiten, Zeitshrift für Angewandte Mathmatik und Mechanik, Band 12 Heft 4, pp.193-215.

Watanabe, A. and Horikawa, K. (1974). Breaking wave forces on a large diameter cell, Proc. of 14th International Conference on Coastal Engineering, Chapter 102, pp.1741-1760.

CHAPTER 169

Transmission of Random Waves Through Pile Breakwaters

Clifford L. Truitt[1] M.ASCE
John B. Herbich,[2] M.ASCE

Abstract

Several previous investigators have conducted experiments leading to expressions for predicting the transformation of waves passing through closely-spaced pile breakwaters. The present study extends those earlier experiments using monochromatic waves to the case of a spectrum of random waves.

Records of incident waves and of waves after transmission through a model pile breakwater were compared to determine a coefficient of transmission. Results are presented for several cases of pile spacing and pile diameter. Good agreement is found between observed transmission coefficients and those predicted using the expression proposed by Hayashi et al. (1966).

Introduction

During the late 1960's and early 1970's considerable interest was generated in the transmission and reflection of waves from both permeable and impermeable structures such as breakwaters. Several investigators (e.g., Costello 1951; Hayashi et al. 1966; Wiegel 1964; Van Weele and Herbich 1972; Massel 1976; Khader 1978, 1981) conducted experiments which led to expressions or procedures for predicting the transformation of waves passing over or through such structures. Unfortunately, no field data of wave transmission through pile breakwaters are available to allow for quantitative evaluation of their effects on incident waves.

One of the basic problems recognized by the earlier researchers and the designers who have used their results was the character of the laboratory waves used in the experiments. The waves were monochromatic and typically small amplitude, while the prototype wave climate consisted of irregular waves forming a relatively broad spectrum. The work summarized in this paper addressed this problem by repeating the basic study of the transmission of waves through an array of closely-spaced model piles, but using spectra of random waves.

[1]Hydraulic Engineer, Coastal Engineering Research Center, U.S. Army Engineer Waterways Experiment Station, Vicksburg, Mississippi 39180.

[2]Professor of Ocean and Civil Engineering, Texas A&M University, College Station, Texas 77843-3136.

The objectives of the investigation were twofold. First, an evaluation was made of the transmission results calculated using different characteristic parameters of the wave spectra. For example, if the transmission coefficient is defined as the ratio of the height of the transmitted wave to that of the incident wave, the question arises as to what height parameter properly characterizes the transmitted and incident spectra. Results are presented using the root-mean-square height of all waves, the arithmetic mean or average of all waves, and the significant wave height. The second objective was to compare transmission coefficients measured for the random wave case with those predicted by expressions based on earlier work with monochromatic waves (Hayashi et al. 1966).

Experimental Procedure

The Hydromechanics Laboratories at Texas A&M University have fitted their existing 120-ft long by 2-ft wide and 2-ft deep (36.6 m by 0.6 m by 0.6 m), glass-walled, wave tank with random sea-generating equipment. This configuration permits the generation of irregular waves through several "library" spectra, or through user-programmed inputs.

The three basic groups of variables in the experiment are the geometry of the pile arrays, the water depths, and the input wave spectra. No attempt was made to rigorously model the experiment based on any prototype conditions. However, a linear scale on the order of approximately 1/50 was convenient and represents typical commercially available piling used in prototype breakwaters and piers.

Two sizes of standard galvanized steel conduit pipe were used to construct the model pile arrays. Steel conduit was selected to assure rigidity in the model and uniformity from pile to pile. The sizes selected were 15/16-in. O.D. (approximately 24mm) and 1-3/16-in. O.D. (approximately 30mm). At a scale of 1/50, these models would represent piles on the order of 48 to 60 in. (122 to 152 cm.) in diameter. The spacings between the piling in the arrays were chosen to be 5, 10, and 20 percent of the pile diameters. Again, while not rigorous, it was felt that these spacings were generally representative of the practical limits which could be achieved in a prototype structure. Consistent and uniform spacings closer than 3 to 4 in. could probably not be economically realized for piles 4 to 6 ft in diameter and typically over one hundred feet in length. A definition sketch is shown in Figure 1.

The model piles were fitted into drilled templates, one at the bottom of the wave tank and one at the top, well above the water surface. Spacings represent the average of measured values and incorporate some variability, as would a prototype structure. In each test run, the array was placed in the tank, plumbed vertically, adjusted to the desired angle relative to the incident wave orthogonal (in this paper, perpendicular), and rigidly clamped in place. Only single-row arrays and circular piles were investigated.

Tests were run with water depths in the tank of 16, 20, and 24 in. (41, 51, and 61 cm). Wire probes were used to measure the water level

fluctuations resulting from the test waves. Each of the two probes was mounted on a movable carriage with one measuring incident wave heights and the other measuring transmitted waves on the opposite side of the model pile array. Tests were run both with the probe carriages moving and with them stationary. The probes recorded directly on standard oscillographs.

The random sea generator was capable of producing both library spectra and user input spectra. The four pre-programmed library spectra were used for these tests. No detailed discussion of the various spectra will be presented here, since results were calculated from actual wave records prior to incidence and after transmission from the arrays, rather than from the theoretical machine input. It was desired to use relatively short sequences or bursts of waves in the tests to minimize the influence of reflection in the tank. Records of a length of 25 to 30 waves were chosen for analysis. The results were examined statistically to assure that they were indeed random and of a satisfactorily significant length. Techniques are available to measure the combination of incident and reflected waves for longer records. However, the simpler approach described provided acceptable results and did not require an energy-based analysis.

It would seem that Reynolds number effects might be important and cause scale effects when comparing model results to prototype applications since a portion of the decrease in transmission in the model may be attributed to viscous damping. However, for prototype pile sizes and spacings, and for free-surface gravity waves the inertial force would likely predominate over the drag force.

Analysis Procedure

Using the described procedures, a total of 30 records were generated, each consisting of an incident wave spectrum and a transmitted wave spectrum. The waves in each record were then

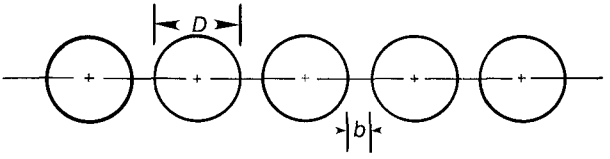

D - PILE DIAMETER

b - PILE SPACING

RATIO (b/D) CHOSEN TO BE 0.05, 0.10, and 0.20

Figure 1. Definition sketch for pile geometry

characterized by actually measuring all recorded heights and calculating the following three parameters.

Root-mean-square wave height:

$$H_{rms} = \sqrt{\frac{1}{N} \sum_{j=1}^{N} H_j^2} \tag{1}$$

Mean, or average wave height:

$$\bar{H} = \frac{1}{N} \sum_{j=1}^{N} H_j \tag{2}$$

Significant wave height:

$$H_s = \text{average height of the one-third highest waves.} \tag{3}$$

With these parameters calculated, both the incident and transmitted waves in each test could be represented by H_{rms}, $\bar{H}$, or H_s. Thompson and Vincent (1984) point out the need to distinguish between the significant wave height, H_s, as defined in equation 3 and the spectral based significant wave height, H_{m_o}, defined from the variance of the wave record. Certainly wave attenuation by a piled breakwater is an energy-based process and the spectral based H_{m_o} may be more appropriate for actual design. However, for the present laboratory case, the water depth and level bottom slope allow treating H_s and H_{m_o} as interchangable.

One concern was to assure that the relatively short sequence lengths in the wave records were indeed long enough to be significant and reasonably random. It has been shown (e.g. Shore Protection Manual 1984) that for a true Rayleigh distribution the following theoretical relationships exist:

$$\bar{H} = 0.886\ H_{rms} \qquad \text{and} \tag{4}$$

$$H_s = 1.416\ H_{rms}\ . \tag{5}$$

Therefore, once H_{rms} had been determined for each incident record, theoretical values of $\bar{H}$, and H_s were calculated from the above relationships. These theoretical values were compared to the $\bar{H}$ and H_s determined from the records and the agreement was taken as an indicator of the significance of the wave sequence length. Figure 2 presents this comparison for H_{rms} and H_s.

In each case the theoretical and actual parameters were within a few percent of each other. While it is certainly desirable to use as long a sequence as possible, the excellent agreement obtained is an

indicator that the record lengths used were acceptable and of value in characterizing any trends present.

Evaluation of Characteristic Parameters

The degree to which wave heights are influenced during transmission through a structure can be described by the ratio of the height of the transmitted wave to the height of the incident wave, or:

$$\text{Coefficient of transmission} = \frac{H_T}{H_I} \tag{6}$$

When considering a spectrum of irregular waves the question arises as to how to characterize the incident and transmitted wave. If all waves in the incident spectrum are affected equally in the transmission process, then the coefficient of transmission can be based on any characteristic parameter, e.g. H_{rms} , $\bar{H}$, or H_s , as long as the same one is used for the transmitted spectrum (and no breaking occurs). However, if a structure "filters" one portion of the incident spectrum to a greater degree than other portions, the coefficient of transmission may vary depending on which parameter is used in the calculation. If we confine the present discussion to wave height parameters, then

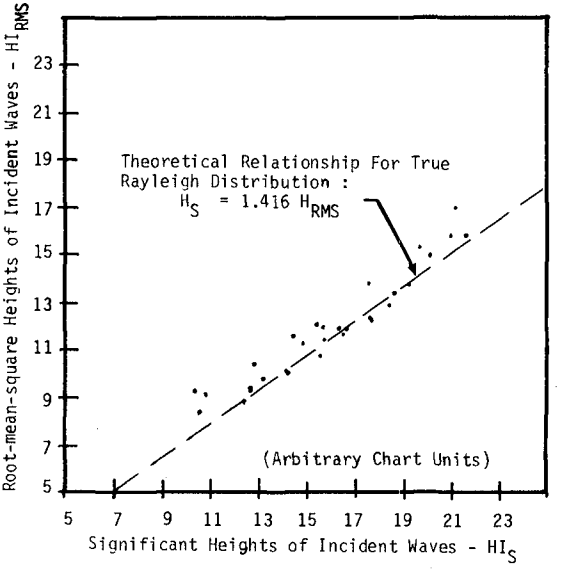

Figure 2. Comparison of observed relationships with theoretical predictors.

the relative variation of the coefficients of transmission calculated using H_{rms} , $\bar{H}$, and H_s may be an indicator of any preferential transmission effects present.

Certainly, other characteristics of the spectra involved may be equally influential and also serve as indicators. Period and wave steepness are proposed most frequently along with analysis of any changes in the relationship between energy density and frequency. All of these procedures require a representation of the wave period. While this may be done for records of actual ocean waves by use of a significant period or similar statistical or numerical methods approximation, such techniques can be difficult for laboratory wave records with all periods in the range of 1 to 2 sec.

For each of the thirty data sets a coefficient of transmission was calculated using the incident and transmitted wave heights given by H_{rms} , $\bar{H}$, and H_s . For a true Rayleigh distribution, linear relationships exist among the mean, root-mean-square, and significant parameters of a function. Therefore, if the Rayleigh distribution is assumed for the incident non-breaking wave spectra, and if the transmitted spectra are not preferentially altered, then the coefficients of transmission for a particular test should be the same whether calculated from root-mean-square, mean, or significant heights. Figure 3 is a comparison of the transmission coefficients calculated using each of the three height parameters. The agreement suggests that the transmission coefficients calculated in this experiment were

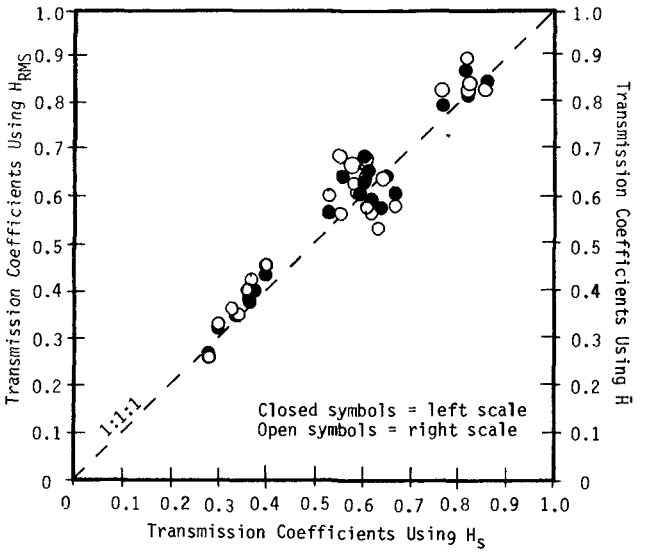

Figure 3. Comparison of transmission coefficients calculated using three different height parameters.

reasonably independent of the parameter used to characterize the wave height spectra. The values based on significant heights were selected for further comparison with predictive models since H_S is widely recognized and easily computed.

Comparison With Predictive Expressions

Wiegel (1961) proposed the following relationship to predict the coefficient of transmission for a single-row pile array:

$$\frac{H_T}{H_I} = \frac{b}{D + b} \tag{7}$$

In this expression b is the spacing and D is the pile diameter as shown on Figure 1. This is a variation on the porosity parameter used in earlier studies of permeable wave absorbers. Wiegel later measured transmitted wave heights typically 25 percent greater than predicted.

Hayashi et al. (1966) proposed the following relationship arising from consideration of the velocity of the water jets discharging through the pile spaces:

$$\frac{H_T}{H_I} = 4\left(\frac{d}{H_I}\right) E \left[- E + \sqrt{E^2 + \frac{H_I}{2d}} \right] \tag{8}$$

$$\text{with } E = C\left(\frac{b}{D + b}\right) \Bigg/ \sqrt{1 - \left(\frac{b}{D + b}\right)^2} \tag{9}$$

The use of b, D, and H are as above, and d is the water depth (still water). The parameter C is a representation of the effects of jet contraction and velocity in Bernoulli's theorem and is recommended as equal to 0.9 to 1.0. It is analogous to a coefficient of discharge, defined as the product of a velocity coefficient, C_v, and a contraction coefficient, C_c. The recommended values of 0.9 to 1.0 suggest that the spacing and well-rounded character of the openings between round piles are such that little decrease in discharge occurs from friction or flow contraction effects. Pile arrays that use other shapes or geometries suggestive of a sharp-edged outlet would require a lower value of C.

For each of the thirty data sets, coefficients of transmission were calculated using the above expression with $C = 0.9$ and again with $C = 1.0$.

The predicted coefficients were then compared to those actually calculated from the observed wave height data. Figures 4 and 5 summarize that comparison. The equation with $C = 1$ tends to predict a somewhat higher transmission coefficient than observed, especially at the closer pile spacings. The use of $C = 0.9$ provided a better general prediction of these tests.

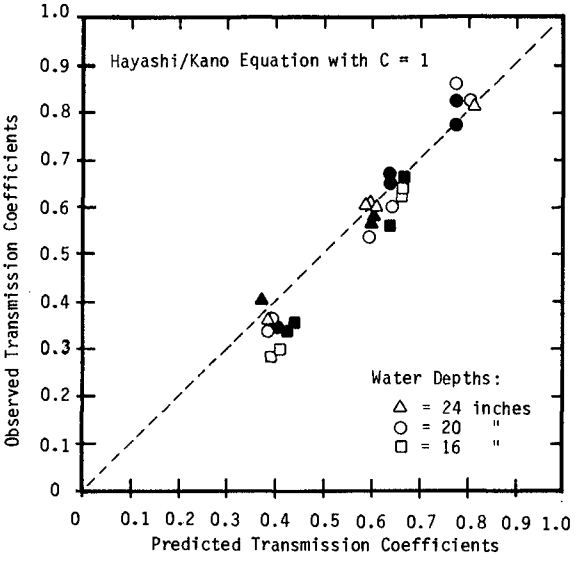

Figure 4. Comparison of observed transmission coefficients with those predicted using equation proposed by Hayashi et al. (1966) (C = 1)

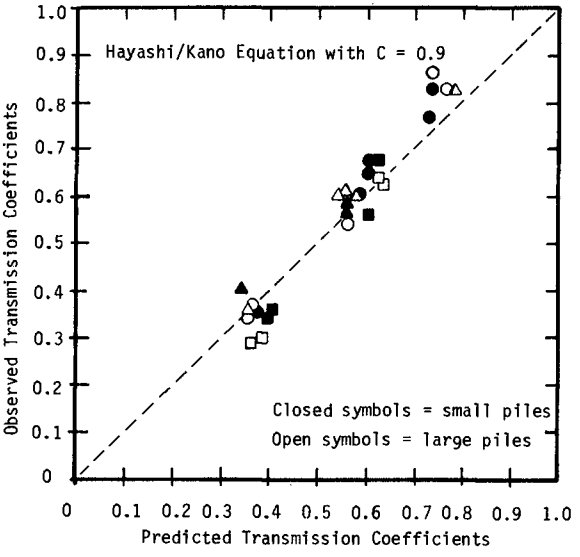

Figure 5. Comparison of observed transmission coefficients with those predicted using equation proposed by Hayashi et al. (1966) (C = 0.9)

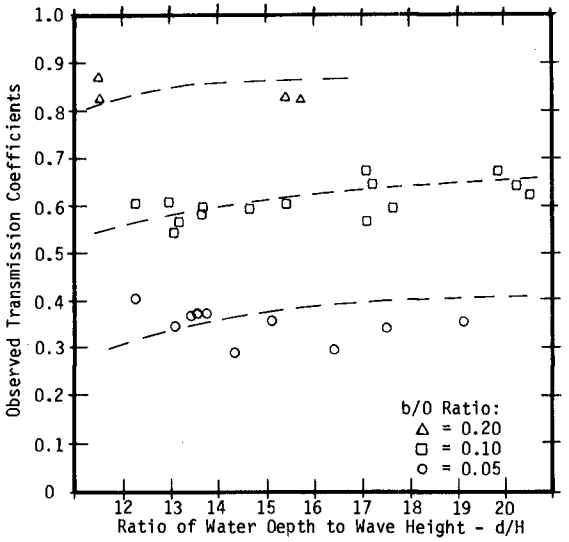

Figure 6. Observed transmission coefficients versus water depth to wave height ratio

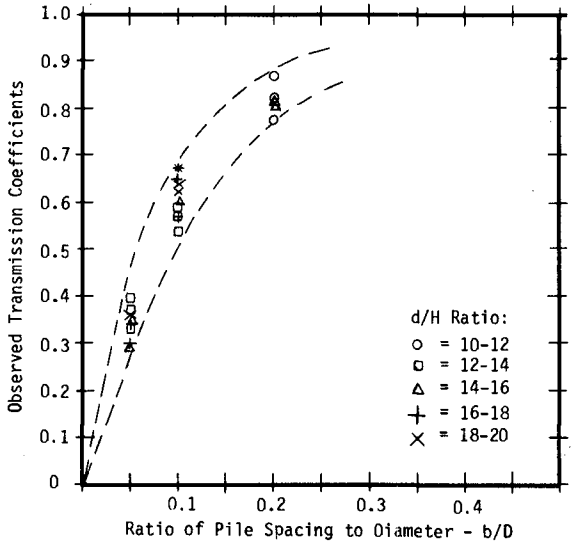

Figure 7. Observed transmission coefficients versus pile spacing to diameter ratio

The additional influences of water depth and of relative spacing were considered. Figures 6 and 7 show the observed transmission coefficients plotted against the ratios of water depth to wave height (d/H_s), and pile spacing to pile diameter (b/D), respectively. Figure 6 clearly shows the influence of the b/D ratio over a range of water depth/wave height values. The influence of d/H_s is not readily apparent in Figure 7. Note that the ratios of water depths to wave heights, d/H_s, in these tests were typically 3 to 5 times larger than those reported by Hayashi et al. (1966). At the lower d/H_s ratios, Hayashi et al. (1966), depicted a strong sorting of the data based on this influence. It appears that as the wave height becomes a smaller precentage of the water depth (larger d/H_s), and/or for random wave spectra consisting of many wave heights, the transmission coefficient is influenced more by the breakwater geometry, b/D, than by the water depth.

Conclusions

As long as the same parameter was used for both incident and transmitted spectra, little difference was noted in transmission coefficients calculated from H_{rms}, $\bar{H}$, or H_s for these laboratory experiments.

The results of these tests indicate that some of the analysis techniques developed earlier for predicting the transmission of monochromatic waves through pile breakwaters can be extended to random waves. Very good agreement was obtained using the equation presented by Hayashi et al., 1966.

The ratio of water depth to wave height (d/H_s) influences the transmission coefficient in the general sense, but the influence of the breakwater geometry, i.e. ratio spacing to diameter (b/D) is more pronounced. Further work should investigate the influences of wave steepness and/or period on transmissions. An energy analysis may be necessary for such an investigation.

Acknowledgement

Preparation of this paper was partially supported by the U.S. Army Corps of Engineers through the Evaluation of Navigation and Shore Protection Structures Civil Works Research Work Unit 31232. Permission was granted by the Chief of Engineers to publish this information.

References

COSTELLO, R. D. (1951). Damping of Water Waves by Vertical Circular Cylinders. Contract Report to the US Navy Office of Naval Research, by the Institute of Engineering Research, Technical Report HE-116-329, University of California, Berkeley, CA.

HAYASHI, T. et al. (1966). Hydraulic Research on Close Spaced Pile Breakwaters. Proceedings of the 10th Coastal Engineering Conference. Vol II, Chapter 50, pp 873-884.

KHADER, M. H. A. and Rai, S. P. (1981). Wave Attenuation Due to Closely Spaced Circular Cylinders. Proceedings of the 19th Congress of I.A.H.R., Vol III, pp 93-102.

MASSEL, S. R. (1976). Interaction of Water Waves with Cylinder Barrier, Journal of the Waterways, Harbors and Coastal Engineering Division, ASCE, Vol. 102, No. WW2, pp 165-187.

THOMPSON, E. F. and VINCENT, C. L. (1984). Shallow Water Wave Height Parameters. Journal of the Waterway, Port, Coastal and Ocean Division, ASCE, Vol. 110, No. WW2, pp 293-299.

VAN WEELE, B. L. and HERBICH, J. B. (1972). Wave Reflection and Transmission for Pile Arrays. Proceedings of the 13th Coastal Engineering Conference ASCE, Vol. III, Chapter 110, pp 1935-1953.

WIEGEL, R. L. (1961). Closely Spaced Piles as a Breakwater. Dock and Harbour Authority, Vol. 42, No. 491.

CHAPTER 170

An Analytical Model for Ocean Wave-Soil-Caisson Interaction

Yau-Tang Tsai[1], William G. McDougal[2], and Charles K. Sollitt[2]

Abstract

An analytical model is developed to predict the soil responses induced by waves and caisson motion. The caisson is founded on a rubble bedding layer overlying a soil of finite depth. The responses are modeled by the Biot consolidation equations. Two approximations are employed to reduce mathematical difficulties: 1) a boundary layer approximation to decouple pore pressure and soil motion in the Biot equations and 2) a contact solution approximation for a thin elastic layer to address mixed-type boundary-value problems.

1. Introduction

Caisson-type structures are commonly employed as breakwaters, bulkheads, and seawalls. Critical failure areas for these types of structures are the toe and underlying foundation. These failures often result from wave-induced scouring, high porewater pressure, and large stresses developed in the foundation soil. These processes may lead to rapid and deep erosion at the toe as well as liquefaction of the foundation material. Hence, an understanding of the failure mechanisms for the foundation and an evaluation of the foundation stability are necessary.

Durand and Monkmeyer (1982), Liu (1985), and Dias and Monkmeyer (1986) have developed analytical solutions to estimate the wave-induced dynamic porewater pressure underneath a fixed caisson or a fixed plate founded on a porous rigid seabed. However, Stematiu and Stera (1985) pointed out that the structure-soil interaction is extremely significant in the foundation design of a caisson. This interaction results in high local stresses in the soil skeleton. Attempts to model the combined effect of porewater pressure and displacements were made by Lindenberg et al. (1982) and Stematiu and Stera (1985) using finite element methods. Finite element models have the disadvantage that they do not provide the physical insight into the problem which is often revealed in an analytical solution. The first steps toward an analytical solution were presented by Mynett and Mei (1982) for a caisson founded directly on the seabed, assuming the soil to be a poroelastic half-space. These assumptions limit the range of application of the model in some practical applications.

[1]Assistant Professor, Ocean Engineering Program, Department of Civil Engineering, Oregon State University, Corvallis, Oregon 97331-2302.
[2]Associate Professor, Ocean Engineering Program, Department of Civil Engineering, Oregon State University, Corvallis, Oregon 97331-2302.

Therefore, the objective of this paper is to develop an analytical model to estimate foundation stresses, porewater pressure, and structure motions for a wave-loaded caisson founded on a rubblemound bedding layer overlying a soil of finite depth.

2. Formulation of the Model

The wave-soil-caisson interaction problem is depicted in Fig. 1, in which h is the still water depth, d is the thickness of the soil skeleton, b is the thickness of the rubble bedding layer, 2c' is the width of the caisson; and 2c is the width of the mound foundation on the mudline through which the displacement repsonse of the caisson completely transfers to the soil skeleton. 2c is approximated employing a 2V:1H slope (Bowles, 1982) and is termed the effective width of the caisson base.

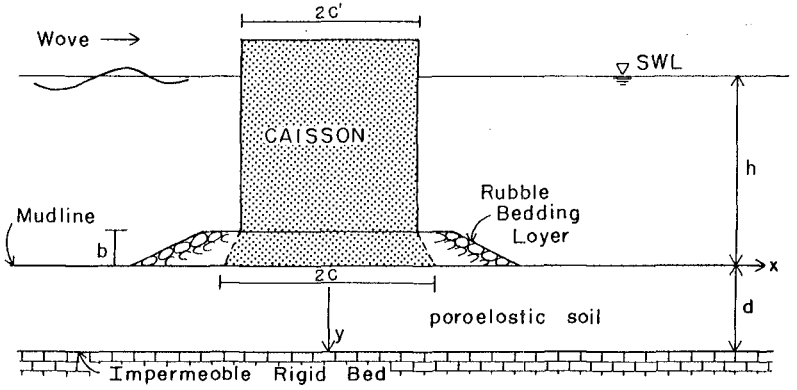

Figure 1. Definition sketch for the coordinate system and wave-soil-caisson system.

The development of the analytical model necessitates a number of assumptions. Among these are:

1. This is a two-dimensional problem.

2. The water depth is constant and small amplitude wave theory is applicable.

3. The soil and wave responses are decoupled.

4. A rigid caisson is founded on a rubble bedding layer which is considered to be hydraulically permeable and mechanically stiff compared with the underlying soil.

5. There is no slip between the caisson and the rubble bedding layer. Caisson displacements are completely transferred to the seabed through the rubble bedding layer.

6. The soil stratum is assumed to be linearly poroelastic, isotropic, and is confined by a horizontal mudline above and a horizontal impermeable, rigid bed below.

Governing Equation

Biot considation theory (Biot, 1941) is applicable to a shift saturated poroelastic medium. It has been successfully employed to model a variety of soil-wave interaction phenomena (Yamamoto et al., 1978; McDougal et al., 1981; and Mei and Foda, 1981). The Biot equations couple the motions of fluid and solid phases. This coupling increases the mathematical difficulty. Mei and Foda (1981) developed a boundary layer approximation which decouples the pore pressure and solid motion. Near the mudline there exists a boundary layer in which drainage is relatively unimpeded and there is significant relative motion between the fluid and the solid. Farther from the mudline there is little drainage so the fluid and solid tend to move in phase. This is termed the outer region problem, which can be reduced to solving a classical elastostatic problem. However, the boundary conditions on the mudline are not satisfied. Hence, corrections are made according to the boundary layer solutions so that the boundary conditions on the mudline are satisfied.

The governing equations for the outer region and boundary layer problems have been developed by Mei and Foda (1981). Their results are summarized in the following.

Outer Region Problem - The governing equations for the outer region problem were derived from the equations of momentum. $()^o$ denotes a parameter in the outer region problem. For sandy sea beds the equations of momentum for the solid and fluid yields

$$\frac{\partial(\tau'^{o}_{ij} - p^o\delta_{ij})}{\partial x_j} = 0 \tag{1}$$

where τ'^{o}_{ij} is the effective stress, p^o is the porewater pressure, δ_{ij} is the Kronecker delta, and x_j is the axis in the Cartesian coordinates system. Introducing the total stress τ^{o}_{ij} to (1) yields

$$\frac{\partial \tau^{o}_{ij}}{\partial x_j} = 0 \tag{2}$$

For convenience, lengths and displacements are scaled by the effective caisson half-width, c, and stresses and pressures are scaled by the mudline pressure amplitude due to the free surface propagating waves, P_o. The dimensionless variables will be denoted by upper case letters.

Applying Hook's law to (2) yields the governing equations for the outer region problem.

$$\nabla^2 U^o + \frac{1}{1-2\nu} \frac{\partial}{\partial X} \left(\frac{\partial U^o}{\partial X} + \frac{\partial V^o}{\partial Y} \right) = 0 \tag{3a}$$

$$\nabla^2 V^o + \frac{1}{1-2\nu} \frac{\partial}{\partial Y} \left(\frac{\partial U^o}{\partial X} + \frac{\partial V^o}{\partial Y} \right) = 0 \tag{3b}$$

in which U^o and V^o are the dimensionless horizontal and vertical displacements, respectively, ν is Poisson's ratio, and X and Y are the dimensionless horizontal and vertical axes in the Cartesian coordinate system, respectively.

First the displacements are determined and then stresses in the soil skeleton may be obtained by applying Hook's law to the displacement solutions. The porewater pressure in the outer region is related to the total stresses by

$$P^o = - \frac{T^o_{xx} + T^o_{yy}}{2 (1+m_o)} \tag{4}$$

in which

$$m_o = \frac{\beta' n_o G}{1-2\nu} \tag{5}$$

and is a parameter indicating the relative stiffness between the solid and pore fluid. In (5) β' is the combined air-water compressibility, n_o is the porosity, and G is the shear modulus.

Boundary Layer Correction - The governing equation for the boundary layer problem was derived from the equation of momentum and the storage equation. Again, $()^b$ denotes a parameter in the boundary layer. The porewater pressure P^b in the boundary layer is governed by the one-dimensional Terzaghi consolidation equation

$$\frac{\partial P^b}{\partial T^b} = \frac{\partial^2 P^b}{\partial (Y^b)^2} \tag{6}$$

in which T^b is dimensionless time scaled by the wave frequency and Y^b is the vertical coordinate and scaled by the boundary layer thickness δ.

The boundary layer correction is summarized as

$$\begin{Bmatrix} P^b \\ T'^b_{xx} \\ T'^b_{yy} \\ T^b_{xy} \end{Bmatrix} = \begin{Bmatrix} 1 \\ \frac{\nu}{1-\nu} \\ 1 \\ 0 \end{Bmatrix} P^b \tag{7}$$

in which T'^{b}_{xx} and T'^{b}_{yy} are the effective dimensionless horizontal and vertical normal stresses, respectively, and T^{b}_{xy} is the dimensionless shear stress. No shear stress correction is required in the boundary layer.

The ratio of the boundary layer thickness and the effective caisson half-width is denoted by

$$\varepsilon = \frac{\delta}{c} \tag{8}$$

in which

$$\delta = \sqrt{\frac{k'}{\sigma}} \left(\beta' n_o + \frac{1}{G} \frac{1-2\nu}{2(1-\nu)}\right)^{1/2} \tag{9}$$

where k' is the intrinsic permeability and σ is the wave frequency. The displacement components for the boundary layer correction are at most of order ε and can be neglected.

Boundary Conditions

The boundary conditions for the wave-soil-caisson problem are:

1. Along the exposed portion of the mudline, the wave pressure and the total normal stress are continuous and the shear stress is negligible (McDougal et al., 1981).

2. Under the structure, the displacements are continuous at the caisson-soil interface.

3. Along the entire mudline, the wave-induced pore pressure is continuous.

4. The soil overlies a rigid bed at which no-slip and no normal fluid flow conditions are imposed.

These boundary conditions are summarized in Fig. 2.

Outer Region Problem - The soil displacement and the caisson motion are coupled. The wave forces along the exposed portion of the mudline induce soil stresses and displacements underneath the caisson. The wave forces on the caisson induce caisson motions which result in stresses and displacements in the soil away from the caisson. Linearity allows these two effects to be decoupled into scattering and radiation problems. In the scattering problem, the caisson is assumed to be fixed and the soil response is completely driven by the wave pressure on the mudline. The forces on the caisson determined in the scattering problem are applied on the caisson in the radiation problem. These forces result in caisson motion on an otherwise static seabed. The sum of these two components, the scattering problem and

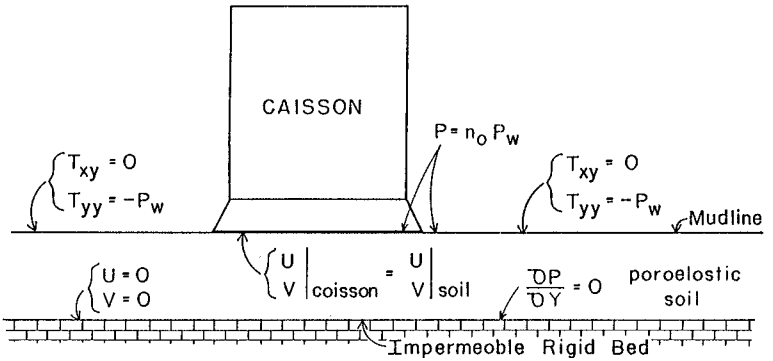

Figure 2. Boundary conditions for the wave-soil-caisson system

the radiation problem, yields the total response. This technique is illustrated in Fig. 3.

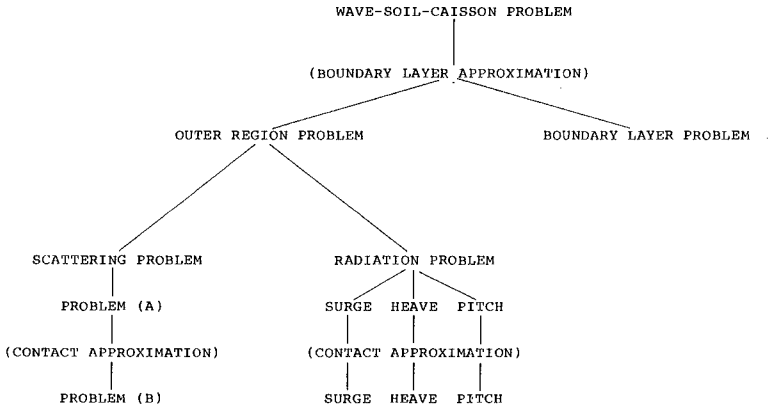

Figure 3. Decomposition of the wave-soil-caisson problem

The Scattering Problem - For the scattering problem the caisson is fixed and the mudline boundary conditions are

$$T^{o}_{xy}(X,0) = 0 \qquad ; 0 \leq |X| < \infty \qquad (10a)$$

$$T^{o}_{yy}(X,0) = -P_{w}(X)e^{-i\sigma t} \qquad ; 1 \leq |X| < \infty \qquad (10b)$$

$$U^{o}(X,0) = 0 \qquad ; |X| \leq 1 \qquad (10c)$$

$$V^{o}(X,0) = 0 \qquad ; |X| \leq 1 \qquad (10d)$$

This results in a mixed boundary-value problem. To solve this problem, a sequence of two solutions is sought: one which satisfies the stress boundary conditions (problem (a)) and then a second solution which satisfies the displacement boundary conditions (problem (b).

The boundary conditions for problem (a) and (b) are shown in Fig. 4. The displacements along the mudline, ${}^{a}U^{o}(X,0)$ and ${}^{a}V^{o}(X,0)$, from the solution for the problem (a) are modified to provide the boundary conditions for problem (b). The first modification is that under the structure the displacements are set equal to zero. The second modification is based on the solution to the contact problem on a thin elastic layer developed by Alblas and Kuipers (1969). This solution provides appropriate displacements adjacent to the structure. Details are presented in Appendix I. The solution to problem (b) satisfies both stress and displacement conditions along the mudline. Thus, it is the solution for the scattering problem.

The Radiation Problem - The radiation problem is a moving caisson on an otherwise static soil. The response of the soil must satisfy the caission displacement conditions on the mudline. The caisson responds to both wave and soil loadings from the scattering problem and a restoring force in the radiation problem. The scattering loads are known but the motion is still unknown. A dynamic boundary condition must be prescribed to solve for the unknown caisson motion. This condition yields the amplitude of the caisson motion. Linearity allows the soil response to be decomposed into three problems corresponding to each of the three degrees of freedom of caisson motion. The caisson is assumed to be rigid and the effects of the structural damping in the caisson are assumed to be negligible compared with the soil.

Underneath the caisson the motions are specified while along the exposed portion of the mudline zero stress conditions apply. The boundary conditions for the radiation problem are depicted in Fig. 5. The respective boundary conditions along the mudline for the problems of surge, heave, and pitch may be defined by appropriate displacement and stress conditons. Displacement conditions over the entire upper boundary may be written by introducing ${}^{1}U^{o}_{f}$, ${}^{2}V^{o}_{f}$, and ${}^{3}V^{o}_{f}$, which account for the unknown displacements along the exposed portion

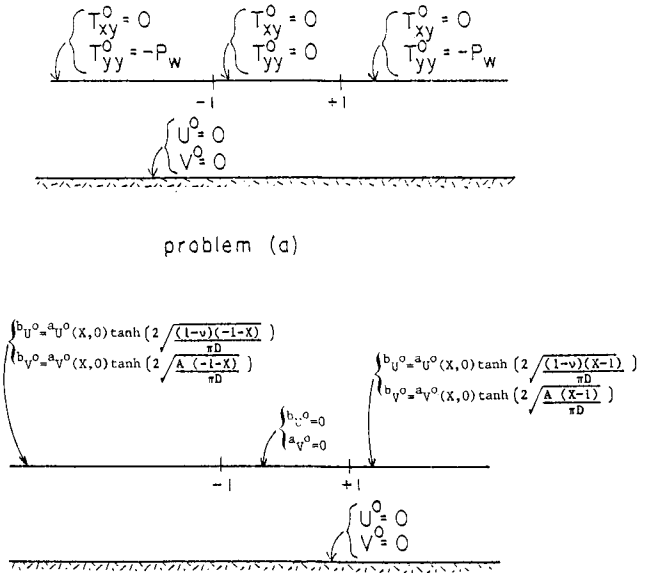

Figure 4. Boundary conditions for the scattering problem

of the mudline. Stress conditions for each degree of freedom of the caisson motion are also reasonably approximated as given by Alblas and Kuipers (1969 and 1970).

(1) surge

$$T^o_{yy}(X,0) = 0 \qquad ; \ 0 \leq |X| \leq \infty \qquad (11a)$$

$$U^o(X,0) = U_c + {}^1U^o_f \qquad ; \ 0 \leq |X| < \infty \qquad (11b)$$

(2) heave

$$T^o_{xy}(X,0) = 0 \qquad ; \ 0 \leq |X| < \infty \qquad (12a)$$

$$V^o(X,0) = V_c + {}^2V^o_f \qquad ; \ 0 \leq |X| < \infty \qquad (12b)$$

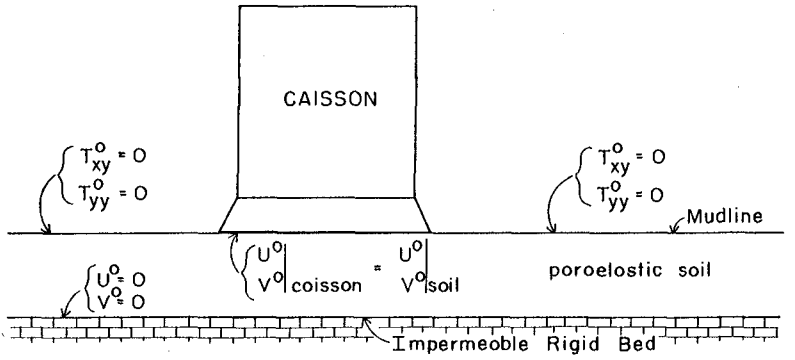

Figure 5. Boundary conditions for the radiation problem

(3) pitch

$$T^o_{xy}(X,0) = 0 \qquad ; 0 \leq |X| < \infty \qquad (13a)$$

$$V^o(X,0) = -\alpha_c X + {}^3V^o_f \qquad ; 0 \leq |X| < \infty \qquad (13b)$$

These are no longer mixed-type boundary conditions, and the boundary-value problem can easily be solved. The displacements ${}^1U^o_f$, ${}^2V^o_f$, and ${}^3V^o_f$ can be evaluated by employing the thin soil layer contact problem solution technique presented in Appendix I.

$${}^1U^o_f = U_c \begin{cases} 1 - \tanh\left(2\sqrt{\dfrac{(1-\nu)(-1-X)}{\pi D}}\right) & ; -\infty < X \leq -1 \\ 1 - \tanh\left(2\sqrt{\dfrac{(1-\nu)(X-1)}{\pi D}}\right) & ; 1 \leq X < \infty \end{cases} \qquad (14a)$$

$${}^2V^o_f = V_c \begin{cases} 1-\tanh\left(2\sqrt{\dfrac{A(-1-X)}{\pi D}}\right) & ; -\infty < X \leq -1 \\ 1-\tanh\left(2\sqrt{\dfrac{A(X-1)}{\pi D}}\right) & ; 1 \leq X < \infty \end{cases} \qquad (14b)$$

$$ {}^{3}V_f^o = \alpha_c \begin{cases} 1-\tanh\left\{2\sqrt{\frac{A(-1-X)}{\pi D}}\,(1 + i\,\hat{S}'_{-}(0))\right\} & ; -\infty < X \leq -1 \\ 1-\tanh\left\{2\sqrt{\frac{A(X-1)}{\pi D}}\,(1 + i\,\hat{S}'_{-}(0)\right\} & ; 1 \leq X < \infty \end{cases} \tag{14c} $$

In (11b), (12b), and (13b), U_c, V_c, and α_c are the displacements of the caisson in surge, heave, and pitch, respectively. Positive α_c is defined as counterclockwise. These displacements are unknown, but may be determined from the dynamic boundary conditions on the soil-caisson interface, i.e., the equation of motion for the caission.

$$ \begin{bmatrix} m & 0 & 0 \\ 0 & m & 0 \\ 0 & 0 & I_m \end{bmatrix} \begin{Bmatrix} \ddot{U}_c \\ \ddot{V}_c \\ \ddot{\alpha}_c \end{Bmatrix} = \begin{Bmatrix} f_{w1} \\ f_{w2} \\ f_{w3} \end{Bmatrix} + \begin{Bmatrix} f_{s1} \\ f_{s2} \\ f_{s3} \end{Bmatrix} + \begin{Bmatrix} f_{r1} \\ f_{r2} \\ f_{r3} \end{Bmatrix} \tag{15} $$

where m and I_m are the mass and mass moment of inertia of the caisson, respectively, $\ddot{U}_c$, $\ddot{V}_c$, and $\ddot{\alpha}_c$ are the accelerations of surge, heave, and pitch of caisson motion, f_{wj} and f_{sj} are the wave and soil loads on the caisson determined in the scattering problem, and f_{rj} are the restoring forces on the caisson. The soil loads are obtained by integrating the stresses along the caisson-seabed interface.

The Boundary Layer Correction - Along the mudline, the summation of the pressure from the boundary correction and outer region solution is equal to the wave-induced porewater pressure. Along the rigid bed underlying the soil, the normal derivative of the pore pressure must be zero, i.e.,

$$ \text{at } Y = 0 \qquad P^o + P^b = n_o\, P_w(X) \qquad ; 0 \leq |X| < \infty \tag{16a} $$

$$ \text{at } Y = D \qquad \frac{\partial(P^o + P^b)}{\partial Y} = 0 \qquad ; 0 \leq |X| < \infty \tag{16b} $$

3. Solution to the Model

The poroelastic layer occupies the strip space $-\infty < X < \infty$; $0 \leq Y \leq D$. A Fourier transform is applied with respect to X in Eq. (3). It follows that the general solution for the outer region problem is in the form of Fourier transform

$$\hat{U}^o(s,Y) = a_1 ch(sY) + a_2 sh(sY) + a_3 Ych(sY) + a_4 Ysh(sY) \qquad (17a)$$

$$\hat{V}^o(s,Y) = -i\{a_1 sh(sY) + a_2 ch(sY) + a_3[Ysh(sY) - \frac{3-4\nu}{s} ch(sY)]$$

$$+ a_4[Ych(sY) - \frac{3-4\nu}{s} sh(sY)]\} \qquad (17b)$$

in which s is a Fourier transform parameter and functions ch and sh are abbreviations of cosh and sinh. The coefficients a_1, a_2, a_3, and a_4 may be quantified by applying boundary conditions for the scattering and radiation problems, respectively. The inverse Fourier transform of the solution can be evaluated with a fast Fourier transform.

For simple harmonic waves, the solution for the boundary layer problem can also be easily solved.

$$p^b = \{[n_o P_w(X) - P^o|_{Y=0}] \frac{\cosh[\frac{1-i}{\sqrt{2}} \frac{D-Y}{\varepsilon}]}{\cosh(\frac{1-i}{\sqrt{2}} \frac{D}{\varepsilon})}$$

$$- \frac{1+i}{\sqrt{2}} \varepsilon \frac{\partial P^o}{\partial Y}|_{Y=D} \frac{\sinh(\frac{1-i}{\sqrt{2}} \frac{Y}{\varepsilon})}{\cosh(\frac{1-i}{\sqrt{2}} \frac{D}{\varepsilon})}\} e^{-iT^b} \qquad (18)$$

The superimposition of the solutions for the scattering problem, radiation problem, and boundary layer problem yields the total solution to the original problem. Since the response of the soil to waves and caisson motions is not readily apparent from the analytical solution, a numerical example will be presented to examine the solution behavior. For this examination the conditions given in Table 1 are assumed.

Contours of the soil response are presented in Fig. 6. These plots are for the wave crest at the face of the caisson (x = -c). Figures 6(a) and (b) show the horizontal and vertical displacements. The horizontal displacement is rather symmetrical with respect to the caisson center line. The surge motion of the caisson tends to dominate this displacement. The vertical displacement is antisymmetrical with respect to the caisson center line because the pitch motion is dominant in this displacement. However, the wave-induced vertical displacement is also significant near the caisson toe. Figures 6(c) through (e) show the shear stress, effective horizontal and vertical normal stresses, respectively. High stress concentrations occur at the caisson toe and heel. Both the shear stress and the effective horizontal normal stress decay with the depth much faster than the

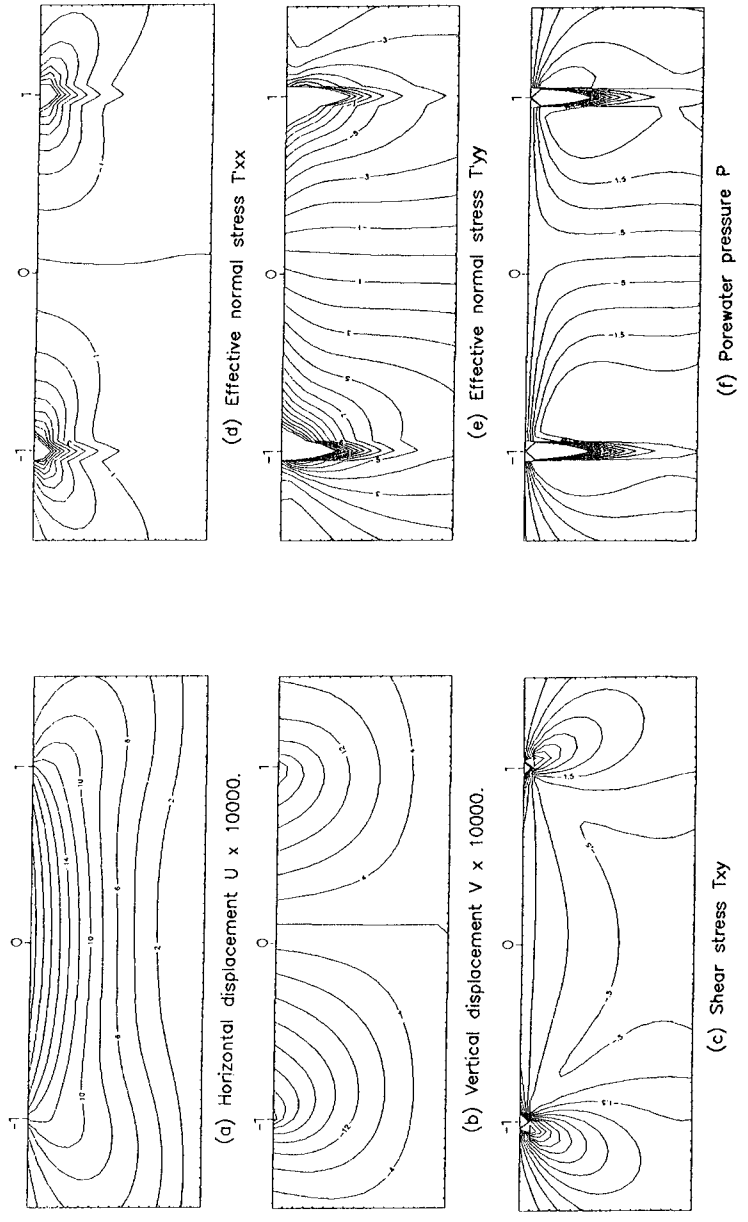

Figure 6. Contours of the soil responses for the total solution

Table 1. Wave, caisson, and soil conditions.

Wave Period	10 sec
Wave Height	6.1 m
Water Depth	12.2 m
Rubblemound Thickness	1.5 m
c'	6.4 m
m	64,240 kg
I_m	6,397,800 kg-m^2
d	7.2 m (dimensionless depth = 1.0)
ν	0.15
G	19,640 KN/m^2
n_ρ	0.3
k^ρ	1.03 x 10^{-8} m^4/sec/N
β'	4.53 x 10^{-10} m^2/N

effective vertical normal stress. Figure 6(f) shows the porewater pressure. Due to the influence of the impermeable rigid bed on the porewater pressure, higher porewater pressures are developed near the impermeable underlying bed rather than near the mudline.

4. Conclusions

1. A linear, two-dimensional analytical model for wave-soil caisson interaction has been developed. The caisson is founded on a rubble bedding layer overlying linearly poroelastic soil of finite depth.

2. Soil displacements, stresses, and porewater pressure as well as caisson motion are predicted.

3. Two approximations are employed: a boundary layer approximation and a contact solution approximation for a thin elastic layer.

4. The pitch motion of the caisson develops the largest soil response while heave is the least significant.

5. The caisson motion induces much larger displacements, stresses, and porewater pressure in the soil than the wave alone. This indicates that a static analysis may significantly underestimate stresses.

5. Acknowledgment

This research was supported by the Oregon State University Sea Grant College Program, National Oceanic and Atmospheric Administration Office of Sea Grant, Dept. of Commerce, under Grant No. NA81AA-D-00086 (Project No. R/CE-13). The U.S. Government is authorized to produce and distribute reprints for governmental purposes, notwithstanding any copyright notation that may appear hereon.

Appendix I. Displacement Boundaries along the Exposed Mudline

A contact solution approximation has been developed for a rectangular block on a thin elastic layer by Alblas and Kuipers (1969). The boundary conditions along the upper boundary of the elastic material are of the mixed type. The displacement condition along the block elastic-layer interface is defined while the stress along the exposed portion of the upper surface are known. Under the assumption of a thin elastic layer, Alblas and Kuipers (1969) developed an approximate solution for the displacement of the elastic layer surface adjacent to the block.

heave

$$V_2'(X) = V_o\left[1-2\sqrt{\frac{A(X-1)}{\pi D}}\right] \qquad ; 0 < X-1 << 1 \qquad (I.1)$$

pitch

$$V_3'(X) = \alpha_c\left\{1-2\sqrt{\frac{A(X-1)}{\pi D}}\,[1 + i\,\hat{S}_-'(0)]\right\} \qquad ; 0 < X-1 << 1 \qquad (I.2)$$

where $A = 2(1-\nu)^2/(1-2\nu)$ and $\hat{S}_-'(0)$ is a function dependent on Poisson's ratio and the layer depth (Alblas and Kuipers, 1970). These solutions are only valid near the structure. Hence, a tanh function is introduced to modify (I.1) and (I.2) to yield approximate solutions which approach the original solutions near the structure and approach the undeformed upper surface at large distances. The tanh function also satisfies the no stress condition along the exposed portion of the elastic layer.

heave

$$V_2(X) = V_c\left\{1-\tanh\left[2\sqrt{\frac{A(X-1)}{\pi D}}\right]\right\} \qquad ; 1 \leq X < \infty \qquad (I.3)$$

pitch

$$V_3(X) = \alpha_c\left[1-\tanh\left\{2\sqrt{\frac{A(X-1)}{\pi D}}\,[1+i\hat{S}_-'(0)]\right\}\right] \qquad ; 1 \leq X < \infty \qquad (I.4)$$

Alblas and Kuipers (1969) did not develop a solution for the surge of the block motion when the block is subjected to a horizontal load. Therefore, an approximate solutions for the horizontal displacement is developed from the solution for the heave, (I.1)

$$U_1'(X) = U_c\left[1-2\sqrt{\frac{(1-\nu)(X-1)}{\pi D}}\right] \qquad ; 0 \leq X-1 << 1 \qquad (I.5)$$

Introducing the tanh function yields

$$U_1(X) = U_c\left[1-\tanh\left(2\sqrt{\frac{(1-\nu)(X-1)}{\pi D}}\right)\right] \quad ; \; 1 < X < \infty \qquad (I.6)$$

Appendix II. References

Albalas, J.B. and M. Kuipers, (1969), "Contact Problems of a Rectangular Block on an Elastic Layer of Finite Thickness, Part I: The Thin Layer," Acta Mechanica, 8:133-145.

Alblas, J.B. and M. Kuipers (1970), "On the Two-Dimensional Problem of a Cylindrical Stamp Pressed into a Thin Elastic Layer," Acta Mechanica, 9:293-311.

Biot, M.A., (1941), "General Theory of Three-Dimensional Consolidation," J. Applied Physics, 12:155-164.

Bowles, J.E., (1982), Foundation Analysis and Design, McGraw-Hill Book Company, New York, 816 pp.

Dias, F.C. and P.L. Monkmeyer, (1986), "The Effects of Wave-Induced Seepage on a Foundation Plate Resting on the Seabed," Ocean Structural Dynamics Symposium '86, Corvallis, Oregon State University, 483-497.

Durand, T.J.P. and P.L. Monkmeyer, (1982), "Wave-Induced Seepage Effects on an Impervious Breakwater," Ocean Structural Dynamics Symposium '82, Corvallis, Oregon State University, pp. 196-210.

Lindenberg, J., J.H. Swart, C.J. Kenter, and K. den Boer, (1982), "Wave Induced Pressures Underneath a Caisson: A Comparison Between Theory and Large Scale Tests," Boss'82, 1:337-357.

Liu, P.F., (1985), "Wave-Induced Pressure Under Gravity Structures," J. WPCOE Div., ASCE, 111:111-120.

McDougal, W.G., C.K. Sollitt, T.S. Vinson, and J.R. Bell, (1981), "Ocean Wave-Soil-Geotextile Interaction," Sea Grant Report, Oregon State University, 143 pp.

Mei, C.C. and M.F. Foda, (1981), "Wave-Induced Responses in a Fluid-Filled Poroelastic Solid with a Free Surface--A Boundary Layer Theory," Geophys. J. R. Astr. Soc., 66:597-631.

Mynett, A.E. and C.C. Mei, (1982), "Wave-Induced Stresses in a Saturated Poroelastic Seabed Beneath a Rectangular Caisson," Geotechnique, 32:235-248.

Stematiu, D. and C. Stera, (1984), "A FEM Model of the Breakwater-Foundation Dynamic Interaction," unpublished.

Yamamoto, T., H.L. Koning, H. Sellmeijer, and E.V. Hijum, (1978), "On the Response of a Poroelastic Bed to Water Wave," J. Fluid Mech., 87:192-206.

CHAPTER 171

ANALYSIS OF BEACH EROSION AROUND LARGE-SCALE COASTAL STRUCTURES

T. UDA*, M. SUMIYA** and Y. KOBAYASHI**

ABSTRACT

The coast of Ibaraki Prefecture, facing the Pacific Ocean, has an alongshore stretch of 181 km. On this coast many structures associated with harbors have been constructed since early 1960s. Since then 25 years have passed, and some notable beach changes due to the influence of the construction of the coastal structures have been observed. This study aims to examine the actual situation of the beach change around large-scale structures and the damages of the coastal structures selecting the coast of Ibaraki Prefecture as the study area. For the purpose aerial photographs were taken along the coast, and the topographic surveys and measurements of median diameter of beach-face materials were made. Data of the soundings having been conducted once a year since 1975 around Oharai Port and Hazaki Fishery Harbor were collected in order to study the beach changes around the large-scale coastal structures. For the analysis of these data the comparison of the shoreline changes were performed by using four sets of aerial photographs since 1947 to the present. Moreover, temporal and spatial changes of the beach topography were investigated by the sounding data.

I. INTRODUCTION

In recent years beach erosion is severe in Japan due to the influences of the decrease of the fluvial sediment supply from rivers and the construction of various large-scale coastal structures built on the coast. Generally the beach should change its form to attain to the new equilibrium condition because the movement of littoral drift is restricted, when coastal structures are built on a coast dominating littoral drift. For the countermeasures against beach erosion concrete armour units have been frequently placed along the coastlines. Furthermore, they have been often placed at the downdrift side of the most severely eroded location, and sometimes deep consideration of keeping the stable beach is lacking. Continuous placement of concrete blocks along the coast brings about the disappearance of the natural sandy beach. These situations can be seen on many Japanese coasts.

The aim of the study is to examine the actual situation of the beach change around large-scale structures and the damages of the coastal structures selecting the Ibaraki Coasts as the study area. On the coast many structures associated with harbors have been constructed since the early 1960s. Since then 25 years have passed, and some notable beach changes due to the influence of the construction of the harbor structures

* Dr. Eng., Head, Coastal Eng. Div., Public Works Research Institute, Ministry of Construction, Ibaraki 305 Japan.

** Public Works Department, Ibaraki Prefectural Office, Ibaraki 310 Japan.

have been observed. In this study the actual situation of the beach erosion on the Ibaraki Coast is investigated using the topographic survey data, aerial photographs and coastal pictures taken in the past.

II. METHOD OF INVESTIGATION

The investigated region of 181.4 km long extends from Ohtsu Fishery Harbor to the mouth of the Tone River (Fig. 1). The region is separated into two coasts: Joban Coast north of Oharai Port and Kashimanada Coast south of the port. First, aerial photographs were taken along the coast, and the soundings and the samplings of beach-face materials were conducted between Oharai Port and the mouth of the Tone River. Second, the sounding data in the past were gathered in order to compare the past with the present state of the beach at three locations around Ohtsu Fishery Harbor (①), Oharai Port (②) and Hazaki Fishery Harbor (④) as expressed in Fig. 1, where the beach was recently eroded to a large extent. The changes of the shoreline positions along the coast were measured from the aerial photographs having been taken 4 times between 1947 and 1984. Temporal and spatial changes of the shoreline positions were also examined at locations where sounding data in the past were obtained. On the north coast of Kashima Port (③ in Fig. 1), pictures of the beach taken in the past were gathered in order to examine the beach condition qualitatively.

III. BEACH EROSION ALONG THE JOBAN COAST

The shoreline changes between Ohtsu Fishery Harbor and Hitachi Port along the Joban Coast are investigated. The shoreline positions were degitalized at 50 m intervals continuously from the aerial photographs, and the changes of the shoreline positions during each subsequent period are calculated (Fig. 2). Regarding the general condition of the coastal landform, there protrude some capes between Ohtsu Fishery Harbor and Unomisaki Cape, and the sandy beaches extend between these capes. The coasts south of Unomisaki Cape generally consist of the coastal cliffs, but locally there exist narrow sandy beaches. For instance, the sand spit is formed around Kawarago Port because of the shelter effect of the offshore rocks[1]. The shoreline changes at locations north of Unomisaki Cape are comparatively larger than those between Unomisaki Cape and Ohse Fishery Harbor, which is mainly due to the types of the coast. The former coast consists of the sandy beach, and the latter one the cliff coast, so that the shoreline change is small. Here, the region between Ohtsu Fishery Harbor and Unomisaki Cape, showing the large shoreline changes, should be discussed in detail. In the region there are three capes, Tenpisan Cape at the mouth of the Ohkita River, Takado and Unomisaki Capes. The existence of the rocky head of the capes, projecting offshore, prevents the longshore sand movement across the head, and thereby some characteristic shoreline changes are noted.

First, it is seen from Fig. 2(a) that the shoreline retreats south of Ohtsu Fishery Harbor and it advances north of Tenpisan Cape. To the contrary the shoreline south of the cape retreats, and again the shoreline north of Takado Cape advances except the

adjacent part of the cape. In addition to these changes, the same features can be observed between Takado and Unomisaki Capes. The shoreline changes as described above have a distinct feature that the shoreline north of the cape advances and that south of it retreats. The shoreline change is due to such reason that the southward longshore drift caused by incident waves from northeast was obstructed at the capes. On the other hand, it is found in Fig. 2(b) that the shoreline changes are totally reversed. Due to the field observation of wave direction having been conducted over 10 years at Ajigaura Beach located south of Joban Coast, southeastern wave direction prevails in summer and northeastern wave direction in the other seasons, and the wave direction has a periodic feature of one year[2]. Taking these features into account, it is concluded that Figs.2(a) and 2(b) designate the shoreline changes after the northeastern and southeastern wave incidences prevailed, respectively. Figure 2(c) shows the different feature from those in Figs.2(a) and 2(b). Between Tenpisan and Takado Capes the shoreline in a region next to the capes retreats and the shoreline advances at the central part of each stretch of the coast. Between Takado and Unomisaki Capes the influence of the river mouth jetty of the Hananuki River to the adjacent beach is newly observed, and the beach is eroded south of the capes and the coastal structure, and vice versa

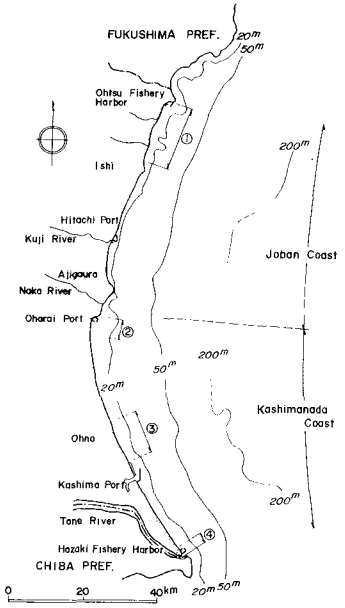

Figure 1 Investigated region along coasts in Ibaraki Prefecture.

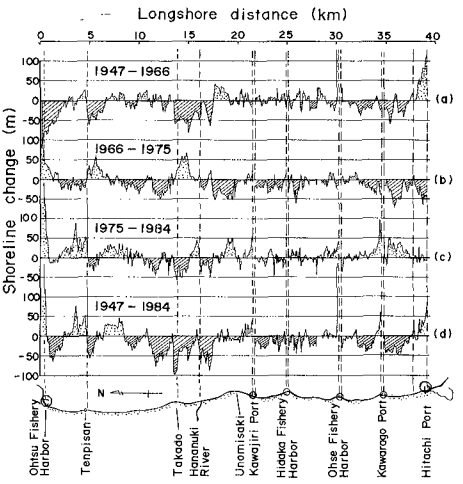

Figure 2 Shoreline changes between Ohtsu Fishery Harbor and Hitachi Port during 37 years from 1947 to 1984.

north of them. The pattern of the shoreline change differs each other. This might be mainly due to the difference of the overall direction of the shoreline configuration, assuming that the incident angle of the waves at far offshore zone is relatively small and takes almost the same value along the coast.

Regarding the shoreline change in Fig.2(d) between 1947 and 1984, the shoreline advances to a great extent on the south side of Ohtsu Fishery Harbor, whereas it retreats far from the harbor. The main cause is considered to be the influence of the construction of the breakwater as described in the following section. In addition, the shoreline retreats in south and north regions around Takado Cape, but the cause of the extensive beach erosion is not known at present.

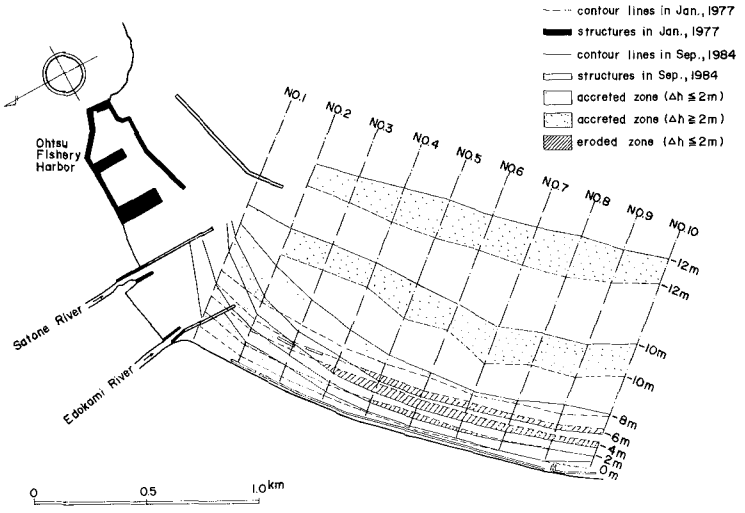

Figure 3 Changes of some contour lines around Ohtsu Fishery Harbor.

Since it is found that the shoreline change is large around Ohtsu Fishery Harbor, the change of the bottom contours is compared as shown in Fig.3, using the sounding data obtained in 1977 and 1984. The construction work of the offshore breakwater finished in 1974, and thereafter large amount of sand accumulated on the southwest side of the harbor. On the other hand, the beach up to 6 m deep below the mean sea level was eroded at No.5 through No.10. The beach erosion at No.7 is so severe in recent years that the coastal revetment fell down in 1983. In the same figure the contours of 10 and 12 m deep have a large change, but they are thought to be the error accompanied with the bottom sounding and not to be the significant change of the beach, considering that large onshore-offshore change of the contours could be observed at a small depth change at the mild slope beach, and that the contours advanced in all region without the difference of the locations. The beach changes stated above are considered to be

caused by the influence of the construction of the breakwater, taking the facts into consideration that sand accumulate inside the harbor and the beach far from the breakwater is eroded. Namely, the nearshore circulation directing toward inside the harbor from outside the shadow zone of the breakwater may develop due to the existence of the offshore breakwater, and the current induces the sand movement toward the lee of the breakwater[3].

In constructing the harbor structures it is necessary to perform the countermeasure works rapidly to prevent the adjacent beach from being eroded. It is ineffective to place the wave breaking works after the initiation of the beach erosion. There are some countermeasure works to be selected. For example, some groins can be constructed to prevent longshore sand movement from outside the harbor and to form a stable shoreline, of which tangent is at right angles with the incident wave direction.

IV. BEACH EROSION ALONG THE KASHIMANADA COAST

The shoreline change along the coast is expressed in Fig.4 with reference to that in 1947. Since there exists Kashima Port at the central part of the coast, the shoreline changes around the port are not shown in the figure. The construction of the breakwater of Kashima Port began in 1963[4], and almost completed in 1976. Regarding the shoreline changes between 1947 and 1965, the beach at 3-4 km south of Oharai Port was eroded locally, and the shoreline tends to advance to the location, of which longshore distance is around 26 km. In further south the shoreline has a tendency to be eroded

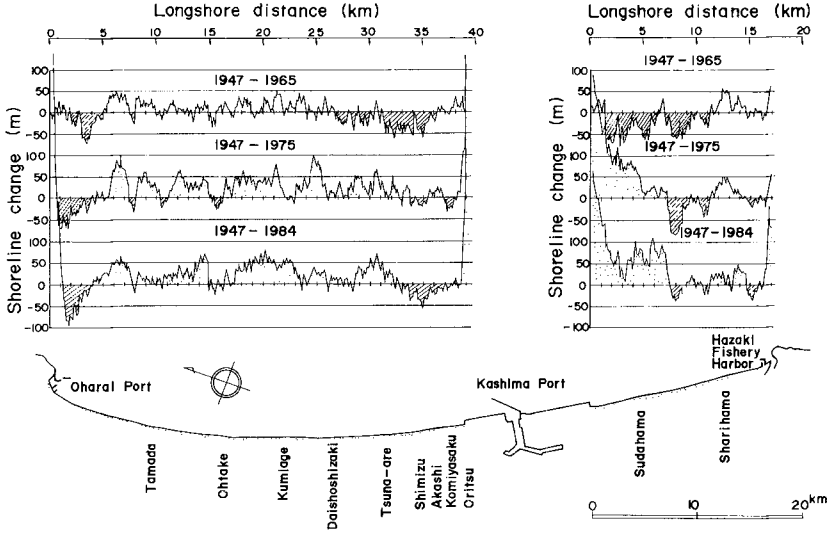

Figure 4 Shoreline changes along the Kashimanada Coast during 37 years from 1947 to 1984.

except the vicinity of Kashima Port and the region between Hazaki Fishery Harbor and the location 5 km north of the harbor. The construction work of Kashima Port began in 1963, and therefore littoral drift could move up and down alongshore freely before 1963. As a result, it may be concluded that for an overall feature of the beach erosion the coasts between Oharai Port and 5 km south of it, and the coasts far south of the longshore distance of 26 km were eroded, and the coasts between the longshore distance of 5 through 26 km were accreted. On the shoreline change around Kashima Port some local changes due to the influence of the existence of the breakwater may be considered to superimpose over the large-scale beach changes as described above.

Comparing the shoreline changes in 1947 and 1975, it is found that the shoreline advanced around 300 m on the south side of Kashima Port. This is due to the artificial nourishment of sand produced by the excavation of the Harbor[4]. Regarding the shoreline changes between Oharai and Kashima Ports, the shoreline tends to advance generally, whereas the shorelines south of Oharai Port and in the vicinity of Kashima Port retreat.

On the shoreline changes between 1947 and 1984, the amount of the retreat increases at the south coast of Oharai Port and the north coast of Kashima Port. Between Kashima Port and Hazaki Fishery Harbor part of sand nourished on the south side of the harbor may have moved southward, and the shoreline inside Hazaki Fishery Harbor advanced to a great extent. Consequently, it is concluded that the littoral cell along the coast was separated into two portions by the existence of the breakwater of Kashima Port, although before the construction of the harbor there existed a northward longshore drift south of the location, of which longshore distance is about 26 km.

In order to study the cause of the shoreline change, wave directions measured at Oharai and Kashima Ports are investigated (Fig.5). The wave gauges of both positions are placed at a depth of around 20 m off the coast as shown by the solid circles in the figure. At Oharai Port the wave data from January, 1980 to February, 1982 are referred[5),6)], and at Kashima Port those in 1980 are used[7)]. The ratio of the period when the wave data were obtained to the total period at Oharai Port is 24%, considering the significant wave height over 1 m, and that at Kashima Port is 97% with regard to the total period. It is clearly understood from Fig.5 that the dominant wave direction is from ENE at both locations. This means that waves are incident from counterclockwise direction with respect to the normal to the coastline in the vicinity of Oharai Port and from clockwise direction near Kashima Port. These wave incidences induce southward and northward longshore transport, respectively, at both locations.

Next, seasonal changes of significant wave height and wave period are examined based on wave observation data of Onahama Port, Ajigaura Beach and Kashima Port during January, 1980 and February, 1982[8),9),10)]. Mean wave height ($\bar{H}1/3$) and wave period ($\bar{T}1/3$) averaged monthly are expressed in Fig.6. Significant wave height measured at Kashima Port is slightly larger than those at two other locations, but almost similar seasonal changes of wave height are observed at Onahama Port and Ajigaura Beach. In summer and winter $\bar{H}1/3$ takes on around 1 m, and in spring and autumn it increases to about 1.4 m. The difference of wave period between three locations is relatively small, and dominant wave period is about 7-8 sec.

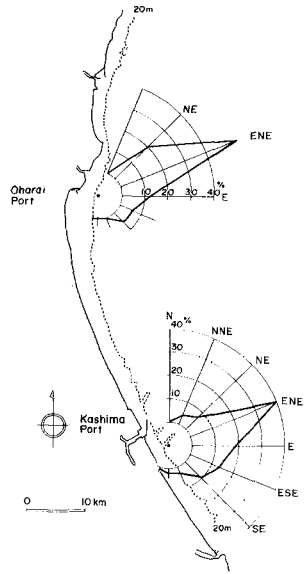

Figure 5 Wave directions at Oharai and Kashima Ports.

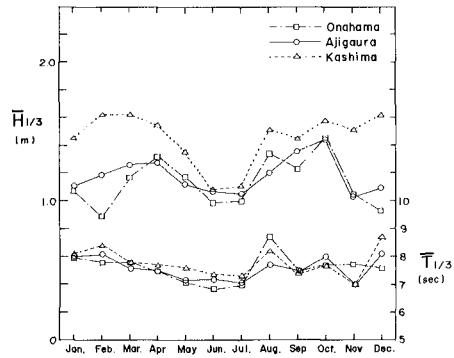

Figure 6 Monthly change of the averaged significant wave height and wave period at Onahama Harbor, Ajigaura and Kashima Port.

In the present study the topographic surveys and the sampling of beach-face materials along the Kashimanada Coast have been carried out. Corresponding to the advance or retreat of the shoreline position, the foreshore slope and the median diameter of the bed materials on the foreshore have also changed to a great extent. Using the topographic survey data, the foreshore slope, defined by the mean slope between 1 m above the mean sea level and 1 m below it, is calculated (Fig.7). The foreshore slope is steep between Oharai Port and the Tamada Coast. On the south of the coast mild slope of around 1/70 continues to the Daishoshizaki Coast, and again the beach slope steepens near Kashima Port. On the south of Kashima Port the beach slope is mild, but again the slope steepens in the vicinity of Hazaki Fishery Harbor. Comparing the foreshore slope with the shoreline changes between 1947 and 1984 shown in Fig.4, it is found that the foreshore slope steepens in the eroded region and it becomes mild in the accreted region. In the comparison between the shoreline change and the foreshore slope, it should be noted that the region of steep foreshore slope is wider than the one where the shoreline actually retreated. This may be partly due to the relatively low accuracy of measurement of the shoreline position, and partly due to the fact that actually the foreshore slope begins to steepen before the change of the shoreline position accompanying with the beach erosion.

The longshore distribution of the median diameter of beach face materials sampled along the shoreline is also expressed in Fig.7. The median diameter takes a

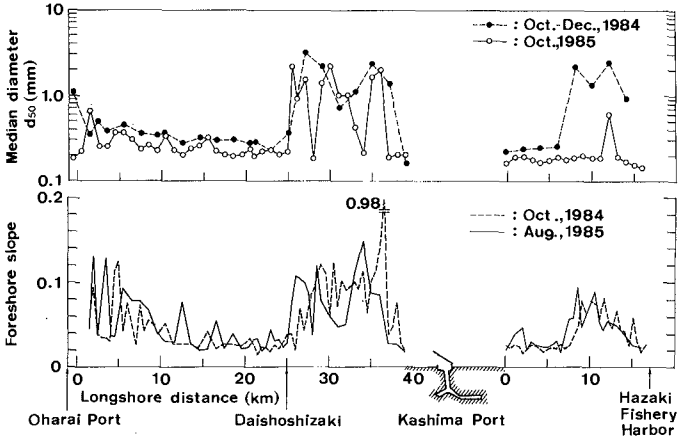

Figure 7 Longshore distribution of median diameter (d_{50}) and foreshore slope along the Kashimanada Coast.

large value between Oharai Port and 5 km south of the port, and the same between the Daishoshizaki Coast and Kashima Port. The median diameters between these areas are fine, that is, $d_{50}=0.2$-0.3 mm. Coaser materials are found between Hazaki Fishery Harbor and the location 10 km north of the harbor, and on further north coast fine materials are seen again. It is found from Figs.4 and 7 that the longshore distribution of the median diameter corresponds well with that of the shoreline change, because large and small grain sizes are found on the eroded and accreted beaches, respectively. It is also understood from Fig.7 that coaser materials can be found on steep beaches. This reason is given by the sorting effect of bed materials due to waves, in which finer materials are carried away first and coarser materials are left on the eroded beach. Furthermore, the region of steep foreshore slope extends in the longshore direction through 1984 and 1985. This means that the eroded region extended in the longshore direction, taking the fact into consideration that the foreshore slope steepened on the eroded beach. It is clear that the foreshore slope and the median diameter on the foreshore become good parameters on judging whether the beach has been eroded or not.

V. DETAILED ANALYSIS OF BEACH CHANGES AROUND COASTAL STRUCTURES

In previous chapter the overall features of beach changes along the Kashimanada Coast were discussed. In the analysis some notable beach changes were observed in the vicinity of Oharai and Kashima Ports, and Hazaki Fishery Harbor. In the following the beach changes of each region will be studied in detail.

5.1 Beach changes around Oharai Port

Oharai Port has been annoyed with the deposition of sand for a long time[3]. The extent of the beach change increased with the completion of the offshore breakwater having been constructed until July, 1984 in order to enlarge the port facility. The shoreline changes of each year with reference to the shoreline positions in April, 1978 are shown in Fig.8. On the coast the wave incidence from ENE dominates as in Fig.5 and in the lee of the breakwater the breaker height lowers, so that clockwise nearshore circulation may develop behind the breakwater and sand accumulate from outside of the port to inside of it. Particularly the accreted zone has expanded southward since the beginning of the construction work of the offshore breakwater in September, 1981. At the same time the beach south of No.9 was eroded. A large part of the eroded sediment may be considered to be transported toward the harbor, taking into consideration that the retreat of the shoreline position decreases with the distance from the port. Moreover, it is found from Fig.8 that the retreat of the shoreline position is much

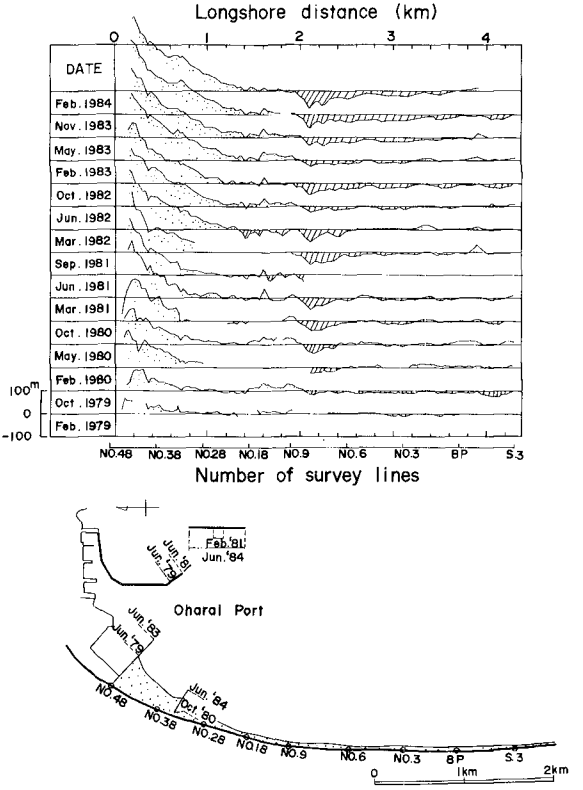

Figure 8 Temporal and spatial change of shoreline position around Oharai Port.

smaller than the advance. This may be interpreted by the reason that high beach cliff was formed by the erosion and therefore the sand supply from the cliff into the sea was large enough not to bring large retreat of the shoreline. The beach erosion is severe between No.9 and No.3 in Fig.8. The coastal revetment fell down over around 300 m long at No.6 in the midst of the region since 1984 due to the beach erosion.

Finally the actual situation of beach erosion will be studied using pictures taken on the coast. Due to Picture 1 taken on the south of Oharai Port in July, 1984, a large amount of sand accumulate inside the harbor accompanying with the construction of the offshore breakwater. In June, 1984 there was a wide beach in front of the coastal revetment at No.6 south of Oharai Port, so that the revetment was stable (Picture 2). Then abrupt change occurred, the foreshore totally disappeared on October 5 in the same year, and the foot of the coastal revetment was exposed to the wave uprush (Picture 3). Finally on February 27, 1985 the revetment fell down (Picture 4) and beach cliff of around 5 m high was formed on the natural sandy beach next to the position of the revetment. It is understood that the coastal revetment may be fallen down easily when the foreshore disappears due to the beach erosion.

Picture 1 Aerial photogragh of Oharai Port taken in July, 1984.

Picture 2 Situation of the beach at survey line No.6 in June, 1984.

Picture 3 Same location as Picture 2. The picture was taken on October 5, 1984.

Picture 4 Same location as Picture 2. The picture was taken on February 27, 1985.

5.2 Beach changes north of Kashima Port

The north coast of Kashima Port has been eroded and particularly the beach erosion was severe in the summer and autumn of 1986, because high waves generated by the tropical storms attacked the coast frequently. In this study many pictures, showing the historical changes of the beach since 1938, were gathered. In order to examine the beach condition qualitatively, the pictures are compared. Picture 5, taken in July, 1980, shows the situation of the beach at the Akashi Coast (For location, see Fig.4) adjacent to Kashima Port. At this stage wide foreshore extends in front of the coastal revetment, and the vegetations can be seen on the foreshore, expressing that the beach has been stable for a fairly long time. On September 15, 1986, the foreshore totally disappeared as shown in Picture 6 due to the beach erosion. These change may be attributed to the beach erosion caused by the imbalance of the littoral transport. Because at the south of the coast a large breakwater of Kashima Port is located, and the northward longshore sediment transport is obstructed at this location.

Picture 5 Situation of the beach of the Akashi Coast north of Kashima Port in July, 1980.

Picture 6 Same location as Picture 5. The picture was taken on September 15, 1986.

5.3 Beach changes around Hazaki Fishery Harbor

The construction work of the breakwater of the fishery harbor began in 1974 at Hazaki next to the mouth of the Tone River. The breakwater was elongated year by year, and until 1984 south and north breakwaters had been completed (Fig.9). With the elongation of the breakwater sand accumulated inside the harbor, and at the same time the north coast of the harbor was eroded. The temporal and spatial changes of the shoreline positions can be examined as shown in Fig.9 because the topograghic surveys around the harbor have been conducting twice a year since 1974. In September, 1976 the lengths of the north and south breakwaters were elongated until about 470 m and 360 m respectively. During the period the shoreline advanced in the vicinity of both breakwaters. On the other hand, the beach between No.12 and No.26 north of the breakwater was eroded. Thereafter both breakwaters were further elongated in the offshore direction until January, 1981 and simultaneously the shoreline inside the harbor gradually advanced. Furthermore, the eroded region extended north over No.0. The

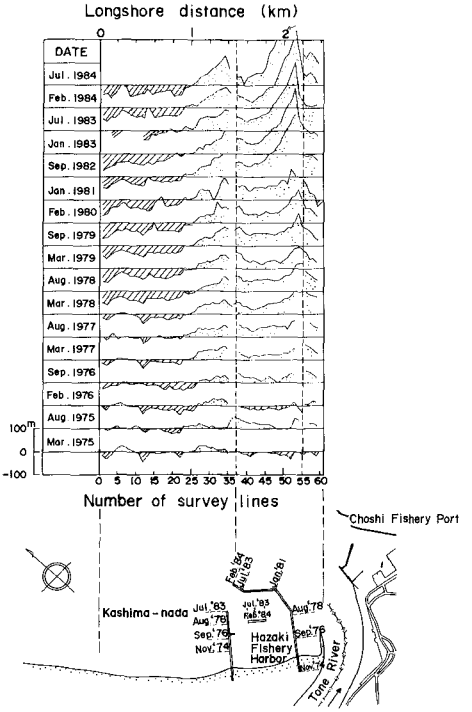

Figure 9 Temporal and spatial changes of shoreline position around Hazaki Fishery Harbor.

breakwater was elongated normal to the direction of the shoreline until January, 1981. During 1981 and 1984 the parallel part of the breakwater was constructed and the north breakwater was also elongated. With these construction works, the shoreline inside the harbor advanced to a great extent to reach to 263 m at maximum. The shoreline on the north side of the harbor advanced with the elongation of the breakwater, but the amount of the advance is smaller than that inside the harbor. The cause may be given by the following reason. First, the predominant direction of the littoral transport is considered to be northwestward at the coast, judging that the eroded zone extended in the northwest direction. In other words, the diminant wave is incident from clockwise with respect to the normal to the initial shoreline. Under such a condition of wave incidence, longshore current directing southeast develops in the lee of the breakwater, and sand accumulate on the north side of the breakwater. Regarding the cause of the beach changes inside the harbor, not only the littoral drift turning around on tip of the breakwater due to the mechanism, but also the deposition of a part of the sediment outflow from the Tone River is thought to be important. Because it is not until 1981, when wave condition inside the harbor was getting calm by the construction of the offshore breakwater, that the shoreline advanced quickly.

VI. DISCUSSIONS

In the previous chapters the actual situation of large-scale beach erosion along the Ibaraki Coast were studied. The types of the beach erosion are separated into two groups. The first is the case, in which the distributions of wave height and wave direction vary due to the influence of the construction of the breakwater first, and hence the beach changes are induced by the littoral drift corresponding to the changed distributions of wave height and wave direction. The second is the case, in which beach change is caused by the obstruction of the longshore drift accompanying with the construction of the coastal structure on a coast, where dominant littoral drift in one direction exists. The former includes the beach changes around Ohtsu Fishery Harbor or Oharai Port, and the latter is the case around Kashima Port or Hazaki Fishery Harbor. Comparing both types, it is considered in the first case that the beach erosion might be confined in a comparatively narrow region, and the construction of a structure to control littoral drift such as a groin is effective for the measures against the beach erosion, if the structure is built in time. To the contrast in the second case the countermeasure work is considerably difficult. If a structure obstructing littoral drift is built along the coast of a long stretch, where littoral transport is dominant and the continuous movement of littoral drift is cut, then there is a high possibility that its influence expands extensively in a long term. In this case the shoreline will change its form to attain to the equilibrium state, in which the normal to the shoreline becomes paralell with the wave direction at the breaker line.

In Japan the sand bypassing method is conducted only experimentally for the measures to ensure the continuity of littoral drift. It is not used for a general method, and therefore it is impossible to maintain the continuity of littoral drift artificially at present. Instead of the sand bypassing method, groins and detached breakwaters are

widely used for the countermeasure works against the beach erosion. In other case concrete armour units or coastal revetments are merely set along the shoreline. In selecting the former method, if once a structure is built along the coast to obstruct the littoral drift, the beach erosion will extend to the downdrift coast. In order to prevent further beach erosion many structures of some longshore intervals have to be built along the coast. Furthermore, the selection of the latter case is not effective only for maintaining the sandy foreshore. The sandy coast of a long stretch will disappear and the sandy beach will be finally replaced by the concrete armour units, since the eroded region extends alongshore gradually. Taking these points into account, fundamentally it is important to consider the method to ensure the continuity of littoral drift. However it is difficult to select the plan for the present because the sand bypassing method is not acknowledged for the countermeasure works in Japan. In addition, it should be noted that the eroded region will extend further with the time elapsing. For the second selection of the measures, a method is considered, in which some coastal structures are built on the coast and the coast is altered to such a coast of stable planform, even if the littoral drift from downdrift end of the structure located on the updrift side becomes zero. At least wider beach could be kept by the method compared with the way using concrete armour units setting along the shoreline.

VII. CONCLUSIONS

Main results of this study are summarized as follows:

(1) Cyclic beach changes of accretion or erosion were observed on both sides of the headlands located between Ohtsu Fishery Harbor and Unomisaki Cape. The cause is considered to be due to the fact that the predominant wave direction changes seasonally from northeast to southeast on the coast.

(2) Severe beach erosion and accretion were caused by the elongation of the offshore breakwater at Ohtsu Fishery Harbor and Oharai Port.

(3) Along the Kashimanada Coast beach erosion is severe at the south site of Oharai Port, the north of Kashima Port and Hazaki Fishery Harbor. It is found quantitatively that the slope of the beach face becomes steep and the armouring of the bed materials on the shore is under way on the eroded beach on the downdrift side of the structure.

(4) A large amount of sand accumulated inside Hazaki Fishery Harbor with the elongation of the breakwater. Especially the shoreline advanced very much after the completion of the construction work of the parallel offshore breakwater with respect to the shoreline. Regarding the cause of the beach changes inside the harbor, the deposition of a part of the sediment outflow from the Tone River is considered to be important because of the formation of the calm water inside the harbor.

(5) The types of the beach erosion along the Ibaraki Coast are separated into two categories. The first is such a case that the beach changes are produced by the littoral transport induced by the longshore changes of wave height and wave direction, which are caused by the influence of the construction of the breakwater. The second is the case, in which the beach change is caused by the obstruction of littoral drift due to the construction of the coastal structure. For the first case, the construction of a coastal

structure to control littoral drift like a groin is effective for the measures against beach erosion, if the structures are built in time. For the second case fundamentally it is important to consider a method to ensure the continuity of littoral drift, and if not, a method to form the shoreline of stable configuration against wave attack by the construction of a structure should be considered.

REFERENCES

1) Uda, T., H. Furukawa and Y. Kanda : Observation of nearshore current around detached breakwaters and headlands, 31st Jap. Conf. on Coastal Eng., pp.416-420, 1984 (in Japanese).
2) Uda, T. : Comparison of long-term and short-period observation data of wave direction and longshore current at Ajigaura Beach, pp.421-425, 31st Jap. Conf. on Coastal Eng., 1984 (in Japanese).
3) Kraus, N. C., S. Harikai and S. Kubota : Simulation of shoreline change at Oharai Coast, 28th Jap. Conf. on Coastal Eng., pp.295-299, 1981 (in Japanese).
4) Sato, S., N. Tanaka and K. Sasaki : On the topograghic changes accompanied with the construction of Kashima Port, 21st Jap. Conf. on Coastal Eng., pp.147-153, 1974 (in Japanese).
5) Ibaraki Prefectural Sanpin Port Office : Report on wave observations at Oharai Port, 332p., 1981 (in Japanese).
6) Ibaraki Prefectural Sanpin Port Office : Report on wave observations at Oharai Port (Climate and Wave observations) No.2, 372p., 1983 (in Japanese).
7) The Second District Port Const. Bureau, Kashima Port Work Office, Ministry of Transport : Waves and Wind at Kashima Port, 299p., 1982 (in Japanese).
8) Takahashi, T., S. Hirose, K. Sugawara and N. Hashimoto : Annual report of wave observations (1980), Technical Note of P.H.R.I., Ministry of Transport, No.417, pp. 80-94, 1982 (in Japanese).
9) Takahashi, T., S. Hirose, K. Sugawara and N. Hashimoto : Annual report of wave observations (1981), Technical Note of P.H.R.I., Ministry of Transport, No.445, pp. 143-157, 1983 (in Japanese).
10) Takahashi, T., S. Hirose, K. Sugawara and N. Hashimoto : Annual report of wave observations (1982), Technical Note of P.H.R.I., Ministry of Transport, No.480, pp. 152-160, 1984 (in Japanese).
11) Uda, T., M. Sumiya and Y. Kobayashi : Beach change along the Ibaraki Coast, Japan, Trans. Japan. Geomorphological Union, Vol. 7-3, pp. 141-163, 1986 (in Japanese).

CHAPTER 172

ENERGY DISSIPATION AND WAVE FORCE AT SLOTTED WALL

Saburo URASHIMA[1], Koichi ISHIZUKA[2] and Hideo KONDO[3]

Abstract

The hydrodynamic coefficients are computed based on the measured total force on the single slotted wall in the wave field, or on the measured head loss in the uniform flow channel. The reflection, transmission and force coefficients on the single slotted wall are computed based on the mean values of the hydrodynamic coefficients. The correlations between these calculated values and measured values are found to be good. A design procedure of the single slotted wall is given the paper.

1 INTRODUCTION

Many studies on wave energy dissipating structures using a pervious wall have been carried out mainly for caisson-type breakwaters, which have a chamber between the pervious front wall and the solid backwall. Although the hydrodynamic characteristics of the single pervious wall are not well-known, it is not so well-known that it can serve as a breakwater itself. The objective of this paper is to establish the optimum form of the vertical parallel piled slits by obtaining the coefficients of reflection, transmission and wave force which are estimated by the drag and mass coefficients.

The hydrodynamic coefficients are computed by measuring the total force on the slotted wall and then employing Morison's equation and the small amplitude wave theory in the wave field, or by measuring the head loss in the uniform flow channel. The reflection and transmission coefficients are determined by making use of the analytical approach to the small amplitude shallow water wave deformation at the pervious wall as explained by the last author in 1979.[1)]

2 EXPERIMENTAL SETUP

The experiments were conducted in a wave flume 0.8 meter deep, 0.4 meter wide and 19.7 meter long. For each test a slotted wall orientation was kept perpendicular to the incident wave direction. The range of wave parameters were as follows:

Wave steepness H_I/L : 0.002 to 0.056
Relative depth h/L : 0.100 to 0.281

The water depth was kept constant at 0.5 meter throughout the experiment. The test apparatus which was used for measurement of wave force is illustrated schematically in Fig. 1. The slotted wall which was tested for measurement of wave force consisted of an acrylic wall, 0.4 meter in width and 0.6 meter long, supported on two frames which were

1 Assistant Professor of Civil Engineering, Tomakomai College of Technology, 443 Nishikioka, Tomakomai, 059-12 JAPAN
2 Professor of Civil Engineering, ditto
3 Professor of Civil Engineering, Muroran Institute of Technology, 27-1 Mizumoto-Cho, Muroran, 050 JAPAN

suspended from the wave flume. These frames were made of steel, 25 by 16 millimeter in section. The wave force was transmitted to the strain-gauges on these frames. Two-dimentional flume tests were made. The reflection coefficients have been computed using Heal's formula.

In addition, the head loss was measured in the uniform flow channel. 21 types of the models with various void ratios and wall thicknesses were tested, as shown in table 1.

3 PROCEDURES EMPLOYED

The ratio of reflected wave amplitude a_R and the incident wave amplitude a_I can be estimated analytically as

$$\frac{a_R}{a_I}=\frac{A_{0,1}}{2+A_{0,1}}=\frac{\frac{\sigma}{kh}\left[\frac{C_l}{2g}|u_{1,1}|+i\frac{\sigma\mathcal{Z}}{g}\right]}{2+\frac{\sigma}{kh}\left[\frac{C_l}{2g}|u_{1,1}|+i\frac{\sigma\mathcal{Z}}{g}\right]} \tag{1}$$

Also the ratio of transmitted wave amplitude a_T to incident wave amplitude is given by

$$\frac{a_T}{a_I}=\frac{2}{2+A_{0,1}}=\frac{2}{2+\frac{\sigma}{kh}\left[\frac{C_l}{2g}|u_{1,1}|+i\frac{\sigma\mathcal{Z}}{g}\right]} \tag{2}$$

where σ is $2\pi/T$ and k is $2\pi/L$. The absolute value of the water particle velocity $|u_{1,1}|$ is approximated by

$$|u_{1,1}|=\frac{8}{3\pi}U_{1,1} \tag{3}$$

where $U_{1,1}$ is the amplitude of horizontal water particle velocity, C_l is the head loss coefficient and $\mathcal{Z}$ is the apparent orifice length.

The forces are divided into two parts, one due to the drag in the case of constant flow, and the other due to acceleration or deceleration of the fluid. The horizontal total force on a slotted wall is given by

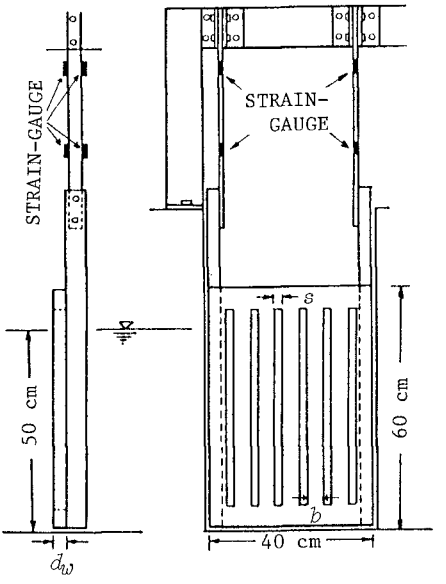

FIG. 1 TEST SETUP FOR THE SLOTTED WALL

Table 1 Geometry of Slotted Walls

Standard Slotted Wall				
λ(%)	b(mm)	s(mm)	d_w(mm)	d_w/s
25	50	17	15	0.90
			30	1.80
			45	2.70
35	43	23	15	0.64
			30	1.29
			45	1.93
50	33	33	15	0.45
			30	0.90
			45	1.35
Array of Square Column				
λ(%)	b(mm)	s(mm)	d_w(mm)	d_w/s
20	40	10	15	1.50
			30	3.00
			45	4.50
30		17	15	0.88
			30	1.75
			45	2.63
40		27	15	0.56
			30	1.12
			45	1.69
50		40	15	0.38
			30	0.75
			45	1.13

$$F_T(t)=F_D(t)+F_I(t)=C_D\cdot f_D(t)+C_M\cdot f_I(t) \tag{4}$$

in which

$$f_D(t)=\int_{-h}^{\eta}\rho\frac{u|u|}{2}dA \tag{5}$$

and

$$f_I(t)=\int_{-h}^{\eta}\rho\dot{u}\,dV \tag{6}$$

and $F_T(t)$ is the horizontal total force, $F_D(t)$ is the horizontal drag force, $F_I(t)$ is the horizontal inertia force, ρ is the mass density of water, η is the water surface elevation, dA and dV refer to the small projected area and volume, u and $\dot{u}$ are particle velocity and acceleration and C_D, C_M are the drag and mass coefficients, respectively.

The force coefficient f is defined as

$$f=\frac{Fmax}{\rho g(1-\lambda)Bhd_w} \tag{7}$$

where $Fmax$ is maximum total force, g is acceleration of gravity, B is wall width and h is water depth.

The relationship between the head loss coefficient C_l and the drag coefficient C_D is given by

$$C_l=(1-\lambda)\cdot C_D \tag{8}$$

and the relationship between the apparent orifice length $\mathcal{L}$ and the mass coefficient C_M is given by

$$\mathcal{L}=\left[1+\frac{(1-\lambda)}{\lambda}\cdot C_M\right]\cdot d_w \tag{9}$$

where λ is the void ratio, d_w is the wall thickness.

4 RESULTS

4.1 Hydrodynamic Coefficient

Fig. 2 presents the head loss coefficients from the wave and from the uniform flow tests. The head loss coefficients from wave test and those from uniform flow test formed smooth continue curve. Evidently, there is a remarkable correlation between the head loss coefficients and Reynolds number. The head loss coefficient is estimated with the Reynolds number Re, as follows.

$$C_l=\frac{A_1}{Re}+B_1 \tag{10}$$

where A_1 and B_1 are constants determined by the experiment. Reynolds number Re is defined by the following equation.

$$Re=\frac{u_{r.m.s}\cdot S}{\nu} \tag{11}$$

where

$$u_{r.m.s}=\frac{1}{T}\sum^{N}\frac{\sqrt{\int_{-h}^{\eta}u^2dy}}{h+\eta}\Delta t \tag{12}$$

and $u_{r.m.s}$ is the root-mean-square velocity. Here $u_{r.m.s}$ is adapted as the presentative velocity.

Fig. 3 shows the head loss coefficient for a standard slotted wall, and Fig. 4 shows one for an array of square columns in uniform flow. In turbulent flow, the head loss coefficient is constant. The head

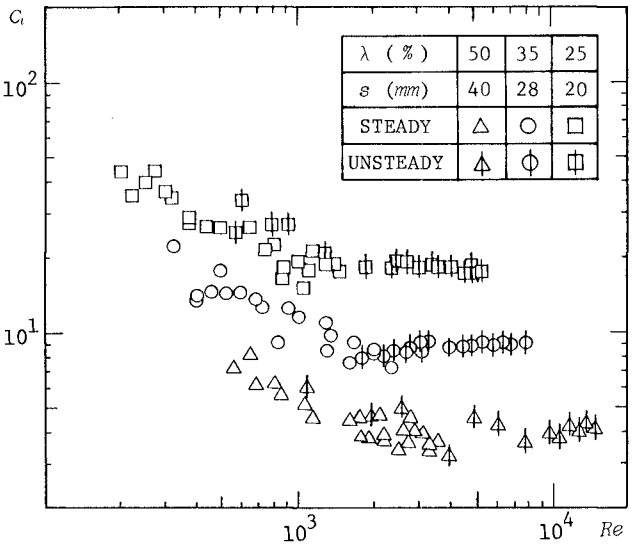

FIG. 2 HEAD LOSS COEFFICIENT VERSUS REYNOLDS NUMBER (d_w = 30 mm)

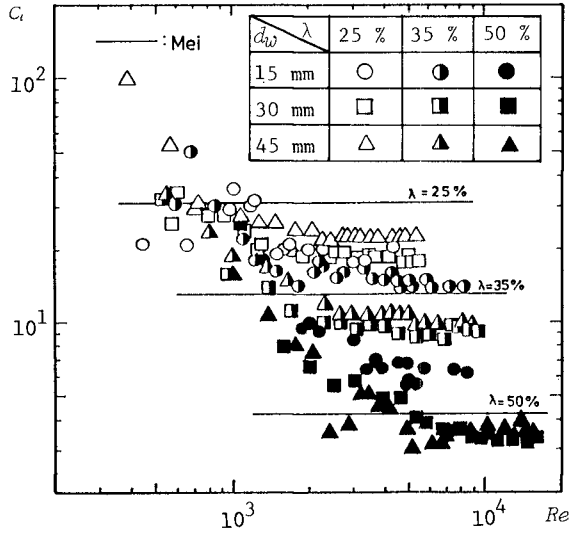

FIG. 3 HEAD LOSS COEFFICIENT VERSUS REYNOLDS NUMBER

loss coefficient is considered to be a function of the void ratio, wall thickness and slit width. The head loss coefficient is approximated by

$$C_l = B_1 = \frac{0.52}{\lambda^{3.0}(d_w/s)^{0.46}} \tag{13}$$

Fig. 5 shows the apparent orifice length versus Keulegan-Carpenter number KC. Evidently, there is a remarkable correlation between the apparent orifice length, wave length and Keulegan-Carpenter number. The apparent orifice length is given as a function of the wave length and the Keulegan-Carpenter number as follows.

$$\frac{\chi}{L} = \frac{A_2}{KC} + B_2 \tag{14}$$

where A_2 and B_2 are constants determined by the experiment. Keulegan-Carpenter number is defined by the following equation.

$$KC = \frac{u_{r.m.s} \cdot T}{d_w} \tag{15}$$

where T is the wave period and d_w is the wall thickness. The constant B_2 is given as a function of the wall thickness as follows.

$$\frac{\chi}{L} = B_2 = 0.00567 \cdot d_w + 0.0033 \tag{16}$$

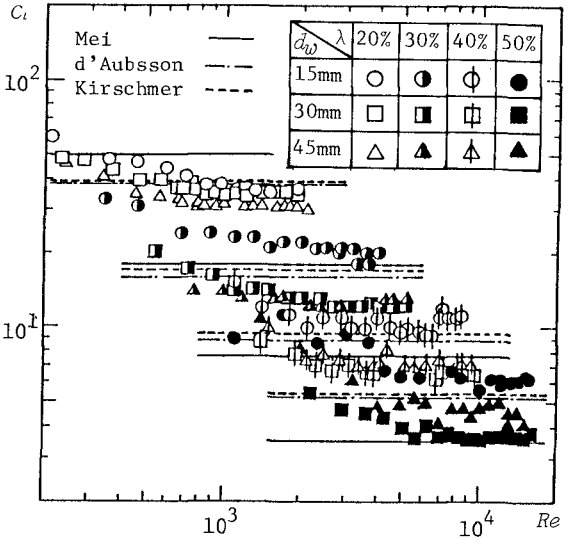

FIG. 4 HEAD LOSS COEFFICIENT VERSUS REYNOLDS NUMBER

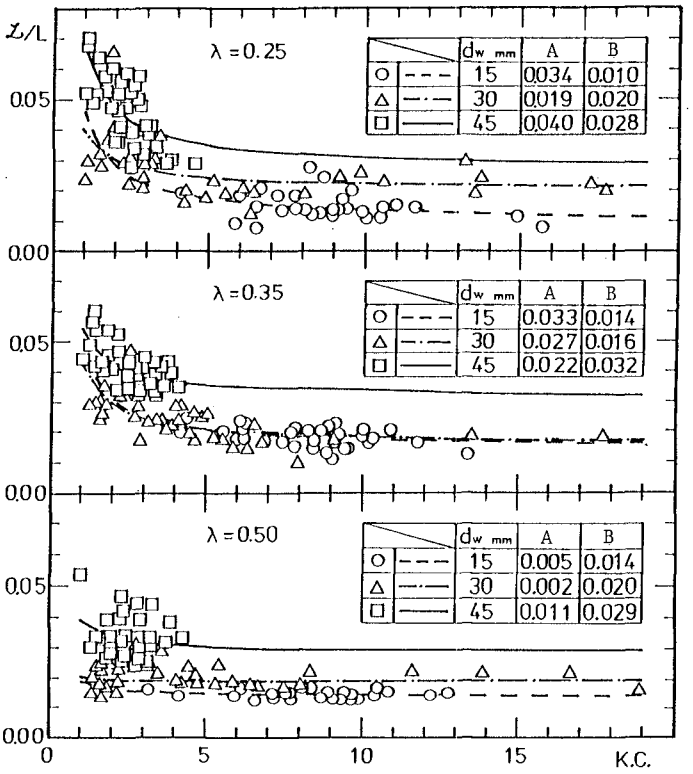

FIC. 5 RATIO OF APPARENT ORIFICE LENCTH TO WAVE LENGTH VERSUS KEULECAN-CARPENTER NUMBER

4.2 The Reflection Coefficient and Transmission Coefficient

Fig. 6 shows the reflection coefficient K_R and the transmission coefficient K_I versus the wave steepness H_I/L for the various values of relative water depth h/L. The theoretical results of Kondo(1979) using an experimental coefficient are superinposed for comparison with the results of the experiment. The agreement between the theoretical and actual results of the experiment is found to be relatively good. In this figure, as the incident wave height increases in the range of smaller height, the reflection coefficient decreases to a certain minimum value, and then increases as the wave height further increases, meanwhile, the transmission coefficient increases to a certain maximum value, and decreases afterwards. It is seen that the wave steepness has an important influence on the reflection and transmission coefficients.

Fig. 7 shows the dependence of reflection and transmission coeffi-

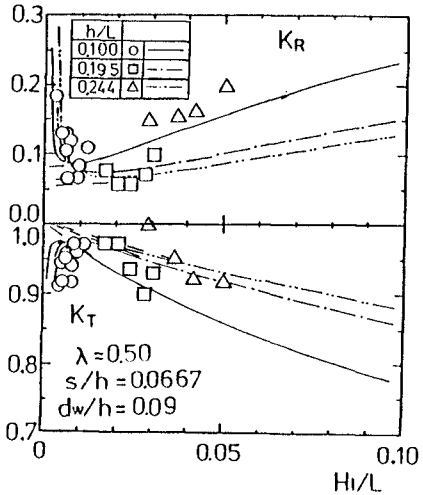

FIG. 6 REFLECTION AND TRANSMISSION COEFFICIENT VERSUS WAVE STEEPNESS

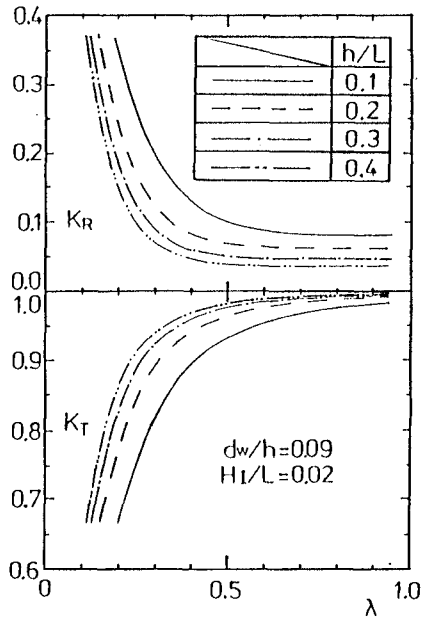

FIG. 7 REFLECTION AND TRANSMISSION COEFFICIENT VERSUS VOID RATIO

cients on the void ratio λ for the various values of relative depth. In this figure, the reflection coefficient decreases rapidly as void ratio increases and gradually decreases to a certain value, while the transmission coefficient increases in the similar manner. It is seen that the void ratio has a great effect on the reflection and transmission coefficients. With wider spacing between the square piles greater energy will be transmitted than reflected or lost and hence the transmission coefficient increases with the void ratio. As the slit size becomes very large, however the effectiveness of the slotted wall as an energy dissipator decreases. The reflection coefficient decreases with increasing slit size as was expected. This can be attributed to the reduction in the net projected area of the slotted wall normal to the direction of wave advance giving rise to greater transmitted energy

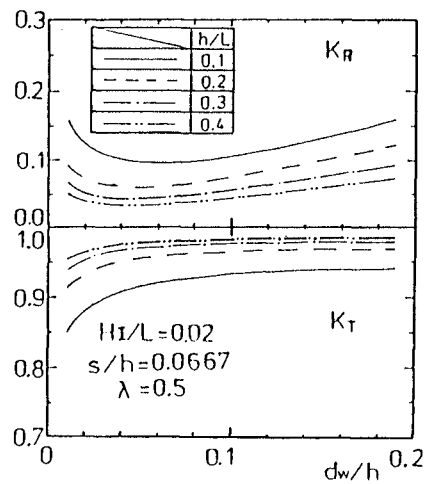

FIG. 8 REFLECTION AND TRANSMISSION COEFFICIENT VERSUS d_w/h

and lesser reflected energy.

Fig. 8 shows the variation of reflection and transmission coefficients with the ratio of wall thickness to water depth d_w/h for the various values of relative depth. In this figure, the reflection and transmission coefficients are not sensitive to the wall thickness. The reflection coefficient decreases as relative water depth increases, and the transmission coefficient increases slightly as relative water depth increases.

4.3 The Force Coefficient

Fig. 9 shows the force coefficient f of Eq.7 versus the wave steepness for the various values of relative depth. The force coefficient increases with wave steepness as expected. The theoretical values which are indicated by the lines on the chart show good agreement with the experimental results within the range of lower values of wave steepness.

Fig. 10 shows the force coefficient versus the void ratio λ for the various values of relative depth. In this figure, the force coefficient decreases at first, then keeps almost constant and increases afterwards, as the void ratio increases. It decreases as the wall thickness increases, and as relative water depth increases.

5 CONCLUSIONS

There is a remarkable correlation between the head loss coefficient and Reynolds number. There is a remarkable correlation between the apparent orifice length, Keulegan-Carpenter number and wave length.

We suggested that the head loss coefficient is given as a function of the void ratio, wall thickness and slit width. We suggested that the apparent orifice length is given as a function of wall thickness.

The theoretical results using these experimental coefficients show relatively good agreement with the results of the experiment.

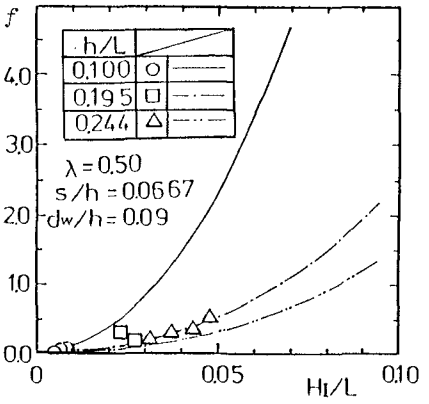

FIG. 9 FORCE COEFFICIENT VERSUS WAVE STEEPNESS

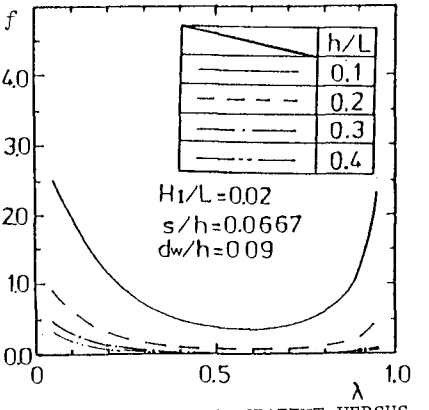

FIG. 10 FORCE COEFFICIENT VERSUS VOID RATIO

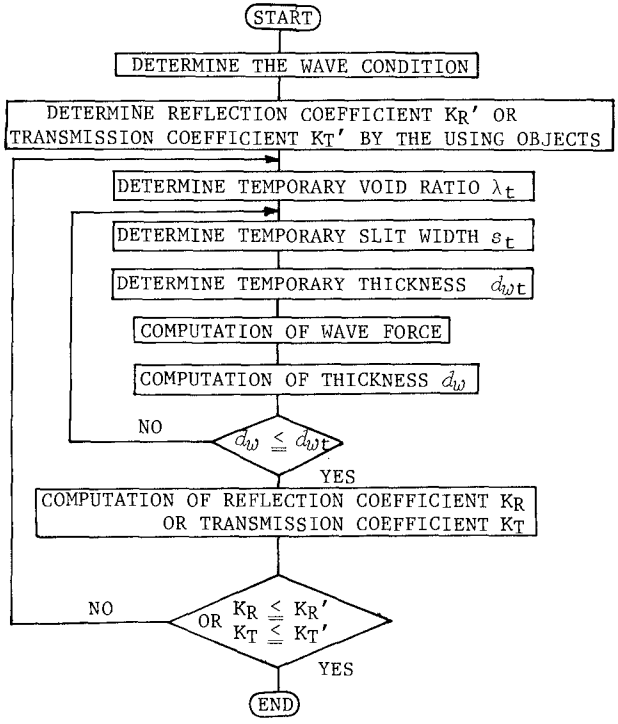

FIG. 11 DESIGN PROCESS OF THE SINGLE PERVIOUS WALL

The optimum void ratio of the slotted wall lies around 0.2 to 0.4 and corresponds to the required conditions of the wall, since the rates of change of the force, reflection and transmission coefficients are large in that range. It can therefore be concluded that using the design process for a single pervious wall to serve as a breakwater, as indicated in Fig. 11 will be effective. The initial value of the void ratio, slit width and thickness may be obtained from Fig. 6 to 8 . However, the actual wall thickness must take into account the level of wave force. In the case of a constant wall thickness, the reflection coefficient can be decreased by increasing the slit width.

REFERENCES

1) Kondo, H. :Analysis of breakwaters having two porous walls, Coastal Structures '79, ASCE, vol.II, 962-977, 1979.

CHAPTER 173

Wave Interception by Sea-Balloon Breakwater

by

Takahiko Uwatoko , Takeshi Ijima , Yukimitsu Ushifusa
and Haruyuki Kojima

Abstract

When a submerged, flexible bag is filled with air about 60～70 % of its full volume (it is called " sea-balloon "), it has a stable shape with vertical axis of symmetry,on which several vertical wrinkles appear with folds of membrane. If two or more such sea-balloons are arranged to the direction of wave travel and connected pneumatically,balloons are deformed periodically and the air flows reciprocally in connecting pipe, following to the fluid pressure fluctuation due to incident waves. Such a system of sea-balloon intercepts incident waves effectively (it is called " sea-balloon breakwater ").

The wave interception by the breakwater is analyzed numerically by three-dimensional boundary integral method, assuming that the fluid motions both in- and out-side of the balloon are potential and that the tension in balloon membrane is proportional to the apparent elongation of membrane with virtual elastic constant.

After analysis and experiments, it is made clear that in relatively long waves the incident wave is canceled by the radiation wave which is generated by volumetric change of sea-balloons, being affected by air-flow resistance in connecting pipe. In short waves, sea-balloons seem to behave like as rigid piles and the incident wave is absorbed by air-flow resistance in pipe and by the turbulence of fluid motion around balloons. Moreover, the effect of gaps between sea-balloons along wave crest on wave interception for relatively long waves is expressed by a simple empirical formula, by which the transmission coefficients at various types of sea-balloon breakwater is easily estimated by two-dimensional computation.

For the improvement of wave interception effect and from the point of practical use, the effects of other sea-balloon breakwater system are investigated by two-dimensional computation and experiments.

1. Introduction

Usual breakwaters are rigid and fixed structures to protect harbours against waves. In contrast with such a rigid structure, the floating breakwater intercepts waves by radiation waves induced by its floating

(1) Associate Professor of Civil Engineering, O-ita National College of Technology, O-ita, Japan
(2) Professor Emeritus, Kyushu University, Fukuoka, Japan
(3) Technical Assistant, Faculty of Engineering,Kyushu University, Japan
(4) Research Assistant, Faculty of Engineering, Kyushu University, Japan

motion. And the radiation wave is generated not only by floating motion of rigid structures but also by the deformation of flexible bodies due to incident waves. Therefore, if the breakwater of flexible structure is able to generate radiation waves of large amplitude enough to reduce the diffraction waves or transmitted waves, it will be able to intercept effectively the incident wave. The authors propose a method of wave interception by flexible bodies in completely submerged state and intend to make clear the wave interception mechanism.

Few years ago, French[1] proposed a method of electric power generation, where a series of flexible air bags in semi-submerged state induces air-flow in the duct under air bags and the air-flow generates electric power. French's air-bag system seems to be similar to the authors' method but is quite different in that the former is semi-submerged, partly exposed in atmosphere and each bag is not isolated but in contact with each other in wave direction. Seymour and Hanes[2] tried to reduce the transmitted waves by great many small, moored balls but they were in effect only to waves of shorter periods than two or three seconds.

2. Construction of the Authors' Method[3]

If a bag 1, as shown in Fig.1, with semi-spherical upper part and cylindrical lower part made by thin, flexible membrane is submerged and filled with air about 60 % of its full volume, it shows a stable shape with vertical axis of symmetry O-O' in Fig.2, which is called " sea-balloon". Points M and M' are inflection points between upper and lower part, where the former is almost spherical and the latter seems like a neck. The air pressure inside the balloon is equal to the hydrostatic pressure at the depth of inflection point M and M'. The most important feature of the sea-balloon is the existence of several vertical wrinkles " 3 " with folds of membrane, as shown by the cross-section

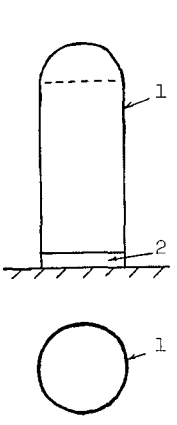

Fig.1 Sea-balloon membrane.

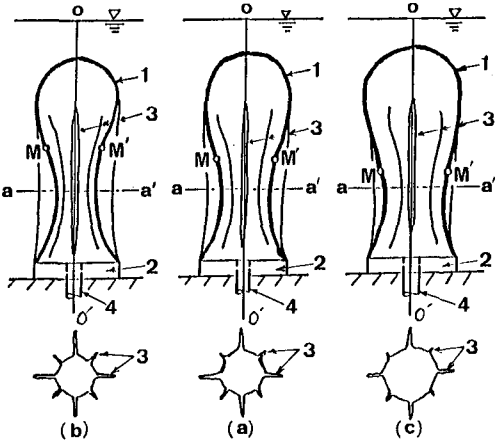

Fig.2 Shape of sea-balloon.

through horizontal plane a-a'. If the air flows out or flows in through the pipe " 4 ", the wrinkles close and grow larger or open and decay smaller, and the volumetric change of the balloon is caused not by the elastic deformation of the balloon membrane but by the growing and the decaying of wrinkles. Therefore, the membrane needs not to be elastic but to be flexible. Many systems of a pair of sea-balloon connected pneumatically by a pipe with length B, if arranged in parallel with the incident wave crest, constitute a " sea-balloon breakwater ", as shown in Fig.3 .

If a train of waves comes into the breakwater, the fluid pressure fluctuation induces shape- and volume-change of sea-balloons and generate radiation waves which affect and decay the transmitted waves. At the same time, a part of wave energy is dissipated by air-flow turbulence in the connecting pipe.

3. Wave Interception Performance of Sea-Balloon Breakwater by Experiments and Calculations [3]

Wave transmission coefficient K_t (= transmitted wave height/incident wave height) at a sea-balloon system fixed on the sea bottom were measured in wave channel with water depth h(=35cm) and width W(=15cm). Two balloons of diameter R(= 11cm),height F(= 20cm),volume of air Q(= 1000cc) made by rubber membrane were attached to base disks with distance B(=3h=105cm) and crown depth A(=2cm from water surface),where the base disks were fixed on the bottom with height c(=13cm) and h_o(=0). Both balloons were connected by a pipe of diameter d(=2.2cm). Measured transmission coefficients are shown with respect to relative depth h/L in Fig.4, where L is wave length and circle O is for the sea-balloon

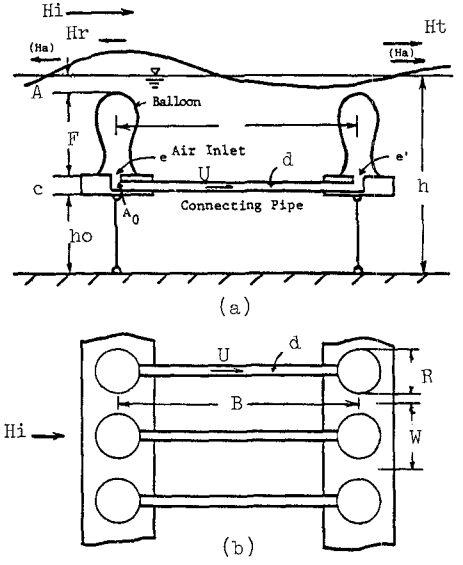

Fig.3 Construction view of sea-balloon breakwater.

system, square □ is for the case when the connecting pipe is removed and balloons are isolated, black square ■ is for the case when sea-balloons are replaced by wooden rigid bodies of the same shape.

It can be seen from the figure that K_t at rigid bodies varies around the value 0.9 without any tendency and K_t at isolated balloons steadily decreases with h/L for $h/L \geq 0.20$. At sea-balloon system, K_t shows the minimum at $h/L \fallingdotseq 0.17$ and then a steep decrease from $h/L \geq 0.3$. Such a tendency is remarkable for the case of a pair of double sea-balloons as shown by black circle ●. These tendencies in the change of K_t with h/L are characteristic in the facts that for long wave region ($h/L < 0.3$) the effect of radiation waves prevails due to the volume change of paired sea-balloons and for short wave region ($h/L \geq 0.3$) the interception effect of nearly isolated submerged balloons prevails by small deformation in shapes.

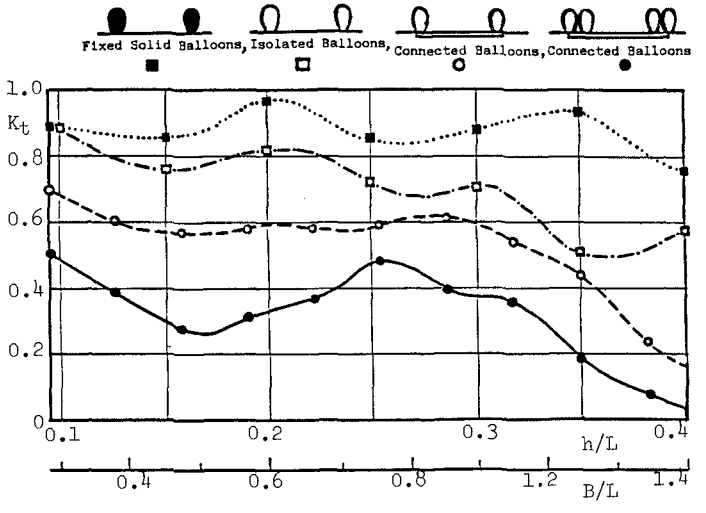

Fig.4 Measured transmission coefficients at fixed solid balloon and various sea-balloon systems.

Fig.5 is another example of measured K_t at sea-balloon breakwater which consists of sea-balloon system with six balloons in floating state moored in wave channel with depth h = 80cm, width W = 60cm. Measured K_t shows the effect of balloon distance B for the height of balloon F = 20cm, volume V = 700cc and crown depth A = 2cm. The distance B is taken as 1.5h and 2.0h. Horizontal axis is shown by $kh = 2\pi h/L$ and B/L for B/h = 1.5 and 2.0.

It can be seen that the minimum point of K_t with respect to kh moves to lower values of kh for larger value of B/h. Furthermore, the minimum point of K_t appears $B/L \fallingdotseq 0.5$ for both value of B/h.

The authors have performed three-dimensional numerical analysis to estimate K_t and reflection coefficient K_r and to clarify the mechanism of wave interception, assuming that the fluid motions outside and inside of the balloons are both potential and then using the boundary integral

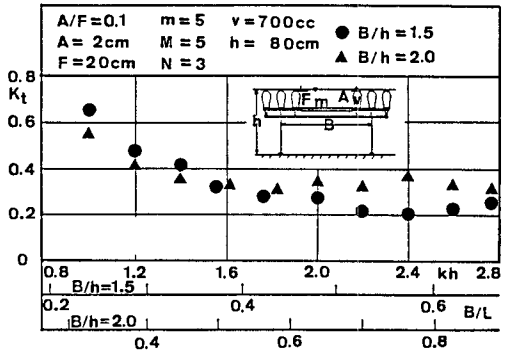

Fig.5 Effect of the distance between grouped balloons on the transmission coefficients.

method by Green's identity formula[4]. Wave interception effects remarkably appear on waves of length about 2·B and waves shorter than 2·B decay monotonically with shortening of wave length as shown in Fig.6, where K_t and K_r are computed (full and broken lines) and measured (plotted for K_t only) for breakwater by a pair of balloons with the same sizes and conditions as those in Fig.4 . Following to the proposed method, the sea-balloon systems of a pair of balloons with different distances between fore- and rear-balloon are computed to give transmission coefficients, which are found to be in good agreement with measured ones.

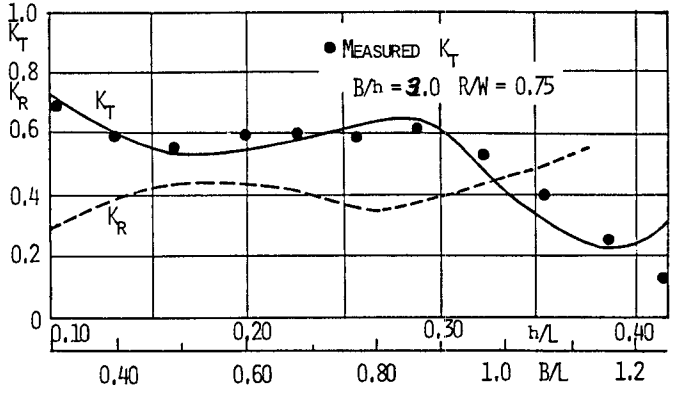

Fig.6 Measured and calculated transmission and reflection coefficients at a system of two balloons.

Fig.7 is the calculated and measured transmission coefficients at a pair of isolated balloons. Comparing Fig.6 with Fig.7, it is made clear that the radiation wave due to the volumetric change of balloons plays the important role of wave interception for relatively long waves.

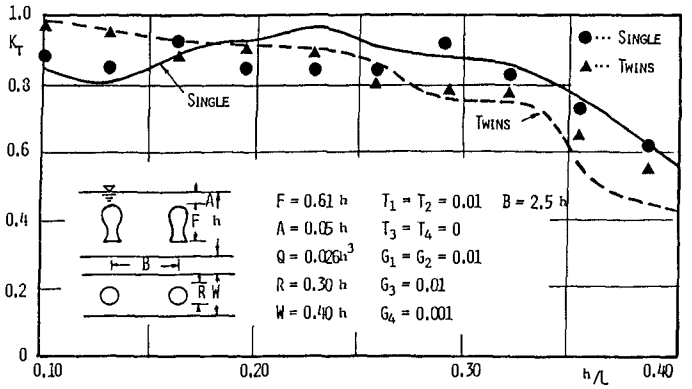

Fig.7 Measured and calculated transmission coefficients at single and a pair of isolated balloons.

4. The Principle of Wave Interception[3)]

The principle of wave interception at a sea-balloon breakwater is interpreted in the following ways as illustrated in Fig.8 :

(1) When the incident wave comes from the left of the figure, the wave crest is at the left balloon and the wave trough is near the right balloon, the fluid pressure around the left and the right balloons is respectively higher and lower than the hydrostatic pressure. When both of the balloons are isolated one by one, their volumes are invariable, though their shapes vary, and most of the incident wave energy travels through the sea-balloon breakwater and the remaining part is reflected. However, if both balloons are connected pneumatically by a pipe, the air in the left one flows to the right due to the pressure gradient between them. Then, it follows that the left and right balloons are compressed and expanded in volume, respectively, and the free water surface falls around the left balloon and rises around the right balloon. The periodical repitition of such a fluctuation of water surface produces the radiation wave, which is composed of two component waves, the one proceeding to the right and the other to the left with the same amplitude as each other. The component wave to the left constitutes the main part of the reflected wave at the breakwater and the one to the right cancels the transmitted wave which is to appear if both balloons are isolated, because of the inverse phase relation between the two waves. Consequently,it is necessary to make the radiation wave amplitude grow as large as possible, in order to improve the wave interception effect of the sea-balloon breakwater.

(2) The equilibrium shape of the sea-balloon is shown by a thick full line in Fig.2(a). Then, as shown in Fig.2(b),(c), if the air inside the balloon flows out through the air inlet " 4 ", the folds grow and the cross-section by the horizontal plane a-a' decays and if the air flows in, the folds decay and the cross-section grows. In this way, most of the volume changes of the sea-balloon occur at its neck part.

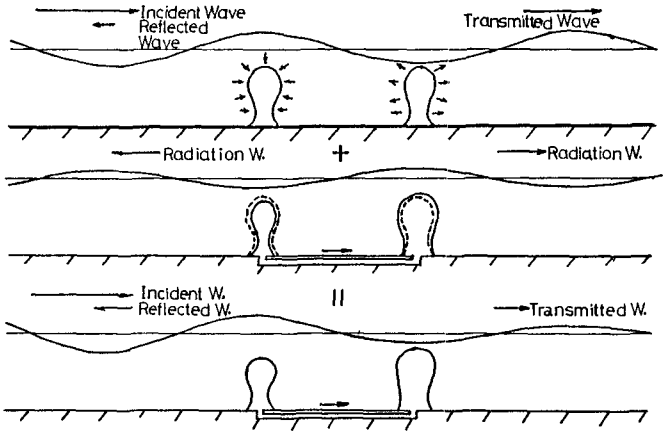

Fig.8 Principle of wave interception by radiation waves.

5. Effect of Gap Width between Adjacent Sea-Balloon Systems on Wave Interception[3)]

So far the width W of fluid region of sea-balloon system and the diameter of balloon R in Fig.3 have been held as constant. However, the wave interception ability of sea-balloon breakwater is greatly influenced by the gap width (W - R) between adjacent sea-balloon systems.

(1) Empirical results on the effect of gap width

In Fig.9, full lines represent computed transmission coefficients at sea-balloon system of three balloons with the same sizes as those in Fig.4, and only the channel width is changed as W/h = 0.30, 0.40, 0.50, 0.75 for balloon diameter R = 0.3h and so as R/W = 1.0, 0.75, 0.60, 0.40,respectively. In the same figure,measured transmission coefficients are illustrated for R/W = 0.90, 0.70, 0.50 and 0.44 .

Comparing the measured with computed values, it is deduced that transmission coefficients at various gap width is empirically expressed as follows:

$$K_t = (W/R)^{1/2} \cdot K_t^* + (W/R - 1.0) \cdot h/L \qquad (1)$$

where K_t^* is the transmission coefficient at W/R = 1.0.

Above representation should be regarded as available for $W/R < 2.0$ and $h/L < 0.4$.

(2) Two-dimensional analysis for sea-balloon system

Since the shape of sea-balloon is, as stated before, three-dimensional with vertical axis of symmetry, the dynamical analysis should be three-dimensional. However, for simplicity, assuming the balloon shape to be two-dimensional with the same cross-section as the three-dimensional one, the breakwater effect of that assumed air bag is analyzed as two-dimensional problem.

(3) Comparison of the results by three-dimensional analysis with those by two-dimensional one and with empirical formula

The broken line in Fig.9 is the computed transmission coefficient by two-dimensional analysis for the same size as those for three-dimensional analysis. It is found that this line almost coincides with the full line by three-dimensional analysis for R/W = 1.0 and it is suggested that the transmission coefficients will be computed through Eq.(1), where K_t^* is replaced by the one obtained by two-dimensional analysis.

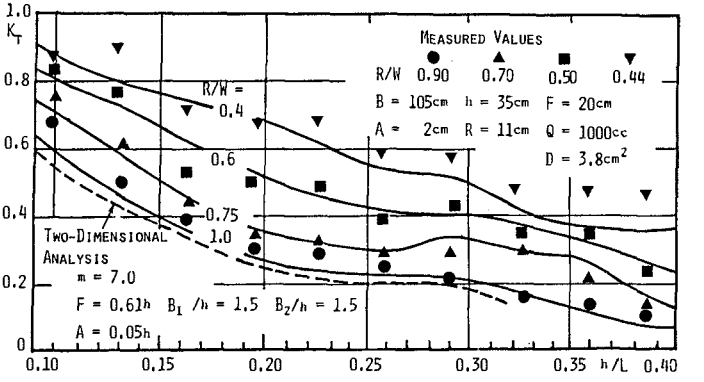

Fig.9 Transmission coefficients at a system of three balloons.

6. The Improvement of Wave Interception Effect of Sea-Balloon Breakwater[3]

In the above description, it is made clear that a pair of sea-balloons connected pneumatically with a distance B between the fore- and the rear-balloons in the direction of wave travel, as shown in Fig.3, has the performance to intercept waves as a kind of breakwater with low reflected waves. For the improvement of wave interception effect of sea-balloon system, the following method are developed by the experiments and the computations of two-dimensional boundary integrals by Green's identity formula.[3][4]

(i) Each balloon is sheltered by a vertical pipe.

(ii) The grouped balloons with small distances or gaps are used in place of the system of the paired balloons.

(iii) The horizontal frame to which balloons and pipes are attached is made impermeable.

(iv) As shown in Fig.10, an impermeable plate is moored in submerged and horizontal conditions in front of the sea-balloon breakwater, instead of making the frame impermeable.

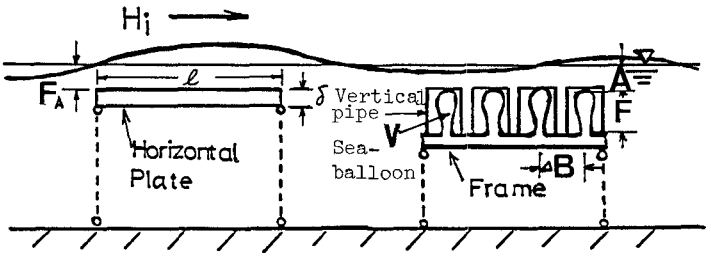

Fig.10 Moored horizontal plate and moored groupe of sea-balloons with vertical pipes.

By the method (i), the vertical pipe has a role to regulate the fluid flow pattern around balloons so as to generate radiation wave efficiently. In the method (ii) , the transmission coefficient with respect to relative depth h/L decreases monotonically with the increase of h/L . In the method (iii), the impermeable frame partly reflects relatively long waves and lowers the transmitted waves. By the method (iv), a flat horizontal plate splits a long incident wave into short waves, which are absorbed effectively by the proposed breakwater of grouped sea-balloons.

6.1 Wave Interception by the Vertical Pipes [5]

Fig.11 (a),(b) illustrates the side and plane views of a system of the sea-balloon breakwater constructed by a pair of two balloons with ΔB =20cm, B =(1.5,2.0,3.0,4.5)h, connected by a pipe with inner diameter Di = 25mm and fixed on the bottom of the wave channel of depth h =35cm, width W = 30cm. The sea-balloon is R = 10cm in diameter, F = 21cm in height, V = 1200cc in volume and A = 4.0cm in crown depth.

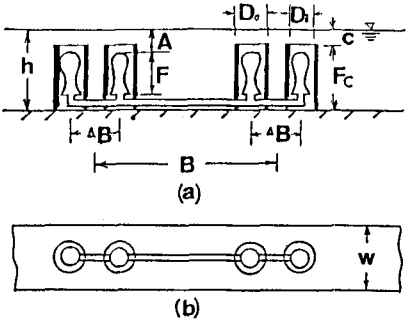

Fig.11 Sea-balloon breakwater provided with vertical pipes.

Fig.12 is the measured transmission coefficient K_t with respect to relative water depth h/L for the above sea-balloon breakwater without a vertical pipe. It is found that K_t falls slowly down with the increase of h/L, showing the minimum value for each B/h, then growing up to the maximum value and finally decaying. For larger values of B/h, the minimum value of K_t appears at smaller value of h/L with K_t value greater than that for smaller B/h.

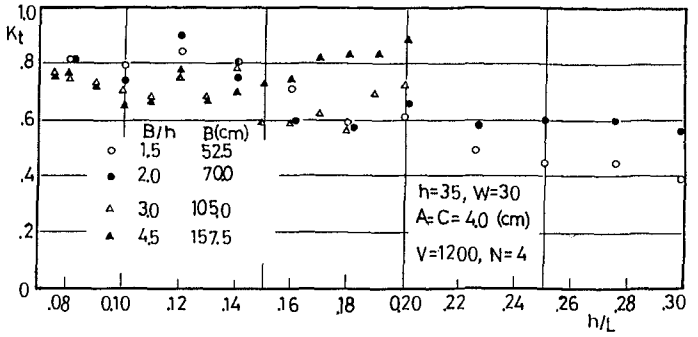

Fig.12 Transmission coefficient at paired-balloon breakwater without vertical pipes.

The transmission coefficients K_t at the sea-balloon breakwater, whose balloons are provided with the vertical pipe of inner diameter Di= 15cm, outer diameter Do = 16.5cm, height Fc = 31.0cm, are measured as shown in Fig.13, where the crown depth of the pipe is the same as that of balloon. Comparing with Fig.12, the effect of the pipes is remarkable, especially for large h/L.

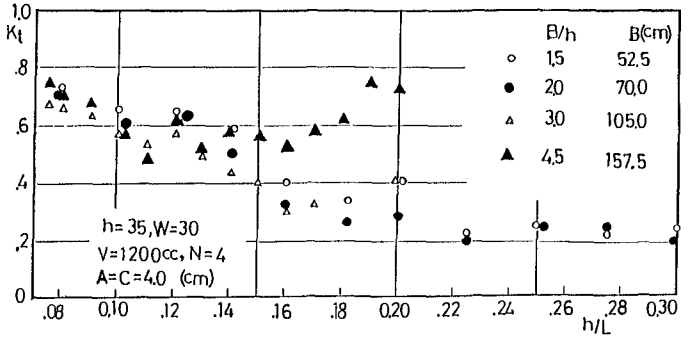

Fig.13 Transmission coefficient at paired-balloon breakwater with vertical pipes.

Fig.14 shows the calculated transmission coefficient for the sea-balloon breakwater whose balloons are provided with the vertical pipe of inner diameter Di = 0.5h, outer diameter Do = 0.6h, height Fc = 0.65h and for the one without the vertical pipe. These systems are constructed by a pair of balloon with B = (3.0,4.0)h, connected by a pipe and assumed to be fixed on the bottom of the wave channel of depth h = 35cm, width W = 30cm. The sea-balloon is R = 0.30h in diameter, F = 0.61h in height, V = 0.13h in volume and A = 0.35h in crown depth. K_t are computed by the method of two-dimensional analysis and it is found that the tendencies of K_t for relatively long waves are similar to those of measured values in Fig.12 and Fig.13 .

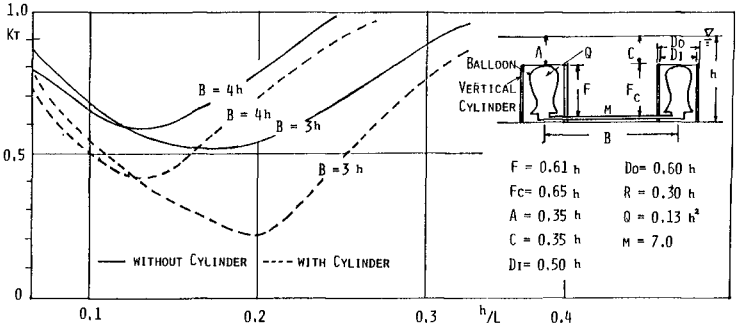

Fig.14 Calculated transmission coefficients at a paired-balloon breakwater with or without vertical pipes.

The above results of experiments and computations are interpreted in the following ways as illustrated in Fig.15. Fig.15(a) shows schematical flow patterns around the balloon,where the shape of the balloon in still state by chain line changes to the shape by full line following to the air inflow and changes to the shape by broken line after the air flows out. Corresponding to the in- and out-flow of the air, arrow lines illustrate the flow patterns around the balloon. And the expansion and reduction of the neck will induce mainly the horizontal direction of fluid flow, which is not so effective to induce the vertical flow for

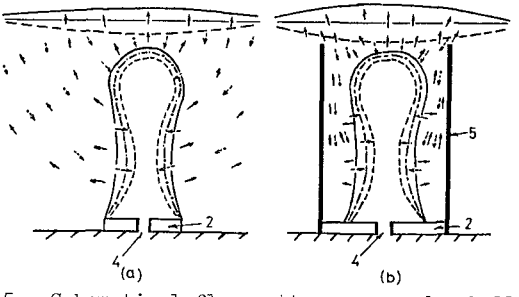

Fig.15 Schematical flow patterns around a balloon.

the water surface fluctuation. While, if the balloon is surrounded with a vertical pipe as shown in Fig.15(b), the horizontal flow due to the volume change of the balloon will be regulated to the vertical flow and then accelerate the formation of surface fluctuation, that is, the generation of radiation waves. It is certified by calculation as shown in Fig.16 that the coefficients of radiation wave height for the sea-balloon system with vertical pipe with the same sizes as those in Fig.14 are larger than those for the sea-balloon without vertical pipe.[3)]

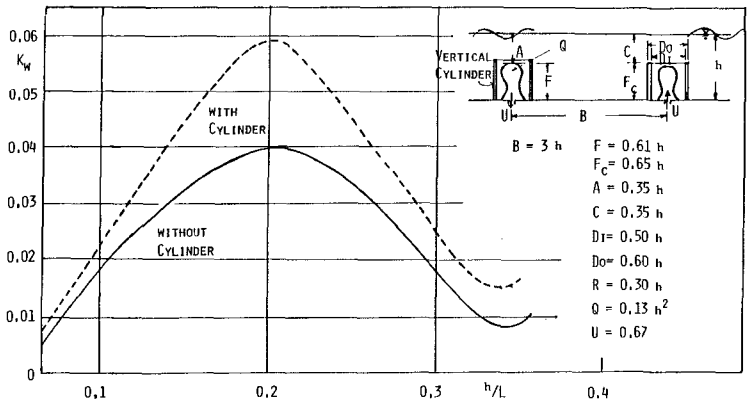

Fig.16 Computed radiation wave height by a pair of balloon with or without vertical pipe.

6.2 Effect of Submerged Horizontal Plate

The question is how to interpret the effect of the submerged plate on the wave interception of the sea-balloon breakwater. To answer the question, a flat plate is submerged and moored at 50cm in front of sea-balloon breakwater as shown in Fig.10. The length of every structure is taken as ℓ = 40.7cm, the depth of upper surface of the plate F_A is as 4.4cm and thickness of the fixed and moored plate δ is 2.4cm. A system of four balloons as shown in Fig.10 with equal distance ΔB to the direction of wave travel is investigated, where balloons are sheltered by pipes. In the experiment, four balloons with diameter R =6.0cm, height F = 10cm, volume V = 175cc are sheltered by vertical pipes with inner diameter Di =8.3cm, outer diameter Do = 8.9cm, height Fc = 14.5cm and arranged with distance ΔB = 13cm. The breakwater system is moored in submerged state with the crown depth of a balloon and pipe as A = C = 4.0cm, in wave channel with depth h = 35cm, width W = 30cm. As shown in Fig.17, the transmission coefficients are measured for five conditions of sea-balloon system with constant incident wave height Hi = 4.0cm as follows:

(1)○ is the case of balloon fixed to the permeable frame and represents the effect of sea-balloon only.

(2)-○- shows the case when the horizontal plate is moored in front of the balloon-breakwater.

(3) □ shows the case when sea-balloons with vertical pipes are fixed to the permeable frame.
(4) ■ is the case when the above permeable frame is changed to impermeable.
(5) -□- is for the case whem the flat plate is moored in front of the balloons with vertical pipes attached to a permeable frame.

The measured K_t values are shown in Fig.17 and the results are explained as follows:
(i) It is clear for case (2) that the moored plate is effective even to the relatively long waves.
(ii) It is shown for case (3) that the vertical pipe is more effective than the flat plate, particularly to the short waves.
(iii) It is shown for case (4) that the horizontal flat plate as the balloon frame is effective to the relatively long waves.
(iv) It is clear for case (5) that the flat plate moored in front of the balloons with vertical pipes is effective to the waves of $h/L > 0.15 \sim 0.2$.

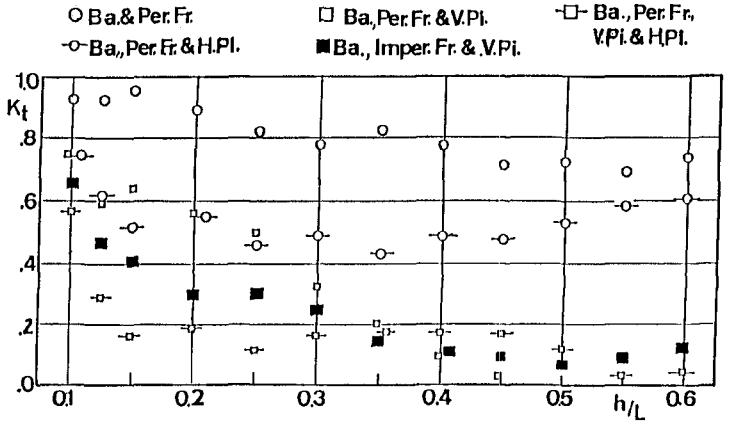

Fig.17 Measured transmission coefficients at sea-balloon breakwater with vertical pipe, permeable or impermeable frame, and with or without horizontal plate.

This means that for waves with small h/L the horizontal flat plate separated from the sea-balloon breakwater is more effective than when it is used as the frame. The reason why the separated plate is so effective is that the incident wave grows in height in fluid region above the plate and the ratio of wave height to wave length becomes so large that the wave deforms sharply due to the nonlinearity with small value of h/L. And after passing the flat plate, the sharply deformed wave splits into two or three trains of solitons, which advance in deep water region and are absorbed effectively by the breakwater of grouped balloons.

A similar tendency of measured K_t is shown theoretically in Fig.18, which is calculated by two-dimensional analysis for similar conditions of sea-balloon systems as shown in Fig.14 and Fig.17 .

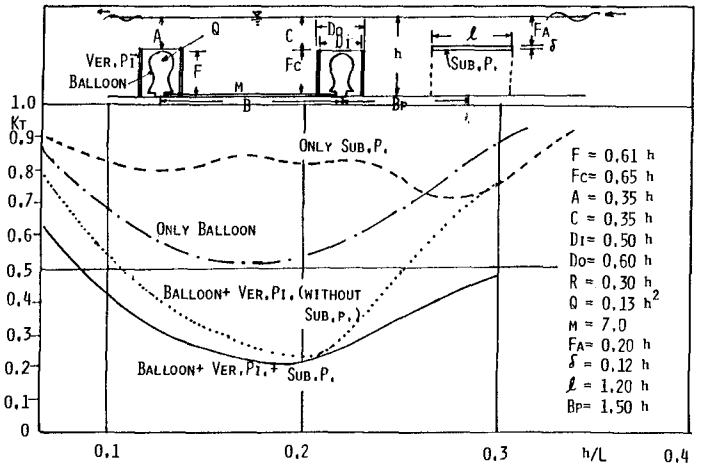

Fig.18 Calculated transmission coefficients at submerged plate and at sea-balloon breakwater with or without vertical pipe, and with or without horizontal plate.

7. Conclusions and Acknowlegement

Above description is summarized as follows:

(1) It is suggested in experiments that almost of the repeating deformation of sea-balloon induced by incident waves is not the elastic deformation of the membrane but caused by the alternate opening and closing of folds along wrinkles on the membrane of balloon.
Therefore,it is certified by experiments on transmission and reflection coefficients that the sea-balloon by polyethylene membrane is similarly effective to the one by rubber membrane. This means that the necessary condition for membrane is not elasticity but flexibility.

(2) Furthermore , fluid motions in- and out-side of sea-balloon are assumed to be potential, so that the boundary integral method by Green's identity formula is applied to numerical analysis of the problem.

(3) After the examination on the accuracy of numerical computation, the results by the authors'method of computation will be almost satisfactory for the estimation of transmission and reflection coefficients in the region of relatively long waves, where the radiation waves due to the deformation of sea-balloon has prevailing effect on wave interception by sea-balloon system.

(4) Following to the proposed method,sea-balloon systems of two balloons with distances between fore- and rear-balloon are computed to give transmission coefficients, which are found to be in good agreement with measured ones. It is clear by the experiments and calculations that the sea-balloon system is able to intercept waves with low reflected waves.

(5) To make clear the mechanism of wave interception, the radiation wave component is computed for the case of two sea-balloons system. After analysis, it becomes clear that the interception of relatively long wave by sea-balloon breakwater is interpreted by the fact that the radiation wave induced by the volume change of sea-balloon under incident wave is

canceled by the transmitted wave at sea-balloon without volume change, due to the anti-phase relation between them. To the contrary, the reflected wave by sea-balloon system without volume change is so small compared with the radiation wave that the resulting reflection coefficient is determined mainly by the latter.
(6) It is found that the transmission coefficient at a sea-balloon breakwater with arbitrary gap width between adjacent sea-balloon system is expressed by a simple empirical formula in terms of the transmission coefficient at sea-balloon breakwater without gap width, the relative water depth and the ratio of gap width to the balloon diameter. Accordingly, the transmission coefficient at sea-balloon breakwater with arbitrary gap width can be easily estimated by simple computation for the virtual two-dimensional sea-balloon breakwater, and various properties of the breakwater are estimated by two-dimensional computation.
(7) A method of sheltering each balloon by a vertical pipe is successful to depress the transmission coefficient for short wave length. This seems to be due to the flow regulation around the balloon and to the effective generation of radiation waves.
(8) The submerged flat plate is more effective to long waves when it is moored in front of the sea-balloon breakwater. This seems to be due not only to the reflection effect of the submerged flat plate, but also to the splitting of long incident waves into two or three short waves which are absorbed individually by the sea-balloon breakwater.

It is concluded that the proposed method to intercept waves by sea-balloon system with connecting pipe has the possibility to be a kind of breakwater with low reflected waves in complete submerged state.

The authors express heartfelt thanks to the following gentlemen who cooperated in experimental works and computations in ages of student at Kyushu University: Mr.Toshiharu Tanaka(Nippon Kokan Co.), Mr.Hitoshi Kitayama (Ministry of Transportation), Mr.Takeshi Nakatsuka (Taisei Kensetsu Co.), Mr.Mitsuyoshi Zaizen (Takenaka Doboku Co.), Mr.Yasuhiro Yoshizuka (Toyo Kensetsu Co.), Mr.Masayuki Niki (The official at Fukuoka Prefecture), Mr.Yuuichi Nishiuchi (The master course student).

References

1) Chaplin R.V. and M.J.French: Aspects of the French flexible device, Power from sea waves, Academic Press, pp.404-424, 1980.
2) Seymour R.J. and D.M. Hanes: Performance analysis of tethered float breakwater, Proc. ASCE, vol.105,ww.3 pp.265-280, 1979.
3) Ijima, T., T.Uwatoko and Y.Ushifusa: Wave interception by sea-balloon breakwater, Memoirs of the Faculty of Engineering Kyushu University , vol.45, No.4, pp.357-392, Dec.1985.
4) Ijima, T., A.Yoshida and H.Kitayama: Numerical analysis on wave reflection in harbours provided with perforated quay wall, Proc.29th. Conf. on coastal eng. JSCE,pp.183-187, Nov.1982.
5) Ijima, T., T.Uwatoko, Y.Ushifusa and H.Kojima: Experiments on the improvement of wave interception effect of sea-balloon breakwater, Memoirs of the Faculty of Engineering Kyushu University, vol.46,No.2, pp.193-206, June 1986.

CHAPTER 174

STRUCTURAL BEHAVIOUR OF TEN TON DOLOS ARMOUR UNITS

S.M. Uzumeri[1] and R. Basset[2]

ABSTRACT

This paper summarizes the results of a research program conducted to examine the structural behaviour of nine full scale ten ton Dolos armour units subjected to a well defined loading regime. Three unreinforced and six reinforced units were tested. The effects of three different types of reinforcement (rebars, hollow steel tubes, and prestressing bars) on the behaviour of the units was determined. Different design approaches for armour units are discussed and one possible new approach is presented.

1. INTRODUCTION

Rubble-mound breakwaters have been used extensively in Canada and throughout the world for harbour protection. The seaward faces of such breakwaters can be subjected to extremely destructive wave actions and thus require some form of protection. This protection is achieved by placing a cover, called the 'armour layer', over the breakwater to help dissipate wave energy and thus protect the breakwater core from direct wave attack. In environmentally demanding locations the armour layer usually consists of concrete armour units which have some interlocking capability. One of the most common is the **'DOLOS'** armour unit developed by Eric M. Merrifield and first used in South Africa (Merrifield, 1968). These units dissipate energy very efficiently and can be manufactured with standard construction contractors' equipment.

During the 1970's a series of failures occurred in breakwaters utilizing Dolosse. One likely cause for these failures was the fracture of individual armour units which lessened their interlocking capability and thus lowered their hydraulic efficiency.

As a result of the situation described it was decided to examine the strength and behaviour of Dolosse from a structural engineering perspective. This paper summarizes the results of a research program (Uzumeri et. al. 1985) conducted to examine the structural behaviour of nine full-scale Dolos armour units subjected to well defined loading regimes. The major variable considered in this project was the effect of different types of reinforcement on the structural behaviour of the armour units.

[1]Professor and Chairman, and [2]Research Engineer
Department of Civil Engineering, University of Toronto,
35 St. George St., Toronto, Ontario, CANADA, M5S 1A4.

2. EXPERIMENTAL PROGRAM

2.1 Specimens

A unit weighing ten tons (proportions shown in Figure 1) was selected for the test program so as to eliminate any scale effects. A total of nine units (designated specimens 0 through 8) were tested with specimen 0 being used as a pilot test to gain familiarity with the handling and testing of the units. Four different types of units were studied in the test program as follows:

Specimens 1,2,3	Unreinforced
Specimens 0,4,5,6	Reinforced with eight rebars
Specimen 7	Reinforced with a steel tube
Specimen 8	Prestressed, Post-tensioned

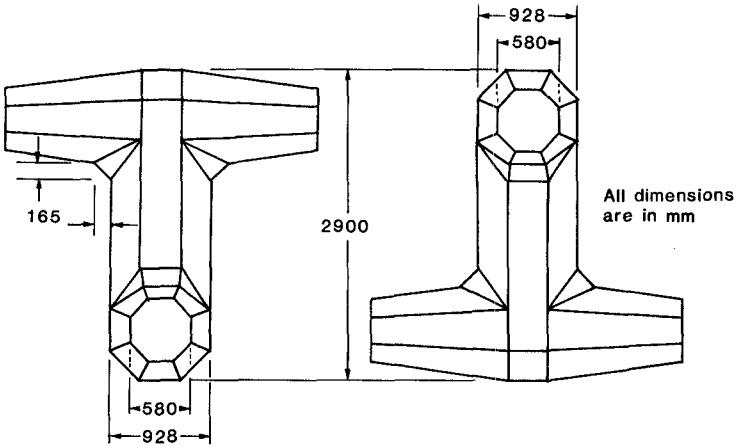

Figure 1: Proportions of Test Unit

All of the reinforcement had a minimum clear cover of 100 mm. The layout of the reinforcement was chosen so as to provide maximum structural benefit combined with ease of fabrication. Table I gives the reinforcement details for the test units.

2.2 Materials

2.2.1 Concrete

The concrete used in this test series was obtained from a ready-mix supplier. The strength was specified to be 25 to 30 Mpa at 28 days with no air entrainment used as only the structural behaviour of the units was being investigated. Table II gives the average observed concrete properties for each of the specimens.

TABLE I

REINFORCEMENT DETAILS

Specimen	Shank Reinforcement		Fluke Reinforcement	
	Number and Type	Total Area (mm^2)	Number and Type	Total area (mm^2)
0,4,5,6	8 - 25 mm dia. rebars	4000	8 - 25 mm dia. rebars	4000
7	1 - Hollow tube 114.3 mm OD 88.9 mm ID	4054	1 - Hollow tube 63.5 mm OD 38.1 mm ID	2027
8	1 - 36 mm dia. Dywidag bar	1018	1 - 26 mm dia. Dywidag bar	548

TABLE II

AVERAGE CONCRETE PROPERTIES

Specimen	f'_c (MPa)	ε_o (mm/mm)
0	33.4	0.0022
1	50.3	0.0024
2	42.1	0.0025
3	58.7	0.0021
4	30.6	0.0017
5	25.9	0.0016
6	31.3	0.0022
7	30.9	0.0018
8	28.2	0.0022

2.2.2 Steel

Three different types of longitudinal steel (rebars, hollow steel tubes and prestressing bars) were used in this investigation. The average properties for each of these types of steel are given in Table III. Values for the rebars were obtained from a minimum of three tensile coupon tests. Since only one each of the hollow tube and prestressed units were tested, it was possible to determine the strength characteristics of the actual bar (or tube) used in the specimen. The results for the prestressing bars were obtained from tensile tests while the tube results were obtained using a compression (stub column) test.

2.3 Test Procedure

The tests were conducted in the Sandford Fleming Structural Laboratory of the Department of Civil Engineering at the University of Toronto. The laboratory contains a 5 metre by 5 metre reaction wall and an 18

TABLE III

AVERAGE LONGITUDINAL STEEL PROPERTIES

Specimen	Reinforcement Type	Area (mm^2)	f_y (MPa)	f_u (MPa)	ε_{sh} (mm/mm)
0	25 mm dia. rebars[a]	500	516	860	0.005
4,5,6	25 mm dia. rebars[a]	500	432	656	0.011
7	Hollow Tubes:				
	Shank : 114.3 mm O.D. 88.9 mm I.D.	4054	380[b]	710[c]	---
	Flukes : 63.5 mm O.D. 38.1 mm I.D.	2027	620[b]	840[c]	---
8	Dywidag prestressing bars:				
	Shank : 36 mm dia. bar	1018	899	1031	0.012
	Flukes : 26 mm dia. bar	548	976	1150	0.013

Notes: a) 8 evenly distributed bars placed on a circle of 760 mm dia.
b) 0.002 offset strain method.
c) Maximum test load.

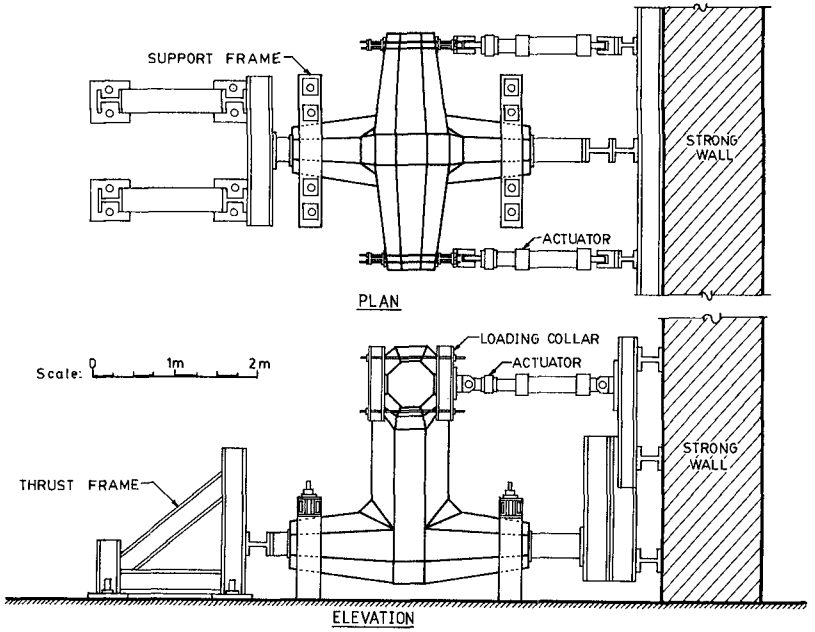

Figure 2: Test set-up

metre by 12 metre strong floor with two-way patterned anchor points on the floor. The test units were placed on the strong floor with the shank in a vertical position. The bottom fluke was supported by concrete pedestals attached to the strong floor. The top fluke was loaded by actuators reacting off the strong wall. The details of the test set-up are shown in Figure 2 while Figure 3 shows a typical test in progress.

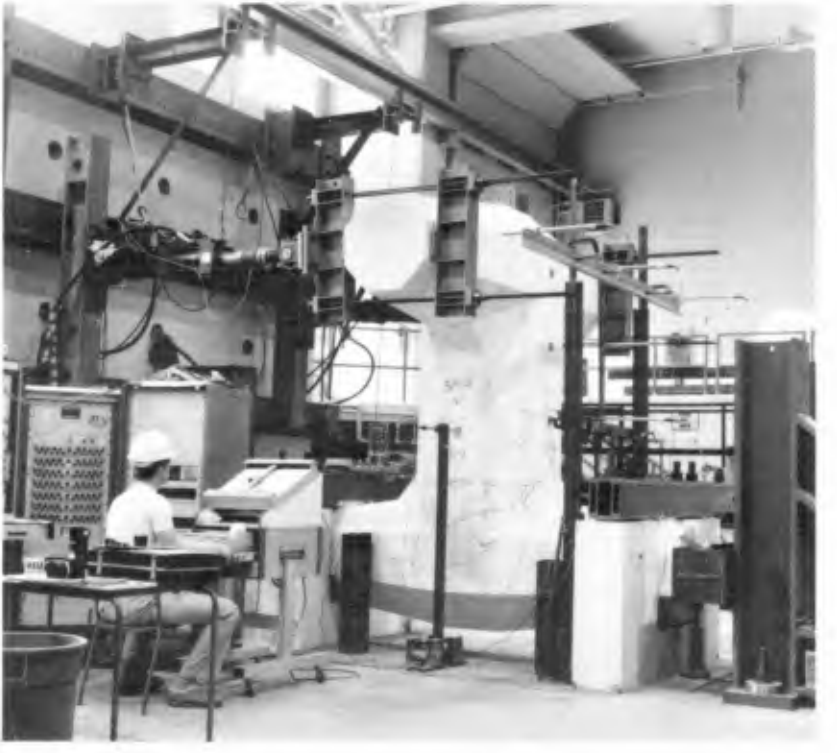

Figure 3: Test in Progress

Three different load combinations were utilized in this investigation as follows:

TYPE I Both ends of top fluke loaded. Loads equal in magnitude and direction. (Bending moment and shear forces generated in the shank).

TYPE II Both ends of top fluke loaded. Loads equal in magnitude but opposite in direction.(Pure torsion generated in the shank).

TYPE III One end of top fluke loaded. (Bending moment, shear and torsion forces generated in the shank).

A schematic representation of the loading types is given in Figure 4.

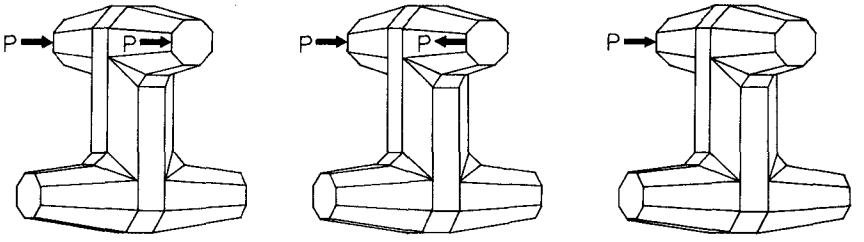

Type I: Moment and Shear | Type II: Pure Torsion | Type III: Moment, Shear and Torsion

Figure 4: Load Types Considered

For each of the three load combinations the same six stage loading sequence was used as follows:

STAGE 1 Monotonic to cracking of specimen in the initial direction.

STAGE 2 Monotonic to cracking in the direction opposite to that in Stage 1.

STAGE 3 Cycle between the two cracking displacements (+/-) for 100,000 cycles.

STAGE 4 Monotonic to overall yielding of specimen in the initial direction.

STAGE 5 Monotonic to yielding of specimen in the direction opposite to that in Stage 4.

STAGE 6 Cycle between the two yield loads until major stiffness deterioration is noted.

The total time required to test each specimen varied from two hours for the unreinforced units to an average of thirty hours for the reinforced specimens.

3. EXPERIMENTAL OBSERVATIONS

3.1 General

Table IV lists the observed cracking and ultimate load capacities for each of the specimens. Figures 5 through 13 show the appearance of the specimens at the end of the tests and the observed response for each of the nine specimens. To give an indication of behaviour, a short summary of the experimental observations for each type of reinforcement will be presented in turn.

TABLE IV

CRACKING AND ULTIMATE STRENGTH SUMMARY

Spec. No.	Force Applied by Actuators (kN)			
	At Cracking		At Ultimate	
	Initial Direction	Opposite Direction	Initial Direction	Opposite Direction
0	241	168	418	417
1	185	---	185	---
2	255	---	255	---
3	130	---	130	---
4	199	190	464	466
5	263	260	263	261
6	153	138	236	228
7	150	149	293	264
8	260	239	332	334

3.2 Unreinforced Specimens

Since specimens 1,2 and 3 were unreinforced, the first crack coincided with failure as expected. The specimens had each separated into two pieces by the end of the test. No ductility was exhibited by any of the unreinforced specimens.

3.3 8-Bar Reinforced Specimens

The four 8-bar reinforced specimens (specimens 0,4,5 and 6) exhibited similar behaviour. They were all very stiff (slightly stiffer than the unreinforced units) up to the appearance of the first crack in the initial direction. During the third stage of loading no stiffness degradation was observed.

Subsequent loading to yield in each direction caused extensive cracking in the shank and a rapid deterioration in stiffness. Maximum crack widths ranged from 30 mm to 40 mm by the end of the test.

3.4 Tube Reinforced Specimen

The first crack for specimen 7 appeared at the base of the shank as expected. Subsequent testing indicated a slight loss in stiffness with continued cycling but difficulties with the control equipment caused the first portion of the test regime to be shortened to 3100 cycles. During stages 4,5 and 6 of the load regime the stiffness deteriorated rapidly. Maximum crack widths were approximately 80 mm.

3.5 Post-Tensioned Specimen

Specimen 8 was very stiff until the first crack developed and remained

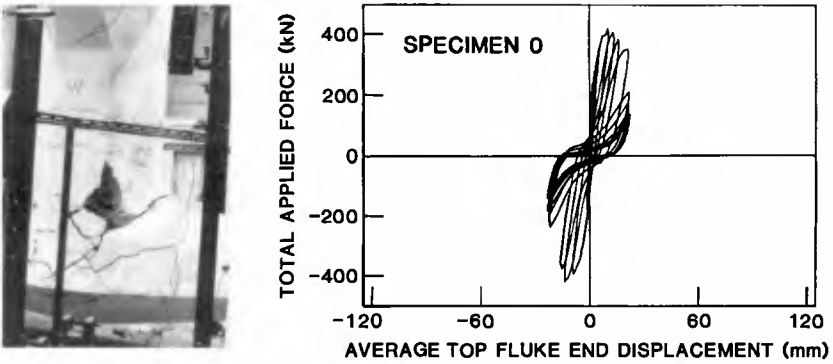

Figure 5: Final Appearance and Observed Response of Specimen 0

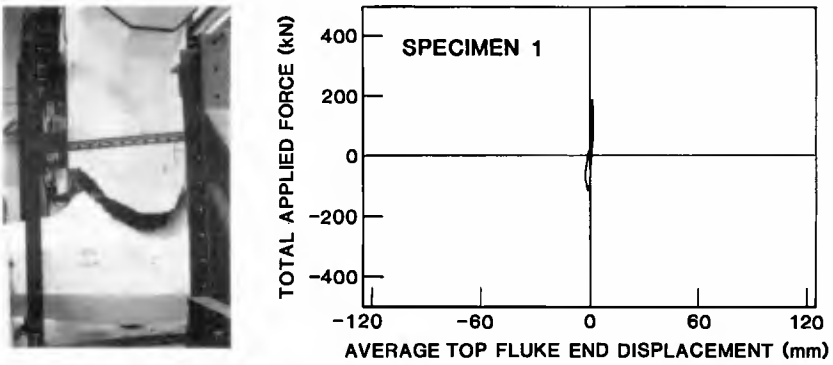

Figure 6: Final Appearance and Observed Response of Specimen 1

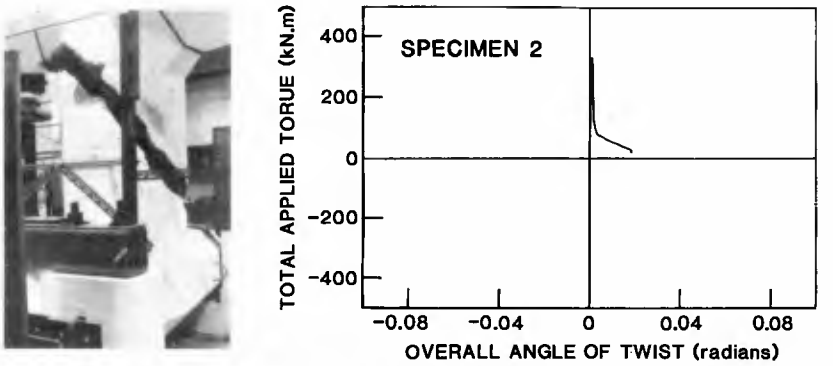

Figure 7: Final Appearance and Observed Response of Specimen 2

Figure 8: Final Appearance and Observed Response of Specimen 3

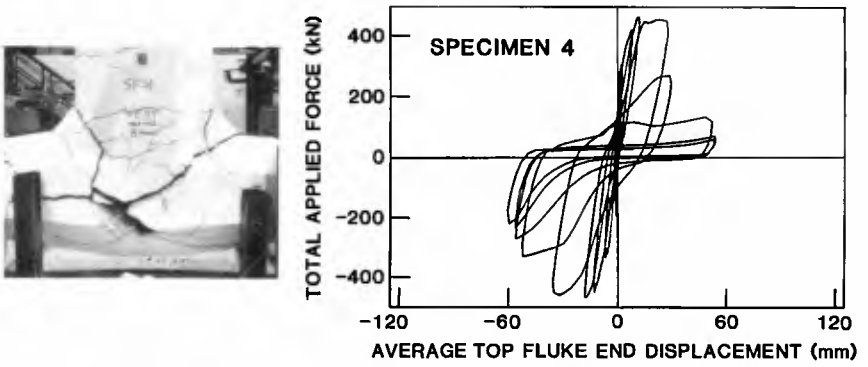

Figure 9: Final Appearance and Observed Response of Specimen 4

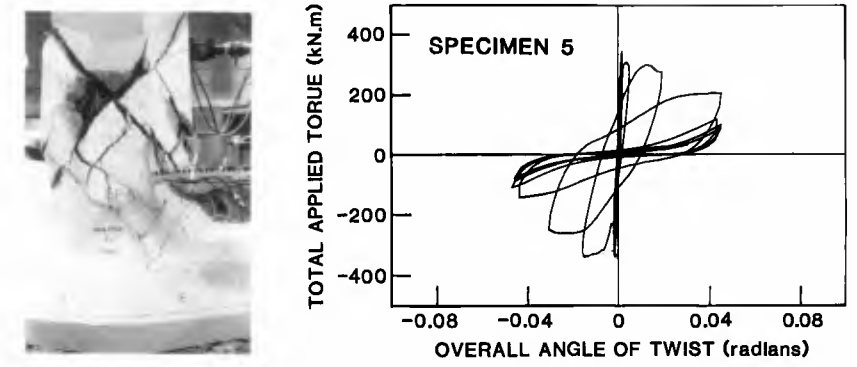

Figure 10: Final Appearance and Observed Response of Specimen 5

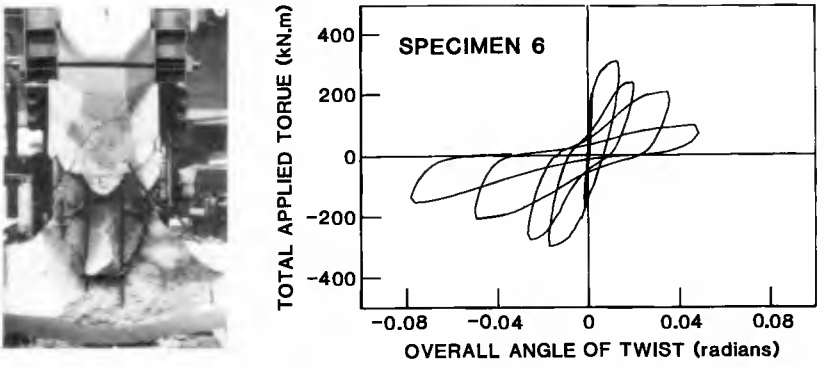

Figure 11: Final Appearance and Observed Response of Specimen 6

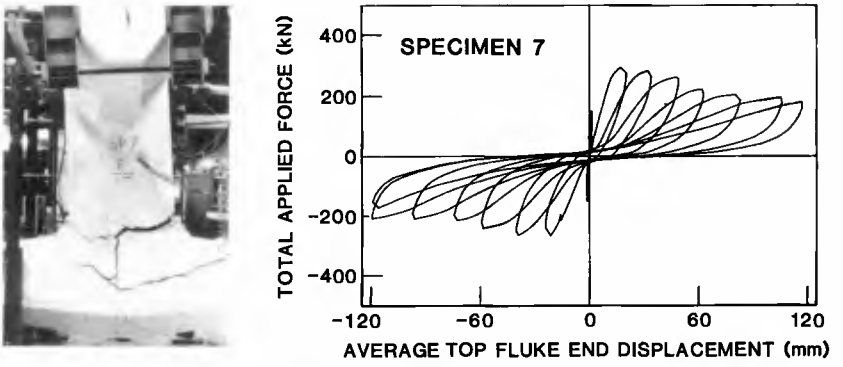

Figure 12: Final Appearance and Observed Response of Specimen 7

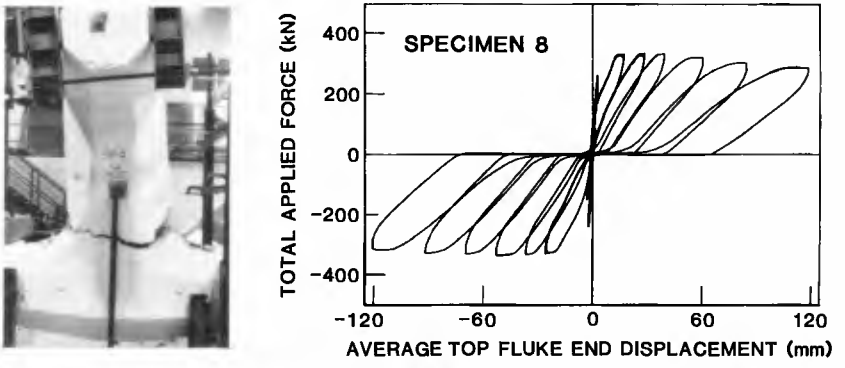

Figure 13: Final Appearance and Observed Response of Specimen 8

stiff with little deterioration during stage 3 of the loading regime. During the final three loading stages the existing crack became wider but no new cracks were formed. Maximum crack widths were of the order of 70 mm.

4. DISCUSSION

4.1 Specimen Comparisons

When one considers the three different load cases applied to both the unreinforced and the 8-bar reinforced specimens it seems apparent that loading type III (combined bending, shear and moment) was the most severe with lower initial cracking loads and ultimate loads. This generalized type of loading is the most likely to occur in the prototype due to the random placing of armour units in a breakwater.

The unreinforced specimens did not behave satisfactorily in a structural sense since they failed as expected at the first crack. No cycling was possible. This brittle behaviour could contribute to breakwater failures.

The reinforced specimens behaved in a satisfactory manner, withstanding 100,000 cycles of low level load reversals and several cycles of high level load reversals. The behaviour of the reinforced specimens was quite similar for the first 100,000 cycles with the units being initially quite stiff and exhibiting little stiffness loss during low level cycling. During the high level load reversals, the stiffness of the reinforced specimens dropped quite rapidly and the cracks became very large. By the conclusion of testing the reinforced specimens had sustained a high degree of damage but were still intact.

Comparing the three different types of reinforcement used in this study it was evident that the 8-bar reinforced units behaved in the most satisfactory manner with the highest resisted loads and the smallest initial crack widths (desirable for corrosion control). This behaviour occurred as a result of the even distribution of the reinforcement located nearer the perimeter of the cross-section as compared to the tube reinforced and prestressed specimens. In all cases the crack widths could have been further reduced by the introduction of reinforcing steel at the shank-fluke intersection.

Considering the effort required to fabricate the test specimens it is evident that the unreinforced units were the simplest to construct. Of the reinforced units, the 8-bar reinforced specimen was the simplest to produce followed by the tube and finally the post-tensioned specimen. All of the specimens were quite simple to cast and strip.

4.2 Alternative Design Approaches For Armour Units

4.2.1 Current design approach

Historically, the design of armour units has been performed by hydraulic and/or coastal engineers. Breakwater design is based partially on results obtained in hydraulic laboratories where the common practice has

been to construct scale models of the actual breakwater and armour units. Unfortunately, although the armour unit can be scaled for size and weight it is very difficult to accurately scale the strength of the unit. Thus, scale armour units used in model breakwaters usually have significantly higher strength than the corresponding prototype units.

The higher strength of the scale armour units results in model tests in which the armour unit rarely fails. Thus, the design of a breakwater is usually based on the assumption that the armour units will not fracture. This assumption is not consistent with prototype experience in which failures of armour units and breakwaters have been observed (Magoon et. al., 1974, and Anonymous, 1982). The effect of armour unit breakage on the performance of a breakwater is not fully understood but it clearly has an effect on performance.

If one were to design an unreinforced concrete armour unit with the criterion that no breakage should occur then the unit will necessarily be larger than optimum since the uncertainties in the determination of the possible loads and the expected concrete strengths must be estimated conservatively to allow a reasonable safety factor. If some of the units were allowed to break then the effects on the stability of the breakwater as a whole must also be examined.

4.2.2 Design based on determination of expected loads

One approach to the design of an armour unit is the determination of the expected loads that the unit will be subjected to. The unit could then be designed to resist these loads.

The determination of the expected loads on the prototype unit is a complex and expensive process which is of questionable value as the loads obtained may only be applicable to the specific site measured. Different wave heights, wave regimes, and breakwater geometries could significantly affect the magnitude and nature of the loads in a manner which is not understood. Thus the loads may not be transferable to another site.

The determination of the loads on a model unit is somewhat easier than for the prototype since one is working under laboratory conditions. Using a model breakwater has the advantage of being able to use different wave heights and regimes and being able to alter the breakwater design. This would allow the determination of the loads for different sites. Unfortunately, the scaling of the loads from the model to the prototype and the determination of a safety factor based on the strength of the units introduces many uncertainties.

4.2.3 Design based on determination of desired response

It may be advantageous to approach the design of concrete armour units from the viewpoint of the response desired from the unit. Thus, if the desired response for the prototype unit is that it emulate the model unit and maintain it's integrity then one must examine the steps required to meet this objective.

In order to maintain it's integrity the unreinforced concrete armour unit must resist the load effect that causes cracking since cracking effectively causes failure of the unit. The load effect which causes cracking for a particular size of unit can be easily calculated and thus the amount of reinforcement required to sustain this load level can be determined. This would be the minimum amount of reinforcement required for ductile behaviour. An additional requirement for reinforcement may be necessary in order to control crack widths since crack sizes could be large, leading to possible corrosion problems. Thus, some level of reinforcement greater than the minimum required for ductile behaviour would seem to be desirable. Placement of additional steel will lead to enhanced ductility, improved crack control, and an increase in load carrying capacity. It is important to note here that the increase in ductility is the fundamental reason for adding reinforcement.

In summary, rather than design unreinforced units for the maximum expected loads, with uncertainties in quantification of both the loads and the resistance of the unit, one could ensure that the armour unit will not fail after cracking and be ductile enough to endure further deformation by the addition of reinforcement. In this manner a ductile unit would spread the load to adjacent units but still remain in one piece thus satisfying the performance objective.

5. CONCLUSIONS

Based on the experiments described in this paper the following conclusions can be drawn:

1) The best approach to the design of Dolosse is likely to be the definition of a desired response and the determination of the amount of reinforcement required to achieve this response.

2) The use of steel reinforcement leads to an increase in both the ultimate strength and ductility of a Dolos concrete armour unit as compared to an unreinforced unit.

3) The best results are obtained when steel is well distributed throughout the unit as close to the perimeter as possible consistent with corrosion control.

4) The cost of a reinforced unit should not be substantially higher than an unreinforced unit since they are simple to construct. The relative cost of reinforcement represents a very small proportion of the cost of a breakwater.

ACKNOWLEDGEMENTS

The research described in this paper was funded by Public Works Canada under a Department of Supply and Services contract (No. 05SU.EN280-2-3-707). The experimental work was performed in the Sandford Fleming Structures Laboratory of the Department of Civil Engineering of the University of Toronto.

REFERENCES

ANONYMOUS (1982). Behind the Sines, Portugal Breakwater Failure. Civil Engineering. A.S.C.E. Vol. 52. No. 4. April 1982. pp. 64-67.

MAGOON, O.T., SLOAN, R.L., and FOOTE, G.L. (1974). Damages to Coastal Structures. Proceedings of the Fifteenth Coastal Engineering Conference. Copenhagen. Denmark.

MERRIFIELD, E.M. (1968). Dolos Concrete Armour Protection. Civil Engineering. A.S.C.E. Vol. 38. No. 12. December 1968. pp. 38-41.

UZUMERI, S.M., BASSET, R. and WILL, G.T. (1985). Structural behaviour of 10 ton Dolos units. Publication No. 85-06. Department of Civil Engineering, University of Toronto, Toronto, Ontario, CANADA. 106 pp. + appendices.

NOTATIONS

ε_o Average longitudinal strain corresponding to the maximum stress in the concrete.

ε_{sh} Strain in steel corresponding to the start of strain hardening.

f'_c Strength of plain concrete as determined from a standard (152 mm diameter x 305 mm long) cylinder test.

f_u Ultimate stress in steel.

f_y Yield stress of steel.

CHAPTER 175

Composite Type Breakwater at Taichung Harbor, R.O.C.

Chung-Chuang Wu*

The composite type breakwater used in Taichung Harbor contributes economical cross section and better consideration of drifting sand control. Also, with the plan of making caissons on the sand beach and installing caissons by using an unprecedented "Island" method, it shorten the construction period of breakwater significantly.

1 Introduction

The government of Rep. of China decided to build a new port in the central part of the west coast of Taiwan, known as Taichung Harbor, about two decades ago. Its purpose was to cope with the problems caused from the rapid economic growth; such as to balance the population distribution, to alleviate inland traffic congestions and to release the burdens of other ports.

Shallow beach and straight coast line with strong seasonal wind and heavy brifting sand are the typical features along the west coast of Taiwan. The variety of meteorology is not only influencing the configuration of the port but also demanding special alternatives to the selection of materials, construction methods, etc.

The design and construction methods of the composite type breakwaters used in Taichung Harbor were trying to triumph most of the meteorological and geographical disadvantages encountered as well as to meet the urgent construction schedule. The effort has been considered successful. The construction processes have appeared highly efficient. Fig. 1 shows the location of Taichung Harbor and the configuration of its breakwaters.

2 Relationships Between Caisson Composite Type Breakwater and Meteorology

During the winter, from October each year to February of the next year, the previaling wind comes from North and North-North-East with average speed of 10 m/sec at Taichung port. The prevailing wind in the summer used to come from South-West with considerably lower speed, not exceeding 9 m/sec except hitting by typhoon. Typhoons attack Taiwan in summer almost every year. They create much more significant waves than the prevailing wind does in the winter. Therefore, the methods of breakwater design of Taichung port were based on the waves created by the typhoons instead of the seasonal prevailing winds. Table 1 gives

* Assistant Engineer, Taichung Harbor Bureau, Taiwan, R.O.C.

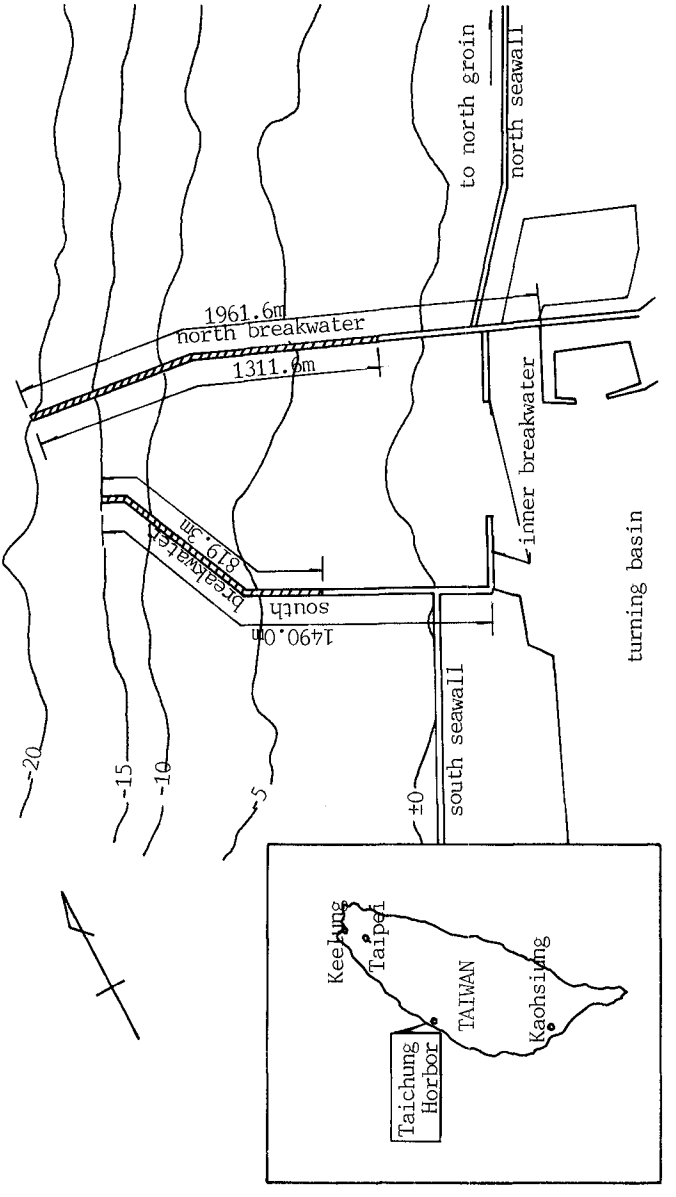

Figure 1. Location of Taichung Harbor and Layout of breakwater, shadow part indicates composite section

the significant wave height, at water depth -20m, of typhoons around Taichung Harbor, which was estimated by the "Wave Tracing Method" suggested by Dr. Ijima [3]. The max. tidal level of +6m was adopted as the H.H.W.L. (highest high water level) for the design.

Table 1. The estimated significant wave height & period at Taichung Harbor.

	Direction	Height (m)	Period (m)	Remarks
During typhoon	NNE	5.0	9.2	water depth = -20 m
	N	5.7	9.7	
	NNW	5.8	9.9	
	NW	5.4	9.9	
	WNW	5.0	9.8	
	W	4.7	9.3	
	WSW	4.6	8.7	
	SW	4.3	8.4	
During winter monsoon	N	4.0	8.0	water depth = -20 m
	NNW	4.0	8.0	

Drifting sand comes from two adjacent rivers; one is Tatu river on the south which carries about 0.2 million m^3 sand drifts northward in the summer, the other is Tachia river on the north with the sand amount around 0.8 million m^3 which goes southward particularly in the winter. There is about 1 million m^3 of sand being transported to the port and vicinity annually. Hence, the effect of preventing sand from settling in this harbor was considered being part of the function of breakwater.

The layout of this port was selected through a series of Model Experiment of Protection. The entrance width is 350m, navigation channel angles with 65°44' westward from the north, i.e. on the skew to the direction of prevailing wind. The length of breakwaters were determined accordingly with that the depth at the seaward end of north breakwater should reach -20m, and should be -15m deep at the end of south breakwater. Also, according to the Sand Drifting Model Test, the breakwater with vertical wall was chosen as typical cross section at places where the water depth is over-4m. The waves reflected by vertical wall breakwater could affect part of the approaching sand load away to the deep water (over -20m) area and the reserved settling place which located between north breakwater and north groin with the area more than 350 hectares. The reserved areas are dredged annually to provide adequate space for future sand deposits. This method provides good means to control sand free from drifting into the harbor [5].

Besides considering of harbor calmness, drifting sand control, vessel operation and construction economy ..., there was another reason for choosing composite type breakwater in Taichung Harbor; to account the property of its faster construction progresses and invulnerable characteristics.

3 Features of Caisson Composite Type Breakwater

3.1 Corresponding Data

The wave pressure acts on breakwater was computed by using Sainflou's Formula at the zoon where the wave is under the non-breaking condition. The Hiroi's Formula was used to calculate the wave pressure wherever the water depth is smaller than twice the height of approaching waves. The initial dimension of the proposed cross sections of composite type breakwater was determined through the estimated wave pressure and the Itoh's Expected Sliding Theory which checked out the possible lateral sliding displacement at any place of the breakwater with the maximum tolerance not exceeding 5 cm [4].

For easily constructing and conveniently towing, also for taking the full usage of caisson dock (its 115m long, 28m wide and 8.9m deep, can cast 4 caissons in one batch), the lengths of concrete caissons were setup to 18m and 24m, the widths varied from 14m to 18m depending on the water depth at the post position.

Final elevation of crown tops for northern and southern breakwaters, according to the estimated overtopping condition at north breakwater during monsoon season and at the south breakwater in the Typhoon period, are +10.2m and +8.6m, respectively [1].

The thickness of rubble mounded foundation was determined to be larger than 2m at any position, despite the good bearing capacity of sea bed around this area (silty sand, the blow count of penetration test at top 10 meters layer, $N > 10$; others $N > 30$) [1]. Mean while, to prevent the sand being washed out from the bottom of foundation by current and tide, vinyl mattress was unfolded to cover the surface of sea bed before rubble mounding. Fig. 2 illustrates the typical cross section of composite type breakwater at Taichung Harbor.

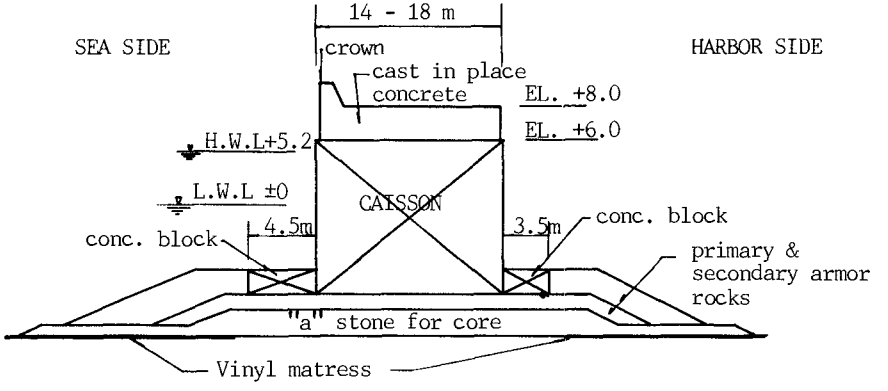

Figure 2. Typical cross section of composite type breakwater at Taichung Harbor

The length of north breakwater is 1961.6 meters with 1311.6 m in composite type. South breakwater is 1490 meters long with composite type 819.3 m.

3.2 Construction Procedure

Totally, 102 breakwater caissons had been completed within the first construction stage (1972-1977); 59 at north, 37 at south, 2 caissons at north groin and 4 at both inner breakwaters. In order to meet the urgent schedule, about 2/3 (71 caissons) of the total amount were built up on the sand beach instead of using dry dock, because the available work yard on beach was almost unlimited for each construction batch. In average, it took only 9.5 days to complete a caisson on the beach -- much shorter than erecting it in dock. Fig. 3 shows the caissons being made on beach were ready for floating out.

A well designed procedure which can be used to float out the caissons safely is the key for successful beach-made-caissons. Experiments of Model Floating and detailed survey during each caisson's floating out were made [2]. At the beginning, the Sit-to-Float method was used on the first two caissons of south breakwater. This kind of method was leading to low down the caisson into water levelly, then enable it floating out at high tide, by dredging and washing out the sand around the bottom of caisson at the same time. Fig. 4 indicates the steps of Sit-to-Float procedure. Unfortunately, stress concentrations were found on the bottom of that two caissons. Therefore, an alternative technique, so called Slide-to-Float method, was adopted as the proper way for all the other beach-made-caissons.

Figure 3. Caissons made on the beach where is dredged for harbor basin later

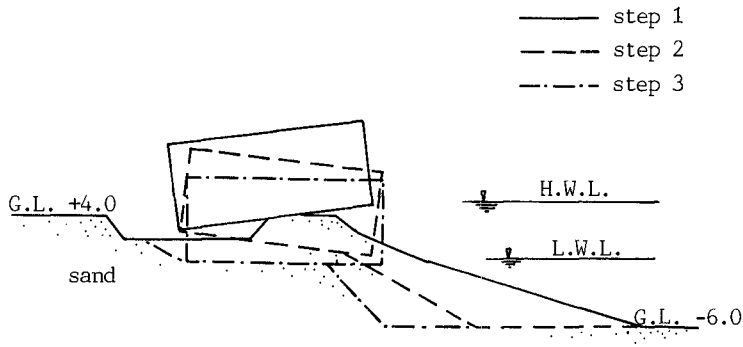

Figure 4. Procedure of caisson floating out -- Sit-to-Float. Steps: 1) dredging and washing out sand around caisson bottom; 2) caisson lowing down at L.W.L.(lowest water level) on its own weight; 3) caisson floating out at H.W.L.(highest water level)

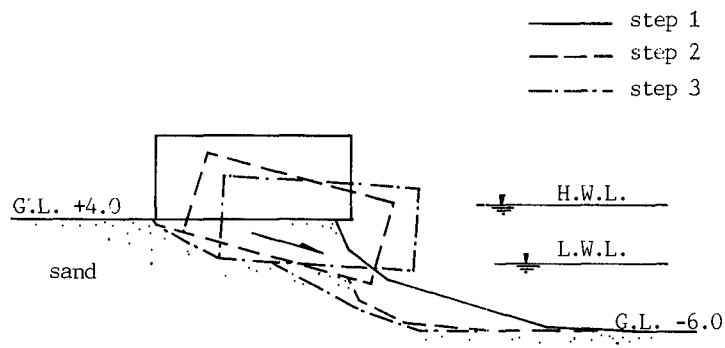

Figure 5. Procedure of caisson floating out -- Slide-to-Float. Steps: 1)dredging out sand under front toe of caisson; 2) caisson sliding toward water deeply at L.W.L.: 3) caisson floating out naturally at H.W.L.

In the method of Slide-to-Float, dredgers were used to cut the sand out from the front toe of each caisson to guide it sliding into water. Then, the caissons would float up for towing when tide flood. Because of the large tidal range (mean spring tide range: 4.59m) and the high friction of sand (angle of friction, ϕ, between 30° and 34°) at this area, caissons would not slide down abruptly. This process neither damaged the structure of the caissons nor hurt the working vessels. Fig. 5 illustrates the processes of Slide-to-Float method. Fig. 6 shows a caisson is sliding toward water under the operation of Slide-to-Float.

Because of the limits of water depth around the caissons' casting yard, wherever at dock or on beach, the constructed height of the caissons should not exceed 14m to ensure the floating out of caissons. Hence, for those caissons which final height beyond 14m were constructed up closely to 14m first. After that, they were towed to the high layer construction site and temporary storage area for continuously completion.

The whole construction sequence of composite type breakwater started from deploying center line, sounding out the elevation of sea bed, and paving PVC mattress. Cobble "a" - the stones with diameter around 30 cm were dumped to the site to constitute as the core of foundation before secondary armor rocks (0.3 - 1 ton) were casted. After the caissons were settled to position, they were filled with sand and gravels. The finishing procedures included pouring cap concrete, placing protective concrete blocks, tetrapods, and primary armor rocks (size 1 - 5 ton). It was considered to be totally completed after the crown had been concreted.

Figure 6. Caisson slides toward water under process of Slide-to-Float method

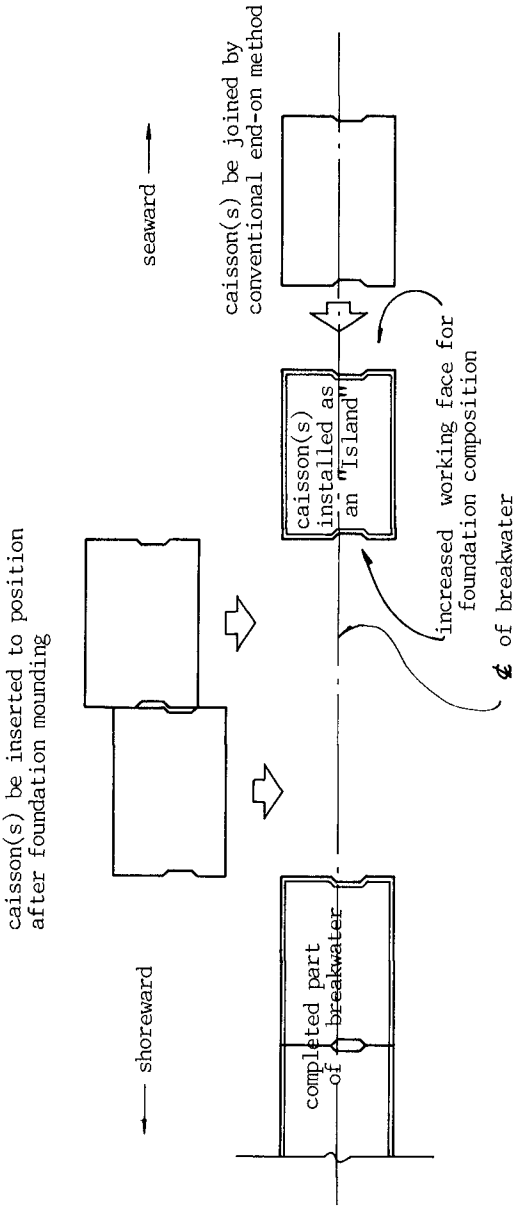

Figure 7. "Island" method of caisson installation

Figure 8. Installation of an "Island" caisson, which is aided by a pre-anchored 80 MT pontoon

Figure 9. Behind an "Island", a caisson is inserting to its position

Since the manufacturing of caissons was shortened significantly, and the workable time on the sea was comparably insufficient (96 caissons should be installed within 3 years), the disposition of installing caissons became critical. In addition to the conventional end-on progressive method, an "Island" method (or might call "Jumping" method) was introduced to increase the working faces to these breakwater construction project. The concept of this scheme, different from the conventional end-on method, is to post caissons some distance apart from the already installed breakwater, promise more working space to conduct consequent foundation rubble mounding, and then to complete this section of breakwater by inserting other caissons [6]. Fig. 7 illustrates the scheme of "Island" method. Fig. 8 shows an "Island" caisson is adjusting its position with the aid of a pre-anchored 80 MT pontoon. Fig. 9 shows a caisson is towed on the way to fill the space between "Island" and the end-on caisson.

4 Conclusion

The workable time on the sea of this project, 120-140 days per year averagely, was very short and urgent. Fortunately, however, the project was smoothly and punctually completed. The success should attribute to the careful and thorough planning, good use of long term and short term weather forecasting informations, etc. The most outstanding tact among these procedures are considered as successfully casting most caissons on the beach area where would be dredged as the channels later, and taking an unprecedented "Island" method to place the caissons.

5 Acknowledgements

The author would like to express his appreciation to Mr. C.C. Sha, Chief Engineer of Taichung Harbor Bureau, for his suggestions and the most help in the successful collection of historical records and data which enabled completion of the work.

6 References

1. CHANG, C.C. et al (1981) Caisson type breakwater of Taichung Harbor. Proc. Third Conf. of Harbor Technique, Taiwan pp. 7-10

2. HSU, C.Y. et al (1976). Report of caissons' construction and out floating from sand beach, Taichung Harbor.

3. JAPAN PORT CONSULTANTS, LTD. (1972) Primary report of wave estimation at Taichung Harbor.

4. TAICHUNG HARBOR BUREAU (1973). Study of engineering design at Taichung Harbor. pp. 2-11

5. TAICHUNG HARBOR BUREAU (1973). Study of model experiments of Taichung Harbor.

6. TAICHUNG HARBOR BUREAU (1976). Report of first stage construction, Taichung Harbor. Vol. II.

CHAPTER 176

METHOD OF ESTIMATING THE POWER EXTRACTED BY FIXED COASTAL TYPE WAVE POWER EXTRACTORS

Kenji YANO,[1] Hideo KONDO,[2] M.ASCE and Tomiji WATABE[3]

ABSTRACT

Study is performed on a vertical flap type energy converter, "Pendulor System". The power absorbed with the system in random waves is estimated using a transfer function of absorbed power (absorption coefficient) in regular waves and wave spectrum. A boundary element technique is applied to compute the hydrodynamic problem associated with the system which is placed in regular waves. The applicability of the method has been examined by a series of field test at a test plant caisson. The agreement between estimation and experiment was found to be good except near the resonance frequency of the system.

1. INTRODUCTION

A large variety of apparatus have been proposed for absorbing wave power and converting to other usable power. These absorbers may be classified roughly into two types, namely, floating type and fixed ones. Initially the fixed type ones had been discarded since the incident wave energy at shallow water area becomes less than that at the deep water. So, they unlikely seem to be attractive. However, since the floating type absorbers accompanies with difficult problems such as mooring or positioning system, energy transportation to land and maintenance which raise the cost of energy. This leads us to a bottom standing fixed type device at the coastal area which can serve as a breakwater and may save the energy cost.

With this point of view, we have studied the fixed type absorbers which can be set within coastal structures and had developed a few systems such as the "Pendulor System", a kind of pendulum with a flat plate. The system has an excellent power absorbing capacity, which had been introduced at the 19th Conference (Kondo et al, 1984). The present report deals with the method to estimate quantitatively the power absorbed by the pendulor system which will be set linearly alongshore in coastal area. This is one of the major problems to be solved in advance of realizing the commercial systems of fixed type.

1 Research Associate of Civil Engineering, Muroran Institute of Technology, 27-1 Mizumoto-cho, Muroran-Shi, Hokkaido, 050 JAPAN
2 Professor of Civil Engineering, ditto
3 Professor of Mechanical Engineering, ditto

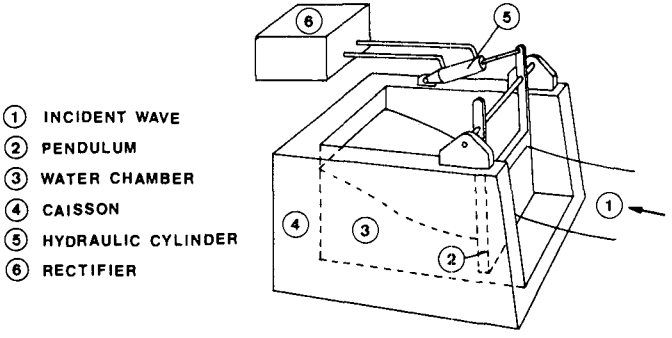

Fig. 1 Schematic diagram of pendulor system

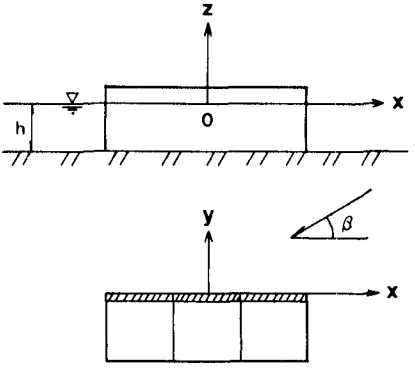

Fig. 2 Co-ordinate system

2. PENDULOR CONCEPT

Fig. 1 shows a concept of the pendulor system. The device consists of an oscillating pendulum around a horizontal axis, a double acting hydraulic cylinder connected to the pendulum, hydraulic circuit, that is a power takeoff mechanism, and a caisson in which a closed water chamber is formed. A kind of standing wave is produced in the chamber by the oscillating pendulum. At the node of standing wave, the pendulum is less affected reacting moment by the wave. Thus the device has high absorption capability under this hydrodynamic condition.

3. THEORETICAL MODEL

3.1 Absorbed Power in Regular and Random Waves

Let's consider m identical pendulor devices connected together to form a string as shown in Fig. 2. Each pendulum is allowed to move roll mode alone in response to regular wave with amplitude a. It is assumed that the mechanism for wave power absorption can be described

by a simple external damper connected to pendulum and that the damping moment caused by power absorption is linearly related to the velocity of the motion of the pendulum.

The motion of pendulums in waves, with their amplitudes varying sinusoidally in time, are calculated by the following equations

$$I_k\ddot{\theta}_k+N_k\dot{\theta}_k+K_k\theta_k=M_k \qquad k=1,2,\cdots,m \tag{1}$$

where I_k, K_k and N_k are the moment of inertia, the restoring moment coefficient of the kth pendulum and the damping moment coefficient of the damper attached to the kth pendulum and θ_k is the angular displacement with complex amplitude $\bar{\theta}_k$. M_k is the hydrodynamic moment acting on the kth pendulum and is represented, as follows

$$M_k = M_{0k} - \sum_{\ell=1}^{m} (I_{k\ell}\ddot{\theta}_\ell + N_{k\ell}\dot{\theta}_\ell) \tag{2}$$

where M_{0k} is wave exciting moment associated with incident and scattering waves and the terms in the parentheses are moments on the kth pendulum due to a radiation wave produced by a motion of the ℓth pendulum. The coefficients I_k and N_k are known as the added moment of inertia and the damping moment coefficient, respectively. The simultaneous linear equations of 1 can be solved for the pendulum motions $\bar{\theta}_k$. Hence, the transfer function of the kth pendulum is defined by Eq. 3.

$$Z_k(f,\beta)=\bar{\theta}_k/a \tag{3}$$

The total power absorbed P_a is given by

$$P_a=\sum_k \frac{1}{2}\omega^2 N_k|\bar{\theta}_k|^2 \quad , \quad \omega=2\pi f \tag{4}$$

The absorbing coefficient κ is defined as

$$\kappa=P_a/(P_w\cdot B_0) \tag{5}$$

where P_w is mean power per unit crest length of incident wave train and B_0 is total width of the series of devices.

It is important for the design of wave power absorbers to know how effectively they absorb power from random waves. In random waves absorbed power $\bar{P}_a$ with the system can be estimated by

$$\bar{P}_a=\rho g\int_0^\infty\int_0^{2\pi}\kappa(f,\beta)S(f,\beta)C_g\,df\,d\beta \tag{6}$$

where $\kappa(f,\beta)$ the absorbing coefficient in waves at frequency f in direction β, and $S(f,\beta)$ the directional wave spectrum, ρ the density of the fluid, g the acceleration of gravity and c_g is the group velocity of waves.

For a case that the wave dimensions are known only at deep water, the following relationship is useful for the transformation of a deep water directional spectrum into a shallow water directional spectrum.

$$S(f,\beta)\,df\,d\beta C_g = S_0(f,\beta_0)\,df\,d\beta_0\,C_{g0}K_r^2 \tag{7}$$

where K_r the refraction coefficient and subscript 0 is used for the symbols at deep water. Substituting Eq. 7 into Eq. 6, the absorbed

power at shallow water area is estimated by deep water spectrum using Eq. 8.

$$\overline{P}_a = \rho g \int_0^{\infty}\int_0^{2\pi} K_r^2(f,h,\beta_0) S_0(f,\beta_0) \times \kappa(f,\lambda(f,\beta_0)) C_{g0}\, df d\beta_0 \qquad (8)$$

$$\beta = \lambda(f,\beta_0)$$

where $\lambda(f,\beta_0)$ is a function of the wave direction.

If we used a spreading function D, the directional spectrum is rewritten as follows

$$S_0(f,\beta_0) = S_0(f) D(f,\beta_0,\overline{\beta}_0) \qquad (9)$$

where $\overline{\beta}_0$ is the dominant wave direction, $S_0(f)$ is a usual frequency spectrum.

The absorbed power with the system is calculated by finite set of directional and frequency-wise components of the absorption coefficient, the wave spectrum, and so on.

3.2 Hydrodynamic Loads

The hydrodynamic loads acting on the pendulums are computed from the velocity potential along the body boundaries. To obtain the potential, we consider separately the fluid region exterior of the string (outer region) and the region interior of the closed chambers (inner region, excluded "harbor" which is shown below).

In the usual manner the velocity potential in the outer region can be decomposed into

$$\Phi(x,y,z;t) = (\phi_0 + \phi_d + \sum_{k=1}^{m} \overline{\theta}_k \phi_k)\, e^{-i\omega t} \qquad (10)$$

where ϕ_0 is the known potential of the incident wave and ϕ_d is the diffraction potential corresponding to scattering of the incident waves by the string with fixed pendulums. ϕ_k represents the radiation potential induced by the forced motion of the kth pendulum in the absence of the incident waves. The boundary condition at the body surface are given by

$$\frac{\partial \phi_d}{\partial n} = -\frac{\partial \phi_0}{\partial n} \qquad \text{on } \Gamma \qquad (11)$$

$$\frac{\partial \phi_k}{\partial n} = -i\omega(z_0 - z) n_y \qquad \text{on } \Gamma_k$$
$$= 0 \qquad \text{on } \Gamma - \Gamma_k \qquad (12)$$

where z_0 represents a depth of the point of rolling axis of the pendulum, Γ_k a wetted surface of the kth pendulum, Γ a wetted surface of the body, n the distance in the direction of the unit normal vector $\mathbf{n}$ directed outward from the boundary and n_y the y-component of $\mathbf{n}$. In the chamber, the potential ϕ' associated with the unit motion of the pendulum can be treated as two dimensional wave making problem and the solution was obtained by Asano (1980).

Assuming the each chamber has same dimensions, the hydrodynamic

loads and the coefficients are expressed as follows

$$M_{0k} = i\omega\rho e^{-i\omega t}\int_{\Gamma_k}(\phi_0+\phi_d)\bar{h}\,d\Gamma \tag{13}$$

$$I_{k\ell} = \frac{1}{\omega^2}\,\mathrm{Re}\left[i\omega\rho\int_{\Gamma_k}(\phi_\ell+\delta_{k\ell}\phi')\bar{h}\,d\Gamma\right] \tag{14}$$

$$N_{k\ell} = \frac{1}{\omega}\,\mathrm{Im}\left[i\omega\rho\int_{\Gamma_k}(\phi_\ell+\delta_{k\ell}\phi')\bar{h}\,d\Gamma\right] \tag{15}$$

in which $\delta_{k\ell}$ is the Kronecker delta function, $\bar{h} = (z_0-z)n_y$, Re[ ] and Im[ ] indicate the real and imaginary parts, respectively.

3.3 Numerical Determination of Potentials

The most general method for calculating the potentials is a boundary element method. A Green's function, G, is chosen as a source potential of unit strength which satisfies the same boundary conditions as the wave potential. As a result of Green's Theorem, the solution for wave potential can be represented as follows

$$-\frac{1}{2}\phi_k(P) = \int_\Gamma\left[\phi_k(Q)\frac{\partial}{\partial n}G(P,Q) - G(P,Q)\frac{\partial}{\partial n}\phi_k(Q)\right] \tag{16}$$

in which P and Q represent points on the boundary of the body Γ. The corresponding integral equation for ϕ_d is obtained from Eq. 16 by replacing ϕ_k by ϕ_d.

Let ψ represents the unknown potential above mentioned and $\hat{\psi}$ is its derivative. Equation 16 is numerically solved for a ψ at a number of discrete points. The surface Γ of the body is divided into N boundary elements. The values of ψ and $\hat{\psi}$ are assumed to be constant on each element and equal to the values at the element center called "nodes". Hence, the integral Eq. 16 for a particular node 'i' can be approximated as

$$\sum_j \hat{H}_{ij}\psi_j = \sum H_{ij}\hat{\psi}_j \tag{17}$$

$$\hat{H}_{ij} = \frac{1}{2}\delta_{ij} + \int_{\Gamma_j}\frac{\partial}{\partial n}G(i,j)\,d\Gamma$$

$$H_{ij} = \int_{\Gamma_j}G(i,j)\,d\Gamma \tag{18}$$

where Γ_j is the boundary of element 'j'. The whole set of equations for N nodes can be expressed in matrix form as follows,

$$\mathbf{\hat{H}U = HQ} \tag{19}$$

where

$$\mathbf{\hat{H}} = [\hat{H}_{ij}] \quad , \quad \mathbf{H} = [H_{ij}]$$

$$\mathbf{U} = \{\psi_1, \psi_2, \cdots, \psi_N\}^T \quad , \quad \mathbf{Q} = \{\hat{\psi}_1, \hat{\psi}_2, \cdots, \hat{\psi}_N\}^T \tag{20}$$

If a single pendulor system has a "harbor" (Ambli et al,1982), consisting of two parallel projecting sidewalls as shown in Fig. 3, corresponding potentials are obtained by a method of combination of regions (e.g. Brebbia, 1980). Consider two separate solution regions, the open sea (region 1) and inside the harbor (region 2). For the first region, the Eq. 16 can be partitioned as follow,

$$[\,\hat{\mathbf{H}}_0^1 \;\; \hat{\mathbf{H}}_I^1\,] \begin{Bmatrix} \mathbf{U}_0^1 \\ \mathbf{U}_I^1 \end{Bmatrix} = [\,\mathbf{H}_0^1 \;\; \mathbf{H}_I^1\,] \begin{Bmatrix} \mathbf{Q}_0^1 \\ \mathbf{Q}_I^1 \end{Bmatrix} \tag{21}$$

where superscript 1 indicates that it belongs to region 1,subscript I and $_0$ indicate the mouth of harbor and other boundary of the region 1, respectively. For the second region we have

$$[\,\mathbf{H}_0^2 \;\; \mathbf{H}_I^2 \;\; \mathbf{H}_P^2\,] \begin{Bmatrix} \mathbf{U}_0^2 \\ \mathbf{U}_I^2 \\ \mathbf{U}_P^2 \end{Bmatrix} = [\,\mathbf{H}_0^2 \;\; \mathbf{H}_I^2 \;\; \mathbf{H}_P^2\,] \begin{Bmatrix} \mathbf{Q}_0^2 \\ \mathbf{Q}_I^2 \\ \mathbf{Q}_P^2 \end{Bmatrix} \tag{22}$$

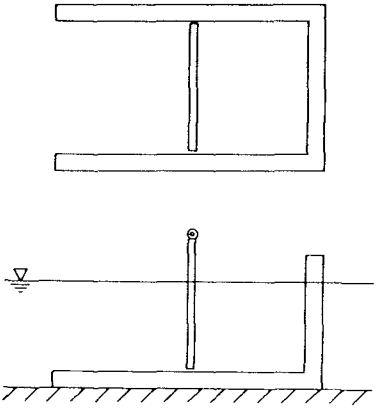

Fig. 3 Geometry of a system added "harbor"

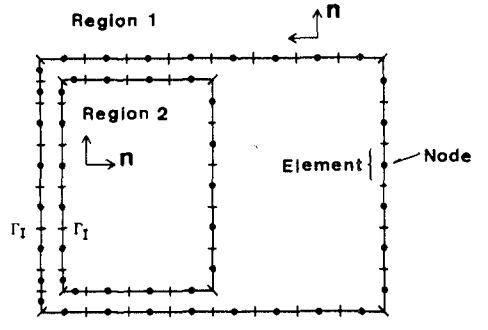

Fig. 4 Body divided into two regions

where subscript P indicate the pendulum part of region 2. According to the definition of the direction of the unit normal vector shown in Fig. 4, the conditions of the mouth of harbor are given by

$$\left.\begin{aligned} U_I^1 &= U_I^2 \\ Q_I^1 &= -Q_I^2 \end{aligned}\right\} \qquad \text{(radiation problem)} \tag{23}$$

$$\left.\begin{aligned} U_I^1 + \underline{U}_I &= U_I^2 \\ Q_I^1 + \underline{Q}_I &= -Q_I^2 \end{aligned}\right\} \qquad \text{(diffraction problem)} \tag{24}$$

where

$$\underline{U} = \{\phi_{0,1}, \phi_{0,2}, \cdots, \phi_{0,N}\} \qquad \underline{Q} = \{\hat{\phi}_{0,1}, \hat{\phi}_{0,2}, \cdots, \hat{\phi}_{0,N}\} \tag{25}$$

Using Eq. 11, 12 and these conditions, Eq. 21 and Eq. 22 can be rewritten as follows.

$$\begin{bmatrix} \hat{H}_0^1 & \hat{H}_I^1 - H_I^1 & 0 & 0 \\ 0 & \hat{H}_I^2 & H_I^2 & \hat{H}_0^2 & \hat{H}_P^2 \end{bmatrix} \begin{Bmatrix} U_0^1 \\ U_I^1 \\ Q_I^1 \\ U_0^2 \\ U_I^2 \end{Bmatrix} = \begin{bmatrix} 0 \\ H_P^2 \end{bmatrix} \{Q_P^2\} \tag{26}$$

(radiation problem)

$$= -\begin{bmatrix} 0 & 0 \\ \hat{H}_I^2 & H_I^2 \end{bmatrix} \begin{Bmatrix} \underline{U}_I \\ \underline{Q}_I \end{Bmatrix} - \begin{bmatrix} H_0^1 \\ 0 \end{bmatrix} \{\underline{Q}_0\} \tag{27}$$

(diffraction problem)

4. FIELD TEST

4.1 Experimental Set-Up

The test plant caisson employed in the field experiment had been constructed seaward of the south breakwater of Port Muroran, as shown in Fig. 5 and Fig. 6. Since the port faces to a bay on the Pacific south west coast of Hokkaido Island, the waves of which significant wave height is greater than 1.0 meter is approximately 12 % and appear mostly in winter.

Fig. 7 shows the dimensions of the caisson. The caisson is partitioned into two chambers by sidewall, and the pendulum had been installed at 2.5 meter inside from the front face of the right hand chamber. The pendulum is of 2.5 ton in weight. Distance between the center of the rolling axis and lower edge of the pendulum is 7.2 meter. The plate to receive wave force at the lower part of it is 2 meter wide and 3.5 meter high.

The wave-induced motion of pendulum is converted into hydraulic

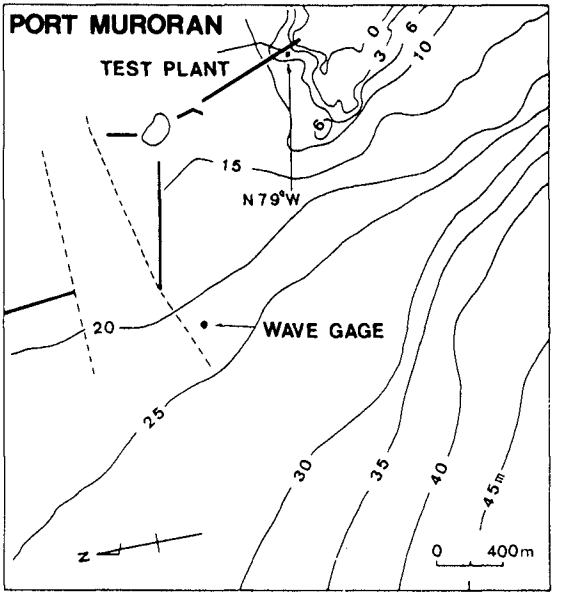

Fig. 5 Location map

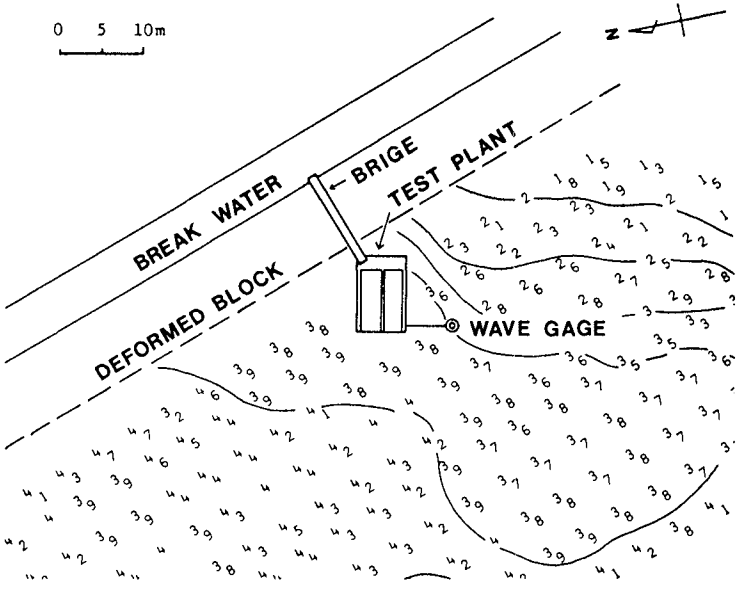

Fig. 6 Bathymetry around test plant

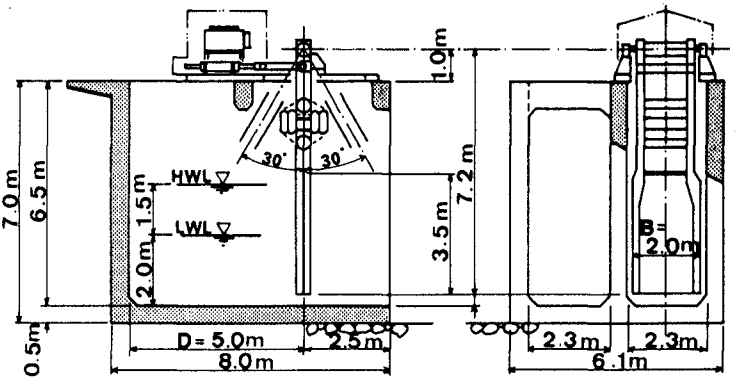

Fig. 7 Dimensions of test plant

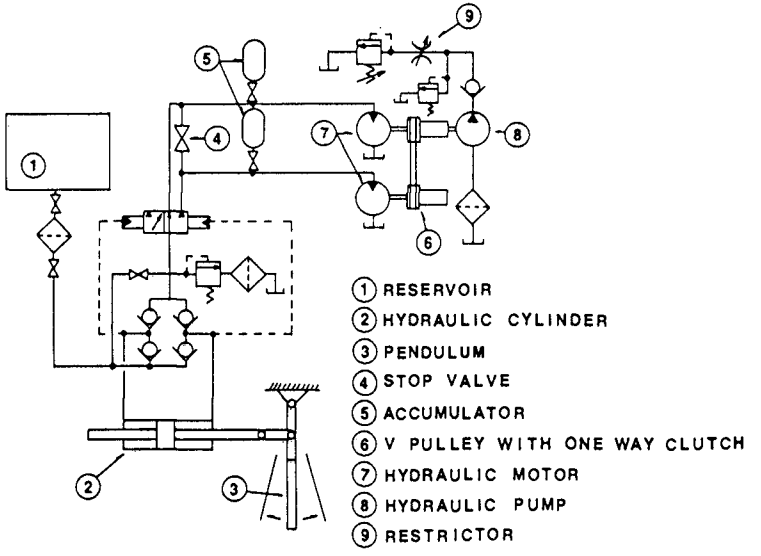

Fig. 8 Hydraulic circuit of test plant

power by the hydro-static power transmission circuit shown in Fig. 8. An electric generator was not equipped in the circuit. The energy absorption is achieved by combination of the hydraulic pump 8 and the restrictor 9, and the energy is finally absorbed by heating oil. In this circuit, the reaction moment of the energy absorption mechanism is non-linear due to the effects of the accumulators 5. Details of the power extracting facilities had been shown by Watabe, et al, in 1986.

The measured quantities in the field tests are the incoming wave profile, displacement of the piston rod, the cylinder pressures P1, P2, total torque of the motors, and the speed of motors. The wave data were measured 5 meter apart from the caisson with the ultrasonic wave gage above sea surface. In addition, the dominant wave direction is measured visually with a compass. In some experiments, the wave data were collected at the location of 1.8 km offshore form the test plant. The data signals were recorded on a magnetic-tape recorder. The measured records were digitized with the sampling rate 2 Hz for a period 1200 seconds giving 2400 data points per measured channel.

4.2 Test Results

(1) Pendulum Motion with/without Damper

Fig. 9 shows the comparison of theoretical and experimental spectra of pendulum motion under the condition of no-load. The former were calculated from the transfer function using measured wave spectrum and a cosine-power spreading function. The influence of the sidewalls protruding in front of the pendulum is considered in the calculation. In the figure, $S_{\theta\theta}$ denotes the power spectrum of the angular displacement of the pendulum and the broken line shows the numerical result for the present pendulor system.

Fig. 10 gives the example of the spectra of wave and pendulum motion with power absorption. In this case, it is necessary a suitable linear approximation of reaction moment of damper to calculate the motion from the mathematical model.

Let's assume that the load system of damper can be defined as follows,

$$M = (i\omega N + K)\bar{\theta}\, e^{i\omega t} \tag{28}$$

where N and K are an equivalent linearized load damping coefficient and restoring moment coefficient, respectively. So, they are given by

$$\begin{aligned} N &= \frac{1}{\omega}\, \mathrm{Im}[S_{\theta M}/S_{\theta\theta}] \\ K &= \mathrm{Re}[S_{\theta M}/S_{\theta\theta}] \end{aligned} \tag{29}$$

where $S_{\theta M}$ is the cross-spectrum of angular displacement of pendulum and the reaction moment from the cylinder. Of course, the coefficients N and K are functions of frequency. For simplicity, we used the values of N and K at peak frequency of the spectrum of reacting moment for calculation at arbitrary frequency.

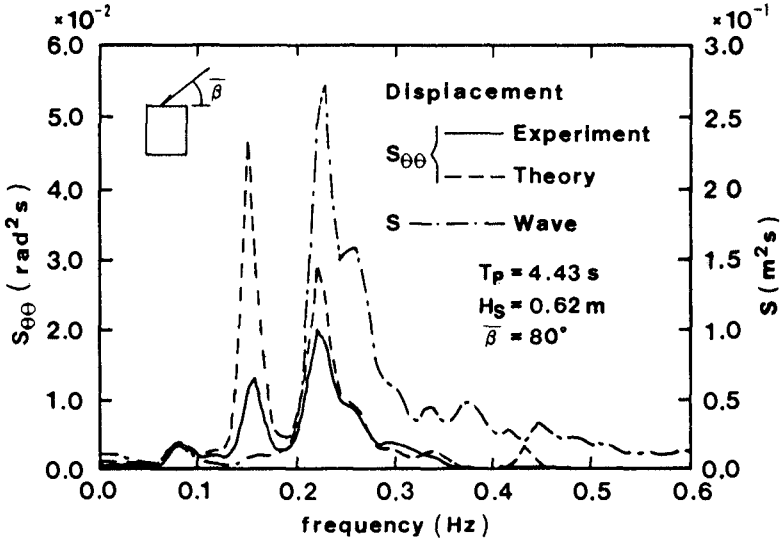

Fig. 9 Spectra of wave and pendulum motion (no-load condition)

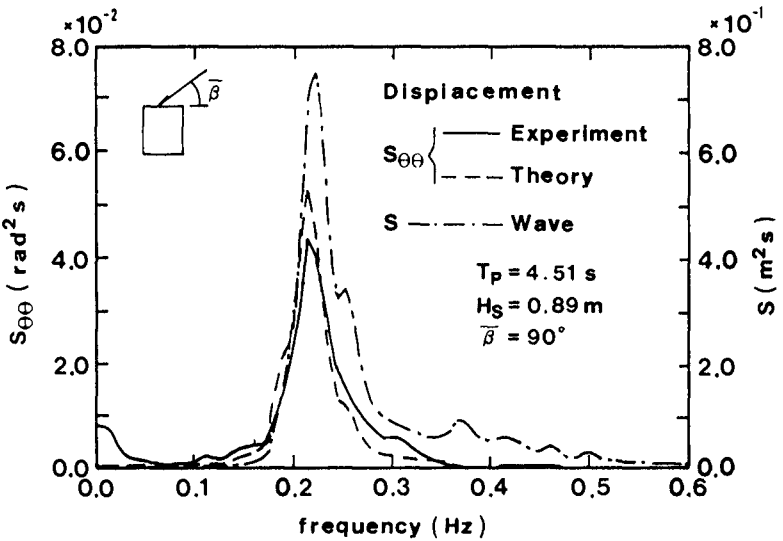

Fig. 10 Spectra of wave and pendulum motion (with power absorption)

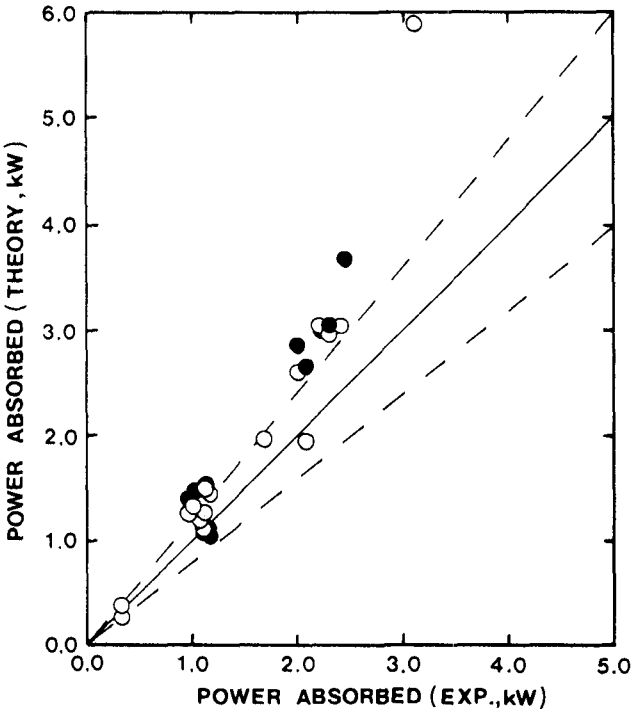

Fig. 11 Comparison of theory with experiment of absorbed power

(2) Absorption Characteristics

Using the estimated spectrum of pendulum motion and the linearized load damping coefficient, we can obtain absorbed power theoretically.

Fig. 11 represents the result of comparison of the theoretical power absorbed with experimental ones at the cylinder. The latter is obtained numerically as follows,

$$\overline{P}_a = \frac{1}{T_m} \int_0^{T_m} A_S (P1-P2) V \, dt \tag{30}$$

where T_m denotes the recording time of data signals, P1,P2 are cylinder pressures, A_S the cross sectional area of piston and V is the velocity of piston.

In the figure, the symbol of solid circle indicates the value estimated from the deep water spectrum. The broken lines represent the range within 20 percent error.

The dominant wave direction of deep water is estimated from wind

direction collected at a small island located nearby the wave gage. The refraction coefficients and wave angles at the plant associated with the deep water waves were determined from wave refraction diagrams.

As concerns the one extreme overestimation plot in the figure, the experimental data was obtained on condition that significant wave height is 1.16 meter and peak frequency of the wave spectrum is near the resonance frequency predicted in the theory.

5. CONCLUDING REMARKS

We have shown a numerical approach to estimate quantitatively the power absorbed by pendulor system of coastal type and confirmed its applicability by the field tests. As expected, one of the main cause of the overestimation above mentioned probably lies that the theory ignores the viscous loss with water motion near the pendulum and that at the mouth of the protruding sidewalls. Another probable cause is due to the partial reflection from the inside surface of the protruding sidewalls, especially the surface of pendulum.

The data obtained from field tests are not enough to allow a more detailed discussion. It is necessary subsequently to asses behavior of the system including the sources of the reduction of absorption in a full range of wave conditions. Stability of the caisson as well as durability of moving components of the system against wave force has been studied and will be disclosed in the near future.

REFERENCES

1) Ambli, N., K. Bonke, O. Malmo and A. Reitan (1982). The Kvaener multiresonant OWC, Proc. of 2nd Int. Symp. on Wave Energy Utilization, Trondheim, pp. 275-295.
2) Asano, S. (1980). Energy absorption efficiency of flap type wave energy converter, JTTC, SK60-14, (in Japanese).
3) Brebbia, C. A. and S. Walked (1980). Boundary element techniques in engineering, Newnes-Butterworths, London, 210p.
4) Kondo, H., T. Watabe and K. Yano (1984). Wave power extraction at coastal structure by means of moving body in the chamber, Proc. 19th Coastal Eng. Conf., Houston, III, pp. 2375-2891.
5) Watabe, T., H. Kondo and K. Yano (1986). Studies on a pendulor-type wave energy converter, Proc. of 3rd Int. Symp. on Wave, Tidal, OTEC, and Small Scale Hydro Energy, Brighton, pp. 281-292.

CHAPTER 177

Wave Diffractions by Rows of Vertical Cylinders of Arbitrary Cross Section

Akinori Yoshida*, Norio Iida**, and Keisuke Murakami***

1. Introduction

Wave diffractions by a number of (a group of or a row of) vertical cylinders have been investigated in connection with, e.g., multilegged offshore structures (Spring and Monkmeyer(1974), Ohkusu(1974), Chakrabarti(1978), Mciver and Evans(1984), etc.); Wave-Power absorption devices (Miles (1983), Falnes(1984), Kyllingstad(1984), etc.); Wave barrier systems (Massel(1976), Kakuno and Oda(1986), etc.). Most of the previous works were, however, mainly aimed at the wave diffractions by cylinders of circular cross section and/or by cylinders of relatively small dimensions compared to wave length.

In this paper, we describe a simple yet versatile analytical method to solve wave diffractions by infinite rows of vertical cylinders. In the method, it is assumed, in addition to usual linearised small amplitude assumptions, that: the row of cylinders is composed of infinite number of surface-piercing evenly spaced equal cylinders fixed on sea bottom; incident wave direction is perpendicular to the row; the number of rows may be arbitrary, at least in principle; the cross sectional shape of the cylinders may be arbitrary as long as it is symmetrical with respect to the incident wave ray; and the cylinders are relatively large compared to incident wave length so that inertial forces are predominant to drag forces.

2. Formulation

We consider the diffractions of a regular plane wave by a row or rows of surface-piercing vertical cylinders fixed in water of uniform depth h. It is assumed that the row is composed of infinite number of equal cylinders evenly spaced (2b distance between adjacent cylinders) and that a plane

* Associate prof., Dept. of Civil Engineering Hydraulics, Kyushu University, 812 Fukuoka, Japan
** Engineer, Japan Port Consultant Ltd., Japan
*** Graduate Student, Kyushu University, 812 Fukuoka, Japan

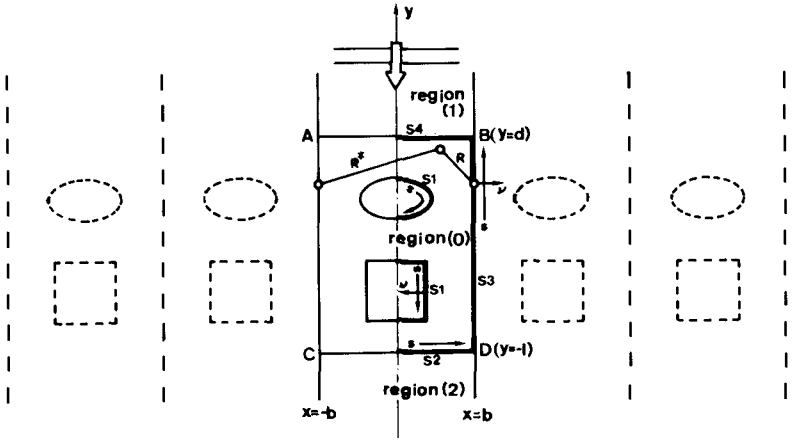

Figure 1. Definition sketch

wave of small amplitude ζ_0, radian frequency σ, wave number k, is incident on the row at right angle. Thus, the wave motion is periodic along the row of cylinders. This situation is equivalent to wave diffraction for a cylinder placed midway in a wave tank of the same width as the spacing interval 2b (e.g., See Sorokosz (1980), Taylor and Hung(1986)).

In the following formulation, we solve the equivalent problem by using an integral-equation and Fourier expansion techniques similar to that adopted by Sorokosz(1980): here in the present method, however, complicated mathematical form of Green function is not needed.

Cartesian co-ordinates are taken with the x and y axes in the horizontal plane of the water surface and the z axis directed vertically upwards. The row is arranged along x axis. A sketch of the horizontal section is given in figure 1.

The fluid is assumed to be inviscid and incompressible and the fluid motion irrotational so that it can be described by a velocity potential which may be expressed in the form

$$\Phi(x, y, z, t) = (g\zeta_0/\sigma)\phi(x, y)Z(z)\exp(i\sigma t) \quad \cdots\cdots\cdots\cdots(1)$$

in which g is acceleration of gravity; $\phi(x,y)$ is dimensionless function which represents horizontal distribution of the velocity potential; $Z(z)=\cosh(k(z+h))/\cosh(kh)$; i = imaginary quantity ($\sqrt{-1}$).

Since the velocity potential satisfies Laplace equation, $\phi(x,y)$ satisfies the following Helmholtz equation,

$$\nabla^2\phi(x, y)+k^2\phi(x, y)=0 \qquad \cdots\cdots\cdots\cdots(2)$$

Now, introducing imaginary boundaries AB (indicated by S4 at y=d) and CD (indicated by S2 at y=-1) as shown in figure 1, we divide the fluid region into three regions, upstream region (1), downstream region (2) and truncated inner region (0).

The inner region (0) is a closed fluid region enclosed with the imaginary boundaries S2 and S4, the cylinder (indicated by S1) and the walls of the wave tank (indicated by S3). Thus, applying Green's theorem to the dimensionless function $\phi_0(x,y)$ in the inner region (0) which satisfies Helmholtz equation (2), it can be expressed by the following Green's Identity Formula:

$$\phi_0(X)=-\frac{i}{\alpha}\int_{S1+S2+S3+S4}\left\{\phi_0(X_b)\frac{\partial}{\partial\nu}G(kR)-G(kR)\frac{\partial}{\partial\nu}\phi_0(X_b)\right\}ds \qquad \cdots(3)$$

where $G(kR)=H_0^{(1)}(kR)+H_0^{(1)}(kR^*)$;

$H_0^{(1)}$ is the Hankel function of the first kind and of order 0; X denotes the co-ordinates (x,y) of any point in the inner region (0) and X_b on the boundary; $R=|X-X_b|$ and $R^*=|X-X_b^*|$ (X_b^* denotes the reflected image point of X_b with respect to the center line of the wave tank.); ν is the outward normal to the boundary; $\alpha=2$ when X is on the boundary and othewise $\alpha=4$.

The integration is taken counterclockwise and along a half of the boundary (indicated by thick lines in figure 1) because the fluid motion is symmetric with respect to the center line of the wave tank.

By representing the dimensionress function of the reflected wave potential and the transmitted wave potential with φ_1 and φ_2, respectively, the function ϕ_1 in the upstream region and ϕ_2 in the downstream region may be written as

$$\phi_1(x,y)=\exp(iky)+\varphi_1(x,y) \qquad \cdots\cdots\cdots\cdots\cdots(4)$$

$$\phi_2(x,y)=\varphi_2(x,y) \qquad \cdots\cdots\cdots\cdots\cdots(5)$$

The function φ_1 and φ_2 also satisfy Helmholtz equation

$$\nabla^2\varphi(x, y)+k^2\varphi(x, y)=0 \qquad \cdots\cdots\cdots\cdots\cdots(6)$$

Applying the method of the separation of variables ($\varphi(x,y)=x(x)Y(y)$) to (6), we obtain the following ordinary differential equations,

$$\left.\begin{aligned} &d^2X/dx^2+k_x^2X=0 \\ &d^2Y/dy^2+k_y^2Y=0 \\ &k_x^2+k_y^2=k^2 \end{aligned}\right\} \qquad \cdots\cdots\cdots\cdots\cdots\cdots(7)$$

Solving (7) under now-flow condition on the wave tank wall and under condition that $\varphi_1(x,y)$ represents waves propagating toward the upstream direction and $\varphi_2(x,y)$ waves propagating toward the downstream direction, we obtain

$$\varphi_1(x,y)=\sum_{n=0}^{\infty} C_n\beta_n(y)\cos(n\pi x/b) \qquad \cdots\cdots\cdots\cdots\cdots\cdots(8)$$

$$\varphi_2(x,y)=\sum_{n=0}^{\infty} D_n\bar{\beta}_n(y)\cos(n\pi x/b) \qquad \cdots\cdots\cdots\cdots\cdots\cdots(9)$$

where

$$\left.\begin{aligned} &\beta_n(y)=\exp\{-iy\sqrt{k^2-(n\pi/b)^2}\} \\ &\bar{\beta}_n(y)=\exp\{iy\sqrt{k^2-(n\pi/b)^2}\} \end{aligned}\right\} \qquad \cdots\cdots\cdots\cdots\cdots\cdots(10)$$

For n which satisfies kb>n (n=0,1,...), $\beta_n(y)$ and $\bar{\beta}_n(y)$ represent progressive wave modes, and otherwise (except for n when kb=n) exponentially decreasing stationary wave modes. For the case of kb=n, (8) and (9) give no-propagating wave mode and imply a standing wave exists across the wave tank.

Equations (8) and (9) show the Fourier series expansion of the dimensionless functions φ_1 and φ_2 across the wave tank, thus for example on the imaginary boundary S4 (at y=d), the coefficients $C_n\beta_n(d)$ can be written as

$$C_n\beta_n(d)=\frac{2e}{b}\int_0^b \varphi_1(x,d)\cos\frac{n\pi x}{b}\,dx \qquad \cdots\cdots\cdots\cdots\cdots\cdots(11)$$

where e=1/2 (n=0) and e=1 (n≠0).
Consequently, we obtain the expression of the dimensionless function $\phi_1(x,y)$ in the upstream region (1) as

$$\phi_1(x,y)=\exp(iky)+\sum_{n=0}^{\infty}\frac{\beta_n(y)}{\beta_n(d)}\left\{\frac{2e}{b}\int_0^b \varphi_1(s,d)\cdot\cos\frac{n\pi s}{b}\,ds\right\}\cos\frac{n\pi x}{b} \qquad \cdots(12)$$

In the same way, in the downstream region (2), we obtain

$$\phi_2(x,y)=\sum_{n=0}^{\infty}\frac{\bar{\beta}_n(y)}{\bar{\beta}_n(-l)}\left\{\frac{2e}{b}\int_0^b \varphi_2(s,-l)\cdot\cos\frac{n\pi s}{b}\,ds\right\}\cos\frac{n\pi x}{b} \qquad \cdots(13)$$

The boundary conditions for the inner region (0) can be written

$$\partial\phi_0/\partial\nu=0 \qquad (S1 \qquad S3) \qquad \text{.....(14)}$$

$$\left.\begin{aligned}&\phi_0=\phi_2\\&\partial\phi_0/\partial\nu=\partial\phi_2/\partial\nu\end{aligned}\right\} \quad (S2:\ y=-l) \qquad \text{.....(15)}$$

$$\left.\begin{aligned}&\phi_0=\phi_1\\&\partial\phi_0/\partial\nu=\partial\phi_1/\partial\nu\end{aligned}\right\} \quad (S4:\ y=d) \qquad \text{.....(16)}$$

By applying (4),(5),(12) and (13) to (15) and (16), equations (15) and (16) are rewritten as

$$\left.\begin{aligned}&\phi_0(x,-l)=\varphi_2(x,-l)\\&\left.\frac{\partial\phi_0}{\partial\nu}\right|_{y=-l}=\sum_{n=0}^{\infty}\frac{2e}{b}\alpha_n\left\{\int_0^b\varphi_2(s,-l)\cdot\cos\frac{n\pi s}{b}ds\right\}\cdot\cos\frac{n\pi x}{b}\\&\phi_0(x,d)=\exp(ikd)+\varphi_1(x,d)\\&\left.\frac{\partial\phi_0}{\partial\nu}\right|_{y=d}=ik\exp(ikd)+\sum_{n=0}^{\infty}\frac{2e}{b}\alpha_n\left\{\int_0^b\varphi_1(s,d)\cdot\cos\frac{n\pi s}{b}ds\right\}\cos\frac{n\pi x}{b}\end{aligned}\right\} \qquad \text{...(17)}$$

where $\alpha_n=\sqrt{k^2-(n\pi/b)^2}$

In order to solve the integral equation (3) under these boundary conditions, we divide the boundary, S1, S2, S3 and S4, into a number of small elements ΔS_j (j=1-N1, 1-N2, 1-N3, 1-N4 on S1, S2, S3 and S4, respectively). Now, assuming that ϕ_0 and its normal derivative $\partial\phi_0/\partial\nu$ are uniform on each element, and denoting them by $\phi_0(j)$ and $\bar{\phi}_0(j)$, we can approximate (3) by the following discretaised equation,

$$\phi_0(X)=\left\{\sum_{j=1}^{N1}+\sum_{j=1}^{N2}+\sum_{j=1}^{N3}+\sum_{j=1}^{N4}\right\}\left(\bar{G}_{Xj}\phi_0(j)-G_{Xj}(j)\,\bar{\phi}_0(j)\right) \qquad \text{.....(18)}$$

where

$$\left.\begin{aligned}G_{Xj}&=-\frac{i}{\alpha}\int_{\Delta S_j}\{H_0^{(1)}(kR)+H_0^{(1)}(kR^*)\}\,ds\\\bar{G}_{Xj}&=-\frac{i}{\alpha}\int_{\Delta S_j}\frac{\partial}{\partial\nu}\{H_0^{(1)}(kR)+H_0^{(1)}(kR^*)\}\,ds\end{aligned}\right\} \qquad \text{.....(19)}$$

When the point X is on the center of any element ΔS_i, equation (18) gives a finite set of linear relations between $\phi_0(j)$ and $\bar{\phi}_0(j)$ as

$$\phi_0(i)=\left\{\sum_{j=1}^{N1}+\sum_{j=1}^{N2}+\sum_{j=1}^{N3}+\sum_{j=1}^{N4}\right\}\left(\bar{G}_{ij}\phi_0(j)-G_{ij}\bar{\phi}_0(j)\right) \quad \cdots\cdots\cdots\cdots(20)$$

$$(i=1\sim N1,\ 1\sim N2,\ 1\sim N3,\ 1\sim N4)$$

Applying the boundary conditions (14) and (17) to (20), we obtain

$$\sum_{j=1}^{N1}(\bar{G}_{ij}-\delta_{ij})\phi_0(j)+\sum_{j=1}^{N2}\left\{(\bar{G}_{ij}-\delta_{ij})-\sum_{p=1}^{N2}G_{ip}Q_{jp}\right\}\varphi_2(j)$$

$$+\sum_{j=1}^{N3}(\bar{G}_{ij}-\delta_{ij})\phi_0(j)+\sum_{j=1}^{N4}\left\{(\bar{G}_{ij}-\delta_{ij})-\sum_{p=1}^{N4}G_{ip}Q_{jp}\right\}\varphi_1(j)$$

$$=-\exp(ikd)\sum_{j=1}^{N4}\{(\bar{G}_{ij}-\delta_{ij})+ikG_{ij}\} \quad \cdots\cdots(21)$$

where $\delta_{ij}=1$ (i=j) and $\delta_{ij}=0$ (i≠j);

$$Q_{jp}=\sum_{n=0}^{\infty}\frac{2e}{b}\alpha_n\Delta S_p\cos\frac{n\pi x_j}{b}\cos\frac{n\pi x_p}{b} \quad \cdots\cdots\cdots\cdots(22)$$

Since equation (21) holds for every i-th element, it provides (N1+N2+N3+N4) linear equations with respect to the same number of unknown quantities, ϕ_0(j) on S1, φ_2(j) on S2, ϕ_0(j) on S3 and φ_1(j) on S4. Thus, solving these linear equations and using the boundary condition (17), we can obtain ϕ_0(j) and $\bar{\phi}_0$(j) for all of the boundary element. The function (X) at any point in the inner region (0) can be evaluated by (18), and ϕ_1(X) and ϕ_2(X) by discretaised form of (12) and (13), respectively.

The ratio of the wave amplitude ζ(X) at any point X to the incident wave amplitude ζ_0 is given by

$$|\zeta(X)/\zeta_0|=|\phi(X)| \quad \cdots\cdots\cdots\cdots(23)$$

The pressure p at the cylinder surface are evaluated from the relation $p=-\rho(\partial\Phi/\partial t)$. Thus, the wave force F acting on the cylinder can be obtained from the integration of p around the cylinder surface

$$F/2\rho g\zeta_0 h^2[\tanh kh/kh]=\left|\sum_{j=1}^{N}\phi_0(j)\Delta x_j/h\right| \quad \cdots\cdots\cdots\cdots(24)$$

where ρ is the density of water; Δxj is the x-compornent of ΔS_j on the cylinder; N is the number of the elements on the cylinder.

The reflection and transmission coefficients can be evaluated from energy flux of the reflected wave and the transmitted wave across the imaginary boundaries. The energy

flux of the reflected wave E_r may be written as

$$E_r=\frac{1}{bT}\int_0^b\int_0^T\int_{-h}^0\left\{\rho Re\left[\frac{\partial\Phi_r}{\partial t}\right]Re\left[\frac{\partial\Phi_r}{\partial y}\right]\right\}dz\,dt\,dx \qquad \text{.....(25)}$$

where Φ_r denotes the velocity potential of the reflected wave and it is given from (1), (4) and (8) by

$$\Phi_r=\frac{g\zeta_0}{\sigma}\left\{\sum_{n=0}^{\infty}C_n\beta_n(y)\cos\frac{n\pi x}{b}\right\}Z(z)\exp(i\sigma t) \qquad \text{.....(26)}$$

Substituting (26) into (25), we have

$$\frac{E_r}{E_i}=\sum_{n=0}^{n^*}\frac{\bar{\varepsilon}\alpha_n}{k}|C_n|^2 \qquad \text{.....(27)}$$

where E_r indicates the energy flux of the incident wave given by $(\rho g\zeta_0^2/8)(1+2kh/\sinh 2kh)(\sigma/k)$; $\bar{\varepsilon}=1$ (n=0) and $\bar{\varepsilon}=1/2$ (n≠0); n is the largest integer value among n's satisfying kb>n. Thus the reflection coefficient K_r is given by

$$K_r=\sqrt{\sum_{n=0}^{n^*}\frac{\bar{\varepsilon}\alpha_n}{k}|C_n|^2} \qquad \text{.....(28)}$$

In the same way, from the energy flux of the transmitted wave across the imaginary boundary CD, the transmission coefficient K_t is given by

$$K_t=\sqrt{\frac{E_t}{E_i}}=\sqrt{\sum_{n=0}^{n^*}\frac{\bar{\varepsilon}\alpha_n}{k}|D_n|^2} \qquad \text{.....(29)}$$

and the following relations should be satisfied

$$\sum_{n=0}^{n^*}\frac{\bar{\varepsilon}\alpha_n}{k}\{|C_n|^2+|D_n|^2\}=1 \qquad \text{.....(30)}$$

3. Numerical Calculations and Experimental Verifications

For the numerical analysis, the infinite series of (17) and (22) are replaced by a finite sum upto N*. The integrations in (17) are evaluated with the following discrete form

$$\int_0^b\varphi(s,d)\cos\frac{n\pi s}{b}ds\approx\sum_{p=1}^{N4}\varphi(p)\cos\frac{n\pi\xi_p}{b}\Delta S_p \qquad \text{.....(31)}$$

and this shows discrete Fourie Transform of φ, thus, it is clear, from the theorem of Finite Fourier Series approximation, that N* should be the same number as that of thek^*

divided elements on the imaginary boundary.

Because the set of the imaginary boundaries is only for the creation of the enclosed fluid region to which Green's theorem is applied, the location of the imaginary boundaries has no physical grounds. Thus, the distance of the imaginary boundaries from the cylinder may be arbitrary and no significant difference occurs in numerical results. In the following numerical calculations, the locations of the imaginary boundaries were taken 3h away from the side of the cylinder and the size of the boundary elements were taken about $\Delta s_j/h=0.2$,

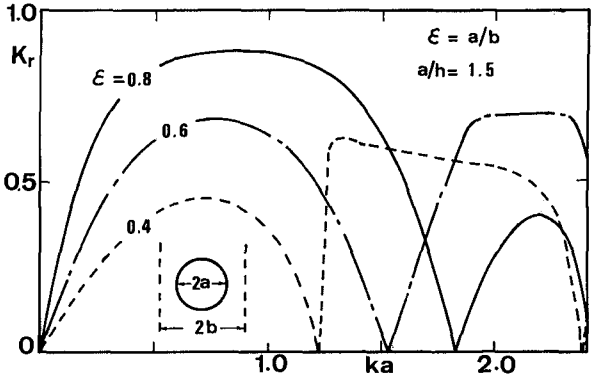

Figure 2. Reflection coefficient for a row of circular cylinders

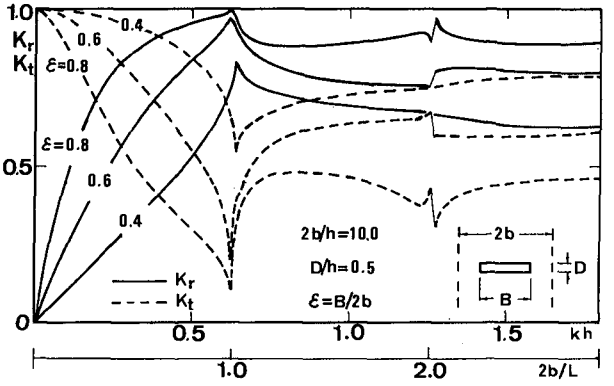

Figure 3. Reflection and transmission coefficients for a row of rectangular cylinders

Figure 2 shows the reflection coefficient for a single row of circular cylinders. The diameter of the cylinder 2a is fixed to 2a/h=3.0 and three different spacing between the cylinders are made to give ε(=2a/2b) of 0.4, 0.6 and 0.8. The reflection characteristics are very much dependent on the incident wave number. Near singular wave number (kb=n) K_r decreases to zero, namely, waves transmits through the cylinder barrier with almost no wave reflection. It is noted that the smaller spacing between the cylinders does not necessarily mean the larger wave reflection.

Figure 3 shows the reflection and transmission coefficients for a single row of rectangular cylinders. The spacing 2b is fixed to 2b/h=10.0, and the width B of the cylinder is changed to give ε(=B/2b) of 0.4, 0.6 and 0.8. The reflection characteristics much differ from those of the circular cylinders, and this shows that the cross-sectional shape of the cylinder is one of main factor for wave reflection-transmission characteristics. At the singular wave numbers where 2b/L=1.0, 2.0,...(L is the incident wave length), it is possible for a standing wave to exist across the wave tank (that is, along the row of the cylinders).

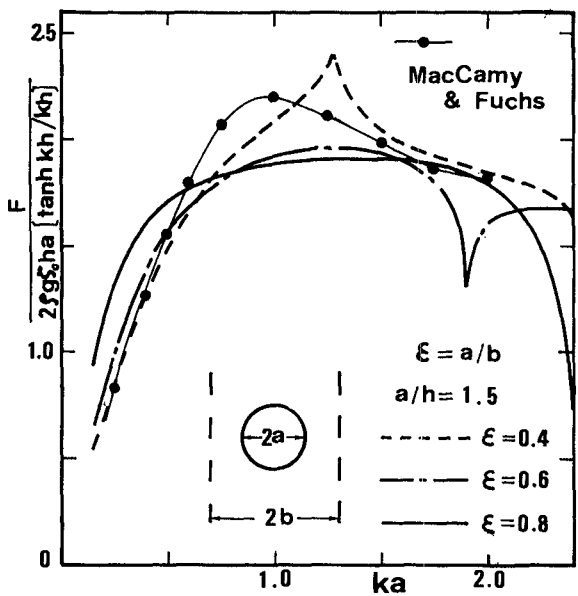

Figure 4. Wave forces for a row of circular cylinders

Wave forces corresponding to figures 2 and 3 are given in figures 4 and 5, respectively. Naturally the forces acting on the cylinders are in line with the direction of the incident wave. Thin solid curve with closed circle in figure 4 represents wave forces acting on a single cylinder in an open-sea given by MacCamy and Fuchs.

Figure 6 shows numerically calculated free surface amplitude around a square cylinder placed on the center line of the wave tank (the case of a row of square cylinders). It is noted that satnding waves appear in the x direction as well as in the upstream direction.

To verify the present method, we conducted wave tank experiments for a row of circular cylinders, a row of rectangular cylinders and two rows of circular cylinders. The wave tank (4m wide × 20m long × 0.6m deep) in the laboratory of Civil Engineering Hydraulics, Kyushu University was used. The diameter of the model cylinders

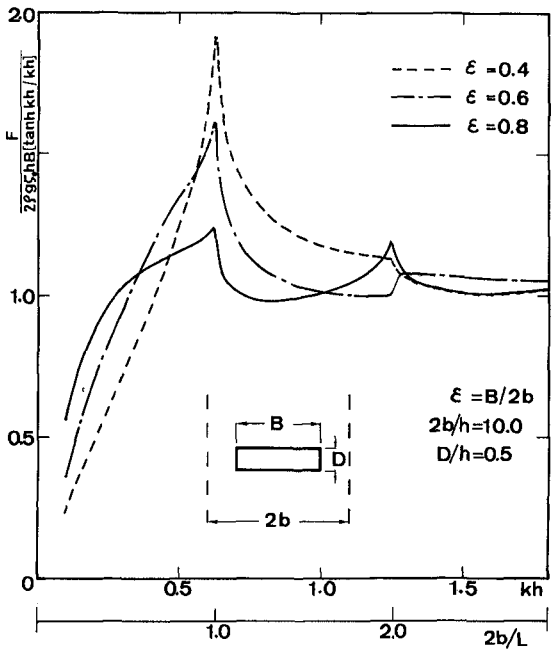

Figure 5. Wave forces for a row of rectangular cylinders

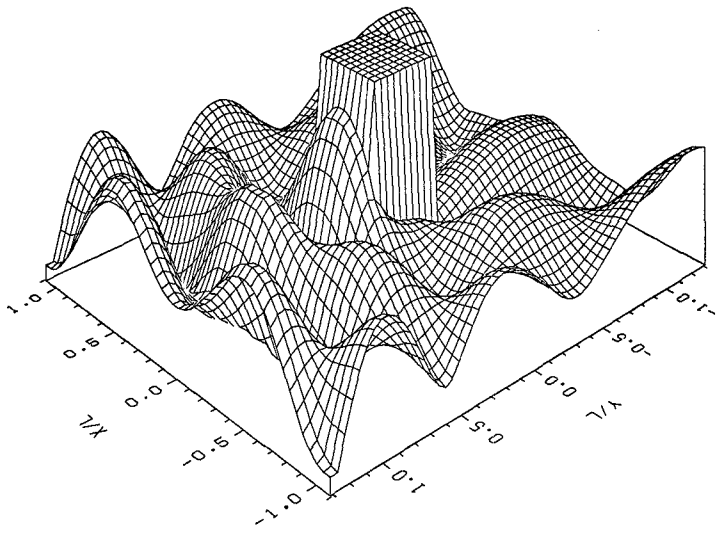

Figure 6. Perspective view of free surface amplitude for a row of square cylinders (kh=1.4, b/h=5.0, B/h=2.0; B is the side length of the square)

were 1.2m, and the size of the rectangular model was 2m by 0.2m. The water depth was kept 0.4m throughout the experiments.

Setting the model cylinders midway of the wave tank, we measured water surface elevation around the cylinders at 20cm by 20cm grid points with 6 capacity type wave gages. The total number of measured grid points were about 200.

The comparisons for perspective view of free surface amplitude between the theory and the experiments are shown in figures 7, 8 and 9. Although the free surface amplitudes drawn from experimental data show rather rough surface compared to the theoretically obtained ones, especially when the free surface is seriously disturbed (for example, figure 9.) because of measured grid points are coarse, overall agreements between the theory and experiments for free surface amplitude are very good.

More precise comparison is given in figure 10 with respect to a contour map of water surface elevation. The number in the contour lines indicates the ratio of free surface amplitude to the incident wave amplitude. Again, very good agreement between the theory and experiment is confirmed.

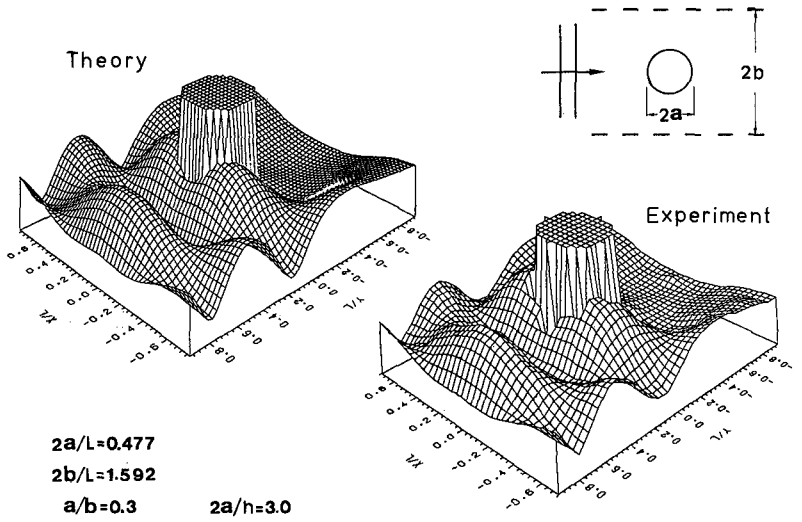

Figure 7. Comparison between theory and experiment for a row of circular cylinders

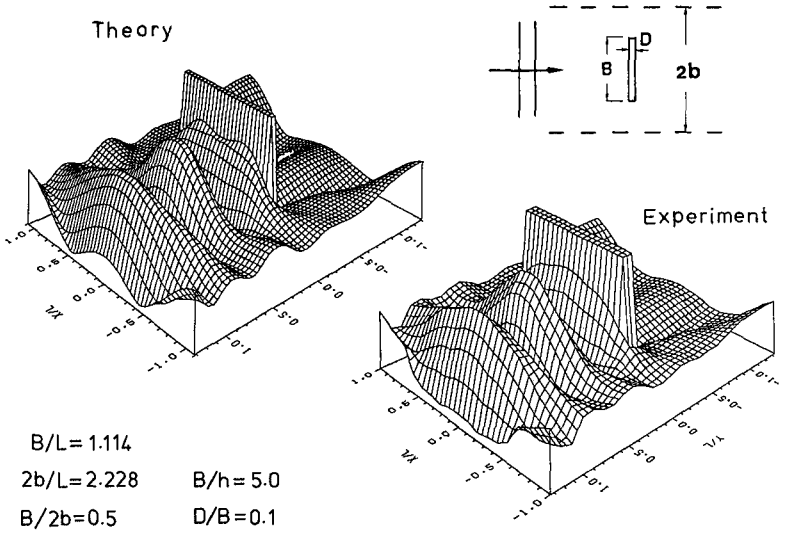

Figure 8. Comparison between theory and experiment for a row of rectangular cylinders

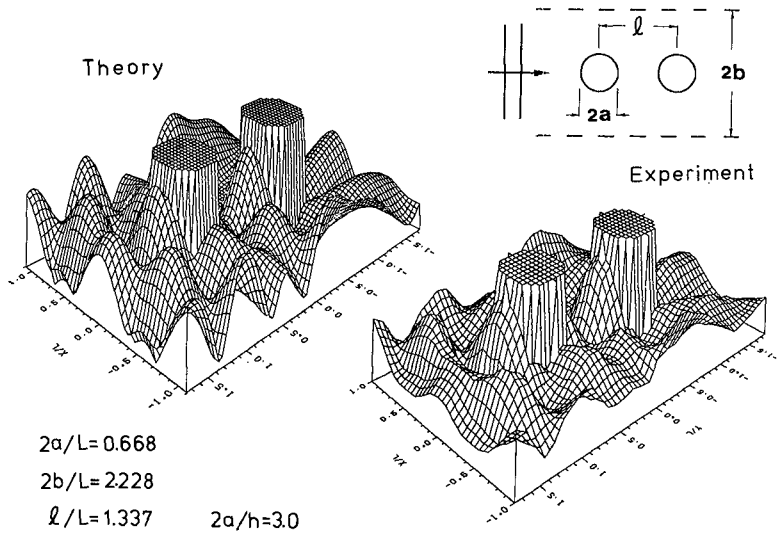

Figure 9. Comparison between theory and experiment for two rows of circular cylinders

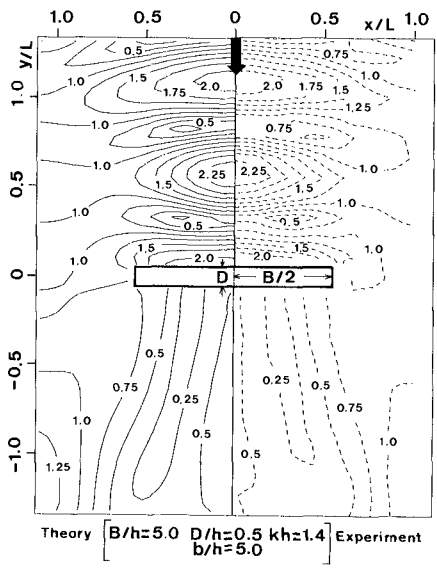

Figure 10. Contour map of free surface amplitude corresponding to figure 8.

4. Conclusions

A simple analytical method using an integral-equation technique has been described for solving wave diffractions by rows of surface-piercing vertical cylinders evenly spaced on sea bottom. The feature of the present method is its easiness to treat diffraction problems of rows of cylinders of arbitrary cross-section and plural row of cylinders: changing the co-ordinates of the boundary elements along the cylinder is the only requirement for variations in the number of the rows and the cross sectional shape of the cylinders.

The method can be easily extended to the case for floating cylinders with flat bottom and for submerged cylinders with flat top, by further applying the Green's Identity Formula for the expression ofthe wave motion in the region between the sea bottom and the bottom of the cylinder and in the region between the free surface and the top of the submerged cylinder. Such cases are related to the problems that frequently occur in Coastal Engineering field, e.g., reflection and transmission problems for rows of floating breakwaters, rows of submerged breakwaters, etc.

The present method is limited to the case that an incident wave direction is perpendicular to the rows of cylinders. More realistic case of oblique incidence needs further study though several studies have been made for a row of circular cylinders by, e.g., Massel (1976) and Miles (1983).

REFERENCES

1 CHAKRABARTI, S.K. (1978). Wave forces on multiple vertical cylinders. Proceedings of American Society of Civil Engineers, 104(ww2): 147-161

2 FALNES, J. (1984). Wave-power absorption by an array of attenuators oscillating with unconstrained amplitudes. Applied ocean research, 6(1): 16-22

3 KYLLINGSTAD,K. (1984). A low-scattering approximation for the hydrodynamic interactions of small wave-power devices, Applied Ocean Research, vol.6, No.3:132-139

4 KAKUNO, S. and ODA, K. (1986). Boundary value analysis on the interaction of cylinder arrays of arbitrary cross-section with a train of uniform waves, Proceedings of Japanese Society of Civil Engineers, No.369, (in japanese)

5 MASSEL, R.M. (1976). Interaction of water waves with cylinder barrier. Proceedings of American Society of Civil Engineers, 102(ww2): 165-187

6 MILES, J.W. (1983). Surface-wave diffraction by a periodic row of submerged ducts. Journal of fluid mechanics, 128: 155-180

7 McIVER, P. and EVANS, D.V. (1984). Approximation of wave forces on cylinder arrays. Applied ocean research, 6(2): 101-107
8 OHKUSU, M. (1974). Hydrodynamic forces on multiple cylinders in waves, Proc. Int. Sympo. Dynamics of Marine Vehicles and Structures in Waves
9 SPRING, B.H. and MONKMEYER, P.L. (1974). Interaction of plane waves with vertical cylinders. Proceedings of the fourteenth coastal engineering conference, 3: 1828-1847
10 SOROKOSZ, M.A. (1980). Some relations for bodies in a canal, with an application to wave-power absorption. Journal of fluid mechanics, 99(1): 145-162
11 TAYLOR, R.E. and HUNG, S.M. (1985). Mean drift forces on an articulated column oscillating in a wave tank. Applied ocean research, 7(2): 67-78

CHAPTER 178

DOLOS ARMOUR DESIGN CONSIDERATIONS

J A ZWAMBORN* and J D P SCHOLTZ**

ABSTRACT

The dolos armour unit has been used all over the world and, although most projects have been successful, there have also been some major failures. When moved around, armour units in general and the rather slender dolosse in particular are prone to structural damage and when dolosse break through the shank, one is left with very unstable pieces of rubble. It is shown in this paper that a safe and economic dolos structure can be obtained if the correct design process is followed. The "optimum" design is based on a reasonable degree of dolos movement which must be established in detailed and representative model tests.

To ensure that the dolosse can withstand these movements, prototype dolos behaviour must be monitored, and such monitoring must be supplemented by representative structural tests, analytical studies and special prototype measurements.

To increase the structural strength of dolosse, the waist to height ratio can be increased and some (simple) form of reinforcing can be included.

1. INTRODUCTION

Much thought has been given to the design of rubble mound breakwaters and considerable effort has gone into obtaining a better understanding of the processes at work and the design techniques after the initial major failures of the Bilboa breakwater in 1976 (35 m depth, 65 t concrete blocks) and the Sines breakwater in 1978/79 (up to 50 m depth, 42 t dolosse; Zwamborn, 1979). In the ten years since these failures progress has been made, particularly in identifying the relevant parameters and in defining the many problems which remain to be solved regarding wave climate, model studies (wave structure interactions), material strength and geotechnical aspects (PIANC, 1985).

Much research will still have to be done on these aspects before a fully reliable design procedure can be developed. In the meantime, however, breakwaters have to be designed with the techniques that are available and particular attention will have to be given to **sensitivity analysis.** This means that the design of the structure should be checked for **realistic variations in the relevant parameters.** The results of this analysis will provide data on the risk of failure or major damage and, at the same time, give an idea of the cost involved in reducing/increasing this task.

* Head, Maritime Structures Division, National Research Institute for Oceanology, Council for Scientific and Industrial Research, South Africa.
** Research Engineer, National Research Institute for Oceanology, Council for Scientific and Industrial Research, South Africa.

These remarks apply to rubble mound breakwaters in general, whether covered with rock armour, simple-shape concrete units (cubes) or complicated-shape units (dolosse) but particularly to the rather slender **dolos armour units.**

It is generally accepted that dolosse have a high hydraulic stability and, in many cases, they offer the most economical solution for breakwaters/shore protection works. Incorrect application of dolosse, however, has resulted in excessive damage due to armour unit breakages.

2. DESIGN APPROACH

There are three different approaches to achieving a safe dolos structure design, namely:

(i) **"No Movement" Design**
In this case the units have to be made to withstand the **in situ** static loads only and the stability can be based on comprehensive and representative hydraulic model tests, using conventional unbreakable model dolosse.

(ii) **"No Breakage" Design**
With this approach the dolosse have to be made "unbreakable" by heavy reinforcing, in one form or other, and stability can be checked by conventional hydraulic model tests aimed at determining acceptable profile changes or unit displacements (the long-term durability of the units/reinforcement must also be considered).

(iii) **"Optimum" Design**
This approach is aimed at a practical and safe design at minimum costs. This is achieved by accepting certain dolos movements, including rocking, and ensuring that the units can withstand these movements without breakage (minimal breakage).

"No Movement Design

Static loading tests on 15 t and 30 t **unreinforced** dolosse have shown that these dolosse can carry 4 to 6 times their own weight under the worst possible loading condition without breakage (Grimaldi and Fontana, 1984).

As no particular problems have been encountered in handling unreinforced dolosse up to 50 t in the casting and placing process (breakages did not exceed 1 to 2 per cent) and because the direct wave forces are of the same order or less than the dead weight forces, a dolos armour consisting of several layers can be designed safely on the basis of hydraulic model test results if these show that there is no significant movement (rocking). In determining the "no movement" criterion, however, **detailed tests** would have to be done, taking into account:

a) realistic and representative design conditions, particularly for waves (wave spectrum/groupiness),
b) possible variation (reliability) of design conditions,
c) storm duration and cumulative effects
d) near-shore effects,
e) variation in test results,
f) the extent of the structure and

g) three-dimensional effects.

Because the "no movement" criterion basically mean that the design must be based on H_{max}, the result could become rather uneconomical.

"No Breakage" Design

The other extreme would be to ensure that the dolosse are **unbreakable** under prototype loading conditions. In this case the design can be based on conventional hydraulic model tests which have to prove that armour displacement will be within acceptable limits, for instance, Figure 1 indicates K_D factors between 25 and 30 for 1 to 2 per cent displacement. **Detailed tests,** as described above, will be necessary to ensure a safe design. The results of these tests could also be used to optimise the design, that is to minimise the total cost (capital investment plus maintenance cost).

This approach is the easiest with regard to model testing but there are two major problems, namely, to determine the **prototype loading conditions** and to make the dolosse **unbreakable** for these conditions without losing the coast advantage of the units' high stability.

Extensive tests have been done with different types of reinforced dolosse (Burcharth, 1981 and Grimaldi and Fontana, 1984). The test results showed limited improvement in impact strength with from 30 kg/m³ up to 120 kg/m³ (0,4 to 1,6 per cent by volume) **steel fibres,** that is, an increase in drop heights from about 20 to 150 per cent at "failure" (major damage and/or breakage). **Conventional steel reinforcement** of 77 to 138 kg/m³ (1 to 1,8 per cent by volume), however, was found to make the dolosse virtually unbreakable. Although first crack formation occurred at drop heights only about 50 percent higher than for unreinforced units, serious damage (major cracking and spalding which exposed the main reinforcing bars) occurred for drop heights 4 to 8 times those of the unreinforced units (0,8 to 1,6 m for 30 t dolosse at Gioia Tauro). Moreover, tests at Gioia Tauro, where a 30 t dolos with a waist ratio of 0,37 and reinforced with conventional steel reinforcement (77 kg/m³ or 1 per cent by volume) was dropped on the breakwater core, showed no serious cracks up to a drop height on 10 m. Although the **in situ** loading is not known, one would intuitively consider this dolos to be strong enough (mechanically) to withstand the **in situ** forces caused by movements/rocking.

Drawbacks of conventionally reinforced dolosse are additional **cost** (50 to 100 per cent more expensive, which could make dolosse unattractive in many applications) and the possibility of **corrosion** causing possible deterioration of the units with time.

"Optimum" Design

It seems obvious that there should be an "optimum" design between the two extremes discussed above whereby a certain amount of **movement/rocking is accepted** while the dolos units are made strong enough to withstand these limited movements without increasing their cost too much.

As early as 1972 it was suggested that the **waist-to-height ratio** (r) of larger dolosse be increased according to:

$$r = 0{,}34\sqrt[6]{\frac{W}{20}}$$

where W is the mass of the dolos in tons, to compensate for the higher stresses occurring in larger dolosse (Zwamborn and Beute, 1972). A simple analysis showed that, when using this formula, dolos stresses would remain about the same with increased dolos mass (Zwamborn, **et al**, 1980). The more rigid structural analysis by Burcharth (1981a) supports this finding (Zwamborn, 1985). The beneficial effect on the structural strength of the dolos was also confirmed by prototype tests on 15 to 30 t units at Gioia Tauro (Grimaldi and Fontana, 1984).

It is obvious that, to get greater unit strength, even larger waist-ratios could be used. However, stability tests with regular waves on dolosse with waist ratios of 0,33, 0,38 and 0,43 showed a gradual reduction in stability for the larger waist ratios, which was to be expected. The reduction in stability from r = 0,33 to 0,38 was relatively small but the test results indicate a significant reduction in K_D for dolosse with r = 0,33 to 0,43 (Scholtz, Zwamborn and Van Niekerk, 1982). As a waist ratio of 0,43 corresponds to an 82 t dolos unit, there is still considerable scope in using the waist ratio in the optimisation of the design (Burcharth, 1981b). Structural performance of dolosse can also be significantly improved by proper mix design and good quality control (Zwamborn, **et al**, 1980).

Single central scrap **rail reinforcement** was used in the original East London dolosse, mainly to lift the units out of the mould. In the redesign of the Gioia Tauro breakwaters (Grimaldi and Fontana, 1984) it was decided (1979) to introduce single-scraprail reinforced 30 t dolosse in the more critical areas on the breakwater heads for extra safety and to reduce maintenance (27,4 kg/m³ steel or 0,35 per cent by volume). Subsequently, the designers (Polytecna Harris of Milan) developed the so-called **double-V rail reinforcement** which consists of a frame with four scraprails in the dolos trunk and one scraprail each in the flukes (53 kg/m³ steel or 0,7 per cent by volume). This solution proved to be both very effective and economical; the critical drop heights were found to come fairly close to those of the conventionally reinforced units while the possibility of corrosion was minimized and the extra cost for the reinforcing was reasonable (extra cost for double-V reinforced dolosse being about 60 per cent in Italy and about 26 per cent in South Africa).

Various relatively cheap methods to improve the strength of dolosse have been discussed above. Unfortunately, it is not possible to define the exact dolos strength required when a certain amount of moving/rocking is allowed to occur under design conditions. Prototype observations have provided reasonable proof that dolos structures designed on the basis of a few per cent (2 to 3) total damage (displacement plus rocking) performed satisfactorily. There is no doubt that strength-improved (e.g. scraprail-reinforced) units will be able to withstand considerably greater movement/rocking but more observations and (full scale) tests are needed to confirm the effectiveness of these improvements, that is, to arrive at the "optimum" design.

3. STABILITY MODEL TESTS

The results of a comprehensive series of dolos stability tests for regular waves are shown in Figure 1. The figure shows damage as a function of

model wave height for different degrees of dolos movements, that is, displacements and rocking. For easier use of the data, a scale for the Hudson stability factors (K_D) has been added.

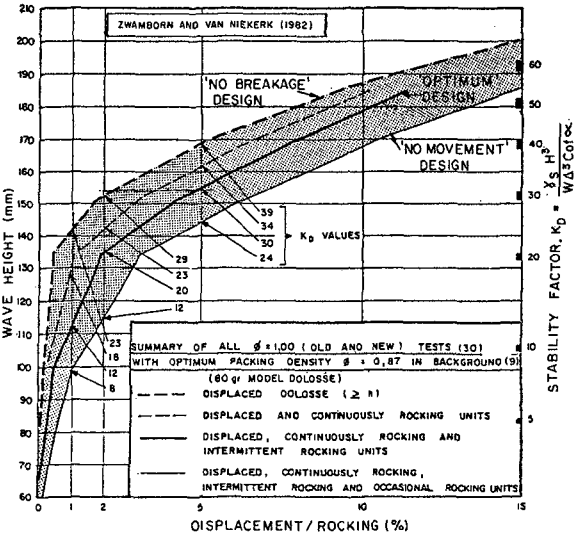

Figure 1: Damage (Displacement/Rocking) versus wave height/stability factor

A similar test programme for irregular waves, under otherwise identical conditions, is underway at present. Results of these tests will become available during 1987.

Although the results shown in Fig. 1 may be used for a first design, detailed and preferably three-dimensional model tests of a specific application using representative wave conditions are a prerequisite for a good design. In these tests, dolos motions/accelerations should be determined as accurately as possible. Dolos motions can be recorded with the now well-known cine and overlay techniques. Alternatively, more advanced measuring techniques can be used to measure accelerations and stresses in individual model armour units but a large number of units would have to be instrumented for each test condition to get statistically reliable results and these results will have to be compared with prototype measurements, as planned in Table Bay and Crescent city (Howell, 1986).

4. PROTOTYPE DOLOS BEHAVIOUR

Details of the behaviour of dolos structures around the world, including ten South African structures, are included in a report entitled "Survey of Dolos Structures" (Zwamborn and Van Niekerk, 1981) which was used extensively for the later survey carried out for PIANC (PIANC, 1985). Further data, for selected South African projects, covering the period 1979 to 1982, are included in Zwamborn (1985) while an update of these projects is given below.

Prototype monitoring in other parts of the world include measurements at Gioia Tauro, Italy (Grimaldi and Fontana, 1984), monitoring of the 2 t dolos breakwater at Cleveland, USA (Markle and Davidson, 1984) and the planned extensive monitoring programme at Crescent City, USA (Howell, 1986).

Richards Bay Breakwater

The Richards Bay main breakwater is protected with 5 t, 20 t and 30 t dolosse placed to slopes of 1 in 1,5 and 1 in 2. This breakwater was completed in Frebruary 1976 and has been monitored at regular intervals since 1978. The monitoring was concentrated on the above-water part of the dolos armour, with the 20 t dolosse on the trunk and the 30 t dolosse on the head of the breakwater. Techniques used were vertical and horizontal photography, visual observations and profiling with a spherical cage, made of reinforcing steel, with a diameter of 2,5 m (0,6 h, were h is the dolos height).
The following survey and storm data have become available since the 1982 review (Zwamborn, 1985):

Breakwater Monitoring		Storm Data						
Date	Type of Survey	Date	H_{s-r} (m)	T_p (s)	Direction (°deep sea)	H_{s-b} (m)	H_{max} (m)	Tide (m+CD*)
24-6-83	Vertical photography	17-2-84	4,3	11,9	140	5,3	10	0,4
		9-4-84	4,0	9,7	117	2,5	5	1,0
		10-4-84	4,1	10,7	147	4,4	8	0,8
		27-4-84	4,5	13,5	140	5,4	10	0,9
		30-5-84	4,3	22,3	160	5,4	10	1,0
4-7-85	Vert. photo. (large scale)	12-7-85	4,1	7,5	120	2,6	5	0,8
24-6-86	Vert. photo.							

*Chart Datum

Only storms with significant wave heights exceeding 4 m have been included in this table. The wave heights (H_{s-r}) and the wave periods (T_p) were recorded by waverider anchored in the 20 m water depth, about 1,5 km seaward of the south breakwater head. Wave directions were recorded by wave clinometer. H_{s-b} values are the wave heights directly in front of the breakwater head, determined from actual measurements made in the original physical model during three-dimensional breakwater stability tests. Because the wave height measurements apply to a 6-hour period, H_{max} = 1,9 H_{s-b} (Longuet-Higgins, 1952). Most of the storms occurred at high tide. The depth at the breakwater head decreased from the original -17 to -12 m CD about 300 m from the breakwater head. This means that at high tide (+1,8 m CD) the maximum breaker height can be about 0,9 x 13,8 = 12,4 m (Jackson, 1968).

Detailed analyses of a section of the breakwater head on which were placed 1 045 30 t dolosse with a waist-to-hight ratio of 0,36 were possible with the use of large-scale vertical photographs. The results of these analyses can be

summed up as follows ("damage" is taken as the sum of the lost and broken units):

Monitoring Date	Storm Data (H_{s-r} > 4 m)		Damage (%)*			
	Date	H_{max} (m)	Lost	Broken	Moved	"Damaged"
28-6-79	24-7-79	8				
	17-4-80	10				
18-6-81	17-8-81	9	0,6	0,8	0,8	1,4
5-12-81	-	-	0	0,2	0,2	0,2
5-6-82	-	-	0	0	0	0
24-6-83	-	-	0,4	0,4	0,2	0,8
	17-2-84	10				
	9-4-84	5				
	10-4-84	8				
	27-4-84	10				
4-7-85	30-5-84	10	0,8	0	0	0,8
24-6-86	12-7-85	5	0	0	0	0
TOTAL OVER 7 YEARS			1,8	1,4	1,2	3,2

*Damage above Low Water based on 500 30 t dolosse

Gansbaai Harbour

The Gansbaai harbour breakwater, described in Zwamborn and Van Niekerk (1981), was repaired between 1979 and 1982 with 505 20 t and 1 630 25 t dolosse at slopes of 1 in 2 and 1,75 respectively. The performance of these dolosse was closely monitored by regular visual observations, including underwater diver surveys, during construction and after the occurrence of large waves (Zwamborn, 1985).

The following data on conditions since completion of the repair work were made available to the Fisheries Development Corporation (no local wave data available after 1982):

Breakwater Monitoring			Storm Data						
Date	Dolos Breakages (%)		Date	H_{s-r} (m)	T_p (s)	H_{s-b} (m)		H_{max} (m)	Tide (m+CD)
	20 t	25 t				WSW	11°N of W		
July 1982	0,2	0,1	12-7-82	3,4	12	1,7	6,0	8	0,6
			17-7-82	3,7	18	2,3	6,4	8,5	1,2
			29-7-82	4,2	14	2,6	6,7	8,5	0,9
April 1984	-	0,25							
May 1984	1,2	0,7	15-5-84	10,8	15,5	(Slangkop)		8,5	1,5
TOTAL	1,4	1,05	Breakages over about 4 years*						

*Some repair work was done after the 16th May 1986 storm.

Koeberg Cooling-Water Intake Basin

The breakwaters forming the Koeberg intake basin are protected with 6 t, 15 t and 20 t dolosse placed at a slope of 1 in 1,5 (Zwamborn and Van Niekerk, 1981). Some 2 295 20 t dolosse were used to armour the main breakwater from chainage 750 to 912 m, which includes the head. The entire main breakwater has depth-limiting design conditions; the depth at its head is -8 m CD and waves with $H_s \geq 3,2$ m were assumed to start breaking on the head (H_{max} = 6,4 m). This means that the design waves (6,4 m breaking waves) occur on average 15 days per year, which was taken into account in deciding on acceptable damage criteria.

The following data have been collected since the previous review (Zwamborn, 1985):

Breakwater Monitoring			Storm Data (H_{s-r} > 3 m)				
Date	Type of Survey	Damage (20 t)	Date	H_{s-r} (m)	T_p (s)	H_{max} (m)	Tide (m+CD)
11-11-81	Horizontal photography						
	(37 storms)		2-1-82 to 10-6-83	3,2 to 5,9	8,8 to 15,5	5,7 to 6,9	0,2 to 1,8
14-6-83	Visual Inspection (9 storms)	(No change)					
			25-6-83 to 31-1-84	3,6 to 5,4	11,9 to 15,5	5,6 to 6,5	0,4 to 1,3
	("100 year" storm)		16-5-84	6,7	15,5	7,4	2,5
29-5-84	Visual, above and below water (11 storms)	0,44					
			29-6-84 to 5-10-84	3,4 to 7,2	11,9 to 18,3	5,9 to 6,6	0,5 to 1,4
17-10-84	Horizontal photography	(No change)					

Concluding Remarks

Prototype measurements of dolos behaviour have provided evidence that 30 t dolosse with a waist ratio of 0,36 placed on the Richards Bay breakwater head can withstand 10 m waves with only about 3 per cent "damage". Applying Figure 1, the expected total damage would be 3 per cent displacement plus all types of rocking, or about 2 per cent when excluding occasional rocking (heavy line in Figure 1).

The newly placed 20 and 25 t dolosse at Gansbaai (waist ratios 0,34 and 0,35 respectively) have withstood four storms with waves reaching 8,5 m with only 1,4 and 1,05 per cent breakages respectively (including the underwater part). For this wave height, Figure 1 indicates 2,5 and 2 per cent "total damage", or 1,5 and 1 per cent excluding occasional rocking, for the 20 and 25 t units respectively.

The 20 t dolosse at Koeberg (waist ratio 0,34) showed little damage (only 0,44 per cent for the "100 year" storm of May 1984) over a period of three years when 6 and 7 m breaking waves attacked the breakwater on 58 occasions. For these wave heights, Figure 1 would indicate 1 per cent "total damage" or 0,5 per cent excluding occasional rocking.

These observations, together with experience in the USA (Markle and David-

son, 1984), provide evidence that well-designed dolos structures (that is, considering different dolos movements) can withstand severe and sustained wave action with nominal damage. However, considerable damage has occurred in certain cased which emphasizes the need for a special and detailed design effort for major dolos projects.

5. STRUCTURAL TESTS ON DOLOSSE

Drop Test on Solid Concrete

In the foregoing, reference has been made to structural tests which provide invaluable data regarding the relative strengths of dolosse of different design, concrete quality and reinforcing. A standard drop test on a solid concrete base has been proposed for dolosse by Burcharth (1981a). Burcharth found that trunk breakage occurred for drop heights (centre of gravity) of 0,12 to 0,17 m using 1,5, 5,4, 10 and 20 t unreinforced dolosse.

The results of similar drop tests carried out at Gioia Tauro, Italy, on 15 t (r = 0,32) and 30 t dolosse (r = 0,37) (Grimaldi and Fontana, 1984) showed a considerable improvement in dolos strength with time (pozzuolana cement was used), the positive effect of the larger waist ratio of the 30 t units, the limited benefit of the steel fibres and the effectiveness of, particularly, the double-V reinforcement.

Gioia Tauro Free Fall Test

The standard drop test is carried out on a rigid base and failure is virtually due to impact loading only. In a breakwater armouring, a dolos will either drop on underlayer stone or on another dolos, both of which will probably move under the impact. A dolos breakage test which more closely represents conditions on an actual breakwater, should, therefore, include a realistic yield comparable to movement of the underlaying dolos and/or stone. Further drop tests and free fall tests were, therefore, done at Gioia Tauro onto a 50 to 1 000 kg rock fill bed and onto the breakwater core (Figure 2).

Test on Rock Test on Core Material

Figure 2: Free-fall tests with 30 t dolosse

The mean results of the tests on 30 t dolosse as interpreted by the author, are given below:

Age (months)	No. Repeat Tests	Type of test	Test bed material	Reinforcement type (kg/m³)	Failure or Damage	
					Fall Height L (m)	Impact Velocity V (m/s)
2,5	2	drop	rock	-	2,4*	5,9*
3,5	1	drop	rock	Twisted fibres (75)	2,4*	5,9*
2,5	3	free fall	rock	-	1,5	5,4+
3,5	2	free fall	rock	Twisted fibres (75) and steel fibres (95)	2,5	7,0
2	1	free fall	rock	Double-V (53)	2,6	7,1
2	2	free fall	core	Double-V (53)	2,5/5,0	7,0/9,9
2	1	free fall	core	Conventional (77)	10	14

*Maximum possible lifting height, no visual damage.

The most significant result of these tests is that the critical fall heights with a realistic yield are about 10 times greater than for the rigid-base case which means that unreinforced dolosse should be able to withstand considerable movements/rocking without breakage, a fact which is born out by prototype observations.

Controlled Yield Tests on 9 t Dolosse

Because tests on rubble are difficult to control fully and because the inclusion of a certain yield is essential to get results more directly comparable with the actual breakwater situation, a test technique by which the impact deceleration is controlled by a given yield has been developed for full scale tests on 9 t dolosse at Cape Town. The test configurations shown in Figure 3 were used for the Table Bay tests, that is, the swing test configuration.

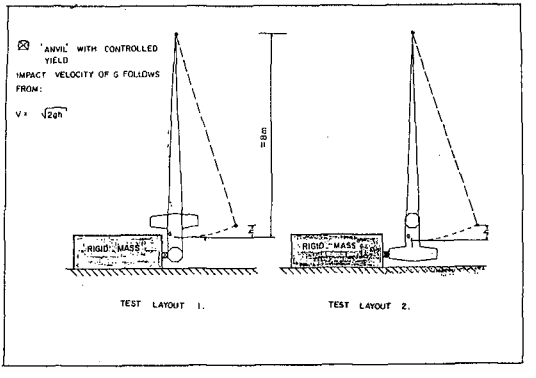

Figure 3: Dynamic Impact Test Arrangements

The height of the 9 t test dolosse was 2,9 m and the waist-to-height ratio was 0,30. The units were made of 40 MPa concrete (28 days). The tests included dolosse without reinforcing and with three types of 43 kg/m **scrap rail reinforcing**, that is a single central rail, the so-called double-V reinforcing designed by Grimaldi and Fontana (1984) and the X-type reinforcing developed by the NRIO (see Figure 4).

Single-rail Reinforcement Double-V Reinforcement X-Type Reinforcement

Figure 4: Rail Reinforcement in 9 t Dolosse

The purpose of the tests, carried out in co-operation with the South African Transport Services, were:

a) to develop a test procedure closely resembling conditions in a breakwater armour;

b) to determine the effectiveness under representative loading conditions of the different types of reinforcement;

c) to determine the effect of repeated impact loading, and

d) to decide on the type and extent of reinforcing for the 25 t dolosse to be used for the breakwater repair.

Figure 5: Free-fall tests on 0,5 to 3 t rock.

To determine a realistic yield, representing the impact of dolosse on underlayer stone or other dolosse, the first test series involved dropping a 9 t (reinforced) dolos onto 0,5 to 3 t underlayer stone (Fig. 5). Decelerations on impact were measured during these tests with two PCB Piezotronics shock accelerometer with 500 g range, fitted on the trunk and on the top shank (Fig. 5).

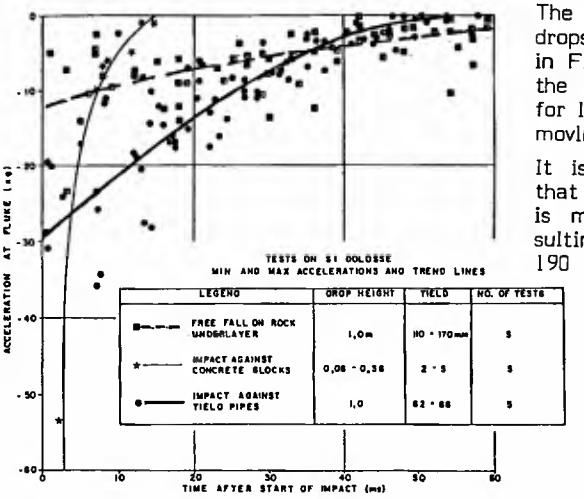

Figure 6: Comparison of accelerations for different test procedures

The results of 5 repeated drops, over 1 m, are plotted in Fig. 6, which also includes the recorded decelerations for impact against solid, non-moving concrete blocks.

It is clear from this figure that the impact on the rock is much more "gentle" (resulting in ayiled of 110 to 190 mm) than that against the rigid concrete blocks and thus, the **resulting stresses in the dolosse are therefore much smaller.**

Because the impact on rock will depend largely on the rock packing and will thus be variable (see spread of points in Fig. 6 for large impact time values), swing test were done using a representative "cushioning device". Considering that, in reality dolosse could either fall onto underlayer rock or on parts of other dolosse, a "cushioning device" consisting of three collapsible "yield pipes" (Fig. 7; 3 pipes: 89 mm OD, 4,5 mm thick and 250 mm long) was designed to give approximately twice the initial deceleration of the free drop-on-rock case but with a similar ultimate impact time of 40 to 60 ms. In this way, a conservative test condition was developed representing breakwater conditions quite realistically.

Figure 7: Cushioning Device

The actual test configuration is shown in Figures 8 and 9. The tests are still underway at present but preliminary results of the tests, according to the Test Layout 2 of Fig. 3, are given in the following table:

Figure 8: General Test Arrangement

Figure 9: Dolos (9t) at impact

Age (Months)	No. Repeat Tests	Type of Tests	Test Bed Material	Reinforcement (kg/m³)	Failure or Major Damage		Mean Yield (m)
					Fall Height (m)	Impact Velocity (m/s)	
19	3	Swing	Yield Pipes		2,3/2,6/2,9	6,7/7,1/7,5	0,16
12/15/18	3	Swing	Yield Pipes	Single Rail (85)	2,6/2,9/2,9	7,1/7,5/7,5	0,17
12	2	Swing	Yield Pipes	X-Rail (115)	3,5/3,5	8,3	0,18
18	2	Swing	Yield Pipes	Double-V (168)	3,8/4,1	8,6/9,0	0,18

The above results show:

(i) similar "failure" drop heights as found at Gioia Tauro,
(ii) the results of repeat tests do not differ much,
(iii) whereas unreinforced dolosse break in the "rigid" drop test for drop heights exceeding about 0,2 m, with a representative yield, the critical drop heights are well above 2 m,
(iv) there appears to be little difference between unreinforced and singrail reinforced dolosse but the latter will be damaged rather than fail,
(v) the double-V and X-type rail reinforcing increase the critical fall heights by 50 to 80 per cent and these are only damaged and did not fail.

Thus the **rail reinforcement** is found to be **very effective** in increasing the dolos strength and preventing dolos failure.

Burcharth (1984) has shown that repeated impact loading rapidly weakens the dolosse. For instance, impact failure will occur after three repeat loadings causing stresses of 10 per cent of the ultimate impact strength compared with 20 loadings in the case of a "pulsating" load/normal fatigue, see Figure 10.

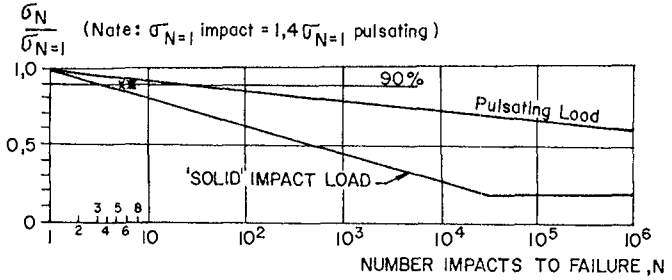

Figure 10: Average Results of Impact Tests on Dolosse (Burcharth)

The results of the first series of fatigue tests done on the 9 t dolosse are:

Type of Dolos	Number of tests	Fall Height	Number of impacts until failure
Unreinforced	2	2,0 m	5 and 7
Double V-reinforcing	1	3,2 m	7

These tests were done with a fall height of 80 per cent of the failure height and the results are plotted in Figure 10*. As expected, considering the inclusion of the cushioning device, the results fall between the pulsating and "rigid" impact lines which means that, in the breakwater situation the dolosse should be able to withstand about twice the number of impact loads predicted by the rigid impact test.

6. CONCLUSIONS

It is concluded that carefully designed dolos structures can withstand large waves with only minor (a few per cent) damage. Shortcomings in the design and/or construction and a lack of understanding of the structural limitations of dolosse can, however, result in significant damage or even local failure of the structure. A detailed and careful design process, as discussed above, will therefore have to be followed to arrive at a safe yet economical design.

An "optimum" dolos armour design should be based on a limited degree of movement using increased waist ratio and/or simple rail reinforcement to strengthen all the dolosse or only those in the more critical areas. Detailed information on **in situ** dolos movements and resulting structural dolos behaviour are required to achieve this. The results of measurements underway in South Africa and elsewhere should provide this information.

7. ACKNOWLEDGEMENT

The assistance of the Harbour Engineer and staff (Cape Town) with the prototype tests is gratefully acknowledged.

*Burcharth (1984) assumed stresses proportional with square root of drop height, thus, for 80 per cent case, $\frac{\sigma N}{\sigma N=1} = \sqrt{0,8} = 0,9$

8. REFERENCES

BURCHARTH, H F (1981a). Full-scale dynamic testing of dolosse to destruction. Coastal Engineering, Vol 4, No 3, Amsterdam.

BURCHARTH, H F (1981b). A design method for impact loaded slender armour units. Proc. ASCE Speciality Conference, New York.

BURCHARTH, H F (1984). Fatigue in breakwater concrete armour units. Report Laboratoriet for Hydraulic of Havnebygning, Aalborg.

GRIMALDI, F and FONTANA, F (1984). Redesign of main breakwater of Gioia Tauro (Italy). Proc. Symposium on Maritime Structures in the Mediterranean Sea, Athens.

HOWELL, G (1986). A system for the measurement of the structural response of dolos armour units in the prototype. Proc, International Conf. on Measuring Techniques, London.

JACKSON, R A (1968). Limiting heights of breaking waves and non-breaking waves on rubble-mound breakwaters. Technical Report No H68.3, WES, Vickburg.

LONGUET-HIGGINS, M S (1952). On the statistical distribution of the heights of sea waves. Journal of Marine Research, Vol XI, No 3.

MARKLE, D G and DAVIDSON, D D (1984). Breakage of concrete armour units; survey of existing Corps structures. Misc. Paper CERC-84-2, Vicksburg.

PIANC, (1985). The Stability of rubble mound breakwaters in deeper water. Supplement to Bulletin No 48 (1985), PIANC, Brussels.

SCHOLTZ, D J P, ZWAMBORN, J A and VAN NIEKERK, M (1982). Dolos stability, effect of block density and waist thickness. Proc. 18th ICCE, Cape Town.

ZWAMBORN, J A and BEUTE, J (1972). Stability of dolos armour units, ECOR Symposium, S71, Stellenbosch.

ZWAMBORN, J A and VAN NIEKERK, M (1981). Survey of dolos structures. CSIR Research Report 385, Stellenbosch.

ZWAMBORN, J A and VAN NIEKERK (1982). Additional model tests, dolos packing density and effect of relative block density. CSIR Research Report 554, Stellenbosch.

ZWAMBORN, J A (1979). analysis of causes of damage to Sines breakwater. Proc. Coastal Structures 79, ASCE Speciality Conference, Alexandria.

ZWAMBORN, J A **et al** (1980). Dolosse: past, present and future? Proc. 17th ICCE, Syndney.

ZWAMBORN, J A (1985). Behaviour of Dolos Structures, particularly in regard to unit strenth. Proc. Workshop on Armour Units, CERC, WES, Vicksburg.

CHAPTER 179

Verification of the Consequences of Wavedirectionality on the Loading of Long Coastal Structures by Field Experiments

J. van Heteren *
H.C. Botma **
A.P. Roskam ***
J.A. Battjes ****

Summary

Field measurements were done at the Haringvliet barrier to verify the theory that loading on long structures shows a considerable reduction if wave directionality is taken into account instead of calculating with uniform long crested waves.

Wave loads were measured with a row of pressure meters at the barrier. Directional parameters of the incoming wave field were calculated from the signals of a 3-component acoustic current meter, mounted 7.5 meter in front of the barrier. These calculations were different from those used for an open sea, since the waves near a reflecting structure are formed by two highly correlated wave fields.
The agreement between the results of the measurements and theory is good.

1. Introduction

In the Oosterschelde, one of the sea arms in the southern part of the Netherlands, a storm surge barrier is being built with a length of 4,500 m and an entrance aperture of 14,000 m^2. At the design of this barrier it turned out that the wave loads on the structure are probably influenced by wave directional properties.

To determine these influences a mathematical model has been developed by Battjes, with the incoming main wave direction, the short crestedness, the wave frequency and the length of the structure element as inputs (Battjes, 1982). It appeared that considerable reductions of wave loads can be expected if wave directionality is incorporated. The mathematical model was verified by comparison with emperical data, but the number of useful data available for this purpose was rather limited. Therefore a field campaign was held at a similar barrier in 1982/1983, covering simultaneous measurements of wave pressures at the barrier and the wave directional spectrum of the approaching waves.

* J. van Heteren, Senior Engineer, Road and Civil Engineering Department, Rijkswaterstaat, The Hague, The Netherlands.
** H.C. Botma, Senior Engineer, TNO-Institute of Applied Physics, Delft, The Netherlands.
*** A.P. Roskam, Project Engineer, Tidal Waters Directorate, Rijkswaterstaat, The Hague, The Netherlands.
**** J.A. Battjes, Professor, Dpt. of Civil Engineering, Delft University of Technology, Delft, The Netherlands.

To eliminate the influence of the foreland in front of the barrier, the wave directional spectrum had to be measured close by the barrier. As a consequence these measurements were made in a combination of two highly correlated wave fields: the incoming and the reflected wave field. This complicates the derivation of the wave directional parameters from a 3-component orbital velocity measurement considerably.

2. Measurements

The measurements were made at one of the gates of the storm surge barrier in the Haringvliet, a sea arm near the Oosterschelde. This barrier is directed from south-west to north-east and is sheltered by shoals from the North Sea and for south-westerly gales also by one of the islands (fig. 1). The local water depth ranges from 12 m close by the barrier to 4 m at the shoals.

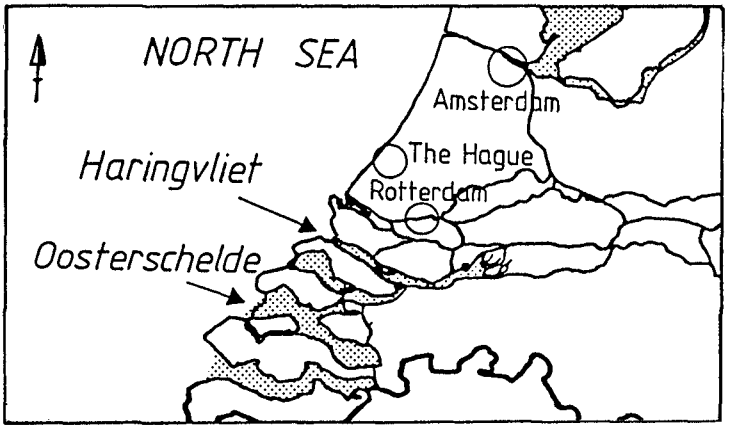

Figure 1. General Topography

Since the depth in the region close to the barrier is relatively large and the bottom is rather flat, the directionality of the wave field close by the barrier is not influenced by refraction. The tidal range in the area is about 1.8 meter. The front of the barrier is not a plane vertical wall, but a smooth cylindrical shaped steel surface.

Pressure was measured at five positions, distributed horizontally along the barrier, covering a width of 14 m.

In front of the barrier a simple steel frame was fixed, carrying 3 pressure gauges A, B and C and the 3-component acoustic current meter V, see figure 2.

In fact the bodies of all four meters were fixed to the central pole of the frame and the pressure intakes and the velocity sensor were fixed to beams, welded to the pole. This ensures that the measurements are taken in parts of the water where the movements are not disturbed too much by the instrument bodies.

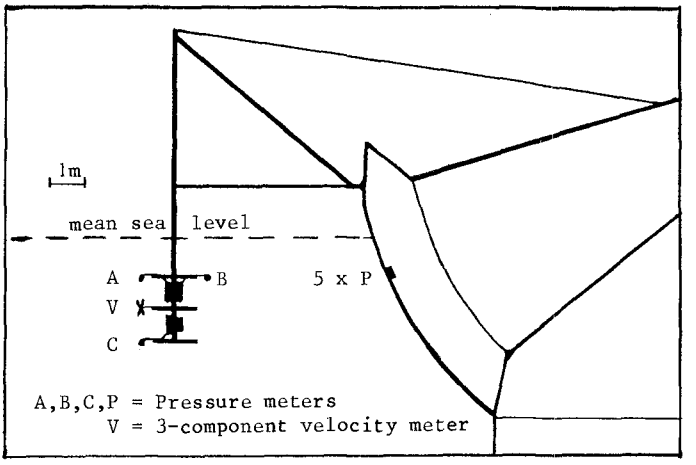

Figure 2. Location of the sensors.

Pressuremeter inlets A and C were positioned in one vertical with 2 m spacing. From pressure signal A the surface waveheights are calculated using linear wave theory. By combining signals A and C linear wave theory could be checked locally. However, afterwards another experiment was performed with simultaneous measurement of surface waves and the associated pressures. The results of these measurements were in good accordance with linear wave theory.

The third pressure gauge B was intended to test standing wave features but it turned out that much more information could be derived from the orbital velocities, so the signals of B were used.

The sensor of the current meter was mounted between pressure intakes A and C. The sensor of this meter is constructed in such a way that it offers little obstruction to the water movements, resulting in good omnidirectional characteristics. It has four pairs of transducers, forming the ends of four measuring lines; the watervelocities along these lines are measured using the average traveltime and the traveltime differences for acoustic pulses in both directions.
The length of the lines is 23 cm and they are directed parallel to the body diagonals of a cube. Because of the redundancy of using four lines instead of three orthogonal lines, a better omnidirectional uniform sensivity has been achieved. In case of steady currents one of the lines can be in the wake of one of its own transducers and then it is an advantage not to use that line for the conversion to orthogonal velocities. (In our case the advantage was that the measurements could be continued when one of the four lines became inoperative).

Signals from the 3 pressure gauges A, B, C, the 5 pressure gauges at the barrier and the 4 velocity signals were recorded during 30 minute intervals with a sampling rate of 8 Hertz.
Wave height seaward of the shoals was measured too, as well as the wind speed and direction.

During the measuring days, the wind directions ranged from south-west to north-west and speeds from 12 to 19 m/s. The significant wave height seaward of the shoals varied between 0.5 and 3 meters.

3. Calculations

The overall scheme of calculations is given in figure 3.

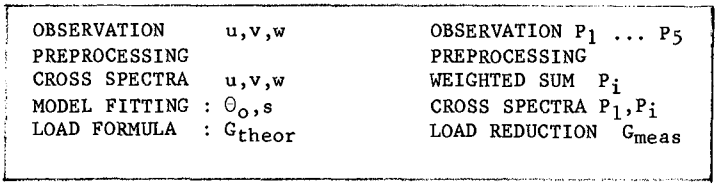

Figure 3. The overall calculation scheme

With one procedure the wavefield parameters are estimated and used as inputs to the theory of Battjes to find the wave loading reduction.

With the other procedure the actual wave loading reduction is derived from the pressures at the barrier. Finally the results are compared.

Cross spectral calculations with the three orbital velocity components are the basis of a method for estimating the wave directional parameters. However, the usual method can not be applied in this case, since it is based on the random phase statistical wave theory which does not hold for correlated wave fields. Therefore, the following method has been used. We assume an incoming unimodel directional wave field which is reflected by the barrier. The directional wave energy distribution in this hypothetic wave field is the well known cos-2s model, modified by cancelling all directions from behind the barrier.

For a given wave frequency the wave length is calculated with linear wave theory. Next, the wave field is split up into a series of elementary waves coming from directions at discrete intervals of 4 degrees. Per elementary wave the orbital velocities of the incoming and reflected waves are easily defined taking into account a reflection coefficient R and the distance to a vertical reflecting wall X_o. (See appendix A).

(In fact, the value of X_o is not simply the distance between the velocity sensor and the barrier, because of the shape of the front of the barrier. In general, the deviation from the vertical at the water-surface is dependant on the mean water level, which implies a variation in the effective value of X_o. Without going into details, it can be further assumed that longer waves will show a stronger influence of the deeper, more tilted part of the barrier, increasing the effective tilt compared to the tilt at the surface.

An investigation was made what this implies for waves with directions normal to the barrier and it appeared that the wavelengths as derived from the measured standing wave patterns fit quite well to the wavelenghts that can be calculated from linear theory. In fact, the waves are not coming from one normal direction, but as a first estimate this is resonable).

Per elementary wave the auto and cross spectral components of the orbital velocities are calculated and these spectral components are integrated for all discrete directions. A finer discrimination than 4 degrees did not alter results significantly, it may be that for the smaller values of s even larger directional steps would have been acceptable.

Since the absolute wave height is not relevant to the directional energy distribution, the spectral components from the calculations as well as from the measurements were normalized by dividing with the sum of the 3 autocorrelation components.

Altering the main wave direction Θ_o, the coefficient s, the effective distance X_o and the reflection coefficient R results in different sets of integrated spectral components. This is used to search for a combination that shows a minimum of the sum of the squared differences between the normalised spectral components of model and measurements. This part of the method is rather similar to that described by Borgman, (1981). In fact, the reflection coefficient R can be estimated also from the phase relation between the vertical velocity-component w and the horizontal component u, perpendicular to the barrier.

As a result we have per frequency a value of Θ_o, s and X_o for a best fit between model and measurements. The parameter X_o is only used to see if it has a reasonable value, taking into account the influence of wavelength and variable tilt of the reflector plane. It can hardly be expected that the fit of the spectral components will be perfect. This can be illustrated if we look at some special features.
In the theoretical model several components can be zero:

$C_{vw} = 0$ in all cases; $C_{uv} = Q_{uw} = 0$ if $R = 1$ and

$C_{uv} = Q_{uv} = Q_{vw} = 0$ if $\Theta_o = 0$.

w = vertical orbital velocity component
u = horizontal component normal to barrier
v = horizontal component parallel to barrier
C_{ij} = co-spectrum of i and j
Q_{ij} = quad-spectrum of i and j
(S_{ii} = auto spectrum of i)
R = reflection coefficient
Θ_o = central wave direction in cos-2s distribution.

Figure 4 shows an example of spectral calculations for one measuring interval. Figure 4a shows the sum of the autospectra $S_{tt} = S_{uu} + S_{vv} + S_{ww}$ divided by the peak value of S_{tt}, together with the three auto-spectra divided by S_{tt}.

Discrepancies with the model are found where the wave energy becomes small relative to the velocity noise. E.g. at low frequencies S_{uu} and S_{ww} show about the same value, where S_{uu} should become much smaller than S_{ww}.
In the frequency range of interest S_{vv} is small, indicating a wave direction nearly normal to the barrier, which is confirmed by the fact that Q_{uv} and Q_{vw} are also small; see figure 4b and 4d.

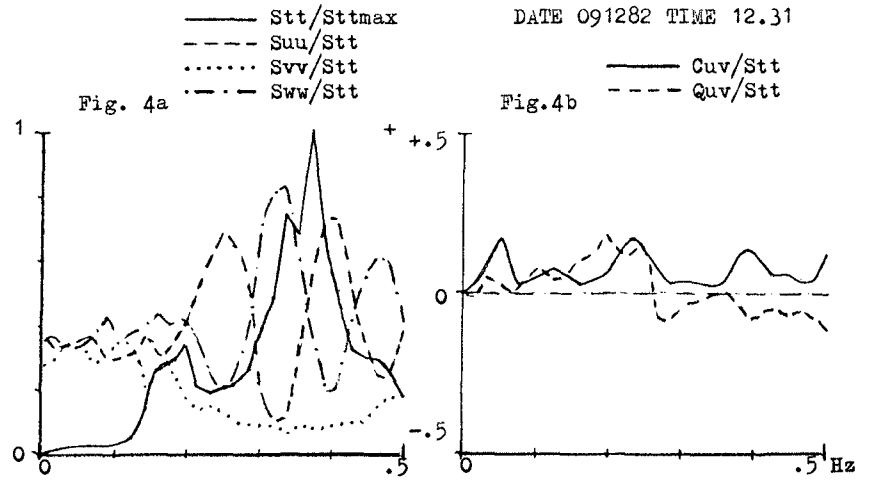

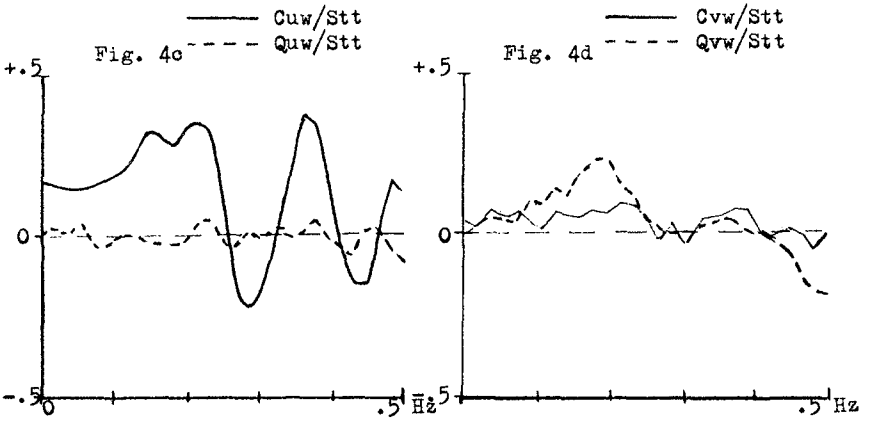

Figure 4. Normalised cross spectra of the orbital velocities.

When comparing the spectra S_{uu} and S_{ww}, the typical standing wave pattern with its nodes and loops can be seen quite distinctly. In general, Q_{uw} is very small; see figure 4c. This means that reflectioncoefficient R is about 1. Values of R greater than 1 do occur. Physically this means that during the measuring interval the reflected parts of the waves were a bit larger than the incoming parts that swept past the velocity meter. In a short crested wavefield that is quite well possible.

According to the theoretical model C_{vw} should be always zero. The measurements do not show this and this again illustrates that the fit can not be perfect.

Nevertheless the results of this best fit procedure give sufficient confidence to use the central wave direction Θ_o and the spreading parameter s as meaningful values.

A confirmation was found from the fact that the values of Θ_o at high frequencies corresponded to the wind direction. At low frequencies the direction of swell, entering from the North Sea, was found.

With Θ_o and s the wave load reduction can be calculated using the formulae given by Battjes (Ref 1). The results of a typical case are given in figure 5 as G_{theory}.

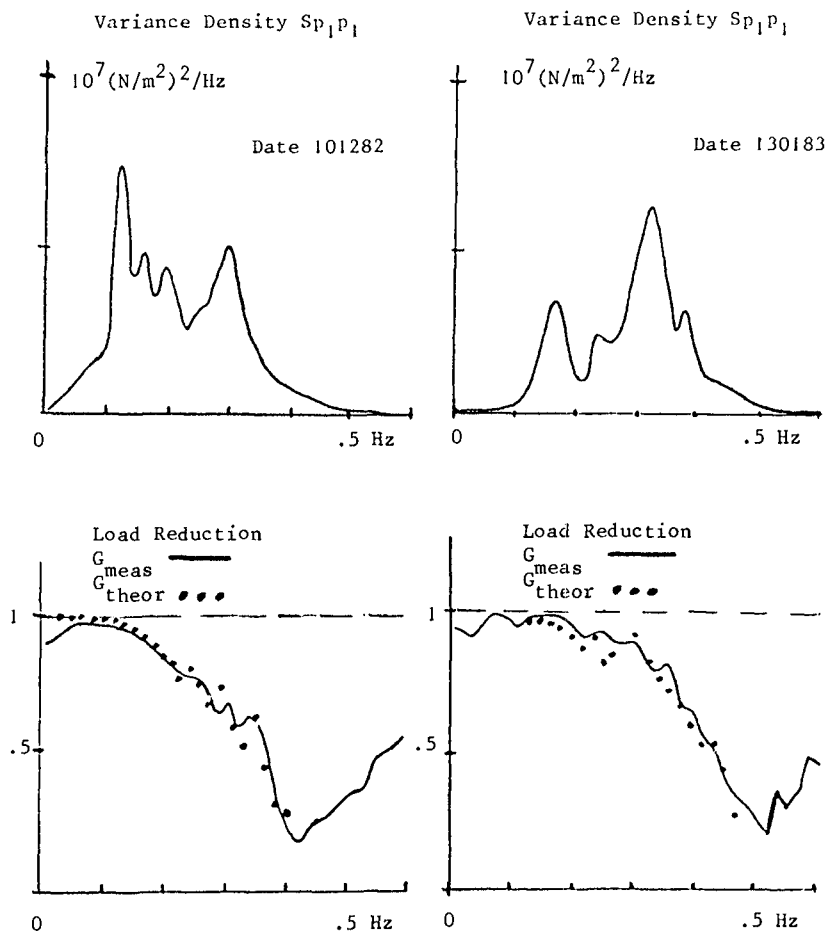

Figure 5. Some results of the waveload verification.

The other calculation path in figure 3 starts with the measured pressure signals at the barrier. After the same preprocessing applied to the other signals, in order to filter out tide and non relevant high frequency noise, the wave load reduction is calculated. The reduction is characterized by the fact that the coherence between pairs of pressure signals decreases if the spacing increases.

By applying to each pressure signal a weight factor, that is representative for a partial area of the barrier, the load reduction can be calculated. The actual load is the sum of products of the partial areas multiplied by the associated pressure signals. The reference load corresponds to the total area multiplied by one of the pressure signals. The results are given in figure 5 as G_{meas}.

Discussion

The agreement between the theoretical and measured load reduction G_{theory} and G_{meas} is very good in the frequency range where the spectral energy is relatively high. At very low frequencies in the formula of Battjes the reduction is 1; the measurement will not reach that value.
Beyond 0.4 Hertz the reduction factor, as calculated from the pressure signals, increases again. This effect is most probably the result of resonant vibrations of the barrier gate and not related to the wave loading.

Conclusions

1. The decrease of the coherence of the wave pressures at the barrier with increasing distance qualitively indicates that the total load will be lower than the product of one local pressure and the total barrier surface.
2. The quantitative verification shows that the wave load reduction as calculated by Battjes, taking into account the effect of short crestedness, does agree with full scale measurements.
3. In spite of the strong interaction between the incoming and reflected waved due to the short distance to the barrier, the main direction and spreading of the incoming wavefield can be estimated well from the three orthogonal velocity components.
   The method for this is the fitting of the spectral components from the measurements to the corresponding spectral components of a theoretical wave field that is a combination of the incoming and the reflected waves.

References

BATTJES, J.A. (1982). Effects of short-crestedness on wave loads on long structures. Applied Ocean Research, 4 (3): 165-172.

BORGMAN, L.E. (1981). A preliminary examination of the estimation of directional wave spectra, 11 pp. (unpublished report to Rijkswaterstaat)

APPENDIX A

The elementary case of reflection of a long-crested periodic wave is illustrated in fig. A1.

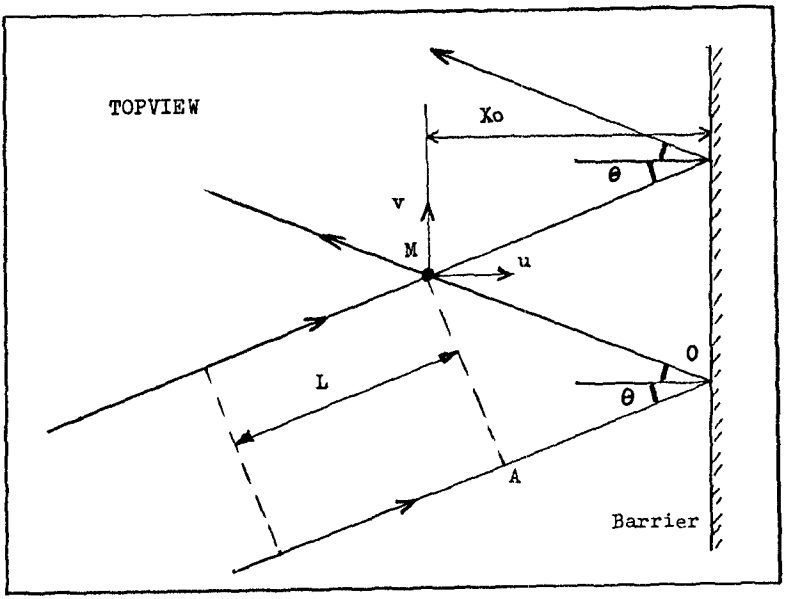

Figure A1. Definition of configuration.

M measuring point
X_o distance from M to the barrier
(The barrier is assumed to be a flat vertical wall)
L wave length
Θ incoming wave direction
u velocity component in direction normal to the barrier
v velocity component in direction parellel to the barrier
w vertical velocity component
R reflection coefficient
a surface elevation amplitude
ω frequency
t time
H_{uv} ratio between surface elevation and horizontal velocity
H_w ratio between surface elevation and vertical velocity

In M the distance between the incoming and reflected waves in the direction of propagation is

$$AO + OM = (\cos 2\Theta+1)OM=(\cos 2\Theta+1)X_o/\cos\Theta = 2X_o\cos\Theta \quad (1)$$

This corresponds to a phase difference

$$\phi = 4\pi X_o \cos\Theta/L \quad (2)$$

For the incoming waves in M, we have

$$u = a\, H_{uv} \cos\Theta \sin\omega t \quad (3)$$

$$v = a\, H_{uv} \sin\Theta \sin\omega t \quad (4)$$

$$w = a\, H_{w} \cos\omega t \quad (5)$$

At the barrier the wave changes direction in such a way, that the phase of u changes π , while the phase of v and w does not change. We assume that the reflection coefficient R is not associated with a phase shift and that R has the same value for u, v and w. This is a simplification.

So the reflected waves in M are described by

$$u = R\, a\, H_{uv} \cos\Theta \sin(\omega t - \phi - \pi) \quad (6)$$

$$v = R\, a\, H_{uv} \sin\Theta \sin(\omega t - \phi) \quad (7)$$

$$w = R\, a\, H_{w} \cos(\omega t - \phi) \quad (8)$$

Adding the incoming and reflected wave signals gives:

$$u = a\, H_{uv} \cos\Theta((1-R)\cos\phi/2 \sin(\omega t-\phi/2) + (1+R)\sin\phi/2 \cos(\omega t-\phi/2)) \quad (9)$$

$$v = a\, H_{uv} \sin\Theta((1+R)\cos\phi/2 \sin(\omega t-\phi/2) + (1-R)\sin\phi/2 \cos(\omega t-\phi/2)) \quad (10)$$

$$w = a\, H_{w} (-(1-R)\sin\phi/2 \sin(\omega t-\phi/2) + (1+R)\cos\phi/2 \cos(\omega t-\phi/2)) \quad (11)$$

These velocities give the following spectral components

$$S_{uu} = 0.5\, a^2\, H_{uv}^2\, (1-2\,R\cos\phi + R^2)\, \cos^2\Theta \quad (12)$$

$$S_{vv} = 0.5\, a^2\, H_{uv}^2\, (1+2\,R\cos\phi + R^2)\, \sin^2\Theta \quad (13)$$

$$S_{ww} = 0.5\, a^2\, H_{w}^2\, (1+2\,R\cos\phi + R^2) \quad (14)$$

$$C_{uv} = 0.5\, a^2\, H_{uv}^2\, (1-R^2)\cos\Theta \sin\Theta \quad (15)$$

$$Q_{uv} = 0.5\, a^2\, H_{uv}^2\, (-2\,R\sin\phi)\, \cos\Theta \sin\Theta \quad (16)$$

$$C_{uw} = 0.5\, a^2\, H_{uv}H_{w}\, (-2\,R\sin\phi)\, \cos\Theta \quad (17)$$

$$Q_{uw} = 0.5\, a^2\, H_{uv}H_{w}\, (1-R^2)\cos\Theta \quad (18)$$

$$C_{vw} = 0 \quad (19)$$

$$Q_{vw} = 0.5\, a^2\, H_{uv}H_{w}\, (1+2\,R\cos\phi + R^2)\sin\Theta \quad (20)$$

In any case $C_{vw} = 0$.
If R = 0 the formulae reduce to the normal single wave case.
If R = 1 then $C_{uv} = 0$ and $Q_{uw} = 0$ (21)

if $\Theta = 0$, then $S_{vv} = 0$, $C_{uv} = 0$, $Q_{uv} = 0$ and $Q_{vw} = 0$ (22)

For each frequency the value of ϕ is calculated via the wavelength L. Then the elementary results (12) to (20) are integrated for various values of Θ , at the same time taking a^2 inaccordance to a cos-2s directional distribution. For $\Theta_o = 0$ again $C_{uv} = 0$, $Q_{uv} = 0$ and $Q_{uw} = 0$ but S_{vv} is no longer zero, except for infinite s.

CHAPTER 180

MECHANICALLY COUPLED BUOYANT FLAPS: THEORY AND EXPERIMENT

by

Charles K. Sollitt, Director of O.H. Hinsdale Wave Research Laboratory, Oregon State University, Corvallis, OR 97331. M, ASCE.

Chung-Pan Lee, Graduate Research Assistant in Ocean Engineering, Oregon State University, Corvallis, OR 97331.

William G. McDougal, Associate Professor of Civil and Ocean Engineering, Oregon State University, Corvallis, OR 97331. AM, ASCE.

Thomas J. Perry, Civil Engineering Student, Oregon State University, Corvallis, OR 97331.

Abstract

A system composed of two buoyant flaps hinged at the sea floor and coupled with weighted mooring lines is modeled analytically and experimentally. The system behavior is described theoretically utilizing an eigenseries representation of linear wave theory in the vicinity of the breakwater. The structure dynamics are modeled in terms of structure weight, inertia, buoyancy, damping, mooring line tension and the wave pressure field.

The mechanically coupled system provides shelter by reflecting incident waves and by attenuating wave energy through structural and viscous damping. The structure can be tuned to minimize wave transmission within a particular frequency range by changing the flap spacing and adjusting the mass and equilibrium position of the mooring line weights.

The theory is validated with experimental results for models fabricated from inflatable, parallel-tube membranes. Buoyancy and inertia are changed by filling tubes with air and/or water. Single and double flaps are examined with and without mooring lines. Incident, reflected, and transmitted waves are measured as well as flap motion. Theoretical results are corroborated by the experiments and the importance of including damping in the model is demonstrated.

Introduction

Floating breakwaters have the desirable characteristics of being transportable, relatively inexpensive, and reusable and rapidly deployable. However, most floating breakwaters are relatively transparent to the incident wave field, e.g., floating parallelepipeds (Adee, 1976), tire-mazes (Harms, 1979), and tethered spheres (Seymour and Harms, 1979). In order to improve the behavior of floating breakwaters, it is necessary for the structure to occupy a major fraction

of the water column or incident wave length. The effectiveness of a floating structure can also be improved by constraining some modes of structural deflection and by tuning the structure natural frequency to avoid design wave frequencies (Leach, McDougal, and Sollitt, 1985).

In this study, a flap-type floating structure is examined which occupies the entire water column and which is hinged at the sea floor. Buoyancy provides a vertical equilibrium position for the structure and additional stiffness is afforded by weighted mooring lines. Wave interference between two structures is obtained by locating the flaps at appropriate spacings. Wave reflection is increased and wave transmission decreased by coupling the flaps with a common weighted mooring line; refer to Fig. 1. The coupled flap system can be tuned to optimize performance by varying the spacing, buoyancy and inertia as well as the mass and equilibrium position of the mooring weights.

The model structure examined during the experimental phase of this study was fabricated from a parallel tube air mattress. The inertia and buoyancy of the flap was changed by filling adjacent tubes with air or water. The membrane fabric which composed the air mattress was cut and glued to change the height and width of the structure and grommets for mooring line attachments were added by gluing additional fabric to the face of the mattress. The structure was anchored with a weighted plate at the sea floor. The utility of the air mattress model has some readily apparent implications for prototype applications in terms of portability and constructibility.

The behavior of the flap system is modeled analytically utilizing an eigenseries representation of linear wave theory in the vicinity of the structure. This contrasts to the numerical solution procedure of Raichlen and Lee (1978) used for inclined plate structures. Linear flap dynamics are modeled in terms of structure weight, inertia, buoyancy, damping, mooring line tension and the wave pressure field. This contrasts to the undamped, unconstrained solution of Evans (1979) and Skrokosz and Evans (1979) for wave power absorbing bodies.

Theoretical and experimental results are compared for single flaps and double flaps, for air and air/water filled mattresses. Examples with and without moorings are included. Both damped and undamped solutions are illustrated. Experimental and theoretical results confirm that structural and viscous damping are important considerations in describing the system behavior.

Theory

Potential Flow Boundary Value Problem (BVP)

In this study, the fluid is considered to be inviscid and incompressible and the flow is assumed to be irrotational. Then a single-valued velocity potential Φ_ℓ, ℓ = I, II, III, can be defined for each flow field separated by the flaps in Fig. 2 as

$$\vec{u}_\ell = -\vec{\nabla}\Phi_\ell \quad ; \qquad \ell = \text{I, II, III} \tag{1}$$

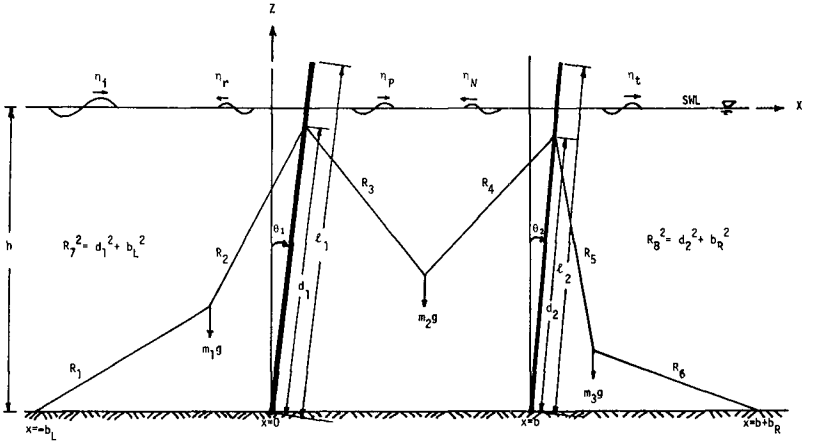

Figure 1. Definition sketch.

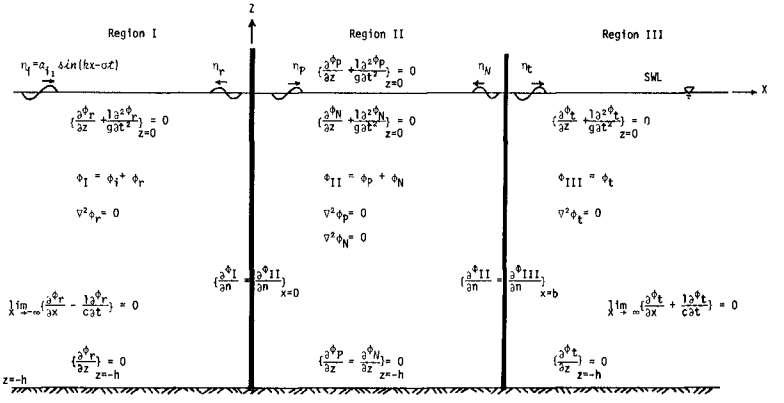

Figure 2. Linearized boundary value problem.

When small amplitude waves are considered, the velocity potentials satisfy the Laplace equation and the boundary conditions shown in Fig. 2. Kinematic boundary conditions, which require continuity of normal velocity across boundaries, are imposed on the impermeable bottom, rigid flaps, and free surface. Dynamic boundary conditions, which require continuity of pressure across a boundary, are imposed on the free surface. An additional radiation condition requiring only outgoing progressive waves at infinity is imposed on the reflected and transmitted waves.

The incident wave velocity potential and water surface profile are specified as

$$\phi_i = R_e\left\{\frac{a_{i1}g}{\sigma}\frac{\cosh K_1(z+h)}{\cosh K_1 h}e^{-(K_1x+i\sigma t)}\right\} \tag{2a}$$

$$\eta_i = R_e\left\{-ia_{i1}e^{-(K_1x+i\sigma t)}\right\} = a_{i1}\sin(kx-\sigma t) \tag{2b}$$

where $K_1 = -ik$, $k = \frac{2\pi}{L}$, L is the wave length, $\sigma = \frac{2\pi}{T}$, T is the wave period, and a_{i1} is the wave amplitude. The velocity potentials satisfying the BVP shown in Fig. 2 are found as follows:

$$\Phi_I = \phi_i + \sum_{j=1}^{\infty}\frac{ga_{rj}}{\sigma}\frac{\cosh K_j(z+h)}{\cosh K_j h}e^{(K_jx-i\sigma t)} \tag{3}$$

$$\Phi_{II} = \sum_{j=1}^{\infty}\frac{g}{\sigma}\frac{\cosh K_j(z+h)}{\cosh K_j h}\left\{a_{pj}e^{-[K_jx+i\sigma t]} + a_{nj}e^{[K_j(x-b)-i\sigma t]}\right\} \tag{4}$$

$$\Phi_{III} = \sum_{j=1}^{\infty}\frac{ga_{tj}}{\sigma}\frac{\cosh K_j(z+h)}{\cosh K_j h}e^{-[K_j(x-b)+i\sigma t]} \tag{5}$$

where the eigenvalues K_j can be determined from the dispersion equation:

$$K_1 = -ik \tag{6a}$$

$$(2j-3)\frac{\pi}{2} < K_j h < (j-1)\pi \quad \text{for } j \geq 2 \tag{6b}$$

$$\sigma^2 = -gK_j \tan K_j h \tag{6c}$$

and

$$a_{rj} = \delta_{j1} a_{i1} - i\beta_j S_1 \tag{7}$$

$$a_{pj} = i\beta_j \left(\frac{S_1 e^{K_j b} - S_2}{2 \sinh K_j b}\right) \tag{8}$$

$$a_{nj} = i\beta_j \left(\frac{S_1 - S_2 e^{K_j b}}{2 \sinh K_j b}\right) \tag{9}$$

$$a_{tj} = i\beta_j S_2 \tag{10}$$

$$\beta_j = \frac{2 \sin K_j h}{K_j^2 h^2 \left(1 + \frac{\sin 2K_j h}{2K_j h}\right)} \left[K_j h \sin K_j h + \cos K_j h - 1\right] \tag{11}$$

for $j \geq 1$ and δ_{j1} is Dirac delta. a_{rj}, a_{pj}, a_{nj}, and a_{tj} are the complex amplitudes of the reflected waves, right-going and left-going waves between the flaps and the transmitted waves, respectively. S_1 and S_2 are the complex amplitudes of the two flaps, referenced to the still water, and related to the flap angle of inclination as

$$\theta_1 \cong \frac{S_1}{h} e^{-i\sigma t} \tag{12}$$

$$\theta_2 \cong \frac{S_2}{h} e^{-i\sigma t} \tag{13}$$

for periodic small motions. S_1 and S_2 are determined by solving the coupled equations of motion of the breakwater flaps.

Each flap is assumed to be rigid yet free to rotate about a fixed point on the seabed. The equation of motion for each flap is found by taking the moment about its hinge point at the seabed as

$$I_\ell \ddot{\theta}_\ell + M_{B\ell} - M_{G\ell} - M_{w\ell} + M_{m\ell} + C_{d\ell} \dot{\theta}_\ell = 0 \quad , \ell = 1,2 \tag{14}$$

where $I\ddot{\theta}$ is the mass moment of inertia of the flap, M_B and M_G are the moments due to the buoyancy F_B and the weight of the flap, M_w is the moment due to wave force, M_m is the moment due to the mooring line, and the last term represents energy dissipation which may be caused by nonconservative forces. For small motions, the moments are found as follows:

$$M_{B\ell} \cong F_{B\ell} B_\ell \theta_\ell \tag{15}$$

$$M_{G\ell} \cong m^*_\ell g G_\ell \theta_\ell \tag{16}$$

$$M_{w\ell} \cong -\frac{h}{S_\ell} \rho g M_\ell \theta_\ell \tag{17}$$

where m* is the mass of the flap per unit width, and B and G are defined in Fig. 3, and

$$M_1 = \sum_{j=1}^{\infty} r_j \{2i\delta_{j1} a_{i1} + \beta_j [S_1 (1+\coth K_j b) - S_2 \operatorname{csch} K_j b]\} \tag{18}$$

$$M_2 = \sum_{j=1}^{\infty} r_j \beta_j [-S_1 \operatorname{csch} K_j b + S_2 (1+\coth K_j b)] \tag{19}$$

$$r_j = \frac{K_j h \sin K_j h + \cos K_j h - 1}{K_j^2 \cos K_j h} \tag{20}$$

The moment due to mooring lines can be found from Fig. 4 as

$$M_{m1} \cong m_1 g d_1 Q_{11} + m_1 g d_1 Q_{12} \theta_1 + m_2 g d_1 Q_{13} \theta_2 - m_1 d_1^2 \theta_{14} \ddot{\theta}_1 + m_2 d_1 d_2 Q_{15} \ddot{\theta}_2 \tag{21}$$

$$M_{m2} \cong m_2 g d_2 Q_{21} + m_2 g d_2 Q_{22} \theta_1 + m_2 g d_2 Q_{23} \theta_2 + m_2 d_1 d_2 Q_{24} \ddot{\theta}_1 - m_2 d_2^2 Q_{25} \ddot{\theta}_2 \tag{22}$$

The subscripted Q_{ij} variables are determined relative to the position of the mooring line weights (Lee et al. 1986).

For a system which has vertical flaps at static equilibrium, a steady-state solution exists as described by Eqs. (12) and (13). The coupled equations of motion are obtained by substituting Eqs. (15), (16), (17), and (21) or (22) into Eq. (14), providing

$$C_{11} S_1 - C_{12} S_2 = -2i a_{i1} \gamma_1 \tag{23}$$

$$C_{21} S_1 - C_{22} S_2 = 0 \tag{24}$$

where

$$C_{11} = C_{01} + P_{11} - \frac{i\sigma}{\rho g h^3} C_{d1} \tag{25}$$

$$C_{12} = C_{02} - P_{12} \tag{26}$$

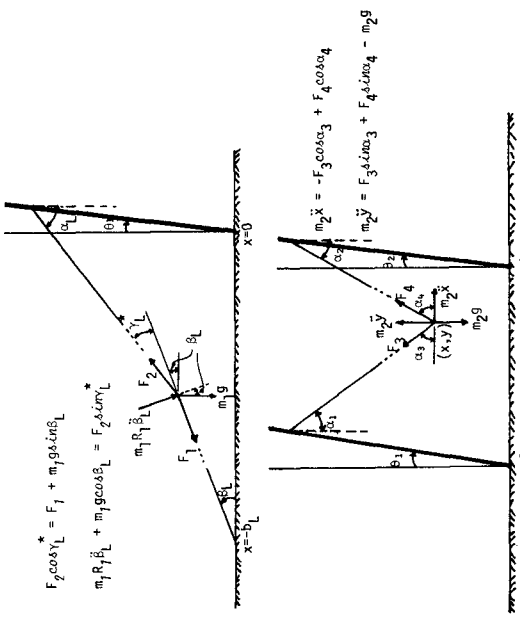

Figure 4. Free body diagrams of mooring weights.

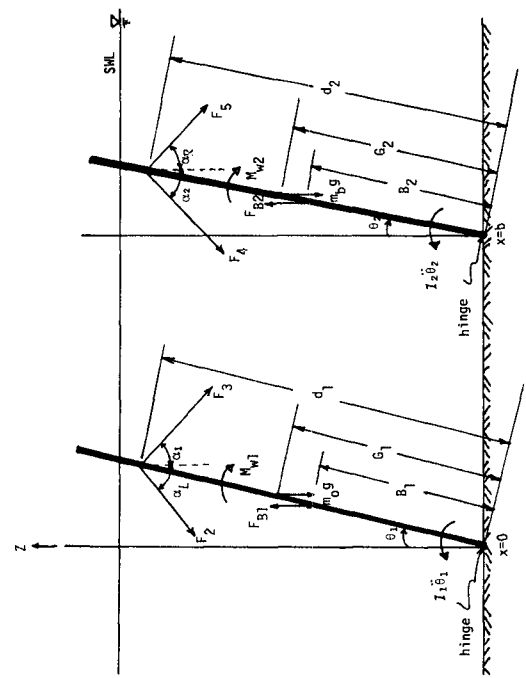

Figure 3. Free body diagrams of buoyant flaps.

$$C_{21} = C_{02} - P_{21} \tag{27}$$

$$C_{22} = C_{01} + P_{22} - \frac{i\sigma}{\rho g h^3} C_{d2} \tag{28}$$

$$C_{01} = \sum_{j=1}^{\infty} \beta_j \gamma_j (1 + \coth K_j b) \tag{29}$$

$$C_{02} = \sum_{j=1}^{\infty} \beta_j \gamma_j \operatorname{csch} K_j b \tag{30}$$

$$P_{11} = \frac{1}{\rho g h^3} [F_{B1} B_1 + m_1 g d_1 Q_{12} - m_1^* g G_1 - \sigma^2 (I_1 - m_1 d_1^2 Q_{14})] \tag{31}$$

$$P_{12} = \frac{1}{\rho g h^3} [m_2 g d_1 Q_{13} - \sigma^2 m_2 d_1 d_2 Q_{15}] \tag{32}$$

$$P_{21} = \frac{-1}{\rho g h^3} [m_2 g d_2 Q_{22} + \sigma^2 m_2 d_1 d_2 Q_{24}] \tag{33}$$

$$P_{22} = \frac{1}{\rho g h^3} [F_{B2} B_2 - m_2 g d_2 Q_{23} - m_2^* g G_2 - \sigma^2 (I_2 - m_2 d_2^2 Q_{25})] \tag{34}$$

Solving Eqs. (23) and (24) simultaneously yields

$$S_1 = i\left[\frac{2\gamma_1 C_{22}}{C_{12} C_{21} - C_{11} C_{22}}\right] a_{i1} \tag{35}$$

$$S_2 = i\left[\frac{2\gamma_1 C_{21}}{C_{12} C_{21} - C_{11} C_{22}}\right] a_{i1} \tag{36}$$

The flap amplitudes are specified by Eqs. (35) and (36). The flap amplitudes are substituted into Eqs. (7) and (10) for j=1 to solve for the reflected and transmitted wave amplitudes, respectively.

Experimental Facilities and Procedures

Experiments were conducted in the Graf Hall wave channel at Oregon State University, USA. The channel is 36 feet long, 2.0 feet wide and 2.2 feet deep. The models were located midway between the wave generator and a 1:10 slope beach. Waves were generated by a flap-style wave board, powered by variable speed electric motor with a right angle gear reduction box and variable eccentric drive shaft. Monochromatic waves were generated in a period range of 0.5 to 1.1 seconds, with wave heights up to 0.27 feet. All tests were conducted in a water depth of 1.5 feet.

Individual flaps for the model breakwaters were constructed from inflatable air mattresses, 1.8 feet wide and 6.0 feet long. The mattresses were composed of seven parallel tube chambers running the length of the mattress, with separate valves in each chamber. The mattresses were fabricated from a woven synthetic textile, sealed with an internal coating.

Mattresses were modified to become breakwater models by cutting each mattress in half to reduce the length and by adhesive fastening a seventh air chamber to provide a flap width equal to the wave channel width. Additional fabric patches were adhesive fastened to each chamber at the water surface to provide a grommet attachment for braided nylon mooring lines. A three yoke bridle distributed the load from each mooring line to three tubes. Two mooring lines were attached to both sides of the moored flaps. Four pound lead weights were suspended from each mooring line to provide a positive restoring force.

The inflated dimensions of the breakwater flap were 2.75 feet high, 2.04 feet wide and 0.22 feet thick. Flaps were inflated to a common pressure head of three feet of water. Some experiments were conducted with all tubes filled with air. Other experiments were conducted with four tubes filled with water to the SWL and three tubes filled with air. Five different breakwater configurations were examined. The characteristics associated with each configuration are identified in Table 1.

Wave profiles were monitored with acoustic water surface sensors, sampling at a rate of 60 hertz. A single fixed wave sensor was placed two water depths beyond the leeward flap to measure the transmitted wave height. A single wave sensor on a sliding carriage was placed on the seaward side of the breakwater to profile the envelope resulting from the superposition of the incident and reflected waves. The incident wave height was calculated from one-half the sum of the relative maxima and minima of the envelope. The reflected wave height was calculated from one-half the diffrence of the relative maxima and minima. Breakwater flap amplitudes were measured visually by scaling flap motion at the still water level.

Table 1. Model characteristics per unit width (ft)

Case	Breakwater Configuration	Weight in Air (lbf/ft)	Displaced Water Weight (lbf/ft)	Center of Gravity (ft)	Center of Buoyancy (ft)	Mass Moment of Inertia ($slug \cdot ft^2/ft$)	Distance Between Breakwaters (ft)	Mooring Weight (lbf/ft)	Damping Coefficient (lbf•ft•sec/ft)
1	Single flap, air filled, without mooring	1.1755	13.9592	1.375	0.75	0.09201	-	-	1.1
2	Single flap, air/water filled*, without mooring	8.8653	13.9592	0.8328	0.75	0.27108	-	-	1.2
3	Double flaps, air/water filled*, without mooring	8.8653	13.9592	0.8328	0.75	0.27108	1.5	-	2.1
4	Double flaps, air/water filled*, with mooring	8.8653	13.9592	0.8328	0.75	0.27108	1.9	4.8483	2.1
5	Double flaps, air/water filled*, with mooring	8.8653	13.9592	0.8328	0.75	0.27108	3.0	4.8483	1.2

*Three tubes filled with air, four tubes filled with water to SWL.

Experimental and Theoretical Results

Reflected and transmitted wave amplitudes are the basis for comparing measured and predicted breakwater performance in this study. The amplitudes are reduced to dimensionless reflection and transmission coefficients by division with the incident wave amplitude. Results are expressed relative to wave frequency in terms of the dimensionless ratio of water depth divided by the linear wave theory deep water wave length, h/Lo. The deep water wave length is the progressive wave solution to the dispersion equation (6), for large water depths, yielding

$$Lo = \frac{gT^2}{2\pi} \tag{37}$$

Results for a single flap, inflated with air without moorings are presented in Fig. 5. This corresponds to Case 1 in Table 1. In general, the reflection coefficient is shown to increase with decreasing wave length (increasing h/Lo) while the transmission coefficient decreases with decreasing wave length. Experimental results are plotted as points in the figure while theoretical results appear as continuous lines. The breakwater becomes a dynamic barrier to high frequency waves (high h/Lo) due to the structural stiffness. However, the breakwater theoretically becomes a kinematic barrier to low frequency waves because breakwater buoyancy can accommodate a head difference across the flap, effectively creating a tidal barrage. The theoretical solution displays this trend at very low frequency; no experimental results are available at this frequency. Note that theory and experiments do follow the same trend, although the theory does overestimate the transmission coefficient for the undamped solution in the upper half of Fig. 5.

A damped solution is compared to experimental results in the lower half of the figure. The damping coefficient is determined empirically by requiring the theoretical solution to dissipate the same energy as the experimental results over the full range of measured data. Resulting damping coefficients are reported in the right hand column of Table 1. Damping does decrease the transmission while increasing the reflection coefficient to a lesser degree. In general, the correlation between theory and experiment is improved for the damped case.

Results for a single flap without moorings but with water to the SWL in four of the seven buoyancy chambers are shown in Fig. 6. This condition (Case 2 in Table 1) tends to give somewhat higher reflection coefficients and slightly lower transmission coefficients at all frequencies. The damped solution in the lower half of the figure more closely follows the experimental results.

A two flap system is illustrated in Fig. 7. The flap spacing is equal to the water depth. The breakwaters are filled with air and water and no moorings are attached. This corresponds to Case 3 in Table 1. The results show that the two flap system is much more frequency selective than the one flap system. Both theory and

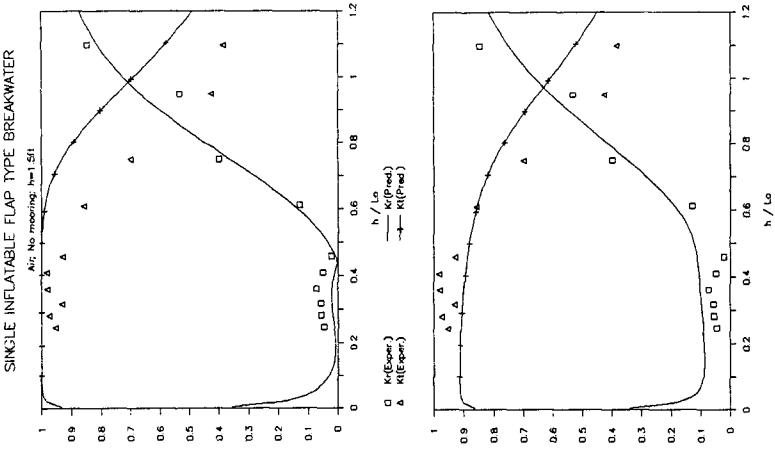

Fig. 5. Experimental and theoretical reflection and transmission coefficients for single flap without mooring, Case 1.

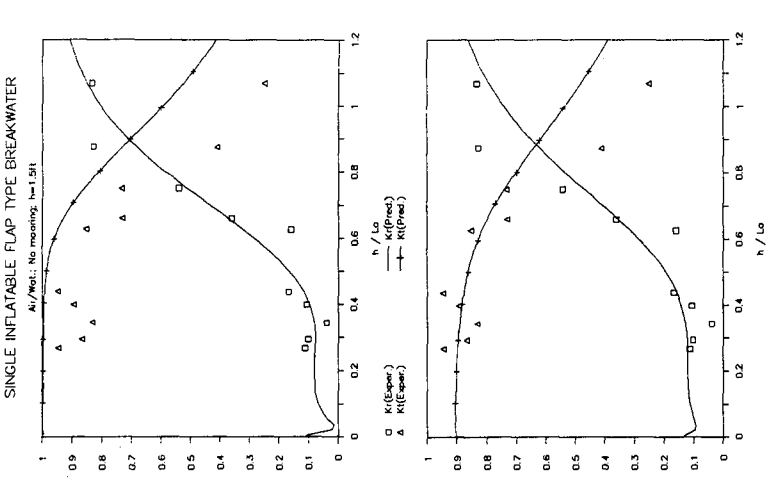

Fig. 6. Experimental and theoretical reflection and transmission coefficients for a single flap without mooring, partially inflated with water, Case 2.

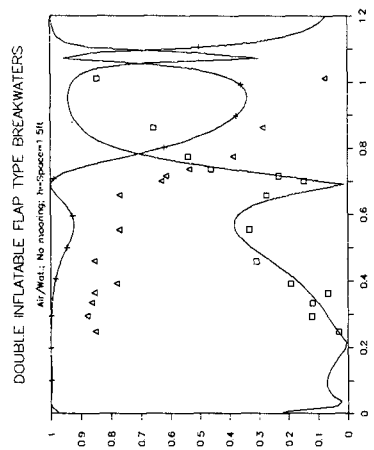

Fig. 7. Experimental and theoretical reflection and transmission coefficients for two flaps without mooring, Case 3.

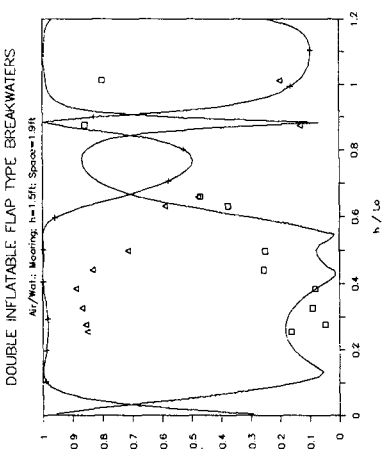

Fig. 8. Experimental and theoretical reflection and transmission coefficients for two flaps with weighted moorings, Case 4.

experiment follow this trend with relative maxima and minima occurring at two points over the data range. Damping improves correlation with the transmission coefficient in the lower figure while the undamped case appears to better reproduce the reflection coefficient behavior at intermediate frequencies.

The effects of moorings for a two flap system, filled with air and water, is shown in Fig. 8. This corresponds to Case 4 in Table 1. The mooring dynamics add additional relative maxima and minima to the breakwater behavior. Damping improves the correlation between theory and experiment at intermediate wave frequencies. The general effect of the mooring is to reduce wave transmission at intermediate frequencies. This is made evident by comparing experimental results in Figs. 7 and 8.

Conclusions and Recommendations

Mechanically coupled buoyant flaps have been proposed and constructed from inflated membranes connected with weighted mooring lines. A closed-form, linear analytical solution to the system behavior has been presented. A model has been constructed from currently available materials, demonstrating the practicality of the application. Comparisons between theoretical and experimental wave reflection and transmission coefficients have validated the analytical model. Theoretical and experimental results suggest that structural and viscous damping are important features in the system behavior.

Damping was quantified with a semi-empirical displacement rate coefficient in the model. This coefficient requires a more deterministic approach for evaluation, utilizing drag force relationships for mooring line motion. Also, signficiant bending of the hinged flap was observed during the experiments, suggesting that the rigid flap approximation may be an oversimplification. Future studies will evaluate the flap behavior as an elastic beam with structural damping quantified relative to the plastic properties of synthetic membranes.

Acknowledgements

This research has been supported by the (Office of Naval Research under Contract No. N00014-86K0687 and the) Oregon State University Sea Grant College Program through the National Oceanic and Atmospheric Administration, Department of Commerce, under Grant No. NA85AA-D-SG095 and project number R/CE18.

References

Adee, B.H., 1976, A review of problems and developments in using floating breakwaters, Proceedings of Offshore Technology Conference.

Evans, D.V., 1976, A theory for wave-power absorption by oscillating bodies, J. Fluid Mech., Vol. 77, Part 1, pp. 1-25.

Harms, V.W., 1979, Design criteria for floating tire breakwaters, J. of WWPCOE Div., ASCE, Vol. 105, No. WW2.

Leach, P.A., McDougal, W.G., and Sollitt, C.K., 1985, Hinged floating breakwater, J. of WWPCOE Div., ASCE, Vol. 111, No. 5, pp. 895-909.

Lee, C.P., Sollitt, C.K., McDougal, W.G., and Perry, T.J., 1986, Mechanically coupled flap-type breakwaters: theory and experiment, Proceedings, Ocean Structural Dynamics Symposium '86, Corvallis, Oregon, pp. 730-757.

Raichlen, F. and Lee, J.J., 1978, An inclined-plate wave generator, Proc. of 16th ICCE, Hamburg, Germany, Vol. I, pp. 358-399.

Srokosz, M.A. and Evans, D.V., 1979, A theory for wave power absorption by two independently oscillating bodies, J. Fluid Mech., Vol. 90, Part 2, pp. 337-362.

Su-Ao Harbor, Taiwan, ROC—R.L. Wiegel

PART IV

COASTAL, ESTUARINE, AND ENVIRONMENTAL PROBLEMS

Aerial View of Taipei City—H.S. Hou

CHAPTER 181

INNOVATIVE DETERMINATION OF NEARSHORE FLOOD FREQUENCY

H. Lee Butler*, and Mark D. Prater**, Members ASCE

ABSTRACT

Reliable estimates of coastal flooding from tides and storm surges are required for making sound engineering decisions regarding the design, operation and maintenance of many coastal projects. A recent investigation of flood frequency along the coast and within the bays of southern Long Island, New York, produced new and optimal approaches to obtain meaningful statistical estimates of flood levels. This paper summarizes various elements of the study and concentrates on the problem of stage-frequency computations in the inland bay areas. Methods for optimizing the number of necessary storm/tide simulations and estimating the accuracy of results are presented.

INTRODUCTION

Efficiency in design of coastal protection is becoming more and more important. Development of coastal regions, costs of damages from storm induced water levels, and costs of protection from these waters are all increasing. Adequate protection for coastal regions is desired; however, due to financial constraints the amount of flood level protection that can be considered adequate becomes a question for which there is no easy answer. Therefore, inherent in any coastal protection project is a need to develop the most accurate possible stage-frequency (frequency of storm/tide induced still-water level above a fixed datum) relationship estimate for the project area, as well as an estimate of the error in this relationship.

The technique in widespread use for the development of coastal flood frequency, especially from hurricane induced water levels, is the joint probability method (JPM) (Myers, 1970). A method to develop error estimates from meteorological uncertainty for stage-frequency relationships derived through the JPM was presented by Prater, et al. (1984). However, a generally accepted method to judge the correctness of the produced flood frequency, or to estimate the error of these frequencies, is not available.

*Chief, Research Division, Coastal Engineering Research Center, U.S. Army Engineer Waterways Experiment Station, P.O. Box 631, Vicksburg, MS 39180.

**Graduate Research Associate, School of Oceanography, University of Washington, Seattle, WA.

A study to investigate the frequency of storm-plus-tide flood levels along the coast and within the bays of southern Long Island, New York, was recently completed at the U.S. Army Engineer Waterways Experiment Station (WES). The offshore study domain is the New York Bight whereas the nearshore area of interest covers a coastal reach of approximately 125 km and includes three inlet/bay systems (Great South, Moriches, and Shinnecock Bays) with interconnecting channels. The problem is further complicated by a variable height dune system along the bayfront barrier islands which is susceptible to overtopping and deterioration during a storm passage.

The approach adopted for estimating stage frequency due to storm-induced surge and wave effects involved conjunctive use of several models. A numerical storm surge model calculated the still water level. A dune breach model permitted an ad hoc determination of dune overtopping and destruction. Several probability models were used to choose events to simulate, assign probabilities to those events, and construct the stage-frequency relationships. Each element of the study is briefly discussed; however, attention here is focused on the optimal methods used for estimating nearshore and inland bay flood frequencies and errors in the development process. A complete report on the study is given in Prater, et al. (1987).

STORM SURGE MODELING

Simulations required in the Long Island study involved application of two numerical surge models, collection of field data for model calibration, and analysis of alternative barrier and inlet configurations. The primary model applied in the study is the WES Implicit Flooding Model (WIFM). The numerical and hydrodynamic features of WIFM are discussed in Butler (1978) and the application to coastal studies is documented in numerous reports including Butler (1980, 1983). WIFM solves the vertically integrated time-dependent shallow water wave equations of fluid motion using an alternating direction implicit finite difference algorithm. The code allows subgrid barriers to be exposed, submerged, or overtopped. An important feature of WIFM is the capability to create an exponentially stretched grid which permits concentration of grid resolution in areas of interest. Also included in the code is the capability to flood or dry individual low-lying cells during a simulation.

A coarse global grid (Figure 1) was constructed to cover the New York Bight from a point south of Atlantic City, New Jersey, to beyond Cape Cod, Massachusetts (and includes New York Harbor and Long Island Sound). The purpose of the global grid is to model large-scale tidal and meteorological events, providing results for input to a small, high-resolution nearshore grid of the main study area. The high-resolution nearshore grid stretches from near Jones Inlet to beyond Shinnecock Inlet (including all back-bay and channel systems) and has variable grid size resolution of 200 to 1200 m.

Both numerical grids were calibrated for the primary M2 astronomical tidal constituent, and verified for a mixed tide condition. Typical results for comparing observed and computed surface elevations are

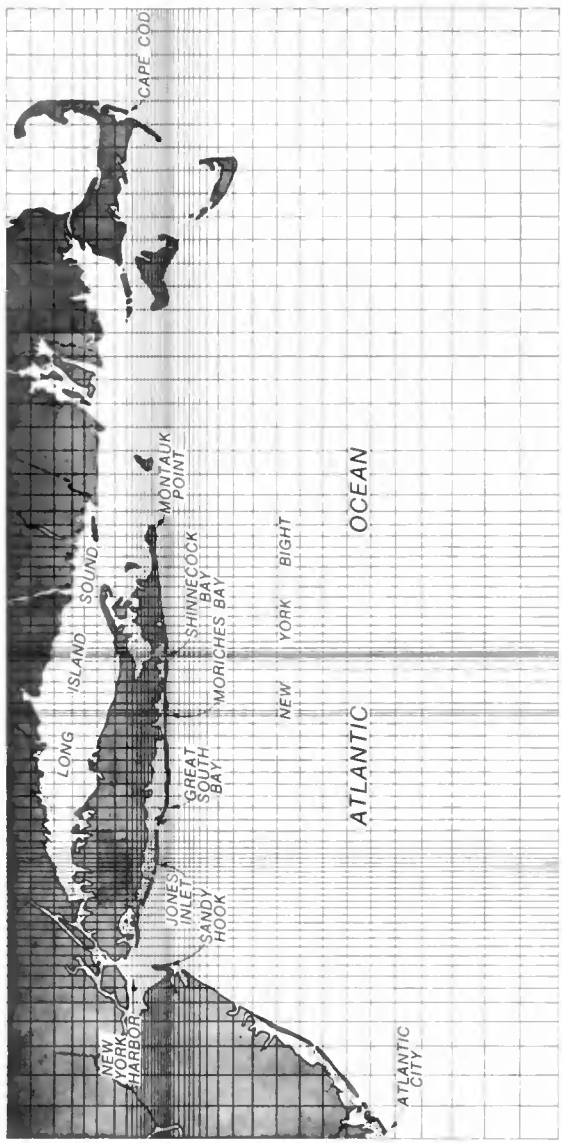

Figure 1. Global grid for storm tide simulations

displayed in Figure 2. Figure 2a shows a comparison of global results to measured data at Sandy Hook, New Jersey, and Figure 2b compares nearshore grid results to measured data at a gage within Great South Bay. Bathymetric and topographic data describing barrier island and inlet configurations for five severe historical storms (hurricanes of 1938, 1954 (Carol), and 1960 (Donna), and the extratropical storms (northeasters) of November 1950 and March 1962) were developed. These storms were hindcasted to verify both the global and nearshore numerical models for storm-plus-tide events.

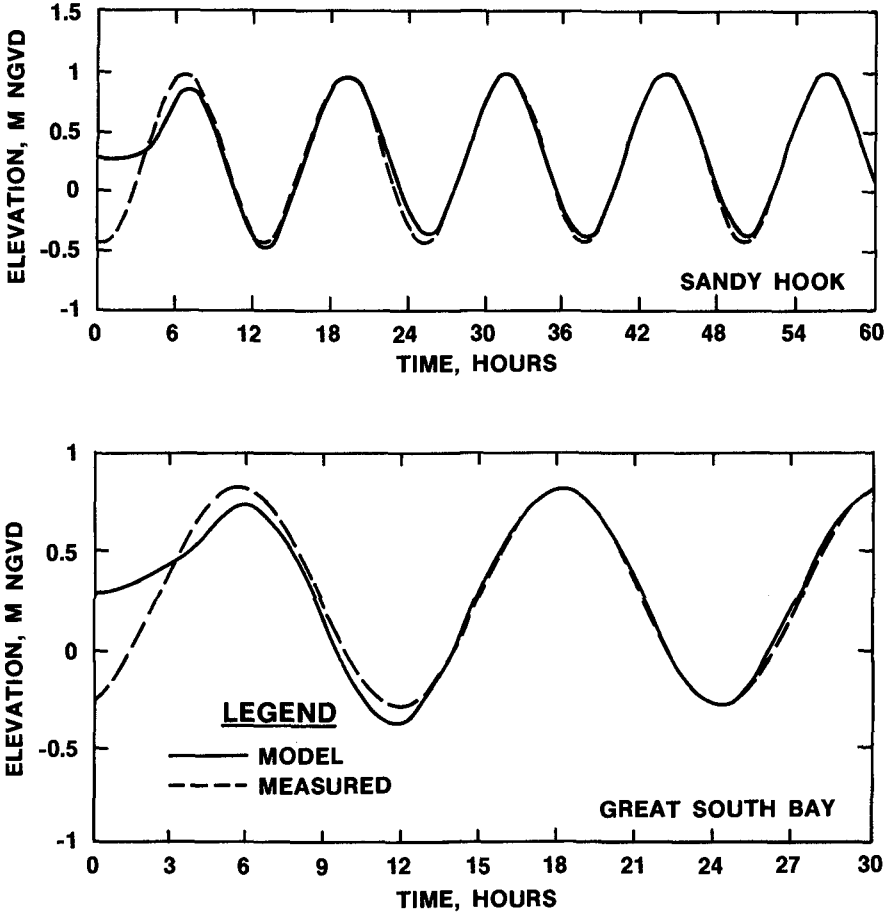

Figure 2. Comparison of global model results to measured data

To provide wind stress from hurricanes to the hydrodynamic model, a parametric model was used to represent the windfield as specified by the Standard Project Hurricane (SPH) criteria (NWS, 1979). Wind speed and direction computed by the SPH model are appropriate to open-coast conditions. The model version used in WIFM permits a reduction of the open-water wind speed at the land-water interface and inland over low-lying land and embayments. For historical northeasters, wind speed and direction and atmospheric pressure were available from archived data (Brooks and Corson, 1984).

Extreme water levels on the coast produce substantial dune destruction and breaching, contributing to higher embayment water levels. In order to simulate these extreme events it was necessary to develop a mechanism to account for dune destruction and breaching. A simple, but deterministic method was adopted to lower the barrier island dunes and permit more water to enter the bays. Using methods given in the Shore Protection Manual (SPM, 1984), an effective water level during wave attack of the dune system is computed and allowed to trigger the lowering (or breaching) of a dune on a cell-by-cell basis. The method was calibrated using historical data from several storms. Destruction/breaching was considered a function of the dune type, height, and base width.

Good comparisons between observed and computed water levels were obtained at open coast gages (Figure 3 displays sample comparisons for Sandy Hook for all five storms mentioned above). Comparison at inland bay gages involve contributions from wave effects and dune breaching as discussed above. Flood potential is increased by the capability of storm-induced waves to enter the inland bays through inlets or over breached dune systems and of waves to develop on shallow inland bays. A method devised by the National Academy of Science (1977) was used to estimate the maximum flood height at inland gages due to surge plus tide plus wave contributions. Table 1 gives an example of comparisons obtained for inland gages spanning the entire nearshore grid domain.

Table 1

Comparison of Meseaured and Computed (Estimated) Flood Levels (m)

	Hurricanes						Northeasters			
	1938		1954		1960		1950		1962	
Gage	M	C	M	C	M	C	M	C	M	C
Amityville	2.4	2.3	1.8	1.5	1.8	2.5	2.1	2.0	1.8	1.7
Patchogue	2.7	2.6	1.5	1.6	1.4*	1.8	1.5	2.0	1.5*	0.7
Moriches CGS	4.6	4.0	1.5*	2.0	1.4	2.1	1.5*	2.0	1.5*	1.1
Pine Neck	4.3	4.5	1.5*	2.4	1.5*	1.9	1.5*	1.8	1.5	1.0

M,C represent measured (M) and computed (C) values
* Limited data available

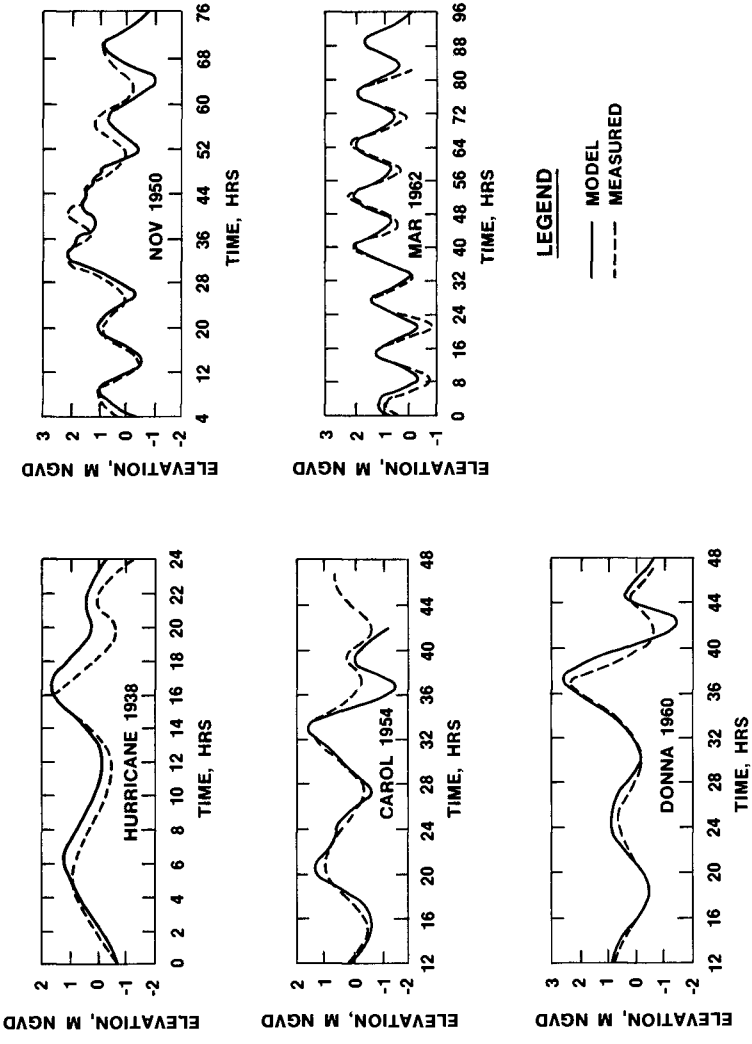

Figure 3. Comparisons of computed and measured water levels at Sandy Hook, New Jersey, for five historical storms

In Table 1, Amityville and Patchogue are located in Great South Bay, the Moriches Bay gage is at the Coast Guard Station, and Pine Neck is located in Shinnecock Bay.

STATISTICAL APPROACH

The two most common approaches to establish frequency curves are called the historical method and the JPM. In the historical method a series of historical events is recreated with pertinent data being saved at necessary grid locations. In effect, it is analogous to operating a "time machine" with the hindsight to know what data to collect and where to collect it. Probability is assigned to each event by a standard ranking method. For the JPM, the storm type is parameterized. For example, hurricane windfields can be defined by three parameters: central pressure deficit (DP), radius to maximum winds (R), and forward speed (F). Then an ensemble of synthethic events is simulated representing those events which are possible in the study area. Probability is assigned to individual events by assigning probabilities to parameter values which determine that event. If the parameters are independent, then the probability of the event will be the product of the probabilities of the component parameters. If dependency among parameters exist, the ensemble is subdivided into sets of events, each containing independent component parameters.

Hurricanes

The JPM approach was adopted to develop hurricane stage frequencies for this study. Five storm parameters were used to describe hurricanes: F, R, DP, track direction, and landfall point. Probability distributions for each parameter were obtained by a thorough review of the historical occurrence of hurricanes in the New York Bight. It was determined that three F's, three R's, six DP's, and five landfall points with three track directions and two track directions for bypassing storms were needed to represent the range of hurricane parameters which could occur. This selection gives a total ensemble of 918 hurricane events to be modeled, each with its own probability of occurrence. The actual number of storm events modeled was reduced. Sensitivity tests determined that water levels resulting from different pressure deficits could be linearly interpolated. Therefore, only two values of DP, values near the extremes of the DP probability distribution, were used in forming the actual computational ensemble of 306 hurricanes.

Northeasters

Because of the difficulty in parameterizing northeasters and the availability of data from frequent storm events, a historical approach was adopted. From previous studies performed for the New York Bight (Myers, 1970; and Camp Dresser and Mckee, 1980) and from historical records, a stage-frequency curve constructed from both northeaster- and hurricane induced water levels show northeasters dominate the higher frequency, lower magnitude events but are generally ineffective in producing the rarer, higher stage events. Consequently, the length of historical record chosen (the 41-year period from 1940 to 1980) is sufficient to adequately cover the area of dominance on the combined event stage-frequency curve.

Historical data from 101 storms over the 41-year span that produced at least a 0.7 m surge at Sandy Hook, New Jersey, were used to develop a partial duration exceedence (PDE) curve. Twenty-seven storms from this set were selected (storms representative of the entire set of 101 storms) and assigned probability masses in proportion to the amount of the PDE distribution each storm is to represent. The mean difference (for the 27 events) between simulated surge elevations and observed values was 8 cm at Sandy Hook and 9 cm at Montauk, New York.

Tide Convolution

Global grid simulations were carried out for surge without tide. Tides were incorporated through the convolution of tidal values with output of the surge-only numerical simulation. This procedure is valid in the open Bight where nonlinear effects of combining surge and tide are negligible. The convolution procedure produced more than 600,000 possible hurricane surge-tide combinations and over 18,000 northeaster surge-tide combinations. These storm-tide event sets were ranked by elevation, and through the use of their probabilities, stage-frequency relationships were developed for open-coast locations throughout the study area.

COASTAL STAGE FREQUENCIES

The surge-tide convolution was performed at all locations in the global grid where a frequency relationship was desired. From these data a probability of exceedence distribution for water levels was developed, from which stage frequencies could be deduced. By adding exceedence probabilities from the hurricane and northeaster curves, the return period between occurrences of water levels equal to or exceeding the specified level from either hurricanes or northeasters were computed. The northeaster storm of record (November 1950) was an outlier for the events chosen. Sensitivity tests on assignment of probability of occurrence for this rare event indicated insignificant impact on the combined stage-frequency curve above the 50-year return period due to the dominance of hurricane events on the longer return periods. Hence, the uncertainty of the return period of the 1950 event will not affect the combined stage-frequency curves in the study area. Figure 4 displays sample combined stage-frequency curves for open-coast locations at Sandy Hook, on the coast fronting Great South Bay, and for the eastern end of the study area (Montauk). Prior to this investigation, a single frequency curve similar to that for Sandy Hook was used for evaluating coastal projects on southern Long Island. These results can reduce costs of future projects by being a yardstick for accurately assessing risk associated with different protection levels. Figure 5 compares stage-frequency curves computed from model results with curves deduced from measurements at Sandy Hook. Historical data used to produce Figure 5 only provide a combined frequency curve out to the 25-year return period.

As stated above, adequately monitored hurricane occurrences are scarce in the north Atlantic Ocean and the development of accurate parameter distributions with limited data becomes difficult. By using a bootstrap technique (Prater, et al., 1984), error estimates on the stage-frequency curve were obtained from the uncertainty of these

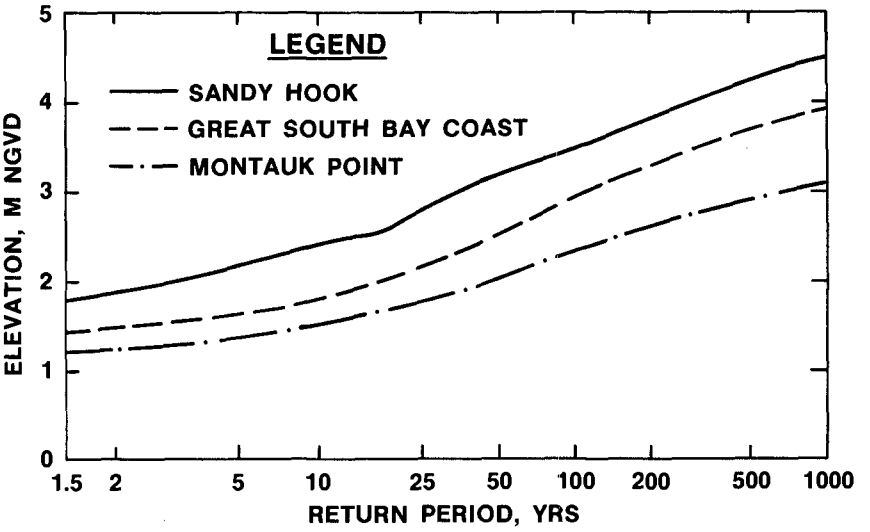

Figure 4. Computed JPM curves for three locations along coastal reach of southern Long Island

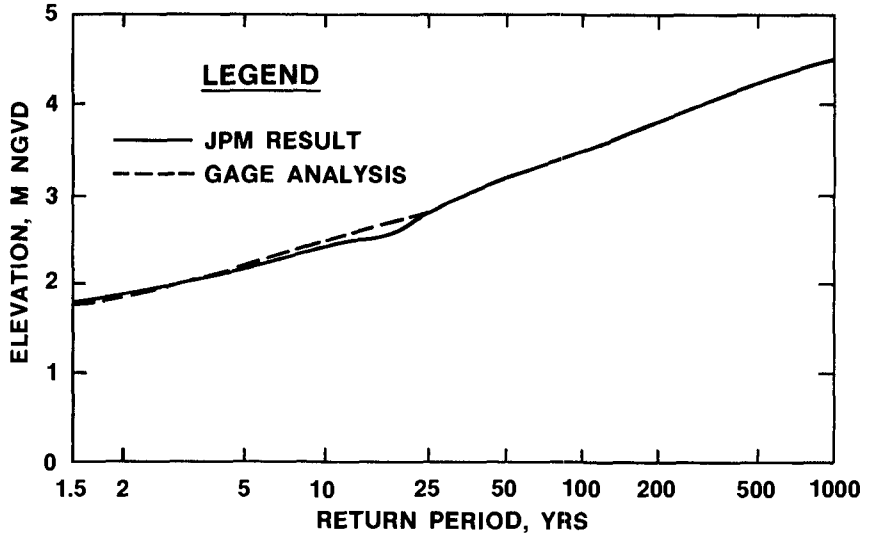

Figure 5. Comparison of computed JPM curve and gage analysis at Sandy Hook, New Jersey

parameter distributions. The procedure consists of assuming the unknown storm population distribution for each hurricane parameter is the same as the parameter distribution obtained from historical information. Synthetic parameter distributions are created by repeated sampling from this assumed population. The variation in the synthtic parameter distributions is due to the small sample sizes. Synthetic stage-frequency curves are then generated by randomly selecting a synthetic distribution for each parameter. About 1000 such curves gave very stable results (little change in final result with increased number of bootstrapped samples) and provided an estimate of error in the selection process. When the process is examined for each return period, an estimate of the uncertainty (due to limited size of sample population) of a stage-frequency curve is obtained (Figure 6).

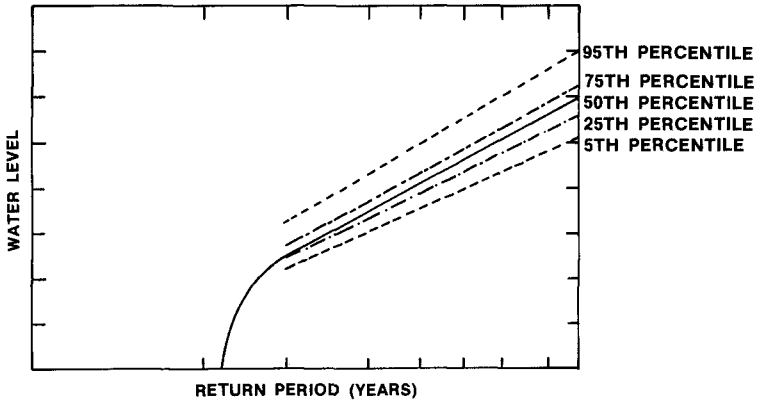

Figure 6. Bootstrapped stage-frequency confidence intervals

INLAND STAGE FREQUENCIES

For nearshore grid simulations, it was necessary to represent the statistics of the thousands of possible global surge-tide events with a much smaller ensemble of events for nearshore simulation. A random sampling of roughly 6000 hurricane-plus-tide events was further reduced to three sets of 17 storm-tide events, with each set chosen to represent a range of storms from moderate to very severe. Weaker events were not emphasized due to the dominance of northeasters for return periods below 50 years. Tests showed that 40 northeaster-plus-tide simulations could reliably represent the full set of extratropical events. Statistical justification in the selection process involves the concept of reduction in dimensionality. Probabilities of each nearshore event were assigned according to what portion of the nearest open-coast stage-frequency curve each event represented. Stage frequencies were developed from results of these simulations. This procedure replaced the typical approach of routing all the open-coast surge events into the back-bay

areas. It provided a clean statistical method to account for the nonlinear effects involved in routing flood waters through inlets and over the barrier islands.

As for the historical storm simulations, the contribution to flood water potential from wave effects was taken into account. Wave set-up estimates were made by applying standard practices in the SPM (SPM, 1984). A procedure was developed which would process previously generated storm simulation output and compute additional bay elevations on a storm-by-storm basis. The accuracy of these results suffers because of the simplifying assumptions made as well as a lack of information available as to the physical processes involved. The results give a good indication of the size of the influence wave setup has on the back-bay stage frequencies. At the 100-year return period, maximum additional water elevation in back-bay areas from influence of wave effects is on the order of 1 m.

CONFIDENCE INTERVALS

Confidence limits on the upper portion of nearshore stage-frequency curves were estimated by observing variability in stage frequencies generated by each of three nearshore sets of 17 hurricane-plus-tide events. The stage frequency curves from these sets were regressed and compared with each other. Assuming for any given return period the calculated stage is a normally distributed random variable, an estimate of the probable error can be calculated using the three stage-frequency curves generated independently from the three sets of selected events. The accepted stage-frequency curve with error bands is formed by processing all 51 events as one set. Figure 7 shows an example of the results obtained for a typical open-coast gage location. Results were presented for specified regions rather than for specific model gage locations. Thus a given stage-frequency curve is applicable, within a specified tolerance level, for a region defined by two endpoints. Regional averages were determined by a weighted average of nearby model gage results. Figure 8 presents an example regional stage-frequency curve for the far eastern region (one of 16 regions) showing the minimum and maximum stages of the data used to develop the curve.

PROJECT ALTERNATIVES

Various project dune heights and other structural alternatives were examined for impact on stage-frequency within the inland bays. Among these were included the 1979 dune configuration, non-overtopping dunes (conservatively built), variable height dune systems design to offer 25-, 50-, 100-, 200-, and 500-year protection, leeved back-bay areas, and inlet and channel surge barriers. Stage-frequency curves for the 1979 dune congiguration were used as a baseline for comparing alternative plan impacts. The non-overtopping dune alternative provided information on the highest level of protection to be obtained in the back bays. A basic result from examining all plan tests is that back-bay flood levels are more effectively minimized by increasing heights of the barrier dune system. Interior channel gates tend to increase flood levels in areas local to the gate. Inlet barriers will reduce surge levels within the gated bay, but unless dune heights are raised inlet gates will not give much protection against severe events. Inlet gates

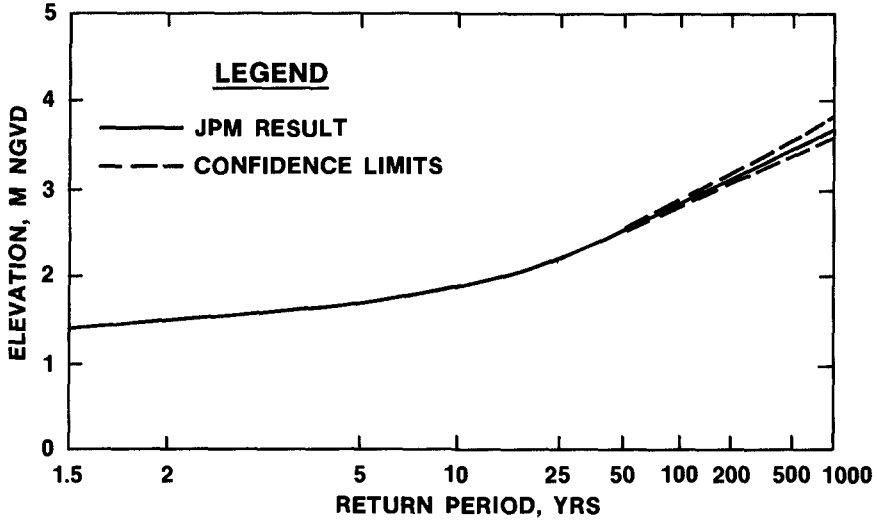

Figure 7. Confidence intervals for the hurricane selection process for a typical open-coast model result

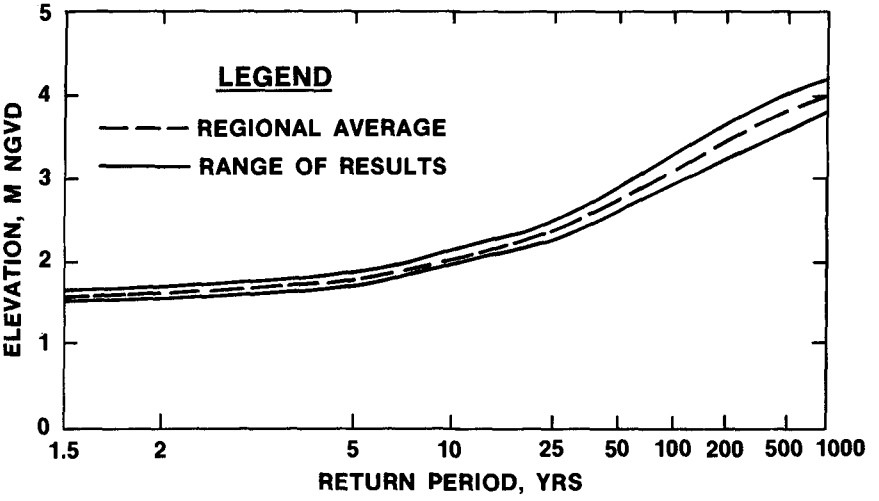

Figure 8. Regional JPM result for southeastern Long Island

do protect against the lower energy events because flood waters are primarily transmitted through the inlets during these events. A plan to levee back-bay areas did not significantly increase bay flood levels.

Variable height dunes were examined by simulating the effect of barrier islands whose protective dune heights are designed according to elevations corresponding to the above mentioned return periods. The design heights include the effect of wave setup. To minimize computational effort, two sets of 17 hurricanes and one set of 13 northeasters (representative storms) were simulated for each of the five alternative barrier conditions. After processing the 25- and 50-year barrier simulations, the number of storms simulated was decreased because the northeaster and several moderate hurricane events have no effect on the higher return period plans. All results were presented in a regional format as exemplified in Figure 8.

SUMMARY AND CONCLUSIONS

A comprehensive investigation of storm-induced flood levels on the southern coast of Long Island, New York was successively completed. Efficient global and nearshore storm surge models were developed to simulate selected storm events. A dune breach model was used to more realistically simulate severe storm events. The most significant development in the progress of the study was the procedure to minimize the computational effort to predict nearshore and inland bay stage frequencies. This procedure permitted economical testing of various alternatives including variable-height dune systems and gated interior channels and inlets. The procedure also permits an estimation of confidence limits in the results. The methods used in this investigation require additonal research, particularly in delineating all sources of error in the estimation of confidence bands. Substantial research is required to accurately simulate contribution of wave setup, wave transmission, and inland bay wave effects. The results from this study also point to the importance of accurately modeling dune erosion and breaching.

ACKNOWLEDGMENTS

The methods developed in this paper were part of a numerical investigation of extreme water levels along the southern coast of Long Island funded by the U.S. Army Engineer District, New York. Permission was granted by the Chief of Engineers to publish this information.

REFERENCES

Brooks, R.M., and Corson, W.D., "Summary of Archived Atlantic Coast Wave Information Study Pressure, Wind, Wave, and Water Level Data," Technical Report WIS Report 13, U.S. Army Engineer Waterways Experiment Station, CE, Vicksburg, MS, 1984.

Butler, H.L., "Coastal Flood Simulation in Stretched Coordinates," 16th International Conference on Coastal Engineering, ASCE, Hamburg, Germany, 27 Aug-1 Sep 1978.

Butler, H.L., "Evolution of a Numerical Model for Simulating Long-Period Wave Behavior in Ocean-Estuarine Systems," Estuarine and Wetland Processes with Emphasis on Modeling, Marine Science Series, Vol. 11, Plenum Press, New York, NY, 1980.

Butler, H.L., "Lake Pontchartrain and Vicinity Hurricane Protection Plan, Report 3, Numerical Model Investigation of Plan Impact on the Tidal Prism of Lake Pontchartrain," Technical Report HL-82-2, U.S. Army Engineer Waterways Experiment Station, CE, Vicksburg, MS, 1983.

Camp Dresser and McKee, "New York City Flood Insurance Study," Reports 1-8, Annandale, VA, 1983.

Myers, V. A., "Joint Probability Method of Tide Frequency Analysis Applied to Atlantic City and Long Beach Island, N.J.," ESSA Technical Memorandum WBTM HYDRO 11, U.S. Department of Commerce, Environmental Science Services Administration, Weather Bureau, Silver Springs, MD, 1970.

National Academy of Sciences, "Methodology for Calculating Wave Action Effects Associated with Storm Surges," National Research Council, NAS, Washington, DC, 1977.

National Weather Service, "Meteorological Criteria for Standard Project Hurricane and Probable Maximum Hurricane Windfields, Gulf and East Coasts of the United States," NOAA Technical Report NWS 23, U.S. Dept. of Commerce, Washington, DC, 1979.

Prater, M.D., Hardy, T.A., and Butler, H.L., "Fire Island to Montauk Point, New York, Storm Surge Model Study," Technical Report in publication, U.S. Army Engineer Waterways Experiment Station, CE, Vicksburg, MS, 1987.

Prater, M.D., Hardy, T.A., Butler, H.L., and Borgman, L.E., "Estimating Error of Coastal Stage Frequency Curves," 19th International Conference on Coastal Engineering, ASCE, Houston, TX, 3-7 September 1984.

Shore Protection Manual, 4th ed., 2 Vols., U.S. Army Engineer Waterways Experiment Station, Coastal Engineering Research Center, CE, U.S. Covernment Printing Office, Washington, DC, 1984.

CHAPTER 182

2-D CIRCULATION IN THE SARONIC GULF

George C. Christodoulou[1], A.M. ASCE
Athanassios E. Kouloumbis[2],
Alice O. Aza[3]

ABSTRACT

The paper refers to mathematical modeling of the 2-D hydrodynamic circulation in the Saronic Gulf, in Greece. The finite element method is followed to evaluate the flow behaviour. Two grids are employed, a coarse one for initial model adaptation and a finer one for a more detailed study of circulation patterns. Actual tide data are obtained at the boundary of the domain and a typical compound tide is introduced; however residual tidal currents are found to be negligible. Wind-generated flow fields under several prevailing wind directions are determined and their comparison to qualitative field evidence is satisfactory. Furthermore, a possible surface tilt along the open boundary associated with large scale circulation in the Aegean Sea, is studied and shown to produce significant motion in the Gulf. Based on circulation patterns obtained, preliminary estimates of dispersion from a proposed sea outfall for Athens sewage can be made. Further work proceeds towards quantitative verification of the model in connection with the proper description of forcing mechanisms and their superposition.

INTRODUCTION

The Saronic Gulf is a coastal water body located in the vicinity of Athens, the capital of Greece, as shown in Fig. 1. Due to its location

1 Assoc. Prof., Dept. of Civ. Engrg., Natl. Tech. Univ. of Athens, Athens, Greece.
2 Grad. Stud., Dept. of Civ. Engrg, Mass. Inst. of Technology, Cambridge, Mass., U.S.A.
3 Res. Collabor., Dept. of Civ. Engrg., Natl. Tech. Univ. of Athens, Athens, Greece.

and the natural beauty of its coastlines and islands it has a high recreational value for over 4 million inhabitants of Athens and nearby towns as well as for many thousands of visitors. Besides, it has economic importance associated with a variety of human activities in the area. However, the marine environment has been threatened in recent years due to increasing pollution loads discharged into the water body, coming from domestic sewage, industrial effluents and also ship traffic to and from the port of Piraeus. Environmental concerns have risen in connection with the planning of a new treatment plant and sea outfall for the sewage of Athens metropolitan area, which could provide the opportunity for significantly reducing one of the major sources of pollution of the gulf. In this context it is desirable to examine the large scale characteristics of flow in the gulf, so that the far field impact of substances introduced into it may be assessed.

Up to now the hydrodynamic behaviour of the gulf is not well understood [1]. Despite considerable field measurement efforts undertaken since the mid-seventies the data base is yet insufficient for evaluating the overall circulation. This is so because the gulf seems to be an extremely complex water body, both in terms of geometrical configuration and in terms of flow-generating mechanisms. In fact, in the absence of a strong tide, as is typical in the Mediterranean Sea, several forcing mechanisms are potentially important, resulting in generally weak but highly variable currents.

The complexity of the problem suggests a mathematical modeling approach. As a first approximation a two-dimensional description of the circulation is sought in this paper, through adaptation of pertinent finite element models. The determination of the circulation patterns under a variety of conditions allows an assessment of the major forcing mechanisms. Furthermore, preliminary estimates of the extent of contamination from the proposed new outfall can be made.

PHYSICAL CHARACTERISTICS OF THE GULF

As shown in Figure 1, the Saronic gulf has an area of approximately 2600 Km^2 and is connected to the Aegean Sea through a 42 Km opening at the SE. Its bathymetry and geometry are highly complex, with irregular boundaries and many islands. The two main islands of Salamina and Aegina essentially divide the gulf into three major parts. The outer gulf, at the SE, is connected to the open sea and has depths gradually decreasing from about 200 m at the boundary to 100 m towards the inner gulf. The latter, at the NE, has depths generally less than 100 m and is of major interest from the environmental point of view. Finally the western gulf has a pronounced depth variability, with depths locally exceeding 400 m; its water masses are only indirectly connected to the open sea, being exchanged through the passages north and south of Aegina island with the inner and outer gulf, respectively.

Temperature and salinity measurements taken at various stations in the gulf have indicated that the density distribution over the water column is essentially uniform during the winter season, while considerable stratification develops during the summer. Therefore the assumption of vertically well-mixed conditions, inherent in the implementation of 2-D model-

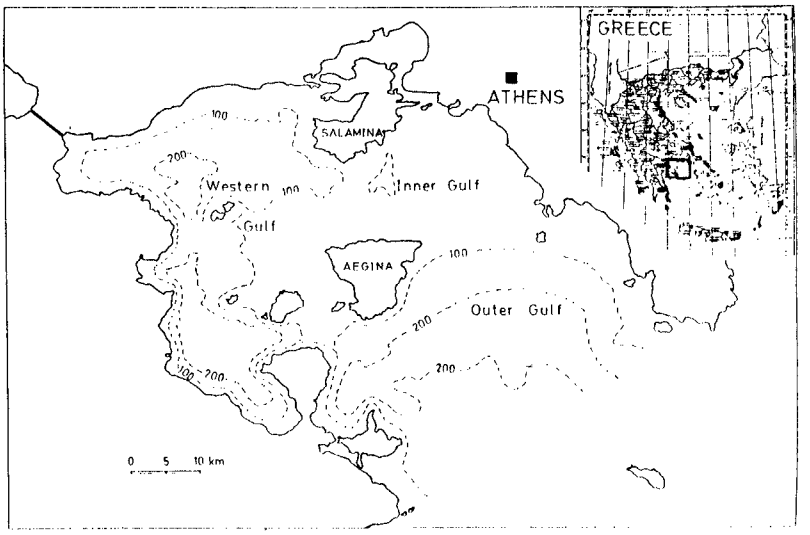

Figure 1. Map of the Saronic Gulf.

ing, is justified by available observations for the winter months, i.e. December to March.

NUMERICAL MODELING

The geometrical complexity of the Saronic Gulf suggests the application of the finite element method. At this stage, a simple and reliable finite element model with linear traingles, code-named CAFE [3], was implemented. The model solves the following depth-integrated equations of continuity and momentum, under the assumptions of constant density and hydrostatic pressure distribution, as described in detail by Wang and Connor [4]:

$$\frac{\partial n}{\partial t} + \frac{\partial q_x}{\partial x} + \frac{\partial q_y}{\partial y} = 0 \tag{1}$$

$$\frac{\partial q_x}{\partial t} + \frac{\partial}{\partial x}(\bar{u}q_x) + \frac{\partial}{\partial y}(\bar{v}q_x) - fq_y = -\frac{\partial F_p}{\partial x} + \frac{\partial F_{xx}}{\partial x} + \frac{\partial F_{xy}}{\partial y} + \frac{1}{\rho}(\tau_x^s - \tau_x^b) + \frac{1}{\rho}(p^s \frac{\partial H}{\partial x} - gn\frac{\partial h}{\partial x}) \tag{2}$$

$$\frac{\partial q_y}{\partial t} + \frac{\partial}{\partial x}(\bar{u}q_y) + \frac{\partial}{\partial y}(\bar{v}q_y) + fq_x = -\frac{\partial F_p}{\partial y} + \frac{\partial F_{xy}}{\partial x} + \frac{\partial F_{yy}}{\partial y} + \frac{1}{\rho}(\tau_y^s - \tau_y^b) +$$

$$+ \frac{1}{\rho} \left(p^s \frac{\partial H}{\partial y} - gn \frac{\partial h}{\partial y} \right) \qquad (3)$$

where:

$-h$, n = bottom and free surface elevation with respect to mean sea level

H = $h + n$ = total depth

q_x = $\int_{-h}^{n} u\,dz = \bar{u}H$ = specific flux along x

q_y = $\int_{-h}^{n} v\,dz = \bar{v}H$ = specific flux along y

$\bar{u}$, $\bar{v}$ = depth-average velocities along x,y

f = $2\omega \sin\varphi$ = Coriolis parameter

p^s = atmospheric pressure, acting on the free surface

τ_x^b, τ_y^b = bottom shear stresses

τ_x^s, τ_y^s = surface shear stresses, due to wind

$F_p = \frac{1}{\rho} \int_{-h}^{n} p\,dz - \frac{1}{2} gh^2$ = hydrostatic force relative to $n=0$

$F_{xx} = \int_{-h}^{n} \left(\nu \frac{\partial \bar{u}}{\partial x} - \overline{u'^2} - u''^2 \right) dz$ = integrated internal stress due to molecular viscosity, turbulent velocity fluctuations and spatial deviations of velocity from depth-average value.

F_{yy}, F_{xy} = respective integrals of internal stresses along yy, xy.

The above equations, with proper parametric expressions for the bottom, surface and internal stresses, are transformed through the Galerkin method to a system of ordinary differential equations in time for the unknowns n, q_x, q_y, which is solved by a split-time integration technique [3,4].

The problem was approached at two levels of detail. Initially a coarse grid was used for model adaptation and calibration in the study area and to obtain an understanding of the importance of the forcing mechanisms at minimum computational effort. The coarse grid is shown in Figure 2. It consists of 112 nodes and 160 triangular elements, with a grid size of the order of 2 to 5 Km. Only two major islands are represented, while the narrow passes between Salamina island and the mainland are considered as closed. Subsequently, a finer grid was applied, in order to study in sufficient detail the circulation generated by the dominant forcing mechanisms and further proceed to preliminary estimates of dispersion from the new sea outfall. This finer grid is shown in Figure 3. It consists of 233 nodes and 373 triangular elements, with a grid size ranging from 0,8 to 3 Km, and it includes three more islands.

In both grids, a zero flux normal to all land boundaries was prescribed, while at the open boundary a specified water level variation was introduced. The computational time step for the coarse grid was 100 sec. and for the fine grid 50 sec. The modeling applications were performed on the CDC Cyber-171 computer of NTUA. The computer time required for the simulation of 1 day real time was about 15 cpu min. for the coarse grid and 60 cpu min. for the finer grid.

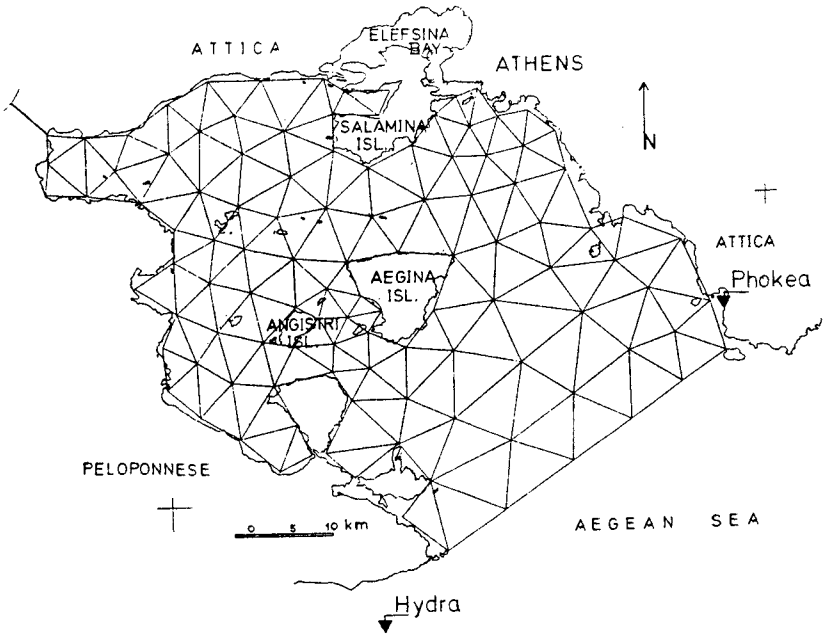

Figure 2. Coarse finite element grid

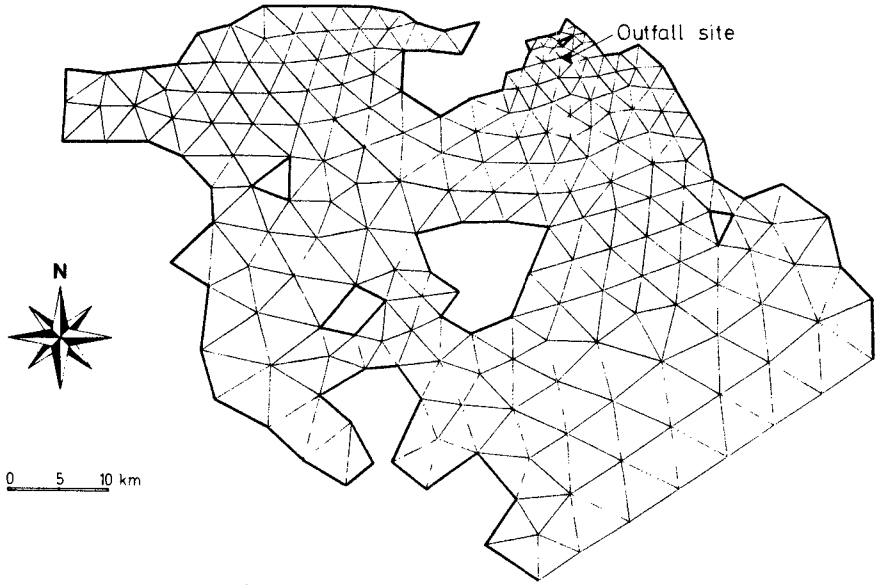

Figure 3. Fine finite element grid

CIRCULATION STUDIES

Coarse grid

Three main forcing mechanisms were examined at a preliminary level with the coarse grid: Tide, wind and a surface filt along the open boundary. In particular, with respect to tide, earlier estimates based on tidal data from Piraeus harbour, at the northern coast of the gulf, have indicated a mean tidal amplitude of about 10cm. Employing such a uniform sinusoidal tidal forcing was found to produce weak and reversing tidal currents resulting in practically no net motion over the entire gulf. In order to determine possible amplitude and phase differences along the open boundary an effort to obtain actual tide data was undertaken. Two self-recording tide gauges were installed near the two ends of the boundary, at Phokea and Hydra, as shown in Fig. 2. Measurements were taken for a period of about three months, from September to December 1984. The half-hourly readings were subsequently analysed by means of Fast Fourrier Transform and harmonic analysis. Four main components were clearly identified, corresponding to two diurnal and two semidiurnal tides, which were found to contain almost all the energy of the signals. These components were then synthesized to produce a "typical" tidal water level variation at the two points, as shown in Figure 4. This typical compound tide of duration 4T= 180,000 sec. was then assumed to repeat itself for numerical modeling purposes. To obtain elevations at intermediate boundary nodes linear interpolation was used at each time step.

As evident from Fig.4, there is a variable elevation difference along the open boundary, therefore some residual currents are to be expected in this case. Figure 5 shows depth-averaged water particle motion obtained for the "typical" tidal forcing acting for 2 weeks. It is seen that appreciable net movement occurs only close to the boundary. Consequently, it may be concluded that tidal flushing cannot be relied upon to reniew the water masses of the Gulf, and especially those of the inner gulf where most of the pollution loads are introduced.

After the above findings, it is clear that the wind-driven circulation should be of primary importance. Still, the resulting depth-averaged currents cannot be very strong due to the relatively large depths of the study area. According to long-term wind records the prevailing winds in the area are from northerly directions. In particular for the winter, excluding periods of no wind, the most frequent wind directions are: N 26.5%, NE 19.0% and S 12.3%. Since reliable wind measurements were available from one station only, a study of uniform wind from several directions over the entire gulf was conducted. In all cases a zero surface elevation at the open boundary was specified. It was found that steady state flow was reached about 1.5 day after the initiation of forcing.

As a third circulation mechanism, a possible small surface tilt along the open boundary was tried. The response of the gulf was found to be quite sensitive to such a forcing. The physical justification for introducing a surface tilt lies in observational evidence of a "permanent" inflow along the eastern coastline of the gulf associated with the large-scale circulation in the Aegean Sea. No quantitative information on this

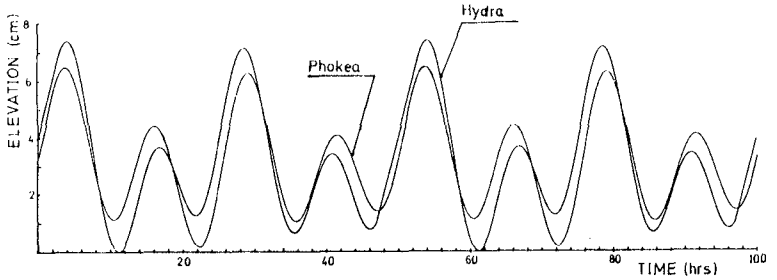

Figure 4. Typical compound tide at open boundary.

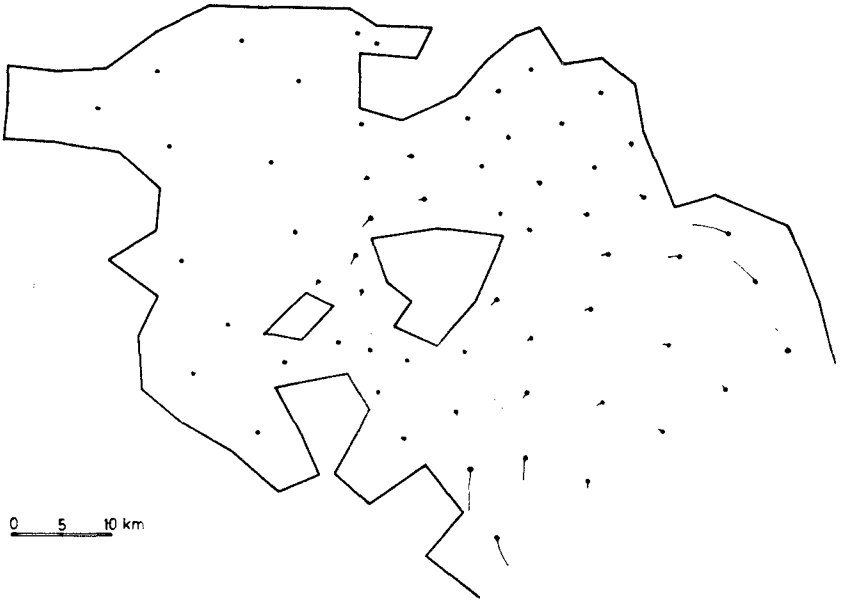

Figure 5. Mean water particle paths under typical tidal forcing for 14 days.

inflow is presently available, and it presumably has significant long-term variability. Yet, its qualitative effect on the circulation of the Saronic Gulf can be possibly simulated by the specification of a higher surface elevation at the eastern end of the open boundary.

Fine Grid

The fine grid was implemented for obtaining more detailed circulation patterns and as a necessary level of discretization for introducing the source of effluent dispersion. With this grid primarily the wind-generated circulation was examined. Figures 6,7 and 8 present the steady-state mean velocity field for the three most frequent wind directions in the study area, that is N, NE and S, respectively. The upper part of each figure, denoted by (a), presents the model results for a constant 20 knot wind, while the lower part, denoted by (b), shows the respective circulation patterns near the surface estimated by Dugdale and Hopkins [2] based on a qualitative synthesis of available oceanographic data and observational evidence at the time.

For the most common north wind the model (Fig. 6a) indicates an inflow from the middle part of the opening and outflow near the two ends. A clockwise gyre develops in the eastern part of the inner gulf and an incomplete counterclockwise motion to its left, leading to outflow towards the western gulf. The upper part of the latter is covered by an extensive clockwise gyre, while a small counterclockwise gyre is seen near the westernmost corner. Two other notable features are the outward coastal current from Athens to the SE and the counterclockwise motion around the island of Aegina. As seen in Fig. 6b the above findings agree reasonably well with the estimates of Dugdale and Hopkins. The major discrepancy lies in the appearance of an opposite current along the northern coast of Aegina, associated with the development of a second, clockwise gyre in the inner gulf.

Results of the model for NE wind (Fig. 7), and S wind (Fig.8) also show generally satisfactory overall qualitative agreement with the respective patterns of Dugdale and Hopkins. Discrepancies are observed primarily in the area between Salamina and Aegina and the adjacent part of the inner gulf. These may well be due to spatial variability of the wind associated with the mountains and other topographical features surrounding the gulf; they could also be caused by local bathymetric detail or even by small horizontal density differences which are not accounted for in the model.

Figure 9 presents the steady-state velocity field for a 1cm elevation difference between the ends of the open boundary. The resulting motion is more pronounced in the outer gulf with inflow at the eastern part and outflow at the western part. An opposite, clockwise, gyre is seen to develop in the inner gulf; flow towards the west is observed in the passage between Salamina and Aegina, while motion continues around Aegina in a counterclockwise sense. It is seen that the effect of such a small surface tilt can be comparable to that of moderate to strong winds and therefore further study is warranted.

Quantitative verification of the model predictions has not yet been made. To this end, limited current meter data obtained at certain locations of the gulf are being analysed; however, preliminary evidence indicates that the model generally underpredicts the velocity magnitude. It is anticipated that satisfactory verification will require further numerical experimentation with improved quantification and superposition of forcing

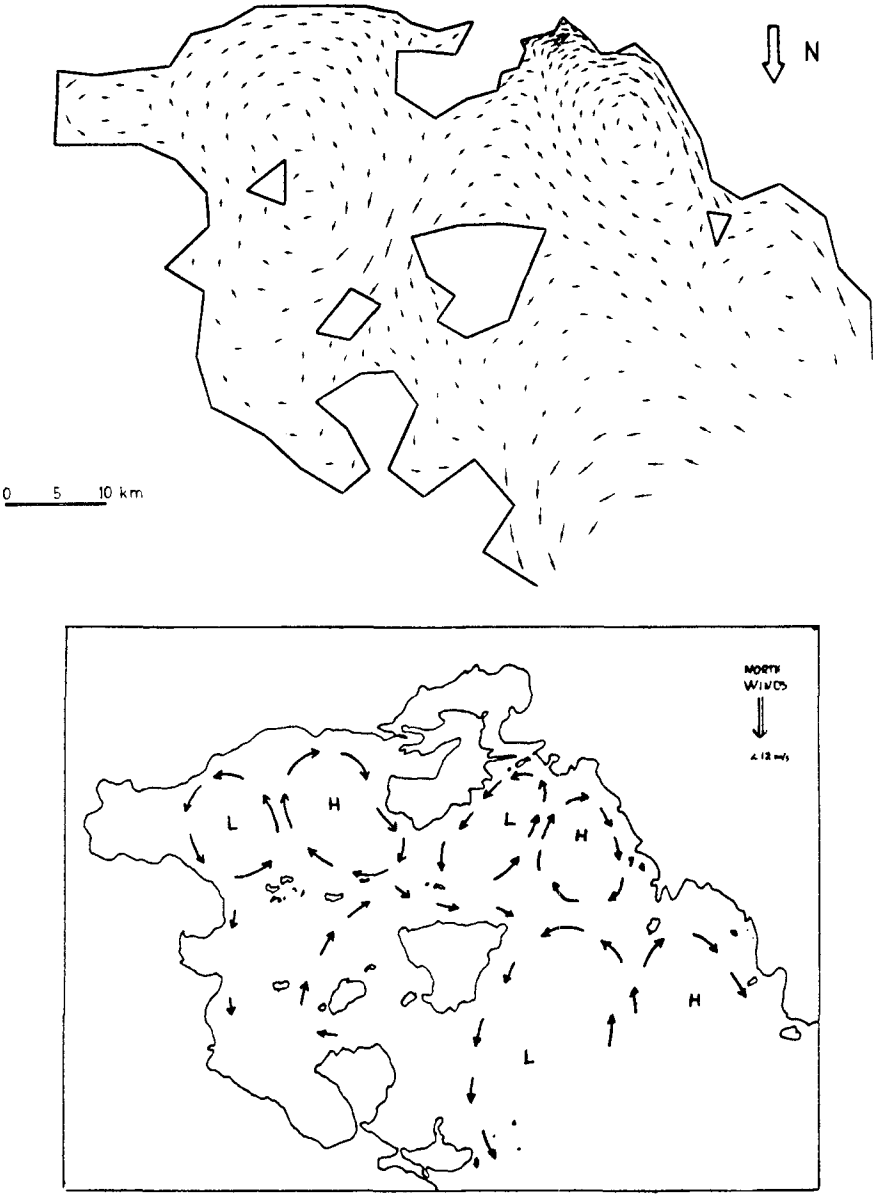

Figure 6. Steady-state circulation for North wind: (a) Model results, (b) Patterns estimated by Dugdale & Hopkins.

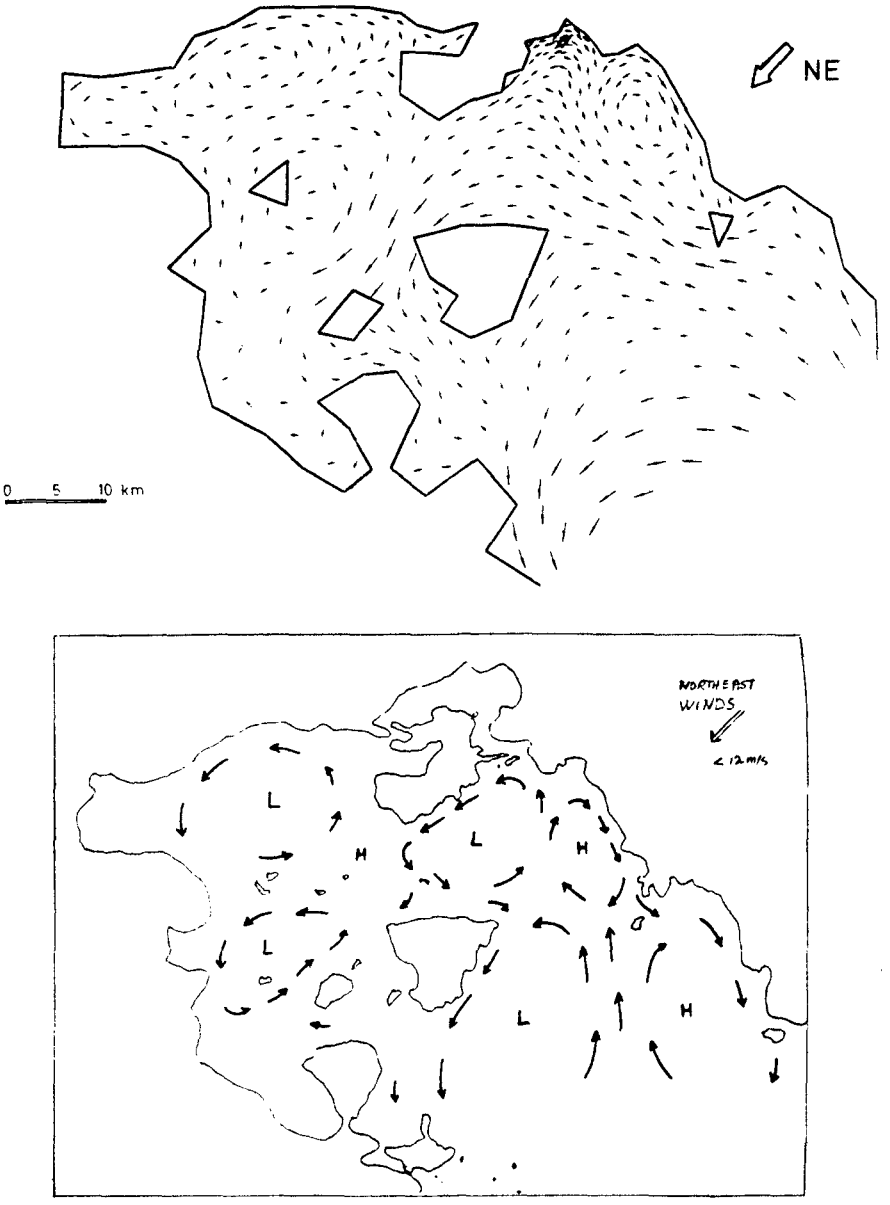

Figure 7. Steady-state circulation for Northeast wind: (a) Model results, (b) Patterns estimated by Dugdale & Hopkins.

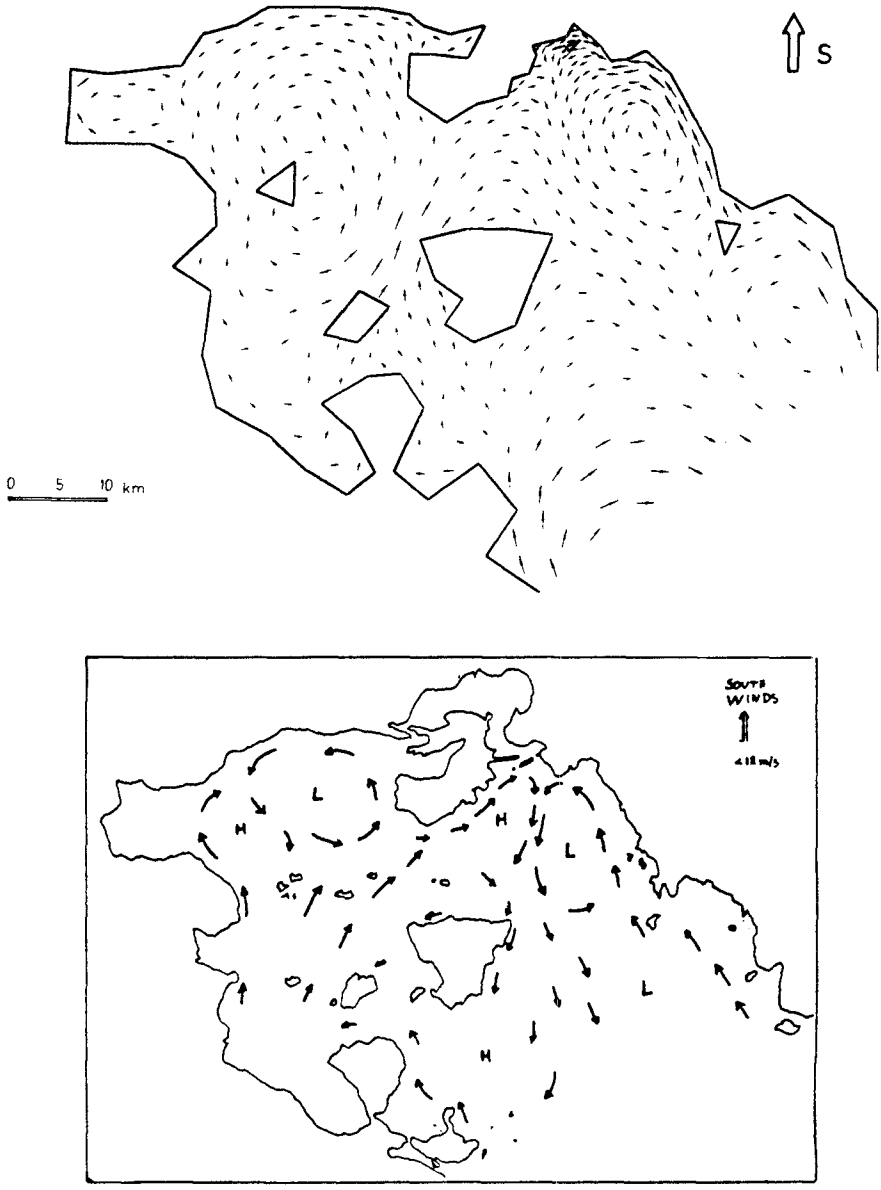

Figure 8. Steady-state circulation for South wind: (a) Model results, (b) Patterns estimated by Dugdale & Hopkins.

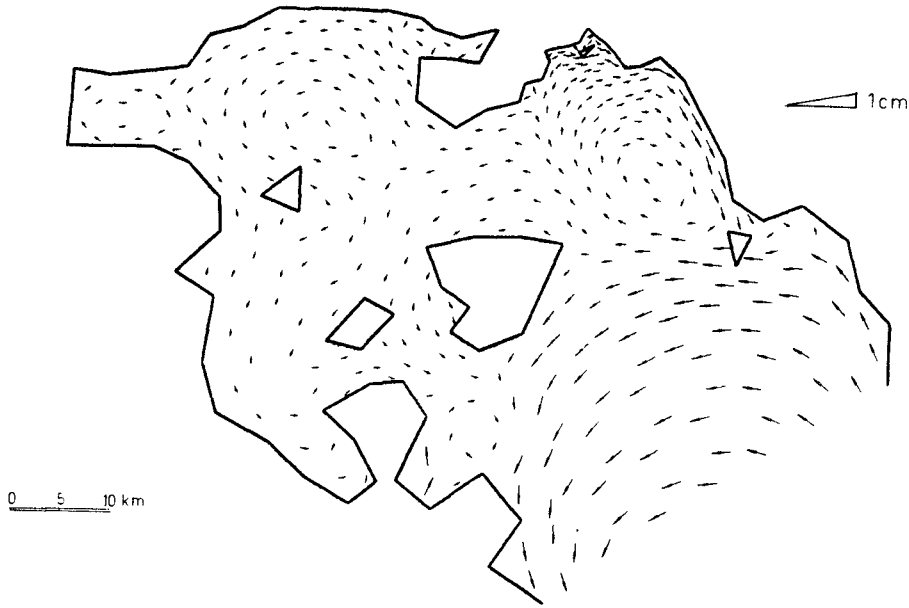

Figure 9. Steady-state circulation for a 1 cm surface tilt of the open boundary.

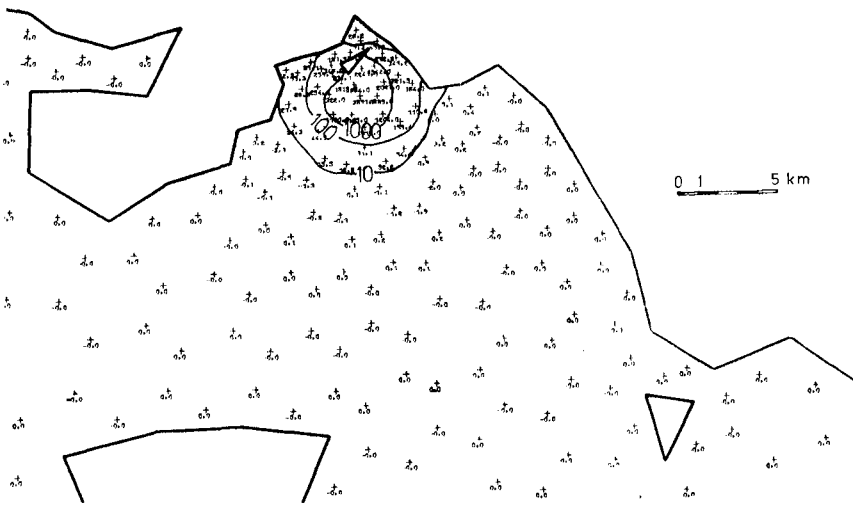

Figure 10. Computed depth-average coliform concentrations (in counts/100 ml) for new outfall.

mechanisms as well as adjustment of some model parameters and boundary conditions.

DISPERSION STUDIES

The dispersion of effluent from the proposed sea outfall was studied with the fine grid shown in Figure 3, where the source is represented by the shaded triangle. The projected annual average discharge of sewage is about $10m^3/sec$. Assuming only preliminary treatment prior to sea disposal, the concentration of coliform in the effluent would be of the order of 10^7 counts/100 ml. Assuming further a decay rate of $k=0.8x10^{-4}sec^{-1}$, corresponding to an average day-night time T_{90}= 8 hrs, and an estimated constant dispersion coefficient of the order of $E = 40m^2/sec$, the dispersion of coliform may be examined for any desired circulation pattern already obtained.

Figure 10 presents steady-state depth-averaged coliform concentration results (in counts/100 ml) under conditions of N wind. It is seen that appreciable concentrations, over 100 counts/100 ml, are confined to a small area around the source, so that no significant contamination of beaches in Attica (to the SE) or Salamina (to the SW) should be expected under the conditions examined. It is further noted that results of other wind cases show little sensitivity of steady-state isoconcentration patterns with wind direction. The above findings strongly depend on the high decay rate used. Evidently, for showly decaying pollutants, e.g. nutrients, the dispersion patterns would be much more extensive and more influenced by meteorological conditions.

CONCLUSIONS

In this paper, the implementation of finite element models for studying the hydrodynamic behaviour of the Saronic Gulf was presented. It was found that wind and a possible surface tilt along the open boundary are of major importance in determining the 2-D circulation in the gulf Actual tide data at the opening were collected and analyzed; yet, the contribution of the tide in the net circulation was found to be negligible. Limited verification with available field evidence was satisfactory in terms of qualitative agreement with model results. But more work is needed on quantitative verification against current meter data, as well as on further examination and quantification of forcing mechanisms, such as the spatial variability of the wind over the study area, the long-term inflow from the Aegean Sea, or any small horizontal density differences that could appreciably change the results of the 2-D circulation. Eventually, the examination of vertical variability will be required for studying the hydrodynamic behaviour under stratified conditions.

The accuracy of circulation patterns will be critical for assessing the dispersion of slowly decaying substances from the proposed sea outfall. However, for fast decaying pollutants, such as coliforms, the extent of appreciable contamination, based on the results presented, is expected to be restricted within the inner gulf.

ACKNOWLEDGMENTS

Financial support for part of this study from the Greek Ministry of

Environment-Planning-Public Works is gratefully acknowledged. The tide gauges used were made available by the Institute of Oceanographic & Fisheries Research.

REFERENCES

1. Christodoulou, G.C., "Hydrodynamic Models in the Saronic Gulf", Proceedings of the International Symposium on Maritime Works in the Mediterranean Sea, Athens, 1984, pp. 3.53-3.60.

2. Dugdale, R.C., and Hopkins, T.S., "Circulation Patterns in the Saronic Gulf as Related to the Wind", Environmental Pollution Research Project, Athens, 1975, Chap. 5.6.

3. Pagenkopf, J.R., Christodoulou, G.C., Pearce, B.R., and Connor, J.J., "A User's Manual for CAFE-1, a Two-Dimensional Finite Element Circulation Model", R.M. Parsons Laboratory for Water Resources and Hydrodynamics Report No. 217, M.I.T., Cambridge, Mass, September 1976.

4. Wang, J.D., and Connor, J.J., "Mathematical Modeling of Near-Coastal Circulation", R.M. Parsons Laboratory for Water Resources and Hydrodynamics Report No. 200, M.I.T., Cambridge, Mass, April 1975.

CHAPTER 183

Numerical Simulation on Thermal Diffusion Concerning Air-Sea Heat Exchange Effects

By

P.C. Chyen[1] C.S. Yang[2]
I.L. Wang[3] H.H. Hwung[4]

Abstract

The numerical simulations on thermal diffusion always concentrated upon the raised temperature and temperature distributions after the heated water discharged from outlet into surrounding water, and the surrounding water temperature was assumed to be a constant. Actually, the water temperature on surface layer in shallow water area varies several centigrade degrees depended upon the weather conditions during a whole day. In order to obtain the absolute water temperature prepared for the ecological changes assessment and even provided for the operation basis of the cooling water system that air-sea heat exchange has to be considered in the numerical simulation of thermal discharges.

For the practical application of this numerical simulation, the first nuclear power plant in Taiwan was taken as an example and simulated in this paper. And the results were presented in figures.

1. Deputy Director, Nuclear Operation Department, Taiwan Power Company, Taipei, R.O.C.
2. Professor of Hydraulic and Ocean Engineering Department, National Cheng Kung University, Tainan, Taiwan, R.O.C.
3. Division Head, Health Physics Division, Nuclear Operation Department , Taiwan Power Company, Taipei, R.O.C.
4. Professor of Hydraulic and Ocean Engineering Department, National Cheng Kung University, Tainan, Taiwan, R.O.C.

1. Introduction

The temperature rise due to air-sea heat exchange is a important factor on the water body where the warmed water discharged from the outlet of a power plant. We know, different species exhibit different tolerant temperature ranges and are restricted within different temperature zones. Under this condition, as the increase in temperature of water body resulting from the discharge of warmed water and air-sea heat exchange is out of the upper tolerant limits that the species will move away and induce ecological changes.

In general, the thermal discharges can be obtaind from numerical model calculations based on the boundary conditions (topography and water depth of computational domain, tide variation and current motion) and initial conditions (include ambient water temperature , intake and outlet discharge and temperature rise of the outlet). However, the variations of water surface temperature resulting from air-sea heat exchange are influenced by solar radiation, water temperature, air temperature, humidity, cloud and wind action. Now, we take the air-sea heat exchange as a source term in the numerical model that the thermal diffusion concerning air-sea heat exchange effects can be obtained in the simulations. And a practical example on the first nuclear power plant in Taiwan was simulated in this paper.

2. Governing Equations

The hydrodynamic equations and equation of heat conservation used in the model for thermal discharge can be written in time-averaged form:

$$\frac{\partial(\rho u)}{\partial t}+\frac{\partial(\rho uu)}{\partial x}+\frac{\partial(\rho uv)}{\partial y}+\frac{\partial(\rho uw)}{\partial z}=-\frac{\partial p}{\partial x}+f\rho v+\frac{\partial \tau_{xx}}{\partial x}+\frac{\partial \tau_{yx}}{\partial y}+\frac{\partial \tau_{zx}}{\partial z} \tag{1}$$

$$\frac{\partial(\rho v)}{\partial t}+\frac{\partial(\rho uv)}{\partial x}+\frac{\partial(\rho vv)}{\partial y}+\frac{\partial(\rho vw)}{\partial z}=-\frac{\partial p}{\partial y}-f\rho u+\frac{\partial \tau_{xy}}{\partial x}+\frac{\partial \tau_{yy}}{\partial y}+\frac{\partial \tau_{zy}}{\partial z} \tag{2}$$

$$\frac{\partial p}{\partial z}+\rho g=0 \tag{3}$$

$$\frac{\partial T}{\partial t}+\frac{\partial(uT)}{\partial x}+\frac{\partial(vt)}{\partial y}+\frac{\partial(wT)}{\partial z}=e_x\frac{\partial^2 T}{\partial x^2}+e_y\frac{\partial^2 T}{\partial y^2}+e_z\frac{\partial^2 T}{\partial z^2}+S_T \tag{4}$$

and the equation of continuity is

$$\frac{\partial \rho}{\partial t}+\frac{\partial(\rho u)}{\partial x}+\frac{\partial(\rho v)}{\partial y}+\frac{\partial(\rho w)}{\partial z}=0 \tag{5}$$

where e_x, e_y, e_z are thermal diffusion coefficients in x,y,z, directions respectively. And S_T is the source terms of heat content flux per unit mass which includes solar radiation, evaporation, heat conduction and so on.

Now, integrating the above equations from bottom to water

surface, that they could be reduced to a two-dimensional flow motion and expressed as follows:

$$\frac{\partial U}{\partial t}+U\frac{\partial U}{\partial x}+V\frac{\partial U}{\partial y}-fV+g\frac{\partial \zeta}{\partial x}+g\frac{U(U^2+V^2)^{1/2}}{C^2H}-\frac{1}{\rho H}\tau_x^s-(K_{x,x}\frac{\partial^2 U}{\partial x^2}+K_{x,y}\frac{\partial^2 U}{\partial y^2})=0 \quad (6)$$

$$\frac{\partial V}{\partial t}+U\frac{\partial V}{\partial x}+V\frac{\partial V}{\partial y}+fU+g\frac{\partial \zeta}{\partial y}+g\frac{V(U^2+V^2)^{1/2}}{C^2H}-\frac{1}{\rho H}\tau_y^s-(K_{x,y}\frac{\partial^2 V}{\partial x^2}+K_{y,y}\frac{\partial^2 V}{\partial y^2})=0 \quad (7)$$

$$\frac{\partial \zeta}{\partial t}+\frac{\partial (HU)}{\partial x}+\frac{\partial (HV)}{\partial y}=0 \quad (8)$$

$$\frac{\partial (HT)}{\partial t}+\frac{\partial (HTU)}{\partial x}+\frac{\partial (HTV)}{\partial y}-\left[\frac{\partial (HD_x\frac{\partial T}{\partial x})}{\partial x}+\frac{\partial (HD_y\frac{\partial T}{\partial y})}{\partial y}\right]-S_T=0 \quad (9)$$

where

$$U=\frac{1}{H}\int_{-h}^{\zeta}u\,dz,\quad V=\frac{1}{H}\int_{-h}^{\zeta}v\,dz$$

3. Air-sea Heat Exchange

The rate of heat exchange on the water surface can be formulated from the algebraic sum of the rates at which heat is transported across the water surface by solar radiation, back radiation, evaporation, heat conduction and so on, it is

$$Q_v=Q_s-(Q_b+Q_e+Q_h) \quad (10)$$

where Q_v is the net rate of heat perpendicular to the water surface, Q_s is the net incoming radiation, Q_b is the back radiation emitted from water surface, Q_e is the heat loss due to evaporation and Q_h is the heat loss or gain due to conduction. All of the above terms have to be obtained from field measurements and will be described as follows.

Since the reflected radiation from water surface is about 6-8% of the total incoming radiation at 25 degree of the latitude that the net incoming radiation can be expressed as

$$Q_s=0.93Q_{s0} \quad (11)$$

And the back radiation is dependent on air and water temperature, cloud, air-vapor pressure and so on. According to the studies

from Central Research Institute of Electric Power Industry (1974), that the back radiation would be

$$Q_b = 1.32\times10^{-12}\theta_a^4(0.49-0.066\sqrt{e(T_a)})(1-0.65n^2)+5.27\times10^{-12}\theta_w^3(T_w-T_a) \quad (12)$$

where $\theta_w=(273°+T_w°C)$, T_w and T_a indicates the water and air temperature respectively, n is the cloud and $e(T_a)$ is the air-vapor pressure which can be calculated from the relationships of humidity and temperature.

As for the heat conduction, it is easy to obtained as

$$Q_h = K_c(T_w - T_a) \quad (13)$$

$$K_c = 2.77\times10^{-4}(0.48+0.272w) \quad (14)$$

here, K_c is the coefficient of heat conduction and W is the wind velocity. And the heat loss due to evaporation can be estimated as

$$Q_e = K_e[e_a(T_w) - fe_a(T_a)] \quad (15)$$

where K_e is the transfer coefficient of evaporation and its value is about $1.5K_c$. f is the relative humidity, $e_a(T_w)$ and $e_a(T_a)$ is the saturation vapor pressure corresponding to the water and air temperature respectively.

According to the above equations the net heat flux between air and sea water surface can be calculated to provide the numerical calculations.

4. Practical Example

For the practical application of this numerical simulation, the first nuclear power plant located in the northern coast of Taiwan was taken as an example and simulated in this paper. Fig-1 is the schematic diagram of the first nuclear power plant and the location of current measurements. Fig-2 is the tide variation of coastal water around this plant. Based on the field measurements of metorological conditions which provided by Taipower Survey Team that the heat flux hour by hour was calculated and listed in Table-1. The currents boundary conditions were set at the east and west sides of the finite-difference grid domain, but the boundary condition at the south was controlled by tides. The numerical model covered an area of 2.88Km×2.88Km with a grid size of 120m. And the numerical simulations were accomplished throughout 4500 time-steps with a value of time step by 30 seconds. Fig-3∿Fig-5 show the simulated flow pattern on the water area of the first nuclear power plant under no wind condition. Fig-6 ∿ Fig-8 are the flow pattern at the same conditions under 5m/sec wind action. And the corresponding temperature distributions were shown in Fig-9∿Fig-14 respectively.

From the results of temperature distributions, we can see the

ambient water temperature rise is about 3.08^{0}C (the initial ambient water temperature is 25^{0}C) for no wind condition and 3.73^{0}C for 5m/sec wind action.

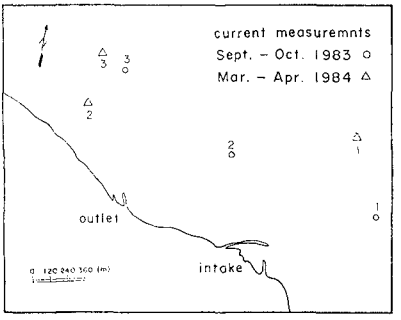

Fig-1

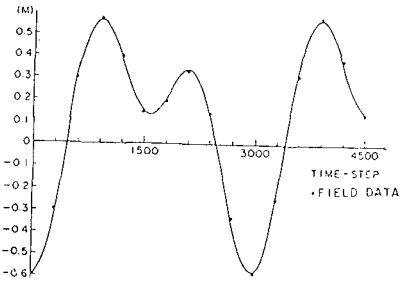

Fig-2

Table-1

Time	3	4	5	6	7	8	9	10
Heat Flux (cal/cm^2·hr)	0.0	0.0	0.0	0.0	0.0	0.0	0.0	62.4
Air Temp.(℃)	27.9	28.0	28.2	28.4	29.0	30.1	31.0	32.0
Time	11	12	13	14	15	16	17	18
Heat Flux (cal/cm^2·hr)	70.8	76.8	78.0	74.4	63.6	44.4	24.0	8.2
Air Temp.(℃)	32.7	32.9	33.4	33.6	33.8	32.0	30.7	30.4
Time	19	20	21	22	23	24	1	2
Heat Flux (cal/cm^2·hr)	2.6	0.0	0.0	0.0	0.0	0.0	0.0	0.0
Air Temp.(℃)	29.8	28.8	28.5	27.9	27.7	27.4	27.0	27.6

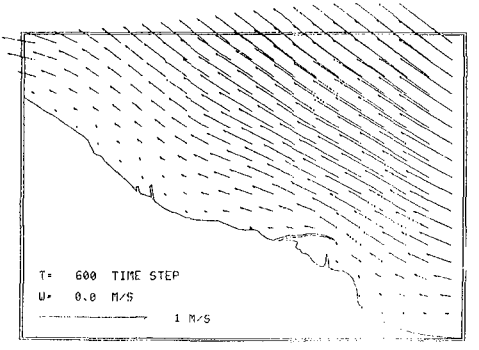

Fig-3

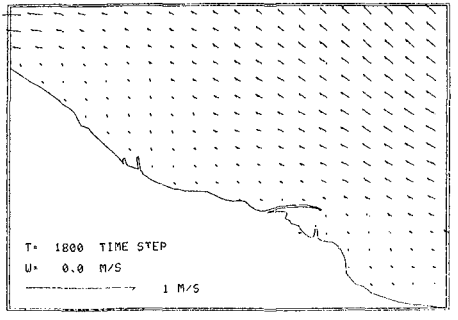

Fig-4

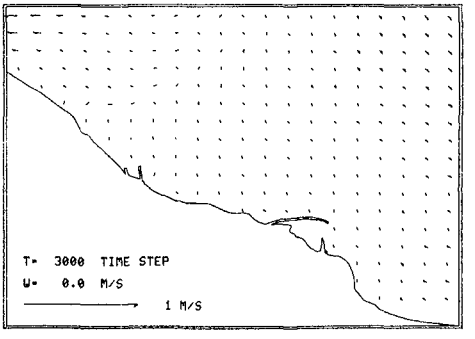

Fig-5

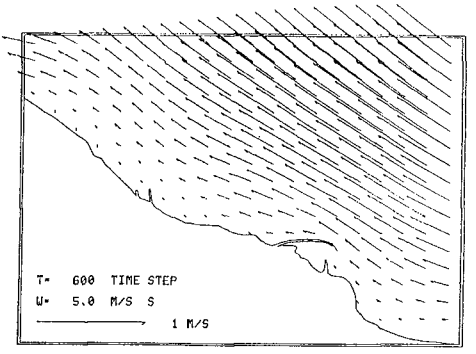

Fig-6

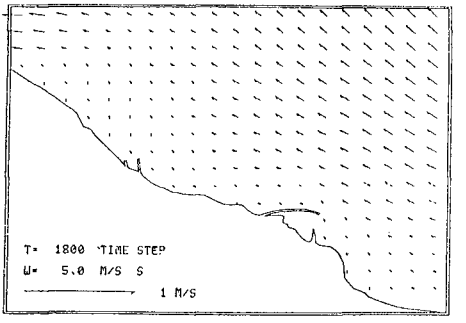

Fig-7

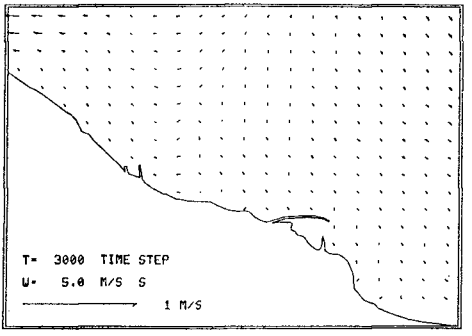

Fig-8

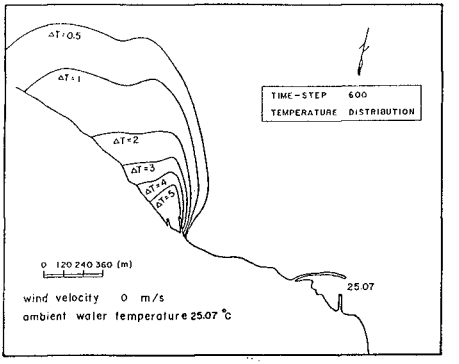

Fig-9

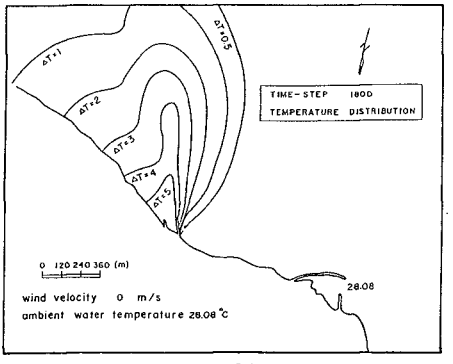

Fig-10

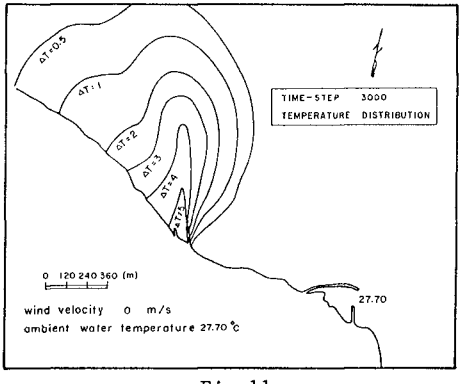

Fig-11

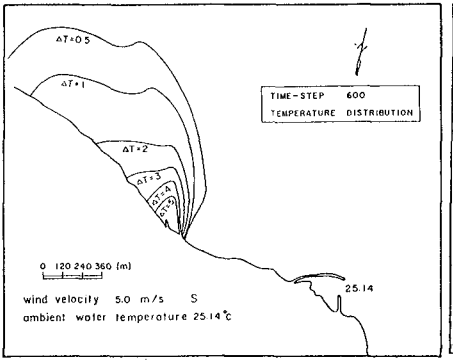

Fig-12

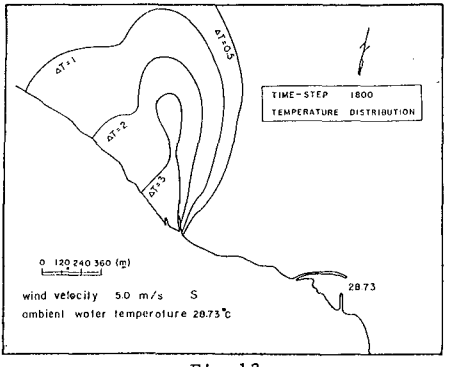

Fig-13

5. Conclusion

From this numerical model simulations, not only the water temperature rise resulting from the thermal discharges of the power plant can be obtained, but also the temperature rise due to air-sea heat exchange will be calculated simultaneouly. That it is more significant to provide enough information for the assessment of ecological changes before a power plant will be planned.

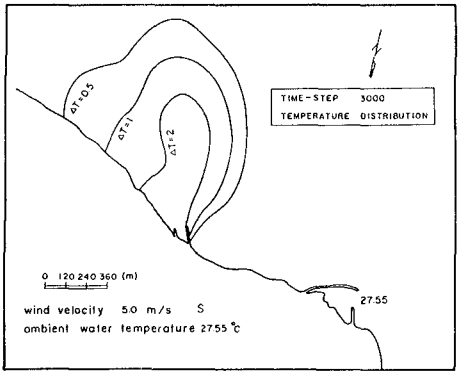

Fig-14

6. Reference

1. Frederick, L.W. Tang and H.H. Hwung (1979). "Studies on the Thermal Diffusion of The Third Nuclear Power and The Field Investigations of Lin-Ko Power Plant", Tainan Hydraulic Laboratory, Bulletin 42.

2. H.H. Hwung, C.S. Yang and Tehfang Lee (1984). "Alarm System Operation Reaerach for The Circulation of The Third Nuclear Power Plant", Tainan Hydraulic Laboratory, Bulletin 68.

3. H.H. Hwung, C. S. Yang (1985). "Development of Two-Dimensional Model on The Thermal Diffusion Study", Tainan Hydraulic Laboratory, Bulletin 78.

4. H.H. Hwung and K.C. Tang (1986). "Two-dimensional Numerical Simulations of Thermal Discharge on The Third Nuclear Power Plant", Tainan Hydraulic Laboratory, Bulletin 89.

5. G.H. Jila, G. Abraham and D.R.F. Harleman (1975). "An Assessment of Techniques for Hydrothermal Prediction", PB 250509, NUREG-0044.

CHAPTER 184

Effect of Breaking Waves on Dissolved Oxygen and Organic Matter

Yoshihiko HOSOI* and Hitoshi MURAKAMI**

Abstract

Water pollution in the near shore area has become a serious problem in coastal engineering. In such a situation, not only wave dissipation but also the functioning of water pollution control is expected from the coastal structure. Since breaking waves are accompanied by many bubbles and intense water turbulence, they promote the contact between organic matter and bacteria and between water and air. Therefore the water quality related to organic matter seems to change under the effect of breaking waves. In this study the variation of the dissolved oxygen and the organic matter near the surf zone were considered. First, a self purification model in the surf zone was developed. Second, the efficiency of breaking waves on reaeration and organic matter decomposition was estimated by an experiment in the laboratory flume and numerical simulation.

1. Introduction

With the expansion of human activities, water pollution in the nearshore area has increased. Organic contaminants discharged into water are decomposed by aerobic bacteria through their metabolic process, which results in the utilization of the dissolved oxygen. The deficit oxygen is compensated for by reaeration which occures through the water surface exposed to the atmosphere. When the rate of oxygen utilization in the decomposition of organic contaminants is within the limit recoverable by the reaeration, the water environment is maintained under desirable conditions. In that sence, the evaluation of natural purification is important in water quality control. Many studies concerning this have been made in rivers.(O'Connor and Dobbins(1956), Churchill et al.(1962), Dobbins(1964)) However, studies of this kind in the sea are few, because the great dilution within a large amount of water plays a principal role in sea water purification.

In general, water turbulence accelerates the contact between the organic matter and bacteria and also between water and air. Therefore it promotes the decomposition of organic matter and the oxygen absorption. Breaking waves produce many bubbles and intense water turbulence. Thus they seem to play a significant role in water purification near the coast, particularly in a bay or water enclosed by breakwaters, where the water exchange with the outer ocean is relatively limited.

* Associate Professor, Technical College, The University of Tokushima, Minamijosanjima, Tokushima, 770 Japan

** Professor, Technical College, The University of Tokushima

Therefore, if we know the characteristics of the natural water purification caused by breaking waves, we can design artificial coasts or coastal structures from the viewpoint of water quality control.

In this study, in order to examine the effect of breaking waves on water quality, we considered the changes of water quality related to organic pollution near the surf zone.

2. Self purification in the nearshore area

As for the decomposition of organic contaminants in a river, the attached bacteria on the bed are considered to play a more significant role than suspended ones. In the case of the coastal area, there are many sites where attached bacteria can grow, for example beaches, breakwaters and so forth. Therefore we can suppose that organic matter is decomposed there by the activity of attached bacteria. Here we propose a model of self purification near the coast as shown in Fig.1.

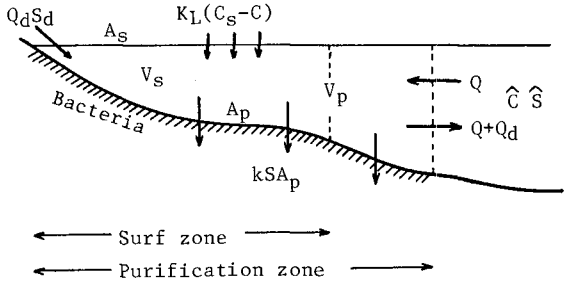

Fig.1 Model of self-purification in nearshore area

The volume of discharged water is represented by Q_d, which includes organic matter whose concentration is S_d. The organic matter is decomposed by the biofilm with the rate of kSA_p. The water volume per unit width in this decomposition zone (which we call in this paper the purification zone) is described by V_p.

The oxygen is supplied through the water surface. As we will describe later, the reaeration efficiency in the surf zone is still greater than that in other areas. Therefore we assume the oxygen is absorbed only at the surf zone whose surface area is A_s.

The mass conservation equations describing the dissolved oxygen and the organic matter are as follows, respectively,

$$d(CV_p)/dt=-kSA_p+K_L(C_s-C)A_s+Q_dC_d+Q\hat{C}-(Q+Q_d)C \quad (1)$$

$$d(SV_p)/dt=-kSA_p+Q_dS_d+Q\hat{S}-(Q+Q_d)S \quad (2)$$

where C and S are the dissolved oxygen concentration and the organic matter concentration, respectinely. $\hat{C}$ and $\hat{S}$ represent the quantities of the outside of the purification zone and C_s the saturated dissolved oxygen concentration. C_d represents the dissolved oxygen in the

discharged water.

We introduce the nondimensional form:

$$C^*=C/C_s, \quad S^*=S/S_r, \quad t^*=t/T \tag{3}$$

where S_r and T are the representative concentration of organic matter and the wave period, respectively.

We rewrite Eqs.(1) and (2) by Eq.(3) as follows,

$$dC^*/dt^*=-k_1TS^*S_r/C_s+k_2T(1-C^*)+TQ_dC_d^*/V_p+TQ\hat{C}^*/V_p-T(Q+Q_d)C^*/V_p \tag{4}$$

$$dS^*/dt^*=-k_1TS^*+TQ_dS_d^*/V_p+TQ\hat{S}^*/V_p-T(Q+Q_d)S^*/V_p \tag{5}$$

where $k_1=kA_p/V_p$ (6), $k_2=K_LA_s/V_p$ (7)

k_1 and k_2 stand for the overall rate constants of decomposition and reaeration in the purification zone, respectively. When the role of suspended bacteria cannot be disregarded, we can include their effects in k_1.

The initial condition is given as follows,

$$t^*=0 : S^*=S_0^*, \ C^*=C_0^* \tag{8}$$

We solve Eqs.(4) and (5) and obtain the following equations.

$$S^*=S_\infty^*+(S_0^*-S_\infty^*)\exp(-\alpha t^*) \tag{9}$$

$$C^*=C_\infty^*-\gamma\exp(-\alpha t^*)+(C_0^*-C\infty^*+\gamma)\exp(-\beta t^*) \tag{10}$$

$$\gamma=(k_1S_r/C_s)(S_0^*-S\infty^*)/(k_2-k_1)$$

α shows water purification efficiency by bacterial decomposition and the water exchange with the outer region, and β shows the efficiency of oxygen supply in reaeration and the water exchange. Each of them are writen as follows, respectively.

$$\alpha=k_1T+T(Q+Q_d)/V_p \tag{11}$$

$$\beta=k_2T+T(Q+Q_d)/V_p \tag{12}$$

The steady state solutions, $S\infty^*$ and $C\infty^*$, are given as follows, respectively,

$$S_\infty^*=F/\alpha=(Q_dS_d^*+Q\hat{S}^*)/(k_1V_p+Q+Q_d) \tag{13}$$

$$C\infty^*=(F+k_2T-k_1TS\infty^*S_r/C_s)/\beta=\frac{Q_dC_d^*+Q\hat{C}^*+k_2V_p-k_1V_pS\infty^*S_r/C_s}{k_2V_p+Q+Q_d} \tag{14}$$

F is the total discharged contaminant load writen as

$$F=(Q_dS_d^*+Q\hat{S}^*)T/V_p \tag{15}$$

The oxygen sag curve obtained by Eq.(10) is shown in Fig.2 and t_1^*, t_2^* and C_{min}^* are given as followas, respectively.

$$t_1^* = \frac{1}{\beta-\alpha} ln \frac{\beta(F+C_\infty^*-C_0^*)}{\alpha F} \tag{16}$$

$$t_2^* = \frac{1}{\beta-\alpha} ln \frac{\beta^2(F+C_\infty^*-C_0^*)}{\alpha^2 F} \tag{17}$$

$$C_{min}^* = C_\infty^* - \gamma \{\frac{\beta(C_0^*-C_\infty^*+\gamma)}{\alpha\gamma}\}^{\frac{\alpha}{\alpha-\beta}} + (C_0^*-C_\infty^*+\gamma)\{\frac{\beta(C_0^*-C_\infty^*+\gamma)}{\alpha\gamma}\}^{\frac{\beta}{\alpha-\beta}} \tag{18}$$

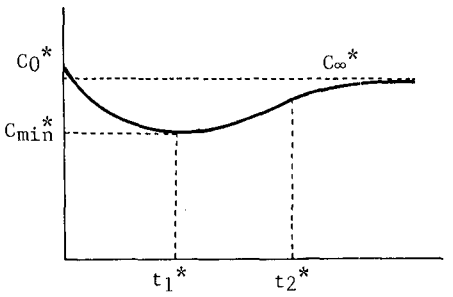

Fig.2 Oxygen sag curve in nearshore area

When C_{min}^* is greater than the critical concentration in which the self purification is possible, the desirable water environment can be recovered. Generally, the minimum DO concentration where aerobic decomposition takes place is said to be 2 mg/l. Thus C_{min} must be greater than 0.15-0.3 (C_s depends on the water temperature and salinity).

In the steady state case, the amount of discharged contaminants into the purification zone is $Q_d S_d^*$ and the amount going out from the purification zone toward the offing is $(Q+Q_d)S_\infty^*$. When we can regard $\widehat{QS}$ as negligibly small compared with $Q_d S_d$, the ratio of both amounts, which gives the purification efficiency, is shown as

$$\frac{(Q+Q_d)S_\infty^*}{Q_d S_d^*} = \frac{1}{1+(k_1 V_p)/(Q+Q_d)}$$

Thus $k_1 V_p/(Q+Q_d)$ is the index which indicates the purification capacity when C_{min}^* satisfies the condition mentioned above.

3. Experimental apparatus and procedure

We examined the behavior of water quality in and near the

purification zone by experiments.

The experiments were performed in a two dimensional wave flume, 14.8 m long, 18.5 cm wide. The water depth was 15.0 cm. The model beach with a plane slope 1/20 was placed in it. Two kinds of experiment were performed as follows.

1) The experiments on reaeration

After the dissolved oxygen (DO) concentration in the flume was reduced with sodium sulfite, waves were generated and broken on the beach. The spatial-temporal DO distribution was observed. The detailed method was reported in Hosoi et al.(1984).

2) The experiments on the decomposition of the organic matter

The aerobic bacteria were added to the water in the flume and waves were generated. Under the presence of waves they were cultured for about 20 days with skim milk fed as a substrate. After the bacteria had grown attached to the sloping bottom, the experiment on the oxidization was conducted as follows.

The initial concentration of organic matter was promoted by skim milk, and waves were generated. The water samples were collected at fixed intervals to capture the spatial-temporal change of DO and the organic matter. The amount of the organic matter was estimated by the chemical oxygen demand (COD) using potassium dichromate.

One series of experiments continued for not longer than 3 days to avoid the influence of the change of biofilm condition.

After one series of experiments was finished, we collected the attached bacteria and observed the biomass and the bacterial activity. The bacterial activity was examined as follows. We put the collected bacteria into a beaker of water which contained organic matter. The water was stirred to suspend bacteria and the temporal changes of COD were observed.

The experiments of 1) and 2) were conducted under some different deep water wave heights.

4. Reaeration

4.1 Theoretical consideration

According to Danckwerts' surface renewal thoery, which explains the gas transfer across the gas-liquid interface in the turbulent flow, the oxygen flux across the interface j and the oxygen transfer coefficient K_L are expressed as follows, respectively,

$$j=K_L(C_s-C) \qquad (19), \qquad K_L \sim (Dr)^{1/2} \qquad (20)$$

where D is the molecular diffusion coefficient. r is the renewal rate which means that water elements near the surface are replaced by the bulk water, and has the dimension of the minus first power of time. It has a close relationship to the turbulent motion.

We assumed the dependence of r on the turbulence as follows (Hosoi et al.(1984)),

$$r \sim (\varepsilon/\nu)^{1/2} \qquad (21)$$

where ε and ν are the energy dissipation rate and the kinematic viscosity, respectively.

If we assume all of the energy which is transported by the wave from the offing toward the shore dissipates in the surf zone, we obtain

$$\varepsilon=g^2H_0^2T/(32\pi V_s) \tag{22}$$

where V_s represents the water volume of the surf zone per unit width.

Placing Eqs.(20), (21) and (22) into Eq.(7), we obtain

$$k_2\sim(T/\nu V_s)^{1/4}(DgH_0)^{1/2}A_s/V_p$$
$$=(T/\nu V_s)^{1/4}(DgH_0)^{1/2}(V_s/V_p)/\overline{h_s} \tag{23}$$

where $\overline{h_s}$ is the mean depth of the surf zone and H_0 the deep water wave height.

If the surf zone has a plane slope, we can say $\overline{h_s}=h_b/2$, where h_b is the breaker depth.

4.2 Experimental results

Fig.3 shows the temporal changes of the dissolved oxygen profile in the experiment on reaeration. The increase rate in the dissolved oxygen is the greatest in the surf zone and becomes smaller as the distance from the shoreline increases.

As we previously indicated (Hosoi and Murakami(1981)), this figure makes us believe that the effect of oxygen absorption in the surf zone is so much greater than in other areas that the oxygen is absorbed only in the surf zone and transferred offshore.

On the basis of this consideration we evaluated the reaeration coefficient (Hosoi et al.(1984)). When we divided the examination area into the boxes as shown in Fig.4, we could obtain the following equation in the i box.

$$dC_iV_i/dt=V_ik_{2i}(C_s-C_i)+q_{i-1}(C_{i-1}-C_i)-q_i(C_i-C_{i+1}) \tag{24}$$

where suffix i represents the quantity in number i box and q_i the water exchange across the boundary between i and i+1 boxes. The box is divided so that the innermost box whose number i=1 becomes the surf zone, i.e., the area between the breaking point and the shoreline, and define the box i=2,3,4,$\cdots\cdots$ in order towards the offing.

Summing up Eq.(24) from i=1 to n, and taking into consideration that the reaeration efficiency in the surf zone is so much greater than other parts that we can neglect their contribution, we obtained

$$d\Sigma C_iV_i/dt=V_1k_{2,1}(C_s-C_1)+q_n(C_{n+1}-C_n) \tag{25}$$

As we saw in Fig.3, the influence of the reaeration in the surf zone did not extend far into the offing. Thus if n-box is taken far from the breaking point where C_n can be regarded as equal to C_{n+1}, Eq.(25) is rewriten as

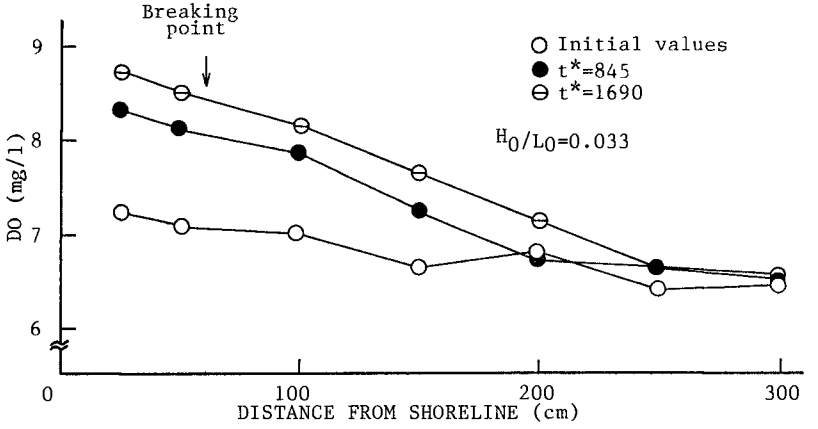

Fig.3 Variation of dissolved oxygen concentration

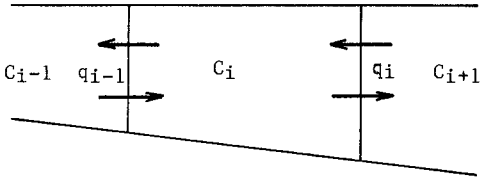

Fig.4 Box model

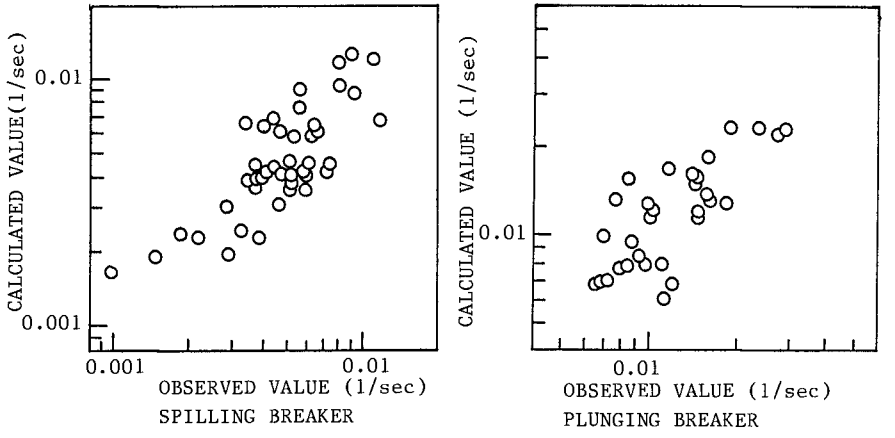

Fig.5 Relationship between observed k_2 and calculated k_2

$$d\Sigma C_i V_i/dt = V_1 k_{2,1}(C_s - C_1) \tag{26}$$

We calculated the reaeration coefficient in the surf zone by Eq.(24) and transformed it to the value at 20°C.

We decided the value of the proportinal constant in Eq.(23) when $V_p = V_s$, from the experimental results. Fig.5 is the comparison between the calculated and the observed values. We obtained the following relation.

$$k_2 = \begin{cases} 0.144(T/\nu V_s)^{1/4}(DgH_0)^{1/2}(V_s/V_p)/\overline{h_s} & \text{(Spilling breaker)} \\ 0.184(T/\nu V_s)^{1/4}(DgH_0)^{1/2}(V_s/V_p)/\overline{h_s} & \text{(Plunging breaker)} \end{cases} \tag{27}$$

The difference in the value of the proportional constant between spilling and plunging breakers is due to the difference of bubble distribution in the surf zone. In spilling breakers, bubbles distribute only near the water surface, while, in plunging breakers, they reach down to the bottom (Hosoi and Murakami(1981)). Thus plunging breakers have a larger area of gas-liquid interface and a greater turbulent intensity than spilling breakers. It may affect the proportional constants in Eq.(27).

5. Decomposition of organic matter

5.1 Variation of COD and DO

The variation of COD and DO is shown in Fig.6. The plane slope extends 3 m from the shoreline, on which there is attached bacterial film.

In the case of Fig.6(a), the initial COD is higher near the shoreline. After 2 hours, COD near the shoreline becomes low, but it scarcely changes at the sites far from the shoreline. As a result the COD profile becomes flat. This shows that the decrease in the organic matter is due to the oxidization in the slope area and not to the diffusion to the offing.

With the decomposition of organic matter the dissolved oxygen is consumed. The decline of DO is noticeable near the site 3 m away from the shoreline. As we have already described, oxygen absorption is far greater in the surf zone. Therefore at this point the main source of oxygen is from the transfer from the surf zone rather than the aeration occurring there. Thus the oxygen supply is not so large as compared with the surf zone. Neverthless here exists the slope with a biofilm and here oxidization of organic matter takes place. As a result the oxygen deficit becomes noticeable in this area.

Fig.6(b) is another example which shows that the initial COD is rather uniform from the shoreline to the offing. COD decreases relatively uniformly. The decrease in DO shows the same trend as in the former case. Here again, we can assume that organic matter is decomposed in the slope area and purified water is transfered to the offing.

5.2 Attached bacteria

The attached biomass on the unit area of the slope bottom is shown

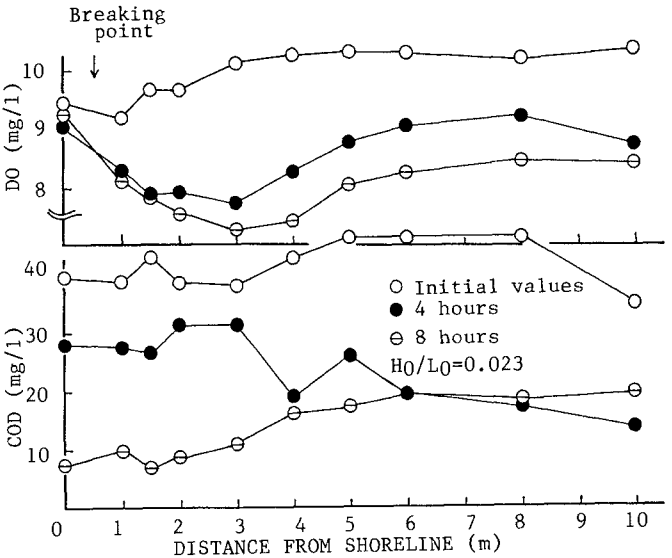

(b)

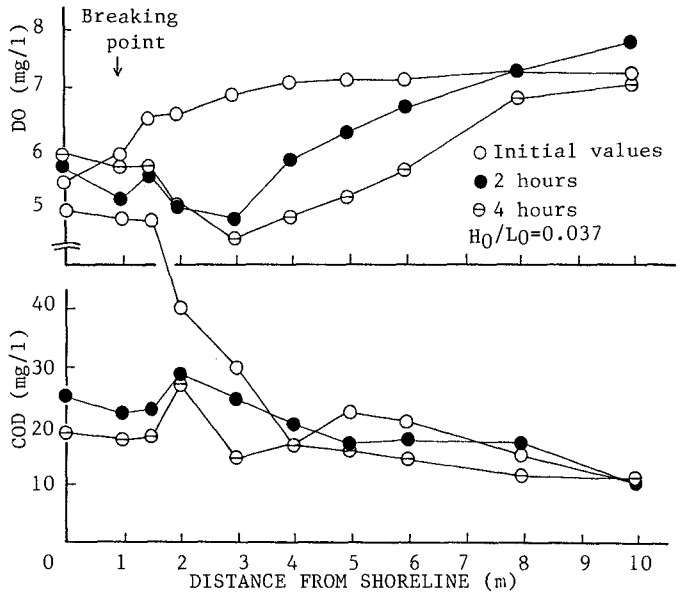

(a)

Fig.6 Variation of DO and COD

in Fig.7. Less biomass grew at the points where wave breaking happened during experiments (0.5-1.0 m away from the shoreline). This shows that the intense turbulence induced by wave breaking prohibits the development of bacterial attachment in the surf zone.

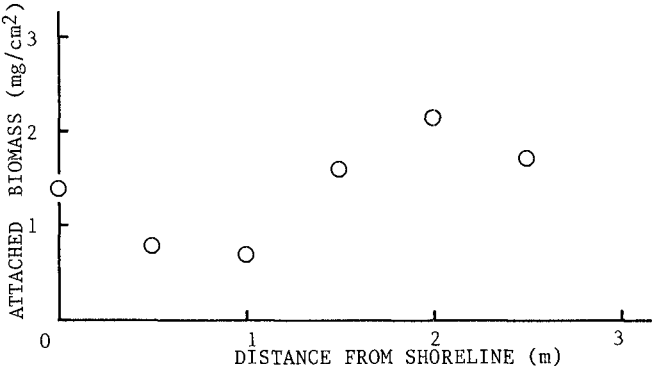

Fig.7 Biomass attached on slope bottom

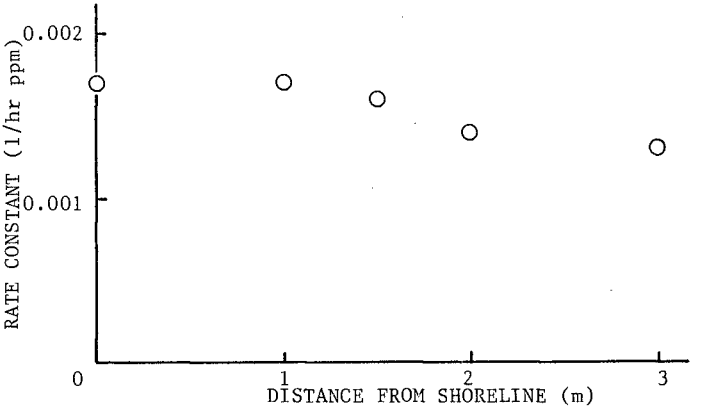

Fig.8 Bacterial activity

The activity of attached bacteria is shown in Fig.8. This shows the decomposition rate to be constant of bacteria suspended in the beaker. There was no significant difference found in the oxidization ability as to the distance from the shoreline.

5.3 Decomposition rate of organic matter on the beach

Generally, the reaction of organic matter oxidization is expressed

as the first power of its concentration. Therefore we write the changes of COD by the following equation.

$$\frac{d}{dt}\int SdV=-kA_pS_p \tag{28}$$

where S_p is the concentration of organic matter in the purification zone. From Eqs.(6) and (28) we obtain

$$k_1V_p=-\frac{1}{S_p}\frac{d}{dt}\int SdV \tag{29}$$

This shows the overall oxidization ability in the purification zone.

Fig.9 shows the relation between the decomposition constant k_1 and the deep water wave steepness. We can see there is a positive relationship. It indicates that the water movement renews the water near the biofilm and promotes the supply of organic matter and DO to the biofilm. It is necessary to examine k_1 in relation to the quantities which represent the water movement structure in the surf zone. Here, however, we obtained the linear relationship shown in Fig.9 for the sake of the next consideration.

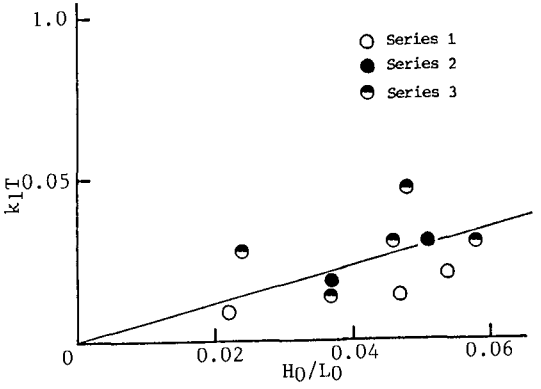

Fig.9 Decomposition rate constant

6. Numerical consideration

In order to consider the effect of incident waves on water quality we used a numerical model. When we take up the box model as shown in Fig.4, we obtain the following equations for DO and COD, respectively,

$$dC_i^*/dt^*=-k_1TS_i^*(S_0/C_s)+k_2T(1-C_i^*)$$
$$+(q_{i-1}T/V_i)(C_{i-1}^*-C_i^*)-(q_iT/V_i)(C_i^*-C_{i+1}^*) \tag{30}$$
$$dS_i^*/dt^*=-k_1TS_i^*+(q_{i-1}T/V_i)(S_{i-1}^*-S_i^*)$$
$$-(q_{i-1}T/V_i)(S_i^*-S_{i+1}^*) \tag{31}$$

where S is transformed into nondimensional form by the initial concentration S_0. The first terms on the right hand side of Eqs.(30) and (31) express the utilization of DO or organic matter through bacterial metabolism. Thus they appear only in the purification zone. The second term on the right hand side of Eq.(30) describes reaeration, and therefore exists only in the surf zone.

The same beach condition as in this experiment was given, i.e., the water depth is 15.0 cm, and the beach slope is 1/20 and there is attached bacteria on the beach.

For the given condition of the deep water wave and the beach slope, the breaker depth was determined by the figure presented by Goda(1970). The wave transformation due to the shoaling effect was calculated by the small amplitude wave theory. The exchanging rate was given with reference to Nadaoka and Kondoh(1982) as follows.(Hosoi et al.(1984))

$$q_i = 0.2\omega\left(\frac{H}{2}\right)^2 \frac{\{1-(H/2h)\}coth kh}{1-(H^2k/8h)coth kh} \tag{32}$$

where H is the wave height, k the wave number and ω the angular frequency with reference to the fixed frames.

The reaeration coefficient was obtained by Eq.(27) and the decomposition rate constant was obtained from the regressive relationship shown in Fig.9.

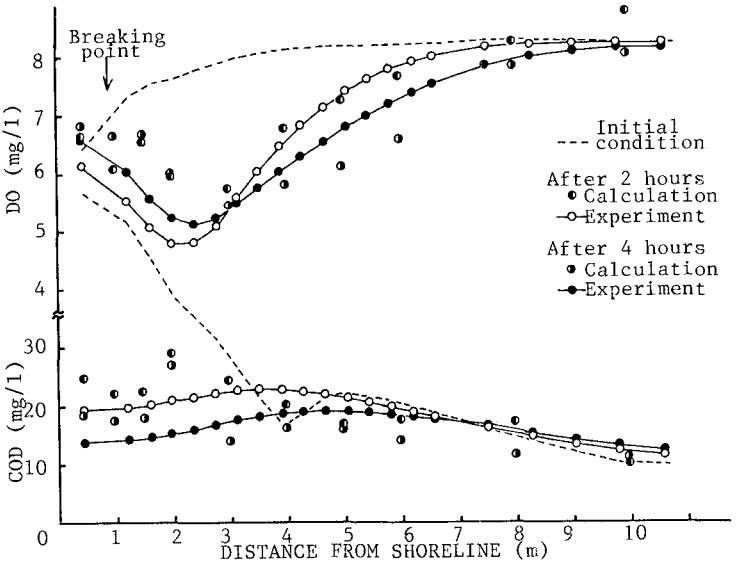

Fig.10 Water quality profiles

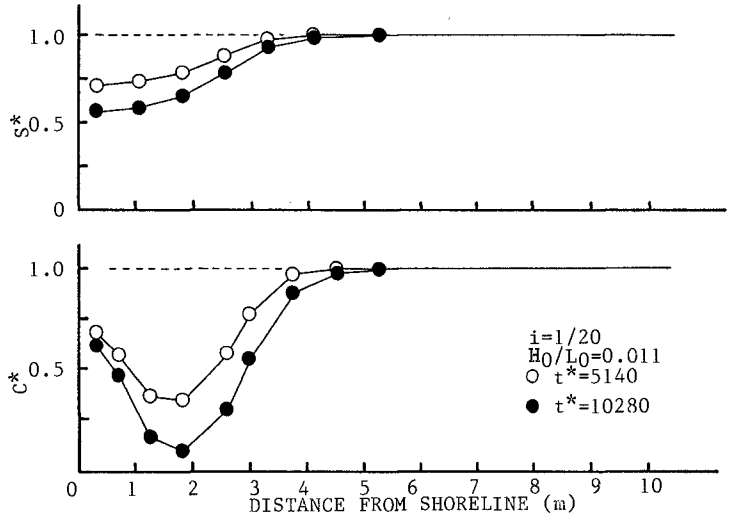

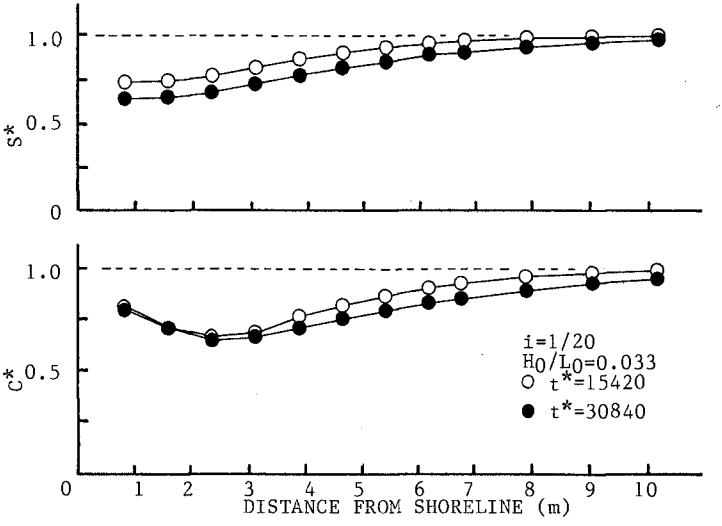

Fig.11 Results of water quality calculation

Fig.10 shows the comparison of water quality profiles between the experiment and the numerical simulation. The simulated results approximately agree with the experimental results. In particular, we could find the feature that DO has a minimum concentration a little outside of the surf zone.

Fig.11 shows the results of calculation under the initial condition that DO is saturated and organic matter distributes uniformly from the shoreline to the offing. In the case of smaller H_0/L_0 (the deep water wave steepness of the incident wave), the area where COD decreases is smaller. The decrease in DO is noticeable a little outside of the surf zone in both cases. When H_0/L_0 is small, the decrease in DO is remarkable and it shifts to the anaerobic condition.

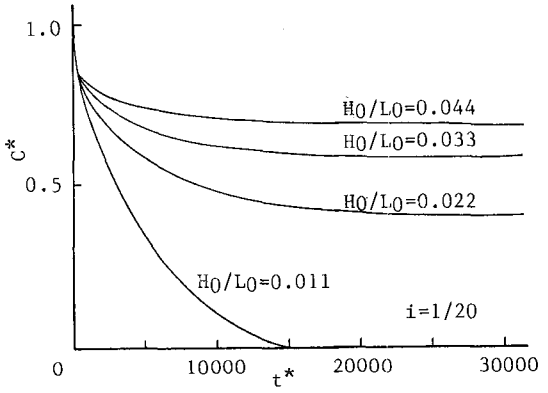

Fig.12 Change of the minimum concentration of the dissolved oxygen

Fig.12 shows the change of DO concentration at the point where it has the minimum value. Under the condition in our consideration, DO is used up completely when $H_0/L_0=0.011$ and the water environment is deteriorated to some extent even when $H_0/L_0=0.022$.

From the considerations so far we suppose that the water pollutant accomodation capacity in the nearshore area can be estimated from the beach shape, the incident wave and the bacterial activity.

7. Conclusions

We have considered the role of breaking waves in water quality near the surf zone. The general expression on DO and organic matter in nearshore area was derived. The variation of DO and organic matter was examined by experiments and a numerical model. Both the relationship between the reaeration coefficient and wave characteristics, and that between the decomposition constant and wave characteristics were shown. At this stage, our conclusion is limited in the experimental flume. The problem of how to apply these results in the field, hereafter still remains.

Acknowledgement

The authors would like to acknowledge the continuing guidance and encouragement of Professor Hisashi Sumitomo, Kyoto University. We were also favored to have the assistance of Tetsushi Iwasaki who contributed his effort to the accomplishment of the experiments and the computer works.

References

Churchill, M.A., H.L. Elmore and R.A. Buckingham (1962) "The prediction of stream reaeration rates", Journal of Sanitary Engineering Division, ASCE, Vol.88, No.SA4, pp.1-46.

Dobbins, W.E. (1964) "BOD and oxygen relationships in streams", Journal of Sanitary Engineering Division, ASCE, Vol.90, No.SA.3, pp.53-78.

Goda, Y. (1970) "A synthesis of breaker indices", Proceedings of JSCE, No.180, pp.39-49 (in Japanese).

Hosoi, Y. and H. Murakami (1981) "An experimental study on dissolved oxygen behavior at surf zone", Proceedings of 28th Japanese Conf. on Coastal Engineering, pp.451-455 (in Japanese).

Hosoi, Y., H. Murakami and M. Oto (1984) "Reaeration by spilling breaker", Coastal Engineering in Japan, Vol.27, pp.97-108.

Nadaoka, K. and T. Kondoh (1982) "Laboratory measurement of velocity field structure in the surf zone by LDV", Coastal Engineering in Japan, Vol.25, pp.125-145.

O'Connor, J.D. and W.E. Dobbins (1956) "The mechanics of reaeration in natural streams", Journal of Sanitary Engineering Division, ASCE, Vol.82, No.SA.6, pp.(1115)1-30.

Feasibility Study of Deep Water Port of Taiwan District, R.O.C.

H.-S. HDU
Institute of Transportation, Ministry of Communications, Republic of China

ABSTRACT

Taiwan is now served by five international ports, two of which were newly opened since 1970. They have been under continuous expansion in recent years to meet the needs of the island's burgeoning foreign trade. Due to recent trend of vessel developed to huge load-capacity, the existing port of Taiwan district is inconvenient to the ULCC or VLCC. For decreasing the shipping cost and accomodating the cargo handing of over 100,000 DWT, the deep water port is urgent to be developed in order to promote the competent capability of port cargo handling.

This research is divided into two parts, at first, the prediction of cargo handling and the cargo sources which are adapted to the huge vessel shipping need to be studied for the development of deep water port. the next, then the oceanographical data for the design and the planning of deep water wharf and breakwater need to be surveyed around this Island for possible site of deep water port.

This study deals with the related problems of deep water breakwater construction and discusses how to apply the present design and construction method to the deep water wharf and breakwater. Further analyses are conducted for this research in the coming three fiscal years.

1. Introduction

In general, relatively small ships are employed in the principal five ports except Kaohsiung. The shipping industry has anticipated the nautical restrictions of the ports of Keelung, Suao, Hualien to receive the range of larger ships and the navigational constraints are much less severe than in the other four ports. Nautical constraints have severe effects on the large vessels, the container trade. Special attention is thus required to keep one or two of Taiwan's ports accessible to larger container vessels in the near future. A deepwater port provides Taiwan with several, distinct advantages. First of all, it allows coal transportation by large bulk carriers, resulting in savings in the costs of transport to Taiwan. For Taichung port the additional costs of inland transportation by barge are more than compensated for by these savings; central handling of coal at other deepwater locations would yield approximately the same outcome. Furthermore, the development of a deepwater port, either in Taichung or Keelung or at another location, would enable Taiwan to create or to include the possibility for creating extra port capacity, which could be used to boost the country's transshipment function in containers and bulk commodities. Moreover, it would facilitate Taiwan's

adequate reaction to suddenly emerging trade opportunities in the region. The proposed "Free Trade Zone" would also fit in well with the deepwater port concept. Finally, such a port can provide the special facilities required for the landing of LNG.

2. Research Procedure

1. Research of requirement and capacity of five international trade-ports in Taiwan district
   (a) Reduce all the data of the future developing plan, facilities, wharves and navigational channel, and then evaluate the present and future burdening operation capacity.
   (b) From the economic growth rate and all item products (including in the agricultural and industrial huge plan), based on the import and export cargo guantity of all harbors and then predict the future (10 or 25 yrs) total gross import and export cargo guantity and operation requirements and finally determine the site of deep water port.

2. Research of the field survey and investigation of the alternative sites of deep water port.
   (a) Investigate and measure all the occanographic data including wind climate, offshore waves, currents, bathymetry, tide, geotechnical conditions and the tansportation system around the hinterland.
   (b) Based on the Taiwan district and international cargo transportation and transshipment, and deal with the requirement guantity of harbor, for considering the long-term developing of port policy, and then the scale of the deep water port and engineering feasibility is determined.

3. Study Under Going

To promote the port integrated development of the Taiwan district, it is suggested that the deep water port construction is necessary in the very near future for the demand of coal import as shown in Table 1. and stevedoring of the large container vessel. To this end, the feasibility study of deep water port of Taiwan district is initiated and studied by the Institute of Transportation, Ministry of Communications and therefore, the author is appointed to take charge of the project research of the deep water port of Taiwan district. This is the first phase study of the project.

The research is divided into three parts. The first part is to study the capacity and requirement of five international ports and predict the future demand, now this part of preliminary study is completed. The second part is based on the study of the first part, if the future demand is required, the result show a positive answer, therefore, the excavation of the deep water port is necessary. So the hydrographic survey and oceanographic measurement is planned and will be under way in the coming fiscal year. The collection and analyses of data on its conditions are necessary for this phase study.

The third part is then proceeded to the harbor planning and detail design. Therefore, the feasibility study will be the base for the future deep water port construction.

4. Coal Terminal is a Part of Deep Water Port

Based on the income requirement of the future coal import until 2000 D.C., in the eastern Taiwan district, coal import to Hualien harbor and then distributed to coal required plants. Accomodation of the construction of coal terminal of the Hualien harbor it does meet the requirement. In the northern Taiwan district, import from Su-Ao harbor could accomodate the civil use, and the coal restoration center of Su-Ao harbor area has much space to use. Therefore, there is no need of any harbor extension for the purpose of coal import either in Hualien port or in Su-Ao harbor.

In the middle of Taiwan district, Taichung harbor could be enlarged as the large scale of coal port. Since coal supplied to Seng-Ao power plant, Linkou power plant and Taichung thermal power plant (under construction) etc., need to use Taichung port coal terminal as the transshipment station. For the demand of huge coal carrier, it is economic to select the vessel of 200,000 DWT or over (See Table 2 & 3) Then, coastal shipping system is need to be planned for transshipment of coal to the above mentioned area. For constructing the deep water coal port, it would be a good idea to take the coal port as the coal storage center and then transferred by coastal shipping or inland transportation toward the concumption unit or power plant as shown in Fig.5. The alternative deep water harbor sites are 1.)the outer area of Taichung port industrical water front, dredging the outer navigational channel and reclaiming the coal wharf space., the layout of the Taichung deep water port is shown in Fig. 1. 2.) An offhore island of the Wai-San-Ding Sand Barrier, is planned as a deepwater coal terminal., the layout is shown in Fig. 2. 3.) Hsin-Ta thermal power plant or LNG terminal will be another deep water port site. 4.) For the northern port site Taoyuan coast offshore area including the single mooring buoy (SMB) for oil unloading toward Taoyuan oil refinery plant will be also the alternative harbor site of deep water port., it is shown in Fig. 4. For the above harbor sites, their orientation and arrangement are determined by using the typhoon attacking track (see Fig. 9) and wind rose and wavedistribution as shown in Fig 10 a & b). Coal import and shipping cost are also analyzed as shown in Fig. 6 & Fig.7 o

5. An Idea of a Central Deepwater Port

The main characteristic of a deepwater port is its ability to permit large vessels of over 100,000 DWT to enter the port by virtue of its depth, entrance channel, turning basin and other special provisions. The primary advantage of a deepwater port lies in its capability to receive large bulk carriers, thus reducing shipping costs for the commodities considerably. The lower handling cost per unit of cargo is, the higher flexibility of a large terminal will be. Therefore, the large investment required for opening up and developing a deepwater port makes it necessary to adopt policies to concentrate

Table 1 Coal Supply and Demand

Unit: Thousand Tonnage

Year	Own Product	Import	Power Use	CSC Use	Other Use	Total Demand
1984	2,011	7,367	4,787	2,460	3,127	10,374
1985	1,800	11,303	6,235	2,540	4,328	13,103
1986	1,600	12,056	6,620	2,640	4,396	13,656
1987	1,400	12,480	6,950	2,640	4,290	13,880
1988	1,200	14,640	8,200	3,540	4,100	15,840
1989	1,200	17,373	9,814	4,430	4,329	18,573
1990	1,200	18,696	10,366	4,960	4,570	19,896
1991	1,200	22,325	13,827	4,960	4,738	23,525
1992	1,100	23,474	14,605	4,960	5,009	24,574
1993	1,100	23,802	14,743	4,960	5,199	24,902
1994	1,100	24,988	14,686	6,010	5,392	26,088
1995	1,100	28,758	17,223	7,040	5,595	29,858
1996	1,100	30,663	18,920	7,040	5,803	31,763
1997	1,100	29,911	17,955	7,040	6,016	31,011
1998	1,100	33,762	21,576	7,040	6,246	34,862
1999	1,100	34,171	22,045	7,040	6,186	35,271
2000	1,100	34,393	21,715	7,040	6,738	35,493
Yearly Mean Growth Rate						
1985 - 1990	-7.8%	10.6%	10.7%	14.3%	1.1%	8.7%
1990 - 2000	-0.9%	6.3%	7.7%	3.6%	4.0%	6.0%
1985 - 2000	-3.2%	7.7%	8.7%	7.0%	3.0%	6.9%

CSC : Chinal Steel Corporation

Table 2 Cost of Island Transportation by Barge

Unit: US dollars/ton

Ship Tonnage OWT / Navigational Oistance (N.M.)	5000	10000	15000	20000	25000	30000
100	2.8	2.4	2.4	2.4	2.5	2.7
120	3.0	2.5	2.5	2.5	2.6	2.7
140	3.1	2.6	2.5	2.6	2.6	2.7
160	3.2	2.7	2.6	2.6	2.7	2.8
180	3.3	2.8	2.7	2.7	2.8	2.8
200	3.5	2.8	2.7	2.7	2.8	2.9

N.M. = Nautical Mile

Table 3 Shipping Cost of Coal Import from Oifferent Navigational line

Unit: US dollars/ton

Ship Tonnage / Navigational line	20000	30000	58000	66000	100000	120000	150000	200000
Australia (5000)	17.8	15.0	11.9	11.4	10.0	9.4	8.7	7.7
Canada (5400)	19.0	16.0	12.6	12.1	10.6	9.9	9.1	8.1
W. Coast.(USA) (6000)	20.8	17.5	15.7	13.2	11.4	10.7	9.8	8.6
South Africa (6300)	21.7	18.3	14.3	13.7	11.8	11.1	10.1	8.9
E. Coast (USA) (9000)	30.0	25.1	19.3	18.4				
E. Coast (USA) (10000)	33.1	27.6	21.1	20.1				

Remark : ( ) indicates the navigational distance.

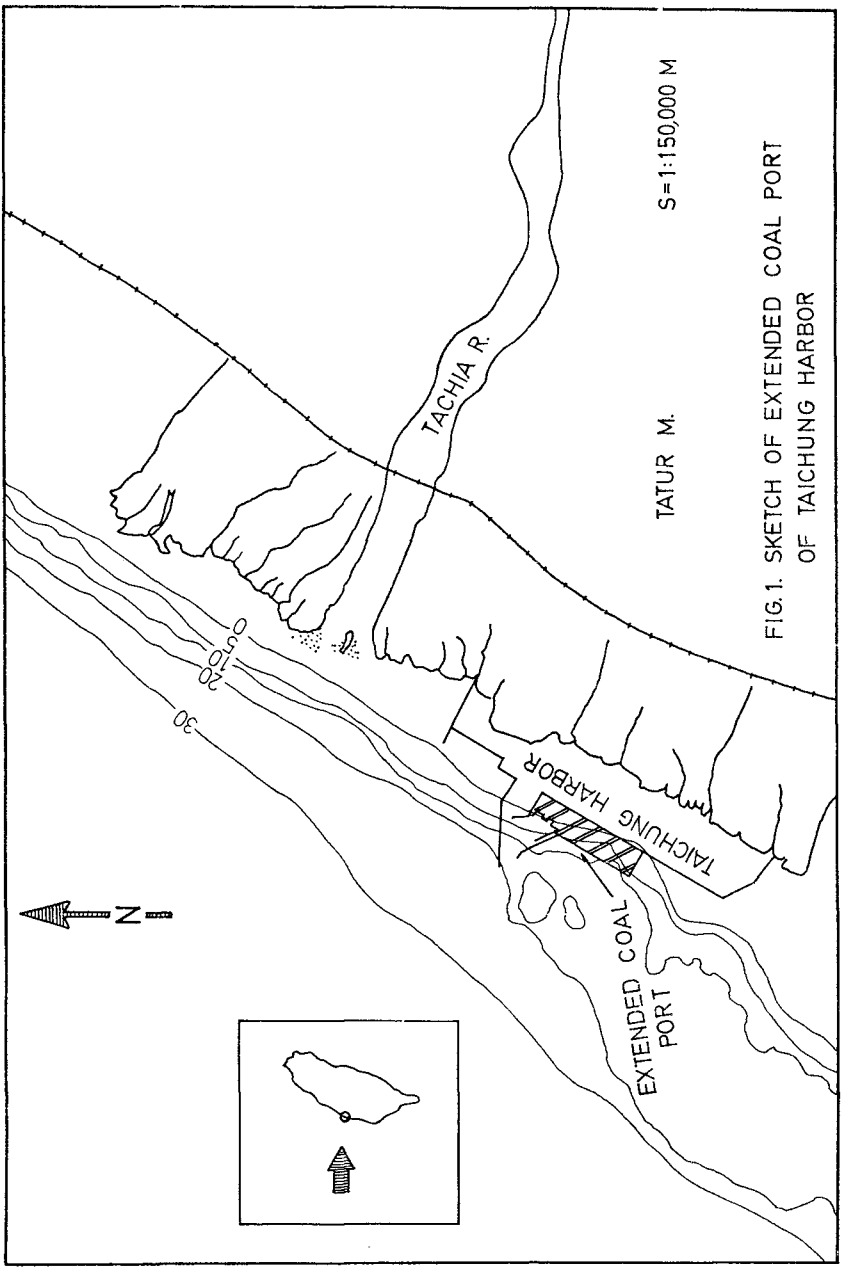

FIG. 1. SKETCH OF EXTENDED COAL PORT OF TAICHUNG HARBOR

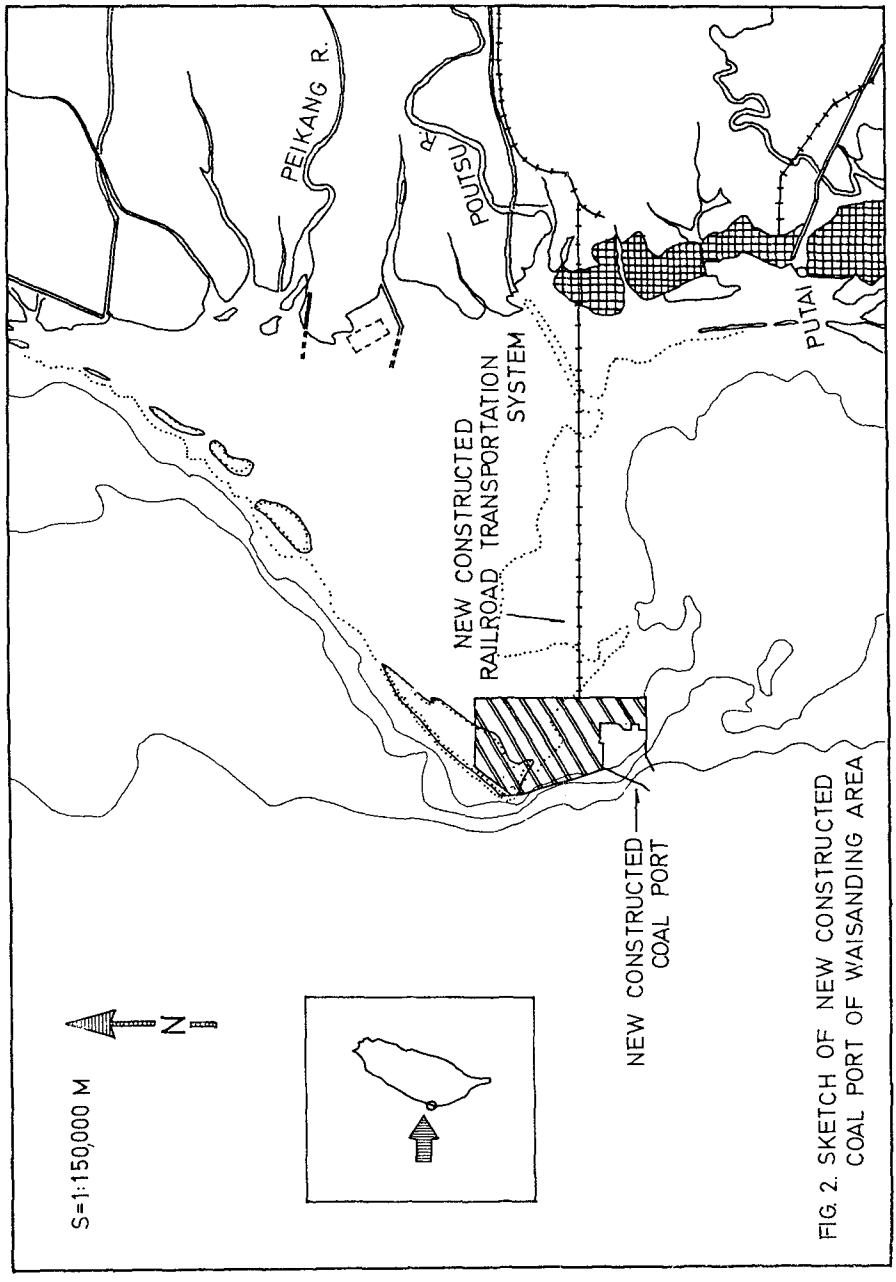

FIG. 2. SKETCH OF NEW CONSTRUCTED COAL PORT OF WAISANDING AREA

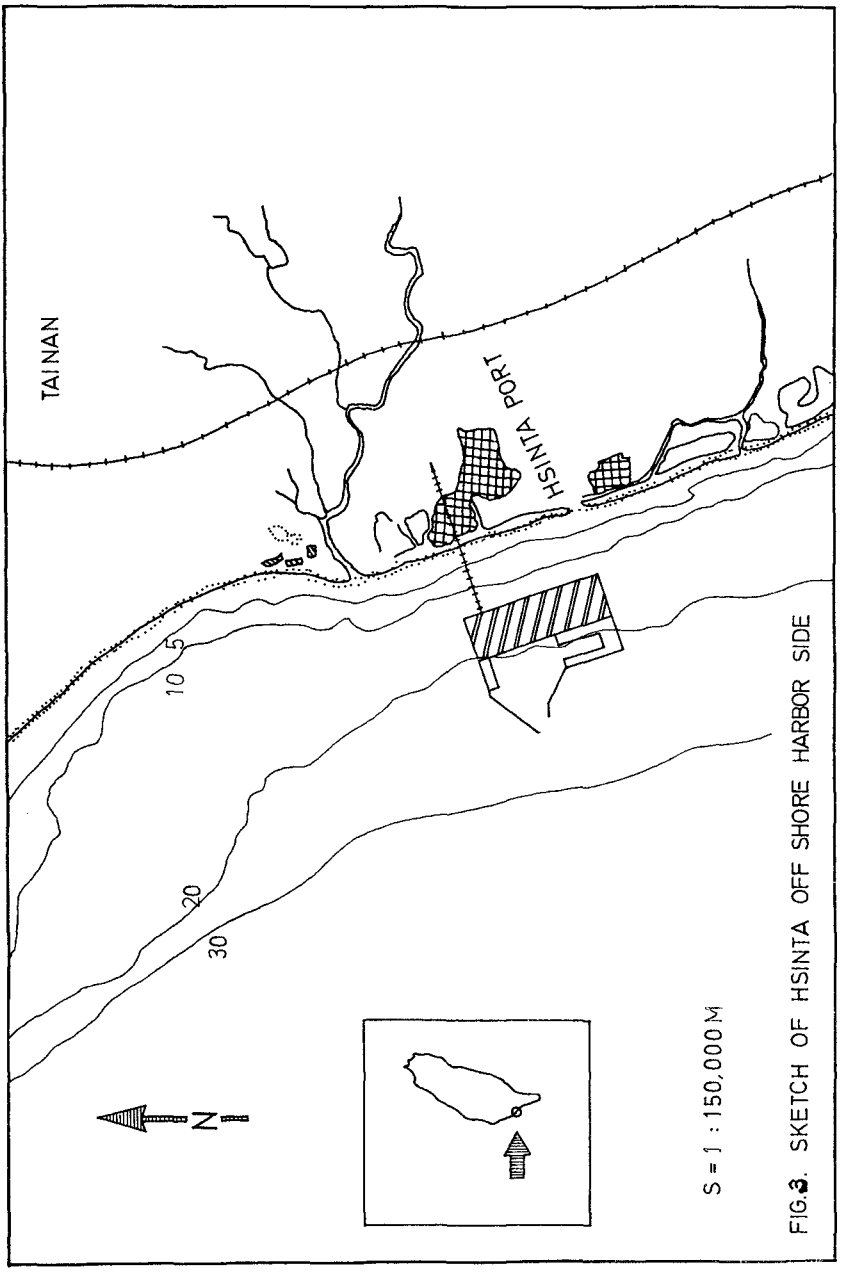

FIG.3. SKETCH OF HSINTA OFF SHORE HARBOR SIDE

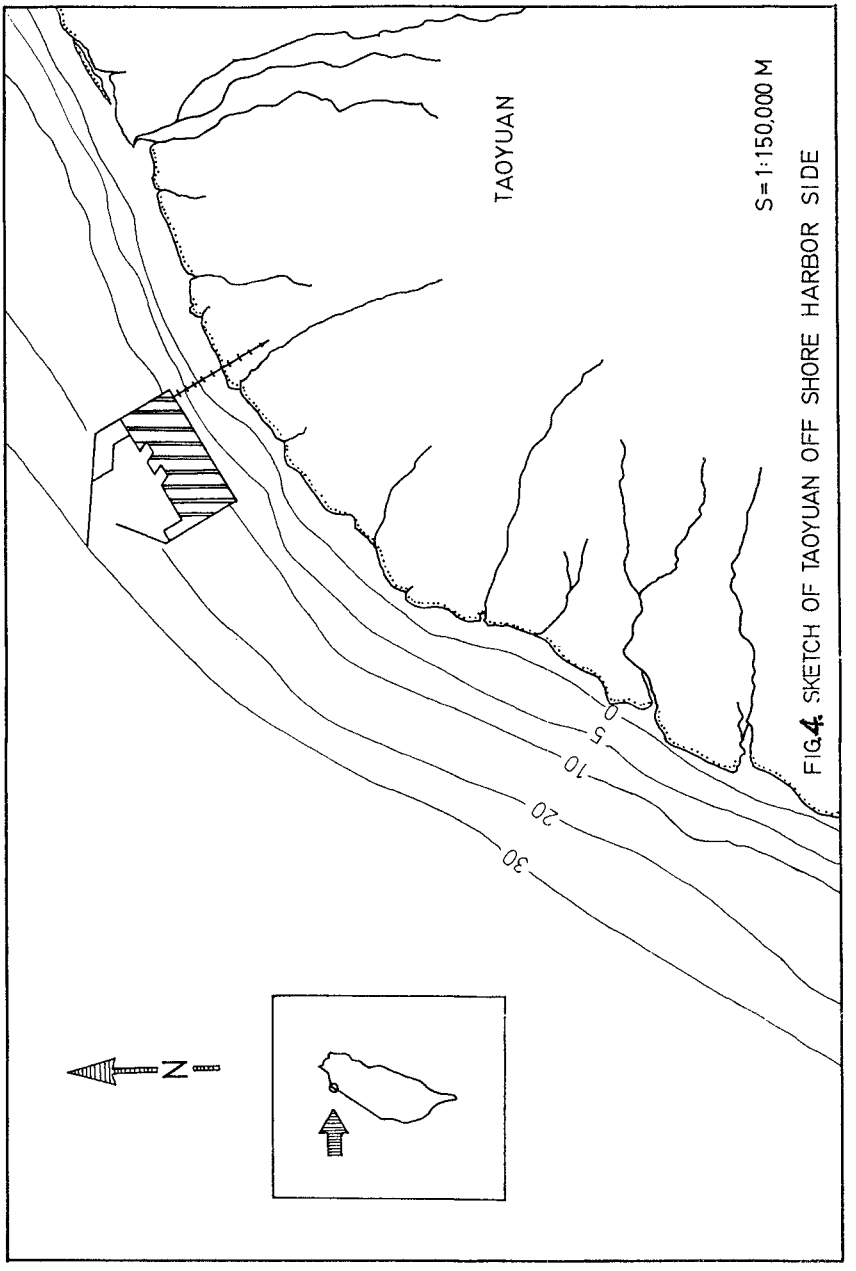

FIG. 4. SKETCH OF TAOYUAN OFF SHORE HARBOR SIDE

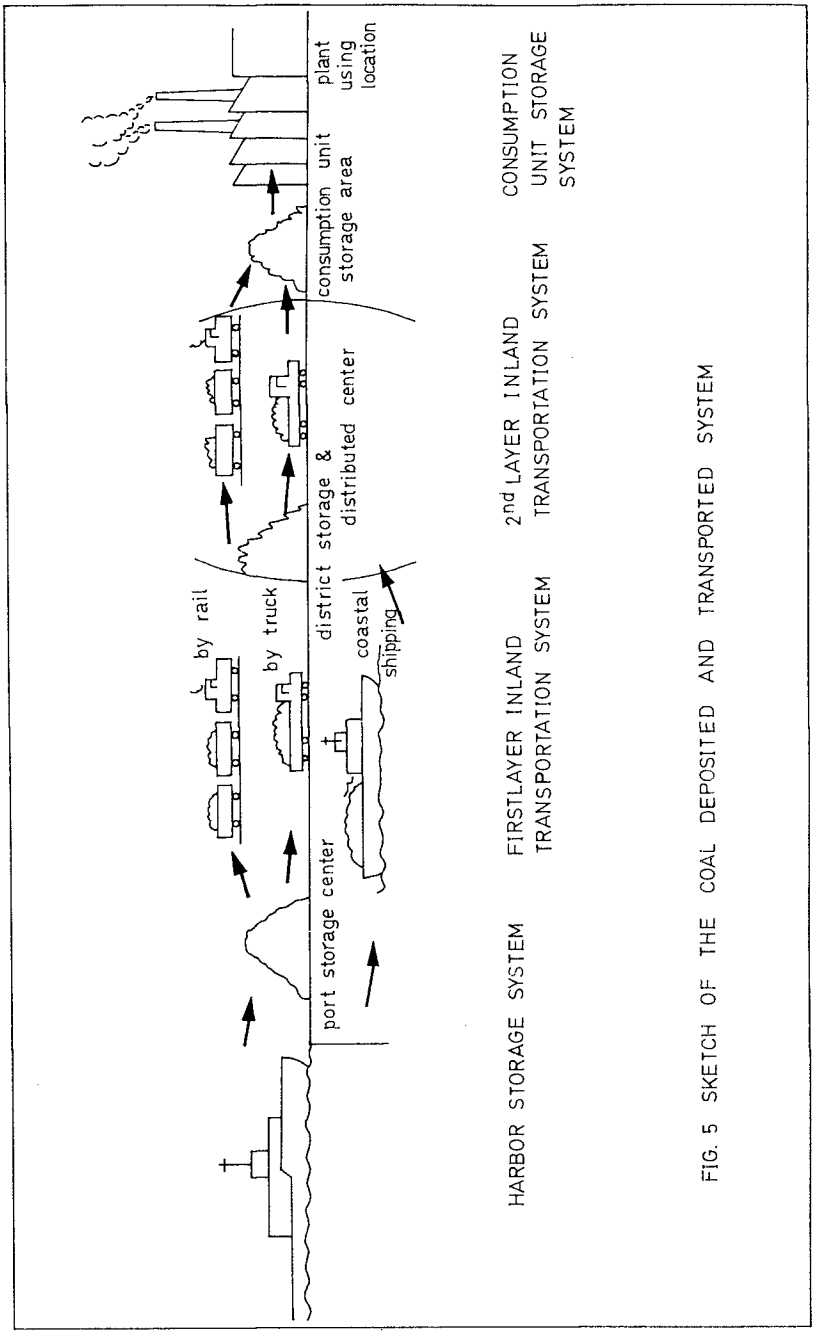

FIG. 5 SKETCH OF THE COAL DEPOSITED AND TRANSPORTED SYSTEM

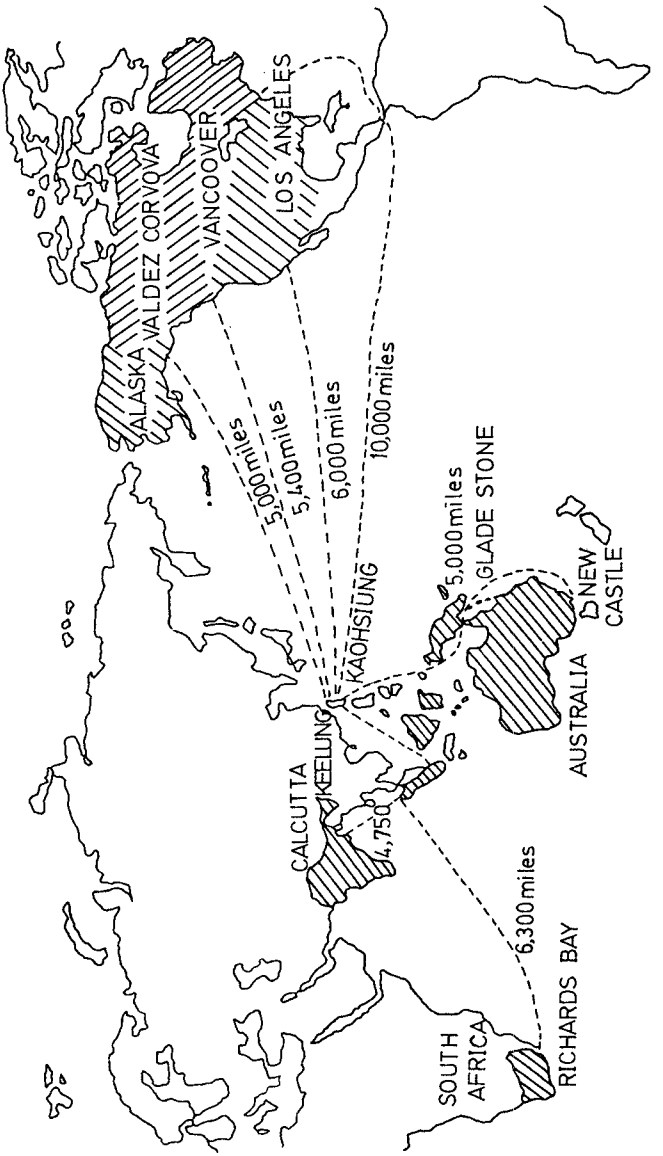

FIG. 6 DISTRIBUTION OF COAL IMPORT FROM FOREIGN COUNTRIES

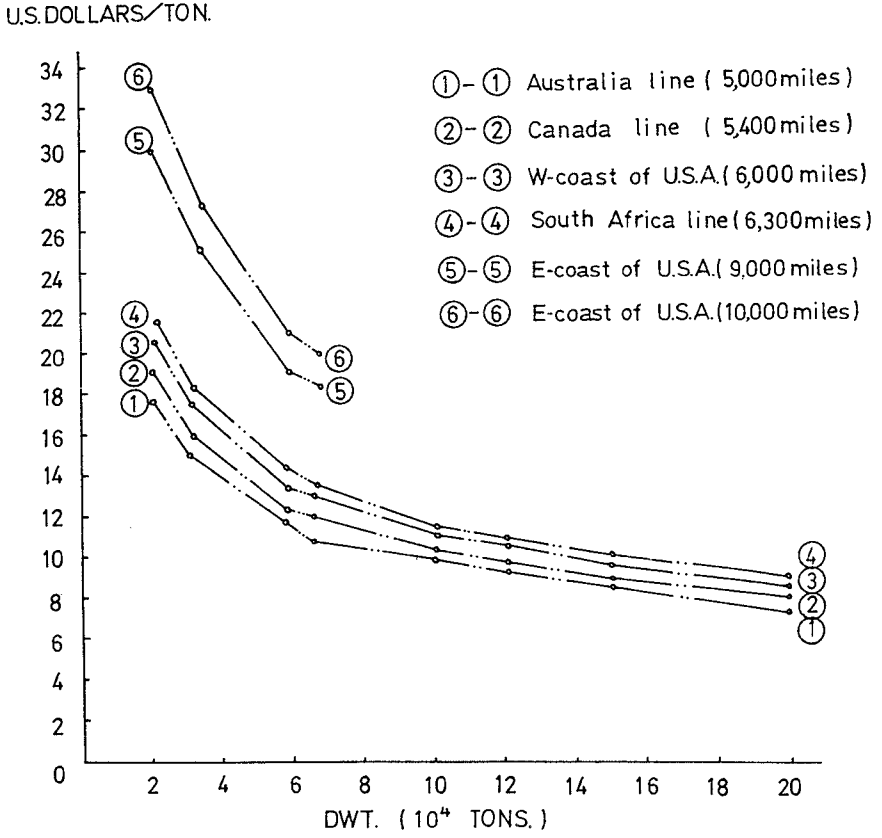

FIG. 7 COAL SHIPPING COST OF EACH NAVIGATIONAL LINE

FIG. 8 COAL SHIPPING QUANTITY RECORD & PREDICTION

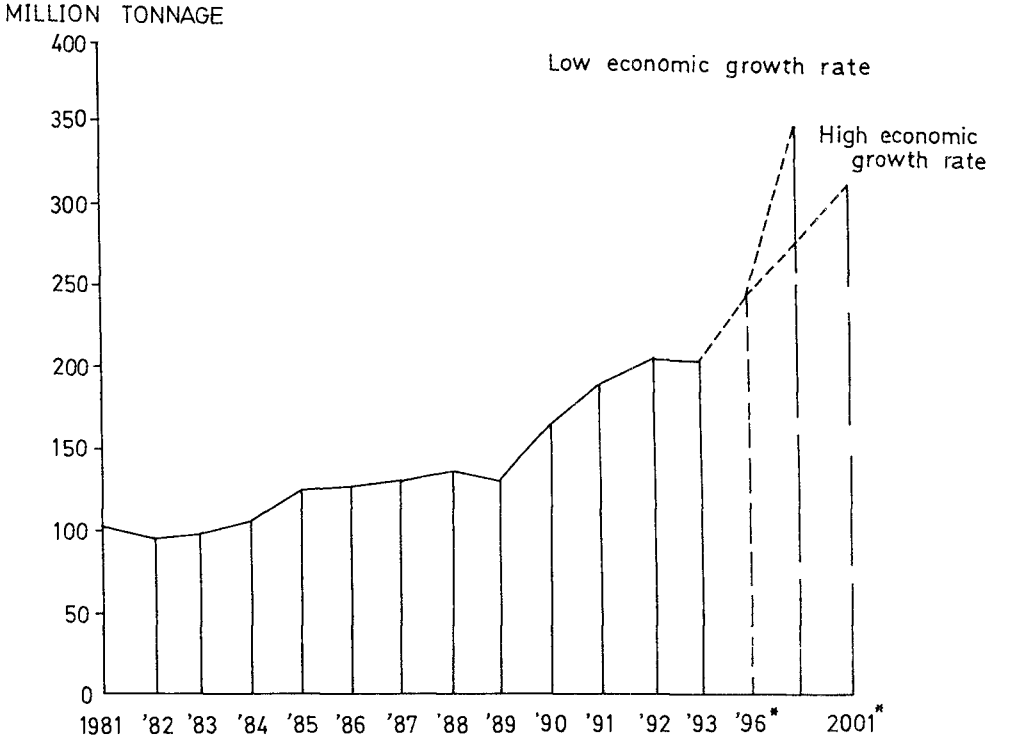

* PREDICTION

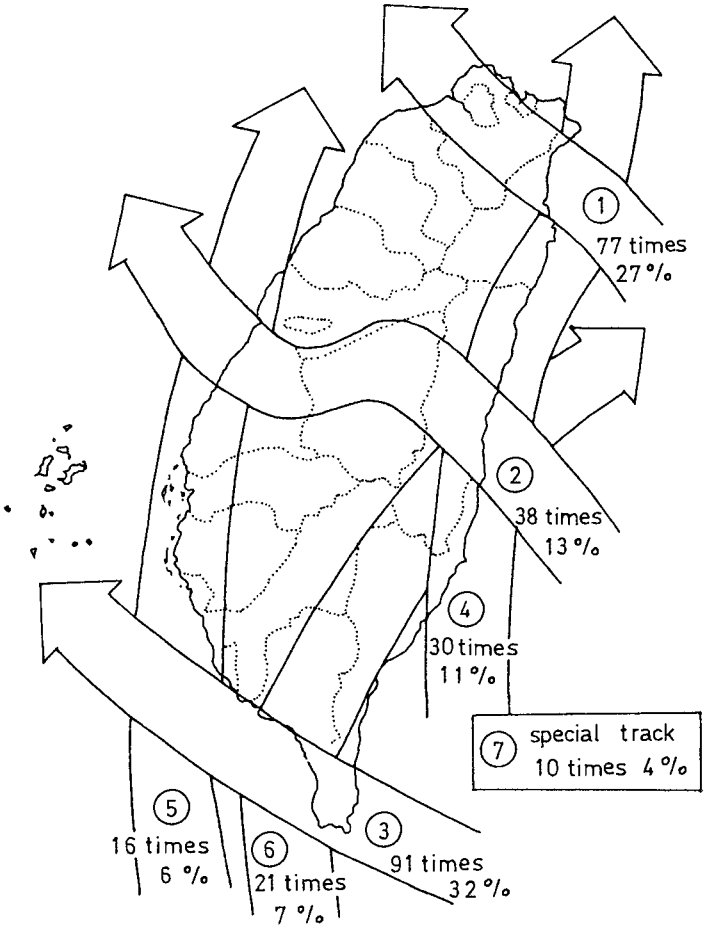

FIG. 9 STATISTICS OF TYPHOON TRACKS
(1897 ~ 1976)

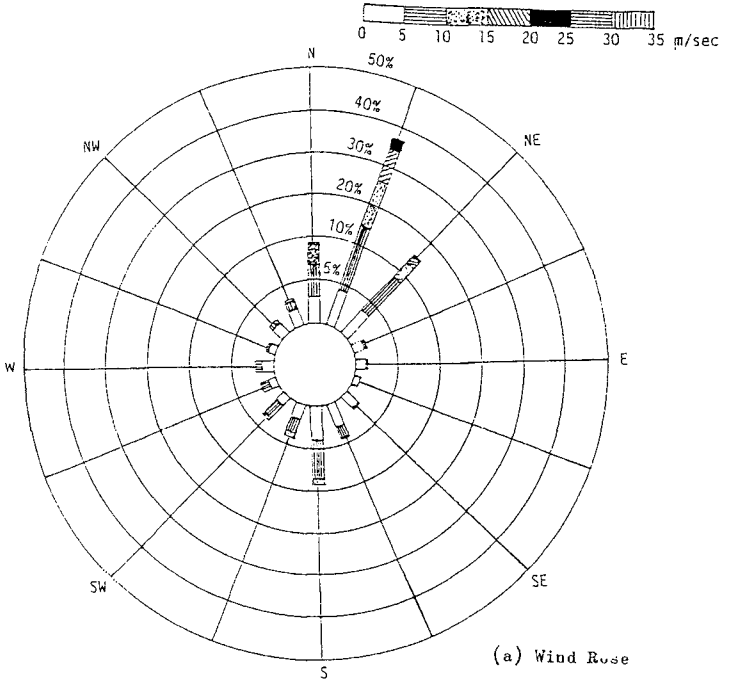

(a) Wind Rose

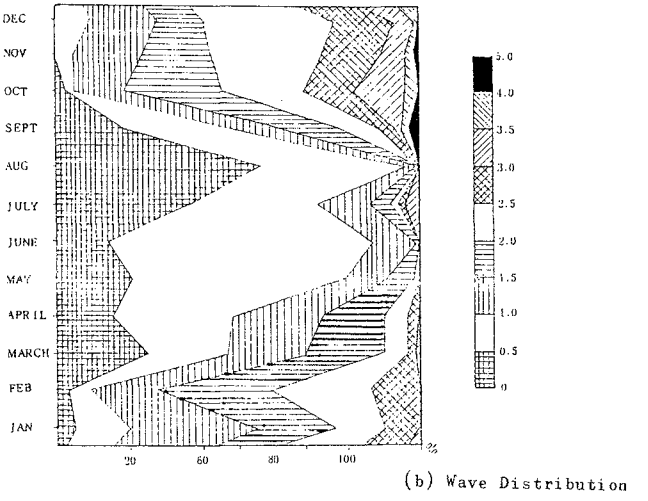

(b) Wave Distribution

Fig.10 a&b Wind Rose and Wave Distribution of Taiwan Strait

the handling of certain commodities as to make the port feasible by the savings thus gained.

For a deepwater port of the Taiwan district, it may be of interest for the extended quantities of coals (see Fig. 8) and containers (Since Keelung port is conjested) to be handled in the near future. A deepwater port would create a large, additional capacity, which would serve as a buffer for Taiwan port developments which cannot be foreseen at this moment. It may become possible to concentrate the capital outlays in one location and to construct, at a lower level of total costs, a safe and well-designed deepwater port instead of having a number of ports complete for the status of deepwater port ---- at a far higher combined cost ---- a status which most of the ports can never attain as a result of their physical and hinterland limitations.

Transshipment of containers, fertilizer and other products are considered as potentially promising port activities of Taiwan district. If transshipment for the East or South-east Asia region is to play an important role, an additional amount of port capacity is to be created over, Taiwan may be called upon to take over one or more port and economic functions from Hong Kong. In the future, Taiwan will import LNG for which a port with relatively large dimensions would be required.

The combined effect of these arguments, an investigation into a possible deepwater port of Taiwan district is warranted to be necessary.

5. Economical and Technical Adaptability of the Proposed Deepwater Harbor Sites.

A. Domestic transportation patterns of export and import commodities

In order to carry out system analysis of the proposed deepwater harbor sites from the viewpoint of transportation economics, domestic transportation patterns of export and import commodities must be estimated. For this purpose, it is desirable to investigate the commodity flow in detail, and to make up the tables of origin and destination. Thereafter, regional demand for international cargo transport is estimated on major items of export and import by above-mentioned pattern.

It is difficult to assume that the present pattern of regional distribution can be applied for the future without adjustment, but the changes are considered to be usually gradual. Our investigation based on present pattern, and modified cases are also calculated for check.

B. Study on proposed deepwater harbor sites based on transportation economics.

The investigation made clear that all the four sites are technically feasible and can reasonably be taken up as alternatives.

Thereafter, adaptability of each proposed site is divided by her locational characteristics as a deepwater port.

C. Natural conditions at the proposed deepwater harbor sites.

For the field occanographic measurements, it is scheduled to be surveyed for the coming fiscal year, the items is listed as follows:

(1) Hydrographic survey: The deeper part from - 20M to - 30M or - 20M to - 40M need to be thoroughly surveyed. Since for the previous data, even nautical chart, there is not so detailly described.

(2) Coastal morphological investigation: The measurement includes the shoreline change, and topographic change of the nearshore area.

(3) Geotechnical investigation: Subsurface boiling, soil sampling and foundation exploring are included.

(4) Wind, wave and current measurements: The offshore measurements are emphasized in each proposed deepwater harbor site.

(5) Coastal hydrology survey: The survey consists of measurements of water temperature, salinity, concentration, conductivity etc., for sufficiently analyzing horizontal & vertical distribution.

(6) Tidal records: This measurement need to be long-term records, at least one-year continuous record.

(7) Sea-bottom topographic change process: The survey need be detailly measured for realizing the deposition and scour around the proposed deepwater harbor sites, especially, for evaluating the littoral transport rate of the harbor sites.

(8) Seismic measurement: Geological distribution of deep layer of the sea-bottom need to be surveyed in detail. For complete seismic survey of the deepwater harbor sits, the design of breakwater and wharf could be carefully considered. The construction of those harbor structure will be safe.

From the above measurement and investigation, the natural conditions of the proposed deepwater harbor sites could be compared, the best conditions of the harbor site is then determined.

Referances

Ho-Shong Hou :" Research on the Development of Deep Water Port of Taiwan District " Annual meeting, 1985 J. of CICHE. Dec. 1985

CEPD, executive Yuan, Taiwan, ROC "Port Development Study Taiwan" under Supervision of NEDECO Dec.1982.

CHAPTER 186

Shore Protection Plan for the Nile Delta Coastline

A.L. Kadib, Member, ASCE[1], A.T. Shak, A. Member, ASCE[2], A.A. Mazen[3], and M.K. Nadar[4]

A Shore Protection Master Plan (SPMP) for the Nile Delta Shoreline, extending from 30 kms west of the city of Alexandria (Arab Republic of Egypt) to 30 kms east of Port Said, is developed and reported. The SPMP was developed in three stages: (1) collection and analysis of relevant data to identify existing and future coastal problems and limits of needed shore protection, (2) development of shore protection alternatives with costs and economic evaluations, and (3) detailed design and technical specifications for the selected shore protection schemes along the SPMP zone. This paper summarizes Tetra Tech, Inc./Honeywell work and achievements on this project while under contract with the Egyptian Shore Protection Authority (SPA). The SPMP considered the Egyptian Government and the SPA national needs to the year 2000.

Introduction and Background

The Nile Delta coastline extending from the western borders of the city of Alexandria to the eastern side of the Port Said (see Figure 1), is presently experiencing some coastal changes. The existing two branches of the River Nile (Rosetta and Damietta) have succeeded over the years in forming two natural sea defense protrusions by depositing a rich supply of sediment load from each branch. In the previous century, the supply of sediment exceeded the natural losses due to wave and current action, and thus resulted in relative land gain from the sea. This trend was reversed around the turn of the 19th century with observed losses from both protrusions.

The principal cause of the shoreline changes presently occurring along the Nile Delta coastline is generally accepted to be the loss of sediments resulting from the construction of control works along the River Nile. Chronic erosion was first observed at the end of the 19th century at several important points along the coast, including the promontories at the mouths of the Rosetta and Damietta branches. This erosion continued during the first half of the 20th century, coinciding with the installation of the first dam at Aswan and the development of

(1) Director, Coastal and Port Engineering Department, Tetra Tech, Inc./Honeywell, 630 N. Rosemead Blvd., Pasadena, CA 91107, U.S.A.
(2) Project Engineer, Tetra Tech, Inc./Honeywell, 630 N. Rosemead Blvd., Pasadena, CA 91107, U.S.A.
(3) Chairman, Egyptian Shore Protection Authority, Ministry of Irrigation, Arab Republic of Egypt
(4) Vice Chairman, Egyptian Shore Protection Authority, Ministry of Irrigation, Arab Republic of Egypt

other dams and barrages, and the increasing diversion of river water for irrigation.

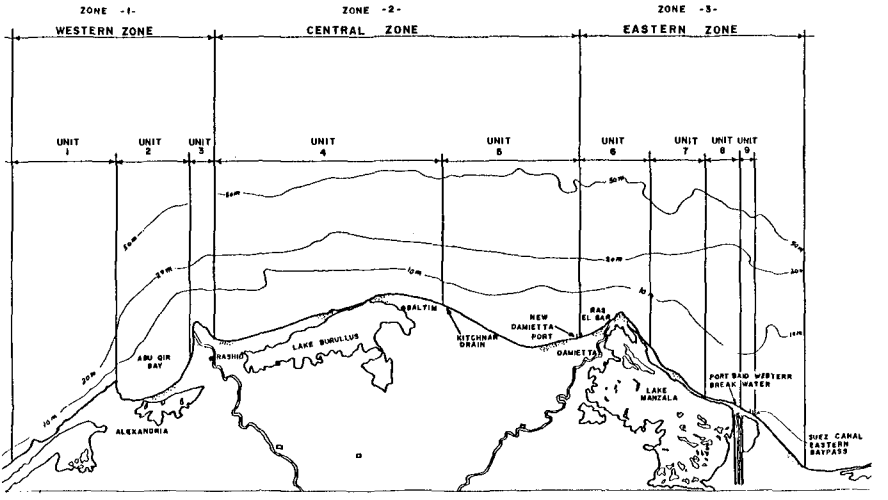

Figure 1. Shore Protection Master Plan Zones and Locations

After the completion of the Aswan High Dam in 1966, erosion along some locations of the Delta coastline accelerated. This erosion has resulted in the loss of resort beach property and flooding of coastal villages. Economic damage to date has been substantial and further serious economic loss is expected if erosion is not controlled. Figures 2 and 3 give examples of the shoreline changes along Rosetta Promontory since 1800 to 1983 (Tetra Tech Progress Report No. 1, ref. 1).

In recognition of the importance of the coastal zone, the Egyptian Government quickly instituted a plan to conduct studies and formulate approaches to manage shoreline erosion. The agency within the Egyptian Government which oversees shore protection projects is the Shore Protection Authority (SPA) of the Ministry of Irrigation formed in 1981. The SPA's responsibilities cover:

1) Planning and design of shore protection works for both short- and long-term considerations.
2) Maintenance and repair work for existing coastal structures.
3) Development and implementation of a shore protection Master Plan for the Nile Delta Coast.

To understand, quantify and assess the recent changes along the Nile Delta Coastline, the Egyptian Government has undertaken many studies since the early 1960's. In 1971, this effort was greatly enhanced when the Egyptian Government secured assistance from the United Nations

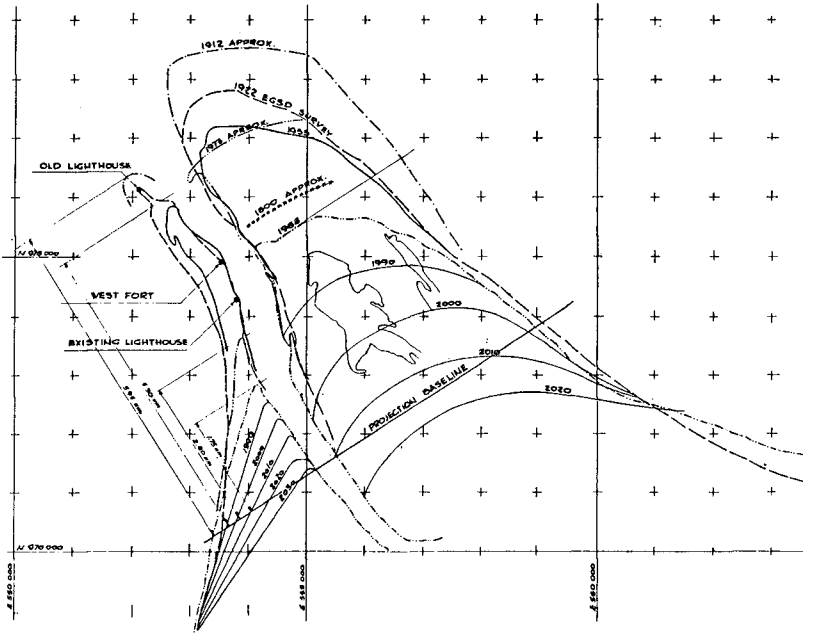

Figure 2. Shoreline Changes along Rosetta Promontory (1800-1983)

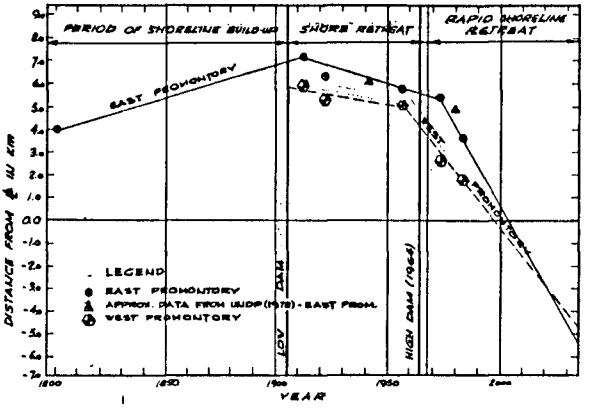

Figure 3. Effect of the Aswan Low and High Dams on Shoreline Changes at Rosetta

Development Programme (UNDP). The UNDP project, which lasted for seven years (1972-1978), conducted geographical, geological, geomorphological, oceanographic, meteorological and hydrodynamic studies of coastal processes along the study area. Coupled with the above effort, the Egyptian Government created the Coastal Research Institute (CRI) to act as the focal point for collection, analysis and monitoring of field information. The CRI has assumed additional responsibilities to assist in the planning and design of a number of shore protection projects along the Delta Coast.

Since its initiation in 1981, the SPA has undertaken many shore protection and maintenance projects and in 1984 awarded a contract to Tetra Tech, Inc. of Pasadena, California, U.S.A., to develop a Shore Protection Master Plan for the Nile Delta Coastline, which is the subject of this paper.

Overall Objectives and Tasks

The objective of this project is to prepare a Shore Protection Master Plan (SPMP) for the Nile Delta Shoreline to manage existing and projected shoreline erosion problems to the year 2000, with special attention to some specific and critical areas such as the Alexandria Coast, Rosetta Promontory, Burullus inlet, Baltim Beach, Ras El Bar, and the coastal strip from Damietta to Port Said. This plan is developed through tasks which were carried out in four stages:

Stage 1 - Collection and Review of Relevant Data
a) Review and evaluation of available data.
b) Detailed field reconnaissance survey.
c) Identification of additional data necessary for the development of the Shore Protection Master Plan.
d) Data analysis and problems definition.

Stage 2 - Preparation of Alternative Shore Protection Schemes
a) Development of alternative shore protection schemes.
b) Assistance to the SPA in the economic evaluation of alternative schemes.
c) Selection of viable shore protection schemes (by SPA).

Stage 3 - Detailed Design of Selected Schemes
a) Elaboration on the detailed design of the selected schemes with technical specifications and tender documents.
b) Identification of needed physical models.

Stage 4 - Final Report
This includes preparation of a comprehensive report describing the detailed aspects of the Master Plan resulting from the analysis of the above activities covering design documents and technical specifications for the selected schemes.

Establishment of SPMP Zoning

Development of the Shore Protection Master Plan for the study area considered three main factors: (a) the existing coastal problems, (b) the proposed uses of the coastal areas; and (c) the physical changes

within each area due to natural and "man-induced" morphological changes. Based on the analysis of these factors, the SPMP was divided into three main planning zones and a number of sub-zones as depicted in Figure 1 and summarized below:

a) Western Zone
The Western Zone extends from Alexandria Western Harbor to the Rosetta Promontory and includes: Alexandria Western Harbor, Alexandria Eastern Harbor, Alexandria Beaches, Montaza Cove, Mamura Beach, Abou Quir Point and Abou Quir Bay and Rosetta Promontory.

b) Central Zone
The Central Zone extends from the east of the Rosetta Promontory to the new Port of Damietta and includes: the saddle area east of Rosetta to Burullus Estuary, Burullus Inlet, El Burg Village, Baltim Beach, 45 kms reach between Baltim and Gamasa and the 20 kms reach from Gamasa to Damietta Port.

c) Eastern Zone
The Eastern Zone extends from the new port of Damietta to 30 kms east of the Port Said area and includes: the new port at Damietta, Ras El Bar Beaches, Damietta Estuary, Damietta Eastern Promontory, Lake Manzala Coastal Barrier, El Gamil area, Port Said Beaches, Port Foad Beaches and the area east of the Suez Canal Eastern Bypass.

Problem Identification

An important aspect of the SPMP development, is the identification of the existing coastal problems along the different planning zones and sub-units. The areas with specific shore protection needs were identified and their problems summarized in Table 1.

Table 1 Summary of SPMP Existing Problems

Planning Sub-units	Specific Problem Definition
	1) WESTERN ZONE
Alexandria western harbor	No major shore protection problem identified.
Alexandria Eastern Harbor	Mooring problems and wave overtopping of parts of the Corniche during storm wave activity.

Table 1 (Continued)

Planning Sub-units	Specific Problem Definition
Alexandria Beaches,	1) Shatbi/Ibrahimiya Lack of recreational beach area due to narrow beach width.
	2) Camp chezar beach Local scour and storms wave action is being corrected by the placement of 1.8m concrete blocks. This effort should continue.
	3) Stanley beach Lack of recreational area and heavily congested beach during summer seasons.
	4) El Asafra beach Recreational and bathing beach areas are very narrow or non-existent.
	5) Mandara beach Beach widths fronting the cabins are narrow and the beach is heavily congested during the summer season.
	6) Montaza Cove a) Inadequate bathing beach area. b) Debris pollution problems adjacent to the Palestine Hotel.
	7) Mamura beach Beach widths are adequate for recreational uses and no erosion problems are identified, however, monitoring is recommended.
Abou Quir point and Abou Quir Bay	1) Abou Quir beaches The beaches are narrow and suffering from the ongoing pollution caused by unauthorized dumping of sewage.
	2) Idku Outlet Sedimentation problem along the navigation channel was corrected by the 2 groins constructed in 1985. Future performance of the outlet should be monitored to evaluate project effectiveness.
	3) Mohamed Ali Seawall Maintenance and monitoring of the existing and ongoing protection is essential for this industrialized area.
Rosetta Promontory	The Rosetta promontory has experienced severe erosion since 1966 and beyond. In 1986 the SPA started a shore protection project using dolosse and stone protection.

Table 1 (Continued)

Planning Sub-units	Specific Problem Definition
	2) CENTRAL ZONE
Saddle area and Lake Burullus coastal barrier	Most of the length of this reach is experiencing accretion, which is expected to continue for at least the next 20 years or so period. Two local areas along the coastal barrier are vulnerable to breaching during severe storm activities, which would affect the existing tidal dynamics of Lake Burullus. Monitoring of this reach is recommended.
Burullus inlet,	The navigation channel in the existing inlet shoals and meanders causing a hazard to navigation.
El Burg area	The existing seawall needs maintenance and rehabilitation. SPA is presently undertaking an extensive rehabilitation program at this reach which seems to be adequate.
Baltim Beach Resort	Long term shoreline observations have indicated an average net recession rate of 4m/year, with superimposed short-term fluctuations of up to 60 m threatening resort property.
Baltim to Gamasa	No coastal engineering problems are identified for this reach.
Gamasa to New port at Damietta	No shore protection problems are identified except for the possibility of some local scour caused by the recently constructed Damietta breakwaters.
	3) EASTERN ZONE
New port at Damietta	Adjustment in shoreline planforms of the shore areas adjacent to the new breakwaters is expected as a result of the adverse effects of these breakwaters.
Ras El Bar	Erosion and storm damages to Ras El Bar summer resort coastal area have resulted in building damages, loss of recreational bathing beach area, and lost tourism and economic development opportunities.
Damietta Estuary	Shoaling along the navigation channel.
Damietta Eastern Promontory	Since 1966, this reach has been deprived from the rich supply of sediment by the Damietta Nile branch. Consequently, the Damietta promontory has experienced continuous erosion.

Table 1 (Continued)

Planning Sub-units	Specific Problem Definition
Lake Manzala coastal barrier	The coastal barrier located to the southeast of Damietta promontory is a low lying sandy area subjected to a strong easterly longshore transport. The spit area next to Damietta promontory is expected to supply Lake Manzala barrier with sediment for many years in the future. The barrier shorelines are, however, unstable and erosional/ accretional fluctuations are occurring along this reach.
El Gamil area	1) Flooding of the Port Said-Damietta road between km 6 to km 10 as measured from Port Said western breakwater. 2) Near km 9, storm waves could damage the road shoulders over a length of 600 m due to the proximity of the road, at this area, to the sea.
Port Said	This Port Said beach area extends from the Suez Canal west breakwater westward, over a shore length of about 6 km. This reach is slowly accreting as longshore sediment transport is impounded by the west breakwater. No shore protection problems are identified for this reach.
Port Foad area	The 2 kms Port Foad area has undergone progressive erosion prior to the construction of the eastern Suez Canal bypass channel and protective breakwaters. However, the above works were completed in the late 1970's, the Port Foad beach area has been confined and is expected to adjust to an equilibrium plan form within the next few years. Consequently, no shore protection work is identified for this area except for some monitoring requirements.
Eastern side of the Suez Canal new bypass	Shoreline retreat is expected due to the adverse effect of the recently constructed Suez Canal breakwaters. No known developments exist in this area and needs for shore protection are not warranted for the next 10-15 years except for shoreline monitoring.

Development of Alternative Solutions

A total of 38 alternative shore protection projects were developed for locations with identified needs or beach enhancement opportunities as shown in Table 1. The development of these alternatives considered the existing problem, beach restoration opportunities, and projections of expected damage under the "no action" alternative. Cost for each of the 38 developed alternatives was estimated and their economic evaluations were computed by the SPA, with Tetra Tech's assistance. Table 2 summarizes the developed shore protection alternative for each planning location.

Table 2 Summary of Developed Shore Protection Alternatives (a)

Main Zone	Planning Location	Alternatives
Western Zone	Alexandria Eastern Harbor	1) 180m Extension of the West Breakwater (b)
		2) 240m Detached Offshore Breakwater
		3) 300m long Corniche Protection
	Chatby/ Ibrahimiya Beach	1) 700m Beachfill retained by detached breakwaters
		2) 700m Beachfill retained by segmented break waters
		3) 700m Beachfill retained by 75m eastern end groin (b)
		4) 1200m Beachfill
	Stanley Beach	1) Beach restoration to add 4,600m^2 of bathing area (b)
	El-Asafra	1) Beachfill retained by west-end groin
		2) Beachfill retained by west end groin and groin pier (b)
	Mandara Beach	1) 700m Beachfill with detached breakwaters (b)
		2) 700m Beachfill
	Montaza Cove	1) 200m wide Beachfill
		2) 50m wide Beachfill with pier extension
		3) Annual Dredging
		4) Dredging with Groin retained Beachfill (b)
Central Zone	Burullus Inlet	1) Trained Eastern Channel
		2) Trained Western Channel (b)
		3) Maintenance dredging
	Baltim Beach Resort	1) Coarse sand nourishment
		2) Beach nourishment from offshore sand sources
		3) Fine sand beach nourishment
		4) T-Groins with sand nourishment
		4A) Above, but sand from offshore sources
		5) Offshore breakwaters and sand nourishment (b)
		5A) Above, but with sand from offshore sources
Eastern Zone	Ras El Bar	1) Groin field starting from existing second groin with Beachfill
		2) Groin field starting from existing third groin with Beachfill
		3) Offshore breakwaters with Beachfill (b)
		4) Artificial Headland
	Damietta Eastern Promontory	1) 11 kms of revetment
		2) 6 kms of revetment (b)
	Lake Manzala Coastal Barrier	Three alternatives are suggested: Shoreline revetment, regulation of construction and relocation, and groins or offshore breakwaters.
	El Gamil Area	1) Revetment and flood dike (b)
		2) Revetment and raise road elevation
		3) Groins field

(a) For more details, see Tetra Tech's Progress Report 2 dated December 1985, Ref. 2.
(b) SPA selected alternative.

Detailed Design and Technical Specifications

Detailed engineering drawings and technical specifications were developed for the 13 selected shore protection projects along the SPMP zones. The engineering designs followed the latest established international and U.S.A. standards. The technical specifications considered the practical application of the International and American specifications to local conditions, including reference to the use of the Egyptian Standard Specifications (ESS) as may be applicable. Both the engineering drawings and technical specifications for each project are given in Reference 3. Examples of some developed projects are shown in Figure 4.

Setting Priorities for Projects Execution

An important element of the SPMP is the establishment of a framework of implementation priorities for the developed projects. This framework should consider a set of measurable objectives such as: a) gains to the national economy; b) encouragement to tourism; (c) degree of protection to valuable developments and land, and (d) the Egyptian government national needs and plans.

As a result of the economic analysis and based on the needed degree of shore protection or beach restoration afforded, the following recommendations are reached:

(1) Projects which may be characterized by "first priority projects" are:

a) With the exception of the Alexandria Eastern Harbor West Breakwater Extension Project, all of the developed beach restoration projects along the Alexandria and Abou Quir area are economically feasible and their implementation should have first priority.

b) Ras El Bar Shore Protection
This relatively exposed and eroding beach, at Ras El Bar, is in urgent need of a shore protection scheme without compromising the availability of bathing areas. The selected project, using detached breakwater and sand nourishment, would solve this problem and enhance the present economic and tourism opportunities.

c) El Gamil Shore Protection and Flood Control Works Project
This project will protect a critical stretch of the Port Said/Damietta road against flooding and localized erosion. Therefore, its implementation should be given first priority.

d) Burullus Inlet Stabilization and Channel Deepening Project
The economy of the Burullus fishing village is centered around securing safe and uninterrupted navigation through this troubled

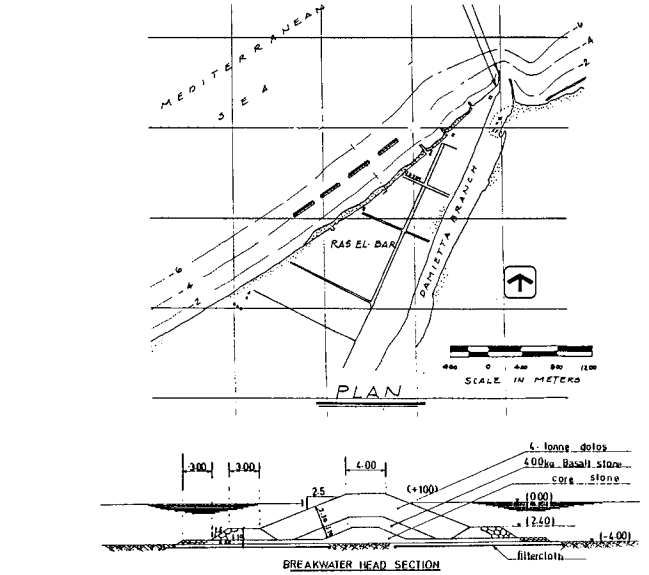

(a) Ras El Bar detached BW and sand nourishment

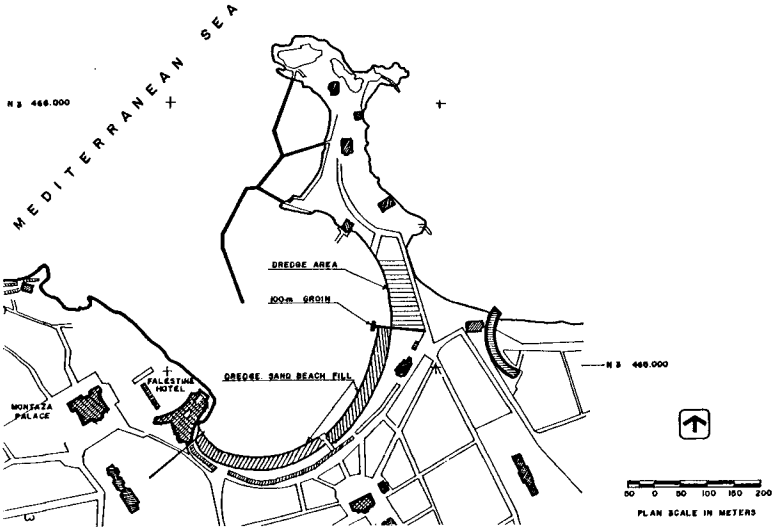

(b) Montaza Cove groin and dredging and sand nourishment

Fig. 4 Example of Shore Protection Projects

inlet. The present hydraulic and sediment situation needs immediate correction to insure safe navigation through a trained channel to check the present sedimentation problem and control channel meandering. This project deserves first priority considerations.

(2) Projects which may be characterized as "second priority projects" are:

a) Alexandria Eastern Harbor West Breakwater Extension
Presently, the Alexandria Eastern Harbor is utilized only by small fishing boats and few pleasure crafts. Under the present level of harbor utilization, additional sheltering is not warranted and only the protection of the Corniche road against spraying and overtopping by waves appears justified. Until future plans for the commercial utilization of the inner harbor area are identified and developed, the economic viability of the selected and designed project would be difficult to justify.

b) Baltim Beaches Replenishment and Stabilization
Due to the complexity of the coastal processes along this beach, the behavior of sand nourishment along this rapidly changing near-shore beach cannot be confidently predicted without further investigations. In addition, the SPA's selected scheme of detached breakwater system could possibly have adverse effects on the surrounding shorelines. It is suggested that before the implementation of the designed project, the SPA has to consider:

- An additional sand nourishment pilot project, with accurate monitoring to gain better understanding of the ongoing beach behavior.

- Employ the use of physical and numerical models combinations to test the relative performance of the other alternatives developed in Tetra Tech's Progress Report No. 2.

The results obtained from the above would give direction for implementation or modification of the designed project. It is therefore recommended that this project deserves a second priority classification until the above additional studies are completed.

c) Damietta Eastern Promontory Shore Protection Project
The Eastern Damietta Promontory is an erosional area supplying sediment to the downdrift sand spit located to the east. Very little information is available on the economic value and the location of the development to be protected along this reach. Priorities of implementation of the developed project lie with the SPA and should consider the Egyptian government overall national interest.

Identification of Model Test Requirements

Table 3 summarizes the SPMP model test requirements and their objectives. These model tests are needed to assist in the alignment of the

protective structures, check their performance and refine the design section's stability and their run-up characteristics.

To date, none of these models have been conducted with the exception of a model for Ras El Bar. It is anticipated that some preliminary model test results could be made available in the near future.

Table 3 Model Test Requirements

Project	Model test requirements and objectives
Alexandria Eastern harbor west breakwater extension (model 1)	* 2-D stability test for the designed cross-section(s). * 3-D physical model to check the alignment of the west breakwater extension and optimize its length.
Asafra and Mandara beach restoration and retention (model 2)	* 3-D physical model with the use of tracers to study the relative performance of the retention structures using variable alignments, spacings and lengths.
Montaza Cove restoration (model 3)	* 3-D fixed bed model with tracers to study wave agitation and circulation conditions under the selected scheme and assist in proper location alignment and extension of the retention groin.
Baltim Beaches Replenishment and stabilization (model 4)	* 3-D physical model with tracers (dye and light density materials) to check the relative performance of a number of alignments, lengths and spacings of the selected protective structures. * For this complex problem, and due to the limitations of the reliability of the available techniques of describing and modeling sedimentation mechanisms in numerical models, their use should be limited as a compliment to the physical model results only with possible future calibration using field and laboratory data on the performance of the executed projects. Another purpose of using numerical models would be the advancement and introduction of related technologies and "state of art" to the SPA technical staff in this field.
Ras El Bar shore protection (model 5)	Same as for Baltim beaches (model 4, above).

Development of a Comprehensive Field Monitoring Program

In coastal engineering, more than one shore protection scheme can be developed to solve the same coastal problem for a given location. The wisdom and merit of using either physical or numerical models or both to assist in the evaluation of these schemes, can be debated for ages before an agreeable and convincing conclusion is reached. This is basically true due to the present degree of complexity of this subject and the practical and academic factors influencing the decision making and the people concerned. Most of these problems can be relaxed if useful field data are available on the performance of similar projects.

There is too much to learn from a well developed and implemented field monitoring program. In addition, monitoring the performance of any selected coastal protection scheme will have considerable benefits in future modifications, maintenance and models calibrations of that scheme.

It is, therefore, essential to carry out a field monitoring program to check, analyze and modify the performance of each project, on an as-needed basis. The field program should be supported by periodic controlled aerial photography for the entire shore protection Master Plan area at, say, 5 year intervals.

"Set-Back Lines"

The so-called "Set-Back Line" or "Red Line" is a concept of delayed and deterent protection. It is used along some areas where long-term future developments are anticipated along eroding shorelines or other areas which could be affected by the adverse effects of projected shore protection structures. In most cases, the establishment of a "Set-Back Line" is based on historical data on shoreline change and its future projections, previous experience on the performance of executed protective structures and other judgmental factors. In this scheme, further projected developments or relocation of existing ones should be regulated or placed at a safe distance back from the existing shoreline.

Other Requirements and Recommendations

Other requirements and recommendations include:

(a) Geotechnical investigations.
(b) Near-shore beach profiling for Alexandria and Abou Quir beaches.
(c) Identification of sand sources for beach nourishment. Presently, the only proven sources of relatively coarse sand (D 50 $\simeq$ 0.5mm) are land sources (Khatatba, Ismailia and others). The costs of mining and transporting this sand to the different project sites are expensive (20-22 LE/m^3). It is estimated that about 1.6×10^6 m^3 of this sand would be needed in the implementation of the SPMP projects. It is, therefore, essential for SPA to consider other sources of medium or coarse sand. Specifically, both offshore and on land sand deposits should be surveyed and the economy of these sources studied, including transportation costs considering available local transportation means, river and inland navigation possibilities, and offshore dredging.

(d) Funding for the SPMP projects
The SPA may elect to approach some of the international financing organizations to secure necessary funds for some of the SPMP aspects. Funding support could consider such subjects as model testing, training, numerical modeling techniques and computer applications and assistance in projects execution, monitoring and construction management.

(e) Other coastal areas outside the present SPMP Zones
It is recommended that the SPA extend the SPMP to the other Egyptian northern coastlines such as the area west of Alexandria to Saloum, the Sinai coasts, and the Red Sea coasts.

(f) Research and developments
The SPA, in cooperation with the Coastal Research Institute, should involve local Egyptian Universities and institutes in sponsoring specialized research and studies on subjects related to the SPMP activities.

(g) Guidelines for coastal developments
SPA should establish guidelines for construction and development regulations along the SPMP Zones guided by the recommended "Set-Back Lines" and coordinate that effort with the concerned Governorates.

(h) Survey and monitoring facilities
SPA should secure the necessary equipment, survey instruments and hydrographic survey facilities at each of the three SPMP Zones.

Acknowledgment

The authors express their appreciation to the UNDP and the U.S. TDP for their financial assistance with this study.

References

Tetra Tech, Inc., "Shore Protection Master Plan for the Nile Delta Coast, Progress Report No. 1", Dec. 1984.

Tetra Tech, Inc., "Shore Protection Master Plan for the Nile Delta Coast, Progress Report No. 2", Dec. 1985, 3 Volumes.

Tetra Tech, Inc., "Shore Protection Master Plan for the Nile Delta Report", Dec. 1986, 14 Volumes.

UNDP, "Coastal Erosion Studies, Findings", Technical Report submitted to the Arab Republic of Egypt, 1978.

U.S. Army, Corps of Engineers, "Shore Protection Manual" published by the Coastal Engineering Research Center, Waterways Experiment Station, 2 Volumes, 1984 Edition.

CHAPTER 187

DESIGN AND PERFORMANCE OF ARTIFICIAL BEACHES FOR THE KUWAIT WATERFRONT PROJECT

Timothy W. Kana,[1] Mohammad Al-Sarawi,[2] and Michael Holland[3]

Introduction

One of the largest recreational waterfront projects ever designed (Sasaki Associates, 1979) is located along 20 kilometers (km) of the City of Kuwait on the Arabian Gulf (Fig. 1). Planning and design were initiated in 1976, and the first phases of construction were completed in 1985. Amenities included artificial beaches, promenades, waterfront parks, and an artificial island. Extensive armoring has also been installed, ranging from 10-ton, dolosse breakwaters to large, quarry-stone revetments. Total investment in the first two phases is upwards of US $100 million.

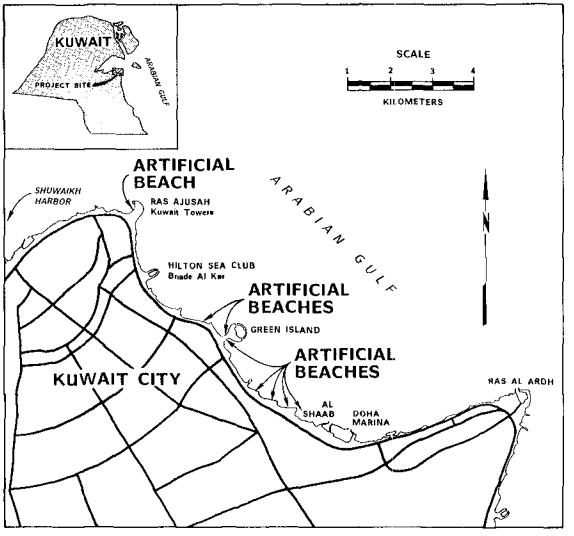

FIGURE 1. Location map of the Kuwait waterfront showing principal features.

1) Coastal Science & Engineering, Inc., P.O. Box 8056, Columbia, SC, USA 29202
2) Faculty of Science, Kuwait University, Safat, Kuwait
3) Sasaki Associates, Inc., 64 Pleasant Street, Watertown, MA, USA 02172

One aspect of the master plan--recreational beaches--required special consideration because of the moderately high tide range of 3.5 m, typical of Kuwait Bay. The present paper describes the participation of the authors since 1977 in developing design criteria [Research Planning Institute, Inc. (RPI), 1979], supervising engineering (Holland, 1981), and monitoring performance (Al-Sarawi et al., 1986) of eight pocket beaches constructed for the waterfront project.

Project Setting

The study area (Fig. 1) is located along the southeast margin of Kuwait Bay at the head of the Arabian Gulf. This is a clastic shoreline composed of sediments derived from the Shatt al-Arab mouth of the Tigris-Euphrates River approximately 50 km to the north. The natural waterfront along Kuwait City consists of a series of perched beaches and low headlands formed of intertidal coral rock. Ras al Ardh, the most prominent headland, marks the division between Kuwait Bay and The Arabian Gulf. West of Kuwait Towers is a commercial shoreline of dhow harbors which predate the rapid build-up of the oil-export industry. With a tide range varying from (est.) 3.0 m to 3.5 m from Ras al Ardh to Shuwaikh, a broad intertidal terrace is exposed at low tide.

East of Kuwait Towers, the project area forms a broad arc bounded by the headland at Ras al Ardh. Midway along the shoreline near the location of Green Island (Fig. 1) is a slight bulge produced by a less prominent headland (beach rock terrace). Between Green Island and Kuwait Towers, Bnade al Kar Sea Club divides the shoreline between recreational beaches to the northwest and a steep rubble edge to the southeast. This area is part of Phases I and II of the Kuwait waterfront (KWF) project.

Coastal Processes

Tide plays a dominant role in the shoreline dynamics along the KWF because of its moderately high range [3.5 m between mean higher, high water (MHHW) and mean lower, low water (MLLW); British Admiralty (1982)]. This limits exposure of the beach to wave action at middle and upper tide levels only. The principal driving force for currents in the Arabian Gulf are the tides which enter through the Strait of Hormuz, 950 km southeast of Kuwait. Local winds play an important secondary role in establishing circulation patterns. Galt et al. (1983) report a net surface flow which is counterclockwise at the head of the gulf under the northwest and southeast winds which are most common. This produces a net ebb-directed flow (time-averaged) in the nearshore area of the KWF project.

Coastal processes and longshore transport are highly variable, being dependent on local winds, nearshore bathymetry, and wave-refraction patterns. Hayes et al. (1977) found that wave energy and longshore transport are low in magnitude along the developed waterfront of Kuwait City. Waves at the shoreline in Kuwait Bay average less than 15 centimeters (cm) and thus produce net sand transport rates on the order of 10^3-10^4 cubic meters per

year (m^3/yr). Longshore transport is higher along the Arabian Gulf shoreline of Kuwait where inshore waves are typically 20-30 cm high. Kana et al. (1986) estimate net southerly rates of 5×10^4 m^3/yr for a site 70 km south of Ras al Ardh.

Long-term erosion rates are unavailable but, based on site-specific data for the Kuwait City shoreline (Hayes et al., 1977), rates are low because of:

1) Protection by the rocky, low-tide terrace.

2) The compartmentalized nature of the shoreline.

3) Low wave energy.

Lacking tropical storms and associated storm surges, beach erosion is limited to periods of highest tides and infrequent shamal winds from northerly components.

Sediments and Beach Morphology

Sediments along the KWF are a mixture of sand, building blocks, rock, and other debris (Hayes et al., 1977). Gravel-sized sediment was found to occur at the base of eroding scarps, the upper swash line (limited small sizes), at the toe of the beach, and at various positions on the low-tide terrace depending on exposure or mining of the beach platform. Sand was found to occur as a thin veneer over the mid-beach face and also as intertidal sand bars on the low-tide terrace. Most remaining beaches prior to construction of the KWF project had moderately to poorly sorted sand ranging from 0.25 millimeters (mm) to 1.0 mm diameter. The principal mode occurs at the break between medium and fine sand (Hayes et al., 1977).

With low wave energy, the active beach slope tends to be steep where beaches exist along the KWF. Hayes et al. (1977) found that slopes ranged from 0.08 to 0.13, or roughly 1 on 10. Berms were widest between Shuwaikh Port and Bnade Al Kar. Typical high-tide berm widths in 1977 were 20-30 m. From a recreational standpoint, Kuwait City beaches are normally usable for bathing only during higher tide stages because of exposure of the low-tide terrace.

Design Planning

A field-monitoring program was initiated in 1977 (Hayes et al., 1977) in order to provide basic criteria for design of improvements to the waterfront edge. These measurements became the basis for a set of design criteria and recommendations for artificial beaches as well as larger-scale structures such as a 400-m-diameter artificial island. Beaches were designed to accommodate the high tide range and high-density recreational use.

A key aspect of the early, field-survey program was measurement of littoral processes over ten days, every quarter for two years at six represen-

tative stations along the KWF. Beach profiles were also measured at over 30 stations every quarter (Fig. 2). For the most part, Kuwait coastal processes are exceedingly weak and changes in the beach profile are minimal (Hayes et al., 1977). However, Kana and Sexton (1978) measured storm processes during a moderate shamal in February 1978 and found that this one event accounted for 25 percent of the gross annual longshore transport. It also produced 2-4 m^3/m of erosion along the active profile where sand beaches existed. These field data provided confirmation of the predominance of northwesterly winds and waves along the waterfront.

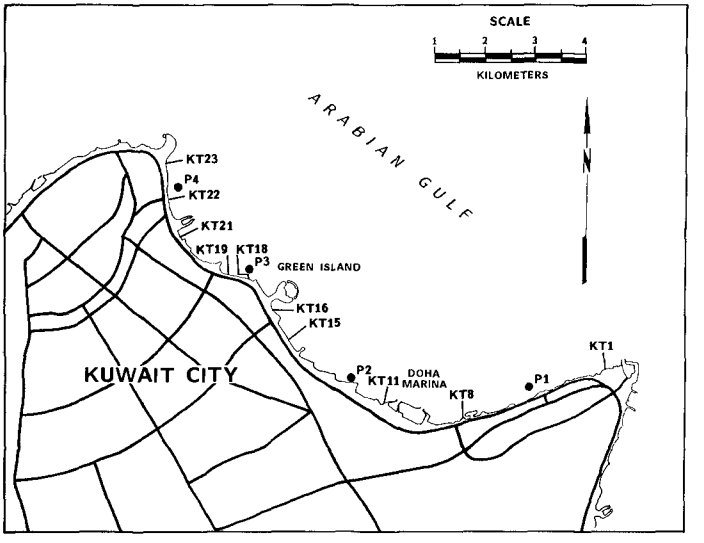

FIGURE 2. Coastal process and selected beach profile stations monitored along the Kuwait waterfront.

Wave-refraction models were developed for Kuwait Bay and the waterfront shoreline by RPI (1979) and Al-Sarawi et al. (1986). Galvin (1979) prepared the original estimate of design waves, using standard hindcasting procedures which were applied in the earlier refraction analysis. The models provided guidance on local longshore transport rates and directions, and the presumed stable configuration of artificial beaches into the incident wave field. Example regional and inshore diagrams are given in Figure 3. These were prepared with a program written by S.J. Siah using a finite-element grid scheme (Al-Sarawi et al., 1986).

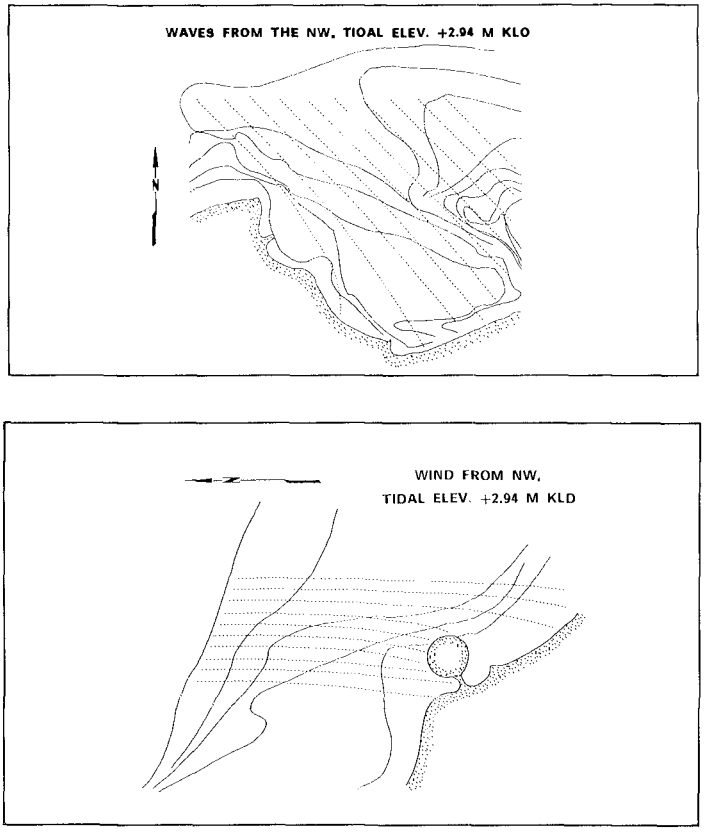

FIGURE 3. Regional (upper) and example inshore refraction diagram (lower) for the area around Green Island. Input parameters are $H_{1/3} = 1.37$ m, $T_{1/3} = 4.6$ s. Tidal elevation approximates MHHW.

It was found that limited reaches of the Kuwait City shoreline would accommodate recreational beaches. Some areas were considered unsuitable because of exposure or proximity to tidal channels. Other areas were eliminated from consideration because of alternative land use such as a marina or aquarium which were integral parts of the master plan. RPI (1979) recommended 6-8 pocket beaches bounded by groins which could double as pedestrian promenades and outfall jetties for upland drainage. Sand compatibility analyses indicated that an inland source would be required since nearshore deposits were considered unsuitable for environmental reasons. Sasaki Associates (1979) incorporated these conceptual designs into the final master plan. Final design proceeded through 1981 with construction of Phase I beginning that year.

Construction

Phases I and II of the KWF project (Kuwait Towers to Doha Marina, Fig. 1) were essentially complete by late 1986. Infrastructure and the major design elements--retaining groins, the artificial island, and the "hook" at Kuwait Towers--were completed before placement of sand in each artificial beach.

Figure 4 illustrates a typical pocket-beach design and postconstruction configuration in December 1985 (Fig. 4b). Given the local orientation of the shoreline oblique to predominant waves refracting from the northwest, a typical configuration consisted of a broad downdrift end with the widest part of the berm measuring 150± m. Typical length of each beach was 500 m. Each beach is backed by a revetment designed to +6.5± m Kuwait Land Datum (KLD). The datum approximates local MLLW, thus placing the crest of each structure about 2.5 m above highest still-water levels. Design berms were set at +4.5 m KLD.

Figure 5 illustrates various stages of sand placement by land-based equipment. The fill was placed in accordance with the design planform of each beach to minimize losses. The beach face and lower part of the profile were allowed to adjust naturally to an equilibrium slope (Fig. 5c).

Comparative profiles (Fig. 6) show the final configuration of two representative beaches in relation to the original profile. Sediment sampling by the authors in 1985 indicated the nourishment sand from upland matched the native sand very well (Fig. 7).

Innovative Features

Two innovative design elements of the KWF project are shown in Figures 8 and 9. The first, Green Island, consists of a 400-m-diameter artificial "island" armored with dolosse and connected to the mainland by a "tombolo" beach. Originally, the master plan called for a tidal channel between the island and shore, but this concept was abandoned in favor of recreational beaches. This design imitates the natural tendency of a shoreline to develop an isthmus (tombolo) in the lee of an offshore island where sediment supply is plentiful.

A second, unusual design element was the "hook" built on the exposed, low-tide terrace adjacent to Kuwait Towers (Fig. 9). This feature anchors a pocket beach facing west into the principal fetch direction.

Postconstruction Monitoring

Postconstruction surveys have been initiated by Al Sarawi et al. (1986) in order to develop preliminary estimates of erosion and changes in local coastal processes produced by the KWF project. These surveys include quarterly rod-and-level measurements and coastal process measurements over ten-day periods. Additional measurements have been taken to monitor inshore

turbidity levels adjacent to the beach fill. Surveyed profiles have been analyzed to compute sediment budgets for several compartments along the shoreline.

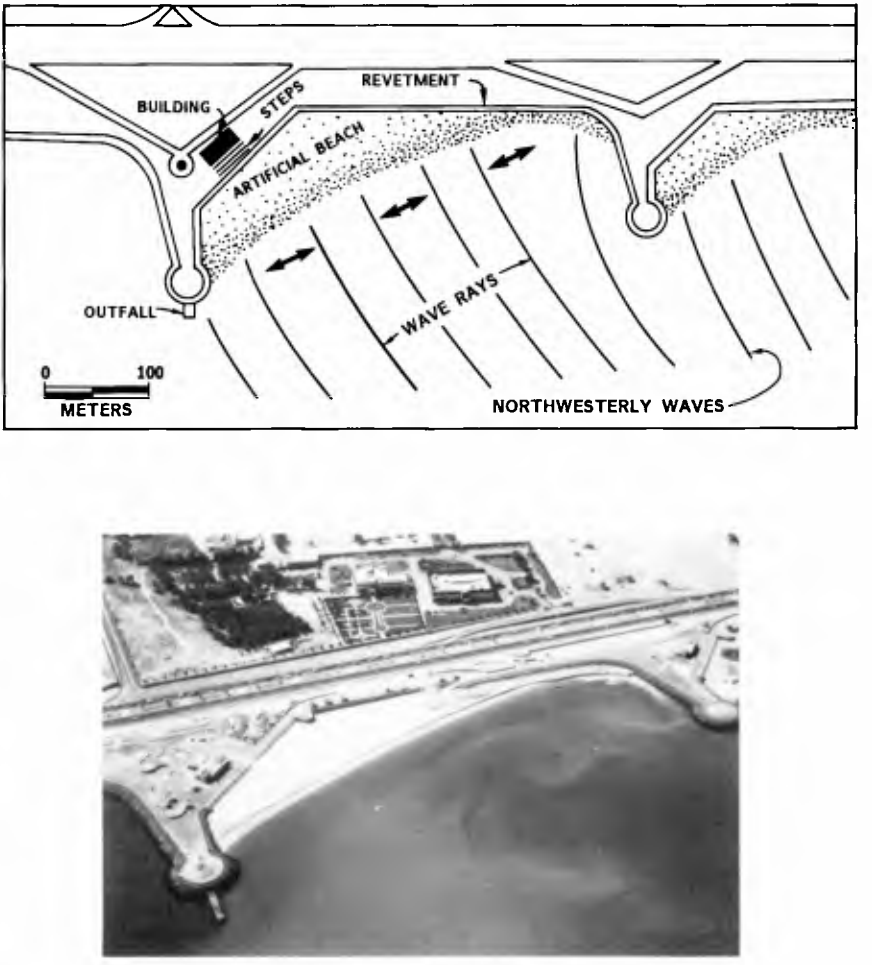

FIGURE 4. (a) Typical pocket beach designed for the KWF project. Alignment is into the predominant wave direction to minimize longshore sand losses. Retaining structures double as promenades and outfalls. (b) Pocket beach nearing completion on 12 December 1985 along the KWF project.

FIGURE 5. Stages of beach construction by land-based equipment beginning with spreading along the profile (top), natural adjustment of the beach face (middle), and final completion in an equilibrium planform (bottom). Photos taken at low tide in March 1985 by T.W. Kana.

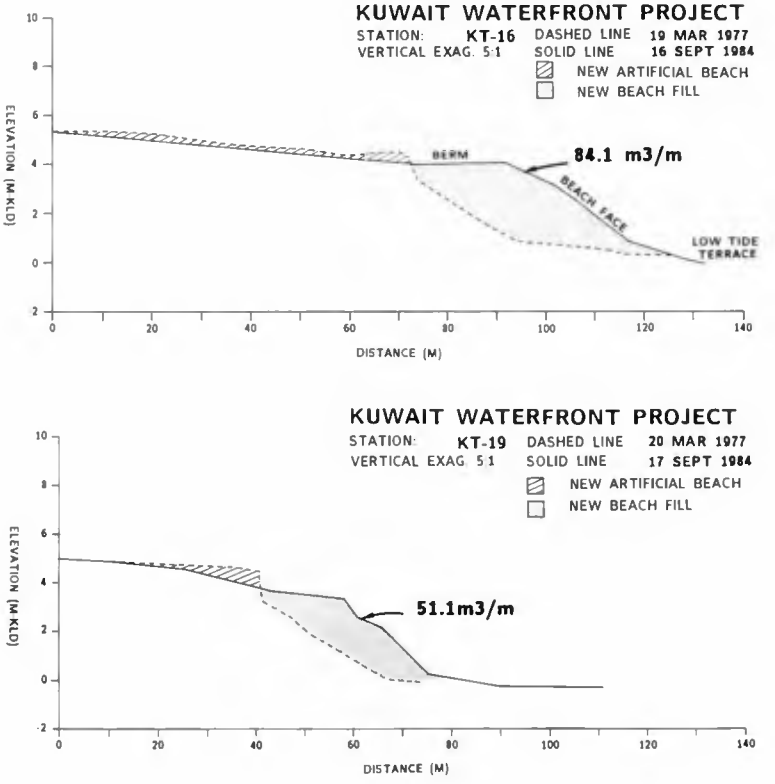

FIGURE 6. Comparative profiles from two representative artificial beaches showing the fill in relation to the preconstruction profile (see Fig. 2 for station location).

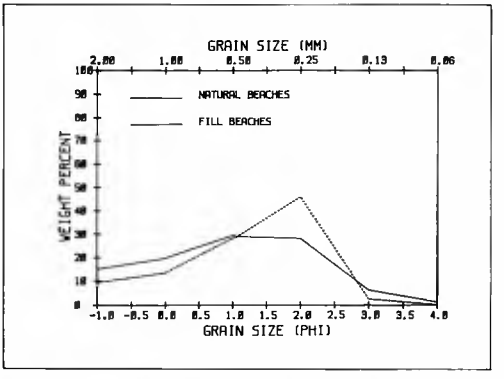

FIGURE 7. Frequency-size curves for composite samples of artificial and natural beach sediments along the KWF study area. Note the slightly better sorting of natural deposits, but generally very good correspondence between the two curves.

FIGURE 8. Conceptual plan for Green Island (Sasaki Associates, 1979) and an aerial photo of the feature nearing completion on 12 December 1985. Note the connecting beaches shaped into a tombolo. Kuwait Towers is in the upper right corner.

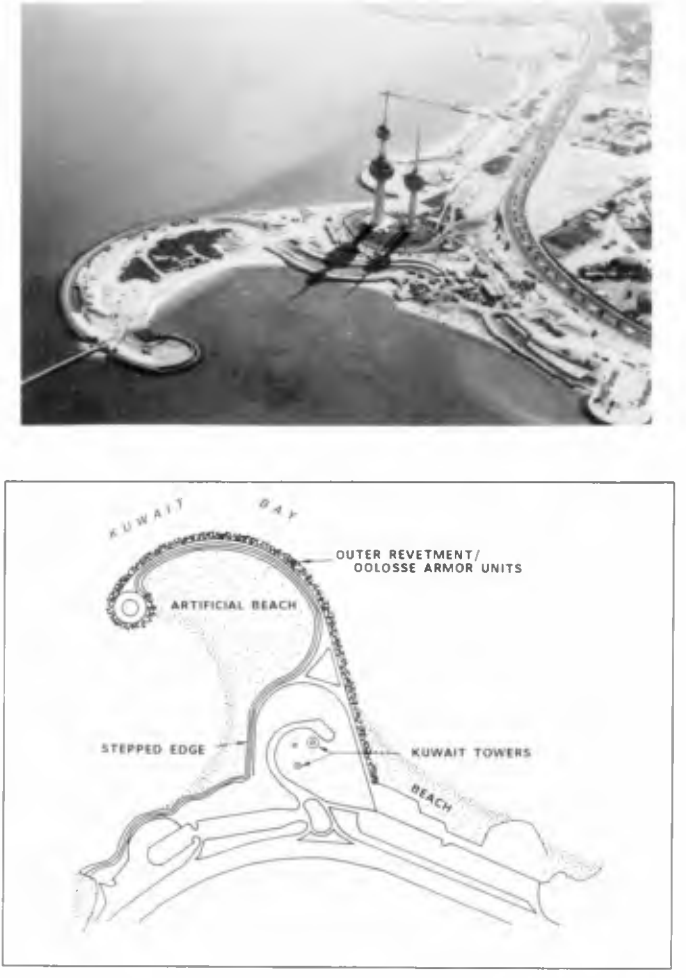

FIGURE 9. Conceptual plan for the artificial beach at Kuwait Towers and an aerial photo of construction on 12 December 1985. The beach is oriented into the primary fetch direction from the west. The jetty shown extending from the hook in the photo is a temporary feature for loading rock imported from Oman for the project.

The typical unit-fill volume for artificial beaches was 50-85 m^3/m. Interestingly, this volume was less than might be expected because each of the new beaches was "perched" on a low-tide terrace. This eliminated much of the profile adjustment normally associated with profile renourishment. On the other hand, the high-tide range required construction of the berm at elevations much higher than typical for beach nourishment. Total quantities of beach fill were unavailable at the time of this writing because some of the beaches had not been completed by the time of the most recent survey (July 1985). However, through that date, approximately 300,000 m^3 of sand had been added to the KWF project in the beach zone. For beaches which had been in place for at least one year, the extent of profile movement (sweep zone) was typically less than 5 m^3/m, or about 6-10 percent of the average, unit-nourishment volume. This compares with typical adjustments of 50 percent or more of the initial fill volume during other beach nourishment projects in order to build up subtidal portions of the profile.

Compared with the 1977-1979 period, measurements of coastal processes indicated little change in wave-energy flux at three monitoring stations (P3 just west of Green Island; P2 at the easternmost pocket beach; and P1, 3 km from Ras al Ardh along the hardened, existing shoreline). Only one station monitored (P4, 1 km southwest of Kuwait Towers) experienced a significant decrease in wave energy, with mean breaker heights decreasing by 40 percent. This is probably a result of construction of the hook at Kuwait Towers which tends to shift incident waves refracting around the headland further downdrift.

Despite the similarities in wave-energy flux at most stations, there was measurably reduced net longshore transport at P3 near Green Island and at P2 near Al Shaab Sea Club (the only two sites where processes were routinely measured along new beaches for comparison with the 1977-1979 surveys). This could be attributed, in part, to sheltering by Green Island during winds from easterly components. Westerly component winds produced comparable wave heights as the 1977-1979 data set, but lower longshore transport rates because of the realignment of the pocket beach into the predominant approach direction. At the other pocket beach, P2, the new shoreline alignment is offset about eight degrees from the strandline, reducing the incident wave angle into the compartment. Thus, net longshore transport has also decreased.

Although long-term monitoring is needed to determine the ultimate success and longevity of each artificial beach, preliminary evidence suggests the fill has rapidly adjusted to an equilibrium planform and profile. Aerial overflights in December 1984 and December 1985, as well as periodic ground inspections, showed no evidence of large sediment plumes, sand spits, or other geomorphic indicators of rapid longshore transport. This contrasts with a situation documented by Hayes et al. (1977) in which a small-scale nourishment project at Al Shaab Sea Club experienced rapid loss of fill because of improper sediment size (too fine) and a design which presumably was out of equilibrium with a natural planform into the predominant wave direction.

Conclusions

Early surveys after construction of artificial beaches along the Kuwait waterfront indicate:

1) It is possible to construct artificial beaches in high tide-range settings (up to 3.5 m) which are usable for swimming throughout most of the tidal cycle.

2) Orientation of artificial beaches should be aligned into the predominant wave approach to minimize sand transport. Wave-refraction models using appropriate hindcast wind frequencies is a minimum design requirement. However, site-specific littoral process measurements should be made to confirm local sand transport patterns, especially where inshore bathymetry is subtle and irregular such as Kuwait's shoreline.

3) Retaining structures were necessary in the Kuwait situation because of other design elements which required separation from recreational beaches. The design of shore-perpendicular structures in this case was modified to incorporate stormwater outfalls, pedestrian promenades, and decorative lighting. Onshore amenities were sited at the downdrift end of each beach where more people would be likely to congregate along the wide part of the berm.

4) Construction of perched beaches on a stable, low-tide platform is facilitated in low-energy, mesotidal areas if the fill is placed at an equilibrium planform and profile slope. Nearby natural beaches provide the best guidance for berm elevations and slope. Provided beach quality fill is used, this reduces turbidity in the nearshore zone and allows artificial beaches to achieve a natural look much faster. Construction by land-based equipment also reduces turbidity levels in comparison to a dredging operation.

Recommendations for Further Study

Given at least eight discrete and independent beaches constructed for the KWF project, it will be possible to develop a controlled data base on each one's response to the prevailing wave and tide regime. Additional profile survey stations should be set up and monitored 2-4 times each year to develop sediment budgets for each compartment. Such surveys will demonstrate whether each beach seeks an equilibrium planform, is retained within the control structures, or tends to shift in the longshore direction under seasonal wave patterns. The low-energy shoreline along Kuwait Bay and the compartmented beach system also provide a workable prototype setting to conduct experiments of onshore/offshore sand transport and the role of natural low-tide sills in stabilizing the profile (i.e., a perched beach). Experience gained from the KWF project beaches should be useful in the design of artificial beaches in other high, tide-range settings.

Acknowledgments

The Kuwait Waterfront Project is being developed by the Municipality of Kuwait. The authors thank the director of the project for permission to publish this work. Monitoring funds included a grant to Dr. Al-Sarawi from the Kuwait Environment Protection Council. We acknowledge the many people from the Municipality of Kuwait, Kuwaiti Engineers' Office, Kuwait University, Sasaki Associates, Research Planning Institute, and Coastal Science & Engineering, Inc., among others, who have assisted in the project.

References

Al-Sarawi, M., A.H. Bu-Olayan, M. Ghannoum, T.W. Kana, B.J. Baca, and S.J. Siah. 1986. Assessment of coastal dynamics and water quality changes associated with the Kuwait waterfront project. Final Report, Environment Protection Council; Faculty of Science, Kuwait University, Safat, 199 pp. + appendices.

British Admiralty. 1982. Northern Arabian Gulf. Chart for Navigation, London, Great Britain.

Galt, J.A., D.L. Payton, G.M. Torgrimson, and G. Watabayashi. 1983. Trajectory analysis for NOWRUS oil spill with specific application to Kuwait. Tech. Rept., U.S. Dept. Commerce, NOAA, 60 pp. + appendices.

Galvin, C.J. 1979. Design wave height calculations for four sites on the Kuwait shore. Tech. Memo. to Research Planning Institute, Inc.; by C.J. Galvin, Coastal Engineer, Springfield, Vir., 5 pp.

Hayes, M.O., J. Michel, and T.W. Kana. 1977. Beach processes study, including morphology and sediments for Kuwait waterfront project. Tech. Rept. to Sasaki Associates, Inc.; by RPI, Columbia, S.C., 52 pp.

Holland, M.F. 1981. Kuwait waterfront project: an interdisciplinary approach to design. In Proc. 7th Conf. Coastal Society, Bethesda, Md., pp. 53-60.

Kana, T.W., and W.J. Sexton. 1978. Beach processes study--Kuwait City waterfront. Tech. Rept. No. 2-KWF to Sasaki Associates, Inc.; by RPI, Columbia, S.C., 31 pp.

Kana, T.W., B.J. Baca, and S.J. Siah. 1986. Chalets at Dubaiyeh: environmental impact and coastal engineering studies. Final Report, Kuwaiti Engineers' Office; Coastal Science & Engineering, Inc., Columbia, S.C., 102 pp. + appendices.

Research Planning Institute, Inc. 1979. Kuwait waterfront project final report on coastal studies (March 1977 through March 1979). Final Rept. to Sasaki Associates, Inc.; by RPI, Columbia, S.C., 105 pp. + appendices.

Sasaki Associates. 1979. Master plan, final report, Kuwait waterfront project. Final Rept. to Municipality of Kuwait; by Sasaki Associates, Inc., Watertown, Mass., 85 pp. + appendices.

Wave Interaction with Moored Sloping Breakwater

S. Kharaghani* and J.J. Lee**

1. ABSTRACT

Interaction of periodic waves with a moored inclined floating breakwater has been studied theoretically and numerically. The floating breakwater is inclined at a well defined angle with the sea bottom; its seaward end in protruding above the water surface. In static equilibrium, without incoming waves, the body weight, the buoyance force, and the restoring forces from the mooring lines which are modeled using linear springs keep the breakwater at a fixed angle. The theoretical formulation is based on a suitable variational principle. For the numerical solution a combination of finite element approximation as well as eigen function expansion technique is used.

The result is obtained in terms of wave transmission and reflection coefficient as well as the sway, heave and roll motion of the breakwater. The sensitivity of the solution on the parameters such as the bottom gap size, angle of inclination, and the mooring line stiffness are investigated over a range of incident wave transmission coefficient for dimensionless wave number $hk > 0.60$ (k is wave number, h is the water depth). The results suggest that a certain degree of sheltering effect can be realized by employing this type of sloping breakwater.

2. INTRODUCTION

Many marine structures are built in the coastal region to withstand the attack of the ocean waves and to proide a sheltered environment. Rubble mound breakwaters are examples for such applications. For certain applications this type of permanent structure might not be the most efficient. For example, during the construction of certain harbor facilities when only temporary protection is needed for a certain period, and when such protection is no longer needed after the construction it would be reasonable to assume that a permanent breakwater would not be necessary. Portable breakwaters could provide the need for such applications. Among many types of portable breakwater, one possible type is the moored inclined floating breakwater which consists of a pontoon structure whose density is so designed that the structure would be neutrally buoyant and

* Research Engineer, University of Southern California, Los Angeles, CA 90089-0231

** Professor of Civil Engineering and Director of the Foundation of Cross-Connection Control and Hydraulic Research, University of Southern California, Los Angeles, CA 90089-0231.

it is placed such that the pontoon is oriented as a well defined angle with the bottom; the seaward side of the pontoon is above the water surface. In static equilibrium, without incoming waves, the body weight, the buoyancy force, and restoring forces from the mooring lines which are modeled using linear springs keep the floating breakwater at a fixed angle. The effectiveness of the floating breakwater described above under the attack of periodic incident waves is studied theoretically and numerically. The bottom edge of the pontoon maintains a varying height of clearance so that it is not necessarily resting directly on the bottom. This clearance would extend the use of the same structure even for a deeper water depth. Of course, the effectiveness of these breakwaters deployed at such water depth must be carefully studied.

3. MATHEMATICAL AND NUMERICAL FORMULATION

For the analysis, the fluid is considered inviscid, incompressible and irrotational. Therefore, the governing equation is the Laplace equation with a mixed boundary condition on the free surface, the homogeneous Neumann condition at the sea bottom, as well as appropriate radiation conditions at infinity which require that the scattered waves are outgoing from the body. An additional boundary condition which requires that the normal velocity of the fluid and the body to be equal of the floating breakwater is also necessary. The boundary conditions are linearlized, the radiation boundary conditions are replaced by a suitable matching boundary condition in the associated functional.

The equivalence of the variational principle and the differential formulations allows for us an adoption of a well known variational form to be applied for the solution of Laplace's equation and its boundary conditions. The associated functional based on the suitable variable variational principle for the present study can be expressed as follows:

$$F(\phi_1,\phi_2,\phi_3)=\int\int_{R_1}\frac{1}{2}(\nabla\phi_1)^2dxdy-\frac{\sigma^2}{2g}\int_{S_F}\phi_1^2dx-\int_{S_R}(\phi_1-\frac{1}{2}\phi_2)\phi_{2,n}dy-$$

$$\int_{S_L}(\phi_1-\frac{1}{2}\phi_3)\phi_{3,n}dy-\int_{S_0}V_n\phi_1ds \qquad (1)$$

where V_n is the normal velocity of floating object, and $\phi_1(x,y)$, $\phi_2(x,y)$, and $\phi_3(x,y)$ are the complex velocity potential describing the flow field in the regions 1, 2 and 3, respectively.

A definition sketch of a moored inclined floating breakwater with its designated boundaries for regions 1, 2, 3 is shown in Fig.1. For the numerical

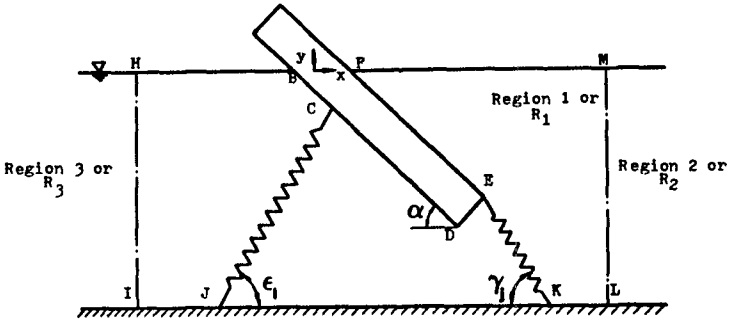

Figure 1. Definition sketch of a moored inclined floating breakwater with its designated boundaries.

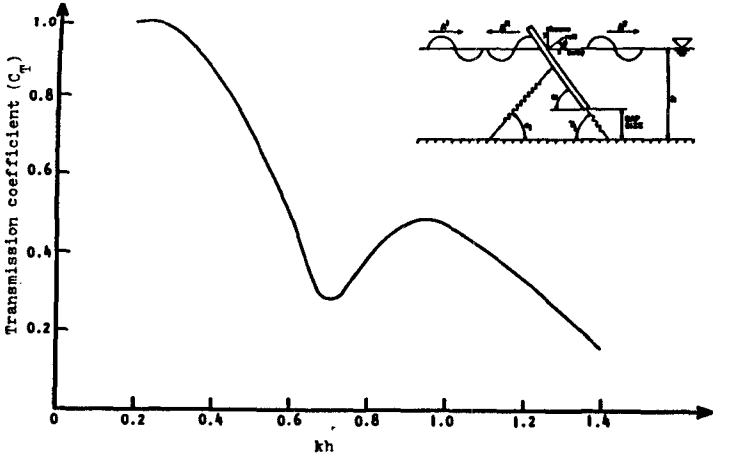

Figure 2. Transmission coefficient for 30% gap size and α=18.43 degree angle of inclination as a function of dimensionless wave number (kh).

computation, the entire fluid region for the present study has been subdivided into regions 1, 2, 3 by drawing two auxilliary vertical lines on both sides of the floating breakwater such that an inner region 1 enclosing the breakwater is formed. This inner region indicates the finite domain of direct computational interest where the functional equation 1 is integrated over with its boundaries. Regions 2 refers to the region to the right of the imaginary boundary line, thus wave would propagate in positive x-direction toward infinity. Region 3 refers to the region to the left imaginary boundary line, thus the scattered waves propagate toward negative x-direction. As a result of impact of an incident wave in the presence of the moored floating body, the total velocity potential can be decomposed as the sum of three components

$$\phi = \phi^I + \phi^D + \phi^R \tag{2}$$

where ϕ^I, ϕ^D and ϕ^R are the velocity potential of the incident wave, diffracted wave, and the radiated wave, respectively. The two dimensional plane motion of the moored inclined floating breakwater can also be decomposed in terms of three unknown modes of motion. These modes of motion are expressed in terms of translation in x-direction (sway), translation in y-direction (heave) and rotation about z-axis (roll motion) so that V_n can be expressed in terms of these three components.

For the numerical implementation the finite element approximation is used near the body and eigenfunction expansions are used to express the solutions away from the floating object. It should be mentioned that the finite element approximation is used to estimate ϕ_1 in region 1 near the breakwater while ϕ_2 and ϕ_3 are approximated by a finite number of the eigenfunction expansions with unknown coefficients in regions 2 and 3, respectively. Then the solution near the body is matched with the eigenfunction expansions along the common boundaries between regions to obtain the final solution. Thus the solution to the system of simultaneous algebraic equations for the unknown node velocity potential, coupled with the three unknown amplitudes of motion of the floating breakwater are sought numerically.

The linearized equations of motion of the floating breakwater can be written as follows:

$$M\ddot{x} = F_{dx} + F_{sx} + \sum_{j=1}^{n} (F_{Mx})_j$$

$$M\ddot{y} = F_{dy} + F_{sy} + \sum_{j=1}^{n} (F_{My})_j \tag{3}$$

$$I\ddot{\theta} = M_{d\theta} + M_{s\theta} + \sum_{j=1}^{n} (F_{M\theta})_j$$

where M is the mass, and I is the mass moment of inertia of the floating body about its center of gravity. The terms $(F_{dx}, F_{dy}, M_{d\theta})$, $(F_{sx}, F_{sy}, M_{s\theta})$ and $(F_{Mx}, F_{My}, F_{M\theta})$ are forces and moments associated with hydrodynamic effects, hydrostatic effects and that due to moorings respectively.

To obtain, for example, the force and moment terms due to the hydrodynamic effect, integrations of hydrodynamic pressure and the moments due to this force must be performed. The pressures are related to the velocity potential function by the well known Bernoulli's equations.

A detailed presentation of the mathematical formulation and the numerical implementation using the finite element approximation is presented in Kharaghani (1986).

4. NUMERICAL RESULTS

A series of numerical calculations using the developed computed model of the theory is carried out to investigate the response of the inclined floating pontoon breakwater. The computed results are expressed in terms of wave transmission and reflection coefficients as well as sway, heave and roll modes of motion. The sensitivity of the solution on the parameters such as bottom gap size, angle of inclination, and mooring line stiffness are inestigated over a range of incident wave periods (see Kharagani,1986).

Fig.2 and 3 show the wave transmission and reflection coefficients as a function of the dimensionless wave number (kh) for a pontoon breakwater inclined at an angle of 18.43 degree with a bottom gap size of 30% as shown in the inserts of the figures. It is seen from Fig.2 that a substantial reduction in the wave transmission coefficient can be achieved for those wave frequency in the range of dimensionless wave number $kh > 0.6$. The wave numver k is defined as 2π/wave length and the water depth, h, is used as a characteristic

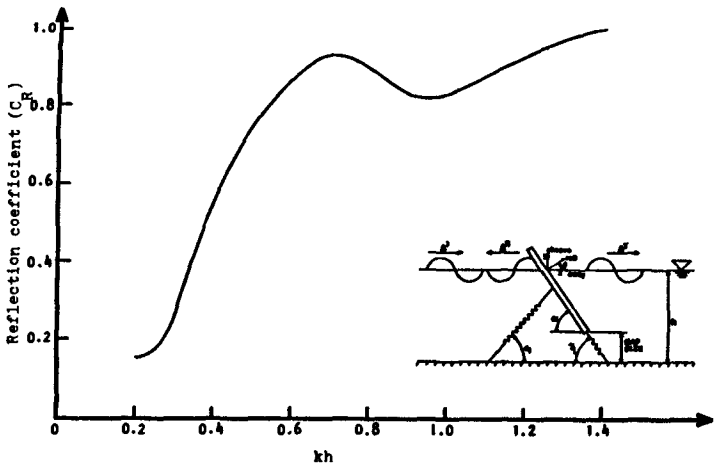

Figure 3. Reflection coefficient for 30% gap size and α= 18.43 degree angle of inclination as a function of dimensionless wave number (kh).

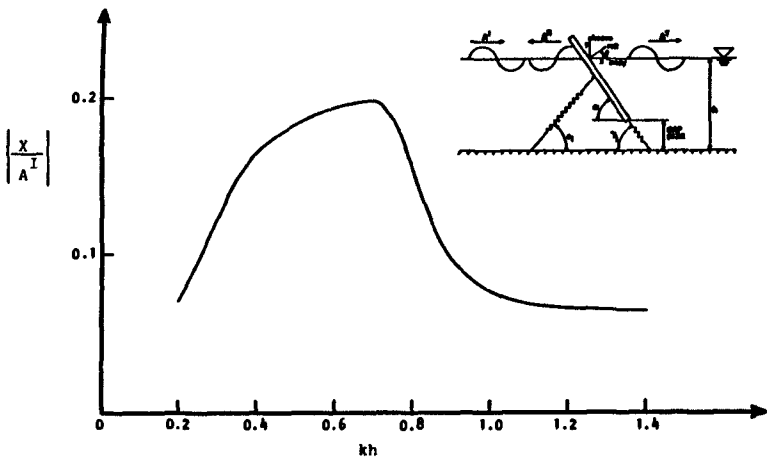

Figure 4. Sway mode of motion for 30% gap size and angle of inclination α=18.43 degree.

depth. It is noted that the transmission coefficient is defined as the transmitted wave amplitude divided by the incident wave amplitude which the reflection coefficient is defined as the reflected wave amplitude divided by incident wave amplitude. The computed amplitude for sway, heave and roll motion of the same sloping potoon breakwater are shown in Fig. 4, 5, and 6. These results indicated the relative dynamical response of the wave-structure interaction in the wave frequency range presented.

As extensive sensitivity analysis for the similar results for different gap size, inclination angle and mooring line stiffness has been conducted by Kharaghani (1986). The interested reader is referred to this for more detail presentation of the results. Similar trend has also been obtained by other investigators using different numerical technique. A comparison of the previous available theorectical results and experiments is given in Fig. 7. This shows a comparison of transmission coefficient for 30% gap size and 18.43 degree inclination angle for two different model thickness of the breakwater. A comparison with prior experimental data and the theoretical result indicates that the major trend is preserved. The result indicates if one could design the structure strong enough to withstand the wave forces a substantial large reduction in wave transmission can be achieved for a fairly large wave frequency range.

5. CONCLUSIONS

A numerical method has been developed to solve the two dimensional problem of the response of a moored inclined floating breakwater subjected to a sinusoidal incident wave. The present method is based on a suitable variational method using the hybrid finite element approximation to a fluid region near the body and the linear equations of motion of the floating breakwater. The body motions, transmitted wave and reflected wave are solved simultaneously. The investigation of the performance of the floating breakwater has been examined by studying the curves of the transmission, reflection, and the three modes of motion with respect to a large range of wave period (kh) that simulate the situation in an idealized incident wave condition from shallow water to deeper water. The results suggest that it is possible to design a moored inclined floating breakwater to be used as a temporary portable wave barrier in providing a sheltered environment against the incident waves in a certain frequency range.

6 ACKNOWLEDGMENTS

The authors appreciate the funding supports from the U.S.C. Foundation for Cross-Connection Control and Hydraulic Research (FCCCHR) and the NOAA Sea Grant Program.

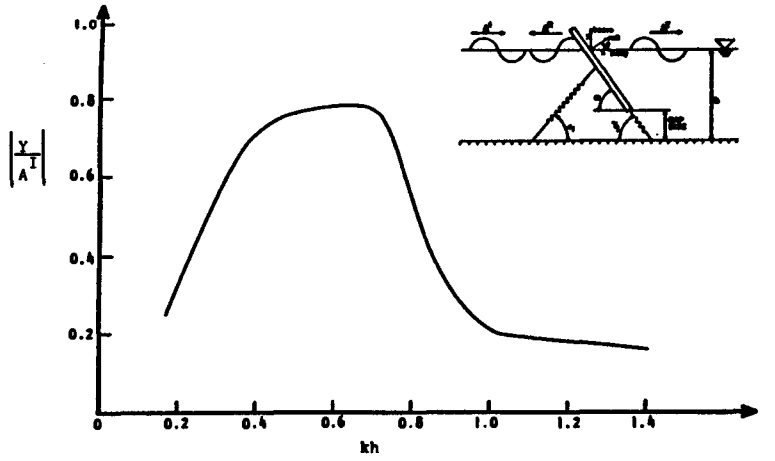

Figure 5. Heave mode of motion for 30% gap size and angle of inclination α=18.43 degree.

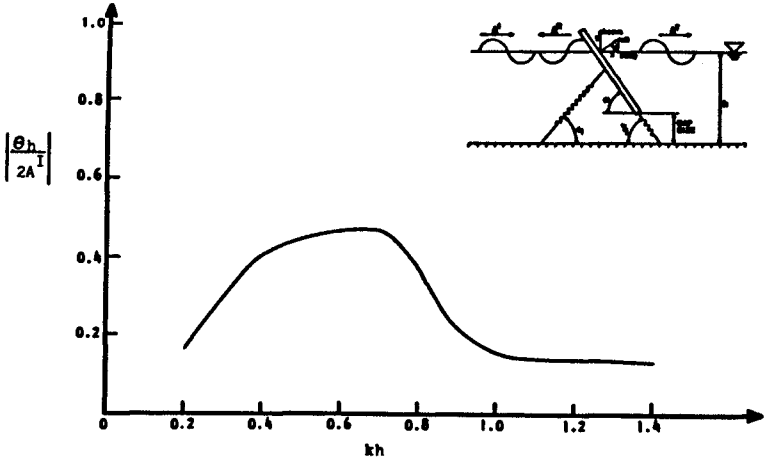

Figure 6. Roll mode of motion for 30% gap size and angle of inclination α=18.43 degree.

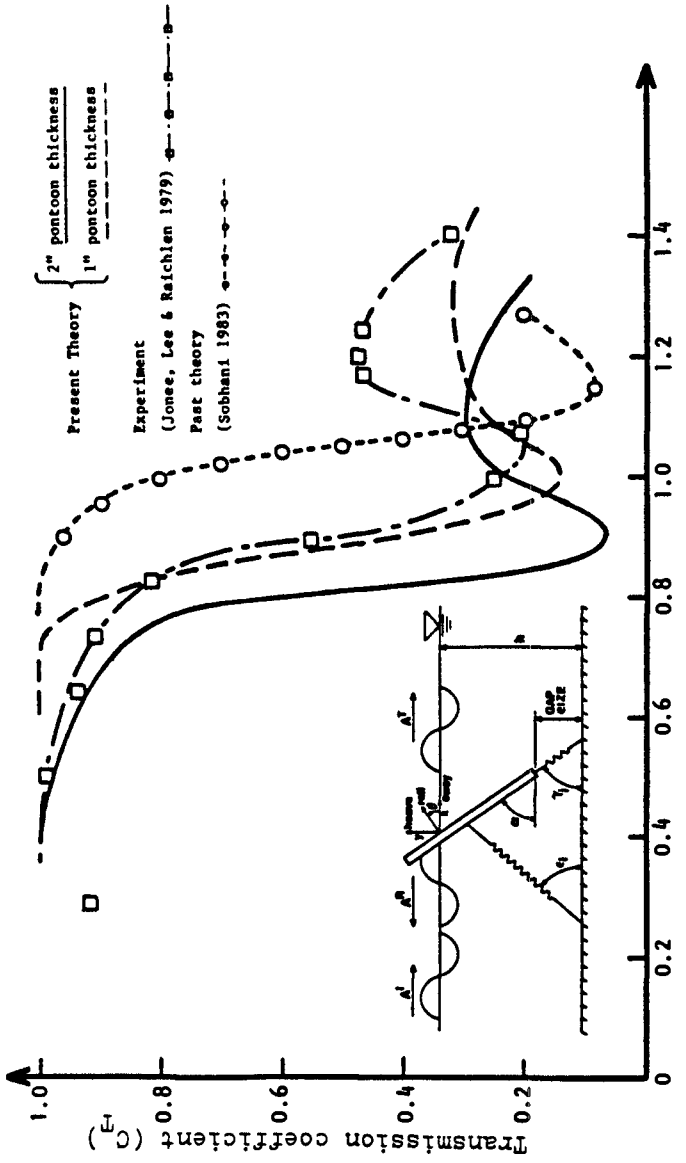

Figure 7. Comparison of wave transmission coefficient for gap size 30%, α=18.43 for two different breakwater thickness and with available theoretical and experimental results.

7. REFERENCES

1. Bai, K.J. and Yeung, R.W. (1974), "Numerical Solution to Free Surface Flow Problems," Proceedings 10th Symposium of Naval Hydrodynamics, Cambridge, MA. pp 609-647.

2. Jones, D.B., Lee, J.J. and Raichlen, F. (1979), "A Transportable Breakwater for Nearshore Applications," Proceeding of the Specialty Conference on Civil Engineering in the Ocean IV. ASCE, San Francisco, CA. pp 433-456.

3. Kharaghani, S.(1986), "Hydrodynamic Response of a Moored inclined Floating Breakwater," Ph.D. thesis, University of Southern California.

4. Leach,P.A., McDougal, W.G. and Sollitt, C.K. (1985),"Hinged Floating Breakwater," Journal Waterway, Port, Coastal and Ocean Engineering, Vol.111, No. 5, pp 895-909.

5. Mei,C.C. (1978), "Numerical Method in Water-Wave Diffraction and Radiation," Annual Reiew of Fluid Mechanics. Vol 10, pp 393-415.

6. Sobhani, S.M. (1983), "Interaction of Waves and Structures, Application to inclined Breakwater," Ph.D. thesis, University of Southern California.

CHAPTER 189

ON THE CONSTRUCTION OF HSIN-TA LNG TERMINAL IN TAIWAN

Shih-sheng Paul Lai*
Cheng-shiun Lee**

ABSTRACT

Since 1984 Hsin-Ta LNG Terminal has been under construction for the purpose of importing liquefied natural gas because of increasing demand and possible depletion of natural gas in Taiwan. Several alternatives were taken into account during the feasibility study. The Terminal is built with only a southern breakwater due to its good natural coastal conditions. Each construction item has been coordinated closely in order to advance the schedule. The first phase of land reclamation was finished by 1986. Three tanks have been under construction since soil improvement was finished. The entire project will be completed in 1989.

1. INTRODUCTION

With a booming of economics in Taiwan, there is an increasing demand for natural gas as new energy resources. In addition, the possible depletion of local natural gas reserves has been taken into account. Hence the Chinese Petroleum Corporation studied the feasibility of importing liquefied natural gas (LNG) in 1979. Since the utilization of LNG is helpful in diversifying the supply of energy resources and decreasing environmental pollution, the government of the Republic of China approved the project in 1984 and decided to establish the LNG Terminal in the Yung-An area. Because there should be no resident within a radius of 1.5 kilometers around the quay of the LNG unloading arm, spacious land is necessary. All of th required area is to be reclaimed by dredging from the locations of navigation channel and turning basin. Because the site for LNG tanks will be built prior to the offshore breakwater, the structure of the revetment should be able to withstand the open sea befoer the completion of breakwater.

2. PLANNING OF HSIN-TA LNG TERMINAL

2.1 Site Selection

The site selection criteria for LNG terminals are quite different from those for typical ports or harbors. In addition to desirable coastal conditions, special considerations must be examined .

* Manager, Planning Dept., BES Engineering Corporation, P.O. Box 335, Taipei, Taiwan, Republic of China.
** Engineer, Planning Dept., BES Engineering Corporation, P.O. Box 335, Taipei, Taiwan, Republic of China.

2.1.1 Soil stability

Taiwan is on the actively seismic circum-Pacific belt. Because of high safety requirements for LNG storage tanks, seismic effects must be taken into consideration. Furthermore the settlement of reclaimed land should be well treated. The sand compaction pile method and the sand drain method have been adopted to improve the soft soil.

2.1.2 Environmental safety

Environmental impacts related to human beings, aquatic vegetation, animals, water and air pollutions must be considered carefully. The required seawater circulation or dredging must not ruin valuable aquatic habitats or ecological systems. In addition, the site should not be chosen in an area where there might be a potential conflict with military training or important public utilities such as gunnery ranges or offshore oil/gas wells.

2.1.3 Storage facilities

There should be large territory available for the building of storage tanks, a regasification system, and control facilities. A buffer zone and a reserve for possible extention must also be included.

2.1.4 Economical transportation cost

The LNG terminal site should have the lowest unit cost for the total transportation system of freight and delivery.

All possible sites in western Taiwan were thoroughly investigated, including Tamsui, Taoyuan, Taichung, Changhau, Yung-An, and Kaohsiung. Since the Yung-An area satisfies the constraints stated above, it was selected to be the site of the first liquefied natural gas terminal in Taiwan, Republic of China.

2.2 Design of Hsin-Ta LNG Terminal

2.2.1 Littoral conditions

The coastline along the site is in the direction of NNW, which is favorable for a harbor in southwestern Taiwan. Since the local coastal data recorded from 1978 were not enough for analysis, data from Kaohsiung harbor had to be frequently referred to.

* Wind: The directions of strong blowing winds range from NW to NNE witn the northern direction most prevailing. Winds less than 10 m/sec occur 96.5% of the year.
* Fog: There are an average of 16.5 days per year.
* Water and tidal level: The highest high water level (HHWL) is 1.99 m above from the local chart datum. The maximum tidal range is 1.30 m in January. The astronomical tide and storm surge with return period of 100 years are +1.36 m and +1.5 m respectively. Hence the tidal level used for the design is +2.86 m.
* Current: Most currents are along the direction of SE-NW. The longshore current speed near the seabed is about 0.5~1.0 m/sec.

*Wave: Wave data show that 93% of the significant wave heights ($H_{1/3}$) are smaller than 1.0 m. Eight model typhoons passing through the site were adopted to calculate the design waves under typhoon conditions. The simulated maximum significant wave is of $H_{1/3}$ = 9.2 m, $T_{1/3}$ = 12.7 sec, S direction, with a return period of 100 years.

* Littoral drift: Since there is a lack of sand for littoral drift and most of the waves approach the beach perpendicularly, the coast is highly eroded with its relatively steeper slope.

2.2.2 Evolution of the Terminal

There are five design alternatives for Hsin-Ta LNG Terminal. They can be classified into three categories: on-shore, off-shore, and shelterless. Each of the former two categories comprises two kinds of storage tank: in-ground and above-ground. The last one is with in-ground tank. Although the general coastal conditions around the site are rather fair, the shelterless layout still can't meet economical and safety requirements. Through various comparisons such as investment, construction period, benifits, etc., on-shore layout is always preferable to off-shore layout except maneuvering security. Hence the general layout of Hsin-Ta LNG Terminal was decided to be an on-shore harbor with in-ground storage tanks, as shown in Fig.1.

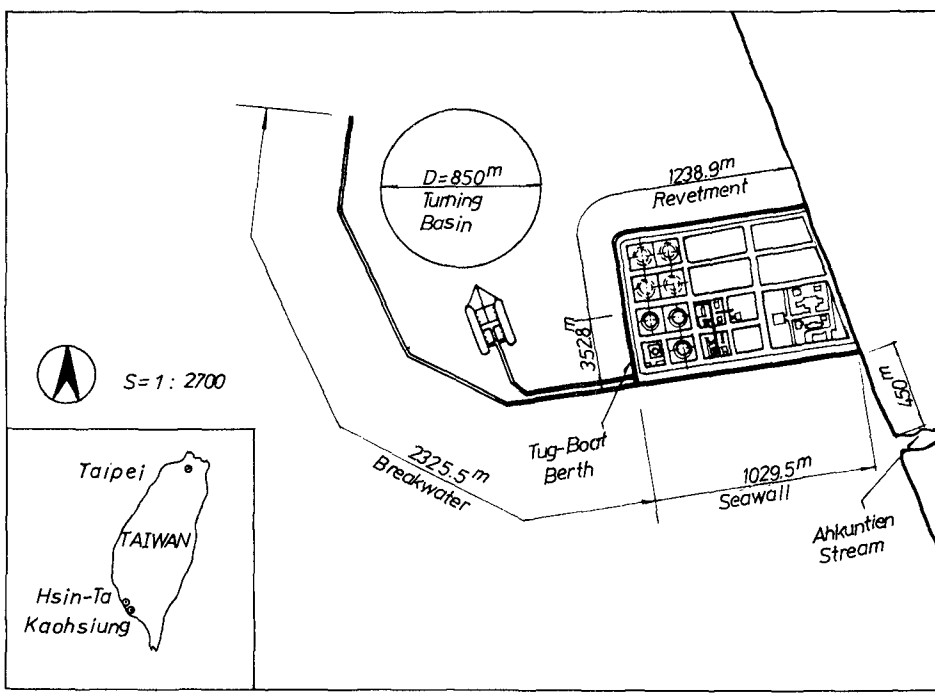

Fig. 1. General Layout of Hsin-Ta LNG Terminal

2.2.3 Cross sections of seawall and revetment

The seawall and revetment of Hsin-Ta LNG Terminal were first divided into a number of sections, and then designed according to each corresponding water depth and local wave conditions. The typical cross sections of rubble mound and composite caission type structures are plotted in Fig.2~Fig.4.

2.3 Feather of the Project

Perhaps the most interesting feature of this project in comparison with other typical ports is the single-armed southern breakwater. The orientation of the coastline along the site is in NNW direction, which effectively protects the Terminal against waves from N to E, whereas waves can approach the site directly from S to W. Hence the single-armed southern breakwater is secure enough to protect the berth from incident waves. The problem of seich is then relatively trivial, due to the opening nature of this harbor entrance.

3. Construction Process

This project has been scheduled to be completed within a short period of 5 years. Therefore the building procedure of the breakwater, land reclamation, storage tanks, and transportation pipes system need to be closely coordinated. In general, Hsin-Ta LNG Terminal consists of three major tasks, i.e., 1) construction of on-shore harbor; 2) land reclamation (about 70 hectares) for working-yards; 3) construction of in-ground LNG storage tanks & associated facilities. The actual execution of the project was started in September, 1984.

3.1 On-shore Harbor

In order to execute the project, BES Engineering Corporation has mobilized a lot of machines, vehicles, agitators, and working vessels. First of all, the rubble mound seawall and revetment were built to protect the reclaimed land from being washed away by waves. Graded seasands were dredged to supersede the soft soil for improving some parts of the foundation of seawall and revetment. Filter fabric was spread out along the orientation of the coastal structure against settlement. Next the rubble was dumped over the filter fabric by dump trucks or bottom-opening stone carriers. After being leveled by bulldozers or divers, the crown wall was then cast in place. The seaward toe of the rubble mound has been protected first by cobble of 4.0cm~10.0cm in size with a slope of 1:1.5 which is 1.5 m thick, and second by 2 layers of concrete armor units which are about 2.0 m thick with a slope of 1:2. On the other side, i.e. harbor side, the coastal structure was backfilled by dredged seasand and covered with a layer of masonry for protection.

As the water depth got deeper than - 8.5 m, the composite caission type structure was adopted. Caissions were made in Anping harbor where is about 30Km to the north of the site, and were towed to the site during suitable maritime conditions. Once the caission was placed on the designated position, concrete blocks were sunk immediately to guard the toe of the caission. in order to keep facilities inside the Terminal safe enough during storms, a "curtain wall " has been built up along the harbor side of the seawall and revetment against wave overtopping. Thus far, 1030.0 m of

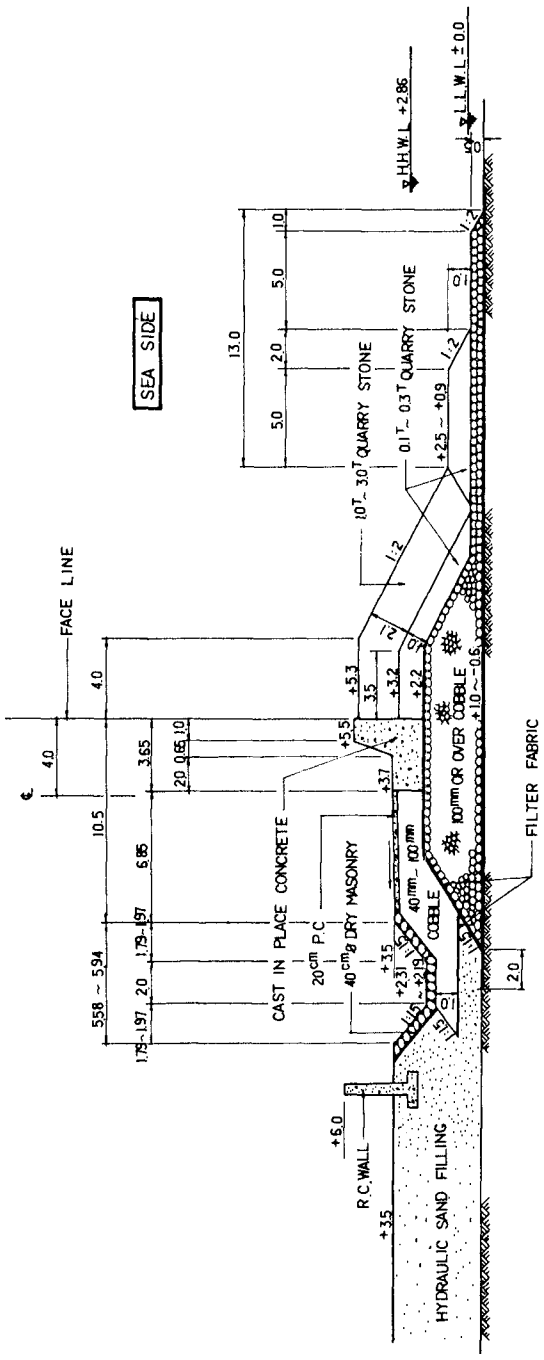

Fig. 2. Typical Cross Section of Revetment (rubble mound)

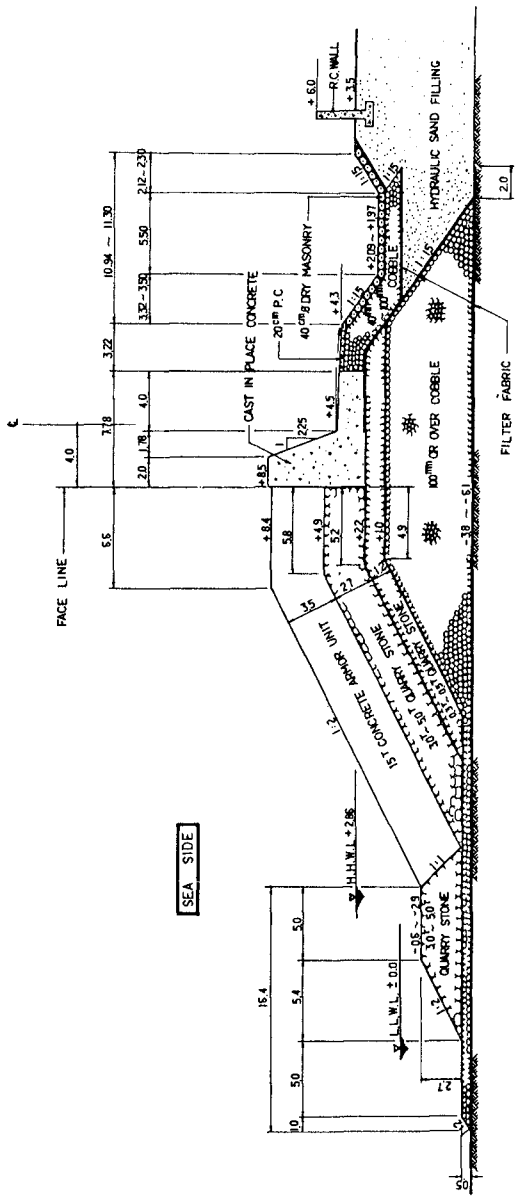

Fig. 3. Typical Cross Section of Seawall (rubble mound)

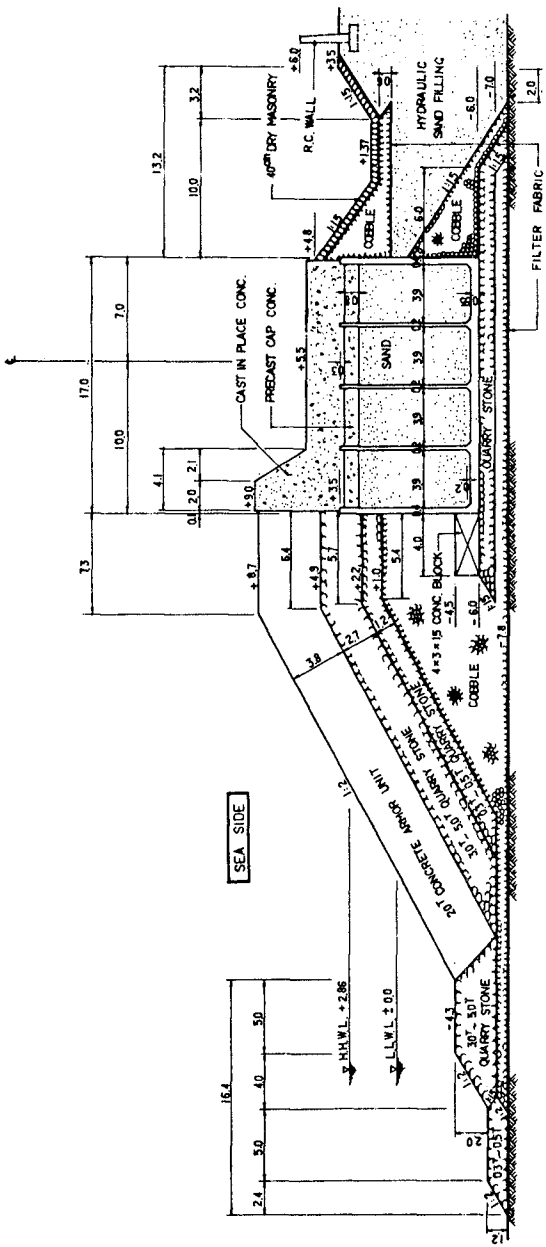

Fig. 4. Typical Cross Section of Seawall/Breakwater (composite caission type)

seawall, 670.0 m of revetment, 703.0 m of permanent and temporary workingboat wharves, and 730.0m of temporary revetment have been completed.

3.2 Land Reclamation

The required working-yards were reclaimed by hydraulic backfilling while building seawall and revetment, as shown in Photo. 1. More than 4.1 million cubic meters of filling volumes have been executed by suction dredger. The total dredged volumes will come to 7.1 million cubic meters.

Owing to the desire of completion by 1989 the storage-yards for the LNG Tanks were reclaimed prior to other places. Several types of concrete armor units were put in place to protect the reclaimed land after each subphase had been finished.

3.3 In-ground LNG Storage Tanks

The tanks are being constructed using the top-down method. The slurry wall was built first. After the excavation of earth was finished, draining filters and steel/butyl waterstops were fixed upon the slurry wall in order to drain and resist possible permeating groundwater respectively. Steel work and form work were subsequently installed. After adjusting each section into its designated position, concrete was then cast in place. With the similar procedure performed downwards, three tanks are expected to be completed by late 1988.

Photo 1. Aerophoto of Hsin-Ta LNG Terminal (under construction)

4. ACKNOWLEDGEMENTS

The authors wish to thank the Chinese Petroleum Corporation and the China Engineering Consultants Inc. for their assistance in providing relevant technical data. The support and encouragement from project manager F.C. Kuo and all colleagues in the Hsin-Ta Construction Station are also highly appreciated by the authors.

CHAPTER 190

THE INFLUENCE OF WAVES ON THE HYDRAULICS OF SEA OUTFALLS

by

Torben Larsen
University of Aalborg
Sohngaardsholmsvej 57, DK-9000 Aalborg, Denmark

1. INTRODUCTION

Most of the larger cities in Denmark are located near the sea. About 60% of the sewage is therefore discharged through sea outfalls. Most of these sea outfalls were built in the seventies. In most cases a plastic pipeline were used, and the pipeline was ballasted with armoured concrete blocks and burried in a trench 1 - 2 m underneath the seabottom. To give the necessary initial dilution a diffusor with one or several contracted, horizontal outlets ends the pipeline.

The Danish coasts are in general shallow and exposed to waves. The littoral sanddrift is considerably and the sea outfalls need to cross one or more bars. The diffusors are often placed outside the bars, but nevertheless sediment transport can occur around the diffusor. Figure 1 gives some typical data for Danish sea outfalls.

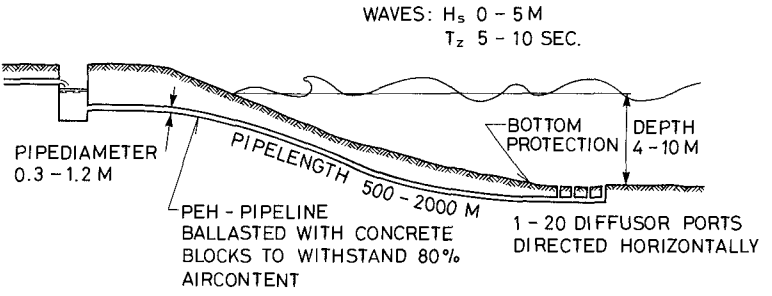

Figure 1. Range of data for Danish sea outfalls.

As a large number of outfalls were designed and established in a short span of time, the practical problems of placing such a rather sophisticated structure in one of the most difficult areas were often underestimated. Many failures have been seen and a considerably num-

ber of sea outfalls have an insufficient function. A typical problem is the sediment intrusion into the diffusor, which can block up the ports, and another example is the lifting of the pipeline due to airpockets and insufficient sandcover of the pipe.

This paper discusses some hydraulic aspects of the influence of waves on the pipeline and the diffusor. These effects have not been reported earlier and they might in some cases be connected to the mentioned failures, but it is not pretended that they are general key points in the design of sea outfalls.

2. NUMERICAL MODEL

It is obvious that the influence of waves on the hydraulics of sea outfalls needs an unsteady description and, furthermore, it is also obvious that due to the important non-linear friction analytical solutions are out of question. The straight-forward procedure is then to apply a numerical computer-model.

The numerical model is basically an extension of a water hammer model. The water hammer theory for the unsteady flow in an elastic pipeline is based on the simultaneous solution of the equations of motion for each discrete pipesection all along the pipeline. The equations of motion are the conservation of momentum (1) and theconservation of mass (continuity) (2) including the elasticity of the water and the pipe (Wylie and Streeter, 1983):

$$g \frac{\partial H}{\partial x} + V \frac{\partial V}{\partial x} + \frac{\partial V}{\partial t} + F \frac{V^2}{2d} = 0 \tag{1}$$

$$\frac{a^2}{g} \frac{\partial V}{\partial x} + \frac{\partial H}{\partial x} + \frac{\partial H}{\partial t} = 0 \tag{2}$$

where

g acceleration of gravity
H hydraulic head
x distance along pipeline
V velocity
t time
f Darcy-Weisbach friction factor
d diameter of pipeline
a wave celerety for unsteady flow

The wave celerety, a, for pressure and velocity changes is app. 300-400 m/sec in a plastic pipeline and 1,100-1,300 m/sec in a steel pipeline, which are the extremes of practical pipelines in this respect.

2.1 The method of characteristics

To solve the equations (1) and (2) the method of characteristics is convenient. The idea of

this method is to choose a computational grid, in which the equations are simplified to a pair of ordinary differential equations (see again Wylie and Streeter, 1983).

The unkowns are the hydraulic head H_p and the velocity in the new point P, figure 2. These are calculated from known values in the two points i−1 and i+1 one time-step earlicr.

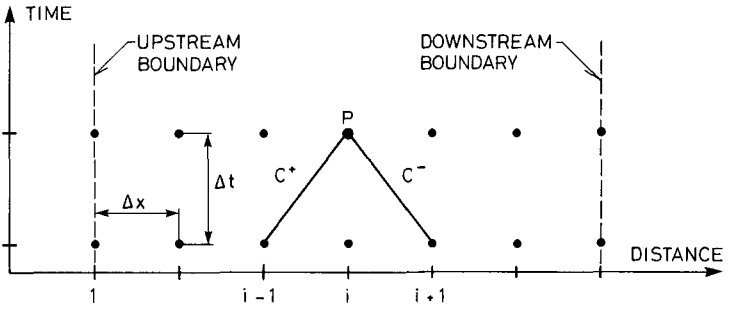

Figure 2. Computational grid for method of characteristics.

2.2 Upstream boundary condition

The upstream boundary condition will often be a pump or a reservoir. Most critical is the reservoir, because of the reflection of the fluctuations. A running pump on the other hand absorbs most of the fluctuations in pressure and flow. But a stopped pump with a closed check valve should be considered if necessary.

In this study the upstream boundary was described by assuming a fixed head in the upstream reservoir and a hydraulic entrance head loss between the reservoir and the pipeline.

2.3 The diffusor boundary

The downstream boundary is the multiport diffusor with the unsteady pressure field from the waves moving across the diffusor ports. From physical arguments it can be stated that the effect of elasticity can be neglected in the diffusor. Consequently the conservation of mass and momentum can be solved in an ordinary finite difference scheme where the non-linear terms required a solution by iteration.

The moving hydraulic head outside the ports was computed based on linear wave theory. Both the effect of monocromatic waves and complex wind waves have been studied. The wind waves were simulated accordingly to the JONSWAP - spectrum (Hasselmann, 1973). This rather narrow spectrum is known to fit well to the fetch limited wave climate around Denmark. It was assumed that the wave energy travelled in the same direction. This assumption showed out to be acceptable as seen later on.

The linear wave theory gives the following hydraulic head outside each diffusor port

$$H_D = \sum_{i=1}^{n} \left[a_i \sin(\omega_i t + k_i x + \varphi_i) \right] / (\cosh(k_i h))$$

where

H_D	head outside the diffusor
a_i	surface amplitude of wave component
$\omega_i = 2\pi f_i$	cyclic frequency of wave component
$k_i = 2\pi / L_i$	wave number
L_i	wave length
φ_i	random phase
h	depth of water

The surface amplitude a_i was found from the JONSWAP - spectrum

$$S(f) = \frac{\alpha g^2}{(2\pi)^4} f^{-5} \exp\left[-\frac{5}{4} \left(\frac{f}{f_m}\right)^{-4} \right] \gamma^{\exp\left[-\frac{1}{2\sigma^2} \left(\frac{f}{f_m} - 1\right)^2 \right]}$$

where

α	$= 0.076 x^{-0.22}$	factor
x	$= g F U_{10}^{-2}$	factor
f_m	$= \dfrac{3.5\, g\, x^{-0.33}}{U_{10}}$	peak frequency
γ	$= 3.3$	factor
σ	$= \begin{cases} 0.07 & \text{if } f \leqslant f_m \\ 0.09 & \text{if } f > f_m \end{cases}$	
F		fetch
U_{10}		wind velocity

3. RESULTS

As the result of this first step of research is the computer model described above, it feels naturally not to give general conclusions but only some typical examples. Figure 3 shows data for the sea outfall used in the following examples.

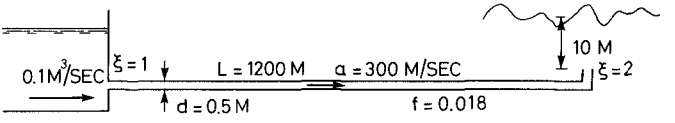

Figure 3. Data for examples.

3.1 Total hydraulic capacity

The total head loss in the pipeline is not significant increased due to the waves in the case of a single port diffusor. For the multiport diffusor a slight increase (0 - 5%) of the head loss can occur.

3.2 Resonance

It is well-known from physics that the wavelength of the basic mode standing wave in a pipeline open in each end is the double of the length of the pipe. The resonance period for a pipeline with L = 1200 m and a = 300 m/sec is then 8 sec. Figure 4 shows a timeplot of how this resonance built up from steady state.

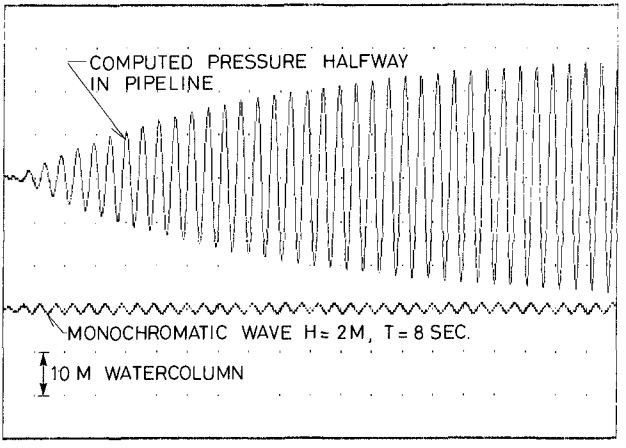

Figure 4. Resonance due to monochromatic waves.

Figure 5 shows the computed results if the waves are irregular according to the JONSWAP - spectrum.

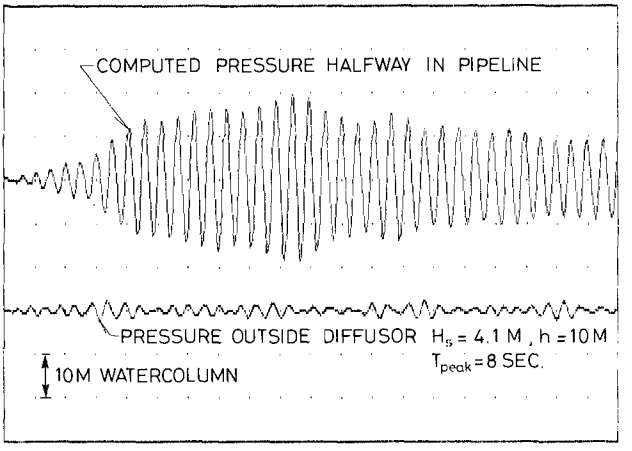

Figure 5. Resonance due to wind waves.

The figures show that the dampening of the standing waves apparently is very small and the pressure fluctuations are surprisingly large. For the moment this has not been experimental verified and the results can only be interpreted as an impulse to further studies.

The above mentioned examples are based on the basic mode of resonance in the pipeline. Resonance should of course be expected on other modes depending on the waves and the pipeline. The resonance periods for a pipeline open in each end are 2 L/a, L/a, 2/3 L/a, 1/2 L/a, etc. If the pipeline is closed in the upstream end (stopped pump and closed check valve) the first resonance periods are 4 L/a, 4/3 L/a, 4/5 L/a, etc. In this connection the long periods are expected to give the strongest resonance because of the lowest dampening.

3.3 Back flow in diffusor

In this example the outfall from figure 3 was connected to a diffusor with 5 ports with a diamater of 0.15 m and a head loss factor $\xi = 2.0$. Over this diffusor wind waves propagated as in figure 5 with $H_s = 4.1$m and $T_{peak} = 8$ sec. Furthermore, the length of the pipeline was L = 1500 m to avoid resonance. Figure 6 shows an instantaneous picture of the flow distribution, where the waves created a back flow in one of the ports.

From an analysis of the results it can be concluded that the unsteady flow in the diffusor to some degree follows the flow near the bottom due to the waves. As the head losses through the ports are smaller than the head fluctuations, it is understood that the local effect of the waves between two adjacent ports is most important. This knowledge can

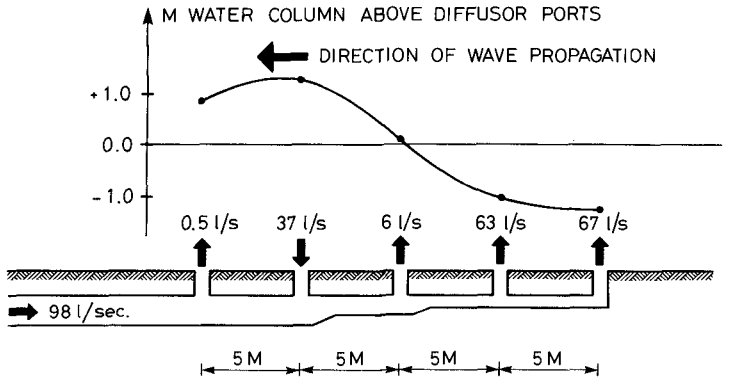

Figure 6. Instantaneous flow in diffusor under waves.

then support the assumption of only applying a uni-directional wave spectrum as the boundary condition to the computation; or with other words, the waves are not short-crested in relation to the distance between two diffusor ports, which only is a fraction of the water depth.

4. CONCLUSION

The results summarized above indicate that waves can cause interesting hydraulic phenomena in sea outfalls on shallow coasts. The results also explain why this has not been realized directly earlier; simply because the resonance in the main pipeline and the back flow in the diffusor cannot be observed in the upstream end of the pipeline.

The author will appreciate very much to be informed about observations on these effects.

5. REFERENCES

Hasselmann, K. et al. (1973): Measurements of Wind - Wave Growth and Swell Decay during the Joint North Sea Wave Project (JONSWAP). Deutsche Hydrographischen Zeitschrifft., Reihe A (8°), Nr. 12.

Wylie, E.B. and Streeter, L. (1983): Fluid Transients. FEB Press, Ann Arbour, Michigan.

CHAPTER 191

FIELD STUDIES OF BUOYANT JET IN COASTAL WATERS

Jeffrey P. Leighton (1), Associate Member, ASCE
Shuen-Wei Scott Tu (2), Member, ASCE

ABSTRACT

Studies were made on a surface buoyant jet from a coastal power plant. The cooling water discharges into shallow waters of irregular bottom topography forming a partially enclosed embayment that connects to the open ocean. Near field mixing was found to be influenced by bottom bathymetry, lateral confinement and a large obstruction. Surface centerline temperature decay, bottom separation and the heat and mass distribution within the embayment were analyzed.

INTRODUCTION

Much of the work on surface buoyant jets has been limited to the case where bottom and side boundary effects are absent. This is not the condition for Diablo Canyon Power Plant on the California Coast of the USA. The cooling water system discharges into shallow waters of irregular bottom topography forming a partially enclosed embayment that connects to the open ocean (see figure 1). Prototype studies were conducted during power ascension testing of both units.

A discharge structure drops the condenser water down to ocean level through two chutes, one for each power plant unit. Cut-outs in the center divider wall allow for cross-over mixing when the unit flow rates are different. There are two cooling water pumps available for each unit; each pump has a maximum capacity of 28 m^3/s. Data were collected during periods when the discharge waters represented: coflowing buoyant and non-buoyant jets (4 cooling water pumps and 1 power plant unit in operation-4P/1U); two coflowing buoyant jets of different densities less than ambient but similar discharge volume (4 pumps and 2 units in operation- 4P/2U); and two coflowing buoyant jets of similar density but different discharge volume (2 pumps and 1 unit in operation- 2P/1U). The tide level controls the initial jet depth. At full load and discharge flow, the temperature rise of the cooling water is 10.8^{o}C.

DATA COLLECTION

A field data collection program was implemented to describe the 3-dimensional receiving water temperature and velocity field. Near-field temperatures in the upper water column were measured along transects with a vertical temperature array. Thermistors were placed down to 10 feet below the surface; data were recorded at 10 second intervals automatically in a self-contained data recording unit. Vertical temperature profiles and far-field surface temperatures were measured with profiling and towed bathythermographs, respectively. A thermistor array with data recorder was configured to be used as a free-floating drogue to determine temperature decay along or near the plume centerline. Plastic drogues were also tracked to determine plume veloci-

(1) Civil Engineer, Pacific Gas and Electric Company, 3400 Crow Canyon Rd., San Ramon, CA 94583
(2) Research Engineer, Pacific Gas and Electric Company, 3400 Crow Canyon Rd., San Ramon, CA 94583

ties and ambient currents. Moored current meters were deployed in some tests at the cove entrances at two depths. Boats were equipped either with a range-azimuth microwave navigation system or with retroprisms for a shore-based laser electronic distance measuring system for boat position. Data were taken on intake and discharge temperatures, tide, wind and wave conditions.

The test methods and data analysis results during power ascension testing of Unit 1 are presented in Leighton et al. (1986), and for Unit 2 in Tu et al. (1986). Emphasis will be given here to test data collected during power ascension testing of Unit 1 (see Table 1). A total of more than 50 field tests were made. A test series usually consisted of multiple data collection periods with a common power plant discharge condition, but with differences in tide, wind, wave and offshore current direction and magnitude.

RESULTS

Centerline surface temperature decay

The excess surface temperature was plotted against the ratio of distance traveled to equivalent discharge diameter, $D = (h_o\, b_o)^{.5}$, where b_o = plume half-width, and h_o = initial plume depth. The power law index, n, was determined for the relation: $\Delta T(x)/\Delta T_o \sim (x/D)^{-n}$, where ΔT_o = discharge temperature rise.

With data for the 2P/1U case, for $x/D < 30$, with one exception, $n = 0$, and for x/D between 30 and 70, $0.5 < n < 1.0$. When the data for 7 tests (2P/1U) are plotted simultaneously, using the equivalent diameter as the length scale, there is significant scatter (see figure 2). When scaling is made with the initial densimetric Froude number (F_o) and aspect ratio (AR), there is significantly reduced scatter (see figure 3). The abscissa is divided by the formula for the transition distance for deep water jets developed by Stolzenbach and Harleman (1971): $12(h_o b_o)^{.5} F_o AR^{.05}$. The ordinate is scaled by the initial densimetric Froude number.

Bottom separation

Bottom detachment was estimated from vertical temperature profiles near the plume centerline, where the bottom excess temperature nearest to the outfall equals zero. The near-field penetration depth varied from 4.5 to 11 meters (see table 2).

The maximum plume depth was not correlated with tide, and poorly correlated with initial densimetric Froude number. The ratio of maximum penetration depth (h_{max}) to initial plume depth (h_o) does show a correlation with initial densimetric Froude number (F_o), based on the initial depth. The results of analyzing 14 tests (2P/1U and 4P/2U) with $5.4 < F_o < 38$ (Tu et al., 1986), gave a best-fit equation of:
$h_{max} = .46\, F_o^{.87}\, h_o$ with a correlation of .91. The empirical equation of Safaie (1978):
$h_{max} = .91\, F_o^{.50}\, h_o$ worked well in the range $5.4 < F_o < 12$, but was a poor predictor at extreme low tides, or high Froude number.

At lift-off (or bottom drop-off), the estimated local densimetric Froude number was of value 1.5, based on the results of 4 tests.

Heat and Mass Flux Balance

Since the discharge cove is semi-enclosed, it was possible to obtain velocity and temperature data sufficient to describe the cross-sectional variation in momentum and buoyancy. Vertical temperature profiles and thermistor transect data were used for temperature; drogues with center of mass at 1.2, 2.5 and 5 meters were tracked for velocity. Results are presented in Table 3.

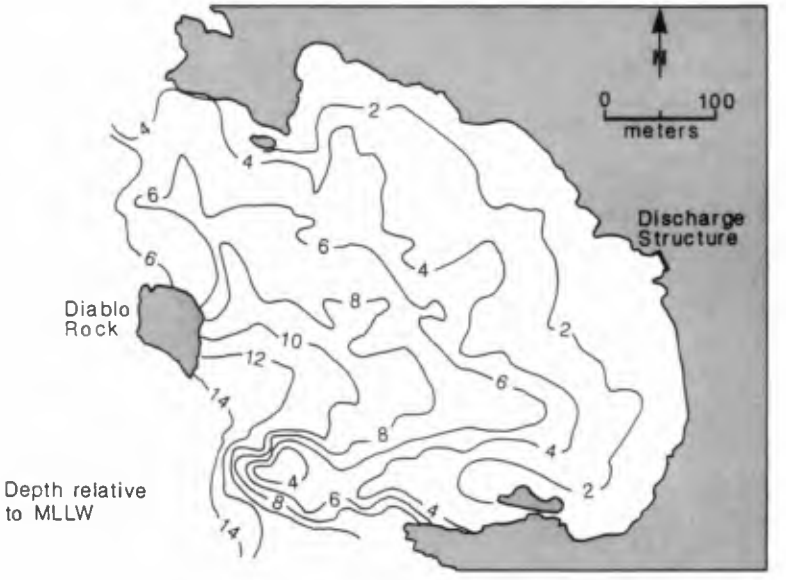

Figure 1. Bathymetry in Diablo Cove

Table 1. Conditions of Selected Tests

Test	Discharge Conditions[1] Unit 1		Unit 2		Tide	Wind[2]	Wave	Offshore[2] Current
	m^3/s	°C	m^3/s	°C	m	m/s	m	m/s
2-HT1	44.1	8.8	40.8	0.3	.6	5.4-	.9	.23-
3-2	34.0	8.6	22.6	8.6	.1	4.5x	.8	.10-
3-3	34.0	9.0	22.6	8.9	.3	5.2+	1.0	.06x
4-1	34.0	9.5	22.6	9.4	.8	5.9-	1.6	.13-
4-3	34.0	9.4	22.6	9.3	.1	2.5-	1.8	.08x
5-1	56.6	10.3	56.6	0.7	.7	3.4x	1.6	.23x
5-2	56.6	10.4	56.6	0.8	.5	6.2+	2.0	.18+
5-4	56.6	11.1	56.6	0.4	.8	2.7+	1.6	.06-
6-2	34.0	10.6	22.6	10.4	.9	1.6+	.7	.15+
6-3	34.0	11.0	22.6	10.7	-.1	2.2-	.8	.28+
6-4	34.0	11.1	22.6	10.9	.9	5.6+	.8	.13+

(1) The cut-outs in the center divider wall allow the cross-over of water whenever unit flows are different. The values given refer to conditions at the end of the discharge structure, after the exchange has occurred (Ryan and Tu, 1985)
(2) The direction in which the wind (or current) is headed. A "+" indicates a downcoast movement, a "-" is for an upcoast movement, and an "x" denotes roughly shore normal movement.

Among the conclusions one can draw from this analysis: The plume is a surface condition outside the discharge cove, with an average of 85% of the excess temperature flux within the top 3 meters of the water column. At low tide, the buoyant jet is deflected more to the north, a result of the presence of parallel rock ridges within 75 meters of the discharge structure, with an orientation towards the north. We have found that this effect is reduced at higher tide level (where the ridges serve as bottom roughness instead of as deflectors) and higher initial momentum (as indicated in test 5-1, with 4 pumps). Consistent over-estimation of the heat flux out of the cove suggests some return flow of buoyant water, most likely on the east side of the north entrance, where data is sparse or non-existent.

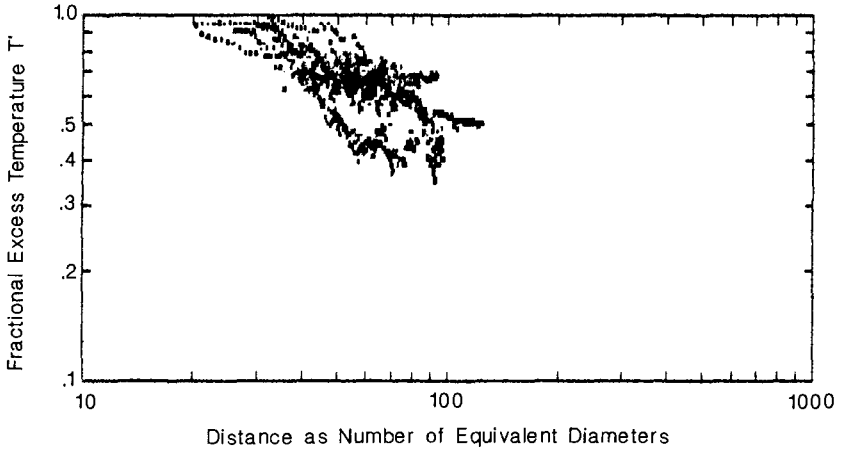

Figure 2. Surface Centerline Temperature Decay

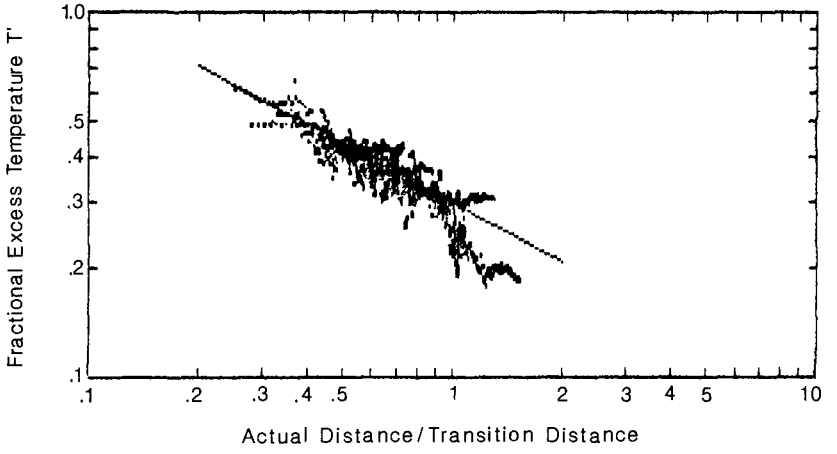

Figure 3. Scaled Temperature Decay

Table 2. Near-field Penetration Depth

Test	Discharge densimetric Froude number	Plume/Jet Depth Initial	Maximum	Local Froude No. At Lift-off
		m	m	
2-HT1	8.3	2.0	9.8	–
3-2	11.5	1.5	4.6	–
3-3	9.2	1.7	4.6	–
4-1	6.6	2.2	6.1	1.4
4-3	11.8	1.5	9.1	>.8
5-2	16.2	1.9	10.7	1.3
6-2	5.7	2.3	4.9	1.5
6-3	16.5	1.1	6.7	–
6-4	5.4	2.3	7.6	1.6

Table 3. Heat and Mass Balance

Test	Percent of Discharge Excess Temperature Flux West	North	Difference	In top 3 meters
2-HT1	82	12	6	ID
3-2	50	57	7	100
3-3	78	24	2	>80
4-1	96	68	64	80
4-3	98	36	34	87
5-1	112	0	12	72
6-2	97	28	25	84
6-3	53	53	6	95
6-4	106	-12	6	77

The effects of a large obstruction

Under most receiving water and discharge conditions, the buoyant jet trajectory is oriented towards Diablo Rock. This large obstruction to the flow has been observed to cause a bifurcation of the plume, upwelling in the wake of the island (see figure 4), and plume deepening on the inward side of the island. On the seaward side of the island, lateral temperature gradients as large as a $7^{o}C$ drop in 90 meters have been observed. The temperature of the water in the wake of the island is near or equal to the offshore ambient conditions. Imberger and McComb (1984) reported upwelling in the wake of Rattray Island in Australia.

Mixing between coflowing jets

Test 5-1 is a case involving coflowing buoyant and non-buoyant jets. We obtained data perpendicular to the jet, which showed the change with distance of the temperature gradient across the interface. Figure 5 shows that mixing between the coflowing jets is limited. The velocity shear between jets is less than between jet and stagnant ambient waters, which may explain why mixing is relatively limited.

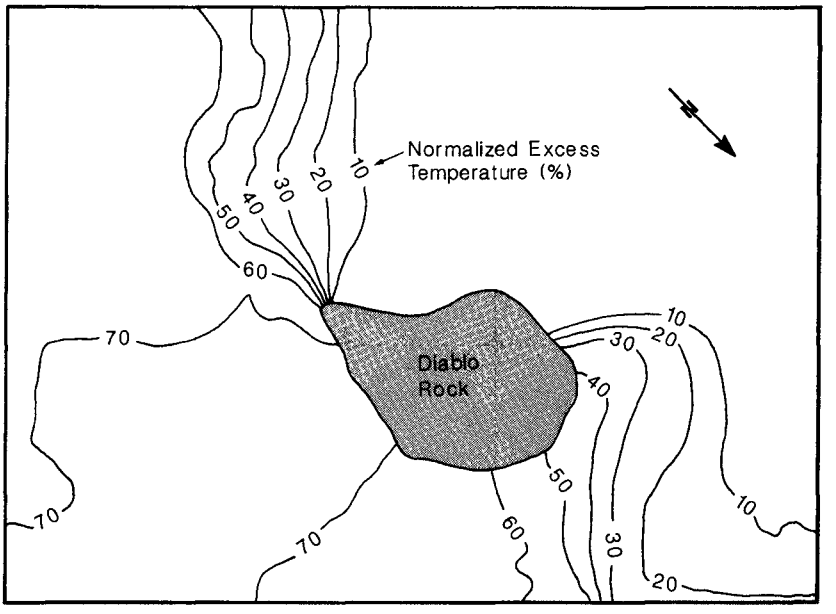

Figure 4. Surface Temperature Pattern around Diablo Rock

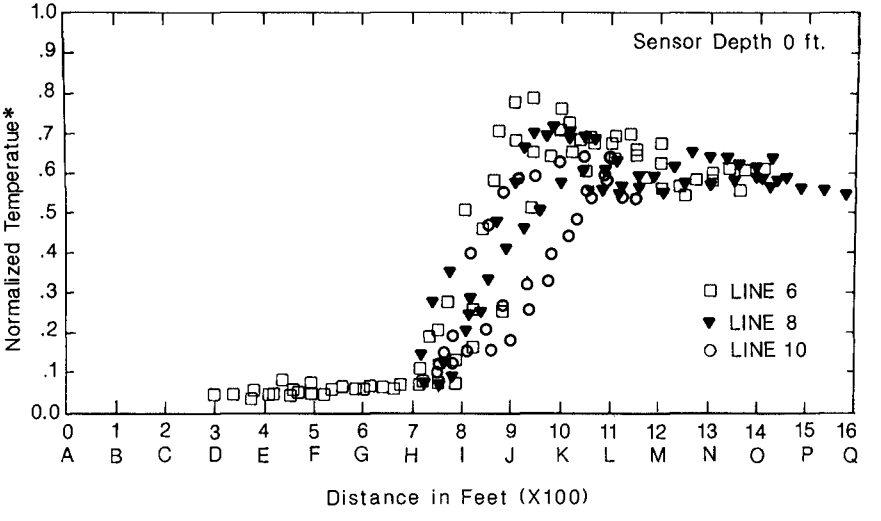

Figure 5. Temperature Transect Data for Test 5-1

Mixing at upcurrent edge between plume and receiving waters

A temperature gradient, as large as $4^{o}C$ in 25 meters, was measured at the upcurrent limit of horizontal spreading of the plume in the far-field. The presence of a warm water front, marked by a slick along which foam collected, has also been observed by Mimura and Horikawa (1982).

Offshore Plume Conditions

The offshore environment was found to have variable current conditions, in terms of both direction and magnitude. We see a variety of offshore plume centerline trajectories in figure 6. The ocean currents were found to be more a function of wind magnitude and directional persistence than the seasonal characteristics of the California Current. The winds at Diablo Canyon typically show a diurnal pattern and the plume can reverse direction within a day.

CONCLUSIONS

Data collection in the field has been made for a buoyant surface jet where near-field mixing is influenced by shallow waters, lateral confinement and a large obstruction. Maximum plume depth and centerline surface temperature decay can be described using standard scaling factors.

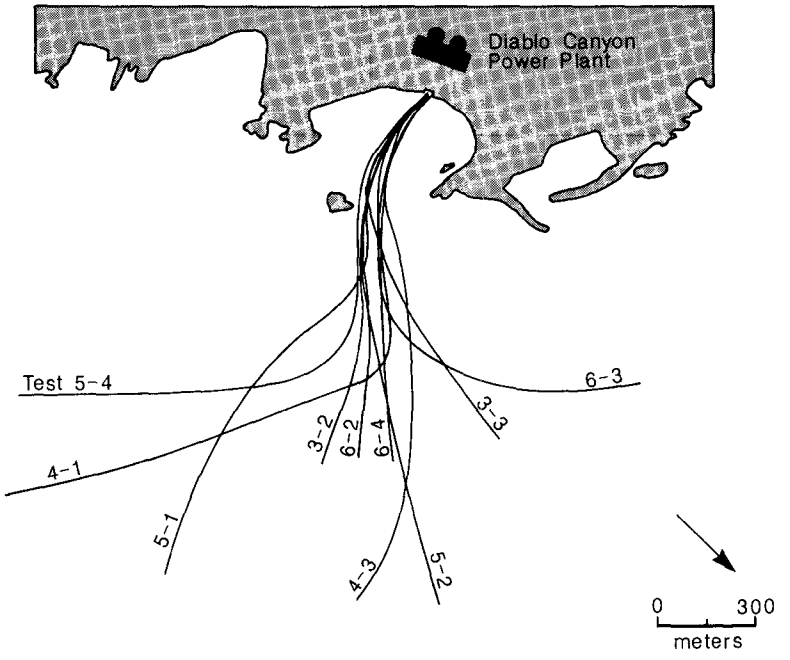

Figure 6. Offshore Plume Centerline Trajectories

REFERENCES

IMBERGER, J. and McCOMB, A.J. (1985), Water research 84. University of Western Australia.

LEIGHTON, J.P., TU, S.W., PETROCCITTO, A.A. and EASTMAN,L.K.,(1986), "Characterization of Receiving Water Temperatures During Power Ascension Testing of Unit 1 of Diablo Canyon Power Plant," Report 420-85.748, Department of Engineering Research, Pacific Gas and Electric Company, San Ramon, California, USA

MIMURA, N. and HORIKAWA, K.,(1982),"Diffusion Characteristics of Large Scale Heated Discharge in the Coastal Region," Coastal Engineering in Japan.

RYAN, P.J. and TU, S.W.,(1985), "Hydraulic Model Studies of Crossflow in the Diablo Canyon Power Plant Discharge Structure," Environmental Investigations At Diablo Canyon, 1984, Pacific Gas and Electric Company, Department of Engineering Research, San Ramon, California, USA

SAFAIE, B.,(1978),"Mixing of Horizontal Buoyant Surface Jet over Sloping Bottom," Ph.D. Dissertation, University of California, Berkeley

STOLZENBACH, K.D. and HARLEMAN, D.R.F.,(1971),"An Analytical and Experimental Investigation of Surface Discharge of Heated Water,"R.M.Parsons Laboratory for Water Resources and Hydrodynamics, Department of Civil Engineering, M.I.T.

TU, S.W., LEIGHTON, J.P., WHITE, C.O. and HSU, C.C.,(1986),"Surface Buoyant Jet Characteristics of the Thermal Discharge Plume At Diablo Canyon Power Plant," Report 420-86.475, Department of Engineering Research, Pacific Gas and Electric Company, San Ramon, California, USA

CHAPTER 192

Studies of Tsunami Hazard
I. Chen Lin[1] and C. C. Tung[2], M.ASCE

ABSTRACT: Tsunami hazard is investigated using the indirect approach with simple seismological and hydrodynamic models. It is assumed that earthquakes of random magnitude may originate anywhere with equal likelihood from a single straight fault and the site is located on the perpendicular plane bisecting the fault. The ground displacement is instantaneous and consists of a block uplift type of movement which may be circular or elongated in the plan view. The hydrodynamic model is based on linear long wave theory wherein the ocean is of constant depth and infinite in the horizontal extent, and the earth is flat. Tsunami hazard is computed for various values of the parameters and a sensitivity study is carried out to examine the effect of certain parameters on hazard.

INTRODUCTION

Tsunami hazard has been investigated using various approaches. Where historical information and measurements regarding tsunami innundation are available, a direct statistical analysis has been used (Houston et al. 1977, Loomis, 1976, Wiegel, 1970). Where such data are scarce, resort has been made to Bayesian estimation (Rascon, 1975) and the concept of indirect analysis (Garcia and Houston, 1975, Houston and Garcia, 1974). The indirect method follows closely the idea underlying seismic hazard analysis for facilities on land (Cornell, 1968, Der Kiureghian and Ang, 1975). The indirect approach, as carried out by Houston and Garcia (1974) and Garcia and Houston (1975), consists essentially of utilizing the information available regarding the magnitude, rate of occurrence and location of past tsunamigenic earthquakes in the region affecting the site, together with the knowledge of tsunami wave propagation based on hydrodynamic considerations to compute the hazard of tsunami at the site. Straightforward application of the indirect method of analysis, however, is time-consuming because of the large amount of numerical computation required to solve the hydrodynamic equations governing the propagation of tsunami waves from source to site. Since the frequency of occurrence, location, and magnitude of tsunamigenic earthquakes are random and there are uncertainties associated with some parameters and characteristics of ground motion, determination of the probability function of the wave elevation at the site due to tsunami by Monte Carlo simulation is difficult to achieve. It is therefore desirable that sensitivity studies be first performed to assess the importance of the various parameters on tsunami hazard. To conduct such an investigation,

[1]Assoc. Prof., Dept. of Hydraulic Engrg., Tam Kang Univ., Taipei, Taiwan Republic of China

[2]Prof., Dept. of Civil Engrg., North Carolina State Univ., Raleigh, NC, United States

the models employed must be sufficiently simple so that the probability computation may be kept at a minimum. For this purpose, an earlier study by Lin and Tung (1982) was undertaken.

In Lin and Tung (1982), it is assumed that earthquakes may originate anywhere with equal likelihood from a well-defined simple straight fault and the site is located on the perpendicular plane bisecting the fault (see Fig. 1a). The ground displacement consists of a block uplift type of movement which takes place instantaneously and is circular in the plan view with a uniform offset (see Fig. 1b). The source area S is empirically determined from the seismic moment m_o (see Fig. 2 and Eq. (4)) characterized by the value of the parameter C_1 and the magnitude of offset $\bar{D}$ is related to the seismic moment m_o by way of definition (see Eq. (3)). The seismic moment in turn depends on the frequency of occurrence of tsunamigenic earthquakes in the region (see Fig. 3) defined by the parameter β from which the probability density function of seismic moment is obtained (see Eq. (12) and Lin and Tung, 1982). The hydrodynamic model is that of linear dispersive waves given by Kajiura (1963) wherein the ocean is infinite in the horizontal extent, sphericity of the earth is ignored and water is of constant depth. The maximum wave elevation at the site due to earthquake of seismic moment m_o is shown by Lin and Tung (1982) to be given by

$$Z = CW\left(\frac{m_o}{r}\right) \tag{1}$$

where C is a constant, $W(\cdot)$ is a nonlinear function and

$$r = (D^2 + r_o^2)^{1/2} \tag{2}$$

is the distance from the source to the site (see Fig. 1) the probability density function of which may be obtained from that of the uniformly distributed random variable D. The tsunami hazard is shown to be simply dependent on $U(z) = P(Z > z) = 1 - F_Z(z)$ where $P(\cdot)$ denotes the probability of the event enclosed in the parentheses and $F_Z(z) = P(Z < z)$ is the probability distribution function of Z which is determined from the probability density functions of the statistically independent random variables m_o and r according to Eq. (1). A sensitivity study is performed to determine the influence of the various parameters on the hazard. The parameters considered are β (see Fig. 3), fault length L (see Fig. 1), C_1 (see Fig. 2) and the upper-bound seismic moment m_{ou}. It is found that values of β and L have little effect on the hazard but the hazard is sensitive to the values of C_1 and m_{ou} if one is interested in large values of tsunami wave elevation at the site. The obvious implication of this finding is that the values of C_1 and m_{ou} must be selected with care when important facilities are designed against extreme conditions.

In the above study, an important feature of the tsunamigenic earthquake that is left out of consideration is the shape of ground displacement. It is known that the ground displacements associated with tsunamigenic earthquakes are generally elongated in the plan view (see Figs. 4 and 5) and their orientation has significant effect on tsunami wave height at the site (Kajiura, 1970).

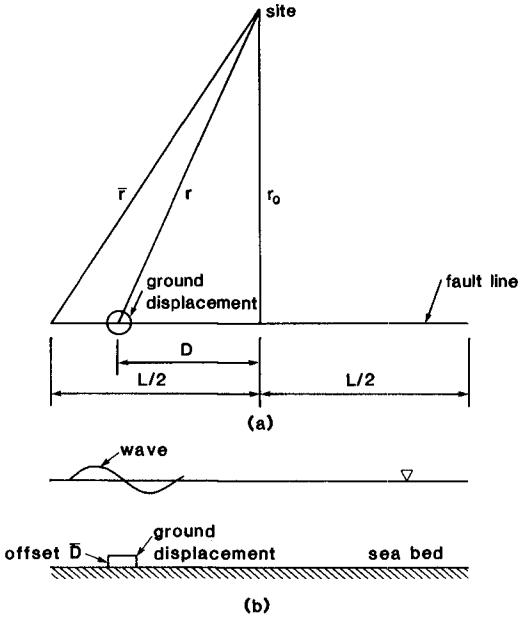

Figure 1. Seismic Model Used in Lin and Tung (1982)

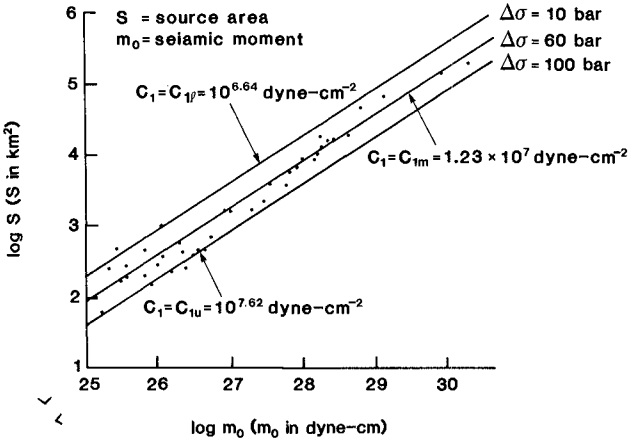

Figure 2. S - m_o Relation

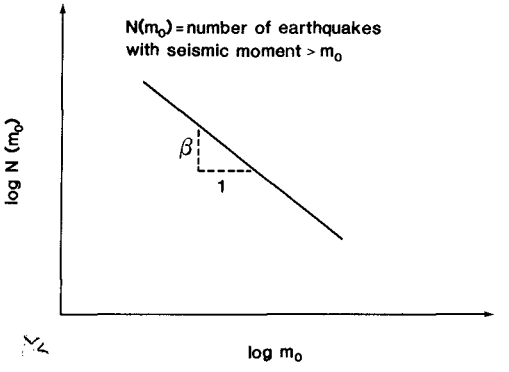

Figure 3. $N(m_o) - m_o$ Relation

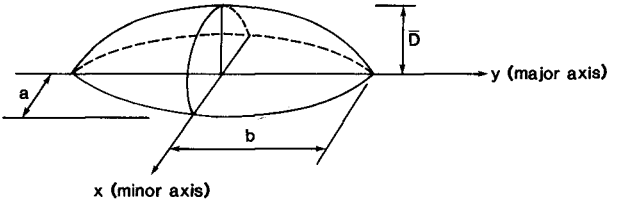

Figure 4. Ground Displacement

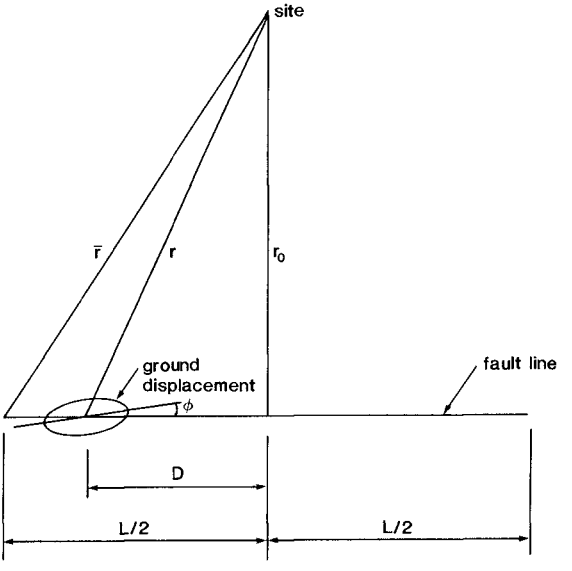

Figure 5. Source - Site Relation

The objective of this study is to consider elongated ground displacement. Specifically, the ground displacement is elliptical in the plan view with an elliptical crest (see Fig. 4). The remaining part of the seismological model is the same as that used in the earlier study (Lin and Tung, 1982) (see Fig. 1). That is, earthquakes may occur anywhere along a straight fault with equal likelihood and the site is situated on the perpendicular bisector of the fault. These assumptions may be removed without causing undue difficulty as pointed out by Der Kiureghian and Ang (1975). In fact, a finite number of fault lines with arbitrary orientation and location with respect to the site may be included. The major axis of the elliptical ground displacement may be inclined making an angle ϕ with the fault (see Fig. 5) and ϕ is taken as a random variable uniformly distributed in the arbitrarily chosen range $(-\pi/12, \pi/12)$. The hydrodynamic model in this study is different from the linear dispersive wave model used in Lin and Tung (1982) and is based on the linear non-dispersive long wave theory given by Kajiura (1970) wherein the ocean floor is also considered flat, the water is of constant depth and infinite in the horizontal extent. The reasons for selecting this particular model are (a) the resulting expression of wave elevation due to tsunami waves at the site is convenient to use and (b) when the elliptical ground displacement (see Fig. 4) is specialized to circular shape, the results may be checked against those obtained in the earlier study (Lin and Tung, 1982) to examine the sensitivity of the hazard to the two different hydrodynamic models used.

Numerical results of tsunami hazard are obtained for various value of the parameters. Since it is found in Lin and Tung (1982) that the values of β (Fig. 3) and fault length L (Fig. 1 or 5) have little effect on the hazard, these quantities are given fixed values. The remaining parameters, the site-fault distance r_o (see Fig. 5) and the shape factor B = b/a (see Fig. 4) are assigned various values in this study. A sensitivity study is performed to evaluate the effect of the upper bound seismic moment m_{ou} and the value of C_1 (see Fig. 2) on the hazard.

In the following, for easy reference, relevant details of the seismological and hydrodynamic models used in this study, shown in more detail in Lin (1985), are given.

SEISMOLOGICAL MODEL

The seismic moment denoted m_o is defined as (Kanamori and Anderson, 1975, Kanamori, 1977)

$$m_o = \mu S \bar{D} \tag{3}$$

where μ is the rigidity of the medium, S is the plane area of ground displacement and $\bar{D}$ is the average offset (see Fig. 4). Based on earthquake data, Kanormi and Anderson (1975) obtained the empirical relation between the seismic moment m_o and the source area S given by

$$m_o = C_1 S^{3/2} \tag{4}$$

as shown in Fig. 2 where the average value of C_1 is $C_{1m} = 1.23 \times 10^7$ dyne-cm^{-2} with S measured in square centimeters. From Eqns. (3) and (4), the average offset $\bar{D}$ is

$$\bar{D} = \frac{(m_o C_1^2)^{1/3}}{\mu} \tag{5}$$

For elliptical ground displacement

$$S = \pi ab = \pi a^2 B \tag{6}$$

where $B = b/a$ is the shape factor so that

$$a = \frac{(m_o/C_1)^{1/3}}{(\pi B)^{1/2}} \tag{7}$$

It is seen that the source area S (hence a and b) and the offset $\bar{D}$ of the ground displacement are all simply related to the seismic moment m_o.

HYDRODYNAMIC MODEL

The hydrodynamic model is that of linear non-dispersive long waves due to Kajiura (1970) in which the earth's sphericity is ignored and the ocean is assumed to be of infinite horizontal extent and constant depth. The maximum wave elevation at the site due to an instantaneous elliptical ground displacement shown in Figs. 4 and 5 is given by

$$Z = A_1 \frac{\sqrt{m_o}}{q} \tag{8}$$

Details of the derivation of Eq. (8) are given in Lin (1985) and are not shown here. In Eq. (8),

$$A_1 = \frac{0.495}{\mu} \left(\frac{C_1^2 B^3}{\pi}\right)^{1/4} \tag{9}$$

is a constant and

$$q = \frac{(A_2 D^2 + A_3 D - A_4 + A_2 r_o^2)^{3/4}}{(D^2 + r_o^2)^{1/2}} \tag{10}$$

where

$$A_2 = 1 + (B^2 - 1)\cos^2\phi$$

$$A_3 = r_o(B^2 - 1)\sin 2\phi \tag{11}$$

and

$$A_4 = r_o^2(B^2 - 1)\cos 2\phi$$

The quantities D, r_o and ϕ are all defined in Fig. 5.

Hazard Analysis

In Eq. (8), the maximum wave elevation Z at the site is a function of the random seismic moment m_o, the uniformly distributed random variable D specifying the location of the source, and the uniformly distributed random variable ϕ, representing the angle between the major axis of the ellipse and the fault line. The three random variables are assumed to be statistically independent and the probability density function of m_o was determined in Lin and Tung (1982) to be

$$f_{m_o}(m_o) = \nu\beta m_{o\ell}^{\beta} \frac{1}{(m_o)^{1+\beta}} \qquad m_{o\ell} \leq m_o < m_{ou} \tag{12}$$

where

$$\nu = \frac{1}{1 - \left(\frac{m_{o\ell}}{m_{ou}}\right)^{\beta}} \tag{13}$$

is a normalizing constant. Since earthquakes with seismic moments smaller than a certain lower limit have no engineering significance and the energy released by an earthquake is also limited, the lower and upper bound magnitudes, denoted $m_{o\ell}$ and m_{ou}, are specified.

The tsunami hazard is defined as the probability that for a given length of time, the water level Z at the site exceeds a certain specified value z. It is shown in Lin and Tung (1982) that the hazard depends on the knowledge of U(z), the probability that $Z > z$, given that an earthquake has occurred, which may be determined by the standard technique of transformation of random variables from Eqns. (8), (10), (11) and (12). Details of the manner in which U(z) is obtained is given in Lin (1985).

RESULTS

To compute U(z), the values of the parameters must be specified. It is assumed that the rigidity of the medium is $\mu = 3 \times 10^7$ dyne-cm^2, and the lower and upper-bound seismic moments are $m_{o\ell} = 10^{22.05}$ and $m_{ou} = 10^{29.55}$ dyne-cm which correspond to earthquake magnitudes $m_\ell = 4$ amd $m_u = 9$, respectively. In Lin and Tung (1980), it is found that the hazard is not sensitive to the values of β and fault length L. Thus, $\beta = 0.8$ and L = 6000 km are used here. In selecting the value of r_o, it is noted that the hydrodynamic model (Kajiura, 1970) used in this study requires that the site be at least moderately far away from the source; therefore values of r_o = 2000, 6000, and 10000 km are selected. To examine the effect of shape factor B = b/a on hazard, values of B = 1 and 5 are assigned, where B = 5 is the case as shown in Fig. 5 and B = 1 represents the case of circular ground displacement.

In Figs. 6 and 7, U(z) are plotted for B = 5 and 1 respectively and for r_o = 2000, 6000 and 10,000 km. The abscissa z is the wave elevation at the site in centimeters. Enlarged insets are inserted. Comparison

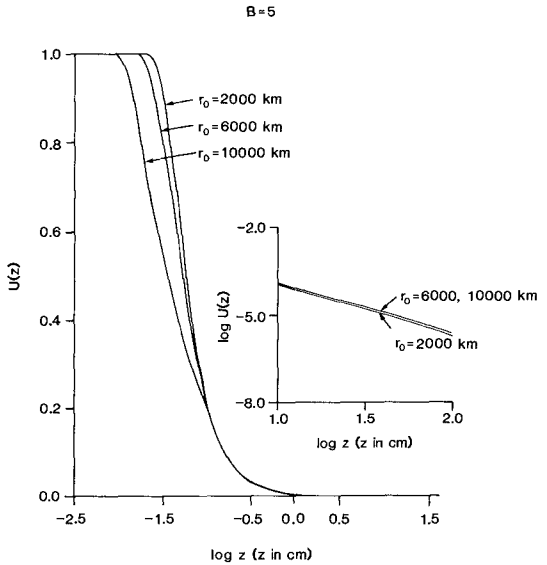

Figure 6. U(z) for B = 5

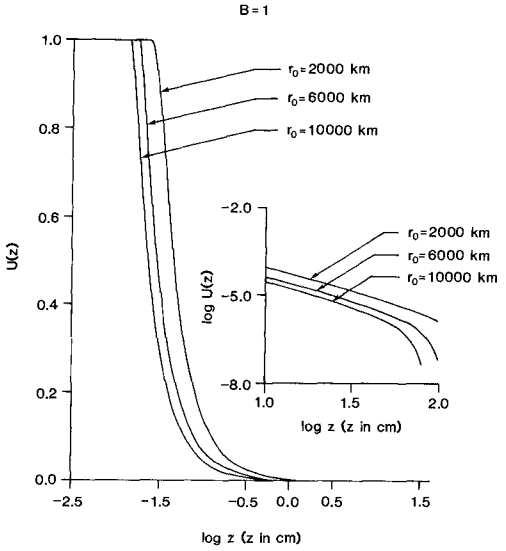

Figure 7. U(z) for B = 1

of Figs. 6 and 7 shows that the elongated ground displacement (B = 5) gives rise to larger values of the hazard.

It is of some interest to compare the results of the case B = 1 with those obtained in Lin and Tung (1982) in which the ground displacement is circular in its plan view. The hazard computed in the present case is much larger than in Lin and Tung (1982). This difference is due primarily to the two different hydrodynamic models used.

In obtaining the results shown in Figs. 6 and 7 we also considered the simplified case in which the angle ϕ between the major axis of the elliptical ground displacement (see Fig. 5) and the fault line is set identically equal to zero in which case the quantity q in Eq. (8) is simply related to the single random variable D as

$$q = \frac{(B^2D^2 + r_o^2)^{3/4}}{(D^2 + r_o^2)^{1/2}} \tag{14}$$

Our results show that the error incurred in U(z) is insignificantly small.

SENSITIVITY STUDIES

Many of the parameters in the models contain uncertainties. It is shown in Lin and Tung (1982) that uncertainties in the values of β and L do not affect the hazard to any significant extent. In this study, only the sensitivity of the hazard to the values of m_{ou} and C_1 are examined for different values of r_o and B.

Sensitivity of Hazard to Upper-bound Seismic Moment

To examine the sensitivity of the hazard to upper-bound seismic moment m_{ou}, U(z) is computed using different values of m_{ou} in much the same way as is done in Der Kiureghian and Ang (1975) and Lin and Tung (1982). For specified water level z, let $U_1(m_{ou})$ be the value of U(z) for the arbitrary value of m_{ou}, and U_2, the value of U(z) for $m_{ou} = 32$ dyne-cm. The ratio $\bar{R} = U_1(m_{ou})/U_2$, termed the hazard ratio, is plotted as a function of m_{ou} in Figs. 8 and 9 for B = 5 and B = 1 respectively for r_o = 2000 km and r_o = 10000 km. Fig. 8a (B = 5, r_o = 2000 km) shows that, for z = 50 cm, for example, if $m_{ou} = 10^{29}$ dyne-cm, the computed hazard is about 75% of that using $m_{ou} = 10^{32}$ dyne-cm. For $m_{ou} = 10^{31}$ dyne-cm, the ratio is close to unity. However, for z = 10 cm, a change of m_{ou} from 10^{32} to 10^{29} dyne-cm would result in a decrease of the hazard of only 3% (versus 25% for z = 50cm). That is, the influence of m_{ou} on the hazard is important when one is interested in large values of the maximum wave elevation at the site. Comparing Fig. 8a with Fig. 8b (r_o = 10000 km), it is seen that as r_o increases the curves become steeper indicating that the hazard is more sensitive to changes in m_{ou} if r_o is larger.

Figs. 9a and 9b are drawn for r_o = 2000 and 10000 km using B = 1 (circular ground displacement). The observations made above for the case B = 5 remain valid. Comparison of Figs. 8 and 9 shows that for the

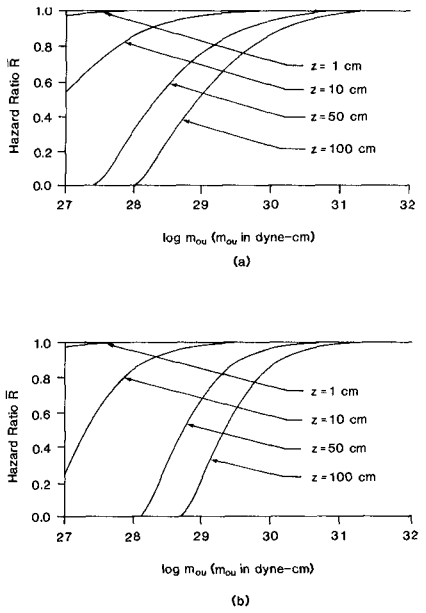

Figure 8. Hazard Ratio $\bar{R}$ for B = 5, r_o = 2000, 10000 km

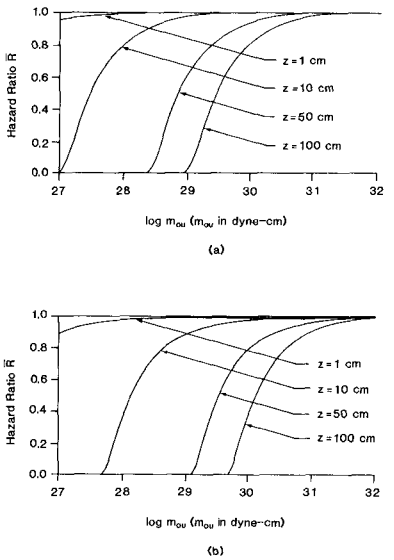

Figure 9. Hazard Ratio $\bar{R}$ for B = 1, r_o = 2000, 10000 km

same values of z and r_o, the curves in Fig. 9 are steeper. That is, the influence of m_{ou} on the hazard is more important when the ground displacement is considered to be circular in the plan view.

Sensitivity of Hazard to Value of C_1

Kanamori and Anderson (1975) used data of 41 earthquakes to construct Fig. 2 relating seismic moment and source area. The data points in the figure are scattered between stress drop values of $\Delta\sigma$ = 10 bars and $\Delta\sigma$ = 100 bars. The value of C_1 in Eq. (9) used in computing U(z) is $C_1 = C_{1m} = 1.23 \times 10^7$ dyne-cm^{-2} and is based on $\Delta\sigma$ = 60 bars. Corresponding to $\Delta\sigma$ = 10 and 100 bars, the values of C_1 are $C_{1\ell} = 10^{6.64}$ and $C_{1u} = 10^{7.62}$ dyne-cm^{-2} respectively. The subscripts ℓ, u and m are introduced to refer to lower and upper limits and mean value of C_1.

To examine the extent the value of C_1 affects the hazard, let $U_\ell(z)$, $U_m(z)$ and $U_u(z)$ be the hazard values corresponding to $C_1 = C_{1\ell}$, C_{1m} and C_{1u} respectively for arbitrary but specified values of z. The ratios $R_1 = U_\ell(z)/U_m(z)$ and $R_2 = U_u(z)/U_m(z)$ may be plotted as functions of z for various values of r_o and B. Fig. 10 gives R_1 and R_2 for r_o = 6000 km and B = 5. From the figure, it is seen that when z < 0.05 cm the ratios are near unity; for a wide range of z, from 0.05 cm to 50 cm, the ratios R_1 = 2.7 and R_2 = 0.4 remain practically constant and when z reaches 50 cm the ratios undergo a rather drastic change.

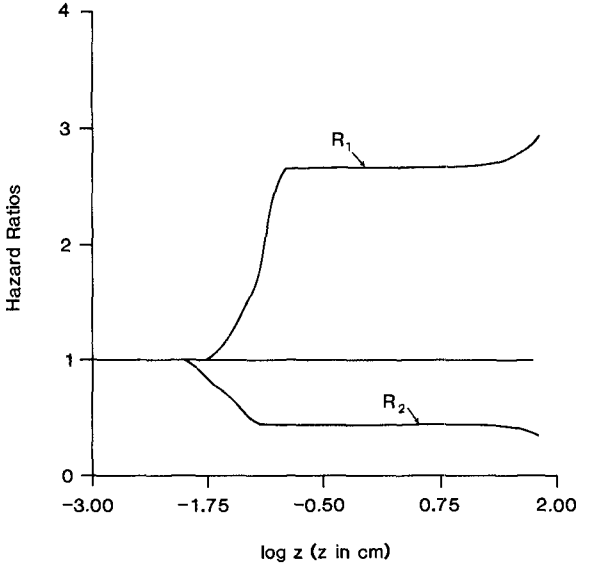

Figure 10. Hazard Ratios R_1 and R_2 for B = 5, r_o = 6000 km

Results were also obtained for B = 5 and r_o = 2000 and 10000 km, and for B = 1, r_o = 20000, 6000 and 10000 km. The ratios are almost identical to those shown in Fig. 10 and are therefore not given. Finally, comparison of these ratios with those of Lin and Tung (1982) shows that influence of C_1 on hazard is much more significant in the present case than in Lin and Tung (1982).

CONCLUSIONS

Based on the results of this study and those of Lin and Tung (1982), the following conclusions may be drawn:

(1) Shape of ground displacement (in plan view) has important effect on hazard; elongated ground displacement gives rise to larger values of hazard than circular ground displacement.

(2) The angle between the major axis of the elliptical ground displacement and the fault line need not be treated as random and may be set equal to zero without affecting hazard to any appreciable degree unless the geological condition indicates that the angle should assume a specific value.

(3) The hazard is critically dependent on water wave theory used.

(4) The value of upper-bound seismic moment has an important effect on the hazard if the maximum wave elevation of interest is large; more so if the site is further removed from the fault line and if ground displacement is circular in plan view.

(5) The hazard is appreciably affected by the value of C_1 for $z > 0.05$ cm.

(6) In future studies, elongated ground displacement should be used unless geological condition indicates otherwise.

ACKNOWLEDGMENTS

This paper is based on the doctoral dissertation of the first author and the research is supported in part by the National Science Foundation through a grant to North Carolina State University.

REFERENCES

Cornell, C. A., "Engineering Seismic Risk Analysis," Bulletin of the Seismological Society of America, Vol. 58, No. 5, 1968, pp. 1583-1606.

Der Kiureghian, A., and Ang, A. H-S., "A Line Source Model for Seismic Risk Analysis," Structural Research Series No. 419, UILU-ENG-75-2023, University of Illinois at Urbana-Champaign, Urbana, Illinois, 1975.

Garcia, A. W. and Houston, J. R., "Type 16 Flood Insurance Study: Tsunami Predictions for Monterey and San Francisco Bays and Puget Sound," Technical Report H-75-17, Hydraulic Laboratory, U. S. Army Engineer Waterways Experiment Station, Vicksburg, Mississippi, 1975.

Houston, J. R., Carver, R. D., and Marckle, D. G., "Tsunami-Wave Elevation Frequency of Occurrence for the Hawaii Islands," Technical Report H-77-16. Hydraulics Laboratory, U. S. Army Engineer Waterways Experiment Station, Vicksburg, Mississippi, 1977.

Hous

Houston, J. R., and Garcia, A. W., "Type 16 Flood Insurance Study: Tsunami Predictions for Pacific Coastal Communities," Technical Report H-74-3, Hydraulics Laboratory, U. S. Army Engineer Waterways Experiment Station, Vicksburg, Mississippi, 1974.

Kajiura, K., "The Leading Wave of a Tsunami," Bulletin of the Earthquake Research Institute, University of Tokyo, Tokyo, Japan, Vol. 41, 1963, pp. 535-571.

Kajiura, K., "Tsunami Source, Energy and the Directivity of Wave Radiation," Bulletin of the Earthquake Research Institute, University of Tokyo, Tokyo, Japan, Vol. 48, 1970, pp. 835-869.

Kanamori, H., "The Energy Release in Great Earthquakes," Journal of Geophysical Research, Vol. 85, No. 20, 1977, pp. 2981-2987.

Kanamori, H., and Anderson, D. L., "Theoretical Basis of Some Empirical Relations in Seismology," Bulletin of the Seismological Society of America, Vol. 65, No. 5, 1975, pp. 1073-1095.

Lin, I-Chen, "An Investigation of Tsunami Hazard," doctoral dissertation, North Carolina State University, Raleigh, North Carolina, 1985.

Lin, I-Chen, and Tung, C. C., "A Preliminary Investigation of Tsunami Hazard," Bulletin of the Seismological Society of America, Vol. 72, No. 6, 1982, pp. 2323-2337.

Loomis, H. C., "Tsunami Wave Run-up Heights in Hawaii," Report No. HIC-76-5, Hawaii Institute of Geophysical Research, University of Hawaii, Honolulu, Hawaii, 1976.

Rascon, O. A., and Villarreal, A. G., "On a Stochastic Model to Estimate Tsunami Risk," Journal of Hydraulic Research, Vol. 13, No. 4, 1975, pp. 383-403.

Wiegel, R. L. (ed.), Earthquake Engineering, Chapter 11, Prentice-Hall, Englewood Cliffs, New Jersey, 1970, pp. 253-306.

CHAPTER 193

A Three Dimensional Model of the Gulf of Alaska

Shiao-Kung Liu and Jan J. Leendertse

Abstract

This paper presents the development of a three dimensional model of the Gulf of Alaska. The model extends between the Vancouver Island and the Aleutian Islands covering approximatedly 1.5 million square kilometers over the northern Pacific Ocean. Formulated on an ellipsoidal horizontal grid and variable vertical grid, the model is schematized over a 81 x 53 x 10 grid structure. The solution scheme is implicit over the vertical and is programmed using one-dimensional dynamic array for the efficient use of machine storage. The turbulence closure scheme for the non-homogeneous vertical shear is formulated so that the potential and kinetic energetics are monitored and transferred in a closed form.

The hydrodynamic model is coupled to a two-dimensional stochastic weather model and an oil-spill trajectory/weathering model. The former also simulates stochastically the cyclogenetic/cyclolytic processes within the modeled area.

The paper also compares the computed results with the available field data. Good agreements are found in tidal amplitude and phases as well as currents.

The Three-Dimensional Modeling System

The model of the Gulf of Alaska uses a modeling system which consists of a three-dimensional hydrodynamic model, a two-dimensional stochastic/deterministic weather model, and an oil spill trajectory/weathering model (Fig 1).

The hydrodynamic model is formulated according to the equations of motion for water and ice, continuity, state, the balance of heat, salt, pollutant and turbulent energy densities on a three-dimensional variable grid. In the vertical, the momentum and constituent transport over the variable layers are solved implicitly. The horizontal grid network coincides with the global ellipsoidal system and has a one-to-one mapping to a Mercator projection for graphical outputs. The derivation of the model equation and the comparison between other layered models are available in the open literature, eg. Liu and Leendertse, 1978, in which aspects such as open boundary conditions, numerical stability, solution discontinuity, and conservation properties are also discussed.

The RAND Corporation, Santa Monica, Calif. 90406, U. S. A.

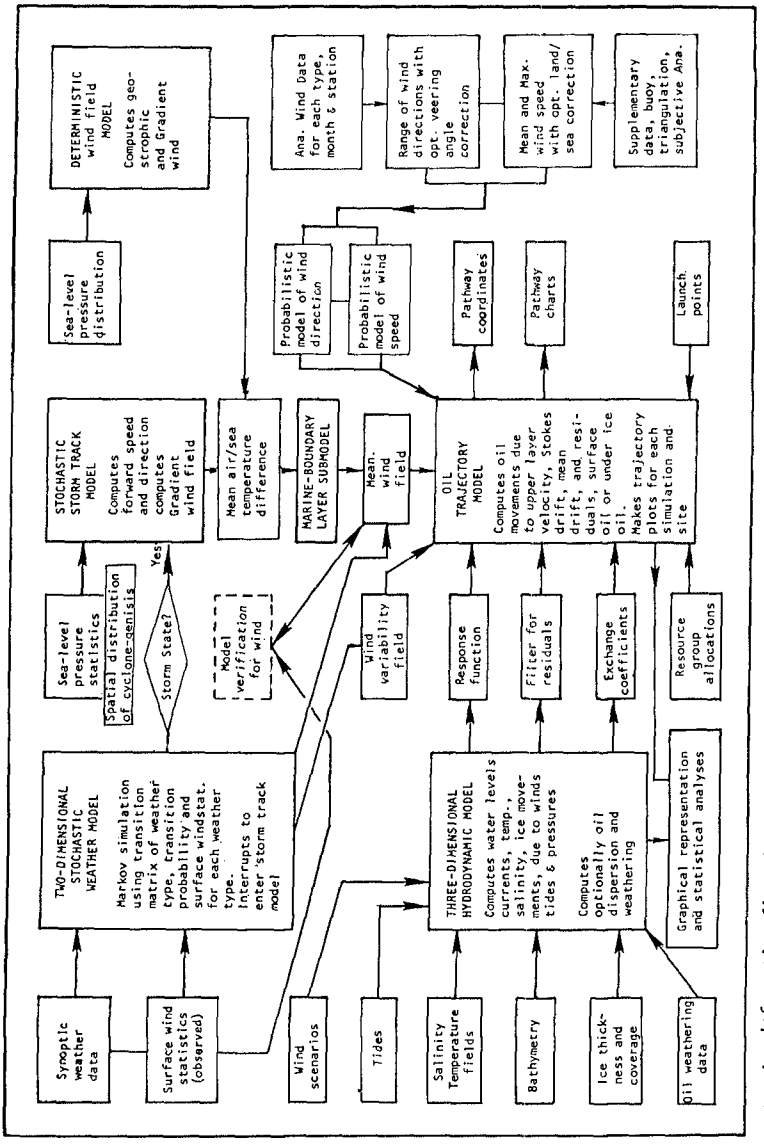

Fig. 1— Information flow chart showing that both the three-dimensional hydrodynamic and the weather model provide important parameters needed by the oil-spill trajectory model. These parameters are difficult and expensive to measure over the entire coastal waters. Observed wind roses, if available, can still be used to drive the trajectory model in its simplist mode.

In the vertical turbulence-closure scheme, the energy production term from the surface layer is computed from the parameterization of the wind-wave generation mechanism. This approach thus circumvents certain difficulties associated with the traditional two-equation model in which a symmetry condition is assumed (as a moving wall, same as the bottom).

The model is capable of having arbitrary layer number and layer thickness, therefore minimizes numerical (pseudo) mixing in deep water. In deep water, the stratification is usually more pronounced than in the shallower, well-mixed areas.

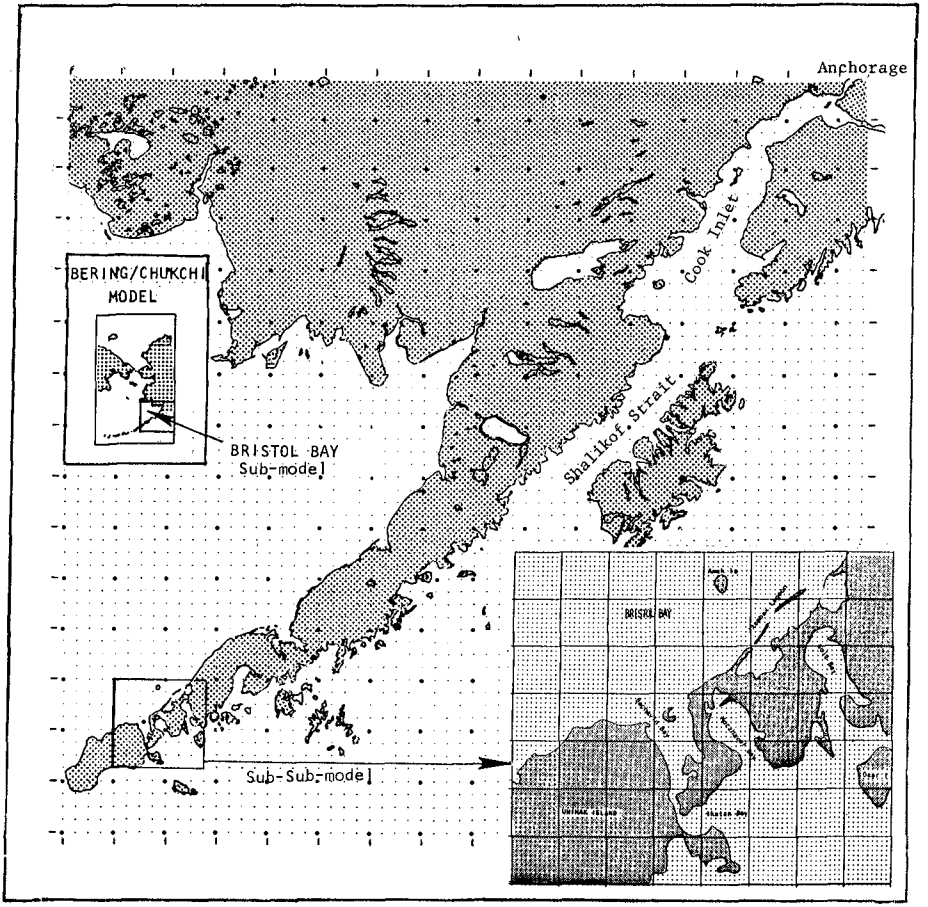

Fig. 2-- A sub-model of Bering Sea covering the area of Bristol Bay and a portion of the Gulf of Alaska. Insert map at the lower left corner is another sub-model of this one, covering the area of Izembak Lagoon.

The model of the Gulf of Alaska

The model of the Gulf of Alaska is the largest model covering the Alaskan coastal waters developed by the authors. Alaskan coast line stretches longer than the other states of the continental U. S. combined. Because of the complex coastal features, a series of nested submodels are needed to resolve the circulation dynamics of the near shore lagoons and the ecologically sensitive passages (Fig. 2). The nested models derive their boundary condition from the larger model because conducting field work in Alaska is both difficult and expensive. The embayment in the NE corner of Fig. 2 is the Cook lnlet, where the largest astronomical tides in the Pacific are found; sometimes reaching 13 meters. Also present are the strong currents and residual circulation induced by the nonlinear interaction between the advective mechanism and bethymetry of the coast.

The three dimensional perspective diagram in the upper part of Fig. 3 illustrates the along-shore view of the higher modes in the water level variation with the highest point at the head of Cook lnlet while the lower diagram shows the cross-shore variations.

Figure 4 shows the computed co-tidal chart for the semidiurnal component and the comparison between the computed amplitudes and phases at four locations where observed data are avaliable (Schumacher and Muench, 1980). Fig. 5 through 8 present the computed horizontal/vertical velocity components and the turbulent energy intensities at levels 1,3,5,7,8,9 at a location near the openning of Cook lnlet (Portlock Bank). At that location, the computed hodograph in Fig 9 nearly matches the observed current ellipse.

The computed tidal ellipses for the entire Gulf of Alaska, from Vancouver lsland to the Aleutian lslands are presented in Fig. 10. ln order to show the strong tidal currents within the Cook lnlet and over shelf areas, the plotting scale is set at 200 cm/sec per grid spacing. The maxmum tidal excursions are found in the middle of Cook Inlet where the tidal currents can reach 140 cm/sec in either direction. Currents over the shelf break can also reach 70 cm/sec. The computed tidal residual current distribution within the Gulf of Alaska is presented in Fig 11. In the figure, the maximum residual current in Cook lnlet is approximately 7.5 cm/sec, which is 5.5 percent of the local maximum tidal current. Over the shelf and in the Shalikof Strait, the direction of the residual current is primarily to the southwest.

Model Behavior and Discussion

In stratified geophysical flow, the density-induced vertical exchange often has a time scale much shorter than its horizontal baroclinic counterpart. lt also plays an important role in the coastal ecological balance via the euphotic/energetic processes.

It therefore creates stringent demands on the accuracy of modeling. On one hand, advances made in other discipline, such as the aerodynamic modeling, can often be applied to the geophysical flows, but, on the other hand, the differences in the free-surface and other boundary treatments makes the closure technique not necessarily identical for stratified flows. Specially

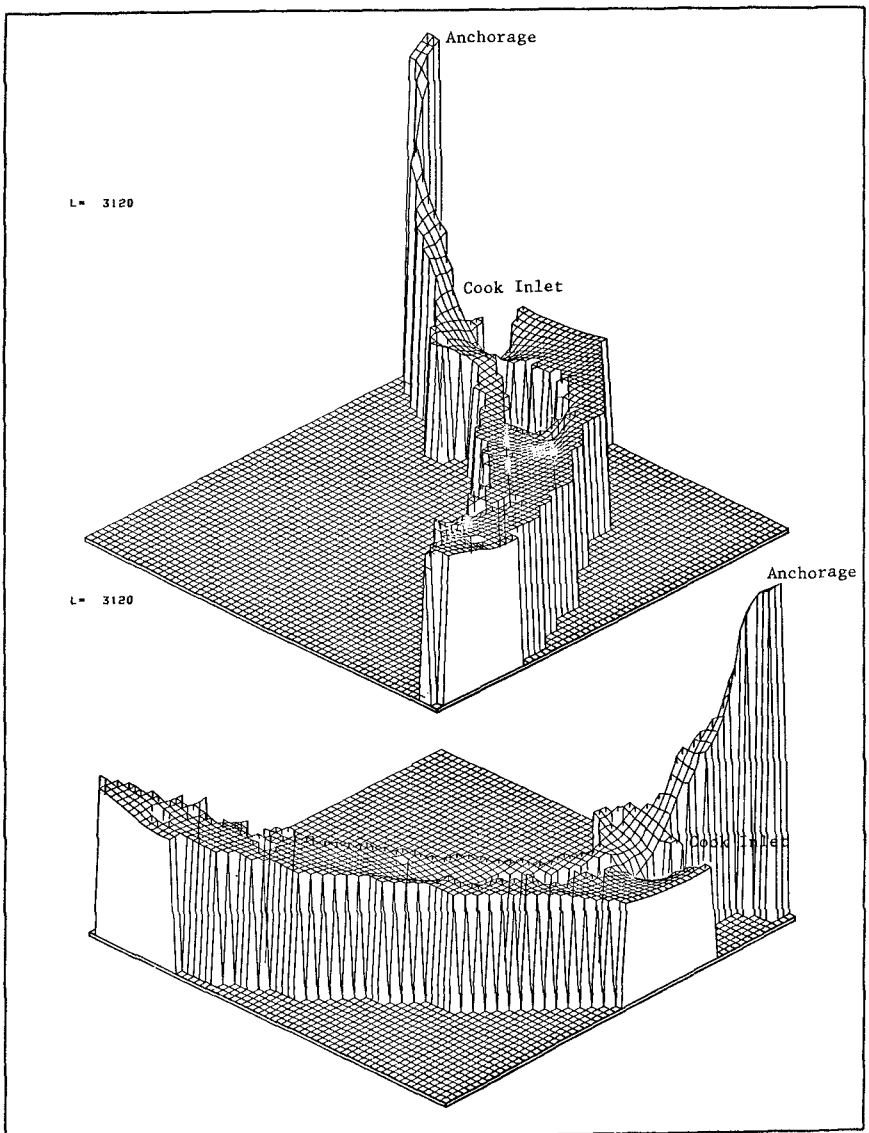

Fig. 3--Three-dimensional perspective diagrams illustrate the along-shore view of higher modes in the water level variation with the highest point at the head of Cook Inlet near Anchorage (upper diagram). The lower diagram shows the cross-shore variation.

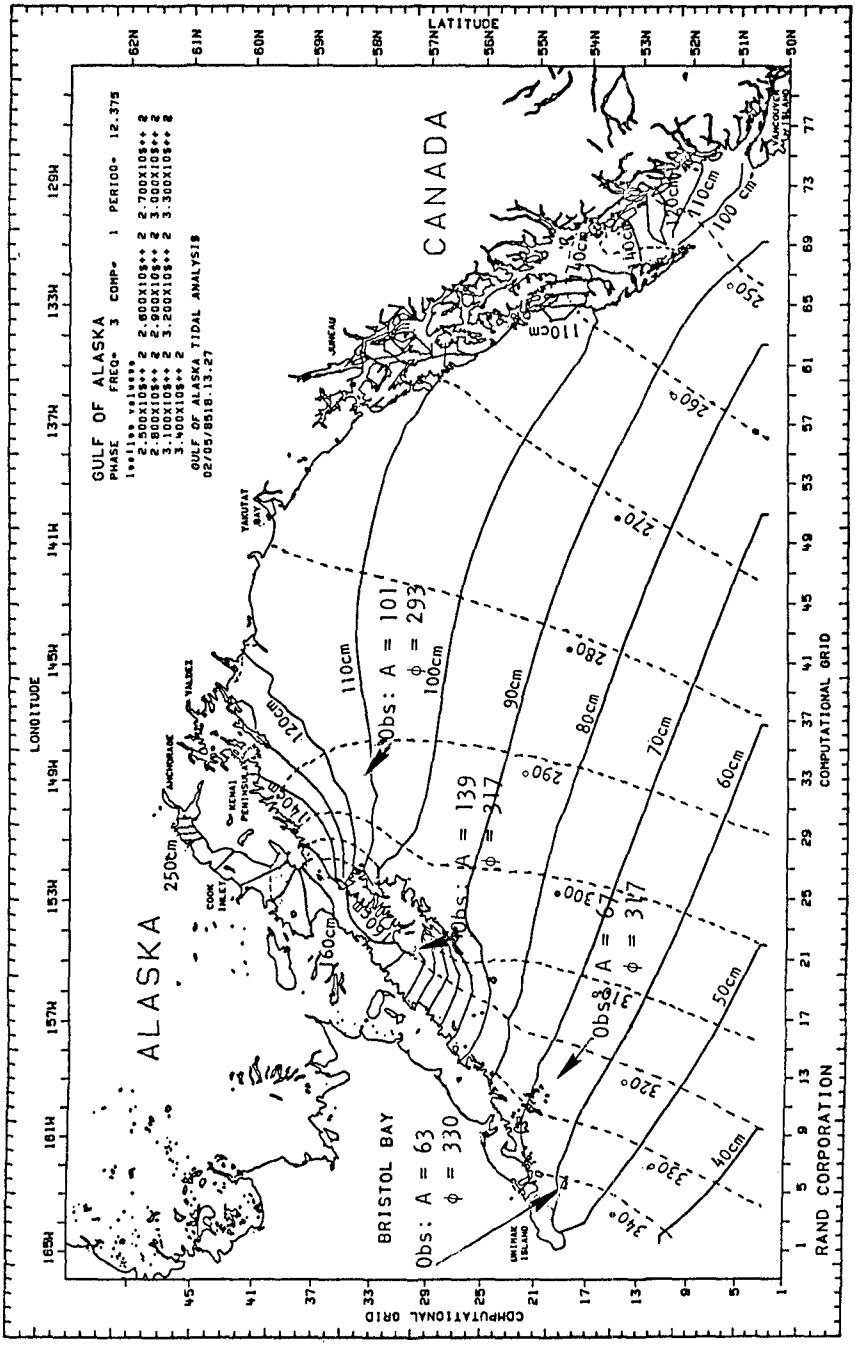

Fig. 4-- Computed co-tidal chart for the semi-diurnal component (primarily M2). Each ten degrees in phase represents approximately 20 minutes lag relative to the Greenwich mean phase. The maximum tidal amplitues are found in the Cook Inlet reaching 250 cm.

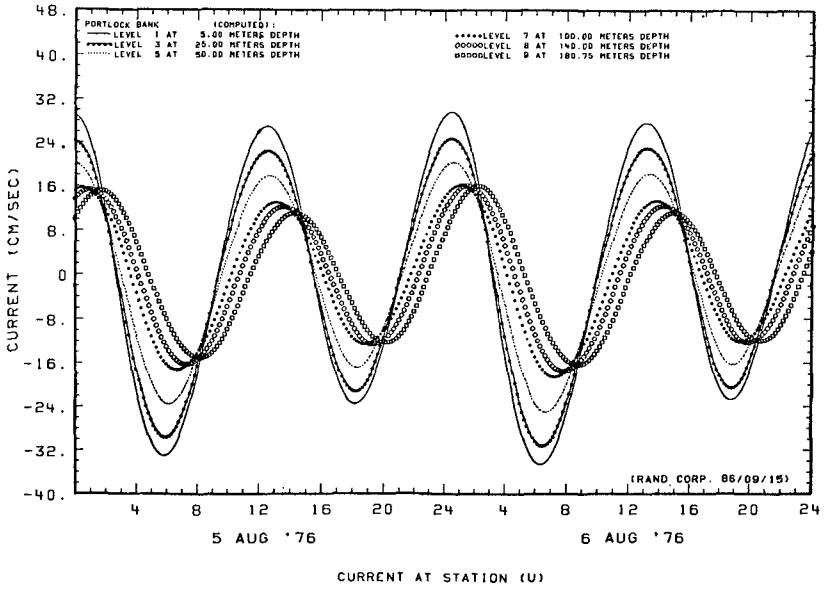

Fig. 5--The computed east-west velocity components at six representative layers near the mouth of Cook Inlet (Portlock Bank).

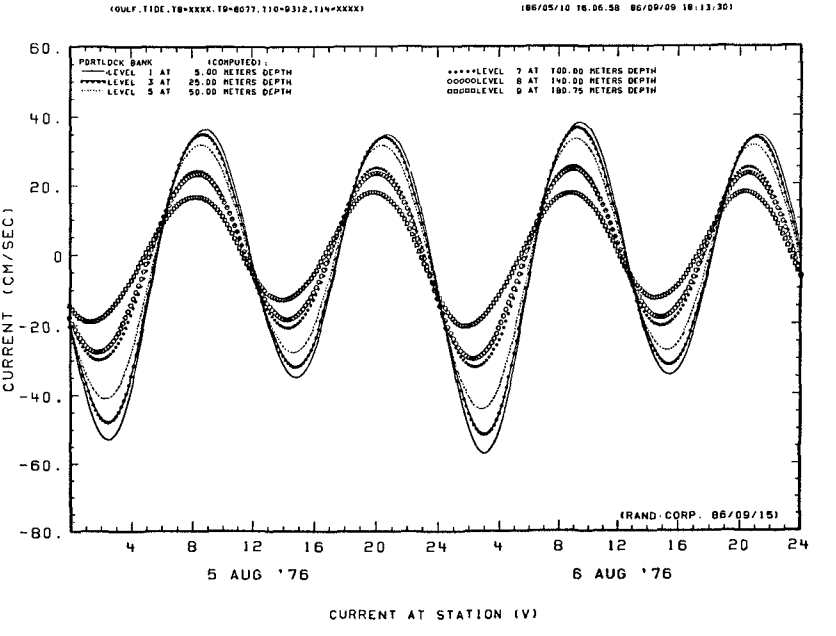

Fig. 6--The computed north-south velocity components at six representative layers near the mouth of Cook Inlet (Portlock Bank).

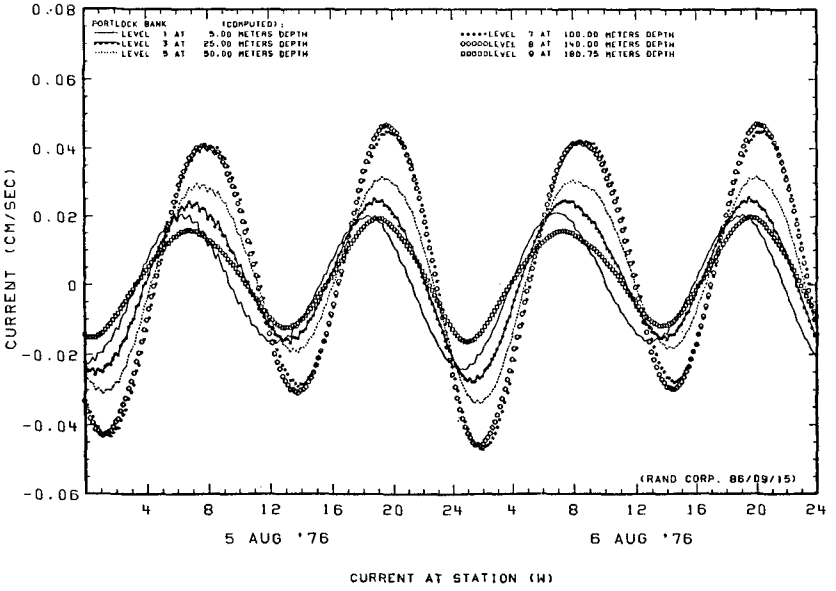

Fig. 7--The computed vertical velocity components at six representative layers near the mouth of Cook Inlet (Portlock Bank).

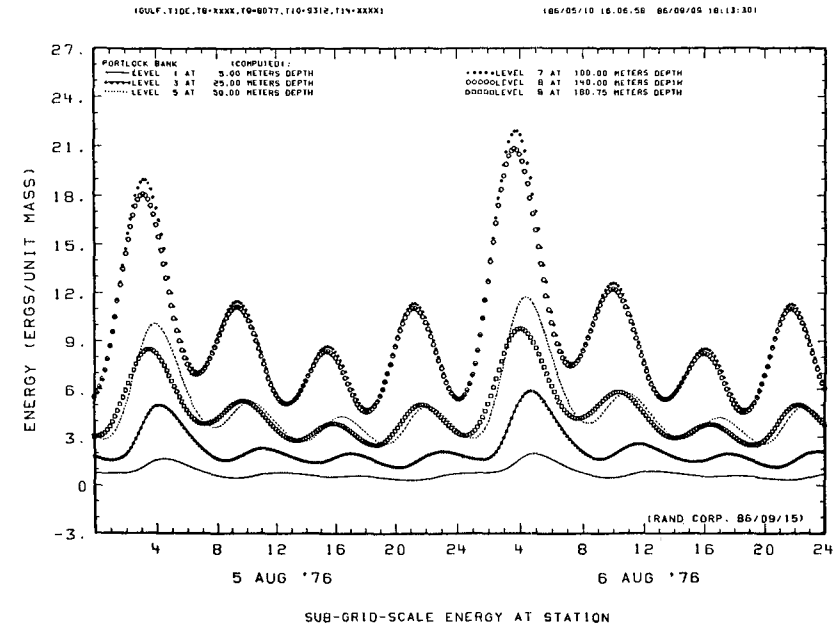

Fig. 8--The computed turbulent energy densities at six representative layers near the mouth of Cook Inlet (Portlock Bank).

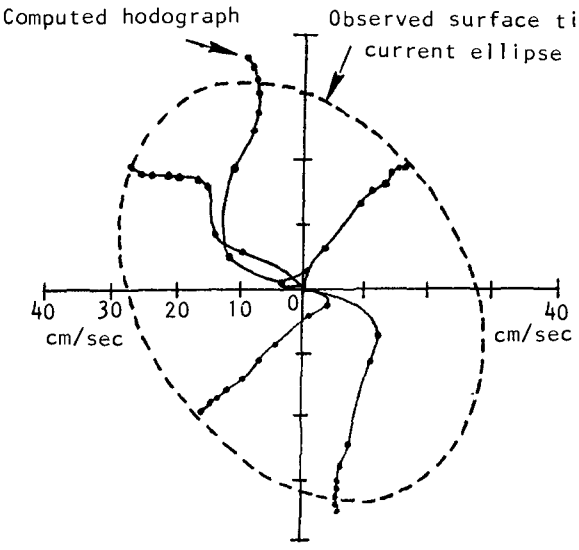

Comparison between the computed hodograph and the measured surface tidal current ellipse

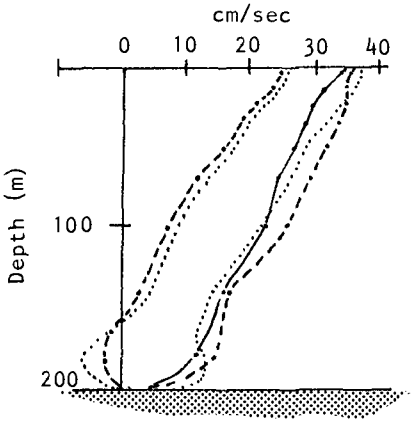

Vertical distribution of magnitude of the computed currents illustrated in the hodograph (near Cook Inlet)

Fig. 9

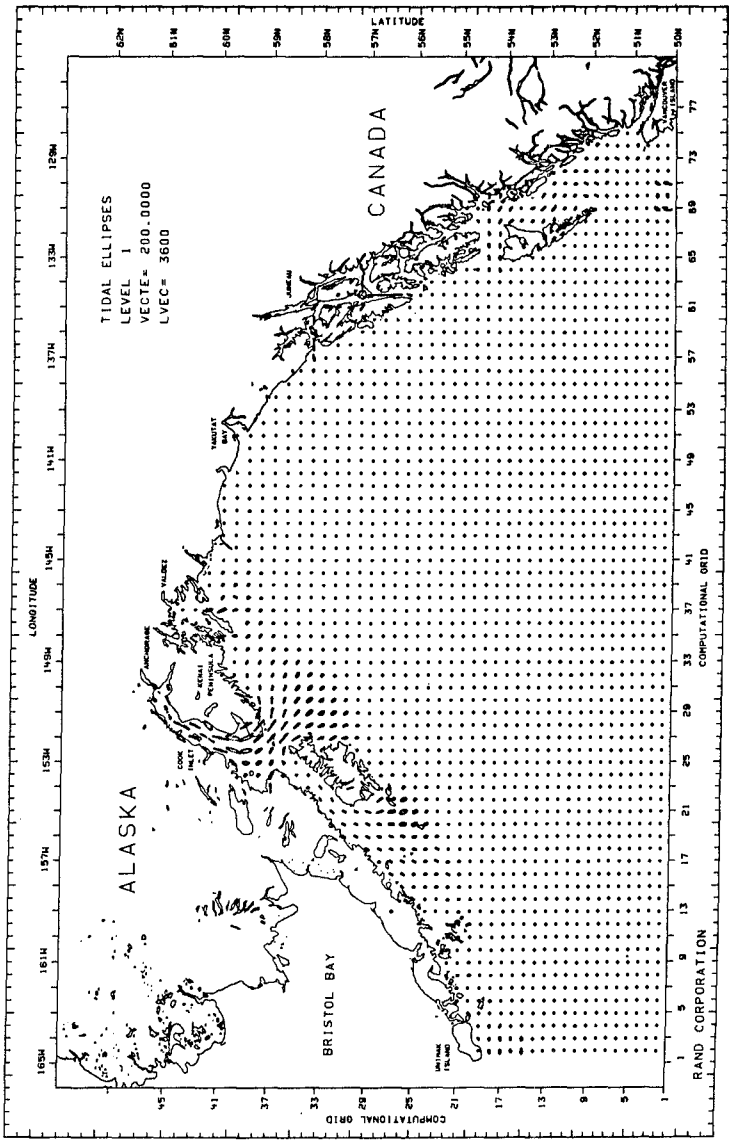

Fig. 10--Computed tidal ellipses in the Gulf of Alaska using a plotting scale of 200 cm/sec per grid spacing. Maximum tidal excursions are found in the middle Cook Inlet where the tidal currents can reach 140 cm/sec in either direction. Currents over the shelf-break near Kodiak are of elliptical rotary-type and can reach a maximum speed of 70 cm/sec.

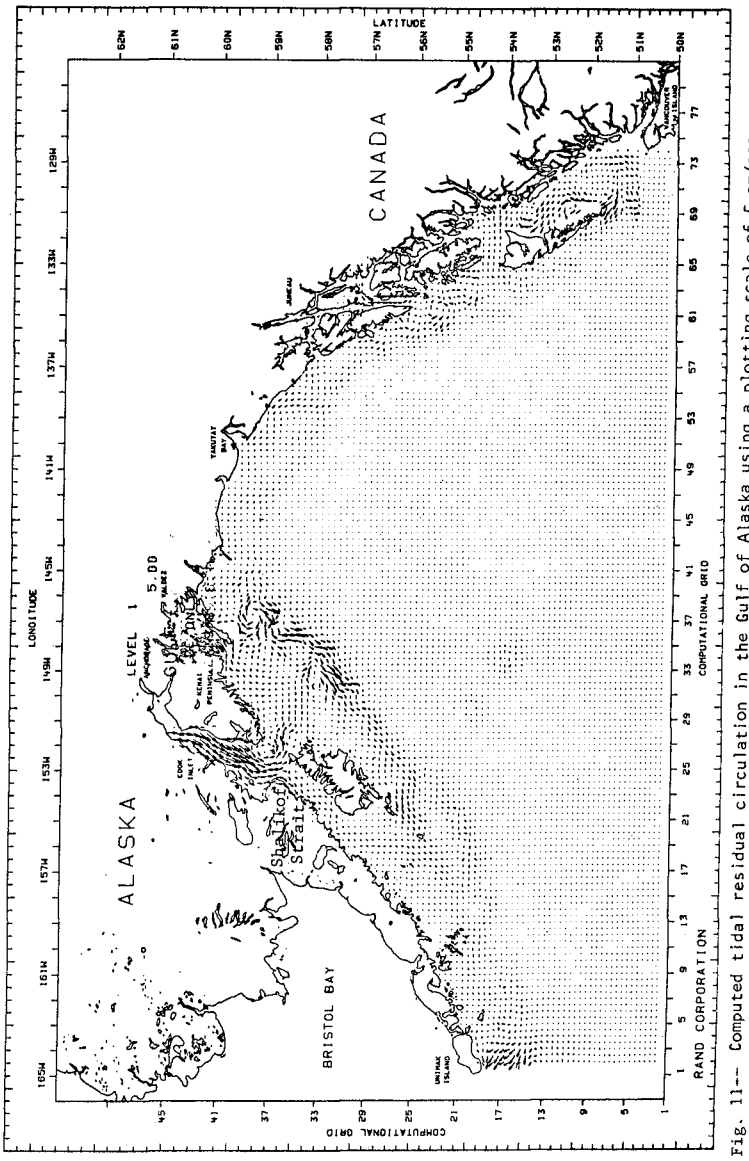

Fig. 11— Computed tidal residual circulation in the Gulf of Alaska using a plotting scale of 5 cm/sec per computational grid. Maximum residual current in the middle Cook Inlet can reach a speed of 7.5 cm/sec which is approximately 5.5% of the local maximum tidal current. Over the shelf break and in the Shalikof Strait, residual currents flow primarily toward the southwest.

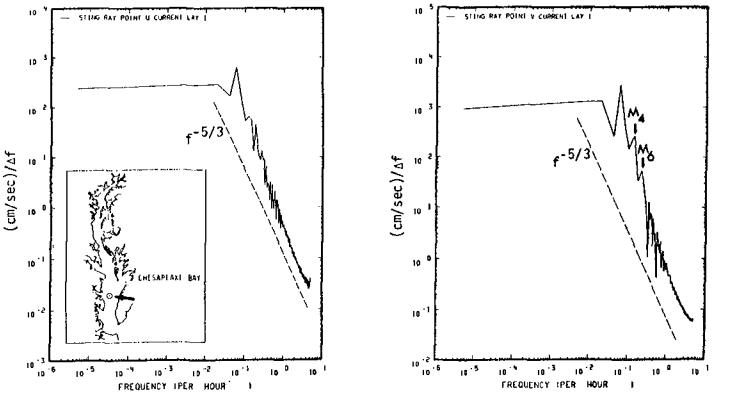

Driven only with M^2 tide (monochromatic wave) at the open boundary the proposed numerical scheme is capable of producing the cascade of energy distribution according to the universal "minus five-third" through the models nonlinear advective process (Hinze, 1959).

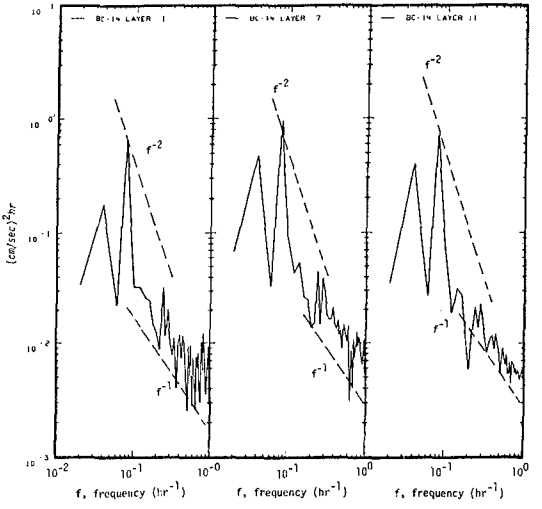

For the stratified fluid, the computed spectra of the vertical displacements (in the surface layer, within pycnocline and near bottom) and significant energy distribution agree with the observed spectra of the first mode of internal waves (Gordon, 1978).

Fig. 12

because coastal flows are primarily two-dimensional. Recent findings on the non-equilibrium statistical characteristics of turbulence have shown that even the universal Kolmogorof-constant of the tubulence spectrum has to be modified for two-dimensional turbulence. Models relying on the Richardson number-related parameters are specially susceptible to field measurement inaccuracies.

Consequently, over the past several years, we have modified our earlier models from requiring Richardson-number-related parameters to an energy balance approach. In the new method, the production and dissipation terms in the vertical energy turbulence-balance equation takes this form:

$$\bar{S}_e^z - D_e = \underbrace{a_3 \overline{L\sqrt{e}}^z \left[(\delta_z \bar{u}^x)^2 + (\delta_z \bar{v}^y)^2\right]}_{(1)} + \underbrace{a_3 \overline{L\sqrt{e}}^z \frac{g}{\bar{h}^z \rho} (\delta_z \bar{\rho}^z)}_{(2)} \underbrace{- a_2 e^{3/2}/L}_{(3)}$$

Where the first term denotes production, the second term represents the portion supplied that is used in potential energy increase, and the third term is dissipation. Some computational results are presented in Figs. 12 and 13. For example, when driven only with M2 tide (a monochromatic wave) at the open boundary, the numerical scheme is capable of producing the cascade of energy partition according to the universal "minus five-third" law through the model's non-linear advective process (top graphs of Fig. 12, also see the recent measurements by

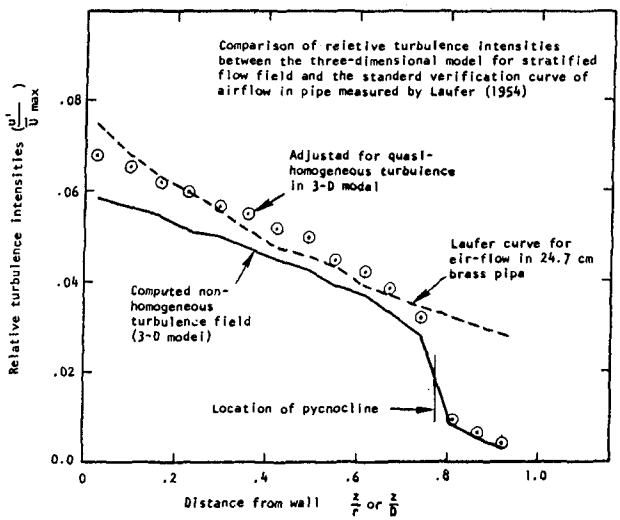

Fig. 13-- When the computed relative turbulence intensities at 15 layers are normalized with respect to the bottom distance, they are nearly the same when compared with the standard verification curve of airflow measured in brass pipe (made by Laufer for NACA, later NASA).

Heathershaw, 1979 and Elliott, 1984). Peaks of the spectra for two-dimensional turbulence are not uniquely located, however, it depends on the energy input and the relative location from the boundary (the so-called localization factor). The lower graphs of Fig 12 show the computed partitions of spectral energy of the vertical displacement near the pycnocline agree with the observed spectra of the first mode of internal waves (Gordon, 1978). When the computed relative turbulence intensities at various layers are normalized with respect to the bottom distance, they are nearly the same when compared with the NASA standard verification curve of airflow measured in brass pipe (made by Laufer). The insulation of momentum transfer across the pycnocline is evident . It is also clear that in stratified flows, more measurements and better model formulation are still needed.

Acknowledgments

This study was supported by the U. S. Bureau of Land Management through interagency agreement with the National Oceanic and Atmospheric Administration (NOAA), under which a multi-year program responding to needs of petroleum development of the Alaska Continental Shelf is managed by the Outer Continental Shelf Environmental Assessment Program Office.

Thanks go to our RAND colleagues Mr. A. B. Nelson and Mrs. G. Coughlan for their indispensable efforts in simulations and report preparation.

References

Elliott, A. J.,(1984): Measurements of the turbulence in an abyssal boundary layer, Jour. Physic. Oceano. Vol. 14, No.11, p 1779-1786.

Gordon, R. L.,(1978): Internal wave climate near the coast of Northwest Africa during JOINT-1, Deep Sea Res. Vol. 25, pp.625-643.

Hinze., J. O., (1959): Turbulence, McGraw-Hill, New York.

Heathershaw, A. D.,(1979): The turbulent structure of the bottom boundary layer in a tidal current. Geophys. J. Roy. Astron. Soc. Vol. 58, pp. 395-430.

Laufer, J.,(1954): The structure of turbulence in fully developed pipe flow, National Adv. Comm. on Aero., TR-1174.

Liu, S. K., and J. J. Leendertse, (1978): Multidimensional numerical modeling of estuaries and coastal seas, in Advances in Hydroscience. Vol 11, Academic Press. New York.

Schumacher, J. D., and R. D. Muench,(1980): Physical oceanography and meteorological conditions in the northwest Gulf of Alaska. NOAA TM-ERL-PMEL-22, Oct. 1980.

CHAPTER 194

Tsunami Threat Evaluation by Historical Documents, Numerical Model and Stochastic Model

Shigehisa Nakamura*

An evaluation of local tsunami threat was studied first refering to the historical documents and the catalogs. Secondly, an example of a numerical model of a finite difference method was discussed in relation to problems for reproducing the past local tsunamis and predicting a forthcoming tsunami. Lastly, a stochastic model was utilized in order to evaluate an exceedance probability of tsunami occurrencein an interested time period at an interesting local area where the concerened information or prediction was in need. The evaluation of a local tsunami threat is useful to get a more effective measure for the tsunami warning system and for protection works.

Introduction

In the coastal area, especially around the circum-Pacific seismic zone, they have had severe tsunami hazards repeatedly for thousands years. With recent higher utilization of the coastal area, they have felt it an urgent need to evaluate the nest tsunami threat of the interested location on the coast by an appropriate scientific techniques. Of cause, they have had learned well theirown way to reduce their loss and mitigate their damage with their experiences. If an evaluation of the threat is obtained properly, it can be a basic information for tsunami warning and protection.

As generally well known, the tsunami threat has locality. The author now wish to extend some concept about tsunami threat evaluation by historical documents, numerical model and stochastic model. With these, evaluation of local tsunami threat can be a more effective measure for establishing the tsunami warning system and for improving the concerned protection works.

Sources of Historical Tsunami Data

In order to get a glance of local tsunami threat, it is essential to refer to a tsunami catalog first. Such a catalog has been well composed afer compilation and reconfirmation of the historical documents. Iida, Cox and Pararas-Carayannis(1967) completed a preliminary catalog of tsunamis in the Pacific. Soloviev and Gao have published the russian editions for the western(1974) and eastern(1976) Pacific respectively. The most recent Japanese edition was published by Watanabe(1986). A more convenient tsunami hazard map was issued by NOAA and it seems very useful.

*Associate Professor, Shirahama Oceanographic Observatory, DPRI, Kyoto University, Katada-Hatasaki, Shirahama, Wakayama, Japan

The first step to compose these tsunami catalogs was to find out the old descriptions which included all of what was concerned the tsunamis and which were mostly kept in form of hand-written. So that, it has been necessary to confirm whether the descriptions are reliable or not at any step of compiling and/or composing them. Even at present, successive effort has been continued to search and reveal the fact out of the historical documents.

These documents are in form of a part of personal diaries, official documents, religious notes kept in Shinto-Shrines, Buddism Temples, Local Office of the Government or simple personal description. Occasionally, some specific merchants left vivid memories. Nakamura (1984a,b, 1985) has been continuing to find out yet any historical description which includes notes concerning the past significant tsunamis in order to get a more precise revision for the local forthcoming hazardous tsunami warning and protection.

As an example, the author take now a local tsunami problem in the coastal area of Tanabe and Shirahama(to the details, refer to the work by Nakamura, 1987, in Bull.DPRI,Kyoto Univ.). Tanabe and Shirahama have had suffered repeatedly from the past hazardous tsunamis accompanied by the big earthquakes, as well known. Tanabe and Shirahama are facing the northwestern Pacific and there are yet many of unpublished materials which inform us the facts which have been left as they have been without any aware of the importance(Nakamura,1984, 1987). A local tsunami catalog can be composed referring to the catalogs introduced above and adding the recently revealed facts out of the unpublished materials. With these additional local documents, a more detailed local tsunami catalog for Tanabe and Shirahama has been composed by Nakamura, 1984).

A brief list is shown as follows referring to the catalog. The significant events are chronologically listed following a format which includes the items of the date in AD or in Japanese era, estimated location of the epicenter taken from Watanabe's recent catalog, the magnitude of the earthquake denoted by M, the tsunami magnitude denoted by S(Nakamura, 1986a) and a brief note about the event.

(1) 684AD Nov.29(Temmu 2) A big earthquake, land falls, destroyed the government offices, warehouses, shrines and temples. Rice fields were drowneded by the tsunami flood. Hot spring ceased at Iyo(Ehime). Tsunami hits Kumano area. Hot spring at Muro also ceased. This is the oldest event confirmed and found in "Nihon-Shoki" and cited everywhere.
(2) 887AD Aug.26 16h(Ninna 9) 135.3E,33.0N, M=8.6, S=3. Big earthquake. Tsunami hits on the coast and lost many lives.
(3) 922AD(Engi 22) 137.7E,33.8N, M=7.0, S=1. A strong earthquake with tsunami.
(4) 1360 Nov.23 0h(Shohei 15) 136.2E,33.4N, M=7.0, S=2. Repeated shocks of the earthquake. On the next day also a big shock felt. Tsunami hits in morning the day after the next day.
(5) 1361 Aug.3(Shohei 16) 135.0E,33.0E, M=8.4, S=3. Description says an earthquake around Kii and tsunami hits Settsu(Osaka).

(6) 1403(Ouei 10) 136.5E,33.7N, M=7.0, S=1. Strong earthquake in Kumano district and tsunami hits.
(7) 1408 Jan.21 18h(Ouei 14) 136.9E,33.8N, M=7.0, S=1. Strong earthquake in Kumano. Possibly tsunami hits.
(8) 1498(Meio 7) High water caused hazards on the coast of Kii.
(9) 1510 Sep.21 4h(Eisho 7) 135.7E,34.6N, M=6.7, S=1. Estimated epicenter is located in Osaka Bay. Tsunami hits.
(10) 1520 Apr.4 18h(Eisho 17) 136.3E,33.6N, M=7.0, S=1. Temple's buildings destroyed by the earthquake. Houses drawnded.
(11) 1605 Feb.3(Keicho 9) 134.9E,33.0N, M=7.9, S=3. Big waves at Kumano. Hiro(1700 families) lost 700 families at the tsunami.
(12) 1707 Oct.28 12h30m(Hoei 4) 135.9E,33.5N, M=8.4, S=4. Details have been kept as the memory to give warning for their successors. Official reports described the damage and the fast-aid request for foods and living materials. After identifying the location appeared in these descriptions, an illustration was completed as a local hazard map which was shown in Fig.1.
(13) 1854 Dec.24 16h(Kaei 7 or Anse 1) 135.6E,33.2E, M=8.4, S=4. The more detailed descriptions of the earthquake and tsunami has been found to make the tsunami hazard map as in Fig.2. At a glance, there are little difference between the two maps of Figs.1 and 2 except learning what were written in the descriptions in 1707 and in 1854.
(14) 1944 Dec.7 13h35m(Showa 19) 136.2E,33.7N(depth 30 km), M=8.0, S=3. On the coast of Kii Peninsula facing the Pacific, houses washed away by the tsunami. No record was kept except only a limitted number of the mareograms which includede the tsunami.
(15) 1946 Dec.21 4h19m(showa 21) 135.6E,33.0N(depth 30 km), M=8.1, S=3. Several scientific records have been kept. With the local descriptions and hearings the tsunami hazard map was made as found in Fig.3 for the event of 1946. This map shows a successful protection works around the mouths of the Rivers, though the protection works have done against the flood of the river discharge. The illustration of Fig.3 shows the other new areas and coasts had the tsunami hit. This means that these areas had never used or lived by the end of the Second World War.
(16) 1960 May 23 19h11mGMT(Showa 35) 73.5W,41.0S, M=8.25, S=4. The Japanese Islands had hit by the tsunami on 24 May 1960 without any seismic shock in advance. The tsunami was highest at Isla Mocha in Chile(20 to 25 m) and it crossed the Pacific to hit the Japan Islands as well as the Chilean coast. In Chile, 909 persons died, 834 persons lost, 667 persons injured and many buildings had severe damage. Even in Japan, 119 persons died, 29 persons lost, 872 persons injured, 2830 houses destroyed, 19,863 houses drownded and the unexpected damage of boats.

Even when we are aware of the difference between the epicenters of 1707 event, 1854 event, 1946 event and 1960 event, the author cannot deny the active effect of the protection works completed by that time looking at and comparing the illustrations in Fig .1 for 1707, Fig.2 for 1854, Fig.3 for 1946 and Fig.4 for 1960. Adding to that, we have to be aware of any type of unexperienced tsunami damage.

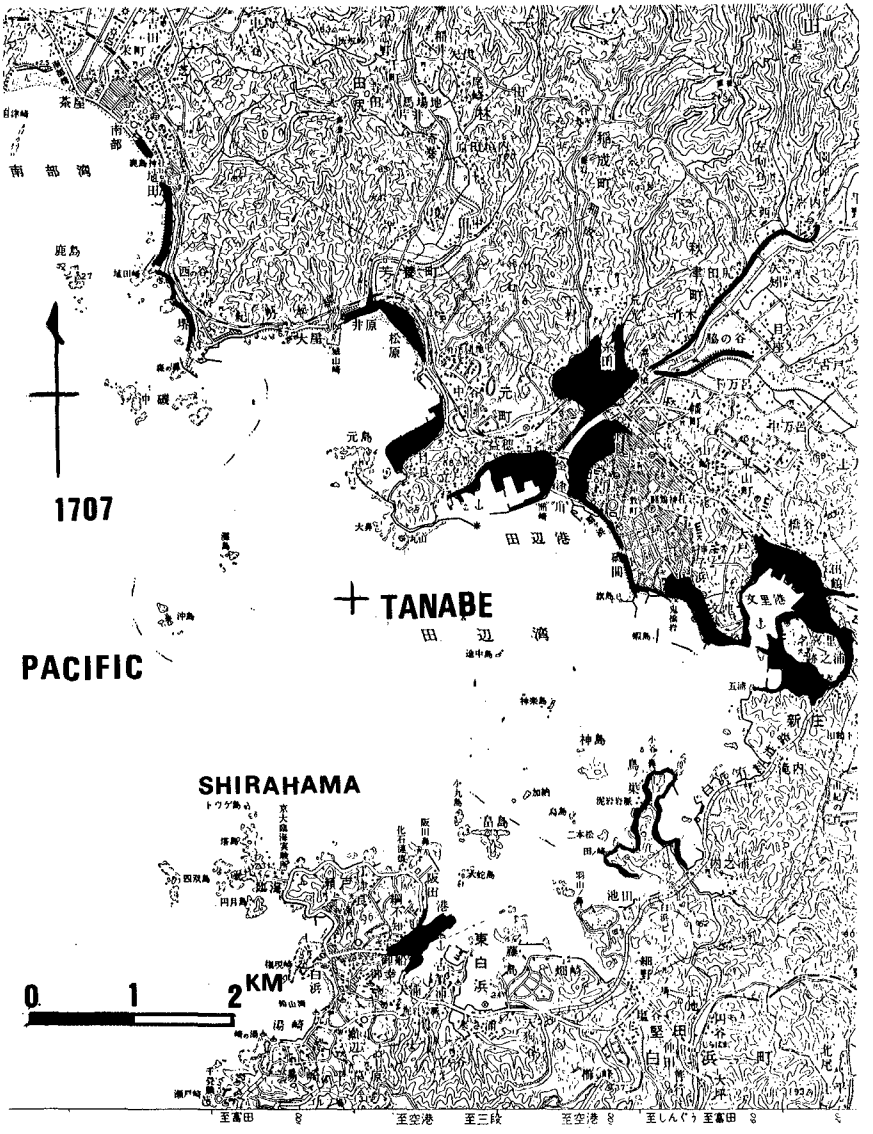

FIG. 1.— Hazard Map of 1707 Hoei Tsunami; Note: The Suffered Area by the Tsunami Flood Was Shown by a Black Coloured Patch or Black Lines along the Coast or along the River Levee and River Bank.
(Location of the cross is 135°21'E, 33°43'N)

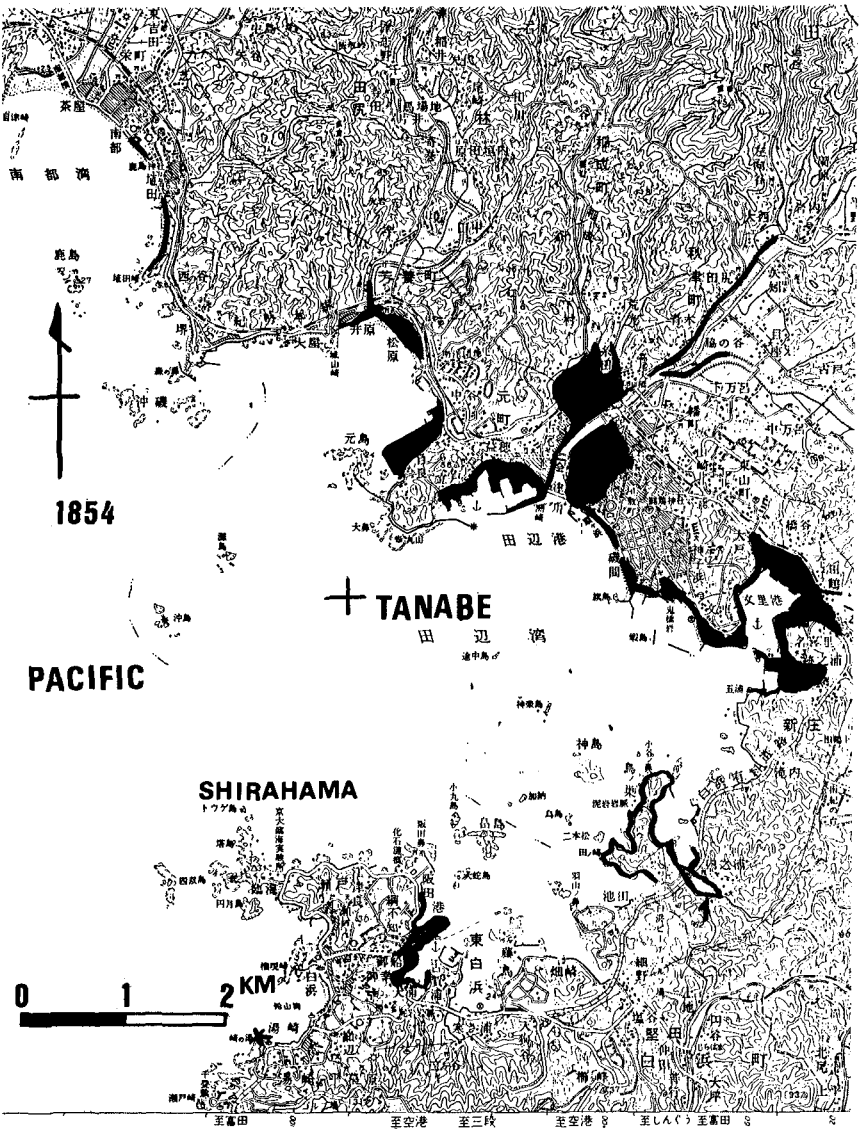

FIG. 2.— Hazard Map of 1854 Ansei Tsunami; Note: The Suffered Area by the Tsunami Flood Was Shown by a Black Coloured Patch or a Black Lines along the Coast or along the River Levee and River Bank. (Location of the cross is 135°21'E, 33°43'N)

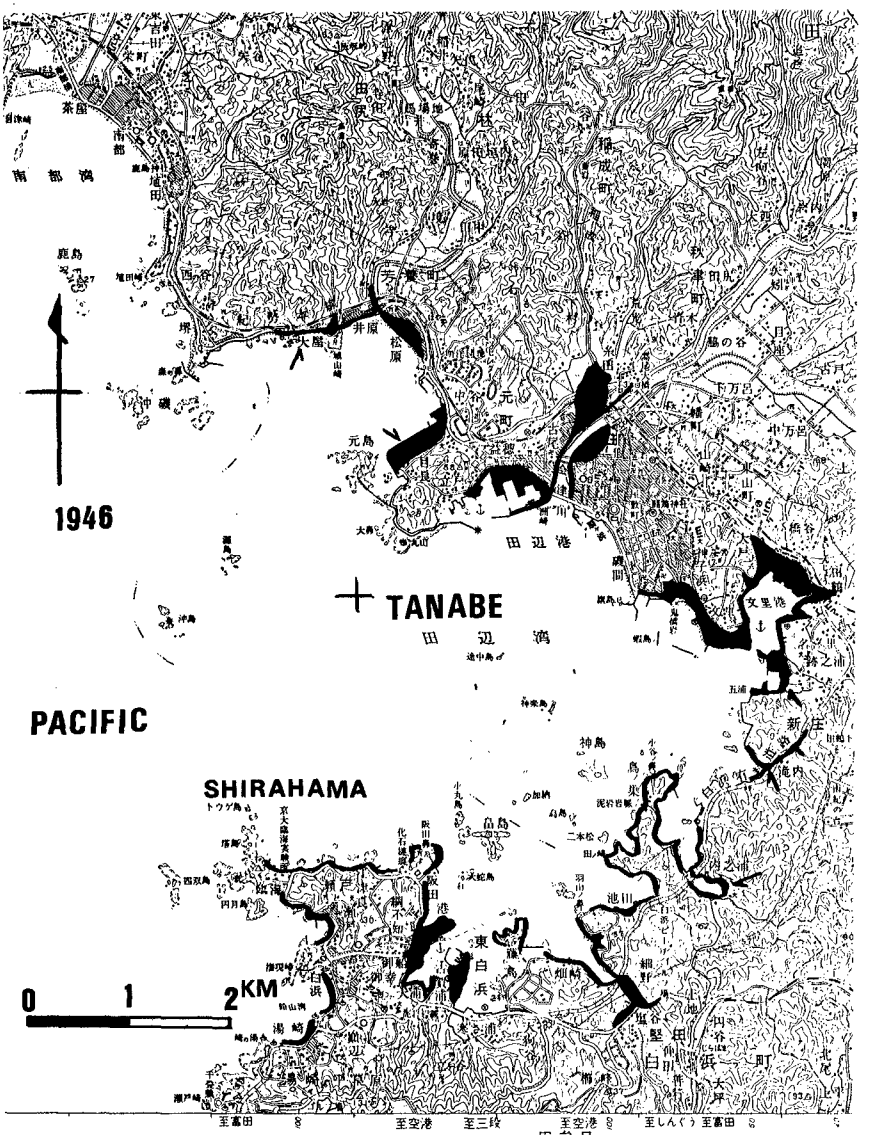

FIG. 3.— Hazard Map of 1946 Nankaido Tsunami; Note: The Suffered Area by the Tsunami Flood Was Shown by a Black Coloured Patch or Black Lines along the Coast or along the River Levee and River Bank (Location of the cross is 135°21'E, 33°43'N)

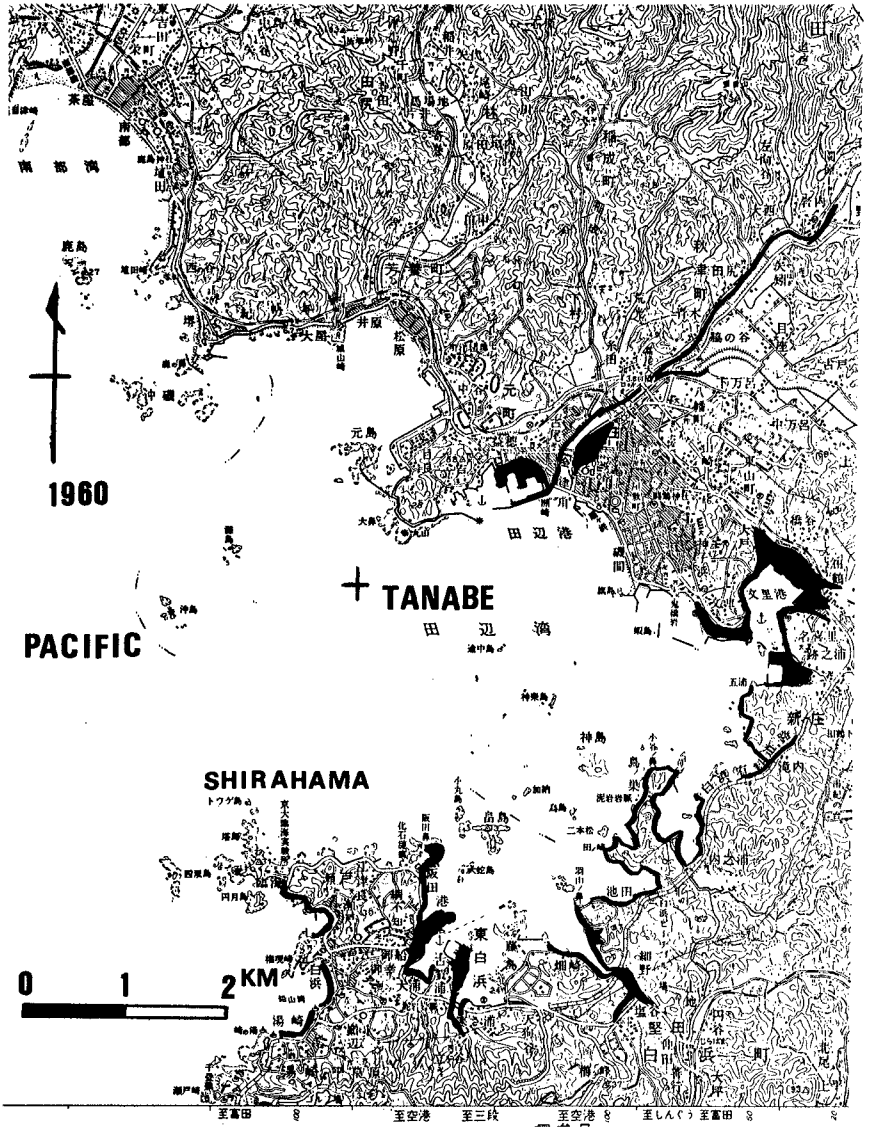

FIG. 4.— Hazard Map of Chilean Tsunami; Note: The Suffered Area by the Tsunami Flood Was Shown by a Black Coloured Patch or Black Lines along the Coast or along the River Levee and River Bank (Location of the cross is 135°21'E, 33°43'N)

Numerical Modelling

Techniques for numerical model has been accepted as a convenient to simulate any local tsunami and to reproduce the forthcoming one. This helpe us to establish an improvement of the present tsunami warning and protection worke. The author feels himself it hard to count up the tsunami model published by thie time. Here, the author introduces only the Japaneee recent works, i.e., by Hatori(1974), Aida(1983), Iwasaki(1983) and Iida et al.(1983). Ando(1982) has tried to reconstruct a fault formed by the main shock of the 1946 earthquake by using the available tsunami data. Nakamura(1983) has ueed and improved Loomis(1972)'s technique for long water waves in a finite difference scheme.

At the author's feeling, the most of the numerical scientists or engineere seem truet that the differential equation is equivalent to a difference equation. When a function u is given as a function of a variable t, it ie correct mathematically that

$$u'=du/dt=\lim_{\Delta t\to 0} \Delta u/\Delta t. \tag{1}$$

However, this does not mean that

$$u'=du/dt=\Delta u/\Delta t, \tag{2}$$

generally. The necessary condition is that the value of Δt is small enough for the given continuoue function, and the limit of (1) have to converge to a certain finite value.

Let ue consider a function $u(t;x,y,z)$ and write it u for our convenience. The first derivative is u'. As for a differential equation $u'=f$,

$$u(t+\Delta t)=u(t)+ f\cdot\Delta t, \text{and } f=f(t;x,y,z), \tag{3}$$

there is no promis to get a finite value of $u(t+\Delta t)$ mathematically if the function f is not continuous or has a specific property. For our convenience, we have to consider a case for

$$f= -u\frac{du}{dx} -v\frac{du}{dy} - \frac{1}{\rho}\cdot\frac{d\zeta}{dx} +\left[\frac{d}{dz}\left(K\frac{du}{dz}\right)\right], \text{ etc.} \tag{4}$$

The differential equation $u'=f$ has a quite similar form to that used for numerical computations of gravitational water waves in a shallow water, i.e., the equation of motion in hydrodynamics. There must bemany of worke not appeared to us as a erroneous solution or ae a simply unexpected solution without any consideration in the scope of mathematics,even if it is reasonable mathematically.

Some other engineer must consider a way to get only for his expected solution using the higher terms of the Taylor's power series expansion of the function u around its variable t. That is,

$$\frac{\Delta u}{\Delta t} = u' + \frac{\Delta t}{2!} u''. \tag{5}$$

Now, consider again similar way as that for (3) and (4), and take $\frac{\Delta u}{\Delta t} = f$, then we have

$$u'' + \left(\frac{2}{\Delta t}\right) u' - f = 0. \tag{6}$$

As for an expected periodical solution in form of $u=u_0\exp(ipt)$, The following relation should be satisfyed in (6).

$$p^2 - \frac{2i}{\Delta t} p + f = 0. \tag{7}$$

From (7),

$$p = \frac{i}{\Delta t} \pm \left[f - \left(\frac{1}{\Delta t}\right)^2 \right]^{1/2} . \tag{8}$$

Hence, the first term in (8) shows that any disturbance decreases monotonously in the model. The second term controls the property of the solution u satisfying (6). If

$$f - \left(\frac{1}{\Delta t}\right)^2 > 0 , \tag{9}$$

the solution u of (6) has a part of an oscillatory solution. If not, this solution must be a monotonous increasing or decreasing function. When the function f is known apriori, it is easy to distinguish whether the solution is oscillatory or not referring to (8) or (9). Although, for example as in case of the function f given by (4) or as a case of an unpredictable function f, we can only control it by a choice of the value of Δt. The necessary condition is that the value of Δt is preferable as small as possible.

This is a remark for a numerical model of a finite difference method which occasionally gives a troublesome unexpected solution or a divergent solution even when so-called"Neumann's criteria" for obtaining a stable solution is well satisfyed. Although, this remark is not neccessarilly exact in the scope of mathematics.

As far as we concern the tsunami researches by this time, one of the tasks for the coastal engineers at present must be to utilize well the numerical model for their successful purposes. When the tsunami source condition is given, we can now utilize a numerical model to simulate and predict a local tsunami only for satisfying given condition. We have to be careful pioneers to introduce some other improved techniques to know when the next tsunami occurs in our interested area in the expected time period. One of them must be that appearing in the next section where the tsunami catalogs are fully utilized as a reference data source.

Stochastic Model

Probability of tsunami occurrence frequency on the coast of California was evaluated first by Wiegel(1970). Rascon and Villareal (1975) worked a stochastic evaluation of possibility of tsunami hit on the Pacific coast of Mexico. Successively, similar studies has been undertaken to know the local property of the tsunami occurrence frequency. Even in Japan, the coastal area in the northwestern Pacific, a simple statistical evaluation about the forthcoming big earthquake and big tsunami. However, it cannot be given as any scientific value for a long time. Only documentation had been

the focus to spend their effort, which is at present highly evaluated in the field of coastal engineering for the basic data of tsunami warning and protection works. Almost all of the studies on tsunami occurrence frequency belongs to a stochastic problem. For example, Nakamura(1986a) has considered to introduce an extensive or modified Poisson process in order to get a better fit to the exceedance probability of local tsunami.

Referring to the tsunami catalogs, we can prepare to make a sequence of annual tsunami occurrence for an interested local area. If we take the tsunami event to be annual or the biggest tsunami in every year, then the annual exceedance frequency of tsunami occurrence in the interested area can be evaluated as a Poisson process or an extended Poisson process. Nakamura(for example, 1986a) has expressed exceedance probability P of tsunami occurrence as a function of an interested time interval t, i.e.,

$$P = 1 - \exp(-\Lambda t), \tag{10}$$

with

$$\Lambda = \Lambda_0 \exp[-\beta(h-h_0)^n], \tag{11}$$

where h is tsunami height and reference tsunami height h_0 is taken to be 1 m in this case. And the value of $\Lambda(=1/378)$ or $\Lambda_0(=58/378)$ is inverse of annual return period for h and h_0 respectively. The specific values of $\beta(=0.34)$ and $n(=1.0)$ characterize locality of the exceedance probability of tsunami occurrence. The above expression corresponds to the case of so-called "Poisson process" if n=1. The author uses tsunami scale S(or m) in the other cases instead of tsunami height h for a convenience. As a result, the author could obtain an exceedance probability of 25 % for a tsunami occurrence of the 1707 class(the local maximum of h was 13 m) at least once in a time period of 100 years.

Lastly, the author wishes to remark that a numerical model and a stochastic model are complementary each other as far as we refer to the historical tsunami descriptions and to the tsunami catalogs.

Conclusions

Evaluation of local tsunami threat was studied (i) using and referring to the historical descriptions and documents compiled by the author with an adjustment of what is written in the tsunami catalogs, (ii) using a numerical model of a finite difference method the author discussed what should be remarked mathematically in a simplified form, and a probability of local tsunami threat was evaluated using a stochastic model for an extended Poisson process. As seen above, evaluation of local tsunami threat is useful to establish a more effective measure for the tsunami warning or protection works.

This work was completed at the agreement for submitting the ASCE Proceedings of the 20th International Conference on Coastal Engineering by Setsuo Okuda, Director of the Disaster Prevention Research Institute, Kyoto University and Yoshito Tsuchiya, Head of the Shirahama Oceanographic Observatory. The author has to express his

thanks to the permission for using the published map of the Geographical Survey Institute at the preparation of the illustrations in this text. In addition, the author cannot forget to appreciate for those who have payed their consideration at the Conference in Taipei as well as for Dr. Billy L. Edge and his fellows.

Appendix – References

Aida, I. (1983). "Numerical simulation of historical tsunami generated off the Tokai District in Central Japan". Tsunamis, Terrapub., Tokyo, pp. 277-291.

Ando, M. (1982). "A fault model of the 1946 Nankaido earthquake derived from tsunami data". Phys. Earth and Planet Int., Vol. 28, pp. 320-336.

Hatori, T. (1974). "Sources of the tsunamis generated off Tokai and Nankaido". Zishin, Ser. 2, Vol. 27, pp. 10-24.

Iida, K., Cox, D., and Praras-Carayannis, G. (1967). "Preliminary catalog of tsunamis in the Pacific". Univ. Hawaii, HIG-67, Data Report No. 5.

Iida, K., Inagaki, K., and Hasegawa, K. (1983) "Finite element method for tsunami wave propagation in Tokai District Japan". Tsunami, Terrapub. pp. 293-301.

Iwasaki, T. (1983). "A hybrid system developed for model tests of tsunamis in a harbor". Tsunamis, Terrapub., Tokyo, pp. 409-421.

Loomis, H. G. (1972). "A package program for time-stepping long waves into coastal regions with application to Haleiwa Harbor Oahu". NOAA-JTRE-79, HIG-72-21, Univ. Hawaii, 33p.

Nakamura, S. (1983). "Numerical tsunami model in Osaka Bay". Bull. Disas. Prev. Res. Inst., Kyoto Univ., Vol. 33, pt. 1, No. 295, pp. 1-14.

Nakamura, S. (1984a). "On tsunamis in Tanabe and Shirahama". Annuals of Disas. Prev. Res. Inst., Kyoto Univ., No. 27B-2, pp. 591-610.

Nakamura, S. (1984b). "Old documents of tsunamis and their evaluation". La mer, Tome 22, pp. 61-72.

Nakamura, S. (1985). "On historical documents of tsunamis around Hidaka River Wakayama-ken". La mer, Tome 23, pp. 26-31.

Nakamura, S. (1986a). "An estimate of exceedance probability of tsunami occurrence in the eastern Pacific". Marine Geodesy, Vol. 10, pp. 124-145.

Nakamura, S. (1986b). "A response of wide-open bay in a numerical model ". Marine Geodesy (manuscript accepted).

Nakamura, S. (1987). "A note on numerical evaluation of tsunami threats by simple hydrodynamic and stochastic models refering to the historical descriptions". Bull. Disas. Prev. Res. Inst., Kyoto Univ., Vol. 37, pt. 1 (to be published).

Rascon, O. A., and Villareal, A. G. (1975). "On a stochastic model to estimate tsunami risk". Jour. Hydraulic Res., Vol. 3, pp. 383-403.

Soloviev, S. L., and Gao, Ch. N. (1974). "Katalog tsunami na zapadnom poberezie Tixogo Okeana". Akad. Nauk (USSR), Izdat. Nauk, 310p.

Soloviev, S. L., and Gao, Ch. N. (1976). "Katalog tsunami na vostochnom poberezie Tixogo Okeana". Akad. Nauk (USSR), Izdat. Nauk, 202p.

Wiegel, R. L. (1970). "Earthquake Engineering". Prentice-Hall, Englewood Cliffs, N. J., 518p.

CHAPTER 195

100 YEARS OF FORESHORE RECLAMATION IN SINGAPORE

S K PUI*, MICE, MASCE

ABSTRACT

Singapore is an island republic with about 10% of her land area reclaimed from foreshore during the last century. In this Paper, past reclamation works are reviewed and possible future reclamation works are predicted.

1 INTRODUCTION

Due to its strategic location, Singapore has since its founding in 1819, been centre for trade and commerce, transportation and other activities in the region. The result was a rapid growth in population, from about 200 in 1819 to 2.5 million todate, in a country with land area of only 636 km^2, inclusive of its 57 offshore islands and 53 km^2 of land reclaimed from foreshore (Information Division, 1986).

The resulting high population density has created a constant need to reclaim land from the foreshore for various development projects along the coastline, especially those related to airports, seaports, maritime and petroleum industries, housing, commerce and recreational parks. The calm wave environment and rather low tidal range (about 3 m) prevail along the coastline of Singapore, has enable the reclamation works to be executed economically.

2 EARLIER RECLAMATION WORKS

Earlier foreshore reclamation works were mainly confined at the southern tip of the main island of Singapore, from Kallang Basin at the east to Tanjong Berlayer at the west. Total land area reclaimed before self-rule in 1959 was about 3 km^2.

The first early major foreshore reclamation works was the reclamation at the then Telok Ayer Bay about 100 years ago, for the construction of a link road between the then commercial centre at Singapore River and a new deep-water port at Keppel Channel. Fill material was obtained by levelling of 2 hills at Tanjong Pagar (Bogaars, 1956). Covering approximately 7 ha, the project took more than 8 years to complete.

*Principal, S K Pui Chartered Consulting Engineers, No. 1 Magazine Road, #04-06B, Central Building, Singapore 0105.

This reclaimed land was subsequently further extended and completed in 1915 with the formation of Telok Ayer Basin. A comprehensive map, drawn 82 years ago, showing earlier reclamation proposals along Singapore coastline was contained in Reith's Handbook to Singapore (1907).

Earlier reclamation works also include reclamation of 9 ha land at the present Container Terminal by the then Tanjong Pagar Land Company in 1880's, and reclamation along Keppel Channel in 1900's for the construction of seaport and shipyards.

At the conference of Kallang and Geylang Rivers, about 1 km^2 of land was reclaimed in 1930's for the construction of Kallang Airport. Seven million m^3 of fill material was obtained from a hill situated some 6 km away from the site. Trains were used for the transportation of the fill material. This project took 4 years to complete. During the same period, the coastline from the mouth of Singapore River to the mouth of Rochore River was also reclaimed for the construction of an esplanade.

3 RECENT RECLAMATION WORKS

With the achievement of self-rule in 1959, and subsequently independence in 1965, various massive reclamation works were initiated to cater for rapid development in public housing, industry, commerce, recreation, air and seaport development, and for construction of express ways. To ensure that reclamation works can be executed without much hinderence, necessary amendments were made to the Land Acquisition and the Foreshore Ordinances in 1964.

Recent reclamation works are mainly carried out by three Statutory Boards as agents to the Government, namely Jurong Town Corporation (JTC), Housing and Development Board (HDB) and Port of Singapore Authority (PSA). Together, these three reclamation agents have reclaimed a total of about 48 km^2 land area, representing more than 90% of the total land area reclaimed from foreshore during the last 100 years. Since 1965, Singapore has been growing in land area at a rate of 8,000 m^2 per day (Radhakrishnan etal, 1983). About 285 million m^3 of fill material was moved in these reclamation works.

Major reclamation works executed by the JTC, mainly for industrial development, are Tuas foreshore reclamation, Jurong Port extension, Loyang Reclamation, Senoko Reclamation, reclamation at Seraya Island, Ayer Merbau Island, Busing Island and Sakra/Bakau Islands. The JTC is now reclaiming a further 6 km^2 of land area off Tuas, a project scheduled to complete in 1988.

Reclaimed lands executed by the HDB are mainly for housing, commercial and recreational purposes. Since 1963, the HDB had reclaimed the entire south-eastern coastline of Singapore Main Island, from Changi at the east to the city centre at the south. These works had been executed in 7 major phases, in tune with public housing development schemes during which hills at Bedok and Tampines were levelled for the building of new towns. The HDB is now reclaiming 9.6 km^2 of foreshore area at Punggol, expected to complete in 1993.

During the last 20 years, the PSA has carried out reclamation works at 21 offshore islands for various purposes, including catering for recreational needs. At the main island, about 10 km^2 of land was reclaimed by the PSA, mainly at Changi, for the building of Singapore Changi Airport, and at Pasir Panjang, for the development of a seaport. Unlike JTC and HDB, fill for the reclamation works executed by the PSA was mostly dredged from seabed.

4 AVAILABILITY OF FILL MATERIAL

Main sources of fill material for reclamation works in Singapore are earth obtained by levelling of hills and seabed sand obtained by dredging.

Before 1974, fill used for reclamation was obtained entirely from levelling of hills, an operation carried out in phase with development of public housing and industrial estates. Borrow area for East Coast Phases III and IV Reclamation Project was subsequently converted into a fresh water reservoir (Wei, 1983).

As land source is rapidly diminishing in capacity, seabed sand is dredged as fill. For the reclamation of offshore islands, seabed sand was the natural fill material. Dredging of seabed has enabled ships with deeper draught to call at Singapore Port, the World's 2nd busiest port after Rotterdam.

During the last 100 years, nearly 165 million m^3 of earth and 120 million seabed sand were moved to reclaim 53 km^2 of land.

5 SHORE-PROTECTION METHODS

When the reclaimed land is not used for wharf construction, shore-protection methods normally adopted for the reclaimed land are either revetment, or headland breakwaters or sandy beach.

Todate, more than 76 km of revetment was built involving at least 2.5 million m^3 of granite blocks, while nearly 20 km of reclaimed coastline is protected by headland break-

waters. The latter is concentrated at the eastern part of Singapore Island, where the reclaimed coastline is mainly catered for recreational purposes.

The remaining 40 km reclaimed coastline is unprotected resulting in formation of sandy beaches wherever sand is used as fill. One typical example of which is the creation of artificial beach at Singapore Changi Airport, where favourable angles of wave approach to the coastline result in negligible littoral drift and thus a remarkable stable beach is formed (Pui, 1983). With mild wave environment prevails around the entire Singapore Island, it is advisable that the sandy beach concept be adopted wherever there is no space limitation for beach formation.

6 FUTURE RECLAMATION IN SINGAPORE

Future reclamation works in Singapore would be executed in deeper water as most of the tidal flats at the fringe of the main island had been reclaimed. It is estimated that another 70 km^2 of land can be reclaimed without much affecting the tidal flows around the island, as well as on limited seaspace for navigation and anchorage, and for submarine services.

As fill is not readily available in large quantity for future major reclamation works, research is now being done in local university on use of marine clay as fill (Information Division, 1986). Marine clay covers much of the seabed around the island. If it is found suitable as fill, future reclamation works could proceed with less imported fill.

7 CONCLUSION AND RECOMMENDATIONS

In view of high population density, there is a constant need in Singapore for reclamation works in foreshore area for various development projects along the coastline.

Earlier foreshore reclamation works, commenced about 100 years ago, were mainly confined at the southern tip of Singapore Main Island. Works included reclamation for construction of road, and building of air and seaports.

Recent reclamation works are mainly carried out by three Statutory Boards as agents to the Government. Together, they have accounted for 90% of the land reclaimed from foreshore during the last 100 years.

Nearly 285 million m^3 of fill material was moved to reclaim 53 km^2 of land area during the last century. As a result, there is little suitable fill source left for further reclamation. Research works are now being done in

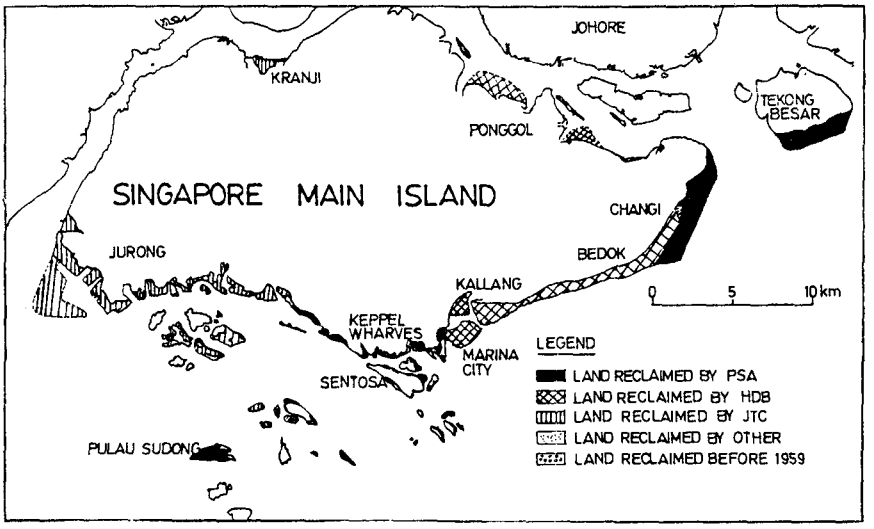

RECLAMATION MAP OF SINGAPORE

local university to verify the suitability of marine clay as fill, a material found in abundant quantity in Singapore.

With mild coastal environment prevails around the Singapore Island, it is suggested that sandy beach concept be adopted as a form of coastal protection method to reclaimed land, wherever there is space for development of beach slope. Saving up to US$1 million per kilometre is envisaged as compared with construction of revetment. Where littoral drift is significant, headland breakwaters can be provided to control the changes of the coastline.

Reclamation works in Singapore are envisaged to continue unabate as it is estimated that another 70 km² of foreshore could be reclaimed economically. This estimated area is more than the total land area reclaimed during the last 100 years.

8 REFERENCES

INFORMATION DIVISION, MINISTRY OF COMMUNICATIONS AND INFORMATION, SINGAPORE (1986). Land Reclamation: Our Resources Stretched. The Mirror, 22(3), pp 1-16.

BOGAARS, G. (1956). The Tanjong Pagar Dock Company (1864 - 1905), Memoirs of the Raffles Museum, No. 3.

REITH, G.M. (1907). Handbook to Singapore. Second edition. Fraser and Neave Ltd., Singapore. 133 pp.

WEI, J. AND CHIEW, L. K. (1983). Reclamation on the east coast of Singapore. Proc. International Land Reclamation Conference, Essex, England, pp. 67 - 100.

RADHAKRISHNAN, R., NG, F.W., RAJENDRA, A.S. and PUI, S.K. (1983). Land Reclamation for Singapore Changi Airport. Proc. International Land Reclamation Conference, Essex, England.

PUI, S.K., RADHAKRISHNAN, R. and RAJENDRA, A.S. (1983). Performance of Artificial Beaches at Changi. Proc. International Conference Coastal and Port Engineering in Developing Countries, Colombo, pp 61 - 73.

CHAPTER 196

WAVE-INDUCED EFFECTS IN A COOLING WATER BASIN

Fredric Raichlen, F.ASCE*

Introduction

Wave-induced effects have been observed in a model of the cooling water intake basin of the Pacific Gas and Electric Company's Diablo Canyon Nuclear Power Plant. This model, built to an undistorted scale of 1:45, was constructed initially to study the design for the repair of the terminus region of the West breakwater damaged in storms of January 28, 1981. It was decided by PC&E to investigate, in the same model, the forces due to waves acting on two air intake structures for the auxiliary saltwater pumps and the pressures on the external and the internal walls and the ceiling of the cooling water intake structure located in the man-made cooling water intake basin. During the course of the experiments it was noticed that the mean water level in the breakwater enclosed basin changed as a function of the incident wave characteristics. This allowed waves to overtop the cooling water intake structure which, without the change in mean water level, would not have occurred. It is this difference between the mean water level and the still water level inside the cooling water basin, defined as ponding, which will be reported herein.

Diskin, et al. (1970) investigated this effect behind low and submerged permeable breakwaters in a two-dimensional wave tank model. As was mentioned by them, in normal breakwater tests it is a common practice to provide some means of communication between the seaward and shoreward side of the breakwater so that precisely this mean water level change due to overtopping of the structure does not occur. For their experiments the change in mean level varied from about 5% of the deep water wave height to 32% of the deep water wave height depending upon the submergence of the breakwater crest; the smallest change corresponded to the largest depth over the breakwater crest.

This effect was discussed by Dalrymple and Dean (1971), and they proposed an analytical model based on the conservation of mass. The estimated inflow was equated to an estimate of the return flow over and through the permeable structure. Some limited agreement with the results of Diskin, et al. (1970) were shown.

Seelig (1983) presents the results of laboratory experiments conducted to investigate reef-lagoon system hydraulics. The laboratory tests were two-dimensional wave flume experiments, and indicated that there could be a significant increase in the mean water level within the lagoon due to a seaward reef. Again, these experiments were two-dimensional.

*Prof. of Civil Eng., W.M. Keck Lab of Hyd. & Water Res., Calif. Inst. of Tech., Pasadena, CA 91125, U.S.A.

The study described here, which is an investigation in a three-dimensional undistorted hydraulic model, is in a sense a more realistic model of the actual dynamics of time-varying storage than the two-dimensional experiments summarized above. Due to complexities associated with the three dimensionality, no attempt has been made to develop a detailed analytical model to describe the observed differences between the still water level and the mean water level denoted here as ponding. Therefore, certain of the data obtained in the course of this experimental program will be presented here and discussed in terms of their physical significance without an attempt at a more general development. Somewhat different definitions of ponding are used for the regular and the irregular wave experiments; these will be defined clearly as the pertinent results are presented.

Experimental Equipment

Figure 1 shows the boundaries of the wave basin which was used and the bathymetric contours in the 1:45 undistorted hydraulic model. The highly contorted bottom contours were accurately represented in the model. The cooling water intake basin is seen in the upper right-hand portion of this figure with the two breakwaters (the West and East) forming the boundaries of the protected basin. The breakwaters are built on rock formations which themselves tend to form natural seaward boundaries to the basin.

Wave guides and the wavemaker plate are shown arranged for waves approaching approximately from the west. Numerical methods were used to refract waves from deep water to the depth of approximately 100 ft where the wavemakers are located. (In this paper all dimensions will be given in prototype units.) The wavemaker was divided into five segments, each driven by a programmable hydraulic system from one function generator; the units were portable and could be aligned to correspond to different wave approach directions.

The original breakwaters were constructed with tribars as their outer armor protection and with a concrete cap with a crest elevation of +20 ft MLLW. A detailed description of the model and the breakwaters is presented by Lillevang, et al. (1984). Two different crest elevations were used in these experiments: +20 ft MLLW and 0 ft MLLW. The latter represented an extreme case where the crest of each breakwater was assumed to have been degraded uniformly to MLLW by storm waves. A third case was tested without breakwaters; certainly an extremely conservative condition.

Both regular and irregular waves were used in these experiments. For periodic waves the cnoidal wave generation procedure presented by Goring and Raichlen (1980) was used. To minimize disturbances and provide more permanent waves in the limited space available, a procedure was developed always to begin the wave machine trajectory at a position which corresponded to a zero plate velocity.

Capacitance wave gages, which could be calibrated remotely, were located throughout the model; the locations are indicated by letter in Figure 1. Waves were not measured at all locations simultaneously.

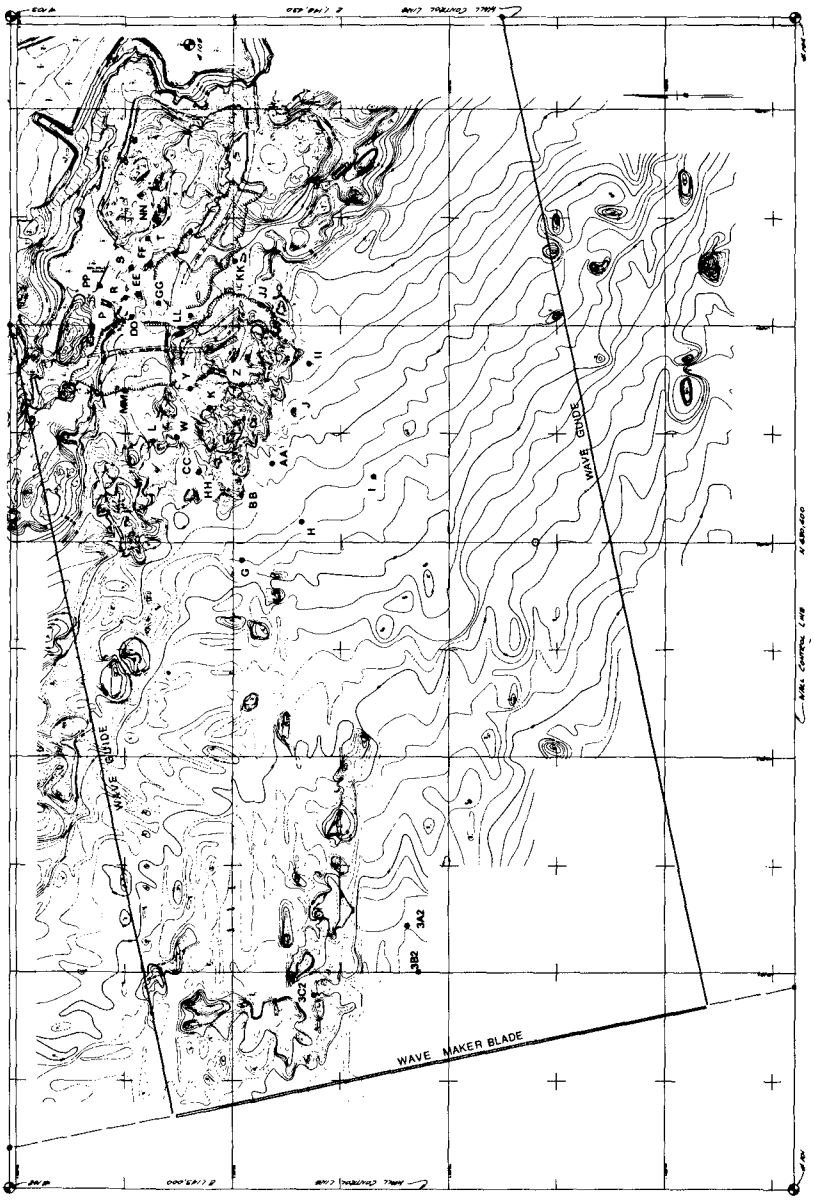

Figure 1 Wavemaker Placement in the Model Basin and Location for Probes, Waves from the West.

The three locations which will be referred to herein are those indicated as: 3B2 near the wave machine, and R and S in front of the cooling water intake structure inside of the cooling water intake basin. (The latter are each located approximately 100 ft seaward of the intake structure and spaced 150 ft apart.) The wave gage at location 3A2 was used with that at 3B2 to define approximately the reflectivity of the breakwater system in the model using a method presented by Goda and Suzuki (1976).

Irregular waves were generated using the wave plate transfer function determined experimentally and spectra defined by either offshore measurements or hindcasting procedures. The method of Goda (1970) was used to transform a spectrum into its harmonic components from which the wave machine trajectory was defined. For the irregular waves discussed herein the wave machine trajectory was determined from a wave spectrum measured on January 28, 1981 at 1800 hrs GMT by the National Oceanic and Atmospheric Administration (NOAA) Buoy 46011 located 18.6 nautical miles southwest of the Diablo Canyon Nuclear Power Plant.

Presentation and Discussion of Results

In this section results will be presented from the experiments conducted with both regular and irregular waves. An example of wave records taken at locations 3B2 near the wave machine and R and S inside the intake basin are presented in Figure 2 for an azimuth direction at the wave machines of 258°. The upper portion of the figure shows cnoidal waves with a period of 12 seconds and a height of approximately 40 ft near the wave machine; the water surface time histories at R and S are shown in the lower part. The breakwater crest for these experiments was degraded to 0 ft MLLW. The effects of wave breaking and overtopping of the structure are evident at stations R and S, and it is noted that the mean level is different from the still water level. As mentioned earlier, the difference between the mean level and the still water level (which is indicated on the figures by a line extending across the figure) for these periodic waves is termed "ponding". Referring back to Figure 1 it is seen that, for this three-dimensional arrangement, in addition to the return flow over and through the permeable breakwaters there is the return flow through the entrance of the basin. This unsteady flow back through the entrance would be defined by the time varying ponding level.

In Figure 3 the variation in the difference between the mean level and the still water level within the basin, denoted as Δ, is shown as a function of offshore wave height. The ponding level was obtained by taking the time average between the second and the sixth waves in the train such as that shown in Figure 2. These figures present data at positions R and S for different breakwater crest elevations (BRKWTR ELEV.), water depths (W.S. ELEV.), wave periods, and incident wave directions (AZIMUTH). (The extreme still water level of +17 ft MLLW was based on the simultaneous occurrence of an extreme high astronomical tide, storm tide, and tsunami.) It is interesting to see, especially at location R, there is a general trend of increasing ponding elevation with offshore wave height with little effect of direction or depth; at S there appears to be more of an influence of both direction and depth. The ponding elevation measured is approximately 10% of the offshore

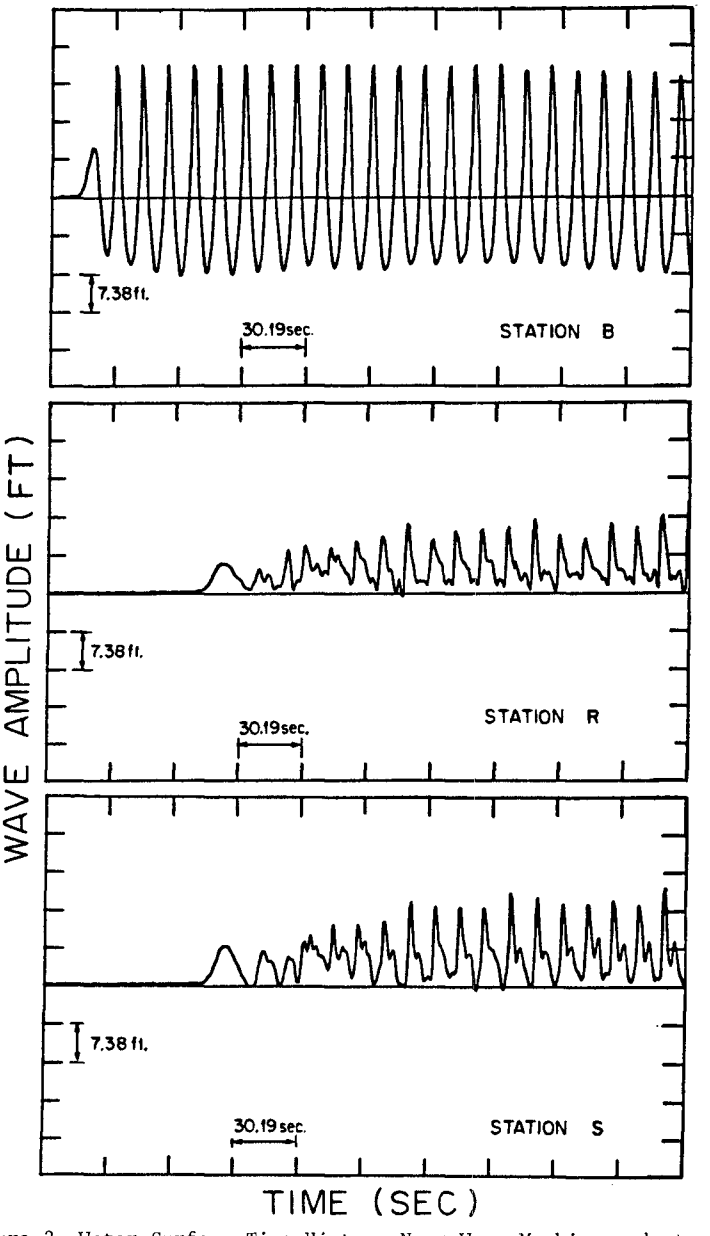

Figure 2 Water Surface Time History Near Wave Machine and at Locations R and S.

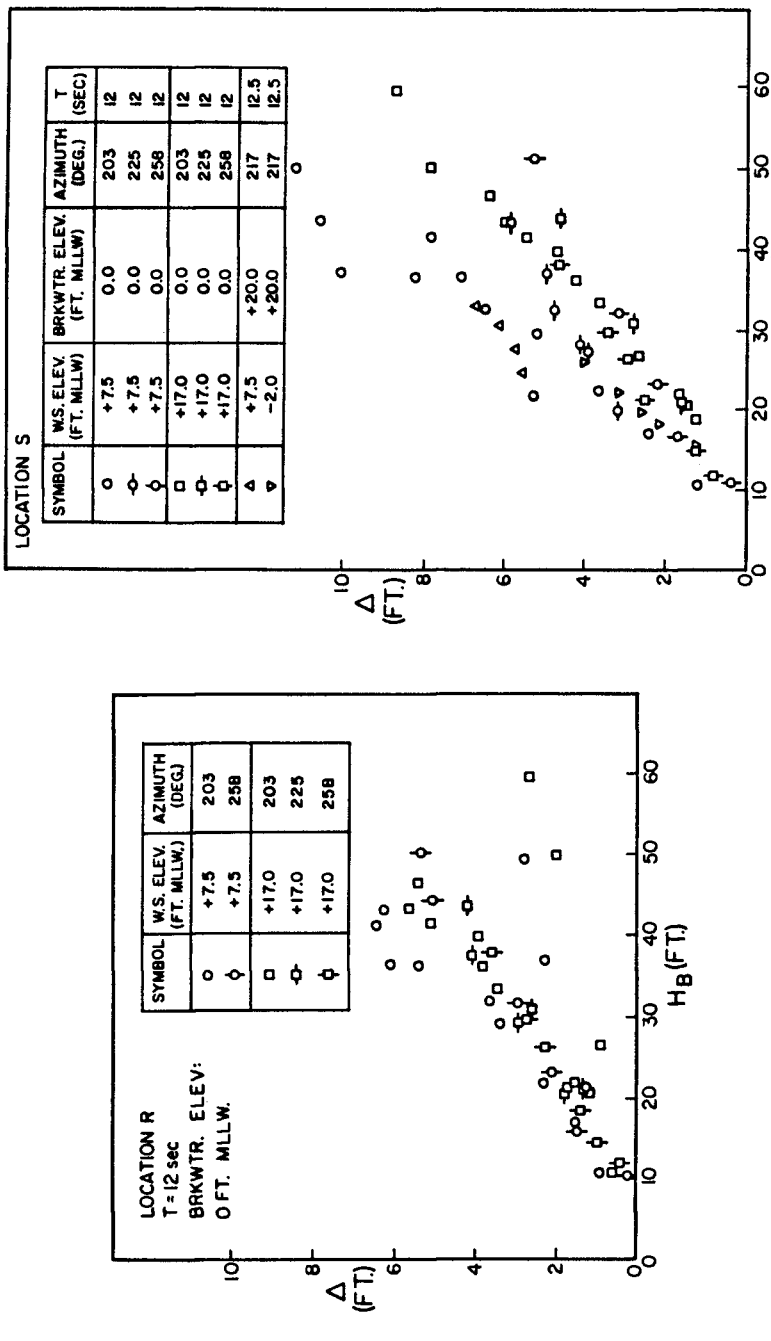

Figure 3 Variation of Ponding at Locations R and S with Offshore Wave Height.

wave height for this case. For the breakwater crest at 0 ft MLLW but with the still water level at +7.5 ft MLLW significantly more scatter of the data is apparent than for the larger depth over the breakwater. This probably can be attributed to the effects of wave breaking and the relatively small depth over the crest through which the broken waves must propagate before entering the intake basin. It should be realized that the width of the breakwater crest is increased significantly for the degraded condition compared to that for the crest at +20 ft MLLW, since in designing the degraded section the volume of the breakwater between 0 ft MLLW and +20 ft MLLW was placed on the shoreward side of the breakwater. (At a crest elevation of +20 ft MLLW the crest width is 21 ft, about three depths, but for the degraded section it would be about 90 ft or about 12 depths.) For the breakwater with its crest at +20 ft MLLW and for mean water levels at +7.5 ft MLLW and -2 ft MLLW the ponding for the former is somewhat greater than for the latter.

In Figure 4 examples are shown of the ponding as a function of the parameter HL; where H and L represent a wave height and wave length, respectively. (The wave height and wave length are defined from linear wave theory using the incident wave height measured at station B near the wave machine, and based on a depth of 50 ft MLLW plus the indicated "tide" elevation, e.g. for a "tide" of +17 ft MLLW a depth of 67 ft was used in the calculations.) This parameter is proportional to the volume under the crest of a periodic wave. The reason for using HL is that the quantity of water which overtops the breakwater and flows into the cooling water basin must be related to the "crestal" wave volume which would be a measure of the volume of the breaking wave which would be associated with overtopping. This is a relatively unsophisticated approach to the problem, and does not consider the detailed intricacies of both overtopping and return flow as, for example, Dalrymple and Dean (1971) did for a two-dimensional problem. The data shown in Figure 4 correspond to an azimuth approach near the wave machines of 203°, some of these data have been presented earlier in Figure 3. In addition, data corresponding to wave periods of 16 sec and 20 sec also are presented.

Data corresponding to the model without the breakwater in place also are presented in Figure 4. These data are for 10 sec and 16 sec waves approaching from 203° with the water surface elevation (W.S. ELEV.) at +7.5 ft MLLW. Generally, it appears that the ponding trends are similar to the cases with the breakwater enclosed basin. However, for a given crestal volume there is less ponding for this case than for the breakwater enclosed cooling basin with the same water depth. Thus, even though the bottom bathymetry acts to form a natural basin it is no doubt the impediment of the return flow imposed by the breakwaters which causes a larger volume storage (and ponding) in the basin.

Average curves obtained from data such as those presented in Figure 4 for R and S are shown in Figure 5; data corresponding to experiments with several different water surface elevations and for the breakwater crest at +20 ft MLLW and at 0 ft MLLW have been used. For convenience, one of the curves in the upper portion of the figure is presented in the lower part at an expanded scale. It is seen that with the exception of the largest depth with the degraded breakwater, all data are in

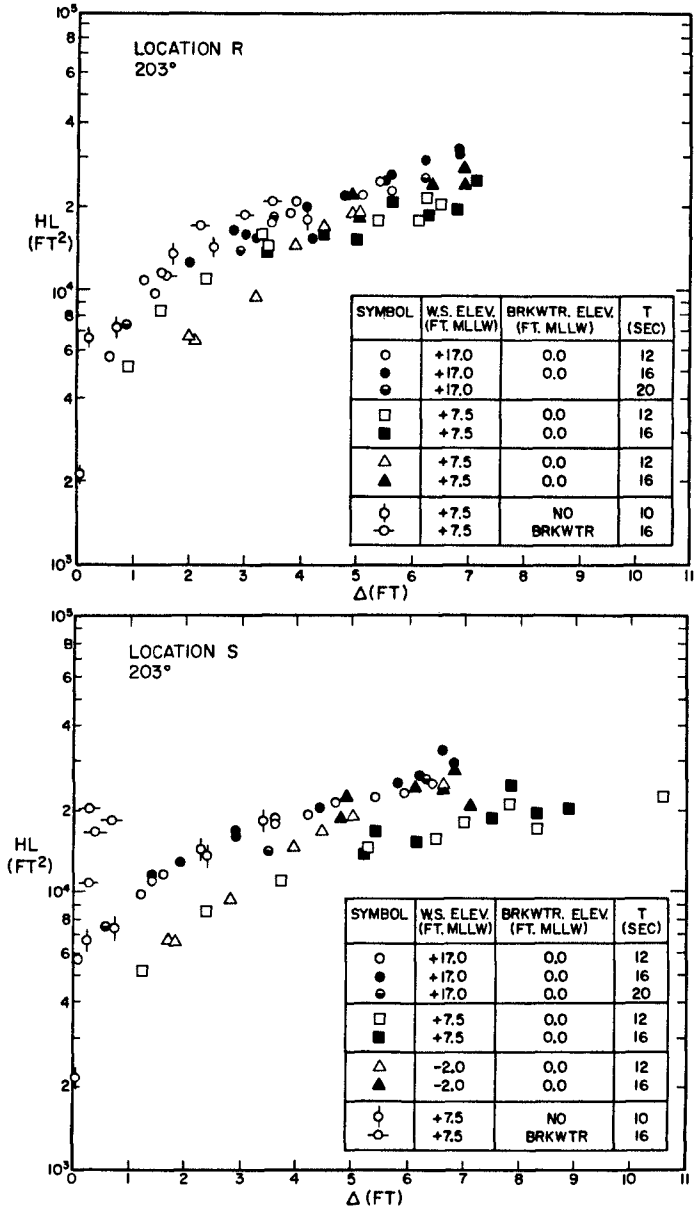

Figure 4 Variation of Ponding at Locations R and S with Wave Crestal Volume Function, HL.

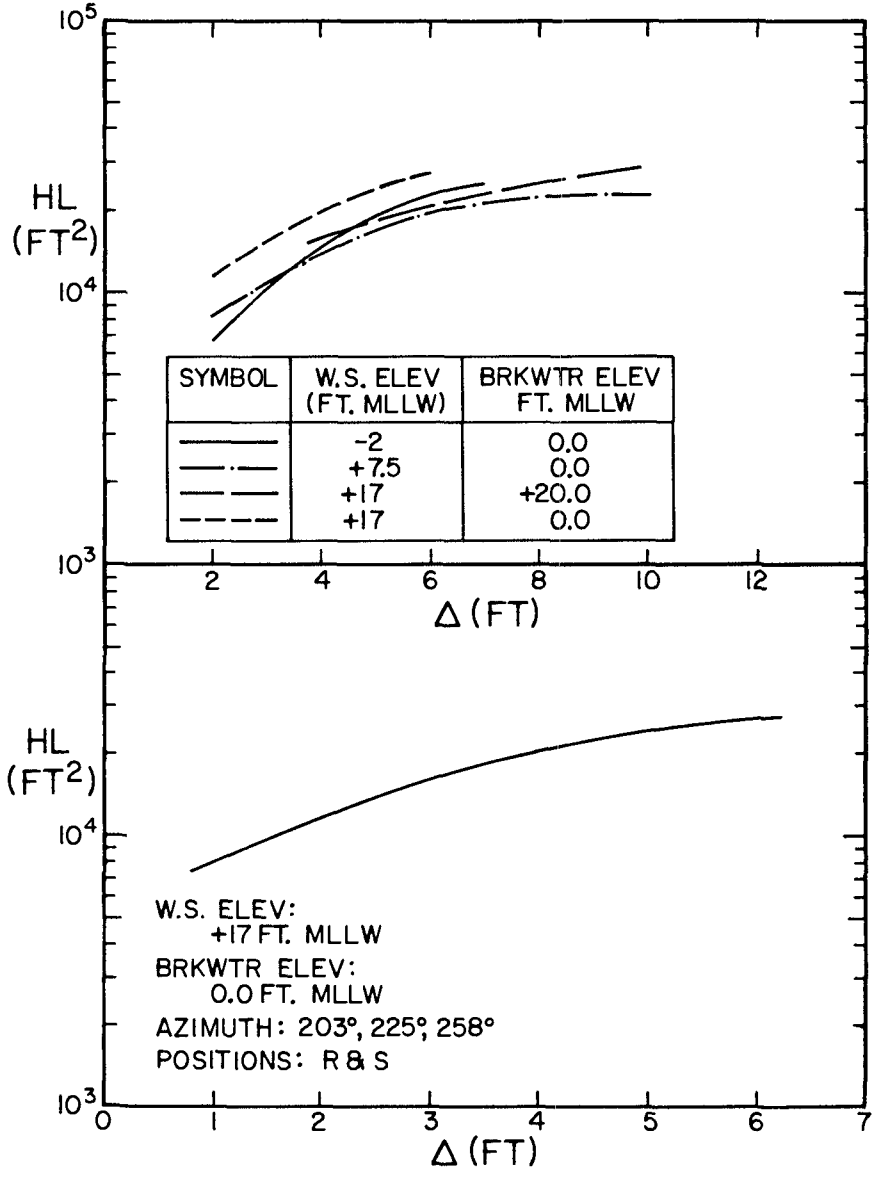

Figure 5 Variation of Average Ponding with Wave Crestal Volume Function, HL.

reasonable agreement when the ponding is presented in terms of the crestal volume parameter.

Experiments were conducted with irregular waves, and data relating to ponding for these cases also are presented. In Figure 6 the water-surface time history near the wave machine is shown for an irregular wave train whose spectral distribution of energy used in constructing the wave machine trajectory was obtained from measurements made by NOAA Buoy No. 46011 on January 28, 1981, at 1800 hrs GMT. (It should be noted that, relative to the still water level, the ordinate is scaled arbitrarily in Figure 6.) The corresponding relatively narrow-band wave spectrum (with the ordinate representing the energy density in units of ft^2sec) is presented in Figure 7 showing a concentration of energy at a frequency of about 0.06 Hz. The significant wave height as determined from the spectrum is about 28 ft.

In Figure 8 the frequency distribution of wave heights offshore as determined from measurements in the model is presented. The ordinate is the wave height normalized by the significant wave height and the abscissa is the percent by number of waves greater than the indicated height. A Rayleigh distribution is fitted to the data for comparison, and the agreement appears reasonably good except at the extremes, which is as would be expected.

The water surface time history measured at position S is shown in Figure 9; the difference between the mean level and the still water level is evident. The corresponding spectrum is presented in Figure 10 showing the modification of the wave spectrum due to the propagation of the waves over the degraded breakwater into the cooling water basin. Wave breaking tends to introduce the higher frequency components seen centered at about 0.15 Hz with a remnant of the original spectrum remaining at a frequency of about 0.045 Hz. A low frequency component, not seen before, appears at a frequency of about 0.02 Hz (50 sec) along with a mean, i.e., a zero frequency component. The latter reflects the direct effect of ponding whereas the former possibly is evidence of a mode of oscillation of the basin which may be excited by the impingement in the basin of breaking waves which overtop the breakwater.

It is interesting to compare Figure 10 with Figure 7. In the latter there is an absence of energy at frequencies less than 0.03 Hz whereas in the former, i.e., the spectrum of waves at location S, energy exists below that frequency. Since it is apparent that the energy below 0.03 Hz is due to the overtopping process, only this energy was retained in investigating ponding in the cooling water basin. This was done by eliminating all harmonic components at frequencies greater than 0.03 Hz; the resultant water surface time history is shown in Figure 11. This is used to determine a frequency distribution of water surface elevation for the filtered water surface time history as well as an average mean level. For irregular waves, where the long period oscillation is easily seen in Figure 11, the ponding is defined from this frequency distribution. It is defined in this way as opposed to evaluating only the mean of the water surface because it is apparent that there is a significant effect of the low frequency "carrier" component on the crest elevation of the wave. It is this elevation

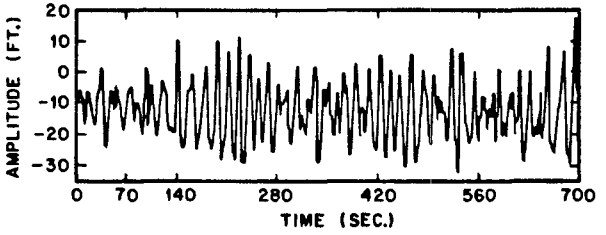

Figure 6 Water Surface Time History Offshore.

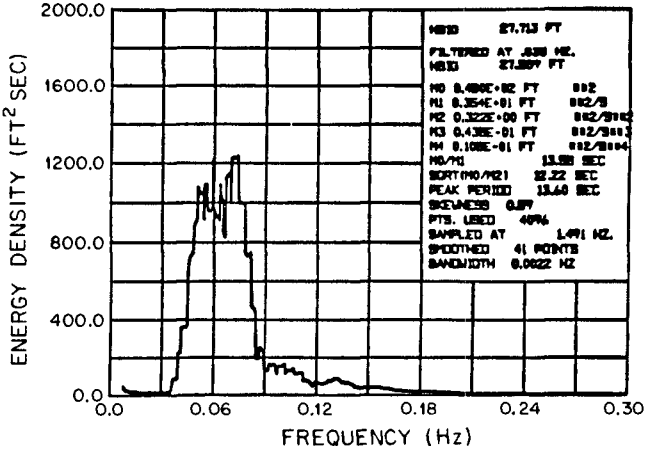

Figure 7 Energy Spectrum Offshore.

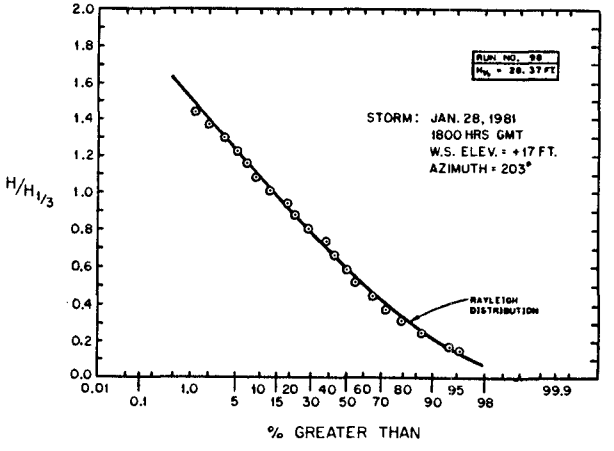

Figure 8 Frequency Distribution of Wave Height Offshore.

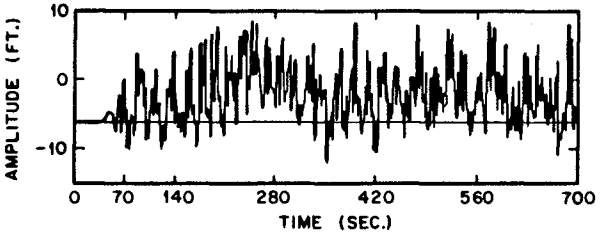

Figure 9 Water Surface Time History at Position S.

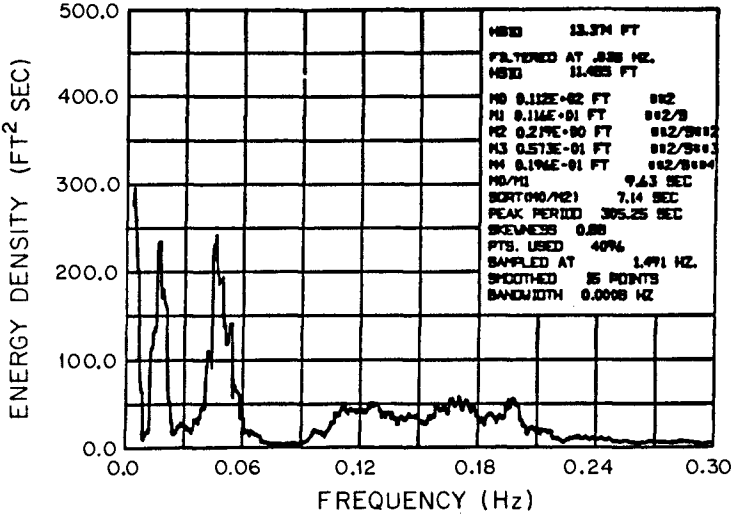

Figure 10 Energy Spectrum at Position S.

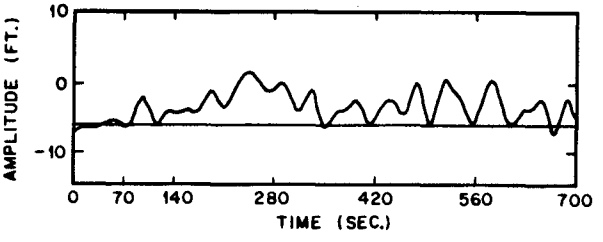

Figure 11 Filtered Water Surface Time History at Location S.

which is most important in the effect of waves in the breakwater protected basin on structures located around its boundary such as the cooling water intake structure. (Data corresponding to the mean alone will be presented also for completeness.)

A typical frequency distribution of the filtered water surface time history is presented in Figure 12. The ordinate is the ponding elevation, i.e., the elevation of the filtered water surface time history relative to the still water level, and the abscissa is the percent by number greater than the indicated elevation. The data shown are for positions R and S for a condition where the tide is -2 ft MLLW with the breakwater degraded such that the crest is at 0 ft MLLW.

Additional data are presented in Figure 13 for several different conditions of still water surface elevation and breakwater crest elevation. In this figure it is observed that the maximum still water surface elevation and the maximum breakwater crest elevation results in the lowest ponding. The maximum ponding occurs for the degraded breakwater with the lower of the two still water levels. If one defines the mean ponding for the irregular wave as the time average of the water surface time history shown in Figure 11 the following values are obtained for experiments 147, 148, and 231: 1.62 ft, 2.6 ft and 1.0 ft, respectively. Thus, there appears to be a somewhat different trend for the irregular wave case as compared to the regular wave results presented in Figure 5; this may be an effect of direction as the waves in experiment 231 are from the south, but those for 147 and 148 are more westerly.

As mentioned earlier, an important effect of the ponding in the cooling water basin is its effect on the elevation of the crest of the wave relative to the still water level. This relates, for example, directly to the overtopping of the cooling water intake structure located along the north boundary of the cooling water basin. Examples of this are shown in Figure 14 for periodic waves for three cases: a still water level of +17 ft MLLW and of -2 ft MLLW with the degraded breakwater and the higher still water level with the breakwater crest at elevation +20 ft MLLW. The ordinate in Figure 14 is the elevation of the crest of the wave in the basin relative to the still water level and the abscissa is the corresponding elevation of the crest of the wave outside of the basin also measured relative to the still water level; a line of equivalence is shown as a solid line in the figure. For 12 sec waves, the distance from the still water level to the crest of the wave at positions R and S appears to be relatively independent of whether the breakwater is at the full elevation of +20 ft MLLW or at 0 ft MLLW for the maximum still water surface elevation (+17 ft MLLW). This indicates, with regard to the elevation of the maximum instantaneous water level in the basin, the effect on the elevation of the wave crest of the elevation of the breakwater crest is small. This means that the effect of ponding must negate to some extent the reduction in wave height due to the increased protection to the cooling water basin afforded by the higher breakwaters.

Conclusions

The following major conclusions can be drawn from this investigation:

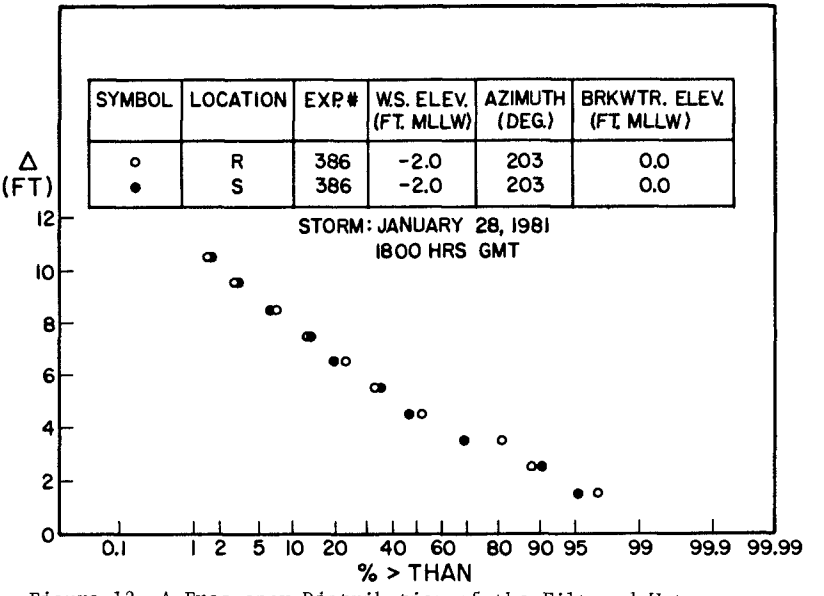

Figure 12 A Frequency Distribution of the Filtered Water Surface Time History.

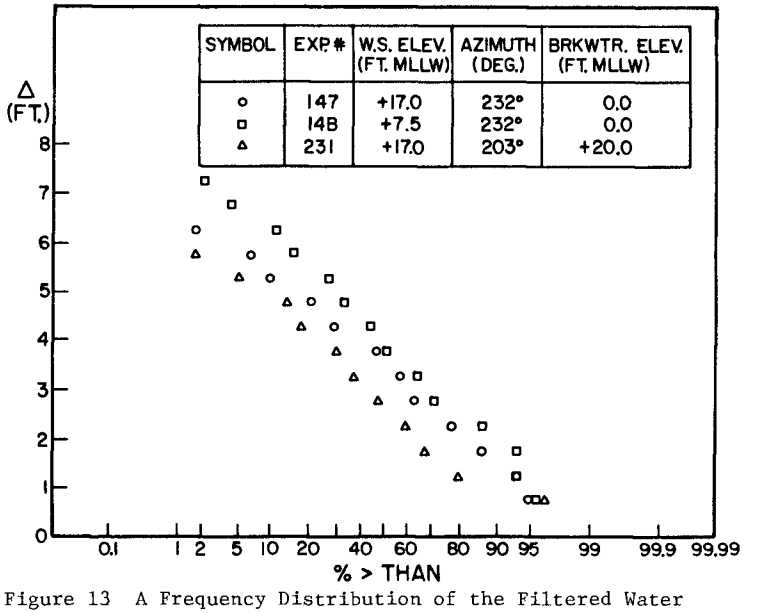

Figure 13 A Frequency Distribution of the Filtered Water Surface Time History.

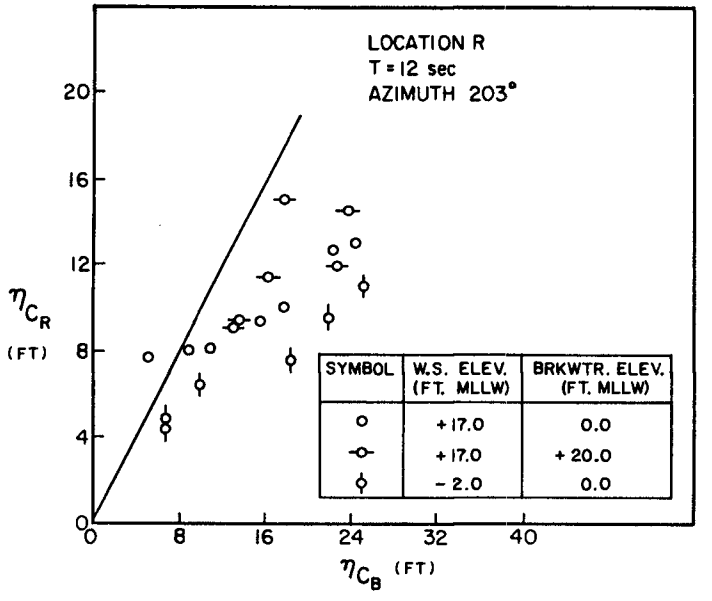

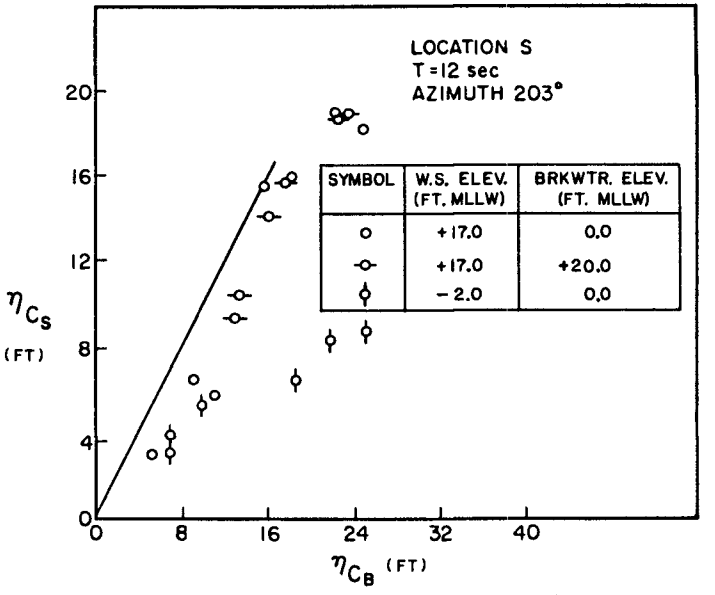

Figure 14 The Variation of the Amplitude of the Crest of the Wave Within the Basin to that Outside.

1. A significant change in the mean water level elevation in the cooling water basin can take place due to the overtopping of the West and East breakwaters. This has been defined in this study as ponding.

2. For regular waves the difference between the mean water level and the still water level can be about 10% of the offshore incident wave height.

3. For regular waves, it appears that the breakwater with its crest at +20 ft MLLW results in larger ponding than when the crest is at 0 ft MLLW.

4. Although the results for periodic waves show a direct dependence of ponding on the wave period, when the data are presented in terms of a measure of the overtopping wave volume, HL, the dependence on wave period is reduced significantly.

5. Irregular wave overtopping of the breakwaters tends to induce oscillations in the cooling water basin and increase the mean water level. Thus, an improvement of wave conditions inside a basin created by breakwaters which may be partially overtopped is, to some extent, reduced by these other wave-induced effects.

Acknowledgement

This study was supported by Pacific Gas and Electric Company; the assistance of Mr. Larry Harrison of PG&E and discussions with Mr. Omar J. Lillevang were appreciated. The Offshore Technology Corporation, Escondido, California, with Dr. J. Ian Collins and Mr. William G. Grosskopf involved, conducted the experiments. Mr. Ross Buchanan, of Bechtel Corporation, assisted in the data reduction.

Appendix--References

Dalrymple, R.A. and Dean, R.G., Discussion of "Piling-up Behind Low and Submerged Permable Breakwaters," Jour. W.W.H., ASCE, Vol. 97, No. WW2, May 1971.

Diskin, M.H., Vajda, M.L. and Amir, I., "Piling-up Behind Low and Submerged Permeable Breakwaters,: Jour. W.W.H., ASCE, Vol. 96, No. WW2, May 1970.

Goda, Y., "Numerical Experiments on Wave Statistics with Spectral Simulation," Report of the Port and Harbor Inst. of Japan, Vol. 9, No. 3, Sept. 1970.

Goda, Y. and Suzuki, Y., "Estimation of Incident and Reflected Waves in Random Wave Experiments," Proc. 15th Intern. Conf. on Coastal Engr., 1976.

Goring, D.G. and Raichlen, F., "The Generation of Long Waves in the Laboratory," Proc. 17th Intern. Conf. on Coastal Engr., 1980.

Lillevang, O.J., Raichlen, F., Cox, J.C., and Behnke, D.L., "A Detailed Model Study of Damage to a Large Breakwater and Model Verification of Concepts for Repair and Upgraded Strength," Proc. 19th Intern. Conf. on Coastal Engr., 1984.

Seelig, W.N., "Laboratory Study of Reef-Lagoon System Hydraulics," Jour. Waterway, Port, Coastal and Ocean Engr., ASCE, Vol. 109, No. 4, Nov. 1983.

CHAPTER 197

Surface currents remotely observed by means of RADAR

F. Schirmer [+]
H.-H. Essen [++]
K.-W. Gurgel [+++]

INTRODUCTION

Surface currents normally are difficult to measure. Only a set of Lagrangian drifters observed from fixed stations or from an aircraft or by satellite can give adequate information. Beneath this there is a new and powerfull field measuring tool which functions with a decametre backscatter radiowave RADAR. Two (or more) such fixed RADAR stations on land or on islands can remotely measure the surface currents in front of them with high resolution in space and time.

This paper has two aims: first, to give a short explanation of the physical principles of the backscatter RADAR and to show its requirements and its limits, and secondly, to demonstrate the possibilities offered by this RADAR with an example of the coastal surface current off Norway.

PHYSICS OF OPERATION

A radio pulse or wave train of frequency 29.85 MHz is transmitted from a place near to the shore. The sea surface acts to the radio wave train as a scattering grid due to BRAGG scattering mechanism: if the wavelength of the transmitted electromagnetic wave is λ_{EL} (approximately 10 m) only those spectral parts of the seas gravity waves (surface waves) with wavelength

$$\lambda_{GR} = 0.5\,\lambda_{EL}$$

are responsible for the intense backscatter of electromagnetic waves. All other elevations of the sea surface act

+ Dr. Florian Schirmer, Dipl.-Phys., member of Hafenbautechnische Gesellschaft e.V. (Association for Port a. Coastal Engineering)
++ Dr. Heinz-Hermann Essen, Dipl.-Phys.
+++ Klaus-Werner Gurgel, Dipl.-Ing.

present address of authors:
University of Hamburg, Institut fuer Meereskunde,
Troplowitzstrasse 7, D 2000 Hamburg 54, W.-Germany.

as scattering targets too, but their combined scattered total energy is some orders less due to destructive interference.

The received backscattered echo from the sea has a somewhat different frequency compared to the transmit signal. This is caused by the phase velocity v_{GR} of those ocean gravity waves which fulfill the BRAGG-condition: If the transmit frequency is f_{EL} and the phase velocity of the gravity waves is

$$v_{GR} = \sqrt{g \cdot \lambda_{GR} / 2\pi}$$

where g is the acceleration due to gravity, the DOPPLER shifted backscattered frequency $f_{EL,D}$ becomes

$$f_{EL,D} = f_{EL} \cdot \left(1 \pm \frac{v_{GR}}{c}\right)^2$$

where c is the speed of light.

The difference in frequency between f_{EL} and the received DOPPLER-echo $f_{EL,D}$ is in the order of one Hertz. Because all variables are known, one can predict this difference. Early observations by D. D. Crombie (1955) turned out that there are differences between predicted and measured frequency shift values. He found, that underlying ocean current is increasing or decreasing the phase velocity of ocean gravity waves thus giving somewhat higher or lower echo frequency shifts. Later on Crombie and many other scientists, in particular D. E. Barrick (1977), B. J. Lipa (1977) and E. D. R. Shearman (1980) used HF-backscatter to remotely measure ocean surface current and wave hight, the latter from the strength of the echo.

THE CODAR

The ocean current mapping HF-RADAR used by us is originally evolved by the U.S.-NOAA's Wave Propagation Laboratory (WPL) in Boulder, Colorado. D. E. Barrick, M. W. Evans and B. L. Weber (1977) and others there developed a RADAR for current mapping which they called CODAR, an acronym for Coastal Ocean Dynamics Application Radar.

The CODAR consists of a transmit antenna near to the shore and a set of four receiving antennas for direction finding of the HF-echos from the sea. The transmitted (and received) electromagnetic wave is a ground wave which follows the curvature of the earth. The water in this case be electric conductive salt water. In the case of fresh water or of sea ice no ground wave is generated.

A single CODAR station can only measure the radial component of the surface current at each point of the sea in front of it. So a minimum of two stations separated by

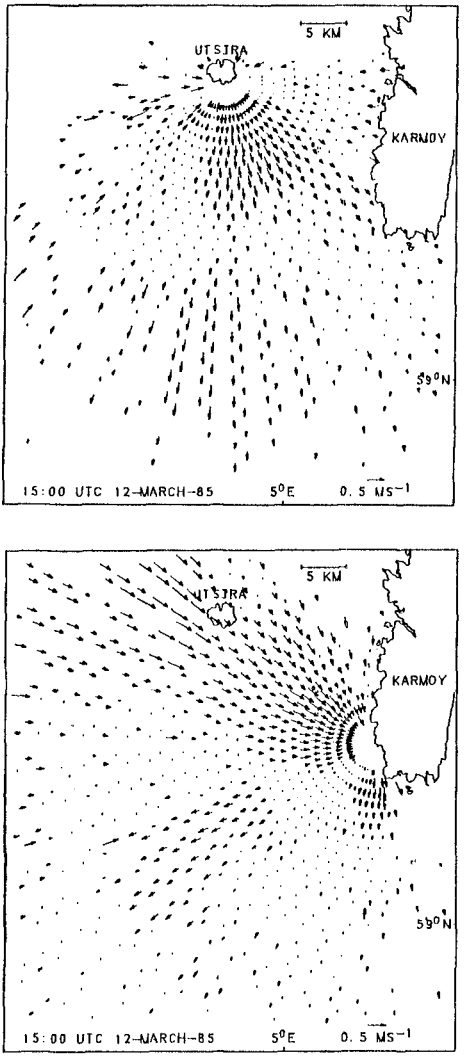

igure 1: The radial portion of the total current field, as seen at the same time from a CODAR station on the island UTSIRA and a second one on the island KARMOY off Norway.

some ten kilometres is capable to give complete information about the two dimensional surface current field. During recent years we developed further both the hardware and the software of our original CODAR transceivers. One of the technical inventors of CODAR, M. W. Evans, founded a company offering CODAR's for sale +). Modern CODAR stations are lightweight and need only some kilowatts electric power.

As a first step each CODAR station is generating a map of measured radial current vectors as shown in figure 1. The azimutal resolution here is 6 degrees while the radial extension is staggered into range cells of 1.2 km depth each. Every radial current vector in fig. 1 is an average over 18 minutes of observation.

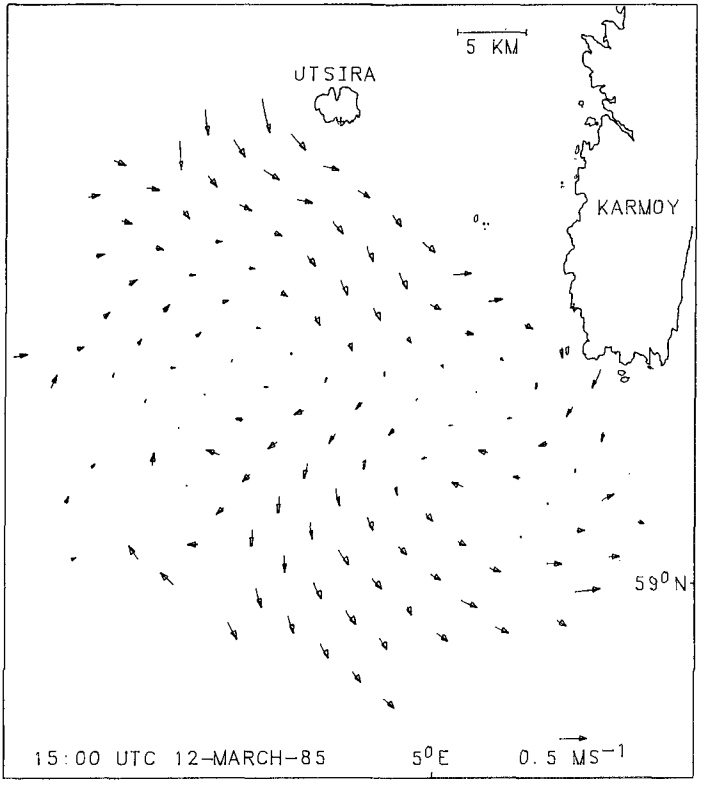

Figure 2: Total surface current field by combination from figures 1.

+) CODAR Technology, Inc., 1428 Florida Ave., Longmont, Colorado 80501, U.S.A.

From two - or more - sets of radial current vectors a final vector map of the total 2-dimensional surface current is produced by combining the radial shares. This is done at each point of a rectangular grid which is adjusted to the observation area. The result of this step is shown in figure 2.

The maximum range we obtained up to now is 50 km, depending on sea state, salinity of water and the place for erection of the antennas. Sometimes there is interference by strange transmitters, but the CODAR can change its own operation frequency.

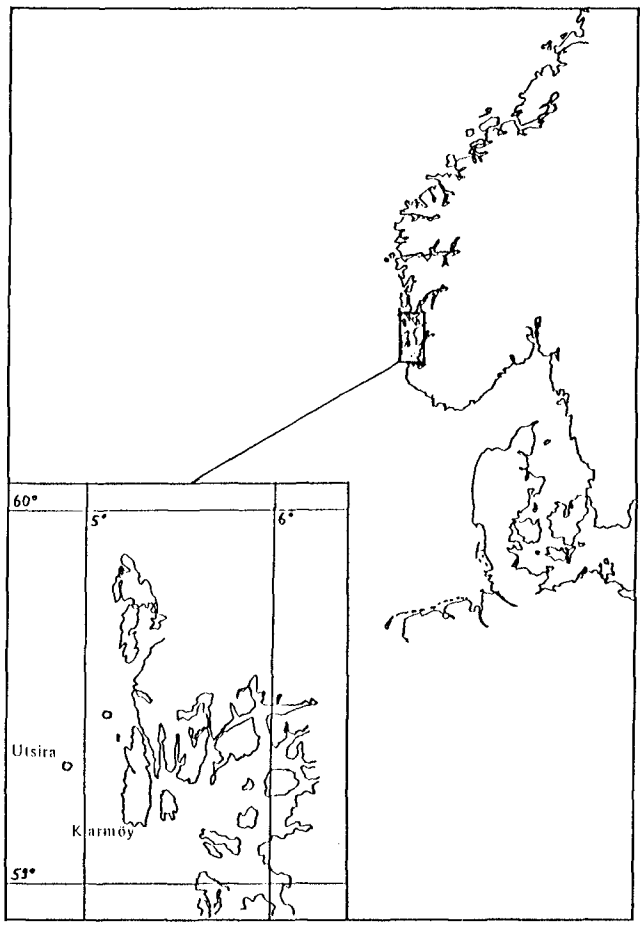

Figure 3, 4: Observation area off Norway. Distance between stations UTSIRA and KARMOY is 21 km.

SURFACE CURRENT MAPS

As an example some measurement results off Norway in 1985 are given here. The area under observation is shown in fig. 3 and enlarged in fig. 4. Two CODAR stations have been installed on the rocks of the coast: one on the island Utsira, the other on the island Karmoy, both sites belonging to Norway.

From satellite pictures it is known that eddies with radii from 10 to 50 km are generated here. Strong tidal and residual currents are typically. It is supposed that a sea bottom topography - given in fig. 5 - which is rich in contrasts is responsible for the generation of eddies. The

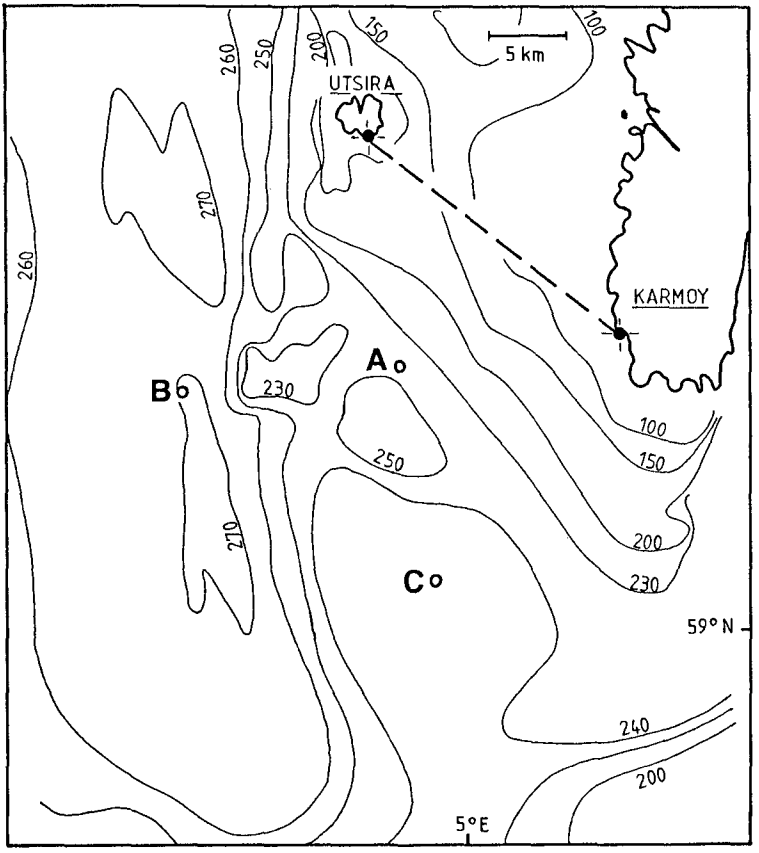

Figure 5: Sea bottom topography; depth given in meters.

consecutive pictures in figure 6, taken during 8 hours of observation, are an example from a set of 150 CODAR observations there.

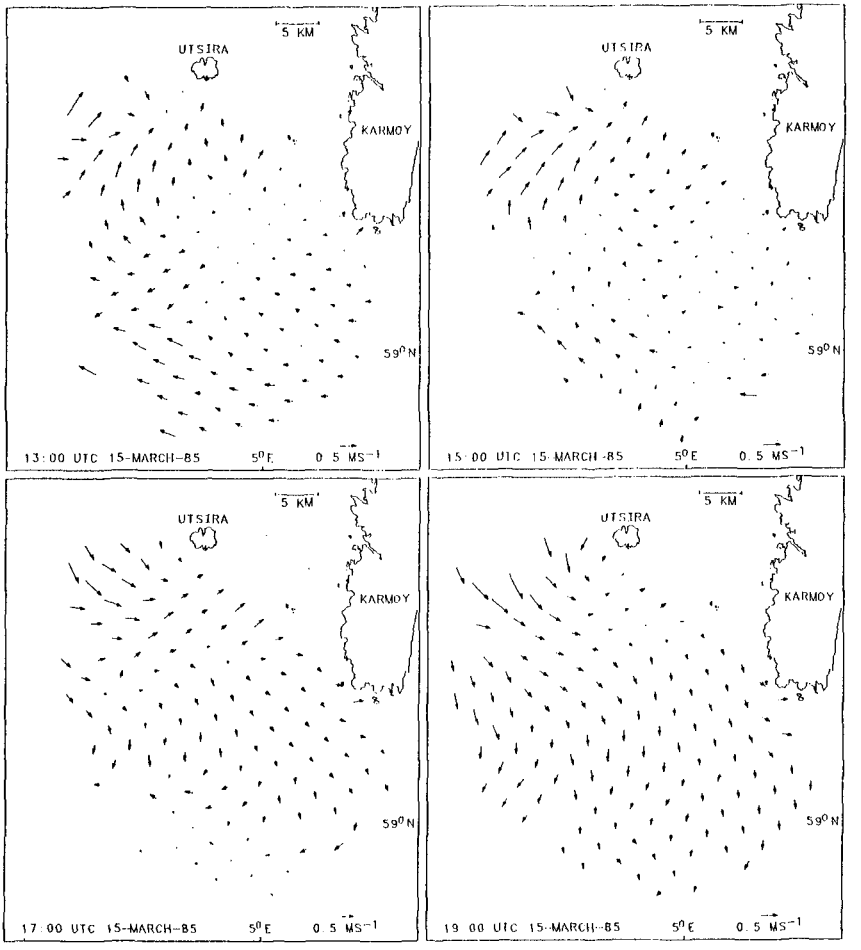

Figure 6: Four consecutive surface current patterns as observed every 2 hours.

TIME SERIES OF SURFACE CURRENT

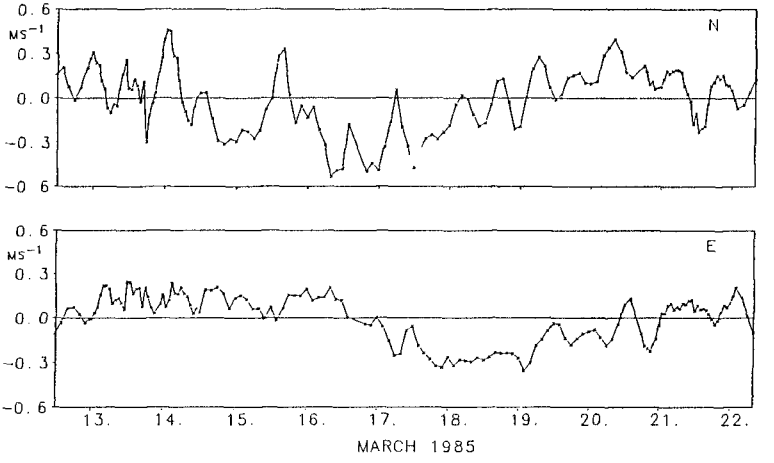

Figure 7: Current velocities at place C versus time.

From a set of consecutive current maps one can compute time series of the current velocity for each place of interest. An example for place C in fig. 5 is given in fig. 7. More detailed analysis of time series obtained from CODAR-results is given by Essen, Gurgel and Schirmer (1983) and by Essen, Freygang, Gurgel and Schirmer (1984).

TIDAL ELLIPSES

Given a set of consecutive CODAR-observations it is possible to compute the tidal ellipses for any place of interest in the current field. In figure 8 a set of 12 of such ellipses is given. Using a frequency filter according to Fourier, only the semi diurnal tidal components are left in this example. In a somewhat similar manner one can extract the residual current only.

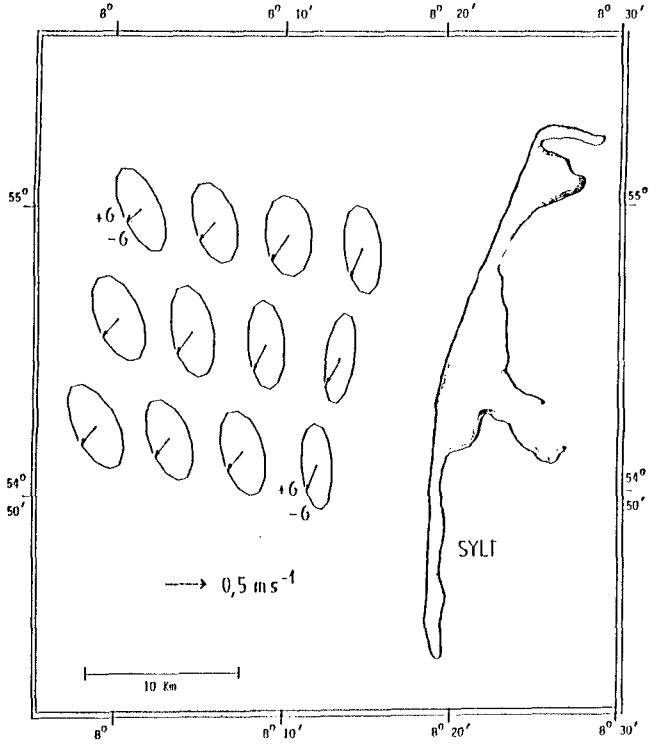

Figure 8: Tidal ellipses in front of the German island SYLT - only the semidiurnal component is given -.

UPWELLING AND DOWNWELLING

From an extensive set of surface current vectors the amount of upwelling or downwelling can be computed. If this is done separately with each snapshot of the surface current field, a time series of upwelling and/or downwelling can be gained. In figure 9 this divergence, taken from the vector fields, is plotted against time for the place A in fig. 5.

In the case of very low current velocities (less than 10 cm/s) the uncertainty becomes to large because differences between small numbers with random noise are to be computed.

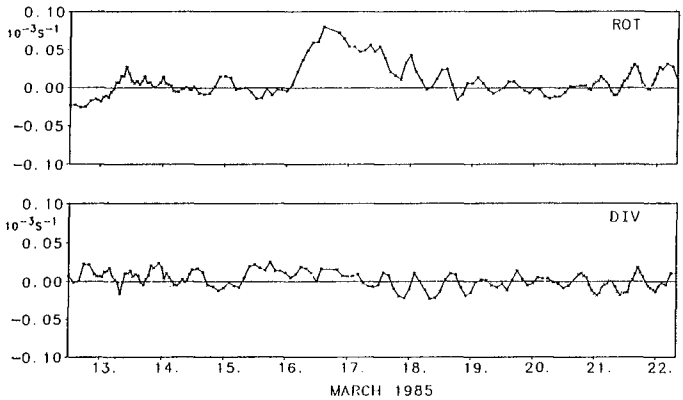

Figure 9 lower part: DIVergence - or upwelling and downwelling respectively - at place A in fig. 5 as a function of time.

upper part: The amount of ROTation at place A in fig. 5.

ROTATION

Finally the amount of rotation can be computed from the vector field of measured surface current. Again this is done - as an example - for place A in fig. 5. The amount of rotation as a function of time is given too in figure 9 - lower curve.

REFERENCES

Crombie, D. D. (1955), Doppler spectrum of sea echo at 13.56 MHz, Nature 175, 681-682.

Barrick, D. E., M. W. Evans and B. L. Weber (1977), Ocean surface currents mapped by radar, Science 198, 138-144.

Lipa, B. J. (1977), Derivation of directional ocean-wave spectra by integral inversion of the second-order radar echoes, Radio Sci. 12, 425-434.

Shearman, E. D. R. (1980), Remote sensing of the sea surface by dekametric radar, Radio Electron. Eng. 50, 611-623.

Essen, H.-H., K.-W. Gurgel and F. Schirmer (1983), Tidal and wind driven parts of surface currents, as measured by radar, DHZ, 36.

Essen, H.-H., T. Freygang, K.-W. Gurgel and F. Schirmer (1984), Oberflächenströmungen vor Sylt - Radarmessungen im Herbst 1983 -, DHZ, 37.

CHAPTER 198

Studies on Thermal Diffusion and Verification of the Third Nuclear Power Plant in Taiwan

By

K.C. Tang[1] M.T. Tsai[2]

Y.R. Hwang[3] H.H. Hwung[4]

Abstract

In general, hydraulic model tests and numerical simulations can be used for securing enough informations in order to assess the environmental impact by thermal discharge after the power plant operation. However, the numerical simulations should be verified by the consequence of hydraulic model tests or the field data. Then, the numerical model can be used as a prediction model to foresee the nature of thermal diffusion when the additional generators will be operated.

The third nuclear power plant in Taiwan has been constructed in 1984. In order to protect the abundant corals which distributed on the rocky bottom around this power plant, a complete studies on thermal diffusion have been performed, accordingly, a verification with field measurements were also made in this paper.

1. Assistant Researcher, Tainan Hydraulics Laboratory, National Cheng Kung University, Tainan, Taiwan, R.O.C.
2. Director, Nuclear Operation Department, Taiwan Power Company,Taipei, Taiwan, R.O.C.
3. Manager, Radiation Laboratory, Taiwan Power Company, Taipei, Taiwan, R.O.C.
4. Professor, Dr. Eng. Director of Tainan Hydraulics Laboratory,National Cheng Kung University, Tainan, Taiwan, R.O.C.

1. Introduction

The third nuclear power plant is located at the southest coast of Taiwan and beside Nan-Wan-Bay, 1984, two units (951MW) have been constructed and attended the commercial operation, afterwards, the other two units also performed at 1985. The intake and outlet are installed on the northern and western coastline of this bay as shown in Fig-1.

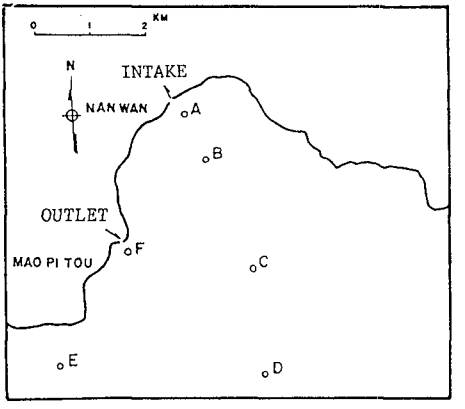

Fig-1

According to the marine ecology studies in the vicinity of Nan-Wan-Bay from August 1976 to December 1977, it showed that the abundant corals distributed on the rocky bottom about from 6m to 30m water depth. From the research of relationships between the growth of corals and water temperature, it points out that the corals will grow well in water below 29^0C,and they can not with stand long periods of exposure at 31^0C, then as water temperature increases more than 32^0C that the corals will die rapidly. Accordingly, in order to prevent the impact on corals resulting from the discharge of heated water, the complete studies on thermal diffusion and verification were made. And the results would be presented in this paper.

2. Field Surveys and Data Analysis

The complete analysis of field survey data had to be done before the hydraulic model tests and numerical simulations were progressed. They are:

(1). Topography, water depth and coastline surveys:

The field surveys should be done at least twice in a year for the necessity to discretize the continuous domain in numerical simulations or to construct the hydraulic model.

(2). Analysis of wind speeds and wind directions:

According to the results obtained from Nan-Wan station, it is obviously to see from Fig-2, that the wind contributes in NE direction for 48.9% of occurence is the main wind at Nan-Wan area. And the average wind velocity is about 10m/sec in this direction.

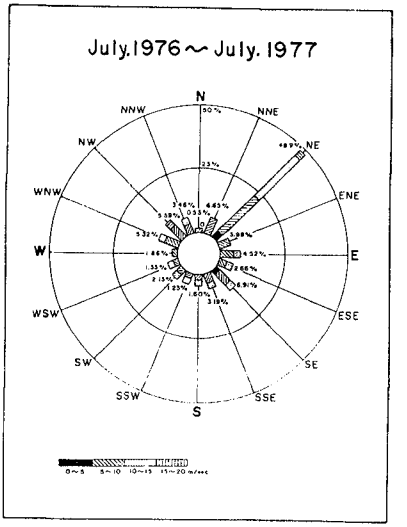

Fig. – 2 Monthly maximum wind velocity and wind direction at Nan–Wan Station

(3). Analysis of water temperature:

The temperature data were collected by Taipower Exploration Team from July, 1976 to July, 1977 at Nan-Wan area. Table-1 indicates the monthly average water temperature, monthly maximum and minimum water temperature throughout the interval.

Table – 1 Water Temperature

Month	Manthly Average Water Temperature°C	Monthly Maximum Water Temperature°C	Manthly Minimum Water Temperature°C
1976 June	28.1	30	24.9
July	29.3	31	27.4
Aug.	29.3	31	28.0
Sep.	28.0	30.1	25.2
Oct.	27.0	29.1	25.1
Nav.	24.4	27.2	21.0
Dec.	23.6	26.0	22.0
1977 Jan.	23.4	25.7	21.4
Feb.	23.2	25.7	20.5
Mar.	24.8	27.5	20.2
Apr.	26.4	28.9	22.5
May	28.2	29.7	26.2
June	27.7	29.5	26.1
July	27.4	30.6	24.5

(4). Analysis of tidal records: Fourteen months of tidal records at Nan-Wan area have been analyzed by least square method in harmonic analysis with twenty-one tidal constituents. Table-2 shows the amplitudes and phase angles for respective tidal constituents. The comparsion between prediction of tidal motion equation created by these tidal constituents and tide records was shown in Fig-3.

Table-2 Analysis results of tidal constituents

consti. name	angular frequency	amplitude (cm)	phase angle (deg.)
M_2	28.9841042	26.842	39.00
K_1	15.0410686	18.772	240.36
O_1	13.9430356	16.042	91.68
MKS_2	29.0662415	0.836	296.81
φ_1	15.0821353	1.770	264.61
OP_1	28.9019669	0.525	294.38
S_1	15.0000000	0.606	268.42
S_2	30.0000000	11.061	191.86
S_4	0.0410686	7.294	54.92
S_{sa}	0.0821373	8.074	147.78
R_2	30.0410667	0.102	219.94
T_2	29.9589333	0.701	353.66
P_1	14.9589314	6.801	263.00
ϕ_1	15.1232059	0.339	297.58
π_1	14.9178647	0.357	330.34
N_2	28.4397295	5.343	280.98
MP_1	14.0251729	1.571	334.90
Q_1	13.3986609	2.829	320.75
K_2	30.0821373	2.900	332.14
$M_{4/3}$	1.0158958	1.994	19.04
ν_2	28.5125831	0.940	353.54
Total		115.7	

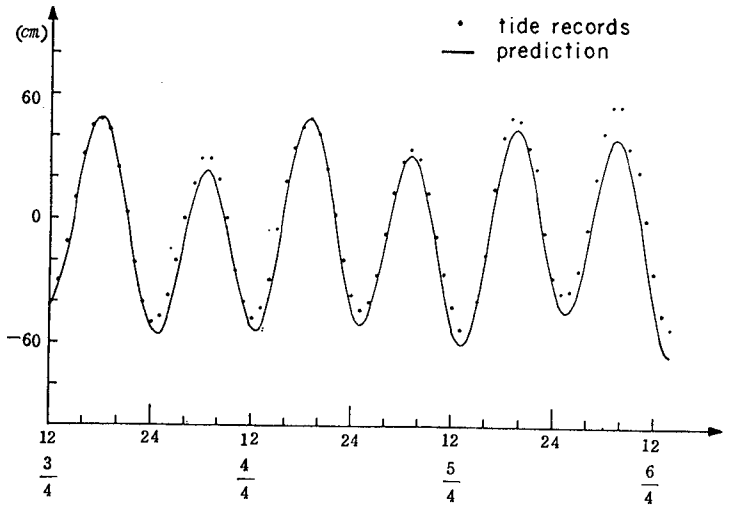

Fig.— 3 Comparison between tide records and prediction

(5). Analysis of measuring currents:

Owing to the ocean current data at Nan-Wan site, four major current constituents at this area are M_2, S_2, K_1 and O_1. And the Analysis results are displayed in Table-3 and Table-4.

Table – 3 Analysis results of current measurement at D station

Name	X – direction amplitude (cm/sec)	phase angle (degree)	Y – direction amplitude (cm/sec)	phase angle (degree)
M_2 = 12.42 hr	27.07	23.90	5.39	123.90
S_2 = 12.00 hr	10.35	7.50	2.81	97.50
K_1 = 23.93 hr	13.07	167.86	2.29	257.86
O_1 = 25.82 hr	16.56	18.24	4.56	108.24

Table – 4 Analysis results of current measurement at E station

Name	X – direction amplitude (cm/sec)	phase angle (degree)	Y – direction amplitude (cm/sec)	phase angle (degree)
M_2 = 12.42 hr	27.99	340.70	8.29	186.78
S_2 = 12.00 hr	26.86	42.33	3.79	237.55
K_1 = 23.93 hr	17.99	43.49	7.54	221.03
O_1 = 25.82 hr	8.40	226.38	5.22	91.41

3. Hydraulic Model Tests

The hydraulic model tests have been completed by Tainan Hydraulics Laboratory according to the previous analysis. A distorted model (horizontal scale is 1/1152, vertical scale is 1/144) was determined by comparing the heat on sea surface which calculated from field data with those examined from laboratory. The results of far-field model tests were shown in Fig-4∿Fig-7.

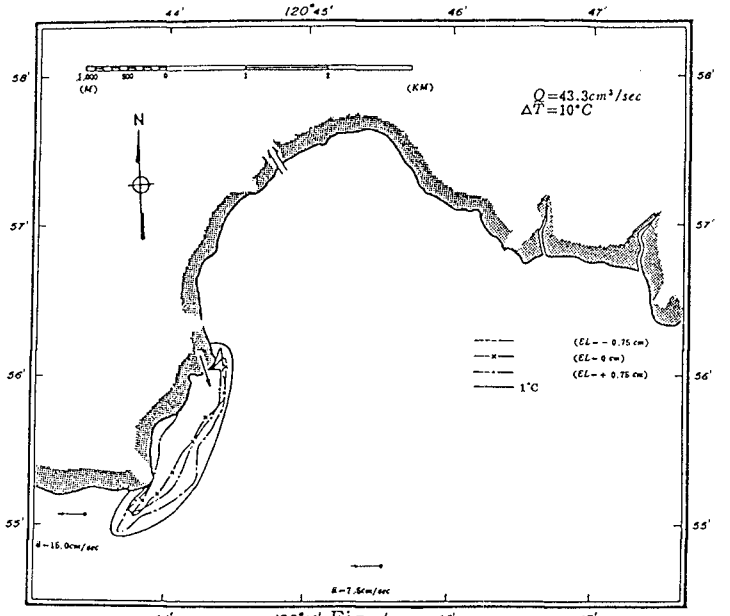
44'
120°45'
46'
47'
58'
57'
56'
55'
(M)
(KM)
Q=43.3cm³/sec
ΔT=10°C
N
(EL=-0.75 cm)
(EL=0 cm)
(EL=+0.75 cm)
1°C
v=15.0cm/sec
v=7.5cm/sec

Fig-4

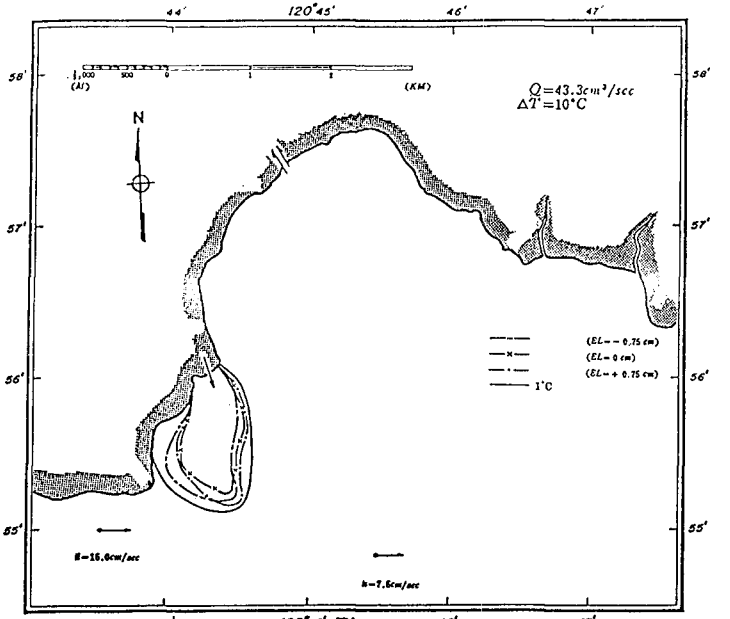
44'
120°45'
46'
47'
58'
57'
56'
55'
(M)
(KM)
Q=43.3cm³/sec
ΔT=10°C
N
(EL=-0.75 cm)
(EL=0 cm)
(EL=+0.75 cm)
1°C
v=15.0cm/sec
v=7.5cm/sec

Fig-5

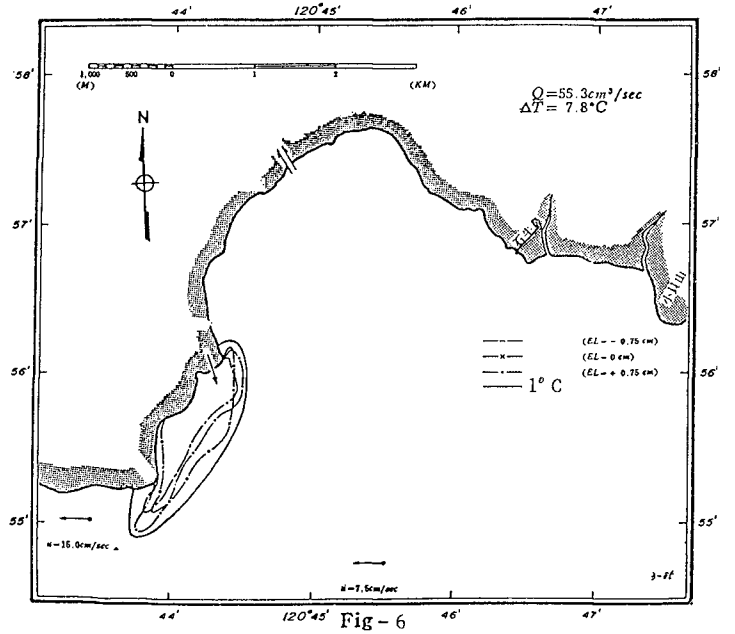
44'
120°45'
46'
47'
58'
57'
56'
55'
(M)
(KM)
Q=55.3cm³/sec
ΔT= 7.8°C
N
(EL – – 0.75 cm)
(EL – 0 cm)
(EL – + 0.75 cm)
1° C
u=15.0cm/sec
u=7.5cm/sec

Fig – 6

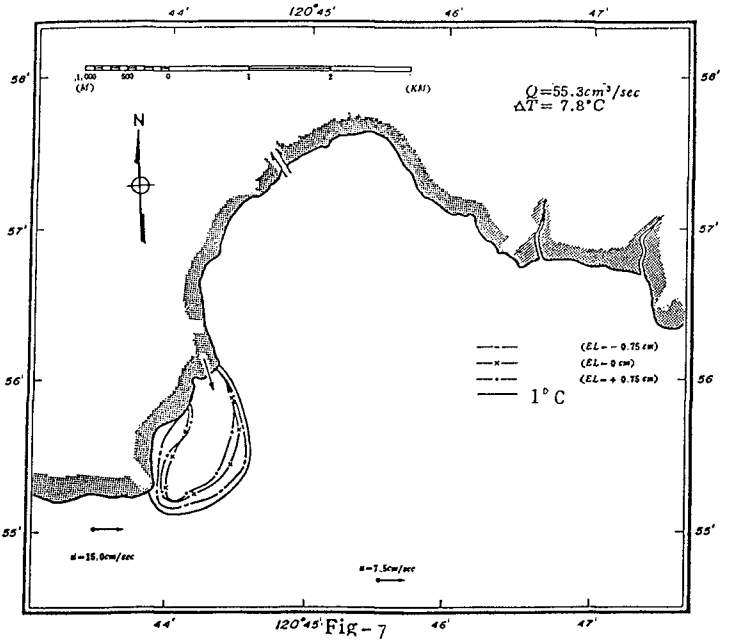
44'
120°45'
46'
47'
58'
57'
56'
55'
(M)
(KM)
Q=55.3cm³/sec
ΔT= 7.8°C
N
(EL – – 0.75 cm)
(EL – 0 cm)
(EL – + 0.75 cm)
1° C
u=15.0cm/sec
u=7.5cm/sec

Fig – 7

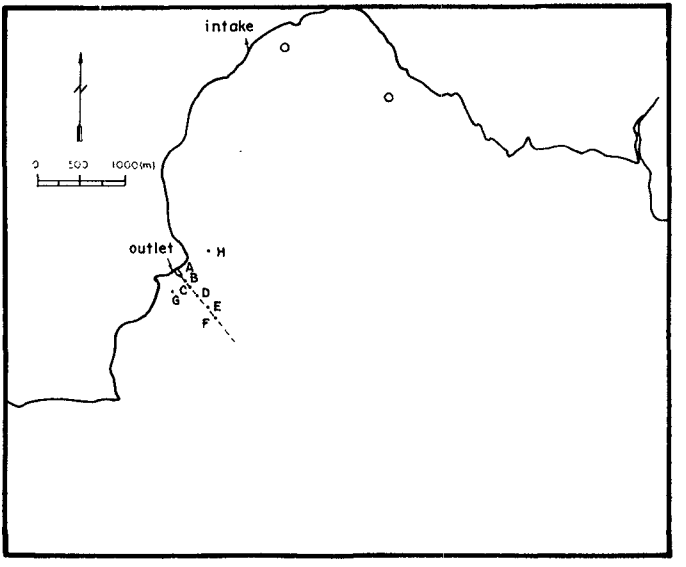

Fig. — 8 Schematic diagram of measuring Points for vertical temperature distribution

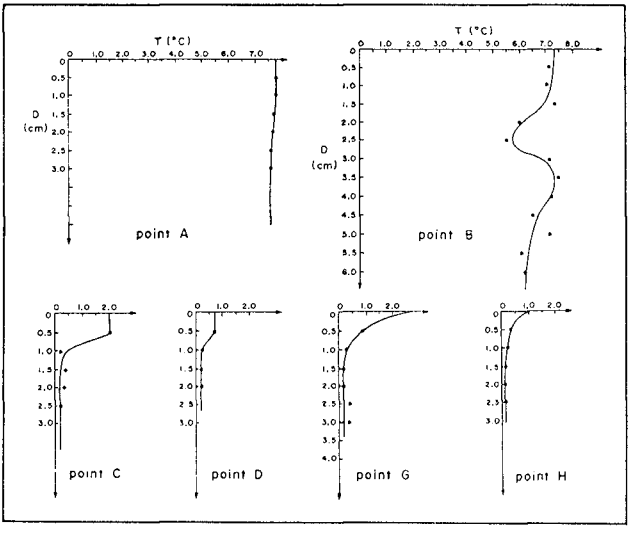

Fig-9

Fig-4 shows the envelope of 1 degree centigrade temperature increasing in conditions of two units operation, the cooling water discharge is 43.3 C.M.S., cooling water temperature rised is 10 degree centigrade and under strong flooding tide action. The result of Fig-5 is in the same conditions as Fig-4 excepts the ocean current is strong ebbing tides. Since the ambient water temperature in Nan-Wan Bay is so high that a great amount of cold water will be pumped from deep sea to mix with the hot water discharged from condensers. The results of this nature are shown in Fig-6 and Fig-7.

Besides, for the request to assure that the coral could grow well, an adjustment was made by installing a 120-meter-long flow-guided breakwater from the outlet to somewhere the water depth is 8 meters that it would keep the heated water floating on the surface layer. And the measuring points for vertical temperature distribution and the corresponding results in an undistorted model were described in Fig-8 and Fig-9 respectively.

4. Numerical Simulations

A two-dimensional model was used to simulate the flow patterns and temperature distributions under tides and currents action. The horizontal diffusion coefficient and thickness of warm water floating on surface layer in the numerical simulations could be determined from the hydraulic model tests. The currents boundary conditions were set at both sides in x-direction of the finite-difference grid domain, but the boundary condition in the south was controlled by tides. The numerical model covered an area of 8.5Km×10.0Km. That meant it had 34 grids in x-direction and 40grids in y-direction with a grid size of 250m. The numerical simulations were accomplished throughout 4500 time steps with a value of time step by 30 seconds. Fig-10∿Fig-13 show the simulated flow patterns at Nan-Wan area by a two-dimensional numerical model when the time level was the 3000th, 3300th, 3600th and 3900th respectively. And the corresponding temperature distributions were shown in Fig-14∿ Fig-17.

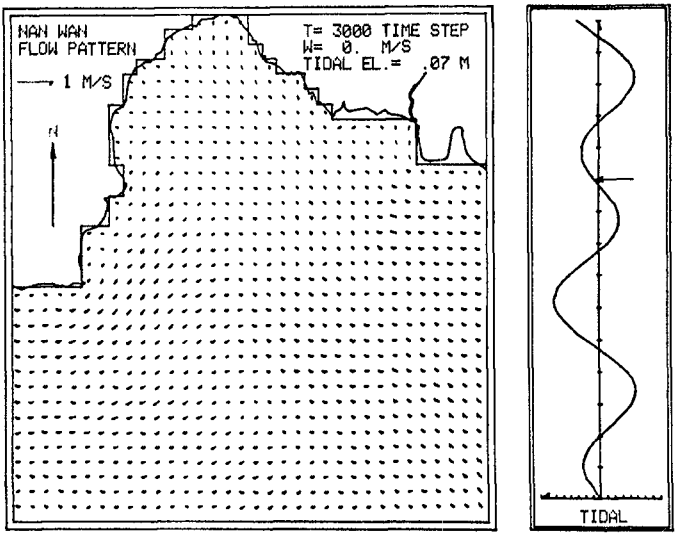
NAN WAN
FLOW PATTERN
1 M/S
N
T= 3000 TIME STEP
W= 0. M/S
TIDAL EL.= .07 M
TIDAL

Fig-10

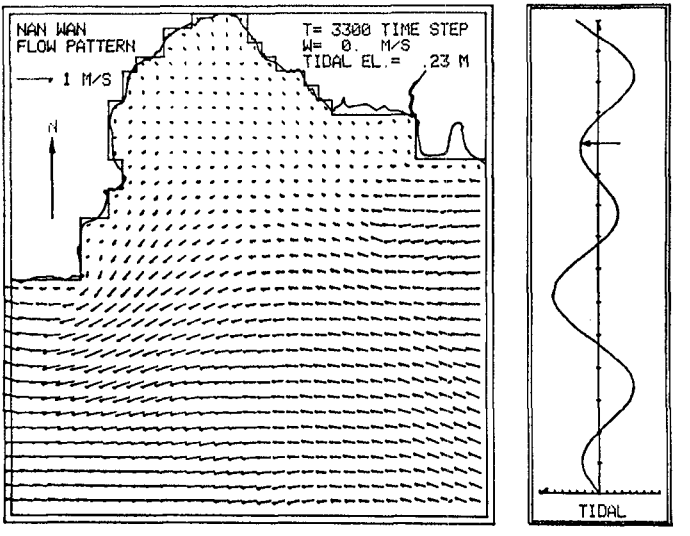
NAN WAN
FLOW PATTERN
1 M/S
N
T= 3300 TIME STEP
W= 0. M/S
TIDAL EL.= .23 M
TIDAL

Fig-11

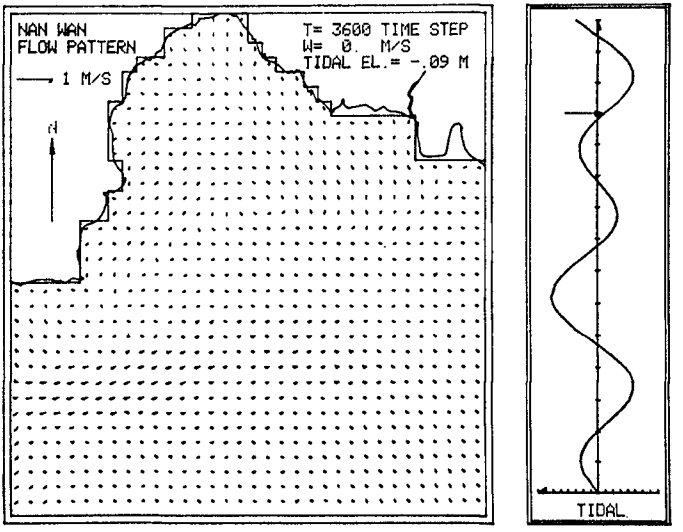
NAN WAN
FLOW PATTERN
1 M/S
N
T= 3600 TIME STEP
W= 0. M/S
TIDAL EL.= -.09 M
TIDAL

Fig-12

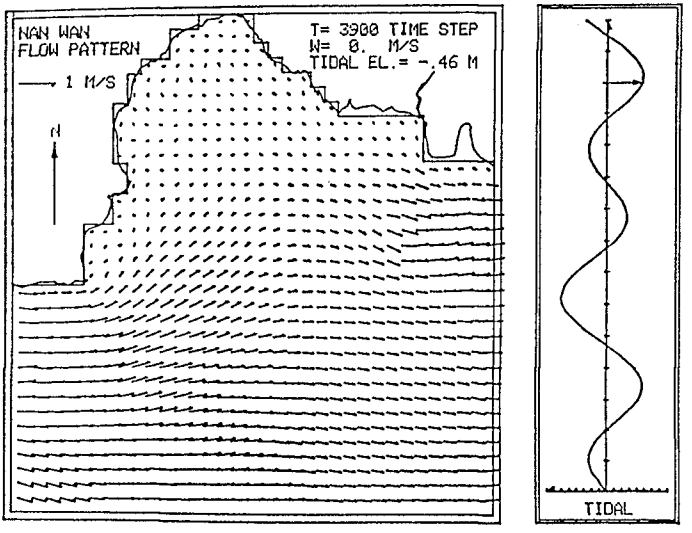
NAN WAN
FLOW PATTERN
1 M/S
N
T= 3900 TIME STEP
W= 0. M/S
TIDAL EL.= -.46 M
TIDAL

Fig-13

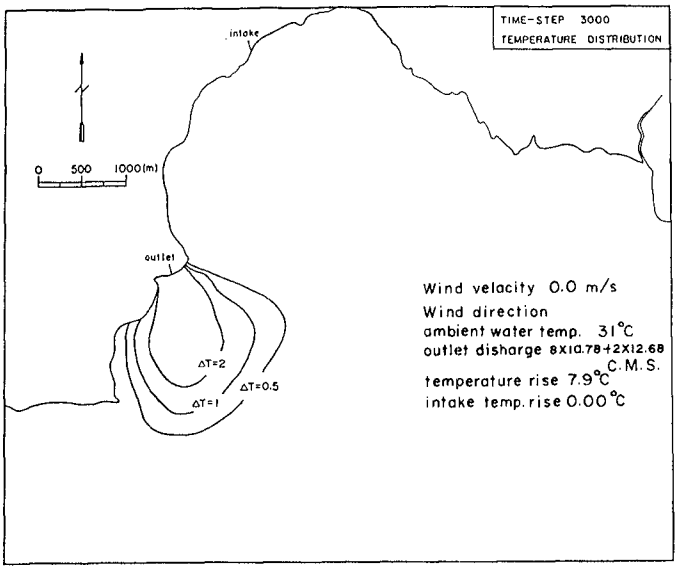
TIME-STEP 3000
TEMPERATURE DISTRIBUTION
intake
0 500 1000(m)
outlet
ΔT=2
ΔT=1
ΔT=0.5
Wind velocity 0.0 m/s
Wind direction
ambient water temp. 31°C
outlet disharge 8X10.78+2X12.68 C.M.S.
temperature rise 7.9°C
intake temp. rise 0.00°C

Fig-14

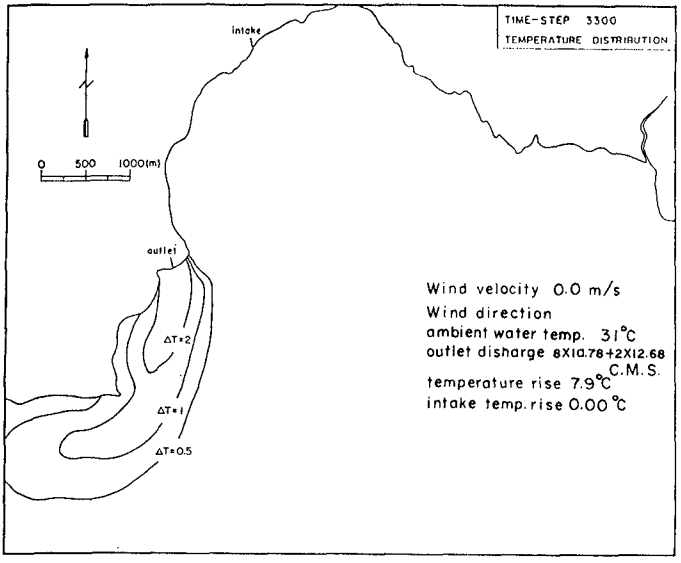
TIME-STEP 3300
TEMPERATURE DISTRIBUTION
intake
0 500 1000(m)
outlet
ΔT=2
ΔT=1
ΔT=0.5
Wind velocity 0.0 m/s
Wind direction
ambient water temp. 31°C
outlet disharge 8X10.78+2X12.68 C.M.S.
temperature rise 7.9°C
intake temp. rise 0.00°C

Fig-15

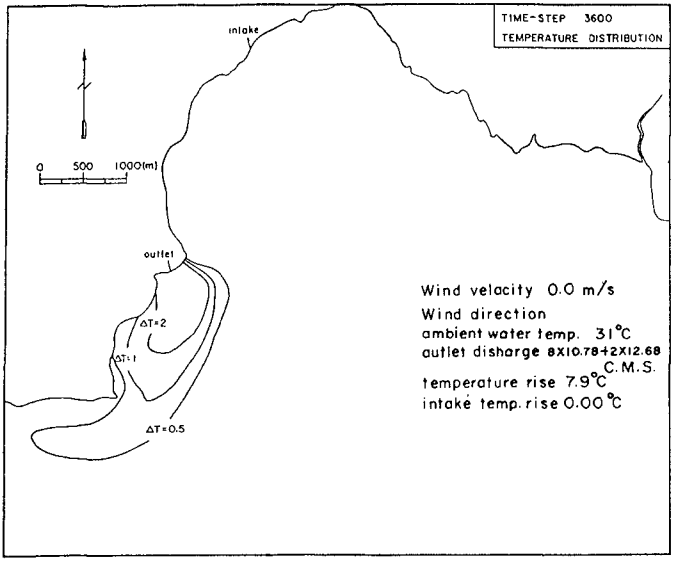
TIME-STEP 3600
TEMPERATURE DISTRIBUTION
intake
0 500 1000(m)
outlet
ΔT=2
ΔT=1
ΔT=0.5
Wind velocity 0.0 m/s
Wind direction
ambient water temp. 31°C
outlet disharge 8X10.78+2X12.68 C.M.S.
temperature rise 7.9°C
intake temp. rise 0.00°C

Fig-16

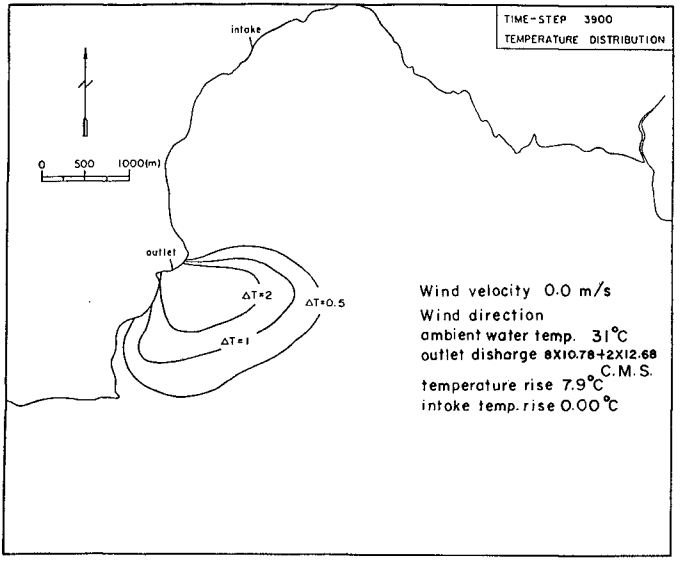
TIME-STEP 3900
TEMPERATURE DISTRIBUTION
intake
0 500 1000(m)
outlet
ΔT=2
ΔT=0.5
ΔT=1
Wind velocity 0.0 m/s
Wind direction
ambient water temp. 31°C
outlet disharge 8X10.78+2X12.68 C.M.S.
temperature rise 7.9°C
intoke temp. rise 0.00°C

Fig-17

5. Verification and Conclusion

After the third nuclear power plant operation from 1984, monitoring program has been proceeded to thermal diffusion in Nan-Wan-Bay. Four fixed monitoring stations were installed around the outlet, and the thermisters (General Ocean 6070-type) were set below the water surface from 0.5m to 5.0m separately. In addition, a large scale survey was also performed by motor-boats for every season. Based on the above results, the numerical calculations of temperature distributions could be verified by field measurements from a large scale surveys. Fig-18 is the temperature distribution obtained from numerical calculation and Fig-19 is the results plotted from field data at the same tide condition . And the comparison of vertical temperature distributions between the hydraulic model tests and field data are also presented in Fig-20.

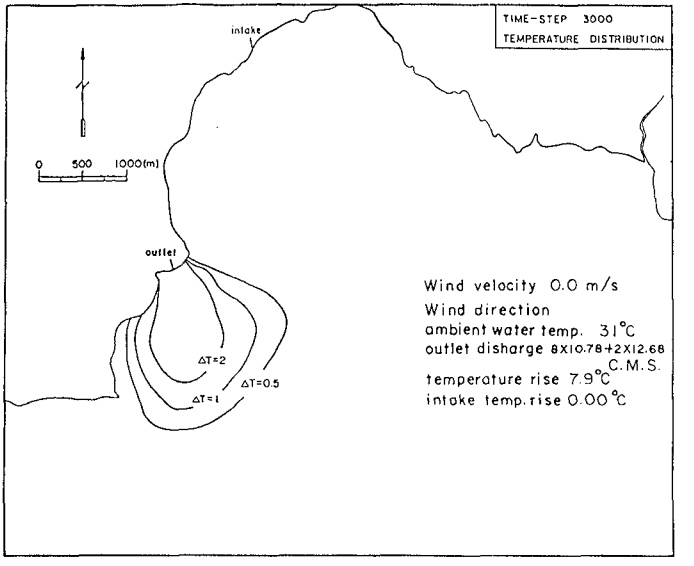

Fig-18

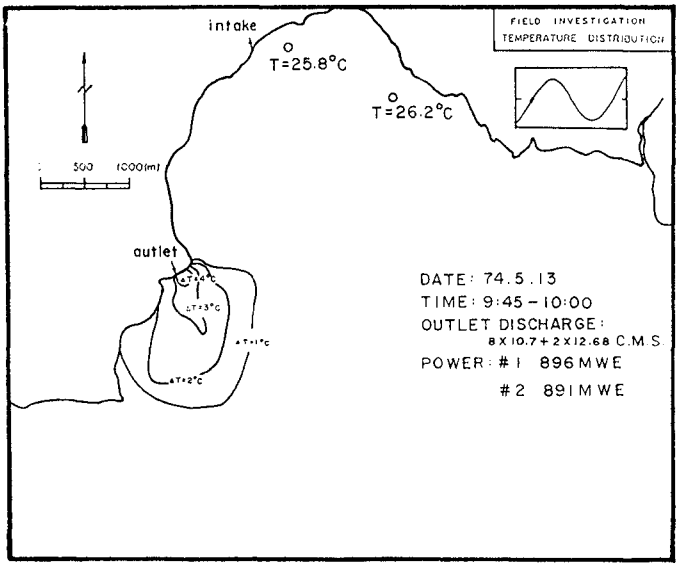
FIELD INVESTIGATION
TEMPERATURE DISTRIBUTION
intake
T=25.8°C
T=26.2°C
500 1000(m)
outlet
ΔT=4°C
ΔT=3°C
ΔT=1°C
ΔT=2°C
DATE: 74.5.13
TIME: 9:45 – 10:00
OUTLET DISCHARGE:
8X10.7+2X12.68 C.M.S
POWER: #1 896MWE
#2 891MWE

Fig-19

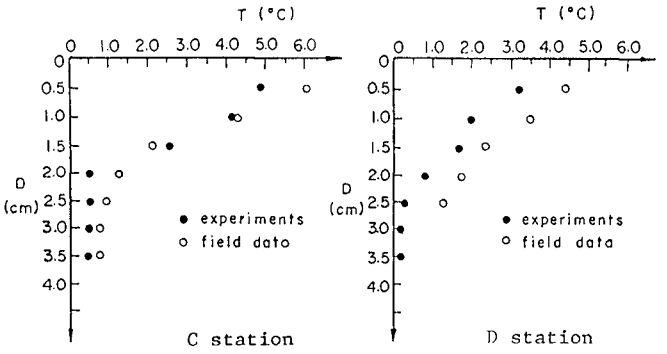
T (°C)
0 1.0 2.0 3.0 4.0 5.0 6.0
D (cm)
0 0.5 1.0 1.5 2.0 2.5 3.0 3.5 4.0
● experiments
○ field data
C station
T (°C)
0 1.0 2.0 3.0 4.0 5.0 6.0
D (cm)
0 0.5 1.0 1.5 2.0 2.5 3.0 3.5 4.0
● experiments
○ field data
D station

Fig-20

According to a number of elaborated hydraulic model tests and numerical simulations on thermal diffusion of the third nuclear power plant in Taiwan, the discharged warm water floating on the surface layer has been proved from field investigations that showed the abundant corals have not affected by warm water and they have grown well until now.

6. References

1. Frederick. L.W. Tang and H.H. Hwung (1979). "Studies on the Thermal Diffusion of The Third Nuclear Power Plant and The Field Investigations of Lin-Ko Power Plant", Tainan Hydraulic Laboratory, Bulletin 42.

2. H.H. Hwung, C.S. Yang and Tehfang Lee (1984). "Alarm System Operation Reaserach for The Circulation of The Third Nuclear Power Plant", Tainan Hydraulic Laboratory, Bulletin 68.

3. H.H. Hwung and C.L. Tsai (1984). "The Studies on The Tidal Frequency Analysis and Variation of Mean Sea Level", Tainan Hydraulic Laboratory, Bulletin 69.

4. H.H. Hwung and K.C.Tang (1986). "Two-dimensional Numerical Simulations of Thermal Discharge on The Third Nuclear Power Plant", Tainan Hydraulic Laboratory, Bulletin 89.

5. G.H. Jika, G. Abraham and D.R.F. Harleman (1975). "An Assessment of Techniques for Hydrothermal Prediction", PB 250509, NUREG-0044.

6. J.J. Leendertse and S.K. Liu (1973). "A Three Dimensional Model for Estuaries and Coastal seas", Vol.1, Principles of Computation, R-1417-ONRR, The Rand Corporation.

7. M. Kato and Akira Wada (1976). "Adaptability of Prediction Method of Hydraulic Model Experiment for Thermal Diffusion", 15th Coastal Engineering Conference, Hawaii.

8. Peter Ackers (1986), "Modeling of Heated-Water Discharge, Engineering Aspects of Thermal Pollution", Chapter 6, pp.177-212. Vanderbilt Univ. Press.

CHAPTER 199

MODEL/FIELD COMPARISON - COASTAL BUOYANT JET

Shuen-Wei Scott Tu (1), Member ASCE
Patrick J. Ryan (2), Member ASCE
Jeffrey P. Leighton (3), Associate Member ASCE

ABSTRACT

Calibration and verification of a 1:75 scale undistorted hydraulic model is described. The model was used to simulate the waste heat distribution in shallow and semi-confined receiving waters. The study was carried out in the laboratory by analyzing the effect of several parameters in comparisons of model and field data. Because of the shallow receiving waters, it was found that the near-field bathymetry, bottom roughness and waves were the critical parameters in achieving a reasonable simulation.

INTRODUCTION

In recent years, there have been numerous studies investigating the behavior of turbulent jets discharging waste heat or sewage into the environment. Extensive non-buoyant and buoyant jets study programs have been carried out for various outfall conditions. In general, they can be characterized as (1) free jets (where no bounding effect is present), (2) submerged jets (where the free surface effect is unimportant), and (3) surface jets (where surface effect is important, but bottom shear is excluded). Few attempts have been made to study the condition of surface jets issuing into rather shallow receiving water. Giger, Jirka and Dracos (1985) conducted a model study for a two dimensional turbulent horizontal jet in both deep and shallow waters. They observed noticeably different jet behavior for the "shallow jets" with a relatively large amplitude meandering motion. For the present study, extensive efforts were made to calibrate a physical model with a comprehensive set of field data. Several factors that affect the jet trajectory and mixing were identified.

MODEL DESCRIPTION AND EXPERIMENTAL APPARATUS

The hydraulic model, constructed in 1975 (Wiegel et al., 1976), is an undistorted densimetric Froude model with a scale of 1:75 (Fig. 1). The model basin is 85 by 64 by 2.5 ft deep (25 X 19 X 0.8 m) and covers a prototype area of 6400 ft (1920 m) along the coast by 4800 ft (1440 m) normal to the coast. It is located at the Richmond Field Station of the University of California, Berkeley, California. The model studies were made under contract with the University, under the direction of Professor R.L. Wiegel.

(1) Research Engineer, Pacific Gas and Electric Company, 3400 Crow Canyon Rd., San Ramon, CA. 94583
(2) Chief Hydrologic Engineer, Bechtel Civil and Mineral Inc., P.O. Box 3965, San Francisco, CA. 94119
(3) Civil Engineer, Pacific Gas and Electric Company, 3400 Crow Canyon Rd., San Ramon, CA. 94583

The offshore current direction and strength can be controlled through a system of valves and pumps. Waves are produced by a piston type paddle. The water level can be programmed to follow a selected sinusoidal tide curve. The temperature measuring system consists of an array of probes (each with five thermistors spaced 4 ft apart (prototype) in the vertical direction) with supporting structures and booms to allow three dimensional movement for sampling. The time constant of the thermistors is approximately 0.3 seconds. Mean values obtained by averaging 20 instantaneous measurements over a period of 200 seconds were found satisfactory for achieving good repetition in the model.

FIELD DATA

In late 1983, photos were taken of the unheated jet from an observation tower at 30 minute intervals. Analysis on these photos indicated that the jet appeared to head towards the north entrance at low tides and towards the west entrance at high tides (Fig. 2)

In late 1984, when the Unit 1 reactor was undergoing power ascension testing, an extensive prototype data collection program was initiated. The field data collection consisted of temperature measurements along five horizontal transects at four depths (Fig. 3), vertical profiles at various locations within Diablo Cove (the discharge cove), and surface temperatures in the offshore area (Leighton et al. (1986A), Leighton and Tu (1986B)).

Two representative power ascension field tests were chosen for model/prototype comparisons (Table 1). The first field test (corresponding to test 5-1 in Leighton et al., 1986A) included a condition of coflowing warm and cold jets from the discharge structure with 4000 cfs (114 m^3/s) total volumetric flow rate. The measured offshore current was 0.7 fps (0.21 m/s) towards the

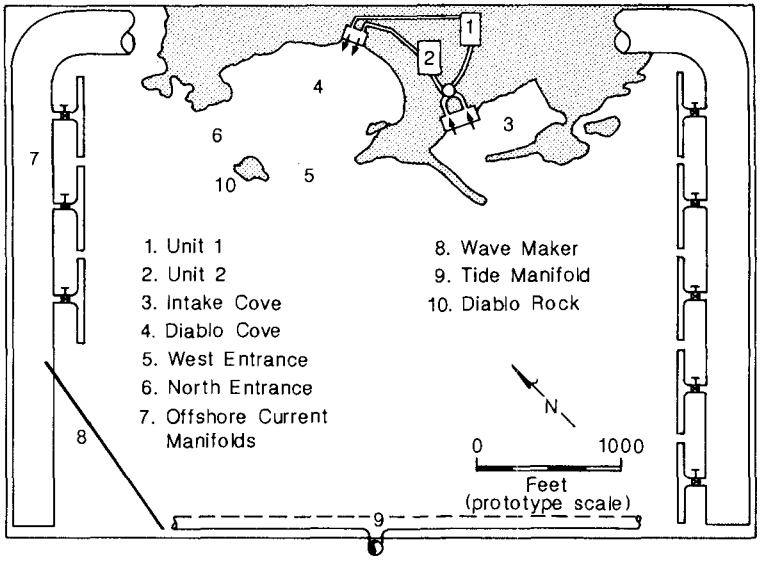

Figure 1. Model Basin Layout

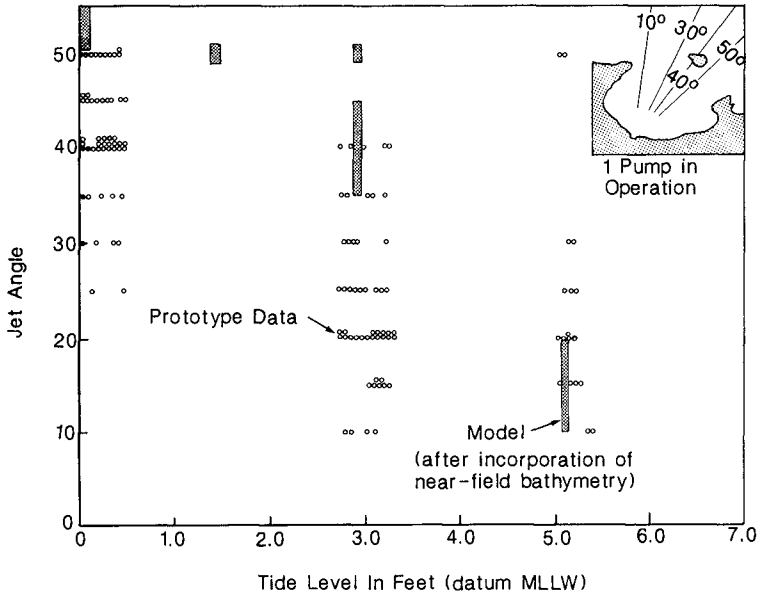

Figure 2. Jet Trajectory Data for Model and Prototype

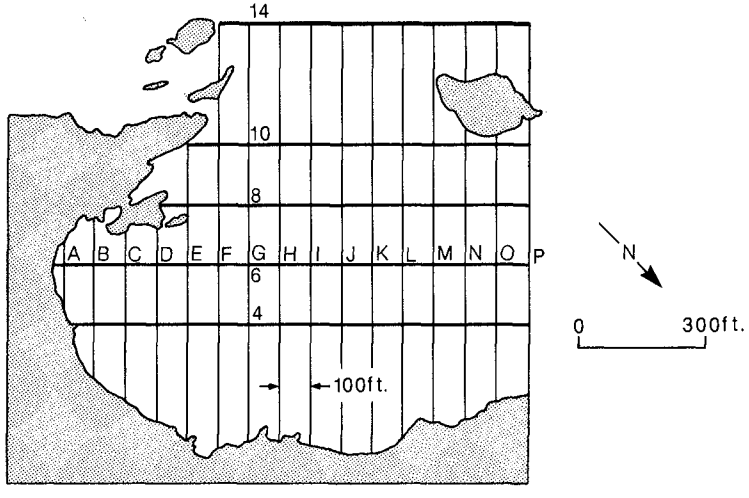

Figure 3. Expanded View and Model Grid for Discharge Cove

Table 1 Field Conditions

	Case 1 (field test 5-1)		Case 2 (field test 6-3)	
Discharge Flow Rate	Unit 1	Unit 2	Unit 1	Unit 2
	2000 cfs (57 m^3/s)	2000 cfs (57 m^3/s)	1200 cfs (34 m^3/s)	800 cfs (23 m^3/s)
ΔT_o	~18°F (10°C)	~0°F	~20°F (11°C)	~20°F (11°C)
Tide	Mean Sea Level		Low Water Level	
Offshore Current	Upcoast 0.7 ft./sec. (21 cm/s)		Strong Downcoast 0.9 ft./sec. (27 cm/s)	
Waves	Sg. Ht.	Period	Sg. Ht.	Period
	5 ft. (1.6m)	7 sec.	3 ft. (1m)	11 sec.

north (upcoast). The tides varied from 1.4 to 3.1 ft (0.4 to 0.9 m) with respect to Mean Lower Low Water (MLLW) datum over the two hour testing period. The second field test (corresponding to test 6-3 in Leighton et al.) consisted of two coflowing warm jets with a total flow rate of 2000 cfs (57 m^3/s). The offshore current was 0.9 fps (0.27 m/s) downcoast (southerly). The tide ranged from -1.3 to -0.7 ft MLLW (-0.4 to -0.2 m).

CALIBRATIONS

Three factors were found to significantly affect the model performance: (1) the near-field bathymetry, (2) the bottom roughness, and (3) waves.

Near-Field Bathymetry

At the start of the calibration, some preliminary model runs using dye visualization had indicated the model jet exhibited a meandering motion (a condition similar to the description by Giger et al., 1985) and exited through the west entrance (Fig. 1) for all tidal levels. The tide-independent plume trajectory in the model was contrary to the observations of the field photo study (Fig. 2). It was found that major bathymetric features near the outfall (covering a prototype area of 100 by 150 ft (30 X 50 m)), absent in the model, were important. In the prototype, striations and rock ridges formed at an oblique angle of 20-30 degrees to the discharge centerline are apparent. During low tides, these rock ridges are close to the surface, and act as a series of vanes to deflect the jet away from the discharge structure centerline. The effect of the incorporation of this bathymetric feature into the model was dramatic and the jet trajectory at low tides was improved (Fig. 2). Nevertheless, the jet meanders in the model still persisted causing too much mixing between the two coflowing jets. The results are depicted as curve 1 in Fig. 4.

Bottom Roughness

As a second step, 3/16" (5 mm) gravel was added to the model as random roughness to represent the presence of 1 to 3 ft (0.3 to 1 m) boulders in the prototype. The addition of the roughness greatly reduced the model jet meandering. In the region about 200 to 600 ft (60 to 180 m,

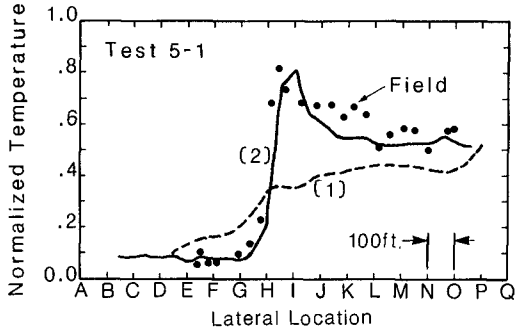

(1) Partially calibrated model - smooth bottom
(2) Final calibrated model

Figure 4. Surface Temperature along Line 4

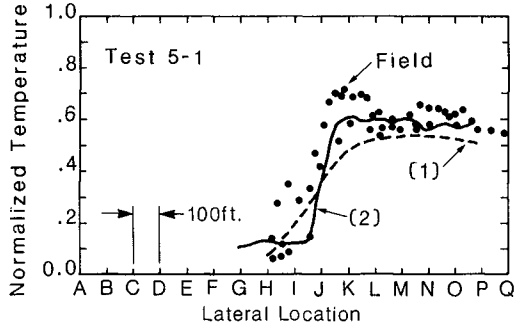

(1) Partially calibrated model - no waves
(2) Final calibrated model - with waves

Figure 5. Surface Temperature along Line 8

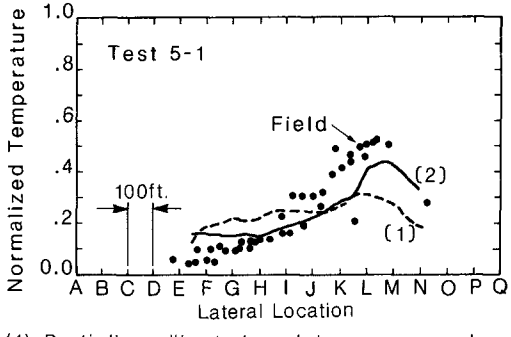

(1) Partially calibrated model - no wave absorber
(2) Final calibrated model

Figure 6. Surface Temperature along Line 14

prototype scale) from the outfall, accurate bathymetric data were not available, and gravel was added in this wave breaking zone as a calibration tool. Model results now showed good agreement with the prototype data for areas within the first 600 ft (180 meters) from the outfall (see curve 2 in Fig. 4), but the agreement deteriorated offshore beyond line 8 (see curve 1 in Fig. 5).

Waves

As the 3rd step, different wave conditions and the corresponding effects were investigated. Waves in the model had a marked effect on profiles in the discharge cove. It was found that model waves scaled relative to the prototype condition had relatively little effect on the inshore temperature profiles (except in extremely shallow areas in the south cove where waves are breaking), but appeared to improve line 8 and line 10. Shown in Figure 5 are two temperature profiles simulated with and without waves. However, on line 14 at the west mouth of the discharge cove, model temperatures still showed poor agreement. It appeared that waves, which were observed breaking and dissipating energy near the seaward side of Diablo Rock (Fig. 1) were actually being reflected in the model. Wave absorption material (horse hair) was put in place in this area to absorb the wave energy. The improvement is shown in Figure 6.

MODEL SIMULATION RESULTS

The final model results are shown in Figures 7-10 for field test 1 and in Figures 11-14 for field test 2. In each figure, the normalized temperature is defined as the ratio of the excess temperature above the ambient to the discharge temperature rise. Figures 7-10 (case 1) and Figures 11-14 (case 2) showed the temperature distribution along transect lines 6,8,10 and 14 at two water depths respectively (i.e., near the surface and 10 ft (3 m) below the surface). Figure 15 (case 1) and Figure 16 (case 2) depict vertical profiles at two locations - one in the north portion and the other in the south portion of the discharge cove (see Fig. 3 for reference coordinates) for both cases. For case 2, inshore line 6 (Fig. 12) shows a marked temperature drop at the surface near the south cove. It was found that breaking waves at low tide in the shallow area in the south cove formed by a number of rock pinnacles produce significant mass transport and pump cold water into the area. During a sensitivity test, placing some wave absorbing material near these wash rocks significantly reduced this discrepancy.

Offshore surface plume behavior was investigated for case 2 and a similar test condition (case 2A). The two field tests examined had similar discharge and environmental conditions, i.e., low tides, low waves and low winds. Both tests had a downcoast (southerly) offshore current, with case 2A having a speed 10% higher than case 2, resulting in some difference in the plume bending (Fig. 17). Both cases were simulated (6-3 026 for case 2 and 6-3 027 for case 2A). The higher cross current model test (6-3 027) was produced with slightly higher waves in comparison to the lower current test (6-3 026). Both model tests showed good agreement with the corresponding prototype data for the plume trajectories (Fig. 17). The isotherm area comparison between model and field exhibited satisfactory results as shown by Figure 18. The isotherm contour configurations for the model test 6-3 027 and field test (case 2A) are shown in Figure 19, and are remarkably similar.

CONCLUSIONS

It appears that the bottom shear has a great impact on the behavior of a shallow water jet. The near-field bathymetry affects the jet trajectory, and random roughness inhibits the development of the jet meandering. Waves also play an important role in the interfacial mixing between two coflowing jets. In shallow areas where waves are breaking and are difficult to scale in a small scale model, material to absorb the wave energy can be used to improve model/field agreement.

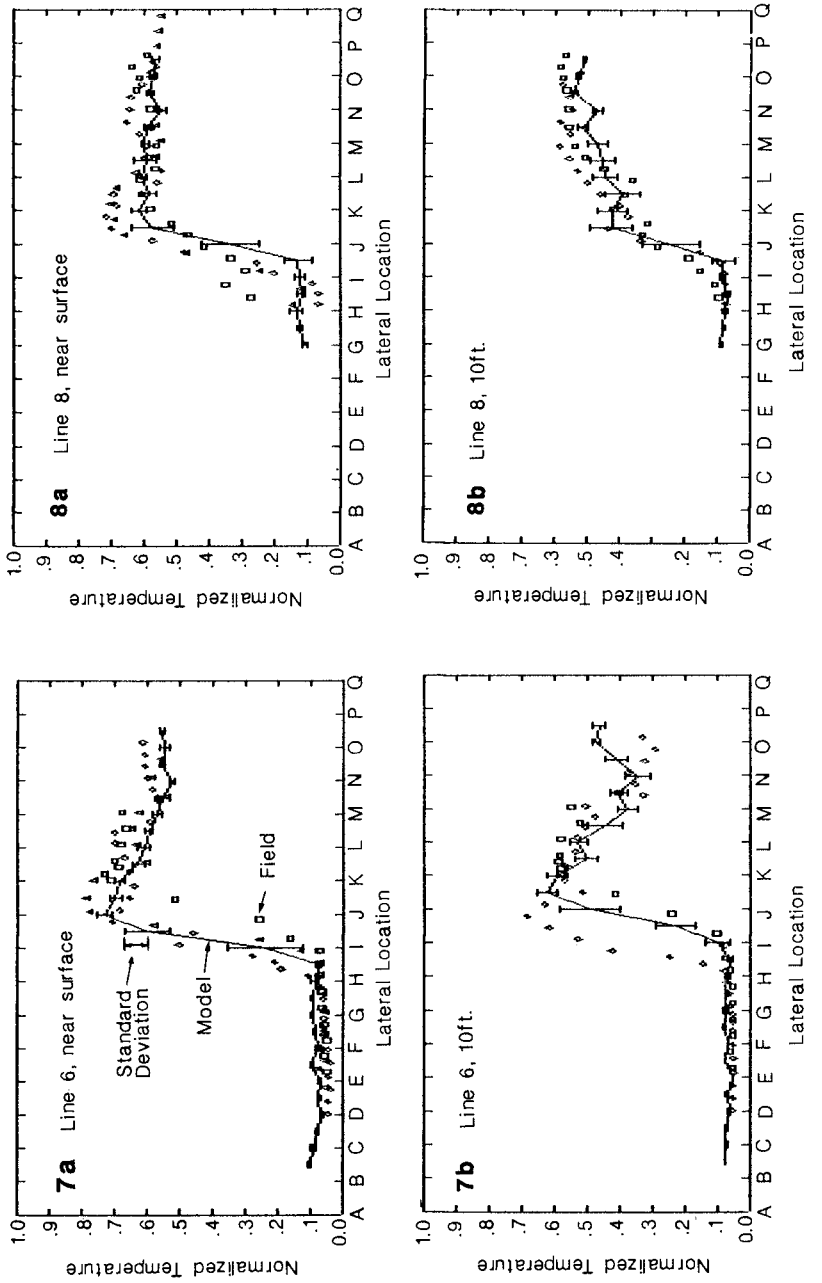

Figures 7 & 8. Comparison of Model and Field Temperature Profiles

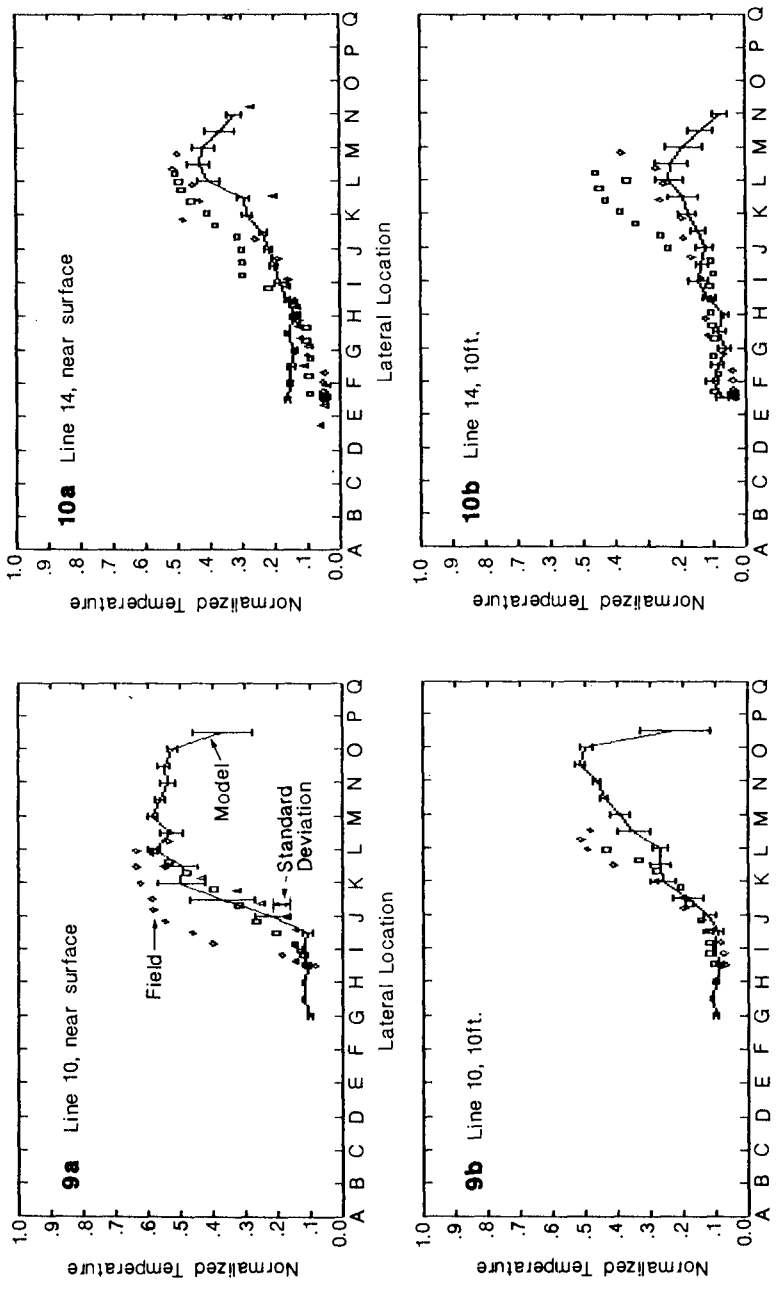

Figures 9 & 10. Comparison of Model and Field Temperature Profiles

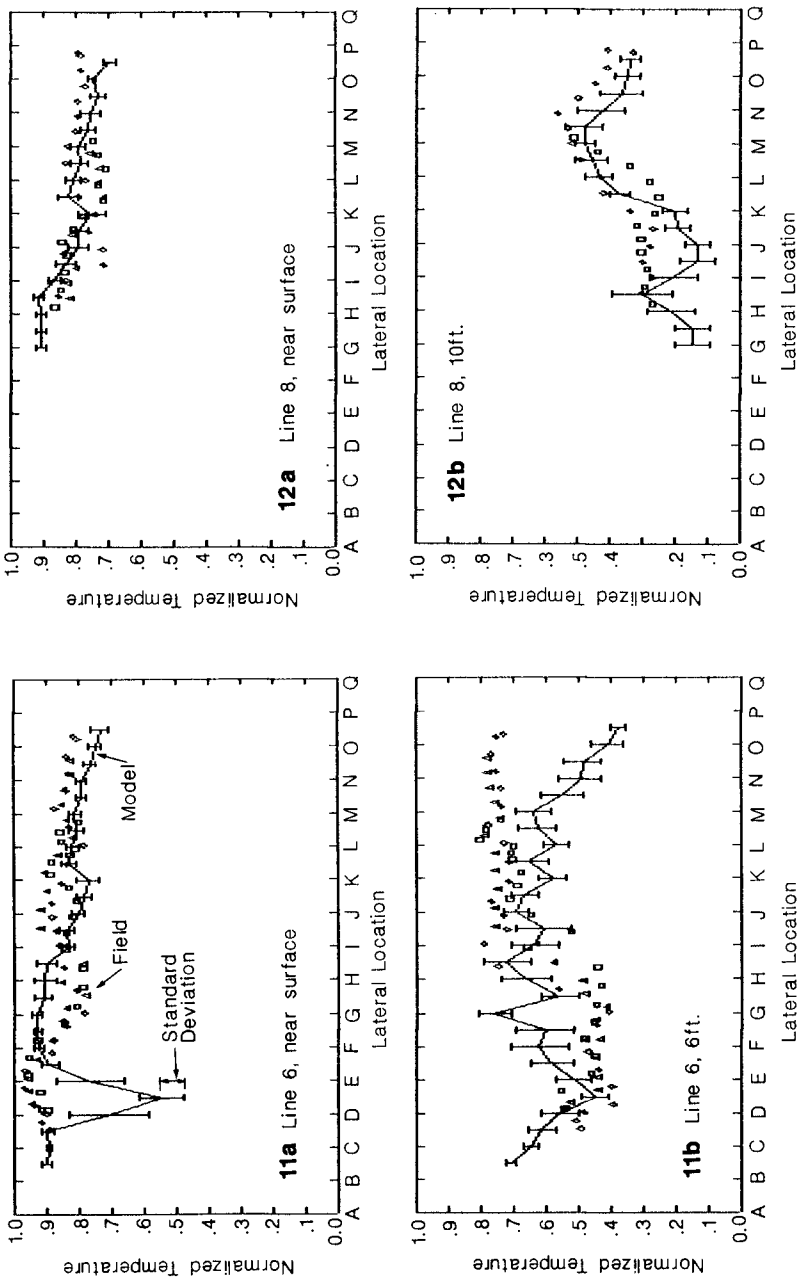

Figures 11 & 12. Comparison of Model and Field Temperature Profiles

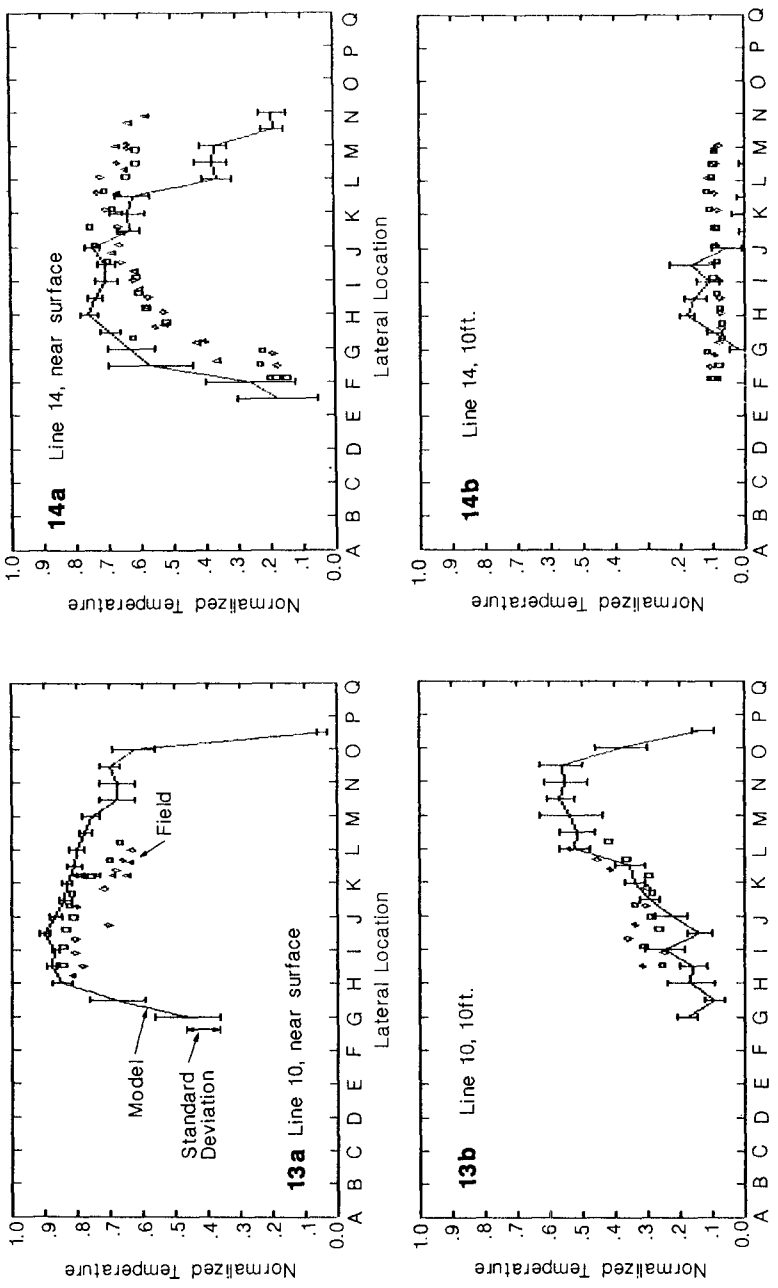

Figures 13 & 14. Comparison of Model and Field Temperature Profiles

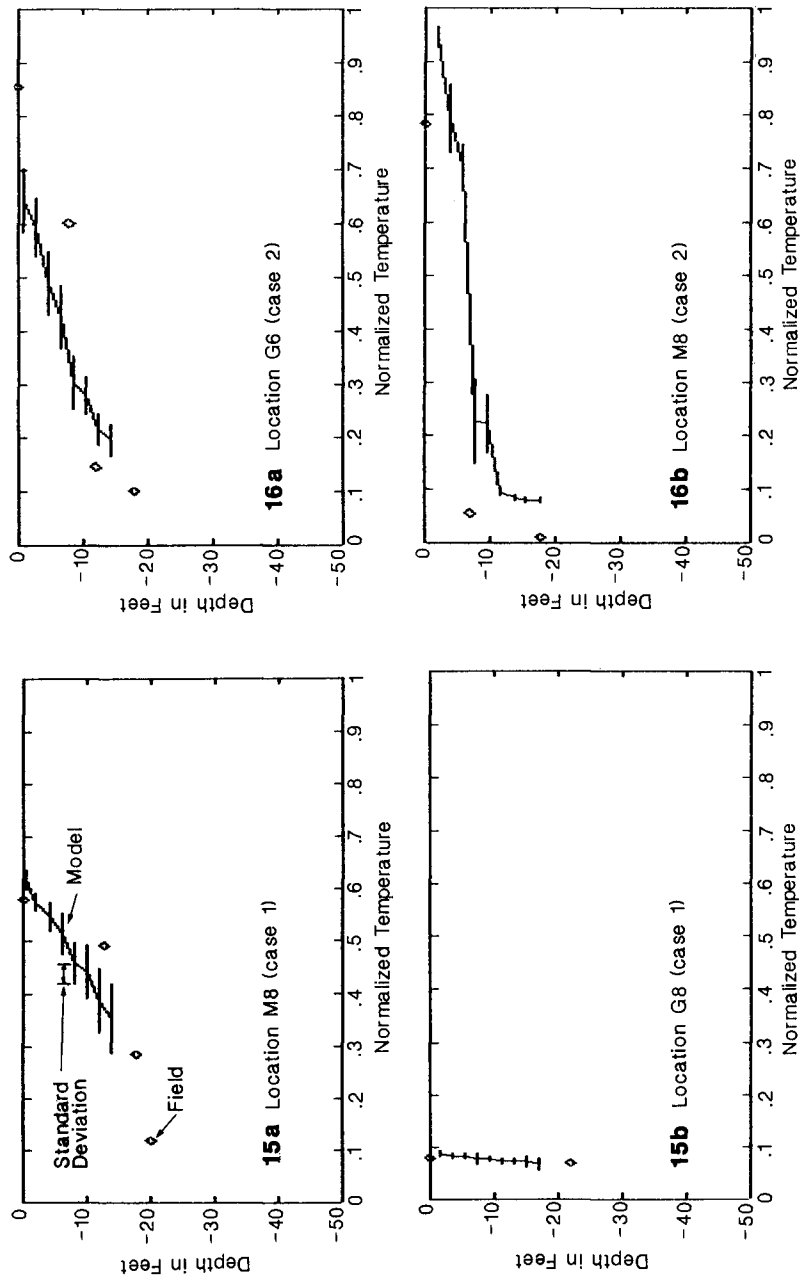

Figures 15 & 16. Comparison of Model and Field Vertical Temperature Profiles

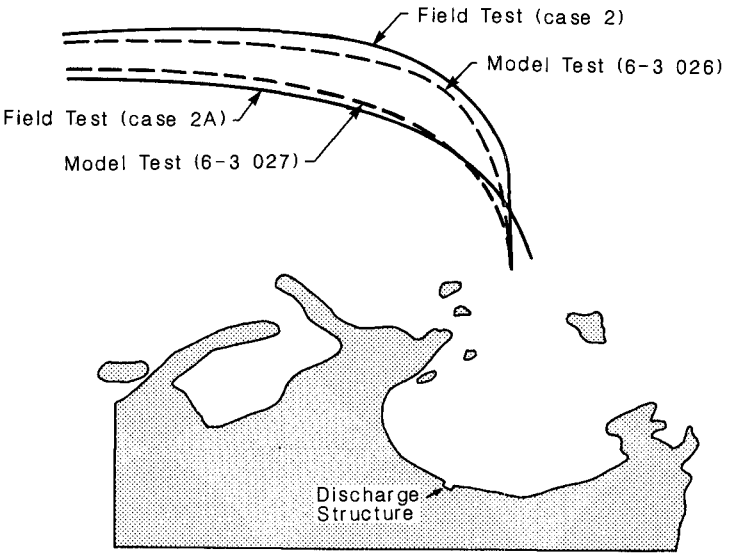

Figure 17. Comparison of Offshore Plume Trajectory between Model and Field data for Case 2 and Case 2A

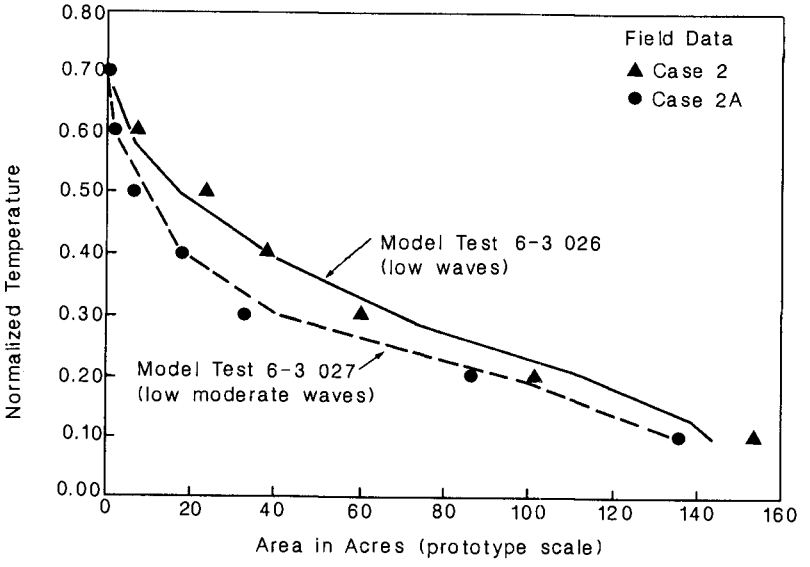

Figure 18. Comparison of Surface Plume Areal Spread between Model and Field Data for Case 2 and Case 2A

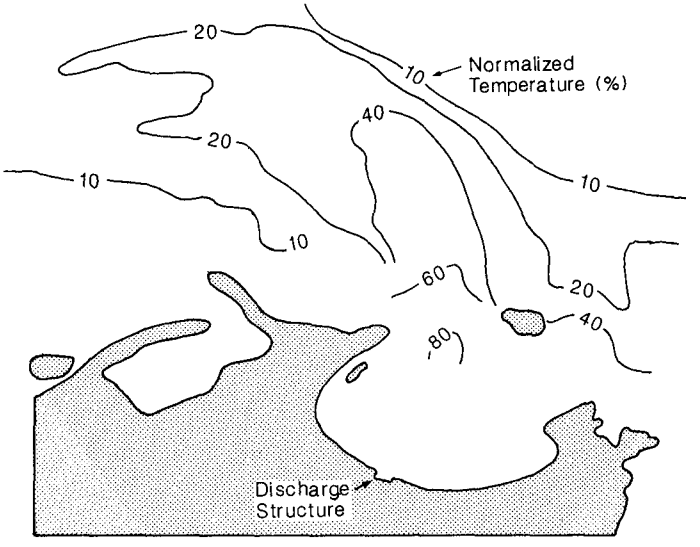

Figure 19a. Offshore Plume Configuration for Model Test 6-3 027

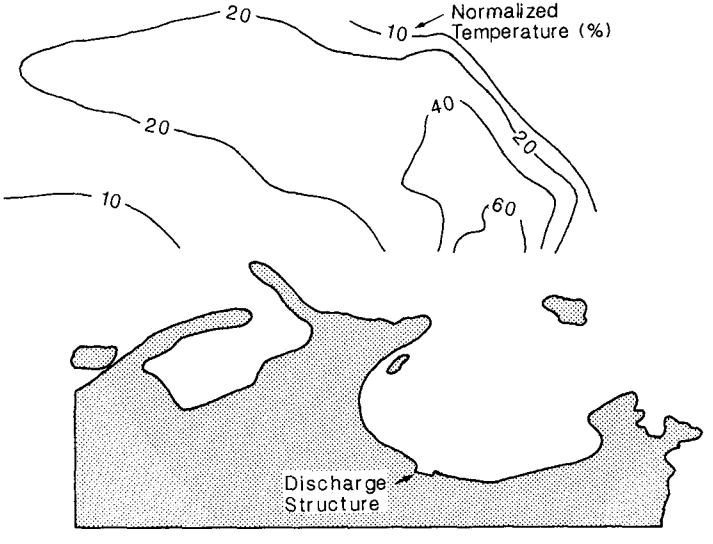

Figure 19b. Offshore Plume Configuration for Field Test Case 2A

REFERENCES

GIGER, M., JIRKA, G.H. and DRACOS T.H., (1985), "Meandering Jets in A Shallow Fluid Layer", Proc. Fifth Symposium on Turbulent Shear Flows, Cornell University, Ithaca, New York.

LEIGHTON, J.P., TU, S.W., PETROCCITTO, A.A. and EASTMAN, L.K., (1986A), "Characterization of Receiving Water Temperatures During Power Ascension Testing of Unit 1 of Diablo Canyon Power Plant", Report 420-85.748, Department of Engineering Research, Pacific Gas and Electric Company, San Ramon, California.

LEIGHTON, J.P. and TU, S.W., (1986B), "Field Studies of Buoyant Jet in Coastal Waters", ASCE, 20th International Conference on Coastal Engineering, Taipei, Taiwan, Republic of China, 9-14 November, 1986

WIEGEL, R.L., HARMS, V.W., SAFAIE, B., CUMMING, J.D., DELLA, R.P., LEIDERSDORF, C.B. and YOUNG, C., (1976), "Report of Model Study of Cooling Water System of Pacific Gas and Electric Company Nuclear Power Plant Located at Diablo Canyon, California", Supplement Report No. 8 to Environmental Report Units 1 and 2 Diablo Canyon Site; also Report No. HEL 27-2, Hydraulic Engineering Lab., University of California at Berkeley, California.

CHAPTER 200

COOLING WATER RECIRCULATION IN THE OCEAN

by

Robert L. Wiegel,[1] F.ASCE, John T. Wells[2] and Michele A. Murdoch,[2] AM. ASCE

Abstract

In some configurations of cooling water systems for thermal-electric power plants, which use sea water as a source, a certain amount of recirculation occurs. A theory is developed to predict this recirculation. The resulting equation for the temperature rise due to a combination of the heat added to the water flowing through the condenser tubes and the build-up of heat by recirculation, the discharge temperature less the ambient temperature, is

$$T_d - T_a = \Delta T_r = \Delta T_0/[1 - (1/D)]$$

where T_d is the discharge water temperature, T_a is the ambient temperature of the sea water, ΔT_0 is the increase in temperature of the water flowing through the condenser tubes, D is the dilution that occurs by turbulent mixing of the warm water discharge with the sea water.

To test the validity of the above equation, a physical model was constructed to simulate the cooling water system, including a constant temperature cooling water source, intake and discharge structures, mixers and a heating system. Digital thermometers were used to measure the water temperatures, and dye was used to visualize the flow and the mixing of the water.

The increase in temperature due only to recirculation, $\Delta T'$, is ΔT_r minus the temperature due to heat added during a cycle, ΔT_0 (i.e., $\Delta T' = \Delta T_r - \Delta T_0 = T_i - T_a$), or

$$\Delta T_t' = T_i - T_a = [\Delta T_0/(1-1/D)] - \Delta T_0$$

where $\Delta T_t'$ is the theoretical value of $\Delta T'$, and T_i is the intake water temperature.

It was found from the experiments that the measured values of temperature increase, $\Delta T'$, were slightly lower (about 10%) in most instances than the values of temperature increase predicted by the equation, $\Delta T_t'$. A later series of tests was run in which the measured values were found to be about 15% higher than the predicted values; these data are suspect, however. If all of the data are considered, in about 60% of the tests the temperature increases were equal to or lower than predicted values, and in about 40% of the tests they were higher than the predicted values.

[1]Professor of Civil Engineering, University of California, Berkeley, CA.
[2]Director, Administrative Services, Dept. Eng. Research, Pacific Gas and Electric Company, San Ramon, CA.
[3]General Engineer, Naval Civil Engineering Laboratory, Port Hueneme, CA.

Introduction

In the cooling water system of a thermal-electric power plant, water is pumped from the ocean (or other source of water), through condenser tubes, and the heated water then discharged back into the ocean. If recirculation occurs, that is, if a portion of the warm water discharge is again taken through the cooling system, there will be a gradual build-up of heat to some equilibrium condition, and this would reduce the thermal efficiency of the plant and increase the effect of the discharge on marine organisms. Ideally, the intake and discharge structures are positioned so that the warm water from the discharge will not be recycled through the cooling system. However, such arrangements are not always possible, and it is desirable to be able to predict how much recirculation might occur.

In 1982, two of the coauthors (RLW and JTW) independently developed an equation for determining the amount of heat build-up that would occur in this type of cooling system, given the temperature of the cooling water source (i.e., the ocean), the amount of heat added to the cooling water during the cooling cycle, and the dilution by turbulent mixing of the recirculated water that occurs between discharge and re-intake. The reliability of this equation was tested by means of a physical model in which the predicted values of heat build-up could be compared to measured values.

This paper describes the theory, the laboratory arrangements and test procedures, the interpretation of the data, and the conclusions based on these experiments.

Theory

The primary assumption in the development of the theory is that cooling water is obtained from a large source, such as the Pacific Ocean, where a gradual temperature rise of the water due to the thermal discharge will not be measurable. This cooling water source maintains a constant ambient temperature, T_a. To simplify the concept of the theory, water is dealt with in terms of units rather than continuous flow until the end of the derivation.

The sketch in Figure 1 represents the circulation system being considered.

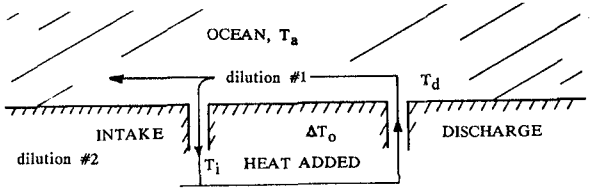

Figure 1. Definition Sketch

Let the amount of heat added to one unit of water during each cycle be proportional to ΔT_o, and the temperature of the discharge water at any time be T_d. When the system is started, one unit (= B) of water is taken in through the intake at temperature T_a, its temperature is increased by ΔT_o, and the discharge temperature after the first cycle is

$$T_d = T_a + \Delta T_o \tag{1}$$

This water is discharged into the ocean, and then diluted as it mixes with the sea water (dilution #1 on the sketch). Most of this diluted water remains in the ocean, becoming further diluted. A small amount is drawn back into the intake where subsequent dilution takes place by the water flowing in through the lower portion of the intake structure (dilution #2). Let the total dilution, from both the ocean and the intake structure, be D. A dilution of $D = 50$ would represent one unit of warm water mixed with 49 units of cool water, for a total of 50 units.

A heat balance gives the temperature of the water after one cycle, from intake to intake including heat added and total dilution:

Temperature after first cycle = $\dfrac{B(T_a + \Delta T_o) + B(D - 1)T_a}{BD}$.

$$T_i = T_a + \Delta T_o/D \tag{2}$$

where $B(T_a + \Delta T_o)$ = heat discharged, $B(D - 1)T_a$ = heat of mixture with sea water, and BD = total water.

For the second cycle, the temperature of the water being discharged, T_d, is

$$T_d = T_a + \Delta T_o/D + \Delta T_o .$$

Placing this value into the heat balance equation gives

$$T_i = \frac{B(T_a + \Delta T_o/D + \Delta T_o) + B(D - 1)T_a}{BD} = T_a + \Delta T_o/D + \Delta T_o/D^2$$

Similarly, for the third cycle,

$$T_i = \frac{B(T_a + \Delta T_o/D + \Delta T_o/D^2 + \Delta T_o) + B(D - 1)T_a}{BD} = T_a + \Delta T_o/D + \Delta T_o/D^2 + \Delta T_o/D^3$$

and so on.

Thus, the series for the intake temperature is

$$T_i = T_a + \Delta T_o/D + \Delta T_o/D^2 + \Delta T_o/D^3 + \cdots \tag{3a}$$

or

$$T_i = T_a + \Delta T_o \sum_{n=1}^{\infty} 1/D^n \tag{3b}$$

The series for the discharge temperature is

$$T_d = T_a + \Delta T_o + \Delta T_o/D + \Delta T_o/D^2 + \Delta T_o/D^3 + \cdots = T_a + \Delta T_o \sum_{n=0}^{\infty} 1/D^n \tag{4a}$$

$$T_d = T_a + \Delta T_o/(1 - 1/D) \tag{4b}$$

Now, consider N units going through the cycle each second; the heat balance equation is

$$\frac{NB(T_i) + NB(D - 1)T_a}{NBD} \tag{5}$$

N cancels out, leaving the resulting temperature the same as it was for discrete units of B. If B is one cubic meter, NB is cubic meters per second, or $NB = Q$ for Q = volumetric flow through the cooling system, and the equation is valid for continuous flow.

The temperature rise, due to the heat added to the water flowing through the condenser tubes and to the build up of heat by recirculation, is the discharge temperature less the ambient temperature

$$\Delta T_r = T_d - T_a = [T_a + \Delta T_o/(1 - 1/D)] - T_a = \Delta T_o/(1 - 1/D) \tag{6}$$

As an example, consider a rather small primary dilution in the ocean of ten to one and a secondary dilution within the intake structure of five to one, for a total dilution of fifty to one, that is, $D = 50$. Assuming the heat added during the cycle to be proportional to 20° F (ΔT_o), the eventual build-up of temperature would be

$$\Delta T_r = \Delta T_o(1 - 1/D) = 20° F/(1 - 1/50) = 20.4° F, \text{ and } \Delta T_l' = 0.4° F.$$

Similarly, dilutions of 100, 25 and 10 to 1 would give ΔT_r = 20.2, 20.8 and 22.2° F, respectively. Note that this is the difference between the discharge and ambient temperatures, and therefore includes the ΔT_o = 20.0° F ($\Delta T_l'$ = 0.2, 0.8, and 2.2° F).

Experimental Arrangements

To test the validity of the above equation, a physical model was constructed to simulate the cooling water system, including a constant temperature cooling water source, intake discharge structures, and a heating system. A value of ΔT_o of about 20° F was used in these tests, as this is the temperature increase used in some power plants. The values of dilution that were obtained were less than 20:1 owing to the small capacity of the current and the discharge available in the test facility.

The cooling water source was simulated by a steady flow of water through a rectangular channel. The amount of dilution occurring could be calculated knowing the speed of the ambient current and the flow of the thermal discharge. A concrete tank 150 feet long, 8 feet wide and 5 feet deep was used. A steady current could be maintained in the tank by means of a large recirculating pump system. The volume of water flowing through this system was sufficiently large that it would not heat up appreciably during the tests. It simulated reasonably well a constant temperature cooling source.

To reduce the scale of the model, which was necessary owing mainly to the limited capacity of the available water heater, a smaller channel was constructed within the large tank, which could carry a steady flow of water, but with a smaller flow rate. The large tank was equipped with a 16' x 8' x 3/4" plywood platform which was suspended from the sides of the tank, and could be adjusted to different depths and angles. The water current in the tank flowed freely both beneath and above this platform mounted in the tank. It was upon this suspended platform that the small channel was built (see Figures 2 and 3).

The platform was placed in a level position at a depth beneath the water surface which would allow the desired current to flow when the recirculating pump was operating at its maximum flow rate. The smaller channel, constructed of two pieces of 3/4" plywood, was 1' wide by 8' long, mounted onto the platform in the tank with the distance between the boards being 18 inches. The joints where the two boards met to form the 16' long channel were sealed with a waterproof putty to prevent infiltration of water from the large tank into the model channel. The leading edges of the barriers were beveled to assure smooth inflow of water into the model channel.

To assure thorough mixing of the thermal discharge and the ambient current, a set of eight mechanical mixers, each of which was geared to a variable speed motor, was suspended in the channel between the discharge and intake (see Figures 4 and 5, and Photo 1). By providing this extra mixing, the dilution of the discharge could be calculated as simply the ratio of the flow through the model to the flow of the discharge.

The intake was located two feet upstream from the end of the channel, to prevent the possibility of water from the "outer" tank further diluting the water at the intake. The intake was drilled through the bottom of the model channel, and a rubber hose (connected to the channel with a steel nipple) was used to carry the water over the side of the large tank to the heater. A pump with a maximum flow of about 20 gpm was used to pump the water from the intake through the heater and out the discharge structure.

The water was heated by a continuous flow type gas operated swimming pool heater. A valve was inserted in the line downstream from the heater to control the discharge flow rate.

A water-mercury manometer connected to a 1/2" orifice was used to determine flow rate through the intake/discharge line. It was calibrated at the start of the tests. The calibration was made by measuring the time required to discharge 100 lbs. of water into a tank, together with the manometer reading.

A pressurized dye injection tank was connected to the line upstream of the discharge outlet. Photo 2 shows the equipment used between the intake and discharge structures.

The discharge water was carried by a rubber hose back to the large tank, and connected to a steel nipple which was threaded through the side of the plywood barriers near the bottom of the channel (see photo 3). Both intake and discharge holes were sealed with waterproof putty to prevent leaking or entrainment of "outside" water. The discharge was located six feet downstream from the mouth of the channel, two feet upstream from the mixers and eight feet upstream from the intake (see Figure 2).

Three digital thermometers were used to monitor the temperature of the water in the intake, in the discharge, and the ambient water flowing through the channel. The temperature probe at the discharge was clipped to the barriers directly over the discharge hole (photo 3), and the probe at the intake gage (photo 4). The probe used to measure the ambient temperature was attached to the outside of the model channel near the mouth to prevent any of the heated water from interferring with the ambient temperature.

The water flow through the model channel was measured by a Kent "miniflow" anemometer-type current meter. The meter reading in hertz represented the number of times per second a propeller blade passed a reference point on the cylinder about which it rotated. The propeller had five blades, so one complete revolution per second would read five hertz. The meter was calibrated prior to the tests. The speed of the current was the most unreliable measurement made during the tests. The meter reading continually fluctuated, making an accurate reading difficult.

Test Procedure

At least thirty minutes before a test was started, the large recirculating pump in the concrete tank was turned on to allow sufficient time for a steady current to develop, and to disperse any temperature stratification that might exist in the water in the tank. The digital thermometers were turned on at the same time, as they required from twenty to thirty minutes to warm up before accurate readings could be made. Then, each of the three thermometers was calibrated relative to the temperature of the water in the trough which was measured with a mercury thermometer. (Note: In some instances the thermometers were not all calibrated to the same temperature due to time limitations; in these instances, the data were adjusted before being inserted into the equation. For example, if two of the thermometers were correctly calibrated to 53.4° F and the third thermometer read 53.5° F, the temperature readings from the third thermometer would be reduced by -0.1° F so that readings on all three thermometers would be in reference to the same base temperature, 53.4° F, in this example.

The intake/discharge cycle was then started, the desired flow rate set, and the manometer reading recorded. The mixers were started, and a small amount of dye injected into the discharge line to check visually that complete mixing was taking place, and that no substantial leaking or infiltration was occurring between the model channel and the outside tank. Dye crystals were dropped into the water near the current meter. As the crystals fell, they formed a dye trail which showed the current pattern through the water column. If the discharge was too high or the mixers were rotating too fast, the current did not flow smoothly into the model channel. If the dye trail did not indicate a smooth steady current, the

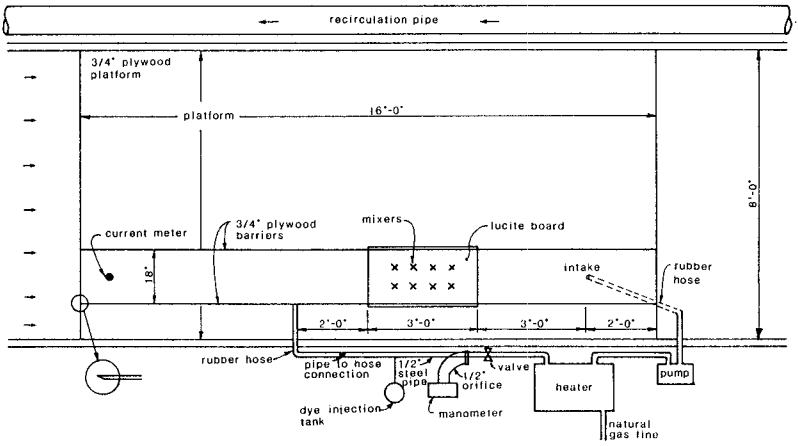

Figure 2. Model Arrangement, Schematic Plan

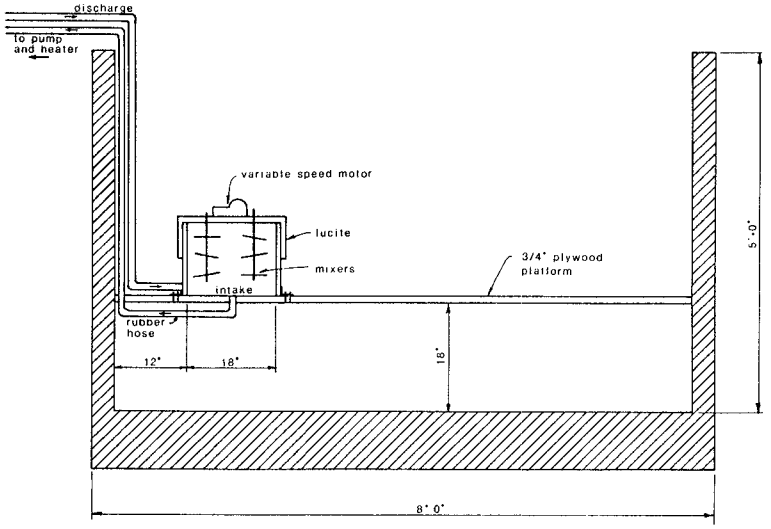

Figure 3. Model Arrangements, Schematic Elevation

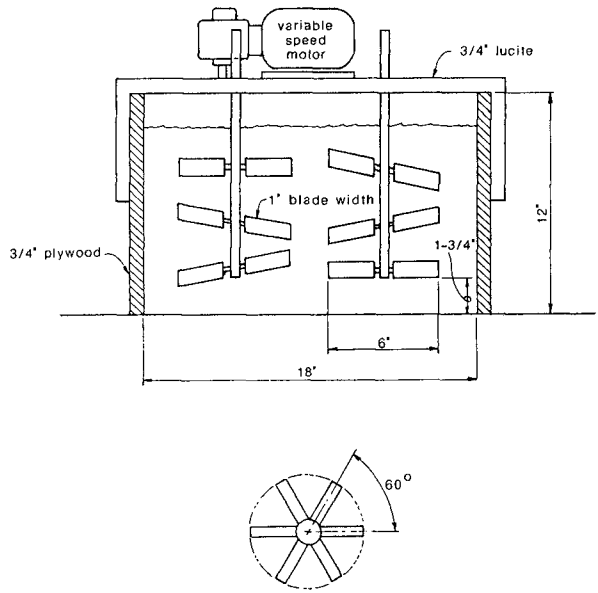

Figure 4. Schematic of Mixers, Elevation

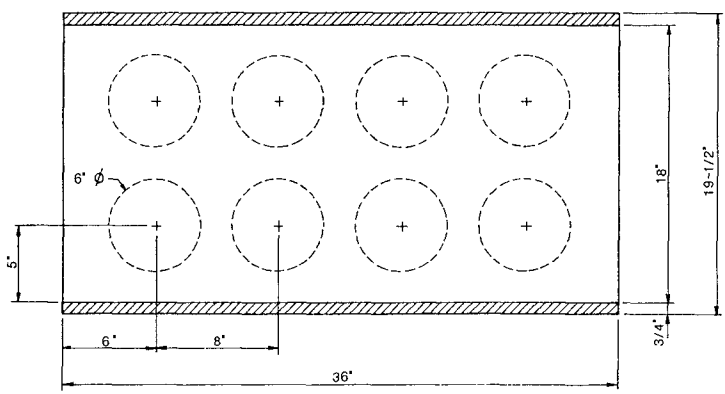

Figure 5. Schematic of Mixers, Plan

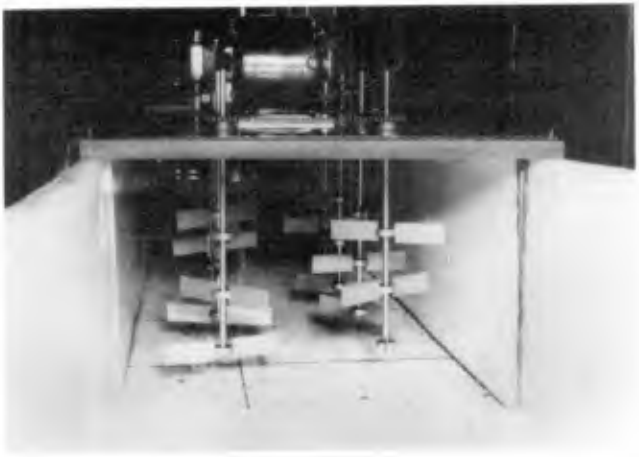

Photo 1.

Photo 2.

Photo 3.

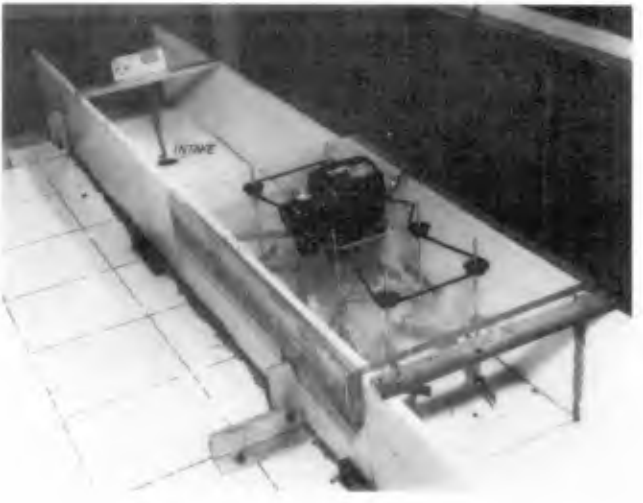

Photo 4.

discharge and mixers were adjusted to provide a good current and thorough mixing.

The heat was then turned on, and the time recorded. While the heater was warming up (this took only two to three minutes), the current meter reading was recorded. The temperatures were recorded at periodic time intervals, usually two to ten minutes, until the test was completed.

After a test was finished the heater was turned off, and cool water pumped through it for about five minutes. Then, the discharge was shut off. The large recirculating pump was left on for about an additional thirty minutes to cause the temperature throughout the tank to become uniform before the next test was begun. This length of time was very conservative as the thermometers indicated that only about five minutes were required to do this.

The thermometers were calibrated again before the next test and any large differences (0.3° F or larger) were noted, as this could be an indication that readings during the previous test were inaccurate. One of the thermometers had to be replaced about half way through the series of tests due to a malfunction. It was replaced by a thermometer which read in degrees Celsius, and these readings converted to °F prior to interpreting the data.

Interpretation of the Data

The velocity and depth of the water in the channel, together with the discharge rate, were used to calculate the dilution, D:

$$D = \frac{\text{total flow (calculated from current meter and depth)}}{\text{discharge flow (calculated from manometer reading)}}$$

A measure of the heat added during a recirculation cycle ΔT_o, was calculated by subtracting the intake temperature, T_i, from the discharge temperature T_d

$$\Delta T_o = T_d - T_i$$

The heat build-up that occurs during the cycle would be proportional to ΔT_r. The heat build-up due only to the recirculation of discharge water would be proportional to ΔT_r less the amount of heat added during a cycle, proportional to ΔT_o. This quantity is given the symbol $\Delta T'$ and is also equal to the temperature difference between intake and ambient waters, or

$$\Delta T' = T_i - T_a$$

$\Delta T'$ can also be calculated using the formula

$$\Delta T_t' = [\Delta T_o/(1 - 1/D)] - \Delta T_o$$

This value for $\Delta T'$ has the subscript "t" as it is calculated from theory.

Results and Conclusions

Measured values of $\Delta T'$ versus predicted values, $\Delta T_t'$, are shown in Figure 6. As can be seen, the measured temperature increases ($\Delta T'$) were slightly lower in most instances than the temperature increases predicted by the equation, $\Delta T_t'$. Thus, the equation gives a slightly conservative approximation to the long term increase of temperature which may be expected due to recirculation. The difference between measured and predicted values is rarely larger than about 10%, and the predicted value is conservative in nearly every case. A few additional tests were run at the end of the experiments in which the opposite effect occurred. That is, the measured temperatures were about 15% greater than the predicted temperatures.

However, other information led the investigators to believe that an error had occurred in the calibration of the digital thermometers at the start of this series of tests. If all of the data are considered, in about 60% of the tests the temperature increases were equal to or lower than predicted values and in about 40% of the tests they were higher than the predicted values.

It was found that during a test the values of ΔT_o gradually increased with time. It is believed that this was due to heat being added by the pump which provided the circulation of the intake/discharge system. The pump only operated at one speed, but the amount of water in the intake/discharge system was controlled by a valve located past the heater and therefore past the pump. When the valve was adjusted so that the flow was less than the maximum flow which could be provided by the pump, the "excess" energy from the pump may have been added to the water as heat. this mechanical heat would be in addition to the provided by the heater. This seemed to be the most reasonable explanation for the increasing ΔT_o.

For temperatures measured to one-tenth of a degree Fahrenheit, only two cycles of recirculation are required before the equation can be used to predict the heat build-up. Two cycles were easily completed in less than three minutes (from a conservative calculation of flow through the system). As the temperature increases described in the above paragraph occurred slowly in comparison, each set of readings taken during a test should truly simulate an individual situation; i.e., each set of readings was analyzed on the basis of the ΔT_o recorded for that instance. This assumption did not appear to affect the results. The results got neither better nor worse with increasing time during a test.

Two other comments regarding the data should be made. First, in a few tests, the mixers were not turned on. The data from these tests are no different than the data of the tests where the mixers were used. It appears from this that the mixers were not needed to obtain the required dilution, as the flow-induced turbulent mixing was sufficient. These data are included in this report. Secondly, in a few tests the ambient temperature changed by 0.1 or 0.2 degrees Fahrenheit (never more than this, however) and this change occurred over times equal to or greater than about thirty minutes. This should not affect the interpretation of the data, since all numbers used in the calculations are relative to the other temperatures. If the ambient temperature was raised 0.1 degree F, say T_i and T_d would also be 0.1 degree F higher, and the increase would cancel out in the equations used to interpret the data.

Despite the limitations of these tests, the consistency in results of the tests shows that the equation presented herein predicts reasonably well the build-up of heat that may occur in a cooling system of the type modeled.

References

Murdoch, Michele A., "Hydraulic Model Tests Performed to Check Validity of Recirculating Cooling Water Model Theory," University of California, Berkeley, CA, Hydraulic Engineering Laboratory Technical Report HEL 27-11, June 1983, 36 pp.

Wiegel, Robert L., "Letter Report on Method for Calculating Recirculation" to Mr. Ramon F. Cayot, Director, Department of Engineering Research, Pacific Gas and Electric Company, 9 June 1982, 3 pp.

Acknowledgments

We would like to thank Hubert L. Burnett whose suggestions and assistance were invaluable during the design and construction of the model; his patience and humor were also appreciated. We would also like to thank Ed White for building the special equipment

needed for the experiment, and Karen Earls for preparing the manuscript of the paper. The work presented herein was supported by a contract between the Pacific Gas and Electric Company and the University of California.

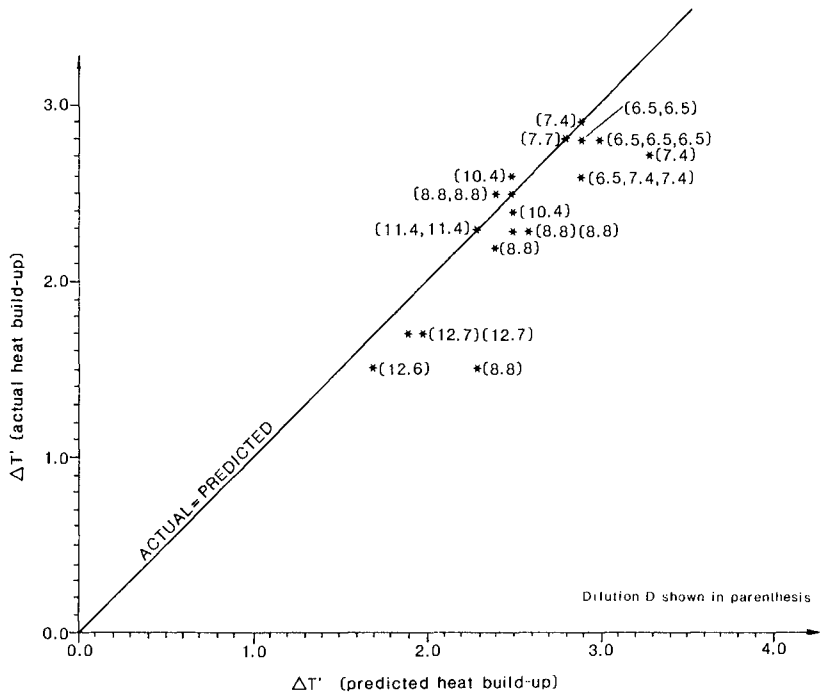

Figure 6. Actual Temperature Build-Up vs. Predicted Temperature Build-Up. 12/29/82, 12/30/82, 12/31/82 and 1/10/83 data. Dilution, D, shown in parentheses.

Keelung Port, Taiwan, ROC—R.L. Wiegel

PART V

SHIP MOTIONS

Composite Breakwater near Taipei—H. Lee Butler

CHAPTER 201

A Numerical Simulation of the Moored Container Ship Movements Induced by Wind

T Z Cheng * & N K Liang **

ABSTRACT

In the past, only the ship motion due to wave is studied. This study is focused on the ship motion induced by a steady oscillating wind. The oscillating wind is assumed to be sinusoidal of a constant frequency. The wind direction θ, number of mooring lines and the wind frequency are the parameters in simulating an Evergreen's Ever Garden class container ship. The results show that the worst angle between the quay and the prevailing wind direction is 45°. Surge and roll are the most significant motions induced by the oscillating wind. By changing the number of mooring lines, the natural frequency can be kept away from the dominant wind frequency, except roll.

INTRODUCTION

The wave affects the ship motion significantly. Hence, in the past only ship motion due to wave is studied (Lewis, 1929; Korvin-Kroukovsky, 1961; Salvesen, et al, 1970). However, there are harbours which are well sheltered by the breakwater from suffering the invasion of waves but attacked by strong moonson wind. It is self-understood that the wind is oscillating. The oscillating wind may induce ship motion. The purpose of this paper is to understand the characteristics of the wind-induced ship motion by numerical simulation qualitatively. The results can be used for the guide line of harbour design.

THEORY

There are two coordinate systems: One is the equilibrium axes (Fig. 1), which is fixed. C.G. is the center of gravity. O is the mean position of ship motion. The other one is the body axes which is moved with the ship (Fig. 2). The definition of 6 ship motions is also shown in Fig. 2. The 3 translation motions are surge $x(t)$, sway $y(t)$ and heave $z(t)$. The 3 angular motions are roll $\phi(t)$, pitch $\theta(t)$ and

* Graduate student, Institute of Oceanography, National Taiwan University, Taiwan, R.O.C.

** Director, Institute of Harbour & Marine Technology, Wuchi, Taiwan R.O.C.

yaw $\psi(t)$. In order to construct the equations of motion, the following assumptions are made:

1. The ship is a rigid body.
2. The ship is symmetric and slender.
3. The ship motion amplitude is small, equations can be linearized.
4. Except roll, the effect of viscosity is neglected.
5. The wind direction is fixed.
6. There is no incident wave.
7. No coupling between the longitudinal motion— surge, heave and pitch, and the transverse motion—sway, roll and yaw.

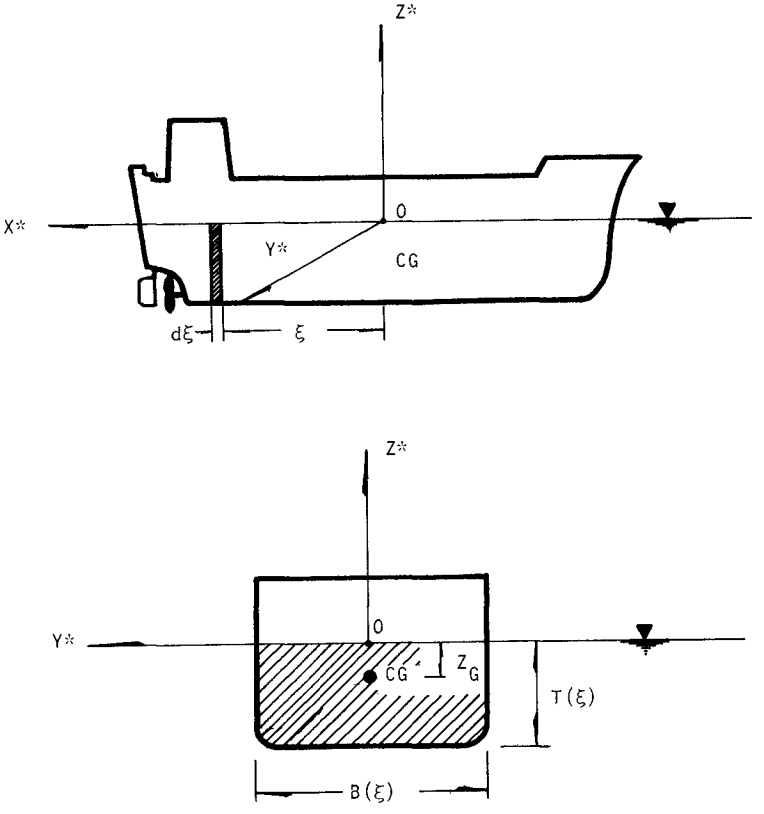

Fig 1. The definition of equilibrium axes

For longitudinal motion

$$\begin{aligned} M'\ddot{x} + M'Z_g\ddot{\theta} &= X_I + X_D + X_H + X_M + X_W \\ M'\ddot{z} &= Z_I + Z_D + Z_H + Z_M + Z_W \\ I_2\ddot{\theta} + M'Z_g\ddot{x} &= M_I + M_D + M_H + M_M + M_W \end{aligned} \tag{1}$$

For transverse motion

$$\begin{aligned} M'\ddot{y} - M'Zg\ddot{\phi} &= Y_I + Y_D + Y_H + Y_M + Y_W \\ I_1\ddot{\phi} - I_{13}\ddot{\psi} - M'Z_g\ddot{y} &= K_I + K_D + K_H + K_M + K_W \\ I_3\ddot{\psi} - I_{13}\ddot{\phi} &= N_I + N_D + N_H + N_M + N_W \end{aligned} \tag{2}$$

where,

M'	mass of ship
M	moment for pitch
K	moment for roll
N	moment for yaw
X	force for surge
Y	force for sway
Z	force for heave
I_1, I_2, I_3	moment of inertial with respect to X^*, Y^* and Z^* axes
I_{13}	Product of inertial with respect to $X^* - Z^*$ axes.

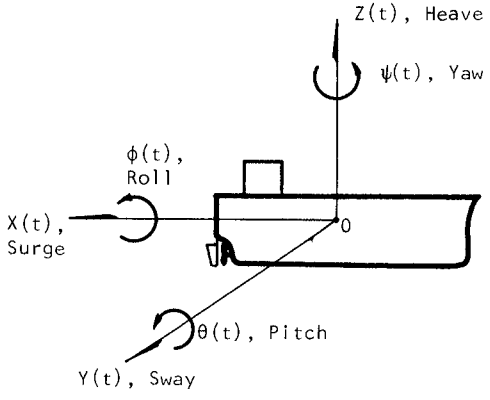

Fig. 2 The definition of six ship motions

the subindex

I	inertial
D	damping
H	hydrostatic restoring
M	mooring line restoring
$\overline{W}$	wind excitation

8. Strip theory approximation
The hydrodynamic forces and moments can be integrated along the ξ - axis, i.e. the longitudinal axis of the ship.

For longitudinal motion

$$X_I = -\int m_x(\xi)d\xi\cdot\ddot{x} + \int Zs(\xi)m_x(\xi)d\xi\cdot\ddot{\theta}$$

$$X_D = -\int n_x(\xi)d\xi\cdot\dot{x} + \int Zs(\xi)n_x(\xi)d\xi\cdot\dot{\theta}$$

$$X_H = 0$$

$$Z_I = -\int m_z(\xi)d\xi\cdot\ddot{z} + \int \xi m_z(\xi)d\xi\cdot\ddot{\theta}$$

$$Z_D = -\int n_z(\xi)d\xi\cdot\dot{z} + \int \xi n_z(\xi)d\xi\cdot\dot{\theta} \qquad (3)$$

$$Z_H = -\rho_w g\int B(\xi)d\xi\cdot z + \rho_w g\int \xi B(\xi)d\xi\cdot\theta$$

$$M_I = \int Zs(\xi)m_x(\xi)d\xi\cdot\ddot{x} + \int \xi m_z(\xi)d\xi\cdot\ddot{z} - \int[\xi^2 m_z(\xi) + Z_s^2(\xi)m_x(\xi)]d\xi\cdot\ddot{\theta}$$

$$M_D = \int Zs(\xi)n_x(\xi)d\xi\cdot\dot{x} + \int \xi n_z(\xi)d\xi\cdot\dot{z} - \int[\xi^2 n_z(\xi) + Z_s^2(\xi)n_x(\xi)]d\xi\cdot\dot{\theta}$$

$$M_H = \rho_w g\int \xi B(\xi)d\xi\cdot z - \rho_w g\int \xi^2 B(\xi)d\xi\cdot\theta$$

where

$m_x(\xi)$	sectional added mass per unit length for surge.
$m_z(\xi)$	sectional added mass per unit length for pitch.
$n_x(\xi)$	sectional damping coefficient per unit length for surge.
$n_z(\xi)$	sectional damping coefficient per unit length for pitch.
$B(\xi)$	sectional width.
$Zs(\xi)$	distance between water surface to the center of the sectional added mass.

For transverse motion

$$Y_I = -\int m_y(\xi)d\xi\cdot\ddot{y} - \int \xi m_y(\xi)d\xi\cdot\ddot{\psi} - \int m_y\phi(\xi)d\xi\cdot\ddot{\phi}$$

$$Y_D = -\int n_y(\xi)d\xi\cdot\dot{y} - \int \xi n_y(\xi)d\xi\cdot\dot{\psi} - \int n_y\phi(\xi)d\xi\cdot\dot{\phi}$$

$$
\begin{aligned}
Y_H &= 0 \\
K_I &= -\int m_{y\phi}(\xi)\,d\xi\cdot\ddot{y} - \int m_{\phi}(\xi)\,d\xi\cdot\ddot{\phi} - \int \xi m_{y\phi}(\xi)\,d\xi\cdot\ddot{\psi} \\
K_D &= -\int n_{y\phi}(\xi)\,d\xi\cdot\dot{y} - \int n_{\phi}(\xi)\,d\xi\cdot\dot{\phi} - \int \xi n_{y\phi}(\xi)\,d\xi\cdot\dot{\psi} \\
&\quad -\int N_{\phi}'(\xi)\,d\xi\cdot\dot{\phi} \qquad (4) \\
K_H &= -\rho_w g \nabla\cdot\overline{GM}\cdot\phi \\
N_I &= -\int \xi m_y(\xi)\,d\xi\cdot\ddot{y} - \int \xi^2 m_y(\xi)\,d\xi\cdot\ddot{\psi} - \int \xi m_{y\phi}(\xi)\,d\xi\cdot\ddot{\phi} \\
N_D &= -\int \xi n_y(\xi)\,d\xi\cdot\dot{y} - \int \xi^2 n_y(\xi)\,d\xi\cdot\dot{\psi} - \int \xi n_{y\phi}(\xi)\,d\xi\cdot\dot{\phi} \\
N_H &= 0
\end{aligned}
$$

where

∇	displaced volume of the ship
$\overline{GM}$	metacentric height
$m_y(\xi)$, $n_y(\xi)$	sectional added mass and damping coefficient per unit length for sway.
$m_\phi(\xi)$, $n_\phi(\xi)$	sectional added mass and damping coefficient per unit length for roll.
$m_{y\phi}(\xi)$, $n_{y\phi}(\xi)$	sectional added mass and damping coefficient per unit length for coupling between roll and sway.
$n_\phi'(\xi)$	sectional damping coefficient due to viscosity for roll.

9. All unit added mass and damping coefficient are only a function of frequency.
Eq.(3) and (4) can be rewritten: (The coefficient Aij, Bij and Cij are calculated according to NSRDC ship-motion and sea-load computer program).

$$
\begin{aligned}
X_I &= -A_{11}\ddot{x} - A_{15}\ddot{\theta} & Y_I &= -A_{22}\ddot{y} - A_{24}\ddot{\phi} - A_{26}\ddot{\psi} \\
X_D &= -B_{11}\dot{x} - B_{15}\dot{\theta} & Y_D &= -B_{22}\dot{y} - B_{24}\dot{\phi} - B_{26}\dot{\psi} \qquad (5) \\
X_H &= 0 & Y_H &= 0
\end{aligned}
$$

where

Aij: added mass coefficient
Bij: damping coefficient
Cij: hydrostatic restoring coefficient

10. The tension of the mooring line follows Hooke's Law, the mooring line is assumed as a straight line.
The static mooring forces & moments and the resistance of fender

at the equilibrium position are balanced with the average wind force. Therefore only the dynamic mooring forces or moments are considered. The dynamic mooring forces and moments are the following:

$$
\begin{aligned}
X_M &= - k_{11}x - k_{13}z - k_{15}\theta \\
Y_M &= - k_{22}y - k_{24}\phi - k_{26}\psi \\
Z_M &= - k_{33}z - k_{31}x - k_{35}\theta \\
K_M &= - k_{44}\phi - k_{42}y - k_{46}\psi \\
M_M &= - k_{55}\theta - k_{51}x - k_{53}z \\
N_M &= - k_{66}\psi - k_{62}y - k_{64}\phi
\end{aligned}
\qquad (6)
$$

And the dynamic mooring line force coefficients are:

$$
\begin{aligned}
k_{11} &= \Sigma(K\cos^2\alpha) \\
k_{13} &= k_{31} = \Sigma(K\cos\alpha\cos\gamma) \\
k_{15} &= k_{51} = \Sigma(KZ_L\cos^2\alpha - KX_L\cos^2\gamma) \\
k_{33} &= \Sigma(K\cos^2\gamma) \\
k_{35} &= k_{53} = \Sigma(KZ_L\cos\alpha\cos\gamma - KX_L\cos^2\gamma) \\
k_{55} &= \Sigma[K(X_L\cos\gamma - Z_L\cos\alpha)^2] \\
k_{22} &= \Sigma(K\cos^2\beta) \\
k_{24} &= k_{42} = \Sigma(-KZ_L\cos^2\beta) \\
k_{26} &= k_{62} = \Sigma(KX_L\cos^2\beta) \\
k_{44} &= \Sigma(KZ_L^2\cos\beta) \\
k_{46} &= k_{64} = \Sigma(-KX_LZ_L\cos^2\beta) \\
k_{66} &= \Sigma(KX_L^2\cos^2\beta)
\end{aligned}
$$

where

E modulus of elasticity
A sectional area of the rope
$K = EA/L$ spring constant , L length of the rope
(X_L, Y_L, Z_L) coordinates of the end of rope on the ship's deck.
(α, β, γ) angles between the rope from the land-end and the X*, Y*, Z* axes (shown in Fig-3)
Σ summantion over the total ropes.

11. The air is an incompressible viscous fluid. It is assumed:

wind force is $F(t) = \frac{1}{2}\rho C_D A U^2(t)$

where

$U(t)$	the wind velocity
ρ	air density
C_D	drag coefficient
A	Projecting area of the object to the plane which is perpendicular to the wind direction.

$$U(t) = \bar{U} + u(t) = \bar{U} + u_o \cos \omega t, \quad u_o << \bar{U}$$

then $U^2(t) \doteq \bar{U}^2 + 2\bar{U} u_o \cos\omega t$

$$F(t) = \tfrac{1}{2}\rho C_D A U^2(t) \doteq \tfrac{1}{2}\rho C_D A\bar{U}^2 + \tfrac{1}{2}\rho C_D A(2\bar{U}u_o)\cos\omega t$$
$$= \bar{F} + f_o \cos\omega t$$

where $\bar{F} = \frac{1}{2}\rho C_D A\bar{U}^2$

$$f_o = \rho C_D A\bar{U}u_o$$

As shown in Fig(4), $F_x(t)$ and $F_y(t)$ are the wind force component in X* and Y* axes, respectively.

Because C_D and A are function of θ_o, then

$$F_x(t;\ \theta_o) = \overline{F_x}(\theta_o) + f_x(\theta_o)\cos\omega t$$
$$F_y(t;\ \theta_o) = \overline{F_y}(\theta_o) + f_y(\theta_o)\cos\omega t$$

where

$$\overline{F_x}(\theta_o) = \tfrac{1}{2}\rho C_{DX}(\theta_o)\ A(\theta_o)\ \bar{U}^2$$
$$\overline{F_y}(\theta_o) = \tfrac{1}{2}\rho C_{DY}(\theta_o)\ A(\theta_o)\ \bar{U}^2$$
$$f_x(\theta_o) = \rho C_{DX}(\theta_o)\ A(\theta_o)\ \bar{U}u_o$$
$$f_x(\theta_o) = \rho C_{DY}(\theta_o)\ A(\theta_o)\ \bar{U}u_o$$

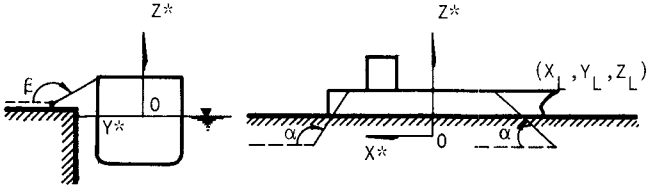

Fig.3 The definition of mooring line parameters

According to the above-mentioned assumptions, 6 second order simultaneous partial differential equations with 6 unknowns are as follows:

$$(M'+A_{11})\ddot{x} + B_{11}\dot{x} + k_{11}x + (A_{15}+M'Z_g)\ddot{\theta} + B_{15}\dot{\theta} + k_{15}\theta + k_{13}z = Xw$$

$$(M'+A_{22})\ddot{y} + B_{22}\dot{y} + k_{22}y + (A_{24}-M'Zg)\ddot{\phi} + B_{24}\dot{\phi} + K_{24}\phi + A_{26}\ddot{\psi} + B_{26}\dot{\psi} + k_{26}\psi = Yw$$

$$(M'+A_{33})\ddot{z} + B_{33}\dot{z} + (C_{33}+k_{33})z + k_{31}x + A_{35}\ddot{\theta} + B_{35}\dot{\theta} + (C_{35}+k_{35})\theta = Zw$$

$$(I_1+A_{44})\ddot{\phi} + B_{44}\dot{\phi} + (C_{44}+k_{44})\phi + (A_{42}-M'Z_g)\ddot{y} + B_{42}\dot{y} + k_{42}y + (A_{46}-I_{13})\ddot{\psi} + B_{46}\dot{\psi} + k_{46}\psi = Kw \quad (7)$$

$$(I_2+A_{55})\ddot{\theta} + B_{55}\dot{\theta} + (C_{55}+k_{55})\theta + (A_{51}+M'Z_g)\ddot{x} + B_{51}\dot{x} + k_{51}x + A_{53}\ddot{z} + B_{53}\dot{z} + (C_{53}+k_{53})z = Mw$$

$$(I_3+A_{66})\ddot{\psi} + B_{66}\dot{\psi} + k_{66}\psi + A_{62}\ddot{y} + B_{62}\dot{y} + k_{62}y + (A_{64}-I_{13})\ddot{\phi} + B_{64}\dot{\phi} + k_{64}\phi = Nw$$

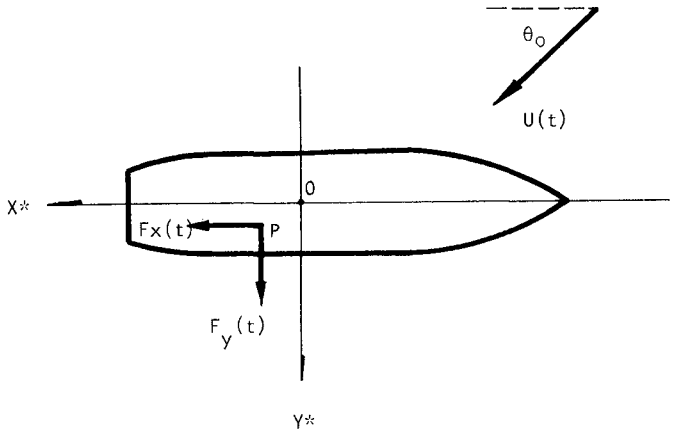

Fig. 4 The definition of wind direction θ_o

The wind force is sinusoidal, it can be represented as follows:

$$\begin{aligned} Xw &= \overline{W}_1 e^{-i\omega t}, & Yw &= \overline{W}_2 e^{-i\omega t} & Zw &= \overline{W}_3 e^{-i\omega t} \\ Kw &= \overline{W}_4 e^{-i\omega t}, & Mw &= \overline{W}_5 e^{-i\omega t} & Nw &= \overline{W}_6 e^{-i\omega t} \end{aligned} \tag{8}$$

$\overline{W}_1$, $\overline{W}_2$, ...$\overline{W}_6$ are the amplitudes of wind forces and moments. At steady state, the solution will be also sinusoidal, then

$$\begin{aligned} x &= x_o e^{-i\omega t}, & y &= y_o e^{-i\omega t}, & z &= z_o e^{-i\omega t} \\ \phi &= \phi_o e^{-i\omega t}, & \theta &= \theta_o e^{-i\omega t}, & \psi &= \psi_o e^{-i\omega t} \end{aligned} \tag{9}$$

substituding eq(8), (9) into eq(7), a new 6 simultaneous linear equcations are obtained.

To make the equations dimensionless M', L and $\sqrt{L/g}$ are used as mass, length and time scale. The index "'" to indicated the dimensionless symbols is omitted.

It can be written in the matrix form:

$$\{([C]+[k]) - \omega^2([M]+[A]) - i\omega[B]\} * [X] = [W] \tag{10}$$

in which

$$[X] = \begin{bmatrix} X_o \\ Y_o \\ Z_o \\ \phi_o \\ \theta_o \\ \psi_o \end{bmatrix}, \quad [W] = \begin{bmatrix} W_1 \\ W_2 \\ W_3 \\ W_4 \\ W_5 \\ W_6 \end{bmatrix}, \quad [M] = \begin{bmatrix} 1 & 0 & 0 & 0 & Z_G & 0 \\ 0 & 1 & 0 & -Z_G & 0 & 0 \\ 0 & 0 & 1 & 0 & 0 & 0 \\ 0 & -Z_G & 0 & I_1 & 0 & -I_{13} \\ Z_G & 0 & 0 & 0 & I_2 & 0 \\ 0 & 0 & 0 & -I_{13} & 0 & I_3 \end{bmatrix}$$

$$[A] = \begin{bmatrix} A_{11} & 0 & 0 & 0 & A_{15} & 0 \\ 0 & A_{22} & 0 & A_{24} & 0 & A_{26} \\ 0 & 0 & A_{33} & 0 & A_{35} & 0 \\ 0 & A_{42} & 0 & A_{44} & 0 & A_{46} \\ A_{51} & 0 & A_{53} & 0 & A_{55} & 0 \\ 0 & A_{62} & 0 & A_{64} & 0 & A_{66} \end{bmatrix}, [B] = \begin{bmatrix} B_{11} & 0 & 0 & 0 & B_{15} & 0 \\ 0 & B_{22} & 0 & B_{24} & 0 & B_{26} \\ 0 & 0 & B_{33} & 0 & B_{35} & 0 \\ 0 & B_{42} & 0 & B_{44} & 0 & B_{46} \\ B_{51} & 0 & B_{53} & 0 & B_{55} & 0 \\ 0 & B_{62} & 0 & B_{64} & 0 & B_{66} \end{bmatrix}$$

$$[C] = \begin{bmatrix} 0 & 0 & 0 & 0 & 0 & 0 \\ 0 & 0 & 0 & 0 & 0 & 0 \\ 0 & 0 & C_{33} & 0 & C_{35} & 0 \\ 0 & 0 & 0 & C_{44} & 0 & 0 \\ 0 & 0 & C_{53} & 0 & C_{55} & 0 \\ 0 & 0 & 0 & 0 & 0 & 0 \end{bmatrix}, [k] = \begin{bmatrix} k_{11} & 0 & k_{13} & 0 & k_{15} & 0 \\ 0 & k_{22} & 0 & k_{24} & 0 & k_{26} \\ k_{31} & 0 & k_{33} & 0 & k_{35} & 0 \\ 0 & k_{42} & 0 & k_{44} & 0 & k_{46} \\ k_{51} & 0 & k_{53} & 0 & k_{55} & 0 \\ 0 & k_{62} & 0 & k_{64} & 0 & k_{66} \end{bmatrix}$$

EXAMPLE

Evergreen's Ever Garden class container ship is used as an example to simulate the ship motion induced by the oscillating wind. The dimensions of the ship and the arrangement of the mooring lines are shown in Fig. 5. The other conditions are as follows:

D.W.T. 42,000 ton
$\bar{U}$ = 60 ft/sec, u_o = 30 ft/sec
wind direction θ_o= 0°, 45° 90°
number of mooring lines, 0, 2, 4, 6, 8, 10

Because the equations are linear, the amplitudes (x, y, z, θ, ψ, ϕ) are proportional to amplitude($\bar{W}$), which is proportional to $\bar{U}u_o$. If $\bar{U}u_o$ is changed, the relationship of the various ship motions remains the same. The results to the wind direction 45° are shown in Fig. (6) (7), (8), (9), (10), (11).

The results are samarized as follows:
1. Increasing the number of the mooring line increases the natural frequency, except roll.
2. The natural periods for different number of mooring lines are as follows:

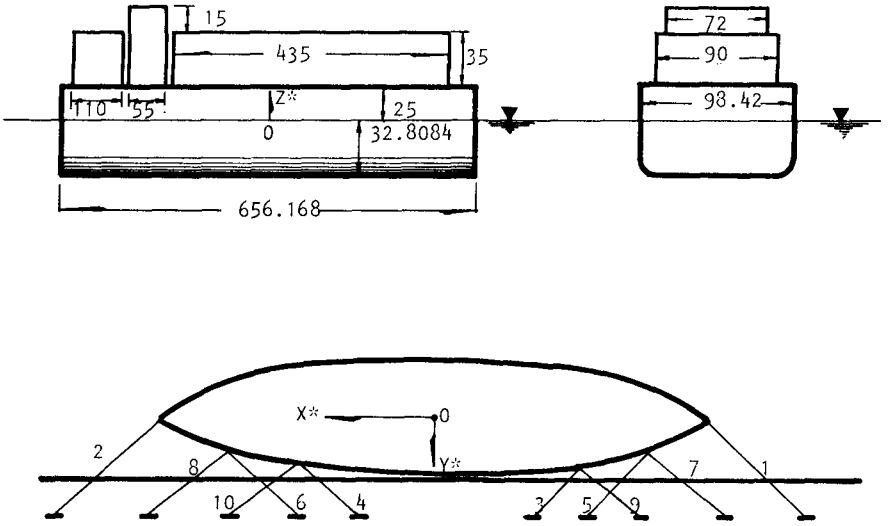

Fig. 5 Dimension of the container ship

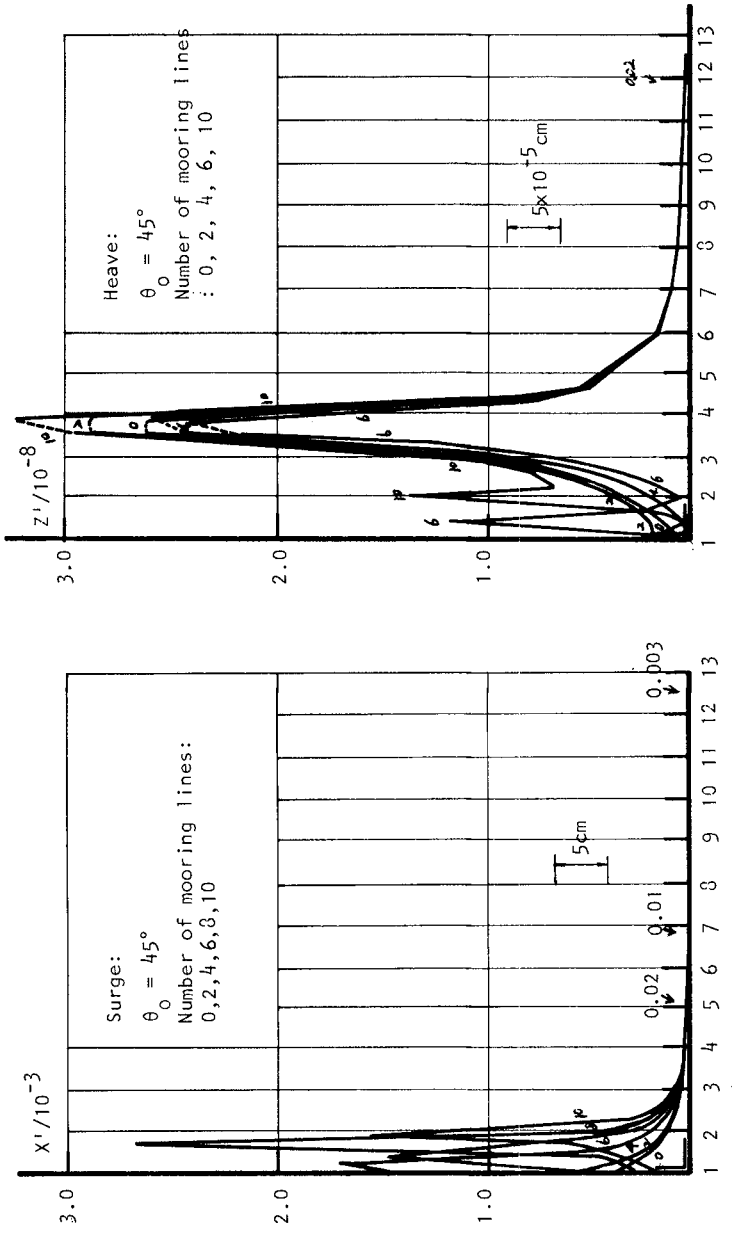

Fig. 6 Amplitude of surge

Fig. 7 Amplitude of heave

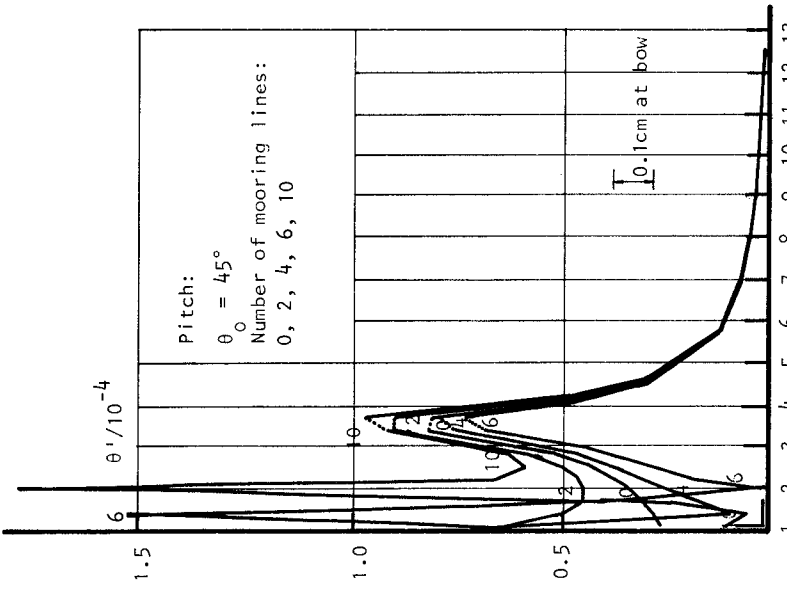

Fig. 8 Amplitude of pitch

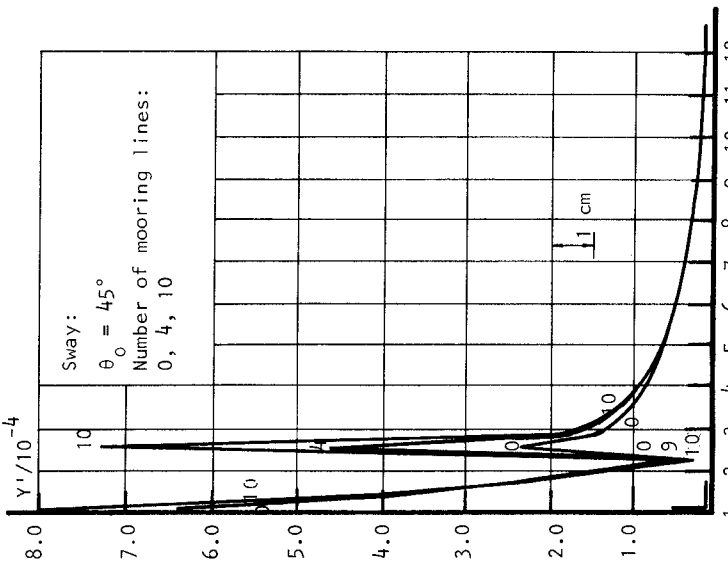

Fig. 9 Amplitude fo sway

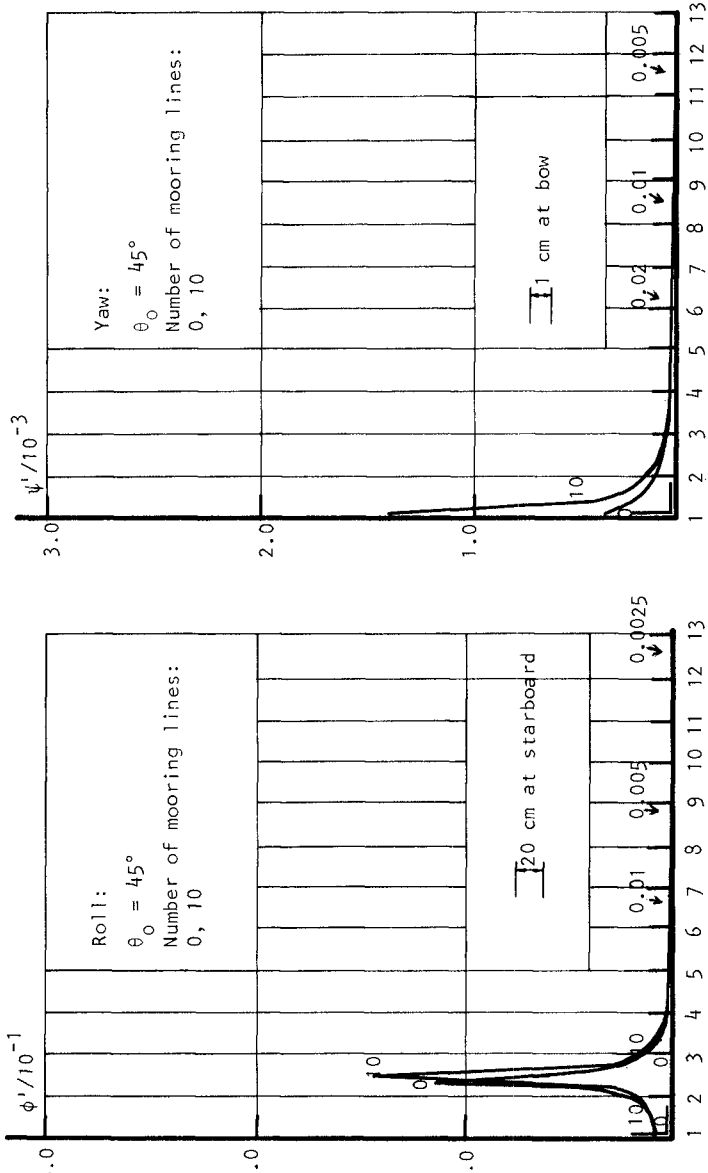

Fig. 10 Amplitude of roll

Fig. 11 Amplitude of yaw

surge	14-28 sec
heave	14-28 sec, 8sec.
pitch	14-28 sec, 8sec.
sway	14-28 sec, 11sec.
roll	11 sec
yaw	> 28 sec

3. Surge, pitch, heave, yaw and roll are maximum for $\theta_o = 45°$. However, sway is maximum for $\theta_o = 90°$.

4. The amplitude in the range of natural frequency for different number of mooring lines and $\theta_o = 45°$ are as follows:

surge	30-50 cm
sway	5-15 cm
heave	very small
yaw	5-15 cm
roll(interpretted as the heave at starboard)	170-220 cm
pitch(interpretted as the heave at bow)	0.7-1.7 cm

5. In the vicinity of natural frequency, the magnitude order of the 6 motions is as follows:

surge > sway >> heave
roll >> yaw > pitch

The only exception is sway (90°) > surge (90°)

CONCLUSIONS

1. The induced ship motions by the oscillating wind are the greatest, as the angle between the quay and the prevailing wind direction is 45°. Of course, the 0°-direction quay is the best design.

2. Surge and roll are the most significant motions induced by the oscillating wind.

3. By changing the number of mooring lines, the natural frequency can be kept away from the dominant wind frequency, except roll.

REFERENCES

1. Korvin-Kroukovsky, B.V. (1961) "Theory of Seakeeping"

2. Lewis, F. M. (1929) "The inertia of water surrounding a vibrating ship" Trans. SNAME, 27, 1-20.

3. Salvesen, N.,E.O. Tuck & O. Faltinsen (1970) "Ship motions and sea load" Trans. SNAME, 78, 250-287

4. "NSRDC ship motion and sea load computer program" NSRDC report No. 3376, 1975.

CHAPTER 204

Physical model test of the moored container ship motion and the related induced mooring force.

H. S. Hou* and G. H. Weng**

*Ho-Shong Hou ph. D. M., ASCE

Head, Transportation Engineering Department,

Institute of Transportation, Minislry of communications, R. O. C.

**Guo-Ho Weng M. E.

Engineer, Transportation Engineering Department,

Institute of Transportation, Ministry of Communications, R. O. C.

ABSTRACT

To optimize structure design it is useful to conduct detail physical model tests. Tests of various basic physical phenomena (e.g. resonance problems), reproducing a sea state ofprototype duration and then from the behavior of entire structure, the optimal design to the wharf structure will be obtained.

Preliminary analyses are made by basing upon experience for structure submitted to the similar action of wave or climates, combined with knowledge of available construction materials. i.e. selection of the rubber fender and the mooring system. Therefore, ship impaction force model simulation could lead to an ideal design.

A lot of experimental research work is conducted in order to facilitate determination of its test value when different factors are involved. Some design recommedations are commonly based on experimental results rather than that from mathematical iterations.

INTRODUCTION

It's well know that, when wave periods are close to the moored ships own periods of oscillation, increase movements take place. The reason for this is that the resonance period of moored ship fall in this range. The internal harbour layout should thus be designed in such a way that no strong resonance occur in this period range.

A differentitation was made between safe mooring and safe operation. Safe operation requires that the ship's movements must not be too great so that loading and offloading operations can be carried out safety. Safe mooring refers to conditions in which cargo handling must be stopped but the vessenal can remain at the berth. Several factors, such as layout of breakwaters, type of quay structure and mooring/fender arrangement, influence the movements of moored ships, It is thus necessary to carry out detailed mooring studies in order to collect safficient data on the behaviour of ship - mooring - fender system. Time and economic constraints make it very difficult to achieve an absolute optimal solution. Systematic testing in the labortory model of various alternatives greatly assisted in arriring at a satistactory solution.

MODEL EXPERIMENT

Model experiment study was carried out in the section channel of the Institute of Harbour and Marine technology at Taichung district in Taiwan. The model is simulated from of 34,500 D.W.T. container ship. The model was built in a 37^m by 7.6^m by 1.0^m have basin with an undistorted scale of one to hundredth. Model ship is moored at nearly the center of the wave basin with six mooring line as shown in Figure 1 & 2.

In the model experiment, following variables such as wave period, wave height, wave direction, characteristics of mooring ropes, loading condition of ship are considered. Ships movement, accelerations of translation, tension of mooring ropes are measured.

The purpose of this research is to arouse to interest of engineers and researchers concerned with ship moored problem. The results of such test may hopefully be used by designers and applied to the harbor planning.

Particular of model ship is given in Table 1. Characteristic of model mooring ropes as shown in Table 2 and Figure 3. Table 3 list experiment cases and variables.

CHARACTERISTICS OF MOVEMENT OF MOORED CONTAINER SHIP

In the section, some characteristics of moored container ship movements, which are obtained from the results of model experiment, are described as follows.

Particularly, the effect of loading condition of ship, characteristics of mooring ropes is described as shown from Figure 4 to Figure 22.

(I) For head sea:

1. Except the short period wave, for the same wave period, surge is increased as wave height increases. As the stiffness of the mooring line increases, then surge motion will be amplified, especially when the long period wave is acting on the vessel. The surge motin will be decreased as the loading the vessel increases, for the long period wave, such phenomena are obvious. For the large stiffness mooring line, the effect of load on the surge motion is small.

2. The obvious effects of the sway motion on the vessel by the wave action, are the test conditions of long period wave, light load vessel and large stiffness of the mooring line. It is found out that the peak value of the sway motion occurs at 15^{sec} wave period.

   The large sway motion occurs during the test conditions of the moored container ship are the light loading, and the large stiffness mooring lines.

3. The peak value of heave motion occurs during the case of the smaller load long period wave action and small stiffness cable. As the small stiffness cable light load vessel, the heave motion will be increased as the longer period wave is acting. While the large stiffness mooring line, large load vessel, the induced heave motion will be decreased as the longer period wave is acting.

4. The roll motion is obviously affected by the big wave action during the ship model is small load, and mooring line is small stiffness. The peak value of the roll motion occurs at the 15^{sec} wave period. The 15^{sec} wave period is possibly named as the natural period of the container ship model.

5. The pitch motion is increased as the wave height increases. The longer wave period action with smaller load vessel condition has the tendency to increase the larger pitch motion.

6. The mangitude of the yaw motion is not so large for this test case. It is probably due to the even anchoring situation. The yaw motion is slightly increased as the wave height increases. The bigger yaw motion occurs at the case of smaller load vessel and larger stiffness of mooring line.

(II) For the oblique sea.

1. For the wave period longer then 15^{sec}, the surge motion has the obvious effect as the wave height increases. The surge motion is general amplified as the incident wave period is longer. For the short wave period and small load of the

vessel, it will cause large surge motion, while the long period wave, the strong stiffness of the mooring line and big load of vessel will cause large surge motion, too.

2. The sway motion and the heave motion will be amplified as the wave height is bigger. The most obvious effect of both motions is during the condition of the longer period wave, the lower load of the vessel and the larger stiffness of the mooring line.

3. The pitch motion is amplified as the long period wave attacking, especially under the condition of lower load of the vessel and the larger stiffness of the mooring line.

4. The roll motion is governed by wave action, it shows the peak value occurring at 15^{sec} wave period, the longer period and large load cause the big roll motion, while the short period and low load also cause the big roll motion. The roll motion is increased under the test conditions of short period wave, large stiffness of mooring and heavy load of the vessel.

5. Both pitch and yaw motions show small effect under the test condition of normal wave action. They have large motion when the ship is of light load and under short wave action.

(III) For Transverse Sea.

1. The surge motion is increased under the test conditions of the long period wave action and light loading ship. It will be amplified during the big wave action and the situation of the large stiffness mooring line.

2. The sway motion is obviously increased under the big wave action. For short period wave action low stiffness cable and heavy loading ship, the induced sway motion is then decreased.

3. The roll motion is increased under the test conditions of the big wave action and the light loading ship. It is shwon that the peak value at 15^{sec} wave period of the light loading ship. For heavy load, the peak value of roll motion will be slightly decreased. The longer wave period and large stiffness cable shows the bigger roll motion against short period wave, small stiffness cable under heavy load of the ship.

4. The pitch motion doesn't show obvious effect. However, during the model ship is of light loading and of small

stiffness mooring line it shows a little effect during wave is acting. For long period wave, the pitch motion shows much effect as wave height increases.

5. The yaw motion has little effect during normal wave action, except long period and big wave. The long period wave and light load vessel will amplify the yaw motion a little bit.

CONCLUSION AND SUGGESTIONS

1. Current design recommendations probably require revision in order to reduce the present extensive destruction of fender on piers, wharves, and dophins beyond normal wear level.

2. The revisions could be provided in accordance with more of results and finding from test performance so far rather them from empirical derivations of simplistic design recommendations.

3. The mooring line and mooring system may be affected by the water depth, therefore it is suggested the dynamic effect of various water depth mooring system is need to be tested for the further study.

4. Short wave disturbance inside the port may cause problems which may result in excessive vertical motions (rolling, pitching and heaving), particularly for smaller ships, but the main problems for the moored VLC'S are caused by the long waves and possible resonances (30 to 150s periods).

REFERENCE

V.

1. "The Berthing Ship", by F. VASCO COSTA, the Bock & Harbour Authority, 1964, May, June, July, Vol. 45, No. 523, 524, 525, PP.22-26, 49-52, 90-94.

2. "The Berthing of a ship to a jettey" by H.L. Fontijn, Journal of The waterway port, Coastal and Ocean Division, 1980, May.

3. "Added Masses of Large Tanlser Berthing to Dolphins" by Hayashi and Masujiro Shirai, Coastal Engineering, 1976, P.2831-2839.

4. "Safety of Ships and Structures During Berthing and Mooring" by Casinir J. Kray, MIT Journal Vo.16 No.1, P.29-38.

5. "Physical Model Test of Ship Motion on Quay to Improve tha Design of Wharf Structure" by H-S Hou and G.-H Weng 5th International Offshore Mechanics and Arctic Engineering (OMAE) Symposium, Tokyo, Japan. April 13-18, 1986.

Table 1 Particular's model ship

	Full	Ballested
L O A (cm)	205	205
L P P (cm)	190	190
DEPTH (cm)	18.7	18.7
BREADTH (cm)	30.6	30.6
DRAFT (cm)	12.0	10.0
DISPLACEMENT (kgs)	409.0	340.8
C_0	0.594	0.577

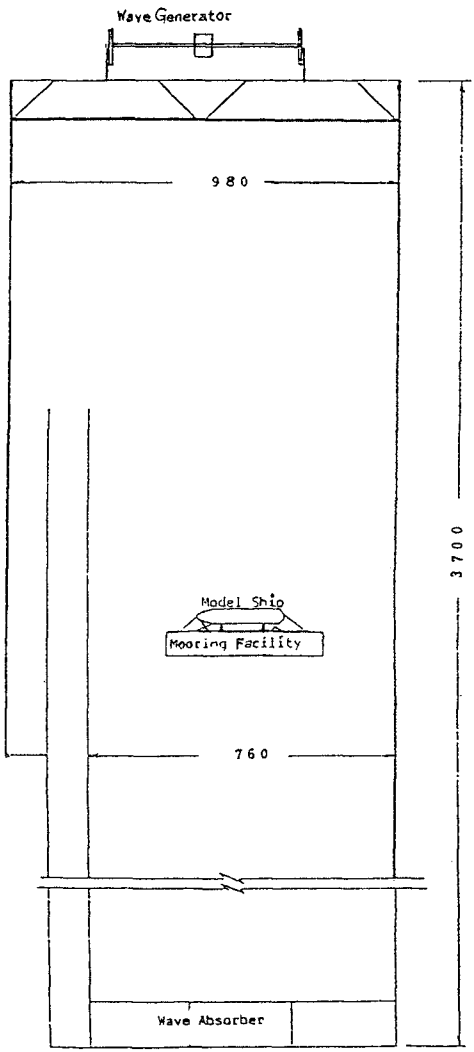

Figure 1 Wave Basin and Arrangement of Equipment

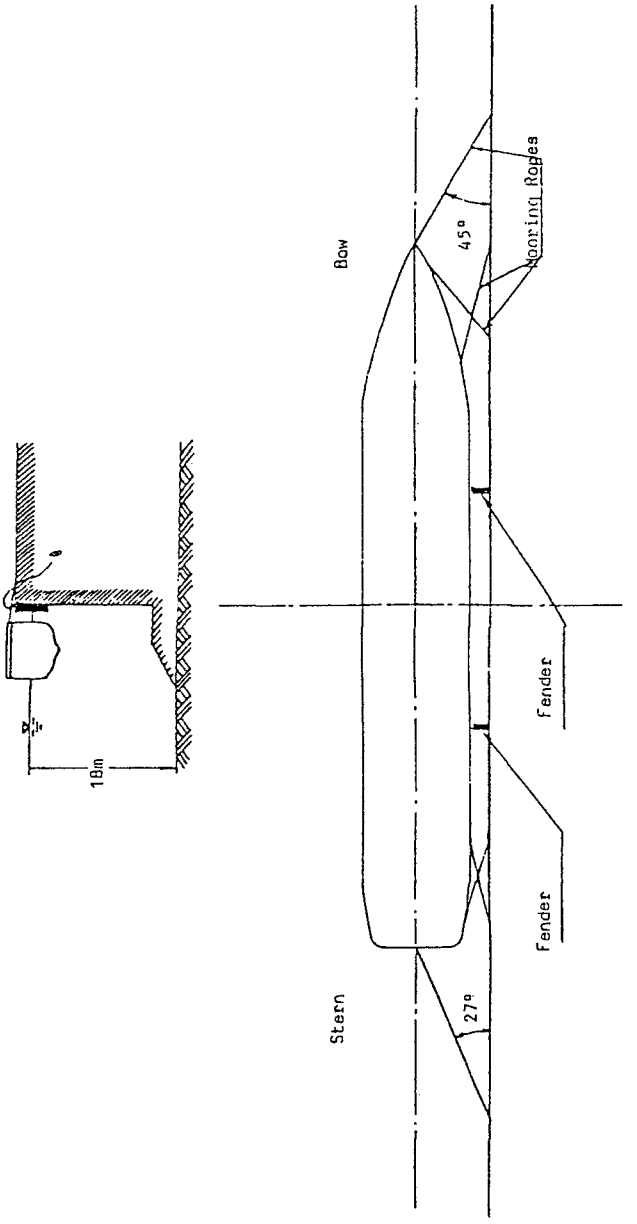

Figure 2 Mooring of Model Ship

Table 2 Characteristics of Model Mooring

	Diameter D (cm)	Load P(kg)	Length L(cm)	Deformation ΔL (cm)
A	0.305	44.0	26.3	5.04
C	0.270	38.0	24.0	8

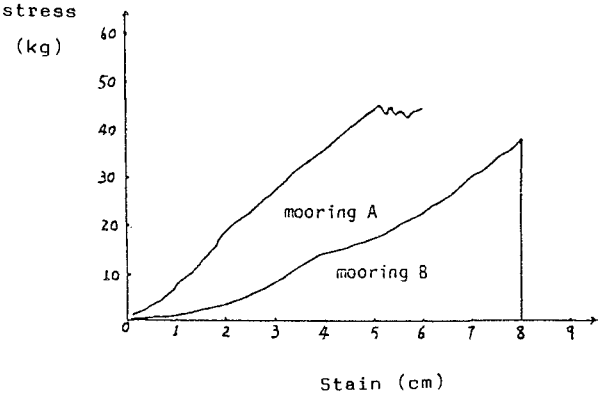

Fig 3. Characteristics of model ropes

Table 3. Experiment Cases and Veriables of the Ship Model

series	Wave Oirection	Load Condition	Mooring Ropes	Wave Height(cm)	Wave Period(sec)	Note
BA00	0°	B	A	R 0.7-2.0	R 1.0-2.0	R=Regular Wave
FA00	0°	F	A	"	"	For mooring rope
BC00	0°	B	C	"	"	A = Rope A
FC00	0°	F	C	"	"	C = Rope C
BA45	45°	B	A	"	"	B = Free
FA45	45°	F	A	"	"	For Load Lond
BC45	45°	B	C	"	"	B = Ballasted
FC45	45°	F	C	"	"	F = Full
BA90	90°	B	A	"	"	
FA90	90°	F	A	"	"	
BC90	90°	B	C	"	"	
FC90	90°	F	C	"	"	
BB00	0°	B	B	"	"	
FB00	0°	F	B	"	"	
BB45	45°	B	B	"	"	
FB45	45°	F	B	"	"	
BB90	90°	B	B	"	"	
FB90	90°	F	B	"	"	

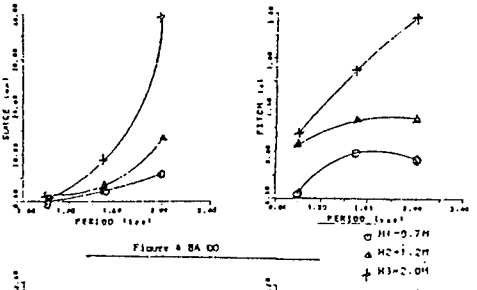

Figure 4 BA 00

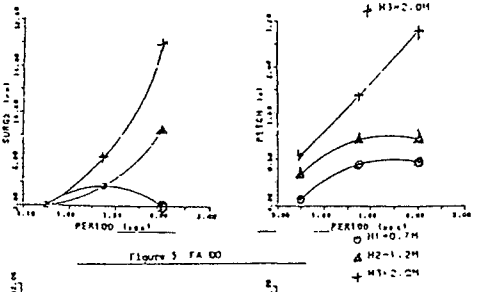

Figure 5 FA 00

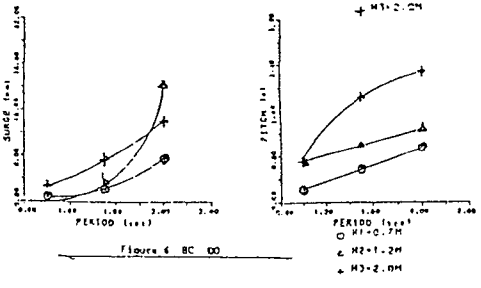

Figure 6 BC 00

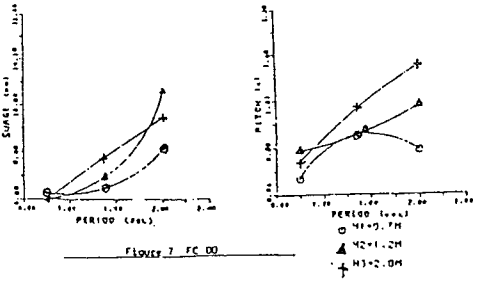

Figure 7 FC 00

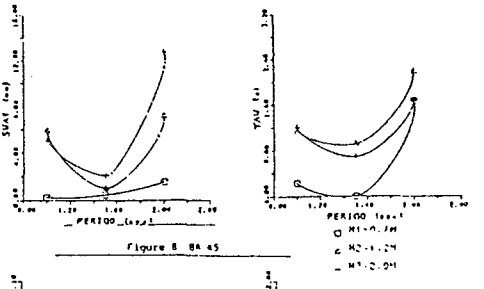

Figure 8 BA 45

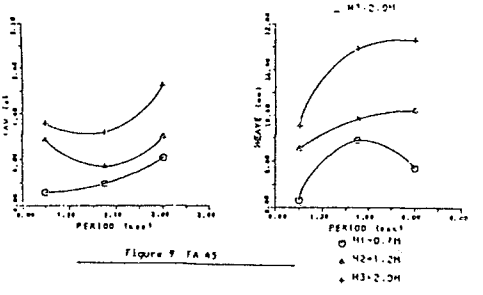

Figure 9 FA 45

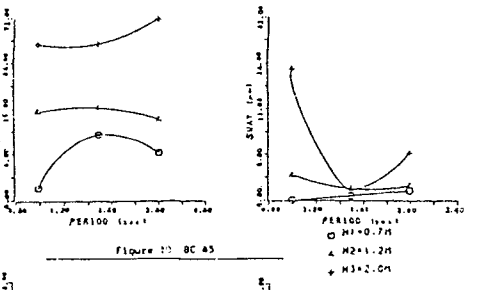

Figure 10 BC 45

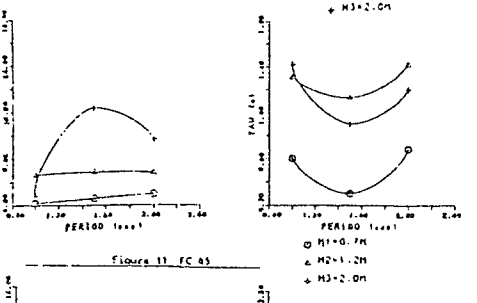

Figure 11 FC 45

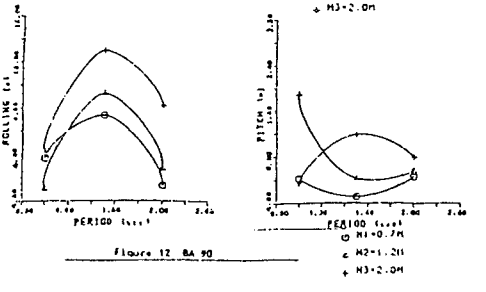

Figure 12 BA 90

Results Of Model Tests (I)

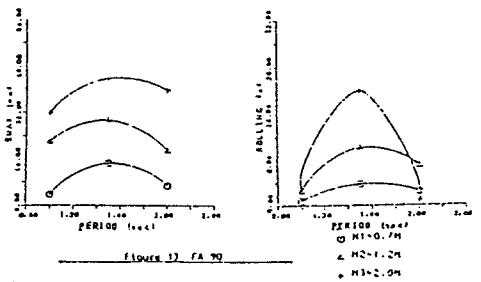

Figure 13 FA 90

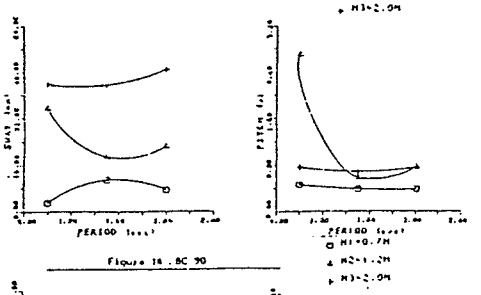

Figure 14 BC 90

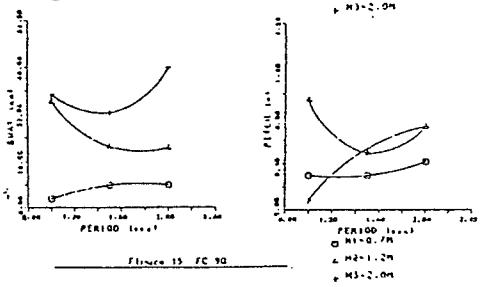

Figure 15 FC 90

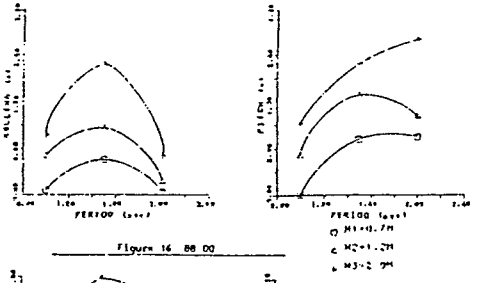

Figure 16 BB 00

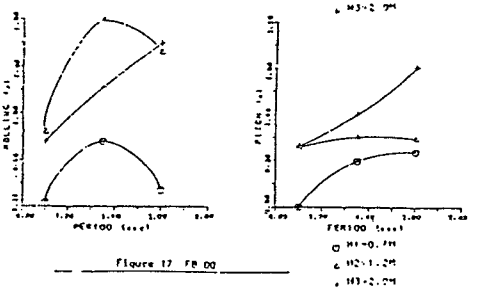

Figure 17 FB 00

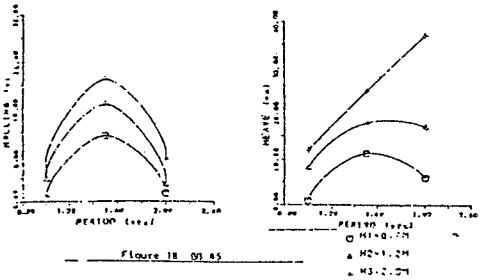

Figure 18 BB 45

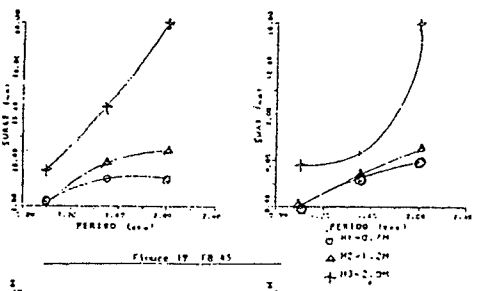

Figure 19 FB 45

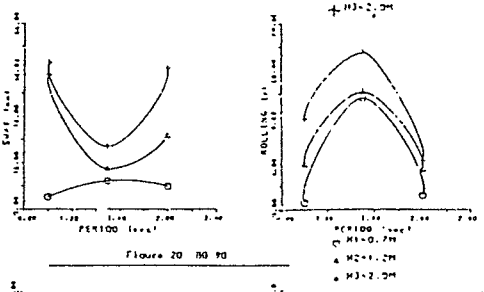

Figure 20 BB 90

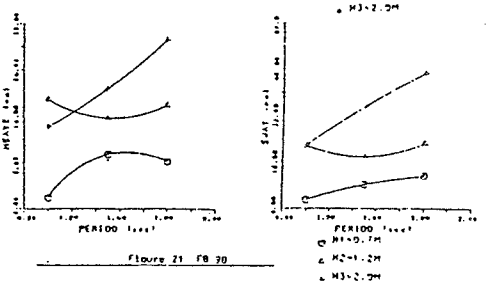

Figure 21 FB 90

Results of Model Tests (II)

CHAPTER 203

An Adjustable Marine Fender System programmed with the Aid of Numerical Models in order to minimize Berthing and Mooring Loads

Tj. J. Risselada M.Sc. *
&
C. Deelen M.Sc. * *

1. Introduction

An adjustable marine fender system, programmed with the aid of mathematical models, can substantially contribute to safer berthing and mooring of ships with various water displacements, operating at high or at low speed under varying wind, wave and current conditions. This doesn't only imply a reduction of risks to vessel and terminal structures but also in case of exposed sites or of unruly waters, a - possible substantial - reduction of ship's costly down-time.

2. The adjustable fender system

2.1. Why an adjustable fender?

Fenders as an interface between ship and rigid or resilient structure (viz. flexile dolphin) are an indispensable protective element both when berthing and when moored. More and more one has become aware that fenders designed to take a certain amount of energy fail to actually dissipate this energy and instead return it to the ship again (the recoiling effect) like the billiard ball against the table frame. Even in a sheltered port like Rotterdam with only modest tidal currents and with ample tug assistance the occurrence of such recoiling effect is not only known but at times even felt as a potential source of risk. This is illustrated in Fig.1 where a ship's movements fore and aft during berthing are rendered, Ref(1).

Also cases are known where the velocity of the far end of the vessel markedly increased or where the velocity during the second approach considerably exceeded that of the first.

This recoiling effect can be observed both when berthing and when mooring alongside. With regard to berthing the fenders are designed to take a certain amount of energy generated by a ship with a certain water displacement hitting them at a certain speed.

Other design specifications, apart from the area of the protective panel, hardly ever are given, primarily so because such specifications thusfar hardly were computable.

* Risselada & Partners, Consulting Engineers, Rotterdam.
** Nautical Research Engineer, Port of Rotterdam Authority.
(former Project Engineer, "Delft Hydraulics").

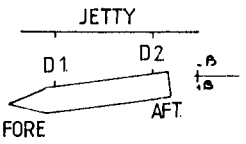

FIGURE 1

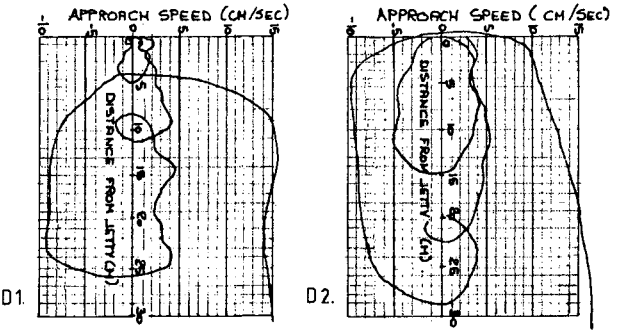

Ships moored alongside an offshore terminal and subject to certain types of waves, or ships moored in a protected harbour and subject to long period waves or seiches might show a very unruly behaviour. In case of swaying and sometimes in case of rolling ships's motions are aggravated instead of dampened when the fenders are not capable of dissipating a sufficient amount of energy or don't possess the required resilience. Also here pertinent specifications lack, be it that a good deal of investigation has been conducted into the functioning of mooring systems as a whole wherefrom it was established that soft fenders perform better.

Basically the problem of recoiling, irrespective whether in case of berthing or of being moored alongside, depends on the degree of hysteresis that occurs in the fender.
None of the current types of fenders is able to meet the demand of economically absorbing a large amount of energy without attaining an excessive compression force and at the same time possesing a high degree of hysteresis, (see reaction force compression and decompression diagrams of Fig.2a, 2b and 2c). Therefore, if not dictated by the outcome of a tender, the as most suitable selected fender(system) can at the best be a compromise on basis of experience.

A universal fender system capable of simultaneously meeting the often conflicting requirements of providing both smooth berthing and quiet mooring facilities under varying wind, wave and current conditions to larger as well as to smaller ships, fully laden or light, can only be achieved by resorting to an adjustable type of fender.

The load/(de)compression relation can now be established more or less arbitrarily, whilst the maximum height of the compression curve is confined by the permissible inside overpressure and the depth of the decompression curve is determined at zero overpressure (see Fig. 2d).

The application of such a universal system implies that first suites of fender characteristics, dealing with every possible situation, must be determined, which necessitates.

a) to thorougly know the wind, wave, and current climate;
b) to have an overview of the type and loading condition of all ships that are going to use a terminal and of the conditions whereunder;
c) to be familiar with the devices and aids for efficiently and reliably accomplishing the successive adjustments to the fender system.

The reguired characteristics can be determined by means of a whole series of scale model tests in a laboratory, but this actually would be prohibitive in view of time and cost.

2.2. The role of numerical models.

However since "Delft Hydraulics" has developed special numerical models to expedite this kind of research, there is no justification any longer for not drawing up more extensive and precise specifications. This in particular applies to terminals off shore or in exposed areas and to sheltered basins where long period waves or swell can penetrate. Thanks to the computer programs "BOTS" and "BAS" fender loads can be quintified more readily, thus enabling to quickly and rather inexpensively determine the required characteristics.

The program "BOTS" applies to ships hitting a resilient body, viz. a flexible dolphin or a rigid structure fitted with fenders. An extrensive description of this program can be found in Ref(2). The phenomena governing these collision processes are highly complicated. Conventional design methods often based on the energy to be absorbed during berthing manoeuvres fail to produce reliable results. A proper mathematical description includes the memory effect in hydronamic forces during the entire collision. This memory effect can be described by impulse reponse theory.

The fluid reactive forces are accounted for by means of freguency dependent hydrodynamic coefficients with regard to the added mass and to the damping, dependent on the ship's hull, water depth, and freguency and direction of motion. By integrating the impulse response functions the behaviour of the total ship-fluid-fender system can be determined. Hence for any specific case it can be computed how the characteristics (viz. kinetic capacity, spring stiffnes and damping power) should be in order to optimize the berthing procedure.

The computer program "BAS" (see Ref(3)) enables to calculate the motion response of the moored ship and the resulting hawser and fender forces for ships subject to every combination of external wind, wave and current forces.
As due to non-linear characteristics of the fender system, the classical solution of cumputing transfer functions by transformation of the equations of motion to freguency domain can not be used, these equations are solved here in the time domain. The main restriction of many mathematical models is that the calculation of the wave exciting forces makes use of linear first order diffraction theory. Present development at "Delft Hydraulics", however, also deals with the calculation of second order slowly varying drift forces.

Once all typical characteristics being known one can thus in conjunction with nautical experts specify for every situation the requirements the fender system has to meet. In case of computer controled operation this means that an all comprehensive program can be drawn up by feeding for every situation of berthing and subsequent mooring the relevant data into the processor. These data can be collected in advance from records together with site observations. But the quickest and most reliable way is to obtain them by means of a wave rider of similar device with respect to wave characteristics, and direction, a current meter for the velocity and direction of the current at the site and an anemometer for the wind. All these data can be automatically recorded in the computer and instantaniously fed into the specific program.

The value of the approach velocity -the most important variable- constitutes a problem apart. Figuring to the square in the calculation it namely can unlike the other variables not be determined in advance but must be instantly decided on it the very last moment when the ship is going to hit the fender. In event - as more and more is to be a rule with important terminals - this velocity is measured by means of special electronic "berthing aids" working either on basis of radar or sonar, this value can together with the angle of approach be directly input in the computer so that the fender further is automatically adjusted.

2.3. Implementation.

The present state of the art enables to devise hollow side or axially loaded compressible pneumatic of hydraulic cylindrical elements fitted with an adjustable valve for regulating the required, computer dictated, internal pump generated pressure. In contrast to current types of rubber fenders, which have heavy walls and consequently a compressibility in the order of 50%, this adjustable type will have much lighter walls consisting of neoprene rubber in a particular way reinforced with a specially designed fabric of aramide fibers, hence a compressibility of some 75%.

Both valve and pum are remote controled and follow exactly the commands from the program selected on the computer. Thus the fenders just can be precisely given those subsequent characteristics which are required

a) to take the amount of energy of a berthing ship with regards to the permissible compression at a varying internal pressure
b) hence to lower that pressure at the end of the travel thus generating sufficient hysteresis to minimize recoiling to the ship
c) to raise the pressure again to such a value that the fender dampens the motions of the moored ship in an optimum way.

As is clear this system entirely roots in the numerical modeling of a whole suite of possible situations with respect to fender characteristics and ship's reactions.

For any situation the appropriate program(s) must be selected, wherein the exogeneneous variables some way or other must be entered.

2.4. Typical fender characteristics.

The first generation fenders, as they may be designated, principally served to prevent direct contact between ship and quay, viz. brushwood bundles, old tyres, timber strips.

The majority of current types of (second generation) fenders consists of side or axially loaded predominantly hollow elements of neoprene rubber or similar material. Requirements as to energy absorption and maximum load to take underly the decision on their dimensions. The selection of the make often is the outcome of a tender, it being thus the price that rules.

It can be distinguished between the "soft" type marked by a convex load compression diagram, secondly the shear type ones which like bending piles habe a nearly linear load compression relation and thirdly the popular buckling types which are characterized by an initially strong concave diagram that conseguently runs horizontal and at the end bends steeply upward.

The shaded area of the typical load/(de)compression diagrams (Fig.2a, 2b, 2c) is indicative for the degree of hysteresis of the above mentioned types, whilst the shaded area of these diagrams (Fig.3a, 3b, 3c) renders their energy absorption capacity at egual ultimate load. In Fig.2d and 3d the same is depicted for a (third generation) adjustable fender, rendering the highest possible compression curve. Actually it can be programmed that the wanted load compression curve takes any random shape within the shaded area shown in Fig.2d. It should be noted that the ultimate compressibility of the current types is assumed to lie around the 50%, and that of the adjustable fenders at about 75%.

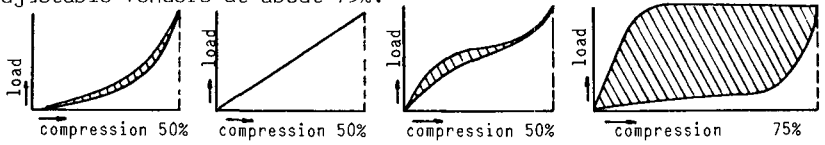

Figure 2. load compression/decompression diagrams and degree of hysteresis of various fender types

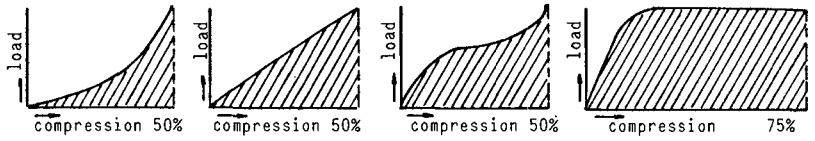

Figure 3. load compression energy absorption diagrams

In case such a fender(cluster) in conjunction with a flexible dolphin is applied a high degree of energy efficiency can be attained, which is greatest when the ultimate reaction forces of the dolphin and of the fenders are equal. In view of theri favorable energy/maximum load relation the buckling type and in particular the adjustable type excel.

2.5. Field of application and cost aspect.

In spite of its higher energy efficiency it is evident that such a custom-designed system is much more expensive than a system by means of one of the current "from the shelf" type fenders. Actually one should not evaluate the adjustable system im comparison with the existing ones solely on basis of the direct cost but also take the indirect returns duely into account.

Apart from a seizable risk reduction in event of unruly wheather conditions, the reduction of ship's downtime might provide sufficient compensation for the higher investment. The application of such a system even lead to bolder and from an operational view point eventually more economical lay-outs, thus (more than) offsetting the extra cost as compared to a traditional fender system fitted to a less exposed lay-out.

In this context it should be noted that such a system ofcourse will have no particular effect on heaving and surging motions.

3. Conclusions.

3.1. The present fenders are inadequate in so far that they more temporarely absorb energy rather than dissipate it and consequently rebound the vessel (recoiling effect), sometimes even aggravating the ship's motions instead of dampening them.

3.2. No current fender at present is universal enough to deal in an optimum way with larger as well as with smaller ships, with fully laden as well as light ones, approaching at higher as well as at lower velocity and operating under varying sea and wind conditions.

3.3. For designing a fender perfectly suited for every possible situation first a set of all the characteristics required hereto must be determined. Theoretically these can be found from scale model laboratory tests, but this actually is prohibitive in view of time and cost.

3.4. The numerical models "BOTS" and "BAS" developed by "Delft Hydraulics" now enable us to compute the desired characteristics in an expeditious and economic way and to compile them in one comprehensive computer program.

3.5. The only way to make a fender meet the many, sometimes conflicting, demands is to make it adjustable.

3.6. With the help of a valve and a pump one can regulate the pneumatic or hydraulic pressure inside a hollow element. viz. cylinder.
Inputting the ad hoc vriable data in a computer allows through said program to adjust the fenders by remote control to the

needs of the moment.

3.7. In exposed sites and in unruly harbour basins better berthing and quieter lying alongside will reduce risks and shorten ship's downtime, hence paying partly or wholly for the higher fender cost.

Appendix

4. References

1) Proceedings of "Ship Handling" symposium, Wageningen, the Netherlands, November 1973.

2) de Vrijer, A., Fender Forces caused by Ship Impacts, Delft Hydraulics Laboratory, publication 309, July 1983.

3) Mynett, A.E., Keuning, P.J., and Vis, F.C., 1985 The dynamic behaviour of moored vessels inside a harbour configuration; Int. Conf. Numerical and Hydraulic Modelling of Ports and Harbours, Birmingham, England, pp 211-220.

CHAPTER 202

Ship Motion Study for the 2010 and 2020 Plan in the San Pedro Bay, California

A.F. Yuen[1], M.G. Burke[2], and T.C. Leung[3]

Introduction

The Port of Long Beach, in cooperation with the Port of Los Angeles and the Corps of Engineers, has been working on the development of a Master Plan for the San Pedro Bay area. This Master Plan, nicknamed the "2020 Plan", is intended to project the Port's land and channel requirements through the year 2020. Any landfill expansion program would be implemented in phases throughout the life of the Master Plan. The initial phases of such a plan would greatly limit the ability of the Port to revise the future configuration of landfill phases, making it important for the Port to determine a final landfill configuration before implementing the early phases.

In developing the 2020 Plan, the Port projected a need for approximately 2,600 acres of additional land. In attempting to turn this 2,600 acre figure into a landfill scheme, the controlling agencies had to take a number of factors into consideration, including (1) water quality and tidal circulation; (2) potential ship motion problems; (3) additional berths required for future development; (4) land and waterside transportation corridors required; (5) availability of dredge material for creating the land; (6) available areas for creating landfills; (7) efficiency of land usage in various configurations; (8) types of ships anticipated to use the new landfills; (9) types of terminals anticipated to be located on the new landfills.

The Port of Long Beach developed two basic schemes which addressed the requirements listed above. In either case, the landfill configuration for the Port of Los Angeles remained the same. The first scheme (called the island scheme, Figure 1) had the advantage of more closely matching the proposed Port of Los Angeles development. Water quality and tidal circulation would be improved with this scheme. The second scheme (called the horseshoe scheme, Figure 2) created a channel on the Long Beach side which did not match the orientation of the channel on the Los Angeles side. This channel was better protected from wave forces than the island scheme, where ships would have to be berthed along the exposed southerly boundary.

(1) Director, Engineering Division, Tetra Tech, Inc./Honeywell, 630 N. Rosemead Blvd., Pasadena, CA 91107, U.S.A.
(2) Civil Engineer, Port of Long Beach, Long Beach, CA, U.S.A.
(3) Senior Engineer, Tetra Tech, Inc./Honeywell, 630 N. Rosemead Blvd., Pasadena, CA 91107, U.S.A.

Since environmental and political pressures were being put on the Port of Long Beach to adopt the island scheme, the Port felt it was necessary to adequately study potential ship motion problems with this configuration. Specifically, the Port wanted to study if it was feasible to berth ships along the southerly boundary line of the island scheme configuration. This area would not have the double breakwater protection afforded most berths in the harbors today, but would only be protected by the federal breakwater from exposure to wave forces.

While not experiencing catastrophic ship motion problems in the Port of Long Beach area, the Port has had a history of minor ship motion problems in its southeast basin. These problems have had a minimal effect on ship loading and unloading efficiencies in the past. The Port's governing criteria in all future developments was to attempt to create no new facilities which would have any potentially greater ship motion problems than those which already exist, and to make sure that any new development does not increase the ship motion problems in any existing facility.

The type of cargo anticipated to be handled at the new landfill was a key issue in studying any potential ship motion problem. Liquid bulk ships, for example, can tolerate a great deal of ship motion, since the main governing criteria is the strength of the mooring lines and the flexibility of the unloading arms. Container ships, on the other hand, have very tight tolerances, since the container crane must be able to pick up a container off the ship with very limited clearances. Unfortunately, the cargo projection in the 2020 Plan indicated that by far the greatest growth in cargo tonnage in the future would be in the container-handling area.

In order to adequately address this potential problem and help decide between the two landfill configuration schemes, the Port contracted with Tetra Tech, Inc., of Pasadena, California, to study a range of ships located along the southerly boundary of the island scheme in two different phases of development. The first phase, shown in Figure 1, was before any landfill will be constructed outside the federal breakwater. The second scheme, shown in Figure 2, was after landfill had been constructed south of the federal breakwater and would probably afford a greater level of protection to the southerly boundary of the island scheme.

While the Port contracted for Tetra Tech to analyze a range of ships, it was anticipated that container ships would be the governing factor, for the reasons listed above.

Environmental Conditions at the Project Site

The environmental conditions associated with ship motion and mooring analyses for this project are discussed in the following sections. These conditions basically include wind, wave, and current statistics over the project site as shown in Figure 3. Based on the derived statistics, a set of design criteria of these environmental conditions were determined for ship motion and mooring analyses.

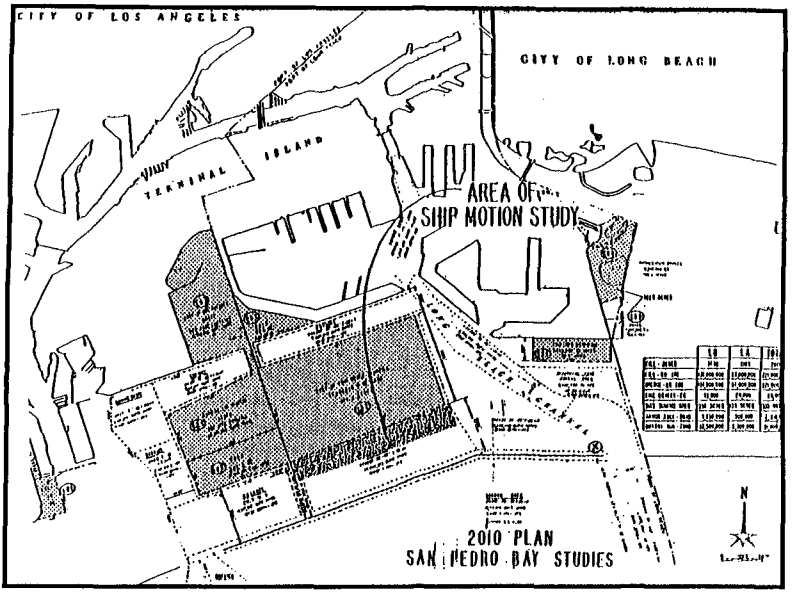

Figure 1 2010 Plan - San Pedro Bay Studies

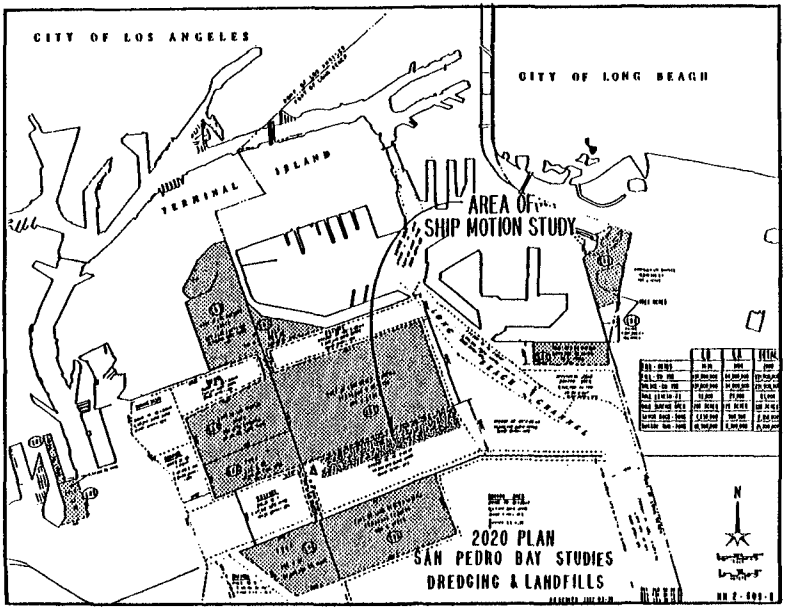

Figure 2 2020 Plan - San Pedro Bay Studies - Dredging and Landfills

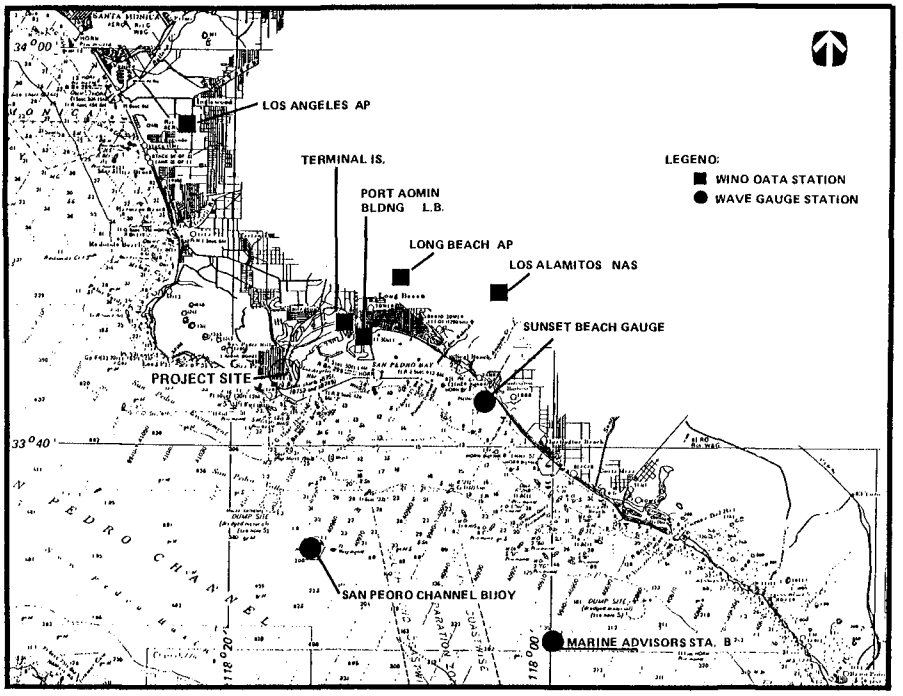

Figure 3 Wind and Wave Gauge Locations

Winds

According to Tetra Tech's previous studies associated with Los Angeles and Long Beach Harbors (Tetra Tech Report TC-3817, 1984), numerous wind information was reviewed and the most applicable wind statistics were discussed and summarized. Stations with available wind data which are used in this analysis are as follows:

	Station Name	Period of Record	Length of Record (Year)
1.	Terminal Island	1955-1977	23
2.	Long Beach AP	1959-1976	18
3.	Los Alamitos NAS	1950-1968	19
4.	Los Angeles AP	1951-1976	26
5.	Port Admin. Bldg. (Long Beach)	1975-1983	9

The locations of these wind stations are shown on Figure 3.

Based on the partial and annual series associated with the ranking of the selected large events and yearly maximum events, respectively, the return periods of the extreme wind speeds were analyzed. The statistics of Terminal Island were selected for study. This is primarily due to

its twenty-three year record and its location within the close proximity of the project site. The estimates of extreme winds, adjusted to an over-water, one-hour duration average from Terminal Island, are 38, 44, 53, and 61 MPH corresponding to 10, 20, 50, and 100 years return period, respectively. The other set of wind statistics derived from 9-year data of Long Beach Port Administration Building are 37, 40, 45, and 48 MPH corresponding to 10, 20, 50, and 100 years return period, respectively. These results have excellent comparison from those of Terminal Island for 10 and 20 year return period. However, it seems to be under estimated for 50 and 100 year return period due to its relatively short duration of wind record. In the ship mooring analysis, the following wind conditions, corresponding to the 60-second duration gust with 5-year return period, were used:

(i) SW wind of 34 knots
(ii) NW wind of 34 knots

Waves

The project site is relatively well protected from wave attack except the direction from south-southeast through south-southwest. Waves with 30 second periods or larger will propagate into the harbor area through the Gulf of Santa Catalina without encountering any effective natural barriers. Whereas the waves with the period less than 30 seconds will experience the effects of wave refraction and island sheltering. The data source of extreme wave condition includes direct measurement inside San Pedro Bay and transformation of hindcasted waves from deep water to the project site.

The relatively short period (less than 30 seconds) extreme waves were associated with major storms or extreme winds. This wave information was obtained by performing deep water wave hindcasting of the selected most severe ten cases during approximately 50 years (IRC, 1976). These deep water waves were transferred into the project site by considering the effects of wave refraction, shoaling, and island sheltering (Tetra Tech Report TC-3817, 1984). Table 1 presents the wave statistics in deep water and in the vicinity outside the breakwater. A 1.7-foot wave height, corresponding to a return period of 1 year, was selected as the representative wave height that would be encountered during daily operations. The transmission coefficient for waves penetrating through the breakwater was adjusted for waves with periods shorter than 16 seconds. Table 2 presents the estimated short period waves, which were used to simulate the ship motions under normal conditions, at the project site of 2010 Plan and 2020 Plan.

Table 1
Wave Statistics in Deep Water and Gate Entrance

Return Period (Yr)	H_{max} (ft, Deep Water)	H_{max} (ft, Gate Entrance)
10	32.8	14.8
20	39.3	19.7
50	45.9	29.5
100	52.5	39.4

Table 2
Estimates of Short Period Waves - Project Site (1-Year Return Period)

Wave Period (sec)	Wave Height (ft)
6	1.1
8	1.3
10	1.4
12 - 14	1.6
16 - 22	1.7

Note: Assume 0.3 transmission coefficient for the waves penetrating through the breakwater.

The characteristics of relatively long period waves (larger than 30 seconds) were measured at Angel's Gate and Queen's Gate during the year of 1971-1972. The long wave statistics are almost impossible to be estimated due to their very limited measurement duration. However, the maximum energy level was measured and the corresponding maximum wave height was estimated by spectral analysis. Wave data were measured by Bottin and Outlaw (1984) at certain locations for the existing conditions. Under the 2010/2020 landfill plans, the wave environment is different from the existing condition. A numerical model was applied to determine the wave environment for the proposed plan. The numerical model geometry and their 290 x 140 grid points for the 2010 and 2020 Plan is shown in Figures 4 and 5, respectively. The maximum long wave heights at the project site were estimated by applying the response factor obtained from the results of the numerical model. Table 3 summarizes the estimated maximum long period wave height at Queen's Gate and the project site of the 2010 and 2020 Plan.

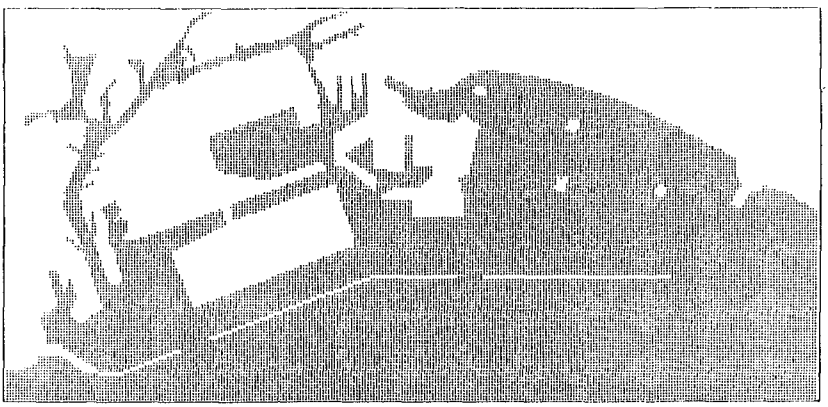

Figure 4 Grid Points in the Numerical Model for 2010 Plan

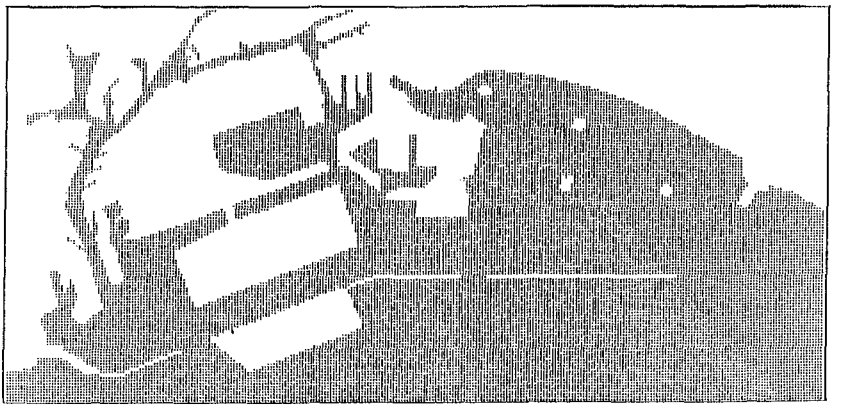

Figure 5 Grid Points in the Numerical Model for 2020 Plan

Table 3
Estimates of Maximum Long Wave Height

Wave Period (sec)	Wave Height (ft) Queen's Gate	Wave Height (ft) 2010 Plan	Wave Height (ft) 2020 Plan
30	0.09	0.30	0.30
40	0.07	0.25	0.25
50	0.05	0.20	0.20
60-70	0.04	0.15	0.10
80-100	0.03	0.15	0.10
110-140	0.02	0.10	0.05
150-180	0.02	0.08	0.08
190-210	0.01	0.10	0.10
220-230	0.01	0.05	0.05
240-300	0.01	0.03	0.03

In order to perform a downtime analysis of the ships, the wave data base in the vicinity outside the breakwater was established by transferring deep water waves to the shallow water site. The deep water waves were obtained from the Sea-State Engineering Analysis System which is maintained by the U.S. Army Engineer Waterways Experiment Station. The joint occurrence probabilities (%) of wave height and period near the breakwater are presented in Table 4.

Table 4
Occurrence Probability (%) of Wave Height and Period
Los Angeles-Long Beach Breakwaters

	Period(s)								
Height (ft)	4.4-6.0	6.1-8.0	8.1-9.5	9.6-10.5	10.6-11.7	11.8-13.3	13.4-15.3	15.4-18.1	18.2-22.2
0.0- 3.2	5.78	20.58	15.23	10.68	14.65	14.25	1.37	0.03	0.01
3.3- 6.5	0.03	0.19	0.49	0.36	0.85	2.91	9.03	0.56	--
6.6- 9.7	0.02	0.07	0.08	0.08	0.14	0.44	0.73	0.94	--
9.8-13.0	--	0.02	0.03	0.02	0.01	0.03	0.26	0.02	--
13.1-16.3	--	0.01	0.04	0.01	--	0.02	--	0.01	--

Currents

The maximum tidal current measured at the project site is approximately 0.5 ft/sec. It is believed that this tidal current should have the least impact on the ship motion and mooring analyses.

Ship Motion and Mooring Analysis

Three representative ships, the D-9 class container ship, 265,000 DWT tanker, and 100,000 DWT dry-bulk carrier, that will frequent the project site of the 2010 Plan and 2020 Plan of the Port of Long Beach, were considered in the study. The principal particulars of these ships are presented in Table 5.

Table 5
Principal Particulars of the "Representative" Container Ship, Tanker, and Dry-Bulk Carrier

Principal Particulars	D-9 Class Container Ship	265,000 DWT Oil Tanker	100,000 DWT Dry-Bulk Carrier
Length Overall (ft)	745	1100	886
Length between Perpendiculars (ft)	699	1060	853
Beam (ft)	100	178	138
Depth (ft)	54	86	69
Draft (ft)	31	67	49

Several mooring configurations, some consisting of steel lines, some dacron lines, and some of a combination of steel and dacron lines, were used to evaluate the ship response under imposed environmental conditions. A typical mooring configuration for the D-9 class container ship is shown in Figure 6. Vessel and berth characteristics, loading condition, mooring line arrangement, fender system, and the excitation force were the input parameters for the Tetra Tech six-degree ship motion analysis program. The detailed description of this numerical solution procedure can be found in the reference report.

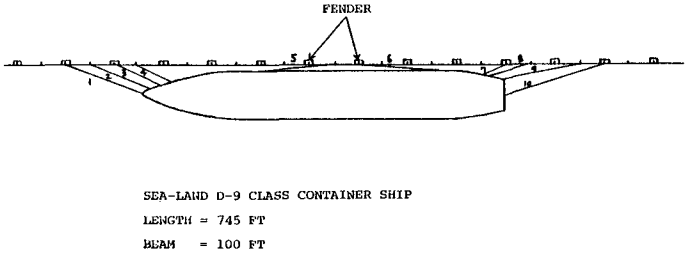

Figure 6 Mooring Line Arrangement - D-9 Class Container Ship Dacron and Steel Lines

Summary of Ship Motion Analysis Results

The primary direction of wave approach was assumed to be zero degree from the stern of the moored ship. It was anticipated that this wave approach angle should provide the information on the maximum longitudinal motion, the surge. For the D-9 class container ship, 265,DDO DWT tanker, and 100,000 DWT dry-bulk carrier, ship responses were computed as a function of the wave period and wave wave height as established in Table 3. Dnly the summary of the results of the maximum surge amplitude for the container ship, tanker and dry-bulk carrier are presented in Table 6. The fender force, hull pressure, and line load under various mooring conditions were determined. The typical line loads due to wave force, wind force, and combination of wave and wind force for a typical case are presented in Table 7.

Table 6
Summary of Maximum Surge Amplitudes

Ship	Plan	Maximum Surge Amplitude (ft)	Mooring Lines	Resonant Wave Period (sec)
Container (D-9 Class)	2D10	4.41	Dacron	100
		0.73	Steel	30
		2.48	Dacron & Steel	60
	2020	2.02	Oacron	120
		0.73	Steel	30
		1.50	Dacron & Steel	70
Oil Tanker (265,000 DWT)	2010	1.28	Dacron	210
		2.23	Steel	80
	2020	1.28	Dacron	210
		2.09	Steel	80
Dry-Bulk Carrier (100,DDD DWT)	2010	2.13	Dacron	190
		0.87	Steel	40
	2020	2.13	Dacron	190
		0.87	Steel	40

Table 7
Line Loads Due to Environmental Forces
D-9 Class Container Ship

Lines	Environmental Force	Maximum Load On Mooring Lines (long tons)									
		1	2	3	4	5	6	7	8	9	10
Dacron & Steel*	60 Sec. wave	40.56	1.76	2.39	4.05	1.36	1.40	6.89	3.38	1.37	31.11
	NW Wind 34kt	20.00	1.90	0.97	1.14	0.09	0.12	6.58	1.88	0.42	19.74
	SW Wind 34kt	9.97	0.44	0.59	1.00	--	0.34	--	--	--	--
	Wave & NW Wind	60.56	3.66	3.36	5.19	1.45	1.52	13.47	5.26	1.79	50.85
Dacron	100 Sec. wave	3.13	4.61	4.61	6.31	10.73	14.37	7.06	4.07	3.04	2.09
	NW Wind 34kt	3.48	5.20	5.20	3.17	4.67	20.91	5.91	2.26	1.27	0.77
	SW Wind 34kt	1.33	1.95	1.95	2.65	4.46	--	--	--	--	--
	Wave & NW Wind	6.61	9.81	9.81	9.48	15.40	35.28	12.97	6.33	4.31	2.86
Steel	30 Sec. Wave	7.63	11.22	1.22	15.03	25.35	34.55	16.70	9.55	6.69	4.88
	NW Wind 34kt	4.84	6.80	6.80	2.76	2.07	19.39	5.70	2.28	1.35	0.85
	SW Wind 34kt	1.33	1.95	1.95	2.65	4.46	--	--	--	--	--
	Wave & NW Wind	12.47	18.02	18.02	17.79	27.42	53.94	22.40	11.83	8.04	5.73

*Note: Steel lines (1 and 10)
Dacron Lines (lines 2 to 9)

Downtime Analysis

Berth downtime is defined as the length of time that the mooring capacity limits are exceeded. The following criteria were considered in establishing the mooring capacity limits:

- o mooring line loads
- o vessel motions
- o fender deflection and hull pressure

Mooring Line Loads

According to the guidelines followed by Butcher et al (1980) an ultimate mooring limit for a particular mooring situation is defined as 65% of the new wire breaking strength. The operating mooring limit, however, is recommended to be equal to the defined ultimate mooring limit divided by a load factor of 1.4 to 1.6. Consequently, 45% of the breaking strength is used as the allowable limit for steel wires. Similarly, the ultimate mooring limit for dacron line is defined as 55% of the breaking strength and 35% of the breaking strength is used as the allowable limit for dacron lines. Line loads in excess of the recommended operating limits are considered excessive and contribute to berth downtime.

Vessel Motions

Oscillatory vessel motions with an amplitude greater than the following limits, in the surge direction, are considered excessive and contribute to berth downtime. The Port of Long Beach provided the following limits for ship surge downtime:

- o Container ships, 0.5 feet of surge
- o Dry-bulk carriers, 5 feet of surge
- o Liquid-bulk carriers, 10 feet of surge

Fender Deflection and Hull Pressure

Hull pressure was taken as the critical condition over fender deflection if excessive lateral motions exist. Consequently, only the allowable hull pressure is checked for downtime analysis. The allowable hull pressure for the three ships considered in the present analysis is listed in the following:

Ship	Maximum Allowable Hull Pressure
D-9 Class Container Ship 265,000 DWT Tanker 100,000 DWT Dry-Bulk Carrier	9.88 long tons/yd^2

Hull pressures greater than these limits are considered excessive and contribute to berth downtime.

Downtime Results

Based upon the calculated results of line loads, vessel motions, and hull pressure presented in the previous section, the vessel downtime can be determined by checking the calculated results with the limiting criteria. The statistics of the short period waves (6-22 seconds) were obtained from Table 4. It should be noted, however, that since there is no data available concerning long period wave ($T > 22$ second) activity in the project sites of the 2010 Plan and 2020 Plan, only vessel response due to waves of periods between 6-22 seconds is considered in the downtime analysis.

Conclusion

Surge is the most significant motion response of the tanker, D-9 Class container ship, and dry-bulk carrier to waves approaching head on (head-sea condition). Since the waves at the project site of Plan 2010 are larger than the waves at the project site of Plan 2020, the ships have larger motion response at Plan 2010. The maximum surge amplitudes of 2.2 and 2.1 feet for the tanker and dry-bulk carrier, respectively, are within the operational limits of surge motion and would not contribute to berth downtime. For the container ship, the mooring system consisting of steel lines induces a smaller maximum surge amplitude than the mooring system consisting of dacron lines, while the mooring system consisting of combination of dacron and steel lines induces a maximum surge amplitude in between of the all steel and all dacron line systems. All the three mooring systems of the container ship result in maximum surge amplitudes larger than 0.5 feet and would contribute to berth downtime. This problem can be mitigated by introducing frictional force between the ship hull and the fender system.

The results of the significant surge amplitude are obtained by letting the ships respond to a spectrum of incoming waves. At the project site of Plan 2010, with the exception of the container ship which is moored by dacron and steel lines, the results of the significant surge amplitude are not smaller than those of the maximum surge amplitude, because the peaks of the ship response spectra sometimes occur close to the peaks of the wave spectra. However, the magnitudes of the significant surge amplitude can be reduced by imposing frictional forces between the ship hull and the fender systems. For instance, the significant surge amplitude of the container ship with the mooring system consisting of dacron and steel lines is redued from 1.96 feet to 1.28 feet when a frictional force of 12,8000 lb is imposed.

For the beam-sea wave conditions, the 1 year waves do not induce significant sway motion or line loads. The maximum fender loads are well within the rated reaction force of the proposed fender. Except for the case of the tanker under high frequency wave conditions (6-7 seconds), the ship hull pressures are also within the maximum allowable hull pressure limit. The problem of excessive hull pressure can be solved by employing additional breast lines to reduce the sway motion during short period beam-sea wave condition. Another solution is to increase the surface area of the fender or the number of fenders.

Tankers and dry-bulk carriers in ballast conditions and container ships in full load condition are more susceptible to wind forces due to the relatively large exposed area above the waterline. Consequently, wind forces are an important factor in regards to mooring safety in the present analysis. Wind forces are higher on the tanker, due to the larger exposed windage areas. The forces induced by the 34kt NW wind load the steel mooring line up to 25%, 25%, and 14% of the line breaking strength for the tanker, D-9 Class container ship, and dry-bulk carrier, respectively. Therefore, the 5-year, 60-second-duration gust does not impose a threat to mooring safety.

Using the wave statistics and the 5-year, 60-second-duration gust wind conditions, the downtime probabilities were calculated to be 0.34, 1.53, and 0% for the tanker, D-9 class, and dry-bulk carrier, respectively.

References

Bottin, R.R., and Outlaw, D.G., Los Angeles and Long Beach Harbors Model Study - Resonant Response of the Harbors for Phase 1 of the Los Angeles Deep-Draft Dry Bulk Export Terminal, prepared for U.S. Army Engineer District, Los Angeles, California, by Coastal Engineering Research Center, U.S. Army Engineer Waterways Experiment Station, Vicksburg, Miss., January, 1984.

Butcher, C.; Leidersdorf, C.; and Wang, S., Mooring Analysis and Berth Downtime Study for Cerrejon Coal Port, prepared for Parsons California, Inc. and Exxon Research and Engineering, Tetra Tech Report TC3303, January, 1980.

Chiang, W.-L., 1979, "Tide Induced Currents in Harbors of Arbitrary Shape," Ph.D. dissertation, University of Southern California. ix+194pp.

Chiang, W.-L., and Lee, J.-J., 1982, "Simulation of large-scale circulation in harbors," Journal of the Waterway, Port, Coastal and Ocean Division, ASCE, 108 (WW1), 17-31.

Durham, D.L., et al., "Analysis of Wave and Ship Motion Data", Los Angeles and Long Beach Harbors Model Study, Part 3, U.S. Army Engineer Waterways Experiment Station, Tech. Report H-75-4, July 1976.

Intersea Research Corporation, Design and Seasonal Waves and Weather Conditions off Port Hueneme, California, prepared for Mobil Oil Corporation, La Jolla, California, January, 1976.

Kim, C.H., "Hydrodynamic Forces and Moments for Heaving, Swaying and Rolling Cylinders on Water of Finite Depth", Journal of Ship Research, June 1969.

Prediction of Wind and Current Loads on VLCC's, International Oil Companies Marine Forum, 1976.

Tetra Tech, Inc., West Channel/Cabrillo Beach Recreational Complex - Wave and Surge Analysis, prepared for City of Los Angeles, Port of Los Angeles, Harbor Department, Tetra Tech Report TC-3817, July, 1984.

Wang, S. and Butcher, C., Arco Tanker Terminal Ship Mooring Study, prepared for Port of Long Beach, Long Beach, California, Tetra Tech Report TC-3330, July, 1980.

Wilson, B.W.; Jen, Y.; Hendrickson, J.A.; and Soot, H., 1968, "Wave and surge-action study for Los Angeles-Long Beach Harbors, Volume I," Final Report, Science Engineering Associates, San Marino, CA.

Yuen, A.F. et al., "Ship Motion analysis for the 2010 and 2020 Plan of Port of Long Beach", prepared for Port of Long Beach, Tetra Tech, Report No. TC-3965, 1985.

CHAPTER 205

IRREGULAR WAVE TRANSFORMATION IN A BOUSSINESQ WAVE MODEL

H.-H. Prüser * / H. Schaper * / W. Zielke *

1. INTRODUCTION

Numerical wave models for shallow water waves are of particular importance for the calculation of the wave climate in harbours and coastal areas. Especially nonlinear time domain models, which are based on the Boussinesq-Wave-Equations, may be helpful in the future for simulating the interaction of currents with refraction, diffraction, reflection and for simulating shoaling of irregular waves in natural areas; a potential which has not yet been fully developed.

During the last ten years numerical models, based on these equations, have been published; such as ABBOTT et. al. , HAUGUEL and SCHAPER / ZIELKE . Research on this topic is currently being carried on.

Some efforts have been made to verify the capability of the models to describe the various physical phenomena. However, up to now, verification has been limited to regular waves. The aim of this paper therefore is, to consider questions concerning irregular, nonlinear waves.

*Zielke, Prof. of Fluid Mechanics
*Prüser, Research Assistant
*Schaper, Research Assistant

Inst. of Fluid Mechanics
University of Hannover
Callinstraße 32
3000 Hannover, FRG

A numerical model, based on the solution of the Boussinesq equations, was used to calculate the behaviour of wave spectra and bichromatic waves in a one dimensional wave flume with constant water depth or with mild slope. The generation of long waves and the energy transfer between individual frequency components in the numerical model was of particular interest. Comparisons with analytical solutions and hydraulic measurements have been made.

2. NUMERICAL MODEL

All computations have been done using the Boussinesq wave model described in detail by SCHAPER / ZIELKE, 1984. Experimental data from a hydraulic wave flume were available. Therefore the study has been restricted to the onedimensional case. The basic equations read:

$$\frac{\delta p}{\delta t} + \frac{\delta}{\delta x}\left(\frac{p^2}{h}\right) + gh\,\frac{\delta \zeta}{\delta x} = \frac{Dh}{2}\,\frac{\delta^3}{\delta x^2 \delta t}\left(\frac{Dp}{h}\right) - \frac{D^2 h}{6}\,\frac{\delta^3}{\delta x^2 \delta t}\left(\frac{p}{h}\right)$$

$$\frac{\delta \zeta}{\delta t} + \frac{\delta p}{\delta x} = 0$$

$h = D + \zeta$: total water depth — D : mean water level

p : vertically integrated flux — ζ : waterelevation

g : acceleration due to gravity

Solitary and cnoidal waves can be regarded as special solutions of the Boussinesq equations. They have been used in the initial stage of model development to investigate the accuracy of the numerical solution for waves up to limiting height.

In short shallow water waves, the nonlinear amplitude-dispersive terms on the left hand side and the nonlinear frequency-dispersive terms on the right hand side are of the

same order. It is therefore necessary to include all these terms into the computation. In the numerical model, the Boussinesq equations are solved with a third order corrected, implicite finite difference method, using two time levels and central differences.

A nonreflecting boundary condition is used at the left end of the flume, instead of a model of the wave maker. Therefore, the re-reflection of waves returning from the right end of the channel is neglected. The input waves can be represented as a prescribed time serie f(t, x=0), which have been obtained from measurements in the flume. The unknown values for the flux and water elevation, as the result of incoming and outgoing waves, can be calculated by using the following equation:

$$p - c\zeta = -2c\, f(t)$$

with: $c = \sqrt{gh - p^4/h^2}$ wave velocity

3. TRANSFORMATION OF PIERSON-MOSKOWITZ SPECTRA

3.1 Hydraulic Test Programme

Hydraulic measurements were taken by Daemrich and Götschenberg from the Franzius-Institute of the University of Hannover to verify the numerical model. In a flume with a constant water depth of 0.5 m, some Pierson-Moskowitz spectra were generated by the wave maker. The amplitudes have been reduced by a constant factor in order to avoid wave breaking, which does occur, if this deep water spectrum is used in shallow water. Several wave gauges were placed along the flume for measuring the time series of the water elevation. Table 1 displays the significant wave parameter of the test program.

Peak-Period [sec] / Peak-Frequency [Hz]			Significant Wave-Height [m]		
1.5	/	0.666	0.04	0.06	0.08
3.0	/	0.333	0.04	0.06	0.08
4.5	/	0.222	0.04	0.06	0.08

Table 1: Test Program

The water elevation, measured at the gauge nearest to the wavemaker, is used to feed the waves into the numerical model at the left boundary.

3.2 Range of Application

Boussinesq equations are long-wave-equations with additional third order terms. They are able to describe wave phenomena in shallow water and in intermediate depths but not in deep water. If one assumes a water depth of 0.5 m, then the deep water waves are shorter than 1.0 m and have a corresponding frequency of higher than 1.25 Hz. Therefore it is to be expected, that the smaller the "deep water" part of the spectrum, the better the calculation of the wave spectra.

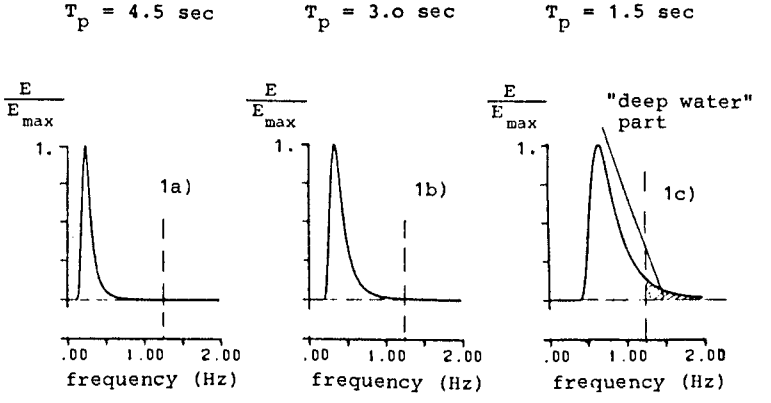

Figure 1: Normalized Pierson-Moskowitz Spectra

Figure 1 displays the normalized Pierson-Moskowitz spectra of the hydraulic test program. The deep water part of spectrum 1c is significant, thus the calculation cannot be accurate in this case. And indeed, verification shows that the Boussinesq wave model reproduces the time series of the water elevation for the spectra 1a) and 1b) very well, but worse for spectrum 1c).

3.2 Calculation and Comparison

3.2.1 Pierson-Moskowitz Spectra in a Flume with even Bottom and a mild Slope

3.2.1.1 Experimental Set-Up

For the hydraulic model, a 54.0 m long flume with even bottom and a slope 1/30 at the right side was used. Two numerical models were created:

The first model was used for verification. The Boussinesq wave model does not contain the possibility of simulating breaking waves, which occur on the upper part of the slope. Instead a nonreflecting boundary was applied at that point of the slope, where the water depth was 0.2 m.

In the second model no slope is taken into account. Therefore, there is a possibility to extract the calculated slope influence by comparing these two numerical models.

The measured time series of the water elevation at gauge 1 is used as wave input for the numerical model. Figure 2 shows the complete experimental set-up.

HYDRAULIC MODEL

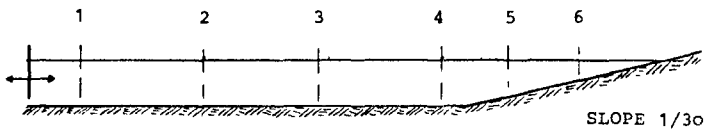

NUMERICAL MODELS

- FOR VERIFICATION

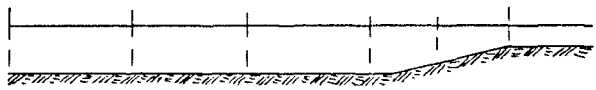

OPEN
BOUNDARY

- FOR COMPARISION

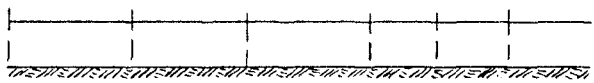

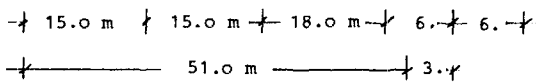

1, 2, 3, 4	GAUGES	WATER DEPTH = .5o m	
5	GAUGE	WATER DEPTH = .4o m	(.5o m)
6	GAUGE	WATER DEPTH = .2o m	(.5o m)

Figure 2: Experimental set-up / flume with slope

3.2.1.2 Results

Figure 3 displays a comparision between measured and calculated time series at different gauges for a Pierson-Moskowitz spectrum (peakperiod period = 3.sec. significant wave height = 0.08m). It can be seen that the numerical model describes the water elevation with a high degree of similarity in the range of horizontal bottom as well as on the slope.

Calculations with both numerical models (with and without a slope) indicate, that the influence of reflection at the mild slope is negligible for the chosen spectra.

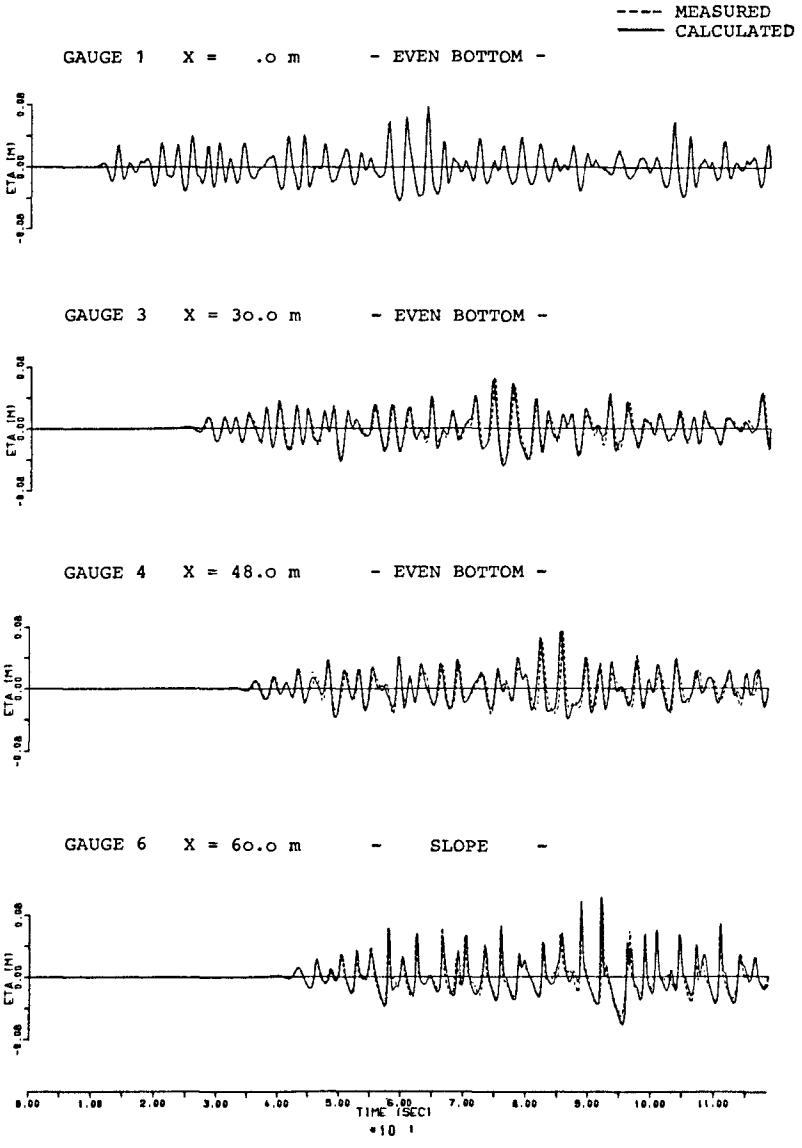

Figure 3: Transformation of wave spectra even bottom / slope, time domain

A better interpretation of the experimental and calculated results is possible by transforming the time series into the frequency domain.

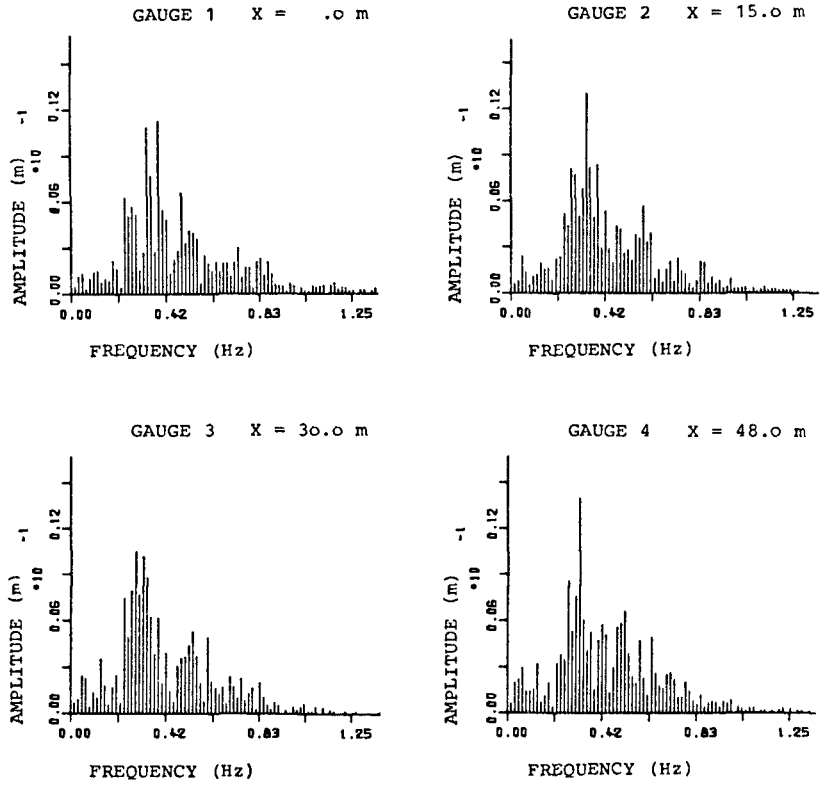

Figure 4: Transformation of wave spectra
even bottom / slope. frequency domain

In linear wave theory, the shape of the spectrum, generated at the wave maker, should not change along the flume if the water depth is constant. However, comparing the amplitude spectra at different locations (see figure 4), an energy transfer between individuel frequency components and the creation and increase of lower frequencies, not included in the original Pierson-Moskowitz spectrum, can be observed in the hydraulic as well as in the numerical model.

At the slope the water depth decreases and the waves turn to the typical cnoidal shape: The crests are higher and shorter and the troughs are longer and less deep than would be predicted for constant water depth.

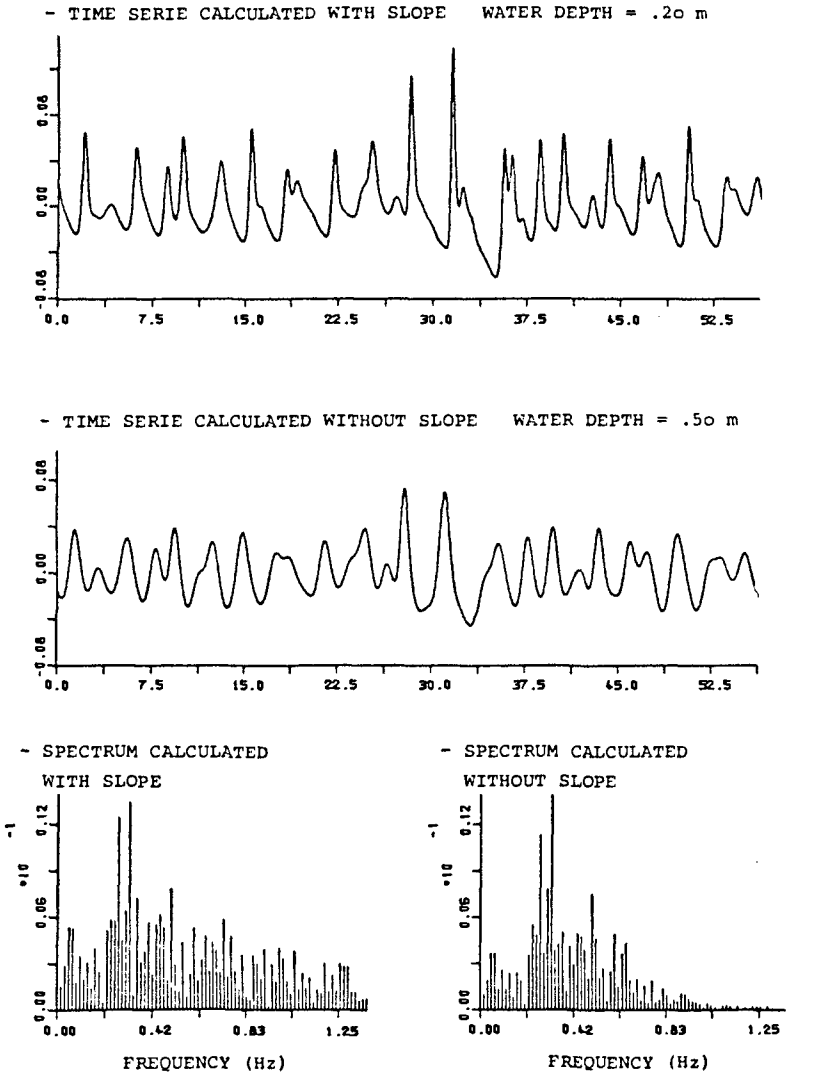

Figure 5: Slope influence calculated at gauge 6. Comparison in time and frequency domain

The increase of the long wave components and the generation of higher frequencies on the slope are results which can be detected in the frequency domain. Figure 5 displays a comparison of the time series and amplitude spectra at gauge 6, calculated with and without a slope.

3.2.2 Pierson-Moskowitz Spectra Reflected at a Wall

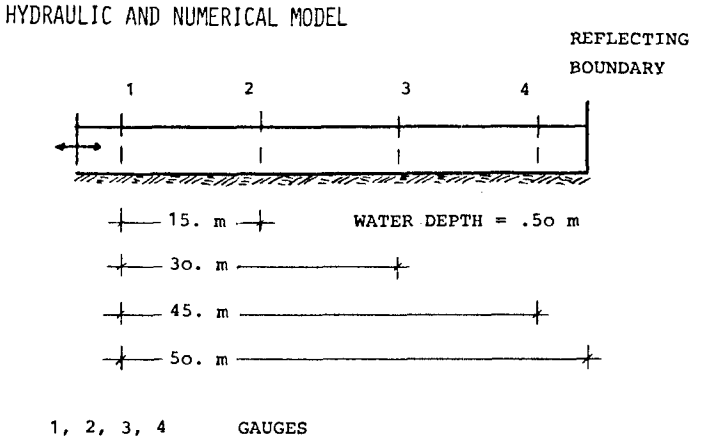

Figure 6: Experimental set-up

The test program was used to verify the reflecting boundary condition at the wall and the capability of the numerical model to calculate the nonlinear interaction of the initial and reflected waves. Figure 6 displays the experimental set-up, figure 7 compares measured and calculated time series of the water elevation at several gauges for the same spectrum used before. The distance between every gauge is 15.0 m. Therefore, it is possible to mark in figure 7, the front of the initial wave, as well as the first reflected wave and the first re-reflected wave. Also the time of the first reflection at the wall and the first re-reflection at the wave maker has been marked. The numerical model is able to describe the resulting wave climate very well. However a

comparison between measurements and calculations is not valid after the reflected wave has reached gauge 1.

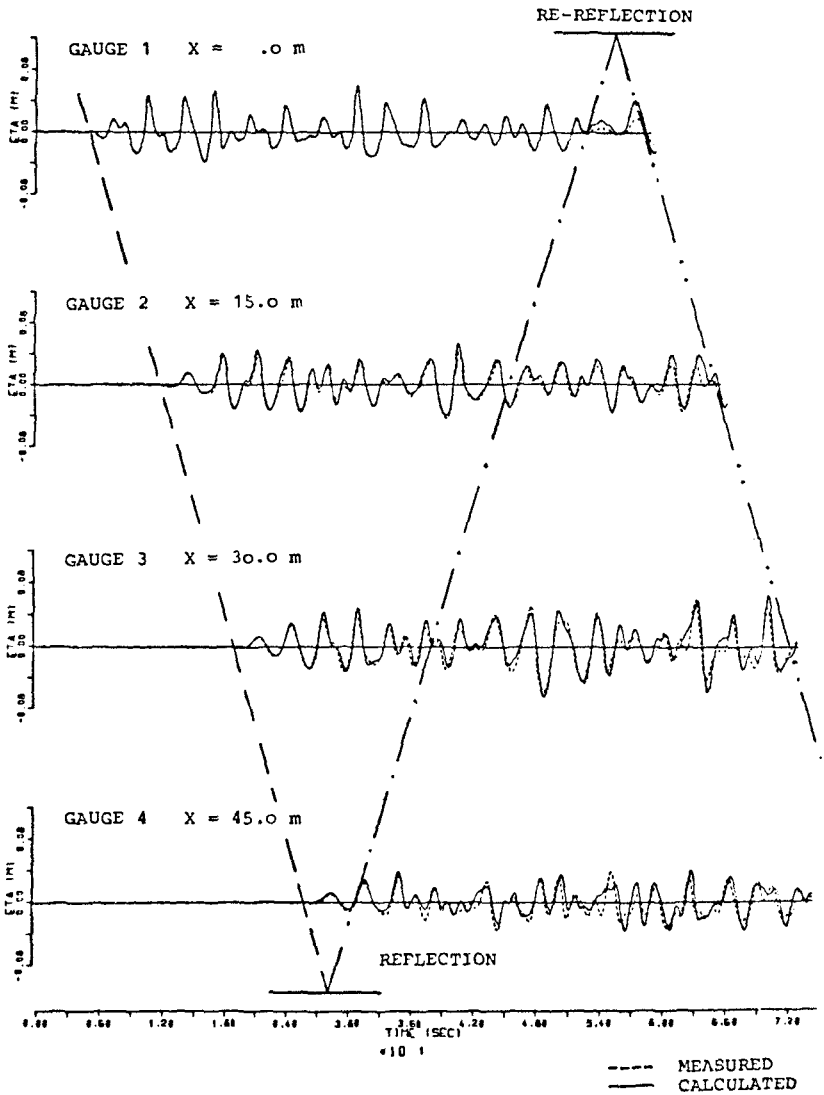

Figure 7: Comparison between measured and calculated time series of the water elevation in a flume with total reflection at a wall

The time series, measured in the hydraulic model at this gauge has been used as input data for the numerical model, which has a non-reflecting boundary at the wave maker. In reality the measurements include the reflection from the wave maker. This leads to significant differences after the first instance of re-reflection, as can be seen in figure 7.

4. LONG WAVES IN A BICHROMATIC WAVE SYSTEM

4.1 Long Wave Generation

OTTESEN-HANSEN pointed out, that two short period waves with the frequencies f_1 and f_2 create a bounded long wave with the frequency $\Delta f = f_1 - f_2$, which propagates with the group velocity. Bounded long waves are of second order with rather limited height. Resonance and shoaling effects can increase their influence.

In traditional first order wave generation, the boundary conditions at the wave board are not fulfilled and various free long waves with the same frequency Δf are generated. These waves appear also in the numerical model. Their velocity and wave length can be calculated by the dispersion relation (KOSTENSE).

Short waves		frequency	f_1 = 0.50 Hz
		amplitude	a_1 = 0.055 m
		frequency	f_2 = 0.40 Hz
		amplitude	a_2 = 0.011 m
Long Waves	Bounded:	frequency	f = 0.10 Hz
		amplitude	a_b = 0.0045 m
		wave length	L_b = 18.0 m
	Free :	frequency	f = 0.10 Hz
		wave length	L_f = 22.1 m

Table 2: Theoretical wave data

The numerical model was used to investigate the generation of bounded and free long waves in a flume with a constant water depth of 0.50 m. Initially a superposition of two harmonic waves was used. However, due to their inherent

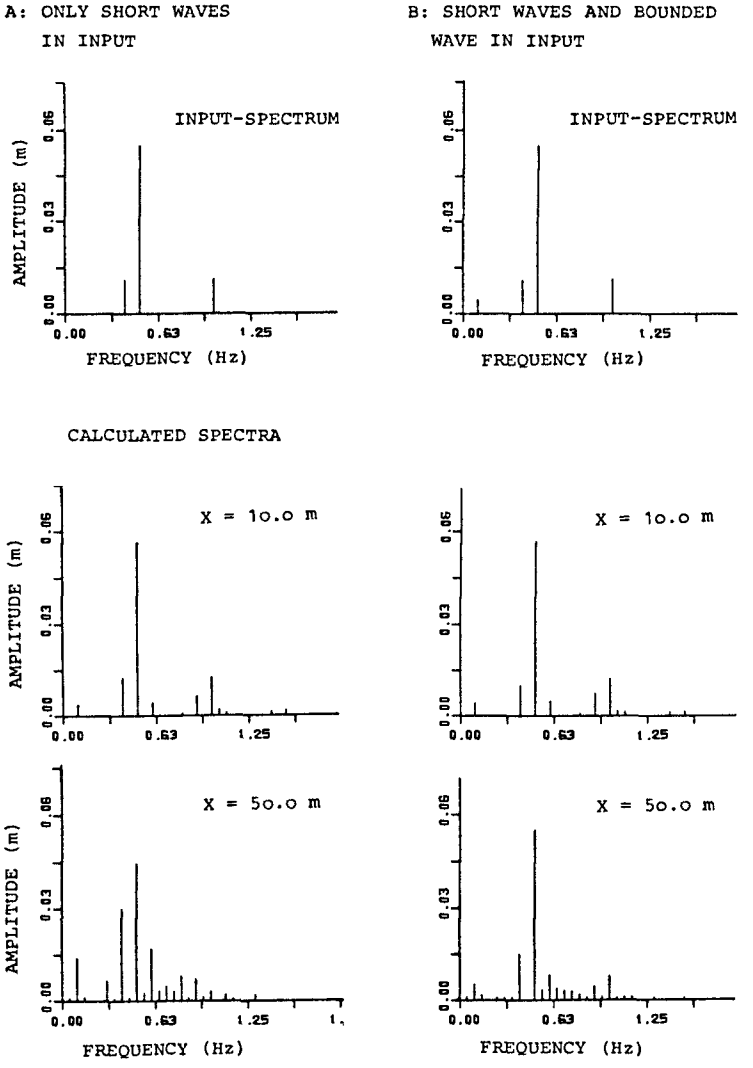

Figure 8: Long wave behaviour in a bichromatic wave system. Flume with horizontal bottom.

instability, complicated transformations occurred, which made the interpretation of the results very difficult. Therefore, a superposition of two cnoidal waves, i.e. waves of permanent form, was used. Table 2 shows a list of the theoretical wave data. The difference in wave lengths of bounded and free long wave leads to a standing wave in the flume, which has been calculated in agreement with theoretical values.

Figure 8A displays wave spectra, calculated at different locations along the numerical flume. It can be seen, that a long period wave, which is not included in the input spectrum has been generated. The input spectrum is unstable and a energy transfer towards the lower frequencies takes place. If, instead the long wave component is added to the input spectrum, the spectrum becomes more stable (see Figure 8B).

4.2 Reflection on a Slope

Investigation of the behaviour of a partial reflection on a slope has been carried out with an input of two short harmonic waves. The influence of the reflection is determined as the difference between calculations with and without a slope. Figure 9 shows the numerical model and the computed incoming and reflected spectra. The reflection coefficient of the long wave is about 3 times as high as that of the short waves. This result is qualitatively correct, but one should be aware that the wave breaking on a real beach has a significant influence on the amplitudes of the reflected waves.

5. CONCLUSIONS

The numerical model has been proven to be numerically stable for nearly breaking waves. The numerical diffusion appears to be insignificant, because cnoidal and solitary waves propagate with permanent form even after several wave lengths.

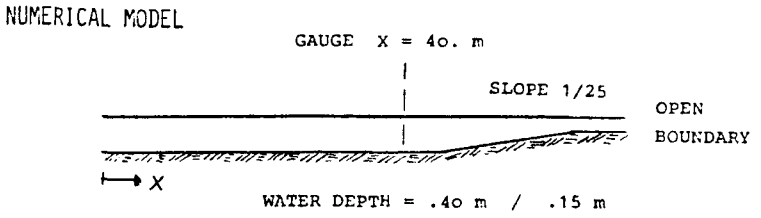

BICNOIDAL WAVE-INPUT:

1. AMPLITUDE = o.o3 m FREQUENCY = o.45 Hz
2. AMPLITUDE = o.o3 m FREQUENCY = o.5o Hz

CALCULATED SPECTRA

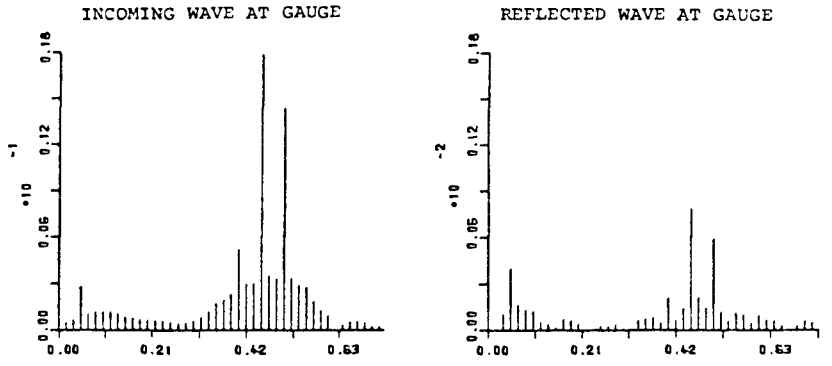

Figure 9: Reflection of bicnoidal waves on a slope

The nonlinear transformation of wave spectra has been studied for an even bottom , for a slope and for a reflection at a wall. A high degree of agreement between computations and measurements has been found, as long as the 'deep water' part of the spectrum is small: i.e. within the range of validity of the Boussinesq-wave-equations.

Long waves from a wave group (bicnoidal waves) are generated in the model in agreement with theoretical values. As should be expected, they are stronger reflected from a bottom slope than short waves.

6. REFERENCES

ABBOTT, M.B., PETERSON, H.M., and SKOOVGAARD, O. (1978): Computation of Short Waves in Shallow Water. Proc. 16th ICCE, Hamburg

HAUGUEL, A., (1980): Adaption of Tidal Numerical Models to Shallow Water Waves Problems. Proc. 18th ICCE, Sydney

KOSTENSE, J.K. (1984) Measurements of Surf Beat and Set-Down Beneath Wave Groups. Proc. 19th ICCE Houston

OTTESEN-HANSEN, N.E., (1978): Long Period Waves in Natural Wave Trains. Inst. Hydrodyn. and Hydraulic Eng., Technical University Denmark, Progress Rep. No. 46

SCHAPER, H., ZIELKE, W. (1984): A Numerical Solution of Boussinesq Type Wave Equations. Proc. 19th ICCE, Houston

Acknowledgements:

The authors express their appreciation to Dr. Daemrich and Dipl.-Ing. Götschenberg for supplying the valuable experimental data. They would also like to thank the German Research Society (Deutsche Forschungsgemeinschaft), which sponsored the research work as part of the scientific program of the "Sonderforschungsbereich" at the University of Hannover.

CHAPTER 206

ON THE SQUATTING OF SHIPS IN SHALLOW AND RESTRICTED WATER

by Drs A M Ferguson and R C McGregor, Department of Naval Architecture and Ocean Engineering, University of Glasgow

1. INTRODUCTION

A major feature of the advances in marine technology is the increasing number, size and speed of ships and, consequently, an increased interest in hydrodynamic problems associated with water restricted in depth and/or lateral extent. The transport of dangerous cargoes and their impact on the benefits of resolving the areas of uncertainty.

Experience of 1,104 vessels of different flags and trades during 1978, shows that grounding/stranding is the third most frequent cause of damage[1]. An examination of the total expenditure of money and time required to repair the resulting damage shows this category to rank highly in both. Indeed, the total repair cost expended as a result of this cause rank top and account for more than 1/5th of the total. Although the shipowner bears a large proportion of the cost of lost revenue, grounding represents a significant cost to underwriters, shipowners and port authorities. The continuous increase in size and draught of vessels in relation to water depth ensures that this situation will continue unless there is a radical development in instrumentation.

To limit the risk of grounding it is extremely important to be able to predict which of a vessel's extremities will experience the greatest sinkage and ground. Where the underkeel clearance is low, reasonable accuracy is demanded in order to ensure safety and to avoid unduly reducing the earning capacity of the vessel by overcaution. This requires a sound knowledge of a vessel's tendency to 'squat'.

2. PRELIMINARY DEFINITIONS

All ships and offshore platforms, when underway, are subject to hydrodynamic pressure changes and friction induced trimming moments which alter their draught and trim in comparison with that when stationary. The term 'squat' includes both the change in draught and the contribution due to trim underway, at any hull extremity of interest. The usual approach to squat is to treat it as a steady-state problem, presenting curves for mean sinkage and trim at varying depths and speeds.

In the plotting of the results, certain non-dimensional parameters have been used:-

(a) The non-dimensional sinkage coefficient,

$$C_S = \frac{100(S_{FP} + S_{AP})}{2L}$$

(b) The non-dimensional trim coefficient,

$$C_\tau = \frac{100(S_{FP} - S_{AP})}{L} = 100\,\tau$$

where S_{FP} and S_{AP} are the sinkages measured at the forward and aft perpendicular, respectively, and τ is the trim angle at radians. Sinkage is assumed negative in the downward z-direction, while trim is defined negative when by-the-bow. Other terminology is explained more fully in reference[1].

3. THE PREDICTION

3.1 Theory

A comprehensive theoretical and experimental study of the ship-to-bottom interaction problem in both laterally restricted and unrestricted shallow water has been completed at the University of Glasgow[2]. It shows that, although both the hydrodynamic and hydraulic theoretical models provide a valuable insight into the squat problem (within the theoretical constraints of each case), a universally applicable theory which allows a routine solution with arbitrary Froude depth number and lateral restrictions, does not exist at present. The subsequent experimental work demonstrated limitations and illustrated features not apparent from the theoretical studies. A wide range of parameters affecting the vertical-plane forces in restricted water were examined, including effects of underkeel clearance, speed, self-propulsion, lateral restrictions, bulbous bow shape, initial trim, draught, a sudden variation in depth and the transverse location in the channel. A full discussion of the theoretical model developed is given in reference[2].

A computer program was written based on the above procedure. Figure 1 demonstrates its utility in predicting model squat in unrestricted shallow water by comparison with experiment. The method is broadly applicable to conventional full-form mono-hull models, towed or self-propelled at steady speed in shallow-water of uniform depth and any width.

3.2 Other Methods

Comparison in the laterally unrestricted shallow water between model data and two recent methods[3] shows that the BMT method gives the better predictions. The model used and the experimental data obtained are considered representative of the considerable data accumulated for the examined block coefficient range. The BMT method is recommended as the more accurate of the methods available and, on this evidence, could be used to derive GO/NO-GO curves, such as in fig. 2, for level or trimmed conditions of full-form vessels.

The inaccuracies of the Barrass formulae[4] stem from the fact that they do not take into account some of the important effects demonstrable by means of theory and model tests. It also appears that, by correlating results obtained on a wide range of hull features (ie, of varying geometry, static draught and trim, etc) and under different environmental conditions (such as water depth and/or lateral restrictions, etc) using various measuring apparatus, reliability has been unduly sacrificed in obtaining convenience. By comparison with model experiments the Barrass formulae are shown not to be conservative and not to possess sufficient limitations on their use under conditions which appear beyond their range of validity. As a result, under some circumstances their use may result in a false sense of security.

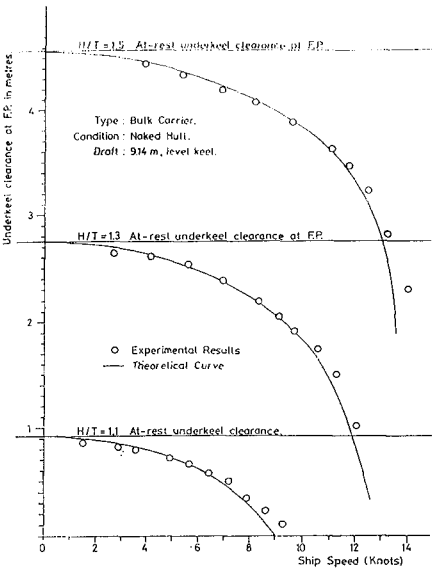

Fig 1: Results for 160m Geosim Ship

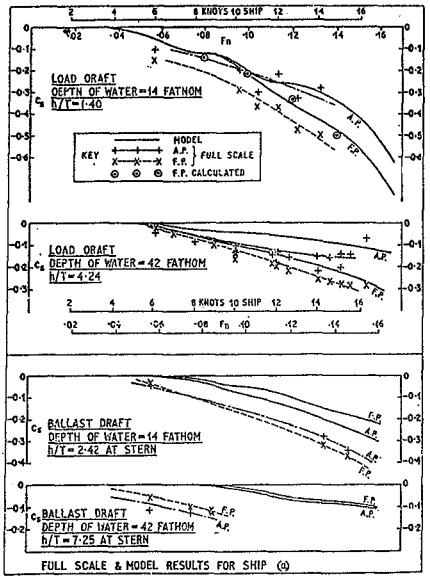

Fig 3

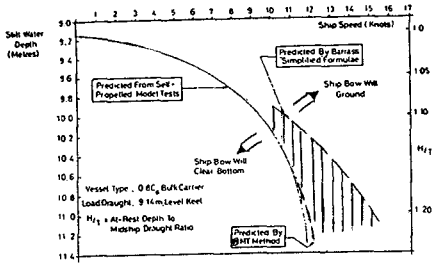

Fig 2: GO/NO-GO Predictions for Level Keel

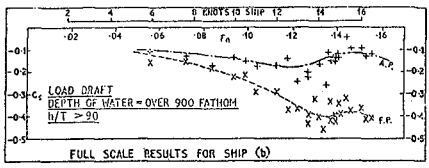

Fig 4

Ship	L_{BP} (m)	B (mld) (m)	D (mld) (m)	Cond	T (m)	Δ Tonnes	C_B	Trim (+ by B/S)	R (m)	Location	Sea State
(A)	304.8	47.2	23.7	L	18.1	215,687	0.82	0	25.6	Cardigan Bay	3 (with long swell)
									76.8	St Georges Channel	
				B	9.2	109,137	-	2.8 B	25.6	Cardigan Bay	2
									76.8	St Georges Channel	
(B)	329.2	58.1	25.6	L	18.9	271,370	0.84	0.4 B	Deep	Off N Spain	3 (with long swell
(C)	329.2	51.8	25.6	L	19.1	274,309	0.84	0.1 B	41-23.5	50NM to Rotterdam	5 decr 3
(D)	313.0	43.7	24.6	L	18.8	195,000	0.84	0	70.0	26NM to Milford Haven	4 decr 2

Table 1: Full Scale Test Conditions

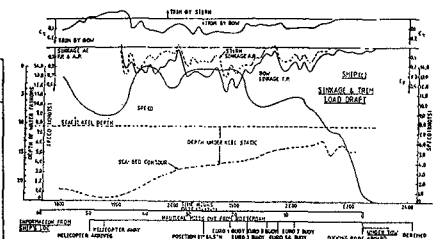

Fig 5

It is important to predict squat with reasonable accuracy particularly where the underkeel clearance is low in order to ensure safety and avoid unduly reducing the earning capacity of a vessel by overcaution. The reluctance of shipboard personnel to hazard vessels at depth-draught ratios less than 1.1 is easily understandable (particularly so when faced with two conflicting methods for predicting vessel behaviour). Because of this, the only significant advances in knowledge may be obtained by model tests.

4. FULL-SCALE MEASUREMENTS

4.1 Experiment Procedure for Full-Scale Measurements

To determine the sinkage and trim to forward speed at sea, it is necessary to record the change in trim and the change in vertical position of any part of the hull and, from such measurements, the sinkage at bow and stern can be computed. Changes in trim are relatively simple to measure and the method which was most successful in these experiments consisted of locating two micromanometers on the centreline of the ship approximately 10 metres apart, connected by a water or oil-filled tube. The recording of changes in sinkage necessitates a datum from which to measure the change in height (which arises from the motion) between a position on the hull and sea.

For this purpose, two ultrasonic transducers were mounted on a light portable boom extending forward from the stem at deck level. The boom was extended well clear of the bow wave system but it proved impossible to project it beyond the symmetrical disturbance of the water surface, which extends well ahead of the stem. The boom used for the most recent experiments extended 15.24m forward of the forward perpendicular. The pressure rise at this position is approximately 0.6m for a 200,000 tonne DW tanker at 14 knots and considerably less for ships of finer trim. Although this pressure rise represents a significant correction to the sinkage signal obtained from the transducer, it is generally accepted that the pressure rise due to the symmetrical disturbance of the water surface ahead of the ship scales linearly.

The effect of sea waves and pitching motion will appear as superimposed undulations on the ultra-sonic and trim signals. In this case, the sinkage and trim values are taken as the average values of the ultra-sonic and trim signals, respectively. To determine the influence of sea state on squat, measurements of ship motions have been included in later experiments.

The overall accuracy of full-scale measurements is estimated to be:-

(±60mm for the ultra-sonic transducer) +

(±30mm for the pressure rise) = ±90mm at the FP,

and (±90mm for the FP) + (±10mm for trim) +

(±70mm for any change in hog or sag under way) = ±170mm at the AP.

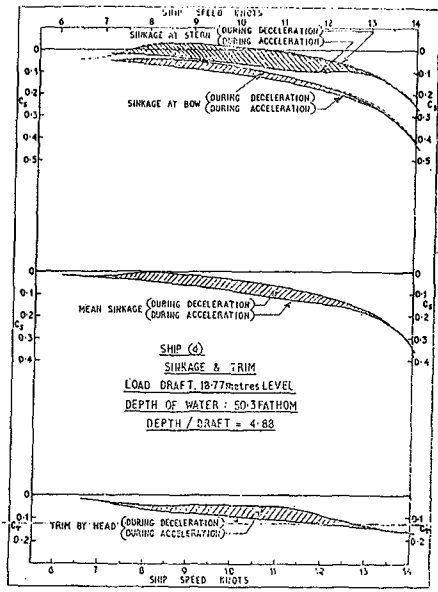

Fig 6: Accelerating and Decelerating

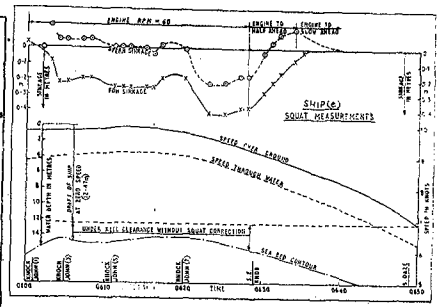

Fig 8

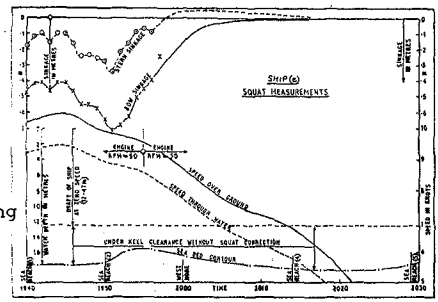

Fig 9

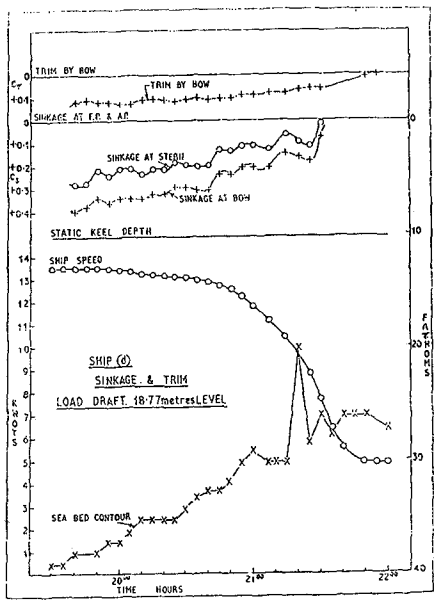

Fig 7

Draught	Incident		Ballast	
Bulb	Original	Glasgow	Original	Glasgow
h/T				
1·05	√ × (1·25)	√	√	
1·1	√ × (1·3)	√ × (1·3)	√	
1·2	√	√		
1·37			√ × (1·64)	√
1·44			√ × (1·70)	√ × (1·70)
1·57			√	√
2·00	√			
2·67			√	

where √ indicate experiments over the level-bed and × ( ) indicate experiments over sandbank with the depth-draught ratio clear of sandbank in parenthesis.

Table 2: Model Test Conditions

4.2 Full-Scale Results

Full-scale results were achieved for five ships, (see figs. 3-9). Ship characteristics and the test sequence for four of them are shown in Table 1. Ship (c) was a sister ship of ship (a).

5. MODEL EXPERIMENTS

It has been shown that even extensive and expensive full-scale tests, as described in the previous section, do not provide the systematic parametric coverage necessary to validate a predictive method close to the crucial point of grounding.

To provide the data needed for this and for the calibration of the squat indicator of section 7, extensive model tests have been undertaken. The Hydrodynamics Laboratory at the University of Glasgow has a 77m x 4.6m x 2.4m towing tank with a specially flat bed and has carried out many model tests in shallow water and restricted water conditions.

The results shown in figs. 10 to 13 are for a bulk carrier with the principal dimensions:

LBP = 160.0m Breadth(mld) = 27.2m

Draught(mld) = 10.19m Block coeff = 0.8

Displacement = 37,000 tonnes.

In this particular series the range of tests were as shown in Table 2 and involved two bulbous bows and level bed and simulated sandbank tests[5]. The tests were conducted with the model propelled by a screw propeller at the model self propulsion point for the speeds tested up to grounding.

6. FACTORS INFLUENCING SQUAT

6.1 Side Bank Interactions

Sway force and yaw moments depart from U^2 behaviour in shallow water with flooded banks. The yaw moment rises more steeply whereas the sway force can reverse at higher speeds. This is caused by the wave interaction between the bow and the bank and implies a higher rudder angle is required because of the bank effects. On some occasions with surface piercing banks, this leads to bodily rejection of a ship approaching a bank at a small incidence. At these times the trim changes from bow down to bow up as the bank approaches. With flooded banks the trim is slightly reduced relative to open water whereas the sinkage is significantly increased[6].

For a vessel travelling along the centre of a channel the effect of lateral restriction is shown in fig. 14. It is seen that sinkage is substantially increased but the effect on trim on this occasion is a small increase. It is found that the percentage changes may be generally used as correction factors to the open water results.

6.2 Underkeel Clearance

The effect of bed proximity is to increase the suction pressures applied to the ships hull and also to cause the ship's boundary layer to

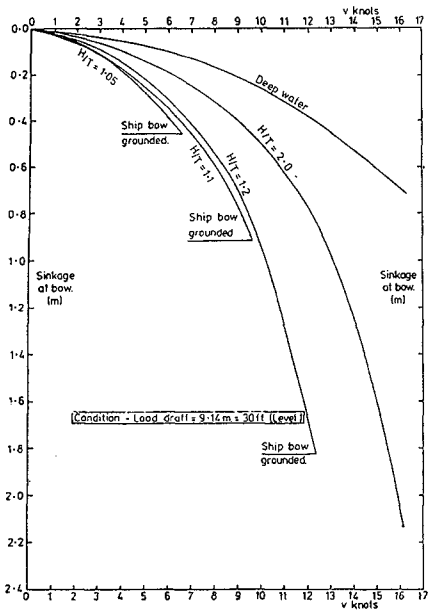

Fig 10

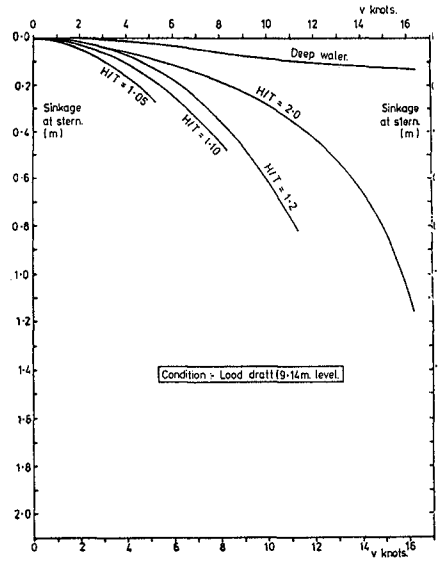

Fig 12

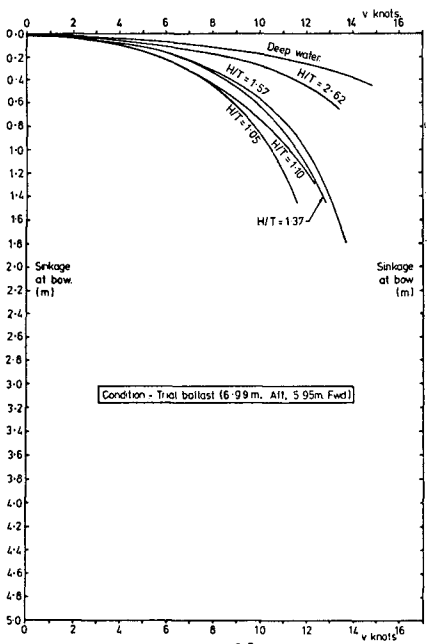

Fig 11

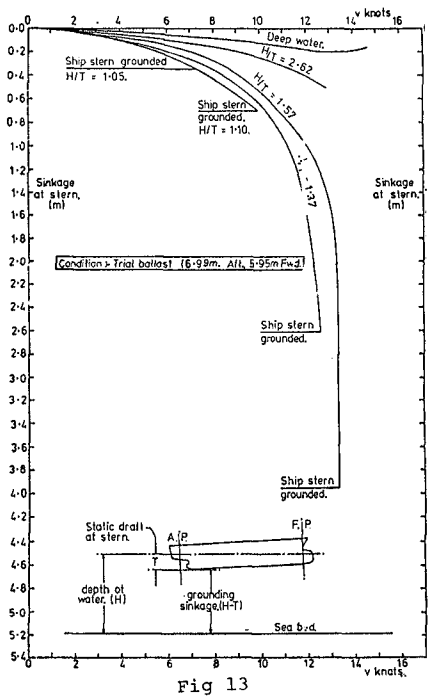

Fig 13

interact with the seabed boundary layer. These effects cause sinkage to increase as the water depth is reduced. Trim also changes rapidly but the manner of change depends on the initial trim as described in section 6.5.

6.3. Sandbanks

The approach to a sandbank leads to the vessel's pressure field interacting with the sandbank and consequently the vessel responds before the bank is reached. Model tests were conducted into a grounding of a bulk carrier in the River Plate. In this case the vessel in load draft experienced a transient trim by the bow (fig. 15) which caused the bow to dive into the sandbank more vigorously than would have been expected under level bed conditions. In ballast conditions (fig. 16) the bow after an initial sinkage is repelled as the stern is attracted leading to the stern being likely to ground almost on leaving the sandbank.

It is possible still to make use of the GO/NO-GO charts (figs. 2 and 17) which were deduced for level bed conditions proved the minimum depth over the sandbank is used.

6.4 The Effect of Hull Geometry

Figure 18 presents a comparison of sinkage and trim data obtained on three models at the load draught, level-keel condition in unrestricted shallow-water. The models represent modern, full-form ships of varying hull parameters and displacement but with the block coefficient limited to between 0.8 and 0.9. The curves represent the mean of the data collected. Although no measurable effect on the mean sinkage may be observed, trim increases with increasing C_B and decreasing B/T ratio. These changes are confirmed by the comprehensive analysis of over 120 models by Ferguson[7] which showed that within the ranges B/T and C_B examined negligible changes in sinkage but marked changes in trim are to be expected. For the most part, the data shows the same trends as the theory but theory indicates that squat is inversely proportional to the L/B ratio while the data suggests the opposite.

The comparison shows that the hull geometry must be incorporated into any prediction method and it is not satisfactory to use simpler measures of ship shape such as C_B or B/T ratio. Consequently, a purely empirical method based on a parent form should be used with caution unless the effects of variations in the hull form are accounted for.

The observations support the view that sinkage results from the pressure changes due to the increased horizontal flow velocity around the hull. In the load draught, level keel condition, the flow velocity is dominated by the long parallel middle-body and negligibly affected by minor hull geometry changes aft and forward. The effect on trim is more complicated since it is the result of the form parameters and the resulting separated flow, depending on factors such as the bulbous-bow and type of propulsion.

The effect of fitting a radically different bulbous-bow design, as shown in fig. 19a, on the vessel's sinkage and trim was also examined by repeating a number of the original experiments[5]. A comparison of the two set of results, fig 19b being typical, showed that the modification leads to minor changes in the force distribution but not its overall magnitude. The resulting changes in close-to-grounding behaviour did not

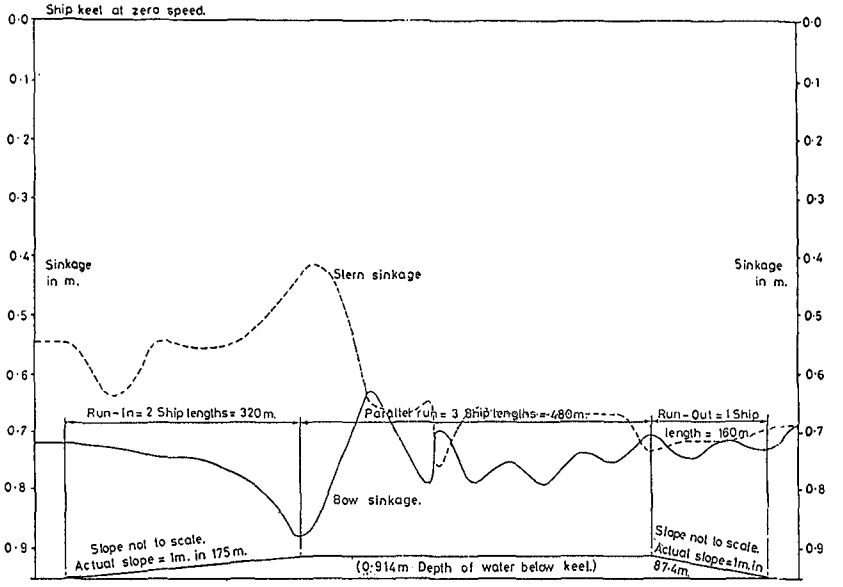

Bow and stern squat over sandbank in the incident condition at a depth-draught ratio of 1·1 over and 1·3 clear of sandbank at a speed of 9·5 knots

Fig 15

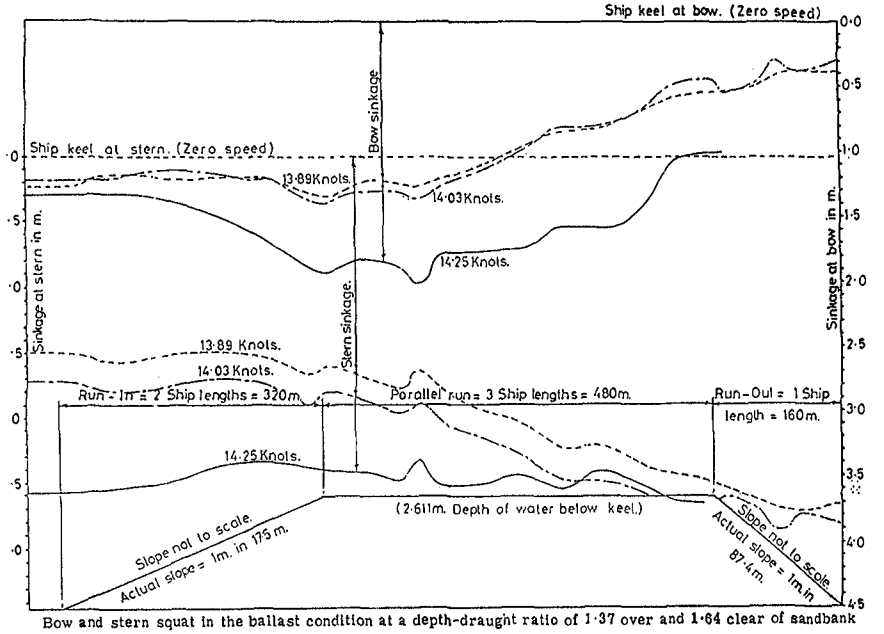

Bow and stern squat in the ballast condition at a depth-draught ratio of 1·37 over and 1·64 clear of sandbank

Fig 16

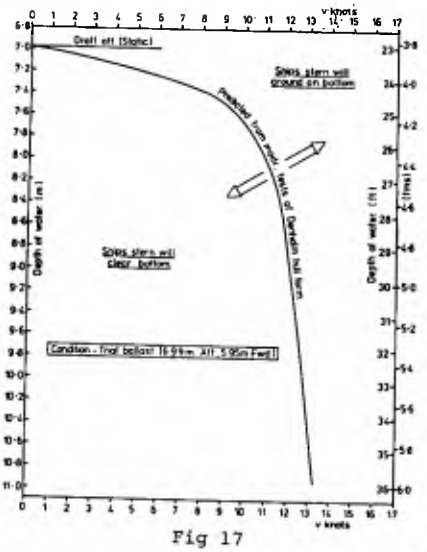

Fig 17

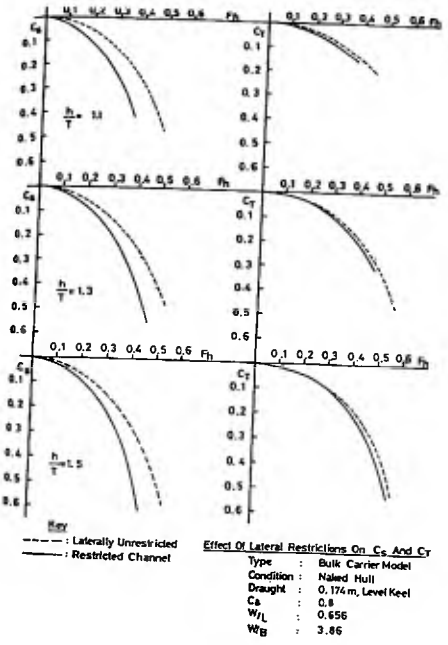

Fig 14

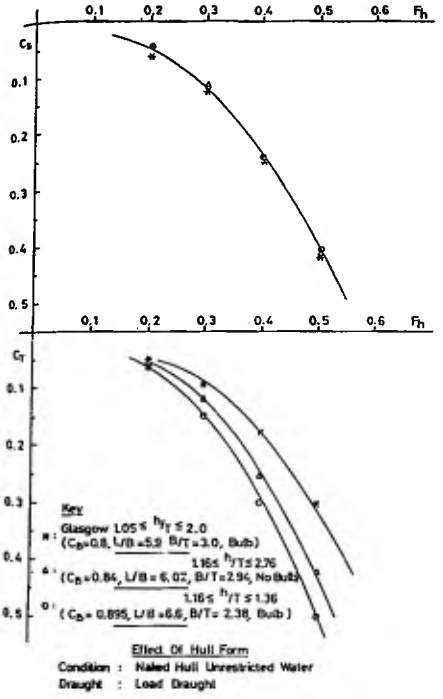

Fig 18

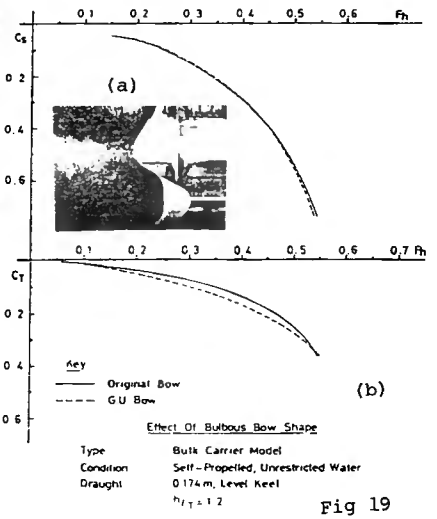

Fig 19

affect the grounding speed or qualitative behaviour and may be considered to have a very small effect and could be omitted from the input hull geometry. However, it should be borne in mind that effects of adding a bulb to an otherwise bulb-less hull will influence the boundary-layer development and the wave system along the hull. It is then to be expected that sinkage and, particularly, trim will be affected to a greater extent than by the above changes in shape.

6.5 Effect of Initial Trim

It is important to recognise that a fully loaded vessel, initially at a level keel in shallow water, will trim progressively by the head and ground with the bow first, whereas a vessel ballasted by the stern (to immerse the screw) will sink progressively with almost constant trim by the stern and ground by the stern, fig. 20. In deeper water the trim by the stern for the ballast condition will decrease with speed.

6.6 Squat and Trim Caused by Bed Mud

In general the sinkage forward and aft above mud appears to be less than above a hard bottom. Moreover, the sinkage values decrease with increasing thickness of the mud layer. There is no clear indication between sinkage above mud of 'winter' and 'summer' densities at the same layer thickness[8].

6.7 Acceleration and Deceleration

Full scale tests on ship(d) in deep water (fig. 6) showed that at moderate speeds an accelerating ship experiences increased sinkage but reduced trim by the bow whereas a decelerating ship sinks less and trims more. If this pattern of behaviour is repeated in shallow water, rapid deceleration could cause the ship to ground.

6.8 Self-Propulsion

The effects of self-propulsion are very important as a correction factor to the theoretical methods and for the model/full scale correlation. Figure 21 shows that sinkage is much increased while trim is substantially reduced.

7. EXTRAPOLATION TO FULL-SCALE

Owing to the significant amount of model data, the model-scale squat component of underkeel clearance is one of a deterministic character. The prediction of the full-scale sinkage and trim is still probabilistic. Consequently, the associated scaling problems present difficulties.

Full scale studies indicate that, at a depth-draught ratio of 1.42, correlation in the load-draught level-keel condition is very reasonable at speeds less than about 12 knots (fig. 3). This is particularly so for trim although the mean sinkage tends to be greater for the ship than for the model. Bearing in mind the importance of viscous effects to the scaling procedure in shallow water, this agreement is unexpected. Frictional resistance constitutes the major proportion of full-form ship resistance at low speeds and since the frictional coefficient is much lower on the full-scale, it is to be expected that model results for the trim component will over-estimate the full-scale. The good agreement is mainly because mean sinkage is almost entirely due to the predominance of pressure changes over the hull, allowing direct scaling of this

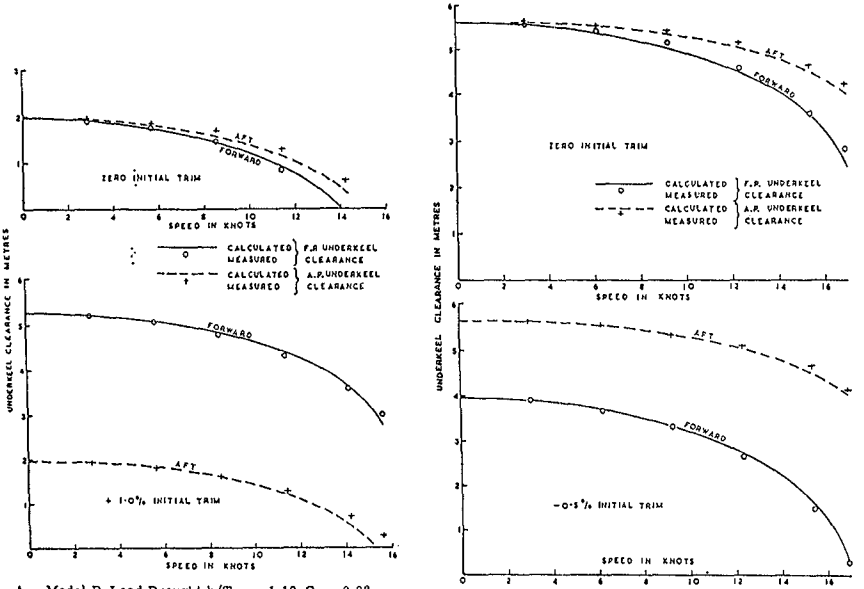

A. Model B, Load Draught $h/T_{AP} = 1{\cdot}10$, $C_B = 0{\cdot}83$
Results scaled to 330·71 L_{PP} Ship

B. Model B, Load Draught $h/T_{AP} = 1{\cdot}28$, $C_B = 0{\cdot}83$
Results scaled to 330·71 L_{PP} Ship.

Effect of Initial Trim on Underkeel Clearance

Fig 20

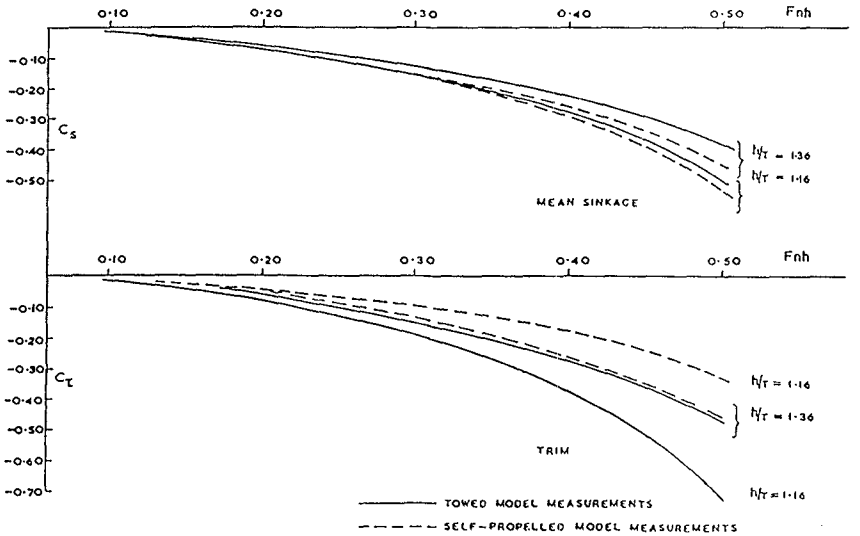

Fig 21 Effect of Self-Propulsion on Mean Sinkage and Trim of a Tanker Model

component without error of practical significance [9].

Although trim has an appreciable viscous component, this is probably counter-balanced by the pressure dominated self-propulsion effects. Any scaling difficulties in the self-propelled, load draught (level keel) condition, therefore, are effectively obscured. However, it is suggested that since the model scale boundary layers are relatively thicker than those at full-scale, they will interact at a greater depth-draught ratio and introduce scaling difficulties in very shallow water.

The model/full-scale comparisons in the self-propelled ballast (trim-by-stern) condition indicate that the normal extrapolation procedure may be in error. The bulb proximity to the free-surface will modify both the hull wave-system and the viscous flow and may induce vertical sinkage or lift forces [9]. It is suggested that since the magnitude of the complex changes induced by the proximity to the free-surface is uncertain, extrapolation to full-scale will be unreliable. Similarly, in the absence of self-propulsion, prediction for the towed, naked-hull condition will be generally unreliable for the trim components in the ballast case.

These problems can only be overcome by careful correlation of model and full-scale results with an adequate computational approach.

8. PRACTICAL NAVIGATION AID

During the trials described in Section 4 it became evident from discussions with Masters and Navigation Officers, that a bridge instrument capable of continually displaying the true dynamic draft, or the amount of squat, would be a useful aid to navigation and contribute to the safe handling of the ship in shallow or restricted waters.

8.1 A Continuous Reading True Draught Indicator

One of the results of the research reported in the preceding sections has been the development of a number of variations of instrumentation systems capable of continuously displaying either the true draught of the vessel, corrected for squat, or the amount of squat present continuously displayed as an increment of draught to be added to the static draught on the ship's bridge.

There is no practical method of obviating squat even though it may be reduced by a given vessel by decreasing speed or, more drastically, by designing a vessel with a higher B/T. Naturally, most operators of large vessels are aware of the dangers and speed is reduced by rule-of-thumb or by the use of squat diagrams posted on the bridge. These diagrams are useful (when accurate) but are easily ignored or overlooked. An instrument capable of continually displaying either the true draught (corrected for squat) or the squat (as an increment to be added to the static draught) would be more useful and more likely to be used. The development of such an instrument is described in Ref 1. Following discussion with tanker fleet operators, the present system is designed to be virtually maintenance free

The signal used is a measure of the water velocity next to the hull. This is responsible for the changes in pressure which cause the squat. In the same way as a particular pressure change results in a particular squat so will the water velocity next to the hull causing that pressure change have a fixed relationship with squat.

The system is shown schematically in fig. 22 and by a block circuit diagram. In an attempt to keep the installation and maintenance costs to a minimum the velocity transducer adopted is an ultra-sonic device which transmits through the hull and reads the velocity close to the hull surface.

8.2 Procedure to Calibrate and Commission the Squat Meter

(a) Using the program described in Section 3 the geometry of the hull is used to compute a complete set of squat information for the practical range of speed and depth of water.

(b) With the instrument properly installed on the ship (an operation which can be carried out during a normal voyage), the ship is sailed over a range of speeds at two or three depths of water. At each combination of speed and depth of water a reading will be displayed on the bridge instrument. This reading is adjusted, using the keyboard input, to read the correct squat according to the computer.

The squat meter should then read the true squat, or dynamic draught if the static draught is keyed in, regardless of the depth under hull and speed combinations even for combinations of speed and depths not covered in the calibration.

9. CONCLUSIONS

The squatting of larger vessels can be an important cause of marine casualties with a serious impact on ship owners and port managers alike. Many factors have a role to play and it should be amphasised that:-

(1) Approaching or leaving port with a trim by the stern does not lead to a more level keel at speed in shallow water.

(2) Transients approaching sandbanks can lead to groundings which may otherwise have been avoided.

(3) Restricted width of fairways has a range of effects and the side forces can exceed the ability of the rudder to control the ship.

(4) Rapid deceleration can lead to larger sinkage at the bow in the short term.

(5) A muddy layer on the seabed reduces sinkage and the idea of effective depth may be necessary for predictions.

It has been demonstrated that a combination of model tests, full scale tests and computer analysis have led to the situation where satisfactory predictions can be made of deterministic squat. The more probabilistic problems involving uncertainties regarding true seabed position, etc, can be ameliorated by a navigational aid as described.

10. REFERENCES

1. FERGUSON, A M, SEREN, D B and McGREGOR, R C, 'The Prediction and Practical Measurement of Ship Squat in Shallow Water', Intl Marine Safety Conf, Sep 83, Glasgow.

2. SEREN, D B, 'Monohulls and Multihulls in Transit: Aspects of Physical and Theoretical Modelling in Restricted Water', PhD Thesis, University of Glasgow, 1982.

3. SEREN, D B, FERGUSON, A M and McGREGOR, R C 'Squat: An Examination of Two Practical Prediction Methods', Naval Architect, Sep 81.

4. BARRASS, C B, 'The Phenomena of Ship Squat, 'Intl Shipbuilding Progress, No 26, 1979.

5. FERGUSON, A M, SEREN, D B and McGREGOR, R C, 'Experimental Investigation of a Grounding on a Shoaling Sandbank', RINA Spring Meetings, London, 1981.

6. DAND, I W, 'On Ship-Bank Interaction', RINA Spring Meetings, London 1981.

7. FERGUSON, A M, 'Factors Affecting the Components of Ship Resistance', PhD Thesis, Glasgow 1976.

8. SELLMEIJER, R and OORTMERSSEN, G van, 'Effect of Mud on Tanker Manoeuvres', Naval Architect, Jun 84.

9. DAND, I W and FERGUSON, A M, 'The Squat of Full Ships in Shallow Water', Trans RINA, Vol 115, 1973.

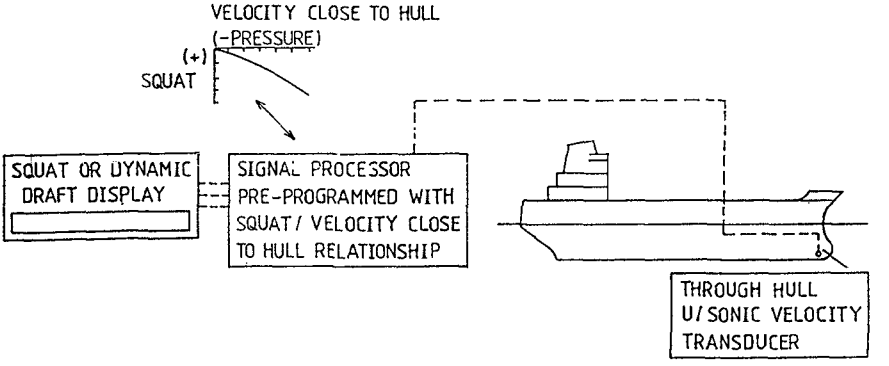

Fig 22

SUBJECT INDEX

Page number refers to first page of paper.

AUTHOR INDEX

Page number refers to first page of paper.